CODEN: JASMAN

ISSN: 0001-4966

The Journal of the Acoustical Society of America

Vol. 118, No. 5 November 2005

(Continued)

THE JOURNAL OF THE ACOUSTICAL SOCIETY OF AMERICA VOL. 118, NO. 5, NOVEMBER 2005

CONTENTS—*Continued from preceding page*

(Continued)

THE JOURNAL OF THE ACOUSTICAL SOCIETY OF AMERICA VOL. 118, NO. 5, NOVEMBER 2005

CONTENTS—*Continued from preceding page*

(Continued)

THE JOURNAL OF THE ACOUSTICAL SOCIETY OF AMERICA VOL. 118, NO. 5, NOVEMBER 2005

CONTENTS—*Continued from preceding page*

ACOUSTICAL NEWS—USA

Elaine Moran
Acoustical Society of America, Suite 1NO1, 2 Huntington Quadrangle, Melville, NY 11747–4502

Editor's Note: *Readers of this journal are encouraged to submit news items on awards, appointments, and other activities about themselves or their colleagues. Deadline dates for news and notices are 2 months prior to publication.*

The 149th meeting of the Acoustical Society of America held in Vancouver, Canada

The 149th meeting of the Acoustical Society of America (ASA) was held 16–21 May at the Hyatt Regency Vancouver Hotel in Vancouver, British Columbia, Canada. The meeting was jointly sponsored by the Canadian Acoustical Association. This is the first time that the Society has met in this city and the fifth time the Society has met in Canada. Previous meetings in Canada were held in Ottawa in 1959, 1968, 1981, and 1993.

The meeting drew a total of 1362 registrants, including 252 nonmembers and 327 students. Attesting to the international ties of our organization, 223 of the registrants (that is, 16%) were from outside North America. There were 41 registrants from the United Kingdom, 33 from Japan, 25 from Germany, 21 from France, 12 from Denmark, 10 each from Korea and Taiwan, 7 each from China and the Netherlands, 6 from Australia, 4 from Singapore, 5 each from Italy, Russia, and Spain, 3 each from Belgium, Brazil, Hong Kong, New Zealand, and Norway, 2 each from Croatia, Cyprus, Finland, Sweden, and Switzerland, and 1 each from Austria, Czech Republic, Greece, Iceland, India, South Africa, and Turkey. North American countries, Canada, Mexico and the United States, accounted for 218, 2, and 841, respectively.

A total of 1068 papers, organized into 100 sessions, covered the areas of interest of all 13 Technical Committees. The meeting also included 17 meetings dealing with standards. The Monday evening tutorial lecture series was continued by Carol Espy-Wilson, University of Maryland. Her tutorial "Automatic Speech Recognition" was presented to an audience of about 140.

The Society's 13 Technical Committees held open meetings during the Vancouver meeting where they made plans for special sessions at upcoming ASA meetings, discussed topics of interest to the attendees and held informal socials after the end of the official business. These are working, collegial meetings and all people attending Society meetings are encouraged to attend and to participate in the discussions. More information about Technical Committees, including minutes of meetings, can be found on the ASA Website <http://asa.aip.org/committees.html> and in the Acoustical News USA section of JASA in the September issue.

The ASA Student Council hosted a Student Reception with 125 people in attendance.

The Technical Committee on Signal Processing in Acoustics sponsored its seventh Gallery of Acoustics at the Vancouver meeting. The winning entry titled "Surf Infrasound" was submitted by Milton Garces, University of Hawaii, who received the $350 prize.

The Technical Committee on Architectural Acoustics sponsored a Student Design Competition which involved the design of a drama theater complex located within an urban mixed-use development. The entries were judged by a panel of architects and acoustical consultants. The first prize winner will receive a cash award of $1000 and entries selected for "commendation" awards will receive $500 each. Announcement of the award winners had not yet been made at the time this report was written.

The Technical Committee on Musical Acoustics sponsored an Instrument Builders Workshop on Friday which drew about 20 participants including musical instrument builders who displayed their crafts and demonstrated their instruments.

The meeting was preceded by the 1st ASA Workshop on Second Language Speech Learning which drew over 115 participants. The workshop was held at Simon Fraser University and included lectures and poster presentations.

Social events included the two social hours held on Tuesday and Thursday, a reception for students, the Fellows Luncheon, and the morning coffee breaks.

FIG. 1. Svein Vagle, recipient of the 2005 Medwin Prize in Acoustical Oceanography.

These social events provided the settings for participants to meet in relaxed settings to encourage social exchange and informal discussions. A special program for students to meet one-on-one with members of the ASA over lunch, which is held at each meeting, was organized by the Committee on Education in Acoustics.

Garry C. Rogers, Research Scientist at the Pacific Geoscience Center, Geological Survey of Canada, was the speaker at the Fellows luncheon, which was attended by over 120 people. The Fellows luncheon is now open to all meeting attendees.

The Women in Acoustics Luncheon was held on Wednesday afternoon and was attended by over 95 people.

The plenary session included a business meeting of the Society, announcements, acknowledgment of the members and other volunteers who organized the meeting, the presentation of society awards, and presentation certificates to newly-elected Fellows.

FIG. 2. ASA President William Kuperman (*r*) presents the Silver Medal in Psychological and Physiological Acoustics to H. Steven Colburn (*l*).

 0001-4966/2005/118(5)/2741/4/$22.50

The 2003 Medwin Prize in Acoustical Oceanography was presented to Svein Vagle "for development of experimental techniques to probe the upper ocean boundary layer" (see Fig. 1). Dr. Vagle presented the Acoustical Oceanography Prize Lecture titled "Acoustic Explorations of the Upper Ocean Boundary Layer" earlier in the meeting.

The Silver Medal in Psychological and Physiological Acoustics was presented to H. Steven Colburn of Boston University "for contributions to psychological and physiological aspects of binaural hearing" (see Fig. 2). The R. Bruce Lindsay Award was presented to Lily M. Wang, University of Nebraska, "for contributions to room and musical acoustics" (see Fig. 3). The Helmholtz-Rayleigh Interdisciplinary Silver Medal in Noise and Physical Acoustics was presented to Gilles A. Daigle, National Research Council of Canada, "for contributions to understanding the effects of micrometeorology, topography and ground properties on outdoor sound propagation" (see Fig. 4). The Gold Medal was presented to Allan D. Pierce, Boston University, "for contributions to physical, environmental, and structural acoustics, acoustics education, and leadership as Editor-in-Chief of the Society" (see Fig. 5).

Election of five members to Fellow grade was announced and fellowship certificates were presented. New fellows are: Catherine T. Best, Bennett M. Brooks, Michael G. Brown, Charles F. Gaumond, and Murray R. Hodgson (see Fig. 6).

ASA William Kuperman expressed the Society's thanks to the Local Committee for the excellent execution of the meeting, which clearly evidenced meticulous planning. He introduced Murray R. Hodgson (see Fig. 7), Chair of the Vancouver meeting, who acknowledged the contributions of the members of his committee including: Stan E. Dosso, Technical Program Chair, Bernadette Duffy, Coordination/Food Service; Mark Cheng and Fred Twefik, Audio-Visual; Claudio Bulfone, Social Events; Wonyoung Yang, Zohreh Razavi, and Katrina Scherebynyj, Signs; Ian Wilson, Student Issues; Nahal Namdaran, Poster Sessions; Bryan Gick, Green Meeting; Herman Li and Connie So, Registration/ASA Office; and Doug Wilson, Promotions/Sightseeing. He also expressed thanks to the members of the Technical Program Organizing Committee: Stan E. Dosso, Technical Program Chair; Michael Wolfson, Acoustical Oceanography; Kathleen M. Stafford, Animal Bioacoustics; Kerrie G. Standlee, Lily M. Wang, Architectural Acoustics; Michael R. Bailey, Biomedical Ultrasound/Bioresponse to Vibration; James P. Cottingham, Education in Acoustics and Musical Acoustics; Stephen C. Thompson, Engineering Acoustics; Jerry G. Lilly, Noise; Thomas J. Matula, Physical Acoustics; Neal F. Viemeister, Psychological and Physiological Acoustics; David I. Havelock, Signal Processing in Acoustics; Terrance M. Nearey, Speech Communication; Claudio Bulfone, Structural Acoustics and Vibration; and Peter H. Dahl, Underwater Acoustics.

A special presentation was held at this plenary, the awarding of a "Telly Award" to the ASA for its 75th Anniversary Film. The "Telly Awards" was founded in 1978 to honor excellence in local, regional and cable television commercials and programs, as well as the finest video and film productions. The presentation of the silver statuette was made to ASA President William Kuperman by Patricia Kuhl and Lawrence Crum who worked with Carol Geertsma of Twisp River Films to produce the video (see Fig. 8).

FIG. 3. ASA President William Kuperman (*r*) presents the 2005 R. Bruce Lindsay Award to Lily M. Wang (*l*).

FIG. 4. ASA President William Kuperman (*l*) presents the 2005 Helmholtz-Rayleigh Interdisciplinary Silver Medal to Gilles A. Daigle (*r*).

FIG. 5. ASA President William Kuperman (*l*) presents the Gold Medal to Allan D. Pierce (*r*).

FIG. 6. ASA Vice President Mark Hamilton (far left) and ASA President William Kuperman (far right) with new Fellows of the ASA.

FIG. 7. Murray R. Hodgson, Chair of the 149th Meeting.

FIG. 8. Patricia Kuhl (*r*) and Lawrence Crum (*l*) present the 'Telly Award' to ASA President William Kuperman (*c*).

The Plenary Session concluded with the presentation of the Vice President's gavel to Mark Hamilton and the President's Tuning Fork to William Kuperman, in recognition of their service to the Society during the past year (see Figs. 9 and 10).

The full technical program and award encomiums can be found in the April 2005 issue of the printed meeting program or online at <scitation.aip.org/JASA> for readers who wish to obtain further information about the Vancouver meeting. We hope that you will consider attending a future meeting of the Society to participate in the many interesting technical events and to meet with colleagues in both technical and social settings. Information about future meetings can be found in the *Journal* and on the ASA Home Page at <http://asa.aip.org>.

WILLIAM A. KUPERMAN
President 2004–2005

FIG. 9. Donna Neff, ASA Vice President-Elect (*r*) presents gavel to Mark Hamilton, Vice President (*l*).

FIG. 10. President-Elect William Yost (*r*) presents Presidents' Tuning Fork to William Kuperman (*l*).

Dissertation Abstract

The interaction of complex harmonic elastic waves with periodically corrugated surfaces and with anisotropic viscoelastic and/or piezoelectric layered media, [43.20.−f, 43.20.Bi, 43.20.El, 43.20.Fn, 43.25.Dc, 43.28.En, 43.30.Gv, 43.30.Hw, 43.30.Ma, 43.55.−n]—Nico F. Declercq, *Soete Laboratory, Department of Mechanical Construction and Production, Ghent University, 12th May 2005 (Ph.D., 717 pages).*

The dissertation describes different aspects of the numerical modeling of ultrasonics, which were encountered when aiming at a quantitative characterization of layered and composite material systems. These aspects include the use of the inhomogeneous wave theory, of complex harmonic waves, and of the radiation mode theory. As an example the characterization of liquids inside containers is described by means of the Schoch effect on the container skin.

The theory of the diffraction of ultrasound on one-dimensional and two-dimensional periodically rough surfaces resulted in an explanation of the backward beam displacement on corrugated surfaces as well as in a physical clarification of the Quetzal echo at the great pyramid of Chichen Itza in Mexico. Part of the dissertation tackles the numerical and experimental use of so-called ultrasonic polar scans for the characterization of layered and anisotropic materials. Previous studies are extended to the propagation in laminates with finite dimensions and in piezoelectric materials subjected to bias fields, such as residual stress. Related to this topic, the interaction of sound with continuously varying mud layers is described, and a study is performed on new techniques to reveal the nautical bottom in rivers and harbors. A last chapter is devoted to acoustic microscopy and to bulk imaging of fiber reinforced composite laminates.

Contact information: Nico F. Declercq, Soete Laboratory, Department of Mechanical Construction and Production, Ghent University, Sint Pietersnieuwstraat 41, B-9000 Gent, Belgium. Electronic mail: NicoF.Declercq@Ugent.be or declercq@ieee.org or declercq@mailaps.org Advisors: Joris Degrieck and Oswald Leroy

USA Meetings Calendar

Listed below is a summary of meetings related to acoustics to be held in the United States in the near future.

2006

9–12 Feb.	46th Annual Convention, Illinois Speech-Language-Hearing Association, Rosemont, IL [ISHA, 230 E. Ohio St., Suite 400, Chicago, IL 60611-3265; Tel.: 312-644-0828; Fax: 315-644-8557; Web:www.aishil.org].
16–18 Feb.	31st Annual Conference, National Hearing Conservation Association, Tampa, FL [NHCA, 7995 E. Prentice Ave., Suite 100 East, Greenwood Village, CO 80111-2710; Tel: 303-224-9022; Fax: 303-770-1614; electronic mail: nhca@gwami.com; WWW: www.hearingconservation.org].
6–9 June	151st Meeting of the Acoustical Society of America, Providence Rhode Island [Acoustical Society of America, Suite 1NO1, 2 Huntington Quadrangle, Melville, NY 11747-4502; Tel.: 516-576-2360; Fax: 516-576-2377; electronic mail: asa@aip.org; WWW: http://asa.aip.org]. Deadline for receipt of abstracts: 24 January 2006.
17–21 Sept.	INTERSPEECH 2006 (ICSLP 2006), Pittsburgh, PA [www.interspeech2006.org <http://www.interspeech2006.org/>]
28 Nov—2 Dec	152nd Meeting of the Acoustical Society of America joint with the Acoustical Society of Japan, Honolulu, Hawaii [Acoustical Society of America, Suite 1NO1, 2 Huntington Quadrangle, Melville, NY 11747-4502; Tel.: 516-576-2360; Fax: 516-576-2377; electronic mail: asa@aip.org; WWW: http://asa.aip.org]. Deadline for receipt of abstracts: 30 June 2006

2008

28 July–1 Aug—9th	International Congress on Noise as a Public Health Problem (Quintennial meeting of ICBEN, the International Commission on Biological Effects of Noise). Foxwoods Resort, Mashantucket, CT [Jerry V. Tobias, ICBEN 9, Post Office Box 1609, Groton, CT 06340-1609, Tel. 860-572-0680; Web: www.icben.org; electronic mail: icben2008@att.net.

Cumulative Indexes to the Journal of the Acoustical Society of America

Ordering information: Orders must be paid by check or money order in United States funds drawn on a United States bank or by Mastercard, Visa, or American Express credit cards. Send orders to Circulation and Fulfillment Division, American Institute of Physics, Suite 1NO1, 2 Huntington Quadrangle, Melville, NY 11747-4502; Tel.: 516-576-2270. Non-U.S. orders add $11 per index.

Some indexes are out of print as noted below.

Volumes 1–10, 1929–1938: JASA, and Contemporary Literature, 1937–1939. Classified by subject and indexed by author, pp. 131. Price: ASA members $5; Nonmembers $10.

Volumes 11–20, 1939–1948: JASA, Contemporary Literature and Patents. Classified by subject and indexed by author and inventor, pp. 395, Out of Print.

Volumes 21–30, 1949–1958: JASA, Contemporary Literature and Patents. Classified by subject and indexed by author and inventor, pp. 952, Price: ASA members $20; Nonmembers $75.

Volumes 31–35, 1959–1963: JASA, Contemporary Literature and Patents. Classified by subject and indexed by author and inventor, pp. 1140, Price: ASA members $20; Nonmembers $90.

Volumes 36–44, 1964–1968: JASA and Patents. Classified by subject and indexed by author and inventor, pp. 485. Out of Print.

Volumes 36–44, 1964–1968: Contemporary Literature. Classified by subject and indexed by author, pp. 1060. Out of Print.

Volumes 45–54, 1969–1973: JASA and Patents. Classified by subject and indexed by author and inventor, pp. 540. Price: $20 (paperbound); ASA members $25 (clothbound); Nonmembers $60 (clothbound).

Volumes 55–64, 1974–1978: JASA and Patents. Classified by subject and indexed by author and inventor, pp. 816. Price: $20 (paperbound); ASA members $25 (clothbound); Nonmembers $60 (clothbound).

Volumes 65–74, 1979–1983: JASA and Patents. Classified by subject and indexed by author and inventor, pp. 624. Price: ASA members $25 (paperbound); Nonmembers $75 (clothbound).

Volumes 75–84, 1984–1988: JASA and Patents. Classified by subject and indexed by author and inventor, pp. 625. Price: ASA members $30 (paperbound); Nonmembers $80 (clothbound).

Volumes 85–94, 1989–1993: JASA and Patents. Classified by subject and indexed by author and inventor, pp. 736. Price: ASA members $30 (paperbound); Nonmembers $80 (clothbound).

Volumes 95–104, 1994–1998: JASA and Patents. Classified by subject and indexed by author and inventor, pp. 632, Price: ASA members $40 (paperbound); Nonmembers $90 (clothbound).

Volumes 105–114, 1999–2003: JASA and Patents. Classified by subject and indexed by author and inventor, pp. 616, Price: ASA members $50; Nonmembers $90 (paperbound).

ACOUSTICAL STANDARDS NEWS

Susan B. Blaeser, Standards Manager
ASA Standards Secretariat, Acoustical Society of America, 35 Pinelawn Rd., Suite 114E, Melville, NY 11747 [Tel.: (631) 390-0215; Fax: (631) 390-0217; e-mail: asastds@aip.org]

George S. K. Wong
Acoustical Standards, Institute for National Measurement Standards, National Research Council, Ottawa, Ontario K1A 0R6, Canada [Tel.: (613) 993-6159; Fax: (613) 990-8765; e-mail: george.wong@nrc.ca]

American National Standards (ANSI Standards) developed by Accredited Standards Committees S1, S2, S3, and S12 in the areas of acoustics, mechanical vibration and shock, bioacoustics, and noise, respectively, are published by the Acoustical Society of America (ASA). In addition to these standards, ASA publishes Catalogs of Acoustical Standards, both National and International. To receive copies of the latest Standards Catalogs, please contact Susan B. Blaeser.

Comments are welcomed on all material in Acoustical Standards News.

This Acoustical Standards News section in JASA, as well as the National and International Catalogs of Acoustical Standards, and other information on the Standards Program of the Acoustical Society of America, are available via the ASA home page: http://asa.aip.org.

Standards Meetings Calendar—National

At the 151st ASA Meeting, Providence, RI, 5–9 June 2006, the ASA Committee on Standards (ASACOS), ASACOS STEERING Committees, and Accredited Standards Committees S1 Acoustics, S2 Mechanical Vibration and Shock, S3 Bioacoustics, and S12 Noise, and the Standards Plenary Group will meet. Times and dates will be published in the January edition.

International Standard Committee Meetings

12–16 December 2005

ISO/TC 108/SC 5 Condition monitoring and diagnostics of machines

This committee and its working groups will meet at the SeaTech Campus of the Florida Atlantic University Graduate School of Ocean Engineering, in Dania Beach, Florida.

ISO/TC 108 Meetings

During the week of 29 August to 2 September 2005, ISO/TC 108 and three of its subcommittees met in Mississauga, Canada at the offices of the Canadian Standards Association. The new CSA building is perfectly designed to host standards meetings, and the 18 working groups that met during the week found the environment to be conducive to their standards development work. The committees that met during this week were ISO/TC 108 *Mechanical vibration and shock*; ISO/TC 108/SC 2 *Measurement and evaluation of mechanical vibration and shock as applied to machines vehicles and structures*; ISO/TC 108/SC 3 *Use and calibration of mechanical vibration and shock measuring instruments*; and ISO/TC 108/SC 6 *Vibration and shock generating systems.*

The official host of the meeting was the Standards Council of Canada, the Canadian member body of ISO. The meeting was organized by George Wong and funded, in part, by contributions received from the ASA Technical Council, as well as contributions from industry and Canadian government sources. Earlier this summer, Canada also hosted the meetings of IEC/TC 29 *Electroacoustics*; ISO/TC 43 *Acoustics*, ISO/TC 43/SC 1 *Noise*; and ISO/TC 43/SC 2 *Building acoustics*.

The U.S. was represented at each of these meetings by a delegation of experts chosen from the U.S. Technical Advisory Group (U.S. TAG) to each committee, which is led by the U.S. TAG Chair. Over the next several months members of the U.S. Technical Advisory Groups to ISO/TC 108 and its subcommittees can expect to review and provide input on the revised editions of the documents that were discussed at the meeting, as they are issued for voting by the ISO member bodies.

There are a few subject areas, however, where additional expertise is needed, in particular "Ground borne noise and vibration from rail systems" and "Vibration of stationary structures." If you would like to find out how you can participate in the development of these or other standards under TC 108, please call the Secretariat.

Photos of a Few of the Working Group Meetings Mississauga

Photo Caption 1: U.S. TAG Chair for ISO/TC 108 and ISO/TC 108/SC 3, David J. Evans (right) is also the convenor of WG 26, "Signal processing methods for the analysis of mechanical vibration and shock." Left to right: Akira Sone (Japan), Torben Licht (Denmark), David Evans (U.S.).

Photo Caption 2: Bruce Douglas, Chairman of ISO/TC 108, and Charles Gaumond, Chair of ASA's Technical Committee on Signal Processing, discuss signal processing standards in the WG. Left to right: Kjell Ahlin (Sweden), Mike Gellatley (U.K.), Charles Gaumond (U.S.), Bruce Douglas (U.S.).

Photo Caption 3: WG 24 "Condition assessment of structural systems from dynamic force measurements." Left to right: Mike Gellatley (U.K.), Talaat Tantawy, WG Convenor (France), Koki Shiohata (Japan), Macinissa Mezache (U.S.).

Photo Caption 4: WG 28, "Vibration materials." Left to right: Kwang Jon Kim (Korea), Walter Madigosky, WG Convenor, Minoru Kato (Japan).

Photo Caption 5: WG 31 "Balancing." Left to right: Hatto Schneider (Germany, back to camera), Macinissa Mezache (U.S.), Rob Herbert, WG Convenor (U.K.), Alan Wattling (U.K.), William Foiles (U.S.), Andrew Hubbard (U.K.), Mike McGuire (U.K.).

Photo Caption 6: ASA Standards Manager, Susan Blaeser, presents a plaque to Arthur Kilcullen, Chair of S2/WG 11, "Measurement and evaluation of mechanical vibration of vehicles," for his leadership in the development of ANSI S2.25-2004 *American National Standard Guide for the Measurement, Reporting, and Evaluation of Hull and Superstructure Vibration in Ships*. Dr. Kilcullen is also the Co-Chair of the U.S. TAG for ISO/TC 108/SC 2.

Accredited Standards Committee on Acoustics, S1

(J. P. Seiler, Chair; G. S. K. Wong, Vice Chair)

Scope: Standards, specifications, methods of measurement and test, and terminology in the field of physical acoustics including architectural acoustics, electroacoustics, sonics and ultrasonics, and underwater sound, but excluding those aspects which pertain to biological safety, tolerance, and comfort.

S1 Working Groups

S1/Advisory —Advisory Planning Committee to S1 (G.S.K. Wong);
S1/WG1 —Standard Microphones and their Calibration (V. Nedzelnitsky);
S1/WG5 —Band Filter Sets (A. H. Marsh);
S1/WG17 —Sound Level Meters and Integrating Sound Level Meters (B. M. Brooks);
S1/WG19 —Insertion Loss of Windscreens (A. J. Campanella);
S1/WG20 —Ground Impedance (K. Attenborough, Chair; J. Sabatier, Vice Chair);

S1/WG22 —Bubble Detection and Cavitation Monitoring (Vacant);
S1/WG25 —Specification for Acoustical Calibrators (P. Battenberg);
S1/WG26 —High Frequency Calibration of the Pressure Sensitivity of Microphones (A. Zuckerwar);
S1/WG27 —Acoustical Terminology (J. Vipperman);
S1/WG28 —Passive Acoustic Monitoring for Marine Mammal Mitigation for Seismic Surveys (A. Thode).

S1 Inactive Working Groups

S1/WG16 —FFT Acoustical Analyzers (R. J. Peppin, Chair).

S1 Standards on Acoustics

ANSI S1.1-1994 (R 2004) American National Standard Acoustical Terminology.
ANSI S1.4-1983 (R 2001) American National Standard Specification for Sound Level Meters.
ANSI S1.4A-1985 (R 2001) Amendment to ANSI S1.4-1983.
ANSI S1.6-1984 (R 2001) American National Standard Preferred Frequencies, Frequency Levels, and Band Numbers for Acoustical Measurements.
ANSI S1.8-1989 (R 2001) American National Standard Reference Quantities for Acoustical Levels.
ANSI S1.9-1996 (R 2001) American National Standard Instruments for the Measurement of Sound Intensity.
ANSI S1.11-2004 American National Standard Specification for Octave-Band and Fractional-Octave-Band Analog and Digital Filters.
ANSI S1.13-2005 American National Standard Measurement of Sound Pressure Levels in Air.
ANSI S1.14-1998 (R 2003) American National Standard Recommendations for Specifying and Testing the Susceptibility of Acoustical Instruments to Radiated Radio-Frequency Electromagnetic Fields, 25 MHz to 1 GHz.
ANSI S1.15-1997/Part 1 (R 2001) American National Standard Measurement Microphones, Part 1: Specifications for Laboratory Standard Microphones.
ANSI S1.15-2005/Part 2 American National Standard Measurement Microphones, Part 2: Primary Method for Pressure Calibration of Laboratory Standard Microphones by the Reciprocity Technique.
ANSI S1.16-2000 (R 2005) American National Standard Method for Measuring the Performance of Noise Discriminating and Noise Canceling Microphones.
ANSI S1.17/1-2000/Part 1 American National Standard Microphone Windscreens- Part 1: Measurements and Specification of Insertion Loss in Still or Slightly Moving Air.
ANSI S1.18-1999 (R 2004) American National Standard Template Method for Ground Impedance.
ANSI S1.20-1988 (R 2003) American National Standard Procedures for Calibration of Underwater Electroacoustic Transducers.
ANSI S1.22-1992 (R 2002) American National Standard Scales and Sizes for Frequency Characteristics and Polar Diagrams in Acoustics.
ANSI S1.24 TR-2002 ANSI Technical Report Bubble Detection and Cavitation Monitoring.
ANSI S1.25-1991 (R 2002) American National Standard Specification for Personal Noise Dosimeters.
ANSI S1.26-1995 (R 2004) American National Standard Method for Calculation of the Absorption of Sound by the Atmosphere.
ANSI S1.40-1984 (R 2001) American National Standard Specification for Acoustical Calibrators.
ANSI S1.42-2001 American National Standard Design Response of Weighting Networks for Acoustical Measurements.
ANSI S1.43-1997 (R 2002) American National Standard Specifications for Integrating-Averaging Sound Level Meters.

Accredited Standards Committee on Mechanical vibration and Shock, S2

(R. J. Peppin, Chair; D. J. Evans, Vice Chair)

Scope: Standards, specifications, methods of measurement and test, and terminology in the field of mechanical vibration and shock, and condition monitoring and diagnostics of machines, including the effects of mechanical vibration and shock on humans, including those aspects which pertain to biological safety, tolerance, and comfort.

S2 Working Groups

S2/WG1 —S2 Advisory Planning Committee (D. J. Evans);
S2/WG2 —Terminology and Nomenclature in the Field of Mechanical Vibration and Shock and Condition Monitoring and Diagnostics of Machines (D. J. Evans);
S2/WG3 —Signal Processing Methods (T. S. Edwards);
S2/WG4 —Characterization of the Dynamic Mechanical Properties of Viscoelastic Polymers (W. M. Madigosky, Chair; J. Niekiec, Vice Chair);
S2/WG5 —Use and Calibration of Vibration and Shock Measuring Instruments (D. J. Evans, Chair; B. E. Douglas, Vice Chair);
S2/WG6 —Vibration and Shock Actuators (G. Booth);
S2/WG7 —Acquisition of Mechanical Vibration and Shock Measurement Data (B. E. Douglas);
S2/WG8 —Analysis Methods of Structural Dynamics (B. E. Douglas);
S2/WG9 —Training and Accreditation (R. Eshleman, Chair;);
S2/WG10 —Measurement and Evaluation of Machinery for Acceptance and Condition (R. Eshleman, Chair; H. Pusey, Vice Chair);
S2/WG10/Panel 1 —Balancing (R. Eshleman);
S2/WG10/Panel 2 —Operational Monitoring and Condition Evaluation (R. Bankert);
S2/WG10/Panel 3 —Machinery Testing (R. Eshleman);
S2/WG10/Panel 4 —Prognosis (R. Eshleman);
S2/WG10/Panel 5 —Data Processing, Communication, and Presentation (K. Bever);
S2/WG11 —Measurement and Evaluation of Mechanical Vibration of Vehicles (A. F. Kilcullen);
S2/WG12 —Measurement and Evaluation of Structures and Structural Systems for Assessment and Condition Monitoring (B. E. Douglas, Chair; R. J. Peppin, Vice Chair);
S2/WG13 —Shock Test Requirements for Commercial Electronic Systems (P. D. Loeffler);
S2/WG39 (S3) —Human Exposure to Mechanical Vibration and Shock — Parallel to ISO/TC 108/SC 4 (D. D. Reynolds, Chair; H. E. von Gierke, Vice Chair).

S2 Inactive Working Group

S2/WG54 —Atmospheric Blast Effects (J. W. Reed).

S2 Standards on Mechanical Vibration and Shock

ANSI S2.1-2000 ISO 2041:1990 Nationally Adopted International Standard Vibration and Shock — Vocabulary.
ANSI S2.2-1959 (R 2001) American National Standard Methods for the Calibration of Shock and Vibration Pickups.
ANSI S2.4-1976 (R 2004) American National Standard Method for Specifying the Characteristics of Auxiliary Analog Equipment for Shock and Vibration Measurements.
ANSI S2.7-1982 (R 2001) American National Standard Balancing Terminology.
ANSI S2.8-1972 (R 2004) American National Standard Guide for Describing the Characteristics of Resilient Mountings.
ANSI S2.9-1976 (R 2001) American National Standard Nomenclature for Specifying Damping Properties of Materials.
ANSI S2.13-1996/Part 1 (R 2001) American National Standard Mechanical Vibration of Nonreciprocating Machines — Measurements on Rotating Shafts and Evaluation Part 1: General Guidelines.
ANSI S2.16-1997 (R 2001) American National Standard Vibratory Noise Measurements and Acceptance Criteria of Shipboard Equipment.
ANSI S2.17-1980 (R 2004) American National Standard Techniques of Machinery Vibration Measurement.
ANSI S2.19-1999 (R 2004) American National Standard Mechanical Vibration — Balance Quality Requirements of Rigid Rotors, Part 1: Determination of Permissible Residual Unbalance, Including Marine Applications.
ANSI S2.20-1983 (R 2001) American National Standard Estimating Airblast Characteristics for Single-Point Explosions in Air, with a Guide to Evaluation of Atmospheric Propagation and Effects.

ANSI S2.21-1998 (R 2002) American National Standard Method for Preparation of a Standard Material for Dynamic Mechanical Measurements.
ANSI S2.22-1998 (R 2002) American National Standard Resonance Method for Measuring the Dynamic Mechanical Properties of Viscoelastic Materials.
ANSI S2.23-1998 (R 2002) American National Standard Single Cantilever Beam Method for Measuring the Dynamic Mechanical Properties of Viscoelastic Materials.
ANSI S2.24-2001 American National Standard Graphical Presentation of the Complex Modulus of Viscoelastic Materials.
ANSI S2.25-2004 American National Standard Guide for the Measurement, Reporting, and Evaluation of Hull and Superstructure Vibration in Ships.
ANSI S2.26-2001 American National Standard Vibration Testing Requirements and Acceptance Criteria for Shipboard Equipment.
ANSI S2.27-2002 American National Standard Guidelines for the Measurement and Evaluation of Vibration of Ship Propulsion Machinery.
ANSI S2.28-2003 American National Standard Guidelines for the Measurement and Evaluation of Vibration of Shipboard Machinery.
ANSI S2.29-2003 American National Standard Guidelines for the Measurement and Evaluation of Vibration of Marine Shafts on Shipboard Machinery.
ANSI S2.31-1979 (R 2004) American National Standard Method for the Experimental Determination of Mechanical Mobility, Part 1: Basic Definitions and Transducers.
ANSI S2.32-1982 (R 2004) American National Standard Methods for the Experimental Determination of Mechanical Mobility, Part 2: Measurements Using Single-Point Translational Excitation.
ANSI S2.34-1984 (R 2005) American National Standard Guide to the Experimental Determination of Rotational Mobility Properties and the Complete Mobility Matrix.
ANSI S2.41-1985 (R 2001) American National Standard Mechanical Vibration of Large Rotating Machines with Speed Range from 10 to 200 rev/s — Measurement and Evaluation of Vibration Severity *in situ*.
ANSI S2.42-1982 (R 2004) American National Standard Procedures for Balancing Flexible Rotors.
ANSI S2.43-1984 (R 2005) American National Standard Criteria for Evaluating Flexible Rotor Balance.
ANSI S2.46-1989 (R 2005) American National Standard Characteristics to be Specified for Seismic Transducers.
ANSI S2.47-1990 (R 2001) American National Standard Vibrations of Buildings — Guidelines for the Measurements of Vibrations and Evaluation of their Effects on Buildings.
ANSI S2.48 -1993 (R 2001) American National Standard Servo-Hydraulic Test Equipment for Generating Vibration — Methods of Describing Characteristics.
ANSI S2.60 -1987 (R 2005) American National Standard Balancing Machines — Enclosures and Other Safety Measures.
ANSI S2.61 -1989 (R 2005) American National Standard Guide to the Mechanical Mounting of Accelerometers.

Accredited Standards Committee on Bioacoustics, S3

(R. F. Burkard, Chair; C. Champlin, Vice Chair)

Scope: Standards, specifications, methods of measurement and test, and terminology in the fields of psychological and physiological acoustics, including aspects of general acoustics, which pertain to biological safety, tolerance, and comfort.

S3 Working Groups

S3/Advisory—Advisory Planning Committee to S3 (R. F. Burkard);
S3/WG35—Audiometers (R. L. Grason);
S3/WG36—Speech Intelligibility (R. S. Schlauch);
S3/WG37—Coupler Calibration of Earphones (B. Kruger);
S3/WG43—Method for Calibration of Bone Conduction Vibrator (J. Durrant);
S3/WG48—Hearing Aids (D. A. Preves);
S3/WG51—Auditory Magnitudes (R. P. Hellman);
S3/WG56—Criteria for Background Noise for Audiometric Testing (J. Franks);
S3/WG59—Measurement of Speech Levels (Vacant);
S3/WG60—Measurement of Acoustic Impedance and Admittance of the Ear (Vacant);
S3/WG62—Impulse Noise with Respect to Hearing Hazard (J. H. Patterson);
S3/WG67—Manikins (M. D. Burkhard);
S3/WG72—Measurement of Auditory Evoked Potentials (R. F. Burkhard);
S3/WG76—Computerized Audiometry (A. J. Miltich);
S3/WG78—Thresholds (W. A. Yost);
S3/WG79—Methods for Calculation of the Speech Intelligibility Index (C. V. Pavlovic);
S3/WG81—Hearing Assistance Technologies (L. Thibodeau and L. A. Wilber, Co-Chairs);
S3/WG82—Basic Vestibular Function Test Battery (C. Wall III);
S3/WG83—Sound Field Audiometry (T. R. Letowski);
S3/WG84—Otoacoustic Emission (G. R. Long);
S3/WG86—Audiometric Data Structures (W. A. Cole and B. Kruger, Co-Chairs);
S3/WG87—Human Response to Repetitive Mechanical Shock (N. Alem);
S3/WG88—Standard Audible Emergency Evacuation and Other Signals (I. Mande);
S3/WG89—Spatial Audiometry in Real and Virtual Environments (J. Besing);
S3/WG90—Animal Bioacoustics (A. E. Bowles);
S3/WG91—Text-to-Speech Synthesis Systems (A. K. Syrdal and C. Bickley, Co-Chairs);
S2/WG39 (S3)—Human Exposure to Mechanical Vibration and Shock — Parallel to ISO/TC 108/SC 4 (D. D. Reynolds).

S3 Liaison Group

S3/L-1 S3 U.S. TAG Liaison to IEC/TC 87 Ultrasonics (W. L. Nyborg).

S3 Inactive Working Groups

S3/WG71 Artificial Mouths (R. L. McKinley);
S3/WG80 Probe-tube Measurements of Hearing Aid Performance (W. A. Cole);
S3/WG58 Hearing Conservation Criteria.

S3 Standards on Bioacoustics

ANSI S3.1-1999 (R 2003) American National Standard Maximum Permissible Ambient Noise Levels for Audiometric Test Rooms.
ANSI S3.2-1989 (R 1999) American National Standard Method for Measuring the Intelligibility of Speech over Communication Systems.
ANSI S3.4-2005 American National Standard Procedure for the Computation of Loudness of Steady Sound.
ANSI S3.5-1997 (R 2002) American National Standard Methods for Calculation of the Speech Intelligibility Index.
ANSI S3.6-2004 American National Standard Specification for Audiometers.
ANSI S3.7-1995 (R 2003) American National Standard Method for Coupler Calibration of Earphones.
ANSI S3.13-1987 (R 2002) American National Standard Mechanical Coupler for Measurement of Bone Vibrators.
ANSI S3.14-1977 (R 1997) American National Standard for Rating Noise with Respect to Speech Interference.
ANSI S3.18 – 2002 ISO 2631-1:1997 Nationally Adopted International Standard Mechanical Vibration and Shock — Evaluation of Human Exposure to Whole-Body Vibration — Part 1: General Requirements.
ANSI S3.18-2003 ISO 2631-4: 2001 Nationally Adopted International Standard Mechanical Vibration and Shock — Evaluation of Human Exposure to Whole-Body Vibration — Part 4: Guidelines for the Evaluation of the Effects of Vibration and Rotational Motion on Passenger and Crew Comfort in Fixed-Guideway Transport Systems.
ANSI S3.20 -1995 (R 2003) American National Standard Bioacoustical Terminology.
ANSI S3.21 -2004 American National Standard Methods for Manual Pure -Tone Threshold Audiometry.
ANSI S3.22-2003 American National Standard Specification of Hearing Aid Characteristics.

ANSI S3.25 -1989 (R 2003) American National Standard for an Occluded Ear Simulator.
ANSI S3.29 -1983 (R 2001) American National Standard Guide to the Evaluation of Human Exposure to Vibration in Buildings.
ANSI S3.34 -1986 (R 1997) American National Standard Guide for the Measurement and Evaluation of Human Exposure to Vibration Transmitted to the Hand.
ANSI S3.35 - 2004 American National Standard Method of Measurement of Performance Characteristics of Hearing Aids under Simulated Real-Ear Working Conditions.
ANSI S3.36-1985 (R 2001) American National Standard Specification for a Manikin for Simulated *in situ* Airborne Acoustic Measurements.
ANSI S3.37-1987 (R 2002) American National Standard Preferred Earhook Nozzle Thread for Postauricular Hearing Aids.
ANSI S3.39-1987 (R 2002) American National Standard Specifications for Instruments to Measure Aural Acoustic Impedance and Admittance (Aural Acoustic Immittance).
ANSI S3.40-2002 ISO 10819:1996 Nationally Adopted International Standard Mechanical Vibration and Shock — Hand-Arm Vibration — Method for the Measurement and Evaluation of the Vibration Transmissibility of Gloves at the Palm of the Hand.
ANSI S3.41-1990 (R 2001) American National Standard Audible Emergency Evacuation Signal.
ANSI S3.42-1992 (R 2002) American National Standard Testing Hearing Aids with a Broad-Band Noise Signal.
ANSI S3.44-1996 (R 2001) American National Standard Determination of Occupational Noise Exposure and Estimation of Noise-Induced Hearing Impairment.
ANSI S3.45-1999 American National Standard Procedure for Testing Basic Vestibular Function.
ANSI S3.46-1997 (R 2002) American National Standard Methods of Measurement of Real-Ear Performance Characteristics of Hearing Aids.

Accredited Standards Committee on Noise, S12

(R. D. Hellweg, Chair; W. J. Murphy, Vice Chair)

Scope: Standards, specifications, and terminology in the field of acoustical noise pertaining to methods of measurement, evaluation, and control, including biological safety, tolerance, and comfort and physical acoustics as related to environmental and occupational noise.

S12 Working Groups

S12/Advisory—Advisory Planning Committee to S12 (R. D. Hellweg);
S12/WG3—Measurement of Noise from Information Technology and Telecommunications Equipment (K. X. C. Man);
S12/WG11—Hearing Protector Attenuation and Performance (E. H. Berger);
S12/WG12—Evaluation of Hearing Conservation Programs (J. D. Royster, Chair; E. H. Berger, Vice Chair);
S12/WG13—Method for the Selection of Hearing Protectors that Optimize the Ability to Communicate (D. Byrne);
12/WG14—Measurement of the Noise Attenuation of Active and/or Passive Level-Dependent Hearing Protective Devices (J. Kalb, Chair; W. J. Murphy, Vice Chair);
S12/WG15—Measurement and Evaluation of Outdoor Community Noise (P. D. Schomer);
S12/WG18—Criteria for Room Noise (R. J. Peppin);
S12/WG23—Determination of Sound Power (R. J. Peppin and B. M. Brooks, Co-Chairs);
S12/WG31—Predicting Sound-Pressure Levels Outdoors (R. J. Peppin);
S12/WG32—Revision of ANSI S12.7-1986 Methods for Measurement of Impulse Noise (A. H. Marsh);
S12/WG33—Revision of ANSI S5.1-1971 Test Code for the Measurement of Sound from Pneumatic Equipment (B. M. Brooks);
S12/WG36—Development of Methods for Using Sound Quality (G. L. Ebbit and P. Davies, Co-Chairs);
S12/WG37—Measuring Sleep Disturbance Due to Noise (K. S. Pearsons);
S12/WG38—Noise Labeling in Products (R. D. Hellweg and J. Pope, Co-Chairs);
S12/WG40—Measurement of the Noise Aboard Ships (S. Antonides, Chair; S. Fisher, Vice Chair);
S12/WG41—Model Community Noise Ordinances (L. Finegold, Chair; B. M. Brooks, Vice Chair);
S12/WG43—Rating Noise with Respect to Speech Interference (M. Alexander).

S12 Liaison Groups

S12/L-1 IEEE 85 Committee for TAG Liaison — Noise Emitted by Rotating Electrical Machines (parallel to ISO/TC 43/SC 1/WG 13) (R. G. Bartheld);
S12/L-2 Measurement of Noise from Pneumatic Compressors Tools and Machines (parallel to ISO/TC 43/SC 1/WG 9) (Vacant);
S12/L-3 SAE Committee for TAG Liaison on Measurement and Evaluation of Motor Vehicle Noise (parallel to ISO/TC 43/SC 1/WG 8) (R. F. Schumacher and J. Johnson);
S12/L-4 SAE Committee A-21 for TAG Liaison on Measurement and Evaluation of Aircraft Noise (J. Brooks);
S12/L-5 ASTM E-33 on Environmental Acoustics (to include activities of ASTM E33.06 on Building Acoustics, parallel to ISO/TC 43/SC 2 and ASTM E33.09 on Community Noise) (K. P. Roy);
S12/L-6 SAE Construction-Agricultural Sound Level Committee (I. Douell);
S12/L-7 SAE Specialized Vehicle and Equipment Sound Level Committee (T. Disch);
S12/L-8 ASTM PTC 36 Measurement of Industrial Sound (R. A. Putnam, Chair; B. M. Brooks, Vice Chair).

S12 Inactive Working Groups

S12/WG27 Outdoor Measurement of Sound-Pressure Level (G. Daigle);
S12/WG8 Determination of Interference of Noise with Speech Intelligibility (L. Marshall);
S12/WG9 Annoyance Response to Impulsive Noise (L. C. Sutherland);
S12/WG19 Measurement of Occupational Noise Exposure (J. P. Barry/R. Goodwin, Co-Chairs)
S12/WG29 Field Measurement of the Sound Output of Audible Public-Warning Devices (Sirens) (P. Graham);
S12/WG34 Methodology for Implementing a Hearing Conservation Program (J. P. Barry).

S12 Standards on Noise

ANSI S12.1-1983 (R 2001) American National Standard Guidelines for the Preparation of Standard Procedures to Determine the Noise Emission from Sources.
ANSI S12.2-1995 (R 1999) American National Standard Criteria for Evaluating Room Noise.
ANSI S12.3-1985 (R 2001) American National Standard Statistical Methods for Determining and Verifying Stated Noise Emission Values of Machinery and Equipment.
ANSI S12.5-1990 (R 1997) American National Standard Requirements for the Performance and Calibration of Reference Sound Sources.
ANSI S12.6-1997 (R 2002) American National Standard Methods for Measuring the Real-Ear Attenuation of Hearing Protectors.
ANSI S12.7-1986 (R 1998) American National Standard Methods for Measurements of Impulse Noise.
ANSI S12.8-1998 (R 2003) American National Standard Methods for Determining the Insertion Loss of Outdoor Noise Barriers.
ANSI S12.9-1988 Part 1 (R 2003) American National Standard Quantities and Procedures for Description and Measurement of Environmental Sound, Part 1.
ANSI S12.9-1992 Part 2 (R 2003) American National Standard Quantities and Procedures for Description and Measurement of Environmental Sound, Part 2: Measurement of Long-Term, Wide-Area Sound.
ANSI S12.9-1993 Part 3 (R 2003) American National Standard Quantities and Procedures for Description and Measurement of Environmental Sound, Part 3: Short-Term Measurements with an Observer Present.
ANSI S12.9-1996 Part 4 (R 2001) American National Standard Quantities and Procedures for Description and Measurement of Environmental

Sound, Part 4: Noise Assessment and Prediction of Long-Term Community Response.

ANSI S12.9-1998 Part 5 (R 2003) American National Standard Quantities and Procedures for Description and Measurement of Environmental Sound, Part 5: Sound Level Descriptors for Determination of Compatible Land Use.

ANSI S12.9-2000 Part 6 American National Standard Quantities and Procedures for Description and Measurement of Environmental Sound Part 6: Methods for Estimation of Awakenings Associated with Aircraft Noise Events Heard in Homes.

ANSI S12.10-2002 ISO 7779:1999 Nationally Adopted International Standard Acoustics — Measurement of Airborne Noise Emitted by Information Technology and Telecommunications Equipment.

ANSI S12.11-2003/Part 1 ISO 10302: 1996 (MOD) American National Standard Acoustics — Measurement of Noise and Vibration of Small Air-Moving Devices — Part 1: Airborne Noise Emission.

ANSI S12.11-2003/Part 2 American National Standard Acoustics — Measurement of Noise and Vibration of Small Air-Moving Devices — Part 2: Structure-Borne Vibration.

ANSI S12.12-1992 (R 2002) American National Standard Engineering Method for the Determination of Sound Power Levels of Noise Sources using Sound Intensity.

ANSI S12.13 TR-2002 ANSI Technical Report Evaluating the Effectiveness of Hearing Conservation Programs through Audiometric Data Base Analysis.

ANSI S12.14-1992 (R 2002) American National Standard Methods for the Field Measurement of the Sound Output of Audible Public Warning Devices Installed at Fixed Locations Outdoors.

ANSI S12.15-1992 (R 2002) American National Standard For Acoustics *B* Portable Electric Power Tools, Stationary and Fixed Electric Power Tools, and Gardening Appliances — Measurement of Sound Emitted.

ANSI S12.16-1992 (R 2002) American National Standard Guidelines for the Specification of Noise of New Machinery.

ANSI S12.17-1996 (R 2001) American National Standard Impulse Sound Propagation for Environmental Noise Assessment.

ANSI S12.18-1994 (R 2004) American National Standard Procedures for Outdoor Measurement of Sound-Pressure Level.

ANSI S12.19-1996 (R 2001) American National Standard Measurement of Occupational Noise Exposure.

ANSI S12.23-1989 (R 2001) American National Standard Method for the Designation of Sound Power Emitted by Machinery and Equipment.

ANSI S12.30-1990 (R 2002) American National Standard Guidelines for the Use of Sound Power Standards and for the Preparation of Noise Test Codes.

ANSI S12.35-1990 (R 2001) American National Standard Precision Methods for the Determination of Sound Power Levels of Noise Sources in Anechoic and Hemi-Anechoic Rooms.

ANSI S12.42-1995 (R 2004) American National Standard Microphone-in-Real-Ear and Acoustic Test Fixture Methods for the Measurement of Insertion Loss of Circumaural Hearing Protection Devices.

ANSI S12.43-1997 (R 2002) American National Standard Methods for Measurement of Sound Emitted by Machinery and Equipment at Workstations and other Specified Positions.

ANSI S12.44-1997 (R 2002) American National Standard Methods for Calculation of Sound Emitted by Machinery and Equipment at Workstations and other Specified Positions from Sound Power Level.

ANSI S12.50-2002 ISO 3740:2000 Nationally Adopted International Standard Acoustics — Determination of Sound Power Levels of Noise Sources — Guidelines for the use of Basic Standards.

ANSI S12.51-2002 ISO 3741:1999 Nationally Adopted International Standard Acoustics — Determination of Sound Power Levels of Noise Sources using Sound Pressure — Precision Method for Reverberation Rooms.

ANSI S12.53/1-1999 (R 2004) ISO 3743-1:1994 Nationally Adopted International Standard Acoustics — Determination of Sound Power Levels of Noise Sources — Engineering Methods for Small, Movable Sources in Reverberant Fields — Part 1: Comparison Method for Hard-Walled Test Rooms.

ANSI S12.53/2-1999 (R 2004) ISO 3743-2:1994 Nationally Adopted International Standard Acoustics — Determination of Sound Power Levels of Noise Sources using Sound Pressure — Engineering Methods for Small, Movable Sources in Reverberant Fields — Part 2: Methods for Special Reverberation Test Rooms.

ANSI S12.54-1999 (R 2004) ISO 3744:1994 Nationally Adopted International Standard Acoustics — Determination of Sound Power Levels of Noise Sources using Sound Pressure — Engineering Method in an Essentially Free Field over a Reflecting Plane.

ANSI S12.56-1999 ISO 3746:1995 Nationally Adopted International Standard Acoustics — Determination of Sound Power Levels of Noise Sources using Sound Pressure — Survey Method using an Enveloping Measurement Surface over a Reflecting Plane.

ANSI S12.57-2002 ISO 3747:2000 Nationally Adopted International Standard Acoustics — Determination of Sound Power Levels of Noise Sources using Sound Pressure — Comparison Method *in situ*.

ANSI S12.60-2002 American National Standard Acoustical Performance Criteria, Design Requirements, and Guidelines for Schools.

ASA Committee on Standards (ASACOS)

ASACOS (P. D. Schomer, Chair and ASA Standards Director).

U.S. Technical Advisory Groups (TAGS) for International Standards Committees

ISO/TC 43 Acoustics, **ISO/TC 43/SC 1** Noise (P. D. Schomer, U.S. TAG Chair).

ISO/TC 108 Mechanical Vibration and Shock (D. J. Evans, U.S. TAG Chair).

ISO/TC 108/SC2 Measurement and Evaluation of Mechanical Vibration and Shock as Applied to Machines, Vehicles, and Structures (A. F. Kilcullen, and R. F. Taddeo U.S. TAG Co-Chairs).

ISO/TC 108/SC3 Use and Calibration of Vibration and Shock Measuring Instruments (D. J. Evans, U.S. TAG Chair).

ISO/TC 108/SC4 Human Exposure to Mechanical Vibration and Shock (D. D. Reynolds, U.S. TAG Chair).

ISO/TC 108/SC5 Condition Monitoring and Diagnostic Machines (D. J. Vendittis, U.S. TAG Chair; R. F. Taddeo, U.S. TAG Vice Chair).

ISO/TC 108/SC6 Vibration and Shock Generating Systems (G. Booth, U.S. TAG Chair).

IEC/TC 29 Electroacoustics (V. Nedzelnitsky, U.S. Technical Advisor).

Standards News from the United States

(Partially derived from *ANSI Reporter*, and *ANSI Standards Action*, with appreciation.)

American National Standards Call for Comment on Proposals Listed

This section solicits comments on proposed new American National Standards and on proposals to revise, reaffirm, or withdrawal approval of existing standards. The dates listed in parenthesis are for information only.

ASA (ASC S12) (Acoustical Society of America)

National Adoptions

BSR S12.5-200X/ISO 6926:1999 Acoustics — Requirements for the Performance and Calibration of Reference Sound Sources Used for the Determination of Sound Power Levels (17 October 2005)

This is a proposed national adoption of ISO 6926 that defines important physical and performance characteristics of reference sound sources and specifies procedures for their calibration, primarily to determine the sound power level of other sound sources. The modification adds an informative guideline to remind those who wish to have their reference sound source calibrated in the 63-Hz and 16-kHz octave bands to specify the need for that requirement.

BSR S12.55-200x/ISO 3745:2003 Acoustics — Determination of sound

power levels of noise sources using sound pressure — Precision methods for anechoic and hemi-anechoic rooms (17 October 2005)

Specifies methods for measuring the sound-pressure levels on a measurement surface enveloping a noise source in anechoic and hemi-anechoic rooms, in order to determine the sound power level or sound energy level produced by the noise source. Gives requirements for the test environment and instrumentation, as well as techniques for obtaining the surface sound-pressure level from which the sound power level or sound energy level is calculated, leading to results which have a grade 1 accuracy. The methods specified are suitable for measurements of all types of noise.

WITHDRAWALS

BSR S12.35-1990 American National Standard Precision Methods for the Determination of Sound Power Levels of Noise Sources in Anechoic and Hemi-Anechoic Rooms (17 October 2005)

This standard describes a precision method for determination of the sound power levels of noise sources in laboratory anechoic or hemi-anechoic rooms. The standard contains information on instrumentation, installation, and operation of the source; methods for determination of the sound-pressure level on the measurement surface; procedures for the calculation of sound power level, directivity index, and directivity factor; and techniques that may be used to qualify the laboratory facilities used for the measurements.

REVISIONS

BSR S12.9-200X/Part 4 Quantities and Procedures for Description and Measurement of Environmental Sound — Part 4: Noise Assessment and Prediction of Long-Term Community Response (Revision of ANSI S12.9-1996/Part 4) (7 November 2005)

Specifies methods to assess environmental sounds and to predict the annoyance response of communities to long-term noise from any and all types of environmental sounds produced by one or more distinct or distributed sound sources. The sources may be separate or in various combinations. Application of the method is limited to areas where people reside and related long-term land uses.

BSR S12.2-200X Criteria for Evaluating Room Noise (Revision of ANSI S12.2-1995) (7 November 2005).

This Standard provides three primary methods for evaluating room noise: a survey method that employs the A-weighted sound level; an engineering method that employs expanded noise criteria (NC) curves; and a precision method that employs room noise criterion (RNC) curves.

Final Actions on American National Standards

The standards actions listed below have been approved by the ANSI Board of Standards Review (BSR) or by an ANSI-Audited Designator, as applicable.

ASA (ASC S1) (Acoustical Society of America)

BSR S1.13-2005 American National Standard Measurement of Sound-Pressure Levels in Air. Specifies requirements and describes procedures for the measurement of sound-pressure levels in air at a single point in space. These apply primarily to measurements performed indoors but may be utilized in outdoor measurements under specified conditions. This is a fundamental standard applicable to a wide range of measurements and to sounds that may differ widely in temporal and spectral characteristics; more specific ANS complement its requirements. A classification is given of the types of sound generally encountered, and the preferred descriptor for each type is identified.

ASA (ASC S2) (Acoustical Society of America)

WITHDRAWALS

BSR S2.45-1983 American National Standard Electrodynamic Test Equipment for Generating Vibration — Methods of Describing Equipment Characteristics (30 June 2005)

This standard provides a method for specifying the characteristics of electrodynamic test equipment for generating vibration and serves as a guide to the selection of such equipment. It applies to electrodynamic vibration generators and power amplifiers, both individually and in combination. The standard provides means to assist a prospective user to calculate and compare the performance of equipment provided by two or more manufacturers, even if the vibration generator and the power amplifier are from different manufacturers.

BSR S2.58-1983 American National Standard Auxiliary Tables for Vibration Generators — Methods of Describing Equipment Characteristics (30 June 2005)

This standard provides a method for specifying the characteristics of eight types of auxiliary tables for vibration generators. It serves as a guide to the prospective user of auxiliary tables to assist him to objectively compare the performance of auxiliary tables available from differing manufacturers.

ASA (ASC S3) (Acoustical Society of America)

REVISIONS

ANSI S3.4-2005 American National Standard Procedure for the Computation of Loudness of Steady Sounds (1 June 2005)

Specifies a procedure for calculating the loudness of steady sounds as perceived by a typical group of listeners with normal hearing, based on the spectra of the sounds. The possible sounds include simple and complex tones (both harmonic and inharmonic) and bands of noise. The spectra can be specified exactly, in terms of the frequencies and levels of individual spectral components, or approximately, in terms of the levels in 1/3-octave bands covering center frequencies from 50 to 16 000 Hz. Sounds can be presented in free field with frontal incidence, in a diffuse field, or via headphones.

Project Initiation Notification System (PINS)

ANSI Procedures require notification of ANSI by ANSI-accredited standards developers of the initiation and scope of activities expected to result in new or revised American National Standards. This information is a key element in planning and coordinating American National Standards.

The following is a list of proposed new American National Standards or revisions to existing American National Standards that have been received from ANSI-accredited standards developers that utilize the periodic maintenance option in connection with their standards. Directly and materially affected interests wishing to receive more information should contact the standards developer directly.

ASA (ASC S3) (Acoustical Society of America)

BSR S1.17/Part 1 — 200X Microphone Windscreens — Part 1: Measurements and Specification of Insertion Loss in Still or Slightly Moving Air.

This document underwent limited revision in 2004. Improvement Comments unrelated to the ballot were received and deemed to justify a new work item proposal. This revision will open the document for improvement.

ASA (ASC S3) (Acoustical Society of America)

BSR S3.47-200X, Hearing Assistance Device Systems (new standard).

Hearing Assistive Devices provide amplification to persons with hearing impairment and need to be verified using standardized procedures so that professionals will know performance characteristics.

ITSDF (Industrial Truck Standards Development Foundation, Inc.)

REVISIONS

BSR/ITSDF B56.11.5–200X, Measurement of Sound Emitted by Low Lift, High Lift, and Rough Terrain Powered Industrial Trucks (revision and redesignation of ANSI/ASME B56.11.5–1992 (R2000))

This standard establishes the conditions, test procedures, environment, and instrumentation for the determination and reporting of the A-weighted sound pressure level of electric battery and internal combustion powered, low lift, high lift, and rouhg terrian industrial trucks. It excludes earthmoving machinery, industrial cranes, and vehicles intended primarily for use on public roads.

EIA (Electric Industries Alliance)

REAFFIRMATIONS

BSR/EIA 364-28D-1999 (R200X), Vibration Test Procedure for Electrical Connectors and Sockets (reaffirmation of ANSI/EIA 364-28D-1999)

Details a method to access the ability of electrical connector components to withstand specified severities of vibration.

Newly Published ISO and IEC Standards

Listed here are new and revised standards recently approved and promulgated by ISO — the International Organization for Standardization.

ISO Standards

Mechanical Vibration and Shock (TC 108)

ISO 7919-5:2005 Mechanical vibration — Evaluation of machine vibration by measurements on rotating shafts — Part 5: Machine sets in hydraulic power generating and pumping plants.

ISO 13373-2:2005 Condition monitoring and diagnostics of machines — Vibration condition monitoring — Part 2: Processing, analysis, and presentation of vibration data.

ISO 14835-1:2005 Mechanical vibration and shock — Cold provocation tests for the assessment of peripheral vascular function — Part 1: Measurement and evaluation of finger skin temperature.

ISO 14835-2:2005 Mechanical vibration and shock — Cold provocation tests for the assessment of peripheral vascular function — Part 2: Measurement and evaluation of finger systolic blood pressure.

ISO 14837-1:2005 Mechanical vibration — Ground-borne noise and vibration arising from rail systems — Part 1: General guidance.

ISO 18437-2:2005 Mechanical vibration and shock — Characterization of the dynamic mechanical properties of visco-elastic materials — Part 2: Resonance method.

ISO 18437-3:2005 Mechanical vibration and shock — Characterization of the dynamic mechanical properties of visco-elastic materials — Part 3: Cantilever shear beam method.

ISO 16063-22:2005 Methods for the calibration of vibration and shock transducers — Part 22: Shock calibration by comparison to a reference transducer.

Noise (ISO/TC 43/SC 1)

ISO 3095:2005 Railway applications — Acoustics — Measurement of noise emitted by railbound vehicles.

ISO 33812005 Railway applications — Acoustics — Measurement of noise inside railbound vehicles.

ISO 17201-1:2005 Acoustics — Noise from shooting ranges — Part 1: Determination of muzzle blast by measurement.

Performance of Household Electrical Appliances (TC 59)

IEC 60704-2-3 Amd.1 Ed. 2.0 b:2005, Amendement 1–Household and similar electrical appliances — Test code for the determination of airborne acoustical noise — Part 2–3: Particular requirements for dishwashers.

IEC 60704-2-5 Ed. 2.0 b:2005, Household and similar electrical appliances — Test code for the determination of airborne acoustical noise — Part 2-5: Particular requirements for electric thermal storage room heaters.

ISO Draft Standards

Mechanical Vibration and Shock (TC 108)

ISO/10326-1:1992/DAmd1 Mechanical vibration — Laboratory method for evaluating vehicle seat vibration — Part 1: Basic requirements.

ISO/DIS 13374-2 Condition monitoring and diagnostics of machines — Data processing, communication and presentation — Part 2: Data-processing.

ISO/DIS 8568.2 Mechanical shock — Testing machines — Characteristics and performance.

Acoustics (TC 43)

ISO/DIS 389-5 Acoustics B Reference zero for the calibration of audiometric equipment B Part 5: Reference equivalent threshold sound-pressure levels for pure tones in the frequency range 8 kHz to 16 kHz.

ISO/FDIS 389-7 Acoustics B Reference zero for the calibration of audiometric equipment B Part 7: Reference threshold of hearing under free-field and diffuse-field listening conditions.

Noise (TC 43/SC 1)

ISO/DTS 4869-5 Acoustics — Hearing protectors — Part 5: Method for estimation of noise reduction using fitting by inexperienced test subjects (*Renumbered from 4869 Part 7*).

Sieves, Sieving and Other Sizing Methods (TC24)

ISO/DIS 20998-1, Particle characterization by acoustic methods — Part 1: Ultrasonic attenuation spectroscopy (14 October 2005).

IEC Draft Standards

Electroacoustics (IEC/TC 29)

29/584/FDIS IEC 60118-8 Electroacoustics — Hearing aids - Part 8: Methods of measurement of performance characteristics of hearing aids under simulated *in situ* working conditions.

29/585/FDIS IEC 60118-7 Electroacoustics — Hearing aids — Part 7: Measurement of the performance characteristics of hearing aids for production, supply, and delivery quality assurance purposes.

14/505/FDIS, IEC 60076-10-1 Ed.1: Power transformers — Part 10–1: determination of sound levels — Application guide (2 September 2005).

BOOK REVIEWS

P. L. Marston
Physics Department, Washington State University, Pullman, Washington 99164

These reviews of books and other forms of information express the opinions of the individual reviewers and are not necessarily endorsed by the Editorial Board of this Journal.

Editorial Policy: *If there is a negative review, the author of the book will be given a chance to respond to the review in this section of the Journal and the reviewer will be allowed to respond to the author's comments. [See "Book Reviews Editor's Note," J. Acoust. Soc. Am.* **81***, 1651 (May 1987).]*

High Frequency Ocean Acoustics (AIP Conference Proceedings)

Edited by Mike Porter, Martin Siderius, and Bill Kuperman

American Institute of Physics, 2004. 549 pp. Price: $165 (hardcover). ISBN: 0735402108

Let me admit immediately that I was favorably disposed towards this volume long before it was sent to me to review. To me, conference proceedings volumes, which give a snapshot overview of a significant part of a technical field (the high frequency component of ocean acoustics in this case), are enormously useful guides and references. We work day to day with our snail's eye view of our own research, augmented by a few of the more relevant references to the problem at hand, and this is certainly adequate and appropriate for detailed research. However, as good researchers, teachers, technical businessmen, etc., we need breadth as well as depth, and the question becomes, "how do we acquire the eagle's eye view of our technical area," as opposed to our more mundane view? There are a few avenues to acquiring such an overview, such as listening to talks at large conferences (which provide the latest view, but often don't provide the hard copy we would like at our fingertips), special issues of various journals (which provide sets of detailed research papers, but very often don't provide a complete overview of the activity in a technical area), 25–30 years of experience in the field (a good avenue for us older folk, but not so good for beginners or students), or conference proceeding volumes such as the one being reviewed. The conference proceeding volume tends to be especially useful if the conference is well attended by the community and if the editorial standards are kept high. Thanks to the spectacular beauty of La Jolla and Scripps, and the vast expertise and professionalism of the three editors, this volume is both complete and of very high quality. So even before I venture into the technical description of the book, let me just make a simple statement: obtain this book if you can. It gives an excellent overview of a major portion of ocean acoustics, and will be a worthy addition to your technical reference library. That having been said, let me proceed to some details.

Let me first address, as the book's editors do in the foreword, just what "high frequency" means in the context of ocean acoustics. To most physicists, high frequency is operationally defined as being the band in which ray theory is the most appropriate description of the propagation or scattering. This is taken as 3 kHz or above by the book's editors. On the other hand, low frequency is operationally defined as the band in which "full wave" theories such as normal modes, parabolic equations (PE), wave number integration, etc., are the most useful descriptors of the physics. This is usually taken to be 1 kHz or below by ocean acousticians, leaving an interesting "no man's land" between one and three kilohertz where ray theory starts to break down, but where modes, PE, and the like also become very awkward to use. This "medium frequency" band, while presenting some computational challenge, is routinely used in the real world by both man and marine animals, and is also welcomed with no discrimination into this volume, which might more appropriately be labeled, "Mostly High Frequency, A Good Deal of Medium Frequency, and Even a Smattering of Low Frequency Ocean Acoustics." The editors have wisely chosen to open their bandwidth in this book beyond the strictly high frequencies, which makes good sense, as many processes and studies routinely cover bands from low to high frequency, and chopping the band arbitrarily would make little sense physically.

The contents of the book are also very broad, as is evidenced by the six overview categories that are needed just to cover the technical areas. These are: (1) sediment acoustics, (2) acoustic communications, (3) boundary scattering and volume fluctuations, (4) marine mammals, (5) experimental and measurement techniques, and (6) target modeling, systems, and applications. Indeed, as the editors state in the foreword, while the propagation physics for high frequency ocean acoustics may be based in good old, plain-vanilla ray theory, the field itself is anything but mundane. Remote sensing of the ocean and seabed, high-speed acoustic communications, the effects of sound on marine mammals, scattering and reverberation in a wildly inhomogeneous medium, time reversal mirrors, advanced naval and civilian sensing applications, state-of-the-art ocean instrumentation, and much more are covered in this 549-page volume. Sixty-one different papers are presented, and the quality of them is uniformly high.

As I mentioned, conference proceedings volumes can be useful introductions to an area, and in that vein I personally most enjoyed reading the articles in the areas of acoustic communications and marine mammal acoustics. These areas are not my particular specialties, but they are ones about which I would like to learn more. T. C. Yang's articles on how environmental variables affect acoustic communications were especially interesting to me in the former category, whereas Whitlow Au's overview of the dolphin's "mediocre" sonar was both informative and entertaining. In addition, the volume also allowed a "low frequency" acoustician like me to catch up on what my colleagues a little higher up in the frequency band have been up to. There is often a considerable difference in the physical processes that affect low and high frequencies, and so this volume was anything but the "same old stuff" to me.

Again, I would strongly advise any ocean acousticians who read this review to get a copy of "High Frequency Ocean Acoustics" for their library. The price, at $165, may be high, but it is well worth the cost. There is a *lot* of great material in this volume, which is a tribute both to the contributors and the editors. As an ocean acoustician, I can only hope to see similar volumes published in the future on shallow water acoustics and long-range acoustics, the two other main research areas of ocean acoustics.

JIM LYNCH
Woods Hole Oceanographic Institution
Woods Hole, MA 02543
(508)289-2230
jlynch@whoi.edu

Structure-Borne Sound: Structural Vibrations and Sound Radiation at Audio Frequencies (3rd Edition)

L. Cremer, M. Heckl, and B. A. T. Petersson

Springer, Berlin, 2005. 607 pp. Price: $199.00 (hardcover), ISBN: 3540226966.

This book, originally published in German in 1966, under the title *Körperschall*, was based on a monograph prepared by Lothar Cremer on propagation of structure-borne sound in structures to which Manfred Heckl added chapters in the areas of transducers, wave types, damping, impedances, attenuation, and radiation. The first English translation by Eric Ungar, which appeared in 1972, was very close to the original German edition, and Ungar took special care to, as he said, "preserve not only the meaning, but also the 'flavor,' of the original text." The second edition in English appeared in 1987. The second edition was nearly identical to the first with the exception of new information on plates, shells, and orthotropic plates. This third edition is a significant reorganization of the material in the earlier editions plus new material, including an expanded list of references usefully grouped at the end of each chapter. There are two new chapters, reflecting the reorganization of the book, that contain some new material, and much new material can be found in the original chapters. The book does have a few shortcomings. When the author deviates from the original translation, the English lacks the smooth elegance of Ungar's prose and often sounds somewhat awkward. A number of graphs that appeared in the earlier editions have been reduced in size, which may make them more difficult to use to obtain numerical information. In addition there are a disturbing number of typographical errors that, hopefully, will be corrected in future editions. On the other hand, the reorganization of the book was sorely needed, has improved the book considerably, and has made the material much more accessible than in the earlier editions.

After a brief introduction the book begins with Chap. 2 under the title "A Little Dynamics." This chapter is new and begins with an elementary discussion of simple oscillators followed by an extension to more complicated systems using Lagrange's equations and Hamilton's principle. This discussion of energy methods is a useful addition to the book and is a theme that continues through many of the subsequent chapters.

Chapter 3 has the same title as Chap. II in the earlier editions, namely "Survey of Wave Types and Characteristics," and much of the material is unchanged. The chapter discusses longitudinal, shear, and bending waves in finite systems and systems of infinite length. It also discusses elastic waves in infinite media and waves in elastic half spaces, including Rayleigh waves. Much of this material has been considerably reorganized and the book benefits from the reorganization. New additions to the chapter include a section on the derivation of the plate equations of motion using Hamilton's principle and a section on structure-borne sound intensity into which all information on power transmission in plates and shells has been gathered.

Chapter 4, "Damping," corresponds to Chap. III of the same name in the earlier editions. It closely follows the material in earlier editions with some new material added. The chapter begins with a discussion of damping mechanisms followed by some new material on damping models. Resonant shear, longitudinal, and bending vibrations of damped beams are discussed followed by descriptions of a number of experimental techniques for obtaining complex moduli of damped materials along with some data on common materials such as metals, plastics, and building materials. Means for estimating the loss factor for plates with a free visco-elastic layer or a constrained visco-elastic layer are provided, including the case of a segmented constraining layer. A new section uses Hamilton's principle to derive the equations of motion of plates with multi-layer damping treatments. Some new material is provided on damping at joints including damping due to both normal and tangential motion relative to the interface.

Chapter 5, "Impedance and Mobility," corresponds to Chap. IV, "Impedances," in earlier editions and contains much of the previous material plus some new material. It begins with the derivation of the point mobility of rods, beams, and plates. It then goes on to a derivation of wave impedances for a number of different structures including orthotropic plates, elastic half spaces, thick plates, strips, and tubes. A very useful table of drive-point impedance formulas is provided that is an expanded version of that table in earlier editions. The chapter concludes with a discussion of point excitation of finite systems with a number of examples, some of which are new, such as excitation from roughness, parametric excitation, and excitation from a sudden release of potential energy.

"Attenuation of Structure-Borne Sound" is the title of Chap. 6, the same as Chap. V in earlier editions. While containing much of the same material as in the earlier editions, this chapter has been totally reorganized with new material interspersed throughout. The material is directed at computing reflection and transmission of longitudinal and bending waves at beam and plate junctions, where the junction may be at a cross-sectional change, a right angle bend, a blocking mass, an elastic layer, or the junction of multiple plates or beams. There is a new section on the use of Hamilton's principle for transmission problems, a section on the transmission of vibration between parallel plates, and a short section on statistical energy analysis.

Chapter 7, "Sound Radiation from Structures," contains similar material and is organized similarly to Chap. VI of the same name in the earlier editions. The chapter contains sections on radiation efficiency, radiation loss factors, and elementary radiators (spheres, cylinders, infinite plates, and impulsive sources) with some new material on force dipole radiators. There are also sections on radiation from baffled finite plates, structural response to sound, and a discussion of the relationship between structural response, radiation, and reciprocity. The chapter concludes with an example of the application of statistical energy analysis to the transmission of sound between acoustic spaces, a somewhat more in depth example than in the earlier editions.

Chapter 8, "Generation and Measurement of Structure-borne Sound," the final chapter, is a new chapter that is the repository for most of the material from Chap. I in the earlier editions. The author was right in placing this material at the end of the book. The chapters now flow together much more logically than before. As with other chapters in the book, this one contains most of the material from the earlier editions but has been thoroughly reorganized and new material added. There are sections that deal with general sensor application issues as well as with specific transducers such as electro-dynamic, electro-magnetic electro-static, and piezo-electric units with some new material on optical and magnetostrictive transducers.

The book has a list of variables at the end and a fairly short (10 pages) index. A more comprehensive index to a book of over 600 pages would be a valuable addition.

When *Structure-Borne Sound* first appeared it filled a void in that no similar collection of material was available in English. While this new edition has a few shortcomings, it is a well-organized work filled with clearly presented, valuable information on the science of structural acoustics. Whether used as a text book by the student or a handbook by the practicing engineer it will continue to fill an important niche in the technical literature and would be a valuable addition to the library of any engineer who has an interest in this technical area.

PAUL J. REMINGTON, Principal Engineer
BBN Technologies,
Cambridge, Massachusetts 02138

 0001-4966/2005/118(5)/2754/1/$22.50

Echolocation in Bat and Dolphins

Jeanette A. Thomas, Cynthia F. Moss, and Marianne Vater

The University of Chicago Press, Chicago, 2004. 631 pp. Price: $45.00 (softcover). ISBN: 0226795993

This edited volume had its origins from a five-day meeting held at Carvoeior, Portugal between 27 May and 2 June 1998. Many may remark that the delay between the meeting and the subsequent publication of the book poses a problem in that the material has become dated. That initial concern should be put to rest by an inspection of the reference sections and readings of the various papers in the volume. The editors have put the time between the meeting and the publication of the book to good use and most of the papers have been updated to reflect the state of science at the 2004 publication data.

This volume is from the last of the six Biosonar meetings, five of which have produced edited works. The Biosonar meetings started in 1966 with the first meeting in Frascati, Italy with 75 registered attendees, many of whom continued to attend the next five meetings. The second meeting was held 12 years later on the Isle of Jersey in April 1978. A third was held in 1986 in Helsingor, Denmark, and the fourth meeting was held in 1991 in Moscow, Russia. A fifth meeting held in 1994 at SPAWARSYSCEN, San Diego, California did not produce a edited volume, but this last meeting in Carvoeior, Portugal produced this nicely edited work.

These meetings all had the same aim and basic agenda—to bring together the leading experts in the fields of bat and dolphin echolocation to share their newest work and (more importantly) foster interdisciplinary understanding of the echolocation systems of these animals. The six volumes together summarize the past 40 years of research and investigation of biological based sonar systems of bats and dolphins. This volume will bring the interested student and professional up to date on the general state of the science.

The book is a large format (8.5×11 in.), softcover volume divided into six parts representing selected topics, each with a separate introduction. This basic design has been used successfully in the past for several books from biosonar conferences and works for this book as well. In this volume the six major topic areas presented are (1) Echolocation Signal Production, Feedback, and Control Systems; (2) Auditory Systems in Echolocating Mammals; (3) Performance and Cognition in Echolocating Mammals; (4) Ecological and Evolutionary Aspects of Echolocating Mammals; (5) Echolocation Theory, Analysis Techniques, and Applications; and (6) Possible Echolocation Abilities in Other Mammals. Whitlow Au leads off the volume with an updated comparison of bat and dolphin biosonar, a theme continued throughout various parts of the book.

This is a handsome book. At first blush, that may seem an odd comment; however, if one looks over the full text of the volume, it is consistent in typeface, article style, and readability of figures. Many past edited volumes arising from the Biosonar conferences tended to suffer from faults in these areas; however, modern electronic word processing and editorial oversight limit these problems. It is obvious that these editors have maintained an overall high quality look and feel of this book. One interesting arrangement, and one that is quite helpful, is the collection of references from each individual section into one reference source located at the end of that section's topic. This will assist the reader in that it tends to reduce repeated citations to the same work after each article. In addition, the interested student will no doubt find that combining references into topic areas makes further literature searches much easier.

Each of the six parts begins with an introductory article followed by selected submissions that follow the theme of the section. An attempt is made to cover both bats and dolphins equally under each part, but due to the vast differences in the accessibility, cost, and regulatory issues, some topics like neuroanatomy and ecology of echolocating mammals are dominated by bat research whereas work on signal production and analysis tends to be more equal.

Part one, "Echolocation Signal Production, Feedback, and Control Systems," provides a good overview of both bat and dolphin sound production systems and bat neuroanatomy. Generally, the take away message is that these animal systems are more plastic than once believed. Concluding remarks discuss the fine adjustments of the system for both bats and dolphins. The ability of bats to develop a plan of attack just before prey capture, the discovery of signal differences between individual Pacific white-sided dolphins, and an elegant model of the click production mechanism in dolphins from Dubrovskiy and Giro are a few of the items addressed. The last article by Goodson, Flint, and Cranford is a testament to Goodson's application of transmission line modeling to the acoustic pathways of signal propagation in the dolphin.

Part two, "The Ears of Whales and Bats," moves through the architecture of the ears of these two echo-locaters. This section clearly displays the degree of understanding that has been achieved of bat neuroanatomy and neurophysiology relative to that of the dolphin. This advanced state of knowledge can be directly related to the number and types of ethical and legal constraints placed upon dolphin researchers that limit their ability to perform the types of research necessary to obtain similar information. The application of behavioral based psychoacoustic studies, and more recently evoked-potential studies, have helped advance the understanding of auditory functions in dolphin research and indicate a new approach to studies of dolphin hearing.

Part three, "Performance and Cognition in Echolocating Mammals," has the fewest number of papers. The introduction by Masters and Harley is quite readable and presents a good overview for the remaining papers. Bat research concerning the ecological significance of echolocation clearly surpasses what is known about the dolphin, whereas studies of cognition are mostly related to dolphins. In "Object Recognition by Dolphins" Roitblat considers the complexity and difficulty of the processes of object recognition and explores the role of context in echolocation, arguing that the complexity of the recognition problem evades simple algorithmic expression.

Part four, "Ecological and Evolutionary Aspects of Echolocating Mammals," considers the results of both bat and dolphin studies of the functional ecology of these echolocating animals. This is where the reader will find the greatest difference in the understanding of the functional significance of echolocation and the environment for bats versus dolphins. Clearly, the role of echolocation in bat ecology is better understood than in dolphin. The reason for this can be explained; bats can be seen flying about using both the aided and unaided eye, whereas dolphins lurk in the deep and mostly turbid littorals of the coastal zone. Only a few hardy researchers have opted to attempt to study these animals in the wild since they are often faced with daunting obstacles of logistics, water clarity, and instrumentation. Part four offers suitable coverage of the subject for both animals.

Part five, "Echolocation Theory, Analysis Techniques, and Applications," considers the signal processing aspects of echolocation. This reflects a more engineering approach to the study of echolocation, an aspect of the science that has traditionally seen less attention than the more biologically based approaches. This part deals with the mathematical model development and computational bases of biosonar. The introduction discusses a multi-element model of the FM bat auditory system. Papers include coverage of the basics of recording and analysis of bat signals, and the development and implementation of standard approaches for the collection and analysis of bat signals. Altes discusses his biologically inspired synthetic aperture sonar approach (now called BioSAS) using multi-aspect echo "snippets" to reconstruct an "image" of the target. Other papers consider biomimetic sonar (transmitter and multiple receivers) combined with computational models based on bats and the use of computer-simulated targets for exploring dolphin echolocation.

Part six, "Possible Echolocation Abilities in Other Mammals," covers the requisite papers which discuss echolocation abilities in other mammals (meaning not bats or dolphins). The introduction deals with what has become a cyclic issue of pinniped echolocation and sets the reader for the remaining papers. Other parts of the section deal with the use of echolocation in rodents and the proposal that baleen whales may use low-frequency sound to probe their environment. These papers draw the reader into the complex notions of what may or may not be considered "echolocation" in other species. Most of the confusion surrounding just what constitutes a dedicated echolocation system comes from the inability to draw a definitive (and rather subjective) line separating the auditory continuum into active echolocation, as used by dolphins and bats, from more passive localization phenomena as demonstrated by humans, pinnipeds, and whales. The papers in this section provide a good background on echolocation issues surrounding pinnipeds and whales that may help the beginning student develop a better understanding as to what is and what is not considered an active echolocation system.

 0001-4966/2005/118(5)/2755/2/$22.50

Although the old adage that "science marches on" still holds true, this book provides a "snap-shot" of the recent science of echolocation along with some in-depth discussion of the leading areas of research. At such a reasonable price, this book should be a part of every marine mammal scientist library as well as that of the serious student.

PATRICK W. MOORE
SPAWARSYSCEN-San Diego
53560 Hull St.,
San Diego, California

REVIEWS OF ACOUSTICAL PATENTS

Lloyd Rice
11222 Flatiron Drive, Lafayette, Colorado 80026

The purpose of these acoustical patent reviews is to provide enough information for a Journal reader to decide whether to seek more information from the patent itself. Any opinions expressed here are those of reviewers as individuals and are not legal opinions. Printed copies of United States Patents may be ordered at $3.00 each from the Commissioner of Patents and Trademarks, Washington, DC 20231. Patents are available via the Internet at http://www.uspto.gov.

Reviewers for this issue:

GEORGE L. AUGSPURGER, *Perception, Incorporated, Box 39536, Los Angeles, California 90039*
JOHN M. EARGLE, *JME Consulting Corporation, 7034 Macapa Drive, Los Angeles, California 90068*
SEAN A. FULOP, *California State University, Fresno, 5245 N. Backer Avenue M/S PB92, Fresno, California 93740-8001*
JEROME A. HELFFRICH, *Southwest Research Institute, San Antonio, Texas 78228*
MARK KAHRS, *Department of Electrical Engineering, University of Pittsburgh, Pittsburgh, Pennsylvania 15261*
DAVID PREVES, *Starkey Laboratories, 6600 Washington Ave. S., Eden Prarie, Minnesota 55344*
DANIEL R. RAICHEL, *2727 Moore Lane, Fort Collins, Colorado 80526*
CARL J. ROSENBERG, *Acentech Incorporated, 33 Moulton Street, Cambridge, Massachusetts 02138*
WILLIAM THOMPSON, JR., *Pennsylvania State University, University Park, Pennsylvania 16802*
ERIC E. UNGAR, *Acentech, Incorporated, 33 Moulton Street, Cambridge, Massachusetts 02138*
ROBERT C. WAAG, *University of Rochester, Department of Electrical and Computer Engineering, Rochester, New York 14627*

6,892,674

43.28.Ra VARIABLE SOUND-EMITTING TOY FOR A PET

Dmitrijs V. Dubinins and Kenneth A. Jellico, assignors to N'Gen New Generation Innovations LLC
17 May 2005 (Class 119/707); filed 12 May 2003

In the interest of entertaining pets that like chewing, the inventors propose a toy that uses air compressed by an elastomeric body **101**. The flow is through the aperature **308** and through the sliding whistle **304** (also see

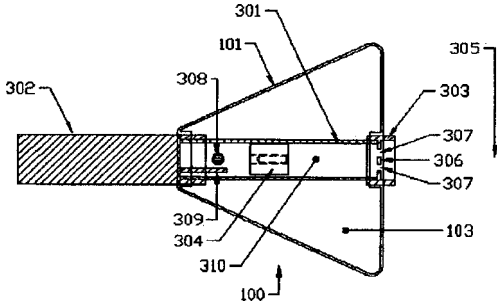

United States Patent 5,590,875) and output aperature **307**. The addition of the end cap **302** (shaded) should permit rolling, thereby enticing the potential abuser.—MK

6,906,982

43.30.Ma MARINE TIME-LAPSE SEISMIC SURVEYING

Rodney William Calvert, assignor to Shell Oil Company
14 June 2005 (Class 367/21); filed 14 April 2003

This patent discusses a procedure for conducting an at-sea, time-lapse, seismic survey that is designed to eliminate multiple surface reflections and changes in the sea state. The seismic sources and receivers are positioned at predetermined locations to record an initial set of data. At a much later point in time, with the sources and receivers at the same locations as before, a second set of monitor signals is recorded. A mathematical model is developed for these first and second data sets that includes the subsurface signal, changes therein, and the effect of multiple reflections within the water channel. A set of filter functions is then developed to filter out multiple reflections. These filter functions, combined with the first and second seismic data sets, are used to calculate any differences in the subsurface layers themselves that are associated with the elapsed time between the measurements of the two data sets.—WT

6,901,029

43.30.Yj TOWED LOW-FREQUENCY UNDERWATER DETECTION SYSTEM

Louis Raillon *et al.*, assignors to Thales
31 May 2005 (Class 367/106); filed in France 30 March 2001

A towed linear array comprises a number of projectors in the form of cylindrical, flextensional, piezoelectric transducers. By means of appropriate time delays of the excitation signals, a number of radiated beams steered to various directions is formed. A linear array of hydrophones is also incorporated within the same array as the projectors.—WT

6,904,188

43.35.Sx ACOUSTO-OPTIC TUNABLE FILTER HAVING IMPROVED WAVE-DAMPING CAPABILITY

Seok-Hyun Yun *et al.*, assignors to Novera Optics, Incorporated
7 June 2005 (Class 385/7); filed 5 February 2002

This acousto-optical tunable filter, of the same kind as described in United States Patent 6,266,461, consists of an optical fiber with two portions fastened securely to mounts at spaced locations on a support, a filtering section between the two mounted portions, a signal generator to generate a

periodic signal, an acoustic transducer that has a terminal connected to the signal generator, and an actuating portion. The electrical signal causes the actuating segment to vibrate. The actuating segment is connected to the interaction length so that the vibration generates an acoustic wave traveling along the interaction length. The filter is said to have the capability of reducing the amplitude of one or more selected wavelengths of light as it travels through the interaction length.—DRR

6,901,802

43.38.Ar ACOUSTIC SENSORS USING MICROSTRUCTURES TUNABLE WITH ENERGY OTHER THAN ACOUSTIC ENERGY

Panagiotis G. Datskos, assignor to UT-Battelle, LLC
7 June 2005 (Class 73/651); filed 30 September 2003

This patent proposes the use of micro-elements with tines that resonate at specific frequencies as a means of detecting very small levels of vibration.

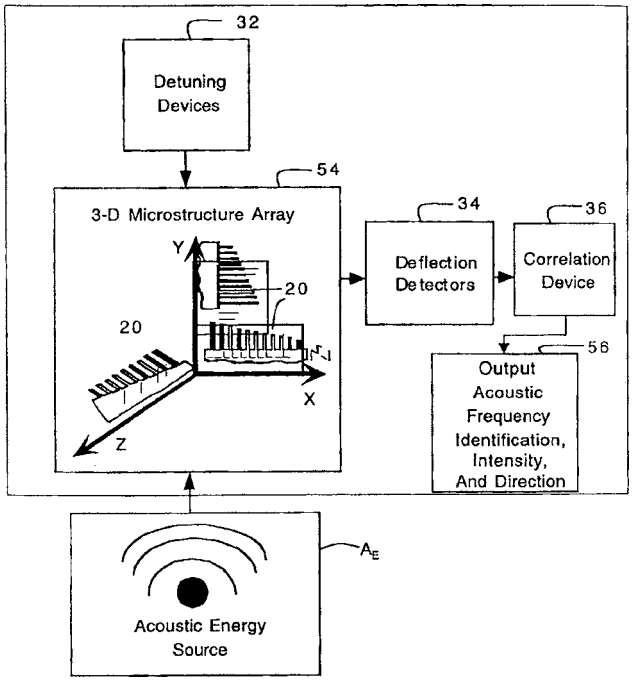

Such devices may be more sensitive, and cost less, than conventional broadband microphones.—JME

6,906,807

43.38.Ar MEMBRANE TYPE OPTICAL TRANSDUCERS PARTICULARLY USEFUL AS OPTICAL MICROPHONES

Alexander Paritsky and Alexander Kots, assignors to Phone-Or Limited
14 June 2005 (Class 356/601); filed 22 March 2002

The patent describes an integral optical transducer in which a light beam is reflected by a moving diaphragm and impinges on a receiver. Sensitivity is maximized by having all reflections take place from the high mobility central portion of the reflective diaphragm.—JME

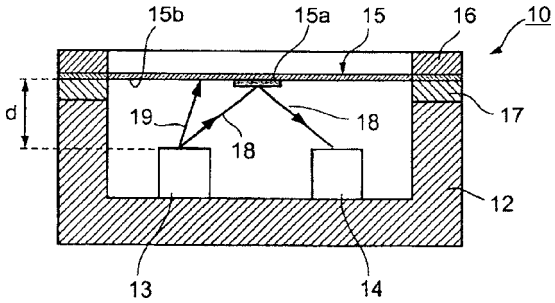

6,901,180

43.38.Bs MEMS OPTICAL SWITCH ON A SINGLE CHIP AND METHOD

Nan Zhang and Hong Zhang, assignors to ADC Telecommunications, Incorporated
31 May 2005 (Class 385/18); filed 24 January 2001

This patent discloses several embodiments of a MEMS optical switch. The construction does not describe the novelties in such designs as pictured

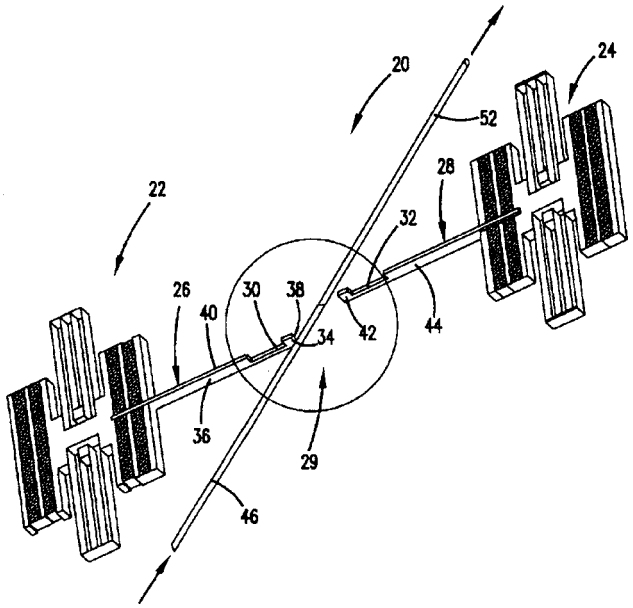

and this reviewer has seen many other designs like it predating this by five or more years.—JAH

6,901,204

43.38.Bs MICROELECTROMECHANICAL SYSTEM (MEMS) VARIABLE OPTICAL ATTENUATOR

Yoon Shik Hong *et al.*, assignors to Samsung Electro-Mechanics Company, Limited
31 May 2005 (Class 385/140); filed in the Republic of Korea 26 December 2002

This patent describes an electrically actuated slider to be used as a beam stop for a fiber optic system. This is a rather standard application of a comb-drive actuator and levers for displacement amplification. There is little that is novel about this arrangement, and practical application of the device would be difficult due to the precise alignment required.—JAH

6,897,601

43.38.Fx PIEZOELECTRIC ELEMENT AND AN OSCILLATION TRANSDUCER WITH A PIEZOELECTRIC ELEMENT

Michael Birth *et al.*, assignors to Holmberg GmbH & Company Kg
24 May 2005 (Class 310/334); filed in Germany 27 July 2001

This patent describes an application of porous PZT to airborne sound transduction. The novel claims are primarily those for the use of a flexible rubber coating to seal the porous sensor surface against air, and the disclosure of a certain optimal elasticity and thickness for the flexible coating. This patent is difficult to read and ignores prior work on the use of porous ceramics dating back to the 1960s.—JAH

6,892,850

43.38.Ja SURROUND FOR SPEAKER SYSTEM AND MANUFACTURING METHOD THEREOF

Takashi Suzuki and Masatoshi Sato, assignors to Pioneer Corporation
17 May 2005 (Class 181/171); filed in Japan 1 April 2002

Half-roll outer suspensions commonly used for woofers must be sufficiently compliant to allow a low resonant frequency and large enough to accomodate long cone excursions. This patent argues that such a suspension can be deformed (''sucked inwards'') by negative air pressure inside the

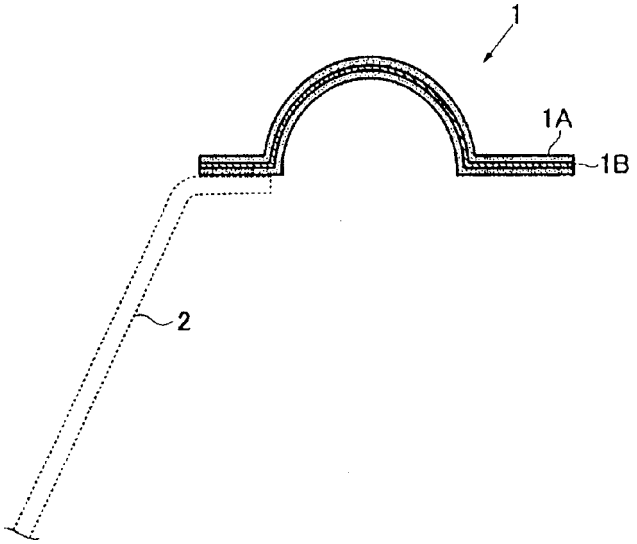

enclosure. A new composite material is described, consisting of a woven fabric impregnated with thermosetting resin **1B**, embedded in molded butyl rubber **1A** or the like. The patent also describes several methods for manufacturing such a suspension.—GLA

6,895,099

43.38.Ja COMPACT SPEAKER FOR PORTABLE PHONE

Chun-Hee Lee and Je-Hyuk Lee, assignors to Samsung Electro-Mechanics Company, Limited
17 May 2005 (Class 381/396); filed in the Republic of Korea 31 August 2001

Minature loudspeakers used in mobile telephones and the like are usually assembled using tooling jigs and adhesives. According to this patent, such an assembly method is not only difficult to carry out, but the speaker's performance is affected by the amount and placement of adhesive used. An

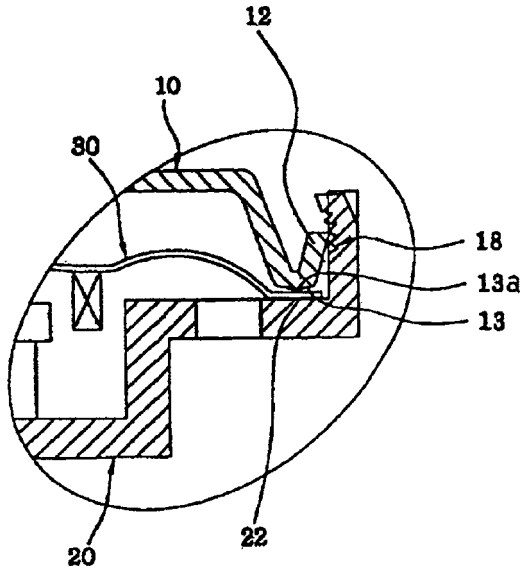

alternative design is proposed in which grill plate **10** is pressed down to secure diaphragm **30** and held in place by serrations **18**. The patent includes response curves demonstrating that a lower resonant frequency and extended high-frequency output can be achieved.—GLA

6,904,157

43.38.Ja STRUCTURE AROUND A SPEAKER UNIT AND APPLIED ELECTRIC OR ELECTRONIC APPARATUS THEREOF

Yoshiharu Shima, assignor to Shima System Company, Limited
7 June 2005 (Class 381/388); filed in Japan 10 August 2000

This device is described as a ''compact lightweight speaker system without a resonance box that can reproduce the original sound with high fidelity.'' After studying the 16 illustrations, reading the text twice, and

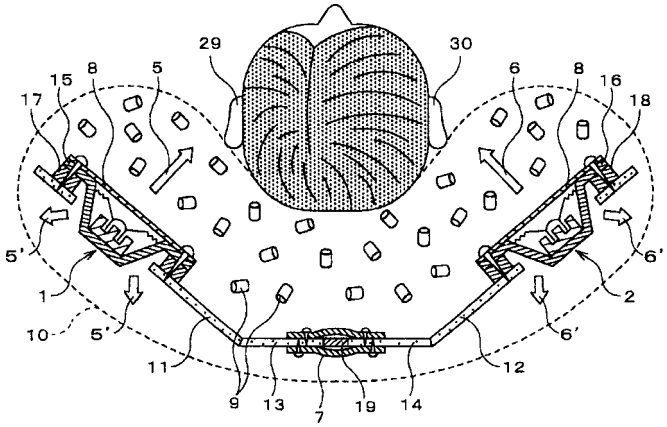

plodding through all 20 claims, this reviewer still does not understand exactly what the author is trying to patent. It appears to be a variant of a pillow speaker in which the speaker assembly is held in place by resilient mountings.—GLA

6,901,150

43.38.Ja PERMANENT MAGNET ACTUATOR WITH ELECTRIC EXCITATION COIL, ESPECIALLY LOUDSPEAKER AND MOBILE TELEPHONE

Marc Anciant, assignor to Sagem, SA
31 May 2005 (Class 381/401); filed in France 19 October 1999

In this unusual speaker design, the motion of voice coil **2** is partially counteracted by the effect of fixed coil **18**. The main goal is to minimize

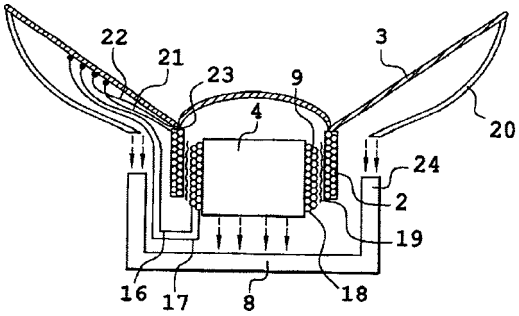

"burst noise" induced into the voice coil from adjacent rf circuitry. However, it is also possible to connect the two coils in various combinations to differentiate between normal and "hands free" operation.—GLA

6,905,001

43.38.Ja SOUNDERS FOR FIRE ALARM SYSTEMS

Dunstan Walter Runciman, assignor to GSBS Development Corporation
14 June 2005 (Class 181/188); filed in South Africa 7 May 1999

Essentially, this is a dual horn transducer with a common diaphragm. The diaphragm **16** has two aperatures **34** and **64**. A lamp **22** is also provided.

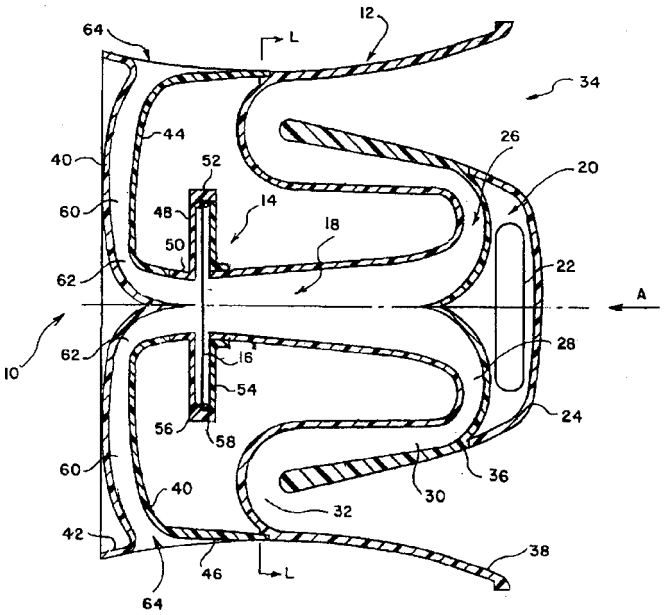

The inventor notes that the length of the air columns should be half the wavelength of the frequency of the vibrating membrane.—MK

6,907,121

43.38.Ja IMPEDANCE MATCHED HORN HAVING IMPEDANCE MATCHED TO IMPEDANCE OF AN EAR

Jonas Andersson, assignor to Telefonaktiebolaget L M Ericsson (publ)
14 June 2005 (Class 379/433.02); filed 16 June 2000

Instead of a conventional miniature loudspeaker, the housing of this mobile telephone contains a tiny horn **27** and an even tinier horn driver **25**. Since the horn mouth **29** is loosely coupled to the user's ear, it can be much smaller than a horn designed for use in free air. The patent claims are quite specific about certain dimensions: "the acoustic horn is about 5 mm in length from the small end to the large end and is about 4 mm wide at the

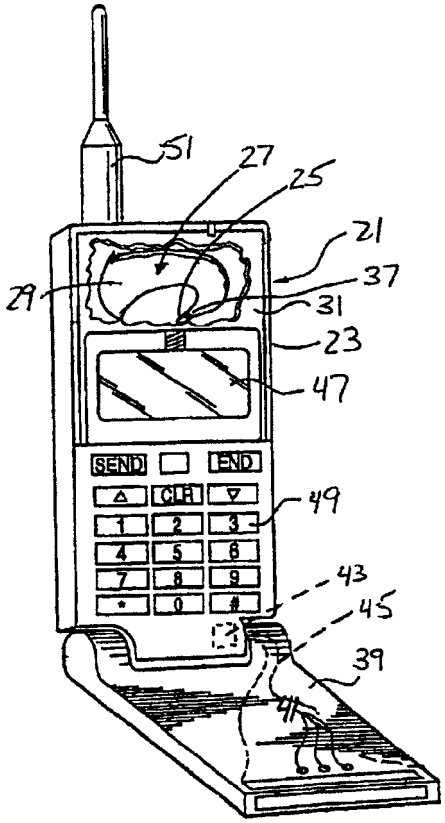

large end." This seems to be at odds with the description of preferred embodiments, which sets forth dimensions, "preferably on the order of 5 mm tall, 1 mm thick, and 34 mm wide at its widest dimension." Visualizing such a device is not easy, but since the driver diaphragm is "preferably on the order of 1 mm or less in diameter," any relation to the real world is questionable anyway.—GLA

6,898,291

43.38.Md METHOD AND APPARATUS FOR USING VISUAL IMAGES TO MIX SOUND

David A. Gibson, Palo Alto, California
24 May 2005 (Class 381/119); filed 30 June 2004

The idea of using colors or images to represent sound is an established graphical technique. Here, the idea is extended to include a 3-D space, where sounds are spheres (music of the spheres?), with textures generated by spectral analysis via the FFT. It is very idiosyncratic.—MK

6,893,317

43.38.Md STORYBOOK LANTERN

James Vlodek, La Grange, Illinois
17 May 2005 (Class 446/147); filed 19 December 2003

The novelty is the physical design: a lantern is combined with ''planar members'' (a.k.a. pages) that turn under motor control via a microprocessor. Naturally this microprocessor can also provide audio entertainment, such as nighttime story telling. The diassembly diagram tells all: the power switch

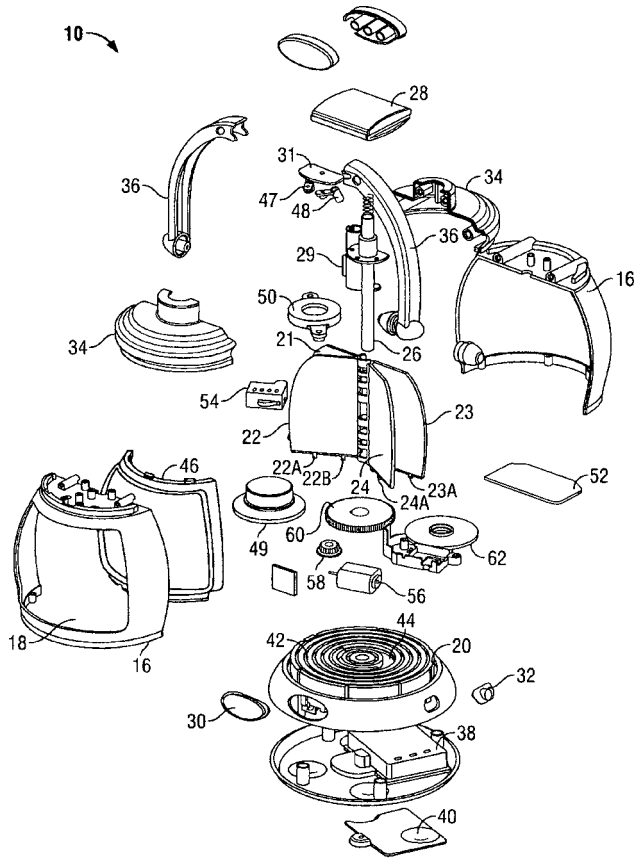

30 and mode switch **32** are connected to the microprocessor PCB **52**, which in turn controls the motor and gears **60**, **62** and the speaker **49**. The ''planar members'' **22**, **23**, and **24** are mounted in concentric rings **42** and **44**. The upper cap **34** holds the pages in place.—MK

6,901,146

43.38.Vk ALL-DIGITAL FM STEREO DEMODULATOR AND DEMODULATION METHOD

Kenichi Taura *et al.*, assignors to Mitsubishi Denki Kabushiki Kaisha
31 May 2005 (Class 381/3); filed in Japan 21 December 1999

FM stereo demodulation in radio receivers has over the years been largely an analog art. This patent describes in detail the application of digital techniques in carrying out the multiple operations involved in this discipline.

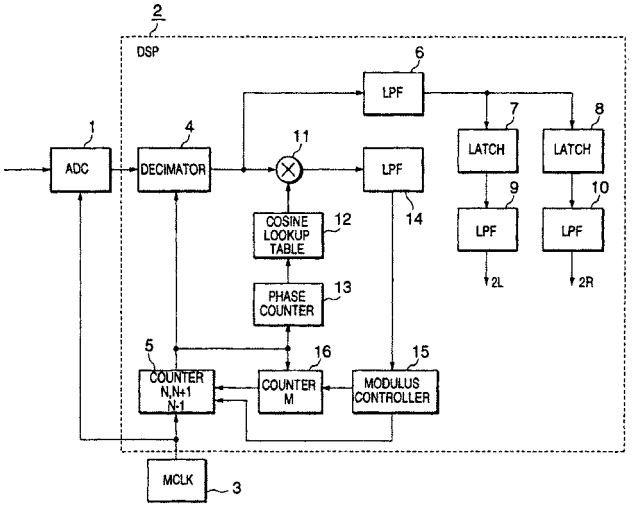

The advantages are reduced costs and space as well as a high level of performance.—JME

6,901,148

43.38.Vk AUTOMATIC SOUND FIELD CORRECTING DEVICE

Hajime Yoshino and Kazuya Tsukada, assignors to Pioneer Corporation
31 May 2005 (Class 381/103); filed in Japan 27 April 2001

Today, there are many systems available (and many more in development) that enable the loudspeakers in a surround sound home system to be automatically aligned with respect to arrival times, levels, and broadband

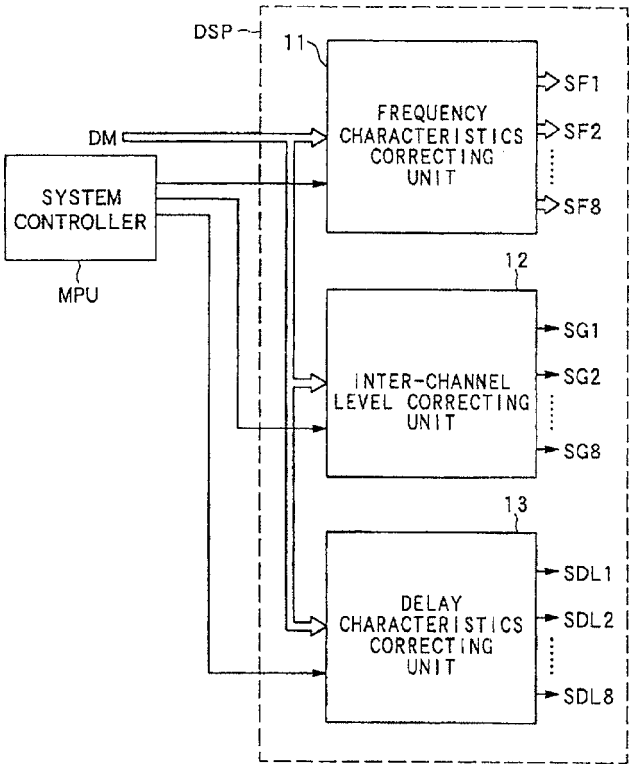

channel equalization, at a predetermined listening position. The patent extends this ''palette'' to include detailed phase relationships among loudspeakers.—JME

6,904,152

43.38.Vk MULTI-CHANNEL SURROUND SOUND MASTERING AND REPRODUCTION TECHNIQUES THAT PRESERVE SPATIAL HARMONICS IN THREE DIMENSIONS

James A. Moorer, assignor to Sonic Solutions
7 June 2005 (Class 381/18); filed 19 April 2000

The patent broadly describes record/playback processes in which spatial harmonics of various orders are used to define the original source directions independent of playback loudspeaker locations. The patent is thorough,

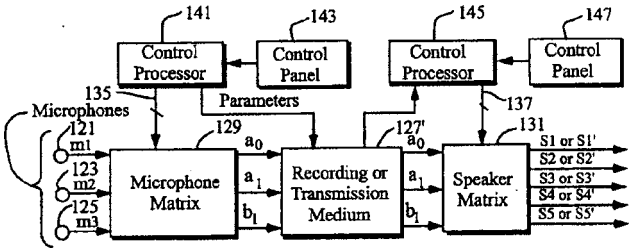

informative, and recommended reading for anyone interested in advanced surround sound technology.—JME

6,894,586

43.40.Dx RADIAL BULK ANNULAR RESONATOR USING MEMS TECHNOLOGY

Brian L. Bircumshaw *et al.*, assignors to The Regents of the University of California
17 May 2005 (Class 333/133); filed 21 May 2003

This patent describes an interesting radial/annular resonator that is electrostatically driven. Design formulas for the resonant frequencies are given, but the scaling laws are not completely described. The discussion is useful as a description of the devices and principles but not as a design guide. Values of resonant frequencies for some different materials of significance to the semiconductor industry are given.—JAH

6,897,744

43.40.Dx LONGITUDINALLY-COUPLED MULTI-MODE PIEZOELECTRIC BULK WAVE FILTER AND ELECTRONIC COMPONENT

Akihiro Mitani *et al.*, assignors to Murata Manufacturing Company, Limited
24 May 2005 (Class 333/189); filed in Japan 21 May 2002

This patent teaches the construction of a bulk acoustic wave bandpass filter having a linear array of interdigitated electrodes. There seems to be little that is novel about this, and the authors do not seem to acknowledge this in the references. The patent is long and full of construction details.—JAH

6,903,489

43.40.Dx PIEZOELECTRIC RESONATOR, PIEZOELECTRIC RESONATOR COMPONENT AND METHOD OF MAKING THE SAME

Toshiyuki Suzuki and Nobuyuki Miki, assignors to TDK Corporation
7 June 2005 (Class 310/320); filed in Japan 25 July 2000

This patent describes a way of mounting and electroding very small fundamental-mode piezo resonators so that the mounting does not spoil the Q or create frequency shifts with aging. The choice and disposition of materials for mounting and electroding is clearly explained and detailed. The techniques described probably have wider applicability, as the broad claims suggest.—JAH

6,903,498

43.40.Dx PIEZOELECTRIC DEVICE, LADDER TYPE FILTER, AND METHOD OF PRODUCING THE PIEZOELECTRIC DEVICE

Toshihiko Unami and Jiro Inoue, assignors to Murata Manufacturing Company, Limited
7 June 2005 (Class 310/366); filed in Japan 28 August 2001

This patent describes the concept of bulk bending wave bandpass filters using interdigitated electrodes. The basic longitudinally periodic structure described is not new, but there are some tricks being played with the cross section in the interest of simplifying fabrication and packaging of the devices.—JAH

6,903,629

43.40.Dx ELECTRODE-FREE RESONATOR STRUCTURES FOR FREQUENCY CONTROL, FILTERS AND SENSORS

Arthur Ballato *et al.*, assignors to The United States of America as represented by the Secretary of the Army
7 June 2005 (Class 333/187); filed 24 September 2003

This patent describes an interesting GHz-frequency, thickness-shear-mode resonant structure that features wells or indentations which have been designed to trap the vibrational energy in an electrode-free region. There are three configurations shown with measurements of mode splittings and cut-offs as a function of the resonator length-to-thickness ratio. The information is useful to those searching for a usable design, but little information is provided on how to extend the energy trapping design to other electrode configurations.—JAH

6,899,197

43.40.Ph METHOD AND APPARATUS FOR ABSORBING ACOUSTIC ENERGY

Abbas Arian *et al.*, assignors to Dresser Industries, Incorporated
31 May 2005 (Class 181/102); filed 23 September 2002

This patent describes improvements to an oil well acoustic logging tool covered by United States Patent 6,564,899 . It is used to determine the acoustic properties of geologic formations as they are traversed by the tool. The device has an elongated body housing one or more acoustic transmitters and receivers. In this upgrade, a variety of cavities and elements are arranged to further attenuate coupling between transmitters and receivers.—GLA

6,892,758

43.40.Tm CHECK VALVE WITH VIBRATION PREVENTION FUNCTION FOR VALVE BODY

Shozo Inage *et al.*, assignors to Advics Company, Limited
17 May 2005 (Class 137/539.5); filed in Japan 12 June 2002

In this check valve design, as in many such designs, the flow in one direction is stopped by a sphere that is pressed against a circular opening by a spring. Here, however, the spring force is made to act on the sphere via a hemispherical body that contacts the sphere off the opening's axis. Thus, when the valve is open, the sphere is forced laterally against a suitably shaped portion of the housing, so that the sphere's tendency to vibrate is reduced.—EEU

6,896,109

43.40.Tm MAGNETORHEOLOGICAL FLUID VIBRATION ISOLATOR

Shawn P. Kelso and Jason E. Lindler, assignors to CSA Engineering, Incorporated
24 May 2005 (Class 188/267.1); filed 7 April 2003

This compact isolator is in the shape of a squat cylinder, the outer circumference of which consists of a metal flexure with relatively high stiffness. Within this cylindrical shape there is provided what amounts to a piston/cylinder arrangement, with a gap between the piston and the cylinder wall that allows a magnetorheological fluid to flow between the two volumes into which the piston divides the total cylinder volume. An electromagnet mounted in the cylinder near this gap permits the viscocity of the fluid to be controlled over a relatively wide range, resulting in desired changes in the stiffness and damping of the isolator.—EEU

6,898,501

43.40.Vn APPARATUS FOR FACILITATING REDUCTION OF VIBRATION IN A WORK VEHICLE HAVING AN ACTIVE CAB SUSPENSION SYSTEM

William L. Schubert, assignor to CNH America LLC
24 May 2005 (Class 701/50); filed 15 July 1999

This patent describes active vibration control systems for the cabs of vehicles such as tractors, bulldozers, and backhoes. These systems, in essence, consist of sensors and of controllers that cause actuators to generate appropriate forces and motions. The suspension system may be integrated via a data bus with systems related to positioning, tool height, steering control, four-wheel-drive control, speed control, and others. Sensors that may be used include conventional vibration sensors, radar that detects terrain irregularities ahead of the vehicle, and global positioning systems.—EEU

6,904,344

43.40.Vn SEMI-ACTIVE SHOCK ABSORBER CONTROL SYSTEM

John A. LaPlante and William T. Larkins, assignors to ActiveShock, Incorporated
7 June 2005 (Class 701/37); filed 4 May 2004

The shock absorber described here consists in essence of a spring and a piston-type damper. The patent presents a methodology that includes defining a number of operating zones based on system parameters (such as relative displacement and velocity) and user-definable or preset inputs, as well as consideration of motion limits. The methodology in general produces a number of valve settings, selection among valve control signals, and applying the selected valve control signal to the valve in a closed-loop feedback system.—EEU

6,892,851

43.50.Gf ACOUSTIC ATTENUATOR

Peng Lee, assignor to Acoustic Horizons, Incorporated
17 May 2005 (Class 181/224); filed 22 October 2003

This device is an acoustical reflective and dissipative attenuation system designed to reduce broadband noise in the air intake duct of a HVAC heat-exchange system. It is said that a significant broadband noise reduction is achieved by positioning a noise-reflecting panel with an appropriate amount of padding at a strategic location. The reflecting panel confines the noise to the intake air duct, thus greatly reducing the amount of noise that will exit the intake duct filter and enter the occupied area of the building.—DRR

6,899,200

43.50.Gf SOUND BARRIER

John Kenneth Roberts, Annandale, and Kenneth James Arcus, Crows Nest, both of New South Wales, Australia
31 May 2005 (Class 181/285); filed in Australia 8 January 1999

This highway sound barrier uses light-weight plastic panels to make a hollow shell that can be filled with a sound attenuating liquid (e.g., water).

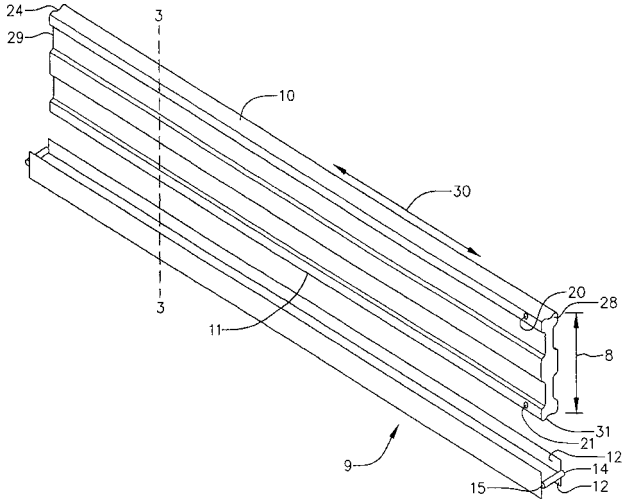

The panels are held in place by vertical posts.—CJR

6,893,711

43.55.Ev ACOUSTICAL INSULATION MATERIAL CONTAINING FINE THERMOPLASTIC FIBERS

Bruce Scott Williamson and Nina Frazier, assignors to Kimberly-Clark Worldwide, Incorporated
17 May 2005 (Class 428/297.1); filed 5 August 2002

A nonwoven web of thermoplastic fibers, with carefully specified size, thickness, and density, provides sound absorption. Contrary to normal sound insulation materials, this web is not very thick or dense. The material can be used in vehicles, appliances, and other locations.—CJR

6,871,545

43.58.Gn SYSTEM AND METHOD FOR MEASURING STIFFNESS IN STANDING TREES

Chin-Linn Huang, assignor to Weyerhaeuser Company
29 March 2005 (Class 73/597); filed 20 June 2003

This portable, electronic tree tester transmits an impact impulse through the wood of a live tree to determine the condition of the wood prior to harvesting the tree. A special spike, outfitted with a microphone, is driven into the tree. A second spike with pickup is also driven into the wood at a distance of several feet from the first. When the first spike is struck with a hammar blow, both mics pick up signals, which are recorded by an analyzer.

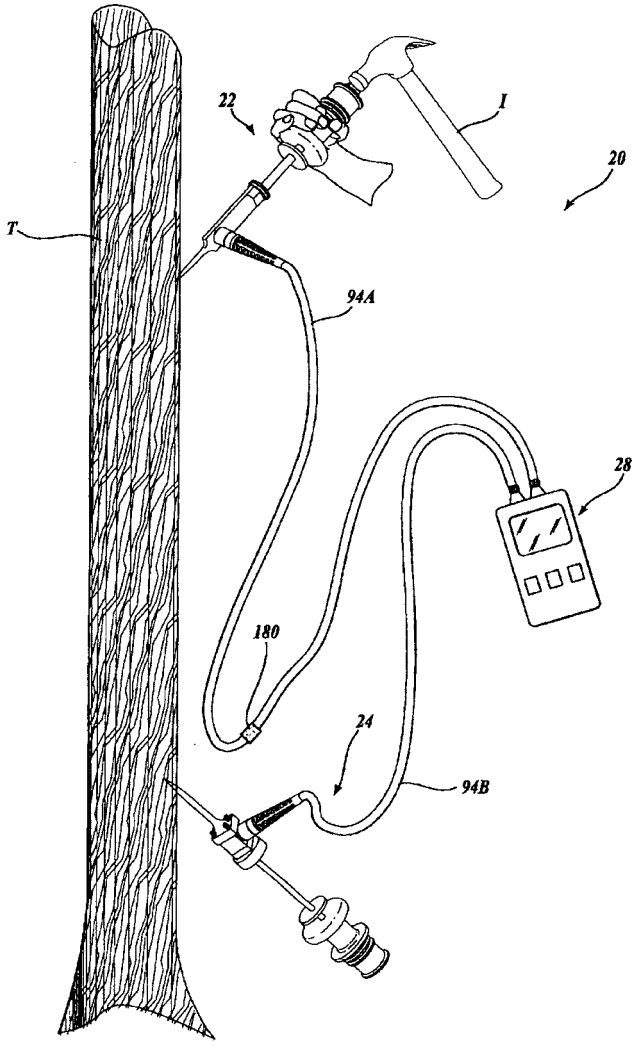

A frequency response of at least 3000 Hz is recommended. The description of the device and its use has much more detail about the nails and the mic pickups than about the analysis procedure.—DLR

6,888,455

43.58.Gn METHOD OF DETECTING FIREARM SHOT

George H. Lerg, assignor to Traptec Corporation
3 May 2005 (Class 340/517); filed 30 July 2003

This gunshot detector analyzes its light and audio inputs for three separate events which, taken together, indicate that a gun has been fired in the area. Audio detectors monitor for the gunpowder explosion and the sonic boom of an object exceeding the speed of sound. A visual detector would note the flash of gunpowder from the barrel. The presence and exact timing

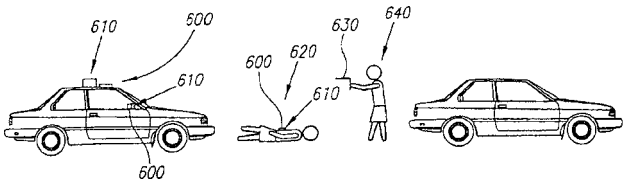

of these events would trigger a gunshot alert, which could then lead to a number of different actions. Deployments **610** may include being mounted on a patrol car or worn on an officer's clothing. The patent would also apply similar technology to other types of event detection, such as the acts of graffiti writers.—DLR

6,894,212

43.58.Hp WRIST MUSICAL INSTRUMENT TUNER

David Capano, Greenfield Center, New York
17 May 2005 (Class 84/454); filed 22 January 2003

If Dick Tracy had been a musician, then Chester Gould would've beaten this inventor to the punch. Simply put, it's a microprocessor pitch detector wrapped around the wrist. The pitch detector is a simple zero crossing detector so the time domain waveform better be nicely periodic.—MK

6,897,743

43.58.Hp ELECTRONIC APPARATUS WITH TWO QUARTZ CRYSTAL OSCILLATORS UTILIZING DIFFERENT VIBRATION MODES

Hirofumi Kawashima, assignor to Piedek Technical Laboratory
24 May 2005 (Class 333/187); filed in Japan 6 March 2002

This patent discloses the use of a quartz crystal as an oscillator element with two different modes of operation, apparently intended to be operated simultaneously. This is said to result in a more compact structure with a higher quality factor than normal clock crystals. The patent gives many details of the construction that are useful for design purposes and the analysis is quite clearly written.—JAH

6,903,618

43.58.Hp QUARTZ CRYSTAL UNIT, AND QUARTZ CRYSTAL OSCILLATOR HAVING QUARTZ CRYSTAL UNIT

Hirofumi Kawashima, assignor to Piedek Technical Laboratory
7 June 2005 (Class 331/158); filed in Japan 6 March 2002

This patent describes the use of holes, slots, and channels in a quartz tuning fork as used in clock crystals. The claim is made that the resulting frequency-determining elements can be made smaller with good stability than they could otherwise be made. Modifications and fabrication processes are described in detail, but evidence of their superiority is not given. It seems to this reviewer that the extra costs of all the proposed cuts will not appeal to many.—JAH

6,874,366

43.58.Kr SYSTEM TO DETERMINE AND ANALYZE THE DYNAMIC INTERNAL LOAD IN REVOLVING MILLS, FOR MINERAL GRINDING

Luis Alberto Magne Ortega *et al.*, assignors to FFE Minerals Corporation
5 April 2005 (Class 73/649); filed in Chile 31 January 2003

Large mills used to crush rock prior to mineral separation and refining are subject to rapid wear. The rate and nature of the deterioration can be controlled to some extent, however, by careful monitoring of loading, load composition, and other factors. A system of wireless acoustic sensors described here would be attached to the outer surface of the mill casing and would transmit the needed parameter data to a receiver and control unit stationed nearby.—DLR

6,880,403

43.58.Kr STRUCTURE INSPECTION DEVICE

Takashi Shimada and Kanji Matsuhashi, assignors to Mitsubishi Denki Kabushiki Kaisha
19 April 2005 (Class 73/652); filed 28 August 2000

This portable concrete tester includes a signal excitation generator in the same device as the signal analyzer unit. In operation, the unit is placed in physical contact with the concrete structure to be tested. A striker **141**, driven by pressurized gas **144**, produces a fairly repeatable elastic wave in

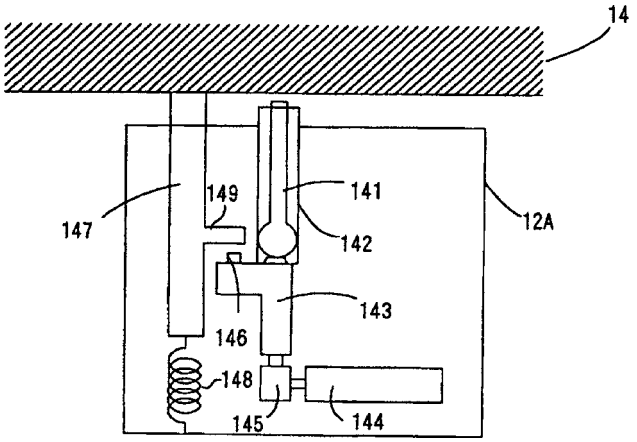

the concrete structure. The sensor **147** consists of a spring-loaded weight having a resonance within the expected range of the return signal, in the range of ''several kHz or less.'' The unit is said to be able to determine the type of a defect, as a crack, a surface peel-off, or a ''honeycomb,'' etc., as well as to determine the depth of such a feature.—DLR

6,895,095

43.60.Bf METHOD OF ELIMINATING INTERFERENCE IN A MICROPHONE

Hans-Jörg Thomas, assignor to DaimlerChrysler AG
17 May 2005 (Class 381/94.7); filed in Germany 3 April 1998

Adaptive equalization, which is widely used in two-way remote conferencing systems to remove noise and other interference components, is put to use here in an automated communication system. The patent is well

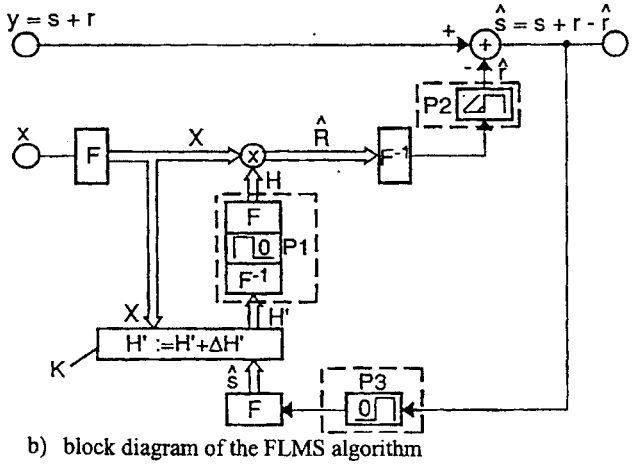

b) block diagram of the FLMS algorithm

written and includes a variety of design options as well as numerous measurements validating the techniques discussed.—JME

6,897,651

43.60.Bf METHOD FOR ELIMINATING EFFECTS OF ACOUSTIC EXCITATIONS IN NMR DATA

Arcady Reiderman *et al.*, assignors to Baker Hughes Incorporated
24 May 2005 (Class 324/303); filed 15 May 2003

A disclosure is made for a method of signal determination in nuclear magnetic resonance (NMR) well logging. Improvement in the signal determination is asserted for this method, directed toward elimination of spurious effects of magneto-acoustic ringing from detected resonance signals. The method entails the application of at least one excitation pulse and also at least one refocusing pulse. The obtained signal is used to numerically construct a synthetic ringing signal sequence. This constructed signal can then be subtracted from an NMR echo signal to lessen the effects of ringing.—DRR

6,901,362

43.60.Bf AUDIO SEGMENTATION AND CLASSIFICATION

Hao Jiang and Hongjiang Zhang, assignors to Microsoft Corporation
31 May 2005 (Class 704/214); filed 19 April 2000

It is not clear what is novel in this patent, as a number of well-known acoustic representations (including linear predictive models and frequency-band periodicity metrics) are cobbled together into Gaussian models stored

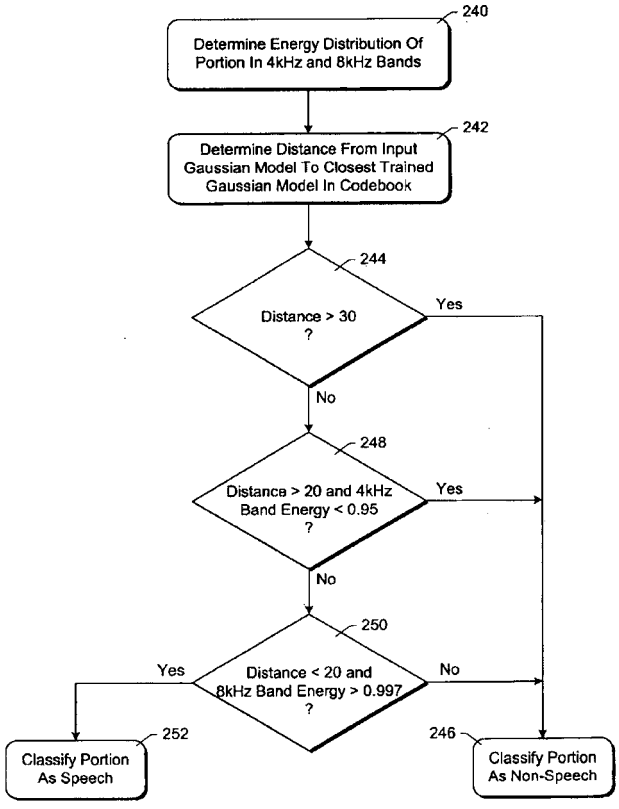

as a codebook, to yield *ad hoc* thresholds for classifying audio signal frames into categories such as ''speech,'' ''non-speech,'' ''silence,'' and ''music.''—SAF

6,895,094

43.60.Mn ADAPTIVE IDENTIFICATION METHOD AND DEVICE, AND ADAPTIVE ECHO CANCELLER IMPLEMENTING SUCH METHOD

Pascal Scalart and Franck Bouteille, assignors to France Telecom
17 May 2005 (Class 381/66); filed in France 26 March 1999

The objective here is one encountered before, viz. to adaptively identify a linear system as characterized by its impulse response to an input signal. After the customary steps of acquiring the input and observed signals and then determining an error signal in terms of some initial identification filter, a novel equation is proposed by which said identification filter's coefficients are to be adaptively updated. Unfortunately, the equation is quite *ad hoc*; no rationale is provided relating to the mentioned prior art for it or its necessary empirically adjusted parameters, nor is there any evaluation in support of the effectiveness of the proposal. The technique is promised to converge faster than prior art methods, which it clearly would, since it is simpler, but it remains mysterious.—SAF

6,907,349

43.60.Rw ACOUSTIC SIGNAL PROCESSING METHOD USING ARRAY COHERENCY

Batakrishna Mandal, assignor to Halliburton Energy Services, Incorporated
14 June 2005 (Class 702/14); filed 20 April 2004

In geological acoustics, a number of acoustic pickups in a borehole can provide information about the surrounding geology by suitable analysis of sound received by them from a multicomponent wave generator. This patent proposes a "coherence method" (see figure) to compute the "semblance" function $E(t,s)$ correlating time delay (or "slowness") of component waves

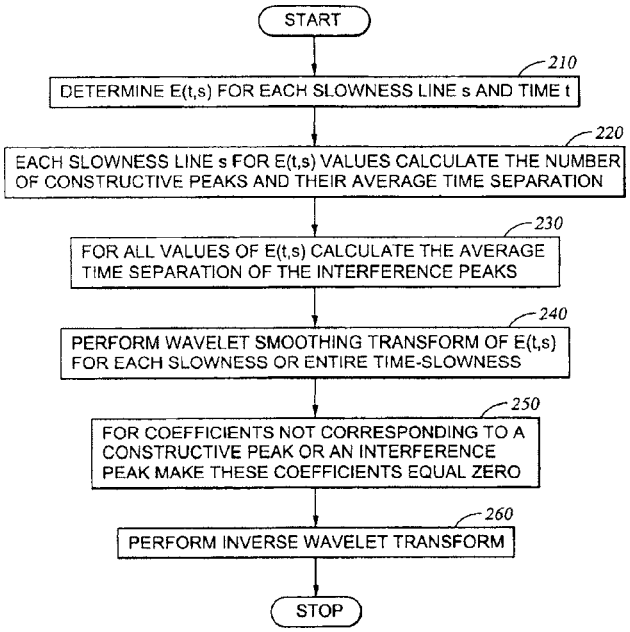

to index time without data windowing. The latter is the novel achievement claimed, by which means truncation errors inherent to windowing are promised to be eliminated. A related method for computing the phase semblance $E(f,s)$ is also described, and these quantities are known to be useful to geology from the prior art.—SAF

6,882,959

43.66.Ba SYSTEM AND PROCESS FOR TRACKING AN OBJECT STATE USING A PARTICLE FILTER SENSOR FUSION TECHNIQUE

Yong Rui and Yunqiang Chen, assignors to Microsoft Corporation
19 April 2005 (Class 702/179); filed 2 May 2003

This model for a machine perception system puts a special emphasis on the ability to fuse the percepts between different modalities, such as auditory and visual inputs. A specific application is the tracking of a particular talker during a conference or other such meeting. Individual sensor modules extract measures of specific interest. For example, a microphone array module would feed source position information to the higher levels of analysis. The fusion module uses particle filtering methods to combine information from the various sensor modules and produce the desired output signals, such as camera controls to track a talker. A detailed technical discussion appears to be quite readable.—DLR

6,895,098

43.66.Ts METHOD FOR OPERATING A HEARING DEVICE, AND HEARING DEVICE

Sylvia Allegro and Michael Büchler, assignors to Phonak AG
17 May 2005 (Class 381/312); filed 5 January 2001

Features of an acoustic signal are extracted and identified at regular or irregular intervals using hidden Markov models and auditory scene analysis. Parameters required for identification are generated in an off-line training session.—DAP

6,898,293

43.66.Ts HEARING AID

Thomas Kaulberg, assignor to Topholm & Westermann ApS
24 May 2005 (Class 381/318); filed 23 December 2003

Some hearing aid acoustic feedback cancellers have a problem with generation of undesirable audio artifacts. To avoid this, a first parameter of the acoustic feedback loop is determined to control the adaptation rate of a set of filter bank coefficients. In one embodiment, the more rapid adaptation

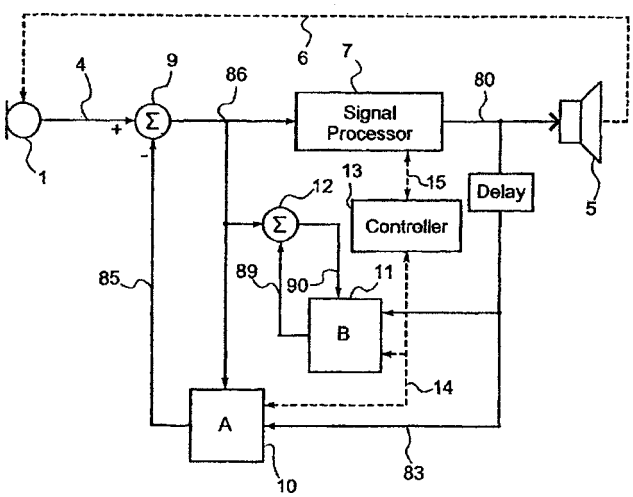

rate of a second filter bank responds to rapid changes in the feedback path and is also used to adjust the adaptation rate of the first adaptive filter bank. In a multichannel implementation, different channels in the filter banks may have different adaptation rates.—DAP

6,904,156

43.66.Ts SYSTEM AND METHOD FOR REDUCING HEARING AID SQUEAL

Remi LeReverend, assignor to Zarlink Semiconductor (U.S.) Incorporated
7 June 2005 (Class 381/312); filed 3 August 2001

This patent assumes that during continuous acoustic feedback oscillation, the hearing aid battery voltage will drop to a lower value. Once it reaches a first predetermined threshold, the amplifier output to the hearing

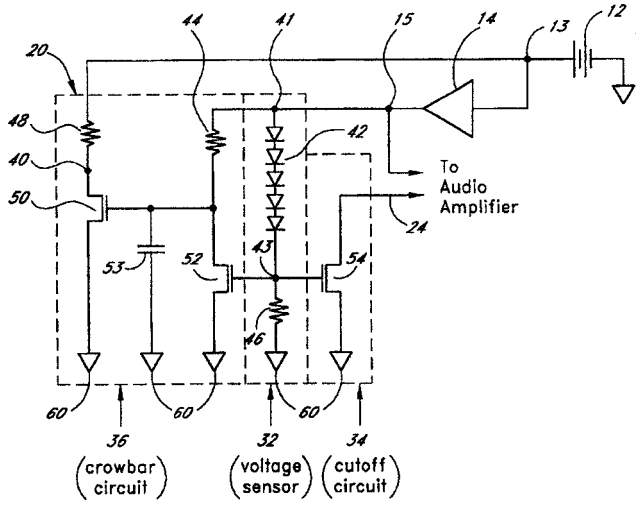

aid receiver is disabled. Hysteresis is provided via an additional load on the battery when the battery voltage reaches a second predetermined threshold.—DAP

6,907,398

43.72.Bs COMPRESSING HMM PROTOTYPES

Harald Hoege, assignor to Siemens Aktiengesellschaft
14 June 2005 (Class 704/265); filed in Germany 6 September 2000

For speech recognition using hidden Markov models (HMMs), many prototypes and a large amount of storage space are required. To reduce the amount of memory needed, especially in mobile devices, a neural network is used as an encoder to map prescribed HMM prototypes onto compressed HMM prototypes which are then stored. A second neural network functions as a decoder.—DAP

6,889,182

43.72.Ew SPEECH BANDWIDTH EXTENSION

Harald Gustafsson, assignor to Telefonaktiebolaget L M Ericsson (publ)
3 May 2005 (Class 704/205); filed 20 December 2001

Standard telephony bandwith is 0.3–3.4 kHz. This patent proposes a number of methods for "fake" bandwidth expansion by a telephone receiver, upon receiving a standard narrow-band signal. By means of upsampling, copying the (flattened) narrow-band harmonic spectrum into the range above 3.4 kHz, bandpass filtering the high range signal, and then combining the high-range signal with the upsampled original, a version of the received speech signal with artificial treble can be produced. By means of pitch tracking, additive sine wave synthesis can add missing harmonics from the fundamental up to 300 Hz, with the amplitude of the sine waves adjusted to match a detected first formant amplitude. These can be combined with the original received signal to yield a version with artificial bass.—SAF

6,895,345

43.66.Yw PORTABLE HEARING-RELATED ANALYSIS SYSTEM

Gordon J. Bye *et al.*, assignors to Micro Ear Technology, Incorporated
17 May 2005 (Class 702/57); filed 31 October 2003

A hearing aid programmer, audiometer, and real ear probe microphone measurement system are packaged in a portable host computer on PCMCIA

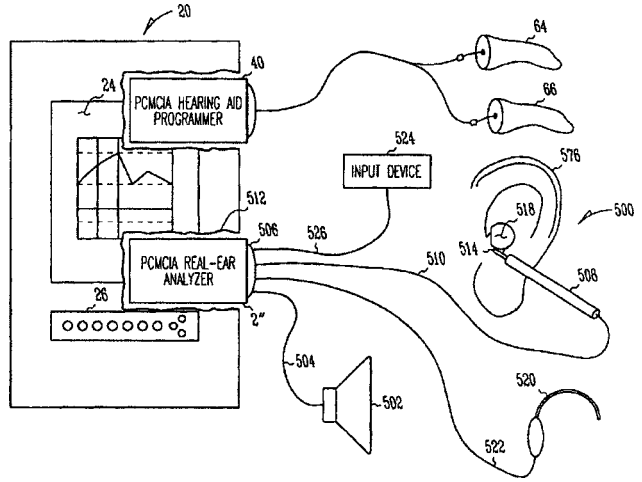

cards. Communication to the hearing aids may be via wireless means.—DAP

6,895,375

43.72.Ew SYSTEM FOR BANDWIDTH EXTENSION OF NARROW-BAND SPEECH

David Malah and Richard Vandervoort Cox, assignors to AT&T Corporation
17 May 2005 (Class 704/219); filed 4 October 2001

A parametric technique is proposed for developing a broadband speech signal from a received narrow-band telephony signal. The idea goes back to the theory of linear predictive coding, by which LPC coefficients obtained from the received signal are used to compute the related reflection coefficients describing a concatenated tube model of the vocal tract. To get a

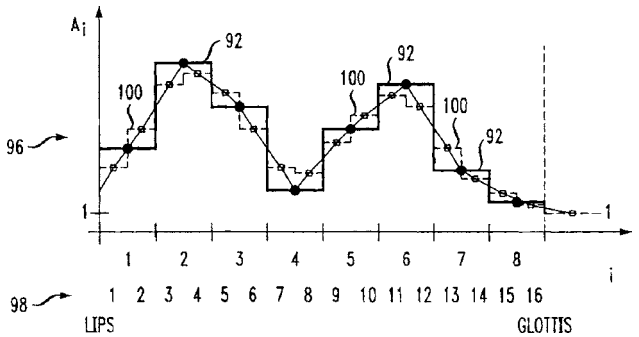

broadband spectrum that extends the original, the calculated tube model (solid line in figure) is interpolated to twice the number of tubes (dashed line). Synthesis involves exciting the resulting interpolated LPC model but eliminating its low band in favor of the original narrow-band signal—thereby only the "fake" part of the signal spectrum is synthesized.—SAF

6,895,376

43.72.Fx EIGENVOICE RE-ESTIMATION TECHNIQUE OF ACOUSTIC MODELS FOR SPEECH RECOGNITION, SPEAKER IDENTIFICATION AND SPEAKER VERIFICATION

Florent Perronnin *et al.*, assignors to Matsushita Electric Industrial Company, Limited
17 May 2005 (Class 704/250); filed 4 May 2001

This patent is related to other work by these inventors under the rubric of their ''eigenvoice method,'' which uses an eigenspace representation of the training speaker population to separate speaker-specific acoustic parameters of phonemes from speaker-independent parameters during training on multiple speakers. With this in hand, standard decision-tree identification of allophone models can be employed in a speaker-independent setting using ''speaker-adjusted'' training data. The methodology is well documented, and context-independent, speaker-dependent phone models are said to be determinable from as little as 20 minutes of training speech from each speaker. Applications to speaker identification tasks are also described.—SAF

6,895,374

43.72.Gy METHOD FOR UTILIZING TEMPORAL MASKING IN DIGITAL AUDIO CODING

Wan-Chieh Pai, assignor to Sony Corporation
17 May 2005 (Class 704/200.1); filed 29 September 2000

To reduce storage and computational requirements, temporal masking signals are derived by a filter from simultaneous masking signals to form a composite masking signal. Overall masking thresholds are then determined

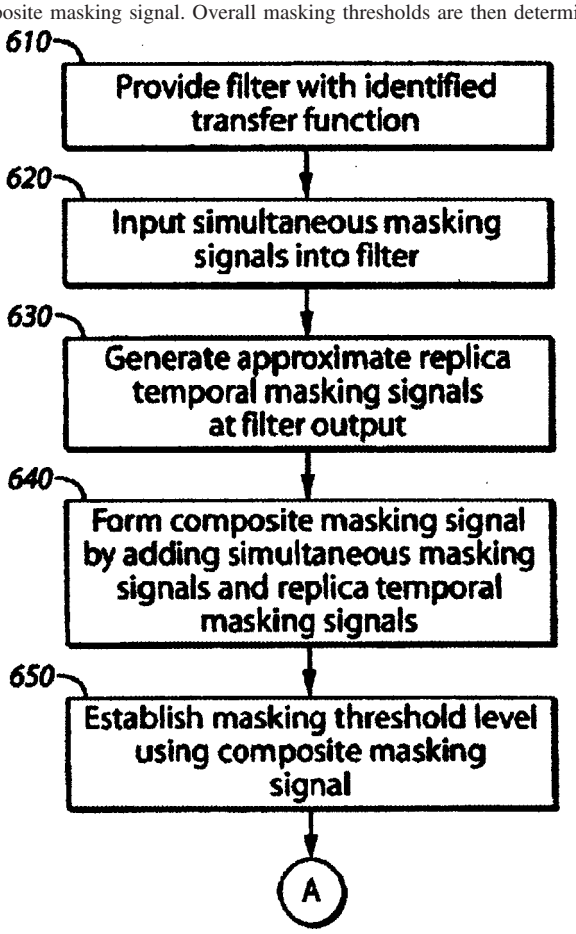

and mapped to the appropriate subband. In the filter design, attention is paid to the effects of masker decay time and masker duration.—DAP

6,885,736

43.72.Ne SYSTEM AND METHOD FOR PROVIDING AND USING UNIVERSALLY ACCESSIBLE VOICE AND SPEECH DATA FILES

Premkumar V. Uppaluru, assignor to Nuance Communications
26 April 2005 (Class 379/88.17); filed 25 January 2002

Here is another patent dealing with the implementation of voice interaction capabilities to be used during access to the Internet. This patent deals specifically with adapting to the user's voice characteristics and operational preferences. Collected personal attributes may include the user's name, address, phone number, ID codes, passwords, voice imprints for identification, and speech training profiles. Preferences might include selection of languages, personal greetings, bookmarks, preferences in ordering various lists, default overrides, and preferred vocabulary. One has to suppose that when the author thought of this, there was not so much spyware around, poised to zero in on your computer and scoop up all of your personal information.—DLR

6,882,972

43.72.Ne METHOD FOR RECOGNIZING SPEECH TO AVOID OVER-ADAPTATION DURING ONLINE SPEAKER ADAPTATION

Ralf Kompe *et al.*, assignors to Sony International (Europe) GmbH
19 April 2005 (Class 704/255); filed in the European Patent Office 10 October 2000

Speaker-independent speech recognition systems most often adapt to each new user by adjusting Gaussian model mixing levels of various phone models in response to successful recognition of an utterance, in the hope of better recognizing each succeeding utterance. ''Over-adaptation'' means the mixture models may be adjusted too much in response to certain frequent words, thus spoiling successful recognition of future content words. This patent proposes to ameliorate this effect by adjusting the amount of model adaptation downward in response to more frequent utterance subunits from a given user.—SAF

6,882,973

43.72.Ne SPEECH RECOGNITION SYSTEM WITH BARGE-IN CAPABILITY

John Brian Pickering, assignor to International Business Machines Corporation
19 April 2005 (Class 704/270); filed in the United Kingdom 27 November 1999

The barge-in capability described in this patent is a step above the run-of-the-mill type, which allows the user to interrupt and stop a machine-generated prompt. Here, the user's input is immediately analyzed to see if certain conditions are met. Only if the input passes these tests, will that input cause the outgoing prompt to be stopped. Conditions tested include the presence of certain predetermined keywords or, for example, the detection of a DTMF tone.—DLR

6,882,974

43.72.Ne VOICE-CONTROL FOR A USER INTERFACE

Frankie James *et al.*, assignors to SAP Aktiengesellschaft
19 April 2005 (Class 704/270.1); filed 28 August 2002

The essence of this patent, first filed in 2002 and dealing with voice activation of an Internet browser, seems to involve issues that were widely known and discussed, if not often implemented, in the 1990s. Much noise was produced decades ago about voice enabling an Internet language, such as HTML, Javascript, or, later, XML. This patent mainly covers the addition of voice-control information to a document, in the form of tag option items, for example, and presents a number of figures showing how the result will appear to the user.—DLR

6,879,953

43.72.Ne SPEECH RECOGNITION WITH REQUEST LEVEL DETERMINATION

Tetsuya Oishi and Humio Saito, assignors to Alpine Electronics, Incorporated
12 April 2005 (Class 704/231); filed in Japan 22 October 1999

This speech recognition system, designed for automobile navigation and control, includes a semantic processor to extract the meaning from ''desire'' phrases, such as ''I'm cold,'' converting these to more specific commands, such as ''Start the heater.'' After the initial conversion of the speech input into a text string, two aspects of the input are determined, a ''desire'' level and a ''request'' level. The former is intended as a measure of the extent to which the input is asking for something to be done, which may or may not appear explictly in the text. The latter is a measure of the urgency with which the request is to be addressed. These aspects are determined both by analysis of the input semantics, as well as from measures taken of the input speech signal, including prosodic cues, such as average pitch or loudness. The patent text includes extensive examples from the Japanese language.—DLR

6,895,117

43.72.Ne RECOGNITION SYSTEM METHOD

Heinz Klemm *et al.*, assignors to Harman Becker Automotive Systems GmbH
17 May 2005 (Class 382/226); filed in Germany 27 March 1998

To reduce processing delay in voice-controlled applications such as voice entry of location names into a vehicle's navigation system, a streamlined method is proposed for storing and transferring character sequences from a reading memory into a working memory.—DAP

6,895,242

43.72.Ne SPEECH ENABLED WIRELESS DEVICE MANAGEMENT AND AN ACCESS PLATFORM AND RELATED CONTROL METHODS THEREOF

Rongyao Fu *et al.*, assignors to International Business Machines Corporation
17 May 2005 (Class 455/420); filed in China 13 October 2000

A speech-enabled Bluetooth device management and access platform controls devices with a speech input. A device management module discovers controlled devices located in proximity of Bluetooth transmission range.

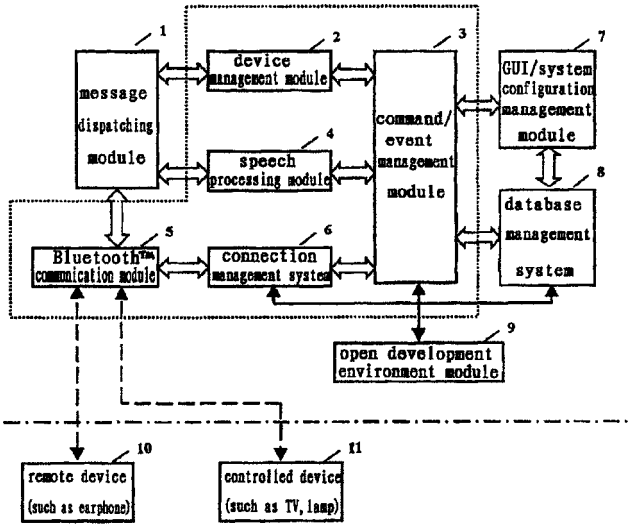

A speech processing module converts a speech command received via Bluetooth into a data command or converts a data response from the controlled device into a speech response.—DAP

6,907,397

43.72.Ne SYSTEM AND METHOD OF MEDIA FILE ACCESS AND RETRIEVAL USING SPEECH RECOGNITION

David Kryze *et al.*, assignors to Matsushita Electric Industrial Company, Limited
14 June 2005 (Class 704/251); filed 16 September 2002

A play list of media files is generated by recognizing speech input from a user of an embedded device. An indexer generates speech recognition grammars based on contents of a media file header or categories in a file

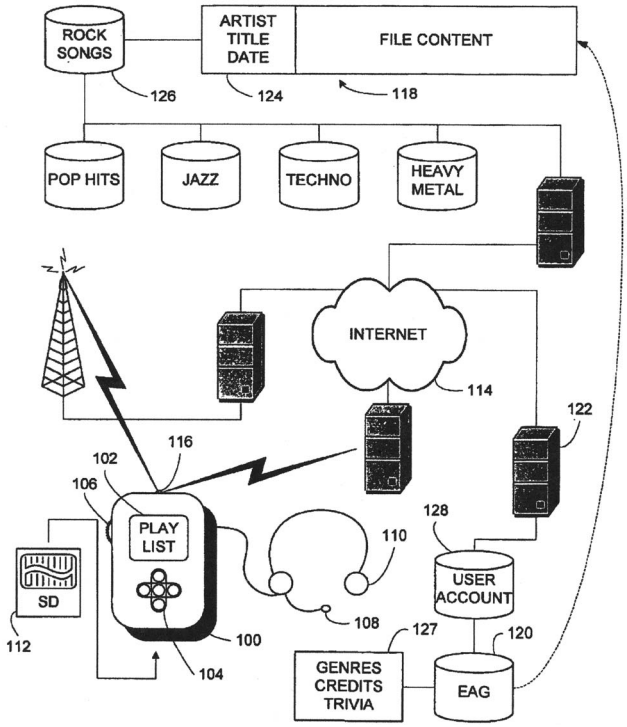

path for retrieving a media file. The system is said to avoid the necessity for the user to create an indexing system for file retrieval.—DAP

6,894,427

43.80.Qf NASAL VIBRATION TRANSDUCER

Susan S. Alfini, assignor to Dymedix Corporation
17 May 2005 (Class 310/338); filed 24 June 2002

This rather intriguing device for monitoring a patient's snoring pattern consists of a thin, flexible laminated vibration transducer that is adapted for placement on a subject's nose. The transducer, which produces an electrical signal indicative of the snoring episodes, has a rectangular portion that

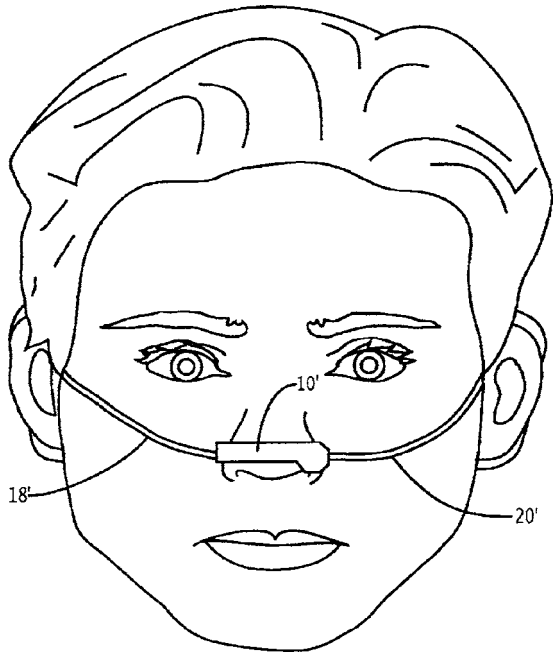

bridges the dorsum and at least one polygonal adhesive area for securing to the ala nasi. The transducer itself is a laminated assembly that incorporates a polyvinylidene fluoride film possessing piezoelectric properties.—DRR

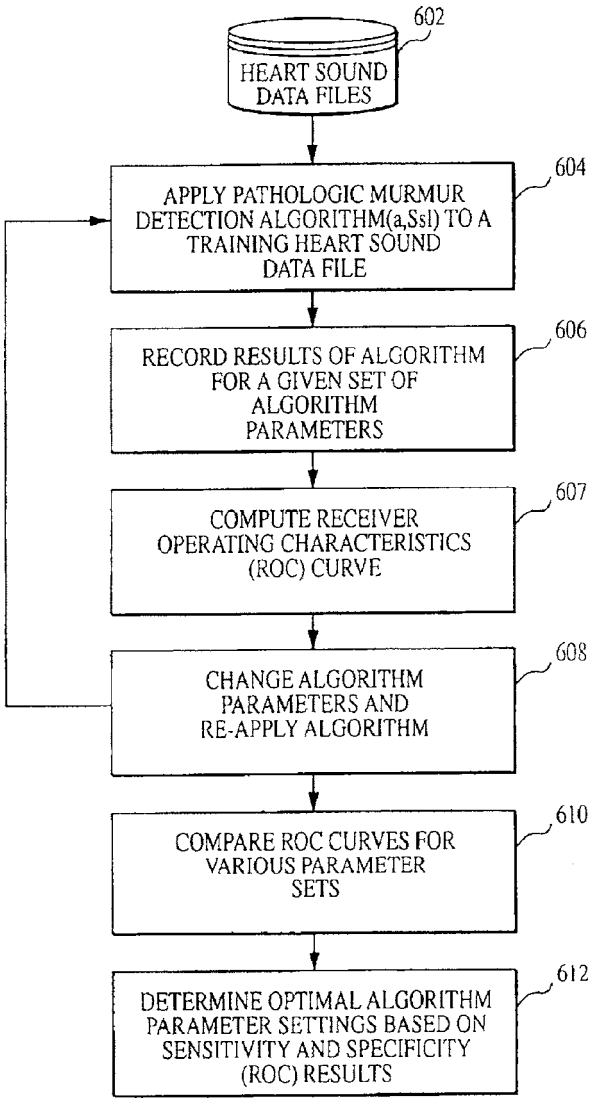

6,898,459

43.80.Qf SYSTEM AND METHOD FOR DIAGNOSING PATHOLOGIC HEART CONDITIONS

Carleton S. Hayek *et al.*, assignors to The Johns Hopkins University
24 May 2005 (Class 600/509); filed 23 February 2001

Heart sounds are used to provide data for diagnosing pathologic heart conditions. This device performs a time-frequency analysis of those sounds. A time series of heart sounds is filtered and parsed into a sequence of individual heart cycles. A systolic interval and subintervals are identified for each heart cycle. An energy value is computed for the systolic subinterval of one or more heart cycles, proportional to the energy level associated with a heart-sound series. A composite energy value is then computed and compared to a threshold level in order to distinguish between a normally functioning heart and a pathologic heart.—DRR

6,899,680

43.80.Qf ULTRASOUND MEASUREMENT TECHNIQUES FOR BONE ANALYSIS

Lars Hoff and Kjell Oygarden, assignors to Odetect as
31 May 2005 (Class 600/449); filed 19 October 2001

A system and method for diagnosing osteoporosis is based on the ultrasound measurement of bone quality through the use of nonlinear analysis in combination with or alternatively using shear waves to provide what is said to be more insightful information on human bone conditions. A method for measuring bone strength consists of software-implemented steps of mea-

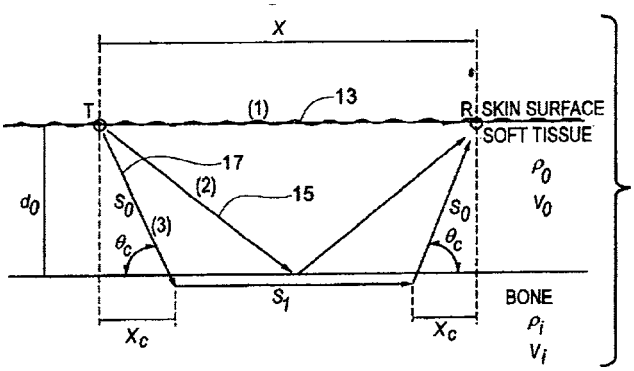

suring the shear wave velocity c_s, estimating the Lamé coefficient shear modulus μ of the bone via the relationship $c_s = \sqrt{\mu/\rho}$ and assigning a bone strength index based on the estimate of shear modulus.—DRR

6,905,468

43.80.Qf THREE-DIMENSIONAL SYSTEM FOR ABDOMINAL AORTIC ANEURYSM EVALUATION

Gerald J. McMorrow *et al.*, assignors to Diagnostic Ultrasound Corporation
14 June 2005 (Class 600/443); filed 18 September 2002

This device consists of a data-acquiring system for three-dimensional ultrasound imaging of the descending abdominal aorta artery. The system processes the information in each converted scan-line plane to determine the

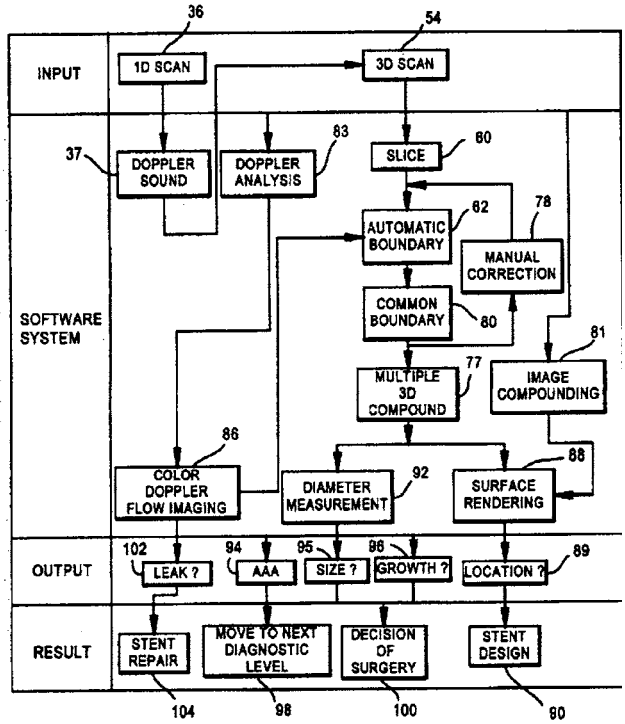

boundaries of the aorta, from which diameter information is then calculated. These diameter measurements over a given region of the aorta can be used to establish and monitor the presence of an aneurysm.—DRR

6,893,399

43.80.Vj METHOD AND APPARATUS FOR B-MODE IMAGE BANDING SUPPRESSION

Satchi Panda *et al.*, assignors to GE Medical Systems Global Technology Company, LLC
17 May 2005 (Class 600/443); filed 27 March 2003

Intensity differences that produce banding between adjacent focal zones in b-scan images are suppressed by determining the intensity along the border of one focal zone and adjusting the intensity along the border of the other focal zone to reduce the difference between the two intensities.—RCW

6,896,658

43.80.Vj SIMULTANEOUS MULTI-MODE AND MULTI-BAND ULTRASONIC IMAGING

Ting-Lan Ji and Glen McLaughlin, assignors to Zonare Medical Systems, Incorporated
24 May 2005 (Class 600/440); filed 20 October 2001

Ultrasound echo signals are digitized and stored. The stored data are then reprocessed as a function of frequency band or alternative encoding.

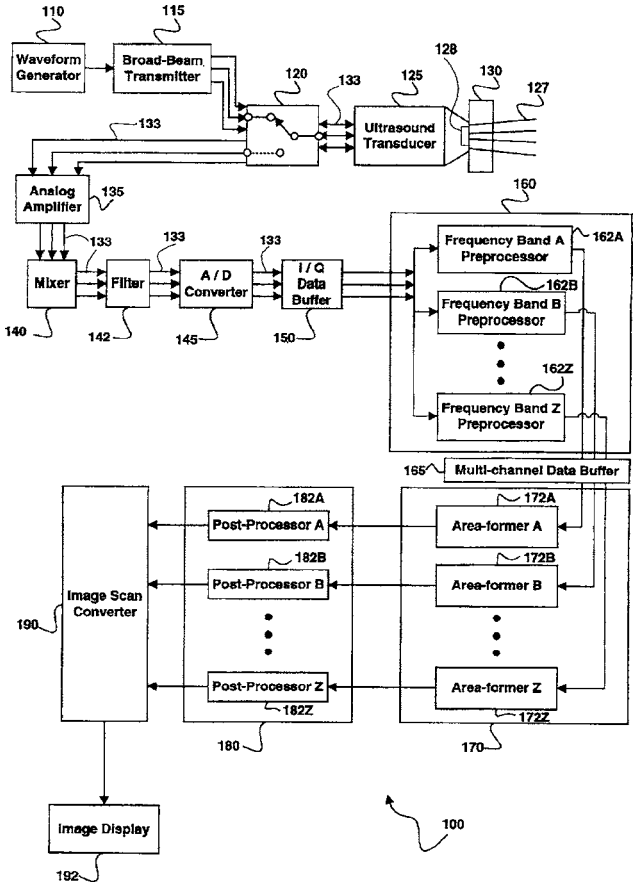

Preprocessor results are used in subsequent parallel processors to obtain data for multimode or multiband images.—RCW

6,896,657

43.80.Vj METHOD AND SYSTEM FOR REGISTERING ULTRASOUND IMAGE IN THREE-DIMENSIONAL COORDINATE SYSTEM

Parker Willis, assignor to SciMed Life Systems, Incorporated
24 May 2005 (Class 600/437); filed 23 May 2003

Ultrasound image data are acquired in one coordinate system and site-of-interest data are acquired in another coordinate system. Based on the location of the ultrasound transducer in each coordinate system, a transformation between the coordinate systems is determined. Ultrasound image data are then registered and displayed in the second coordinate system along with the sites of interest.—RCW

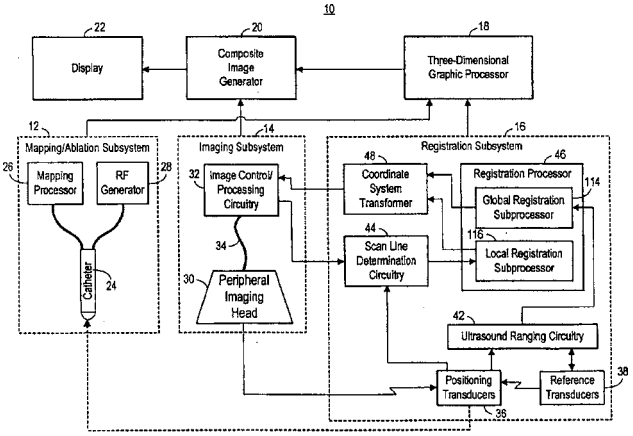

6,896,659

43.80.Vj METHOD FOR ULTRASOUND TRIGGERED DRUG DELIVERY USING HOLLOW MICROBUBBLES WITH CONTROLLED FRAGILITY

Stanley R. Conston *et al.*, assignors to Point Biomedical Corporation
24 May 2005 (Class 600/458); filed 22 October 2001

Therapeutic or diagnostic agents are delivered to a region in a fluid-filled cavity, vessel, or tissue by using an agent-loaded microbubble population. The population has a controlled fragility characterized by a uniform wall thickness-to-diameter ratio that determines the ultrasound intensity at which microbubble rupture occurs in the population. The location of the microbubbles can be monitored to determine their presence in the region of interest prior to application of ultrasonic power that ruptures the microbubbles.—RCW

6,899,681

43.80.Vj AUTOMATED POWER LEVEL FOR CONTRAST AGENT IMAGING

Patrick J. Phillips *et al.*, assignors to Acuson Corporation
31 May 2005 (Class 600/458); filed 15 February 2002

Transmit power used to image contrast agents with minimum destruction of the contrast agent and with maximum signal-to-noise ratio is determined by analysis of echo data produced by different transmit power levels, different delays between acquisition, or different acquisition sequences.—RCW

6,905,465

43.80.Vj CORRECTIONS FOR PULSE REVERBERATIONS AND PHASEFRONT ABERRATIONS IN ULTRASOUND IMAGING

Bjørn A. J. Angelsen and Tonni F. Johansen, both of Trondheim, Norway
14 June 2005 (Class 600/437); filed 7 April 2003

Pulse reverberation is estimated using two transmissions in which the second transmission is determined by processing echos from the first transmission. Reverberation can also be estimated from a single transmission by using two receive beams and processing echos in those beams. Strong reverberation is reduced by adjustment of the active transmit aperture.—RCW

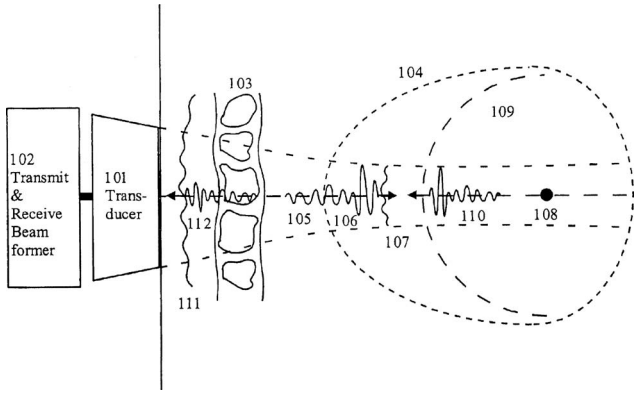

6,905,466

43.80.Vj IMAGING ULTRASOUND TRANSDUCER TEMPERATURE CONTROL SYSTEM AND METHOD USING FEEDBACK

Ivan Salgo *et al.*, assignors to Koninklijke Philips Electronics, N.V.
14 June 2005 (Class 600/437); filed 21 August 2003

The temperature of an ultrasound transducer in an imaging system is controlled by operating system parameter changes based on feedback from temperature sensors in the transducer. The system parameters that are changed may be preset, controlled by the user, or a combination of the two. System parameter adjustments can be made proportional to the difference between the current temperature and a preferred operating temperature or can be made by switching to a lower power imaging mode when temperature feedback indicates a threshold temperature has been reached.—RCW

LETTERS TO THE EDITOR

This Letters section is for publishing (a) brief acoustical research or applied acoustical reports, (b) comments on articles or letters previously published in this Journal, and (c) a reply by the article author to criticism by the Letter author in (b). Extensive reports should be submitted as articles, not in a letter series. Letters are peer-reviewed on the same basis as articles, but usually require less review time before acceptance. Letters cannot exceed four printed pages (approximately 3000–4000 words) including figures, tables, references, and a required abstract of about 100 words.

Consonant identification in *N*-talker babble is a nonmonotonic function of *N* (L)

Sarah A. Simpson[a] and Martin Cooke[b]
Department of Computer Science, University of Sheffield, Regent Court, 211 Portobello Street, Sheffield, S1 4DP, England

(Received 18 March 2005; revised 12 August 2005; accepted 18 August 2005)

Consonant identification rates were measured for vowel-consonant-vowel tokens gated with *N*-talker babble noise and babble-modulated noise for an extensive range of *N*, at a fixed signal-to-noise ratio. In the natural babble condition, intelligibility was a nonmonotonic function of *N*, with a broad performance minimum from $N=6$ to $N=128$. Identification rates in babble-modulated noise fell gradually with *N*. The contributions of factors such as energetic masking, linguistic confusion, attentional load, peripheral adaptation, and stationarity to the perception of consonants in *N*-talker babble are discussed. © *2005 Acoustical Society of America.* [DOI: 10.1121/1.2062650]

PACS number(s): 43.71.Es, 43.66.Dc, 43.66.Lj, 43.50.Fe, 43.72.Dv [RLD] Pages: 2775–2778

I. INTRODUCTION

Speech communication frequently takes place in environments in which other talkers are active. For this reason, babble (i.e., the summed waveform of several simultaneous talkers) is often used as a masker in studies of everyday speech perception in noise. However, the masking effect of babble is heavily dependent on the number (*N*) of simultaneous talkers in the mixture. Recent studies employing babble noise, such as Snell *et al.* (2002), Markham and Hazan (2004) and Cutler *et al.* (2004) used $N=\{4,6,20\}$, respectively. The widely used speech intelligibility test of Kalikow *et al.* (1977) contains babble with $N=12$.

Single-talker maskers ($N=1$) and speech-shaped noise ($N=\infty$) are the extremes of the babble continuum. Speech reception threshold (SRT) gains of around 6–8 dB for the single-talker masker over speech-shaped noise have been reported (Duquesnoy, 1983; Festen and Plomp, 1990). The release from masking produced by a single talker relative to speech-shaped noise is usually explained by the assumption that listeners take advantage of temporal fluctuations in masker energy to listen in intervals of favorable local signal-to-noise ratio (SNR) (Assmann and Summerfield, 2004). If this were the only factor underlying speech perception in babble noise, one would expect that as *N* increases, intelligibility would decline monotonically to the level observed in speech-shaped noise.

Miller's classic study of masking (Miller, 1947) was the first to investigate intermediate values of *N*. Miller measured the intelligibility of words in *N*-babble for $N=\{1,2,4,6,8\}$. He found that the difference in masking effect for a single talker over two talkers was equivalent to an SRT difference of about 8 dB. Babble with $N=\{4,6,8\}$ produced an additional 3–4 dB of masking over the two-talker condition. Miller's results on their own indicate a monotonic decrease in intelligibility as *N* increases. However, taken together with those of Duquesnoy (1983) and Festen and Plomp (1990), they suggest that babble for $N=\{4,8\}$ is a more effective masker than speech-shaped noise. Other studies support this hypothesis. Danhauer and Leppler (1979) observed that consonants in a background of babble with $N=\{4,9\}$ talkers were recognized less well than in white noise at SNRs below 5 dB. Miller's own data suggest than the $N=8$ condition provides marginally less masking that $N=\{4,6\}$ for SNRs of 3 dB and below. Finally, in a pilot study, the authors found significantly greater masking of consonants in an $N=8$ babble condition than in speech-shaped noise at SNRs of 0, −6, and −12 dB. Bronkhorst (2000) summarizes data on speech intelligibility in multitalker backgrounds for $N<9$.

The purpose of the current study was to discover the shape of the intelligibility function for an extensive range of *N* values. The study was motivated by: (i) The possibility of a nonmonotonic change in intelligibility as *N* increases, (ii) the difficulty in comparing results from previous studies, as noted by Bronkhorst (2000), (iii) the relatively narrow range of *N* tested to date, and (iv) the observation that babble constructed using larger values of *N* is used routinely in speech

[a]Electronic mail: s.simpson@dcs.shef.ac.uk
[b]Electronic mail: m.cooke@dcs.shef.ac.uk

perception testing. In fact, a study by Carhart *et al.* (1975) did employ babble with a wide range of N values. They measured the intelligibility of spondees in N-talker babble for $N=\{1,2,3,16,32,64,128,\infty\}$. Their results appeared to confirm the suggestion of a nonmonotonic intelligibility function, but since their findings appeared only as an abstract, it is difficult to appreciate the precise pattern and significance of the results.

In the current study, listeners identified consonants presented in vowel-consonant-vowel (VCV) contexts in N-talker babble for $N=\{1,2,3,4,6,8,16,32,64,32,64,128,512,\infty\}$. In addition, intelligibility in babble-modulated speech-shaped noise was measured for the same values of N.

II. EXPERIMENT: CONSONANT IDENTIFICATION IN *N*-TALKER BABBLE

A. Stimuli

Speech stimuli were chosen from the VCV corpus collected by Shannon *et al.* (1999). Sixteen consonants (b, d, g, p, t, k, m, n, l, r, f, v, s, z, ʃ, tʃ) in the context of the vowel /ɑ/ were used. Two examples of each consonant from five male talkers were chosen, leading to a test set of 160 items. An additional 32 VCVs were used as practice items.

Speech stimuli were presented in 23 masking conditions consisting of N-talker babble (11 conditions), speech-shaped noise modulated by N-talker babble (11 conditions), and unmodulated speech-shaped noise. Babble stimuli were constructed from subsets of 1056 utterances spoken by 132 male talkers from dialect regions 1–3 of the TIMIT corpus (Garofolo *et al.*, 1992). TIMIT "shibboleth" sentences spoken by all talkers were not used. All utterances were normalized to have the same RMS energy prior to forming babble noise to ensure that they all contributed equally to the masker. Speech-shaped noise was created by processing white noise with a filter whose magnitude response was equal to the long-term magnitude spectrum of the entire set of sentences. Speech-shaped noise was multiplied by the envelope of N-babble waveforms to create N-babble-modulated speech-shaped noise. Following Brungart *et al.* (2001), the envelope was computed by convolving the absolute value of the base signal with a 7.2 ms rectangular window.

Masked VCVs were formed by adding a randomly selected fragment of masking noise to each consonant at a constant target-to-masker ratio of −6 dB. The masker and VCV were gated, i.e., started and stopped at the same time. Stimuli were presented at approximately 68 dB SPL.

B. Listeners

Twelve listeners (10 M and 2 F) participated in the experiment. All received a hearing test and were found to have normal hearing (better than 20 dB hearing level in the range 250–8000 Hz). All listeners passed a pretest which required them to recognize VCV tokens in clean conditions at an identification rate of at least 98%.

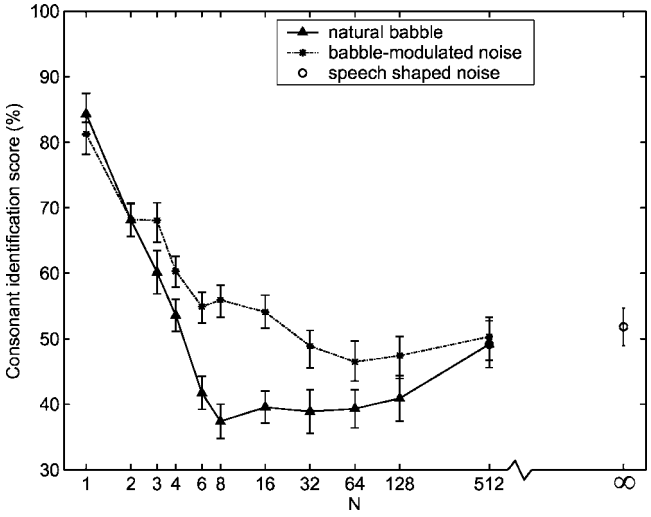

FIG. 1. Consonant identification rates in N-talker babble as a function of the number of talkers, for natural babble (solid line), babble-modulated noise (dashed line), and speech-shaped noise (circle). The error bars represent 95% confidence intervals in each condition.

C. Procedure

Listening sessions took place in an IAC single-walled acoustically isolated booth. Stimuli were resampled to 25 kHz and presented via a Tucker-Davis Technologies System 3 RP2.1. Stimulus presentation and results collection were controlled by a computer situated outside the booth. Signals were presented diotically over Sennheiser HD250 headphones.

Each participant completed the 23 conditions over 4–6 sessions. Every condition consisted of 192 tokens, and required about 6–7 minutes to complete. The initial 32 practice tokens were not scored, although participants were not aware of this. Condition orders were balanced across listeners, and token order within each condition was randomized.

III. RESULTS

Figure 1 summarizes consonant identification rates in all masking conditions. The data have been averaged across the 12 listeners and the error bars in the figure represent the 95% confidence interval at each data point. In natural babble, performance falls rapidly to a minimum at $N=8$. Little improvement is observed between $N=8$ and $N=128$ before a recovery to the level of speech-shaped noise by $N=512$. In contrast, babble-modulated noise is a less effective masker at all values of $N>2$ and shows a more gradual decrease in performance with increasing N. The difference between natural babble and babble-modulated noise also varied with N, reaching a maximum at $N=8$ (Fig. 2). The error bars in figure 2 represent the Bonferroni-adjusted 95% confidence intervals in each masking condition.

A repeated-measures ANOVA with factors of N and masker type showed a significant ($p<0.01$) effect for both factors and their interaction (effect size $\eta^2=0.924$ for masker type, 0.964 for N and 0.682 for their interaction). Results were partitioned by masker type and post-hoc tests (with Bonferroni adjustment for multiple comparisons) computed to investigate the effect of N.

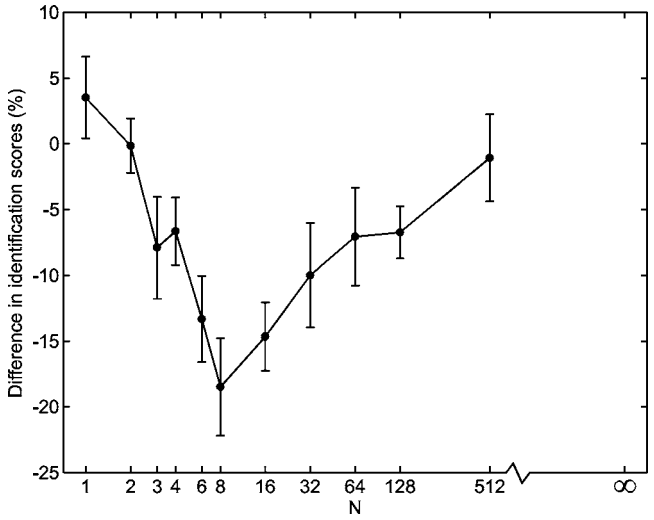

FIG. 2. Difference in consonant identification rate between natural babble and babble-modulated noise. The error bars represent Bonferroni-adjusted 95% confidence intervals in each condition.

For natural babble, conditions in the set $N=\{1,2,3,4\}$ differed ($p<0.01$) from each other and from all other values of N, apart from the pairs (3, 4), (4, 512), and $(4,\infty)$ which were not significantly different ($p>0.05$). All pairs of conditions in the subset $N=\{6,8,16,32,64,128\}$ were statistically equivalent. The $N=512$ condition differed from all others apart from $N=\{4,6,\infty\}$.

For babble-modulated noise, conditions $N=\{1,2,3,4\}$ differed from each other and all other conditions apart from the pairs (2, 3) and (4, 8). No conditions with $N>6$ differed significantly from speech-shaped noise, although the $N=\{6,8\}$ conditions differed from $N=\{64,128\}$.

IV. DISCUSSION

The experiment demonstrated that the masking effectiveness of N-talker babble varies nonmonotonically with N. This confirms the findings reported in the abstract of Carhart *et al.* (1975) and extends to speech-shaped noise the results of Danhauer and Leppler (1979). Masking by babble-modulated noise increased monotonically up to $N=6$ then leveled out. This confirms and extends to larger N the results of Bronkhorst and Plomp (1992) who measured the SRT of babble-modulated noise for $N=\{1,2,4,6\}$. The difference between the babble-modulated noise and natural babble conditions also varied with N.

An unexpected outcome of the study was the finding that all babble noises consisting of between 8 and 128 talkers have approximately the same masking effectiveness. The difference between the babble-modulated noise and natural babble conditions is usually attributed to the perceptual masking (Carhart *et al.*, 1969) which occurs when portions of the masker are wrongly attributed to the target speech. Phonetic cues are audible in the masker for small N, but become progressively inaudible as N increases. It is difficult to see how the factors which govern overall masking (energetic and informational) at $N=8$ could be the same as those which limit performance at $N=128$. Several studies have suggested that what is presumably the "linguistic uncertainty" component of informational masking effects is most potent for $N=2$ (Freyman *et al.*, 2004) or $N=3$ (Carhart *et al.*, 1975), and is almost absent by $N=10$ (Freyman *et al.*, 2004). In fact, the effect of informational masking may be underestimated because, for low values of N, listeners may be able to use level differences between the target and individual talkers in the background to help overcome some of the effects of linguistic confusions (Brungart, 2001).

Several factors might contribute to the breadth of the dip between $N=8$ and 128. Babble is identifiable as a signal composed of multiple speech sources for this range of N. Consequently, it is possible that attentional resources are devoted to monitoring the background in case some important speech event emerges. A related factor is the auditory system's response to fluctuating stimuli and, in particular, the enhancement of onsets. As N increases, the number of onsets in the background will increase, perhaps distracting attention from the target speech. Forward masking may also increase with N. However, the difference in masking effectiveness between natural babble and babble-modulated noise remains significant for large N, so any effects of distracting onsets and forward masking must be greater in the natural babble background. Another possibility is that the auditory system, like most systems for robust automatic speech recognition, makes use of background noise estimates to improve identification of the target. As the background becomes more stationary, the accuracy of the estimate increases. Ainsworth and Meyer (1994) found that the identification of syllables in steady-state noise was better when the noise was continuously present than when it was gated with the syllables. It is possible that, even though gated presentation was used in the current study, repeated exposure to the noise in the presence of a static /ɑ/ context is sufficient to provide a better noise estimate for $N>128$ than for smaller values of N. However, if the slight reduction in masking observed in babble-modulated noise for $N>64$ reflects increasing masker stationarity, then its effect is small.

These findings have yet to be generalized to other SNRs and different speech material, although a similar pattern of results was observed in a pilot study at SNRs of 0 and −12 dB. For the task and SNR condition investigated in this study (consonant identification in a VCV context at a SNR of −6 dB) an eight-talker babble provided the greatest amount of masking. Maximal informational masking for sentence material is usually reported to occur for small values of N (e.g., Freyman *et al.*, 2004). For consonants embedded in a static vowel context, listeners are likely to focus on brief acoustic cues present in the central region of the VCV in the absence of the wider contextual cues present in words and sentences. Conflicting cues to brief acoustic events are certainly salient in eight-talker babble and are perhaps sufficiently numerous in this condition to be at their most disruptive.

The N-babble continuum presents a challenge for accounts of speech perception in noise. The observed pattern of results appears to represent the combined contribution of several factors, each of which vary with N. Energetic masking increases with N, while linguistic masking reaches a peak at small values of N. Attentional demands resulting from

monitoring a speechlike background, the distracting effects of numerous onsets and nonstationarity may continue to have a role for larger values of *N*.

ACKNOWLEDGMENTS

The authors would like to thank Jon Barker for discussion on an earlier draft of this letter. They also thank Jose Benki, one other reviewer, and the editor for their useful comments on the manuscript.

Ainsworth, W. A. and Meyer, G. F. (**1994**). "Recognition of plosive syllables in noise: Comparison of an auditory model with human performance," J. Acoust. Soc. Am. **96**, 687–694.

Assmann, P. and Summerfield, Q. (**2004**). "The perception of speech under adverse acoustic conditions," in *Speech Processing in the Auditory System*, Springer Handbook of Auditory Research Vol. 18, edited by S. Greenberg, W. A. Ainsworth, A. N. Popper, and R. R. Fay (Springer, Berlin).

Bronkhorst, A. W. (**2000**). "The cocktail party phenomenon: A review of research on speech intelligibility in multiple-talker conditions," Acust. Acta Acust. **86**, 117–128.

Bronkhorst, A. W. and Plomp, R. (**1992**). "Effect of multiple speechlike maskers on binaural speech recognition in normal and impaired hearing," J. Acoust. Soc. Am. **92**, 3132–3139.

Brungart, D. S. (**2001**). "Informational and energetic masking effects in the perception of two simultaneous talkers," J. Acoust. Soc. Am. **109**, 1101-1109.

Brungart, D. S., Simpson, B. D., Ericson, M. A., and Scott, K. R. (**2001**). "Informational and energetic masking effects in the perception of multiple simultaneous talkers," J. Acoust. Soc. Am. **110**, 2527–2538.

Carhart, R., Johnson, C., and Goodman, J. (**1975**). "Perceptual masking of spondees by combinations of talkers," J. Acoust. Soc. Am. **58**, 535.

Carhart, R., Tillman, T. W., and Greetis, E. S. (**1969**). "Perceptual masking in multiple sound backgrounds," J. Acoust. Soc. Am. **45**, 694–703.

Cutler, A., Weber, A., Smits, R., and Cooper, N. (**2004**). "Patterns of English phoneme confusions by native and non-native listeners," J. Acoust. Soc. Am. **116**, 3668–3678.

Danhauer, J. L. and Leppler, J. G. (**1979**). "Effects of four noise competitors on the California Consonant Test." J. Speech Hear Disord. **44**, 354–362.

Duquesnoy, A. J. (**1983**). "Effect of a single interfering noise or speech source upon the binaural sentence intelligibility of aged persons," J. Acoust. Soc. Am. **74**, 739–743.

Festen, J. M. and Plomp, R. (**1990**). "Effects of fluctuating noise and interfering speech on the speech-reception threshold for impaired and normal hearing," J. Acoust. Soc. Am. **88**, 1725-1736.

Freyman, R. L., Balakrishnan, U., and Helfer, K. S. (**2004**). "Effect of number of masking talkers and auditory priming on informational masking in speech recognition," J. Acoust. Soc. Am. **115**, 2246–2256.

Garofolo, J. S., Lamel, L. F., Fisher, W. M., Fiscus, J. G., Pallett, D. S., and Dahlgren, N. L. (**1992**). "DARPA TIMIT Acoustic Phonetic Continuous Speech Corpus CDROM," NIST, Md.

Kalikow, D. N., Stevens, K. N., and Elliott, L. L. (**1977**). "Development of a test of speech intelligibility in noise using sentence materials with controlled word predictability," J. Acoust. Soc. Am. **61**, 1337–1351.

Markham, D. and Hazan, V. (**2004**). "The effect of talker- and listener-related factors on intelligibility for a real-word, open-set perception test," J. Speech Lang. Hear. Res. **47**, 725-737.

Miller, G. A. (**1947**). "The masking of speech," Psychol. Bull. **44**, 105–129.

Shannon, R. V., Jensvold, A., Padilla, M., Robert, M. E., and Wang, X. (**1999**). "Consonant recordings for speech testing," J. Acoust. Soc. Am. **106**, L71–L74.

Snell, K. B., Mapes, F. M., Hickman, E. D., and Frisina, D. R. (**2002**). "Word recognition in competing babble and the effects of age, temporal processing, and absolute sensitivity," J. Acoust. Soc. Am. **112**, 720–727.

Measurements of tortuosity in stereolithographical bone replicas using audiofrequency pulses (L)

Keith Attenborough, Ho-Chul Shin,[a] Qin Qin, and Michael J Fagan
Department of Engineering, University of Hull, Cottingham Road, Hull, HU6 7RX, United Kingdom

Christian M Langton
University of Hull & Hull Royal Infirmary, Hull, HU3 2RW, United Kingdom

(Received 28 January 2005; accepted 19 August 2005)

The tortuosity of five air-filled stereolithographical cancellous bone replicas has been obtained from measurements using audiofrequency pulses in a rectangular waveguide. The data obtained from the replicas yields information about anisotropy with respect to orthogonal axes of the passages that would be marrow filled *in vivo*. A strong relationship has been found between the acoustically measured tortuosity and the independently measured porosity. Use of stereolithographical bone replicas has the potential to simulate perforation and thinning of cancellous bone and hence evaluate the dependence of acoustic properties on cancellous bone microstructure. As an "extreme" illustration of such use, "inverses" of the original replicas have been manufactured and acoustic measurements have been made on them. The data reveal significantly greater tortuosity of the passages that are geometrically equivalent to the original solid bone structures. © *2005 Acoustical Society of America.* [DOI: 10.1121/1.2062688]

PACS number(s): 43.20.Bi, 43.20.Hq, 43.20.Jr, 43.80.Cs [TDM] Pages: 2779–2782

I. INTRODUCTION

Recently,[1] it has been shown that a modified Biot theory is able to describe ultrasonic propagation in cancellous bone, i.e., bone with a less than 70% volume fraction of solids. An ultrasonic pulse, with a center frequency near 2 MHz, incident on three water-filled bone samples between 3.8 and 7 mm thick machined from human cancellous bone in femoral heads, was found to give rise to two transmitted pulses associated with "fast" and "slow" waves with varying degrees of overlap. The measured transmitted pulse shapes were found to be predicted well using parameters deduced in part from ultrasonic measurements on the same samples in air. On the basis of a sensitivity analysis using the modified Biot theory, it has been predicted that, as well as porosity, sample thickness, solid bulk modulus, and skeletal frame compressibility, tortuosity plays an important role simultaneously on both fast and slow waves since it affects the inertial coupling between them. An approximately 20% increase in tortuosity, from 1.05 to 1.26, is predicted to decrease the fast wave speed by approximately 10% and amplify its amplitude by nearly 300%. The same change in tortuosity is predicted to reduce the slow wave speed by just over 10% and decrease its amplitude by more than 60%. Strelitzki *et al.*[2] have made measurements using conventional ultrasonic equipment in air-saturated samples of bone. They have demonstrated that an airborne "slow" compressional wave can be measured, in a repeatable manner, during pulse transmission through 21.5 mm diameter, 2.5 to 6.7 mm thick circular disks of cancellous bone, using conventional 1 MHz transducers, and that such measurements have the potential to give structural information, viz., the tortuosity of the trabecular framework. Nevertheless, since the 0.4 mm wavelength used at 800 kHz was comparable with typical trabecular dimensions of 0.1 mm, the inevitable scattering reduced the accuracy of their tortuosity deductions.

Micro Computer Tomography (μCT) has been suggested as a method for characterizing porous foams. The scanning of μCT images of aluminum foam, magnified ten times, has been used to deduce porosity and thermal characteristic length.[3] μCT is one method by which the three-dimensional (3-D) template for the construction of stereolithographical replicas can be obtained. It has been shown that broadband ultrasound attenuation and velocity values in stereolithographical bone replicas made from resin and saturated with castor oil are commensurate with those measured in a commercial phantom.[4] The use of stereolithographical bone replicas has the potential to enable systematic investigations of the influences of perforation and thinning in cancellous bone on the acoustical and mechanical properties of the bone structure.

The stereolithographical models used in this work are 13 times the actual size of the bone microstructure, and are in the form of 57 mm cubes. Five bone replicas have been used. Views of these replicas are shown in Fig. 1 and the associated bone characteristics are identified in Table I.

Ultrasonic measurements on such replicas would be greatly affected by scattering. However, measurements using sufficiently low frequencies should avoid this. As is the case with the solid constituent of bone, the solid resin of the replica framework has much greater density and rigidity than air. Air-filled replicas behave essentially as rigid-framed porous media so that the reflection and transmission of acoustic pulses are determined primarily by the slow wave traveling through the air-filled pores. The reflection and transmission

[a]Current address: Department of Engineering, University of Cambridge, Cambridge, United Kingdom.

FIG. 1. Views of five stereolithographical cancellous bone replicas.

TABLE I. The bone replicas and two properties of the bones.

Replica number	Body part	Code name	Porosity	Bulk density (kg/m^3)
1	Iliac crest	ICF	0.8386	200.1
2	Femoral head	FRA	0.7426	316.9
3	Lumbar spine (LS2)	LS2B	0.9173	100.9
4	Calcaneus	CAB	0.8822	139.1
5	Lumbar spine (LS4)	LS4A	0.9121	102.3

FIG. 2. Views of the "inverse" stereolithographical bone replicas.

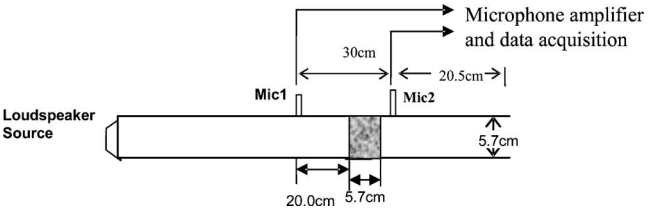

FIG. 3. Measurement arrangement using loudspeaker-generated pulses and two microphones.

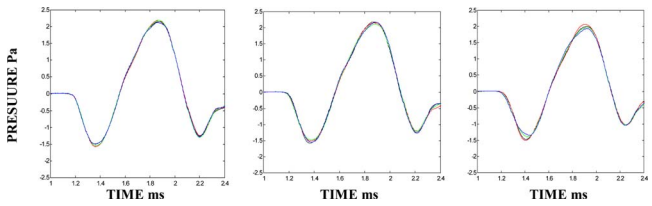

FIG. 4. Transmitted pulses obtained after each of four rotations about each of three orthogonal axes (left to right = X, Y, Z) through the stereolithographical replica of calcaneus bone using loudspeaker-generated pulses.

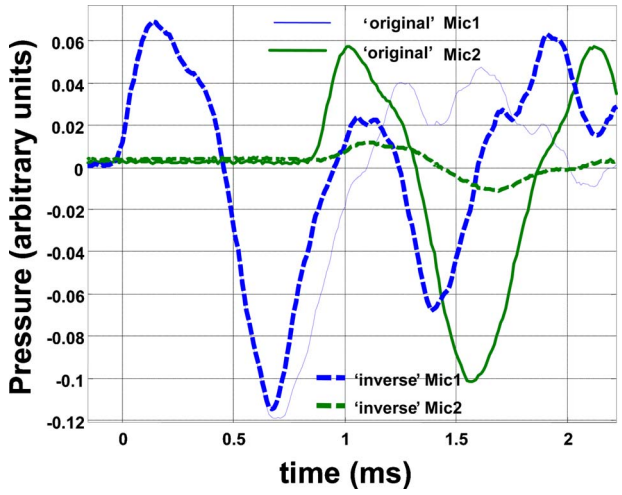

FIG. 5. Examples of direct and reflected pulses at microphone 1 and transmitted pulses at microphone 2 for "original" and "inverse" calcaneus replicas.

of audiofrequency pulses has been used to deduce the porosity and tortuosity of thick samples of several air-filled rigid-porous media[5] on the basis of a high-frequency approximation of the Johnson–Allard model.[6,7] Since porosity and tortuosity are unaffected by scaling, measurements on stereolithographical bone replicas should yield values representative of bone.

Here, we describe the use of audiofrequency pulse transmission on stereolithographical bone replicas to determine tortuosity along three orthogonal axes and to investigate the relationship between the resulting values and independent measurements of porosity. Also, to illustrate an "extreme" experiment that can be carried out using stereolithographical replicas, we report results of audiofrequency pulse measurements on "inverse" air-filled replicas in which the solid framework and the pore structure of the original replicas have been reversed. The "inverse" replicas corresponding to the five original cases are shown in Fig. 2.

II. MEASUREMENTS

The arrangement used for measurements with loudspeaker-generated pulses is shown in Fig. 3.

The bone replicas were placed in a square cross section tube, which acted as a sample holder and a waveguide. A Tannoy 75W loudspeaker driver at one end of the waveguide was used to emit pulses with measured peak-to-peak voltages between 0.18 and 1 V centered on 1 or 2 kHz. The other end of the waveguide was open. Microphones were located on either side of the replica and signals from these were amplified and captured by a computer-based data acquisition card with a sampling frequency of 1 MHz. Measurements were conducted in two stages. First, pulses were recorded inside the empty tube to determine the speed of sound in air. Subsequently, the replica was placed in the tube and transmission measurements were made four times for each axis of interest. The replica was rotated about the relevant axis (labeled X, Y, and Z, respectively) between each measurement.

Figure 4 demonstrates the repeatability of the transmit-

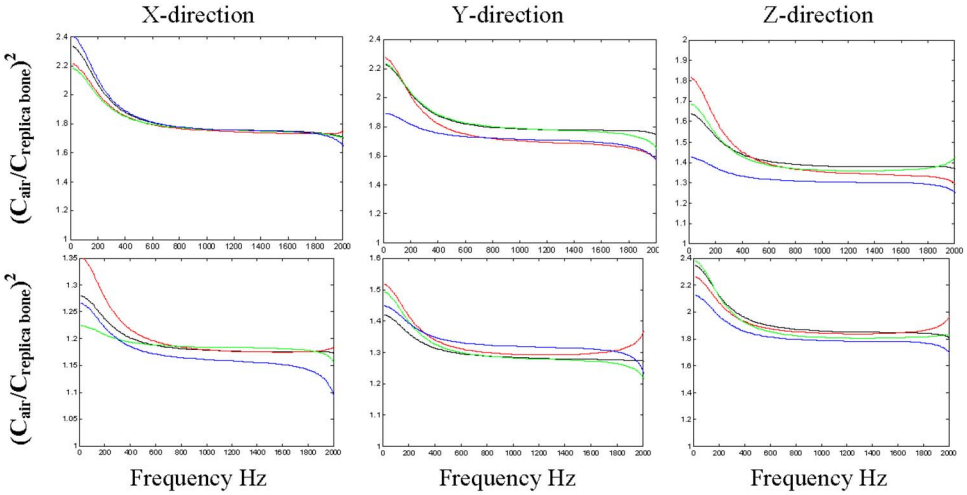

FIG. 6. Squared ratios of the phase speed in air to those in two of the bone replicas deduced from loudspeaker-generated pulse transmission data [upper, iliac crest: lower, calcaneus]. Each plot shows data from four rotations of the replicas.

ted pulses, along each axis, after four rotations of the replica within the waveguide. Five measured pulses for each replica and each axis were averaged in the time domain to remove possible fluctuations due to the measurement system. The pulses were windowed to remove any higher-order modes. The pulses transmitted through the original replicas were well separated from the pulses reflected from the surface. Consequently, it was possible to use the FFT of the complete transmitted pulses in a subsequent analysis. The phase information from the FFT analysis was unwrapped to compare the difference between the incident and transmitted pulses. Finally, the difference was converted to the phase speed, using the known distance between the transducers.

The amplitudes of the pulses transmitted through the "inverse" replicas were relatively small. Moreover, as a consequence of the greater reflection, there was overlap between the transmitted and reflected pulses. This is illustrated for the "original" and "inverse" calcaneous replicas in Fig. 5. Hence, only the first (positive-going) part of the incident and transmitted pulses have been used for the FFT-based analysis of the pulses transmitted through the "inverse" replicas.

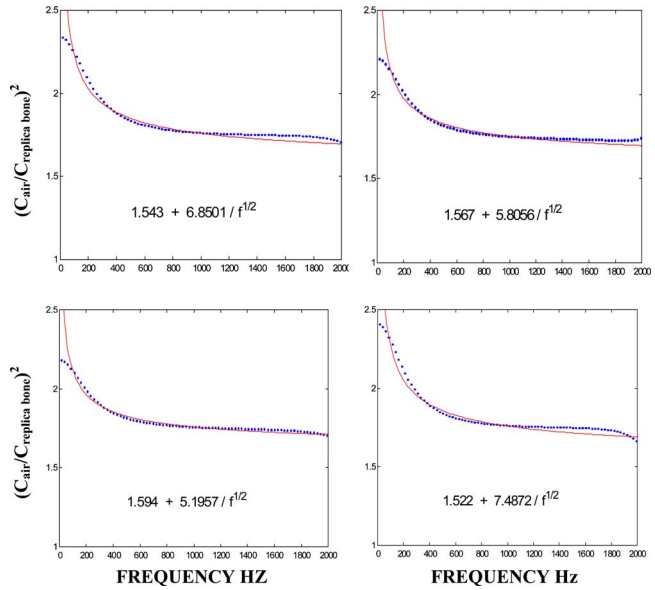

FIG. 7. Example fits of function (1) (lines) to data (points) obtained with loudspeaker pulses centered on 1 kHz. Each plot represents a fit to data between 200 and 1200 Hz for a particular rotation of the bone replica (iliac crest, X direction) within the sample holder.

III. ANALYSIS AND DISCUSSION

Figure 6 shows the squared ratios of the phase speeds in the frequency domain, obtained by the FFT of the time series from the loudspeaker-generated pulses for four rotations about each of the three orthogonal directions in two of the "original" replica bone samples.

A high-frequency approximation of the squared ratio of the sound speed in air to that of the slow wave in a rigid-porous material has the form[5]

$$F(f) = a_1 + a_2 \frac{1}{\sqrt{f}}, \tag{1}$$

where a_1 represents the tortuosity. Since, according to Fig. 6, there is a tendency for anomalous results to be obtained at the higher end of the frequency range where scattering is likely to be more important, the frequency range for fitting was reduced. Figure 7 shows example results from fitting function (1) to a reduced frequency range. Resulting values of tortuosity for the five original bone replicas are shown in Table II.

From Table II, it appears that the direction labeled Z in the iliac crest replica and the direction labeled X in the femoral head bone replica are significantly less tortuous than the other two directions. The Z direction in the calcaneus replica yields a significantly higher tortuosity than the other two directions. Visually, this direction is almost "blocked" by the plate-like character of the model trabeculae.

The Y and Z directions through the femoral head replica and the Z direction in the calcaneus replica yield the highest dispersion. The dispersions in the lumbar spine replicas are significantly lower than in the other replicas.

The results from a single measurement along each axis of the "inverse" replicas are given in Table III.

With the exception of the data for the inverse iliac crest replica, these indicate similar forms of anisotropy to the "originals."

Figure 8 shows the relationship between the acoustically deduced tortuosity values and the independently measured

TABLE II. Tortuosity values deduced by fitting data for squared sound speed ratios in "original" replicas.

	Iliac Crest (ICF)			Femoral Head (FRA)		
	X	Y	Z	X	Y	Z
Rotation 1	1.543	1.613	1.280	1.299	1.889	1.739
Rotation 2	1.567	1.480	1.171	1.283	1.554	1.770
Rotation 3	1.594	1.610	1.234	1.205	1.674	1.510
Rotation 4	1.522	1.639	1.257	1.309	1.659	1.628
Mean	**1.557**	**1.586**	**1.236**	**1.274**	**1.694**	**1.662**
St. Dev.	0.031	0.072	0.047	0.047	0.141	0.118
	Lumbar Spine (LS2B)			Calcaneus (CAB)		
	X	Y	Z	X	Y	Z
Rotation 1	1.086	1.172	1.047	1.136	1.228	1.671
Rotation 2	1.078	1.190	1.167	1.109	1.208	1.683
Rotation 3	1.084	1.175	1.119	1.168	1.199	1.598
Rotation 4	1.085	1.122	1.190	1.117	1.266	1.662
Mean	**1.083**	**1.165**	**1.131**	**1.133**	**1.225**	**1.654**
St. Dev.	0.004	0.030	0.063	0.026	0.030	0.038
	Lumbar Spine (LS4A)					
	X	Y	Z			
Rotation 1	1.047	1.062	1.154			
Rotation 2	1.063	1.134	1.193			
Rotation 3	1.034	1.091	1.142			
Rotation 4	1.025	1.136	1.207			
Mean	**1.042**	**1.106**	**1.174**			
St. Dev.	0.017	0.036	0.031			

porosity. In Fig. 8, the minimum, middle, and the maximum tortuosity values for each sample are represented by diamonds, squares, and circles, respectively. As expected from studies of other rigid-porous media and from expressions for the relationships between tortuosity and porosity deduced for idealized media, there is a tendency for the tortuosity in the bone replicas to decrease as porosity increases. In the "original" replicas, the relationship between tortuosity and porosity is clearest for the middle tortuosity values.

IV. CONCLUSIONS

Measurements of the reflection and transmission of acoustic "slow wave" pulses by stereolithographical bone replicas in air offer the potential for evaluating the dependence of acoustical properties on cancellous bone structure. This preliminary study has clearly revealed anisotropy in the tortuosity, the mean of which has been found to decrease as porosity increases. The tortuosity value (1.041) deduced from 800 kHz measurements on a calcaneus sample *in vitro* by Strelitzki *et al.*[4] is a little less than the lower range of those reported here in the X direction through the calcaneus replica (1.109–1.168). The values (1.02 to 1.05) measured ultrasonically by Fellah *et al.*[1] in the "trabecular alignment" direction of air-filled femoral head samples are somewhat lower than the values (1.274±0.047) obtained in the least tortuous direction in the femoral head replica.

TABLE III. Tortuosity values deduced by fitting data for squared sound speed ratios in "inverse" replicas.

	Axis and corresponding tortuosity		
"Inverse" replica	**X**	**Y**	**Z**
Iliac crest	2.676	3.041	3.052
Femoral head	1.983	2.321	2.965
Lumbar spine (LS2B)	2.451	3.300	3.610
Calcaneu	2.243	2.814	3.544
Lumbar spine (LS4A)	2.339	4.312	4.409

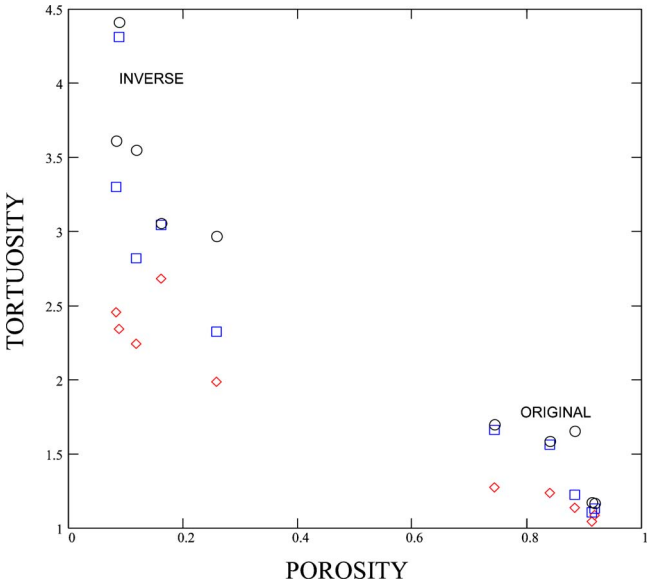

FIG. 8. Relationship between acoustically deduced tortuosity and independently measured porosity for "original" and "inverse" bone replicas.

The possibility for using bone replicas to explore the variation of acoustically deduced parameters with a microstructure has been illustrated by the "extreme" example of inverse replicas. The "inverse" replicas are found to have considerably higher tortuosity than the "original" replicas.

In principle,[5] data for the frequency dependence of the phase speed, reflection coefficient, and attenuation constant, from measurements on air-filled replica bones, could be used to deduce other "slow wave" parameters (e.g., porosity, flow resistivity, and viscous and thermal characteristic lengths).

[1]Z. E. A. Fellah, J. Y. Chapelon, S. Berger, W. Lauriks, and C. Depollier, "Ultrasonic wave propagation in human cancellous bone: Application of Biot theory," J. Acoust. Soc. Am. **116**, 61–73 (2004).
[2]R. Strelitzki, V. Paech, and P. H. F. Nicholson, "Measurement of airborne ultrasonic slow waves in calcaneal cancellous bone," Med. Eng. Phys. **21**, 215–223 (1999).
[3]C. Perrot, R. Panneton, X. Olny, and R. Bouchard, "Mesostructural approach for characterising macroscopic parameters of open cell foams with computed microtomography," Proc. Inst. Acoust. **25**, 169–175 (2003).
[4]C. M. Langton, M. A. Whitehead, D. K. Langton, and G. Langley, "Development of a cancellous bone structural model by stereolithography for ultrasound characterisation of the calcaneus," Med. Eng. Phys. **19**, 599–604 (1997).
[5]O. Umnova, K. Attenborough, H.-C Shin, and A. Cummings, "Deduction of tortuosity and porosity from acoustic reflection and transmission measurements on thick samples of rigid-porous materials," Appl. Acoust. **66**, 607–624 (2005).
[6]D. L. Johnson, J. Koplik, and R. Dashen, "Theory of dynamic permeability and tortuosity in fluid saturated porous media," J. Fluid Mech. **176**, 379–402 (1987).
[7]Y. Champoux and J.-F. Allard, "Dynamic tortuosity and bulk modulus in air-saturated porous media," J. Appl. Phys. **70**, 1975–1979 (1991).

Retrieving the Green's function in an open system by cross correlation: A comparison of approaches (L)

Kees Wapenaar[a] and Jacob Fokkema
Department of Geotechnology, Delft University of Technology, Delft, The Netherlands

Roel Snieder
Center for Wave Phenomena, Colorado School of Mines, Golden, Colorado 80401

(Received 11 March 2005; revised 7 July 2005; accepted 2 August 2005)

We compare two approaches for deriving the fact that the Green's function in an arbitrary inhomogeneous open system can be obtained by cross correlating recordings of the wave field at two positions. One approach is based on physical arguments, exploiting the principle of time-reversal invariance of the acoustic wave equation. The other approach is based on Rayleigh's reciprocity theorem. Using a unified notation, we show that the result of the time-reversal approach can be obtained as an approximation of the result of the reciprocity approach. © *2005 Acoustical Society of America.* [DOI: 10.1121/1.2046847]

PACS number(s): 43.20.Fn, 43.40.Ph, 43.60.Tj [RLW] Pages: 2783–2786

I. INTRODUCTION

Since the work of Weaver and Lobkis,[1,2] many researchers have shown theoretically and experimentally that the cross correlation of the recordings of a diffuse wave field at two receiver positions yields the Green's function between these positions. In most cases it is assumed that the diffuse wave field consists of normal modes (with uncorrelated amplitudes) in a closed system. Less attention has been paid to the theory of Green's function retrieval in arbitrary inhomogeneous open systems. Nevertheless, the first result stems from 1968, albeit for one-dimensional media, when Claerbout[3] showed that the seismic reflection response of a horizontally layered earth can be synthesized from the autocorrelation of its transmission response. Recently we generalized this to three-dimensional (3D) arbitrary inhomogeneous media.[4–6] Using reciprocity theorems of the correlation type, we showed in those papers that the cross correlation of transmission responses observed at the earth's free surface, due to uncorrelated noise sources in the subsurface, yields the full reflection response (i.e., the ballistic wave and the coda) of the 3D inhomogeneous subsurface. Weaver and Lobkis[7] followed a similar approach for a configuration in which the 3D inhomogeneous medium is surrounded by uncorrelated sources. Independently, Derode *et al.*[8,9] derived expressions for Green's function retrieval in open systems using physical arguments, exploiting the principle of time-reversal invariance of the acoustic wave equation. Their approach can be seen as the "physical counterpart" of our derivations based on reciprocity. In this letter we compare the time-reversal approach of Derode *et al.*[8,9] with our approach based on Rayleigh's reciprocity theorem.[4–6] Using a unified notation, we show that the result of the time-reversal approach can be obtained as an approximation of the result of the reciprocity approach.

It should be noted that in both derivations we consider the situation of impulsive point sources, uniformly distributed over a surface surrounding the configuration. We briefly indicate how the resulting expressions can be modified for the situation of uncorrelated noise sources.

II. TIME-REVERSAL APPROACH

In this section we summarize the time-reversal approach of Derode *et al.*[8,9] for deriving expressions for Green's function retrieval. Consider a lossless arbitrary inhomogeneous acoustic medium in a homogeneous embedding. In this configuration we define two points with coordinate vectors $\mathbf{x}_A$ and $\mathbf{x}_B$. Our aim is to show that the acoustic response at $\mathbf{x}_B$ due to an impulsive source at $\mathbf{x}_A$ [i.e., the Green's function $G(\mathbf{x}_B,\mathbf{x}_A,t)$] can be obtained by cross correlating passive measurements of the wave fields at $\mathbf{x}_A$ and $\mathbf{x}_B$ due to sources on a surface S in the homogeneous embedding. The derivation starts by considering another physical experiment, namely an impulsive source at $\mathbf{x}_A$ and receivers at $\mathbf{x}$ on S. The response at one particular point $\mathbf{x}$ on S is denoted by $G(\mathbf{x},\mathbf{x}_A,t)$. Imagine that we record this response for all $\mathbf{x}$ on S, revert the time axis, and feed these time-reverted functions $G(\mathbf{x},\mathbf{x}_A,-t)$ to sources at all $\mathbf{x}$ on S. The superposition principle states that the wave field at any point $\mathbf{x}'$ in S due to these sources on S is then given by

$$u(\mathbf{x}',t) \propto \oint_S \underbrace{G(\mathbf{x}',\mathbf{x},t)}_{\text{'propagator'}} * \underbrace{G(\mathbf{x},\mathbf{x}_A,-t)}_{\text{'source'}} d^2\mathbf{x}, \tag{1}$$

where $*$ denotes convolution and $\propto$ "proportional to." According to this equation, $G(\mathbf{x}',\mathbf{x},t)$ propagates the source function $G(\mathbf{x},\mathbf{x}_A,-t)$ from $\mathbf{x}$ to $\mathbf{x}'$ and the result is integrated over all sources on S. Due to the invariance of the acoustic wave equation for time-reversal, the wave field $u(\mathbf{x}',t)$ focuses for $\mathbf{x}'=\mathbf{x}_A$ at $t=0$. McMechan[10] exploited this property in a seismic imaging method which has become known as reverse time migration. Derode *et al.*[8,9] give a new interpretation to Eq. (1). Since $u(\mathbf{x}',t)$ focuses for $\mathbf{x}'=\mathbf{x}_A$ at $t=0$, the

[a]Electronic mail: c.p.a.wapenaar@citg.tudelft.nl

wave field $u(\mathbf{x}',t)$ for arbitrary $\mathbf{x}'$ and t can be seen as the response of a virtual source at $\mathbf{x}_A$ and $t=0$. This virtual source response, however, consists of a causal and an anticausal part, according to

$$u(\mathbf{x}',t) = G(\mathbf{x}',\mathbf{x}_A,t) + G(\mathbf{x}',\mathbf{x}_A,-t). \tag{2}$$

This is explained as follows: the wave field generated by the anticausal sources on S first propagates to all $\mathbf{x}'$ where it gives an anticausal contribution, next it focuses in $\mathbf{x}_A$ at $t=0$, and finally it propagates again to all $\mathbf{x}'$ giving the causal contribution. The propagation paths from $\mathbf{x}'$ to $\mathbf{x}_A$ are the same as those from $\mathbf{x}_A$ to $\mathbf{x}'$, but are traveled in opposite direction. Combining Eqs. (1) and (2), applying source-receiver reciprocity to $G(\mathbf{x},\mathbf{x}_A,-t)$ in Eq. (1), and setting $\mathbf{x}'=\mathbf{x}_B$ yields

$$G(\mathbf{x}_B,\mathbf{x}_A,t) + G(\mathbf{x}_B,\mathbf{x}_A,-t) \propto \oint_S G(\mathbf{x}_B,\mathbf{x},t) * G(\mathbf{x}_A,\mathbf{x},-t)d^2\mathbf{x}. \tag{3}$$

The right-hand side of Eq. (3) can be interpreted as the integral of cross correlations of observations of wave fields at $\mathbf{x}_B$ and $\mathbf{x}_A$, respectively, due to impulsive sources at $\mathbf{x}$ on S; the integration takes place along the source coordinate $\mathbf{x}$. The left-hand side is interpreted as the superposition of the response at $\mathbf{x}_B$ due to an impulsive source at $\mathbf{x}_A$ and its time-reversed version. Since the Green's function $G(\mathbf{x}_B,\mathbf{x}_A,t)$ is causal, it can be obtained from the left-hand side of Eq. (3) by taking the causal part. The reconstructed Green's function contains the ballistic wave as well as the coda due to multiple scattering in the inhomogeneous medium.

III. RECIPROCITY APPROACH

In this section we summarize our derivation based on Rayleigh's reciprocity theorem.[4–6] A reciprocity theorem relates two independent acoustic states in one and the same domain.[11,12] Consider an acoustic wave field, characterized by the acoustic pressure $p(\mathbf{x},t)$ and the particle velocity $v_i(\mathbf{x},t)$. We define the temporal Fourier transform of a space- and time-dependent quantity $p(\mathbf{x},t)$ as $\hat{p}(\mathbf{x},\omega) = \int \exp(-j\omega t)p(\mathbf{x},t)dt$, where j is the imaginary unit and ω the angular frequency. In the space-frequency domain the acoustic pressure and particle velocity in a lossless arbitrary inhomogeneous acoustic medium obey the equation of motion $j\omega\rho\hat{v}_i + \partial_i\hat{p} = 0$ and the stress-strain relation $j\omega\kappa\hat{p} + \partial_i\hat{v}_i = \hat{q}$, where ∂_i is the partial derivative in the x_i direction (Einstein's summation convention applies for repeated lowercase subscripts), $\rho(\mathbf{x})$ the mass density of the medium, $\kappa(\mathbf{x})$ its compressibility, and $\hat{q}(\mathbf{x},\omega)$ a source distribution in terms of volume injection rate density. We introduce two independent acoustic states, which will be distinguished by subscripts A and B, and consider the following combination of wave fields in both states: $\hat{p}_A\hat{v}_{i,B} - \hat{v}_{i,A}\hat{p}_B$. Note that these products in the frequency domain correspond to convolutions in the time domain. Rayleigh's reciprocity theorem is obtained by applying the differential operator ∂_i, according to $\partial_i\{\hat{p}_A\hat{v}_{i,B} - \hat{v}_{i,A}\hat{p}_B\}$, substituting the equation of motion and the stress-strain relation for states A and B, integrating the result over a spatial domain V enclosed by S with outward pointing normal vector $\mathbf{n}=(n_1,n_2,n_3)$ and applying the theorem of Gauss. This gives

$$\int_V \{\hat{p}_A\hat{q}_B - \hat{q}_A\hat{p}_B\}d^3\mathbf{x} = \oint_S \{\hat{p}_A\hat{v}_{i,B} - \hat{v}_{i,A}\hat{p}_B\}n_i d^2\mathbf{x}. \tag{4}$$

Since the medium is lossless, we can apply the principle of time-reversal invariance.[13] In the frequency domain time-reversal is replaced by complex conjugation. Hence, when $\hat{p}$ and $\hat{v}_i$ are a solution of the equation of motion and the stress-strain relation with source distribution $\hat{q}$, then $\hat{p}^*$ and $-\hat{v}_i^*$ obey the same equations with source distribution $-\hat{q}^*$ (the asterisk denotes complex conjugation). Making these substitutions for state A we obtain

$$\int_V \{\hat{p}_A^*\hat{q}_B + \hat{q}_A^*\hat{p}_B\}d^3\mathbf{x} = \oint_S \{\hat{p}_A^*\hat{v}_{i,B} + \hat{v}_{i,A}^*\hat{p}_B\}n_i d^2\mathbf{x}. \tag{5}$$

Next we choose impulsive point sources in both states, according to $\hat{q}_A(\mathbf{x},\omega) = \delta(\mathbf{x}-\mathbf{x}_A)$ and $\hat{q}_B(\mathbf{x},\omega) = \delta(\mathbf{x}-\mathbf{x}_B)$, with $\mathbf{x}_A$ and $\mathbf{x}_B$ both in V. The wave field in state A can thus be expressed in terms of a Green's function, according to

$$\hat{p}_A(\mathbf{x},\omega) = \hat{G}(\mathbf{x},\mathbf{x}_A,\omega), \tag{6}$$

$$\hat{v}_{i,A}(\mathbf{x},\omega) = -(j\omega\rho(\mathbf{x}))^{-1}\partial_i\hat{G}(\mathbf{x},\mathbf{x}_A,\omega), \tag{7}$$

where $\hat{G}(\mathbf{x},\mathbf{x}_A,\omega)$ obeys the wave equation

$$\partial_i(\rho^{-1}\partial_i\hat{G}) + (\omega^2/\rho c^2)\hat{G} = -j\omega\delta(\mathbf{x}-\mathbf{x}_A), \tag{8}$$

with propagation velocity $c(\mathbf{x}) = \{\kappa(\mathbf{x})\rho(\mathbf{x})\}^{-1/2}$; similar expressions hold for the wave field in state B. Substituting these expressions into Eq. (5) and using source-receiver reciprocity of the Green's functions gives

$$2\Re\{\hat{G}(\mathbf{x}_B,\mathbf{x}_A,\omega)\} = \oint_S \frac{-1}{j\omega\rho(\mathbf{x})}(\partial_i\hat{G}(\mathbf{x}_B,\mathbf{x},\omega)\hat{G}^*(\mathbf{x}_A,\mathbf{x},\omega) - \hat{G}(\mathbf{x}_B,\mathbf{x},\omega)\partial_i\hat{G}^*(\mathbf{x}_A,\mathbf{x},\omega))n_i d^2\mathbf{x}, \tag{9}$$

where $\Re$ denotes the real part. Note that the left-hand side is the Fourier transform of $G(\mathbf{x}_B,\mathbf{x}_A,t) + G(\mathbf{x}_B,\mathbf{x}_A,-t)$; the products $\partial_i\hat{G}\hat{G}^*$, etc., on the right-hand side correspond to cross correlations in the time domain. Expressions like the right-hand side of this equation have been used by numerous researchers (including the authors) for seismic migration in the frequency domain. Esmersoy and Oristaglio[14] explained the link with the reverse time migration method, mentioned in Sec. II. What is new (compared with migration) is that Eq. (9) is formulated in such a way that it gives an exact representation of the Green's function $\hat{G}(\mathbf{x}_B,\mathbf{x}_A,\omega)$ in terms of cross correlations of observed wave fields at $\mathbf{x}_B$ and $\mathbf{x}_A$. Note that, unlike in Sec. II, we have not assumed that the medium outside surface S is homogeneous. The terms $\hat{G}$ and $\partial_i\hat{G}$ under the integral represent responses of monopole and dipole sources at $\mathbf{x}$ on S; the combination of the two correlation products under the integral ensures that waves propagating outward from the sources on S do not interact with those propagating inward and vice versa. When a part of S is a free

surface on which the acoustic pressure vanishes, then the surface integral in Eq. (5) and hence in Eq. (9) need only be evaluated over the remaining part of S. Other modifications of Eq. (9), including the elastodynamic generalization, are discussed in Refs. 4–6. Van Manen and Robertsson[15] propose an efficient modeling scheme, based on an expression similar to Eq. (9).

Note that for the derivation of expressions (3) and (9) we assumed that impulsive point sources were placed on the surface S. This is the approach taken, e.g., by Bakulin and Calvert[16] in their experiment on virtual source imaging. Our derivation also holds for uncorrelated stationary noise sources on S whose source-time function satisfies $\langle N(\mathbf{x},t)*N(\mathbf{x}',-t)\rangle=\delta(\mathbf{x}-\mathbf{x}')C(t)$, where $\langle\cdot\rangle$ denotes a spatial ensemble average and $C(t)$ the autocorrelation of the noise (which is assumed to be the same for all sources). When the noise is distributed over the surface, the cross-correlation of the observations at $\mathbf{x}_A$ and $\mathbf{x}_B$ leads to a double surface integral. The delta function reduces this to the single surface integral in the theory presented here.[4–7,9,17] A further discussion is beyond the scope of this letter.

IV. COMPARISON

Equation (9) is an exact representation of the real part of the Green's function $\hat{G}(\mathbf{x}_B,\mathbf{x}_A,\omega)$. In comparison with Eq. (3), the right-hand side of Eq. (9) contains two correlation products instead of one. Moreover, each of the correlation products in Eq. (9) involves a monopole and a dipole response instead of two monopole responses. Last but not least, Eq. (9) is formulated in the frequency domain and Eq. (3) in the time domain.

First we discuss how we can combine the two correlation products in Eq. (9) into a single term. To this end we assume that the medium outside S is homogeneous, with constant propagation velocity c and mass density ρ. In the high frequency regime, the derivatives of the Green's functions can be approximated by multiplying each constituent (direct wave, scattered wave, etc.) by $-j(\omega/c)|\cos\alpha|$, where α is the angle between the pertinent ray and the normal on S. The main contributions to the integral in Eq. (9) come from stationary points on S.[17–19] At those points the ray angles for both Green's functions are identical (see also the example in Sec. V). This implies that the contributions of the two terms under the integral in Eq. (9) are approximately equal (but opposite in sign), hence

$$2\Re\{\hat{G}(\mathbf{x}_B,\mathbf{x}_A,\omega)\}\approx\frac{-2}{j\omega\rho}\oint_S\partial_i\hat{G}(\mathbf{x}_B,\mathbf{x},\omega)\hat{G}^*(\mathbf{x}_A,\mathbf{x},\omega)n_i d^2\mathbf{x}. \tag{10}$$

The accuracy of this approximation is demonstrated with a numerical example in Sec. V.

Our next aim is to express the dipole response $n_i\partial_i\hat{G}$ in terms of the monopole response $\hat{G}$. As explained earlier, this could be done by multiplying each constituent by $-j(\omega/c)|\cos\alpha|$. However, since α may have multiple values and since these values are usually unknown (unless the inhomogeneous medium as well as the source positions are accurately known), we approximate $n_i\partial_i\hat{G}$ by $-j(\omega/c)\hat{G}$, hence

$$2\Re\{\hat{G}(\mathbf{x}_B,\mathbf{x}_A,\omega)\}\approx\frac{2}{\rho c}\oint_S\hat{G}(\mathbf{x}_B,\mathbf{x},\omega)\hat{G}^*(\mathbf{x}_A,\mathbf{x},\omega)d^2\mathbf{x}. \tag{11}$$

This approximation is quite accurate when S is a sphere with very large radius so that all rays are normal to S (i.e., $\alpha\approx0$). In general, however, this approximation involves an amplitude error that can be significant, see the numerical example in Sec. V. However, since this approximation does not affect the phase it is considered acceptable for many practical situations. Transforming both sides of Eq. (11) back to the time domain yields Eq. (3) (i.e., the result of Derode *et al.*[8,9]), with proportionality factor $2/\rho c$.

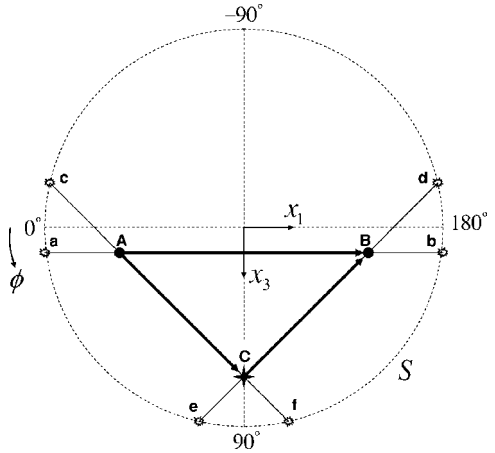

FIG. 1. Single point diffractor (C) in a homogeneous model. The receivers are at A and B. The numerical integration is carried out along the sources on the surface S. The main contributions come from the stationary points a–d. The contributions from stationary points e and f cancel.

V. NUMERICAL EXAMPLE

We illustrate Eq. (10) with a simple example. We consider a two-dimensional configuration with a single point diffractor at $(x_1,x_3)=(0,600)$m in a homogeneous medium with propagation velocity $c=2000$ m/s, see Fig. 1, in which C denotes the diffractor. Further, we define $\mathbf{x}_A=(-500,100)$m and $\mathbf{x}_B=(500,100)$m, denoted by A and B in Fig. 1. The surface S is a circle with its center at the origin and a radius of 800 m. The solid arrows in Fig. 1 denote the propagation paths of the Green's function $G(\mathbf{x}_B,\mathbf{x}_A,t)$. For the Green's functions in Eq. (10) we use analytical expressions, based on the Born approximation (hence, the contrast at the point diffractor is assumed to be small). To be consistent with the Born approximation, in the cross correlations we also consider only the zeroth- and first-order terms. Figure 2(a) shows the time-domain representation of the integrand of Eq. (10), convolved with a wavelet with a central frequency of 50 Hz. Each trace corresponds to a fixed source position $\mathbf{x}$ on S; the source position in polar coordinates is $(\phi,r=800)$. The sum of all these traces (multiplied by $rd\phi$) is shown in Fig. 2(b). This result accurately matches the time-domain version of the left-hand side of Eq. (10), i.e., $G(\mathbf{x}_B,\mathbf{x}_A,t)+G(\mathbf{x}_B,\mathbf{x}_A,-t)$, convolved with a wavelet, see

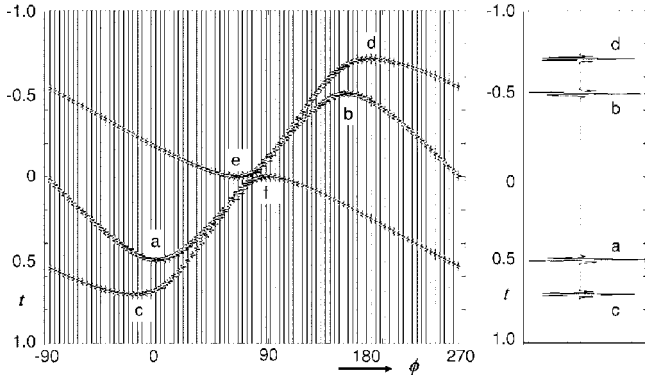

FIG. 2. (a) Time domain representation of the integrand of Eq. (10). (b) The sum of all traces in (a).

Fig. 3. The events labeled "a" and "c" in Fig. 2 are the direct and scattered arrivals; the events "b" and "d" are the corresponding anticausal arrivals. This figure clearly shows that the main contribution to these events come from Fresnel zones around the stationary points of the integrand.[17–19] The sources at these stationary points are marked in Fig. 1 with the same labels. We discuss event "c" in more detail. The path "cCB" in Fig. 1 represents the scattered wave in $G(\mathbf{x}_B,\mathbf{x},t)$, for $\mathbf{x}$ at the stationary point "c." The path "cA" represents the direct wave in $G(\mathbf{x}_A,\mathbf{x},t)$. By correlating these two waves, the travel time along the path "cA" is subtracted from that along the path "cCB," leaving the travel time along the path "ACB," which corresponds to the travel time of the scattered wave in $G(\mathbf{x}_B,\mathbf{x}_A,t)$. This correlation result is indicated by "c" in Fig. 2(a) and the integral over the Fresnel zone around this point is event "c" in Fig. 2(b). The other events in Fig. 2(b) can be explained in a similar way. Finally, note that there are two more stationary points, indicated by "e" and "f" in Figs. 1 and 2(a), of which the contributions cancel each other.

The numerical evaluation of Eq. (11) for the same configuration yields the result represented by the dashed curve in Fig. 3. We observe that the travel time of the scattered wave is accurately captured by this equation, but the amplitude is overestimated (apparently the assumption $\alpha \approx 0$ is not fulfilled here). By increasing the radius of S to 10 000 m we obtained a result with Eq. (11) that again accurately matches the directly modeled wave field (not shown).

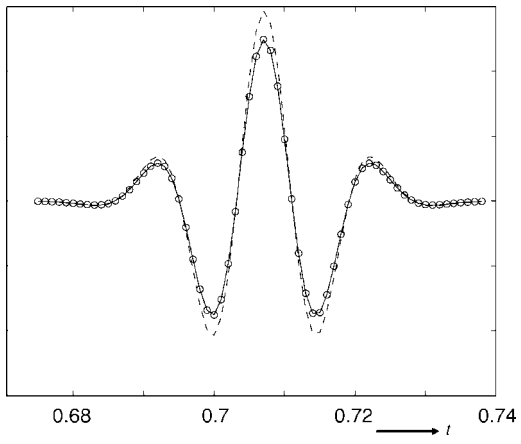

FIG. 3. Zoomed-in version of event c in Fig. 2(b). The solid line is the time-domain version of the left-hand side of Eq. (10). The circles represent the numerical integration result of the right-hand side of Eq. (10) [i.e., the sum of the traces in Fig. 2(a)]. The dashed line represents the numerical integration result of Eq. (11).

VI. CONCLUSIONS

In the literature several derivations have been proposed for Green's function retrieval from cross correlations of wave fields in inhomogeneous open systems. In this letter we compared a derivation based on the time-reversal approach[8,9] with one based on Rayleigh's reciprocity theorem.[4–6] One of the conclusions is that the expression obtained by the time-reversal approach is an approximation of that based on Rayleigh's reciprocity theorem.

[1] O. I. Lobkis and R. L. Weaver, "On the emergence of the Green's function in the correlations of a diffuse field," J. Acoust. Soc. Am. **110**, 3011–3017 (2001).

[2] R. L. Weaver and O. I. Lobkis, "Ultrasonics without a source: Thermal fluctuation correlations at MHz frequencies," Phys. Rev. Lett. **87**, 134301-1–134301-4 (2001).

[3] J. F. Claerbout, "Synthesis of a layered medium from its acoustic transmission response," Geophysics **33**, 264–269 (1968).

[4] K. Wapenaar, "Synthesis of an inhomogeneous medium from its acoustic transmission response," Geophysics **68**, 1756–1759 (2003).

[5] K. Wapenaar, "Retrieving the elastodynamic Green's function of an arbitrary inhomogeneous medium by cross correlation," Phys. Rev. Lett. **93**, 254301-1–254301-4 (2004).

[6] K. Wapenaar, D. Draganov, J. Thorbecke, and J. Fokkema, "Theory of acoustic daylight imaging revisited," Proceedings of the 72nd Annual SEG Meeting (Society of Exploration Geophysicists, Tulsa, 2002), pp. 2269–2272.

[7] R. L. Weaver and O. I. Lobkis, "Diffuse fields in open systems and the emergence of the Green's function (L)," J. Acoust. Soc. Am. **116**, 2731–2734 (2004).

[8] A. Derode, E. Larose, M. Campillo, and M. Fink, "How to estimate the Green's function of a heterogeneous medium between two passive sensors? Application to acoustic waves," Appl. Phys. Lett. **83**, 3054–3056 (2003).

[9] A. Derode, E. Larose, M. Tanter, J. de Rosny, A. Tourin, M. Campillo, and M. Fink, "Recovering the Green's function from field-field correlations in an open scattering medium (L)," J. Acoust. Soc. Am. **113**, 2973–2976 (2003).

[10] G. A. McMechan, "Migration by extrapolation of time-dependent boundary values," Geophys. Prospect. **31**, 413–420 (1983).

[11] A. T. de Hoop, "Time-domain reciprocity theorems for acoustic wave fields in fluids with relaxation," J. Acoust. Soc. Am. **84**, 1877–1882 (1988).

[12] J. T. Fokkema and P. M. van den Berg, *Seismic Applications of Acoustic Reciprocity* (Elsevier, Amsterdam, 1993).

[13] N. N. Bojarski, "Generalized reaction principles and reciprocity theorems for the wave equations, and the relationship between the time-advanced and time-retarded fields," J. Acoust. Soc. Am. **74**, 281–285 (1983).

[14] C. Esmersoy and M. Oristaglio, "Reverse-time wave-field extrapolation, imaging, and inversion," Geophysics **53**, 920–931 (1988).

[15] D.-J. van Manen, J. O. A. Robertsson, and A. Curtis, "Modeling of wave propagation in inhomogeneous media," Phys. Rev. Lett. **94**, 164301-1–164301-4 (2005).

[16] A. Bakulin and R. Calvert, "Virtual source: New method for imaging and 4D below complex overburden," Proceedings of the 74th Annual SEG Meeting (Society of Exploration Geophysicists, Tulsa, 2004), pp. 2477–2480.

[17] R. Snieder, "Extracting the Green's function from the correlation of coda waves: A derivation based on stationary phase," Phys. Rev. E **69**, 046610-1–046610-8 (2004).

[18] G. T. Schuster, J. Yu, J. Sheng, and J. Rickett, "Interferometric/daylight seismic imaging," Geophys. J. Int. **157**, 838–852 (2004).

[19] K. Wapenaar, D. Draganov, J. van der Neut, and J. Thorbecke, "Seismic interferometry: A comparison of approaches," Proceedings of the 74th Annual Meeting of the SEG (Society of Exploration Geophysicists, Tulsa, 2004), pp. 1981–1984.

On errors in estimating seabed scattering strength from long-range reverberation (L)

Charles Holland
Applied Research Laboratory, The Pennsylvania State University, State College, Pennsylvania 16804

(Received 29 April 2005; revised 9 August 2005; accepted 10 August 2005)

Shallow water acoustic reverberation is sometimes exploited to estimate properties of the seabed. In the process of estimating these properties, the scattering kernel (the dependence of the scattering on incident and scattered angle) is often assumed. That is, the scattering kernel is generally not known *a priori*. The errors associated with assuming an incorrect scattering kernel are explored and quantified for several types of scattering kernels. Choosing an incorrect scattering kernel can lead to significant errors in the frequency dependence of the estimated scattering strength. Finally, it is shown that the sonar equation approach for obtaining scattering strength from reverberation assumes that the scattering strength is independent of both incident and scattered angle. This assumption appears to be contrary to a large body of evidence that indicates the scattering strength decreases at low grazing angles. © *2005 Acoustical Society of America.* [DOI: 10.1121/1.2048947]

PACS number(s): 43.30.Pc, 43.30.Ma [RAS] Pages: 2787–2790

I. INTRODUCTION

Long-range reverberation in shallow water is sensitive to the properties of the seabed as well as the ocean volume and sea surface. In some environments, reverberation from the seabed may dominate the overall observed reverberation. Reverberation in such instances provides an attractive way to rapidly probe seabed properties. Numerous techniques have been developed that invert the seabed properties from the reverberation (e.g., Refs. 1–4 which is not intended to be an exhaustive list). The objective of this paper is to examine errors that may occur when *a priori* assumptions are made about the form of the scattering kernel.

II. THEORY

A variety of formulas have been developed for waveguide propagation[5] and reverberation[6,7] using ray invariants and acoustic flux. These formulas are useful to show the kinds of errors that may occur if the scattering kernel is guessed incorrectly. In general, the monostatic reverberation from a Pekeris waveguide can be written as

$$I = I_o \frac{1}{H^2 r} \frac{c\tau}{2} \int_0^{\theta_c} \int_0^{\theta_c} \int_{\psi-\gamma/2}^{\psi+\gamma/2} M(\theta_i, \theta_o, \phi) \times \exp(-\alpha r \theta_i^2/2H) \exp(-\alpha r \theta_o^2/2H) d\theta_i d\theta_o d\phi, \quad (1)$$

where I_o is the source intensity, r is the range, θ_c is the critical angle, ψ is the steering direction, γ is the horizontal beam width, c is the sound speed, τ is pulse length, H is water depth, and M is the scattering kernel which depends upon incoming and outgoing vertical angles, θ_i, θ_o and azimuthal angle ϕ. Finally α is the slope of the plane wave intensity reflection coefficient, R, where below the critical angle, $R \sim \exp(-\alpha\theta)$ (see Ref. 5).[8]

Solutions to Eq. (1) for various scattering kernels are given in Refs. 6 and 7. Reference 7 shows how the time (or range) dependent decay of the reverberation is a function of the scattering kernel, e.g., Lamberts law,

$$M = \mu \sin\theta_i \sin\theta_o, \quad (2)$$

leads to

$$I = I_o \frac{\mu}{\alpha^2 r^3} \frac{\gamma c \tau}{2} [1 - \exp(-\alpha r \theta_c^2/2H)]^2. \quad (3)$$

Reference 7 considers solutions to Eq. (1) for two other kinds of scattering kernels, a scattering function M independent of incoming and outgoing vertical angles,

$$M = \mu \quad (4)$$

and the Lommel-Seeliger scattering law,

$$M = \mu \sin\theta_i \sin\theta_o / (\sin\theta_i + \sin\theta_o). \quad (5)$$

The backscattering strength for these three scattering kernels is shown in Fig. 1. Many measurements of seabed scattering strength appear to roughly follow a Lommel-Seeliger law, Lambert's law or somewhere in between.[9–14] The reverberation intensity for these three scattering kernels can be written as

$$I = I_o \frac{\mu\varepsilon}{\alpha^m r^{m+1}} \frac{\gamma c \tau}{2} \left(\frac{\pi}{2H}\right)^{2-m} \{[1 - \exp(-\alpha r \theta_c^2/2H)]^{2m-2} \times [\mathrm{erf}(\sqrt{\alpha r \theta_c^2/2H})]^{2(2-m)}\} \quad (6)$$

which is a generalization of results in Ref. 7 where parameter m represents the scattering kernel, $m=1$ corresponds to angle-independent scattering, $m=3/2$ corresponds to the Lommel-Seeliger law, and $m=2$ corresponds to Lambert's law. The variable $\varepsilon = 1 - \log[\mathrm{sqrt}(2)+1]/\mathrm{sqrt}(2)$ when $m=3/2$, otherwise $\varepsilon=1$. Note that Ref. 7 is in error by a factor of 2 for the case of $m=3/2$ [see Eq. (35) in Ref. 7] and that there is a typographical error in the definition of ε. Equation (6) is exact for $m=1,2$ and is a very good approximation when $m=3/2$.[15]

Equation (6) is a simple but useful way to understand the relationship between seabed properties and the observed reverberation. In order to extract the seabed properties from a

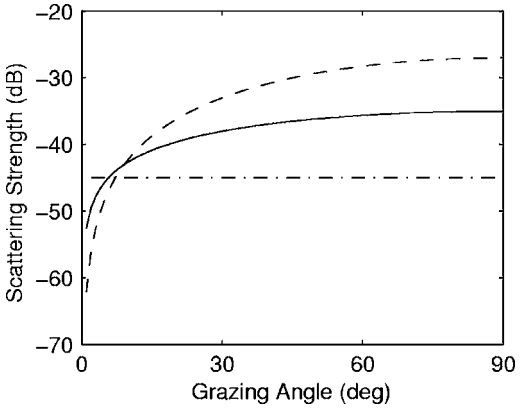

FIG. 1. Comparison of various scattering kernels: Lambert's law (dashed), Lommel-Seeliger (solid), and angle-independent (dashed-dotted). The scattering strengths are −27, −32, and −45 dB, respectively.

reverberation measurement, four fundamental properties of the seabed must be recovered, the angular dependence of the scattering kernel M (which of course may or may not be one of these scattering kernels) the scattering coefficient, μ, the reflection parameter α and the critical angle θ_c.

Two general approaches to estimating seabed properties from reverberation data will be addressed here. The standard sonar equation approach developed by Urick[1] and used by others (e.g., Ref. 2) is to measure transmission loss and then estimate the scattering coefficient μ. In the other approach, the reverberation is exploited to solve for the scattering coefficient μ and reflection parameter α and θ_c (e.g., Refs. 3 and 4) which equivalently may take the form of a geoacoustic model or a reflection coefficient. It is the intent of this paper to clarify the assumptions about the scattering kernel M in both approaches and to show how those assumptions may lead to biases in the resulting seabed parameters.

III. ESTIMATION OF μ: URICK (OR SONAR EQUATION) APPROACH

Urick[1] developed a method for estimating the bottom scattering strength from measured reverberation and transmission loss. In the context of the above expressions, transmission loss (TL) observations essentially contain information about the reflection coefficient parameter, α. Urick derived an expression for monostatic reverberation intensity which can be written as

$$I = I_o \delta^2 \frac{c\tau}{2} \mu \gamma r, \tag{7}$$

where I_o is the source intensity, δ is a transmission factor from the source to the scattering patch [$-10\log_{10}(\delta)$ is the one-way transmission loss]. Sometimes it is written in its sonar equation form,

$$\mathrm{RL} = \mathrm{SL} - 2\,\mathrm{TL} + \mathrm{BSS} + 10\log_{10}(A), \tag{8}$$

where RL is received level, SL is source level, TL is transmission loss, BSS is scattering strength, and A is insonified area, in this case equal to $c\tau\gamma r/2$.

The attraction of this sonar equation approach is its simplicity. Given a measurement of reverberation and transmission loss, one can immediately produce an estimate of μ. However, we pose the question, what is the assumed underlying form of the scattering kernel? It is the author's opinion that many in the community have (incorrectly) interpreted μ in Eq. (7) and BSS in Eq. (8) as having an arbitrary angular dependence. However, Eqs. (7) and (8) for waveguide propagation[16] are only valid under the assumption that the scattering strength is independent of angle. We can show this by substituting an expression for δ from a Pekeris waveguide,[7]

$$\delta = \sqrt{\frac{2\pi}{H\alpha r^3}}\,\mathrm{erf}(\theta_c\sqrt{\alpha r/2H}) \tag{9}$$

into Eq. (7) to obtain the expression for monostatic reverberation intensity as

$$I = I_o \frac{2\pi}{H\alpha r^2}\frac{c\tau}{2}\mu\gamma[\mathrm{erf}(\sqrt{\alpha r\theta_c^2/2H})]^2 \tag{10}$$

which is identical to the expression for reverberation with angle-independent scattering [see Eq. (6)] when the incident field on the seabed is assumed to be the full field [i.e., in Eq. (25) of Ref. 7 $Q^2=4$, rather than one-half the full field, $Q^2=1$].

Given that the Urick approach assumes an angle-independent scattering kernel, we wish to determine if that assumption is reasonable and what kind of biases it would create if the scattering kernel were something different. For the former, it is noted that an angle-independent scattering kernel seems unlikely, given measurements to date of backscatter from the seabed (e.g., Refs. 9–14). The implications of this are that estimates of μ using the Urick approach may be incorrect both as to the level and the frequency dependence (discussed below).

The bias error introduced when angle-independent scattering [Eq. (4)] is assumed but when the scattering kernel is not angle independent can be quantified for a few representative cases using Eq. (6).[17] For example, if the correct scattering law for the seabed in a given area was well represented by Lambert's law, but the Urick approach was used, the relationship between the estimated, μ_{Urick} and the true scattering strength μ_{Lambert} would be

$$\mu_{\mathrm{Lambert}} = \mu_{\mathrm{Urick}} 4\frac{\pi\alpha r}{2H}\frac{[\mathrm{erf}(\sqrt{\alpha r\theta_c^2/2H})]^2}{[1-\exp(-\alpha r\theta_c^2/2H)]^2} \tag{11}$$

and if the true scattering kernel were represented by Lommel-Seeliger, μ_{LS} then

$$\mu_{\mathrm{LS}} \cong \mu_{\mathrm{Urick}}\frac{4}{\varepsilon}\sqrt{\frac{\pi\alpha r}{2H}}\frac{\mathrm{erf}(\sqrt{\alpha r\theta_c^2/2H})}{1-\exp(-\alpha r\theta_c^2/2H)}, \tag{12}$$

where the factor of 4 comes from the assumption in the Urick approach that the incident field on the seabed is equal to the full field. Note that the final factor in Eqs. (11) and (12) is ~1 in the long range limit (roughly greater than 20 water depths). Inspection of these two equations shows that the estimated scattering strength from the Urick approach contains a bias that is a function of frequency (since α is generally a function of frequency, e.g., Ref. 6, Fig. 1), and also a function of range.

The range dependence of the bias may not be easily observable, that is, typically a limited time window is taken for estimating μ_{Urick} so that the bias may be small. For example, in Ref. 2, μ_{Urick} was obtained from ranges from 3.5 to 10 km. If Lommel-Seeliger scattering were the underlying scattering kernel, then there would be only a maximum of ±1 dB difference relative to fitting an angle-independent scattering kernel over that entire range. For Lambert scattering, the maximum difference would be ±2 dB. Given that reverberation data exhibit rapid fluctuations in time/range, these small differences in the rate of decay would probably not be detectable.

The frequency bias is expected to be more significant. The frequency dependence in Eqs. (11) and (12), is contained in α. For a homogeneous fluid sediment half-space, α is independent of frequency since the reflection coefficient is independent of frequency. However, given the natural variability of the seabed (e.g., layering and roughness) the reflection coefficient and hence α is in general expected to be frequency dependent. The frequency dependence of α in a given environment will depend upon many factors including the attenuation and sound speed profile in the seabed, and roughness. Experimental observations indicate that α tends to increase with increasing frequency. For example, in Ref. 6, the frequency dependence of α for 11 different environments varies roughly from an $f^{1/2}$ to f^2 dependence; for several environments α varies roughly linearly with frequency. Unpublished results from the author (using transmission loss data) in several shallow water environments also indicate a nearly linear frequency dependence. While other frequency dependencies are possible, a linear dependence is explored here to give a rough idea of the magnitude of errors that might be expected.

As a concrete example of the kinds of errors that can occur, the biases predicted in Eqs. (11) and (12) are computed for a specific range [5 km (Ref. 18)] and environment, water depth=100 m, $\alpha=\kappa f$ where f is frequency in kHz and $\kappa=2$ rad^{-1} kHz^{-1} and $\theta_c=25°$. If the true scattering followed the Lommel-Seeliger law and the scattering strength was nearly independent of frequency (solid line in Fig. 2), the biased estimate using the Urick (or sonar equation) approach, μ_{Urick}, would be that shown by the chain-dashed line. If the scattering followed Lambert's law (dashed line in Fig. 2), the biased estimate using the Urick approach would again be that shown by the chain-dashed line. In summary, μ_{Urick} may badly bias the true frequency dependence of the scattering strength μ. If α is a monotonic increasing function of frequency, μ_{Urick} will always increase with frequency more slowly than either μ_{Lambert} or μ_{LS} [see Eqs. (11) and (12)].

IV. JOINT ESTIMATION OF μ AND α

Another method of obtaining seabed properties from reverberation data is to estimate both μ and α simultaneously (e.g., Refs. 3 and 4). In this method, the scattering law M is chosen *a priori*. Various scattering laws have been chosen in various approaches, but the most widely assumed form of the scattering kernel is Lambert's law. For a Pekeris waveguide, the error in the case of an assumed Lambert's law, where the scattering actually followed the Lommel-Seeliger law would be in the long-range limit,

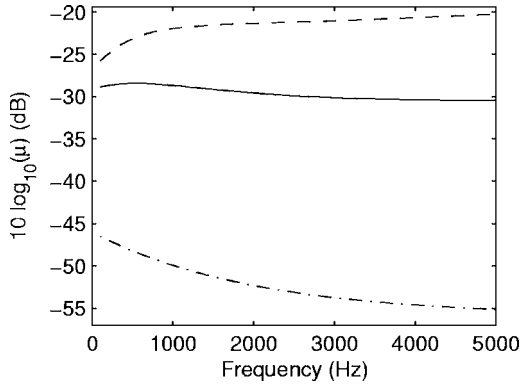

FIG. 2. The scattering coefficient μ for the same reverberation at a fixed range (5 km) showing biases associated with an incorrect assumption of the scattering law [see Eqs. (11) and (12)]. If the true scattering strength followed Lommel-Seeliger law (solid line), then the biased estimate assuming angle-independent scattering (Urick approach) would be the chain dashed line. The biased estimate assuming Lambert's law would be given by the dashed line. Likewise if the true scattering strength followed Lamberts law, then the biased estimate assuming angle-independent scattering (Urick approach) would be the chain dashed line and the biased estimate assuming Lommel-Seeliger law would be the solid line. At other ranges, the frequency dependence of the dashed and solid curves would be identical, but shifted in level [see Eqs. (11) and (12)].

$$\mu_{\text{LS}} = \mu_{\text{Lambert}} \sqrt{\frac{2H}{\pi r}} \frac{\alpha_{\text{true}}^{3/2}}{\alpha_{\text{Lambert}}^2} \varepsilon^{-1}, \tag{13}$$

where α_{Lambert} is the estimated value of α (which may or may not be the true value α_{true}). If α_{Lambert} has the correct frequency dependence and monotonically increases with frequency, then μ_{Lambert} will increase more rapidly with frequency than the true scattering strength. In other words, if the scattering kernel is "flatter" with angle than the assumed Lambert's law, the bias in the estimated scattering strength will increase with frequency.

In most instances, the scattering strength would be estimated at ranges such that the long-range limit would be satisfied and Eq. (13) can be employed. In cases where this condition is not met, the error in assuming Lambert's law depends also on errors in the estimated critical angle, $\theta_{c\_\text{Lambert}}$,

$$\mu_{\text{LS}} = \mu_{\text{Lambert}} \sqrt{\frac{2H}{\pi r}} \frac{\alpha_{\text{true}}^{3/2}}{\alpha_{\text{Lambert}}^2} \varepsilon^{-1} \times \frac{[1-\exp(-\alpha_{\text{Lambert}} r\theta_{c\_\text{Lambert}}^2/2H)]^2}{[1-\exp(-\alpha_{\text{true}} r\theta_{c\_\text{true}}^2/2H)]\text{erf}(\sqrt{\alpha_{\text{true}} r\theta_{c\_\text{true}}^2/2H})}. \tag{14}$$

As a concrete example, if $\alpha_{\text{Lambert}}=\alpha_{\text{true}}$, $\theta_{c\_\text{Lambert}}=\theta_{c\_\text{true}}$ and $\alpha \sim 2f$ then the bias error is that shown in Fig. 2 for μ_{Lambert} versus μ_{LS}. The bias errors increase from ~3 dB at 100 Hz to ~10 dB at 4000 Hz.

V. CONCLUSION

Bias errors occur when estimating seabed properties from reverberation when the incorrect scattering kernel is

assumed. These errors were discussed and quantified for a Pekeris waveguide. On the one hand, it may be argued that these errors are not important because an incorrect scattering kernel with remaining parameters fitted to the reverberation curve will (by definition) reproduce the observed reverberation. However, this is only true if the fitted seabed parameters are used to predict reverberation under precisely the same environmental conditions and sonar settings (e.g., depth and vertical beam pattern).

If, on the other hand, the seabed parameters were used to predict reverberation in other environmental conditions (i.e., a different sound speed profile) and/or different sonar settings, the predictions could be quite incorrect since the angles (modes) probing the seafloor would sample a different angular region of the scattering kernel. In this case, the bias errors may be quite important. Another reason to examine the issue of errors is related to the emergence of seabed scattering databases. In a database, it is important that the parameters have some connection to the actual physical properties of the seabed so that the spatial variation of the parameters reflects the spatial variations in the seabed at least in a gross sense. Thus, the seabed parameters from reverberation data should accurately reflect the correct scattering law.

ACKNOWLEDGMENTS

The author gratefully acknowledges the support of the Office of Naval Research, Code OA 321.

[1]R. J. Urick, "Reverberation-derived scattering strength of the shallow sea bed," J. Acoust. Soc. Am. **48**, 392–397 (1970).
[2]P. G. Cable, K. D. Frech, J. C. O'Connor, and J. M. Steele, "Reverberation-derived shallow-water bottom scattering strength," IEEE J. Ocean. Eng. **22**, 534–540 (1997).
[3]J. R. Preston, D. D. Ellis, and R. C. Gauss, "Geoacoustic parameter extraction using reverberation data from the 2000 boundary characterization experiment on the Malta Plateau," IEEE J. Ocean. Eng. (to be published).
[4]M. Sundvik, E. Rabe, and M. Vaccaro, "Mapping seabed acoustic reflection and scattering coefficients using tactical sonar systems," MTS/IEEE Oceans 99 proceedings, 1999, Vol. **2**, pp. 1070–1075.
[5]D. E. Weston, "Intensity-range relations in oceanographic acoustics," J. Sound Vib. **18**, 271–287 (1971).
[6]J. Zhou, D. Guan, E. Shang, and E. Luo, "Long-range reverberation and bottom scattering strength in shallow water," Chinese J. Acoust. **1982**, 54–63 (1982).
[7]C. H. Harrison, "Closed-form expressions for ocean reverberation and signal excess with mode stripping and Lambert's law," J. Acoust. Soc. Am. **114**, 2744–2756 (2003).
[8]Note that in Zhou *et al.* (Ref. 6), the reflection parameter Q is defined based on the plane wave pressure reflection coefficient so that $Q=\alpha/2$. This Q should not be confused with the same symbol used in Ref. 7 to account for differences in the definition of the incident field on the seabed.
[9]K. V. Mackenzie, "Bottom reverberation for 530 and 1030 cps sound in deep water," J. Acoust. Soc. Am. **33**, 1498–1504 (1961).
[10]H. M. Merklinger, "Bottom reverberation measured with explosive charges fired deep in the ocean," J. Acoust. Soc. Am. **44**, 508–513 (1968).
[11]P. B. Schmidt, "Monostatic and bistatic backscattering measurements from the deep ocean bottom," J. Acoust. Soc. Am. **50**, 326–331 (1971).
[12]I. C. Smailes, "Bottom reverberation measurements at low grazing angles in the NE Atlantic and Mediterranean Sea," J. Acoust. Soc. Am. **64**, 1482–1486 (1978).
[13]C. W. Holland, R. Hollett, and L. Troiano, "A measurement technique for bottom scattering in shallow water," J. Acoust. Soc. Am. **108**, 997–1011 (2000).
[14]C. W. Holland, "Shallow water coupled scattering and reflection measurements," IEEE J. Ocean. Eng. **27**, 454–470 (2002).
[15]The approximation is worst at small values of the argument of the exponent, however, even at very small values of the argument, the error in the approximation is modest. For example, when the argument is $5e$-3, the difference between the approximation and the exact solution is less than 0.5 dB.
[16]Eqs. (7) and (8) do allow an arbitrary angular dependence for the scattering for a direct path geometry, i.e., single interaction with the seabed, but do not allow an arbitrary dependence for a waveguide propagation.
[17]We make the assumption in the following that there are no bias errors in estimating α and θ_c from the transmission loss. In practical cases, errors in α and θ_c may further add to the predicted errors.
[18]At this range, the long-range limit criteria (i.e., $\alpha r\theta_c^2/2H \gg 1$) is met at all frequencies except below a few hundred hertz. That is, above a few hundred hertz, the biases would be well estimated by setting the last terms in Eqs. (11) and (12) equal to unity.

Subspace algorithms for noise reduction in cochlear implants (L)

Philipos C. Loizou,[a] Arthur Lobo, and Yi Hu
Department of Electrical Engineering, University of Texas at Dallas, Richardson, Texas 75083-0688

(Received 28 March 2005; revised 22 August 2005; accepted 22 August 2005)

A single-channel algorithm is proposed for noise reduction in cochlear implants. The proposed algorithm is based on subspace principles and projects the noisy speech vector onto "signal" and "noise" subspaces. An estimate of the clean signal is made by retaining only the components in the signal subspace. The performance of the subspace reduction algorithm is evaluated using 14 subjects wearing the Clarion device. Results indicated that the subspace algorithm produced significant improvements in sentence recognition scores compared to the subjects' daily strategy, at least in stationary noise. Further work is needed to extend the subspace algorithm to nonstationary noise environments. © *2005 Acoustical Society of America.* [DOI: 10.1121/1.2065847]

PACS number(s): 43.66.Ts, 43.71.Ky [AJO] Pages: 2791–2793

I. INTRODUCTION

Several noise-reduction algorithms have been proposed for cochlear implant (CI) users (van Hoesel and Clark, 1995; Hamacher *et al.*, 1997; Wouters and Vanden Berghe, 2001). Most of these algorithms, however, were based on the assumption that two or more microphones were available. van Hoesel and Clark (1995) tested an adaptive beamforming technique with four Nucleus-22 implantees using signals from two microphones—one behind each ear—to reduce noise coming from 90° of the patients. Results indicated that adaptive beamforming with two microphones can bring substantial benefits to CI users in conditions for which reverberation is moderate, and only one source is predominantly interfering with speech. Adding, however, a second microphone contralateral to the implant is ergonomically difficult without requiring the CI users to wear headphones or a neckloop (bilateral implants might provide the means, but their benefit is still being investigated). Alternatively, monaural multimicrophone techniques can be used and such techniques are now becoming commercially available (e.g., BEAM in Nucleus devices).

In general, single-microphone noise reduction algorithms are more desirable and cosmetically more appealing than the algorithms based on multiple-microphone inputs. A few single-microphone noise-reduction strategies (Weiss, 1993; Hochberg *et al.*, 1992; Yang and Fu, 2005) have been proposed for cochlear implants, some of which were implemented on old cochlear implant processors based on feature extraction strategies (F0/F1/F2 and MPEAK strategies) and some of which were implemented on the latest processors. Weiss (1993) demonstrated that preprocessing the signal with a standard noise reduction algorithm could reduce the errors in formant extraction. The latest speech processors, however, are not based on feature extraction strategies but are based on vocoder-type strategies. Recently, Yang and Fu (2005) evaluated a spectral-subtractive algorithm using the latest implant processors. Significant benefits in sentence recognition were observed for all subjects with the spectral-subtractive algorithm, particularly for speech embedded in speech-shaped noise.

In brief, only a few studies (e.g., Yang and Fu, 2005) were conducted to investigate the benefits of preprocessing the noisy speech signal by a noise reduction algorithm and feeding the enhanced signal to implant listeners. In the present study we evaluate the performance of a subspace noise reduction algorithm that is used as a preprocessor for signal enhancement.

II. EXPERIMENT 1: EVALUATION OF SUBSPACE ALGORITHM

In this experiment, we investigate the potential benefits of first preprocessing the noisy signal with a noise reduction algorithm and then feeding the "enhanced" signal to the CI processor. For noise reduction, we use a custom subspace-based algorithm (Hu and Loizou, 2002).

A. Subjects

A total of 14 Clarion implant users participated in this experiment consisting of 9 Clarion CII patients and 5 Clarion S-series patients. The majority of the CII patients were fitted with the CIS strategy, and the S-series patients were fitted with the SAS strategy. All subjects had at least 1 yr of experience with their implant device (see Table I).

B. Subspace algorithm

The signal subspace algorithm was originally developed by Ephraim and Van Trees (1995) for white input noise and was later extended to handle colored noise (e.g., speech-shaped noise) by Hu and Loizou (2002). The underlying principle of the subspace algorithm is based on the projection of the noisy speech vector (consisting of, say, a segment of speech) onto two subspaces: the "signal" subspace and the "noise" subspace. The noise subspace contains only signal

[a]Address correspondence to Philipos C. Loizou, Ph.D., Department of Electrical Engineering, University of Texas at Dallas, P.O. Box 830688, EC 33, Richardson, Texas 75083-0688. Electronic mail: loizou@utdallas.edu; phone: (972) 883-4617; fax: (972) 883-2710.

TABLE I. Subject information.

Subject	Age	Implant	CI use (yr)	HINT score (quiet)
S1	41	Clarion CII	2	57
S2	26	Clarion CII	2	55
S3	39	Clarion CII	1	90
S4	41	Clarion CII	2	52
S5	70	Clarion CII	2	60
S6	55	Clarion CII	1	86
S7	58	Clarion CII	2	88
S8	66	Clarion CII	3	95
S9	38	Clarion CII	4	35
SS1	56	Clarion S series	1	60
SS2	45	Clarion S series	1	94
SS3	40	Clarion S series	1	55
SS4	52	Clarion S series	1	79
SS5	43	Clarion S series	1	80

components due to the noise, and the signal subspace contains primarily the clean signal. Therefore, an estimate of the clean signal can be made by removing the components of the signal in the noise subspace and retaining only the components of the signal in the signal subspace.

Let $\mathbf{y}$ be the noisy vector, and let $\hat{\mathbf{x}}=\mathbf{H}\mathbf{y}$ be an estimate of the clean signal vector, where $\mathbf{H}$ is a transformation matrix. The noise reduction problem can be formulated as that of finding a transformation matrix $\mathbf{H}$, which, when applied to the noisy vector, would yield the clean signal. After applying such a transformation to the noisy signal, we can express the error between the estimated signal $\hat{\mathbf{x}}$ and the true clean signal $\mathbf{x}$ as $\epsilon=\hat{\mathbf{x}}-\mathbf{x}=(\mathbf{H}-\mathbf{I})\mathbf{x}+\mathbf{H}\,\mathbf{n}$, where $\mathbf{n}$ is the noise vector. Since the transformation matrix will not be perfect, it will introduce some speech distortion, which is quantified by the first term of the error term, i.e., by $(\mathbf{H}\text{-}\mathbf{I})\mathbf{x}$. The second term $(\mathbf{H}\,\mathbf{n})$ quantifies the amount of noise distortion introduced by the transformation matrix. As the speech and noise distortion (as defined above) are decoupled, one can find the optimal transformation matrix $\mathbf{H}$ that would minimize the speech distortion subject to the noise distortion falling below a preset threshold. The solution to this constrained minimization problem for colored noise is given by (Hu and Loizou, 2002):

$$\mathbf{H_{opt}} = \mathbf{V^{-T}}\mathbf{\Lambda}(\mathbf{\Lambda}+\mu\mathbf{I})^{-1}\mathbf{V^{T}}, \tag{1}$$

where μ is a parameter (typical values for $\mu=1-20$), $\mathbf{V}$ is an eigenvector matrix, and $\mathbf{\Lambda}$ is a diagonal eigenvalue matrix obtained from the noisy speech vector (more details can be found in Hu and Loizou, 2002, 2003). In our implementation, we used a variable μ that took values in the range of 1 to 20 depending on the estimated short-term signal-to-noise ratio (see Hu and Loizou, 2003).

The above equation has the following interesting interpretation. The matrix $\mathbf{V^{T}}$ acts like a data-dependent transform and projects the noisy speech vector into the noise and signal subspaces. The diagonal matrix $\mathbf{\Lambda}(\mathbf{\Lambda}+\mu\mathbf{I})^{-1}$ multiplies the components of the signal in the signal subspace by a gain while zeroing out the components of the signal in the noise subspace. Finally, the matrix $\mathbf{V^{-T}}$ transforms back the projected signal, i.e., it acts like an inverse transform.

The implementation of the above signal subspace algorithm can be summarized into two steps. Step (1): For each frame of noisy speech ($\mathbf{y}$), use the above transformation given in Eq. (1) to obtain an estimate of the clean signal vector $\hat{\mathbf{x}}$, i.e., $\hat{\mathbf{x}}=\mathbf{H_{opt}}\mathbf{y}$. Step (2): Use the estimated signal $\hat{\mathbf{x}}$ as input to the CI processor.

The above estimator was applied to 4 ms duration frames of the noisy signal, which overlapped each other by 50%. The enhanced speech vectors were Hamming windowed and combined using the overlap and add approach. No voice activity detection algorithm was used in our approach to update the noise covariance matrix needed to compute the matrix $\mathbf{V}$. The noise covariance matrix was estimated using speech vectors from the initial silent frames of the sentences. Although this procedure for estimating the noise covariance matrix is adequate for stationary noise (such as the one used in this study), it is not adequate for nonstationary environments in which the background spectra (and consequently the noise covariance matrices) constantly change. In nonstationary environments (e.g., restaurant noise), the noise covariance matrix could be estimated and updated whenever a speech-absent segment is detected based on a voice activity detector or a noise-estimation algorithm.

C. Procedure

HINT sentences (Nilsson *et al.*, 1994) corrupted in +5 dB S/N speech-shaped noise (taken from the HINT database) were used for evaluation. Six lists (60 sentences) were processed offline in MATLAB by the subspace noise reduction algorithm. The processed sentences were presented directly to the subjects via the auxiliary input jack of their CI processor at a comfortable listening level. Subjects were fitted with their daily strategy. For comparative purposes, subjects were also presented with six different lists (60 sentences) of HINT sentences corrupted in +5 dB speech-shaped noise, i.e., unprocessed sentences. The presentation order of preprocessed and unprocessed sentences was randomized between subjects.

D. Results and discussion

The sentences were scored in terms of the percent of words identified correctly (all words were scored). Figure 1 shows the percent correct scores for all subjects. The mean score obtained with sentences preprocessed by the subspace algorithm was 44% correct, and the mean score obtained with unprocessed sentences was 19% correct. ANOVA (repeated measures) tests indicated that the sentence scores obtained with the subspace algorithm were significantly higher $[F(1,13)=33.1,\ p<0.0005]$ than the scores obtained with the unprocessed sentences. As can be seen from Fig. 1, most subjects benefited from the noise reduction algorithm. Subject's SS4 score, for instance, improved from 0% correct to 40% correct. Similarly, subjects' SS1 and SS2 scores improved from roughly 0% to 50% correct.

The above results indicate that the subspace algorithm can provide significant benefits to CI users in regard to the

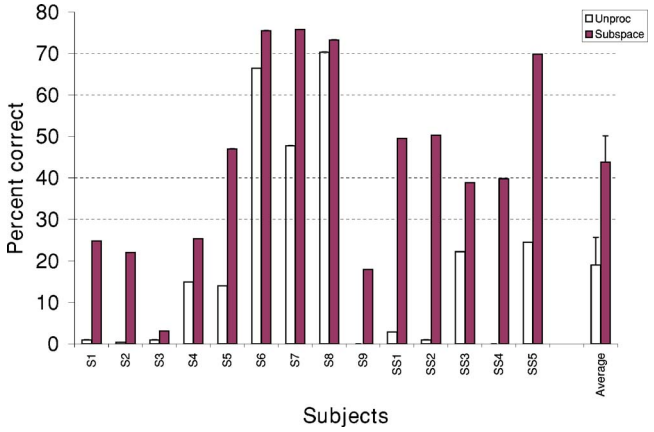

FIG. 1. (Color online) The subjects' performance on the identification of words in sentences embedded in +5 dB S/N speech-shaped noise and preprocessed (dark bars) by the subspace algorithm or left unprocessed (white bars). Subjects S1–S9 were Clarion CII patients and subjects SS1–SS5 were Clarion S-series patients. Error bars indicate standard errors of the mean.

recognition of sentences corrupted by stationary noise. It should be noted that the above signal subspace algorithm was only tested in stationary noise, and it is not clear whether such an intelligibility benefit would be maintained if the algorithm was tested in nonstationary environments (e.g., restaurant, multitalker babble). Further work is needed to extend the subspace algorithm to nonstationary noise environments, particularly with regard to updating the noise covariance matrix based on perhaps a voice activity detector or a noise-estimation algorithm.

ACKNOWLEDGMENTS

This research was supported by Grant No. R01-DC03421 from NIDCD/NIH. The authors would like to thank the anonymous reviewers and Dr. Andrew Oxenham for their valuable comments.

Ephraim, Y., and Van Trees H. L. (**1995**). "A signal subspace approach for speech enhancement," IEEE Trans. Speech Audio Process. **3**, 251–266.

Hamacher, V., Doering, W., Mauer, G., Fleischmann, H., and Hennecke, J. (**1997**). "Evaluation of noise reduction systems for cochlear implant users in different acoustic environments," Am. J. Otol. 18, S46–S49.

Hochberg, I., Boorthroyd, A., Weiss, M., and Hellman, S. (**1992**). "Effects of noise and noise suppression on speech perception by cochlear implant users," Ear Hear. **13**, 263–271.

Hu, Y., and Loizou P. (**2002**). "A subspace approach for enhancing speech corrupted with colored noise," IEEE Signal Process. Lett. **9**, 204–206.

Hu, Y., and Loizou, P. (**2003**). "A generalized subspace approach for enhancing speech corrupted with colored noise," IEEE Trans. Speech Audio Process. **11**, 334–341.

Nilsson, M., Soli, S., and Sullivan, J. (**1994**). "Development of the hearing in noise test for the measurement of speech reception thresholds in quiet and in noise," J. Acoust. Soc. Am. **95**, 1085–1099.

van Hoesel, R., and Clark, G. (**1995**). "Evaluation of a portable two-microphone adaptive beamforming speech processor with cochlear implant patients," J. Acoust. Soc. Am. **97**, 2498–2503.

Weiss, M. (**1993**). "Effects of noise and noise reduction processing on the operation of the Nucleus-22 cochlear implant processor," J. Rehabil. Res. Dev. **30**, 117–128.

Wouters, J., and Vanden Berghe, J. (**2001**). "Speech recognition in noise for cochlear implantees with a two-microphone monaural adaptive noise reduction system," Ear Hear. **22**, 420–430.

Yang, L., and Fu, Q. (**2005**). "Spectral subtraction-based speech enhancement for cochlear implant patients in background noise," J. Acoust. Soc. Am. **117**, 1001–1004.

Profile analysis: The effects of rove on sparse spectra (L)

Jennifer J. Lentz[a)]
Department of Speech and Hearing Sciences, Indiana University, 200 S. Jordan Avenue, Bloomington, Indiana 47405

(Received 28 July 2004; revised 25 July 2005; accepted 12 August 2005)

Profile-analysis thresholds were measured in the presence and absence of overall level variation at different stimulus levels to determine whether nonlinear changes in the shape of the edges of excitation pattern peaks contribute to poorer spectral-shape sensitivity observed under roving levels. Roving levels decreased sensitivity for stimuli having few components separated widely in frequency to a greater extent than for stimuli having more densely spaced components. The stimulus level did not influence sensitivity when overall level variation was absent, suggesting that listeners rely on peaks in the excitation patterns and not the edges of the peaks (as would have been predicted by the near miss to Weber's law). Because the edges of the peaks were not used in the absence of roving levels, it follows that the larger rove effects for sparse stimuli were not likely due to excitation pattern inconstancy. © *2005 Acoustical Society of America.* [DOI: 10.1121/1.2062187]

PACS number(s): 43.66.Fe, 43.66.Jh, 43.66.Ba [GDK] Pages: 2794–2797

I. INTRODUCTION

Experiments that test the ability of listeners to detect changes in the spectral shape of sound (profile-analysis experiments) have often included randomly altered stimulus levels on every presentation. Commonly referred to as "rove", this variation was meant to ensure that the level difference created by the spectral-shape change did not provide a confounding cue (e.g., Speigel *et al.*, 1981; Green *et al.*, 1983; Mason *et al.*, 1984; see Green, 1988 for a history). The few studies that have evaluated the effects of rove consistently have demonstrated better sensitivity in conditions that have no level randomization (Henn and Turner, 1990; Kidd *et al.*, 1991; Drennan and Watson, 2001). No study or model has fully accounted for this sensitivity decrease accompanying overall level variation.

It has been proposed that the decrease in sensitivity associated with rove might be due, in part, to: (1) elimination of intensity-based cues (Speigel *et al.*, 1981); (2) increased uncertainty (Drennan and Watson, 2001); and (3) adoption of different listening strategies (Lentz and Leek, 2002). Roving levels might also lead to varied shapes of the internal spectrum (i.e., the excitation pattern) at different levels through nonlinear changes in auditory filter shape with level (Mason *et al.*, 1984). Rather than the spectrally dense stimuli used by Mason *et al.* (1984), the following experiment employs spectrally sparse stimuli to determine whether the inconstancy of the shape of the internal spectrum on a presentation-by-presentation basis contributes to the decrease in spectral-shape sensitivity provided by level variation.

Stimuli with sparsely spaced components make strong candidates for establishing whether excitation pattern inconstancy leads to elevated thresholds in the presence of rove because the shape of their excitation patterns will vary more with level than stimuli having dense spectra. This reasoning is illustrated in Fig. 1, which shows normalized excitation patterns of multitonal stimuli created using the auditory filters described by Glasberg and Moore (1990). Stimuli are 3, 7, and 21 components equally spaced between 200 and 5000 Hz. Figure 1 indicates that the excitation patterns at the two levels for the three-component stimuli are rather different in shape (due to audibility and auditory filter nonlinearity). These differences are located primarily on the high-frequency edges of the peaks and in the valleys of the excitation pattern. The peaks themselves have very similar shapes at the two different stimulus levels. The differences between the 45 dB and 65 dB excitation patterns decrease as the number of components is increased, as can be seen in the 7- and 21-component excitation patterns (middle and right-hand side panels).

To the extent that the auditory system relies on the edges of the peaks in the excitation pattern to discriminate sounds with different spectral shapes (i.e., the entire excitation pattern is used when comparing stimuli), roving levels should have a larger effect on spectral-shape sensitivity for sparsely spaced spectra, and a smaller effect on sensitivity for densely spaced spectra. An auditory system which uses the entire excitation pattern to make discriminations should also exhibit improvements in the discrimination threshold at higher stimulus levels for conditions without rove. For intensity discrimination of tones, this result is known as the "near miss"

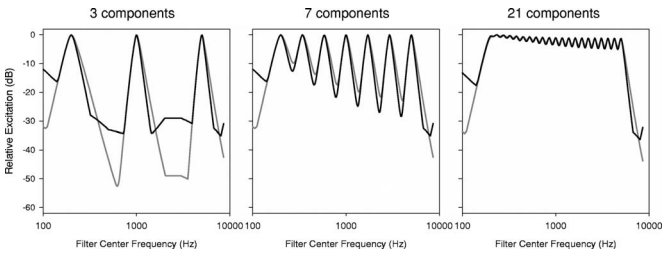

FIG. 1. Normalized excitation patterns for standard stimuli are shown at two different stimulus levels (45 dB SPL per component as the black line; 65 dB SPL per component as the gray line). 0 dB corresponds with the maximum excitation for each excitation pattern.

a)Electronic mail: jjlentz@indiana.edu

to Weber's law (e.g., Riesz, 1928; Viemeister, 1972; Moore and Raab, 1974; Jesteadt *et al.*, 1977), and is likely due to the auditory system placing a high importance on the high-frequency edge of the tonal excitation pattern where the change in excitation is greatest (McGill and Goldberg, 1968; Florentine and Buus, 1981). If excitation pattern inconstancy contributes to decreased sensitivity to spectral shape (implicating the edges of the excitation pattern in spectral-shape discrimination), the near miss to Weber's law should also be observed. Previous profile-analysis experiments showed no near miss (Mason *et al.* 1984; Green and Mason, 1985), but these experiments used spectrally dense profiles. Spectrally sparse stimuli should be tested to maximize the possibility of revealing behavior reflecting the near miss to Weber's law in profile-analysis tasks.

II. METHODS

A. Stimuli

The standard stimuli were the sum of 3, 5, 7, 11, 17, or 21 equal-amplitude sinusoids ranging from 200 to 5000 Hz, spaced equidistantly on a logarithmic scale, and rounded to the nearest 4 Hz. On each stimulus presentation, the starting phases of the component tones were selected randomly and independently from a uniform distribution ranging from 0 to 2π rad. The signal stimulus was generated by adding a 1000-Hz tone in phase to the 1000-Hz component of the standard stimulus. The signal strength is described as the signal level relative to the standard in dB, equal to $20\log(\Delta A/A)$, in which ΔA is the change in amplitude of the added tone relative to A, the mean amplitude of the component to which it was added. Three different stimulus levels were tested, in which the components had mean levels of 35, 55, and 75 dB SPL per component. Stimuli were generated digitally, played through one channel of a 24-bit digital-to-analog converter (TDT System III RP2.1) at a sampling rate of 4096×10^{-5} s (about 24 414 Hz). [1] The output was fed into the right headphone of a Sennheiser HD 250 II Linear headset. The stimuli were 200 ms in duration, including 30 ms cosine-squared rise/decay ramps.

Measurements were obtained both with and without across-interval level randomization (rove and no rove, respectively). When rove was applied, the overall levels of the stimuli were varied on every presentation through the use of an external attenuator. The value of the attenuator was randomly altered based on draws from a uniform distribution with a 20 dB range and a 0.1 dB gradation.

B. Procedure

A modified two-alternative forced-choice task was used to estimate thresholds, with trial-by-trial signal levels chosen according to a three-down, one-up adaptive tracking procedure estimating the 79% correct point on the psychometric function (Levitt, 1971). Observers were seated in a sound-attenuating room and heard the three sounds separated by 400 ms. The standard was always presented in the first interval. The signal and standard were presented in the second and third interval, the order of which was selected randomly with equal likelihood. Listeners indicated which interval contained the signal stimulus by responding with a button box. Feedback was provided to the listener following each trial.

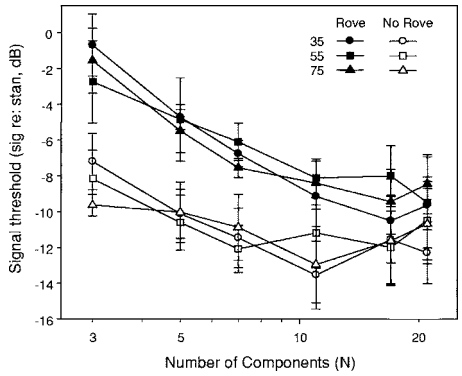

FIG. 2. Thresholds averaged across four listeners are plotted as a function of the number of stimulus components. Filled and unfilled symbols denote rove and no-rove data, respectively. The different symbols indicate thresholds obtained at three different stimulus levels: 35, 55, and 75 dB SPL per component. Error bars are standard errors of the mean.

At the beginning of every track, the mean level of the signal tone was set to 10 or 15 dB above an estimate of the listener's final threshold. The initial step size of the tracking procedure was 4 dB, and after three reversals the step size was reduced to 2 dB. The mean of the signal levels at the last six reversal points (from a total of nine) was taken as threshold.

C. Observer characteristics and order of data collection

Four normal-hearing listeners, ranging in age from 21 to 30 years, participated. All listeners had pure tone audiometric thresholds less than 15 dB HL between 250 and 8000 Hz. All observers were naïve to psychoacoustic experiments.

Observers received at least 2 h of practice on various experimental conditions before data collection began. After practice, a randomized block design was used to collect 12 threshold estimates per condition. For each observer, stimulus level, number of components (N), and rove type were chosen at random. Four threshold estimates were obtained for the condition selected, and then four estimates were obtained for the other rove type. A new N was selected randomly, and after all Ns were tested for the rove and no-rove types, a new randomly chosen stimulus level was selected, and the process repeated. After four thresholds were obtained in all conditions, four new thresholds were estimated with the conditions run in reverse order, and a final set of four thresholds estimates was collected with conditions in their original order. Thresholds reported here represent the average of the last eight threshold estimates in each condition.

III. RESULTS

Figure 2 shows thresholds averaged across the four listeners as a function of the number of components. Sensitivity consistently improves from $N=3$ to $N=21$. The rove data indicate a larger change in threshold than the no-rove data between $N=3$ and 21 (7.5 dB for rove and 2.8 dB for no

rove). Rove thresholds are always higher than the no-rove thresholds at the same N, indicating poorer sensitivity in the rove conditions. All rove thresholds are below the detection limit that would be expected if listeners used only intensity cues for a single component (+2 dB; Green, 1988), indicating that listeners used only spectral-shape cues in the rove conditions.

A repeated-measures ANOVA with three within-subjects factors—rove type, number of components, and stimulus level—was used to establish the main effects and interactions in the data set. Two significant main effects were revealed by the ANOVA: Sensitivity was poorer for the rove condition than for the no-rove condition [$F(1,3)=187.86$; $p<0.001$], and sensitivity generally improved with increasing numbers of components [N; $F(5,15)=3.60$; $p<0.03$]. A two-way interaction between rove type and N [$F(5,15)=4.33$; $p<0.02$] suggests that the main effect of N is dominated by data in the rove condition, with the rove data reflecting greater improvements in sensitivity with increasing N (7.5 versus 2.8 dB). The data of Henn and Turner (1990) and Kidd *et al.* (1991) directly contrast this finding; their studies showed a similar change in threshold with increasing N for rove and no-rove conditions. In both of their studies, increasing numbers of components led to increases in the stimulus bandwidth and not spectral density. Here, the stimulus bandwidth was fixed, and increases in N led to increases in spectral density. The different effects present between Kidd *et al.*'s (1991) data set and the current data set suggest that rove impacts sparsely spaced stimuli to a greater extent than densely spaced stimuli. A significant three-way interaction [$F(10,30)=2.70$; $p<0.02$] was also revealed.

In Fig. 2, the data obtained at the different levels overlap greatly, indicating no effect of stimulus level on sensitivity [$F(2,6)=0.09$; $p=0.9$] and, therefore, no evidence for the near miss to Weber's law. However, it was anticipated that behavior reflecting the near miss to Weber's law might be evident only for very sparse stimuli (e.g., N of 3, 5, or 7) for the no-rove conditions. Even at these small Ns, no-rove sensitivity is similar regardless of the stimulus level tested, and better performance at higher stimulus levels was only observed with the three-component stimulus where thresholds were 2.4 dB higher for the 35 dB stimulus than for the 75 dB stimulus. The absence of the near miss to Weber's law is not consistent with a hypothesis that the auditory system relies on changes in excitation at the edges of the peaks in the excitation pattern to detect a spectral change. It seems more likely that only the peaks in the excitation pattern are used for discrimination.

IV. DISCUSSION

The results of the current experiment indicate that rove decreased the sensitivity to changes in spectral shape more for sparsely spaced stimuli than for densely spaced stimuli. The near miss to Weber's law also was not generally observed in no-rove conditions for sparsely spaced stimuli. This result implies that the auditory system does not greatly rely on the edges of peaks to make spectral-shape discriminations in no-rove conditions. A logical consequence of that result is that even when rove is not present, the peaks of the excitation pattern are primarily used for spectral-shape discrimination. Because it seems unlikely that roving levels would encourage the use of the peak edges (as these are loci of unreliable information), it also follows that the poorer sensitivity to changes in spectral shape under roving levels is not due to changing shapes of the edges of the excitation patterns. Thus, the larger effects of rove for sparse stimuli may be due to the greater availability of single-channel intensity cues for those stimuli.

Because reliance on the various cues that are available in no-rove conditions would lead to different patterns of threshold versus N, it can be determined which cues are used by listeners for this task. First, the difference in overall level between two stimuli with different spectral shapes could cue the spectral-shape change. Second, the change in level within the critical band of a single component might also cue a spectral-shape difference, and finally, a spectral-shape cue is also present. The use of each of these cues leads to different predictions regarding the shape of the function relating no-rove thresholds to N and also the effects of rove as a function of N.

First, most profile-analysis data collected in the absence of roving levels are inconsistent with an overall level cue. In their seminal profile-analysis paper, Spiegel *et al.* (1981) argued that listeners must have been using a spectral-shape cue, even in the absence of roving levels, because sensitivity was too good to be explained by overall intensity cues alone. Also, for stimuli in which the spectral-shape change is created by incrementing the level of a component, increasing the number of stimulus components necessitates a greater increment to maintain a constant criterion for detection. As more and more tones are added to the stimulus, the single increment (and therefore threshold) would have to increase to produce a constant change in overall level. In direct contrast to this prediction, spectral-shape discrimination data measured in the absence of roving levels indicate that thresholds decrease with increasing N (Henn and Turner, 1990; Kidd *et al.*, 1991).

Second, if the decision variable is based on the change in level within the critical band of the signal component and additional stimulus components are ignored (i.e., single-channel intensity cues), sensitivity would be independent of N under no-rove conditions (e.g., Green, 1992). However, the typically observed increase in sensitivity with increasing N in the absence of rove also suggests that, while listeners might use a single-channel level cue to some degree, it is not the only cue present in no-rove conditions. Lentz and Leek (2002) found support for this interpretation and argued that both single-channel and spectral-shape cues are used in the absence of rove.

If listeners use multiple cues in the absence of rove, it is expected that rove could differentially impact spectral-shape discrimination thresholds at various Ns. When rove is absent, increasing N leads to an increase in the reliability of a spectral-shape cue, and consequently, an increase in sensitivity. With this improved sensitivity comes a decrease in the strength of the single-channel level cue, and listeners might be required to rely less on that level cue. Then, when roving

levels are imposed on these stimuli, the level cue is rendered unreliable and listeners are forced to use only the spectral-shape cue. If the single-channel auditory cue were more available for the stimuli with few components, it would be anticipated that rove would decrease sensitivity for the stimuli with fewer components by a greater amount.

However, in contrast to the differential effects of rove observed in this experiment, Henn and Turner (1990) and Kidd *et al.* (1991) found similar effects of rove for all *N*. Therefore, differences between the stimulus designs of the three studies may have encouraged the differential use of single-channel cues in the current experiment, but not in Henn and Turner's and Kidd *et al.*'s experiments under no-rove conditions. The major difference between the present experiment and Henn and Turner (1990) and Kidd *et al.*'s (1991) studies is that, here, increases in the number of components led to increasing spectral density, whereas in the other experiments increasing *N* led to a wider stimulus bandwidth. The greatest contrast among the studies is apparent for the stimuli with few components. The frequency ratios of the three-component stimulus are 5, 1.38, and 1.175 for the current experiment, Henn and Turner's experiment, and Kidd *et al.*'s experiment, respectively. The wider frequency spacing used in the current experiment may have encouraged listeners to rely on single-channel level cues to a greater extent than the other experiments. Spectral separation of frequency components may allow a tone to be perceived as separate from a complex stimulus. Moore and Ohgushi (1993) have shown that the resolvability of components will affect whether a listener can perceive a stimulus component as being separate from a complex stimulus. When components are more closely spaced, it is much more difficult for listeners to perceive the tone as separate. However, when components are spaced distantly in frequency, the perception of tonal separation is clearer. For the sparse stimuli used in the current experiment, the separation between tones is much larger than used by either Henn and Turner and Kidd *et al.* Therefore, listeners (while not necessarily consciously perceiving the 1000 Hz tone as being separate from the other tones) are better able to use the intensity change of that component than when the stimuli are spectrally dense.

The relative contribution of the single-channel, overall level, and spectral-shape cues could differ depending on stimulus construction, range of rove, and strength of the spectral-shape cue. It appears, then, that a portion of the increase in threshold due to roving levels might be attributed to the contribution of single-channel intensity-based cues in the no-rove conditions. It is likely that these cues may influence sparsely spaced stimuli to a greater extent than densely spaced stimuli.

V. SUMMARY AND CONCLUSIONS

The current experiment indicated that roving levels decreased sensitivity to spectral shape more for stimuli with sparse spectra than for stimuli with dense spectra. In addition, stimulus level had little effect on spectral-shape discrimination thresholds. Taken together, these results suggest that the auditory system selectively uses peaks in the excitation pattern for discrimination, and that changes in the shape of the excitation pattern at different levels do not contribute to elevated thresholds due to rove. Greater availability of single-channel intensity cues for stimuli with sparse spectra than for stimuli with dense spectra might account for the larger effects of rove on sparse stimuli.

ACKNOWLEDGMENTS

This work was supported by Grant No. DC 005825 from the National Institute on Deafness and Communication Disorders. The author thanks T. Beth Trainor-Hayes, Jamie Vittum, and Melissa Ferrello for assistance during data collection. Dr. Marjorie Leek, Dr. Virginia Richards, and Dr. Michael Akeroyd also provided helpful comments on this manuscript. Software used to generate the Glasberg and Moore (1990) excitation patterns in MATLAB was developed by Jens Appell, Carl-von-Ossietzky-Universitat, Germany.

[1]The TDT RP2.1 does not generate aliased stimuli below the sampling rate, eliminating the need for an antialiasing filter.

Drennan, W. R. and Watson, C. S. (**2001**). "Sources of variation in profile analysis. II: Component spacing, dynamic changes, and roving level," J. Acoust. Soc. Am. **110**, 2498–2504.

Florentine, M. and Buus, S. (**1981**). "An excitation-pattern model for intensity discrimination," J. Acoust. Soc. Am. **70**, 1646–1654.

Glasberg, B. R. and Moore, B. C. J. (**1990**). "Derivation of auditory filter shapes from notched-noise data," Hear. Res. **47**, 103–138.

Green, D. M. (**1988**). *Profile Analysis: Auditory Intensity Discrimination* (Oxford University Press, New York).

Green, D. M. (**1992**). "The number of components in profile analysis tasks," J. Acoust. Soc. Am. **91**, 1616–1623.

Green, D. M., Kidd, G., Jr., and Picardi, M. C. (**1983**). "Successive versus simultaneous comparison in auditory intensity discrimination," J. Acoust. Soc. Am., **73**, 639–643.

Green, D. M. and Mason, C. R. (**1985**). "Auditory profile analysis: Frequency, phase, and Weber's law," J. Acoust. Soc. Am. **77**, 1155–1161.

Henn, C. C. and Turner, C. W. (**1990**). "Pure-tone increment detection in harmonic and inharmonic backgrounds," J. Acoust. Soc. Am. **88**, 126–131.

Jesteadt, W., Wier, C. C., and Green, D. M. (**1977**). "Intensity discrimination as a function of frequency and sensation level," J. Acoust. Soc. Am. **61**, 169–177.

Kidd, G., Jr., Mason, C. R., Uchanski, R. M., Brantley, M. A., and Shah, P. (**1991**). "Evaluation of simple models of auditory profile analysis using random reference spectra," J. Acoust. Soc. Am. **90**, 1340–1354.

Lentz, J. J. and Leek, M. R. (**2002**) "Decision strategies of hearing-impaired listeners in spectral shape discrimination," J. Acoust. Soc. Am. **111**, 1389–1398.

Levitt, H. (**1971**). "Transformed up-down methods in psychoacoustics," J. Acoust. Soc. Am. **49**, 467–477.

Mason, C. R., Kidd, G., Jr., Hanna, T. E., and Green, D. M. (**1984**). "Profile analysis and level variation," Hear. Res. **13**, 269–275.

McGill, W. J. and Goldberg, J. P. (**1968**). "Pure-tone intensity discrimination and energy detection," J. Acoust. Soc. Am. **44**, 576–581.

Moore, B. C. J. and RaabD. H.. (**1974**). "Pure-tone intensity discrimination: some experiments relating to the "near-miss" to Weber's law," J. Acoust. Soc. Am. **55**, 1049–1054

Moore, B. C. J. and Ohgushi, K. (**1993**) "Audibility of partials in inharmonic complex tones," J. Acoust. Soc. Am. **93**, 452–461.

Riesz, R. R. (**1928**). "Differential intensity sensitivity of the ear for pure tones," Phys. Rev. **31**, 867–875.

Spiegel, M. F., Picardi, M. C., and Green, D. M. (**1981**). "Signal and masker uncertainty in intensity discrimination," J. Acoust. Soc. Am. **70**, 1015–1019.

Viemeister, N. F. (**1972**) "Intensity discrimination of pulsed sinusoids," J. Acoust. Soc. Am. **51**, 1265–1269.

Phonation thresholds as a function of laryngeal size in a two-mass model of the vocal folds (L)

Jorge C. Lucero[a)]
Department of Mathematics, University of Brasília, Brasília 70910-900, Brazil

Laura L. Koenig[b)]
Haskins Laboratories, 300 George Street, New Haven, Connecticut 06511 and Long Island University, Brooklyn, New York 11201-8423

(Received 4 April 2005; revised 11 July 2005; accepted 29 August 2005)

This letter analyzes the oscillation onset-offset conditions of the vocal folds as a function of laryngeal size. A version of the two-mass model of the vocal folds is used, coupled to a two-tube approximation of the vocal tract in configuration for the vowel /a/. The standard male configurations of the laryngeal and vocal tract models are used as reference, and their dimensions are scaled using a single factor. Simulations of the vocal fold oscillation and oral output are produced for varying values of the scaling factor. The results show that the oscillation threshold conditions become more restricted for smaller laryngeal sizes, such as those appropriate for females and children. © *2005 Acoustical Society of America.* [DOI: 10.1121/1.2074987]

PACS number(s): 43.70.Aj, 43.70.Bk [DOS] Pages: 2798–2801

I. INTRODUCTION

The purpose of this letter is to analyze how phonation onset-offset conditions change according to laryngeal size, as in cases of phonation by men, women, and children. Since the biomechanical parameters of the vocal folds, the interaction between the vocal folds and airflow, and other terms of glottal aerodynamics depend on the anatomical dimensions of the glottis, variations of the oscillatory behavior of the vocal folds as functions of those dimensions might be expected. Such variations might influence the strategies for controlling voicing onset and offset during speech by women versus men, and might be important for understanding the development of laryngeal motor control in children.

In recent works, a version of the two-mass model of the vocal folds (Ishizaka and Flanagan, 1972) was used to simulate speech production of adults (Lucero and Koenig, 2005) and children (Lucero and Koenig, 2003) in the vicinity of an abduction gesture. The objective was to determine control strategies of voicing onset and offset used by speakers, and detect possible differences between female, male, and child speakers. There, an inverse dynamic approach was used, in which the model was fitted to collected speech records. The results showed that devoicing during the abduction-adduction gesture for /h/ is achieved by the combined action of vocal fold abduction, decrease of subglottal pressure, and increase of vocal fold tension. Each of these actions has the effect of inhibiting the vocal fold oscillation, suppressing it when reaching an offset threshold. Also, more restricted oscillation regions for women than for men were detected, probably as a consequence of their smaller laryngeal size.

To take a closer look at this result, the following sections will analyze the oscillation threshold conditions versus laryngeal dimensions. We remark that our goal is not to develop a new model or present detailed simulations of vocal output; rather, this letter is a brief analytical exercise to explore qualitative relations among laryngeal parameters in the well-established two-mass model of the vocal folds.

II. MODELS

The larynx is modeled using our version of the two-mass model (Lucero and Koenig, 2005), schematically shown in Fig. 1, coupled to a two-tube approximation of the vocal tract in configuration for the vowel /a/ (Titze, 1994). As in our previous work, the standard values of the models' parameters (Ishizaka and Flanagan, 1972; Titze, 1994) are used as reference for a male configuration. To vary their size, a single scaling factor β is used for all dimensions.[1] According to reported experimental data (Goldstein, 1980; Titze, 1989), an adult female configuration would then correspond to an approximate factor of $\beta=0.72$, and a 5-year-old configuration to $\beta=0.64$.

Masses are accordingly scaled by multiplying by β^3, to compensate for the volume change. For the tissue stiffness, a constant elasticity modulus is assumed for all sizes. In this case, the stiffness coefficient is directly proportional to the cross-sectional area of the tissues, and inversely proportional to their length. Hence, scaling of all dimensions by a factor β implies that stiffness is also scaled by this same factor (see also Titze and Story, 2002). We also incorporate a Q factor for the natural frequencies of the model (Ishizaka and Flanagan, 1972), which may be used to control its oscillation frequency. All masses are divided and stiffness coefficients are multiplied by Q. Finally, a constant damping ratio ξ of tissues is assumed for all sizes, which implies that the damping coefficient $r=2\xi\sqrt{mk}$ (where m is the mass and k is the stiffness coefficient) must be multiplied by β^2. The use of a single scaling factor for all dimensions and the assumptions of constant elasticity modulus and damping ratio are conve-

a)Electronic mail: lucero@mat.unb.br
b)Electronic mail: koenig@haskins.yale.edu

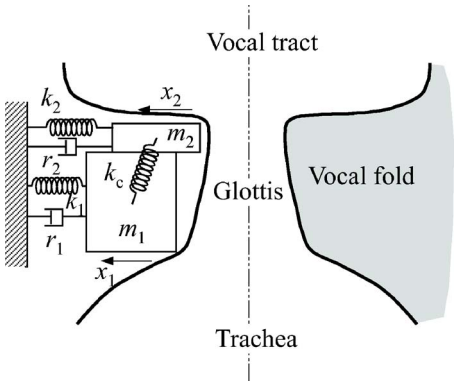

FIG. 1. Two-mass model of the vocal folds.

nient simplifications of the actual variations of size and tissue composition among men, women, and children (e.g., Hirano *et al.*, 1983; Titze, 1989). Such simplifications are justified by our intention to analyze the oscillatory behavior of the vocal folds versus laryngeal size qualitatively, rather than producing detailed simulations of vocal output.

Figure 2 shows plots of simulated oral airflow, as an example of the model's output. The simulations were obtained by varying the glottal half-width from 0.02 to 0.1 cm, and then back to the original value, following a sinusoidal pattern. This variation pattern imitates the glottal abduction-adduction gesture during the production of the utterance /aha/ in running speech (Lucero and Koenig, 2003, 2005). All other parameters were kept fixed at their standard values.

Comparing the plots, we see that the male flow has larger amplitude and lower fundamental frequency, as expected due to the larger size. As the size is reduced, the flow amplitude decreases because of the increased glottal resistance. Also, the oscillation frequency [computed from the ac component of the flow, as described in Lucero and Koenig (2005)] increases: From top to bottom, approximately 123, 165, and 187 Hz. Note that the oscillation frequency is

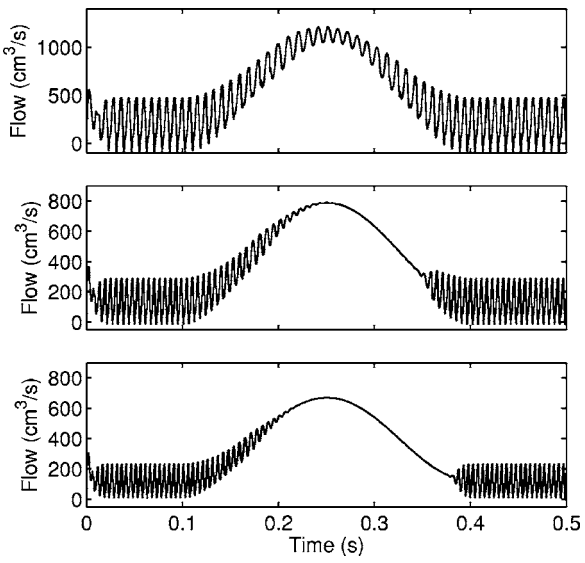

FIG. 2. Oral airflow patterns during a vocal fold abduction-adduction gesture. Top panel: $\beta=1$ (male adult), middle: panel $\beta=0.72$ (female adult), bottom panel: $\beta=0.64$ (5-year-old child).

$2\pi f=\sqrt{(\beta k)/(\beta^3 m)}=(\sqrt{k/m})/\beta$, and so it is inversely proportional to β. The frequency differences are actually smaller than expected, suggesting that the simplifications adopted leave out some aspects of the population differences. In the female case, the glottal pulses stop at the peak abduction, and restart at the end of the following adduction, in a clear oscillation hysteresis phenomenon. In the child case, the glottal pulses stop even earlier than the female case, at a lower value of the glottal width. The plots clearly show that the oscillation region becomes more restricted as the laryngeal size decreases.

III. STABILITY ANALYSIS

The dynamics of the two-mass model in the vicinity of its rest position has been analyzed in previous studies (e.g., Lucero, 1993; Steinecke and Herzel, 1995). According to the theory of dynamical systems (e.g., Perko, 1991), the stability of that position may be determined by taking the linear part of the equations of motion in its vicinity. Simplifying those equations by neglecting losses due to air viscosity, and assuming that the load presented by the vocal tract to the vocal folds is negligible, we find an equilibrium position at the rest position of the vocal folds. The linearized differential equations of the two-mass model around that position are

$$m_1\ddot{x}_1 + r_1\dot{x}_1 + (k_c + k_1)x_1 - k_c x_2 = \frac{2d_1 l_g P_s}{x_0}(x_1 - x_2),$$
$$m_2\ddot{x}_2 + r_2\dot{x}_2 + (k_c + k_2)x_2 - k_c x_1 = 0, \tag{1}$$

where m_i, with $i=1, 2$, are the masses, x_i are their horizontal displacements measured from a rest (neutral) position $x_0 > 0$, r_i are the damping coefficients, k_i and k_c are the stiffness coefficients, d_1 is the lower mass width, l_g is its length, and P_s is the subglottal pressure. Introducing the size scaling factor β and the Q factor, as explained earlier (i.e., doing the substitutions $m_i \to \beta^3 m_i/Q, r_i \to \beta^2 r_i, k_i \to \beta Q k_i, d_1 \to \beta d_1, l_g \to \beta l_g$) and computing the characteristic equation of this system, we obtai

$$\beta^4 s^4 + \beta^3 Q(\mu_1 + \mu_2)s^3 + \beta^2 Q^2(\omega_1^2 + \omega_2^2 + \mu_1\mu_2)s^2 + \beta Q^3(\mu_1\omega_2^2 + \mu_2\omega_1^2)s + Q^4(\omega_1^2\omega_2^2 - \kappa) = 0, \tag{2}$$

where $\mu_1=r_1/m_1$, $\mu_2=r_2/m_2$, $\omega_1^2=(k_1+k_c-\Gamma)/m_1$, $\omega_2^2=(k_2+k_c)/m_2$, $\kappa=k_c(k_c-\Gamma)/(m_1m_2)$, $\Gamma=2\beta d_1 l_g P_s/(Qx_0)$, and s is a complex variable.

Changing next the variable to $p=\beta s/Q$, the above noted characteristic equation simplifies to

$$p^4 + (\mu_1 + \mu_2)p^3 + (\omega_1^2 + \omega_2^2 + \mu_1\mu_2)p^2 + (\mu_1\omega_2^2 + \mu_2\omega_1^2)p + (\omega_1^2\omega_2^2 - \kappa) = 0. \tag{3}$$

This last polynomial equation has the general form $p^4 + a_1p^3 + a_2p^2 + a_3p + a_4 = 0$. According to the Routh-Hurwitz criterion (Ogata, 1970), a pair of complex roots cross the imaginary axis from left to right when

$$a_1a_2a_3 - a_3^2 - a_1^2a_4 = 0. \tag{4}$$

This fact signals the occurrence of a Hopf bifurcation, at which the rest position becomes unstable and a limit cycle is

produced, determining the onset threshold of the vocal fold oscillation. Equations (3) and (4) show that the onset threshold condition depends on the value of β only through $\Gamma(\beta)$: note that when substituting the values of the coefficients a_i in Eq. (4), Γ will appear within the expressions for ω_1 and κ; and further, that Γ will be the only factor related to β. For the standard values of the parameters (Ishizaka and Flanagan, 1972), Eq. (4) has a solution at $\Gamma_{\text{th}}=47.80$ N/m. Using also the standard values of d_1 and l_g, we have the threshold relation

$$\left.\frac{\beta P_s}{x_0 Q}\right|_{\text{threshold}} = 6.83 \times 10^5 \text{ N/m}^3. \quad (5)$$

This relation indicates that, for smaller larynges (smaller values of β), the threshold value of the subglottal pressure to start the vocal fold oscillation must be higher (larger P_s), or the vocal folds must be driven closer together (smaller x_0, or larger adduction), or the vocal fold tissues must be more relaxed (smaller Q). Let us also note that factor β appears in the expression for Γ due to the reduction in the medial surface of mass m_1, on which the air pressure acts (if this surface were constant, then the previous conclusions would be just the opposite). Hence, smaller larynges have more restricted phonation regions because their glottal surface is smaller, and so they absorb less energy from the airflow to fuel the vocal fold oscillation.

IV. PHONATION THRESHOLD PRESSURE

The analysis of Sec. III was done under the simplifying assumption of neglecting the effects of air viscosity and vocal tract loading. That simplification was necessary to permit the analytical treatment, and obtain the qualitative relation between size and main control parameters expressed by Eq. (5). However, the question naturally arises: what happens when the model's full equations are considered? We consider here the oscillation threshold for the subglottal pressure; similar results may be obtained for the thresholds on x_0 and Q.

To determine the oscillation threshold pressure, simulations of vocal fold oscillation were performed, while varying the subglottal pressure from 0 to 1000 Pa and back to 0 over a period of 1 s, following a sinusoidal curve as shown in Fig. 3. The simulations were done using both the complete equations of the model, as given in our previous work (Lucero and Koenig, 2005), and also a simplified version without the effects of air viscosity and the vocal tract, which matches the conditions adopted in the previous stability analysis.

From the simulated glottal airflow, the rms amplitude of its ac component was computed cycle-by-cycle, using a zero-crossing algorithm with low pass filtering (Titze and Liang, 1993). The oscillation onset was determined as the instant of time at which the rms flow amplitude increased above a threshold value of 1 cm^3/s. Similarly, the offset was determined as the instant of time at which the rms flow decreased below 1 cm^3/s.

Figure 4 shows the computed values of the oscillation thresholds for the subglottal pressure. We can see that there are two different levels of the thresholds, one for onset, and

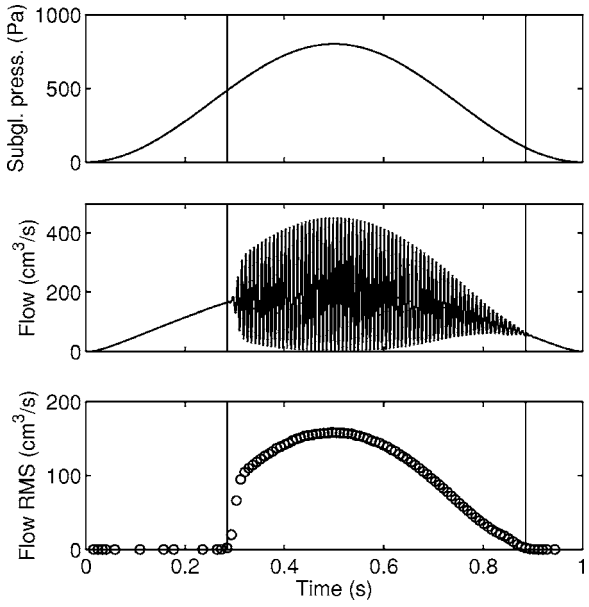

FIG. 3. Simulation results to compute the oscillation threshold value of subglottal pressure. Top panel: subglottal pressure, middle panel: glottal airflow, bottom panel: rms value of the ac glottal airflow. The left and right vertical lines mark the position of the oscillation onset and offset, respectively.

a lower value for offset. Both thresholds increase when the larynx size is reduced, as predicted by Eq. (5). The observed differences between the theoretical values from the stability analysis and simulated results for the same simplifying assumptions (the squares in the plot) come from two sources. One is the computing error inherent to the technique used to detect the thresholds, which overestimates the time of oscillation onset and underestimates the offset. Another source is the time-varying subglottal pressure, which is assumed constant in the stability analysis. It may be verified that the slower its rate of variation, the closer the simulated results are to the theoretical ones. We also note that the onset threshold is higher when using the full equations (circles in the

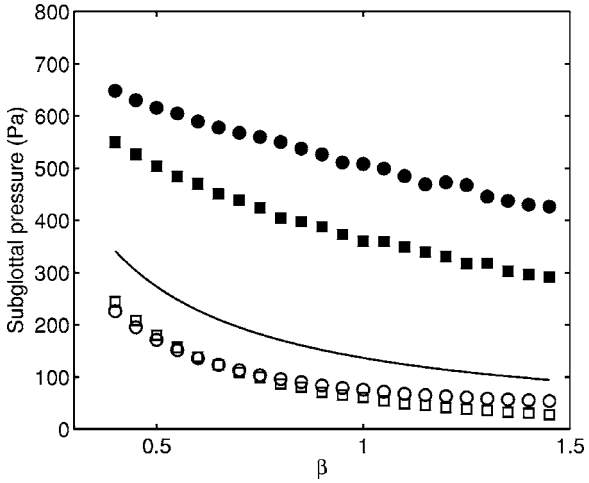

FIG. 4. Oscillation thresholds of subglottal pressure. Circles: thresholds when using the full equations of the model; squares: thresholds when neglecting the effects of air viscosity and the vocal tract. In both cases, the closed marks indicate the oscillation onset, and the open marks indicate the offset. Full line: value predicted by Eq. (5).

plot). One possible explanation is that pressure losses for air viscosity have the consequence of leaving less energy to fuel the oscillation, and therefore of increasing the onset threshold.

V. CONCLUSIONS

In general, the results show that the oscillation conditions of the vocal folds become more restricted as laryngeal size is reduced. This restriction seems to result from a reduction of the glottal area in contact with the airflow, where the energy is transferred from the flow to fuel the vocal fold oscillation. According to this result, women will have in general more restricted conditions for vocal fold oscillation due to a smaller laryngeal size. This would explain their larger occurrence of devoicing in glottal abduction-adduction gestures (Koenig, 2000). As the vocal folds are abducted, the offset threshold position would be easier to reach for women than men. Similarly, child vocal folds will have more restricted oscillation conditions than adults. This restriction could result in their higher values of subglottal pressures observed during speech (e.g., Stathopoulos and Sapienza, 1993; Stathopoulos and Weismer, 1985). In the literature, higher subglottal pressures in children have usually been attributed to higher resistances as a result of smaller airways, although Stathopoulos and Weismer (1985) also suggested that children may simply choose higher speaking volumes. Our results seem to offer a different explanation for the higher pressure values, or at least some motivation behind Stathopoulos and Weismer's suggestion: children may need those higher pressures to get phonatory patterns within acceptable perceptual limits.

The results also suggest the possibility of different strategies for speakers to achieve similar patterns of voicing offset-onset during speech. Equation (5) confirms the results of our previous paper (Lucero and Koenig, 2005), indicating that voice onset may be achieved by the combined action of glottal adduction, increase of subglottal pressure, and decrease of vocal fold tension (for voice offset, the actions are the opposite). Thus, speakers (within a size group) could adopt different vocal tract postures and adjust accordingly the vocal fold tension to arrive at the same phonatory result. Consistent with this hypothesis, our recent experiemntal data from women (Koenig *et al.*, 2005) provide evidence for interspeaker differences in voicing control.

We remark that the above-noted conclusions must be considered within the simplifying assumptions of the two-mass model. For example, the stability analysis assumes a constant subglottal pressure, independent of the glottal area. This simplification derives from a constant lung pressure and neglect of pressure variations in the subglottal airways. Recent works (Neubauer *et al.*, 2005) have detected a potentially significant influence of the subglottal system on the phonation thresholds, even suppressing onset-offset hysteresis effects. However, we believe that our main conclusions should hold in general qualitative terms, when using more sophisticated models. Certainly, the influence of the subglottal system on phonation is an interesting subject, which deserves further exploration.

ACKNOWLEDGMENTS

This work was supported by Grant No. DC-00865 from the National Institute on Deafness and Other Communication Disorders of the National Institutes of Health, CT-Info/MCT/CNPq and Finatec (Brazil). The results reported here were presented at the Fourth International Conference on Voice Physiology and Biomechanics (ICVPB) in Marseille, 18–20 August 2004.

[1]In our previous article (Lucero and Koenig, 2005), we used β as scaling factor from a female reference. We have here inverted the factor and adopt a male reference. This simplifies interpretation of the results, since the β values are directly proportional to laryngeal size.

Goldstein, U. (**1980**). "An articulatory model for the vocal tracts of growing children," Doctoral dissertation, Massachusetts Institute of Technology, Cambridge, MA.

Hirano, M., Kurita, S., and Nakashima, T. (**1983**). "Growth, development, and aging of human vocal folds," *Vocal Fold Physiology: Contemporary Research and Clinical Issues*, edited by D. M. Bless and J. H. Abbs (College-Hill, San Diego), pp 22–43.

Ishizaka, K., and Flanagan, J. L. (**1972**). "Synthesis of voiced sounds from a two-mass model of the vocal folds," Bell Syst. Tech. J. **51**, 1233–1268.

Koenig, L. L. (**2000**). "Laryngeal factors in voiceless consonant production in men, women, and 5-year-olds," J. Speech Lang. Hear. Res. **43**, 1211–1228.

Koenig, L. L., Mencl, W. E., and Lucero, J. C. (**2005**). "Multidimensional analysis of voicing offsets and onsets in female speakers," J. Acoust. Soc. Am. (in press).

Lucero, J. C. (**1993**). "Dynamics of the two-mass model of the vocal folds: Equilibria, bifurcations, and oscillation region," J. Acoust. Soc. Am. **94**, 3104–3111.

Lucero, J. C., and Koenig, L. L. (**2003**). "Simulations of VhV sequences in children," *Proceedings of the 15th International Congress on Phonetic Sciences*, pp. 2605–2608.

Lucero, J. C., and Koenig, L. L. (**2005**). "Simulations of temporal patterns of oral airflow in men and women using a two-mass model of the vocal folds under dynamic control," J. Acoust. Soc. Am. **117**, 1362–1372.

Neubauer, J., Zhang, Z., and Berry, D. (**2005**). "Effects of subglottal acoustics on phonation onset," J. Acoust. Soc. Am. **117**, 2542.

Ogata, K. (**1970**). *Modern Control Engineering* (Prentice-Hall, Englewood Cliffs), pp. 252–258.

Perko, L. (**1991**). *Differential Equations and Dynamical Systems* (Springer, New York).

Stathopoulos, E. T., and Sapienza, C. (**1993**). "Respiratory and laryngeal measures of children during vocal intensity variation," J. Acoust. Soc. Am. **94**, 2531–2543.

Stathopoulos, E. T., and Weismer, G. (**1985**). "Oral airflow and air pressure during speech production: A comparative study of children, youths and adults," Folia Phoniatr. **37**, 152–159.

Steinecke, I., and Herzel, H. (**1995**). "Bifurcations in an asymmetric vocal fold model," J. Acoust. Soc. Am. **97**, 1878–1884.

Titze, I. R. (**1989**). "Physiologic and acoustic differences between male and female voices," J. Acoust. Soc. Am. **85**, 1699–1707.

Titze, I. R. (**1994**). *Principles of Voice Production* (Prentice-Hall, Englewood Cliffs).

Titze, I. R., and Liang, H. (**1993**). "Comparison of F0 extraction methods for high-precision voice perturbation measurements," J. Speech Hear. Res. **36**, 1120–1133.

Titze, I. R., and Story, B. H. (**2002**). "Rules for controlling low-dimensional vocal fold models with muscle activation," J. Acoust. Soc. Am. **112**, 1064–1076.

A probability density function method for acoustic field uncertainty analysis

Kevin R. James and David R. Dowling[a)]
Department of Mechanical Engineering, University of Michigan, Ann Arbor, Michigan 48109-2133

(Received 10 March 2005; revised 15 August 2005; accepted 15 August 2005)

Acoustic field predictions, whether analytical or computational, rely on knowledge of the environmental, boundary, and initial conditions. When knowledge of these conditions is uncertain, acoustic field predictions will also be uncertain, even if the techniques for field prediction are perfect. Quantifying acoustic field uncertainty is important for applications that require accurate field amplitude and phase predictions, like matched-field techniques for sonar, nondestructive evaluation, bio-medical ultrasound, and atmospheric remote sensing. Drawing on prior turbulence research, this paper describes how an evolution equation for the probability density function (PDF) of the predicted acoustic field can be derived and used to quantify predicted-acoustic-field uncertainties arising from uncertain environmental, boundary, or initial conditions. Example calculations are presented in one and two spatial dimensions for the one-point PDF for the real and imaginary parts of a harmonic field, and show that predicted field uncertainty increases with increasing range and frequency. In particular, at 500 Hz in an ideal 100 m deep underwater sound channel with a 1 m root-mean-square depth uncertainty, the PDF results presented here indicate that at a range of 5 km, all phases and a 10 dB range of amplitudes will have non-negligible probability. Evolution equations for the two-point PDF are also derived. [DOI: 10.1121/1.2062269]

PACS number(s): 43.20.Bi, 43.20.Mv, 43.30.Bp [DKW] Pages: 2802–2810

I. INTRODUCTION

Acoustic predictions can be made using either analytical or numerical means, with the latter continually allowing more complicated environments and geometries to be tackled ([see Jensen *et al.* (1994)], for examples in underwater acoustics). However, even if perfect analytical or numerical techniques are used, or model and numerical errors are negligible, the accuracy of either analytic or numerical acoustic field predictions will be limited if the parameters describing the acoustic environment and the boundary or initial conditions used in the solution technique are uncertain. The effects that uncertain environmental, boundary, or initial conditions (hereafter referred to as input parameter uncertainties) have on predicted acoustic fields is not readily ascertained from the field prediction technique itself, and may depend in a complicated and nonlinear manner on the particular input parameters involved.

Quantifying the uncertainty in predicted acoustic fields produced by input parameter uncertainties is potentially important for any application of acoustics that relies on a field model to generate predictions. Such applications include matched-field techniques in sonar, nondestructive evaluation, bio-medical ultrasound, acoustic holography, and atmospheric and other types of remote sensing. In these applications, mismatch between actual acoustic propagation and predicted acoustic propagation may lead to erroneous results. Plus, recent studies [Sha and Nolte (2005a), (2005b)] have determined that sonar detection performance is degraded in uncertain environments. Given the accuracy of modern computational techniques, predicted-field uncertainty may dominate other sources of uncertainty, especially at higher frequencies and longer source-receiver ranges where input parameter uncertainties cause greater predicted-field uncertainties. Thus, an underlying assumption made here is that the interested acoustician has a means for predicting acoustic fields but may not have any means to assess the uncertainty of the predicted fields.

The primary purpose of this paper is to present a potentially useful means for quantifying predicted-field uncertainty arising from input parameter uncertainties. Here, uncertainty is quantified in terms of a probability density function (PDF), and this PDF's evolution equation is derived using mathematical identities developed from the relevant fine-grained PDF [Lundgren (1967)] and wave mechanics, in a manner similar to that developed for the study of turbulence [see Pope (2000)]. This PDF approach is new to acoustics and the examples presented here are meant to be illustrative, not exhaustive. Indeed, analyzing predicted-field uncertainty via PDFs is potentially challenging because the relationship between uncertain-input-parameter PDFs and the predicted-field PDFs may be complicated and nonlinear. Furthermore, the additional and possibly difficult task of determining *a priori* input-parameter PDFs is not addressed here. Thus, future investigations that surpass the one reported here will be necessary to determine the ultimate utility of these PDF techniques for quantifying predicted acoustic-field uncertainty.

The material presented here is a new application of the PDF transport formalism developed for turbulence and turbulent combustion. However, fundamental differences exist

a)Author to whom correspondence should be addressed.

between turbulence PDFs and those in acoustic uncertainty analysis. For example, the turbulent-velocity-fluctuation PDF is intended to statistically describe actual fluid velocity fluctuations. Hence, its form is constrained or limited by the nonlinear physical conservation laws for mass, momentum, and energy. In acoustic uncertainty analysis, the pressure-field PDF is intended to statistically describe the possible acoustic pressure fields that might arise from a set of input parameter uncertainties. In the acoustic case, each possible field obeys linearized versions of the conservation laws, but the input parameter uncertainties themselves are nearly unconstrained by conservation laws or other physical limits. Therefore, acoustic-field-uncertainty PDFs are inherently less constrained than turbulence PDFs. Although this may mean that acoustic-field-uncertainty PDFs will be even more elusive than turbulence PDFs, the prospects for developing effective PDF prediction techniques for acoustics might actually be better than that for turbulence because the underlying phenomena in the acoustic case are linear while turbulence is inherently nonlinear.

For the present discussion, random and uncertain acoustic environments are not the same. The goal of the research effort presented here is to quantify acoustic field uncertainties in primarily deterministic environments where one (or perhaps a few) input parameter(s) is (are) uncertain. To this end, one- and two-dimensional cases of ideal range-independent sound channels, each with a single uncertain scalar parameter, are presented in Secs. II and III. Acoustic propagation in random environments is different because it is likely to require many uncertain input parameters. Consider a random-depth range-dependent sound channel with constant average depth. Here, a randomly rough bottom with a finite horizontal correlation length would necessitate the inclusion of an uncertain parameter (depth, slope, etc.) for each range increment—for example, a roughness correlation length—between the source and receiver. Thus, this situation could entail many uncertain input parameters at long ranges. For comparison, the example in Sec. III involves a sound channel with a constant range-independent depth that is uncertain, a situation described by a single random variable for any source-receiver range.

Wave propagation in random media is commonly analyzed via moments of the acoustic (or electromagnetic) field and an extensive literature exists for field-moment equations for random media [see Uscinski (1977), Ishimaru (1978)]. It is conjectured that the PDF methods presented here can be formally connected to these established results when the uncertain input parameters are sufficiently numerous and appropriately distributed in space, and moments are extracted from the appropriate PDF evolution equation. However, proof of this conjecture is beyond the scope of this paper.

At least two other means for quantifying predicted-field acoustic uncertainty and its impact on signal processing have recently been reported. Sibul *et al.* (2004), using maximum entropy methods, discusses how randomness and uncertainty in the environmental, boundary, and source parameters affects the probability of detection of a narrowband sound source. Finette (2005) describes how uncertainty can be imbedded into ocean acoustic propagation models through expansions of the input parameter uncertainties in orthogonal polynomials. Both of these techniques, and the one described in this paper, hold the promise of significant computational efficiency compared to Monte Carlo simulations, the common and robust but computationally expensive means for assessing field statistics in uncertain or random media.

For simplicity, this paper only addresses the PDF equations for time harmonic fields at radian frequency ω. Thus, two probability variables must be considered, R and I, the real and imaginary parts of the predicted acoustic field, or A and Θ, the amplitude and phase of the predicted acoustic field. Here the former are emphasized over the later. An advantage of this PDF formulation of the predicted-field uncertainty is that a PDF carries more information than its first few moments alone. This advantage is particularly important because the PDF of R and I may depart drastically from joint-Gaussian even when the input parameter uncertainty is Gaussian distributed. Extension of this effort to broadband time-dependent pressure fields is possible but is not pursued here.

The remainder of this paper is divided into four sections. The next section presents the development of the predicted-field PDF transport equation in one spatial dimension. This equation is then solved for the case of uncertain wave number or sound speed. The third section extends the development to two spatial dimensions and a numerical solution for an ideal waveguide with uncertain depth is presented. The fourth section shows how the techniques presented in the first two sections can be extended to derive an equation for the two-point predicted-field PDF. The final section summarizes this effort, presents its conclusions, and describes possible extensions of this work.

II. PDF UNCERTAINTY ANALYSIS IN ONE SPATIAL DIMENSION

The purpose of this section is to illustrate how an evolution equation for the PDF of a predicted acoustic field can be obtained from the fine-grained PDF [Lundgren (1967)] and one-dimensional wave propagation relationships for harmonic waves. The resulting equation is then solved by direct analytical means for acoustic waves propagating in an ideal duct with uncertain wave number (or sound speed). Here, pressure has a harmonic time dependence with radian frequency ω, $p(x,t)=\mathrm{Re}\{\hat{p}(x)e^{-i\omega t}\}$ where $\hat{p}(x)=p_R(x)+ip_I(x)$, and x is the spatial coordinate. The PDF of interest is the one-point, joint PDF for the real and imaginary parts of the pressure, $f_P(R,I;x)$, where R and I are the probability sample space variables for the real and imaginary parts of the pressure. Throughout this paper the letter f with subscripts will denote a PDF. Capital-letter arguments will refer to probability space variables and lowercase-letter arguments will refer to field variables, spatial coordinates, or other parameters.

The evolution equation for $f_P(R,I;x)$ can be obtained by manipulating its fine-grained PDF, f_P, a function that can be thought of as a single realization in the infinite ensemble of trials represented by $f_P(R,I;x)$ [Lundgren (1967)]. In this paper, and in PDF transport work in turbulence [Pope (2000)] and turbulent combustion [Dopazo (1994)], the fine-

grain PDF plays the role of a generating function that can be transformed into $f_P(R,I;x)$ by computing its expected value. Here, the fine-grain PDF is written explicitly as a product of Dirac delta-functions,

$$\mathcal{f}_P = \delta(p_R - R)\,\delta(p_I - I), \tag{1}$$

and its expected value, denoted $\langle \mathcal{f}_P \rangle$, is

$$\begin{aligned}\langle \mathcal{f}_P \rangle &= \int_{-\infty}^{+\infty}\int_{-\infty}^{+\infty} \delta(\tilde{R}-R)\,\delta(\tilde{I}-I) f_P(\tilde{R},\tilde{I};x)\,d\tilde{R}\,d\tilde{I} \\ &= f_P(R,I;x).\end{aligned} \tag{2}$$

The properties of the fine-grained PDF and the structure of its arguments allow it to be the basis for constructing mathematical identities involving its derivatives with respect to the independent spatial and probability-space variables. These identities for $\mathcal{f}_P$ can be converted to identities for $f_P(R,I;x)$ by computing an expected value. Then, substitution for the pressure-field derivatives appearing in the identity for $f_P(R,I;x)$ from established wave-physics relationships produces an evolution equation for $f_P(R,I;x)$. This procedure is illustrated in the next few paragraphs of this section, and in the first few paragraphs of Secs. III and IV.

An important identity for the fine-grained PDF can be derived from Bayes' theorem for any function or variable b with probability space variable B:

$$\begin{aligned}\langle b\mathcal{f}_P \rangle &= \int_{-\infty}^{+\infty}\int_{-\infty}^{+\infty}\int_{-\infty}^{+\infty} B\,\delta(\tilde{R}-R)\,\delta(\tilde{I}-I) f_{BP}(B,\tilde{R},\tilde{I})\,dB\,d\tilde{R}\,d\tilde{I} \\ &= \int_{-\infty}^{+\infty} B f_{BP}(B,R,I)\,dB \\ &= f_P(R,I)\int_{-\infty}^{+\infty} B\frac{f_{BP}(B,R,I)}{f_P(R,I)}\,dB \\ &= f_P(R,I)\int_{-\infty}^{+\infty} B f_{B|P}(B|R,I)\,dB \\ &= f_P(R,I)\langle B|R,I\rangle\end{aligned} \tag{3}$$

[see Pope (2000)] where f_{BP} is the joint PDF of B, R, and I, and $f_{B|P}$ is the conditional PDF for B given values of R and I. Here the vertical bar denotes conditioning, i.e., $\langle B|R,I\rangle$ is the expected value of B given the information $p_R=R$ and $p_I=I$. This use of Bayes' theorem involves the higher-level distributions $f_{BP}(B,R,I)$ and $f_{B|P}(B|R,I)$, which may not be available in general. However, construction of these distributions and/or their moments may be possible when an analytical field model exists, as is shown in the remainder of this section. Alternatively, models for the requisite conditional moment $\langle B|R,I\rangle$ may be developed directly as is done in PDF work in turbulence [Pope (2000), Lou and Miller (2001), Waclawczyk *et al.* (2004)] and turbulent combustion [Dopazo (1994), Pope (2004), James *et al.* (2005)]. A general means for determining $f_{BP}(B,R,I)$ or its moments is beyond the scope of this paper.

For acoustic field uncertainty analysis, the most important relationships that can be obtained from the fine-grained PDF involve spatial derivatives. For example, partial differentiation with respect to the independent spatial variable x produces

$$\begin{aligned}\frac{\partial \mathcal{f}_P}{\partial x} &= \delta'(p_R - R)\frac{\partial p_R}{\partial x}\delta(p_I - I) + \delta(p_R - R)\,\delta'(p_I - I)\frac{\partial p_I}{\partial x} \\ &= -\frac{\partial \mathcal{f}_P}{\partial R}\frac{\partial p_R}{\partial x} - \frac{\partial \mathcal{f}_P}{\partial I}\frac{\partial p_I}{\partial x},\end{aligned} \tag{4}$$

an identity for $\mathcal{f}_P$. Here the prime denotes differentiation with respect to the argument. Taking the expected value of Eq. (4) and using Eq. (3) produces an identity for $f_P(R,I;x)$:

$$\begin{aligned}\left\langle \frac{\partial \mathcal{f}_P}{\partial x} \right\rangle = \frac{\partial f_P}{\partial x} &= \left\langle -\frac{\partial \mathcal{f}_P}{\partial R}\frac{\partial p_R}{\partial x} - \frac{\partial \mathcal{f}_P}{\partial I}\frac{\partial p_I}{\partial x} \right\rangle \\ &= -\frac{\partial}{\partial R}\left\langle \mathcal{f}_P \frac{\partial p_R}{\partial x} \right\rangle - \frac{\partial}{\partial I}\left\langle \mathcal{f}_P \frac{\partial p_I}{\partial x} \right\rangle \\ &= -\frac{\partial}{\partial R}\left(f_P \left\langle \frac{\partial p_R}{\partial x}|R,I \right\rangle \right) - \frac{\partial}{\partial I}\left(f_P \left\langle \frac{\partial p_I}{\partial x}|R,I \right\rangle \right).\end{aligned} \tag{5}$$

This identity can be converted into an evolution equation for $f_P(R,I;x)$ by introducing wave-propagation physics through the pressure derivatives. Here, unidirectional plane-wave $[\hat{p}(x) \propto e^{+ikx}]$ propagation relationships are used: $\partial p_R/\partial x = -kp_I$ and $\partial p_I/\partial x = +kp_R$, where $k=\omega/c$ is an uncertain wave number based on the uncertain speed of sound c. These relationships allow the conditional moments in Eq. (5) to be rewritten, $\langle \partial p_R/\partial x|R,I\rangle = \langle -kp_I|R,I\rangle = -I\langle k|R,I\rangle$ and $\langle \partial p_I/\partial x|R,I\rangle = \langle +kp_R|R,I\rangle = R\langle k|R,I\rangle$, so it is converted into an evolution equation for $f_P(R,I;x)$:

$$\frac{\partial f_P}{\partial x} = I\frac{\partial}{\partial R}(f_P\langle k|R,I\rangle) - R\frac{\partial}{\partial I}(f_P\langle k|R,I\rangle). \tag{6}$$

The remainder of this section presents a solution of Eq. (6) for the simple case of an acoustic source with uncertain amplitude and zero phase at $x=0$ that radiates plane waves in the positive x-direction along an ideal constant-cross-sectional area duct having a uniform but uncertain speed of sound. The first step is to rewrite the derivatives in Eq. (6) in terms of amplitude, $A=\sqrt{R^2+I^2}$, and phase Θ $(\tan\Theta = I/R)$ using $\partial/\partial R = (R/A)\partial/\partial A - (I/A^2)\partial/\partial\Theta$ and $\partial/\partial I = (I/A)\partial/\partial A + (R/A^2)\partial/\partial\Theta$ to find:

$$\frac{\partial f_P}{\partial x} = -\frac{\partial}{\partial\Theta}(f_P\langle k|R,I\rangle). \tag{7}$$

For a known input frequency, ω, the solution for $f_P(R,I;x)$ can be obtained in terms of the *a priori* PDFs for the uncertain wave number $f_K(K)$ and the uncertain amplitude $f_A(A)$. The initial condition on f_P is:

$$f_P(x=0) = \frac{1}{A} f_A(A)\,\delta(\Theta); \tag{8}$$

the factor of $1/A$ in Eq. (8) ensures the normalization: $\int\int f_P(x=0)\,A\,dA\,d\Theta = 1$.

The primary difficulty in solving Eq. (7) comes from relating the conditional expectation $\langle k|R,I\rangle$ to the other in-

dependent or dependent variables. For this simple case, $\langle k|R,I\rangle$ can be determined analytically in terms of Θ, x, and $f_K(K)$. Here, phases between 0 and $+2\pi$ are considered, and the range of the arctangent is set to $[0,\pi]$. The relationship between wave number and phase is thus

$$\Theta = \left\{ \begin{array}{ll} \tan^{-1}(I/R) & \text{for } I>0 \\ \tan^{-1}(I/R)+\pi & \text{for } I<0 \end{array} \right\} = \mathrm{mod}(kx, 2\pi). \tag{9}$$

Thus, for a given R and I, k must take one of the discrete values:

$$K_n = \frac{\Theta - 2\pi n}{x}, \quad n = 0, \pm 1, \pm 2, \ldots \tag{10}$$

so the conditional PDF of k, $f_{K|P}$, is a sum of δ-functions appropriately weighted by $f_K(K)$:

$$f_{K|P}(K|R,I) = \frac{\sum_n \delta(K-K_n) f_K(K_n)}{\sum_n f_K(K_n)}, \tag{11}$$

where the denominator factor merely provides the requisite normalization. The conditional expectation in Eq. (7) can be evaluated in terms of K_n and f_K using Eq. (11):

$$\langle k|R,I\rangle = \int_{-\infty}^{+\infty} K f_{K|P}(K|R,I)\,dK = \frac{\sum_n K_n f_K(K_n)}{\sum_n f_K(K_n)}. \tag{12}$$

Formally, the summation is over all possible n; however, only a finite number of the K_n occur where f_K is nonzero and this set of n is used in the summations.

The form of Eq. (12), with K_n providing the dominant combination of the independent variables x and Θ, motivates a solution to Eq. (7) based on the K_n as separate variables:

$$f_P = g(A,x)\sum_n h(K_n). \tag{13}$$

Here, g and h are unknown functions, and, as a recap: $A = \sqrt{R^2+I^2}$ is the pressure field amplitude, x is the lone spatial coordinate, and K_n is the nth possible wave number value at location x for a given value of R and I. Using Eq. (13), Eq. (7) becomes

$$\begin{aligned} \frac{\partial g}{\partial x}\sum_n h - \frac{g}{x}\sum_n K_n h' &= -g\frac{\partial}{\partial\Theta}\left(\langle k|R,I\rangle \sum_n h\right) \\ &= -\frac{g}{x}\frac{\partial}{\partial K_n}\left(\langle k|R,I\rangle \sum_n h\right), \end{aligned} \tag{14}$$

where derivative relationships, $\partial K_n/\partial x = -K_n/x$ and $\partial K_n/\partial\Theta = -1/x$, from Eq. (10) have been used as well. In Eq. (14), the unspecified dependence of $\langle k|R,I\rangle$ and the argument of h are both K_n, and $\partial/\partial K_n$ implies term by term differentiation of the sums that form $\langle k|R,I\rangle \Sigma_n h$. The two ends of Eq. (14) can be used to find:

$$-\frac{x}{g}\frac{\partial g}{\partial x} = \left[\frac{\partial}{\partial K_n}\left(\langle k|R,I\rangle \sum_n h\right) - \sum_n K_n h'\right] \Big/ \sum_n h. \tag{15}$$

The left side of Eq. (15) depends only on A and x, while the right side depends only on K_n. Thus, both sides must equal a constant yielding two equations:

$$-\frac{x}{g}\frac{\partial g}{\partial x} = \alpha \tag{16}$$

and

$$1 + \left[\frac{\partial}{\partial K_n}\left(\langle k|R,I\rangle \sum_n h - \sum_n K_n h\right)\right] \Big/ \sum_n h = \alpha, \tag{17}$$

where α is the separation constant, and the derivative relationship $(\partial/\partial K_n)(\Sigma K_n h) = \Sigma K_n h' + \Sigma h$ has been used to expand the K_n-derivative in Eq. (15) to fill the [,]-brackets. Equations (12) and (17) produce an equation for h:

$$\frac{\partial}{\partial K_n}\left(\frac{\sum K_n f_K}{\sum f_K}\sum h - \sum K_n h\right) = (\alpha - 1)\sum h, \tag{18}$$

where the n-designation has been dropped from the summations to save space. The value of α can be determined by considering the form of the solution for x approaching zero. Here, the pressure PDF must match the conditions at the source where the phase is deterministic. Thus, as $x \to 0$ only one value of n can contribute to the various sums, so the terms in parentheses in Eq. (18) become: $(K_n f_K/f_K)h - K_n h = 0$ which means that $\alpha = 1$, and more generally that:

$$\sum K_n f_K \sum h - \sum K_n h \sum f_K = 0, \tag{19}$$

which is solved by simply setting $h = f_K$. Returning to Eq. (16), $\alpha = 1$ implies $\partial g/\partial x = -g/x$, which has the simple solution $g(A,x) = \tilde{g}(A)/x$ where $\tilde{g}$ is an undetermined function of A alone.

Thus, the solution for the pressure field PDF is

$$f_P = \frac{\tilde{g}(A)}{x}\sum_n f_K\left(\frac{\Theta - 2\pi n}{x}\right). \tag{20}$$

Applying the initial condition, Eq. (8), while recognizing that for any distribution f_K that goes to zero when its argument goes to infinity,

$$\lim_{x\to 0}\left\{\frac{1}{x}\sum_n f_K\left(\frac{\Theta - 2\pi n}{x}\right)\right\} = \delta(\Theta), \tag{21}$$

allows the identification $\tilde{g} = f_A/A$, so that the final solution for this example is:

$$f_p(R,I;x) = \frac{f_A(\sqrt{R^2+I^2})}{x\sqrt{R^2+I^2}}\sum_n f_K\left(\frac{\tan^{-1}(I/R) - 2\pi n}{x}\right) \quad \text{for } I>0 \tag{22}$$

where $2\pi n$ in the argument of f_K should be replaced by $2\pi(n-1/2)$ when $I<0$.

The evolution of f_P based on Eq. (22) for increasing x is shown in the four parts of Fig. 1 for known amplitude A_o, i.e., $f_A(A) = \delta(A - A_o)$, and a Gaussian wave number distribu-

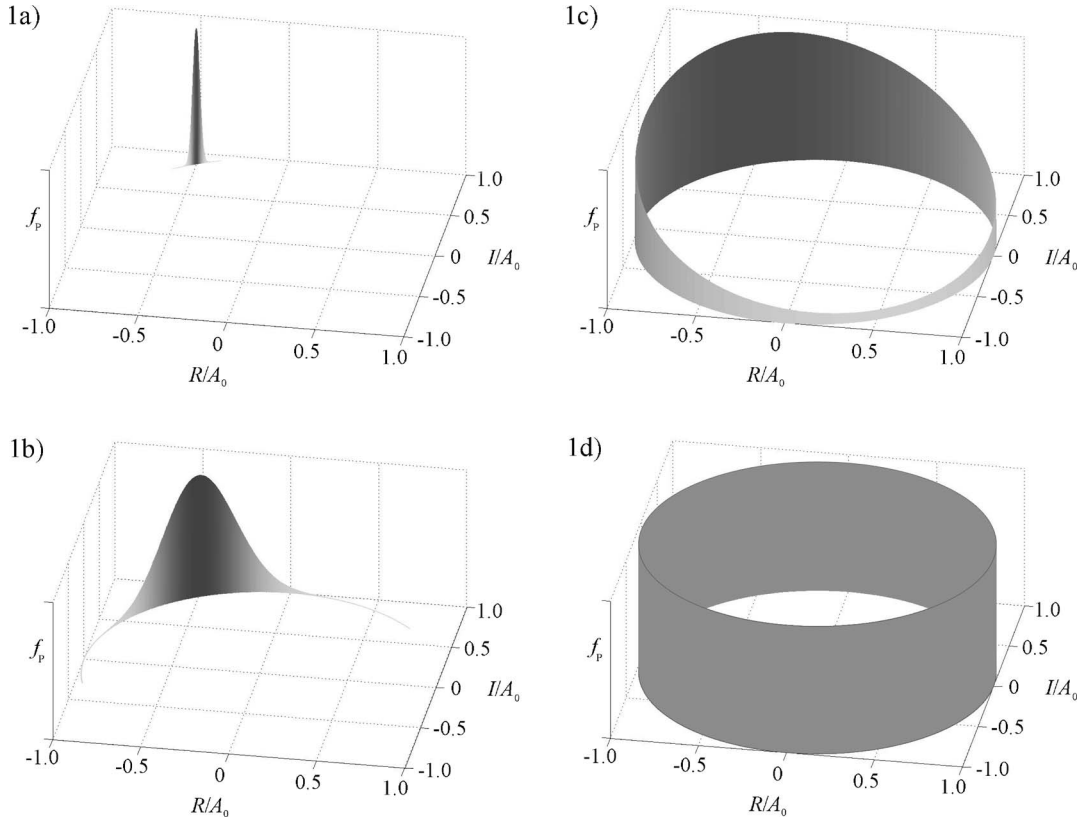

FIG. 1. Isometric views of the probability density function, f_P, for the real, R, and imaginary, I, parts of a unidirectional acoustic plane wave propagating in an ideal duct with an uncertain wave number at four distances from the sound source. These results are based on Eq. (22). Here the wave number uncertainty has a standard deviation of 1% of the average wave number and A_o is the sound amplitude produced by the zero-phase plane wave source at $x=0$. The four distances from the source are: (a) $x=\lambda/3$, (b) $x=10\lambda/3$, (c) $x=58\lambda/3$, and (d) $x=178\lambda/3$, where λ is the average acoustic wavelength. The vertical axis is linear not logarithmic.

tion centered on $2\pi/\lambda$ with a standard deviation of $0.01(2\pi/\lambda)$ for $x=\lambda/3$, $10\lambda/3$, $58\lambda/3$, and $178\lambda/3$, where λ is the average acoustic wavelength. The figure renders f_P in an isometric view with the independent R and I axes lying in a horizontal plane. The predicted-field amplitude is independent of x, a direct consequence of the plane wave assumption, while f_P spreads in phase as x increases. The phase starts out known, but as x increases, the uncertainty in wave number results in a growing uncertainty in phase. This phase uncertainty growth eventually saturates so that sufficiently far from the source all phases are essentially equally likely. At such distances, the value of the acoustic field calculations for a coherent signal processing application would be severely degraded. Thus, if more realism can be included, the type of analysis presented here could lead to guidelines for knowing when acoustic-field phase predictions are likely to be useful.

Interestingly, the solution to this example problem, Eq. (22), could have been obtained by direct PDF transformations [see Papoulis (1965)] using known analytical results for one-dimensional acoustic waves. Thus, the value of the preceding derivation lies in its illustration of the procedure for generating and solving an equation for the evolution of f_P. In more complicated uncertain acoustic environments, direct PDF transformation techniques may not be feasible, but methods paralleling this one-dimensional example may still be possible when exact or approximate values for the conditional moments can be found. In particular, recent PDF-method calculations of turbulence [Lou and Miller (2001), Waclawczyk *et al.* (2004)] and turbulent combustion [Pope (2004), James *et al.* (2005)] follow such an approach using approximate models for the conditional moments.

III. PDF UNCERTAINTY ANALYSIS IN TWO OR MORE SPATIAL DIMENSIONS

An equation for the evolution of f_P in two or more spatial dimensions can be found in a manner similar to that given in the previous section where differentiation of Eq. (1) is used to produce Eqs. (5) and (6), except here the Laplacian of the fine-grained PDF in Eq. (1),

$$\nabla^2 f_P = -\frac{\partial f_P}{\partial R}\nabla^2 p_R - \frac{\partial f_P}{\partial I}\nabla^2 p_I + \frac{\partial^2 f_P}{\partial R^2}|\nabla p_R|^2 + \frac{\partial^2 f_P}{\partial I^2}|\nabla p_I|^2 + 2\frac{\partial^2 f_P}{\partial R \partial I}\nabla p_R \cdot \nabla p_R \tag{23}$$

is needed to create the appropriate mathematical identity for f_P,

$$\nabla^2 f_P = -\frac{\partial}{\partial R}(f_P\langle\nabla^2 p_R|R,I\rangle) - \frac{\partial}{\partial I}(f_P\langle\nabla^2 p_I|R,I\rangle) + \frac{\partial^2}{\partial R^2}(f_P\langle|\nabla p_R|^2|R,I\rangle) + \frac{\partial^2}{\partial I^2}(f_P\langle|\nabla p_I|^2|R,I\rangle) + 2\frac{\partial^2}{\partial R\partial I}(f_P\langle\nabla p_R\cdot\nabla p_I|R,I\rangle), \quad (24)$$

and the Helmholtz equation, $\nabla^2\hat{p}=-k^2\hat{p}$ is used to convert this identity [Eq. (24)] into an evolution equation for f_p.

$$\nabla^2 f_P = 2f_P\langle k^2|R,I\rangle + R\frac{\partial}{\partial R}(f_P\langle k^2|R,I\rangle) + I\frac{\partial}{\partial I}(f_P\langle k^2|R,I\rangle) + \frac{\partial^2}{\partial R^2}(f_P\langle|\nabla p_R|^2|R,I\rangle) + \frac{\partial^2}{\partial I^2}(f_P\langle|\nabla p_I|^2|R,I\rangle) + 2\frac{\partial^2}{\partial R\partial I}(f_P\langle\nabla p_R\cdot\nabla p_I|R,I\rangle). \quad (25)$$

This is a general evolution equation for the PDF of acoustic pressure when the wave number is uncertain; it is the three-dimensional extension of Eq. (6). It is derived solely from identities and the Helmholtz equation, so it is applicable to all geometries. Unfortunately, it contains four conditional expectations and three terms involving acoustic pressure gradients. These terms prevent a direct solution of Eq. (25) because they cannot be readily determined from the other dependent and independent variables.

Without attempting to approximate or model the conditional expectations, their effect on PDF evolution can be illustrated by examining a solution to Eq. (25) based on direct PDF transformation between the PDF of the uncertain input parameter (an *a priori* PDF) and f_p. In this example, a deterministic acoustic point source radiates sound into an isospeed, uniform-density sound channel having uncertain channel depth D, a situation that has been the subject of a prior study on environmental mismatch and matched-field processing [Shang and Wang (1991)]. The solution is constructed directly from the functional dependence of $\hat{p}$ on D.

$$f_P(R,I;r,z) = \int_{-\infty}^{+\infty} \delta(p_R(r,z,D)-R)\,\delta(p_I(r,z,D)-I) \times f_D(D)\,dD. \quad (26)$$

Here, r and z are the usual range and depth coordinates used in underwater acoustics, the source is located at $r=0$ and $z=z_s$, f_D is the *a priori* PDF of the depth, and $\hat{p}(r,z,D)=p_R+ip_I$ is given by

$$\hat{p}(r,z;D) = iS\sqrt{\frac{8\pi}{r}}\exp\left(-i\frac{\pi}{4}\right) \times\sum_m \frac{\sin(k_{zm}(D)z_s)\sin(k_{zm}(D)z)}{D\sqrt{k_{zm}(D)}}\exp(ik_m(D)r) \quad (27)$$

[see Kinsler *et al.* (2000)] where S sets the source strength, k_m is the mth mode's horizontal wave number, and k_{zm} is the mth mode's vertical wave number. The sound channel geometry and parameters are provided on Fig. 2.

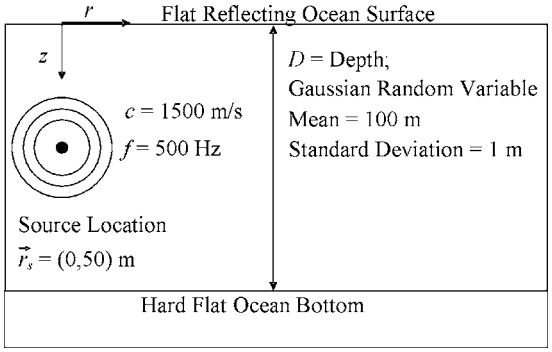

FIG. 2. The ideal range-independent sound channel and coordinate system.

The primary difficulty in evaluating of Eq. (26) arises from the delta functions which set $f_P(R,I;r,z)$ to zero at nearly all points in the R-I plane. Thus, for a chosen spatial location (r,z), the evaluation of Eq. (26) was done numerically by first finding the locus of points in the R-I plane where $f_P(R,I;r,z)$ is nonzero. This locus traces a contour in the R-I plane determined by $\hat{p}(r,z;D)=R+iI$ as D is varied from its lower to its upper extreme value. Nonzero, relative values of $f_P(R,I;r,z)$ were then computed by assigning the appropriate value of f_D on this locus of points. The discontinuities where the contour crosses itself were ignored. This simple approach is computationally tractable for a single uncertain parameter, but its computational effort grows exponentially with the number of uncertain parameters.

Sample results are presented in Fig. 3 for a source with acoustic frequency of 500 Hz, a sound speed of 1500 m/s, a Gaussian distribution of depth having a mean of 100 m and a standard deviation of 1 m, and source and receiver depths of $z_s=z=50$ m at nominal ranges of 200 m, 1 km, 5 km, and 20 km. In addition, only the first ten propagating modes were included in the sum specified in Eq. (27) as a crude means of modeling real-ocean bottom losses that preferentially attenuate higher-order propagating modes.

The down-range evolution of f_P shown on Fig. 3 has several interesting features. Near the source, the field uncertainty is low and f_P resembles a delta-function spike in the R-I plane, but it spreads along a thin curve as the range increases. This curve is shown in Fig. 4 as an overhead view of Fig. 3(d). In this example, unlike in the one-dimensional one, the spreading curve is neither circular nor centered at the origin, and changes shape with range, so acoustic field uncertainty occurs in both amplitude and phase. Furthermore, the shape of f_P, most noticeably at the three longer ranges, is quite different from the familiar bell-shaped distribution of a joint Gaussian, indicating that an assumption of Gaussian field statistics may be very inaccurate. Furthermore, for ranges greater than 5 km or so, all acoustic-field phases have a non-negligible probability of occurring, and there exists at least a 10 dB range of probable amplitudes, so acoustic field predictions at a single point at such distances might be considered too uncertain to be useful.

Revisiting Eq. (25) in light of the Fig. 3 results, it is seen that this complicated behavior must arise from the character of the conditional expectations, so any simplification or approximation to these expectations must keep this character

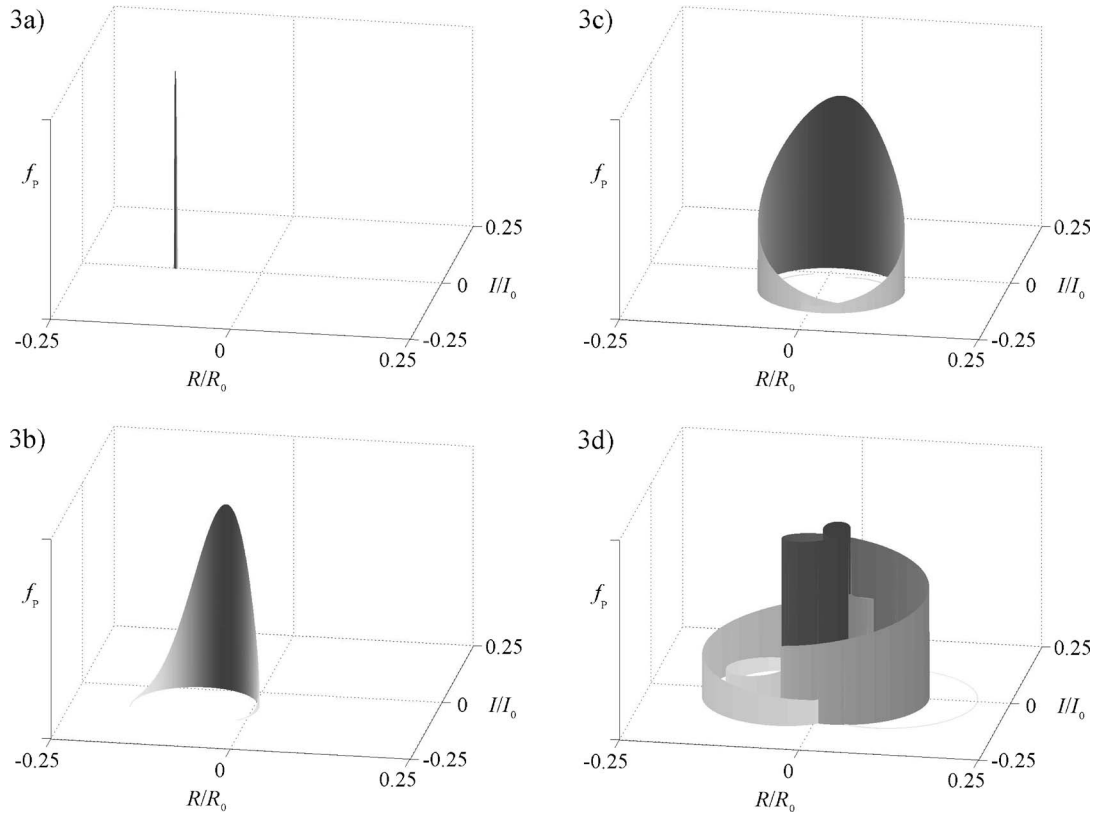

FIG. 3. Isometric views of the probability density function, f_P, for the real, R, and imaginary, I, parts of the acoustic field propagating in the ideal range-independent sound channel of Fig. 2 with an uncertain depth at four distances from a 500 Hz sound source. These results are based on numerical evaluation of Eqs. (26) and (27). Here, the depth uncertainty has a standard deviation of 1 m, the average depth is 100 m, the source and receiver depths are the same (50 m), and $R_0=I_0=S\sqrt{8\pi/r}$ [see Eq. (27)]. The four nominal source-receiver ranges are: (a) $r=200$ m, (b) $r=1$ km, (c) $r=5$ km, and (d) $r=20$ km. As in Fig. 1, the vertical axis is linear not logarithmic.

intact. However, if manageable expressions can be developed for these expressions, then PDF evolution analysis has potential as a useful tool for acoustic uncertainty analysis. Such expressions have been developed in other fields where PDF analysis has been applied [see Dopazo (1994), Pope (2000), James *et al.* (2005)].

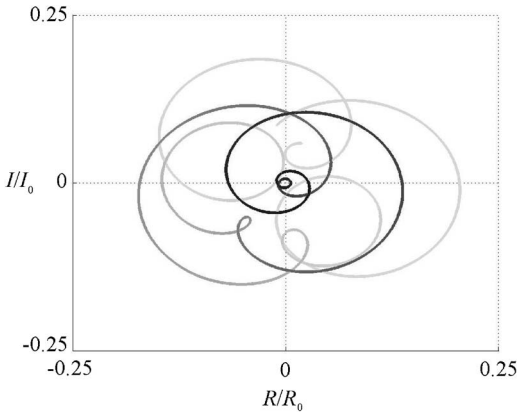

FIG. 4. Overhead view of Fig. 3(d). The spread of f_P is non-Gaussian even though the *a priori* input PDF, f_D, for the uncertain channel depth was Gaussian. As in Figs. 1 and 3, darker shades imply higher probability.

IV. MULTIPOINT PDF UNCERTAINTY ANALYSIS IN TWO OR MORE SPATIAL DIMENSIONS

In acoustic array signal processing, the structure of the acoustic field may be as or more important than the phase and amplitude of the field at any particular point. Thus, the two-point PDF of acoustic pressure might also be of interest in uncertain acoustic environments. The following short derivation presents the two-point version of Eq. (25). Generalization to n-point PDF equations can be obtained by appropriate extension of the following steps.

Following Lundgren (1967), the equation for the two-point acoustic field PDF, f_{12}, can be built from the two-point fine-grained PDF,

$$\mathcal{f}_{12} = \delta(p_{R1} - R)\,\delta(p_{I1} - I)\,\delta(p_{R2} - R)\,\delta(p_{I2} - I) \tag{28}$$

where the extra numerical subscripts throughout this section refer to the two field points, $\mathbf{x}_1$ and $\mathbf{x}_2$. Computing the Laplacians of this equation with respect to the first and second field points produces two equations like Eq. (23) with "1" and "2" subscripts. Taking the expected value of these two equations and substituting from the Helmholtz equation results in two equations for f_{12} with conditional moments that depend on the complex pressure at $\mathbf{x}_1$ and $\mathbf{x}_2$. The first of these equations is

$$\nabla_I^2 f_{12} = 2f_{12}\langle k^2|1,2\rangle + R_1\frac{\partial}{\partial R_1}(f_{12}\langle k^2|1,2\rangle) + I_1\frac{\partial}{\partial I_1}(f_{12}\langle k^2|1,2\rangle) + \frac{\partial^2}{\partial R_1^2}(f_{12}\langle|\nabla_1 p_{R1}|^2|1,2\rangle) + \frac{\partial^2}{\partial I_1^2}(f_{12}\langle|\nabla_1 p_{I1}|^2|1,2\rangle) + 2\frac{\partial^2}{\partial R_1 \partial I_1}(f_{12}\langle\nabla_1 p_{R1}\cdot\nabla_1 p_{I1}|1,2\rangle) \quad (29)$$

where $\langle\ldots|R_1,R_2,I_1,I_2\rangle$ has been abbreviated as $\langle\ldots|1,2\rangle$. The second equation is identical to Eq. (29) with the "1"-subscripts on ∇, p_R, p_I, R, and I replaced by "2"-subscripts.

For an N-dimensional geometry, the two-point PDF exists in a $2N$-dimensional space consisting of all possible locations of both points (where the value of f_{12} at each point is a function of R_1, I_1, R_2, and I_2). The two equations for f_{12} describe its evolution in this space. For an n-point joint PDF, there would be n such equations, with the expectations conditioned on the pressure values at all n points.

V. SUMMARY AND CONCLUSIONS

This paper has presented a technique for constructing the evolution equation for the probability density function (PDF) of an uncertain harmonic acoustic field in an uncertain environment. The technique was illustrated through examples involving one and two independent spatial dimensions. One-point and multi-point PDFs and their equations were considered. It has been assumed throughout this research effort that the PDFs of uncertain acoustic fields contain information that may be valuable in applications of acoustics. The following three conclusions can be drawn from this effort.

First, the wavelength scaling for distances, or ranges, that arises in both examples suggests that the behavior of the acoustic-field PDF for fixed frequency and increasing range—as investigated here—will be essentially the same for fixed ranges and increasing frequencies. Thus, even for small input parameter uncertainties, there will be a range at any fixed frequency, or a frequency at any fixed range, beyond or above which the use of a perfect acoustic field model may no longer be useful for predicting the phase of the acoustic field. Thus, the present harmonic-field results provide some insight into broadband-sound acoustic uncertainty, even though it was not explicitly addressed.

Second, uncertain wave propagation involving one or more independent spatial dimensions may not be adequately described by an expected value and a variance (the first two moments of a PDF). In the two-dimensional example provided in Fig. 3, the resulting PDF is far from joint-Gaussian, even when the only uncertain input parameter is Gaussian. Although this effect may be less pronounced if a larger number of uncertain input parameters is considered, it prevents an immediate retreat to field-moment-based techniques, like those used for wave propagation in random media, for acoustic uncertainty analysis. Additional investigation could determine if the predicted-field PDF approaches Gaussian behavior when more input parameters are uncertain.

Third, the PDF equations derived here contain complications that were partially overcome in the two examples through the existence of an analytical field model. Significant complications arise, however, in realistic geometries where, at best, a computational field model is available. When there is no invertible, analytic relationship between the uncertain parameters and the pressure, the PDF evolution equations contain terms that cannot be explicitly evaluated. If tractable and robust expressions can be found for these terms, the methods described here may become useful tools in acoustic uncertainty analysis.

As a final note, the equations presented herein are not the only candidates for describing the evolution of acoustic-field PDFs. For example, when the acoustic waves travel in nearly the same direction, a PDF equation could be developed from the parabolic approximation to the Helmholtz equation instead of from the Helmholtz equation itself. The different conditional expectations that arise in such an effort may prove to be more or less tractable in certain situations. Uncertainty in acoustic-ray equations could also be analyzed by the PDF-equation construction approach described here. In addition, this approach might be successfully applied to other fields where physical laws are stated via partial differential equations for relevant field quantities such as electricity and magnetism, wave propagation in solids and other media, or physical systems involving thermal or species diffusion. In general, not all PDF equations so generated can be applied to boundary value problems, but they might still provide insight into the origins and propagation of uncertainty in a variety of physical systems.

ACKNOWLEDGMENT

This research was sponsored by the Ocean Acoustics Program of the Office of Naval Research under Grant Nos. N00014-96-1-0040 and N00014-05-1-0243.

Dopazo, C. (**1994**). "Recent developments in PDF methods," in *Turbulent Reacting Flows*, edited by P. A. Libby and F. A. Williams (Academic Press, London), Ch. 7, pp. 375–474.

Finette, S. (**2005**). "Embedding uncertainty into ocean acoustic propagation models," J. Acoust. Soc. Am. **117**, 997–1000.

Ishimaru, A. (**1978**). *Wave propagation and scattering in random media*, Vol **II** (Academic press, San Diego), Chap. 20.

James, S., Zhu, J., and Anand, M. S. (**2005**). "Lagrangian PDF transport method for simulations of axisymmetric turbulent reacting flows," AIAA Paper No. 2005-156.

Jensen, F. B., Kuperman, W. A., Porter, M. B., and Schmidt, H. (**1994**). *Computational Ocean Acoustics* (AIP Press, New York).

Kinsler, L. E., Frey, A. R., Coppens, A. B., Sanders, J. V. (**2000**). *Fundamentals of Acoustics*, 4th Ed. (Wiley, New York), p. 261.

Lou, H., and Miller, R. S. (**2001**). "On the scalar probability density function transport equation for binary mixing in isotropic turbulence at supercritical pressure," Phys. Fluids **13**, 3386–3399.

Lundgren, T. S. (**1967**). "Distribution functions in the statistical theory of turbulence," Phys. Fluids **10**, 969–975.

Papoulis, A. (**1965**). *Probability, Random Variables, and Stochastic Processes* (McGraw Hill, New York), Chap. 5.

Pope, S. B. (**2000**). *Turbulent Flows* (Cambridge University Press, Cambridge, UK). Ch. 12, Appendix H.

Pope, S. B. (**2004**). "Advances in PDF methods for turbulent reacting flows," Proceedings of the 10th Conference on Turbulence, Paper No. 801, pp. 1–8.

Sha, L., and Nolte, L. W. (**2005a**). "Effects of environmental uncertainties on sonar detection performance prediction," J. Acoust. Soc. Am. **117**, 1942–1953.

Sha, L., and Nolte, L. W. (**2005b**). "Bayesian sonar detection performance prediction in the presence of interference in uncertain environments," J. Acoust. Soc. Am. **117**, 1954–1964.

Shang, E. C., and Wang, Y. Y. (**1991**). "Environmental mismatch effects on source localization processing in mode space," J. Acoust. Soc. Am. **89**, 2285–2290.

Sibul, L. H., Coviello, C. M., and Roan, M. J. (**2004**). "Detection of high frequency sources in random/uncertain media," in *High Frequency Ocean Acoustics*, edited by M. B. Porter, M. Siderious, and W. A. Kuperman (Am. Inst. Phys., Melville, NY), pp. 237–244.

Uscinski, B. J. (**1977**). *The elements of wave propagation in random media* (McGraw Hill, New York).

Waclawczyk, M., Pozorski, J., and Minier, J.-P. (**2004**). "Probability density function computation of turbulent flows with a new near-wall model," Phys. Fluids **16**, 1410–1422.

Doubly focused backscattering from finite targets in an Airy caustic formed by a curved reflecting surface

Benjamin R. Dzikowicz[a] and Philip L. Marston
Department of Physics, Washington State University, Pullman, Washington 99164-2814

(Received 6 June 2005; revised 29 July 2005; accepted 3 August 2005)

Caustics can be formed in the water column when sound scatters off a curved-reflecting surface such as the ocean floor or surface. The simplest caustic is an Airy caustic formed by the merging of two rays. Small targets lying in or near Airy caustics have backscattered echoes that can be focused both to the target and upon return. For a point target, the doubly focused backscattering amplitude is proportional to the square of an Airy function whose argument depends on the target location through the changes in relative return times of contributing rays. For a finite sized target, the symmetry is broken and the amplitude unfolds into a hyperbolic umbilic catastrophe. The arguments for the hyperbolic umbilic function are calculated using the relative return times of transient echoes. These doubly focused echoes can lead to amplitudes larger than that of direct or singly focused echoes (echoes which focus once, either to the target or upon return). Experiments using a cylindrical half-pipe as a reflecting surface confirm these predictions. © *2005 Acoustical Society of America.* [DOI: 10.1121/1.2046867]

PACS number(s): 43.20.El, 43.30.Gv, 43.20.Dk [TDM] Pages: 2811–2819

I. INTRODUCTION

In a prior paper,[1] the authors studied the enhanced backscattering due to single focusing caused by a nearby curved surface. The signal returned to a source/receiver from a target residing in an Airy wave field was studied for the case where there is focusing for either the outgoing signal or the incoming one. This paper treats the case of a target when the signal is focused both to the target and upon return. The solution for a point target with this double focusing is presented first. A finite sized target involves an additional complication; the target can reside not only in the shadow region or the insonified region, but may reside partially in each region. This situation is emphasized in this paper.

Prior research associated with sound reflected from curved surfaces in water has emphasized the description of the caustics and associated wave fields[2–4] and the statistical properties of the intensity fluctuations.[5,6] The branch of singularity theory commonly known as catastrophe theory provides a framework for describing the wave fields.[7–10] Caustics are also produced in the refractions and reflections of sound associated with long-range propagation, and catastrophe theory is successfully applied to those situations. These types of caustics also contribute to volume reverberation.[11] Although in many situations the reverberation from reflecting surfaces may be considered noise or interference, focused reflections can be used to enhance the amplitude of the backscattering.[1]

In order to study these doubly focused echoes, the same geometry in the previous paper[1] is used and figures in that paper can be referred to for additional clarification. A projection down the axis of the cylindrical reflecting surface with a point target and source/receiver is shown here in Fig. 1. The source/receiver and the target are separated in the Z direction to prevent reverberation from unwanted additional echoes. In Fig. 1 the target is in the completely insonified region on the left side of the caustic, shown as a light gray line. In this region there are three rays connecting the target to the source/receiver. There is a direct ray, and two rays which reflect off the cylindrical surface. As the target is moved from this region into the shadow region to the right of the caustic, the two rays reflecting off the surface merge at the surface and vanish. Additional studies on the scattering and wave fields within circular cylinders can be found in the literature.[12–14]

The various rays extending from the source/receiver to the target and back to the source/receiver will be identified in the same manner as in the previous paper.[1] The ray traveling directly to the target and back without reflecting off the surface is called the *direct ray* (D). Two rays travel directly to the target and return by reflecting off one of two points on the surface. Two additional rays, degenerate to these, travel in the opposite direction giving four *single bounce rays* (SB). The shorter two of these paths are labeled SB1 and the longer, SB2. *Double bounce rays* (DB) are rays which reflect off the curved surface twice, once on the way to the target and once on return. There are also four of these paths, one taking the shorter path in both directions (DB1), one taking the longer path in both directions (DB2) and two degenerate rays taking the shorter in one direction and the longer in the other, the *cross double bounce* (XDB).

For the experiments and discussions here the target moves from the shadow region into the fully insonified region crossing an Airy, or fold, caustic[7–10,15,16] along the way. Airy caustics in the reflected wave field involve the merging of two rays and are modeled using cubic distance functions because that function has the appropriate evolution of stationary points. In the insonified region both roots for the ray location are real and in the shadow region they are both

[a]Now with: NSWC-Panama City, Code R-21, 110 Vernon Ave., Panama City, FL, 32407; electronic mail: benjamin.dzikowicz@navy.mil

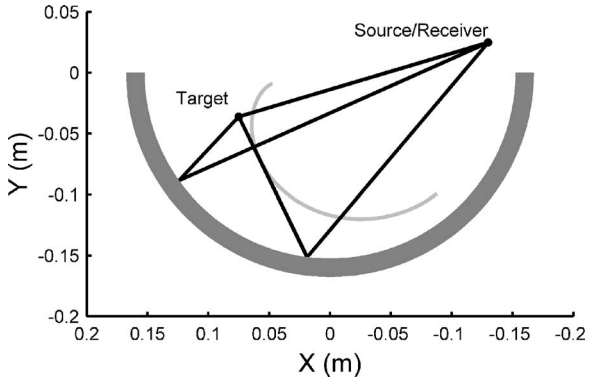

FIG. 1. In this projection down the z-axis, a point target located on the illuminated side of the Airy caustic shows two reflected rays connecting the target and the source/receiver. With the target to the right of the caustic, there are reflected rays to the target. The caustic is shown in light gray.

imaginary. Directly at the caustic, the roots are real and identical. When sending a short pulse from the source/receiver each of these rays can be identified. In Fig. 2 the target is located on the caustic and three returns are seen: the direct return, the single bounce returns, and the double bounce returns. With the target at the caustic, each of the two groups of reflecting rays has merged and enhancements relative to the direct return can be seen. The merging of the DB rays gives the greatest enhancement since they have been doubly focused. In Fig. 3, with the target in the insonified region transient echoes can be identified for each of the separate rays. The XDB returns and both of the SB returns each represent two degenerate rays. The experimental conditions and techniques used to obtain these plots are explained in Sec. IV.

II. THEORY

This analysis concerns the situation where the incident pulses are of sufficient duration so that certain ray contributions overlap in time at the hydrophone. The resulting superposition echoes produce a sequence of quasisteady state sig-

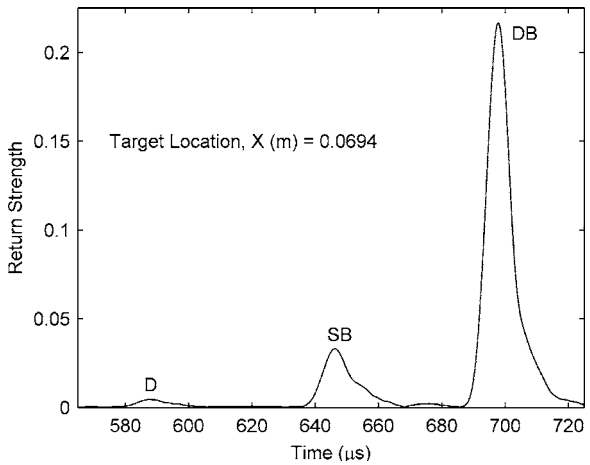

FIG. 2. The envelope of recorded echoes for a single short pulse with the target lying near the caustic. Both the singly (SB) and doubly (DB) focused echoes can be seen along with the direct one. Note the enhancements associated with focusing.

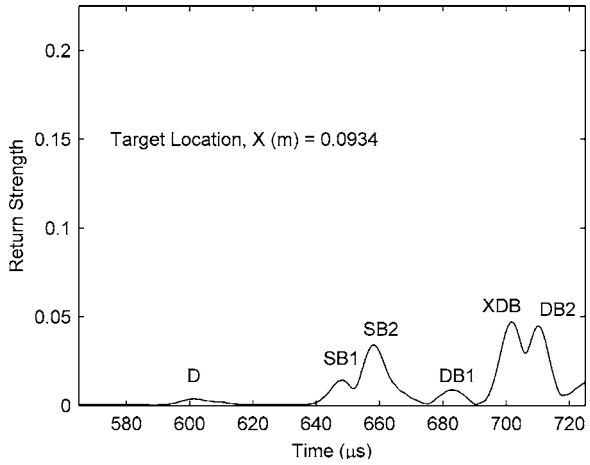

FIG. 3. With the target in the fully illuminated area the envelopes of the individual echoes can be seen from a short pulse. The SB1 and SB2 returns and the DB1, XDB, and DB2 echoes were merged when the target was near the caustic giving the enhancement seen in Fig. 2.

nals shown in Fig. 4 and in Fig. 5 of Ref. 1. In order to find the pressure at the receiver due to the merging of the rays, the following expression is used:

$$p(0,0,z) \approx \frac{ik}{2\pi z}\int_{-\infty}^{\infty}\int_{-\infty}^{\infty} A(x,y)e^{ik\phi(x,y)}dx\,dy. \tag{1}$$

This corresponds to a fixed receiver location of a more general expression.[9] Throughout the paper, lowercase letters will be used to describe the Cartesian coordinates of a wave field, whereas the capital letters, X, Y, and Z, will be used to denote the Cartesian coordinates of the target. The convention $e^{-i\omega t}$ is used to denote the time dependence of the quasistationary signal and $k=\omega/c$. The field point at the receiver is chosen on the z axis. It is illuminated in the far field by an incoming wave that can be attributed to a virtual wave front defined by a distance function $\phi(x,y)$ and amplitude $A(x,y)$. The wave front is described as virtual since it is specified at a location beyond the curved reflecting surface. The function

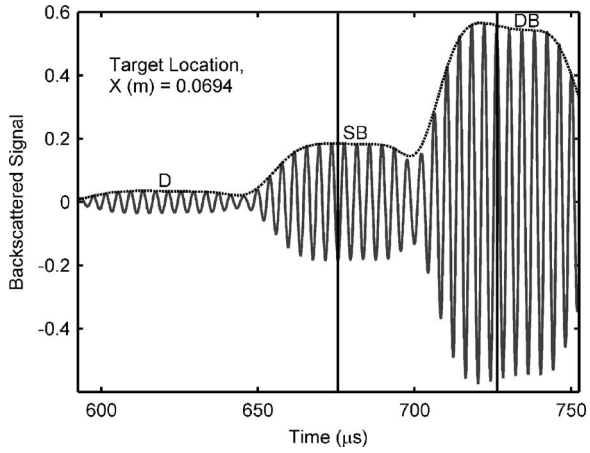

FIG. 4. A typical backscattered return with the target near the caustic. Each of the three types of return can be seen. The direct reflection (D), the singly focused returns (SB), and the doubly focused returns (DB) can be seen. Each focusing gives a greater return than the one before it. The Hilbert transform is used to find the envelope of the return also plotted here. The target radius was 30 mm and $ka \approx 30$.

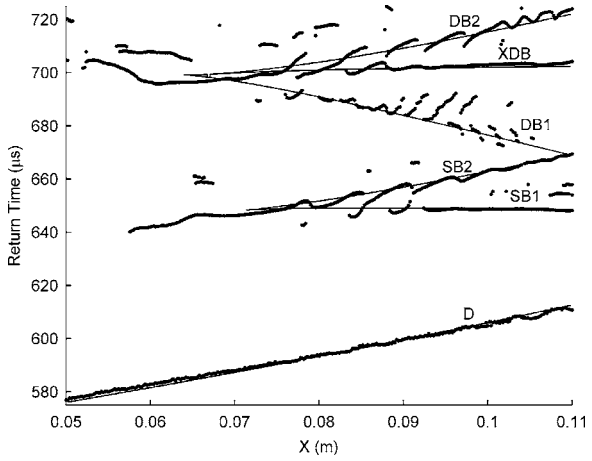

FIG. 5. Round trip return times for a short pulse plotted with respect to the target position as it moves across the caustic. The solid lines are the calculated return times using a numerical ray finding technique. (Due to limitations in the technique there are points missing near the caustic.) Each of the different types of returns is labeled: the lone direct return (D), two single bounce (SB) returns, and the double bounce returns (DB and XDB). The target radius was 30 mm. The points are extracted from local envelope maxima as explained in Ref. 1.

ϕ (sometimes described as the generating function) gives the distance from the receiver at $(x,y,z)=(0,0,z)$ to a point on the wave front in some reference frame. Equation (1) is used to calculate the backscattered echo and this paper concerns itself with finding $\phi(x,y)$ and $A(x,y)$ for the merging of DB rays and applying the integral to the experimental results. The functions, $\phi(x,y)$ and $A(x,y)$, also depend on the target coordinates X, Y, and Z.

A. Singly focused solutions

Previously,[1] the backscattered pressure for the merging of the SB rays was found using a cubic distance function,

$$\phi(x,y) = \gamma x^3 + \alpha x + \beta y^2 + z_0, \tag{2}$$

and $A(x,y)=p_0$ assuming the amplitude does not vary significantly over the wave front. These assumptions lead to a backscattered pressure of

$$p(Q) \approx -\frac{i\pi^{1/2}k^{1/6}p_0}{z_0(3\gamma)^{1/3}\beta^{1/2}} \exp\left[i\left(kz_0+\frac{\pi}{4}\right)\right] \times \mathrm{Ai}\left(-\left(\frac{3}{4}\omega\Delta t_{\mathrm{SB}}\right)^{2/3}\right). \tag{3}$$

The locations of the source/receiver and the target are denoted by Q. Since the determination of γ and β is not central to the following discussions and only the relative magnitudes can be determined using the experiment described in the following section, Eq. (3) can be written more simply,

$$|p_{\mathrm{SB}}(Q)| = S\omega^{1/6}\left|\mathrm{Ai}\left(-\left(\frac{3}{4}\omega\Delta t_{\mathrm{SB}}\right)^{2/3}\right)\right|, \tag{4}$$

where S is determined experimentally and is in units of pressure$\times$time$^{1/6}$. As explained in Ref. 1, the prefactor neglects any ω dependence of the intrinsic scattering by the target. The argument of the Airy function $-[(3/4)\omega\Delta t_{\mathrm{SB}}]^{2/3}$ has been written as a function of the difference in return times of the two SB times. These return times can be found experimentally using short pulse return times as in Fig. 3 or by applying a numerical ray finding algorithm.[17] The latter method is more desirable and is used here since the finiteness of the short pulses makes these times difficult to resolve. The time difference, Δt_{SB}, is seen in Fig. 5 as the difference in the return times between SB2 and SB1.

B. Doubly focused point target solution

The merging of the three DB echoes for a point target is relatively straightforward. There are four rays merging at the same place (Fig. 1, and recall the center return, XDB, is degenerate). The same $\omega\Delta t_{\mathrm{DB}}$ describes both mergers with XDB and the form of the pressure for double bounce focusing is proportional to the square of the SB result given in Eq. (4),

$$|p_{\mathrm{DB}}(Q)| \approx D\omega^{1/3}\left|\left\{\mathrm{Ai}\left[-\left(\frac{3}{4}\omega\Delta t_{\mathrm{DB}}\right)^{2/3}\right]\right\}^2\right|. \tag{5}$$

D is an experimentally determined coefficient in units of pressure$\times$time$^{1/3}$. This simple result is for a point target. It is important to note that the frequency dependence of the coefficient in Eq. (4) goes like $k^{1/6}$ contrasting with the $k^{1/3}$ dependence on the DB result. Some qualifications on what is meant here by a point target are appropriate. The target must be sufficiently small relative to the surface radius of curvature that the modifications introduced by the result in Eq. (24) may be neglected. Since the prefactor neglects any ω dependence of the intrinsic scattering by the target, the target must not be too small and there are conditions on the material properties. For Styrofoam targets used in the experiment it is necessary for ka to exceed 8 to neglect the ω dependence. The spheres used were sufficiently large that they could not be treated as point scatterers.

C. Doubly focused finite target result

The measured return times for a short pulse, as in Fig. 5, are difficult to analyze because of the finite nature of the pulse, especially at the caustic where the echoes interfere with each other. The short pulses are not perfectly transient; their echoes overlap when they are close together and result in interference between the return times, such as between the SB1 and SB2 times in Fig. 5. Furthermore, the transient signals are distorted near caustics.[9,15] In order to evaluate the return times, a numerical ray finding technique was developed.[17] This allows calculation of the theoretical return times in Fig. 5 as well as plots of the rays and the targets (Figs. 1, 6–8, and 10) to help understand the nature of the ray mergings.

For a point target, geometry shows that $\omega\Delta t_{\mathrm{DB}}$ is the same for both the DB mergings. Figure 5 shows that this is not the case either experimentally or with the numerical ray finding technique. That is, the return time difference between DB2 and XDB is less than the difference between XDB and DB1. Figure 5 also shows that the DB rays do not merge at the same target position as the SB rays do as expected by

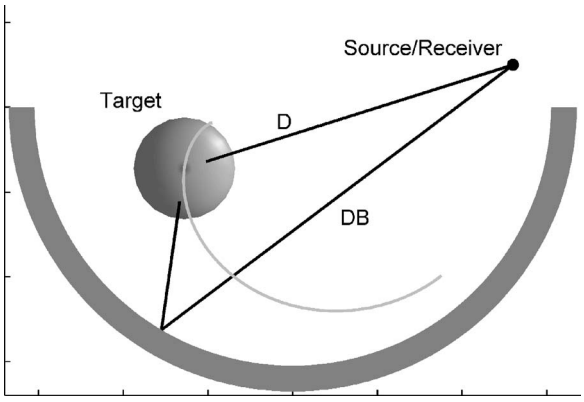

FIG. 6. A projection down the z axis with the large target. The source/receiver is located at $(-0.13, 0.025, 0)$ m and the target at $(0.0639, -0.036, 0.409)$ m. The caustic due to the source/receiver is shown in light gray. Here the first ray appears: a DB ray striking the target normally. There are two returns here, the direct echo and the one DB echo.

analysis of a point target. Behavior of the different types of rays is determined by close examination of the results of the numerical ray finding algorithm. As the target moves from the shadow region to the fully insonified it goes through seven distinct regions where different numbers of rays pass between the source/receiver and the target. A ray touching a caustic focuses as it touches the caustic surface, this leads to a phase advance of $\pi/2$.[18–20] This is important when examining limits when the rays are far apart.

1. Shadow region

In this region, there are no rays save the direct one. The target can lie partially in the insonified region of the Airy caustic and still be in the shadow region since there are no roundtrip rays to the receiver. Thus, even though there are rays traveling to the target they do not reflect off it in a way that returns them to the receiver.

2. DB merger 1

As shown in Fig. 6, the first echo to appear is DB. Since it does not strike at the same location as the direct ray, there is no way for it to return except along the path it arrived.

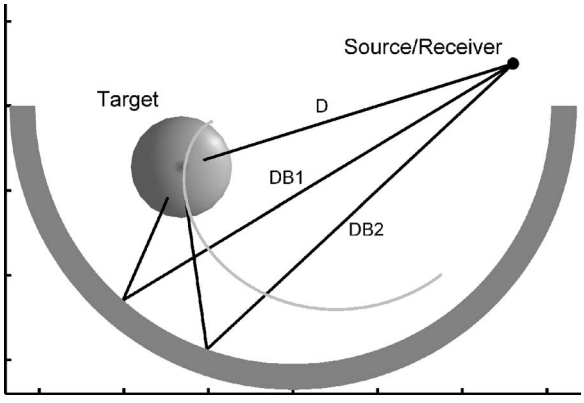

FIG. 7. A projection down the z axis with the large target. The source/receiver is located at $(-0.13, 0.025, 0)$ m and the target at $(0.065, -0.036, 0.409)$ m. The caustic due to the source/receiver is shown in light gray. Here the two DB rays have separated and there are three returns: the direct echo two DB echoes.

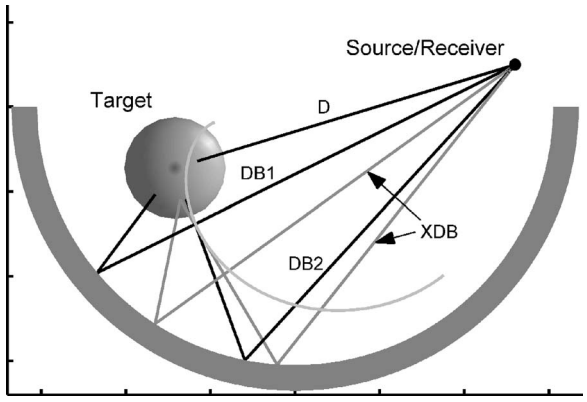

FIG. 8. A projection down the z axis with the large target. The source/receiver is located at $(-0.13, 0.025, 0)$ m and the target at $(0.071, -0.036, 0.409)$ m. The caustic due to the source/receiver is shown in light gray. Here all the DB rays have appeared and can be seen clearly. There are the same five returns: the direct echo, the two normal DB echoes, and two degenerate XDB echoes.

Thus, there is no SB ray associated with it. This ray appears at a point on the target on the lit side of the caustic surface but does not appear on the caustic itself, nor does it touch a caustic and pick up a phase advance.

3. Middle region

After the first merger the DB ray splits in two. Each of these DB rays strike the target normally. Thus, there is *no* XDB ray in this region. Neither of these rays touch a caustic so there is no phase shift for these rays in this middle region. As the target passes through this region, one of the rays moves toward the caustic and one moves away. The ray moving toward the caustic eventually hits it and when it does, an XDB ray appears.

4. DB merger 2

In Fig. 7, the XDB ray has just formed at the source/receiver caustic. This happens when the one normal DB ray touches the caustic at the target. In addition, as the normal DB ray moves away from the caustic it has picked up a phase shift, as it now touches the caustic.

5. Fully lit DB region

Figure 8 shows the target in the lit region with all the DB rays distinct. Here we have the same rays as expected from the point target analysis with the same caustic touches.

6. SB merger

After all the DB rays have appeared there is a merger of the SB rays. Here the rays appear on the caustic of the source/receiver. This is merger was the subject of the prior paper.[1]

7. Fully lit region

After crossing the SB merging position, all the rays have appeared. The now fully separated SB rays act the same as in the point case, that is, one of them touches a caustic and the other does not.

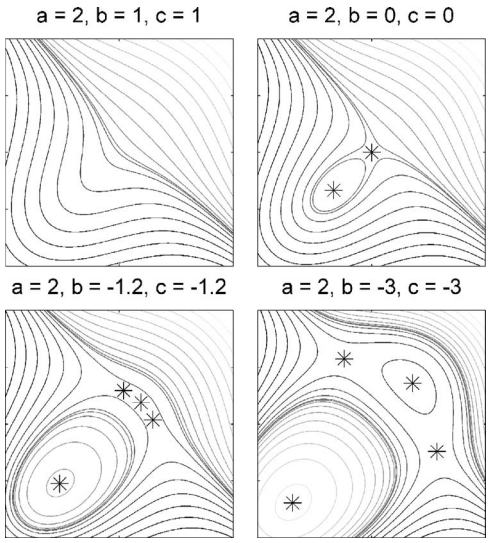

FIG. 9. Contour plots of the hyperbolic umbilic function for constant a with $b=c$. Stationary points are marked with a star. Going left to right, top to bottom: shadow region (no stationary points), after merger 1 (two stationary points one maximum and one saddle), just after merger 2 (four stationary points a max, a min, and two saddles), deep in the lit region (four stationary points a max, a min, and two saddles). Lighter contours are higher values.

Imagine the sphere size going from a point to some finite size well within the insonified region; that is, going from Fig. 1 to the situation in Fig. 8. Allowing for degeneracy, there must still be four DB rays. However, the rays may be shifted because the contact angles on the sphere's surface have equal incident and reflection angles. Note that the rays appear in order of contact angles: the DB rays reflect normally, the XDB at a slight angle, and the SB rays at a much larger contact angle.

A catastrophe function must be found with the correct number and type of stationary points as described earlier to be used as the distance function, $\phi(x,y)$, in Eq. (1). Thom[7] tabulated the standard catastrophe functions, and study of these indicates that the hyperbolic umbilic matches the stationary points in the proper way[8,9] with a u and v dependence of the form:

$$F(u,v) = u^3 + v^3 + auv + bu + cv. \tag{6}$$

This has regions of zero, then two, then four rays (recall the XDB ray is degenerate). This is the only catastrophe function that has the proper ray sequence and the proper point target limit. In order to get the proper degeneracy one must set $b=c$. Figure 9 shows the evolution of the hyperbolic umbilic as $b=c$ is varied and the stationary points appear. Literature provides additional discussion on this type of catastrophe function as well as plots in different spaces.[21–23]

To ease the upcoming transformations a term having the form of Eq. (6) is inserted for $k\phi$ in Eq. (1). The result is written with $A(x,y)=p_0$ taken to be constant:

$$p_{\mathrm{DB}}(Q) \approx \frac{-ik^{1/3}p_0}{2\pi\chi^2 z_0}\int_{-\infty}^{\infty}\int_{-\infty}^{\infty} e^{i\Phi(u,v)}du\,dv \tag{7}$$

with

$$\Phi(u,v) = u^3 + v^3 + auv + bu + bv + d + kz_0. \tag{8}$$

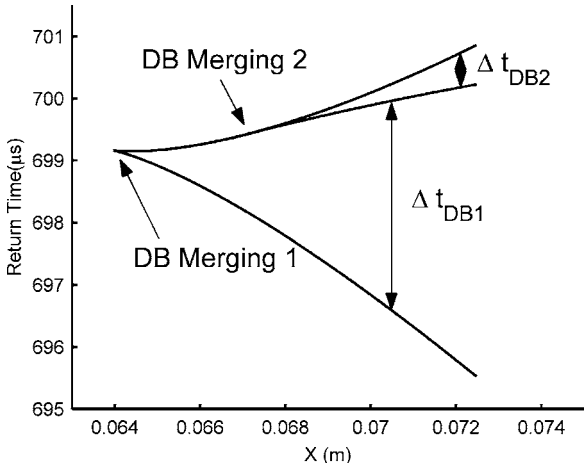

FIG. 10. Double bounce merging for the large target. This is a blowup of the numerical portion of the mergers shown in Fig. 4. It shows the double bounce returns and the return time differences used to calculate the argument of the hyperbolic umbilic function.

Equation (8) is in the standard form given by Thom. The variables u and v along with the function $\Phi(u,v)$ are dimensionless; this is accomplished by inserting the constant χ with units of length to the minus two-thirds. The overall phase, $d+kz_0$, contains the distance to the reference plane,[17] z_0, and a constant d to simplify an upcoming transformation. To make this equation useful the pressure must be written as a function of ray return-time differences, Δt_{DB1} and Δt_{DB2}. These time differences are shown in Fig. 10, which depicts a blow up of the DB merging region as drawn by the numerical ray finding program.[17] Equation (8) proves unwieldy so a different space with one-to-one mapping suggested by Poston and Stewart[24] is used,

$$\Phi(\tilde{v},\tilde{u}) = \frac{\tilde{u}^3}{6} + \frac{\tilde{u}\tilde{v}^2}{4} + B(\tilde{u}^2+\tilde{v}^2) + f\tilde{u} + kz_0 \tag{9}$$

with

$$u = \frac{1}{2}\left(\frac{2}{3}\right)^{1/3}\left(\tilde{u} + \frac{\tilde{v}}{2} + 3B\right), \quad v = \frac{1}{2}\left(\frac{2}{3}\right)^{1/3}\left(\tilde{u} - \frac{\tilde{v}}{2} + 3B\right) \tag{10}$$

and

$$a = 2^{1/3}3^{2/3}B, \quad b = \left(\tfrac{3}{2}\right)^{1/3}\left(f - \tfrac{3}{2}B^2\right),$$
$$d = -3B\left(f - \tfrac{3}{2}B^2\right) = -ab. \tag{11}$$

Now B and f must be found in terms of Δt_{DB1} and Δt_{DB2}.

The conditions for the stationary points are found and matched to the transient echo time data. First, the derivatives of Eq. (9) are found and set to zero, then making the substitution $f=-f'+2B^2$ to simplify the algebra; the roots are then

$$\tilde{u}_{\pm} = -2B \pm \sqrt{2f'}, \quad \tilde{v}_{\pm} = 0 \tag{12}$$

and

$$\tilde{u}_0 = -4B, \quad \tilde{v}_0 = \sqrt{4(f' - 2B^2)}. \tag{13}$$

The root in Eq. (13) is doubly degenerate, indicating that there can be up to four stationary points.

These locations can be plugged back into the dimensionless distance function, Eq. (9):

$$\Phi_0 = kz_0 - \tfrac{8}{3}B^3 + 4Bf' \tag{14}$$

and

$$\Phi_\pm = kz_0 - \frac{4B^3}{3} + 2Bf' \mp \frac{(2f')^{3/2}}{3}. \tag{15}$$

Examination of (14) and (15) reveals that $\Phi_\pm$ can be written partially in terms of Φ_0,

$$\Phi_\pm = \frac{kz_0 + \Phi_0}{2} \mp \frac{(2f')^{3/2}}{3}. \tag{16}$$

The echo time differences labeled in Fig. 10 are the ones used to find the coefficients B and f' and thus a, b, and d. The earliest echo time in that figure is Φ_- and the latest Φ_+. The degenerate XDB echoes are in between them and modeled by Φ_0.

The relevant nondimensional combination of time differences are written as

$$\sigma = \omega\Delta t_{\mathrm{DB1}} + \omega\Delta t_{\mathrm{DB2}}, \quad \delta = \omega\Delta t_{\mathrm{DB1}} - \omega\Delta t_{\mathrm{DB2}}. \tag{17}$$

When written in this manner these parameters can be described by what they represent physically; σ is responsible for the overall merging rate and δ regulates the asymmetry of the merger of rays. Thus, δ is a function of the finiteness of the target, if the target size vanishes so does δ. These temporal echo relationships can then be written in terms of the dimensionless distance functions:

$$\begin{aligned} &\sigma = \Phi_+ - \Phi_-, \\ &\delta = (\Phi_0 - \Phi_+) - (\Phi_- - \Phi_0) = 2\Phi_0 - \Phi_+ - \Phi_-. \end{aligned} \tag{18}$$

Then putting these in Eqs. (14)–(16) gives

$$\sigma = \tfrac{2}{3}(2f')^{3/2}, \quad \delta = \Phi_0 - kz_0 = -\tfrac{8}{3}B^3 + 4Bf'. \tag{19}$$

Using these results and Eq. (11) along with the f' substitution the steps to find coefficients a, b, and d in the fully lit region can be obtained. As explained in Sec. III, a must vanish with δ. Thus,

1. a is the root, which vanishes when δ vanishes, of

$$\tfrac{4}{27}a^3 - \sigma^{2/3}a + \delta = 0. \tag{20}$$

2. Using a from the above, b is then found using

$$b = -3^{1/3}\left(\tfrac{3}{8}\sigma\right)^{2/3} + \tfrac{1}{12}a^2. \tag{21}$$

3. The condition on d becomes,

$$d = -ab. \tag{22}$$

The cubic equation in Eq. (20) can be solved,[17] but this form suffices for the discussion here. These coefficients can be put into Eqs. (7) and (8) to give the pressure in the fully lit region. Since these coefficients are undefined in the other regions (shadow region or the middle region between the mergers) they must be extrapolated into these regions.

III. ANALYSIS

The integral needed to solve for the pressure given in Eq. (8) is not trivial. In general, for these types of integrals, the region where the phase varies slowly is identified and numerically calculated then asymptotic solutions are used for the remainder of space.[25,26] Since a is expected to be small we can use a method given by Uzer *et al.*[27] to take advantage of the Airy function results. They define

$$U[a,b,c] = \frac{1}{(2\pi)^2}\int_{-\infty}^{\infty}\int_{-\infty}^{\infty} e^{i(x^3+y^3+axy+bx+cy)}dx\,dy. \tag{23}$$

With this definition a simpler form of Eq. (7) can be written in the same manner and for the same reasons as Eqs. (4) and (5),

$$|p_{\mathrm{DB}}(Q)| = D\omega^{1/3}|U[a,b,b]|, \tag{24}$$

where again, D is an experimentally determined coefficient in units of pressure $\times$ time$^{1/3}$.

For small a the function $U[a,b,c]$ goes over to two Airy functions and can be written as a series in $a^n/n!$ as shown by Connor,[28]

$$U[a,b,c] = 3^{-2/3}\sum_{n=0}^{\infty}\frac{(-i3^{-2/3}a)^n}{n!}\mathrm{Ai}^{(n)}[3^{-1/3}b]\mathrm{Ai}^{(n)}[3^{-1/3}c], \tag{25}$$

where $\mathrm{Ai}^{(n)}(w)$ is the nth derivative of the Airy function. To find the derivatives of the Airy function the Airy differential equation can be used,[29]

$$w''(z) = zw(z), \tag{26}$$

to give the recursion relation

$$\mathrm{Ai}^{(n)}[w] = (n-2)\mathrm{Ai}^{(n-3)}[w] + w\mathrm{Ai}^{(n-2)}[w]. \tag{27}$$

An algorithm is written using this method to calculate $U[a,b,c]$ and confirmed by comparison to published results.[27] This form of the integral is also useful to demonstrate some of the limits of the result.

The most obvious limit to consider is the point target limit. Consider what happens to σ and δ for a point target. By geometry and as discussed earlier, the two echo time differences ($\omega\Delta t_{\mathrm{DB1}}$ and $\omega\Delta t_{\mathrm{DB2}}$) are equal for a point target. Thus δ vanishes and σ is simply written $2\omega\Delta t_{\mathrm{DB}}$. Then the arguments of the hyperbolic umbilic integral become

$$a = 0, \quad b = -3^{1/3}\left(\tfrac{3}{4}\omega\Delta t_{\mathrm{DB}}\right)^{2/3}, \quad d = 0. \tag{28}$$

Approximating $U[a,b,c]$ for small a by taking only the first term, the correct point target limit given by Eq. (5) is found. The integral in Eq. (23) was previously analyzed[9] for $a=0$ for the purpose of explaining aspects of the scattering of light by spheroidal drops.[21]

Less obvious limits bearing investigation are the large argument limits. As the rays get further and further apart in time and space, they behave more like individual rays. This should be reflected in the large argument limits of each of the magnitudes. Starting with the large target limit of the Airy function as given by Abramowitz and Stegun,[29]

$$\mathrm{Ai}[-z] \approx \pi^{-1/2} z^{-1/4} \left\{ \sin\left(\xi + \frac{\pi}{4}\right) \sum_{k=0}^{\infty} (-1)^n c_{2k} \xi^{-2k} - \cos\left(\xi + \frac{\pi}{4}\right) \right\} \sum_{k=0}^{\infty} (-1)^n c_{2k+1} \xi^{-2k-1} \tag{29}$$

with

$$\xi = \frac{2}{3} z^{3/2}, \quad c_0 = 1, \quad c_k = \frac{\Gamma\left(3k + \frac{1}{2}\right)}{54^k k! \Gamma\left(k + \frac{1}{2}\right)}. \tag{30}$$

To leading order in ξ this becomes

$$\mathrm{Ai}(-z) \approx \pi^{-1/2} z^{-1/4} \cos\left(\xi - \frac{\pi}{4}\right) = \pi^{-1/2} \left(\frac{3}{2}\xi\right)^{-1/6} \cos\left(\xi - \frac{\pi}{4}\right). \tag{31}$$

For the SB case $\xi = (\omega/2)\Delta t = (\omega/2)(t_2 - t_1)$ this can be rewritten (using the Euler equation) as

$$\mathrm{Ai}\left[-\left(\frac{3}{4}\omega\Delta t\right)^{2/3}\right] \approx \frac{e^{i\pi/4}}{2\pi^{1/2}\left(\frac{3}{4}\omega\Delta t\right)^{1/6}} \exp\left(-i\frac{\omega}{2}(t_1 + t_2)\right) \times (e^{i\omega t_1} + e^{-i\pi/2} e^{i\omega t_2}). \tag{32}$$

Equation (32) gives the results expected for two rays far apart in time. Note that ωt_1 and ωt_2 are the geometrically calculated propagation phase shifts and the temporal factor of the wave field is $e^{-i\omega t}$. Recall that each time a ray is focused as it touches a caustic it picks up a phase advance of $\pi/2$.[19,30] This is reflected in Eq. (32) by the extra phase in the second term.

For the finite target DB case, when σ is sufficiently large the rays can be treated separately. Equation (20) can be rewritten,

$$a = \frac{\frac{4}{27}a^3 + \delta}{\sigma^{2/3}} \tag{33}$$

making it apparent that a vanishes in the large σ limit. Then b becomes

$$b = -3^{1/3}\left(\tfrac{3}{8}\sigma\right)^{2/3} = -3^{1/3}\left(\tfrac{3}{8}[\omega t_3 - \omega t_1]\right)^{2/3}, \tag{34}$$

with $\sigma = \omega\Delta t_{\mathrm{DB2}} + \omega\Delta t_{\mathrm{DB1}} = \omega t_3 - \omega t_1$. Now $a = 0$ and b can be put into Eq. (25) and with Eq. (32) this can be rewritten for large argument

$$U(0,b,b) \approx \frac{3^{-2/3} e^{i\pi/2} e^{-i(\omega/2)(t_3+t_1)}}{4\pi\left(\frac{3}{8}\omega[t_3 - t_1]\right)^{1/3}} \times \{e^{i\omega t_1} + 2e^{-i(\pi/2)} e^{i(\omega/2)(t_1+t_3)} + e^{-i\pi} e^{i\omega t_3}\}. \tag{35}$$

Studying Eq. (35) along with Figs. 8 and 10 shows that each of the echoes is represented. The shorter of the two normal DB echoes, t_1, touches no caustics either to or from the target thus it has no caustic phase shift. The longer one, t_3, touches twice, once to the target and once upon return, and thus has two $\pi/2$ advances. The XDB echoes are represented by the second term. A coefficient of two accounts for the degeneracy and a $\pi/2$ phase advance accounts for the single touching, to the target for one echo and on the way back for the other.

IV. EXPERIMENTS

The experiments and data here are gathered along with the data for the SB analysis reported previously,[1,17] and the reader is referred to Ref. 1 for details of the experiments. All dimensions and distances in Ref. 1 are the same for the experiments presented here. The experiments are run twice at each position once with a short pulse (6 cycle Gaussian envelope burst at 400 kHz) to get return time information and again with a tone burst (70 μs at 250 kHz smoothed with 25 μs cosine-squared tails at either end) to find the DB overlap magnitudes. The magnitudes are recorded at the average of the two DB return times as calculated by the numerical ray finding algorithm. The vertical lines in Fig. 4 indicate where the SB and DB magnitudes were recorded for this particular target position.

There are two target sizes: a larger target with a radius of 0.030 m giving $ka \approx 30$ for the tone burst, and a small target with a radius of 0.009 95 m, giving $ka \approx 10.5$ where the wave number k is evaluated at 250 kHz. The reflecting surface is a closed-cell Styrofoam cylindrical half-pipe of radius 0.1524 m. The target is located approximately 0.34 m away. Figures 6–8 are to scale for the larger of the two targets. Figures 2–5 are also based on the large target experimental data. Figures 5 and 10 contain numerical ray finding data based on the large target. The large target is used for explanation here since the deviation from the point target is more obvious; both targets will be addressed in the results. Figure 4 of Ref. 1 gives the small target timing data and Fig. 5 of Ref. 1 shows a small target tone burst return.

V. RESULTS AND DISCUSSION

The return times used to find the arguments a, b, and d for the hyperbolic canonical integral function as well as the argument of the Airy function for the SB case are calculated using the numerical ray finding technique, shown in Fig. 5. The data are not available in the shadow region so the arguments must be extrapolated into this region. The functions are smooth enough so that a simple cubic polynomial fitting technique works well. This is shown along with the values of the arguments from the numerical model in Fig. 11. In the

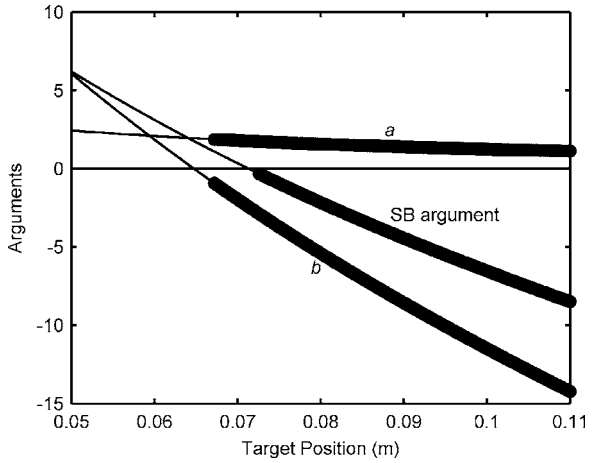

FIG. 11. Dimensionless arguments for the large target. With the source/receiver at $(-0.13, 0.025, 0)$ m and the target at $(X, -0.036, 0.409)$ m, each of the coefficients is calculated (X is the target position): the SB argument of the Airy function as in Eq. (4) and the DB arguments a and b from Eqs. (20) and (21). The dots (so close together they look like a line) are from the numerical calculation using the computed travel time differences. The thin lines are a polynomial extrapolation for the shadow region.

shadow region, there is simply a decay of the backscattering so this region is of less interest. Methods exist for treating the rays (which are now complex) in the shadow region.[31] These are not examined here, as the extrapolation proves sufficient.

Figures 12 and 13 show the magnitudes of the DB mergers for each of the two target sizes. For the small target experiment the target is located at $(X, -0.042, 0.275)$ m and the source at $(-0.13, 0.032, 0)$ m where the target moves from $X=0.05$ to 0.10 m. For the large target experiment the target is located at $(X, -0.036, 0.409)$ m and the source at $(-0.13, 0.025, 0)$ m where the target moves from $X=0.05$ to 0.11 m. The model used is given in Eq. (24) with the arguments for the large target plotted in Fig. 11. No attempt is made to take into account variations in the virtual wave front amplitude, $A(x, y)$, although it is plausible that it might be done by extending the method explained for the SB

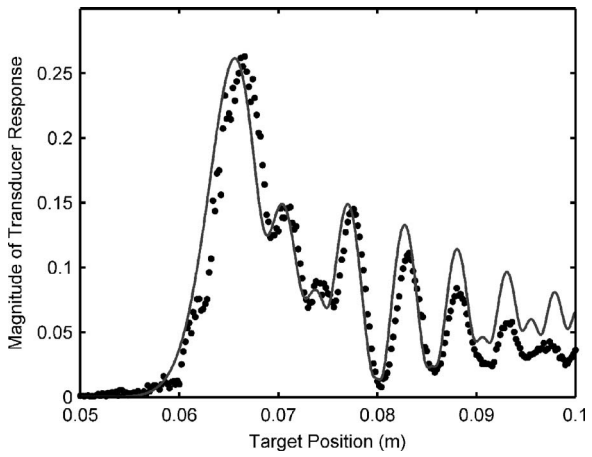

FIG. 12. The solid dots are the magnitudes of the double bounce merging as found using the experimental method described for the small target ($ka \approx 10$). The solid line is the hyperbolic umbilic canonical integral model from Eq. (24). The magnitude in this equation, D, has been adjusted to fit the data.

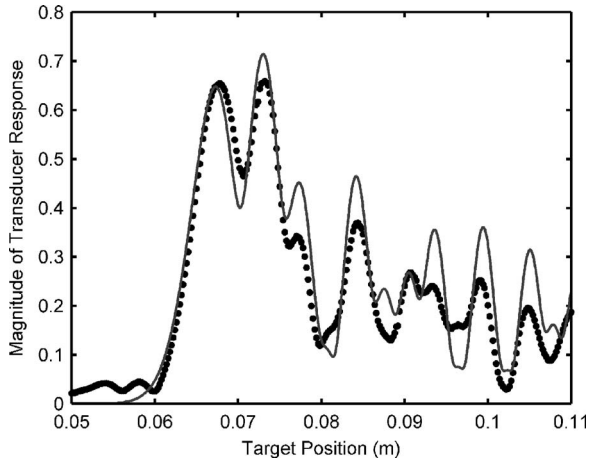

FIG. 13. The solid dots are the magnitudes of the double bounce merging as found using the experimental method described for the large target ($ka \approx 30$). The solid line is the hyperbolic umbilic canonical integral model from Eq. (24). The magnitude in this equation, D, has been adjusted to fit the data.

case.[1,17] For both target sizes the theory shows qualitative agreement, each experimental peak has a theoretical analogue. Similar experiments with the small target using frequencies from 200 to 300 kHz also show qualitative agreement with Eq. (24).[17] The small target results match the experiment much more closely than large target results. The approximation for the large target breaks down for a variety of reasons including: (a) failure of the DB returns to completely overlap as the target moves deeper into the fully lit region,[17] (b) encroachment of the SB rays into the DB region (see Fig. 5), and (c) edge diffraction from the cylindrical half-pipe. Deep into the fully lit region the surface of the target comes close to the edge of the cylindrical half-pipe.

The most important result of this research is the enhancement of the backscatter with the presence of a focusing surface. This is seen in Fig. 2 for the short pulse and in Fig. 4 for the longer tone burst. In addition, the results here may allow location of a target at a greater distance by observing the way in which the return times merge and its size by the shape of the doubly focused return. Imagine a surface wave passing over a target thus moving the target in and out of a caustic field, the changing magnitude of the singly and doubly focused echo would provide information about the target. Although the nature of caustic fields is well understood, study of targets in caustic regions is ripe with unsolved problems. Here only the simplest caustic and convex target were examined; many other cases remain. If the doubly focused case were to be analyzed for slightly oblate or prolate targets, from Thom's theorem, the general features visible in Fig. 10 would be preserved although the evolution of time differences would change. Consequently, the arguments in Eq. (25) would be modified. With modifications to allow for forward scattering, our approach should be applicable to the double focusing of prereverberation diagrammed in Fig. 5 of Ref. 11.

ACKNOWLEDGMENT

This work was supported by the Office of Naval Research.

[1]B. R. Dzikowicz and P. L. Marston, "Singly focused backscattering from small targets in an Airy caustic formed by a curved reflecting surface," J. Acoust. Soc. Am. **116**, 2751–2758 (2004).
[2]K. L. Williams, J. S. Stroud, and P. L. Marston, "High-frequency forward scattering from Gaussian spectrum, pressure release, corrugated surfaces. I. Catastrophe theory modeling," J. Acoust. Soc. Am. **96**, 1687–1702 (1994).
[3]C. K. Frederickson and P. L. Marston, "Transverse cusp diffraction catastrophes produced by the reflection of ultrasonic tone bursts from a curved surface in water: Observations," J. Acoust. Soc. Am. **92**, 2869–2877 (1992).
[4]C. K. Frederickson and P. L. Marston, "Travel time surface of a transverse cusp caustic produced by reflection of acoustical transients from a curved metal surface in water," J. Acoust. Soc. Am. **95**, 650–660 (1994).
[5]J. S. Stroud, P. L. Marston, and K. L. Williams, "Intensity moments of underwater sound scattered by a Gaussian spectrum corrugated surface: Measurements and comparison with a catastrophe theory approximation," Proceedings from NATO SCLANTCEN, edited by N. G. Pace, E. Pouliquen, and O. Bergem, Lerici, Italy, 30 June–4 July 1997, pp. 532–535.
[6]J. C. Preisig and G. B. Dean, "Surface wave focusing and acoustic communications in the surf zone," J. Acoust. Soc. Am. **116**, 2067–2080 (2004).
[7]R. Thom, *Structural Stability and Morphogenesis* (Benjamin/Cummings, Reading, MA, 1975).
[8]M. V. Berry, "Waves and Thom's theorem," Adv. Phys. **25**, 1–26 (1976).
[9]P. L. Marston, "Geometrical and catastrophe optics methods in scattering," Phys. Acoust. **21**, 1–234 (1992).
[10]J. F. Nye, *Natural Focusing and Fine Structure of Light; Caustics and Wave Dislocations* (IOP, Bristol, 1999).
[11]V. S. Gostev and R. F. Shvachko, "Caustics and volume prereverberation in a surface oceanic waveguide," Acoust. Phys. **46**, 559–562 (2000).
[12]C. J. Chapman, "Caustics in cylindrical ducts," Proc. R. Soc. London, Ser. A **455**, 2529–2548 (1999).
[13]E. Topuz, E. Niver, and L. Felsen, "Electromagnetic fields near a concave perfectly conducting cylindrical surface," IEEE Trans. Antennas Propag. **AP-30**, 280–292 (1982).
[14]W. Wasylkiwskyj, "Diffraction by a concave perfectly conducting circular cylinder," IEEE Trans. Antennas Propag. **AP-23**, 480–492 (1975).
[15]M. G. Brown, "The transient wave fields in the vicinity of the cuspoid caustics," J. Acoust. Soc. Am. **79**, 1367–1384 (1986).
[16]M. G. Brown and F. D. Tappert, "Catastrophe theory, caustics and travel time diagrams in seismology," Geophys. J. R. Astron. Soc. **88**, 217–229 (1987).
[17]B. Dzikowicz, "Backscattering of sound from targets in an Airy caustic formed by a curved reflecting surface," Ph.D. dissertation, Washington State University, 2003.
[18]M. G. Brown and F. D. Tappert, "Causality, caustics, and the structure of transient wave fields," J. Acoust. Soc. Am. **80**, 251–255 (1986).
[19]R. W. Boyd, "Intuitive explanation of the phase anomaly of focused light beams," J. Opt. Soc. Am. **70**, 877–880 (1980).
[20]B. Dzikowicz, "Backscattering of sound from targets in an Airy caustic formed by a curved reflecting surface," Ph.D. dissertation, Washington State University, 2003.
[21]P. L. Marston and E. H. Trinh, "Hyperbolic umbilic diffraction catastrophe and rainbow scattering from spherical drops," Nature (London) **312**, 529–531 (1984).
[22]M. J. Sewell, "On Legendre transformations and umbilic catastrophes," Math. Proc. Cambridge Philos. Soc. **83**, 273–288 (1978).
[23]H. Trinkaus and F. Drepper, "On the analysis of diffraction catastrophes," J. Phys. A **10**, L11–L16 (1977).
[24]T. Poston and T. Stewart, *Catastrophe Theory and its Applications* (Dover, New York, 1978).
[25]J. N. L. Conner and P. R. Curtis, "A method for the numerical evaluation of the oscillatory integrals associated with the cuspoid catastrophes: Application to Pearcey's integral and its derivatives," J. Phys. A **15**, 1179–1190 (1982).
[26]J. N. L. Connor, "Evaluation of multidimensional canonical integrals in semiclassical collision theory," Mol. Phys. **26**, 1371–1377 (1973).
[27]T. Uzer, J. T. Muckerman, and M. S. Child, "Collisions and umbilic catastrophes, The hyperbolic umbilic canonical diffraction integral," Mol. Phys. **50**, 1215–1230 (1983).
[28]J. N. L. Conner, "Multidimensional canonical integrals for the asymptotic evaluation of the S-matrix in semiclassical collision theory," Faraday Discuss. Chem. Soc. **55**, 51–58 (1972).
[29]*Handbook of Mathematical Functions*, edited by P. B. Abramowitz and I. A. Stegun, National Bureau Standards, Applied Mathematics Series Vol. **55** (U.S. GPO, Washington, D.C., 1964).
[30]M. G. Brown, "The transient wave fields in the vicinity of the elliptic, hyperbolic, and parabolic ubilic caustics," J. Acoust. Soc. Am. **79**, 1385–1401 (1986).
[31]D. W. White and M. A. Pedersen, "Evaluation of shadow-zone fields by uniform asymptotics and complex rays," J. Acoust. Soc. Am. **69**, 1029–1059 (1981).

Acoustic scattering by a metallic tube with a concentric solid polymer cylinder coupled by a thin water layer. Influence of the thickness of the water layer on the two Scholte–Stoneley waves

Farid Chati,[a] Fernand Léon, and Gérard Maze
Laboratoire d'Acoustique Ultrasonore et d'Electronique, UMR CNRS 6068, Université du Havre, Place Robert Schuman, BP 4006, 76610, Le Havre, France

(Received 20 September 2004; revised 25 April 2005; accepted 22 August 2005)

The problem of a plane acoustic wave scattered by a layered cylinder submerged in water is considered. This cylinder consists of a tube made of aluminum with a solid Lucite cylinder concentrically fitt inside it. These two components are coupled by a thin layer of water. A particular investigation is made on the influence of the thickness of the water layer on the presence of the bending wave A on the tube and the Scholte–Stoneley wave on the cylinder. The presence of these waves is examined in the function of the varying water layer thickness: two special cases are discussed. First, for a layer thickness greater than the tube thickness, it is shown that both the A wave on the aluminum tube and the Scholte–Stoneley wave on the Lucite cylinder are generated. Second, for a thickness much smaller than the tube thickness, a different wave is generated, which is a combination of both waves. These two cases are experimentally verified in a setup that employs a short pulse method. © *2005 Acoustical Society of America.* [DOI: 10.1121/1.2065807]

PACS number(s): 43.20.Fn, 43.20.Ks [MO] Pages: 2820–2828

I. INTRODUCTION

In various studies involving ultrasonic scattering by cylindrical targets, the Scholte–Stoneley wave plays a significant part in resonance scattering. It is often referred to by many researchers as the bending wave A in the case of elastic cylindrical shells. For elastic metallic tubes filled with a fluid and immersed in water, it has already been established that the presence of the A wave depends on the thickness of the tube walls.[1–6] Indeed, it has further been shown that resonances related to this wave are only detected on tubes of small thickness;[4–6] in addition, these resonances are observable in a frequency window whose position depends also on the thickness of the tubes. However, in a recent publication, it has been shown that the Scholte–Stoneley wave can also be generated on the circumference of a solid Lucite cylinder.[7] This polymer material is characterized by a low absorption and a shear velocity that is lower than the sound velocity in water. Favretto-Anrès pointed out that the Scholte–Stoneley wave at a plane interface between a fluid and a viscoelastic solid is sensitive to the variation of the shear velocity.[8] Experimentally, its resonances are detectable at low frequencies because of the loss of acoustic energy due to absorption in the polymer,[7] which increases with frequency.[9,10]

The scattering of a normally incident plane wave from an aluminum tube containing a Lucite cylinder is investigated both theoretically and experimentally. The two objects are coupled by a thin water layer. In this study, we seek to determine whether the A wave on the shell and the Scholte–Stoneley wave on the cylinder can also be generated around layered cylinders. The influence of the thickness of the water layer on the generation of these two waves is shown. To this end, two significant water layer thicknesses are considered. The first is relatively bigger in comparison to the wall thickness of the tube whereas the second is relatively smaller.

The study of the two cylinders with different water layer thicknesses is organized as follows. First, a theoretical analysis is carried out at low frequencies so as to lessen energy loss due to absorption in the polymer cylinder. Our interest is thus focused on the waves that can be experimentally observed. Second, a theoretical asymptotic analysis of dispersion curves of the phase velocities of these waves on the layered cylinder is carried out over a wide frequency range. This approach enables us to identify waves that are generated. In order to show the influence of the water layer thickness, the obtained results are confronted with those of the two elementary constituents of the target (cylinder and tube) separately. Last, an experimental verification is made by means of a short-pulse measurement method called MIN (Méthode Impulsionnelle Numérisée).[11]

II. THEORETICAL ANALYSIS: PLANE OF MODAL IDENTIFICATION—DISPERSION CURVE OF THE PHASE VELOCITY

Numerical computations are performed for an aluminum tube (outer radius a, inner radius b) with a Lucite cylinder (radius c) concentrically fitt inside it [Fig. 1(a)]. The lengths of both objects are assumed infinite. The wall thickness of the tube has been chosen such that the experimental observation windows of the A wave related to the tube and the Scholte–Stoneley wave related to the Lucite cylinder can be located within the same frequency range. The location of the

[a]Author to whom correspondence should be addressed. Electronic mail: farid.chati@univ-lehavre.fr

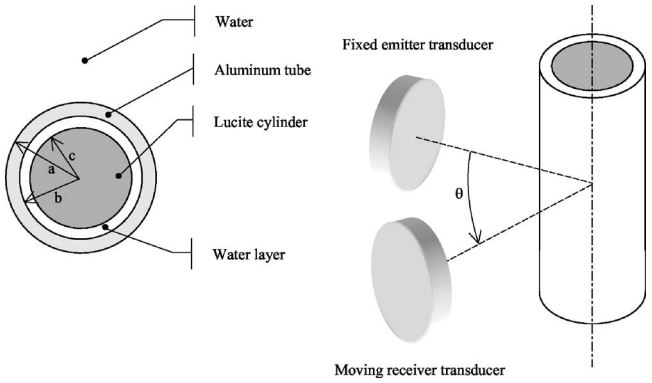

FIG. 1. (a) Geometry of the problem. (b) Experimental bistatic setup.

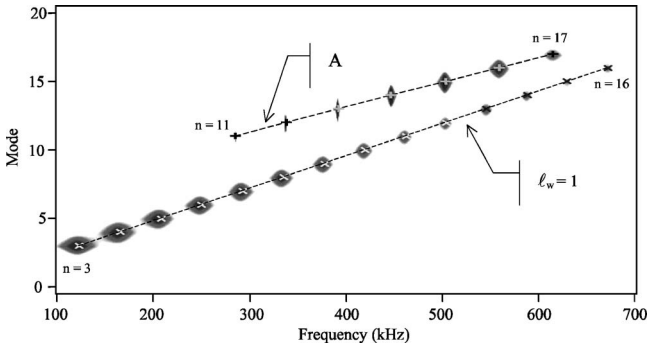

FIG. 2. Theoretical plane of modal identification of an aluminum tube containing a Lucite solid cylinder coupled by a water layer with a thickness h = 1.03 mm (gray level representation). Dashed lines concern the two constituents (+: bending wave A of the tube filled by water, ×: Scholte–Stoneley wave l_w=1 of the Lucite cylinder).

wave A depends on the thickness of the tube.[5,6] Computations have been carried out with two particular water layer thicknesses $h(h=b-c)$. The first is larger than the wall thickness of the tube $(a-b)$, whereas the second is much smaller. Values of the physical parameters used are as follows:

Aluminum tube: a=5.5 mm, b/a=0.924, ρ_2=2765 kg/m^3, C_{L2}=6440 m/s, C_{S2}=3133 m/s;
Lucite cylinders: ρ_4=1180 kg/m^3, C_{L4}=2673 m/s, C_{S4}=1383 m/s, β_{L4}=0.003 48 Np, β_{S4}=0.005 31 Np,
Cylinder 1: c=4.05 mm(h=1.03 mm),
Cylinder 2: c=5 mm(h=0.08 mm);
Water: $\rho_1=\rho_3$=1000 kg/m^3, $C_1=C_3$=1470 m/s,

where ρ_1, ρ_2, ρ_3, ρ_4 are the densities of, respectively, the surrounding liquid (water), aluminum, the coupling layer (water), and Lucite. C_{L2} and C_{S2} are the longitudinal and shear velocities in aluminum, C_{L4} and C_{S4} are the longitudinal and shear velocities in Lucite. β_{L4} and β_{S4} are, respectively, the longitudinal and shear absorption factors characterizing the loss of the acoustic energy in Lucite. C_1 and C_3 are the sound velocities in, respectively, the surrounding and coupling liquids.

In this section, we seek to identify resonances (i.e., the resonance frequency f_n and the associated vibration mode n) and the corresponding waves. The starting point is the knowledge of the farfield scattering pressure, obtained from the following classical expression:[12]

$$P_{\mathrm{sc}}(\omega,\theta) = P_0 \frac{1-i}{\sqrt{\pi k_1 r}} \exp i(k_1 r - \omega \mathbf{t}) \sum_{n=0}^{\infty} \varepsilon_n \frac{D_n^{[1]}}{D_n} \cos n\theta, \tag{1}$$

where r is the distance between the axis of the layered cylinder and the observation point. k_1 is the modulus of the wavelength vector in surrounding water, θ is the azimuth angle, ω the pulsation and n the vibration mode, ε_n is the Neumann factor (ε_n=1 if n=0; ε_n=2 if $n \neq 0$). By applying the boundary conditions at the three surfaces of the cylinder ($r=a$, $r=b$, and $r=c$), the unknown scattering coefficient $D_n^{[1]}/D_n$ can be determined by continuity of the radial displacements, continuity of the radial stresses, nullity of the tangential, and shear stresses (Appendix A). For each value of the summation index n, this scattering coefficient can be found from a system of the eight linear homogenous equations (Appendix A). $D_n^{[1]}$ and D_n are two determinants of the eighth order whose terms are provided in Appendix B.[13]

In our numerical study we consider that P_0=1. The time origin is defined as the instant when the incident wave passes through the cylinder axis. In order to have the same time origin as the experimental case, a new time origin is defined by

$$t' = t + t_1, \tag{2}$$

where t_1 is the time required to cover the distance between the source of the incident wave and the cylinder axis. Its expression is $t_1=(u+a)/c_1$ (where u is the distance between the source and the cylinder surface). The change in variable leads to the following scattered pressure expression [the term $\exp i(2k_1u-\omega t')$ is omitted]:[12]

$$P_{sc}(\omega,\theta) = \frac{1-i}{\sqrt{\pi k_1 r}} \exp(2ik_1 a) \sum_{n=0}^{\infty} \varepsilon_n \frac{D_n^{[1]}}{D_n} \cos n\theta. \tag{3}$$

The temporal pulse responses $T(t,\theta)$ are then determined by applying the inverse Fast Fourier Transforms on $P_{sc}(\omega,\theta)$ $(0 \leqslant \theta \leqslant \pi)$. At a given angle θ, the real part of the inverse transform represents the temporal acoustic response. Each response is composed of echoes related to both nonresonant and resonant contributions.[14,15] In order to identify modes and resonance frequencies, the modulus of double Fast Fourier Transforms on $T(t,\theta)$ devoid of the nonresonant contribution are calculated. The dual variable of θa is χ (expressed in m^{-1}).[16] It is associated to the modulus of the wavelength vector in the layered cylinder k by the relation $k=2\pi\chi$. The results of these two-dimensional (2D) transforms are represented as a function of f and n. The vibration mode n is given by the relation $n=ka$. Thus, only the case where ka is an integer is considered.

The numerical results are then plotted as a gray level representation called the *plane of modal identification* (as shown in the example, Fig. 2). The darker the gray shade is the bigger the magnitude. Modes n and resonance frequencies f_n are easily determined by searching for coordinates of peak of amplitudes. One of the main advantages of this numerical processing is the possibility to determine, at the same time, all the resonances. Nevertheless, in this section

only resonances that can be excited are considered; i.e., resonances whose attenuation is neither "too big" nor "too small." An attenuation too big is due to the strong coupling between the surface wave and the incident wave,[5,6] thus the wave reradiates all its energy into the surrounding liquid as soon as it is generated. An attenuation too small is due to the weak coupling; the wave reradiates insufficient energy in the surrounding medium. In both cases, resonances cannot be observed experimentally.

The identification of resonances (n, f_n) is carried out in low frequencies in order to observe the Scholte–Stoneley wave on the solid Lucite cylinder.[7] It has already been established that the absorption due to the viscosity of a polymer depends on the frequency, and, in particular, absorption increases with the frequency. This absorption causes a decrease of the magnitude of resonances. Therefore, the studied frequency shall be limited in the range 100–700 kHz.

The identification of waves is performed from the knowledge of phase velocities. A theoretical analysis of the dispersion curves of phase velocities of waves on the layered cylinder is carried out in large frequency ranges (0–5 MHz and 0–2.5 MHz). The phase velocity C_{ph} is calculated from the expression

$$C_{\mathrm{ph}} = \frac{x_{\mathrm{n1}} C_1}{n}, \tag{4}$$

where x_{n1} is the dimensionless resonance frequency. For each mode n, the numerical value is determined by searching for the roots of the equation $D_n(\tilde{x}_1)=0$,[17] whose solutions are complex, given by the expression $\tilde{x}_1 = x_{\mathrm{n1}} + i\Gamma/2$. The real part represents the resonance frequency and the imaginary part the half-width of the resonance. In Sec. IV, both the identification of waves on the layered cylinder and their behavior for the two coupling layer thicknesses are discussed using phase velocities. Numerical results from the layered tube are confronted with those from both elementary constituents (tube and cylinder). The dispersion curves of phase velocities of the A wave on the tube and the Scholte–Stoneley on the cylinder are taken as references. For the aluminum tube, in the high-frequency limit the phase velocity of the A wave tends toward the speed of sound in water (1470 m/s),[18] whereas in the case of the Lucite cylinder the phase velocity of the Scholte–Stoneley tends toward the speed of the Scholte–Stoneley mode (about 1050 m/s) that may propagate in the Lucite–water plane interface.[7] In all these computations, absorption is not taken into account ($\beta_{L4}=\beta_{S4}=0$). This assumption is justifiable because values of resonance frequencies are only very slightly modified by absorption,[10] and thus phase velocities are not depended on it either.

III. EXPERIMENTAL SETUP

The cylindrical aluminum shell containing, successively, the two Lucite cylinders is analyzed. The lengths of the shell and of cylinders are, respectively, equal to 300 and 245 mm. Appropriate adjustment tools ensure that the shell's axe coincides with the cylinder's one. The two objects are fixed together at the cylindrical shell extremities. The whole structure is not watertight: openings let water fill the thin space between the shell and the cylinder when the target is immersed in water. This water layer ensures the coupling between them. Two water layer thicknesses ($h=1.03$ mm, $h=0.08$ mm) are successively considered. Each layered cylinder is vertically immersed in a rectangular tank, 2 m long, 1.50 m wide, and 1 m deep filled with water. The target is suspended at the center of this tank. The short-pulse bistatic setup of the MIN (Méthode Impulsionnelle Numérisée) is used to obtain experimental results.[11] Broadband Panametrics transducers, model V389, with a central frequency equal to 500 kHz are employed; their useful frequency range is about 100–700 kHz. This setup comprises a fixed emitter transducer and a mobile receiver transducer moving around the layered cylinder under study [Fig. 1(b)]. The receiver transducer is rotated in an azimuthal plane, normal to the layered cylinder axis, in one degree displacements. At each azimuth angle θ, the time-domain response of the insonified layered cylinder is measured and recorded. The temporal responses consist of echo waveforms made up specular reflections and elastic wave reradiations. In a similar way as in Sec. II, double FFT of the time-domain responses, devoid of nonresonant contributions (specular reflections), are carried out. The obtained results are represented as planes of modal identification. In order to compare numerical and experimental planes, a correction of the passbands of the transducers is carried out.

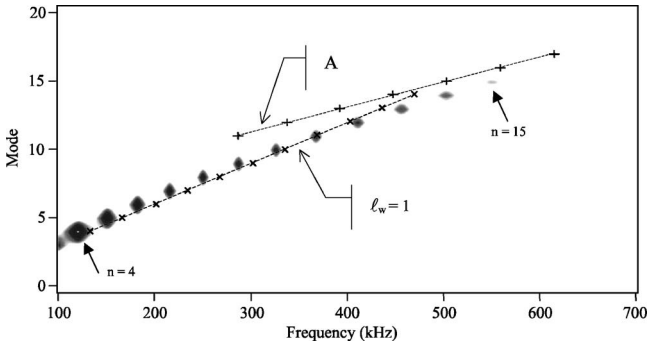

FIG. 3. Theoretical plane of modal identification of an aluminum tube containing a Lucite solid cylinder coupled by a water layer with a thickness $h=0.08$ mm (gray level representation). Dashed lines concern the two constituents (+: bending wave A of the tube filled by water, ×: Scholte–Stoneley wave $l_w=1$ of the Lucite cylinder).

IV. DISCUSSION

Figures 2 and 3 present the planes of modal identification calculated using coupling water layer thicknesses of, respectively, $h=1.03$ mm and $h=0.08$ mm. The coordinates of external modes related to the two primary objects separately (solid Lucite cylinder and aluminum tube filled with water) are superimposed on these planes. The curve representing the wave that propagates around the solid cylinder imbedded in water is labeled $l_w=1$, while one representing the wave that propagates at the surface of the tube immersed in water is labeled A. These planes of modal identification enable us to show, at low frequencies, the presence of both waves and their behavior when h changes. In a study of cylindrical targets it is common practice to use dimensionless

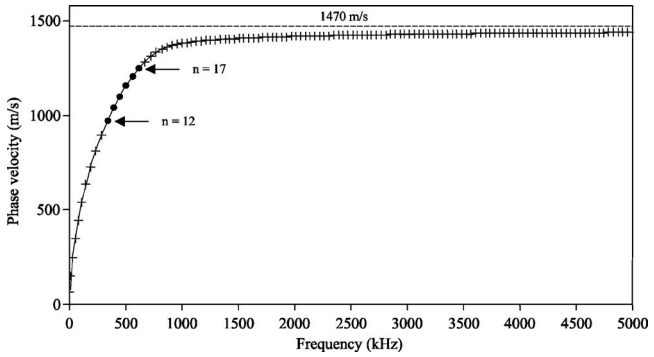

FIG. 4. Theoretical dispersion curves of phase velocity of the A wave; solid line: curve concerning the aluminum filled by water, + and ●: modes concerning the aluminum tube containing a Lucite solide cylinder coupled by a water layer with a thickness $h=1.03$ mm (●: mode that can be experimentally observed).

frequency ($x_1=2\pi$ radius/speed of sound in the outer fluid). However, in the present case, it is not judicious to use the dimensionless frequency because the primary constituent objects have different radii ($a>c$). Thus, the use of the frequency expressed in Hertz makes the analysis and the comparison of numerical results easier. Further, the two planes only reveal those vibration modes that are experimentally detectable.

Figures 4–6 depict different dispersion curves of phase velocities of the waves for the two layered cylinders characterized by different values of h. Those of the A and $l_w=1$ waves and their asymptotes (i.e., the values of the boundary velocities) are also plotted. The values of asymptotes are, respectively, the speed of sound in water (1470 m/s) and the speed of the Scholte–Stoneley mode at the plane interface Lucite–water (1050 m/s). For the reason mentioned in the previous paragraph, the abscissa axis is graduated in Hertz. Here, all modes are considered (experimentally observable or not).

For $h=1.03$ mm, the theoretical plane in Fig. 2 yields two waves whose identification of resonances is easily realized throughout the studied frequency range (100–700 kHz). One of these waves comprises 14 vibration modes from $n=3$ to $n=16$. The other comprises seven modes, from $n=11$ to $n=17$. Let us recall that theses figures display only the vibration modes that can be experimentally observed. Other modes associated with these waves are excluded by fixing a minimum amplitude threshold (i.e., resonances of small magnitudes are not considered). Modes associated with whispering gallery waves (internal waves of the cylinder and the tube) are equally excluded by applying numerical filters. This plane of modal identification shows a clear closeness between waves of this layered cylinder and external waves of the two constituent objects. Thus, it seems quite likely that the generated modes belong to the $l_w=1$ and the A waves. Tables I and II and Fig. 2 corroborate this observation. At low frequencies, in Tables I and II, the confrontation of resonance frequencies related to the layered cylinder with those related to both reference objects shows a good agreement. The comparison is made between columns 2 and 3.

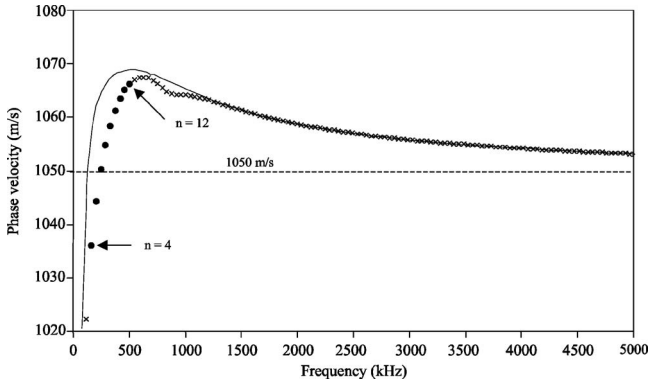

FIG. 5. Theoretical dispersion curves of phase velocity of the Scholte–Stoneley wave; solid line: curve concerning the solid Lucite cylinder, × and ●: modes concerning the aluminum tube containing a Lucite solide cylinder coupled by a water layer with a thickness $h=1.03$ mm (●: mode that can be experimentally observed).

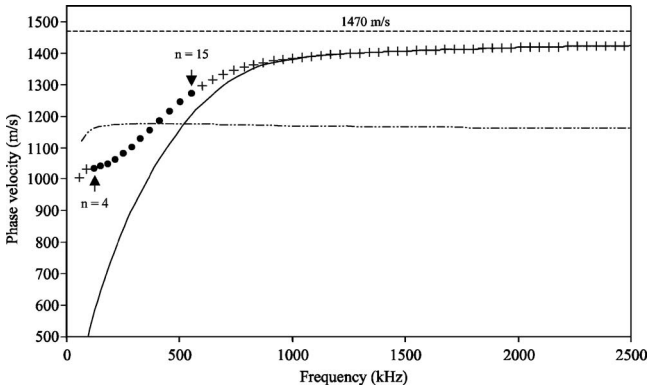

FIG. 6. Theoretical dispersion curves of phase velocity; + and ●: modes concerning the aluminum tube containing a Lucite solid cylinder coupled by a water layer with a thickness $h=0.08$ mm (●: mode that can be experimentally observed), solid line: curve concerning the wave A of the aluminum tube filled by water; dashed line (——): curve concerning the Scholte–Stoneley wave of the Lucite cylinder (velocity calculated by taking the outer radius of the tube).

TABLE I. Aluminum tube containing a Lucite cylinder coupled by a water layer thickness $h=1.03$ mm. Theoretical and experimental results relating to the Scholte–Stoneley wave of the Lucite cylinder.

	Theoretical results f(kHz)		Experimental results f(kHz)
Mode	Layered cylinder	Cylinder	Layered cylinder
3	119.4	122.9	-
4	162.0	165.3	154.1
5	204.6	207.8	204.5
6	247.1	250.3	247.2
7	289.7	292.4	289.9
8	332.3	334.7	332.6
9	374.9	377.0	373.8
10	417.4	419.2	419.6
11	460.0	461.3	462.3
12	502.6	503.4	502.0
13	544.1	545.4	-
14	586.7	589.1	-
15	628.2	629.1	-
16	670.8	671.1	-

TABLE II. Aluminum tube containing a Lucite cylinder coupled by a water layer thickness $h=1.03$ mm. Theoretical and experimental results relating to the A wave of the tube.

	Theoretical results f(kHz)		Experimental results f(kHz)
Mode	Layered cylinder	Cylinder	Layered cylinder
11	284.5	285.6	-
12	336.4	337.5	337.0
13	390.4	391.5	390.6
14	445.5	446.5	447.1
15	501.5	502.6	502.0
16	557.6	558.7	558.5
17	617.7	614.2	614.9

The theoretical dispersion curves plotted in Figs. 4 and 5 confirm that waves of the layered cylinder correspond to the A and $l_w=1$ waves. Indeed, although some modes undergo speed shifting at low frequencies, the shapes of dispersion curves are very similar to those of A and $l_w=1$ waves. Within the limits of high frequencies, the two waves of the layered cylinder tend toward the characteristic boundary speeds, i.e., 1470 and 1050 m/s. Figure 4 shows that the A wave is practically not disturbed by the Lucite cylinder. As for the $l_w=1$ wave, it is observed in Fig. 5 that speed gaps between the two dispersion curves become smaller as the frequency rises. These gaps are due to the fact that the wavelength in water λ_1 ($\lambda_1=C_1/f$) is bigger than h at low frequencies and becomes smaller than h at high frequencies. They are nil for $h>\lambda_1$, i.e., $f>1.43$ MHz. In this case the water layer thickness is sufficiently "big" such that the incident wave excites the two objects separately. Conversely, when $h<\lambda_1$, these objects are excited simultaneously by the incident wave; the propagation of the $l_w=1$ wave is only slightly modified. For this particular value of h, in spite of the complex geometry of the layered cylinder, the A and $l_w=1$ waves can both be excited. The generation of some modes has been verified experimentally at low frequencies (100–700 kHz). The experimental plane of modal identification plotted in Fig. 7 shows the presence of the A and $l_w=1$ waves. The confrontation of theoretical results with experimental ones in Tables I and II depicts a good agreement (see columns 2 and 4).

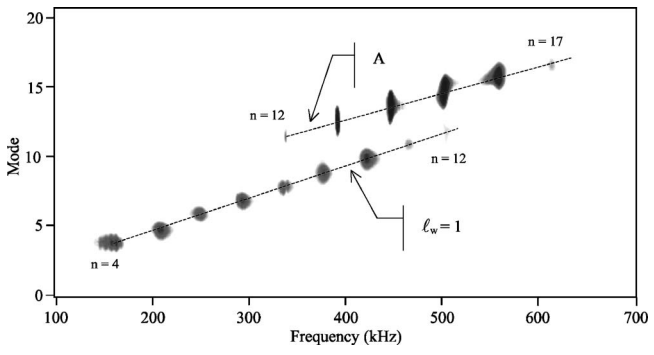

FIG. 7. Experimental plane of modal identification of an aluminum tube containing a Lucite solid cylinder coupled by a water layer with a thickness $h=1.03$ mm (gray level representation). Dashed lines concern the two contituents (A wave relating to the tube filled by water; Scholte–Stoneley wave relating to the solid Lucite cylinder: $l_w=1$).

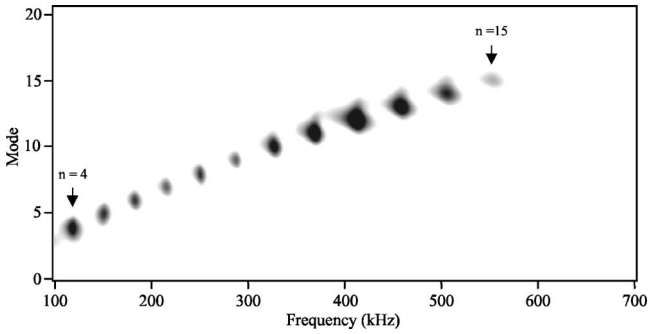

FIG. 8. Experimental plane of modal identification of an aluminum tube containing a Lucite solid cylinder coupled by a water layer with a thickness $h=0.08$ mm (gray level representation).

For $h=0.08$ mm, and in the frequency range 100–700 kHz, the wavelength in water, λ_1, is much bigger than to h ($\lambda_1 \gg h$, 2.1 mm $\leqslant \lambda_1 \leqslant$ 14.7 mm), as a result the incident wave excites the two constituent targets simultaneously. Let us recall that parameters of the aluminum tube are maintained unchanged and only the radius c of the Lucite cylinder is changed ($c=5$ mm). In this case, the theoretical plane of modal identification depicted in Fig. 3 reveals the presence of only a single wave type that can be generated on the circumference of the layered cylinder. In this low-frequency range (100–700 kHz), the wave in question comprises 12 modes ranging from $n=4$ to $n=15$. In comparison with the $l_w=1$ wave that propagates at the surface of the Lucite cylinder, the first eight modes tend to shift toward the low-frequency zone while the last four modes tend toward the high-frequency zone. Despite the fact that there exists a difference in the positions of the curves representing these two waves, it appears that all of the observed modes are "rather" attributable to the $l_w=1$ wave. It also appears that these modes are close to those of the $l_w=1$ wave. The A wave is no longer present; none of its modes is observed in the frequency range 100–700 kHz. Unlike in the previous case, where $h=1.03$ mm, here the A wave is strongly disturbed by the presence of the Lucite cylinder.

In fact, in a large frequency range (0–2500 kHz), dispersion curves of phase velocities plotted in Fig. 6 show that the wave at the surface of the layered cylinder is neither the $l_w=1$ wave nor the A wave, but appears to be a combination of these two waves. Indeed, the modes observed in the low frequencies are attributed to the $l_w=1$ wave while those in the high frequencies are attributed to the A wave. The evolution of its phase velocity becomes similar to that of the A wave at high frequencies. Hence, as the frequency increases, the generated wave becomes more and more external. It should be specified that all phase velocities have been computed by taking into account the radius a; consequently, those concerning the Lucite cylinder are multiplied by a/c.

The experimentally observed modes are therefore related to the Lucite cylinder. The experimental plane represented in Fig. 8 bears out the theoretical plane (Fig. 3). Here 12 modes have been easily measured (from $n=4$ to $n=15$). Table III summarizes the obtained results and shows a good agreement between experimental and theoretical results (see columns 2 and 5).

TABLE III. Aluminum tube containing a Lucite cylinder coupled by a water layer thickness $h=0.08$ mm. Theoretical and experimental results.

	Theoretical results f(kHz)			Experimental results f(kHz)
Mode	Layered cylinder	Tube filled by water	Cylinder	Layered cylinder
4	119.4	-	133.9	117.6
5	149.5	-	168.3	149.7
6	181.7	-	202.7	181.8
7	214.9	-	236.8	215.4
8	249.2	-	271.1	250.4
9	286.6	-	305.4	287.2
10	325.0	-	339.6	326.9
11	368.6	285.6	373.7	368.1
12	410.2	337.5	407.8	412.4
13	456.9	391.5	441.8	458.2
14	501.6	446.5	477.2	504.1
15	549.3	502.6	509.6	551.1
16	598.1	558.7	543.6	-
17	-	614.2	577.4	-

V. CONCLUSION

The scattering from a layered cylinder immersed in water is analyzed. The target is made up of an aluminum shell fitted with a concentric solid Lucite cylinder and the two are coupled by a thin water layer. We show that the observation of the A wave on the tube and of the Scholte–Stoneley wave on the cylinder depends on the thickness of the coupling water layer. When this thickness is greater than that of the tube, it is possible to generate both external waves. Conversely, for a thickness much smaller than that of the tube, it is not possible to observe either of them, instead, a new wave appears; it is a combination of both waves. At low frequencies, its modes are close to those of the Scholte–Stoneley wave on the solid Lucite cylinder ($l_w=1$), while at high frequencies, its modes are those of the A wave on the tube filled with water. These two cases are analyzed in detail both theoretically and experimentally.

ACKNOWLEDGMENTS

The authors are grateful to Dr. J. G. Chiumia for its careful reading of this manuscript and useful suggestions.

APPENDIX A: BOUNDARY CONDITIONS

(1) Continuity of the radial displacements:

$$r=a, \quad u_{r1}=u_{r2},$$

$$r=b, \quad u_{r2}=u_{r3},$$

$$r=c, \quad u_{r3}=u_{r4};$$

(2) continuity of the radial stresses:

$$r=a, \quad T_{rr1}=T_{rr2},$$

$$r=b, \quad T_{rr2}=T_{rr3},$$

$$r=c, \quad T_{rr3}=T_{rr4};$$

(3) nullity of the tangential and shear stresses:

$$r=a, \quad T_{r\theta 2}=0,$$

$$r=b, \quad T_{r\theta 2}=0,$$

$$r=c, \quad T_{r\theta 4}=0.$$

$(M).(A)=(C)$; the elements of the matrix (A) are the unknown coefficients.

APPENDIX B: DETERMINANTS ELEMENTS

$$D_n=|M|$$

$$D_n^{[1]}=\begin{vmatrix} C(1) & M(1,2) & M(1,3) & M(1,4) & M(1,5) & M(1,6) & M(1,7) & M(1,8) & M(1,9) \\ C(2) & M(2,2) & M(2,3) & M(2,4) & M(2,5) & M(2,6) & M(2,7) & M(2,8) & M(2,9) \\ C(3) & M(3,2) & M(3,3) & M(3,4) & M(3,4) & M(3,6) & M(3,7) & M(3,8) & M(3,9) \\ C(4) & M(4,2) & M(4,3) & M(4,4) & M(4,4) & M(4,6) & M(4,7) & M(4,8) & M(4,9) \\ C(5) & M(5,2) & M(5,3) & M(5,4) & M(5,4) & M(5,6) & M(5,7) & M(5,8) & M(5,9) \\ C(6) & M(6,2) & M(6,3) & M(6,4) & M(6,4) & M(6,6) & M(6,7) & M(6,8) & M(6,9) \\ C(7) & M(7,2) & M(7,3) & M(7,4) & M(7,4) & M(7,6) & M(7,7) & M(7,8) & M(7,9) \\ C(8) & M(8,2) & M(8,3) & M(8,4) & M(8,4) & M(8,6) & M(8,7) & M(8,8) & M(8,9) \\ C(9) & M(9,2) & M(9,3) & M(9,4) & M(9,4) & M(9,6) & M(9,7) & M(9,8) & M(9,9) \end{vmatrix}$$

1. Data

$$x_1 = k_1 a,$$

$$x_{L2} = k_{L2} a, \quad x_{S2} = k_{S2} a, \quad y_{L2} = k_{L2} b, \quad y_{S2} = k_{S2} b,$$

$$y_3 = k_3 b, \quad z_3 = k_3 c,$$

$$\tilde{k}_{L4} = k_{L4}(1 + i\beta_{L4}), \quad \tilde{k}_{S4} = k_{S4}(1 + i\beta_{S4}),$$

$$\tilde{z}_{L4} = \tilde{k}_{L4} c, \quad \tilde{z}_{S4} = \tilde{k}_{S4} c,$$

where $k_1 = k_3 = \omega / c_1$, $k_{L2} = \omega / c_{L2}$, $k_{S2} = \omega / c_{S2}$, $k_{L4} = \omega / c_{L4}$, $k_{S4} = \omega / c_{S4}$.

2. Elements $M(i,j)$

$$M(1,1) = -{x_{S2}}^2 H_n^{(1)}(x_1),$$

$$M(1,2) = [2n(n-1) - {x_{S2}}^2] J_n(x_{L2}) + 2x_{L2} J_{n+1}(x_{L2}),$$

$$M(1,3) = [2n(n-1) - {x_{S2}}^2] Y_n(x_{L2}) + 2x_{L2} Y_{n+1}(x_{L2}),$$

$$M(1,4) = 2n[(n-1) J_n(x_{S2}) - x_{S2} J_{n+1}(x_{S2})],$$

$$M(1,5) = 2n[(n-1) Y_n(x_{S2}) - x_{S2} Y_{n+1}(x_{S2})],$$

$$M(1,6) = 0,$$

$$M(1,7) = 0,$$

$$M(1,8) = 0,$$

$$M(1,9) = 0,$$

$$M(2,1) = \rho_2/\rho_1 [n H_n^{(1)}(x_1) - x_1 H_{n+1}^{(1)}(x_1)],$$

$$M(2,2) = n J_n(x_{L2}) - x_{L2} J_{n+1}(x_{L2}),$$

$$M(2,3) = n Y_n(x_{L2}) - x_{L2} Y_{n+1}(x_{L2}),$$

$$M(2,4) = n J_n(x_{S2}),$$

$$M(2,5) = n Y_n(x_{S2}),$$

$$M(2,6) = 0,$$

$$M(2,7) = 0,$$

$$M(2,8) = 0,$$

$$M(2,9) = 0,$$

$$M(3,1) = 0,$$

$$M(3,2) = 2n[(1-n) J_n(x_{L2}) + x_{L2} J_{n+1}(x_{L2})],$$

$$M(3,3) = 2n[(1-n) Y_n(x_{L2}) + x_{L2} Y_{n+1}(x_{L2})],$$

$$M(3,4) = [2n(1-n) + {x_{S2}}^2] J_n(x_{S2}) - 2x_{S2} J_{n+1}(x_{S2}),$$

$$M(3,5) = [2n(1-n) + {x_{S2}}^2] Y_n(x_{S2}) - 2x_{S2} Y_{n+1}(x_{S2}),$$

$$M(3,6) = 0,$$

$$M(3,7) = 0,$$

$$M(3,8) = 0,$$

$$M(3,9) = 0,$$

$$M(4,1) = 0,$$

$$M(4,2) = n J_n(y_{L2}) - y_{L2} J_{n+1}(y_{L2}),$$

$$M(4,3) = n Y_n(y_{L2}) - y_{L2} Y_{n+1}(y_{L2}),$$

$$M(4,4) = n J_n(y_{S2}),$$

$$M(4,5) = n Y_n(y_{S2}),$$

$$M(4,6) = \rho_2/\rho_3 [y_{L3} J_{n+1}(y_{L3}) - n J_n(y_{L3})],$$

$$M(4,7) = \rho_2/\rho_3 [y_{L3} Y_{n+1}(y_{L3}) - n Y_n(y_{L3})],$$

$$M(4,8) = 0,$$

$$M(4,9) = 0,$$

$$M(5,1) = 0,$$

$$M(5,2) = [2n(n-1) - {y_{S2}}^2] J_n(y_{L2}) + 2y_{L2} J_{n+1}(y_{L2}),$$

$$M(5,3) = [2n(n-1) - {y_{S2}}^2] Y_n(y_{L2}) + 2y_{L2} Y_{n+1}(y_{L2}),$$

$$M(5,4) = 2n[(n-1) J_n(y_{S2}) - y_{S2} J_{n+1}(y_{S2})],$$

$$M(5,5) = 2n[(n-1) Y_n(y_{S2}) - y_{S2} Y_{n+1}(y_{S2})],$$

$$M(5,6) = {y_{S2}}^2 J_n(y_{L3}),$$

$$M(5,7) = {y_{S2}}^2 Y_n(y_{L3}),$$

$$M(5,8) = 0,$$

$$M(5,9) = 0,$$

$$M(6,1) = 0,$$

$$M(6,2) = 2n[y_{L2} J_{n+1}(y_{L2}) + (1-n) J_n(y_{L2})],$$

$$M(6,3) = 2n[y_{L2} Y_{n+1}(y_{L2}) + (1-n) Y_n(y_{L2})],$$

$$M(6,4) = [2n(1-n) + {y_{S2}}^2] J_n(y_{S2}) - 2y_{S2} J_{n+1}(y_{S2}),$$

$$M(6,5) = [2n(1-n) + {y_{S2}}^2] Y_n(y_{S2}) - 2y_{S2} Y_{n+1}(y_{S2}),$$

$$M(6,6) = 0,$$

$$M(6,7) = 0,$$

$$M(6,8) = 0,$$

$$M(6,9) = 0,$$

$$M(7,1) = 0,$$

$$M(7,2) = 0,$$

$$M(7,3) = 0,$$

$$M(7,4) = 0$$

$$M(7,5) = 0,$$

$$M(7,6) = nJ_n(z_3) - z_3 J_{n+1}(z_3),$$

$$M(7,7) = nY_n(z_3) - z_3 Y_{n+1}(z_3),$$

$$M(7,8) = \rho_3/\rho_4[\tilde{z}_{L4} J_{n+1}(\tilde{z}_{L4}) - nJ_n(\tilde{z}_{L4})],$$

$$M(7,9) = -n\rho_3/\rho_4 J_n(\tilde{z}_{S4}),$$

$$M(8,1) = 0,$$

$$M(8,2) = 0,$$

$$M(8,3) = 0,$$

$$M(8,4) = 0,$$

$$M(8,5) = 0,$$

$$M(8,6) = -\tilde{z}_{S4}^2 J_n(z_{L3}),$$

$$M(8,7) = -\tilde{z}_{S4}^2 Y_n(z_{L3}),$$

$$M(8,8) = [2n(1-n) + \tilde{z}_{S4}^2]J_n(\tilde{z}_{L4}) - 2\tilde{z}_{L4} J_{n+1}(\tilde{z}_{L4}),$$

$$M(8,9) = 2n[\tilde{z}_{S4} J_{n+1}(\tilde{z}_{S4}) + (1-n)J_n(\tilde{z}_{S4})],$$

$$M(9,1) = 0,$$

$$M(9,2) = 0,$$

$$M(9,3) = 0,$$

$$M(9,4) = 0,$$

$$M(9,5) = 0,$$

$$M(9,6) = 0,$$

$$M(9,7) = 0,$$

$$M(9,8) = 2n[(n-1)J_n(\tilde{z}_{L4}) - \tilde{z}_{L4} J_{n+1}(\tilde{z}_{L4})],$$

$$M(9,9) = [2n(n-1) - \tilde{z}_{S4}^2]J_n(\tilde{z}_{S4}) + 2\tilde{z}_{S4} J_{n+1}(\tilde{z}_{S4}).$$

3. Elements *C*(*i*)

$$C(1) = x_{S2}^2 J_n(x_1),$$

$$C(2) = \rho_2/\rho_1[x_1 J_{n+1}(x_1) - nJ_n(x_1)],$$

$$C(3) = 0,$$

$$C(4) = 0,$$

$$C(5) = 0,$$

$$C(6) = 0,$$

$$C(7) = 0,$$

$$C(8) = 0,$$

$$C(9) = 0,$$

[1] J. L. Rousselot, "Comportement acoustique d'un tube cylindrique mince en basse fréquence," Acustica **58**, 1291–1297 (1985).
[2] J. L. Izbicki, G. Maze, and J. Ripoche, "Diffusion acoustic par des tubes immergés dans l'eau: nouvelles résonances observées en basse fréquence," Acustica **61**, 137–139 (1986).
[3] J. L. Izbicki, J. L. Rousselot, A. Gérard, G. Maze, and J. Ripoche, "Analyse of resonances related to Scholte–Stoneley waves around circular cylindrical shells," J. Acoust. Soc. Am. **90**, 2602–2608 (1991).
[4] N. D. Veksler, J. L. Izbicki, and J. M. Conoir, "Bending A wave in the scattering by a circular cylindrical shell: Its relation with the bending free modes," J. Acoust. Soc. Am. **96**, 287–292 (1994).
[5] G. Maze, F. Léon, J. Ripoche, A. Klauson, J. Metsaveer, and H. Überall, "Nature de l'onde d'interface de Scholte sur une coque cylindrique," Acustica **81**, 201–213 (1995).
[6] G. Maze, F. Léon, J. Ripoche, and H. Überall "Repulsion phenomena in the phase-velocity curves of circumferential waves on elastic cylindrical waves," J. Acoust. Soc. Am. **105**, 1695–1701, (1999).
[7] F. Chati, F. Léon, and G. Maze, "Theoretical and experimental studies of the Scholte–Stoneley wave on a solid cylinder," Acoust. Lett. **24**, 1–4 (2000).
[8] N. Favretto-Anrès, "Theoretical study of the Stoneley–Scholte wave at the interface between an ideal fluid and a viscoelastic solid," Acust. Acta Acust. 82, 829–838 (1996).
[9] B. Hartmann and J. Jarzynski, "Ultrasonic hysteresis absorption in polymers," J. Appl. Phys. **43**, 4304–4312 (1972).
[10] V. M. Ayres and G. C. Gaunaurd, "Acoustic resonances scattering by viscoelastic cylinders," J. Acoust. Soc. Am. **82**, 301–311 (1987).
[11] P. Pareige, P. Rembert, J. L. Izbicki, G. Maze, and J. Ripoche, "Méthode impulsionelle numérisée (MIN) pour l'isolement et l'identification des résonances de tubes immergés," Phys. Lett. A **135**, 143–146 (1989); P. Rembert, A. Cand, P. Pareige, M. Talmant, G. Quentin, and J. Ripoche, "The short pulse method of isolation and identification of resonances: Comparison with a quasiharmonic method and application to axisymmetrical scatterers," J. Acoust. Soc. Am. **92**, 3271–3277 (1992).
[12] G. Maze, "Acoustic scattering from submerged cylinders. MIIR Im/Re: Experimental and theoretical study," J. Acoust. Soc. Am. **89**, 2559–2566 (1991).
[13] F. Chati, "Diffusion acoustique par des objets cylindriques comportant un matériau viscoélastique," Ph. D. thesis, University of Le Havre, France, 1998.
[14] L. Flax, L. R. Dragonette, and H. Überall, "Theory of elastic resonance excitation by sound scattering," J. Acoust. Soc. Am. **63**, 723–731 (1978).
[15] A. Derem, Rev. Cethedec 58, 43–79 (1979).

[16]L. Martinez, "Nouvelles méthodes d'identication d'ondes de surfaces—Etude de l'onde A sur une cible courbe," Ph.D. thesis, University of Le Havre, France, 1998.
[17]H. Überall, L. R. Dragonette, and L. Flax, "Relation between creeping waves and normal modes of vibration of a curved body," J. Acoust. Soc. Am. **61**, 711–715 (1977).
[18]G. V. Frisk, J. W. Dickey, and H. Überall, "Surface wave modes on elastic cylinders," J. Acoust. Soc. Am. **58**, 996–1008 (1975).

Temporal analysis of tissue displacement induced by a transient ultrasound radiation force

Samuel Callé,[a] Jean-Pierre Remenieras, Olivier Bou Matar,
Melouka Elkateb Hachemi, and Frédéric Patat
GIP ULTRASONS-LUSSI, FRE 2448 CNRS, 2 bis boulevard Tonnellé, 37032 Tours Cedex, France

(Received 20 January 2005; revised 24 June 2005; accepted 18 August 2005)

One of the stress sources that can be used in dynamic elastography imaging methods is the acoustic radiation force. However, displacements of the medium induced by this stress field are generally not fully understood in terms of spatial distribution and temporal evolution. A model has been developed based on the elastodynamic Green's function describing the different acoustic waves generated by focused ultrasound. The function is composed of three terms: two far-field terms, which correspond to a purely longitudinal compression wave and a purely transverse shear wave, and a coupling near-field term which has a longitudinal component and a transverse component. For propagation distances in the shear wavelength range, the predominant term is the near field term. The displacement duration corresponds to the propagation duration of the shear wave between the farthest source point and the observation point. This time therefore depends on the source size and the local shear modulus of the tissue. Evolution of the displacement/time curve profile, which is directly linked to spatial and temporal source profiles, is computed at different radial distances, for different durations of force applications and different shear elastic coefficients. Experimental results performed with an optical interferometric method in a homogeneous tissue-mimicking phantom agreed with the theoretical profiles.
 [DOI: 10.1121/1.2062527]

PACS number(s): 43.20.Gp, 43.25.Qp [PEB] Pages: 2829–2840

I. INTRODUCTION

A. Background

Elastography imaging has recently shown its potential to differentiate soft tissues on the basis of their mechanical properties. An effective way to investigate elastic properties is to generate transient acoustic waves in the body, and to follow the associated transient motion in the time/space domain. This method makes it possible to overcome various artifacts linked to static methods due for example to the unknown boundary conditions. It is possible to create stress by using external mechanical vibration[1–5] or by using an acoustic radiation force created by a focused ultrasound beam.[6–14] In the latter case, the stress field is distributed deep in the body, and has considerable advantages in comparison to external force sources. First, the excitation force can be applied inside the tissue, and thus the technique is not limited to superficial organs.[15] Moreover, no precise information about boundary conditions is needed. Last, the stress can be modulated as needed in terms of spatial distribution and temporal duration.

The radiation force is induced by the momentum transfer from the acoustic wave to the medium. In an attenuating homogeneous medium and assuming plane wave propagation, this force applied to the tissue is expressed as follows:[16,17]

$$F = \frac{2\alpha I}{c_0}, \tag{1}$$

where $F[\mathrm{kg/(s^2\,cm^2)}]$ is the acoustic radiation force, $c_0[\mathrm{m/s}]$ is the speed of sound in the medium, $\alpha[\mathrm{m^{-1}}]$ the absorption coefficient of the tissue, and $I[\mathrm{W/cm^2}]$ the average temporal intensity of the acoustic beam at a given point in the tissue. Intensity I is related to acoustic pressure p by

$$I \propto \overline{\left(\frac{\partial p}{\partial t}\right)^2}, \tag{2}$$

where the overbar denotes averaging over the ultrasound wave period. If we assume that the radiation force acts only in the x_j direction, we can express the i projection F_i of this force by:[18]

$$F_i \simeq \frac{b}{\rho^{(0)} c_0^3}\overline{\left(\frac{\partial p}{\partial \tau}\right)^2}\delta_{ij}, \tag{3}$$

where δ_{ij} represents the Kronecker symbol, b the effective dissipation, and $\tau = t - x/c_0$ the retarded time (time in the moving coordinate system commonly used in nonlinear acoustics). This expression implies weakly focused fields in the paraxial approximation. In this paper, the force is applied along x_3. When ultrasound is emitted in continuous mode, the intensity amplitude (at a specific space point) is constant over time, and therefore the radiation force is constant. However, when the pressure is amplitude-modulated, a radiation force is generated modulated at the modulation frequency in addition to the static force.[8] If the beams are strongly fo-

[a]Electronic mail: calle_s@med.univ-tours.fr

cused, this radiation force is like a "virtual finger" which alternately pushes the medium in depth. This corresponds to remote palpation of tissue with ultrasound.

In all dynamic elastography methods, the force applied generates shear waves in the tissue. These shear waves are directly linked to the shear elastic modulus μ, whose variations can be significant between healthy and pathological tissue when even the bulk elastic modulus $K=\lambda+\frac{2}{3}\mu$ has small variations.[19] λ and μ are called the compression and shear elastic Lamé coefficients, respectively. Sugimoto *et al.*,[6] Greenleaf *et al.*,[8] and Sarvazyan *et al.*[9] first introduced the use of radiation force to provide information about the elastic properties of tissues.

The source can have an alternative temporal profile. Shear wave elasticity imaging developed by Sarvazyan *et al.*[9,20] is based on the alternative radiation force created by an amplitude-modulated focused ultrasound beam. The modulation frequency f_{LF} is typically in the kilohertz range. The acoustic shear wave resulting from this acoustic radiation force is generated in the medium at the modulation frequency, detected by an imaging transducer or surface acoustic radiator, and then used to characterize the medium being studied. In Vibro-acoustography (Fatemi and Greenleaf[8,21]) the amplitude modulation giving rise to a low-frequency (LF) alternative radiation force originates from the combination of two focused primary beams emitted at two slightly different frequencies (f_1 and $f_2=f_1+f_{LF}$). The amplitude or the phase of the shear wave thus generated (acoustic response of the object to mechanical excitation) is then measured with a low frequency hydrophone and used to form the image.

Another way to investigate the tissue is to generate a constant source (in the millisecond range). Nightingale *et al.*[11] use the same transducer to push the tissue with focused ultrasound and to follow the displacements induced in depth using a succession of tracking beams. *In vitro* and *in vivo* images of displacement of different tissues have been performed. Walker *et al.*[10] developed a similar system allowing generation of a localized radiation force and measurement of displacements with ultrasound correlation-based methods. Relative elasticity and viscosity are calculated using the Voigt model. Lizzi *et al.*[12] used radiation force imaging to compare the motion data before and after a HIFU exposure, and then to identify lesions as regions with altered mechanical properties.

Finally, a short pulse can be applied to generate the localized stress field. In this way, Bercoff *et al.*[13,22] recently obtained images of shear wave propagation in two dimensions with an ultrafast imaging system. Elasticity can be deduced from the shear wave propagation data using inversion algorithms.

B. Purpose

In the present study, displacements generated by a localized radiation force in the case of soft tissue were investigated. Green's function[23,24] solution to the elastic wave propagation equation in homogeneous, isotropic, and infinite solids was used to model these displacements. The results emphasize the role of the near field term of the Green's function in the shape of the time/displacement curves. This explains the importance of spatial and temporal stress profiles as well as the importance of the shear elastic coefficient in the amplitude and duration of the displacement curves.

In sec. II, a model is developed based on the elastodynamic Green's function describing the waves generated by focused ultrasound. This shows that shear waves are the predominant waves created in soft tissues. Calculations of displacements were carried out for different spatial source shapes and temporal force profiles. Moreover, the evolution of the shape of the displacement/time curves was studied as a function of the radial distance x_1 and the shear elastic coefficient μ. Section III shows the experimental results of displacements induced by a localized radiation force in a tissue-mimicking phantom (gelatine-based phantom) created by a focused ultrasound beam. An optical interferometric method was used to study both the displacement induced by the radiation force at the focal point and the axial shear displacement along the radial direction around the focal point of the transducer, with a sensitivity of 2 nm. Evolution of the displacement as a function of both the transmit voltage amplitude and the duration of emission was investigated. Comparison between theoretical results (where the experimental source spatial distribution was used as source profile in the model) and experimental results showed that theoretical profiles agreed with experimental curves. The evolution of the displacement/time curves as a function of different parameters (spatial source profile, temporal force profile, radial distance and shear wave velocity) is discussed in Sec. IV.

II. ANALYTICAL MODEL

The aim of the analytical model we developed was to simulate displacements induced by an external force (radiation force) in an infinite medium. We then sought to determine this displacement $\boldsymbol{u}$ by solving the elastic-wave equation with an unidirectional force $\boldsymbol{F}$ in a homogeneous, isotropic, and unbounded solid medium. An analysis (in the frequency and time domains) of the elastodynamic Green's function solution to this equation is presented in Sec. II A. In Sec. II B, the temporal Green's function is used to compute the displacements generated by an impulse radiation force. Different spatial source profiles were tested. Finally the influence of different parameters on the shape of the time/displacement curves is presented in Sec. II C.

A. Elastodynamic Green's function

1. Frequency analysis

The wave propagation equation in an elastic medium can be expressed as follows:

$$\rho^{(0)}\frac{\partial^2 u_i}{\partial t^2}=\frac{\partial T_{ij}}{\partial x_j}+F_i=C_{ijkl}\frac{\partial}{\partial x_j}\frac{\partial}{\partial x_k}u_l+F_i, \tag{4}$$

where $\rho^{(0)}$ is the mass density and u_i the displacement in the x_i direction. Moreover, T_{ij} represents the stress tensor and C_{ijkl} the fourth order tensor of the elastic constants. The latter allows expression of the stress tensor according to the strain

tensor S_{kl} (Hooke's law). In the case of a force applied in the x_i direction on the surface j, we obtain

$$T_{ij} = C_{ijkl} S_{kl}. \tag{5}$$

In an isotropic medium, C_{ijkl} has the form:

$$C_{ijkl} = \mu(\delta_{ik}\delta_{jl} + \delta_{jk}\delta_{il}) + \lambda\,\delta_{kl}\delta_{ij}. \tag{6}$$

In the case of a point sinusoidal force proportional to $e^{j(\omega t - \boldsymbol{\xi}\boldsymbol{x})}$, Eq. (4) becomes

$$-\rho^{(0)}\omega^2 g_{im} = C_{ijkl}\frac{\partial}{\partial x_j}\frac{\partial}{\partial x_k} g_{lm} + \delta_{im}\delta(\boldsymbol{x}), \tag{7}$$

where ω is the angular frequency and g_{ij} the Green's function solution to Eq. (4) for a point force. Index i corresponds to the component of the displacement observed, and index j indicates the force application direction. The inverse Fourier transform of Eq. (7) gives

$$\delta_{im} = C_{ijkl}\xi_j\xi_k G_{lm}(\xi) - \rho^{(0)}\omega^2 G_{im}(\xi), \tag{8}$$

where G_{ij} is the spatial Fourier transform of g_{ij} and ξ_i the spatial wave vector (*ith* component). Equation (8) can be written as follows:

$$\delta_{im} = [(\lambda + \mu)\xi_i\xi_l + \mu(\xi^2 - k_s^2)\delta_{il}]G_{lm}(\xi) = K_{il}(\xi)G_{lm}(\xi), \tag{9}$$

where $k_s = \sqrt{\rho\omega^2/\mu}$ is the shear wave number. To obtain the Green's function g_{lm}, we use inversion of the matrix $K_{il}(\xi)$:

$$K_{il}^{-1}(\xi) = \frac{\delta_{il}}{\mu(\xi^2 - k_s^2)} - \frac{\xi_i\xi_l}{\mu k_s^2(\xi^2 - k_s^2)} + \frac{\xi_i\xi_l}{(\lambda + 2\mu)k_c^2(\xi^2 - k_c^2)}, \tag{10}$$

where $k_c = \sqrt{\rho\omega^2/(\lambda + 2\mu)}$ represents the compression wave number. $G_{\ell m}(\xi)$ can be expressed as follows:

$$G_{\ell m}(\xi) = K_{i\ell}^{-1}\delta_{im} = \frac{\delta_{\ell m}}{\mu(\xi^2 - k_s^2)} - \frac{\xi_\ell\xi_m}{\mu k_s^2(\xi^2 - k_s^2)} + \frac{\xi_\ell\xi_m}{(\lambda + 2\mu)k_c^2(\xi^2 - k_c^2)}.$$

The inverse Fourier transform of $G_{\ell m}(\xi)$ provides

$$g_{ij}(\boldsymbol{x},\omega) = \frac{1}{4\pi\rho^{(0)}\omega^2}\left[\delta_{ij}k_s^2\frac{\exp(jk_s r)}{r} - \frac{\partial}{\partial x_i}\frac{\partial}{\partial x_j}\left(\frac{\exp(jk_c r) - \exp(jk_s r)}{r}\right)\right], \tag{11}$$

where $r = |\boldsymbol{x}| = \sqrt{x_1^2 + x_2^2 + x_3^2}$ is the distance between the point source and the observation point. Equation (11) can be developed:

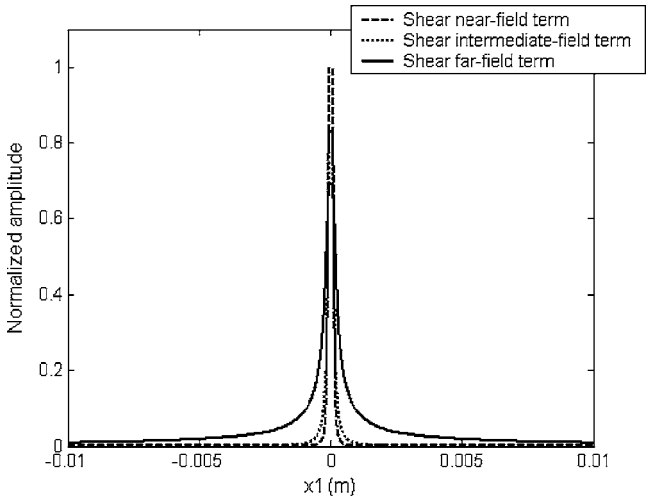

FIG. 1. Amplitude of the near, intermediate, and far field terms of the shear part of the Green's function g_{33}. The compression and shear wave velocities were $V_c = 1500$ m/s and $V_s = 5$ m/s, respectively, and the frequency was 10 kHz.

$$g_{ij}(\boldsymbol{x},\omega) = \frac{1}{4\pi\rho^{(0)}\omega^2}\left\{\left[\frac{\delta_{ij}}{r^2}(1 - k_c r) - \frac{\gamma_i\gamma_j}{r^2}(3 - 3jk_c r - k_c^2 r^2)\right]\frac{\exp(jk_c r)}{r} + \left[-\frac{\delta_{ij}}{r^2}(1 - k_s r - k_s^2 r^2) + \frac{\gamma_i\gamma_j}{r^2}(3 - 3jk_s r - k_s^2 r^2)\right]\frac{\exp(jk_s r)}{r}\right\} \tag{12}$$

with $\gamma_i = x_i/r = \partial r/\partial x_i$ the direction cosines for the vector x_i.

As described by Aki and Richards,[23] three terms are linked to the shear wave and three to the compression wave. Terms related to r^{-1} are called the far field terms, terms related to r^{-2} the intermediate field terms, and terms related to r^{-3} the near field terms. We can divide the compression and shear terms:

$$g_{ij}(\boldsymbol{x},\omega) = \frac{1}{4\pi\rho^{(0)}\omega^2}\left\{\left[\frac{\gamma_i\gamma_j k_c^2}{r} + \frac{(3j\gamma_i\gamma_j - \delta_{ij})k_c}{r^2} + \frac{(\delta_{ij} - 3\gamma_i\gamma_j)}{r^3}\right]\exp(jk_c r) + \left[\frac{(\delta_{ij} - \gamma_i\gamma_j)k_s^2}{r} + \frac{(\delta_{ij} - 3j\gamma_i\gamma_j)k_s}{r^2} + \frac{(3\gamma_i\gamma_j - \delta_{ij})}{r^3}\right]\exp(jk_s r)\right\}. \tag{13}$$

Figure 1 illustrates the three terms linked to the shear part of g_{33}. The force is applied along the x_3 axis and we represent the displacements in the direction x_3. It can be seen that the far field term is rapidly predominant.

Figures 2(a) and 3(a) represent the displacement vectors at 5 cm from the point source for the compression and shear waves, respectively. Vector F symbolizes the radiation force direction vector. Directivity of these waves is represented using polar coordinates in Figs. 2(b) and 3(b). Amplitudes were normalized with the maximum of the compression wave directivity amplitude. It can be seen that the compression wave directivity is mainly situated in the axial direction, and that the shear wave directivity is perpendicular to this

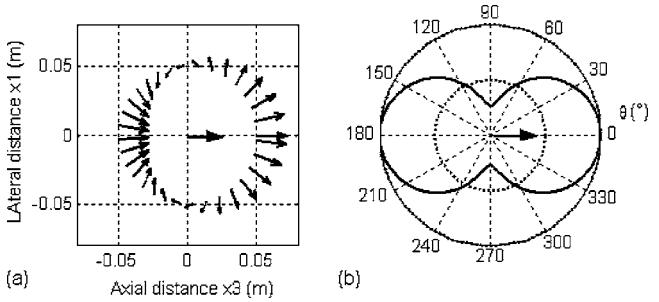

FIG. 2. 2D representation (a) of the displacement vectors of the compression wave at $r=0.05$ m ($V_c=1500$ m/s and $f=10$ kHz) created by a sinusoidal point force F parallel to the horizontal axis applied at the origin O, and (b) its angular directivity in polar coordinates.

direction. In fact, the compression and shear wavelengths are $\lambda_c=15$ cm and $\lambda_s=0.5$ cm, respectively. As the observation point is situated 5 cm from the force point, we are in the near field for the compression wave and in the far field for the shear wave. From Eq. (13) it can be seen that the compression wave is not purely longitudinal in the near field domain: there is a transverse component. On the other hand, the far field term of the shear contribution is described by the expression $(\delta_{ij}-\gamma_i\gamma_j)$. In the case of a force point acting in the x_3 direction, this term gives zero displacements in the x_1 direction on the x_1 axis and non zero displacements in the x_3 direction. Moreover, it gives on the x_3 axis zero displacements along x_1 and x_3. As described by Eq. (13), shear wave amplitude is higher than compression wave amplitude. As the factor $(V_c/V_s)^2$ between the compression and shear terms is high in tissue, shear wave generation is predominant.

2. Temporal analysis

In order to study the temporal evolution of displacements generated by a finite duration radiation force, expression of the Green's function is needed as a function of time t. This can be obtained[24] from Eq. (13) or developed directly from the propagation wave equation in an elastic medium. In this case, Lamé's theorem is used.[23] In homogeneous, infinite and isotropic solids, the elastodynamic Green's function in the temporal domain is

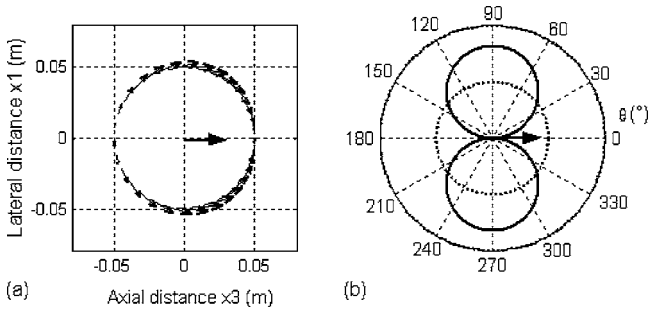

FIG. 3. 2D representation (a) of the displacement vectors of the shear wave at $r=0.05$ m ($V_s=5$ m/s and $f=10$ kHz) created by a sinusoidal point force F parallel to the horizontal axis applied at the origin O, and (b) its angular directivity in polar coordinates.

$$g_{ij}(\boldsymbol{x},t)=\frac{(3\gamma_i\gamma_j-\delta_{ij})}{4\pi\rho^{(0)}}\frac{1}{r^3}\int_{r/V_c}^{r/V_s}\tau\delta(t-\tau)d\tau+\frac{\gamma_i\gamma_j}{4\pi\rho^{(0)}}\frac{1}{r}\frac{\delta(t-r/V_c)}{V_c^2}+\frac{(\delta_{ij}-\gamma_i\gamma_j)}{4\pi\rho^{(0)}}\frac{1}{r}\frac{\delta(t-r/V_s)}{V_s^2},\tag{14}$$

where δ is the Dirac function. As in the previous paragraph, different contributions can be distinguished. The first term including $r^{-3}\int_{r/V_c}^{r/V_s}\tau\delta(t-\tau)d\tau$ corresponds to a coupling term linked to both the compression and shear waves. This term behaves like r^{-2} for times that are short compared to $r/V_s-r/V_c$, and the remaining terms behave as r^{-1}. Since r^{-2} dominates r^{-1} as $r\to 0$, it is called the near field term in comparison with the other two terms. In fact, the second and third terms are classical far field terms, corresponding to compression and shear waves, respectively. Their contributions, purely longitudinal and purely transverse, respectively, are Dirac functions occurring at times r/V_c and r/V_s. The near field term is a temporal ramp between r/V_c and r/V_s. It can be seen that it plays the most important role in the shear wave propagation. In fact, the shear wavelength in shear wave elasticity imaging techniques is generally in the millimeter range, which corresponds to the propagation distances of this wave. This coupling term has a longitudinal component and a transverse component. It is therefore neither irrotational nor solenoidal.

The importance of this term has recently been investigated by Sandrin *et al.*[25] in the case of transient elastography. However, the Sandrin study evaluated an external vibration source, whereas we are evaluating a radiation force source.

B. Computation of impulse displacement for different spatial sources

A force (applied in the x_j direction) $\boldsymbol{f}_i(\boldsymbol{x},t)$ induces displacements inside the medium in the x_i direction described by the following spatio temporal convolution:

$$u_i(\boldsymbol{x},t)=\boldsymbol{f}_i(\boldsymbol{x},t)\underset{\text{Time Space}}{\otimes}g_{ij}(\boldsymbol{x},t).\tag{15}$$

In the present study, stress was applied in the x_3 direction. Displacements were calculated for different source profiles.

1. Point source

A point source was applied in the x_3 direction at point O (origin) at time $\tau=0$. The observation point was placed at $x_1=2$ mm. In this case, the force can be expressed as

$$\boldsymbol{f}_i(\boldsymbol{x},t)=A\,\delta(t)\,\delta(\boldsymbol{x})\,\delta_{i3}.\tag{16}$$

In expressions (15) and (16), dimensions of Green's function $g_{ij}(\boldsymbol{x},t)$, force $\boldsymbol{f}_i(\boldsymbol{x},t)$, impulse amplitude A, $\delta(\boldsymbol{x})$ and $\delta(t)$ were speed per force unit, force per volume unit, force per time unit, 1/volume and 1/time, respectively. With this representation, the displacement had the correct dimension (distance).

Figure 4 represents displacements in the x_3 direction calculated at $x_1=2$ mm from the point source. If we look at the

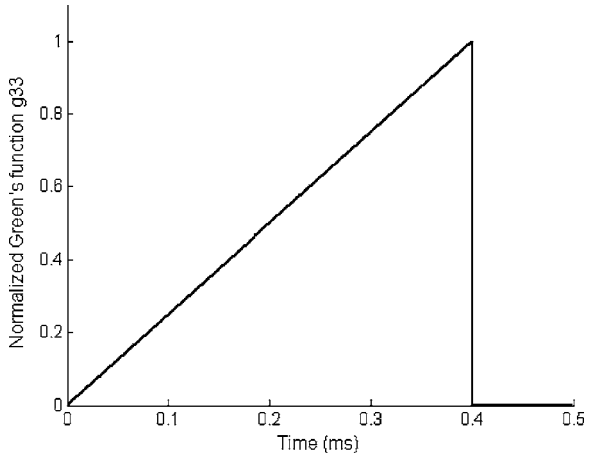

FIG. 4. Normalized Green's function g_{33} of one point source. The point force is applied at the origin O and the receiver is placed at $x_1=2$ mm. Compression and shear wave velocities are $V_c=1500$ m/s and $V_s=5$ m/s, respectively.

displacement component u_3 in the x_1 direction, g_{33} can be calculated with the following simplifications: $\delta_{33}=1$, $\gamma_1=1$, and $\gamma_3=0$. From Eq. (14) it can be seen that the far field compression term is zero and the far field shear term is negligible. The near field term is predominant and has a triangular shape. The beginning of displacement occurs at $\tau_{V_c}=1.3$ μs (propagation duration at the compressional velocity between the point source and the receiver) and the end at $\tau_{V_s}=0.4$ ms (time of flight between the source and the receiver at the shear velocity). Time τ_{V_s} being much greater than time τ_{V_c}, the total duration of displacement is linked to the shear wave velocity with

$$\tau_{\text{total}} \simeq \tau_{V_s} = r/V_s. \tag{17}$$

The maximum displacement amplitude $D_{\max}$ can be determined from Eq. (14) :

$$D_{\max} = \frac{A}{4\pi\rho^{(0)}}\frac{1}{r^2 V_s}, \tag{18}$$

where A is the impulse amplitude. The displacement velocity Σ (slope of displacement) corresponding to

$$\Sigma = \frac{D_{\max}}{\tau_{V_s}} = \frac{A}{4\pi\rho^{(0)}}\frac{1}{r^3} \tag{19}$$

is independent of the shear velocity value.

2. Linear source

In this case, the spatial source is composed of 401 points identical to those defined in the previous paragraph, aligned along the x_3 direction. Figure 5(a) illustrates the Green's functions originating from each point source. The sum of all these displacements gives the total displacement generated at the observation point by the source line [Fig 5(b)]. It can be seen that the end of displacement corresponds to the duration of propagation at the shear velocity between the farthest point source and the observation point ($\tau_{\text{total}} \simeq 1.88$ ms). The largest contribution is from the point of the source situated exactly at 90° of the observation point (see Fig. 3), which is

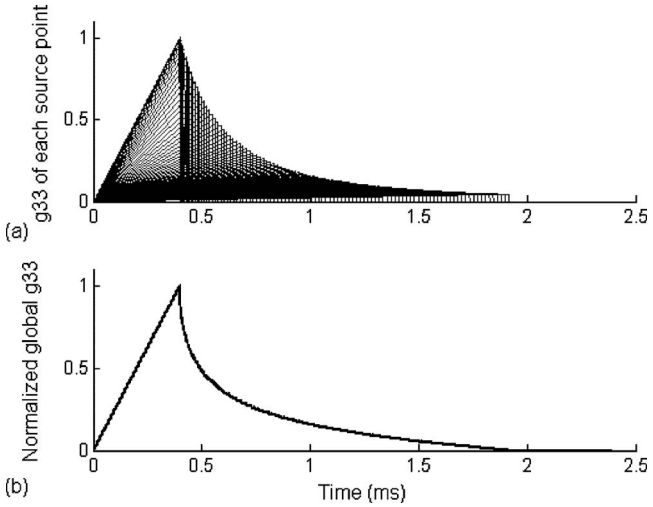

FIG. 5. Representation (a) of Green's functions g_{33} of each source point and (b) normalized overall displacement u_3 generated by all these sources. The origin O is placed in the middle of this 1.88 cm length linear stress source and the receiver at $x_1=2$ mm.

the source point that is the closest distance to the observation point. The contributions of the other source points have smaller amplitudes and occur later. Moreover, it is important to observe the decrease in the displacement curve. This is due to diffraction effects and not to attenuation.

3. Rectangular source

In this section the spatial source consists of 37 parallel lines. This force therefore has a rectangular spatial profile. Figure 6 describes the set of displacements induced by each line source [Fig. 6(a)] and the overall displacement generated by the summation of all these lines [Fig. 6(b)].

4. Three dimensional source

In order to compare the theoretical results with the experimental data, the displacements generated by a stress induced by the transducer used in the experimental part must

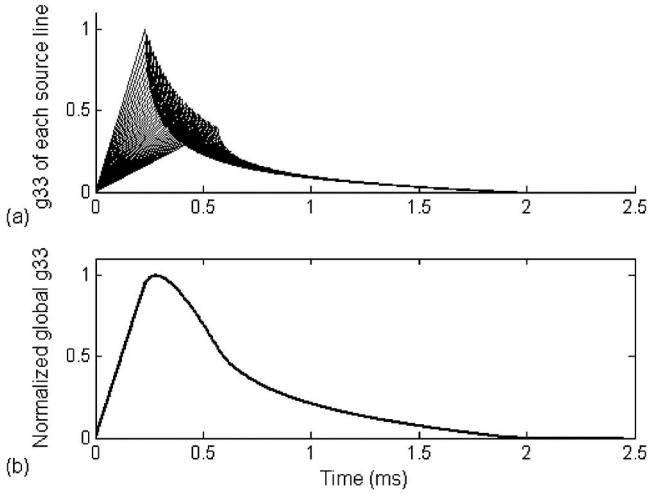

FIG. 6. Representation (a) of Green's functions g_{33} of each source line and (b) normalized overall displacement u_3 generated by all these sources. This rectangular stress source (18.8×1.7 mm^2) is centered on the origin point O and the receiver is placed at $x_1=2$ mm.

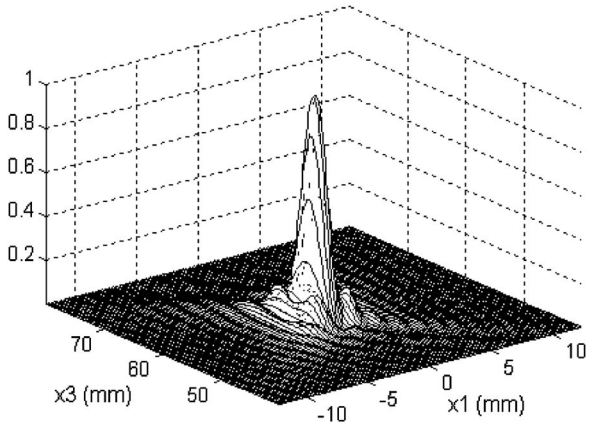

FIG. 7. : Representation in plane (x_1,x_3) of the normalized amplitude of the radiation force generated by a circular transducer (4.16 cm radius and 6 cm focal length).

be predicted. The acoustic pressure generated by a focused transducer (4.16 cm radius) was calculated in three dimensions. The central frequency was 1 MHz and the focal distance was fixed at 6 cm. We used classical angular spectral decomposition[26] associated with a source condition described by Levin *et al.*[27] for the calculation of the ultrasound pressure generated by the focused transducer. Figure 7 shows the normalized amplitude of the radiation pressure in the (x_1,x_3) plane computed using the square of the envelope of the ultrasound pressure [see Eq. (3)]. It can be seen that the radiation force was well localized in space and measured 6 mm in the axial direction and 2 mm in the radial direction. The "virtual finger" which pushes the medium in depth therefore has cylindrical symmetry around the propagation axis. This symmetry has consequences on the LF wave propagation (Fig. 8): this wave has a plane wave front in the planes (x_1,x_3) and (x_2,x_3), and has a ring shape in the plane (x_1,x_2) perpendicular to the propagation direction.

Figure 9 illustrates the impulse displacement at $x_1=0.5$ mm originating from the three dimensional (3D) convolution of the elastodynamic Green's function with the spatial source calculated previously. We used a 3D grid with 576 points along x_1 and x_2, and 274 points along x_3. The spatial resolution of this numerical grid was 1.875×10^{-4} m in the

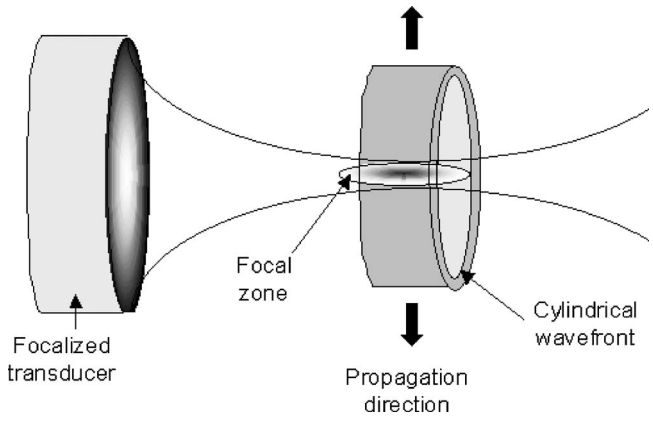

FIG. 8. Representation of the cylindrical shear wave induced by a focused transducer: the cylindrical symmetry around the propagation axis is due to the cigar shape of the pressure field.

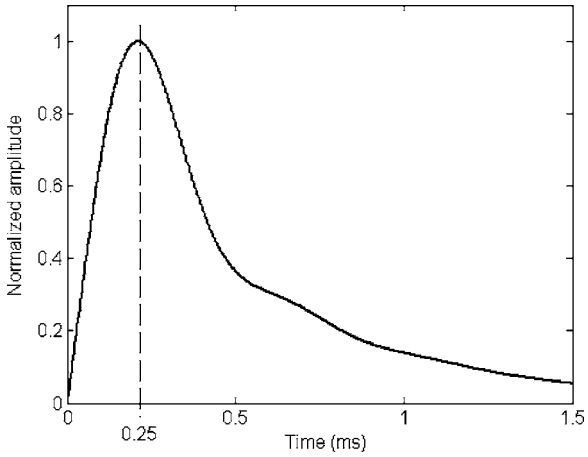

FIG. 9. Normalized impulse displacement in the case of a 3D source generated by a focused transducer (4.16 cm radius and 6 cm focal length) at $x_1=0.5$ mm. The shear velocity is $V_s=2.5$ m/s.

three dimensions. Each point of the discrete grid contributed to the displacement with a triangular function. The summation of all these contributions is represented in Fig. 9. It was obtained after filtering (in this example, signals of frequency greater than 2.5 kHz have been removed) in order to delete possible contributions due to spatial discretization. In this example of displacement curve $\tau_{max}=250\ \mu$s and $\tau_{total}=1.8$ ms.

C. Influence of different parameters

The previously described 3D spatial source is used in the following. The influence of emission duration, radial distance, and shear velocity is studied and discussed.

1. Influence of emission duration

Figures 10 and 11 represent the displacement curves at $x_1=0.5$ mm with the 3D spatial source for different durations of emission T. It can be seen that in the case of short emission duration, the longer the emission duration, and the higher the displacement amplitude (Fig. 10). Moreover, the

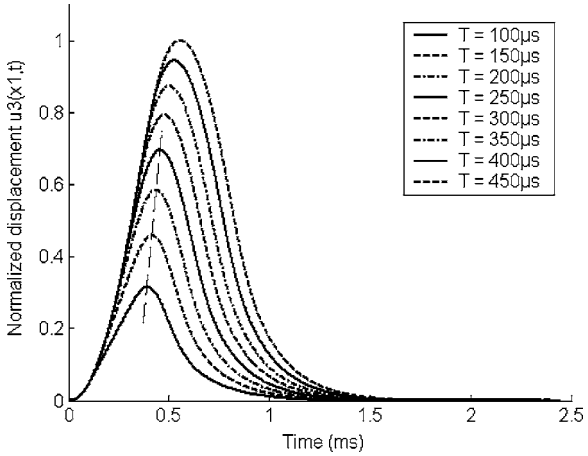

FIG. 10. Normalized displacement $u_3(x_1,t)$ vs emission duration T: case of short emissions (ranging from 100 to 450 μs). This calculation is performed at $x_1=0.5$ mm with the 3D spatial source. The displacement amplitude is proportional to the emission duration (dotted line).

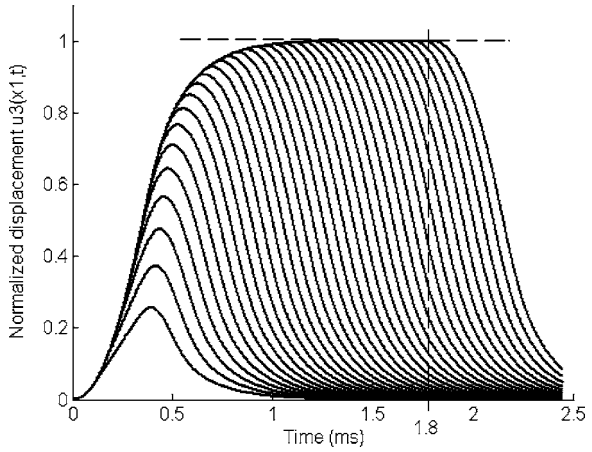

FIG. 11. Normalized displacement $u_3(x_1,t)$ vs emission duration T: case of long emissions. Source and receiver position are the same as in Fig. 10. A plateau occurs at $t=1.8$ ms (dotted line).

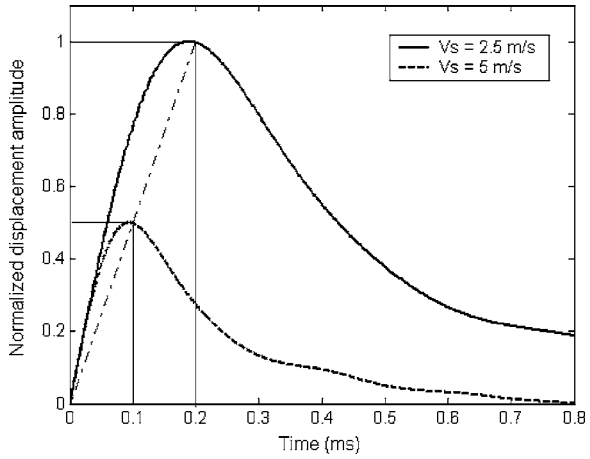

FIG. 13. Displacement curves vs time for two different shear velocities ($V_s=2.5$ m/s and $V_s=5$ m/s) in the case of an impulse temporal source. The receiver is placed at $x_1=0.5$ mm.

displacement slope (deformation velocity) was the same whatever the duration of emission T. However, when the emission duration was too long, the displacement amplitude reached a plateau (Fig. 11). This can be explained by the fact that a convolution occurs between the short impulse response and a gate function (corresponding to the temporal profile of the radiation force). The temporal shape of the convolution result leads to a gate function. The inclination of the displacement slope begins when the duration T is longer than time $\tau_{\max}$, corresponding to the maximum displacement in the impulse case (here 250 μs). The plateau occurs when T is longer than the total duration of displacement τ_{total} in the impulse case (in this example, 1.8 ms). That means that the medium has a static deformation: i.e., there is a balance between the radiation force generated and the passive viscoelastic force of the medium.

2. Influence of the radial distance

The displacement was calculated at different radial distances x_1 (Fig. 12). The different curves represent the propagation of the shear wave along the axis x_1 at 5 m/s, perpendicular to the stress application direction x_3. The distance

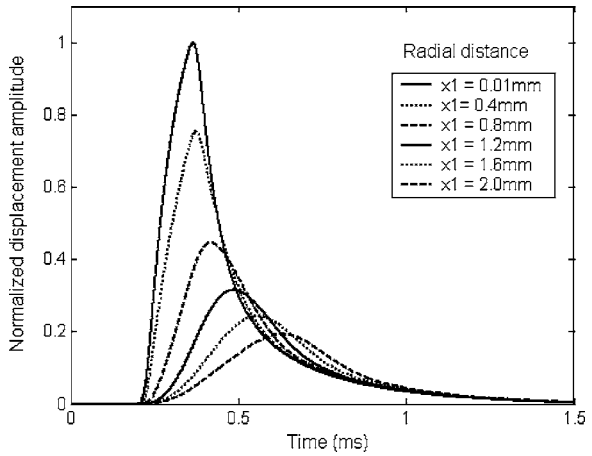

FIG. 12. Displacement amplitude $u_3(x_1,t)$ vs radial distance x_1 (ranging from 0.01 to 2 mm). In this example, the emission duration is $T=200$ μs and begins at $t=0.2$ ms. The shear velocity is $V_s=5$ m/s.

between the shear wave front and the beam axis then increased as a function of $V_s \times t$. The decrease in wave amplitude was due only to the wave divergence (diffraction effects) because the viscosity was not taken into account in this model. As previously noted, the shape of this wave was cylindrical. This explains why diffraction attenuation was high, as seen in the figure (amplitude divided by a factor of 5 after 2 mm propagation). The beginning of displacement was linked to velocity V_c and the maximum displacement to V_s, explaining the spread of the temporal representation of displacement when the radial distance increased.

3. Influence of shear velocity

The influence of velocity V_s, and hence the influence of the shear elastic coefficient μ, is investigated in this paragraph. Figure 13 represents the displacement curves *versus* time for two different shear velocities ($V_s=2.5$ m/s and $V_s=5$ m/s). It can be seen that when V_s increased, i.e., when the coefficient μ increased ($E=3\mu$), both the maximum displacement amplitude $D_{\max}$ and the time $\tau_{\max}$ to reach this maximum displacement decreased. In fact, the shear contributions of each point source occurred earlier than the observation point. It is not hard to foresee intuitively that the medium was less "elastic" when V_s increased, and the amplitude and duration of displacement were smaller.

There was a stretching of the coordinates in the two dimensions, corresponding to the ratio between the two velocities (factor of the dilatation scale of 2). In fact, these curves represent the summation of all the triangular signals originating from each point source. As previously observed, the amplitude and duration of displacement of all these points were inversely proportional to the shear velocity. The sum of all these contributions therefore had the same properties. When the velocity was divided by 2, the amplitude and duration of displacement of each point of the displacement curve in the case of this 3D source were multiplied by this factor of 2.

Moreover, the two curves had the same slope of displacement, i.e., the same deformation velocity. In fact, this

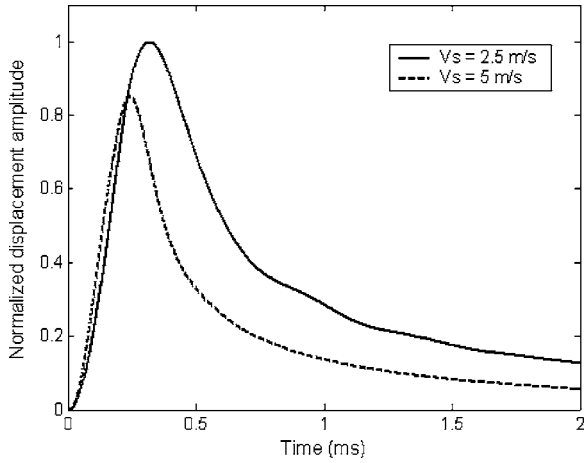

FIG. 14. Same plots as in Fig. 13 in the case of a 200 μs temporal source.

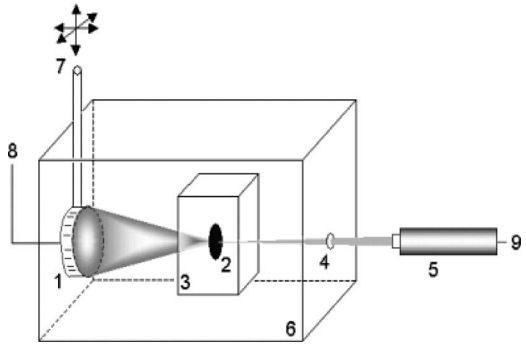

FIG. 15. Experimental setup of the optic interferometric method.

slope was composed of the summation of the displacement slopes Σ of each point source which were independent of V_s.

The maximum of amplitude $D_{\max}$ and the time $\tau_{\max}$ to reach this maximum seem therefore to be two interesting parameters to use in the study of the variations in V_s, and hence the variations in the shear elastic coefficient μ. Moreover, it can be seen that if there is a variation in the radiation force amplitude, the displacement amplitude varies but the displacement duration remains constant. It would therefore be more appropriate to follow the variations in $\tau_{\max}$ to image the coefficient μ. However, the parameters $D_{\max}$ and $\tau_{\max}$ are directly linked to r and thus to the spatial profile of the stress source. They vary when the spatial shape of the source varies (by diffraction on an inhomogeneity for example). The ultrasound beam generated by the system has thus to be as constant as possible when the source application area is moved.

As described by Sarvazyan *et al.*,[19] shear elastic coefficients can vary by 1 kPa to 2 MPa between healthy and malignant mammalian tissues. For example, if we consider a healthy biological medium with a 10 kPa shear coefficient and a malignant medium with a 1 MPa shear coefficient, the respective shear velocities are 3 and 30 m/s. We can then conclude that, as the two velocities differ by a factor of 10, it may in a homogeneous medium result in two displacement curves which are very different in terms of amplitude and duration of displacement. However, the images presented by Nightingale *et al.*[28] showed the real difficulties of this technique in *in vivo* applications. These can be explained by the results presented in Fig. 14. The simulation was the same as the previous one, but with a finite emission duration of $T = 200$ μs. It can be seen that there was no longer dilatation of a factor of 2 between the two curves. In fact, convolution with a finite temporal profile involves compression of the two curves and thus it is no longer possible to evaluate the real ratio between the two shear velocities. These curves are therefore not easily exploited in comparison with the curves obtained with a temporal impulse emission. To lessen the impact of this loss of information, one hypothesis might be (from displacement curves obtained with emissions of hundred microseconds, which allow measurable displacements) to perform a numerical deconvolution with the temporal stress profile to obtain the impulse response. However, this is not always easily feasible in practice.

4. Discussion

Some authors have analytically studied the shapes of displacement/time curves. Andreev *et al.*[29] used Eq. (3) and ignored the compression terms in order to reach the shear wave propagation equation. Approximation of a cylindrical wave was achieved and a simplified expression of displacement in the impulse case is described. This approximation was not performed by Sarvazyan *et al.*[8] Similarly, terms linked to the compression wave were ignored, as in the model of Andreev *et al.* The force expression described by Eq. (3) was resolved using an analytical expression of the pressure solution (focused Gaussian beam) of the linear parabolic propagation equation. Simulations for impulse emission and for continuous amplitude-modulated emission have been tested and comparisons between our model and these models have been made.[30,31] We emphasize that in the near field of the source created by the radiation force, shear and compression waves are coupled. It is therefore important to take into account the compression term in the displacement description. It is only in the far field of the source (for distances greater than a few millimeters) that these two waves can be studied independently. Lizzi *et al.*[12] previously developed a numerical model (using finite-difference algorithms) which takes into account the compressional component of the displacement.

III. EXPERIMENTAL RESULTS

A. Experimental setup

In this section, we present briefly the materials and methodology used in our technique of visualizing shear waves excited by focused ultrasound. Figure 15 represents the experimental setup. A tissue-mimicking phantom (3) ($10\times10\times8$ cm^3 gel with 8% gelatin) including a 1-μm-thick metallized sheet of Mylar (2) is placed in a water tank (6). While the transient shear wave propagates, this reflective target moves with the tissue. The central plane of the phantom was positioned between the transducer (1) and the optical interferometer (5), perpendicular to both ultrasound and laser beams. The 8.32-cm-diam transducer emitting at 1 MHz focuses at the optical focal point. The laser probe (SH 140, BMI, France) was a compact Mach-Zender heterodyne

interferometer, equipped with a doubled YAG laser.[32] The laser beam enters the water tank through an optical window (4) specially coated for the YAG wavelength to avoid reflection, propagates in the optically transparent phantom, and is reflected back by the Mylar. A PC controls the emission (8) and the position (7) of the transducer, and the output (via an oscilloscope) of the laser probe (9).

The displacement of the Mylar sheet induces modulation of the phase of the optical wave. The optical phase-shift $\Delta\Phi$ is given by

$$\Delta\Phi = \frac{4\pi}{\lambda} u(t), \tag{20}$$

where $u(t)$ is the displacement at the surface of the sheet.

In order to see the shear wave propagation, the transducer was moved in the radial direction x_1. The laser beam then measured the displacement $u(t)$ in the direction of propagation at a radial distance x_1 around the focal point. A high frequency (HF) filtering suppressed the HF burst. During our experiments, the displacements observed were around 10 μm for burst durations in the millisecond range at frequencies varying from 1 to 2 MHz.

Andreev *et al.*[29] previously developed a technique allowing visualization of displacements generated by an ultrasound radiation force in a gel with a laser source. This emission reception method between a laser and a diode provided similar curve profiles to our method. However, this technique requires a precise calibration procedure before each measurement and has a noise level varying from 1 to 3 μm.

B. Predominant contribution of displacement

Reflection of the emission acoustic beam (emitted at $f_0 = 1$ MHz) on the membrane and the radiation force induced by the attenuation of emission beam in the gelatin phantom both contribute to the displacements of the membrane. Comparison of two characteristic values will help to distinguish which provides the main contribution.

We first calculated the reflection coefficient R. Mylar sheet thickness was $e_M = 1.3$ μm and its density $\rho_M = 1374$ kg/m^3. The longitudinal wave velocity in Mylar was approximately $V_M = 3000$ m/s. If Z_g is the gelatine impedance and Z_M the Mylar impedance, the reflection coefficient is given by

$$R = \frac{1}{4}\left(\frac{Z_g}{Z_M} - \frac{Z_M}{Z_g}\right)^2 \sin^2(k_M e_M), \tag{21}$$

where $k_M = 2\pi f_0 / V_M$ is the wave number of the Mylar sheet. As $V_g = 1500$ m/s and $\rho_g = 1000$ kg/m^3 are the ultrasound velocity in the gelatin and the phantom density, respectively, the reflection coefficient is: $R \simeq 10^{-3}$. The reflection radiation force term is also $2 \cdot 10^{-3}$.

We then compared this force contribution with a term due to the radiation force induced by the gel attenuation. This term is αl_c where l_c is the characteristic length (the length of the focal region) and α the attenuation coefficient in the phantom in Np/m. We measured $\alpha_{\mathrm{dB}} = 0.05$dB/cm in the gel. The following expression:

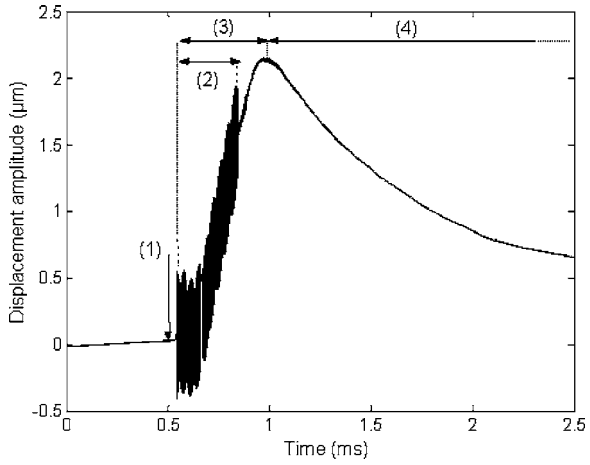

FIG. 16. Example of demodulated laser signal before filtering at the focal point in the case of a 300 μs temporal source beginning at $t = 500$ μs (transmit voltage amplitude: 25 V).

$$\alpha_{\mathrm{dB}} = -20 \log(e^{-\alpha}) \tag{22}$$

provides the value of α. As the focal region length is in the centimeter range, $\alpha l_c \simeq 6 \cdot 10^{-3}$.

We can conclude that the difference between attenuation and reflection contributions to radiation force is a factor 3. Even if the term linked to the gel attenuation is preponderant, this setup may introduce a non-negligible reflection radiation force term. Moreover, the membrane may slightly stiffen the gel surrounding it, which can reduce the measured displacement.

C. Experimental results

1. Displacement at the focal point

Figure 16 presents an example of displacement curve induced by the radiation force before filtering. The ultrasound emission began at 0.5 ms (1). After 40 μs, corresponding to the propagation duration between the transducer and the Mylar sheet, the ultrasound wave can be seen (in the present case, 300 periods at 1 MHz), which rapidly moves the reflective target. The acoustic HF pressure at the focal point of the transducer (in the present study 4.2 MPa) can be calculated from this HF displacement (2). In our case, a constant averaged pressure at the focal point induced a LF displacement (3). This displacement was followed by a period of relaxation (4). In this case, the displacement induced by the radiation force was 2 μm and the displacement noise level was 2 nm, whereas the ultrasound methods usually used to measure these tissue displacements have a noise level of 1 μm.[11]

Figure 17 represents the displacement amplitude of the Mylar sheet for emission burst durations varying from 100 to 600 periods at 1 MHz. It can be seen that the displacement amplitude is proportional to the high frequency burst duration (0.95 μm displacement for a 0.2 ms emission duration and 1.9 μm displacement for a 0.4 ms emission duration). Moreover, the slope of the displacement/time curve is independent of the emission duration. The velocity of displacement (here 5 mm/s), analyzed by Yamakoshi *et al.*[2] and more recently by Chen,[33] could then characterize the me-

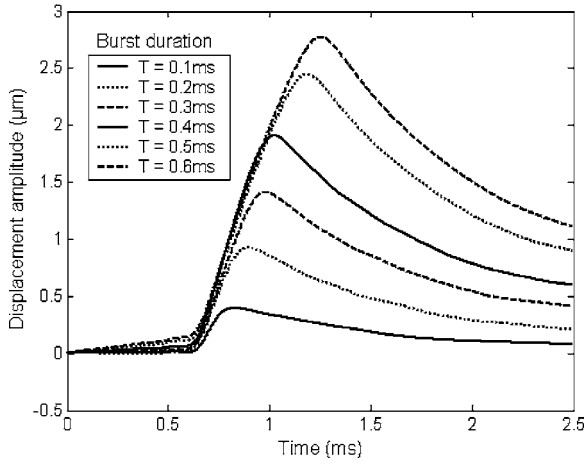

FIG. 17. Displacement amplitude vs emission burst duration T (varying from 0.1 ms to 0.6 ms). The onset of transducer emission (transmit voltage amplitude: 20 V) occurs at $t=500$ μs.

dium. However, this velocity depends on the radiation force amplitude [see Eq. (19)], which can vary with a change in the structure of the medium studied.

Displacement amplitude of the Mylar sheet as a function of the transmit voltage amplitude U is represented in Fig. 18. It can be seen that when U increased, the displacement amplitude also increased, and that the duration of displacement remained constant whatever the amplitude U: a constant time, corresponding to the time between beginning emission and the maximum displacement, is thus a characteristic constant of the tissue. In this case, the time between burst reception on the reflective sheet and the end of displacement was 0.43 ms. The ratio of the measured displacements for the different transmit voltages is consistent with the predicted quadratic relationship between pressure and applied radiation force magnitude, assuming a linear relationship between force magnitude and displacement: when the transmit voltage amplitude was multiplied by 2 (10 and 20 V, respectively), the displacement amplitude was multiplied by 4 (0.35 and 1.4 μm, respectively).

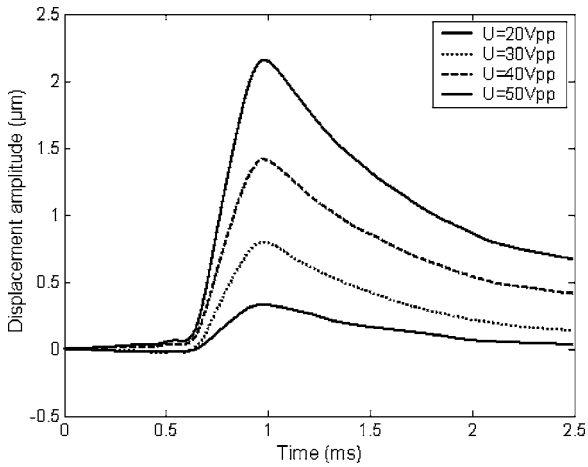

FIG. 18. Displacement amplitude vs transmit voltage amplitude U (varying from 10 V to 25 V). The emission corresponds to a burst of 300 periods at 1 MHz.

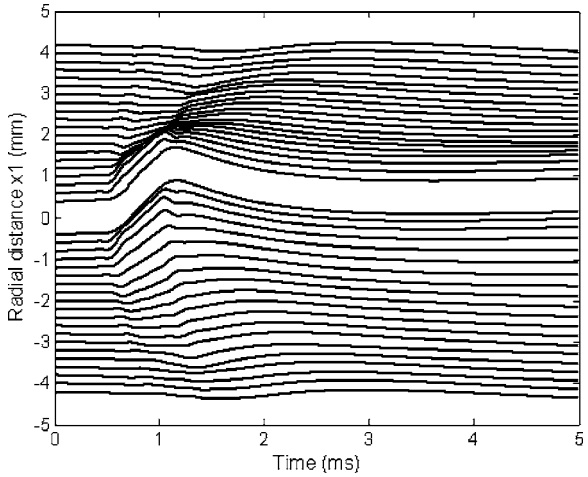

FIG. 19. Seismic representation of shear wave propagation.

2. Shear wave generation

In this section, shear wave propagation was investigated. The 1 MHz transducer emits a 0.5 ms burst with an emission amplitude of $U=40$ V. The Mylar sheet was inserted in a gel constituted of 8% gelatin. A scan was performed in the radial direction around the focal point, with a displacement step of 200 μm. Figure 19 represents a seismic view of the shear wave propagation.

The displacement amplitude of the shear wave at different radial distances x_1 from the focal point is shown in Fig. 20. In this case, the shear wave amplitude was around 7 and 3.2 μm at $x_1=1$ mm and $x_1=2$ mm, respectively, for an emission of 50 V.

D. Comparison between theoretical and experimental results

In order to compare the experimental measurements with the analytical model, we performed an experimental 3D scan of the pressure beam generated by the transducer used in the experiments. Sections in the $(\boldsymbol{x}_1,\boldsymbol{x}_3)$ and $(\boldsymbol{x}_1,\boldsymbol{x}_2)$ planes are represented in Fig. 21. The cigar shape of the

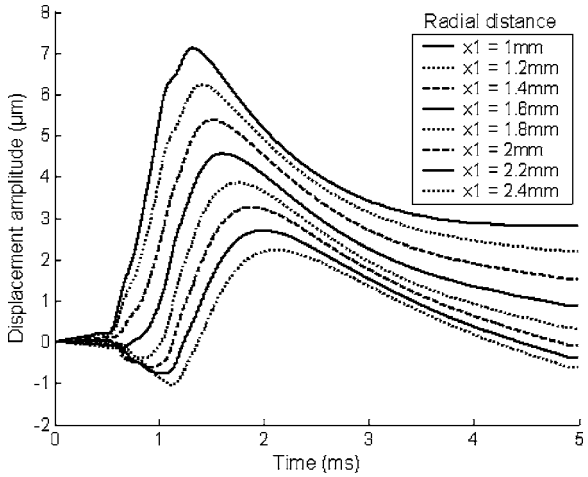

FIG. 20. Displacement amplitude vs radial distance x_1 (ranging from 1 to 2.4 mm). The transmit voltage amplitude is 50 V and the emission burst duration 500 μs.

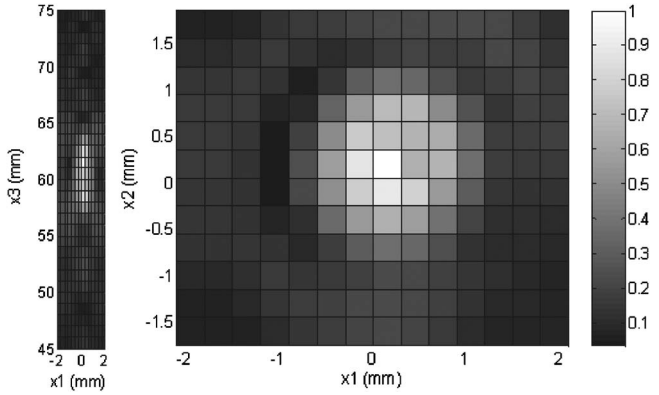

FIG. 21. Sections in the (x_1, x_3) and (x_1, x_2) planes of the pressure field emitted by the 1 MHz focused transducer.

pressure field is clearly seen. Axial and radial dimensions were 7 and 1.5 mm, respectively. This 3D pressure field made it possible to calculate the three-dimensional spatial profile of the radiation force used in the theoretical model. Thus the stress source in the experiment and the model was the same. The experiment was carried out with a phantom composed of 8% gelatin. Emission began at $t=500$ μm, duration was $T=500$ μm and measurement was performed at $x_1=1.2$ mm. These parameters were taken into account in the analytical model. The shear wave velocity was varied to obtain the best fit between the experimental and theoretical curves. $V_s=1.3$ m/s was chosen, which is within the expected range of shear velocity in gelatin phantoms,[34] corresponding to a shear elasticity coefficient $\mu=1.7$ kPa and a Young modulus $E\approx 5$ kPa. This comparison between theoretical and experimental displacement curves is presented in Fig. 22. It can be seen that the theoretical profile agrees with the experimental curve. The beginning of displacement, displacement slope, and time of displacement are in good agreement. A difference in the decreasing part of the curves can be seen. This may be due to the viscosity, which is not taken into account in the analytical model, relaxation times of a medium being increased by viscosity. Moreover, the experimental measurement may not have been performed exactly at the focal point of the transducer, which is very thin.

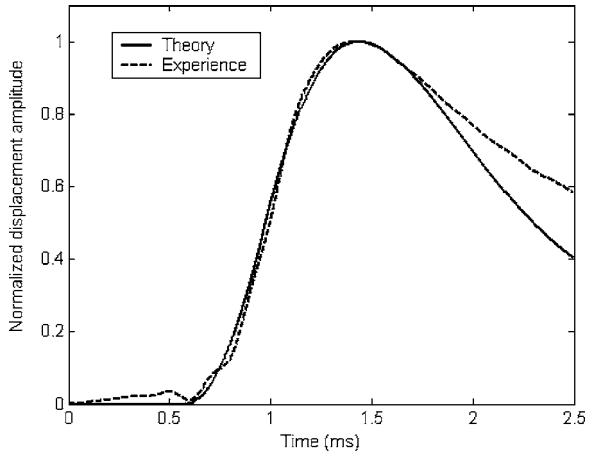

FIG. 22. Comparison between theoretical (solid line) and experimental (dash line) displacement curves.

IV. CONCLUSION

The purpose of this study was to provide an analytical model for predicting the displacement generated inside tissue in dynamic elastography methods based on the radiation force. The approach developed for thus purpose is based on the elastodynamic Green's function. The importance of the source geometry and the near field term of this Green's function on the calculation of the temporal deformation induced by ultrasound radiation pressure are emphasized. Expression of the displacement $u(\boldsymbol{x},t)$ is simply the convolution of this Green's function by the spatial force source and the temporal evolution of the ultrasound emission. The shape of the displacement curve was studied for different shear wave velocities, different emission times, and different amplitudes of the radiation force. The importance of parameters obtained directly from the displacement curves such as the maximum amplitude $D_{\max}$, the time $\tau_{\max}$ corresponding to the duration of the rising edge and the slope Σ of displacement curves was studied theoretically. These analytical results were compared with experimental measurements obtained in tissue-mimicking phantoms and performed using an optical interferometric technique. The shape of the experimental displacement curve and the evolution of this curve in relation to the emission configuration or the description of the medium agreed with the theoretical results. We propose that, with an appropriate temporal deconvolution technique used to compensate for the deformation effect linked to the finite duration of the emission $X_0(t)$, the rising time $\tau_{\max}$ of the displacement curve seems to be a reliable parameter to form an image directly proportional to the shear elasticity modulus μ.

ACKNOWLEDGMENTS

The authors express their gratitude to the Ministère de la Recherche and to the Association pour la Recherche sur le Cancer for funding this work and thank François Le Clésiau for his valuable contribution to this study.

[1] K. J. Parker, S. R. Huang, R. A. Musulin, and R. M. Lerner, "Tissue response to mechanical vibrations for sonoelasticity imaging," Ultrasound Med. Biol. **16**, 241–246 (1990).
[2] Y. Yamakoshi, J. Sato, and T. Sato, "Ultrasonic imaging of the internal vibration of soft tissue under forced vibration," IEEE Trans. Ultrason. Ferroelectr. Freq. Control **37**, 45–53 (1990).
[3] R. Muthupillai, D. J. Lomas, P. J. Rossman, J. F. Greenleaf, A. Manduca, and R. L. Ehman, "Magnetic resonance elastography by direct visualization of propagating acoustic strain waves," Science **269**, 1854–1857 (1995).
[4] S. Catheline, F. Wu, and M. Fink, "A solution to diffraction biases in sonoelasticity: The acoustic impulse technique," J. Acoust. Soc. Am. **105**, 2941–2950 (1999).
[5] L. Sandrin, M. Tanter, S. Catheline, and M. Fink, "Shear modulus imaging with 2-D transient elastography," IEEE Trans. Ultrason. Ferroelectr. Freq. Control **49**, 426–435 (2002).
[6] T. Sugimoto, S. Ueha, and K. Itoh, "Tissue hardness measurement using the radiation force of focused ultrasound," *IEEE International Ultrasonics Symposium*, 1990, pp. 1377–1380.
[7] M. Fatemi and J. F. Greenleaf, "C-scan imaging by radiation force stimulated acoustic emission method," *IEEE International Ultrasonics Symposium*, 1996, pp. 1459–1462.
[8] M. Fatemi and J. F. Greenleaf, "Ultrasound-stimulated vibro-acoustic spectrography," Science **280**, 82–85 (1998).
[9] A. P. Sarvazyan, O. V. Rudenko, S. D. Swanson, J. B. Fowlkes, and G. E.

Trahey, "Shear wave elasticity imaging: A new ultrasonic technology of medical diagnostics," Ultrasound Med. Biol. **24**, 1419–1435 (1998).
[10]W. F. Walker, "Internal deformation of a uniform elastic solid by acoustic radiation force," J. Acoust. Soc. Am. **105**, 2508–2518 (1999).
[11]K. Nightingale, M. L. Palmeri, R. W. Nightingale, and G. E. Trahey, "On the feasibility of remote palpation using acoustic radiation force," J. Acoust. Soc. Am. **110**, 625–634 (2001).
[12]F. L. Lizzi, R. Muratore, C. X. Deng, J. A. Ketterling, S. K. Alam, S. Mikaelian, and A. Kalisz, "Radiation-force technique to monitor lesions during ultrasonic therapy," Ultrasound Med. Biol. **29**, 1593–1605 (2003).
[13]J. Bercoff, M. Tanter, S. Chaffai, and M. Fink, "Ultrafast imaging of beamformed shear waves induced by the acoustic radiation force," *IEEE International Ultrasonics Symposium*, 2002.
[14]S. Callé, J. P. Remenieras, O. Bou Matar, M. Defontaine, and F. Patat, "Application of nonlinear phenomena induced by focused ultrasound to bone imaging," Ultrasound Med. Biol. **29**, 465–472 (2003).
[15]G. E. Trahey and B. Fahey, "Abdominal acoustic radiation force impulse imaging," *IEEE International Ultrasonics Symposium*, 2004.
[16]W. Nyborg, *Physical Acoustics* (Academic, New York, 1965), Vol. **IIB**, Chap. 11.
[17]H. C. Staritt, F. A. Duck, and V. F. Humphrey, "Forces acting in the direction of propagation in pulsed ultrasound fields," Phys. Med. Biol. **36**, 1465–1474 (1991).
[18]O. V. Rudenko, A. P. Sarvazyan, and S. Y. Emilianov, "Acoustic radiation force and streaming induced by focused nonlinear ultrasound in a dissipative medium," J. Acoust. Soc. Am. **99**, 2791–2798 (1996).
[19]A. P. Sarvazyan, A. R. Skovoroda, S. Y. Emilianov, J. B. Fowlkes, J. G. Pipe, R. S. Adler, R. B. Buxton, and P. L. Carson, "Biophysical base of elasticity imaging," Acoust. Imaging **21**, 223–240 (1995).
[20]A. P. Sarvazyan, "Method and device for shear wave elasticity imaging," US Patent Number 5,606,971 (1997).
[21]M. Fatemi and J. F. Greenleaf, "Vibro-acoustography: An imaging modality based on ultrasound-stimulated acoustic emission," Proc. Natl. Acad. Sci. U.S.A. **96**, 6603–6608 (1999).
[22]J. Bercoff, S. Chaffai, M. Tanter, L. Sandrin, S. Catheline, M. Fink, J. L. Genisson, and M. Meunier, "In vivo breast tumor detection using transient elastography," Ultrasound Med. Biol. **29**, 1387–1396 (2003).
[23]K. Aki and P. G. Richards, *Quantitative seismology–Theory and Methods* (Freeman, San Francisco, 1980), Vol. **1**, Chap. 4.
[24]Y. H. Pao and V. Varatharajulu, "Huygens' principle, radiation conditions, and integral formulas for the scattering of elastic waves," J. Acoust. Soc. Am. **59**, 1361–1371 (1976).
[25]L. Sandrin, D. Cassereau, and M. Fink, "The role of the coupling term in transient elastography," J. Acoust. Soc. Am. **115**, 73–83, (2004).
[26]J. W. Goodman, *Introduction to Fourier optics* (McGaw-Hill, New York, 1968).
[27]V. M. Levin, O. I. Lobkis, and R. G. Maev, "Field of spherical focusing transducer with arbitrary aperture angle," Sov. Phys. Acoust. **33**, 87–89 (1987).
[28]K. Nightingale, M. Scott Soo, R. W. Nightingale, and G. E. Trahey, "Acoustic radiation force impulse imaging: In vivo demonstration of clinical feasibility," Ultrasound Med. Biol. **28**, 227–235 (2002).
[29]V. G. Andreev, V. N. Dmitriex, Y. A. Pishchal'nikov, O. V. Rudenko, O. A. Sapozhnikov, and A. P. Sarvazyan, "Observation of shear waves excited by focused ultrasound in a rubber-like medium," Acoust. Phys. **43**, 123–128 (1997).
[30]S. Callé, J. P. Remenieras, O. Bou Matar, and F. Patat, "Application of vibro-acoustography to tissue elasticity imaging," Acustica **89**, 936–941 (2003).
[31]S. Callé, "Application de la force de radiation ultrasonore á l'imagerie d'élasticité des tissus biologiques (Application of the acoustic radiation force to elasticity imaging of biological tissues)," Ph. D. thesis, University of Tours, France, 2003 (in French).
[32]D. Royer and O. Casula, "Quantitative imaging of transient acoustic fields by optical heterodyne interferometry," *IEEE International Ultrasonics Symposium*, 1994, pp. 1153–1162.
[33]S. Chen, "Shear property characterization of viscoelastic media using vibrations induced by an ultrasound radiation force," Ph. D. Thesis, Faculty of the Mayo Graduate School (2002).
[34]T. J. Hall, M. Bilgen, M. F. Insana, and T. A. Krouskop, "Phantom materials for elastography," IEEE Trans. Ultrason. Ferroelectr. Freq. Control **44**, 1355–1365 (1997).

Symmetric mode resonance of bubbles attached to a rigid boundary

Edward M. B. Payne,[a] Suhith J. Illesinghe,[b] and Andrew Ooi[c]
Department of Mechanical and Manufacturing Engineering, The University of Melbourne, Parkville Melbourne, Victoria 3010, Australia

Richard Manasseh[d]
CSIRO Manufacturing and Infrastructure Technology, Energy and Thermofluids Engineering, P.O. Box 56 (Graham Road), Highett Melbourne, Victoria 3190, Australia

(Received 9 March 2005; revised 15 July 2005; accepted 12 August 2005)

Experimental results are compared with a theoretical analysis concerning wall effects on the symmetric mode resonance frequency of millimeter-sized air bubbles in water. An analytical model based on a linear coupled-oscillator approximation is used to describe the oscillations of the bubbles, while the method of images is used to model the effect of the wall. Three situations are considered: a single bubble, a group of two bubbles, and a group of three bubbles. The results show that bubbles attached to a rigid boundary have lower resonance frequencies compared to when they are in an infinite uniform liquid domain (referred to as free space). Both the experimental data and theoretical analysis show that the symmetric mode resonance frequency decreases with the number of bubbles but increases as the bubbles are moved apart. Discrepancies between theory and experiment can be explained by the fact that distortion effects due to buoyancy forces and surface tension were ignored. The data presented here are intended to guide future investigations into the resonances of larger arrays of bubbles on rigid surfaces, which may assist in surface sonochemistry, sonic cleaning, and micro-mixing applications.
 [DOI: 10.1121/1.2062268]

PACS number(s): 43.20.Ks, 43.30.Dr [AJS] Pages: 2841–2849

I. INTRODUCTION

Modeling the compressible oscillations of gas bubbles dates back to 1917 with the work of Rayleigh[1] who gave the first mathematical formulation of the dynamics of a single oscillating bubble. In the family of Rayleigh-Plesset equations the radial expansion and contraction of the bubble is given by the spherically symmetric momentum equation for the liquid only; the ideal gas law is often used to give the boundary condition at the bubble wall. Minnaert[2] independently developed a simple linear relationship for the resonance frequency of a freely pulsating spherical bubble, known as the Minnaert frequency, which was derived using an energy balance approach that inherently assumed linear behavior. Extensive work has since been done toward developing a model to describe the oscillations of multiple gas bubbles in a liquid medium,[3–11] mostly analyzing pairs of bubbles. Furthermore, many investigators have been interested in how bubbles interact with each other, and in the natural frequencies of a system of an arbitrary number of bubbles.

A coupled-oscillator model based on the self-consistent approach, such as that introduced by Tolstoy[4] and later developed by Feuillade,[12] is one way to describe the collective oscillations of bubbles. This approach inherently eliminates an inconsistency in the coupled equations owing to multiple bubble re-reflections and has been shown to qualitatively predict the acoustic pressure distribution around a bubble chain.[13,14] In his work, Feuillade[12] modeled an arbitrary number of bubbles in free space, showing how the symmetric mode (where all bubbles oscillate in phase) has a lower resonance frequency than the asymmetric modes (where some, or all of the bubbles oscillate out of phase).

Due to the complex nature of surface tension and buoyancy effects, most modeling of bubbles attached to a rigid boundary has been done numerically. A good review of bubble deformation near rigid and free boundaries is given by Blake and Gibson.[15] Other workers include Chahine,[16,17] who has used a numerical boundary element method to describe bubble collapse near a solid wall. However, in terms of the current framework, for which experimental results can be easily compared to a simple linear model, numerical calculations are not required. In this paper, therefore, an image theory approach developed by Strasberg[18] will be incorporated into Feuillade's work to model the effect of the boundary.

Strasberg performed an analysis of the effect of a nearby rigid boundary on the resonance frequency of a single spherical bubble. He showed that a bubble pulsating next to the rigid boundary is equivalent to two bubbles pulsating in phase in free space, which in this paper will be referred to as the "image effect." The result of this image effect is that bubbles next to a rigid boundary have lower resonance frequencies than the same bubbles in an unbounded domain.

[a]Electronic mail: embp@ecr.mu.oz.au
[b]Electronic mail: s.illesinghe@gmail.com
[c]Electronic mail: a.ooi@unimelb.edu.au
[d]Electronic mail: Richard.Manasseh@.csiro.au

Including this into Feuillade's model is easily done and will be shown in the following. Other work, by Howkins[19] and Blue,[20] also adopted Strasberg's image theory to try to explain their experimental findings. In their work, they experimentally measured the resonance frequency of a bubble which was actually attached to a rigid boundary, and showed that the resonance frequency was lower compared to that of an equivalent bubble in free space. However their work only considered single bubble arrangements of different bubble radii, and only n different bubble radii, where $n=2$ for Blue's work and $n=11$ for Howkins' work. This paper is intended to determine whether the image theory is applicable for larger bubble groups attached to a rigid boundary, by providing original and detailed experimental results over a range of bubble sizes.

Apart from these limited experimental and theoretical studies on the resonance frequencies of multiple bubble arrangements attached to a rigid boundary, the majority of work has been carried out for bubbles in free space. For example, lower resonance frequencies for groups of bubbles has been shown by Nicholas *et al.*[21] for bubble clouds, by Feuillade[12] for up to three bubbles, and by Manasseh *et al.*[22] for a bubble chain. Furthermore, Hsiao *et al.*[8] and Leroy *et al.*[11] experimentally showed that the symmetric mode resonance frequency for two bubbles in free space is lower than the resonance frequency of a single bubble in free space. In addition, Weston[23] and Tolstoy *et al.*[24] have modeled line and plane arrays of bubbles.

The present paper thus fills a gap in the literature, in that it is concerned theoretically, but primarily experimentally, with the symmetric mode resonance frequency of multiple bubble arrangements attached to a plate, over a range of bubble sizes. From a theoretical standpoint, the current work builds upon a simplified version of Feuillade's coupled-oscillator model, in which a mirror image of bubbles is introduced to model the presence of a rigid boundary. The resulting system of equations is reduced to an analytical expression which gives the symmetric mode natural frequency of an arrangement of up to three bubbles attached to a rigid boundary, whose spacing between bubble centers is identical. Although unequal bubble spacings are an interesting added possibility, as is the possibility of unequal bubble sizes, effects of these parameters are not considered in this paper.

Experimental results for the symmetric mode resonance frequency of different arrangements of bubbles attached to a glass plate are presented. One, two, and three bubble arrangements are considered, where in each case the system was excited by a varying frequency (chirp) signal, covering the expected resonance frequency of the given bubble arrangement. The response with and without bubbles was detected by a hydrophone, allowing the symmetric mode resonance frequency to be determined. Comparison between the theoretical natural frequency and the experimental resonance frequency can be made since for the relatively large bubble sizes involved, the resonance frequency and natural frequency are essentially the same.

For ease of experimental setup, bubbles of order millimeter size were used, with natural frequencies of the order of 1000 Hz. As a result, the acoustic wavelengths in the experimental tank were large ($\approx$1.5 m) relative to the spacing between the bubbles (which was approximately three times the equilibrium radius; a typical value being 7.5 mm). Hence the symmetric mode was preferentially excited over the asymmetric modes because a given bubble arrangement was under the same pressure field at any one point in time, albeit with slight variations in the pressure amplitude and phase.

From this work, predictions of the resonance frequencies of multiple bubbles attached to a rigid boundary will potentially help in the manufacture and operation of devices for the medical-pathology field such as those already demonstrated by Liu *et al.*[25] as well as for surface sonochemistry and sonic cleaning applications.

II. THEORY

A. Development of the model

Under adiabatic conditions, the natural frequency of a spherical, millimeter-sized, linearly oscillating bubble is given by Minnaert's equation[2]

$$\omega_0 = \frac{1}{R_0}\sqrt{\frac{3\gamma P_0}{\rho}}, \tag{1}$$

where ω_0 is the circular natural frequency, γ is the ratio of gas specific heats, P_0 is the absolute liquid pressure, ρ is the liquid density, and R_0 is the equilibrium radius of the bubble.

Feuillade's model[12] is used to describe the dynamics of an arbitrary number of bubbles located in free space, driven by an external pressure field. Mathematically this is given by the following coupled differential equation:

$$m_i\ddot{v}_i + b_i\dot{v}_i + \kappa_i v_i = -P_i e^{I(\omega t+\phi_i)} - \sum_{j\neq i}^{N}\frac{\rho}{4\pi s_{ji}}\ddot{v}_j(t - s_{ij}/c), \tag{2}$$

where v_i represents the differential volume of the ith bubble (i.e., the difference between the instantaneous and equilibrium bubble volumes), $m_i(=\rho/4\pi R_{0_i})$ is the inertial "mass" of bubble i, having radius R_{0_i}, b_i describes the damping, and $\kappa_i(=3\gamma P_0/4\pi R_{0_i}^3)$ is the "adiabatic stiffness." The amplitude and phase of the external field experienced by the ith bubble are denoted by P_i and ϕ_i, respectively, and s_{ji} denotes the center-to-center distance between bubbles i and j. The angular driving frequency is denoted by ω and t is time. The imaginary unit is denoted by I. The last term on the right-hand side describes the time delay coupling between the bubbles due to their oscillating pressure fields. The speed of sound in water is denoted by c.

Since only the natural frequencies are required, the external field acting on each bubble is neglected. Later it will be shown that the natural frequency is a very close approximation to the resonance frequency, given the relatively large bubble sizes considered. The time delay in the second term on the right-hand side of Eq. (2) can be neglected since there is negligible time for the sound to propagate from one bubble to another. In other words, because of the small bubble separations considered (e.g., $s_{ij}=7.5$ mm) and the relative speed of sound in water (i.e., $c=1480$ m/s), the time delay term $s_{ij}/c \approx 5\times10^{-6}$ s and will be assumed to be small enough,

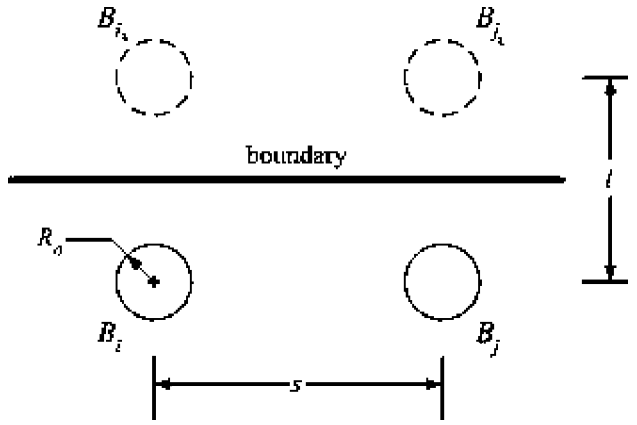

FIG. 1. Schematic of bubble image model for $N=2$. The solid line represents the real bubble and the dashed line represents the image bubble.

compared to the natural period of an oscillating bubble, to neglect. Further, it has been shown by Doinikov *et al.*[14] that time delays only affect the damping but not the natural frequencies of the natural modes of the system when the bubbles are not too far apart. Since the interest of this paper is only on the natural frequencies of the system, it is anticipated that neglecting time delays will not affect any of the data presented in this paper. As a further simplification it is assumed that the bubbles have identical radii and the same physical properties (i.e., $R_{0_1}=R_{0_2}=\ldots=R_{0_N}=R_0$, $m_1=m_2=\ldots=m_N=m$, etc.). Therefore Eq. (2) reduces to

$$m\ddot{v}_i + b\dot{v}_i + \kappa v_i = -\sum_{j\neq i}^{N} \frac{\rho}{4\pi s_{ji}}\ddot{v}_j. \tag{3}$$

It can be seen that the solution of the above gives N different eigenmodes each having an associated eigenfrequency.

B. Introduction of a rigid boundary

Consider the dynamics of a planar array of bubbles situated a distance $l/2$ from a rigid boundary. A bubble next to a rigid boundary creates an acoustic image of itself,[12] which oscillates in phase with the original bubble and is coupled to it. Under the above-mentioned assumptions, the bubble produces a velocity field like a potential-flow source or sink; hence the rigid boundary can be modeled by a mirror image. This is depicted in Fig. 1 for the simple case of two bubbles B_i and B_j. Note that $l(=s_{ii_\iota})$ is the separation between a bubble and its image (e.g., B_i and B_{i_ι}).

It can be seen by examining Eq. (3) with j set to i_ι that the image bubble (which simulates the solid wall) has the effect of increasing the effective mass on the real bubble. Physically this is because the boundary forces the streamlines to be parallel to itself and hence into a new (more constrained) topology. Thus, an extra term (given by R_0/l) arises as part of the inertial coefficient for bubble i. Also an extra term (given by $\rho/4\pi l_{j_\iota i}$) arises because of the coupling between a given bubble i and all the other bubble images j_ι. Equation (3) thus becomes

$$\left(m + m\frac{R_0}{l}\right)\ddot{v}_i + b\dot{v}_i + \kappa v_i = -\sum_{j\neq i}^{N}\left(\frac{\rho}{4\pi s_{ji}} + \frac{\rho}{4\pi l_{j_\iota i}}\right)\ddot{v}_j, \tag{4}$$

where $l_{j_\iota i}(=\sqrt{s^2+l^2})$ denotes the radial distance between image bubble j_ι and bubble i.

An analytical expression is obtained for the undamped natural symmetric mode frequency for $N\leqslant 3$ bubbles,[26] in which the separation between bubble centers, s, is identical. Since the symmetric mode is assumed all bubbles pulsate with the same amplitude and phase, it follows that for the undamped case, Eq. (4) reduces to one independent equation given by

$$\left(m + m\frac{R_0}{l}\right)\ddot{v} + \kappa v = -(N-1)\frac{\rho}{4\pi}\left(\frac{1}{s} + \frac{1}{l_\iota}\right)\ddot{v}, \tag{5}$$

where $l_\iota=\sqrt{s^2+l^2}$. Grouping inertia terms, dividing through by m and noting that $m=\rho/(4\pi R_0)$ and $\kappa/m=3\gamma P_0/(\rho R_0^2)=\omega_0^2$, yields

$$\left(1 + \frac{R_0}{l} + (N-1)R_0\left(\frac{1}{s} + \frac{1}{l_\iota}\right)\right)\ddot{v} + \omega_0^2 v = 0. \tag{6}$$

The damping term has been neglected because Strasberg[18] showed that its impact on the resonance frequency is negligible for relatively large bubbles. However, it does influence the resonance frequency of small (submicron radii) bubbles, as shown by Khismatullin.[27] The natural frequency (in rad/s) of Eq. (6) is thus given by

$$\omega_{\mathrm{sym}_N} = \frac{\omega_0}{\sqrt{1 + \frac{R_0}{l} + (N-1)R_0\left(\frac{1}{s} + \frac{1}{l_\iota}\right)}}, \tag{7}$$

which holds for $N\leqslant 3$. This limitation arises because it has been assumed that the separation between bubble centers is identical and a group of three bubbles is the largest number of bubbles which satisfies the condition for a planar array. Note that $N=3$ corresponds to a group of three bubbles arranged in an equilateral triangle.

A justification for the comparison between the resonance frequency of the bubbles in the experiments and the natural frequency given by Eq. (7) is as follows. The resonance frequency is identical to the natural frequency when there is no damping. Since the bubbles considered in this paper are quite large, damping is small, meaning that the resonance frequency can be very closely approximated by the undamped natural frequency given by Eq. (7). To show this, a plot of the amplitude response (in terms of a change in radius) of a group of two bubbles attached to a rigid boundary and driven by an external source is given in Fig. 2, where $R_0=2.5$ mm, $s=5R_0$, and $l=2R_0$. In this numerical example, the bubbles have been driven in phase (to excite the symmetric mode), and damping has been included. The amplitude has been divided by the driving amplitude to give a normalized response amplitude and is denoted by the solid line in Fig. 2. The dashed line highlights the undamped natural frequency as calculated using Eq. (7). Clearly the difference between the undamped natural frequency and the resonance frequency

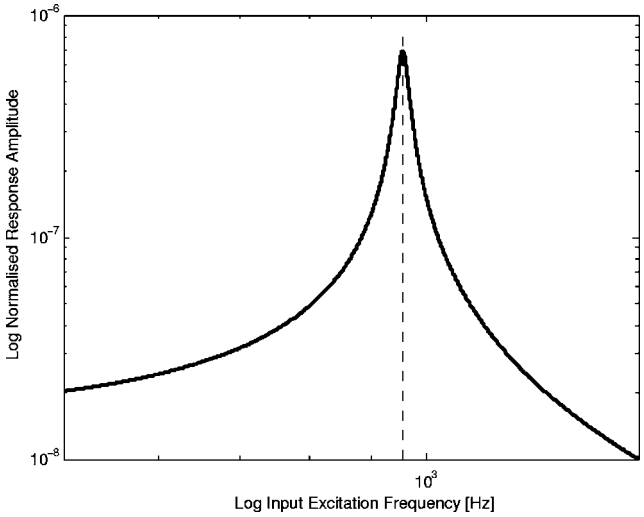

FIG. 2. Resonance frequency compared to the undamped natural frequency for a group of two bubbles attached to a rigid boundary, each with $R_0 = 2.5$ mm. Separation distance $s = 5R_0$ and $l = 2R_0$. Equation (7) is used to calculate the undamped natural frequency which is highlighted by the dashed vertical line. The resonance frequency coincides with the undamped natural frequency at approximately 956 Hz.

(the frequency at which maximum amplitude occurs) is negligible. For this example resonance occurs at approximately 956 Hz.

Bubbles are considered "attached" to the boundary when $l = 2R_0$ (the smallest physical value for l), such that the perpendicular distance from the center of a bubble to the plate is equal to R_0. Equation (7) does not allow for divergence from sphericity due to the flattening of the buoyant bubble, which in the experiment was trapped under a rigid boundary. It is therefore expected that the expression will be more valid for smaller bubbles which are closer to spherical shape. For larger bubbles however there is a significant contact area between the bubble and the boundary, resulting in reduced bubble-wall velocity near the boundary as the bubble pulsates. In this situation the image theory is no longer appropriate. Instead, the dynamics of larger bubbles are better described by hemispheres or domes as previously investigated by Blue.[20]

To do this, a hemispherical shape is assumed, equivalent in volume to half a spherical bubble. Therefore, in determining the resonance frequency of a hemispherical bubble, the radius of a spherical bubble with twice the volume of the hemispherical bubble is calculated and substituted into Minnaert's equation [Eq. (1)]. This has the effect of reducing the resonance frequency by a factor of $2^{-(1/3)}$ compared to that of a spherical bubble with the same volume as the hemisphere. It is therefore suggested that the dynamics of a large (approximately hemispherical) bubble which is attached to a boundary is equivalent to the dynamics of a single bubble (with twice the volume) pulsating in free space. This is what was implied from Blue's work. In the absence of surface tension and friction, this seems a reasonable approximation.

The above-noted consideration, which is consistent with the work of Strasberg, Blue, and Howkins, means that the resonance frequency of a bubble attached to a rigid boundary will be lower than that of a bubble with the same size in free space. But due to nonsphericity of the bubbles the resonance frequency will be slightly increased.

III. EXPERIMENT

Experiments were carried out to detect the response of air bubbles in water trapped under a glass plate when driven by an acoustic pressure field, as depicted in Fig. 3. The tank was made from 12-mm-thick Perspex with a 300 mm square base. The glass plate (of thickness 3 mm) was securely maintained at a height of 20 mm above the face of a piston which was attached to a modified speaker. A circular hole in the bottom of the tank allowed direct transfer of sound from the speaker to the water, thereby setting up an acoustic pressure field within the tank. Adhesive tape was used to seal the area adjoining the water and the face of the piston.

Air bubbles were generated with a syringe (50 μl, ALLTECH Associates Australia) with a volumetric accuracy of ±5% and were arranged as close to the center-line of the piston as possible (±0.25 mm) so as to receive maximum power from the speaker. A chirp signal was used to excite the bubbles which was preamplified before passing through the speaker. In the first set of single bubble experiments, a chirp signal of 80 ms was used, while for the second set of single bubble experiments, as well as for the two and three bubble experiments, a chirp signal of 180 ms was used. The difference in chirp duration for the two sets of single bubble ex-

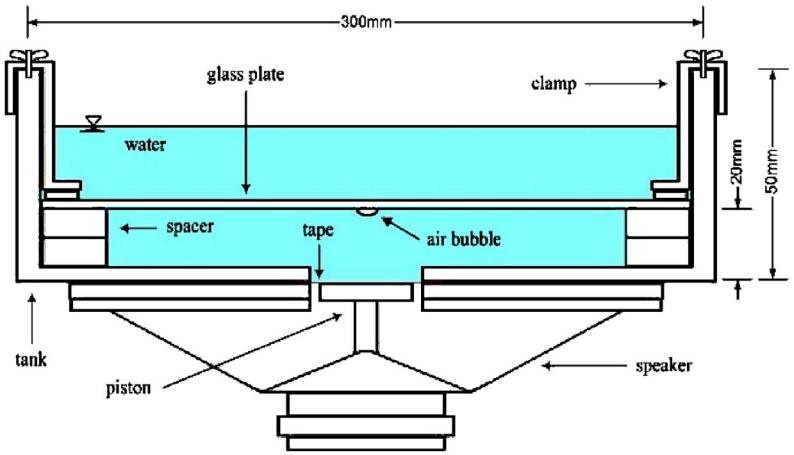

FIG. 3. (Color online) Schematic cross-sectional view of the main experimental apparatus with a single air bubble. The bubble is excited by the speaker.

TABLE I. Experimental parameters and conditions.

Density of water	1000 kg/m^3
Temperature of water	20°C
Equilibrium water pressure	10^5 Pa
Speaker driving pressure amplitudes	$<$100 Pa
Frequency range	400–3000 Hz
Polytropic index	1.33

periments is shown not to affect the resonance frequency. The applied sound pressures directly above the piston near the glass plate were typically of the order of 100 Pa or less, so as to remain in the linear regime. Frequencies employed were mostly in the 400–3000 Hz range. Table I gives a summary of the experimental conditions and parameters.

The small pressure fluctuation caused by the response of the bubbles was detected by a hydrophone (Brüel & Kjaer 8103, 9.5 mm diameter and 50 mm in length, with an essentially constant frequency response from 0.1 Hz to 20 kHz). The distance from the hydrophone's acoustic center to the closest bubble wall was approximately 7 mm. The output of the hydrophone was then fed into a charge amplifier (Brüel & Kjaer type 2634, with an essentially constant frequency response from 1 Hz to 20 kHz), and connected to a digital oscilloscope (HP54600A) for data acquisition and storage on a PC. A schematic of the setup is given in Fig. 4.

Thirty time-domain responses were captured for a given bubble volume and arrangement, and each one converted to a frequency-domain response. Likewise, 30 responses without bubbles were captured, thus measuring the response of the tank and speaker assembly only. The difference in the frequency-domain responses at each frequency with and without bubbles was scaled by dividing by the average response with no bubbles present. If the maximum "scaled" difference in power was statistically significant, the frequency at which this difference occurred was considered to be the resonance frequency of the bubble arrangement. A sample time-domain and corresponding frequency-domain response are shown in Figs. 5 and 6, respectively, for a 45 μl bubble. In Fig. 6 the maximum scaled difference occurs at around 1100 Hz, indicating that that is the resonance frequency of the bubble, when attached to the glass plate.

Although the dominant response detected by the hydrophone was believed to be pressure fluctuations caused by the radial pulsation of the bubble (the breathing mode), there was the possibility that surface modes[28] would interfere with the response. Surface modes were visually observed, but only when the system was driven at very high amplitudes. At the amplitudes used during experimentation, surface modes were not observed. Given the relatively large size of the hydrophone head compared to the small scale pressure variations caused by surface modes, any surface modes that were present would have had little influence on the hydrophone. Therefore it is quite reasonable to assume that the above-determined resonances were indeed associated with the radial pulsation of the bubble.

It should be emphasized that the purpose of this paper is to investigate the symmetric mode resonance frequency of the bubble groups, and not the other possible modes (e.g., the asymmetric mode). While the experiments were intended to excite the symmetric mode, small differences in the pressure amplitude applied to each bubble, as well as slight phase

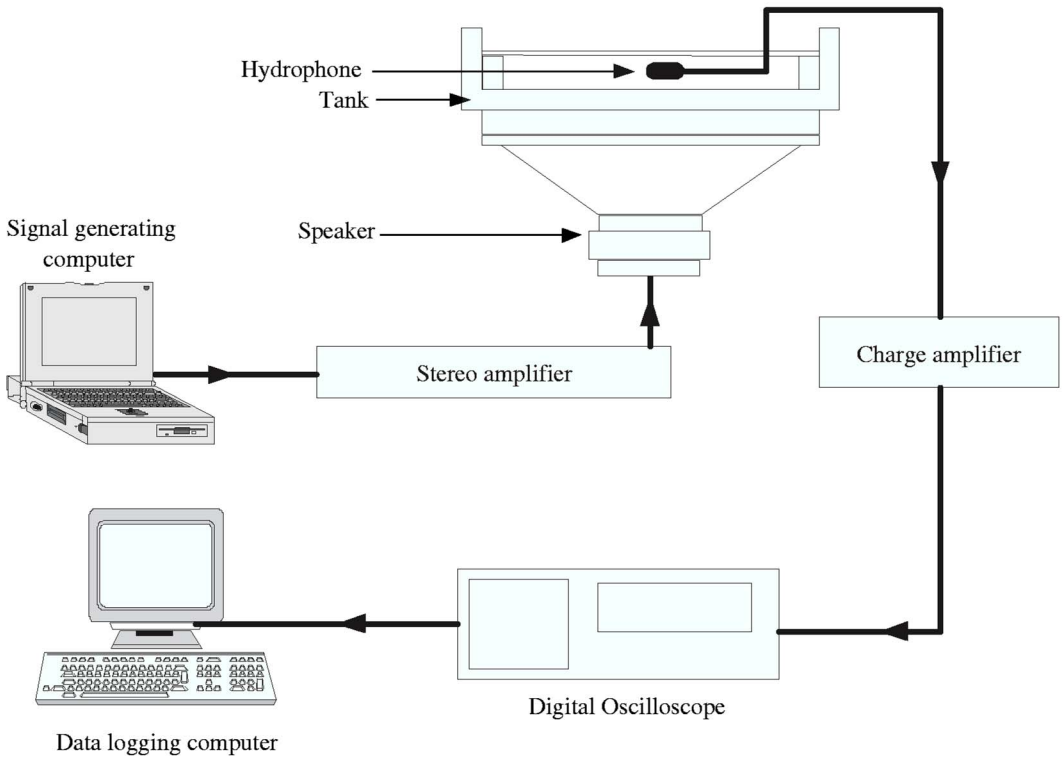

FIG. 4. (Color online) Schematic of the experimental setup. See Table I for experimental conditions.

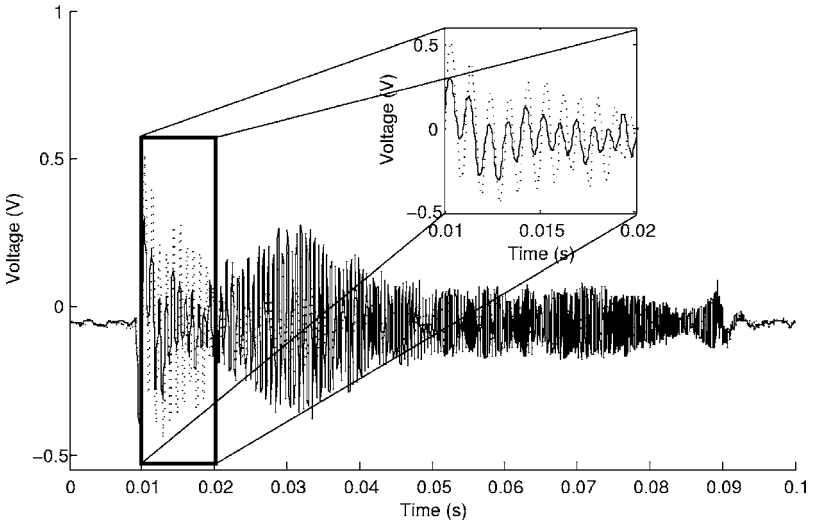

FIG. 5. Time-domain response of the system with and without bubbles. The dotted line denotes the response with a 45 μl bubble. The solid line represents the case when the bubble was removed. This test used an 80 ms chirp signal sweeping from 900 to 3500 Hz. A enlarged region from 0.01 to 0.02 s is highlighted to distinguish the response with a bubble from the response without a bubble.

differences, tended to excite asymmetric modes as well. However the symmetric mode appeared to be dominant for most of the conditions investigated. In the conditions where this was not the case, only the contribution of the symmetric mode was identified. Investigation of the asymmetric modes is beyond the scope of this paper and will be the focus of future work.

IV. RESULTS AND DISCUSSION

A. Single bubble arrangement with varying bubble size

Figure 7 shows the symmetric mode resonance frequency versus bubble radius for the case of a single bubble attached to the glass plate. Superimposed is Minnaert's relationship and the analytical expression from Eq. (7) for $N=1$, as well as the half-bubble approximation. Clearly the image theory (the analytical expression) gives a better agreement to the experimental data than Minnaert's relationship. The error bars on the experimental results are included, but are barely visible due to the tight confidence limits on the results. The radii given on the horizontal axis represent the radius of a spherical bubble with a volume (V_{inj}) equal to the bubble which was injected (i.e., $R_0=(3V_{\text{inj}}/4\pi)^{1/3}$).

As predicted by the theory, the experimental data show that smaller bubbles have higher resonance frequencies than larger ones. This is expected and confirms that the resonance response of the bubble has been detected by the hydrophone. Also, both the image theory and the experimental data lie below Minnaert's relationship, which is consistent with the data of previous investigators;[18–20] and from the present work, enough data points are now available for the functional form of the relation to be confirmed. According to the image theory, this can be reasoned as follows. The effect of the boundary is equivalent to introducing an image bubble adjacent to the real bubble. Since the image bubble will exactly "mirror" the real bubble, there is a symmetric coupling between the real bubble and the image bubble. This increases the effective mass of the system, resulting in a decrease in

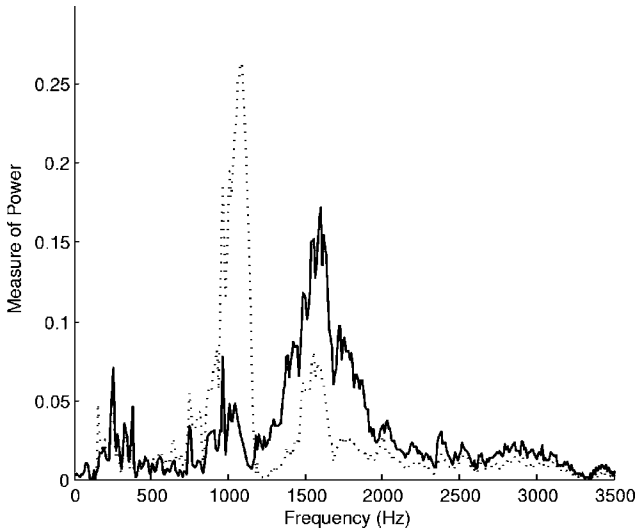

FIG. 6. Frequency-domain response of the system with and without bubbles. The dotted line denotes the response with a 45 μl bubble. The solid line represents the case when the bubble was removed.

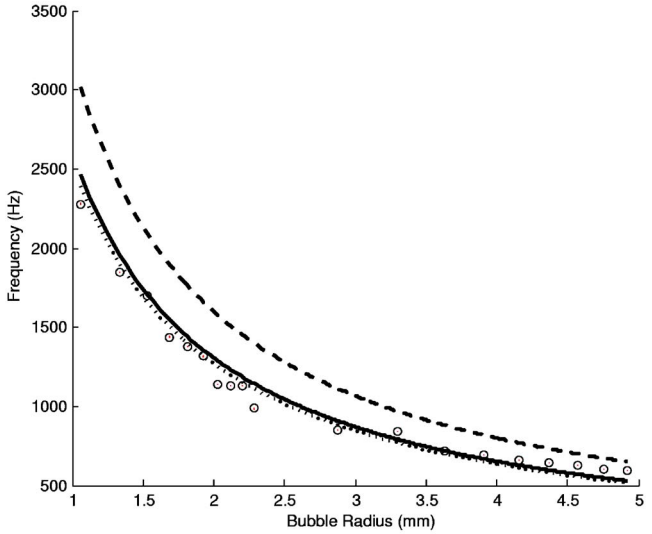

FIG. 7. Comparison of experimental resonance frequencies and theoretical undamped natural frequencies for a single bubble of varying radius. (---) Minnaert's equation and (—) represents the analytical expression for $N=1$. (···) The half-bubble approximation. The points denoted ◯ are the experimental results, with error bars shown by vertical lines.

resonance frequency. This is analogous to a mass-spring system where an increase in the mass will lower the resonance frequency.

Although a bubble (especially a large bubble) is flattened when attached to a plate (due to buoyancy and surface tension) the deviation from spherical shape does not appear to greatly affect the resonance frequency. Strasberg's work on the resonance frequency of oblate spheroids is consistent with this observation. In his work, he showed that as a bubble is deformed from sphericity its pulsation frequency increases, but slightly, increasing by only 2% when the bubble becomes a spheroid with a ratio of major to minor axes equal to 2 (see Table I of Strasberg's work[18]). Admittedly, his work was for a bubble in free space, but it appears to be consistent with the trend observed in our experimental data.

For small bubbles the experimental data show close agreement with the analytical expression, but on closer analysis (for radii less than about 3 mm) there is a slight downwards shift in the experimental data. A possible explanation for this is as follows. Recall that the analytical expression was based on the assumption that the bubble is spherical and is just touching the boundary, meaning that distance between the real bubble and its image is given by $l=2R_0$. However, even the smallest bubbles used in the experiments were slightly flattened, giving $l<2R_0$. This increases the effective mass and hence decreases the resonance frequency. Consequently the experimental data points are lower than the analytical expression. There may be other reasons for the slight downwards shift; such as damping effects. It is known from elementary mechanics that the damped resonance frequency of a simple harmonic oscillator (such as a bubble) is lower than the damped natural frequency. The fact that there is a downwards shift for smaller bubbles is consistent with damping having a greater influence on the resonance frequency of smaller bubbles, as proposed by Khismatullin.[27]

The upwards shift in experimental data points from the image theory for larger bubble radii (>3 mm) is not as clearly justified. The measured eccentricity of the spheroidal-shaped bubbles used in the experiments was approximately equal to 2, and so the increase in resonance frequency according to Strasberg's[18] work is insignificant. Furthermore, the above-mentioned flattening effect (which has a greater impact on larger bubbles), would tend to decrease the resonance frequency, making the fit even worse. Even with the half-bubble approximation, which is a worse fit than the image theory (but a more realistic physical approximation), the increase in resonance frequency caused by the flattening of the bubble would be less than 2%, hardly enough to explain the significant upward shift.

Thus, at this point there seems to be no reasonable explanation for the upwards shift in experimental data points for larger bubbles. Nonetheless, the limited results of Blue and Howkins have been found to be consistent with the present data, in that for small bubbles (which were used by Blue) the experimental data lie below both Minnaert and the image (equivalent to Strasberg's) theory, while for larger bubbles (which were used by Howkins) the experimental data lie between Minnaert and Strasberg's theory. The transition from a downwards to upwards shift in the experimental results as the bubble size increases suggests that for a bubble attached to a rigid boundary, there is a critical bubble size greater than which surface tension and buoyancy forces significantly alter the dynamics and hence resonance frequency of the system.

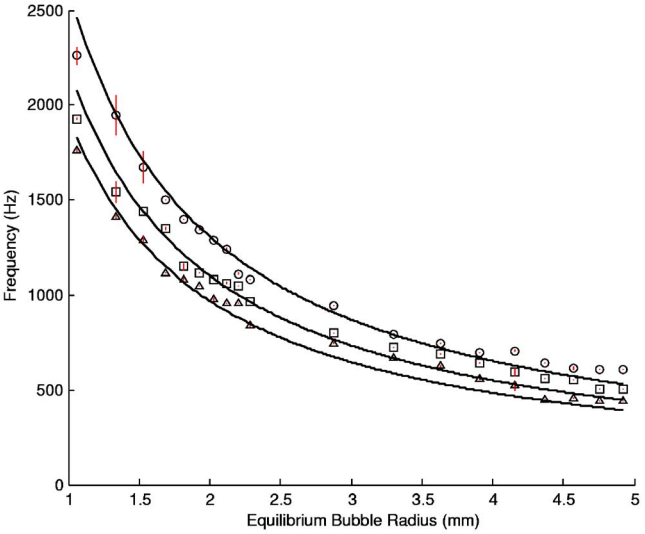

FIG. 8. (Color online) Comparison of experimental resonance frequencies and theoretical undamped natural frequencies for one, two, and three bubble arrangements vs bubble radius at a fixed separation, $s=3R_0$. (—) The analytical expression for one bubble (top curve), two bubbles (middle curve), and three bubbles (bottom curve). The points denoted ◯, □, and △ are the experimental results for one, two, and three bubbles, respectively, with error bars shown by vertical lines.

B. Multiple bubble arrangements with varying bubble size

Figure 8 shows the experimental data for a three bubble group arranged in an equilateral triangle, a two bubble group, and a single bubble. The respective analytical expressions for $N=3$, $N=2$, and $N=1$ are superimposed. For the arrangements with two and three bubbles, the separation between bubble centers was kept constant at approximately $3R_0$, in which the radius of the bubble was known from the injected volumetric measurement. Small variations in the volume of air injected to make the bubbles had negligible impact on the bubble radius (less than 1.7%).

As with the previous single bubble case, a similar trend (in terms of variation of resonance frequency with bubble size) is seen here; where for large bubble radii there is an upwards divergence from the analytical expression while for smaller bubble radii there is a downwards shift.

As evident in Fig. 8, the analytical curves are displaced downwards as N increases. This agrees with the trend in the experimental data. The downwards shift can be explained by the increase in effective mass for larger bubble groups, resulting in a lower resonance frequency. There is a clear distinction between each arrangement which is statistically significant since the error bars do not overlap for any given bubble size.

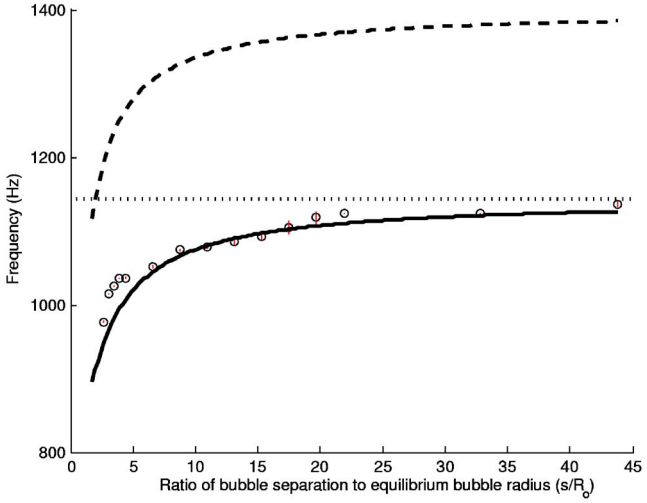

FIG. 9. (Color online) Resonance frequency vs ratio of bubble separation to bubble radius for two 50 μl bubbles (R_0=2.29 mm). (---) The undamped symmetric mode frequency for two spherical bubbles in free space. (—) The analytical expression (7) for N=2 and l=2R_0. (···) The limit as s approaches infinity. The points denoted ◯ are the experimental results, with error bars shown by vertical lines.

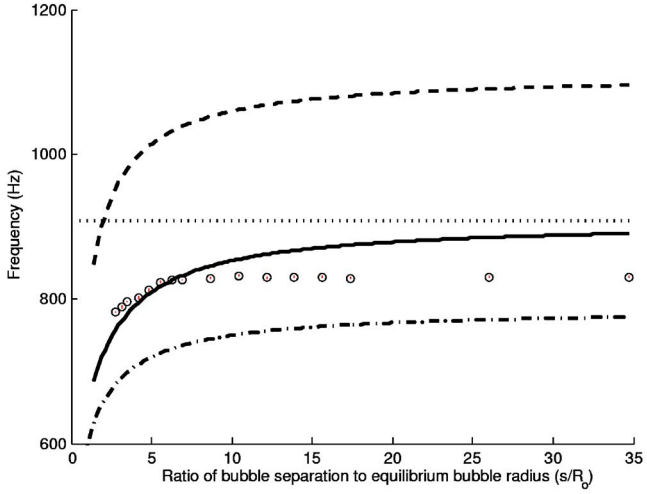

FIG. 10. (Color online) Resonance frequency vs ratio of bubble separation to bubble radius for two 100 μl bubbles (R_0=2.88 mm). (---) The undamped symmetric mode frequency for two spherical bubbles in free space. (—) The analytical expression (7) for N=2 and l=2R_0, while (–.–) represents the analytical expression for l=R_0. (···) shows the limit as s approaches infinity. The points denoted ◯ are the experimental results, with error bars shown by vertical lines.

C. Variation of resonance frequency with bubble separation

Hsiao *et al.*[8] gave experimental results for the case of two bubbles interacting in free space at varying separation. Their results agree with that predicted by their theory, showing that the symmetric mode resonance frequency decreases as the bubbles are brought closer together. However, there does not appear in the literature to be results for the case of two and three bubbles attached to a rigid boundary. Hence the purpose of the present results, which show that the same trend as documented for bubbles in free space, also holds for bubbles attached to a rigid boundary. The results also clearly show that the image theory is a much better approximation than the theory for groups of bubbles in an unbounded domain.

Figure 9 shows how the symmetric mode resonance frequency decreases as two identical 50 μl bubbles are brought closer together. The reduction in frequency for smaller separations is due to the increased effective mass on each bubble.[12] Conversely, when the bubbles are further apart, the image loading due to the interaction of the pair is weaker and the frequency approaches that of a single bubble attached to a boundary, shown by the dotted horizontal line in Fig. 9 and subsequent figures.

As mentioned, the radius of a given bubble was known from the volumetric measurement. Thus for a 50 μl bubble the nominal spherical radius is 2.29 mm. For a 100 μl bubble the radius is 2.88 mm. In order to change the ratio of bubble separation to bubble radius, s/R_0, the radii of the bubbles were kept constant while the bubble separation was varied (by moving one of the bubbles and keeping the other fixed). The analytical expression [Eq. (7)] is given by the solid line in Fig. 9. The expression for two bubbles in an unbounded domain is equivalent to setting l=∞ in Eq. (7) with N=2, resulting in the same expression given by Hsiao *et al.*[8] This is also plotted in Fig. 9 and is given by the dashed line.

Figure 10 shows the same as Fig. 9 but for two 100 μl bubbles. The same trend is observed, verifying that the results are reproducible, but there is a larger discrepancy between the experiment and theory for large values of s/R_0. Also plotted is the image theory for l=R_0, given by the dash-dot line. This has been plotted because the bubbles are squashed and the center distance to their image is less than 2R_0. On comparison with this line however, there still remains a significant discrepancy, which is possibly due to surface tension and buoyancy force effects.

The variation in symmetric mode resonance frequency with bubble separation was also performed on a group of three equi-spaced bubbles. Figure 11 shows the results for three 10 μl bubbles (nominal spherical radius of 1.34 mm). A consistent trend is observed in reasonable agreement with the theory. The fact that this trend is observed supports the assumption that the interaction between the pair of bubbles is caused by the coupled radial pulsations, rather than surface modes.

V. CONCLUSIONS

The results from this work show that bubbles attached to a rigid boundary have similar resonance trends to bubbles in free space, while the actual frequencies are lower. It has been shown theoretically and experimentally that smaller bubbles have higher resonance frequencies than larger bubbles, and that larger groups of bubbles have lower resonance frequencies than smaller groups. The deviation from sphericity was shown to have a minor effect on the frequencies predicted by the analytical expression, and is clearly less dominant than the increase in image loading caused by the decrease in separation between a real bubble and its image. Furthermore,

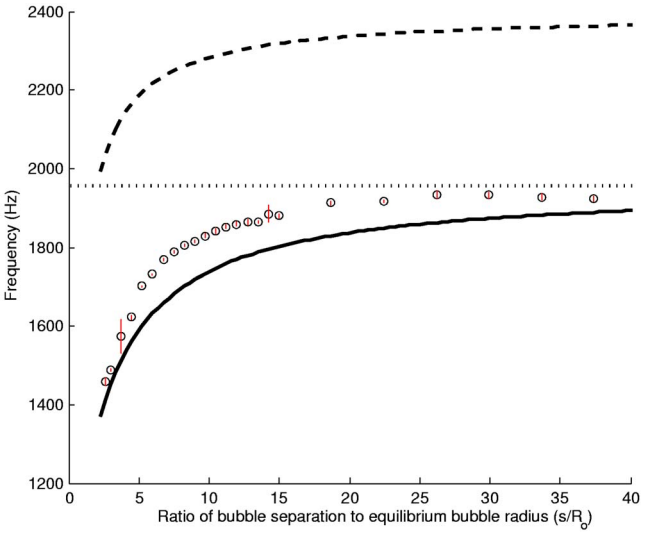

FIG. 11. (Color online) Resonance frequency vs ratio of bubble separation to bubble radius for three 10 μl bubbles (R_0=1.34 mm). (---) The undamped symmetric mode frequency for three spherical bubbles in free space. (—) The analytical expression (7) for N=3 and l=2R_0. (···) The limit as s approaches infinity. The points denoted ◯ are the experimental results, with error bars shown by vertical lines.

despite the assumptions of spherical bubble shape and the neglect of surface tension and damping, overall the analytical expression shows good agreement with the experimental results. This is a useful outcome, because it means that the resonance frequency of bubble arrays with greater number of bubbles can be predicted with a certain degree of accuracy. However, for very small bubbles, damping would have to be more rigorously considered. Future experimental work in this direction would help validate such predictions and provide guidance for the investigation of acoustic streaming from bubble arrays as well as sonic cleaning applications.

ACKNOWLEDGMENTS

The authors are very grateful to CSIRO Manufacturing & Infrastructure Technology for providing assistance throughout the experimental stage of this work. We are also appreciative of the assistance of Professor Ray Watson (Department of Mathematics and Statistics, University of Melbourne), who instructed us on the statistical analysis of the experimental results. Thanks also to Darren Waters and Nicholas Adler for their help in the design of the tank.

[1]L. Rayleigh, "On the pressure developed in a liquid during the collapse of a spherical cavity," Philos. Mag. **34**, 94–98 (1917).
[2]M. Minnaert, "On musical air bubbles and the sound of running water," Philos. Mag. **16**, 235–248 (1933).
[3]E. A. Zabolotskaya, "Interaction of gas bubbles in a sound field," Sov. Phys. Acoust. **30**, 365–368 (1984).
[4]I. Tolstoy, "Superresonant systems of scatterers. I," J. Acoust. Soc. Am. **80**, 282–294 (1986).
[5]H. Ogũz and A. Properetti, "A generalization of the impulse and virial theorems with an application to bubble oscillations," J. Fluid Mech. **218**, 143–162 (1990).
[6]A. A. Doinikov and S. T. Zavtrak, "On the mutual interation of two gas bubbles in a sound field," Phys. Fluids **7**, 1923–1930 (1995).
[7]K. Ohsaka and E. H. Trinh, "A two frequency acoustic technique for bubble resonant oscillation studies," J. Acoust. Soc. Am. **107**, 1346–1351 (2000).
[8]P. Y. Hsiao, M. Devaud, and J. Bacri, "Acoustic coupling between two air bubbles in water," Eur. Phys. J. E **4**, 5–10 (2001).
[9]M. Ida, "A characteristic frequency of two mutually interating gas bubbles in an acoustic field," Phys. Lett. A **297**, 210–217 (2002).
[10]M. Ida, "Number of transition frequencies of a system containing an arbitrary number of gas bubbles," J. Phys. Soc. Jpn. **71**, 1214–1217 (2002).
[11]V. Leroy, M. Devaud, and J. Bacri, "The air bubble: Experiments on an unusual harmonic oscillator," Am. J. Phys. **70**, 1012–1019 (2002).
[12]C. Feuillade, "Scattering from collective modes of air bubbles in water and the physical mechanism of superresonances," J. Acoust. Soc. Am. **98**, 1178–1190 (1995).
[13]R. Manasseh, A. Nikolovska, A. Ooi, and S. Yoshida, "Anisotropy in the sound field generated by a bubble chain," J. Sound Vib. **278**, 807–823 (2004).
[14]A. A. Doinikov, R. Manasseh, and A. Ooi, "Time delays in coupled multibubble systems," J. Acoust. Soc. Am. **116**, 1–4 (2005).
[15]J. R. Blake and D. C. Gibson, "Cavitation bubbles near boundaries," Annu. Rev. Fluid Mech. **19**, 99–123 (1987).
[16]G. L. Chahine, "Experimental and asymptotic study of non-spherical bubble collapse," Appl. Sci. Res. **38**, 187–197 (1982).
[17]G. L. Chahine, "Cavitation dynamics at microscale level," J. Heart Valve Dis. **3**, 102–116 (1994).
[18]M. Strasberg, "The pulsation frequency of nonspherical gas bubbles in liquids," J. Acoust. Soc. Am. **25**, 536–537 (1953).
[19]S. D. Howkins, "Measurements of the resonant frequency of a bubble near a rigid boundary," J. Acoust. Soc. Am. **37**, 504–508 (1965).
[20]J. E. Blue, "Resonance of a bubble on an infinite rigid boundary," J. Acoust. Soc. Am. **41**, 369–372 (1967).
[21]M. Nicholas, R. A. Roy, and L. A. Crum, "Sound emissions by a laboratory bubble cloud," J. Acoust. Soc. Am. **95**, 3171–3181 (1994).
[22]R. Manasseh, R. F. LaFontaine, J. Davy, I. C. Shepherd, and Y. Zhu, "Passive acoustic bubble sizing in sparged systems," Exp. Fluids **30**, 672–682 (2001).
[23]D. F. Weston, "Acoustic interaction effects in arrays of small spheres," J. Acoust. Soc. Am. **39**, 316–322 (1966).
[24]I. Tolstoy and A. Tolstoy, "Line and plane arrays of resonant monopole scatterers," J. Acoust. Soc. Am. **87**, 1038–1043 (1990).
[25]R. H. Liu, J. Yang, M. Z. Pindera, M. Athavale, and P. Grodzinski, "Bubble-induced acoustic micromixing," Lab Chip **2**, 151–157 (2002).
[26]A. Ooi and R. Manasseh, "Coupled nonlinear oscillations of microbubbles," Aust N. Z. Ind. Appl. Math. J. **46**, C102–C116 (2005).
[27]D. B. Khismatullin, "Resonance frequency of microbubbles: Effect of viscosity," J. Acoust. Soc. Am. **116**, 1463–1473 (2004).
[28]H. Lamb, *Hydrodynamics* (Cambridge University Press, Cambridge, 1997).

Dispersion anomalies of shear horizontal guided waves in two- and three-layered plates

V. I. Alshits
A.V. Shubnikov Institute of Crystallography, The Russian Academy of Sciences, Leninskii pr. 59, Moscow 119333, Russia

M. Deschamps[a)]
Laboratoire de Mécanique Physique, Université Bordeaux 1, CNRS, UMR 5469, 351, Cours de la Libération, 33405-Talence Cedex, France

V. N. Lyubimov
A.V. Shubnikov Institute of Crystallography, The Russian Academy of Sciences, Leninskii pr. 59, Moscow 119333, Russia

(Received 17 February 2005; revised 11 July 2005; accepted 2 August 2005)

The dispersion spectra of SH guided waves are studied both analytically and numerically for two-layered plates with a plane of propagation being the plane of transverse isotropy. The boundary-value problems are considered for a plate with free, clamped, or clamped/free surfaces. It is noticed that formally the problem is very similar to that for symmetric and antisymmetric Lamb waves in a homogeneous plate. On this basis the Mindlin's approach of a bound grid is applied for an analysis. It is found that the studied spectra are characterized by the following specific features. They have two asymptotic levels c_{t1} and c_{t2} corresponding to the speeds of SH bulk waves in both layers. In the vicinity of the upper level (c_{t2}) dispersion curves form a step-like pattern tending to c_{t2} in succession one by one with further going down to the lower asymptote c_{t1}. Over the level c_{t2} there is a zone, where dispersion curves have a wavy form similar to that in spectra of Lamb waves in homogeneous plates. It is shown that the families of dispersion branches related to the boundary conditions of free and clamped surfaces cross each other at the same types of nodes of Mindlin's grid as those for symmetric and antisymmetric Lamb waves in a free homogeneous plate. The tracing speed level $v=v_0$ is found where the appropriate families of dispersion curves cross each other beyond the nodes of Mindlin's grid. It is proved that the spectra of symmetric and antisymmetric SH guided waves in symmetric three-layered plates with free or clamped faces are described by the same four equations as for the studied two-layered plates with free, clamped, free/clamped or clamped/free surfaces. © *2005 Acoustical Society of America.*
[DOI: 10.1121/1.2046807]

PACS number(s): 43.20.Ks, 43.20.Mv [AJMD] Pages: 2850–2859

I. INTRODUCTION

Guided waves in plates, both homogeneous and layered, due to their multiple applications in modern devices attract more and more attention in the acoustic literature. Here one can find monographs,[1–4] review articles (e.g., see the paper by Chimenti[5] with four hundred references), and numerous original publications. There are several different approaches to the problem: general theoretical studies,[6–13] explicit calculations,[14–24] and computer analysis.[25–28] Of course, this list is very incomplete (we recall approximately 400 references in Ref. 5). In addition, there are also various combined approaches. We shall be interested in a combination of explicit calculations and a computer analysis such as that given by Auld *et al.*,[29] who studied the propagation of SH waves in periodically layered composites. In such a problem, due to the simplicity of analytical description of SH waves in isotropic media (even multilayered), one can go rather far in an explicit analysis. This provides a good level of qualitative understanding of physical results. And additional computing makes them more exact and quantitatively complete.

We shall consider a more local problem of the same type being interested in specific features of spectra of guided SH waves in a two-layered plate for a series of boundary-value problems. The first motivation for this study was an intent to find out analytically how many asymptotes occur in a spectrum of such waves: the only one equal to the minimum of the two shear wave velocities (c_{t1} and c_{t2}) for two layers, or the largest velocity (say c_{t2}) also represents an asymptotical level. In the latter case in the vicinity of this level one could expect quite specific behavior of dispersion lines, which should tend to it in succession, not crossing each other, approaching the asymptote one by one with further going down to the lower asymptote c_{t1}. As a result, dispersion lines should form around the upper asymptote a step-like terracing pattern discussed earlier in Ref. 11 for spectra of homogeneous anisotropic plates. Figure 1 of Ref. 29 gave us hope that indeed this expected anomaly in spectra of two-layered

a)Author to whom correspondence should be addressed; electronic mail: deschamps@lmp.u-bordeaux1.fr

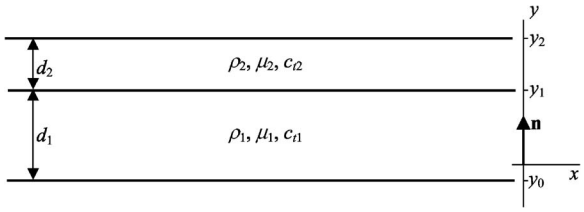

FIG. 1. The two-layered plate with its material parameters and geometrical characteristics in the chosen coordinate system.

plates might occur. So, we made some calculations and checked the situation. The results have turned out to be very unexpected: we found not only mentioned spectral anomalies in the vicinity of c_{t2}, but also some other very unusual features, like a *wavy* form of dispersion lines over the level c_{t2} in the zone occupied by Mindlin's grid.[14,19] The number of "zigzags" on the lines increases with growing frequency. We have also established an intimate similarity between studied spectra of SH guided waves in two-layered plates with those of symmetric and antisymmetric Lamb waves in homogeneous plates. Furthermore, the deduced dispersion equations for a two-layered plate with free, clamped, free/clamped or clamped/free faces have proved to be simultaneously governed equations describing spectra of symmetric and antisymmetric SH waves in symmetric three-layered plates with free or clamped surfaces. In the following all these observations will be presented analytically with exact computer illustrations.

II. BASIC EQUATIONS

Consider a two-layered elastic plate with the plane of transverse isotropy orthogonal to the surfaces. We choose the coordinate system with the y axis along the normal $\mathbf{n}$ to the upper surface, the x axis parallel to the plane of transverse isotropy and the z axis perpendicular to this plane (Fig. 1). In the chosen Cartesian system the lower face is indicated by the coordinate $y=y_0$, the interface by $y=y_1$, and the upper face by $y=y_2$, so that the thickness of the lower layer is equal to $y_1-y_0=d_1$ and the thickness of the upper layer is $y_2-y_1=d_2$. We shall be interested in SH guided waves propagating in the sagittal plane of transverse isotropy (xy) and polarized along z. For their characterization it is sufficient to fix the moduli $c_{44}^{(j)}=\mu_j$ and the densities $\rho_j (j=1,2)$ of the layers (Fig. 1). Then the phase velocities of the corresponding SH bulk waves in the lower and upper layers are given, respectively, by

$$c_{t1}=\sqrt{\mu_1/\rho_1}, \quad c_{t2}=\sqrt{\mu_2/\rho_2}. \tag{1}$$

In the following for definiteness we shall suppose that $c_{t1}<c_{t2}$.

The basic vector characteristics of such waves, displacements $\mathbf{u}$, and tractions $\boldsymbol{\sigma}\mathbf{n}$, are directed along z. So, we shall describe them by the scalar steady-state fields,

$$u_z=u(x,y,t)=A(y)\exp[ik(x-vt)], \tag{2}$$

$$\sigma_{yz}=\sigma(x,y,t)=-ikL(y)\exp[ik(x-vt)], \tag{3}$$

characterized by the frequency $\omega=2\pi f$ and the tracing speed $v=2\pi f/k$. It is convenient to form the unknown two-component vector function

$$\boldsymbol{\eta}(y)=\begin{pmatrix} A(y) \\ L(y) \end{pmatrix}, \tag{4}$$

which can be expressed as a superposition

$$\boldsymbol{\eta}(y)=\begin{cases} \boldsymbol{\eta}^{(1)}(y), & y_0<y<y_1 \\ \boldsymbol{\eta}^{(2)}(y), & y_1<y<y_2. \end{cases} \tag{5}$$

The functions $\boldsymbol{\eta}^{(j)}(y)$ describing the y profiles of fields (2) and (3) in the separate layers ($j=1,2$) can be written as the two-partial combinations

$$\boldsymbol{\eta}^{(j)}(y)=c_1^{(j)}\boldsymbol{\xi}_1^{(j)}\exp(ikp_1^{(j)}y)+c_2^{(j)}\boldsymbol{\xi}_2^{(j)}\exp(ikp_2^{(j)}y). \tag{6}$$

Here $c_{1,2}^{(j)}$ are amplitudes supposed to be found from conditions at the surfaces and the interface, and the pairs $\boldsymbol{\xi}_{1,2}^{(j)}, p_{1,2}^{(j)}$ are the eigenvectors and eigenvalues of the matrix $\mathbf{N}_{\mathrm{SH}}^{(j)}$, which is an appropriate 2×2 modification of the general 6×6 Stroh matrix.[30] According to Ref. 31

$$\boldsymbol{\xi}_1^{(j)}=\frac{i}{\sqrt{2}}\begin{pmatrix} (\mu_j p_j)^{-1/2} \\ -(\mu_j p_j)^{1/2} \end{pmatrix}, \quad \boldsymbol{\xi}_2^{(j)}=\frac{1}{\sqrt{2}}\begin{pmatrix} (\mu_j p_j)^{-1/2} \\ (\mu_j p_j)^{1/2} \end{pmatrix}, \tag{7}$$

$$p_{1,2}^{(j)}=\pm p_j=\pm\sqrt{(v/c_{tj})^2-1}, \tag{8}$$

where $c_{tj} (j=1,2)$ are the shear velocities given by Eq. (1).

III. FOUR TYPES OF BOUNDARY-VALUE PROBLEMS

A formulation of boundary-value problems for a considered layered plate is seriously simplified in terms of the propagator matrix $\mathbf{W}_{\mathrm{SH}}^{(k)}(y_2|y_0)$,[9,13] which directly relates to each other the amplitudes of displacements and tractions at both surfaces:

$$\begin{pmatrix} A_2 \\ L_2 \end{pmatrix}=\mathbf{W}_{\mathrm{SH}}^{(k)}(y_2|y_0)\begin{pmatrix} A_0 \\ L_0 \end{pmatrix}. \tag{9}$$

The corresponding 2×2 matrix $\mathbf{W}_{\mathrm{SH}}^{(k)}(y_2|y_0)$ is defined by

$$\mathbf{W}_{\mathrm{SH}}^{(k)}(y_2|y_0)=\mathbf{W}_{\mathrm{SH}}^{(k2)}(y_2|y_1)\mathbf{W}_{\mathrm{SH}}^{(k1)}(y_1|y_0), \tag{10}$$

where

$$\mathbf{W}_{\mathrm{SH}}^{(kj)}(y_j|y_i)=\sum_{\alpha=1}^{2}\boldsymbol{\xi}_\alpha^{(j)}\otimes\mathbf{T}\boldsymbol{\xi}_\alpha^{(j)}\exp[ikp_\alpha^{(j)}(y_j-y_i)],$$
$$\mathbf{T}=\begin{pmatrix} 0 & 1 \\ 1 & 0 \end{pmatrix}. \tag{11}$$

Combining Eqs. (10) and (11) with Eq. (7) one can easily find

$$\mathbf{W}_{\mathrm{SH}}^{(k)}(y_2|y_0)=\begin{pmatrix} \cos\alpha_1\cos\alpha_2-\dfrac{a_1}{a_2}\sin\alpha_1\sin\alpha_2 & -i\left[\dfrac{\sin\alpha_1\cos\alpha_2}{a_1}+\dfrac{\cos\alpha_1\sin\alpha_2}{a_2}\right] \\ -i[a_1\sin\alpha_1\cos\alpha_2+a_2\cos\alpha_1\sin\alpha_2] & \cos\alpha_1\cos\alpha_2-\dfrac{a_2}{a_1}\sin\alpha_1\sin\alpha_2 \end{pmatrix}\equiv\begin{pmatrix} W_1 & W_2 \\ W_3 & W_4 \end{pmatrix}, \tag{12}$$

where the notation is introduced

$$\alpha_j=kd_jp_j,\quad a_j=\mu_jp_j,\quad j=1,2. \tag{13}$$

In terms of the components W_i Eq. (9) reduces to the system

$$A_2=W_1A_0+W_2L_0,$$

$$L_2=W_3A_0+W_4L_0. \tag{14}$$

Now we can consider the following four types of boundary conditions.

A. Both faces of the plate are free of tractions ($L_0=L_2=0$)

In this case system (14) transforms into

$$A_2=W_1A_0,$$

$$W_3A_0=0. \tag{15}$$

The second of these equations is homogeneous and has a nontrivial solution only if $W_3(k,v)=0$, which is the form of dispersion equation for the plate with free surfaces. By Eqs. (12) and (13), this dispersion equation has the following explicit form:

$$\Phi^f(v,k)=\tan(kd_1p_1)\cot(kd_2p_2)+a_2/a_1=0. \tag{16}$$

Quite similarly one can derive dispersion equations for the other boundary-value problems.

B. Both faces of the plate are clamped ($A_0=A_2=0$)

$$\Phi^c(v,k)=\tan(kd_1p_1)\cot(kd_2p_2)+a_1/a_2=0. \tag{17}$$

C. The lower face is clamped and the upper face is free ($A_0=L_2=0$)

$$\Phi^{c/f}(v,k)=\cot(kd_1p_1)\cot(kd_2p_2)-a_2/a_1=0. \tag{18}$$

D. The lower face is free and the upper face is clamped ($L_0=A_2=0$)

$$\Phi^{f/c}(v,k)=\cot(kd_1p_1)\cot(kd_2p_2)-a_1/a_2=0. \tag{19}$$

Transcendental Eqs. (16)–(19) determine the four infinite sets of dispersion branches $v=f_n(k)$ or (after substituting here $k=2\pi f/v$ and extracting v), in more convenient terms, $v=g_n(f)$.

IV. ANALYSIS OF DISPERSION EQUATIONS (16) and (17)

A convenient method of analysis of dispersion equations of this type was first introduced by Mindlin[14] for symmetric and antisymmetric Lamb modes in a homogeneous isotropic plate (see also Refs. 19–21). The idea was to find a discreet series of points belonging to dispersion curves and simultaneously being the nodes of an infinite grid formed by the two families of supplementary curves, the so-called bounds. Now we shall analyze Eqs. (16) and (17) based on Mindlin's idea. It is rather evident that both mentioned dispersion equations must be simultaneously satisfied in the points of intersection of bound curves solving the two systems

$$\tan[kd_1p_1(v)]=\pm\infty,$$

$$\cot[kd_2p_2(v)]=0; \tag{20a}$$

$$\tan[kd_1p_1(v)]=0,$$

$$\cot[kd_2p_2(v)]=\pm\infty. \tag{20b}$$

Both systems are solved by

$$kd_1p_1(v)\equiv\frac{2\pi fd_1}{v}p_1(v)=\frac{\pi}{2}n,$$

$$kd_2p_2(v)\equiv\frac{2\pi fd_2}{v}p_2(v)=\frac{\pi}{2}m. \tag{21}$$

For odd numbers $n=2r+1$ and $m=2t+1$ $(r,t=0,1,2,\ldots)$, Eq. (21) gives a solution of first system (20a) and for even numbers $n=2l$ and $m=2s$ $(l,s=1,2,\ldots)$ it solves second system (20b). Combining Eqs. (21) and (8) one can easily find an explicit form for the bound curves in coordinates $v\div k$ or $v\div f$. In practice it is more convenient and customary to use for an argument a frequency f rather than a wave number k, so we present the bound functions in the form $v=\bar{v}_{n,m}^{(1,2)}(f)$, where

$$\bar{v}_n^{(1)}(f)=\frac{c_{t1}}{\sqrt{1-(nc_{t1}/4d_1f)^2}},$$

$$\bar{v}_m^{(2)}(f)=\frac{c_{t2}}{\sqrt{1-(mc_{t2}/4d_2f)^2}}. \tag{22}$$

These two families of bounds, $\bar{v}_n^{(1)}(f)$ and $\bar{v}_m^{(2)}(f)$, include infinite sets of monotonic curves tending for $f\to\infty$ to the horizontal asymptotes c_{t1} or c_{t2}, respectively, and with decreasing frequency—to individual vertical asymptotes

$$f_n^{(1)}=\frac{nc_{t1}}{4d_1},\quad f_m^{(2)}=\frac{mc_{t2}}{4d_2},\quad n,m=1,2,\ldots, \tag{23}$$

also respectively. The crossing points of these two bound families are given by

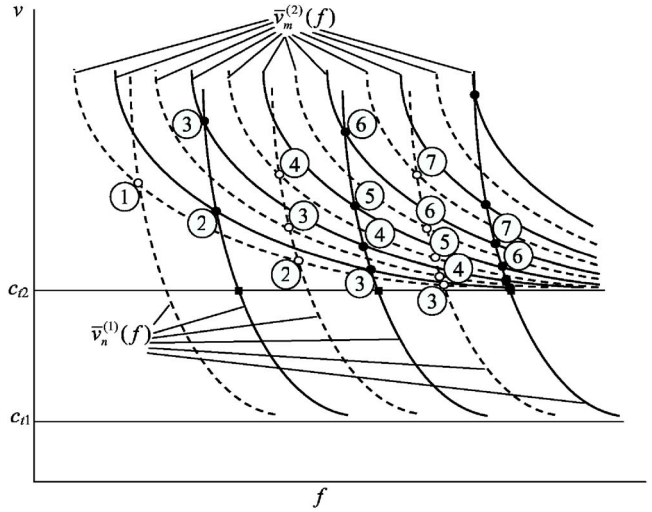

FIG. 2. Schematic plot of Mindlin's grid of crossing bounds [Eq. (22)]. White and black circle points correspond to intersections of odd-odd (dashed lines) and even-even bounds, respectively; circles with the equal numbers (l) inside indicate crossing points belonging to the same dispersion branches $v_l^{f,c}(f)$.

$$f_{nm} = \frac{1}{4}\sqrt{\frac{(n/d_1)^2 - (m/d_2)^2}{c_{t1}^{-2} - c_{t2}^{-2}}}, \tag{24a}$$

$$v_{nm} = \sqrt{\frac{(n/d_1)^2 - (m/d_2)^2}{(n/d_1c_{t2})^2 - (m/d_2c_{t1})^2}}. \tag{24b}$$

We stress that n and m in Eqs. (22)–(24) must be of the same evenness. And in Eq. (24) they must be chosen so that the expressions under the square roots would be positive. Consequently, with the accepted condition $c_{t2} > c_{t1}$, the choice of numbers n and m in Eq. (24) is limited by the criterion

$$\frac{m}{n} < \frac{d_2 c_{t1}}{d_1 c_{t2}} \equiv \kappa. \tag{25}$$

Thus, each crossing point (24) must simultaneously belong to the two dispersion curves, $v_l^f(f)$ and $v_l^c(f)$, which solve problems (16) and (17) for free and clamped surfaces, respectively. It is evident that neither of the dispersion curves could intersect any bound line beyond the above-mentioned nodes of Mindlin's grid (that is why they are *bounds*), this would contradict Eq. (16) or Eq. (17). Thus, Mindlin's grid provides a discreet frame for dispersion curves $v_l^f(f)$ and $v_l^c(f)$.

Figure 2 schematically shows the grid of bounds (22) and the "even-even" and "odd-odd" crossing points (24) belonging to our dispersion curves. As is clear from this figure, all bounds of the system $\bar{v}_m^{(2)}(f)$ are crossed by the infinite number of bounds from the other family $\bar{v}_n^{(1)}(f)$. However, at $\kappa \leqslant 1$ some number of first branches $\bar{v}_n^{(1)}(f)$ will go beyond the bounds $\bar{v}_m^{(2)}(f)$ without intersections. Let the first odd branch $\bar{v}_n^{(1)}(f)$, which crosses $\bar{v}_1^{(2)}(f)$, have the number $n = 2n_0 + 1$. Then that will be the first bound of the family (1), which takes part in forming Mindlin's grid, and it is convenient to start counting curves of this series from that particular branch. In accordance with this principle, in the following in this section the lth branch $\bar{v}_l^{(1)}(f)$ in the grid zone will be supposed to be defined by Eq. (22a), where $n = 2n_0 + l$.

Of course, the coincidence of a pair of the curves $v_l^f(f)$ and $v_l^c(f)$ in a series of discrete points (24) does not mean that these curves are identical. Let us evaluate slopes of the branches $v_l^f(f)$ and $v_l^c(f)$ at the found crossing points. It can be done based on Eqs. (16), (17), and (20):

$$\left.\frac{\partial v_l^f}{\partial f}\right|_{\substack{n=2r \\ m=2s}} = -\frac{v_{nm}}{f_{nm}}\left\{v_{nm}^2 \frac{\rho_1 d_1 + \rho_2 d_2}{\mu_1 d_1 + \mu_2 d_2} - 1\right\},$$

$$\left.\frac{\partial v_l^f}{\partial f}\right|_{\substack{n=2r+1 \\ m=2s+1}} = -\frac{v_{nm}}{f_{nm}} \frac{\mu_1 d_2 + \mu_2 d_1}{\dfrac{\mu_1 d_2}{p_2^2(v_{nm})} + \dfrac{\mu_2 d_1}{p_1^2(v_{nm})}}, \tag{26}$$

$$\left.\frac{\partial v_l^c}{\partial f}\right|_{\substack{n=2r \\ m=2s}} = -\frac{v_{nm}}{f_{nm}} \frac{\mu_1 d_2 + \mu_2 d_1}{\dfrac{\mu_1 d_2}{p_2^2(v_{nm})} + \dfrac{\mu_2 d_1}{p_1^2(v_{nm})}},$$

$$\left.\frac{\partial v_l^c}{\partial f}\right|_{\substack{n=2r+1 \\ m=2s+1}} = -\frac{v_{nm}}{f_{nm}}\left\{v_{nm}^2 \frac{\rho_1 d_1 + \rho_2 d_2}{\mu_1 d_1 + \mu_2 d_2} - 1\right\}. \tag{27}$$

Hence, the f and c branches have different slopes at the same points. As is seen from Fig. 2, along these branches even-even and odd-odd points must be situated in succession. And by Eqs. (26) and (27), in these neighboring points the derivatives $\partial v_l^f / \partial f$ and $\partial v_l^c / \partial f$ represent analytical continuations for each other. But then, the both dispersion curves $v_l^f(f)$ and $v_l^c(f)$ must abruptly change a slope at each next point of the grid. Consequently, the closer the dispersion line to the level c_{t2}, the less is the distance between neighboring nodes and the more pronounced should be wavy form of dispersion curves.

The considered nodes of our grid occur only in the region $v > c_{t2}$, where both families of bond lines (22) coexist (Fig. 2). And even in this region nodes occupy only some band. As follows from Fig. 2 and Eq. (24a), in this band the density of grid nodes grows with an increase of the frequency. And accordingly the greater number of nodes on the dispersion lines $v_l^{f,c}(f)$, the greater is l. In Fig. 2, the first branches $v_1^{f,c}(f)$ contain only one node, the second branches—two, the third branch—three, and so on. On the other hand, as we know, the more nodes there are on a line, the more "zigzags" it contains. So, we come to the conclusion: *the greater the frequency the wavier the spectrum*, however only inside the grid band just over c_{t2}.

The separate problem is related to an estimation of a width of the grid band. For each fixed n it can be evaluated as $v_{nm}^{\max} - c_{t2}$ where $v_{nm}^{\max}$ is given by Eq. (24b) taken at the maximum $m = m_{\max}$ admitted by inequality (25). Let us estimate $v_{nm}^{\max}$ for large enough numbers n. At any n and κ their product always belongs to some interval between two integers: $l < n\kappa \leqslant l+1$. So, we put $m_{\max} = l$ and introduce the parameter $\alpha_n = n\kappa - l$, which by definition belongs to the interval $0 < \alpha_n \leqslant 1$. For large enough $n\kappa$ to a first approximation: $l \approx n\kappa$. With the same accuracy

$$v_{nm}^{\max} = \sqrt{\frac{(c_{t2}n\kappa)^2 - (c_{t1}l)^2}{(n\kappa)^2 - l^2}} \approx \sqrt{\frac{\kappa n}{2\alpha_n}(c_{t2}^2 - c_{t1}^2)}. \qquad (28)$$

Thus, roughly, the upper limit of the grid band is proportional to $n^{1/2}$, i.e., to $f^{1/2}$. Of course, the parameter α_n dependent on n provides some fluctuations of this dependence, which might be even rather large. For instance, if the parameter κ (25) slightly exceeds some integer which corresponds to a resonance relation between definite pairs of cut-off frequencies (23), we arrive at very small $\alpha_n \ll 1$ for a series of numbers n and at respective coherent fluctuations of $v_{nm}^{\max}$. On the other hand, if κ is close from above to a rational fraction (e.g., to 7/4), we shall have resonance situations for a series of separate n (e.g., for each fourth $n=4s$, where the number of resonant integers s depends on κ). Such "resonances" for any n can be artificially arranged by a special choice of parameters determining κ (25).

Figure 3 demonstrates the numerically found spectra of SH guided waves in the two-layered plate with free or clamped faces. It is seen that at large f the upper boundary of the grid is indeed roughly proportional to $f^{1/2}$ [the dashed curve in Fig. 3(a)]. Going up along dispersion curves $v_l^{f,c}(f)$ through the grid, after the last node on it we should fall within a smooth zone between a pair of neighboring not intersecting bonds. That is exactly what we see in Fig. 3(a). With decrease of frequency our curves approach their own vertical asymptotes situated between the corresponding pairs of the cut-off frequencies (23). On the other hand, as is seen from Fig. 3(b), a pronounced wavy character of dispersion curves occurs only in the bottom part of the grid zone.

Let us study the situation at $v \leqslant c_{t2}$. In this region the dispersion equations (16) and (17) remain valid but it is convenient to change them so that they would not contain the imaginary parameter p_2. Substituting into Eqs. (16) and (17) $p_2 = i\bar{p}_2$ where

$$\bar{p}_2 = \sqrt{1 - (v/c_{t2})^2}, \qquad (29)$$

we obtain the following new form for these dispersion equations:

$$\tan(kd_1p_1) = \frac{\mu_2\bar{p}_2}{\mu_1 p_1}\tanh(kd_2\bar{p}_2), \qquad (30)$$

$$\tan(kd_1p_1) = -\frac{\mu_1 p_1}{\mu_2\bar{p}_2}\tanh(kd_2\bar{p}_2). \qquad (31)$$

Let us start from the free surfaces boundary-value problem (30). On the level $v=c_{t2}$ we have $\bar{p}_2=0$, which leads to the equation $\tan(kd_1p_1)=0$, coinciding with the first equation of system (20b). This means that our dispersion curves $v_l^f(f)$ cross the level $v=c_{t2}$ at the same points f_l as the bond lines $\bar{v}_{2l}^{(1)}(f)$ (22) (the black square points in Fig. 3):

$$f_l = \frac{c_{t2}l}{2d_1p_1(c_{t2})}. \qquad (32)$$

The slopes of the dispersion curves at these points can be found similar to Eqs. (26) and (27):

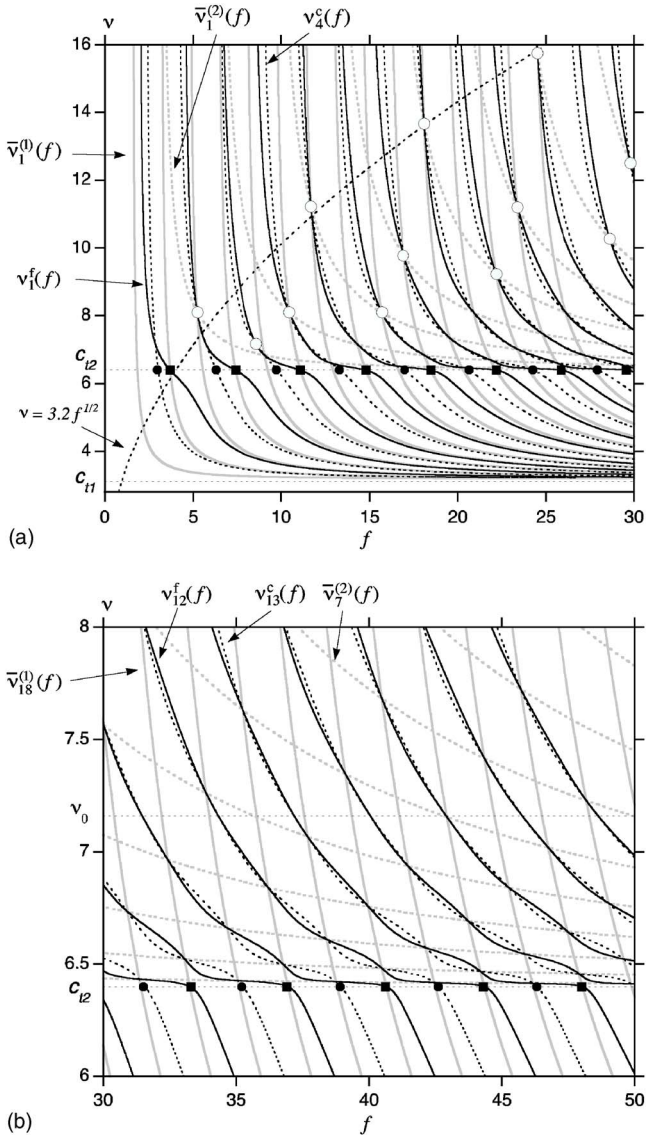

FIG. 3. Numerical plot of dispersion curves $v_l^f(f)$ (—) and $v_l^c(f)$ (···) on the background of Mindlin's bounds $\bar{v}_l^{(1)}(f)$ and $\bar{v}_l^{(2)}(f)$ (grey lines, solid and dotted, respectively). The black square and circle points show intersections of the curves $v_l^f(f)$ and $v_l^c(f)$, respectively, with the level c_{t2}. The white circle points in (a) indicate the upper nodes of the grid along bound lines. (b) demonstrates a large scale image of the high frequency part ($30<f<50$) of the same dependencies. In computations the following parameters were used: $d_1=d_2=0.5$; $\rho_1=\rho_2=2.7$; $c_{t1}=3.2$; $c_{t2}=6.4$.

$$\frac{\partial v_l^f}{\partial f_l} = -\frac{c_{t2}}{f_l}\frac{p_1^2(c_2)}{1 + 2\mu_2 d_2/\mu_1 d_1}. \qquad (33)$$

Hence, with increasing frequency $f\to\infty$ the slope of the dispersion curves on this level tends to zero. This shows that we have met in our spectrum a very specific asymptotic level. Dispersion branches should tend to it in succession, one by one, changing each other and going down to the next asymptote $v=c_{t1}$. This is just a behavior, which one can see in Fig. 3(b). Analogous step-like terracing patterns in spectra of homogeneous anisotropic plates were described in Ref. 11.

After crossing the level $v=c_{t2}$ the branch $v_l^f(f)$ goes down between the two bound curves,

$$\bar{v}_{2l}^{(1)}(f) < v_l^f(f) < \bar{v}_{2l+1}^{(1)}(f). \tag{34}$$

With increase of f when the both bounding curves (34) tend to c_{t1}, the function $p_1(v)$ in Eq. (30) is close to zero and the dispersion equation (30) acquires the limiting form $\tan(kd_1p_1) \to +\infty$ identical to the first equation of system (20a). This means that at large f,

$$v_l^f(f) \approx \bar{v}_{2l+1}^{(1)}(f), \tag{35}$$

which is illustrated by Fig. 3(a).

The analysis of the dispersion equation (31) for a plate with clamped surfaces can be done in the same manner. The results are similar: the family of curves $v_l^c(f)$ also demonstrates an asymptotic behavior on the level $v=c_{t2}$ [Fig. 3(b)]. Below this level they go down between the appropriate bound lines:

$$\bar{v}_{2l-1}^{(1)}(f) < v_l^c(f) < \bar{v}_{2l}^{(1)}(f) \tag{36}$$

[Fig. 3(a)]. With increase of the number l the crossing points of the curves $v_l^c(f)$ with the level $v=c_{t2}$ [the black round points in Figs. 3(a) and 3(b)] are approaching those for the bounds $\bar{v}_{2l-1}^{(1)}(f)$ with the same level. However at large f the curves $v_l^c(f)$, approach from below to the opposite (upper) limit in Eq. (36), like in the previous case (34) and (35):

$$v_l^c(f) \approx \bar{v}_{2l}^{(1)}(f), \tag{37}$$

see Fig. 3(a).

V. ANALYSIS OF DISPERSION EQUATIONS (18) and (19)

The pair of boundary-value problems related to plates with clamped/free and free/clamped surfaces, Eqs. (18) and (19), can be analytically analyzed in a completely analogous manner. And Fig. 4 shows the results of a numerical analysis. The solutions $v_l^{c/f}(f)$ and $v_l^{f/c}(f)$ also go through coinciding nodes of the grid formed by the same families of bound lines (22). However this time the "active" nodes correspond to intersections of bounds having different evenness: $\bar{v}_{2l}^{(1)}(f)$ with $\bar{v}_{2s+1}^{(2)}(f)$ and $\bar{v}_{2l+1}^{(1)}(f)$ with $\bar{v}_{2s}^{(2)}(f)$. Above the grid zone the dispersion lines $v_l^{c/f}(f)$ and $v_l^{f/c}(f)$ must be limited from both sides by some bound lines. And inside the zone of crossing bounds the branches $v_l^{c/f}(k)$ and $v_l^{f/c}(k)$ have derivatives again different both from each other at the same nodes and, for one curve, at neighboring crossing points of the above-mentioned two types. The latter difference indicates a wavy configuration of dispersion lines in this zone. The number of "zigzags" on a line reflects the number of Mindlin's nodes on it. And both numbers increase with the order of the eigenwave. In the vicinity of c_{t2}, as before, a step-like asymptotic pattern occurs. The curves $v_l^{c/f}(f)$ cross the level $v=c_{t2}$ at the same points as the bound lines $\bar{v}_{2l-1}^{(1)}(f)$ (the white square points in Fig. 4) and go down between the pairs

$$\bar{v}_{2l-1}^{(1)}(f) < v_l^{c/f}(f) < \bar{v}_{2l}^{(1)}(f), \tag{38}$$

closing at large f as before to the upper limit in Eq. (38) (Fig. 4),

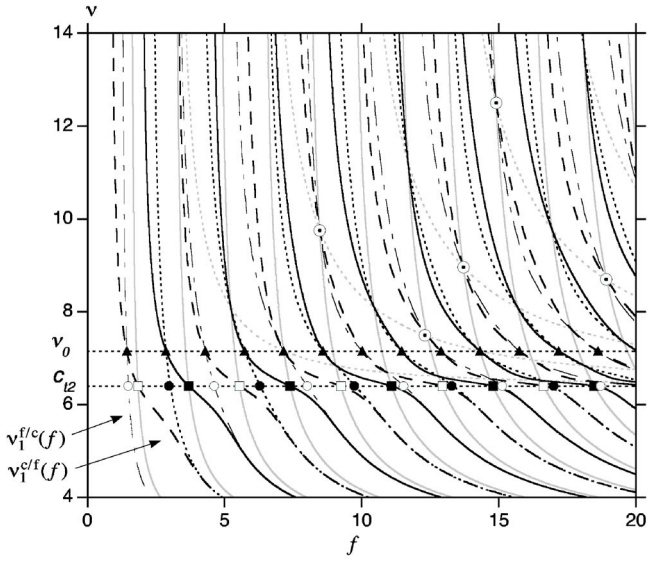

FIG. 4. Numerical plot of dispersion curves $v_l^f(f)$ (—), $v_l^c(f)$ (···), $v_l^{f/c}(f)$ (---), and $v_l^{c/f}(f)$ (---) on the background of the grid bounds $\bar{v}_l^{(1)}(f)$ and $\bar{v}_l^{(2)}(f)$ (grey lines). The white square and circle points indicate intersections of branches $v_l^{c/f}(f)$ and $v_l^{f/c}(f)$, respectively, with the level c_{t2}. The black triangles show the points of intersection of the branches $v_l^f(f)$ with $v_l^c(f)$ and $v_l^{f/c}(f)$ with $v_l^{c/f}(f)$ not coinciding with nodes of the grid and belonging to the level $v=v_0$. Other notations and used parameters are the same as in Fig. 3.

$$v_l^{c/f}(f) \approx \bar{v}_{2l}^{(1)}(f), \tag{39}$$

and smoothly approaching together with this curve to the asymptote c_{t1}.

The branches $v_l^{f/c}(f)$ go down between the same pairs as $v_{l-1}^f(f)$, Eq. (34),

$$\bar{v}_{2l-2}^{(1)}(f) < v_l^{f/c}(f) < \bar{v}_{2l-1}^{(1)}(f). \tag{40}$$

With increasing number l the crossing points f_l of the lines $v_l^{f/c}(f)$ with the level $v=c_{t2}$ (the white round points in Fig. 4) approach the corresponding points for the bound lines $\bar{v}_{2l-2}^{(1)} \times(f)$. And for large f the branches $v_l^{f/c}(f)$ are closing to the same bounds as $v_{l-1}^f(f)$, Eq. (35),

$$v_l^{f/c}(f) \approx \bar{v}_{2l-1}^{(1)}(f). \tag{41}$$

However, one can check that everywhere

$$v_{l-1}^f(f) < v_l^{f/c}(f). \tag{42}$$

As is seen from Fig. 4, the above two curves are approaching each other much faster than they both tend to the bound line $\bar{v}_{2l-1}^{(1)}(f)$. As follows from an analytical analysis, at sufficiently large l the branches $v_{l-1}^f(f)$ and $v_l^{f/c}(f)$ become exponentially close to each other in almost all the zone $v<c_{t2}$. The same is valid also for the pair $v_l^{c/f}(f)$, $v_l^c(f)$ and the bound $\bar{v}_{2l}^{(1)}(f)$. Summing up, we can state that by Eqs. (34), (36), (38), (40), and (42) at and below c_{t2} there is a definite order between the four series of dispersion curves with the same numbers (Fig. 4):

$$v_l^{f/c}(f) < v_l^{c/f}(f) < v_l^c(f) < v_l^f(f). \tag{43}$$

VI. INTERSECTIONS OF DISPERSION CURVES BEYOND THE NODES OF MINDLIN'S GRID

As is seen from Figs. 3(b) and 4, apart from intersections of the two studied pairs of families of dispersion curves in nodes of Mindlin's grid there is the other group of crossing points related to a constant speed level, $v=v_0\approx 7.16$ conv. units. Its interpretation is automatically obtained from the observation that at $a_1=a_2$ Eq. (16) becomes identical to Eq. (17) and Eq. (18) coincides with Eq. (19). Combining the equation $\mu_1 p_1=\mu_2 p_2$ with Eq. (8) we immediately find this level:

$$v_0=\sqrt{\frac{\mu_2^2-\mu_1^2}{\rho_2\mu_2-\rho_1\mu_1}}=\sqrt{\frac{\rho_2^2c_{t2}^4-\rho_1^2c_{t1}^4}{\rho_2^2c_{t2}^2-\rho_1^2c_{t1}^2}}. \tag{44}$$

Clearly it exists until the material parameters admit a real square root in Eq. (44). On the other hand, with $\mu_1 p_1=\mu_2 p_2$ the dispersion equations (16) and (17) coincide into one,

$$\sin\left[\frac{2\pi f}{v_0}(d_1p_1(v_0)+d_2p_2(v_0))\right]=0, \tag{45}$$

which in turn determines the coordinates of the considered set of crossing points at the level v_0:

$$f_r=\frac{rv_0}{2[d_1p_1(v_0)+d_2p_2(v_0)]}=\frac{r}{2(d_1\mu_2+d_2\mu_1)}\sqrt{\frac{\mu_2^2-\mu_1^2}{c_{t1}^{-2}-c_{t2}^{-2}}},\quad r=1,2,\ldots\ . \tag{46}$$

Quite similarly one can find that on the same level v_0 (44) the dispersion lines $v_l^{c/f}(f)$ and $v_l^{f/c}(f)$ must cross each other at the points

$$f_s=\frac{2s+1}{4(d_1\mu_2+d_2\mu_1)}\sqrt{\frac{\mu_2^2-\mu_1^2}{c_{t1}^{-2}-c_{t2}^{-2}}},\quad s=1,2,\ldots\ . \tag{47}$$

Bearing in mind that all numerical calculations for the above-mentioned plots were accomplished for a particular case $\rho_1=\rho_2$, we obtain in this case, instead of Eq. (44),

$$v_0=\sqrt{c_{t1}^2+c_{t2}^2}, \tag{48}$$

which for the used parameters $c_{t1}=3.2$, $c_{t2}=6.4$ immediately gives $v_0\approx 7.16$ (conventional units) fitting our observations in Figs. 3(b) and 4.

VII. APPLICATION TO A SYMMETRIC THREE-LAYERED PLATE

Consider a symmetric three-layered plate $d_1\div d_2\div d_1$ (Fig. 5) with the same materials parameters as in the above-mentioned two-layered plate $d_1\div d_2$. We shall suppose the boundary conditions to be also symmetric: let both surfaces of the plate be either free or clamped. In such a structure the spectrum of eigenwaves must be split into two parts, symmetric and antisymmetric. In the coordinate system with the plane xz coinciding with the middle plane of the structure (Fig. 5) for symmetric modes there must be

$$u(-y)=u(y), \tag{49a}$$

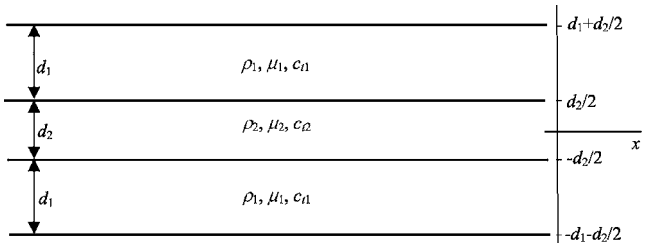

FIG. 5. The three-layered plate with its material parameters and geometrical characteristics in the chosen coordinate system.

$$\sigma(-y)=-\sigma(y), \tag{49b}$$

and for antisymmetric modes, conversely,

$$u(-y)=-u(y), \tag{50a}$$

$$\sigma(-y)=\sigma(y). \tag{50b}$$

As follows from Eq. (49b), for symmetric modes the middle plane $y=0$ of the plate must be free of tractions,

$$\sigma(0)=0. \tag{51}$$

Similarly, by Eq. (50a), for antisymmetric modes the middle plane is automatically "clamped,"

$$u(0)=0. \tag{52}$$

Accordingly, the *f/f boundary-value problem of the considered three-layered plate for a symmetric part of the spectrum* reduces to the f/f problem for the half of the structure, i.e., for a two-layered plate (say, $d_1\div d_2/2$). The corresponding spectrum is determined by Eq. (16), where one should replace d_2 by $d_2/2$:

$$\tan(kd_1p_1)\cot(kd_2p_2/2)+a_2/a_1=0. \tag{53}$$

And the same *f/f boundary-value problem for the antisymmetric part of the spectrum* is equivalent to the f/c problem for the two-layered plate $d_1\div d_2/2$, i.e., is described by the dispersion equation

$$\cot(kd_1p_1)\cot(kd_2p_2/2)-a_1/a_2=0, \tag{54}$$

compare with Eq. (19).

Similarly, the above-mentioned three-layered plate with *clamped surfaces for symmetric waves* has the same spectrum as the two-layered plate $d_1\div d_2/2$ with clamped/free faces which leads to the dispersion equation analogous to Eq. (18):

$$\cot(kd_1p_1)\cot(kd_2p_2/2)-a_2/a_1=0. \tag{55}$$

And the *c/c boundary-value problem for antisymmetric waves* reduces to the c/c problem for the two-layered plate $d_1\div d_2/2$ [see Eq. (17)]:

$$\tan(kd_1p_1)\cot(kd_2p_2/2)+a_1/a_2=0. \tag{56}$$

Thus, the three-layered plate with free or clamped faces has the spectrum given by the pairs of equations (53) and (54) or (55) and (56) respectively. But as we know, these pairs of equations determine the dispersion curves, which go through different (not coinciding) sorts of Mindlin's nodes. This explains why symmetric and antisymmetric branches of

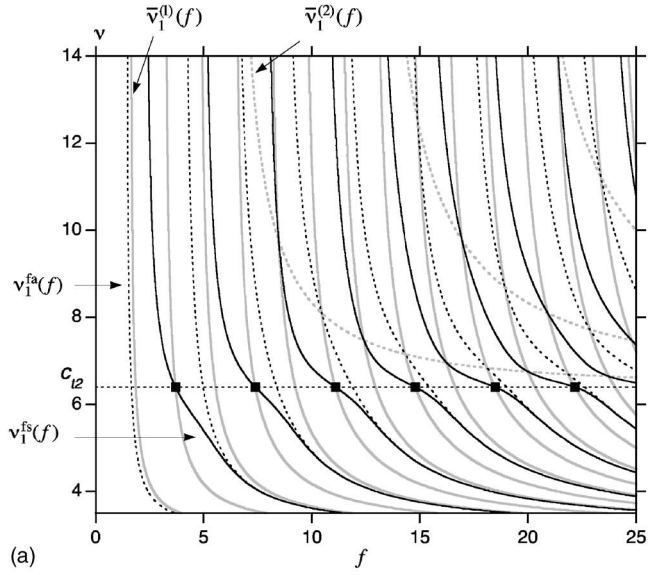

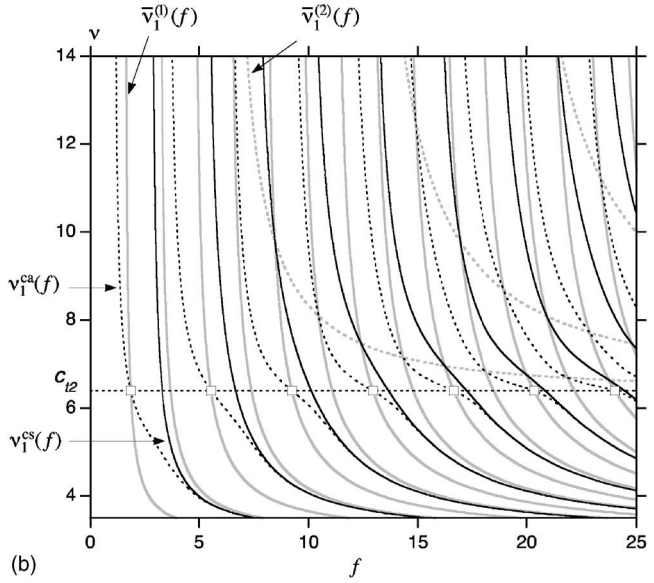

FIG. 6. Spectra of symmetric (—) and antisymmetric (···) waves in the three-layered plate shown in Fig. 5 with the parameters coinciding with those for the above-mentioned two-layered plates, i.e., $d_1=d_2=0.5$; $\rho_1=\rho_2=2.7$; $c_{t1}=3.2$; $c_{t2}=6.4$; (a) both surfaces are free, (b) both surfaces are clamped.

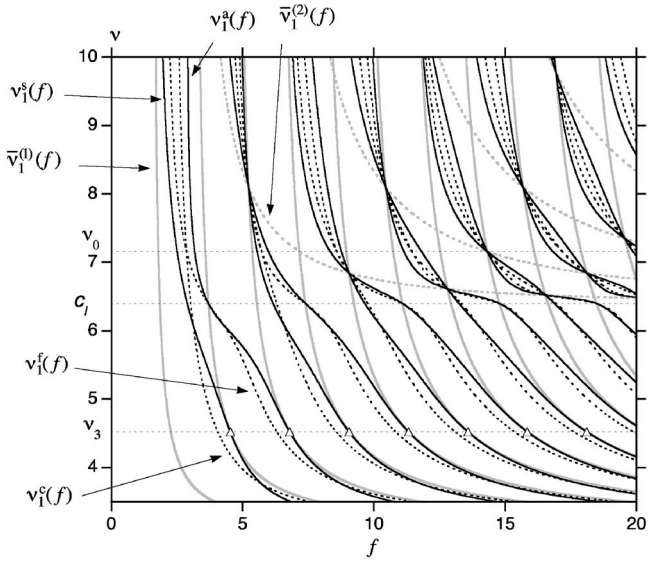

FIG. 7. Numerical plot of dispersion curves for symmetric and antisymmetric Lamb waves in a free homogeneous plate, $v_l^{s,a}(f)$ (—), and for SH guided waves in a two-layered plate with free or clamped faces, $v_l^{f,c}(f)$ (···). The grid bounds, as before, are shown by grey lines. The used parameters were $d=d_1+d_2=1$, $d_1=d_2=0.5$; $c_t=c_{t1}=3.2$; $c_l=c_{t2}=6.4$; $\rho=\rho_1=\rho_2=2.7$.

SH guided waves in the considered three-layered plate do not cross each other [see Figs. 6(a) and 6(b)], in contrast to Lamb waves in a homogeneous plate.

As is seen from Fig. 6, for both types of boundary conditions the symmetric and antisymmetric branches below the level c_{t2} are fast closing to each other and for large enough frequency f practically coincide in almost all the zone $v<c_{t2}$. This observation is similar to analogous behavior of corresponding branches for a two-layered plate (Fig. 4). The reason for that becomes quite clear if one compares the appropriate dispersion equations [say, Eqs. (53) and (54)] with each other in the region $v<c_{t2}$. Indeed, in view of the relation $p_2=i\bar{p}_2$, Eq. (29), and the identity $\tan(ix)=i\tanh(x)$, for $v<c_{t2}$ the above pair of dispersion equations respectively transforms to

$$\tan(kd_1p_1)=\frac{\mu_2\bar{p}_2}{\mu_1p_1}\tanh(kd_2\bar{p}_2/2),$$
$$\tan(kd_1p_1)=\frac{\mu_2\bar{p}_2}{\mu_1p_1}\coth(kd_2\bar{p}_2/2), \tag{57}$$

i.e., their right-hand sides differ from each other only by the replacement

$$\tanh(kd_2\bar{p}_2/2)\leftrightarrow\coth(kd_2\bar{p}_2/2). \tag{58}$$

But for a large enough argument $kd_2\bar{p}_2\gg1$ these functions differ from each other only by exponentially small terms $\sim\exp(-kd_2\bar{p}_2)$. Of course, at the level $v=c_{t2}$, by Eq. (29), $\bar{p}_2=0$ and the right-hand sides of the equations in Eq. (57) are essentially different. However, for any level $v<c_{t2}$ there always exists such a large parameter $kd_2\gg1$, which provides the condition $kd_2\bar{p}_2\gg1$ and the corresponding closeness of appropriate dispersion curves (see Figs. 4 and 6).

VIII. CONCLUSION

As was mentioned earlier, formally the studied boundary-value problems for SH guided waves in a two-layered plate (and, as we now understand, in symmetric three-layered plate) are very similar to those for symmetric and antisymmetric Lamb waves in a homogeneous plate. For instance, in the latter case the dispersion equations for *symmetric* and *antisymmetric* waves differ from Eqs. (16) and (17), respectively, only by the following replacements in the latter equations: c_{t1} by c_t, c_{t2} by c_l, $d_1=d_2$ by $d/2$ and the parameter $a_2/a_1=\mu_2p_2/\mu_1p_1$ by $4p_1p_2/(p_1^2-1)^2$ for free faces[1] and by p_1p_2 for clamped faces.[22] So the bound grids for SH and Lamb waves will be quite similar and the most of the features of the spectra found above will remain valid. In particular, symmetric branches must cross the level c_l at the

same set of points f_i (32) as the bound lines $\bar{v}_{2i}^{(1)}(f)$ (22) (with the above-mentioned renormalizing parameters).

Figure 7 shows the numerical plot of dispersion curves for symmetric and antisymmetric Lamb waves in a homogeneous plate with free faces and for SH guided waves in a two-layered plate with free or clamped faces. The choice of parameters provides the same Mindlin's bounds (22) for Lamb's and SH waves. One can see that all qualitative features of spectra of these two types of waves are indeed very similar. All dispersion branches, $v_l^{f,c}(f)$ and $v_l^{s,a}(f)$, go through the same nodes of bound grid and for sufficiently large numbers l manifest both an asymptotic behavior at the level $c_{t2}=c_l$ and a wavy form over that. The latter proves to be more pronounced for the Lamb's branches $v_l^{s,a}(f)$. In principle, as was shown by Mindlin[14] (see also Ref. 19), crossings of curves $v_l^s(f)$ and $v_l^a(f)$ can also occur beyond nodes of the grid at the two different fixed speed levels $v=v_{1,2}$. They represent the two roots (additional to the Rayleigh velocity) of the corresponding cubic equation $4p_1p_2/(p_1^2-1)^2=1$. The condition for their existence reduces to the inequality: $c_t/c_l>0{,}567$,[32] which is not satisfied for our choice of parameters. Accordingly they are absent in Fig. 7.

As is seen from Fig. 7, the third specific speed level v_3 exists for Lamb wave branches, where tangency occurs of the curves $v_l^{s,a}(f)$ with the bound lines $\bar{v}_l^{(1)}(f)$. One can easily deduce that these points relate to the condition $p_1(v_3)=1$, i.e.,

$$v_3 = c_t\sqrt{2}. \tag{59}$$

The coordinates f_n of the considered set of points are given by

$$f_n = (v_3/2d)n. \tag{60}$$

The slopes at the tangent points are decreasing with growing f_n as

$$\left[\frac{\partial v}{\partial f}\right]_{f=f_n} = -\frac{v_3}{f_n} = -\frac{2d}{n}. \tag{61}$$

For the parameters applied in Fig. 7 the level (59) corresponds to $v_3 \approx 4.38$ which fits the numerical results. If unlike our choice of parameters the level v_3 turns out to be more than c_l (when $c_l < c_t\sqrt{2}$), we would obtain at the same level the additional set of tangent points of the curves $v_l^{s,a}(f)$ also with the second family of the bond lines $\bar{v}_l^{(2)}(f)$. The coordinates f_m of the new tangent points additional to Eq. (60) and the slopes of common tangent lines at the points of this type of contact are equal

$$f_m = \frac{v_3 m}{2dp_2(v_3)}, \quad \left[\frac{\partial v}{\partial f}\right]_{f=f_m} = -\frac{v_3 p_2^2(v_3)}{f_m} = -\frac{2dp_2^3(v_3)}{m}. \tag{62}$$

It is worthwhile to mention that the above-discussed features of Lamb wave spectra, a specific asymptotic behavior at the level c_l, and a wavy character of Lamb dispersion curves over c_l become even more pronounced in pre-stressed compressible plates.[33]

ACKNOWLEDGMENTS

The authors are grateful to A.L. Shuvalov for helpful discussions. V.I.A. and V.N.L. were supported in part by the Russian Foundation for Basic Research (Grant No. 05-02-16666). V.I.A. also acknowledges partial support from the Polish-Japanese Institute of Information Technology (Research Grant No. PJ/MKT/02/2005) and from the Kielce University of Technology.

[1] I. A. Viktorov, *Rayleigh and Lamb Waves: Physical Theory and Applications* (Plenum, New York, 1967).
[2] L. M. Brekhovskikh, *Waves in Layered Media* (Academic, New York, 1980).
[3] B. A. Auld, *Acoustic Fields and Waves in Solids* (Krieger, Malabar, FL, 1990).
[4] A. H. Nayfeh, *Wave Propagation in Layered Anisotropic Media* (North-Holland, Amsterdam, 1995).
[5] D. E. Chimenti, "Guided waves in plates and their use in materials characterization," Appl. Mech. Rev. **50**, 247–284 (1997).
[6] T. C. T. Ting and P. Chadwick, "Harmonic waves in periodically layered anisotropic composites," in *Symposium of Wave Propagation in Structural Composites*, edited by A. K. Mal and T. C. T. Ting (ASME, New York, 1988), Vol. **90**, pp. 69–79.
[7] A. H. Nayfeh, "The general problem of elastic wave propagation in multilayered anisotropic media," J. Acoust. Soc. Am. **89**, 1521–1531 (1991).
[8] A. Norris, "Low frequency wave propagation in periodically layered anisotropic elastic solids," in *Modern Theory of Anisotropic Elasticity and Applications*, edited by J. J. Wu, T. C. T. Ting, and D. M. Barnett (SIAM, Philadelphia, 1991), Chap. 17, pp. 255–262.
[9] A. M. B. Braga and G. Herrmann, "Floquet waves in anisotropic periodically layered composites," J. Acoust. Soc. Am. **91**, 1211–1227 (1992).
[10] A. L. Shuvalov, "On the theory of wave propagation in anisotropic plates," Proc. R. Soc. London, Ser. A **456**, 2197–2222 (2000).
[11] V. I. Alshits, M. Deschamps, and G. A. Maugin, "Elastic waves in anisotropic plates: Short-wavelength asymptotics of the dispersion branches $v_n(k)$," Wave Motion **37**, 273–292 (2003).
[12] A. L. Shuvalov, O. Poncelet, and M. Deschamps, "General formalism for plane guided waves in transversely inhomogeneous anisotropic plates," Wave Motion **40**, 413–426 (2004).
[13] V. I. Alshits and G. A. Maugin, "Dynamics of multilayers: Elastic waves in an anisotropic graded or stratified plate," Wave Motion **41**, 357–394 (2005).
[14] R. D. Mindlin, "Waves and vibrations in isotropic, elastic plates," in *Structural Mechanics*, edited by J. N. Goodier and N. Hoff (Pergamon, New York, 1960), pp. 199–232.
[15] V. I. Alshits, J. Lothe, and V. N. Lyubimov, "Surface and exceptional body elastic waves in a plate of a hexagonal crystal," Sov. Phys. Crystallogr. **28**, 378–380 (1983).
[16] G. A. Maugin, "Elastic surface waves with transverse horizontal polarization," Adv. Appl. Mech. **23**, 373–434 (1983).
[17] V. I. Alshits and V. N. Lyubimov, "Anomalous dispersion of surface elastic waves in an anisotropic plate," Sov. Phys. Crystallogr. **33**, 163–166 (1988).
[18] S. I. Rokhlin and Y. J. Wang, "Equivalent boundary conditions for thin orthotropic layer between two solids: Reflection, refraction, and interface waves," J. Acoust. Soc. Am. **91**, 1875–1887 (1992).
[19] A. Freedman, "The variation, with the Poisson ratio, of Lamb modes in a free plate," J. Sound Vib. **137**, 209–266 (1990).
[20] Q. Zhu and W. G. Mayer, "On the crossing points of Lamb wave velocity dispersion curves," J. Acoust. Soc. Am. **93**, 1893–1895 (1993).
[21] A. Freedman, "Comment on 'On the crossing points of Lamb wave velocity dispersion curves' [J. Acoust. Soc. Am. **93**, 1893–1895 (1993)]," J. Acoust. Soc. Am. **98**, 2363–2364 (1995).
[22] V. I. Alshits, W. Gierulski, V. N. Lyubimov, and A. Radowicz, "Resonance excitation of quasi-Rayleigh waves in plates on soft or hard substrates," Crystallogr. Rep. **42**, 20–27 (1997).
[23] V. I. Alshits, V. N. Lyubimov, and A. Radowicz, "Quasi-Rayleigh waves in sandwich structures: Dispersion equation, eigenmodes, and resonance reflection," Crystallogr. Rep. **45**, 457–465 (2000).
[24] V. I. Alshits and V. N. Lyubimov, "Anomalous dispersion of SH acoustic waves in a piezoelectric sandwich structure," Phys. Solid State **45**, 832–835 (2003).

[25]M. Castaings and B. Hosten, "Transfer matrix of multilayered absorbing and anisotropic media. Measurements and simulations of ultrasonic wave propagation through composite materials," J. Acoust. Soc. Am. **94**, 1488–1495 (1993).
[26]M. J. S. Lowe, "Matrix techniques for modeling ultrasonic waves in multilayered media," IEEE Trans. Ultrason. Ferroelectr. Freq. Control **42**, 525–542 (1995).
[27]L. Wang and S. I. Rokhlin, "Stable reformulation of transfer matrix method for wave propagation in layered anisotropic media," Ultrasonics **39**, 413–424 (2001).
[28]E. R. Green, "Channelling of high-frequency elastic waves in laminated plates," Wave Motion **35**, 247–255 (2002).
[29]B. A. Auld, D. E. Chimenti, and P. J. Shull, "Shear horizontal wave propagation in periodically layered composites," IEEE Trans. Ultrason. Ferroelectr. Freq. Control **43**, 319–325 (1996).
[30]A. N. Stroh, "Steady state problems in anisotropic elasticity," J. Math. Phys. **41**, 77–103 (1962).
[31]V. I. Alshits and J. Lothe, "Comments on the relation between surface wave theory and the theory of reflection," Wave Motion **3**, 297–310 (1981).
[32]V. N. Lyubimov and V. I. Alshits, "Brewster reflections of elastic waves in hexagonal crystals," Sov. Phys. Crystallogr. **27**, 512–516 (1982).
[33]E. V. Nolde, L. A. Prikazchikova, and G. A. Rogerson, "Dispersion of small amplitude waves in a pre-stressed, compressible elastic plate," J. Elast. **75**, 1–29 (2004).

Plane wave propagation in generalized multiply connected acoustic filters

S. N. Panigrahi and M. L. Munjal[a)]
Facility for Research in Technical Acoustics, Department of Mechanical Engineering, Indian Institute of Science, Bangalore-560012, India

(Received 26 October 2004; revised 10 August 2005; accepted 12 August 2005)

A generalized algorithm is developed for studying the sound wave propagation in a system of interconnected rigid walled acoustic filter elements. The algorithm is based on the transfer matrix approach of analysis. Interconnection between various elements is represented by a connectivity matrix. Equations of mass velocity continuity and pressure equilibrium at the interconnections are generated using this connectivity matrix and are solved to get the overall transfer matrix of the system. The algorithm used for generalized labeling of the network and computation of transmission loss is discussed. The algorithm is applied to investigate multiply connected automobile mufflers as a network of acoustic elements. Results for some configurations have been compared with those from the finite element model analysis and experiments cited in the literature. A parametric study with respect to some geometric variables is carried out. While the results are illustrated here for a few configurations, the approach holds for all kinds of combinations of acoustic elements with any degree of complexity. The acoustical similarity between apparently different networks is discussed. The approach is flexible to incorporate any other acoustic elements, provided the acoustic variables at the junctions of the element can be related by a transfer matrix *a priori*. © *2005 Acoustical Society of America.* [DOI: 10.1121/1.2049127]

PACS number(s): 43.20.Mv [SFW] Pages: 2860–2868

I. INTRODUCTION

Acoustic wave propagation through a combination of acoustic filter or muffler elements has been studied for a very long time in the history of acoustic filters. Study of two tubes in parallel connection, for varying lengths and cross-sectional areas, has been carried out since the 19th century, first by Herschel and Quincke[1,2] and later refined by Stewart and Lindsay[3–5] in the early 20th century. Stewart's analysis, however, was a restricted one in a way that it forced the cross-sectional areas of the parallel ducts to be equal and the sum of the cross-sectional areas of the two branch ducts to be the same as that of the entrant and the exit duct. A general analytical expression for the transmission loss of a simple two-node, two-duct configuration [i.e., the Herschel-Quincke (HQ) tube] was developed and the numerical and experimental verification of the same was carried out by Selamet *et al.*[6] In their work, the conservation equations for mass, momentum, and internal energy, coupled with the ideal gas equation of state were formulated and solved using numerical methods.

Historically, the use of the HQ tube has been restricted to the suppression of tones of specific frequencies. The sound attenuation that can be achieved by use of such tube networks has not been exploited as it has been argued that the attenuation bands are too narrow.[7] But their attenuation bandwidth may be enhanced by removing the restrictions imposed by Stewart and by increasing the number of parallel ducts. Selamet and Easwaran[8] developed a close form expression for the transmission loss characteristics and resonance locations for an *n*-duct configuration. The analysis, however, was restricted to the configuration where inlets and outlets of all the "*n*" ducts were connected together, respectively.

The physical connection of two or more acoustic elements makes the pressure equal in all of the elements associated at the point of connection. In the present work, it is assumed that the lateral dimensions of all the elements are such that the disturbances (the higher order modes) that are created at the junction of elements or at any sharp bend that may be present, die out within a very small distance (as compared to the lengths of the converging tubes) from the junction or the bend for the whole frequency range of interest. So, the pressure field outside this small region of disturbance can be considered as plane in nature and this pressure has been considered equal in all the elements at the junctions. While using complex acoustic elements, the only care that must be taken is to ensure that plane wave assumption holds good in the frequency range of interest in all of the constituting elements of the network. Insofar as the present work is concerned, the walls of all the acoustic elements are assumed to be strictly rigid so as to avoid any dispersive effect in the waves carried through them. The summation of volume velocity is also zero at these points. Such points of connection of elements, hereafter, in analogy to the electrical circuitry terminology, are referred to as nodes in the present paper. Similarly, the acoustic element connecting any two nodes is referred to as a branch to keep the discussion general with respect to the elements constituting an acoustic filter (explicit mention of some of the used elements has been made in the next section). Such systems or acoustic filters with many nodes and branches are referred to as acoustic

[a)]Electronic mail: munjal@mecheng.iisc.ernet.in

networks in the present paper. So, as an example, the configuration taken up by Selamet and Easwaran in their work[8] shall be referred to here as a 2-node, *n*-branch network of rigid walled ducts.

In the existing literature, generally, two methods, namely, the transfer matrix method and stiffness matrix method, are followed to analyze suchlike mufflers or any acoustic network in general. Chainlike networks similar to a muffler or a long duct with many changes of cross sectional area and many segments for which individual transfer matrices are known, have been dealt with as a cascade by means of the transfer matrix approach.[9,10] Apart from the attempt to get a broad band sound attenuation, as in the case of automobile mufflers and multiply tuned quincke tubes, there is another objective of the analysis of networks of acoustic wave guides. In the gas piping systems, the knowledge of resonance frequencies is more important than the overall sound attenuation. Simplified analyses have been used to study resonance in pipelines.[11] To[12,13] analyzed the acoustic propagation in piping systems by developing a computer program based on the transfer matrix approach. In applying his approach, one needs to first locate the subsystems with certain input/output combination. For example, one-input–one-output, one-input–two-output, two-input–one-output, etc. This task becomes very complicated when one deals with a fairly complex network of filter elements. Again, at times, it can be very difficult to distinguish a two-input–one-output subsystem from a one-input–two-output subsystem, and so on.

Craggs *et al.*[14] have used the stiffness matrix method to analyze the attenuation behavior of sound waves in pipe networks. They have used a two-dimensional finite element model (FEM) of the bends and junctions of the network and combined these solutions with exact solutions for the pipe to study the overall sound attenuation in a certain network of pipes, which they have verified experimentally.

Recently, Dowling and Peat[15] have used the transfer matrix approach to analyze silencers of general geometry. They have devised a path fraction algorithm to break the complete network into subsystems of simpler elements. This method uses a fork (similar to the one-input–two-output subsystem of To[12]) to connect a single input to two outputs. But, if a number of branches emerge from a single point and all of them are connected to some different locations, which in turn may be the confluence point of many other branches of the network, it may not be possible to break the network using only forks, particularly in the case of three-dimensional networks, which is common in all realistic gas piping systems.

The present paper suggests a transfer matrix based approach to analyze a generalized *m*-node, *n*-branch, two-port network of ducts (e.g., see Fig. 1). The fifth configuration of the figure below shows two ducts emerging from the same point and they seem to be overlapping. This confusion can be avoided if the network is visualized in a three-dimensional space. An example of such a configuration has been shown in Fig. 2 where several branches emerge from the same point of the network. So, the concept of line diagram has been used to represent the networks and is discussed in the next section. A scheme has been proposed to label the network. A connectivity matrix is formed using the network labeling. The connectivity matrix gives an indication of acoustically similar networks with different physical appearance. An algorithm has been developed to use the connectivity matrix to automate the generation of the pressure balance equations, and volume-velocity continuity equations along with the proper transfer matrices between the nodes. The final transfer matrix, which relates the acoustic variables at the upstream and downstream points, is then evaluated from which the transmission loss can be calculated.[9,10] Investigation of complex, multiply connected mufflers is carried out using the present method. This generalized network can be used to analyze many other acoustic elements which cannot be thought of as networks on a first look. Some such cases are analyzed to show the usefulness of this generalized network analysis.

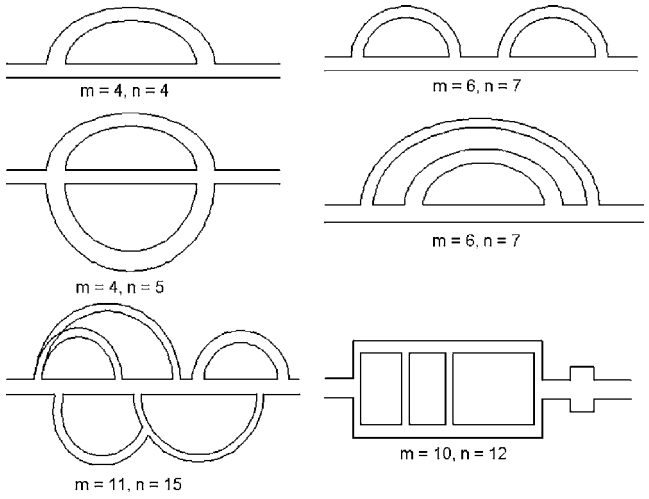

FIG. 1. Schematic of some representative *m*-node, *n*-branch acoustic filters.

The present study consists of four sections. Following this Introduction, the algorithm developed is discussed.

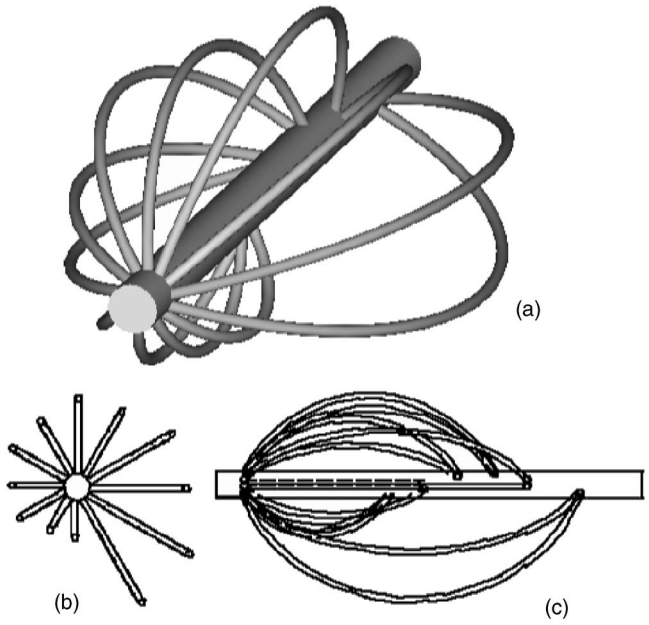

FIG. 2. (a) 3D view, (b) left side view, and (c) front view of a multiply tuned Quincke tube.

Then, the predictions are validated and some configurations are analyzed to show the flexibility and usefulness of the approach. One section exclusively deals with the investigation of multiply connected mufflers. The study is then summarized and concluded with some final remarks.

II. ALGORITHM

As pointed out previously, some times it becomes difficult to comprehend from the two-dimensional representation of networks. The three-dimensional figures are not suitable for analysis either. So, the line diagram representation is used in the present work to represent the networks. A general m-node, n-branch network can be drawn by first noting the nodes of the network. As indicated above, a node represents a branching of a certain duct into several elements or the confluence of several elements at a specific point. Then the nodes can be connected by appropriate number of elements referred to as branches or edges as indicated in a preceding section. The lateral dimensions of these elements have been considered small so as to have the plane wave region up to the maximum frequency of interest. The medium inside the elements is assumed to be a gaseous fluid so that the rigidity assumption for the walls can be relied upon to a reasonable degree of accuracy. These elements can be simple rigid walled ducts, expansion chambers with or without any extended inlet/outlet, concentric tube resonators, duct with any number of mutually interacting perforated ducts,[16] or for that matter, any other newly developed element. The theory of deriving the transfer matrices for many of these filter elements has been discussed in the literature.[9,10] The detailed derivation of transfer matrix for some particular acoustic element may become very involved at times. The simplicity of the present method lies in the fact that the transfer matrix (derived rigorously) of such complex elements can also be used directly without going into the intricacies of the derivation. The cutoff frequency for the constituting elements, however, can be calculated from their geometrical parameters by referring to the respective literature.

A statement is worth noting regarding the above-mentioned elements. Complex elements like concentric tube resonators or similar can be used directly in the network if the transfer matrix for the same is known *a priori*. Otherwise these elements can themselves be analyzed as networks made of simpler elements. The end terminations can be directly incorporated as separate elements and the transfer matrices for such terminations take into account the impedance of the termination. So, no special treatment is needed to handle such situations. However, the rigid terminations can be dealt with in a much simpler way. A rigid duct of very small cross-sectional area (nearing zero) and a very large length (arbitrarily large) can be imagined to be emerging from such a termination and can be connected to any point of the network. When two or more such terminations exist, they can be connected to each other in this manner. This kind of treatment of the termination has been illustrated in subsequent sections. The lengths of the network branches need not be considered while drawing these line diagrams. An example of a line diagram is shown in Fig. 3 (the inlet and the outlet tubes have not been considered) with its corresponding two-dimensional network representation. A sudden change in area can also be handled by introducing nodes at such discontinuities. Such configurations are analyzed later in a subsequent section.

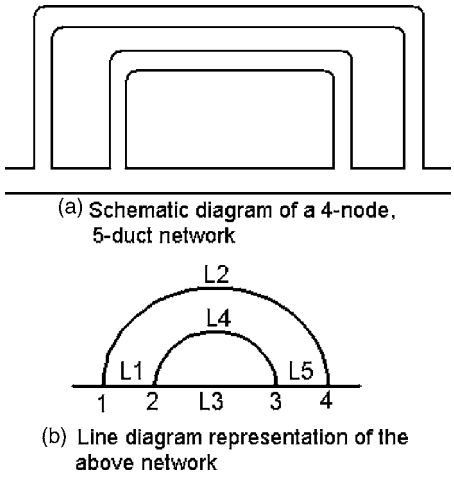

FIG. 3. An example of line diagram representation of general network.

Once the line diagram is prepared, the next step is to number the nodes. The nodes are numbered sequentially, starting from 1, and this is assigned to the inlet of the network. The numbering of intermediate nodes can be done arbitrarily except that the outlet of the network must be assigned the highest node number. The complete algorithm has been implemented through a computer program using MATLAB Version 6. In the data input stage, which is the first stage of the algorithm, the program involves gathering data regarding the connectivities among the different elements as user input with the help of the line diagram. It also involves gathering information about the type of elements for each connection, physical data (radii, lengths, perforation parameters, etc.) for each element, and then storing the complete information as an editable data file. When multiple interacting ducts are to be included in the network some more data (information about the nodes that are associated with the multiply interacting duct) must be entered so that the program can identify all the nodes which are associated with these interacting ducts. To enter this information correctly, the line diagram itself is modified with dotted lines (instead of solid lines) between the nodes which are part of these interacting nodes. Use of this kind of line diagram has been illustrated in subsequent sections through examples. This data file can later be edited manually to make small changes for some parametric study which would help in reducing the total designing time of any particular filter or muffler configuration. Each node may or may not be connected to all the other nodes, and between any pair of nodes there can be several branches. In the analysis stage, the program reads data from the stored file and generates the program variables. The connectivity information is stored in the form of a matrix, hereafter called the connectivity matrix. For the network shown in Fig. 3, this would look like the matrix $[\mathbf{C}]$ in Eq. (1),

$$[\mathbf{C}] = \begin{bmatrix} \times & 1 & 0 & 1 \\ 1 & \times & 2 & 0 \\ 0 & 2 & \times & 1 \\ 1 & 0 & 1 & \times \end{bmatrix}. \tag{1}$$

The cross marks in the diagonal position suggests that each node is connected to itself. Nonzero values in other positions denote the number of branches between the pair of nodes, the pair being decided by the position in the matrix. For example, $[\mathbf{C}]_{23}=1$ indicates that there is only one branch connecting the pair of nodes 2 and 3, and so on. A zero at any position implies that the corresponding nodes are not connected directly. The upper diagonal part of this connectivity matrix is then traversed for getting the information about the number of branches between each pair of nodes, and labels are assigned to them sequentially as $L_1, L_2, \ldots$, etc., up to the last branch. For the present configuration, $[\mathbf{C}]_{12}=1$, $[\mathbf{C}]_{14}=1$ suggest that the name of the branches between nodes 1–2 and 1–4 is L_1 and L_2, respectively. Between nodes 2 and 3 there are two branches ($[\mathbf{C}]_{23}=2$) which are labeled as L_3 and L_4. This labeling can be done without any preference to any of the branches between these nodes. This labeling is done automatically through the program. The physical parameters are input at this stage of operation. The upstream and the downstream ends are also assigned to the corresponding branches. Once all this information is gathered, the transfer matrix equations are generated, assuming plane wave propagation, for each branch between their corresponding nodes. The state variables at the upstream and the downstream ends of each branch are related by the transfer matrix as

$$\begin{Bmatrix} p \\ v \end{Bmatrix}_{L_i}^{u} = [\mathbf{TM}] \begin{Bmatrix} p \\ v \end{Bmatrix}_{L_i}^{d}, \tag{2}$$

where p is the acoustic pressure and v is the acoustic mass velocity. $[\mathbf{TM}]$ is the transfer matrix, superscripts "u" and "d" denote the upstream/downstream points and "L_i" denotes the branch for which the equation is being written. The above equations could also have been written in terms of the progressive forward and rearward moving pressure waves.[6] The advantage of writing in the transfer matrix form is that, any acoustic element (or a cascade of elements) for which transfer matrix is known can directly be incorporated between any pair of nodes; a branch does not have to be a uniform tube, duct or pipe. This makes the algorithm more general in terms of analyzing various networks with different acoustic elements. The equations are generated using the symbolic arithmetic so that final results can be evaluated in two different forms. One can assign numerical values to all parameters and solve the final equation numerically. Alternatively, the equations can be solved symbolically and later on the numerical values can be assigned. The second method generally takes much longer time to solve and is computationally more demanding on the resources. But once this solution is obtained the parametric studies become much easier and faster. So, if the network is made of tubes only, which happens to be the case in the current example, Eq. (2) becomes

$$\begin{Bmatrix} p \\ v \end{Bmatrix}_{L_i}^{u} = \begin{bmatrix} \cos(kL_i) & jY_i \sin(kL_i) \\ \frac{j}{Y_i} \sin(kL_i) & \cos(kL_i) \end{bmatrix} \begin{Bmatrix} p \\ v \end{Bmatrix}_{L_i}^{d}, \tag{3}$$

where $k=\omega/a_0$ and $Y_i=a_0/S_i$. k is the wave number and Y_i denotes the characteristic impedance of ith branches labeled as L_i. ω is the driving frequency, a_0 is the speed of sound in air, and S_i represents the cross-sectional area of ith branch. The transfer matrix equations for the first duct of the present example that are generated in the program are given as

$$p_u^{L_1} - \cos(kL_1) p_d^{L_1} - \frac{ja_0 \sin(kL_1) v_d^{L_1}}{S_1} = 0, \tag{4}$$

$$v_u^{L_1} - \frac{jS_1 \sin(kL_1) p_d^{L_1}}{a_0} - \cos(kL_1) v_d^{L_1} = 0. \tag{5}$$

Each such equation introduces four new unknowns in the total list of unknowns.

Conditions for pressure equilibrium at each node or junction of acoustic elements can be expressed as Eq. (6) and the corresponding equations for the case at hand are given as Eq. (7),

$$p_{u,d}^{L_i} = p_{u,d}^{L_j}, \tag{6}$$

$$p_d^{L_1} - p_u^{L_3} = 0, \quad p_d^{L_1} - p_u^{L_4} = 0, \quad p_d^{L_3} - p_d^{L_4} = 0, \quad p_d^{L_3} - p_u^{L_5} = 0. \tag{7}$$

Here, j traverses through all the elements (except the element with the lowest serial number) present at a particular junction of elements and i represents the element which bears the lowest serial number among the set of elements present at that junction. The "up" or the "down" status is read from the matrix generated during the file reading process to obtain the connectivity matrix. Equation (6) represents the pressure equilibrium equation at the intermediate nodes. The corresponding equations for the inlet and the outlet ports, respectively, are as follows:

$$p_u = p_u^{L_i}, \tag{8}$$

$$p_d = p_d^{L_i}. \tag{9}$$

For the present example network, the pressure equilibrium equations are given as

$$p_u - p_u^{L_1} = 0, \quad p_u - p_u^{L_2} = 0, \tag{10}$$

$$p_d - p_d^{L_5} = 0, \quad p_d - p_d^{L_2} = 0. \tag{11}$$

Continuity of mass velocity (assuming uniform density) at the nodes is expressed as

$$v_u + v_u^{L_{b1}} + \cdots + v_u^{L_{bn}} = 0 \tag{12}$$

at the inlet of the network, as

$$v_d + v_d^{L_{b1}} + \cdots + v_d^{L_{bn}} = 0 \tag{13}$$

at the outlet of the network, and as

$$v_{u,d}^{L_{b_1}} \pm v_{u,d}^{L_{b2}} \cdots \pm v_{u,d}^{L_{bn}} = 0 \tag{14}$$

at the intermediate junctions. For the present example network (Fig. 3), the equations for continuity of volume velocity are given as

$$v_u + v_u^{L_1} + v_u^{L_2} = 0, \quad v_d + v_d^{L_2} + v_d^{L_5} = 0, \tag{15}$$

for the inlet and outlet on the network, respectively, and

$$v_d^{L_1} - v_u^{L_3} - v_u^{L_4} = 0, \quad v_d^{L_3} + v_d^{L_4} - v_u^{L_5} = 0 \tag{16}$$

for the intermediate nodes.

It is worth noting that addition of each new branch introduces four more equations. For example, when a new branch is added to a single tube having six equations, to form the Herschel-Quincke tube, the number of equations increases to 10. So, for an n-duct configuration the total number of equations would be $4n+2$. Each transfer matrix equation introduces four additional unknown variables. Therefore, there would be $4n$ unknowns. The state variables at the inlet and the outlet ports, namely p_u, v_u, p_d, and v_d, add four more unknowns making the total number of unknowns $4n+4$. On eliminating the intermediate unknown variables, the pressure and the volume velocity at the inlet of the network can be expressed in terms of those at the outlet of the network. Then, setting $v_d=0$ and $p_d=1$ in the pressure equation, T_{11} can be found out. Similarly, the other three terms, namely, T_{12}, T_{21}, and T_{22} of the transfer matrix can also be evaluated. Then the two upstream variables at the inlet port can be expressed in terms of the two downstream variables at the outlet port as

$$\begin{Bmatrix} p \\ v \end{Bmatrix}_u = \begin{bmatrix} T_{11} & T_{12} \\ T_{21} & T_{22} \end{bmatrix} \begin{Bmatrix} p \\ v \end{Bmatrix}_d, \tag{17}$$

where $T_{ij}(i,j=1,2)$ are known as the four-pole parameters of the system. The transmission loss for the network can be expressed in terms of these four-pole parameters as[9]

$$\mathrm{TL}_a = 20 \log_{10} \frac{(T_{11} + T_{12}/Y + YT_{21} + T_{22})}{2}, \tag{18}$$

where Y is the characteristic impedance of the upstream duct (inlet port) or the downstream duct (outlet port), assumed to be equal in Eq. (18).

III. VALIDATION OF THE ALGORITHM

Some self-consistency checks have been carried out for validation of the algorithm described above. For a 2-node, 2-branch (L_1, L_2 being the lengths of the two branches) network the transmission loss has been calculated. This network is supposed to be acoustically identical to a simple expansion chamber[8] when the two branches become equal in length, the area of expansion chamber being equal to the combined area of the two ducts. In this case the expression for TL is given by Davis *et al.*[7] as

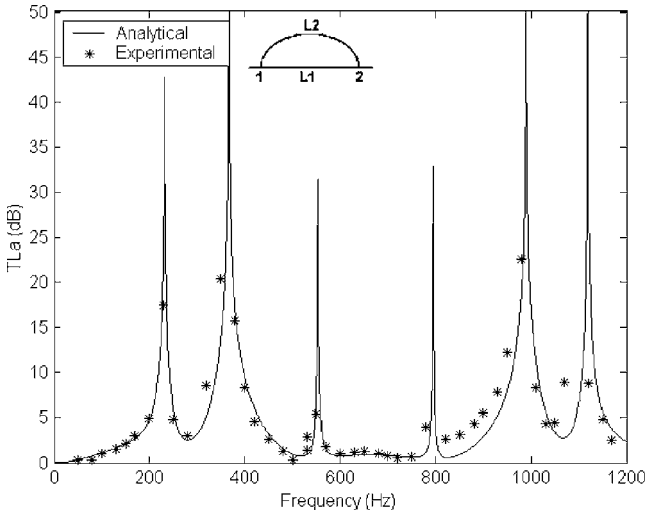

FIG. 4. Transmission loss spectra for the network ($L_1=0.3935$ m, $L_2=0.9065$ m, $r_1=0.0243$ m, $r_2=0.019\,05$ m) investigated by Selamet *et al.* (Ref. 6). Comparison of network analysis and the experimental results.

$$\mathrm{TL} = 10 \log_{10}\left[1 + \tfrac{1}{4}(m - 1/m)^2 \sin^2(kl)\right], \tag{19}$$

where m, the area ratio, is given by $(S_1+S_2)/S_u$. S_1, S_2 are the area of cross section of the two branches and S_u is the cross-sectional area of the upstream duct. The TL predicted from the present network analysis has been verified to be identical to that from Eq. (19) as expected. The TL curve for unequal lengths ($L_2 \neq L_1$) has been observed to be above the TL curve for equal lengths of the branches. This comparison brings out the importance of the role of unequal branch lengths in wave cancellation.

Figure 4 shows the comparison of the predicted results with the experimental[6] ones for a 2-node, 2-branch network ($L_1=0.3935$ m, $L_2=0.9065$ m, $r_1=0.0243$ m, $r_2=0.019\,05$ m) with unequal lengths and unequal cross-section areas of the branch ducts.

The present approach has been used to analyze a 2-node, n-branch network as a special case of the m-node, n-branch network. The results obtained for 2-node, 2- and 3-branch configurations ($L_1=0.4$ m, $L_3=0.8$ m, $r_1=0.025$ m, $r_2=0.025$ m, $r_3=0.025$ m) have been checked to have an exact match with those of Selamet *et al.*[8] as shown in Fig. 5. After validating for a 2-node, n-branch configuration, the approach has been used to predict transmission loss for an m-node, n-branch (6-node, 7-branch) network of tubes. The experimental results obtained by Craggs *et al.*[14] for the network have been compared in Fig. 6 with those obtained from the present approach. The two can be seen to be matching well. The dimensions (in meters) and other parameters used here are the same as those used in Ref. 14 and are as follows:

$$L_1 = 0.2, \quad L_2 = L_3 = L_4 = L_5 = L_6 = 0.453.$$

The branch denoted by L_7, in fact, is an expansion chamber with inlet length of 0.1555 m, expanded chamber length of 0.05 m and area expansion ratio of 3.25 to confirm with the dimensions used in the cited reference. They have used a square cross section for the tubes of the network. For the present study, tubes with the same area of cross

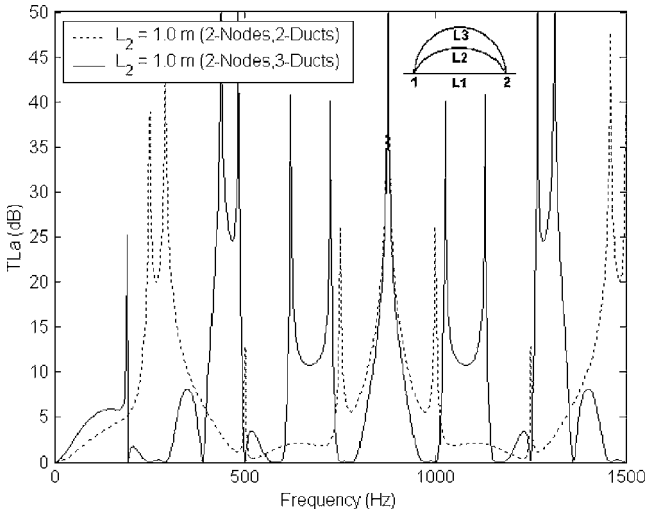

FIG. 5. Transmission loss spectra for the network (L_1=0.4 m, L_3=0.8 m, r_1=0.025 m, r_2=0.025, r_3=0.025 m) investigated by Selamet *et al.* (Ref. 8) predicted from the present analysis.

section (with r=0.027 m) have been considered in modeling the equivalent general network.

IV. SOME PARAMETRIC STUDIES

A general 4-node, 5-branch network is shown in Fig. 7(a). Figures 7(b) and 7(c) show similar networks with expansion chambers in one and two of their branches, respectively. All these networks can be analyzed as 4-node networks if the transfer matrix for the branches with expansion chambers is used directly between the corresponding nodes. They can also be analyzed by introducing more number of nodes in the branches and this method has been used here for the analysis. The line diagrams for the above configurations are shown in the inset of Fig. 8. The curves show the transmission loss predicted for the networks shown in the inset

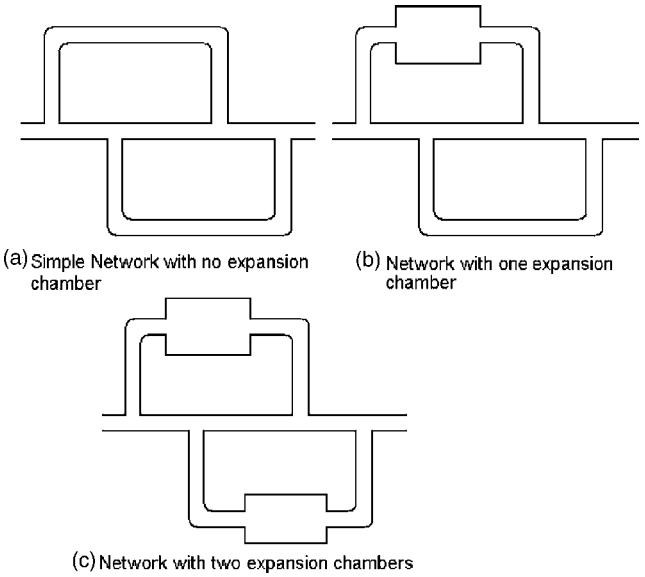

FIG. 7. A network with (a) zero, (b) one, and (c) two expansion chambers on the branches.

comprising a number of tubes and expansion chambers. For the configuration (a) of Fig. 8, the dimensions (in meters) used are

$$r_u = r_1 = r_2 = r_3 = r_4 = r_5 = r_d, \quad r_u = 0.02,$$

$$L_1 = 0.1, \quad L_2 = 2L_1, \quad L_3 = 1.5L_1, \quad L_4 = 2.5L_1, \quad L_5 = L_1.$$

The configuration (b) shown in the inset of Fig. 8 consists of an expansion chamber on its upper branch between nodes 3 and 4 (denoted by L_5). Dimensions for this configuration are considered in such a way that the total length of the upper branch of configurations (a) and (b) remains the same, i.e.,

$$(L_2)_a = (L_2 + L_5 + L_6)_b,$$

where $L_2 = L_6 = L_1/2$, $L_5 = L_1$, and $r_5 = 3r_u$.

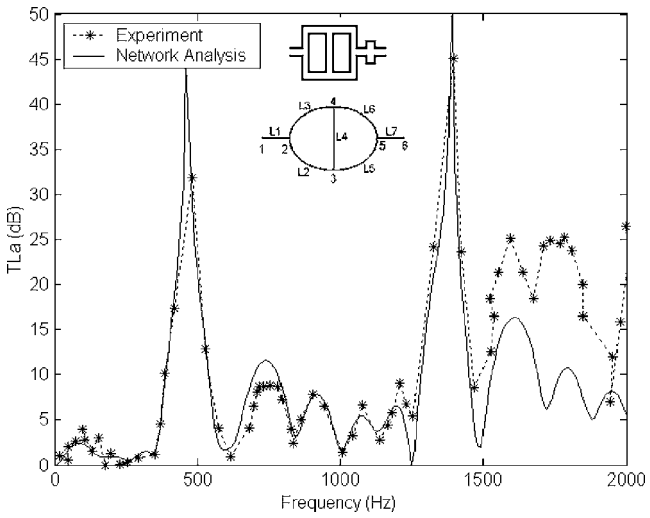

FIG. 6. Transmission loss spectrum for a 6-node, 7-branch, acoustic filter (L_1=0.2 m, L_2=L_3=L_4=L_5=L_6=0.453 m, r=0.027 m, L_7=expansion chamber with inlet length of 0.1555 m, expansion ratio=3.25, length of expanded chamber=0.05 m). Comparison of predicted results from present analysis with the experimental results of Craggs *et al.* (Ref. 14).

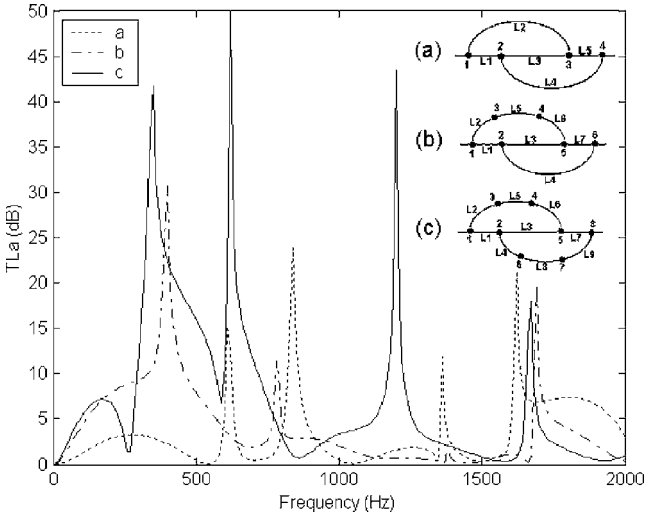

FIG. 8. Comparison of the axial transmission loss spectra of networks containing (a) zero, (b) one, and (c) two expansion chambers on the branch ducts. (a) r_u=r_1=r_2=r_3=r_4=r_5=r_d, r_u=0.02 m, L_1=0.1 m, L_2=2L_1, L_3=1.5L_1, L_4=2.5L_1, L_5=L_1; (b) L_2 of (a)=(L_2+L_5+L_6) of (b); L_5=L_1, L_2=L_6=L_1/2, r_5=3r_u; (c) L_4=1.5L_1, L_8=L_9=L_1/2, r_5=r_8=3r_u.

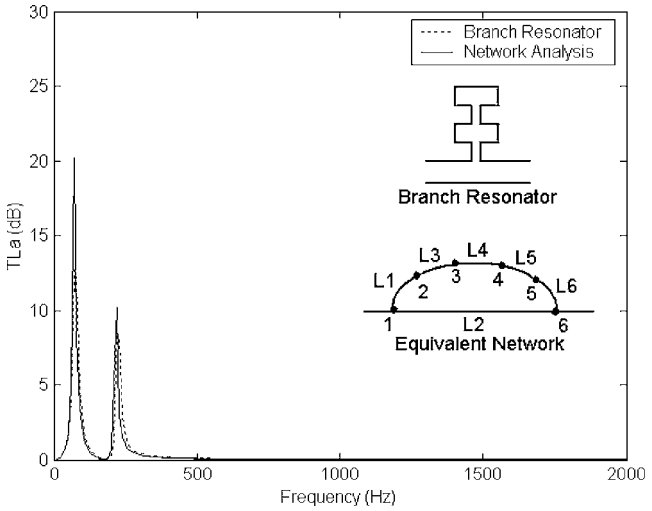

FIG. 9. Transmission loss spectrum for the branch resonator. Comparison with the predicted results from the equivalent network. L_1=0.02 m, L_3 =0.08 m, L_4=0.02 m, L_5=0.13 m, r_1=0.005 m, r_2=0.02 m, r_3=0.04 m, r_4 =0.005 m, r_5=0.04 m. L_6 is arbitrarily large. r_6=arbitrarily small.

In a similar way, the configuration (c) consists of an additional expansion chamber on its lower branch between nodes 6 and 7 (denoted by L_8),

$$\text{where } L_4 = 1.5L_1,\ L_8 = L_9 = L_1/2, \text{ and } r_5 = r_8 = 3r_u.$$

From the TL curves of Fig. 8 it can be inferred that by inclusion of multiple expansion chambers in the side branches it is possible to enhance the attenuation bandwidth.

The present approach can be used for analysis of other acoustical elements. Figure 9 shows such an example where a branch resonator has been analyzed as a special case of the equivalent network shown in the inset. The corresponding line diagram also has been included in the inset figure. The dimensions (in meters) used are L_1=0.02, L_3=0.08, L_4 =0.02, L_5=0.13, r_1=0.005, r_2=0.02, r_3=0.04, r_4=0.005, r_5 =0.04. In order to simulate the above effect, the radius of the duct between nodes 5 and 6 (r_6) has been taken as almost zero as has been discussed previously. Length L_2 was chosen to be 0.02 m which, in fact, may be assigned any value. It can be seen from the figure that the result from one-dimensional analysis correlates well with the prediction from the present approach. The above equivalence motivates analysis of other desired special acoustic elements using an appropriate equivalent network having side branches at many places of the network. By properly choosing the lengths and radii of various ducts and branches, the attenuation behavior can be controlled to obtain better performance over a desired frequency range.

A. Analysis of multiply connected mufflers

The present approach can be applied to analyze mufflers containing multiply connected components. One simple example of such a muffler and its line diagram representation are shown in Fig. 10. It can be seen from the diagram that the pressure field inside the perforated inlet and in the outer annular duct at plane "*A*" are interacting with the pressure field in the main duct at plane "*B*." So, this multiple connection

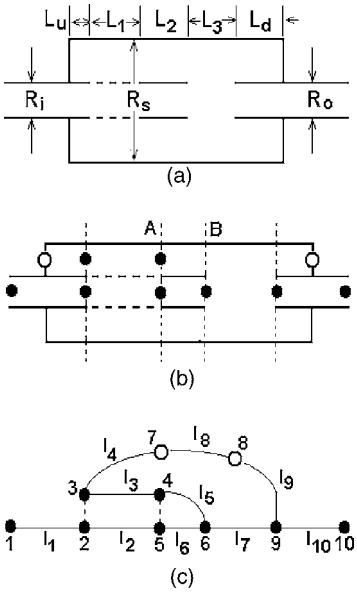

FIG. 10. (a) Schematic of a multiply connected muffler. (b) Node marking scheme. (c) The branches have been numbered through the algorithm. L_u =L_d=0.1 m, L_1=0.12 m, L_2=0.12 m, L_3=0.08 m, R_i=R_o=0.02 m, R_s =0.05 m.

inside the muffler has been dealt with in the line diagram. Representation of the rigid terminations as long, narrow duct also has been illustrated in this example. The branch representing this long duct is shown by the length "l_8" in the figure. The dimensions (in meters) of the muffler are as follows:

$$L_u = L_d = 0.1, \quad L_1 = 0.12, \quad L_2 = 0.12, \quad L_3 = 0.08,$$

$$R_i = R_o = 0.02, \quad R_s = 0.05.$$

The nondimensional perforate impedance, ζ, for the perforated portion of the extended inlet has been calculated according to the following expression:[9]

$$\zeta = [6 \times 10^{-3} + jk(t + 0.75d_h)]/\sigma, \tag{20}$$

where t is the thickness of the duct wall and d_h is the diameter of the holes in the perforated region, and σ represents the porosity of the perforated portion given by the ratio of open area to the total area of that part. The perforate impedance has been nondimensionalized with respect to the characteristic impedance of air medium. It is to be noted that for these dimensions, the cut-on frequency for the first higher order mode is calculated to be about 2.0 kHz. The sound speed is assumed to be 340 m/s for the above calculation of cut-on frequency.

The predicted transmission loss spectrum from the present approach has been shown in Fig. 11. A comparison has been made with the results from the 3D-FEM analysis of the same muffler performed with SYSNOISE®, a commercial FEM package.[17] The results can be seen to be in good agreement for the whole frequency range of interest. The computational time (~200 millisecond per frequency) for the FEM analysis is not much as compared to the network analysis, for the mesh required for reasonable accurate results for the case under discussion. But, the modeling and the

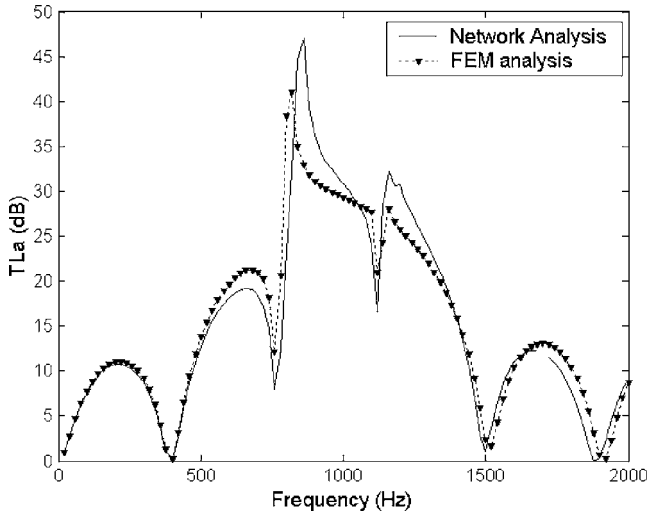

FIG. 11. The predicted TL spectra for the multiply connected muffler shown in Fig. 10. Comparison between 3D FEM and the 1D Network analyses.

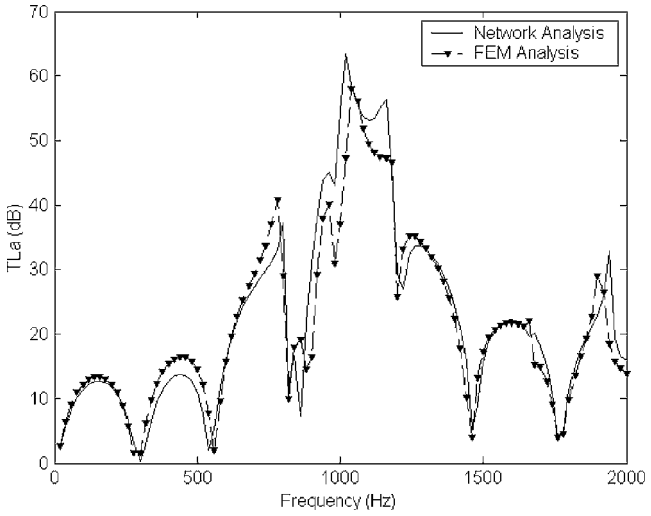

FIG. 13. The predicted TL spectra for the multiply connected muffler shown in Fig. 12. Comparison between 3D FEM and the 1D Network analyses.

mesh generation takes a good amount of time as compared to the data input time for the present analysis. The present analysis even presents a simpler data input scheme as compared to the path fraction algorithm[15] discussed in the introductory section. So, when it comes to parametric study for optimizing the muffler dimensions, the FEM analysis is not a convenient tool as compared to the network analysis. Figure 12 shows a still more complex multiply connected muffler and the predicted TL spectrum is shown in Fig. 13. It can be seen that the predicted result correlates well with the FEM results. The same perforate impedance expression has been used for both the perforated regions of the muffler. The convenience of using this approach vis-a-vis any FEM package can be realized during the parametric study (with respect to geometrical variables) of any system. Though the execution time for the FEM analysis (with a fine mesh) is comparable with that for the present approach, the geometrical model and the FE mesh must be generated afresh for each variation, which is very time consuming, particularly for conducting a parametric study required for design purposes.

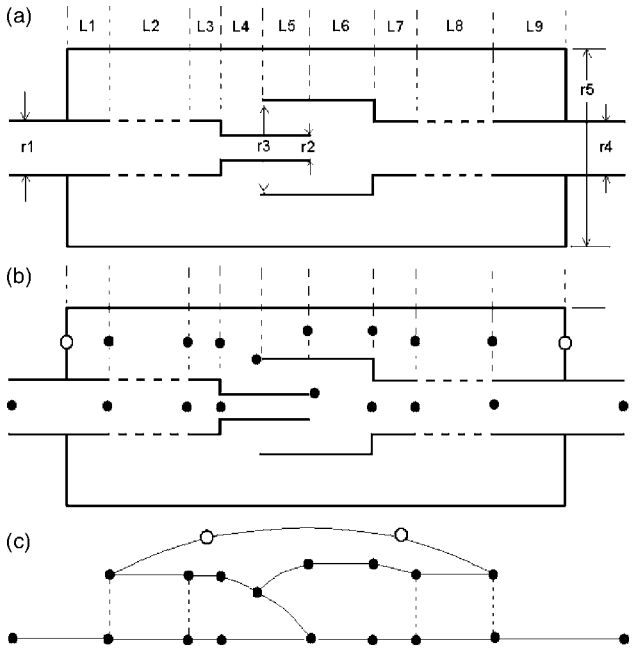

FIG. 12. (a) Schematic of a complex, multiply connected muffler. (b) Node marking scheme. (c) The branches have been numbered through the algorithm. L_1=0.05 m, L_2=0.131 m, L_3=0.054 m, L_4=0.05 m, L_5=0.05 m, L_6=0.07 m, L_7=0.025 m, L_8=0.091 m, L_9=0.054 m, r_1=0.02 m, r_2=0.01 m, r_3=0.04 m, r_4=0.02 m, r_5=0.06 m.

B. Example of acoustically equivalent but physically different networks

Figure 14 shows TL curves for the two configurations shown in the inset. The curves are indeed overlapping. Though the two configurations seem to be physically very different from one another, yet their acoustic behavior, at least in the plane wave range, is identical. The figures of the network in the inset have not been drawn to scale for a quick appreciation of the fact that is being emphasized. For analysis, however, the corresponding lengths between each pair of

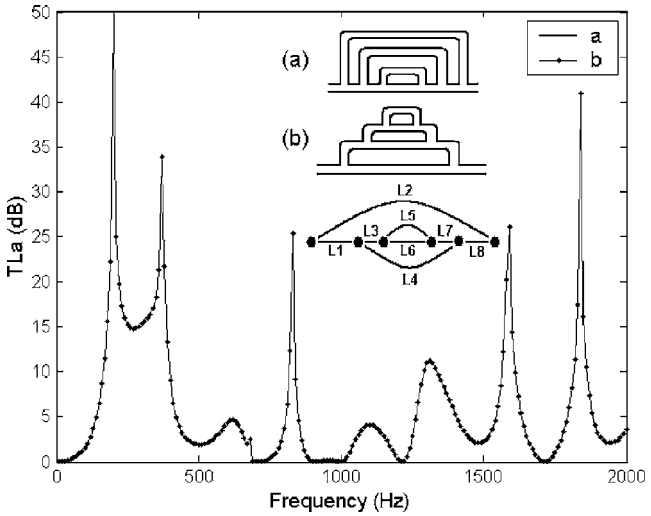

FIG. 14. The predicted TL spectra for two apparently different but acoustically equivalent filter configurations. L_1=0.1 m, L_2=9L_1, L_3=1.5L_1, L_4=7L_1, L_5=2L_1, L_6=3L_1, L_7=1.5L_1, L_8=L_1, r_1=0.02 m, r_2=r_3=r_4=r_5=r_6=r_7=r_8=r_1.

node have been kept the same for the two networks to become equivalent. Thus the approach outlined here can be used to verify different networks with different physical appearance for their acoustical equivalence.

V. CONCLUSIONS

A generalized approach for analyzing the sound attenuation behavior of complex networks (comprising m nodes and n branches) of acoustic filter elements containing gaseous, nondispersive fluids has been presented based on the plane wave assumption. Results for known acoustical elements have been reproduced using the approach as limiting cases, and have been shown to correlate well. The transmission loss predictions have been validated against experimental results from available literature. Higher order modes may affect the accuracy of the approach at higher frequencies for complex networks. The locations of the resonant frequencies however can be predicted with better accuracy. Use of the proposed method has been made to analyze some complex, multiply connected automobile mufflers. Validation has been done through comparison with some analytical closed form results, experimental results, and FEM solutions in some cases where they were available. The approach has also been used to show acoustical equivalence of apparently different networks which in turn can be utilized for designing networks with better space utilization. Apart from networks of simple tubes, networks with multiple expansion chambers at various branches and side branch resonators have been investigated for their pattern of sound attenuation. The results obtained reveal the acoustic resonant frequencies of the configuration under consideration and can be used for analyzing complex network systems with different acoustical elements in the constituent branches.

ACKNOWLEDGMENTS

Financial support of the Department of Science and Technology of the Government of India for the Facility for Research in Technical Acoustics (FRITA) is gratefully acknowledged.

[1] J. F. W. Herschel, "On the absorption of sound by coloured media viewed in connection with undulatory theory," Philos. Mag. **3**, 401–412 (1833).
[2] G. Quincke, "Ueber interferenzapparate für schallwallen," Ann. Phys. Chem. **128**, 177–192 (1866).
[3] G. W. Stewart, "The theory of Herschel-Quincke tube," Phys. Rev. **31**, 696–698 (1928).
[4] G. W. Stewart and R. B. Lindsay, *Acoustics* (Van Nostrand, Princeton, NJ, 1930).
[5] G. W. Stewart, "The theory of Herschel-Quincke tube," J. Acoust. Soc. Am. **17**, 107–108 (1945).
[6] A. Selamet, N. S. Dickey, and J. M. Novak, "The Herschel-Quincke tube: A theoretical computational and experimental investigation," J. Acoust. Soc. Am. **96**, 3177–3185 (1994).
[7] D. D. Davis, Jr., G. M. Stokes, D. Moore, and G. L. Stevens, Jr., "Theoretical and experimental investigation of mufflers with comments on engine-exhaust muffler design," National Advisory Committee for Aeronautics Report No. 1192, 1954.
[8] A. Selamet and V. Easwaran, "Modified Herschel-Quincke tube: Attenuation and resonance for n-duct configuration," J. Acoust. Soc. Am. **102**, 164–169 (1997).
[9] M. L. Munjal, *Acoustics of Ducts and Muffler* (Wiley-Interscience, New York, 1987).
[10] M. L. Munjal, "Muffler acoustics," in *Formulas of Acoustics*, edited by F. P. Mechel (Springer-Verlag, Berlin, 2002), Chap. K.
[11] M. W. Kellogg Company, *Design of Piping Systems* (Wiley, New York, 1956).
[12] C. W. S. To, "The acoustic simulation and analysis of complicated reciprocating compressor piping systems, I: Analysis technique and parameter matrices of acoustic elements," J. Sound Vib. **96**, 175–194 (1984).
[13] C. W. S. To, "The acoustic simulation and analysis of complicated reciprocating compressor piping systems, II: Program structure and applications," J. Sound Vib. **96**, 195–205 (1984).
[14] A. Craggs and D. C. Stredulinsky, "Analysis of acoustic wave transmission in a piping network," J. Acoust. Soc. Am. **88**, 542–547 (1990).
[15] J. F. Dowling and K. S. Peat, "An algorithm for the efficient acoustic analysis of silencers of any general geometry," Appl. Acoust. **65**, 211–227 (2004).
[16] T. Kar and M. L. Munjal, "Generalized analysis of a muffler with any number of interacting ducts," J. Sound Vib. **285**, 585–596 (2005).
[17] SYSNOISE Rev 5.6, Users manual, LMS International, 2003.

Reflection of the s_0 Lamb mode from a flat bottom circular hole

O. Diligent and M. J. S. Lowe[a)]
Department of Mechanical Engineering, Imperial College London, London SW7 2AZ, United Kingdom

(Received 31 March 2005; revised 25 August 2005; accepted 26 August 2005)

A study of the interaction of the s_0 Lamb wave with a flat bottom circular hole in a plate is presented. The majority of the study was performed using a three-dimensional finite element model, representing an area of the plate with a circular flat-bottom hole (33% or 50% of the plate thickness deep). In the first part of the work, the incident s_0 wave was specified to be a plane wave. The specular reflection was predicted and showed the importance of several factors: the interference phenomena between reflections from the leading and trailing edges of the hole and secondary reflections, and the decay in amplitude of the reflected wave. Some results of this case are also compared with analytical solutions based on modal superposition. In the second part of the work, the Lamb wave mode is excited by a small circular source. The specular reflection is predicted and compared with experimental results. An assessment is made of the significance of the path lengths, wavelengths, and defect sizes on the reflection characteristics. Good agreement is found between all techniques. [DOI: 10.1121/1.2074947]

PACS number(s): 43.20.Mv [YHB] Pages: 2869–2879

I. INTRODUCTION

The motivation of the work presented in this paper is the development of a guided wave inspection technqiue which will test large areas of thick walled structures such as pressure vessels or petro-chemical storage tanks for localized loss of thickness caused by corrosion.

The inspection of such large areas is usually performed by measuring the thickness of the plate on a point-by-point basis, usually using electromagnetic techniques. This approach can find corrosion on either side of the plate, provided that the spacing of the sampling positions is close enough not to miss localized defects, but it is very time consuming and thus expensive. Conventional ultrasonic equipment can also be used to measure the thickness at any location, by measuring the time of propagation of sound through the thickness of the plate, but this is no faster, and it also suffers from difficulties of coupling if the surface is rough, dirty, or painted.

An alternative method is to use ultrasonic Lamb waves which propagate along the plate and may be reflected by any defects. These waves can inspect all positions along a line, thus reducing the time of inspection. In recent years, there has been a large and increasing number of publications relating to the exploitation of Lamb waves for the inspection of flat plate[1–10] or cylindrical shell[11–17] structures. Much of the literature relates to the practical use of guided waves in order to inspect pipes. This is essentially a one-dimensional problem as the waves propagate unidirectionally, whereas the propagation of guided waves in plates is a two-dimensional problem. However the findings on pipes can be extended to the plate study.[18]

This approach of using Lamb waves has been implemented by Wilcox *et al.* in a prototype plate tester device.[18,19] This is a phased array transducer, employing electromagnetic acoustic transducers (EMATs).[20–22] It generates a controlled signal in a chosen direction in the structure and then receives the reflections coming from defects and other features. Conceptually, the operation of the array may be regarded as a number of pulse-echo tests, each looking in a different direction at the surrounding plate. The final output from the array is displayed to the operator as a two-dimensional map of the plate.

This paper presents the results of research on the behavior when the s_0 Lamb mode is incident at a part-depth circular hole in a plate, representing, to a first approximation, a corrosion patch. The aim is to improve understanding of the practical results obtained by the plate tester device and to estimate its sensitivity for target inspection tasks. This paper follows as a progression from an earlier study by the authors on the interaction of the s_0 Lamb mode with a through-thickness hole.[23] In the earlier work the structure was perfectly symmetric with respect to the mid-plane of the plate, and only symmetric waves were scattered when a symmetric wave was incident. In the present work the part-depth hole adds considerable complexity: mode conversions between symmetric and antisymmetric waves must now be included, and a three-dimensional analysis domain is required. This work thus develops understanding of a more realistic representation of target corrosion defects then previously. Clearly the regular part-depth hole is not strictly representative of a corrosion patch, but it is believed that the nature of the behavior found from this study will have generic application to the behavior in real cases; this has certainly been the true in the previous work on Non Destructive Evaluation (NDE) of pipelines, cited earlier, in which regular notches were used as an approximate representation of corrosion patches.

The study assesses the problem for two different kinds of sources: a plane wave field coming from a straight plane source, and a cylindrical wave field coming from a small circular source. The former is typical of the assumed field for many works on scattering, including the earlier paper.[23] The

[a)]Electronic mail: m.lowe@imperial.ac.uk

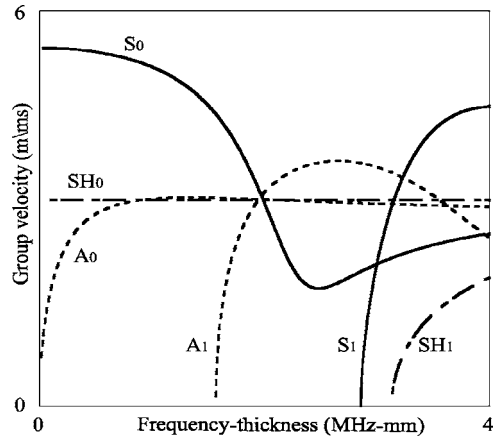

FIG. 1. Group velocity dispersion curves for Lamb waves in an aluminum plate.

latter represents the field most easily generated in a practical experimental setup. Both cases are studied using finite element (FE) predictions, and the results are compared with analytical and experimental data for the plane wave case and the circular source case, respectively. The analytical model is derived directly from the model which was used in the earlier paper[23] and was presented in full detail in a separate paper by co-author Grahn.[24] The experimental data are obtained from the plate tester device and from single EMAT transducers.

Mode characteristics and frequency range of interest

The study was performed using an aluminum plate, since this was easier to handle than a steel plate for the experimental work. However the principles of the findings will be relevant to any elastic material, and, since the properties of waves in aluminum are very similar to those in steel, the specific results presented here will also be applicable to steel plates.

Figure 1 shows the group velocity dispersion curves for an aluminum plate. The group velocity curves describe the speed at which a guided wave packet travels and are therefore of particular interest for long-range NDE applications. These dispersion curves were calculated using the predictive model DISPERSE.[25,26] The material properties of aluminum are presented in Table I. Since the frequency axis may be scaled with the plate thickness, the scale is plotted as frequency thickness for generality.

At low frequency, the s_0 Lamb mode has very little dispersion, which is ideal for long-range NDE. The effect of dispersion on a propagating wave packet is that the energy

TABLE I. Material properties for aluminum.

Density (ρ)	Poisson's ratio (ν)	Young modulus (E)
2.7 g/cm^3	0.33	70.75 GPa

spreads in time and space as it propagates. This means that close to the source the signal is similar to the input wave, but as the distance increases, the signal duration increases and the peak amplitude decreases. However, resolution requirements and an increase in the sensitivity to defects with increasing frequency normally force the frequency of choice upwards, thus a compromise between these characteristics must be found.[27,28] In previous papers,[23,28] a sensible upper limit was proposed to be around 1.6 MHz mm, in order to avoid the a_1 cut-off frequency. In fact the work which is presented here is limited to the very low end of the range, that is below about 1.2 MHz mm, where the s_0 mode is essentially nondispersive.

Figure 2 shows stress and displacement mode shapes of the s_0 mode through the plate at 750 kHz mm. The direction z is the normal to the surface of the plate, y is the normal to the plane of plane strain, and x is the direction of propagation of the wave; displacements are denoted u and stresses σ or τ. It can be seen here that the mode shapes of this mode at low frequency are extremely simple, being dominated by the in-plane components. This will enable a very simple finite element to be employed for the modeling. Furthermore, these shapes show that, at this frequency, this mode is equally sensitive to defects at any location through the thickness of the plate. Additional attractions are that it has low dispersion, and if the plate is immersed in a fluid, then the attenuation due to leakage is very small.

II. METHODOLOGY FOR FINITE ELEMENT PREDICTIONS

In the following two FE models are described: (1) a model with a plane wave excitation and (2) a model with a small circular source.

In both cases, the presence of the part-depth hole requires that the plate be modeled using a three-dimensional (3D) domain. The 3D FE modeling was performed using the program FINEL, which is developed at Imperial College.[29] 3D solid elements, with eight nodes, each node having three degrees of freedom (X,Y,Z displacements in Fig. 3) and linear shape functions were used in the models. The spatial discretization in both cases was chosen to be certain of satisfying the rule:

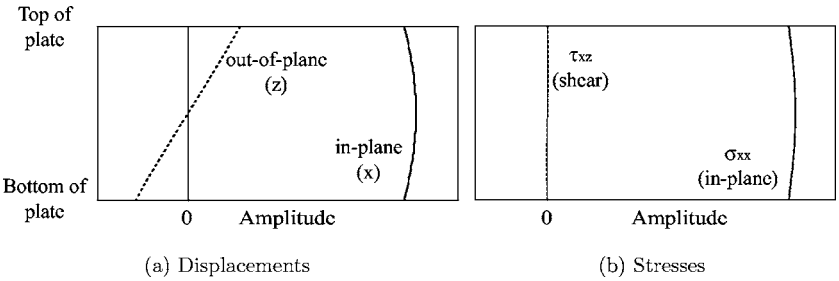

FIG. 2. Mode shapes of the s_0 mode in an aluminum plate at 750 kHz mm; (a) displacements and (b) stresses.

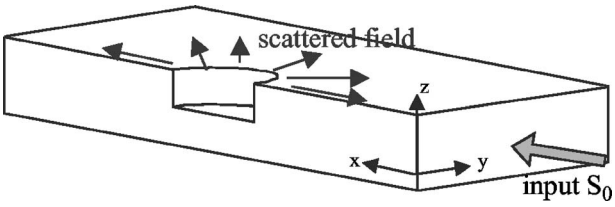

FIG. 3. Schematic illustration of finite element spatial discretization: outline of the mesh for the plane wave source study.

$$\lambda_{\min} \geqslant 8\Delta x, \tag{1}$$

where $\lambda_{\min}$ is the shortest wavelength, within the bandwidth of the signal, of any waves which may travel in the structure, and Δx is the biggest dimension across any single element in the model. This rule has been found to be effective for ensuring accurate modeling, see for example Ref. 16.

The program uses a diagonal mass matrix, allowing an efficient explicit time marching algorithm to be exploited. The explicit algorithm is stable provided that the time step is short enough to meet the stability criterion stated, for example, by Bathe.[30] To be safe, a time step δt of 80% of the strict limit was used, given by

$$\delta t \leqslant 0.8\frac{\Delta s}{c}, \tag{2}$$

where c is the velocity of the wave and Δs is the shortest side-length of any element.

A. Simulation with plane wave excitation

Three-dimensional finite element models are computationally very intensive, so just two or three elements were used through the thickness of the plate for the majority of the study.

To be sure that two or three elements through the thickness are enough to model the different waves properly, a test model with six elements through the thickness was used and compared with the less refined models. The same results were achieved (not shown here) and this confirmed the choice of having few elements through the thickness in order to reduce computational time. However caustion must be taken with any conclusions from this finding: the simple model works well only because the frequency is low enough that the mode shapes are very simple; at higher frequencies it would be necessary to use more elements through the thickness.

Plates of 5 and 7.5 mm thickness were modeled, each with a 2.5-mm-deep hole. Thus the depths of the holes were 50% and 33%, respectively, of the plate thickness. The two other dimensions (X and Y axes) of the element were 3 mm. Also, to reduce computation time, only half of the plate was modeled, applying symmetry in the X/Z plane through the center of the hole (see Fig. 3). The holes were modeled simply by removing elements from the mesh.

An s_0 wave input was excited by prescribing displacements in the X direction along the whole edge at the end of the plate, as shown in Fig. 3. The wave signal was five cycles of 100 kHz in a Hanning window. Its propagation along the plate was then simulated in the time domain. Following the interaction of the input s_0 with the hole, the s_0,a_0, and sh_0 components of the signal are reflected or scattered. Of these, only the specular reflection of the s_0 wave was studied since this is the principal mode of interest for practical testing. This was monitored at 33 points along a line on the plane of symmetry, at a distance of about 900 mm from the hole. At these points the symmetry ensures that only the s_0 and a_0 modes are present, while the distance allows the input and reflected signals to be separated in time. In order to monitor the s_0 mode separately from the a_0 mode, signals from the top and bottom surfaces of the plate were summed: since a_0 is antisymmetric, this addition cancels its contribution to the field, leaving only s_0.

A series of models was run covering the two different hole depths and a range of diameters of the hole.

B. Simulation with small circular source excitation

The simulation studies with the small circular source considered only the 50% depth hole, and so used just two elements through the thickness of the plate. The two other dimensions of the element (X and Y axes) were of 1.5 mm. Note that this mesh was then finer than in the preceding study, where elements were 3 mm in the X and Y directions.

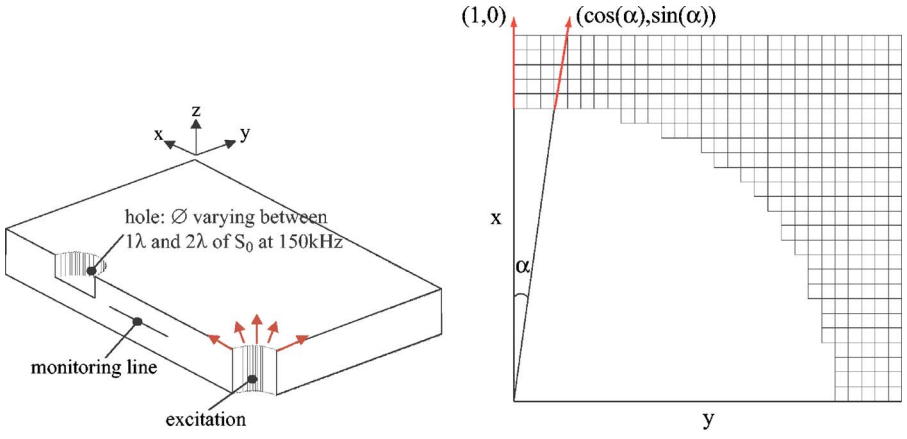

(a) Full mesh (b) Excitation

FIG. 4. (Color online) (a) Outline of the finite element model, showing the monitoring line and the small circular source; (b) details of the excitation.

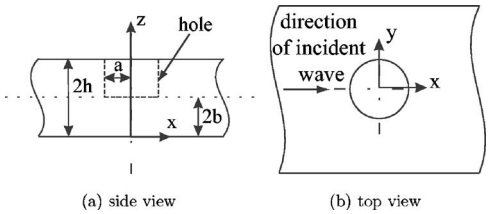

FIG. 5. Geometry of the analytical problem with: (a) side view and (b) top view.

It is not possible to excite motion at a single point in all the in-plane directions. Thus in order to model a localized source, excitation from the edge of a circular hole was introduced, as shown in Fig. 4. Excitation could have been applied to a circle of nodes, without creating a hole, but in this case there would have been an additional component of the signal caused by waves propagating back through the center of the circle. Therefore the use of a hole enables a cleaner signal to be simulated. The wave was excited by prescribing in-plane displacement radially to the edge of the source circle all through the thickness of the plate and at all circumferential positions. The wave signal was five cycles of 150 kHz in a Hanning window. In order to be sure that the wave field was cylindrical and uniform with angle, the incident wave was monitored at 420 mm after leaving the source and at three angles (0°, 45°, and 90°) around the excitation source. No discernible difference between the three monitored signals could be observed.

Following the interaction of the incident s_0 wave with the hole, s_0, a_0, and sh_0 are reflected and scattered. For comparison with the experimental data, the authors are particularly interested in the s_0 specular reflection, and the same routine to remove the a_0 mode as in the plane wave study was performed.

A series of models was run covering the 50% depth hole with a range of diameters of the hole. The reflected s_0 signal was monitored in the same way as was described for the plane wave source. The monitoring line (Fig. 4) consisted of 30 points with 12 mm spacing, starting at a position 150 mm away from the edge of the hole.

III. ANALYTICAL MODEL

The analytical model for this problem, developed by Grahn, is very similar to that which was summarized in the earlier paper on the through-thickness hole[23] and discussed elsewhere in detail by Grahn,[24] and only the differences with respect to the through-hole case will be summarized here.

A key difference is that the calculation of the scattered wave field now needs to include the antisymmetric Lamb modes which are expected to be generated by mode conversion when the s_0 Lamb mode is incident. Whereas the a_0 mode is not of specific interest in this study, it is essential that its existence is enabled in the analysis in order that the scattering is calculated correctly.

The second difference is that the analysis now requires a change in the boundary conditions, to represent the part-depth hole. The boundary conditions are of two kinds, continuity of displacements and stresses. For the displacements, continuity must hold at $r=a$ (see Fig. 5) in the region of material beneath the hole, thus

$$\mathbf{u}^{\text{inc}} + \mathbf{u}^{>} = \mathbf{u}^{<}, \quad 0 < z < 2b, \quad r = a, \tag{3}$$

where $\mathbf{u}^{>}$ is the scattered field in the outer region ($r<-a$ and $r>a$) and $\mathbf{u}^{<}$ is the displacement field in the inner region ($-a<r<a$). The boundary conditions for the stress are continuity at $r=a$ in the region below the hole and that the hole is stress free, thus

$$(\boldsymbol{\sigma}^{\text{inc}} + \boldsymbol{\sigma}^{>}) \,.\, \hat{\mathbf{e}}_{\mathbf{r}} = \begin{cases} \mathbf{0}, & 2b < z < 2h, \quad r = a \\ \boldsymbol{\sigma}^{<} \,.\, \hat{\mathbf{e}}_{\mathbf{r}}, & 0 < z < 2b, \quad r = a, \end{cases} \tag{4}$$

where $\hat{\mathbf{e}}_{\mathbf{r}}$ is the unit vector in the radial direction.

The model predicts the field at any chosen location in the plate, resulting from a plane wave incident at the hole. The field is given by the displacement at the mid-plane of the plate ($z=h$) at any chosen monitoring location.

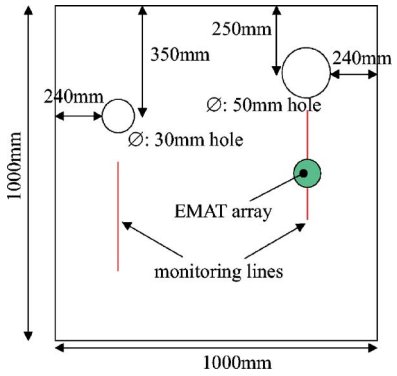

FIG. 6. (Color online) Experimental setup using the phased array transducer.

IV. METHODOLOGY OF THE EXPERIMENTAL STUDIES

It is much more difficult to create a uniform plane wave field in a plate than a cylindrical field from a localized source. Therefore the experimental study was limited to the case of the small circular source. The validation of the FE results is thus achieved by comparison with the analytical model for the incident plane wave and with the experimental measurements for the incident cylindrical wave.

Two experimental setups were used, one with a single EMAT transducer element, and the other with the plate tester EMAT array device.[18,19] The single EMAT was constructed in the laboratory to be similar to one element of the array

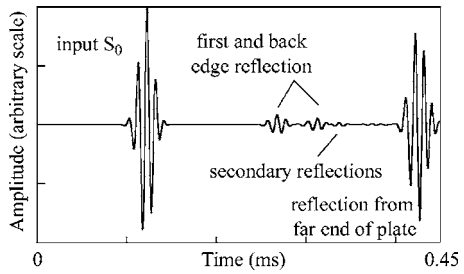

FIG. 7. Typical time record from finite element simulation; hole diameter 114 mm, 50% of the plate thickness deep and monitored at 390 mm from the near edge of the hole.

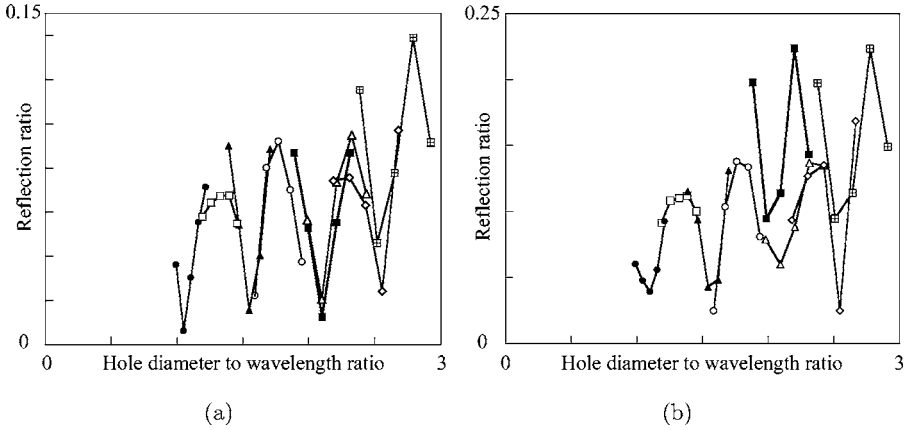

FIG. 8. Predicted variation of s_0 reflection ratio with hole diameter normalized to wavelength, when hole depth is (a) 33% and (b) 50% of plate thickness; results for hole diameters 60 mm (●), 72 mm (□), 84 mm (▲), 96 mm (○), 114 mm (■), 120 mm (△), 132 mm (◇), and 144 mm (⊞) for different frequencies. These results are for the plane wave source study.

device. Each EMAT transducer element is designed to generate an axially symmetric s_0 field, with relatively little of the unwanted a_0 mode and practically none of the unwanted sh_0 mode, and to operate in the frequency range of about 150–300 kHz.

A. Single EMAT transducer study

The major practical problem when working with time traces is to separate unwanted edge echoes from the wanted echoes from the hole. The simplest way to do this is to use a very large plate, but this becomes practically inconvenient to handle and to machine the holes. Furthermore, as the thickness increases, the amount of the unwanted a_0 mode which is generated increases, but if the plate is very thin then it can be difficult to machine the holes accurately. As a compromise between these factors, a 1 m square aluminum plate of thickness 3 mm was chosen. Three such plates were obtained, and a flat-bottomed hole was machined in each of them. The hole diameters were 30, 40, and 50 mm, and all had a depth of 50% of the plate thickness.

The positions of the transducers were chosen such as to optimize the separation of the different components of the received signal. Thus a different measurement distance was used for each hole. For the 50-mm-diam hole, the emitter was positioned at 125 mm from the leading edge of the hole and the receiver was positioned at a further 300 mm away, but on the same radial line. For the 40-mm-diam hole the emitter was placed at 130 mm from the leading edge of the hole and the receiver 300 mm further. The emitter for the experiment on the 30-mm-diam hole was placed at 140 mm from the edge of the hole and the receiver at 250 mm further. Thus in all cases the receiver was placed at a greater distance from the hole than the emitter, the opposite way round to the arrangement for the FE simulations. The implication is that in the experimental study the "incident signal," which travels directly from the transmitter to the receiver, travels in the direction away from the hole, whereas in the FE simulations it travels toward the hole. However, because of the reciprocity theorem, the measurement of the scattered signals remains the same for both cases.

The excitation wave signal was five cycles in a Hanning window. Measurements were made with five different values of the carrier frequency, corresponding to frequency-thickness products of 450, 570, 660, 810, and 1020 kHz mm.

B. Full array study

A 1 m by 1 m by 5 mm thick aluminum plate was used for the full array experiments. Two holes, 30 and 50 mm in diameter and 50% of the plate thickness deep, were machined in a single plate as shown in Fig. 6.

The plate tester array device[19] has a diameter of 200 mm and it is configured to act in "pulse-echo" mode, that is to say, it can both generate and detect the waves. It is tuned to maximize the generation and reception of the s_0 mode while avoiding as far as possible the unwanted a_0 mode. It is configured such that an emitted Lamb wave beam can be steered in any chosen direction with uniform omni-directional performance. The instrument is controlled by computer to per-

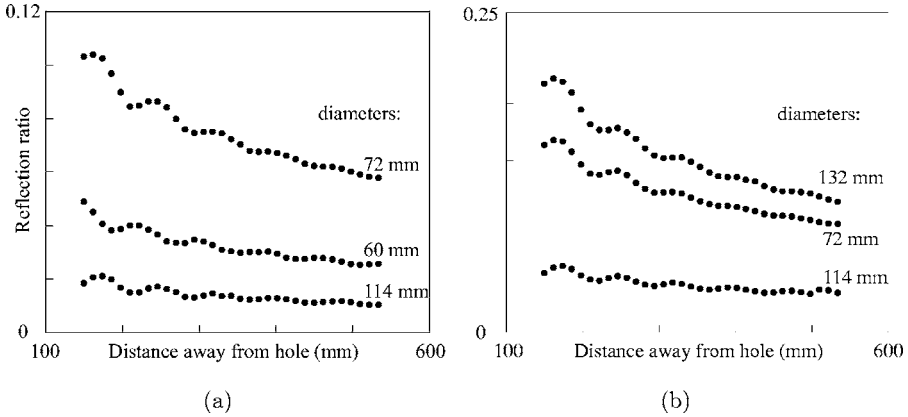

FIG. 9. FE predictions of the amplitude of the reflected wave as a function of distance of the receiver from the hole: (a) a 33% of the plate thickness deep hole and (b) 50% of the plate thickness deep hole. These results are for the plane wave source study, and the amplitude is of the Fourier transform at the center frequency (100 kHz) of the complete signal from the hole.

form a series of angular measurements, yielding as its output an area scan of the plate. The scan is displayed to the operator as a two-dimensional map of the plate, where a color scale indicates the amplitude of any reflected signal at each point in the plate. Because the array is of finite size, its directionality is not perfect, and it cannot resolve the angular position of a reflector precisely. Instead, a single reflector produces a characteristic arc shaped signal on the output map as will be seen later.

The array was used in a range of positions along two monitoring lines, as shown in Fig. 6. The s_0 mode which was excited was a five cycle 150 kHz tone burst modified by a Hanning window.

V. RESULTS AND DISCUSSION

A. FE results and comparison with results of analytical model, for plane wave source

Figure 7 shows a typical finite element time history signal monitored at 390 mm from the edge of a hole which is 114 mm in diameter and has a depth of 50% of the plate thickness. The incoming s_0 Lamb wave on its way to the hole is separated from the s_0 wave reflected by the hole.

The reflection ratio was calculated by dividing the spectrum of the full signal reflected from the hole by that of the input, in the frequency domain. The curve thus obtained displays amplitude (reflection radio) against frequency. To compare curves for different cases, it is helpful to recognize that for any given depth of the hole, the problem is defined by three spatial parameters: diameter of the hole, wavelength, and distance of the monitoring position from the hole (this was discussed in the earlier paper[23]). One approach to normalization, which is consistent with most scattering work, is to take the ratio of the size of the scatterer to the wavelength. Therefore the reflection ratio results here have been plotted against the axis "hole-diameter to wavelength ratio." The results for 33% and 50% deep holes are presented in Figs. 8(a) and 8(b), respectively. The wavelengths of the s_0 mode correspond to frequencies of 90, 95, 100, 105, and 110 kHz for each point extracted from each plate.

Maxima in amplitude are observed at hole diameters corresponding to odd multiples of quarter-wavelength, and minima at even multiples. The reason for these peaks and troughs of the function is understood to be the interference between two signals which reflect from the hole, one from the leading edge and the other from the trailing edge (having traveled across the flat bottom of the hole). The reflection from the trailing edge is, of course, retarded with respect to the signal from the leading edge, so their superposition in the resulting wave packet is either constructive or destructive, depending on the duration of the delay. Furthermore, the reflections at both edges can experience phase shifts too, due to the impedance change. For the leading edge, there is a decrease in impedance, whereas there is an increase for the trailing edge.[28] Consequently, the constructive interference occurs when the trailing edge reflection is half a cycle behind the leading edge reflection, that is when the hole is a quarter of a wavelength in diameter. Similarly, a hole diameter of half a wavelength delays the reflection by one cycle, thereby causing the destructive effect. However, these maxima and minima do not occur exactly at a quarter or half wavelength. This is because the reflection is not only composed of the s_0 mode, but is a combination of influence from both the a_0 and the s_0 modes in the flat bottom of the hole.

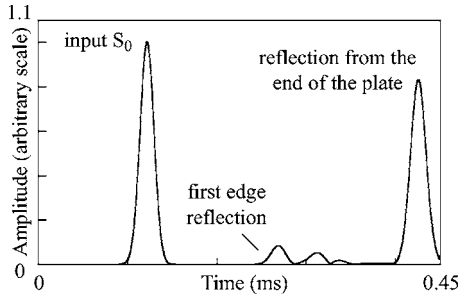

FIG. 10. Envelope of time signal shown in Fig. 7.

Interference patterns can also be seen when plotting the amplitude of the reflection from the hole at a given frequency against distance of the receiver from the hole. Figure 9 shows the magnitude of the Fourier transform at the center frequency (100 kHz) of the full signal reflected from the hole shown in Fig. 7 as a function of distance away from the hole. The waviness of these curves does not come from interference between the leading edge and trailing edge signals, because all the results are plotted for a single value of frequency. Instead the interference here is between the s_0 Lamb waves reflected by the hole (leading and trailing edges) and secondary reflections which come later than the trailing edge signal, which are evident in Fig. 7 (labeled "secondary reflections"). The secondary reflections are composed of cir-

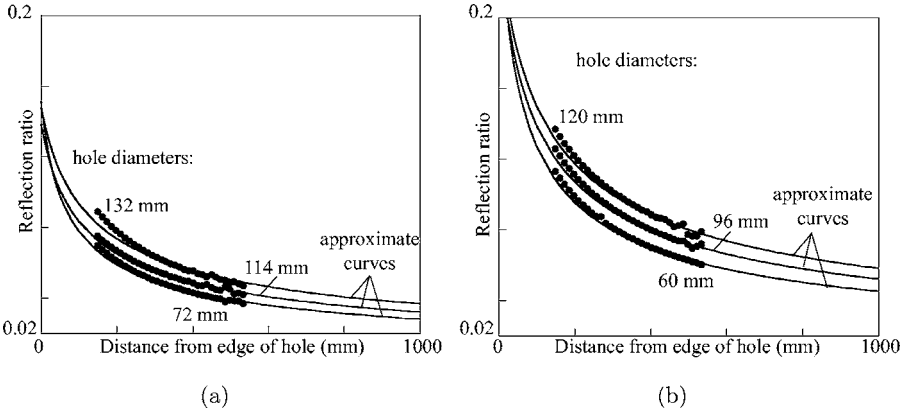

FIG. 11. Comparison between finite element results and approximate curves for (a) 33% and (b) 50% of the thickness deep hole. Note that the results are only shown for three diameters (for each hole depth) in order to clarify the graph.

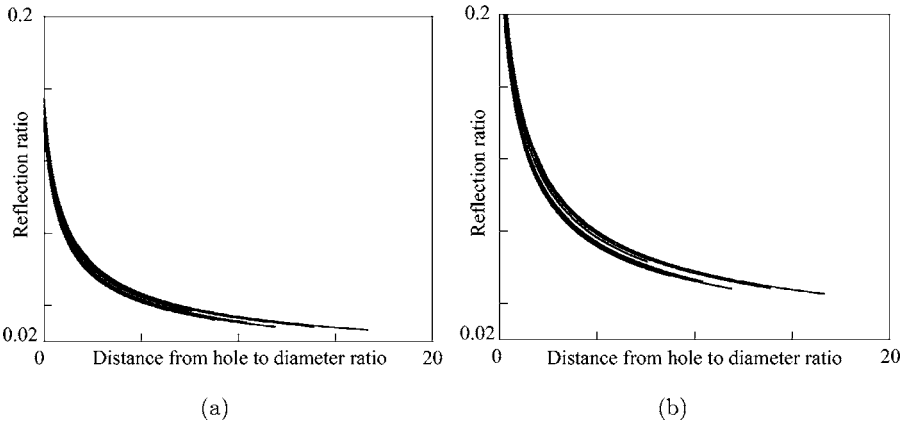

FIG. 12. Approximations calculated from the finite element results, plotted as ratio of distance away from hole to hole diameter for: (a) 33 % of the plate thickness deep hole and (b) 50 %. All data points for eight diameters between 60 and 144 mm are shown.

cumferential creeping waves and mode converted sh_0 waves. Since these are scattered from any location on the circumference of the hole (not just along the axis), their interference with the main reflections on the axis depends on the distance from the hole, being constructive at some distances and destructive at others.

The other important information to come from Fig. 9 is the overall decay of the signal with distance from the hole. In order to compare this with a simple spreading function, the interference of the secondary waves can be avoided by measuring only the s_0 part of the signal. This has been done using an envelope of the signals in the time domain (this is more reliable than attempting to separate the two parts of the signal for a frequency analysis). Figure 10 represents the Hilbert transform of the signal in Fig. 7, this being a convenient way of obtaining the envelope of the time domain signal. The reflection ratio for the leading edge s_0 signal was extracted from the figure by dividing the peak amplitude of the first-edge reflection by the peak amplitude of the input signal. This was repeated for a range of distances from the hole and for several hole diameters.

Results are presented in Fig. 11, for cases of three of the diameters. As expected, the curves are smooth, and the reflection ratio increases with diameter and decreases with distance from the hole, also the difference in amplitude between the 33% and 50% deep hole results can be observed.

If the hole is assumed to function as a cylindrical emitter of reflected waves, then the decay of the amplitude of a signal is inversely proportional to the square root of the propagated distance, as should reasonably be expected. Taking the center of the hole as the center of spreading of the scattered cylindrical wave field, and fitting this cylindrical decay function to the monitored points, it can be seen that this assumption works well: the curves labeled "approximate curves" are drawn using this decay function and they fit very well with the FE predictions. This agrees with the earlier findings for the through-thickness hole.

The "approximate curves" were calculated for the other sizes of holes and are plotted together in Fig. 12, employing a horizontal axis in which the distance of the monitoring point from the hole is normalized to the diameter of the hole. The curves are seen to overlie fairly closely for each of the hole depths, confirming that, as with the throught-thickness hole, this choice of normalization enables results of different hole sizes, distances, and wavelengths to be plotted together. This means that, at a given distance from the hole measured in multiple diameters, all reflection ratios at a given frequency are approximately the same, whatever the hole size.

The scattered field around the hole is illustrated well by a polar plot, and this also allows comparison between the FE results and the predictions of the analytical model. Figure 13 shows the predicted amplitudes of the scattered modes for a hole which is 100 mm in diameter, when the receiver is at a distance of 250 mm away from the edge of the hole. The

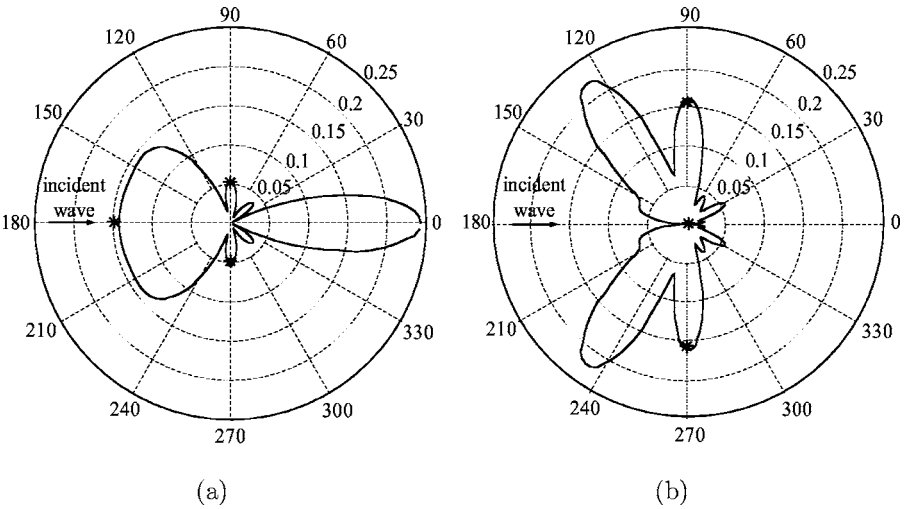

FIG. 13. Polar plots comparing analytical (solid line) and finite element (*) predictions for a hole 100 mm in diameter, when the wave is received at 250 mm away from the hole. The radial distance in the plots represents the amplitude of the received signal. The s_0 mode is incident at 100 kHz mm. Plots show scattering of (a) s_0 mode; (b) sh_0 mode.

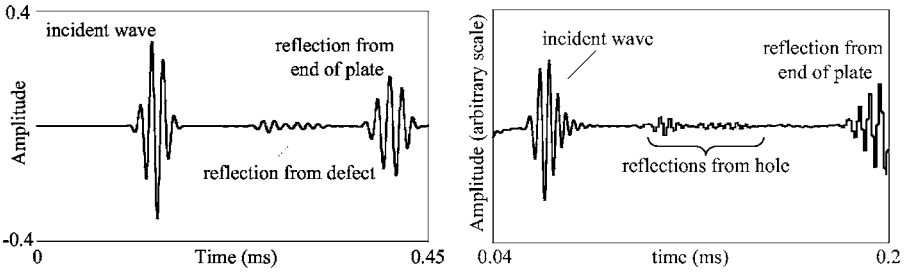

(a) Finite Element (b) Single EMAT

FIG. 14. Example for a 50-mm-diam hole of (a) a monitored FE time signal at 350 mm away from the edge of the hole; and (b) a monitored single EMAT time signal at 425 mm away from the edge of the hole. These time traces are for the small circular source.

circumferential axis of the plots corresponds directly to the angular location with respect to the center of the hole; the origin (180°) corresponds to the direction of the incident wave. The radial axis of the plots corresponds to the magnitude of the displacement.

The dominant displacement components are shown, that is the radial component, u_r [Fig. 13(a)], for the s_0 mode and the circumferential component, u_θ [Fig. 13(b)], for the sh_0 mode. Note that these results show that there is significant mode conversion of the incoming s_0 wave to laterally propagating sh_0 waves. The solid lines are calculated from the analytical model developed by Grahn[24] for a single frequency of 100 kHz. The amplitude plotted here is the whole Lamb mode reflected amplitude from the hole, that is to say the combination of the first edge and the back edge waves. Results from the finite element models are also included at some specific angles and those points are calculated by measuring in the frequency domain the reflected or scattered Lamb wave amplitude at 100 kHz.

Very good agreement is found between the two techniques. The reflected s_0 wave is scattered mainly forwards and backwards (at 0° and 180°), while the reflected sh_0 is scattered mainly in the transverse direction. Note that the incoming s_0 wave is not plotted.

B. FE results and comparison with results from EMATs, for small circular source

1. Comparison of FE predictions with measurements made with a single EMAT

Finite element predictions of the received signals at a series of points along the axis were made in the same way as for the plane wave source. Similarly, measurements were made using a single EMAT transmitter and a single EMAT receiver, as explained earlier. All of the holes had a depth of 50% of the plate thickness.

Figure 14 illustrates the kind of signals which were seen, and the quality of the measured signals. Figure 14(a) shows a typical FE predicted time signal at a location on this monitoring line and 350 mm from the hole. This shows the incident s_0 mode on its way to the hole, which was in this case 50 mm in diameter, and the s_0 reflection from the hole. The secondary reflections can also be seen. Figure 14(b) shows a measured time signal at a location 425 mm from the hole. The center frequency of the five cycle tone burst is 810 kHz. This shows the direct s_0 mode signal from the transmitter to the receiver (the incident signal"), followed by the s_0 reflections from the hole, which was in this case 50 mm in diameter.

The processing of the results was performed using the time domain envelope method which had the benefit of smoothing the undulations out of the signal, and so clarifying the comparisons for different distances. The reflection ratio was extracted from the Hilbert envelopes by dividing the peak amplitude of the s_0 leading edge reflection by the peak amplitude of the input s_0 wave.

Figure 15 compares the experimental measurements with the FE predictions for a range of distances of the receiver from the hole. Also shown in the figure is the cylindrical decay function, as used earlier with the plane wave study, and fitted here to a single FE data value. This result confirms the consistency of the measurements with the EMAT transducers and the expected cylindrical decay of the reflection function with distance from the hole.

Results for the full received signal, including the effects of interference of the components of the signal, are shown in Fig. 16. In this case the reflection ratio was calculated by dividing the spectrum of the full signal reflected from the hole by that of the input in the frequency domain, for both the FE and experimental data. The curve thus obtained displays amplitude (reflection ratio) against the ratio of the diameter of the hole to the wavelength. The points on the graph correspond to ten frequency-thickness measurements from the finite element results and five frequency measurements from the experimental data within the frequency-thickness

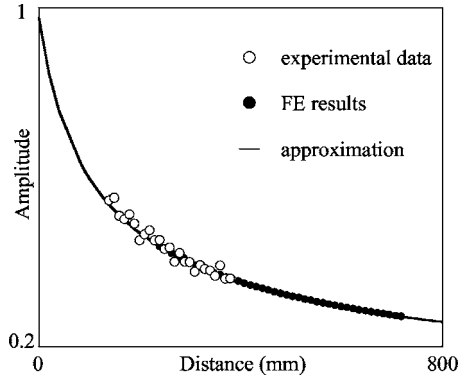

FIG. 15. Confirmation between finite element predictions (●) and experimental data using a single EMAT (◯) of the incident s_0 mode plotted as a function of distance from the source. Values are taken from the Hilbert envelope calculation. The line shows the cylindrical decay function which has been fitted to just one point.

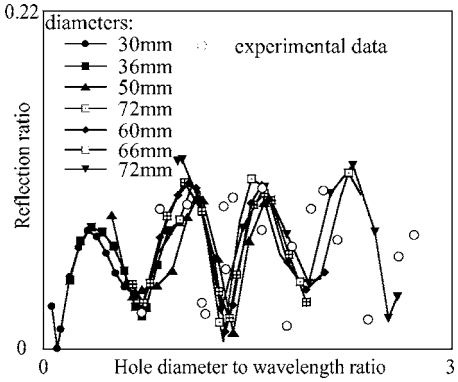

FIG. 16. Comparison between predicted and experimental variation of s_0 reflection ratio with hole diameter normalized to wavelength, when hole depth is 50% of plate thickness; FE results for hole diameters 30 mm (●), 36 mm (■), 50 mm (▲), 57 mm (⊞), 60 mm (♦), 66 mm (□), and 72 mm (▼) and experimental data for 30, 40, and 50 mm (◯).

bandwidth 500–1000 kHz mm. Some normalization of the experimental results to account for beam spreading has also been applied. The experimental incident wave has traveled only 125 mm on its way to the hole, compared with the 900 mm for the FE calculations; and the receiver is placed at 425 mm away from the hole in both cases. In order to compensate for the difference in amplitude between the two incident waves when they reach the hole, the beam spreading, or decay in amplitude, has been taken from Fig. 15 and normalized to that of the FE predictions. Thus the experimental signal has the amplitude it would be expected to have if it traveled the distance of the FE model.

In general good agreement is found between the predictions and the measurements, although the latter show some scatter. As in the plane wave case, maxima in amplitude are observed at diameters corresponding to odd multiples of quarter-wavelength, and minima at even multiples, and this is now confirmed experimentally.

Unlike the incident plane wave case, the distance between the small source and the hole affects the results, and, not surprisingly, the results can be normalized to take this additional distance parameter into account. The signal from the small source decays according to the cylindrical spread function in the same way as was seen for the signal traveling from the hole to the receiver, and thus a cylindrical decay

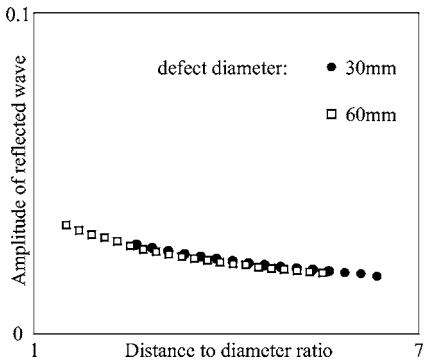

FIG. 17. FE predicted decay function when the distance from the hole is normalized to the diameter of the hole and the distance between the edge of the source and the hole is taken into account. Results shown for a 30-mm-diam hole (●) and a 60-mm-diam hole (□). Source has unit amplitude.

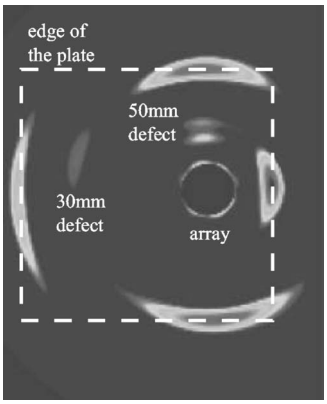

FIG. 18. Map of the plate obtained with the plate tester device (Ref. 19). Scale: 27 dB (white 0 dB, black −27 dB).

function can be used to describe the whole propagation path. To normalize the source signal, its amplitude can be scaled according to its distance from the hole. Alternatively, a convenient approach in this study is just to scale the diameter of the circle which defines the small source. A pair of FE models was used to illustrate and confirm this. The first model had a source diameter of 120 mm and the hole was placed at eight source diameters away (960 mm) from the edge of the source circle. A second model had a 60-mm-diam source and again the distance between the edge of the source and the hole was eight source diameters (480 mm). The results for two different hole diameters are shown in Fig. 17, in which the horizontal axis has been normalized in the usual way to account for the hole-receiver distance. It can be seen that the two reflection amplitude curves overlay.

2. Comparison of FE predictions with measurements made with the plate tester device

Figure 18 shows an example of a map obtained by the plate tester system described earlier and in detail by Wilcox.[19] The edges of the plate can be clearly seen as well as the two holes. Only one wave reflected by the 30-mm-diam hole is detected, as the near edge and the far edge reflections overlay in time. On the other hand, these two reflections can be seen separately for the 50-mm-diam hole.

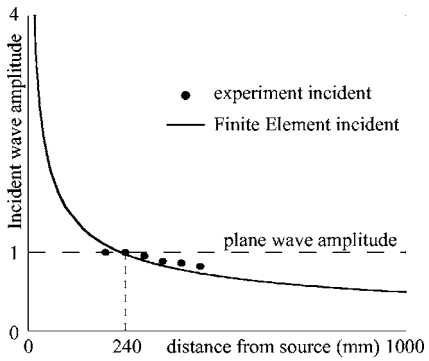

FIG. 19. Comparison between experimental and FE results of the decay of the amplitude of the incident wave. According to normalization in the array instrument, the incident wave has unit amplitude at 240 mm from the center of the source.

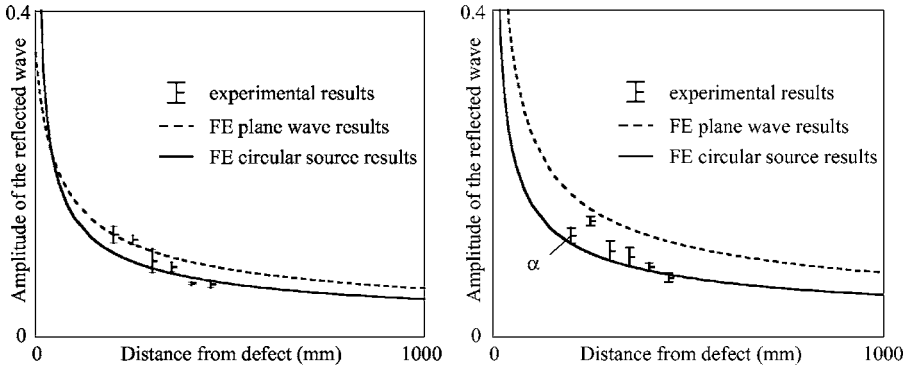

FIG. 20. Comparison between experimental and FE results of the decay of the amplitude of the reflected wave for (a) a 30-mm-diam hole and (b) a 50-mm-diam hole. Incident wave has unit amplitude at 240 mm from center of source.

In order to compare FE predictions with these experiments, the FE incident wave needs to be scaled to the amplitude of that from the experiments. In the FE model, the incident wave has unit amplitude at the edge of the source circle. In the experiment, the normalization performed by the instrument is such that the incident wave has unit amplitude at its first reflection, this being the near edge of the plate (240 mm, see Fig. 6).

It is interesting to see the nature of the decay, or beam spreading, of the outgoing wave from the experimental transducer before it gets to the hole. This is needed in order to check if the approximation of cylindrical decay from a point source is correct for this instrument in this range of propagation distance. Figure 19 shows a comparison between the FE predictions and the experimental results for the outgoing wave. The dashed line shows the constant amplitude which would be expected for a plane wave source (unity), the solid line is the amplitude predicted by FE for a point source, and the closed circles are the experimental data. In general, good agreement is found between FE and experiments. It seems, not surprisingly, that the decay of the incident wave follows the predicted point source decay at distances greater than the reference distance (240 mm).

Figures 20(a) and 20(b) show a comparison between the experimental data (symbols) and the FE results (dashed line: plane wave; solid line: circular source excitation) for the wave reflected from a 30- and a 50-mm-diam hole, respectively. The symbols representing the experimental data are calculated as follows: the middle point is the rms of five values; the upper and lower points are the rms plus or minus one standard deviation, respectively. Generally good agreement is found between the predictions and the experiments, although there is one anomalous experimental point marked α in Fig. 20(b).

VI. CONCLUSION

Following work presented earlier on related two-dimensional problems,[23] three-dimensional finite element studies have been performed in order to investigate the nature of the specular reflection of the simple extensional mode s_0 from a circular part-depth hole in a plate.

This case differs significantly from the previous work of a through-hole in that the asymmetry of the defect with respect to the mid-plane of the plate generates three-dimensional phenomena in the response, including mode conversion from the s_0 mode to the a_0 mode, and cross-diameter propagation of modes across the remaining material at the bottom of the hole. Such effects have previously been studied for long notches using two-dimensional plane strain models, but in those cases the models could not consider the finite size of the scatterer in plane of the plate, or the effects of the circular geometry. This study presents for the first time a full three-dimensional analysis.

Studies have been carried out when the s_0 wave signal was created by a plane wave or by a small circular source. The following has been found.

(a) When the reflection ratio of the full reflection from the hole is plotted as a function of hole diameter to wavelength ratio, maxima in amplitude are observed at diameters corresponding to an odd multiple of quarter-wavelengths, and minima at even multiples. This comes from the constructive or destructive interference between the separate reflections from the front and the back edge of the hole.
(b) As expected the signal decays as a function of one over the square root of distance from the center of the hole.
(c) The reflection bahavior for a circular source can be normalized to account for the source diameter, the hole diameter, and the distance between them.
(d) Secondary waves, consisting of creeping waves and sh_0 waves, also interfere with the reflected signal, and this is seen as undulations in the reflection ratio plotted as a function of receiver distance from the hole.
(e) The results of the plane wave finite element model agree well with the results of the analytical model for the specular reflection of the s_0 Lamb mode and the mode conversion to the sh_0 mode.
(f) The results of the small source finite element model agree well with experimental results obtained using a single EMAT and the prototype plate tester instrument.

ACKNOWLEDGMENT

The authors are grateful to Dr. T. Grahn for the use of his analytical model and for helpful discussions.

[1]T. Mansfield, "Lamb wave inspection of aluminium sheet," Mater. Eval. **33**, 96–100 (1975).
[2]D. Alleyne and P. Cawley, "The interaction of Lamb waves with defects,"

IEEE Trans. Ultrason. Ferroelectr. Freq. Control **39**, 381–397 (1992).
[3]D. Alleyne and P. Cawley, "Optimization of Lamb wave inspection techniques," NDT & E Int. **25**, 11–22 (1992).
[4]Y. Cho and J. Rose, "A boundary element solution for a mode conversion study on the edge reflection of Lamb waves," J. Acoust. Soc. Am. **99**, 2097–2109 (1996).
[5]Y. Cho, D. Hongerholt, and J. Rose, "Lamb wave scattering analysis for reflector characterization," IEEE Trans. Ultrason. Ferroelectr. Freq. Control **44**, 44–52 (1997).
[6]T. Ghosh, T. Kundu, and P. Karpur, "Efficient use of Lamb modes for detecting defects in large plates," Ultrasonics **36**, 791–801 (1998).
[7]J. Paffenholz, W. Fox, X. Gu, G. Jewett, S. Datta, and H. Spetzler, "Experimental and theoretical study of Rayleigh-Lamb waves in a plate containing a surface-breaking crack," Res. Nondestruct. Eval. **1**, 197–217 (1990).
[8]J. McKeon and M. Hinders, "Lamb wave scattering from a through hole," J. Sound Vib. **224**, 843–862 (1999).
[9]A. Norris and C. Vemula, "Scattering of flexural waves on thin plates," J. Sound Vib. **181**, 115–125 (1995).
[10]Z. Chang and A. Mal, "Scattering of Lamb waves from a rivet hole with edge cracks," Mech. Mater. **31**, 197–204 (1999).
[11]W. Mohr and P. Holler, "On inspection of thin-walled tubes for transverse and longitudinal flaws by guided ultrasonic waves," IEEE Trans. Sonics Ultrason. **SU-23**, 369–378 (1976).
[12]W. Bottger, H. Schneider, and W. Weingarten, "Prototype EMAT system for tube inspection with guided ultrasonic waves," Nucl. Eng. Des. **102**, 356–376 (1987).
[13]J. Rose, J. Ditri, A. Pilarski, K. Rajana, and F. Carr, "A guided wave inspection technique for nuclear steam generator tubing," NDT & E Int. **27**, 307–310 (1994).
[14]J. Ditri, "Utilization of guided elastic waves for the characterization of circumferential cracks in hollow cylinders," J. Acoust. Soc. Am. **96**, 3769–3775 (1994).
[15]D. Alleyne and P. Cawley, "Long range propagation of Lamb waves in chemical plant pipework," Mater. Eval. **55**, 504–508 (1997).
[16]D. Alleyne, M. Lowe, and P. Cawley, "The reflection of guided waves from circumferential notches in pipes," J. Appl. Mech. **65**, 635–641 (1998).
[17]M. Lowe, D. Alleyne, and P. Cawley, "The mode conversion of a guided wave by a part-circumferential notch in a pipe," J. Appl. Mech. **65**, 649–656 (1998).
[18]P. Wilcox, M. Lowe, and P. Cawley, "Lamb and Shear wave transducer arrays for the inspection of large areas of thick plates," in *Review of Progress in Quantitative NDE*, edited by D. Thompson and D. Chimenti (Plenum, New York, 2000), Vol. 19, pp. 1049–1056.
[19]P. Wilcox, M. Lowe, and P. Cawley, "An EMAT array for the rapid inspection of large structures using guided waves," in *Review of Progress in Quantitative NDE*, edited by D. Thompson and D. Chimenti (American Institute of Physics, New York, 2003), Vol. 22, 761–768.
[20]B. Maxfield, A. Kuramoto, and J. Hulbert, "Evaluating EMAT designs for selected application," Mater. Eval. **45**, 1166–1183 (1987).
[21]G. Alers and L. Burns, "EMAT designs for special applications," Mater. Eval. **45**, 1184–1189 (1987).
[22]R. Thompson, "Physical principles of measurements with EMAT transducers," in *Physical Acoustics* (Academic, New York, 1990), Vol. XIX, pp. 157–200.
[23]O. Diligent, T. Grahn, A. Boström, P. Cawley, and M. Lowe, "The low-frequency reflection and scattering of the S_0 Lamb mode from a circular through-thickness hole in a plate: Finite element, analytical and experimental studies," J. Acoust. Soc. Am. **112**, 2589–2601 (2002).
[24]T. Grahn, "Lamb wave scattering from a circular partly through-thickness hole in a plate," Wave Motion **37**, 63–80 (2003).
[25]M. Lowe, "Matrix techniques for modeling ultrasonic waves in mutilayered media," IEEE Trans. Ultrason. Ferroelectr. Freq. Control **42**, 525–542 (1995).
[26]B. Pavlakovic, M. Lowe, D. Alleyne, and P. Cawley, "DISPERSE: A general purpose program for creating dispersion curves," in *Review of Progress in Quantitative NDE*, edited by D. Thompson and D. Chimenti (Plenum, New York, 1997), Vol. 16, pp. 185–192.
[27]P. Wilcox, M. Lowe, and P. Cawley, "Long range Lamb wave inspection: The effect of dispersion and modal selectivity," in *Review of Progress in Quantitative NDE*, edited by D. Thompson and D. Chimenti (Plenum, New York, 1999), Vol. 18, pp. 151–158.
[28]M. Lowe and O. Diligent, "The low frequency reflection characteristics of the fundamental symmetric Lamb wave S_0 from a rectangular notch in a plate," J. Acoust. Soc. Am. **111**, 64–74 (2002).
[29]D. Hitchings, "FE77 user manual," Tech. Rep., Imperial College of Science, Technology and Medicine, London, 1994.
[30]K.-J. Bathe, *Finite Element Procedures in Engineering Analysis* (Prentice-Hall, Englewood Cliffs, NJ, 1982).

Two-dimensional axisymmetric numerical simulation of supercritical phase conjugation of ultrasound in active solid media

Olivier Bou Matar,[a] Vladimir Preobrazhensky,[b] and Philippe Pernod
Institut d'Electronique, de Micro-électronique et de Nanotechnologie (IEMN-DOAE UMR CNRS 8520), Ecole Centrale de Lille, BP 48, 59651 Villeneuve d'ascq Cedex, France

(Received 24 September 2004; revised 28 April 2005; accepted 17 August 2005)

In the present study a two-dimensional axisymmetric numerical model is developed for supercritical parametric phase conjugation of ultrasound in a solid active element of cylindrical shape and finite length. The pseudospectral time domain algorithm (PSTD) is used owing to its efficiency to model large-scale problems. PSTD solves elastic wave equation in time-dependent heterogeneous isotropic and axisymmetric anisotropic solids using FFTs for high order approximation of the spatial differential operator on staggered grid, and a fourth-order Adams–Bashforth time integrator. In order to truncate the computational domain absorbing boundary conditions are introduced with complex frequency shifted perfectly matched layers. This procedure is highly effective at absorbing signals of long time-signature. The free surface of the active ceramic rod is introduced through the method of images. A systematic study of the influence of lateral limitations of the active medium on parametric wave phase conjugation of sound is made. It is shown that retro-focusing of the incident pulse takes place even in the case of mode conversions inside the active zone. Nevertheless, amplitude and form of the obtained conjugate pulse depend on the simulated configuration. Numerical simulation correctly describes the parametric amplification and retro-focusing of ultrasound observed in experiments. © *2005 Acoustical Society of America.*
[DOI: 10.1121/1.2062467]

PACS number(s): 43.25.Dc [MFH] Pages: 2880–2890

I. INTRODUCTION

Parametric wave phase conjugation (WPC) of ultrasound using supercritical electromagnetic pumping in solids is known as one of the basic principles of wave front reversal in modern physical acoustics.[1,2] As was demonstrated experimentally[2] this principle provides compensation of phase distortions and automatic retro-focusing of ultrasound beams in inhomogeneous media both in quasilinear and nonlinear modes of wave propagation. The potential of the parametric method of WPC is of interest for various applications in nondestructive testing, medical imaging, and power ultrasonics. The experiments show a multitude of factors influence on power of emission and quality of acoustic field reproduction by parametric conjugation device (conjugator). Among them one can mention the geometry of active element of conjugator (see Fig. 15 in Ref. 1). Another factor follows from the principle of parametric WPC based on modulation of elasticity moduli of active material by electromagnetic field. As usual different acoustic modes of real active materials have different modulation efficiency, therefore multiple mode conversions influence essentially the dynamics of parametric WPC. While some general aspects of supercritical WPC problem in acoustics were studied successfully by multiscale analytical methods,[3–7] simulation of WPC processes in real conjugators requires elaboration of numerical approaches. Recently, numerical studies of WPC supercritical dynamics were made for the linear[8] and nonlinear[9] pumping modes, in a one-dimensional configuration. To study the influence of geometrical factors, reverberations and multiple mode conversions inside the active element of the conjugator on the parametric WPC process, simulations have to be extended in two (2D) or three dimensions.

In the present paper the pseudospectral time domain algorithm (PSTD)[10] is developed for 2D axisymmetric geometry of solid state phase conjugator. The difference of modulation efficiency for longitudinal and transversal waves is taken into account. The acoustic field within cylindrical active element is calculated for various stages of supercritical parametric WPC. Influences of lateral and axial size limitations on retro-focusing quality, output intensity, and pulse shape of phase conjugate wave are studied.

II. THE ELASTIC WAVE SOLVER

In the present study, a 2D axisymmetric numerical model is developed for elastic wave propagation in a cylindrical solid with an active zone of finite length L. Reversing and amplification of an incident elastic wave of frequency ω are produced by modulating the elastic constants (or similarly the sound velocities) in the active zone of the solid at the frequency $\Omega=2\omega$. In our experimental configuration this

[a]On leave from GIP Ultrasons/LUSSI, Université de Tours, 2 bis Bd. Tonnellé, 37032 Tours, France; electronic mail: olivier.boumatar@iemn.univ-lille1.fr
[b]Also with Wave Research Center of General Physics Institute (RAS), 38 Vavilova Str., 119991 Moscow, Russia.

sound velocities modulation is created in a limited zone of a magnetostrictive ceramic by pumping it with an alternating magnetic field.[1]

A. Governing equations

Consider the propagation of elastic waves in an heterogeneous solid medium where the elastic coefficients change with time according to an electric or magnetic external field. Newton's second law is written:

$$\frac{\partial v_i}{\partial t} = \frac{1}{\rho_0}\frac{\partial \tau_{ij}}{\partial x_j}, \tag{1}$$

where x_j are the components of the position vector, ρ_0 is the density, v_i are the components of the particle velocity vector, τ_{ij} are the components of the stress tensor, and t is time. The constitutive relation for a linear elastic solid is given by Hooke's law:

$$\tau_{ij} = C_{ijkl}(t)\varepsilon_{kl}, \tag{2}$$

where the linear approximation of the strain tensor ε is

$$\varepsilon_{kl} = \frac{1}{2}\left(\frac{\partial u_k}{\partial x_l} + \frac{\partial u_l}{\partial x_k}\right). \tag{3}$$

$C_{ijkl}(t)$ are the time-dependent elastic coefficients, and u_k are the components of the displacement vector given by

$$\frac{\partial u_i}{\partial t} = v_i. \tag{4}$$

In our case, we are interested in the axisymmetric wave propagation problem in a transversely isotropic solid. It is thus convenient to take cylindrical coordinates (r,θ,z). In such a medium the elastic coefficients tensor in Voigt notations $(xx\rightarrow 1, yy\rightarrow 2, zz\rightarrow 3, yz, zy\rightarrow 4, xz, zx\rightarrow 5,$ and $xy, yx\rightarrow 6$ in the case of axisymmetry about the z axis) has the general form[11]

$$C = \begin{bmatrix} C_{11} & C_{12} & C_{13} & 0 & 0 & 0 \\ C_{12} & C_{11} & C_{13} & 0 & 0 & 0 \\ C_{13} & C_{13} & C_{33} & 0 & 0 & 0 \\ 0 & 0 & 0 & C_{44} & 0 & 0 \\ 0 & 0 & 0 & 0 & C_{44} & 0 \\ 0 & 0 & 0 & 0 & 0 & C_{66} \end{bmatrix}, \tag{5}$$

where $C_{12}=C_{11}-2C_{66}$, and the following constraints $C_{11} \geqslant C_{66} \geqslant 0, C_{33} \geqslant 0, C_{44} \geqslant 0,$ and $C_{13}^2 \leqslant C_{33}(C_{11}-C_{66})$. Because of the symmetry properties, the equations of motion and the constitutive equations are given as follows:

$$\frac{\partial v_r}{\partial t} = \frac{1}{\rho_0}\left(\frac{\partial \tau_{rr}}{\partial r} + \frac{\partial \tau_{rz}}{\partial z} + \frac{\tau_{rr}-\tau_{\theta\theta}}{r}\right), \tag{6a}$$

$$\frac{\partial v_z}{\partial t} = \frac{1}{\rho_0}\left(\frac{\partial \tau_{rz}}{\partial r} + \frac{\partial \tau_{zz}}{\partial z} + \frac{\tau_{rz}}{r}\right), \tag{6b}$$

$$\frac{\partial u_r}{\partial t} = v_r, \tag{6c}$$

$$\frac{\partial u_z}{\partial t} = v_z, \tag{6d}$$

$$\tau_{rr} = C_{11}\frac{\partial u_r}{\partial r} + C_{13}\frac{\partial u_z}{\partial z} + C_{12}\frac{u_r}{r}, \tag{6e}$$

$$\tau_{rz} = C_{44}\left(\frac{\partial u_z}{\partial r} + \frac{\partial u_r}{\partial z}\right), \tag{6f}$$

$$\tau_{zz} = C_{13}\left(\frac{\partial u_r}{\partial r} + \frac{u_r}{r}\right) + C_{33}\frac{\partial u_z}{\partial z}, \tag{6g}$$

$$\tau_{\theta\theta} = C_{12}\frac{\partial u_r}{\partial r} + C_{13}\frac{\partial u_z}{\partial z} + C_{11}\frac{u_r}{r}. \tag{6h}$$

In the active zone of the solid, the elastic coefficients modulations ΔC_{IJ} induced by the magnetic pumping are introduced by

$$C_{IJ} = C_{IJ}^0 + \Delta C_{IJ}, \tag{7}$$

where

$$\Delta C_{IJ} = C_{IJ}^0 m_{C_{IJ}} \cos(\Omega t + \psi_{C_{IJ}}). \tag{8}$$

Here, $C_{IJ}^0 (I,J=1,\ldots,6)$ represent elastic coefficients in the magnetostrictive ceramic when a static magnetic field has been applied, and ΔC_{IJ} correspond to small variations $(\Delta C_{IJ} \ll 1)$ induced by the dynamic magnetic pumping at the frequency Ω. For an isotropic ceramic, these elastic coefficient variations are linked to modulation depths m_l and m_t of the longitudinal c_l and transverse c_t sound velocities, introduced by Ben Khelil *et al.*[8] as

$$c_l^2(t) \approx c_{l0}^2(1 + m_l \cos(\Omega t + \psi_l)), \tag{9}$$

$$c_t^2(t) \approx c_{t0}^2(1 + m_t \cos(\Omega t + \psi_t)), \tag{10}$$

where the longitudinal and transverse wave speeds in the absence of pumping are, respectively, given by $c_{l0} = \sqrt{C_{11}^0/\rho_0}$ and $c_{t0} = \sqrt{C_{44}^0/\rho_0}$. In this case, the following relations are obtained: $m_{C_{11}} = m_{C_{33}} = m_l$, $m_{C_{44}} = m_t$, $m_{C_{12}} = m_{C_{13}} = (C_{11}^0/C_{12}^0)m_l - 2(C_{44}^0/C_{12}^0)m_t$.

B. The pseudospectral method

The solver developed uses a pseudospectral method to calculate the spatial derivatives involved in Eqs. (6a)–(6h). To reduce numerical artifacts in pseudospectral simulations for a heterogeneous medium, a staggered grid implementation is used.[10] For example, the derivative $\partial \tau_{zz}/\partial z$ is computed by taking the Fourier transform of $\tau_{zz}(z)$ over z, multiplying each point in the resulting spectrum by $jk_z e^{jk_z \Delta z/2}$, and performing the inverse Fourier transform:

$$\frac{\partial \tau_{zz}(z)}{\partial z} = \mathrm{FT}^{-1}[jk_z e^{jk_z \Delta z/2} \mathrm{FT}[\tau_{zz}(z)]], \tag{11}$$

where FT is a forward Fourier transform, FT^{-1} is an inverse Fourier transform, and k_z is the wave number in the z direction. Δz is the spatial step of the numerical grid in the z direction.

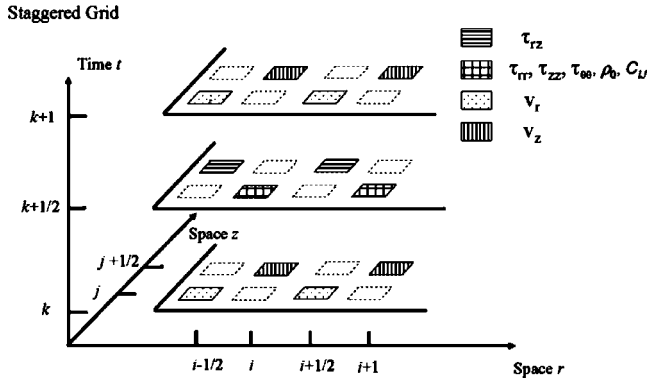

FIG. 1. Spatial and temporal staggered grid geometry showing the placement of the field variables and the material parameters.

The spatial derivatives in the radial direction have to be calculated differently to take into account the cylindrical geometry of our problem. Indeed, Eqs. (6a)–(6h) includes terms divided by r, introducing a singularity on the symmetry axis. In fact, both $v_r(r=0)$ and $T_{rz}(r=0)$ vanish. Therefore, using a staggered grid with v_r and T_{rz} located on the axis instead of $v_z, T_{rr}, T_{\theta\theta}$, and T_{zz}, no field component has to be calculated. The stress and particle velocity components have the following symmetric and antisymmetric properties with r:

$$v_r(-r,z) = -v_r(r,z), \tag{12a}$$

$$v_z(-r,z) = v_z(r,z), \tag{12b}$$

$$\tau_{rr}(-r,z) = \tau_{rr}(r,z), \tag{12c}$$

$$\tau_{\theta\theta}(-r,z) = \tau_{\theta\theta}(r,z), \tag{12d}$$

$$\tau_{zz}(-r,z) = \tau_{zz}(r,z), \tag{12e}$$

$$\tau_{rz}(-r,z) = -\tau_{rz}(r,z). \tag{12f}$$

Let $f(r,\cdot)$ represent a field variable defined along the radial direction in cylindrical coordinates. The r differentiation can be performed by the following scheme including as described above a staggered Fourier differentiation process. First, $f(n\Delta r,\cdot)$ with $(n=0,\ldots,N-1)$ for field variable with antisymmetric extension and $f((n+1/2)\Delta r,\cdot)$ for field variable with symmetric extension are copied into the latter half of a work vector of length $2N$. N is the length of the grid in the radial direction. The first half of this vector is assigned the values $-f(n\Delta r,\cdot)$ for antisymmetric extension and $f((n+1/2)\Delta r,\cdot)$ for symmetric extension, with $n=-N,\ldots,-1$. Then, a usual Fourier differentiation is done on the work vector, and the radial differentiation $\partial f/\partial r$ corresponds to the latter half of the resulting vector.

The solver uses a staggered fourth-order Adams–Bashforth method, by which stress and particle velocity are updated at alternating half time steps, to integrate forward in time.[12] The resulting staggered grid in space and in time is shown in Fig. 1.

To circumvent wraparound inherent to FFT-based pseudospectral simulation, perfectly matched layers (PML) boundary condition is used. In our case a novel implementation of the complex frequency-shifted (CFS) PML, named convolutional PML(CPML) has been chosen and extended to the axisymmetrical case. This method has been introduced in electromagnetic simulations with finite difference time domain (FDTD) method,[13] and studies have shown that CFS-PML is highly effective at absorbing evanescent waves and signals of long time signature.[14]

C. The CPML

The CPML method is introduced based on a stretched-coordinate formulation of Eqs. (6a)–(6h). The choice of the complex stretching variables will be that proposed by Kuzuoglu and Mittra[14] extended to cylindrical coordinates using the complex coordinates.[15–17] We introduce the complex coordinate transformation:

$$\tilde{z} = \int_0^z s_z(z')dz', \tag{13a}$$

$$\tilde{r} = \int_0^r s_r(r')dr', \tag{13b}$$

where

$$s_z(z) = \kappa_z(z) + \frac{\sigma_z(z)}{\alpha_z + j\omega}, \tag{14a}$$

$$s_r(r) = \kappa_r(r) + \frac{\sigma_r(r)}{\alpha_r + j\omega}, \tag{14b}$$

where s_z and s_r are the stretched-coordinate metrics, $\alpha_z, \sigma_z, \alpha_r$, and σ_r are assumed to be positive and real, and κ_z and κ_r are real and $\geqslant 1$. Introducing Eq. (14b) in Eq. (13b), the radial complex coordinate can be written explicitly as

$$\tilde{r} = S_r = \mathrm{K}_r(r) + \frac{\mathrm{P}_r(r)}{\alpha_r + j\omega}. \tag{15}$$

The originally split PML, proposed by Berenger[18] and first introduced for elastic waves propagation by Chew and Liu,[19] is retrieved imposing $\alpha_{z,r}=0$ and $\kappa_{z,r}=1$.

In the frequency domain and stretched-coordinate space given by Eqs. (13a) and (13b), Eqs. (6a)–(6h) becomes:

$$j\omega v_r(\omega) = \frac{1}{\rho_0}\left(\frac{1}{s_r}\frac{\partial \tau_{rr}}{\partial r} + \frac{1}{S_r}(\tau_{rr} - \tau_{\theta\theta}) + \frac{1}{s_z}\frac{\partial \tau_{rz}}{\partial z}\right), \tag{16a}$$

$$j\omega v_z(\omega) = \frac{1}{\rho_0}\left(\frac{1}{s_r}\frac{\partial \tau_{rz}}{\partial r} + \frac{1}{S_r}\tau_{rz} + \frac{1}{s_z}\frac{\partial \tau_{zz}}{\partial z}\right), \tag{16b}$$

$$\tau_{rr}(\omega) = C_{11}(\omega) \otimes \left[\frac{1}{s_r}\frac{\partial u_r}{\partial r}\right] + C_{12}(\omega) \otimes \left[\frac{1}{S_r}u_r\right] + C_{13}(\omega) \otimes \left[\frac{1}{s_z}\frac{\partial u_z}{\partial z}\right], \tag{16c}$$

$$\tau_{rz}(\omega) = C_{44}(\omega) \otimes \left[\frac{1}{s_r}\frac{\partial u_z}{\partial r}\right] + C_{44}(\omega) \otimes \left[\frac{1}{s_z}\frac{\partial u_r}{\partial z}\right], \tag{16d}$$

$$\tau_{zz}(\omega) = C_{13}(\omega) \otimes \left[\frac{1}{s_r} \frac{\partial u_r}{\partial r} \right] + C_{13}(\omega) \otimes \left[\frac{1}{S_r} u_r \right] + C_{33}(\omega) \otimes \left[\frac{1}{s_z} \frac{\partial u_z}{\partial z} \right], \tag{16e}$$

$$\tau_{\theta\theta}(\omega) = C_{12}(\omega) \otimes \left[\frac{1}{s_r} \frac{\partial u_r}{\partial r} \right] + C_{11}(\omega) \otimes \left[\frac{1}{S_r} u_r \right] + C_{13}(\omega) \otimes \left[\frac{1}{s_z} \frac{\partial u_z}{\partial z} \right]. \tag{16f}$$

Equations (16a)–(16f) are next transformed back to the time domain. Due to the frequency dependence of the stretched-coordinate metrics, a convolution appears in the resulting equations. Nevertheless the convolution terms may be eliminated by introducing so-called memory variables.[13] They are replaced by a first-order differential equation for each memory variable as described in the Appendix.

Finally, the system to be solved becomes

$$\frac{\partial v_r}{\partial t} = \frac{1}{\rho_0} \left(\frac{1}{\kappa_r} \frac{\partial \tau_{rr}}{\partial r} + \frac{1}{\mathrm{K}_r} (\tau_{rr} - \tau_{\theta\theta}) + \frac{1}{\kappa_z} \frac{\partial \tau_{rz}}{\partial z} + \frac{A_r}{\kappa_r} + \frac{B_r}{\mathrm{K}_r} + \frac{C_z}{\kappa_z} \right), \tag{17a}$$

$$\frac{\partial v_z}{\partial t} = \frac{1}{\rho_0} \left(\frac{1}{\kappa_r} \frac{\partial \tau_{rz}}{\partial r} + \frac{1}{\mathrm{K}_r} \tau_{rz} + \frac{1}{\kappa_z} \frac{\partial \tau_{zz}}{\partial z} + \frac{D_r}{\kappa_r} + \frac{E_r}{\mathrm{K}_r} + \frac{F_z}{\kappa_z} \right), \tag{17b}$$

$$\tau_{rr} = \frac{C_{11}}{\kappa_r} \frac{\partial u_r}{\partial r} + \frac{C_{12}}{\mathrm{K}_r} u_r + \frac{C_{13}}{\kappa_z} \frac{\partial u_z}{\partial z} + \frac{C_{11}}{\kappa_r} G_r + \frac{C_{12}}{\mathrm{K}_r} H_r + \frac{C_{13}}{\kappa_z} I_z, \tag{17c}$$

$$\tau_{rz} = \frac{C_{44}}{\kappa_r} \frac{\partial u_z}{\partial r} + \frac{C_{44}}{\kappa_z} \frac{\partial u_r}{\partial z} + \frac{C_{44}}{\kappa_r} J_r + \frac{C_{44}}{\kappa_z} L_z, \tag{17d}$$

$$\tau_{zz} = \frac{C_{13}}{\kappa_r} \frac{\partial u_r}{\partial r} + \frac{C_{13}}{\mathrm{K}_r} u_r + \frac{C_{33}}{\kappa_z} \frac{\partial u_z}{\partial z} + \frac{C_{13}}{\kappa_r} G_r + \frac{C_{13}}{\mathrm{K}_r} H_r + \frac{C_{33}}{\kappa_z} I_z, \tag{17e}$$

$$\tau_{\theta\theta} = \frac{C_{12}}{\kappa_r} \frac{\partial u_r}{\partial r} + \frac{C_{11}}{\mathrm{K}_r} u_r + \frac{C_{13}}{\kappa_z} \frac{\partial u_z}{\partial z} + \frac{C_{12}}{\kappa_r} G_r + \frac{C_{11}}{\mathrm{K}_r} H_r + \frac{C_{13}}{\kappa_z} I_z, \tag{17f}$$

where the memory variables $A_r, B_r, C_z, D_r, E_r, F_z, G_r, H_r, I_z, J_r$, and L_z are obtained by the following first-order differential equations:

$$\frac{\partial A_r}{\partial t} = -\delta_r \frac{\partial \tau_{rr}}{\partial r} - \beta_r A_r, \tag{18a}$$

$$\frac{\partial B_r}{\partial t} = -\bar{\delta}_r (\tau_{rr} - \tau_{\theta\theta}) - \bar{\beta}_r B_r, \tag{18b}$$

$$\frac{\partial C_z}{\partial t} = -\delta_z \frac{\partial \tau_{rz}}{\partial z} - \beta_z C_z, \tag{18c}$$

$$\frac{\partial D_r}{\partial t} = -\delta_r \frac{\partial \tau_{rz}}{\partial r} - \beta_r D_r, \tag{18d}$$

$$\frac{\partial E_r}{\partial t} = -\bar{\delta}_r \tau_{rz} - \bar{\beta}_r E_r, \tag{18e}$$

$$\frac{\partial F_z}{\partial t} = -\delta_z \frac{\partial \tau_{zz}}{\partial z} - \beta_z F_z, \tag{18f}$$

$$\frac{\partial G_r}{\partial t} = -\delta_r \frac{\partial u_r}{\partial r} - \beta_r G_r, \tag{18g}$$

$$\frac{\partial H_r}{\partial t} = -\bar{\delta}_r u_r - \bar{\beta}_r H_r, \tag{18h}$$

$$\frac{\partial I_z}{\partial t} = -\delta_z \frac{\partial u_z}{\partial z} - \beta_z I_z, \tag{18i}$$

$$\frac{\partial J_r}{\partial t} = -\delta_r \frac{\partial u_z}{\partial r} - \beta_r J_r, \tag{18j}$$

$$\frac{\partial L_z}{\partial t} = -\delta_z \frac{\partial u_r}{\partial z} - \beta_z L_z, \tag{18k}$$

with $\delta_{r,z} = \sigma_{r,z}/\kappa_{r,z}$, $\bar{\delta}_r = \mathrm{P}_r/\mathrm{K}_r$, $\beta_{r,z} = \alpha_{r,z} + \sigma_{r,z}/\kappa_{r,z}$, $\bar{\beta}_r = \alpha_r + \mathrm{P}_r/\mathrm{K}_r$ and where the memory variables are zero outside the PML zones. The particle displacements are calculated everywhere with Eqs. (6c) and (6d). The choice of the CPML parameters ($\sigma_{r,z}, \kappa_{r,z}, \mathrm{P}_r, K_r$, and $\alpha_{r,z}$) used in our simulations are the same as the ones given in Ref. 13.

The CPML offers the advantage over the traditional implementation of the PML to be a nonsplitting PML corresponding to perturbations to the original wave equations where the perturbed equations reduce automatically to the original wave equation outside the PML absorbing layers. So, the fact that the CPML treats the boundary layers in the same way as the rest of the computational domain, greatly simplifies the computer implementation.

D. Free-surface implementation

In a Fourier pseudospectral simulation, the introduction of free surfaces is not easy due to the nonlocal behavior of the spatial derivatives, even if this problem has been reduced by the use of a staggered grid. In the solver, a method of images, first introduced by Levander[20] and described in detail by Robertsson,[21] is used. The idea is as follows: for example, a vertical free surface is chosen to be located on a τ_{rr} node. On this node, the condition $\tau_{rr}=0$ is imposed. To guarantee that τ_{rz} is also zero on this free boundary, it is mirrored around the free surface as an odd function when calculating its radial spatial derivative. The radial spatial derivative of all the nonzero variables on the free surface is calculated after their mirroring around the free surface as even functions.

In the solver the CPML zones are suppressed behind a free surface, because no waves are supposed to propagate in this zone. Thus, behind a free surface, we do not need to

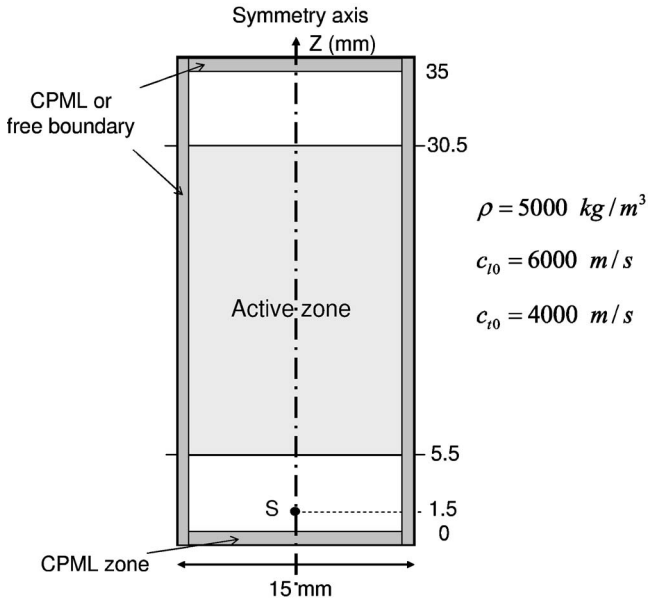

FIG. 2. Geometry of the simulated solid wave phase conjugator with a 2.5 cm active zone. *S* is a point or 750-μm-diam stress source inside the solid.

absorb any wave. Nevertheless, in this case the effects of the domain periodicity inherent in FFT-based calculations reappear. For this reason the stress and the particle velocity are smoothly reduced to zero using an apodization window near the limits of the numerical domain when a stress free boundary is present.

This complex free surface implementation is linked to the domain periodicity inherent in the Fourier pseudospectral method. A better way to solve this problem should be to use the multidomain PSTD method based on Chebychev polynomials as described by Zheng *et al.*[22] In this case free boundaries (and material discontinuities also) are directly included in the polynomials expansion.

III. RESULTS AND DISCUSSION

The main objective of this part is to determine the influence of lateral limitation of the active medium on parametric WPC, and more precisely the influence of reverberations and mode conversions within the active zone of the conjugator.

Numerical simulations presented in this section were made for the configuration shown in Fig. 2. The incident acoustic wave is a three period wave train, with a frequency of 10 MHz, emitted by a point source or a 750-μm-diam disc source placed in position *S*. The wave phase conjugator is a 3.5 cm length (L) solid rod with a diameter of 1.5 cm, and the following parameters:

$$\rho = 5000\ \text{kg/m}^3, \quad C_{l0} = 6000\ \text{m/s}, \quad C_{t0} = 4000\ \text{m/s}. \tag{19}$$

These values correspond to the polycrystalline ferrite sample N1 described in Ref. 23, and used in experiments. In the simulations the active zone length is always 2.5 cm and the boundary conditions at the upper (z=3.5 cm) and lateral (r =0.75 cm) boundaries can be a CPML absorbing zone or a free boundary (solid/air interface), depending on the studied configuration. In all cases the electromagnetic pumping is switched on when the acoustic wave arrives in the active zone. A T=19 μs pumping duration is chosen because it corresponds, for the experimental sample simulated, to the maximal duration before nonlinear effects induce a pumping depletion[5,9] and therefore an amplitude limitation of the conjugate wave.

As described by the linear theory of the supercritical amplification stage in active coupled wave system[3,4] the first part of the envelop of the phase conjugate wave corresponds to an exponential amplification with gain Γ given by the following system:

$$\Gamma = \sqrt{\left(\frac{\omega m_l}{4}\right)^2 - \left(\frac{Xc_0}{L}\right)^2}, \quad 1 + \frac{\Gamma}{X}\frac{L}{c_0} tg(X) = 0, \tag{20}$$

where $c_0 = c_{l0}$ for longitudinal wave and $c_0 = c_{t0}$ for transverse wave. An analytical expression of the gain increment can be obtained in the case where the excess over parametric instability threshold is small:[5]

$$\Gamma = \frac{\pi}{2}\left[\frac{\omega m_l}{4} - \frac{\pi c_0}{2L}\right]. \tag{21}$$

From the gain increment Γ=0.6 μs^{-1} measured in Ref. 23 one can estimate a typical transverse modulation depth $m_t = 4.1 \times 10^{-2}$, obtained in experimental configuration. To maintain the same gain increment in the case of longitudinal wave active zone, e.g., an active zone where only the longitudinal wave velocity is modulated, the modulation depth has to be increased to the value $m_l = 4.8 \times 10^{-2}$. These two values of m_t and m_l are chosen successively for all the simulations, excepted as otherwise noted.

A. Validation of pseudospectral results

First, to test the accuracy of the PSTD code implementation, the wave propagation in a homogeneous elastic plate test case proposed by Schubert *et al.*[24] is used. The plate is cylindical with thickness of 5 cm and radius of 10 cm. The elastic parameters of the plate are as follows: ρ =7820 kg/m^3, c_{l0}=5900 m/s, and c_{t0}=3200 m/s. A normal force impact with a 2 μs duration is applied in the center of one surface of the plate. The displacement u_z at the center of the opposite surface (receiver position R1) and the dispacement u_r also on the opposite surface, but 4 cm away from the center (receiver position R2) obtained are shown in Figs. 3(a) and 3(b), respectively. They are in excellent agreement with the results presented in Ref. 24 (Figs. 6 and 7, respectively) in the case of the finer FDTD grid and the analytical model.

Now, in order to validate the implementation of active medium, a longitudinal plane wave incident on an active zone with $m_t = 0$ and $m_l = 4.8 \times 10^{-2}$ is simulated. In this case, the particle velocity v_z obtained in the source plane [Fig. 4(a)] can be favorably compared to one-dimensional (1D) simulation results already obtained[8] and analytical expressions.[5] More precisely, the first part of the envelop of the conjugate wave is effectively described by an exponential function of time with an estimated gain (by fitting) of Γ =0.512 μs^{-1}. This gain is lower than the one predicted by Eq. (21), but corresponds perfectly to solution of Eq. (20)

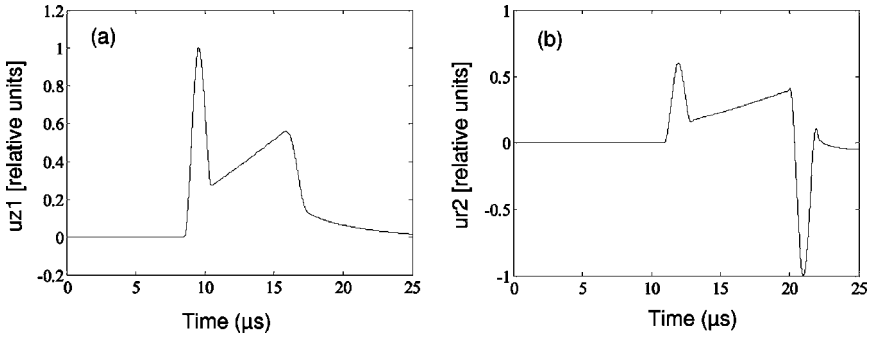

FIG. 3. (a) Displacement u_z at receiver position R1, and (b) displacement u_r at receiver position R2 obtained in the PSTD simulation of the homogeneous media test case of Ref. 24.

($\Gamma=0.507\ \mu s^{-1}$) and to numerical integration of the parametrically coupled system of equations obtained, for the problem treated here, for slowly varying forward and reverse wave amplitudes.[3,6,7] The second part of the signal, after the end of the pump excitation, corresponding to the spatial amplitude distribution of the acoustic conjugate wave inside the active zone at the end of the pumping, is described by a truncated sinusoidal function.[4,6]

Figure 5 presents the axial component of the time averaged (on the acoustic wave period $T=1/f$) Poynting vector P_z given by

$$P_z = -\frac{1}{T}\int_0^T (\tau_{rz} v_r + \tau_{zz} v_z) dt. \tag{22}$$

This term provides the perpendicular energy flow across the surface $z=C^e$. The giant amplification ($\sim$57 dB) of the conjugate wave (CW) compared to the incident wave is clearly shown. The negative sign of P_z for the conjugate wave represents its backward propagation toward the source. When $\Gamma=0$ we obtain the parametric instability threshold, which corresponds from Eq. (21) to a modulation depth $m_l=\lambda_l/L=2.410^{-2}$, where λ_l is the longitudinal acoustic wavelength. Then, as shown in Fig. 4(b), after the incident acoustic pulse has traveled a double path across the active zone ($t \geqslant T_0=2L/c_{l0} \approx 8.3\ \mu s$ if $t=0$ is the time of electromagnetic pumping beginning) the conjugate wave is stabilized to a constant value. Finally, when m_l is lower than the threshold value [$m_l=1.8\times10^{-2}$ in Fig. 4(c)], the conjugate wave still exists but without any amplification according to the physical meaning of the threshold.

B. Influence of lateral limitation of the active medium on parametric WPC

Consider now a point source, inside the solid, at position S corresponding to $z=1.5$ mm, when only the transverse wave velocity is modulated. For the first computation, the active zone has a limited size (2.5 cm length and 1.5 cm diameter), but the medium is unlimited. As shown in Fig. 6 the axial stress applied on the symmetry axis of the wave phase conjugator creates a longitudinal and transverse spherical waves propagating away from the source. When the transverse wave arrives in the active zone, the electromagnetic pumping is switched on and a CW retropropagating to the source appears. This conjugate wave is then amplified during all the pumping duration, even when the incident shear wave has left the active zone. At the end of the pumping duration ($t=20\ \mu s$) the stored energy inside the active zone is evacuated in the forward (FAW) and backward (BKW) directions. This latter part of the stored energy continues to retro-focalize at the source, achieving a maximum amplitude at $t=23\ \mu s$.

The obtained time evolution of the stress τ_{zz} at the source position is presented in Fig. 7(a). As in the plane wave simulation, the first part of the conjugate wave has an exponential increase with time, but with a lower gain increment $\Gamma \approx 0.44\ \mu s^{-1}$ here. This lowering of the increment gain is probably induced by the fact that the amplitude maximum of the incident transverse wave impinges the active zone with a large angle of incidence, and then crosses it only in a limited zone, lowering the effective length L of the wave phase conjugator. As described by Eq. (21), the increment gain is then decreased. Moreover, each component in the spatial frequency domain, corresponding to an angle of incidence on the active zone, crosses a different active zone length, and is then differently amplified. So, the direction of maximum amplitude of the conjugate wave follows during the amplification process the direction of the spatial frequency component of the incident wave which propagates inside the active zone along the longest length (compare $t=5\ \mu s$ and $t=20\ \mu s$ in Fig. 6, where straight lines have been plotted to guide the eye). In the presented case, it changes from the direction of the incident wave (here $\sim$45° relative to the symmetry axis) at the beginning of the process, to the direction defined by the line linking the source position to the outside upper corner of the active zone ($r=7.5$ mm and $z=30$ mm), when the incident transverse wave leaves the active zone. Now, the second part of the conjugate wave envelop no longer has a sinusoidal shape due to the modification of the spatial amplitude distribution of the acoustic wave inside the active zone at the end of the electromagnetic pumping (Fig. 6, $t=20\ \mu s$).

Figures 7(b)–7(d) present the influence of the solid wave phase conjugator size limitation on the phase conjugate wave at the source position. First, when the conjugator is a 1.5-cm-diam rod of infinite axial size [Fig. 7(b)], the axial stress τ_{zz} of the conjugate wave is greatly amplified compared to the case of an infinite solid, and the increment gain is now nearly the same as the one obtained in the plane wave case: $\Gamma \approx 0.52\ \mu s^{-1}$. The shape of the axial stress, as a function of time in this case, is very similar to the shape measured experimentally and presented in Fig. 4 of Ref. 6. The power of the conjugate wave at the source position in this radial lim-

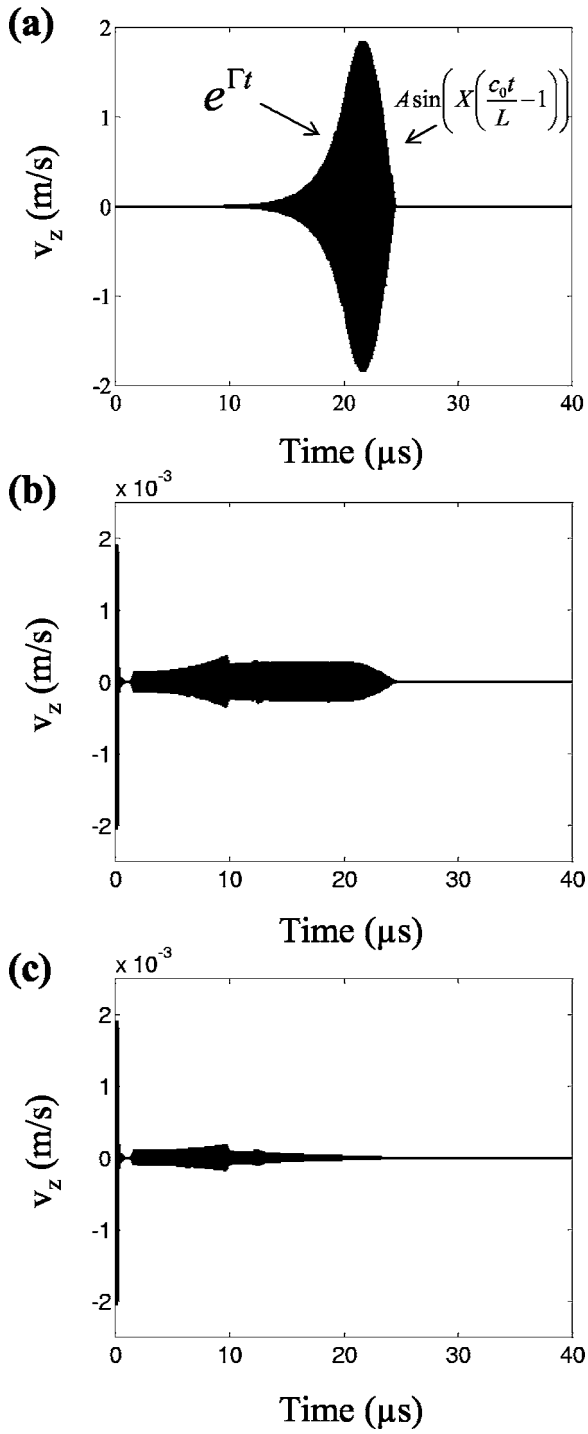

FIG. 4. Time evolution of particle velocity v_z in the source plane for longitudinal incident plane wave with a modulation depth (a) $m_l=4.8\times10^{-2}$, (b) $m_l=2.4\times10^{-2}$, and (c) $m_l=1.8\times10^{-2}$. The case (b) corresponds to the parametric instability threshold: $m_l=\lambda_l/L$, where λ_l is the longitudinal wavelength and L the active zone length.

ited configuration is more than two orders of magnitude higher [Fig. 8(a)] than in an unlimited solid, and the maximum amplitude temporal position is 2 μs delayed. Moreover, the radial resolution of the retro-focused wave at its focus is greatly enhanced: 300 μm (at −3 dB) in comparison with 1 mm in the preceding configuration. To understand this radial resolution enhancement, let us look to Fig. 9, which presents the particle velocity (in dB scale referenced at

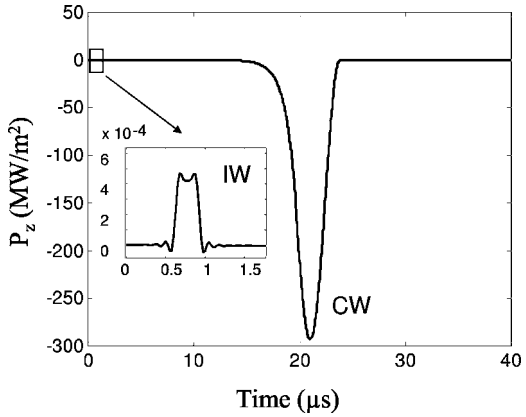

FIG. 5. Axial component of the Poynting vector P_z in the source plane as a function of time. The inserted curve is a zoom of the incident wave (IW). CW—conjugate wave.

0.16 m/s) at four chosen time moments of the WPC process. As shown at $t=24.4$ μs, corresponding to the time when the conjugate wave at the focal point is maximum, the conjugate wave comes from two sources: one created by the transverse wave directly incident on the active zone and the other by the transverse wave induced by the reflection of the longitudinal incident wave on the radial boundary of the rod (indicated by arrows). Note that even inside the active zone the conjugate wave retro-focuses to the source position following the incident wave path. These two sources of conjugate wave are more clearly shown in Fig. 10 where the axial component P_z of the Poynting vector in the lower side of the active zone ($z=5$ mm) is plotted as a function of time for an unlimited solid (a) and a 15-mm-diam rod (b). When the solid is unlimited the conjugate wave propagates outside the active zone at the end of the electromagnetic pumping closer from the symmetry axis than the incident transverse wave, as described before. The direction of energy flow across the lower boundary of the active zone, given by Poynting vector **P**, is also shown in Fig. 10. The radial component P_r of **P** is calculated in the same way as P_z by

$$P_r = -\frac{1}{T}\int_0^T (\tau_{rr}v_r + \tau_{rz}v_z)dt. \tag{23}$$

In Fig. 10(a), it shows the direction of retro-focusing of the conjugate wave. When the wave phase conjugator is a rod of infinite axial length, interference pattern is shown on P_z axial distribution, corresponding well to the two sources of conjugate wave.

Now, when the conjugator is still a 1.5-cm-diam rod of infinite length and the point source is replaced by a 750-μm-diam stress source, the major part of the incident transverse elastic energy is concentrated around the axial direction. So, reflections and mode conversions influence less the wave phase conjugation process, and the radial resolution enhancement is lowered, even if the amplitude of the conjugate wave is higher.

Finally, a free boundary is introduced at $z=35$ mm, and identical parameters than the preceding simulations are kept. As shown in Fig. 8, the wave phase conjugation process is not modified: the amplitude of the conjugate wave and the

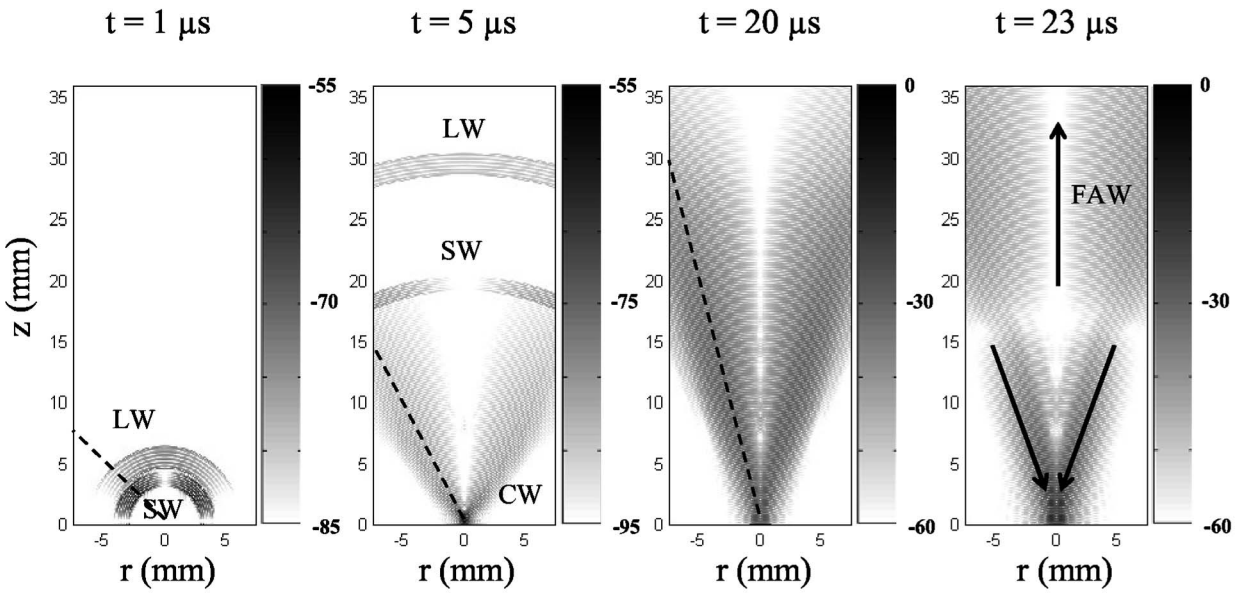

FIG. 6. Particle velocity (in dB scale referenced at 0.04 m/s) at four time moments in the WPC process in the case of an incident wave emitted by a point source, on a transverse wave active zone. The active zone has limited size (2.5 cm length and 1.5 cm diameter), but the ceramic is unlimited. $t=20$ μs corresponds to the end of the magnetic pumping and $t=23$ μs to the time when the conjugate wave at the focal point is maximum. LW—longitudinal wave, SW—transverse wave, CW—conjugate wave, FAW—Forward amplified wave. Arrows indicate directions of energy flow.

quality of the retro-focusing are the same. The only difference noticeable is the appearance of a trail after the conjugate pulse due to reflections of the forward amplified wave on the upper free boundary. Contrary to 1D simulations[8] these reflections do not have the same shape and amplitude as the retro-focused conjugate wave. Indeed, the forward amplified wave is no more a plane wave and its reflection on the free boundary and its following backpropagation to the source does not take place in a coherent way, resulting in a lower amplitude trail. This trail is always seen in experiments, as shown for example in Fig. 3 of Ref. 6.

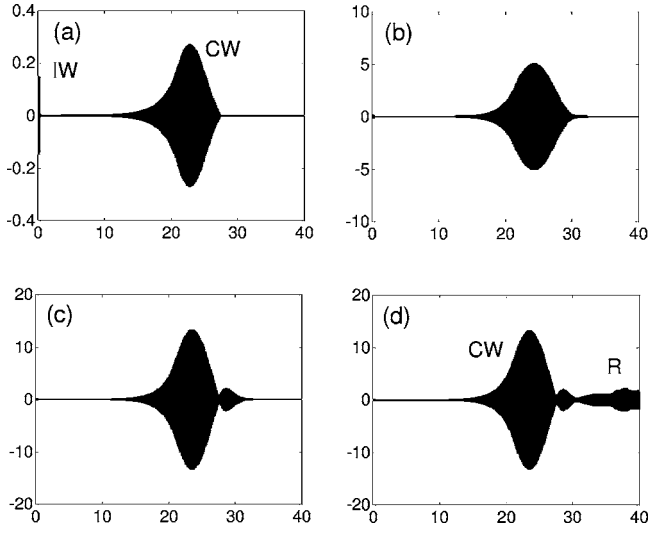

FIG. 7. Axial stress τ_{zz} at the source position vs time in the case of an incident wave, emitted by a point source (a), (b) or a 750-μm-diam source (c), (d), on a transverse wave active zone. The active zone has limited size (2.5 cm length and 1.5 cm diameter), but the ceramic is unlimited (a) or is a 1.5 cm diameter rod (b)–(d). The axial dimension is unlimited (a)–(c) or has a free boundary at $z=35$ mm (d). IW—incident wave, CW—conjugate wave, R—reverberations due to the limited axial size of the sample.

Similar results are obtained when only the longitudinal wave is modulated in the active zone (Fig. 11). The radial limitation of the conjugator increases the retro-focused

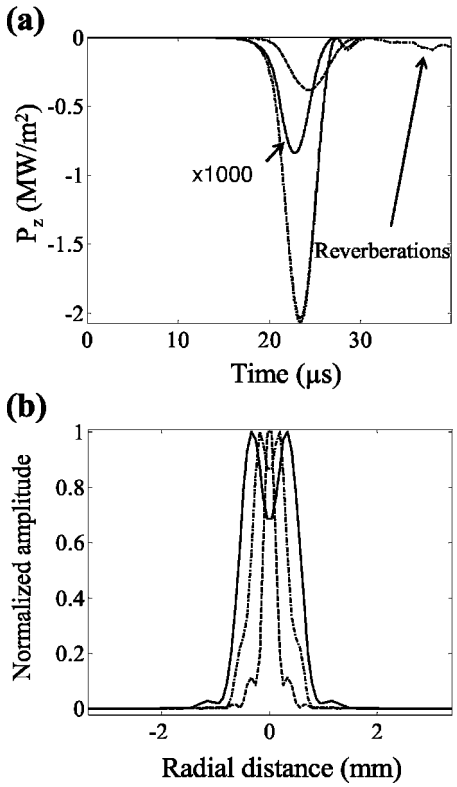

FIG. 8. (a) Axial component at the source position of the averaged Poynting vector as a function of time, and (b) normalized amplitude of the Poynting vector in the source plane as a function of radial distance. The four simulated configurations are the same as described in Fig. 7. Case (a) of Fig. 7 corresponds to the solid line multiplied by a factor 1000, case (b) to the dashed line, case (c) to the dotted line, and case (d) to the dash-dotted line.

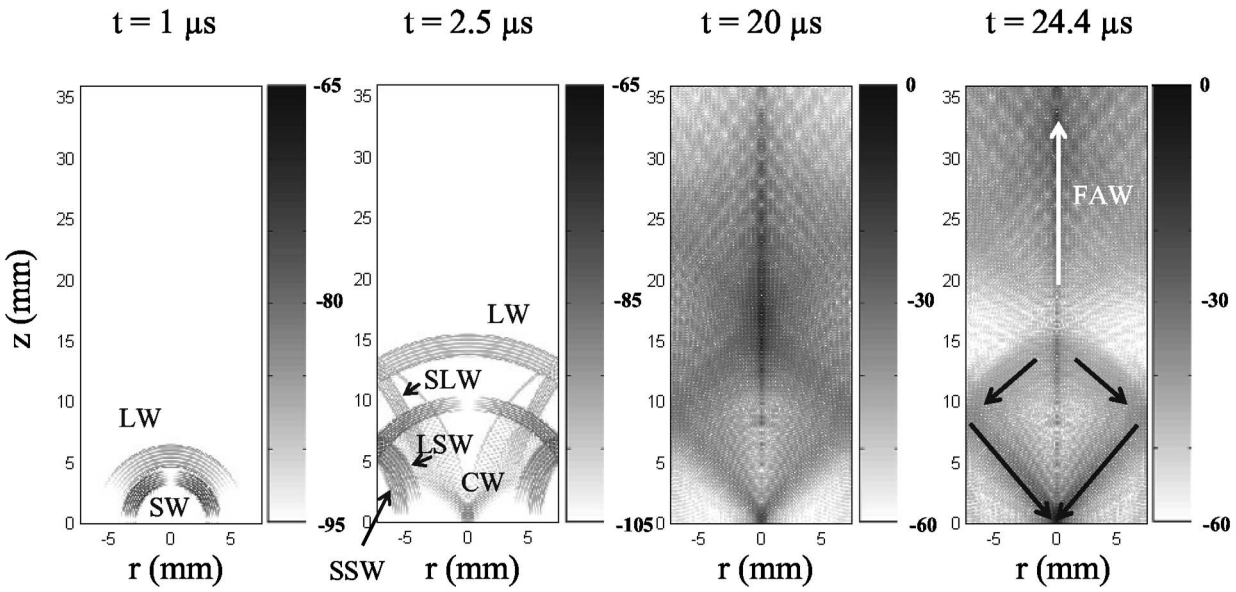

FIG. 9. Particle velocity (in dB scale referenced at 0.16 m/s) at four time moments in the WPC process in the case of an incident wave emitted by a point source in a 1.5-cm-diam rod. In the active zone only the transverse wave velocity is modulated. $t=20$ μs corresponds to the end of the magnetic pumping and $t=24.4$ μs to the time when the conjugate wave is maximum at the focal point. LW—longitudinal wave, SW—transverse wave, CW—conjugate wave, LSW—longitudinal wave created by reflection of the SW, SLW—transverse wave created by reflection of the LW, SSW—transverse wave created by reflection of the SW, FAW—forward amplified wave. Arrows indicate directions of energy flow.

power [Fig. 11(a)] and enhances its radial resolution [Fig. 11(b)] in the case of a point source. When the stress source is extended to a 750-μm-diam size (dash-dotted line) the great majority of the incident longitudinal elastic energy arrives nearly at normal incidence on the active zone. So, reflections and mode conversions do not greatly influence any more the wave phase conjugation process, and the radial resolution enhancement is lost, even if the amplitude of the conjugate wave is higher. In all three cases considered the obtained increment gain is identically equal to $\Gamma=0.5$ μs^{-1}.

IV. CONCLUSION

The presented results demonstrate high efficiency of PSDT method for simulation of multiscale parametric processes in solid active media. The method is applicable both for sub- and supercritical parametric modes. Comparison with analytical results for 1D configuration shows perfect agreement of obtained gain increment and pulse shape of conjugate waves. Extension of the method for 2D provided simulation of dynamics of WPC for real axisymmetric geometry of solid parametric conjugators. Calculations show that acoustic mode conversion inside of a conjugator does not prevent high quality retro-focusing of the phase conjugate wave. Moreover lateral limitation of the active element leads to increase of output power of a conjugator and to enhancement of radial resolution of the retro-focused wave compared with model of unlimited active medium. The numerical simulation correctly describes the parametric amplification and retro-focusing of ultrasound observed in experiments and can be used for optimization of conjugators design. The proposed numerical approach is developed now also for description of phase conjugate wave emission from parametrically active solid to liquid in the cases of plane and crimped interfaces between the media. The results are prepared for following publication.

ACKNOWLEDGMENTS

The research described in this publication was made within the CNRS-RAS PICS program 1573, Interreg IIIa No. 56, and in part by support of the French embassy in Moscow (MAE), Award No. RP-2367-MO-02 of the U.S. Civilian Research & Development Foundation for the Independent States of the Former Soviet Union (CRDF), grant 02-02-16916 from RFBR, and Grant No. 1553.2003.2 of the president of RF.

APPENDIX

In this Appendix the procedure to eliminate the convolutions appearing in Eqs. (16a)–(16f) is described in the case of Eq. (16c). First, we define $\bar{s}_z=s_z^{-1}$, $\bar{s}_r=s_r^{-1}$, and $\bar{S}_r=S_r^{-1}$. Then, transforming back to the time domain Eq. (16c) gives

$$\tau_{rr}=C_{11}\left[\bar{s}_r\otimes\frac{\partial u_r}{\partial r}\right]+C_{12}[\bar{S}_r\otimes u_r]+C_{13}\left[\bar{s}_z\otimes\frac{\partial u_z}{\partial z}\right], \tag{A1}$$

Roden and Gedney[13] have shown that the impulse response of $\bar{s}_z$ is given by

$$\bar{s}_z(t)=\frac{\delta(t)}{\kappa_z}+\zeta_z(t), \tag{A2}$$

where $\delta(t)$ is the unit impulse function,

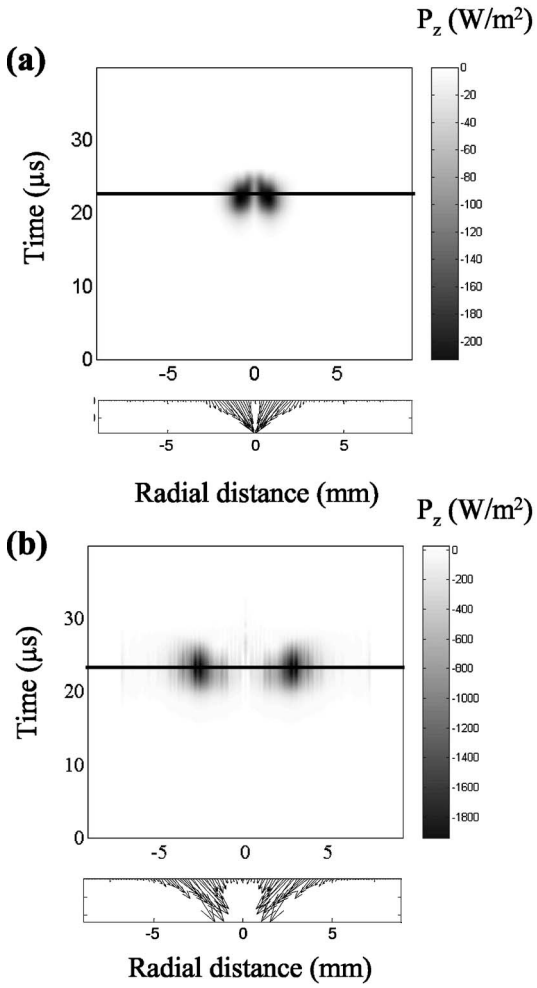

FIG. 10. Axial component P_z of the Poynting vector for an incident wave, emitted by a point source, on a transverse wave active zone in the lower side of the active zone as a function of time. The solid wave phase conjugator is of (a) unlimited size, and (b) radial diameter of 15 mm. In both cases the active zone has limited size (2.5 cm length and 1.5 cm diameter), and the lower graph presents the direction of energy flow **P** across the lower side of the active zone, when its amplitude is maximum.

$$\zeta_z(t) = -\frac{\sigma_z}{\kappa_z^2} e^{-(\sigma_z/\kappa_z+\alpha_z)t} h(t), \tag{A3}$$

and $h(t)$ is the step function. Similar results are obtained for $\bar{s}_r$, and $\bar{S}_r$:

$$\bar{s}_r(t) = \frac{\delta(t)}{\kappa_r} + \zeta_r(t), \tag{A4a}$$

$$\bar{S}_r(t) = \frac{\delta(t)}{K_r} + \bar{\zeta}_r(t) \tag{A4b}$$

with

$$\zeta_r(t) = -\frac{\sigma_r}{\kappa_r^2} e^{-(\sigma_r/\kappa_r+\alpha_r)t} h(t), \tag{A5a}$$

$$\bar{\zeta}_r(t) = -\frac{P_r}{K_r^2} e^{-(P_r/K_r+\alpha_r)t} h(t). \tag{A5b}$$

Inserting Eqs. (A2), (A4a), and (A4b) into Eq. (A1) leads to

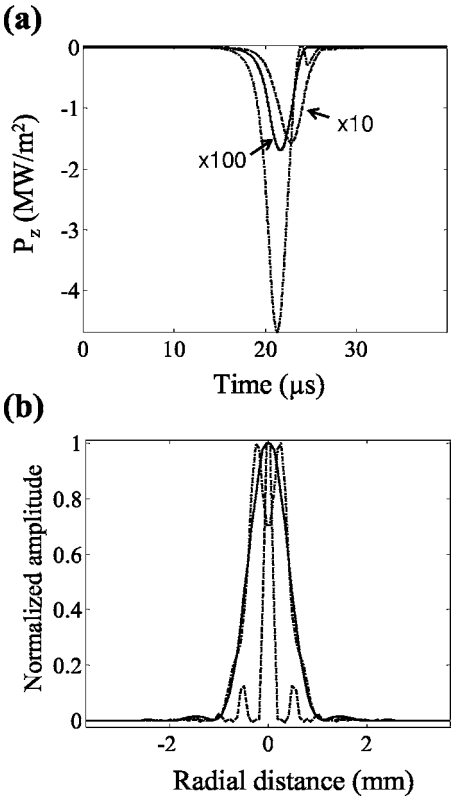

FIG. 11. (a) Axial component P_z of the averaged Poynting vector at the source position as a function of time, and (b) normalized amplitude of the Poynting vector in the source plane as a function of radial distance in the case of an incident wave emitted on a longitudinal wave active zone by a point source (solid and dashed lines) or a 750-μm-diam source (dash-dotted line). The active zone has limited size (2.5 cm length and 1.5 cm diameter), but the ceramic is unlimited (solid line) or is a 1.5-cm-diameter rod (dashed and dash-dotted line). Note that the solid line corresponds to 100 P_z, and the dashed line to 10 P_z.

$$\tau_{rr} = \frac{C_{11}}{\kappa_r}\frac{\partial u_r}{\partial r} + \frac{C_{12}}{\mathrm{K}_r}u_r + \frac{C_{13}}{\kappa_z}\frac{\partial u_z}{\partial z} + \frac{C_{11}}{\kappa_r}G_r + \frac{C_{12}}{\mathrm{K}_r}H_r + \frac{C_{13}}{\kappa_z}I_z, \tag{A6}$$

where the following memory variables have been introduced:

$$G_r = \kappa_r \zeta_r(t) \otimes \frac{\partial u_r}{\partial r}, \tag{A7a}$$

$$H_r = K_r \bar{\zeta}_r(t) \otimes u_r, \tag{A7b}$$

$$I_z = \kappa_z \zeta_z(t) \otimes \frac{\partial u_z}{\partial z}. \tag{A7c}$$

The introduction of memory variables leads to replacing the convolution in Eq. (16c) by a supplementary differential equation for each variable, as will be shown now. Taking, for example, the derivative of I_z and using properties of the convolution operator leads to

$$\frac{\partial I_z}{\partial t} = \kappa_z \frac{\partial}{\partial t}\left(\zeta_z(t) \otimes \frac{\partial u_z}{\partial z}\right) = \kappa_z \frac{\partial u_z}{\partial z} \otimes \frac{\partial \zeta_z(t)}{\partial t}. \tag{A8}$$

Taking time derivative of Eq. (A3) gives

$$\frac{\partial \zeta_z(t)}{\partial t} = -\frac{\sigma_z}{\kappa_z^2}\delta(t) - \left(\frac{\sigma_z}{\kappa_z} + \alpha_z\right)\zeta_z(t). \tag{A9}$$

Finally, inserting the last results into Eq. (A8) leads to the following first-order differential equation for the memory variable I_z:

$$\frac{\partial I_z}{\partial t} = -\frac{\sigma_z}{\kappa_z}\frac{\partial u_z}{\partial z} - \left(\frac{\sigma_z}{\kappa_z} + \alpha_z\right)I_z. \tag{A10}$$

Similar results are obtained for the two other memory variables G_r and H_r. All the equations of Eqs. (16a)–(16f) can be treated in a similar way, resulting in Eqs. (17a)–(17f) with the memory variables of Eqs. (18a)–(18k).

[1] A. P. Brysev, L. M. Krutyansky, and V. L. Preobrazhensky, "Wave phase conjugation of ultrasound beams," Usp. Fiz. Nauk **168**, 877–890 (1998).
[2] A. P. Brysev, L. M. Krutyansky, and V. L. Preobrazhensky, "Modern problems of the parametric ultrasonic wave phase conjugation," Phys. Vib. **9**, 52–70 (2001).
[3] D. L. Bobroff and H. A. Haus, "Impulse response of active coupled wave systems," J. Appl. Phys. **38**, 390–403 (1967).
[4] R. B. Thompson and C. F. Quate, "Nonlinear interaction of microwave electric fields and sound in $LiNbO_3$," J. Appl. Phys. **42**, 907–919 (1971).
[5] V. L. Preobrazhensky, "Overthreshold nonlinearity of parametric sound wave phase conjugation in solids," Jpn. J. Appl. Phys., Part 1 **32**, 2247–2251 (1993).
[6] P. Pernod and V. L. Preobrazhensky, "Parametric phase conjugation of a wide-band acoustic pulse in supercritical mode," Appl. Phys. Lett. **76**, 387–389 (2000).
[7] A. P. Brysev, F. V. Bunkin, D. V. Vlasov, L. M. Krutyanskii, V. L. Preobrazhenskii, and A. D. Stakhovskii, "Regenerative amplification of acoustic waves with phase conjugation in a ferrite," Sov. Phys. Acoust. **34**, 567–569 (1988).
[8] S. Ben Khelil, A. Merlen, V. L. Preobrazhensky, and P. Pernod, "Numerical simulation of acoustic conjugation in active media," J. Acoust. Soc. Am. **109**, 75–83 (2001).
[9] A. Merlen, V. L. Preobrazhensky, and P. Pernod, "Supercritical parametric phase conjugation of ultrasound. Numerical simulation of nonlinear and non-stationary mode," J. Acoust. Soc. Am. **112**, 2656–2665 (2002).
[10] T. Özdenvar and G. A. McMechan, "Causes and reduction of numerical artifacts in pseudospectral wavefield extrapolation," Geophys. J. Int. **126**, 819–828 (1996).
[11] J. Dellinger and F. Muir, "Axisymmetric anisotropy I: Kinematics," SEP Report **42**, 1–24 (1985).
[12] M. Ghrist, B. Fornberg, and T. A. Driscoll, "Staggered time integrators for wave equations," SIAM (Soc. Ind. Appl. Math.) J. Numer. Anal. **38**, 718–741 (2000).
[13] J. A. Roden and S. D. Gedney, "Convolution PML (CPML): An efficient FDTD implementation of the CFS-PML for arbitrary media," Microwave Opt. Technol. Lett. **27**, 334–339 (2000).
[14] M. Kuzuoglu and R. Mittra, "Frequency dependence of the constitutive parameters of causal perfectly matched anisotropic absorbers," IEEE Microw. Guid. Wave Lett. **6**, 447–449 (1996).
[15] W. C. Chew, J. M. Jin, and E. Michelssen, "Complex coordinate system as a generalized absorbing boundary condition," Microwave Opt. Technol. Lett. **15**, 363–369 (1997).
[16] F. L. Teixeira and W. C. Chew, "PML-FDTD in cylindrical and spherical grids," IEEE Microw. Guid. Wave Lett. **7**, 285–287 (1997).
[17] Q. H. Liu, "Perfectly matched layers for elastic waves in cylindrical and spherical coordinates," J. Acoust. Soc. Am. **105**, 2075–2084 (1999).
[18] J. P. Berenger, "A perfectly matched layer for the absorption of electromagnetic waves," J. Comput. Phys. **114**, 195–200 (1994).
[19] W. C. Chew and Q. H. Liu, "Perfectly matched layers for elastodynamics: A new absorbing boundary condition," J. Comput. Acoust. **4**, 72–79 (1996).
[20] A. R. Levander, "Fourth-order finite-difference P-SV seismograms," Geophysics **53**, 1425–1436 (1988).
[21] J. O. A. Robertsson, "A numerical free-surface condition for elastic/viscoelastic finite-difference modeling in the presence of topography," Geophysics **61**, 1921–1934 (1996).
[22] Z. Q. Zeng and Q. H. Liu, "A multidomain PSTD method for 3D elastic wave equations," Bull. Seismol. Soc. Am. **94**, 1002–1015 (2004).
[23] A. P. Brysev, P. Pernod, and V. L. Preobrazhensky, "Magneto-acoustic ceramics for parametric sound wave phase conjugators," Ultrasonics **38**, 834–837 (2000).
[24] F. Schubert, A. Peiffer, B. Köhler, and T. Sanderson, "The elastodynamic finite integration technique for waves in cylindrical geometries," J. Acoust. Soc. Am. **104**, 2604–2614 (1998).

Numerical simulation of finite amplitude wave propagation in air using a realistic atmospheric absorption model[a)]

Mark S. Wochner,[b)] Anthony A. Atchley, and Victor W. Sparrow
Graduate Program in Acoustics, The Pennsylvania State University, 217 Applied Science Building, University Park, Pennsylvania 16802

(Received 11 November 2004; revised 26 July 2005; accepted 3 August 2005)

A nonlinear system of fluid dynamic equations is modeled that accounts for the effects of classical absorption, nitrogen and oxygen molecular relaxation, and relative humidity. Total variables rather than acoustic variables are used, which allow for the inclusion of frequency-independent terms. This system of equations is then solved in two dimensions using a fourth-order Runge-Kutta scheme in time and a dispersion-relation-preserving scheme in space. It is shown that the model accurately simulates wave steepening for propagation up to one shock formation distance. For a source amplitude of 157 dB re 20 μPa, the Fourier component amplitudes of the analytical and computed waveforms differ by 0.21% at most for the first harmonic in a lossless medium and 0.16% at most for the first harmonic in a medium that includes thermoviscous losses. It is shown that the absorption due to classical effects and molecular relaxation demonstrated by the model is within 1% of the analytical model and the computed dispersion due to molecular relaxation of nitrogen and oxygen is within 0.7% over a large frequency range. Furthermore, it is shown that the model can predict the amplification factor at a rigid boundary, which in a nonlinear system will be greater than two, to within 0.015%. © *2005 Acoustical Society of America.* [DOI: 10.1121/1.2047109]

PACS number(s): 43.28.Js, 43.25.Cb, 43.25.Vt [RR] Pages: 2891–2898

I. INTRODUCTION

The motivation for this research is to create a versatile computational model that can simulate nonlinear propagation of sound in air more realistically than numerical models that are currently available. To achieve this goal, a number of criteria need to be met. First, the model needs to recreate nonlinear phenomena accurately; second, it needs to simulate the absorption and dispersion due to shear and bulk viscosity, thermal conductivity, and molecular relaxation processes; third, it needs to be able to include spatially varying sound speed, frequency-independent velocity, ambient temperature, and ambient pressure profiles in order to accurately represent realistic atmospheric conditions; fourth, it needs to be able to do this multidimensionally using a reasonable amount of computational resources in a reasonable amount of time. The first two criteria are met using a set of nonlinear fluid-dynamic equations taken from Pierce[1] that include terms for shear and bulk viscosity, thermal conductivity, and molecular relaxation. The third criterion is met using a time-domain numerical solver that uses the total variables rather than the perturbed values, allowing for the imposition of spatially dependent, frequency-independent terms in the solution. The fourth criterion is met using an efficient time-domain numerical solver.

Previous work by others in the acoustics community has met some of the above-described criteria. The work of Sparrow and Raspet[2] had a similar aim, however their simulations contained only up to second-order nonlinear terms, and did not include the total variables or explicit relaxation mechanisms. In other work, modified Burgers equations have been developed and solved using either combination time/frequency domain solvers or exclusively time domain solvers.[3] These methods have been tailored for quite specific cases, e.g., sonic boom propagation, and all model only one-dimensional propagation, hindering the general utility of such models. More detailed explanations of these kinds of models can be found in the work by Cleveland.[4] Computational fluid dynamics algorithms, such as those developed by Morris[5] and Tam,[6] have been implemented in two or three dimensions and are nonlinear, but they do not include the effects of molecular relaxation, which affects the accuracy of the solution since molecular relaxation is the dominant attenuation mechanism over a large frequency range and causes a considerable amount of dispersion. Detailed explanations of these types of algorithms can be found in the literature by Tam,[7] Long,[8] and Kurbatskii.[9]

In this paper, the system of equations, which is mostly taken from Pierce,[1] is described. Following this, a description of the numerical solver is provided. This solver allows one to model all of the above-described absorption mechanisms. Some preliminary results are then shown that confirm that the system of equations does indeed match known analytical solutions. Finally, future improvements of the model are discussed.

[a)]Portions of this work were presented in "Numerical simulation of finite amplitude waves in air including the effects of molecular relaxation," Proceedings of the 18th International Conference on Acoustics, Kyoto, Japan, April 2004.

[b)]Electronic mail: msw192@psu.edu

II. SYSTEM OF EQUATIONS

The fluid dynamic equations using the total variables, rather than the perturbed (acoustic) variables, that govern wave propagation are the continuity equation,[10]

$$\frac{\partial \rho}{\partial t} + \nabla \cdot (\rho \mathbf{v}) = 0, \tag{1}$$

the Navier-Stokes equation (also known as the momentum equation),

$$\rho \frac{D\mathbf{v}}{Dt} = -\nabla p + \nabla(\mu_B \nabla \cdot \mathbf{v}) + \mu \sum_{ij} e_i \frac{\partial \phi_{ij}}{\partial x_j}, \tag{2}$$

the entropy-balance equation,

$$\rho \frac{Ds_{\mathrm{fr}}}{Dt} + \sum_{\nu} \frac{\rho}{T_\nu} c_{v\nu} \frac{DT_\nu}{Dt} - \nabla \cdot \left(\frac{\kappa}{T} \nabla T \right) = \sigma_s, \tag{3}$$

and the relaxation equation,

$$\frac{DT_\nu}{Dt} = \frac{1}{\tau_\nu}(T - T_\nu). \tag{4}$$

In the above equations, ρ is the density, t the time, $\mathbf{v}$ the velocity, p the pressure, μ and μ_B the shear and bulk viscosities, e_i the unit vector in the ith dimension, ϕ the rate of shear tensor, s_{fr} the frozen entropy, T the absolute temperature, κ the coefficient of thermal conduction, $c_{v\nu}$ the specific heat at constant volume associated with the ν-type molecule, σ_s a variable used to represent the source terms of the entropy equation [Eq. (3)], and T_ν and τ_ν the apparent vibration temperature and relaxation time of the ν-type molecule, respectively. In this investigation, the ν-type molecules considered are nitrogen and oxygen, although more could be added to the calculation.

Equations (1)–(4) are called the constitutive equations. To obtain a closed set of equations that may be solved, the variables contained on the right-hand sides of the constitutive equations need to be determined at each time step of the calculation. They are given as follows:[11]

$$\sigma_s = \frac{\mu_B}{T}(\nabla \cdot \mathbf{v})^2 + \frac{\mu}{2T} \sum_{ij} \phi_{ij}^2 + \frac{\kappa}{T^2}(\nabla T)^2 + \frac{\rho}{T} \sum_{\nu} A_\nu \frac{DT_\nu}{Dt}, \tag{5}$$

$$\phi_{ij} = \frac{\partial v_i}{\partial x_j} + \frac{\partial v_j}{\partial x_i} - \frac{2}{3} \nabla \cdot \mathbf{v} \delta_{ij}, \tag{6}$$

$$A_\nu = \left(\frac{T}{T_\nu} - 1 \right) c_{v\nu}, \tag{7}$$

and

$$c_{v\nu} = \frac{n_\nu}{n} R \left(\frac{T_\nu^*}{T_\nu} \right)^2 e^{-T_\nu^*/T_\nu}. \tag{8}$$

Here A_ν is the affinity associated with the ν-type molecule, v_i the ith component of velocity, δ_{ij} the Kronecker delta, n_ν/n the fraction of all molecules that is of species ν, R the gas constant, and T_ν^* the molecular constant of molecule ν.

In addition to the constitutive equations, the van der Walls form of the state equation and the entropy relation are used:[12]

$$p = \frac{\rho RT}{M} + \frac{\rho^2}{M^2}[RTb - a] + \frac{\rho^3}{M^3}[RTb^2] \tag{9}$$

and

$$T = T_0 e^{(s_{\mathrm{fr}} - s_{\mathrm{fr}_0} - R \ln[\rho_0/\rho])/c_v}, \tag{10}$$

where M is the molar mass of air, given as 28.96 kg kmol^{-1}, c_v the specific heat of air at constant volume, given as 720.4 J kg^{-1} K^{-1}, s_{fr_0} the ambient entropy, T_0 the ambient temperature, given as 293.15 K, and the values of a and b used[13] are 1.361×10^5 J m^3 kmol^{-2} and 0.03649 m^3 kmol^{-1}, respectively.

The constitutive equations need to be recast in conservative form so that they can be solved by an explicit time-domain finite-difference scheme. An equation is in conservative form if there are no dependent variables in front of the partial derivatives. Usually, one can reduce the nonconservative form to conservative form by inserting the left-hand side of the continuity equation, Eq. (1), which is by definition equal to zero, on the left-hand side of the nonconservative equation. This addition allows all of the terms on the left-hand side to be regrouped within the partial derivatives, leaving the equation in conservative form. A particularly clear explanation of this approach is given in Anderson's text.[14] In a two-dimensional Cartesian coordinate system the conservative forms of the constitutive equations are

$$\frac{\partial \rho}{\partial t} + \frac{\partial(\rho u)}{\partial x} + \frac{\partial(\rho v)}{\partial y} = 0, \tag{11}$$

$$\frac{\partial(\rho u)}{\partial t} + \frac{\partial(\rho u u)}{\partial x} + \frac{\partial(\rho u v)}{\partial y} = -\frac{\partial p}{\partial x} + \mu_B \left(\frac{\partial^2 u}{\partial x^2} + \frac{\partial^2 v}{\partial x \partial y} \right) + \mu \left(\frac{\partial \phi_{xx}}{\partial x} + \frac{\partial \phi_{xy}}{\partial y} \right), \tag{12}$$

$$\frac{\partial(\rho v)}{\partial t} + \frac{\partial(\rho v u)}{\partial x} + \frac{\partial(\rho v v)}{\partial y} = -\frac{\partial p}{\partial y} + \mu_B \left(\frac{\partial^2 v}{\partial y^2} + \frac{\partial^2 u}{\partial y \partial x} \right) + \mu \left(\frac{\partial \phi_{yx}}{\partial x} + \frac{\partial \phi_{yy}}{\partial y} \right), \tag{13}$$

$$\frac{\partial(\rho s_{\mathrm{fr}})}{\partial t} + \frac{\partial(\rho u s_{\mathrm{fr}})}{\partial x} + \frac{\partial(\rho v s_{\mathrm{fr}})}{\partial y} = \sigma_s - \sum_{\nu} \frac{\rho}{T_\nu} c_{v\nu} \frac{DT_\nu}{Dt} + \nabla \cdot \left(\frac{\kappa}{T} \nabla T \right), \tag{14}$$

and

$$\frac{\partial(\rho T_\nu)}{\partial t} + \frac{\partial(\rho u T_\nu)}{\partial x} + \frac{\partial(\rho v T_\nu)}{\partial y} = \frac{\rho}{\tau_\nu}(T - T_\nu), \tag{15}$$

where u and v are the x and y components of the velocity, respectively. Because the calculations presented in this paper are two-dimensional, the Navier-Stokes equation, Eq. (2), has only x and y components, leading to Eqs. (12) and (13).

The computational domain resulting from these equations is essentially a slice of a three-dimensional field that is invariant in the third dimension. Therefore, the units used in the calculation are the physical, three-dimensional units, e.g., the units of pressure are pascals as opposed to pascals/meter. An extension to three dimensions is straightforward. It requires the inclusion of the z component of the Navier-Stokes equation and the reworking of some of the source terms in the constitutive equations to account for the third dimension. It should also be noted that although the equations are in a Cartesian coordinate system, they are equally applicable to other coordinate systems.

The last parameter that needs to be included is the relative humidity. The humidity of the air can change the relaxation frequencies of nitrogen and oxygen by several orders of magnitude and hence it needs to be included in the model. Relative humidity is incorporated using the following semiempirical relations:[15]

$$f_{N_2} = \frac{1}{2\pi\tau_{N_2}} = \frac{p}{p_{\text{ref}}}\left(24 + 4.04 \times 10^6 h \frac{0.02 + 100h}{0.391 + 100h}\right), \tag{16}$$

and

$$f_{O_2} = \frac{1}{2\pi\tau_{O_2}} = \frac{p}{p_{\text{ref}}}\left[\left(\frac{T_{\text{ref}}}{T}\right)^{1/2}(9 + 2.8 \times 10^4 h e^{-\eta})\right], \tag{17}$$

where

$$h = \frac{10^{-2}(\text{RH})p_{\text{vp}}(T)}{p}, \tag{18}$$

and

$$\eta = 4.17\left[\left(\frac{T_{\text{ref}}}{T}\right)^{1/3} - 1\right]. \tag{19}$$

Using the above-presented equations, the relaxation frequencies (f_{N_2} and f_{O_2}) or the relaxation times (τ_{N_2} and τ_{O_2}) of nitrogen and oxygen can be determined. Here, p_{vp} is the saturation vapor pressure of water, h is the fraction of molecules in air that is H_2O, RH is the relative humidity percentage, and the values used for T_{ref} and p_{ref} are 293.16 K and 1.01325×10^5 Pa, respectively. The equation for the saturation vapor pressure, which is a function of the absolute temperature and pressure of the medium, is quite long and is omitted, although it may be found in the work by Bass *et al.*[15] Equations (16)–(19) are solved using the initial, unperturbed values of pressure and temperature to determine the values of f_{N_2} and f_{O_2}. The relaxation frequencies are assumed to be constants thereafter.

III. NUMERICAL SOLUTION

Upon examination of the constitutive equations in conservative form, Eqs. (11)–(15), it is apparent that they are all of similar type and may be written together in the following vector form:

$$\frac{\partial \mathbf{w}}{\partial t} + \frac{\partial \mathbf{F}}{\partial x} + \frac{\partial \mathbf{G}}{\partial y} = \mathbf{H} \tag{20}$$

where the time derivatives of the constitutive equations are rows in the **w** vector, the x derivatives rows in the **F** vector, the y derivatives rows in the **G** vector, and the source terms rows in **H**. This gives the following vectors for **w**, **F**, **G**, and **H**:

$$\mathbf{w} = \begin{pmatrix} \rho \\ \rho u \\ \rho v \\ \rho s_{\text{fr}} \\ \rho T_{N_2} \\ \rho T_{O_2} \end{pmatrix}, \tag{21}$$

$$\mathbf{F} = \begin{pmatrix} \rho u \\ \rho u u \\ \rho u v \\ \rho u s_{\text{fr}} \\ \rho u T_{N_2} \\ \rho u T_{O_2} \end{pmatrix}, \tag{22}$$

$$\mathbf{G} = \begin{pmatrix} \rho v \\ \rho v u \\ \rho v v \\ \rho v s_{\text{fr}} \\ \rho v T_{N_2} \\ \rho v T_{O_2} \end{pmatrix}, \tag{23}$$

and

$$\mathbf{H} = \begin{pmatrix} 0 \\ -\frac{\partial p}{\partial x} + \mu_B\left(\frac{\partial^2 u}{\partial x^2} + \frac{\partial^2 v}{\partial x \partial y}\right) + \mu\left(\frac{\partial \phi_{xx}}{\partial x} + \frac{\partial \phi_{xy}}{\partial y}\right) \\ -\frac{\partial p}{\partial y} + \mu_B\left(\frac{\partial^2 v}{\partial y^2} + \frac{\partial^2 u}{\partial y \partial x}\right) + \mu\left(\frac{\partial \phi_{yx}}{\partial x} + \frac{\partial \phi_{yy}}{\partial y}\right) \\ \sigma_s - \sum_\nu \frac{\rho}{T_\nu} c_{v\nu} \frac{DT_\nu}{Dt} + \nabla \cdot \left(\frac{\kappa}{T} \nabla T\right) \\ \frac{\rho}{\tau_{N_2}}(T - T_{N_2}) \\ \frac{\rho}{\tau_{O_2}}(T - T_{O_2}) \end{pmatrix}. \tag{24}$$

Equations in this form, in which all of the variables on the left-hand sides of the equations are within the derivative operators of t, x, or y, may be solved by many explicit finite-difference approximations. In the current investigation, a fourth-order-accurate Runge-Kutta method is used in time and the dispersion-relation-preserving (DRP) scheme intro-

duced by Tam[16] using a seven point stencil is implemented in space. The DRP scheme has been shown to foster a numerical solution that exhibits a minimal amount of numerical dissipation and dispersion. The increased accuracy is especially important for the work discussed here, in which atmospheric absorption and dispersion is what one wishes to capture. The Runge-Kutta method used is of the form:

$$\mathbf{w}^{(0)} = \mathbf{w}^{n}, \tag{25}$$

$$\mathbf{w}_{l,m}^{(1)} = \mathbf{w}_{l,m}^{(0)} - \tfrac{1}{2}\Delta t \mathbf{K}_{l,m}^{(0)}, \tag{26}$$

$$\mathbf{w}_{l,m}^{(2)} = \mathbf{w}_{l,m}^{(0)} - \tfrac{1}{2}\Delta t \mathbf{K}_{l,m}^{(1)}, \tag{27}$$

$$\mathbf{w}_{l,m}^{(3)} = \mathbf{w}_{l,m}^{(0)} - \Delta t \mathbf{K}_{l,m}^{(2)}, \tag{28}$$

$$\mathbf{w}_{l,m}^{n+1} = \mathbf{w}_{l,m}^{(0)} - \Delta t \sum_{q=0}^{3} b_q \mathbf{K}_{l,m}^{(q)}, \tag{29}$$

where $b=[1/6, 1/3, 1/3, 1/6]$ and

$$\mathbf{K}_{l,m} = \frac{1}{\Delta x}\left(\sum_{j=-3}^{3} a_j \mathbf{F}_{l+j,m}\right) + \frac{1}{\Delta y}\left(\sum_{j=-3}^{3} a_j \mathbf{G}_{l,m+j}\right) - \mathbf{H}_{l,m}, \tag{30}$$

where[16]

$$a_0 = 0,$$

$$a_1 = -a_{-1} = 0.799\,266\,43,$$

$$a_2 = -a_{-2} = -0.189\,413\,14,$$

$$a_3 = -a_{-3} = 0.026\,519\,95. \tag{31}$$

Using the above-described scheme, the system of equations is solved over an incremental time spacing of Δt using a spatial spacing of Δx. Sources are introduced by adding a Gaussian spatially distributed density perturbation in the computational domain. A mass disturbance can be added just once at the beginning of the calculation to simulate an acoustic pulse or a time dependent mass source can be inserted anywhere in the spatial domain to simulate a continuous source.

A useful feature incorporated into the model is a set of on/off switches that allow each individual absorption mechanism to be turned on or off without affecting the others. If, for example, the nitrogen relaxation mechanism is not wanted, it is eliminated by simply imposing that $f_{N_2}=0$. The bulk viscosity, shear viscosity, or the coefficient of thermal conductivity are individually made equal to zero if the respective absorption mechanism is not wanted. This feature is especially helpful when investigating the effect that each specific absorption mechanism has upon the propagation characteristics of the medium and allows better comparison of the computational results to a variety of published data.

IV. RESULTS

The model was written in FORTRAN 90 and run on a 3.2 GHz Pentium 4 with 2 Gbytes of RAM. A typical run time for 20 000 computational iterations on a spatial grid of 22 500 points is about 150 min. It should be noted that the following results are calculated on a two-dimensional grid, but because plane waves are used in the calculations, the results are essentially one-dimensional. These conditions are used to allow comparison to the relatively abundant one-dimensional analytical results. It should also be noted that with the exception of the results in which the amplification factor on a rigid boundary is measured, boundary conditions are not implemented since the waves do not encounter the boundaries.

The first result given demonstrates the ability of the model to simulate wave steepening. A Gaussian-distributed source of the form

$$\rho = \rho_0 = A \exp\left(-\frac{\ln(2)(x-x_0)^2}{\alpha^2}\right)\sin \omega t \tag{32}$$

was inserted into the center of the domain. Here ρ_0 is the ambient density, A the amplitude of the disturbance, x the spatial variable, x_0 the position of the source, α the half-width of the Gaussian, and ω the angular frequency. Because in this case the Gaussian is a function of x only, the wave is invariant in the y direction, resulting in a plane-wave-like source in the x direction. The half-width of the Gaussian is set to be small to approximate the plane wave sources used in the analytical results given in the following. A high frequency source will be used in order to clearly demonstrate the effect of atmospheric absorption within a reasonably small computational domain. Using the above-described source, 1 MHz plane waves with a Gaussian half-width of 10% of the wavelength at 157 dB re 20 μPa ($\rho-\rho_0 = 0.0173$ kg/m^3) were propagated through a lossless domain of $20\,001\times 7$ points using 800 points per wavelength and a Courant-Friedrichs-Levy (CFL) number of 0.99, where

$$\mathrm{CFL} \equiv c\frac{\Delta t}{\Delta x}. \tag{33}$$

Fifty-three virtual microphones were placed in the computational domain at regular intervals along the path of the wave. The spectrum of the recorded time waveforms received from each microphone were normalized and compared to the Fubini solution:[1]

$$B_n = \frac{2}{n\sigma} J_n(n\sigma), \tag{34}$$

where B_n is the Fourier component amplitude for harmonic n, J_n the Bessel function of the first kind, n the harmonic number, $\sigma = x/\bar{x}$, and $\bar{x}$ the plane wave sinusoidal shock formation distance, given as

$$\bar{x} = \frac{1}{\beta \epsilon k}, \tag{35}$$

where β is the coefficient of nonlinearity, ϵ the acoustic mach number, and k the wave number. The comparison between the Fubini solution and the numerical results are shown in Fig. 1 for $n=1$, 2, and 3. Only the first three harmonics are included for clarity, but it should be noted that

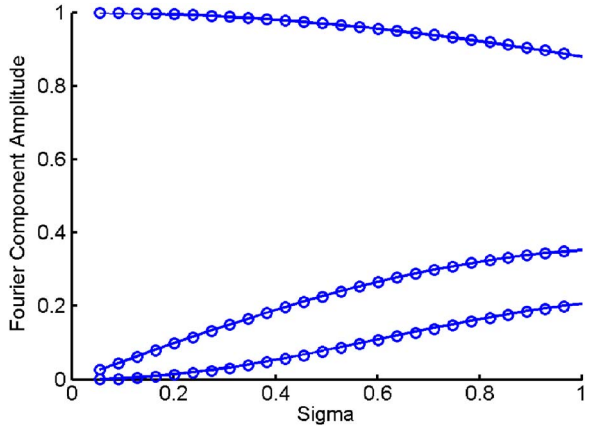

FIG. 1. (Color online) Graph of Fourier component amplitudes as a function of shock formation distance showing the comparison between the Fubini solution (solid line) and the normalized computed solution (circles) for the first three harmonic components of a 1 MHz plane wave traveling in a lossless medium. For clarity, every other data point for the computed solution has been omitted.

the Fubini solution matches the numerical solution far beyond the third harmonic. The percent difference between the two approaches is at most 0.23% for the first harmonic throughout the entire domain. The time waveforms at four different propagation distances are given in Fig. 2.

Using the same computational parameters, the test was rerun with thermoviscous losses turned on. This includes bulk viscosity, shear viscosity, and thermal conductivity. The results were compared to Mendousse's solution of Burgers' equation given by Pierce:[1]

$$\frac{p}{p_0} = \frac{\frac{4}{\Gamma}\sum_{n=1}^{\infty}(-1)^{n+1}I_n\left(\frac{\Gamma}{2}\right)ne^{-n^2\sigma/\Gamma}\sin(n\omega t')}{I_0\left(\frac{\Gamma}{2}\right)+2\sum_{n=1}^{\infty}(-1)^{n}I_n\left(\frac{\Gamma}{2}\right)ne^{-n^2\sigma/\Gamma}\cos(n\omega t')} \tag{36}$$

where

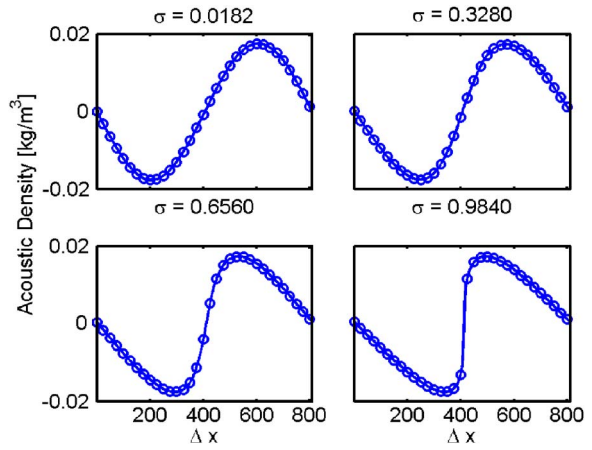

FIG. 2. (Color online) Graph showing the comparison between the time waveforms resulting from the analytical solution (solid line) and the computed solution (circles) at four different propagation distances in a lossless medium. The y axis is the acoustic density (kg/m^3), $\rho-\rho_0$, and the x axis is the grid point number.

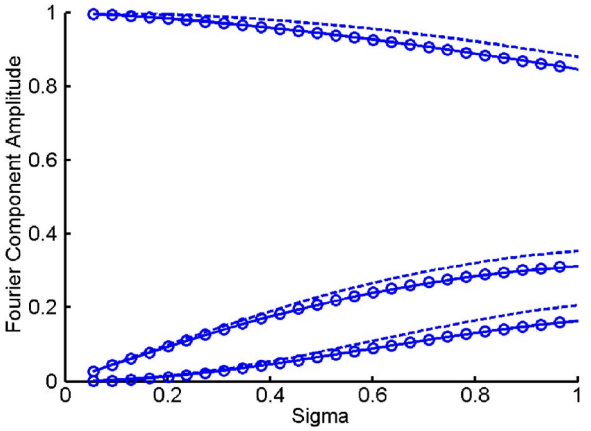

FIG. 3. (Color online) Graph of Fourier component amplitudes as a function of shock formation distance showing the comparison between the Fubini solution (dashed line) for a lossless medium, and the Burgers solution (solid line) and the computational model's solution (circles) for a medium including classical absorption and molecular relaxation of nitrogen and oxygen. For clarity, every other data point for the computed solution has been omitted.

$$\Gamma = \frac{c^3}{\delta\omega^2\bar{x}}, \tag{37}$$

$$\delta = \frac{\mu}{2\rho}\left[\frac{4}{3}+\frac{\mu_B}{\mu}+\frac{(\gamma-1)\kappa}{c_p\mu}\right], \tag{38}$$

t' the retarded time, I_n the modified Bessel functions, c_p the specific heat at constant pressure, and γ the ratio of specific heats. The comparison of the two is shown in Fig. 3 again for only the first three harmonics. The difference between the two solutions is at most 0.16% for the first harmonic. The time waveforms at various propagation distances are given in Fig. 4.

The next test demonstrates the ability of the code to predict amplification factors at a rigid boundary. In a linear system pressure doubling occurs at a rigid boundary, but for nonlinear systems of large enough incident pressure ampli-

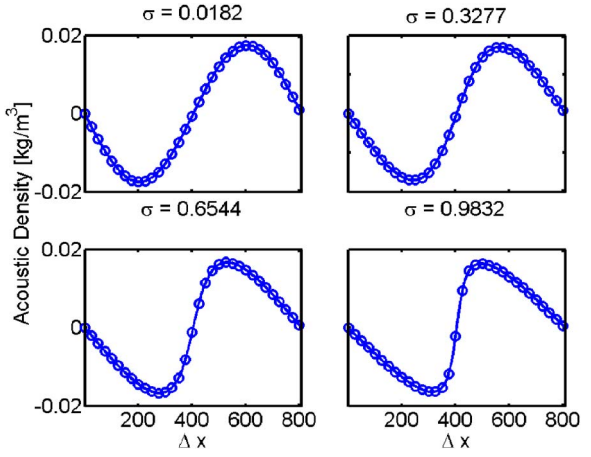

FIG. 4. (Color online) Graph showing the comparison between the time waveforms resulting from the analytical solution (solid line) and the computed solution (circles) at four different propagation distances at 1 MHz and in a medium including classical absorption and molecular relaxation of nitrogen and oxygen. The y axis is the acoustic density (kg/m^3) and the x axis is the grid point number.

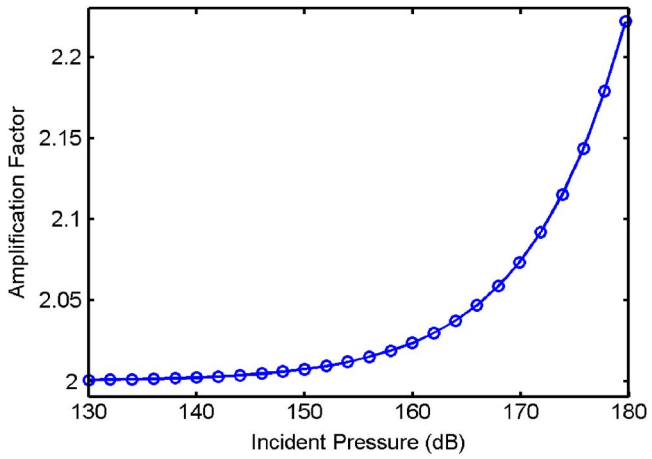

FIG. 5. (Color online) Graph of amplification factor for a plane wave pulse incident upon a perfectly rigid boundary in a lossless medium as a function of incident pressure comparing the Pfriem solution (solid line) and the computed solution (circles).

tudes, amplification factors will be greater than two. This amplification factor for normal incidence may be determined using the Pfriem solution:[17]

$$\mathbf{a} = \frac{[2(p_{\text{inc}}/p_0)^{1/\chi} - 1]^{\chi} - 1}{p_{\text{inc}}/p_0 - 1}, \tag{39}$$

where

$$\chi = \frac{2\gamma}{\gamma - 1}. \tag{40}$$

Here, p_{inc} is the total incident pressure and **a** the amplification factor, which again equals two in the linear acoustic regime. The test was performed by propagating Gaussian-distributed plane wave pulses of varying amplitude through a lossless domain and onto a rigid boundary. The rigid boundary was created by imposing on an $N \times M$ sized grid that for all j,

$$\rho(N,j) = \rho(N-1,j), \tag{41}$$

$$u(N,j) = -u(N-1,j), \tag{42}$$

$$v(N,j) = v(N-1,j), \tag{43}$$

$$s_{\text{fr}}(N,j) = s_{\text{fr}}(N-1,j), \tag{44}$$

$$T_{N_2}(N,j) = T_{N_2}(N-1,j), \tag{45}$$

and

$$T_{O_2}(N,j) = T_{O_2}(N-1,j). \tag{46}$$

Waves at 1 MHz were propagated in a lossless domain of 4001×7 points using a value of 8.575×10^{-8} m for Δx and 3.125×10^{-11} s for Δt. A virtual microphone was placed on the boundary and a time history of the pressure was recorded as the plane wave pulse approached and reflected off the rigid boundary. The peak pressure was then taken and used in the calculation of the amplification factor. The comparison between the Pfriem solution, Eq. (39) and the computational results are shown in Fig. 5. The percent difference between the two results is within 0.015% over the entire range of amplitudes.

The next set of results demonstrate the ability of the code to simulate the effects of classical absorption (including bulk viscosity) and molecular relaxation absorption of nitrogen and oxygen. First, Gaussian-distributed line sources were propagated over a frequency range of 10 Hz–1 MHz with only the modified classical absorption mechanisms (shear viscosity, bulk viscosity, and thermal conductivity) included in the calculation. Typical computational parameters included a grid size of $10\,001 \times 7$ points with 200 points per wavelength, a CFL number of 0.99, and amplitude of 108 dB re 20 μPa. Line sources were used so that the cylindrical spreading inherent to the propagation in the two-dimensional computational domain was avoided, and the only nonnumerical loss observed was due to the particular mechanism that was turned on. The analytical, modified classical absorption equation is given by[1]

$$\alpha'_{\text{cl}} = \frac{\omega^2 \mu}{2\rho_0 c^3}\left[\frac{4}{3} + \frac{\mu_B}{\mu} + \frac{(\gamma-1)\kappa}{c_p \mu}\right]. \tag{47}$$

The absorption coefficient values were determined using the decay envelope of the propagated wave.

Absorption tests using the same parameters used in the classical absorption calculation were performed with only nitrogen relaxation and then only oxygen relaxation turned on. The analytical relaxation absorption equation is given by[1]

$$\alpha_\nu = \frac{1}{\lambda}(\alpha_\nu \lambda)_m \frac{2\omega\tau_\nu}{1 + (\omega\tau_\nu)^2}, \tag{48}$$

where

$$(\alpha_\nu \lambda)_m = \frac{\pi}{2}\frac{(\gamma-1)c_{u\nu}}{c_p} \tag{49}$$

and λ is the wavelength. All of the absorption mechanisms (classical absorption and molecular relaxation) were then turned on and the total absorption of the model was tested. The analytical absorption curve for the combination of classical absorption and nitrogen and oxygen relaxation has been shown analytically[18] and experimentally[19] to be equal to a sum of the three for frequencies below 10 MHz; thus, the following analytical form is used in the comparison:

$$\alpha = \alpha'_{\text{cl}} + \alpha_{N_2} + \alpha_{O_2}. \tag{50}$$

The results for all four tests described above are given in Fig. 6. The percent differences for all four tests stay within 1% of the analytical results, and it is the authors' belief that finer grids would decrease this difference further. However, the results are sufficient to show that the model can accurately recreate atmospheric absorption, and any further tests are left for future work.

The next results show the effect of molecular relaxation upon the propagation speed of waves of different frequencies. Again, using a Gaussian-distributed line source, the speed of propagation of monofrequency waves was determined over a variety of frequencies and using a variety of atmospheric conditions. The model used 200 points per wavelength, a grid size of 7501×3 points, a Gaussian half-

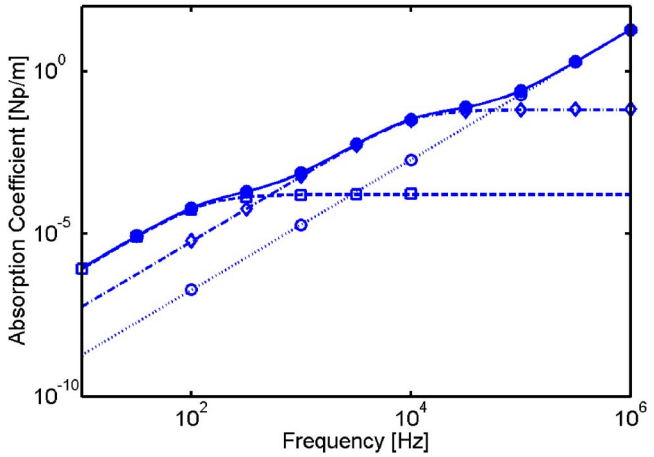

FIG. 6. (Color online) Summary of the absorption calculated for four different conditions: analytical modified classical absorption (dotted line) and calculated modified classical absorption (open circles); analytical nitrogen relaxation absorption (dashed line) and calculated nitrogen relaxation absorption (squares); analytical oxygen relaxation absorption (dash-dot line) and calculated oxygen relaxation absorption (diamonds); and analytical total atmospheric absorption (solid line) and calculated total atmospheric absorption (closed circles).

width equal to 10% of a wavelength, and a source amplitude of 108 dB re 20 μPa. The analytical result for the variation of sound speed as a function of frequency is given as[1]

$$v_{\mathrm{ph}} = c - \frac{c}{\pi}\sum_{\nu}\frac{(\alpha_\nu \lambda)_m}{1+\omega^2\tau_\nu^2}, \tag{51}$$

where v_{ph} is the phase velocity. Using only nitrogen relaxation, the wave speed of the computational model was determined and is compared to the analytical result in Fig. 7. The difference between the equilibrium (low-frequency limit) sound speed and the frozen (high-frequency limit) sound speed,[20] another important parameter in molecular dispersion, was determined to be approximately 0.0209 m/s over the frequency range given. The analytical result for this is given by[1]

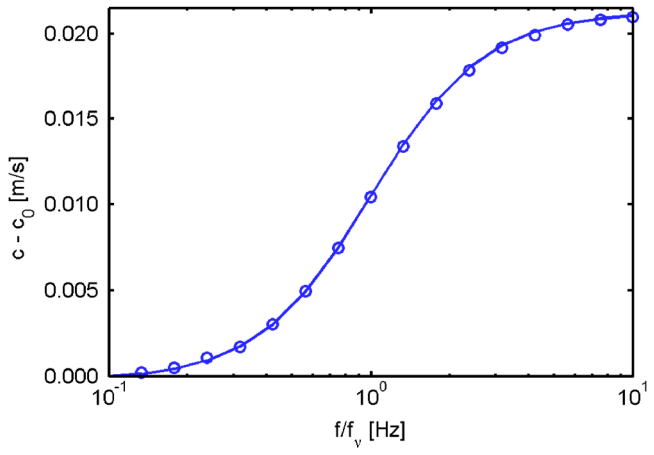

FIG. 7. (Color online) Graph of the calculated sound speed minus the equilibrium sound speed as a function of frequency normalized by the relaxation frequency showing the comparison between the analytical dispersion curve (solid line) and the computed solution (circles) for a medium including nitrogen relaxation only.

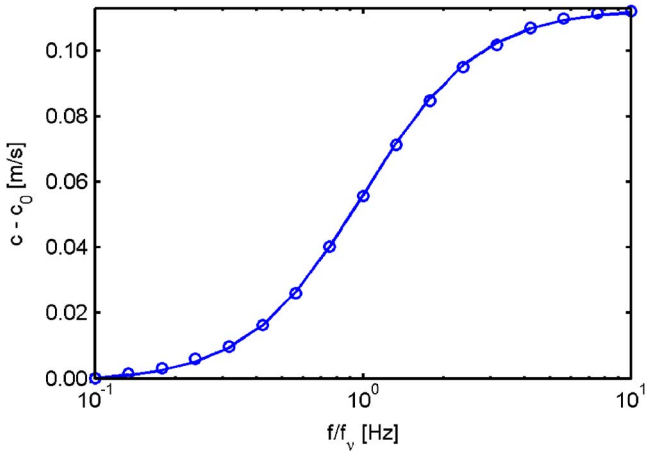

FIG. 8. (Color online) Graph of the calculated sound speed minus the equilibrium sound speed as a function of frequency normalized by the relaxation frequency showing the comparison between the analytical dispersion curve (solid line) and the computed solution (circles) for a medium including oxygen relaxation only.

$$\Delta c_\nu = \frac{c}{\pi}(\alpha_\nu \lambda)_m, \tag{52}$$

where Δc_ν the difference between the equilibrium and frozen sound speeds, which is equal to 0.0211 m/s for the frequencies used in the calculation, a percent difference of 0.731%.

Next, the dispersion due to oxygen relaxation was investigated using the same parameters as that for nitrogen. Using only oxygen relaxation, the wave speed of the computational model was measured and is compared to the analytical result in Fig. 8. The value of Δc_ν for oxygen was determined to be approximately 0.112 m/s over the frequencies used in the calculation, compared to the analytical result of 0.111 m/s using Eq. (53), a percent difference of 0.503%.

Finally, the dispersion that occurs with both oxygen and nitrogen relaxation included was investigated using the same parameters as those used earlier. The resulting analysis and its comparison to the analytical result is given in Fig. 9. The

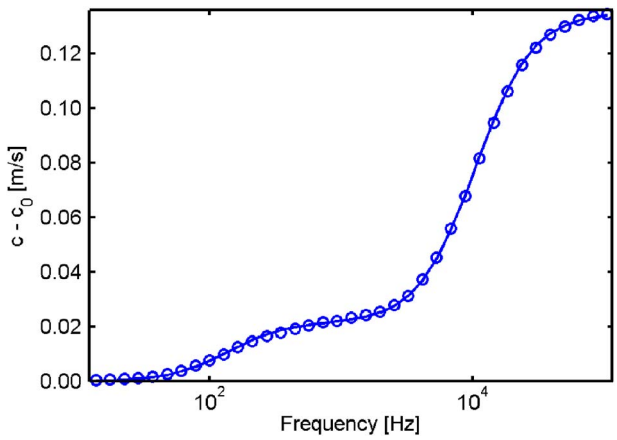

FIG. 9. (Color online) Graph of the calculated sound speed minus the equilibrium sound speed as a function of frequency showing the comparison between the analytical dispersion curve (solid line) and the computed solution (circles) for a medium including nitrogen and oxygen relaxation only.

difference between the analytical and computational dispersion is at most 0.280%.

V. CONCLUSIONS

This investigation has shown that by solving a set of nonlinear fluid dynamic equations that include the effects of shear viscosity, bulk viscosity, thermal conductivity, molecular relaxation and relative humidity using an accurate time-domain finite-difference solution scheme, realistic absorption, dispersion, and nonlinear phenomena can be simulated. In essence, a computational acoustical workspace has been created: one that can handle complex acoustical phenomena and simulate atmospheric absorption and dispersion. Although the numerical solution has proven itself to be accurate and reliable, improvements are possible, such as using sophisticated boundary conditions like the perfectly matched layer described by Berenger[21] that would allow for high-quality nonreflecting boundary conditions. For the long-range propagation of shock waves, another region of interest in nonlinear acoustics, a weighted essentially nonoscillatory (WENO) scheme such as the one described by Shu[22] may eventually replace the dispersion-relation-preserving algorithm used currently. The WENO scheme has been shown to propagate discontinuities with very low oscillatory behavior and also to have a similarly high order of accuracy.

ACKNOWLEDGMENTS

The authors would like to thank Dr. Said Boluriaan for his helpful discussions. The authors would also like to thank the reviewers of this manuscript for their thoroughness and helpful suggestions, in particular Dr. Richard Raspet for his suggestions on proper state equations for this numerical model. This work is supported by the Office of Naval Research and the Exploratory and Fundamental Program of the Applied Research Laboratory at The Pennsylvania State University.

[1]A. D. Pierce, *Acoustics: An Introduction to Its Physical Principles and Applications* (Acoustical Society of America, New York, 1989).
[2]V. W. Sparrow and R. Raspet, "A numerical method for general finite amplitude propagation in two dimensions and its application to spark pulses," J. Acoust. Soc. Am. **90**, 2683–2691 (1991).
[3]R. O. Cleveland, "Time-domain modeling of finite-amplitude sound in relaxing fluids," J. Acoust. Soc. Am. **99**, 3312–3318 (1996).
[4]R. O. Cleveland, J. P. Chambers, H. E. Bass, R. Raspet, D. T. Blackstock, and M. F. Hamilton, "Comparison of computer codes for the propagation of sonic boom waveforms through isothermal atmospheres," J. Acoust. Soc. Am. **100**, 3017–3027 (1996).
[5]P. J. Morris, L. N. Long, T. E. Scheidegger, and S. Boluriaan, "Simulations of supersonic jet noise," Int. J. Aeroacoust. **1**, 17–41 (2002).
[6]C. K. W. Tam and K. A. Kurbatskii, "Multi-size-mesh multi-time-step dispersion-relation-preserving scheme for multiple-scales aeroacoustics problems," Int. J. Comput. Fluid Dyn. **17**, 119–132 (2003).
[7]C. K. W. Tam, "Computational aeroacoustics: An overview of computational challenges and applications," Int. J. Comput. Fluid Dyn. **18**, 547–567 (2004).
[8]L. N. Long, P. J. Morris, and A. Agarwal, "A review of parallel computing in computational aeroacoustics," Int. J. Comput. Fluid Dyn. **18**, 493–502 (2004).
[9]K. A. Kurbatskii and R. R. Mankbadi, "Review of computational aeroacoustics algorithms," Int. J. Comput. Fluid Dyn. **18**, 533–546 (2004).
[10]Reference 1. Equations (1)–(4) are given in Pierce as equations (1-2.4), (10-7.19), (10-7.20), and (10-7.22), respectively.
[11]Reference 1. Equations (5)–(8) are given in Pierce as equations (10-17.18), (10-1.10), (10-7.14), and (10-7.15), respectively.
[12]F. W. Sears and G. L. Salinger, *Thermodynamics, Kinetic Theory, and Statistical Thermodynamics* (Addison-Wesley, Reading, 1975).
[13]K. Wark, *Thermodynamics* (McGraw-Hill, New York, 1977).
[14]J. D. Anderson, *Computational Fluid Dynamics: The Basics with Applications* (McGraw-Hill, New York, 1995).
[15]H. E. Bass, L. C. Sutherland, A. J. Zuckerwar, D. T. Blackstock, and D. M. Hester, "Atmospheric absorption of sound: Further developments," J. Acoust. Soc. Am. **97**, 680–683 (1995).
[16]C. K. W. Tam and J. C. Webb, "Dispersion-relation-preserving finite difference schemes for computational acoustics," J. Comput. Phys. **107**, 262–281 (1993).
[17]D. T. Blackstock, "Nonlinear acoustics (theoretical)," in *American Institute of Physics Handbook*, 3rd ed., edited by D. E. Gray (McGraw Hill, New York, 1972), pp. 3-183–3-205.
[18]H.-J. Bauer, "Influences of transport mechanisms on sound propagation in gases," Adv. Mol. Relax. Processes **2**, 319 (1972).
[19]L. B. Evans, H. E. Bass, and T. G. Winter, "Precautions with classical absorption," J. Acoust. Soc. Am. **48**, 771–772 (1970).
[20]In order to avoid confusion it should be noted that for Fig. 10-12(b) in Pierce (Ref. 1), the labels for equilibrium and frozen sound speed are printed in reverse positions.
[21]J. Berenger, "A perfectly matched layer for the absorption of electromagnetic waves," J. Comput. Phys. **114**, 185–200 (1994).
[22]C.-W. Shu, "Essentially non-oscillatory schemes for hyperbolic conservation laws," in *Advanced Numerical Approximation of Nonlinear Hyperbolic Equations*, edited by B. Cockburn, C. Johnson, C.-W. Shu, and E. Tadmor, Lecture Notes in Mathematics (Springer, Berlin, 1998), Vol. 1697, pp. 325–432.

Ocean sound channel ray path perturbations from internal-wave shear and strain

Timothy F. Duda
Applied Ocean Physics and Engineering Dept., MS 11, Woods Hole Oceanographic Institution, Woods Hole, Massachusetts 02543

(Received 16 December 2004; revised 13 July 2005; accepted 1 August 2005)

The relative importance of internal-wave strain and internal-wave shear on perturbation of acoustic ray trajectories in the ocean is analyzed. Previous estimates based on the Garrett-Munk internal-wave spectral model are updated using data from recent field studies of internal waves. Estimates of the ratio of the rms shear effect to the rms strain effect based on data from the upper kilometer of ocean are as high as 0.25–0.4, exceeding the estimates of 0.08–0.17 stemming from the model. Increased strength of three phenomena that have shear to strain ratios higher than the internal-wave average can cause this effect. These are near-inertial waves, internal tides, and vortical modes. © *2005 Acoustical Society of America.* [DOI: 10.1121/1.2062127]

PACS number(s): 43.30.Cq, 43.30.Ft, 43.30.Re [WLS] Pages: 2899–2903

I. INTRODUCTION

Small-scale temporally variable perturbations to the average ocean sound channel have been known for some time to cause acoustic field variability. Based on work motivated by reciprocal-transmission measurement of currents [Worcester (1977)], studies of variability generally neglect the effect of fluctuating current shear with respect to the effect of the fluctuating vertical derivative of sound-speed [Colosi, Flatté, and Bracher (1994); Flatté (1983) Sec. II D; Munk, Worcester, and Wunsch (1995)]. Those studies use the Garrett-Munk (GM) spectral model of internal waves to describe perturbation strain in the ocean. [GM describes both strain and shear in the case of Worcester (1977)]. The strain is responsible for sound-speed perturbations. However, measurements from the ocean suggest that conditions may vary from GM. In particular, stronger shear to strain ratios have been observed than are consistent with GM, so the relative strength of the two terms is revisited here and in another paper [Colosi (2005)].

The relative effects of strain and shear on ray-path perturbations are chosen for analysis, rather than some other aspect of the acoustic field, because a ramification of ocean medium fluctuations is temporally variable ray-path alteration, which is one manner of describing acoustic field fluctuations [Simmen, Flatté, and Wang (1997)]. Also, the path perturbations themselves have been suggested to be an important indicator of sound field variability (Beron-Vera and Brown (2003); Brown *et al.* (2003); Brown and Viechnicki (1998); Smith, Brown, and Tappert (1992); Virovlyansky (2003))]. Ray paths can fluctuate rapidly because of two internal wave effects: changes to the vertical gradient of sound-speed caused by internal-wave vertical strain, and to the vertical component of internal-wave shear.

Here, it is reported that the rms shear effect on rays may be as large or larger than one-quarter the rms strain effect, which is roughly double the 13% effect predicted using GM. Both ratios refer to effects on rays in the upper ocean, where both effects will have their maximum effect on rays. This means that it may be important to include shear effects in some situations. For completeness, expressions that govern ray trajectories in the presence of internal wave currents that have an angle/depth form are derived. This form facilitates comparison by having terms related to shear and strain in only one equation. Next, the rms magnitudes of various perturbation terms controlling ray curvature are examined as functions of depth in the ocean sound channel, and are compared with curvature imposed by the mean profile of sound speed.

The paper is organized in the following way. In Sec. II, the ray equations valid in a moving medium in the form appropriate for the deep-ocean sound channel are given. In Sec. III, the sizes of various perturbation terms in the ray angle equation are investigated, showing the relative importances of various small-scale effects. Results obtained using the GM model and using oceanic data are computed and are compared to each other. Sec. IV is a summary.

II. RAY TRAJECTORIES IN A MOVING INHOMOGENEOUS MEDIUM

The analysis uses an angle/depth version of the equations governing ray trajectories in an inhomogeneous medium with inhomogeneous motion. These equations can be derived using the calculus of variations and Fermat's principle of least time. This approach is outlined in one reference [Munk, Worcester, and Wunsch (1995)], and appears in a report [Bowlin *et al.* (1993)] (The report may be found online). To apply Fermat's principle to long-range propagation in the ocean sound channel, we must assume that the ray approximation, as derived from Helmholtz equation via the eikonal equation [Ostashev (1997), for example], a high-wavenumber model, provides a valid description of the physics at the frequency of interest. The ray approximation has been shown to hold at frequencies as low as 75 Hz [Colosi *et al.* (1999)].

Mathematically, Fermat's principle is expressed by setting the variation of the time to zero,

$$\delta T = \delta \int dt = 0, \tag{1}$$

where the integral on the right hand side is over the path of the ray with fixed limits of integration and where δ is any (differentiable) variation in the path that keeps the end points fixed. In order to find the path we convert the integral over dt to an integral over path length ds using the slowness in the moving medium

$$Q = dt/ds = 1/(c + u_s) = 1/(c + u_r \cos\theta + u_z \sin\theta), \tag{2}$$

where c is the sound speed, u_r and u_z are medium velocity components along horizontal r axis and vertical z axes, and u_s is the medium velocity in the direction of the ray. θ is the angle between the ray and the horizontal. Out-of-plane velocity is disregarded. This gives

$$\delta T = \delta \int Q ds. \tag{3}$$

The path length can be expressed in terms of Cartesian coordinates x_i as $ds = (dx_i dx_i)^{1/2}$ where we use the summation convention of implicitly summing over repeated indices.

Using manipulations common in the calculus of variations yields

$$\delta T = \int \delta x_i \left(\partial_i Q - \frac{d}{ds}(Q\dot{x}_i) \right) ds, \tag{4}$$

where a dot over a quantity indicates the total derivative of the quantity with respect to s. For this expression to be zero for any and all variations, the term within parentheses must equal zero. This yields the ray equation, which may be also be written

$$\ddot{x}_i = \frac{\partial_i Q}{Q} - \dot{x}_i \left(\dot{x}_j \frac{\partial_j Q}{Q} \right). \tag{5}$$

The components $\dot{x}_i$ form a unit vector pointing along the direction of the ray. The second term on the right hand side is the projection of $\nabla Q/Q$ in the $\dot{x}$ direction. Thus $\ddot{x}$ is equal to that part of $\nabla Q/Q$ which is perpendicular to the path of the ray.

To put this into a more familiar form used in ocean acoustics, and applying the typically used restriction of propagation only within a plane, consider the ray angle θ. The r component of the resulting ray equation is an expression for $\dot{\theta}$,

$$Q\dot{\theta} = \partial_z Q \cos\theta - \partial_r Q \sin\theta. \tag{6}$$

The slowness $S = 1/c$ is typically used in derivations of this type, instead of the quantity Q used here. The inclusion of medium velocity in the slowness implies that an advective push of the sound does not invalidate Fermat's principle, which may be intuitive. Intuition does not constitute a proof, however. Fortunately, a proof that Fermat's principle is valid for a moving medium has recently been published [Godin and Voronovich (2004)].

A few manipulations yield

$$\frac{d\theta}{dr} = -Q(\partial_z c + \partial_z u_r \cos\theta + \partial_z u_z \sin\theta) + Q\tan\theta(\partial_r c + \partial_r u_r \cos\theta + \partial_r u_z \sin\theta). \tag{7}$$

Now, expand Q with u_i/c as a small parameter, giving

$$\frac{d\theta}{dr} = -c^{-1}(1 - u_r\cos\theta/c - u_z\sin\theta/c)(\partial_z c + \partial_z u_r \cos\theta + \partial_z u_z \sin\theta) + c^{-1}\tan\theta(1 - u_r\cos\theta/c - u_z\sin\theta/c) \times (\partial_r c + \partial_r u_r \cos\theta + \partial_z u_z \sin\theta). \tag{8}$$

Eighteen terms remain on the right hand side. With no motion this is the basic ray angle equation. The other terms show the effects of advection, which are small in the ocean. If the sound speed is written as a basic profile plus perturbations $c(r,z) = c_o(z) + c'(r,z)$, and if we delete most of the derivatives with respect to range, which are smaller than derivatives with respect to vertical because the ocean is known to have anisotropic perturbations, then we can write an expression that includes the effects of velocity and sound speed perturbations

$$\frac{d\theta}{dr} = -c_o^{-1}(1 - c'/c_o - u_r\cos\theta/c_o - u_z\sin\theta/c)(\partial_z c_o + \partial_z c' + \partial_z u_r \cos\theta + \partial_z u_z \sin\theta - \partial_r c_o \tan\theta), \tag{9}$$

where terms of higher order in c'/c_o have been omitted. Further analysis in the next section shows the relative influences of the anomaly c', the shear $\partial_z u_r$, the strain $\partial_z u_z$, and the velocities u_r and u_z.

An additional equation needed to trace rays is that for ray height

$$\frac{dz}{dr} = \tan\theta. \tag{10}$$

If travel time is of interest, it is given to first order in u_i/c by this expression:

$$\frac{dt}{dr} = \frac{\sec\theta}{c}(1 - u_r\cos\theta/c - u_z\sin\theta/c). \tag{11}$$

The advective effect of the medium velocity enters in an intuitive way.

Note that (9)–(11) have the same meaning as the sets of equations appearing in other works [Franchi and Jacobson (1972); Lamancusa and Daroux (1993); Ostashev (1997)], which might have been chosen for analysis instead. However, the form used here contains medium properties in only one of the two geometry equations, facilitating the analysis.

III. COMPARISON OF PERTURBATION TERMS

To first order in u_i/c_o and c'/c_o, rewrite (9) as

$$\frac{d\theta}{dr} = -c_o^{-1}[\partial_z c_o(1 - c'/c_o - u_r\cos\theta/c_o - u_z\sin\theta/c_o) + \partial_z c' + \partial_z u_r \cos\theta + \partial_z u_z \sin\theta - \partial_r c_o \tan\theta]. \tag{12}$$

Here, we have taken advantage of the fact that small-scale ocean sound-speed and velocity perturbations have red spec-

tra [Garrett and Munk (1975); Pinkel (1984)], so that most of the energy is at low wavenumbers, below order $2\pi/(500\ \mathrm{m})$ in the horizontal and order $2\pi/(100\ \mathrm{m})$ in the vertical. This means that the differentiation operation on perturbations (multiplication by wavenumber for members of a Fourier expansion) reduces magnitude, so that many derivative terms have been omitted.

There are eight terms on the right-hand side of (12). Although many small terms have already been neglected, many remaining terms are typically also quite small and could sensibly be omitted for almost all ocean acoustic situations. There is no danger in retaining these terms, however, although their presence may obscure the essential physics. The danger lies in incorrectly omitting significant terms. The first and last terms in (12) represent the effect of the unperturbed sound channel. Between them are six perturbation terms. The first three perturbation terms are corrections to the rate of change of θ versus r that arise because the sound is not traveling at the background speed c_o. These are very small and are not considered any further. Term 7 is expected to be much less than term 2 and is also not evaluated. (The ratio of term 7 to term 2 for a wave of angular frequency ω is $\omega/\partial_z c_o$.) The relative sizes of the remaining perturbation terms (5 and 6, $\partial_z c'$ and $\partial_z u_r \cos\theta$) are examined in the next section using two methods: Computations involving GM model internal-wave spectra, and evaluation in terms of directly observed small-scale velocities and sound-speed perturbations. Because a number of papers have shown that realistically scaled perturbations c' can lead to large ray path alterations about a mean state [Beron-Vera and Brown (2003); Virovlyansky (2003)], we must only show that $\partial_z u_r \cos\theta$ is similar to $\partial_z c'$ in magnitude in order to verify its importance.

A. Analysis of terms using a spectral model

The GM model spectrum, which fits observed internal wave spectra in most regions of the deep ocean (away from the uppermost 500 m) within about a factor of three, provides expressions for variances of internal wave horizontal velocity $\hat{u}=\hat{r}u_r+\hat{y}u_y$, shear $d\hat{u}/dz$, displacement η, and strain $\partial_z\eta$. Hat indicates vector. $\hat{r}$ and $\hat{y}$ are unit vectors. The square roots of these provide useful estimates of typical perturbation term magnitudes. Worcester (1977) has already analyzed the relative sizes of terms 5 and 6 using the GM model spectrum and a canonical sound-speed profile. Only a few numbers are given, however, and subsequent work has formalized the relationship between shear variance and strain variance in the model, so a similar analysis is included here. Also, the GM model was new at the time of that publication, and details concerning how it compares with oceanic data have since been uncovered. These are discussed here.

The GM model expresses wave spectral density in terms of frequency and vertical mode number. Manipulations allow spectra in terms of frequency, horizontal wavenumber, and vertical wavenumber to also be written. The dispersion relation, which relates wavenumber angle from the horizontal to frequency, constrains the model, so that only two of those three are independent. The primary features of GM are symmetry in vertical wavenumber, horizontal isotropy, and separable wavenumber and frequency dependencies. The fair agreement with observation stems in part from the fact that the model parameters were deduced from observations [Garrett and Munk (1975)]. Some of the differences between GM and actual ocean spectra are pertinent to this work and are discussed later.

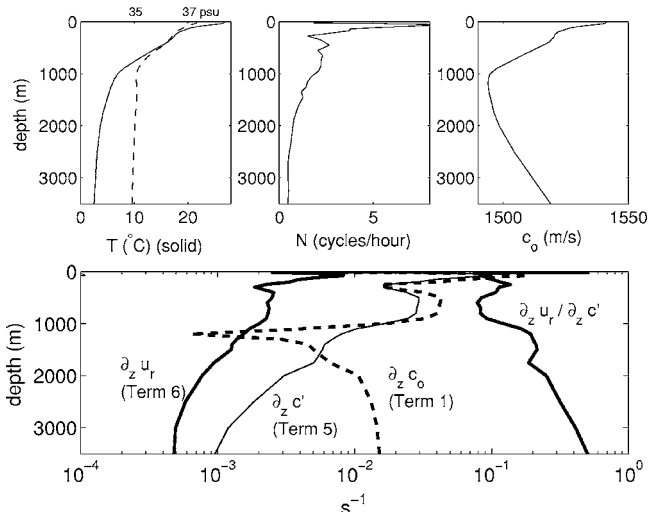

FIG. 1. The top left panel shows temperature $T(z)$ and salinity $S(z)$ (dashed line) profiles used in the GM model computation of fluctuation term rms values. The top center and top right panels show buoyancy-frequency and sound-speed profiles computed from $T(z)$ and $S(z)$. The lower panel shows rms magnitudes of terms 1 (mean profile), 5 (strain), and 6 (shear) in Eq. (12). The lower panel also shows the dimensionless ratio of shear to strain rms magnitudes at the right, as a function of depth. The shear to strain ratio R_ω is 3 in the GM model. Higher R_ω have been observed in the ocean, implying a higher ratio of shear to strain effects.

For given temperature and salinity profiles, the GM model yields expressions for the four variances of interest that are functions of depth, with depth-dependence parameterized in terms of the buoyancy frequency $N(z)$, which is proportional to the density gradient. For this computation, profiles from the summer Levitus database for the position 27° N, 48° W in the North Atlantic are chosen [Levitus (1982)]. From these, $N(z)$ and $c_o(z)$ are computed (Fig. 1). For the GM76 version of the model, the variances are given as follows [Gregg (1989)]

$$\langle u^2\rangle = \langle u_r^2\rangle + \langle u_y^2\rangle = (3/2)b^2 E N_0^2 (N/N_0), \tag{13}$$

$$\langle (\partial_z u)^2\rangle_{k_u} = (3/2)\,\pi E b j_* N_0^2 k_u (N/N_0)^2, \tag{14}$$

$$\langle \eta^2\rangle = (1/2)Eb^2 (N/N_0)^{-1}, \tag{15}$$

$$\langle (\partial_z \eta)^2\rangle_{k_u} = \langle (\partial_z u)^2\rangle_{k_u}/(R_\omega N^2), \tag{16}$$

where $E=6.3\times10^{-5}$ is the dimensionless energy parameter, $N_0=5.2\times10^{-3}$ (3 cph), f is the Coriolis frequency, $b=1300$ m is the stratification length scale, and $j_*=3$ is the internal wave bandwidth parameter. The shear to strain ratio R_ω is 3 for the GM model. The notation $\langle\ \rangle_{k_u}$ means integrated up to cut-off vertical wavenumber k_u. The final expression stems from a different paper than the others [Polzin, Toole, and Schmitt (1995)]. Note that b

=1300 m is almost universally chosen when the GM spectrum is evaluated, despite the fact that the $N(z)$ profile rarely has the form $\exp(z/1300)$, particularly in the upper 500 m.

Rms values of $u_r, \partial_z u_r, \eta$, and strain $\partial_z \eta$ are found by taking the square roots. Rms magnitudes of the horizontal velocity and shear terms (third and sixth) of (12) can then be computed directly. The c' terms (second and fifth) require conversion of displacement to sound speed perturbation via $c' = \eta(\partial_z c_o - \gamma_a c_o)$ where γ_a is the adiabatic sound speed gradient, typically 1.1×10^{-5} m^{-1}, and via $\partial_z c' \approx \partial_z \eta(\partial_z c_o - \gamma_a c_o)$

The lower part of Fig. 1 shows the magnitudes of the rms values of three of the five terms chosen for analysis, as functions of depth. Terms 2 and 3 lie off the left edge of the plot, varying between 10^{-7} at great depths and 10^{-4} at shallow depths. The shear term (number 6) is a little smaller than the $\partial_z c'$ strain term (number 5). Both exceed the magnitude of the background term (number 1) near the sound channel axis. The strain term is seen to give an appreciable effect in the upper water column, consistent with the results of the papers showing ray path fluctuation cited previously. The shear term approaches the strain term in magnitude at depth, but each are smaller than $\partial_z c_o$ (term 1) there.

Shear term rms values are smaller than strain term rms values at all depths for this model, with the ratio ranging from 0.08 to 0.15 in the upper kilometer. (These are different values than obtained by Worcester using the canonical profile). However, we have two reasons to believe that the GM model underestimates shear with respect to strain. One reason is that GM does not include near-inertial waves, which have high shear and low strain, to the degree sometimes observed in the field, and does not include the spectral peaks at tidal bands (internal tides) that are apparent in some data [Nash *et al.* (2004)]. An excess of these types of waves at the low-frequency end of the internal-wave band would increase the shear to strain spectral ratio above the GM value of $R_\omega = 3$. (Some data sets do not provide enough information to compute $R_\omega = 3$.) Another reason is that $R_\omega > 3$ have been observed in the upper kilometer of water at many locations [Polzin *et al.* (2003)], implying that excess low-frequency waves and/or finescale velocity features such as zero-frequency geostrophically balanced vortical modes (not included in GM), may be prevalent. The shear variances at those locations exceed that of GM, while the strain variances are in line with GM. This would boost the shear term contribution to trajectory perturbations a factor of about three in the extreme cases, increasing the shear-effect to strain-effect ratios to the range 0.24 to 0.45.

B. Observational evidence

The GM model is a useful benchmark for intercomparison of observed internal wave spectra. However, even with adjustments such as made at the end of the previous section, it does not fully describe many observed spectra, particularly those in the upper ocean [Duda and Cox (1989); Pinkel (1984); Pinkel (1985)]. The separability criterion is notably troublesome. Thus, it is prudent to estimate perturbation term sizes by looking directly at shear and strain data. Multiplication of the GM spectrum by a scaling factor so that it matches observed rms shear, for example, might not produce rms strain that also matches the observations.

Data sets providing concurrent estimates of rms shear $\partial_z u_r$ and rms $\partial_z c'$ are available. One such data set was collected in the North Atlantic Tracer Release Experiment (NATRE) in the North Atlantic Ocean at 25-27°N, 28-35°W [Duda and Jacobs (1995); Ledwell, Watson, and Law (1998)]. Using data from a profiling float, rms shear values from a depth range of approximately 250–425 m were measured to be 0.005 s^{-1} in the fall of 1992 and 0.007 s^{-1} in the spring of 1993 [Duda and Jacobs (1995)]. These must be multiplied by 0.707 to get standard deviation for a single component. The resulting rms $\partial_z u_r$ values of 0.0035 and 0.005 s^{-1} are a bit higher than the term 6 predictions of order 0.002 s^{-1} shown in the lower part of Fig. 1. Rms high-frequency strain values obtained from the same float were always near $(\partial_z \eta)_{\text{rms}} = 0.3$ s^{-1}. These strain values differ from the values of Polzin *et al.* (2003) mentioned at the end of the previous section because these do not include static finestructure signatures (possibly vortical modes), which those do (i.e., these data contain only strain and shear effects in the internal-wave frequency band). Because measured $|\partial_z c_o|$ is ~ 0.04 s^{-1} and $|\partial_z c_o - \gamma c_o|$ is ~ 0.06 s^{-1}, resulting rms $\partial_z c'$ values are about 0.018 s^{-1}, close to the term 5 prediction shown in Fig. 1, but only about four times larger than the higher of the two rms $\partial_z u_r$ values. Thus, the ratio of shear and strain term rms values is 0.25 rather than the GM value near 0.1.

Consistent with this, shear to strain ratios R_ω measured in NATRE ranged from 7 to 19, always exceeding the GM value of $R_\omega = 3$. Additional finescale shear estimates were collected with a mooring during the experiment, and temporally variable shear intensity was observed, sometimes attaining values far exceeding GM [Ledwell, Watson, and Law (1998)].

The nature of the measurements may make the separation of sub-inertial band and internal-wave band signals difficult [Polzin *et al.* (2003)]. Note that although NATRE internal-wave strain measurements were consistent with rms $\partial_z c' \sim 0.02$ s^{-1}, observed $\partial_z c'$ values exceeded this by up to a factor of two in individual profiles, stemming from "static finestructure" that was removed before estimation of high-frequency strain (i.e., internal-wave strain). This means that although the ratio of rms $\partial_z u_r$ to rms wave-induced $\partial_z c'$ exceeded the GM prediction, the overall ratio of $\partial_z u_r$ to $\partial_z c'$ effects may, by chance, be closer to that given by GM.

IV. CONCLUSION

It has been shown that the ray-refracting effects of vertical shear of horizontal currents in the ocean can have magnitudes exceeding one-quarter those of strain-induced sound speed perturbations. Ratios of rms shear to strain effects are up to 0.25 in the spring 1993 NATRE observations [Duda and Jacobs (1995)], and of that same magnitude for other data sets [Polzin *et al.* (2003)]. Because ocean sound-speed perturbations are widely believed to be large enough to in-

fluence ray geometry in long-range propagation, the shear is thus large enough to do the same. This value of 0.25 in the upper few hundreds of meters in the ocean exceeds values of 0.13–0.17 for those depths computed earlier from an internal-wave model [Worcester (1977)], and exceeds values of 0.08–0.15 similarly computed here. Thus, precise study of long-range acoustics may require that shear effects be included rather than neglected. Finally, the analysis shown here uses angle-depth ray geometry equations, rather than other canonical variable or vector forms, which place all of the effects into a single equation, simplifying the comparison of shear, strain, and mean-profile effects.

ACKNOWLEDGMENTS

This work was funded by grants from the U.S. Office of Naval Research. Helpful discussions with John Colosi are acknowledged. Comments made by the anonymous reviewers helped to greatly improve this work. This is WHOI contribution 11278.

Beron-Vera, F. J., and M. G. Brown (**2003**), "Ray stability in weakly range-dependent sound channels," J. Acoust. Soc. Am. **114**, 123–130.

Bowlin, J. B., J. L. Spiesberger, T. F. Duda, and L. F. Freitag (**1993**), Ocean acoustical ray-tracing software RAY, Woods Hole Oceanographic Institution, WHOI Tech. Report 93-10, Woods Hole, MA.

Brown, M. G., J. A. Colosi, S. Tomsovic, A. L. Virovlyansky, M. A. Wolfson, and G. M. Zaslavsky (**2003**), "Ray dynamics in long-range deep ocean sound propagation," J. Acoust. Soc. Am. **113**, 2533–2547.

Brown, M. G., and J. Viechnicki (**1998**), "Stochastic ray theory for long-range sound propagation in deep ocean environment," J. Acoust. Soc. Am. **104**, 2090–2104.

Colosi, J. A. (**2005**), "Geometric sound propagation through an inhomogeneous and moving ocean: Scattering by small scale internal wave currents," J. Acoust. Soc. Am. (to be published).

Colosi, J. A., S. M. Flatté, and C. Bracher (**1994**), "Internal-wave effects on 1000 km oceanic acoustic pulse propagation: Simulation and comparison with experiment," J. Acoust. Soc. Am. **96**, 452–468.

Colosi, J. A., E. K. Scheer, S. M. Flatté, B. D. Cornuelle, M. A. Dzieciuch, W. H. Munk, P. F. Woecester, B. M. Howe, J. A. Mercer, R. C. Spindel, K. Metzger, T. G. Birdsall, and A. B. Baggeroer (**1999**), "Comparisons of measured and predicted acoustic fluctuations for a 3250 km propagation experiment in the eastern North Pacific Ocean," J. Acoust. Soc. Am. **105**, 3202–3218.

Duda, T. F., and C. S. Cox (**1989**), "Vertical wave number spectra of velocity and shear at small internal wave scales," J. Geophys. Res. **94**, 939–950.

Duda, T. F., and D. C. Jacobs (**1995**), "Comparison of shear measurements and mixing predictions with a direct observation of diapycnal mixing in the Atlantic thermocline," J. Geophys. Res. **100**, 13,481–13,498.

Flatté, S. M. (**1983**), "Wave propagation through random media: Contributions from ocean acoustics," Proc. IEEE **71**, 1267–1294.

Franchi, E. R., and M. J. Jacobson (**1972**), "Ray propagation in a channel with depth-variable sound speed and current," J. Acoust. Soc. Am. **52**, 316–331.

Garrett, C. J. R., and W. H. Munk (**1975**), "Space-time scales of internal waves: A progress report," J. Geophys. Res. **80**, 291–297.

Godin, O. A., and A. G. Voronovich (**2004**), "Fermat's principle for non-dispersive waves in non-stationary media," Proc. R. Soc. London, Ser. A **460**, 1631–1647.

Gregg, M. C. (**1989**), "Scaling turbulent dissipation in the thermocline," J. Geophys. Res. **94**, 9686–9698.

Lamancusa, J. S., and P. A. Daroux (**1993**), "Ray tracing in a moving medium with two-dimensional sound speed variation and application to sound propagation over terrain discontinuities," J. Acoust. Soc. Am. **93**, 1716–1726.

Ledwell, J. R., A. J. Watson, and C. S. Law (**1998**), "Mixing of a tracer in the pycnocline," J. Geophys. Res. **103**, 21,499–21,529.

Levitus, S. (**1982**), A Climatological Atlas of the World Ocean, NOAA Prof. Pap. 13, Princeton, NJ.

Munk, W., P. Worcester, and C. Wunsch (**1995**), *Ocean Acoustic Tomography* (Cambridge University Press, New York).

Nash, J. D., E. Kunze, J. M. Toole, and R. W. Schmitt (**2004**), "Internal tide reflection and turbulent mixing on the continental slope," J. Phys. Oceanogr. **34**, 1117–1134.

Ostashev, V. E. (**1997**), *Acoustics in Moving Inhomogeneous Media* (E & FN Spon, London).

Pinkel, R. (**1984**), "Doppler sonar observations of internal waves: The wavenumber-frequency spectrum," J. Phys. Oceanogr. **14**, 1249–1270.

Pinkel, R. (**1985**), "A wavenumber-frequency spectrum of upper ocean shear," J. Phys. Oceanogr. **15**, 1453–1469.

Polzin, K. L., E. Kunze, J. M. Toole, and R. W. Schmitt (**2003**), "The partition of finescale energy into internal waves and subinertial motions," J. Phys. Oceanogr. **33**, 234–248.

Polzin, K. L., J. M. Toole, and R. W. Schmitt (**1995**), "Finescale parameterizations of turbulent dissipation," J. Phys. Oceanogr. **25**, 306–328.

Simmen, J., S. M. Flatté, and G.-Y. Wang (**1997**), "Wavefront folding, chaos, and diffraction for sound propagation through ocean internal waves," J. Acoust. Soc. Am. **102**, 239–255.

Smith, K. B., M. G. Brown, and F. D. Tappert (**1992**), "Ray chaos in underwater acoustics," J. Acoust. Soc. Am. **91**, 1939–1949.

Virovlyansky, A. L. (**2003**), "Ray travel times at long ranges in acoustic waveguides," J. Acoust. Soc. Am. **113**, 2523–2532.

Worcester, P. F. (**1977**), "Reciprocal acoustic transmission in a midocean environment," J. Acoust. Soc. Am. **62**, 895–905.

A new method for estimating shear-wave velocity in marine sediments from radiation impedance measurements

Masao Kimura[a)]
School of Marine Science and Technology, Tokai University, 3-20-1 Shimizu-Orido, Shizuoka, Shizuoka 424-8610, Japan

(Received 29 July 2004; revised 8 August 2005; accepted 8 August 2005)

Shear-wave velocity is one of the important parameters that characterize the physical properties of marine sediments. In this study, a new method is proposed for measuring shear-wave velocity in marine sediments by using radiation impedance. Shear-wave velocities for three kinds of urethane rubber with different Japanese Industrial Standards hardness values were obtained by radiation impedance and time-of-flight measurement techniques. It was shown that the values of the shear-wave velocity measured by the radiation impedance method were consistent with those of time-of-flight measurements. It was then shown that the shear-wave velocities for air- and water-saturated beach sands are different. It was also found that the indicated shear-wave velocity is dependent on the vibrating plate radius because the instrument measures an average shear-wave velocity within a depth window beneath the plate; the larger the plate radius, the deeper the averaging window. Finally, measurements were made on two-layered media in which air-saturated beach sand or urethane rubber was covered with air-saturated clay, and the relationship between the thickness of the clay layer and the indicated shear-wave velocity was investigated. © *2005 Acoustical Society of America.* [DOI: 10.1121/1.2047187]

PACS number(s): 43.30.Ma [RAS] Pages: 2904–2912

I. INTRODUCTION

Shear-wave velocity is one of the important parameters for characterizing the properties of the marine sediments. It is normally measured by using a bimorph type piezoelectric transducer.[1] However, it is difficult to conduct *in situ* measurements for marine sediments with slow shear-wave velocities.

In this study, a new measuring method that utilizes the radiation impedance of a circular vibrating plate on the surface of the sediment is proposed.[2,3] In our previous study, we developed "an open acoustic tube method" for measuring sound velocity and attenuation in marine sediments.[4,5] During the development, the radiation impedance viewed from the tube end was investigated in detail, and the possibility of measuring the shear-wave velocity by using radiation impedance was discovered. Dunlop proposed a radiation impedance method for measuring the longitudinal-wave velocity and attenuation; however, his method cannot be used for shear-wave velocity measurements.[6] As a result of our extensive research on radiation impedance measurements,[3,7,8] a new method has been developed as a nonintrusive technique for measuring shear-wave velocity. In this paper, first, the usefulness of this method is shown for three kinds of urethane rubber with different JIS (Japanese Industrial Standards) hardness values. Next, measurements in air- and water-saturated beach sands were carried out, and the results of the measurements were compared and investigated. The variation of the indicated shear-wave velocity as a function of the radius of the plate was then investigated. Finally, the measurements of two-layered media, in which air-saturated beach sand or urethane rubber is covered with air-saturated clay, were made, and the relationship between the thickness of the air-saturated clay and the indicated shear-wave velocity was investigated.

II. RADIATION IMPEDANCE

In marine sediments, the assemblage of the mineral grain is saturated with seawater. In this study, the marine sediment is assumed to be a homogeneous elastic medium.[9]

Robertson[10] derived the radiation impedance for an elastic medium. According to his derivation, the radiation impedance of a circular vibrating plate of radius a on a semi-infinite elastic medium is expressed as follows:

$$z_r = r_r + jx_r = \frac{4a\mu}{j\omega(1-\sigma)} \int_0^1 \theta(t)dt, \tag{1}$$

where σ denotes Poisson's ratio; μ, shear modulus; and ω, angular frequency. $\theta(t)$ satisfies the Fredholm integral equation of the second kind,

$$\theta(t) + \frac{1}{\pi} \int_0^1 K(t,\tau)\theta(\tau)d\tau = 1, \tag{2}$$

where $K(t,\tau)$ denotes the kernel of the integral equation, as follows:

[a)]Electronic mail: mkimura@scc.u-tokai.ac.jp

$$K(t,\tau)=\frac{jk_sa}{2(1-\sigma)}\left\{\frac{-\pi s_r\sqrt{s_r^2-\gamma^2}\exp(jk_sat s_r)\cos(k_sa\tau s_r)}{f'(s_r)}+\int_0^{\gamma}\frac{\xi\sqrt{\gamma^2-\xi^2}\exp(jk_sat\xi)\cos(k_sa\tau\xi)}{(\xi^2-0.5)^2+\sqrt{\gamma^2-\xi^2}\sqrt{1-\xi^2}\xi^2}d\xi\right.$$
$$\left.+\int_{\gamma}^{1}\frac{\xi^3(\xi^2-\gamma^2)\sqrt{1-\xi^2}\exp(jk_sat\xi)\cos(k_sa\tau\xi)}{(\xi^2-0.5)^4+(1-\xi^2)(\xi^2-\gamma^2)\xi^4}d\xi\right\}. \tag{3}$$

In Eq. (3), s_r is the root of

$$f(s)=(s^2-0.5)^2-s^2\sqrt{s^2-\gamma^2}\sqrt{s^2-1}=0, \tag{4}$$

$$\gamma^2=\frac{1-2\sigma}{2(1-\sigma)}=\frac{\mu}{\lambda+2\mu}=\left(\frac{c_s}{c_l}\right)^2, \tag{5}$$

$$k_s=\frac{\omega}{c_s}, \tag{6}$$

$$c_s=\sqrt{\frac{\mu}{\rho}}, \tag{7}$$

where λ and μ are the Lamé constants; c_l and c_s, the longitudinal- and shear-wave velocities, respectively; and ρ, the density.

Equation (3) is satisfied in the case of $t>\tau$. In the case of $t<\tau$, it is necessary to interchange t and τ in the equation.

III. NUMERICAL CALCULATIONS FOR RADIATION IMPEDANCE

Equation (2)—the Fredholm integral equation of the second kind—cannot be solved analytically. Robertson derived the approximate equations for $k_sa<1$, but not for $k_sa>1$. It is necessary to obtain the solution of Eq. (2) for $k_sa>1$ in this study. We obtained the radiation impedance for $k_sa>1$ by approximating the second term on the left-hand side of Eq. (2) using a numerical integration method.[11,12] Thus,

$$\theta(t)+\frac{1}{\pi}\sum_{j=1}^{n}K(t,\tau_j)\theta(\tau_j)\Delta\tau=1, \tag{8}$$

where $\Delta\tau$ is assumed to be divided by n in [0,1]. It is expressed as follows:

$$\Delta\tau=\frac{1-0}{n}=\frac{1}{n}. \tag{9}$$

In addition, since the range of t is [0,1], at $t=t_1=1/n$,

$$\theta(t_1)+\frac{1}{\pi n}\sum_{j=1}^{n}K(t_1,\tau_j)\theta(\tau_j)=1.$$

At $t=t_2=2/n$,

$$\theta(t_2)+\frac{1}{\pi n}\sum_{j=1}^{n}K(t_2,\tau_j)\theta(\tau_j)=1.$$

At $t=t_n=1$,

$$\theta(t_n)+\frac{1}{\pi n}\sum_{j=1}^{n}K(t_n,\tau_j)\theta(\tau_j)=1.$$

Generally at $t=t_i=i/n$, the following equation is obtained:

$$\theta(t_i)+\frac{1}{\pi n}\sum_{j=1}^{n}K(t_i,\tau_j)\theta(\tau_j)=1\ (i=1,2,\ldots,n), \tag{10}$$

where we put $K_{ij}=(1/\pi n)K(t_i,\tau_j)$, $\theta_i=\theta(t_i)$, $\theta_j=\theta(\tau_j)$, and abbreviate Eq. (10) to the

$$\theta_i+\sum_{j=1}^{n}K_{ij}\theta_j=1. \tag{11}$$

Moreover, we use the Kronecker δ_{ij} and obtain

$$\sum_{j=1}^{n}(\delta_{ij}+K_{ij})\theta_j=1\ (i=1,2,\ldots,n). \tag{12}$$

Rewriting the upper equation in matrix form, the following can be obtained:

$$\begin{bmatrix}1+K_{11} & K_{12} & K_{13} & \cdots & K_{1n}\\ K_{21} & 1+K_{22} & K_{23} & \cdots & K_{2n}\\ K_{31} & K_{32} & 1+K_{33} & \cdots & K_{3n}\\ & & & \cdots & \\ \vdots & \vdots & \vdots & \vdots & \vdots\\ & & & \cdots & \\ K_{n1} & K_{n2} & K_{n3} & \cdots & 1+K_{nn}\end{bmatrix}\begin{bmatrix}\theta_1\\ \theta_2\\ \theta_3\\ \vdots\\ \\ \theta_n\end{bmatrix}=\begin{bmatrix}1\\ 1\\ 1\\ \vdots\\ \\ 1\end{bmatrix}. \tag{13}$$

By solving this n-dimensional simultaneous equation, the values of θ_i $(i=1,2,\ldots,n)$ can be obtained. Hence, the radiation impedance can be calculated from Eq. (1). Throughout the paper, the radiation impedance is calculated with relatively large number of division, $n=100$. The number of division, $n=100$, was determined to be adequate because a larger number of divisions (e.g., 200) did not lead to any significant improvements in the calculation of radiation impedance results. In the case $\mu/(\lambda+2\mu)=0.000\,03, 0.0003, 0.003, 0.03$, the calculated results of the normalized radiation resistance $r_{r_0}(=r_r/z_0, z_0=\pi a^2\rho c_l)$ and the normalized radiation reactance $x_{r_0}(=x_r/z_0)$ are shown in Figs. 1 and 2, respectively. The radiation resistance increases with the value of $\mu/(\lambda+2\mu)$. Each normalized radiation reactance curve is plotted as a function of the dimensionless frequency k_la and has a deep notch. The

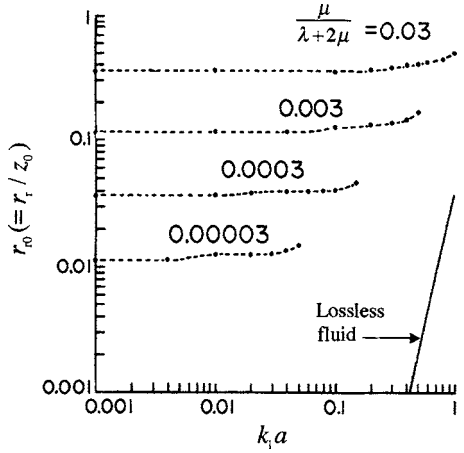

FIG. 1. Calculated normalized radiation resistance as a function of $k_l a$. The values of $\mu/(\lambda+2\mu)=(c_s/c_l)^2$ as the parameter are 0.000 03, 0.0003, 0.003, and 0.03.

radiation reactance is negative to the left of the notch, as indicated by the minus sign. To the right of the notch, it is positive and approaches the case of the lossless fluid at a high $k_l a$. At the center of the notch, its magnitude is zero.

IV. NEW EXPRESSION FOR SHEAR WAVE VELOCITY

The relationship between the value of $k_l a$ $(k_l=\omega/c_l)$ where the value of the radiation reactance reaches zero $k_l a|_{x_{r_0}=0}$, and the square of the shear- to longitudinal-wave velocity ratio $\mu/(\lambda+2\mu)=(c_s/c_l)^2$ from Fig. 2 is shown in Fig. 3. In Fig. 3, the results for the case where the square of the shear- to longitudinal-wave velocity ratio is higher than 0.03 are also shown. From Fig. 3, it can be observed that a line exists up to a higher limit of 0.03 in $(c_s/c_l)^2$, and that the value of $k_l a|_{x_{r_0}=0}$ is proportional to the half-power of $\mu/(\lambda+2\mu)$ in this range, which can be obtained from the slope of the line in Fig. 3. That is,

$$k_l a|_{x_{r_0}=0} = 2.5\sqrt{\frac{\mu}{\lambda+2\mu}} = 2.5\frac{c_s}{c_l}. \tag{14}$$

The following simple equation can be derived from Eq. (14):

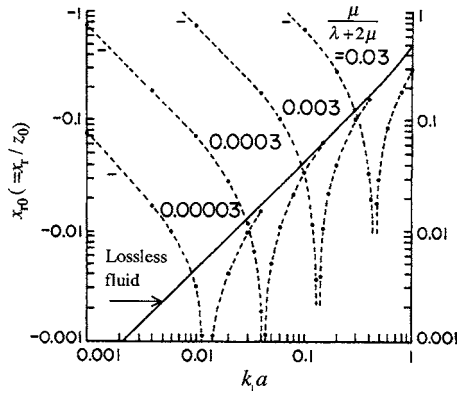

FIG. 2. Calculated normalized radiation reactance as a function of $k_l a$. The values of $\mu/(\lambda+2\mu)=(c_s/c_l)^2$ as the parameter are 0.000 03, 0.0003, 0.003, and 0.03.

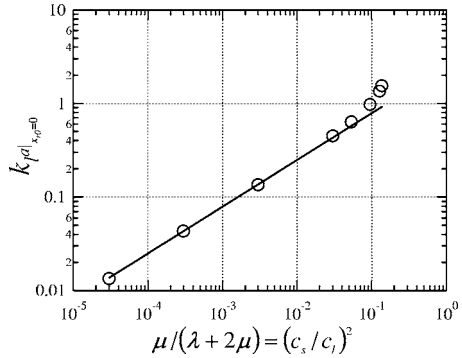

FIG. 3. Dimensionless zero-reactance frequency $k_l a|_{x_{r_0}=0}$ as a function of $\mu/(\lambda+2\mu)=(c_s/c_l)^2$. The linear relationship exists up to 0.03 for the value of $(c_s/c_l)^2$.

$$c_s = \frac{2\pi a}{2.5} f|_{x_{r_0}=0}. \tag{15}$$

Equation (15) implies that the shear-wave velocity c_s can be obtained by measuring the frequency at which x_{r_0} becomes zero. The frequency $f|_{x_{r_0}=0}$ will be termed the "zero-reactance frequency."

This linear relationship between $k_l a|_{x_{r_0}=0}$ and c_s/c_l is considered to exist for the following reason. The radiation reactance consists of the radiation mass M_r and the medium compliance C_r. Assuming that $k_s a<0.7$, the radiation mass and the medium compliance are given approximately by[13]

$$M_r = \frac{4\rho a^3 A_1}{1-\sigma}, \tag{16}$$

$$C_r = \frac{1-\sigma}{4\rho c_s^2 a}, \tag{17}$$

where A_1 is approximately constant, in the range of the Poisson's ratio concerned. Using Eqs. (16) and (17), the following linear relationship between $k_l a|_{x_{r_0}=0}$ and c_s/c_l can be obtained:

$$k_l a|_{x_{r_0}=0} = \frac{1}{\sqrt{A_1}}\sqrt{\frac{\mu}{\lambda+2\mu}} = \frac{1}{\sqrt{A_1}}\frac{c_s}{c_l}. \tag{18}$$

It is considered that for $k_l a>1$, the radiation mass decreases as $k_l a$ increases, and the linear relationship between $k_l a|_{x_{r_0}=0}$ and c_s/c_l does not hold, from the consideration of the characteristics of radiation reactance for lossless fluid.

V. EXPERIMENTS

A. Measurements in urethane rubber (Ref. 7)

The shear-wave velocities of three kinds of urethane rubber with the different JIS hardness values, 30, 60, and 90 (UR30, UR60, and UR90) were measured by employing the radiation reactance method. Each urethane rubber sample was cylindrical in shape, with a diameter of 100 mm and length of 150 mm. Each sample was set in a water vessel with a volume of approximately 60 l, thus equating the surfaces of the medium and the water. The radiation reactance is obtained from

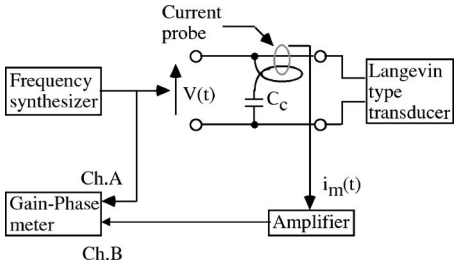

FIG. 4. Block diagram of the shear-wave velocity measurement system using input admittance for urethane rubber. Input admittance is obtained by measuring input voltage and current at the electrical terminals of a Langevin-type transducer.

$$x_{r_0} = \frac{RQ\left(\frac{f_0}{f_T} - \frac{f_T}{f_0}\right)}{\left(\frac{\rho c_l S}{A^2}\right)}, \tag{19}$$

where f_0, R, and Q denote the resonance frequency, resonance resistance, and quality factor of the unloaded transducer, respectively; f_T is the resonance frequency in the loaded condition where the surface of the transducer is in contact with that of the medium; S, the area of the surface of the transducer; and A, the force factor of the transducer. The transducers are Langevin-type with diameters of 20, 10, and 5 mm, lengths of approximately 100 mm, and a resonance frequency of approximately 21 kHz. In case of the measurements at smaller diameters, a half-wavelength aluminum horn with the diameters of 2.5, 1.5, and 1.2 mm is attached to the surface of the transducer. The density of each sample is obtained from the measured values of the weight and the volume. The longitudinal-wave velocities are measured using the ultrasonic pulse method. The block diagram for the shear-wave velocity measurement system is shown in Fig. 4. The frequency characteristics of the radiation reactance were obtained by using input admittance. Input admittance is obtained by measuring input voltage and current at the electrical terminals of a Langevin-type transducer. The measurements are carried out at a temperature of 25–32 °C. The measured results of the radiation reactance are shown in Fig. 5. It is evident

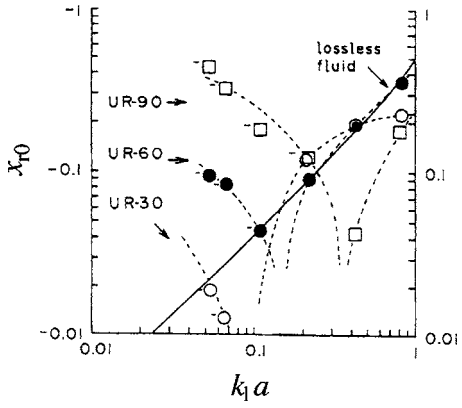

FIG. 5. Measured normalized radiation reactance as a function of $k_l a$ for three kinds of urethane rubber. The curve for the case of the lossless fluid is also shown.

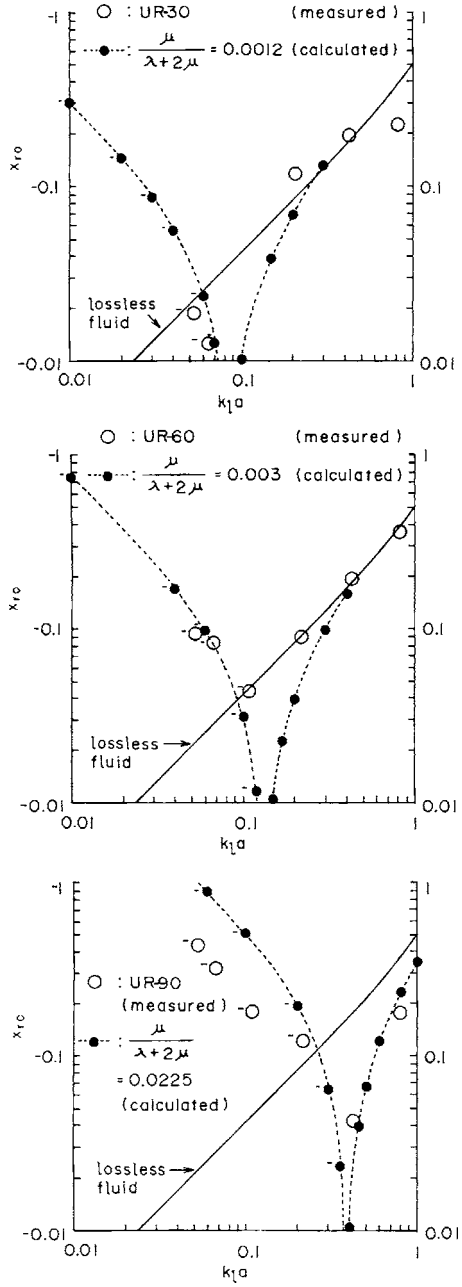

FIG. 6. Measured and calculated radiation reactance as a function of $k_l a$ for three kinds of urethane rubber. The curves for the case of the lossless fluid are also shown.

that there is a notch in each curve. The value of $k_l a$ at which x_{r_0} becomes zero increases with the JIS hardness value. The measured and calculated radiation reactance for the three kinds of urethane rubber is shown in Fig. 6. The measured results are consistent with the calculated curves.

The shear-wave velocity is obtained from the zero-reactance frequency by using Eq. (15). The results are shown in Table I. In this table, the values of the shear-wave velocities by using the bimorph type piezoelectric transducer are also shown for comparison. The measured values obtained by the radiation impedance method are in good agreement with those obtained by the bimorph type piezoelectric transducer method. It is evident that the measurement method for

TABLE I. Measured values of shear-wave velocities for three kinds of urethane rubber by using radiation impedance and a bimorph type piezoelectric transducer.

	c_s (m/s) from radiation impedance (f=20 kHz)	c_s (m/s) measured using bimorph transducer (f=3.5 kHz)
UR30	52	60
UR60	82	80
UR90	225	205

shear-wave velocity by using radiation impedance is useful because it is a nonintrusive method by which the medium for measurement does not suffer any disturbance.

B. Measurements in air- and water-saturated sands (a=50 mm)—Ref. 3

The measurements of radiation impedance for air- and water-saturated sands were carried out. In the laboratory, the sand was set in an acrylic vessel with the dimensions of 90 $\times$90$\times$30 cm. A circular vibrating plate was set on the center of the sand surface. The plate was made of aluminum with a radius of 50 mm, and thickness of 25 mm. A force pickup (PF-31, Rion Co.) was attached to the center of the lower surface of the vibrating plate and an acceleration pickup (PV-02, Rion Co.) was attached to the upper surface. The frequency characteristics of the radiation reactance were obtained by measuring the force and acceleration signals. Transducers were used for undertaking measurements in urethane rubbers. By this method, it was necessary to use many transducers to vary the values of $k_l a$. Therefore, force and acceleration pickups were used after these measurements because a wide frequency range could be covered by using one vibrator. The block diagram of the measurement system is shown in Fig. 7. In Shizunami beach, the measurements were carried out on air- and water-saturated beach sands; the latter was almost completely saturated with seawater. The measured results of the frequency characteristics of the radiation reactance, from the laboratory and *in situ* on the beach, are shown in Fig. 8. The zero-reactance frequencies obtained

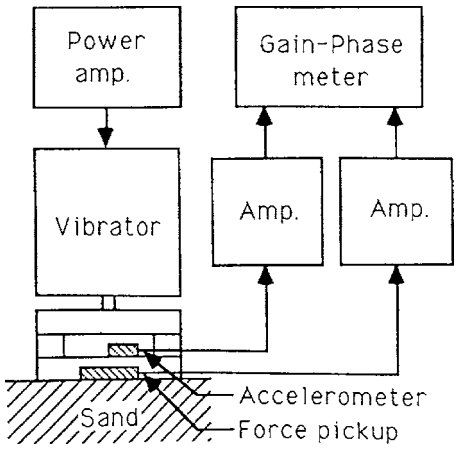

FIG. 7. Block diagram of the shear-wave velocity measurement system using force and acceleration pickups for sand.

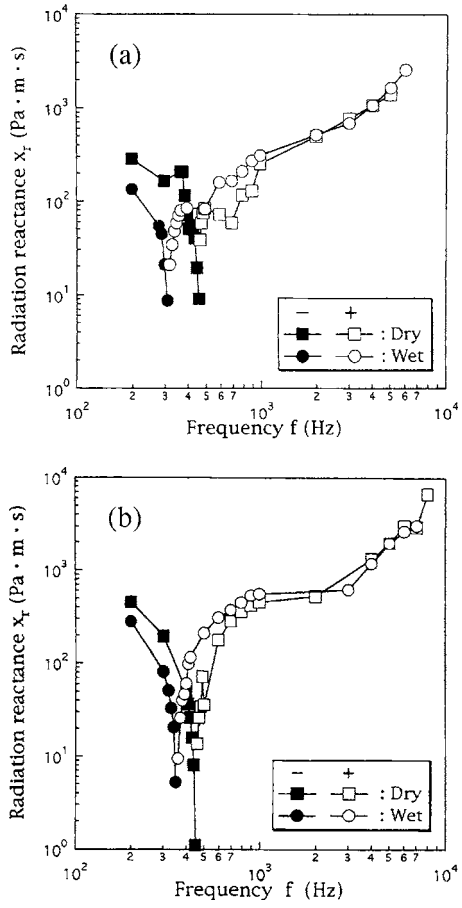

FIG. 8. Measured radiation reactance as a function of frequency for air- and water-saturated Shizunami sand (a) in laboratory and (b) on the beach.

from these figures and the shear-wave velocities computed from the frequencies by using Eq. (15) are shown in Table II. It can be observed that the shear-wave velocity in the water-saturated sand is smaller than that in the air-saturated sand, both in the laboratory and *in situ* on the beach. This is most likely due to the density difference between the water- and air- saturated sands and the difference of the depth dependence of the shear-wave velocity in air- and water-saturated sands; the increasing rate with the depth of shear-wave velocity in air-saturated sand is larger that in water-saturated sand. The measured values in the laboratory are relatively close to those obtained on the beach.

TABLE II. Measured values of the zero-reactance frequencies and the corresponding values of shear-wave velocities for air- and water-saturated Shizunami sands in the laboratory and on the beach.

		Zero-reactance frequency $f\|_{x_{r_0}=0}$ (Hz)	Shear wave velocity c_s (m/s)
Laboratory	Air-saturated	462	58
	Water-saturated	318	40
Beach	Air-saturated	454	57
	Water-saturated	350	44

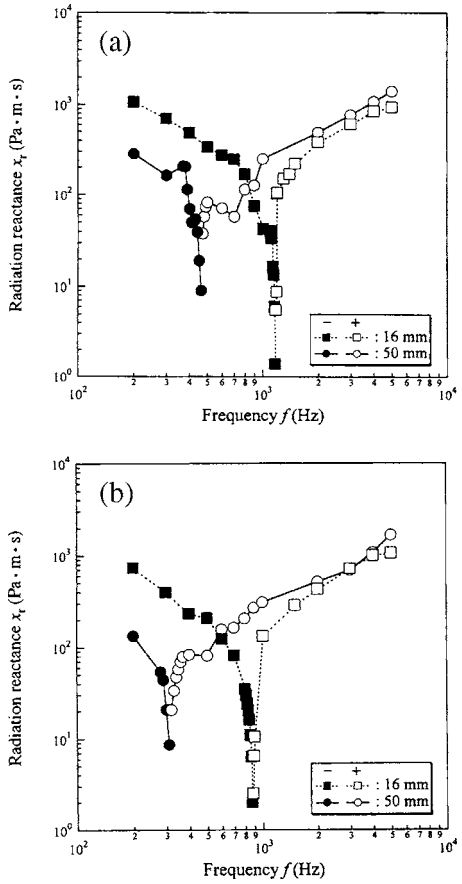

FIG. 9. Measured radiation reactance as a function of frequency for Shizunami sand in laboratory (a=16 and 50 mm) (a) air-saturated and (b) water-saturated.

C. Indicated shear-wave velocity as a function of the radius of the vibrating plate (a=16,50 mm)—Ref. 3

In the measurements of the radiation impedance of the air- and water-saturated sands in the laboratory, a vibrating plate with a radius of 50 mm was used, as mentioned in Sec. V B. The effect of the plate radius on the indicated value of the shear-wave velocity will be examined. A second vibrating plate with a radius of 16 mm was also used. The measured frequency dependence of the radiation reactance for the air- and water-saturated sands is shown in Fig. 9. The zero-reactance frequencies obtained from these figures and the shear-wave velocities computed from the frequencies by using Eq. (15) are shown in Table III. With both the plates, it is seen that the shear-wave velocity in the water-saturated sand is always smaller than that in the air-saturated sand in a relative sense.

TABLE III. Measured values of the zero-reactance frequencies and the corresponding values of shear-wave velocities for air- and water-saturated Shizunami sands, with vibrating plate radii of 50 and 16 mm.

		Zero-reactance frequency $f\|_{x_r=0}$ (Hz)	Shear wave velocity c_s (m/s)
Air-saturated	a=50 mm	463	58
	a=16 mm	1163	47
Water-saturated	a=50 mm	315	40
	a=16 mm	877	35

The indicated absolute values of shear-wave velocity appear to change with the plate radius. This may be explained in terms of the penetration depth of the measurement: (1) The measured reactance is influenced by the property of the medium within an averaging window that extends from the surface to an effective penetration depth, which increases with wavelength. From Eq. (15), it is seen that the zero-reactance wavelength (frequency) increases (decreases) with the radius of the vibrating plate. (2) In sand, both the shear-wave velocity and the overburden stress are known to increase with the depth.[14] These two facts combine to produce an indicated shear-wave velocity that appears to increase with the plate radius. In fact, the instrument yields an average shear-wave velocity, averaged over a depth window that changes with the plate diameter. For these reasons, the indicated shear-wave velocity obtained from a vibrating plate with a radius of 16 mm would be less than that obtained from a radius of 50 mm; this observation is consistent with the results in Table III.

D. Measurements using two-layered media

1. Kibushi clay on Miho sand (Ref. 3)

From the measured results for the air- and water-saturated beach sands in Sec. V C, it was observed that the indicated shear-wave velocity varies as a function of the radius of the vibrating plate. This is due to the effect of the depth dependence of stress in sand. The frequency characteristics of the radiation reactance of a two-layered medium, composed of a layer of air-saturated Kibushi clay on a half-space air-saturated Miho sand, were measured to investigate this phenomenon in greater detail. In this experiment, the thickness of Miho sand was 30 cm and that of Kibushi clay, overlaying the Miho sand, was 0 (that is, only Miho sand), 1, 2, 4, and 30 cm (that is, only Kibushi clay). The changes in the frequency characteristics of the radiation reactance as a function of the thickness of the clay were investigated. An example of the measured radiation reactance (radius of the vibration plate a=16 mm, and clay layer thickness d=1 cm) is shown in Fig. 10. From this figure, a zero-reactance frequency is easy to determine with depth dependent shear-wave velocity. The measured values of zero-reactance frequencies and the computed values of the shear-wave velocities are shown in Tables IV and V by using the 50- and 16-mm plate radii, respectively. The indicated shear-wave velocity values from Tables IV and V are plotted in Fig. 11.

The following observations are made from Fig. 12.

(1) In case of pure Miho sand or Kibushi clay, the indicated shear-wave velocity is greater for the plate with a larger radius than for one with a smaller radius. As explained previously, the indicated shear-wave velocity is an average value over an averaging depth window that increases with the plate radius. Both the sand and the clay have overburden stresses that increase with depth; hence, the

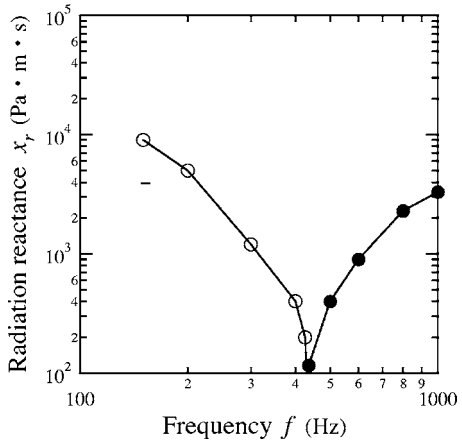

FIG. 10. An example of the measured radiation reactance as a function of frequency for the clay-sand two-layered medium (a=16 mm, d=1 cm).

TABLE IV. Measured values of the zero-reactance frequencies and the corresponding values of shear-wave velocities for two-layered media: Kibushi clay on Miho sand (a=50 mm).

Thickness of clay d (cm)	$f\|_{x_{r_0}=0}$ (Hz)	c_s (m/s)
0	351	44.1
1	195	24.5
2	187	23.5
4	167	21.0
30	165	20.7

TABLE V. Measured values of the zero-reactance frequencies and the corresponding values of shear-wave velocities for two layered mediua: Kibushi clay on Miho sand (a=16 mm).

Thickness of clay d (cm)	$f\|_{x_{r_0}=0}$ (Hz)	c_s (m/s)
0	749	30.1
1	450	18.1
2	415	16.7
4	409	16.4
30	412	16.6

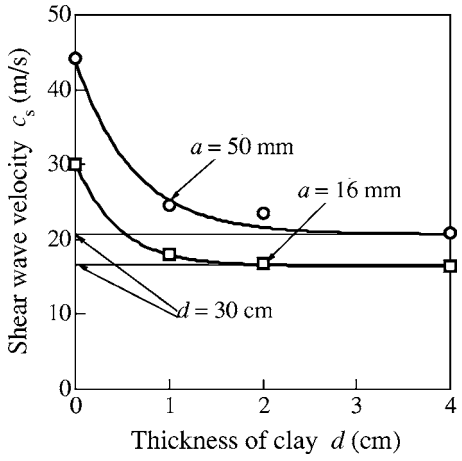

FIG. 11. Shear-wave velocity by the radiation impedance method vs the thickness of clay for the clay-sand two-layered medium. Two horizontal lines indicate the shear wave velocities for d=30 mm.

shear-wave velocities also increase with depth. For these reasons, the indicated shear-wave velocities should increase with the plate radius.

(2) The shear-wave velocity decreases as the thickness of Kibushi clay increases. It is observed that the indicated value approaches the shear-wave velocity for pure Kibushi clay because the influence of Miho sand decreases as the thickness of Kibushi clay increases.

(3) Vibration plates with two different radii produce different shear-wave velocities for the clay layer of thickness d=30 cm. This is solely due to the overburden stresses in the clay layer.

2. Kibushi clay on urethane rubber (Ref. 8)

The frequency characteristics of the radiation reactance for two-layered media composed of air-saturated Kibushi clay on urethane rubber with the different JIS hardness values 30 and 60 (UR30, UR60) were measured. The diameter of the urethane rubber samples is 100 mm and the thickness is 150 mm. In this experiment, the thickness of Kibushi clay, overlaying the urethane rubber, varied from 3 to 80 mm. Circular vibrators of radii 3 and 16 mm were used. The changes in the frequency characteristics of radiation reactance as a function of the thickness of the clay were investigated. The measured values of the zero-reactance frequency and the corresponding values of the shear-wave velocity are shown in Table VI. The plots of shear-wave velocity versus the thickness of clay are shown in Fig. 12: the closed triangles and closed circles indicate the shear-wave velocities for pure ure-

TABLE VI. Measured values of the zero-reactance frequencies and the corresponding values of shear-wave velocities for Kibushi clay-urethane rubber two-layered media. (a) UR30, (b) UR60.

	Thickness of clay (mm)	Frequency $\|x_r=0$ (Hz)		Shear wave velocity (m/s)	
		a=3 mm	a=16 mm	a=3 mm	a=16 mm
(a)	3	6521	1266	49.17	50.91
	5	4412	958	33.27	38.52
	10	2719	672	20.50	27.02
	15	2299	529	17.33	21.27
	20	2011	495	15.16	19.91
	30	1709	431	12.89	17.33
	40	1540	419	11.61	16.85
	50	1519	415	11.45	16.69
	60	1515	412	11.42	16.57
	70	1511	411	11.39	16.53
	80	1510	411	11.39	16.53
(b)	3	8566	1705	64.59	68.56
	5	6547	1360	49.36	54.69
	10	5109	1082	38.52	43.51
	15	3532	826	26.63	33.22
	20	2684	665	20.24	26.74
	30	1716	509	12.94	20.47
	40	1538	430	11.60	17.29
	50	1525	413	11.50	16.61
	60	1515	412	11.42	16.57
	70	1513	411	11.41	16.53
	80	1511	410	11.39	16.49

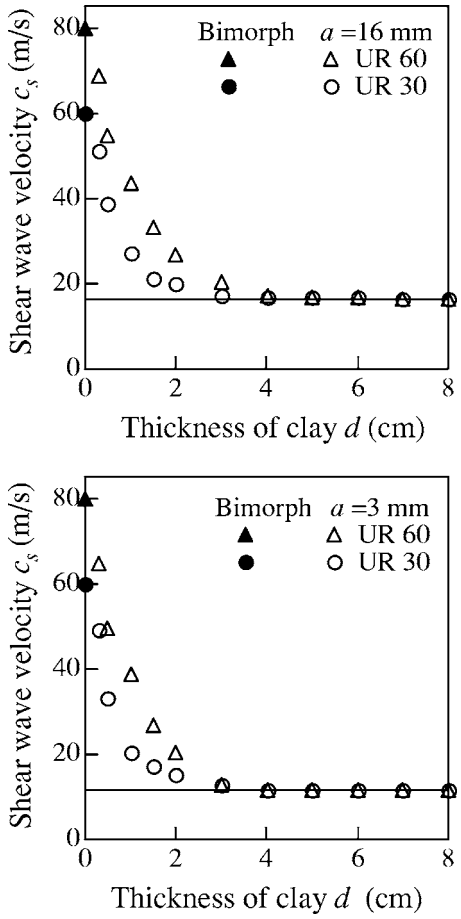

FIG. 12. Shear-wave velocity by the radiation impedance method vs the thickness of clay for the clay-urethane rubber two-layered medium. Upper panel: for $a=16$ mm, lower panel: for $a=3$ mm.

thane rubber measured by a bimorph type piezoelectric transducer. The solid lines show the shear-wave velocity for pure Kibushi clay. A thickness of 30 cm was sufficient to approximate a semi-infinite half-space.

The indicated shear-wave velocity decreases as the thickness of Kibushi clay increases. It is observed that this velocity approaches the shear-wave velocity for pure Kibushi clay. This is because the influence of urethane rubber decreases as the thickness of Kibushi clay increases. On the other hand, the shear-wave velocity approaches that of pure urethane rubber—as measured by a bimorph type piezoelectric transducer—as the thickness of Kibushi clay approaches zero.

The indicated shear-wave velocity of the clay obtained by using a larger vibrating plate is greater than that obtained by using a smaller vibrating plate for reasons discussed in Sec. V C. However, the indicated shear-wave velocities of the urethane rubber samples were independent of plate radius because the rubber properties are uniform and devoid of any depth dependence.

VI. CONCLUSIONS

It is shown by numerical analysis that the shear-wave velocity of an elastic medium can be obtained from a frequency at which the radiation reactance of a circular vibrating plate on the surface of the medium becomes zero. This frequency was referred to as the "zero-reactance frequency." This was demonstrated for three grades of urethane rubber with three different JIS hardness values; it was shown that the values of shear-wave velocity measured by the radiation impedance method were consistent with those obtained by using a bimorph type piezoelectric transducer. These results demonstrate the usefulness of the new radiation impedance method. The measured results of shear-wave velocity by the radiation reactance method on air- and water-saturated sands indicated that the shear-wave velocity in the air-saturated case is greater than the corresponding water-saturated case. They also showed that the indicated shear-wave velocity is dependent on the radius of the vibrating plate. The indicated shear-wave velocity increases with the diameter of the vibrating plate. This is because the overburden stress and shear-wave velocity of granular media, such as sand and clay, increase with depth, and the radiation impedance method measures the average shear-wave velocity within an averaging window that proportionally increases in depth with the plate radius. Finally, measurements on two-layered media, particularly Kibushi clay on Miho sand and Kibushi clay on urethane rubber, were carried out. The relationship between the thickness of the clay layer and the indicated shear-wave velocity was obtained. As mentioned earlier, the effective penetration depth of the measurement increases with the vibrating plate radius. Therefore, it is suggested that the depth dependence of the shear-wave velocity in the surficial marine sediment can be obtained by the radiation impedance method using vibrating plates with a wide range of radii.

ACKNOWLEDGMENTS

The author wishes to acknowledges Professor Robert D. Stoll and Professor Henrik Schmidt for their valuable comments and expresses his appreciation to Dr. Nicholas P. Chotiros for his suggestions and revising the manuscript.

APPENDIX: RADIATION IMPEDANCE OF A CIRCULAR VIBRATING PLATE ON A SEMI-INFINITE ELASTIC MEDIUM

In this section, the Robertson[10] derivation of the radiation impedance for a circular vibrating plate on a semi-infinite elastic medium is summarized.

In an axisymmetric problem in cylindrical coordinates, the displacement (r,θ,z) may be written as $(u_r,0,u_z)e^{-j\omega t}$, where u_r and u_z satisfy

$$(\lambda+2\mu)\frac{\partial}{\partial r}\left[\frac{1}{r}\frac{\partial}{\partial r}(ru_r)\right]+\mu\frac{\partial^2 u_r}{\partial z^2}+(\lambda+\mu)\frac{\partial^2 u_z}{\partial r\partial z}+\rho\omega^2 u_r=0, \tag{A1}$$

$$(\lambda+2\mu)\frac{\partial^2 u_z}{\partial z^2}+\frac{\mu}{r}\frac{\partial}{\partial r}\left(r\frac{\partial u_z}{\partial r}\right)+\frac{\lambda+\mu}{r}\frac{\partial}{\partial r}\left(r\frac{\partial u_r}{\partial z}\right)+\rho\omega^2 u_z=0. \tag{A2}$$

The stress σ_{zz} and σ_{rz} can be expressed as follows:

$$\sigma_{zz} = -\mu \int_0^\infty p[\alpha^{-1}A(2p^2 - k^2)e^{-\alpha z} + 2\beta C e^{-\beta z}]J_0(pr)dp \cdot e^{-j\omega t}, \quad \text{(A3)}$$

$$\sigma_{rz} = -\mu \int_0^\infty [2Ap^2 e^{-\alpha z} + C(2p^2 - k^2)e^{-\beta z}]J_1(pr)dp \cdot e^{-j\omega t}, \quad \text{(A4)}$$

where A and C are arbitrary constants, and

$$\alpha = \begin{cases} \sqrt{p^2 - h^2} & (p > h) \\ -i\sqrt{h^2 - p^2} & (0 \leqslant p \leqslant h), \end{cases}$$
$$\beta = \begin{cases} \sqrt{p^2 - k^2} & (p > k) \\ -i\sqrt{k^2 - p^2} & (0 \leqslant p \leqslant k), \end{cases} \quad \text{(A5)}$$

with $h^2 = \rho\omega^2/(\lambda + 2\mu)$, $k^2 = \rho\omega^2/\mu$.

The stress field in an elastic half-space $z \geqslant 0$ when a smooth rigid circular disc of unit radius is pressed against its surface at $z=0$ is considered. The displacement of the disc is given in the form $b + ce^{-i\omega t}(b \geqslant c)$. In order to derive a solution for the normal reaction, the following boundary conditions need to be satisfied:

$$u_z(r,0) = c \quad (0 \leqslant r \leqslant 1),$$
$$\sigma_{zz}(r,0) = 0 \quad (r > 1), \quad \text{(A6)}$$
$$\sigma_{rz}(r,0) = 0 \quad (r > 0).$$

The normal stress under the disc is obtained by putting $z=0$ in Eq. (A3) and satisfying the above-noted boundary conditions. The following result is obtained:

$$\sigma_{zz}(r,0) = \frac{2\sigma c e^{-j\omega t}}{\pi(1-\sigma)r} \frac{d}{dt} \int_r^1 \frac{\tau\theta(\tau)d\tau}{\sqrt{\tau^2 - r^2}} \quad (0 \leqslant r < 1), \quad \text{(A7)}$$

where σ is Poisson's ratio, and $\theta(t)$ is satisfied by the Fredholm integral equation of the second kind as follows:

$$\theta(t) + \frac{1}{\pi} \int_0^1 K(t,\tau)\theta(\tau)d\tau = 1. \quad \text{(A8)}$$

The total load that must be applied to the disc to produce the displacement $ce^{-j\omega t}$ is given by

$$P = -\frac{4\mu c}{1-\sigma} e^{-j\omega t} \int_0^1 \theta(\tau)d\tau. \quad \text{(A9)}$$

Finally, the radiation impedance can be obtained as follows:

$$z_r = \frac{4\mu}{j\omega(1-\sigma)} \int_0^1 \theta(t)dt. \quad \text{(A10)}$$

[1] D. J. Shirley and L. D. Hampton, "Shear-wave measurements in laboratory sediments," J. Acoust. Soc. Am. **63**, 607–613 (1978).
[2] M. Kimura, "A measuring method for shear wave velocity of marine sediment using radiation impedance," J. Acoust. Soc. Am. **103**, 2934(A) (1998).
[3] M. Kimura, "Shear wave velocity measurements in marine sediment model using radiation impedance," Technical Report of IEICE, US99-36, 1999, pp. 47–54.
[4] M. Kimura and H. Shimizu, "A new method of simply measuring acoustic properties for marine sediments and its basic experiments," J. Acoust. Soc. Jpn. **45**, 274–281 (1989).
[5] M. Kimura and H. Shimizu, "An open acoustic-tube method for measuring sound velocity and attenuation constant of marine sediments," Jpn. J. Appl. Phys. **29**, Suppl. 29-206–209 (1990).
[6] J. I. Dunlop, "An open tube technique for the measurement of acoustic parameters of porous absorbing materials," J. Acoust. Soc. Am. **77**, 2173–2178 (1985).
[7] M. Kimura and H. Shimizu, "Radiation impedance of a circular piston vibrator for viscoelastic medium," Technical Report of IEICE, US89-19, 1989, pp. 23–30.
[8] M. Kimura, "Shear wave velocity measurements of layered sediment models using radiation impedance," J. Acoust. Soc. Am. **107**, 2773(A) (2000).
[9] E. L. Hamilton *et al.*, "Velocities of compressional and shear waves in marine sediments determined in situ from a research submersible," J. Geophys. Res. **75**, 4039–4049 (1970).
[10] I. A. Robertson, "Forced vertical vibration of a rigid circular disc on a semi-infinite elastic solid," Proc. Cambridge Philos. Soc. **62**, 547–553 (1966).
[11] J. Kondo, *Integral Equation* (Baifukan, Tokyo, 1971).
[12] K. Isoda and Y. Oono, *Numerical Calculation by Fortran* (Oomu, Tokyo, 1975).
[13] M. H. Safar, "On the determination of the downgoing P-waves radiated by the vertical seismic vibrator," Geophys. Prospect. **32**, 392–405 (1984).
[14] M. Kimura and S. Kawashima, "Depth dependence of shear wave velocity in sands," Jpn. J. Appl. Phys., Part 1 **34**, 2936–2939 (1995).

Performance and limitations of spectral factorization for ambient noise sub-bottom profiling

Chris H. Harrison[a)]
NATO Undersea Research Centre, Viale San Bartolomeo, 400, 19138 La Spezia, Italy

(Received 25 May 2005; revised 11 August 2005; accepted 11 August 2005)

Using a drifting vertical array as a means to measure noise directionality one can infer reflection coefficient vs angle and frequency. This can be converted to a time-varying impulse response, i.e., a sub-bottom profile, by using spectral factorization to recover the phase. Limitations of the technique are discussed with simulations and experiment. First, spectral factorization provides a minimum phase realization of the impulse response for the given spectrum, whereas the true reflection coefficient may not actually be minimum phase. Second, the beam width, determined by array length, slightly smudges the interference fringes that are characteristic of the reflection coefficient. This reduction in frequency resolution reduces the maximum depth to which layers can be detected. Consideration of the detailed mechanism leads to a way of improving frequency resolution and hence maximum depth. Spectral factorization tends to function well unless the impedance contrast between water and upper layers is very small. The depth limitations due to beam width will usually be more important than those of spectral factorization even with the proposed recovery of frequency resolution. At 4 kHz design frequency the layer structure thus determined during a 6 km drift compares well with a seismic boomer down to 15 m. [DOI: 10.1121/1.2048967]

PACS number(s): 43.30.Pc [AIT] Pages: 2913–2923

I. INTRODUCTION

Finding seabed characteristics from acoustic measurements, i.e., geoacoustic inversion, is by now a mature discipline with a large literature (see, for instance, Tolstoy *et al.*, 1998; Caiti *et al.*, 2004; Collins and Kuperman, 1991). In recent years interest has included geoacoustic inversion of ambient noise, and a number of approaches have been proposed based on sea surface noise spatial coherence (Buckingham and Jones, 1987; Carbone, 1998), surface noise directionality (Harrison and Simons, 2002; Aredov and Furduev, 1994), individual ships (Heaney, 2002), light aircraft (Giddens and Buckingham, 2004). Most recently it has been possible to extract coherent features from ambient noise, for instance, by investigating the time-domain cross correlation between separated hydrophones to obtain the Green's function (Roux *et al.*, 2004; Roux *et al.*, 2005; Sabra *et al.*, 2005), and also by using spectral factorization to recover the phase and so transform reflection coefficient into sub-bottom layer profiles (Harrison, 2004).

The underlying theory of noise directionality with multiple sources arranged in a sheet near the sea surface can be seen equivalently in terms of mode theory (Kuperman and Ingenito, 1980; Buckingham, 1980) or ray theory (Harrison, 1996; Chapman, 1988). Quite generally, wind-generated ambient noise emanates from a sheet of sound sources near the sea surface and therefore provides a useful source of broadband plane waves at all angles. Simple flux arguments (amongst others) show that the vertical directionality of the noise can be used to plot and map out the reflection properties of the seabed over a substantial frequency band and angle range (Harrison and Simons, 2002). Because the deduced reflection loss is, in fact, a local measurement one can survey the bottom properties by using a drifting vertical array. Furthermore the reflection loss is essentially the frequency response of the bottom at each angle, and it has been shown that (Harrison, 2004) under certain common conditions one can reconstruct the reflection phase using spectral factorization (SF). Given this complex reflection coefficient one can determine the impulse response of the seabed by Fourier transformation. A plot of the slowly varying impulse response (acoustic delay time vs drift time) then constitutes a sub-bottom profile showing layer boundaries in which zero delay time corresponds to the local water-sediment interface.

Limitations of the measurement technique when using a vertical line array (VLA) have been discussed elsewhere (Harrison and Baldacci, 2003) and comparisons made with more conventional measurements of reflection loss (Holland and Harrison, 2003). Here we investigate the performance of spectral factorization and associated processing in this context. In this paper we take two approaches. First we apply SF to simulated layer echoes and compare results with the known layer starting point. Second we compare experimental results with an alternative experimental method (seismic boomer), that we deem to be a "ground-truth."

The limitations manifest themselves in the time domain (i.e., in the impulse response) in two ways, one as a "ghosting" effect in which the SF introduces an artificial repeat of a true earlier or later layer echo; the other way as a depth limitation resulting from the beam pattern's degrading of the reflection loss's frequency resolution. As a result of understanding this mechanism it is possible partially to recover this frequency resolution, and the experimental results show

[a)]Electronic mail: harrison@nurc.nato.int

TABLE I. Parameters used for the 20 random layers in cases 1 and 2 (layer thickness, sound speed, density, attenuation). The uniform value in each layer consists of a linear (depth-dependent) part and a random part with given SD. The water sound speed, density, and attenuation are 1500, 1, 0.

	Parameter	h (m)	c (m/s)	ρ (g/cc)	α (dB/λ)
Case 1	LO	1	1550	1.4	0.14
	HI	1.2	1600	1.6	0.16
	SD	0.5	10	0.05	0.01
Case 2	LO	1	1510	1.1	0.14
	HI	1.2	1600	1.6	0.16
	SD	0.5	10	0.05	0.01

how, with a design frequency of 4167 Hz, the initial depth limit of about 3 m can be extended to 10 m and possibly beyond. The experiment, whose details are given later, was one of a series of six drifting array experiments in the Mediterranean in 2003 accompanied by subsequent seismic boomer runs along the same track and parallel with small offsets.

II. TYPICAL REFLECTION PHASE BEHAVIOR

It is straightforward to model reflection loss from multiple layers. One convenient method for arbitrary fluid layering[1] is described by Jensen *et al.* (1994). Knowing the reflection coefficient R_{nm} for each boundary *in isolation* and the phase change in crossing the nth layer ϕ_n one can build the *joint* reflection coefficient $\Re_{nm}$ by accumulating layers from the substrate (layer M) upwards to the water (layer 0). The joint reflection coefficient for all boundaries below layer n is

$$\Re_{nM} = \frac{R_{n,n+1} + \Re_{n+1,M} \exp(2i\phi_{n+1})}{1 + R_{n,n+1}\Re_{n+1,M} \exp(2i\phi_{n+1})}. \tag{1}$$

Thus starting with $n=M-2$ (the second boundary up) and $\Re_{M-1,M}=R_{M-1,M}$ we work back to $n=0$ which is the joint reflection coefficient for all boundaries below the water. Before using Eq. (1) numerically it is interesting to note the similarity (for any n) between it and the equation for a digital infinite impulse response (IIR) filter,

$$H(Z) = \frac{B(Z)}{A(Z)}, \tag{2}$$

where $Z=\exp(i\omega T)$ in Z transform notation (ω being angular frequency and T being sample interval), and A and B are polynomials in Z (Proakis and Manolakis, 1996). The denominator in Eq. (1) represents multiple reflections (feedback) and if we were to ignore all terms except unity in the denominator (for instance, if all R were small) the final result would be a simple sum of all the in-isolation-reflection-coefficients multiplied by their phase terms—in other words a feed-forward network or finite impulse response (FIR) filter. Note that if the layers are not uniformly spaced, this representation may require a high order but sparse polynomial.

Spectral factorization has been developed in filter theory applied to geophysical prospecting (Claerbout, 1985) as a means of restoring the phase from a frequency-dependent amplitude. The simple Kolmogoroff form,

$$R' = \exp(\mathcal{H}\{\ln(|R|)\}), \tag{3}$$

where $\mathcal{H}$ constructs the "analytic signal" (whose real part is the unchanged argument of $\mathcal{H}$ and whose imaginary part is the Hilbert transform of the same argument), was used by Harrison (2004). Numerically the Hilbert transform operation is done by zeroing the negative frequencies and multiplying the amplitudes of the positive frequencies by two, strictly without zero padding (see for instance, Bellanger, 1994, pp. 247–249; an example of this will be seen later in Appendix A). It is well known (Proakis and Manolakis, 1996) that the solution R' is minimum phase, and for an IIR or FIR filter this means that all zeros and poles are inside the unit circle ($|Z|<1$). A more intuitive explanation is as follows. The phase angle is $\phi=a\tan[\mathrm{Im}(R)/\mathrm{Re}(R)]$ and its progress may be followed in the complex R plane as frequency changes. Depending on the complexity of R (number of boundaries and their respective reflection coefficients), as frequency increases from zero, R will follow an epicycloidlike curve which may loop around the origin many times, or may occasionally loop the origin, or may never do so. In the first case the phase angle ϕ increases monotonically; in the last case it oscillates back and forth but always returns to zero once per cycle. The latter condition can be regarded as a simpler definition of minimum phase [see Proakis and Manolakis (1996), p. 360], and it provides an easy way of testing whether a given reflection coefficient is, in fact, minimum phase. Knowing $R(f,\theta)$ we can unwrap the phase along frequency independently for each ray angle θ and normalize the result by π to count the number of half-revolutions.

$$U = \mathrm{unwrap}(\phi)/\pi. \tag{4}$$

Minimum phase behavior is then indicated by $|U|<1$. In practice one can often find one frequency range where this is obeyed but another where it is not. Provided this frequency range where it is obeyed coincides with the measurement range we deem R to be minimum phase, and therefore complex R' to be a good approximation for complex R.

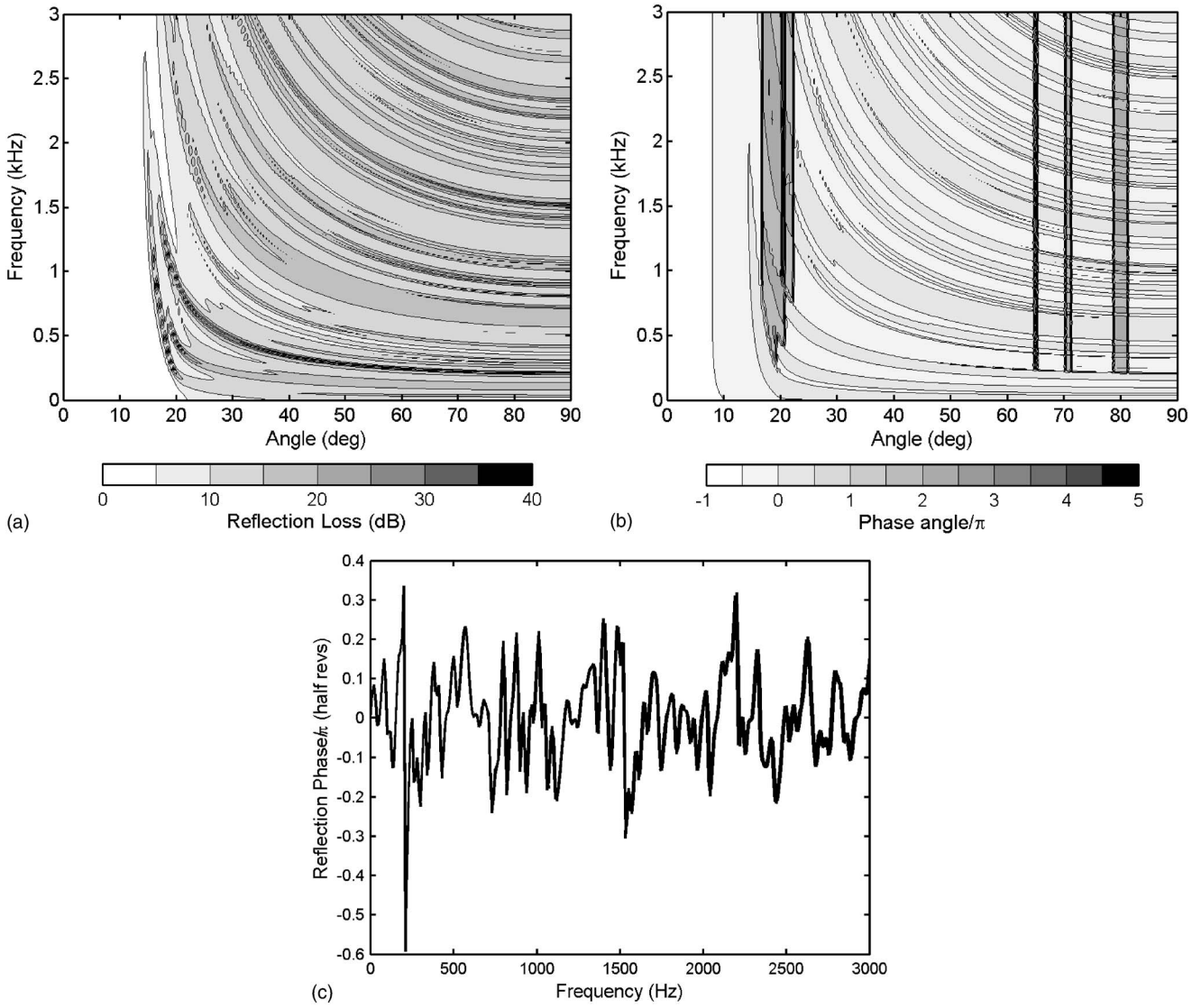

FIG. 1. Case 1, SF good. (a) Reflection loss $[-20\ln(R)]$, (b) unwrapped reflection phase angle normalized by π, (c) unwrapped reflection phase angle for 10 ray angles between 85° and 90°.

An example: Using code based on Eq. (1) we calculate first $R(f,\theta)$ then $U(f,\theta)$ for two cases, one where SF performs well and one where it does not, then we suggest a criterion or condition under which R is minimum phase.

The first case uses the parameters shown in Table I to construct a uniform value in each of 20 layers, having a random part with the given standard deviation (SD) superimposed on a linear trend between "LO" and "HI." For convenience in these examples we take the upper frequency limit to be 3 kHz with an assumed hydrophone spacing of 0.5 m leading to a design frequency of 1500 Hz. Identical reflection coefficients would be obtained for different frequency ranges by scaling layer thickness h and frequency f such that the product $h\times f$ is constant. The resulting reflection loss $[\mathrm{RL}=20\log_{10}(|R|)]$ and unwrapped phase angle are shown, respectively, in Figs. 1(a) and 1(b). A phase angle plot for near vertical is shown in Fig. 1(c). Clearly, despite the prominent interference fringes, there are large regions where $|U|<1$ is obeyed. In the ray angle direction there are some, at first sight, rather surprising discontinuities; within an infinitesimal angle range R jumps from maximum phase (a monotonic rise in U as a function of frequency only) to minimum phase ($|U|<1$). However, remembering the discussion on looping the origin it is clear that sudden changes are easily explained by infinitesimal changes in the diameter of the complex $R(f)$ curve which depends on relative changes in the individual layer reflection amplitudes. Most importantly dark grey to black indicates regions where SF will break down, whereas white to pale grey predicts good SF performance. Note that for sub-bottom profiling where we select only angles close to 90°, only the behavior of U at these angles matters, as in Fig. 1(c).

The second case uses parameters shown on the right-hand side of Table I. Figures 2(a)–2(c) show equivalent plots of R and U, and Fig. 2(c) shows that, unlike Fig. 1(c), the phase angle increases monotonically—distinctly not minimum phase behavior, suggesting poor SF performance. In Fig. 2(b) this corresponds to almost the entire grey-black area.

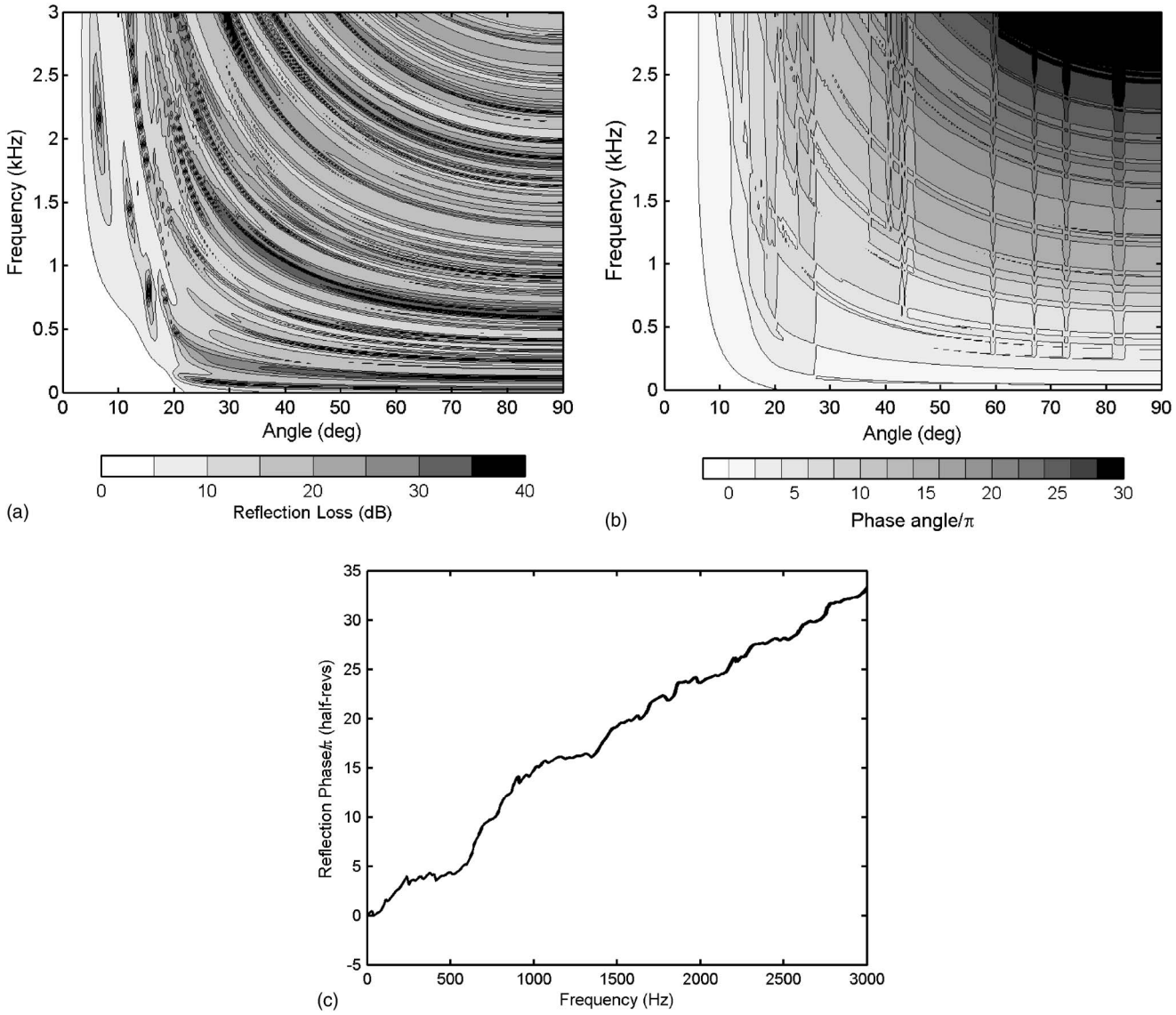

FIG. 2. Case 2, SF poor. (a) Reflection loss $[-20\ln(R)]$, (b) unwrapped reflection phase angle normalized by π, (c) unwrapped reflection phase angle for 10 ray angles between 85° and 90°.

III. A CRITERION FOR GOOD SPECTRAL FACTORIZATION PERFORMANCE

Without loss of generality, the impulse response of a multilayered seabed [equivalent to Eqs. (1) and (2)] can be written as

$$h(t) = a_0\delta(t) + \sum_n a_n\delta(t - t_n) \tag{5}$$

or the equivalent frequency response as

$$H(\omega) = a_0 + \sum_n a_n \exp(i\omega t_n). \tag{6}$$

Appendix A shows that a sufficient condition for R being minimum phase (though possibly too stringent) is that the sum of the later arrival amplitudes a_n must be smaller than the first a_0,

$$C \equiv \sum_n |a_n/a_0| < 1. \tag{7}$$

A less stringent form might be the square root of the sum of squares, i.e., RMS. Equation (7) is easy to understand in terms of the vector addition of the complex components in Eq. (6). It is the multiple a_n and their varying rotation rates t_n (as a function of ω) that determine the epicyclic orbits of R in the complex plane. If the a_n are small then the orbit cannot possibly loop a round the origin, so the solution must be minimum phase. Equation (7) can only be true if the a_n are *all* small compared with a_0. In this case the a_0, a_n correspond to R_{01}, $R_{n,n+1}$.

Interestingly Eq. (7) is also the condition that the only significant spikes in the autocorrelation function of the impulse response [Eq. (5)] lie at the same delays as in the impulse response itself because all the cross terms ($a_n \times a_m/a_0^2$) are much smaller still. From this view point it is also clear that the first impulse in the impulse response must

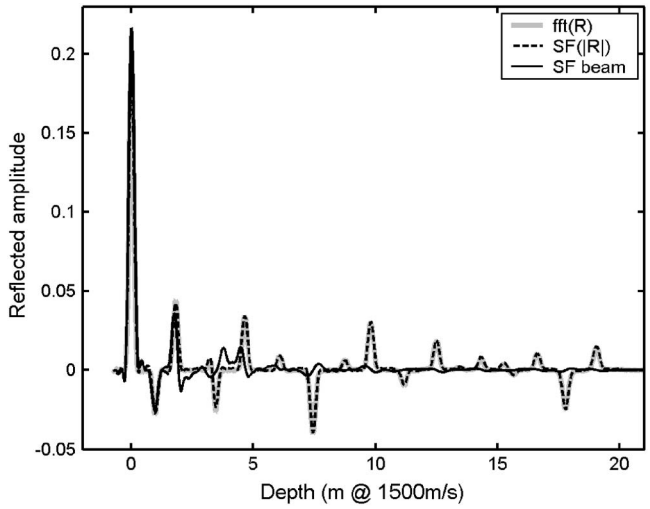

FIG. 3. Impulse responses for case 1, FT of reflection coefficient (grey, but partially hidden by black dashed); spectral factorized modulus of reflection coefficient (black dashed); spectral factorized simulated beam response (black solid).

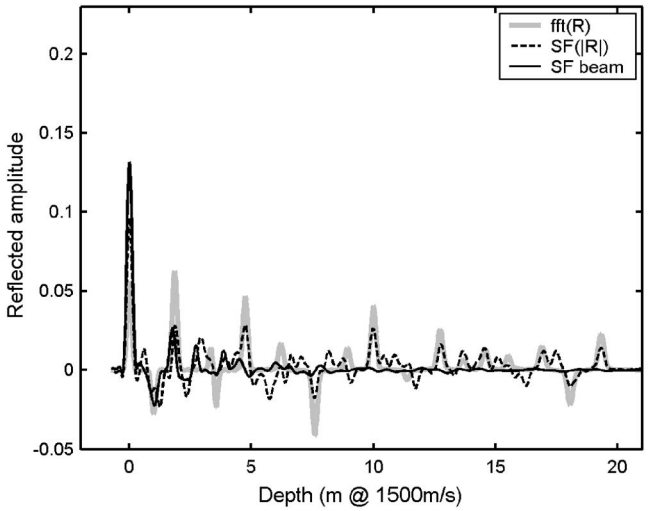

FIG. 4. Impulse responses for case 2, FT of reflection coefficient (grey); spectral factorized modulus of reflection coefficient (black dashed); spectral factorized simulated beam response (black solid).

be strongest otherwise the ordering in the autocorrelation function will be different. Fortuitously in underwater acoustics this is often the case (even though sound speeds and densities tend to rise with depth) because the impedance difference between the water and the first sediment layer is much greater than between subsequent layers. Unfortunately a single measured impulse response, even of this form, does not prove minimum phase behavior. However when SF fails, the spatial variation of the impulse response as the array moves horizontally may reveal tell-tale ghosting (where a pair of impulses follow the undulations of a single boundary). The ghost corresponds to a crossterm in the autocorrelation function.

IV. A NUMERICAL SPECTRAL FACTORIZATION TEST

SF performance can be checked straightforwardly by choosing an arbitrary impulse response $h(t)$ and comparing it with the spectral factorized version [which requires Fourier transformation (FT) to the frequency domain and back to time]. A more realistic starting point is to take the impulse response to be the FT of the reflection coefficient at a given angle in Fig. 1 or 2. We then take SF of $|R|$ and inverse FT to obtain the SF impulse response. The example from Fig. 1 at 90° is shown in Fig. 3 (thick grey line is FT; black dashed line is SF). There are a number of positive and negative impulses corresponding to the assumed 20 layers. As expected agreement of the SF version is extremely good, and indeed is indistinguishable from the true impulse response in this plot. As expected, the goodness coefficient is rather high, $C=2.2$. The less stringent RMS criterion has $C_{\mathrm{RMS}}=0.62$, which therefore appears to be a better indicator.

The SF impulse response for case 2 (cf. Fig. 2), shown in Fig. 4 (black dashed line), is a poorer match to the true impulse response (thick grey line), and although the main peaks occur at the correct times there are additional smaller spurious peaks. The values of the two goodness coefficients are $C=9.2$ and $C_{\mathrm{RMS}}=2.5$.

An additional factor of interest in the case of reflection loss derived from ambient noise is the effect of the preprocessing. As explained in Harrison and Simons (2002) and Harrison (2004) the available frequency band when deriving reflection loss from noise is limited by the parameters of the array. At the low frequency end one could shift the band to zero and compensate with a linear phase multiplication post-FFT. Here we have continued to use the extrapolation technique proposed by Harrison (2004). Although not demonstrated here, extrapolation by itself has little effect on the impulse response. Beam forming has the undesirable effect of blurring the interference fringes (Harrison and Baldacci, 2003). A numerical estimate is given in Appendix B; essentially the mechanism is as follows. The fringes roughly follow lines of constant $f \sin\theta$ (where f is frequency and θ is grazing angle) and although near vertical these variations are small, the endfire beam of the VLA is quite wide ($\sim 15°$) and so the integration in angle blurs the variation in frequency, i.e., degrades its resolution. When we take the IFT back to the time domain this reduces the maximum detectable depth to $Mc/(9f_o)$ (where, as in Appendix B, M is the number of hydrophones, c is the sound speed assumed for beam forming, and f_o is the design frequency), i.e., 3 m for a 32 element array designed for 1500 Hz. Therefore it is interesting to investigate the behavior of SF applied to the simulated noise-derived power reflection coefficient, i.e., the ratio of the up-down beam responses to noise in a shallow water environment with the given reflection properties. The third line (solid black) in the two plots (Figs. 3 and 4) shows this SF of inverted noise. Performance even in the good case (Fig. 3) is indeed worse, indicating that beam forming, or at least the limitation of array size, is a more serious problem for sub-bottom profiling with noise than is spectral factorization. Nevertheless it is worth pointing out that the array was chosen for determining reflection coefficient versus angle rather than selecting a narrow vertical up and down beam. It is easy to confirm this point in simulation by simply increasing the number of hydrophones to narrow the endfire beam,

for instance, the predicted maximum depth for 128 hydrophones is 12 m. In principle one could design an array with a broader horizontal baseline to improve angle, and therefore frequency, resolution and thereby increase depth range. In the meantime an alternative is suggested in the next section.

V. A DESMEARING CORRECTION

Closer inspection of Eq. (B4) in Appendix B reveals that it is a homogeneous Volterra equation of the first kind (Morse and Feshbach, 1953). In other words the integral has a kernel $K(x,x_0)$ and a variable limit, and can be written as

$$G(x_0) = \int_{-\infty}^{x_0} K(x,x_0)g(x)dx. \tag{8}$$

Also in this instance $K(x,x_0)$ can be written as $K(x_0-x)$, and the variable limit can be taken care of by inventing a function $K'(x_0-x)$ where

$$K'(x) = K(x), \quad x \leqslant x_0,$$
$$= 0, \quad x > x_0.$$

So the integral can also be written as a convolution

$$G(x_0) = \int_{-\infty}^{\infty} K'(x_0 - x)g(x)dx. \tag{9}$$

Now because the function K' has a sharp edge (effectively containing all frequencies) the integral can be inverted, either by matrix inversion (the inverse is guaranteed nonsingular) or by inverse filtering using FFTs. The truth of these statements is easily demonstrated numerically and in at least one case can be demonstrated analytically (Appendix C). In effect the inverse filter will boost high frequencies, and although the filter response is finite it is sensitive to rapid fluctuations in g regardless of their cause. Therefore one needs to be especially careful when processing real data in this way. Otherwise this offers a way of countering the frequency smearing that results from the substantial endfire beam width.

Figure 5 is a demonstration of successful application of this (matrix) inversion before spectral factorization to the simulated beam response already seen in Fig. 3 (i.e., case 1, where spectral factorization, by itself worked well, but beam-smearing spoilted the result). Now there is a dramatic recovery of the impulse response (the peaks in the solid black line match those in the thick grey line). The equivalent for case 2 is shown in Fig. 6, but now recovery is not possible because spectral factorization failed.

VI. EXPERIMENTS

A vertical array was allowed to drift in six Mediterranean experiments during the three *NRV Alliance* cruises of BOUNDARY2002, BOUNDARY2003, BOUNDARY2004. The buoy's movements were predominantly towards the southeast following local currents, and the drift tracks are shown in Fig. 7. During BOUNDARY2003 a *Geoacoustics 5813B* seismic boomer was deployed at the sites of the longest 2002 and 2003 drifts. The boomer is a downward looking active sonar operating with pulse length about 0.2 ms (bandwidth 10 kHz) and maximum pulse energy 280 joules. The receiver is a very short horizontal array. The resulting layer profiles were used as "ground-truth," and the 2002 drift which used 32 elements with design frequency 1500 Hz (0.5 m spacing) has already been reported in Harrison (2004). Later drifts used a medium frequency array (MFA) still with 32 elements but a design frequency of 4167 Hz (0.18 m separation) and benefited from the weaker shipping noise at higher frequencies. Here we concentrate on the 6 km drift in 2003. There are three corresponding boomer tracks, one a straight line joining the drift's endpoints (deviating slightly from the mildly erratic drifting buoy), the other two, parallel but offset 50 m on either side. The aim was to allow for actual deviations in the drift path, uncertainties in position which was inferred from the ship's radar, and to obtain an estimate of the true lateral variability of the layers. Using ship's navigation one can plot all four sub-bottom profiles

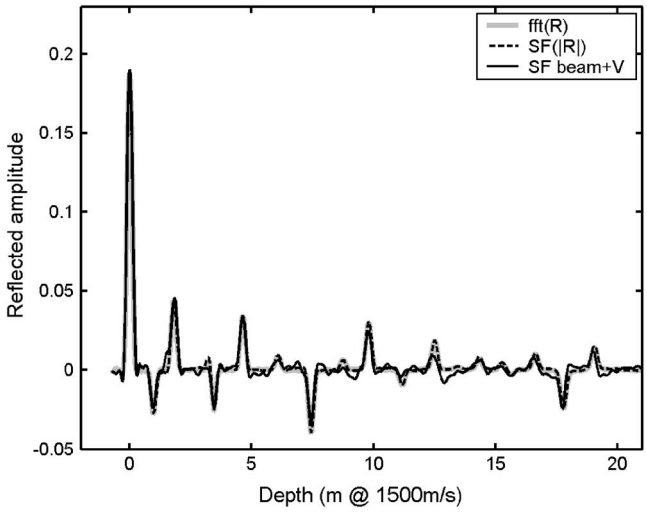

FIG. 5. Recovered impulse responses for case 1, FT of reflection coefficient (grey, but partially hidden by black); spectral factorized modulus of reflection coefficient (black dashed); inverse filtered, spectral factorized simulated beam response (black solid).

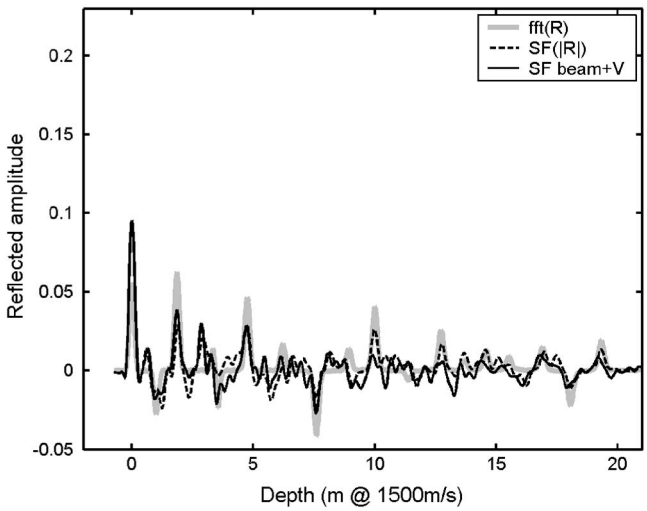

FIG. 6. Unsuccessfully recovered impulse responses for case 2, FT of reflection coefficient (grey); spectral factorized modulus of reflection coefficient (black dashed); inverse filtered, spectral factorized simulated beam response (black solid).

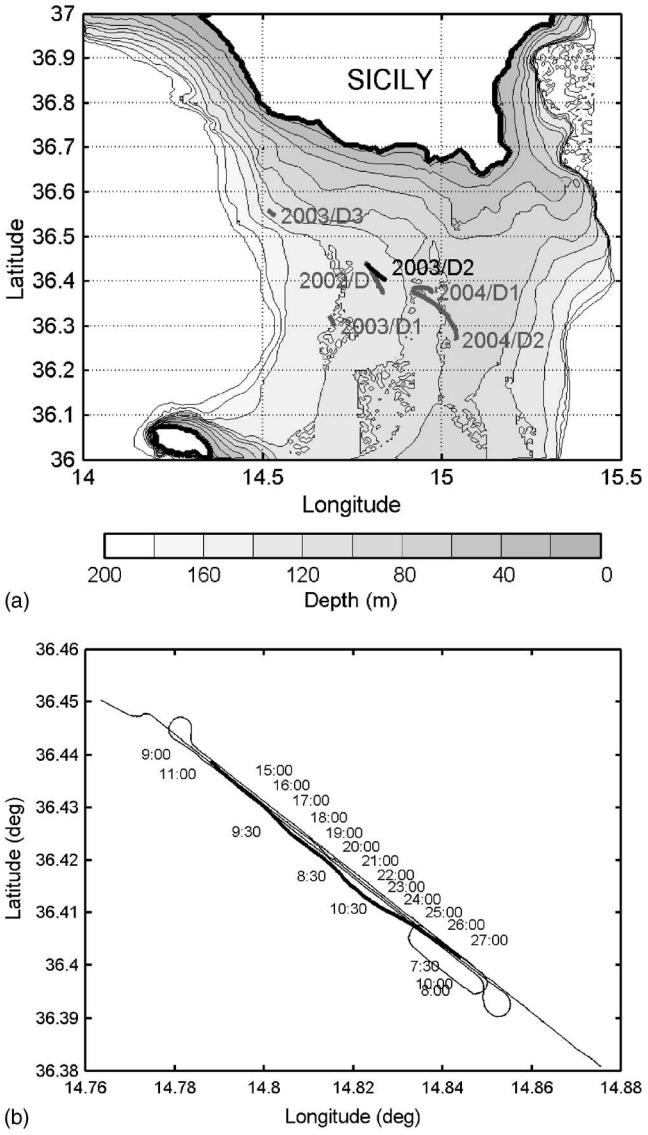

FIG. 7. (a) Map showing drift tracks during BOUNDARY experiments, and (b) detailed VLA drift tracks and three parallel boomer tracks during BOUNDARY2003.

aligned with a linear length scale. Clock times then appear nonlinearly on the same plots. In Harrison (2004) the noise-derived profiles were displayed in color to show positive and negative arrival amplitudes in the impulse response. In contrast, a common procedure with the boomer is to show only the negative side of the wave form. To compare like with like, Fig. 8 shows the noise profile and zero-referenced boomer (i.e., zero delay is adjusted to the first bottom arrival) all processed in this way.

A. Beam-smeared results

In the first instance we have applied extrapolation and spectral factorization but not the anti-beam-smear correction. The original noise spectrum is derived from a 128 point FFT of the 12 kHz sampled time series. After spectral factorization an IFFT is performed to obtain the impulse response, but regardless of the number of points in the IFFT the maximum delay corresponds to the original frequency resolution, namely $12\,000/128=93.75$ Hz. Rejecting times beyond Nyquist leads to a maximum time of $128/(2\times12\,000)=5.33$ ms. Converting this two-way travel time to a depth @ 1500 m/s gives $1500\times128/(2\times2\times12\,000)=4.0$ m, as shown in all panels of Fig. 8.

First of all we note from the bottom three panels of Fig. 8 that the boomer shows significant differences in moving laterally by ±50 m. The left half of the noise profile (top panel) shows more similarity with the boomer than the right. This is likely to be because the first half of the drift track was more straight and coincided better with the boomer track. Otherwise the main similarities are the curving ("s"-shaped) features between 1 and 3 m and 4.7 and 5.3 km, the deep returns between 5.5 and 7.5 km, and the return at depths of 1 m increasing to 3 m at ranges beyond 8.5 km including two sawtooth features at about 9.5 km.

Interestingly there are often repeat echoes (same shape line, displaced in delay) in both noise and boomer profiles though not in the same places. To the right of 5.5 km in all three boomer records there is a pronounced double echo that appears not to be a multiple reflection since there are no other layers with related time delays. In the noise profile it is in principle possible to see multiple reflections since they would have been incorporated in the original frequency response [see Eq. (1)]. A hint of this repeat echo behavior is seen between 8 and 9 km, but again, and for the same reasons, we do not suspect a multiple reflection on this occasion. It is also possible to see "ghost" echoes that are neither multiple reflections nor parallel layers. Such a case is the repeat "s"-shaped line at 4.9 km. Since the later return appears to agree very well in shape and depth with all boomer records we assume that it is the earlier one that is false. This cannot be a multiple reflection because it is not causal, i.e., it occurs before the main reflection. In this case it is believed to be an artefact of spectral factorization. In fact it is a manifestation of the criterion, Eq. (7) being violated.

This can be understood as follows. If we had taken the FT of $|R|^2$ instead of complex R we would have obtained the autocorrelation of the impulse response. Clearly this function contains impulses at delays corresponding to all possible layer separations. If the first peak in the impulse response is significantly stronger than the others, as required by the criterion, then, to first order, the peaks to the right of the origin of the autocorrelation function are at the same delays as the peaks in the actual impulse response, and they have proportional amplitudes. All the rest are much weaker. In short, the impulse response resembles its autocorrelation function.

The implication is that spectral factorization is really only operating on the amplitudes of the peaks in the autocorrelation function; it does not alter any time delays or add or subtract impulses. It therefore works when the impulse response resembles the autocorrelation function, i.e., when the first peak is strongest. For all other layer arrangements (except for the possibility of the *last* impulse being the strongest) the impulse response does not resemble its autocorrelation function. Under these conditions the spectral factorized result still resembles the autocorrelation function, but differs from the true impulse response in including ghost echoes.

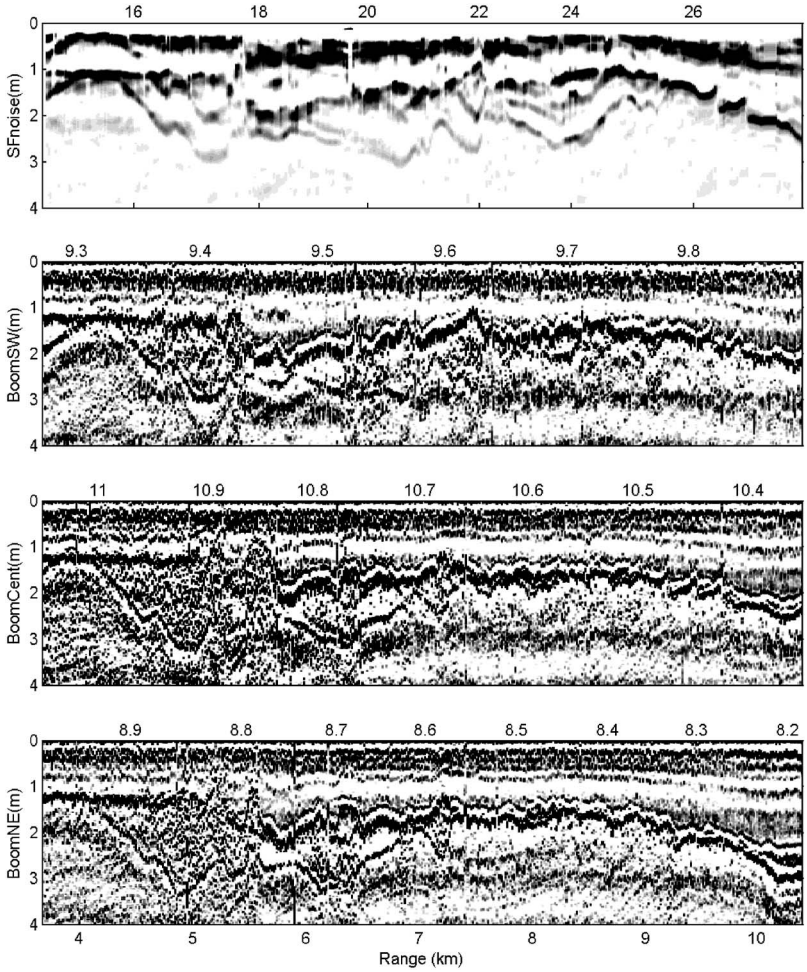

FIG. 8. Noise sub-bottom profile (top panel) compared with parallel boomer tracks displaced +50 m, 0 m, −50 m either side. The maximum depth is determined by the FFT size of 128, and beam-smear processing was excluded.

B. Results including a beam-smearing correction

The restoration process discussed in Sec. V is now applied to the same experimental data. To see any fluctuations at all we need to use a larger FFT size (e.g., 256, 512 rather than 128), but as already noted we need to take care of fluctuations in $|R|$ other than those truly caused by beam forming. Typically even after averaging one sees fluctuations in $|R(\omega)|$ that are unchanging with angle and therefore not due to beam forming. These can be removed to a certain extent by averaging along the fringe lines, as follows. The behavior of the fringes with angle within about 10° of vertical is almost entirely geometrical so the fringes always spread apart in frequency as angle departs from vertical. Locally one can assume $R(\omega,\pi/2)=R(\omega/\sin\theta,\theta)$ (see Appendix B). Thus unwanted angle-independent fluctuations can be removed by averaging over a limited range of angle along the fringe crests, i.e., keeping this condition true.

As a check, the first example shown in Fig. 9 has the correction applied to the original data with no increase in FFT size (i.e., still 128). As far as layer depth is concerned the image is the same as Fig. 8, however there is an increase in clarity (i.e., impulse amplitude) at the deeper depths near 4 m. Figure 10 shows the extension to 8 m with an FFT size of 256 including the correction. There is clearly additional layer structure at these depths that compares well with the boomer, in particular at 4 and 6 m on the left and rising layers between 8 and 4 m on the right. Figure 11 shows extension to 16 m (FFT size 512) where the rising layers on the right are again visible down to about 15 m and there are layers at about 10 and 11 m on the left. Overall, we find that this technique does indeed provide a substantial improvement in the strength and penetration depth of the returns.

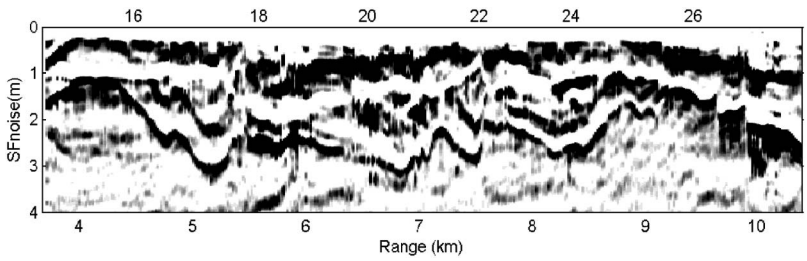

FIG. 9. Noise sub-bottom profile for the same depth range as in Fig. 8 but including beam-smear processing.

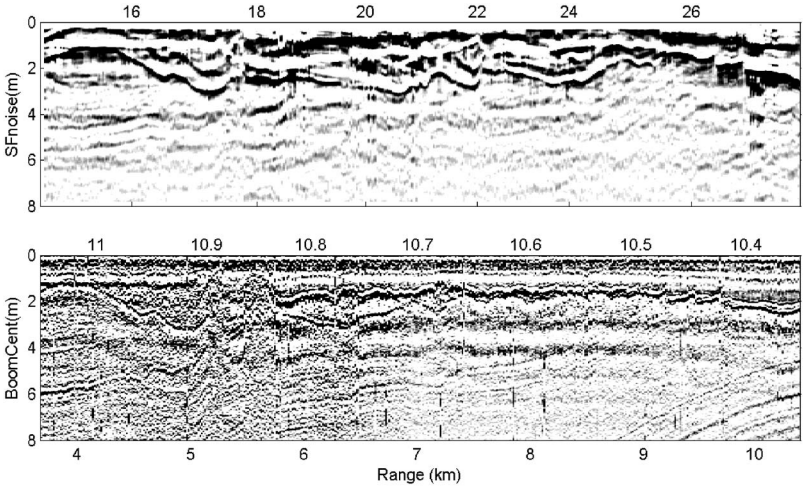

FIG. 10. Noise sub-bottom profile (top panel) compared with the central boomer track result. The maximum depth of 8 m is determined by the FFT size of 256. Beam-smear processing was included.

VII. CONCLUSIONS

In underwater acoustics there is a wide range of layered seabeds for which spectral factorization can successfully reconstruct the reflection phase. Here we have investigated the factors that determine the degree of success. Essentially one needs high impedance contrast at the water sediment interface and relatively low contrast at subsequent layer boundaries. Alternatively, in terms of filter theory one can state that the spectral factorized solution is always minimum phase, therefore its validity requires that the layer structure, regarded as a filter, be minimum phase. Pragmatically the spectral factorized solution is closely related to the autocorrelation of the impulse response, so when the (right-hand side of the) autocorrelation function has the same shape as the impulse response the solution is valid. Furthermore, the shape of the autocorrelation is actually the same as the impulse response to a good approximation when the first arrival is significantly stronger than the others. This occurs under the condition already stated, that there is high impedance contrast at the water sediment interface but weaker elsewhere. Two multiple layer simulations were chosen to demonstrate good and bad performance. In each case the true impulse response and the spectral factorized results were known, one could investigate the unwrapped phase of the reflection coefficient, and one could therefore invent a criterion for likely success. It was possible to see that the actual phase of the reflection coefficient had deviations of only a small fraction of π in the successful case (i.e., minimum phase behavior) but increased monotonically in the unsuccessful case.

In the case where one derives the near vertical reflection loss from ambient noise it appears that the width of the endfire beam can effectively smudge the frequency resolution which, in turn, limits the maximum detectable depth. If one includes this effect in simulating the spectral factorized impulse response, performance is more seriously degraded. Therefore the technique of sub-bottom profiling with noise (as opposed to determination of the reflection coefficient or geoacoustic inversion) could be improved by designing an array with an increased horizontal baseline and narrower vertical beam.

Surprisingly it is possible partly to recover this frequency smeared information. Beam forming can be thought of as a convolution in angle with a beam pattern, but this, usually smooth function, has an abrupt edge at endfire. By making use of the characteristic shape of the fringes one can rewrite the angle convolution integral for the endfire case as a frequency convolution where the smoothing function is one sided. This class of filter function is always invertible so one can reconstruct the presmoothed fringe pattern. In simulation this more or less eliminates the beam-smearing degradation.

Experiments with a drifting array (design frequency 4167 Hz) during BOUNDARY2003 produced sub-bottom

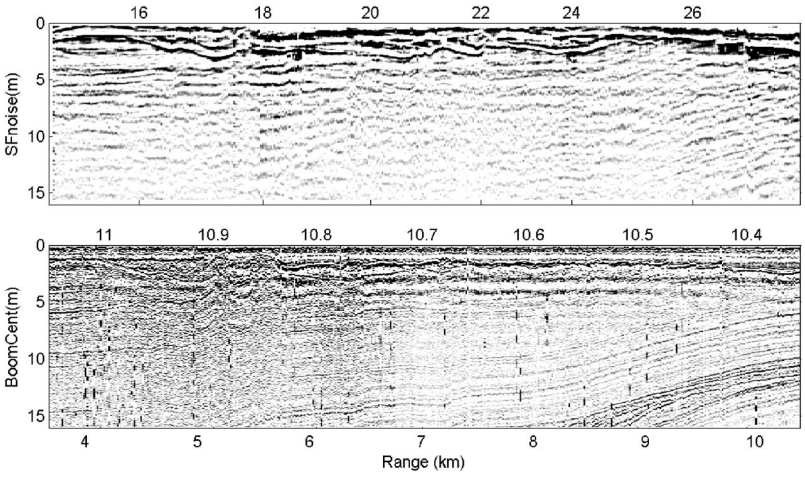

FIG. 11. Noise sub-bottom profile (top panel) compared with the central boomer track result. The maximum depth of 16 m is determined by the FFT size of 512. Beam-smear processing was included.

profiles that are remarkably similar to seismic boomer results obtained along the same track on another occasion during the same cruise. The natural maximum depth dictated by the FFT size was 4 m. Applying the desmearing correction to the noise enabled one to see features common to the boomer down as far as 15 m. Precautions were taken against introducing spurious responses by inadvertently restoring fluctuations from mechanisms other than beam smearing.

ACKNOWLEDGMENTS

The author thanks the Captain and crew of the *NRV Alliance*, Enzo Michelozzi for engineering coordination, Piero Boni for data acquisition, and particularly Peter Nielsen who acted as Scientist-in-charge of the three cited BOUNDARY experiments.

APPENDIX A: A CRITERION FOR GOOD SPECTRAL FACTORIZATION PERFORMANCE

The spectral factorization of the reflection coefficient R [Eq. (3)] can be written as

$$R' = \exp(\mathcal{H}\{\ln(|R|)\}) = \exp\left(\mathcal{H}\tfrac{1}{2}\{\ln(|R|^2)\}\right). \tag{A1}$$

Inserting Eq. (6) as a representation of complex R we have

$$|R|^2 = \left(a_0 + \sum_n a_n \exp(i\omega t_n)\right)\left(a_0 + \sum_n a_n \exp(-i\omega t_n)\right). \tag{A2}$$

Initially we assume Eq. (7) to be true and all the t_n to be positive delays, so

$$\ln(|R|^2) = 2\ln a_0 + \ln\left(1 + \sum_n (a_n/a_0)\exp(i\omega t_n)\right) + \ln\left(1 + \sum_n (a_n/a_0)\exp(-i\omega t_n)\right). \tag{A3}$$

Writing the sums, respectively, as g_+ and g_- we temporarily substitute the Taylor expansion of $\ln(1+g)$ as

$$\ln(|R|^2) = 2\ln a_0 + (g_+ - g_+^2/2 + g_+^3/3 + \cdots) + (g_- - g_-^2/2 + g_-^3/3 + \cdots). \tag{A4}$$

Since the t_n are, by assumption, all positive, the g_+^k are entirely positive frequencies whereas the g_-^k are entirely negative frequencies. Now, application of an ideal Hilbert transform multiplies the amplitudes of the positive frequencies by 2 and rejects the negative frequencies [Eq. (2) of Harrison (2004)]. The result is

$$\begin{aligned} R' &= \exp[\ln a_0 + (g_+ - g_+^2/2 + g_+^3/3 + \cdots)] \\ &= a_0\left(1 + \sum_n (a_n/a_0)\exp(i\omega t_n)\right) \\ &= \left(a_0 + \sum_n a_n \exp(i\omega t_n)\right) = R. \end{aligned} \tag{A5}$$

In other words the SF result R' is exactly the original R provided Eq. (7) is obeyed, otherwise the Taylor expansion does not converge. Furthermore, if the strongest impulse a_0 is not earliest then some of the t_n must be negative, so we can be certain that the g_+^k are no longer all positive frequencies and the g_-^k are no longer all negative frequencies. It follows, in general, that $R' \neq R$.

APPENDIX B: ENDFIRE FREQUENCY SMUDGING

In the vicinity of the vertical, the interference fringes in the reflection coefficient and therefore also in the noise (Harrison, 1996) closely follow lines of constant $f \sin\theta$. Therefore the noise power can roughly be written in terms of a function of a single variable as

$$N(f,\theta) = N_o(f\sin\theta). \tag{B1}$$

The beam responses $A(\theta_s)$ (up and down) are then formed by multiplying by the appropriate beam pattern $B(f,\theta,\theta_s)$ and integrating over angle. It is easy to show that, for a M element VLA with design frequency f_o, B is of the following form, and that a hamming shaded beam can be approximated as a Gaussian:

$$\begin{aligned} B(f,\theta,\theta_s) &= B[(\sin\theta_s - \sin\theta)fM/2f_o] \\ &\Rightarrow \exp\{-[(\sin\theta_s - \sin\theta)fM/\alpha f_o]^2\}, \end{aligned} \tag{B2}$$

where $\alpha = 2\sqrt{2/\pi} \approx 1.6$. This has the property that at the design frequency and broadside ($\theta_s = 0$), beamwidth is α/M, whereas at endfire ($\sin\theta_s = 1$) beamwidth is $\sqrt{\alpha/M}$. The beam response is

$$A(\theta_s) = \int_{-\pi/2}^{\pi/2} N(f\sin\theta)\exp\{-[(\sin\theta_s - \sin\theta)/(\alpha f_o/fM)]^2\}\cos\theta\, d\theta. \tag{B3}$$

If we change variable to $F = f\sin\theta$ this becomes

$$A(\theta_s) = \int_{-f}^{f} N(F)\exp\{-[(f\sin\theta_s - F)/(\alpha f_o/M)]^2\} dF/f. \tag{B4}$$

For all steer angles θ_s (other than endfire) this can clearly be regarded as multiplication of the noise function (of modified frequency F) by a smoothing function of full width $2\alpha f_o/M$. At endfire only one-half of the smoothing function is effective and the width is $\delta f = 2\alpha f_o/M$. Thus with $M = 32$ we expect smoothing on a scale of 1/20 of the design frequency. It is interesting to compare this with the frequency sampling chosen (on pragmatic grounds) to date (Harrison and Simons, 2002) where a FFT size of 128 combined with sample frequency 6 kHz led to $\Delta f = 93.75$ Hz; with $f_o = 1500$ Hz we find $\alpha f_o/M$ is 75 Hz which is close. When the reflection coefficient is calculated from the ratio of the endfire beam responses it suffers the same degradation, and consequently layering derived from its FT has a maximum round-trip travel time[2] of $1/(\pi\delta f) = M/(\pi\alpha f_o)$, or maximum depth $Mc/(2\pi\alpha f_o)$ which for $M = 32$, $c = 1500$ m/s, $f_o = 1500$ Hz is 3 m.

APPENDIX C: INVERTIBLE FILTERS

An array's beam response can be regarded as a filtered version of the directional field to which it responds. The filter is always a low-pass or smoothing filter. In general the rapid angular variation is lost, so inversion is impossible. With this

prejudice it is surprising to find that one can (in principle) invert the corresponding convolution in frequency [Eq. (B4), Appendix B, or Eq. (9) in the main text],

$$G(x_0) = \int_{-\infty}^{x_0} K(x_0 - x) g(x) dx. \tag{C1}$$

There are three pertinent viewpoints, (1) Fourier analysis, (2) matrix rank, (3) straightforward solution of a Volterra integral equation (Morse and Feshbach, 1953).

From the Fourier analysis point of view a convolution in time can be written as the product of the FTs of the filter and the input. Since the inverse filter is the reciprocal of the forward filter it is clear that, to be invertible, the modulus of the latter must be nonzero for all frequencies, so the filter shape in time cannot be smooth; it must contain steps or spikes (slope or higher order discontinuities, while important for continuous functions, are less important for discrete systems).

Equation (C1) can be written in matrix form as $\mathbf{G}=\mathbf{K}\mathbf{g}$. If $\mathbf{K}$ represents a beam pattern, for instance a Gaussian, then it is Toeplitz and symmetrical about the diagonal. On the other hand, if $\mathbf{K}$ represents the kernel of the frequency integral of Appendix B then it is still Toeplitz but either the upper or lower triangle is zero. It is easy to show numerically that the rank of $\mathbf{K}$ in the first example tends to unity (the determinant tends to zero) but in the second is the size of the matrix (i.e., the number of linearly independent rows or columns). Therefore the second is invertible but the first is not.

Finally in the special case where $K(x_0,x)=K(x_0-x)=\exp[-a(x_0-x)]$, an exponentially weighted filter, invertibility can be demonstrated explicitly since there is an analytical solution. Differentiating Eq. (8) with respect to x_0 we find

$$\frac{\partial G}{\partial x_0} = \int_{-\infty}^{x_0} \frac{\partial K}{\partial x_0} g(x) dx + g(x_0), \tag{C2}$$

but $\partial K/\partial x_0 = -aK$ so

$$\frac{\partial G}{\partial x_0} = -aG(x_0) + g(x_0) \tag{C3}$$

and the inverted solution is

$$g(x_0) = \frac{\partial G}{\partial x_0} + aG(x_0). \tag{C4}$$

In other words the output of an exponentially weighted filter can be inverted to find the original raw signal $g(x)$. The $\partial G/\partial x_0$ term makes clear that $g(x)$ is sensitive to fine changes in $G(x_0)$ whether due to the true convolution or due to unknown and unwanted causes.

[1]This approach can be marginally extended to the case where the substrate alone is solid since there will still be a unique speed, and therefore phase, in each of the upper layers.

[2]The product of the half-width of a Gaussian in frequency and the half-width of its FT is $\delta t \delta f = \pi$

Aredov, A. A., and Furduev, A. V. (**1994**). "Angular and frequency dependencies of the bottom reflection coefficient from the anisotropic characteristics of a noise field," Acoust. Phys. **40**, 176–180.

Bellanger, M. (**1994**). *Digital Processing of Signals* (Wiley, New York).

Buckingham, M. J. (**1980**). "A theoretical model of ambient noise in a low-loss shallow water channel," J. Acoust. Soc. Am. **67**, 1186–1192.

Buckingham, M. J., and Jones, S. A. S. (**1987**). "A new shallow-ocean technique for determining the critical angle of the seabed from the vertical directionality of the ambient noise in the water column," J. Acoust. Soc. Am. **81**, 938–946.

Caiti, A., Chapman, R., Hermand, J., and Jesus, S. (2004). "Acoustic inversion methods and experiments for assessment of the shallow water environment," 2nd Workshop 28–30 June 2004, Ischia, Italy.

Carbone, N. M., Deane, G. B., and Buckingham, M. J. (**1998**). "Estimating the compressional and shear wave speeds of a shallow-water seabed from the vertical coherence of ambient noise in the water column," J. Acoust. Soc. Am. **103**, 801–803.

Chapman, D. (**1988**). "Surface-generated noise in shallow water: A model," Proceedings of (UK) Institute of Acoustics, Conference, Vol. **9**, pp. 1–11.

Claerbout, J. (**1985**). *Fundamentals of Geophysical Data Processing* (Blackwell Scientific, Palo Alto).

Collins, M. D., and Kuperman, W. A. (**1991**). "Focalization: Environmental focusing and source localization," J. Acoust. Soc. Am. **90**, 1410–1422.

Giddens, E. M., and Buckingham, M. J. (**2004**). "Geoacoustic inversions in shallow water using Doppler-shifted modes from a moving source," J. Acoust. Soc. Am. **116**, 2557.

Harrison, C. H. (**1996**). "Formulas for ambient noise level and coherence," J. Acoust. Soc. Am. **99**, 2055–2066.

Harrison, C. H. (**2004**). "Sub-bottom profiling using ocean ambient noise," J. Acoust. Soc. Am. **115**, 1505–1515.

Harrison, C. H., and Baldacci, A. (**2003**). "Bottom reflection properties deduced from ambient noise: simulation and experiment," in *Theoretical and Computational Acoustics 2003*, edited by A. Tolstoy, Y.-C. Teng, and E. C. Shang (World Scientific, New Jersey), pp. 162–177.

Harrison, C. H., and Simons., D. G. (**2002**). "Geoacoustic inversion of ambient noise: a simple method," J. Acoust. Soc. Am. **112**, 1377–1389.

Heaney, K. D. (**2002**). "Rapid geoacoustic characterization from a surface ship of opportunity," J. Acoust. Soc. Am. **111**, 2334.

Holland, C. W., and Harrison, C. H. (**2003**). "Measurement of the seabed reflection coefficient in shallow water: a comparison of two techniques," in *Theoretical and Computational Acoustics 2003*, edited by A. Tolstoy, Y.-C. Teng, and E. C. Shang (World Scientific, New Jersey), pp. 178–191.

Jensen, F. B., Kuperman, W. A., Porter, M. B., and Schmidt, H. (**1994**). *Computational Ocean Acoustics* (AIP, New York).

Kuperman, W. A., and Ingenito, F. (**1980**). "Spatial correlation of surface-generated noise in a stratified ocean," J. Acoust. Soc. Am. **67**, 1988–1996.

Morse, P. M., and Feshbach, H. (**1953**). *Methods of Theoretical Physics* (McGraw-Hill, New York).

Proakis, J. G., and Manolakis, D. G. (**1996**). *Digital Signal Processing Principles, Algorithms, and Applications* (Prentice-Hall, Englewood Cliffs, NJ).

Roux, P., Kuperman, W. A., Colosi, J. A., Cornuelle, B. D., Dushaw, B. D., Dzieciuch, M. A., Howe, B. M., Mercer, J. A., Munk, W., Spindel, R. C., and Worcester, P. F. (**2004**). "Extracting coherent wave fronts from acoustic ambient noise in the ocean," J. Acoust. Soc. Am. **116**, 1995–2003.

Roux, P., Sabra, K. G., Kuperman, W. A., and Roux, A. (**2005**). "Ambient noise cross correlation in free space: Theoretical approach," J. Acoust. Soc. Am. **117**, 79–84.

Sabra, K. G., Roux, P., and Kuperman, W. A. (**2005**). "Arrival-time structure of the time-averaged ambient noise cross-correlation function in an oceanic waveguide," J. Acoust. Soc. Am. **117**, 164–174.

Tolstoy, A., Chapman, N. R., and Brooke, G. (**1998**). "Workshop'97: Benchmarking for geoacoustic inversion in shallow water," J. Comput. Acoust. **6**, 1–28.

Source localization in the Haro Strait primer experiment using arrival time estimation and linearization

Zoi-Heleni Michalopoulou[a)]
Department of Mathematical Sciences, New Jersey Institute of Technology, Newark, New Jersey 07102

Xiaoqun Ma
Watermark Management Corporation, Princeton, New Jersey 08542

(Received 8 June 2005; revised 16 August 2005; accepted 17 August 2005)

Modeling sound propagation in the Haro Strait is a challenging task, the site being complex and the sediment structure exhibiting a strong range dependence. The environmental complexities create difficulties for source localization using matched field processing because many of the parameters needed for replica calculation are uncertain or rapidly varying. Received time series from signal propagation at the site provide a wealth of information that can be exploited for source localization obviating the need for extensive environmental knowledge. In this paper, a Gibbs sampling-maximum *a posteriori* estimator is used to extract the direct path, first surface bounce, and first bottom bounce arrival times from time series received at vertical line arrays. Those times provide source and receiving phone location and water column depth estimates through a set of linear relationships. Estimates obtained with the proposed method for data collected during the Haro Strait primer experiment are very close to reference values for the unknown parameters. © *2005 Acoustical Society of America.* [DOI: 10.1121/1.2062287]

PACS number(s): 43.30.Pc, 43.60.Jn [AIT] Pages: 2924–2933

I. INTRODUCTION

This paper presents a two-stage estimation procedure, combining efficient arrival time estimation and linearization, for source localization. In stage 1, arrival times are estimated using a Gibbs sampling-maximum *a posteriori* (GS-MAP) process, presented in Ref. 1 and modified here for greater efficiency. This new estimator is applied for the first time to real data collected in the Haro Strait.[2] In stage 2, estimated ray path arrival times from stage 1 are used for source localization by employing a simple linear system.

Inverse theory plays a critical role in underwater acoustics for the estimation of geometric parameters (source and receiver location, bottom depth) and environmental parameters (sound speed profiles, sediment densities, attenuations and sediment layer depths). A popular approach for inversion is matched-field processing (MFP),[3–5] in which replica fields are computed using sound propagation models and then correlated to the measured field. Values of the unknown parameters that maximize the similarity between replica and true acoustic fields are the desired estimates.

MFP has been used with excellent results on many data sets, both real and synthetic.[5–11] This desirable efficacy is, however, bought at the significant cost of intensive computation for the calculation of the full acoustic field at a set of receiving phones. Necessary for these calculations are assumptions about the numerous parameters that define the structure of the transmission environment, many of which critically affect localization results and may not be dismissed. Information on these parameters is often vague, so that inaccuracies and uncertainties are inevitable even in carefully considered situations. Uncertainties on factors including water column depth and bottom sediments must be incorporated in the estimation process to ensure accurate inversion. The resulting computational load of matched-field inversion is often substantial.

In order to circumvent the need for multiple replica field calculation, necessary to properly manage the information uncertainties just outlined, attempts have been made to simplify modeling. Two such simplifications are inversion using distinct arrivals[12–18] and linearization.[6,19,20,15–18,21,22] Linearized inversion comparing direct path arrival times at spatially separated phones was demonstrated in Refs. 15–17 with excellent results in array element localization; bottom reflected paths were used for array element localization in Ref. 18 for a known (range dependent) bathymetry and known sound speed. While linearization for acoustic inversion using arrival times does simplify the computational task, it does so at the cost of requiring identification of the nature of each arrival observed in the ocean impulse response: how many bounces, if any, each path has gone through and with which interfaces it has interacted. Such identification is not always straightforward, especially when only limited prior information is available on the propagation environment. We propose a method tailored specifically to this challenge.

In Ref. 1, a GS-MAP method was developed for arrival identification. The method produced excellent arrival time and amplitude estimates with synthetic data and did not suffer from instabilities or convergence to local extrema. In this paper, a modified GS-MAP method with improved efficiency is employed for arrival time estimation of three paths (direct, surface, and first bottom bounce) from time series recorded during the Haro Strait experiment. The relationship between arrival times and unknown source location parameters and

[a)]Electronic mail: michalop@njit.edu

bottom depth is linearized using the GS-MAP time estimates as measured arrival times, yielding a simple-to-solve localization problem.

In essence, the presented method combines time delay estimation and linearization to build a model-based time-delay algorithm, which compares arrival time estimates of the aforementioned paths to theoretically predicted arrival times for paths of the same nature. The latter arrival times, which are also referred to here as replica arrival times, are generated using geometry ignoring refraction because of the simplicity of the water-column sound speed profile in the Haro Strait. Accurate results were readily obtained.

The structure of this paper is as follows: Section II provides a brief presentation of the GS-MAP method of Ref. 1, which we have modified for faster arrival time estimation. Section III presents the approximating linear system linking arrival time estimates to source and receiver location and water column depth. Section IV presents and discusses results from the application of the combined GS-MAP and linearization algorithm to Haro Strait data. Section V summarizes the work and presents conclusions.

II. GIBBS SAMPLING FOR TIME DELAY ESTIMATION

As explained in Ref. 1, estimates of time delays and amplitudes (as well as variance of the noise corrupting the signal) are obtained through maximization of the posterior distribution of the unknown parameters given the observed signal $r(n)$ and a Gaussian model for the noise; $r(n)$ is written as

$$r(n) = \sum_{i=1}^{M} a_i s(n - n_i) + w(n), \tag{1}$$

where $n=1,\ldots,N$ (N is the number of samples of the received signal), $s(n)$ is the transmitted waveform, a_i is the amplitude of the ith path, and n_i is the arrival time of the ith path. Quantity $w(n)$ is additive, white normally distributed noise with zero mean and variance ϕ^2. It is assumed that the number of arrivals is known. The amplitudes are real numbers (positive or negative, the sign indicating polarity of the arrivals). The assumption of lack of dispersion, implicit in the distortionless arrivals of Eq. (1), is often reasonable for propagation at frequencies above a few hundred hertz.

For the amplitudes we consider uniform, noninformative, improper prior distributions:[23]

$$p(a_i) = 1, \quad -\infty < a_i < \infty, \; i = 1,\ldots,M. \tag{2}$$

We set uniform priors for the delays:

$$p(n_i) = \frac{1}{N}, \quad 1 \leqslant n_i \leqslant N, \quad i = 1,\ldots,M. \tag{3}$$

For variance ϕ^2, the noninformative prior

$$p(\phi^2) = \frac{1}{\phi^2}, \tag{4}$$

was selected.[1,24]

A uniform prior distribution is selected for M, the number of arrivals present in the time series:

$$p(M) = \frac{1}{M_2 - M_1 + 1}, \tag{5}$$

where M_1 and M_2 are the lowest and highest values, respectively, that M can take.

Taking into account the Gaussian model for the data and the above-mentioned prior distributions, we can write the posterior probability distribution function of all amplitudes and delays (a_i and n_i for $i=1,\ldots,M$), variance ϕ^2, and number of arrivals M as follows:

$$\begin{aligned} &p(n_1,n_2,\ldots,n_M,a_1,a_2,\ldots,a_M,\phi^2,M|r(t)) \\ &\quad = K\frac{1}{(M_2 - M_1 + 1)}\frac{1}{N^M}\frac{1}{(\sqrt{2\pi})^N \phi^{N+2}} \\ &\qquad \times \exp\left(-\frac{1}{2\phi^2}\sum_{n=1}^{N} (r(n) - \sum_{i=1}^{M} a_i s(n - n_i))^2 \right). \end{aligned} \tag{6}$$

Quantity K is a constant ensuring correct scaling of the probability distribution.

MAP estimates of all unknowns can be obtained through the maximization of Eq. (6), not a trivial task for a high-dimensional search space. In Ref. 1 a Gibbs sampler was implemented for optimizing the search, drawing samples from the conditional distributions of each parameter given all other parameters and the data. The proposed method was shown to produce excellent results for amplitudes and delays. For the estimation of the number of arrivals, M, the method was applied to the received time series for several values of M. The Schwartz-Rissanen criterion was then used to select an estimate for M;[25] time-delay, amplitude, and variance estimates from the Gibbs sampler run corresponding to the selected value for M were then identified.

Although the process was successful, it required running the Gibbs sampler for several values for M. Here, we modified the processor, so that M is included in the sampling process, thus improving the efficiency of the procedure. The conditional posterior probability distribution of M given all other parameters and the data is obtained; then values for M are sampled from this conditional distribution in every Gibbs sampling iteration as was done for all other parameters.

III. THE LINEAR SYSTEM

The arrival time of the direct, first surface reflected, and first bottom reflected ray path depends on the geometry and environmental parameters of the underwater problem of interest: source range r, source depth z_s, receiving phone depths z_r, bottom (water column) depth D, sound speed profile $c(z)$ in water, and the source instant t_s. For the Haro Strait experiment, sound speed is a known, depth-independent quantity: $c(z)=c=1482.5$ m/s. Formally, a received arrival time (assuming no noise in the measurements) can be written as

$$t_r = t(r, z_s, z_r, D) + t_s, \tag{7}$$

where $t(\cdot)$ represents the ray travel time. Now we equate this functional expression for arrival time to the estimate obtained with the GS-MAP processor of Sec. II: $t(r, z_s, z_r, D) = n/f_s$, where n is a time delay estimate obtained with the Gibbs sampler and f_s is the sampling frequency for the received data.

The transmitted signals travel in the ocean and are received at multiple hydrophones. For the SW and NE arrays of the Haro Strait experiment measurements at 16 hydrophones ($L=16$) are available; only 12 hydrophones were operational ($L=12$) for the NW array. For an array with L hydrophones, if three characteristic ray paths (direct, first surface bounce, first bottom bounce) are employed, there will be a total of $3L$ arrival time measurements (data) which depend on $2L+3$ parameters (two spatial variables for each hydrophone, source depth, bottom depth, and source instant). These measurements can be described as

$$\mathbf{t_r} = \mathbf{f}(\mathbf{q}), \tag{8}$$

where $\mathbf{t_r}$ is the vector of measured (estimated) travel times; $\mathbf{f}$ represents the forward method, or acoustic model, that relates travel times to the unknown parameters; $\mathbf{q}$ represents the vector of these parameters:

$$\mathbf{q} = [r_1 r_2 \ldots r_L z_s z_{r1} z_{r2} \ldots z_{rL} D t_s]^T. \tag{9}$$

For the acoustic inverse problem, vector $\mathbf{q}$ is estimated using the measured data and forward model $\mathbf{f}$. The inverse process is nonlinear, tractable only with considerable computational effort; linearizing the problem locally may lead to accurate solutions with vastly reduced effort. A linear approximation to Eq. (8) can be obtained as[15,21,22]

$$\mathbf{t_r} = \mathbf{t_0} + \mathbf{J}(\mathbf{q} - \mathbf{q_0}), \tag{10}$$

where $\mathbf{t_0}$ is a vector of arrival times calculated for initial conditions $\mathbf{q_0}$ for $\mathbf{q}$ and $\mathbf{J}$ is the Jacobian matrix which contains time derivatives with respect to each of the unknown parameters along specific paths. By introducing $\delta\mathbf{t} = \mathbf{t_r} - \mathbf{f}(\mathbf{q_0}) = \mathbf{t_r} - \mathbf{t_0}$ and $\delta\mathbf{q} = \mathbf{q} - \mathbf{q_0}$, Eq. (10) yields

$$\mathbf{J}\delta\mathbf{q} = \delta\mathbf{t}. \tag{11}$$

Alternatively, one can write

$$\mathbf{J}\mathbf{q} = \mathbf{t_r}. \tag{12}$$

Equations (11) and (12) reflect a linear relationship between arrival times and parameters $\mathbf{q}$. Both equations typically lead to overdetermined systems that can be solved using least squares, several iterations being necessary for convergence of the method. Although the two equations look very similar, choosing the one over the other could lead to slightly different results (depending on the nullspace of $\mathbf{J}$); results from the system of Eq. (11) are more sensitive to the particular choice of initial conditions than results from Eq. (12).[26] It is therefore preferable to work with Eq. (12) which is also more flexible than Eq. (11) and can be refined to give more accurate results, as will be shown in the following. [In our case, matrix $\mathbf{J}$ is full-rank and Eqs. (11) and (12) would give identical results.]

Solving the system of Eq. (12) requires computation of the entries of matrix $\mathbf{J}$. These are arrival time derivatives with respect to the unknown parameters. For the Haro Strait data, the isovelocity profile of the water column makes these calculations very simple, since refraction does not need to be accounted for. Using simple geometry, one can write

$$t_{di} = t_s + \frac{\sqrt{r_i^2 + (z_s - z_{ri})^2}}{c}, \tag{13}$$

$$t_{si} = t_s + \frac{\sqrt{r_i^2 + (z_s + z_{ri})^2}}{c}, \tag{14}$$

$$t_{bi} = t_s + \frac{\sqrt{r_i^2 + (2D - z_s - z_{ri})^2}}{c}, \tag{15}$$

where t_{di}, t_{si}, and t_{bi} are the arrival times for the direct path, first surface, and first bottom bounce at the ith receiver, respectively ($i=1,\ldots,L$); r_i is the distance between source and the ith receiver, and z_{ri} is the depth of the ith phone.

Time derivatives with respect to range r_i, source depth z_s, receiver depth z_{ri}, bottom depth D, and t_s can be calculated in a straightforward manner from Eqs. (13)–(15).

As previously mentioned, overdetermined systems of the form of Eq. (12) are often solved with least squares. The least-squares method solves an inverse problem by finding parameter values that minimize the Euclidean distance $\Sigma_{j=1}^{3L}(\mathbf{J}_{jx}\mathbf{q} - \mathbf{t_r}_j)^2$, where $\mathbf{J}_{jx}$ is the jth row of $\mathbf{J}$, and $\mathbf{t_r}_j$ is the jth element of measured arrival times $\mathbf{t_r}$. Parameter values that maximize the likelihood function formulated under the Gaussian assumption are also those that minimize the error in a least-squares sense for a linear model.[21,22] The assumption of Gaussian statistics is reasonable in our case, because arrival times are typically modeled with zero mean Gaussian distributions with a standard deviation σ of a few hundred microseconds to a few millseconds. It should be noted that variance σ^2 is different than ϕ^2; σ^2 is the variance of the estimates of arrival times, whereas ϕ^2 is the variance of the noise that had been added to the received sequence.

The least-squares solution of Eq. (12) is

$$\mathbf{q} = (\mathbf{J}^T\mathbf{J})^{-1}\mathbf{J}^T\mathbf{t_r}. \tag{16}$$

In the above-given formulation, the assumption is that uncertainty variance σ^2 is the same in all arrival times.

If matrix $\mathbf{J}^T\mathbf{J}$ is not singular, its inverse can be obtained and $\mathbf{q}$ can be easily calculated. Setting heavily correlated parameters (as source and receiver depths) as unknown, however, results in stability problems in the solutions of the system caused by the ill-conditioned $\mathbf{J}^T\mathbf{J}$ matrix; even tiny noise levels in the data can generate highly oscillating and unreliable estimates. Remedying the problem involves stabilization of the ill-conditioned matrix which can be done through singular value decomposition and truncation (truncating singular values below a threshold) or diagonal loading, to name the two most popular approaches. More elegantly and meaningfully, the problem can be regularized to incorporate prior knowledge on the unknowns as done in Refs. 26 and 15–18.

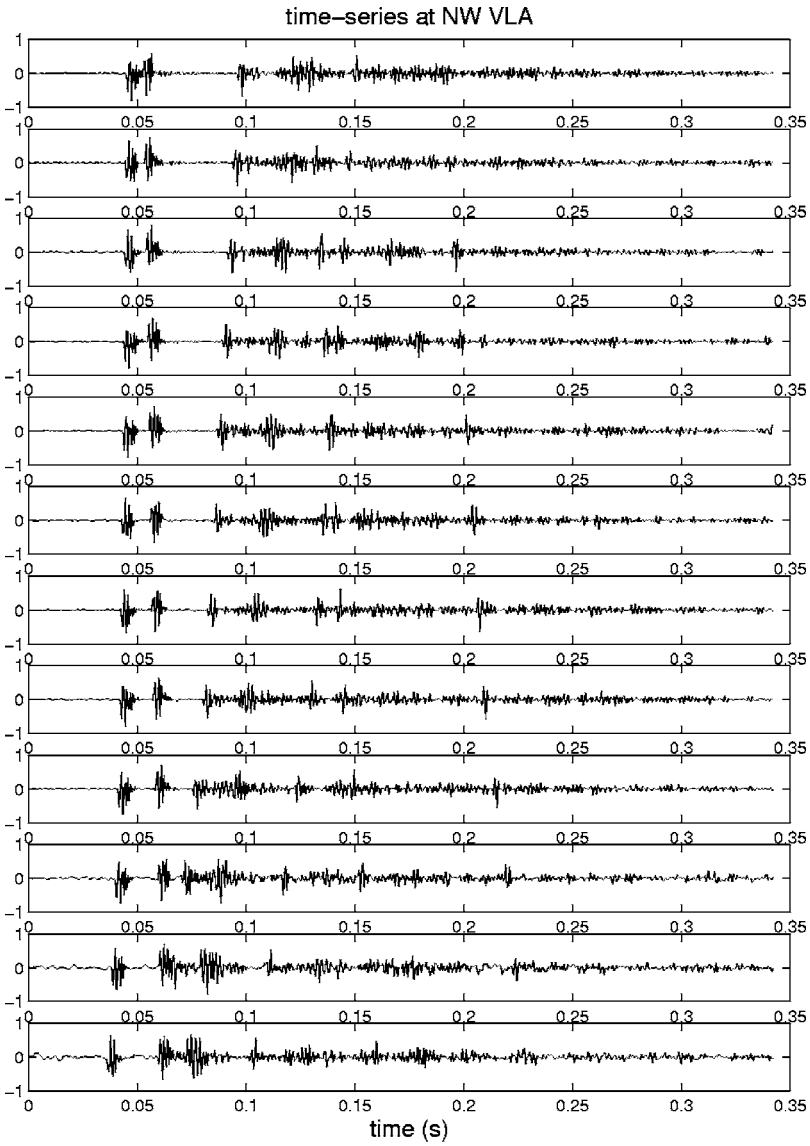

FIG. 1. Time series recorded at the NW array (NW024).

Regularization makes use of the system formulation of Eq. (12) and minimizes a new objective function $g(\mathbf{q})$, where g is a combination of misfit between true data and predicted data with the chosen forward model and the error between parameter values and prior knowledge on those. Function g can be written as

$$g(\mathbf{q}) = \|\mathbf{G}(\mathbf{J}\mathbf{q} - \mathbf{t_r})\|^2 + \alpha^2\|\mathbf{H}(\mathbf{q} - \mathbf{q_p})\|^2, \tag{17}$$

where $\mathbf{H}$ is the regularization weighting matrix, including uncertainties on those parameters with available *a priori* information, and $\mathbf{q_p}$ is the vector containing prior information of the components of vector $\mathbf{q}$. Assuming that the error in the measured data (arrival times) follows a zero mean Gaussian distribution with standard deviation σ_i, $\mathbf{G}$ is a diagonal matrix defined as

$$\mathbf{G} = \mathrm{diag}[1/\sigma_1, 1/\sigma_2, \ldots, 1/\sigma_{3L}]. \tag{18}$$

(In our case, we assume that $\sigma_1 = \sigma_2 = \ldots = \sigma_{3L}$.)

The regularized solution is obtained as[27,15]

$$\mathbf{q} = (\mathbf{J}^T\mathbf{G}^T\mathbf{G}\mathbf{J} + \alpha^2\mathbf{H}^T\mathbf{H})^{-1}(\mathbf{J}^T\mathbf{G}^T\mathbf{G}\mathbf{t_r} + \alpha^2\mathbf{H}^T\mathbf{H}\mathbf{q_p}). \tag{19}$$

Parameter α^2 is a Lagrange multiplier. Quantity $\alpha^2\mathbf{H}^T\mathbf{H}$ of Eq. (19) stabilizes and "smooths" the inversion solution by removing the ambiguities of the unregularized inverse problem,[27,26,22] resolving the instability induced by the ill-conditioned matrix $\mathbf{J}^T\mathbf{J}$ previously mentioned. Determination of an "optimal" value for α^2 is a point of active research and it really depends on the specific estimation problem. Large values of α^2 place a large weight on prior information; small values for α^2 place the weight on the data-model mismatch. In Ref. 15, α^2 is selected by applying the discrepancy principle;[27] that is, by conducting a search for a value of α^2 that will make a χ^2 statistic (defined in the following) obtain or approach its expected value of $3L-(2L+3)$ (number of available arrival times minus the number of unknowns):

$$\chi^2 = 3L - (2L + 3). \tag{20}$$

Here χ^2 is defined as

$$\chi^2 = \|\mathbf{G}(\mathbf{f}(\mathbf{q}) - \mathbf{t_r})\|^2, \tag{21}$$

where $\mathbf{t_r}$ is the measured data, vector $\mathbf{f}$ is the forward model (simple geometric equations relating time to unknowns), and

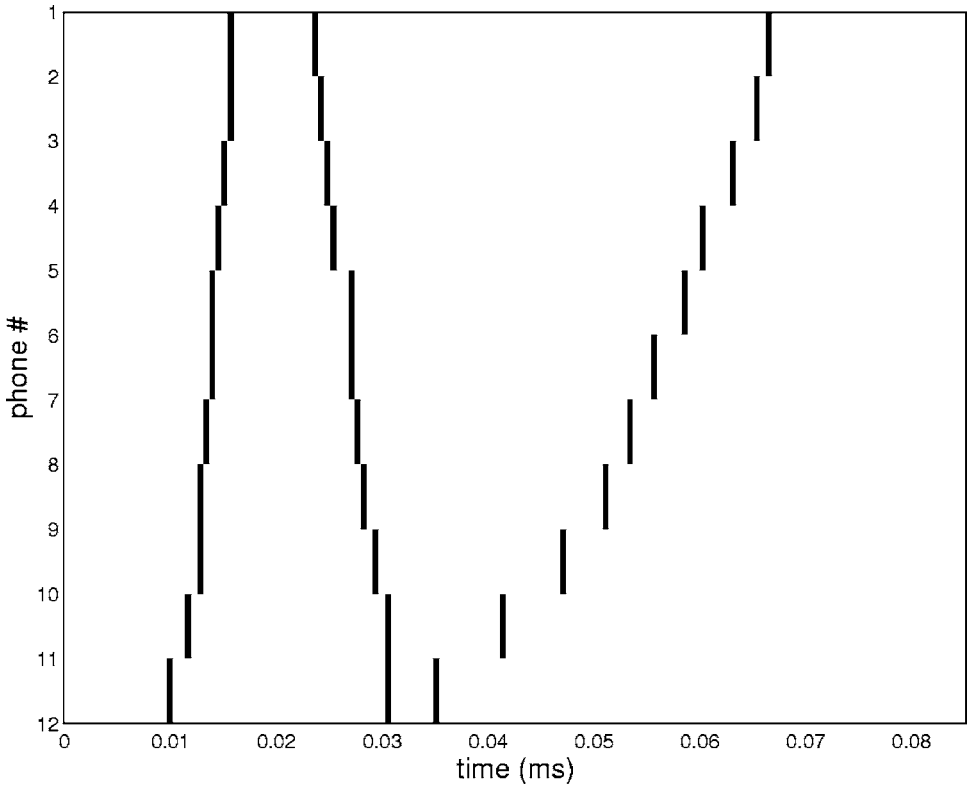

FIG. 2. Extracted arrival times from the received time series at the NW array (NW024).

q is the vector of estimates of model parameters. We eschew the discrepancy principle in favor of a different criterion, the L curve, for choosing α^2 which we believe is more suitable to our problem. The L curve is the plot of $\|\mathbf{H}(\mathbf{q}-\mathbf{q_p})\|^2$ vs $\|\mathbf{G}(\mathbf{f}(\mathbf{q})-\mathbf{t_r})\|^2$ [the χ^2 quantity of Eq. (21)] for solutions of Eq. (19) for different values of α^2; it thus reveals the tradeoff between regularization error and model-data fit.

The L curve takes its name from its shape. which resembles a letter L. The value of α^2 corresponding to the corner of the L curve balances the two errors, χ^2 and squared weighted difference between the solution and prior information. This is the value of α^2 that is often selected in regularization; the value is typically smaller than the α^2 required to achieve $\chi^2=3L-(2L+3)$. There have been many efforts to

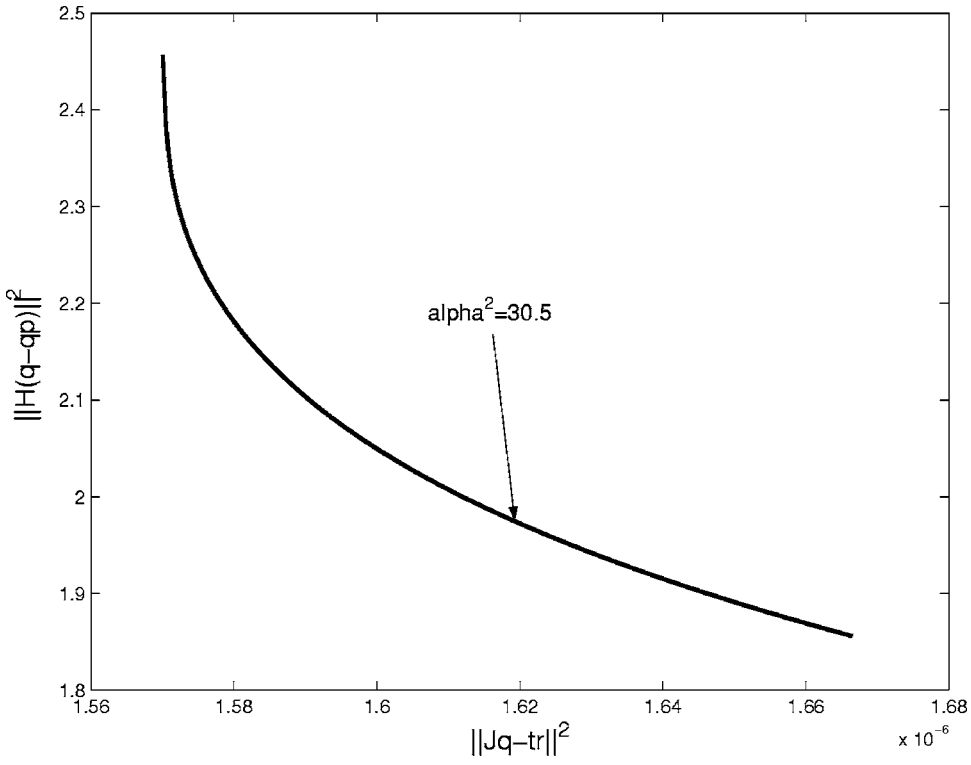

FIG. 3. The L curve for time-series NW024.

further refine the choice of α^2. To keep a low bound on the estimation error, it has been recommended in Ref. 28 to select a value of α^2 leading to a point on the L curve slightly to the right of the corner. We follow that recommendation herein.

In inversion, the choice of α^2 is largely dictated by the specific problem and the degree of belief in the validity of the prior information. For example, in well controlled situations where many of the parameters are known within tight intervals, the best choice of α^2 might be a value that keeps the deviation from the prior information as small as possible, placing more weight on that error than on the χ^2 error component. This choice leads to an α^2 that corresponds to an L-curve point more to the right of the corner than the one we select [such as the one resulting in the χ^2 quantity of Eq. (21)]. Treating our problem as a source localization problem with a large degree of uncertainty (and also not knowing explicitly arrival time noise variance), we eschew this selection process, placing less weight on the prior information.

There are various methods for the formulation of regularization matrix **H** based on different *a priori* information. Here, **H** is selected as in Ref. 15:

$$\mathbf{H} = \mathrm{diag}[1/\theta_1, 1/\theta_2, \ldots, 1/\theta_{2L+3}], \tag{22}$$

where θ_i represents the uncertainty or "spread" for the ith parameter. For those parameters without *a priori* information, the corresponding term in **H** is set to zero, the obvious implication being that, if there is no prior information on any of the parameters, matrix **H** would be the **0** matrix and the problem would revert to simple least squares with its attendant solution instabilities.

TABLE I. Source location and water column depth for NW024.

Parameter	Estimate	Reference
r_1(m)	509.0	512.9
z_s(m)	60.7	70.0
D(m)	201.7	200.0

IV. INVERSION WITH THE HARO STRAIT DATA

The Haro Strait experiment was conducted in the Summer of 1996 at Haro Strait, east of South Vancouver Island.[2,14,13] The experiment involved several broadband sources and three vertical line arrays (VLAs). The broadband sources were light bulb shots with frequency content between 100 and 800 Hz. The underwater sound speed profile was roughly independent of depth with a value of approximately 1482.5 m/s. The bathymetry of the site was range dependent; depth varied between 150 and 230 m. The three VLAs (denoted as NW, SW, and NE) consisted of 16 hydrophones roughly located between 50 and 150 m (only 12 hydrophones were operational for the NW VLA). The sampling rate was 1750 Hz.

We applied the combination of the two methods, Gibbs sampling for time delay estimation and linearization using the time delay estimates, to several sets of received data from the Haro Strait experiment. Once the Gibbs sampler was run on the data, we selected the first three arrivals that consistently appeared in the time series received at the VLAs and formed measurements for the direct path and first surface and bottom bounce arrivals to be used for the inversion. The noise variance required for the formulation of matrix **G** in Eqs. (19) and (21) was unknown. Observing that from different applications of the Gibbs sampler to the same data, we

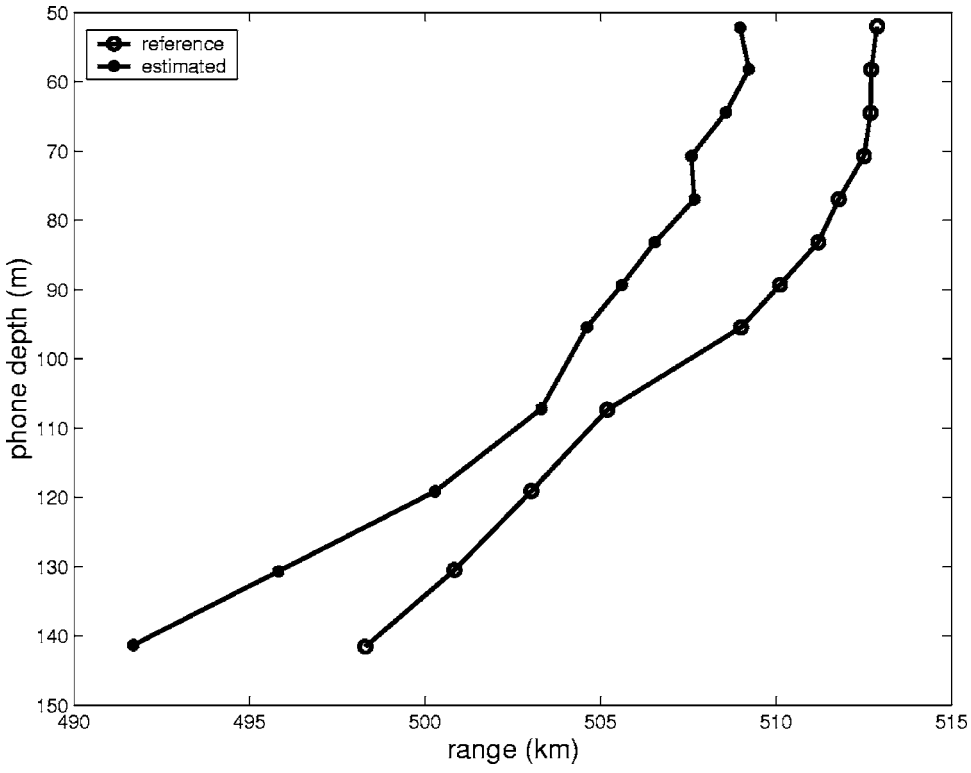

FIG. 4. Source-receiver ranges and phone depths for time-series NW024.

TABLE II. Source location and water column depth for SW032.

Parameter	Estimate	Reference
r_1(m)	1332.2	1348.9
z_s(m)	50.5	50.0
D(m)	195.1	190.0

TABLE III. Source location and water column depth for SW029.

Parameter	Estimate	Reference
r_1(m)	865.8	894.7
z_s(m)	77.0	70.0
D(m)	202.0	190.0

sometimes obtained differences of one to two samples (0.0011 s) in the estimated arrival times, we selected $\sigma = 0.001$ s.

One set of the time series that we processed for the NW array (NW024) is shown in Fig. 1. Figure 2 shows the first three arrival time estimates for those time series.

The linear system for source location and bottom depth estimation for NW024 was constructed with prior values of 1 km for all horizontal distances between source and phones, 20 m for the source depth, and 200 m for the water column depth. The receiver depths were set at the reference depths available for the NW VLA. Prior knowledge (although available) was not provided to the algorithm for the ranges, source depth, or source instant. Uncertainty of the water column depth was taken to be ±20 m around 200; uncertainty for the phone depths was ±5 m around the reference values.

Figure 3 shows the L curve for inversion using this data set (since $\mathbf{G}$ is not accurately known here, we plot $\|\mathbf{H}(\mathbf{q}-\mathbf{q_p})\|^2$ vs $\|(\mathbf{f}(\mathbf{q})-\mathbf{t_r})\|^2$). The arrow indicates the L-curve point that is taken as our "balance" between regularization error and misfit; the value of α^2 corresponding to that point was 30.5. Table I shows reference values for source range, depth, and water column depth for that case as well as the estimates obtained here. Range and water column depth estimates are very close to the reference values; the source depth estimate is roughly 9 m away from its reference value. Phone-source ranges and phone depths are shown in Fig. 4. The array shape as seen from the NW024 source was estimated in Ref. 13. Our results are plotted along with the results of Ref. 13 and the match is very good. The array shape obtained with our approach matched very closely that of Ref. 13; an offset of less than 10 m is observed in range between reference measurements and estimates.

It should be noted that reference values used in our tables were calculated by translating latitude and longitude coordinates of sources and receivers into distance. Depending on the algorithm used for the conversion, slightly different reference values could be obtained.

Source location and bottom depth estimates were next obtained for data received at the SW VLA for shot 32. Results, presented in Table II, show excellent agreement with the reference values for the data. The water depth for this case changed with range between source and receiver. It was close to 210 m for the array location and to 180 m at the source. The value of 180 m was selected both as initial condition for the depth and as prior information. The initial values for source range and depth were 1 km and 20 m, respectively. Using the L curve, α^2 was selected to be 25.

The results of Table II are also corroborated by the estimates of Table III for case SW029. Source 029 lay approximately on the line segment connecting source 032 and the SW array; it was located closer to the array than source 032.

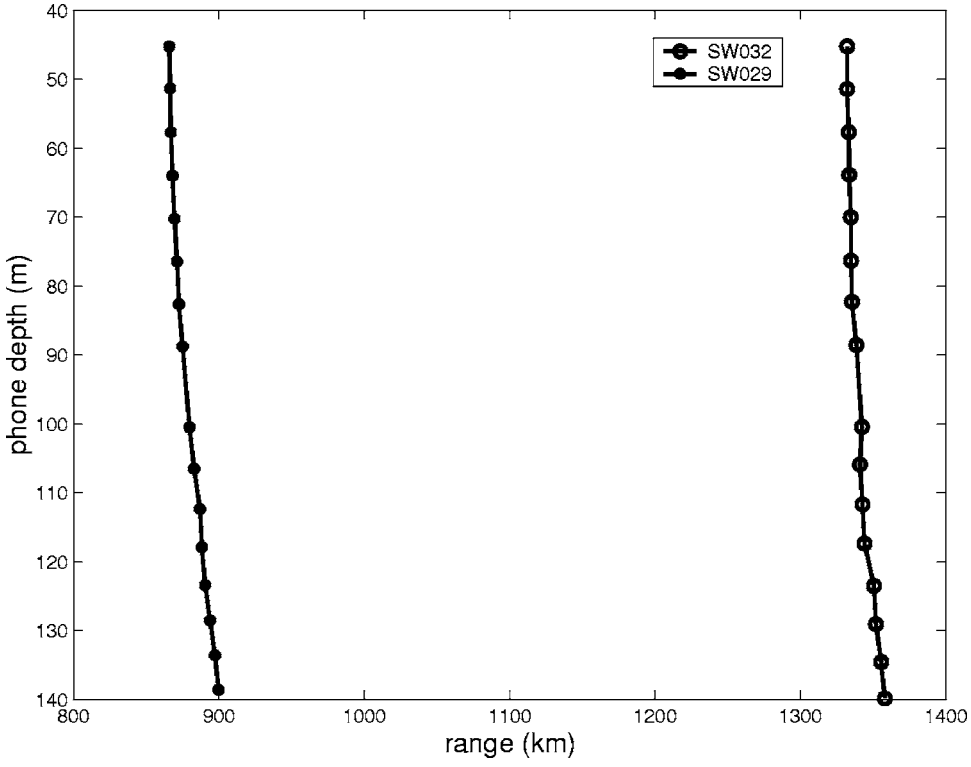

FIG. 5. Source-receiver ranges and phone depths for time-series SW032 and SW029.

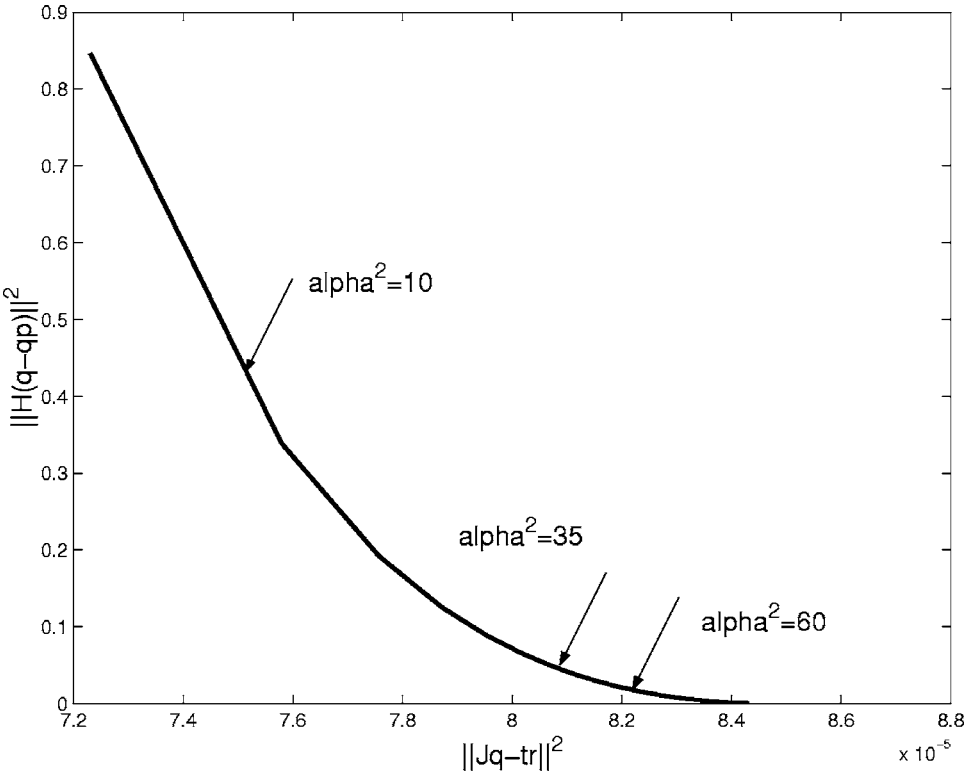

FIG. 6. The L curve for time-series SW032.

This is exactly what comparison of the two sets of results reveals. Also a bathymetric map of the region shows that the water was slightly deeper at source 029 than at source 032; again the results demonstrate this relationship.

Figure 5 shows estimates of phone depths and ranges for the two cases SW029 and SW032. Because both sources lie on the same line segment that connects them to the SW VLA, we expect the array shape "seen" from both sites to be the same; indeed, the two array shapes are very similar.

We selected case SW032 to illustrate the effect of multiplier α^2. Figure 6 shows the L curve for that case. Arrows indicate which values of α^2 correspond to points on the curve. We selected $\alpha^2=35$ for our problem following the recommendation of finding the corner of the curve and moving a little to the right. An α^2 of 10 would put less weight on the prior information leading to a point on the curve to the left of the corner (small χ^2 error but large deviation for prior information). A value of 60 for α^2 weighs prior information more heavily resulting in a smaller deviation from prior and larger χ^2 error. The inversion results from different values of α^2 are shown in Table IV.

TABLE IV. Source location and water column depth for SW032 for $\alpha^2=10$ and $\alpha^2=60$.

α^2	Parameter	Estimate	Reference
10	r_1(m)	1389.9	1348.9
10	z_s(m)	53.5	50.0
10	D(m)	199.2	190.0
60	r_1(m)	1296.2	1348.9
60	z_s(m)	48.7	50.0
60	D(m)	192.6	190.0

As can be seen from Table IV, the estimation process for $\alpha^2=60$ attempts to match the prior value of 180 for the bottom depth and adjusts the other parameters accordingly. For $\alpha^2=10$ and $\alpha^2=35$ (Table II) the value of 180 for the depth is not too restrictive and the process converges to parameter values that give a good data-model fit.

Table V contains inversion results for case NE020; the corresponding L curve is shown in Fig. 7. This case is probably the most challenging studied in this paper because (i) the two first arrivals for several of the receivers almost coincide and are difficult to identify and (ii) the bathymetry between the NE array and source 020 is highly variable. Using previously selected initial conditions for range and source depth and 190 m for water depth (as an average value), we obtained reasonable estimates for all parameters. The assumption of range independence inherent in our calculations can easily explain the difference in range between reference value and estimate.

V. CONCLUSIONS

In this paper an inversion method was developed for source and hydrophone localization of a real broadband source in a shallow water environment; bottom depth was estimated as well. The method produces estimates through a

TABLE V. Source location and water column depth for NE020.

Parameter	Estimated	Reference
r_1(m)	2921.5	2740.0
z_s(m)	66.1	70.0
D(m)	189.9	150.0–230.0

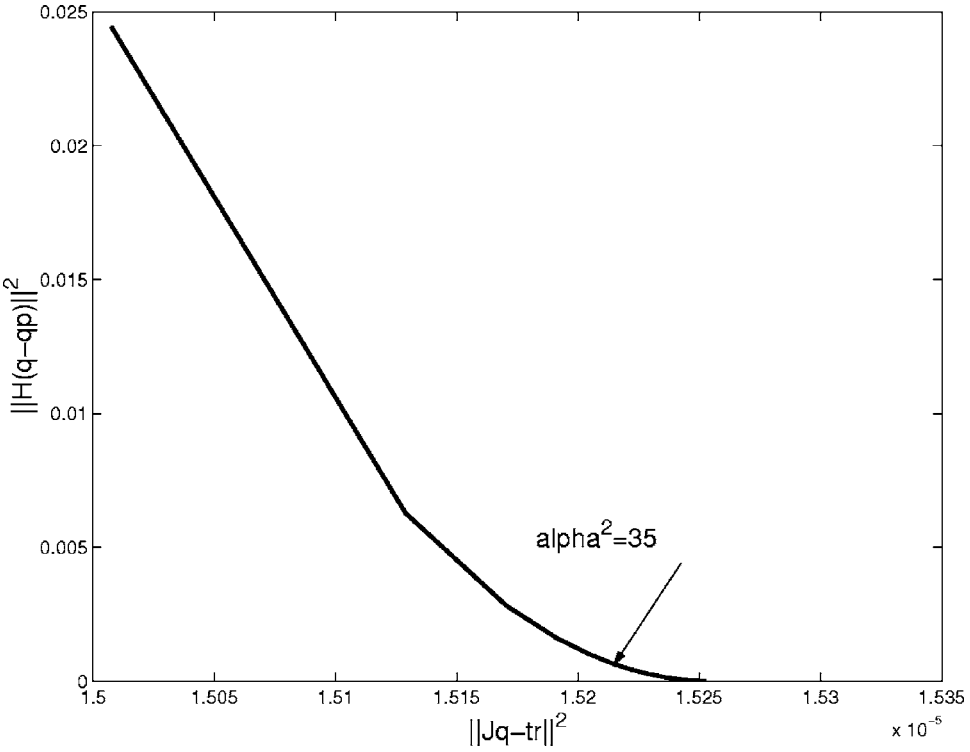

FIG. 7. The L curve for time-series NE020.

two stage procedure: (i) Gibbs sampling-maximum *a posteriori* estimation of arrival times and (ii) a matching process between estimated and replica arrival times of different ray paths exploiting a linear approximation. The linear system employs derivatives of time with respect to the unknown parameters and is solved using regularization.

The method, requiring limited prior knowledge on bottom depth and receiving element locations, consistently gave reliable source localization results with real data from the Haro Strait primer experiment. The process was also efficient. Although a computational load was associated with the first stage of the procedure (time delay estimation and path identification), the actual source localization process (second stage) has minimal computational requirements in contrast to full-field matching methods.

As the method requires identification of the direct path and first surface and bottom reflections, it is appropriate for problems in which the three distinct paths can be detected. Short-range problems, including the Haro Strait primer experiment studied, are natural candidates. More generally, the path identification requirement provides an immediate indication of viability: if, for a given data set, path identification is not sufficiently feasible (and some diagnostic uncertainty criteria need to be developed here), then alternative, more demanding techniques will be required for accurate source localization.

ACKNOWLEDGMENTS

This work was supported by the Office of Naval Research through Grant Nos. N00014-00-1-0051, N00014-97-1-0600, and N00014-05-1-0262. The authors wish to thank Dr. N. Ross Chapman for making the Haro Strait data available and Dr. Stan Dosso for insightful discussions.

[1]Z.-H. Michalopoulou and M. Picarelli, "Gibbs sampling for time-delay and amplitude estimation in underwater acoustics," J. Acoust. Soc. Am. **117**, 799–808 (2005).
[2]L. Jaschke and R. Chapman, "Matched field inversion of broadband data using the freeze bath method," J. Acoust. Soc. Am. **106**, 1838–1851 (1999).
[3]A. Tolstoy, *Matched Field Processing for Underwater Acoustics*. Singapore (World Scientific, Singapore, 1993).
[4]M. B. Porter and A. Tolstoy, "The matched field processing benchmark problems," J. Comput. Acoust. **2**, 161–185 (1994).
[5]A. Baggeroer, W. Kuperman, and H. Schmidt, "Matched field processing: Source localization in correlated noise as an optimum parameters estimation problem," J. Acoust. Soc. Am. **83**, 571–587 (1988).
[6]A. Tolstoy, "Simulated performance of acoustic tomography via matched field processing," J. Comput. Acoust. **2**, 1–10 (1994).
[7]Z.-H. Michalopoulou, M. B. Porter, and J. P. Ianniello, "Broadband source localization in the Gulf of Mexico," J. Comput. Acoust. **4**, 361–370 (1996).
[8]Z.-H. Michalopoulou and M. B. Porter, "Matched-field processing for broad-band source localization," IEEE J. Ocean. Eng. **21**, 384–392 (1996).
[9]Z.-H. Michalopoulou and M. B. Porter, "Source tracking in the Hudson Canyon experiment," J. Comput. Acoust. **4**, 371–383 (1996).
[10]E. K. Westwood, "Broadband matched-field source localization," J. Acoust. Soc. Am. **91**, 2777–2789 (1992).
[11]A. Baggeroer, W. Kuperman, and H. Schmidt, "Matched field processing: Source localization in correlated noise as an optimum parameters estimation problem," J. Acoust. Soc. Am. **83**, 571–587 (1988).
[12]E. K. Westwood and D. P. Knobles, "Source track localization via multipath correlation matching," J. Acoust. Soc. Am. **102**, 2645–2654 (1997).
[13]L. Jaschke, "Geophysical inversion by the freeze bath method with an application to geoacoustic ocean bottom parameter estimation," Master's thesis, University of Victoria, 1997.
[14]P. Pignot and R. Chapman, "Tomographic inversion for geoacoustic properties in a range dependent shallow water environment," J. Acoust. Soc. Am. **104**, 1338–1348 (1998).
[15]S. E. Dosso, M. R. Fallat, B. J. Sotirin, and J. L. Newton, "Array element localization for horizontal arrays via Occam's inversion," J. Acoust. Soc. Am. **104**, 846–859 (1998).
[16]S. E. Dosso, G. H. Brooke, S. J. Kilistoff, B. J. Sotirin, V. K. McDonald, M. R. Fallat, and N. E. Collison, "High-precision array element localization for vertical line arrays in the Arctic Ocean," IEEE J. Ocean. Eng. **23**, 365–379 (1998).

[17]S. E. Dosso and B. Sotirin, "Optimal array element localization," J. Acoust. Soc. Am. **106**, 3445–3459 (1999).
[18]S. E. Dosso and M. Reidel, "Array element localization for towed marine seismic arrays," J. Acoust. Soc. Am. (in press).
[19]A. Tolstoy, "Linearization of the matched field processing approach to acoustic tomography," J. Acoust. Soc. Am. **91**, 781–787 (1992).
[20]A. Tolstoy, "Tomographic inversion for geoacoustic parameters in shallow water," J. Comput. Acoust. **8**, 285–293 (2000).
[21]A. Tarantola, *Inverse Problem Theory* (Elsevier, Amsterdom, 1987).
[22]W. Menke, *Geophysical Data Analysis: Discrete Inverse Theory* (Academic, New York, 1989).
[23]J. O. Berger, *Statistical Decision Theory and Bayesian Analysis*, 2nd ed. (Springer, Berlin, 1985).
[24]G. Box and G. Tiao, *Bayesian Inference in Statistical Analysis* (Addison Wesley, Reading, MA, 1973).
[25]M. Wax and T. Kailath, "Detection of signals by information theoretic criteria," IEEE Trans. Acoust., Speech, Signal Process. **32**, 387–392, (1985).
[26]A. Scales, P. Docherty, and A. Gersztenkorn, "Regularization of nonlinear inverse problems: Imaging the near-surface weathering layer," Inverse Probl. **6**, 115–131 (1990).
[27]R. Aster, B. Borchers, and C. Thurber, *Parameter Estimation and Inverse Problems* (Academic, New York, 2004).
[28]P. C. Hansen, *Rank-Deficient and Discrete Ill-Posed Problems: Numerical Aspects of Linear Inversion* (SIAM, Philadelphia, 1998).

Ray-theoretic localization of an impulsive source in a stratified ocean using two hydrophones

E. K. Skarsoulis
Institute of Applied and Computational Mathematics, Foundation for Research and Technology Hellas, P.O. Box 1527, 711 10 Heraklion, Crete, Greece

M. A. Kalogerakis
Technological Education Institute of Crete, P.O. Box 1939, 710 04 Heraklion, Crete, Greece and Institute of Applied and Computational Mathematics, Foundation for Research and Technology Hellas, P.O. Box 1527, 711 10 Heraklion, Crete, Greece

(Received 7 April 2005; revised 27 July 2005; accepted 27 July 2005)

A method is presented for passive localization of impulsive acoustic sources in a stratified ocean by measuring relative times of direct and surface-reflected arrivals at two hydrophones. The proposed method is based on ray theory and takes into account the effects of refraction on the geometry of acoustic paths (ray bending) and travel times, generalizing previous approaches based on the homogeneous-ocean assumption (straight-line localization). If the hydrophone depths are known, then the source depth and distance from each hydrophone can be estimated from the three differential arrival times. If in addition the hydrophone separation is known, the bearing of the source can be estimated as well. Apart from the effects on ray geometry and travel times, stratification affects localization by introducing shadow zones and caustics. For source locations in the neighborhood of caustics, the localization problem accepts two solutions, one of which is the true source location and the other one which is an artifact (ghost solution). This ambiguity can be resolved in the case of tracking moving sources since as the source moves away from the caustic only the track corresponding to the true source position will be continued. The present method has been developed primarily for monitoring the dive behavior of sperm whales producing acoustic clicks, yet it is general and can be applied for the localization and tracking of any kind of impulsive acoustic source in the ocean. [DOI: 10.1121/1.2041267]

PACS number(s): 43.30.Wi, 43.60.Jn, 43.30.Cq, 43.30.Sf [AIT] Pages: 2934–2943

I. INTRODUCTION

This work addresses passive localization of impulsive acoustic sources in a stratified ocean environment based on the measurement of differential arrival times of direct and surface-reflected receptions at a pair of hydrophones and taking into account the effects of refraction on ray geometry (ray bending) and travel times. The particular approach has been developed for monitoring sperm whales, but it can be applied in general for the localization and tracking of any kind of impulsive acoustic source, either biological or man-made, in the ocean.

Sperm whales take long dives to depths of 1000 m or more in search of food. A single dive may last up to 90 min, during which the animal produces long series of pulsed sounds (regular clicks) with interclick intervals (ICI) between 0.5 and 2 s.[1,2] Each click is composed by a series of uniformly spaced pulses of 1–2-ms duration and rapidly decaying amplitude, corresponding to successive internal reflections of a primary pulse in the head of the animal.[3,4] Regular clicks of sperm whales are broadband signals with frequency bandwidth extending from ~300 Hz to ~30 kHz. According to recent studies,[5] their high-frequency part (3–30 kHz) is characterized by high directionality whereas the remaining low-frequency part (<3 kHz) is nearly omni-directional. In this connection, regular clicks have the potential both for echolocation (high directionality) and communication (omni-directionality) at the same time.

The localization and tracking of whales during dives is essential for mitigation operations and behavioral studies, as well as for the quantitative description of a number of characteristics of the produced sounds such as source level and directionality. Animal localization can be carried out either by passive acoustic techniques based on the analysis of clicks received at a hydrophone array,[6,7] or by active methods including the use of active sonar[8] and tagging,[9–11] or by a combination of the above.[12,13] Passive monitoring is the most discreet observing method, provided that the animal of interest is acoustically active. It can be implemented at different levels of sophistication, from a single hydrophone for simple recording of sounds to complicated array configurations for localization based on the measurement of differential arrival times.[6,7,14–16] In some cases even a single hydrophone can be used for localization by exploiting the reflections from the sea surface and bottom.[17]

A simple array configuration commonly used for marine mammal observation involves two hydrophones; estimates for the animal's bearing can be obtained by measuring the time difference of the direct arrivals at the two hydrophones.[6,18,19] By exploiting both direct and surface-reflected arrivals at a pair of hydrophones, three-dimensional localization can be achieved, subject to left-right ambiguity,

as shown in the case of a homogeneous ocean (straight-line localization).[20,21] The localization accuracy in that case increases with increasing depth and horizontal separation of the hydrophones. The errors in distance estimation are largest when the source (vocalizing animal) is close to the sea surface or lies at the broadside of the hydrophone array, i.e., right below or at the side of the two hydrophones, and increase with distance. In contrast, the errors in bearing estimation are largest for source locations close to the vertical hydrophone plane, where the errors in distance estimation are smallest.

Localization errors are the cumulative result of measurement and modeling errors. Measurement errors are caused by uncertainties in measuring hydrophone positions and differential arrival times. Modeling errors are due to simplifications imposed by the theoretical propagation model used, such as the assumption of a flat sea surface or the absence of refraction effects. Surface roughness, associated with gravity waves at the sea surface, causes fluctuations in the travel times of surface-reflected arrivals[22,23] and thus introduces variability to the localization results. The refraction effects, on the other hand, can be neglected in case of near-uniform sound-speed distribution (nearly constant sound speed in the water column) or in the case of moderate nonuniformity but small source-receiver distances (less than 1 km). In cases of strongly nonuniform sound-speed distribution, such as in the Mediterranean Sea in summer, it is shown here that the omission of refraction effects can lead to significant errors even for short rages. An approximate expression for the travel-time error arising from the straight-line assumption in the case of a linear sound-speed profile was derived by Spiesberger and Firstrup.[24,25] In a first attempt to take into account refraction effects in localization with two hydrophones, the assumption was made that the wave fronts corresponding to the direct arrivals at the two hydrophones are parallel to each other (same assumption for the surface-reflected arrivals).[20] This assumption is justified only in the case of very small hydrophone separations, which in turn limits the applicability to very short ranges, for which the ray bending effects are not significant anyway.

The present work addresses passive localization of an impulsive source in a general stratified ocean environment, with known sound-speed profile, by measuring the differential arrival times of direct and surface-reflected arrivals at two hydrophones of arbitrary separation. The method is free from the above parallelism assumption and thus applies for any separation between the hydrophones, enabling localization at longer ranges, up to several kilometers. If the hydrophone depths are known, then the three differential arrival times—resulting from the direct and surface-reflected arrivals at the two hydrophones—can be used for the estimation of range (horizontal distance from each hydrophone) and depth of the target source. If, in addition, the horizontal distance of the two hydrophones is known, then the azimuth angle (bearing) of the target source can also be estimated (with left-right ambiguity). These findings generalize previous results obtained under the homogeneous-ocean assumption.[20,21]

Acoustic propagation in a stratified ocean is characterized in general by the presence of shadow zones, caustics and multipath, such that—depending on the source location—there may be no acoustic paths from the source to the hydrophones or multiple acoustic paths, i.e., multiple arrivals with nearby arrival times, especially in the neighborhood of caustics. The present approach assumes that there are two acoustic paths from the source to each hydrophone, a direct and a surface reflected one, which is the more usual case. The exploitation of additional arrivals, due to multipath or bottom reflections, is associated with a more difficult identification problem and is not addressed here. Bottom-reflected arrivals are often not available and, even if they are present, they are difficult to detect since they are weaker and more spread in time depending on the geometry and composition of the sea bed. On the other hand, surface-reflected arrivals of sperm whale clicks are recorded 90% of the time when the animals are less than 2 km away from the hydrophones, and even when the ocean surface is agitated.[21]

The contents of this work are organized as follows: Section II introduces basic ray-theoretic notions. Section III describes the localization method for a general stratified ocean environment using differential times of direct and surface-reflected arrivals at two arbitrarily positioned hydrophones. Section IV presents some numerical results for localization (range and depth estimation) in a synthetic strongly stratified ocean environment resembling Mediterranean conditions in summer, including localization errors due to uncertainties in the measurements of hydrophones depths and differential arrival times as well as due to sea-surface roughness. Finally, Sec. V contains a discussion and summarizes the main conclusions of this work.

II. RAY TRACING

In the context of ray theory (high-frequency asymptotic approximation to the acoustic field),[26] the geometry of propagation paths (acoustic rays) in a stratified ocean, with sound speed $c(z)$ varying with depth z, is governed by Snell's refraction law

$$\frac{\cos\varphi}{c} = \text{const}, \tag{1}$$

where φ is the grazing angle of propagation. By applying Snell's law the time of flight along an acoustic ray from depth z_0 to depth z can be obtained from the expression

$$T = \int_{z_0}^{z} \frac{|dz'|}{c(z')\sin(\varphi(z'))} = \int_{z_0}^{z} \frac{|dz'|}{c(z')\sqrt{1-c^2(z')/\hat{c}^2}}, \tag{2}$$

where $\hat{c}=c_0/\cos\varphi_0$, φ_0 is the initial grazing angle, and $c_0=c(z_0)$. Equation (2) applies under the condition that the ray depth is a monotonous function of range. If an acoustic path has turning points or surface reflections, then Eq. (2) can be used piecewise between turning/reflection points, and thus the total travel time can be calculated.

If the sound speed varies linearly with depth, $c(z)=a-bz$, where a and b are constants, the acoustic rays are circular arcs with radius depending on the initial conditions.[26] In this case the travel time along a ray path from depth z_0 to

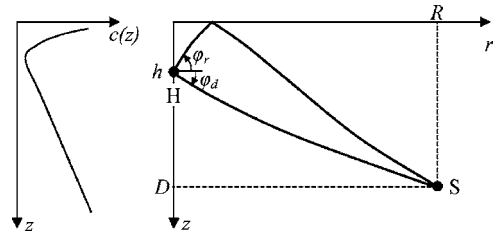

FIG. 1. Schematic diagram of the geometry of the direct and surface-reflected acoustic paths connecting an acoustic source S and a hydrophone H.

depth z_1 can be calculated in closed form and the final expression in the case of a monotonous ray (in the absence of reflection or turning points) is the following,

$$T = \left| \frac{1}{b} \ln \frac{c_0(\hat{c} + \sqrt{\hat{c}^2 - c_1^2})}{c_1(\hat{c} + \sqrt{\hat{c}^2 - c_0^2})} \right|, \tag{3}$$

where $c_0 = a - bz_0$ and $c_1 = a - bz_1$. In case there is a turning point, the above formula has to be applied to the two monotonous parts separately, and the final expression becomes

$$T = \left| \frac{1}{b} \ln \frac{\hat{c} + \sqrt{\hat{c}^2 - c_1^2}}{c_1} \right| + \left| \frac{1}{b} \ln \frac{\hat{c} + \sqrt{\hat{c}^2 - c_0^2}}{c_0} \right|. \tag{4}$$

The contribution at the turning point in this case vanishes since the grazing angle at the turning point is zero, and, thus, according to Snell's law, the sound speed c_{tp} at the turning point equals $\hat{c}$. In the case of piecewise linear sound-speed profiles, ray tracing and arrival time calculation can be carried out by following each ray as it moves through the different water layers, characterized by constant sound-speed gradient, and using the circular arc representation in each layer.

Refraction causes multipath propagation. This means that a signal emitted by an acoustic source will reach a distant receiver over a multitude of acoustic paths whose geometry is governed by Snell's law (1) and whose number increases with range. For relatively short ranges (1–2 km) multipath is mainly due to reflection of the source signal at the sea surface. Bottom reflections are usually weaker and more spread in time, depending on the geometry and composition of the sea bed, and are not considered here. Thus, assuming deep water, a hydrophone H (at depth h) will receive the signal emitted by an acoustic source S (at depth D and range R—horizontal distance from the hydrophone) over a direct (d) and a surface-reflected (r) path (see Fig. 1). The arrival angles (grazing angles) of the direct and surface-reflected arrival are denoted by φ_d and φ_r, and the corresponding source-receiver travel times by T_d and T_r, respectively.

The source location (range and depth) with respect to the hydrophone H can be alternatively described as the intersection of the direct and surface-reflected rays launched from H with launch angles φ_d and φ_r, respectively, depending also on the hydrophone depth h and the sound-speed profile $c(z)$. Thus, assuming a flat sea surface, the depth D and the range R of the source can be written as functions of the above quantities

$$R = R(\varphi_d, \varphi_r; h; c), \tag{5}$$

$$D = D(\varphi_d, \varphi_r; h; c). \tag{6}$$

In general, for a given environment $[c(z)]$ and initial conditions $(\varphi_d, \varphi_r, h)$, there are more than one intersection point. In this case R and D are considered as the range and depth of the first intersection, i.e., the one closest to H.

The travel times from the hydrophone to the intersection point over the direct and the surface-reflected path, T_d and T_r, respectively, can be calculated simultaneously with the ray tracing and can also be expressed in the form

$$T_d = T_d(\varphi_d, \varphi_r; h; c), \tag{7}$$

$$T_r = T_r(\varphi_d, \varphi_r; h; c). \tag{8}$$

Thus, for fixed hydrophone depth h and sound-speed profile $c(z)$, any values of the angles φ_d and φ_r will result in an intersection point, i.e., in particular values for R and D, and also in particular values for the travel times T_d and T_r from the hydrophone to the intersection point over the direct and surface reflected path.

III. RAY-THEORETIC LOCALIZATION WITH TWO HYDROPHONES

This section describes a method for passive localization of an impulsive acoustic source by measuring differential travel times of direct and surface-reflected arrivals at two hydrophones (H_1 and H_2) at arbitrary locations in a general stratified environment characterized by a known sound speed profile $c(z)$. Denoting the hydrophone depths by $h_i, i = 1, 2$, the corresponding range (horizontal distance) and depth of the intersection point with respect to each hydrophone can be written as

$$R_i = R_i(\varphi_{d,i}, \varphi_{r,i}; h_i; c), \quad i = 1, 2, \tag{9}$$

$$D_i = D_i(\varphi_{d,i}, \varphi_{r,i}; h_i; c), \quad i = 1, 2. \tag{10}$$

The meaning of these relations is that two rays starting at the point H_i (depth h_i) with launch angles $\varphi_{d,i}$ and $\varphi_{r,i} (\varphi_{d,i} \neq \varphi_{r,i})$ will intersect each other at a range R_i (horizontal distance from the starting point H_i) and depth D_i, which will depend on the initial conditions $(\varphi_{d,i}, \varphi_{r,i}, h_i)$ and $c(z)$. Similarly, the corresponding travel times can be written in the form

$$T_{d,i} = T_{d,i}(\varphi_{d,i}, \varphi_{r,i}; h_i; c), \quad i = 1, 2, \tag{11}$$

$$T_{r,i} = T_{r,i}(\varphi_{d,i}, \varphi_{r,i}; h_i; c), \quad i = 1, 2. \tag{12}$$

If the two hydrophones have a common time reference, then the differential travel times $\tau_{1r1} = T_{r,1} - T_{d,1}$, $\tau_{21} = T_{d,2} - T_{d,1}$, and $\tau_{2r2} = T_{r,2} - T_{d,2}$ can be measured (the common time reference is needed for obtaining τ_{21}). The measured quantities will be denoted in the following by the superscript (m). The quantities $\tau_{1r1}^{(m)}$, $\tau_{21}^{(m)}$, and $\tau_{2r2}^{(m)}$ are the input data driving the localization. Having established the functional relations (9)–(12), through ray tracing, the equations to be solved are the following:

$$\tau_{1r1}^{(m)} = T_{r,1}(\varphi_{d,1}, \varphi_{r,1}; h_1; c) - T_{d,1}(\varphi_{d,1}, \varphi_{r,1}; h_1; c), \quad (13)$$

$$\tau_{2r2}^{(m)} = T_{r,2}(\varphi_{d,2}, \varphi_{r,2}; h_2; c) - T_{d,2}(\varphi_{d,2}, \varphi_{r,2}; h_2; c), \quad (14)$$

$$\tau_{21}^{(m)} = T_{d,2}(\varphi_{d,2}, \varphi_{r,2}; h_2; c) - T_{d,1}(\varphi_{d,1}, \varphi_{r,1}; h_1; c). \quad (15)$$

Equations (13)–(15) link the measured data (differential travel times) on the left-hand side and model expressions, obtained through ray tracing, on the right, stating that the measured differential travel times have to agree with those predicted from ray theory. Since the two intersection points (one for each hydrophone) describe a single target, the depths D_1 and D_2 must be equal:

$$D_1(\varphi_{d,1}, \varphi_{r,1}; h_1; c) = D_2(\varphi_{d,2}, \varphi_{r,2}; h_2; c). \quad (16)$$

The ranges R_1 and R_2 (horizontal distances from each hydrophone) will in general be different since the hydrophones are at different locations. Solving the system of equations (13)–(16) the unknown angles $\varphi_{d,1}$, $\varphi_{r,1}$, $\varphi_{d,2}$, and $\varphi_{r,2}$ can be obtained. The horizontal distance of the target from each hydrophone, as well as its depth, can then be obtained from Eqs. (9) and (10).

A method for solving Eqs. (13)–(16) is described in the following. From Eq. (13) a relation between the angles $\varphi_{d,1}$ and $\varphi_{r,1}$ of the direct and surface-reflected rays at H_1 can be obtained: $\varphi_{r,1} = \varphi_{r,1}(\varphi_{d,1})$; the dependence on the quantities h_1, $c(z)$, and $\tau_{1r1}^{(m)}$ is omitted in the following since they are assumed known. Substituting this relation into Eqs. (9)–(11) for $i=1$, the range and depth of the intersection point with respect to H_1, as well as the corresponding travel time along the direct propagation path, can be written as functions of $\varphi_{d,1}$ only:

$$R_1 = R_1(\varphi_{d,1}), \quad D_1 = D_1(\varphi_{d,1}), \quad T_{d,1} = T_{d,1}(\varphi_{d,1}). \quad (17)$$

In a similar way, from Eq. (14) a relation of the form $\varphi_{r,2} = \varphi_{r,2}(\varphi_{d,2})$ can be obtained, which can be substituted into Eqs. (9)–(11) for $i=2$ to obtain the range of the intersection point with respect to H_2, its depth, and the corresponding travel time along the direct propagation path as functions of $\varphi_{d,2}$ only:

$$R_2 = R_2(\varphi_{d,2}), \quad D_2 = D_2(\varphi_{d,2}), \quad T_{d,2} = T_{d,2}(\varphi_{d,2}). \quad (18)$$

By substitution of the relations (17) and (18) into Eqs. (15) and (16), the latter take the form

$$T_{d,1}(\varphi_{d,1}) + \tau_{21}^{(m)} = T_{d,2}(\varphi_{d,2}), \quad (19)$$

$$D_1(\varphi_{d,1}) = D_2(\varphi_{d,2}). \quad (20)$$

The solution of this system can be obtained on the (T_d, D) plane, as shown schematically in Fig. 2: The $(T_{d,1}, D_1)$ pairs resulting from the various values of $\varphi_{d,1}$ are plotted on the (T_d, D) plane (H_1 curve). Similarly, the $(T_{d,2}, D_2)$ pairs resulting for the various values of $\varphi_{d,2}$ are plotted on the same plane (H_2 curve). The H_1 curve is then shifted along the T_d axis by an amount equal to the measured differential time $\tau_{21}^{(m)}$. The intersection point(s) between the shifted H_1 curve and the H_2 curve is the solution. The system of equations (19) and (20) is called the *characteristic* system, since its solution underlies the solution of the localization problem. Equivalently, the solution is the root of the difference $T_{d,2} - (T_{d,1} + \tau_{21}^{(m)})$ as a function of depth D; in this connection, the corresponding time-depth curve is called the *characteristic* curve of the localization problem.

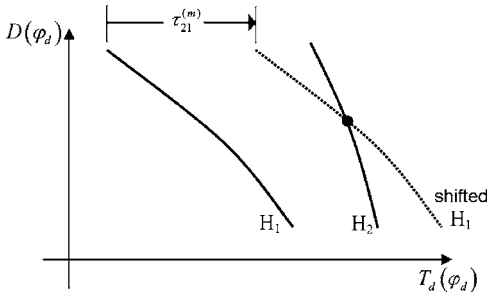

FIG. 2. Schematic diagram of the intersection method for target-depth and travel-time estimation.

The intersection method described above provides the target depth $D = D_1 = D_2$, the absolute travel times $T_{d,1}$ and $T_{d,2}$ from the target to the two hydrophones along the direct paths, and implicitly also the angles $\varphi_{d,1}$ and $\varphi_{d,2}$. By substituting the latter into the relations (17) and (18) for the range, the horizontal distances R_1 and R_2 from the hydrophones H_1 and H_2, respectively, can be obtained. Thus, for known hydrophone depths h_1, h_2 and sound velocity profile $c(z)$, the source depth D and ranges R_1, R_2 can be obtained from the differential travel times $\tau_{1r1}^{(m)}$, $\tau_{21}^{(m)}$, and $\tau_{2r2}^{(m)}$ without needing to know the horizontal separation Δ between the two hydrophones. This fact generalizes previous results obtained under the homogeneous-ocean assumption (straight-line localization),[21] and it is particularly important since hydrophone separation is difficult to measure.

If in addition the hydrophone separation Δ can be measured, then it can be combined with the calculated ranges R_1 and R_2 to obtain an estimate of the azimuthal angle of the source, as shown in Fig. 3. Using the law of cosines, the azimuthal deviation of the source from the vertical plane defined by the two hydrophones is given by

$$\theta = \arccos\left(\frac{\Delta^2 + R_1^2 - R_2^2}{2\Delta R_1}\right). \quad (21)$$

With a two-hydrophone configuration, a left-right ambiguity remains in the azimuthal direction, as in the homogeneous-ocean case.

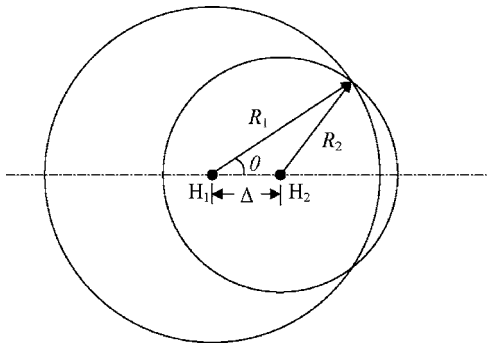

FIG. 3. Bearing estimation using two hydrophones with known separation Δ (top view). The estimation is subject to left-right ambiguity.

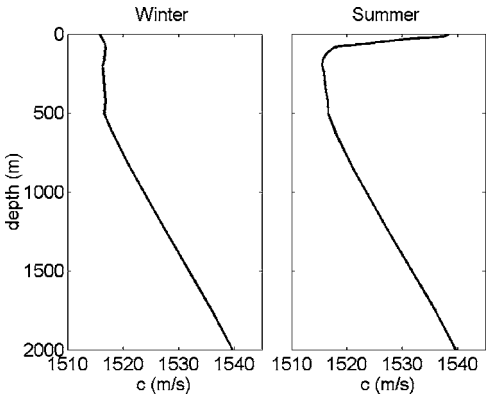

FIG. 4. Typical sound-speed profiles off southern Crete—South-Eastern Mediterranean.

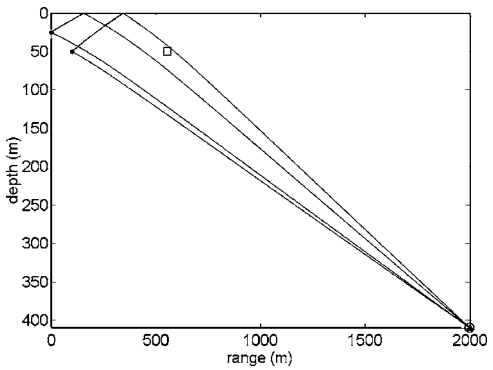

FIG. 6. Ray-theoretic (○) versus straight-line (□) localization of an impulsive source at 2-km range and 410-m depth (▲—lower right corner) using two hydrophones (●) in summer.

IV. NUMERICAL RESULTS

This section presents some localization results in a stratified ocean environment representing typical conditions in the eastern Mediterranean Sea using synthetic data. Figure 4 shows a typical winter and summer sound-speed profile for the sea area off southern Crete (Greece), a favorable area for the encounter of sperm whales.[27] The underlying temperature and salinity profiles have been extracted from the Mediterranean Ocean Data Base (MODB),[28] whereas the sound-speed profile has been obtained using the Chen-Millero formula.[29] The main difference between the two profiles in Fig. 4 is in the seasonal thermocline in the upper 200 m. In winter the surface layer is mixed and thus characterized by a nearly uniform temperature and sound-speed distribution, whereas in summer intense warming leads to strong temperature and sound-speed gradients. Accordingly, strong refraction is expected to take place in the surface layer in summer.

Figure 5 shows the modeling error due to refraction of the straight-line localization approach[20,21] for distance estimation (slant range $\Lambda=\sqrt{R_1^2+D^2}$ with respect to H_1), as a function of target (source) location on the vertical plane defined by the two hydrophones, in the direction of hydrophone H_2. The errors have been calculated for the winter and summer sound-speed profiles of Fig. 4 and for two geometrical configurations, one with 50-m and one with 100-m horizontal separation Δ between the two hydrophones; the hydrophone depths in both cases are $h_1=25$ m and $h_2=50$ m. For each target location the direct and surface-reflected ray paths (eigenrays) and the corresponding travel times $(T_{d,1}, T_{r,1}, T_{d,2}, T_{r,2})$ to each of the two hydrophones is calculated using ray theory, i.e., taking refraction into account, and then the straight-line localization formula[20,21]

$$\Lambda = -\frac{c}{2}\frac{h_1\tau_{21}^2 + h_2\tau_{1r1}^2 - h_1\tau_{2r1}^2}{h_1\tau_{21} + h_2\tau_{1r1} - h_1\tau_{2r1}} \tag{22}$$

is applied for estimating the source distance from the three differential travel times, where c is the average sound speed, and $\tau_{21}=T_{d,2}-T_{d,1}$, $\tau_{1r1}=T_{r,1}-T_{d,1}$, and $\tau_{2r1}=T_{r,2}-T_{d,1}$ are the differential travel times based on the above ray-theoretic results.

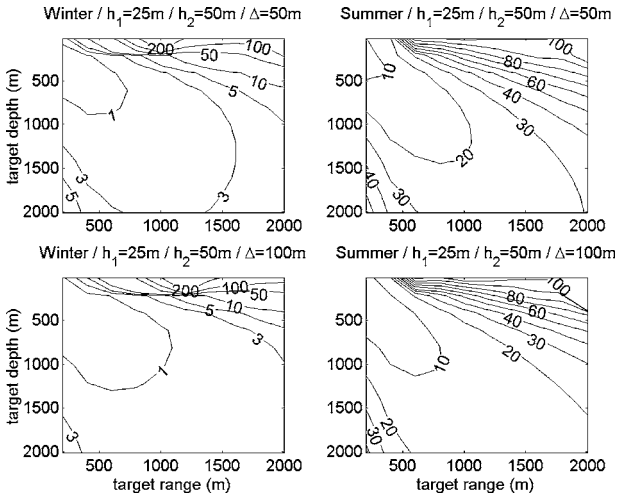

FIG. 5. Straight-line localization (homogeneous-ocean assumption): modeling error (%) in the estimated slant distance of the target (source) from H_1 due to refraction in winter/summer as a function of the source location on the vertical hydrophone plane for two receiving configurations. The target range (horizontal axis) is measured from H_1 in the direction of H_2.

It is seen from Fig. 5 that the modeling errors of straight-line localization increase significantly from winter to summer. This is due to the intense refraction taking place close to the surface in summer (large deviation from homogeneity assumption) that affects localization in the whole water column. Since the two-hydrophone system is most sensitive to errors when the source lies close to the surface or at the broadside of the hydrophones, i.e., at the side or below the two hydrophones,[20,21] the modeling errors are largest in those areas as well. By increasing the horizontal hydrophone separation from 50 to 100 m, the modeling errors are reduced but still remain significant in summer. These errors are eliminated by the ray-theoretic localization approach proposed here.

Figure 6 shows the ray-theoretic versus straight-line localization result for a source located on the vertical hydrophone plane at a horizontal distance 2 km from H_1 in the direction of H_2 and at a depth of 410 m in an environment characterized by the summer sound-speed profile (Fig. 4) and a flat sea surface. The hydrophones are considered at depths $h_1=25$ m and $h_2=50$ m, and separated by $\Delta=100$ m in the horizontal. The ray-theoretic localization manages to reproduce the source location exactly, whereas the straight-line approach estimates a much smaller range (~550 m) and

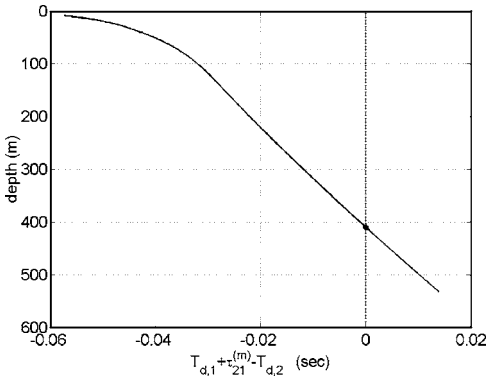

FIG. 7. Characteristic curve (solid line) underlying the ray-theoretic localization presented in Fig. 6. The solution (●) of the localization problem corresponds to $T_{d,1}+\tau_{21}^{(m)}-T_{d,2}=0$.

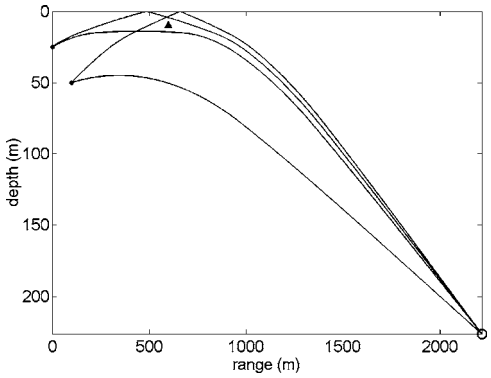

FIG. 9. Ghost solution (○) in ray-theoretic localization of an impulsive source at 600-m range and 10-m depth (▲) using two hydrophones (●) in summer.

depth (~49 m). The geometry of the direct and surface-reflected eigenrays, connecting the source and the two hydrophones, resulting from the ray-theoretic localization, are also shown on Fig. 6. A slight bending of the eigenrays, especially of the surface-reflected ones in the surface layer, is visible. It is the deviation from straight-line propagation and the effect of the variable sound speed on the travel-times that causes the straight-line approach to result in a false source location—the error in this case is in agreement with the results shown in the lower right panel in Fig. 5. No uncertainties in the travel times and hydrophone depths have been considered in this example—their effect is addressed later on.

Figure 7 shows the characteristic curve underlying the ray-theoretic localization in Fig. 6. This is a time-depth plot extending in the vertical over the common depths (~20 to ~530 m) of the two geometrical loci $(T_{d,i}, D_i)$, $i=1,2$, with travel-time differences between direct and surface-reflected arrivals equal to the measured time difference $\tau_{1r1}^{(m)}$ and $\tau_{2r2}^{(m)}$ (H_1 and H_2 curve), respectively—in the synthetic examples considered here, "measured" means calculated from direct ray tracing. The horizontal axis measures the difference between the measured relative time $\tau_{21}^{(m)}$ of the direct arrival times at the two hydrophones and the corresponding theoretical relative time $T_{d,2}-T_{d,1}$, for points of equal depth on the above geometrical loci. The solution of the localization problem is the point where the difference $\tau_{21}^{(m)}-(T_{d,2}-T_{d,1})$ is zero. In Fig. 7 this difference changes monotonously with depth, from −57 to +13 ms, such that there is a clear solution at 410-m depth.

Figure 8 shows another localization case with the same hydrophone configuration as before but with the target (source) much shallower, at a depth of 10 m, and also closer to H_1, at a range of 600 m. In this case the straight-line localization approach results in a shorter range (460 m) and a negative depth, i.e., the source is localized above the sea surface, which means that the straight-line solution is rejected. The ray-theoretic approach manages to recover the true source location. However, in this case there exists a second ray-theoretic solution (ghost solution), far away from the true source location as shown in Fig. 9; the range of this second estimated source location is ~2200 m and the depth ~226 m. Hence, localization in this case is associated with ambiguity. In the following, the underlying reason for this behavior is studied.

Figure 10 shows the characteristic curve corresponding to source range 600 m and depth 10 m. In contrast to the previous case (Fig. 7), the characteristic curve is no longer a monotonous function of depth and this gives rise to two solutions, one corresponding to the true source depth (10 m) and one with a depth of ~226 m. The shape of the rightmost part of the characteristic curve is similar to travel-time patterns observed in the neighborhood of caustics.[30] Figure 11 (panels on the left) shows the ray diagrams in the upper

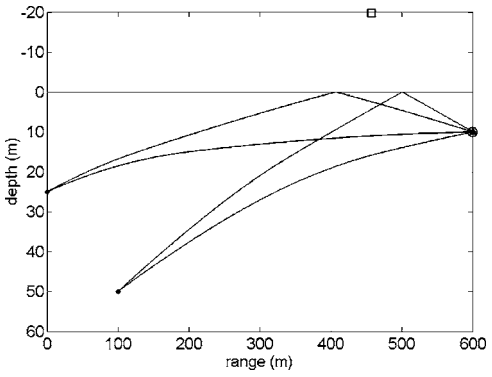

FIG. 8. Ray-theoretic (○) versus straight-line (□) localization of an impulsive source at 600-m range and 10-m depth (▲) using two hydrophones (●) in summer.

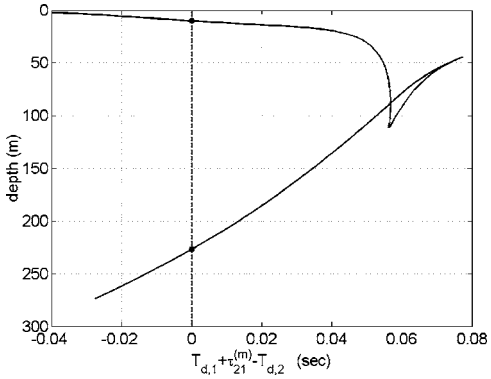

FIG. 10. Characteristic curve (solid line) underlying the ray-theoretic localization presented in Figs. 8 and 9. The two solutions (●) correspond to $T_{d,1}+\tau_{21}^{(m)}-T_{d,2}=0$.

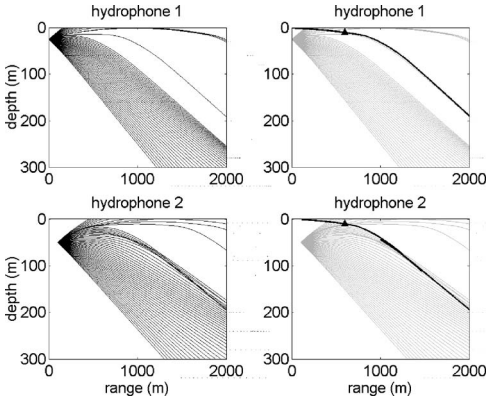

FIG. 11. Ray diagrams for hydrophones 1 and 2 in summer along with geometrical loci (heavy solid lines on the right panels) of points with differential travel time between direct and surface-reflected arrivals equal to $\tau_{1r1}^{(m)}$ and $\tau_{2r2}^{(m)}$, respectively, corresponding to source location at 600-m range and 10-m depth (▲).

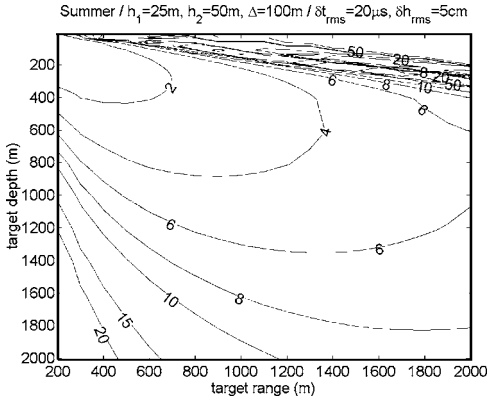

FIG. 13. Ray-theoretic localization: rms measurement error (%) in the estimated slant distance from H_1 in summer due to travel-time and hydrophone-depth uncertainties, as a function of the source location on the vertical hydrophone plane. The target range (horizontal axis) is measured from H_1 in the direction of H_2.

300 m and for ranges up to 2 km from H_1 of the rays starting at the locations of the two hydrophones. While H_1 has a regular ray diagram, a smooth caustic is formed in the case of the deeper hydrophone H_2. Surface reflections are not shown on this figure. In the two panels on the right of Fig. 11 the ray diagrams are repeated (in gray) and superimposed on the geometrical loci of the points with differential travel times between direct and surface reflected arrivals equal to the measured travel times $\tau_{1r1}^{(m)}$ and $\tau_{2r2}^{(m)}$, respectively, and corresponding to the true source location (range 600 m and depth 10 m), which is also plotted. While the geometrical locus in the case of H_1 is a smooth curve (top right panel), the locus in the case of H_2 encounters the caustic and its geometry is affected.

Figure 12 presents a detailed view of the geometrical locus corresponding to H_2 in the neighborhood of the caustic—a higher ray coverage is used in this figure. As the grazing angle at H_2 decreases, the depth on the geometrical locus increases and for a particular value of the launch angle the locus encounters the caustic. Then as the launce angle further decreases, the locus is set back (the depth decreases) up to a certain point and then it moves downward again, but with a different inclination and nearly follows the caustic. The encounter of the caustic, the setback, and the continuation with different inclination affects the travel times and gives rise to the folding of the characteristic curve in Fig. 10, leading to a double solution. Thus, in the presence of caustics, double-valued localization solutions are expected for source locations in their neighborhood.

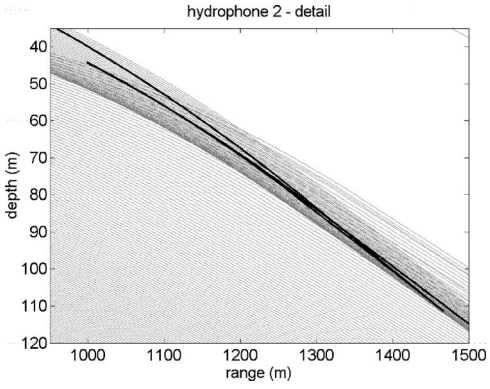

FIG. 12. Detailed view of ray diagram for hydrophone 2 (higher coverage than in Fig. 11) in the area where the geometrical locus ($T_{2r}-T_2=\tau_{2r2}^{(m)}$)—heavy line—encounters the caustic.

Uncertainties in the hydrophone depths and differential travel times introduce errors in the estimated source location. In the following, some results for the errors in distance estimation are shown for source locations on the vertical hydrophone plane. In the framework of a linear perturbation approach,[7] small changes in hydrophone depths $(\delta h_1, \delta h_2)$ and differential travel times $(\delta\tau_{1r1}, \delta\tau_{2r2}, \delta\tau_{21})$ will cause the estimated distance Λ of the source S from hydrophone H_1 to change by

$$\delta\Lambda = \frac{\partial\Lambda}{\partial h_1}\delta h_1 + \frac{\partial\Lambda}{\partial h_2}\delta h_2 + \frac{\partial\Lambda}{\partial\tau_{1r1}^{(m)}}\delta\tau_{1r1} + \frac{\partial\Lambda}{\partial\tau_{2r2}^{(m)}}\delta\tau_{2r2} + \frac{\partial\Lambda}{\partial\tau_{21}^{(m)}}\delta\tau_{21}. \tag{23}$$

Assuming that the errors $(\delta h_1, \delta h_2, \delta\tau_{1r1}, \delta\tau_{2r2}, \delta\tau_{21})$ are uncorrelated, the variance of the error $\delta\Lambda$ can be then expressed as

$$\langle\delta\Lambda^2\rangle = \left(\frac{\partial\Lambda}{\partial h_1}\right)^2\langle\delta h_1^2\rangle + \left(\frac{\partial\Lambda}{\partial h_2}\right)^2\langle\delta h_2^2\rangle + \left(\frac{\partial\Lambda}{\partial\tau_{1r1}^{(m)}}\right)^2\langle\delta\tau_{1r1}^2\rangle + \left(\frac{\partial\Lambda}{\partial\tau_{2r2}^{(m)}}\right)^2\langle\delta\tau_{2r2}^2\rangle + \left(\frac{\partial\Lambda}{\partial\tau_{21}^{(m)}}\right)^2\langle\delta\tau_{21}^2\rangle. \tag{24}$$

Thus, the root mean square (rms) error $\delta\Lambda_{\rm rms}=\sqrt{\langle\delta\Lambda^2\rangle}$ for the source distance can be calculated in terms of the underlying rms errors in depth and travel-time measurement. Unlike the straight-line localization, in a ray-theoretic framework there is no closed-form expression relating the distance Λ with the parameters $h_1, h_2, \tau_{1r1}^{(m)}, \tau_{2r2}^{(m)}, \tau_{21}^{(m)}$. Hence, the evaluation of the partial derivatives appearing in (24) has to be carried out numerically.

For an environment characterized by the summer sound-speed profile (Fig. 4) and a hydrophone configuration with $h_1=25$ m, $h_2=50$ m, and $\Delta=100$ m, Fig. 13 shows the rms

error in distance estimation, due to measurement errors (rms) of 5 cm in hydrophone depths and 0.02 ms in differential travel times, as a function of the source location on the vertical hydrophone plane in the direction of H_2. The error is presented as a percentage of the true source distance from H_1. From this figure it is seen that the errors are largest for source locations close to the surface and below the two hydrophones. When the source is close to the surface, the temporal separation between direct and surface-reflected arrivals at each hydrophone is very small and at the limit (source at the surface) the two arrivals degenerate into one. Still, refraction causes a nonmonotonous increase of the error towards the surface. Thus, for source range 2 km the error reaches a maximum 50% for source depth 310 m, drops to 8% at 250 m depth, and rises again for smaller depths. Furthermore, stratification gives rise to shadow zones close to the surface (cf. Fig. 11) for ranges larger than 1 km. When the source lies within the shadow zones of both hydrophones there are no arrivals and thus localization (or even detection) is impossible. When the source lies below the hydrophones the differential arrival time between the direct and the surface-reflected arrivals is affected mainly by the hydrophone depth and hardly by the source distance—hence the large uncertainty in distance estimation.

Besides the errors in the measurement of travel times and hydrophone depths, the localization accuracy is also affected by surface roughness associated with the presence of propagating gravity waves at the sea surface. Surface roughness causes fluctuations in the travel times of surface-reflected arrivals[22] and thus contributes to the error in differential travel times between direct and surface-reflected arrivals. In the case of large-scale surface roughness and homogeneous medium, Godin and Fuks[23] derived the following estimate for the travel-time variance of arrivals subject to a single reflection at the rough surface: $\langle \delta T_r^2 \rangle = (2\sigma \sin\varphi/c)^2$, where σ is the surface roughness—rms deviation from the unperturbed (flat) surface, φ is the acoustic grazing angle at the unperturbed surface, and c is the sound speed. This estimate is of local nature (it does not depend on propagation length) and describes a mechanism of travel-time modification at the surface; the travel-time changes are largest in near-vertical propagation (e.g., source below the receiver) and smallest for propagation close to the horizontal. The variability due to surface roughness affects the differential travel times τ_{1r1} and τ_{2r2} involving the surface-reflected arrivals—the travel-time difference τ_{21} involves only direct arrivals and thus it is not affected by surface roughness.

Figure 14 shows the rms error in distance estimation (%) caused by travel-time and hydrophone-depth uncertainties (same as considered in Fig. 13) and by surface roughness of 0.1 m rms (corresponding to wave height $H_S \simeq 0.3$ m). By comparing Figs. 13 and 14 it is seen that the effects of surface roughness are significant even in the case of small amplitude waves. A possible way to eliminate these effects is by taking travel-time averages—for the short ranges considered here the bias $\langle \delta T_r \rangle$ is negligible.[22,23] Nevertheless, in the case of a moving source the size of the averaging sample should be carefully selected, taking into consideration the pulse repetition rate, the source speed, and the sought localization accuracy.

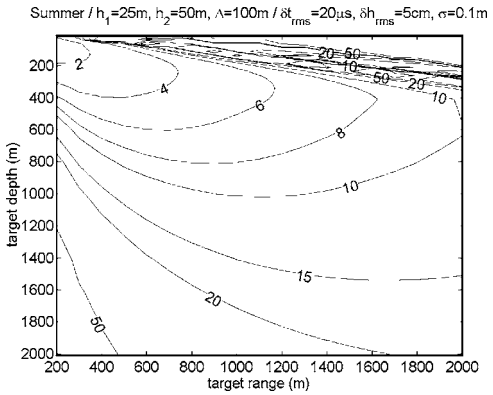

FIG. 14. Ray-theoretic localization: rms measurement error (%) in the estimated slant distance from H_1 in summer due to sea surface roughness and travel-time/hydrophone-depth uncertainties, as a function of the source location on the vertical hydrophone plane. The target range (horizontal axis) is measured from H_1 in the direction of H_2.

V. DISCUSSION AND CONCLUSIONS

A simple two-hydrophone configuration can be used for the passive localization of impulsive sources by measuring relative travel times of direct and surface-reflected arrivals. A major advantage of this technique, besides the simplicity of the receiving array, is that it does not require control over the exact location of the two hydrophones but merely the knowledge of the two hydrophone depths in order to provide source range (horizontal distance from each hydrophone) and depth estimates. If in addition the horizontal separation of the two hydrophones is known, then an estimate for the azimuthal direction (bearing) of the source can be obtained as well subject to left-right ambiguity. A way to raise this ambiguity is to perform two sets of measurements, by placing the hydrophones in two different azimuthal directions, and combine the results.

Up to the present, the two-hydrophone localization method was developed assuming a homogeneous ocean (straight-line localization). This assumption limits application to short ranges or to environments of weak stratification. In the presence of strong stratification, such as in the Mediterranean Sea in summer, the effects of refraction on localization are significant even for short ranges, cf. Fig. 5, and they have to be taken into account. To address this issue, a ray-theoretic approach was used taking into account the effects of variable sound speed on ray geometry and travel times, and thus extending the applicability of the two-hydrophone localization to longer ranges. The method of solution presented here reduces the localization problem to a problem of finding the root(s) of a characteristic function (curve). The form of the characteristic curve offers insight to the behavior of the solution, e.g., in the neighborhood of caustics. Further, the particular method allows for targeted search of the source location with the same numerical accuracy, independently of its distance from the hydrophones. The localization problem can also be solved by using more

straightforward methods based on precalculated travel times along a set of fixed direct and surface-reflected rays launched from the two hydrophones. These methods are in general faster since the basic ray tracing calculations are not repeated as long as the environment and the hydrophone depths remain unchanged. On the other hand, their accuracy decreases with distance, due to the increasing spread of the rays.

The problem of the source range/depth estimation is uncoupled from that of the bearing estimation problem. In this connection, the examples of ray-theoretic calculation of source range and depth given in Sec. IV for source locations on the vertical hydrophone plane (zero azimuth) would be identical with examples of nonzero source azimuth θ and larger hydrophone separation Δ, according to Eq. (21). Although the source range and depth are estimated independently of the source azimuth, their errors depend on the azimuthal direction, as in the homogeneous-ocean case.[20,21] Some indicative results for the error in distance estimation caused by hydrophone-depth and travel-time uncertainties as well as by surface roughness were presented here in the case of zero azimuth. A further source of errors is associated with uncertainties in the sound-speed profile; this type of uncertainty was not considered here assuming a perfectly known ocean environment.

Besides the direct influence of refraction on localization, due to ray bending and travel-time effects, there are further consequences of stratification such as shadow zones, caustics, and multipath. If the source lies in the shadow zone of the two hydrophones, then there is no reception and accordingly the source cannot be localized or even detected. If the source is received by one hydrophone only, then it has to be in the shadow zone of the other hydrophone. Although no precise localization can be performed in that case, still some indication about the source location can be obtained by considering the intersection of the shadow zone of the nonreceiving hydrophone with the geometrical locus of points with fixed (measured) differential travel time between direct and surface-reflected arrivals at the receiving hydrophone. In the neighborhood of surface shadow zones caused by downward refraction, the localization problem becomes increasingly indefinite since the difference between the refracted and the surface-reflected paths becomes smaller.

As far as multipath is concerned, the present approach assumes that there exist only two acoustic paths from the source to each hydrophone, a direct and a surface-reflected one, which is the usual case for relatively short ranges, up to a couple of kilometers. For longer ranges in the presence of stratification/refraction there will be in general multiple direct paths from the source to each hydrophone leading to additional direct arrivals that can be exploited for solving the localization problem. On the other hand, for source locations in the neighborhood of caustics there are multiple direct acoustic paths even for short ranges. Nevertheless, the difference in travel times along such paths is very small (of the order of 0.1 ms in the cases considered) such that the corresponding multiple arrivals cannot be resolved—the major effect in this case will be an increased error in arrival-time estimation.

A further consequence of caustics is the existence of double solutions for source locations in the neighborhood of the caustics. One of the two solutions corresponds to the true source location while the other one is an artifact (ghost solution). Accordingly the localization of sources in the neighborhood of caustics is associated with ambiguity. However, in environments such as the Mediterranean in summer, where the minimum of the sound speed (channel axis) is at relatively small depths ($\sim$100 m), and for practical hydrophone depths (less than 100 m) and ranges (up to a couple of kilometers), the caustics—if present—are expected to be formed near the surface, up to depths of 200–300 m. Thus, they pose no problem for localization at larger depths of interest for marine-mammal observation. In deep-ocean environments with channel axis at large depths ($\sim$1000 m) the caustics are expected to be formed at larger distances,[31] hence they do not enter the localization picture.

A similar double-solution behavior in the presence/neighborhood of caustics has been encountered in seismic imaging problems;[32,33] the solution ambiguity in that case is resolved by using multiple excitation sources. For passive localization under the conditions described above, the double solutions—if present—are likely to be for source locations close to the surface. In the case of monitoring diving whales, the double-solution ambiguity can be resolved by the diving tracks themselves, since after a particular depth only one of the two solutions will be continued.

In the case of multiple sources the arrivals from each individual source have to be identified prior to localization. This can be done by comparing the bearings estimated from the differential arrival times at the two hydrophones or by studying the time difference between consecutive arrivals at each single hydrophone.[21]

ACKNOWLEDGMENTS

The authors would like to thank the anonymous reviewers for helpful comments and suggestions.

[1]N. Jaquet, S. Dawson, and L. Douglas, "Vocal behavior of male sperm whales: Why do they click?" J. Acoust. Soc. Am. **109**, 2254–2259 (2001).
[2]J. C. Goold and S. E. Jones, "Time and frequency-domain characteristics of sperm whale clicks," J. Acoust. Soc. Am. **98**, 1279–1291 (1995).
[3]K. S. Norris and G. W. Harvey, "A theory for the function of the spermaceti organ of the sperm whale *Physter catodon*," in *Animal Orientation and Navigation*, edited by S. R. Galler, K. Schmidt-Koenig, G. J. Jacobs, and R. E. Belleville, SP-262 NASA, Washington, DC., pp. 397–417 (1972).
[4]B. Møhl, "Sound transmission in the nose of the sperm whale *Physeter catodon*. A *post mortem* study," J. Comp. Physiol., A **187**, 335–340 (2001).
[5]W. M. X. Zimmer, P. L. Tyack, M. P. Johnson, and P. T. Madsen, "Three-dimensional beam pattern of regular sperm whale clicks confirms bent-horn hypothesis," J. Acoust. Soc. Am. **117**, 1473–1485 (2005).
[6]W. A. Watkins and W. E. Schevill, "Sound source location by arrival times on a non-rigid three-dimensional hydrophone array," Deep-Sea Res. **19**, 691–706 (1972).
[7]M. Wahlberg, B. Møhl, and P. T. Madsen, "Estimating source position accuracy of a large-aperture hydrophone array for bioacoustics," J. Acoust. Soc. Am. **109**, 397–406 (2001).
[8]V. Papastavrou, S. C. Smith, and H. Whitehead, "Diving behavior of the sperm whale *Physter macrocephalus* off the Galapagos Islands," Can. J. Zool. **67**, 839–846 (1989).
[9]W. A. Watkins, M. A. Daher, N. A. DiMarzio, A. Samuels, D. Wartzok, K. M. Fristrup, D. P. Gannon, P. W. Howey, R. R. Maiefski, and T. R. Spra-

dlin, "Sperm whale surface activity from tracking by radio and satellite tags," Marine Mammal Sci. **15**, 1158–1180 (1999).
[10]P. T. Madsen, R. Payne, N. U. Kristiansen, M. Wahlberg, I. Kerr, and B. Møhl, "Sperm whale sound production studied with ultrasound time/depth-recording tags," J. Exp. Biol. **205**, 1899–1906 (2002).
[11]M. Johnson and P. L. Tyack, "A digital acoustic recording tag for measuring the response of wild marine mammals to sound," IEEE J. Ocean. Eng. **28**, 3–13 (2003).
[12]W. A. Watkins, M. A. Daher, K. M. Fristrup, and T. J. Howald, "Sperm whales tagged with transponders and tracked underwater by sonar," Marine Mammal Sci. **9**, 55–67 (1993).
[13]W. M. X. Zimmer, M. P. Johnson, A. D'Amico, and P. L. Tyack, "Combining data from a multisensor tag and passive sonar to determine the diving behavior of a sperm whale *Physeter macrocephalus*," IEEE J. Ocean. Eng. **28**, 13–28 (2003).
[14]B. Møhl, M. Wahlberg, P. T. Madsen, L. A. Miller, and A. Surlykke, "Sperm whale clicks: Directionality and source level revisited," J. Acoust. Soc. Am. **107**, 638–648 (2000).
[15]B. Møhl, M. Wahlberg, and A. Heerfordt, "A large-aperture array of nonlinked receivers for acoustic positioning of biological sound sources," J. Acoust. Soc. Am. **109**, 434–437 (2001).
[16]M. Wahlberg, "The acoustic behaviour of diving sperm whales observed with a hydrophone array," J. Exp. Mar. Biol. Ecol. **281**, 53–62 (2002).
[17]R. Aubauer, M. O. Lammers, and W. W. L. Au, "One-hydrophone method of estimating distance and depth of phonating dolphins in shallow water," J. Acoust. Soc. Am. **107**, 2744–2749 (2000).
[18]R. Leaper, O. Chappell, and J. Gordon, "The development of practical techniques for surveying sperm whale populations acoustically," Rep. Int. Whal. Comm. **42**, 549–560 (1992).
[19]G. D. Hastie, R. J. Swift, J. C. D. Gordon, G. Slesser, and W. R. Turrell, "Sperm whale distribution and seasonal density in the Faroe Shetland Channel," J. Cetacean Res. Manage. **5**, 247–252 (2003).
[20]E. K. Skarsoulis, A. Frantzis, and M. Kalogerakis, "Passive localization of pulsed sound sources with a 2-hydrophone array," in *Seventh European Conference on Underwater Acoustics*, Delft, The Netherlands, 2004.
[21]A. Thode, "Tracking sperm whale (*Physeter macrocephalus*) dive profiles using a towed passive acoustic array," J. Acoust. Soc. Am. **116**, 245–253 (2004).
[22]J. F. Lynch, J. H. Miller, and C. S. Chiu, "Phase and travel-time variability of adiabatic acoustic normal modes due to scattering from a rough sea surface, with applications to propagation in shallow-water and high-latitude regions," J. Acoust. Soc. Am. **85**, 83–89 (1989).
[23]O. A. Godin and I. M. Fuks, "Travel-time statistics for signals scattered at a rough surface," Waves Random Media **13**, 205–221 (2003).
[24]J. L. Spiesberger and K. M. Fristrup, "Passive location of calling animals and sensing of their acoustic environment using acoustic tomography," Am. Nat. **135**, 107–153 (1990).
[25]J. L. Spiesberger, "Locating animals from their sounds and tomography of the atmosphere: Experimental demonstration," J. Acoust. Soc. Am. **106**, 837–846 (1999).
[26]L. Brekhovskikh and Y. Lysanov, *Fundamentals of Ocean Acoustics* (Springer Verlag, New York, 1982).
[27]A. Frantzis, P. Alexiadou, G. Paximadis, E. Politi, A. Gannier, and M. Corsini-Foka, "Current knowledge of the cetacean fauna of the Greek Seas," J. Cetacean Res. Manage. **5**, 219–232 (2003).
[28]P. Brasseur, "The MED2 hydrographic data base (http://modb.oce.ulg.ac.be)," Lit. Rev. **42**, 414–415 (1995).
[29]C.-T. Chen and F. J. Millero, "Speed of sound in sea water at high pressures," J. Acoust. Soc. Am. **62**, 1129–1135 (1977).
[30]C. K. Frederickson and P. L. Marston, "Travel time surface of a transverse cusp caustic produced by reflection of acoustical transients from a curved metal surface in water," J. Acoust. Soc. Am. **95**, 650–660 (1994).
[31]Y. A. Kravtsov and Y. I. Orlov, *Geometrical Optics of Inhomogeneous Media* (Springer Verlag, Berlin, 1990).
[32]M. G. Brown and F. D. Tappert, "Catastrophe theory, caustics and travel-time diagrams in seismology," Geophys. J. R. Astron. Soc. **88**, 217–229 (1987).
[33]C. J. Nolan, "Scattering in the presence of fold caustics," SIAM J. Appl. Math. **61**, 659–672 (2000).

Localization of multiple acoustic sources in the shallow ocean

Tracianne B. Neilsen[a)]
Applied Research Laboratories, The University of Texas at Austin, Austin, Texas 78713-8029

(Received 12 October 2004; revised 20 June 2005; accepted 1 August 2005)

An iterative, rotated coordinates inversion technique is applied in conjunction with spatial narrowband filters in matrix form to localize multiple acoustic sources in the shallow ocean. When the iterative, rotated coordinates inversion technique is applied to broadband horizontal line array data designed to simulate a group of moving ships, the bearing of the loudest source is quickly identified. Both passband and stop band matrix filters are constructed for an angular sector centered on the identified bearing. Data filtered with the passband filters are used in the inversion to obtain estimates of the remaining source parameters, range, depth, course angle and speed, and prominent environmental parameters. Additional inversions applied to data modified by the stop band filters yield the bearing of the next loudest source. The procedure is repeated until all detectable sources have been localized. Results of applying this strategy to several simulated cases are presented.
 [DOI: 10.1121/1.2041307]

PACS number(s): 43.30.Wi, 43.30.Pc [WLS] Pages: 2944–2953

I. INTRODUCTION

A central goal in many areas of underwater acoustics research is the localization of acoustic sources. Traditionally, the first task is to identify the number of sources and their bearings. Next, the ranges from the receiver array to the sources are estimated. In contrast, the goals of the present work are to find the locations and trajectories of multiple acoustic source without *a priori* knowledge of the number of sources present by applying an optimization algorithm[1,2] and narrowband matrix filters[3] to broadband horizontal line array (HLA) data.

Identification of the bearing of an acoustic source can be accomplished with many techniques. A large number of these methods are based on beamforming, in which the responses of the array for sound received from multiple bearing angles, referred to as look-directions, are compared to plane-wave replica vectors: the response expected on the array for a plane-wave arrival from a source in the far-field at that bearing. A detailed description of beamforming can be found in Ref. 4. For the present, the relevant point is that while advanced beamforming techniques accurately identify source bearings in a wide variety of cases, they must be used in conjunction with other algorithms to obtain source ranges and trajectories.

Another set of techniques developed for source localization are referred to as matched field processing (MFP) algorithms. In contrast to plane-wave beamforming, the array response in each look-direction is compared, in MFP, to the replica vectors calculated when the effects of the ocean environment on the plane-wave propagation are included. Thus, the replica vectors depend inherently on the assumed environmental properties. When the environment is well known, MFP can yield good values for source locations in bearing, range, and depth.[5–7] But if the assumed environmental characteristics are incorrect, a case referred to as environmental mismatch, the accuracy of MFP decreases.

To tackle the problems of environmental mismatch, a number of match-field inversion methods,[8] also known as geoacoustic inversions, have emerged. The goal of these optimizations is to obtain accurate estimates for the environmental properties of the shallow-ocean. References 9 and 10 contain reports of benchmark workshops in which such inversion algorithms are applied to synthetic data for range-independent and range-dependent environments, respectively. The articles therein illustrate the wide variety of optimizations currently in use.

A few geoacoustic optimization algorithms have been adapted to invert for the location of a single source along with the environmental parameters. For example, in Refs. 11–13, range and depth of the source are found along with environmental parameters. In Ref. 1, estimates of bearing, range, depth, course angle, and speed of a moving source, as well as environmental characteristics, are found for broadband, HLA data designed to simulate a moving source. The *posteriori* distributions in Ref. 11 and the rotated coordinates in Ref. 1 confirm that the acoustic field is much more sensitive to changes in the source parameters than changes in the environmental properties, as described in Ref. 14.

Building on the work in Refs. 1 and 2, the iterative, rotated coordinates inversion method is applied herein in conjunction with spatial, narrowband filters in matrix form[3] to synthetic, broadband, HLA data generated for multiple, moving, acoustic sources. With no *a priori* knowledge about the number of sources present, the inherently single-source inversion quickly identifies the bearing of the strongest source. Two kinds of narrowband matrix filters are then designed about the identified angle. First, passband matrix filters[3] are constructed to isolate sound originating from an angular sector about the source bearing and are applied to the original data. The resulting filtered data set is used in the inversion to obtain estimates of the source's range, depth, and trajectory. Second, stop band matrix filters remove sound

[a)]Electronic mail: neilsen@arlut.utexas.edu

corresponding to sources in an angular sector about the identified bearing. The resulting modified data are basically equivalent to broadband, HLA data from one less source than the original data. Application of the inversion technique to the modified data yields the bearing of the next strongest source. New sets of matrix filters are created, and the process is repeated until all detectable sources have been localized.

Details and examples of applying this iterative invert-and-filter technique are presented in this paper, which is organized as follows. Section II describes the inversion technique and the procedure for constructing the matrix filters. The performance of the iterative invert-and-filter strategy is demonstrated in Sec. III, for cases of two, four, and ten moving sources. Gaussian noise is added to the ten-source case. The case of environmental mismatch is explored in Sec. III D. Section IV contains conclusions that have been obtained thus far and further potential applications of these techniques.

II. METHODOLOGY

Brief overviews of the inversion method and the matrix filters are presented. Further details about the techniques are available in Refs. 1–3. All computations use complex spectral values at multiple frequencies obtained when a fast Fourier transform (FFT) is performed on time series received on an array of hydrophones.

A. Iterative inversion method

Inversion methods are characterized by three main components: the forward model, the cost function to be minimized, and the search algorithm. For the work presented in this paper, a range-independent, normal mode model, ORCA,[15] is used to produce the modeled field. The modeled field is compared to the data in a cost function based on a cross-phone correlation that is summed coherently over both frequencies and time (range) sequences. The search algorithm is the iterative inversion method referred to as systematic decoupling using rotated coordinates (SDRC),[1,2] which uses multiple sets of rotated coordinates in a series of fast simulated annealing optimizations.

1. Cost function

The cost function minimized in our analysis, based on the coherent, broadband correlation first introduced in Ref. 6, is defined as

$$E(\mathbf{x}) = 1 - \frac{1}{n}\sum_{t} C_1(\mathbf{x},t), \tag{1}$$

where n is the number of time sequences. $C_1(\mathbf{x},t)$ is the coherent, broadband, cross-phone correlation between data and model, at time sequence t, for the set of physical parameters $\mathbf{x}$:

$$C_1(\mathbf{x},\mathbf{t}) = \sum_{f}\sum_{j}\sum_{i>j} D_i(f,t)D_j^*(f,t)M_i^*(f,t,\mathbf{x})M_j(f,t,\mathbf{x}), \tag{2}$$

with i and j indicating the receivers. $D_i(f,t)$ is the measured spectra on the ith hydrophone at frequency f and is normalized at each time t such that

$$\sqrt{\sum_{f}\sum_{j}\sum_{i>j} |D_i(f,t)D_j^*(f,t)|^2} = 1. \tag{3}$$

A single set of source parameters and environmental parameters in $\mathbf{x}$ are used to calculate the modeled spectral values $M_i(f,t,\mathbf{x})$ (complex pressure field), which are normalized in the same manner. In the examples, the data $\mathbf{D}$ are produced by multiple sources, but the modeled values $\mathbf{M}$ are generated assuming only a single source.

2. The SDRC algorithm

The cost function E is minimized by a series of fast simulated annealing optimizations in a process called SDRC. The SDRC approach developed in Refs. 1 and 2 is designed to quickly identify the most sensitive parameters, defined as those which have the largest influence on the cost function, without *a priori* decisions regarding which parameters are not to be varied during the optimization.

The SDRC method uses rotated coordinates, introduced in Ref. 16, to navigate the parameter search space because often there is a correlation between how various parameters influence the cost function E. The application of rotated coordinates transforms the inversion problem from the N physical parameters in $\mathbf{x}$ to a coordinate system that is better aligned with the prominent valleys and gradients of the search space. The transformation is accomplished via diagonalizing $\mathbf{K}$, the covariance matrix of the cost function gradients. The components of $\mathbf{K}$ are defined by

$$K_{ij} = \int_{\Omega} \frac{\partial E}{\partial \hat{x}_i}\frac{\partial E}{\partial \hat{x}_j} d\Omega, \tag{4}$$

and $i,j=1,\ldots,N$. The integration is performed over the N-dimensional volume Ω using an efficient Monte Carlo algorithm.[17] The values of $\hat{\mathbf{x}}$ are dimensionless: the dimensions have been removed from the physical parameters by dividing them by the difference between the respective maximum and minimum values of the parameters in the volume Ω.

An eigenvalue decomposition of $\mathbf{K}$ yields eigenvectors $\mathbf{v_i}$ and eigenvalues s_i. The eigenvectors $\mathbf{v_i}$, which are referred to as the rotated coordinates, indicate how the parameters are coupled, and are used in constructing the explicit expression for the parameter perturbations in the fast simulated annealing optimization.[16,18] Specifically, at each step in the inversion, a single eigenvector $\mathbf{v_j}$ is used to change the set of parameters in $\hat{\mathbf{x}}$ to the new values $\hat{\mathbf{x}}'$ by

$$\hat{\mathbf{x}}' = \hat{\mathbf{x}} + \tfrac{1}{2}\gamma^3\mathbf{v_j}, \tag{5}$$

where γ is randomly selected from the interval $(-1,1)$. Equation (5) is chosen because it tends toward small perturbations but allows large perturbations and works well with

the fast simulated annealing algorithm.[16,18] The eigenvalues s_i indicate which rotated coordinates or, equivalently, which combinations of parameters, have the largest effect on the cost function. Both the parameter couplings and the relative sensitivities depend on Ω, the bounds on the integration in Eq. (4).

Although the use of rotated coordinates, as compared to standard coordinates, in the annealing increases the efficiency of the optimization, it is, nevertheless, extremely difficult to obtain reliable estimates for a large number of parameters from a single inversion in which all the rotated coordinates are varied; the difficulty arises from the wide range of the cost function's sensitivities to changes in the different parameters. The SDRC method[1] has been designed to take advantage of the diverse sensitivities and to find estimates for the most sensitive parameters first before trying to obtain the less sensitive parameters. In SDRC multiple sets of rotated coordinates, each corresponding to a subsequently smaller set of parameter bounds, are used in a series of inversions. For each annealing, only the primary rotated coordinates, defined as those with large corresponding eigenvalues, are used to vary the parameters as in Eq. (5). As the most sensitive parameters become better defined and the bounds on these parameters in the volume Ω are reduced as described in Ref. 2, subsequent sets of primary rotated coordinates change and different parameters are varied more substantially. It is important to note that throughout the iterative algorithm the bounds on the annealing search space are not changed.

B. Spatial filters

Once an approximate source bearing is obtained, narrowband, spatial filters in matrix form, centered on the estimated source bearing, are computed for the frequencies of interest: $f_1, \ldots, f_P$. Matrix filters were originally developed as frequency selective filters for short time series[19] and have been employed for source localization in passive SONAR problems.[20] Many design algorithms are computationally expensive and are not practical in situations where new matrix filters may have to be created and used in real time. The matrix filters applied in the present work are constructed with an efficient method based on the solution of a set of least-squares (LS) problems.[3]

For an array with N_e elements the filtering operation is the matrix-vector product $\mathbf{GD}$, where the $N_e \times N_e$ matrix filter $\mathbf{G}$ is complex, non-Hermitian, rank-deficient, and a function of both the angular window W and frequency f.

The filter design requires the construction of a matrix of steering vectors $\mathbf{Y}(f)$ whose columns are the plane-wave replica vectors. Each replica vector $\mathbf{y_i}(f)$ is an N_e vector giving the plane-wave, array element response due to a single far-field source at angle ϕ_i.

The response of the matrix filter $\mathbf{G}$, for a given frequency f, is given by

$$\mathbf{G}y_i = \ell_i y_i, \quad i = 1, \ldots, M, \tag{6}$$

where M is the number of discrete angles $\{\phi_i, \ldots, \phi_M\}$ covering the bearing space. In the applications presented here, $\ell_k \in \{0,1\}$. For a spatial passband filter about the angular window $W=[\phi_i, \phi_j]$, $\ell_k=1$, for $i \leqslant k \leqslant j$, and $\ell_k=0$, otherwise. Similarly, for the spatial stop band filter, $\ell_k=0$, for $i \leqslant k \leqslant j$, and $\ell_k=1$, otherwise. By defining $\mathbf{\Lambda} = \mathrm{diag}(\ell_1, \ldots, \ell_M)$, the M equations in Eq. (6) can be written as $\mathbf{GY}=\mathbf{Y\Lambda}$. This leads to the rank-deficient least-squares problem:

$$\min_{g_{ij}} \|\mathbf{GY} - \mathbf{Y\Lambda}\|^2 = \min_{g_{ij}} \|\mathbf{Y}^H\mathbf{G}^H - \mathbf{\Lambda}^H\mathbf{Y}^H\|^2, \tag{7}$$

where the superscript H denotes conjugate transpose. A standard numerical method for the solution of rank-deficient linear LS problems[21] based on calculating the psuedo-inverse $\mathbf{P}=(\mathbf{Y}^H)^{+}$[17] is used such that the solution to Eq. (7) is

$$\mathbf{G} = \mathbf{Y\Lambda P}^H. \tag{8}$$

The computation of the matrix filters $\mathbf{G}$, as a function of the angular window W and the frequency f, is efficient enough for practical applications because (1) the replica vectors Y and corresponding pseudo-inverses P for frequencies and angles of interest can be calculated once and stored, and (2) the filtering operation can be calculated with only a few vector inner products instead of a full matrix-vector product because of the low rank of the filters.

Studies by Stotts[22] have shown that optimum matrix filters can be designed if the array configuration is taken into account when choosing the rank of the psuedo-inverse. This work has proven useful, especially for nonuniform arrays.[23] In the present work, however, the array elements are uniformly spaced and a standard threshold is used.

III. EXAMPLES

Examples are presented to show how multiple applications of the SDRC inversion method and the matrix filters on broadband, HLA data can locate and track multiple sources in an uncertain ocean environment. The iterative invert-and-filter strategy proceeds as follows. First, a SDRC inversion is performed with the broadband, HLA data. The inversion algorithm computes the modeled field $M_j(f,t,\mathbf{x})$ in Eq. (2) based on a single set of source parameters in $\mathbf{x}$. The source bearing found by the inversion, θ_1, is the initial bearing of the source with the loudest received level on the HLA. Stop band filters, also referred to as notch filters, are constructed about θ_1 and applied to the original data to effectively remove the contribution of the loudest source in the element-level data. The resulting filtered data are processed in the inversion to obtain the bearing of the next loudest source, θ_2. A new set of notch filters is created about θ_2 and applied to the data. The process is repeated until all discernible source bearings are found. In parallel to this source-bearing identification and source-removal procedure, passband filters are constructed about each angle θ_i that is identified as an initial source bearing. Data filtered with passband filters contain sound originating in the designated angular sector, which ideally contains only one source. These filtered data sets, one for each θ_i, can be used in a SDRC inversion to find additional source parameters, depth z_s, range r_0, course angle ϕ, and speed v, as well as environmental characteristics.

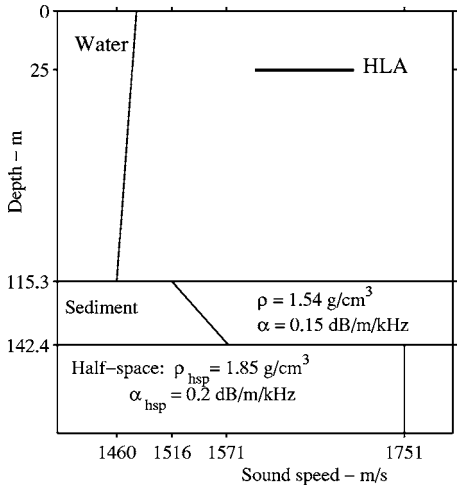

FIG. 1. Shallow ocean environment for the examples in Sec. III. The bold, horizontal line represents the HLA at a depth of 25 m. The other bold, solid lines show the sound speed c in the water, sediment, and half-space. The density ρ and the attenuation α in the sediment and the half-space are specified.

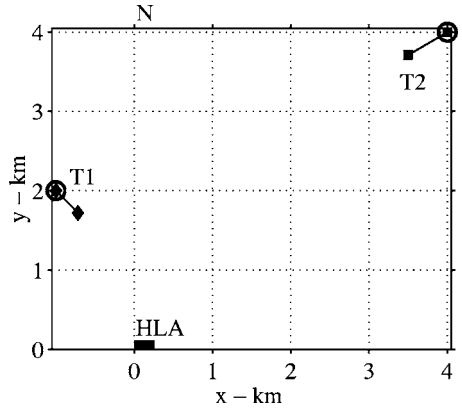

FIG. 2. Geometry of the sources and receivers for the example in Sec. III A. The initial locations are shown as circles and the final as a diamond for T1 and a square for T2. The horizontal aperture covered by the array is illustrated as a box on the x axis.

Some of the questions that arise when considering the above strategy include the following. (1) Is there a ratio of source levels for which the bearing θ_i found by the inversion does not correspond to an actual source bearing? (2) How many sources can be identified by successive applications of the inversions and matrix filters? (3) In what cases is the invert-and-filter scheme unable to locate sources? (4) What influence does an incorrect description for the ocean environment have on the estimates of the source parameters obtained by the inversion? (5) Can estimates of the environmental characteristics be identified while applying the SDRC inversion method to data filtered to isolate a loud source? Three test cases are used to explore these questions.

The data for the test cases are generated in the following manner. First, ORCA[15] is used to obtain the broadband modal eigenvalues for the specified environment. These modal eigenvalues are combined with the individual, unique source spectra, broadband source level, initial location, and trajectory for each source to generate the acoustic field received at the array. The resulting data file contains the FFT of the time series produced by the designated moving sources in the specified environment. For the ten-source case, noise is added to the acoustic field.

The environment and array specifications are the same for all cases. The environment is based on one of the test cases from the 1997 Geoacoustic Inversion Workshop,[9] illustrated in Fig. 1. The HLA is located at a depth of 25 m and consists of 65 elements that are spaced 4 m apart for a total horizontal aperture of 256 m.

A. Two sources with varying source levels

Multisource field data from two sources are simulated with different ratios of the source levels to explore (1) whether or not the inherently single-source SDRC inversion algorithm can reliably obtain a valid source bearing when applied to the field from two sources and (2) if an ambiguous source bearing is found when the sound received on the array from two sources is approximately equivalent. Specifically, the complex spectra from two, concurrent sources at 41 evenly spaced frequencies from 50 to 250 Hz received on the HLA at eleven time sequences that cover a 3-min time interval are generated with different source levels. The positions of the two sources during the 3 min and the HLA are illustrated in Fig. 2. Table I lists the sources' characteristics.

In this example, the SDRC inversion method is applied to data generated for different ratios of the broadband source levels of T1 and T2, and the bearing obtained by the inversion always matches one of the correct source bearings. The broadband source level is the total intensity of the source integrated over the specified frequency band. The source level of T2 is held at 140 dB, while the source level of T1 is varied from 105 to 130 dB. For cases when the source level of T1 is less than 123 dB, the inversion properly identifies an initial bearing of $45° \pm 0.5°$, the bearing of T2. In addition, good estimates are obtained for the range r (within 200 m), the course angle ϕ (within 4°), and the speed v (within 0.3 m/s) by inversions performed starting with several different sets of initial source parameters and with the parameter bounds on the inversions listed in Table I. When the source level of T1 is greater than 125 dB, the initial bearing of T1 is found within 0.3°, and r, ϕ, and v are found with the same accuracy as cited earlier. When the T1 source level is 123 dB, the initial bearing of T2 is found, and good estimates of r, ϕ, and v are obtained from about half of the inversions. Similarly, inversions based on data with a T1

TABLE I. Characteristics of the two sources (T1 and T2) for the synthetic data described in Sec. III A: the source depth z_s, the initial range r_0 and initial bearing θ from the array, the course angle ϕ, the speed v. All angles are measured relative to North (0°). The last two columns list the bounds on the parameters for the inversions.

Parameters	T1	T2	Min	Max
z_s (m)	40	6	1	70
r_0 (km)	2.236	5.657	0.1	10
θ (deg)	−26.6	45	−90	90
ϕ (deg)	135	240	0	360
v (m/s)	2.2	3.2	1	10

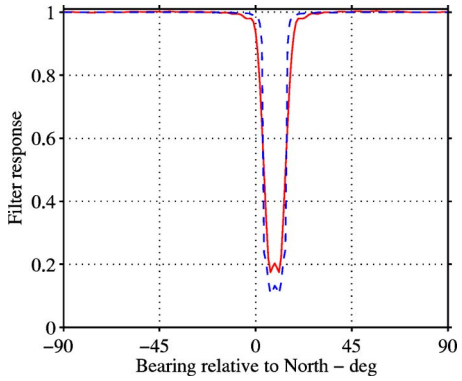

FIG. 3. A 10° notch filter about 11° at 50 Hz (dashed line) and 250 Hz (solid line) for the environment and array in Fig. 1.

source level of 125 dB find the initial bearing of T1 reliably and sometimes find good estimates for the other source parameters. For a source level of 124 dB, the sources have the same received level on the array; the inversion identifies either −26.6° (T1) or 45° (T2) as the source bearing and often obtains approximately correct values for the corresponding r, ϕ, and v. The inversion does not converge to an incorrect bearing even when the sound level received on the array from the two sources is equivalent. If one of the sources is louder than the other, then r, ϕ, and v can also be well approximated by a single SDRC inversion.

B. Four well-separated targets

For the second example, a series of SDRC inversions and notch filters are applied to the field produced by four sources (T1–T4), which are well separated in bearing, to obtain estimates of the source locations and trajectories. Examples of 10° notch filters at 50 and 250 Hz are shown in Fig. 3.[24] The source configuration used to create the data are listed in Table II, and the locations and motion of the sources over the 3-min interval are illustrated in Fig. 4. Each source has a unique source spectra.

One way to examine the progress of the iterative, invert-and-filter method is to view scatter plots of the cost function E versus the individual parameters for all states visited in each SDRC inversion.[1] Envelopes of the scatter plots,[2] which essentially trace the minimum values of E found for each parameter, are shown in Figs. 5–9. The line representations of the scatter plots include on the order of 10 000 model realizations.

TABLE II. Characteristics of the four sources (T1–T4) for the synthetic data described in Sec. III B. The last two columns list the bounds on the parameters for the inversions.

Parameters	T1	T2	T3	T4	Min	Max
z_s (m)	30	20	6	40	1	85
r_0 (km)	2.828	5.099	5.000	6.325	0.1	10
θ (deg)	45	11.3	−36.9	−71.6	−90	90
ϕ (deg)	45	0	180	90	0	360
v (m/s)	2.0	2.0	2.0	2.0	0	10
SL (dB)	125	130	140	125		

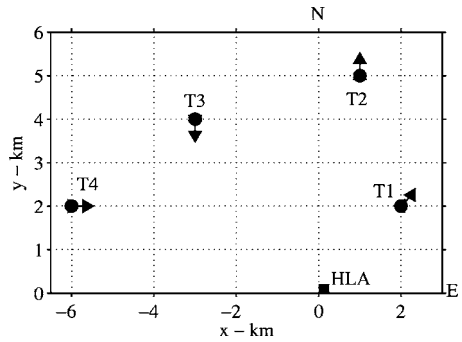

FIG. 4. Source configuration for examples in Sec. III B. The circles denote the starting location, and the arrows indicate the source positions 3 min later. The rectangle near the origin shows the horizontal aperture covered by the HLA.

Figure 5 contains plots of E versus initial source bearing θ for each of the four, successive, SDRC inversions and illustrates how application of the invert-and-filter method systematically obtains all four source bearings. The first inversion, performed on the original data, finds a minimum value of E at θ=11°, the initial bearing of T2, as depicted in Fig. 5(a); a second deep minimum is also visible at θ=−37°, the initial bearing of T3. The results of the second inversion performed after notch filters remove T2, shown in Fig. 5(b), yield a well-defined minimum of the E at θ=−37° (T3). Figure 5(c) shows how the third inversion (after T2 and T3 have been removed) results in θ=45° (T1). The plot of E vs θ for the fourth and final inversion, Fig. 5(d), reveals a sharp minimum at the initial bearing of T4, θ=−72°.

Figures 6–9 show the inversion results for the remaining four source parameters obtained by the four, successive inversions detailed Fig. 5. The width of the minima indicates the relative uncertainty in the inversion results: the wider the valley around the minimum, the more uncertain the estimate obtained by the inversion. The vertical dashed lines show the correct values, except in Fig. 6(c) where the correct answer is

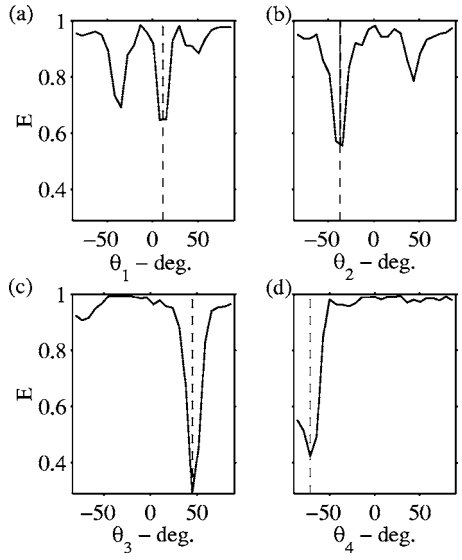

FIG. 5. Distribution envelopes of bearing θ vs cost function E for the four, successive, SDRC inversions in Sec. III B. The vertical dashed lines show correct bearings for (a) T2, (b) T3, (c) T1, and (d) T4.

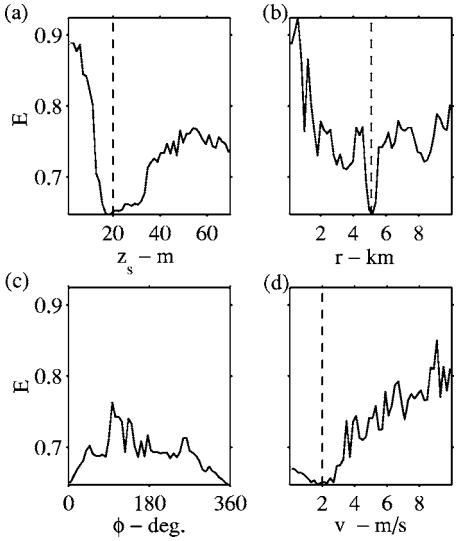

FIG. 6. Distribution envelopes of (a) z_s, (b) r, (c) ϕ, and (d) v vs cost function E for the first SDRC inversion in Sec. III B on the original four source data. The vertical dashed lines are the correct values for source T2.

$\phi=0°=360°$. In Fig. 6, all four source parameters for T2 are well approximated by the first SDRC inversion on the original four-source data. Figure 7 shows the results of the second inversion on data modified by notch filters to remove 10° about $\theta=11°$, the initial bearing of T2, in which good estimates are obtained for r, ϕ, and v of T3 but not for z_s. The correct z_s for T3 is 6 m, and as has been stated in Refs. 1 and 2, it is very difficult to find a shallow source depth accurately. Figures 8 and 9 show similar results: the source parameters for T1 and T4 are well approximated by the third and fourth SDRC inversions based on data modified by notch filters. Thus, the four sources have been localized, with the exception of one source depth, and tracked over the 3-min time interval by successive application of the single-source, SDRC inversion method and notch filters.

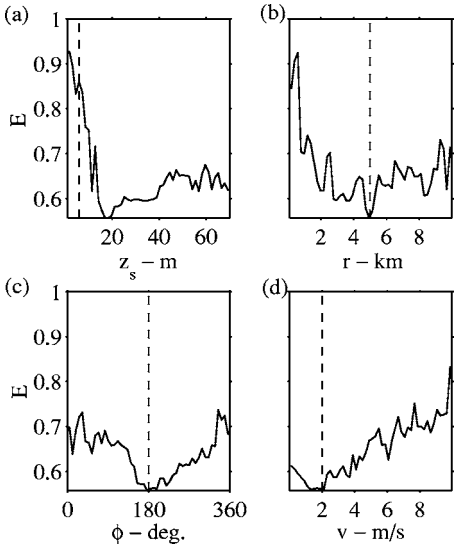

FIG. 7. Distribution envelopes of (a) z_s, (b) r, (c) ϕ, and (d) v vs cost function E for the second SDRC inversion in Sec. III B after T2 has been filtered out. The vertical dashed lines are the correct values for source T3.

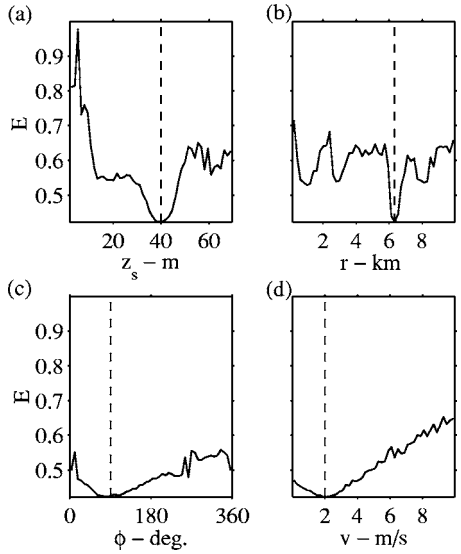

FIG. 8. Distribution envelopes of (a) z_s, (b) r, (c) ϕ, and (d) v vs cost function E for the third SDRC inversion in Sec. III B after T2 and T3 have been removed by notch filters. The vertical dashed lines are the correct values for source T1.

C. Ten targets

The iterative invert-and-filter approach is applied to data from ten, concurrent sources (T1–T10), designed to simulate a noisy, high-traffic area of the ocean, to explore how many sources can be localized and tracked with this approach. The bearing identification and notch filters are applied as in Sec. III B. In addition, passband filters are constructed around each identified bearing and applied to the data. The resulting filtered data sets are used in SDRC inversions to localize and track the sources. The positions of the sources during a 3 -min time interval are illustrated in Fig. 10. Five of the ten sources (T2, T6–T9) are loud surface ships (with $z_s \leqslant 10$m) traveling in parallel directions ($\phi=135°$ or 315°). The remaining five sources are located at a wide variety of depths

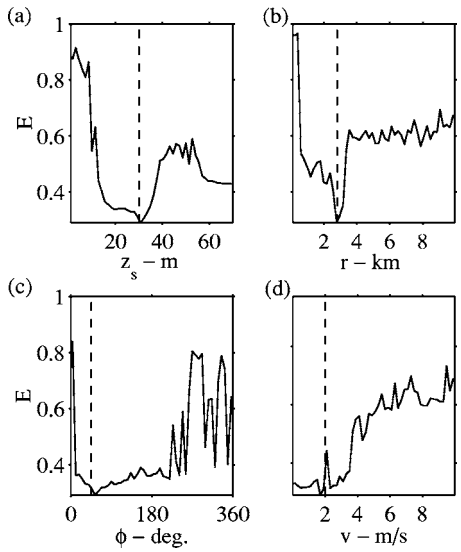

FIG. 9. Distribution envelopes of (a) z_s, (b) r, (c) ϕ, and (d) v vs cost function E for the fourth and final SDRC inversion in Sec. III B after T1, T2, and T3 have been removed by notch filters. The vertical dashed lines are the correct values for source T4.

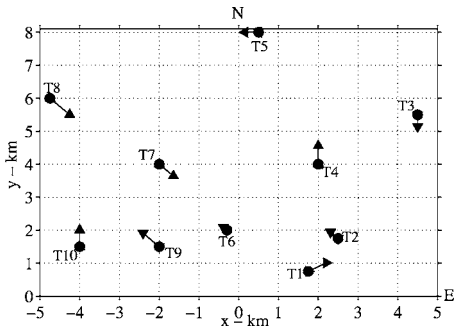

FIG. 10. Source configuration the ten sources (T1–T10) used in Sec. III C.

and ranges, with T5 being the quietest source and furthest from the array. In addition, a Gaussian noise background is added such that the signal-to-noise ratio with respect to the quietest source, T5, is 3 dB. The same frequencies, array configuration, and time sequences are used in these inversions as in the previous examples.

To follow the performance of the invert-and-filter method, envelopes of the distribution of the initial source bearing θ versus the cost function E for the successive SDRC inversions are plotted in Fig. 11. The dashed line in each plot is the initial bearing of the source shown in Fig. 10 that is closest to the bearing associated with the minimum value of

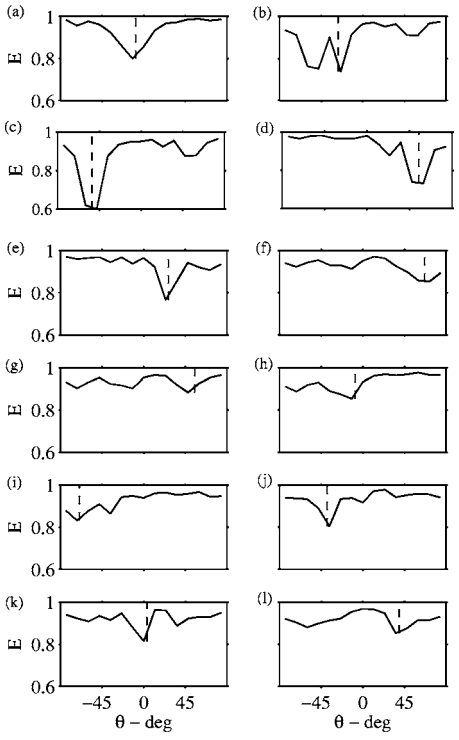

FIG. 11. Envelopes of the distributions of initial source bearing θ vs cost function E for the inversions described in Sec. III C. The dashed line in each plot is the initial bearing of the source shown in Fig. 10 that is closest to the value corresponding to the minimum E. In (a), the first SDRC inversion performed on the ten-source data finds the minimum values of E to be at $\theta=-11°$, close to the bearing of source T6. Each inversion (b)–(l) is performed using data modified by notch filters that remove one additional source. The source bearings identified by this method are (a) T6, (b) T7, (c) T9, (d) T2, (e) T4, (f) T1, (g) T2, (h) T6, (i) T10, (j) T8, (k) T5, (l) T3. The bearing of T2 and T6 are found twice because the initial notch filters are not wide enough to remove large sidelobes associated with T2 and T6.

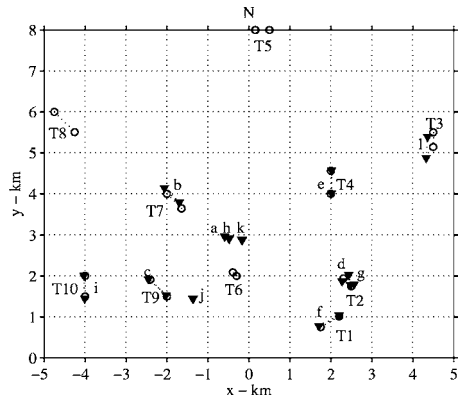

FIG. 12. Source locations resulting from inversions performed on data filtered about the bearings obtained in Fig. 11. Triangles mark the initial and final positions. The corresponding letters (a)–(l) label which filtered data set produced which trajectory. The actual beginning and ending source positions are shown as open circles and labeled T1–T10 as in Fig. 10.

E found in that inversion. In between the inversions, notch filters are created that remove 10° about each bearing identified thus far, and the filters are applied to the original data. Thus, the nth inversion uses data modified by notch filters with $n-1$ angular sectors removed. The first SDRC inversion performed on the ten-source data finds the minimum values of E at $\theta=-11°$, close to the initial bearing of source T6, as shown in Fig. 11(a). Figures 11(b)–11(f) display the results of the next five inversions that obtain good estimates for the bearings of sources (b) T7, (c) T9, (d) T2, (e) T4, and (f) T1. The loudest sources' bearings are found first. The next two inversion, shown in Figs. 11(g) and 11(h), yield bearings that are close to the values already found for T2 and T6 indicating that the 10° window removed by the notch filter is not sufficiently large to remove the main sidelobes of T2 and T6. Additional notch filters are used to extend the nulled angular sector about the estimated bearings. The remaining four inversions, Figs. 11(i)–11(l), find a miniumum near the initial bearings of (i) T10, (j) T8, (k) T5, and (l) T3. Thus it appears that all ten source bearings have been obtained using the invert-and-filter approach.

The next task is to obtain estimates of depth, range, and trajectory for each source whose bearing is identified by the invert-and-filter technique. First, separate filters are designed to pass 15° about each θ obtained by the 12 inversions displayed in Fig. 11. Next, the filters are applied to the original data, and the twelve filtered data sets, labeled (a)–(l) in accordance with Fig. 11, are processed in SDRC inversions to obtain estimates of z_s, r, ϕ, and v for each source. All twelve data sets are used, even though two of them are essentially duplicates because in realistic applications the true source bearings are not known.

A plot of the source locations over the 3-min time interval as obtained by the 12 inversions are plotted in Fig. 12, with triangles at the beginning and end locations, and are labeled (a)–(l) to indicate which of the filtered data sets yield which source parameters. The beginning and ending locations of the original, ten sources are shown as open circles. The HLA is located at the origin and extends along the $+x$ axis. From this plot, it is seen that the inversion using data filtered to pass 15° about the bearing identified in Fig. 11(f)

TABLE III. Source depths for the true source configuration in Fig. 10 and those obtained by the inversions in Figs. 12, 13(b), and 14(b). Inverted source depths are not listed for T5 and T8 because they are not localized by the inversion method.

Source	True	Inverted	B1	C1
T1	30	33	33	31
T2	6	16	14	14
T3	50	49	66	49
T4	20	19	27	20
T5	40	*X*	*X*	*X*
T6	6	34	38	33
T7	6	27	11	14
T8	10	*X*	*X*	*X*
T9	10	16	12	12
T10	15	14	5	16

of $\theta=66°$ obtains good estimates for the range, course angle, and speed of T1. Similarly, inversions based on filtered data sets (d) and (g) both yield good values for T2, confirming the idea that the bearing obtained in inversion (g) converges to a portion of the signal from T2 that is not removed by notching out a 10° angular sector about the bearing obtained by inversion (d). T3 is found using filtered data set (l), T4 by (e), T7 by (b), T9 by (c), and T10 by (i). Sources T5 and T8 are not identified using any of the filtered data sets.

Four of the 12 inversions did not converge accurately to correct source locations. Inversions (a) and (f) have the same bearing as T6, which is the loudest source, but the range is incorrect. This error occurs because T6 is the slowest of all the sources, $v=0.7$ m/s, and is moving too slowly for the range to be adequately determined by this cost function. Although the range estimates from inversions (a) and (f) are too large, the bearing, course angle and slow speed are found correctly. The other two inversions with poor results correspond to Figs. 11(j) and 11(k), even though the estimated bearings are close to the bearings of T8 and T5. The probable reasons for the inability to localize T5 and T8 are (1) the larger distance from the HLA and (2) the proximity to the loudest source T6. In addition, the results labeled (j) and (k) have very slow speeds similar to (a) and (f).

The source property that is not represented in Fig. 12 is the source depth. Table III lists the correct source depths and those obtained by the inversions performed on the filtered data sets. Although there is difficulty in obtaining accurate estimates for very shallow source depths, $z_s<10$ m, the remaining source depth estimates are within a few meters of the correct values.

The error in the inversions (j) and (k) and the inability to isolate the bearings of T5 and T8 demonstrate the limits of the invert-and-filter approach. At some point, after many angular sectors have been removed by the notch filters, the inversion can converge on either sidelobes of louder sources or on some feature of the interference between sidelobes of different sources. Thus, remaining sidelobe features can mask quieter sources. To locate quiet targets, a better way of removing the entire signal of the loud sources is required.

D. Environmental mismatch

In the previous examples, the properties of the shallow ocean environment are assumed to be known exactly. In cases where an approximately correct environment is used, then inversion such as those in Sec. III C generally yield reasonable source locations and trajectories. If the environmental information is very incorrect, it is still possible to obtain bearings of the sources with the invert-and-filter method. In the case of corrupt environmental information, a SDRC inversion, on data filtered to pass a loud source, in which both the source and environmental parameters are allowed to vary yields a modified description of the environment that can then be used to get improved estimates of the remaining sources' locations.

To examine the effect of environmental mismatch on the source localization process, two environments, listed as "B" and "C" in Table V, are considered. Environment B corresponds to a softer sediment with a ratio of water to sediment sound speed rc_1 less than one, while C represents a harder sediment. The process in Sec. III C is repeated twice more with the incorrect environments held fixed. In both cases, the source-bearing identification and source-removal procedure yields results equivalent to those in Fig. 11. The ability of the inversion to obtain correct source bearings with incorrect environments is evidence of the lack of coupling between the source bearing and the environment.[1] In addition, the matrix filters are based on plane-wave replica vectors and thus are independent of the assumed environment.

Once approximate source bearings have been estimated, data filtered to about each bearing are used in separate SDRC inversions for source parameters holding the incorrect environments fixed. In most instances, fairly good estimates are obtained for the course angle and speed but poorer estimates are obtained for the range and the depths. The ability of the inversions to determine relatively good estimates of ϕ and v independent of the environment is expected because they are not as significantly coupled to the environment as are z_s and r_0.

The inversion estimates are improved if a modified environment is used. The properties of the incorrect environment are allowed to vary along with the source parameters in the inversion based on data filtered around the source at −53°, a loud surface ship (T9), because it was the second bearing identified. (In general, the first bearing could be used, but in this case T6, the loudest source, is moving too slow to yield good results, as described in Sec. III C.) The bounds on the environmental parameters used in the inversion are listed in Table IV. The estimates of the environmental properties obtained by SDRC inversions on the loud source T2 are listed in Table V as B1 and C1 and are referred to hereafter as the modified environments. The estimates obtained for the most sensitive feature, rc_1, are closer to the correct value. The inversions on the filtered data sets for the other sources are performed again holding the modified environments fixed, and the resulting source locations and trajectories are shown in Fig. 13(b) for environment B1 and Fig. 14(b) for C1. The source depths are listed in Table III under B1 and C1.

TABLE IV. Environment used to generate the simulated data set in Sec. III is given in the column labeled "True." The last two columns contain the bounds on the nine environmental parameters varied in the inversions in Sec. III D. The ratio of the sound speed across interface i is labeled as rc_i; gc_i is the gradient of the sound speed in layer i.

Parameters	True	Min	Max
h_w (m)	115.3	112	118
h_1 (m)	27.1	25	50
ρ_1 (g/cm^3)	1.54	1.0	2.5
rc_1	1.038	0.98	1.30
gc_1 (1/s)	2.103	0	5
c_1 (m/s)	1516		
c_2 (m/s)	1573		
α_1 (dB/m/kHz)	0.15	0.0	0.5
ρ_{hsp} (g/cm^3)	1.85	1.5	2.5
rc_{hsp}	1.113	1.0	1.5
c_{hsp} (m/s)	1751		
α_{hsp} (dB/m/kHz)	0.2	0.05	0.8

The source locations and trajectories produced when the modified environments are used are very similar to those obtained using the correct environment. Thus, the overall invert-and-filter approach to obtaining multiple source locations and trajectories can be applied in cases where little is known about the seafloor.

IV. CONCLUSIONS

The iterative invert-and-filter technique has been tested on several synthetic cases to locate and track multiple, concurrent targets in both known and uncertain shallow ocean environments. The inherently single-source, SDRC inversion algorithm successfully identifies the bearing of the strongest source when applied to simulated, broadband, HLA data.

When a passband filter designed about the identified bearing is applied to the data, the resulting filtered data are processed in a SDRC inversion to obtain good estimates for the source range, course angle, speed, and source depth with two exceptions. (1) Incorrect range estimates are often found for source speeds less than 1 m/s using the the cost function specified in Eq. (1), which includes a summation over time sequences. (2) It is difficult to obtain accurate estimates for shallow source depths, i.e., less than 10 m.

Stop band or notch filters are also designed about the identified bearing and applied to the data effectively removing the sound originating from that angular sector. A SDRC inversion on this filtered data yields the bearing of the next loudest source. Additional applications of filters and inver-

TABLE V. Two test environments, B and C, used in Figs. 13(a) and 14(a), respectively. Two modified environments, B1 and C1, obtained by a SDRC inversion on a loud source, that are used for Figs. 13(b) and 14(b), respectively.

Parameters	B	C	B1	C1
h_w (m)	115	115	117.5	114
h_1 (m)	25	30	33	23
ρ_1 (g/cm^3)	1.4	1.7	1.86	1.34
rc_1	0.99	1.13	1.023	1.035
gc_1 (1/s)	2	2.8	3.03	4.65
c_1 (m/s)	1450	1650	1493	1511
c_2 (m/s)	1500	1735	1595	1617
α_1 (dB/m/kHz)	0.1	0.16	0.24	0.23
ρ_{hsp} (g/cm^3)	1.67	2.0	1.58	2.13
rc_{hsp}	1.117	1.110	1.218	1.11
c_{hsp} (m/s)	1675	1925	1942	1970
α_{hsp} (dB/m/kHz)	0.18	0.22	0.31	0.18

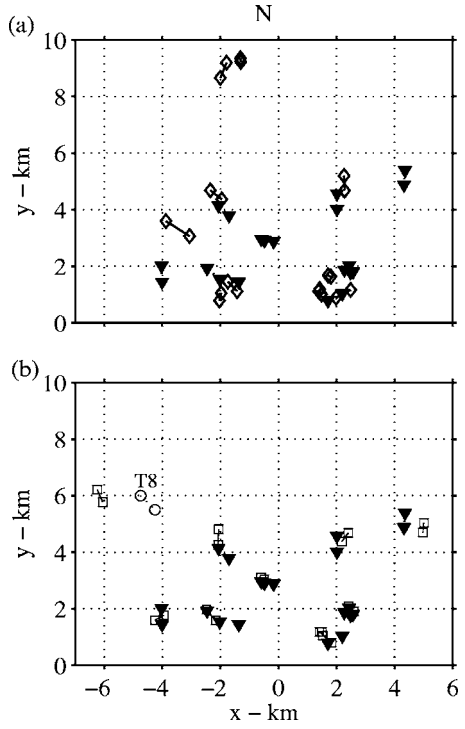

FIG. 13. Comparison of source locations obtained using correct environment (closed triangles, the same as in Fig. 12) in (a) to those found with environment B (open diamonds) and in (b) to those found using the modified environment B1 (open squares) obtained from a loud source.

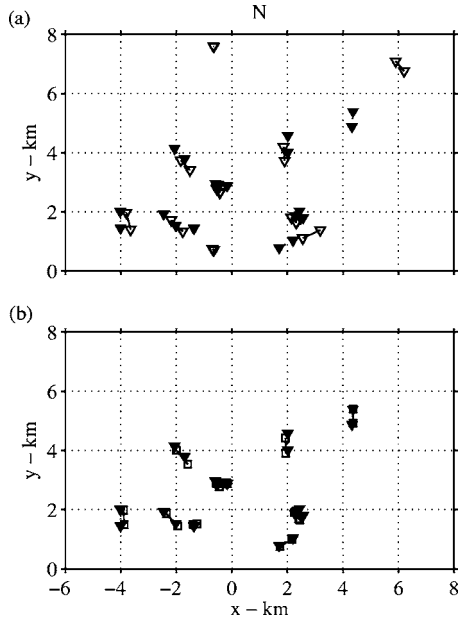

FIG. 14. Similar to Fig. 13 except environment C is used in (a) and modified environment C1 is used in (b).

sions reveal additional source bearings. If the notch filter is not sufficiently large, the inversion may converge on a main sidelobe of a source that has been previously identified. In such cases, the subsequent inversion on the pass-filtered data converges to the same location as a previous source indicating a duplication of source bearing. While it is possible for a source to be too quiet to be detected or for it to be masked by sidelobes or interference patterns remaining after other sources are removed by the filters, in most cases, many sources can be accurately localized with the invert-and-filter technique.

The performance of the invert-and-filter scheme in the presence of environmental mismatch has been investigated. Incorrect environmental information does not impede the bearing-identification and source-removal procedure. In cases of large environmental mismatch, the estimates of source range and depth can be improved when a modified environment, obtained from an inversion based on filtered data corresponding to a loud source, is used.

It is possible that filters based on the environment, instead of on the plane-wave assumption, might improve the effectiveness of the notch filter.[25] However, the sensitivity of such filters to environmental mismatch could be substantial and needs to be investigated.

ACKNOWLEDGMENTS

This work was supported by the Office of Naval Research. The author wishes to acknowledge that Dr. Craig S. MacInnes introduced her to the passband matrix filters and that Dr. Gary Wilson first suggested that the inversion method be applied directly to multisource problems. The author also wishes to thank Dr. David Knobles and Dr. Robert Koch, Dr. Steven Stotts, and Eric Ridderman for their helpful comments and discussions regarding this work. In addition, gratitude is expressed to the reviewers who made valuable suggestions and comments.

[1]T. B. Neilsen, "An iterative implementation of rotated coordinates for inverse problems," J. Acoust. Soc. Am. **113**, 2574–2586 (2003).
[2]T. B. Neilsen and D. P. Knobles, "Geoacoustic inversion of range-dependent data with added Gaussian noise," IEEE J. Ocean. Eng. **28**, 446–453 (2003).
[3]C. S. MacInnes, "Source localization using subspace estimation and spatial filtering," submitted IEEE J. Ocean. Eng. (submitted).
[4]H. Cox, R. M. Zeskind, and M. M. Owen, "Robust adaptive beamforming," IEEE Trans. Acoust., Speech, Signal Process. **35**, 1365–1376 (1987).
[5]A. Tolstoy, *Matched Field Processing for Underwater Acoustics* (World Scientific, Englewood Cliffs, NJ, 1993).
[6]E. K. Westwood, "Broadband matched-field source localization," J. Acoust. Soc. Am. **91**, 2777–2789 (1992).
[7]A. B. Baggeroer, W. A. Kuperman, and P. N. Mikhalevsky, "An overview of matched-field methods in ocean acoustics," IEEE J. Ocean. Eng. **18**, 401–424 (1993).
[8]*Full Field Inversion Methods in Ocean and Seismo-acoustics*, edited by O. Diachok, A. Caiti, P. Gerstoft, and H. Schmidt (Kluwer Academic, Dordrecht, 1995).
[9]A. Tolstoy, N. R. Chapman, and G. Brooke, "Workshop '97: Benchmarking for geoacoustic inversion in shallow water," J. Comput. Acoust. **6**, 135–150 (1998).
[10]N. R. Chapman, S. Chin-Bing, D. King, and R. B. Evans, "Benchmarking geoacoustic inversion methods for range-dependent waveguides," Phys. Lett. A **28**, 320–330 (2000).
[11]S. E. Dosso, "Quantifying uncertainty in geoacoustic inversion. I. A fast Gibbs sampler approach," J. Acoust. Soc. Am. **111**, 129–142 (2002).
[12]S. E. Dosso and P. L. Nielsen, "Quantifying uncertainty in geoacoustic inversion. II. Application to broadband, shallow-water data," J. Acoust. Soc. Am. **111**, 143–159 (2002).
[13]Z. Michalopoulou and U. Ghosh-Dastidar, "Tabu for matched-field source localization and geoacoustic inversion," J. Acoust. Soc. Am. **111**, 135–145 (2004).
[14]M. D. Collins and W. A. Kuperman, "Focalization: Environmental focusing and source localization," J. Acoust. Soc. Am. **90**, 1410–1422 (1991).
[15]E. K. Westwood, C. T. Tindle, and N. R. Chapman, "A normal mode model for acousto-elastic environments," J. Acoust. Soc. Am. **100**, 3631–3645 (1996).
[16]M. D. Collins and L. Fishman, "Efficient navigation of parameter landscapes," J. Acoust. Soc. Am. **98**, 1637–1644 (1995).
[17]W. H. Press, A. Teukolsky, W. T. Vetterling, and B. P. Flannery, *Numerical Recipes in FORTRAN: The Art of Scientific Computing* (Cambridge University Press, Cambridge, 1992), Sec. 7.8.
[18]H. Szu and R. Hartley, "Fast simuated annealing," Phys. Lett. A **122**, 157–162 (1987).
[19]R. J. Vaccaro and B. F. Harrison, "Optimal matrix filter design," IEEE Trans. Signal Process. **44**, 705–709 (1996).
[20]R. J. Vaccaro and B. F. Harrison, "Matrix filters for passive SONAR," in Proceedings of the ICASSP 2001 International Conference on Acoustics, Speech and Signal Processing, Salt Lake City, UT, May 2001.
[21]G. H. Golub and C. F. Van Loan, *Matrix Computations*, 3rd ed. (Johns Hopkins University Press, Baltimore, 1996).
[22]S. A. Stotts, "A robust spatial filtering technique for multisource localization and geoacoustic inversion" J. Acoust. Soc. Am., **118**, 139–162 (2005).
[23]E. A. Ridderman and D. Knobles, University of Texas at Austin (private communication).
[24]For bearings close to endfire of the array, the matrix filters have large sidelobes for frequencies not well sampled by the array elements because the spacing between array elements is greater than one half the wavelength.
[25]R. J. Vaccaro, A. Chetri, and B. F. Harrison, "Matrix filter design for passive sonar interference suppression," J. Acoust. Soc. Am. **115**, 3010–3020 (2004).

Reverberation effects in acoustical resonators used for bubble measurements

David M. Farmer
Graduate School of Oceanography, University of Rhode Island, Narragansett, Rhode Island 02882

Svein Vagle
Institute of Ocean Sciences, PO Box 5000, Sidney, British Columbia, Canada V8L4B2

Donald Booth
Autonetics, 5490 Sooke Road, Sooke, British Columbia, Canada V0S1N0

(Received 1 March 2005; revised 14 July 2005; accepted 4 August 2005)

Attention has recently been drawn to the potential for errors to arise in the classical interpretation of bubble behavior in a reverberant cavity. The bubbles contribute to the reverberant field and, in a reciprocal effect, their response is modified by it. These reverberant loading effects have been shown to be important in the case of a bubble placed in a reverberant cavity. Here, the related topic of reverberant loading in a parallel plate acoustical resonator within which the bubbles are randomly distributed is addressed. Calculations are carried out for random bubble distributions consistent with measured populations. It is shown that, although large reverberation effects do occur, these are confined to relatively narrow bandwidths. Only when these narrow bands coincide with the resonator harmonics are resonator measurements significantly affected. For the specific geometry used to measure ocean bubble populations, reverberation effects turn out to be small. Other resonator dimensions or designs, however, could lead to greater effects, and the calculations presented here emphasize the importance of properly evaluating the reverberation influence for any specific application. Procedures for implementing corrections are identified. © *2005 Acoustical Society of America.* [DOI: 10.1121/1.2047148]

PACS number(s): 43.30.Xm, 43.20.Ks, 43.20.Ye, 43.30.Ft [WMC] Pages: 2954–2960

I. INTRODUCTION

The freely flooding acoustical resonator (Farmer, Vagle, and Booth, 1998) is one of several devices that allows measurement of bubble-size distributions through inversion of the bulk acoustic properties of the fluid. A reverberant cavity between two parallel plates (see Fig. 1) is ensonified with broadband noise, producing multiple resonant modes that are detected with a hydrophone. Excitation of the bubbles modifies the bulk complex sound speed of the fluid, leading to attenuation and frequency changes of the resonator response. The broadband sensitivity of the resonator allows incorporation of both the resonant and off-resonant contributions to acoustic properties over a wide frequency range, providing data that may be inverted to recover the distribution of bubbles of different sizes within the cavity. The instrument operates at low signal intensity, justifying application of linear acoustical theory to the inversion. Quasicontinuous transmission of sound into the cavity avoids uncertainties in the time-dependent acoustic response of bubbles to short pulses; multiple reflections of the reverberant signal increase the effective signal-to-noise ratio of the detection.

Farmer, Vagle, and Booth (1998) provide a rather detailed mathematical analysis of the resonator operation. However, in common with the implementation and analysis of other bubble-sensing techniques that rely on the bulk acoustic properties of the medium, the analysis includes an important simplification. Specifically, it is assumed that the formulations based on the work of Minneart (1933) can be applied without accounting for effects due to the presence of reflecting surfaces. That is, we assume that although the detected signal is attenuated and suffers a change in sound speed due to the bulk summation of single-scatter bubble effects, the resonant response of individual bubbles may be calculated on the basis of free-field conditions. Conversely, it is also assumed that the contribution of each individual bubble to the source field is negligible. Leighton *et al.* (1998) showed that, when a bubble is placed in a pipe, its resonant frequency is changed from the free-field value, thus raising the interesting possibility that the free-field approximation may not be generally valid within a resonant cavity. The problem was further explored both theoretically and experimentally by Leighton *et al.* (2002) for the case of a bubble within a rectangular cavity. These prior studies emphasize the necessity for proper consideration of reverberant loading effects when inverting acoustic measurements to recover bubble populations.

It is the purpose of this paper to examine the corresponding problem for the freely flooding acoustical resonator. Specifically, we explore the implications of the reverberation effects on bubble resonance identified by Leighton *et al.* (1998, 2002) for accurate measurement of bubble-size distributions. Leighton *et al.* used the applicable Green's function (Morse and Ingaard, 1986) to derive the reverberant effects. In the present case we need to calculate the effects of a random field of scatterers, requiring a stochastic description of bubbles, each of which contributes to, and is affected

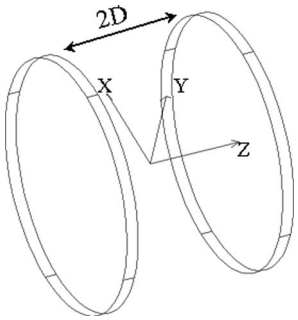

FIG. 1. Schematic diagram of the acoustical resonator showing the two circular steel plates separated by a distance $2D$. The coordinate system used in the numerical simulations has origin on the axis of the plates, halfway between them with the z component pointing along the axis.

by, the reverberant field. Multiple scattering must be considered both between the bubbles and also for successive reflections within the resonator cavity.

II. SIMULATION

The resonator exploits the modification of the complex sound speed caused by the presence of bubbles lying between the two resonator plates. Broadband noise is transmitted into the cavity between the plates, and the resulting signal is detected with a hydrophone consisting of an acoustically sensitive PVDF sheet covering one of the plates. The white noise excites resonant modes between the plates and is detected with the hydrophone. The sound speed and attenuation due to the bubbles reduces the amplitude and slightly shifts the frequency of the resonant peaks. These effects may be inverted to recover the original bubble population.

Instead of restricting attention to the bulk properties of the medium, we now examine the contributions from, and influence on, individual bubbles. Consider the signal received at a point (x_0, y_0, D) on the receiving plate due to all of the scatterers as well as their reflections at the resonator plates. Signals are received both directly from a bubble, and also indirectly from one or more reflections in the plates. We make no distinction in what follows between a bubble and its multiple reflections, treating each as a distinct and separate entity. We need to sum over the signals received from each bubble and each reflected image bubble, recognizing that in addition to scattering losses due to the presence of bubbles lying along the propagation path, there are also losses associated with each reflection and losses through the open boundaries which reduce the effective quality factor of the resonance, as discussed in detail by Farmer, Vagle, and Booth (1998). In practice, these losses limit the total number of reflections that need to be incorporated in any practical calculation. In the following derivation, it is assumed that the origin (0,0,0) of the coordinate system is at the center of the resonant cavity, halfway between the two plates (Fig. 1). This makes the derivation of reflections from the two plates symmetrical. Thus, the plate spacing is assumed to be $2D$. Furthermore, we assume that the resonant forcing field in the cavity is fully stabilized and can be represented by

$$G\cos(k(D+z)+\omega t), \tag{1}$$

where

$$G=\frac{\cos(kD)}{\sqrt{1+|\gamma|^4-2|\gamma|^2\cos(\xi_0-\xi_k)}} \tag{2}$$

is the field distribution function in the resonator for angular frequency ω, k is the complex wave number at sound speed c, and z is the distance perpendicular to the plates. The term $\xi_0-\xi_k$ is the difference in modal frequencies of the resonator, and

$$\gamma=\exp(-2Dk_{\mathrm{im}}) \tag{3}$$

is the absolute value of the complex eigenvalue determining the resonance characteristics of the resonator cavity, with k_{im} being the imaginary part of the complex wave number (see Farmer, Vagle, and Booth, 1998, for detailed description).

When bubbles are randomly distributed in the resonant cavity at positions (x_i, y_i, z_i) and exposed to the resonant field (1), the resulting pressure field P at our observation point (x_0, y_0, D) is given by

$$P=p_0\sum_i \frac{\Re}{r_i}\sqrt{\frac{\sigma_s}{4\pi}}\exp(-k_{\mathrm{im}}r_i) \times G\cos(k(D+z_i+r_i+\varphi_i)+\omega t), \tag{4}$$

where r_i is the distance between a bubble at (x_i, y_i, z_i) and the observation point (x_0, y_0, D) or the distance between one of its reflections in a plate boundary of the resonator and the observation point, φ_i, is the acoustic phase change occurring at any boundary (taken as zero if there are no reflections), σ_s is the scattering cross section of the bubble, p_0 is the transmitted signal, and $\Re$ is the frequency-dependent reflectivity coefficient of the resonator plates. The total pressure P_{tot} at the point (x_0, y_0, z_0) consists of the sum of the driving field (1) and the bubble-generated pressure field (4)

$$P_{\mathrm{tot}}=p_0\left[G\cos(k(D+z_0)+\omega t)+\sum_i a_i\cos(\phi_i+\omega t)\right], \tag{5}$$

where

$$a_i=\frac{\Re\exp(-k_{\mathrm{im}}r_i)}{r_i}\sqrt{\frac{\sigma_s}{4\pi}}, \tag{6}$$

and

$$\phi_i=k(D+z_i+r_i+\varphi_i). \tag{7}$$

Equation (5) can be reduced to the form

$$P_{\mathrm{tot}}=p_0B\cos(\omega t+\Phi), \tag{8}$$

where a is generic and not to be confused with the a used in Leighton *et al.* (1998), Eqs. (42), (43), and

$$B=G\sqrt{\left(\cos(\eta_0)+\sum_i a_i\cos(\phi_i)\right)^2+\left(\sin(\eta_0)+\sum_i a_i\sin(\phi_i)\right)^2}, \tag{9}$$

$$\eta_0 = k(D + z_0), \tag{10}$$

and

$$\tan(\Phi) = \frac{\left(\sin(\eta_0) + \sum_i a_i \sin(\phi_i)\right)}{\left(\cos(\eta_0) + \sum_i a_i \cos(\phi_i)\right)}. \tag{11}$$

Inclusion of the reverberant field will modify the free-field "Minneart" resonant frequency of any particular bubble (Leighton *et al.*, 2002) such that

$$\frac{\omega_0}{\omega_{0f}} \approx \frac{1}{\sqrt{1 + \sum_i a_i \cos(\phi_i)}}, \tag{12}$$

where the subscript f represents the free-field quantity. This ratio is subsequently referred to as the reverberant frequency correction. Leighton *et al.* (2002) also derived a reverberant damping correction

$$\frac{\delta}{\delta_f} = 1 + \sum_i a_i \sin(\phi_i), \tag{13}$$

where δ is the damping coefficient in the presence of the reverberant field and δ_f is the corresponding free-field damping coefficient, proportional to the real part of the total acoustic impedance presented to a particular bubble in free space.

III. RESULTS

Calculations were carried out using measurements acquired with the resonator described by Farmer, Vagle, and Booth (1998). Bubble populations were obtained at a depth of 1 m in the Gulf of Mexico, during an extended deployment that included a storm. The sample size distributions used in our subsequent calculations are derived from 0.5-s averages and are selected from a 65-s period, during passage of a bubble cloud, when the wind speed was approximately 10 ms^{-1}. Measurements were also acquired from deeper instruments, but as shown subsequently, the potential for error due to the reverberant effect increases with bubble concentration, and the concentrations used here approach the maximum at which reliable, single-scatter inversions are achieved (void fraction of $\sim 5 \times 10^{-5}$). We are concerned here with an upper bound to the reverberant contribution.

Figure 2 shows an example of the bubble-size distribution evaluated using the method described in Farmer, Vagle, and Booth (1998), expressed both as number density [Fig. 2(a)] and as volume conserved density (bubble-size distribution scaled by the bubble volume at each radius) [Fig. 2(b)] as functions of bubble radius. The reverberant effects discussed below were not included in the inversion used to derive this population. However, it will become apparent that the bias due to these effects is minor, and the resulting bubble populations provide a reasonable starting point for considering reverberant effects.

As predicted by Garrett, Li, and Farmer (2000), the volume-conserving distribution exhibits a prominent peak at ~ 160 μm, corresponding to a resonant frequency of ~ 20 kHz. This is apparent in the corresponding relative spectral intensity measured by the resonator shown in Fig. 3.

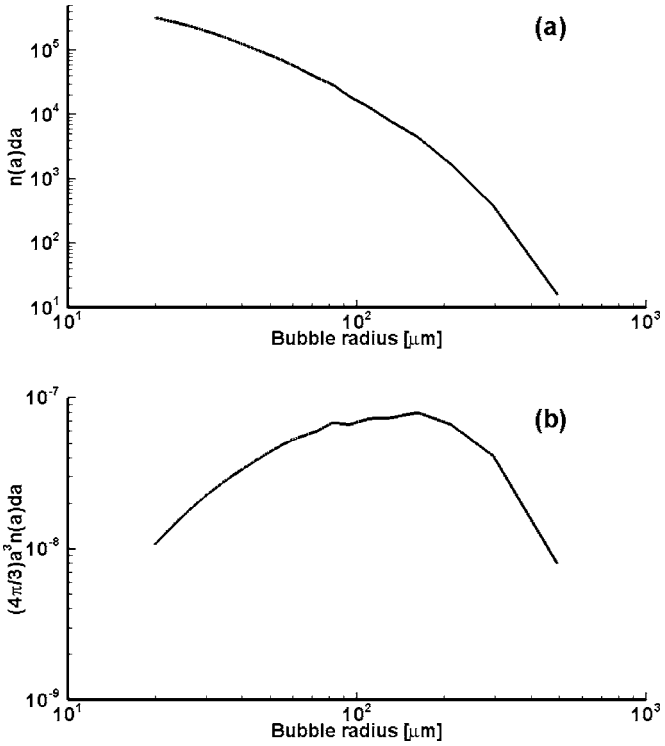

FIG. 2. (a) Sample bubble-size distribution in number of bubbles per unit volume per 1-μm radius increment and (b) volume-scaled bubble-size distribution measured at a depth of 1 m in the Gulf of Mexico during a storm. The corresponding resonator spectrum is shown in Fig. 3(b).

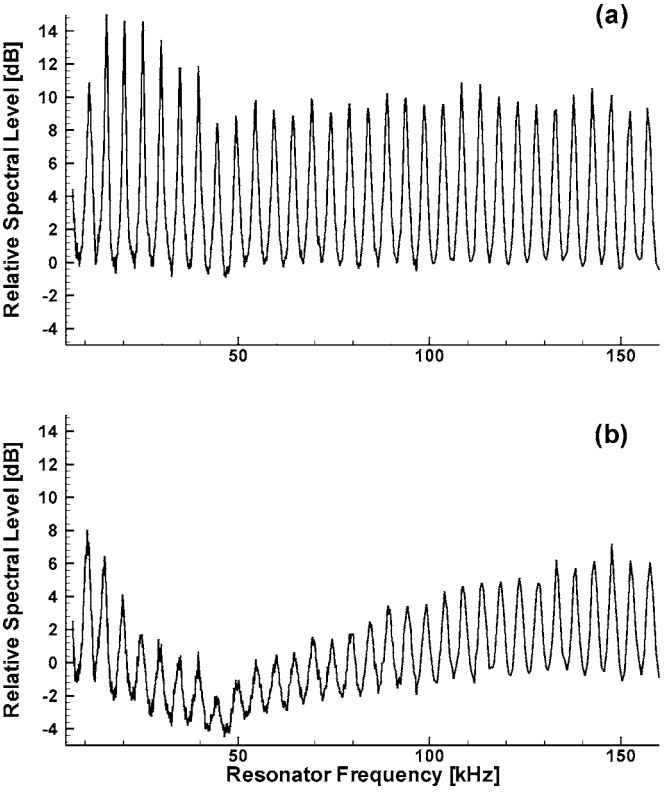

FIG. 3. Resonator response function (a) in the absence of bubbles and (b) with bubbles present.

Figure 3(a) shows the spectral response in the absence of bubbles. This response varies significantly over the total range, with a minimum sensitivity at 45 kHz and maximum at ~15 kHz. In the presence of bubbles, all of the spectral peaks are depressed. Figure 3(b) shows the response during passage of a fairly dense cloud of bubbles corresponding to the bubble distribution given in Fig. 2. The bubbles attenuate the measured signal, causing the height of the peaks to decrease and the valleys between the peaks also to be reduced. Only the peak heights are used in the inversion, although small shifts in peak frequency provide additional information that can be useful, as described by Farmer, Vagle, and Booth (1998). The greatest decrease of approximately 12 dB occurs at 25 kHz. At 45 kHz the spectral peak in Fig. 3(b) is smaller, but this is just a consequence of the lower sensitivity at this frequency.

A test of the validity of the discrete scatter calculation was made by deriving the expected absorption of a monotonic acoustic signal propagating through a given bubble distribution and comparing it with the bulk formula. The selected bubble distributions are described in more detail below. The calculation leads to some statistical uncertainty, but the discrete calculation agrees with the bulk formula subject to deviations of ~10%. Bubbles do not respond instantaneously to an imposed signal, but gradually adjust to the ambient driving signal over a time of order Q breathing cycles, where Q is the quality factor of the bubbles at resonance. This depends on the bubble radius, but for the worst case is $\sim 1.5 \times 10^{-3}$ s, which is much less than the instrument's insonification period of 0.2 s and is therefore unlikely to be a significant factor in the response. For the propagation and reflection losses applicable here, a maximum of eight reflections was found to provide accurate results, and this number has been used throughout.

The calculated signal intensity at a given bubble is singular in the pathological case where the signal is received from another bubble that is spatially coincident. This special case is easily avoided in the simulation, but, more generally, calculations of this sort normally exclude bubbles lying within a few bubble radii of each other. However, this is unduly restrictive, as may be shown by a 3D calculation of bubble distributions relevant to the present problem. Calculations with exclusion zones of various distances around each bubble caused no noticeable difference, and for completeness we incorporate all values in the final results. Large values for small separations are so rare that they are lost in the overall summation. The calculations were carried out with a random distribution of bubbles, with the bubble density similar to the observed bubble density. The representative observed bubble distribution was divided into radius increments of 1 μm and the corresponding bubble density used to generate a random distribution of bubbles within the resonator cavity. This was carried out for each radius increment to generate a representative bubble distribution. A number of different random number generators were used with different random number sources. There was no significant difference between their outputs. To ensure a uniform distribution between the plates, three axial coordinates were obtained for each bubble and the resulting point tested to make sure that it was within the resonant cavity. Distributions were calculated 1000 times and the results averaged.

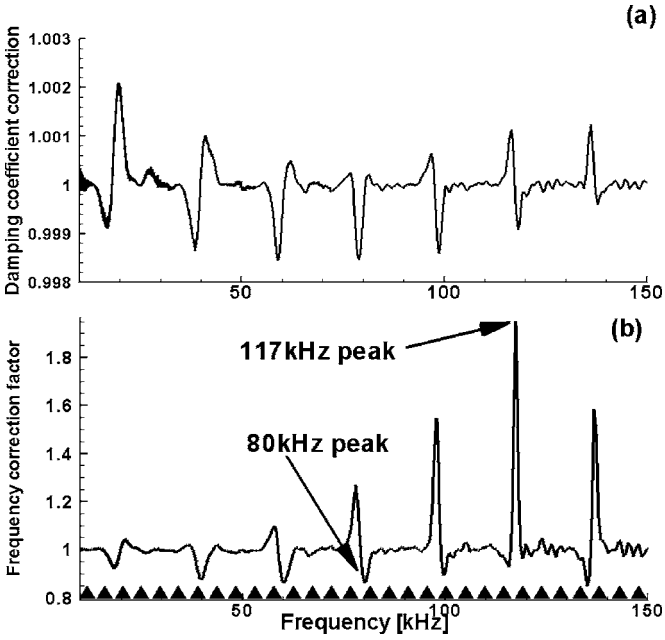

FIG. 4. (a) Multiplicative damping correction defined in (12) associated with reverberation effects. (b) Reverberation-induced frequency correction factor. The triangles along the bottom of the figure identify the location of the resonator frequency response peaks.

Figure 4(a) shows the reverberant damping correction factor defined in (12) for the sample bubble population of Fig. 2(a) derived from (12). This multiplicative correction is of order 1.002. This is much smaller than the damping found by Leighton *et al.* (1998). Factors that could affect the damping include the open-ended geometry of the resonator, which significantly reduces the Q factor especially at lower frequencies, and the higher frequencies involved. These low damping factors are not explicitly included in the subsequent analysis. However, it must be emphasized that designs that differ from the present one might have completely different reverberant loading responses which would need to be calculated in each case. The reverberant frequency correction [Fig. 4(b)] derived from (11) can be much greater, up to a factor of 1.9 for the largest peak at ~117 kHz. The dominant corrections are greater than unity, but corrections less than unity also occur, for example at 80 kHz in Fig. 4(b). Although the dominant corrections are large, they occur over relatively narrow bandwidths. Their potential impact can only be evaluated by considering their location relative to the resonator peaks used in the bubble inversion. At this point, it appears that a straightforward exclusion of resonator peaks coinciding with these discrete narrow-band error peaks might suffice to avoid problems; however, we explore the implications more closely for the two representative error peaks identified in Fig. 4(b).

Figure 5 shows expanded views of both the reverberant frequency corrections for these two examples together with the resonator response. The reverberant frequency correction at 80 kHz, which has a value of 1.25, occurs to the right of the 78-kHz resonator peak. At the resonator response peak

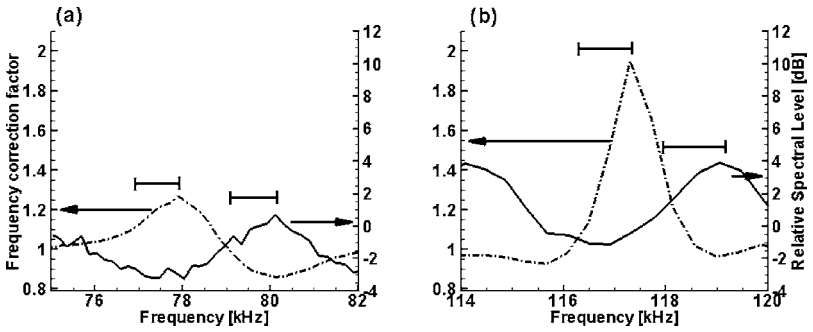

FIG. 5. Expanded view of frequency correction factor and resonator response at frequencies between (a) 75 and 82 kHz and (b) 114 and 120 kHz. Dashed line: Reverberation frequency correction factor with corresponding scale to the left. Solid line: resonator response for the given bubble population with corresponding scale to the right. Horizontal bars above frequency correction and resonator response peaks indicate the shifts in these curves that result from measured variations in bubble concentration as the resonator passes through the bubble cloud.

the reverberant frequency correction is 0.85. In Fig. 5(b), the large positive reverberant frequency correction at 117.5 kHz occurs in the resonator response valley to the left of the 119-kHz peak. At the peak of the resonator response the frequency correction is approximately 1.1.

These two examples illustrate the way in which the precise shape and location of the reverberant frequency correction need to be taken into account when evaluating its significance to bubble measurements, which are based on the height of the resonator peaks. Large reverberant frequency corrections could have a significant impact on bubble inversions if they coincide with the resonator peaks, but may otherwise exert only a modest influence.

The locations of both the resonator peaks and the reverberant frequency corrections change slightly with sound speed. The horizontal bars in Fig. 5 positioned above the reverberant frequency correction peaks and resonator response peaks illustrate the range of corresponding frequency shifts encountered with measured variations in bubble cloud density.

Figure 6 shows a time series of properties for the most extreme reverberant frequency correction, evaluated for a sequence of bubble populations during passage of a bubble cloud past the sensor. Note that we show values corresponding to the maximum reverberant correction, which is not located at a resonator response peak. Figure 6(a) shows the location (in frequency) of the maximum correction, which changes by about 2 kHz as the bubble cloud passes. Figure 6(b) shows the size of the reverberant frequency correction, which is approximately 2 for much of the time. The corresponding air fraction is given in Fig. 6(c).

A first-order correction can be applied to the data by noting that the bubble radius corresponding to any given resonator peak differs from that calculated for the free-field

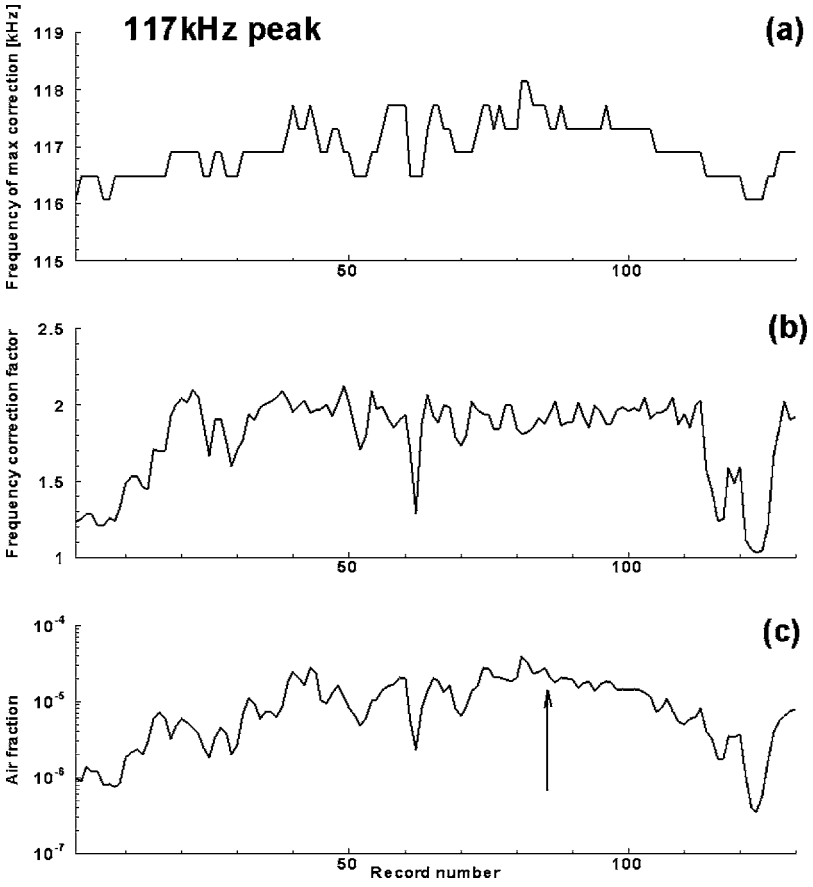

FIG. 6. Time series of reverberant frequency correction factor properties for the peak centered at around 117 kHz shown for the most extreme example of Fig. 4(b) during passage of a bubble cloud. Each record is separated by approximately 0.5 s. (a) Location in frequency of maximum correction. (b) Size of the reverberant frequency correction. (c) Air fraction derived from integration over all measured bubble sizes. Vertical arrow in (c) indicates location of individual measurement used in the preceding examples. Note that the properties shown here do not correspond to values occurring at the nearest resonator peak and are therefore not directly applicable to the bubble inversion.

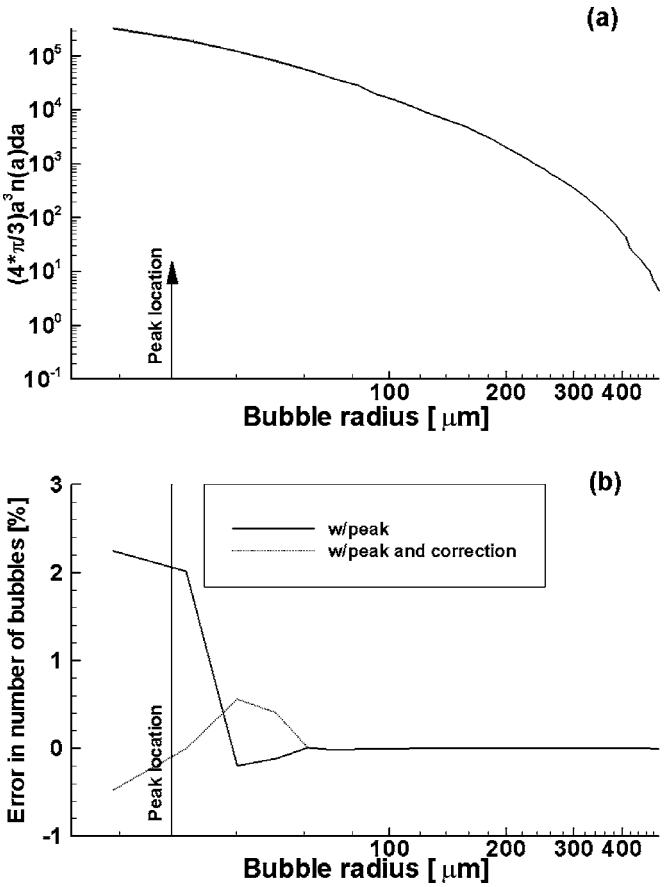

FIG. 7. First-order bubble density corrections for measurements corresponding to a single free-field resonance frequency of 117 kHz. (a) Uncorrected bubble distribution. Arrow shows radius corresponding to 117-kHz free-field bubble resonance. (b) Solid line: Percentage error due to effect of reverberant frequency shift of bubble resonance at the corresponding resonator peak. Dotted line: Percentage error after first-order correction.

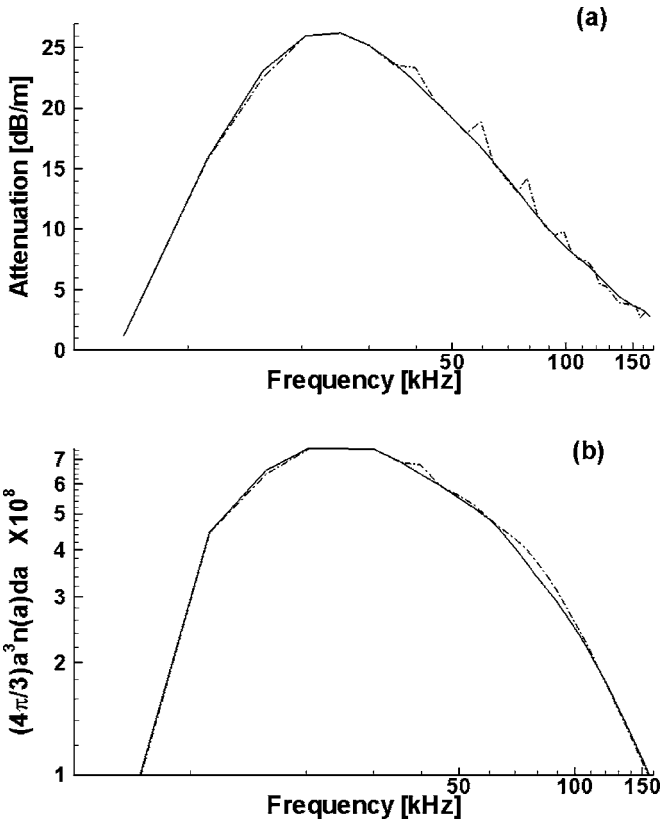

FIG. 8. Bubble inversions illustrating the effect of reverberant frequency corrections. (a) Solid line: Model attenuation curve representing a smooth approximation to measured attenuation as a function of frequency. Dashed line: Frequency shifted attenuation obtained by frequency shifting the corresponding attenuation values using the reverberant frequency corrections of Fig. 4(b). (b) Bubble populations found by inverting the original and corrected attenuation curves of (a).

bubble resonance. For the data used in Fig. 4(b), the corresponding frequency shift is evaluated and can therefore be applied to each resonator peak accordingly. Strictly, this should be interpreted as the first step in an iterative procedure, with the bubble-size distribution being updated at each step, but for the resonator geometry used here the corrections turn out to be small. This is illustrated for bubble density estimates corresponding to a single free-field resonance frequency of 117 kHz in Fig. 7. Figure 7(a) shows the bubble population without correction. Figure 7(b) shows the percentage error in bubble population obtained at the bubble radius having a free-field resonance coinciding with the nearest resonator peak at 117 kHz, before and after the first-order correction. The error is approximately 2% over the bandwidth corresponding to the resonator peak separation, reducing to ±0.5% after correction.

It might seem surprising that the quite large reverberant frequency correction identified in Fig. 4(b) results in such a small error. This is partly due to the fact that the reverberant frequency corrections have a fairly narrow bandwidth and do not coincide with the resonator peaks, and partly to the fact that the volume-scaled bubble population is quite flat at this radius, so that a frequency shift in bubble resonance frequency is proportionately less important. A given correction would be more important at lower frequencies, corresponding to steeper portions of the bubble spectrum, and for strongly peaked distributions. However, the corrections are much smaller at lower frequencies (see Fig. 4).

We can gain insight as to the overall magnitude of the errors in a different way. If we start with a smooth attenuation function representative of a measured population, and apply the reverberant frequency corrections of Fig. 4(b), we derive a modified attenuation function [see Fig. 8(a)] corresponding to the expected measurement. Note the noisy character relative to the initial function. We may then invert this attenuation function to recover a "corrected" bubble spectrum and compare it with the corresponding spectrum derived from the initial model attenuation curve. The two spectra [Fig. 8(b)] are essentially indistinguishable, given the natural variability of bubble populations. Previously published bubble-size spectra acquired with the resonators described here have not incorporated the corrections indicated above. Errors comparable to the fluctuations seen in Fig. 8 would be present in these results. While discrepancies should be noted, it does not appear that they are significant in this case, given the very large variability of bubble populations. It should also be pointed out that small variations in resonator response tend to be smoothed out by Commander and

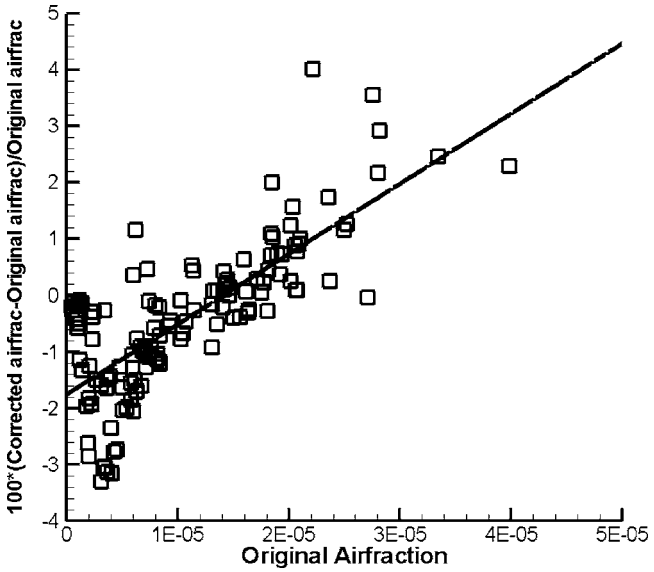

FIG. 9. Comparison of air fraction integrated over all measured bubble radii before and after first-order correction for reverberant effects. The data correspond to the time series illustrated in Fig. 6. Solid line is a least-squares fit. Note that errors are always within 4% for this particular resonator design.

McDonald's (1991) inversion approach, which we have used. Alternative inversions may be much more sensitive to small discrepancies.

Finally, we compare the air fraction integrated over the measured bubble population for the observations used in Fig. 6, with the air fraction derived from the first-order correction in which the bubble radius corresponding to each peak is shifted according to the reverberant loading value calculated from the model. This correction is carried out for all resonator peaks, and the scattering model has been run separately for each measurement in the time series. The comparison is shown in Fig. 9. The results display some variability, with a positive trend having an origin at an air fraction of 1.5×10^{-5}, but everywhere the correction is less than 4%.

In practice, this correction procedure is computationally heavy, since the full model must be run for each sample. If corrections are more significant than in the present case and need to be included in the data analysis, a practical approach is to delete those resonator peaks, which are significantly affected by the reverberation-induced modification of bubble resonance. We note that the reverberant effects for both damping and frequency shifts are essentially colocated (Fig. 4), so that removing a resonator peak from the inversion would avoid both types of error. For the resonator dimensions we have used, the effects are modest, but this result is entirely fortuitous and can in no way be generalized to other geometries. Careful calculation along the lines indicated appears to be necessary for any specific resonator design, so as to ensure that the results are not subject to significant bias.

IV. CONCLUSIONS

The effects of the reverberation field on resonance of bubbles in a cavity have been investigated using a numerical model and resonator measurements acquired in the Gulf of Mexico. The reverberation can induce large shifts in resonance frequency within a set of confined bands in the spectrum. Unless the resonator peaks coincide with large values in the reverberation effect, however, the impact on bubble measurement is modest. This is the case for the particular resonator geometry and dimensions that we have used. However, reverberation effects can occur even if the resonator and reverberation peaks do not coincide. A procedure for estimating errors and implementing corrections has been described. Errors for the largest reverberation peaks caused errors in the calculated bubble spectrum at the corresponding resonant bubble radius of around 2%, reducing to 0.5% with a first-order correction. Errors in air fraction integrated over the measured bubble spectrum showed errors that were always less than 4% for our specific resonator design. Given the natural variability in bubble populations, these errors can be considered minor. An alternative correction procedure involves deleting data from the few resonator peaks found subject to reverberation effects.

It cannot be too strongly emphasized that, although the particular resonator dimensions we have adopted led to quite minor reverberation loading effects on derived bubble populations, this result cannot be assumed to apply to other designs or dimensions. Different geometries and dimensions could lead to closer coincidence of error peaks with resonator peaks, with correspondingly greater effects on the inversion. Our calculations illustrate that the reverberation effect identified by Leighton *et al.* (1998) should be considered for any bubble measuring system in which free-field resonance is inhibited by the presence of reflecting boundaries.

ACKNOWLEDGMENTS

This work was supported by the U.S. Office of Naval Research. We are grateful to Dr. T. Leighton (Southampton University) for drawing our attention to the potential effects of reverberation on bubble resonance characteristics, for making available to us a preprint of his, work and for insightful comments. We also acknowledge valuable comments and corrections by Dr. H. Medwin.

Commander, K. C., and McDonald, R. J. (**1991**). "Finite-element solution of the inverse problem in bubble swarm acoustics," J. Acoust. Soc. Am. **89**, 592–597.

Farmer, D. M., Vagle, S., and Booth, A. D. (**1998**). "A free flooding acoustical resonator for measurement of bubble size distributions," J. Atmos. Ocean. Technol. **15**(5), 1132–1146.

Garrett, C., Li, M., and Farmer, D. (**2000**). "The connection between bubble size spectra and energy dissipation rates in the upper ocean," J. Phys. Oceanogr. **30**, 2163–2171.

Leighton, T. G., Ramble, D. G., Phelps, A. D., Morfey, C. L., and Harris, P. P. (**1998**). "Acoustic detection of gas bubbles in a pipe," Acta Acust. (Beijing) **84**, 801–814.

Leighton, T. G., White, P. R., Morfey, C. L., Clarke, J. W. L., Heald, G. J., Dumbrell, H. A., and Holland, K. R. (**2002**). "The effect of reverberation on the damping of bubbles," J. Acoust. Soc. Am. **112**(4), 1366–1376.

Minneart, M. (**1933**). "On musical air-bubbles and sounds of running water," Philos. Mag. **16**, 235–248.

Morse, P. M., and Ingaard, K. U. (**1986**). *Theoretical Acoustics* (Princeton University Press, Princeton, NJ), pp. 500–503.

Acoustic signals of underwater explosions near surfaces

John R. Krieger and Georges L. Chahine
Dynaflow, Inc., 10621-J Iron Bridge Road, Jessup, Maryland 20794

(Received 12 November 2004; revised 13 July 2005; accepted 4 August 2005)

Underwater explosions are conventionally identified and characterized by their seismic and/or acoustic signature based on spherical models of explosion bubbles. These models can be misleading in cases where the bubble is distorted by proximity to the free surface, the bottom, or to a solid object. An experimental and numerical study of the effects of various nearby surfaces on the bubble's acoustic signature is presented. Measurements from high-speed movie visualizations and acoustic signals are presented which show that the effect of proximity to a rigid surface is to increase the first period, weaken the first bubble pulse, and affect significantly the second period, resulting in a peak value at standoffs of the same order as the maximum bubble radius. These results are compared to results under a free surface, over a bed of sand, and over a cavity in a rigid surface. In all cases, the first period is increasingly lengthened or shortened as the motion of fluid around the bubble is increasingly or decreasingly hindered. The effect of bubble distortion is to weaken the first bubble pulse and increase the bubble size and the duration of the second cycle. © *2005 Acoustical Society of America.* [DOI: 10.1121/1.2047147]

PACS number(s): 43.30.−k, 43.30.Lz [WMC] Pages: 2961–2974

I. INTRODUCTION

Underwater explosions produce bubbles of gas and vapor that alternately expand and collapse, generating a train of acoustic pulses that propagates acoustically through the water, and seismically through the seafloor. The timing of these pulses can be used to determine the yield of the explosion, provided its depth can be estimated. In some cases, reverberations from the sea surface and ocean bottom provide information about the explosion depth (Baumgardt and Der, 1998). If the explosion is far from the free surface and the bottom and is otherwise unconstrained, the classic formula, as presented for example by Cole (1948), serves to define the "bubble pulse" period (T in seconds) in terms of the explosive yield (W in pounds), its depth (Z in feet), and a parameter ($K=4.25$ for TNT) characterizing the explosive

$$T = K\frac{W^{1/3}}{(Z+33)^{5/6}}. \tag{1}$$

The ability to assess the character of an underwater explosion (UNDEX) and estimate its yield and depth is important for a variety of reasons. For example, the use of explosives as underwater acoustic sources has a long and rich history (Weston, 1960). A common method of surveying ocean geoacoustic properties is to detonate calibrated charges and measure the propagated signal from acoustic sensors or arrays at various ranges (Potty *et al.*, 2004, 2003; Spiersberger, 2003; Godin *et al.*, 1999; Popov and Simakina, 1998). In addition, the bubble pulse signature is also vital in the context of nuclear test-ban verification (Weinstein, 1968), where a key issue is to distinguish an UNDEX from an underwater earthquake (Baumgardt, 1999) and in tracking dynamite fishing practices (Woodman *et al.*, 2003). Exploiting dynamite fishing explosions as sound sources of opportunity provides another motivation to this study (Lin *et al.*, 2004).

In all cases, erroneous conclusions result from the use of Eq. (1) if the explosion is near an obstacle, the bottom, or if it is partly contained. In particular, the bubble generated by an UNDEX can be severely distorted from the presumed spherical geometry by a nearby object or surface. This could result in "bubble pulse periods" that correspond to a yield substantially different from that predicted by Eq. (1).

Considerable efforts have been devoted to experimental and theoretical understanding of the physics of underwater explosions as sound sources. These attempts have typically used *ad hoc* models of bubble migration (Buratti *et al.*, 1999) or have been based on tests with actual full-scale explosives (Chapman, 1985, 1988; Hannay and Chapman, 1999). This paper presents controlled scaled laboratory tests to define the multicycle motion and geometry of the explosion bubble, and compares with a sophisticated numerical simulation based on the dynamics of bubbles near boundaries. Quantitative results (in particular, depths and time of acoustic radiations) that are most important for defining impulse point sources of acoustic propagation are presented. Section II describes the basic physics, Sec. III describes the experimental and numerical conditions of the study, Sec. IV presents the results of the study, and Sec. V provides a discussion of these results in terms of characterization of explosions.

II. BACKGROUND

The detonation of an explosive charge underwater results in the emission of a shock wave and the creation of a high-pressure gas and vapor bubble. The shock wave constitutes the first of a series of acoustic pulses detectable at long ranges, and the remaining bubble pulses are generated by the subsequent motion of the bubble. The pressure of the bubble initially causes it to expand, but inertia of the liquid carries the bubble past its equilibrium point, causing it to overexpand, and then collapse again. The final stages of the collapse are quite violent, and return the bubble nearly to its original state, generating large pressures and another acoustic

pulse. The bubble then begins the cycle again and continues until it has broken up and its energy has been dissipated.

The shock and subsequent bubble pulses radiate sound as point- or compact impulsive sources at different depths and times. While boundaries affect the sound propagation from a point source in well-understood ways, the problem of how the boundaries affect the multicycle motion of the bubble acoustic source is the focus of this paper.

A. Numerical model

Following an underwater explosion detonation, and after a very short period of time where compressible effects are important, the characteristic liquid velocities become small compared to the velocity of sound, enabling one to neglect the liquid compressibility. Similarly, viscous effects can be neglected and one can consider the water flow field as potential, with $\mathbf{u}=\nabla\Phi$, where $\mathbf{u}$ is the liquid velocity vector and $\mathbf{\Phi}$ is the velocity potential. $\mathbf{\Phi}$ satisfies Laplace's equation in the fluid domain, D

$$\nabla^2\Phi(\mathbf{x},t)=0, \quad x\in\mathcal{D}, \tag{2}$$

where $\mathbf{x}$ is the spatial variable and t is time (Chahine and Perdue, 1989). On the bubble surface S_b, of local normal, $\mathbf{n}$, Φ satisfies the kinematic boundary condition, which expresses equality between the fluid and the free-surface normal velocities

$$d\mathbf{x}/dt\cdot\mathbf{n}=\nabla\Phi\cdot\mathbf{n}, \quad \mathbf{x}\in S_b, \tag{3}$$

and the dynamic boundary condition

$$\frac{\partial\Phi}{\partial t}=-\frac{1}{2}|\nabla\Phi|^2+\frac{P_\infty-P_b}{\rho}-gz|_{x\in S_b}, \tag{4}$$

where P_∞ is the hydrostatic pressure at the point of initiation of the explosion, $P_b(x,t)$ is the local pressure in the liquid at the bubble interface, and z is the vertical coordinate at point x.

The pressure inside the bubble is assumed spatially homogeneous, and the bubble content is assumed to be composed of noncondensable gas arising from the explosion products, which follow a polytropic compression law of constant k. These assumptions have been shown, for a wide range of free-field bubbles, to lead to an excellent fit between experimental data and numerical results (Chahine *et al.*, 1995). This leads to the following form of the normal stress boundary condition at the bubble interface:

$$P_b(\mathbf{x},t)=P_{g0}\left[\frac{\mathsf{V}(t)}{\mathsf{V}_0}\right]^k+P_v-\sigma\mathsf{C}, \tag{5}$$

where P_{g0} is the initial pressure of the noncondensable gas inside the bubble and P_v is the water vapor pressure. V_0 is the initial volume of the bubble, σ is the surface tension coefficient, and $\mathsf{C}(x_s,t)$ is twice the local mean curvature at x_s given by

$$\mathsf{C}=\nabla\cdot\mathbf{n}. \tag{6}$$

The local normal to the surface, $\mathbf{n}$, is defined as

$$\mathbf{n}=\pm\frac{\nabla f}{|\nabla f|}, \tag{7}$$

where f is the bubble surface equation. The appropriate sign is chosen so that the normals point towards the liquid.

In addition to conditions (3) and (4), the boundary condition on any nearby solid body S_t is given by

$$\frac{\partial\Phi}{\partial n}=u_n, \quad \mathbf{x}\in S_t, \tag{8}$$

where u_n is the local normal velocity of the solid body in response to the bubble loading. This includes body motion and deformation (Kalumuck *et al.*, 1995; Chahine and Kalumuck, 1998). At infinity, the fluid velocities due to the bubble dynamics vanish, and the boundary condition is

$$\lim|_{x\to\infty}|\nabla\Phi|=0. \tag{9}$$

To complete the description of the problem, appropriate initial conditions are used. At the initiation of the computation, and only at that instant, the bubble dynamics is assumed to be that due to a spherical explosion bubble in a free field. The Rayleigh–Plesset equation (Plesset, 1948) governing spherical bubble dynamics is used to obtain these initial conditions (i.e., a relationship between the initial bubble radius and the initial bubble wall velocity or gas pressure). This results in the following relationship between the initial bubble radius, R_0, and the initial gas pressure inside the bubble, P_{g0}, for $R_0=0$:

$$P_{g0}=\frac{3(1-k)}{1-\varepsilon_0^{3k-3}}\left[\frac{p_\infty-p_v}{3}(1-\varepsilon_0^{-3})+\frac{\sigma}{R_0}(1-\varepsilon_0^{-2})\right]; \quad \varepsilon_0=\frac{R_0}{R_{\max}}. \tag{10}$$

Thus, a closed system of equations is obtained to solve for Φ using Green's identity

$$\Omega\Phi(\mathbf{x})=\int_S\mathbf{n}_\mathbf{y}\cdot\nabla_\mathbf{y}\Phi(\mathbf{y})G(\mathbf{x},\mathbf{y})ds_y-\int_S\mathbf{n}_\mathbf{y}\cdot\nabla_\mathbf{y}G(\mathbf{x},\mathbf{y})\Phi(\mathbf{y})ds_y, \tag{11}$$

where $\mathbf{x}$ is selected on the boundary, $\mathbf{y}$ is an integration variable on the surface S, $\mathbf{n}_y$ is the normal to S, and

$$G(\mathbf{x},\mathbf{y})=\frac{1}{|\mathbf{x}-\mathbf{y}|} \tag{12}$$

is the Green's function. Ω is the solid angle subtended in the fluid at the point $\mathbf{x}$.

Equation (11) is an integral equation which relates the potential at any point $\mathbf{x}$ to the values of Φ and its normal derivatives on the boundary of the liquid domain, S. We can use Eq. (11) to determine at a given computation time the unknown quantities: Φ on solid surfaces and normal derivative of the potential, $\partial\Phi/\partial n$, on the free surface, knowing the normal velocities on the solid surfaces and the velocity potential on the free surface. To start the computations, we

know the potential on the initial bubble surface through ($\Phi = R_0\dot{R}_0$), and we assume a zero body velocity.

Once the flow variables are known at a given time step, values at subsequent steps can be obtained by integrating Eqs. (3) and (4), and using an appropriate time-stepping technique. The material derivative, $D\Phi/Dt$, is then computed using the Bernoulli equation (4), and noting that $\mathbf{u}=\nabla\Phi$

$$\frac{D\Phi}{Dt} = \frac{\partial\Phi}{\partial t} + \nabla\Phi\cdot\nabla\Phi = \frac{\partial\Phi}{\partial t} + |\mathbf{u}|^2. \tag{13}$$

This time stepping proceeds throughout the bubble growth and collapse, resulting at each time step in the knowledge of all flow-field quantities and the shape of the bubble.

This is the basis of the numerical method used in this paper and which has been extensively used and validated for both axisymmetric (Zhang *et al.*, 1993; Choi and Chahine, 2003) and three-dimensional interactions between UNDEX bubbles and nearby structures [e.g., Chahine and Perdue (1989); Chahine (1996); Chahine, Kalumuck, and Hsiao, (2003)].

B. Discussion and definitions for analysis

The acoustic bubble pulses, generated by the bubble volume and shape changes, may be treated theoretically primarily as a monopole radiation in the far field with strength dependent on the volume acceleration of the bubble, plus a dipole with strength dependent on the bubble migration, and higher-order poles dependent on its deformation.

In the absence of gravity effects or nearby objects, the bubble remains spherical in shape, and the period of its volume oscillations can be predicted analytically. Rayleigh (1917) analyzed the collapse of empty spherical cavities and found the time of collapse to be

$$T_{\text{collapse}} = 0.915 R_{\max}\sqrt{\frac{\rho}{P_\infty}}, \tag{14}$$

where $R_{\max}$ is the initial (maximum) radius of the cavity, and ρ and P_∞ are the density and pressure of the ambient fluid, respectively. This dependence of the period on the ambient pressure and the bubble size is another formulation of Eq. (1). The effects of vapor pressure, noncondensable gas, surface tension, viscosity, and a time-varying ambient pressure could also be included, to produce the Rayleigh–Plesset equation (Plesset, 1948), the equation of wall motion for a collapsing and rebounding spherical bubble. For given conditions, the period of the bubble oscillation can be predicted from the solutions of this equation.

If the explosion occurs near an object or at shallow depths where the effects of gravity are strong, the bubble collapses asymmetrically, resulting in reentrant jet and toroidal bubble formation, or if both effects are strong and in opposite directions, a pear shape and bubble splitting (Chahine, 1996, 1997), and the bubble does not produce the same series of pulses as it would in deep submergence and away from boundaries.

The effect of a nearby surface is quantified in terms of the normalized standoff distance

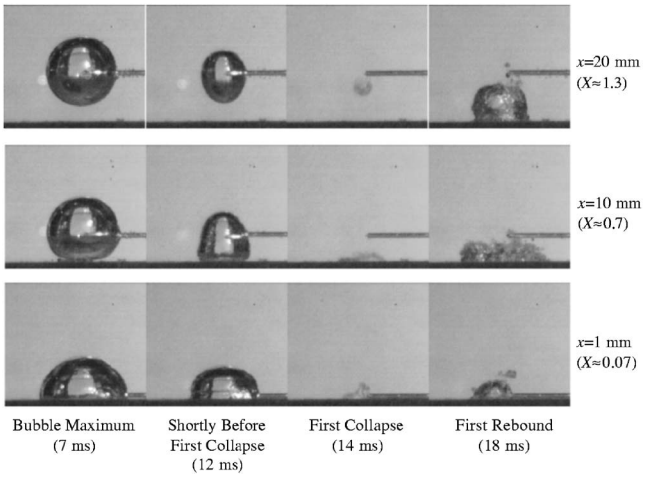

FIG. 1. Spark-generated bubbles over a rigid surface. Horizontally, four different times are shown—the time of the first volume maximum, just prior to the first collapse, the time of the first collapse, and the time of the second volume maximum—and vertically three different standoff distances are shown, with standoff distance increasing from bottom to top. The ambient pressure was approximately 60 mbar, and $R_{\max}$ was approximately 15 mm.

$$X = \frac{x}{R_{\max}}, \tag{15}$$

where x is the standoff distance, i.e., the shortest distance from the initial explosion center to the surface, and $R_{\max}$ is the maximum radius the bubble would achieve if the explosive were detonated in an infinite medium at the same depth.

For large values of the standoff parameter, the bubble is essentially spherical and unaffected by the boundary. As the standoff distance is reduced, the bubble becomes more and more affected by the boundary. At values near unity, the bubble nearly touches the surface on its first expansion, and at values near zero, the first bubble pulsation is quasihemispherical. Examples of this behavior for small-scale explosions generated by a spark in a water tank (Chahine *et al.*, 1995) are shown in Fig. 1.

The effect of buoyancy is quantified in terms of the Froude number (Chahine, 1997)

$$\mathrm{F} = \frac{P_\infty - P_v}{2\rho g R_{\max}}. \tag{16}$$

This parameter is the ratio of the difference between the ambient pressure at the charge location and the vapor pressure to the difference in pressure between the top and bottom of the bubble. It expresses the relative importance of the compressional force tending to collapse the bubble and the gravity force tending to deform and migrate the bubble upward. For large values of the Froude number, the effect of gravity is relatively weak, and the bubble remains spherical. For small Froude numbers, upward motion and bubble distortion due to gravity are important. This parameter is strongly responsible for differences between UNDEX bubble behaviors at different geometric scales. The Froude number (or the gravity acceleration term) does not appear explicitly in the equations, but the gravity term can be seen in the boundary condition (4) on the bubble and free-surface walls.

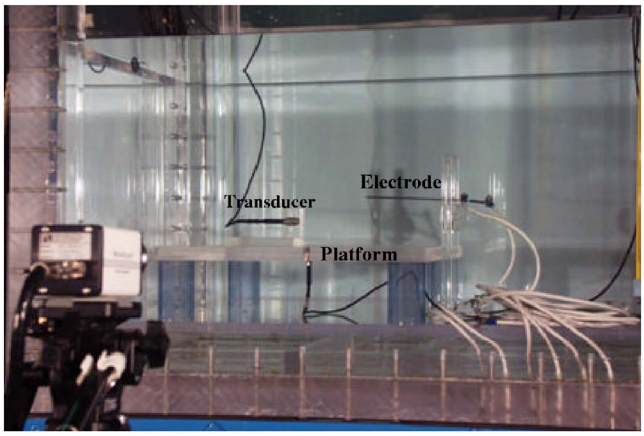

FIG. 2. The experimental arrangement for recording bubble dynamics near a rigid surface.

For problems of interaction between an UNDEX bubble and the ocean bottom, or an obstacle located below the bubble, gravity acts in an opposite direction than the bottom, i.e., it tends to force the bubble to have a reentrant jet moving upward, while the bottom induces a downward motion. This results, at small Froude numbers, in large differences in the bubble behavior between two different Froude number conditions for otherwise similar UNDEX conditions.

III. EXPERIMENTAL AND NUMERICAL ANALYSIS

A. Experimental methods

Bubbles generated by the underwater discharge of a high-voltage charge between two coaxial electrodes, exposed to each other at their ends and contained within a transparent vacuum cell, were used as laboratory-scale models of underwater explosions (Chahine *et al.*, 1995). The cell is $3\times3\times3$ ft.^{3} made of 1-in.-thick Plexiglas wall, which enables it to withstand reduced pressure down to 0.5 psi. By reducing the pressure in the cell, relatively large and slow-collapsing bubbles were generated, and the transparent walls allowed recording of the bubble dynamics by a high-speed digital camera (Redlake Imaging model PCI8000S). The acoustic signals of the bubbles were measured with a piezoelectric transducer having a 1-μs rise time (PCB Piezotronics model 102A03). A photograph of the experimental arrangement is shown in Fig. 2. Concerning the physics of the problem, the arrangement electrodes/nearby boundary is quite simple and is further illustrated in the bubble pictures in this paper, such as in Fig. 1. Note that the acoustic properties of the acrylic platform are close to those of water, making the reflection coefficient near zero over the relevant range of reflection angles. Furthermore, reflections from walls and other distant objects resulted in path lengths much longer than the straight-line path from bubble to transducer. Because of this, only the pulses propagating directly from the bubble to the transducer were strong enough to be detectable.

The energy of the bubble was controlled by adjusting the voltage supplied to the capacitor of the spark generator. The effects of the tank pressure and of the variations in the discharge output were removed from the data by measuring $R_{\max}$ and normalizing periods using a characteristic time (equal to the Rayleigh collapse time omitting the factor 0.915) as in Eq. (15). The bubble maximum radius is used to normalize the standoff distance, and is obtained by direct measurement from the video pictures corresponding to each signal. When the bubble was significantly distant from the bottom, it retained a spherical shape at maximum volume and a radius could easily be measured. In cases where the bubble was distorted by the presence of the nearby boundary, an equivalent radius, equal to the radius of a sphere of equal volume, was used. Simulations of identical initial bubbles at various distances show that the bubble achieves the same volume, within ±1%, at the time of its maximum growth regardless of the standoff distance, so that the equivalent $R_{\max}$ is a consistent measure of bubble size. The volumes of distorted experimental bubbles were calculated from the observed bubble outline at the time of maximum growth, as the volume of a solid of revolution around its vertical axis. The validity of the assumption of axisymmetry is supported by top views, which show circular profiles, and by the mirror symmetry seen in side views.

The ambient pressure was calculated based on the absolute pressure in the vacuum cell and the depth of the electrodes, and the vapor pressure was calculated based on the measured ambient water temperature. All times, t, and distances, r, were normalized using the quantities ρ, $R_{\max}$, and $P_{\text{amb}}-P_v$

$$\bar{t} \equiv \frac{t}{R_{\max}\sqrt{\dfrac{\rho}{P_{\text{amb}}-P_v}}}, \tag{17}$$

$$\bar{r} \equiv \frac{r}{R_{\max}}. \tag{18}$$

Although spark-generated bubbles are considerably smaller than typical explosion bubbles, surface tension and viscosity effects remain negligible, and the bubble dynamics is an accurate scaled representation of a full-scale case having the same normalized standoff and Froude number (Chahine *et al.*, 1995). Conversion between scales is accomplished using the characteristic length $l_{\text{charac}}=R_{\max}$ and the characteristic time $T_{\text{charac}}=R_{\max}(\rho/\Delta P)^{1/2}$, as above. Differences between various scaled results obviously exist if the Froude numbers, i.e., the relative influence of gravity, are not the same.

B. Error estimates

One of the principal sources of experimental uncertainties lies in the determination of $R_{\max}$ for each case, which affects both the normalized standoff distance and the normalized period. Repeated measurements for several different cases give a standard deviation of about 1% of the mean. In cases where an equivalent $R_{\max}$ was measured for the bubble at its second maximum, the standard deviation was about 4%, since the axisymmetric assumption probably introduces more significant errors in these cases. Vapor pressure is a function of temperature, and uncertainty in the temperature measurement led to errors of about 2% or less. The least significant digit on the pressure gauge is 1 mbar, or about

2% for low-pressure tests. For high-pressure tests, in which the bubbles are small, the dominant source of uncertainty lay in the measurement of standoff, which could have been as much as 10%. In the graphs presented here, it was decided to rely upon the scatter among a large number of data points as an indication of repeatability. One series of tests was conducted with each test repeated five times, which produced standard deviations in normalized period and normalized standoff of approximately 5%.

C. Numerical approach

DYNAFLOW's boundary element method code 2DYNAFS© (Choi and Chahine, 2003) was used to conduct simulations of bubbles under conditions matching those of the spark tests. 2DYNAFS© is based on the boundary element method described in Sec. II for solving potential flows with arbitrary boundaries, and calculates the motion of one or more interfaces in an axisymmetric geometry. Each interface is discretized in a meridional plane, each node is advanced at each time step using the velocities and the unsteady Bernoulli equation, and the new velocity potentials and normal velocities are calculated using a discretized version of Green's equation (Zhang *et al.*, 1993). In cases where a reentrant jet impacts the opposite wall of the bubble, the dynamic cut relocation algorithm of Best (1994) was used to continue computations with a new toroidal bubble. For laboratory-scale simulations, the initial conditions of the bubble were specified as the same ambient pressure as the corresponding experimental test, and an initially spherical explosion bubble with a radius and pressure such as to produce an R_{max} value of 1.3 cm, which is a typical value for the spark tests in the pressure range tested.

IV. RESULTS

A. Bubble dynamics near a rigid surface

Figure 3 shows an example series of pressure signals from bubbles generated by spark discharges at varying distances above a flat, rigid plate, with each signal offset vertically in the figure by an amount proportional to its corresponding standoff distance. The time has been normalized as in Eq. (15). Each signal contains initial strong fluctuations composed of a combination of the initial shock wave and electrical noise associated with the spark discharge, followed by two and sometimes three detectable peaks generated by the bubble collapses. Two principal differences among the signals can be observed. First, the timing of the first collapse pulses appears in general delayed for bubbles near the plate. Second, the first bubble pulse decreases in strength dramatically as the bubble approaches the plate.

For bubbles at moderate distances from a rigid surface, Chahine and Bovis (1983) have demonstrated, using matched asymptotic expansions for large X, that

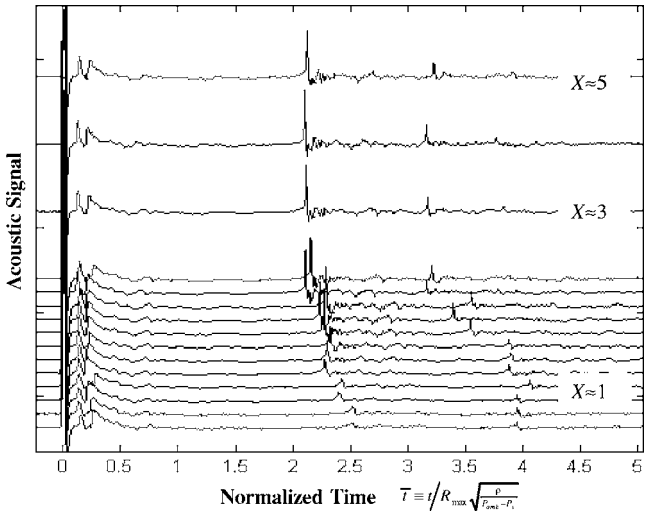

FIG. 3. Pressure signals from a spark-generated bubble with varying standoff distance. Signals were measured using a quartz pressure transducer several inches to one side of the bubble. The ambient pressure was 1 atmosphere and the maximum bubble radius about 6 mm. All signals have been offset vertically by an amount proportional to the respective standoff distance.

$$T^* \cong 1.83\left(1+\frac{1}{4X}\int_{R_0}^{R_{\max}} R(t)dt\right) \approx 1.83\left(1+\frac{0.79}{4X}\right), \tag{19}$$

where T^* is the normalized period of the bubble in the presence of the surface. This first-order approximation provides a useful theoretical comparison for moderate values of standoff distance, although it is not valid for small values.

In order to investigate the effects of proximity to a rigid boundary over the entire range of standoff distances, several series of spark tests were conducted using approximately constant energy but varying standoff distances, including a concentrated series of measurements for values of X less than 1, and these results were compared to the results from a series of simulations using 2DYNAFS©. The measured and calculated first bubble periods are shown in Fig. 4 along with a curve calculated from Eq. (19), and a correlation calculated from Eq. (20), presented below.

Both the measurements and the simulations agree with the predictions of the first-order asymptotic expansion (19)

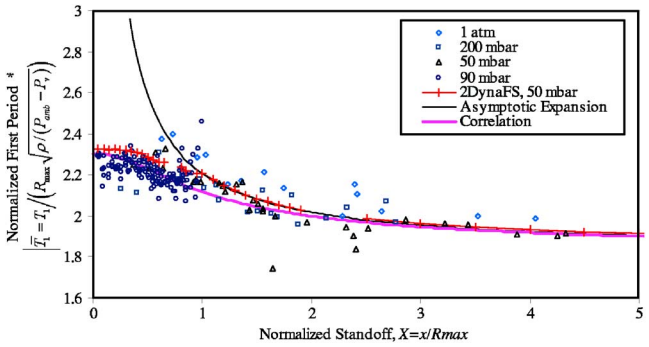

FIG. 4. First bubble period as a function of standoff distance. Experimental data were collected for several cell pressures, and simulations were conducted using an ambient pressure of 50 mbar plus a correction for depth, and an R_{max} value of 1.3 cm.

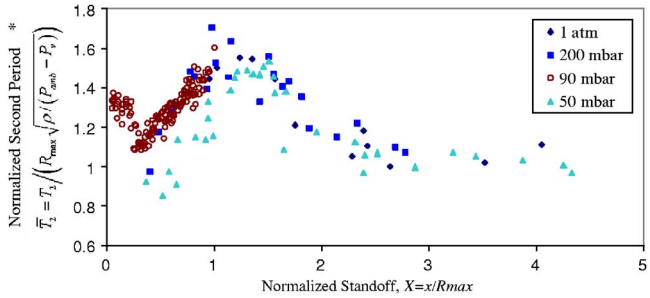

FIG. 5. Normalized second period as a function of standoff. Experimental data are shown from the same set of tests as in Fig. 4, normalized using Eqs. (17) and (18).

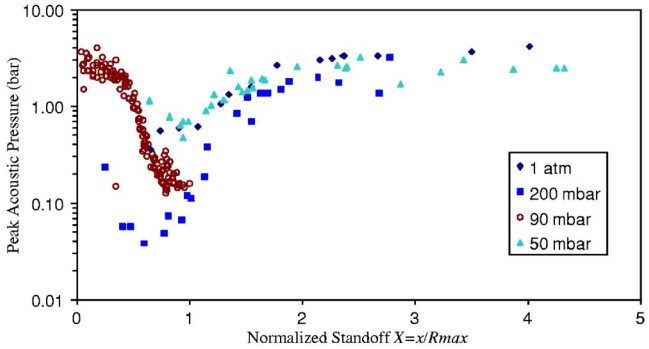

FIG. 6. First bubble pulse strength as a function of standoff. The maximum pressure recorded by the transducer 3 in. from the bubble during the first bubble pulse is shown from the same tests as in Fig. 4 and Fig. 5.

for values of X larger than 1, where the period is approximately twice the characteristic time, as expected. The contribution of this work is the description of a nonasymptotic region where larger bubble deformations occur. As the bubble nears the bottom, the period shows a steady gradual increase, up to a value at the bottom approximately 20%–25% greater than the "free" value. This increase is consistent theoretically with the additional energy due to an image bubble on the opposite side of the surface. If a hemispherical bubble is generated exactly at the surface, it will act with its mirror image as a single spherical bubble having twice the energy as the actual bubble, and according to the period–energy relation will have a period greater than the actual bubble if it were spherical by a factor of $2^{1/3}=1.26$. Thus, the theory predicts a normalized period of $2\times0.915=1.83$ for free bubbles, and with the image a period of $2\times0.915\times2^{1/3}=2.31$ for bubbles on a rigid surface. Both experimental measurements and numerical simulations using 2DYNAFS© agree with these extrema and show a steady progression in between, while, as expected, the asymptotic expansion (and the classical corrections) fails at the lower values of X.

A general analytic prediction of the bubble first period over all standoff distances is lacking. However, the empirical expression

$$T^* \cong 1.83\left(1+\frac{0.1975}{\sqrt{0.5776+X^2}}\right), \tag{20}$$

does a reasonably good job as a correlation, as shown in Fig. 4. This expression matches the theoretical values for $X=0$ and $X\to\infty$, and agrees with the asymptotic expansion formula for large X. It may be used to predict the period of an explosion bubble of any size near a large, flat, rigid surface, as long as the effects of buoyancy are not too strong, i.e., as long as the Froude number is above approximately 10. Similar expression could be derived for other values of F but were not attempted here.

The period of the second cycle, shown in Fig. 5, depends on the history of the bubble through the first cycle, and exhibits more variation with standoff than does the first period. The second period is normalized using the same characteristic time as the first period. At large standoff distances, the second period is nearly half that of the first cycle, which according to the period–energy relation for spherical bubbles, and for negligible migration, corresponds to an energy of $(\frac{1}{2})^3$ or 13% of the original energy, or an energy loss at the first collapse of about 87%. This differs slightly from period ratios and energy losses for free-explosion bubbles (Cole, 1948), but is consistent with reported values for laser-generated bubbles (Vogel *et al.*, 1989; Vogel and Lauterborn, 1988). As the standoff distance decreases to a value of $X\approx1$, the second period increases to a large fraction of its original value, suggesting a reduction in the bubble energy loss during the first collapse. A reduction in energy loss is also suggested by a reduction in emitted acoustic energy, as is indicated in Fig. 6, which shows a pronounced minimum in the peak pulse pressure near $X=1$. However, a change in period is also to be expected for these standoff distances simply due to the formation of a vortex ring bubble, whose period is known to be larger than that of a spherical bubble of equal energy (Chahine and Genoux, 1983). As the standoff distance decreases below $X\approx1$, the period again decreases. This behavior of exhibiting an extremum near $X\approx1$ is also shown in the measurements of Lindau and Lauterborn (2003), who measured maximum and minimum volumes of laser-generated bubbles near a plate and found that the ratio of maximum to minimum volume near $X\approx1$ was reduced by roughly 2 orders of magnitude from its value very near and very far from the plate. In other words, the strength of compression of the bubble contents is greatly weakened when the standoff distance is approximately 1 bubble radius from the surface.

Note that the value of peak pressure shown in Fig. 6 is probably lower than the actual value due to the extreme brevity of the pulse (laser-induced bubbles produce pulses with a duration of tens of nanoseconds; see Vogel and Lauterborn, 1988), and the relatively large size and slow response (rise time of 1 μs) of the quartz transducer. The pressures in all cases were measured several inches to the side, and were normalized to correspond to a 3-in. separation between electrodes and transducer, using an assumed $1/r$ dependence of pressure with distance.

Since standoff values much less and much greater than the bubble size correspond, respectively, to hemispherical and spherical symmetry, while standoff values nearly equal to the bubble size result in highly nonspherical bubbles and in the development of strong linear and rotational motion, it seems reasonable to explain the extrema in all of these properties in terms of bubble distortion during the first cycle and

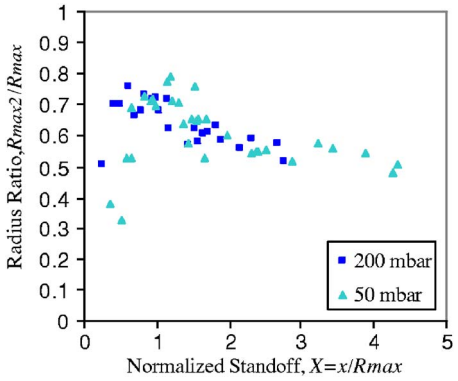

FIG. 7. Ratio of second maximum radius to first maximum radius as a function of standoff distance. Data are shown from the same set as shown in previous figures.

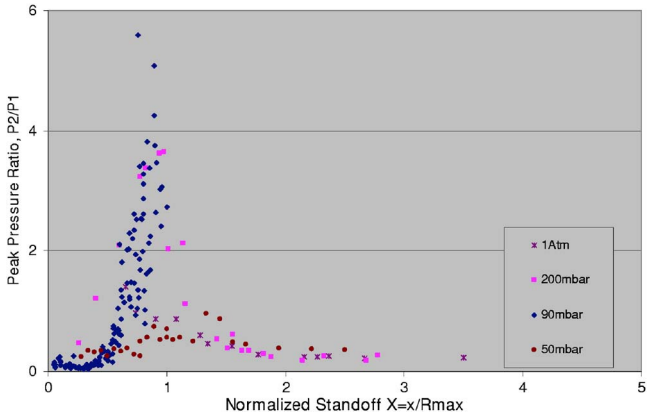

FIG. 9. Ratio of second peak pressure to first peak pressure as a function of standoff distance. Data are shown from the same experimental tests as shown in previous figures.

energy loss during the first collapse. For hemispherically and spherically symmetric bubble collapse, all of the energy of the fluid is directed into compression of the gaseous contents of the bubble, producing small minimum volumes, large maximum pressures, and large energy losses due to acoustic radiation. For values of $X \approx 1$, much of the fluid energy goes into the formation of a jet and a toroidal bubble, and the asymmetric collapse deprives the gas of some of its compression energy, producing larger minimum volumes, smaller pressures, and weaker acoustic emission.

Larger second-cycle bubble volumes, as well as larger second periods, are also observed near $X=1$. Figure 7 shows approximate measurements of the bubble equivalent radius at the second volume maximum ($R_{\max 2}$), as a fraction of the first $R_{\max}$ value. Similar to the second period, the second maximum radius displays a maximum near $X=1$. Furthermore, the similarity between the radius ratio and the ratio of second to first period, shown in Fig. 8, suggests that the period scales approximately as the equivalent maximum radius for nonspherical bubbles as for spherical bubbles, and both are decreased in nearly the same proportion by the loss of energy during the first collapse. Note that Cole (1948) reports a period ratio of approximately 0.77 for free-explosion bubbles, and a decrease in the ratio as the explosion approaches the bottom, while a period ratio between 0.5 and 0.6 is consistently obtained for free spark-generated bubbles in the ambient pressure conditions considered here, and this ratio increases as the bubbles approach the bottom. The energy losses for spark-generated bubbles are consistent, however, with reported energy losses for laser-produced bubbles (Vogel *et al.*, 1989). Also, the influence of gravity in the two cases is very different, since the Froude number for the conditions reported by Cole is approximately half of the value for a typical spark test reported here, and the opposing effects of gravity and a nearby bottom produce significantly different effects from the effects of a surface alone, such as bubble lengthening and splitting (Chahine, 1996). In addition, energy losses between one bubble cycle and the following for free-field bubble have been shown experimentally, over a very large range of explosion conditions, to depend on a parameter equivalent to the Froude number, i.e., $R_{\max}/Z$, where Z is the hydrostatic head at the explosion center (Snay, 1962; Chahine and Harris, 1997).

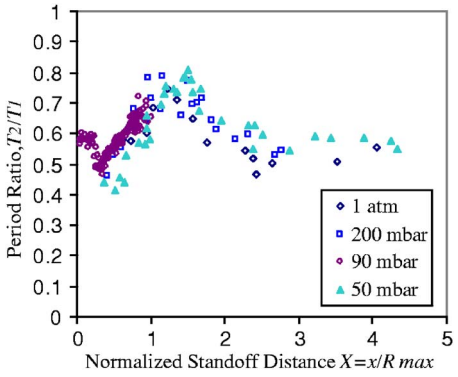

FIG. 8. Ratio of second period to first period as a function of standoff distance. Data are shown from the same experimental tests as shown in previous figures.

The ratio of the peak pressures between the second and the first bubble cycle is also very instructive, and shows a very distinctive peak at a normalized standoff distance of approximately $X=0.9$. This is clearly illustrated in Fig. 9.

B. Bubble dynamics near a free surface

It is well known that proximity to a free surface reduces the first period of an explosion bubble. An analysis using the image theory can be applied to a free surface, similar to that for a rigid surface but with an opposite sign, resulting in an analogous formula (Chahine and Bovis, 1983)

$$T^* \approx 1.83\left(1 - \frac{0.79}{4X}\right). \tag{21}$$

In this case, X is the normalized depth, or standoff distance from the free surface. This formula is essentially the same as that given by Cole (1948), and except for depths shallower than 1 bubble radius, agrees quite well with both laboratory-scale experimental data, and with simulations, as shown in Fig. 10. Note that the Froude number for the experimental conditions is approximately 8, indicating a mild influence of buoyancy, while Eq. (21) assumes negligible influence of buoyancy ($\mathrm{F} \gg 1$). Also note that data are unavailable below approximately $X=0.5$, as the spark-generated bubbles vent

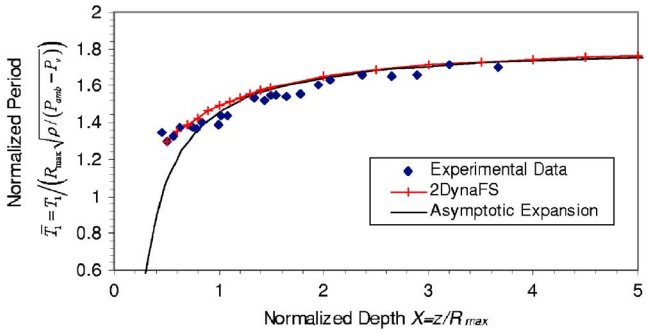

FIG. 10. Normalized first period versus normalized depth for bubbles near the free surface.

their contents to the atmosphere in this region, lose their identity, and fail to emit bubble pulses. In the range $0.5 < X < 1.0$, the top of the bubble does rise above the equilibrium free-surface level, but the surface is not breached—it maintains its integrity and exhibits behavior resembling an elastic membrane, and a water layer remains between the bubble and the free surface (Chahine, 1977).

As with bubbles near a rigid surface, the first bubble pulse and the second cycle behavior of bubbles near a free surface show more complex variations than the period of the first cycle. The first bubble pulse strength, and the ratios of second to first period and second cycle bubble size to first cycle bubble size, are shown in Fig. 11. When the bubble is close to the surface, the surface has a repulsive effect which forces the bubble downward during and after the collapse. When the bubble is sufficiently deep, the effect of buoyancy dominates over the effect of the free surface, and the bubble is distorted and lifts upward. At some intermediate depth, the two opposing effects cancel each other, and the bubble is observed to remain nearly spherical and to pulsate without rising or descending. Under the laboratory conditions shown here, this occurs at a normalized depth of approximately 2. Unfortunately, when the bubble remains spherical and stationary it collapses at the tip of the electrode, and this tends to make the bubble pulse magnitudes somewhat erratic in this region.

Figure 11 shows that, near a normalized depth of 2, the strength of the first bubble pulse is relatively strong, and that the second bubble cycle is relatively short with a small maximum bubble radius. Thus, just as for bubbles near a rigid surface, when the collapse is symmetric the compression of the bubble contents is relatively strong, resulting in relatively large energy losses and weaker second cycles. When the bubble is distorted during collapse, the compression is weakened, resulting in smaller energy losses and stronger second cycles.

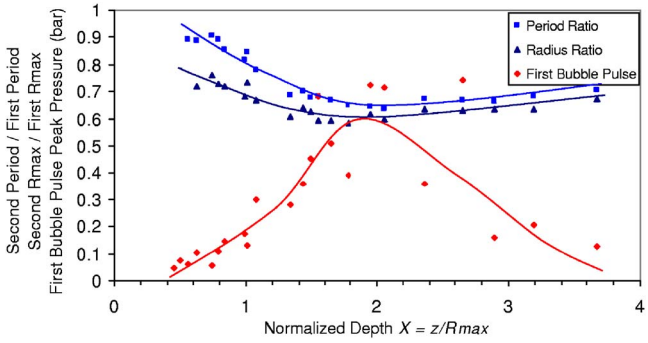

FIG. 11. Size and duration of the second bubble cycle, and magnitude of the first bubble pulse for bubbles near a free surface.

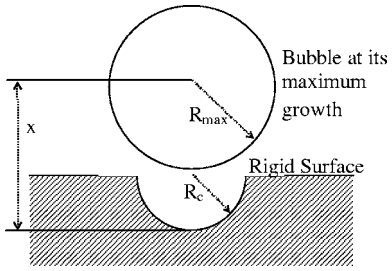

FIG. 12. Schematic of spark-generated bubbles over a hemispherical cavity in a rigid surface.

C. Bubble dynamics near a nonflat rigid surface

In addition to being nonrigid, surfaces near explosion bubbles are often not perfectly flat. Explosions near the seafloor may result in a crater. Explosions near or on an object may interact with a cavity in the object. As a simple model of a bubble interaction with a nonflat surface, a series of simulations and experimental tests of a bubble near a flat surface containing a hemispherical cavity was conducted. These tests are characterized not only by the normalized standoff distance $x/R_{\max}$, but also by the ratio of cavity size to maximum bubble size, $R_c/R_{\max}$. The standoff distance for these tests is defined relative to the bottom of the cavity, as shown in Fig. 12 in order to avoid ambiguities in the limit as the wall cavity radius becomes very large.

If the explosion bubble is very much larger or very much smaller than the cavity, the behavior of the bubble resembles that near a flat surface, with the bubble interacting with a large region of the surface around the cavity, or with the bottom of the cavity, respectively. If the bubble size is of the same order as the cavity size, however, the behavior is different. If the bubble is initiated at the bottom of the cavity, it splits during collapse, as shown in Fig. 13. The most prominent effect of the cavity on the acoustic signals is the significant increase in first period for bubbles partially enclosed within the cavity. Figure 14 shows the normalized first period as a function of normalized standoff for various ratios of cavity size to bubble size, with Fig. 14(a) showing experimental data, and Fig. 14(b) showing the results of simulations. In both cases, a curve similar to the normalized period curve for flat surfaces is produced when the cavity to bubble

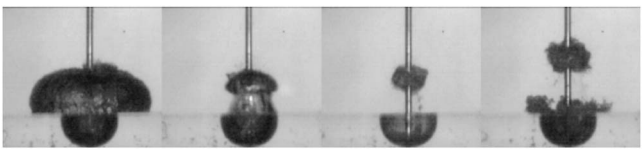

FIG. 13. Collapse, splitting, and rebound of an explosion bubble initiated at the bottom of a moderately sized hemispherical cavity.

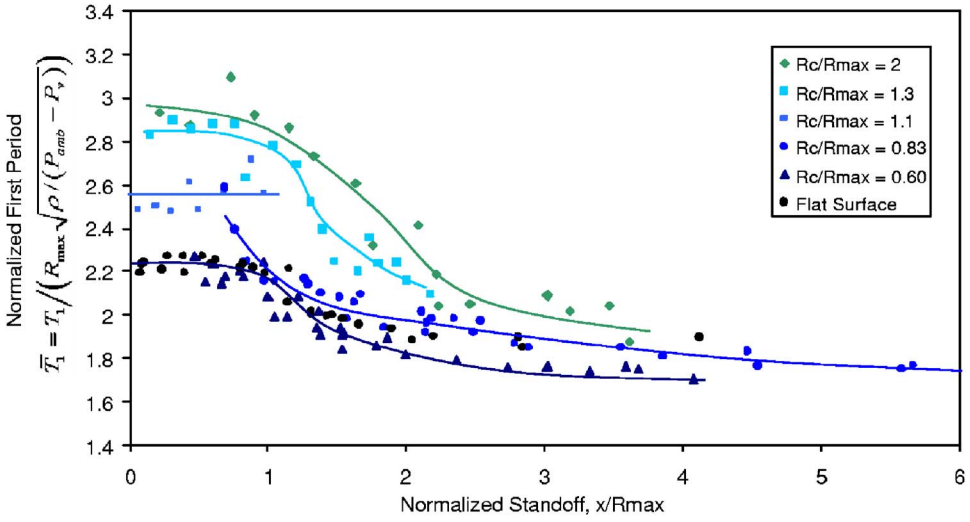

(a) Experimental Results

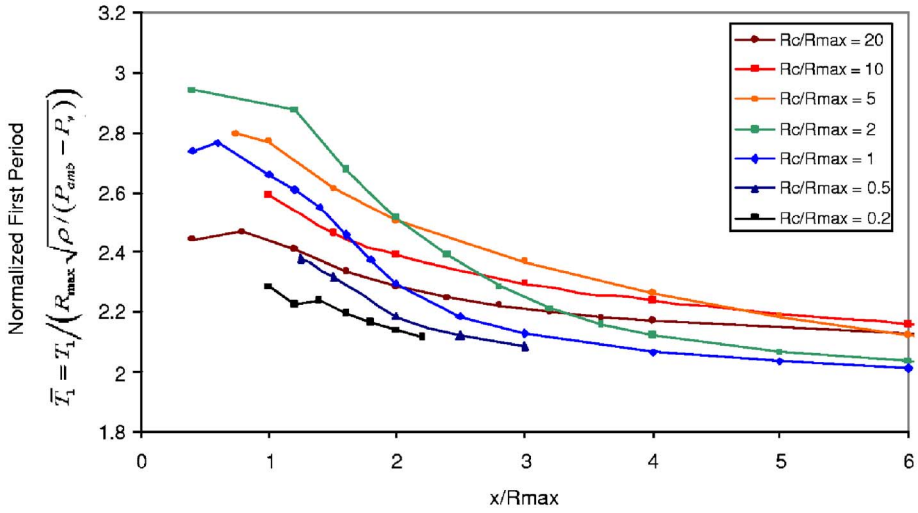

(b) Simulation Results using 2DynaFS

FIG. 14. Normalized first period of bubbles over a cavity in a rigid surface.

size ratio tends towards very small or very large values, since, in the limit of very small cavities, the bubble should interact with a flat surface with negligible influence of the cavity, and in the limit of very large cavities, the bubble should interact with the bottom of the cavity as if it were a very large flat surface. Note that curves for large values of $R_c/R_{\max}$ maintain higher values than curves for small values of $R_c/R_{\max}$ at large standoff distances, since smaller bubbles imply that larger normalized standoff distances are required to emerge from and to escape the effects of the wall cavity. If the wall cavity to bubble size ratio is not extremely large or small, i.e., if the wall cavity and maximum bubble radii are of the same order, then there is a marked increase in the bubble period when the explosion is initiated near or within the wall cavity, demonstrating the effect of increased inertia of the surrounding water due to increasing confinement of the explosion.

Figure 15 shows more clearly the effect of the relative cavity and bubble sizes. The normalized first period is shown from experiments and simulations of explosion bubbles initiated at the bottom of the crater, for various values of $R_c/R_{\max}$. As expected, the period approaches the theoretical value for an infinite flat surface for large and small values of $R_c/R_{\max}$, and increases by a factor of almost 2 in the range $R_c/R_{\max} \sim 2-3$, indicating a maximum restriction of bubble motion when the bubble size is a large fraction of the size of the containing cavity.

Figure 16 and Fig. 17 show the experimental results for the second bubble oscillation period, and the amplitude of the first bubble pressure pulse, for bubbles near a cavity. Overall behavior is similar to that near a flat surface, except that the curves are shifted towards larger standoff values as the bubbles become smaller, due to the fact that smaller bubbles must be further away from the bottom of the cavity in order to escape its effects.

D. Bubble dynamics near a bed of sand

In order to investigate the effect of nonrigid surfaces, a series of experimental tests over a bed of sand was conducted, for comparison to the rigid surface. Commercial playground-quality sand (grain size approximately 0.1–1.0 mm) was thoroughly rinsed and poured into a bed

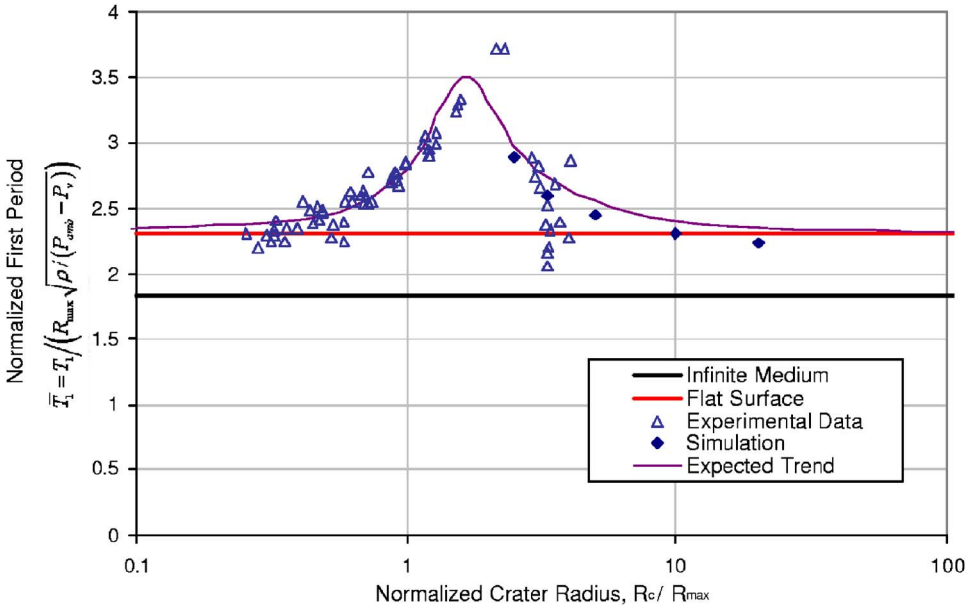

FIG. 15. Normalized first period of explosion bubbles initiated at the bottom of a cavity, as a function of the cavity size relative to the bubble size.

2 cm deep. Each bubble growth and collapse disturbed the surface of the sand to a certain extent, so the surface was smoothed flat before each test.

When the bubble is within approximately 2 radii from the surface, the bubble tends to lift the sand underneath it into a mound during its collapse, as shown in Fig. 18. The dynamics of the first cycle appears otherwise unaffected compared to behavior over a rigid surface, and shows similar distortions and similar jetting behavior at similar standoff distances. Furthermore, the first period of the bubble over sand is within experimental variability of the first period over a rigid surface, as shown in Fig. 19, indicating that the ability of a solid surface to deform slightly or fluidize within a shallow region is not sufficient to significantly alter the hydrodynamics around a bubble near the surface. Greater elasticity, such as that of a free surface, is required to produce large variations in the bubble behavior.

The most pronounced difference between the effect of a sandy bottom and of a rigid bottom lies in the behavior following the impact of the bubble with the sand. For a rigid surface, the bubble and remnants of the bubble may be observed in motion for a long time, but when a bubble strikes the sandy surface, the sand appears to immediately swallow the bubble, with fragments occasionally reemerging only after a long time. A second bubble pulse is normally detectable, indicating a second collapse, but the strength of this pulse is much diminished for bubbles very near to the sand, as shown in Fig. 20. (As in Fig. 3, each signal has been offset vertically by an amount proportional to the standoff distance. Note that several signals are overlaid at certain standoff distances, representing multiple tests at those distances.) The second period, shown as the ratio of second to first period in Fig. 21, shows a similar trend to the period ratio for bubbles over a rigid surface, except for somewhat diminished values for small standoff distances. The reduced period of the second cycle shown in Fig. 20 and Fig. 21 for standoff distances less than about 1, which is the region where the bubble collapses directly against the sandy surface, indicates a weakened rebound and second cycle, presumably due to dissipation of the bubble's energy as it rebounds within and moves through the sand. The weakened second bubble pulse is consistent with greater energy losses as the pulse propagates from deeper within the sand bed.

E. Spectra of the first bubble pulse

In cases where the explosion occurs near a rigid surface, the bubble pulse is often not a single peak, but has a smaller,

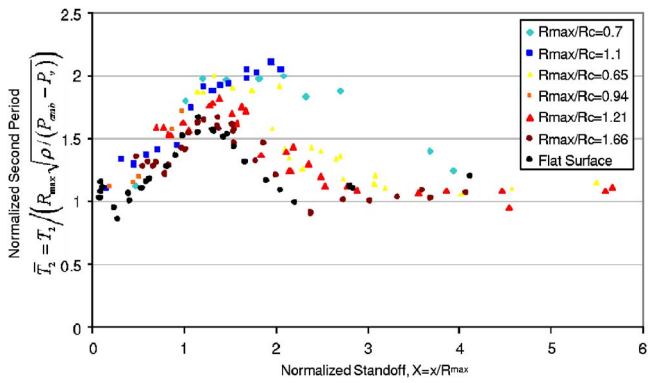

FIG. 16. Normalized second period of the bubble oscillations.

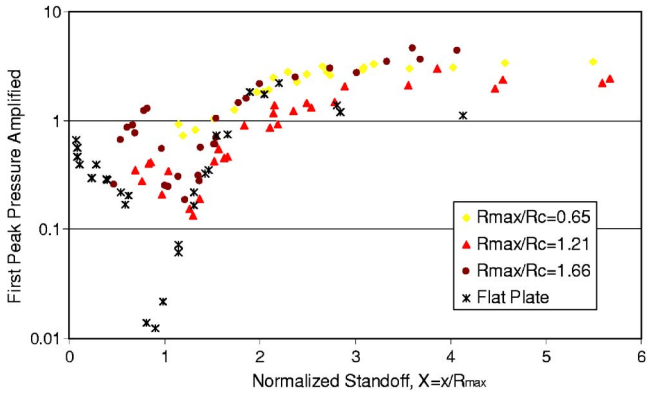

FIG. 17. Amplitude of the first bubble pulse peak pressure.

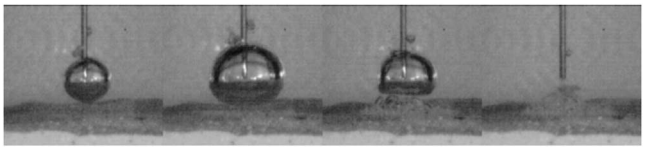

FIG. 18. Growth and collapse of an explosion bubble over a bed of sand.

initial peak preceding the primary collapse peak, as shown in Fig. 22, which shows typical peak profiles for normalized standoff distances of 0.06, 0.30, 0.45, and 0.69. The initial, or precursor, peak is evident for $X=0.06$ and quite pronounced at $X=0.3$. Also evident is the decrease in peak amplitude for standoff distances near $X=1$. A multitude of peaks, such as Fig. 22(c), is often observed for standoff values in the neighborhood of $X=1$, and sometimes for bubbles strongly influenced by gravity as well, and is probably a result of partial or complete bubble breakup during collapse. The precursor peak is known to occur as a result of impact of the reentrant jet on the surface (Chahine and Duraiswami, 1994; Thrun *et al.*, 1992), while the main peak is produced at the bubble's volume minimum. This precursor peak, which is most pronounced at a normalized standoff value of approximately 0.3, may also hold some explanation for the minimum in the second bubble period which occurs at this standoff value, due to increased energy loss accompanying the jet impact and pulse emission. Bubble collapse is an unstable process, and any perturbations, such as disruption of flow around an electrode, or any other object present in a nonideal flow field, will promote breakup of the bubble. This breakup has sometimes been observed in overhead views to produce daughter bubble fragments which collapse separately.

In order to identify the effect of the changing features of the bubble pulse on spectra of the acoustic signal, a series of spectra of the first bubble pulse has been compared. Figure 23 shows profiles of the first bubble pulse and precursor peak, with the primary peak centered at $t=0$, while Fig. 24 shows spectra of the first bubble pulse for standoff distances less than approximately unity. In Fig. 23, the signals from five repeated tests at each standoff distance have been overlaid, as an indication of variability in the signals. As is evident in Fig. 23, the jet impact peak becomes pronounced at $X\approx 0.3$, although with variable delay between it and the primary peak, and both the precursor peak and the collapse peak become more variable before nearly vanishing as the

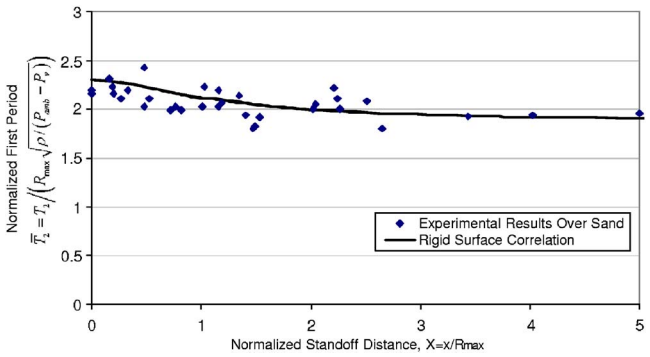

FIG. 19. First period of a bubble over a bed of sand.

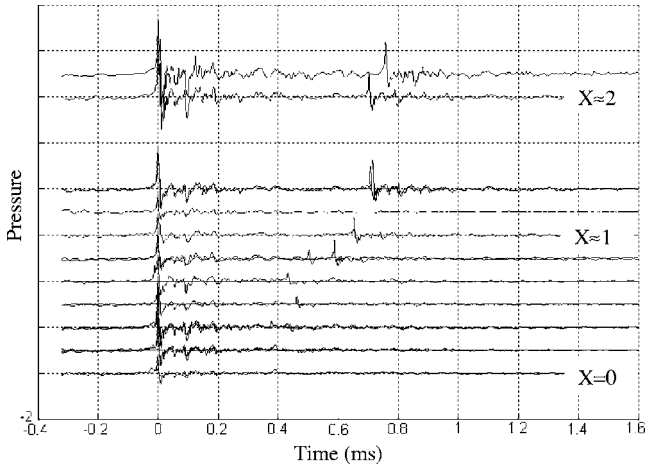

FIG. 20. The first and second bubble pulses of bubbles over a bed of sand. Signals were measured using a quartz pressure transducer several inches to one side of the bubble. The ambient pressure was 1 atmosphere and the maximum bubble radius about 6 mm. All signals have been offset vertically by an amount proportional to the respective standoff distance.

standoff distance approaches $X\approx 1$. Similar behavior may be observed in the spectra. The full width at half-maximum of the bubble pulse is typically approximately 16 μs, the logarithm of the reciprocal of which is 4.8. A distinct peak in the average spectra can be discerned at a value of 4.8, at least for the lower standoff distances where the pulse is strong. At standoff distances of approximately 0.5, where the bubble pulses become more erratic, the spectra do as well. At standoff distances of approximately 0.3, where the jet impact peak is most distinct and the interval is approximately 80 μs, the spectra show a faint rise at $10^{4.1}$ Hz$=1/80$ μs.

V. CONCLUSIONS

We have presented measurements of the acoustic signals of spark-generated bubbles (laboratory-scale underwater explosion bubbles), as well as simulations for similar conditions, which demonstrate the effects of bubble deformations on the acoustic signals. The influence of a nearby rigid surface increases the first period up to a value of approximately 25% greater than the free-field value when the explosion is right at the wall, and increases the second period significantly near a normalized standoff value of $X=1$, due to jet

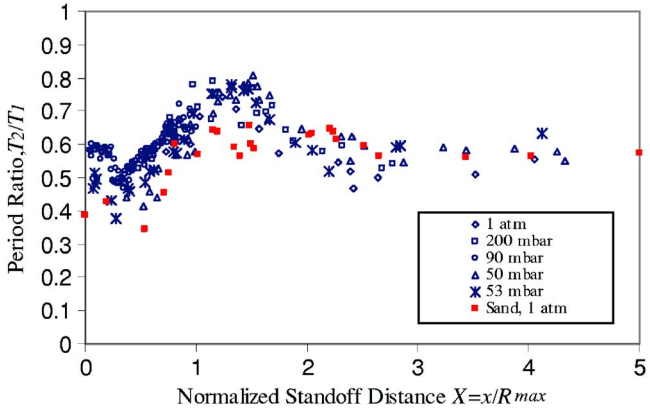

FIG. 21. Ratio of second period to first period for explosion bubbles over sand.

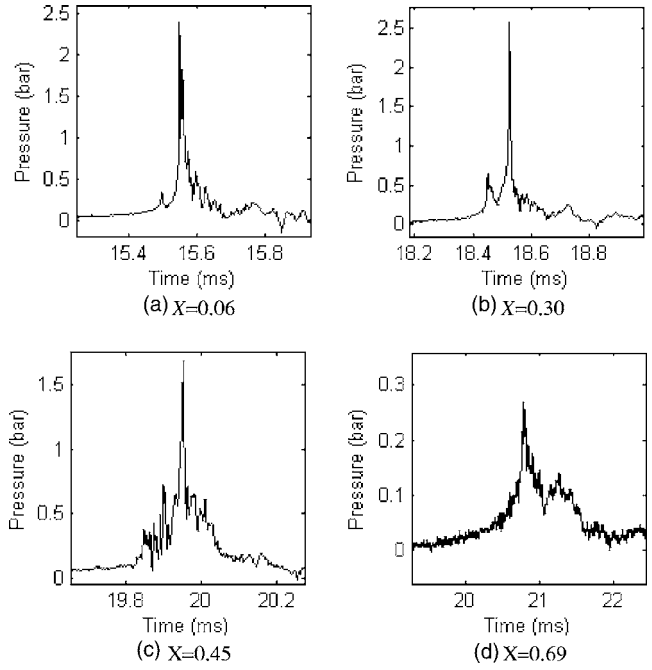

FIG. 22. Experimentally measured acoustic pressure profiles taken around the time of the first bubble pulse. At the lower standoffs, a precursor pulse can be seen (noted 1), and is attributed to reentrant jet impact.

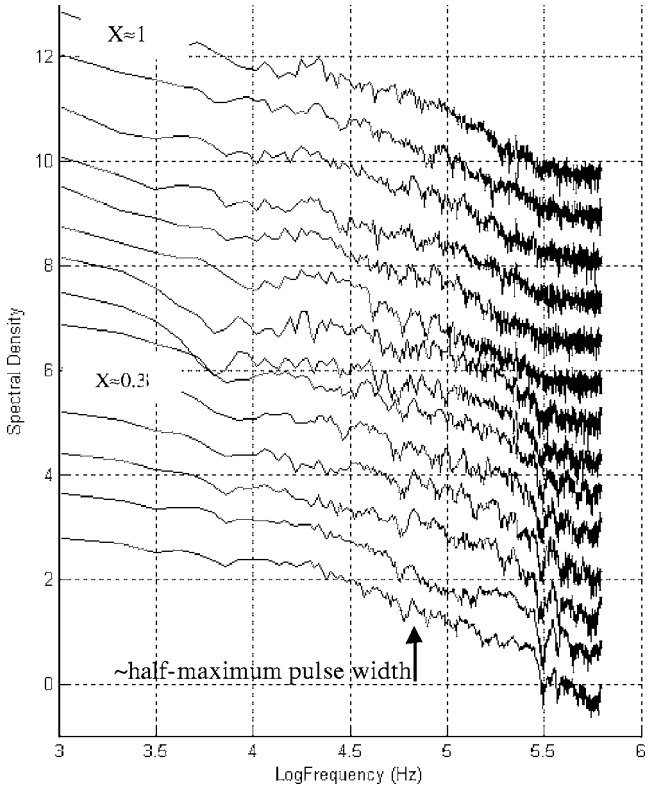

FIG. 24. Averaged spectra of the first bubble pulses from bubbles near a rigid surface. Each spectrum has been offset vertically by an amount proportional to the standoff distance.

and toroidal bubble formation during the first collapse. This increase in the second period corresponds to reductions in the first bubble pulse pressure and increases in the second cycle bubble size near $X=1$.

The presence of a free surface produces similar but opposite effects for moderate distances, causing a decrease in the bubble period for bubbles close to the surface. In addition, the distortion caused by the free surface has similar effects on the bubble pulse and second period as the distortion caused by a rigid surface, namely a weakening of the bubble pulse and a lengthening of the second period of the bubble. The influence of a sandy surface produces similar effects to a rigid surface for moderate distances, but the sand tends to engulf the bubble and dissipate its energy for small standoff distances, greatly reducing the strength of later bubble pulses and the period of later cycles. An explosion bubble near or within a hemispherical cavity in a rigid surface exhibits behaviors similar to a bubble near a flat rigid

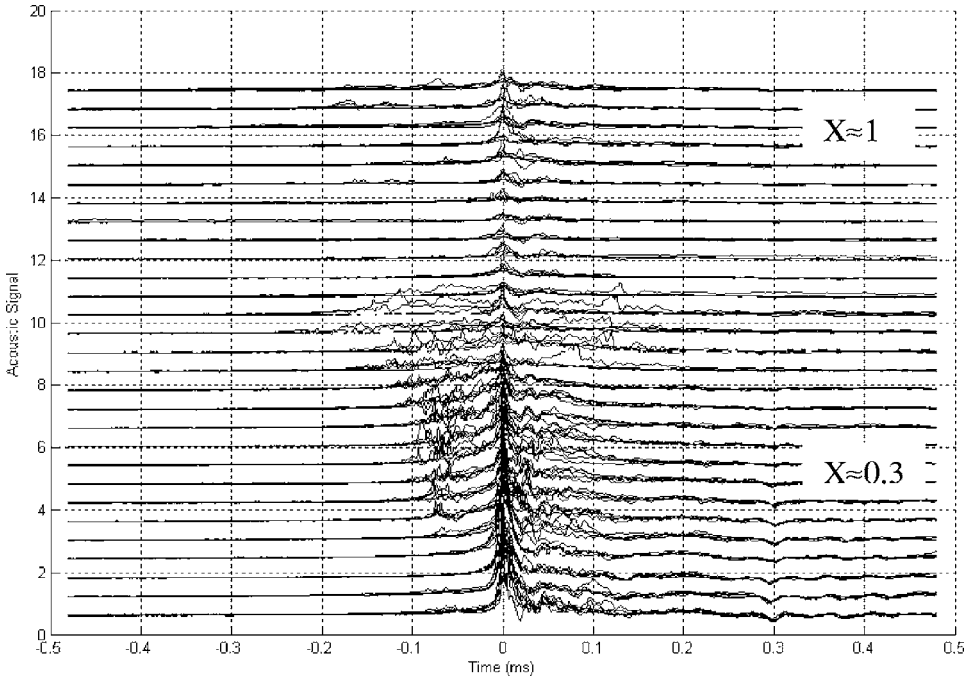

FIG. 23. Precursor peaks for bubbles within approximately 1 maximum bubble radius of a rigid surface. Each signal has been offset vertically by an amount proportional to the standoff distance. Five signals from repeated tests have been overlaid over each other for each standoff distance.

wall if the bubble is very much larger or smaller than the size of the cavity, but if the bubble size is of the same order as that of the cavity, the restriction of motion caused by the cavity surrounding the bubble causes significant increases in the duration of the bubble cycle and the period between pulses.

These results are consistent with general rules summarized as follows: Any factors which tend to confine the bubble, i.e., which restrict the motion of the fluid around the bubble, will tend to increase the first period. Any factors which tend to distort the bubble, e.g., large buoyancy forces or the presence of nearby objects, will tend to increase the minimum volume of the bubble during its collapse and thus tend to weaken the compression during collapse, resulting in weaker bubble pulses and longer periods in subsequent cycles.

The significance of these results to seismo-acoustic signals can be demonstrated by considering a standard 1.8 -pound signal charge, which at a depth of 56 ft. produces a maximum bubble radius of about 1 m, and a first bubble period of about 0.12 s. If the explosion is within 1 m of the bottom at this depth, the period will be larger than this, and could be as much as 0.15 s, according to the data presented here. The period is weakly dependent on the yield, as indicated by Eq. (1), so that this difference in the periods will produce an even greater difference in estimates of the yield. Given the same depth, a period of 0.15 s would correspond in the inverse problem to an overestimate of the yield of 3.3 pounds, if Eq. (1) is used. This factor of 2 excess could also be predicted from the observation that a hemispherical bubble on the bottom will have a period corresponding to a spherical bubble of twice the energy. The results for explosions over a hemispherical cavity indicate that, if the explosion is near a partial enclosure, the first bubble period could be increased by as much as a factor of 2, depending on the proximity and size of the enclosure. A factor of 2 increase in the period would result in an overprediction of the yield by a factor of 8.

Finally, we remark that, given this new ability to make accurate predictions of bubble pulse, depths, and times, one can numerically model the multiple impulsive point sources (shock and bubble pulses) to simulate a pressure time series that defines more realistically the acoustic radiation from an underwater explosion. This capability could be useful for refined geoacoustic measurements using calibrated explosives, since each impulse occurs at a different depth and time. It should also be possible, by inverting bubble pulse measurements to estimate yield and depth of an explosion (Gumerov and Chahine, 2000), to calibrate dynamite fishing and other "explosions of opportunity."

ACKNOWLEDGMENTS

This work was sponsored by the DCI Postdoctoral Fellowship Program and was conducted at DYNAFLOW, INC., ⟨www.dynaflow-inc.com⟩. The authors wish to thank many colleagues at DYNAFLOW, who have contributed to one aspect or another of this study, and most particularly Dr. Jin-Keun Choi, Dr. Chao-Tsung Hsiao, and Mr. Gary Frederick. We are also very grateful to Dr. John Cyranski of the Department of the Navy for his critical guidance and his support.

Baumgardt, D. R. (**1999**). "Seismic characterization of underwater explosions and undersea earthquakes using spectral/cepstral modeling and inversion," 21st Seismic Research Symposium.

Baumgardt, D. R., and Der, Z. (**1998**). "Identification of presumed shallow underwater chemical explosions using land-based regional arrays," Bull. Seismol. Soc. Am. **88**, No. 2, 581–595.

Best, J. P. (**1994**). "The rebound of toroidal bubbles," in *Bubble Dynamics and Interface Phenomena*, edited by J. R. Blake, J. M. Boulton-Stone, and N. H. Thomas (Kluwer, Dordrecht), pp. 405–412.

Buratti, R. H., Dionne, J. E., Cusanelli, M. A., Flynn, D. F. X., Tralies, J. M., and Russo, D. M. (1999). "Shallow-water explosive model," U.S. Navy Journal of Underwater Acoustics **49**, No. 2, 493–500 (Unclassified).

Chahine, G. L. (**1977**). "Interaction between an oscillating bubble and a free surface," J. Fluids Eng. **99**, 709–716.

Chahine, G. L. (**1996**). "Bubble dynamics near a cylindrical body: 3-D boundary element simulation of the ONR Snay/Goertner bubble benchmark problems," Proceedings of the 67th Shock and Vibration Symposium, Monterey, CA.

Chahine, G. L. (**1997**). "Numerical and experimental study of explosion bubble crown jetting behavior," DYNAFLOW Technical Report 96003–1ONR, 1997.

Chahine, G. L., and Bovis, A. G. (**1983**). "Pressure field generated by non-spherical bubble collapse," ASME J. Fluids Eng. **105**, 356–363.

Chahine, G. L., and Duraiswami, R. (**1994**). "Boundary element method for calculating 2-D and 3-D underwater explosion bubble behavior in free water and near structures," NSWC Weapons Research and Technology Department Development, White Oak Detachment, Report NSWCDD/TR-93/44. (limited distribution)

Chahine, G. L., and Genoux, Ph. (**1983**). "Collapse of a cavitation vortex ring," J. Fluids Eng. **105**, 400–405.

Chahine, G. L., and Harris, G. (**1997**). "Development and validation of a multicycle bubble model for UNDEX application," 68th Shock and Vibration Symposium, Hunt Valley, MD, November 1997.

Chahine, G. L., and Kalumuck, K. (**1998**). "BEM software for free surface flow simulation including fluid structure interaction effects," Int. J. Comput. Appl. Technol. **11**, Nos. 3/4/5 177–198.

Chahine, G. L., and Perdue, T. O. (**1989**). "Simulation of the three-dimensional behavior of an unsteady large bubble near a structure," 3rd International Colloquium on Drops and Bubbles, Monterey, California, September **1988**, AIP Conf. Proc. 197, edited by T. G. Wang, **1989**.

Chahine, G. L., Kalumuck, K. M., and Hsiao, C.-T. (**2003**). "Simulation of surface piercing body coupled response to underwater bubble dynamics utilizing 3DYNAFS©, a three-dimensional BEM code," Comput. Mech. **32**, Nos. 4-6, 319–326.

Chahine, G. L., Frederick, G. S., Lambrecht, C. J., Harris, G. S., and Mair H. U. (**1995**). "Spark generated bubbles as laboratory-scale models of underwater explosions and their use for validation of simulation tools," Proceedings of the 66th Shock and Vibration Symposium, Biloxi, MS.

Chapman, N. R. (**1985**). "Measurement of the waveform parameters of shallow explosive charges," J. Acoust. Soc. Am. **78**, No. 2, 672–681.

Chapman, N. R. (**1988**). "Source levels of shallow explosive charges," J. Acoust. Soc. Am. **84**, No. 2, 607–702.

Choi, J.-K., and Chahine, G. L. (**2003**). "Non-spherical bubble behavior in vortex flow fields," in *Computational Mechanics* (Springer, Berlin), Vol. **32**, No. 4-6, pp. 281–290.

Cole, R. H. (**1948**). *Underwater Explosions* (Princeton University Press, Princeton, NJ).

Godin, O. A., Chapman, N. R., Laidlaw, M. C. A., and Hannay, D. E. (**1999**). "Head wave data inversion for geoacoustic parameters of the ocean bottom of Vancouver Island," J. Acoust. Soc. Am. **106**, No. 5, 2540–2550.

Gumerov, N., and Chahine, G. L. (**2000**). *An Inverse Method for the Acoustic Detection, Localization, and Determination of the Shape Evolution of a Bubble* (IOP on Inverse Problems, London), Vol. **16**, pp. 1741–1760.

Hannay, D. E., and Chapman, N. R. (**1999**). "Source levels of shallow underwater sound charges," J. Acoust. Soc. Am. **105**, No. 1, 260–263.

Kalumuck, K. M., Duraiswami R., and Chahine, G. L. (**1995**). "Bubble dynamics fluid–structure interaction simulation by coupling fluid BEM and structural FEM codes," J. Fluids Struct. **9**, 861–883.

Lin, Y-T, Lynch, J. F., Chotiros, N., Chen, C.-F., Newhall, A., Turgut, A., Schock, S., Chiu, C.-S., Bartek, L., and Liu, C.-S. (**2004**). "An estimate of

the bottom compressional wave speed profile in the Northeastern South China Sea using 'sources of opportunity'," IEEE J. Ocean. Eng. **29**, No. 4, 1231–1248.
Lindau, O., and Lauterborn, W. (**2003**). "Cinematographic observation of the collapse and rebound of a laser-produced cavitation bubble near a wall," J. Fluid Mech. **479**, 327–348.
Plesset, M. S. (**1948**). "Dynamics of cavitation bubbles," J. Appl. Mech. **16**, 228–231.
Popov, R. Yu., and Simanika, E. V. (**1998**). "Estimation of the temporal variability of explosive signal propagation conditions in the Black Sea," Acoust. Phys. **44**, No. 5, 614–615.
Potty, G. R., Miller, J. H., and Lynch, J. F. (**2003**). "Inversion for sediment geoacoustic properties in the New England Bight," J. Acoust. Soc. Am. **114**, No. 4, 1874–1887.
Potty, G. R., Miller, J. H., Dahl, P. H., and Lazanki, C. J. (**2004**). "Geoacoustic inversion results from the ASIAEX East China Sea experiment," IEEE J. Ocean. Eng. **29**, No. 4, 1000–1010.
Rayleigh, Lord (**1917**). "On the pressure developed in a liquid during the collapse of a spherical cavity," Philos. Mag. **34**, 94–98.
Snay, H. G. (**1962**). "Underwater explosion phenomenon: The parameters of migrating explosion bubbles," NAVORD Report 4135, 12 Oct. 1962.
Spiesberger, J. L. (**2003**). "U.S. Navy sources and receivers for studying acoustic propagation and climate change in the ocean," (L) J. Acoust. Soc. Am. **114**, No. 5, 2557–2560.
Thrun, R., Goertner, J. F., and Harris, G. S. (**1992**). "Underwater explosion bubble collapse against a flat plate. 1992 Seneca Lake test series data report," Naval Surface Warfare Center, Dahlgren Division, NSWCDD/TR-92/482.
Vogel, A., and Lauterborn, W. (**1988**). "Acoustic transient generation by laser-produced cavitation bubbles near solid boundaries," J. Acoust. Soc. Am. **84**, 719–731.
Vogel, A., Lauterborn, W., and Timm, R. (**1989**). "Optical and acoustic investigations of the dynamics of laser-produced cavitation bubbles near a solid boundary," J. Fluid Mech. **206**, 299–338.
Weinstein, M. W. (**1968**). "Spectra of acoustic and seismic signals generated by underwater explosions during chase experiment," J. Geophys. Res. **73**, No. 2, 5473–5476.
Weston, D. E. (**1960**). "Underwater explosions as acoustic sources," Proc. Phys. Soc. London **LXXVI**, No. 2, 233–249.
Woodman, G. H., Wilson, S. C., Li, V. Y. F., and Renneberg, R. (**2003**). "Acoustic characteristics of fish bombing: Potential to develop an automated blast detector," Mar. Pollution Bull. **46**, 99–106.
Zhang, S., Duncan, J., and Chahine, G. L. (**1993**). "The final stage of the collapse of a cavitation bubble near a rigid wall," J. Fluid Mech. **257**, 147–181.

On three-dimensional edge waves in semi-infinite isotropic plates subject to mixed face boundary conditions

J. Kaplunov[a)]
Department of Mathematics, University of Manchester, Oxford Road, Manchester, M13 9PL, United Kingdom

D. A. Prikazchikov[b)] and G. A. Rogerson
Centre of Applied Mathematics, University of Salford, Salford, M5 4WT, United Kingdom

(Received 15 October 2004; revised 17 June 2005; accepted 18 August 2005)

This paper is concerned with the propagation of three-dimensional waves localized near the edge of a semi-infinite elastic plate subject to mixed face boundary conditions. In the linear isotropic case it is shown that the problem is closely related to that of Rayleigh surface wave propagation along the free surface of the corresponding half-space. The cut-off frequencies of the analyzed edge waves coincide with the natural frequencies of the associated cross-sectional semi-infinite strip. It is also demonstrated that the eigenspectrum of a rectangular rod can be expressed in terms of the considered three-dimensional waves. The results are then generalized to a prestressed isotropic incompressible material. It is noted that the density of the edge wave spectrum is strongly influenced by the prestress. It is illustrated that the areas of negative group velocity may exist for large primary deformation. Long-wave asymptotic expansions in the vicinity of the cut-off frequencies are presented. © *2005 Acoustical Society of America.* [DOI: 10.1121/1.2062487]

PACS number(s): 43.35.Cg [PEB] Pages: 2975–2983

I. INTRODUCTION

Edge waves in plates are well known within the framework of two-dimensional approximate theories, describing long-wave low-frequency motion. The simplest example of such waves is that propagating along the edge of a semi-infinite plate subject to a generalized plane stress state. The edge wave speed c_E is defined from the following see, e.g., Kaplunov *et al.*:[1]

$$\left(2-\frac{c_E^2}{c_2^2}\right)^2=4\sqrt{1-\frac{c_E^2}{c_3^2}}\sqrt{1-\frac{c_E^2}{c_2^2}}, \tag{1}$$

where

$$c_2=\sqrt{\frac{\mu}{\rho}},\quad c_3=\sqrt{\frac{8(\mu+2\lambda)(\mu+\lambda)^2}{\rho(2\mu+\lambda)(2\mu+3\lambda)}},$$

with ρ denoting density and λ and μ Lamé coefficients. This wave is a natural analog of a Rayleigh wave, which may propagate along the surface of the corresponding half-space. Equation (1) is very similar to the classical Rayleigh equation; the only difference is the appearance of the "plate" longitudinal velocity c_3, which in three-dimensional (3D) elasticity is replaced by

$$c_1=\sqrt{\frac{2\mu+\lambda}{\rho}}.$$

In contrast to long-wave, low-frequency, symmetric wave, its antisymmetric analog is dispersive. This wave was first considered by Konenkov[2] within the framework of Kirchhoff plate theory and then "rediscovered" several times; for history of the issue and more literature on the subject see, e.g., Norris *et al.*[3] and Zakharov.[4] The speed value, denoted by c_K, may be presented explicitly as

$$c_K=\alpha\sqrt{c_3\omega h}, \tag{2}$$

where

$$\alpha=\sqrt[4]{\frac{\lambda+2\mu}{12(\lambda+\mu)^2}\left[(2\mu-\lambda)+2\sqrt{2(\lambda+\mu)^2+2\mu^2}\right]},$$

and ω and h denote the frequency and the half-thickness of the plate, respectively, see Konenkov.[2] We also remark that the flexural edge waves were later considered for anisotropic plates, see Fu,[5] Norris,[6] and Zakharov and Becker,[7] and also for plates immersed in fluid, see, for example, Kouzov and Louk'yanov,[8] Goldstein *et al.*,[9] and Abrahams and Norris.[10]

In our present paper we are trying to construct three-dimensional edge waves for certain mixed face boundary conditions. Our approach is motivated by a recently discovered link between the localized spectrum of a flat semi-infinite strip with mixed face boundary conditions and Rayleigh-type waves propagating along the edge, see Kaplunov *et al.*.[1] Similar observation has also been established for edge modes of a prestressed isotropic elastic semi-strip, see Kaplunov *et al.*.[11]

We begin by considering a semi-infinite plate, composed of linear, isotropic, elastic material, and investigate three-dimensional edge waves. The link between the edge eigenmodes and the Rayleigh wave is established, being a generalization of that for two-dimensional case. Predictably, the

[a)]Current address: School of Information Systems, Computing & Mathematics, Brunel University, Uxbridge UB8 3PH, United Kingdom.
[b)]Current address: ITE Research Laboratory, The Russian State Open Technical University of Railways, Chasovaya 22/2, Moscow, 125993, Russia; electronic mail: prikazchikovda@yandex.ru

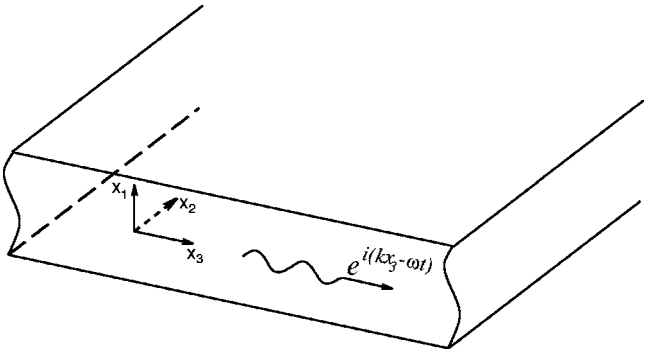

FIG. 1. The geometry of the problem.

cut-off frequencies coincide with edge natural frequencies of a flat longitudinal cross section of the semi-infinite plate.

To illustrate further applications, we investigate the problem of free edge vibration in a semi-infinite rectangular rod. We note that a rod subject to the considered boundary conditions possesses a clear physical interpretation as an insertion into a stiffer media.

The next stage concerns applying the same idea to a prestressed semi-infinite plate. This case is more difficult from both technical and informational points of view, due to the fact that for a prestressed material the Rayleigh wave speed depends on the direction of propagation. We remark that the edge spectrum density may increase significantly in the vicinity of two critical points of normal static stress σ_2, this fact being a generalization of a result previously obtained by the present authors, see Kaplunov *et al.*.[11] It is also demonstrated that in case of large primary deformation this type of waves may possess negative group velocity. Simple long-wave asymptotic expansions in the vicinity of the cut-off frequencies are developed.

II. 3D EDGE WAVES IN A SEMI-INFINITE PLATE

We consider the problem of three-dimensional edge wave propagation in a linear isotropic elastic material. The analysis is carried out with respect to a semi-infinite plate (see Fig. 1), occupying the region

$$-h \leqslant x_1 \leqslant h, \quad 0 \leqslant x_2 < \infty, \quad -\infty < x_3 < \infty. \tag{3}$$

The stress components are given by

$$\sigma_{ij} = \lambda u_{k,k}\delta_{ij} + \mu(u_{i,j} + u_{j,i}), \tag{4}$$

where λ and μ are the Lamé constants and $\mathbf{u}=(u_1,u_2,u_3)$ the displacement vector. The equations of motion are taken in their classical form

$$\sigma_{ij,j} = \rho\ddot{u}_i, \quad i=1,2,3, \tag{5}$$

which in view of Eq. (4) may be represented as

$$(\lambda+\mu)u_{j,ji} + \mu u_{i,jj} - \rho\ddot{u}_i = 0, \quad i=1,2,3. \tag{6}$$

We consider mixed boundary conditions on the faces $x_1=\pm h$, part of which is precluding some of the displacement components while the other part imposes restrictions on the traction components. These will allow us to separate the thickness variable. In fact there are three possible types of mixed face boundary conditions that may be considered. The first type allows only in-plane displacements on both sides and therefore may be interpreted as the plate being surrounded by stiff frictionless enclosure; the second type allows only transverse displacements on both sides and may be thought of as having the plate covered by a thin inextensible membrane; the third type is a mixture of the previous two, having only in-plane displacements on one face and only transverse displacements on the other face. This interpretation was already discussed by the authors in more detail, see Kaplunov *et al.*.[11] For the sake of definiteness, throughout this paper we investigate symmetric motions for the case of a frictionless enclosure, noting that the calculations for the other cases are very similar.

The face boundary conditions may be expressed as

$$u_1 = 0, \quad \sigma_{12} = 0, \quad \sigma_{13} = 0 \quad \text{at } x_1 = \pm h, \tag{7}$$

precluding the displacements in the x_1 direction, however not preventing displacements in other directions. We note that the surface $x_2=0$ might be better referred to as an end face, but as is common in the literature, we will call it an edge. We impose traction-free edge boundary conditions

$$\sigma_{21} = 0, \quad \sigma_{22} = 0, \quad \sigma_{23} = 0 \quad \text{at } x_2 = 0. \tag{8}$$

We shall seek solutions which satisfy the face boundary conditions (7) and decay away from the edge $x_2=0$, namely

$$\begin{aligned} u_1 &= \mathcal{A}\sin\left(\frac{\pi n x_1}{h}\right)\exp\{-rx_2 + i(kx_3 - \omega t)\},\\ u_2 &= \mathcal{B}\cos\left(\frac{\pi n x_1}{h}\right)\exp\{-rx_2 + i(kx_3 - \omega t)\},\\ u_3 &= \mathcal{C}\cos\left(\frac{\pi n x_1}{h}\right)\exp\{-rx_2 + i(kx_3 - \omega t)\}, \end{aligned} \tag{9}$$

where $r>0, n=1, 2, 3,\ldots$, and $\mathcal{A}$, $\mathcal{B}$, and $\mathcal{C}$ are disposable constants. It can be readily verified that displacements (9) satisfy the boundary conditions (7). We note that the antisymmetric family of solutions is easily obtained from the symmetric case by changing πn to $\pi(2n+1)/2$ and interchanging sin and cos.

Substituting expressions (9) into the equations of motion (6), we arrive at a system of three homogeneous equations with respect to $\mathcal{A}$, $\mathcal{B}$, and $\mathcal{C}$,

$$\begin{aligned} &\mathcal{A}h^2\{\rho\omega^2 + \mu[r^2 - k^2] - [\lambda+2\mu](\pi n/h)^2\}\\ &\quad + \mathcal{B}(\lambda+\mu)\pi n r h - \mathcal{C}(\lambda+\mu)ikh\pi n = 0,\\ &-\mathcal{A}(\lambda+\mu)\pi n r h + \mathcal{B}h^2\{\rho\omega^2 - \mu\mathcal{K}^2/h^2 + (\lambda+2\mu)r^2\}\\ &\quad - \mathcal{C}(\lambda+\mu)ikh^2 r = 0,\\ &-\mathcal{A}(\lambda+\mu)\pi nikh + \mathcal{B}(\lambda+\mu)ikh^2 r\\ &\quad + \mathcal{C}h^2\{\rho\omega^2 + \mu[r^2 - (\pi n/h)^2] - [\lambda+2\mu]k^2\} = 0, \end{aligned} \tag{10}$$

with

$$\mathcal{K}^2 = (\pi n)^2 + (kh)^2, \tag{11}$$

which possesses nontrivial solutions provided the corresponding determinant is equal to zero. The latter requirement takes form

$$(r^2 - r_1^2)(r^2 - r_2^2)^2 = 0, \tag{12}$$

where

$$r_1 = \sqrt{\frac{\mathcal{K}^2}{h^2} + \frac{\omega^2}{c_1^2}}, \quad r_2 = \sqrt{\frac{\mathcal{K}^2}{h^2} + \frac{\omega^2}{c_2^2}}. \tag{13}$$

Substituting $r=r_1$ and $r=r_2$ into Eq. (10), it is possible to obtain the eigenfunctions for displacements as

$$u_1 = (\pi n \mathcal{D}_1 e^{-r_1 x_2} + (r_2 h \mathcal{D}_2 - ikh\mathcal{D}_3)e^{-r_2 x_2}) \times \sin\left(\frac{\pi n x_1}{h}\right) e^{i(kx_3 - \omega t)},$$

$$u_2 = (r_1 h \mathcal{D}_1 e^{-r_1 x_2} + \pi n \mathcal{D}_2 e^{-r_2 x_2}) \cos\left(\frac{\pi n x_1}{h}\right) e^{i(kx_3 - \omega t)}, \tag{14}$$

$$u_3 = (-ikh\mathcal{D}_1 e^{-r_1 x_2} + \pi n \mathcal{D}_3 e^{-r_2 x_2}) \cos\left(\frac{\pi n x_1}{h}\right) e^{i(kx_3 - \omega t)}.$$

In view of Eq. (14) the edge boundary conditions (8) take form of a homogeneous system of algebraic equations with respect to the constants $\mathcal{D}_1, \mathcal{D}_2$, and $\mathcal{D}_3$,

$$2\pi n r_1 h \mathcal{D}_1 + [(\pi n)^2 + (r_2 h)^2]\mathcal{D}_2 - ikh^2 r_2 \mathcal{D}_3 = 0, \tag{15}$$

$$\left[(\pi n)^2 + (kh)^2 - \frac{\omega^2 h^2}{2c_2^2}\right]\mathcal{D}_1 + \pi n r_2 h \mathcal{D}_2 = 0, \tag{16}$$

$$2ikh^2 r_1 \mathcal{D}_1 + ikh\pi n \mathcal{D}_2 - r_2 h \pi n \mathcal{D}_3 = 0, \tag{17}$$

which possesses nontrivial solutions provided

$$\left[\mathcal{K}^2 - \frac{(\omega h)^2}{2c_2^2}\right]^2 = \mathcal{K}^2 \sqrt{\mathcal{K}^2 - \frac{(\omega h)^2}{c_1^2}} \sqrt{\mathcal{K}^2 - \frac{(\omega h)^2}{c_2^2}}. \tag{18}$$

Equation (18) is in fact the famous Rayleigh equation provided $\omega h = c_R \mathcal{K}$. The frequency of the family of edge waves is then given by

$$\omega_n = \sqrt{k^2 + (\pi n/h)^2}\, c_R. \tag{19}$$

We remark that within the framework of linear isotropic elasticity c_R does not depend on the direction of propagation. This fact will be noted later when we generalize this approach for a prestressed material. The considered edge waves are fully 3D, being a generalization of the two-dimensional edge waves for a semi-infinite strip. The corresponding two-dimensional results may be easily obtained from Eq. (19) by substituting $kh=0$. It is also possible to obtain in the long-wave limit (when kh is small in comparison with n) that

$$\frac{\omega h}{c_R} = \pi n + \frac{(kh)^2}{2\pi n} + O(kh)^4. \tag{20}$$

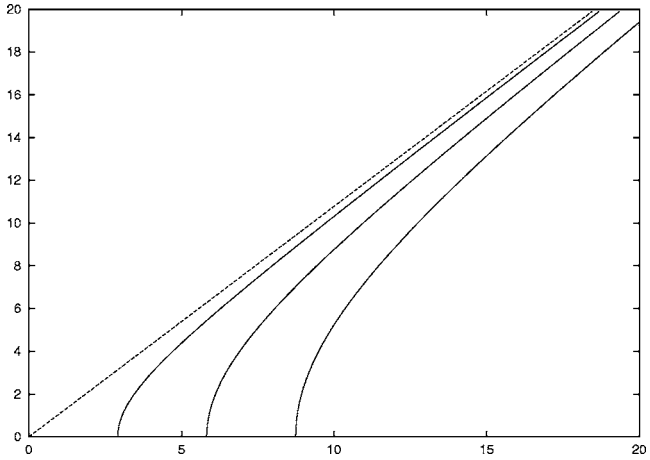

FIG. 2. Numerical solutions of the first three branches of the dispersion relation (18), solid lines; and the short-wave limit, dashed line (the calculations are performed for $\lambda = 1.5\mu$).

Finally in this section, we present a typical graph of dispersion curves for the Rayleigh equation (18), see Fig. 2, the calculations being performed for $\lambda = 1.5\mu$. The three solid curves in Fig. 2 are numerical solutions of Eq. (18) for $n = 1, 2, 3$. Their points of intersection with $kh=0$ correspond to the first three cut-off frequencies, which coincide with the edge natural frequencies of the associated semi-strip, being a longitudinal cross section of the plate. The dotted line is defined by $\omega h = c_R kh$ and is the short-wave asymptotic limit for each curve as $kh \to \infty$.

III. EDGE STANDING MODES OF A RECTANGULAR ROD

To illustrate some possible applications we note that the results of Sec. II may be applied to a rectangular rod, occupying the domain

$$-h_1 \leqslant x_1 < h_1, \quad 0 \leqslant x_2 \leqslant \infty, \quad -h_3 < x_3 < h_3, \tag{21}$$

see Fig. 3.

The equations of motion and the stress components are again taken in their classical form (6) and (4). In addition to

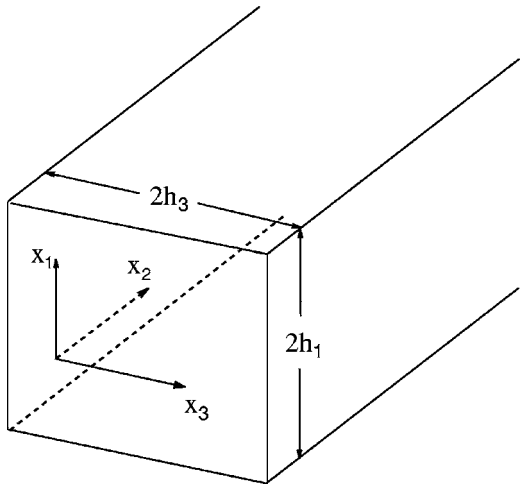

FIG. 3. The geometry of the rod.

the traction-free edge boundary conditions (8) and mixed boundary conditions (7) on $x_1=\pm h_1$, we will also impose similar conditions on $x_3=\pm h_3$, namely

$$u_3=0, \quad \sigma_{31}=0, \quad \sigma_{32}=0 \quad \text{at } x_3=\pm h_3. \tag{22}$$

It is worth mentioning that a rod subject to mixed boundary conditions (7) and (22) possesses a clear physical interpretation, it can be thought of as an insertion into a stiffer media.

Symmetric solutions for displacements decaying away from the edge $x_2=0$ and satisfying the mixed face boundary conditions (7) and (22), may be written as

$$\begin{aligned} u_1 &= \mathcal{A}\sin\left(\frac{\pi n x_1}{h_1}\right)\sin\left(\frac{\pi m x_3}{h_3}\right)\exp\{-\beta x_2-i\omega t\},\\ u_2 &= \mathcal{B}\cos\left(\frac{\pi n x_1}{h_1}\right)\cos\left(\frac{\pi m x_3}{h_3}\right)\exp\{-\beta x_2-\omega t\},\\ u_3 &= \mathcal{C}\cos\left(\frac{\pi n x_1}{h_1}\right)\cos\left(\frac{\pi m x_3}{h_3}\right)\exp\{-\beta x_2-\omega t\}. \end{aligned} \tag{23}$$

Substituting Eq. (23) into the equations of motion (6), it is possible to find the roots for β as

$$\beta_j^2=\left(\frac{\pi n}{h_1}\right)^2+\left(\frac{\pi m}{h_3}\right)^2-\frac{\omega^2}{c_j^2}, \quad j=1,2, \tag{24}$$

these being analogous to the roots of Eq. (12). Similar to Sec. II, satisfying the edge boundary conditions (8), it is possible to obtain the Rayleigh equation, from which the set of edge modes for the rod may be found in the form

$$\omega_{nm}=\pi c_R\sqrt{\frac{n^2}{h_1^2}+\frac{m^2}{h_3^2}}. \tag{25}$$

IV. 3D EDGE WAVES IN A PRESTRESSED INCOMPRESSIBLE ISOTROPIC SEMI-INFINITE PLATE

In this section we extend the results of Sec. II to a semi-infinite plate composed of prestressed incompressible isotropic elastic material. We are considering the domain given in Eq. (3), see Fig. 1. The Cartesian axes Ox_1,x_2,x_3 are chosen to coincide with the principal axes of the primary deformation. The equations of motion are written in the form

$$\begin{aligned} &B_{1111}u_{1,11}+B_{2121}u_{1,22}+B_{3131}u_{1,33}+(B_{1122}+B_{1221})u_{2,12}\\ &\quad+(B_{1133}+B_{1331})u_{3,13}-p^*_{,1}=\rho\ddot{u}_1, \end{aligned} \tag{26}$$

$$\begin{aligned} &(B_{1122}+B_{1221})u_{1,12}+B_{1212}u_{2,11}+B_{2222}u_{2,22}+B_{3232}u_{2,33}\\ &\quad+(B_{2233}+B_{2332})u_{3,23}-p^*_{,2}=\rho\ddot{u}_2, \end{aligned} \tag{27}$$

$$\begin{aligned} &(B_{1133}+B_{1331})u_{1,13}+(B_{2332}+B_{2233})u_{2,23}+B_{1313}u_{3,11}\\ &\quad+B_{2323}u_{3,22}+B_{3333}u_{3,33}-p^*_{,3}=\rho\ddot{u}_3, \end{aligned} \tag{28}$$

where B_{ijkl} denote the fourth-order elasticity tensor components, and p^* is the incremental pressure, see, e.g., Rogerson and Sandiford.[12] We are also paying respect to the incompressibility condition

$$u_{1,1}+u_{2,2}+u_{3,3}=0. \tag{29}$$

The incremental traction components may be expressed as

$$\tau_i^{(m)}=(B_{jilk}u_{k,l}+\bar{p}u_{j,i}-p^*\delta_{ij})\delta_{jm}, \tag{30}$$

where $\tau_i^{(m)}$ denote the incremental traction components, acting on an element of surface area normal to Ox_m, and $\bar{p}$ is static pressure, see, e.g., Dowaikh and Ogden.[13] Throughout Sec. IV we specifically employ only six components of the incremental traction, which are given explicitly

$$\begin{aligned} \tau_1^{(1)} &= (B_{1111}+\bar{p})u_{1,1}+B_{1122}u_{2,2}+B_{1133}u_{3,3}-p^*,\\ \tau_2^{(1)} &= B_{1212}u_{2,1}+(B_{1221}+\bar{p})u_{1,2},\\ \tau_3^{(1)} &= B_{1313}u_{3,1}+(B_{1331}+\bar{p})u_{1,3},\\ \tau_2^{(2)} &= B_{1122}u_{1,1}+(B_{2222}+\bar{p})u_{2,2}+B_{2233}u_{3,3}-p^*,\\ \tau_1^{(2)} &= B_{2121}u_{1,2}+(B_{1221}+\bar{p})u_{2,1},\\ \tau_3^{(2)} &= B_{2323}u_{3,2}+(B_{2332}+\bar{p})u_{2,3}. \end{aligned} \tag{31}$$

We also note a useful relation between $\bar{p}$ and the normal Cauchy stress σ_2

$$\sigma_2=B_{2121}-B_{2112}-\bar{p}=B_{2323}-B_{2332}-\bar{p}, \tag{32}$$

see Ogden.[14]

Symmetric family of solutions decaying away from the edge $x_2=0$ is given by

$$\begin{aligned} u_1 &= U\sin\left(\frac{\pi n x_1}{h}\right)\exp\{qx_2+ikx_3-i\omega t\},\\ u_2 &= V\cos\left(\frac{\pi n x_1}{h}\right)\exp\{qx_2+ikx_3-i\omega t\},\\ u_3 &= W\cos\left(\frac{\pi n x_1}{h}\right)\exp\{qx_2+ikx_3-i\omega t\},\\ p^* &= \frac{\pi n}{h}P\cos\left(\frac{\pi n x_1}{h}\right)\exp\{qx_2+ikx_3-i\omega t\}, \end{aligned} \tag{33}$$

where $\Re(q)<0$. The boundary conditions may be expressed as

$$u_1=0, \quad \tau_2^{(1)}=0, \quad \tau_3^{(1)}=0 \quad \text{at } x_1=\pm h, \tag{34a}$$

$$\tau_1^{(2)}=0, \quad \tau_2^{(2)}=0, \quad \tau_3^{(2)}=0 \quad \text{at } x_2=0. \tag{34b}$$

These conditions are completely analogous to conditions (7) and (8), allowing only in-plane displacements on the faces $x_1=\pm h$, with the edge $x_2=0$ being traction-free.

It can be verified that the face boundary conditions (34a) are satisfied automatically for the forms of solution indicated in Eq. (33). Substituting Eq. (33) into Eqs. (26)–(29), we arrive at

$$\begin{aligned} &[\rho(\omega h)^2-B_{1111}(\pi n)^2+B_{2121}(qh)^2-B_{3131}(kh)^2]U\\ &\quad-qh\pi n(B_{1122}+B_{1221})V-ikh\pi n(B_{1133}+B_{1331})W\\ &\quad+(\pi n)^2P=0, \end{aligned} \tag{35}$$

$$[\rho(\omega h)^2 - B_{1212}(\pi n)^2 + B_{2222}(qh)^2 - B_{3232}(kh)^2]V + qh\pi n(B_{1122} + B_{1221})U + ikqh^2(B_{2332} + B_{2233})W - qh\pi nP = 0, \tag{36}$$

$$[\rho(\omega h)^2 - B_{1313}(\pi n)^2 + B_{2323}(qh)^2 - B_{3333}(kh)^2]W + ikh\pi n(B_{1133} + B_{1331})U + ikqh^2(B_{2332} + B_{2233})V - ikh\pi nP = 0, \tag{37}$$

$$\pi nU + qhV + ikhW = 0. \tag{38}$$

The condition for Eqs. (35)–(38) to yield nontrivial solutions, which is often referred to as a secular equation, takes the form of a bi-cubic equation for q,

$$q^6h^6\gamma_{21}\gamma_{23} + q^4h^4\{\rho(\omega h)^2[\gamma_{21} + \gamma_{23}] - \alpha_1\} + q^2h^2[\rho^2(\omega h)^4 - \alpha_2\rho(\omega h)^2 + \alpha_3] - [\rho(\omega h)^2 - \alpha_4] \times\{\rho\omega^2h^2[(\pi n)^2 + (kh)^2] - \alpha_5\} = 0, \tag{39}$$

with the following notation introduced:

$$\gamma_{ij} = B_{ijij}, \quad 2\beta_{ij} = B_{iiii} + B_{jjjj} - 2(B_{iijj} + B_{ijji}),$$

$$\mu_{ik} = \beta_{ik} - \beta_{ij} - \beta_{jk},$$

$$\alpha_1 = (kh)^2[\gamma_{23}\gamma_{31} + 2\beta_{23}\gamma_{21}] + (\pi n)^2[\gamma_{21}\gamma_{13} + 2\beta_{12}\gamma_{23}],$$

$$\alpha_2 = (kh)^2[\gamma_{21} + \gamma_{31} + 2\beta_{23}] + (\pi n)^2[\gamma_{13} + \gamma_{23} + 2\beta_{12}], \tag{40}$$

$$\alpha_3 = (\pi n)^4[\gamma_{12}\gamma_{23} + 2\beta_{12}\gamma_{13}] + (kh)^4[\gamma_{32}\gamma_{21} + 2\beta_{23}\gamma_{31}] + (\pi nkh)^2[\gamma_{12}\gamma_{21} + \gamma_{13}\gamma_{31} + \gamma_{23}\gamma_{32} + 4\beta_{12}\beta_{23} - \mu_{13}^2],$$

$$\alpha_4 = \gamma_{12}(\pi n)^2 + \gamma_{32}(kh)^2,$$

$$\alpha_5 = \gamma_{13}(\pi n)^4 + \gamma_{31}(kh)^4 + 2(\pi nkh)^2\beta_{13}.$$

It is now possible to express the displacements and the pressure increment as linear combinations of exponentially decaying solutions, namely,

$$u_1 = \sum_{m=1}^{3} U^{(m)}\exp\{q_m x_2 + ikx_3 - i\omega t\}\sin\left(\frac{\pi n x_1}{h}\right),$$

$$u_2 = \sum_{m=1}^{3} V^{(m)}\exp\{q_m x_2 + ikx_3 - i\omega t\}\cos\left(\frac{\pi n x_1}{h}\right),$$

$$u_3 = \sum_{m=1}^{3} W^{(m)}\exp\{q_m x_2 + ikx_3 - i\omega t\}\cos\left(\frac{\pi n x_1}{h}\right),$$

$$p^* = \sum_{m=1}^{3} \frac{\pi n}{h}P^{(m)}\exp\{q_m x_2 + ikx_3 - i\omega t\}\cos\left(\frac{\pi n x_1}{h}\right), \tag{41}$$

where $U^{(m)}, V^{(m)}, W^{(m)}$, and $P^{(m)}(m=1,2,3)$ form a set of disposable constants, and $q_m(m=1,2,3)$ are the three roots of the secular equation (39) satisfying the exponential decay condition $\Re(q) < 0$. Using Eqs. (35)–(38) and introducing for notational convenience

$$\begin{aligned}
\mathcal{U}(q,\omega) &= \rho(\omega h)^2 + \gamma_{23}(qh)^2 - \gamma_{13}(\pi n)^2 + \mu_{12}(kh)^2,\\
\mathcal{W}(q,\omega) &= \rho(\omega h)^2 + \gamma_{21}(qh)^2 - \gamma_{31}(kh)^2 + \mu_{23}(\pi n)^2,\\
\mathcal{V}(q,\omega) &= (\pi n)^2\mathcal{U}(q,\omega) + (kh)^2\mathcal{W}(q,\omega),\\
\mathcal{P}(q,\omega) &= \mathcal{U}(q,\omega)\mathcal{W}(q,\omega) + (\pi n)^2\mathcal{U}(q,\omega)[B_{2233} + B_{2332} - B_{1133} - B_{1331}]\\
&\quad + (kh)^2\mathcal{W}(q,\omega)[B_{1122} + B_{1221} - B_{1133} - B_{1331}],
\end{aligned} \tag{42}$$

it is possible to present the displacements and the pressure increment in terms of only three disposable constants $V^{(m)}$ as

$$\begin{aligned}
u_1 &= \sum_{m=1}^{3} \frac{q_m h\pi n\mathcal{U}(q_m,\omega)V^{(m)}}{\mathcal{V}(q_m,\omega)} \times\exp\{q_m x_2 + ikx_3 - i\omega t\}\sin\left(\frac{\pi n x_1}{h}\right),\\
u_2 &= \sum_{m=1}^{3} V^{(m)}\exp\{q_m x_2 + ikx_3 - i\omega t\}\cos\left(\frac{\pi n x_1}{h}\right),\\
u_3 &= \sum_{m=1}^{3} \frac{ikh^2 q_m\mathcal{W}(q_m,\omega)V^{(m)}}{\mathcal{V}(q_m,\omega)} \times\exp\{q_m x_2 + ikx_3 - i\omega t\}\cos\left(\frac{\pi n x_1}{h}\right),\\
p^* &= \sum_{m=1}^{3} \frac{q_m\mathcal{P}(q_m,\omega)V^{(m)}}{\mathcal{V}(q_m,\omega)} \times\exp\{q_m x_2 + ikx_3 - i\omega t\}\cos\left(\frac{\pi n x_1}{h}\right).
\end{aligned} \tag{43}$$

Substituting the eigenmodes (43) into the traction free edge boundary conditions (34b), we obtain

$$\begin{aligned}
&\sum_{m=1}^{3} \frac{\mathcal{T}_1(q_m,\omega)V^{(m)}}{\mathcal{V}(q_m,\omega)} = 0,\\
&\sum_{m=1}^{3} \frac{q_m\mathcal{T}_2(q_m,\omega)V^{(m)}}{\mathcal{V}(q_m,\omega)} = 0,\\
&\sum_{m=1}^{3} \frac{\mathcal{T}_3(q_m,\omega)V^{(m)}}{\mathcal{V}(q_m,\omega)} = 0,
\end{aligned} \tag{44}$$

where

$$\begin{aligned}
\mathcal{T}_1(q,\omega) &= \gamma_{21}(qh)^2\mathcal{U}(q,\omega) + (\gamma_{21} - \sigma_2)\mathcal{V}(q,\omega),\\
\mathcal{T}_3(q,\omega) &= \gamma_{23}(qh)^2\mathcal{W}(q,\omega) + (\gamma_{23} - \sigma_2)\mathcal{V}(q,\omega),\\
\mathcal{T}_2(q,\omega) &= \mathcal{U}(q,\omega)(\pi n)^2(\gamma_{21} - \sigma_2 - \mu_{13}) - \mathcal{U}(q,\omega)\mathcal{W}(q,\omega) + \mathcal{W}(q,\omega)(kh)^2(\gamma_{23} - \sigma_2 - \mu_{13}).
\end{aligned} \tag{45}$$

Equation (44) forms a homogeneous algebraic system with respect to the constants $V^{(1)}, V^{(2)}$, and $V^{(3)}$. The necessary and

sufficient condition for this system to possess nontrivial solutions is given by

$$\det \mathbf{T}(q_1,q_2,q_3,\omega)=0, \tag{46}$$

where matrix $\mathbf{T}$ is defined as

$$\mathbf{T}(q_1,q_2,q_3,\omega)=\begin{pmatrix} \mathcal{T}_1(q_1,\omega) & \mathcal{T}_1(q_2,\omega) & \mathcal{T}_1(q_3,\omega) \\ q_1\mathcal{T}_2(q_1,\omega) & q_2\mathcal{T}_2(q_2,\omega) & q_3\mathcal{T}_2(q_3,\omega) \\ \mathcal{T}_3(q_1,\omega) & \mathcal{T}_3(q_2,\omega) & \mathcal{T}_3(q_3,\omega) \end{pmatrix}. \tag{47}$$

We remark that in view of the definition of $\mathbf{T}$, Eq. (46), for a fixed mode number n is a relation between the wave number kh and the frequency ω, and therefore may be regarded as a dispersion relation. This relation may be also derived using scaled parameters, namely

$$\{\xi,\eta,\zeta\}=\frac{\{x_1,x_2,x_3\}}{h}, \quad \{\hat{q},\hat{\omega}\}=\frac{\{qh,\sqrt{\rho}\omega h\}}{\sqrt{(\pi n)^2+(kh)^2}},$$
$$\{\cos\theta,\sin\theta\}=\frac{\{\pi n,kh\}}{\sqrt{(\pi n)^2+(kh)^2}}, \tag{48}$$

where θ may be thought of as a propagation angle. In view of Eq. (48), the secular equation (39) will coincide exactly with the known secular equation for wave propagation in a prestressed isotropic material, see for example Pichugin and Rogerson.[15] Rewriting the dispersion relation (46) in terms of parameters (48), we obtain an equation, which may be shown to coincide with the three-dimensional surface wave equation for a half-space composed of a prestressed incompressible elastic material, see Rogerson and Sandiford,[12] provided $\hat{\omega}=\sqrt{\rho}c_R$, therefore

$$\frac{\omega h}{\sqrt{(\pi n)^2+(kh)^2}}=c_R(n,kh), \tag{49}$$

where c_R is the Rayleigh wave speed for a prestressed material. It can be observed that Eq. (49) is in fact a generalization of Eq. (19), however there is a significant difference due to the fact that the Rayleigh wave speed in a prestressed material depends on the direction of propagation.

It is worth mentioning that the set of cut-off-frequencies coincides with the edge natural frequencies for the corresponding two-dimensional problem for a semi-strip, see Kaplunov *et al.*.[11] We will now present graphical illustrations of the dispersion relation (46). In order to reduce tedious algebra we consider a particular case, in which the secular equation is completely factorized. Therefore we specify the primary deformation to bi-axial with the principal stretches $\lambda_1=\lambda_2=\Lambda$, and, as follows from the incompressibility condition, $\lambda_3=\Lambda^{-2}$. We also impose some restrictions on the strain-energy function, namely

$$\gamma_{ij}+\gamma_{ji}=2\beta_{ij}. \tag{50}$$

Similar deformations and restrictions on the strain-energy function have previously been exploited with respect to surface wave problems, see for example Prikazchikov and Rogerson.[16] Using these restrictions, expressions for the roots may be presented as

$$q_1=-\frac{\sqrt{(\pi n)^2+(kh)^2}}{h},$$
$$q_2=-\sqrt{\frac{\gamma_{21}(\pi n)^2+\gamma_{31}(kh)^2-\rho(\omega h)^2}{\gamma_{21}h^2}}, \tag{51}$$
$$q_3=-\sqrt{\frac{\gamma_{13}(\pi n)^2+\gamma_{31}(kh)^2-\rho(\omega h)^2}{\gamma_{13}h^2}}.$$

It has previously been shown that a real surface wave speed in an incompressible elastic half-space will only exist providing σ_2 lies between two critical values, see Rogerson and Sandiford.[12] These two critical values depend on the angle of propagation and are denoted by $\sigma_0^-(\theta)$ and $\sigma_0^+(\theta)$, with the real surface wave propagating within angle θ existing provided $\sigma_0^-(\theta)<\sigma_2<\sigma_0^+(\theta)$. Therefore, in the three-dimensional case the stability interval may be written as $\sigma_0^-<\sigma_2<\sigma_0^+$ with its limits defined by

$$\sigma_0^-=\sup_{0\leqslant\theta\leqslant 90^\circ}\sigma_0^-(\theta), \quad \sigma_0^+=\inf_{0\leqslant\theta\leqslant 90^\circ}\sigma_0^+(\theta), \tag{52}$$

with these usually achieved at either $\theta=0$ or $\theta=90^\circ$.

We remark that there exist some unstable configurations when $\sigma_0^+<\sigma_0^-$, not allowing real surface wave propagation in all directions. These configurations are excluded from our consideration. It is now convenient for us to introduce a scaling parameter

$$d=\frac{2\sigma_2-\sigma_0^--\sigma_0^+}{\sigma_0^+-\sigma_0^-}, \quad d\in(-1;1), \tag{53}$$

which will be used later.

We note that all further numerical illustrations are carried out with respect to the Mooney-Rivlin strain-energy function, which is given explicitly by

$$W=c_{10}(\lambda_1^2+\lambda_2^2+\lambda_3^2-3)+c_{01}(\lambda_1^2\lambda_2^2+\lambda_1^2\lambda_3^2+\lambda_2^2\lambda_3^2-3), \tag{54}$$

see, e.g., Ogden,[14] with the constants taken as $c_{01}=c_{10}$. Also, it is worth mentioning that all numerical calculations, except for Fig. 5, are performed for a specific value of the normal Cauchy stress, corresponding to the middle of the stability interval, namely

$$\sigma_2=\frac{\sigma_0^-+\sigma_0^+}{2}. \tag{55}$$

Figures 4–6 illustrate relation between the scaled frequency $\bar{\omega}h=\sqrt{\rho/c_{01}}\omega h$ and the scaled wave number kh. The first three dispersion curves are presented in Figs. 4(a) and 4(b) for $\Lambda=1.1$ and $\Lambda=1.5$, respectively. The behavior of the curves in the long-wave region depends crucially on the prestress. The curves presented in Fig. 4, where the effect of prestress is small, look rather similar to those previously obtained for isotropic material, see Fig. 2. However, increase in primary deformation to the value of $\Lambda=1.5$ [see Fig. 4(b)] effects the curves significantly, changing completely the long-wave behavior. It is observed that in the vicinity of $kh=0$ the curves flatten and a distinct region of negative group velocity appears. An-

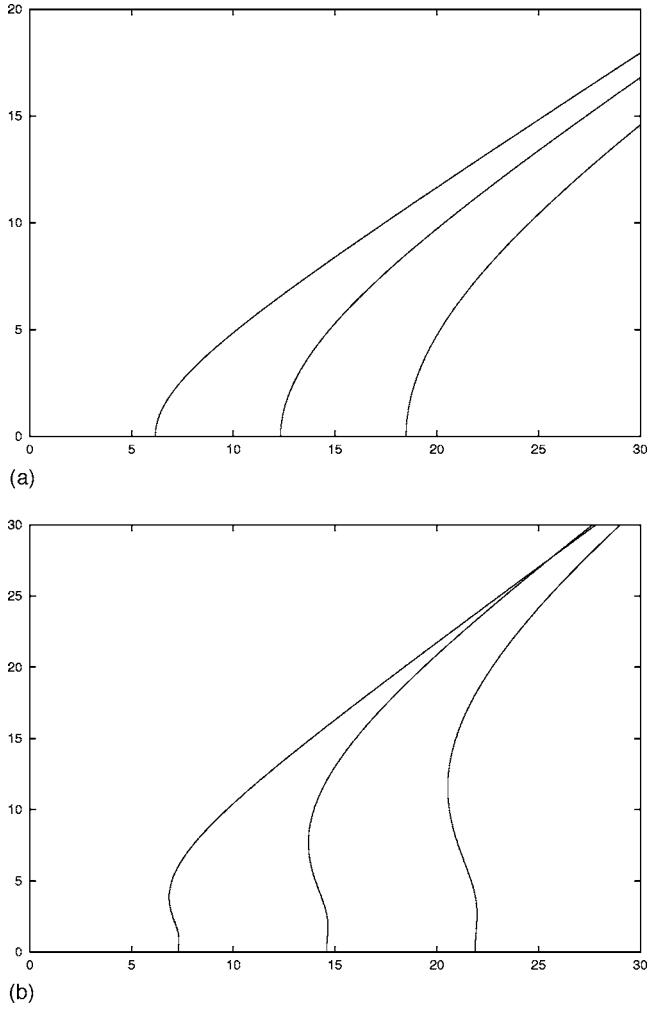

FIG. 4. The first three modes of the dispersion relation (46) in case of (a) $\Lambda=1.1$ and (b) $\Lambda=1.5$.

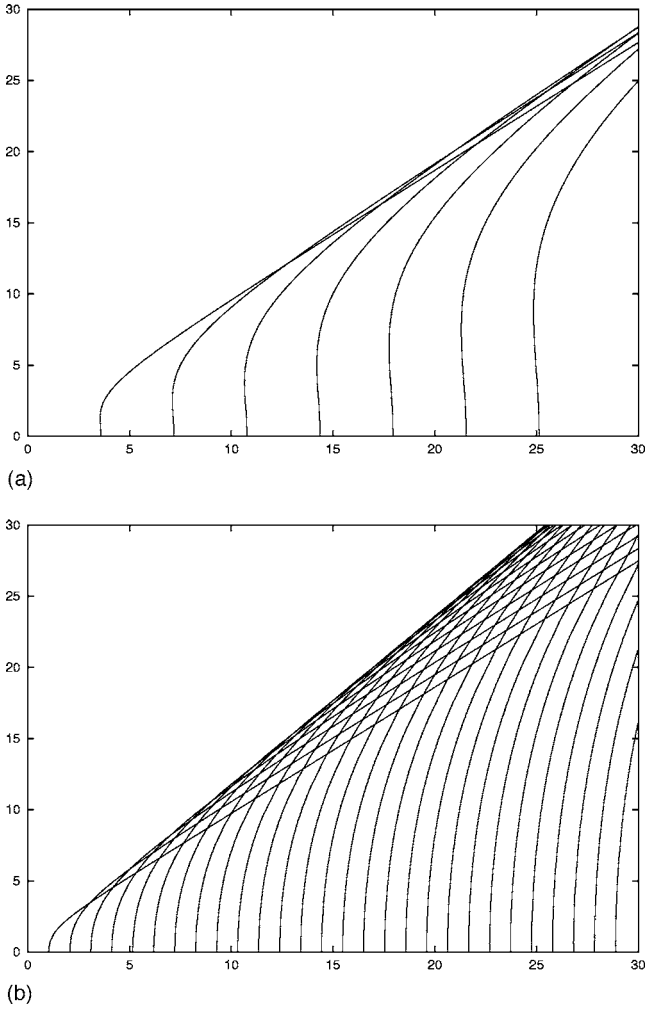

FIG. 5. Modes of the dispersion relation (46) for $\Lambda=1.5$ with σ_2 tending to a value associated with a critical σ_2^+ value.

other clear difference between the curves in Figs. 4(a) and 4(b) lies in the fact of their coalescing in the case of relatively large prestress. Regarding the short-wave region, the curves on both graphs tend to their asymptotic limits, given by

$$\omega h = c_R^\infty kh, \quad c_R^\infty = \lim_{kh\to\infty} c_R(n,kh), \quad n=1,2,3,\ldots . \tag{56}$$

It is worth mentioning that the edge spectrum density may increase very significantly when σ_2 tends to either σ_0^- or σ_0^+. This fact, revealed by the authors in their previous two-dimensional studies, see Kaplunov *et al.*,[11] is now be re-established in three dimensions. In order to illustrate this situation, for example, when $\sigma_2\to\sigma_0^+$, or, equivalently, $d\to 1$, we compare Figs. 4(b), 5(a), and 5(b) (the calculations are performed for $\Lambda=1.5$).

We start from Fig. 4(b), where σ_2 is in the middle of the stability interval, corresponding to $d=0$. We anticipate that as σ_2 tends to a critical value, the edge spectrum density will increase. Figure 5(a), corresponding to $d=0.875$, presents evidence of such an increase. We may now observe seven dispersion curves within the same frequency range, compared with three in Fig. 4(b). The effect becomes stronger as we proceed to Fig. 5(b), for which $d=0.99$. Another remark regards the sign of the group velocity in Figs. 4(b), 5(a), and 5(b). It can be clearly seen that as σ_2 tends to the critical value, the region of negative group velocity disappears. We note that similar illustrations may be readily obtained when σ_2 tends to the left end of the stability interval, and for other values of primary deformation and other strain-energy functions.

We will now present the long-wave asymptotic approximations of the dispersion relation (46). Introducing

$$c_R^{(0)} = c_R(n,0), \tag{57}$$

and expanding $\omega(n,kh)$ from Eq. (46) as a Taylor series in the vicinity of $kh=0$, it is possible to obtain

$$\omega h = c_R^{(0)}\pi n + \frac{(kh)^2}{2}\chi + \mathcal{O}(kh)^4, \tag{58}$$

where

$$\chi = -\left.\frac{\mathcal{G}_2(k,k)\mathcal{G}_1^2(\omega) - 2\mathcal{G}_2(k,\omega)\mathcal{G}_1(k)\mathcal{G}_1(\omega) + \mathcal{G}_2(\omega,\omega)\mathcal{G}_1^2(k)}{\mathcal{G}_1^3(\omega)h}\right|_{k=0}, \tag{59}$$

and

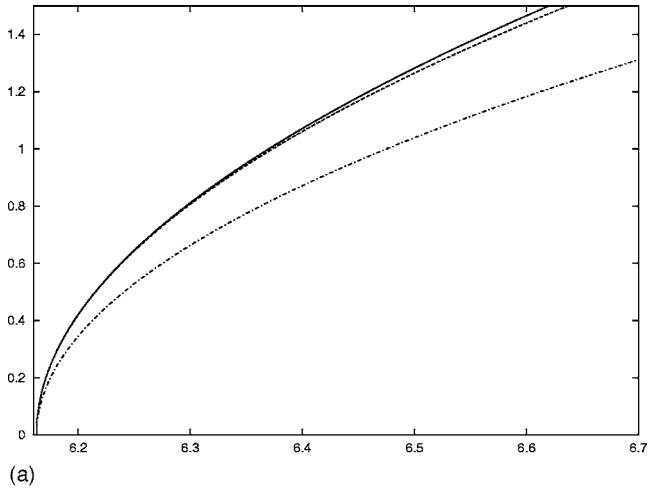

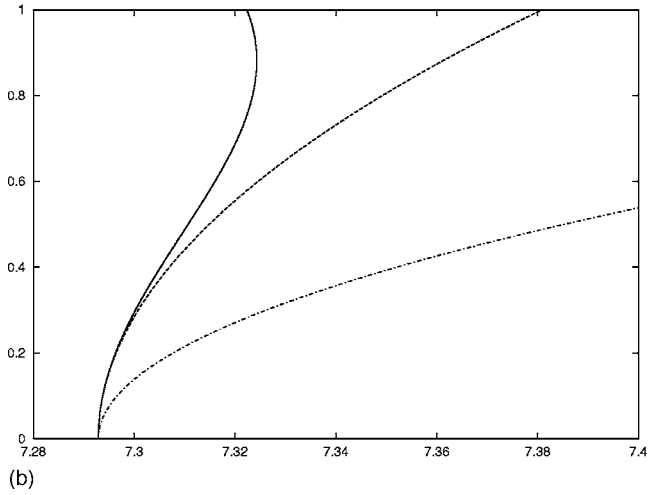

FIG. 6. Vibration modes of the dispersion relation (46) and their long-wave approximations in the vicinity of the cut-off frequencies for (a) $\Lambda=1.1$ and (b) $\Lambda=1.5$.

$$\mathcal{G}_2(x,y)=\frac{\partial T_{iA}}{\partial x}\frac{\partial T_{jB}}{\partial y}(S_{Ai}S_{Bj}-S_{Aj}S_{Bi})+\frac{\partial^2 T_{iA}}{\partial x\,\partial y}S_{Ai},$$

$$\mathcal{G}_1(x)=\frac{\partial T_{iA}}{\partial x}S_{Ai},\quad T_{iA}=T_{iA}(q_1,q_2,q_3,\omega),\quad \mathbf{S}=\mathbf{T}^{-1}. \tag{60}$$

Here T_{iA} and S_{Ai} denote the elements of matrix $\mathbf{T}$ and $\mathbf{S}$, respectively, and q_1, q_2, and q_3 are given explicitly in Eq. (51). We also note that summation over repeated suffices is tacitly assumed in Eq. (60).

We now proceed to the graphical illustrations of the obtained long-wave asymptotic approximations.

Figures 6(a) and 6(b) contain the first eigenmode (solid lines), its long-wave asymptotic approximation (58) (dashed lines), and also the corresponding approximation within the framework of linear isotropic elasticity (depicted by dashed-dotted line), given by Eq. (20).

Not surprisingly, it is observed from the first case ($\Lambda=1.1$), see Fig. 6(a), that the asymptotic expansion based on linear theory is still approximating the exact numerical solution. This may be explained by the fact that the primary deformation is relatively small, so the result is anticipated to be rather close to that for linear isotropic elasticity. Even so it may be seen that the other asymptotic expansion, derived in assumption that the surface wave speed depends on the wave number, works better. The preference of expansions (58) over approximations (20) becomes very clear in the second case ($\Lambda=1.5$), see Fig. 6(b).

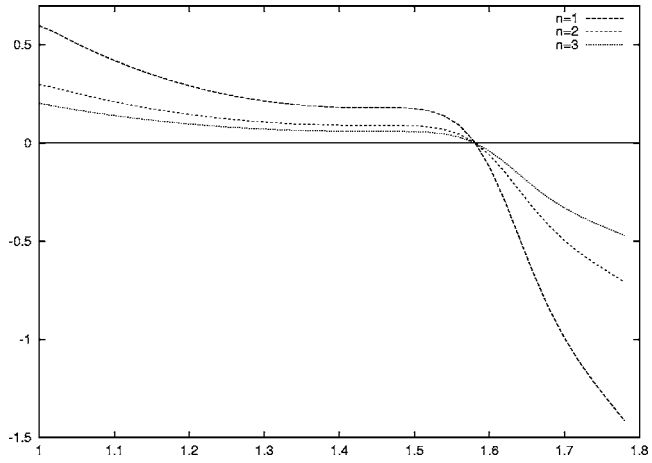

FIG. 7. The dependence of the scaled quantity $\bar{\chi}$ on the principal stretch Λ.

From Fig. 6(a) we observe that the asymptotic approximation (58) works remarkably well, probably due to the parabolic shape of the exact dispersion curve, allowing the second-order Taylor expansion to almost coincide with the exact solution. However, it is not so smooth in the second case, illustrated in Fig. 6(b), from which one may notice that a region of negative group velocity appears, which is not reflected in the asymptotic approximations. In order to overcome this difficulty a higher order Taylor expansion has to be computed. This may be quite complicated algebraically, though of no principal difficulty.

The coefficient χ seems to play a significant role in the dispersion behavior, and for each mode clearly depends on the pre stress parameters only. Figure 7 illustrates the behavior of the scaled coefficient $\bar{\chi}=\sqrt{\rho/c_{01}}\chi$ in respect of the prestress Λ for $n=1, 2, 3$. It can clearly be observed that at the point $\Lambda=1$, corresponding to linear isotropy, the value of $\bar{\chi}$ is positive, and then decreases with increase in Λ.

We also present the dependence of the scaled surface wave speed $\bar{c}_R=\sqrt{\rho/c_{01}}c_R$ over the dimensionless wave number kh for the cases of $\Lambda=1.1$ and $\Lambda=1.5$ (see Fig. 8). It can be noticed that in Fig. 8(a), illustrating the case which is close to the classical linear isotropy, the surface wave speed is changing slowly in the small vicinity of $kh=0$, being in a sense close to a constant. However, the second case reveals a completely different type of behavior.

V. CONCLUDING REMARKS

As previously mentioned, in this paper we restricted ourselves to considering symmetric motions for only one type of mixed face boundary conditions. Antisymmetric motion can be investigated in a similar way, as may the other two types of face boundary conditions. More details can be found in Kaplunov *et al.*[11] with respect to two-dimensional edge vibration.

Other important remarks are connected with possible ways of generalizing this approach. First of all, it should be

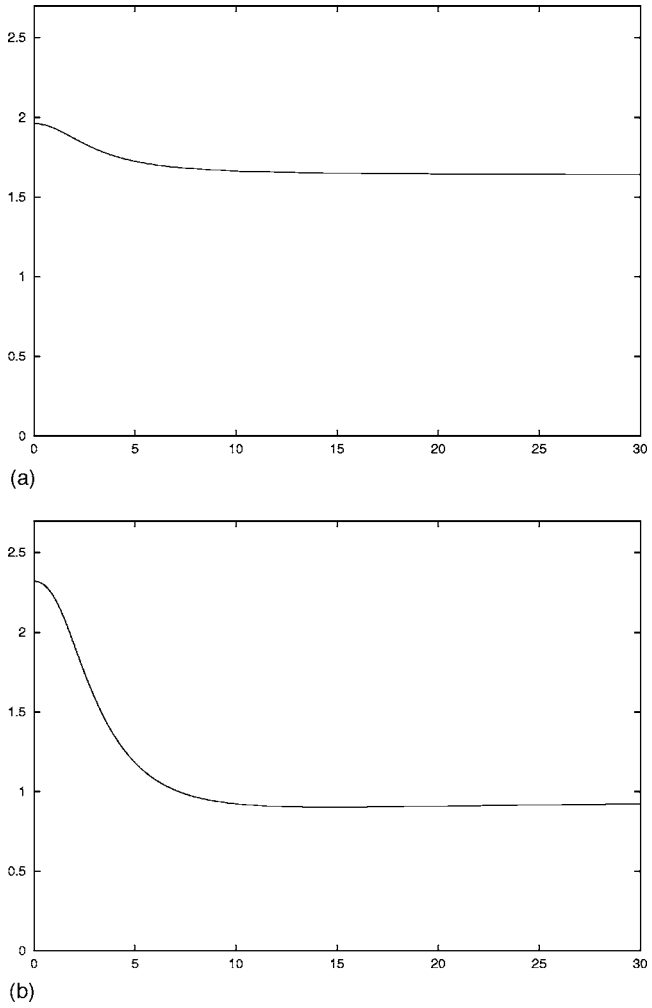

FIG. 8. The dependence of the scaled surface wave speed $\bar{c}_R$ on the wave number kh for (a) $\Lambda=1.1$ and (b) $\Lambda=1.5$.

possible to apply it to plates composed of anisotropic elastic media. Another problem which may be considered is the propagation of short wavelength edge waves in curved thin walled bodies. It is well known, see Kaplunov *et al.*,[17] that short-wave motion is not considerably influenced by curvature. Therefore, the ideas utilized in this paper may be applied, say, for a semi-infinite cylinder of a general curvature. Finally, the most difficult possible generalization is connected with a semi-infinite plate subject to some nonmixed face boundary conditions.

ACKNOWLEDGMENTS

The work of D. A. Prikazchikov is supported by an ORS Award and a University of Salford Postgraduate Award. These awards are gratefully acknowledged. The authors are also very grateful to Professor Y. Fu and Dr. E. V. Nolde for fruitful discussions.

[1]J. D. Kaplunov, L. Yu. Kossovich and M. V. Wilde, "Free localized vibrations of a semi-infinite cylindrical shell," J. Acoust. Soc. Am. **107**, 1383–1393 (2000).
[2]Yu. K. Konenkov, "A Rayleigh-type flexural wave," Sov. Phys. Acoust. **6**, 122–123 (1960).
[3]A. N. Norris, V. V. Krylov, and I. D. Abrahams, "Flexural edge waves and comments on 'A new bending wave solutions for the classical plate equation ," J. Acoust. Soc. Am. **107**, 1781–1784 (2000).
[4]D. D. Zakharov, "Analysis of the acoustical edge flexural mode in a plate using refined asymptotics," J. Acoust. Soc. Am. **116**, 782–788 (2004).
[5]Y. Fu, "Existence and uniqueness of edge waves in a generally anisotropic elastic plate," Q. J. Mech. Appl. Math. **56**, 605–616 (2003).
[6]A. N. Norris, "Flexural edge waves," J. Sound Vib. **174**, 571–573 (1994).
[7]D. D. Zakharov and W. Becker, "Rayleigh type bending waves in anisotropic media," J. Sound Vib. **261**, 805–818 (2003).
[8]D. P. Kouzov and V. D. Louk'yanov, "On the waves propagating along the edges of plates," Sov. Phys. Acoust. **18**, 129–135 (1972).
[9]R. V. Goldstein and A. V. Marchenko, "The diffraction of plane gravitational wave by the edge of an ice corner," J. Appl. Math. Mech. (PMM) **53**, 731–736 (1983).
[10]I. D. Abrahams and A. N. Norris, "On the existence of flexural edge waves on submerged elastic plates," Proc. R. Soc. London, Ser. A **456**, 1559–1582 (2000).
[11]J. D. Kaplunov, D. A. Prikazchikov, and G. A. Rogerson, "Edge vibration of a pre-stressed semi-infinite strip with traction-free edge and mixed face boundary conditions," J. Appl. Math. Phys. (ZAMP) **55**, 701–719 (2004).
[12]G. A. Rogerson and K. J. Sandiford, "Harmonic wave propagation along a non-principal direction in a pre-stressed elastic plate," Int. J. Eng. Sci. **37**, 1663–1691 (1999).
[13]M. A. Dowaikh and R. W. Ogden "On surface waves and deformations in a pre-stressed incompressible elastic solid," IMA J. Appl. Math. **44**, 261–284 (1990).
[14]R. W. Ogden *Non-linear Elastic Deformations* (Ellis Harwood, Dover, 1997).
[15]A. V. Pichugin and G. A. Rogerson, "An asymptotic membrane-like theory for long-wave motion in a pre-stressed elastic plate," Proc. R. Soc. London, Ser. A **458**, 1447–1468 (2002).
[16]D. A. Prikazchikov and G. A. Rogerson, "On surface wave propagation in incompressible, transversely isotropic, pre-stressed elastic half-spaces," Int. J. Eng. Sci. **42**, 967–986 (2004).
[17]J. D. Kaplunov, L. Yu. Kossovich and E. V. Nolde, *Dynamics of Thin Walled Elastic Bodies* (Academic, San Diego, 1998).

Transmission loss of viscoelastic materials containing oriented ellipsoidal coated microinclusions

Michael R. Haberman,[a] Yves H. Berthelot, and Mohammed Cherkaoui
Woodruff School of Mechanical Engineering, Georgia Tech Lorraine, 2 rue Marconi, 57070- Metz, France and Woodruff School of Mechanical Engineering, Georgia Institute of Technology Atlanta, Georgia 30332-0405 and Laboratoire de Physique et Mécanique des Matériaux, Institut Supérieur de Génie Mécanique et Productique, UMR 7554 CNRS, Université de Metz, 57045, Metz, France

(Received 2 February 2005; revised 20 May 2005; accepted 18 August 2005)

The three-phase self-consistent (SC) micromechanical model of Cherkaoui *et al.* [J. Eng. Mater. Technol. **116**, 274–278 (1994)] is employed to model the anisotropic effects induced by identically oriented, coated, and ellipsoidal microinclusions embedded in a viscoelastic matrix. Numerical predictions of the lossy and anisotropic behavior of the viscoelastic composite material are obtained. This study is an extension of a previous paper [J. Acoust. Soc. Am. **112** (5), 1937–1943 (2002)], where the agreement of the micromechanical approach with the long wavelength scattering model of Baird *et al.* [J. Acoust. Soc. Am. **105** (3), 1527–1538 (1999)] was demonstrated for the case of spherical inclusions. The use of the SC model for the special case of a biphase effective material is also considered and compared with the complex bounds available in the literature. Parametric studies are presented for the transmission loss in the 0–100 kHz frequency range of a 1 cm thick composite material slab containing oblate spheroidal inclusions of varying aspect ratios when the slab is submerged under water. The results are compared with the case of an isotropic composite material having identical constituent material properties and volume fractions. © *2005 Acoustical Society of America.* [DOI: 10.1121/1.2062648]

PACS number(s): 43.35.Mr, 43.20.Fn, 43.40.Fz [PEB] Pages: 2984–2992

I. INTRODUCTION

The acoustical properties of viscoelastic (VE) materials containing microinclusions have been a subject of interest for well over thirty years. Most models are derived using wave propagation techniques that require finding analytical solutions to the problem of a single inclusion (or coated inclusion) to an incident plane wave. The resulting relations are then expanded based on the low-frequency limit ($ka \ll 1$, k being the incident wave number and a the radius of the inclusion), and high-order terms are truncated. The resulting relations are generally only valid for a low volume fraction of inclusions and for spherical inclusions. Seminal papers in this area include those of Kuster-Toksöz[1] and Ying and Truell.[2] In order to improve the approximation of the lossy behavior for high volume fraction inclusions, several different multiple scattering and self-consistent (SC) approaches have been proposed, most notably by Gaunaurd and Überall,[3] Waterman and Truell (WT),[4] Varadan *et al.*,[5] and others.[6–8] Unfortunately, these methods break down when the composite contains nonspherical inclusions. An exception is the model proposed by Berryman,[9] which is limited to biphase composites with randomly oriented ellipsoidal inclusions yielding a globally isotropic effective material having different properties than that of a composite containing spherical inclusions. The objective of this paper is to present a three-phase model that predicts the effective material and acoustical properties of a viscoelastic matrix containing coated spheroidal microinclusions. The approach selected here is not based on wave propagation models but rather on a SC micromechanical model of Haberman *et al.*[10]

It was previously shown that the micromechanical models can be used to approximate the global dynamic behavior of isotropic three-phase lossy composites in the low-frequency, or quasi-static, regime.[10] This is due to the fact that the main features of the dynamics of the composite are correctly captured in the quasi-static regime because the micromechanical approach takes the small strains in the neighborhood of an inclusion into account using homogenization techniques. Thus, it accounts for losses during propagation directly due to that strain and not by using the scattering approximations. This approach has the added advantage of being amenable to the modeling of the anisotropic behavior of the material when the inclusions are no longer spherical and are similarly oriented with respect to the coordinate system of reference.

II. MODEL

Consider a fluid medium of density ρ and sound speed c in which an acoustic plane wave of the form $e^{i(kx_3-\omega t)}$ is normally incident on an infinitely long slab of thickness L, as shown in Fig. 1. The slab is made of a VE material with complex Lamé constants, λ_M and μ_M and density ρ_M. Consider the orthotropic case where the slab contains oblate spheroidal inclusions all oriented such that their minor axes are along the x_3 direction of propagation. The inclusions are defined by their Lamé constants λ_I and μ_I and density ρ_I, the coating by λ_C and μ_C, density ρ_C, and the thickness Δa, where $\Delta a/a$ is assumed to be much less than unity. If the

[a]Author to whom correspondence should be addressed; electronic mail: mhaberma@georgiatech-metz.fr

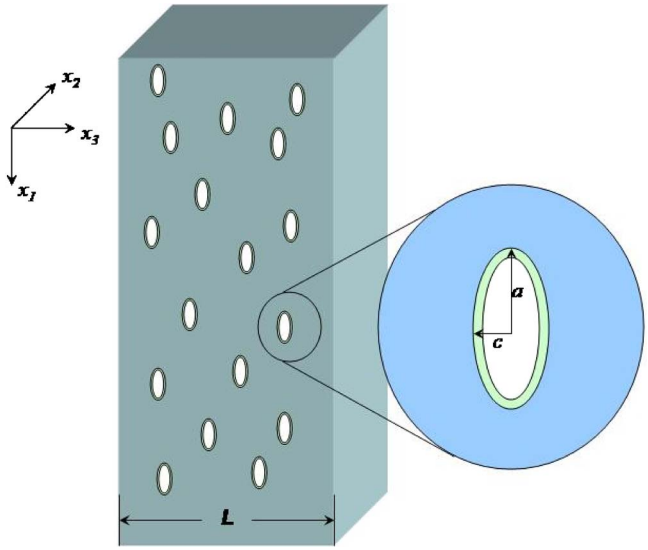

FIG. 1. (Color online) Diagram of a slab of viscoelastic composite material containing oblate spheroidal coated inclusions showing the major axes of interest and the orientation of coordinate system used in TL calculations.

inclusions are much smaller than the wavelength, and if they are distributed uniformly throughout the slab, it is reasonable to model the composite as a homogeneous material defined by its complex effective elastic stiffness tensor C_{ijkl}^{eff}. For plane wave transmission along the x_3 axis, through the slab submerged in water, the transmission loss (TL), in decibels, is defined in terms of the transmission coefficient T by[11]

$$\text{TL} = -10\log_{10}(TT^*) \tag{1}$$

with

$$T = 2\left[2\cos(k^{\text{eff}}L) - i\left(\frac{Z^{\text{eff}}}{(\rho c)^{\text{water}}} + \frac{(\rho c)^{\text{water}}}{Z^{\text{eff}}}\right)\sin(k^{\text{eff}}L)\right]^{-1}, \tag{2}$$

where the effective wave number in the x_3 direction is given by

$$k^{\text{eff}} = \omega\sqrt{\frac{\rho^{\text{eff}}}{M^{\text{eff}}}} = k'_{\text{eff}} + i\alpha^{\text{eff}}. \tag{3}$$

The effective density and impedance of the composite are, respectively,

$$\rho^{\text{eff}} = \rho^M - \phi\left[\rho^M - \rho^C\left(3\frac{\Delta a}{a}\right) - \rho^I\left(1 - 3\frac{\Delta a}{a}\right)\right], \tag{4}$$

and

$$Z^{\text{eff}} = \rho^{\text{eff}}c^{\text{eff}} = \sqrt{M^{\text{eff}}\rho^{\text{eff}}}. \tag{5}$$

In the above equations, $M^{\text{eff}} = C_{33}^{\text{eff}}$ is the complex plane wave modulus of the material in the direction of wave propagation, c^{eff} is the longitudinal phase velocity in the x_3 direction, α^{eff} is the longitudinal wave amplitude attenuation coefficient in the x_3 direction, ϕ is the volume fraction of coated inclusions, and the asterisk denotes the complex conjugate.

In the micromechanical approach, the global behavior of the composite material is approximated by writing the constitutive stress and strain relations for the smallest element that is assumed to fully describe the material. This element is called the representative volume element (RVE). For the SC model used here, it consists of a coated ellipsoidal inclusion embedded in an effective matrix of unknown properties (see Fig. 2). The derivation of this model for the static case is given by Cherkaoui *et al.*[12] and its extension to the long-wavelength (low-ka) regime is given by Haberman[10] for the case of coated spherical inclusions. For convenience, the tensor relations for the frequency dependent effective material properties of a composite consisting of a frequency dependent VE matrix containing inclusions coated by a third phase are included in Eq. (6):

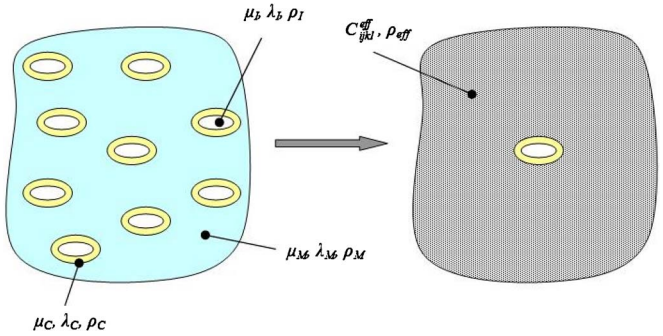

FIG. 2. (Color online) RVE of SC approach to model the effective material.

$$C_{ijmn}^{\text{eff}}(f) = C_{ijmn}^{M}(f) + f_I\left[C_{ijkl}^{I}(f) - C_{ijkl}^{M}(f)\right]A_{klmn}^{I} + f_C\left[C_{ijkl}^{C}(f) - C_{ijkl}^{M}(f)\right]A_{klmn}^{C}. \tag{6}$$

The elastic properties of the matrix, inclusion, and coating are given by the stiffness tensors $C_{ijkl}^{M}(f)$, $C_{ijkl}^{I}(f)$, and $C_{ijkl}^{C}(f)$, respectively, f_I and f_C are the volume fractions, and A_{ijrs}^{I} and A_{ijrs}^{C} are the strain localization tensors for the inclusion and coating, respectively. It should also be noted that the equations given here were developed for the homothetic case, that is the case where $\Delta a_i/a_i = \Delta a_j/a_j$. We emphasize that the model has no restrictions on the frequency dependent behavior of the matrix, inclusion, or coating material and, in general, all three phases may display very different frequency dependent behavior without loss of applicability of the SC model in the low-ka limit. In what follows, however, only the frequency dependence of the VE matrix material is taken into account as it often dominates the lossy behavior of composites of interest.

The key to the evaluation of this or any micromechanical model lies in the evaluation of the strain localization tensors. These tensors can be understood to be intelligently calculated weights on the law of mixtures approximation to the global behavior of the composite. The function of these tensors is to relate the globally observed strain of the composite, denoted as E_{ij}, to the average strain (which, after the work of Eshelby,[13] is assumed to be uniform) in its respective phase χ, $\bar{\varepsilon}_{ij}^{\chi}$. These two strains are related by $\bar{\varepsilon}_{ij}^{\chi} = A_{ijkl}^{\chi}E_{kl}$. The specific relations for the coating and inclusion strain localization tensors are given in Refs. 10 and 12, and are rewritten here for convenience

$$A^I_{ijrs} = \left\{ \frac{f_I}{f_I + f_C} \left(I_{ijrs} + T^I_{ijkl}(C^{\text{eff}}) \Delta C^I_{klrs} \right) + \frac{f_C}{f_I + f_C} \left(I_{ijmn} + T^I_{ijkl}(C^{\text{eff}}) \Delta C^C_{klmn} \right) \times \left(I_{mnrs} + T^I_{ijkl}(C^C) \Delta C^{IC}_{klrs} \right) \right\}^{-1}, \tag{7a}$$

$$A^C_{ijpq} = \left(I_{ijmn} + T^I_{ijkl}(C^C) \Delta C^{IC}_{klmn} \right) A^I_{mnpq}, \tag{7b}$$

where the contrast tensors ΔC^X_{ijkl} are given below:

$$\Delta C^I_{ijkl} = C^I_{ijkl} - C^{\text{eff}}_{ijkl}, \tag{8a}$$

$$\Delta C^C_{ijkl} = C^C_{ijkl} - C^{\text{eff}}_{ijkl}, \tag{8b}$$

$$\Delta C^{IC}_{ijkl} = C^I_{ijkl} - C^C_{ijkl}. \tag{8c}$$

Since Eqs. (7) and (8) depend on the effective elastic tensor, Eq. (6) must be solved *implicitly* for C^{eff}_{ijkl}. In Eq. (7), the tensor $T^I_{ijkl}(C^X)$ is the integral of the modified Green's tensor, $\Gamma_{ijkl}(r-r')$, defined in Eq. (9):

$$C^X_{ijkl} G_{km,lj}(r-r') + \delta_{im}\delta(r-r') = 0, \tag{9a}$$

$$\Gamma_{mnij}(r-r') = -\frac{1}{2}\{G_{mi,nj}(r-r') + G_{ni,mj}(r-r')\}, \tag{9b}$$

$$T^I_{ijkl}(C^X) = \int_{V_I} \Gamma_{ijkl}(r-r')dr, \qquad r' \in V_I. \tag{9c}$$

The Green's tensor, $G_{km}(r-r')$, is used in the static regime to represent the displacement in the k direction at point r when a unit force, $f_i = \delta_{im}(r-r')$, is applied at point r' in the m direction. This unit force is proportional to the stress caused by the accommodation of the matrix due to the presence of the inclusion at point r'. $T^I_{ijkl}(C^X)$ can be calculated for the cases of elliptical inclusions embedded in an *isotropic* matrix according to the results of Eshelby[13] as cited in Mura.[14] However, in the case of oriented ellipsoidal inclusions and/or anisotropic constituents, the calculation of $T^I_{ijkl}(C^{\text{eff}})$ becomes complicated due to the resultant anisotropic effective stiffness tensor and, therefore, numerical approximation techniques must be adopted to resolve the system. Numerical evaluation can be done either by the method of Fourier transforms (FTs) or that of potential functions.[14] The current implementation of the SC model employs the FT technique as the means of approximating the tensor. For evaluation using the FT technique, the assumption is made that the displacement field caused by the presence of the inclusion can be represented by the superposition of an infinite sum of spatially regular displacement fields. This assumption, by the very nature of the FT, implies that the spacing of inclusions is regular. Though this can be a gross estimate, the method has been proven to provide very good approximations to true composite material behavior.[14] Numerical approximation of the implementation of this method is briefly discussed in the Appendix.

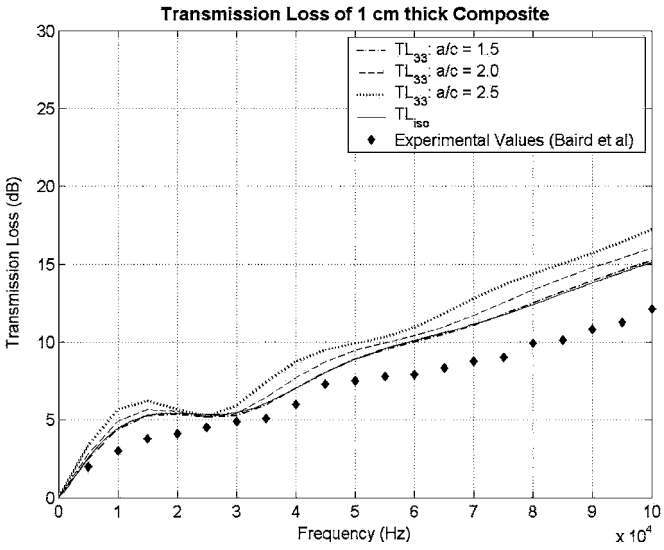

FIG. 3. TL of 1 cm thick slab of composite material having the orientation shown in Fig. 1 and containing 13% by volume of oblate coated inclusions of varying aspect ratios. —- $a/c=1$, –.- $a/c=1.5$, - - - $a/c=2$, ... $a/c=2.5$.

III. RESULTS

The model is used to predict sound transmission through a VE slab, 1 cm thick, containing 13% volume fraction of coated oblate inclusions of varying aspect ratios. The constituent materials are taken to be the same as those used by Baird *et al.*[7] for the case of a stiff matrix. Figure 3 gives the TL as a function of frequency for various aspect ratios: $a/c=1$ (spherical inclusions), $a/c=1.5$, 2.0, and 2.5, while keeping the volume fraction constant at $\phi=0.13$. The oscillations in TL observed at the lower frequencies of the observed range are caused by resonances in the finite thickness of the slab. Maximum transmission, i.e., minimum TL, occurs at the half-wavelength resonances while maximum TLs occur at the odd quarter-wavelength resonances. It is observed that increasing the aspect ratio a/c results in a small increase in TL (less than 2 dB in the 0–100 kHz range) because of the increased shear strain in the neighborhood of the inclusion caused by the form of the inclusion. In other words, for the same traveling compressional stress wave field, more deformation occurs in the neighborhood of the oblate inclusions as compared to the spherical inclusion. Thus, more mode conversion to shear occurs, with subsequent increased losses. This trend is also confirmed by plotting the attenuation coefficient, α^{eff}, of the longitudinal wave number as a function of the angle in the x_1-x_3 plane, as shown in Fig. 4. The angle is the polar angle, here denoted as θ, in spherical coordinates and the plot shows the attenuation coefficient for a longitudinal wave traveling in the direction, $\mathbf{n}$, defined as $\mathbf{n}=\langle \sin\theta\cos\varphi\hat{\mathbf{i}}, \sin\theta\sin\varphi\hat{\mathbf{j}}, \cos\theta\hat{\mathbf{k}}\rangle$, in an infinite medium containing oriented ellipsoidal inclusions (where φ is the azimuthal angle). It is in this way that the influence of changing the orientation of inclusions with respect to the coordinate system shown in Fig. 1 (i.e., rotating the inclusions about the x_2 axis in the material) for a slab of composite material can be studied. The attenuation coeffi-

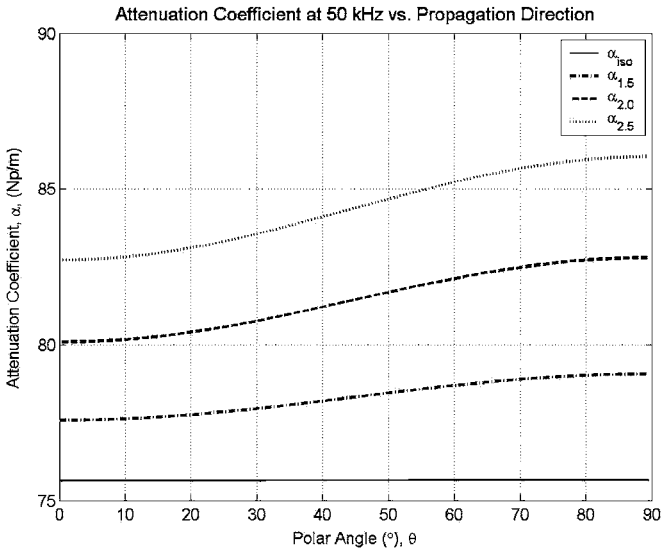

FIG. 4. Attenuation coefficient as a function of angle in the x_1-x_3 plane of material containing oblate ellipsoidal inclusions of varying aspect ratios ($\theta=0$ coincides with x_3 axis). The volume fraction of inclusions is 13% and the frequency of the incident wave is 50 kHz. —- $a/c=1$, –.- $a/c=1.5$, - - - $a/c=2$, ... $a/c=2.5$.

cient in the x_1-x_3 plane ($\varphi=0$) as a function of polar angle is calculated as shown below:

$$\alpha^2(\theta) = \alpha_{11}^2 \sin^2\theta + \alpha_{33}^2 \cos^2\theta. \tag{10}$$

As expected, both the attenuation coefficient (in Np/m) and the anisotropy factor, defined as $(\alpha_{11}-\alpha_{33})/\alpha_{33}$, increase as the aspect ratio increases. One interesting point is that as the angle of propagation increases, the attenuation coefficient is seen to increase. Here, it is noted that there are competing factors to the increase or decrease in the lossy behavior with respect to the polar angle, namely effective shearing area of the inclusions based on their form and increases or decreases in effective material stiffness of the composite due to coated-inclusion properties. For the case shown in Fig. 4, the increase in shearing area parallel to the propagation direction

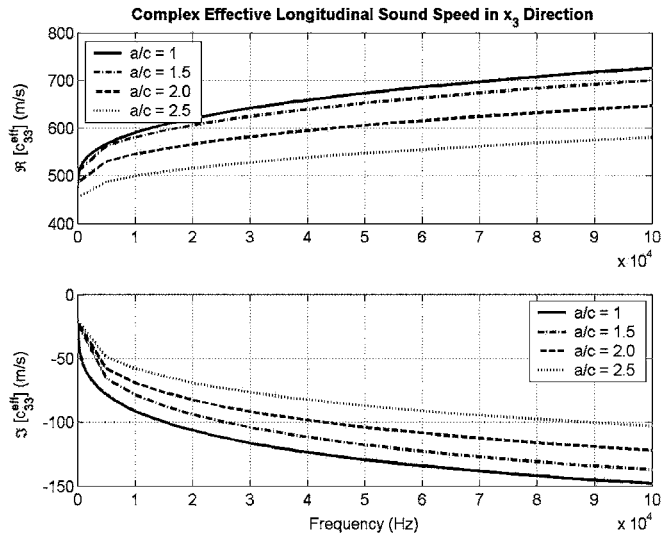

FIG. 5. Real and imaginary parts of effective complex longitudinal wave speed in x_3 direction as function of frequency for a volume fraction inclusions of 13%. —- $a/c=1$, –.- $a/c=1.5$, - - - $a/c=2$, ... $a/c=2.5$.

TABLE I. Material properties of coating and inclusion for material modeled in Fig. 6.

	μ (GPa)	ν	ρ (kg/m^3)
Coating	1.40	0.40	1200
Inclusion	28.5	0.23	2300

due to the oblate form of the inclusions dominates, and thus causes an increase in lossy behavior which results in the observed increase in attenuation coefficient with polar angle. As will be seen below, the opposite trend is observed when an overall increase in stiffness due to inclusion and coating materials dominates the increase in shearing area. Figure 5 plots the real and imaginary parts of the complex wave speed in the x_3 direction as a function of frequency for aspect ratios $a/c=1, 1.5, 2.0$, and 2.5, again for a fixed volume fraction $\phi=0.13$. The results show another aspect of the change in inclusion form, specifically that at a fixed frequency, the real part of the phase velocity decreases as the aspect ratio is increased. This corresponds to a relative softening in the x_3 direction of the composite for increasing aspect ratios, a result of the increased strain energy in the neighborhood of the inclusion for the same stress levels due to the oblate inclusion geometry. At the same time, at a fixed frequency, the absolute value of the imaginary part of the phase velocity also decreases as the aspect ratio is also increased, though proportionally less than the decrease of the real part. This corresponds to an increase in attenuation in the x_3 direction for the oblate geometry.

The above discussion is for a specific case of a VE matrix containing oblate coated inclusions. However, the SC model can be used to study the effects of prolate, needle-shaped, and penny-shaped inclusions, among others. In order to investigate such effects, the SC model is applied to the case of composite material consisting of the same VE matrix used previously and containing inclusion and coating materials with the properties given in Table I. To display this capability, five types of inclusions are considered: Oblate, prolate, penny-shaped, and needle-shaped ellipsoids, as well as spherical inclusions. For each of these cases, the ratios of the minor radii, a/b and a/c, are given in Table II. In Fig. 6, the variation of the calculated attenuation coefficient in the x_1-x_3 plane is plotted as a function of polar angle. As expected, the minimum attenuation is observed for propagation along the x_3 axis ($\theta=0$) for a composite containing needle-shaped inclusions aligned with this axis. The attenuation increases monotonically when the angle between incident plane wave and the long axis of the needle-shaped inclusions is increased. The attenuation is also reduced for propagation along the x_1 axis (and therefore, by symmetry, the x_2 axis) for a composite containing penny-shaped inclusions with

TABLE II. Minor radius ratios for composite modeled in Fig. 6.

	Sphere	Oblate	Penny	Prolate	Needle
a/b	1	1	1	1	1
a/c	1	3	10	1/3	1/10

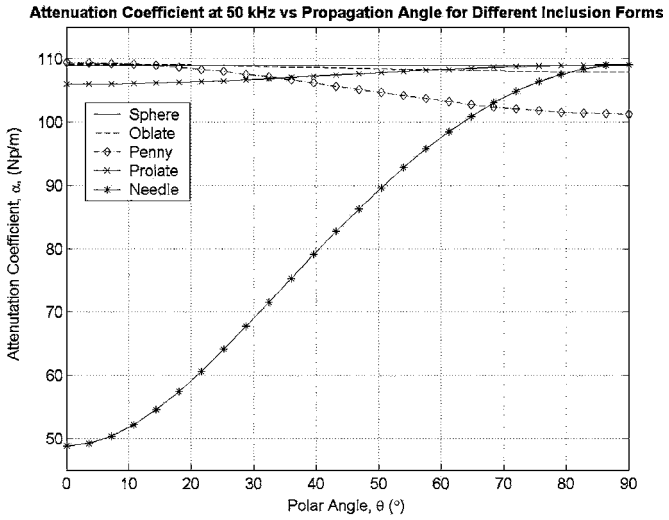

FIG. 6. Attenuation coefficient as a function of angle in the x_1-x_3 plane for a composite consisting of a VE matrix with Lucite coated glass ellipsoidal inclusions of different forms (θ=0 coincides with x_3 axis). The volume fraction of inclusions is 10% and the frequency of the incident wave is 50 kHz.

large radii in the x_1-x_2 plane. As discussed in the previous paragraph where the opposite was observed for different coated inclusions having different properties, this decrease in attenuation is due to the stiffening of the material in that direction due to the material properties of the inclusions and coating, which dominate the increase in shearing area. This also explains why the decrease in attenuation coefficient for the oblate and penny-shaped inclusions is much less than that of the needle-shaped inclusions, namely that the increase in shearing area of these inclusions, which tends to cause more lossy behavior, is competing with the increase in stiffness, which decreases losses. For this case, the increase in stiffness dominates, but its effects are reduced as the shearing area is significantly raised in this form of inclusion. As expected, the composite containing spherical inclusions has a constant attenuation regardless of propagation direction, and the oblate and prolate inclusion cases fall somewhere in between the limits of the penny-shaped and needle-shaped inclusions. One point of interest is that the attenuation coefficient for propagation along the x_3 axis for materials containing both oblate and penny-shaped inclusions is slightly superior to that of the material containing spherical inclusions. This is due to the fact that the shape of the inclusion leads to stronger mode conversion at the boundaries.

At this point, it is interesting to point out that the factors discussed above give a few guidelines for the design of composite materials for a desired lossy behavior. First, if inclusions are softer than the matrix material, an increase in aspect ratio will lead to increases in lossy behavior over that of spherical inclusions in all directions, and even higher losses will be observed in directions perpendicular to the outward normals of increased shear areas, such as is the case of the oblate spheroids shown in Fig. 4. Second, if stiffness is required in one direction while high losses are desired in an orthogonal direction, high modulus needle-shaped inclusions are an ideal solution (see, for example, Fig. 6). This type of inclusion leads to low losses and high reinforcement along the longest major axis of the inclusions, while maintaining a lossy behavior nearly identical to spherical inclusions (twice the attenuation as observed along the longest axis) for propagation in the perpendicular plane.

IV. DISCUSSION

A. Bounds

When modeling the effective mechanical properties of composite materials with any effective medium theory (EMT), it is well known that the predicted elastic moduli must fall within certain accepted limits, or bounds. These bounds are based on high- and low-energy restrictions for a given concentration of material phases, the most restrictive of which are based on variational principles. Bounding techniques for purely elastic materials (i.e., no losses, real moduli) are well established. For information on these bounds, the reader is referred to Hashin and Shtrikman,[15] Walpole,[16] Hill,[17,18] and to the review by Hashin.[19] It is well known that the n-phase SC model falls within accepted bounds in the purely elastic case.[20] However, there has been comparatively less work done on the bounds of the effective material properties of composites having complex effective material properties. The problem has been addressed in several papers starting with Hashin,[21–23] Christensen,[24] and Roscoe.[25,26] More recently, rigorous bounding techniques based on variational techniques first introduced by Cherkaev and Gibiansky,[27] and Milton[28] have been introduced. These techniques have resulted in a series of related papers by Gibiansky and Milton,[29] Milton and Berryman,[30] Gibiansky and Lakes,[31,32] and Gibiansky and Torquato.[33] These methods all rely on bounding the effective bulk and/or shear moduli of the composite in zones of the complex plane prescribed by arcs which are functions of the complex moduli of the constituent phases. Their approach reduces, in the purely elastic case, to the Hashin–Shtrikman bounds for an isotropic biphase composite.

Currently, there seems to be no bounding techniques for anisotropic three-phase VE composites. The bounds proposed Gibiansky and Lakes[31] for the complex effective bulk modulus and by Milton and Berryman[30] for the complex shear modulus, though three-dimensional, are restricted to the case of a biphase isotropic composite. Both of these approaches bound the complex effective values to a lens-shaped region in the complex plane for a given volume fraction of inclusion and frequency. The results of the SC model, as applied to hypothetical material properties for 50% inclusion volume fraction as given in Refs. 31 and 30, are shown in Figs. 7 and 8, respectively. The material properties are summarized in Table III for convenience. The complex bulk and shear moduli calculated by the self-consistent approach, discussed in Sec. I, are shown to fall within the complex bounds of both Gibiansky and Lakes[31] and Milton and Berryman.[30]

B. Numerical implementation

Successful implementation of the general SC model depends on the ability to evaluate numerically the solution to the implicit problem given in Eqs. (1)–(4). Because of the

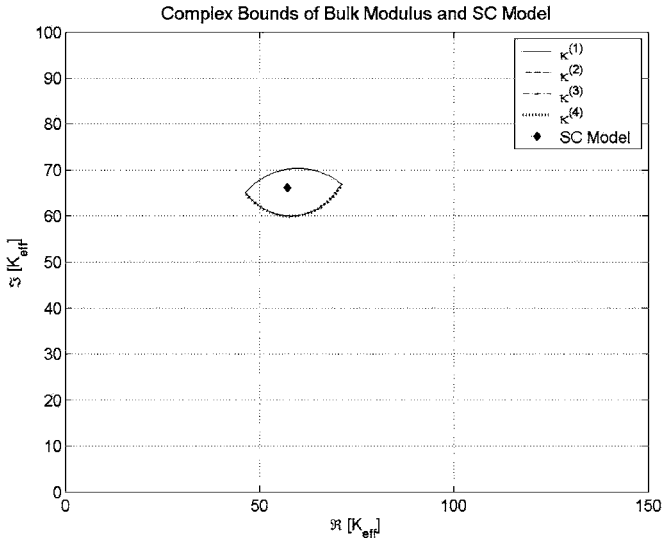

FIG. 7. Bounds in the complex bulk modulus plane calculated from Ref. 31 and SC model approximation, ♦, of same composite. Bounds are delineated by four, sometimes overlapping, lines: $\kappa^{(1-4)}$.

complexity of the implicit tensor relationships, careful consideration must be made in the selection of the numerical root-finding and/or minimization techniques to find the solution for the effective tensor C_{ijkl}^{eff}. For the case of spherical-coated inclusions, the resulting effective properties are isotropic and Eqs. (1)–(4) can be reduced to two implicit equations for the effective Lamé constants, μ^{eff} and λ^{eff}. These relations are given in Appendix A of Haberman *et al.*[10] Solutions to this set of equations can be obtained by using a two-dimensional Newton–Raphson numerical root-finding scheme. This technique for the isotropic effective material is very robust and no convergence problems have been observed regardless of material contrasts or volume fraction of coated inclusions.

The implicit solution to the general anisotropic case is neither simple nor guaranteed to converge for all combinations of material stiffness contrasts, inclusion aspect ratios,

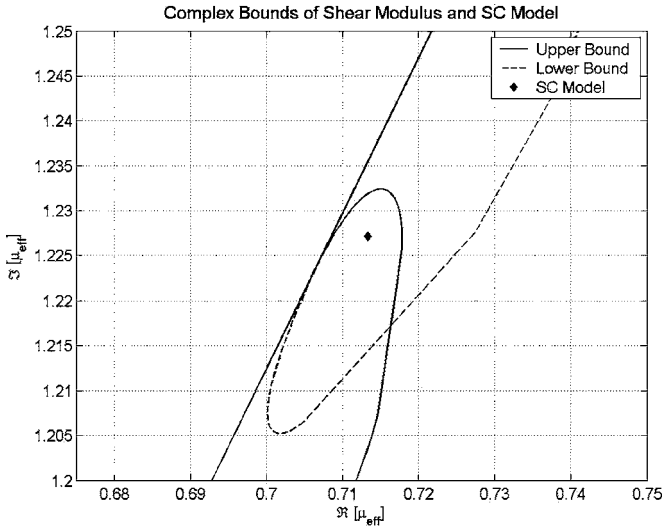

FIG. 8. Bounds on the complex effective shear modulus given in Ref. 30. —- Upper bound; - - - Lower bound. Calculated SC model point, ♦, is shown to fall within ellipsoidal bounded area.

TABLE III. Material properties and inclusion volume fractions used for Figs. 7 and 8.

	Vol. Fract.	μ_1	K_1	μ_2	K_2
Figure 7	50%	$40+0i$	$100+0i$	$0+30i$	$0+65i$
Figure 8	50%	$0.5+0.866i$	$0.66+0.33i$	$1+1.732i$	$1.33+0.833i$

Note: Values taken from Refs. 30 and 31 for verification.

or volume fractions. For the case of orthotropic materials, fully described by nine independent elastic constants, the coefficients of the effective stiffness tensor can be rearranged as a 9×1 vector, $C_{ijkl}^{\text{eff}}\rightarrow\mathbf{v}^{\text{eff}}$. A function of this vector, to be minimized, can then be defined in order to approximate the solution of the effective material stiffness to an acceptable degree of accuracy. For our application, this function is defined in Eq. (11):

$$h(\mathbf{v}^{\text{eff}}) = \text{SC}(\mathbf{v}^{\text{eff}}) - \mathbf{v}^{\text{eff}}, \tag{11}$$

where $h(\mathbf{v}^{\text{eff}})$ is the function to be minimized and $\text{SC}(\mathbf{v}^{\text{eff}})$ is understood to be the result in vector form of the SC model given in Eqs. (1)–(4) for an input of $\mathbf{v}^{\text{eff}}\rightarrow C_{ijkl}^{\text{eff}}$. The evaluation of the tensor $T_{ijkl}^{I}(C^{X})$ given in Eq. (4c) is done by numerical integration of the modified Green's tensor by an n-point Gauss–Legendre quadrature integration, after using FT techniques to transform the ellipsoidal inclusions into spheres in the Fourier domain as outlined in the Appendix. A nine-dimensional simplex method[34] is then used to minimize the implicit relationship given in Eq. (11). The simplex method is robust and effective because it does not require the calculation of rates of change in the function with respect to each individual variable. The technique involves the evaluation of the SC model at ten points suspected to surround the solution in the nine-dimensional space. During implementation, these points are chosen by varying each of the nine elements of $\mathbf{v}^{\text{eff}}$ of the previous volume fraction step by a small percentage (1% used for this evaluation), yielding nine initial guess points and then using the unaltered elements of $\mathbf{v}^{\text{eff}}$ for the tenth point. The algorithm then uses a series of reflections and contractions of the ten points until an acceptable level of convergence is found. Though the technique is robust, it is not guaranteed to converge to the correct solution and calculation time can be significant for a high volume fraction of inclusions.

Several factors can cause significant problems in the convergence of the numerical evaluation of the general SC model. Therefore, a few qualitative observations may help for the successful implementation of the method. The parameter that has the strongest influence on the convergence of the model is the contrast of the moduli of the constituent phases. If the moduli of the inclusion materials are significantly lower than that of the matrix (as is the case with air inclusions), the numerical scheme has great difficulty in converging to the correct solution. This is also the case when the inclusions are coated. Indeed, glass coated voids embedded in a soft matrix prove to be one of the most difficult set of parameters for the resolution of the general SC model. Another parameter that has a strong influence on the convergence of the general model is the aspect ratio of the inclu-

sions. As the aspect ratio (either a/b or a/c) increases, the likelihood of poor convergence behavior also increases. It should be noted that poor convergence due to the inclusion aspect ratio is coupled with the contrast of the material properties; the higher the material contrast, the less stable the SC method for any given aspect ratio. However, no obvious practical guidelines can be given. Here, it is emphasized that, even with large aspect ratios, the model is strictly valid in the low-ka regime. Yet another parameter that can influence convergence, though to a lesser extent, is the ratio of $\Delta a/a$, i.e., the normalized coating thickness. It has been observed that values of this parameter below 10^{-3} can lead to poor convergence behavior, though, like the effect of the aspect ratio, the influence of $\Delta a/a$ on the convergence is coupled to the material contrast and therefore smaller ratios can be tolerated for lower contrast situations. Other known issues are usual user-defined parameters of root-finding techniques, such as the initial values for the numerical search algorithm, the volume fraction step size, and the number of points chosen for Gauss–Legendre evaluation of the integral of the modified Green's tensor.

V. CONCLUSIONS

A SC model has been used to evaluate the effective elastic constants of an isotropic viscoelastic matrix containing coated, ellipsoidal elastic inclusions. The model relies on a careful evaluation of the strain localization tensors, which are well known in micromechanics, as the averaging technique for EMT calculations. Then, the lossy behavior of the anisotropic composite is captured by introducing the frequency dependence of the complex moduli of the matrix material. This approach is fundamentally different from the scattering formulation of Refs. 1–8 which are derived from wave-propagation considerations. It was, therefore, shown that the implicit formulation accounts for multiple scattering through micromechanical homogenization techniques. A simplex minimization algorithm has been used to calculate the effective elastic tensor in the orthotropic case where the coated ellipsoidal inclusions are all aligned in the same directions. The complex effective sound speed of the material has been evaluated as a function of frequency, constituent properties, and volume fraction. The TL of a normally incident plane wave, in water, through a 1 cm thick slab of such a composite, has been calculated for oblate-ellipsoidal coated inclusions with aspects ratios ranging from 1.0 (sphere) to 2.5. For the range of material properties used, the effect of the inclusion geometry on the TL was modest, less than 2 dB. The effects of different inclusion geometries, such as penny-shaped, needle-shaped, oblate, and prolate, have also been studied. The results show that variations with direction on the lossy behavior of a composite can be obtained using the quasi-static SC model. It has also been shown that the model predicts values of effective complex moduli for two-phase media (uncoated inclusions) that are within the complex bounds established by Gibiansky and Lakes,[31] and Milton and Berryman.[30] The given calculations and discussion further verify that the micromechanical model allows for a level of generality in modeling of lossy composites, where other modeling approaches are limited. As such, it is possible that it could be a useful tool in the design of new anisotropic damping materials for numerous applications, including for cases where the anisotropy of such materials is induced due to loading conditions or manufacturing processes.

ACKNOWLEDGMENTS

The authors gratefully acknowledge support from the Conseil Régional de Lorraine in France.

APPENDIX: NUMERICAL EVALUATION OF GREEN'S TENSOR BY FOURIER TRANSFORM TECHNIQUES

Implementation of the SC technique requires the numerical approximation of the modified Green's tensor for cases where the surrounding matrix is anisotropic (this includes cases when the actual material phases are anisotropic or when the inclusions are ellipsoidal and oriented). The numerical evaluation is done via Fourier transform techniques as explained in Mura.[14] The method is rather involved, but stated simply involves using the Fourier integral to transform the ellipsoid into a sphere in Fourier domain (where the transform variable is the "wave number" of the spatial regularity of the strain field in an infinite homogeneous medium due to the presence of inclusions). The transformation allows for numerical integration around a spherical volume using numerical techniques (Gauss–Legendre quadrature is the method currently employed) to evaluate Eq. (9c).

Let the FT of the Green's tensor and its inverse be defined as follows:

$$\tilde{G}_{km}(k) = \int_{-\infty}^{\infty} G_{km}(r) e^{ik\cdot r} dr,$$
$$G_{km}(r) = \frac{1}{(2\pi)^3} \int_{-\infty}^{\infty} \tilde{G}_{km}(k) e^{-ik\cdot r} dk, \tag{A1}$$

where the vector k is the wave number of the displacement (and therefore strain) field in an infinite homogeneous medium due to the presence of the coated inclusion. Applying the Fourier transform to Eq. (9a) leads to

$$C^{\chi}_{ijkl} k_l k_j \tilde{G}_{km}(k) = \delta_{im}. \tag{A2}$$

If the inclusion is ellipsoidal, it is convenient to introduce the following change of variables:

$$\vec{r} = \begin{Bmatrix} x_1 \\ x_2 \\ x_3 \end{Bmatrix} \Rightarrow R = \begin{Bmatrix} X_1 = x_1 \\ X_2 = \dfrac{a}{b}x_2 \\ X_3 = \dfrac{a}{c}x_3 \end{Bmatrix} \text{ and } k = \begin{Bmatrix} k_1 \\ k_2 \\ k_3 \end{Bmatrix} \Rightarrow K$$
$$= \begin{Bmatrix} K_1 = k_1 \\ K_2 = \dfrac{b}{a}k_2 \\ K_3 = \dfrac{c}{a}k_3 \end{Bmatrix}. \tag{A3}$$

The following equalities are then useful:

$$k \cdot r = K \cdot R, \tag{A4}$$

$$k_i = \Phi_{it}K_t, \quad \text{where } [\Phi_{it}] = \begin{bmatrix} 1 & 0 & 0 \\ 0 & \dfrac{a}{b} & 0 \\ 0 & 0 & \dfrac{a}{c} \end{bmatrix}. \tag{A5}$$

Equation (A2) can then be expressed as for the case of an ellipsoidal inclusion:

$$C^{\chi}_{ijkl}K_t\Phi_{lt}K_u\Phi_{ju}\tilde{G}_{km}(k) = \delta_{im}. \tag{A6}$$

Then, defining $K_t = K\chi_t$, where K is the magnitude and χ_t are the direction cosines, leads to:

$$C^{\chi}_{ijkl}\Phi_{lt}\Phi_{ju}\chi_t\chi_u = M_{ki},$$
$$K^2\tilde{G}_{km}(K) = M^{-1}_{km}, \tag{A7}$$

which depends only on the magnitude of the vector K. This expression can then be substituted into the inverse FT in order to evaluate t^I_{ijkl}, and therefore $T^I_{ijkl}(C^{\chi})$ as follows:

$$t^I_{klmj} = \frac{abc}{3}\int_0^{\pi} \sin\theta d\theta \int_0^{2\pi} \left[K^2\tilde{G}_{km}(K)\right]\chi_t\Phi_{lt}\chi_u\Phi_{ju}d\varphi, \tag{A8}$$

$$T^I_{klmj}(C^{\chi}) = \frac{1}{2}\left\{t^I_{klmj} + t^I_{lkmj}\right\}. \tag{A9}$$

For efficient and accurate numerical evaluation of the integral in Eq. (A9), an n-point Gaussian–Legendre quadrature has been employed. It was found that, for most cases studied, a ten-point quadrature was sufficient. Finally, it should also be noted here that the integral of the modified Green's tensor is related to Eshelby's tensor through the following relationship:

$$S_{mnkl} = \frac{1}{V}T^I_{mnij}(C^{\chi})C^{\chi}_{ijkl}. \tag{A10}$$

[1] G. T. Kuster and M. N. Toksöz, "Velocity and attenuation of seismic waves in two-phase media: Theoretical formulation," Geophysics **39**, 587–606 (1974).
[2] C. F. Ying and R. Truell, "Scattering of a plane longitudinal wave by a spherical obstacle in an isotropically elastic fluid," J. Acoust. Soc. Am. **27**, 1086–1097 (1956).
[3] G. C. Gaunaurd and H. Überall, "Resonance theory of the effective properties of perforated solids," J. Acoust. Soc. Am. **71**(2), 282–295 (1982).
[4] P. C. Waterman and R. Truell, "Multiple scattering of waves," J. Math. Phys. **2**, 513–537 (1961).
[5] V. K. Varadan, Y. Ma, and V. V. Varadan, "A multiple scattering theory for elastic wave propagation in discrete random media," J. Acoust. Soc. Am. **77**, 375–385 (1985).
[6] F. Kerr, "The scattering of a plane elastic wave by spherical elastic inclusions," Int. J. Eng. Sci. **30**, 169–186 (1992).
[7] A. M. Baird, F. H. Kerr, and D. J. Townend, "Wave propagation in a viscoelastic medium having fluid-filled microspheres," J. Acoust. Soc. Am. **105**, 1527–1538 (1999).
[8] A. N. Norris, "Scattering of elastic waves by spherical inclusions with applications to low-frequency wave propagation in composites," Int. J. Eng. Sci. **24**, 1271–1282 (1986).
[9] J. G. Berryman, "Long-wavelength propagation in composite elastic media II. Ellipsoidal inclusions," J. Acoust. Soc. Am. **68**(6), 1820–1831 (1980).
[10] M. Haberman, Y. Berthelot, J. Jarzynski, and M. Cherkaoui, "Micromechanical modeling of viscolelastic voided composites in the low-frequency approximation," J. Acoust. Soc. Am. **112**(5), 1937–1943 (2002).
[11] D. T. Blackstock, *Fundamentals of Physical Acoustics* (Wiley, New York, 2000), pp. 163–164.
[12] M. Cherkaoui, H. Sabar, and M. Berveiller, "Micromechanical approach of the coated inclusion problem and applications to composite materials," J. Eng. Mater. Technol. **116**, 274–278 (1994).
[13] J. D. Eshelby, "The determination of the elastic field of an ellipsoidal inclusion, and related problems," Proc. R. Soc. London, Ser. A **241**, 376–396 (1957).
[14] T. Mura, *Micromechanics of Defects in Solids*, 2nd ed. (Kluwer Academic, 1987).
[15] Z. Hashin and S. Shtrikman, "A variational approach to the theory of the elastic behavior of multi-phase materials," J. Mech. Phys. Solids **11**, 127–140 (1963).
[16] L. J. Walpole, "On the bounds for the overall elastic moduli of inhomogeneous systems I," J. Mech. Phys. Solids **14**, 151–162 (1966).
[17] R. Hill, "The elastic behaviour of a crystalline aggregate," Proc. Phys. Soc., London, Sect. A **65**, 349–354 (1952).
[18] R. Hill, "Elastic properties of reinforced solids: Some theoretical principles," J. Mech. Phys. Solids **11**, 357–372 (1963).
[19] Z. Hashin, "Analysis of composite materials," J. Appl. Mech. **50**, 481–505 (1983).
[20] R. Hill, "A self-consistent mechanics of composite materials," J. Mech. Phys. Solids **13**, 213–222 (1965).
[21] Z. Hashin, "Viscoelastic behavior of heterogeneous media," J. Appl. Mech. **32**, 630–636 (1965).
[22] Z. Hashin, "Complex moduli of viscoelastic composites I: General theory and application to particulate composites," Int. J. Solids Struct. **6**, 539–552 (1970).
[23] Z. Hashin, "Complex moduli of viscoelastic composites II: Fiber reinforced materials," Int. J. Solids Struct. **6**, 797–807 (1970).
[24] R. M. Christensen, "Viscoelastic properties of heterogeneous media," J. Mech. Phys. Solids **17**, 23–41 (1969).
[25] R. Roscoe, "Bounds for real and imaginary parts of the dynamic moduli of composite viscoelastic systems," J. Mech. Phys. Solids **17**, 17–22 (1969).
[26] R. Roscoe, "Improved bounds for real and imaginary parts of complex moduli of isotropic viscoelastic composites," J. Mech. Phys. Solids **20**, 91–99 (1972).
[27] A. V. Cherkaev and L. V. Gibiansky, "Variational principles for complex conductivity, viscoelasticity, and similar problems I: Media with complex moduli," J. Math. Phys. **35**(1), 127–145 (1994).
[28] G. W. Milton, "On characterizing the set of possible effective tensors of composites: The variational method and the translation method," Commun. Pure Appl. Math. **43**, 63–125 (1990).
[29] L. V. Gibiansky and G. W. Milton, "On the effective viscoelastic moduli of two-phase media. I: Rigorous bounds on the complex bulk modulus," Proc. R. Soc. London, Ser. A **440**, 163–188 (1993).

[30]G. W. Milton and J. G. Berryman, "On the effective viscoelastic moduli of two-phase media. II: Rigorous bounds on the complex shear modulus in three dimensions," Proc. R. Soc. London, Ser. A **453**, 1849–1880 (1997).
[31]L. V. Gibiansky and R. Lakes, "Bounds on the complex bulk modulus of a two-phase viscoelastic composite with arbitrary volume fractions of the components," Mech. Mater. **16**, 317–331 (1993).
[32]L. V. Gibiansky and R. Lakes, "Bounds on the complex bulk and shear moduli of a two-dimensional two-phase viscoelastic composite," Mech. Mater. **25**, 79–95 (1997).
[33]L. V. Gibiansky and S. Torquato, "New method to generate three-point bounds on effective properties of composites: Application to viscoelasticity," J. Mech. Phys. Solids **46**(4), 749–783 (1998).
[34]W. H. Press, B. P. Flannery, S. A. Teukolsky, and W. T. Vetterling, *Numerical Recipes in Fortran: The Art of Scientific Computing* (Press Syndicate of the University of Cambridge, Cambridge, UK, 1992), pp. 402–406.

Computation of the temperature distortion in the stack of a standing-wave thermoacoustic refrigerator

David Marx and Philippe Blanc-Benon
Centre Acoustique, LMFA, UMR CNRS 5509, Ecole Centrale de Lyon, 36 avenue Guy de Collongues, 69134 Ecully cedex, France

(Received 21 February 2005; revised 1 August 2005; accepted 19 August 2005)

The numerical computation of the flow and heat transfer in the vicinity of a stack plate in a standing wave refrigerator is performed. Temperature distortion is observed, which appears only in the stack region, even if the acoustic standing wave outside the stack is itself sinusoidal. The distortion takes place above the whole plate surface when the length of the plate is equal to or shorter than four times the particle displacement. This condition may occur at high drive ratios and is favored by plate positions close to the velocity antinode. The thermal distortion decreases the thermoacoustic heat pumping along the plate. At high drive ratios, if the length of the plate is not large enough, the thermal distortion can typically explain a difference of about 10% between the calculated heat flux and the heat flux predicted using linear theory. © *2005 Acoustical Society of America.*
[DOI: 10.1121/1.2063087]

PACS number(s): 43.35.Ud, 43.25.−x [RR] Pages: 2993–2999

I. INTRODUCTION

To design and predict the performance of thermoacoustic devices, the most widely used tool is the standard "linear theory."[1] Although very advanced, this theory does not take into account some phenomena such as nonlinear effects, including complex flows. Complex flows include turbulence and motions resulting from abrupt changes of section. Vortical motions at the extremities of the stack plates and heat exchangers have been observed both experimentally and numerically.[2] They can generate minor losses[3–5] that are detrimental to performance. Acoustic nonlinear effects consist of acoustic streaming[6–8] and harmonics generation. In some cases acoustic streaming has been identified and successfully suppressed.[3] The most obvious reason for harmonics generation is the nonlinear propagation of a high-amplitude wave in the resonator.[9–12] Using an appropriate shape for the resonator[13] (or more simply inserts at the harmonics velocity antinode) these harmonics can be removed. From a different nature are the thermal harmonics resulting from the thermal interaction between the stack and the oscillating gas, which were theoretically predicted by use of an inviscid nonlinear model.[14] Some results previously reported by the authors confirmed the distortion of the temperature oscillation at high acoustic amplitudes in the stack region.[15]

All together, nonlinear phenomena have a very important effect on thermoacoustic device performance, and their knowledge is especially important to predict the saturation amplitude of thermoacoustic engines. The parameter used in thermoacoustics to describe the amplitude of the wave is the drive ratio, defined as the ratio of the acoustic pressure amplitude at the pressure antinode to the mean pressure in the resonator. For standing wave devices, nonlinear effects are generally considered to appear when the drive ratio is more than about 2% or 3%.[16,17] Though this limit is somewhat arbitrary since it depends on the configuration of the system and on the type of nonlinearity that happens to be the critical one in the system. Nevertheless, for practical drive ratios of 10%, a typical 10% error on the heat flux is observed in standing-wave devices, even in precisely controlled experiments.[10,18] Results reported here may explain part of the difference between theoretical predictions and experimental results. In the paper we deal with the computation of nonlinear temperature effects in a standing wave thermoacoustic refrigerator. In Sec. II the numerical modeling of the problem is briefly explained. Results of the simulations are then presented in Sec. III. They concern mainly the distortion of the time variation of the temperature in the stack region. A discussion is made in Sec. IV, where results are interpreted using the previous analysis by Gusev *et al.*[14] Some implications of the temperature distortion on the thermoacoustic heat pumping are also given. The main conclusions are drawn in Sec. IV.

II. METHODS

To include most of the physical phenomena involved in thermoacoustic heat pumping (boundary layers, nonlinear acoustics, heat transfer, temperature gradient, two-dimensional flow), a numerical solver has been developed.[15,19] It is based on the solution of the two-dimensional compressible and unsteady Navier–Stokes equations, coupled with mass and energy conservation equations. The governing equations for a perfect gas are

$$p = \rho r T, \tag{1}$$

$$\frac{\partial \rho}{\partial t} + \nabla \cdot (\rho \mathbf{u}) = 0, \tag{2}$$

$$\frac{\partial (\rho \mathbf{u})}{\partial t} + \nabla \cdot (\rho \mathbf{u}\mathbf{u}) + \nabla p = \nabla \cdot \boldsymbol{\tau}, \tag{3}$$

$$\frac{\partial T}{\partial t} + \mathbf{u}\cdot\boldsymbol{\nabla} T + (\gamma - 1) T \boldsymbol{\nabla}\cdot\mathbf{u} = \frac{(\gamma - 1)}{\rho r}[\Phi + \boldsymbol{\nabla}\cdot(K\,\boldsymbol{\nabla} T)], \tag{4}$$

where the components of the viscous stress tensor $\boldsymbol{\tau}$ are

$$\tau_{xx} = \frac{4}{3}\mu\frac{\partial u}{\partial x} - \frac{2}{3}\mu\frac{\partial v}{\partial y},$$

$$\tau_{xy} = \tau_{yx} = \mu\left(\frac{\partial u}{\partial y} + \frac{\partial v}{\partial x}\right), \tag{5}$$

$$\tau_{yy} = \frac{4}{3}\mu\frac{\partial v}{\partial y} - \frac{2}{3}\mu\frac{\partial u}{\partial x},$$

and the viscous dissipation, Φ, is defined by

$$\Phi = 2\mu\left[\left(\frac{\partial u}{\partial x}\right)^2 + \left(\frac{\partial v}{\partial y}\right)^2 + \frac{1}{2}\left(\frac{\partial u}{\partial y} + \frac{\partial v}{\partial x}\right)^2 - \frac{1}{3}\left(\frac{\partial u}{\partial x} + \frac{\partial v}{\partial y}\right)^2\right]. \tag{6}$$

In these expressions T is the temperature, p is the pressure, ρ is the density, $\mathbf{u}=[u;v]$ is the velocity vector; r is the gas constant, γ is the ratio of specific heats, μ is the shear viscosity, and K is the thermal conductivity. The temperature dependence of μ and K is not taken into account, which is a reasonable approximation because the temperature gradients are small in the present case. For air, $\mu = 1.8\times10^{-5}$ Pa s; $K = 2.5\times10^{-2}$ W K^{-1} m^{-1}; $r = 287$ J K^{-1} kg^{-1}; $\gamma = 1.4$. Equations (1)–(4) are used to solve for the variables p, ρ, $\mathbf{u}$, and T. The calculation is started from a initial state consisting of ambient values for the thermodynamic variables and zero velocity, and is performed until the rate of growth becomes negligible. To solve Eqs. (1)–(4), fourth-order dispersion-relation-preserving finite differences are used for calculating spatial derivatives, and time integration is performed using a four-step Runge–Kutta method. Dispersion-relation-preserving methods are used to minimize the error between physical and numerical dispersion relations.[20] These accurate methods are chosen to calculate second-order quantities (thermoacoustic heat pumping, mass streaming, and potentially minor losses[5]) superimposed on a first-order acoustic field. As they introduce little dissipation, spurious waves can appear and are filtered using high-order filters.[21] The solver allows the simulation of the flow and heat transfer in the vicinity of a stack plate in the presence of an acoustic standing wave. The plate may be either of negligible or finite thickness, and be either heat conducting or isothermal. The more complex are the geometry and the thermal model, the more important the computational cost will be. It can sometimes be prohibitive. In the present paper we will focus on the case of an isothermal plate of negligible thickness. The effect of the plate is to impose a fixed temperature (as well as a no-slip) condition on its surface, so that no additional energy conservation equation needs to be solved for the plate. The isothermal plate model has already been used in some other numerical simulations, mostly for its simplicity.[22,23] It should be noticed that despite this model prevents one from getting a temperature gradient in the plate itself, it allows a temperature gradient to establish within the fluid above the plate. This gradient if somewhat reduced because of the isothermal condition, but this indeed tends to increase the thermoacoustic heat pumping along the plate. It turns out that the use of an isothermal boundary condition does not modify the validity of the results presented below, as will be mentioned below.

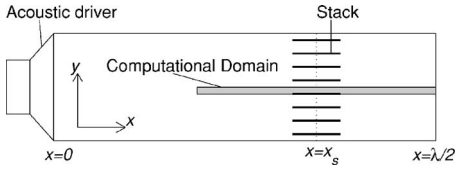

FIG. 1. Sketch of the thermoacoustic refrigerator.

The thermoacoustic refrigerator is represented in Fig. 1, where the grayed-out area is the computational domain. The abscissa origin is taken at the acoustic driver. The length of the resonator is half the wavelength, λ. The position of the stack middle point is x_s. The computational domain is shown in Fig. 2. The computational domain takes advantage of the periodic nature of the stack and includes only one plate of the stack. Symmetric boundary conditions are used on the lateral boundaries of the domain, an approach that has been used in all thermoacoustic simulations[22–24] in order to decrease the computational time. The acoustic standing wave that is required in a standing wave refrigerator is created in a physical way: by superimposing two counterpropagating traveling waves. More precisely, a traveling wave is continuously injected into the domain through the S_{wave} boundary. This wave travels up to the rigid end, where it is reflected. There is thus also a reflected traveling wave that travels from the rigid end toward the surface S_{wave}, where it goes out of the domain. The S_{wave} surface has a double role: to inject the direct right-traveling wave and to let escape the reflected left-traveling wave. Numerically this is done using the method of characteristics.[25] The superimposition of the direct and reflected traveling waves creates a standing wave. The total distance covered by the traveling wave (first direct and then reflected) during its stay in the domain is twice the length of the domain; this is less than a wavelength. As a consequence, the wave has not enough time to be modified by nonlinear effects during its propagation, even at the high

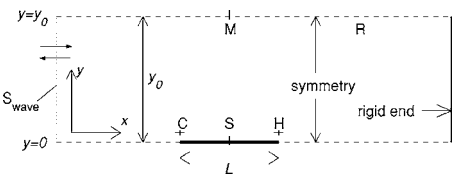

FIG. 2. Sketch of the computational domain. Point S is in the middle of the plate. Point C is in the fluid just above the plate extremity, in the cold region. Point H is in the fluid just above the other extremity, in the hot region.

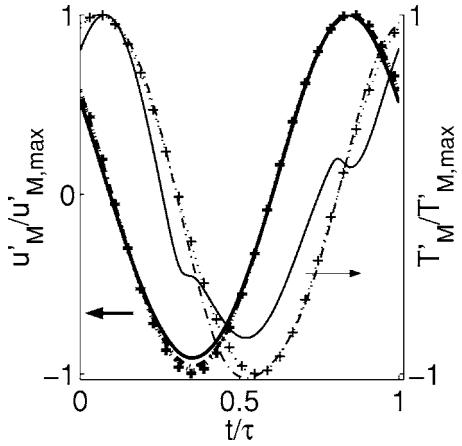

FIG. 3. Time variation of the temperature at point M, T'_M, divided by the maximum value of this variation, $T'_{M,\max}$, and time variation of the velocity at point M, u'_M, divided by the maximum value of this variation, $u'_{M,\max}$. The values for the drive ratio are +++, D_r=0.7%; ⋯, D_r=2.8%; − − −, D_r=5.6%; —, D_r=11.2%. Thin symbols are for temperature; bold symbols are for velocity.

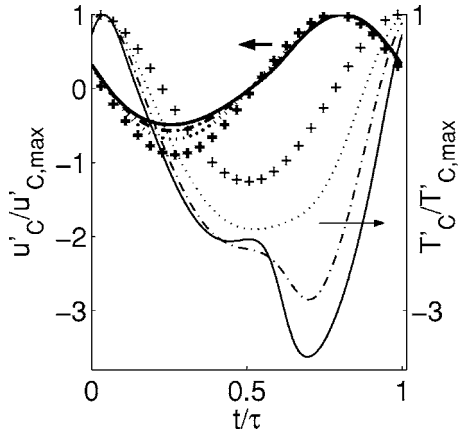

FIG. 4. Time variation of the temperature at point C, T'_C, divided by the maximum value of this variation, $T'_{C,\max}$, and time variation of the velocity at point C, u'_C, divided by the maximum value of this variation, $u'_{C,\max}$. The values for the drive ratio are +++, D_r=0.7%; ⋯, D_r=2.8%; − − −, D_r=5.6%; —, D_r=11.2%. Thin symbols are for temperature; bold symbols are for velocity.

amplitudes that will be considered in the following. This allows to get a high-amplitude standing wave with nearly no harmonics.

III. RESULTS

In the following, any quantity, ψ, will be written $\psi=\psi_0+\psi'$, where the subscript 0 indicates a quantity at rest, and the prime indicates the perturbation of that quantity when there is an acoustic wave in the domain. Hence, ψ' includes the first-order perturbation (ψ_1) as well as all the terms of higher order, including harmonics and time-averaged terms. With these notations, the drive ratio is $D_r=p'(\lambda/2)/p_0$. This is the ratio of the acoustic pressure at the rigid end of the resonator (located at $x=\lambda/2$; see Fig. 1) to the pressure p_0 when the system is at rest. The density, temperature, and pressure at rest are $\rho_0=1.2\ \mathrm{kg\ m^{-3}}$, $T_0=298$ K, and $p_0=100$ kPa, respectively. The velocity at rest is simply $u_0=0$. The speed of sound is $c_0=\sqrt{\gamma r T_0}$. Important quantities in thermoacoustic are the viscous and thermal penetration depth defined, respectively, by $\delta_\nu=\sqrt{\mu/\rho_0\pi f}$ and $\delta_\kappa=\sqrt{K/\rho_0 c_p \pi f}$, where $c_p=\gamma r(\gamma-1)$ is the isobaric specific heat, and f is the frequency. The height, y_0, of the computational domain is such that $y_0/\delta_\kappa=2.5$, a typical value for thermoacoustic stacks. The mesh size is equal to $\delta_\kappa/7.3$ (except for Fig. 6, later, where it is $\delta_\kappa/10$), a value that has proved sufficient for these simple calculations.[19] The plate length, L is such that $L=\lambda/40$. The position of the plate will be expressed in the normalized form kx_s, where $k=2\pi/\lambda$ is the wave number. This position will be fixed at $kx_s=2.13$, except in Fig. 6 (later)

As a nonlinear behavior generally implies some distortion, the time variations of the velocity and temperature were recorded at several points of the computational domain. The temperature time variation at point M of the domain (see Fig. 2) is shown in Fig. 3 for different values of the drive ratio. Temperature T'_M is made dimensionless using its maximal value during the acoustic cycle $T'_{M,\max}$. Time is made dimensionless using the acoustic period, τ. At lower drive ratios, D_r=0.7% and D_r=2.8%, the temperature variation is sinusoidal. For a higher drive ratio, D_r=5.6%, the temperature time variation slightly departs from a sinusoidal curve. For the higher drive ratio represented, D_r=11.2%, the temperature variation is clearly distorted, showing the importance of nonlinear effects. The computed variations of the temperature are periodic of the acoustic period τ; thus the temperature distortion is made of harmonics of the fundamental. This was also verified using a Fast Fourier Transform. Hence, in the following, *temperature distortion* and *temperature harmonics generation* will have the same meaning. In all the cases considered in this paper, the FFT showed also that only five or six harmonics had a non-negligible amplitude, with the first and second having a major contribution. The time variation of the velocity at point M for different drive ratios is also shown in Fig. 3. As can be seen, the velocity time variation, unlike the temperature variation, remains sinusoidal, even for the highest value of the drive ratio, D_r=11.2%. The normalized velocity is indeed slightly modified in its most negative values when the drive ratio increases, in such a way that the time-averaged velocity at point M over one acoustic cycle becomes slightly positive. This is consistent with observation of acoustic streaming above the plate[26] (here the nonzero mean velocity is due to "inner" vortices[8]). Nevertheless, this effect remains small.

The temperature time variation was also recorded at point C of the domain (see Fig. 2), located in the fluid, just above the extremity of the plate, in the cold region (the stack is pumping heat from cold point C to hot point H). This variation is shown in Fig. 4 for different values of the drive ratio. Even for the lower drive ratios, $D_r<5.6\%$, the temperature variation is not sinusoidal. At the highest drive ratio, D_r=11.2%, the nonsinusoidal behavior of the temperature at point C is much more pronounced than that at point M at the same drive ratio. Velocity variation at point C is also shown in Fig. 4. Again, unlike the temperature variation, the velocity variation at point C remains sinusoidal for the whole range of the drive ratio. It is almost obvious from Fig. 4 that the time-averaged temperature and velocity over one acous-

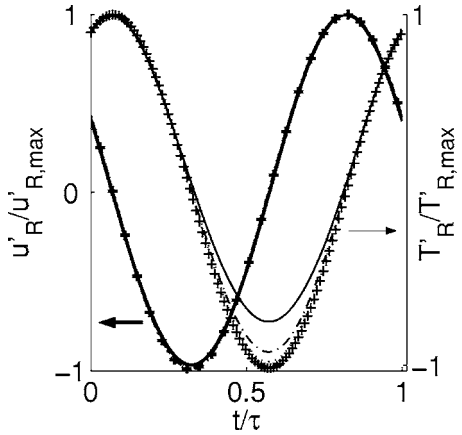

FIG. 5. Time variation of the temperature at point R, T'_R, divided by the maximum value of this variation, $T'_{R,\max}$, and time variation of the velocity at point R, u'_R, divided by the maximum value of this variation, $u'_{R,\max}$. The values for the drive ratio are $+++$, $D_r=0.7\%$; $\cdots$, $D_r=2.8\%$; $---$, $D_r=5.6\%$; —, $D_r=11.2\%$. Thin symbols are for temperature; bold symbols are for velocity.

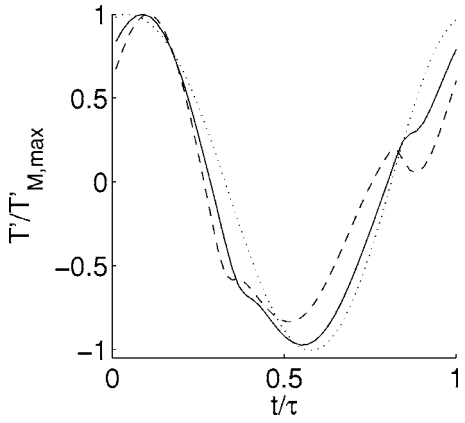

FIG. 6. Temperature time variation at point M, T'_M, divided by its maximum value, $T'_{M,\max}$, for several positions of the plate in the domain: ---, $kx_s=2.07$; —, $kx_s=2.35$; $\cdots$, $kx_s=2.81$. For all three curves, $D_r=11.2\%$.

tic cycle are not zero. The mean value of the temperature is logically negative, since point C is located in a cold region. The nonzero value of the time-averaged velocity comes from time-averaged motions at the end of the plate.[26] These mean motions can roughly be explained as follows. First note that the fluid in, say, the viscous boundary layer above the plate, is almost at rest. This means that although the plate itself has a negligible thickness, the plate plus the fluid at rest just above it may be considered as a plate of nonzero thickness. Thus, the flow of the fluid located outside the viscous layer sees a "step" at the junction between the resonator and the plate. At point C, during the half of the acoustic period when the fluid moves leftward there is a decreasing step, with the creation of anticlockwise vortices. During the half of the acoustic period when the fluid moves rightward, there is a raising step, which creates much less vorticity. On average, there is a mean anticlockwise vortical flow at the end of the plate at point C, which explains why the mean velocity at this point is not zero.

The temperature and velocity variations at point R of the domain are given in Fig. 5 for different values of the drive ratios. Point R is located in the core of the resonator, at an equal distance from the plate and the end wall. At this location both temperature and velocity variations remain sinusoidal, unlike what happens at point M or point C. This also confirms that the method used to sustain the wave in the resonator creates a high drive ratio standing wave without any wave steepening. Note that the mean temperature at point R is positive, since point R is located in the hot part of the resonator located between the stack and the rigid end.

It was stated in a previous study[15] that the temperature distortion tend to disappear when the plate is moved toward the velocity node, which is toward the rigid end of the resonator. This is indeed shown in Fig. 6. In this figure, the time variation of the temperature at point M is plotted for different values of the normalized position kx_s, at a drive ratio $D_r=11.2\%$. For a position close to the velocity antinode, $kx_s=2.07$, temperature harmonics are visible. They disappear when the plate is located at $kx_s=2.81$, closer to the velocity node.

IV. DISCUSSION

The results given above show that in the stack region (points C and M) the temperature may be nonsinusoidal, while the velocity remains harmonic. Far from the stack region (point R), the temperature and velocity both remain sinusoidal, even at high drive ratios. It means that temperature harmonics creation is taking place in the stack only. Moreover this creation is more effective at the extremities of the stack plates, since harmonics, when present at both points M and C, are stronger at point C. It also means that in the stack region, the nonlinear term of the momentum equation $(u\cdot\nabla u)$ has a much less important effect than the corresponding term in the energy equation $(u\cdot\nabla T)$. This is partly taken into account in the linear theory, since in the linearization the term $(u\cdot\nabla u)$ disappears, while the term $(u\cdot\nabla T)$ is kept and replaced by $(u\cdot\nabla T_m)$, where T_m is the mean temperature. But even if they take into account the effect of mean temperature variation, the linearized equations cannot account for the temperature harmonics observed above.

The results presented above can be explained by considering the analysis made by Gusev *et al.*[14] Using an inviscid but nonlinear model (the term $u\cdot\nabla T$ is fully preserved in their energy equation), these authors have shown that the nonlinear convective term $u\cdot\nabla T$ in the energy equation is responsible for temperature harmonics generation at the edges of the plate. This generation exists because of the energy exchange between the plate and the fluid at that location.[22] This exchange itself occurs because of the thermoacoustic heat flux entering or leaving the plate at its extremities. The point at which the temperature harmonics generation occurs are located within two particle displacements from the extremities of the stack. Moreover, harmonics generation is more important closer to the extremity of the plate. In Fig. 7(a), the grayed-out regions at each extremity of the plate represent regions in which there is harmonics generation. The height of these regions are simply of the order of the thermal penetration depth (that is of the order of y_0),

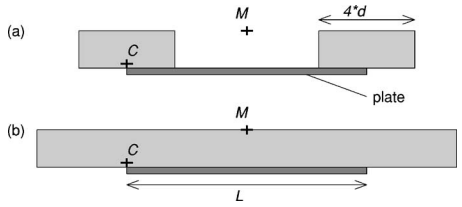

FIG. 7. In a grayed-out area, the temperature variation has a nonlinear behavior, that is, harmonics are created. Two cases are represented: (a) The acoustic displacement amplitude, d, is small compared with the plate length, L; (b) the particle displacement amplitude, d, is of the order of L.

since it is the characteristic length for heat transfer between the fluid and the plate. Their length is four times the particle displacement, d, defined by

$$d = \frac{u'}{2\pi f}. \tag{7}$$

For a standing wave in the resonator, the particle displacement at the stack position is

$$d = \gamma D_r \frac{\lambda}{2\pi} \sin(kx_s). \tag{8}$$

Importantly, the particle displacement increases with the drive ratio, and depends on the position x_s of the stack. In their analysis, Gusev *et al.* comment the case when the particle displacement is small compared with the plate length. This happens at low drive ratios. This case is represented in Fig. 7(a). In particular, in this figure point C belongs to the grayed-out region, but not point M. This explains why at low drive ratios, temperature harmonics are observed at point C (Fig. 4) but not at point M (Fig. 3). When the drive ratio increases, the particle displacement increases as well, and the situation may correspond to the sketch of Fig. 7(b). In this figure, both points C and M belong to the grayed-out region, which explains why at high drive ratios, temperature harmonics are observed at both locations (Fig. 3 and Fig. 4). Actually, the nonlinear region extends gradually when the drive ratio increases, and is expected to reach point M and cover the whole plate when the drive ratio is such that $L = 4d$, that is when

$$L = 4\gamma D_r \frac{\lambda}{2\pi} \sin(kx_s). \tag{9}$$

This equation defines a critical length for the stack, and is expected from the analysis. It is obtained using Eq. (8), which does not take into account the presence of the plate. It has indeed been observed in the computations that the temperature nonlinearities are observed at point M when $L \sim 4d_M$, where d_M is the actual (computed) value of the particle displacement at point M. Considering the critical length defined by Eq. (9), whether the temperature variation above the plate is nonsinusoidal is expected to depend on two parameters: the drive ratio and the position of the plate. The dependence on the drive ratio has just been explained. The effect of plate position was demonstrated in Fig. 6: at a fixed drive ratio, harmonics may appear if the plate is close to the velocity antinode (small kx_s), but not if the plate is moved toward the velocity node (large kx_s).

Hence, all the results obtained numerically may be explained using the theory by Gusev *et al.*[14] Let us mention that the analysis of Gusev *et al.* dealt with a nonviscous fluid. In an earlier part of the work and in an attempt to decouple as much as possible the different sources of nonlinearity, inviscid simulations were performed so that only the thermal interaction with the stack was accounted for. In terms of temperature variation the results were very similar to those presented in the present paper, where viscosity is taken into account. It appears that taking into account the viscosity in the present calculations does not prevent the apparition of nonlinear temperature harmonics, nor does it create any velocity harmonic. One consequence of taking viscosity into account is that the velocity is canceled on the plate surface due to no-slip boundary conditions. This effect may be compared to the thermal effect of the plate, which is to cancel the fluid temperature variation on the plate surface (due to isothermal boundary condition, or, more generally, due to the large specific heat of the plate). Despite this similarity, the velocity and temperature have different behaviors. One reason for this is that no momentum is exchanged between the plate and the fluid, while thermal energy is, particularly at the extremities of the plate. One could questions whether the use of an isothermal boundary has an important effect on the thermal harmonics generation. The thermal generation occurs as soon as there is a heat exchange between the plate and the fluid, with large associated temperature gradients. Hence, it is expected to appear with a plate having itself a variable temperature (solved using a solid energy conservation equation). Indeed harmonics generation has been observed for isothermal and nonisothermal plates, of negligible or finite thickness.[19] Petculescu and Wilen[27] conclude from their experiments that the linear theory can be used to describe the thermoacoustic heat pumping along a plate, even when the particle displacement is larger than the plate. Their conclusion is different from the one given in the present paper. But their experimental condition is also very different. In the experiment of Petculescu and Wilen, the plate is embedded within a wall. This wall can thermally interact with the fluid particle when the particle just leaves the plate surface. This is very different from the present configuration, where the fluid that is outside the plate has nothing to interact with and has an adiabatic movement. The present configuration is indeed more representative of a practical stack. Nevertheless it can be inferred that the thermal harmonics generation could possibly be decreased by the presence of heat exchangers, since these exchangers would reduce the heat transfer discontinuity between the fluid and the plate.

One effect often associated with harmonics generation in a signal is the saturation of the amplitude of this signal. The maximal value of the temperature variation at point M, $T'_{M,\max}$, is plotted as a function of the drive ratio in Fig. 8. For low drive ratios, $T'_{M,\max}$ is a linear function of the drive ratio. For a drive ratio of about 5.6%, the temperature maximal value is almost saturating. This corresponds to the appearance of harmonics at point M.

The effect of temperature harmonics creation on heat flux carried along the plate is now discussed. The mean

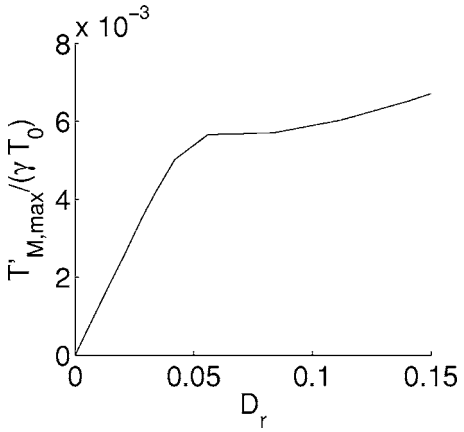

FIG. 8. Effect of the drive ratio, D_r, on the maximum value of the temperature variation at point M, $T'_{M,\max}$.

(time-averaged) thermoacoustic enthalpy flux integrated over the cross section SM of the computational domain is[1]

$$H_{xm}(x_s) = \int_{y=0}^{y=y_0} h_{xm}(x_s, y)dy, \tag{10}$$

where

$$h_{xm}(x,y) = c_p\langle[\rho_0 + \rho'(x,y)]u'(x,y)T'(x,y)\rangle_t, \tag{11}$$

where $\langle\cdot\rangle_t$ is the time average operator. The nonintegrated mean enthalpy flux h_{xm} depends on the vertical position y. The integrated mean enthalpy flux is calculated in section SM located at $x=x_s$ (see Figs. 1 and 2). A term $c_pT_0\langle(\rho_0+\rho')u'\rangle_t$ has been implicitly omitted in Eq. (11) because the section average of this term in Eq. (10) is zero, no net mass flux being possible in a closed-end device. It is also recalled that $u_0=0$. Equation (11) is very well approximated by $h_{xm}=\rho_0 c_p\langle u'T'\rangle_t$, the effect of the density fluctuation being small. Since H_{xm} depends on T', any harmonics generation in T' will have an effect on H_{xm}. In particular, the maximal temperature saturation has a limiting effect on the enthalpy flux. This is shown in Fig. 9, where H_{xm} is plotted as a

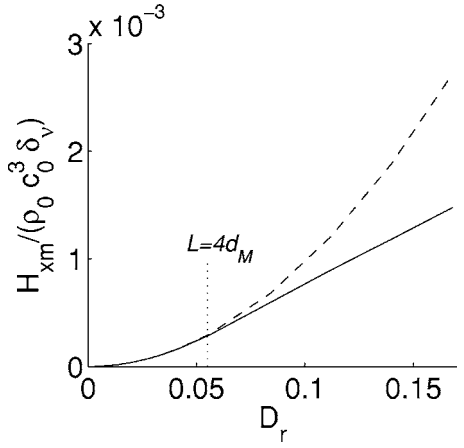

FIG. 9. Section-averaged mean enthalpy flux carried along the plate, H_{xm}, as a function of the drive ratio, D_r: —, calculated flux; ---, D_r^2 fitting at low values of D_r. A vertical dotted line is plotted at $D_r=5.6\%$, which is such that the length of the plate, L, is four times the particle displacement at point M, d_M.

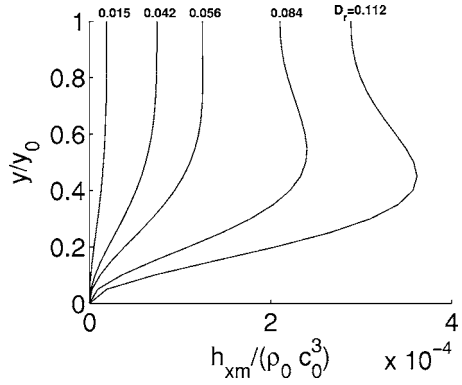

FIG. 10. Spatial variation of mean enthalpy flux, h_{xm}, over the section SM of the computational domain, with the drive ratio as a parameter.

function of the drive ratio. Also plotted in the figure is a fitting at low drive ratios, which dependence is in D_r^2. Such a dependence is being expected from the linear theory. The enthalpy flux matches the fitting curve up to a drive ratio of about 5%, when temperature harmonics appear first at point M. For drive ratios above 5%, H_{xm} depends only linearly on D_r. Given the saturation of the temperature observed in Fig. 8, this linear dependence comes from the velocity term in Eq. (11). In Fig. 9 is also indicated the drive ratio for which the length of the plate, L, is equal to four times the computed particle displacement at point M, d_M.

When a temperature harmonic is created, the thermal boundary layer thickness associated with this harmonic is different from the thermal boundary layer thickness associated with the fundamental (since the thermal boundary layer depends on the frequency). As a result, the temperature waveform above the plate is modified. This also has an effect on the distribution of the enthalpy flux within one cross section above the plate. The spatial variation of $h_{xm}(x_s,y)$ (the mean enthalpy flux within section SM of the computational domain) is shown in Fig. 10 for several values of the drive ratios. The profile of the enthalpy flux is modified for drive ratios above 5.6%. This is because the profile of the temperature itself changes.

Hence, the apparition of thermal harmonics may have an effect on the enthalpy flux carried along the plate. The effect is negligible at low drive ratios when harmonics only appear at the extreme edges of the stack. If the length of the plate is such that the harmonics spread onto the plate at high drive ratios, their effect is to decrease the heat pumping by the plate. The criterion $L=4d_M$ can roughly be used to decide whether it is the case. It has been observed, for example, that this reduction in heat flux decreases the temperature difference between the extremities of a stack plate placed in an acoustic resonator.[28] Typically, harmonics generation may account for a 10% difference between measurements and linear theory predictions. In Fig. 9, at $D_r=0.10$, the difference between the computed curve and the fitting is about 20%, for a plate located close to the velocity antinode where harmonics generation is easily observed.

V. CONCLUSION

The numerical computation of flow and heat transfer in the vicinity of an isothermal plate of negligible thickness

placed in an acoustic standing wave has been performed. A distortion of the temperature oscillation has been observed, and all observations could be explained by referring to a former nonlinear analysis. The temperature harmonics appear only in the stack region, even when the acoustic standing wave itself is sinusoidal and contains no harmonic. They are present above the whole plate surface when the length of the plate is equal to or shorter than four times the particle displacement. This condition may occur at high drive ratios and is favored by plate positions close to the velocity antinode. The thermal harmonics generation decreases thermoacoustic heat pumping by the plate. Fortunately, in standing wave thermoacoustic devices, the optimal position of the stack is closer to the pressure antinode than to the velocity antinode. Nevertheless, at high enough drive ratios, if the length of the plate is not large enough, a difference of about 10% between obtained and predicted heat fluxes can typically occur.

ACKNOWLEDGMENTS

The authors acknowledge the French Ministry of Defense (DGA, Délégation Générale pour l'Armement) for its financial support. Calculations were partially performed using the IDRIS (Institut du Développement et des Ressources en Informatique Scientifique) computing center.

[1]G. W. Swift, "Thermoacoustic engines," J. Acoust. Soc. Am. **84**, 1145–1180 (1988).
[2]Ph. Blanc-Benon, E. Besnoin, and O. Knio, "Experimental and computational visualization of the flow field in a thermoacoustic stack," C. R. Mec. **331**, 17–24 (2003).
[3]S. Backhaus and G. W. Swift, "A thermoacoustic Stirling heat engine: detailed study," J. Acoust. Soc. Am. **107**, 3148–3166 (2000).
[4]R. S. Wakeland and R. M. Keolian, "Influence of velocity profile non uniformity on minor losses for flow exiting thermoacoustic heat exchangers," J. Acoust. Soc. Am. **112**, 1249–1252 (2002).
[5]P. J. Morris, S. Boluriaan, and C. M. Shieh, "Numerical simulation of minor losses due to a sudden contraction and expansion in high amplitude acoustic resonators," Acta. Acust. Acust. **90**, 393–409 (2004).
[6]R. Waxler, "Stationary velocity and pressure gradients in a thermoacoustic stack," J. Acoust. Soc. Am. **109**, 2739–2750 (2001).
[7]H. A. Bailliet, V. Gusev, R. Raspet, and R. A. Hiller, "Acoustic streaming in closed thermoacoustic devices," J. Acoust. Soc. Am. **110**, 1808–1821 (2001).
[8]M. F. Hamilton, Y. A. Ilinskii, and E. A. Zabolotskaya, "Acoustic streaming generated by standing waves in two-dimensional channels of arbitrary width," J. Acoust. Soc. Am. **113**, 153–160 (2003).
[9]A. A. Atchley, H. E. Bass, and T. J. Hofler, "Development of nonlinear waves in a thermoacoustic prime mover," in *Frontiers of Nonlinear Acoustics: 12th ISNA*, edited by M. F. Hamilton and D. T. Blackstock (Elsevier, New York, 1990), pp. 603–608.
[10]G. W. Swift, "Analysis and performance of a large thermoacoustic engine," J. Acoust. Soc. Am. **92**, 1551–1563 (1992).
[11]M. F. Hamilton, Y. A. Ilinskii, and E. A. Zabolotskaya, "Nonlinear two-dimensional model for acoustic engines," J. Acoust. Soc. Am. **111**, 2076–2086 (2002).
[12]S. Karpov and A. Prosperetti, "A nonlinear model of thermoacoustic devices," J. Acoust. Soc. Am. **112**, 1431–1444 (2002).
[13]C. C. Lawrenson, B. Lipkens, T. S. Lucas, D. K. Perkins, and T. W. Van Doren, "Measurements of macrosonic standing waves in oscillating closed cavities," J. Acoust. Soc. Am. **104**, 623–636 (1998).
[14]V. Gusev, P. Lotton, H. Bailliet, S. Job, and M. Bruneau, "Thermal wave harmonics generation in the hydrodynamical heat transport in thermoacoustics," J. Acoust. Soc. Am. **109**, 84–90 (2001).
[15]D. Marx and Ph. Blanc-Benon, "Numerical simulation of stack-heat exchangers coupling in a thermoacoutic refrigerator," AIAA J. **42**, 1338–1347 (2004).
[16]M. E. Poese and S. L. Garrett, "Performance measurements on a thermoacoustic refrigerator driven at high amplitudes," J. Acoust. Soc. Am. **107**, 2480–2486 (2000).
[17]A. A. Atchley, T. J. Hofler, M. L. Muzerall, M. D. Kite, and C. Ao, "Acoustically generated temperature gradients in short plates," J. Acoust. Soc. Am. **88**, 251–263 (1990).
[18]D. L. Gardner and G. W. Swift, "A cascade thermoacoustic engine," J. Acoust. Soc. Am. **114**, 1905–1919 (2003).
[19]D. Marx, "Simulation numérique d'un réfrigérateur thermoacoustique," Ph.D. thesis 2003–34, Ecole Centrale de Lyon, 2003.
[20]C. K. W. Tam and J. C. Webb, "Dispersion-relation-preserving difference schemes for computational aeroacoustics," J. Comput. Phys. **107**, 262–281 (1993).
[21]C. Bogey and C. Bailly, "A family of low dispersive and low dissipative explicit schemes for flow and noise computations," J. Comput. Phys. **194**, 194–214 (2004).
[22]N. Cao, J. R. Olson, G. W. Swift, and S. Chen, "Energy flux density in a thermoacoustic couple," J. Acoust. Soc. Am. **99**, 3456–3464 (1996).
[23]H. Ishikawa and D. J. Mee, "Numerical investigations of flow and energy fields near a thermoacoustic couple," J. Acoust. Soc. Am. **111**, 831–839 (2002).
[24]A. S. Worlikar and O. Knio, "Numerical simulation of a thermoacoustic refrigerator. Part 2: Stratified flow around the stack," J. Comput. Phys. **144**, 299–324 (1998).
[25]K. W. Thompson, "Time dependent boundary conditions for hyperbolic systems," J. Comput. Phys. **68**, 1–24 (1987).
[26]D. Marx and Ph. Blanc-Benon, "Computation of the mean velocity field above a stack plate in a thermoacoustic refrigerator," C. R. Mec. **332**, 867–874 (2004).
[27]G. Petculescu and L. A. Wilen, "High-amplitude thermoacoustic effects in a single pore," J. Acoust. Soc. Am. **109**, 942–948 (2001).
[28]D. Marx and Ph. Blanc-Benon, "Numerical calculation of the temperature difference between the extremities of a thermoacoustic stack plate," Cryogenics **45**, 163–172 (2005).

Micromachined microphones with diffraction-based optical displacement detection

Neal A. Hall,[a] Baris Bicen, M. Kamran Jeelani, Wook Lee,
Shakeel Qureshi, and F. Levent Degertekin
G.W. Woodruff School of Mechanical Engineering, Georgia Institute of Technology, Atlanta, Georgia 30332

Murat Okandan
Sandia National Laboratories, Albuquerque, New Mexico 87185

(Received 11 July 2005; revised 8 August 2005; accepted 17 August 2005)

Micromachined microphones with diffraction-based optical displacement detection are introduced. The approach enables interferometric displacement detection sensitivity in a system that can be optoelectronically integrated with a multichip module into mm^3 volumes without beamsplitters, focusing optics, or critical alignment problems. Prototype devices fabricated using Sandia National Laboratories' silicon based SwIFT-Lite™ process are presented and characterized in detail. Integrated electrostatic actuation capabilities of the microphone diaphragm are used to perform dynamic characterization in vacuum and air environments to study the acoustic impedances in an equivalent circuit model of the device. The characterization results are used to predict the thermal mechanical noise spectrum, which is in excellent agreement with measurements performed in an anechoic test chamber. An A weighted displacement noise of 2.4×10^{-2} Å measured from individual prototype 2100 μm $\times$ 2100 μm diaphragms demonstrates the potential for achieving precision measurement quality microphone performance from elements 1 mm^2 in size. The high sensitivity to size ratio coupled with the ability to fabricate elements with precisely matched properties on the same silicon chip may make the approach ideal for realizing high fidelity miniature microphone arrays (sub-cm^2 aperture) employing recently developed signal processing algorithms for sound source separation and localization in the audio frequency range. © *2005 Acoustical Society of America.* [DOI: 10.1121/1.2062429]

PACS number(s): 43.38.Gy, 43.38.Ar, 43.38.Bs, 43.38.Kb [YHB] Pages: 3000–3009

I. INTRODUCTION

The application space for microphones is large, extending from commodity microphones such as those used in cellular phones where total system and integration costs are the most important factor, to scientific measurement microphones where sensitivity and bandwidth are typically the most important criteria. There are applications in the middle of this spectrum such as hearing aid microphones where performance and affordability are both important considerations.[1,2] Many of these and other applications have unique performance requirements with regard to size, dynamic range, insensitivity to vibration and temperature fluctuations, resistance to moisture, resistance to shock, etc. For some specialty applications, a microphone with a high sensitivity to size ratio may be advantageous. Such a microphone may be placed on the end of a thin pin or rod to perform broadband, high fidelity, noninvasive measurements in small or difficult to reach places. High fidelity to sensor size ratio is also advantageous in the realization of miniature microphone arrays that utilize recently developed signal processing algorithms to perform multiple sound source separation and localization in the audio frequency range using less than a 1-cm-diam total aperture size.[3] In the case of miniature arrays, precise phase response matching between elements is also advantageous.

Similarly, the range of microphone technologies that have been explored is also wide.[4] Over the past two decades, the potential of microelectromechanical system (MEMS)—based microphones to cover various regions of the application space has been investigated.[1,5] Such microphones have potential manufacturing cost advantages due to the batch nature of micromachining processes and the potential for on chip electronic integration.[6] In addition, micromachining offers the capability of making small microphone elements, and nearly identical elements with matched dynamic properties in close proximity on the same silicon chip due to the tight control of material properties and lateral and vertical dimensions associated with micromachining. Arnold *et al.*, for example, have shown phase response matching within 1° between 16 piezoelectric microphones fabricated on the same silicon wafer and used for the construction of an array for aeroacoustic measurements.[7] All of these attributes of microfabrication are ideal for realizing miniature microphone arrays on a single silicon chip. However, capacitive detection, which has proven to be the most popular MEMS sensing method, does not scale favorably with size reduction as the ratio of active to parasitic capacitance becomes smaller. In addition, capacitive detection presents conflicting

[a]Current affiliation: Sandia National Laboratories, Albuquerque, NM 87185; electronic mail: nahall@sandia.gov

design goals that make achieving high sensitivity challenging. Although measurement quality MEMS capacitive microphones have recently been demonstrated by performing rigorous optimization of the coupled and conflicting design parameters inherent to capacitive sensing, there is motivation to pursue alternative sensing techniques for high fidelity miniature form factor microphone applications that uncouple performance parameters and present new design spaces.[8]

The design conflicts and tradeoffs of capacitive microphones are well documented.[4,5] Displacement detection sensitivity of the integrated diaphragm improves with the use of small gap heights (on the order of a few microns) and large electrostatic bias voltage. However, the small gap limits the electrostatic bias voltage that can be applied to the device due to electrostatic pull-in. Furthermore, the displacement detection is most sensitive when the sensor is operated close to electrostatic pull-in, but linearity and dynamic range are reduced under these conditions. These design conflicts exist in the electrical or displacement sensing domain, but design conflicts also exist across the mechanical and electrical design space. For example, the microphone backplate is perforated to alleviate squeeze film damping at high frequencies, but this perforation reduces the active capacitance which, due to parasitic effects, can adversely affect the displacement detection sensitivity and, in turn, the pressure sensitivity of the microphone. A microphone using vacuum sealed capacitive micromachined ultrasonic transducer (cMUT) membranes configured to form a radio frequency interferometric transmission line has recently been demonstrated.[9] This design uncouples the dynamic response of the device from the detection sensitivity, and microphones with a flat response from 0.1 Hz to over 100 kHz have been demonstrated. However, since the scheme still requires measuring a change in capacitance, the method is sensitive to parasitic effects and is subject to the design conflicts in the electrical domain.

Optical interferometry is an ideal way to uncouple the electrical and mechanical design space and achieve high displacement sensitivity independent of the lateral area interrogated. In addition, optical methods offer the possibility of force feedback operation for large dynamic range applications. Many optical microphone techniques that have been explored, however, have proven difficult to integrate or use crude intensity modulation schemes with little or no improvement in sensitivity over capacitive sensing.[10] A recently demonstrated micromachined diffraction-based optical displacement detection method has shown advantages over other optical techniques in terms of integration, stability, and power consumption.[11] This technique has the sensitivity of a full scale Michelson interferometer and can be assembled in a robust, nearly monolithically integrated package without beamsplitters or critical alignment problems. Lee *et al.* have demonstrated integration of the method using custom designed CMOS photodiodes in a 2 mm^3 volume.[12] The method has been used to create optical-cMUTs with improved dynamic range and sensitivity per unit area as compared to cMUTs employing capacitive detection. In this case, interferometric detection sensitivity from individual 160 μm elements in an array enabled phased array imaging in-air using only a 4 mm $\times$ 4 mm aperture.[13]

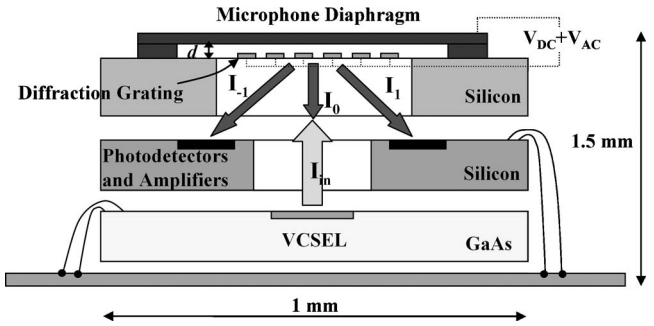

FIG. 1. Schematic of a fully integrated diffraction-based optical microphone.

In this work, we characterize in detail the performance of a bulk and surface micromachined microphone structure with integrated diffraction-based optical displacement detection. This work shows the potential of the method for achieving precision measurement microphone performance using sensors occupying only a few mm^3 volume, making the method ideal for small form factor applications and miniature microphone arrays. Also, since optical detection removes the small microphone gap height requirement, the method may be ideal for exploring novel mechanical-acoustic designs such as biomimetic teeter-totter microphones.[14,15] In what follows, the detection scheme is summarized followed by a description of the device fabrication and experimental testing setup. The diaphragm displacement detection sensitivity is characterized, and the dynamic response of the structure is studied in both air and vacuum environments using integrated electrostatic actuation capabilities to isolate the study of parameters in an equivalent circuit model of the device. The completed model is used to predict the thermal noise limited response in air which is in agreement with noise measurements performed in an anechoic testing facility. The significance of the results is then discussed with reference to existing measurement microphones.

II. DIFFRACTION-BASED OPTICAL MICROPHONES

A schematic of the diffraction-based optical microphone under study is shown in Fig. 1. The displacement sensing structure is similar to previously demonstrated interleaved gratings which have been used in the design of high resolution accelerometers and interdigital cantilevers for atomic force microscopy.[16–18] In the system under consideration, the microphone diaphragm rests above a rigid diffraction grating back electrode. When illuminated from the back side with an integrated semiconductor laser such as vertical cavity surface emitting laser (VCSEL) as shown in Fig. 1, a diffracted field consisting of a zero and higher orders results whose angles remain fixed but whose intensities are modulated by the diaphragm deflection to produce the interference curves of a regular Michelson interferometer. The optical properties of the grating structure when illuminated with diverging beams such as those from a VCSEL have been studied in detail using both a near field Fresnel analysis and rigorous coupled wave modeling.[13,19] These results show more than adequate separation between orders for 1 mm^3 integration as sug-

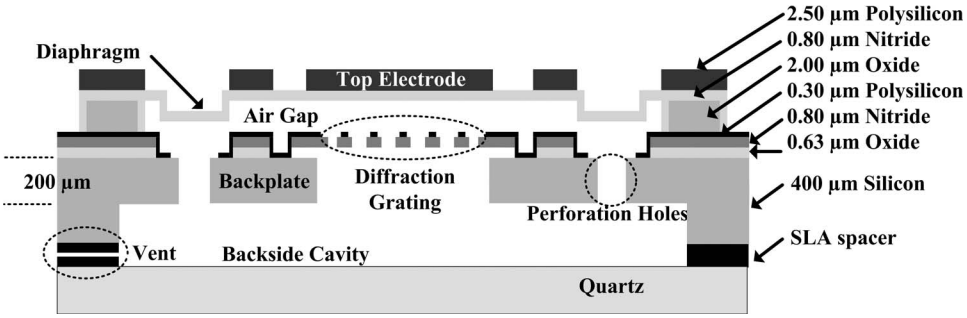

FIG. 2. Detailed schematic of the microphone structure fabricated with SwIFT-Lite™ and the additional packaging used for prototype testing.

gested in Fig. 1. These analyses also show that the intensities of the zero and first diffracted orders as a function of the microphone gap height, d, labeled in Fig. 1 closely resemble the particularly simple expressions obtained using a far field approximation,

$$I_0 = I_{\text{in}} \cos^2\left(\frac{2\pi d}{\lambda}\right), \tag{1}$$

$$I_{\pm 1} = \frac{4I_{\text{in}}}{\pi^2} \sin^2\left(\frac{2\pi d}{\lambda}\right), \tag{2}$$

where I_{in} and λ are the incident light intensity and wavelength, respectively. The zero order beam intensity is complementary to all higher order beams which enables a differential detection scheme for sensitivity doubling and laser intensity noise cancellation without any additional optical components. A self-contained sensor requires only the integration of photodiodes and simple detection electronics on a separate silicon chip as shown in Fig. 1. Since both the diaphragm and backplate can be made electrically conductive, the design also directly integrates electrostatic actuation capabilities, as suggested in Fig. 1, which enables tuning of the displacement sensitivity, generation of self-calibration signals, and force feedback operation for high dynamic range.[4] Since all three component chips in Fig. 1 are micromachined, the approach is readily adaptable to fabricating arrays of such elements with the multiple chip module shown.

III. PROTOTYPE DEVICE FABRICATION AND EXPERIMENTAL SETUP

Prototype diffraction-based optical microphones have been fabricated using Sandia National Laboratories dedicated silicon-based SwIFT-Lite™ process, which uses predefined layer thicknesses and material types to enable assembly line processing for tight variance control and high yield.[20] The fabrication process flow used to create the diffraction-based optical microphone structure has been described in detail previously.[21,22] A schematic of a completed structure is shown in Fig. 3, where both the layer materials and thicknesses used in SwIFT-Lite™ as well as the functional components of the fabricated structure are labeled. All layers are deposited using low pressure chemical vapor deposition processes, with the exception of the first 0.63-μm-thick oxide layer which is thermally grown. All etches are performed using dry chemistries, with a tetraethylorthosilicate (TEOS) process used for patterning the 2.0-μm-thick sacrificial oxide. The top silicon nitride layer forms the microphone diaphragm and is deposited with approximately 100 MPa residual tension which dominates the diaphragm's stiffness. The 2.5-μm-thick polysilicon layer is patterned on top of the diaphragm to form the optical reflector as well as additional regions of a top electrode used for electrostatic actuation. Similarly, polysilicon and nitride layers are used to form a diffraction grating with 5 μm period and additional regions of the bottom electrode. The SwIFT-Lite™ process includes a back side deep reactive ion etch through the bulk silicon wafer which is used to create the optical port to the diffraction grating and to perforate the microphone backplate. This step is preceded by a counterbore etch half-way through the bulk silicon substrate which results in a 200-μm-thick microphone backplate as labeled in Fig. 2. In a fully integrated embodiment such as that shown in Fig. 1, the dies containing the photodetection electronics and light source form the enclosed back side cavity of the microphone. In this work, the microphone structures are characterized using an external hand-held test-bed and the microphone cavity is sealed using a quartz window to provide optical access as shown in Fig. 2. A barometric pressure vent is created using a spacer with a small hole fabricated using stereo lithography and is also shown in Fig. 2.

The details of the fabricated silicon structure are made clear in micrographs of the completed devices. A back side view of a sensor with a 900 μm $\times$ 900 μm membrane is shown in Fig. 3(a), where the first plane observed along the perimeter is the surface of the 400-μm-thick bulk silicon wafer. At a distance 200 μm deeper into the back side of the wafer lies the backsurface of the backplate with five perforation holes etched completely through the silicon—one large hole in each corner and a smaller hole in the center. Note that the use of such large size holes in the corners would severely reduce the microphone sensitivity if using capacitive sensing but does not affect the sensitivity using optical detection. Focusing on a plane 200 μm deeper into the structure through the center hole makes visible the diffraction grating. For the remaining four openings in the corners, this plane makes visible the back side of the transparent nitride membrane which is suspended above the thin 2 μm microphone air gap defined by the sacrificial oxide layer. A separate zoomed micrograph showing the details of the diffraction grating is presented Fig. 3(b). The top-surface of the same device is shown in Fig. 3(c), which makes visible the top electrode and the optical reflector. As shown schematically in Fig. 2, the polysilicon is patterned such that the top electrode exists above the diaphragm anchor (which provides

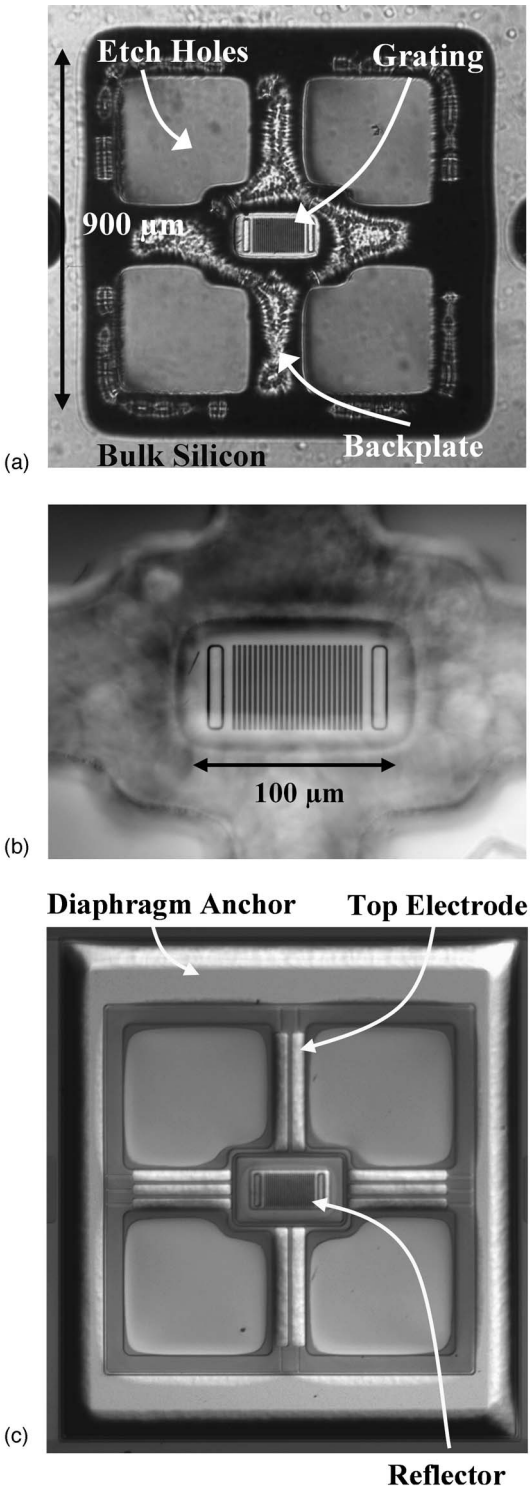

FIG. 3. Micrographs of the [(a) and (b)] back side and (c) front side of a 900 μm $\times$ 900 μm microphone structure.

a wire-bonding surface) and above the backplate regions where the bottom electrode exists and electrostatic actuation is effective. Several prototype devices with different diaphragm sizes and backplate architectures were fabricated. The remainder of this work focuses on the characterization of the device shown in Fig. 4 which has a 2100 μm $\times$2100 μm diaphragm and a more traditional microphone backplate design.

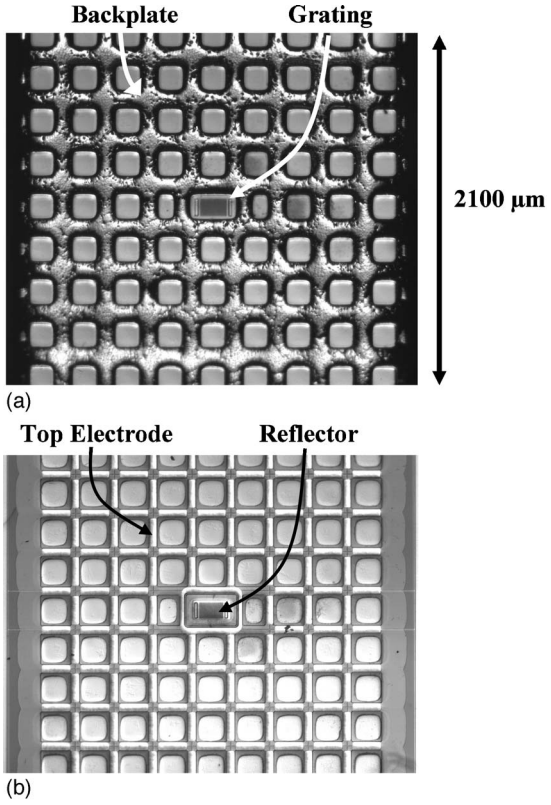

FIG. 4. Micrographs showing the (a) back and (b) top side of a 2100 μm $\times$2100 μm diaphragm.

The fabricated prototypes are assembled on a handheld test-bed as summarized schematically in Fig. 5. Light from a 640 nm wavelength laser diode is focused to a 20-μm-diam spot through a 20 mm working distance lens and illuminates the back side of the sensor which is mounted with a vertical tilt to direct the reflected plane beneath the laser diode and lens where a photodiode array and amplifiers are placed to capture signals from the zero and first diffracted orders. A function generator is used to apply dc and ac electrostatic signals for sensitivity tuning and dynamic characterization as demonstrated in the following sections.

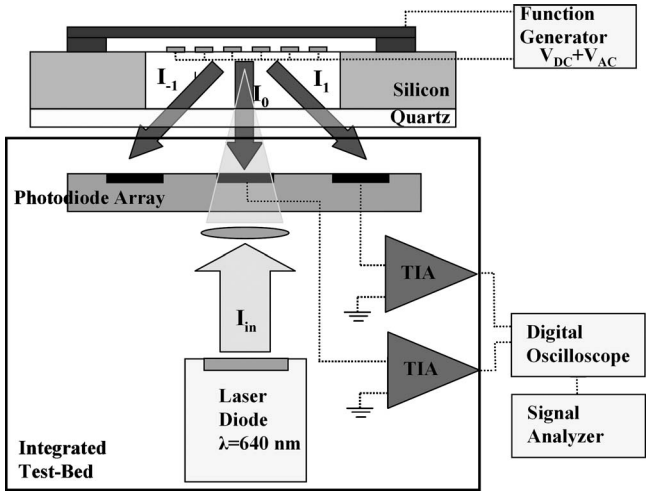

FIG. 5. Schematic of an integrated hand-held test bed used for experimental characterization.

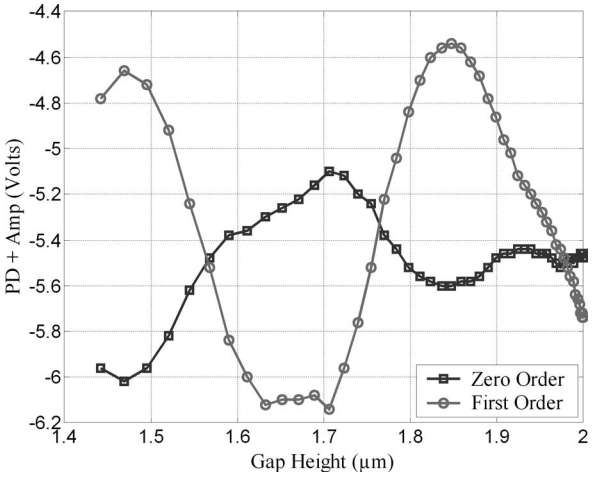

FIG. 6. Experimental tracing of the optical interference curves obtained using the integrated electrostatic actuation capabilities of the microphone diaphragm.

IV. DISPLACEMENT SENSITIVITY CALIBRATION

The diffracted order intensity versus gap height behavior predicted in Eqs. (1) and (2) is experimentally traced using capacitive actuation to pull the microphone diaphragm toward the substrate while simultaneously recording the signals from the photodiodes and the membrane deflection profile as measured from the front side using an external optical Wyko profilometer (not shown in Fig. 5).[23] With these data, the intensities of the zero and a single first diffracted order are plotted versus gap height as shown in Fig. 6 where data have been obtained from the 2100 μm diaphragm shown in Fig. 4. The voltage values are negative as the transimpedance amplifiers are inverting in this particular case. The period of the interference curves can be approximated using the distance between the two peaks of the zero order curve as 350 nm, which is in relatively good agreement with the theoretical prediction of $\lambda/2$, or 320 nm for the diode laser used.[24] Although the zero and first orders are 180° out of phase as expected, the curves do not exhibit a full swing in intensity. The first order curve in Fig. 6, for example, should pass through zero at its nulls (corresponding to microphone gap heights of $\lambda/2$ multiples) as the system acts as a flat mirror under these conditions regardless of the grating period and fill factor. As argued in detail in previous work, the reduced intensity swing is most likely due to optical scatter caused by corrugations in the polysilicon reflector, which are transferred from the grating topography through the sacrificial oxide layer during processing.[21,22] Since the displacement sensitivity and dynamic range of the detection scheme improve with the intensity swing, the elimination of this topography is recommended in future runs via chemical mechanical polishing (CMP) of the sacrificial oxide—an available option with SwIFT-Lite™. As apparent in Fig. 6, optimal displacement sensitivity is obtained when biasing the gap height to 1.55 or 1.75 μm, where the slopes are at a maximum. At 1.75 μm, for example, the displacement detection sensitivity for the particular 2.5 mW laser power and transimpedance amplifier gains used in these experiments is 20 V/μm using single first order detection, and 30 V/μm using differential detection of the zero and first order which is obtained as the sum of the two slopes. The calibrated sensitivity is useful for characterizing the dynamics of the microphone structure and is also necessary for assessing internal noise of the microphone as discussed in detail in the remaining sections.

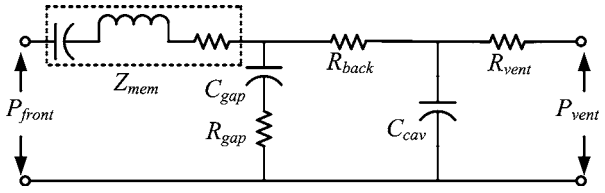

FIG. 7. Equivalent circuit model of the packaged microphone structure shown in Fig. 2.

V. DYNAMIC CHARACTERIZATION AND MODELING

Characterizing the dynamics of the microphone structure is not only important for assessing the microphone's bandwidth, but also for studying the parameters that determine the thermal mechanical noise response of the device, which typically limits the pressure detection resolution for low noise devices such as measurement and hearing aid microphones. Thompson *et al.* demonstrated the benefit of combining equivalent circuit models with dynamic frequency response characterization in both air and vacuum environments to isolate the study of acoustic impedances in the model which affect the thermal noise response.[25] A similar approach is taken here using the integrated electrostatic actuation port to generate the input signals, which eliminates the need for the external electrostatic actuation heads used with condenser microphone characterization. During operation, this integrated feature of the optical microphone can be used for *in situ* self-calibration.

An equivalent circuit model of the packaged device in Fig. 2 is shown in Fig. 7, with Table I providing a description of the elements in the circuit. The model is similar to those commonly used to study condenser and other microphone types. Such models have been presented in detail in many references.[26] The effort and flow variables in the circuit of Fig. 7 are pressure and volume flow rate, respectively, so that all impedances are acoustic impedances with units of $\mathrm{Ra/m^2}$. When the microphone responds to sound, the pressure outside the vent is equal to the pressure acting at the microphone diaphragm and the model captures the low frequency limit of the microphone diaphragm response in this case. When the diaphragm is excited electrostatically as in the following experiments, the vent pressure is zero. Furthermore, the impedances of all elements in Fig. 7 other than the diaphragm impedance are zero in vacuum—providing a means to isolate this parameter for study. In a previous work, the displacement of the 2100 μm diaphragm in Fig. 4 in response to an applied electrostatic pressure impulse in vacuum was recorded via capturing the signal from a first diffracted order with a digital oscilloscope using the system in Fig. 5.[21,22] The dynamic frequency response—obtained by taking the Fourier transform of the displacement signal—showed a fundamental diaphragm resonance at 44.8 kHz and

TABLE I. Description of parameters in the equivalent circuit model of the microphone structure.

Parameter	Description	Acoustic Impedance (Ra/m^2)
P_{front}	Acoustic pressure acting on the microphone diaphragm	NA
Z_{mem}	Total diaphragm impedance in vacuum	NA
C_{gap}	Compliance of the thin air gap between the diaphragm and bottom electrode (i.e., squeeze film compliance)	$1/(j\omega C_{gap})$
R_{gap}	Resistance associated with compression of air in the air gap (i.e., squeeze film resistance)	R_{gap}
R_{back}	Resistance of air displacing laterally in the thin air gap and out through the diffraction grating and perforation holes into the back side cavity (i.e., backplate resistance)	R_{back}
C_{cav}	Compliance of the air volume in the back side cavity	$1/(j\omega C_{cav})$
R_{vent}	Resistance of air flow through the acoustic vent	R_{vent}

several higher order resonances. This measurement, combined with a finite element model modal analysis which takes into account the distributed mass of the polysilicon top electrode, provides a means to determine the effective diaphragm mass and compliance as described in detail previously.[21,22] The compliance of this particular diaphragm is 44 Å center point deflection per 1 Pa uniform diaphragm pressure.

With the diaphragm impedance characterized, the remaining relevant circuit elements in Fig. 7 are determined from dynamic response measurements in air. The back side cavity compliance and the vent resistance are important parameters affecting the lower limiting frequency of the microphone response to sound, but do not affect the electrostatic response as the cavity impedance is substantially smaller than the backplate resistance and the gap impedance. Furthermore, the thin microphone air gap is typically at least an order of magnitude stiffer than the diaphragm itself.[26] The backplate resistance is the most important parameter affecting the microphone bandwidth and the dampening of the diaphragm resonance. In addition to the backplate perforation hole design, this resistance is sensitive to the microphone gap height as the air in the thin gap must displace laterally to reach the perforation holes. Simulations of the 2100 μm diaphragm response using the circuit in Fig. 7 and various backplate resistance values are shown in Fig. 8. For this particular diaphragm with a 44.8 kHz resonance, the ideal backplate resistance is close to 1×10^8 Ra/m^2, which dampens the resonant peak but does not limit the bandwidth below the diaphragm resonant frequency. As shown in Fig. 8, larger backplate resistance values result in overdamped systems with reduced bandwidth.

The dynamic response in air of the 2100 μm diaphragm in Fig. 4 is measured using a procedure identical to that used in the above-described vacuum measurement with the microphone gap height biased to an arbitrary value of 1.90 μm. Figure 9(a) shows time traces of the input electrostatic pressure applied to the diaphragm and the resulting displacement, and the curve in Fig. 9(b) with the 1.90 μm gap height label shows the Fourier transform of the displacement signal or the dynamic frequency response. For this particular backplate design and gap height, the microphone is overdamped with a 3 dB cutoff frequency [corresponding to 30 Å/Pa in Fig. 9(b)] close to 4 kHz, which is well below the 44.8 kHz diaphragm resonant frequency. To verify that the observed cutoff frequency is caused by the backplate resistance as proposed by the model and simulations in Figs. 7 and 8, respectively, the measurement is performed using smaller gap heights—controlled via the applied dc bias voltage—and the expected lowering in the cut-off frequency due to the increased backplate resistance is observed in the additional measurements shown in Fig. 9(b). The equivalent circuit model has been fitted to the measured data to obtain an estimate of the backplate resistance as 7.4×10^9 Ra/m^2. In addition to limiting the microphone bandwidth, this backplate resistance dominates the thermal noise response across the audio frequency range as shown by measurements presented in Sec. VI.

VI. DISPLACEMENT AND SOUND PRESSURE DETECTION RESOLUTION

The displacement detection resolution of the microphone diaphragm (i.e., the displacement measured with a signal-to-noise ratio of 1) is measured as the output noise

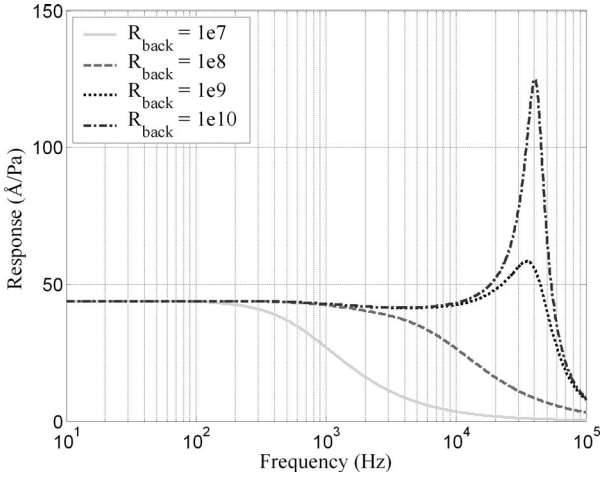

FIG. 8. Simulation of the microphone structure dynamic response for various backplate resistance values in units of Ra/m^2 using the equivalent circuit model in Fig. 7.

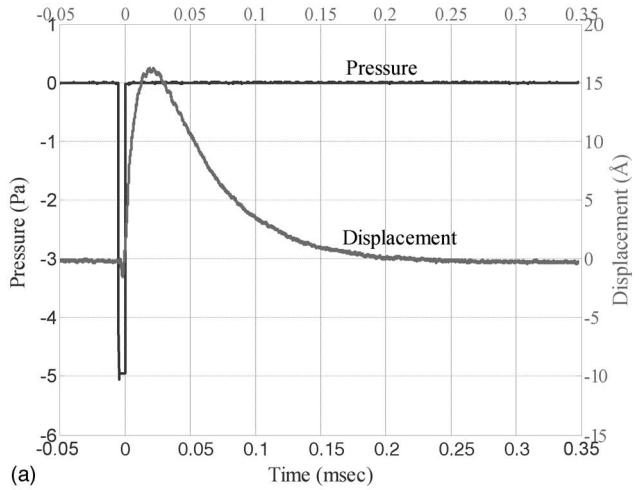

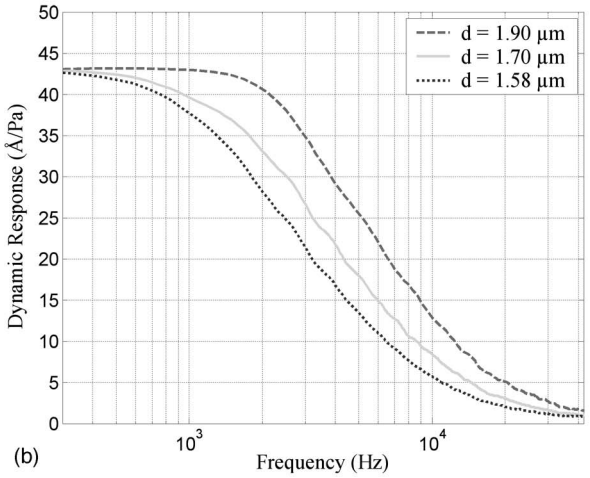

FIG. 9. (a) Time traces of the applied electrostatic impulse pressure and resulting diaphragm displacement measured in air, and (b) the dynamic frequency response for three different microphone gap heights.

voltage spectral density divided by the displacement sensitivity calibrated in Fig. 6. To suppress ambient acoustic and vibration noise so that the internal or self noise of the sensor can be studied, these measurements are performed in an anechoic test chamber using the integrated test-bed in Fig. 6, with signals from the zero and a first diffracted order routed to a dynamic signal analyzer stationed outside the test chamber. A precision Larson Davis measurement microphone is used to measure the ambient pressure noise floor inside the chamber, and these results are converted to equivalent diaphragm displacement in the spectrum labeled "chamber" shown in Fig. 10.[27] The signal at 1 kHz is applied acoustically and serves to generate a known reference displacement. The internal noise of the sensor is limited by the dominant internal detection noise sources, which consists of laser intensity noise, photodetector shot noise, and thermal mechanical noise of the microphone diaphragm and flow channels. The affect of laser phase noise in interferometric systems is proportional to the difference in optical path lengths, and is negligible due to the compact integration of the approach. The displacement noise of the 2100 μm device under study is measured under several conditions to study the dominant noise sources across the audio frequency range.

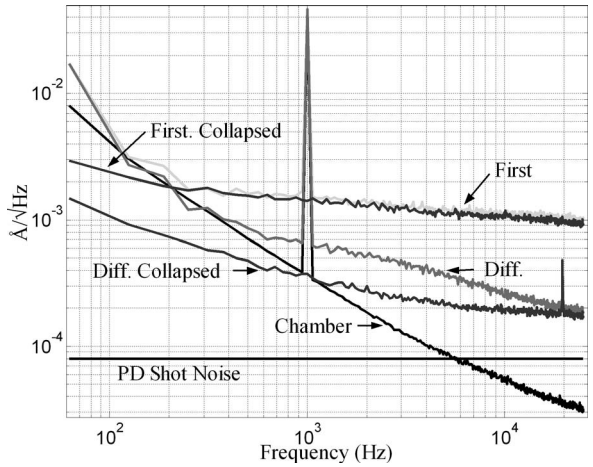

FIG. 10. Displacement noise spectrum of the microphone measured under several conditions.

The noise spectrum is first recorded with the microphone diaphragm held rigidly collapsed against the backplate using electrostatic actuation, thereby eliminating thermal mechanical noise and any unsuppressed ambient noise. This measurement is analogous to measurements on capacitive microphones performed with clamped capacitor heads to isolate internal electrical noise. The measured spectra using a single first order and differential detection of the zero and first order are shown in Fig. 10, with the latter showing a 14 dB improvement near 10 kHz. Only 3.5 dB of this improvement can be attributed to the gain in detection sensitivity, implying that more than 10 dB of laser intensity noise cancellation is observed using differential detection. Above 10 kHz, the differential measurement is observed to approach the fundamental photodetection shot noise limit which has been computed for these particular conditions. Below 10 kHz, uncancelled laser intensity noise limits the detection resolution. Note that the acoustically applied reference signal at 1 kHz does not appear in either of these spectra implying that electrostatic actuation is indeed holding the diaphragm completely rigid.

The noise spectra using first and differential order detection are then recorded with the diaphragm released from collapse and biased to a 1.75 μm gap height where maximum displacement detection sensitivity is achieved. With first order detection, the noise floor is dominated by the ambient acoustic noise in the test chamber at frequencies below 200 Hz where the spectrum is observed to match the chamber noise, and is limited by laser intensity noise at frequencies above 200 Hz where the spectrum is identical to the first order collapsed measurement. With differential detection, however, the displacement detection is limited by the ambient chamber noise up to 600 Hz, and by an internal noise source associated with the diaphragm motion in the 600 Hz–10 kHz frequency range. Simulations using the equivalent circuit model and the dynamic characterization results show that the internal noise is thermal mechanical noise caused by the backplate flow resistance. Figure 11 shows the complete thermal noise equivalent circuit which consists of thermal agitation induced pressure sources with

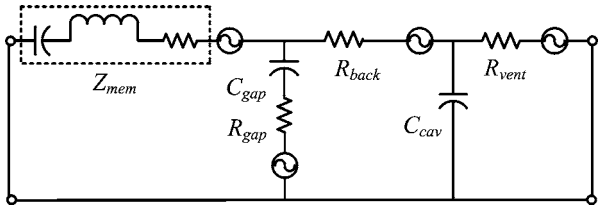

FIG. 11. Thermal noise equivalent circuit model of the microphone structure.

uniform frequency distribution in series with the resistive impedance elements in the circuit. The amplitude spectral density of these sources is given by

$$P_n = \sqrt{4kTR}, \tag{3}$$

where k is Boltzmann's constant, T is the ambient temperature, and R is the acoustic impedance.[28,29] Experiments in vacuum show that the resistive impedance of the diaphragm itself is at least an order of magnitude smaller than the backplate resistance. The vent resistance, which has not been characterized in this work, can be large and the thermal mechanical pressure fluctuations induced can cause significant actuation of the diaphragm at low frequencies, but become shunted by the large cavity compliance at frequencies above the lower limiting frequency of the microphone. [As can be verified from the model in Fig. 11, the fraction of the thermal mechanical pressure induced by the vent resistance that is applied across the diaphragm decreases at 20 dB/decade above the lower limiting frequency of the microphone, determined as $1/(2\pi R_{\text{vent}} C_{\text{cav}})$. Thermal noise caused by the vent resistance is not directly observed in this study which may be due to high ambient chamber noise.] The pressure induced by the backplate resistance, however, is essentially applied directly across the backplate and diaphragm in series which gives rise to the frequency dependence in the measured noise spectrum in Fig. 10. A complete circuit simulation using the measured diaphragm impedance and backplate resistance of 7.4×10^9 Ra/m^2 is shown in Fig. 12 along with the measured differential noise spectrum repeated from Fig. 10 for comparison. The simulated response in Fig. 12 includes the incoherent addition of the uncancelled laser intensity noise represented by the collapsed diaphragm measurement—also repeated from Fig. 10 for comparison. The similarity in both scale and frequency dependence confirm that the thermal noise induced by the backplate resistance is the dominant noise source over the 600 HZ–10 kHz frequency range.

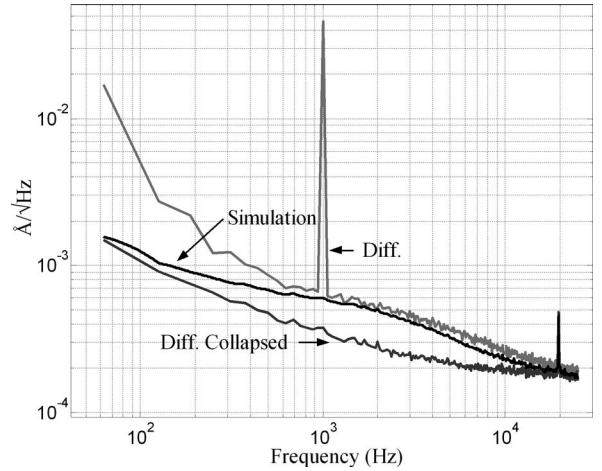

FIG. 12. Measured and simulated thermal noise spectrum.

The sound pressure noise spectrum of the microphone is obtained by dividing the displacement noise spectrum by the dynamic frequency response of the microphone measured in Fig. 9(b). The upper 3 dB cut-off frequency of 4 kHz for the prototype 2100 μm device under study results in high equivalent pressure noise above this frequency and adversely affects the microphone's overall A weighted noise rating, which can be computed as 39.9 dB(A). It should be noted that, in general, the frequency response to sound pressure can have an upper cut-off frequency well beyond the electrostatic response due to interaction of the measured sound field with the microphone package at higher frequencies.[4,8] The electrostatic response was used in this case to be conservative as the prototype microphones presented here have not been packaged for a specific application.

VII. DISCUSSION

The performance of the particular prototype microphones presented in this work will improve significantly with a lower backplate resistance, which can be achieved with an improved backplate design or the use of a thicker sacrificial oxide layer which defines the air gap thickness. For example, the simulations in Fig. 8 show that a backplate resistance of 1×10^8 Ra/m^2 would effectively dampen the diaphragm resonance while maintaining the full 44.8 kHz diaphragm resonance limited bandwidth. The equivalent thermal agitation pressure for this resistance value computed using Eq. (3) is 1.3 μPa/$\sqrt{\text{Hz}}$ which results in 6×10^{-5} Å/$\sqrt{\text{Hz}}$ diaphragm displacement. Since this value is below even the shot noise detection limit shown in Fig. 10, the internal displacement noise spectrum for such a device is expected to be identical to the differential data measured with the diaphragm collapsed which has corresponding A weighted displacement amplitude computed as 2.4×10^{-2} Å. With the 44 Å/Pa diaphragm currently in use, the resulting A weighted noise level would be 29.0 dB(A). For comparison, a Bruel & Kjaer model 4939 $\frac{1}{4}$ in. measurement microphone which has a diaphragm resonance near 80 kHz has an internal noise floor near 32 dB(A) when used with a model 2670 preamplifier.[30] Future designs will also benefit from a single layer polysilicon diaphragm as opposed to tensioned silicon nitride as this will enable softer diaphragms occupying smaller area. For example, less than 1.5-mm-diam micromachined diaphragms with 20 kHz resonance and approximately 200 Å/Pa compliance are common.[31,32] The A weighted pressure noise level of a microphone using such a diaphragm with the 2.4×10^{-2} Å displacement resolution demonstrated here would be 17.5 dB(A), a figure comparable to precision $\frac{1}{2}$-in.-diam condenser microphones.[33]

The above-noted comparisons are based on the displacement resolution measured in this work. The displacement resolution, however, can also be significantly improved. By

eliminating the topography in the optical reflector, which can be done using a CMP step with the current process for example, the troughs in the interference curves shown in Fig. 6 can be reduced by a factor of 5, thereby improving the intensity swing, slope, displacement sensitivity, and displacement detection resolution by a factor of 5, or 14 dB. Alternatively, improvements in the interference slope can be used to achieve a displacement detection resolution comparable to that measured in this work but with significantly less laser power than the 2.5 mW used in these experiments. For example, shot noise detection levels of 1.2×10^{-4} Å/$\sqrt{\text{Hz}}$ (close to the 0.8×10^{-4} Å/$\sqrt{\text{Hz}}$ level shown in Fig. 10) have been achieved with ultrasonic transducers exhibiting nearly ideal interference curves and using only 61 μW of optical power. Since the shot noise detection limit is inversely proportional to the square root of the optical power used as discussed and demonstrated in detail in previous work, achieving the same detection limit demands roughly 30× less power due to the 5× improvement in slope.[12] For applications with strict power budgets such as hearing aids and unattended field sensors, the average laser power can be further reduced using pulsed modulation of the integrated semiconductor laser. Considering that light sources such as VCSELs can be modulated in the GHz frequency range, duty cycles well below 1% can be used for acoustic detection up to 100 kHz.

VIII. CONCLUSIONS

Micromachined microphones with integrated diffraction-based optical displacement detection have been presented. An A weighted microphone diaphragm displacement detection resolution of 2.4×10^{-2} Å has been measured from 2100 μm prototype devices fabricated with a surface and bulk micromachining process using Sandia National Laboratories SwIFT-Lite™ platform. Measurements of the dynamic frequency response in air show a 3 dB upper cut-off frequency of 4 kHz which is far below the 44.8 kHz diaphragm resonant frequency in vacuum and is caused by the large backplate flow resistance of these particular prototype devices. The thermal mechanical noise induced by the backplate resistance is the dominant internal noise source over the 600 Hz–10 kHz frequency range. The backplate resistance can be reduced in future designs with the use of a larger gap height and/or a redesigned backplate—neither of which will adversely affect the displacement detection sensitivity with the optical approach. Additional recommendations for future designs include the CMP of the sacrificial oxide defining the microphone gap to eliminate topography in the microphone diaphragm for improved optics, and the use of polysilicon diaphragms which can be made smaller and more compliant than tensioned nitride diaphragms. Using parameters of such diaphragms characterized in the literature and the displacement detection resolution measured in this work, the potential for realizing precision $\frac{1}{2}$ in. measurement quality microphones using diaphragms only 1 mm in size is shown. The compact optoelectronic integration capabilities coupled with the microfabrication aspect may make the approach ideal for realizing high fidelity, miniature, chip module microphone arrays employing recently developed signal processing techniques to enable source localization and separation in the audio frequency range using apertures on the order of 1 cm^2. The technology is also ideal for single element applications where sensitivity to size ratio is an important performance parameter.

ACKNOWLEDGMENTS

This work is supported by the Defense Advanced Research Projects Agency Microsystems Technology Office (Contract No. DAAD19-00-1-0174) and the National Institutes of Health (Grant No. 1 R01 DC005762-01A1). The authors would also like to thank the Microsystems and Engineering Sciences Applications (MESA) Institute at Sandia National Laboratories. Sandia is a multiprogram laboratory operated by Sandia Corporation, a Lockheed Martin Company, for the United States Department of Energy's National Nuclear Security Administration under contract DE-AC04–94AL85000.

[1] S. Bouwstra, T. Storgaard-Larsen, P. R. Scheeper, J. Ole Gullov, J. Bay, M. Mullenborg, and P. Rombach, "Silicon microphones—a Danish perspective," J. Micromech. Microeng. **8**, 64–68 (1998).
[2] J. Mason, "Companies compete to be heard on the increasingly noisy MEMS phone market," *Small Times*, 2003.
[3] M. Stanacevic, G. Cauwengberghs, and G. Zweig, "Gradient flow adaptive beamforming and signal separation in a miniature microphone array," Proceedings of the IEEE International Conference on Acoustics Speech and Signal Processing, 2002, pp. 416–419.
[4] M. Gayford, *Microphone Engineering Handbook* (Focal Press, Oxford, 1994).
[5] P. R. Scheeper, A. G. H. Van Der Donk, W. Olthuis, and P. Bergveld, "A review of silicon microphones," Sens. Actuators, A **44**, 1–11 (1994).
[6] M. Pederson, W. Olthuis, and P. Bergveld, "High-performance condenser microphone with fully integrated CMOS amplifier and DC-DC voltage converter," J. Microelectromech. Syst. **7**, 387–394 (1998).
[7] D. P. Arnold, T. Nishida, L. N. Cattafesta, and M. Sheplak, "A directional acoustic array using silicon micromachined piezoresistive microphones," J. Acoust. Soc. Am. **113**, 289–298 (2003).
[8] P. R. Scheeper, B. Nordstrand, J. O. Gullov, B. Liu, T. Clausen, L. Midjord, and T. Storgaard-Larsen, "A new measurement microphone based on MEMS technology," J. Microelectromech. Syst. **12**, 880–891 (2003).
[9] S. T. Hansen, A. S. Ergun, W. Liou, B. A. Auld, and B. T. Khuri-Yakub, "Wideband micromachined capacitive microphones with radio frequency detection," J. Acoust. Soc. Am. **116**, 828–842 (2004).
[10] N. Bilaniuk, "Optical microphone transduction techniques," Appl. Acoust. **50**, 35–63 (1997).
[11] N. A. Hall and F. L. Degertekin, "Integrated optical interferometric detection method for micromachined capacitive acoustic transducers," Appl. Phys. Lett. **80**, 3859–3861 (2002).
[12] W. Lee, N. A. Hall, Z. Zhou, and F. L. Degertekin, "Fabrication and characterization of a micromachined acoustic sensor with integrated optical readout," IEEE J. Sel. Top. Quantum Electron. **10**, 643–651 (2004).
[13] N. A. Hall, W. Lee, and F. L. Degertekin, "Capacitive micromachined ultrasonic transducers with diffraction-based integrated optical displacement detection," IEEE Trans. Ultrason. Ferroelectr. Freq. Control **50**, 1570–1580 (2003).
[14] C. Gibbons and R. N. Miles, "Design of a biomimetic directional microphone diaphragm," American Society of Mechanical Engineers, Noise Control and Acoustics Division Publication No. 27, 2000, pp. 173–179.
[15] L. Tan, R. N. Miles, M. G. Weinstein, R. A. Miller, Q. Su, W. Cui, and J. Gao, "Response of a biologically inspired MEMS differential microphone diaphragm," Proc. SPIE **4743**, 91–98 (2002).
[16] N. C. Loh, M. A. Schmidt, and S. R. Manalis, "Sub-10 cm^3 interferometric accelerometer with nano-g resolution," J. Microelectromech. Syst. **11**, 182–187 (2002).
[17] T. Sulchek, R. J. Grow, G. G. Yaralioglu, S. C. Minne, C. F. Quate, S. R. Manalis, A. Kiraz, A. Aydine, and A. Atalar, "Parallel atomic force microscopy with optical interferometric detection," Appl. Phys. Lett. **78**,

1787–1789 (2001).
[18]G. G. Yaralioglu, A. Atalar, S. R. Manalis, and C. F. Quate, "Analysis and design of an interdigital cantilever as a displacement sensor," J. Appl. Phys. **83**, 7405–7415 (1998).
[19]W. Lee and F. L. Degertekin, "Rigorous coupled-wave analysis of multilayered grating structures," J. Lightwave Technol. **22**, 2359–2363 (2004).
[20]M. Okandan, P. Galambos, S. Mani, and J. Jakubczak, "Development of surface micromachining technologies for microfluidics and BioMEMS," Proc. SPIE **4560**, 133–139 (2001).
[21]N. A. Hall, "Micromachined broadband acoustic transducers with integrated optical displacement detection," PhD thesis, G. W. Woodruff School of Mechanical Engineering, Georgia Institute of Technology, Atlanta, GA, 2004.
[22]N. A. Hall, M. Okandan, and F. L. Degertekin, "Surface and bulk silicon micromachined optical displacement sensor fabricated with SwIFT—Lite™," J. Microelectromech. Syst. (submitted).
[23]www.veeco.com, "Wyko Profilometer NT3300," 7 July, 2005.
[24]www.coherentinc.com, "31-0144-000," 7 July, 2005.
[25]S. C. Thompson, J. L. LoPresti, E. M. Ring, H. G. Nepomuceno, J. J. Beard, W. J. Ballad, and E. V. Carlson, "Noise in miniature microphones," J. Acoust. Soc. Am. **111**, 861–866 (2002).
[26]L. L. Beranek, *Acoustic Measurements* (Wiley, New York, 1949).
[27]www.lardav.com, "Model 2541, 1/2 inch freefield microphone," 7 July, 2005.
[28]T. B. Gabrielson, "Mechanical-thermal noise in micromachined acoustic and vibration sensors," IEEE Trans. Electron Devices **40**, 903–909 (1993).
[29]T. B. Gabrielson, "Fundamental noise limits for miniature acoustic and vibration sensors," J. Vibr. Acoust. **117**, 405–410 (1995).
[30]www.bksv.com, "Model 4939," 7 July, 2005.
[31]A. Torkkeli, O. Rusanen, J. Saarilahti, H. Seppa, H. Sipola, and J. Hietanen, "Capacitive microphone with low-stress polysilicon membrane and high-stress polysilicon backplate," Sens. Actuators, A **85**, 116–123 (2000).
[32]P. R. Scheeper, W. Olthuis, and P. Bergveld, "The design, fabrication, and testing of corrugated silicon nitride diaphragms," J. Microelectromech. Syst. **3**, 36–42 (1994).
[33]www.bksv.com, "Model 4189," 7 July, 2005.

Coupling of flexural and longitudinal wave motion in a periodic structure with asymmetrically arranged transverse beams

Lars Friis[a] and Mogens Ohlrich[b]
Acoustic Technology, Ørsted•DTU, Technical University of Denmark, Building 352, DK-2800 Kgs. Lyngby, Denmark

(Received 1 December 2004; revised 15 August 2005; accepted 22 August 2005)

In this paper we investigate the coupling of flexural and longitudinal wave motions in a waveguide with structural side branches attached at regular intervals. The analysis is based on periodic structure theory, and considers wave transmission in a fully tricoupled and semidefinite periodic assembly of beam-type elements (or plane-wave transmission for normal incidence in a similar plate assembly). Receptances of a composite periodic element with offset resonant beams are derived and used for computing the frequency-dependent propagation constants of three coupled wave types as well as the distribution of motion displacements in each wave type. This is used for calculating the spatial variation of the forced harmonic responses of a semi-infinite periodic structure to point excitations by a longitudinal force and by a moment. Numerical simulations reveal the complicated wave coupling phenomena, which are clarified by calculating the ratio of flexural and longitudinal kinetic energies in the wave-carrying component for each wave type. In contrast to a corresponding, but uncoupled, system with significant broadband attenuation of flexural waves, the numerical results further show that the flexural-longitudinal wave coupling in a system with resonant side branches results in a highly enhanced wave transmission with very little attenuation from element to element. © *2005 Acoustical Society of America.* [DOI: 10.1121/1.2065767]

PACS number(s): 43.40.At, 43.40.Cw, 43.20.Bi [MO] Pages: 3010–3020

I. INTRODUCTION

Many types of engineering structures are built up of an assembly of nominally identical elements that are coupled together in an identical manner to form a so-called "spatially periodic structure." Examples are offshore accommodation modules, ship structures, and some buildings. The vibration and transmission of structural waves, say, from floor to floor in multistory buildings or from deck to deck in a ship, often give rise to noise problems in removed areas. A full three-dimensional analysis of such audiofrequency problems is very difficult due to the vibrational interactions between the large numbers of structural components. However, a fundamental understanding of the transmission may be obtained from studies of less complicated models that consider only a single transmission path comprising an assembly of beam-type components, or assume plane-wave transmission for normal incidence in a similar periodic assembly of plate elements.

A periodic system composed of repeated elements that are coupled with one another through n motion coordinates is known to support n characteristic-free, harmonic wave-types, which can exist simultaneously and independently at any frequency.[1–3] These wave-types occur in n pairs of positive- and negative-going waves, where each of the waves types is governed by a pair of complex characteristic "propagation constants" $\mu=\pm(\mu_R+i\mu_I)$; the real part μ_R is the so-called attenuation constant and the imaginary part μ_I is the phase constant. Here μ_R and μ_I are defined as positive. So, if only a single positive-going characteristic harmonic wave with propagation constant $\mu=-(\mu_R+i\mu_I)$ and angular frequency ω travels through the system, then the complex displacements $q(x)=q(\xi)$ and $q(\xi+l)$ at identical positions ξ in adjacent elements of length l are related by $q(\xi+l)e^{i\omega t}=e^{\mu}q(\xi)e^{i\omega t}$. This shows that free wave motion is possible only in frequency bands where μ is purely imaginary. These bands are known as "propagation zones" or "pass bands." For negligible structural damping, the wave thus propagates throughout the system without a change in amplitude. The frequency bands in which μ is real are called "attenuation zones" or "stop bands," since no transport of vibrational energy is possible and the wave amplitude is attenuated (reduced) from element to element.

Some years ago Ohlrich[4] investigated the propagation characteristics of longitudinal and flexural waves in beam- or column-type transmission paths with symmetrically arranged "point loads" in the form of resonant transverse beams. With such symmetrical cross beams the longitudinal wave motion in the structure was effectively uncoupled from flexural wave motion. This structure was used as a model of an inner or center-core-type transmission path in multistory buildings with floor supporting beams. For typical dimensions it was found that longitudinal waves propagate at almost all frequencies in the low-frequency range, say up to 300 Hz, only being interrupted by narrow-band, resonant attenuation zones caused by modes of the cross beams. Flexural waves were found to be more effectively attenuated by both resonant and smooth attenuation zones, and wave propagation occurred only in narrow bands constituting about 20% of the considered frequency range. A brief description of these findings is given in Ref. 5. However, experimental results also revealed[4]

[a]Electronic mail: lf@oersted.dtu.dk
[b]Electronic mail: mo@oersted.dtu.dk

that inertia loads attached on one side only of the transverse beams provoked longitudinal-flexural wave coupling because of the introduced eccentricity or asymmetry. The implication of this was a significant enhancement of the overall transmission of locally excited flexural wave motion, due to the conversion of flexural wave motion into predominantly longitudinal wave motion, which is generally transmitted with much less attenuation.

An understanding of the wave coupling that occurs in *asymmetrically* loaded transmission paths is of considerable practical interest, for example, in the prediction of vibration levels and structure-borne sound transmission in web-stiffened panels, in ship hulls that have deck structures to one side only and in outer supporting column structures in building skeletons or façade panels of buildings. In such periodic structures the longitudinal and flexural waves will, in general, be fully coupled, which significantly complicates the associated propagation properties and the underlying analysis, as will be revealed in this paper.

Wave motion in various kinds of periodic structures such as multisupported beams, plates, and shells have been studied for many years, but apparently no work has been done on the addressed problem of longitudinal–flexural wave coupling in semidefinite periodic structures with asymmetrical *and* multiresonant structural components, as are found in practical structures with resonating cross members such as one-sided decks, deep ribs, webs, and the like. Nearly half a century ago, Müller[6] observed an enhanced wave transmission in rib-reinforced concrete floors and this behavior was modeled by using eccentrically attached inertia loads at regular intervals on an otherwise continuous beam. In addition to Ohlrich's experimental observation,[4] Mead and Markus[7] later demonstrated the occurrence of longitudinal–flexural wave conversion in a simply multisupported beam loaded eccentrically with simple oscillators on levers. Their study also revealed that wave coupling diminishes as the structural damping is increased. Coupling of different wave types in periodic structures with lumped point loads has been studied in Refs. 8–11. Manfred Heckl[8] demonstrated four methods for calculating the structure-borne sound propagation in beams with many nonresonant discontinuities. In three of the methods coupling between longitudinal and flexural waves was taken into account. More recently, Maria Heckl[9] modeled a profiled cladding as a periodic structure consisting of long narrow panels attached to each other. Propagation characteristics of the coupled flexural–longitudinal wave motion and the transmission of airborne sound through the cladding were calculated numerically. Maria Heckl[10] also presented a mathematical model for the propagation and coupling of waves in a periodically supported Timoshenko beam. This coupling included flexural, longitudinal, and torsional waves. Roy and Plunkett[11] used transfer matrices to examine attenuation of flexural waves in an undamped beam with flexible but nonresonant ribs, which were attached either symmetrically or asymmetrically. However, they did not consider coupling between flexural and longitudinal waves.

In the present paper we examine such longitudinal–flexural wave coupling in periodic structures with asymmetrical and resonant point loadings caused by *continuous* cross-members. An investigation of this important problem has not been done before to the best of our knowledge. The effect of coupling on wave propagation and response levels in this type of semidefinite system is investigated and the results obtained are compared with the properties of a similar, but symmetrically loaded, periodic structure in order to ease the understanding of the wave conversion. Both types of structures are presented in Sec. II. The employed analytical analysis is based on the receptance approach to the periodic structure theory developed by Mead.[3,12,13] This theory is briefly summarized in the beginning of Sec. III for ease of reference, and as a basis for the analysis that follows. Basically, this approach utilizes that harmonic displacements and forces of a single periodic element are related by its dynamic receptances. Therefore, in Sec. III we derive expressions for the receptances of a composite periodic element that are required for determining the propagation constants of the considered type of discrete periodic structure. Next, expressions are presented for determining the coupled response of semi-infinite periodic systems from the eigenvectors of the characteristic wave types. This technique, which was developed by Mead,[13] utilizes so-called normalized force vectors and displacement vectors together with a set of generalized wave coordinates. This is put into use in Sec. IV, where receptances, propagation constants, and total response are derived for the target structure, the asymmetrically point-loaded periodic structure. Finally, the results of a numerical investigation are presented in Sec. V for a choice of structural parameters that clearly illustrates the longitudinal–flexural wave coupling. In a companion paper[14] the response of a similar, but *finite* periodic structure will be examined and predicted responses will be compared with experimental results.

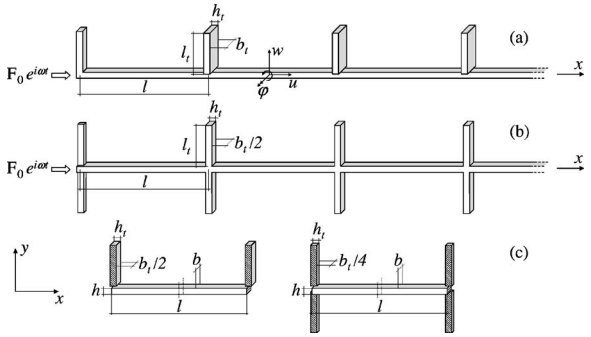

FIG. 1. Semi-infinite periodic structures with load components in the form of (a) asymmetrical beam loadings and (b) symmetrical beam loadings. (c) Corresponding periodic elements that are symmetrical with respect to $x = l/2$.

II. STRUCTURES WITH PERIODIC CROSS-MEMBERS

Consider a semi-infinite periodic structure that extends to infinity in the positive x direction, as shown in Fig. 1(a). The structure is driven at the end by an external forcing vector $\mathbf{F}_0 e^{i\omega t}$ that represents both longitudinal and transverse force excitations as well as moment excitation. The response is governed by three motion degrees of freedom, comprising displacements $u(x,t)$, $w(x,t)$, and $\varphi(x,t)$ in the longitudinal, transverse, and rotational directions. Note that the application of any single one of the external force components will

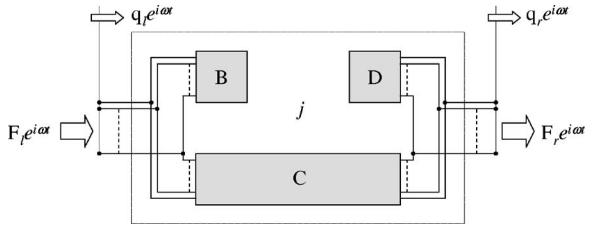

FIG. 2. Free body diagram of a multicoupled, composite periodic element, consisting of a wave-carrying component C and load components B and D. Shown are the force vectors on a single periodic element and the associated displacement vectors.

generate a *mixed* response comprising both longitudinal and flexural wave motions in the column components of such an asymmetric periodic structure. In order to comprehend the effects of coupling between flexural and longitudinal wave motions, it is useful to compare the derived results of response and propagation characteristics with those of a periodic structure in which longitudinal and flexural wave motions are not coupled. Figure 1(b) shows such a structure consisting of a continuous column loaded periodically with symmetrically arranged transverse beams. This type of structure is similar to one previously investigated in Refs. 4 and 5. Due to the symmetrical loadings, longitudinal and flexural wave motions are uncoupled, and excitation by either an external longitudinal (axial) force or a moment thus solely generates longitudinal wave motions or flexural wave motions, respectively. The periodically attached transverse beams have the same weight and same natural frequencies of antisymmetric and pinned modes as those of the structure in Fig. 1(a).

The periodic *elements* of the two structures are shown in Fig 1(c); for convenience in analysis these elements are chosen to be symmetrical about the middle of the column component, which means that the periodic element can be rotated about the y axis without changing its dynamic properties. This is achieved by dividing each transverse beam into beams of half-width. Thus, when periodic elements are physically connected to one another, the transverse beams of half-width become interconnected to form transverse beams of full width.

III. THEORY

A. Outline of theory

In a general one-dimensional periodic system, each periodic element is coupled at either end to the adjacent element through n motion coordinates. These n coordinates at the left- and right-hand end of the element are represented by the generalized displacement vectors $\mathbf{q}_l$ and $\mathbf{q}_r$, each being a column vector with n entries. Forces acting on the element's ends are similarly denoted by the force vectors $\mathbf{F}_l$ and $\mathbf{F}_r$, as illustrated in Fig. 2. This shows a free body diagram of a periodic element consisting of three *components*, being the wave-carrying component C and two structural loadings, components B and D. By assuming harmonic wave motion at angular frequency ω, we can relate the complex displacements $\mathbf{q}$ and forces $\mathbf{F}$ through a $2n\times 2n$ receptance matrix $\boldsymbol{\alpha}$ of the periodic element as[15] $\mathbf{q}e^{i\omega t}=\boldsymbol{\alpha}\mathbf{F}e^{i\omega t}$. With the time dependence suppressed this gives, in a partitioned form,

$$\begin{pmatrix}\mathbf{q}_l\\ \mathbf{q}_r\end{pmatrix}=\begin{bmatrix}\boldsymbol{\alpha}_{ll} & \boldsymbol{\alpha}_{lr}\\ \boldsymbol{\alpha}_{rl} & \boldsymbol{\alpha}_{rr}\end{bmatrix}\begin{pmatrix}\mathbf{F}_l\\ \mathbf{F}_r\end{pmatrix}, \tag{1}$$

where $\boldsymbol{\alpha}_{ll}$ and $\boldsymbol{\alpha}_{rr}$ are the direct receptance matrices of the periodic element, and $\boldsymbol{\alpha}_{lr}$ and $\boldsymbol{\alpha}_{rl}$ are the corresponding transfer receptance matrices. The first subscript refers to the response location and the second to the point of applied unit force excitation (other forces are absent). For linear elastic systems we have $\boldsymbol{\alpha}_{lr}=\boldsymbol{\alpha}_{rl}^T$, where superscript T denotes a "transposed" matrix.

If only a single characteristic wave travels through a periodic structure, then continuity of displacements and equilibrium of forces at the ends of a periodic element ensure that the displacement vectors $\mathbf{q}_l$ and $\mathbf{q}_r$, and force vectors $\mathbf{F}_l$ and $\mathbf{F}_r$, are related by[3]

$$\mathbf{q}_r=e^{\mu}\mathbf{q}_l,\quad \mathbf{F}_r=-e^{\mu}\mathbf{F}_l, \tag{2}$$

where $\mu=\mu_R+i\mu_I$ is the complex, frequency-dependent propagation constant. The real part of μ, the "attenuation constant" μ_R, expresses the decay rate in wave amplitude per element, whereas the imaginary part, the "phase constant" μ_I, describes the phase change of the wave motion per element. Equations (1) and (2) yield a relationship between displacements and forces at the same position, i.e.,

$$\mathbf{q}_l=[\boldsymbol{\alpha}_{ll}-e^{\mu}\boldsymbol{\alpha}_{lr}]\mathbf{F}_l. \tag{3}$$

From the same equations a general system equation can be derived, giving

$$[\boldsymbol{\alpha}_{ll}+\boldsymbol{\alpha}_{rr}-e^{\mu}\boldsymbol{\alpha}_{lr}-e^{-\mu}\boldsymbol{\alpha}_{rl}]\mathbf{F}_l=\mathbf{0}. \tag{4}$$

This represents a quadratic eigenvalue problem for e^{μ}; for nontrivial solutions the determinant of this matrix must be zero,

$$|\boldsymbol{\alpha}_{ll}+\boldsymbol{\alpha}_{rr}-e^{\mu}\boldsymbol{\alpha}_{lr}-e^{-\mu}\boldsymbol{\alpha}_{rl}|=0. \tag{5}$$

At any given frequency this yields up to n different pairs of propagation constants $\mu=\pm\mu_i$, where $i=1,2,\ldots,n$. If the real and imaginary parts of μ_i are defined as positive, then the corresponding n positive-going waves have propagation constants $\mu_{i,+}=-\mu_i$, and the n negative-going waves are associated with the propagation constants $\mu_{i,-}=\mu_i$.

B. Receptances of a composite periodic element

Receptances of a periodic element, expressed explicitly in terms of the component receptances, can be derived from the free body diagram in Fig. 2. Displacements and internal forces at the coupling points of the wave-carrying component C are in a similar manner to Eq. (1) related through the $2n\times 2n$ receptance matrix $\boldsymbol{\gamma}$ as

$$\begin{pmatrix}\mathbf{q}_{l,C}\\ \mathbf{q}_{r,C}\end{pmatrix}=\begin{bmatrix}\boldsymbol{\gamma}_{ll} & \boldsymbol{\gamma}_{lr}\\ \boldsymbol{\gamma}_{rl} & \boldsymbol{\gamma}_{rr}\end{bmatrix}\begin{pmatrix}\mathbf{F}_{l,C}\\ \mathbf{F}_{r,C}\end{pmatrix}. \tag{6}$$

Further, the displacements and forces of the load components B and D are related by the $n\times n$ receptance matrices $\boldsymbol{\beta}$ and $\boldsymbol{\delta}$ as

$$\mathbf{q}_B=\boldsymbol{\beta}\mathbf{F}_B, \tag{7}$$

$$\mathbf{q}_D = \boldsymbol{\delta}\mathbf{F}_D. \tag{8}$$

Combining Eqs. (6)–(8) and including the continuity of displacements and equilibrium of forces, the receptance submatrices of the periodic element yield[4]

$$\boldsymbol{\alpha}_{rl} = \mathbf{D}^{-1}, \tag{9}$$

$$\boldsymbol{\alpha}_{ll} = [-\boldsymbol{\gamma}_{lr}\boldsymbol{\delta}^{-1} + \boldsymbol{\gamma}_{ll}\boldsymbol{\gamma}_{rl}^{-1}[\mathbf{I} + \boldsymbol{\gamma}_{rr}\boldsymbol{\delta}^{-1}]]\mathbf{D}^{-1}, \tag{10}$$

$$\boldsymbol{\alpha}_{lr} = (\mathbf{D}^{-1})^T, \tag{11}$$

$$\boldsymbol{\alpha}_{rr} = [-\boldsymbol{\gamma}_{rl}\boldsymbol{\beta}^{-1} + \boldsymbol{\gamma}_{rr}\boldsymbol{\gamma}_{lr}^{-1}[\mathbf{I} + \boldsymbol{\gamma}_{ll}\boldsymbol{\beta}^{-1}]](\mathbf{D}^{-1})^T, \tag{12}$$

where

$$\mathbf{D} = -\boldsymbol{\beta}^{-1}\boldsymbol{\gamma}_{lr}\boldsymbol{\delta}^{-1} + [\boldsymbol{\beta}^{-1}\boldsymbol{\gamma}_{ll} + \mathbf{I}]\boldsymbol{\gamma}_{rl}^{-1}[\mathbf{I} + \boldsymbol{\gamma}_{rr}\boldsymbol{\delta}^{-1}]. \tag{13}$$

Here superscript -1 denotes a matrix inversion and $\mathbf{I}$ is the unity matrix.

Submatrices of *symmetric* periodic elements take on special forms,[13] and it is thus mathematically convenient to consider the load components as being identical, i.e., $\boldsymbol{\beta}=\boldsymbol{\delta}$, and to separate the end displacements into two types of motion coordinates that are denoted as type I and type II. In a symmetrical flexural mode, for example, the transverse displacements at the ends have the *same* sign whereas rotations have *opposite* signs. All kinds of motion coordinates belong to one of these categories, which are denoted type I and type II coordinates, respectively. It is readily seen that longitudinal displacements are type II coordinates. By using this, the displacements and forces in Eqs. (1)–(4) can be written in the following partitioned form:

$$\mathbf{q}_l = \begin{pmatrix} \mathbf{q}_{l_{\mathrm{I}}} \\ \mathbf{q}_{l_{\mathrm{II}}} \end{pmatrix}, \quad \mathbf{q}_r = \begin{pmatrix} \mathbf{q}_{r_{\mathrm{I}}} \\ \mathbf{q}_{r_{\mathrm{II}}} \end{pmatrix}, \quad \mathbf{F}_l = \begin{pmatrix} \mathbf{F}_{l_{\mathrm{I}}} \\ \mathbf{F}_{l_{\mathrm{II}}} \end{pmatrix}, \quad \mathbf{F}_r = \begin{pmatrix} \mathbf{F}_{r_{\mathrm{I}}} \\ \mathbf{F}_{r_{\mathrm{II}}} \end{pmatrix}. \tag{14}$$

Likewise, the periodic element's subreceptance matrices can be partitioned with respect to type I and II coordinates and the following relationships can be shown to apply:[13]

$$\boldsymbol{\alpha}_{ll} = \begin{bmatrix} \boldsymbol{\alpha}_{ll_{\mathrm{I,I}}} & \boldsymbol{\alpha}_{ll_{\mathrm{I,II}}} \\ \boldsymbol{\alpha}_{ll_{\mathrm{I,II}}}^T & \boldsymbol{\alpha}_{ll_{\mathrm{II,II}}} \end{bmatrix},$$

$$\boldsymbol{\alpha}_{rr} = \begin{bmatrix} \boldsymbol{\alpha}_{ll_{\mathrm{I,I}}} & -\boldsymbol{\alpha}_{ll_{\mathrm{I,II}}} \\ -\boldsymbol{\alpha}_{ll_{\mathrm{I,II}}}^T & \boldsymbol{\alpha}_{ll_{\mathrm{II,II}}} \end{bmatrix}, \tag{15}$$

$$\boldsymbol{\alpha}_{lr} = \boldsymbol{\alpha}_{rl}^T = \begin{bmatrix} \boldsymbol{\alpha}_{lr_{\mathrm{I,I}}} & \boldsymbol{\alpha}_{lr_{\mathrm{I,II}}} \\ -\boldsymbol{\alpha}_{lr_{\mathrm{I,II}}}^T & \boldsymbol{\alpha}_{lr_{\mathrm{II,II}}} \end{bmatrix}.$$

Herein submatrices $\boldsymbol{\alpha}_{ll_{\mathrm{I,I}}}$, $\boldsymbol{\alpha}_{ll_{\mathrm{II,II}}}$, $\boldsymbol{\alpha}_{lr_{\mathrm{I,I}}}$, and $\boldsymbol{\alpha}_{lr_{\mathrm{II,II}}}$ are all symmetric. Thus, in the case of systems with symmetric periodic elements the receptance submatrices given by Eq. (15) lead to the following special forms of equations, Eqs. (4) and (5):

$$\left[\begin{bmatrix} \boldsymbol{\alpha}_{ll_{\mathrm{I,I}}} & \mathbf{0} \\ \mathbf{0} & \boldsymbol{\alpha}_{ll_{\mathrm{II,II}}} \end{bmatrix} - \cosh\mu \begin{bmatrix} \boldsymbol{\alpha}_{lr_{\mathrm{I,I}}} & \mathbf{0} \\ \mathbf{0} & \boldsymbol{\alpha}_{lr_{\mathrm{II,II}}} \end{bmatrix} - \sinh\mu \begin{bmatrix} \mathbf{0} & \boldsymbol{\alpha}_{lr_{\mathrm{I,II}}} \\ -\boldsymbol{\alpha}_{lr_{\mathrm{I,II}}}^{\mathrm{T}} & \mathbf{0} \end{bmatrix}\right] \begin{pmatrix} \mathbf{F}_{l_{\mathrm{I}}} \\ \mathbf{F}_{l_{\mathrm{II}}} \end{pmatrix} = \mathbf{0} \tag{16}$$

and

$$\left|\begin{bmatrix} \boldsymbol{\alpha}_{ll_{\mathrm{I,I}}} & \mathbf{0} \\ \mathbf{0} & \boldsymbol{\alpha}_{ll_{\mathrm{II,II}}} \end{bmatrix} - \cosh\mu \begin{bmatrix} \boldsymbol{\alpha}_{lr_{\mathrm{I,I}}} & \mathbf{0} \\ \mathbf{0} & \boldsymbol{\alpha}_{lr_{\mathrm{II,II}}} \end{bmatrix} - \sinh\mu \begin{bmatrix} \mathbf{0} & \boldsymbol{\alpha}_{lr_{\mathrm{I,II}}} \\ -\boldsymbol{\alpha}_{lr_{\mathrm{I,II}}}^{T} & \mathbf{0} \end{bmatrix}\right| = 0. \tag{17}$$

C. Determination of total response of semi-infinite periodic structure

Consider a semi-infinite periodic structure driven by an external force vector $\mathbf{F}_0$, e.g., the tricoupled structure in Fig. 1(a). Mead[13] has shown that each wave propagation constant is associated with a particular force eigenvector, $\mathbf{F}_l$, which is a column vector with n entries according to Eq. (4) or (16). This eigenvector was also shown to be conveniently written as

$$\mathbf{F}_l = \mathbf{f}\psi, \tag{18}$$

where $\mathbf{f}$ is a so-called "normalized force vector" and ψ is an associated single "generalized wave coordinate." The normalized force vector specifies the relative amounts of different force components in the wave type under consideration. This force vector is obtained from Eq. (4) or (16), and it may be normalized in any desired form, but it is usually convenient to make the first element unity. While $\mathbf{f}$ depends solely on the element receptances and the considered propagation constant, then ψ is also influenced by the nature of the external excitation, that is, by the contents of the n elements force vector $\mathbf{F}_0$. Further, by analogy to Eq. (18) there is also a particular displacement vector $\mathbf{q}_l$ corresponding to each propagation constant; this is given by

$$\mathbf{q}_l = \boldsymbol{\zeta}\psi, \tag{19}$$

where $\boldsymbol{\zeta}$ is a so-called "normalized displacement vector," which specifies the relative amounts of different motion components in the wave type in question.

Now consider a single, positive-going wave with propagation constant $\mu_{i,+}=-\mu_i$, force eigenvector $\mathbf{F}_{i,+}=\mathbf{f}_{i,+}\psi_{i,+}$ and displacement vector $\mathbf{q}_{i,+}=\boldsymbol{\zeta}_{i,+}\psi_{i,+}$. Substituting these into Eq. (3) yields the following relationship between the normalized force vector $\mathbf{f}_{i,+}$ and normalized displacement vector $\boldsymbol{\zeta}_{i,+}$:

$$\boldsymbol{\zeta}_{i,+} = \boldsymbol{\alpha}_{ll}\mathbf{f}_{i,+} - \boldsymbol{\alpha}_{lr}\mathbf{f}_{i,+}e^{-\mu_i}. \tag{20}$$

If a semi-infinite periodic structure is excited at the finite left-hand end by the force vector $\mathbf{F}_0$, having n different components, then n characteristic positive-going waves are generated and these will all govern the response. The sum of the force eigenvectors corresponding to each of these waves must be in equilibrium with the applied force vector $\mathbf{F}_0$, that is,

$$\mathbf{F}_0 = \sum_{i=1}^{n} \mathbf{F}_{i,+} = \sum_{i=1}^{n} \mathbf{f}_{i,+}\psi_{i,+} = \mathbf{f}_+ \boldsymbol{\psi}_+, \tag{21}$$

where $\mathbf{f}_+$ is an $n \times n$ matrix containing n columns of normalized force vectors $\mathbf{f}_{i,+}$, where $i=1,2,\ldots,n$, and $\boldsymbol{\psi}_+$ is a column vector containing n generalized wave coordinates $\psi_{i,+}$, each of which is associated with a normalized force vector. The vector containing the generalized wave coordinates can now be found by a matrix inversion as

$$\boldsymbol{\psi}_+ = \mathbf{f}_+^{-1}\mathbf{F}_0. \tag{22}$$

By analogy to Eq. (21), the total displacement vector $\mathbf{q}_0$ at the excitation point reads as

$$\mathbf{q}_0 = \sum_{i=1}^{n} \mathbf{q}_{i,+} = \sum_{i=1}^{n} \boldsymbol{\zeta}_{i,+}\psi_{i,+} = \boldsymbol{\zeta}_+ \boldsymbol{\psi}_+. \tag{23}$$

The response at j junctions to the right, q_j, can now be expressed as

$$\mathbf{q}_j = \sum_{i=1}^{n} \mathbf{q}_{i,+} e^{-j\mu_i} = \sum_{i=1}^{n} \boldsymbol{\zeta}_{i,+} e^{-j\mu_i}\psi_{i,+} = \boldsymbol{\zeta}_+ \mathbf{e}_d^{-\mathbf{j}\boldsymbol{\mu}} \boldsymbol{\psi}_+, \tag{24}$$

where $\mathbf{e}_d^{-\mathbf{j}\boldsymbol{\mu}}$ is an $n \times n$ diagonal matrix containing the $(-j\mu_i)$'s for every wave type in the appropriate order. By using Eqs. (20) and (22), this expression finally yields

$$\mathbf{q}_j = (\boldsymbol{\alpha}_{ll}\mathbf{f}_+ - \boldsymbol{\alpha}_{lr}\mathbf{f}_+\mathbf{e}_d^{-\boldsymbol{\mu}})\mathbf{e}_d^{-\mathbf{j}\boldsymbol{\mu}}\mathbf{f}_+^{-1}\mathbf{F}_0. \tag{25}$$

IV. ASYMMETRICALLY LOADED PERIODIC STRUCTURE

We now consider the specific case of the asymmetrically loaded periodic structure in Fig. 1(a). According to Eq. (15), the submatrices of the periodic element's receptance matrix of this tricoupled periodic structure can be written in the partitioned form

$$\boldsymbol{\alpha}_{ll} = \begin{bmatrix} \alpha_{ll_{22}} & \alpha_{ll_{23}} & \alpha_{ll_{21}} \\ \alpha_{ll_{23}} & \alpha_{ll_{33}} & \alpha_{ll_{31}} \\ \alpha_{ll_{21}} & \alpha_{ll_{31}} & \alpha_{ll_{11}} \end{bmatrix},$$

$$\boldsymbol{\alpha}_{rr} = \begin{bmatrix} \alpha_{ll_{22}} & -\alpha_{ll_{23}} & -\alpha_{ll_{21}} \\ -\alpha_{ll_{23}} & \alpha_{ll_{33}} & \alpha_{ll_{31}} \\ -\alpha_{ll_{21}} & \alpha_{ll_{31}} & \alpha_{ll_{11}} \end{bmatrix}, \tag{26}$$

$$\boldsymbol{\alpha}_{lr} = \boldsymbol{\alpha}_{rl}^{\mathrm{T}} = \begin{bmatrix} \alpha_{lr_{22}} & \alpha_{lr_{23}} & \alpha_{lr_{21}} \\ -\alpha_{lr_{23}} & \alpha_{lr_{33}} & \alpha_{lr_{31}} \\ -\alpha_{lr_{21}} & \alpha_{lr_{31}} & \alpha_{lr_{11}} \end{bmatrix},$$

where subscripts 1, 2, and 3 denote longitudinal, transversal, and rotational variables, respectively. These submatrices can be obtained numerically from Eqs. (9)–(13), in which the receptance submatrices of the wave-carrying column component as well as the receptance matrix of the transverse beam load components take on the forms

$$\boldsymbol{\gamma}_{ll} = \begin{bmatrix} \gamma_{ll_{22}} & \gamma_{ll_{23}} & 0 \\ \gamma_{ll_{23}} & \gamma_{ll_{33}} & 0 \\ 0 & 0 & \gamma_{ll_{11}} \end{bmatrix},$$

$$\boldsymbol{\gamma}_{rr} = \begin{bmatrix} \gamma_{ll_{22}} & -\gamma_{ll_{23}} & 0 \\ -\gamma_{ll_{23}} & \gamma_{ll_{33}} & 0 \\ 0 & 0 & \gamma_{ll_{11}} \end{bmatrix}, \tag{27}$$

$$\boldsymbol{\gamma}_{lr} = \boldsymbol{\gamma}_{rl}^{T} = \begin{bmatrix} \gamma_{lr_{22}} & \gamma_{lr_{23}} & 0 \\ -\gamma_{lr_{23}} & \gamma_{lr_{33}} & 0 \\ 0 & 0 & \gamma_{lr_{11}} \end{bmatrix},$$

and

$$\boldsymbol{\beta} = \begin{bmatrix} \beta_{22} & 0 & 0 \\ 0 & \beta_{33} & \beta_{13} \\ 0 & \beta_{13} & \beta_{11} \end{bmatrix}. \tag{28}$$

Closed form expressions of all the individual component receptances in Eqs. (27) and (28) may be found in Ref. 15. In the present analysis all components are modeled by using Bernoulli–Euler beam theory, albeit with a correction for shear deformation,[16] which is required especially for obtaining correct natural frequencies of the periodic element in the considered frequency range. Note that it is the receptance β_{13}, which is solely responsible for the coupling between longitudinal and flexural wave motions in this type of periodic structure. Receptance β_{13}, of course, becomes an integral part of $\alpha_{ll_{21}}$, $\alpha_{ll_{31}}$, $\alpha_{lr_{21}}$, and $\alpha_{lr_{31}}$ when these receptances of Eq. (26) are computed from Eqs. (10) and (11).

Having derived expressions for the receptances, we are now able to determine the propagation constants for the possible wave types in the periodic structure and, subsequently, the total response that they generate. Propagation constants are determined from Eq. (17), and for the considered tricoupled system this yields

$$\left| \begin{bmatrix} \alpha_{ll_{22}} & 0 & 0 \\ 0 & \alpha_{ll_{33}} & \alpha_{ll_{31}} \\ 0 & \alpha_{ll_{31}} & \alpha_{ll_{11}} \end{bmatrix} - \cosh\mu \begin{bmatrix} \alpha_{lr_{22}} & 0 & 0 \\ 0 & \alpha_{lr_{33}} & \alpha_{lr_{31}} \\ 0 & \alpha_{lr_{31}} & \alpha_{lr_{11}} \end{bmatrix} - \sinh\mu \begin{bmatrix} 0 & \alpha_{lr_{23}} & \alpha_{lr_{21}} \\ -\alpha_{lr_{23}} & 0 & 0 \\ -\alpha_{lr_{21}} & 0 & 0 \end{bmatrix} \right| = 0. \tag{29}$$

From this equation three pairs of propagation constants $\pm\mu_i$ are found, where $i=A,B,C$. Due to wave conversion, all three wave types contain contributions of axial, transversal, and rotational motions, and the total response of the semi-infinite periodic structure of Fig. 1(a) is thus the sum of contributions from the three, positive-going waves. Hence, from Eq. (25) we obtain the total response at the jth junction; when written in full this yields

$$\begin{pmatrix} q_{j_2} \\ q_{j_3} \\ q_{j_1} \end{pmatrix} = \left(\left(\begin{bmatrix} \alpha_{ll_{22}} & \alpha_{ll_{23}} & \alpha_{ll_{21}} \\ \alpha_{ll_{23}} & \alpha_{ll_{33}} & \alpha_{ll_{31}} \\ \alpha_{ll_{21}} & \alpha_{ll_{31}} & \alpha_{ll_{11}} \end{bmatrix} \mathbf{f}_+ - \begin{bmatrix} \alpha_{lr_{22}} & \alpha_{lr_{23}} & \alpha_{lr_{21}} \\ -\alpha_{lr_{23}} & \alpha_{lr_{33}} & \alpha_{lr_{31}} \\ -\alpha_{lr_{21}} & \alpha_{lr_{31}} & \alpha_{lr_{11}} \end{bmatrix} \right. \right.$$
$$\left. \left. \times \mathbf{f}_+ \begin{bmatrix} e^{-\mu_A} & 0 & 0 \\ 0 & e^{-\mu_B} & 0 \\ 0 & 0 & e^{-\mu_C} \end{bmatrix} \right) \begin{bmatrix} e^{-j\mu_A} & 0 & 0 \\ 0 & e^{-j\mu_B} & 0 \\ 0 & 0 & e^{-j\mu_C} \end{bmatrix} \right.$$
$$\left. \times \mathbf{f}_+^{-1} \begin{pmatrix} F_{0_2} \\ F_{0_3} \\ F_{0_1} \end{pmatrix}, \right. \tag{30}$$

where the matrix $\mathbf{f}_+$ containing the three normalized force vectors $\mathbf{f}_{i,+}$ is given as

$$\mathbf{f}_+ = [\mathbf{f}_{A,+} \quad \mathbf{f}_{B,+} \quad \mathbf{f}_{C,+}] = \begin{bmatrix} 1 & 1 & 1 \\ X_{A,+_{32}} & X_{B,+_{32}} & X_{C,+_{32}} \\ X_{A,+_{12}} & X_{B,+_{12}} & X_{C,+_{12}} \end{bmatrix}. \tag{31}$$

Here $X_{i,+_{32}}$ is the ratio between excitations from moment and transversal force and $X_{i,+_{12}}$ is the ratio between axial force and transversal force; these force ratios for the ith wave are derived in Appendix A.

Now, in order to explain why each wave may contribute differently to the total response, it is necessary to quantify the relative amounts of flexural and longitudinal wave motion contained in each wave type. As shown in Ref. 7, this can be done by introducing the ratio $E_{\mathrm{kin},F}/E_{\mathrm{kin},L}$, which expresses the ratio between the maximum kinetic energies of flexural and longitudinal motion in the wave-carrying column component. In order to find these energies it is therefore necessary to determine the longitudinal and transversal motions at all positions in the column component caused by a single wave. Expressions for these "interior" motions are derived in Appendix B in terms of the displacements at the element's left-hand end and the propagation constant of the wave type considered. Note that any second-order contributions, say, transverse motion in quasilongitudinal waves and longitudinal motion in flexural waves are neglected in the calculations, and so is the rotational part of the flexural kinetic energy. Now, for the ith wave, the junction displacements at the left-hand end are found from the ith term in the series Eq. (24), giving

$$\begin{bmatrix} q_{i,j,+_2} \\ q_{i,j,+_3} \\ q_{i,j,+_1} \end{bmatrix} = \begin{bmatrix} \zeta_{i,+_2} \\ \zeta_{i,+_3} \\ \zeta_{i,+_1} \end{bmatrix} e^{-j\mu_i} \psi_{i,+}$$
$$= \left(\begin{bmatrix} \alpha_{ll_{22}} & \alpha_{ll_{23}} & \alpha_{ll_{21}} \\ \alpha_{ll_{23}} & \alpha_{ll_{33}} & \alpha_{ll_{31}} \\ \alpha_{ll_{21}} & \alpha_{ll_{31}} & \alpha_{ll_{11}} \end{bmatrix} \begin{pmatrix} 1 \\ X_{A,+_{32}} \\ X_{A,+_{12}} \end{pmatrix} \right.$$
$$\left. - \begin{bmatrix} \alpha_{lr_{22}} & \alpha_{lr_{23}} & \alpha_{lr_{21}} \\ -\alpha_{lr_{23}} & \alpha_{lr_{33}} & \alpha_{lr_{31}} \\ -\alpha_{lr_{21}} & \alpha_{lr_{31}} & \alpha_{lr_{11}} \end{bmatrix} \begin{pmatrix} 1 \\ X_{A,+_{32}} \\ X_{A,+_{12}} \end{pmatrix} e^{-\mu_i} \right) e^{-j\mu_i} \psi_{i,+}. \tag{32}$$

Notice that all three junction displacements of the considered periodic element are proportional to $(e^{-j\mu_i}\psi_{i,+})$, and so are also the displacements in the column component. However, $(e^{-j\mu_i}\psi_{i,+})$ cancels out in the expression for the energy ratio $E_{\mathrm{kin},F}/E_{\mathrm{kin},L}$ since both energies are proportional to the square of the column displacements. This implies that the energy ratio only depends upon the normalized displacements in the vector $\zeta_{i,+}$ and not on the actual displacements, which additionally depend upon position j and the external excitation of the periodic structure.

V. NUMERICAL INVESTIGATION AND DISCUSSION

Numerical analyses and parameter studies have been conducted for both asymmetric and symmetric types of semi-infinite periodic structures in order to examine and reveal the effects of wave conversion. In both types of structures the mass and natural frequencies of the transverse beam components are taken to be identical in order to facilitate a direct comparison of the system's properties. The results presented herein are for relatively short beam loads that are tuned to have their fundamental natural frequency well within the considered frequency range. The purpose of this parameter choice is to illustrate clearly the different and complicated wave conversion phenomena that take place. All computations and matrix manipulations have been done using MATLAB, version 6.5.

Apart from the above-mentioned dimensions of the beam loads, the structural properties and dimensions of the element components used in these simulations are similar to those used in an experimental investigation, being presented in a companion paper.[14] The material is acrylic with Young's modulus $E=5.4\times10^9\ \mathrm{N/m^2}$ and a density of $\rho=1200\ \mathrm{kg/m^3}$. Material damping is modeled by letting Young's modulus become complex as $\underline{E}=E(1+i\eta)$, where η is the damping loss factor. In the simulations, an arbitrarily low value of $\eta=0.001$ has been chosen in order to clearly reveal the wave coupling phenomena. The dimensions of the wave-carrying column component are length $l=235$ mm, thickness $h=15$ mm, and width $b=20$ mm, whereas the transverse load beam has length $l_t=l/8$, thickness parameter $h_t=h$, and width parameter $b_t=2b$. Results herein are presented as a function of the nondimensional frequency parameter $\Omega=(k_b l)^2$, where k_b is the wave number for free flexural waves in the column component. Substituting the bending stiffness of the column yields

$$\Omega = (k_b l)^2 = \omega(12\rho/E)^{1/2}(l^2/h). \tag{33}$$

A. Propagation constants

It is recalled that in the simpler case of a symmetrically loaded structure,[4,5] there is no longitudinal–flexural wave coupling, and the response is therefore governed by a purely longitudinal wave type and by two purely flexural wave types. In other words, flexural waves cannot be excited by a longitudinal excitation force, and *vice versa*. By contrast, all three wave types are coupled in the case of an asymmetrically loaded structure; these waves (and the resulting response) thus include contributions of longitudinal and flex-

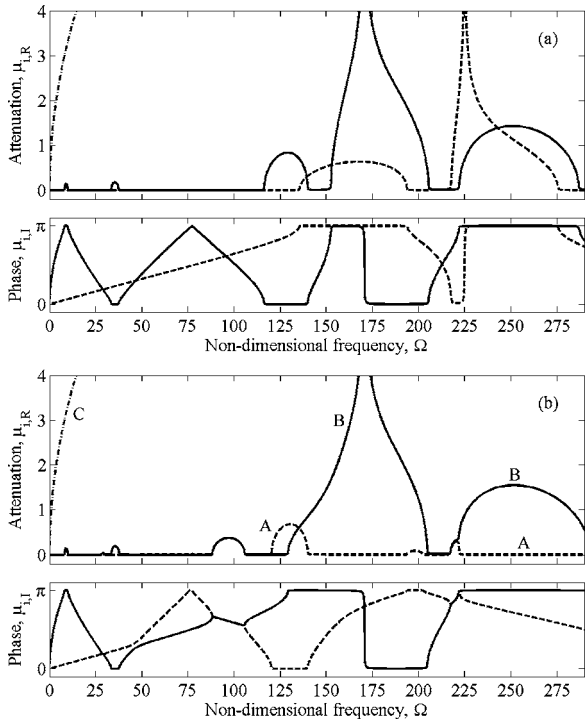

FIG. 3. Frequency variation of the real and imaginary parts of the propagation constants $\mu_i=\mu_{i,R}+i\mu_{i,I}$ for the three wave types. (a) Symmetrically loaded column-structure: - - -, longitudinal wave; —, flexural wave; -·-, flexural near field. (b) Asymmetrically loaded column-structure: - - -, flexural–longitudinal wave A; —, flexural-longitudinal wave B; -·-, primarily flexural near-field C. Loss factor $\eta=0.001$.

ural wave motions, i.e., all three wave types as well as the total response contain contributions from longitudinal (axial), transverse, and rotational displacements. The wave characteristics for both types of structures are presented in Fig. 3, which shows the frequency variation of the real and imaginary parts of the propagation constants associated with the three wave types.

Results for the *symmetrically* loaded column structure are shown in Fig. 3(a). The longitudinal wave motion, which is governed by a single characteristic wave, is seen to propagate (without attenuation in wave amplitude) over a broadband of frequencies up to $\Omega=135$, and with a phase change per element, μ_I, that is almost proportional to Ω. From there on, the transmission characteristics for longitudinal waves exhibit both smooth and resonant attenuation zones with intermediate zones of propagation. The frequency position and "bandwidth" of the resonant attenuation zone(s) is controlled by the mass, length, and modal characteristic of the load components; the peak attenuation thus occurs at a frequency at which the transverse beam-load components vibrate in a virtually midpoint-fixed, symmetrical mode. For clarity we have chosen a system with relatively short beam components that has only a single resonant attenuation zone within the considered frequency range. (For a system with somewhat longer beam components, say $l_t=0.8l$, there are four resonant attenuation zones[4,5] in the considered frequency range, and similarly four resonant attenuation zones for flexural wave motion). Such resonant attenuation zones are bounded by the natural frequencies of a single *periodic* element with both ends free. The magnitude and bandwidth of the smooth attenuation zone is controlled by the modal mass of the load components. The lower bounding frequency of a smooth attenuation zone is identical to the natural frequency of a single element with both ends free, whereas the upper bounding frequency is identical with the natural frequency of a single element with both ends fixed.

The flexural wave motion is governed by two waves, of which one is associated with a very high attenuation constant and can be regarded as a near field. For the sake of simplicity the phase constant of this wave has been omitted in Fig. 3(a). The other flexural wave also has the pattern of smooth and resonant attenuation zones. Apart from two very weak attenuation zones, this flexural wave is seen to propagate up until $\Omega=115$. At the peak attenuation frequency there is virtually neither rotation nor transverse displacement at the column–beam junctions. This frequency is related to the natural frequency of the midpoint-fixed mode of the transverse beam components that vibrate in an antisymmetric mode as opposed to the symmetric mode at the same frequency that governs the longitudinal resonant attenuation zones. However, peak attenuation of the flexural wave occurs at a somewhat lower frequency. This shift is caused by a minimum in $\alpha_{ll_{23}}=\alpha_{ll_{32}}$ at an even lower frequency, which creates zero transverse displacement due to moment excitation and zero rotation due to transverse force excitation. Further, at the frequency of peak attenuation the two flexural waves become complex conjugates. It is well known[4] that the lower bounding frequencies of smooth flexural attenuation zones are controlled by element modes of zero rotation at the junctions, whereas all other bounding frequencies of attenuation zones are controlled by element modes with zero transverse displacements.

We now consider the results in Fig. 3(b) for the *asymmetrically* loaded periodic structure. Due to longitudinal–flexural wave coupling, all three wave types contain axial, transversal, and rotational motions. The denoted wave type C, however, is again associated with a very large attenuation constant, and it can be regarded primarily as a flexural near-field, as will be revealed in the next section. Apart from the gross overall resemblance with the results for the symmetric structure, a number of important differences can be observed regarding the propagation constants of the remaining two wave types in the asymmetric structure, say, waves A and B.

From the phase constants, it is seen that the two curves do not cross over in a straightforward manner, as was the case in Fig. 3(a). Instead the curves either (i) diverge from one another or (ii) they merge, so that the propagation constants almost become complex conjugates with a nonzero attenuation constant. The first phenomenon is seen to occur at $\Omega=46$; at this frequency the phase constant of the apparently longitudinal-type wave, A, change over to a steeper phase characteristic that is usually associated with a flexural-type wave. This appears to be a clear indicator of the occurrence of a strong wave coupling or wave conversion. The second phenomenon of strong wave coupling is seen to occur in the bands of $\Omega=28$ to 30, 88 to 106 and 217 to 222, in which the coupled longitudinal–flexural waves are also attenuated as they progress through the periodic structure. Such complex conjugate zones, or "amber bands," have also

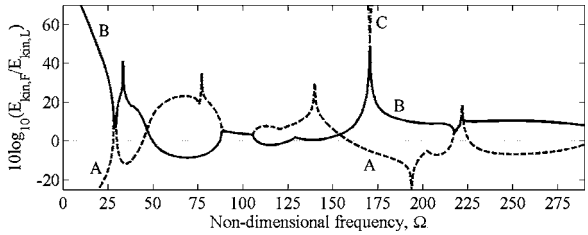

FIG. 4. Energy ratios $E_{\mathrm{kin},F}/E_{\mathrm{kin},L}$ for wave types in an asymmetrically loaded column structure. - - -, flexural–longitudinal wave A; —, flexural–longitudinal wave B; -·-, primarily flexural near-field C. Loss factor $\eta=0.001$.

been examined in Refs. 17,18. It should be mentioned that these two types of coupling phenomena occur most strongly in lightly damped systems, whereas they may disappear more or less completely in systems with high structural damping. Mead and Markus[7] observed this in their study of a simply loaded periodic system.

From the attenuation constants in Fig. 3(b) it is seen that only a *single* resonant attenuation zone is present and that this is associated with wave type B, whereas wave type A has a full propagation zone in more or less the same frequency band. The peak attenuation is noted to occur at a frequency of $\Omega=170$, which is nearly the same as for the symmetric system in Fig. 3(a). Another important observation is that the coupling enforces a merging of the previously uncoupled, flexural resonant attenuation zone and the smooth longitudinal attenuation zone into a single attenuation zone. A parameter study reveals that this merging generally takes place when the two types of attenuation zones (in the uncoupled symmetric case) appear close to one another or are actually coinciding.

What remains is a characterization of the type of wave motions that occur in the different frequency bands. The propagation constants presented in Fig. 3(b) do not solely facilitate such a classification of the actual wave nature, but this can be revealed by computing the normalized displacement vectors, $\boldsymbol{\zeta}_{i,+}$, as given by Eq. (32).

B. Nature of wave types

The relative amounts of flexural and longitudinal motions contained in each wave type can be quantified by the kinetic energy ratio $(E_{\mathrm{kin},F}/E_{\mathrm{kin},L})$, which was defined in Sec. IV. This quantity has been calculated numerically for each wave type in terms of the normalized displacement vector, $\boldsymbol{\zeta}_{i,+}$ and propagation constant $\mu_{i,+}=-\mu_i$ for its positive-going wave.

Figure 4 show such results in the form of energy ratio levels for the three wave types in the asymmetrically loaded column structure; corresponding propagation constants are given in Fig. 3(b). At low frequencies a distinction between the wave types is readily made. Wave type A is clearly longitudinal and wave type B is clearly flexural, whereas wave type C is a flexural near-field with an energy ratio level exceeding 70 dB! This behavior of type A and B waves extends up until about $\Omega=27$. From there on both wave types must be classified as being longitudinal–flexural as each of them alternates in a complicated manner between being predominantly longitudinal and predominantly flexural, or fully mixed, with approximately equal contributions. In complex conjugate zones the relative amount of flexural and longitudinal motions in the two mixed wave types are seen to be of the same order of magnitude. Further, wave types B and C become complex conjugate at $\Omega=170$, at an energy level of about 40 dB. At some frequencies (around $\Omega=46$ and 154) and in complex conjugate zones both of the two mixed wave types are predominantly flexural.

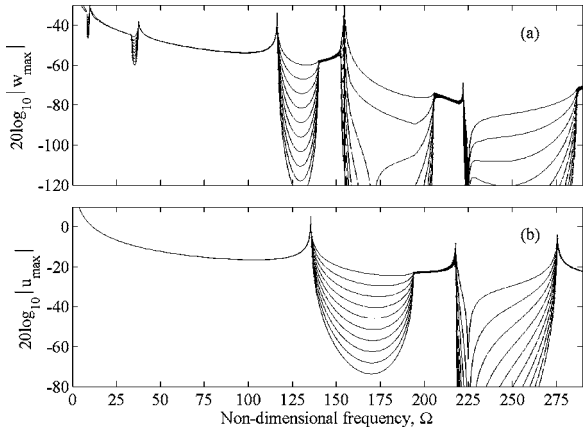

FIG. 5. Maximum displacement amplitudes in the column component of the first ten elements of the semi-infinite, symmetrically loaded structure. (a) Maximum transverse displacement $|w_{\max}|$ of flexural motion generated by an external harmonic moment M_0. (b) Maximum longitudinal displacement $|u_{\max}|$ generated by an external harmonic force F_0. Loss factor $\eta=0.001$.

C. Response of semi-infinite periodic structures

Finally, we shall demonstrate the effect of wave coupling on the response of semi-infinite periodic structures to external point excitation. Two types of external harmonic excitations are considered, namely a nondimensional moment of amplitude $M_0=(EI)/l$, and a nondimensional longitudinal (axial) force of amplitude $F_0=ES$, where I is the second moment of area of the column component and S is its cross-sectional area. Again, the results for a symmetrically loaded structure are first shown in order to clearly demonstrate what happens when the asymmetrically loaded structure is considered.

For the symmetrically loaded system Fig. 5 shows the maximum displacements in the first ten column components in terms of the transverse displacement $|w_{\max}|$ in the uncoupled flexural wave motion and the longitudinal displacement $|u_{\max}|$ in the purely longitudinal wave motion. These interior, maximum responses of the column components are calculated from the expressions in Appendix B by using the displacements for each wave type at the left-hand end of the considered element, as given in Eq. (32). Figure 5 clearly shows the occurrence and effect of the pass bands and stop bands that are associated with the corresponding propagation constants in Fig. 3(a). Further, it is seen that the system responds strongly at the bounding frequencies, which are governed by the natural frequencies of a single periodic element.

In the asymmetrically loaded system [see Fig. 1(a)] the harmonic response results from a combination of contributions from the coupled positive-going waves. The signifi-

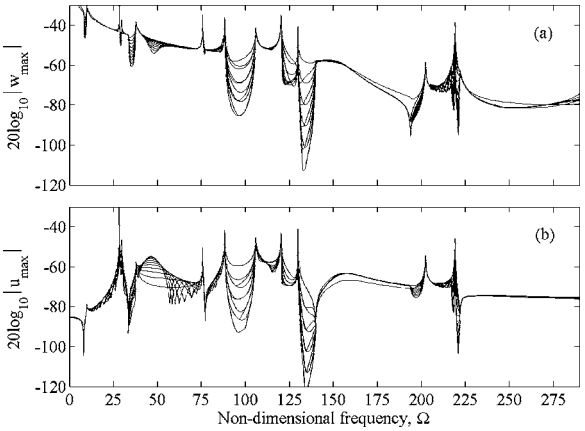

FIG. 6. Maximum displacements in the column component of the first ten elements of a semi-infinite, asymmetrically loaded structure, excited by an external harmonic moment M_0. (a) Maximum transverse displacement $|w_{max}|$ of flexural motion; (b) Maximum longitudinal displacement $|u_{max}|$. Loss factor $\eta=0.001$.

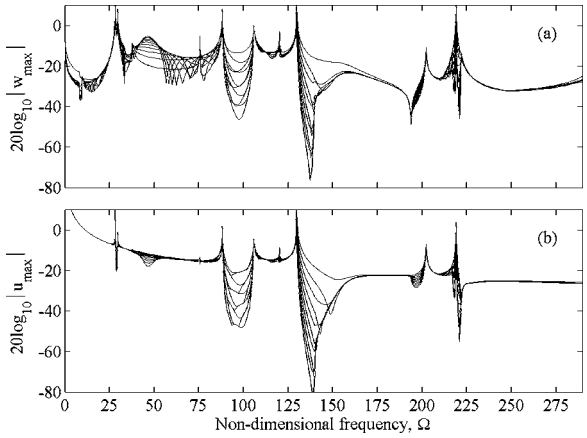

FIG. 7. The same as in Fig. 6, but for an external harmonic axial force excitation F_0.

cance and contribution of each wave with respect to the total response does not only depend upon the type of external excitation, but also on the energy ratios and the propagation constants. This implies that the calculated displacement responses can be explained from the results in Fig. 3(b) and Fig. 4. The maximum displacement responses for the case of the asymmetrically loaded periodic system driven by an external harmonic moment M_0 are shown in Fig. 6. Compared to the symmetrically loaded system, it is seen that the wave coupling has a drastic effect; with the exception of a few narrow stop bands, the waves are seen to propagate unattenuated in most parts of the considered frequency range. Thus, in the bands from $\Omega=140$ to 205 and from $\Omega=222$ and up, in which the type B wave is predominantly flexural (see Fig. 4), the strong attenuation zones have no significant effect on either of the groups of responses in Fig. 6. The reason for this is that the propagating type-A wave is dominating, even though it is predominantly longitudinal. Generally, this is found to be the case whenever one of the wave types is propagating and the other wave type is *strongly* attenuated. A close inspection further reveals that for most frequencies exceeding $\Omega=165$, the longitudinal displacements in Fig. 6(b) are even higher than the transverse flexural displacements in Fig. 6(a). It is only at low frequencies, below $\Omega\approx25$, that longitudinal displacement responses are insignificant. From $\Omega=30$ to 88 the longitudinal displacements are about 13 dB lower than the transverse displacements, and they become very similar in the range from $\Omega=88$ to 165.

Moreover, an appreciable but uneven attenuation from element to element is noted to occur in narrow frequency zones where wave types A and B are both governed by appreciable attenuation constants; see $\Omega\approx95$ and 135 in Fig. 3(b) and Fig. 6. Small attenuation also occurs when the two wave types are both propagating, and their contributions of transverse and longitudinal displacements are of the same order of magnitude. When superimposed the waves cancel one another either partly or completely. This is seen to be the case in the frequency range from $\Omega=38$ to 75 in Fig. 6.

Results for harmonic excitation with an external longitudinal (axial) force F_0 are shown in Fig. 7. From Fig. 7(b) it is seen again that the wave coupling has a very strong effect when compared to the results for the uncoupled longitudinal responses in Fig. 5(b). Overall the results are very similar to those in Fig. 6, although the stop band at $\Omega\approx135$ is slightly wider. Apart from the stop bands and the peaks at some of the bounding frequencies, the longitudinal displacement responses in Fig. 7(b) may readily be shown to follow closely the asymptotic response of a simple continuous and semi-infinite column structure of the same cross-sectional area S. This means that the corresponding longitudinal *velocity* responses are grossly independent of frequency in the considered frequency range. Very similar are also the spectral shapes of the system's "cross-properties," that is, the transverse flexural displacements in the column elements generated by the longitudinal force F_0 [see Fig. 7(a)] and the longitudinal displacements generated by the moment excitation M_0; see Fig. 6(b). In the case of longitudinal force excitation it is the transverse displacement that is insignificant at the low frequencies below $\Omega=27$. From $\Omega=30$ to 165 the longitudinal and transverse displacements are very similar in amplitude, and from there on the longitudinal displacement is about 6 dB higher than the transverse, as was the case with moment excitation.

VI. CONCLUSIONS

A new model based on *composite* element receptances has been developed for studying phenomena of flexural–longitudinal wave coupling in fully tricoupled *periodic* waveguides. Specifically examined are lightly damped periodic structures with multiple and resonant side branches in the form of offset transverse beams attached at regular intervals. This may resemble a one-dimensional model of column-beam skeletons in buildings or idealized plane-wave, normal incidence models of web-stiffened panels, ship hulls with decks to one side only, etc. Computed results of complex propagation constants, which govern the wave fields in periodic structures, have clearly revealed *pass* and *stop* band characteristics and wave coupling phenomena, which are shown to enhance the long-range transmission when the periodic structure is unconstrained and hence allowed to vi-

brate freely in its plane. This system can support three coupled wave types, and their importance is clarified and quantified from computations of their contribution to ratios of maximum flexural and longitudinal kinetic energies in the wave-carrying components. For this *asymmetrically* point-loaded periodic structure it is found that two wave types can be categorized as being *coupled* flexural–longitudinal waves in major parts of the considered frequency range, because both types alternate in a complicated manner between being either fully mixed or occasionally predominantly longitudinal or predominantly flexural. The remaining third wave type is a flexural type "near-field" as is the case for a corresponding, but *symmetrical* system in which longitudinal and flexural wave types are *uncoupled*.

The determined distribution of displacements in each wave type is furthermore used for calculating the spatial variation of the responses of a semi-infinite periodic structure that is subjected to end-point harmonic excitations by either a longitudinal force or by a moment. In contrast to the corresponding uncoupled symmetrical system with significant broadband attenuation of flexural-type waves, the numerical results show that the flexural–longitudinal wave coupling in a system with resonant side branches has a drastic effect on the wave propagation properties. Despite the system is excited by an external moment — and one of the two wave types is predominantly flexural with a broad stop band — it is unexpectedly found that the inherent wave coupling results in a highly enhanced wave transmission with very little attenuation of flexural motion from element to element. This enhanced transmission is caused by the other wave type, which is predominantly longitudinal and propagates with significant components of both flexural and longitudinal displacements. Also in the case of longitudinal force excitation, wave propagation similarly occurs at most frequencies and both types of response displacements are of the same order of magnitude. For the structural components and dimensions considered in this study the longitudinal responses along the periodic structure are furthermore found to be only little influenced by the transverse beam loads; hence, responses follow grossly the asymptotic response of a simple continuous waveguide of the same cross-sectional area. With the present composite-receptance approach other types of structural side-branches components or other boundary conditions can easily be incorporated in the developed prediction model.

APPENDIX A: DERIVATION OF FORCE RATIOS FOR THE *i*TH WAVE

For a characteristic positive-going wave traveling through the periodic system with propagation constant $-\mu_i$, the corresponding force eigenvector can be found from Eq. (16). For the tricoupled structure this yields

$$\begin{bmatrix} \alpha_{ll_{22}} - \alpha_{lr_{22}} \cosh \mu_i & -\alpha_{lr_{23}} \sinh \mu_i & -\alpha_{lr_{21}} \sinh \mu_i \\ \alpha_{lr_{23}} \sinh \mu_i & \alpha_{ll_{33}} - \alpha_{lr_{33}} \cosh \mu_i & \alpha_{ll_{31}} - \alpha_{lr_{31}} \cosh \mu_i \\ \alpha_{lr_{21}} \sinh \mu_i & \alpha_{ll_{31}} - \alpha_{lr_{31}} \cosh \mu_i & \alpha_{ll_{11}} - \alpha_{lr_{11}} \cosh \mu_i \end{bmatrix} \begin{pmatrix} F_{i,+_2} \\ F_{i,+_3} \\ F_{i,+_1} \end{pmatrix} = \begin{pmatrix} 0 \\ 0 \\ 0 \end{pmatrix}. \tag{A1}$$

The first and second of these equations can be written as

$$(\alpha_{ll_{22}} - \alpha_{lr_{22}} \cosh \mu_i) F_{i,+_2} - (\alpha_{lr_{23}} \sinh \mu_i) F_{i,+_3} - (\alpha_{lr_{21}} \sinh \mu_i) F_{i,+_1} = 0,$$

$$(\alpha_{lr_{23}} \sinh \mu_i) F_{i,+_2} + (\alpha_{ll_{33}} - \alpha_{lr_{33}} \cosh \mu_i) F_{i,+_3} + (\alpha_{ll_{31}} - \alpha_{lr_{31}} \cosh \mu_i) F_{i,+_1} = 0. \tag{A2}$$

By multiplying the first equation with $(\alpha_{ll_{31}} - \alpha_{lr_{33}} \cosh \mu_i)$ and the second equation with $(\alpha_{lr_{21}} \sinh \mu_i)$, and finally subtracting the two, $F_{i,+_1}$ is eliminated:

$$(\alpha_{ll_{22}} - \alpha_{lr_{22}} \cosh \mu_i)(\alpha_{ll_{31}} - \alpha_{lr_{31}} \cosh \mu_i) F_{i,+_2} - (\alpha_{lr_{23}} \sinh \mu_i)(\alpha_{ll_{31}} - \alpha_{lr_{31}} \cosh \mu_i) F_{i,+_3} + (\alpha_{lr_{23}} \sinh \mu_i)(\alpha_{lr_{21}} \sinh \mu_i) F_{i,+_2}$$
$$+ (\alpha_{ll_{33}} - \alpha_{lr_{33}} \cosh \mu_i)(\alpha_{lr_{21}} \sinh \mu_i) F_{i,+_3} = 0. \tag{A3}$$

From this the ratio between $F_{i,+_3}$ and $F_{i,+_2}$ can be found as

$$X_{i,+_{32}} = \frac{F_{i,+_3}}{F_{i,+_2}} = -\frac{(\alpha_{ll_{22}} - \alpha_{lr_{22}} \cosh \mu_i)(\alpha_{ll_{31}} - \alpha_{lr_{31}} \cosh \mu_i) + (\alpha_{lr_{23}} \sinh \mu_i)(\alpha_{lr_{21}} \sinh \mu_i)}{(\alpha_{ll_{33}} - \alpha_{lr_{33}} \cosh \mu_i)(\alpha_{lr_{21}} \sinh \mu_i) - (\alpha_{lr_{23}} \sinh \mu_i)(\alpha_{ll_{31}} - \alpha_{lr_{31}} \cosh \mu_i)}. \tag{A4}$$

The use of any other two equations from the matrix in Eq. (A1) would result in the same ratio. The ratio between $F_{i,+_1}$ and $F_{i,+_2}$ is found likewise by multiplying the first equation with $(\alpha_{ll_{33}} - \alpha_{lr_{33}} \cosh \mu_i)$ and the second equation with $(-\alpha_{lr_{23}} \sinh \mu_i)$, and further subtracting the two in order to eliminate $F_{i,+_3}$. This yields

$$X_{i,+_{12}} = \frac{F_{i,+_1}}{F_{i,+_2}} = -\frac{(\alpha_{ll_{22}} - \alpha_{lr_{22}} \cosh \mu_i)(\alpha_{ll_{33}} - \alpha_{lr_{33}} \cosh \mu_i) + (\alpha_{lr_{23}} \sinh \mu_i)(\alpha_{lr_{23}} \sinh \mu_i)}{(\alpha_{ll_{31}} - \alpha_{lr_{31}} \cosh \mu_i)(\alpha_{lr_{23}} \sinh \mu_i) - (\alpha_{lr_{21}} \sinh \mu_i)(\alpha_{ll_{33}} - \alpha_{lr_{33}} \cosh \mu_i)}. \tag{A5}$$

APPENDIX B: LONGITUDINAL AND TRANSVERSAL RESPONSES IN THE COLUMN COMPONENT

The response at an arbitrary position x in a column component or in a transverse beam component can be obtained in terms of the displacements and rotations at the ends of the periodic element. The longitudinal displacements, transverse displacements, and rotations at the left- and right-hand ends of an element due to the ith wave type are now denoted $u_{l,i}$, $u_{r,i}$, $w_{l,i}$, $w_{r,i}$, $\varphi_{l,i}$, and $\varphi_{r,i}$, respectively. Index l and r refer to left- and right-hand end. Thus, for a single harmonic wave type with propagation constant $-\mu_i$, the complex displacement amplitudes at the right- and left-hand ends of the periodic element are related as

$$u_{r,i} = u_{l,i}e^{-\mu_i}, \quad w_{r,i} = w_{l,i}e^{-\mu_i}, \quad \text{and} \quad \varphi_{r,i} = \varphi_{l,i}e^{-\mu_i}. \tag{B1}$$

Utilizing these relationships, we can express the displacements in the column component in terms of the element's displacements at the left-hand end and the propagation constant for the wave considered. The displacements at the left-hand end of the jth element are given in Eq. (32); hence

$$u_{l,i} = q_{i,j,+_1}, \quad w_{l,i} = q_{i,j,+_2} \quad \text{and} \quad \varphi_{l,i} = q_{i,j,+_3}. \tag{B2}$$

By using general wave theory,[1] the local x dependence of the longitudinal displacement $u_i(x)$ in the column component, due to the ith wave, takes the form

$$u_i(x) = A_i \cos k_l x + B_i \sin k_l x, \tag{B3}$$

where k_l is the wave number for free longitudinal waves. Applying Eq. (B1), this can be expressed as

$$u_i(x) = u_{l,i}[\cos k_l x + \sin k_l x(e^{-\mu_i} - \cos k_l l)/\sin k_l l]. \tag{B4}$$

In a similar form the transverse displacement $w_i(x)$ in the column component due to the ith wave is given by

$$w_i(x) = a_i(\cos k_b x - \cosh k_b x) + b_i(\sin k_b x - \sinh k_b x) + w_{l,i}\cosh(k_b x) + (\varphi_{l,i}/k_b)\sinh(k_b x), \tag{B5}$$

and by applying Eq. (B1), a_i and b_i are expressed as

$$a_i = [[w_{l,i}(\cosh k_b l \cos k_b l - \sinh k_b l \sin k_b l - 1) - e^{-\mu_i}(\cos k_b l - \cosh k_b l)] + \varphi_l/k_b[(\sinh k_b l \cos k_b l - \cosh k_b l \sin k_b l) + e^{-\mu_i}(\sin k_b l - \sinh k_b l)]]/[2(\cos k_b l \cosh k_b l - 1)] \tag{B6}$$

and

$$b_i = [a_i(\cos k_b l - \cosh k_b l) + w_l(\cosh k_b l - e^{-\mu_i}) + \varphi_l/k_b \sinh k_b l]/[\sinh k_b l - \sin k_b l], \tag{B7}$$

where k_b is the wave number for free flexural waves.

According to Eq. (24), the total response is a sum of response contributions from all three positive-going waves and by using linear superposition, the longitudinal displacement $u(x)$ and the transverse displacement $w(x)$ in the column yield

$$u(x) = \sum_{i=A}^{C} u_i(x) = \sum_{i=A}^{C} u_{l,i}[\cos k_l x + \sin k_l x(e^{-\mu_i} - \cos k_l l)/\sin k_l l] \tag{B8}$$

and

$$w(x) = \sum_{i=A}^{C} w_i(x) = \sum_{i=A}^{C} [a_i(\cos k_b x - \cosh k_b x) + b_i(\sin k_b x - \sinh k_b x) + w_{l,i}\cosh(k_b x) + (\varphi_{l,i}/k_b)\sinh(k_b x)]. \tag{B9}$$

[1] L. Cremer and H. O. Leilich, "Zur theorie der Biegekettenleiter" ("On theory of flexural periodic systems"), Arch. Elektr. Uebertrag. **7**, 261–270 (1953).

[2] L. Cremer, M. Heckl, and E. E. Ungar, *Structure-Borne Sound* (Springer-Verlag, Berlin, 1973), translated from German; original 1967.

[3] D. J. Mead, "A general theory of harmonic wave propagation in linear periodic systems with multiple coupling," J. Sound Vib. **27**, 235–260 (1973).

[4] M. Ohlrich, "Wave propagation in periodic systems representing models of building structures: A theoretical and experimental study," Ph.D. thesis, Institute of Sound and Vibration Research, Southampton University, England, 1977.

[5] M. Ohlrich, "Harmonic vibration of a column structure with transverse beams," *Proceeding of the Institute of Acoustics*, Spring Meeting, Southampton, England, Paper 20.I2, 1979.

[6] H. L. Müller, "Biegewellen-Dämmung an symmetrischen und exzentrischen Sperrmassen" ("Attenuation of bending waves caused by symmetrical and eccentric blocking masses"), Dr.-Ing. Dissertation, Institut für Technische Akustik der Technischen Universität, Berlin, 1957.

[7] D. J. Mead and S. Markus, "Coupled flexural–longitudinal wave motion in a periodic beam," J. Sound Vib. **90**, 1–24 (1983).

[8] M. Heckl, "Körperschallausbreitung auf Balken mit vielen Störstellen" ("Structure-borne sound propagation on beams with many discontinuities"), Acustica **81**, 439–449 (1995).

[9] M. A. Heckl, "Acoustic properties of profiled cladding on buildings," Acust. Acta Acust. 87, 560–581 (2001).

[10] M. A. Heckl, "Coupled waves on a periodically supported Timoshenko beam," J. Sound Vib. **252**, 849–882 (2002).

[11] A. K. Roy and R. Plunkett, "Wave attenuation in periodic structures," J. Sound Vib. **104**, 395–410 (1986).

[12] D. J. Mead, "Wave propagation and natural modes in periodic systems: I. Mono-coupled systems," J. Sound Vib. **40**, 1–18 (1975).

[13] D. J. Mead, "Wave propagation and natural modes in periodic systems: II. Multi-coupled systems, with and without damping," J. Sound Vib. **40**, 19–39 (1975).

[14] L. Friis and M. Ohlrich, "Coupled flexural-longitudinal wave motion in a finite periodic structure with asymmetrically arranged transverse beams," J. Acoust. Soc. Am. (in press).

[15] R. E. D. Bishop and D. C. Johnson, *The Mechanics of Vibration* (Cambridge University Press, Cambridge, 1960).

[16] G. L. Rodgers, *Dynamics of Framed Structures* (Wiley, New York, 1959).

[17] E. Rebillard and J. L. Guyader, "Vibrational behaviour of lattices of plates: Basic behaviour and hypersensitivity phenomena," J. Sound Vib. **205**, 337–354 (1997).

[18] S. Y. Lee and W. F. Yeen, "Free coupled longitudinal and flexural waves of a periodically supported beam," J. Sound Vib. **142**, 203–211 (1990).

Time-resolved modal decomposition based on the Linear Prediction Method—Applied for crack detection

István A. Veres[a] and Dieter M. Profunser[b]
Swiss Federal Institute of Technology, Institute of Mechanical Systems, Center of Mechanics, ETH Zentrum, Zürich CH-8092, Switzerland

(Received 13 January 2005; revised 29 July 2005; accepted 19 August 2005)

A nondestructive technique for testing and monitoring structures is presented, this uses guided waves to avoid a long scanning process. In contrast to other techniques that use guided waves this method can be applied to any structure made of a material that can be dispersive, strongly attenuating, and anisotropic, without the need of special adaptation. This is demonstrated on beams made of aluminum and wood. The propagating waves are reflected at any acoustic discontinuity, for example, by cracks and defects. In strongly attenuating materials such as wood, it is necessary to work with low frequencies, but due to the correspondingly long wavelength, the incident and reflected (from defects and boundaries) waves superimpose. The presented new signal processing technique allows the determination of the wave modes and their propagation direction very accurately in the time domain. Incident and reflected waves can easily be distinguished by the propagation direction. Since the wave mode is known from signal processing the right group velocity is applied for an accurate calculation of the defect location. © *2005 Acoustical Society of America.* [DOI: 10.1121/1.2062652]

PACS number(s): 43.40.At, 43.20.Hq, 43.40.Cw, 43.60.Gk [ANN] Pages: 3021–3030

I. INTRODUCTION

Since cracks in load bearing structures may cause fatal damage, nondestructive inspection is very important before and during use to guarantee safe operation. In this work we deal with the nondestructive long-range inspection of structures made of an arbitrary material. The most common inspection method is the use of ultrasound.[1,2] The high attenuation of ultrasound at high frequencies limits the inspection area, therefore a scanning process over the complete structure is unavoidable. Other methods work by monitoring the vibrations in the structures[3] or by measuring displacement of the structure under load.[4,5] In most of these methods it is necessary to measure the displacement at several points on the structure. Therefore the complete structure must be accessible. Long-range inspection by means of guided wave propagation in different structures like plates, beams and pipes which has the advantage of defect localization over a wide region with only a few measurement points has also been reported.[6,7] In contrast to the technique presented in this paper, in the previously presented methods of long-range inspection it is necessary to excite only one guided wave mode. Mostly the mode with the lowest dispersion is chosen. In some anisotropic structures like wood or composites the excitation of only one mode can be very difficult and can differ for each material and each configuration. However, the excitation of the presented technique is realized with only one transducer and the separation of the wave modes is realized with a new signal processing technique.

The goal of the presented research is a general method that can be used for long-range NDE of structures made of any material. With this new technique it is only necessary to measure over a small section of the structure, which allows the use of this technique for *in situ* monitoring or for structures that are only partly accessible. This is achieved by using guided acoustic waves. Guided acoustic waves have the advantage that they cover a large distance before their amplitude is attenuated, which make them interesting for characterizing and testing of structures with small cross section compared to their length. Usually beams used in different structures have such dimensions. In our case the guided waves are excited with a piezoelectric transducer and the displacement caused by the guided waves is measured over a short section of the beam by means of an optical interferometer.

Two completely different materials—aluminum and wood—are chosen for the demonstration of this new technique. In contrast to aluminum, which behaves isotropically, the behavior of wood is generally orthotropic. Due to the biological (micro-) structure of wood with grains oriented in the length scale, the stiffness in the length scale is several times higher than in the cross section. Only in some special cases can the stress–strain relation be simplified to a transversely isotropic behavior.

While the attenuation of propagating waves in aluminum is very small and it is possible to work in a higher-frequency range, in wooden structures the high damping is one of the crucial facts. Since the attenuation increases strongly with increasing signal frequency it is necessary to work in wooden structures with guided waves with a frequency content not higher than several kHz. Apart from the frequency the attenuation also depends on the sort of wood and, as might be intuitively expected, is higher in soft than in hard

[a]Electronic mail: istvan.veres@imes.mavt.ethz.ch
[b]Electronic mail: dieter@profunser.com, now at Hokkaido University, Japan.

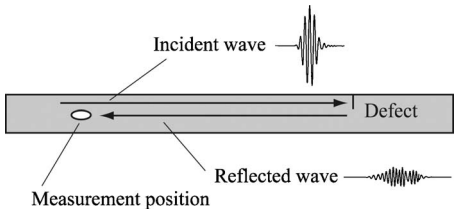

FIG. 1. Illustration of the basic measurement principle: the incident guided wave is partially reflected by a defect and the reflected wave is detected in the measurement.

wood. The localization of defects in wooden structures using existing ultrasound techniques at some MHz is almost impossible or only possible on a very limited scale.

II. PROBLEM STATEMENT

The basic principle of this technique according to Fig. 1 is very simple. An incident guided wave is partially reflected by a defect, in the experiments described here this is a notch. The time of flight of the guided wave package to the defect and back to the measurement position is evaluated and with the known group velocity of the guided wave package the distance of the defect from the point of measurement is calculated. If necessary the material properties and wave velocity can first be determined with the same measurements.[8] In NDE using ultrasonic pulses the amplitude of the measured signal (normally referring to the displacement) is discussed directly in the time domain, which usually fails to work with guided wave because:

- the wavelength is much larger than the defect and therefore the reflected amplitude can be very small, depending on the size of the defect.
- guided waves are in a lower-frequency range (therefore they are longer than the ultrasonic pulses) that lead to overlapping wave packages.
- due to anisotropy several different modes are excited and overlapped.

A new signal processing technique based on the powerful Linear Prediction Method[9,10] is proposed. The use of other basic techniques, such as 2D-FFT[11] or Matrix Pencil[12] is also possible. With this technique it is possible to determine in the time domain the propagation direction and the phase velocity (wave number) at a certain position on the beam. With the phase velocity the temporal presence of the different wave modes can be determined. So, even if there are several wave modes excited and the dispersion is very high as in wood, for instance, the time of flight of the wave packages of each mode can be determined and with it the distance from the measurement point to the defect.

This technique can also be applied in other applications where it is necessary to discuss temporal phenomena separately of each mode. For example, in an application of the crack detection with Rayleigh waves it has also been successfully applied. In this case, however, only one wave mode needs to be considered.

III. ANALYSIS OF MULTIMODE SIGNALS

A measurement signal, a time history, of guided waves is usually composed of several different wave packets. These packets can consist of different wave modes and, also, of the reflections of the waves from the boundaries. The different modes propagate with different wave numbers at the same frequency. The reflected waves propagate backward; therefore the signs of the wave numbers are reversed. In the time domain it may not be possible to separate these wave packets.

One possibility is the use of the modal decomposition method,[13] which calculates reflection and transmission coefficients for the interaction of waves with boundaries and cracks. However, the signals can also be analyzed directly by signal processing methods, such as 2D-FFT,[11] the Linear Prediction Method,[9] or the Matrix Pencil Method.[12] Using the 2D-FFT method,[11] the two-dimensional measurement series in the time–space domain will be transformed by two Fourier transforms (in the time and in the space domain) into the frequency–wave number plane, where the different wave numbers at one frequency can be separated. This method is commonly used and allows a fast determination of the included wave numbers of the signal. By applying this method at different frequencies, the complete dispersion relation can also be determined.[11]

Instead of applying the Fourier transformation a second time, the Linear Prediction Method (LPM) or Matrix Pencil Method can be used in the space domain to evaluate the wave numbers.[8,14] These techniques provide the following advantages:

- higher resolution;[15] if the wave numbers are well separated, FFT in the space domain is efficient for the estimation of wave numbers. However, if the wave numbers are closely spaced, a high-resolution technique is required.[9]
- possibility of noise reduction;[9] LPM enables the application of the singular value decomposition[16] (SVD). This decomposition is able to distinguish the noise from the signal and reduces its influence.
- the possibility of the detection of complex frequencies or wave numbers[17] or the determination of the damping.[10]

All these methods can distinguish the different wave numbers in the measured signals but usually provide no information on the temporal occurrence of the determined wave numbers. However, a temporal discussion of the decomposed multimode signal is only possible if these methods are combined with a short, sliding window in the time domain.[18] This sliding window is used to separate the wave packets and evaluate the wave numbers in the time domain.

The presented signal processing method includes the following steps: A short, sliding temporal (Hanning) window is introduced to separate the wave packets in the time domain. Using FFT in the time domain the signals will be transformed into the frequency domain. In the space domain the LPM will be used to evaluate the wave numbers. This process will be repeated at different positions of the temporal (Hanning) window, which enables the determination of the wave numbers as a function of the time.

IV. SIGNAL PROCESSING USING THE LINEAR PREDICTION METHOD

The Linear Prediction Method (LPM) can be applied in signal processing to determine, for example, the unknown frequencies of a signal composed by sinusoids. In the following the basic steps of this method are shown, more details can be found in the paper of Tufts *et al.*[9] and Kannan *et al.*[10]

A function $y(t)$ composed of M complex sinusoids can be described as

$$y(t) = \sum_{j=1}^{M} a_j e^{i\omega_j t}, \tag{1}$$

where a_j is the set of unknown complex amplitudes and ω_j the set of unknown angular frequencies. The discrete data sequence of this function observed in N time points with sampling interval dt is given by the formula

$$y(n) = \sum_{j=1}^{M} a_j e^{i\omega_j n\, dt} = \sum_{j=1}^{M} a_j (e^{i\omega_j\, dt})^n = \sum_{j=1}^{M} a_j (\mu_j)^n, \quad n = 1,2,\ldots,N, \tag{2}$$

with $\mu_j = e^{i\omega_j\, dt}$. If there is no noise in the data, then it can be observed that there exist L complex constants $g_1, g_2, \ldots, g_L$ so that Eq. (3) is fulfilled

$$\begin{bmatrix} y(L) & y(L-1) & \cdots & y(1) \\ y(L+1) & y(L) & \cdots & y(2) \\ \vdots & \vdots & & \vdots \\ y(N-1) & y(N-2) & \cdots & y(N-L) \end{bmatrix} \begin{bmatrix} g_1 \\ g_2 \\ \vdots \\ g_L \end{bmatrix} = \begin{bmatrix} y(L+1) \\ y(L+2) \\ \vdots \\ y(N) \end{bmatrix}. \tag{3}$$

This system of linear equations is the prediction equation (see Tufts *et al.*[9] and Kannan *et al.*[10]). It can be written in matrix form as

$$\mathbf{A}\mathbf{g} = \mathbf{f}. \tag{4}$$

It can be seen that the system of linear equations can be underdetermined or overdetermined depending on the value of L (prediction filter order). The matrix $\mathbf{A}$ can be written in terms of its singular value decomposition,[19]

$$\mathbf{A} = \mathbf{U}\mathbf{D}\mathbf{V}. \tag{5}$$

In the diagonal matrix $\mathbf{D}$ are the singular values of $\mathbf{A}$, the positive roots of the eigenvalues of $\mathbf{A}^*\mathbf{A}$, where "*" denotes the complex conjugate transpose. In $\mathbf{U}$ and $\mathbf{V}$ are the left- and right-singular vectors, the eigenvectors of $\mathbf{A}\mathbf{A}^*$ and $\mathbf{A}^*\mathbf{A}$, respectively. In the noiseless case there are M nonzero singular values. In a real case there is always noise in the measurement, so every singular values are nonzero, however, the first M of them are large and well separated in magnitude. The magnitudes of the singular values can be interpreted as the representation of the amplitude of the components. Usually, the number of frequencies M is unknown and it can be determined using this property of the singular values. The influence of the noise can be reduced considering only the M largest singular values and recalculating $\mathbf{A}$ by Eq. (5).

Equation (4) can be solved using the pseudoinverse of $\mathbf{A}$,

$$\mathbf{g} = \begin{cases} (\mathbf{A}^*\mathbf{A})^{-1}\mathbf{A}^*\mathbf{f} \\ \mathbf{A}^*(\mathbf{A}\mathbf{A}^*)^{-1}\mathbf{f} \end{cases} \tag{6}$$

depending on whichever is appropriate. Using the notation in Eq. (2), an equation (for example, the first one) of the linear equation system in (3) can be written as

$$\sum_{j=1}^{M} a_j (\mu_j)^{L+1} - g_1 \sum_{j=1}^{M} a_j (\mu_j)^L - \cdots - g_L \sum_{j=1}^{M} a_j (\mu_j)^1 = 0, \tag{7}$$

or

$$\sum_{j=1}^{M} a_j \mu_j [\mu_j^L - g_1 \mu_j^{L-1} - \cdots - g_L] = 0. \tag{8}$$

The polynomial in the brackets is the prediction-error filter and it must vanish to satisfy Eq. (8). The polynomial has M of its zeros according to Tufts *et al.*[9] on the unit circle on the complex plane (noiseless case) or close to this circle (with noise). The M solutions of the prediction-error filter ($\mu_p, p = 1,2,\ldots,M$) closest to the unit circle are the solutions that represent the unknown frequencies,

$$\omega_p = \frac{\ln \mu_p}{i\, dt}, \quad p = 1,2,\ldots,M. \tag{9}$$

V. APPLICATION IN WAVE PROPAGATION PROBLEMS

The displacements of a harmonic wave including M components, propagating in the positive z direction, is given as

$$u(z,t) = \sum_{j=1}^{M} c_j e^{i(\omega t - k_j z)}, \tag{10}$$

where c_j is the set of unknown complex amplitudes and k_j the set of unknown wave numbers. By the Fourier transformation of Eq. (10) the time and frequency dependence of this function can be eliminated

$$F\{u(z,t)\} = U(z,\omega) = \sum_{j=1}^{M} C_j(\omega) e^{-ik_j z}. \tag{11}$$

Measurements usually include spatially discrete sequences. The Fourier transformation of a measurement observed in N points with sampling interval dz is given as

$$U(n,\omega) = \sum_{j=1}^{M} C_j(\omega) e^{-ik_j n\, dz} = \sum_{j=1}^{M} C_j(\omega)(\mu_j)^n, \quad n = 1,2,\ldots,N, \tag{12}$$

with $\mu_j = e^{-ik_j\, dz}$. This form is identical with the form in Eq. (2). However, in this case the unknowns are the wave numbers k_j and the measurements are in the space domain at one known frequency. Consequently, Eq. (9) will be modified as

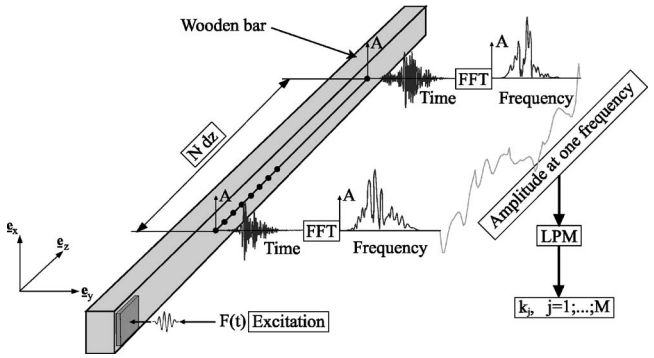

FIG. 2. Evaluation of the dispersion curves of a bar: the ordinates of the Fourier transformation build for each frequency a sum of exponential functions. These will be analyzed by LPM and it results in the dispersion diagram.

$$k_p = \frac{\ln \mu_p}{-i\,dz}, \quad p = 1,2,\ldots,\mathrm{M}. \tag{13}$$

This method can be applied, for example, to determine the dispersion curves, the frequency–wave number relationship, of a bar[8] (Fig. 2).

A. Detection of reflected waves

The method is the following: the signals are multiplied by a short Hanning window, transformed into the frequency plane and the wave numbers are evaluated by LPM at one frequency. In the next step (Fig. 3) the Hanning window is moved in the time by a short interval Δ, the signals are multiplied with the window and analyzed by LPM. The Hanning window will be moved step by step along the complete signals. The signals will be transformed into the frequency plane and analyzed in every step by LPM and the resulting wave numbers or phase velocities are plotted against the time.

At the beginning the signals contain only the information of the incident waves; only positive wave numbers are determined. After a certain shift of the Hanning window in the time domain, negative wave numbers are determined. These negative wave numbers correspond to reflected waves that are propagating in the opposite direction than the incident waves. The time difference between the detection of the incident wave and the reflected wave can be calculated and, if the group velocity of the wave at the frequency of the evaluation is known, the origin of the reflected wave can easily be determined.

B. Practical steps of the application

The Linear Prediction Method is able to identify the components of a harmonic wave in a measurement series. To optimize the application of this method, some rules of thumb can be formulated for the measurement length and interval. The whole length of the measurement should be at least one-half of the longest wavelength, and the shortest wavelength should be scanned at least ten times per wavelength. Respecting these conditions, the method is able to identify one wave mode in a signal without noise, but in a real measurement usually more than one wave mode is excited and the rules should be satisfied for all waves with its different wavelength. Therefore more measurement points and a longer measurement distance are sometimes necessary. Moreover, if there is a strong noise in the measurement, an increased number of measurement points in the space domain reduce its effect. For the evaluation the following steps are suggested:

(1) Multiplication of the signals by a Hanning window.
(2) Discrete Fourier-transformation of the signals.
(3) Assembling a vector with the values of the Fourier transformation at one frequency.
(4) Evaluation of this vector by the LPM.
(5) Plot the evaluated phase velocities and the singular values against time (the evaluated phase velocities can be plotted, for example, against the first point of the Hanning window in every step).
(6) Movement of the Hanning window.
(7) Go to step (1) and repeat until end of signal.

The evaluated diagram shows the phase velocities as a function of time. Therefore the time difference Δt between the arrival of the incident wave (positive velocity) and the reflected wave (negative velocity) can be determined. The distance to the origin of the reflected wave can be calculated as

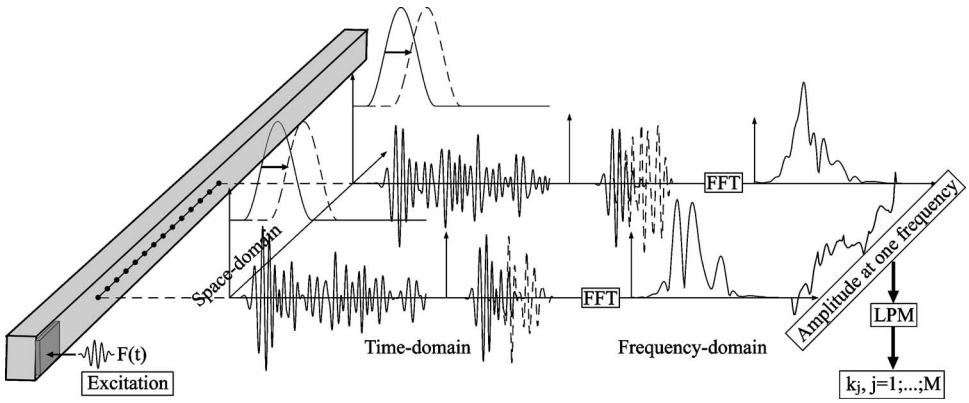

FIG. 3. Basic idea of the method; before the transformation using FFT the signals are multiplied by a short Hanning window, and the LPM will be only at the main frequency applied. In the next step the Hanning window will be moved by Δ, and the signals are analyzed by LPM.

$$L = \frac{1}{2}\Delta t\, c_g, \tag{14}$$

where c_g denotes the group velocity. The dispersion curves can be determined by LPM, as described in Sect. V. It results in the frequency–wave number relationship and the group velocity can be determined by the derivation of this curve with respect to the wave number.

To guarantee a result with high precision, some points have to be considered. A very short Hanning window ($T^H \approx 1/f^{\text{main}}$, where f^{main} denotes the main frequency of the excitation) can influence the frequency spectrum of the signal. Therefore the length of the Hanning window should be five to ten times larger than the period of the exciting wave.

It can be seen that in the first measurement point the waves arrive earlier than in the last one, because the waves need some time to propagate between the two points. Therefore the application of the same Hanning window in the time domain for every signal has an effect also in the space domain. A wave can be included for the first points by a Hanning window but excluded for the other parts of the measurement. This can be interpreted as a multiplication by a Hanning window in the space domain. It was shown at the beginning of this section that there is an optimal configuration and some rules of thumb for LPM that are not respected in this case. As a result, the evaluated wave number will be inaccurate in some steps.

With the movement of the Hanning window, the waves are detected in some intervals. The inaccuracy of the evaluation described above acts at the beginning and at the end of the intervals. Therefore the exact detection of the beginning and the end of these interval is almost impossible, so the determination of the time difference will be also imperfect. An accurate result is yielded by calculating the time difference by the use of the singular values of the wave modes. It was shown that the Hanning window applied in the time domain has the same effect also in the space domain. The result is that the singular values of a wave have several maxima in the time. It can be shown that the singular values have a maximum, as the Hanning window is centered above the middle point of the measurement. Hence, the distance calculated from the time difference between the peaks is the distance of the middle of the measurement and the notch (Fig. 4).

It is difficult to determine the absolute arrival time of the wave at an arbitrary point of the spatial measurement series, because the analysis is performed in the time–space plane. The phase velocities are determined from the whole measurement series, so it cannot be determined at which time in an arbitrary point the wave arrives, but nevertheless it can be determined at which time the wave passes the center of the measurement.

The measurement signals are discrete data sequences with sampling interval dt. This is the lower limit in the time domain for the movement of the Hanning window. Therefore, the resolution of the peaks and the time differences is limited by this sampling interval. In our measurements a sampling interval of $dt = 8 \times 10^{-8}$ s was used, which enables a very high resolution in the time domain. The accuracy of the group velocity c_g is therefore more restrictive for the determination of the origin of the reflected wave in Eq. (14).

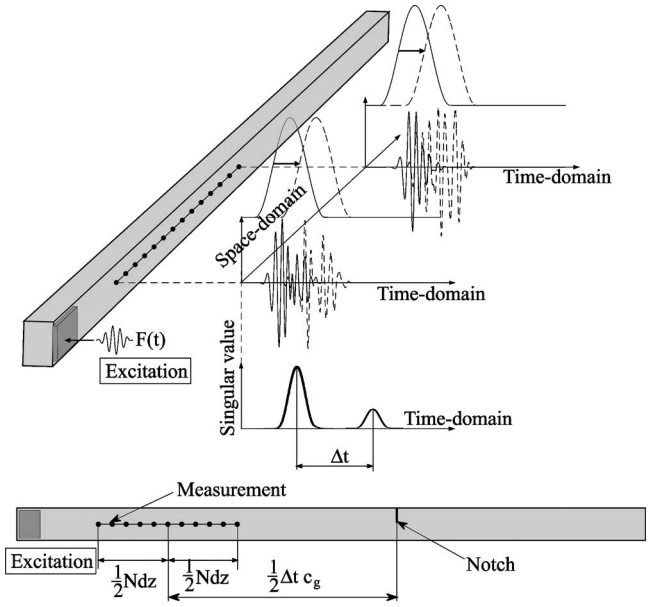

FIG. 4. Time difference and coupled distance; the difference of two peaks in the time domain represents the double distance of the middle of the measurement and the reflection point.

VI. RESULTS

In this section some examples are presented. First, an isotropic bar, an aluminum one, is considered. In the second example a wooden bar with orthotropic material properties is examined. The dispersion curves of the bars were determined by experiments, as described in Sec. V, so the phase and group velocities were known. The measurement setup shown in Fig. 5 were used in the experiments. A computer controls the measurement process. The function generator triggers the measurement and creates a voltage signal. It is amplified and applied to the transducer. The transducer, which is glued at the end of the bar, converts the voltage signal into mechanical force and excites waves. The displacement or the velocity at the surface of the bar is measured by the laser interferometer. The detected signal is filtered and recorded by the computer. The measurement cycle is repeated a few hundred times and averaged to reduce the noise. In the next step the positioning system moves the laser interferometer into the next measurement point.

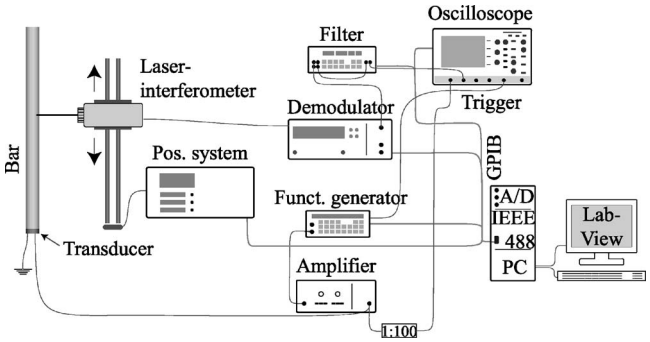

FIG. 5. Measurement setup.

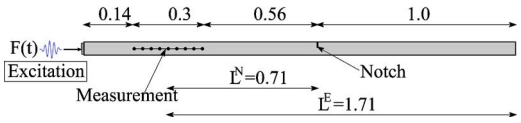

FIG. 6. Geometry of the aluminum bar and measurement configuration.

A. Aluminum bar

Two aluminum bars were used in the experiments with the same geometry ($10\times10\times2000$ mm) and with slightly different material properties. Two measurements are presented. In both measurements, longitudinal waves were excited at a 100 kHz center frequency, however, it is impossible to avoid the excitation of other wave types, for example, transverse waves in this case. The velocities on the surface were measured at 200 points over a distance of 300 mm, and the first point was at 0.14 m (Fig. 6). The sampling frequency was 12.5 MHz ($dt=8\times10^{-8}$ s), and 20 000 points were recorded in the time domain.

In the first case there was no notch in the bar. In the second measurement the second bar has a large notch in the middle. The dispersion curves of the bars, the phase, and group velocities, were determined in a separate experiment using the method described in Sec. V.

1. Bar without notch

The length of the Hanning window was $3000\times dt$, the step of the movement $20\times dt$, and the measurement was evaluated at 100 kHz. Figure 7 shows a typical measurement signal, and the two diagrams in Fig. 8 show the results of the first measurement. On the diagram above, the detected phase velocities in the function of the time can be seen. The diagram below shows the calculated singular values of the waves.

First the incident longitudinal and transverse waves are detected (the two positive velocities, I and II). Two peaks of the singular values on the lower diagram correspond to these velocities. The first and largest one is the incident longitudinal wave; the second smaller one is the incident transverse wave. On the diagram above, it can be seen that after 0.4 ms some reflected longitudinal and transverse waves are detected. However, on the lower diagram, it can be seen that the amplitudes of the singular values—and so also the amplitude of the waves—are very small.

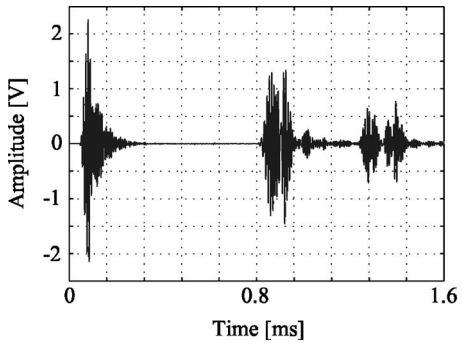

FIG. 7. A typical measurement signal for the aluminum bar.

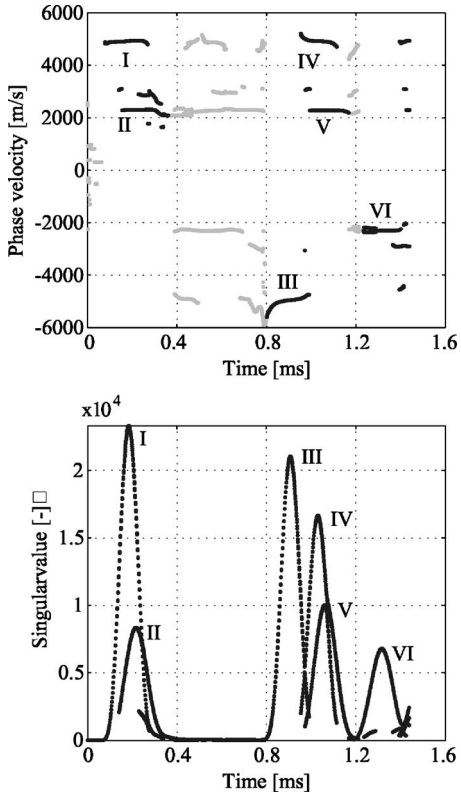

FIG. 8. Evaluated diagrams of the first measurement (aluminum bar without notch); above the evaluated phase velocities, below the singular values calculated by LPM can be seen.

The longitudinal wave reflects at the end of the bar and propagates backward in the bar. It arrives at the measurement positions after 0.8 ms (third peak, III).The fourth peak represents again a positive velocity (IV), the reflection of the longitudinal wave at the beginning of the bar. This reflection causes a mode conversion, also a transverse wave propagates forward (fifth peak, V). The reflection of the transverse wave from the end of the bar (sixth peak, VI) arrives only now the position of the measurement.

The second peak shows that a transverse wave is also excited. This is not unusual because the gluing is not normally concentric and the transducers are never perfectly polarized. These effects cause in this case a transverse wave with a high amplitude (peak II) and they can also explain the strong mode conversion at the reflection of the longitudinal wave (peaks III, IV, and V). In this paper we do not deal with the explanation of wave propagation in bars, however, this example shows how difficult it is to excite only one chosen wave mode and to interpret a real measurement. Moreover, it can be seen that this technique can be successfully applied to interpret a measurement.

The analysis can be proved by calculating the traveled distance of the wave using the time difference between the first and the third peaks, and the group velocity. In the first column of Table I the evaluation of this measurement can be seen. It shows that the distance is evaluated very accurately ($e<1\%$).

2. Bar with large notch

In this measurement the second bar was used, this has a large notch (3 mm deep) in the middle. (See Figs. 6 and 9.)

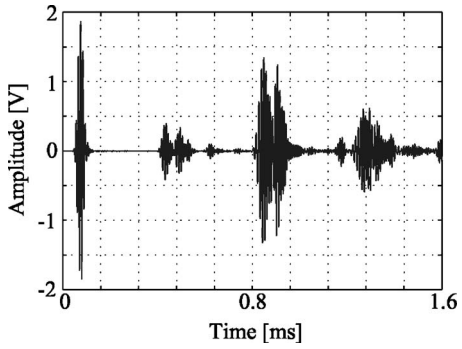

FIG. 9. Typical measurement signal (second measurement).

The length of the Hanning window was $3000 \times dt$ and the step of the movement $20 \times dt$. The analysis of the measurement (Fig. 10) shows a clear result. The incident waves (longitudinal and transverse) will be detected at the beginning, however, the arrival time is slightly different because of the different wave velocities in this bar ($c_g^l = 4850$ m/s). The two peaks of the singular values between 0.8–1.2 ms represent the reflection of the longitudinal waves from the end of the bar, the backward and then forward propagating longitudinal wave. In this case there are two other smaller peaks between the peaks of the incident and reflected waves. These peaks represent the reflected longitudinal waves from the notch.

It can be seen that in this case the excited transverse wave has a smaller amplitude (the second peak) than in the first measurement, and there is no mode conversion after the reflection of the longitudinal wave at the beginning of the bar. In Table I the diagrams are evaluated and the origin of the reflected waves is calculated. The results show that these distances are calculated with a very high precision ($e \approx 0.5\%$). This experiment was also evaluated using FFT instead of LPM in the space domain. A 3D view of the results can be seen in Fig. 11. A direct comparison of both evaluations is presented in Fig. 12. In the time domain the resolutions of both methods are similar, because the same sliding temporal (Hanning) window is used. However, for the wave number or phase velocity determination, the LPM has a much better resolution and gives exactly one value as an accurate estimation of the phase velocity.

B. Wooden bar

In the second part of the experiments a wooden bar was used. The geometry of the bar was $20 \times 25 \times 2348$ mm. Two

TABLE I. Results of the measurements.

Bar	Aluminum		Wood	
Measurement	1	2	1	2
Group velocity (m/s)	4750	4850	1190	1190
Time difference notch (ms)	-	0.294	-	1.490
Distance notch (m)	-	0.713	-	0.887
Distance notch (exact) (m)	-	0.710	-	0.898
Error (%)	-	0.4	-	1.2
Time difference end (ms)	0.723	0.709	3.04	3.04
Distance end (m)	1.717	1.719	1.809	1.809
Distance end (exact) (m)	1.710	1.710	1.798	1.798
Error (%)	0.4	0.5	0.6	0.6

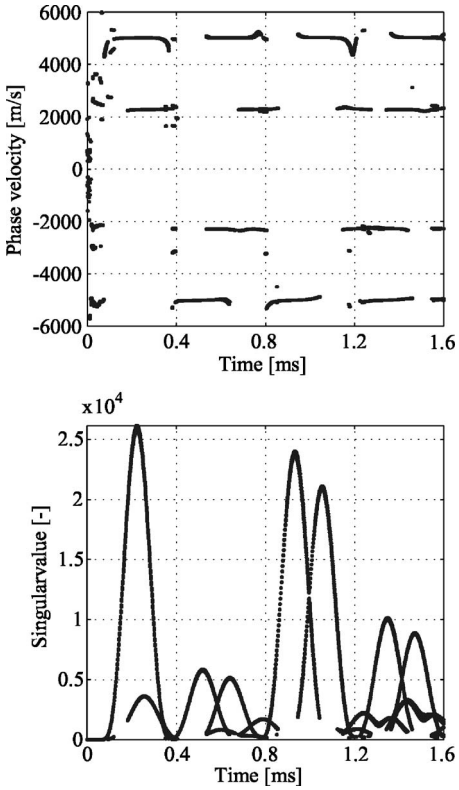

FIG. 10. Evaluation of the measurement on the second bar with large notch. The smaller peaks between 0.4 and 0.8 ms represents the reflected waves.

measurements were carried out with transverse waves. Frequencies between 0.5 and 5 kHz were excited and the measurement was evaluated at 3.5 kHz. In this case a low frequency was chosen, because wood has very high damping at higher frequencies. Transverse waves were used because longitudinal waves at this frequency range have a long wavelength. It would be necessary to measure a long distance (1–2 m) to detect this wave type.

The velocities of the surface were measured at 250 points over a distance of 500 mm, and the first point was at 0.3 m (Fig. 13). The sampling frequency was 1 MHz ($dt = 1 \times 10^{-6}$ s), and 10 000 points were recorded in the time domain.

In this case the same measurement data were used to determine the dispersion curves of the bar and to detect a notch. The method, described in Sect. V, was used to evaluate the dispersion curves of the bar in the range of the excitation, between 0.5 and 5 kHz.

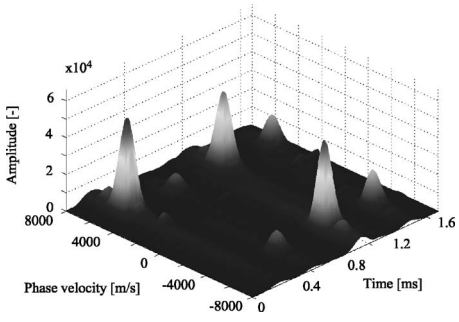

FIG. 11. Evaluation of the second measurement using FFT also in the space domain; a 3D view.

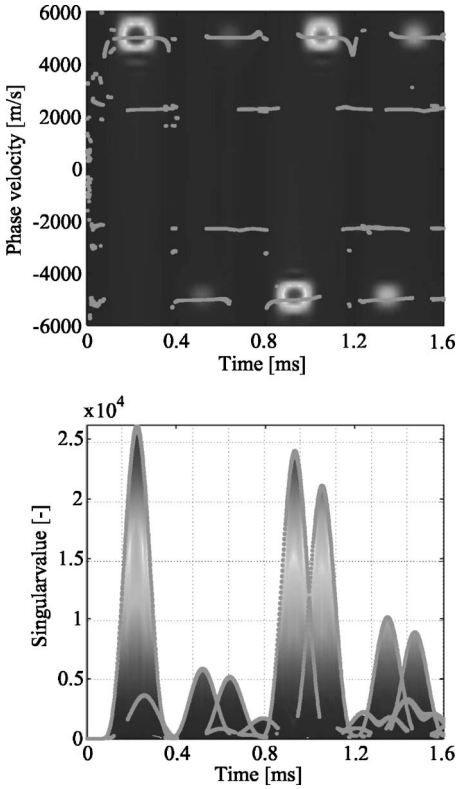

FIG. 12. A comparison of the evaluation by LPM and FFT. The amplitude of the FFT is scaled to the amplitude of the singular values.

1. Bar without notch

In the first measurement there was no notch in the bar. However, in wood there are always some inhomogeneities, such as knots or annual rings, and they cause some reflections. In this bar there is no large discontinuity (knot), but the natural inhomogeneity of the wood causes some disturbances. Furthermore, the influence of the lower wave velocity, higher damping and longer excitation on this method should be proved and compared with the results on the aluminum bar in this measurement and evaluation.

The length of the Hanning window was $3000\times dt$ and the step of the movement $20\times dt$. The analysis of the measurement is shown in Fig. 14. The peaks of the singular values are wider and they are closer than in case of the aluminum bar, which is caused by the lower frequencies (longer excitation). In Sec. IV it was referred to that the singular values represent the amplitude of the waves. In Fig. 14 the high attenuation of the wood is demonstrated; the amplitude of the reflected wave, represented by the second peak, is much smaller than the amplitude of the incident wave (first peak). The ratio of these peaks is 0.49 (for aluminum it is 0.9).

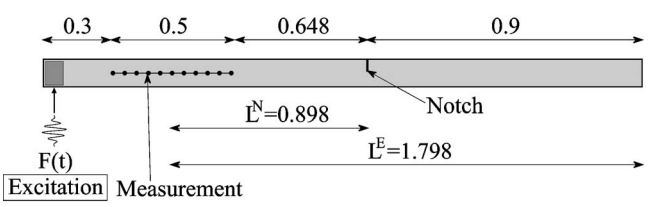

FIG. 13. Geometry of the wooden bar and measurement configuration.

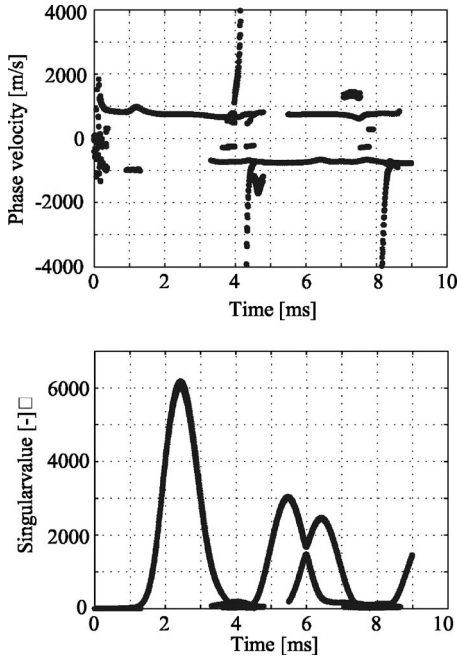

FIG. 14. Analysis of the measurement on the wooden bar; the peaks are wider and closer than for the aluminum bar; the high attenuation of wood is demonstrated by the second smaller peak of the reflected wave.

Between the peaks of the singular values there are disturbances such as in the case of the aluminum bar. The amplitudes of them are small, though they are clearly higher, like for the aluminum bar. The results of the measurement are presented in Table I. The origin of the reflected wave (end of the bar) is evaluated with high precision ($e \approx 0.6\%$).

2. Bar with notch

A notch was cut in the wooden bar for the second measurement (8 mm deep). As a consequence of the inhomogeneity and the high attenuation of wood it can be hard to differ the reflection from a small notch and the disturbances caused by the inhomogeneities. (See Figs. 15 and 16.) To avoid an erroneous result a large notch was used.

The length of the Hanning window was $3000\times dt$ and the step of the movement $20\times dt$. The measurement is evaluated in Fig. 17 and the results are presented in Table I. Even

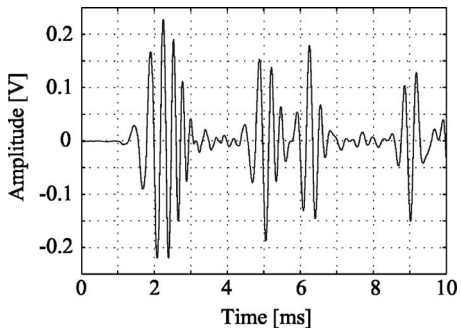

FIG. 15. Typical measurement signal; wooden bar without notch.

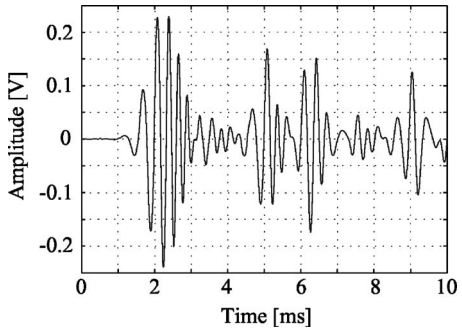

FIG. 16. Typical measurement signal; wooden bar with notch.

though the notch is large, the high damping and the anisotropy of wood causes the reflected wave to have a small amplitude (compare Fig. 14 and Fig. 17). However, the peak of the reflected wave can be explicitly identified and the origin of the wave determined accurately ($e \approx 1.3\%$).

VII. CONCLUSION AND OUTLOOK

In this paper we presented an accurate long-range inspection technique for beams by means of guided acoustic waves. With the presented technique defects can be localized without a scanning process across the complete structure. For analyzing the measured displacement a new signal processing technique is used, which is based on the Linear Prediction Method (LPM). The mentioned signal processing technique has the following main advantages:

- each mode of the propagating guided wave can be identified.
- the propagation direction of each mode can be determined. A differentiation between incident and reflected waves is easily possible.

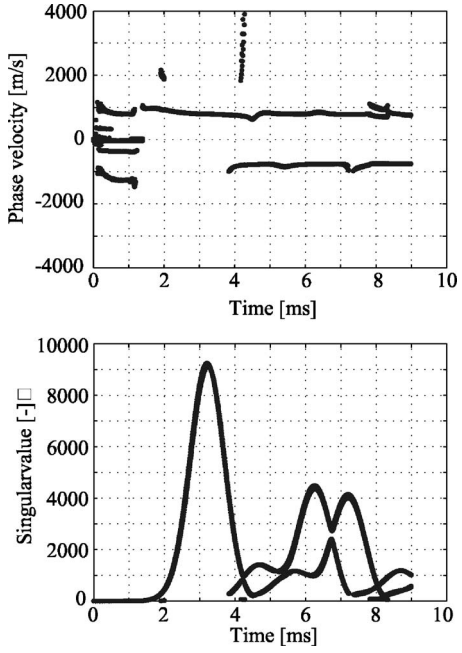

FIG. 17. Analysis of the measurement on the wooden bar with notch; the peak of the reflected wave can be identified, however, the peaks are not so well separated as in case of the aluminum bar.

- a temporal discussion of the occurrence of each mode can also be performed and with it the localization of the defects.

These advantages enable this technique to be successfully used in structures made of materials, which are strongly dispersive, attenuating, and anisotropic without any adaptation of the experimental setup for the excitation or measurement of a special single mode. Good results were shown by a comparison of measurements in an aluminum and a wooden beam. In each of the presented measurements the distance of the artificially made notches from the measurement position is determined with an accuracy of about 1%. In aluminum, the position of a larger defect is determined with the accuracy of the distance of 0.5%. In a case that is not discussed in detail in this paper the accuracy of the detection of a very small notch, whose damaged area is only 0.5% of the cross section, can have an error as low as 5%. Also in a wooden bar the accuracy was very high (0.6%), despite the dispersion and attenuation of the guided waves being very high. Additionally, the dimensions of the damaged cross section can be estimated. For the accurate localization of the defects it is necessary to determine the frequency-dependent group velocity of the traveling wave. This can easily be done using the same measured data as for the crack detection and also the Linear Prediction Method (LPM) combined with a numerical derivation of the determined phase velocity.

The localization of several cracks in the same beam is much more challenging and is limited by several reasons such as the distance between the cracks and the size of the cracks. Furthermore, these limitations are also depending on the accuracy of the determined group velocity and the temporal resolution used for the signal processing. An investigation of these limitations will be the subject of further research.

Applications in other experiments have also shown that this technique can be applied, for example, to Lamb wave or Rayleigh wave experiments, for time-resolved modal decomposition.

[1]J. L. Rose, *Ultrasonic Waves in Solid Media* (Cambridge University Press, Cambridge, 1999).
[2]D. E. Asraf and M. G. Gustafsson, "Phenomenological detectors for crack echo families in elastic solids," J. Acoust. Soc. Am. **116**, 379–388 (2004).
[3]E. Douka, S. Loutridis, and A. Trochidis, "Crack identification in beams using wavelet analysis," Int. J. Solids Struct. **40**, 3557–3569 (2003).
[4]A. V. Ovanesova and L. E. Suarez, "Applications of wavelet transforms to damage detection in frame structures," Eng. Struct. **26**, 39–47 (2004).
[5]S.-T. Quek, Q. Wang, L. Zhang, and K.-K. Ang, "Sensitivity analysis of crack detection in beams by wavelet technique," Int. J. Mech. Sci. **43**, 2899–2910 (2001).
[6]D. N. Alleye, B. Pavlakovic, M. J. S. Lowe, and P. Cawley, "Rapid, long range inspection of chemical plant pipework using guided waves," Key Eng. Mater. **270–273**, 434–441 (2004).
[7]P. Fromme and M. B. Sayir, "Measurement of the scattering of a Lamb wave by a through hole in a plate," J. Acoust. Soc. Am. **111**, 1165–1170 (2002).
[8]I. A. Veres and M. B. Sayir, "Wave propagation in a wooden bar," Ultrasonics **42**, 495–499 (2004).
[9]D. W. Tufts and R. Kumaresan, "Estimation of frequencies of multiple sinusoids: Making linear prediction perform like maximum likelihood," Proc. IEEE **70**, 975–989 (1982).
[10]N. Kannan and D. Kundu, "Estimating parameters in the damped expo-

nential model," Signal Process. **81**, 2343–2351 (2001).
[11]D. Alleyne and P. Cawley, "A two-dimensional Fourier transform method for the measurement of propagating multimode signals," J. Acoust. Soc. Am. **89**, 1159–1168 (1991).
[12]Y. Hua and T. K. Sarkar, "Matrix pencil method for estimating parameters of exponentially damped/undamped sinusoids in Noise," IEEE Trans. Acoust., Speech, Signal Process. **38**, 814–824 (1990).
[13]M. Castaings, E. Le Clezio, and B. Hosten, "Modal decomposition method for modeling the interaction of Lamb waves with cracks," J. Acoust. Soc. Am. **112**, 2567–2582 (2002).
[14]J. Vollmann, R. Breu, and J. Dual, "High-resolution analysis of the complex wave spectrum in a cylindrical shell containing a viscoelastic medium: Experimental results versus theory, J. Acoust. Soc. Am. **102**, 909–920 (1997)
[15]S. Guan and A. G. Marshall, "Linear prediction Cholesky decomposition vs. Fourier transform spectral analysis for ion cyclotron resonance mass spectrometry," Anal. Chem. **69**, 1156–1162 (1997).
[16]L. L. Scharf, "The SVD and reduced rank signal processing," Signal Process. **25**, 113–133 (1991).
[17]K. Grosh, "Complex wave-number decomposition of structural vibrations," J. Acoust. Soc. Am. **93**, 836–848 (1993).
[18]L. Martinez, B. Morvan, and J. L. Izbicki, "Space-time-wave number-frequency $Z(x,t,k,f)$ analysis of SAW generation on fluid filled cylindrical shells," Ultrasonics **42**, 383–389 (2004).
[19]I. N. Bronstein, K. A. Semendjajew, G. Musiol and H. Mühlig, *Taschenbuch der Mathematik*, 5th ed. (Harri Deutsch, City, 2000).

Energy sinks: Vibration absorption by an optimal set of undamped oscillators

I. Murat Koç
Mechanical Engineering Department, Carnegie Mellon University, Pittsburgh, Pennsylvania 15213

Antonio Carcaterra
Universita Degli Studi di Roma "La Sapienza," Dipartimento di Meccanica e Aeronautica, Via Eudossiana 18, 00184 Roma, Italy

Zhaoshun Xu and Adnan Akay[a)]
Mechanical Engineering Department, Carnegie Mellon University, Pittsburgh, Pennsylvania 15213

(Received 7 December 2004; revised 6 June 2005; accepted 23 August 2005)

This paper describes a new concept referred to here as "energy sinks" as an alternative to conventional methods of vibration absorption and damping. A prototypical energy sink envisioned here consists of a set of oscillators attached to, or an integral part of, a vibrating structure. The oscillators that make up an energy sink absorb vibratory energy from a structure and retain it in their phase space. In principle, energy sinks do not dissipate vibratory energy as heat in the classical sense. The absorbed energy remains in an energy sink permanently (or for sufficiently long durations) so that the flow of energy from the primary structure appears to it as damping. This paper demonstrates that a set of linear oscillators can collectively absorb and retain vibratory energy with near irreversibility when they have a particular distribution of natural frequencies. The approach to obtain such a frequency distribution is based on an optimization that minimizes the energy retained by the structure as a function of frequency distribution of the oscillators in the set. The paper offers verification of such optimal frequency spectra with numerical simulations and physical demonstrations. © *2005 Acoustical Society of America.* [DOI: 10.1121/1.2074807]

PACS number(s): 43.40.At, 43.40.Kd [RLW] Pages: 3031–3042

I. INTRODUCTION

Considerable advances over the years have been made in reducing structural vibrations by means of damping. These range from passive methods to active-control methods. Passive methods include contact damping, fluid-layer damping, and those that use energy absorption materials, such as viscoelastic and granular materials. Selection of damping methods is based on cost and suitability to a given application; contact damping for jet engine blade vibrations, fluid layer damping for rotating thin disks, and viscoelastic layers for stationary large panels are such examples.

Energy sinks function as a substructure attached to, or an integral part of, a primary structure from which they can absorb and trap vibrational energy without adversely affecting its performance. As such, energy sinks provide a suitable alternative to application of conventional damping treatments under conditions when they are not suitable. For example, transient vibrations of large structures that have very low frequencies such as naval vessels and those deployed in space and buildings fall into this category.

The energy sinks described here consist of a set of linear oscillators. When attached to a primary structure, for example an oscillating rigid platform, the set of oscillators absorbs and retains the vibratory energy from the primary structure. Energy sinks described here, in principle, do not require the presence of loss mechanisms, or damping in the classical sense. Energy is conserved and the absorbed energy remains in the collective phase space of the attached oscillators. Depending on design parameters of the set, the absorbed energy may remain in the set permanently (or for sufficiently long duration) so that the flow of energy from the primary structure appears as damping. As such, energy sinks induce "apparent damping" to the primary structure.[1]

Irreversible absorption of energy is usually associated with nonlinear systems, such as a lattice of atoms in a solid excited by friction.[2] Corresponding linear systems normally require the presence of loss mechanisms to irreversibly absorb energy because in a conservative linear system energy exchange between a primary structure and its satellites is known to exhibit periodicity, or recurrence, determined by the system configuration. For example, considering transient cases, when a primary structure responds to an initial excitation, energy transferred to the attached oscillators returns to the primary structure after a delay during which the oscillators undergo their own periodic motions. However, as shown in this paper, under certain conditions conservative linear systems may also absorb and retain energy with near irreversibility.

The concept of energy sink described here differs from the previous similar proposals, such as spatial containment or single nonlinear attachments, or those that consider influence of internal degrees of freedom on a structure, viz. Refs. 3–7. The method used here relies on the use of a *set* of lossless,

[a)]Electronic mail: akay@cmu.edu

linear oscillators that absorbs the vibratory energy of the primary structure to which it is attached.

Multiple tuned mass dampers with linear stiffness and damping function effectively under steady-state excitation. Zuo and Nayfeh in a series of studies showed optimum distributions of these properties for vibration reduction in single- and multiple-degree-of-freedom systems.[8,9]

Among the many studies that examined energy absorption from a primary structure by attached oscillators, viz., Refs. 10–24, several showed that numerous oscillators attached to a primary structure collectively act like a viscous damper.[10,12–14] Most of these studies also demonstrate a trade off between the number of oscillators and the need for presence of a loss mechanism in the oscillators; a set of oscillators absorbs energy even for vanishing values of loss factor in each oscillator so long as the number of oscillators remain large, approaching infinity.[12]

For practical cases, however, where the primary structure has a finite number of oscillators attached to it, the assertions for vanishing loss factors hold true only during a transient period, described as the return time t^*, during which energy flows into the satellite oscillators before returning to the primary structure. If the attached oscillators do not possess any loss mechanisms, even for very large number of oscillators, energy returns to the master with a return time that depends on the number of oscillators.[1,16] For a very large number of oscillators, the transient part has a very long duration. The return time corresponds to the smallest difference among the natural frequencies of the oscillators.

The present study shows that energy can be trapped with near irreversibly by a finite number of linearly attached oscillators even in the absence of dissipative mechanisms. In this case, energy absorption by the oscillators is governed by their frequency distribution, a subject which has not yet received much attention. The results show the existence of an optimal frequency distribution that minimizes the total energy returned to the primary structure from the set of oscillators.

The underlying physics of energy absorption also relates to the return times associated with the optimum set of frequencies. The optimization method described in the following produces an optimal distribution for the fundamental frequencies of the oscillators such that the combination of the associated return times minimizes the energy retained by the primary structure. Corresponding experiments demonstrate the feasibility of energy sinks.

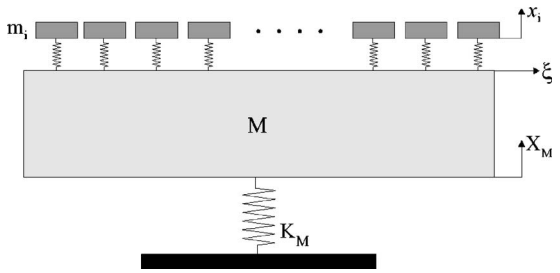

FIG. 1. Schematic description of a primary structure and attached set of oscillators.

II. MODEL

The prototypical system under consideration consists of a rigid primary structure with a substructure comprised of a set of oscillators attached to it as depicted in Fig. 1. The system does not possess any mechanism of dissipation in the classical sense, thus stiffness alone characterizes the connections between the substructure and the primary structure. The total mass, m ($m=\Sigma m_i$), of the attachments is a fraction of the primary mass, M, always $m/M \leqslant 0.1$

Dynamic response of such a system can be described by a set of coupled equations:

$$M\ddot{x}_M + K_M x_M + \sum_{i=1}^{N} k_i[x_M - x_i] = 0, \tag{1}$$

$$m_i\ddot{x}_i + k_i[x_i - x_M] = 0, \tag{2}$$

where k_i and m_i represent the stiffness and mass of individual oscillators, respectively, and $x_M(t)$ is the displacement of the primary structure and $x_i(t)$ is the displacement of the ith oscillator in the set. [For brevity, the time variable t is omitted in $x_M(t)$ and $x_i(t)$.] For a given mass ratio m/M, energy trapped by the attached set is determined largely by the properties of the mass and stiffness m_i, k_i, or the uncoupled natural frequency distribution ω_i, of the attached oscillators.

Figure 2(b) shows a typical impulse response of the primary structure in the prototype problem described by Eqs. (1) and (2) that has a linear frequency distribution as shown in Fig. 2(a). In this simple example, the natural frequencies of the oscillators have a constant frequency difference between the neighboring frequencies. As expected of linear oscillators with a linear frequency distribution, the response shows a recurrence; as shown in Fig. 2(c), energy periodically returns to the primary structure when the number of

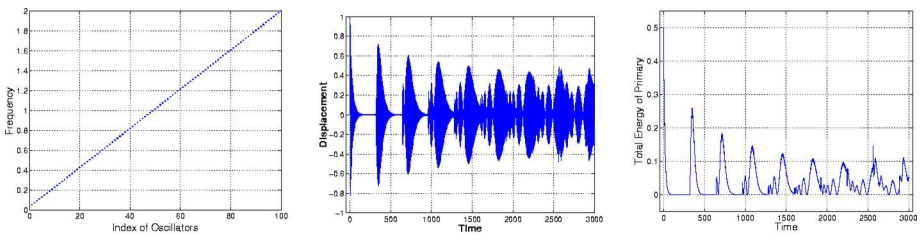

(a) (b) (c)

FIG. 2. (Color online) Simulation results using $N=99$ oscillators: (a) linear frequency distribution of the attached oscillators, (b) displacement response, and (c) total energy of the primary structure.

oscillators is finite, in this case $N=100$. The return time corresponds to the constant frequency difference $t^*=2\pi/\Delta\omega$. The optimization method described next seeks to determine a frequency distribution for the attached oscillators that reduces the response amplitude of the primary structure and diminishes the energy it retains.

III. OPTIMIZATION

The optimum distribution of the natural frequencies of attached oscillators is sought by finding the frequencies that minimize the objective function, which is based on the integral of the energy of the primary structure:

$$\mathcal{L}_M \sim \int_0^\infty x_M^2(t)dt. \tag{3}$$

Because the approach used here requires that the integral is finite, a small amount of "damping" will be introduced for optimization to find the desired distribution. However, the frequency distribution obtained from this approach will then be used in the absence of any damping in the system. With Parseval's theorem, an equivalent expression to Eq. (3) in the frequency domain becomes

$$\mathcal{L}_M \sim \int_{-\infty}^{+\infty} |X_M(\omega)^2| d\omega. \tag{4}$$

Using nondimensional parameters, substituting in Eq. (4) the equations of motion of the system (1) and (2) produces

$$\mathcal{L}_M \sim \int_{-\infty}^{+\infty} \frac{d\Omega}{\left|1+j\eta_M-\Omega^2-(m/MN)\sum_{i=1}^N \frac{\Omega^2(1+j\eta_i)}{1+j\eta_i-(\Omega/\Omega_i)^2}\right|^2}, \tag{5}$$

where $\Omega=\omega/\omega_M$, $\Omega_i=\omega_i/\omega_M$, with $\omega_M=\sqrt{K_M/M}$ and $\omega_i=\sqrt{k_i/m_i}$, and η_i, η_M represent the loss factors associated with the oscillators and primary structure, respectively.

Optimization searches for the minima of the multivariable function $\mathcal{L}_M(\mathbf{\Omega})$ by solving the set of coupled nonlinear equations:

$$\frac{\partial \mathcal{L}_M}{\partial \Omega_i}=0, \quad i=1,\ldots,N. \tag{6}$$

For the solution $\mathbf{\Omega}=[\Omega_1,\Omega_2,\ldots,\Omega_N]$ of Eq. (6) to be a local minimum solution of $\mathcal{L}_M(\mathbf{\Omega})$ requires that the Hessian Matrix H_{kj}, evaluated at $\mathbf{\Omega}$, is positive definite with all eigenvalues that satisfy:

$$H_{kj}=\frac{\partial^2 \mathcal{L}_M(\mathbf{\Omega})}{\partial\Omega_k\,\partial\Omega_j}>0, \quad k=1,\ldots,N, \quad j=1,\ldots,N. \tag{7}$$

The numerical results reported in Sec. IV are obtained using the Quasi-Newton optimization method and ODE23t solver, which avoid introduction of numerical damping.

IV. NUMERICAL RESULTS

The optimization process starts with an estimated frequency distribution, seeks to minimize the integral of the energy, $\mathcal{L}_M$, by continuously adjusting the frequency distribution, and stops when $\mathcal{L}_M$ reaches its minimum value. The frequency distribution that produces the lowest value of $\mathcal{L}_M$ is accepted as the optimum distribution. The time it takes for optimization of a particular case depends on the number of oscillators and the value of the loss factor as shown in the following. The effectiveness of the resulting optimum frequency distribution is judged by the vibration amplitude of the primary mass and the total energy it retains following, in this case, an impulsive excitation as compared with the case shown in Fig. 2 for which the attached oscillators have a linear frequency distribution. In the optimization and simulations results presented in this paper, frequencies are normalized with respect to that of the primary oscillator and the frequencies for the energy sinks range between 0 and twice the primary mass resonant frequency.

A. Influence of initial frequency estimates

Optimization starting with different sets of initial estimates for the frequency distribution of the attached oscillators do not show a discernible difference in the case of $N=29$ oscillators. Some differences in the optimum results appear for $N=99$ oscillators, particularly when using very low loss factors, but not enough to affect the response of the primary and the energy it retains, as shown later with simulations.

As shown in Fig. 3, the three different initial estimates of frequency distributions, constant, linearly varying and a nonlinearly varying power-law distribution, which we refer to here as a polynomial distribution, produce nearly identical optimized frequency distributions. Also shown in Fig. 3 is the change in the value of the integral energy, represented by $\mathcal{L}_M$, throughout the optimization process, starting with the result of the first step of optimization. Its initial value and rate of decline depend on the selection of the initial frequency distribution shown in the first column. Each of the initial frequency distributions produce nearly the same minimum integral of energy, within 0.3% of each other.

Similar optimum distributions result in the case of a larger number of attached oscillators ($N=99$), however, with some variation at either end of each frequency distribution as shown in Fig. 4. The largest difference in the minimum value of integral among the three cases changes with the loss factors used in the integral. The values of $\mathcal{L}_M$ corresponding to the optimum frequency distributions shown in Fig. 4 vary 0.5% for $\eta_i=0.01$ and the variation increases to about 16% when $\eta_i=0.001$ is used. The differences that also appear in the corresponding frequency distributions indeed become less if optimization process is continued.

B. Role of loss factor used in optimization of $\mathcal{L}_M$

The loss factors used to ensure a finite value for $\mathcal{L}_M$ in Eq. (4) also determine the duration of the integral considered for optimization. Ideally, the lower the loss factors used, the closer the integral energy represents the energy sink, which does not embody dissipation sources. A lower loss factor leads to minimization of the energy of the primary structure over a longer period of time, which also requires longer computation times. A higher loss factor, on the other hand, short-

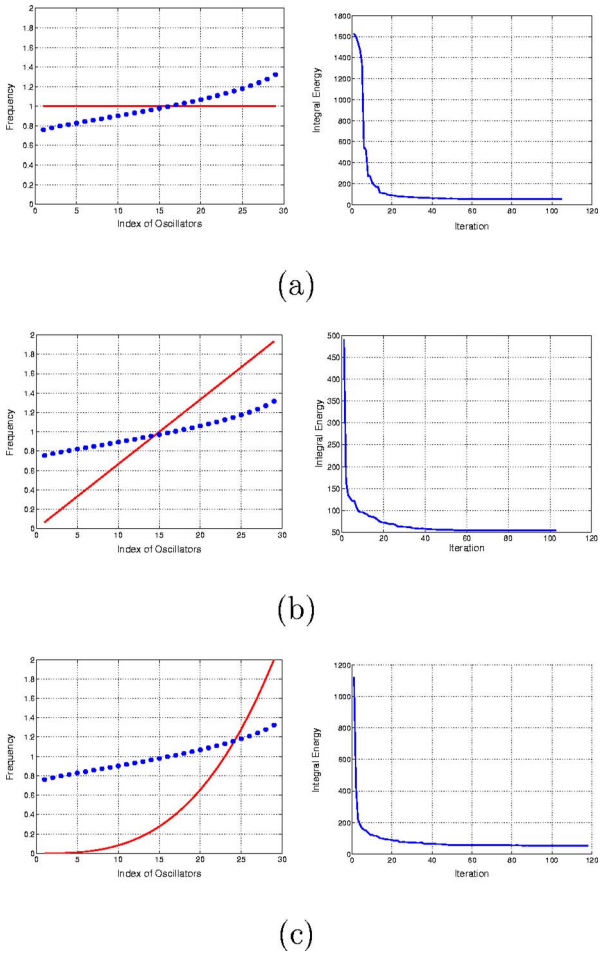

FIG. 3. (Color online) Optimized frequency distributions (dotted lines) for a system of $N=29$ oscillators each with a loss factor $\eta_i=0.001$. The change of the integral of the energy of the primary structure, Eq. (5), (right-hand column) at each iteration illustrates the optimization process for different initial estimates for the frequency distribution from which optimization starts: (a) all oscillators have the same frequency as the primary structure $\omega_i=1$, (b) linear distribution, and (c) polynomial distribution.

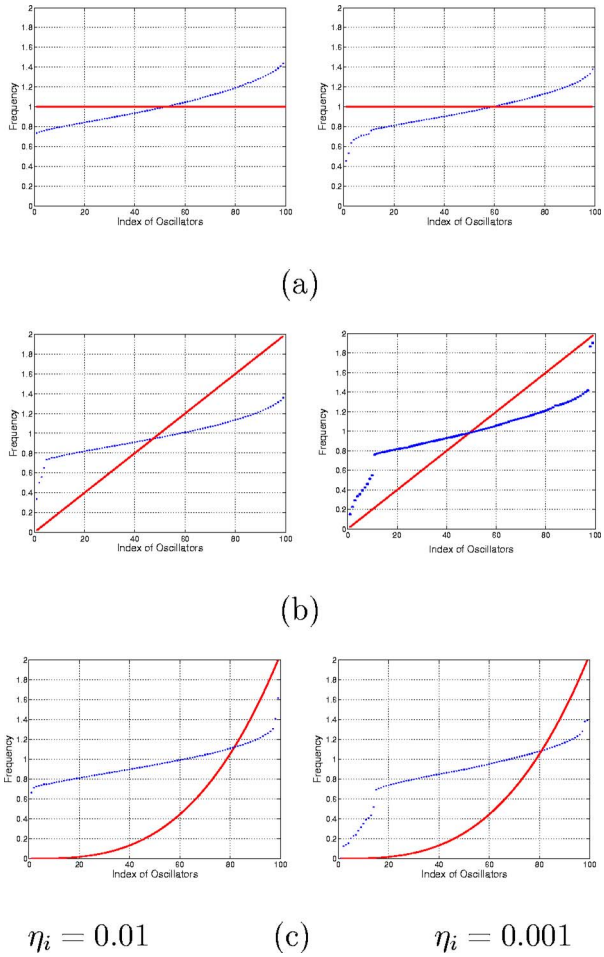

FIG. 4. (Color online) Optimized frequency distributions for $N=99$ oscillators that result from different initial frequency distributions for two different loss factors η_i: (a) all oscillators have the same frequency as the primary structure $\omega_i=1$, (b) linear distribution, and (c) polynomial distribution.

ens the period of the integral, thus reducing the time over which energy should be minimized. However, loss factors η_i also reduce the vibration amplitude of individual oscillators in the energy sink and thus reducing their effectiveness in transferring energy from the primary structure as simulations demonstrate.

Figures 5 and 6 show examples of optimization results for low and moderate values of loss factors for $N=29$ and 99 oscillators, respectively. In each case, the initial frequency distribution of the set has a constant value the same as that of the primary mass, $\omega_M=1$, as indicated by the solid line.

Optimization spreads the frequencies over a band with a higher density around the frequency of the primary mass. The optimum frequency sets in Fig. 5, obtained using loss factors $\eta_i=0.1$, 0.01, and 0.001, display very similar distributions except at each end of the frequency bands. The corresponding optimum frequency distributions for $N=99$ oscillators, shown in Fig. 6, also exhibit similar trends.

The simulations presented next show the relative effectiveness of optimum frequency distributions in reducing the vibration amplitude of the primary mass and the energy it retains. Results also show that the use of large loss factors speeds up the optimization process but produces less than optimal distributions as demonstrated later with simulations. Very small values of loss factors prolong the optimization process and introduce computational errors.

C. Simulations

The simulation results presented in the following use the optimum frequency distributions, obtained as described earlier, in solving Eqs. (1) and (2) without any damping in the system.

As an example, Fig. 7 demonstrates simulation results that correspond to the optimum frequency set shown in Fig. 5(c) obtained for $N=29$ oscillators with loss factors $\eta_i=0.001$ and compares them with the corresponding responses for the initial frequency distribution with which optimization started. The amplitude response and the total energy of the primary mass presented over a long time period show a distinct reduction from the initial conditions from which optimization started when all oscillators had the same frequency as the primary, making the initial configuration essentially a two-degree-of-freedom system. The response spectrum 7(b) of the primary mass reflects the presence of a distributed set

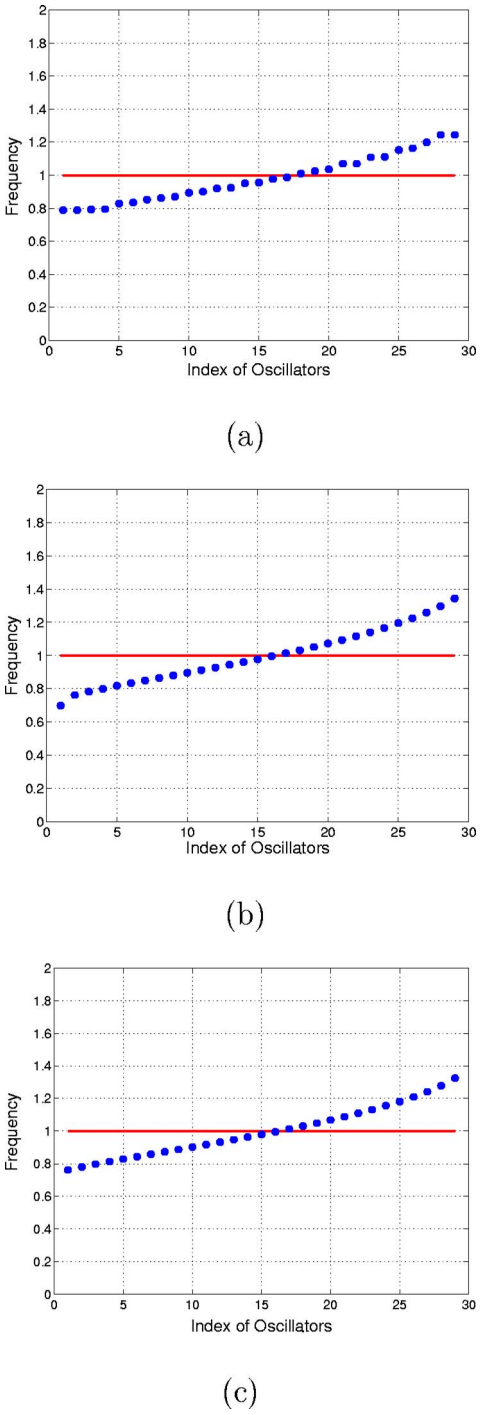

FIG. 5. (Color online) Influence of loss factors η_i on the resulting optimized frequency distributions for a system with $N=29$ oscillators, which initially have the same frequencies as that of the primary $\omega_i=\omega_M=1$. (a) $\eta_i=0.1$, (b) $\eta_i=0.01$, and (c) $\eta_i=0.001$.

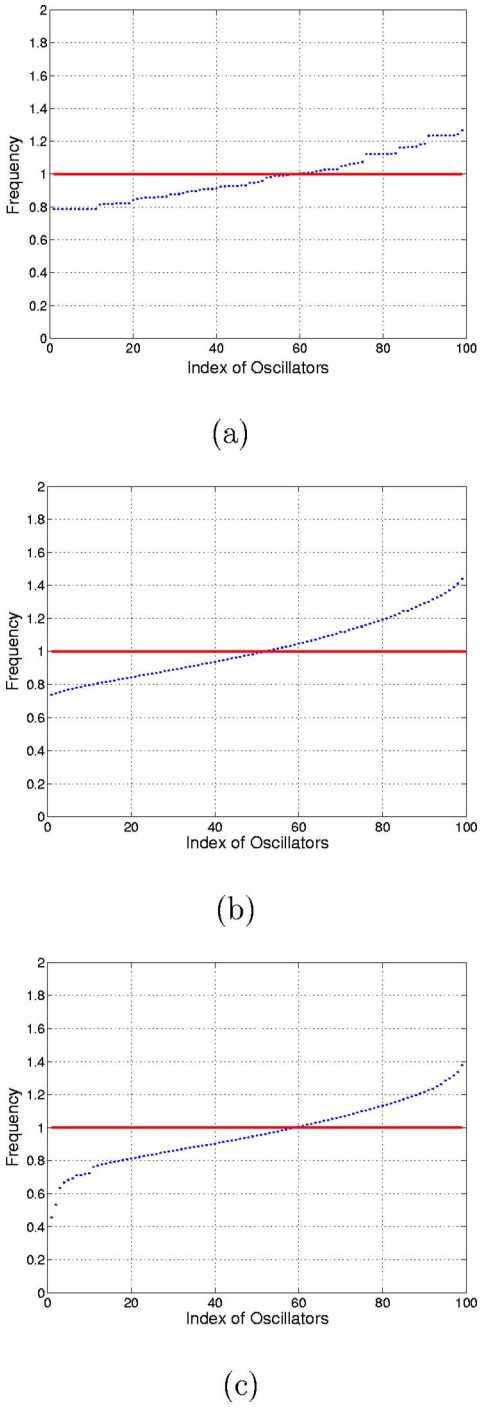

FIG. 6. (Color online) Effect of loss factor on the optimized frequency distribution for $N=99$. Optimization begins with the same initial frequencies for all oscillators and the primary structure. (a) $\eta_i=0.1$, (b) $\eta_i=0.01$, and (c) $\eta_i=0.001$.

of frequencies that contains the effects of each of the 29 oscillators, distinct from the two frequencies with which the initial estimate started out. While the initial amplitude and the energy of the primary structure exhibits a periodic behavior with a constant amplitude, the optimized frequency distribution reduces both the response amplitude and the retained energy each to a fraction of the corresponding initial values.

The impulse response of the primary structure shows that the envelop of its displacement amplitude remains within 40% of its initial response for $N=29$ and the retained energy within 20% of its initial value. The energy initially contained in the two frequencies spreads over to 29 frequencies, each with an amplitude less than 10% of the initial spectral amplitudes. As shown later, increasing oscillator number in the set further reduces the amplitude and retained energy.

Simulations that correspond to the optimized frequency sets obtained from different initial distributions presented in Fig. 4 produce responses shown in Figs. 8 and 9. The slight

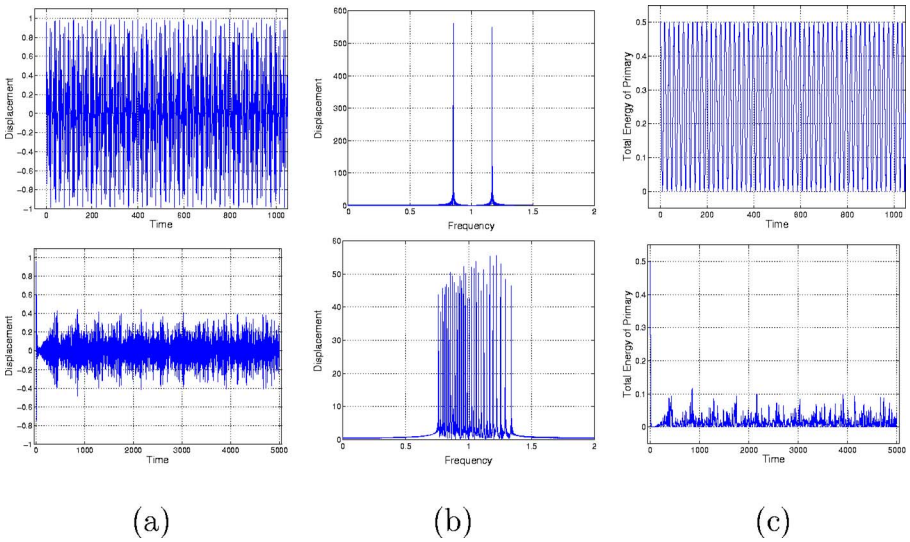

FIG. 7. (Color online) Simulation results for a set of $N=29$ attached oscillators each with a loss factor of $\eta_i=0.001$. The top row shows the response of the primary when all attached oscillators and the primary have the same frequency $\omega_i=\omega_M=1$. The bottom row shows the results obtained using the optimum frequency distribution: (a) displacement time, (b) displacement-frequency response, and (c) total energy of the primary structure.

variations among the optimal frequency distributions lead to barely discernible differences in the response amplitude of the primary and the energy it retains over time. While the differences are small, in this case the optimum frequencies resulting from an initial estimate of constant frequencies and loss factors $\eta_i=0.001$ show a better performance, Fig. 9(a).

An example of how nonoptimal frequency distributions that result from use of large loss factors in Eq. (5) affect the performance of an energy sink is shown in Fig. 10. The frequency distribution presented in Fig. 6(a), obtained using $\eta_i=0.1$, yields larger amplitudes for the displacement of and the energy retained by the primary than the corresponding cases with distributions obtained using lower loss factors. These results are consistent with the observation that the lower the loss factors used in equations of motion (5) the closer they represent the energy sink, which does not have any dissipation at all.

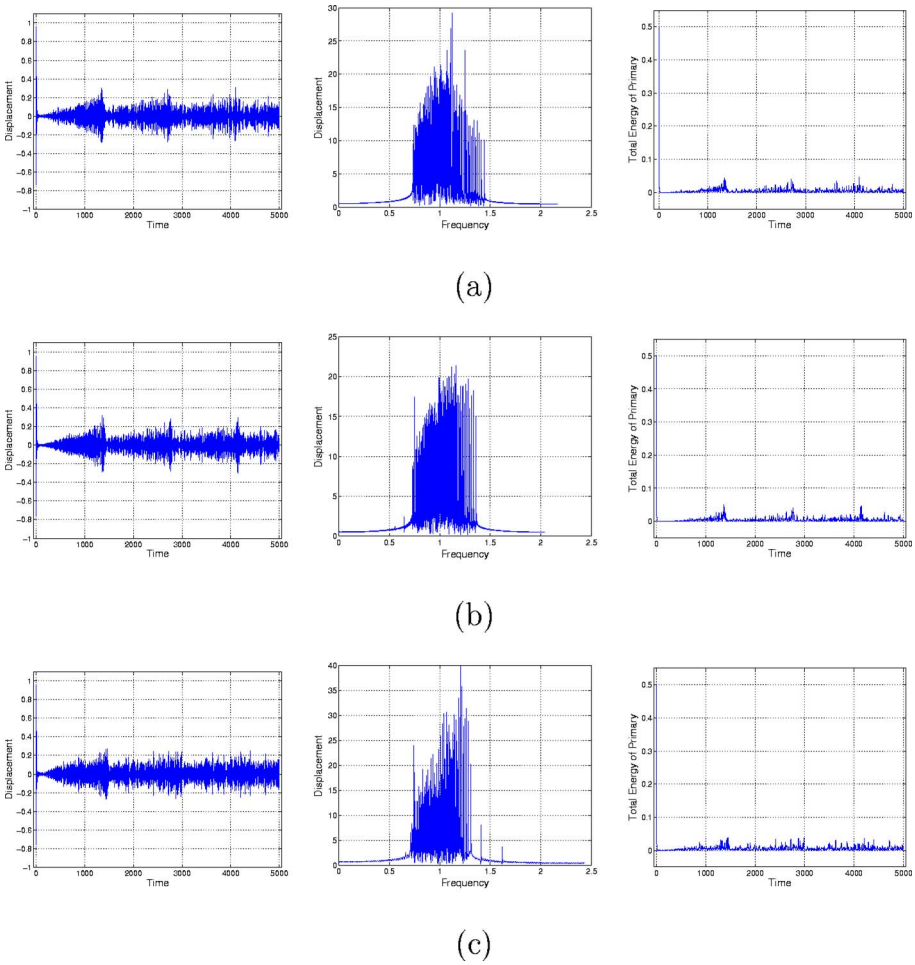

FIG. 8. (Color online) Simulation results for the optimum frequency distributions obtained starting with initial frequencies that correspond to those in Fig. 4 ($\eta_i=0.01$) show negligible difference in the displacement response of the primary in time and frequency domains as well as the total energy it retains. $N=99$. Optimum frequency used in each row corresponds to a different set of initial frequency estimates used in optimization: (a) all oscillators have the same frequency as the primary structure $\omega_i=1$, (b) linear distribution, and (c) polynomial distribution.

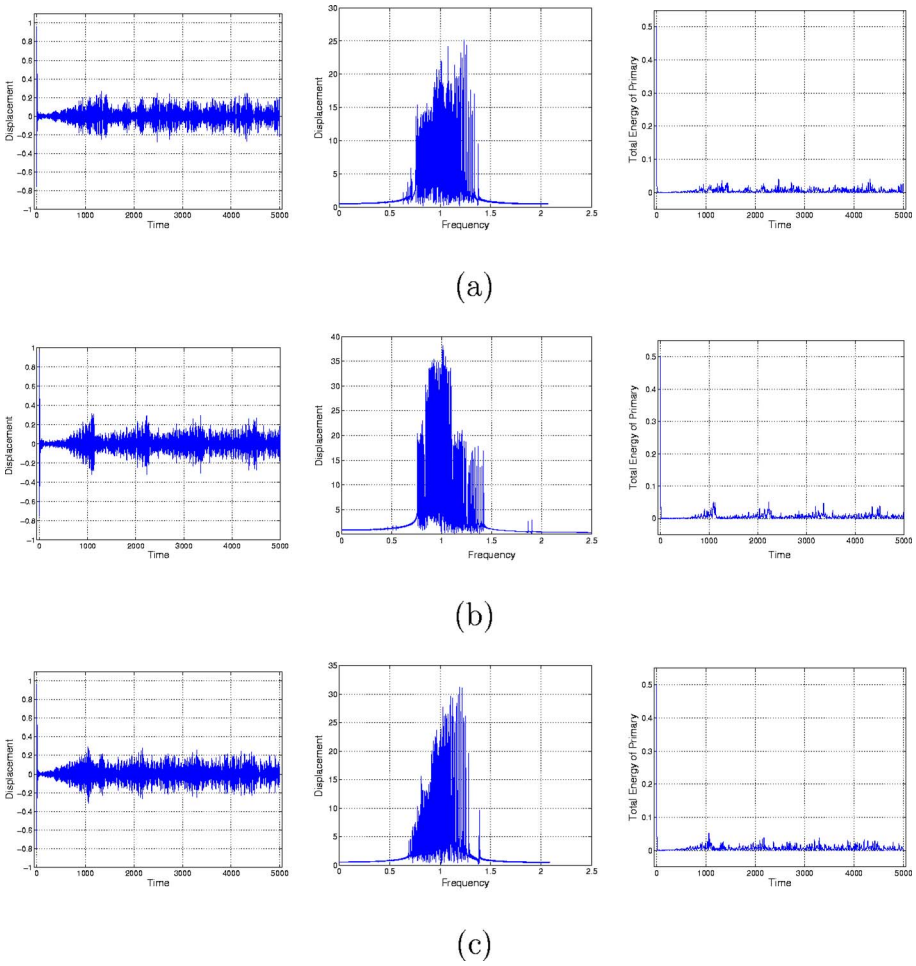

FIG. 9. (Color online) Simulation results for the optimum frequency distributions obtained starting with initial frequencies that correspond to those in Fig. 4 (η_i=0.001): (a) all oscillators have the same frequency as the primary structure ω_i=1, (b) linear distribution, and (c) polynomial distribution. Results show negligible difference in the displacement response of the primary in time and frequency domains as well as the total energy it retains. N=99.

D. Role of damping in an energy sink

Since physical systems have inherent dissipation mechanisms, it is worth examining the influence of losses present in an energy sink on its performance. For low values of loss factors, $\eta_i \simeq 0.01$, the main role of dissipation in the oscillators is to further reduce the oscillation amplitude of the primary structure as seen in Fig. 11 compared with Fig. 9(a). However, the presence of large damping in the system, for example $\eta_i \geqslant 0.1$, reduces the effectiveness, and perhaps the need, for an energy sink.

E. Multiple-degree-of-freedom systems

When optimization is applied to a primary structure with two degrees of freedom depicted in Fig. 12, oscillator frequencies distribute themselves around each of the primary frequencies and absorb energy from both masses. In the example shown, for comparison, the mass ratio between the oscillators and the two-component primary mass has the same value as in the previous examples. As a result of optimization, oscillators assume frequency distributions about the natural frequencies of the primary structure, $\omega_M^{\{1\}}=0.618$ and $\omega_M^{\{2\}}=1.618$, similar to those that resulted for a single-degree-of-freedom platform. As before, simulations show that the optimized frequency distributions reduce the vibration amplitude and the retained energy by the primary structures. The responses of the primary structures have a higher amplitude than the corresponding case with a single primary, in part, as a result of the effectively reduced number of oscillators for each mass.

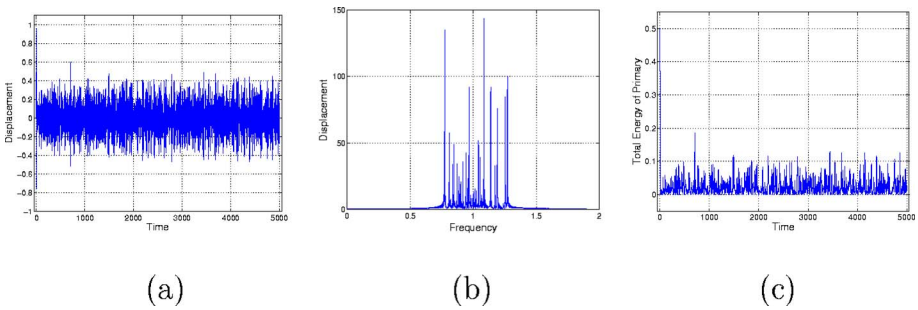

FIG. 10. (Color online) Simulation results for an energy sink with N=99 oscillators. The optimum frequency distribution, shown in Fig. 6(a), is obtained using a rather large loss factor η=0.1 for each of the oscillators: (a) linear frequency distribution of the attached oscillators, (b) displacement response, and (c) energy of the primary structure.

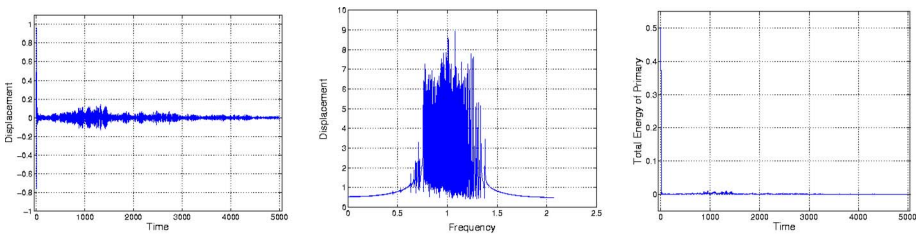

FIG. 11. (Color online) Simulated response of the primary with $N=99$ oscillators corresponding to Fig. 9(a) but each oscillator has a loss factor $\eta_i=0.001$.

F. An analytical expression for optimal frequency distribution

The frequency distributions obtained by the above-described optimization can be approximated by an analytical expression that depends on a single parameter α:

$$\omega(\xi) = A\left[\frac{2\xi-1}{|2\xi-1|}\frac{e^{\alpha|2\xi-1|}-1}{e^{\alpha}-1}+1\right], \tag{8}$$

where $0<\xi\leqslant 1$. Discrete values $\omega_i(\xi)$ of frequency distribution are obtained with $\xi_i=i/N$.

Figure 13 shows a representative set of frequency distributions for different values of α with corresponding simulations in Fig. 14. Very small values of α represent a nearly linear frequency distribution with the same periodic energy return to the primary structure. Values of $\alpha>5$ assign most of the oscillators the same frequency, producing essentially a two-degree-of-freedom system, with the corresponding results in rows (c) and (d) of Fig. 14 and as discussed earlier. Among these, the distribution that corresponds to $\alpha\approx 2.5$ yields the most optimum result yielding minimum average energy retention by the primary.

An alternative method to reduce the computation time in cases involving a large number of attached oscillators uses the distribution that results from optimization for a small number of oscillators. Figure 15 displays and compares the distributions obtained for $N=29$ and $N=99$ oscillators by direct optimization. Repopulating the distribution for $N=29$ with 99 oscillators and simulating the response of the primary structure as before produces results very close to those obtained by a distribution obtained through direct optimization. A comparison of the results based on interpolated distribution given in Fig. 16 with those in Fig. 9 shows very little difference.

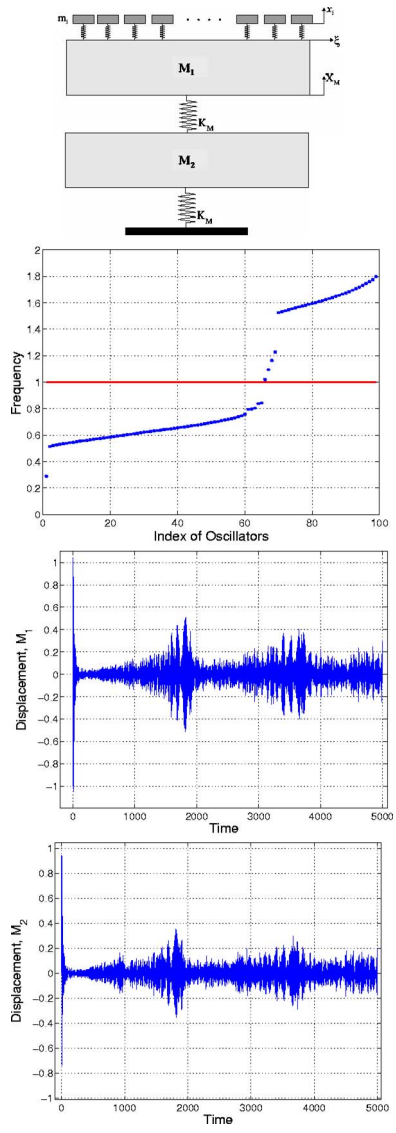

FIG. 12. (Color online) Optimized frequency distribution of $N=99$ oscillators attached to a two-degree-of-freedom primary structure and the responses of the platform with the attached oscillators and platform attached to ground (bottom). The natural frequencies of the primary structure are $\omega_M^{\{1\}}=0.618$ and $\omega_M^{\{2\}}=1.618$.

V. EXPERIMENTS

The two energy sinks with different physical configurations demonstrate the efficacy of the proposed energy sinks.

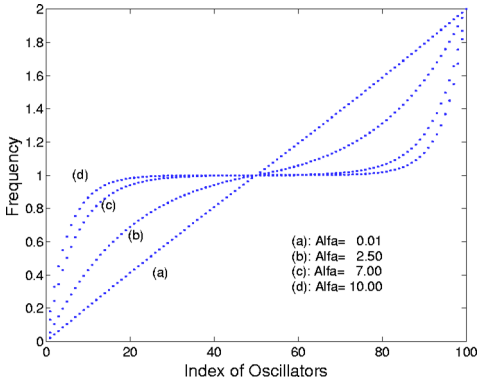

FIG. 13. (Color online) Examples of frequency distribution for different values of α in Eq. (8).

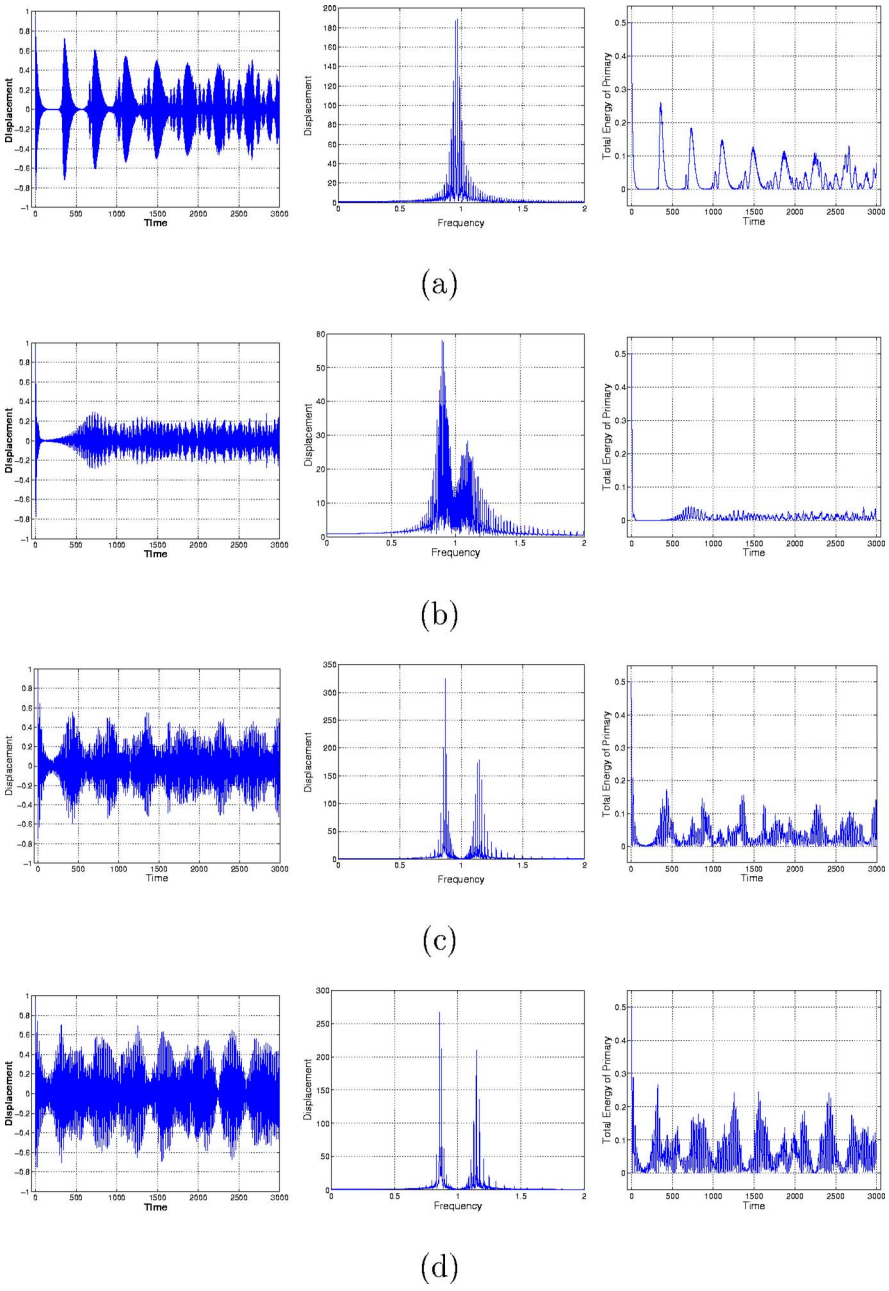

FIG. 14. (Color online) Simulation results for displacement response in time and frequency domains and the energy retained by the primary mass using values of α in Eq. (8): (a) α=0.01, (b) α=2.5, (c) α=7.0, and (d) α=10.0.

The ubiquitous presence of inherent losses in physical systems precludes construction of either a primary structure or an energy sink that can oscillate indefinitely. However, use of different frequency distributions delineates the effects of losses in the system from energy absorbed by the attached oscillators.

A. A set of thin beams attached to a *T*-configuration

Figure 17 shows the impulse response of a *T*-configuration of joined beams with and without a set of thin beams attached to it. The first natural frequencies of the thin beams follow the optimum distribution described by the analytical expression in Eq. (8). Without the oscillators, the response of the structure decays as a result of dissipation due to connections and material losses. However, the corresponding response with the attached oscillators exhibit the same behavior as those obtained through simulations in both time

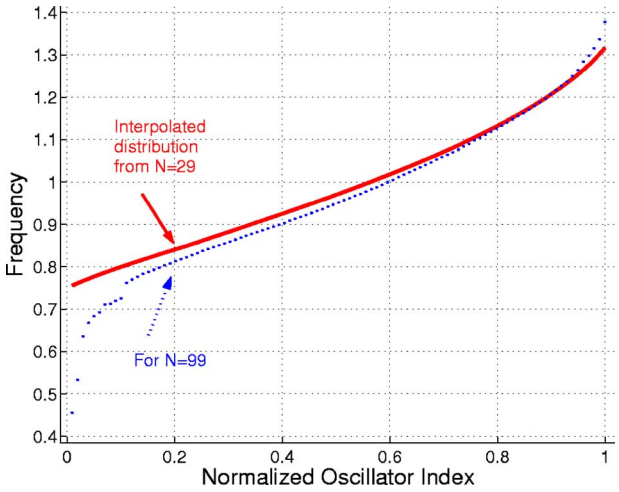

FIG. 15. (Color online) A comparison of the frequency distribution for N=99 oscillators obtained by two approaches. Dotted line represents result by direct optimization and the solid line represents interpolation for N=99 using the optimum distribution obtained for N=29 oscillators.

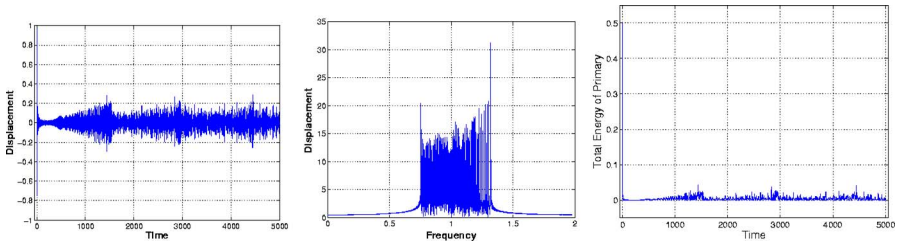

FIG. 16. (Color online) Response of the primary structure with an interpolated frequency distribution. Optimized frequency distribution obtained using $N=29$ oscillators interpolated for $N=99$ oscillators. $\eta_i=0.001$.

and in frequency domains. The response of the primary structure in the frequency domain, shown with both linear and logarithmic scales, clearly shows the effects of the oscillators.

B. A set of flexible beams attached to a rigid oscillator

This demonstration uses as the primary structure a single degree of freedom oscillator that consists of a rigid block which can freely slide in an air bearing. A pair of springs at one end anchors it to an optical table. As displayed in Fig. 18, a lightweight structure built on the block carries a set flexible cantilever wire beams, each with a mass along its axis that acts as an oscillator. Natural frequency of each oscillator is determined by adjusting the position of the mass along the beam. Figure 19 presents velocity response of the block to an impulse for two cases: the oscillators have either a linear or an optimum frequency distribution. When the distribution follows the optimum values obtained using the method described earlier, the energy returned to the block is distributed both in time and frequency compared with the case when oscillators have a linear distribution. The recurrence observed with the linear distribution has a lower amplitude than expected, in part due to the inexact values of the oscillator frequencies. The inherent damping in the physical system also reduces the response amplitudes. To better reflect the effects of losses in the system, the simulation results presented in Fig. 20 include their values as measured from the experimental setup. The simulated responses, both in time and frequency domain, represent the same characteristics as those produced by measurements.

VI. CONCLUDING REMARKS

An energy sink that consists of a set of oscillators can absorb vibration energy from a structure to which it is attached. Following transient excitation of a structure, energy that flows into the oscillators remains in their phase space.

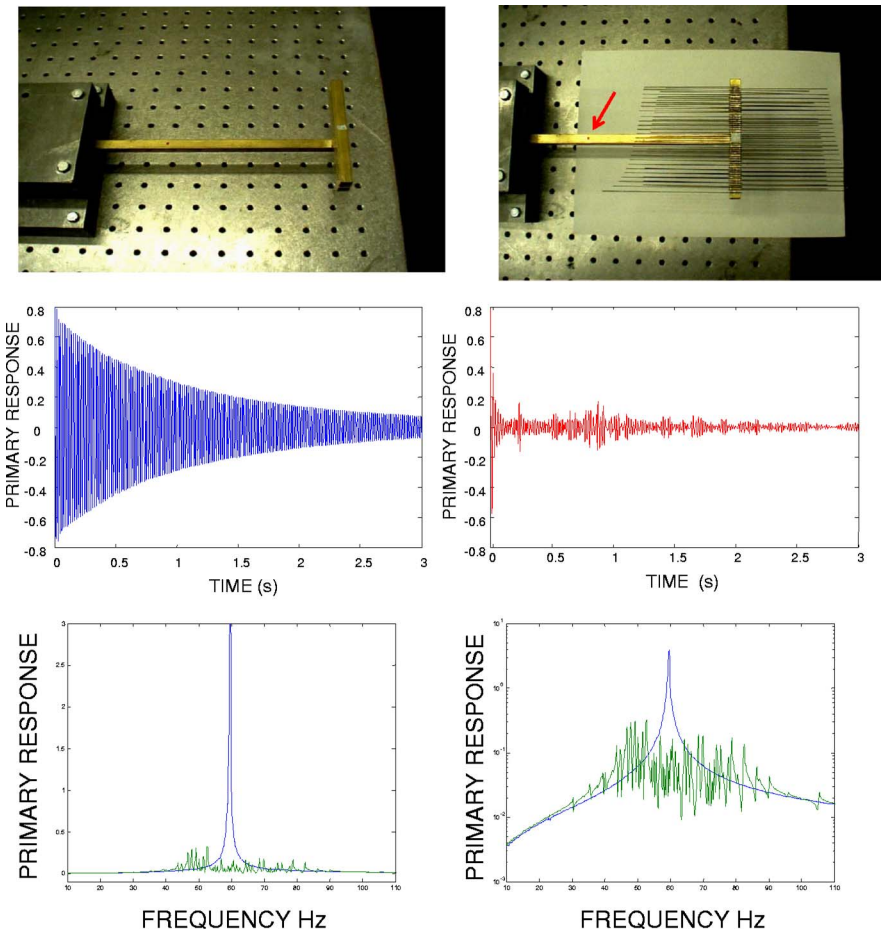

FIG. 17. (Color online) Response of a structure (top) shown with and without the oscillators that make up an energy sink. The first bending frequency of the thin beams that act as oscillators follow the analytical optimum frequency distribution given in Eq. (8). Response of the structure with and without the oscillators is shown (bottom row) in frequency domain using both linear and logarithmic scales.

The net force they collectively exert on the primary structure, and thus the total energy that returns to the primary, stays below a fraction of its initial value.

Because energy sinks, in principle, do not require conventional dissipation sources, they are particularly useful in high temperature or chemically hazardous environments where materials and mechanisms that provide dissipation may not be as effective. The unavoidable loss mechanisms in physical systems, however, induce dissipation in the primary and the attached oscillators. As long as these dissipation rates remain moderate, they do not adversely affect the performance of energy sinks, but assist in reducing the vibration amplitude of the oscillators as well as the primary structure.

Energy absorption by a set of linear oscillators relates to their frequency distribution. The optimization method presented in this paper finds such a distribution. The optimization used here minimizes the energy of the primary mass over a selected time period. Optimization results show a degree of robustness of the process with respect to the initial frequency distributions and the values of loss factors. Optimum distributions increase the density of oscillators near the frequencies of interest, as demonstrated for a two-degree-of-freedom primary structure. This result is consistent with the observation that with linear frequency distributions (and thus constant frequency difference); oscillators near the primary frequency respond with a higher level of energy absorption than those with frequencies away from it. Such a distribution also de-emphasizes the need to finely tune the frequencies as in conventional vibration absorbers.

The simulations and the physical demonstrations support the viability of reducing vibrations of structures with linear energy sinks and that the concept can be extended to primary structures with multiple degrees of freedom. Ability of linear energy sinks to absorb energy independent of dissipation sources sets it apart from many other similar approaches. In particular, energy sinks have an advantage in transient and low frequency applications.

Although this manuscript primarily addresses the role of optimum frequency distribution of energy sinks, their ability

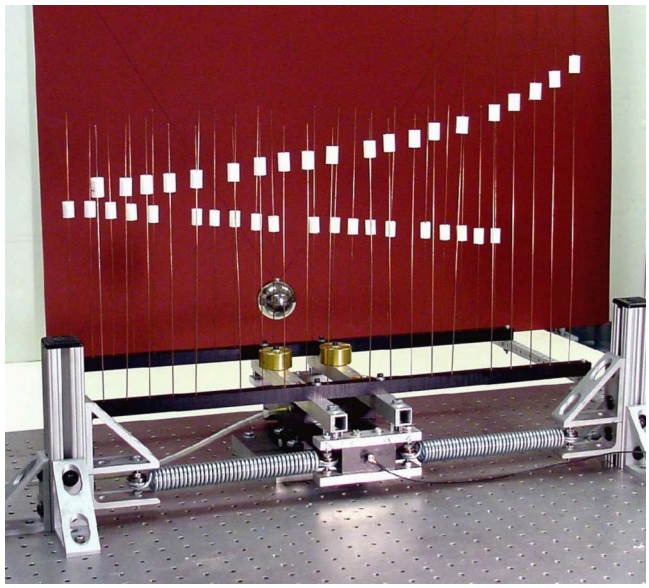

FIG. 18. (Color online) A set of 40 oscillators attached to a primary structure.

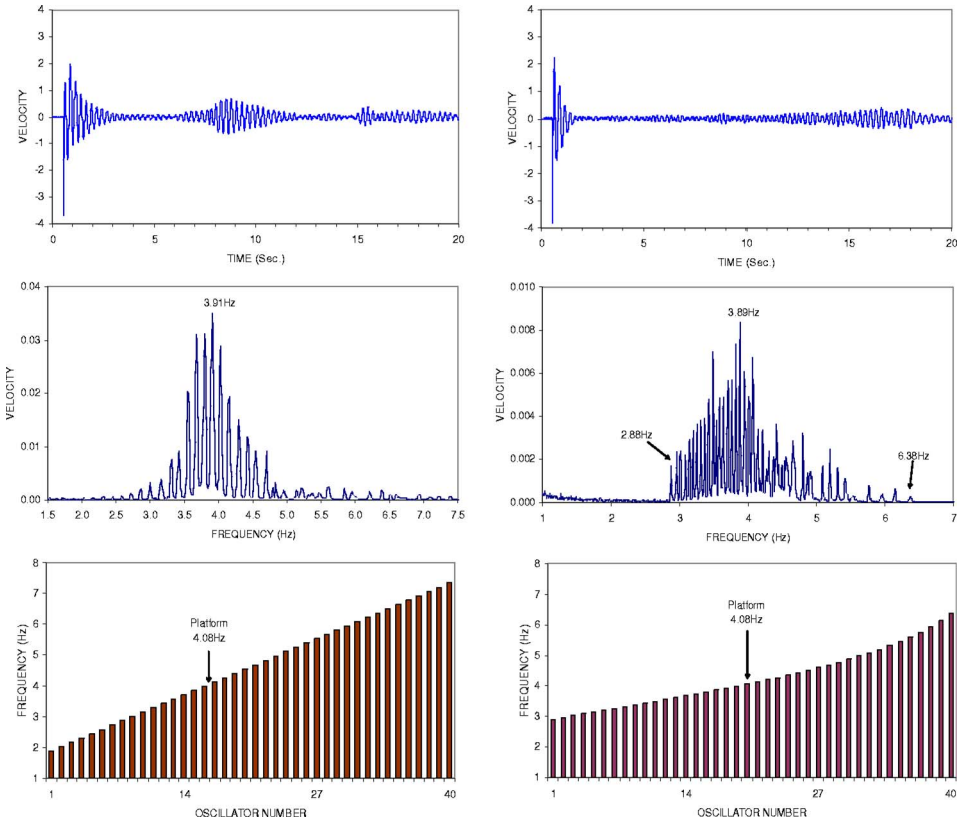

FIG. 19. (Color online) Response of the block with 40 oscillators to an impulse excitation shows that oscillators with an optimum frequency distribution (right) spread the return energy over both time and frequency and reduce its amplitude. Inherent damping in the system also reduces the amplitude of recurrence for the linear distribution, at $t \simeq 8$ s.

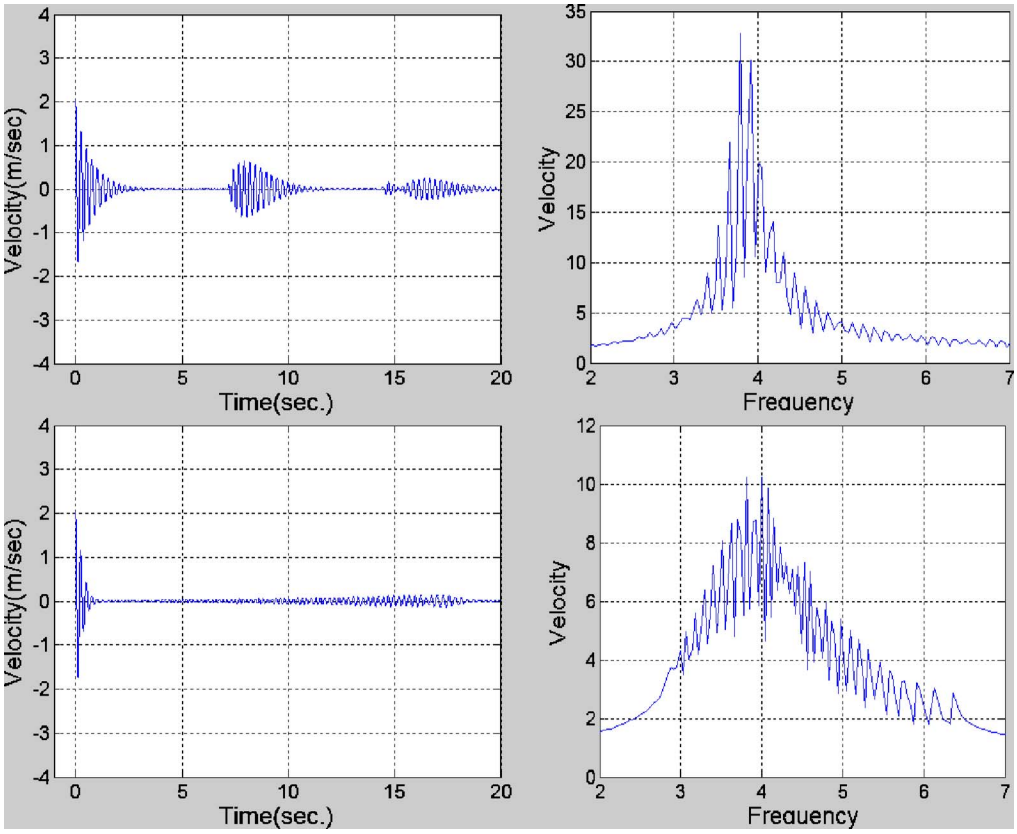

FIG. 20. (Color online) Simulated response of the block corresponding to conditions in Fig. 19 using loss factors measured from the experimental setup as $\eta_M=0.008$ and $\eta_i=0.008$.

to absorb energy also depends on other parameters such as the number of oscillators and their mass ratio as discussed in earlier studies, viz. Ref. 1.

[1]A. Carcaterra and A. Akay, "Transient energy exchange between a primary structure and a set of oscillators: Return time and apparent damping," J. Acoust. Soc. Am. **115**, 683–696 (2004).
[2]C. E. Celik and A. Akay, "Dissipation in solids: Thermal oscillations of atoms," J. Acoust. Soc. Am. **108**, 184–191 (2000).
[3]A. F. Vakakis, "Inducing passive nonlinear energy sinks in vibrating systems," J. Vibr. Acoust. **123**, 324–332 (2001).
[4]O. Gendelman, L. I. Manevitch, A. F. Vakakis, and R. M'Closkey, "Energy pumping in nonlinear mechanical oscillators. I. Dynamics of the underlying Hamiltonian systems," J. Appl. Mech. **68**, 34–41 (2001).
[5]A. F. Vakakis and O. Gendelman, "Energy pumping in nonlinear mechanical oscillators. II. Resonance capture," J. Appl. Mech. **68**, 42–48 (2001).
[6]J. Aubrecht, A. F. Vakakis, T.-C. Tsao, and J. Bentsman, "Experimental study of nonlinear transient motion confinement in a system of coupled beams," J. Sound Vib. **195**, 629–648 (1996).
[7]A. F. Vakakis, "Passive spatial confinmement of impulsive responses in coupled nonlinear beams," AIAA J. **32**, 1902–1909 (1994).
[8]L. Zuo and S. A. Nayfeh, "Optimization of the individual stiffness and damping parameters in multiple-tuned-mass-damper systems," ASME J. Vibr. Acoust. **127**, 77–83 (2005).
[9]L. Zuo and S. A. Nayfeh, "Minimax optimization of multiple-degree-of-freedom tuned-mass dampers," J. Sound Vib. **272**, 893–908 (2004).
[10]K. Xu and T. Igusa, "Dynamic characteristics of multiple substructures with closely spaced freuencies," Earthquake Eng. Struct. Dyn. **21**, 1059–1070 (1992).
[11]C. Soize, "A model and numerical method in the medium frequency range for vibroacoustic predictions using the theory of structural fuzzy," J. Acoust. Soc. Am. **94**, 849–865 (1993).
[12]A. D. Pierce, V. W. Sparrow, and D. A. Russell, "Fundamental structural-acoustic idealizations for structures with fuzzy internals," J. Vibr. Acoust. **117**, 339–348 (1995).
[13]M. Strasberg and D. Feit, "Vibration damping of large structures induced by attached small resonant structures," J. Acoust. Soc. Am. **99**, 335–344 (1996).
[14]M. Strasberg, "Continuous structure as 'fuzzy' substructures," J. Acoust. Soc. Am. **100**, 3456–3459 (1996).
[15]R. J. Nagem, I. Veljkovic, and G. Sandri, "Vibration damping by a continuous distribution of undamped oscillators," J. Sound Vib. **207**, 429–434 (1997).
[16]R. L. Weaver, "The effect of an undamped finite degree of freedom 'fuzzy' substructure: Numerical solutions and theoretical discussion," J. Acoust. Soc. Am. **100**, 3159–3164 (1996).
[17]R. L. Weaver, "Mean and mean-square response of a prototypical master/fuzzy structure," J. Acoust. Soc. Am. **101**, 1441–1449 (1997).
[18]R. L. Weaver, "Multiple-scattering theory for mean responses in a plate with sprung masses," J. Acoust. Soc. Am. **101**, 3466–3474 (1997).
[19]R. L. Weaver, "Mean-square responses in a plate with sprung masses, energy flow and diffusion," J. Acoust. Soc. Am. **103**, 414–427 (1998)
[20]R. L. Weaver, "Equipartition and mean-square response in large undamped structures," J. Acoust. Soc. Am. **110**, 894–903 (2001).
[21]G. Maidanik and K. J. Becker, "Noise control of a master harmonic oscillator coupled to a set of satellite harmonic oscillators," J. Acoust. Soc. Am. **104**, 2628–2637 (1998).
[22]G. Maidanik and K. J. Becker, "Characterization of multiple-sprung masses for wideband noise control," J. Acoust. Soc. Am. **106**, 3109–3118 (1999).
[23]G. Maidanik and K. J. Becker, "Criteria for designing multiple-sprung masses for wideband noise control," J. Acoust. Soc. Am. **106**, 3119–3127 (1999).
[24]G. Maidanik, "Induced damping by a nearly continuous distribution of nearly undamped oscillators: Linear analysis," J. Sound Vib. **240**, 717–731 (2001).

Experiments on vibration absorption using energy sinks

Adnan Akay[a] and Zhaoshun Xu
Mechanical Engineering Department, Carnegie Mellon University, Pittsburgh, Pennsylvania 15213

Antonio Carcaterra
Universita Degli Studi di Roma "La Sapienza," Dipartimento di Meccanica e Aeronautica, Via Eudossiana 18, 00184 Roma, Italy

I. Murat Koç
Mechanical Engineering Department, Carnegie Mellon University, Pittsburgh, Pennsylvania 15213

(Received 24 January 2005; revised 13 June 2005; accepted 2 August 2005)

This paper presents experiments that demonstrate the concept of energy sinks, which when attached to a vibrating structure can absorb most of its energy. Energy sinks consist of a set of undamped linear oscillators and, in principle, do not require presence of damping in the classical sense. The set of undamped oscillators that make up an energy sink collectively absorb the vibratory energy and retain it in their phase space. Earlier optimization studies by the authors have shown the feasibility of vibration absorption and energy retention by energy sinks if the set of oscillators have a particular frequency distribution. Experimental results presented in this paper support the concept of energy sinks. Different physical realizations of energy sinks demonstrate the significance of frequency distributions and the ability of energy sinks to reduce vibration amplitude of a primary structure to which they are attached.
 [DOI: 10.1121/1.2046767]

PACS number(s): 43.40.At, 43.40.Kd [RLW] Pages: 3043–3049

I. INTRODUCTION

Compared with the conventional methods of vibration reduction, the concept of energy sinks presents a unique and viable alternative for cases where the classical vibration absorption or damping techniques have limited applicability, particularly at low frequencies and under transient conditions. An energy sink, consisting of a set of oscillators, absorbs and retains energy when attached to a vibrating structure. An energy sink admits flow of energy from a transiently excited structure and retains it in the collective phase space of the oscillators.[1]

In principle, energy sinks do not require dissipation mechanisms to reduce vibration amplitudes of the structures to which they are attached. However, because of the inherent losses in physical systems, a certain amount of dissipation becomes unavoidable when constructing energy sinks. Presence of moderate losses in the oscillators enhances the performance of an energy sink, particularly in long times. Large dissipation in the oscillators, however, reduces the performance of energy sinks as effective vibration absorbers.[1]

While analogous in terms of their energy pathways, the concept of energy sinks differs from vibration absorption and damping observed in complex systems that employ "fuzzy" attachments or multiple tuned absorbers. Studies on energy absorption from a primary structure by attached oscillators (viz., Refs. 2–17) show that a trade-off exists between the number of oscillators and the need for presence of a loss mechanism in the oscillators. Attached oscillators absorb energy even for vanishing values of loss factor in each oscillator so long as the number of oscillators remains large, approaching infinity.[5] Energy sinks also differ from proposed multiple tuned mass dampers, which have similar energy absorption mechanisms but rely on the presence of damping and are designed for steady-state vibrations.[18,19] The concept of energy sinks described here relies on the use of a *set* of undamped, linear oscillators making it different than previous similar proposals, such as spatial containment or single nonlinear attachments, or those that consider influence of internal degrees of freedom on a structure (viz., Refs. 20–24).

As shown earlier by the authors,[1] there exists an optimum frequency distribution for the oscillators in an energy sink that enables it to rapidly absorb vibration energy from a transiently excited structure and retain most of it.

This paper presents physical demonstrations of energy exchange phenomenon between a simple structure and an attached set of oscillators. Measurement results demonstrate the viability of energy sinks and the significance of frequency distribution of the oscillators.

II. EXPERIMENTS

The primary goal of the experiments described in the following is to investigate the energy exchange process between a primary structure (in this case a rigid platform or a flexible beam) and a set of oscillators attached to it, and to demonstrate the performance of an energy sink. For an ideal demonstration of energy exchange with an energy sink, neither the primary structure nor the attached set should have any losses. However, the ubiquitous nature of inherent losses in any physical system precludes building a prototype struc-

[a]Electronic mail: akay@cmu.edu

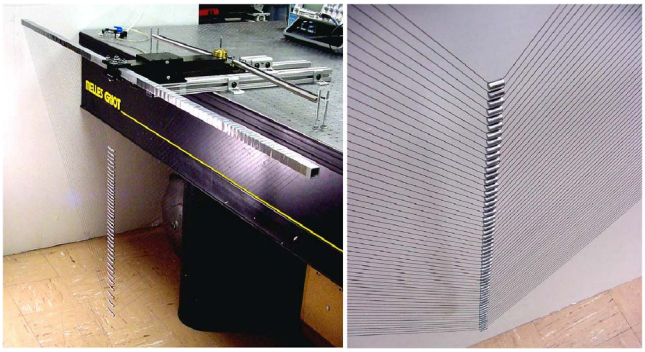

FIG. 1. (Color online) A primary mass that consists of a steel block in an air bearing and a set of pendulums that act as an energy sink.

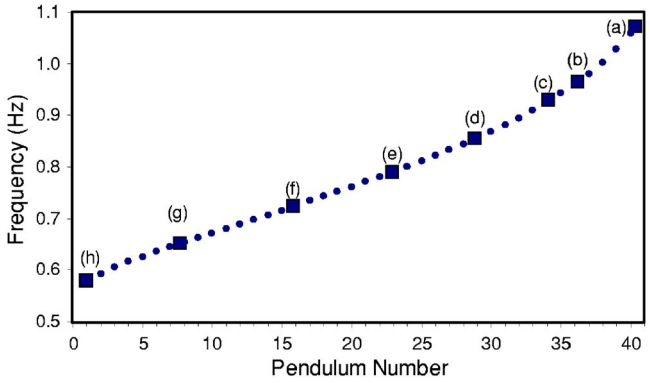

FIG. 2. Frequency distribution of the pendulums in Fig. 1. The closed squares indicate the uncoupled frequency ω_M of the primary mass corresponding to the measurements in Fig. 3.

ture and an energy sink that can oscillate indefinitely. Thus, an important criterion in the design of experiments addresses minimization of dissipation.

The number of oscillators used in an energy sink also becomes important in circumventing the effect of losses when investigating energy exchange. The larger the number of oscillators in an energy sink, the more energy it absorbs from the primary and the longer is the return time after which energy may return to the primary structure.[2] Presence of damping reduces vibration amplitudes in long times, obscuring investigation of whether or not energy returns from the sink to the primary. Use of lower numbers of oscillators reduces the return time, thus allowing better observation of energy exchange. Also, using the same set of oscillators, but with different frequency distributions, helps to bring out the role of frequency distribution and to delineate the role of inherent losses. The measurements, made using three different experimental configurations reported in the following, validate the concept of energy sinks and also demonstrate how the energy absorption process depends on the frequency distribution of the oscillators. In each of the configurations described in the following, the mass ratio between the set of oscillators and the primary structure always remains below 10%.

A. A set of pendulums attached to an oscillator

A steel block that can freely slide in an air bearing, and attached to a pair of springs at one end, acts as the primary structure. It carries at its free-end a set of 40–60 pendulums suspended concentrically from a quasirigid beam as shown in Fig. 1. Motion of the primary oscillator is in horizontal plane and parallel to the small-amplitude motion of the pendulums. The natural frequencies of the pendulums are selected by varying their lengths. The uncoupled natural frequency, ω_M, of the primary structure can be adjusted by selecting the stiffness of the springs that anchor it to the optical table on which the air bearing is mounted. Measurements represent a range of natural frequencies ω_M that span the band of pendulum frequencies as illustrated in Fig. 2, which also shows the distribution of the uncoupled frequencies of the 40-pendulum set.

Measurements were conducted by imposing an initial displacement to the primary structure and recording the subsequent acceleration, velocity, or displacement response of the primary structure. Response measurements were made using accelerometers and a laser-doppler velocimeter.

Representative velocity-time histories of the primary oscillator in response to an initial displacement of 30 mm are shown in Fig. 3. Each response corresponds to a different natural frequency of the primary oscillator, obtained by changing the springs that anchor it but otherwise leaving the system, including the attached set, unchanged. Each figure compares the free-vibration of the primary block with and without the attached set of oscillators, while maintaining the same total mass. The differences in the decay rates among the uncoupled free-vibration responses of the primary arise from the different loss factors introduced by the springs used for each case.

The measurements presented in Fig. 3 show unambiguously a reduction of the primary structure response due to the attached oscillators and the significance of the natural frequency of the primary structure relative to those of the pendulum set. As shown in Figs. 3(b)–3(g), when its frequency falls within the range of frequencies of the set, response of the primary structure decays rapidly. In some cases, energy exchange continues with some energy returning to the primary. However, Figs. 3(a) and 3(h) show that when the frequency of primary falls near the limits of the same frequency range, its response has similar characteristics as its free uncoupled vibrations, although in this case its amplitude decays at a faster rate due to additional dissipation through the pendulums. In such cases the pendulums do not act as an energy sink. These results are consistent with the analytical model proposed by Carcaterra and Akay.[2]

The collective dynamic behavior of the pendulums is just as instructive. During the first few cycles, when periodic energy exchange is under way between the primary oscillator and the attached set, the pendulums exhibit a coherent motion maintaining a wave-like configuration. During the latter part, when the primary oscillator yields its energy, pendulums appear to have a random phase distribution due to the differences in their natural frequencies, as illustrated in Fig. 4.

B. Flexible beams as oscillators

In the configuration shown in Fig. 5, the energy sink consists of a set of cantilever beams, each constructed of

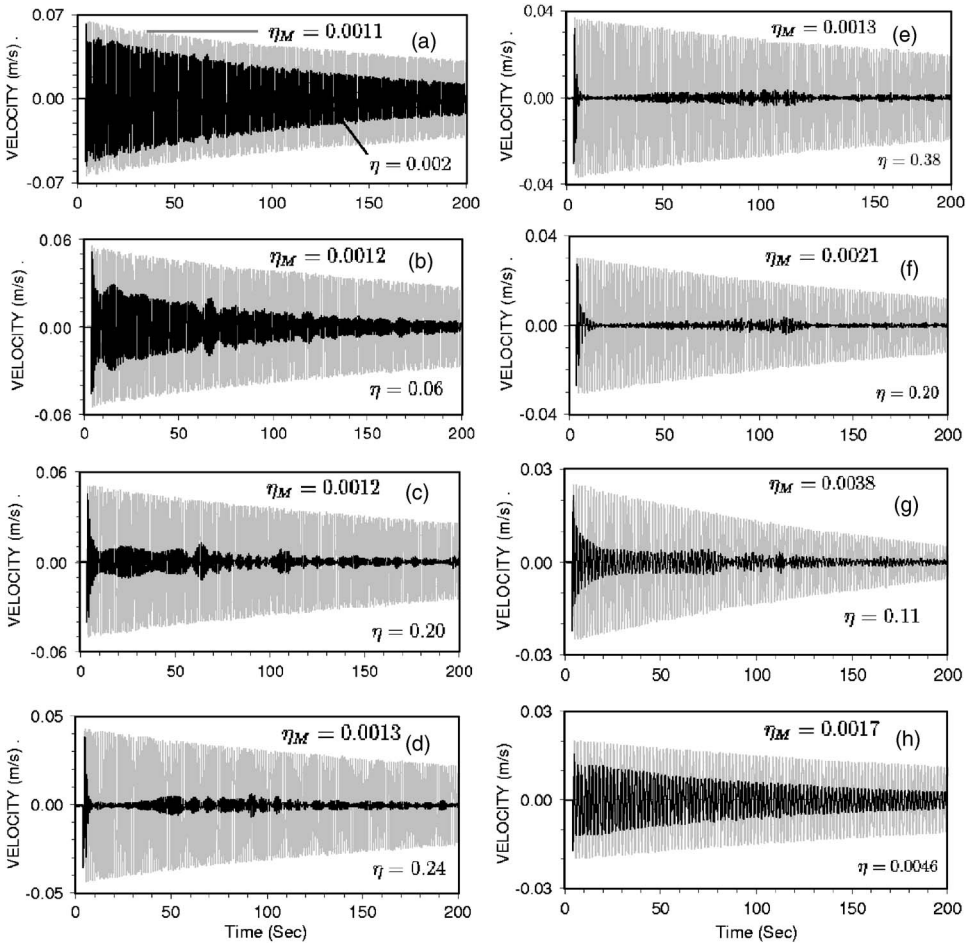

FIG. 3. Response of the primary mass in Fig. 1 with (dark) and without (gray) the attached pendulums. Each figure corresponds to a different uncoupled natural frequency ω_M of the primary structure obtained by using springs that have different stiffness. The differences in the decay of free vibration amplitude result from the different loss factors associated with each spring pair. In each figure η_M represents the loss factor of the primary alone, and η represents the loss factor of the primary with the attached oscillators. In each case the mass ratio is 9% and the frequency distribution of the pendulums is unchanged, ranging between 0.58 and 1.06 Hz. (a) f_M =1.07 Hz, (b) f_M=0.97 Hz, (c) f_M =0.93 Hz, (d) f_M=0.86 Hz, (e) f_M =0.79 Hz, (f) f_M=0.72 Hz, (g) f_M =0.65 Hz, (h) f_M=0.58 Hz.

steel wire and carrying a small mass, mounted on a structure attached to the same air bearing described earlier. Such a configuration permits easy modification of frequency distribution of the oscillators by sliding the small masses along the thin beams to obtain the desired frequency. Uncoupled natural frequency of each oscillator is calibrated using an optical sensor to measure its period.

Figure 6 shows the uncoupled free-oscillation response of the block and one of the oscillators. The decay of amplitude in each response represents the baseline value of the inherent damping of the primary structure and the individual oscillators.

Figure 7 shows different cases for the response of the block where all oscillators in the energy sink have the same frequency, but with three different values with respect to that of the primary structure, the block. When the frequency of the oscillators is close to that of the block, as expected, beats develop. The observed decay of amplitude in the time domain results from the inherent damping in the system much as the decay of free vibrations of the primary in Fig. 6.

Figure 8 shows the response of the block when the oscillators have a linear frequency distribution (with a constant frequency difference $\Delta\omega$). Consistent with the results of earlier simulations,[2] vibration energy returns to the block after a return time determined by $t^*=2\pi/\Delta\omega$, in this case 8 s. The returned energy for the case of constant $\Delta\omega$ appears less pronounced than expected, primarily due to the inherent damping present in the physical system and the inexactness of the frequencies of the attached pendulums, and thus $\Delta\omega$ between them, which spreads the return times and brings its performance closer to that by the optimum distribution. Figure 8 also shows the case when the oscillators have frequencies that follow an optimum distribution.[1] In this case the returned energy is spread over time with a consequent reduction of its amplitude. Use of larger number of oscillators produces similar but more effective energy absorption, with a larger reduction in the amplitude of the primary.

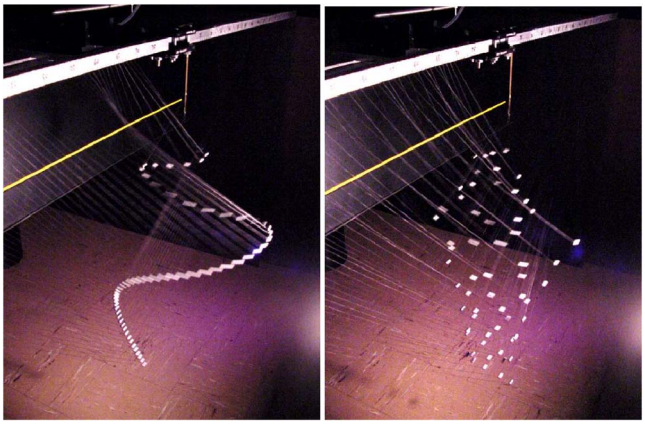

FIG. 4. (Color online) Snapshots of pendulums following an initial displacement provided to the primary mass. During the initial periodic energy exchange between the primary, pendulums maintain a coherent wave-like configuration (left) and after a time when energy is retained mostly by the pendulums.

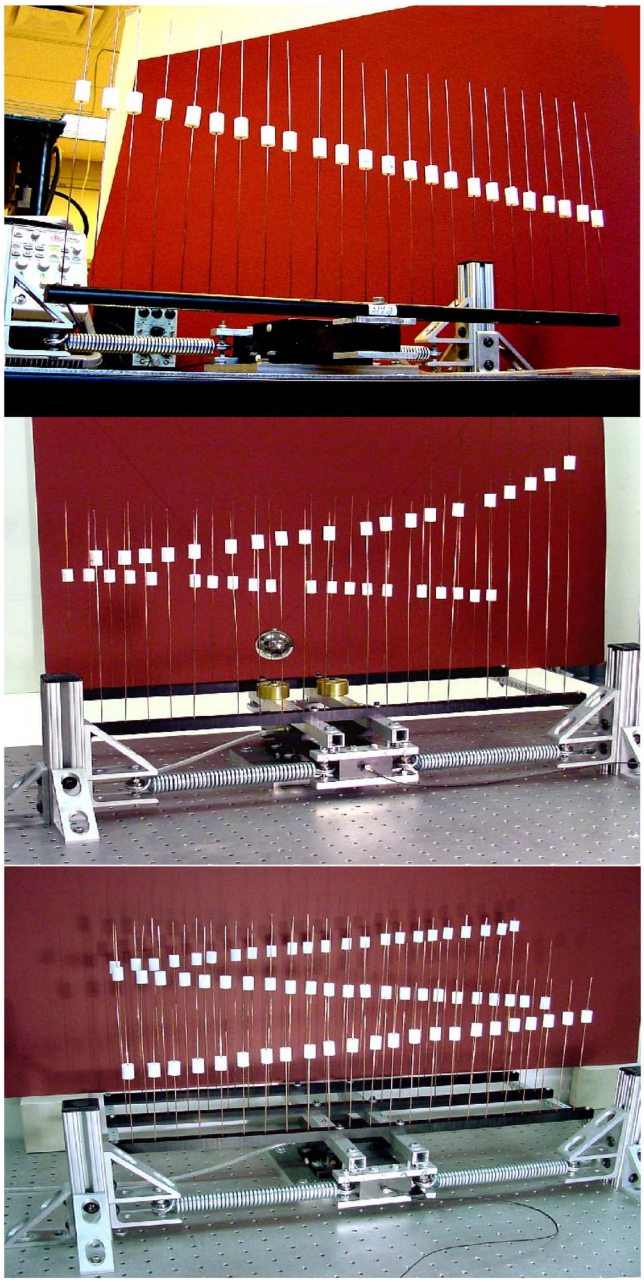

FIG. 5. (Color online) Oscillators attached to the same primary structure shown in Fig. 1 through a light-weight superstructure built on it. Each oscillator consists of a small mass attached to a steel wire that permits adjustment of its natural frequency by changing the position of the mass on the wire. The figures show sets of 24, 40, and 69 oscillators.

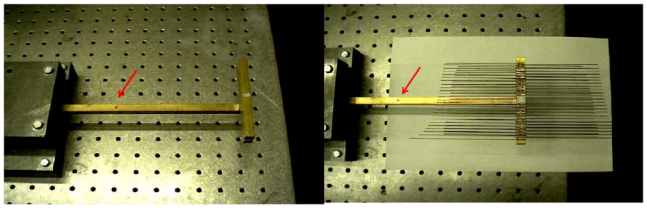

FIG. 9. (Color online) A primary structure that consists of two beams connected in a T-configuration. Attached thin beams act as a set of oscillators vibrating at their fundamental frequencies, which follow an optimum distribution. Impulse excitation is applied at the point indicated by the arrow.

C. A flexible beam as a primary structure

The application described in this section involves reduction of vibration response of a continuous system with an energy sink. The primary structure in this case consists of two beams joined in a T-configuration as shown in Fig. 9. The energy sink consists of an assembly of 100 thin beams attached to the structure as shown in the figure. Each beam, constructed of a thin steel wire, acts as an oscillator vibrating primarily in its first mode. Second modes do not become excited and, thus, have negligible effect on the response of the structure. The lengths of the attached beams are selected to produce an optimum distribution[1] as shown in Fig. 10.

The inherent damping of the primary structure is evident in the impulse response of the structure without the attached oscillators as shown in Fig. 11(a). Figures 11(b)–11(d) represent the impulse response of the same structure with the attached oscillators. In each case, the primary structure has a different uncoupled fundamental frequency but with the same energy sink attached in the same position. The fundamental frequency of the primary structure is modified by adjusting the length of the flexible beam. When the primary structure frequency falls in the middle of the bandwidth of the energy sink, most of its energy is absorbed by the set of beam-oscillators that make up the energy sink. As the primary frequency approaches to the limits of the frequency band of the sink, energy absorption decreases correspondingly, similar to the pendulum responses in Fig. 3 and as shown by the previous analytical results.[1,2]

The change in the frequency response of the primary structure with and without the attached beams, given in Fig. 12, illustrates how the energy associated with the fundamental frequency of the primary structure spreads over the frequency band of the energy sink.

In all of the cases shown above, the attached set of oscillators absorbs the vibratory energy from the primary structure and distributes it throughout the set. The response of the

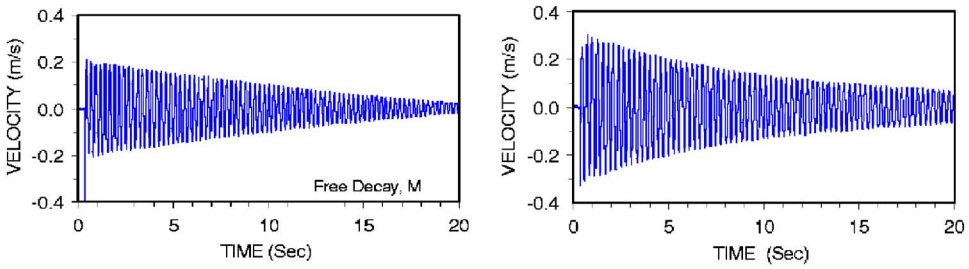

FIG. 6. Impulse response of the block (left) without the attached oscillators and that of an individual oscillator shown in Fig. 5.

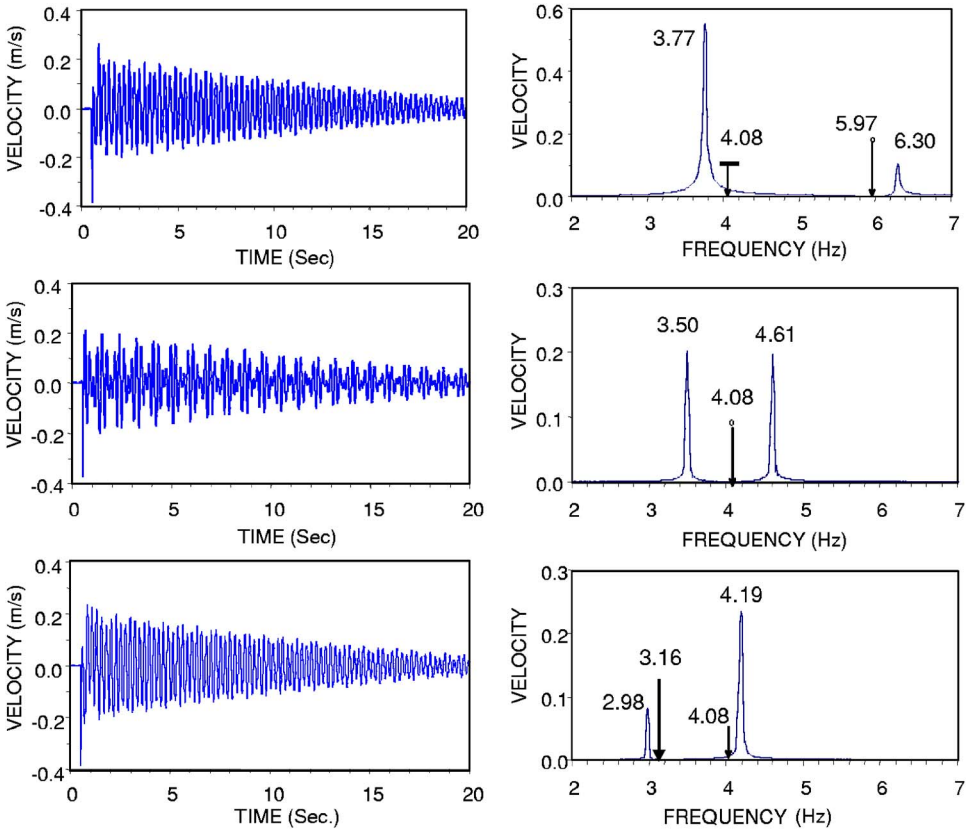

FIG. 7. (Color online) Response of the primary structure (block) with a set of 40 oscillators all with the same natural frequency, effectively reducing the system freedom to two degrees. In each case the uncoupled natural frequency of the block is f_M=4.08 Hz. From top the oscillators have a constant frequency of f_m=5.97, 4.08, and 3.16 Hz as indicated by the arrows. The response in time domain shows the expected beats.

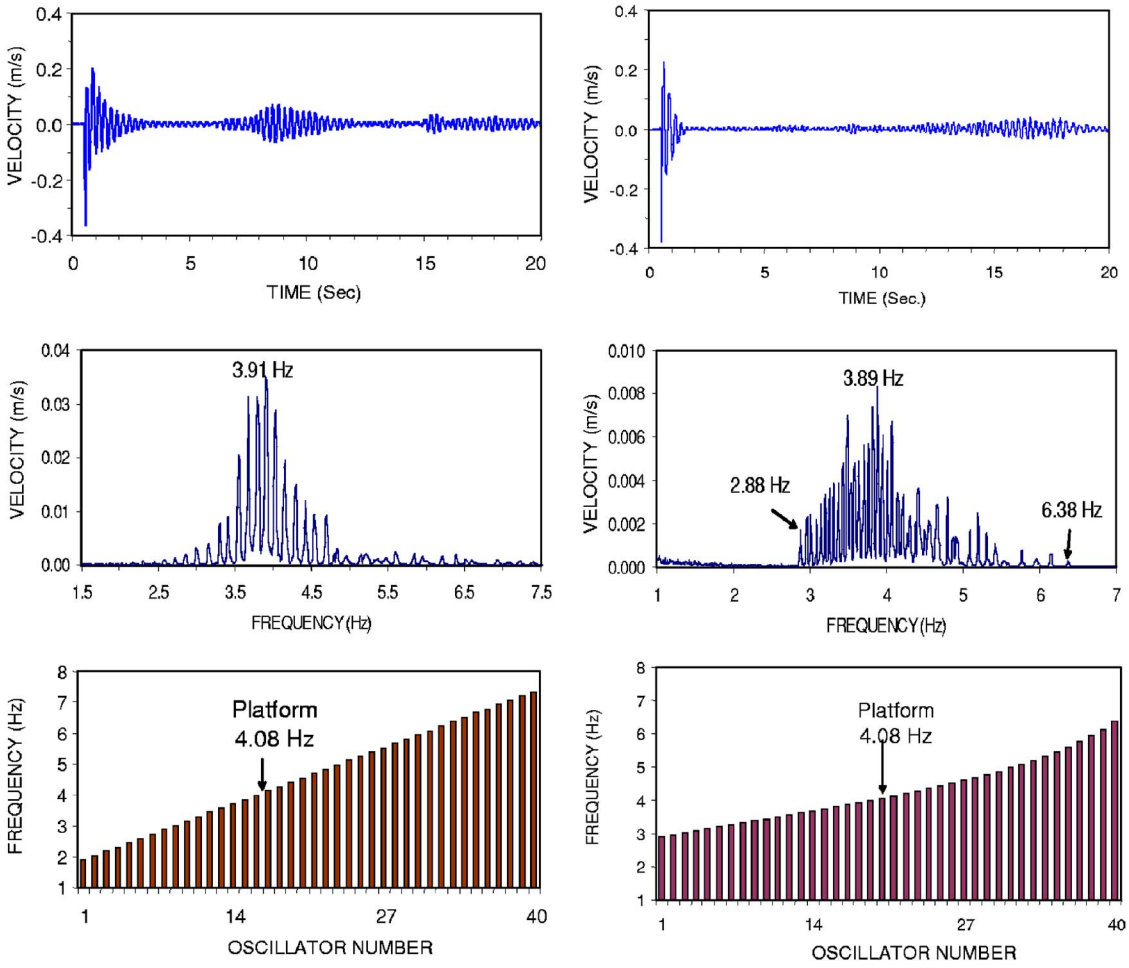

FIG. 8. (Color online) Response of the same system shown in Fig. 6 but with linear and optimum frequency distributions. In both cases the vibration amplitude of the block is reduced significantly. The optimum distribution (right) further reduces the response and spreads the energy over a larger set of frequencies.

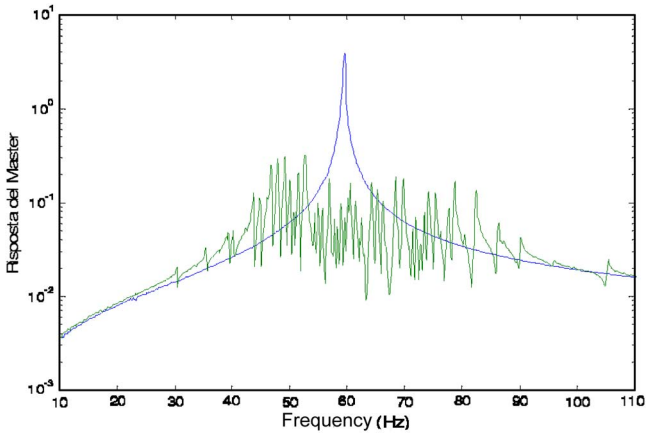

FIG. 12. (Color online) A comparison of the response of the primary structure shown in Fig. 9 with and without the attached oscillators. The presence of thin beam oscillators spreads the energy over their frequency band, reducing the amplitude of the primary significantly.

primary structure shows both a reduction in amplitude and a distribution of energy over a band of frequencies corresponding to the oscillators within the energy sink.

III. CONCLUDING REMARKS

Experiments described in this paper demonstrate the viability of energy sinks corroborating previous analytical results[1] that show how a set of undamped linear oscillators can absorb energy from a structure to which it is attached.

The three different configurations described earlier had small enough inherent losses that allowed observation of energy exchange, albeit for finite time durations. Use of small

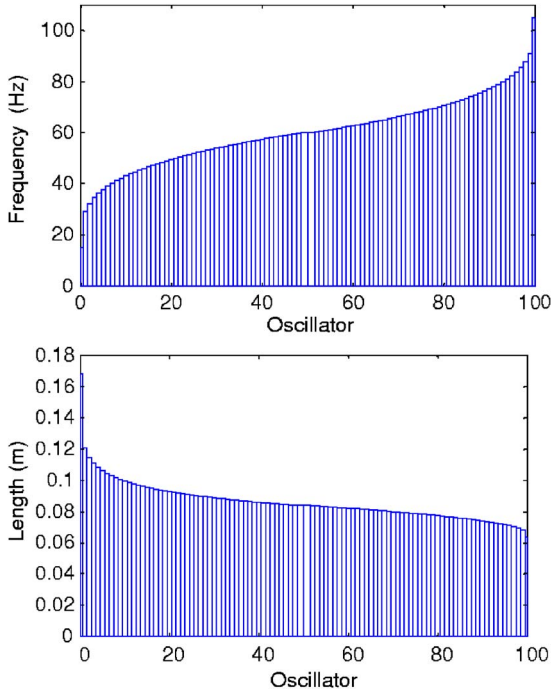

FIG. 10. (Color online) The lengths of the thin beams (bottom) in Fig. 9 produce fundamental frequencies (top) that follow the optimum distribution that leads to maximum absorption of energy (Ref. 1).

numbers of oscillators and changing the relative frequency of the primary with respect to the frequency band of the set also helped to demonstrate the role of frequency distribution on energy exchange.

In addition to obscuring long-time observations in experiments, damping in the attached oscillators can also re-

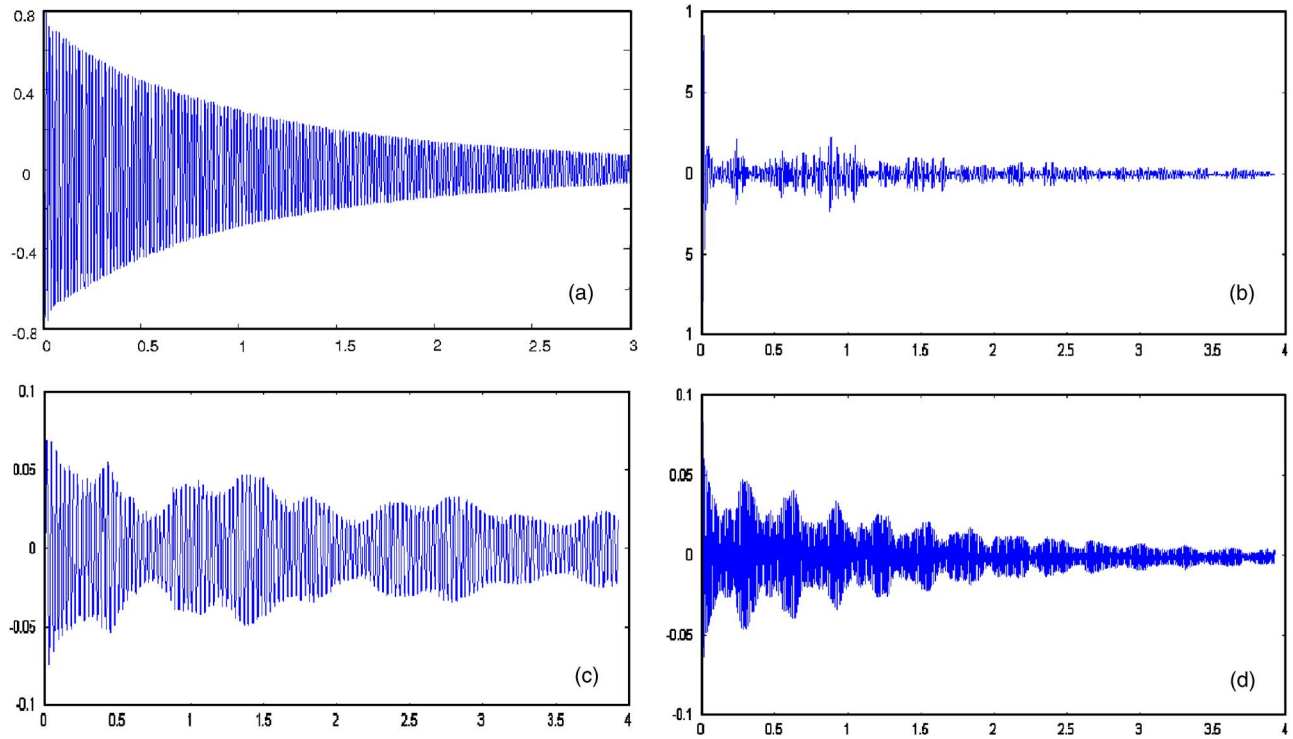

FIG. 11. (Color online) A comparison of the response of the primary structure shown in Fig. 9 without (a) and with (b)–(d) the attached oscillators. In (c) and (d), the fundamental frequency of the primary structure coincides with the lowest (30 Hz) and the highest (90 Hz) value in the frequency band of the oscillators, respectively. In both (a) and (b), the primary natural frequency is 60 Hz. The comparison clearly shows the effects of the attached thin beams.

duce the effectiveness of the energy sink if it is high enough to strongly couple the oscillators to the primary structure. As long as these dissipation rates remain moderate, they do not adversely affect the performance of energy sinks, but reduce the vibration amplitude of the oscillators and that of the primary structure.

As expected, the oscillators with natural frequencies in the neighborhood of that of the primary structure exhibit a higher level of energy absorption than those with frequencies away from it. Such high-amplitude oscillations can introduce nonlinear behavior of the oscillators, which can have additional consequences on the energy exchange process. However, measurements with very low initial energy input produced results similar to those reported here suggesting negligible effects due to the observed high-amplitude pendulum oscillations.

The key to energy absorption observed here relates to the frequency distribution of the oscillators in an energy sink. In the transient cases considered here, the underlying physics of energy absorption can be explained better in terms of energy trapping. The energy from an impulsively excited primary structure flows to the oscillators of the attached energy sink. Once the attached oscillators begin to oscillate, the net force they exert back on the primary structure, and thus the net energy transferred back to the primary structure, becomes inhibited as a result of their frequency distribution.[2]

The prototype system described here has analogies to simple, tuned vibration absorbers. In both cases the attached oscillators remove the vibratory energy from the primary structure. However, unlike the tuned absorbers, the proposed energy sinks also work under transient conditions and without the need for fine-tuning to a particular frequency. Energy sinks can function either as a substructure attached to or as an integral part of a vibrating structure from which they can absorb and retain vibrational energy.

Because energy sinks do not require conventional dissipation strategies, they can be particularly useful in high temperature or chemically hazardous environments where classical damping or vibration absorption techniques may not be effective. Energy sinks present two advantages over the conventional absorption and dissipation sources: they are particularly effective at low frequencies and under transient conditions that are commonly found in large structures such as naval vessels and those deployed in space and buildings.

[1]I. M. Koç, A. Carcaterra, Z. Xu, and A. Akay, "Energy sinks: Vibration absorption by an optimal set of undamped oscillators," J. Acoust. Soc. Am. **118**, 3031–3042 (2005).

[2]A. Carcaterra and A. Akay, "Transient energy exchange between a primary structure and a set of oscillators: Return time and apparent damping," J. Acoust. Soc. Am. **115**, 683–696 (2004).

[3]K. Xu and T. Igusa, "Dynamic characteristics of multiple substructures with closely spaced frequencies," Earthquake Eng. Struct. Dyn. **21**, 1059–1070 (1992).

[4]C. Soize, "A model and numerical method in the medium frequency range for vibroacoustic predictions using the theory of structural fuzzy," J. Acoust. Soc. Am. **94**, 849–865 (1993).

[5]A. D. Pierce, V. W. Sparrow, and D. A. Russell, "Fundamental structural-acoustic idealizations for structures with fuzzy internals," J. Vibr. Acoust. **117**, 339–348 (1995).

[6]M. Strasberg and D. Feit, "Vibration damping of large structures induced by attached small resonant structures," J. Acoust. Soc. Am. **99**, 335–344 (1996).

[7]M. Strasberg, "Continuous structures as 'fuzzy' substructures," J. Acoust. Soc. Am. **100**, 3456–3459 (1996).

[8]R. J. Nagem, I. Veljkovic, and G. Sandri, "Vibration damping by a continuous distribution of undamped oscillators," J. Sound Vib. **207**, 429–434 (1997).

[9]R. L. Weaver, "The effect of an undamped finite degree of freedom 'fuzzy' substructure: Numerical solutions and theoretical discussion," J. Acoust. Soc. Am. **100**, 3159–3164 (1996).

[10]R. L. Weaver, "Mean and mean-square response of a prototypical master/fuzzy structure," J. Acoust. Soc. Am. **101**, 1441–1449 (1997).

[11]R. L. Weaver, "Multiple-scattering theory for mean responses in a plate with sprung masses," J. Acoust. Soc. Am. **101**, 3466–3474 (1997).

[12]R. L. Weaver, "Mean-square responses in a plate with sprung masses, energy flow and diffusion," J. Acoust. Soc. Am. **103**, 414–427 (1998).

[13]R. L. Weaver, "Equipartition and mean-square response in large undamped structures," J. Acoust. Soc. Am. **110**, 894–903 (2001).

[14]G. Maidanik and K. J. Becker, "Noise control of a master harmonic oscillator coupled to a set of satellite harmonic oscillators," J. Acoust. Soc. Am. **104**, 2628–2637 (1998).

[15]G. Maidanik and K. J. Becker, "Characterization of multiple-sprung masses for wideband noise control," J. Acoust. Soc. Am. **106**, 3109–3118 (1999).

[16]G. Maidanik and K. J. Becker, "Criteria for designing multiple-sprung masses for wideband noise control," J. Acoust. Soc. Am. **106**, 3119–3127 (1999).

[17]G. Maidanik, "Induced damping by a *nearly* continuous distribution of *nearly* undamped oscillators: Linear analysis," J. Sound Vib. **240**, 717–731 (2001).

[18]L. Zuo and S. A. Nayfeh, "Optimization of the individual stiffness and damping parameters in multiple-tuned-mass-damper systems," ASME J. Vibr. Acoust. **127**, 77–83 (2005).

[19]L. Zuo and S. A. Nayfeh, "Minimax optimization of multiple-degree-of-freedom tuned-mass dampers," J. Sound Vib. **272**, 893–908 (2004).

[20]A. F. Vakakis, "Inducing passive nonlinear energy sinks in vibrating systems," J. Vibr. Acoust. **123**, 324–332 (2001).

[21]O. Gendelman, L. I. Manevitch, A. F. Vakakis, and R. M'Closkey, "Energy pumping in nonlinear mechanical oscillators. I. Dynamics of the underlying Hamiltonian Systems," J. Appl. Mech. **68**, 34–41 (2001).

[22]A. F. Vakakis and O. Gendelman, "Energy pumping in nonlinear mechanical oscillators. II. Resonance capture," J. Appl. Mech. **68**, 42–48 (2001).

[23]J. Aubrecht, A. F. Vakakis, T.-C. Tsao, and J. Bentsman, "Experimental study of nonlinear transient motion confinement in a system of coupled beams," J. Sound Vib. **195**, 629–648 (1996).

[24]A. F. Vakakis, "Passive spatial confinement of impulsive responses in coupled nonlinear beams," AIAA J. **32**, 1902–1909 (1994).

An experimental investigation of two active segmented partition arrays

Timothy W. Leishman[a)]
Acoustics Research Group, Department of Physics and Astronomy, Brigham Young University, Eyring Science Center, Provo, Utah 84602

Jiri Tichy
Graduate Program in Acoustics, The Pennsylvania State University, Applied Science Building, University Park, Pennsylvania 16802

(Received 20 December 2004; revised 27 July 2005; accepted 3 August 2005)

This paper addresses the construction, measurement, and analysis of two active segmented partition arrays (ASP arrays) for use in active sound transmission control. The control objective for each array was to actively minimize principal transmitting surface vibrations to induce high transmission loss. The arrays incorporated four adjacent lightweight modules with composite single or double leaves and small loudspeakers as actuators. A normal-incidence transmission loss measurement system was developed to evaluate their performances under passive and active conditions. Measurement results were compared to results for passive benchmark partitions and theoretical predictions. Four decentralized single-error-input, single-output filtered-x controllers were used with the arrays. They were shown to perform at least as well as a centralized multiple-error-input, multiple-output controller, with good error signal reductions and stability. Scanning laser vibrometer measurements confirmed the ability of the double-composite-leaf ASP to efficiently and globally minimize its transmitting surface vibrations to produce high transmission loss. Its average transmission loss over the active measurement bandwidth (30–290 Hz) was 56 dB—a full 34 dB greater than that of the single-composite-leaf ASP. The work confirms that a properly configured lightweight ASP can produce very high transmission loss through vibration control techniques. [DOI: 10.1121/1.2047348]

PACS number(s): 43.40.Vn, 43.50.Ki, 43.55.Rg [KAC] Pages: 3050–3063

I. INTRODUCTION

An active segmented partition (ASP) is a contiguous array of interconnected modules or elements that are specifically configured and controlled to reduce sound transmission between a source space and a receiving space. Several authors have investigated ASPs in recent years for distinct purposes.[1–9] The authors of this paper have explored them with the general aim of controlling sound transmission through lightweight structures via efficient, global control of transmitting surface vibrations.[10–17] One recent investigation[16] explored background and basic concepts of ASP design and use, focusing on modeling, theoretical analysis, and numerical transmission loss predictions for four individual module configurations. Two modules involved single-composite-leaf (SCL) configurations and two involved double-composite-leaf (DCL) configurations. Each was considered a candidate to fulfill one or more design and performance criteria established earlier.[10] Analytical and numerical results predicted that the two DCL arrangements would provide much greater transmission loss than the two SCL arrangements. However, only one of the DCL configurations (configuration 4 of Ref. 16) incorporated specialized segmentation and isolation to reduce coupling between adjacent partition modules. These characteristics were expected to enhance the effectiveness of the configurations in extended arrays using simple decentralized controllers.

A recent experimental study[17] validated the modeling and theoretical predictions for two individual modules from Ref. 16: configuration 2 (a SCL arrangement) and configuration 3 (a DCL arrangement). Experimental testing of configuration 1 (a SCL arrangement) and configuration 4 (a DCL arrangement), and evaluations of *arrays* of modules then became primary focuses of the present work. Because arrays of modules more closely represent practical ASPs, their distinguishing characteristics must be carefully considered.

Two experimental ASP arrays were designed and constructed for this investigation. Both consisted of four adjacent lightweight modules in square patterns. A normal-incidence transmission loss measurement system was also built for their evaluation. The properties of the arrays were determined under passive and active conditions and compared to theoretical predictions and properties of passive benchmark partitions. Scanning laser vibrometer measurements demonstrated the ability of the DCL arrangement to efficiently and globally minimize its transmitting surface vibrations.

The investigation also compared the normal-incidence transmission loss performance of the DCL ASP with that of the SCL ASP. It explored behaviors of decentralized (decoupled) and centralized (coupled) adaptive controllers in con-

a)Electronic mail: tim_leishman@byu.edu

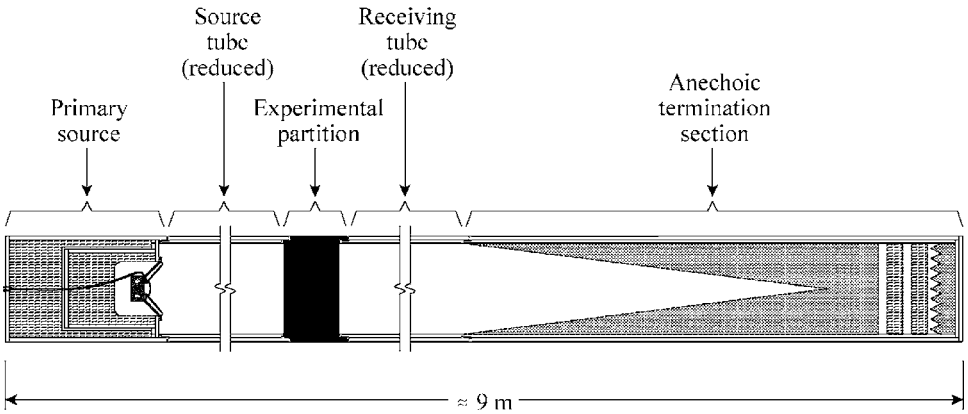

FIG. 1. A system for measuring normal-incidence transmission losses of test partitions (shown with an arbitrary partition positioned between the source tube and receiving tube).

junction with the arrays.[18] While the experimental arrays primarily used multiple single-error-input, single-output (multiple SISO or MSISO) filtered-x controllers, the DCL ASP also used a centralized multiple-error-input, multiple-output (MIMO) filtered-x controller for comparison.

The following sections discuss the apparatuses, techniques, and challenges associated with the evaluations. They also present key experimental results, draw pertinent conclusions, and provide recommendations for further research.

II. EXPERIMENTAL METHODS

The experimental methods used in this work were generally similar to those described in Ref. 17. However, many of the specific measurement apparatuses and capabilities were different. The transducers and electronics also varied in types and numbers. The following sections outline several details of the experimental approach.[19]

A. Normal-incidence measurement system

The normal-incidence measurement system is depicted in Fig. 1, with an arbitrary partition (ASP array or passive benchmark partition) positioned between the source and receiving tubes. The square tubes were basically identical in construction, with 47.6 cm $\times$ 47.6 cm interior cross-sectional dimensions and 244 cm nominal lengths. Their walls were constructed of two laminated layers of 1.9-cm-thick medium density fiberboard (MDF).

The primary source shown to the left of the source tube was an NHT 1259 loudspeaker (25.4 cm effective radiating diameter) that was front mounted on a double-walled sealed enclosure. All sections of the measurement system were constructed with undersized male and oversized female ends for convenient interconnection and isolation. Thick resilient double gaskets and adjustable clamps produced required airtight seals. The overall length of the entire plane-wave tube system was approximately 9 m, although its exact length depended upon the particular partition under evaluation.

To limit the fields incident upon partitions to normally propagating plane waves, the source tube was consistently driven below the cutoff frequency of its first cross mode (approximately 360 Hz). At sufficient axial distances from the primary source and partition, the total upstream and downstream fields were accordingly dominated by plane waves. However, because residual effects of the first cross mode[20] or corruption due to vibrating tube walls became conspicuous in the measured field above 290 Hz, this latter frequency was considered the maximum plane-wave frequency of interest.

Most experimental partitions measured in the system produced boundary conditions that yielded significant axial source tube resonances. To address resulting measurement problems, the source loudspeaker was driven more vigorously at some frequencies (i.e., near tube antiresonance frequencies) than at others (i.e., near tube resonance frequencies). Because of its inconsistent vibration amplitude, structure-borne or air-borne flanking transmission often became more conspicuous near the source tube *antiresonance* frequencies. The tube walls were significant paths in flanking transmission at these and other frequencies.

As shown in Fig. 1, the receiving tube was bounded by a large anechoic termination. It was an inverted pyramidal structure cut from blocks of 25.6 kg/m^3 open-cell polyurethane foam rubber. When assembled, it tapered from a 47.6 cm $\times$ 47.6 cm opening to a central point over a 180.3 cm span. The base behind the point was a 25.4-cm-thick continuous extension of the wedge pieces, backed by a 38.1-cm-thick air cavity filled with layers of fiberglass insulation and open-cell polyurethane foam rubber. The cavity was capped with a rigid plug consisting of two laminated layers of 1.9-cm-thick MDF. The overall absorptive length of the termination was approximately 244 cm. Its measured cutoff frequency was about 45 Hz, but its absorption coefficient exceeded 0.7 down to nearly 10 Hz.[21]

B. ASP arrays

As indicated earlier, the first experimental ASP array consisted of a cluster of four adjacent SCL modules in a square pattern. The second consisted of a similar pattern of DCL modules. Both used Aura AS4-75-8 FR moving-coil loudspeakers as actuators. The drivers were designed with radially oriented neodymium magnet structures that permitted compact size, relatively low total mass (214 g), and reasonable low-frequency output. Their diaphragm dust domes were coated with several layers of epoxy to provide sufficiently rigid surfaces for accelerometer mounting. The following sections consider the design and construction of the two arrays in greater detail.

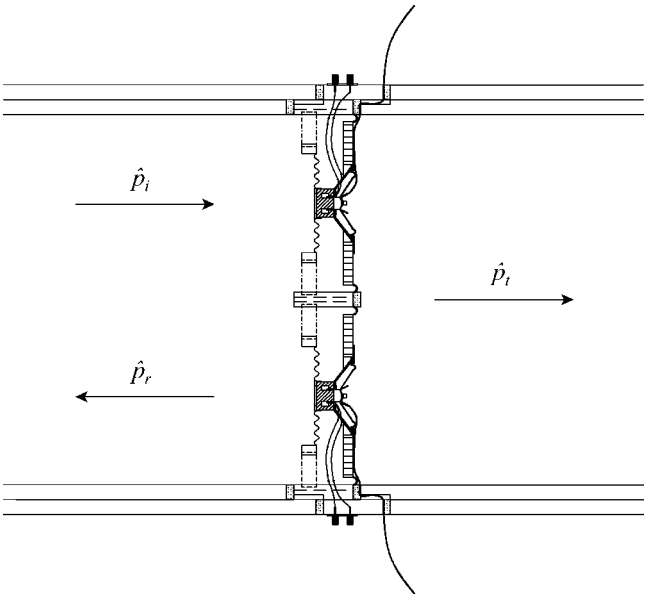

FIG. 2. A cutaway side view of the SCL ASP array. The view exposes two of the four adjacent modules with accelerometers mounted to the actuator dust domes. The array is connected to the source and receiving tubes via resilient airtight gaskets.

1. Single-composite-leaf (SCL) array

Figure 2 illustrates the SCL array in a cutaway side view that exposes two of the four modules. It also shows the interconnection of the array to the source and receiving tubes. Photographs of the array, taken from both the source side and transmitting side, are shown in Fig. 3. The actuators were mounted and sealed within centered 9.3-cm-diam openings of square resiliently suspended support panels. The panels were lightweight aluminum honeycomb sandwich constructions with dimensions of $20.9\ \text{cm} \times 20.9\ \text{cm} \times 1.6\ \text{cm}$ $(H \times W \times D)$ and average net masses of 87 g. They were stiffness controlled over the bandwidth of interest, exhibiting an average fundamental bending mode resonance frequency of about 940 Hz with no surround or actuator attached (i.e., with free boundary conditions). When these elements were attached, the frequency dropped slightly to approximately 865 Hz.

The panels were centered and resiliently attached within $22.9\ \text{cm} \times 22.9\ \text{cm}$ openings of an MDF frame using square half-roll compressed foam-rubber surrounds. They effectively behaved as large finite impedance interstices.[16] The 1.9-cm-thick MDF frame elements might also be termed interstices, but their large stiffnesses and small cross-sectional areas were expected to have very little effect on sound transmission.

The rear portions of the actuator magnet structures were firmly attached to perforated circular disks that were suspended from perforated support structures with porous secondary suspensions (spiders). These suspensions and the accompanying supports were intended to be acoustically unobtrusive over the frequency range of interest. The primary function of the spiders was to operate in conjunction with the support panel surrounds to produce spaced dual suspensions that helped constrain translational rigid-body motion of the support panels.

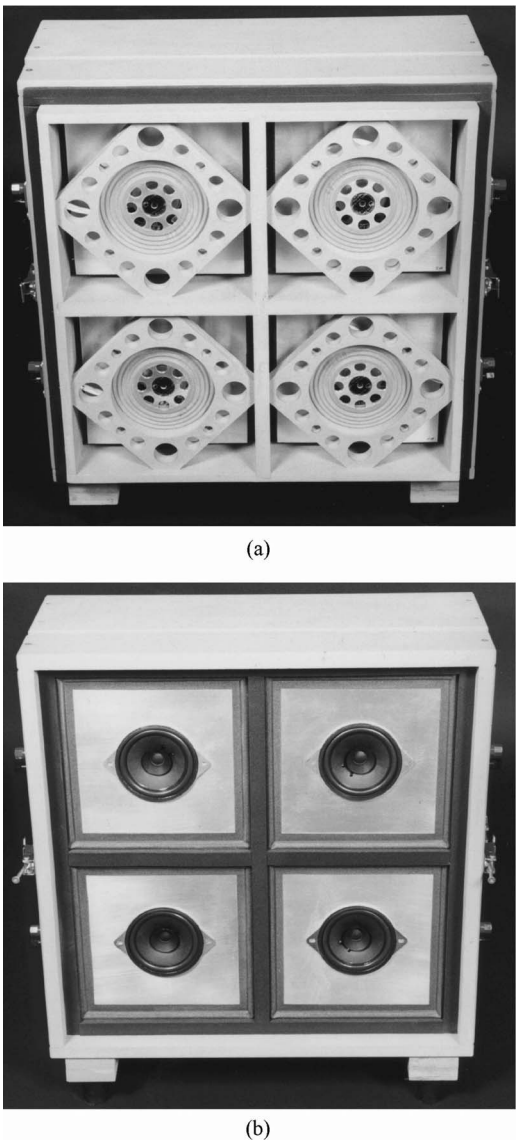

FIG. 3. Photographs of the experimental SCL array. (a) Source side. (b) Transmitting side.

As a rule-of-thumb, half of the flexing surface areas and masses of the suspensions were added to the surface areas and masses of the support panels for numerical predictions of array behaviors. The other halves were added to the presumably rigid MDF interstices. The net masses of the actuators (their total masses minus the moving masses of their diaphragm assemblies), the masses of the perforated secondary suspension mounting disks, and the masses of various adhesives were also added to the masses of the support panels to yield an average moving mass of approximately 340 g. This mass and the actuator diaphragm mass could vary slightly, depending upon accelerometer mounting and other conditions.

The array was intended to be tested in both its passive and active modes. The passive mode involved open-circuited actuator terminals, whereas the active mode involved the minimization of all normal actuator diaphragm accelerations.

2. Double-composite-leaf (DCL) array

Figure 4 shows a cutaway side view of the DCL array. Once again, each module of the array included a circular

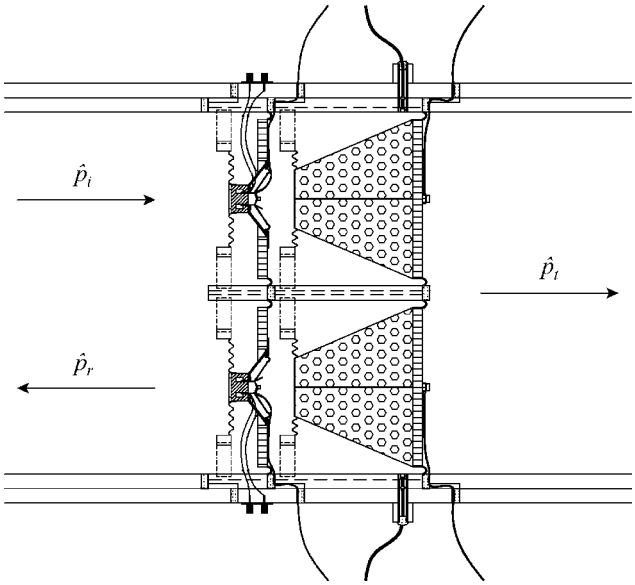

FIG. 4. A cutaway side view of the DCL ASP array. The view exposes two of the four adjacent modules with accelerometers mounted to the actuator dust domes and passive transmitting diaphragms. Cavity microphones are positioned behind the transmitting diaphragm surrounds. The actuator and transmitting diaphragm assemblies are joined by a resilient airtight connection.

moving-coil actuator surrounded by a square resiliently suspended support panel. In fact, the SCL array was an integral part of the DCL array. The photograph in Fig. 5 shows the actuator section being joined to the transmitting diaphragm section. In this arrangement, the actuators drove isolated rectangular cavities with passive transmitting diaphragms on the opposite sides.

The transmitting diaphragms were lightweight aluminum honeycomb sandwich panels similar in fabrication to the actuator support panels. They were centered and resiliently attached within 22.9 cm $\times$ 22.9 cm openings using similar half-roll compressed foam rubber surrounds. Perforated 0.8-mm-thick aluminum fins were attached in a crossing pattern to the back faces of the panels. They extended perpendicularly from the panels to thin perforated circular aluminum plates, which in turn were connected to spaced secondary suspensions (spiders). The fins were mounted to the panels along the crossing nodal lines of their first bending modes to help reduce mechanical excitation of those modes. The spiders were similar to those used in the SCL array and were again intended to help constrain translational piston-like motion of the transmitting diaphragms. Photographs of the transmitting diaphragm sections, taken from both the cavity and transmitting sides, are shown in Fig. 6.

FIG. 5. A photograph of the experimental DCL array, being formed by joining the SCL actuator array to the passive transmitting diaphragm array.

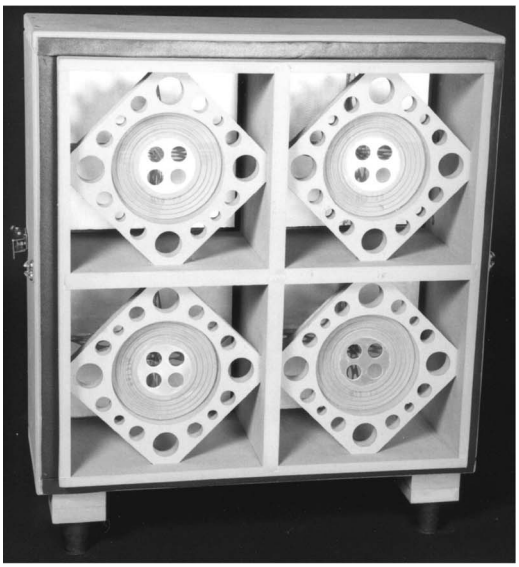

(a)

(b)

FIG. 6. Photographs of the transmitting diaphragm array portion of the experimental DCL array. (a) Cavity side. (b) Transmitting side.

The transmitting diaphragms were stiffness-controlled over the bandwidth of interest, exhibiting an average fundamental bending mode frequency of approximately 1020 Hz with all elements attached. Accounting for the masses of the fin structures, one half the masses of the suspensions, and the masses of adhesives, the average total moving mass of a transmitting diaphragm assembly was approximately 185 g. This mass could also vary slightly, depending upon accelerometer mounting and other conditions.

The DCL array was intended to be tested in both its passive mode (actuator terminals open-circuited) and in its active mode (normal transmitting diaphragm accelerations

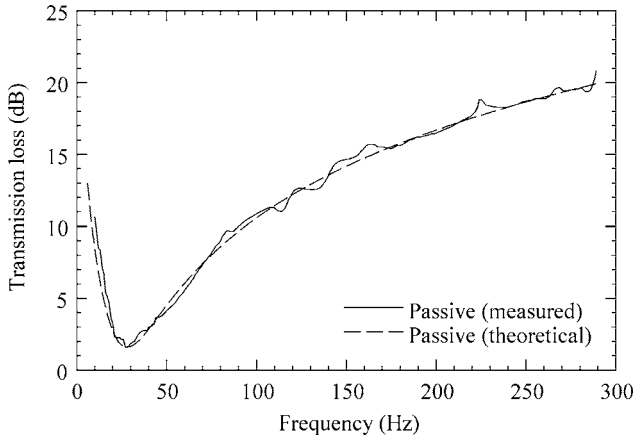

FIG. 7. The measured transmission loss for the passive transmitting diaphragm array. The measured curve is plotted against a theoretical prediction.

minimized). Acoustic pressures at positions within the module cavities could also be directly minimized through active control. However, the results produced by this scheme were very similar at low frequencies to those produced by the acceleration control scheme. This paper reports only the latter.

C. Passive benchmark partitions

Several passive benchmark partitions were developed to validate the performances of both the measurement system and the ASP arrays. Five structures were used for this purpose: (1) an open tube (no partition in place), (2) a lightweight single-leaf partition segmented into four modules, (3) a massive single-leaf partition filled with concrete, (4) a massive single-leaf partition filled with sand, and (5) a massive double-leaf partition consisting of both the concrete-filled and sand-filled leaves with various leaf spacings.

The measured transmission loss of the first benchmark "partition" (open tube) had an average value[22] of less than 0.3 dB over the passive measurement bandwidth (20–290 Hz). It gradually rose from very small values ($\approx$0 dB) at lower frequencies to around 2 dB at higher frequencies. The simple arrangement was tested to verify the ability of the system to measure very small transmission losses and to quantify system losses.

The second benchmark partition (segmented single-leaf partition) was the isolated passive transmitting diaphragm section of the DCL ASP array (see Fig. 6). The measured transmission loss for the partition is shown in Fig. 7, along with a theoretical prediction. The theoretical curve is based on modeling results from Refs. 13 and 16, the average moving diaphragm mass of the modules, the effective suspension compliance (derived from the mass and the 28 Hz resonance frequency), and an effective suspension resistance (derived from the transmission loss at resonance).[23] As suggested earlier, it assumes that the effective transmitting surface areas of the modules incorporate the inner flexing halves of their surrounds. The outer halves are treated as though they formed portions of the presumably rigid surrounding interstices.

The third benchmark partition was constructed using spaced MDF panels that spanned the partition cross section to form a 15.2-cm-thick cavity that was filled solid with concrete. The overall partition mass was approximately 85 kg. The fourth benchmark partition was similar to the concrete-filled partition, but it had a 10.2-cm-thick cavity filled with dry sand. Its overall mass was approximately 40 kg. The fifth benchmark partition provided the highest passive transmission loss. It consisted of a double-leaf structure involving both the concrete-filled and sand-filled leaves, with varying spacings and interconnections. The spacings included (1) a minimal separation of approximately 1 cm (provided only by compressed resilient gaskets), (2) a moderate separation of approximately 17 cm (provided by a spacer and resilient gaskets), and (3) a wide separation of approximately 175 cm with no direct structural connection. For the first two spacings, the adjustable gasket compression clamps could be configured with or without resilient rubber pads between their sections.

As detailed in Ref. 13, these massive benchmark partitions produced transmission loss curves that followed theoretical predictions to an extent. They also revealed measurement system limitations. Analyses showed that the system was capable of measuring partition transmission losses up to about 60 dB—except between 155 and 190 Hz, and above 225 Hz. In these isolated regions, flanking transmission reduced the reliability of measured values greater than about 45 dB. Interesting transmission loss anomalies were consistently found in regions near 175 and 245 Hz, both of which were axial antiresonance frequencies of the source tube. Measurements of partitions with very high transmission loss could produce higher values (at some frequencies) than those indicated. However, because much higher values could have been corrupted (e.g., from downstream interference produced by multiple transmission paths), they were generally considered with a degree of uncertainty.

D. Transducers

Small Kistler and PCB Piezotronics accelerometers were used to measure normal accelerations of several vibrating surfaces: actuator diaphragms, actuator support panels, and passive transmitting diaphragms. The accelerometers were wax mounted to these surfaces and, with the exception of the actuator support panels, were positioned at their cross-sectional centers. In the case of the actuator support panels, they were mounted just outside the actuator diameters.

Up to eight Sennheiser KE 4-211-2 electret microphones (with custom amplifiers, power supplies, and housings) were used for multichannel measurements at key positions in the measurement system. The closeup view of the transmission loss measurement system in Fig. 8 shows holes drilled into the tops of the source and receiving tubes to accept relatively calibrated microphone pairs with 39.2 or 85.8 cm spacings. The upstream and downstream fields could then be decomposed following the two-microphone transfer function technique[24–26] for assessment of key partition properties within specified bandwidths and error constraints.[27] Another microphone was positioned in a hole approximately 2 cm from the source-side face of each partition to provide a reference pressure signal for automatic level adjustment of the

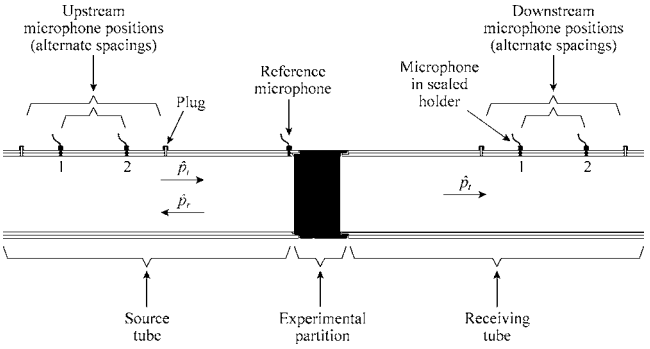

FIG. 8. A closeup view of the normal-incidence transmission loss measurement system near the arbitrary test partition. The drawing shows various microphone positions used in the measurements.

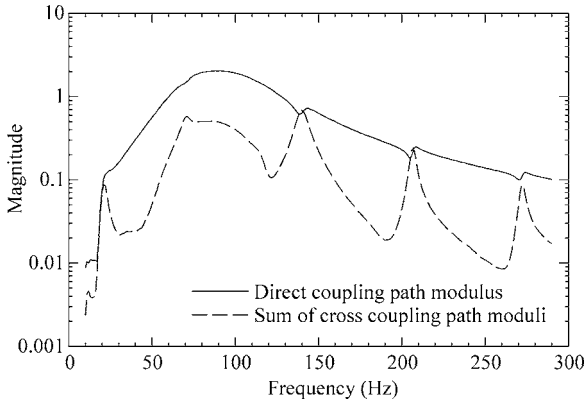

FIG. 9. The direct control path transfer function modulus and sum of cross-coupling control path transfer function moduli for one module of the DCL array.

swept sine wave stimulus used to drive the source loudspeaker.[17] As suggested in Fig. 4, four additional microphones were used to probe acoustic pressures within the cavities of the DCL ASP array. Signals derived from the microphones were used for simple monitoring purposes or to provide alternative error signals. When microphones and housings were removed from any of the holes in the system, they were replaced with airtight plugs. Brüel & Kjær model 4135 microphones (with 2633 preamplifiers and 2801 or 2803 power supplies) were also used for some measurements and as relative calibration standards for the Sennheiser microphones.

A Polytec PSV-200 scanning laser Doppler vibrometer system was used to measure transmitting normal surface vibrations of the DCL ASP. It generated operating deflection shapes[28] that increased understanding of transmitting surface behaviors. Additional details of its use are given in Sec. II F.

E. Electronics

While the electronics used in the experiments were similar to those described in Ref. 17, several of their functions were duplicated because of the increased number of controlled channels. A Hewlett-Packard 3566A PC Spectrum/Network analyzer was expanded to 16 channels. Three Krohn-Hite 3364 filter/amplifier sets (four channels each) were used instead of one. An Adcom GFA-555 power amplifier was used to drive the source loudspeaker, freeing four channels of a Luxman M-111 amplifier to drive the module actuators. Only a single dbx 1046 quad compressor/limiter was available, so it was used only to process the controller reference signal—not the four module error signals.

As indicated earlier, multiple single-error-input/single-output (MSISO) and multiple-error-input/multiple-output (MIMO) filtered-x controllers were used with the ASP arrays. Both utilized only a single reference signal derived from the signal driving the source loudspeaker amplifier. Both were implemented using a Spectrum DSP96002 system board (based on the Motorola DSP 96002 digital signal processor) and multichannel Spectrum I/O boards. While centralized multichannel controllers are commonly used in active noise control applications, a key objective of this research was to develop an ASP capable of achieving very high transmission loss over a broad bandwidth using multiple single-channel controllers. This was motivated by the expectation that individually packaged single-channel controllers could provide simplified local control for each module and thereby increase the practicality of large ASP arrays. Because the DCL ASP array was expected to produce very high transmission loss, its ability to utilize the MSISO controllers was of particular interest.

A sufficient condition for stable operation of such decentralized controllers[29] requires that the sum of cross-coupling control path transfer function moduli not exceed the direct control path transfer function modulus for any given module. Figure 9 shows these two frequency-dependent functions for one module of the array. (Because of array symmetry, plots for the other three modules were nearly identical.) The two curves reveal that the sufficient condition for stable MSISO control is met, except perhaps near 140, 206, and 272 Hz (near specific axial source tube resonance frequencies), and below about 20 Hz. In other words, the multichannel control path coupling matrix is diagonally dominant, except in these very limited spectral regions. Nevertheless, because the stated conservative condition is a sufficient but not necessary condition for guaranteed stability, the chances for successful operation across the entire bandwidth remained high.

F. Measurement capabilities and limitations

Because transducer calibration, signal derivation, signal conditioning, and postprocessing of data were conducted in manners similar to those described in Ref. 17, many of the capabilities and limitations of the experimental approach were also similar. However, several important distinctions arose in this investigation. The longer anechoic termination and wider microphone separation distances enabled lower frequency measurements. On the other hand, the square cross-sectional areas of the arrays and source and receiving tubes were much larger than those of their circular counterparts in the previous work. The highest measurement frequency was therefore much lower. Nevertheless, because the low-frequency capabilities of active partitions are of most practical interest, this limitation posed no serious problem. The more important consequence of the size and materials of the system related to an increase in flanking transmission.

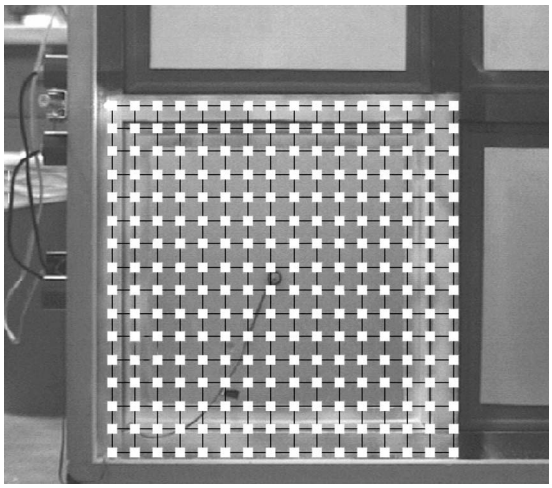

FIG. 10. Transmitting surface scan points for the scanning laser vibrometer measurement of one DCL array module.

The passive benchmark partitions discussed in Sec. II C had a variety of characteristics that helped establish the maximum bandwidth and transmission loss capabilities of the system. Through other measurements, the electroacoustic signal-to-noise ratio of the system was found to have an average value of approximately 87 dB and a minimum value no lower than 73 dB.[13] Electronic crosstalk was consistent with that discussed in Ref. 17. Neither of these concerns posed a limitation for most transmission loss measurements.

The scanning laser vibrometer measurements were only performed for the DCL ASP to verify that its transmission loss performance was in fact a by-product of efficient global control of transmitting surface vibrations. Furthermore, only a single transmitting diaphragm, its surrounding suspension, and interstice were measured as a representative sampling of the entire array. The receiving tube was removed from the measurement system to allow optical access to these transmitting surfaces. The vibrometer scanning head was positioned approximately 1.4 m away from the array. To enhance laser light detection by the head, the transmitting surfaces were coated with white (optically reflective) powder. The vibrometer system was then programmed to sequentially measure the surface vibrations at the 256 scan points indicated in Fig. 10. Using the measured results, the system generated surface plot animations representing time-harmonic structural responses (operating deflection shapes) of the surfaces. These responses were determined at different frequencies, in both passive and active states. During the measurements, the array frame was no longer sandwiched between the source and receiving tubes. It could thus vibrate against the resilient source tube gaskets with greater freedom than usual.

G. Other experimental challenges

Some of the experimental challenges discussed in Ref. 17 were again encountered with the measurements of this work. Simultaneous dynamic range requirements of the adaptive controllers and measurement systems had to be carefully addressed. Adaptive controller tracking of swept sine wave stimuli also remained a consistent challenge.

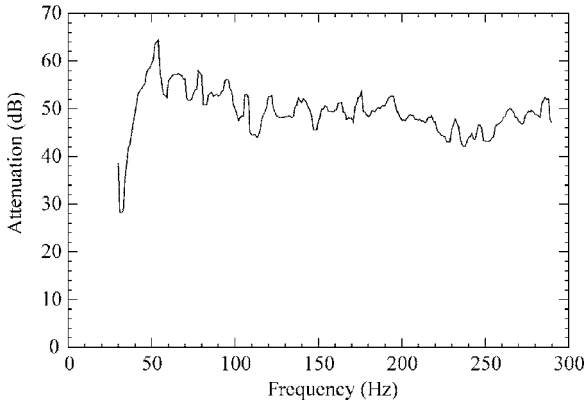

FIG. 11. The average normal acceleration error signal attenuation for the four actuator diaphragms of the SCL array.

However, flanking transmission became the matter of more serious concern as the larger experimental measurement system exacerbated its effects. Construction of sufficiently rigid and massive source and receiving tubes was difficult because of several practical constraints. Efforts were made to measure mechanical properties of their materials, fabricate rigid and massive walls, and provide resilient connections between adjacent tube sections and the floor beneath. However, the inherent structural characteristics of the large, flat tube surfaces made it difficult to minimize their vibrations sufficiently.

Another experimental challenge involved the difficulty of constraining sufficient translational piston-like motions of the ASP actuator support panels and the passive transmitting diaphragms. Even if these aluminum honeycomb sandwich panels were assumed to behave as perfect rigid bodies, nonuniformities in their spaced dual suspensions could have produced rotational components of vibration. Significant effort was expended to create suspensions that helped constrain translational motions, but both physical and fabrication limitations bounded their capabilities. Additional design effort and more precise manufacturing might have improved their behaviors.

III. RESULTS

A. Single-composite-leaf (SCL) array

The SCL array depicted in Figs. 2 and 3 was first evaluated in its passive mode, with all actuator terminals open circuited. It was subsequently evaluated when the normal accelerations of its actuator diaphragms were minimized through MSISO adaptive control (see Sec. II E). This section considers error signal reductions achieved in the latter state then presents the normal-incidence transmission losses measured in both states.

The error signal attenuations measured for each of the four modules were very similar. The average attenuation is plotted in Fig. 11 as a function of frequency. The frequency-averaged value of this curve over the controlled measurement bandwidth (30–290 Hz) was 50 dB. The steep drop to relatively poor attenuation below 50 Hz was likely caused by actuator nonlinearities below their resonance frequencies. The actuators were not effective below about 30 Hz.

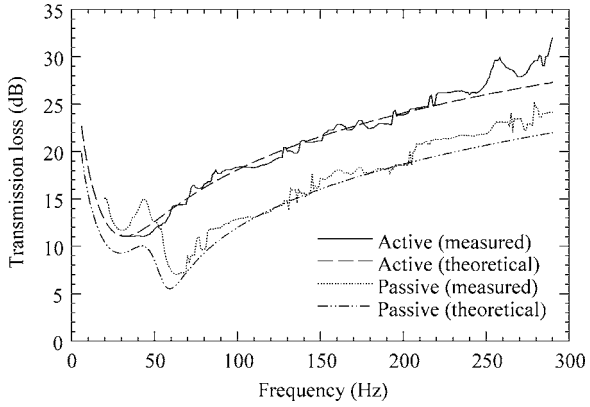

FIG. 12. Measured transmission losses for the SCL array in its active and passive states. The measured curves are plotted against theoretical predictions.

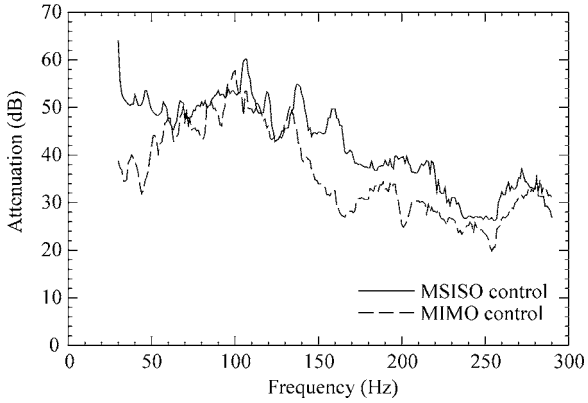

FIG. 13. Average normal acceleration error signal attenuations for the four transmitting diaphragms of the DCL array under MSISO and MIMO control.

Measured normal-incidence transmission losses of the array are plotted in Fig. 12 for both passive and active control conditions. They are also plotted against theoretical predictions based on analytical results,[16,30] as well as published, measured, and estimated parameter values.[23] In the passive mode, the array produced an average transmission loss of approximately 17 dB over the measurement bandwidth (20–290 Hz). The curve exhibits a small dip to 12 dB centered at 30 Hz and a much deeper dip to 7 dB centered at 63 Hz (near the resonance frequency of the accelerometer-loaded actuators). The array appears to be mass-controlled above 63 Hz, with a consistent rise in transmission loss of approximately 6 dB per octave. It agrees reasonably well with theoretical predictions. Once the normal accelerations of the actuator diaphragms were actively minimized, transmission loss noticeably increased over most of the measurement bandwidth. Over the controlled bandwidth, the average transmission loss was 22 dB. The resulting curve demonstrates a consistent increase of approximately 6 dB per octave at higher frequencies. It also agrees well with theoretical predictions.

B. Double-composite-leaf (DCL) array

The DCL array depicted in Figs. 4 and 5 was similarly evaluated with all actuator terminals open circuited, then with its normal transmitting diaphragm accelerations minimized through adaptive control. The control was alternately implemented using the MIMO and MSISO controllers (see Sec. II E). This section first investigates error signal reductions, controller convergences, and observed stability for the two schemes. It subsequently presents normal-incidence transmission losses for the array and compares them to those of the massive benchmark partitions and the SCL array. It then concludes with a discussion of scanning laser vibrometer measurements.

1. Error signal reduction, controller convergence, and stability

Similar error signal attenuations were again measured for each of the four modules. Average attenuations produced by the MIMO and MSISO schemes are plotted in Fig. 13 as a function of frequency. Under MIMO control, attenuations varied from 20 to 58 dB, with a frequency-averaged value of 36 dB over the controlled measurement bandwidth. Notable declines in attenuation were evident above and below 100 Hz. Attenuation under MSISO control varied from 22 to more than 60 dB, producing a frequency-averaged value of 42 dB—a full 6 dB greater than that produced by the MIMO controller. It exhibited notable improvement in attenuation below 60 Hz and between 135 and 280 Hz. In some cases, the improvement was greater than 15 dB. Outside these bandwidths, the two control schemes performed on par with one another.

It is worthwhile to consider the mechanism by which the transmitting diaphragm accelerations were minimized. As discussed in Ref. 16, the net volume velocities into the module cavities were expected to approach zero. To validate this prediction for a single module, the normal acceleration of an actuator diaphragm and that of its surrounding support panel were measured in the actively controlled state using relatively calibrated accelerometers. The volume velocities of the elements were then estimated from these measurements and the effective radiating surface areas (including pertinent surround halves). (The estimation assumed that the surfaces behaved as ideal translational pistons.) Relative levels and phases of the computed volume velocities varied slightly over frequency. However, when averaged over the controlled measurement bandwidth, the levels were within 0.7 dB and the phase difference was 162 degrees. Thus, although the agreement between the theoretical prediction and these rough experimental measurements was not exact, the primary mechanism for controlling normal transmitting diaphragm motion was basically validated.

The convergence behaviors of the two adaptive control systems were measured near source tube resonance and antiresonance frequencies for comparison. Figure 14 shows typical error signal convergences for all channels of the MIMO controller at 65 Hz (near the resonance frequency of 70 Hz). The relatively long 20 s convergence time was common near many of the source tube resonance frequencies. It is immediately evident from the plots that the convergences of all modules were in unison, as expected for the MIMO

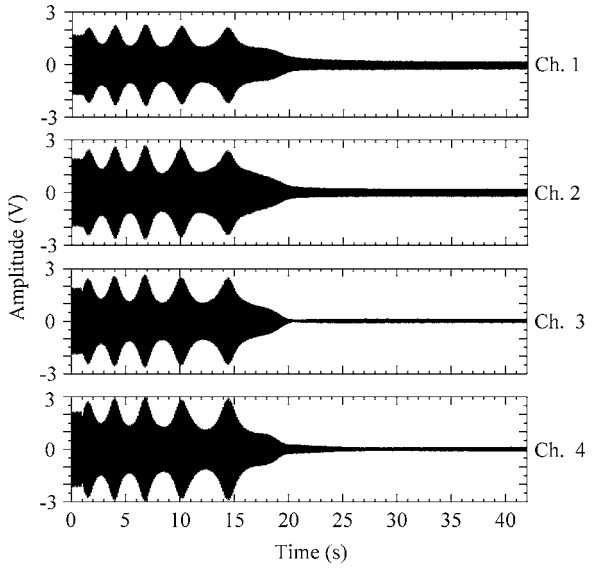

FIG. 14. Initial error signal convergences for the four channels of the MIMO controller when controlling the DCL array at 65 Hz (near the source tube resonance frequency of 70 Hz). The adaptation process begins at time approximately equal to 1 s.

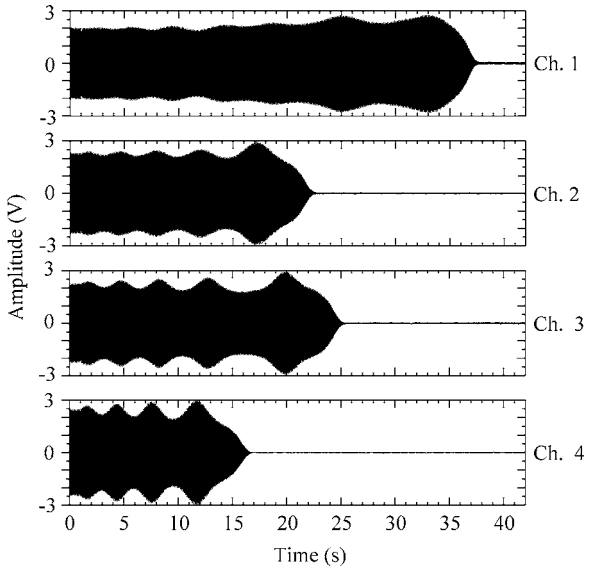

FIG. 16. Initial error signal convergences for the four SISO controllers when controlling the DCL array at 65 Hz (near the source tube resonance frequency of 70 Hz). The adaptation process begins at time approximately equal to 1 s.

controller. Several oscillatory cycles were required to reach the final steady-state condition that minimized the sum of mean-square-error values.

Figure 15 shows initial convergence plots for the MIMO controller operating at 100 Hz (near the antiresonance frequency of 105 Hz). In this case, the convergence time was only 2 s. Convergence of all channels was again simultaneous, but it proceeded with minimal oscillation and yielded notably smaller residual mean-square error values.

Initial convergence characteristics for the MSISO controllers were also investigated at these same two frequencies. Figure 16 shows typical convergence plots at 65 Hz. It is obvious from the plots that the modules did not generally converge in unison. Several oscillatory cycles were again required to reach the final steady state conditions that minimized individual mean-square-error values. The residual error signals were relatively small in comparison to those produced by the MIMO controller at this frequency. The convergence times for the various modules varied from 16 to 37 s, with an average of about 25 s. Although convergence parameters of the four SISO controllers were identical, different initial coefficient values for their passive on-line system identification algorithms may have affected individual convergence times.

The MSISO convergences at 100 Hz are shown in Fig. 17. They proceeded with few oscillatory cycles, producing

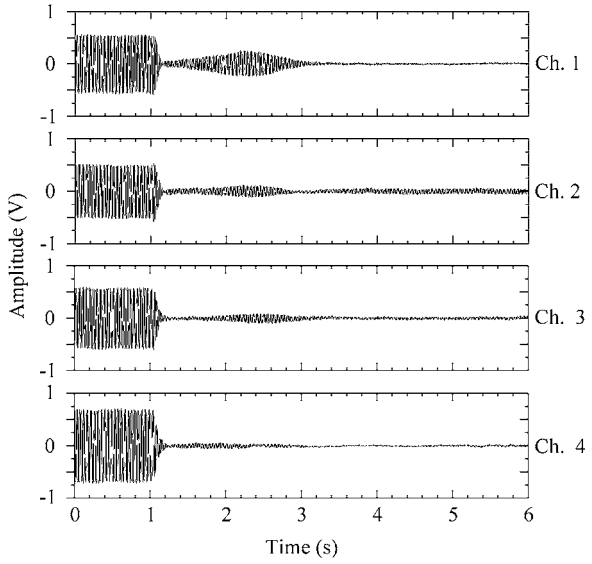

FIG. 15. Initial error signal convergences for the four channels of the MIMO controller when controlling the DCL array at 100 Hz (near the source tube antiresonance frequency of 105 Hz). The adaptation process begins at time approximately equal to 1 s.

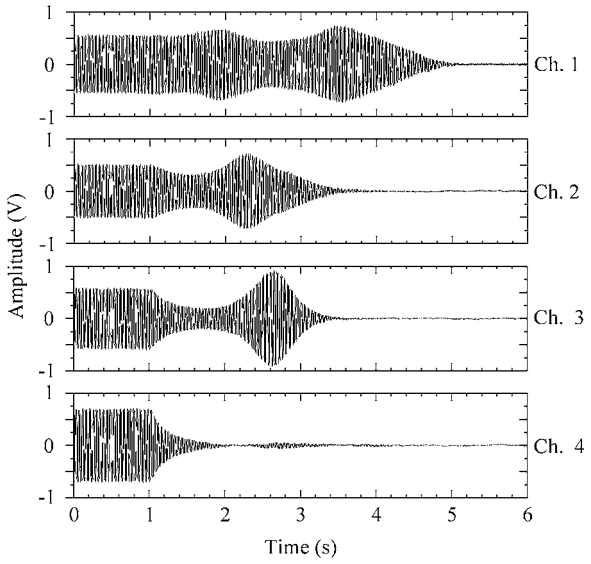

FIG. 17. Initial error signal convergences for the four SISO controllers when controlling the DCL array at 100 Hz (near the source tube antiresonance frequency of 105 Hz). The adaptation process begins at time approximately equal to 1 s.

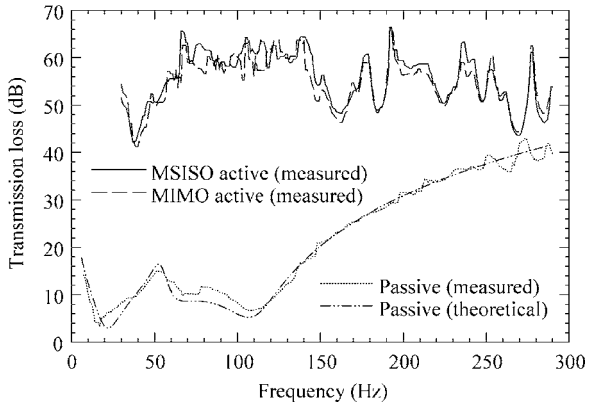

FIG. 18. Measured transmission losses for the DCL array in its active and passive states. The two active states involve either MSISO control or MIMO control. The passive transmission loss is plotted against a theoretical prediction.

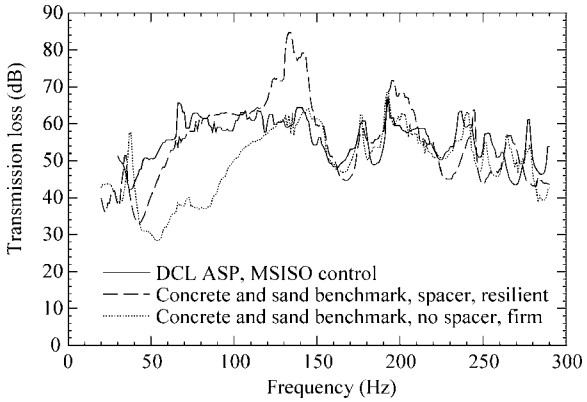

FIG. 19. Measured transmission loss for the DCL array under MSISO control. The curve is plotted against measured transmission losses for the massive double-leaf benchmark partition (concrete and sand-filled leaves) with two spacing and interconnection conditions.

convergence times between 2.5 and 4 s, and an average of about 3 s. Residual steady state error signals were again relatively small.

In addition to the convergence characteristics just considered, the stability and robustness of the controllers were matters of concern. From this standpoint, the initial convergence plots of Figs. 14–17 are somewhat misleading. Although the MIMO controller did converge well at most fixed frequencies, it had difficulty tracking the swept sine wave stimulus in certain spectral regions (e.g., near the first source tube resonance frequency of 70 Hz) with sufficient stability. In such problematic regions, the MIMO controller would often appear to converge after a long period, only to become unstable and diverge sometime later. Yet there was no indication that the control path transfer function matrix was ill conditioned for MIMO control at these or any other frequencies within the controlled measurement bandwidth.[31] It thus became necessary to adjust convergence parameters to sufficiently slow and guarantee convergence with changing stimulus frequencies. Invariably, the MSISO controllers were more stable than the MIMO controller under these same conditions. As shown earlier, their error signal attenuations were also generally superior.

The stability of the MSISO controllers was investigated under other circumstances of practical interest. The behaviors of the converged controllers were observed when control signals supplied to one or more of the array actuators were abruptly disconnected. These behaviors might be considered representative of their behaviors in applications wherein one or more ASP modules became unexpectedly disturbed. Again, these characteristics were monitored near axial resonance and antiresonance frequencies of the source tube. In every case tested, slight disturbances were noted in the other module error signals, but the controllers remained stable and quickly reconverged (i.e., in less than 1 s).

2. Normal-incidence transmission losses

Normal-incidence transmission losses of the DCL ASP are plotted in Fig. 18 for the one passive and two active conditions. The passive curve is also plotted with good agreement against a theoretical curve determined from analytical results,[16,30] as well as published, measured, and estimated module parameters.

In the passive mode, the array behaved much like a double-leaf partition. It exhibited a fundamental resonance frequency at about 17 Hz and something similar to a mass-air-mass resonance frequency at about 108 Hz. The partition appeared to be stiffness controlled below 17 Hz and produced an increase in transmission loss of slightly more than 18 dB per octave above 108 Hz. The average transmission loss over the measurement bandwidth was 22 dB.

Under MIMO transmitting diaphragm acceleration control, the average transmission loss over the controlled bandwidth (30–290 Hz) rose to 55 dB. However, the curve did exhibit several notable undulations. The minimum measured value was 41 dB, whereas the maximum measured value was 66 dB, pushing the measurement capabilities discussed in Sec. II C.

Under MSISO control, the average transmission loss over the controlled measurement bandwidth was 56 dB. This was a 33 dB improvement over that produced by the passive mode. Between 30 and 150 Hz the average improvement was 47 dB. Once again, the controlled transmission loss curve had no specific trend over frequency. In similarity to the MIMO control case, there was a prominent dip to a value of 42 dB centered at 38 Hz and other dips to values near 45 dB surrounding the source tube antiresonance frequencies of 175 and 245 Hz. The minimum measured transmission loss was 42 dB and the maximum was again 66 dB.

3. Transmission loss comparisons

To better understand the transmission loss characteristics under active control, it is worthwhile to make a few important comparisons. Because MSISO control produced slightly better performance, it alone is considered in this discussion. Measured results for the massive double-leaf benchmark partition (see Sec. II C) and the SCL array are used as standards of comparison.

The transmission loss for the active DCL array is again plotted in Fig. 19 against two measured transmission losses for the massive benchmark partition with both concrete and

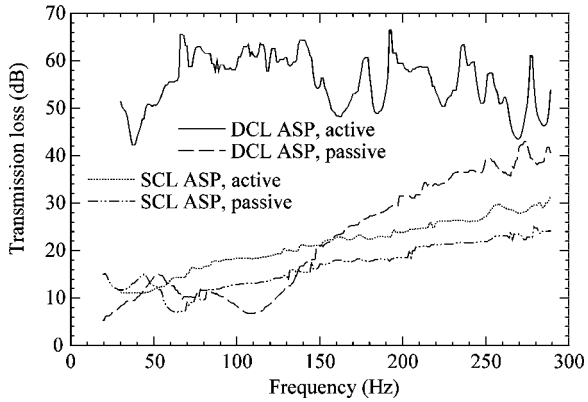

FIG. 20. Measured transmission losses for the SCL and DCL ASP arrays in their completely passive modes (actuator terminals open circuited) and under diaphragm acceleration control.

sand-filled leaves. The first benchmark measurement was made with the spacer and resilient clamping between leaves; the second was made with no spacer and firm clamping. The actively controlled array appears to perform on par with the much more massive benchmark partition in its two embodiments. (Recall from Sec. II C that transmission loss values much greater than 60 dB are considered to be uncertain.) When averaged over the controlled measurement bandwidth, the transmission loss of the array is basically equal to that of the benchmark partition involving the spacer and resilient clamping. In some spectral regions (e.g., near the benchmark low-frequency resonance dip) it performs better, but in other regions it performs worse. The ASP array produces an average 6 dB transmission loss improvement over that of the benchmark partition with small spacing and firm clamping. It performs much better than the structure between 40 and 120 Hz, the general region of its resonance dip. The array might have performed even better at the lowest control frequencies had the actuators not exhibited an increase in nonlinear behavior below 50 Hz. Limitations in controller performance may have produced other deficiencies. Based on the discussion in Sec. II C, it is also possible that flanking transmission limited the measurable transmission loss values for the array over much of the measurement bandwidth.

Additional insights follow from direct comparison of the DCL and SCL array transmission losses, as measured in their passive and active states. Figure 20 shows that the active DCL array consistently produced much higher transmission loss than the active SCL array, but its improvement was generally greater at lower frequencies than at higher frequencies. Within the controlled measurement bandwidth, the average improvement was 34 dB. The maximum improvement was 51 dB at 66 Hz and the minimum improvement was 16 dB at 269 Hz. Thus, although the objective of controlling normal principal transmitting surface vibrations was the same for both arrays, a dramatic increase in transmission loss performance was accomplished through a simple configurational change.

4. Scanning laser vibrometer measurements of transmitting surfaces

Normal vibrations of the DCL array transmitting surfaces were measured using the Polytec scanning laser vibrometer as discussed in Secs. II D and II F. Point-by-point measurements (see Fig. 10) were taken at 100 and 200 Hz in the passive state and in the active state produced by MSISO control.

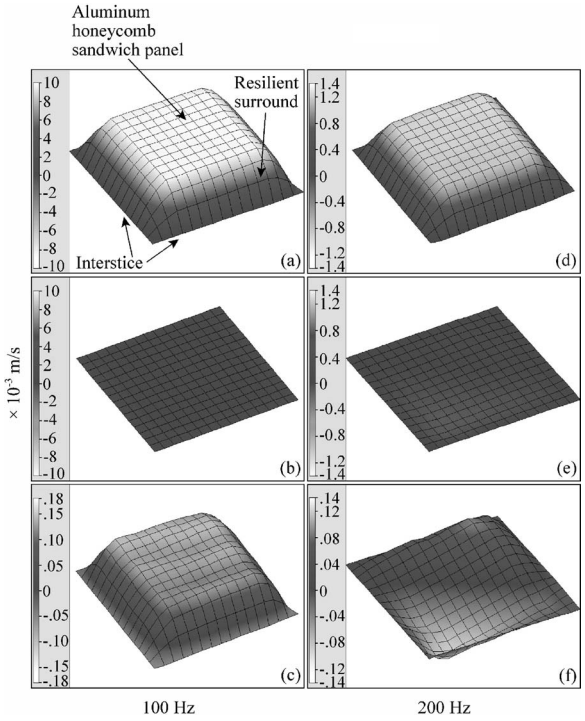

FIG. 21. Operating deflection shape images for the transmitting surfaces of an individual DCL ASP module. (a) Passive mode, 100 Hz. (b) Normal transmitting diaphragm acceleration control, 100 Hz. (c) Normal transmitting diaphragm acceleration control, magnified scale, 100 Hz. (d) Passive mode, 200 Hz. (e) Normal transmitting diaphragm acceleration control, 200 Hz. (f) Normal transmitting diaphragm acceleration control, magnified scale, 200 Hz.

Figure 21(a) shows an operating deflection shape visualization of the transmitting diaphragm, resilient suspension, and interstice for a single passive module with 100 Hz excitation. Figure 21(d) shows a similar result for 200 Hz excitation. Animations of the shapes showed that the transmitting diaphragm (central portion of each image) behaved as a nearly ideal translational piston at both frequencies. Though not apparent from Fig. 21(d), there was a slight "wobble" detectable in the response at 200 Hz, but it was almost insignificant. The resilient surround appeared to flex consistently around the periphery of the piston at both frequencies. Interstice vibration, represented by the outermost points of the images, was undetectable in the 100 Hz animation, and was only slightly detectable in the 200 Hz animation.

When normal acceleration at the center of the transmitting diaphragm was actively minimized, the surfaces exhibited the responses shown in Figs. 21(b) and 21(e) at 100 and 200 Hz, respectively. From these images, it is clear that normal vibration was efficiently and globally minimized at both frequencies—fulfilling a key design objective. Fine details of the minute residual vibrations were difficult to ascertain with the same amplitude scales used for the passive mode. The scales were consequently adjusted to magnify the responses as shown in Figs. 21(c) and 21(f). These images reveal several interesting characteristics.

At 100 Hz, the maximum normal vibration was reduced by approximately 37 dB. Judging from the 53 dB normal acceleration attenuation shown for this frequency in Fig. 13, it is evident that the reduction did not represent the maximum that might have been achieved. There are a few reasons for this. First, the vibrometer measurements were intended chiefly to demonstrate spatial responses of the vibrating surfaces under passive and active conditions. The same attention to signal gain structures and control optimization was therefore not considered as important for these measurements. Because the normal acceleration of the panel was reduced to nearly the threshold of the centrally mounted accelerometer, the accelerometer could not reliably provide signal for further attenuation. Initial excitation levels (seen in the passive state) might have been increased or an accelerometer with a lower threshold might have been employed to demonstrate greater vibration attenuation capabilities. In addition, control filter coefficients were adapted *a priori* for this case, then held constant over the duration of the vibrometer scans to enable reasonably time-invariant conditions for the point-by-point measurements. Without the typical continuous adaptation of control filter coefficients (which might have produced ambiguous operating deflection shapes), a less-than-maximal error signal attenuation resulted.[32]

It is apparent from Fig. 21(c) that the residual transmitting diaphragm vibration at 100 Hz continued to be piston-like in nature. A small amount of rippling is evident over the diaphragm area that may have been an artifact of measurement noise. The surround also continued to flex in a consistent manner around the diaphragm at all measurement points. A small in-phase residual interstice vibration was apparent from the animations at the magnified scale. As suggested earlier, such motion should be expected—even for a perfectly stiff frame—because the array was mounted resiliently to the source tube, and was not sandwiched between it and the receiving tube. Despite the motion, the small cross-sectional area of the interstice would have produced inefficient radiation into a receiving space.

The 200 Hz residual response shown in Fig. 21(f) reveals a more interesting vibrational pattern. The maximum normal vibration (near the opposing deflected corners) was reduced by approximately 21 dB relative to the passive piston-like amplitude. Once again, this attenuation might be contrasted with the 40 dB normal acceleration attenuation found in Fig. 13 at the same frequency for the center point of the transmitting diaphragm. Figure 21(f) shows this point to have more significantly reduced motion than many other positions. Animations also clarified that the residual vibration consisted of a rocking motion about a nearly diagonal line. The motion appeared to be a combination of the two rotational rigid-body modes about the centered Cartesian axes parallel to the module edges.

Fortunately, this dipole-like motion is known to produce very inefficient radiation into a receiving space. In the case of the plane-wave receiving tube, a surface dipole with zero volume velocity would produce zero radiation to downstream positions. In a three-dimensional receiving space, its radiation would be finite but very small if the dimensions of the diaphragm were small compared to wavelength. At 200 Hz, the dimensions certainly met this requirement. Furthermore, when several adjacent modules demonstrate this type of vibrational behavior, the overall multipole order of the ASP can become much higher than a dipole, producing even less efficient radiation.[33]

Additional vibrometer measurements verified that the tendency of the transmitting diaphragm to exhibit residual rotational rigid-body motion was greater at higher frequencies than at lower frequencies. The field behind the diaphragm became less and less uniform with increasing frequency and would therefore tend to excite the diaphragm with a less symmetric pressure distribution. However, it is likely that this residual rocking motion could have been reduced through improved manufacturing processes. Any nonuniformities or imbalances in the diaphragm suspensions or fin structures might have induced the problem—even with a uniform pressure distribution behind the diaphragm.

IV. SUMMARY AND CONCLUSIONS

Experimental methods have been developed to measure normal-incidence transmission losses of two lightweight active segmented partitions (ASPs) in their passive and active states. The first ASP consisted of four single-composite-leaf (SCL) modules with lightweight moving-coil actuators mounted within resiliently suspended support panels. The second consisted of four double-composite-leaf (DCL) modules that used the first array to electroacoustically actuate isolated cavities that were bounded on the opposite sides by passive transmitting diaphragms. The control objective for each array was to globally reduce normal transmitting surface vibrations through the simple actuation and sensing of principal transmitting surfaces, and to consequently produce high transmission loss.

The DCL ASP used this vibration control scheme much more efficiently than the SCL ASP. It also satisfied several other design and performance criteria established earlier. Its high transmission loss capabilities could not be completely evaluated because of flanking transmission limitations in the measurement system. Nevertheless, its average transmission loss over the measurement bandwidth was determined to be 56 dB—a full 34 dB greater than that of the SCL ASP. In addition, its average value was 47 dB higher in the typically challenging low-frequency range between 30 and 150 Hz. These substantial increases resulted from a simple configurational change in the array—not from considerable changes in underlying control objectives or system complexities.

The measured passive and active transmission losses agreed well with theoretical estimates, suggesting that previously developed models had useful predictive capabilities. Other measurements verified that a predicted zero source-side volume velocity condition for the DCL modules was principally responsible for controlling their normal transmitting diaphragm vibrations.

The DCL ASP was successfully controlled using multiple-error-input, multiple-output (MIMO) and multiple single-error-input/single-output (MSISO) filtered-x controllers. The decentralized MSISO controllers produced an aver-

age error signal attenuation (in transmitting diaphragm acceleration) that was approximately 6 dB greater than that produced by the centralized MIMO controller. Although average convergence times were slightly longer for the decentralized controllers, they remained very stable when one or more of the array actuators were abruptly disturbed. They were also more stable than the MIMO controller near source tube resonance frequencies. These results demonstrate that the ASP was amenable to independent single-channel controllers—a matter of importance for practical implementations.

Scanning laser vibrometer measurements of the DCL ASP verified that its high transmission loss was produced primarily by efficient global reductions in its normal transmitting surface vibrations. Although minute residual vibrations were detectable in its controlled state, they were either so small in amplitude or produced such inefficient transmission into the receiving space that they were of minor importance.

This work has shown that lightweight ASPs can be practically and locally controlled to produce very high transmission loss at lower audible frequencies, far exceeding transmission losses of passive partitions with comparable masses. When properly configured, they can achieve this result through global reduction of normal transmitting surface vibrations. While this work and previous work have demonstrated promising results for DCL configurations, they have also increased awareness of issues requiring further investigation. Transmission losses of ASPs should be carefully investigated using oblique and random-incidence fields. Sound transmission should be analyzed in near fields and far fields of three-dimensional receiving spaces. The impact of vibrating interstices and their flexural responses should also be studied. Alternative types of actuators and controllers should be developed and work should be conducted to further decrease overall ASP masses and thicknesses. Bidirectional capabilities of ASPs (i.e., their abilities to produce active sound transmission control in either direction between adjacent acoustic spaces) should also be studied and developed. The authors encourage research in these and other areas to enhance the viability of ASPs as sound transmission control tools.

ACKNOWLEDGMENTS

The authors gratefully acknowledge financial and other support for portions of this project from the Penn State University Graduate Program in Acoustics. They also acknowledge the Penn State Applied Research Laboratory, Rapid Die and Molding Company, Hewlett-Packard Company, Young-Cheol Park, Scott Sommerfeldt, Karl Reichard, and Courtney Burroughs for their contributions and input to the project. They finally thank Joye, Lara, Lane, and Rachel Leishman for meaningful assistance in the assembly of the transmission loss measurement system.

[1]J. E. Cole, III and M. C. Junger, "Active noise control for machinery enclosures," NSF Final Report U-1944-379F, 1991.
[2]D. R. Thomas, P. A. Nelson, and S. J. Elliott, "An experimental investigation into the active control of sound transmission through stiff light composite panels," Noise Control Eng. J. **41**, 273–279 (1993).
[3]D. R. Thomas, P. A. Nelson, R. J. Pinnington, and S. J. Elliott, "An analytical investigation of the active control of the transmission of sound through plates," J. Sound Vib. **181**, 515–539 (1995).
[4]S. L. Sharp, G. H. Koopmann, and W. Chen, "Transmission loss characteristics of an active trim panel," Proceedings of Noise-Con 97, University Park, PA, 1997, Vol. **2**, pp. 149–160.
[5]M. E. Johnson and S. J. Elliott, "Active control of sound radiation from vibrating surfaces using arrays of discrete actuators," J. Sound Vib. **207**, 743–759 (1997).
[6]R. L. St. Pierre, Jr., G. H. Koopmann, and W. Chen, "Volume velocity control of sound transmission through composite panels," J. Sound Vib. **210**, 441–460 (1998).
[7]J. E. Cole, K. F. Martini, and A. W. Stokes, "Active noise control for machinery enclosures," NSF Final Report U-2413-393, 1996.
[8]S. M. Hirsch, J. Q. Sun, and M. R. Jolly, "An analytical study of interior noise control using segmented panels," J. Sound Vib. **231**, 1007–1021 (2000).
[9]S. M. Hirsch, N. E. Meyer, M. A. Westervelt, P. King, F. J. Li, M. V. Petrova, and J. Q. Sun, "Experimental study of smart segmented trim panels for aircraft interior noise," J. Sound Vib. **231**, 1023–1027 (2000).
[10]T. W. Leishman and J. Tichy, "A fundamental investigation of the active control of sound transmission through segmented partition elements," Proceedings of Noise-Con 97, University Park, PA, 1997, Vol. **2**, pp. 137–148.
[11]T. W. Leishman and J. Tichy, "An experimental evaluation of individual partition segment configurations for the active control of sound transmission," J. Acoust. Soc. Am. **104**, 1776(A) (1998).
[12]T. W. Leishman and J. Tichy, "An experimental investigation of a novel active segmented partition for sound transmission control," J. Acoust. Soc. Am. **105**, 1156(A) (1999).
[13]T. W. Leishman, "Active control of sound transmission through partitions composed of discretely controlled modules," Ph.D. thesis, The Pennsylvania State University, University Park, PA, 2000.
[14]T. W. Leishman, "Vibration-controlled modules for use in active segmented partitions," J. Acoust. Soc. Am. **114**, 2385(A) (2003).
[15]T. W. Leishman, "Research in the field of active sound transmission control," J. Acoust. Soc. Am. **114**, 2390(A) (2003).
[16]T. W. Leishman and J. Tichy, "A theoretical and numerical analysis of vibration-controlled modules for use in active segmented partitions," J. Acoust. Soc. Am. **118**, 1424–1438 (2005).
[17]T. W. Leishman and J. Tichy, "An experimental investigation of two module configurations for use in active segmented partitions," J. Acoust. Soc. Am. **118**, 1439–1451 (2005).
[18]Previously established criteria for effective ASPs have suggested that adjacent modules should have sufficiently weak cross-coupling control paths to facilitate use of decentralized single-channel adaptive controllers.
[19]Additional details concerning the measurement system and procedures are found in Refs. 13 and 17.
[20]P. E. Doak, "Excitation, transmission and radiation of sound from source distributions in hard-walled ducts of finite length. I. The effects of duct cross-section geometry and source distribution space-time pattern," J. Sound Vib. **31**, 1–72 (1973).
[21]Slight transmission loss measurement errors were caused by the nonanechoic condition below 45 Hz.
[22]Arithmetic decibel averages are used in this paper.
[23]B. E. Anderson and T. W. Leishman, "An acoustical measurement method for the derivation of loudspeaker parameters," AES 115th Convention, New York, 2003, Preprint 5865, pp. 1–13.
[24]J. Y. Chung and D. A. Blaser, "Transfer function method of measuring in-duct acoustic properties. I. Theory," J. Acoust. Soc. Am. **68**, 907–913 (1980).
[25]J. Y. Chung and D. A. Blaser, "Transfer function method of measuring in-duct acoustic properties. II. Experiment," J. Acoust. Soc. Am. **68**, 914–921 (1980).
[26]"Standard test method for impedance and absorption of acoustical materials using a tube, two microphones, and a digital frequency analysis system," American Society for Testing and Materials, ASTM Designation: E 1050-90, 1990.
[27]H. Bodén and M. Åbom, "Influence of errors on the two-microphone method for measuring acoustic properties in ducts," J. Acoust. Soc. Am. **79**, 541–549 (1986).
[28]M. H. Richardson, "Is it a mode shape, or an operating deflection shape?," Sound Vib. **31**, 54–61 (1997).

[29]S. J. Elliott and C. C. Boucher, "Interaction between multiple feedforward active control systems," IEEE Trans. Speech Audio Process. **2**, 521–530 (1994).
[30]The analytical predictions of Ref. 16 were adapted to account for the small surface areas of the rigid MDF interstices.
[31]P. A. Nelson and S. J. Elliott, *Active Control of Sound* (Academic, London, 1992).
[32]One might assume a one-to-one correspondence between transmitting surface vibration attenuation and transmission loss increase. However, transmission loss is a function of both transmitted and incident sound power. The latter cannot always be considered constant. The introduction of active sound transmission control changes the terminating boundary condition of the source tube and therefore changes the source tube field, including the incident sound power.
[33]I. L. Vér and C. L. Holmer, "Interaction of sound waves with solid structures," in *Noise and Vibration Control*, revised ed., edited by L. L. Beranek (Institute of Noise Control Engineering, Washington, DC, 1988), Chap. 11.

The ensemble statistics of the vibrational energy density of a random system subjected to single point harmonic excitation

R. S. Langley
Department of Engineering, University of Cambridge, Trumpington Street, Cambridge CB2 1PZ United Kingdom

V. Cotoni
ESI US R&D, 12555 High Bluff Drive, Suite 250, San Diego CA 92130

(Received 1 March 2005; revised 30 June 2005; accepted 2 August 2005)

This paper is concerned with the ensemble statistics of the energy density of a random system subjected to a harmonic point load. Both the mean and variance of the reverberant energy density (i.e., the total response minus the direct field) are investigated. It is shown that the ensemble average of the reverberant energy density is not spatially homogeneous, but rather the value at the drive point is between two and three times the spatially averaged value, depending on the modal overlap factor. This result is closely analogous to established results regarding the case of transient excitation. Expressions are also derived for the relative variance of the reverberant energy density both remote from the drive point and at the drive point, and a number of anomalies are found in existing results. A comparison is made with simulation results for a randomized plate, and this comparison highlights the importance of the ensemble size considered in the simulations. The present analysis is based on a random point process model of the system natural frequencies, and both Gaussian orthogonal ensemble (GOE) statistics and Poisson statistics are considered. [DOI: 10.1121/1.2046827]

PACS number(s): 43.40.Qi, 43.20.Ks, 43.40.Dx [RLW] Pages: 3064–3076

I. INTRODUCTION

The high-frequency dynamic response of an engineering system can be sensitive to small random imperfections that occur during manufacture. This phenomenon has been demonstrated by Kompella and Bernhard (1993) who measured structural-acoustic transfer functions in 98 nominally identical automotive vehicles. Beyond the first few modes of vibration, a huge variation in response levels was found, meaning that a detailed and accurate mathematical model of a single vehicle would produce inaccurate results for all the other vehicles. To fully describe the behavior of this type of system it is therefore necessary to consider the statistics of the response over an ensemble of random realizations of the system. In principle this problem can be addressed by employing a standard analysis technique such as the finite element method to produce a model of the system, and then solving numerous randomized versions of this model. However, a realistic finite element model of the high-frequency vibration of a complex system may involve hundreds of thousands of degrees of freedom, and the solution for a single realization of the system, let alone a random ensemble, can present a significant computational challenge. For this reason much research has been directed at the development of more efficient techniques that take advantage of certain universal tendencies of the statistics of the system mode shapes and natural frequencies. As described in detail in what follows, the present work is concerned with application of this type of approach to study spatial inhomogeneity in the statistics of the response of a linear system subjected to concentrated loading. The energy density of the system can be expected to have fairly uniform properties well away from the forcing point, but the behavior in the immediate vicinity of the forcing point has yet to be fully determined. This has application to the consideration of stress concentrations at the forcing point, and also to the calculation of coupling loss factors in point coupled SEA (statistical energy analysis) subsystems (Lyon and DeJong, 1995).

A key result in the study of random systems is that the natural frequencies of a single random subsystem (such as a metal block, a plate, or an acoustic volume) tend to have statistical properties governed by the Gaussian orthogonal ensemble (GOE). The GOE is a special type of random matrix (Mehta, 1991), and the evidence for the appearance of GOE statistics in engineering systems has been reviewed by Langley and Brown (2004a). In brief, the GOE can be expected to apply when the random perturbations are sufficient to cause "statistical overlap." Statistical overlap is said to occur when the random changes in any particular natural frequency exceed the mean spacing between neighboring natural frequencies, so that there is strong mixing and veering between modes across the ensemble. An exception to the GOE occurs when the system has many symmetries, so that distinct groups of modes occur with no coupling between these groups, in which case Poisson natural frequencies can be expected (Mehta, 1991). The GOE has been used to study the steady-state response of a single subsystem by Langley and Brown (2004a, b), Weaver (1989), Burkhardt and Weaver (1996), and Lobkis *et al.* (2000), and general built-up systems by Langley and Cotoni (2004). In contrast,

the steady-state response of a single subsystem with Poisson statistics has been studied by Lyon (1969) and Davy (1981), and a Poisson-based analysis has been applied to built-up systems by Lyon and DeJong (1995).

The existing literature raises several questions regarding the statistics of the energy density of a single subsystem subjected to point forcing, and these are addressed in the present paper. When considering the statistics of the transfer function between the forcing point and some other point on the subsystem, it is usual to consider the ensemble mean of the transfer function separately from the random part. The ensemble mean is termed the "direct field" and the random part the "reverberant field." Similarly the energy density associated with the random part can be termed the "reverberant energy density." Physically the reverberant field can be viewed as the component of response arising from random scattering of waves associated with the direct field. Intuitively it might be expected that the features that distinguish the forcing point from other points on the plate should be contained in the direct field, so that the reverberant field should not have any special properties at this point. However, Lyon (1969) has concluded that, assuming Poisson natural frequency statistics, the ensemble average reverberant energy density at the forcing point is a factor of $\frac{9}{4}$ times that at remote points for 2-D systems, and this factor becomes $\frac{27}{8}$ for 3-D systems. Lyon (1969) has also suggested that the relative variance of the reverberant energy density has a different form at the forcing point compared to remote points. Away from the forcing point, Eq. (65) of Lyon (1969) predicts that the relative variance tends to unity at high values of modal overlap, while it is suggested by Eq. (67) of Lyon (1969) that the relative variance at the forcing point grows without limit with increasing modal overlap. These unexpected results are reconsidered here, and also a comparison is made with results associated with GOE natural frequency statistics.

Weaver (1989), Burkhardt and Weaver (1996), and Lobkis *et al.* (2000) have already considered the relative variance of the reverberant energy density at a point remote from the forcing point, as given by GOE statistics. Burkhardt and Weaver (1996) extended the approximate GOE analysis of Weaver (1989) to random modal damping (i.e., decay curvature), and Lobkis *et al.* (2000) further extended this analysis to a more exact treatment of the GOE statistical functions. In all cases, agreement was found with the Lyon (1969) prediction that the relative variance tends to unity with increasing modal overlap. However, the ensemble average energy density and the relative variance at the forcing point were not considered by these authors, so that the other general predictions of Lyon (1969) were neither confirmed nor refuted. However, Weaver and Burkhardt (1994) have considered the related problem of the reverberant energy density of a system subjected to impulsive point forcing. It was found that at early times the ensemble average at the forcing point is twice that at remote points, while at later times this factor asymptotes to 3; these predictions have subsequently been confirmed by experiment by Weaver and Lobkis (2000), and the factor of 2 at early times has also been demonstrated by de Rosny *et al.* (2000). Although the impulsive loading case clearly differs from steady-state excitation, the special properties found at the forcing point are consistent with the results found by Lyon (1969) for the ensemble-averaged energy density. The present work considers the missing elements of (*i*) the ensemble average reverberant energy density at the forcing point and (*ii*) the relative variance at the forcing point, for a system with GOE natural frequency statistics driven by steady-state excitation.

The ensemble average reverberant energy density, both away from and near to the forcing point, is considered in Sec. II. Both Poisson and GOE natural frequencies are considered, and a comparison is made with numerical simulations for a plate with randomly located lumped masses. The relative variance of the energy density is then considered in Sec. III, and again the theory is compared with numerical simulations for a mass loaded plate. A relation between the energy density at the forcing point and the total energy of the system is derived in Sec. IV, and conclusions are given in Sec. V.

II. THE ENSEMBLE AVERAGE OF THE ENERGY DENSITY

A. General considerations

Consider a dynamic system that is subjected to a unit point load of frequency ω, acting at a spatial location $\mathbf{x}_0$. The displacement response H of the system at spatial location $\mathbf{x}$ can be written in the form of a modal sum [see, for example, Meirovitch (1986)], so that

$$H(\omega,\mathbf{x}_0,\mathbf{x}) = \sum_n \frac{\phi_n(\mathbf{x}_0)\phi_n(\mathbf{x})}{\omega_n^2(1+i\eta)-\omega^2}, \tag{1}$$

where ω_n and ϕ_n are respectively the natural frequency and mode shape (scaled to unit generalised mass) for the nth mode, and hysteretic damping with a constant loss factor η has been assumed. The more general case of a nonconstant loss factor has been considered by other authors [for example, Burkhardt and Weaver (1996) and Lobkis *et al.* (2000)], but in the present work it is assumed that η is constant, at least over the modes that contribute significantly to the response at any particular frequency. The validity of this assumption will depend on the nature of the dissipation; for example, Burkhardt and Weaver (1996) have shown that the loss factor can fluctuate significantly if discrete point dampers act on a system. On the other hand, a fairly constant loss factor can be expected if the loss mechanisms are spatially distributed, arising, for example, from a damping layer bonded to a system, and this is the type of situation considered here.

For the purposes of later analysis, Eq. (1) can also be written in the form

$$H(\omega,\mathbf{x}_0,\mathbf{x}) = \int_{-\infty}^{\infty} h(\omega,\omega')\xi(\omega')\mathrm{d}\omega', \tag{2}$$

$$\xi(\omega') = \sum_n c_n \delta(\omega'-\omega_n), \tag{3}$$

$$c_n = \phi_n(\mathbf{x}_0)\phi_n(\mathbf{x}), \tag{4}$$

$$h(\omega,\omega') = \frac{1}{\omega'^2(1+i\eta)-\omega^2} \approx \frac{1}{2\omega(\omega'-\omega+i\omega\eta/2)}, \quad (5)$$

where $\delta(\omega)$ is the Dirac delta function. The approximation employed in Eq. (5) simplifies the following analysis without significant loss of accuracy: $h(\omega,\omega')$ makes most contribution to Eq. (2) in the vicinity of $\omega \approx \omega'$, and in this vicinity $\omega'^2-\omega^2 \approx 2\omega(\omega'-\omega)$, leading to Eq. (5).

The present work is concerned with the statistics of H over an ensemble of random systems, i.e., the modes shapes ϕ_n, the natural frequencies ω_n, and the coefficients c_n are each considered to be random. The natural frequencies can be considered to form a sequence of random points on the frequency axis, and thus the problem is amenable to analysis by random point process theory. The main results of this theory will be employed here without proof, but full details of the background mathematics can be found in the texts by Stratonovich (1963) and Lin (1967). The theory is phrased in terms of a set of functions $g_s(\omega_1,\omega_2,\ldots,\omega_s)$, $s=1,2,\ldots,\infty$, that describe the statistics of the placement of the random points; these are called the correlation functions by Stratonovich (1963) and the cumulant functions by Lin (1967)—the latter terminology will be adopted here. The cumulant functions are symmetric with respect to the arguments, and, if the point process is stationary, i.e., the statistical properties are constant along the frequency axis, then g_s depends upon only $s-1$ arguments and can be written in the form $g_s(\omega_2-\omega_1,\ldots,\omega_s-\omega_1)$. Strictly, the natural frequency point process can only be stationary if the modal density of the system (ν, the average number of natural frequencies in a unit frequency band) is constant, and in many cases this is not true—for example the modal density increases with increasing frequency for a membrane, an acoustic volume, or the in-plane modes of a plate, although the modal density is actually constant for the bending modes of a plate. On the other hand, only a limited number of modes make a significant contribution to Eq. (1) at any specified frequency ω, and, providing the modal density is approximately constant over the span of these modes, then it is reasonable to assume that the point process is stationary. The number of modes that contribute is approximately equal to the modal overlap factor, $m=\omega\eta\nu$, and so the requirement is that the modal density is approximately constant over the frequency bandwidth $\omega\eta$. The natural frequency point process will be assumed to be stationary here, since this approximation will be accurate for most practical systems.

As mentioned previously, the cumulant functions g_s govern (or describe) the statistics of the system natural frequencies. The first cumulant function g_1 is always equal to the modal density ν, but the higher-order cumulant functions vary significantly across different statistical models. For example, if the natural frequencies are assumed to be Poisson, then $g_s=0$ for $s>1$, but if the natural frequencies are taken to have GOE statistics, then all of the cumulant functions are nonzero, and the lengthy formulas given by Mehta (1991) apply. Stratonovich (1987) has shown that the cumulants of the process $\xi(\omega')$ that appears in Eq. (3) can be written in terms of the functions g_s. For example, the first cumulant (i.e., the mean value) has the form

$$\kappa_1[\xi(\omega')] = \mathrm{E}[c_n]g_1 = \mathrm{E}[c_n]\nu. \quad (6)$$

Similarly, the second cumulant (i.e., the covariance function) is given by

$$\kappa_2[\xi(\omega_1'),\xi(\omega_2')] = \mathrm{E}[c_n]^2 g_2(\omega_2'-\omega_1') + \mathrm{E}[c_n^2]\delta(\omega_2'-\omega_1')g_1. \quad (7)$$

The third and fourth cumulants are also of interest in the present work, and these are given by

$$\begin{aligned}\kappa_3[\xi(\omega_1'),\xi(\omega_2'),\xi(\omega_3')] &= \mathrm{E}[c_n]^3 g_3(\omega_2'-\omega_1',\omega_3'-\omega_1') + 3\mathrm{E}[c_n^2]\mathrm{E}[c_n] \\ &\quad\times\{\delta(\omega_2'-\omega_1')g_2(\omega_3'-\omega_1')\}_s + \mathrm{E}[c_n^3]\delta(\omega_2'-\omega_1') \\ &\quad\times\delta(\omega_3'-\omega_1')g_1, \end{aligned} \quad (8)$$

$$\begin{aligned}\kappa_4[\xi(\omega_1'),\xi(\omega_2'),\xi(\omega_3'),\xi(\omega_4')] &= \mathrm{E}[c_n]^4 g_4(\omega_2'-\omega_1',\omega_3'-\omega_1',\omega_4'-\omega_1') + 6\mathrm{E}[c_n^2] \\ &\quad\times\mathrm{E}[c_n]^2\{\delta(\omega_2'-\omega_1')g_3(\omega_3'-\omega_1',\omega_4'-\omega_1')\}_s \\ &\quad + 3\mathrm{E}[c_n^2]^2\{\delta(\omega_2'-\omega_1')\delta(\omega_4'-\omega_3')g_2(\omega_3'-\omega_1')\}_s \\ &\quad + 4\mathrm{E}[c_n^3]\mathrm{E}[c_n]\{\delta(\omega_2'-\omega_1')\delta(\omega_3'-\omega_1')g_2(\omega_4'-\omega_1')\}_s \\ &\quad + \mathrm{E}[c_n^4]\delta(\omega_2'-\omega_1')\delta(\omega_3'-\omega_1')\delta(\omega_4'-\omega_1')g_1. \end{aligned} \quad (9)$$

The notation here is such that $\{X\}_s$, for any function X, represents the symmetric form of X, i.e., the sum of possible permutations of the arguments, divided by the number of possible permutations. In addition to the assumption that the point process is stationary, Eqs. (6)–(9) incorporate two further assumptions: (*i*) the coefficients c_n are statistically independent of each other and of the natural frequencies, and (*ii*) the statistical moments of c_n are the same for each mode n (at least for those modes that are close to the excitation frequency). These assumptions are consistent with existing models of random structures and can be expected to apply when the system has "statistical overlap," meaning that random variations in the system cause changes in the natural frequencies that exceed the mean frequency spacing. In this case any particular mode shape will vary considerably over the ensemble, thus promoting conditions (*i*) and (*ii*).

Equations (6)–(9), in conjunction with Eq. (2), allow expressions to be derived for the statistical moments of the transfer function. For example, taking the expectation of Eq. (2) and using Eq. (6) yields

$$\begin{aligned}\mathrm{E}[H(\omega,\mathbf{x}_0,\mathbf{x})] &= \int_{-\infty}^{\infty} h(\omega,\omega')\kappa_1[\xi(\omega')]\mathrm{d}\omega' \\ &= -i\mathrm{E}[c_n]\pi\nu/(2\omega). \end{aligned} \quad (10)$$

It is interesting to consider this result at the forcing point $\mathbf{x}=\mathrm{x}_0$, where $c_n=\phi_n^2(\mathbf{x}_0)$. Given that the mode shapes are scaled to unit generalized mass, it follows that $\mathrm{E}[\phi_n^2]=1/M$, where M is the total mass of the system. Equation (10) thus becomes

$$\mathrm{E}[H(\omega,\mathbf{x}_0,\mathbf{x}_0)] = -i\pi\nu/(2M\omega). \quad (11)$$

Now both the modal density ν and the total mass M scale in proportion to the size of the system, meaning that the result

given by Eq. (11) is actually independent of the system size. In fact, Eq. (11) agrees with a known result (Cremer *et al.*, 1990) for the imaginary part of the response of an infinite system to a point force. The physics behind this result can be explained by noting that the total response of the finite system consists of the response of an infinite system (called the "direct field"), together with reflections of this response from the system boundaries (known as the "reverberant field"). Equation (11) states that the reverberant field averages to zero across the ensemble, to leave the direct field, although it should be noted that any real component of the direct field is missing from Eq. (11). This is because the modal density has been assumed to be constant in the present analysis, which is correct for a plate in bending, but incorrect for a beam, for example. Equation (11) is fully correct for a plate, but to compute the nonzero real part of the response for a beam, a modified analysis must be used, as described by Langley (1994). The imaginary part of the response is sometimes called the "resistive" component, being associated with the transmission of power, as opposed to the real or "reactive" component which does not contribute to the transmission of power. Thus from an energy balance point of view, the imaginary component of the direct field is the key quantity, and this is predicted correctly by the present level of approximation. In what follows the statistics of the reverberant field (i.e., the total response minus the direct field) is considered in detail, and thus any errors regarding the real part of the direct field do not propagate through the analysis.

The following sections consider the higher statistical moments of the response under two different models of the natural frequency statistics: Poisson statistics and GOE statistics. The main concern is with the properties of the modulus squared response at a general location $\mathbf{x}$, a quantity which is directly proportional to the *energy density* at this location.

B. Poisson natural frequency statistics

It follows from Eq. (2) that the squared modulus of the response can be written in the form

$$|H(\omega,\mathbf{x}_0,\mathbf{x})|^2 = \int_{-\infty}^{\infty}\int_{-\infty}^{\infty} h(\omega,\omega_1')h^*(\omega,\omega_2')\xi(\omega_1')\xi(\omega_2')\mathrm{d}\omega_1'\,\mathrm{d}\omega_2'. \quad (12)$$

Now if the reverberant response H_{rev} is defined as the total response minus the direct field given by Eq. (11), then it follows that

$$\mathrm{E}[|H_{\mathrm{rev}}(\omega,\mathbf{x}_0,\mathbf{x})|^2] = \int_{-\infty}^{\infty}\int_{-\infty}^{\infty} h(\omega,\omega_1')h^*(\omega,\omega_2')\kappa_2[\xi(\omega_1')\xi(\omega_2')]\mathrm{d}\omega_1'\,\mathrm{d}\omega_2', \quad (13)$$

where κ_2 is the covariance function given by Eq. (7). If the natural frequencies are assumed to have Poisson statistics, then $g_2=0$, and Eq. (13) can readily be evaluated to yield

$$\mathrm{E}[|H_{\mathrm{rev}}(\omega,\mathbf{x}_0,\mathbf{x})|^2] = \mathrm{E}[c_n^2]\pi\nu/(2\omega^3\eta) = \mathrm{E}[\phi_n^2(\mathbf{x}_0)\phi_n^2(\mathbf{x})]\pi\nu/(2\omega^3\eta). \quad (14)$$

Away from the drive point, where $\mathbf{x}$ and $\mathbf{x}_0$ are well separated so that $\phi_n(\mathbf{x}_0)$ and $\phi_n(\mathbf{x})$ can be considered to be statistically independent, the expectation in Eq. (14) yields $\mathrm{E}[\phi_n^2(\mathbf{x}_0)\phi_n^2(\mathbf{x})]\approx 1/M^2$, so that

$$\mathrm{E}[|H_{\mathrm{rev}}(\omega,\mathbf{x}_0,\mathbf{x})|^2]_{\mathrm{far}} = \pi\nu/(2M^2\omega^3\eta). \quad (15)$$

Here the subscript "far" indicates the value in the far field of the point load. Equation (15) is fully consistent with a power balance analysis of the type that would be performed in statistical energy analysis (Lyon and DeJong, 1995): Eq. (11) implies that the ensemble average power input to the system by a unit load is $\mathrm{E}[P_{\mathrm{in}}]=\pi\nu/4M$, and this must equal the power dissipated by the system, which is given by $\omega\eta\mathrm{E}[E]$, where $\mathrm{E}[E]$ is the ensemble average of the total energy. Writing $\mathrm{E}[E]=\mathrm{E}[|H|^2]\omega^2M/2$ (the total energy is twice the time averaged kinetic energy) then leads to Eq. (15).

At the drive point ($\mathbf{x}=\mathbf{x}_0$) the expectation in Eq. (14) becomes $\mathrm{E}[\phi_n^4]$. Having assumed that the natural frequencies have a Poisson distribution, it is consistent to assume that the mode shapes are sinusoidal (Lyon, 1969); this is exactly the situation that applies to a rectangular plate or a box-shaped acoustic space. In this case $\mathrm{E}[\phi_n^4]=9/4M^2$ for a two-dimensional system and $\mathrm{E}[\phi_n^4]=27/8M^2$ for a three-dimensional system. It then follows that

$$\mathrm{E}[|H_{\mathrm{rev}}(\omega,\mathbf{x}_0,\mathbf{x}_0)|^2]/\mathrm{E}[|H_{\mathrm{rev}}(\omega,\mathbf{x}_0,\mathbf{x})|^2]_{\mathrm{far}} = \begin{cases} 9/4, & \text{2-D system,} \\ 27/8, & \text{3-D system.} \end{cases} \quad (16)$$

Hence the Poisson assumption leads to the conclusion that there is a concentration of the reverberant field at the drive point, and the concentration factor is something greater than 2. Equation (16) has previously been derived by Lyon [1969, Eq. (62)]. It can be noted that the mode shapes associated with Poisson natural frequency statistics are not necessarily sinusoidal, and thus Eq. (16) can be considered to be a special case, limited to systems with a simple geometry.

C. GOE natural frequency statistics

For GOE natural frequency statistics the cumulant function g_2 is nonzero, and Eqs. (7) and (12) lead to the result

$$\mathrm{E}[|H_{\mathrm{rev}}(\omega,\mathbf{x}_0,\mathbf{x})|^2] = \mathrm{E}[c_n]^2\int_{-\infty}^{\infty}\int_{-\infty}^{\infty} h(\omega,\omega_1')h^*(\omega,\omega_2')g_2(\omega_2'-\omega_1') \times \mathrm{d}\omega_1'\,\mathrm{d}\omega_2' + \mathrm{E}[c_n^2]\pi\nu/(2\omega^3\eta). \quad (17)$$

By putting $\chi=\omega_2'-\omega_1'$ and changing the integration variables from (ω_1',ω_2') to (ω_1',χ), the integral over ω_1' can be performed by contour integration to yield

$$\int_{-\infty}^{\infty}\int_{-\infty}^{\infty} h(\omega,\omega_1')h^*(\omega,\omega_2')g_2(\omega_2'-\omega_1')\mathrm{d}\omega_1'\,\mathrm{d}\omega_2'$$

$$=\int_{-\infty}^{\infty}\frac{i\pi g_2(\chi)\mathrm{d}\chi}{2\omega^2(-\chi+i\omega\eta)}. \tag{18}$$

This integral can also be written in the form

$$\int_{-\infty}^{\infty}\frac{i\pi g_2(\chi)\mathrm{d}\chi}{2\omega^2(-\chi+i\omega\eta)}=\int_{-\infty}^{\infty}s(\theta)G_2(\theta)\mathrm{d}\theta, \tag{19}$$

where

$$s(\theta)=\frac{1}{2\pi}\int_{-\infty}^{\infty}\frac{i\pi e^{i\theta\chi}\,\mathrm{d}\chi}{2\omega^2(-\chi+i\omega\eta)}$$

$$=\begin{cases}(\pi/2\omega^2)e^{-\omega\eta\theta},\theta>0,\\ 0,\quad \theta<0,\end{cases} \tag{20}$$

$$G_2(\theta)=\int_{-\infty}^{\infty}g_2(\chi)e^{-i\chi\theta}\,\mathrm{d}\chi. \tag{21}$$

Equation (19) is a statement of Parseval's theorem [see, for example, Morfey (2001)], with Eqs. (20) and (21) representing the Fourier transforms of the two functions that appear in the integrand on the left-hand side of the equation. For GOE natural frequency statistics, the Fourier transform of the second cumulant function is given by (Mehta, 1991)

$$G_2(\theta)=-\nu b(\theta/2\pi\nu), \tag{22}$$

$$b(\theta)=\begin{cases}1-2|\theta|+|\theta|\ln(1+2|\theta|), & |\theta|\leqslant 1,\\ -1+|\theta|\ln\left(\dfrac{2|\theta|+1}{2|\theta|-1}\right), & |\theta|\geqslant 1.\end{cases} \tag{23}$$

The integral appearing in Eq. (19) has previously been evaluated by Langley and Brown (2004a) in a study concerning the variance of the total energy of a random system. The result is $\pi\nu q(m)/(2\omega^3\eta)$, where $m=\omega\eta\nu$ is the modal overlap of the system and the function $q(m)$ is given by

$$q(m)=-1+\frac{1}{2\pi m}[1-\exp(-2\pi m)]+\mathrm{E}_1(\pi m)$$

$$\times\left[\cosh(\pi m)-\frac{1}{\pi m}\sinh(\pi m)\right], \tag{24}$$

where E_1 is the exponential integral (Abramowitz and Stegun, 1964). By combining this result with Eqs. (18) and (19), the ensemble average of the squared modulus of the reverberant response can be written in the form

$$\mathrm{E}[|H_{\mathrm{rev}}(\omega,\mathbf{x}_0,\mathbf{x})|^2]=\frac{\pi\nu}{2\omega^3\eta}\{\mathrm{E}[c_n^2]+\mathrm{E}[c_n]^2q(m)\}. \tag{25}$$

It can be recalled that $c_n=\phi_n(\mathbf{x}_0)\phi_n(\mathbf{x})$, so that further progress in evaluating Eq. (25) requires knowledge of the statistical properties of the mode shapes. It is often postulated that the mode shapes associated with the GOE are Gaussian (Mehta, 1991), although a number of studies have revealed slight variations from Gaussian statistics for practical systems (Langley and Brown, 2004a, b; Weaver, 1989; Burkhardt and Weaver, 1996; Lobkis *et al.*, 2000). This issue is discussed further in Sec. III and the Appendix, but, nonetheless, the Gaussian hypothesis is a good first approximation, in which case

$$\mathrm{E}[c_n^2]=\mathrm{E}[\phi_n^2(\mathbf{x}_0)\phi_n^2(\mathbf{x})]$$

$$=\mathrm{E}[\phi_n^2(\mathbf{x}_0)]\mathrm{E}[\phi_n^2(\mathbf{x})]+2\mathrm{E}[\phi_n(\mathbf{x}_0)\phi_n(\mathbf{x})]^2. \tag{26}$$

Now, as mentioned previously, the fact that the mode shapes are scaled to unit generalized mass implies that $E[\phi_n^2(\mathbf{x})]=1/M$. Furthermore, taking the mode shapes to form a homogeneous random field, the final expectation appearing in Eq. (26) can be written as

$$\mathrm{E}[\phi_n(\mathbf{x}_0)\phi_n(\mathbf{x})]=R(\mathbf{x}-\mathbf{x}_0)/M, \tag{27}$$

where R is the correlation function. From wave-mode duality arguments [see for example Weaver and Burkhardt (1994) and also Berry 1983], it can be deduced that the appropriate value of R is the *diffuse field correlation function*, which for two- and three-dimensional systems has the form (Cremer *et al.*, 1990)

$$R(\mathbf{x}-\mathbf{x}_0)=\begin{cases}J_0(kr), & \text{2-D system},\\ \sin(kr)/kr, & \text{3-D system},\end{cases} \tag{28}$$

where k is the wave number of the vibrations and $r=|\mathbf{x}-\mathbf{x}_0|$. By employing Eqs. (26) and (27), Eq. (25) becomes

$$\mathrm{E}[|H_{\mathrm{rev}}(\omega,\mathbf{x}_0,\mathbf{x})|^2]=\frac{\pi\nu}{2M^2\omega^3\eta}\{1+R^2(\mathbf{x}-\mathbf{x}_0)[2+q(m)]\}. \tag{29}$$

At points remote from the drive point, where $R\approx 0$, Eq. (15) is recovered, so that the GOE result agrees with both the Poisson result and the energy balance argument. More generally, the concentration factor near to the drive point can be written as

$$\mathrm{E}[|H_{\mathrm{rev}}(\omega,\mathbf{x}_0,\mathbf{x})|^2]/\mathrm{E}[|H_{\mathrm{rev}}(\omega,\mathbf{x}_0,\mathbf{x})|^2]_{\mathrm{far}}$$

$$=1+R^2(\mathbf{x}-\mathbf{x}_0)[2+q(m)]. \tag{30}$$

Now the function $q(m)$ tends to 0 for low values of m, and to -1 for high values of m. Thus at the drive point, where $R=1$, the concentration factor has the following properties:

$$\mathrm{E}[|H_{\mathrm{rev}}(\omega,\mathbf{x}_0,\mathbf{x}_0)|^2]/\mathrm{E}[|H_{\mathrm{rev}}(\omega,\mathbf{x}_0,\mathbf{x})|^2]_{\mathrm{far}}=\begin{cases}3, & m\to 0,\\ 2, & m\to\infty.\end{cases} \tag{31}$$

This result can be compared with results obtained by Weaver and Burkhardt (1994) concerning the impulsive excitation of a random system. It was found that at early times the concentration factor at the drive point is 2, while at later times this factor tends to 3. There is a physical analogy between time in a transient analysis and the modal overlap factor in a steady-state analysis: at low times and high modal overlap factor, the response consists of relatively few reflections from the system boundaries; at later times and low modal overlap factor, the input waves reflect many times from the boundaries. Weaver and Burkhardt (1994) have further de-

scribed how the factor of 2 might be anticipated from a time-reversal argument.

The result given by Eq. (30) is quite different from that resulting from the assumption of Poisson natural frequency statistics, Eq. (16). A comparison is made with simulation results for a mass loaded plate in the following section.

D. Numerical simulations

In this section simulation results are presented for the concentration factor of the reverberant response of a random system near to the drive point. The example consists in a flat plate excited by a harmonic transverse point force. Only bending motion is considered (i.e., in-plane motion is not included). The plate is rectangular and simply supported, of size 1.35×1.2 m^2 and thickness 5 mm. The construction material is aluminium (Young's modulus 7.2×10^{10} N/m^2, density 2800 kg/m^3, and Poisson ratio 0.3), and the plate is damped with a damping loss factor of either 1% or 0.1%. Randomization of the plate has been achieved by adding ten point masses at random locations, with each mass having 2% of the total mass of the plate, and three rotational springs randomly located on each edge.

Benchmark Monte Carlo simulation results have been obtained by using the Lagrange-Rayleigh-Ritz method with the sine-sine mode shapes of the bare plate as basis functions. The added masses and springs are accounted for in the analysis by adding the appropriate kinetic and potential energies to the Lagrangian. An ensemble of 200 systems has been generated and solved. Since the primary interest here is in the reverberant response, the direct field from the point load was systematically subtracted from the complete response. As explained below Eq. (11), the direct field is the ensemble mean of the complex response, $H_{\mathrm{dir}}(\omega,\mathbf{x}_0,\mathbf{x})=\mathrm{E}[H(\omega,\mathbf{x}_0,\mathbf{x})]$, and the remaining reverberant part of the response, $H_{\mathrm{rev}}=H-H_{\mathrm{dir}}$, has zero mean.

The concentration factor at the drive point was first computed over the frequency range $[0,3000]$ Hz. This was done by calculating the ensemble mean of the squared modulus reverberant response at the drive point and then dividing by the ensemble mean of the spatially averaged response. This ratio was obtained for each of 20 drive points distributed over the plate area: the location of each point was held fixed for all realizations, and the locations were chosen to be remote from the plate edges to avoid near-field and correlation effects that are not covered by the present theory. Although the theory applies to any one of the 20 drive points, the simulated concentration ratios were averaged over the 20 points in order to improve the convergence afforded by the limited ensemble size.

The predictions yielded by the present theory were obtained by using the theoretical asymptotic modal density for the plate, $\nu=S(\rho h/D)^{1/2}/4\pi$, where S is the area of the plate, ρ is the density, h is the thickness, and D is the flexural rigidity. This yields $\nu=0.0168$ Hz^{-1}, while the actual value obtained from the eigensolution of the Monte Carlo realizations was around 0.0160 Hz^{-1} (i.e., less than 5% error). The investigated frequency range therefore encompasses approximately 314 resonant modes of the plate. For the damping cases of $\eta=1\%$ and $\eta=0.1\%$, the modal overlap at 3000 Hz is respectively $m=3.14$ and $m=0.314$. Since the modal overlap is a linear function of frequency for plates with constant damping, the value of m can readily be deduced for any frequency.

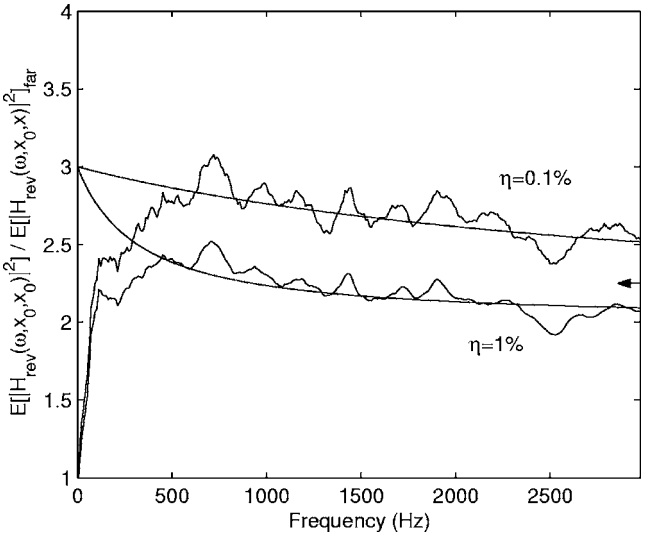

FIG. 1. The concentration factor at the drive point of a random plate, as a function of frequency, for two values of damping. The simulation results are the fluctuating curves; the GOE predictions from Eq. (30) are the solid lines; and the arrow indicates the Poisson frequency independent prediction according to Eq. (16).

The simulated concentration factor is shown in Fig. 1 as a function of frequency for both values of damping, and a comparison is made with the theoretical result yielded by Eq. (30). Reasonable agreement between theory and simulation is obtained above 400 Hz in the highly damped case and above 800 Hz in the lightly damped case. Below these frequencies, it is believed that the randomization is not strong enough to produce statistical overlap, i.e., the added masses and springs are insufficient to completely randomize the plate at low frequencies, and thus the present theory does not apply. It can be noted that despite averaging over the 20 drive point locations, and over the 200 realizations of the ensemble, the simulation results are not entirely smooth functions of frequency. This behaviour can be traced primarily to lack of convergence due to the finite size of the ensemble.

For the case of 0.1% damping, the spatial variation of the concentration factor was investigated at the frequency 3000 Hz. Simulation results were obtained in the vicinity of the drive point, along ten lines of length $L=0.4$ m, starting in different directions from ten driving locations. Here again, although the theory describes any of the 10×10 spatial distributions, the simulated results were averaged over all the cases to accelerate convergence. At 3000 Hz, the flexural wavelength is $\lambda=0.127$ m, so that around three wavelengths lie along the measurement lines.

The concentration factor is shown in Fig. 2 as a function of the normalized distance from the drive point, and a comparison is made with the analytical result yielded by Eq. (30). The modal overlap is 0.314, yielding $q(m)=-0.48$ in Eq. (30), so that the concentration factor at the drive point is

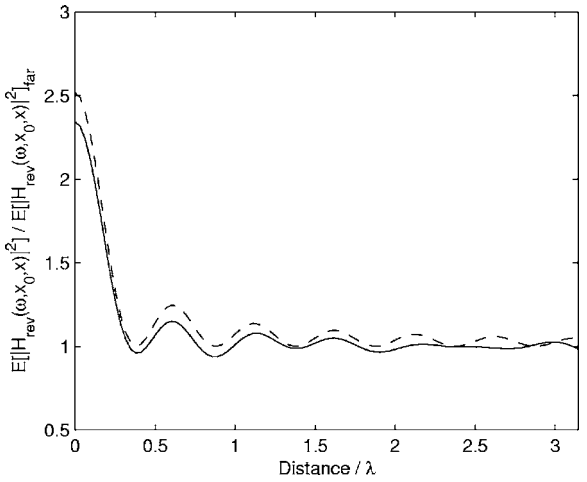

FIG. 2. Spatial variation of the concentration factor of the reverberant field along a line starting at the drive point of a random plate. Solid: simulation result; dotted: GOE prediction from Eq. (30).

predicted to be 2.52. This is slightly larger than the simulation result, and this can be traced largely to the fact that Eq. (30) is based on the assumption of Gaussian mode shapes; the validity of this assumption is explored in detail in Sec. III D. The oscillatory behavior predicted by Eq. (30) is clearly visible in the simulation results, with the position of the nodes and antinodes being determined by the nodes and antinodes of the diffuse field correlation function. Finally, in this section, it can be noted that the present theory concerns the ratio of ensemble mean quantities; however, it might be expected that a frequency-band average performed on the response of a single realization would yield similar results [see, for example, de Rosny *et al.* (2000)].

III. THE RELATIVE VARIANCE OF THE ENERGY DENSITY

A. General considerations

The aim of this section is to compute the relative variance of the energy density at the location $\mathbf{x}$. Since the energy density is directly proportional to the modulus squared response, the relative variance can be written in the form

$$r^2 = \frac{\mathrm{E}[|H_{\mathrm{rev}}(\omega,\mathbf{x}_0,\mathbf{x})|^4] - \mathrm{E}[|H_{\mathrm{rev}}(\omega,\mathbf{x}_0,\mathbf{x})|^2]^2}{\mathrm{E}[|H_{\mathrm{rev}}(\omega,\mathbf{x}_0,\mathbf{x})|^2]^2}. \tag{32}$$

The second term in the numerator is available from either Eq. (14) for Poisson statistics or Eq. (29) for GOE statistics, and thus the remaining task is to derive an expression for the first term. Progress can be made by noting the following relation (Stratonovich, 1963) between the fourth central moment of H and the cumulants of H (omitting the arguments of H for clarity):

$$\mathrm{E}[|H_{\mathrm{rev}}|^4] = \kappa_4[H,H,H^*,H^*] + 2\kappa_2^2[H,H^*] + \kappa_2[H,H]\kappa_2[H^*,H^*]. \tag{33}$$

Now by definition $\kappa_2[H,H^*]=\mathrm{E}[|H_{\mathrm{rev}}|^2]$, and it can readily be shown from an analysis similar to that presented in Sec. II C that $\kappa_2[H,H]=0$. It therefore follows from Eqs. (32) and (33) that

$$r^2 = 1 + \frac{\kappa_4[H,H,H^*,H^*]}{\mathrm{E}[|H_{\mathrm{rev}}(\omega,\mathbf{x}_0,\mathbf{x})|^2]^2}. \tag{34}$$

Now it follows from Eq. (2) that

$$\kappa_4[H,H,H^*,H^*] = \int_{-\infty}^{\infty}\int_{-\infty}^{\infty}\int_{-\infty}^{\infty}\int_{-\infty}^{\infty} h(\omega,\omega_1') \times h(\omega,\omega_2')h^*(\omega,\omega_3')h^*(\omega,\omega_4')\cdots \cdots \kappa_4[\xi(\omega_1'),\xi(\omega_2'),\xi(\omega_3'),\xi(\omega_4')] \times \mathrm{d}\omega_1'\,\mathrm{d}\omega_2'\,\mathrm{d}\omega_3'\,\mathrm{d}\omega_4', \tag{35}$$

where the joint cumulant function that appears inside the integral is given by Eq. (9). Equations (34) and (35) will be evaluated in the following sections for the two cases of Poisson and GOE natural frequency statistics.

B. Poisson natural frequency statistics

In the case of Poisson natural frequency statistics, only the first cumulant function g_1 is nonzero, and hence Eqs. (9) and (35) lead to the result

$$\kappa_4[H,H,H^*,H^*] = \mathrm{E}[c_n^4]\nu\int_{-\infty}^{\infty}|h(\omega,\omega_1')|^4\,\mathrm{d}\omega_1'. \tag{36}$$

The integral in this equation is readily evaluated by contour integration, and Eqs. (14), (34), and (36) then yield

$$r^2 = 1 + \frac{\mathrm{E}[c_n^4]}{\mathrm{E}[c_n^2]^2}\left(\frac{1}{\pi m}\right). \tag{37}$$

At large values of modal overlap this equation yields $r=1$, which agrees with a result derived by Schroeder (1987). Schroeder (1987) assumed on the basis of the central limit theorem that, above a frequency known as the Schroeder frequency, the transfer function can be taken to be a complex Gaussian process, meaning that the modulus squared transfer function has an exponential distribution (and hence $r=1$). The Schroeder frequency is often taken to be the frequency at which $m=3$, and this is consistent with the second term in Eq. (37) making a small contribution to the relative variance.

At points distant from the drive point $\phi_n(\mathbf{x})$ can be considered to be statistically independent of $\phi_n(\mathbf{x}_0)$, and Eq. (37) yields

$$r_{\mathrm{far}}^2 = 1 + \left(\frac{\mathrm{E}[\phi_n^4]}{\mathrm{E}[\phi_n^2]^2}\right)^2\left(\frac{1}{\pi m}\right) = \begin{cases} 1 + 5.06/(\pi m), & \text{2-D systems,} \\ 1 + 11.39/(\pi m), & \text{3-D systems,} \end{cases} \tag{38}$$

where, as in Eq. (16), sinusoidal mode shapes have been assumed. This result is in agreement with Eq. (65) of Lyon (1969). At the drive point, where $\phi_n(\mathbf{x})=\phi_n(\mathbf{x}_0)$, Eq. (37) yields

$$r_{\mathrm{drive}}^2 = 1 + \left(\frac{\mathrm{E}[\phi_n^8]}{\mathrm{E}[\phi_n^4]^2}\right)\left(\frac{1}{\pi m}\right) = \begin{cases} 1 + 3.78/(\pi m), & \text{2-D systems,} \\ 1 + 7.35/(\pi m), & \text{3-D systems.} \end{cases} \tag{39}$$

This result does *not* agree with Eq. (67) of Lyon, which in the present notation reads

$$r^2_{\text{drive}} = 1 + \left(\frac{\mathrm{E}[\phi_n^8]}{\mathrm{E}[\phi_n^4]^2}\right)\left(\frac{1}{\pi m}\right) + \left(\frac{\mathrm{E}[\phi_n^2]^2}{\mathrm{E}[\phi_n^4]}\right)\pi m + 8\left(\frac{\mathrm{E}[\phi_n^6]\mathrm{E}[\phi_n^2]}{\mathrm{E}[\phi_n^4]^2}\right). \quad (40)$$

Equation (40) predicts that the relative variance increases with increasing modal overlap, which is very different to the far-field result, Eq. (39), and Lyon (1969) makes special mention of this behavior. However, a close inspection of the derivation of Eq. (40) reveals that the computed result is not the relative variance of the reverberant field: rather it is the ratio $\{\mathrm{E}[|H|^4]-\mathrm{E}[|H|^2]^2\}/\mathrm{E}[|H_{\text{rev}}|^2]^2$, meaning that the numerator includes the direct field but the denominator does not. Equation (39) therefore provides a more consistent comparison with the far-field result, Eq. (38), and in both cases the relative variance decreases with increasing modal overlap.

C. GOE natural frequency statistics

In the case of GOE natural frequency statistics, all of the cumulant functions that appear in Eq. (9) are nonzero, and thus the evaluation of the integral that appears in Eq. (35) is far from trivial. In the far field of the drive point the condition $\mathrm{E}[c_n]=0$ applies, and in this case Eq. (35) simplifies to

$$\kappa_4[H,H,H^*,H^*] = \mathrm{E}[c_n^2]^2\left\{2\int_{-\infty}^{\infty}\int_{-\infty}^{\infty}|h(\omega,\omega_1')|^2|h(\omega,\omega_2')|^2 g_2(\omega_2'-\omega_1')\times \mathrm{d}\omega_1'\,\mathrm{d}\omega_2' + \int_{-\infty}^{\infty}\int_{-\infty}^{\infty}h^2(\omega,\omega_1')h^{*2}(\omega,\omega_2')g_2(\omega_2'-\omega_1')\times \mathrm{d}\omega_1'\,\mathrm{d}\omega_2'\right\} + \mathrm{E}[c_n^4]\nu\int_{-\infty}^{\infty}|h(\omega,\omega_1')|^4\,\mathrm{d}\omega_1'. \quad (41)$$

As in Sec. III C, the first two integrals that appear in this expression can be evaluated by putting $\chi=\omega_2'-\omega_1'$ and changing the integration variables from (ω_1',ω_2') to (ω_1',χ). All of the integrals over ω_1' can then be performed by contour integration, and the remaining integral over χ can be reexpressed in a similar fashion to Eq. (19). Equation (34) then yields

$$r^2_{\text{far}} = 1 + \left(\frac{1}{\pi m}\right)\left\{\frac{\mathrm{E}[c_n^4]}{\mathrm{E}[c_n^2]^2} - f(m)\right\}, \quad (42)$$

where

$$f(m) = 4\pi m\int_0^{\infty} b(\theta)[1+(\pi m\theta)^2]e^{-2\pi m\theta}\,\mathrm{d}\theta, \quad (43)$$

and $b(\theta)$ is given by Eq. (23). Equations (42) and (43) have previously been derived by Lobkis *et al.* (2000), although the result quoted for $f(m)$ in that reference contains a number of small typographical errors. The corrected version, in the same format as (Lobkis *et al.*, 2000), is

$$f(m) = \left(\frac{\pi m}{4}+2-\frac{5}{4\pi m}\right) + e^{-2\pi m}\left(\frac{\pi m}{4}+\frac{1}{2}+\frac{5}{4\pi m}\right) - \mathrm{E}_1(\pi m)e^{-\pi m}\left(\frac{\pi^2m^2}{4}+\frac{3\pi m}{4}+\frac{5}{2}+\frac{5}{2\pi m}\right) - \mathrm{E}_1(\pi m)e^{\pi m}\left(\frac{\pi^2m^2}{4}-\frac{3\pi m}{4}+\frac{5}{2}-\frac{5}{2\pi m}\right). \quad (44)$$

The function $f(m)$ varies between 0 and 3 as the modal overlap factor increases from zero to infinity, so that Eq. (42) has the behavior

$$r^2_{\text{far}} = \begin{cases} 1+K^2/(\pi m), & m\to 0,\\ 1+(K^2-3)/(\pi m), & m\to\infty, \end{cases} \quad (45)$$

where

$$K = \frac{\mathrm{E}[\phi_n^4]}{\mathrm{E}[\phi_n^2]^2}. \quad (46)$$

For Gaussian mode shapes $K=3$, although for various types of dynamic systems it has been found that the mode shapes have a small negative excess of kurtosis, and Langley and Brown (2004a, b) have suggested that $K\approx 2.7$ provides closer agreement with both experimental and numerical data. Other authors have also found values of $K<3$, and in some cases it has been postulated that this could be due to the fact that the mode shapes are complex for nonproportionally damped systems [for example, Lobkis *et al.* (2000)]. In both Langley and Brown (2004a, b) and the present work, proportional damping is considered and thus a value of $K<3$ cannot be explained by the occurrence of complex modes, since the modes are purely real. An alternative explanation is suggested in the Appendix, based on the eigenvalue statistics reported by Brody *et al.* (1981).

For $K=2.7$, Eq. (45) yields $r^2_{\text{far}}=1+7.29/(\pi m)$ at low modal overlap, and $r^2_{\text{far}}=1+4.29/(\pi m)$ at high modal overlap; these results enclose the Poisson result given by Eq. (38) for 2-D systems, $r^2_{\text{far}}=1+5.06/(\pi m)$, but both results lie below the Poisson prediction for 3-D systems, $r^2_{\text{far}}=1+11.39/(\pi m)$.

At the drive point $\mathrm{E}[c_n]\neq 0$ and all of the terms in Eq. (9) contribute to Eq. (35). An exact analysis of the relative variance would be extremely difficult in this case due to the presence of the higher-order cumulant functions g_3 and g_4 in Eq. (9). Furthermore, Eq. (9) includes terms involving the eighth statistical moment of the mode shape at the drive point, and it can be argued that uncertainties in the mode shape statistics do not justify a fully rigorous analysis. A compromise is to neglect the higher-order correlations associated with g_3 and g_4 in Eq. (9) and retain only the more tractable terms involving g_2. The penultimate term in Eq. (9) adds the following contribution to Eq. (41):

$$\kappa_4[H,H,H^*,H^*] = \kappa_4[H,H,H^*,H^*]_{\text{far}} + 4\mathrm{E}[c_n^3]\mathrm{E}[c_n]\mathrm{Re}\times\int_{-\infty}^{\infty}\int_{-\infty}^{\infty}h(\omega,\omega_1')h(\omega,\omega_2')h^{*2}(\omega,\omega_2')\times g_2(\omega_2'-\omega_1')\mathrm{d}\omega_1'\,\mathrm{d}\omega_2'. \quad (47)$$

The integral in this equation can be evaluated by using the same technique employed for Eqs. (17) and (41). The final result for the relative variance, as given by Eq. (34) with $\mathbf{x}=\mathbf{x}_0$, is

$$r^2_{\text{drive}} = 1 + \frac{\mathrm{E}[\phi_n^8] - \mathrm{E}[\phi_n^4]^2 f(m) - \mathrm{E}[\phi_n^6]\mathrm{E}[\phi_n^2] s(m)}{\pi m \{\mathrm{E}[\phi_n^4] + \mathrm{E}[\phi_n^2]^2 q(m)\}^2}, \quad (48)$$

where

$$s(m) = 4\pi m \int_0^\infty b(\theta)[1 + \pi m \theta] e^{-2\pi m \theta} \, \mathrm{d}\theta. \quad (49)$$

This integral can be evaluated to yield

$$s(m) = \left(3 - \frac{2}{\pi m}\right) + e^{-2\pi m}\left(1 + \frac{2}{\pi m}\right) - \mathrm{E}_1(\pi m) e^{-\pi m} \times \left(\pi m + 3 + \frac{3}{\pi m}\right) + \mathrm{E}_1(\pi m) e^{\pi m}\left(\pi m - 3 + \frac{3}{\pi m}\right). \quad (50)$$

The function $s(m)$ varies between 0 and 4 as m increases from zero to infinity. If it is assumed that the mode shapes are Gaussian, then Eq. (48) can be rewritten in the form

$$r^2_{\text{drive}} = 1 + \frac{105 - 9f(m) - 15s(m)}{\pi m \{3 + q(m)\}^2}, \quad (51)$$

and the limiting values of the relative variance are

$$r^2_{\text{drive}} = \begin{cases} 1 + 11.7/(\pi m), & m \to 0, \\ 1 + 4.5/(\pi m), & m \to \infty. \end{cases} \quad (52)$$

Were the mode shapes assumed to be Gaussian in Eq. (45), then the corresponding numerators of the $1/(\pi m)$ term would be 9 and 6 for the far field response. Equation (52) thus suggests that at high modal overlap the relative variance at the drive point is slightly lower than that in the far field, and this is consistent with the Poisson results, Eqs. (38) and (39). It should be emphasized that Eq. (52) is based on the neglect of g_3 and g_4 and the assumption of Gaussian mode shapes, and conclusions based on this equation should thus be considered with some degree of caution.

D. Numerical simulations

The same ensemble of 200 random plates employed in Sec. II D has been used to assess the theoretical predictions of the relative variance of the response. For the two damping cases already noted ($\eta=1\%$ and 0.1%), the squared modulus reverberant response at the drive point and at a point distant from the drive point were each computed over the frequency range $[0, 3000]$ Hz. For each random realization of the plate, 20 drive points were considered and the ensemble relative variance results were averaged over these points to improve convergence. As noted in Sec. II D, the plate modal density is $\nu=0.0168$ Hz^{-1}, and for the damping cases of $\eta=1\%$ and $\eta=0.1\%$ the modal overlap ranges from $m=0$ to respectively 3.14 and 0.314 at 3000 Hz.

Before considering the relative variance of the response, it is instructive to investigate the statistical moments of the mode shapes which appear in Eqs. (38), (39), (42), and (48).

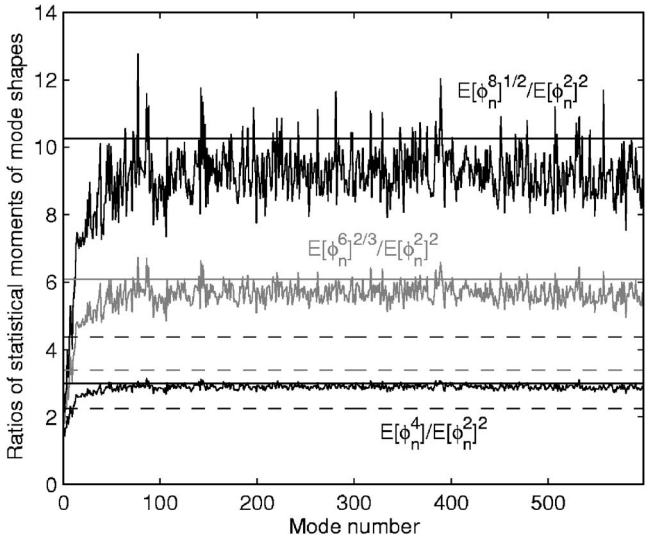

FIG. 3. Ratio of the statistical moments of the mode shapes of a random plate, as a function of the mode number. The fluctuating curves are the simulation results; the solid horizontal lines are the values for Gaussian mode shapes; and the dotted lines are the values for sinusoidal mode shapes.

These moments have been computed by performing an eigenanalysis for each realization in the ensemble: the first 598 modes were extracted, and the corresponding value at a fixed location $\mathbf{x}$, $\phi_n(\mathbf{x})$, was used to derive ensemble average quantities of the type $\mathrm{E}[\phi_n^P(\mathbf{x})]$, with $P=2$, 4, 6 or 8. Various computed ratios, together with predictions for Gaussian and sinusoidal modes, are shown in Fig. 3 as a function of the mode number n. It can be seen that beyond $n=50$ the ratios are more or less independent of the mode number, as implicitly assumed in the theory. The average results from the simulations are $\mathrm{E}[\phi_n^4]/\mathrm{E}[\phi_n^2]^2=2.87$, $\mathrm{E}[\phi_n^6]/\mathrm{E}[\phi_n^2]^3=13.3$, and $\mathrm{E}[\phi_n^8]/\mathrm{E}[\phi_n^2]^4=83.7$, which compares with 3, 15, and 105 for Gaussian mode shapes and 2.25, 6.25, and 19.14 for sinusoidal two-dimensional mode shapes. The assumption of sinusoidal mode shapes therefore strongly underestimates the actual values of the ratios, while the assumption of Gaussian mode shapes leads to a slight overestimation. This is in qualitative agreement with observations made in previous work concerning the first ratio, $K=\mathrm{E}[\phi_n^4]/\mathrm{E}[\phi_n^2]^2$: for example the experimental results reported by Weaver (1989) suggest that $K=2.6$, while the simulation results of Langley and Brown (2004a, b) suggest that $K=2.7$. Both of these results are less than the present value of $K=2.87$, and the problem-dependent nature of K clearly requires further investigation. In what follows the simulation results for the statistical moments of the mode shapes are employed in the theoretical variance equations.

For each of the two selected values of damping, the relative variance of the squared modulus reverberant response at a point remote from the drive point is shown in Fig. 4 as a function of frequency. The simulation results are compared with the present GOE prediction given by Eq. (42), and with the Poisson prediction given by Eq. (38). It can be seen that for both values of damping, the GOE prediction apparently overestimates the relative variance over the whole frequency range. In contrast, the Poisson prediction appears to yield better agreement with the simulation

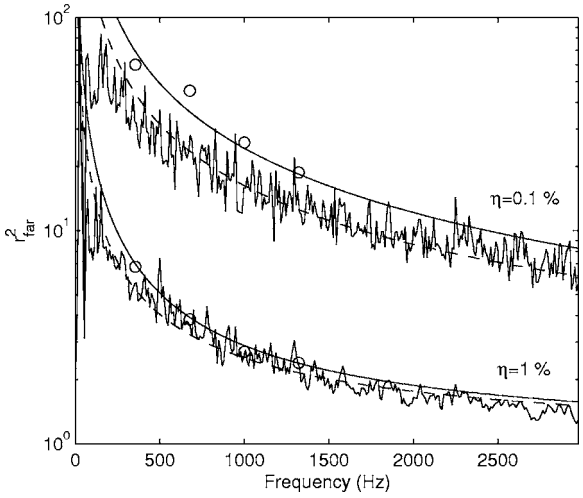

FIG. 4. Relative variance of the squared modulus displacement at a point remote from the drive point of a random plate, as a function of frequency. The simulation results are the fluctuating curves. Solid line: GOE prediction from Eq. (42) with actual statistics of mode shapes ($K=2.87$); dotted line: Poisson prediction from Eq. (38). The circles are the simulation results at four discrete frequencies with 10 000 samples (instead of 200 for the fluctuating curves).

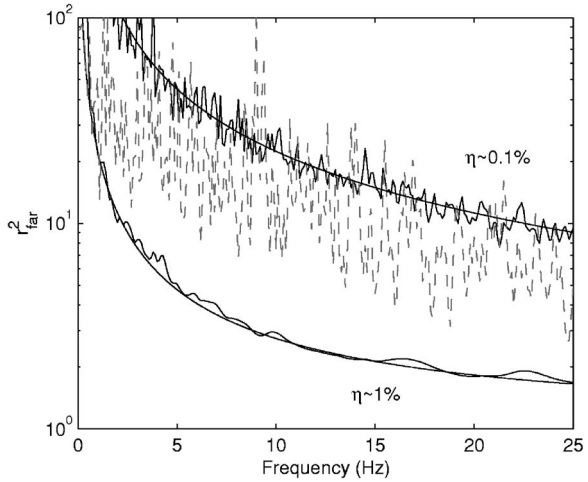

FIG. 6. Relative variance of the squared modulus displacement at a point remote from the drive point of an artificial GOE system, as a function of frequency. The simulation results with 20 000 samples are the fluctuating black curves. The dotted gray curve is the simulation result with 200 samples. The smooth lines are the GOE prediction from Eq. (42) with the statistics of Gaussian mode shapes.

results, particularly at low modal overlap. This unexpected result has been traced to the use of insufficient realizations (200) in the random ensemble. Additional simulations have been performed using 10 000 realizations at four discrete frequencies, and the results are shown as circles in Fig. 4. Clearly the relative variance is increased by considering more realizations, and the resulting value is in closer agreement with the GOE prediction. The convergence behavior of the relative variance is shown in Fig. 5 for the frequency 1322 Hz; convergence of the response at two locations is shown for each of the two values of damping. Very clear "jumps" are apparent, particularly for the case of light damping. Each jump can be traced to the occurrence of a realization that has a natural frequency very close to the excitation frequency *and* a corresponding mode shape that is large at both the drive point and the receiver point. This is a very rare

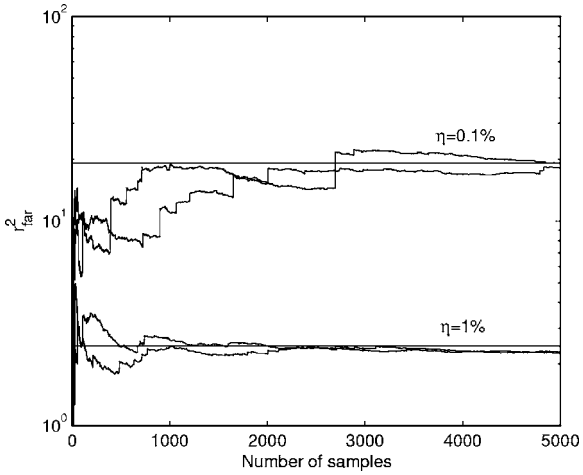

FIG. 5. Estimated relative variance of the squared modulus displacement at two points away from the drive point of a random plate, as a function of the number of samples in the simulation ensemble. The GOE predictions from Eq. (42) are the horizontal lines.

event, but it leads to a very large response, and the ensemble must include a sufficient number of these events to yield a converged result for the response statistics. At the higher level of damping, where there is a greater modal overlap, the properties of any single mode have less influence on the response and the jumps are less noticeable, leading to more rapid convergence.

When considering the present validation example, it should be noted that the plate is not guaranteed to have GOE statistics; rather the occurrence of GOE statistics in this type of system is a hypothesis based on previous experimental and simulation results. It is of interest to consider a second example for which this issue does not arise, and to this end an artificially constructed GOE random system has been studied. The natural frequencies of this system have been generated from the eigenvalues of a GOE matrix (Mehta, 1991), the mode shapes have been taken to be Gaussian random variables, and the response has been computed from Eq. (1). Results for this system are shown in Fig. 6. Although the parameters of the system (modal density, loss factor, etc.) are different to those of the plate, the two curves shown in Fig. 6 have the same range of modal overlap as those shown in Fig. 4, i.e., from $m=0$ to either 3.14 or 0.314. Very good agreement between simulation and theory is obtained when a large number of realizations (20 000) is employed, but, as for the plate, the simulations yield a lower relative variance when insufficient realizations (200) are considered. The convergence issue is therefore not a feature specific to the plate, but rather can be expected for all systems with low modal overlap.

Thus far the results presented in this section have concerned the relative variance of the response at a point remote from the drive point. The relative variance of the plate response *at* the drive point is shown in Fig. 7. In this case the GOE prediction is given by Eq. (48) and the Poisson prediction by Eq. (39). Simulation results with 10 000 realizations, as opposed to 200 realizations, are shown with circles at four

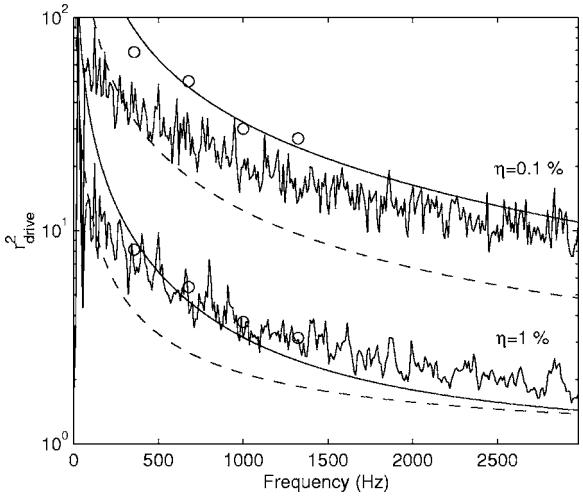

FIG. 7. Relative variance of the squared modulus displacement at the drive point of a random plate, as a function of frequency. The Monte Carlo simulation results are the fluctuating curves. Solid line: GOE prediction from Eq. (48) with actual statistics of mode shapes; dotted line: Poisson prediction from Eq. (39). The circles are the simulation results at four discrete frequencies with 10 000 samples (instead of 200 for the fluctuating curves).

discrete frequencies. In this case an increase in the number of simulations does not cause a significant shift in the results for heavy damping, which remain above the GOE prediction, but for light damping the relative variance is significantly increased to give good agreement with the GOE prediction. It can be noted that the GOE prediction represented by Eq. (48) is approximate, since the third- and fourth-order GOE cumulant functions were neglected in the derivation. The disagreement between theory and simulation for the heavily damped system could be due to this approximation or due to a deviation of the plate behavior from GOE statistics. To investigate this issue, drive point results are presented in Fig. 8 for the previously considered GOE system. Clearly the trends are very similar to those shown for the plate, and this suggests that the higher-order cumulant functions must be considered if an accurate estimate of the drive point relative

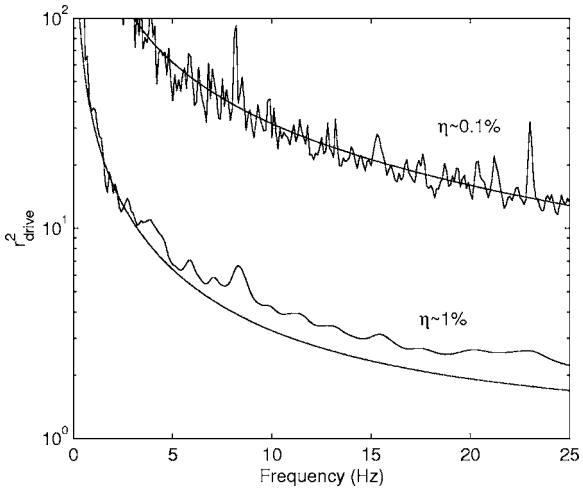

FIG. 8. Relative variance of the squared modulus displacement at the drive point of an artificial GOE system, as a function of frequency. The smooth lines are the GOE prediction from Eq. (48) with the statistics of Gaussian mode shapes.

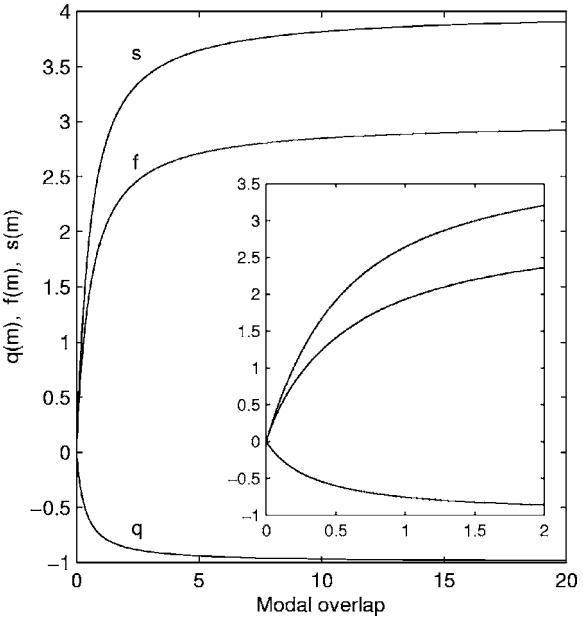

FIG. 9. Functions q from Eq. (24), f from Eq. (44), and s from Eq. (50) versus the modal overlap.

variance is required for $m>1$. Below this value, Eq. (48) represents a good approximation.

The main analytical results of this paper, Eqs. (30), (42), and (48), each have a fairly simple form, although the functions $q(m)$, $f(m)$, and $s(m)$ that appear in these equations are fairly involved. To make the equations more amenable to hand calculation, the three functions are plotted in Fig. 9 for a wide range of modal overlap factor.

IV. A RELATION BETWEEN THE STATISTICS OF THE ENERGY DENSITY AND THE TOTAL ENERGY

The function $q(m)$ that appears in the expression for the ensemble-averaged modulus squared response, Eq. (29), also appears in Langley and Brown (2004a) in an expression for the variance of the total energy of the system. This raises the question of a possible relation between the statistics of the energy density and the total energy, and this is explored in the present section. Firstly, it can be noted that the power input to the system by a point load of complex amplitude F has the form

$$P_{\text{in}} = \left(\tfrac{1}{2}\right)\text{Re}\{i\omega H(\omega,\mathbf{x}_0,\mathbf{x}_0)FF^*\} = \left(\tfrac{1}{4}\right)i\omega|F|^2\{H-H^*\}. \tag{53}$$

The second cumulant (i.e., the variance) of the power is therefore given by

$$\text{Var}(P_{\text{in}}) = (\omega^2/16)|F|^4\{-\kappa_2(H,H)-\kappa_2(H^*,H^*) + 2\kappa_2(H,H^*)\}. \tag{54}$$

As mentioned below Eq. (33), the first two terms on the right-hand side of this expression are zero, and, hence, in the notation of the previous sections,

$$\text{Var}(P_{\text{in}}) = (\omega^2/8)|F|^4\text{E}[|H_{\text{rev}}(\omega,\mathbf{x}_0,\mathbf{x}_0)|^2]. \tag{55}$$

Now from power balance, the total energy E say, is given by $P_{\text{in}}/\omega\eta$ so that

$$\mathrm{Var}(E) = (1/8\eta^2)|F|^4 \mathrm{E}[|H_{\mathrm{rev}}(\omega, \mathbf{x}_0, \mathbf{x}_0)|^2]. \quad (56)$$

If e_{rev} is used to represent the energy density at the drive point (equal to twice the kinetic energy density for a resonant system), then $e_{\mathrm{rev}} = (\rho\omega^2/2)|FH_{\mathrm{rev}}|^2$ where ρ is the mass density of the system. Also, as discussed below Eq. (15), the average value of the total energy can be found by $\mathrm{E}[E] = \pi\nu|F|^2/(4M\omega\eta)$, where M is the total mass of the system and ν is the modal density. Equation (56) can then be written in the form

$$\mathrm{Var}(E) = (1/\pi m)\mathrm{E}[E]\mathrm{E}[Ae_{\mathrm{rev}}(\omega, \mathbf{x}_0, \mathbf{x}_0)], \quad (57)$$

where A is the area (or equivalent) of the system. Thus the *ensemble variance* of the total energy is proportional to the *ensemble mean* of the energy density at the drive point. If Eq. (29) is substituted into Eq. (57), then the result for the variance of the total energy agrees with the expression given by Langley and Brown (2004a), apart from the fact that Eq. (38) of that reference contains a factor of K [referred to as α by Langley and Brown (2004a)] in place of a factor of 3 that appears in the present result. The constant K is given by Eq. (46) and takes the value 3 for Gaussian mode shapes, as assumed here in Eq. (26).

V. CONCLUSIONS

This paper has considered various aspects of the response of a random system to a harmonic point load. In particular, expressions have been derived for the mean and variance of the energy density of the reverberant part of the response, under the assumption of GOE natural frequency statistics. The main findings are as follows.

(1) The spatial distribution of the ensemble-averaged energy density is given by Eq. (30). It should be noted that this result *excludes* the direct field, and thus the energy concentration near to the drive point predicted by Eq. (30) is *not* a direct field effect. A similar result has previously been derived for impulsive loading (Weaver and Burkhardt, 1994), where a time reversal argument was used to account for the concentration factor at early times (analogous to high damping in the present case). For harmonic loading, a concentration factor at the drive point has previously been predicted under Poisson natural frequency statistics (Lyon, 1969). A comparison with numerical simulations for a plate has shown that Eq. (30) captures the main features of the response; it is thought that the small differences between theory and simulation are largely due to assumptions regarding the statistics of the system mode shapes, which are not quite Gaussian.

(2) The relative variance of the reverberant energy density at points remote from the drive point is given by Eq. (42). This result was previously derived (reported with small typographical errors) by Lobkis *et al.* (2000), as part of a more general study that included the effect of random modal damping factors. A comparison with simulation results has revealed the importance of ensemble size when the modal overlap is low: convergence is very slow due to the (rare) occurrence of realizations that have a very large response. With an insufficient number of samples the false impression is created that the GOE prediction overestimates the relative variance.

(3) The relative variance of the reverberant energy density at the drive point is given by Eq. (48). This is an approximate result, since the third- and fourth-order GOE cumulant functions were neglected in the derivation. A comparison with numerical simulations shows that the result is accurate for $m < 1$. In contrast to an earlier result due to Lyon (1969) (for Poisson statistics), the relative variance is predicted to decrease with increasing modal overlap. The reason for this discrepancy has been explained, and a modified version of Lyon's Poisson result has been presented.

(4) The *mean* energy density at the drive point is closely related to the *variance* of the total energy of the system. This relationship is given by Eq. (57), which explains why the function $q(m)$, derived by Langley and Brown (2004a) when considering the total energy, reappears in the present result for the mean energy density.

It can be noted that, when comparing the plate simulation results with the GOE analytical predictions, the simulated values of the mode shape statistics were employed in the theory. The fact that good agreement was then obtained suggests that the plate natural frequencies conform closely to GOE statistics, although the mode shapes are not quite Gaussian. This issue has been raised by previous authors [for example, Langley and Brown (2004a), Weaver (1989), and Lobkis *et al.* (2000)]. It seems that the statistics of the mode shapes, as measured, for example, by the parameter K, may depend on the effective dimension of the system (as discussed in the Appendix), and more work is required in this area.

ACKNOWLEDGMENTS

This work was sponsored by the Air Force Research Laboratory, Space Vehicles Directorate, Kirtland AFB, NM, USA under SBIR Phase II Contract F29601-02-C-0109.

APPENDIX: A NOTE ON EIGENVECTOR STATISTICS

Brody *et al.* (1981) have derived the statistics of a d-dimensional eigenvector based on the assumption that the statistics are orthogonally invariant. The $2\nu'$th statistical moment of an entry of the eigenvector is given by

$$\mathrm{E}[\phi_n^{2\nu}] = \frac{(2\nu - 1)!!(d-2)!!}{(d + 2\nu - 2)!!}. \quad (A1)$$

The factor K that appears in Eq. (46) would in this case have the value

$$K = \frac{\mathrm{E}[\phi_n^4]}{\mathrm{E}[\phi_n^2]^2} = 3\left(\frac{d}{d+2}\right). \quad (A2)$$

Clearly, $K < 3$ with $K \to 3$ as $d \to \infty$. This raises the possibility that the value of $K < 3$ observed in the earlier work [for example, Langley and Brown (2004a,b)] is due to a limited number of degrees of freedom d interacting over the random ensemble. For example, the reported value of $K = 2.7$ (Lan-

gley and Brown, 2004a,b) corresponds to $d=18$. It is not unreasonable that the number of interacting degrees of freedom should be of this order for a structural dynamic system, and further investigation of this issue is warranted.

Abramowitz, M., and Stegun, I. A. (**1964**). *Handbook of Mathematical Functions* (Dover, New York).

Berry, M. V. (**1983**). "Semi classical mechanics of regular and irregular motion," in *Les Houches, Lecture Series Session XXXVI*, edited by G. Jooss, R. H. G. Helleman, and R. Stora (North Holland, Amsterdam), pp. 171–271.

Brody, T. A., Flores, J., French, J. B., Mello, P. A., Pandey, A., and Wong, S. S. M. (**1981**). "Random-matrix, physics-spectrum and strength fluctuations," Rev. Mod. Phys. **53**, 385–479.

Burkhardt, J., and Weaver, R. L. (**1996**). "The effect of decay rate variability on statistical response prediction in acoustical systems," J. Sound Vib. **196**, 147–164.

Cremer, L., Heckl, M., and Ungar, E. E. (**1990**). *Structure Borne Sound: Structural Vibrations and Sound Radiation at Audio Frequencies*, 2nd ed. (Springer-Verlag, New York).

Davy, J. L. (**1981**). "The relative variance of the transmission loss of a reverberation room," J. Sound Vib. **77**, 455–479.

de Rosny, J., Tourin, A., and Fink, M. (**2000**). "Coherent backscattering of an elastic wave in a chaotic cavity," Phys. Rev. Lett. **84**, 1693–1695.

Kompella, M. S., and Bernhard, B. J. (**1993**). "Measurement of the statistical variation of structural-acoustic characteristics of automotive vehicle," in *Proceedings of the SAE Noise and Vibration Conference*, Warrendale, PA, USA.

Langley, R. S. (**1994**). "Spatially averaged frequency response envelopes for one- and two-dimensional structural components," J. Sound Vib. **178**, 483–500.

Langley, R. S., and Brown, A. W. M. (**2004a**). "The ensemble statistics of the energy of a random system subjected to harmonic excitation," J. Sound Vib. **275**, 823–846.

Langley, R. S., and Brown, A. W. M. (**2004b**). "The ensemble statistics of the band-averaged energy of a random system," J. Sound Vib. **275**, 847–857.

Langley, R. S., and Cotoni, V. (**2004**). "Response variance prediction in the statistical energy analysis of built-up systems," J. Acoust. Soc. Am. **115**, 706–718.

Lin, Y. K. (**1967**). *Probabilistic Theory of Structural Dynamics* (McGraw-Hill, New York).

Lobkis, O. I., Weaver, R. L., and Rozhkov, I. (**2000**). "Power variances and decay curvature in a reverberant system," J. Sound Vib. **237**, 281–302.

Lyon, R. H. (**1969**). "Statistical analysis of power injection and response in structures and rooms," J. Acoust. Soc. Am. **45**, 545–565.

Lyon, R. H., and DeJong, R. G. (**1995**). *Theory and Application of Statistical Energy Analysis* (Butterworth-Heinemann, London).

Mehta, M. L. (**1991**). *Random Matrices* (Academic, New York).

Meirovitch, L. (**1986**). *Elements of Vibration Analysis*, 2nd ed. (McGraw-Hill, New York).

Morfey, C. L. (**2001**). *Dictionary of Acoustics* (Academic Press, San Diego).

Schroeder, M. R. (**1987**). "Statistical parameters of the frequency response curves of large rooms," J. Audio Eng. Soc. **35**, 289–304.

Stratonovich, R. L. (**1963**). *Topics in the Theory of Random Noise* (Gordon and Breach, New York).

Weaver, R. L. (**1989**). "On the ensemble variance of reverberation room transmission functions, the effect of spectral rigidity," J. Sound Vib. **130**, 487–491.

Weaver, R. L., and Burkhardt, J. (**1994**). "Weak Anderson localization and enhanced backscatter in reverberation rooms and quantum dots," J. Acoust. Soc. Am. **96**, 3186–3190.

Weaver, R. L., and Lobkis, O. I. (**2000**). "Enhanced Backscattering and Modal Echo of Reverberant Elastic Waves," Phys. Rev. Lett. **84**, 4942–4945.

Effect of flow on the drumlike silencer

Y. S. Choy and Lixi Huang[a)]
Department of Mechanical Engineering, The Hong Kong Polytechnic University, Kowloon, Hong Kong

(Received 21 February 2005; revised 8 August 2005; accepted 8 August 2005)

This study examines the effects of a mean flow and turbulent flow excitation on the performance of the recently conceived device which was tested under the no-flow condition [J. Acoust. Soc. Am. **112**, 2014–2035 (2002)]. The silencer consists of two cavity-backed membranes lining part of the duct walls. When a certain optimal tension is applied, the silencer gives a broad stopband in the low-frequency regime. Similar performance is predicted for the condition with a mean flow, and tests conducted for flow speeds from 5 to 15 m/s validated these predictions. The spectrum of transmission loss without flow features three resonance peaks, and the mean flow is found to smooth out all peaks and shift two of them through cross-modal coupling. The silencer was tested in a wind tunnel, and no flow induced flexural instability was found on the membrane in the range of flow speeds tested. Insertion loss measurement was also conducted in a natural ventilation condition where a turbulence intensity of 3% was recorded, and the results were close to those without flow. It is concluded that no noticeable extra sound is produced by the turbulent excitation of the membrane under the optimal tension required by the silencer. © *2005 Acoustical Society of America.* [DOI: 10.1121/1.2047207]

PACS number(s): 43.50.Gf, 43.20.Tb, 43.20.Ks [DKW] Pages: 3077–3085

I. INTRODUCTION

Ventilation and air conditioning systems provide thermal comforts, but often they are accompanied by noise propagating to the working area through the air conveying ducts. Traditionally, fibrous duct lining is installed and it is only effective in the range of medium to high frequencies (Ingard, 1994). Actually, the low-frequency noise is the most difficult to control and it still remains a technical challenge. Apart from this acoustical difficulty, the use of some fibers may also aggrevate the problem of indoor air pollution. A team of acousticians led by Fuchs has been very successful in finding fiberless solutions to the problem of medium- to low-frequency noise (Fuchs, 2001a). It may be said that a simple expansion chamber is also a method to avoid the use of fibrous duct lining. However, it creates considerable pressure loss (back pressure) and the frequency range of noise control is not wide. To reduce the back pressure, silencers in practical use are often fitted with a perforated, flow-through tubing, such as the straight-through resonator studied by Thawani and Jayaraman (1983). There are three main types of multiple duct perforated tube resonators: concentric tube resonator, plug muffler, and three-duct cross-flow muffler, and their performances are well verified by experiments (Munjal *et al.*, 1993). Among all these designs, the ones with good performance, such as the plug muffler, still tend to carry a penalty of high back pressure, so a compromise has to be reached. The design of the two-chamber, three-duct, open-ended muffler is recommended by Gogate and Munjal (1995). It works for a wide frequency range and the pressure drop is not very large. However, it is larger than the concentric and plug-type mufflers. As the pressure loss in the muffler connected to an engine or pump consumes power, more noise is generated by the additional power required to overcome the pressure loss. So, apart from the consideration of the environmental aspects and the space occupied, back pressure is one of the most important attributes of a muffler.

In order to control the pressure drop, a silencer has to be designed in such a way that there is little change of cross-sectional area. A device called membrane absorber box is one such example (Ackermann *et al.*, 1988, 1994). Its practical performance as an exhaust stack silencer has been reported by Ackermann and Fuchs (1989). The working principle of the device is based on the sound absorption by an array of smart Helmholtz resonators. Recently, Huang (1999) introduced the idea of using tensioned membranes to reflect low-frequency noise and the device is called a drumlike silencer as its highly tensioned membrane resembles a drum (Huang, 2002). The noise reduction performance has been experimentally verified (Choy and Huang, 2002). The objective of developing the drumlike silencer is identical to that of many patented devices by Fuchs and his colleagues, which is to provide a fiber-free solution (Fuchs *et al.*, 1988; Fuchs, 2001a, b). In addition to achieving this objective, there are other potential bonuses for the drumlike silencer. First, it provides a total noninvasiveness for the flow conduit, and almost eliminates the undesirable pressure loss. Second, it occupies a minimal space outside the main flow conduit. To further this goal of space-saving, helium can be introduced to fill shallow cavities, and such a device has also been studied both theoretically and experimentally (Choy and Huang, 2003).

However, all the analyses and experiments on the drumlike silencer have been conducted without flow in the duct. The current study is a step forward in extending the results to the flow duct. The effect of flow is divided into two parts in the current study. The first is the effect of a uniform flow on

[a)]Author to whom correspondence should be addressed. Electronic mail: mmlhuang@polyu.edu.hk

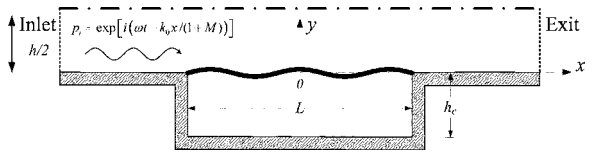

FIG. 1. The schematic diagram of the drumlike silencer.

the capability of the membrane to reflect noise; the second is the effect of flow turbulence on the membrane vibration. Turbulence levels may be high in the air conditioning system with elbows (Fry, 1988). The first question is dealt with in Sec. II by numerical study and in Sec. III A by experimental studies in a quiet wind tunnel. The results show that the transmission loss spectrum shifts, but the overall performance is not seriously affected as long as an optimum tension higher than that for the no-flow condition is found and applied. The second question is answered experimentally, and this is reported in Secs. III B and III C. The specific question asked here is whether the inevitable vibration induced by the flow turbulence radiates significant noise in addition to the incident noise from the upstream. To avoid the uncertainty of sound measurement in a turbulent flow, an insertion loss measurement is also conducted. The conclusion is that the sound radiated from the turbulence-induced vibration is too small to affect the performance of the drumlike silencer under such a high tension.

II. THEORETICAL MODELING

In previous studies, good agreement between analytical (Huang, 2002) and experimental results was achieved for the drumlike silencer without flow (Choy and Huang, 2002). In this paper, finite element computation is adopted in the hope that it would pave the way for engineering design tasks involving complex configurations in the near future. The response of the membrane motion to an incident sound is found through solving a fully coupled problem, and the transmission loss is predicted. The geometry of the drumlike silencer is shown in Fig. 1 for half of the device which is symmetrical about the duct center plane drawn as a solid line on the top. It resembles a standard, two-dimensional expansion chamber with a main channel height h, and two identical cavities of length L and depth h. Note that the cavity depth can differ from the duct height, but it is kept the same in this study to avoid unnecessary parametric variations. The geometrical optimization is described in Huang (2004). Note also that, in the experimental studies described later, the silencer was three-dimensional and the membrane was two-dimensional on the plane of (x,z). However, the two lateral edges at $z=\pm w/2$, where $w=h$ was the membrane width, were allowed to move freely. This experimental configuration simulates a two-dimensional duct, or channel, with a one-dimensional membrane, or a string. The same configuration was used in the earlier studies (Choy and Huang, 2002) for comparison with theory and was proved to be effective.

The software package of Femlab®, which works under the popular programming language of Matlab®, is chosen. Femlab solves properly composed partial differential equations and it has a strong multi-physics capability which is found particularly suitable for the current vibroacoustic coupling problem. In the numerical simulation, there are two domains. One is the two-dimensional domain for the fluid (air) in the duct with cavity, the cavity and the duct being geometrically disconnected. Another is the one-dimensional domain for the membrane, which is in fact a string. The fluid inside the duct flows and it is assumed to be uniform and inviscid. The mean flow has a density ρ_0, velocity U, and Mach number $\mathrm{M}=U/c_0$, where c_0 is the speed of sound. The unsteady fluid dynamics of the air in the duct is governed by the convective wave equation with velocity potential ϕ (Howe, 1998),

$$(1-\mathrm{M}^2)\frac{\partial^2\phi}{\partial x^2}+\frac{\partial^2\phi}{\partial^2 y}-\frac{2\mathrm{M}}{c_0}\frac{\partial^2\phi}{\partial x\partial t}-\frac{1}{c_0^2}\frac{\partial^2\phi}{\partial t^2}=0, \tag{1}$$

which is related to pressure p and the horizontal component of the acoustic particle velocity u as

$$p=-\rho_0\left(\frac{\partial\phi}{\partial t}+Uu\right), \quad u=\frac{\partial\phi}{\partial x}. \tag{2}$$

The sound in the duct is coupled by a kinematic boundary condition on the membrane surface $(y=0+)$ with displacement $\eta(x,t)$,

$$\left.\frac{\partial\phi}{\partial y}\right|_{y=0+}=\frac{\partial\eta}{\partial t}+U\frac{\partial\eta}{\partial x}. \tag{3}$$

The same equations govern sound in cavity by substituting $M=0$ in the above equations. The membrane vibration is driven by the air pressure difference across the interface at $y=0$,

$$T\frac{\partial^2\eta}{\partial x^2}+p|_{y=0-}-p|_{y=0+}=m\frac{\partial^2\eta}{\partial t^2}, \quad \eta|_{x=\pm L/2}=0, \tag{4}$$

where T and m are, respectively, the tensile force applied on and the mass per unit distance of the membrane. For frequencies below the cut-on frequency of the duct, the inlet and exit boundaries are governed by simple traveling wave relationships:

$$\phi_\pm=A_\pm\exp[i\omega t\mp ik_0x/(1\pm\mathrm{M})], \quad p_\pm=\pm\rho_0c_0u, \tag{5}$$

where a time dependence of $\exp(i\omega t)$ has been assumed, $k_0=\omega/c_0$, and the two signs of $\pm$ apply to the downstream and upstream traveling waves, respectively. At the exit boundary, an anechoic boundary is assumed so that $p=\rho_0c_0u$ or

$$\frac{\partial\phi}{\partial n}+\frac{ik_0\phi}{1+\mathrm{M}}=0, \tag{6}$$

where the outward normal direction n coincides with x. Assuming that the incident wave is one with a unit velocity potential amplitude,

$$\phi_+ = \exp\left[i\left(\omega t - \frac{k_0 x}{1+\mathrm{M}} \right) \right], \quad u_+ = \frac{\partial \phi_+}{\partial x} = -\frac{ik_0 \phi_+}{1+\mathrm{M}} = \frac{p_+}{\rho_0 c_0}. \tag{7}$$

The reflection wave, $p_- = p - p_+$, satisfies the upstream traveling wave relationship: $p_- + \rho_0 c_0 u_- = 0$. Hence the total sound wave satisfies

$$p + \rho_0 c_0 u = p_+ + \rho_0 c_0 u_+ = 2\rho_0 c_0 u_+, \tag{8}$$

which can be rewritten as

$$(1-\mathrm{M})\frac{\partial \phi}{\partial n} + ik_0 \phi = -2u_+ = \frac{2ik_0 \phi_+}{1+\mathrm{M}}. \tag{9}$$

The wall of the duct and cavity are assumed to be acoustically rigid, so the particle velocity normal to the wall vanishes. Therefore, the boundary condition on the walls is

$$\frac{\partial \phi}{\partial n} = 0. \tag{10}$$

Equations (1)–(10) are solved in a coupled manner in Femlab, and the final result is a sound transmission loss (TL) defined as the ratio of the Blokhintsev sound intensity (Blokhintsev, 1946),

$$I = \left(\frac{p}{\rho_0} + Uu \right)(\rho_0 u + \rho U), \quad I_\pm = \frac{1}{2}\rho_0 c_0 k_0^2 |\phi_\pm|^2,$$

$$\mathrm{TL} = 10 \log_{10} \frac{I_+}{I_-}, \tag{11}$$

where $\rho = p/c_0^2$ is the density fluctuation in the fluid, I is the total sound intensity while I_+ and I_- are the intensity of waves traveling in $+x$ and $-x$ directions, respectively.

In the following presentations, all parameters are normalized by a set of three basic quantities: air density ρ_0, speed of sound c_0, and the duct height h. So, the frequency f is normalized by c_0/h, tensile force per unit depth T by $\rho_0 c_0^2 h$, and membrane mass per unit area m by $\rho_0 h$. For the sake of simplicity, the same symbols are used for both dimensional and dimensionless variables at times. A quantity is deemed dimensional when a physical unit, e.g., Newton for force, is given, so there is little risk of confusion.

The accuracy of the finite element simulation depends on the solver and the mesh size. To ensure that the prediction is reliable, it is necessary to validate it. The validation is conducted by comparison with the analytical solution for $\mathrm{M}=0$ [see Huang (2002) for details], and the result is shown in Fig. 2. The normalized mass (or mass ratio) is $m=1.3$ and the normalized tension is $T=0.54$. The analytical solution is shown as a solid line, and the numerical prediction is given as open circles. In the numerical simulation, a total of around 17 000 Lagrangian, quadratic, triangular elements are used for the fluid domain and 101 nodes are used for the one-dimensional membrane. There is no visible deviation between the two TL curves except minor frequency shifts around the spectral peaks. As another check for the accuracy of the Femlab solver, the conservation of acoustic energy at the absence of any dissipation mechanism is examined. The reflection sound energy found at the inlet and the transmitted

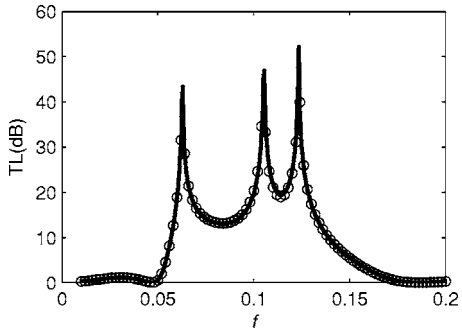

FIG. 2. Comparison between the Femlab calculation (open circles) and the analytical solution (solid line) for the dimensionless parameters of length $L=5$, mass $m=1.3$, and tension $T=0.54$.

sound energy at the exit are added up and compared with the specified incident sound. The error is calculated as

$$\delta E = \int_{\text{inlet}} |\phi - \phi_{\text{in}}|^2 \, dy + \int_{\text{exit}} |\phi|^2 \, dy - \int_{\text{inlet}} |\phi_{\text{in}}|^2 \, dy, \tag{12}$$

where subscripts "in" denote the incident wave evaluated at the inlet boundary. When compared with the incident sound power, the maximum normalized error, $\delta E / \int_{\text{inlet}} |\phi_{\text{in}}|^2 \, dy$, for all the calculated frequencies is less than 10^{-11}. The comparison is very satisfactory and the same mesh is used for predictions with flow. In a parametric study conducted by Huang (2004), the stopband is defined as a continuous frequency band, $f \in [f_1, f_2]$, in which $\mathrm{TL} > \mathrm{TL}_{cr}$ and the criterion value of $\mathrm{TL}_{cr} = 10.4$ dB is used for a drumlike silencer with two cavities of depth h and length $L=5h$, which is exactly the configuration used in the current study. The criterion value of 10.4 dB is calculated on the basis of the total volume used for the cavities in Huang (2004). There is no reason why it cannot be rounded down to 10 dB, but the use of 10.4 dB would certainly make the comparison with earlier results easier. It is found in Huang (2004) that the best performance is given by a membrane of vanishing mass. In real applications, the membrane with practically minimal mass is chosen. For the given mass ratio m, an optimization procedure is constructed to search for the best tension T on the membrane that gives the highest frequency ratio of f_2/f_1, which is found, for $m=1.3$, to be 2.42 at $T=0.54$. Part of the reason for optimizing the frequency ratio instead of the frequency difference is the desire to give emphasis to the low-frequency region which is difficult for traditional duct linings.

The mechanisms behind the peaks have been analyzed (Huang, 2002) by decomposing the membrane displacement η into *in vacuo* string modes of index j:

$$\eta_j = \sin\left[j\pi\left(\frac{x}{L} + \frac{1}{2} \right) \right]. \tag{13}$$

It is found that the first two modes, $j=1,2$, play the dominant role. The first peak is mainly contributed by the combination of the first and second *in vacuo* modes, while the second and third peaks are attributed mostly to the first and

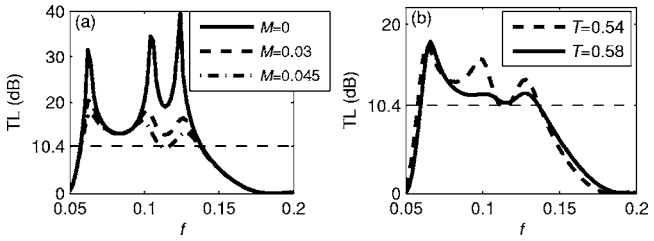

FIG. 3. Predicted spectra for (a) fixed tension $T=0.54$ with varying Mach number M and (b) fixed M=0.045 with different T.

second *in vacuo* modes, respectively. When the fluid loading caused by a modal vibration of the jth mode is transformed into a sine series to find its coefficient of the lth *in vacuo* mode, the result is defined as modal impedance matrix $\{Z_{jl}\}$,

$$Z_{jl}=\frac{2}{L}\int_{-L/2}^{L/2}\left[p_{y=0-}-p_{y=0+}\right]\big|_{\eta=\eta_j(x)e^{i\omega t}}\eta_l(x)dx. \tag{14}$$

It is found that there is no cross-modal interaction between the odd and even modes. In other words, $Z_{jl}=0$ when j is odd and l is even, or when j is even and l is odd.

The flow effect on the performance of the drumlike silencer is now investigated numerically. Tension is kept constant at $T=0.54$ while the Mach number M varies. The results are shown in Fig. 3(a). The solid curve with three sharp peaks is the reference case without flow (M=0). When the flow velocity is increased, the levels of all three peaks are decreased and they are also smoothed out. Compared with the peak height, the TL between the first and second peaks has less noticeable changes. However, the second and third peaks drift apart. As a result, the trough between them, around $f=0.12$, dips below the 10.4 dB criterion value for M=0.045 (dash-dot line). This spectral movement is very similar to that which occurs when the tension is reduced for the no-flow case (Huang, 2002). Therefore, the effect of flow on the sound-membrane interaction is similar to the reduction of membrane tension. The reason behind such an effect is rather complex, but preliminary analysis of the modal impedance reveals its essence. The modal impedance is easily calculated by changing the present coupled problem into one in which the membrane vibration is specified and there is no incident wave. Sine transform is applied to the resultant fluid loading to find the modal impedance. The absence of the cross-modal interaction for M=0 is easily validated, and serious cross modal interaction is found for $M\neq 0$. For example, the following numerical results (Table I) are obtained for the first two modes. The values of the cross-modal coefficients for M=0, $|Z_{12}|=0.0017$ and $|Z_{21}|=0.0023$, are an indication of the numerical error which can be shown to be further diminishing with the mesh size. The changes of the magnitude of cross modal impedance, $|\Delta Z_{12}|=0.1467$ and $|\Delta Z_{21}|=0.1465$, are found to be much larger than the change of the self-impedance, $|\Delta Z_{11}|=0.0071$ and $|\Delta Z_{22}|=0.0178$. The fact that there is cross-modal interaction with flow is readily comprehensible. The extra term in the boundary condition Eq. (3), $U\partial\eta/\partial x$, gives rise to terms of $\cos\left[j\pi(x/L+\frac{1}{2})\right]$, which spreads over many *in vacuo* modes of $\sin\left[j\pi(x/L+\frac{1}{2})\right]$.

TABLE I. Computed modal impedance with and without flow.

	$\lvert Z_{M=0}\rvert$			$\lvert Z_{M=0.045}$-$Z_{M=0}\rvert$	
	$l=1$	$l=2$		$l=1$	$l=2$
$j=1$	2.7739	0.0017	$j=1$	0.0071	0.1467
$j=2$	0.0023	2.2304	$j=2$	0.1465	0.0178

Figure 3(b) shows that, when a higher tension of $T=0.58$ is used, the TL spectral trough between the second and third peaks can be lifted above the threshold value of $TL_{cr}=10.4$ dB again. This reconfirms the earlier observation that the net effect of flow is similar to the reduction of membrane tension. It also means that a different optimal tension has to be found for each flow condition.

III. EXPERIMENTAL STUDIES

Experimental studies were conducted to answer three important questions.

(1) Can the drumlike silencer maintain its broadband performance in flow when a higher tension is applied on the membrane?
(2) Is there flow-induced flexural instability which converts flow energy into vibration and subsequently sound energy?
(3) Is there significant noise radiation by the turbulence excitation on the membrane?

Note that there is an important distinction between questions 2 and 3. In question 2, the flow is nominally uniform and there is no incident sound. The instability and vibration grow out of infinitesimal disturbances due to an intrinsic mechanism of energy transfer from the mean flow (zero frequency) to the vibration of a finite frequency (Huang, 2001). If such instability exists, it would only get quenched by nonlinear effects. Because of this, vibration induced by such an instability mechanism can certainly be measured and is expected to be much larger in magnitude than that induced by an incident sound or the local flow turbulence. Question 3 differs from 2 in that it deals with the forced vibration instead of self-induced vibration. When there is a flow turbulence, excitation exists on the membrane and there must be a finite response. The question is whether such vibration radiates a significant amount of sound. The question of how much sound is significant can only be answered by comparing the sound pressure level associated with a realistic flow condition. The plan in this section is as follows. Questions 1 and 2 will be answered by tests conducted in a wind tunnel where the mean flow is smooth, while question 3 is dealt with by using a realistic flow generated by a fan attached to a duct. To avoid uncertainties of signal processing for the sound measured in flow, the insertion loss is measured by placing a microphone in the no-flow region in an anechoic chamber into which the turbulent flow is discharged.

A. Wind tunnel test

The transmission loss measurement was conducted in a quiet mini-wind-tunnel in which the noise of the fan driving

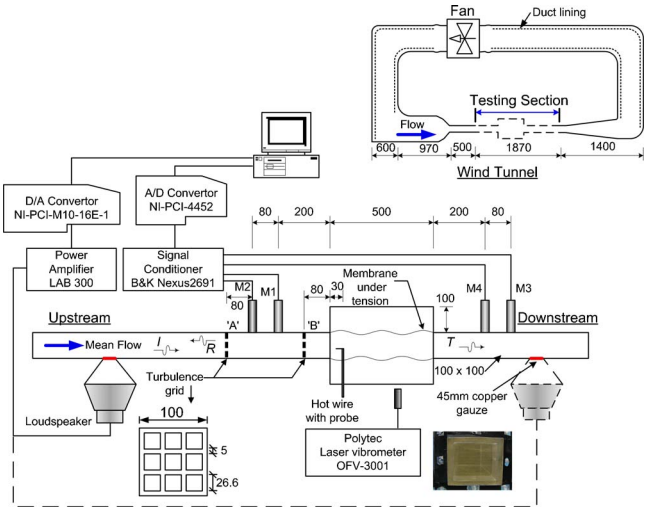

FIG. 4. The setup of the measurement system using the four-microphone, two-source position method. The hot-wire measures the flow speed and the laser vibrometer measures the membrane vibration velocity. Turbulence is generated by a screen upstream of the drumlike silencer.

the closed-loop flow was mostly absorbed by the acoustic linings. The schematic of the setup is given in Fig. 4. The overall layout of the wind tunnel is illustrated in the upper right corner of Fig. 4. The working section of the wind tunnel was 100 mm by 100 mm in cross section and 1.8 m in length. This length is very long compared with normal wind tunnel designs and it is deliberately chosen for the duct acoustics testing. The turbulence intensity at the upstream sections was less than 0.1%. As shown in Fig. 4, a turbulence trigger made of a screen covering the duct cross section was installed at an upstream position when a high level of turbulence was needed. The length of the membrane and the cavity was $L=500$ mm and the mass per unit area of the membrane was $m=0.17$ kg/m^2. The tensile force applied on the membrane was measured by a strain gauge glued to the surface of the membrane. The dimension of the strain gauge sensor (TML FLA-3-11) was 3 mm. More details are described in Choy and Huang (2003). The duct and cavity height was $h=100$ mm and so was the width of the membrane. The duct wall was made of 15-mm-thick acrylic. The magnitude of the vibration velocity on this wall was found to be, typically, 1% of that in the membrane. It was therefore considered to be acoustically rigid. The first cut-on frequency of the duct was 1700 Hz. Two pairs of B&K $\frac{1}{2}$ in. condenser microphones (type no. 4187) were installed flush with the duct walls. A wide separation distance of 80 mm was used for the microphone pairs in order to have a good measurement accuracy at low frequencies. The microphones were supported by a B&K Nexus four-channel conditioning amplifier (type 2691), and the signals were acquired through the National Instruments AD conversion card (type PCI-4452). The testing sound was generated by a loudspeaker driven by the amplified DA signals. Both the AD and the DA processes were controlled by a Labview program, which was made to run through a range of testing frequencies from 20 to 1000 Hz in a loop with a frequency interval of 10 Hz. The output signal from the DA converter (National Instruments PCI-M10-16E-1) was passed to the loudspeaker via a

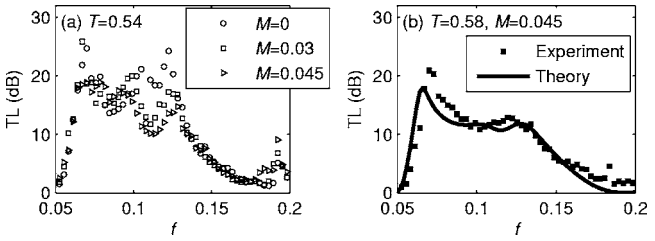

FIG. 5. Measured transmission loss of the drumlike silencer with flow. (a) Fixed tension $T=0.54$ and various flow speeds. (b) Comparison between the Femlab prediction and the measured data for M=0.045, $T=0.58$.

B&K power amplifier (LAB Gruppen 300). The natural advantage of the pure tone tests is the high signal-to-noise ratio, which is especially important in the wind tunnel where there is a background flow noise and the local pressure fluctuation on the flush-mounted microphone. In addition, the sampling rate and period can be adjusted automatically in the Labview code such that an integer number of cycles are guaranteed for all frequencies tested. No digital windowing is needed for the subsequent FFT analyses.

The exact locations of the microphones are shown in Fig. 4 with the labels of M1-4. The travelling wave components in the upstream and downstream sides can be resolved by one pair of microphones in each side. The convection effect was taken into consideration in the two-microphone method. The method of two sources at two positions (Munjal and Doige, 1990) was used to find the transmission loss. The first test was conducted with the loudspeaker on the left-hand side (upstream). The loudspeaker was flush mounted to the wind tunnel wall via a 45 mm by 45 mm copper gauze with a mesh size of about 1 mm, of which a photo is attached in Fig. 4. This avoided the flow separation and large scale turbulence, and this installation did not affect the uniformity of the flow and the turbulence intensity along the membrane of the drumlike silencer. Another set of measurements was taken by moving the loudspeaker to the downstream section while the opening in the upstream was sealed by a rigid plate. The linear combination of the intensity fluxes for the two tests then gave a virtual test in which the downstream was strictly anechoic.

The flow velocity inside the tunnel was measured by a hot-wire which was calibrated by a flow manometer and was connected to the filtered anemometer with constant current. There were three positions for measuring the flow turbulence over the membrane: the leading edge of the membrane, 200 mm downstream from the leading edge and 50 mm upstream from the trailing edge. To ensure the uniformity of the flow, the turbulence intensity and the flow velocity were checked by traversing the hot wire along the height of the working section with a vertical interval of 5 mm.

The results of the transmission loss measurement are shown in Fig. 5. Figure 5(a) shows the spectra for $T=0.54$ with M=0 (open circles), M=0.03 (or 10 m/s, open squares), and M=0.045 (or $U=15$ m/s, open triangles). The level of TL in the frequency range between the second and third peaks is generally reduced by flow. As explained earlier, the flow has the effect of lowering the effective tension so the second peak shifts towards lower frequencies as com-

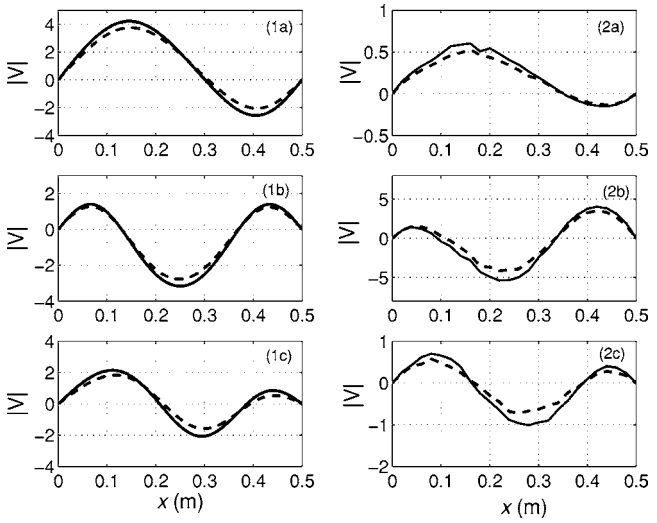

FIG. 6. The response of the membrane. The first column is the Femlab prediction while the second column is the experimental results at the frequencies of (a) 200 Hz, (b) 330 Hz, and (c) 420 Hz. All solid lines are for M=0 and dashed lines for M=0.026. A turbulence intensity of 6% is used in the experiment with loudspeaker sound excitation.

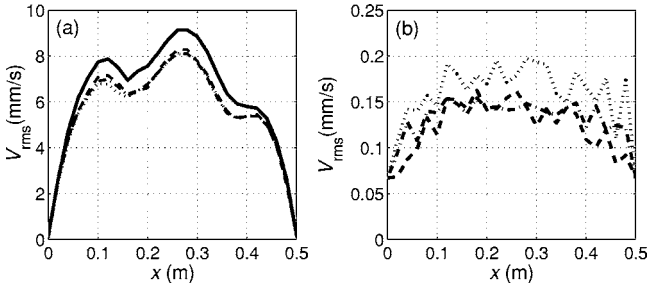

FIG. 7. The membrane vibration velocity under the tension of $T=0.54$. (a) is the response under random sound excitation from a side-branch loudspeaker and (b) is without such excitation. The solid line is for the no-flow condition, and the others are with a mean flow velocity of 10 m/s (M=0.03) and a turbulence intensity of 0.04% (dashed line), 3% (dash-dot line), and 6% (dotted line), respectively.

pared with the no-flow condition (M=0). The shift and the change in the second and third peaks cause TL to fall below the criterion value of 10.4 dB. So, an increase in tension is required. Figure 5(b) shows the improvement of performance by the increased membrane tension of $T=0.58$ for M =0.045 (filled squares), which agrees closely with the theoretical predictions (solid line). Note that, in all numerical predictions, the losses of wall friction, thermal conduction, and flow turbulence are not considered and the predicted transmission loss is expected to be a little lower than the measured values.

B. Vibration measurement

As shown in the lower part of Fig. 4, a laser vibrometer (Polytec type with controller FV-3001 and sensor head OFV-303) picked up signals of the membrane vibration through the transparent cavity walls installed outside the wind tunnel working section. The vibration signal was referenced against the driving voltage sent to the loudspeaker, and the measurement was repeated by moving the sensor in the streamwise direction with an interval of 20 mm. When the results for all points were compiled, a distribution of vibration velocity as a function of membrane coordinate x with correct phase was obtained. There are two purposes for the vibration measurements: to study the modal response of the membrane and to answer the question of whether there is flow-induced flexural instability.

The response of the membrane under the acoustic excitation has been explained in detail by Huang (2002). It is found that the first and second *in vacuo* modes are dominant while the third mode also plays some role. The same phenomenon is found in the measured results here. Figure 6 compares the membrane response between the Femlab prediction (left column) with the measured results (right column) for the frequencies of 200 Hz (first row), 330 Hz (second row), and 420 Hz (third row) corresponding to three peaks in the TL spectrum in Fig. 2. In the Femlab prediction shown in the left column, the solid lines represent the condition without flow while the dashed lines with flow of M =0.026 ($U=9$ m/s). In the experimental data shown in the right column, solid lines also represent the condition of no flow, and the dashed line represents a flow of M=0.026 (U =9 m/s) and 6% turbulence intensity. In fact, the effect of turbulence on vibration is little in this case, and this is discussed in the next figure. Note that the two columns have different coordinate scales and only the shapes should be compared. The comparison of the two columns shows that there is a general agreement in terms of the membrane response although there are quantitative differences. Comparisons between the membrane response for the no-flow and with-flow conditions shows that the flow decreases the membrane response, and that there is also an agreement in this between the Femlab prediction and the measurement.

Having obtained the conclusion that the measured modal response agrees with the prediction, the focus is now on the rms values of the membrane vibration velocity under different flow conditions. Four flow conditions are considered: (1) no flow, (2) a uniform flow, which is, strictly speaking, a flow with a low turbulence intensity of 0.04%, (3) a flow with 4% turbulence intensity, and (4) 6% turbulence intensity. The flow velocity for conditions (2–4) was 9 m/s (M =0.026). Two types of tests were conducted. In the first, random excitation was given to the loudspeaker, and the results for various flow conditions are shown in Fig. 7(a). In the second test, shown in Fig. 7(b), the loudspeakers were switched off, and the recorded membrane vibration was purely caused by the flow turbulence and wind tunnel background noise. As shown in Fig. 7(a) for the loudspeaker excitation, there is a certain difference between the results of no-flow (solid line) and those with flow conditions, and this is consistent with the trend of reduced membrane response by flow as shown in Fig. 6. The results for the flow with three different values of turbulence intensity, 0.04% (mean flow, dashed line), 4% (dash-dot line), and 6% (dot line), show very little difference. The reason is found in Fig. 7(b) where the loudspeaker is switched off. The comparison between Figs. 7(a) and 7(b) shows that the level of sound-induced vibration dominates over the turbulence-induced vibration, so the three flow conditions in Fig. 7(a) do not make

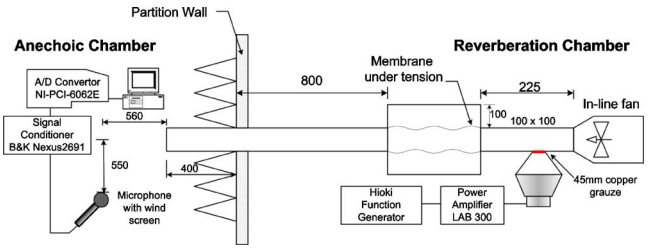

FIG. 8. Experimental setup for the insertion loss measurement.

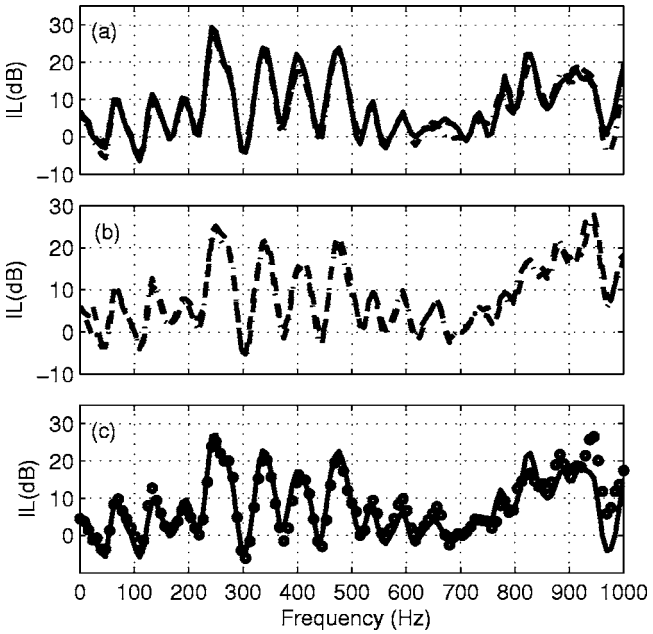

FIG. 9. Insertion loss under different flow and loudspeaker excitation conditions. (a) Loudspeaker on without flow (solid line), a flow of 5 m/s (dashed line) and a flow of 10 m/s (dash-dot line). (b) Loudspeaker off with a flow of 5 m/s (dashed line) and 10 m/s (dash-dot line). (c) Comparison of the results with loudspeaker-on and 10 m/s (solid line) with the loudspeaker-off with 10 m/s flow (filled circles).

much impact on the results. In terms of the turbulence-induced vibration shown in Fig. 7(b), clear differences are found between the 4% and 6% turbulence, but little difference is found between the mean flow (0.04%) and 4% turbulence. The similarity in the latter two conditions indicates that the background noise may have contributed to the recorded vibration whose magnitude is probably of the same order as that caused by the 4% flow turbulence.

When the vibration energy is integrated over the whole membrane, an overall rms value is found for each case in Fig. 7. For the no-flow case shown in Fig. 7(a), the overall V_{rms} is found to be 6.9 mm/s. The incident wave due to the random noise generated by the loudspeaker in the no-flow condition can be resolved unambiguously by the two-microphone method, and the total sound pressure level is found to be 61.6 dB. The overall vibration induced by the 6% turbulence, as shown in Fig. 7(b), is $V_{rms}=0.17$ mm/s. The amount of sound required to induce the same amount of turbulence induced vibration is calculated as $61.6+20\log_{10}(0.17/6.9)=29.4$ dB. This is not a very loud noise, and the comparison serves to highlight the dominance of the sound-induced vibration over the turbulence-induced vibration.

C. Insertion loss measurement

Measurement of sound inside a flow duct is always subject to uncertainties related to aerodynamic pressure fluctuations within the boundary layer where the microphone is placed. This can be avoided if the microphone is located outside the air stream measuring the sound radiation through the exit of a flow duct. If two such measurements, one with and another without the silencer, are compared, the difference gives the so-called insertion loss (IL). Insertion loss differs from transmission loss (TL) in that its result depends partly on the impedance of the noise source upstream of the silencer as well as the exit impedance at the downstream. On the contrary, TL depends solely on the silencer properties. The setup for the IL measurement is shown in Fig. 8. The flow was generated by an in-line fan attached to one end of the duct. The duct and the silencer were installed across a partition window between an anechoic chamber (left) and a reverberation chamber (right). The only measurable acoustic communication between the two chambers was the duct at the partition wall was well built and all window edges were sealed. The fan ran at 2800 rpm at its design condition and was located inside the reverberation chamber, while a measurement microphone (B&K 4187) was used in the anechoic chamber at an axial distance of 56 cm from the duct exit and 55 cm below the duct. For each IL test, two noise measurements by the same microphone at the same position were taken, one with the silencer installed and another with the silencer replaced by a rigid duct of the same length. It is well known that the insertion loss can be negative at some frequencies due to the impedance conditions at the source and the exit. Such phenomenon would not be a concern if there is no flexible structure. However, the use of a vibrating membrane causes a concern of whether the negative value of IL signifies extra noise radiated by the flow-induced membrane vibration. To be certain, a side-branch loudspeaker was also installed to measure IL without flow. The loudspeaker was driven by a function generator (Hioki) coupled with an amplifier, and its connection with the duct was similar to the arrangement made for the wind-tunnel test. The loudspeaker was always present even when it was switched off and the noise source was provided naturally by the fan and its generated flow. The fan can generate a maximum flow of 9 m/s and the turbulence level was found to be 3% at the upstream end of the membrane while the level decays to 2% in the middle of the membrane section. The optimal tension of 780 N (dimensionless $T=0.54$) was used for the drumlike silencer. In order to avoid the transmission of the mechanical vibration from the fan and motor to the testing rig, a 50-mm-long flexible duct made of plastics was inserted between the fan and the entrance of the test rig.

The first IL test was conducted with the loudspeaker switched on and the fan switched off. The result is shown in Fig. 9(a) as the solid line. Then the fan was switched on to produce a flow speed of about 5 m/s with 2% turbulence intensity at the upstream edge of the membrane, and the result is given as the dashed line in the figure. The result

obtained when the fan operated at the full speed of 2800 rpm, producing a speed of 9 m/s with 3% turbulence, is shown as the dash-dot line. Note that the sound pressure level measured when the fan operated at this speed was about 50 dB when the loudspeaker was switched off, and the SPL was 60 dB when the fan was switched off and the loudspeaker was switched on. A margin of 10 dB was obtained for the loudspeaker sound dominance during this set of tests. Several observations are now made. First, the results for 5 and 9 m/s are hardly distinguishable. But when they are compared with the result without flow, approximately 1–2-dB reduction in IL is found at the IL peaks with the introduction of the flow. This reduction is consistent with the prediction shown in Fig. 3(a) where spectral peaks are rounded off by the flow even when there is no damping mechanisms present. The second observation is that IL reaches about 20 dB at 250, 330, 400, and 480 Hz, and the frequencies of the first three peaks coincide with those of the predicted TL curve for the optimal tension of 780 N. The third observation is that negative IL is found around 45, 105, and 300 Hz. Due to the dominance of the loudspeaker sound, the negative IL is deemed to be a result of source and exit impedance conditions instead of extra sound radiation from the membrane in the silencer.

The results obtained when the loudspeaker was switched off and when the flow speed was 5 and 9 m/s are given in Fig. 9(b) as the dashed line and the dash-dot line, respectively. Again, there is no noticeable difference between these two. The comparison between the 9-m/s flow test with and without the loudspeaker sound excitation is shown in Fig. 9(c). The difference between them is also small, around 1–2 dB at some peak positions. There is a general agreement of IL tests with loudspeaker excitation with flow and the excitation by the flow noise alone at different flow speeds. There is also qualitative agreement between the IL tests between the no-flow condition and the conditions with flow. These results lead to two important conclusions.

(a) There was no flow-induced instability in the range of flow speed tested. Should there be such instability, energy in the mean flow would have been transferred to the membrane vibration and the IL results for different flow speeds would have been quite different.
(b) There was no significant extra noise radiated by the turbulence-induced vibration. Should there be such extra noise, the source of noise would have been on the membrane and the IL results in Fig. 9 would also have been quite different. The absence of any significant difference in IL means that the membrane only acted as a passive wave reflector.

IV. CONCLUSIONS

The effect of flow on the drumlike silencer has two aspects. In the first, the use of the tensioned membrane is seen as a potential hazard of flow-induced flexural instabilities and turbulence-induced vibration, leading to extra noise generation. In the second, the effect of a mean flow is looked at quantitatively, and the concern is whether the good silencing performance predicted for the silencer without flow can be maintained when there is flow. The first aspect was investigated mainly experimentally, while the second one was done both theoretically and experimentally. Several conclusions are drawn:

(1) It has been shown experimentally that, for the flow speed common in ventilation applications, there is no flow-induced flexural instability. This is partly due to the high tension applied on the membrane, high tension being a result of acoustic optimization for a broadband wave reflection. In an example of wind tunnel test with 9-m/s flow superimposed by 6% turbulence intensity, the amount of vibration induced was found to be equivalent to that induced by an incident sound of about 30 dB. This result serves to highlight how small the turbulence-induced vibration is when the tension is high.
(2) The question of whether there is significant extra noise radiated by the turbulence-induced vibration was also investigated by an insertion loss measurement using a realistic ventilation flow generated by an in-line fan. The insertion loss measured by using a loudspeaker excitation was essentially the same as that by the natural fan noise excitation. It means that all the noise sources were upstream of the silencer and the possible noise radiated by the turbulence-induced vibration was insignificant. Negative insertion loss was found only where the no-flow test also showed such result.
(3) The quantitative effect of flow on the silencing performance is mainly the smoothing and the shifting of the peaks, especially the second one, in the transmission loss spectrum. This was predicted by the finite element method and validated by the wind tunnel experiment. In a typical TL spectrum, there are three peaks featuring the wave reflection by the combination of the first and second, first, and second *in vacuo* modes of the membrane, respectively. The main effect of flow is to deteriorate the silencer performance between the second and third peaks, for which the remedy is found with the increased membrane tension. The reason for such effect is identified as the cross-modal coupling which is absent without flow.

ACKNOWLEDGMENTS

The research reported here is supported by a grant from the Research Grants Council of the Hong Kong SAR (Grant No. PolyU 5169/02E).

Ackermann, U., and Fuchs, H. V. (**1989**). "Technical note: noise reduction in an exhaust stack of a papermill," Noise Control Eng. J. **33**(2), 52–60.
Ackermann, U., Fuchs, H. V., and Rambausek, N. (**1988**). "Sound absorbers of a novel membrane construction," Appl. Acoust. **25**, 197–215.
Ackermann, U., Fuchs, H. V., and Sheng, S. (**1994**). "Acoustic performance of membrane absorbers," J. Sound Vib. **170**, 621–636.
Blockhintsev, D. I. (**1946**). *Acoustics of a nonhomogeneous moving medium*, English translation NACA-TM-1399, 1956.
Choy, Y. S., and Huang, L. (**2002**). "Experimental studies of Drum-like Silencer," J. Acoust. Soc. Am. **112**, 2026–2035.
Choy, Y. S., and Huang, L. (**2003**). "Drum silencer with shallow cavity filled with helium," J. Acoust. Soc. Am. **114**, 1477–1486.
Fry, A. T. (**1988**). *Noise Control in Building Services* (Sound Research Laboratories Ltd., Pergamon Press, New York).
Fuchs, H. V. (**2001a**). "Alternative fibreless absorbers—new tool and mate-

rials for noise control and acoustic comfort," Acta Acust. (Beijing) **87**, 414–422.
Fuchs, H. V. (**2001b**). "Technical and applied papers—From advanced acoustic research to novel silencing procedures and innovative sound treatments," Acta Acust. (Beijing) **87**, 407–413.
Fuchs, H. V., Ackermann, U., and Rambausek, N. (**1988**). "Sound attenuating box," United States Patent, 4,787,473.
Gogate, G. R., and Munjal, M. L. (**1995**). "Analytical and experimental aeroacoustic studies of open-ended three-duct perforated elements used in muffler," J. Acoust. Soc. Am. **97**, 2919–2927.
Howe, M. S. (**1998**). *Acousitcs of Fluid Structure Interaction* (Cambridge U.P., Cambridge).
Huang, L. (**1999**). "A theoretical study of duct noise control by flexible panels," J. Acoust. Soc. Am. **106**, 1801–1809.
Huang, L. (**2001**). "Viscous flutter of a finite elastic membrane in Poiseuille flow," J. Fluids Struct. **15**, 1061–1088.
Huang, L. (**2002**). "Modal analysis of a drumlike silencer," J. Acoust. Soc. Am. **112**, 2014–2025.
Huang, L. (**2004**). "Parametric study of a drum-like silencer," J. Sound Vib. **269**, 467–488.
Ingard, K. U. (**1994**). *Note on Sound Absorption Technology*, Noise Control Foundation, U.S.A.
Munjal, M. L., and Doige, A. G. (**1990**). "Theory of a two source-location method for direct experimental evaluation of the four-pole parameters of an aeroacoustic system," J. Sound Vib. **141**, 323–333.
Munjal, M. L., Krishnan, S., and Reddy, M. M. (**1993**). "Flow-acoustic performance of perforated element mufflers with application to design," Noise Control Eng. J. **40**, 159–167.
Thawani, P. T., and Jayaraman, K. (**1983**). "Modelling and application of straight-through resonators," J. Acoust. Soc. Am. **73**, 1387–1389.

Optimal virtual sensing for active noise control in a rigid-walled acoustic duct

Dick Petersen,[a] Anthony C. Zander,[b] Ben S. Cazzolato,[c] and Colin H. Hansen[d]
Active Noise and Vibration Control Group, School of Mechanical Engineering, The University of Adelaide, SA 5005, Australia

(Received 23 November 2004; revised 28 July 2005; accepted 3 August 2005)

The performance of local active noise control systems is generally limited by the small sizes of the zones of quiet created at the error sensors. This is often exacerbated by the fact that the error sensors cannot always be located close to an observer's ears. Virtual sensing is a method that can move the zone of quiet away from the physical location of the transducers to a desired location, such as an observer's ear. In this article, analytical expressions are derived for optimal virtual sensing in a rigid-walled acoustic duct with arbitrary termination conditions. The expressions are derived for tonal excitations, and are obtained by employing a traveling wave model of a rigid-walled acoustic duct. It is shown that the optimal solution for the virtual sensing microphone weights is independent of the source location and microphone locations. It is also shown that, theoretically, it is possible to obtain infinite reductions at the virtual location. The analytical expressions are compared with forward difference prediction techniques. The results demonstrate that the maximum attenuation, that theoretically can be obtained at the virtual location using forward difference prediction techniques, is expected to decrease for higher excitation frequencies and larger virtual distances. [DOI: 10.1121/1.2047127]

PACS number(s): 43.50.Ki [KAC] Pages: 3086–3093

I. INTRODUCTION

Local active noise control systems aim to create zones of quiet at specific locations, for instance at the passenger's ears inside a vehicle cabin. Unfortunately, the greatest noise reductions are generally achieved at the error sensor locations, which might not always be where the maximum attenuation is required. This is further complicated by the fact that the created zones of quiet tend to be very small. It has been shown both analytically and experimentally that the zone of quiet, in which the noise is reduced by 10 dB or more, typically has the shape of a sphere with a diameter of one-tenth of an acoustic wavelength.[1] Consequently, the error sensors usually need to be placed close to an observer's ear, which might not always be a possible or convenient solution. For local control to be practical, a nonintrusive sensor is required, which is placed remotely from the desired measurement location. This nonintrusive sensor can be used to estimate the pressure remote from the location of the physical transducers. The estimated pressure at the remote location can then be minimized by a local active noise control system. As a result, the zone of quiet can be moved away from the physical location of the transducers to the desired location of maximum attenuation, such as a person's ear. This concept, which is called virtual sensing, has been investigated previously by a number of authors.

Elliott and David[2] suggested a virtual sensing method called the virtual microphone arrangement. This method requires a preliminary system identification step in which the transfer functions between the secondary sources and the physical and virtual microphones are estimated. Furthermore, it is assumed that the primary pressures at the physical and virtual microphones are equal. This assumption, together with the knowledge of the estimated transfer functions, allows the estimation of the pressures at the virtual microphones. The virtual microphone arrangement has been thoroughly investigated by a number of authors.[3,4]

Roure and Albarrazin[5] and Popovich[6] independently suggested a virtual sensing method called the remote microphone technique. This method requires a preliminary system identification step in which three transfer functions are estimated. The first two are the transfer functions between the secondary sources and the physical and virtual microphones, which are also needed in the virtual microphone arrangement of Elliott and David.[2] However, the remote microphone technique requires the estimation of a third transfer function that models the transfer path between the primary field pressures at the physical and virtual microphones. The virtual microphone arrangement assumes this transfer function to be unity and thus is a simplified version of the remote microphone technique.

Cazzolato[7] suggested an alternative approach to the virtual microphone arrangement based on forward difference prediction techniques. In this approach, the pressure at the virtual location is estimated by summing the weighted pressures from a number of microphones in an array. The weights for each of the elements in the microphone array are determined using forward difference prediction techniques. The forward difference prediction approach has been extensively investigated for a rigid-walled acoustic duct and a free field.[8,9] A linear prediction method using a two-microphone

[a]Electronic mail: cornelis.petersen@adelaide.edu.au
[b]Electronic mail: anthony.zander@adelaide.edu.au
[c]Electronic mail: benjamin.cazzolato@adelaide.edu.au
[d]Electronic mail: colin.hansen@adelaide.edu.au

array and a quadratic prediction method using a three-microphone array were evaluated both theoretically and experimentally. While the quadratic prediction method theoretically gave the highest attenuation at the desired location, experiments showed that the linear prediction method proved to be better, in practice.[10–12] This was attributed to the high sensitivity of the quadratic prediction method to short-wavelength extraneous noise. In an effort to overcome this problem, higher-order virtual microphone arrays were investigated.[9] This method uses a higher number of microphones in the array than the order of the prediction algorithm, resulting in an overconstrained problem that can be solved by a least squares approximation. The higher-order prediction algorithm then acts to spatially filter out the extraneous noise. The experimental results showed that the accuracy of these higher-order prediction algorithms was very much affected by the phase and sensitivity mismatches and relative position errors between the microphones in the array.[13] These mismatches and position errors are generally unavoidable, especially if the number of microphones used is increased.

In an effort to overcome the problem of phase mismatches, sensitivity mismatches, and relative position errors encountered in the forward difference prediction techniques, Cazzolato[14] explored the use of the adaptive LMS algorithm to determine the optimal weights for each of the microphone elements. This technique places a microphone at the virtual location, after which the microphone weights are adapted by the LMS algorithm so as to optimally predict the sound pressure at this location. After the weights have converged, the microphone is removed from the virtual location and the weights are fixed to their optimal value. Munn[9] theoretically investigated the use of the adaptive LMS virtual microphone technique for a rigid-walled acoustic duct. It was found that the LMS algorithm could completely compensate for relative position errors and sensitivity mismatches and partly compensate for phase mismatches. Real-time control results for a rigid-walled acoustic duct showed that the adaptive LMS virtual microphone technique outperformed the forward difference prediction techniques.[9,15] Gawron and Schaaf[16] suggested a virtual sensing method very similar to the adaptive LMS virtual microphone technique, which was applied to local active noise control inside a car cabin. Experimental results showed the potential of this virtual sensing method.

Our aim in this paper is to derive analytical expressions for the optimal microphone weights for the case of virtual sensing in a rigid-walled acoustic duct with arbitrary termination conditions. These analytical expressions can be compared with the forward difference prediction microphone weights, and with the adaptive LMS virtual microphone technique weights that should converge to the optimal microphone weights. The analytical expressions are derived for tonal excitations, and are obtained by employing a traveling wave model of a rigid-walled acoustic duct with arbitrary termination conditions. It is shown that the optimal microphone weights are independent of the source location, the microphone locations, and the termination conditions.

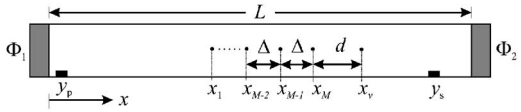

FIG. 1. Schematic diagram of a rigid-walled acoustic duct of length L, and arbitrary termination conditions characterized by $\Phi_{1,2}$.

II. THEORY

A. Traveling wave model

Figure 1 shows a schematic diagram of a rigid-walled acoustic duct of length L, and with arbitrary termination conditions characterized by

$$\Phi_{1,2} = \pi\alpha_{1,2} - j\pi\beta_{1,2}. \tag{1}$$

The termination phasors $\Phi_{1,2}$ in Eq. (1) are related to the reflection coefficients by $R_{1,2}=e^{-2\Phi_{1,2}}$.[17] The coefficients $\alpha_{1,2}$ and $\beta_{1,2}$ are thus determined by the acoustic properties of the termination at each end of the duct. A rigid, totally reflective termination is achieved for $\alpha_{1,2}=\beta_{1,2}=0$, while an anechoic termination is obtained for $\alpha_{1,2}=\infty$.

The complex acoustic pressure $p(x)$ at a point x in the rigid-walled duct due to a source of complex volume velocity q located at y, is given by[18,19]

$$p(x) = A[e^{-jk|y-x|} + e^{-jk(y+x)-2\Phi_1} + e^{jk(y+x)-j2kL-2\Phi_2} + e^{jk|y-x|-j2kL-2\Phi_1-2\Phi_2}]T_r, \tag{2}$$

where the amplitude A is defined as

$$A = \frac{\rho c q}{2S}, \tag{3}$$

and the reverberation factor T_r of the duct is given by

$$T_r = \frac{1}{1 - e^{-j2kL-2\Phi_1-2\Phi_2}}. \tag{4}$$

In the above equations, ρ is the density of air, c is the speed of sound, S is the cross-sectional area of the duct, and k is the acoustic wave number. Furthermore, it is assumed that no higher-order modes are present in the duct. It can be shown that for $0 \leqslant x \leqslant y$, Eq. (2) can be written more succinctly as

$$p(x) = \frac{\rho c q \cos[k(L-y) - j\Phi_2]\cos[kx - j\Phi_1]}{jS \sin[kL - j(\Phi_1 + \Phi_2)]}. \tag{5}$$

Similarly, for $y \leqslant x \leqslant L$, Eq. (2) can be written as

$$p(x) = \frac{\rho c q \cos[ky - j\Phi_1]\cos[k(L-x) - j\Phi_2]}{jS \sin[kL - j(\Phi_1 + \Phi_2)]}. \tag{6}$$

For totally reflective termination conditions, such that $\Phi_{1,2}=0$, Eqs. (5) and (6) reduce to the expressions discussed by Nelson and Elliott.[20]

B. Virtual sensing algorithm

In this section we introduce the algorithm utilized for virtual sensing in a rigid-walled acoustic duct. This algorithm requires an array of M physical microphones located at $\mathbf{x}$, as illustrated in Fig. 1, with the vector $\mathbf{x}$ of length M given by

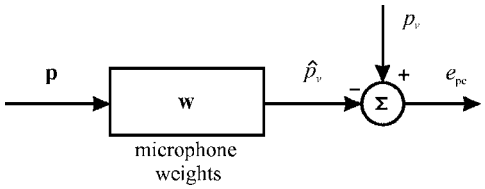

FIG. 2. Block diagram of a virtual sensing algorithm.

$$\mathbf{x} = [x_1\ x_2\ \ldots\ x_M]^T = [x_1\ x_1 + \Delta\ \ldots\ x_1 + (M-1)\Delta]^T, \tag{7}$$

where Δ is the microphone separation distance, and $(\cdot)^T$ is the transpose of the term inside the brackets. The aim of the virtual sensing algorithm is to obtain an estimate $\hat{p}_v$ of the pressure p_v at the virtual location $x_v = x_M + d$, where d is the virtual distance as shown in Fig. 1. This estimate is calculated as

$$\hat{p}_v = \mathbf{w}^T\mathbf{p}, \tag{8}$$

where $\mathbf{p}$ is a vector of length M containing the complex pressures at the physical microphone locations defined as

$$\mathbf{p} = [p_1\ p_2\ \ldots\ p_M]^T, \tag{9}$$

and $\mathbf{w}$ is a vector of length M containing the real-valued microphone weights defined as

$$\mathbf{w} = [w_1\ w_2\ \ldots\ w_M]^T. \tag{10}$$

The algorithm is illustrated in Fig. 2, where e_{pe} is the prediction error given by

$$e_{pe} = p_v - \mathbf{w}^T\mathbf{p}. \tag{11}$$

The aim of the virtual sensing algorithm is to minimize this prediction error by choosing a set of suitable microphone weights $\mathbf{w}$.

III. OPTIMAL MICROPHONE WEIGHTS FOR TONAL EXCITATION

Suppose there is a primary source located at y_p, a secondary source at y_s, two physical microphones at $\mathbf{x}$, and a virtual microphone at x_v. The locations of all these components are such that $0 \leqslant y_p \leqslant x_1 \leqslant x_2 \leqslant x_v \leqslant y_s \leqslant L$, as illustrated in Fig. 1. First, the optimal microphone weights $\mathbf{w}_0$ are calculated for the primary field, such that

$$p_{p,v} = \mathbf{w}_0^T\mathbf{p}_p = [w_{01}\ w_{02}]\begin{bmatrix} p_{p1} \\ p_{p2} \end{bmatrix}, \tag{12}$$

with $\mathbf{p}_p$ the complex primary pressures at the physical microphone locations, and $p_{p,v}$ the complex primary pressure at the virtual microphone location. Using Eq. (6), this can be written as

$$\cos[k(L-x_v) - j\Phi] = [w_{01}\quad w_{02}]\begin{bmatrix} \cos[k(L-x_1) - j\Phi] \\ \cos[k(L-x_2) - j\Phi] \end{bmatrix}, \tag{13}$$

where it is assumed for convenience that $\Phi_1 = \Phi_2 = \Phi$, as this will not make a difference in the final result. Using the fact that $\cos\theta = \frac{1}{2}(e^{j\theta} + e^{-j\theta})$, and taking together the terms in e^{jkL} and e^{-jkL}, Eq. (13) can be transformed into the following matrix equation:

$$\mathbf{A}\mathbf{w}_0 = \mathbf{b}, \tag{14}$$

where the matrix $\mathbf{A}$ is given by

$$\mathbf{A} = \begin{bmatrix} e^{-jkx_1+\Phi} & e^{-jkx_2+\Phi} \\ e^{jkx_1-\Phi} & e^{jkx_2-\Phi} \end{bmatrix}, \tag{15}$$

and the vector $\mathbf{b}$ is defined as

$$\mathbf{b} = \begin{bmatrix} e^{-jkx_v+\Phi} \\ e^{jkx_v-\Phi} \end{bmatrix}. \tag{16}$$

The optimal microphone weights $\mathbf{w}_0$ can now be calculated from Eq. (14) as

$$\mathbf{w}_0 = \mathbf{A}^{-1}\mathbf{b}, \tag{17}$$

which can be concisely written as

$$\mathbf{w}_0 = \frac{1}{\sin k\Delta}\begin{bmatrix} -\sin kd \\ \sin k(d+\Delta) \end{bmatrix}. \tag{18}$$

It can be shown that exactly the same expression results for $\mathbf{w}_0$ for the secondary field. Equation (18) shows that the optimal microphone weights depend on the wave number k, the microphone separation distance Δ, and the virtual distance d. Moreover, the optimal microphone weights are independent of the location of the source, the physical and virtual microphone locations, and the termination conditions. With these equations, the dependence of the optimal microphone weights on the microphone separation distances Δ, the virtual distances d, and the frequency $\omega = kc$ can be analyzed. If the optimal microphone weights $\mathbf{w}_0$ are used in the virtual sensing method illustrated in Fig. 2, a perfect estimate of the pressure at the virtual location is obtained.

From Eq. (18), it can be seen that no solution exists for the optimal weights if $k\Delta = n\pi$. In this instance, an integer multiple n of half an acoustic wavelength $\lambda = 2\pi/k$ exactly fits within the microphone separation distance Δ. It can be shown from Eqs. (5) and (6) that for this case, the pressures at the physical microphone locations x_1 and $x_2 = x_1 + \Delta$ are such that $p_1 = -p_2$. As a result, the matrix $\mathbf{A}$ in Eq. (15) becomes singular, and the inverse in Eq. (17) does not exist. To avoid this problem, the microphone separation distance should be such that $\Delta \neq \lambda/2$.

IV. COMPARISON WITH FORWARD DIFFERENCE PREDICTION TECHNIQUES

Another method of determining the microphone weights is to use forward difference prediction techniques.[7] These techniques have been investigated extensively by a number of authors for a rigid-walled acoustic duct.[8,9] Forward difference prediction techniques calculate the microphone weights by fitting a polynomial through the pressures $\mathbf{p}$ at the physical microphone locations $\mathbf{x}$, and by extrapolating this polynomial to the virtual location x_v in order to obtain an estimate $\hat{p}_v$ of the pressure at the virtual location.

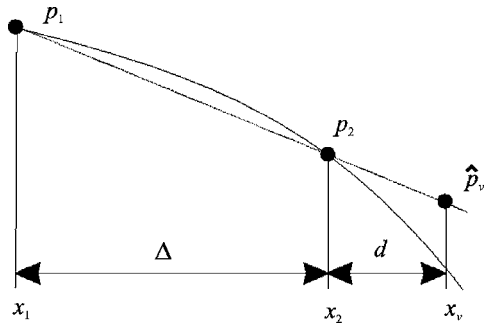

FIG. 3. Two-microphone linear forward difference prediction.

A. Two-microphone linear forward difference prediction

The linear forward difference prediction method, which uses two physical microphones, is illustrated in Fig. 3. In this case, a first-order polynomial is fitted through the pressures at the two physical microphones, which is then extrapolated to obtain an estimate $\hat{p}_v$ of the pressure at the virtual location. This pressure estimate is calculated as

$$\hat{p}_v = \begin{bmatrix} \frac{d}{\Delta} & 1 \end{bmatrix} \begin{bmatrix} -1 & 1 \\ 0 & 1 \end{bmatrix} \begin{bmatrix} p_1 \\ p_2 \end{bmatrix}. \tag{19}$$

The two-microphone linear forward difference prediction microphone weights $\mathbf{w}_{\mathrm{fl}}$ are given by[21]

$$\mathbf{w}_{\mathrm{fl}} = \begin{bmatrix} -\frac{d}{\Delta} \\ \frac{d+\Delta}{\Delta} \end{bmatrix}. \tag{20}$$

These weights can be compared with the optimal microphone weights defined in Eq. (18). If the wave number k, the virtual distance d, and the microphone separation distance Δ are such that $kd \ll 1$ and $k\Delta \ll 1$, the optimal microphone weights can be approximated by the weights defined in Eq. (20), where use has been made of small angle approximations, such that

$$\sin\theta \approx \theta, \quad \theta \ll 1. \tag{21}$$

This is illustrated in Figs. 4 and 5, which show both the optimal weights $\mathbf{w}_0$ and the linear forward difference prediction weights $\mathbf{w}_{\mathrm{fl}}$ plotted against frequency $f=k/2\pi c$ and virtual distance d, for a microphone separation distance $\Delta=50$ mm. These results are based on a traveling wave model of a rigid-walled acoustic duct of length $L=4.83$ m, and with termination conditions $\Phi_1=\Phi_2=0.025k$. The primary source is located at $y_p=0$ m, and the secondary source is located at $y_s=4.33$ m. The physical microphones are assumed to be located at $\mathbf{x}=[2.53\ 2.58]$ m. These parameters are chosen in order to compare the results with previous work.[8,9] Figure 4 shows that for a virtual distance $d=2\Delta=0.1$ m, the linear prediction weights approximate the optimal weights at low frequencies. Figure 5 shows that for an excitation frequency $f=249$ Hz, which is the natural frequency of the seventh axial mode of the rigid-walled acoustic duct under consideration, the linear prediction weights approximate the optimal weights for small virtual distances. These figures also indicate that the prediction accuracy of the linear forward difference prediction method is expected to deteriorate for larger virtual distances and increasing excitation frequencies. The excitation frequency, microphone separation distance, and virtual distance used to generate Figs. 4 and 5 were chosen to coincide with previous work in which these analytical results have been confirmed through simulations and experiments.[8,9]

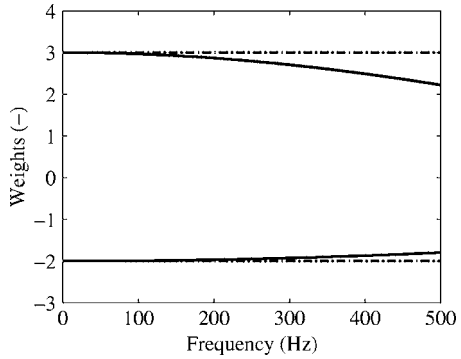

FIG. 4. Optimal microphone weights $\mathbf{w}_0$ and linear forward difference prediction microphone weights $\mathbf{w}_{\mathrm{fl}}$ plotted against frequency for a virtual distance $d=2\Delta=0.1$ m. —, optical weights; ---, forward difference prediction weights.

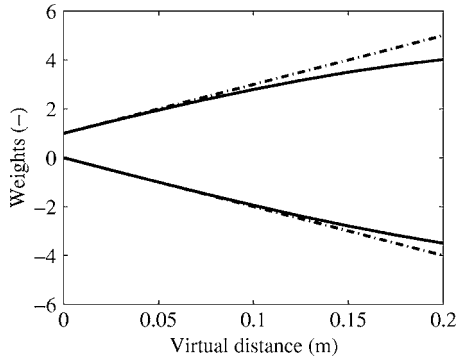

FIG. 5. Optimal microphone weights $\mathbf{w}_0$ and linear forward difference prediction microphone weights $\mathbf{w}_{\mathrm{fl}}$ plotted against the virtual distance for a frequency $f=249$ Hz. —, optimal weights; ---, forward difference prediction weights.

B. Three-microphone linear forward difference prediction

The three-microphone linear forward difference prediction method, which uses three physical microphones, is illustrated in Fig. 6. In this instance, a first-order polynomial is fitted through the pressures at the three physical microphones, resulting in an overconstrained problem that can be solved by a least squares approximation. The pressure estimate $\hat{p}_v$ is then calculated as

$$\hat{p}_v = \mathbf{w}_{\mathrm{fl3}}^T \begin{bmatrix} p_1 \\ p_2 \\ p_3 \end{bmatrix}, \tag{22}$$

where $\mathbf{w}_{\mathrm{fl3}}$ are the three-microphone linear forward difference prediction microphone weights, given by[13]

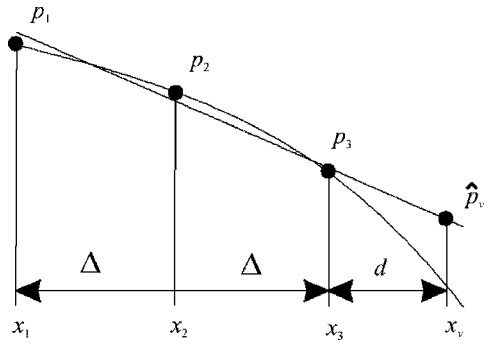

FIG. 6. Three-microphone linear forward difference prediction.

$$\mathbf{w}_{\mathrm{fl3}} = \begin{bmatrix} -\dfrac{3d+\Delta}{6\Delta} \\ \dfrac{1}{3} \\ \dfrac{3d+5\Delta}{6\Delta} \end{bmatrix}. \tag{23}$$

These weights can be compared with the optimal microphone weights $\mathbf{w}_0$ for the three-microphone case, which can be found in a similar way, as described in Sec. III, where the optimal microphone weights were calculated for the case of two physical microphones. Similar to Eqs. (14)–(17), the following matrix equation can be solved in order to find the optimal microphone weights:

$$\mathbf{A}\begin{bmatrix} w_{01} \\ w_{02} \\ w_{03} \end{bmatrix} = \begin{bmatrix} \mathrm{e}^{-jkx_v+\Phi} \\ \mathrm{e}^{jkx_v-\Phi} \end{bmatrix}, \tag{24}$$

with the matrix $\mathbf{A}$ given by

$$\mathbf{A} = \begin{bmatrix} \mathrm{e}^{-jkx_1+\Phi} & \mathrm{e}^{-jkx_2+\Phi} & \mathrm{e}^{-jkx_3+\Phi} \\ \mathrm{e}^{jkx_1-\Phi} & \mathrm{e}^{jkx_2-\Phi} & \mathrm{e}^{jkx_3-\Phi} \end{bmatrix}. \tag{25}$$

Equation (24) is an underdetermined system of equations, which requires the introduction of an additional constraint in order to obtain a unique solution for the optimal microphone weights $\mathbf{w}_0$. A common additional constraint is to minimize $\mathbf{w}_0^{\mathrm{H}}\mathbf{w}_0$ while setting the prediction error e_{pe} in Eq. (11) to zero.[20] The optimal microphone weights $\mathbf{w}_0$ are then given by

$$\mathbf{w}_0 = \mathbf{A}^{\dagger}\begin{bmatrix} \mathrm{e}^{-jkx_v+\Phi} \\ \mathrm{e}^{jkx_v-\Phi} \end{bmatrix}, \tag{26}$$

where $\mathbf{A}^{\dagger}$ is the pseudoinverse of the matrix $\mathbf{A}$ from Eq. (25). This pseudoinverse is defined as

$$\mathbf{A}^{\dagger} = \mathbf{A}^{\mathrm{H}}(\mathbf{A}\mathbf{A}^{\mathrm{H}})^{-1}, \tag{27}$$

where $(\cdot)^{\mathrm{H}}$ is the Hermitian transpose of the term inside the brackets. It can be shown that Eq. (26) can be written in compact form as

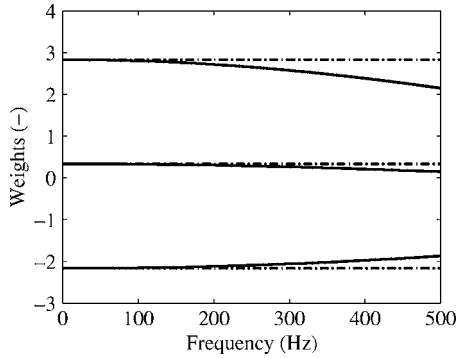

FIG. 7. Optimal microphone weights $\mathbf{w}_0$ and three-microphone linear forward difference prediction microphone weights $\mathbf{w}_{\mathrm{fl3}}$ plotted against frequency for a virtual distance $d=4\Delta=0.1$ m. —, optimal weights; ---, forward difference prediction weights.

$$\begin{bmatrix} w_{01} \\ w_{02} \\ w_{03} \end{bmatrix} = \begin{bmatrix} -\dfrac{2\sin[k(d+\Delta)]+\sin[k(d-\Delta)]}{3\sin[k\Delta]+\sin[3k\Delta]} \\ \dfrac{\cos[k(d+\Delta)]}{2+\cos[2k\Delta]} \\ \dfrac{2\sin[k(d+\Delta)]+\sin[k(d+3\Delta)]}{3\sin[k\Delta]+\sin[3k\Delta]} \end{bmatrix}. \tag{28}$$

Following the discussion at the end of Sec. III, Eq. (28) shows that no solution exists for the optimal weights if $k\Delta = n\pi$. For small angle approximations, the sinusoidal terms in Eq. (28) reduce to Eq. (23). This is illustrated in Figs. 7 and 8, which show both the optimal weights $\mathbf{w}_0$ and the three-microphone linear forward difference prediction weights $\mathbf{w}_{\mathrm{fl3}}$ plotted against frequency $f=k/2\pi c$ and virtual distance d for a microphone separation distance $\Delta=25$ mm. Again, these results are based on a traveling wave model of a rigid-walled acoustic duct of length $L=4.83$ m, and with termination conditions $\Phi_1=\Phi_2=0.025k$. The primary source is located at $y_p=0$ m, and the secondary source is located at $y_s=4.33$ m. The physical microphones are assumed to be located at $\mathbf{x}=[2.530\ 2.555\ 2.580]$ m. These parameters are chosen in order to compare the results with previous work.[8,9] Figure 7 shows that for a virtual distance $d=4\Delta=0.1$ m, the three-microphone linear prediction weights approximate the optimal weights at low frequen-

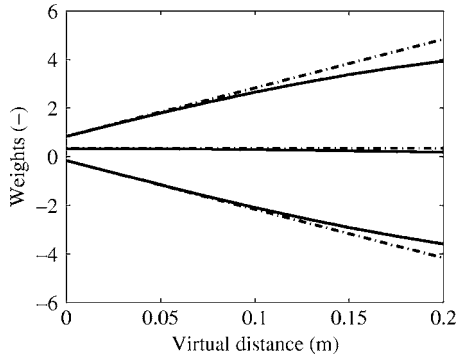

FIG. 8. Optimal microphone weights $\mathbf{w}_0$ and three-microphone linear forward difference prediction microphone weights $\mathbf{w}_{\mathrm{fl3}}$ plotted against the virtual distance for a frequency $f=249$ Hz. —, optimal weights; ---, forward difference prediction weights.

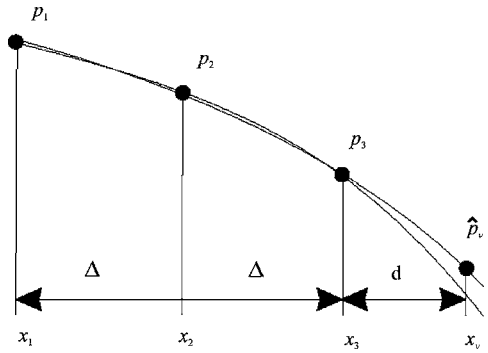

FIG. 9. Three-microphone quadratic forward difference prediction.

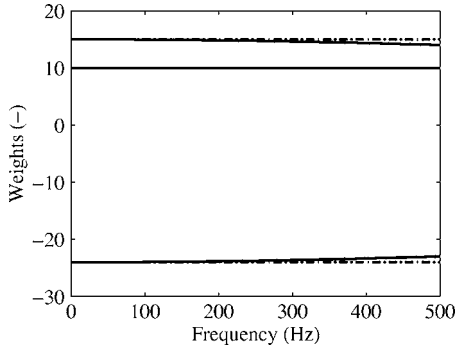

FIG. 10. Optimal microphone weights $\mathbf{w}_0$ and three-microphone quadratic forward difference prediction microphone weights $\mathbf{w}_{\mathrm{fq}}$ plotted against frequency for a virtual distance $d=4\Delta=0.1$ m. —, optimal weights; ---, forward difference prediction weights.

cies. Figure 8 shows that for an excitation frequency $f=249$ Hz, the three-microphone linear prediction weights approximate the optimal weights for small virtual distances. These figures also indicate that the prediction accuracy of the three-microphone linear forward difference prediction method is expected to deteriorate for larger virtual distances and increasing excitation frequencies. These analytical results have been confirmed through simulations and experimental work on a rigid-walled acoustic duct.[8,9]

C. Three-microphone quadratic forward difference prediction

The three-microphone quadratic forward difference prediction method, which uses three physical microphones, is illustrated in Fig. 9. For this case, a second-order polynomial is fitted through the pressures at the three physical microphones. The pressure estimate $\hat{p}_v$ is then calculated as

$$\hat{p}_v = \mathbf{w}_{\mathrm{fq}}^T \begin{bmatrix} p_1 \\ p_2 \\ p_3 \end{bmatrix}, \tag{29}$$

where $\mathbf{w}_{\mathrm{fq}}$ are the three-microphone quadratic forward difference prediction microphone weights given by[21]

$$\mathbf{w}_{\mathrm{fq}} = \begin{bmatrix} \dfrac{d(d+\Delta)}{2\Delta^2} \\ -\dfrac{d(d+2\Delta)}{\Delta^2} \\ \dfrac{d^2+3d\Delta+2\Delta^2}{2\Delta^2} \end{bmatrix}. \tag{30}$$

These weights can be compared with the optimal microphone weights $\mathbf{w}_0$, which can be found in a similar way as described in Sec. IV B. Again, the optimal microphone weights can be found from Eq. (24) by introducing an additional constraint. In order to make a comparison with the quadratic forward different prediction microphone weights $\mathbf{w}_{\mathrm{fq}}$, one of the weights of $\mathbf{w}_0$ is constrained to be equal to that weight of $\mathbf{w}_{\mathrm{fq}}$. Here, the weights w_{fq1} and w_{01} for the physical microphone located at x_1 are constrained to be equal. Equation (24) can then be modified to

$$\mathbf{A}\begin{bmatrix} w_{01} \\ w_{02} \\ w_{03} \end{bmatrix} = \begin{bmatrix} \dfrac{d(d+\Delta)}{2\Delta^2} \\ \mathrm{e}^{-jkx_v+\Phi} \\ \mathrm{e}^{jkx_v-\Phi} \end{bmatrix}, \tag{31}$$

with the matrix $\mathbf{A}$ given by

$$\mathbf{A} = \begin{bmatrix} 1 & 0 & 0 \\ \mathrm{e}^{-jkx_1+\Phi} & \mathrm{e}^{-jkx_2+\Phi} & \mathrm{e}^{-jkx_3+\Phi} \\ \mathrm{e}^{jkx_1-\Phi} & \mathrm{e}^{jkx_2-\Phi} & \mathrm{e}^{jkx_3-\Phi} \end{bmatrix}. \tag{32}$$

Equation (31) is a fully determined system of equations that can be solved for the microphone weights $\mathbf{w}_0$ as

$$\mathbf{w}_0 = \mathbf{A}^{-1}\begin{bmatrix} \dfrac{d(d+\Delta)}{2\Delta^2} \\ \mathrm{e}^{-jkx_v+\Phi} \\ \mathrm{e}^{jkx_v-\Phi} \end{bmatrix}, \tag{33}$$

which can be compactly written as

$$\begin{bmatrix} w_{01} \\ w_{02} \\ w_{03} \end{bmatrix} = \begin{bmatrix} \dfrac{d(d+\Delta)}{2\Delta^2} \\ -\dfrac{d(d+\Delta)\sin[2k\Delta]+2\Delta^2\sin[kd]}{2\Delta^2\sin[k\Delta]} \\ \dfrac{d(d+\Delta)\sin[k\Delta]+2\Delta^2\sin[k(d+\Delta)]}{2\Delta^2\sin[k\Delta]} \end{bmatrix}. \tag{34}$$

Following the discussion at the end of Sec. III, Eq. (34) shows that no solution exists for the optimal weights if $k\Delta=n\pi$. For small angle approximations, the sinusoidal terms in Eq. (34) reduce to Eq. (30). This is illustrated in Figs. 10 and 11, which show both the optimal weights $\mathbf{w}_0$ and the three-microphone quadratic forward difference prediction weights $\mathbf{w}_{\mathrm{fq}}$ plotted against frequency $f=k/2\pi c$ and virtual distance d for a microphone separation distance $\Delta=25$ mm. Again, these results are based on a traveling wave model of a rigid-walled acoustic duct of length $L=4.83$ m, and with termination conditions $\Phi_1=\Phi_2=0.025k$. The primary source is located at $y_p=0$ m, and the secondary source is located at $y_s=4.33$ m. The physical microphones are assumed to be located at $\mathbf{x}=[2.530\ 2.555\ 2.580]$ m. These parameters are chosen in order to compare the results with

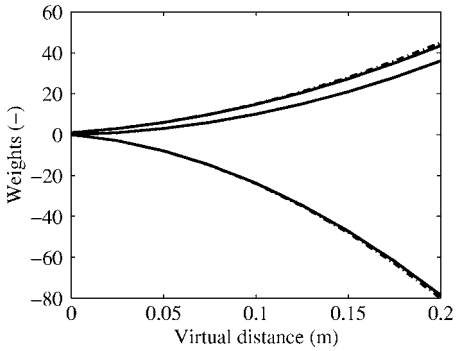

FIG. 11. Optimal microphone weights $\mathbf{w}_0$ and three-microphone quadratic forward difference prediction microphone weights $\mathbf{w}_{\text{fq}}$ plotted against the virtual distance for a frequency $f=249$ Hz. —, optimal weights; ---, forward difference prediction weights.

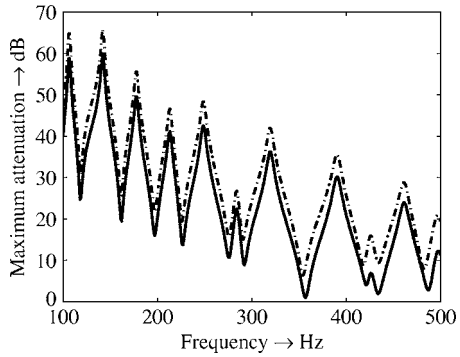

FIG. 12. Maximum theoretical attenuation η that can be obtained with forward difference prediction techniques plotted against frequency f for a virtual distance $d=0.1$ m. —, linear prediction; ---, quadratic prediction.

previous work.[8,9] Figure 10 shows that for a virtual distance $d=4\Delta=0.1$ m, the quadratic prediction weights approximate the optimal weights at low frequencies. Figure 11 shows that for an excitation frequency $f=249$ Hz, the quadratic prediction weights approximate the optimal weights for small virtual distances. These figures also indicate that the prediction accuracy of the three-microphone quadratic forward difference prediction method is expected to deteriorate for larger virtual distances and increasing excitation frequencies. These analytical results have been confirmed through simulations and experimental work on a rigid-walled acoustic duct.[8,9]

V. THEORETICAL LIMIT ON CONTROL PERFORMANCE

The performance of a local active noise control system incorporating a virtual sensor will heavily depend on the prediction accuracy of the virtual sensing algorithm. In this section, an expression for the maximum attenuation that theoretically can be achieved with a local active noise control system incorporating the virtual sensing method under consideration is derived.

From Eq. (8), the estimated complex pressure $\hat{p}_v$ at the virtual microphone location is given by

$$\hat{p}_v = \mathbf{w}^T\mathbf{p}_p + \mathbf{w}^T\mathbf{p}_s = \hat{p}_{p,v} + \hat{p}_{s,v}, \tag{35}$$

with $\hat{p}_{p,v}$ the estimated complex primary pressure at the virtual microphone location, and $\hat{p}_{s,v}$ the estimated complex secondary pressure at the virtual microphone location. Equation (35) can also be written as

$$\hat{p}_v = \mathbf{w}^T\mathbf{p}_p + \mathbf{w}^T\mathbf{Z}_s q_s, \tag{36}$$

where q_s is the complex secondary source strength, and $\mathbf{Z}_s$ is a vector of length M containing the complex acoustic transfer impedances between the secondary source and the physical microphones. These acoustic transfer impedances can be calculated from Eqs. (5) and (6) as

$$Z_{s,m} = \frac{p(x_m)}{q_s}, \tag{37}$$

where $Z_{s,m}$ is the complex acoustic transfer impedance between the secondary source located at y_s and a microphone located at x_m. From Eq. (36), it can be seen that the secondary source strength q_s that minimizes the estimated pressure $\hat{p}_v$ at the virtual location is given by

$$q_s = -(\mathbf{w}^T\mathbf{Z}_s)^{-1}\mathbf{w}^T\mathbf{p}_p. \tag{38}$$

From Eq. (11), the residual pressure p_v at the virtual location is now given by

$$p_v = e_{pe} + \hat{p}_v = e_{pe}, \tag{39}$$

since the estimated pressure at the virtual location $\hat{p}_v=0$ with the secondary source strength as defined in Eq. (38). The residual pressure at the virtual location is thus equal to the prediction error e_{pe} of the virtual sensing algorithm, which was defined in Eq. (11). The maximum attenuation η that can be achieved at the virtual microphone location is therefore given by

$$\eta = 20\log_{10}\left|\frac{e_{pe}}{p_{p,v}}\right|. \tag{40}$$

It can be shown that this can also be written as

$$\eta = 20\log_{10}\left|1 - \frac{Z_{s,v}\hat{Z}_{p,v}}{\hat{Z}_{s,v}Z_{p,v}}\right|, \tag{41}$$

with $\hat{Z}_{s,v}$ the estimated acoustic transfer impedance between the secondary source and the virtual microphone, given by

$$\hat{Z}_{s,v} = \mathbf{w}^T\mathbf{Z}_s, \tag{42}$$

and $\hat{Z}_{p,v}$ the estimated acoustic transfer impedance between the primary source and the virtual microphone defined in a similar way. If the virtual sensing algorithm provides perfect estimates of these transfer impedances, Eq. (41) shows that, theoretically, infinite reductions can be achieved at the virtual location for tonal excitations. Since the derived optimal microphone weights $\mathbf{w}_0$ are able to provide perfect estimates of the transfer impedances in Eq. (41), it is theoretically possible to obtain infinite reductions at the virtual location for tonal excitations.

The maximum attenuation that theoretically can be achieved using forward difference prediction techniques can now be calculated from Eq. (41). Figure 12 shows the maximum achievable attenuation η plotted against frequency f for a virtual distance $d=0.1$ m for the case of using linear and

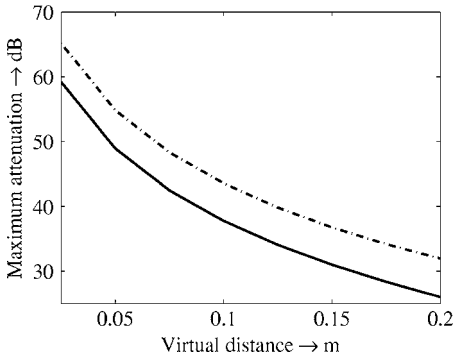

FIG. 13. Maximum theoretical attenuation η that can be obtained with forward difference prediction techniques plotted against virtual distance d for an excitation frequency $f=249$ Hz. —, linear prediction; --, quadratic prediction.

quadratic forward difference prediction techniques. Figure 13 shows the maximum achievable attenuation η plotted against virtual distance d for an excitation frequency $f=249$ Hz. The three-microphone linear forward difference prediction results are not shown in these figures, as the results are similar to the two-microphone linear prediction results. A traveling wave model of the rigid-walled acoustic duct with parameters as discussed in Sec. IV, was used to generate these figures. Both figures illustrate that, theoretically, the quadratic prediction technique outperforms the linear prediction technique. However, previous experimental results indicated otherwise,[10–12] for reasons that were discussed in Sec. I.

VI. CONCLUSION

Analytical expressions have been derived for the optimal microphone weights for virtual sensing in a rigid-walled acoustic duct with arbitrary termination conditions. The analytical expressions show that the optimal microphone weights depend on the acoustic wave number, the microphone separation distance, and the virtual distance. Moreover, the optimal microphone weights are independent of the source location, the physical and virtual microphone locations, and the termination conditions.

The analytical expressions for the optimal microphone weights have been compared with the weights obtained using various forward difference prediction techniques. The results indicate that the forward difference prediction weights match the optimal weights at low frequencies and small virtual distances, but that they become increasingly different for higher frequencies and larger virtual distances. This reduces the maximum attenuation that can be obtained at the virtual location using forward difference prediction techniques in combination with a local active noise control system.

An expression for the maximum theoretical attenuation that can be achieved with the virtual sensing algorithm discussed here has been derived. Using this expression, it was shown that the quadratic forward difference prediction technique theoretically outperforms the linear forward difference prediction technique. It was also shown that, theoretically, it is possible to obtain infinite reductions at the virtual location for tonal excitations.

ACKNOWLEDGMENTS

The author gratefully acknowledges The University of Adelaide for providing an ASI scholarship, and the Australian Research Council for supporting this research.

[1]S. J. Elliott, P. Joseph, A. J. Bullmore, and P. A. Nelson, "Active cancellation at a point in a pure tone diffuse sound field," J. Sound Vib. **120**, 183–189 (1988).
[2]S. J. Elliott and A. David, "A virtual microphone arrangement for local active sound control," *Proceedings of the 1st International Conference on Motion and Vibration Control*, Yokohama, 1992, pp. 1027–1031.
[3]J. Garcia-Bonito, S. J. Elliott, and C. C. Boucher, "A virtual microphone arrangement in a practical active headrest," *Proceedings of Inter-noise '96*, Liverpool, 1996, pp. 1115–1120.
[4]J. Garcia-Bonito, S. J. Elliott, and C. C. Boucher, "Generation of zones of quiet using a virtual microphone arrangement," J. Acoust. Soc. Am. **101**(6), 3498–3516 (1997).
[5]A. Roure and A. Albarrazin, "The remote microphone technique for active noise control," *Proceedings of Active '99*, 1999, pp. 1233–1244.
[6]S. R. Popovich, "Active acoustic control in remote regions," U.S. Patent No. 5,701,350, 1997.
[7]B. S. Cazzolato, "Sensing systems for active control of sound transmission into cavities," Ph.D. thesis, Department of Mechanical Engineering, The University of Adelaide, SA 5005, 1999.
[8]C. D. Kestell, "Active control of sound in a small single engine aircraft cabin with virtual error sensors," Ph.D. thesis, Department of Mechanical Engineering, The University of Adelaide, SA 5005, 2000.
[9]J. M. Munn, "Virtual sensors for active noise control," Ph.D. thesis, Department of Mechanical Engineering, The University of Adelaide, SA 5005, 2003.
[10]C. D. Kestell, C. H. Hansen, and B. S. Cazzolato, "Active noise control in a free field with virtual error sensors," J. Acoust. Soc. Am. **109**, 232–243 (2000).
[11]C. D. Kestell, C. H. Hansen, and B. S. Cazzolato, "Active noise control with virtual sensors in a long narrow duct," Int. J. Acoust. Vib. **5**, 1–14 (2000).
[12]J. M. Munn, C. D. Kestell, B. S. Cazzolato, and C. H. Hansen, "Real-time feedforward control using virtual error sensors in a long narrow duct," *Proceedings of the Annual Australian Acoustical Society Conference*, 2001.
[13]J. M. Munn, B. S. Cazzolato, C. H. Hansen, and C. D. Kestell, "Higher-order virtual sensing for remote active noise control," *Proceedings of Active 2002*, ISVR, Southampton, UK, 2002, pp. 377–386.
[14]B. S. Cazzolato, "An adaptive LMS virtual microphone," *Proceedings of Active 2002*, ISVR, Southampton, UK, 2002, pp. 105–116.
[15]J. M. Munn, B. S. Cazzolato, and C. H. Hansen, "Virtual sensing: Open loop vs adaptive LMS," *Proceedings of the Annual Australian Acoustical Society Conference*, 2002, pp. 24–33.
[16]H. J. Gawron and K. Schaaf, "Interior car noise: Active cancellation of harmonics using virtual microphones," *Proceedings of the 2nd International Conference on Vehicle Comfort: Ergonomic*, Vibrational and Thermal Aspects, Bologna, Italy, 1992, pp. 739–748.
[17]P. M. Morse and K. U. Ingard, *Theoretical Acoustics* (McGraw-Hill, New York, 1968).
[18]A. C. Zander and C. H. Hansen, "A comparison of error sensor strategies for the active control of duct noise," J. Acoust. Soc. Am. **94**, 841–848 (1993).
[19]B. S. Cazzolato, D. Petersen, C. Q. Howard, and A. C. Zander, "Active control of energy density in a one-dimensional waveguide: A cautionary note (L)," J. Acoust. Soc. Am. **117**, 3377–3380 (2005).
[20]P. A. Nelson and S. J. Elliott, *Active Control of Sound*, 1st ed. (Academic, New York, 1992).
[21]J. M. Munn, B. S. Cazzolato, C. D. Kestell, and H. C. Hansen, "Virtual sensing for active noise control in a one-dimensional waveguide: Performance prediction versus measurement (L)," J. Acoust. Soc. Am. **113**, 35–38 (2003).

Sound-field analysis by plane-wave decomposition using spherical microphone array

Munhum Park
Institute of Sound and Vibration Research, University of Southampton, Highfield, Southampton SO17 1BJ, United Kingdom

Boaz Rafaely
Department of Electrical and Computer Engineering, Ben-Gurion University of the Negev, Beer-Sheva, 84105, Israel

(Received 21 December 2004; revised 19 August 2005; accepted 20 August 2005)

Directional sound-field information is becoming more important in sound-field analysis and auditorium acoustics, and, as a consequence, a variety of microphone arrays have recently been studied that provide such information. In particular, spherical microphone arrays have been proposed that provide three-dimensional information by decomposing the sound field into spherical harmonics. The theoretical formulation of the plane-wave decomposition and array performance analysis were also presented. In this paper, as a direct continuation of the recent work, a spherical microphone array configured around a rigid sphere is designed, analyzed using simulation, and then used experimentally to decompose the sound field in an anechoic chamber and an auditorium into waves. The array employs a maximum of 98 measurement positions around the sphere, and is used to compute spherical harmonics up to order 6. In the current paper we investigate the factors affecting the performance of plane-wave decomposition, showing that the direct sound and several reflections in an auditorium can be identified experimentally. This suggests that the microphone arrays studied here can be employed in various acoustic applications to identify the characteristics of reverberant sound fields. © *2005 Acoustical Society of America.* [DOI: 10.1121/1.2063108]

PACS number(s): 43.55.Mc, 43.60.Fg, 43.55.Br [NX] Pages: 3094–3103

I. INTRODUCTION

Directional analysis of reverberant sound fields is becoming essential in areas such as speech enhancement, music recordings, and auditorium acoustics. Since it was found in the 1960s that the subjective impression is dependent on the lateral reflections of the sound field,[1] new room acoustics indicators such as the early/late lateral energy fraction[1,2] and the front-back ratio[3] were developed. These require spatial sound-field information, typically measured by microphone arrays, in contrast to the previous measures, such as the reverberation time, which employed a single microphone. As a result, measurement devices and techniques for spatial sound-field analysis are being developed continuously. Thiele[4] studied a microphone that was made directional using a parabolic reflector. Okubo *et al.*[5] used five microphones to detect four directional impulse responses corresponding to each quadrant and could produce several directional sound-field indicators. A four-element microphone array on a tetrahedron was employed by Sekiguchi *et al.*[6] to detect the arrival direction of time-separated wave fronts.

More recent microphone array designs have employed a larger number of microphones to improve spatial resolution. Rigelsford and Tennant[7] used a volumetric array with 64 microphones, while Gover *et al.*[8] used a spherical array with 32 elements and calculated various spatial room acoustics measures. Spherical microphone arrays, particularly those based on spherical harmonics processing, attracted special attention recently due to the inherent rotational symmetry in the spatial analysis. Spherical arrays were suggested for beamforming,[9] sound recording,[9] and sound-field analysis.[10–12] One form of the sound-field analysis is by plane-wave decomposition, where the sound field is decomposed into plane-wave components. The formulation of the plane-wave decomposition from the pressure distribution on a sphere was presented by Rafaely,[11] employing the spherical Fourier transform and spherical convolution.[13] The plane-wave decomposition can provide spatial information about the individual reflections in an enclosure, which can then be used to compute several spatial room acoustics measures, thus supporting a more detailed architectural acoustics design.

In this paper we describe the design, implementation, and an experimental investigation of a spherical microphone array used for plane-wave decomposition in an auditorium. The array is composed of a rigid sphere with a maximum of 98 positions on the sphere sampled by a single microphone, relocated to measure the impulse response from a loudspeaker at each location. Following a brief review of the plane-wave decomposition, we present the performance analysis of the array through a simulation study and experimental investigation, first in an anechoic chamber and then in an auditorium.

II. PLANE-WAVE DECOMPOSITION

In this section we provide a brief review of spherical harmonics,[14] the spherical Fourier transform,[13] and array

processing for the plane-wave decomposition,[11] which are used in this paper. The reader is referred to the references above for further reading.

The spherical Fourier transform p_{nm} of a square-integrable function on the unit sphere, $p(\Omega)$, is defined as[13]

$$p_{nm} = \int_{\Omega \in S^2} p(\Omega) Y_n^{m^*}(\Omega) d\Omega, \tag{1}$$

and the orthonormality of the spherical harmonics gives the closed form of the inverse transform:

$$p(\Omega) = \sum_{n=0}^{\infty} \sum_{m=-n}^{n} p_{nm} Y_n^m(\Omega), \tag{2}$$

where $\Omega = (\theta, \phi)$ defines a position in the angular sense, using the standard spherical coordinate system (r, θ, ϕ).[14] The integral over the unit sphere is evaluated as

$$\int_{\Omega \in S^2} d\Omega = \int_0^{2\pi} \int_0^{\pi} \sin\theta \, d\theta \, d\phi \tag{3}$$

and the spherical harmonics are defined as

$$Y_n^m(\Omega) = Y_n^m(\theta, \phi) = \sqrt{\frac{(2n+1)}{4\pi} \frac{(n-m)!}{(n+m)!}} P_n^m(\cos\theta) e^{im\phi}, \tag{4}$$

where n is the order of the spherical harmonics, $i = \sqrt{-1}$, and P_n^m is the associated Legendre function. When M microphones sample the sound pressure on a sphere at positions Ω_j, the spherical Fourier integral is approximated by a summation to give

$$p_{nm} = \sum_{j=1}^{M} a_j p(\Omega_j) Y_n^{m^*}(\Omega_j). \tag{5}$$

This approximation can be exact with a careful choice of the sampling positions[12] and an appropriate choice of the constants a_j, if the function p_{nm} is bandlimited, i.e., $p_{nm} = 0, \ \forall n > N$. The reader is referred to Rafaely[12] for a further description of sampling methods. One particular method used here is Gaussian sampling, where the azimuth angle ϕ is sampled at $2(N+1)$ equiangle positions, and the elevation angle θ is sampled at $(N+1)$ nearly equiangle positions, such that $M = 2(N+1)^2$.[2] In this case, Eq. (5) can be computed more efficiently by separating the summations over the angles and using the fast Fourier transform over ϕ.[11]

The spherical Fourier transform is now used in plane-wave decomposition. The pressure due to a single unit-amplitude plane wave scattered by a rigid sphere can be represented using the spherical harmonics as[15]

$$p(\Omega, \Omega_l) = \sum_{n=0}^{\infty} \sum_{m=-n}^{n} b_n(kr, ka) Y_n^{m^*}(\Omega_l) Y_n^m(\Omega), \tag{6}$$

where $b_n(kr, ka)$ is given for a rigid sphere of radius a by[9,15]

$$b_n(kr, ka) = 4\pi i^n \left(j_n(kr) - \frac{j_n'(ka)}{h_n'(ka)} h_n(kr) \right). \tag{7}$$

Here $k = \omega/c$ is the wave number for frequency ω and the speed of sound c, and $\Omega_l = (\theta_l, \phi_l)$ is the wave arrival direction. j_n and h_n are the spherical Bessel and Hankel functions, and j_n' and h_n' are their derivatives.

When the sound field is composed of an infinite number of plane waves, each with directional amplitude density denoted by $w(\Omega_l)$, the integration over all possible angles and the use of the spherical Fourier transform gives a simple and important relation between the pressure and the waves directional amplitude density in the spherical Fourier domain:[11]

$$p_{nm} = w_{nm} b_n, \tag{8}$$

such that w is calculated as

$$w(\Omega_l) = \sum_{n=0}^{N} \sum_{m=-n}^{n} \frac{p_{nm}}{b_n} Y_n^m(\Omega_l), \tag{9}$$

where the summation over n was truncated, since it was assumed that p_{nm} is calculated up to order $n \leq N$. The computation of the plane-wave decomposition using a microphone array is therefore performed in two stages for each frequency. First, the coefficients p_{nm} up to order N are calculated using Eq. (5), and then the waves directional amplitude density at each frequency, i.e., plane-wave decomposition, is computed at the desired directions using Eq. (9).

III. SPHERICAL MICROPHONE ARRAY DESIGN

There are several important issues to be considered when designing a spherical microphone array. These include the choice between an open and a rigid sphere, the number of microphones affecting the harmonic order and thus the spatial resolution, and the realization in practice, with issues such as positioning accuracy, transducer noise, and aliasing, all of which affect the useful operating frequency range. A theoretical analysis of the factors affecting the performance and design considerations have recently been presented by Rafaely.[12]

The microphone array implemented in this work was configured around a rigid (wooden) sphere, of radius $a = 10.9$ cm, which had been chosen to avoid singularities involved with an open sphere.[11] Two sampling configurations were employed, both using the Gaussian sampling scheme,[12] one with $M = 50$ samples and the other with $M = 98$ samples, providing a good approximation of Eq. (1) by Eq. (5) for orders $N = 4$ and $N = 6$, respectively. In both cases, a single microphone was used to measure a full set of frequency responses from loudspeakers to all the sampling points by repositioning the sensor. This type of microphone array realization is suitable for non-real-time applications in stationary sound fields, such as impulse response analysis. The accuracy in microphone positioning is limited, while the use of a single microphone reduces the microphone mismatch problem. Furthermore, additional inaccuracy could be introduced, in particular during long measurement sessions, when conditions in the room change and the sound field is no longer stationary.

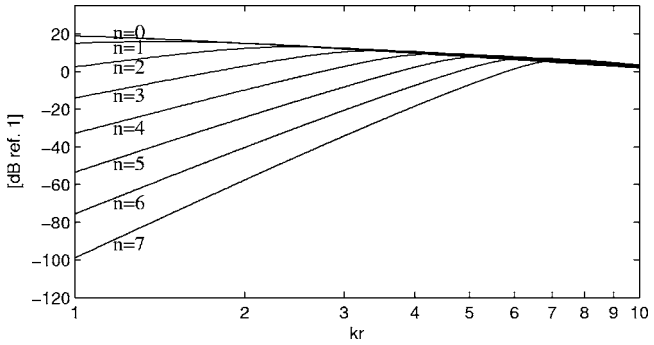

FIG. 1. Magnitude of $b_n(kr,kr)$ for $n \leqslant 7$.

Microphone array analysis[12] shows that this type of array operates best around $kr \simeq N$, for $r=a$, i.e., when the pressure is sampled on the surface of a sphere. At lower kr, transducer noise and positioning errors severely affect the array performance, as does the aliasing error at higher kr. Figure 1 shows $b_n(kr,kr)$, which explains this behavior. For $kr \ll N$, it will not be possible to precisely measure high-order terms since they have a very low magnitude. Dividing by these terms as required by Eq. (9) will introduce noise, while ignoring them will reduce the array order and degrade the spatial resolution. On the other hand, for $kr > N$, terms with $n > N$ are significant so that the sampling of this non-bandlimited pressure may result in aliasing. The frequency corresponding to $kr \simeq N$ can therefore be considered optimal and is written as $f_N^{\text{opt}} \simeq cN/2\pi a$, assuming $r=a$.

As another way of examining the array performance and robustness, Rafaely[12] showed that the white noise gain (WNG) of the current spherical microphone array can be represented as

$$\text{WNG} = \frac{(N+1)^4}{\sum_{j=1}^{M} a_j^2 \left| \sum_{n=0}^{N} \frac{2n+1}{b_n} P_n(\cos \Theta_j) \right|^2}, \tag{10}$$

where Θ_j is the angle between the array look direction and the pressure sampling positions. The WNG curves shown in Fig. 2 have been obtained for the arrays considered in this study (see Table I), from which the optimal frequency f_N^{opt} as well as the operational frequency range can be roughly estimated.

The two array configurations used in this work are summarized in Table I. The spatial resolution of the two arrays,

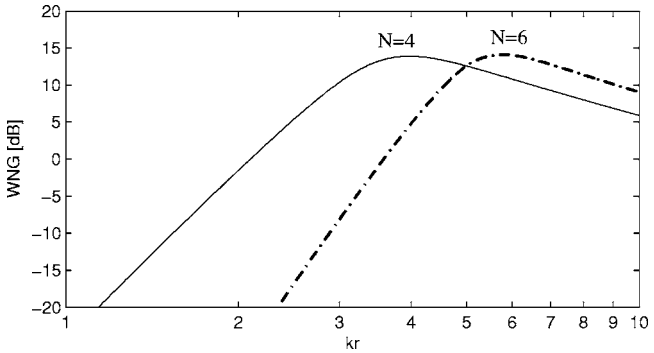

FIG. 2. White noise gain obtained for $N=4$ and 6.

TABLE I. Design specifications of the two spherical microphone arrays based on Gaussian sampling. Optimal frequencies are computed assuming that the system operates in air with a solid sphere of 10.9 cm radius.

Order N	Number of pressure samples	Optimal frequency, f_N^{opt}	Spatial resolution, Θ_r
4	10 azim. $\times$ 5 elev. = 50	$\sim$2000 Hz	45°
6	14 azim. $\times$ 7 elev. = 98	$\sim$3000 Hz	30°

denoted by Θ_r in Table I, represents half of the zero-to-zero width of the array response to a plane wave,[11] or its beampattern in this case, and is approximated by[11]

$$\Theta_r \simeq \frac{\pi}{N}. \tag{11}$$

A photograph of the wooden sphere and the measuring microphone is given in Fig. 3.

IV. SIMULATION STUDY

The two spherical microphone arrays presented in Table I were studied by numerical simulations in this section, with the aim of investigating the expected performance and the limitations of the arrays. Sound fields composed of one and two plane waves scattered around a rigid sphere were simulated by using Eq. (6) with n running up to 50, where supplemental simulations have shown that the terms in the summation have little significance for $n \gtrsim 20$. The pressure was then sampled at the positions determined by the Gaussian sampling method so that a matrix of pressure responses could be produced from 0 to 5000 Hz at every 6.25 Hz, where the sampling frequency is assumed to be 10 kHz. These specifications in frequency domain are made identical to those to be used in the measurements. This pressure matrix was then used to compute the plane-wave decomposition as discussed above, producing w bandlimited at $N=4$, 6.

A. Spatial resolution and frequency bandwidth

Figures 4(a) and 5(a) represent the plane-wave decomposition for a single plane wave arriving from direction $(\theta,\phi)=(90°,180°)$, showing $w(\theta,\phi)$ for the two arrays at

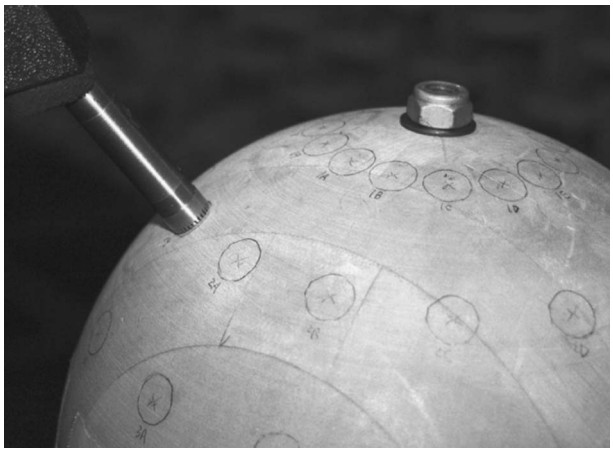

FIG. 3. Microphone positioned on one of the sample points.

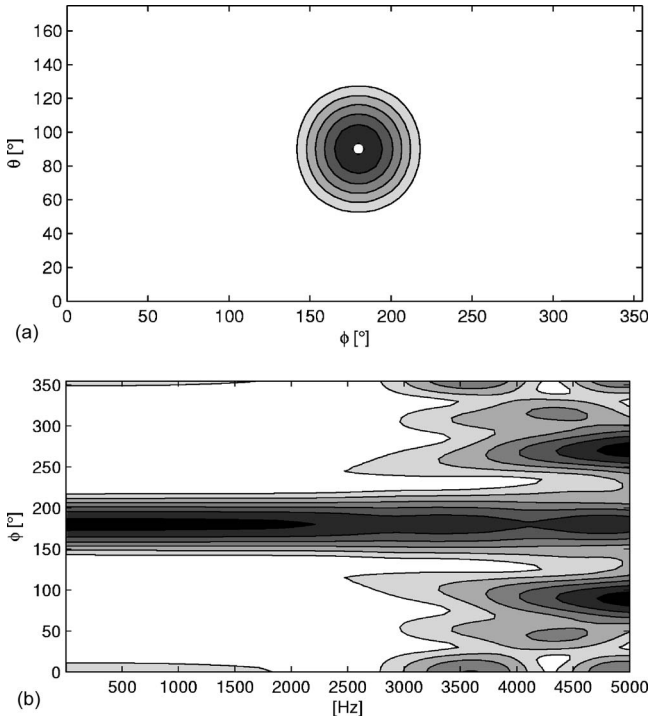

FIG. 4. (a) Simulated directional amplitude density $w(\theta,\phi)$ using the fourth-order array for a single plane-wave sound field at 2000 Hz; (b) $w(90°,\phi)$ for the same array and the sound field as a function of frequency.

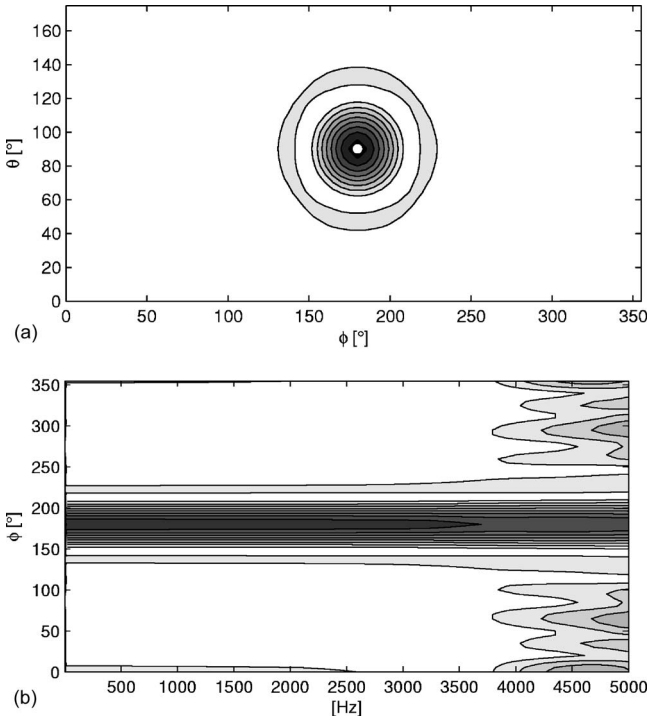

FIG. 5. (a) Simulated directional amplitude density $w(\theta,\phi)$ using the sixth-order array for a single plane-wave sound field at 3000 Hz; (b) $w(90°,\phi)$ for the same array and sound field as a function of frequency.

their optimal frequencies. The figures indicate that the designed arrays are capable of detecting the incident direction of the plane waves, marked by the white dot on the figures. It is clear that the array with $N=6$ gives a better spatial resolution compared to the array with $N=4$, evident by the narrower circle in the figure.

Figures 4(b) and 5(b) show $w(90°,\phi)$ as a function of frequency, providing the frequency dependence of the array azimuthal directivity. The width of the main lobe corresponds to about $2\Theta_r$, as detailed in Table I, confirming the design goal. Since the transducer noise and the positioning errors were not included in these simulations, the array performance is good down to very low frequencies, while the high frequencies are affected by aliasing as expected, which increases significantly beyond the optimal frequencies detailed in Table I.

B. Measurement errors

Errors in positioning the microphone can produce noise at the array output.[12] This is particularly important here since a single microphone is continuously repositioned, making it more difficult to keep it in place with high accuracy. In order to show significant changes in the array output over frequency, the directional gain (DG) has been considered as a scalar measure for array performance.[8] It is defined as the peak-to-average directional response and can be computed by

$$\mathrm{DG(dB)} = 20\log\frac{\max\{|w(\theta,\phi,\omega)|\}_{\theta,\phi}}{\langle|w(\theta,\phi,\omega)|\rangle_{\theta,\phi}}. \tag{12}$$

The solid lines in Figs. 6(a) and 6(b) show the directional gains for the two arrays before taking into account the positioning errors. The directional gain decreases above f_N^{opt} in both cases due to aliasing.

If d_θ and d_ϕ are assumed to be positioning errors in the direction of θ and ϕ, the associated angular perturbations are given by

$$\theta_n = \frac{d_\theta}{r}, \quad \phi_n = \frac{d_\phi}{r}\frac{1}{\sin\theta}, \tag{13}$$

and the actual measurement position (θ_p,ϕ_p) can be represented by

$$\theta_p = \theta + \theta_n, \quad \phi_p = \phi + \phi_n. \tag{14}$$

The nonsolid lines in Figs. 6(a) and 6(b) illustrate the effect of the positioning error on the directional gain when d_θ and d_ϕ vary independently having zero-mean Gaussian distributions with standard deviation σ_d. The figure shows that for both arrays the directional gain is degraded at low frequencies more significantly for larger positioning errors, consequently narrowing the array bandwidth. The array with $N=6$ is more susceptible to microphone positioning error since it includes additional higher-order terms compared to the array with order 4.

Another significant error factor is transducer noise, or measurement noise. A theoretical analysis of measurement noise has been recently presented,[12] where it is shown to have similar behavior to positioning error. Figure 9 (dotted curves), later, shows the simulated combined effect of positioning error with $\sigma_d=3$ mm and a signal-to-noise-ratio (SNR) of 40 dB at the array input. In both arrays the direc-

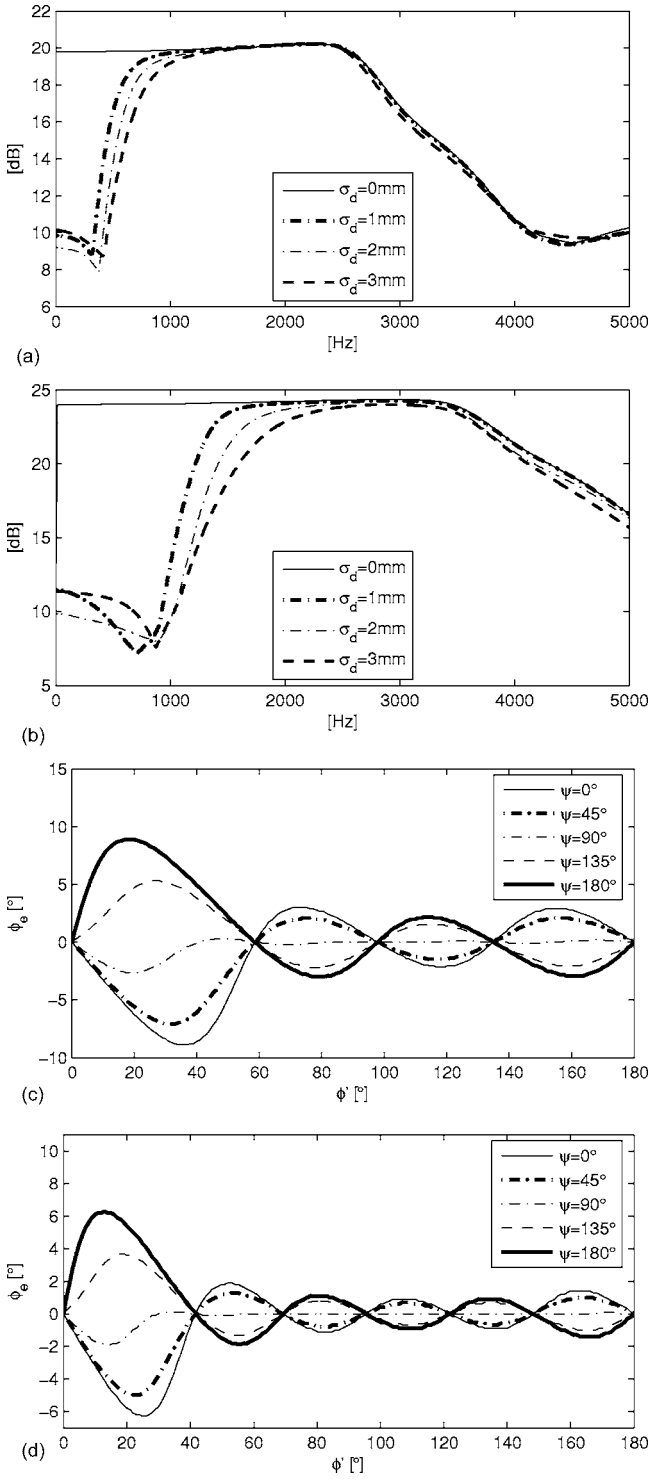

FIG. 6. Effect of microphone positioning error on the directional gain: (a) $N=4$, (b) $N=6$. Error in direction finding shown for a varying phase difference: (c) $N=4$, (d) $N=6$. The amplitude of the target sound wave is two times greater than the other.

tional gain at low frequencies is degraded, but, as expected, the fourth-order array has been shown to be more robust.

C. Spatial resolution with two plane waves

In practice, the sound field may be composed of more than one wave at the same frequency; therefore the array may be required to distinguish between two (or more) waves with similar arrival directions. In conjunction with such a requirement, a sound field with two plane waves was simulated, for which the plane-wave decomposition is investigated here.

When the spatial separation between the two waves is significant compared to the spatial resolution, i.e. Θ_r, plane-wave decomposition is expected to work efficiently in discriminating the waves. This is because the w functions of the two waves have a small interaction, i.e. their peaks are not significantly affected by the presence of the other wave. However, when the two waves are relatively close to each other, the two w functions will interact strongly. As seen below, the error in detection of wave arrival direction depends not only on the spatial separation but also on the relative phase and amplitude of the two waves. For example, the w function of the two separate waves can add or substract, producing a different overall w in each case.

Consider two plane waves separated by an angle of ϕ', incident from $(90°, 180° \pm \phi'/2)$, having phase difference ψ with relative amplitude ratio R. The error of the array in direction finding is defined as $\phi_e = \phi_s - \phi_m$, where ϕ_s is the azimuth of the wave arrival direction, and ϕ_m is the detected azimuth of the wave incidence. As a function of ϕ', the error in direction finding is illustrated in Figs. 6(c) and 6(d) for the two arrays where the target wave amplitude is assumed to be two times greater than the interfering wave, i.e. $R=2$.

It is obvious that the detection error is greater for small ϕ' $\left(\phi' \lesssim \frac{4}{3}\Theta_r\right)$ than for the larger separation angles, where it oscillates every time a peak or dip in the directional amplitude density function w of the target wave is added to or subtracted from that of the interfering wave. The maximum error, the range of the transient behaviour for small ϕ', and the period of the late oscillations all decrease for the higher-order array. In Figs. 6(c) and 6(d), it is also shown that the arrays are less accurate in detecting two sound waves incident either in phase or out of phase, since the corresponding w functions interact most significantly in those cases. A detailed analysis for other values of the amplitude ratio R confirmed that weaker sound waves are harder to detect with accuracy.

The presence of multiple sound waves degrades the array performance even for very large separation angles, and such limitations on the wave detection can restrict the application of the plane-wave decomposition in practical sound fields with many waves. However, in the case of the plane-wave decomposition based on impulse responses, as performed in this work, additional separation is possible by means of time windowing so that waves can be separated even in reverberant sound fields, which will be presented in Sec. VI.

D. Directional response

The directional response of the array to a single plane wave arriving from $(\theta, \phi) = (90°, 180°)$ was calculated and plotted for $\theta = 90°$ as a dash–dotted curve in Fig. 7. The narrower main lobe of the array with $N=6$ and the side lobes of both arrays are clearly depicted, confirming the spatial resolution detailed in Table I.

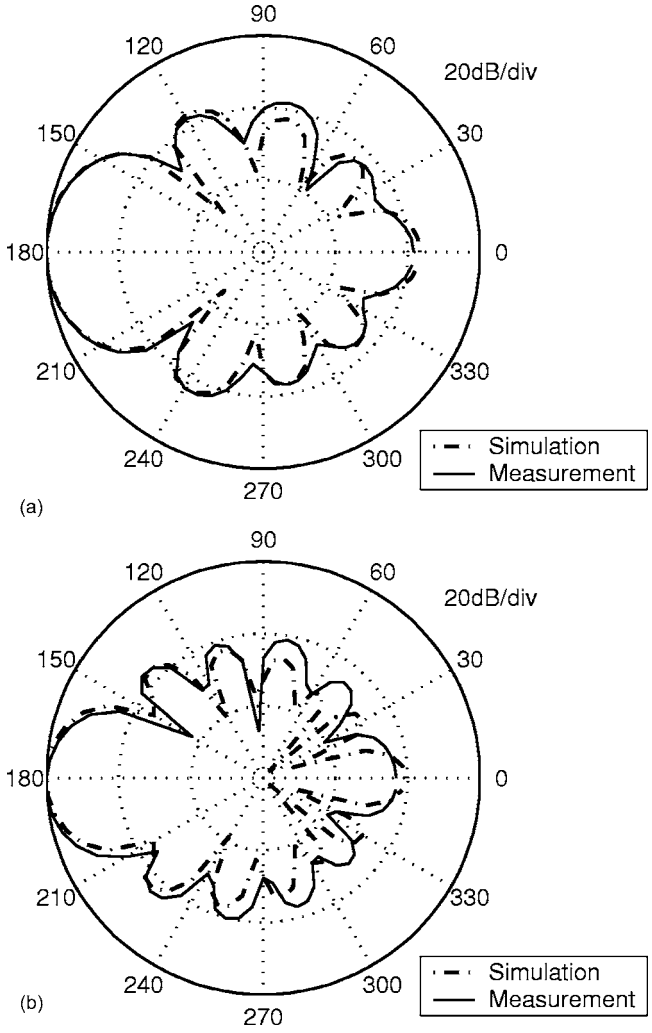

FIG. 7. Directional response obtained from measurement, compared with simulation: (a) $N=4$ at 2000 Hz, (b) $N=6$ at 3000 Hz. Measured response was normalized to the simulation result for a comparison.

V. ANECHOIC CHAMBER MEASUREMENTS

The microphone arrays were implemented and investigated experimentally in an anechoic chamber under a well-controlled condition. The microphone array system included a rigid wooden sphere of radius 10.9 cm, with either 50 or 98 sample points, as detailed in Table I. A B&K microphone type 4132, connected to a B&K measuring amplifier type 2608, was placed very close to the sample point on the surface of the sphere. The measurement of the frequency response between the input signal to a loudspeaker and the microphone output was performed using a spectrum analyzer (Adventest, R9211C FFT Servo Analyzer), with sample rate and frequency resolution as described in the introduction of Sec. IV. For each set of measurements, frequency responses were taken for all the microphone positions by relocating the single microphone.

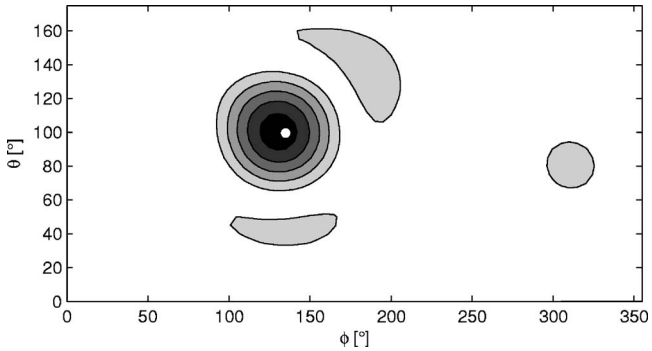

FIG. 8. $w(\theta,\phi)$ measured at 2000 Hz with the fourth-order array.

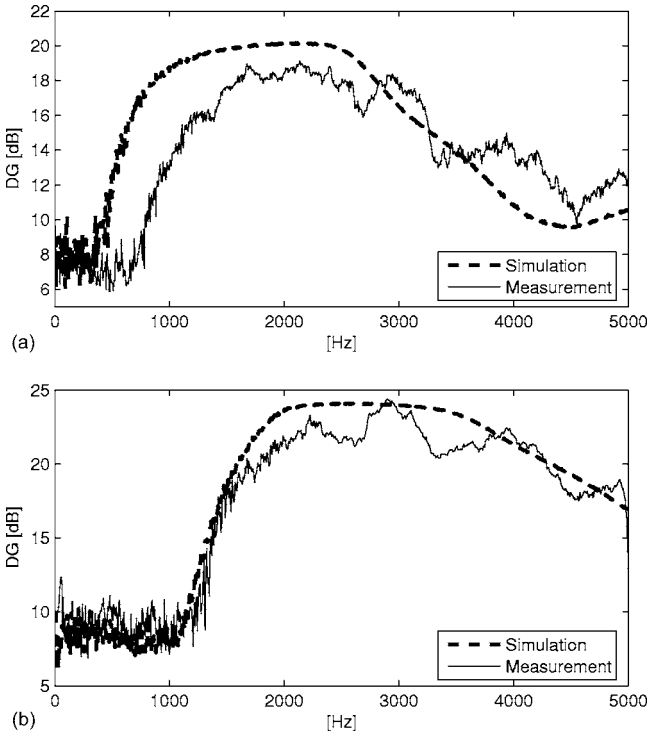

FIG. 9. Directional gain by measurement compared with one of the simulation results (40 dB SNR and $\sigma_d=3$ mm in sensor-positioning error): (a) $N=4$, (b) $N=6$.

The experiment was performed in the large anechoic chamber at the Institute of Sound and Vibration Research, University of Southampton, measuring 9.15 m $\times$ 9.15 m $\times$ 7.32 m. A total of four loudspeakers were installed on the supportive metal meshed floor. Different combinations of loudspeakers were driven by a white-noise input signal generated by the spectrum analyzer. The frequency response functions obtained by the analyzer at each sensor position were used as the complex pressure $p(\Omega_j)$ in Eq. (5).

Figure 8 shows an example of $w(\theta,\phi)$ for a single-source sound field as detected by the fourth-order array, with

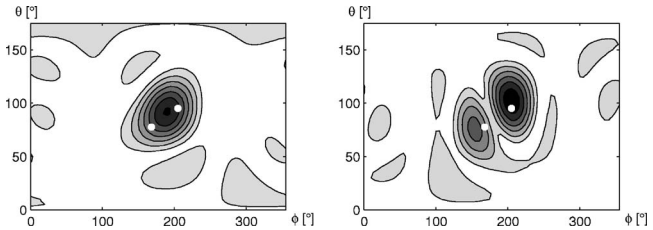

FIG. 10. $w(\theta,\phi)$ of the double-source (locations marked by two white dots) sound field measured by the fourth-order array in an anechoic chamber. At 1768.75 Hz (left), a fused peak of two sources is shown while at 1850 Hz (right), they are more distinguishable with a changing degree of separation.

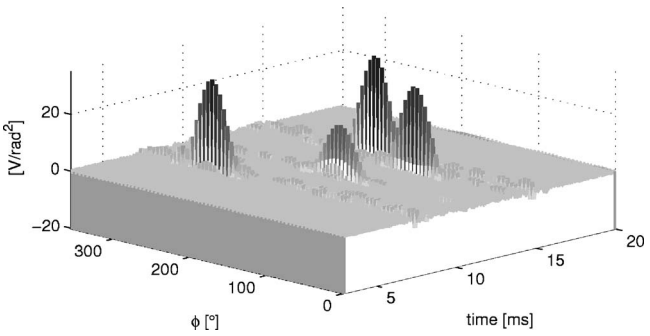

FIG. 11. Directional impulse responses for $\theta=90°$. Four sources are clearly seen by the peaks at their expected arrival times.

the actual direction of arrival approximated from geometrical measurements (white dot on the figure). The approximated source direction is about 4° away from the detected direction, which is a reasonable difference given the limited accuracy of the setup. The noise at directions away from the source direction originates from side lobes and measurement noise.

The actual effect of measurement noise on array performance is investigated through an analysis of the directional gain for a single-source sound field. Figure 9 shows the directional gain for both arrays as a function of frequency. Array performance is comparable to the simulated performance assuming a 40 dB SNR, and $\sigma_d=3$ mm. This comparison gives an idea of the affecting factors in practice. Both arrays have their best performance around the optimal

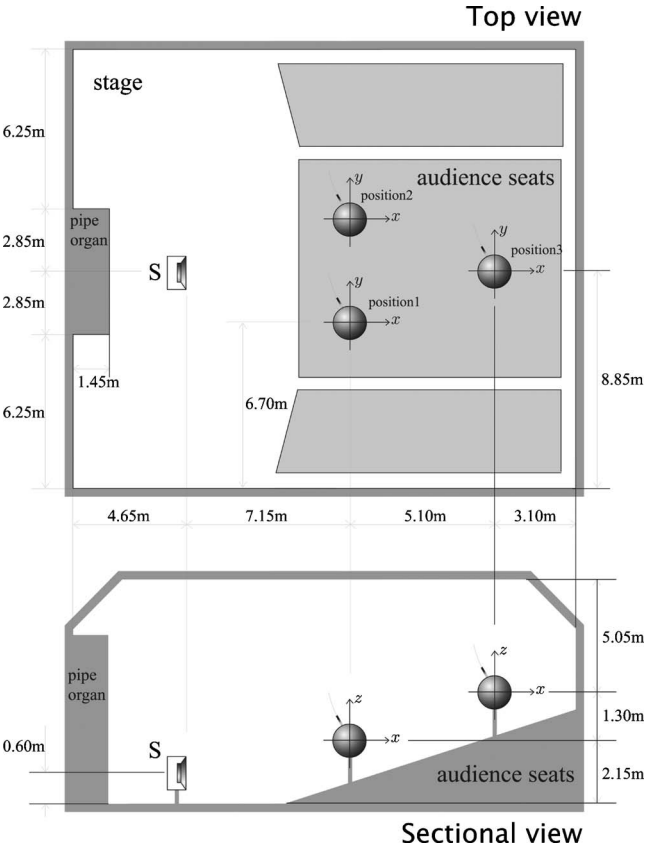

FIG. 12. The sketch of the building plan of the Turner Sims Concert Hall in the University of Southampton. Measurement setup is also shown.

FIG. 13. A photograph showing the auditorium measurement site.

frequencies detailed in Table I, which also agrees with the analysis of the WNG presented with Fig. 2. In addition, the measured directional response is compared to the simulated one in Fig. 7, showing good agreement between simulated and measured directivities.

The next experiment involves two sources, and as discussed in the simulations section, separation ability depends, among other factors, on the relative phase of the waves, which can translate to the dependence on frequency (through kr). Figure 10 shows sources marked by two white dots and the way they were detected by the fourth-order array at two nearby frequencies, where the separation between the two peaks keeps changing with frequency. The two sources had a 1.4 m path difference to the microphone, such that the phases of the two sources correlate every 245 Hz. This was confirmed by a detailed inspection of the plane-wave decomposition across the frequency range. The figure illustrates that although the sources are fixed in position, the separation ability changes with relative sources phases, as shown in Sec. IV.

The final test in the anechoic chamber involved four sound sources, but this time the directional amplitude density function $w(\theta,\phi)$ was calculated at each frequency, and the inverse FFT was used to compute the directional impulse response for each (θ,ϕ). At low frequencies, the array suffers from high noise originating mainly from the high-order terms, which can be detrimental for the computation of the directional impulse responses. Therefore, an order limiting filter is applied, denoted as $c_n(f)$, $n\leqslant N$, such that Eq. (9) becomes

$$w(\Omega_l)=\sum_{n=0}^{N}\sum_{m=-n}^{n}c_n\frac{p_{nm}}{b_n}Y_n^m(\Omega_l). \tag{15}$$

In order to maintain low noise at the entire frequency range, the filter c_n can be chosen so that the microphone array system have an increasing order at higher frequencies. Since b_n for $n>kr$ starts to decay rapidly with increasing n, c_n was chosen to ensure that a given b_n will only contribute for $n<kr$:

TABLE II. Performance of the array system in the auditorium. θ_e and ϕ_e represent errors in elevation and azimuth angles, respectively, while the expected locations have been obtained by means of the image source method.

Measure position	Traveling path	Traveling time (ms)	Expected location	Errors θ_e(°)	Errors ϕ_e(°)
2	Direct	22.4	(102°,199°)	+2	+2
	Stage floor	23.3	(110°,199°)	+4	+2
	Ceiling	46.9	(29°,199°)	+3	+1
	Stage floor → ceiling	50.1	(26°,199°)	+3	+3
	Right sidewall	50.7	(95°,114°)	+5	+1
	Left sidewall	63.8	(94°,251°)	+6	+1
	Stage wall → right sidewall	66.8	(94°,136°)	+6	+6
	Stage wall → left sidewall	77.0	(93°,231°)	+4	−5
	Ceiling → rear wall	80.5	(59°,354°)	−3	−1
3	Direct	36.6	(103°,179°)	+4	+5
	Stage floor	37.6	(108°,179°)	+7	+4
	Ceiling	52.0	(43°,179°)	+5	+4
	Stage floor → ceiling	54.5	(41°,179°)	+1	+2
	Left sidewall	63.9	(98°,236°)	+5	+6
	Right sidewall	65.1	(97°,124°)	+7	+5

$$c_n(f) = \begin{cases} 1, & n < 2\pi fr/c, \\ 0, & n \geqslant 2\pi fr/c. \end{cases} \tag{16}$$

Although this additional process reduces noise, it distorts plane-wave decomposition as a lower spatial resolution is achieved at low frequencies. Nevertheless, directional impulse responses were computed with an order-limiting filter, as detailed in Eq. (16). Figure 11 illustrates the directional impulse responses for all azimuth angles obtained thereby, in which the four peaks corresponding to the four sound sources are clearly distinguishable at their expected arrival times, and the comparison of source strengths is easily made. This spatial–temporal separation will be used below in the analysis of the sound field in a concert hall to improve spatial resolution by analyzing time-windowed responses.

VI. AUDITORIUM MEASUREMENTS

The final part of the experimental study aimed at evaluating the performance of the spherical microphone array in a real reverberant sound field. The experiment was therefore performed in a concert hall, the Turner Sims Concert Hall in the University of Southampton, which measures approximately 18 m × 20 m × 8.5 m, accommodating 406 seats (see Figs. 12 and 13). A single loudspeaker positioned at the center of the stage (in the front part) was used throughout the experiment, and three measurement positions were chosen for a comparison between seats, two of which were in the front seating area, and the third at the rear seating section. Both the loudspeaker and the measurement device were positioned well above the floor, roughly taking into account the height of orchestral instruments and audience ear positions.

As shown in Fig. 12, the coordinate systems chosen for each measurement position take the center of the sphere as

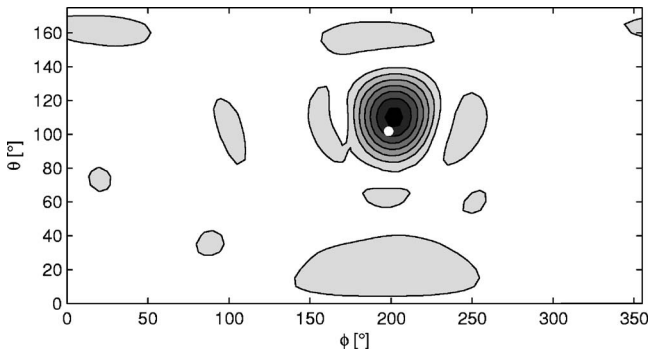

FIG. 14. $w(\theta, \phi)$ at 3000 Hz (position 2). The white dot indicates the position of the loudspeaker.

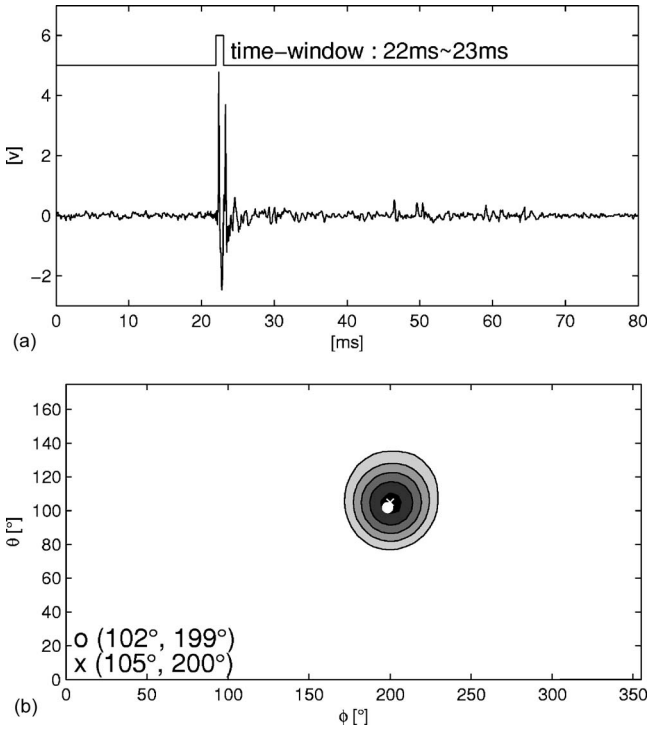

FIG. 15. (a) An example of time windowing shown for the impulse response at (90°,180°). (b) $w(\theta, \phi)$ at 3000 Hz (position 2) after time windowing. (The white dot indicates the loudspeaker location, while the circle and the cross show the expected and detected wave incident directions, respectively.)

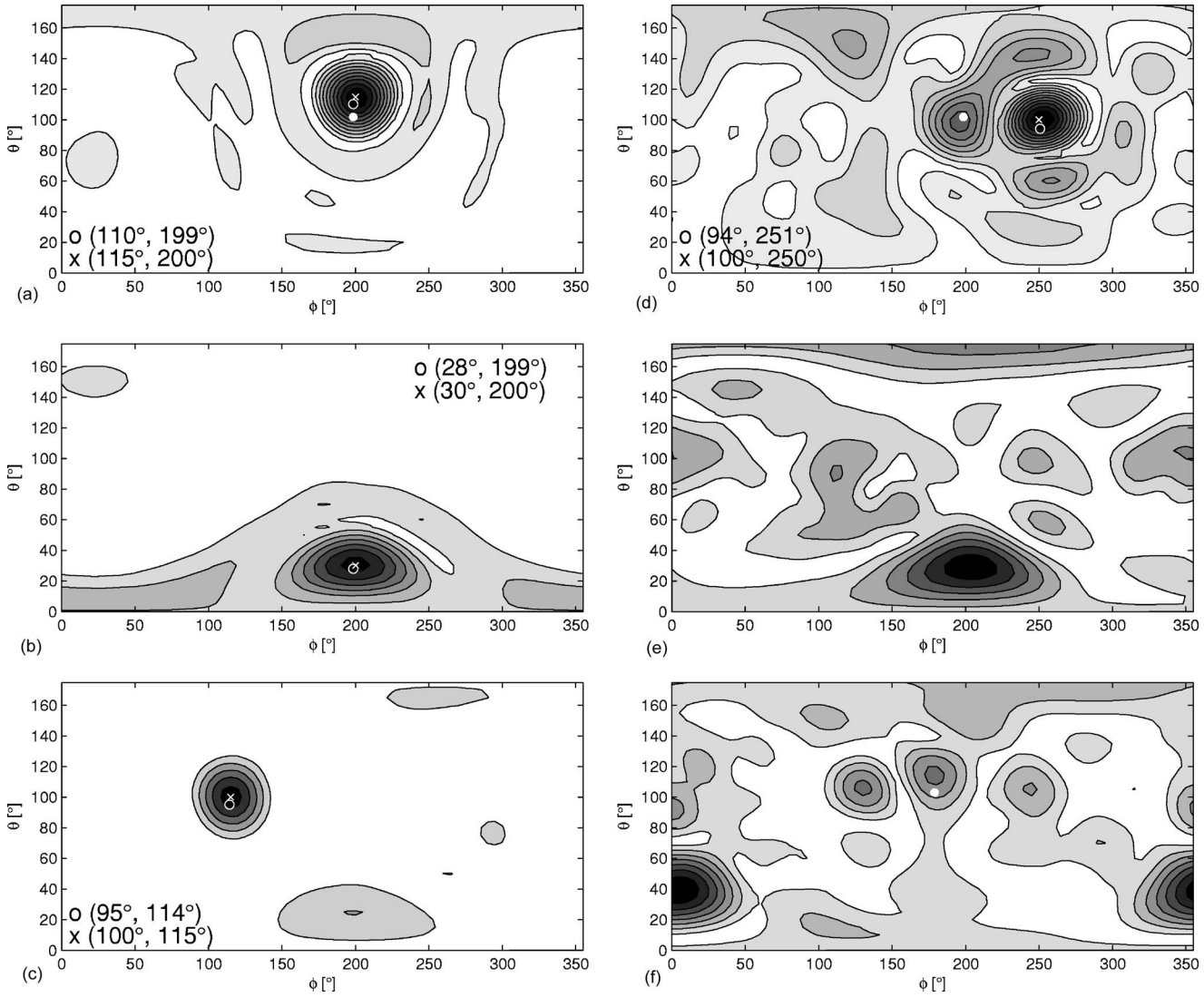

FIG. 16. $w(\theta, \phi)$ at 3000 Hz (position 2) after time windowing to show the wave bounced from the (a) stage floor, (b) ceiling, (c) right sidewall, and (d) left sidewall. Panels (e) and (f) show $w(\theta, \phi)$ for the early periods (5–80 ms after direct sound). (The white dot for the loudspeaker, and the circle and the cross for the expected and detected directions, respectively) The reflections from the ceiling are dominant at the position 2 [panel (f)], while the sound waves from the front are more evenly distributed at position 3 [panel (e)].

the origin, and the line directing backward therefrom as the base line of azimuth angle ϕ, while the elevation angle θ is measured from the line stretching to the ceiling, the z axis.

A sixth-order array was used to give a better resolution, while the analysis was performed only at the optimal frequency, 3000 Hz, to achieve the best performance. The rest of the measurement specifications are identical to those used in the anechoic chamber.

The arrival times and directions of the direct sound as well as the following reflections were approximated from the hall geometry by considering the locations of the real and image sources. Table II lists various wave paths for the two of the array positions with their travel times. These travel times were used to produce a set of time windows to truncate the corresponding peaks in the impulse responses.

Figure 14 shows the plane-wave decomposition applied to the measured response at 3000 Hz before time windowing. The figure shows no clear wave directions except a peak resulting from the dominance of the direct sound and the first reflection from the floor. As a consequence, the detection of individual waves is not possible.

In order to improve plane-wave decomposition, a time window was applied around the peaks of the impulse responses in the time domain, assuming that the waves are separated to a reasonable extent in the spatial–temporal domain. The frequency responses of these windowed impulses were then evaluated at 3000 Hz, which formed the data for plane-wave decomposition.

One of the examples of the time-windowed plane-wave decomposition is shown in Fig. 15 for the sound field at measurement position 2. The impulse responses were windowed around the arrival time of the direct sound [panel (a)], emphasizing its incidence direction at the peak value [panel (b)].

In a similar manner, the first reflection bounced from the stage floor could be captured by a predetermined time win-

dow, which exactly selected the second peak of the impulse responses. As listed for a few wave paths in Table II, incidence directions could be detected in this way and compared to those predicted by the image source method, where errors could be found in the range of $-3° \sim +7°$ [see Figs. 16(a)–16(d)]. In the early period, the errors are ascribed to the imprecise measurement of the hall dimension and the device positions, thus, the misplacement of the image sources. However, it is obvious that the complete isolation of a specific incident sound wave becomes more difficult with an increasing number of reflected waves, which is responsible for the errors in the later period. A finer time resolution is required to identify the waves in this period.

Inspections showed that the sound fields at the two front measurement positions are practically symmetric, but, as expected, the one at the position 3 distinguished itself from the former in many ways. For example, it contained more acoustic energy from the back wall rather than the ceiling, and the waves from the front were more evenly incident in contrast to the emphasized right-wall reflection in case of position 2 [see Figs. 16(e) and 16(f)].

Directional impulse responses can be obtained from these measurements and used to acquire several room acoustics indicators such as the directional reverberation times, etc.,[8] although in its current form the system cannot perform broadband analysis at high order, or resolution. Ways to improve the SNR and increase bandwidth are topics of current research.

VII. CONCLUSION

In this paper we presented an experimental study of plane-wave decomposition using a spherical microphone array, which is supported by simulations and theory. It was shown that using impulse response information, the direction of arrival of the direct sound and initial reflections were reasonably accurately detected by the array, therefore showing a potential for a practical architectural acoustics measurement tool. Microphone measurement arrays of orders $N=4$ and $N=6$ were implemented and studied. The low-order array achieved lower spatial resolution but suffered less from errors due to measurement noise and microphone misplacement, therefore achieving a broader operating frequency range.

Array performance was enhanced when time windowing of the impulse responses was employed before plane-wave decomposition. The detected incident directions agreed well with the image source locations computed beforehand, implying a successful application of this type of microphone array system to reverberant sound field analysis. An interesting factor affecting wave detection was found to be the relative phase and amplitude of adjacent sources, which implies that spatial resolution could also be affected by the sources signal.

Future work aims at the design of a microphone array and array processing with improved performance and robustness, such that more accurate plane-wave decomposition could be achieved in a wider frequency range in practice.

[1] M. Barron and A. H. Marshall, "Spatial impression due to early lateral reflections in concert halls: the derivation of physical measure," J. Sound Vib. **77**, 211–232 (1981).

[2] J. S. Bradley, "The Gulbenkian Great Hall, Lisbon, : an acoustic study of a concert hall with variable stage," Appl. Acoust. **66**, 91–108 (2000).

[3] M. Morimoto and K. Iida, "A new physical measure for psychological evaluation of a sound field: front back energy ratio as a measure for envelopment," J. Acoust. Soc. Am. **93**, 2282 (1993).

[4] R. Thiele, "Richtungsverteilung and zeitfolge der schallrückwürfe in Räumen (directional distribution and time sequence of acoutic reactions in rooms)," Acustica **3**, 291–302 (1953).

[5] H. Okubo, M. Otani, E. Ikezawa, S. Komiyama, and K. Nakabayashi, "A system for measuring the directional room acoustical parameters," Appl. Acoust. **62**, 203–215 (2001).

[6] K. Sekiguchi, S. Kimura, and T. Hanyuu, "Analysis of sound field on spatial information using a four-channel microphone system based on regular tetrahedron peak point method," Appl. Acoust. **37**, 305–323 (1992).

[7] J. M. Rigelsford and A. Tennant, "A 64 element acoustic volumetric array," Appl. Acoust. **61**, 469–475 (2000).

[8] B. N. Gover, J. G. Ryan, and M. R. Stinson, "Microphone array measurement system for analysis of directional and spatial variation of sound fields," J. Acoust. Soc. Am. **112**, 1980–1991 (2002).

[9] J. Meyer and G. Elko, "A highly scalable spherical microphone array based on an orthonormal decomposition of the soundfield," *Proceedings of ICASSP*, 2002, Vol. **2**, pp. 1781–1784.

[10] T. D. Abhayapala and D. B. Ward "Theory and design of high order sound field microphones using spherical microphone array," *Proceedings of ICASSP*, 2002, Vol. **2**, pp. 1949–1952.

[11] B. Rafaely, "Plane-wave decomposition of the sound field on a sphere by spherical convolution," J. Acoust. Soc. Am. **116**, 2149–2157 (2004).

[12] B. Rafaely, "Analysis and design of spherical microphone arrays," IEEE Trans. Speech Audio Process. 2005, **13**, 135–143 (2005).

[13] J. R. Driscoll and D. M. Healy, Jr., "Computing Fourier transform and convolutions on the 2-sphere," Adv. Appl. Math. **15**, 202–250 (1994).

[14] G. Arfken, *Mathematical Methods For Physicists*, 3rd ed. (Academic, New York, 1985).

[15] E. G. Williams, *Fourier Acoustics* (Academic, New York, 1999).

Flat-walled multilayered anechoic linings: Optimization and application

Jingfeng Xu[a)]
School of Architecture, Design Science and Planning, University of Sydney, NSW 2006, Australia

Jörg M. Buchholz
MARCS Auditory Laboratories, University of Western Sydney, Locked Bag 1797, Penrith South DC, NSW 1797, Australia

Fergus R. Fricke
229 Rowntree Street, Balmain, NSW 2041, Australia

(Received 12 June 2005; revised 25 August 2005; accepted 25 August 2005)

The concept of flat-walled multilayered absorbent linings for anechoic rooms was proposed three decades ago. Flat-walled linings have the advantage of being less complicated and, hence, less costly to manufacture and install than the individual units such as wedges. However, there are difficulties in optimizing the design of such absorbent linings. In the present work, the design of a flat-walled multilayered anechoic lining that targeted a 250 Hz cut-off frequency and a 300 mm maximum lining thickness was first optimized using an evolutionary algorithm. Sixteen of the most commonly used commercial fibrous building insulation materials available in Australia were investigated and fourteen design options (i.e., material combinations) were found by the evolutionary algorithm. These options were then evaluated in accordance with their costs and measured acoustic absorption performances. Finally, the completed anechoic room, where the optimized design was applied, was qualified and the results showed that a large percentage (75%–85%) of the distance between the sound source and the room boundaries, on the traverses made, were anechoic. © *2005 Acoustical Society of America.* [DOI: 10.1121/1.2074907]

PACS number(s): 43.55.Pe, 43.55.Ev [NX] Pages: 3104–3109

I. INTRODUCTION

The MARCS Auditory Laboratories at the University of Western Sydney recently decided to construct an anechoic room for its research in the area of speech communication and auditory processes. The internal size of the room is 4500 mm long, 3600 mm wide, and 3500 mm high. The maximum anechoic lining thickness was limited to 300 mm due to the small size of the room and the desired cut-off frequency was 250 Hz. (The cut-off frequency is the frequency above which no pressure reflection factor exceeds 10%; this corresponds to an energy absorption exceeding 99%.) As the budget for the project was limited, the conventional anechoic lining system using individual units such as wedges was not affordable. An alternative anechoic lining system was therefore required.

The concept of flat-walled multilayered absorbent linings for anechoic rooms was proposed three decades ago. Flat-walled linings have the advantage of being less complicated and, hence, less costly to manufacture and install than the individual units such as wedges. Recently, flat-walled multilayered absorbent linings were also applied as the anechoic termination for other types of enclosures, such as the duct-type noise measurement enclosure,[2] which require anechoic conditions for their internal surfaces.

Davern[3] studied experimentally the design of flat-walled multilayered anechoic linings. The approach used was to design a flat-walled lining system by using conventional measurements in an impedance tube. However, the work proved to be tedious and time consuming because of the numerous trial and error measurements involved. The subsequent work undertaken by Dunn and Davern[4] proved that the overall impedance of a flat-walled multilayered system could be calculated by the repeated application of a single layer impedance equation. The inputs to the equation were simply the bulk acoustic properties (characteristic impedance and propagation constant) and the thickness of each layer of material. Xu, Nannariello, and Fricke[5] demonstrated that an evolutionary algorithm (EA) could be successfully employed as an optimizer to aid and speed up the design of flat-walled multilayered anechoic linings. The material investigated in the work was polyurethane open cell foams and the target cut-off frequency was 100 Hz. A further investigation[6] carried out by Xu, Buchholz, and Fricke on the application of multilayered polyurethane foams as the flat-walled anechoic lining indicated that for low (100 Hz) and mid (250 Hz) cut-off frequencies to achieve the minimum overall lining thickness the minimum number of layers of linings required is three. However, the materials used in the optimum designs of the above mentioned two works[5,6] might not be commercially available because the bulk acoustic properties of the materials were calculated using Delany and Bazley[7] type curve-fitting equations developed by Dunn and Davern[4] and Cummings[8] and it was assumed that any required thickness of the material was available. The MARCS Auditory Laboratories was also reluctant to use polyurethane foams for the

[a)]Electronic mail: jixu4247@mail.usyd.edu.au

anechoic lining material because of the fire hazard and mechanical durability problems related to this type of material so fibrous materials were required.

In the present work, the bulk acoustic properties of sixteen of the most commonly used commercial fibrous building insulation materials available in Australia were measured and on the basis of the measurement results the same evolutionary algorithm as that introduced in previous work[5] was used to optimize the design of the flat-walled multilayered anechoic lining to meet the design criteria, namely a 250 Hz cut-off frequency with a maximum lining thickness of 300 mm. The lining system for the anechoic room at the MARCS Auditory Laboratories was then selected from the design options provided by the EA on the basis of their costs and acoustic absorption performance measured using an impedance tube.[9] Finally, the completed anechoic room, where the optimized design was applied, was qualified and the results showed that a large percentage (75%–85%) of the distance between the sound source and the room boundaries, on the traverses made, were anechoic.

II. FUNDAMENTALS OF FLAT-WALLED MULTILAYERED ANECHOIC LININGS

An ideal acoustic absorbent material should have a low frontal acoustic reflection and a high internal acoustic attenuation. However, these two requirements for the same material are in conflict with each other. A method of partially overcoming this conflict is to use a multilayered lining system.[4] By selecting a front layer material with appropriate characteristic impedance, one can obtain a low primary reflection by encouraging the incoming acoustic wave train to enter the composite layer structure. Then, the inner layers of material can be selected to attenuate the wave energy within the material as much as possible without at the same time causing a substantial interlayer reflection.

Dunn and Davern[4] proved that the surface impedance, Z, at the front of a multilayered lining could be calculated by applying the single-layer equation to each material successively, i.e.,

$$Z_i = W_i \frac{Z_{i-1}\cosh(\gamma_i L_i) + W_i \sinh(\gamma_i L_i)}{Z_{i-1}\sinh(\gamma_i L_i) + W_i \cosh(\gamma_i L_i)}, \tag{1}$$

where the subscript i refers to the ith layer, starting from the layer closest to solid backing; L is the thickness of the layer; and W and γ are, respectively, the characteristic impedance and propagation constant of the layer. Both W and γ are complex numbers. When a material is backed by a solid surface ($Z_0=\infty$), the single layer equation can be written as

$$Z_1 = W_1 \coth(\gamma_1 L_1). \tag{2}$$

The pressure reflection factor at normal incidence, r, is the ratio of the pressure amplitude of the reflected wave to the incident wave in the reference plane for a plane wave at normal incidence and can be calculated by[9]

TABLE I. Materials investigated.

Type	Material ID	Fixed thickness (mm)	Density (kg/m^3)	Flow resistivity (Pas/m)
Low-density glasswool	1	50	10.4	3190
Mid-density glasswool	2	25	20.0	11180
	3	25	29.5	12378
	4	25	30.0	13915
High-density glasswool	5	25	108.0	47637
Mid-density polyester	6	25	33.0	6221
	7	25	40.0	7153
Low-density polyester	8	25	10.5	1410
	9	35	7.9	453
	10	65	8.8	535
	11	75	10.8	458
	12	85	10.8	594
	13	90	11.6	659
	14	30	9.6	562
	15	40	8.2	483
	16	50	9.3	663

$$r = \left| \frac{Z_i/\rho c - 1}{Z_i/\rho c + 1} \right|, \tag{3}$$

where ρ is the air density and c is the velocity of sound in air. The relationship between r and the normal incidence sound absorption coefficient α_n[9] is

$$\alpha_n = 1 - r^2. \tag{4}$$

III. MATERIALS INVESTIGATED

As indicated previously sixteen of the most commonly used commercial fibrous building insulation materials available in Australia were investigated in the present work. Measurements of thickness, density, and flow resistivity[10] of each material were made and results of these measurements are presented Table I. The bulk acoustic properties of each material were also measured using a two-thickness method.[11] Generally, the cost for the glasswool type material is higher than the polyester type material.

IV. OPTIMIZATION

Since the pressure reflection factor r of an anechoic lining at any frequency above the cut-off frequency shall not exceed 10%,[1] the design of an anechoic lining can be considered as a multiobjective optimization problem (MOP). The previous work[5] demonstrated that a Genetic and Evolutionary Algorithm Toolbox for use with Matlab (GEATbx)[12] could be successfully employed to tackle this MOP. In the present work, GEATbx was again applied.

A. Application of GEATbx

In the present work the sixteen materials investigated all have their own measured bulk properties and fixed thicknesses and the overall thickness of a material can only be multiples of its fixed thickness, i.e., variables in the present work all have a discrete nature. In order to apply GEATbx,

TABLE II. Optimization results.

	Material ID of each layer			Multiples of the fixed thickness of each layer's material				Pressure reflection factor at each midband frequency of one-third-octave bands ranging from 250 Hz to 1 kHz						
Option ID	Layer 1	Layer 2	Layer 3	Layer 1	Layer 2	Layer 3	Overall thickness of the lining system (mm)	250 Hz	315 Hz	400 Hz	500 Hz	630 Hz	800 Hz	1 kHz
1	4	1	16	4	2	1	250	9.6	7.7	1.7	4.5	0.8	4.6	6.3
2	7	1	15	3	2	2	255	1.3	2.6	6.2	8.4	4.5	1.3	11.6
3	5	2	15	2	4	3	270	8.6	8.4	3.7	1.5	0.7	6.1	8.6
4	2	1	16	5	2	1	275	10.2	10.3	5.1	7.4	4.9	2.6	4.7
5	7	1	16	3	3	1	275	8.1	11.6	8.2	9.1	4.4	3.9	3.2
6	3	1	15	2	3	2	280	7.6	2.6	8.6	10.1	7.5	2.5	10.2
7	4	1	15	2	3	2	280	7.0	3.3	9.1	10.4	7.1	2.3	9.8
8	2	1	15	4	2	2	280	4.2	6.5	6.2	7.0	5.0	0.9	11.8
9	2	1	15	2	3	2	280	8.0	0.8	8.5	10.3	7.9	3.2	10.1
10	7	1	15	2	3	2	280	5.6	5.0	10.3	11.3	6.9	2.1	11.2
11	5	1	15	2	3	2	280	9.9	8.1	4.4	8.1	5.3	6.6	5.3
12	7	1	15	3	2	3	295	5.9	11.7	9.6	2.7	3.6	7.2	11.3
13	5	1	16	2	4	1	300	8.4	10.3	7.8	10.5	6.0	5.2	1.4
14	7	1	16	4	3	1	300	11.0	11.1	6.9	6.5	3.0	5.6	3.3

the bulk properties and fixed thicknesses of the materials were organized into matrices with the index of each column of the matrix, ranging from one to sixteen, representing each material. Another variable required is the integer multiples of the fixed thickness of each material. During the EA searching process, the program would pick up the material of interest by pointing at the corresponding column of the matrix and vary the overall thickness of the material by assigning a certain integer multiple.

B. Optimization results

In the present work, a three-layered lining system was investigated because of its high efficacy compared with a two-layered lining system.[6] Taking into account the expected errors resulting from Eq. (1) and the measurements of the materials' bulk properties, it was considered that a reflection factor of no larger than 12 was acceptable during the EA search. It was also considered that frequencies below 1000 Hz were the most critical ones in the design of anechoic linings and thus the EA search was limited to one-third-octave band frequencies between 250 and 1000 Hz. Table II shows the optimization results provided by GEATbx.

Using the sixteen materials investigated, the program found fourteen options (i.e., material combinations) that could achieve a 250 Hz cut-off frequency with an overall thickness of the lining system no larger than 300 mm. Among the fourteen options, Options 2 and 12 are the cheapest because the least amount of glasswool material was required. The only difference between Options 2 and 12 was that Option 12 uses 40 mm more of Material 15 for Layer 3 than Option 2 does. The absorption performances of Options 2 and 12, in terms of the pressure reflection factor, were measured using an impedance tube.[9] The measurement results are plotted in Fig. 1. The difference between the measured pressure reflection factors presented in Fig. 1 and predicted ones shown in Table II appears to be due to the errors associated with Eq. (1) and the measurement of bulk properties of the single layer of materials. Since the measured pressure reflection factors of Option 2 at frequencies of 250 and 315 Hz are larger than 12, it was decided to apply Option 12 as the lining system for the anechoic room at the MARCS Auditory Laboratories.

V. INSTALLATION OF THE LINING

Layers of insulation materials were attached to each other and the internal surfaces of the room using spikes affixed to the internal surfaces of the room. Care was taken to eliminate air cavities between the layers of insulation materials and between the internal surfaces of the room and the most inner layer of insulation material.

At the joints where two sheets of the same layer of material meet each other large gaps were avoided by placing them tightly against each other. The joints at different layers were staggered to ensure that they did not overlap. Also, at corners of the room, multilayers of insulation materials were staggered to ensure that their edges overlapped. Figure 2 provides an illustration of the arrangement of multilayered

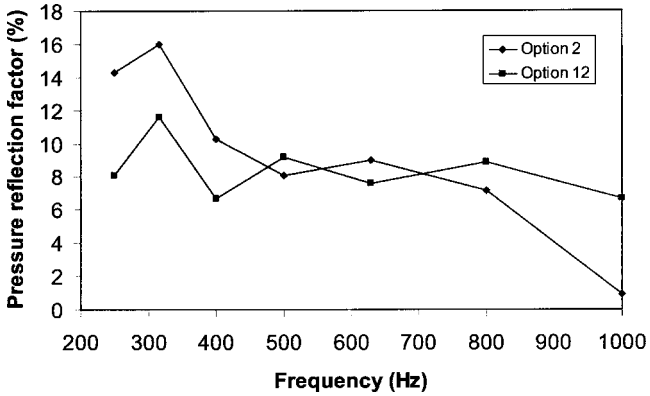

FIG. 1. Impedance tube measurement results of Option 2 and Option 12.

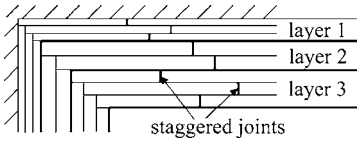

FIG. 2. Installation arrangements of multilayered materials.

materials. For the layer that is exposed to the air the adjoining sheets of material were loosely sewed together.

VI. QUALIFICATION OF THE ANECHOIC ROOM

The completed anechoic room was qualified in accordance with the procedure set out in ISO 3745:2003.[13] The sound source was located so that the assumed position of its acoustic center was at the geometric center of the room. Five straight microphone traverses were used. Four of the five traverses were from the geometric center of the room to the room corners (the lower Southeast, lower Southwest, upper Northeast, and upper Northwest corners) and lay in an imaginary plane that passed through the geometric center of the room. The fifth traverse was from the geometric center of the room to the West wall, which is one of the parallel walls closest to the geometric center of the room. One-third-octave band-filtered pink noise with the sequential mid-band frequencies from 250 Hz to 10 kHz was used as the test signal. The test signal was generated and digitally filtered[14] using Matlab.[15] For the five traverses, the measurement of the sound pressure level was carried out starting 0.5 m from the geometric center of the room and extending to the maximum distance that the measurement microphone could reach. The spacing between the measurement points was 0.1 m.

A. Sound sources

For the qualification of the room the directionality of the sound source must be uniform to within the allowable deviations as set out in ISO 3745:2003.[13] These limits are reproduced in Table III. For the mid-band frequencies below 800 Hz, a Bruel & Kjaer Type 4296 OmniPower Loudspeaker, which meets the requirements of ISO 140-3,[16,17] was used as the sound source.[13] For the higher frequency bands from 800 Hz to 10 kHz, a compression driver (TOA Electric TU-50) attached to a 1.5m-long and 6-mm-i.d. cylindrical tube was used as the sound source. The compression driver was acoustically shielded by a box wrapped with mass loaded vinyl material. As there was no directionality information for the custom-made high frequency sound source, its directionality was measured in accordance with the procedure set out in ISO 3745:2003.[13] The measurement was conducted in an anechoic room, with a 50 Hz cut-off frequency,[18] at the Australian National Acoustic Laboratories. Figure 3 shows the measured deviations in directionality of the custom-made high frequency sound source.

TABLE III. Maximum allowable deviation in directionality of the sound source for an anechoic room qualification as per ISO 3745:2003 (Ref. 13).

One-third-octave band frequency (Hz)	Allowable deviations in directionality (dB)
800–5000	±2.0
6300–10 000	±2.5

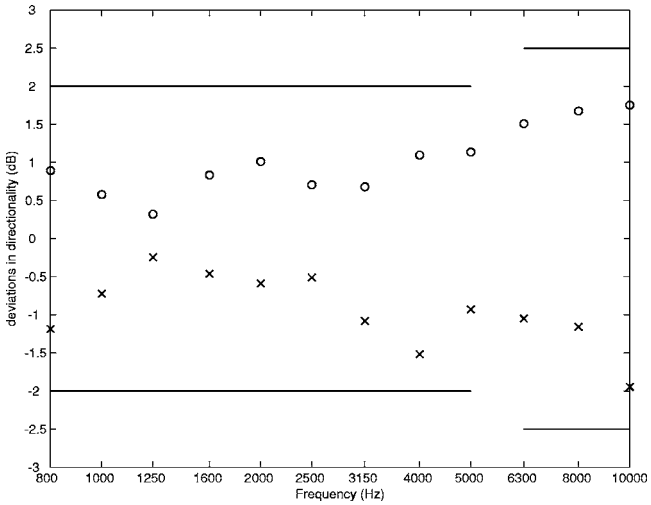

FIG. 3. Measured deviations in directionality for the custom-made high frequency sound source.

During the measurements a reference microphone was located at an arbitrary but fixed position in the room to check the variation of the sound source output. The drift of the sound power level of the sound sources (with the associated signal generation and amplification system) in any one-third-octave band, from 250 to 630 Hz for the low frequency sound source and from 800 Hz to 10 kHz for the high frequency sound source, was less than ±0.2 dB at any time during the measurement.

B. Qualification results

The maximum allowable deviation of the measured sound pressure levels from the theoretical levels, using the inverse square law as per ISO 3745:2003,[13] is reproduced in Table IV. Figure 4 shows the measured deviations for the traverse into the lower Southeast corner of the room. Similar results can be observed for the traverses into other corners. Figure 5 shows the measured deviations for the traverse into the West wall of the room.

VII. CONCLUSIONS

In the present work an EA was successfully applied to optimize the design of a flat-walled multilayered lining system for the anechoic room at MARCS Auditory Laboratories at the University of Western Sydney. Results of the EA search indicated that for the sixteen materials investigated

TABLE IV. Maximum allowable deviation of measured sound pressure levels from the theoretical level using the inverse square law in an anechoic room as per ISO 3745:2003 (Ref. 13).

One-third-octave band frequency (Hz)	Allowable deviations (dB)
≤630	±1.5
800–5000	±1.0
≥6300	±1.5

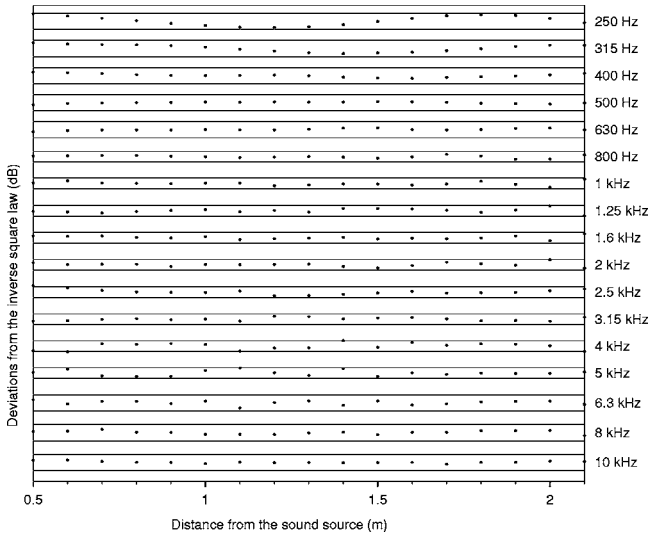

FIG. 4. Measured deviations for the traverse into the lower Southeast corner of the room. The frequency labels along the right vertical axis define the position of the 0-dB deviation for that frequency; the lines above and below the 0-dB position are the permissible variations from free-field performance in accordance with Table IV.

there were fourteen options that could achieve a cut-off frequency of 250 Hz with the overall lining thickness less than 300 mm. For all of the options the materials in the lining system exhibit a trend of a graduated increase of density and flow resistivity from the front layer (Layer 3) to the back layer (Layer 1).

The options found by EA were evaluated on the basis of their costs and two options were short listed. The acoustic absorption performances of the short-listed options were then measured in an impedance tube. Only slight differences were observed between the measured acoustic absorption performances and the predicted ones. The option that had the lower

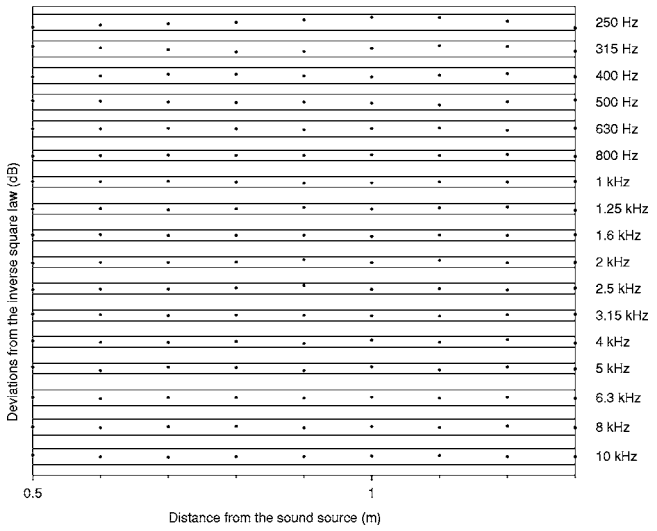

FIG. 5. Measured deviations for the traverse into the West wall of the room. The frequency labels along the right vertical axis define the position of the 0-dB deviation for that frequency; the lines above and below the 0-dB position are the permissible variations from free-field performance in accordance with Table IV.

pressure reflection factors at low frequencies was used as the lining system for the anechoic room at the MARCS Auditory Laboratories.

The lining system finally used in the anechoic room has an overall thickness of 295 mm, which is about 45 mm less than a quarter of a wavelength at the cut-off frequency of 250 Hz. The material cost of the applied lining system was about fifty Australian dollars per square meter. The qualification procedure carried out in the completed anechoic room indicates that

(1) A minimum anechoic distance of 2.1 m is achieved for the traverses to the four corners that are on an imaginary plane passing the geometric center of the room. This approximately corresponds to 75% of half of the diagonal distance (without taking into account the anechoic lining thickness) of the imaginary plane.
(2) A minimum anechoic distance of 1.3 m is achieved for the traverse to one of the walls closest to the geometric center of the room. This approximately corresponds to 85% of half of the distance (without taking into account the anechoic lining thickness) between the two parallel walls closest to the geometric center of the room.

ACKNOWLEDGMENTS

The authors are grateful to John Bassett, Rick Moss, and Ken Stewart at the University of Sydney for their technical support and assistance throughout the present work. The present research was conducted under an Australian Postgraduate Award and a School of Architecture Design Science and Planning Supplementary Scholarship.

[1]L. L. Beranek and H. P Sleeper, "The design and construction of anechoic sound chambers," J. Acoust. Soc. Am. **18**, 140–150 (1946).
[2]A. Bracciali and G. Cascini, "Measurement of the lateral noise emission of an UIC 60 rail with a custom device," J. Sound Vib. **231**, 653–665 (2000).
[3]W. A. Davern, "Flat-walled graded density anechoic lining," Tenth International Congress on Acoustics, Sydney, 1980.
[4]I. P. Dunn and W. A. Davern, "Calculation of acoustic impedance of multi-layer absorbers," Appl. Acoust. **19**, 321–334 (1986).
[5]J. Xu, J. Nannariello, and F. R. Fricke, "Optimising flat-walled multilayered anechoic linings using evolutionary algorithms," Appl. Acoust. **165**, 1009–1026 (2004).
[6]J. Xu, J. Buchholz, and F. R. Fricke, "Application of multi-layered polyurethane foams for flatwalled anechoic linings," Appl. Acoust. (in press).
[7]M. E. Delany and E. N. Bazley, "Acoustical properties of fibrous absorbent materials," Appl. Acoust. **3**, 105–116 (1970).
[8]A. Cummings and S. P. Beadle, "Acoustic properties of reticulated plastic foams," J. Sound Vib. **175**, 115–133(1993).
[9]ISO, ISO 10534-1:1996, "Acoustics—Determination of sound absorption coefficient and impedance in impedance tubes Part 1: Method using standing wave ratio," International Organization for Standardization, Geneva, 1996.
[10]ASTM, ASTM C522-03, "Standard test method for airflow resistance of acoustical materials," American Society for Testing and Materials, Philadelphia, 2003.
[11]C. D. Smith and T. L. Parrott, "Comparison of three methods for measuring acoustic properties of bulk materials," J. Acoust. Soc. Am. **74**, 1577–1582 (1983).
[12]H. Pohlheim, "Genetic and evolutionary algorithm toolbox for use with matlab version 3.5," http://www.geatbx.com/, Berlin, 2004.
[13]ISO, ISO 3745:2003, "Acoustics—Determination of sound power levels of noise sources using sound pressure—Precision methods for anechoic and hemi-anechoic rooms," International Organization for Standardization, Geneva, Switzerland, 2003.
[14]IEC, IEC 1260:1995, "Electroacoustics: Octave band and fractional-

octave band filters," International Electrotechnical Commission, Geneva, Switzerland, 1995.
[15]MathWorks, "MATLAB reference guide (Version 6.5 R13)," The MathWorks Inc, Natick, MA, 2002.
[16]ISO, ISO 140-3:1995(E), "Acoustics—Measurement of sound insulation in buildings and of building elements—Part 3: Laboratory measurements of airborne sound insulation of building elements," International Organization for Standardization, Geneva, Switzerland, 2003.
[17]Bruel & Kjaer, "Product data—Sound sources for building acoustics: Omnipower sound source-type 4269, Omnisource sound source—Type 4295, tapping machine—Type 3207, including power amplifier—Type 2716", http://www.bksv.com/, Nœrum, Denmark, 2005.
[18]Australian National Acoustic Laboratories, "Research and development annual report 2002/2003," Australian National Acoustic Laboratories, Sydney, 2003, pp. 50–51.

Technique for the calibration of hydrophones in the frequency range 10 to 600 kHz using a heterodyne interferometer and an acoustically compliant membrane

Pete D. Theobald, Stephen P. Robinson, Alex D. Thompson, and Roy C. Preston
National Physical Laboratory, Teddington, Middlesex TW11 0LW, United Kingdom

Paul A. Lepper
Loughborough University, Loughborough, Leicestershire LE11 3TU, United Kingdom

Wang Yuebing
Hangzhou Applied Acoustics Research Institute, 80 Guihuaxi Road, Hangzhou, Zhejiang, 311400, China

(Received 31 January 2005; revised 15 August 2005; accepted 19 August 2005)

A technique for the calibration of hydrophones using an optical method is presented. In the method, a measurement is made of the acoustic particle velocity in the field of a transducer by use of a thin plastic pellicle that is used to reflect the optical beam of a laser vibrometer, the pellicle being acoustically transparent at the frequency of interest. The hydrophone under test is then substituted for the pellicle, and the hydrophone response to the known acoustic field is measured. A commercially available laser vibrometer is used to undertake the calibrations, and results are presented over a frequency range from 10 to 600 kHz. A comparison is made with the method of three-transducer spherical-wave reciprocity, with agreement of better than 0.5 dB over the majority of the frequency range. The pellicle used is in the form of a narrow strip of thin Mylar©, and a discussion is given of the effect of the properties of the pellicle on the measurement results. The initial results presented here show that the method has the potential to form the basis of a primary standard method, with the calibration traceable to standards of length measurement through the wavelength of the laser light. [DOI: 10.1121/1.2063068]

PACS number(s): 43.58.Vb [AJZ] Pages: 3110–3116

I. INTRODUCTION

In underwater acoustics, hydrophones are typically used to make absolute measurements of acoustic fields.[1] For example, they may be required to measure the level of ambient noise in the ocean, or the level of unwanted sound produced in the ocean by manmade sources. Alternatively, hydrophones may be used to characterize the output of transducers used in active sonar systems, where the source level and transmit sensitivity are vital in determining the system range or detection limits. If absolute measurements are to be meaningful, the hydrophone used must be calibrated using an appropriate method and the calibration must be traceable to agreed standards.[2]

The free-field receive sensitivity of a hydrophone is the quotient of the open-circuit voltage developed by the hydrophone in response to the acoustic pressure from a plane wave. In the definition, the pressure used is that which exists at the position of the acoustic center of the hydrophone, but in the absence of the hydrophone from the field. The established methods for the calibration of hydrophones are the classic methods based on the principle of reciprocity,[2,3] and there is an international standard specifying the free-field calibration of a hydrophone by the method of three-transducer spherical-wave reciprocity.[4] In this method, three hydrophones are required, at least one of which must be a reciprocal device. For a device to be reciprocal, it must be linear, passive, and reversible, with the ratio of the transmitting and receiving response of the device equal to a constant. The hydrophones are paired off in three measurement arrangements, for each of which one device is used as a transmitter and one as a receiver. At each stage, measurements are made of the current used to drive the transmitting device, and the voltage developed by the receiver. Knowledge is also required of the acoustic transfer impedance, which is equal to the quotient of the sound pressure at the position of the receiver to the volume velocity produced by the transmitter.[5] For a spherical-wave field, this depends upon the acoustic frequency, the density of the medium, and the separation distance. This is common to each of the measurement arrangements and is often given in terms of a constant factor, termed the reciprocity factor.[6] From these purely electrical measurements, and knowledge of the reciprocity factor, the absolute sensitivity of any of the three transducers may be determined, with the calibration traceable to electrical primary standards.

The strength of the reciprocity method is that it does not require any absolute measurement of an acoustic field parameter, and this is one of the main reasons why it displaced other calibration methods as the preferred choice for a primary acoustical calibration method. However, it does have weaknesses in that it depends on the nature of the acoustic field (for example, on the existence of a spherical-wave field), and on the availability of a transducer that is reciprocal (not an easy property to validate).[3] From a metrological

perspective, it may also be considered less satisfactory, in that it does not provide a direct realization of the acoustic pascal.

Optical methods have long been used as a nonperturbing way of detecting acoustic fields, usually by measuring the acoustic particle velocity or displacement using an interferometer-based technique or a technique based on measuring the Doppler shift of scattered light. Optical methods have the advantage that they do not depend on a transducer being reciprocal, or whether the acoustic field has a particular geometry, and may facilitate a more direct realization of an acoustic quantity. They also provide the potential for accurate measurement, with traceability to primary standards of length via the wavelength of the laser light.

An example of such a technique is that of laser Doppler anemometry, which has been used to measure the acoustic particle velocity in air.[7] This method involves intersecting two laser beams and detecting the Doppler shift of the light scattered from the particles crossing the small intersecting volume. This method has been configured to provide free-field calibrations of microphones.[8,9] The same method has also been reported for use in water.[10] However, this method has been shown to have limitations when measurements are required at a point in a water-borne field. This is because the optical beam responds not only to the movement of the particles, but also to refractive index changes along the paths of the beam caused by the compressional and rarefractional pressure variations in the medium during the passage of the acoustic wave. Although not significant for measurements made in air, when measuring in water this acousto-optic interaction can lead to difficulty in interpreting the measurements.[11]

This acousto-optic effect has been exploited to provide a technique for measuring acoustic fields in water, where the optical beam is configured to be orthogonal to the direction of the acoustic beam (parallel to the acoustic wave fronts) in order to maximize the interaction.[12] When combined with tomographic techniques, this provides a potentially powerful and rapid technique for mapping acoustic fields.[13,14] However, for the calibration of hydrophones, a measurement is required of a field parameter at a point in the field. Since methods utilizing the acousto-optic interaction almost invariably rely on an integrated effect along the length of the optical beam, this limits the usefulness of the methods for hydrophone calibration.

For ultrasonic frequencies in the range from 500 kHz to 20 MHz, optical methods are now well established.[15] At the National Physical Laboratory, UK, such a method is used for the primary calibration of miniature ultrasonic hydrophones.[16,17] The methods use optical interferometry to measure the displacement of a thin plastic membrane (termed a pellicle) placed in the farfield of an ultrasonic transducer. The membrane is used to reflect the optical signal beam of a Michelson interferometer, the pellicle being thin enough to be acoustically transparent at the frequency of interest. The interferometer is sensitive to the optical phase changes induced by movement of the pellicle and provides a measurement of acoustic particle displacement, the acoustic pressure then being derived from the measured displacement. In the method, the optical beam is arranged to be parallel to the direction of the acoustic beam (orthogonal to the wave fronts). In such a configuration, the effect of the acousto-optic interaction is minimized and is amenable to the simplified theoretical treatment of Bacon.[18] Modified versions of such methods have recently been extended to frequencies as high as 60 MHz at NPL,[19] and to 70 MHz at PTB in Germany using a similar method, where the acousto-optic effect is eliminated by placing the membrane on the water surface so that the entire optical path is through air.[20]

Recently, initial attempts to extend pellicle-based calibration methods down to the lower kilohertz range have been reported using a commercial laser vibrometer to measure the acoustic particle velocity.[21,22] A report has already been given of a comparison of this method with the NPL primary standard interferometer at frequencies of 500 kHz to 1 MHz,[23] and of initial attempts to use the technique at NPL at lower frequencies.[24]

Presented in this paper are the results of a feasibility study of applying the same technique to the calibration of underwater acoustic hydrophones.[25,26] Initial results are presented for the calibration of a hydrophone in the frequency range of 10 to 600 kHz using a commercial vibrometer to undertake the optical measurement, and a comparison is made with results obtained by the method of three-transducer spherical-wave reciprocity. In the paper we further consider the response of the pellicle and its effect on the results, with a theoretical and practical study of the membrane behavior in the presence of an acoustic field.

II. OPTICAL MEASUREMENT OF ACOUSTIC PARTICLE VELOCITY

In order to perform a free-field calibration of a hydrophone, it must be exposed to a known acoustic pressure, p, in a plane-wave field. The acoustic pressure used in the calculation of the free-field sensitivity is that which exists in the field at that position when the hydrophone is absent from the field. Although optical interferometry does not provide a direct measure of acoustic pressure, it offers a method to measure the acoustic particle velocity, u, from which the acoustic pressure can be derived using the following:

$$p = \rho\, c\, u, \tag{1}$$

where ρ is the density and c is the speed of sound in the medium. The direct measurement of acoustic particle velocity can be achieved by employing a laser Doppler interferometric technique, where the interferometer is designed to be sensitive to a frequency shift between the reference arm and the measurement arm. The Doppler frequency shift, $\delta\nu$, can be related to the laser wavelength, λ, and the particle velocity vector, u, by the following equation:[15]

$$\delta\nu = \frac{2u}{\lambda}\cos\beta\cos\left(\frac{1}{2}\phi\right), \tag{2}$$

where β is the angle the velocity vector u makes with the bisector of the incident and reflected beams. In practice, the incident and reflected beams are aligned so that they traverse similar paths such that $\phi \rightarrow 0$, where ϕ is the angle between

the incident and reflected beams. The Doppler shift can therefore be written as

$$\delta\nu = \frac{2u}{\lambda}\cos\beta. \tag{3}$$

With knowledge of the laser wavelength, this Doppler beat frequency obtained from the detector allows a determination of the absolute particle velocity and thus the acoustic pressure.

The use of a Doppler heterodyne interferometer is favored over a conventional homodyne phase-locked interferometer for this application due to the potentially large dynamic range required of up to 5 mm/s and the requirement for a relatively low-frequency measurement capability down to 1 kHz. Phase-locked homodyne interferometers do have the advantage that they do not require Doppler decoding electronics but they are limited in dynamic range to the linear section of the fringe pattern and the phase-locking prohibits low-frequency measurements because of the necessary vibration compensation.[15]

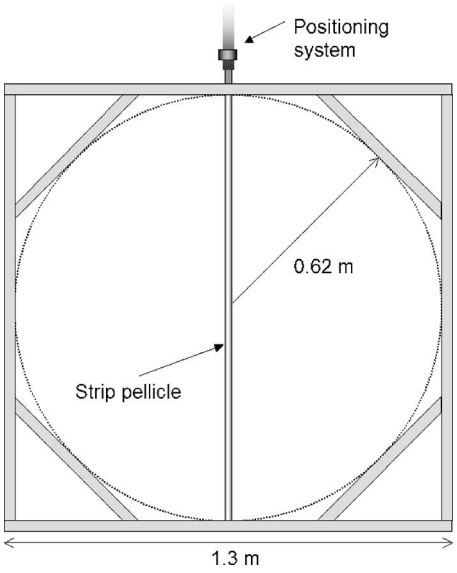

FIG. 1. Mounting frame and strip pellicle.

III. EXPERIMENTAL METHODOLOGY

Measurements of the acoustic particle velocity at a point in the field of an acoustic transducer were performed using a commercial laser Doppler vibrometer. The measurement was conducted by reflecting the laser light from a thin plastic pellicle suspended in the field. The principle behind the use of a pellicle is to enable the measurement to be made at a specific point in the field, with pellicle thickness being small compared to the acoustic wavelength and the acoustic impedance being similar to that of water so that the motion of the pellicle follows the motion of the water particles. The vibrometer provides an output that is proportional to velocity, and the time-resolved signal may be displayed on a digitizing oscilloscope in the same manner as a hydrophone signal. From the measured velocity, the acoustic pressure was calculated using the expression given in Eq. (1). The hydrophone under test was then substituted for the pellicle and the hydrophone voltage measured, with the hydrophone sensitivity calculated from the quotient of the hydrophone voltage and the acoustic pressure.

The vibrometer used was a Polytec PSV-3000 scanning vibrometer, which provided a maximum measurement bandwidth of 1.5 MHz.

The test tank used for the measurements has dimensions of 2 m long by 1.5 m wide by 1.5 m deep and incorporates a two-carriage precision positioning system for positioning and orienting devices. A glass window is set into one end of the tank to allow optical interrogation of the acoustic field.

The pellicle used was in the form of a narrow plastic strip, which was made from a 23 μm thick Mylar© membrane coated on one side with 40 nm of aluminium so as to render it a specular reflector of the optical beam. A number of different widths of pellicle were tried during the measurements, from strips as narrow as 2 mm to strips as broad as 12.6 mm. The pellicle was tensioned over a frame measuring 1.3 m square and constructed from 30 mm extruded aluminium, as shown in Fig. 1. The mounting frame provided a reflection-free time window of around 0.65 ms for a transmitter–receiver separation of 0.5 m. The frame was mounted on one of the carriages of the positioning system adjacent to the optical window, with the acoustic projector mounted on the other carriage, as shown in Fig. 2. The vibrometer beam was then aligned through the optical window of the tank on the acoustic center of the projector. For the flat face piston projectors used, the limited optical reflection from the surface of the transducer was used to align the optical beam of the vibrometer with the acoustic axis of the transducer. The membrane was then positioned to intercept the laser beam and reflect the light back through the glass window and into the optical collection head of the vibrometer. It was possible to align the optical beam very precisely with the pellicle because of its specular reflecting properties. The above procedure ensured that the acoustic beam was colinear with both the incident and return paths of the optical beam. A transmitter–receiver separation of 0.5 m was used, which was sufficient to ensure a measurement in the acoustic farfield. To undertake measurements with the hydrophone, it was substituted for the pellicle mount and aligned using the positioning system so the laser beam was incident on the acoustic center of the hydrophone. The device under test was a Reson TC4034 reference hydrophone, which has a 6 mm diameter spherical element and a resonance frequency of ap-

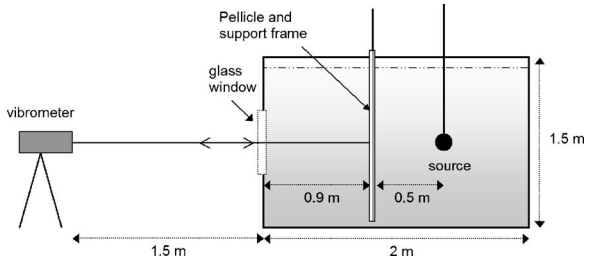

FIG. 2. Measurement arrangement used to measure acoustic velocity using an optical vibrometer.

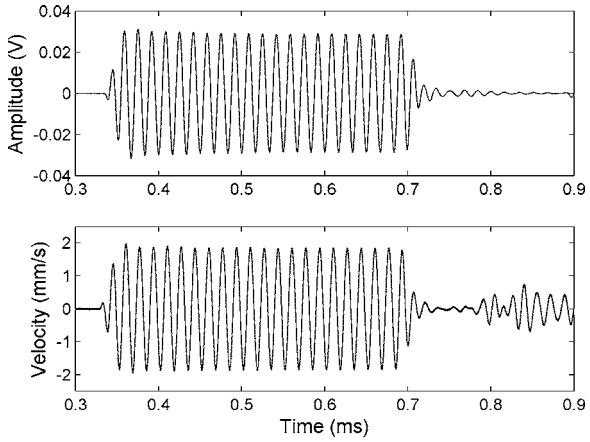

FIG. 3. A comparison of waveforms recorded by the reference hydrophone (upper plot) and the vibrometer (lower plot) for an acoustic signal of 60 kHz.

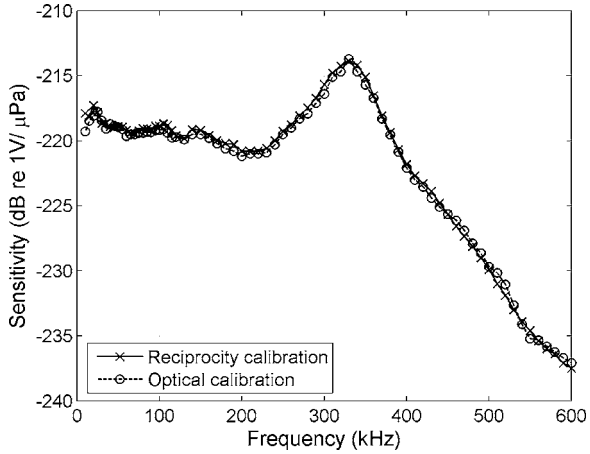

FIG. 4. A comparison of sensitivities for a TC4034 hydrophone obtained by the free-field reciprocity method and the optical method using a 2 mm wide pellicle.

proximately 350 kHz. The hydrophone had previously been calibrated using the method of three-transducer spherical-wave reciprocity.

Three transducers were used as acoustic projectors to cover a frequency range from 10 to 600 kHz: an ITC1042, 25 mm diameter spherical transducer with a resonance frequency of 75 kHz was used for the range 10 to 120 kHz; a 1.5 inc. diameter piston transducer manufactured by Ultran with a resonance frequency of 250 kHz was used for the range 100 to 400 kHz; a 1 inc. diameter piston transducer with a resonance frequency of 500 kHz manufactured by Panametrics was used for the range 300 to 600 kHz. The acoustic projectors were driven with discrete frequency tone-burst signals, with time-gating techniques used to isolate reflections from the tank boundaries. The tone bursts were produced by a HP33120A arbitrary waveform generator and an electronic gating unit, a B&K2713 power amplifier being used with the ITC1042 projector, and a Krohn-Hite 7500 power amplifier being used with the piston transducers. Both amplifiers were set to a 40 dB gain, the maximum peak voltages driving the projectors being 60 V for the ITC1042, 40 V for the 250 kHz piston and 15 V for the 500 kHz piston.

The output voltages for both the vibrometer and the reference hydrophone were captured using a HP89410A vector signal analyzer, after amplification using a Reson VP1000 preamplifier and electronic filtering by a Krohn-Hite 3944 filter. The voltage measurements were performed by measuring the steady-state portion of the tone-burst signals. When using the optical vibrometer, the velocities were calculated using the manufacturer's stated calibration factor of 25 (mm/s)/V.

IV. RESULTS

Figure 3 shows a comparison of waveforms recorded with the optical method and with the hydrophone for an acoustic frequency of 60 kHz. The waveform obtained from the vibrometer has been scaled by the sensitivity setting of the vibrometer to provide a reading of velocity in millimeters per second, whereas the hydrophone waveform is in Volts. The two waveforms compare very well with the arrival of the direct path signal occurring at approximately 0.33 ms and a similar shape to the tone-burst envelope apparent in both signals. For the vibrometer waveform, the reflected signal from the pellicle frame is observed arriving at approximately 0.77 ms (this is absent from the hydrophone waveform since the frame is not in place during the hydrophone measurement).

Figure 4 shows the calibration results obtained using the optical method in the frequency range from 10 to 600 kHz for the TC4034 reference hydrophone. The measurements of acoustic particle velocity were obtained using a 2 mm wide pellicle. Also shown on the plot are data from the calibration of the hydrophone by the three-transducer spherical-wave reciprocity method. Good agreement can be seen between the two methods, and this is highlighted by Fig. 5, where the difference between the results is plotted (the optical results have been subtracted from the reciprocity results to give a positive difference when the reciprocity results are of a higher value). Agreement between the results is better than 0.5 dB over the majority of the frequency range. The overall uncertainty for the free-field reciprocity calibration varies with frequency but is typically of the order of 0.5 dB when

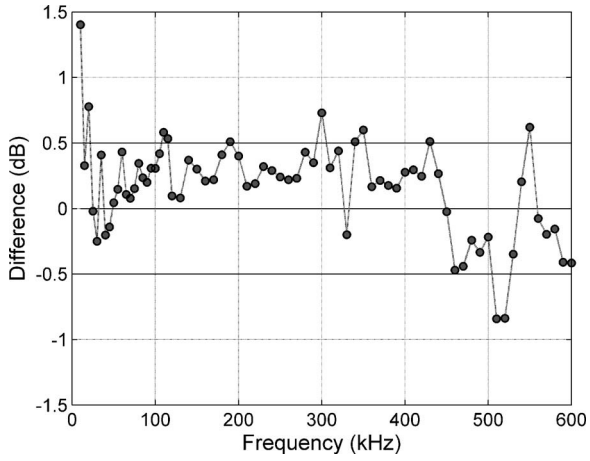

FIG. 5. The difference between hydrophone sensitivity determined using the free-field reciprocity method and the optical method using a 2 mm wide pellicle.

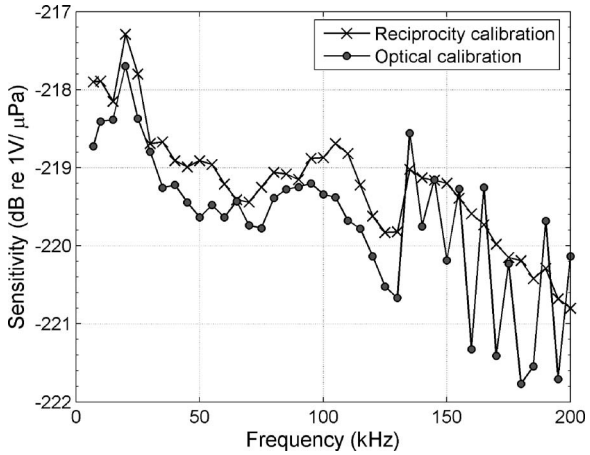

FIG. 6. A comparison of sensitivities for a TC4034 hydrophone obtained by the free-field reciprocity method and the optical method using a 12.6 mm wide pellicle.

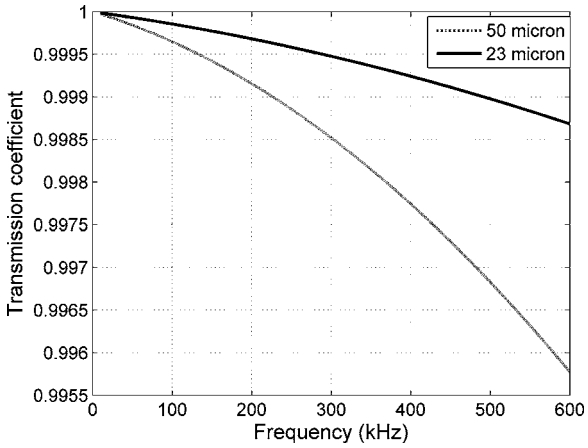

FIG. 7. The results of modeling the pellicle acoustic transmission coefficient for infinite planar membranes of thickness of 23 and 50 μm.

expressed as an expanded uncertainty for a coverage factor of $k=2$. A definitive uncertainty analysis has not yet been completed for the optical method.

Measurements were also performed using a wider pellicle made from a 12.6 mm strip of Mylar© film. Figure 6 shows a comparison of the hydrophone sensitivities for the TC4034 hydrophone obtained using the ITC1042 projector and the 12.6 mm pellicle in the frequency range from 7 to 200 kHz. The low-frequency agreement is again of the order of 0.5 dB or better, but at frequencies greater than about 120 kHz the results from the two methods depart from each other with the results for the optical method showing rapid fluctuations with frequency.

An examination of the results clearly showed that the fluctuations are present in the velocity data measured by the vibrometer (they were not observed in the hydrophone voltage).

The method depends on the pellicle following the motion of the water particles, and if this assumption is violated, inaccuracies will be introduced to the measurements made using the optical method. The material properties and the geometry of the pellicle used may affect the accuracy of the measurements, preventing the pellicle from moving in sympathy with the water particles. An investigation was undertaken into the effect of the pellicle properties on the measurements, and this is described in the next section.

V. DISCUSSION

When using interferometry for the measurement of the movement of a thin membrane in an acoustic field, there are several factors that could contribute to the overall uncertainty of the measurement.

A. Pellicle transmission loss

The measurement of velocity at the pellicle surface is made on the "back surface," i.e., after the acoustic wave has passed through the pellicle. Therefore, any reflection or absorption in the pellicle membrane will influence the measured velocity. The effect of pellicle transmission was investigated by Bacon,[16] and later by Esward and Robinson[19] using an insertion method to experimentally determine the extent of transmission loss at higher frequencies. The transmission losses at frequencies of 10 MHz and more were small but measurable, and allowed a correction to be made when calibrating miniature ultrasonic hydrophones at megahertz frequencies.[17] At the lower frequencies of interest in the work reported here (below 500 kHz), the transmission loss is expected to be negligible. To predict the transmission losses at lower frequencies, a simple layered model was used to represent an infinite water layer, a Mylar© layer, an aluminium layer, and a second infinite water layer.[27] The results of the model agree well with the experimental data from megahertz frequencies where the measurable proportion of the incident sound field is reflected from the membrane.[19] The model prediction for frequencies below 600 kHz are shown in Fig. 7 and are based on a 23 and a 50 μm thick infinite membrane of Mylar© coated with a 40 nm aluminium film and surrounded by water.

The model predictions show that the transmission loss is essentially negligible for a 23 μm membrane at frequencies below 500 kHz. Increasing the thickness of the membrane causes the expected increase in the transmission loss, although this is still very small for a 50 μm membrane at 500 kHz. Note that over this frequency range, such thin pellicles show a monotonic variation in transmission loss with no fluctuations apparent with frequency.

However, this very simple model assumes that the membrane is of an infinite extent and the incident wave is a plane wave. For the NPL primary standard interferometer at megahertz frequencies, this assumption is reasonable. The pellicle used is in the form of a sheet of Mylar© supported by a 100 mm diameter annular ring, and the collimated acoustic fields produced by the piston projectors used pass through the support ring without a significant sound being scattered from the support itself. This type of pellicle was not considered practical for work at the frequencies used here since the support ring would have to be of the order of 1 m or more in diameter to avoid reflected sound from the support ring impinging on the pellicle before acoustic steady-state conditions are

achieved. For the work reported here, the pellicle chosen has a finite width, and this can influence the motion of the pellicle in response to the acoustic wave.

B. Pellicle modes

The displacement or velocity of a pellicle or membrane in response to an acoustic field may not always be fully representative of particle movement in the surrounding medium. There is a possibility that pellicle movement is governed by modes excited by the acoustic field. In the case of the pellicle membrane stretched across an annular ring, as used with the NPL primary standard interferometer for megahertz frequencies, the radial modes (the "drum-skin modes") occur at very low frequencies and are in any case heavily damped by the surrounding water. However, Bacon has shown that for certain angles of incidence, the acoustic field may excite Lamb waves in the pellicle membrane.[16]

The pellicle used in this work is in the form of a strip and does not approximate to an infinite plane. The modes of vibration of such a structure will depend on the boundary conditions imposed. The mounting method for the pellicle (see Fig. 2) dictates that the ends are clamped, while the edges of the pellicle can move freely within the medium. To investigate the vibration modes of the pellicle in this configuration, the vibration of the pellicle strip was determined experimentally by scanning the vibrometer beam across the pellicle strip in the water tank shown Fig. 2.

Scans of the vibration profile of the pellicle were performed using the Polytec PSV-3000 scanning vibrometer, consisting of an OFV 056 scanning head and a PSV-Z-040-F control unit. The vibrometer scans the beam across the width of the pellicle by changing the angle at which the laser beam exits the optical aperture of the vibrometer, thus changing the angle of the optical beam subtended to the pellicle surface. This deviation of the laser beam from the central axis of the pellicle could potentially lead to an error since the vibrometer measures the component of velocity along the axis of the optical beam. A correction is therefore applied for the cosine of the angle at which the laser beam is incident on the pellicle surface. The incident angle of the optical beam with the pellicle was minimized by maximizing the standoff distance of the vibrometer from the pellicle, thus reducing this effect. This also minimizes any acousto-optic influences due to the incident and reflected optical beams traversing slightly different paths. A number of different pellicle widths were investigated using the same experimental arrangement as that used for the hydrophone calibration measurements. Figure 8 shows the velocity magnitude obtained for a one-dimensional line scan across the width of a 5 mm pellicle. The spatial scan resolution of the vibrometer limited the number of scan points that could be obtained across the 5 mm width of the pellicle.

The line profiles shown in Fig. 8 clearly show the presence of modes across the width of the pellicle at certain frequencies. Due to the limited spatial resolution of the scans, it is not possible to be certain about the wavelength of a given mode at, say, 250 kHz, where it appears that approximately one wavelength occurs across the 5 mm width of the

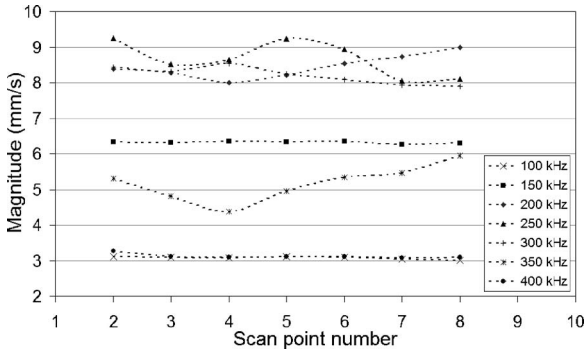

FIG. 8. Velocity magnitude obtained for a one-dimensional line scan across the width of a 5 mm pellicle at selected frequencies in the range 100 to 400 kHz.

pellicle since it is impossible to exclude the possibility of aliasing. The results do, however, show that modes do exist and that they are a function of frequency. There appears to be very limited variation across the 5 mm wide pellicle at 100, 150, and 400 kHz, but significant velocity variation across the pellicle between 250 and 350 kHz. The presence of these modes could lead to uncertainties in the hydrophone calibration using the optical method and are believed to be the reason for the fluctuations above 120 kHz observed in the optical calibration data shown in Fig. 6.

C. Other sources of error

Other sources of error in the method include the presence of signals due to the acousto-optic interaction in addition to the signals due to the pellicle movement. The rate of change of the refractive index along the optical pathlength can give rise to signals that are effectively interpreted as velocities by the vibrometer. This effect is exploited in configurations where the optical beam and acoustic beam are arranged to be orthogonal, as in the work of Harland.[14] The configuration for the work reported here is designed to measure only the pellicle movement, but if the laser beam subtends an angle to the direction of acoustic propagation, there may be some component of the signal due to the refractive index variation along the optical beam, leading to an error in the measurement of pellicle velocity.

Due to the specular reflecting properties of the pellicle, the optical beam can be aligned very precisely with the pellicle. However, alignment of the optical beam or the pellicle with the acoustic beam is more difficult. For spherical projectors, this problem is solved by first aligning the optical beam on the acoustic center of the projector and then inserting the pellicle into the path of the optical beam, ensuring that the acoustic beam and the pellicle are both aligned with the optical beam. For flat-faced piston-type projectors where the acoustic beam is produced at a normal incidence to the face of the projector, the small component of the optical beam reflected from the surface of the projector can be used to aid in alignment. However, the optical scattering produced at the surface of the transducer may give rise to a small angular error. The work of Bacon has shown the error in a hydrophone calibration to be insignificant for a small angular error of around 0.5°.[28]

One difficulty when using a commercial vibrometer is that of reliance on the calibration of the instrument, for example, reliance on the 25 (mm/s)/V setting on the Polytec system used for much of the work described here. For use in metrology, the instrument calibration must be traceable. As described in Sec. II, the velocity is dependent on the Doppler shift of the optical frequency, which in turn is traceable to standards of length via the laser wavelength. However, a vibrometer requires the Doppler shift to be converted to a voltage proportional to the velocity if a time-resolved signal is to be derived, and this typically requires the use of frequency mixing, filtering, and phase-lock loop circuitry.[25] The errors introduced by this signal processing are crucial in governing the absolute accuracy of the vibrometer, and for the most accurate work, the signal processing circuitry should be carefully characterized. Since this is not easy to do for a "black-box" commercial unit, it is necessary to design a custom-made vibrometer where each stage of the system can be characterized independently.[26]

VI. CONCLUSIONS

A novel technique for the absolute calibration of hydrophones in water using an optical method based on laser vibrometry has been presented. The method relies on the use of a thin plastic pellicle that is used to reflect the signal beam of a commercial laser vibrometer, the pellicle being thin enough to be acoustically transparent at the frequency of interest. The pellicle motion is taken to represent the acoustic particle velocity in the medium. The hydrophone response to a known acoustic field is measured and the hydrophone sensitivity derived. Results have been presented of the calibration of a reference measuring hydrophone over the frequency range 10 to 600 kHz. Excellent agreement has been achieved with the classic method of three-transducer spherical-wave reciprocity, with agreement to better than 0.5 dB over the majority of the frequency range.

An initial discussion of some of the sources of uncertainty has been presented. In particular, the influence of the properties of the pellicle has been the subject of preliminary study, both experimentally and theoretically. This has shown that the modes of vibration of the pellicle strip used can significantly degrade the accuracy of the results. However, if the pellicle is made sufficiently narrow the resonant modes are forced above the measurement frequency of interest, allowing accurate measurements to be performed. The method has been shown to offer the potential for a new primary standard method, with the calibration traceable to standards of length measurement through the wavelength of the laser light. More extensive studies are required to assess the sources of uncertainty before definitive conclusions can be drawn as to the accuracy.

ACKNOWLEDGMENT

The authors gratefully acknowledge the financial support of the UK Department of Trade & Industry (National Measurement System Directorate).

[1]R. J. Urick. *Principles of Underwater Sound*, 3rd ed. (McGraw-Hill, New York, 1983).
[2]R. J. Bobber, *Underwater Electroacoustic Measurements*, 2nd ed. (Peninsula Press, Los Altos, 1988).
[3]W. R. Maclean, "Absolute measurement of sound without a primary standard," J. Acoust. Soc. Am., **12**, 140–146 (1940).
[4]IEC 565, The Calibration of Hydrophones, International Electrotechnical Commission, Geneva, Switzerland, 1977.
[5]L. E. Kinsler and A. R. Frey, *Fundamentals of Acoustics* (Wiley, New York, 1982).
[6]R. J. Bobber, "General reciprocity parameter," J. Acoust. Soc. Am. **39**, 680–687 (1966).
[7]K. J. Taylor, "Absolute measurement of acoustic particle velocity," J. Acoust. Soc. Am., **59**, 691–694 (1976).
[8]K. J. Taylor, "Absolute calibration of microphones by a laser Doppler technique," J. Acoust. Soc. Am. **70**, 939–945 (1981).
[9]T. MacGillivray, D. Campbell, C. Greated, and R. Barham, "The development of a microphone calibration technique using laser Doppler anemometry," Acta. Acust. Acust. **88**, 135–141 (2002).
[10]P. S. Dubbleday and H. C Shau, "Laser Doppler anemometry detection of hydroacoustic particle velocity," J. Acoust. Soc. Am. **86**, 891–894 (1989).
[11]R. I. Crickmore, S. H. Jack, D. B. Hann, and C. A. Greated, "Laser Doppler anemometry and the acousto-optic effect," Opt. Laser Technol. **31**, 85–94 (1999).
[12]A. R. Harland, J. N. Petzing, and J. R. Tyrer, "Non-invasive measurements of underwater pressure fields using laser Doppler velocimetry," J. Sound Vib. **252**, 169–177 (2002).
[13]T. A. Pitts and J. F. Greenleaf, "Three-dimensional optical measurement of instantaneous pressure," J. Acoust. Soc. Am. **108**, 2873–2883 (2000).
[14]A. R. Harland, J. N. Petzing, and J. R. Tyrer, "Nonperturbing measurements of spatially distributed underwater acoustic fields using a scanning laser Doppler vibrometer," J. Acoust. Soc. Am. **115**, 187–195 (2004).
[15]C. B. Scruby and L. E. Drain, *Laser Ultrasonics* (Adam Hilger, Bristol, 1990).
[16]D. R. Bacon, "Primary calibration of ultrasonic hydrophones using optical interferometry," IEEE Trans. Ultrason. Ferroelectr. Freq. Control **35**, 152–161 (1988).
[17]R. C. Preston, S. P. Robinson, B. Zeqiri, T. J. Esward, P. N. Gelat, and N. D. Lee, "Primary calibration of membrane hydrophones in the frequency range 0.5 MHz to 60 MHz," Metrologia **36**, 331–343 (1999).
[18]D. R. Bacon, R. C. Chivers, and J. N. Som, "The acousto-optic interaction in the interferometric measurement of ultrasonic transducer surface motion," Ultrasonics **31**, 321–325 (1993).
[19]T. J. Esward and S. P. Robinson, "Extending the frequency range of the National Physical Laboratory primary standard laser interferometer for hydrophone calibrations to 60 MHz," IEEE Trans. Ultrason. Ferroelectr. Freq. Control **46**, 737–744 (1999).
[20]C. Koch and W. Molkenstruck, "Primary calibration of hydrophones with extended frequency range 1 to 70 MHz using optical interferometry," IEEE Trans. Ultrason. Ferroelectr. Freq. Control **46**, 1303–1314 (1999).
[21]W. Yuebing and H. Yongjun, "Calibration of hydrophones using an optical technique," Acta Acust. (Beijing) **26**, 29–33 (2001).
[22]W. Yuebing, "The application of optical interferometry in the measurement of hydrophones," *Proceedings of the Institute of Acoustics*, 2003, Vol. **25**.
[23]A. R. Harland, J. N. Petzing, C. Bickley, S. P. Robinson, J. R. Tyrer, and R. C. Preston, "Application and assessment of laser Doppler velocimetry for underwater acoustic measurements," J. Sound Vib. **265**, 627–645 (2003).
[24]P. D. Theobald, C. J. Bickley, and S. P. Robinson, "Recent progress at NPL in the use of optical techniques for hydrophone calibration," *Proceedings of the Institute of Acoustics*, 2003, Vol. **25**.
[25]P. D. Theobald, S. P. Robinson, A. D. Thompson, R. C. Preston, P. Lepper, W. Yuebing, C. Swift, and J. Tyrer, "Fundamental standards for acoustics based on optical methods—Phase two report for sound in water," NPL Report CAIR 3, 2002.
[26]P. D. Theobald, A. D. Thompson, S. P. Robinson, R. C. Preston, P. Lepper, W. Yuebing, C. Swift, and J. Tyrer, "Fundamental standards for acoustics based on optical methods—Phase three report for sound in water," NPL Report CAIR 9, 2004.
[27]L. M. Brekhovskikh, *Waves in Layered Media*, 2nd ed. (Academic, New York, 1980).
[28]D. R. Bacon, "The improvement and evaluation of a laser interferometer for the absolute measurement of ultrasonic displacements in the frequency range up to 15 MHz," NPL Report Ac 109, 1986.

Source localization in the presence of internal waves

Ralph N. Baer and Michael D. Collins
Naval Research Laboratory, Washington, DC 20375

(Received 29 March 2005; revised 11 July 2005; accepted 1 August 2005)

The possibility of determining the location of an acoustic source in the presence of internal waves is investigated. Source localization problems require environmental information as inputs. Internal waves cause uncertainties in the sound speed field. In previous work [J. Acoust. Soc. Am. **90**, 1410–1422 (1991)], it was found that a source can often be localized in an uncertain environment by including environmental parameters in the search space and tweaking them, but usually not determining their true values. This is possible due to a parameter hierarchy in which the source position is more important than the environmental parameters. The parameter hierarchy is shown to also apply to uncertainties associated with internal waves. Due to differences in the nature of the parameter space, this problem is solved with a statistical approach rather than a parameter search technique such as simulated annealing. [DOI: 10.1121/1.2041331]

PACS number(s): 43.60.Kx, 43.30.Wi [WLS] Pages: 3117–3121

I. INTRODUCTION

Matched-field processing is an approach for estimating the location of an acoustic source by analyzing data measured on an array of hydrophones.[1–3] The measured field is compared with replica fields, which are obtained by solving the acoustic wave equation for different locations of a test source. The estimate for the source location is the test source location that corresponds to the best match with the data.

Several factors may cause matched-field processing to fail. For example, there are usually uncertainties in the sound speed field and other environmental parameters. This is an important issue because small uncertainties can have large effects on the acoustic field. Focalization is a special type of matched-field processing that has been designed to deal with the problem of environmental uncertainty.[4–6] Environmental parameters are included along with the source location in the space of unknown parameters. Due to a parameter hierarchy in which the source location outranks environmental parameters, it is often possible to determine the source location without recovering the true environmental parameters. This is a fortunate situation when the main objective is to locate the source. Focalization can be an effective approach for solving matched-field processing problems, even when the signal-to-noise ratio is low.[5]

In this paper, we investigate the possibility of performing focalization in the presence of internal waves, which for many years have been regarded as a serious limiting factor in matched-field processing. In practical applications, it is not feasible to determine the internal wave field accurately. If the source is sufficiently far from the hydrophones, internal waves can cause matched-field processing to break down. We present simulations based on the Garrett–Munk internal wave spectrum[7,8] that indicate that the parameter hierarchy also applies to internal waves. It is often possible to locate a source by including the internal wave field in the space of unknown parameters. In many cases, the correct source location can be obtained reliably without obtaining the correct internal wave field.

II. THE PARAMETER SPACE

One of the keys to solving an inverse problem is to have a basic understanding of the parameter space. The source position is the only unknown in the classical matched-field processing problem. Environmental parameters are the unknowns in the tomography[9,10] and geoacoustic inversion[11–13] problems. Both types of parameters were considered in the original work on focalization,[4] which we refer to as deterministic focalization. Before the concept of a parameter hierarchy was introduced, the problem of environmental uncertainty appeared to severely restrict the applicability of matched-field processing, and research on this topic was limited to illustrating the failure of matched-field processing under different types of uncertainties[14–17] and attempting to reduce the problem by designing ambiguity functions that are relatively insensitive to uncertainties.[18–20] The inverse problem involving both types of parameters had never been considered because it seemed impossible to simultaneously determine both types of parameters. Although this is indeed true in many cases, it turns out that the source position can often be determined simply by tweaking the environmental parameters without actually determining their true values.[4]

Three additional types of parameters arise when a stochastic process, such as internal waves, is included in the parameter space. We refer to such problems as stochastic focalization, which may involve stochastic parameters (such as length scales and amplitudes), purely random parameters (such as the random numbers used to generate a realization of the stochastic process), and nonacoustic environmental parameters. There are two stochastic parameters in the Garrett–Munk model for internal waves,

$$\delta c = \frac{\mu c}{g} N^2 \zeta, \tag{1}$$

$$F_\zeta(j,\omega) = \frac{4\zeta_0^2}{\pi M} \frac{N_0}{N} \frac{f}{\omega^3} \frac{\sqrt{\omega^2 - f^2}}{j^2 + j_*^2}, \tag{2}$$

$$f \equiv 2\Omega \sin\phi, \tag{3}$$

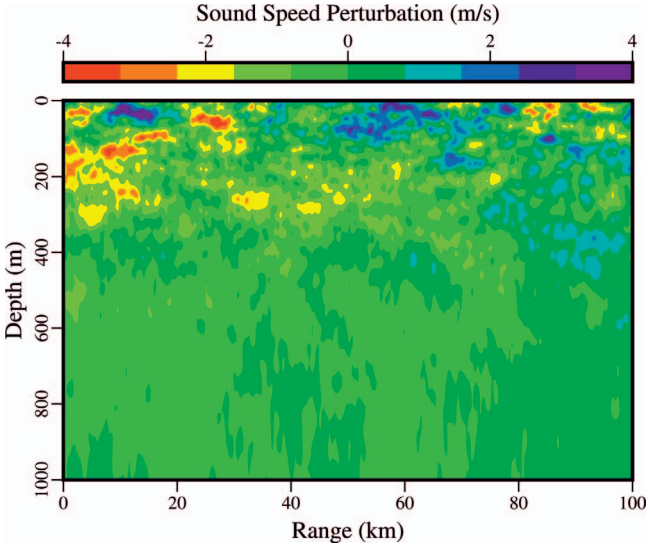

FIG. 1. Sound speed perturbation due to a realization of the Garrett–Munk internal wave spectrum.

$$M \equiv \sum_{j=1}^{\infty} (j^2 + j_*^2)^{-1}, \tag{4}$$

where N is the buoyancy frequency, N_0 is the buoyancy frequency near the surface, ζ is the vertical displacement of a fluid parcel, ζ_0^2 is the mean square displacement near the surface, c is the speed of sound, μ is a dimensionless constitutive parameter, g is the acceleration due to gravity, δc is the perturbation in c due to internal waves, ω is the internal wave frequency, F_ζ is the internal wave spectrum, j is the internal wave mode number, ϕ is the latitude, and Ω is the diurnal circular frequency. The empirical constants j_* and ζ_0 are the stochastic parameters, which affect the shape and amplitude of the spectrum. The nonacoustic parameters μ, N, and N_0 are not considered in deterministic focalization problems.

A realization of the sound speed perturbation due to internal waves appears in Fig. 1. This example illustrates the extreme complexity of internal wave fields and suggests that it is not feasible to map them by tomography over the large horizontal distances (several kilometers or more) that are typically of interest in source localization problems. Since deterministic parameters can often be estimated over such ranges by tomography, stochastic focalization appears to be in some sense a harder problem than deterministic focaliza-

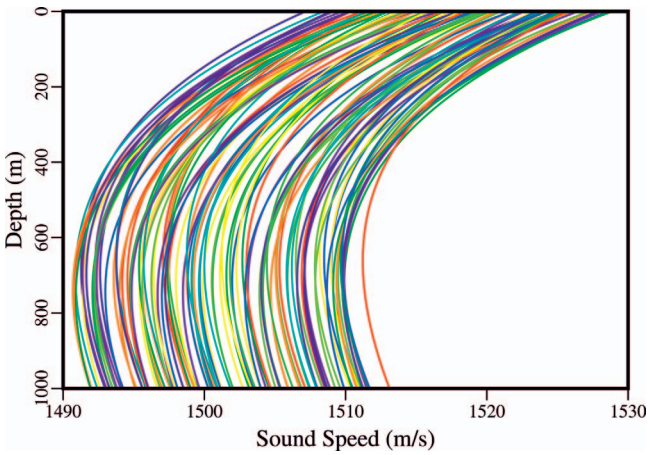

FIG. 2. Randomly selected sound speed profiles within the parameter bounds in Eqs. (9), (10), and (11).

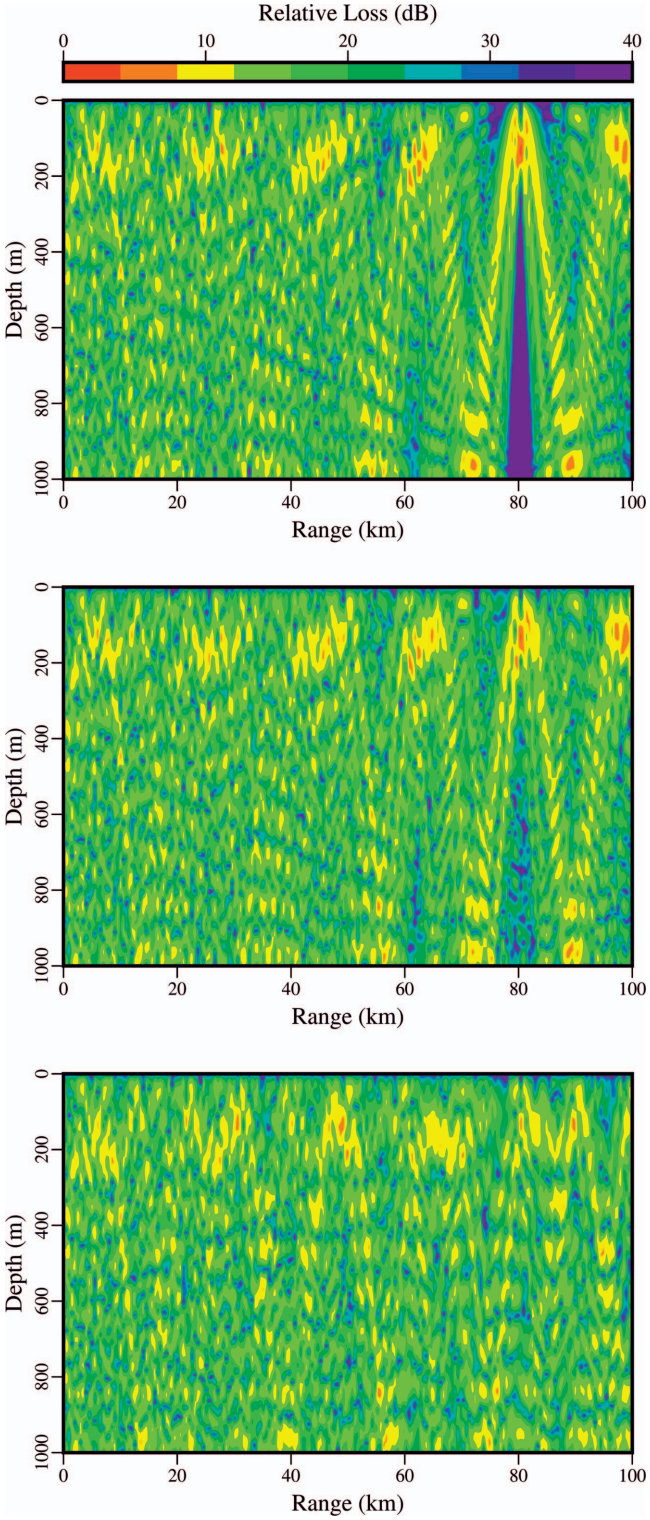

FIG. 3. Ambiguity surfaces for the 80 km stochastic case. There is a well-defined peak at the source location when the internal wave field is known exactly (top frame). The main peak is weakened but occurs at the source location for some realizations of the internal wave field (middle frame). The main peak occurs at the wrong location for some realizations (bottom frame).

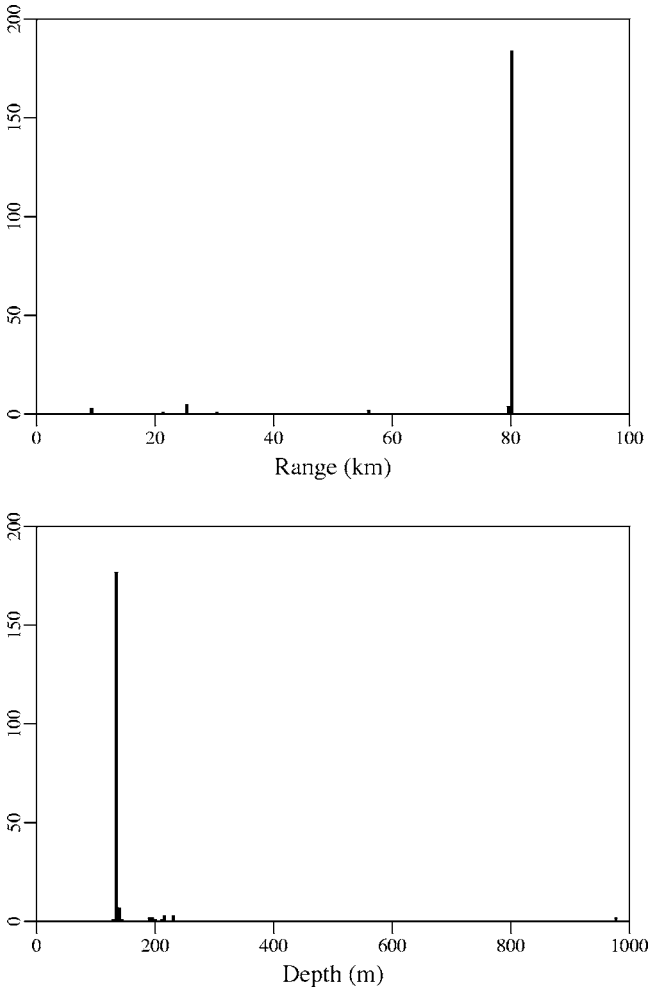

FIG. 4. Histograms for the 80 km stochastic case. The main peak is near the correct source location for most of the realizations of the internal wave field.

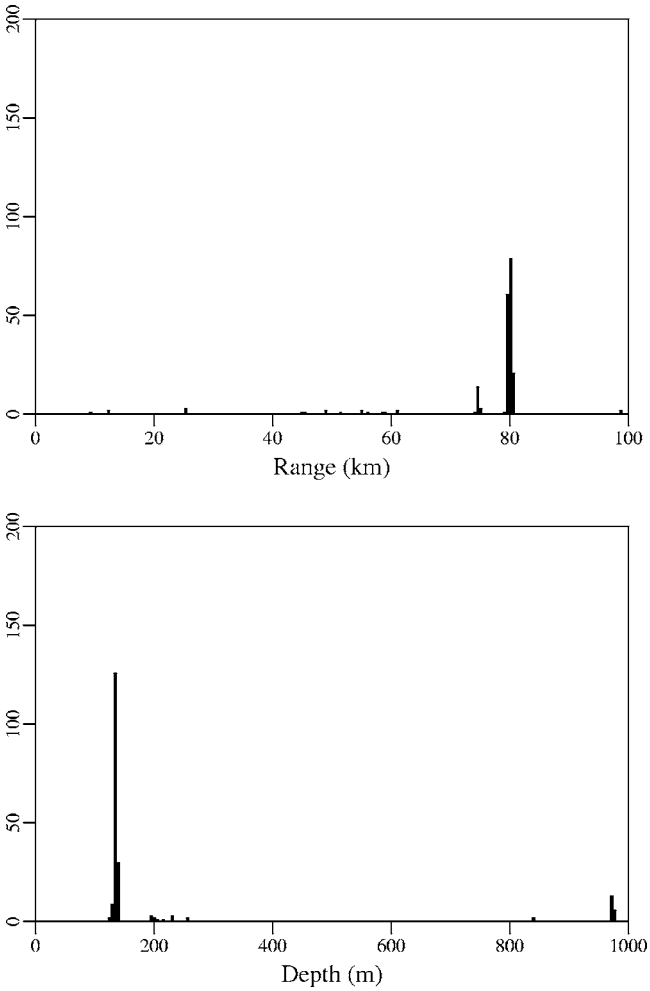

FIG. 5. Histograms for the 80 km stochastic–deterministic case. The inclusion of uncertainties in the background profile causes the main peak to occur more frequently at the wrong position.

tion. Since internal waves cause perturbations to the sound speed field, however, their effect is a form of environmental uncertainty, and we would expect the parameter hierarchy to apply.

III. IMPLEMENTATION AND TESTING

Focalization and geoacoustic inversion have been implemented using simulated annealing,[21–23] an optimization method that uses gradient information to search for the global minimum of a cost function. This approach is effective for deterministic problems in which the parameter landscape consists of smooth hills and valleys. Simulated annealing searches involve a series of perturbations of the parameters that are selected from a distribution that is biased toward small perturbations, which sense the gradient, but allows some large perturbations, which are useful for escaping local minima. For stochastic problems, it is not natural to consider small perturbations of the purely random parameters. For example, internal wave fields are highly complex and each realization tends to be as unique as a fingerprint. We apply a histogram approach to the stochastic focalization problem. We randomly sample the parameters, construct an ambiguity surface for each sample, and consider histograms of the location of the largest peak in the ambiguity surfaces.

For the examples, we use the field on a vertical array that spans all depths and construct ambiguity surfaces using phase conjugation and back-propagation.[24] With this approach, the complex pressure that is received on the array is conjugated and propagated away from the array. If the correct environmental information is used, the field will focus at the source location. This efficient approach only requires one solution of the wave equation. In contrast, the construction of the closely related Bartlett processor requires one solution of the wave equation for each receiver in the array.

The examples involve a 50 Hz source 132 m below the surface in an ocean with the background sound speed profile,[25]

$$c = c_0\left[1 + \alpha\left(2\frac{z - z_0}{B} + \exp\left(-2\frac{z - z_0}{B}\right) - 1\right)\right], \tag{5}$$

where $z_0 = 700$ m is the channel depth, $c_0 = 1500$ m/s is the channel sound speed, $B = 1000$ m is the channel thickness, and $\alpha = 0.0071$. A parabolic equation model is used to solve the acoustic wave equation with the sound speed $c + \delta c$, where δc is obtained using Eq. (1) and the approach described in Ref. 8. We use the exponential buoyancy profile described in Ref. 8 and take $\mu = 24.5$, $j_* = 3$, and

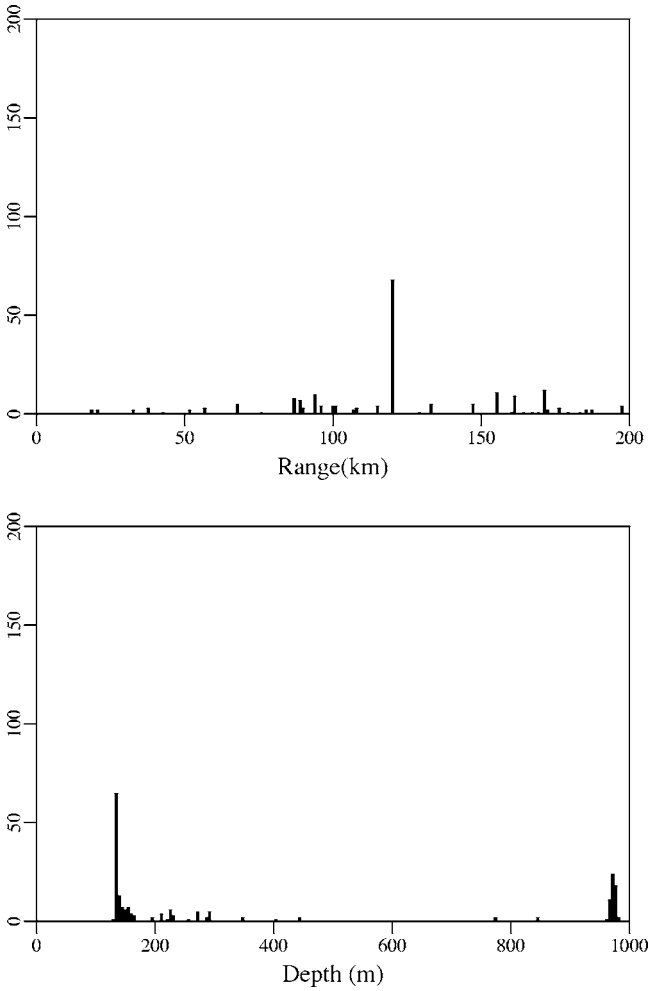

FIG. 6. Histograms for the 120 km stochastic case. The influence of internal waves increases with range, and the main peak occurs more frequently at the wrong position.

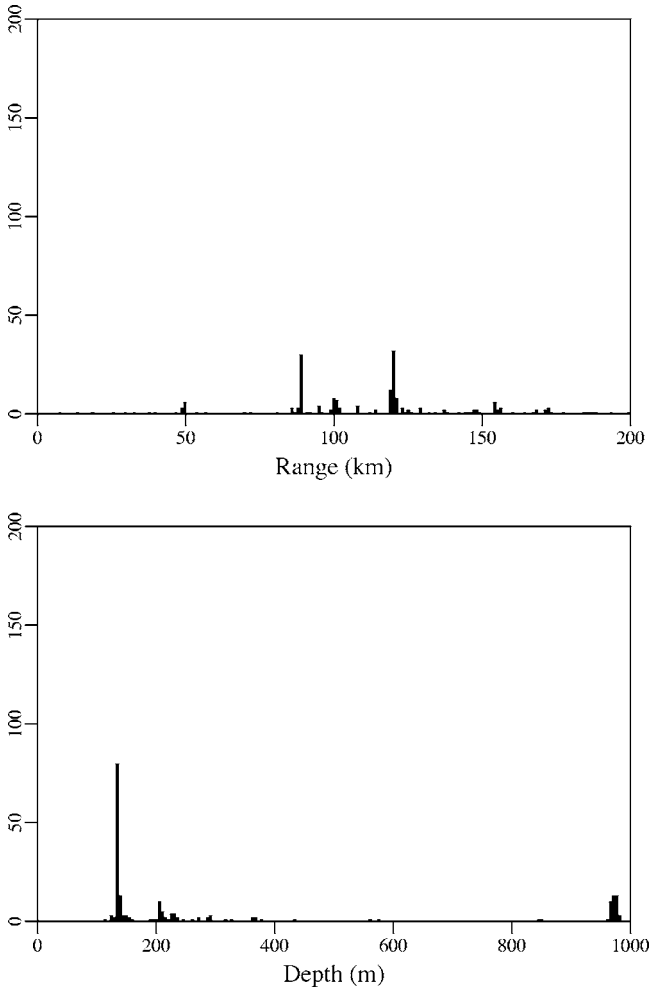

FIG. 7. Histograms for the 120 km stochastic–deterministic case. Although the main peak occurs more frequently at the source position than at any other position, this example illustrates the difficulty of the localization problem when the source range is large, there are uncertainties in the background profile, and there are internal waves.

ζ_0=5.61 m. The parameter search is conducted within the bounds,

$$10 \leqslant \mu \leqslant 25, \tag{6}$$

$$2 \leqslant j_* \leqslant 6, \tag{7}$$

$$5 \text{ m} \leqslant \zeta_0 \leqslant 10 \text{ m}, \tag{8}$$

$$650 \text{ m} \leqslant z_0 \leqslant 750 \text{ m}, \tag{9}$$

$$1490 \text{ m/s} \leqslant c_0 \leqslant 1510 \text{ m/s}, \tag{10}$$

$$980 \text{ m} \leqslant B \leqslant 1020 \text{ m}. \tag{11}$$

Each realization is generated by selecting values from within these bounds using a uniform distribution. We consider source ranges of 80 and 120 km for a stochastic case in which the background profile is known and a stochastic–deterministic case in which all of the parameters are unknown. For each example, we generated 200 realizations of $c+\delta c$ and used them to construct 200 ambiguity surfaces. The randomly generated background profiles appear in Fig. 2.

Ambiguity surfaces appear in Fig. 3 for the 80 km stochastic case. When the correct background profile and internal waves are used, the ambiguity surface has a well-defined peak at the source position. When a different realization of the internal wave field is used, the peak is either degraded or lost. The histograms in Fig. 4 illustrate that the main peak frequently occurs near the source location and the source is reliably localized. Since the main peak occurs at other locations for some realizations, conventional matched-field processing is not reliable for this problem. Histograms appear in Fig. 5 for the 80 km stochastic–deterministic case. The source is still reliably localized, but the main peak occurs more frequently at the wrong location. Histograms appear in Figs. 6 and 7 for the 120 km cases. Since the effect of the internal waves accumulates with range, stochastic focalization is less reliable than for the corresponding 80 km cases. For the stochastic–deterministic case, an ambiguous peak occurs nearly as frequently as the peak at the source location. In a practical application, it might be possible to rule out this peak since its location is very deep.

IV. CONCLUSION

Focalization is an effective approach for localizing a source in the presence of internal waves. When internal waves cause conventional matched-field processing to fail, the source location can often be determined reliably by considering a series of realizations of the internal wave field. Due to the parameter hierarchy, the source position can often be determined without determining the internal wave field. Deterministic focalization was originally implemented using simulated annealing. A histogram approach appears to be more effective for stochastic focalization.

ACKNOWLEDGMENTS

This work was supported by the Office of Naval Research. The authors thank John A. Colosi, Charles F. Gaumond, B. Edward McDonald, and William L. Siegmann for providing helpful comments and suggestions.

[1]H. P. Bucker, "Use of calculated sound fields and matched-field detection to locate sound sources in shallow water," J. Acoust. Soc. Am. **59**, 368–373 (1976).
[2]A. B. Baggeroer, W. A. Kuperman, and H. Schmidt, "Matched field processing: Source localization in correlated noise as an optimum parameter estimation problem," J. Acoust. Soc. Am. **83**, 571–587 (1988).
[3]A. B. Baggeroer, W. A. Kuperman, and P. N. Mikhalevsky, "An overview of matched field methods in ocean acoustics," IEEE J. Ocean. Eng. **18**, 401–424 (1993).
[4]M. D. Collins and W. A. Kuperman, "Focalization: Environmental focusing and source localization," J. Acoust. Soc. Am. **90**, 1410–1422 (1991).
[5]L. T. Fialkowski, M. D. Collins, J. S. Perkins, and W. A. Kuperman, "Source localization in noisy and uncertain ocean environments," J. Acoust. Soc. Am. **101**, 3539–3545 (1997).
[6]C. Soares, M. Siderius, and S. M. Jesus, "Source localization in a time-varying waveguide," J. Acoust. Soc. Am. **112**, 1879–1889 (2002).
[7]C. Garrett and W. H. Munk, "Space-time scale of internal waves: A progress report," J. Geophys. Res. **80**, 291–297 (1975).
[8]J. A. Colosi and M. G. Brown, "Efficient numerical simulation of stochastic internal-wave-induced sound-speed perturbation fields," J. Acoust. Soc. Am. **103**, 2232–2235 (1998).
[9]W. Munk and C. Wunsch, "Ocean acoustic tomography: A scheme for large scale monitoring," Deep-Sea Res., Part A **26A**, 123–161 (1979).
[10]W. H. Munk and P. F. Worcester, "Ocean acoustic tomography," Oceanogr. **1**, 8–10 (1988).
[11]M. D. Collins, W. A. Kuperman, and H. Schmidt, "Nonlinear inversion for ocean-bottom properties," J. Acoust. Soc. Am. **92**, 2770–2783 (1992).
[12]S. E. Dosso, M. J. Wilmut, and A. L. S. Lapinski, "An adaptive-hybrid algorithm for geoacoustics inversion," IEEE J. Ocean. Eng. **26**, 324–336 (2001).
[13]P. Gerstoft and C. F. Mecklenbrauker, "Ocean acoustic inversion with estimation of *a posteriori* probability distributions," J. Acoust. Soc. Am. **104**, 808–819 (1998).
[14]M. B. Porter, R. L. Dicus, and R. G. Fizell, "Simulations of matched-field processing in a deep water Pacific environment," IEEE J. Ocean. Eng. **12**, 173–181 (1987).
[15]A. Tolstoy, "Sensitivity of matched field processing to sound-speed profile mismatch for vertical arrays in a deep water Pacific environment," J. Acoust. Soc. Am. **85**, 2394–2404 (1989).
[16]R. M. Hamson and R. M. Heitmeyer, "Environmental and system effects on source localization in shallow water by the matched-field processing of a vertical array," J. Acoust. Soc. Am. **86**, 1950–1959 (1989).
[17]D. F. Gingras, "Methods for predicting the sensitivity of matched-field processors to mismatch," J. Acoust. Soc. Am. **88**, 423–433 (1990).
[18]H. Schmidt, A. B. Baggeroer, W. A. Kuperman, and E. K. Scheer, "Environmentally tolerant beamforming for high-resolution matched field processing: Deterministic mismatch," J. Acoust. Soc. Am. **88**, 1851–1862 (1990).
[19]A. M. Richardson and L. W. Nolte, "*A posteriori* probability source localization in an uncertain sound speed, deep ocean environment," J. Acoust. Soc. Am. **89**, 2280–2290 (1991).
[20]J. L. Krolik, "Matched-field minimum variance beamforming in a random ocean channel," J. Acoust. Soc. Am. **92**, 1408–1419 (1991).
[21]N. Metropolis, A. W. Rosenbluth, M. N. Rosenbluth, A. H. Teller, and E. Teller, "Equations of state calculations by fast computing machines," J. Chem. Phys. **21**, 1087–1091 (1953).
[22]S. Kirkpatrick, C. D. Gellatt, and M. P. Vecchi, "Optimization by simulated annealing," IBM Thomas J. Watson Research Center, Yorktown Heights, New York, 1982.
[23]H. Szu and R. Hartley, "Fast simulated annealing," Phys. Lett. A **122**, 157–162 (1987).
[24]F. D. Tappert, L. Nghiem-Phu, and C. S. Daubin, "Source localization using the PE method," J. Acoust. Soc. Am. **78**, S30 (1985).
[25]W. H. Munk, "Sound channel in an exponentially stratified ocean with applications to SOFAR," J. Acoust. Soc. Am. **55**, 220–226 (1974).

Development of a multiview time-domain imaging algorithm with a Fermat correction

Karl A. Fisher[a)]
Lawrence Livermore National Laboratory, L-333, Livermore, California 94566

Sean K. Lehman[b)]
Lawrence Livermore National Laboratory, L-154, Livermore, California 94566

Dave H. Chambers[c)]
Lawrence Livermore National Laboratory, L-154, 7000 E. Avenue, Livermore, California 94566

(Received 3 February 2005; revised 3 August 2005; accepted 7 August 2005)

An imaging algorithm is presented based on the standard assumption that the total scattered field can be separated into an elastic component with monopolelike dependence and an inertial component with dipolelike dependence. The resulting inversion generates two separate image maps corresponding to the monopole and dipole terms of the forward model. The complexity of imaging flaws and defects in layered elastic media is further compounded by the existence of high contrast gradients in either sound speed and/or density from layer to layer. To compensate for these gradients, we have incorporated Fermat's method of least time into our forward model to determine the appropriate delays between individual source-receiver pairs. Preliminary numerical and experimental results are in good agreement with each other. © *2005 Acoustical Society of America.* [DOI: 10.1121/1.2048927]

PACS number(s): 43.60.Pt, 43.60.Ac, 43.35.Zc [EJS] Pages: 3122–3128

I. INTRODUCTION

Typically, a tomographic reconstruction is derived from a series of *projections*, where a projection is defined as the integral of the image in the direction specified by that angle. Experimentally, this is usually obtained by systematically measuring the transmitted or reflected energies from the object, as it is insonified through a series of angular directions defined by the source-receiver pair.[1] Traditional methods of acoustic/seismic tomography rely on algorithms that can generate a two-dimensional velocity map from a set of line integrals representing the travel time of numerous rays throughout the medium of interest.[2,3] To that end, most straight-ray backprojection algorithms yield single-valued reconstructions of either the medium velocity, density, or attenuation, depending on the forward propagation model used and the nature of the probing system.[1] Recently, techniques have been developed to invert acoustic data sets and reconstruct either, density or compressibility maps under specified conditions in tissue.[4,5]

The motivation for our development is driven by the need to detect and generate two-dimensional images of flaws in multilayered structures. Application of ultrasonic reflection tomography to nondestructive evaluation of materials is possible, owing to the fact that flaws generally result in weak and localized signals. Thus, the Born approximation can be applied to the scattered field.[6] Common time-domain imaging methods include migration algorithms used in geophysics,[7] and B-scan algorithms used in medical ultrasound imaging.[8] Our imaging algorithm is based on implementing monopole and dipole expansion terms of a long-wavelength scattering result. The implementation we will present generates dual valued reconstructions of the image space, corresponding to the monopole and dipole components of the field scattered from each point in the image. If the scattered field is generated by a collection of pointlike scatterers, the monopole and dipole images correspond to compressibility and density contrast between the medium and each scatterer (neglecting multiple interactions). The algorithm permits the selection of arbitrary source and receiver locations, thus it can be applied to numerous multistatic data collection geometries and procedures. Though originally intended to be implemented in the time domain, the algorithm could also be implemented in the frequency domain.

In most nondestructive evaluation (NDE) problems however, there can be large contrast differences in the acoustic impedances between adjacent layers resulting in significant refraction effects. Various backprojection algorithms have been developed to account for ray bending due to gradients in the background velocity distribution.[9] The significant difference with our application is that a considerable amount of prior knowledge of the internal structure of the part is known, either through blueprints or some other type of manufacturing specification. Thus, for NDE purposes, it is reasonable to assume that the material properties and geometry of the individual layers are well known and understood. In this case, the inverse wave imaging is used to identify deviations, defects, and or flaws in the assembled part.

Although the algorithm is developed around a long-wavelength (point scatterer) limit, it is not related to the classical time-reversal algorithms which form *detection maps* using MUSIC rather than actual images of physical

[a)]Electronic mail: fisher34@llnl.gov
[b)]Electronic mail: lehman2@llnl.gov
[c)]Electronic mail: chambers2@llnl.gov

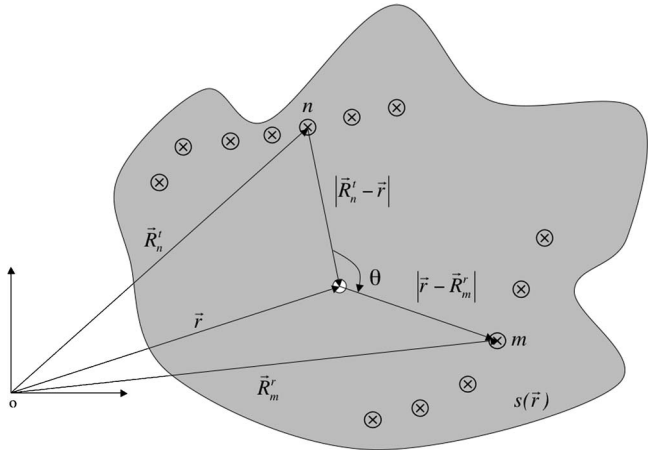

FIG. 1. Arbitrary wave probing system where the sensor locations are denoted as ⊗. The slowness distribution for the medium is given by $s(\mathbf{r}) = 1/v(\mathbf{r})$, where $v(\mathbf{r})$ is the corresponding bulk velocity distribution of the background medium.

properties.[10] Nor can the algorithm be considered as a member of the backpropagation family of algorithms since it is based upon straight-ray scattering and there are now fields being back propagated.

In the following section, we will present a derivation of our multiview, time-domain imaging tomography algorithm (MTDI). This is followed by a generalized correction to the forward model for highly refractive media using Fermat's principle of least time.[11] The section ends with an application of the corrected forward model to a representative two-layer aluminum-copper part. A description of the simulation and experiment are given in Sec. III. Finally, results for simulated and experimental reconstructions of the two-layered part are presented in Sec. IV. Conclusions are discussed in Sec. V.

II. THEORETICAL FORMULATION

A. Derivation of the forward model

From Morse and Ingard,[12] Eqs. 8.2.15 and 8.2.19, the *long-wavelength* approximation of the scattered field due to a point scatterer is

$$\psi^{\text{scat}}(\mathbf{R}_m^r, \mathbf{R}_n^t, \mathbf{r}, \omega) = \frac{1}{3}\Phi(\omega)\frac{e^{ikr_m}}{r_m}k^2a^3[\gamma_\kappa + \gamma_\rho \cos\,\theta_{mn}(\mathbf{r})], \tag{1}$$

where $\psi^{\text{scat}}(\mathbf{R}_m^r, \mathbf{R}_n^t, \mathbf{r}, \omega)$ is the measured scattered field at the mth receiver located at $\mathbf{R}_m^r$ from the nth source located at $\mathbf{R}_n^t$; $\mathbf{r}$ is the point scatterer location; $\mathbf{r}_m \equiv |r - R_m^r|$ is the distance from the point scatter to the mth receiver; ω is the narrow band frequency; $k \equiv \omega/c$ is the narrow band wave number; $\Phi(\omega)$ is the spectrum of the incident pulse; $\gamma_\kappa \equiv \kappa_s - \kappa_o/\kappa_o$ is the relative compressibility ratio; $\gamma_\rho \equiv 3(\rho_s - \rho_o)/(2\,\rho_s + \rho_o)$ is the relative density ratio; θ_{mn} is the scattering angle; a is the point scatterer radius.

The scattering geometry is presented in Fig. 1. The compressibility and density of the scatterer are given as κ_s and ρ_s; and for the background as, κ_o and ρ_o, respectively.

We obtain the time-domain representation of the scattered field via

$$\psi^{\text{scat}}(\mathbf{R}_m^r, \mathbf{R}_n^t, \mathbf{r}, t) = \frac{a^3}{3c^2 r_m (2\pi)}[\gamma_\kappa + \gamma_\rho \cos\,\theta_{mn}(\mathbf{r})] \times \int_{-\infty}^{\infty} d\omega\, \omega^2 \Phi(\omega) e^{i\omega r_m/c} e^{-i\omega t}. \tag{2}$$

The inverse Fourier transform yields

$$\begin{aligned}\frac{1}{2\pi}\int_{-\infty}^{\infty} d\omega\, \omega^2 \Phi(\omega) e^{i\omega r_m/c} e^{-i\omega t} &= \frac{1}{2\pi}\int_{-\infty}^{\infty} d\omega\, \Phi(\omega)\frac{d^2}{dt^2} e^{-i(t - r_m/c)\omega} \\ &= \frac{1}{2\pi}\frac{d^2}{dt^2}\int_{-\infty}^{\infty} d\omega\, \Phi(\omega) e^{-i(t - r_m/c)\omega} = \frac{1}{2\pi}\frac{d^2}{dt^2}\phi(t - r_m/c),\end{aligned} \tag{3}$$

resulting in

$$\psi^{\text{scat}}(\mathbf{R}_m^r, \mathbf{R}_n^t, \mathbf{r}, t) = \frac{a^3}{6\pi c^2 r_m}[\gamma_\kappa + \gamma_\rho \cos\,\theta_{mn}(\mathbf{r})]\frac{d^2}{dt^2} \times \phi(t - r_m/c), \tag{4}$$

as our forward model where $\phi(t)$ is the time-domain pulse.

We consider the arbitrary probing system of Fig. 1. A transmitter located at $\mathbf{R}_n^t$ launches an incident field that propagates into the medium. The field interacts with a point scatter located at $\mathbf{r}$, and the scattered field is measured at a receiver located at $\mathbf{R}_m^r$. The scattering angle is θ. In succession, each source transmitter is excited and the scattered field is measured at all of the receivers. (Technically, the *total* field is measured. The *scattered* field is obtained from the difference between the *total* field and the *incident* field.) Thus, at each receiver, m, we measure the scattered field time series from source, n, to a scatterer located at $\mathbf{r}$. These time series are represented by $\psi(\mathbf{R}_m^r, \mathbf{R}_n^t, \mathbf{r}, t)$.

In the case where all sources are excited simultaneously, we can view Eq. (4) as representing the *multistatic scattering matrix* and express it as

$$\psi_{mn}(\mathbf{r}) = \frac{1}{r_m}[\hat{\gamma}_\kappa + \hat{\gamma}_\rho \cos\,\theta_{mn}(\mathbf{r})]\frac{d^2}{dt^2}\phi(t - r_m/c), \tag{5}$$

where the time dependence is implicit but we maintain the spatial dependence to indicate the data are due to a point scatterer at $\mathbf{r}$, and we have introduced the modified compressibility and density relative ratios, defined as

$$\hat{\gamma}_\rho \equiv \frac{a^3}{6\pi c^2}\gamma_\rho, \tag{6}$$

$$\hat{\gamma}_\kappa \equiv \frac{a^3}{6\pi c^2}\gamma_\kappa. \tag{7}$$

Given a complete set of measurements in the multistatic data matrix, we wish to solve for the modified relative compressibility and relative density ratios. Equation (5) represents a set of $N_c = N_{src} \times N_{rcv}$ measurements for the two unknowns where N_{src} is the number of transmitters and N_{rcv} is the number of receivers. In matrix form, Eq. (5) reads

$$\begin{bmatrix} 1/r_1 & \cos\theta_{1,1}(\mathbf{r})/r_1 \\ 1/r_1 & \cos\theta_{1,2}(\mathbf{r})/r_1 \\ 1/r_1 & \cos\theta_{1,N_t}(\mathbf{r})/r_1 \\ 1/r_2 & \cos\theta_{2,1}(\mathbf{r})/r_2 \\ 1/r_2 & \cos\theta_{2,N_t}(\mathbf{r})/r_2 \\ 1/r_{N_r} & \cos\theta_{N_r,N_t}(\mathbf{r})/r_{N_r} \end{bmatrix} \begin{bmatrix} \hat{\gamma}_\kappa \\ \hat{\gamma}_\rho \end{bmatrix} = \begin{bmatrix} \psi_{1,1}(\mathbf{r}) \\ \psi_{1,2}(\mathbf{r}) \\ \psi_{1,N_t}(\mathbf{r}) \\ \psi_{2,1}(\mathbf{r}) \\ \psi_{2,N_t}(\mathbf{r}) \\ \psi_{N_r,N_t}(\mathbf{r}) \end{bmatrix}. \tag{8}$$

It should be noted that Eq. (8) is valid only in a least-squares sense. The scattering angle is given by

$$\cos\theta_{mn}(\mathbf{r}) \equiv -\frac{(\mathbf{r}-\mathbf{R}_m^r)(\mathbf{R}_n^t-\mathbf{r})}{|\mathbf{r}-\mathbf{R}_m^r||\mathbf{R}_n^t-\mathbf{r}|}. \tag{9}$$

Equation (8) is of the form

$$A\mathbf{g}=\mathbf{k}, \tag{10}$$

where A, is an $N_c\times 2$ matrix of $1/r_m$ and cosine terms of the scattering angle, $\mathbf{g}$ is the 2×1 vector of unknown modified relative compressibility and relative density ratios, and $\mathbf{k}$ is the $N_c\times 1$ vector of values from the multistatic data matrix.

The $\psi_{mn}(\mathbf{r})$ values are obtained in one of two different methods. The first method, the *time-domain method*, is to compute the total travel time, using the background velocity, from the source to the scatterer, and then from the scatterer to the receiver, and select the time series value at that time. One can optionally add to this travel time a delay to the pulse maximum. For example, if $\phi(t)$ is the transmitted pulse, and T_d is the time to the pulse maximum defined as

$$T_d \equiv \arg\max_t |\phi(t)|, \tag{11}$$

then $\psi_{mn}(\mathbf{r})$ is the value of the received time series evaluated at

$$t_{mn}(\mathbf{r}) \equiv |\mathbf{R}_n^t-\mathbf{r}|s_o + |\mathbf{r}-\mathbf{R}_m^r|S_o + T_d, \tag{12}$$

where s_o, is the slowness of the background medium defined as $s_o=1/v_o$. where v_o is the bulk velocity of the background media. The second method is a *frequency-domain method* in which the Fourier transform of the multistatic data matrix series is computed, and $\psi_{mn}(\mathbf{r})$ is set equal to the value of the Fourier series peak at the frequency multiplied by a phase delay given by $e^{\pm i t_{m,n}(\mathbf{r})\omega}$ where the ± depends upon the sign of the forward Fourier transform.

In this development, we have chosen the *time-domain* method. Equation (10) is solved in the least-squares sense by

$$\mathbf{g}=(A^\dagger A)^{-1}A^\dagger\mathbf{k}, \tag{13}$$

where the superscript † denotes transpose. Explicitly, we have

$$A^\dagger A = \begin{bmatrix} N_t\sum_{mn}\frac{1}{r_m^2} & \sum_{mn}\frac{\cos\theta_{mn}(\mathbf{r})}{r_m^2} \\ \sum_{mn}\frac{\cos\theta_{mn}(\mathbf{r})}{r_m^2} & \sum_{mn}\left(\frac{\cos\theta_{mn}(\mathbf{r})}{r_m}\right)^2 \end{bmatrix}, \tag{14}$$

$$A^\dagger\mathbf{k} = \begin{bmatrix} \sum_{mn}\frac{\psi_{mn}(\mathbf{r})}{r_m} \\ \sum_{mn}\frac{\cos\theta_{mn}(\mathbf{r})\psi_{mn}(\mathbf{r})}{r_m} \end{bmatrix}. \tag{15}$$

Thus

$$(A^\dagger A)^{-1} = \frac{1}{\Delta}\begin{bmatrix} \sum_{mn}\left(\frac{\cos\theta_{mn}(\mathbf{r})}{r_m}\right)^2 & -\sum_{mn}\frac{\cos\theta_{mn}(\mathbf{r})}{r_m^2} \\ -\sum_{mn}\frac{\cos\theta_{mn}(\mathbf{r})}{r_m^2} & N_t\sum_{mn}\frac{1}{r_m^2} \end{bmatrix}, \tag{16}$$

where the determinant is

$$\Delta \equiv \left(N_t\sum_{mn}\frac{1}{r_m^2}\right)\sum_{mn}\left(\frac{\cos\theta_{mn}(\mathbf{r})}{r_m}\right)^2 - \left(\sum_{mn}\frac{\cos\theta_{mn}(\mathbf{r})}{r_m^2}\right)^2. \tag{17}$$

Solving for $\mathbf{g}$, we find

$$g = \frac{1}{\Delta}\begin{bmatrix} \sum_{mn}\left(\frac{\cos\theta_{mn}(\mathbf{r})}{r_m}\right)^2\left(\sum_{mn}\frac{\psi_{mn}(\mathbf{r})}{r_m}\right) - \left(\sum_{mn}\frac{\cos\theta_{mn}(\mathbf{r})}{r_m^2}\right)\left(\sum_{mn}\frac{\cos\theta_{mn}(\mathbf{r})\psi_{mn}(\mathbf{r})}{r_m}\right) \\ \left(N_t\sum_{mn}\frac{1}{r_m^2}\right)\left(\sum_{mn}\frac{\cos\theta_{mn}(\mathbf{r})\psi_{mn}(\mathbf{r})}{r_m}\right) - \left(\sum_{mn}\frac{\cos\theta_{mn}(\mathbf{r})}{r_m^2}\right)\left(\sum_{mn}\frac{\psi_{mn}(\mathbf{r})}{r_m}\right) \end{bmatrix}. \tag{18}$$

Finally,

$$\kappa_s = (1+\hat{\gamma}_\kappa)\kappa_o \tag{19}$$

and

$$\rho_s = \frac{3+\hat{\gamma}_\rho}{(2\hat{\gamma}_\rho-3)}\rho_o. \tag{20}$$

B. Generalize the forward model to a variable background velocity

The analysis thus far has assumed a constant slowness $s(\mathbf{r})=s_o$ throughout the imaged region. Implicit in this assumption is that the incident and scattered acoustic fields propagate following straight ray paths from transmitter location $\mathbf{R}_n^t$ to the scatterer at $\mathbf{r}$ and from the scatterer to the receiver location $\mathbf{R}_m^r$. Depending upon the severity of the

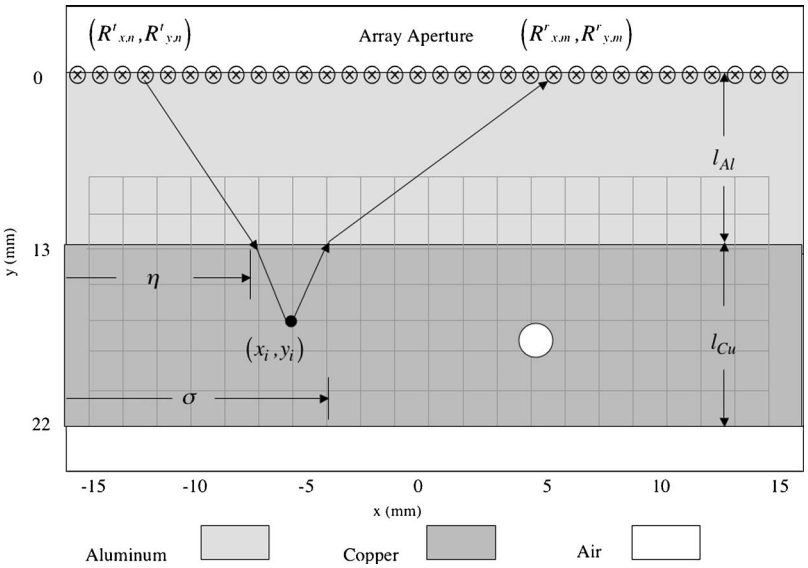

FIG. 2. The planar multilayered system. The grid locations correspond to the image reconstruction region. The finite difference time domain grid is much finer and not shown. The longitudinal sound speed and density of the system are defined where, c_{Al}=6.32 mm/us and ρ_{Al}=2.7 g/cm^3 are the longitudinal sound speed and density of aluminum respectively; and c_{Cu} =4.66 mm/us, ρ_{Cu}=8.98 g/cm^3, are the longitudinal sound speed and density of copper. The longitudinal sound speed and density of air is c_{air}=0.344 mm/us, ρ_{air}=0.012 gm/cm^3.

spatial velocity gradients, this assumption is often a very poor approximation. In this section, we will present a correction to the forward model given in Eq. (4) that utilizes Fermat's principle of least time.

Fermat's principle of least time selects the ray that minimizes the travel time between two locations. Let us consider an arbitrary path P denoted in this case by the vectors $(\mathbf{R}_n^t - \mathbf{r})$ and $(\mathbf{r} - \mathbf{R}_m^r)$. These vectors denote the path from the source to an arbitrary scatterer location, r and back to a receiver location. A typical source-scatter-receiver path is illustrated in Fig. 1. The travel time for this path is denoted as

$$\tau^p(s) = \int_P s(\mathbf{x}) dl^P, \tag{21}$$

with $\mathbf{x}$ describing the vector connecting the source-receiver pair through the scatterer at $\mathbf{r}$ and dl^P corresponding to an infinitesimal distance along path P. Fermat's principle states that the *correct* ray path is one that connects the source-scatter-receiver path with the minimum travel time. Stated another way, Fermat's principle stipulates that the travel time integral given by Eq. (21) is *stationary* with respect to variations in the source-scatter-receiver ray path.[13] Following from Fig. 1, the travel time between a given source-scatter-receiver path is

$$t^f_{m,n} = \min_{P_1 \in \text{Paths}} \left(\int_{P_1} s(x) dl^{P_1} \right) + \min_{P_2 \in \text{Paths}} \left(\int_{P_2} s(x) dl^{P_2} \right), \tag{22}$$

where P_1 is the path from transmitter $\mathbf{R}_n^t$ to scattering location $\mathbf{r}$, P_2 is the path from the scattering location to the receiver $\mathbf{R}_m^r$. The notation, $P_i \in$ paths, means that P is a member of the set of possible paths connecting the source-receiver pair. We will now apply this generalized formulation to a two-dimensional planar problem.

C. Two-dimensional aluminum-copper planar structure

Consider the planar multilayer geometry shown in Fig. 2. We assume that the aperture of the imaging array is located along the upper surface of layer 1, and that at each sensor location the transducer can act as either a transmitter or as a receiver of acoustic energy. As before, n, is the index number for a defined set of transmitters $(n=1, N_{src})$ and m, is the index number for a defined set of receivers $(m=1, N_{rcv})$. The planar geometry gives rise to the following set of functional equations. The first relates the time of flight from a transmitter location $[R^t_{x,n}, R^t_{y,n}]$ to a scatterer at location (x_i, y_i),

$$t^f_n(x_i, y_i) = \min_{\eta \in \text{Paths}} \left(\frac{[(\eta - R^t_{x,n})^2 + (l_{\text{Al}} - R^t_{y,n})^2]^{1/2}}{c_{\text{Al}}} + \frac{[(x_i - \eta)^2 + (y_i - l_{\text{Al}})^2]^{1/2}}{c_{\text{Cu}}} \right), \tag{23}$$

and the second relates the time of flight from the scatterer at (x_i, y_i), to a receiver at location $[R^r_{x,m}, R^r_{y,m}]$

$$t^f_m(x_i, y_i) = \min_{\sigma \in \text{Paths}} \left(\frac{[(x_i - \sigma)^2 + (y_i - l_{\text{Al}})^2]^{1/2}}{c_{\text{Cu}}} + \frac{[(l_{\text{Al}} - R^r_{y,m})^2 + (R^r_{x,m} - \sigma)^2]^{1/2}}{c_{\text{Al}}} \right). \tag{24}$$

Here the notation, $\eta \in$ paths refers to the set of all possible ray intersections from a transmitter location $[R^t_{x,n}, R^t_{y,n}]$, through the interface at l_{Al} to the location (x_i, y_j). Similarly, $\sigma \in$ paths refers to the set of all possible ray intersections from the location (x_i, y_j), through the interface at l_{Al} to a receiver located at $[R^r_{x,m}, R^r_{y,m}]$. The minimum total time between the source to the scattering location and then to the receiver is simply

$$t^f_{mn}(x_i, y_i) = t^f_n(x_i, y_i) + t^f_m(x_i, y_i) + T_d. \tag{25}$$

Equation (25) defines the variable velocity *minimum* travel time for our planar geometry, where the similarities to Eq. (12) are apparent.

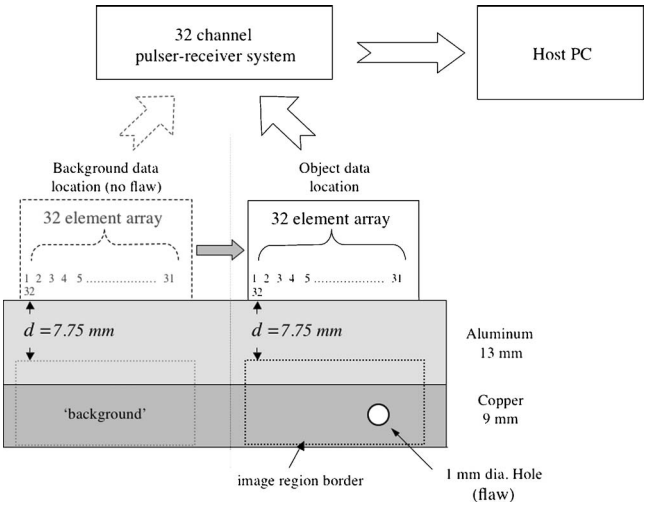

FIG. 3. Experimental setup and multi-channel data acquisition hardware.[11] Two separate multistatic data sets are obtained, a *background* scan and then an *object* scan. The background scan location is chosen in a region free of flaws. The object scan location is chosen such that the flaw is insonified by the imaging array.

III. EXPERIMENTAL AND NUMERICAL SIMULATION

The experimental data were collected using a computer controlled 32-channel pulser-receiver data acquisition system connected to a single 32-element 5 MHz ultrasonic array.[14] The system has the capability of transmitting arbitrary wave forms and receiving on all channels. The array was mounted on the upper surface of two-layer aluminum-copper test part. The aluminum layer was 13 mm thick; the copper layer was 9 mm thick. A "defect" in the form of a 1 mm hole was drilled into the copper layer such that the axis of the hole was parallel with the planar layer interfaces. A schematic of the test part and the array are shown in Fig. 3. Data sets were recorded in a full multistatic process whereby each source sequentially ensonified the medium with a broadband pulse centered at 5 MHz and the corresponding scattered field was recorded on all of the receivers. Following this procedure, one would obtain a three-dimensional data set comprising the sampled time record for all possible source and receiver locations. Mathematically this corresponds to data matrix A of the form $N_{src} \times N_{rcv} \times N_t$ where N_t, is the number of samples in the voltage time form, N_{src} are the number of transmitters and, N_{rcv}, is the number of receivers.

In addition to the experiment, a two-dimensional numerical simulation was performed to generate additional data sets for comparison. The simulation results were obtained using E3D, an explicit finite-difference time domain-code developed at Lawrence Livermore National Laboratory.[15–20] The code can simulate full wave scattering phenomena in elastic or coupled fluid-elastic systems in either two or three dimensions. The required input parameters are a longitudinal velocity distribution, a transverse velocity distribution, and a density distribution. The model is comprised of four layers, air, aluminum, copper, and air. The "defect" is an air filled circular region 1 mm in diameter in the copper layer. The numerical region and the material properties are listed in Fig. 2.

Simulations and the experiments used the same Gaussian windowed pulse shape,

$$u(t) = \sin(\omega_o t) e^{-t^2/(2\sigma^2)}, \tag{26}$$

where $\omega_o \neq 2\pi f_o$, $\sigma \neq N_{\text{cyc}}/\omega_o$ and N_{cyc} is the number of cycles in the pulse. We used $f_o = 5$ MHz and $N_{\text{cyc}} = 5$ cycles. For the experiment, this pulse is actually defined in terms of voltage. However, in the simulation, it is defined as a normal stress applied at a source location. A spectral comparison conducted on an experimental pulse measured in a simple pulse-echo geometry, and the corresponding simulated pressure pulse reveal only slight differences in their respective frequency content. We can assert, that the voltage-to-pressure transfer function is constant over the bandwidth of the applied pulse. Thus, normalized images created using numerical data and experimental data can be compared directly. All the experimental measurements were taken using the aforementioned 32-channel RDTech system. This custom hardware-software system allows for the individual control of each transducer element with arbitrary transmit-pulse capabilities. The transmit-receive array was designed to operate at 5 MHz with an element to element pitch of approximately 1 mm. The element height is 10 mm. Voltage-time records for each receive element can easily be recorded and stored as RF wave forms on the host PC. Reconstruction algorithms were conducted on a separate computer.

The reconstruction process requires a multistatic data set representing the *scattered* field in the elastic region of interest. Multistatic data refers to the process in which one element of the array acts as a transmitter to ensonify the test region. The return time-series signals (echoes) are subsequently recorded on *all* of the elements; this process is repeated at all of the transmit-receive locations. To that end, we began by recording a *background* data set. See Fig. 3. The *background* data can be obtained from an identical part, or a region on the same part, that is free of defects. (Recall, that because we are applying this algorithm as a nondestructive imaging technique we have access to *a priori* knowledge of the system without defects either through initial inspections or mechanical specifications.) For our purposes, the *background* data were obtained by locating the transducer array over a region of the aluminum-copper plate far enough away from the hole to eliminate any reflections. A complete multistatic background data set was recorded. The array was then moved to a region over the flaw, as shown in Fig. 3, and a second complete multistatic data set was recorded. This data set is referred to as the *object* data set. The complete multistatic *scattered* data set is then the difference between the *object* data set and the *background* data set. In a similar manner, numerical simulations of the multistatic data were generated for the *background* (no flaw) and *object* (flaw present) data sets.

IV. RESULTS

The resulting reconstructions using simulated and experimental data are shown in Figs. 4 and 5, respectively. The upper figure represents a map of the *modified* relative *com-*

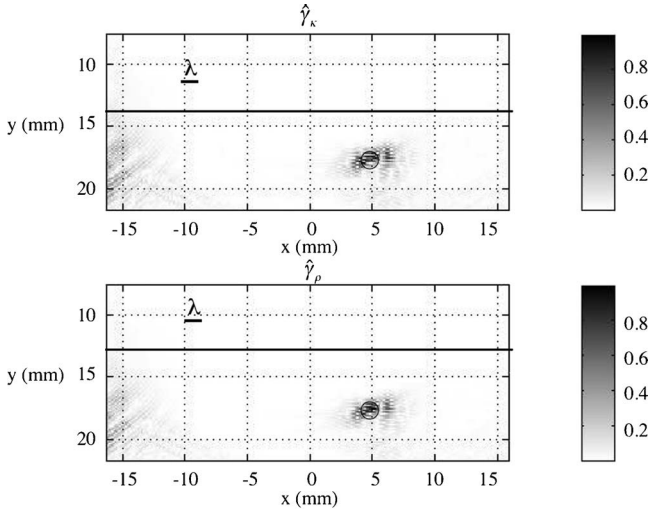

FIG. 4. Reconstructions of *simulated* data using the MTDI algorithm. Limited view aperture. The aluminum-copper interface and location of the hole are superimposed on the image for reference. The images clearly show the flaw correctly located in the copper layer. The λ metric is the wavelength of the field in the top aluminum layer at f_o=5 MHz.

pressibility ratio, while the lower figure represents a map of the *modified* relative *density* ratio [see Eqs. (6) and (7)] for the imaged region. The actual location of the aluminum-copper interface and the flaw are included for reference. The lambda metric is the wavelength in the aluminum layer at f_o=5 MHz.

The reconstruction of the simulated data clearly shows the flaw correctly located in the copper layer. The moderate haloing effect around the hole is a result of diffraction and shear wave effects in the immediate region surrounding the hole. The artifacts to the far left of the hole are a result of multiple reflections in the *scattered* field occurring in the aluminum and copper layers. Even with the subtraction process, which effectively removes the incident field and its multiples, the scattered field will become more complex with time reducing the quality of the reconstruction. The present algorithm does not take into account multipath scattering effects. However, if we limit the length of the time records used for the reconstruction to approximately the time of flight of a return arrival from the lower copper boundary, then these types of errors can be mitigated.

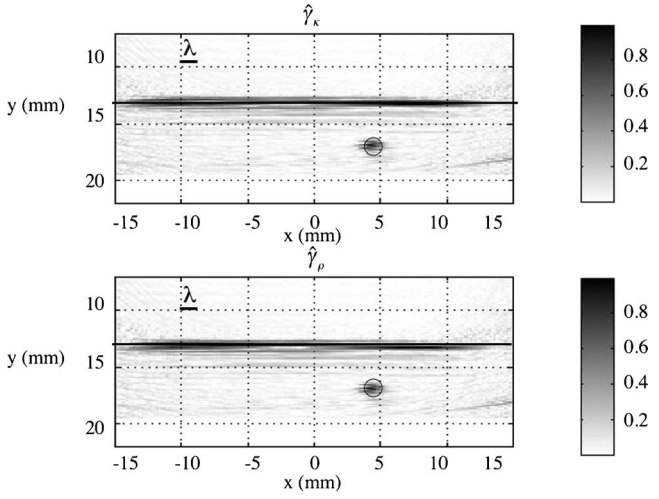

FIG. 5. Reconstructions of *experimental* data using the MTDI algorithm. Limited view aperture. The aluminum-copper interface and location of the hole are superimposed on the image. A strong indication of the interface between the aluminum and copper layers is also present. In this case the subtraction process did not remove the incident field completely. This could result from slight changes between the background data set and the object data set due to location and bond differences. The λ metric is the wavelength of the field in the top aluminum layer at f_o=5 MHz.

Reconstructions of the experimental data show a visible flaw, correctly located in the lower copper layer. A strong indication of the interface between the aluminum and copper layers is also present. In this case the subtraction process did not remove the incident field completely. This could result from slight changes between the background data set and the object data set due to location and bond differences. Note, that this type of effect could be included into the simulated data. In the actual part, the bond line between the aluminum and the copper has a finite thickness of approximately 0.003 in.(0.076 mm) and with significantly different acoustic impedance (Z_{epoxy}=3.2 mks Rayles, verses Z_{Al}=17 mks Rayles and Z_{Cu}=42 mks Rayles). A finite bond thickness is not accounted for in the reconstruction model. The experimental image contains more artifacts than the simulated image, owing to the systematic problems associated with subtracting the background data from the object data, random noise in the recorded data and part variability. Even with these issues, the images clearly show accurate localization and acceptable contrast of the flaw within the part geometry.

V. CONCLUSIONS

An algorithm has been developed for imaging and characterization of elastic structures that have high contrast gradients in either compressibility (velocity) and or density. Applying the standard monopole and dipole expansion terms of a long-wavelength acoustic scattering approximation, in conjunction with a concise matrix approach, we have obtained separate image maps corresponding to these monopole and dipole terms. A bent ray correction method utilizing Fermat's method of least time is incorporated into the forward model to accommodate ray-bending effects in the layered system. The method will also image any number of scatterer locations in the image region. The limit being the wavelength resolution and the discretization of all possible scatterer locations, (x_i, y_i), as defined in the image region. Future work will be directed towards developing a quantitative version of this algorithm where by the inversion generates reconstructions that are directly proportional to the mediums density and compressibility.

ACKNOWLEDGMENTS

The authors thank Dr. Jim Candy for use of his data acquisition system. This work was performed under the auspices of the U. S. Department of Energy by the University of California, Lawrence Livermore National Laboratory under Contract No.W-7405-48.

[1]A. C. Kak and M. Slaney, *Principles of Computerized Tomographic Imaging* (IEEE, New York, 1988).
[2]J. G. Berryman, "Stable iterative reconstruction algorithm for nonlinear

traveltime tomography," Inverse Probl. **6**, 21–42 (1990).
[3]S. A. Enright, S. M. Dale, V. A. Smith, R. D. Murch, and R. T. Bates, "Towards solving the bent-ray tomographic problem," Inverse Probl. **8**, 83–94 (1992).
[4]S. J. Norton, "Generation of separate density and compressibility images in tissue," Ultrason. Imaging **5**, 240–252 (1983).
[5]S. Mensah and J. P. Lefebvre, "Enhanced compressibility tomography," IEEE Trans. Ultrason. Ferroelectr. Freq. Control **44**, 1245–1252 (1997).
[6]J. P. Lefebvre, P. Recotillet, and P. Lasaygues, "NDE application of ultrasonic reflection tomography," *IEEE Ultrasonics Symposium Proceedings* (IEEE, New York, 1994), pp. 11289–11292.
[7]J. Gazdag and P. Sguazzero, "Migration of seismic data," *Proceedings of the IEEE* (IEEE, New York, 1984), pp. 1302–1351.
[8]M. Fatemi and A. C. Kak, "Ultrasonic b-scan imaging: Theory of image formation and a technique for restoration," Ultrason. Imaging **2**, 1–47 (1980).
[9]M. Kueger, V. Burow, K. M. Hiltawsky, and H. Everet, "Limited angle ultrasonic tomography of the compressed female breast," *IEEE Ultrasonics Symposium Proceedings* (IEEE, New York, 1998), pp. 1345–1348.
[10]S. K. Lehman and A. J. Devaney, "Transmission mode time-reversal super- resolution imaging," J. Acoust. Soc. Am. **113**, 2742–2753 (2003).
[11]J. A. Scales, *Theory of Seismic Imaging* (Samizdat Press, 1994, White River Junction, Vermont).
[12]P. M. Morse and K. U. Ingard, *Theoretical Acoustics* (Princeton University Press, Princeton, NJ, 1968).
[13]M. Born and E. Wolf, *Principles of Optics* (Pergamon, London, 1959), pp. 127–129.
[14]R/D Tech, TomoScan System, 4495, Wilfrid-Hamel Blvd., Québec (Québec), G1P2J7, Canada.
[15]A. R. Levendar, "Forth-order finite-difference p-sv seismograms," Geophysics **53**, 1425–1436 (1988).
[16]S. Larsen and J. Greiger, "Elastic modeling initiative, part III: 3-D computational modeling," *Proceedings of the 68th Ann. Internat. Mtg: of Soc. Expl. Geophys.*, 1803–1806 (1998).
[17]S. Larsen *et al.*, "3D simulations of scenario earthquakes in the San Francisco Bay Area," EOS Trans. Am. Geophys. Union **78**, 487 (1997).
[18]R. Madariaga, "Dynamics of an expanding circular fault," Bull. Seismol. Soc. Am. **66**, 639–666 (1976).
[19]J. Viriux, "P-SV wave propagation in heterogeneous media, Velocity-stress finite-difference method," Geophysics **51**, 889–901 (1986).
[20]S. Larsen and D. Harris, "Seismic wave propagation through a low-velocity nuclear rubble zone," Technical Report, Lawrence Livermore National Laboratory, Livermore, CA, 1993.

Time-reversal-based imaging and inverse scattering of multiply scattering point targets

Anthony J. Devaney, Edwin A. Marengo, and Fred K. Gruber
Department of Electrical and Computer Engineering, Northeastern University, Boston, Massachusetts 02115

(Received 17 September 2004; revised 17 July 2005; accepted 1 August 2005)

The treatment of time-reversal imaging of multiply scattering point targets developed by the present authors in Gruber *et al.* ["Time-reversal imaging with multiple signal classification considering multiple scattering between the targets," J. Acoust. Soc. Am., **115**, 3042–3047 (2004)] is reformulated and extended to the estimation of the target scattering strengths using the Foldy–Lax multiple scattering model. It is shown that the time-reversal multiple signal classification (MUSIC) pseudospectrum computed using the background Green function as the steering vector yields accurate estimates of the target locations, even in the presence of strong multiple scattering between the targets, and that the target scattering strengths are readily computed from the so-determined target locations using a nonlinear iterative algorithm. The paper includes computer simulations illustrating the theory and algorithms presented in the paper. © *2005 Acoustical Society of America.* [DOI: 10.1121/1.2042987]

PACS number(s): 43.60.Pt, 43.35.Zc [DRD] Pages: 3129–3138

I. INTRODUCTION

Wave field imaging methods based on the decomposition of the time-reversal operator ("D.O.R.T.") technique,[1–3] usually referred to as "time-reversal imaging," have been of interest for a number of years in connection with sonar, underwater communications, and medical and nondestructive testing applications.[4] One of these methods is the so-called time-reversal imaging with multiple signal classification (time-reversal MUSIC) method developed by Devaney[5] and Lev-Ari and Devaney[6] and elaborated further in Lehman and Devaney,[7] Prada and Thomas,[8] and Gruber *et al.*[9] A similar method has been investigated by Miwa and Arai.[10] Time-reversal MUSIC, like classical time-reversal imaging as performed using the D.O.R.T. method,[1–3] is designed to locate M point targets (representing scatterers that are small relative to the relevant wavelength) embedded in a rather arbitrary background medium from knowledge of the multistatic data matrix K of the collection of targets as measured by an active array of $N>M$ transceivers. Unlike the D.O.R.T. method, time-reversal MUSIC enables the super-resolved location of closely spaced targets[5–8] and is ideally suited for interrogation with sparse transceiver arrays.[5]

The vast majority of these developments have been established within the linear framework of the distorted wave Born approximation (DWBA),[11,12] which ignores multiple scattering between the targets, although the experimental results of Prada and Thomas[8] suggest the practicality of the technique, even for multiply scattering targets. The latter finding has been investigated theoretically in a more recent paper,[9] which shows how the time-reversal imaging with the MUSIC method can be generalized to incorporate multiple scattering between the targets. In that paper we employ the exact scattering formalism of the Neumann series to show that the same method actually holds, even if there is significant multiple scattering between the targets.

In the present paper, the treatment of time-reversal MUSIC for the location of multiply scattering point targets developed by Gruber *et al.*[9] is reformulated and extended to the estimation of the target scattering strengths using the Foldy–Lax multiple scattering model.[13–15] It is shown that even in the presence of strong multiple scattering, the time-reversal MUSIC pseudospectrum computed using the *background* Green function as a steering vector yields accurate estimates of the target locations, and that the target scattering strengths are readily computed from the so-determined target locations using a nonlinear iterative algorithm. The paper includes computer simulations illustrating the theory and algorithms presented in the paper. Unlike the numerical examples in Gruber *et al.*,[9] which focus on comparing the first-order (Born-approximated) versus the second-order (quadratic) scattering models, the present examples consider the full multiple scattering interactions between the targets as incorporated numerically via the Foldy–Lax equations.

II. FOLDY–LAX FORMULATION OF THE MULTIPLE SCATTERING PROBLEM

Consider a system of N acoustic or electromagnetic wave transceivers located at spatial positions $\boldsymbol{\alpha}_k$, $k=1,2,\ldots,N$ that interrogate a set of M point targets (scatterers) located at $\mathbf{x}_m$, $m=1,2,\ldots,M$. In the frequency domain, the field ψ_k generated by the interaction of the incident field $\psi_k^{(\mathrm{in})}$ generated by the kth transceiver element with the M point targets is given by the equation

$$\psi_k(\mathbf{r},\omega)=\psi_k^{(\mathrm{in})}(\mathbf{r},\omega)+\sum_{m=1}^{M}\tau_m(\omega)G_0(\mathbf{r},\mathbf{x}_m,\omega)\psi_k(\mathbf{x}_m,\omega), \tag{1}$$

where $\tau_m(\omega)$ is the scattering strength of the mth target and G_0 is the Green function corresponding to the background medium in which the targets are embedded. This Green

function will be referred to as *the background Green function*. Equation (1) is readily derived from the Lippman-Schwinger equation[11] in the special case of a set of M point scatterers. From this point on, we will work exclusively in the frequency domain and will no longer explicitly display the frequency ω, with the understanding that the results apply equally well to both narrow band and wide band applications.

Equation (1) applies at all space points except at the actual target locations $\mathbf{r}=\mathbf{x}_m$, where the background Green function is singular. At the target locations the "self-field" contribution is absorbed into the definition of the target scattering strengths τ_m and Eq. (1) is replaced by the so-called Foldy–Lax equations,[13–15]

$$\psi_k(\mathbf{x}_m) = \psi_k^{(\mathrm{in})}(\mathbf{x}_m) + \sum_{m' \neq m} \tau_{m'} G_0(\mathbf{x}_m, \mathbf{x}_{m'}) \psi_k(\mathbf{x}_{m'}). \tag{2}$$

If the incident field $\psi_k^{(\mathrm{in})}$, target locations $\mathbf{x}_m$, $m=1,\ldots,M$ and target scattering strengths τ_m, $m=1,\ldots,M$ are known, then the Foldy–Lax equations are a set of M coupled linear equations that can be solved for the field amplitudes $\psi_k(\mathbf{x}_m)$ at the target locations $\mathbf{x}_m$. Indeed, Eq. (2) can be expressed in the matrix form

$$H\Psi_k = \Psi_k^{(\mathrm{in})}, \tag{3}$$

where

$$\Psi_k = [\psi_k(\mathbf{x}_1), \psi_k(\mathbf{x}_2), \ldots, \psi_k(\mathbf{x}_M)]^T, \tag{4a}$$

$$\Psi_k^{(\mathrm{in})} = [\psi_k^{(\mathrm{in})}(\mathbf{x}_1), \psi_k^{(\mathrm{in})}(\mathbf{x}_2), \ldots, \psi_k^{(\mathrm{in})}(\mathbf{x}_M)]^T, \tag{4b}$$

are M-dimensional column vectors (where the superscript letter T denotes the transpose) whose elements are the total and incident field amplitudes, respectively, at the target locations, and where H is the $M \times M$ matrix whose diagonal elements are unity and whose off-diagonal elements are given by the product of the target scattering strengths with the background Green function evaluated at the target locations; in particular,

$$H_{m,m'} = \delta_{m,m'} - (1 - \delta_{m,m'}) \tau_{m'} G_0(\mathbf{x}_m, \mathbf{x}_{m'}). \tag{5}$$

The matrix equation, Eq. (3), clearly has a unique solution for any given incident wave and set of targets. Once the field strengths $\psi_k(\mathbf{x}_m)$ are computed at the various target locations the field can be evaluated at an arbitrary field point by using Eq. (1).

III. IMAGING AND INVERSE SCATTERING FROM THE MULTISTATIC DATA MATRIX

The imaging problem for point targets can be roughly defined to be that of forming an "image" of the distribution of target scattering centers $\mathbf{x}_m$, $m=1,2,\ldots,M$ from measurements of the fields $\psi_k(\mathbf{r})$, $k=1,2,\ldots,N$ generated in a suite of N scattering experiments that employ the set of incident fields $\psi_k^{(\mathrm{in})}$. The inverse scattering problem goes one step beyond the imaging problem and has as its goal the quantitative determination of *both* the target positions $\mathbf{x}_m$, $m=1,2,\ldots,M$ and the target scattering strengths τ_m, $m=1,2,\ldots,M$ from the available scattered field data. Of particular interest in this paper is the inverse scattering problem, but aspects of the associated imaging problem will be discussed as well. It is assumed that one knows the background Green function G_0 of the medium in which the targets are embedded. In the simplest case this is free space and G_0 is the well-known free space Green function, but the background medium can also be heterogeneous with possible sharp boundaries and reflecting surfaces.

In this work it is assumed that the field measurements are performed at the same set of N transceivers that are used to interrogate the targets; thus a "coincident" array is assumed. It is also assumed that the transceivers are all identical and small compared with the wavelength so that they can be approximated as point elements. Although these assumptions are not necessary, they simplify the discussion and do not severely limit the generality of the development. Under these conditions the incident waves $\psi_k^{(\mathrm{in})}(\mathbf{r})$, $k=1,2,\ldots,N$, due to unit-amplitude excitations, are equal to the background Green function $G_0(\mathbf{r},\mathbf{r}')$ evaluated for a source point $\mathbf{r}'=\boldsymbol{\alpha}_k$ at a transmitter location and the measured outputs from the set of transceivers are equal to the full Green function $G(\mathbf{r},\mathbf{r}')$ of the combined background plus the target medium for a source point $\mathbf{r}'=\boldsymbol{\alpha}_k$ at the kth transmitter location and a field point $\mathbf{r}=\boldsymbol{\alpha}_j$ at the jth receiver location. Within the present formulation the inverse scattering problem then reduces to that of deducing the target positions $\mathbf{x}_m$ and scattering strengths τ_m from knowledge of the full Green function specified at all transmitter/receiver pairs as well as of the background Green function $G_0(\mathbf{r},\mathbf{r}')$ at all pairs of points $(\mathbf{r},\mathbf{r}')$ within the background medium.

Under our assumption of point transceivers, Eqs. (1) and (2) become

$$G(\mathbf{r},\boldsymbol{\alpha}_k) = G_0(\mathbf{r},\boldsymbol{\alpha}_k) + \sum_{m=1}^{M} \tau_m G_0(\mathbf{r},\mathbf{x}_m) G(\mathbf{x}_m,\boldsymbol{\alpha}_k), \tag{6a}$$

$$G(\mathbf{x}_m,\boldsymbol{\alpha}_k) = G_0(\mathbf{x}_m,\boldsymbol{\alpha}_k) + \sum_{m' \neq m} \tau_{m'} G_0(\mathbf{x}_m,\mathbf{x}_{m'}) G(\mathbf{x}_{m'},\boldsymbol{\alpha}_k), \tag{6b}$$

where $G(\mathbf{r},\mathbf{r}')$ is the full Green function of the combined background plus target medium. The data for the inverse scattering problem are the outputs from the various transceivers, which, as discussed above, are simply the full Green function $G(\mathbf{r},\boldsymbol{\alpha}_k)$ evaluated at the transceiver locations $\mathbf{r}=\boldsymbol{\alpha}_j$, $j=1,2,\ldots,N$. However, since the background Green function G_0 is assumed known one can also regard the data for the inverse scattering problem to be the scattered field component of this Green function, which is the second term in Eq. (6a). This component of the Green function when evaluated between various transceiver elements is known as *the multistatic data matrix* and is given by the expression

$$K_{j,k} = G(\boldsymbol{\alpha}_j,\boldsymbol{\alpha}_k) - G_0(\boldsymbol{\alpha}_j,\boldsymbol{\alpha}_k) = \sum_{m=1}^{M} \tau_m G_0(\boldsymbol{\alpha}_j,\mathbf{x}_m) G(\mathbf{x}_m,\boldsymbol{\alpha}_k). \tag{7}$$

The inverse scattering problem then reduces to solving for the set of unknown target locations $\mathbf{x}_m$, $m=1,2,\ldots,M$ and

target scattering strengths τ_m, $m=1,2,\ldots,M$ given the background Green function G_0, the measured multistatic data matrix K, and the Foldy–Lax model, Eqs. (6).

Up to this point, care has been exercised in preserving the order of the two arguments of the background and the full Green functions. However, in the following, attention will be restricted to the usual case of *reciprocal media*, where the background and full Green functions obey the standard reciprocity conditions:

$$G_0(\mathbf{r},\mathbf{r}') = G_0(\mathbf{r}',\mathbf{r}), \quad G(\mathbf{r},\mathbf{r}') = G(\mathbf{r}',\mathbf{r}).$$

Reciprocity of the Green functions allows us to employ a standard form where the transceiver coordinates will always be placed *second* in the arguments of the Green functions. Thus, with this standard notation, Eq. (7) defining the multistatic data matrix can be expressed as

$$K_{j,k} = \sum_{m=1}^{M} \tau_m G_0(\mathbf{x}_m, \boldsymbol{\alpha}_j) G(\mathbf{x}_m, \boldsymbol{\alpha}_k). \tag{8}$$

Note for future reference that because of the reciprocity of the two Green functions the multistatic data matrix K is also symmetric, as can be verified readily using Eq. (7).

IV. IMAGING AND INVERSE SCATTERING WITHIN THE DISTORTED WAVE BORN APPROXIMATION

A standard approximation that is used in time-reversal studies is the DWBA. The DWBA ignores all multiple scattering between the various targets so that the Foldy–Lax equations (6) return the approximate solution,

$$G(\mathbf{x}_m, \boldsymbol{\alpha}_k) \approx G_0(\mathbf{x}_m, \boldsymbol{\alpha}_k),$$

which, when used in Eq. (8), yields the following approximate expression for the multistatic data matrix within the DWBA:

$$K_{j,k} \approx K^b_{j,k} = \sum_{m=1}^{M} \tau_m G_0(\mathbf{x}_m, \boldsymbol{\alpha}_j) G_0(\mathbf{x}_m, \boldsymbol{\alpha}_k), \tag{9}$$

where we have denoted the DWBA approximation of the multistatic data matrix by $K^b_{j,k}$. Within the DWBA the full Green function does not appear and the only unknowns are the target locations $\mathbf{x}_m, m=1,2,\ldots M$ and the target scattering strengths τ_m.

The DWBA approximation, Eq. (9), for the multistatic data matrix can be expressed in the matrix form

$$K^b = \sum_{m=1}^{M} \tau_m g_0(\mathbf{x}_m) g_0^T(\mathbf{x}_m), \tag{10}$$

where

$$g_0(\mathbf{x}) = [G_0(\mathbf{x}, \boldsymbol{\alpha}_1), G_0(\mathbf{x}, \boldsymbol{\alpha}_2), \ldots, G_0(\mathbf{x}, \boldsymbol{\alpha}_N)]^T \tag{11}$$

is *the background Green function vector* and $K^b = \{K^b_{j,k}\}$ is the DWBA approximation to the multistatic data matrix.

It was shown some time ago in a now classic paper[1] (see also Prada *et al.*[2] and Mordant *et al.*[3]) that within the DWBA the target locations $\mathbf{x}_m$ and target scattering strengths τ_m can be estimated from the multistatic data matrix as long as the number of targets is less than or equal to the number of transceiver elements ($M \leqslant N$) and the targets are "well resolved." This condition requires that the targets are sufficiently separated from each other that they can be "resolved" by the transceiver array.[1,5] In the case of well-resolved targets it was shown that within the DWBA there exists a one-to-one relationship between the individual targets and the singular vectors and singular values of the multistatic data matrix. Moreover, in this case the locations of the individual targets can be determined by forming "time-reversal images" from the singular vectors associated to nonzero singular values using the background Green function and the target scattering strengths can be determined from the set of singular values. Unfortunately, this imaging approach fails (in the sense of not yielding selective focusing) if the targets are not "well resolved," as will be the case, for example, if the targets are not well separated from each other. In this case strong multiple scattering will exist between the various targets and the DWBA will not even be valid.

A. Time-reversal MUSIC within the DWBA

The "well-resolved" requirement of the original time-reversal imaging method can be removed if instead of forming estimates of the target locations using time-reversal imaging a generalized MUSIC algorithm is employed.[5–8] In this approach the singular vectors and singular values of the multistatic data matrix are still employed as in standard time-reversal imaging,[1] but the singular vectors associated to zero singular values are now used in the image formation process rather than the singular vectors associated with nonzero singular values, as are used in standard time-reversal imaging. As mentioned earlier, the latter method requires that $M \leqslant N$ (the number of targets be less than or equal to the number of transceiver elements) and that the targets be well resolved. The time-reversal MUSIC scheme does not require that the targets be well resolved, but it does require that the number of targets be *less* than the number of transceiver elements ($M < N$). In fact, as also mentioned earlier, this holds, even in the presence of multiple scattering, as shown in Prada and Thomas[8] and in a contribution coauthored by the current authors.[9] These early results are explained next from an alternative perspective based on the Foldy–Lax model, including the associated estimation of the target scattering amplitudes that was not considered in those papers.

Both the D.O.R.T. method[1–3] as well as the time-reversal MUSIC method are based on the singular value decomposition (SVD) of the K matrix that we write in the form

$$K v_p = \sigma_p u_p, \quad K^\dagger u_p = \sigma_p v_p, \tag{12a}$$

$$K = \sum_{p=1}^{N} \sigma_p u_p v_p^\dagger. \tag{12b}$$

It is clear from Eq. (10) that within the DWBA the multistatic data matrix K maps C^N, the vector space of complex N-tuples, to the subspace $\mathcal{S}_0 = \mathrm{Span}\{g_0(\mathbf{x}_m), m=1,2,\ldots,M\} \subseteq C^N$ spanned by the background Green function vectors evaluated at the scatterer locations $\mathbf{x}_m$. It was shown by Devaney[5] that except in certain special and unusual remote sensing geometries and as long as $M \leqslant N$, the

background Green function vectors form a linearly independent set so that $\{g_0(\mathbf{x}_m), m=1,2,\ldots,M\}$ forms a basis for $\mathcal{S}_0$. On the other hand, it follows from Eq. (12b) that $\mathcal{S}_0 = \mathrm{Span}\{u_p, \sigma_p > 0\}$. Moreover, since $\mathcal{S}_0 = \mathrm{Span}\{u_p, \sigma_p > 0\} \perp \mathcal{N}_0 = \mathrm{Span}\{u_p, \sigma_p = 0\}$ and $\{g_0(\mathbf{x}_m), m=1,2,\ldots,M\}$ is also a basis for $\mathcal{S}_0$, it then follows that

$$u_p^\dagger g_0(\mathbf{x}_m) = 0, \quad \sigma_p = 0. \tag{13}$$

The locations of the scatterers can then be determined from the time-reversal MUSIC pseudo-spectrum,

$$\Phi(\mathbf{x}) = \frac{1}{\sum_{\sigma_p=0} |u_p^\dagger g_0(\mathbf{x})|^2}, \tag{14a}$$

which will peak (ideally to infinity) when $\mathbf{x}=\mathbf{x}_m, m=1,2,\ldots,M$. Thus, the target (scatterer) location within the DWBA reduces to finding the maxima of the pseudospectrum defined in Eq. (14a), generated using the background Green function vector $g_0(\mathbf{x})$ as a steering vector.

Since the multistatic data matrix is symmetric, it follows that $v_p = u_p^*$, so that the pseudospectrum can also be written in the alternative form

$$\Phi(\mathbf{x}) = \frac{1}{\sum_{\sigma_p=0} |v_p^\dagger g_0^*(\mathbf{x}_m)|^2}. \tag{14b}$$

Note also that time-reversal MUSIC will fail if the "noise subspace" $\mathcal{N}_0 = \mathrm{Span}\{u_p, \sigma_p = 0\}$ is empty. This will occur if the rank of the K matrix is equal to the number of transceivers N that will occur if $M \geqslant N$. Thus, generally, time-reversal MUSIC requires that $M < N$.

It is worth emphasizing that the above analysis has been based on the DWBA and should not be expected to be valid in the presence of strong multiple scattering, where the DWBA approximation, Eq. (9), will fail. In this latter case there is no reason to believe from the above development that the pseudospectra in Eqs. (14), when computed using the singular system $\{u_p, v_p, \sigma_p\}$ of the exact (e.g., measured) multistatic data matrix as defined in Eq. (8) together with the background Green function vector as a steering vector, will peak at the correct scatterer locations. Amazingly, as suggested in Prada and Thomas[8] and as shown in Gruber *et al.*[9] and in the following section, these pseudospectra actually do apply even when computed using exact scattering data.

B. Scattering strength computation within the DWBA

Equation (9) for the multistatic data matrix within the DWBA can be regarded as a matrix equation relating the unknown scattering coefficients τ_m to the observed values of $K_{j,k}$ expressed as an N^2 long column vector as follows:

$$\overbrace{[K_{j,k}]}^{N^2\times 1} = \overbrace{[G_0(\mathbf{x}_m, \boldsymbol{\alpha}_j) G_0(\mathbf{x}_m, \boldsymbol{\alpha}_k)]}^{N^2\times M} \overbrace{[\tau_m]}^{M\times 1}, \tag{15}$$

where $[K_{j,k}] = [K_{1,1}, K_{1,2}, \ldots, K_{N,N}]^T$, $[\tau_m] = [\tau_1, \tau_2, \ldots, \tau_M]^T$ and

$$[G_0(\mathbf{x}_m, \boldsymbol{\alpha}_j) G_0(\mathbf{x}_m, \boldsymbol{\alpha}_k)] = \begin{bmatrix} G_0(\mathbf{x}_1, \boldsymbol{\alpha}_1) G_0(\mathbf{x}_1, \boldsymbol{\alpha}_1) & \cdots & G_0(\mathbf{x}_M, \boldsymbol{\alpha}_1) G_0(\mathbf{x}_M, \boldsymbol{\alpha}_1) \\ G_0(\mathbf{x}_1, \boldsymbol{\alpha}_1) G_0(\mathbf{x}_1, \boldsymbol{\alpha}_2) & \cdots & G_0(\mathbf{x}_M, \boldsymbol{\alpha}_1) G_0(\mathbf{x}_M, \boldsymbol{\alpha}_2) \\ \vdots & \vdots & \vdots \\ G_0(\mathbf{x}_1, \boldsymbol{\alpha}_N) G_0(\mathbf{x}_1, \boldsymbol{\alpha}_N) & \cdots & G_0(\mathbf{x}_M, \boldsymbol{\alpha}_N) G_0(\mathbf{x}_M, \boldsymbol{\alpha}_N) \end{bmatrix}.$$

Since the values of the target locations $\mathbf{x}_m$ and background Green functions are known, using, for example, the time-reversal MUSIC algorithm described in the previous section, a least squares solution of Eq. (15) will yield the $M < N$ scattering coefficients τ_m. Because the DWBA model is only approximate and because there will always be some noise sources in the measurement process, the fact that Eq. (15) is overdetermined and requires a least squares solution is a desirable property of the inversion process.

V. IMAGING AND INVERSE SCATTERING IN THE PRESENCE OF MULTIPLE SCATTERING

In the case where multiple scattering between the point targets becomes important, the DWBA can no longer be employed and the coupled set of Eqs.(6) must be employed in the imaging and inverse scattering problems. Remarkably, as shown in Gruber *et al.*[9] *the time-reversal MUSIC algorithm established in the preceding section can still be employed to determine the target locations* $\mathbf{x}_m$. In Gruber *et al.*[9] this conclusion was reached within the exact scattering formalism of the Neumann series using the fact that the multistatic data matrix K is symmetric even in the presence of multiple scattering between the targets. Here, a different approach is employed to establishing this result that has the advantage of adding insight into the estimation process. This approach also has the advantage that it can be generalized to cases of non-coincident transceiver arrays for which the multistatic data matrix is not symmetric so that the treatment employed in Gruber *et al.*[9] is not applicable.

A. Time-reversal MUSIC in the presence of multiple scattering

The exact expression, Eq. (8), for the multistatic data matrix, including multiple scattering between the set of point scatterers, can be expressed in the form

$$K = \sum_{m=1}^{M} \tau_m g_0(\mathbf{x}_m) g^T(\mathbf{x}_m), \tag{16}$$

where g_0 is the background Green function vector defined in Eq. (11) and g is *the total Green function vector*, defined as

$$g(\mathbf{x}) = [G(\mathbf{x}, \boldsymbol{\alpha}_1), G(\mathbf{x}, \boldsymbol{\alpha}_2), \ldots, G(\mathbf{x}, \boldsymbol{\alpha}_N)]^T. \tag{17}$$

It is clear from Eq. (16) that, as was the case within the DWBA, the exact scattering model for K maps C^N to the M-dimensional subspace $\mathcal{S}_0 = \mathrm{Span}\{g_0(\mathbf{x}_m), m=1,2,\ldots,M < N\} \subset C^N$ spanned by the background Green function vectors evaluated at the scatterer locations and that this set of Green function vectors forms a basis as long as $M < N$. On the other-hand, unlike the DWBA approximation, the adjoint $K^\dagger$ maps C^N to the M-dimensional subspace $\mathcal{S} = \mathrm{Span}\{g^*(\mathbf{x}_m), m=1,2,\ldots,M\} \subset C^N$ spanned by the full

Green function vectors again evaluated at the scatterer locations rather than the background Green function vectors evaluated at these locations. If one again makes use of the SVD of the K matrix via Eqs. (12), then it is apparent that $\mathcal{S}_0=\mathrm{Span}\{u_p,\sigma_p>0\}$ and that $\mathcal{S}=\mathrm{Span}\{v_p,\sigma_p>0\}$. Moreover, since $\mathcal{S}_0=\mathrm{Span}\{u_p,\sigma_p>0\}\perp\mathcal{N}_0=\mathrm{Span}\{u_p,\sigma_p=0\}$ and $\mathcal{S}=\mathrm{Span}\{v_p,\sigma_p>0\}\perp\mathcal{N}=\mathrm{Span}\{v_p,\sigma_p=0\}$ it then follows that

$$u_p^\dagger g_0(\mathbf{x}_m)=0, \quad \text{if } \sigma_p=0, \tag{18a}$$

$$v_p^\dagger g^*(\mathbf{x}_m)=0, \quad \text{if } \sigma_p=0. \tag{18b}$$

Equations (18) then lead to the two time-reversal MUSIC pseudospectra

$$\Phi_1(\mathbf{x})=\frac{1}{\sum_{\sigma_p=0}|u_p^\dagger g_0(\mathbf{x})|^2}, \tag{19a}$$

$$\Phi_2(\mathbf{x})=\frac{1}{\sum_{\sigma_p=0}|v_p^\dagger g^*(\mathbf{x})|^2}, \tag{19b}$$

whose peaks (pole) locations theoretically yield the sought after target locations.

The pseudospectrum Φ_1 is quite remarkable, in that it is functionally identical to the DWBA pseudospectrum defined in Eq. (14a). This, of course, means that even in the presence of multiple scattering, the target locations can still be determined knowing only the background Green function rather than the full (unknown) Green function. This is precisely the result obtained in Gruber *et al.*[9] by using the fact that the multistatic data matrix is symmetric, even in the presence of multiple scattering due to the reciprocity of the full and background Green functions. Also, as mentioned by Gruber *et al.*,[9] this result is independent of the specific multiple scattering model and depends only on the assumption of a point scattering model of the form given in Eq. (6a) and the assumed reciprocity of the full and background Green functions. By this we mean that the result does not depend on the use of the Foldy–Lax model. Indeed, in Gruber *et al.*[9] the Neumann expansion was employed as the multiple scattering model.

The pseudospectrum Φ_2 uses the full Green function vector as a steering vector and although it will peak at the same target locations as Φ_1, the two pseudospectra will generally be different; e.g., will have a different lobe structure. Also, we note that since the K matrix is symmetric, even in the presence of multiple scattering, it follows that $v_p=u_p^*$, so that $|u_p^\dagger g_0|=|v_p^T g_0|=|v_p^\dagger g_0^*|$, so that the pseudospectrum Φ_1 is, in fact, identical to the other form of the DWBA pseudospectrum given in Eq. (14b). This alternate form for Φ_1 coincides with Φ_2 under the replacement of the full Green function vector with the background Green function vector.

It is interesting to note that the pseudospectrum $\Phi_1\equiv\Phi$ computed using either DWBA or exact (multiple scattering) data will be identical. To see this we represent the singular system computed using the DWBA model, Eq. (10), by $\{u_p^b,v_p^b,\sigma_p^b\}$ and the system generated using the exact multiple scattering model Eq. (16) by the usual $\{u_p,v_p,\sigma_p\}$. Now the subspaces spanned by both sets of singular vectors $u_p^b,\sigma_p^b>0$ and $u_p,\sigma_p>0$ are identical since they are both equal to $\mathcal{S}_0=\mathrm{Span}\{g_0(\mathbf{x}_m),m=1,2,\ldots,M\}\subset C^N$. From this it follows from Parseval's theorem that

$$\sum_{\sigma_p^b=0}|u_p^{b\dagger}g_0(\mathbf{x})|^2=\sum_{\sigma_p=0}|u_p^\dagger g_0(\mathbf{x})|^2,$$

from which it follows that the pseudospectra computed from either DWBA or exact scattering data are precisely the same.

B. Scattering strength computation in the presence of multiple scattering

In analogy with what was done in the case of the DWBA, one can express the exact multistatic data matrix, Eq. (16), in the form of Eq. (15) where, however, the matrix $[G_0(\mathbf{x}_m,\boldsymbol{\alpha}_j)G_0(\mathbf{x}_m,\boldsymbol{\alpha}_k)]$ is replaced by the matrix

$$[G_0(\mathbf{x}_m,\boldsymbol{\alpha}_j)G(\mathbf{x}_m,\boldsymbol{\alpha}_k)]=\begin{bmatrix} G_0(\mathbf{x}_1,\boldsymbol{\alpha}_1)G(\mathbf{x}_1,\boldsymbol{\alpha}_1) & \cdots & G_0(\mathbf{x}_M,\boldsymbol{\alpha}_1)G(\mathbf{x}_M,\boldsymbol{\alpha}_1) \\ G_0(\mathbf{x}_1,\boldsymbol{\alpha}_1)G(\mathbf{x}_1,\boldsymbol{\alpha}_2) & \cdots & G_0(\mathbf{x}_M,\boldsymbol{\alpha}_1)G(\mathbf{x}_M,\boldsymbol{\alpha}_2) \\ \vdots & \vdots & \vdots \\ G_0(\mathbf{x}_1,\boldsymbol{\alpha}_N)G(\mathbf{x}_1,\boldsymbol{\alpha}_N) & \cdots & G_0(\mathbf{x}_M,\boldsymbol{\alpha}_N)G(\mathbf{x}_M,\boldsymbol{\alpha}_N) \end{bmatrix}.$$

In the case of the DWBA, the matrix equation, Eq. (15), only involved the (known via MUSIC) target locations $\mathbf{x}_m$ and known background Green function G_0 and, hence, was least squares invertible. In the multiple scattering case this equation contains the full Green function $G(\mathbf{x}_m,\boldsymbol{\alpha}_k)$, which is unknown and must also be determined in the inversion process. Moreover, in this case the set of equations (15) are no longer linear, in that products of the two sets of unknowns (full Green function and scattering strengths) appear in the equations.

Besides being related by the modified form of Eq. (15), the scattering strengths and full Green function are coupled by the Foldy–Lax equations, which are written in matrix form for general transceivers in Eq. (3). For the special case of point tranceivers under consideration here, this set of equations still applies with the following definitions of the column vectors Ψ_k and $\Psi_k^{(\mathrm{in})}$:

$$\Psi_k=[G(\mathbf{x}_1,\boldsymbol{\alpha}_k),G(\mathbf{x}_2,\boldsymbol{\alpha}_k),\ldots,G(\mathbf{x}_M,\boldsymbol{\alpha}_k)]^T, \tag{20a}$$

$$\Psi_k^{(\mathrm{in})}=[G_0(\mathbf{x}_1,\boldsymbol{\alpha}_k),G_0(\mathbf{x}_2,\boldsymbol{\alpha}_k),\ldots,G_0(\mathbf{x}_M,\boldsymbol{\alpha}_k)]^T, \tag{20b}$$

and where the $M\times M$ matrix H is still defined according to Eq. (5) that we reproduce here for clarity:

$$H_{m,m'}=\delta_{m,m'}-(1-\delta_{m,m'})\tau_{m'}G_0(\mathbf{x}_m,\mathbf{x}_{m'}).$$

Equation (3), with Ψ_k and $\Psi_k^{(\mathrm{in})}$ defined as above, can be expressed in the shortened form

$$H[G(\mathbf{x}_m,\boldsymbol{\alpha}_k)]=[G_0(\mathbf{x}_m,\boldsymbol{\alpha}_k)], \quad k=1,2,\ldots,N, \tag{21}$$

where $[G(\mathbf{x}_m,\boldsymbol{\alpha}_k)]$ and $[G_0(\mathbf{x}_m,\boldsymbol{\alpha}_k)]$ are the column vectors defined in Eqs. (20).

C. Iterative inversion

Equations (15) (with $[G_0(\mathbf{x}_m,\boldsymbol{\alpha}_j)G_0(\mathbf{x}_m,\boldsymbol{\alpha}_k)]$ replaced by $[G_0(\mathbf{x}_m,\boldsymbol{\alpha}_j)G(\mathbf{x}_m,\boldsymbol{\alpha}_k)]$) and (21) are a set of coupled nonlinear equations that can be solved via iteration for the scattering strengths τ_m and the full Green functions $G(\mathbf{x}_m,\boldsymbol{\alpha}_k)$. In particular, consider next a sequence $\{G^{(n)}(\mathbf{x}_m,\boldsymbol{\alpha}_k)\}, n=0,1,\ldots$, of estimated Green functions and a sequence of $\{\tau_m^{(n)}\}, n=1,2,\ldots$, of estimated scattering strengths, where the target locations are first computed using the MUSIC pseudospectrum Φ defined in Eqs. (14a) or (14b), and the iteration begins with the DWBA estimate for the Green function; i.e., $G^{(0)}(\mathbf{x}_m,\boldsymbol{\alpha}_k)=G_0(\mathbf{x}_m,\boldsymbol{\alpha}_k)$. The iteration then proceeds to compute the sequence of scattering strength estimates and Green function estimates using the following set of equations:

$$[K_{j,k}]=[G_0(\mathbf{x}_m,\boldsymbol{\alpha}_j)G^{(n)}(\mathbf{x}_m,\boldsymbol{\alpha}_k)][\tau_m^{(n+1)}], \tag{22a}$$

$$H^{(n+1)}=\delta_{m,m'}-(1-\delta_{m,m'})\tau_{m'}^{(n+1)}G_0(\mathbf{x}_m,\mathbf{x}_{m'}), \tag{22b}$$

$$H^{(n+1)}[G^{(n+1)}(\mathbf{x}_m,\boldsymbol{\alpha}_k)]=[G_0(\mathbf{x}_m,\boldsymbol{\alpha}_k)]. \tag{22c}$$

The above iteration scheme has been implemented in MATLAB and employed in simplified examples presented in the following section. In the absence of noise and perfect data it works perfectly, as expected, but experiences convergence problems in cases of closely clustered targets separated by less than a few wavelengths in the presence of additive noise and/or error in the target location estimates. The convergence properties of the iteration scheme will not be discussed in this paper. The interested reader is instead referred to standard treatments of such schemes that are available in the literature.[16–18]

VI. COMPUTER SIMULATIONS

In this section we present the results of a MATLAB simulation study of two-dimensional scattering from a set of $M=4$ point scatterers embedded in free space and being interrogated by a set of $N=7$ coincident point transceivers. A basic image grid was employed involving quarter-wavelength ($\lambda/4$) spacing with 256 points along the horizontal (x) axis corresponding to spatial locations varying from $x=-32\lambda$ to $x=32\lambda$ and 128 points along the vertical (z) axis corresponding to spatial locations varying from $z=0$ to $z=-32\lambda$. The transceiver array was a uniform linear array having six λ element-element separation and was centered along the x axis at the top of the image grid (at $z=0$). The four targets were located at positions $(-2.25,-14.75)$, $(-0.25,-14.75)$, $(0.75,-15.75)$, and $(2.75,-15.75)$, all in units of a wavelength. Unit-amplitude target scattering strengths were chosen for all targets, i.e., $\tau_m=1$, $m=1,2,3,4$, and the targets were placed sufficiently close to each other so as to simulate conditions involving strong multiple scattering between the targets.

The scattering data in the form of the multistatic data matrix $K=\{K_{j,k}\}$, $j,k=1,2,\ldots,7$ were computed according to Eq. (8) with the background Green function,

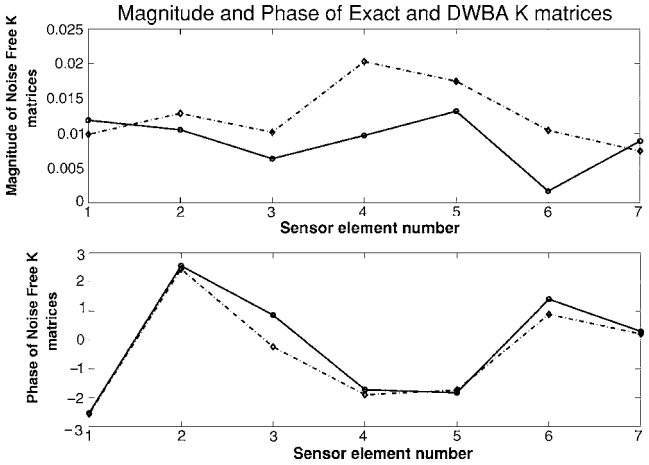

FIG. 1. Plots of the magnitude and phase of the third column of the multistatic data matrix K computed using the DWBA and the Foldy-Lax multiple scattering models.

$$G_0(\mathbf{x}_m,\boldsymbol{\alpha}_j)=\frac{i}{4}H_0(k_0|\mathbf{x_m}-\boldsymbol{\alpha}_j|),$$

where H_0 is the zeroth-order Hankel function of the first kind and $k_0=2\pi/\lambda$ is the free space wave number. The full Green function $G(\mathbf{x}_m,\boldsymbol{\alpha}_k)$ appearing in the expression for the multistatic data matrix was computed using the Foldy–Lax equations (6b) for the specified set of scatterer locations $\mathbf{x}_m$ and scattering strengths τ_m with $m=1,2,3,4$. The Foldy–Lax equations were solved directly via the matrix equation (21). In the first simulation we also computed, for comparison purposes, DWBA data, where the free space Green function $G_0(\mathbf{x}_m,\boldsymbol{\alpha}_k)$ was employed in place of the full Green function in the computation of the multistatic data matrix.

A. Comparison of time-reversal MUSIC using noise free DWBA and multiple scattering data

The first simulation examined the effect of multiple scattering on scatterer location estimation and scatterer strength estimation using noise-free (perfect) simulated data and the generalized MUSIC algorithm. Figure 1 shows plots of the third column of the multistatic data matrices computed using the DWBA approximation and the Foldy–Lax multiple scattering model. It is apparent from the figure that the two data matrices differ significantly, indicating the presence of strong multiple scattering between the various point scatterers.

The SVDs of the two data matrices shown in Fig. 1 were employed to generate two pseudospectra across the basic image grid of 256×128 points using quarter-wavelength spacing. These spectra were also interpolated (using a standard MATLAB command) over a small region centered within the target region using $\lambda/40$ spacing. The pseudospectra have large amplitudes in the immediate vicinity of the transceiver array so that we only employ and plot these quantities over a 256×122 grid that is displaced by two wavelengths in the vertical (z) direction from the transceiver array. Mesh plots of the two pseudospectra are shown in Fig. 2, where in the top of the figure we show the raw pseudospectra displayed over the 256×122 grid with $\lambda/4$ spacing and in the bottom the interpolated quantities using $\lambda/40$ spacing. It is clear

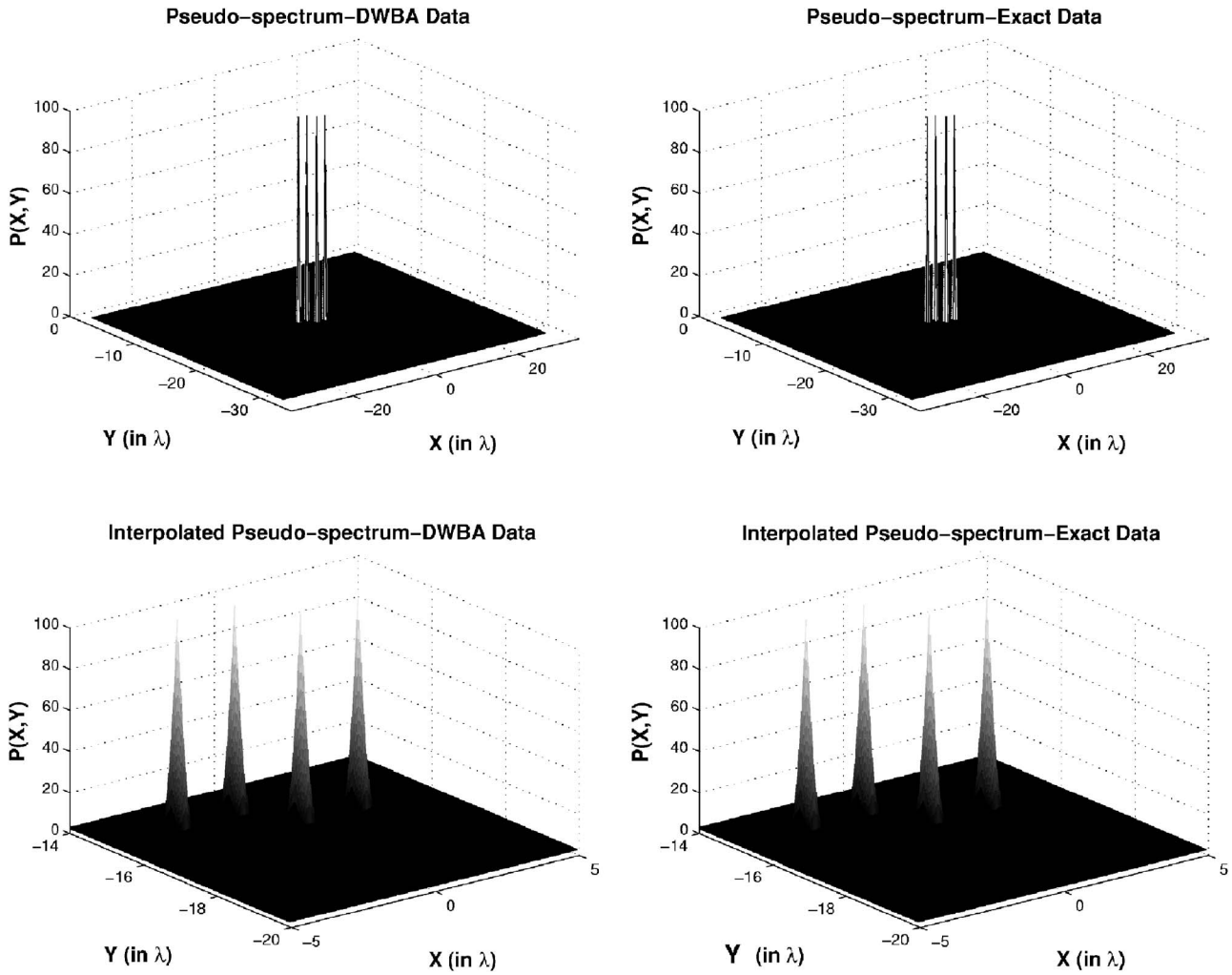

FIG. 2. Mesh plots of the noise-free time-reversal MUSIC pseudospectra for the DWBA (left) and Foldy–Lax model (right) cases. The upper plots correspond to the raw data while the lower plots correspond to the MATLAB-interpolated data. The positions of the peaks in these pseudospectra coincide exactly with the target locations, as desired.

from the figure that the two pseudospectra are virtually identical, as required by the theory presented in Sec. V. An actual numerical comparison of these two pseudospectra shows them to be the same to within 11 decimal places.

The noise-free data described above was used to estimate the scatterer locations $\mathbf{x}_m$ and scattering strengths τ_m using both the DWBA algorithm, Eq. (15), and the iterative algorithm described in Sec. V. The scatterer locations were determined by a simple grid search for maxima of the pseudospectra illustrated in Fig. 2 and were found to yield exact target location estimates. These locations were then input into both the DWBA and exact inversion algorithms to generate estimates $\hat{\boldsymbol{\tau}}$ of the scattering strength vector $\boldsymbol{\tau} = [1,1,1,1]$. The accuracy of the estimates was quantified by using a normalized percent error, defined by

$$E = 100 * \frac{\|\hat{\boldsymbol{\tau}} - \boldsymbol{\tau}\|}{\|\boldsymbol{\tau}\|},$$

where $\|x\|$ is the usual $L2$ norm of the vector x. The DWBA inversion algorithm applied to DWBA data and the iterative exact algorithm applied to multiple scattering data both returned essentially exact estimates of the $\boldsymbol{\tau}$ vector. On the other hand, the DWBA inversion algorithm applied to the multiple scattering data returned an estimate having a 32% error. Other runs of the simulation code using differing choices of the scatterer locations and transceiver element separations yielded similar results.

B. Time-reversal MUSIC performance in the presence of additive noise

To determine the effect of additive noise on the scatterer location and strength estimation algorithms we added complex additive white Gaussian noise (AWGN) to the multiple scattering data and performed the same estimation procedures employed in the above example. In this and the later examples we employed only multiple scattering data since the noise-free simulation results presented above clearly demonstrate the inadequacy of the DWBA data model for this particular scattering configuration. The signal model was of the form

$$\hat{K} = K + \mathcal{N},$$

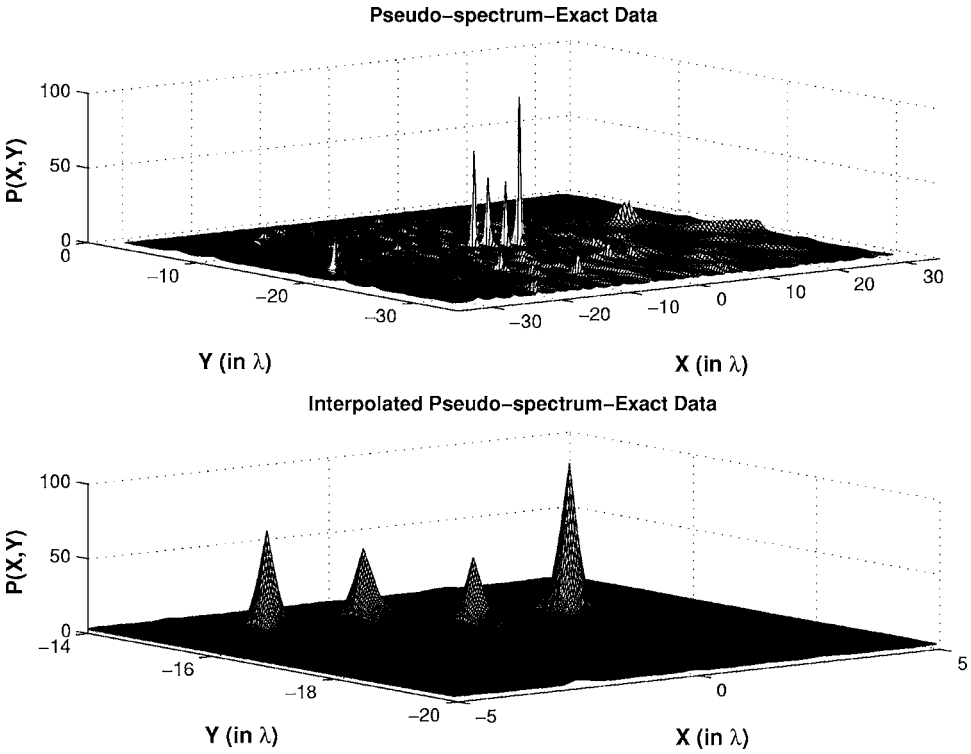

FIG. 3. Mesh plots of the time-reversal MUSIC pseudospectrum computed from noisy multiple scattering data with AWGN yielding a signal-to-noise ratio of about 25 dB. The positions of the peaks in the pseudospectrum coincide exactly with the target locations, as desired, despite the presence of additive noise.

where K is the noise-free multiple scattering multistatic data matrix and $\mathcal{N}$ is an uncorrelated, zero mean complex Gaussian process (AWGN). The noise level was quantified by the usual signal-to-noise ratio in dB defined according to the equation

$$S/N = 20 \log_{10} \frac{\|K\|}{\|\mathcal{N}\|}.$$

Figure 3 shows the pseudospectrum computed from a single realization of noisy data having a signal-to-noise ratio of roughly 25 dB. The plot on the top of the figure is displayed over the 256×122 image grid using $\lambda/4$ spacing while the plot displayed in the bottom is of the interpolated pseudospectrum using $\lambda/40$ spacing. The effect of the noise is evident from the raw pseudospectrum in the form of spurious maxima surrounding the maxima due to the scatterer locations. The scatterer locations as estimated from the raw pseudospectrum had an error of less than a tenth of one percent, even in the presence of the additive noise. The DWBA and multiple scattering-based iterative inversion algorithms were employed to estimate the scattering amplitudes $\tau_m, m = 1,2,3,4$, yielding errors of 33.7% and 1.76%, respectively. Different noise realizations having similar signal-to-noise ratios yielded comparable results.

As a final example, a Monte Carlo simulation was ran where the Foldy–Lax multiple scattering data was subjected to zero mean AWGN. This noisy data was then used to estimate the target locations using the raw (noninterpolated) MUSIC pseudospectrum and these location estimates were then employed in the DWBA and multiple scattering-based iterative inversion algorithms to estimate the scattering amplitudes $\tau_m, m = 1,2,3,4$. A thousand noise realizations were considered for each of ten noise variances and, for each noise variance, the resulting signal-to-noise ratios and target location and scattering strength error estimates were averaged over the number of noise realizations.

The results of the Monte Carlo simulation are shown in Fig. 4. It is seen from the figure that there is a high degree of correlation between the location error estimates shown in the upper left-hand portion of the figure and the DWBA and multiple scattering inversion algorithm errors shown in the upper right- and lower left-hand portions of the figure, respectively. The raw (noninterpolated) pseudospectrum and a simple grid search algorithm were used in obtaining the location estimates. One should expect us to obtain better results using the interpolated pseudospectra and a more refined search algorithm. Improved location error estimates translate directly into improved coefficient estimates as is clear from the figure.

Finally, we wish to mention that, unlike conventional MUSIC that depends on having several statistical signal realizations, the present approach can handle the worst-case scenario of a single realization or snapshot (single snapshot data) as has been, in fact, the focus in the examples above. The fact that we considered only the most restrictive case of single snapshot data also explains why large errors occur at relatively low noise levels. Clearly, the performance can be better, in practice, if one manages to record more than a single field realization (sample) since then the different noise contributions will statistically cancel out.

VII. CONCLUSION

This paper reformulated, by means of the Foldy–Lax multiple scattering model, the treatment of a previous paper[9] concerning time-reversal imaging with MUSIC for the loca-

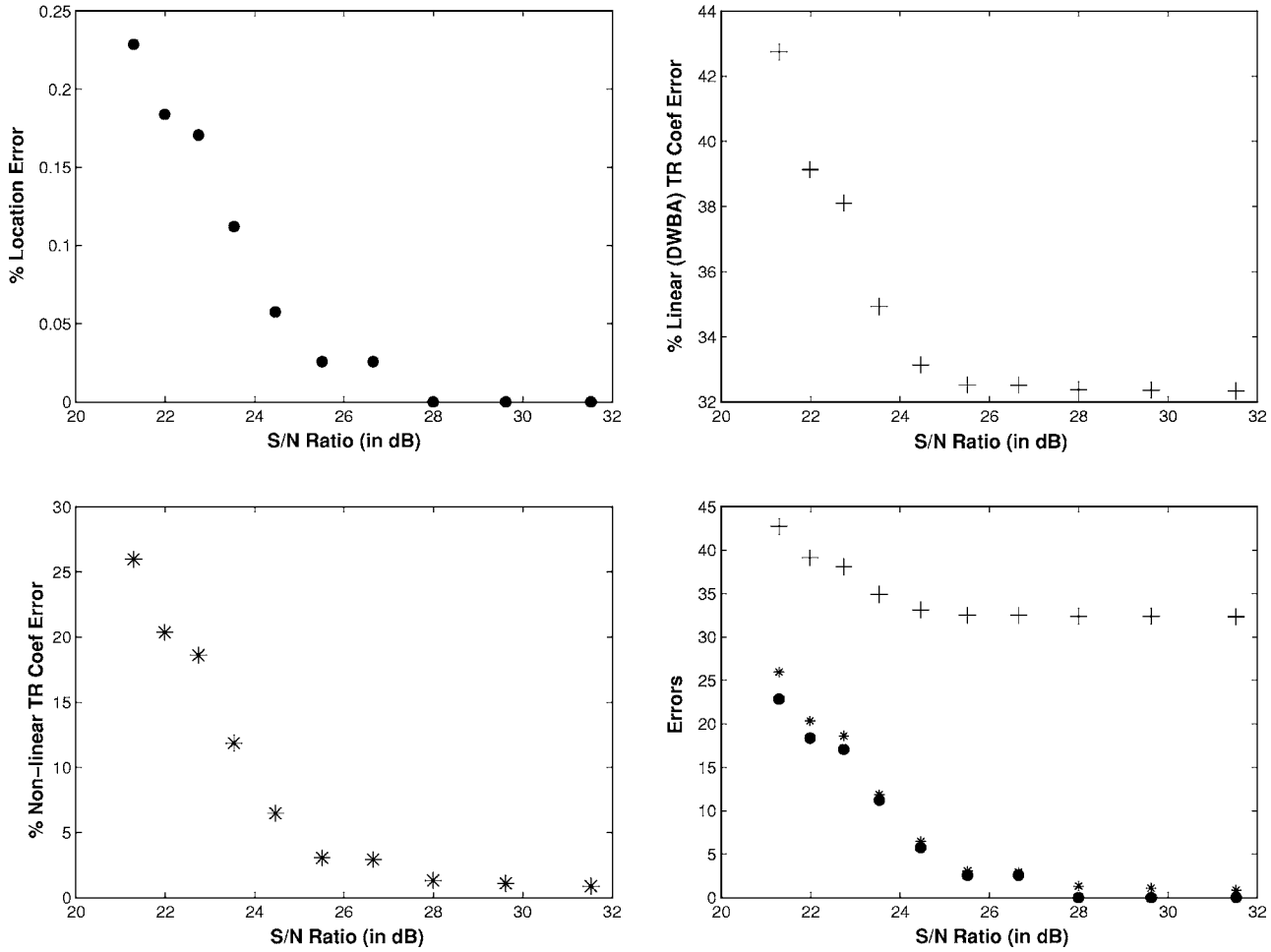

FIG. 4. Plots of the target location and target scattering strength estimation errors of the time-reversal-based inverse scattering method developed in the paper as a function of the signal-to-noise ratio. For reference, these percentage errors are presented within the same plot at the bottom right, with the error in target position appearing multiplied by a factor of 100.

tion of multiply scattering point targets embedded in a known linear and reciprocal but otherwise arbitrary background medium. In the present paper we went a step beyond both in theoretical insight and in the inversion algorithm, addressing within a common theoretical footing based on the Foldy–Lax multiple scattering model both the target location problem and the associated target scattering strength estimation problem. The theoretical results were illustrated with computer simulations that validated the main theoretical expectations on both target location and scattering strength estimations under significant multiple scattering conditions. The examples of this paper were based on numerical simulations of exact scattering derived from the Foldy–Lax equations and illustrated also the role of noise in the data.

It was shown that the MUSIC pseudospectrum computed using the background Green function as a steering vector yields accurate estimates of the target locations, and that the target scattering strengths can be computed from the so-determined target locations by means of a nonlinear iterative routine. These developments corroborate via a detailed formulation that complements the one in Gruber *et al.* (which was based on the Neumann series) the main finding that the time-reversal imaging with a MUSIC method for the target location can be used, not only in the usual DWBA framework but also in more general nonlinear scattering frameworks, where there is significant multiple scattering between the targets. This result is important toward practical implementations of both time reversal and MUSIC methods in, e.g., sonar, underwater communications, medicine, nondestructive evaluation, and imaging, in general.[4,8,10] The nonlinear scattering strength estimation routine derived in the present paper completes the full target inversion (target location plus scattering strength estimation) of multiply scattering point targets from multistatic array data and it also provides a new general framework applicable to other inverse problems.

ACKNOWLEDGMENTS

The authors gratefully acknowledge support under Grant No. FA9550-04-1-0187 from the Defense Advanced Research Projects Agency (DARPA) and the Air Force Office of Scientific Research (AFOSR) for the research reported here. This work is affiliated with CenSSIS, the Center for Subsurface Sensing and Imaging Systems, under the Engineering Research Centers Program of the National Science Foundation (Award No. EEC-9986821).

[1]C. Prada and M. Fink, "Eigenmodes of the time-reversal operator: A solution to selective focusing in multiple target media," Wave Motion **20**, 151–163 (1994).
[2]C. Prada, S. Manneville, D. Spoliansky, and M. Fink, "Decomposition of the time-reversal operator: Application to detection and selective focusing on two scatterers," J. Acoust. Soc. Am. **99**, 2067–2076 (1996).
[3]M. Mordant, C. Prada, and M. Fink, "Highly resolved detection and selective focusing in a waveguide using the D.O.R.T. method," J. Acoust. Soc. Am. **105**, 2634–2642 (1999).
[4]M. Fink, D. Cassereau, A. Derode, C. Prada, P. Roux, M. Tanter, J. L. Thomas, and F. Wu, "Time-reversed acoustics," Rep. Prog. Phys. **63**, 1933–1995 (2000).
[5]A. J. Devaney, "Super-resolution processing of multi-static data using time reversal and MUSIC," unpublished manuscript available on the web site www.ece.neu.edu/faculty/devaney, 2000.
[6]H. Lev-Ari and A. J. Devaney, "The time-reversal technique reinterpreted: Subspace-based signal processing for multi-static target location," *IEEE Sensor Array and Multichannel Signal Processing Workshop*, Cambridge, MA, 2000, pp. 509–513.
[7]S. Lehman and A. J. Devaney, "Transmission mode time-reversal superresolution imaging," J. Acoust. Soc. Am. **113**, 2742–2753 (2003).
[8]C. Prada and J. L. Thomas, "Experimental subwavelength localization of scatterers by decomposition of the time-reversal operator interpreted as a covariance matrix," J. Acoust. Soc. Am. **114**, 235–243 (2003).
[9]F. K. Gruber, E. A. Marengo, and A. J. Devaney, "Time-reversal imaging with multiple signal classification considering multiple scattering between the targets," J. Acoust. Soc. Am. **115**, 3042–3047 (2004).
[10]T. Miwa and I. Arai, "Super-resolution imaging for point reflectors near transmitting and receiving array," IEEE Trans. Antennas Propag. **52**, 220–229 (2004).
[11]J. H. Taylor, *Scattering Theory* (Wiley, New York, 1972).
[12]A. J. Devaney and M. Oristaglio, "Inversion procedure for inverse scattering within the distorted wave Born approximation," Phys. Rev. Lett. **51**, 237–240 (1983).
[13]L. L. Foldy, "The multiple scattering of waves," Phys. Rev. **67**, 107–119 (1945).
[14]R. K. Snieder and J. A. Scales, "Time-reversed imaging as a diagnostic of wave and particle chaos," Phys. Rev. E **58**, 5668–5675 (1998).
[15]L. Tsang, J. A. Kong, K.-H. Ding, and C. O. Ao, *Scattering of Electromagnetic Waves: Numerical Simulations* (Wiley, New York, 2001).
[16]J. M. Ortega and W. C. Rheinboldt, *Iterative Solution of Nonlinear Equations in Several Variables* (Academic, New York, 1970).
[17]M. N. Vrahatis, G. D. Magoulas, and V. P. Plagianakos, "From linear to nonlinear iterative methods," Appl. Numer. Math. **45**, 59–77 (2003).
[18]M. S. Bazaraa and C. M. Shetty, *Nonlinear Programming: Theory and Algorithms* (Wiley, New York, 1979).

Near field acoustic holography with particle velocity transducers[a)]

Finn Jacobsen[b)] and Yang Liu[c)]
Acoustic Technology, Ørsted·DTU, Technical University of Denmark, Building 352, Ørsteds Plads, DK-2800 Kgs. Lyngby, Denmark

(Received 14 June 2005; revised 26 August 2005; accepted 31 August 2005)

Near field acoustic holography is usually based on measurement of the pressure. This paper describes an investigation of an alternative technique that involves measuring the normal component of the acoustic particle velocity. A simulation study shows that there is no appreciable difference between the quality of predictions of the pressure based on knowledge of the pressure in the measurement plane and predictions of the particle velocity based on knowledge of the particle velocity in the measurement plane. However, when the particle velocity is predicted close to the source on the basis of the pressure measured in a plane further away, high spatial frequency components corresponding to evanescent modes are not only amplified by the distance but also by the wave number ratio (k_z/k). By contrast, when the pressure is predicted close to the source on the basis of the particle velocity measured in a plane further away, high spatial frequency components are reduced by the reciprocal wave number ratio (k/k_z). For the same reason holography based on the particle velocity is less sensitive to transducer mismatch than the conventional technique based on the pressure. These findings are confirmed by an experimental investigation made with a *p-u* sound intensity probe produced by Microflown.
[DOI: 10.1121/1.2082687]

PACS number(s): 43.60.Sx, 43.60.Pt, 43.20.Rz [EJS] Pages: 3139–3144

I. INTRODUCTION

Near field acoustic holography is a powerful experimental technique for analyzing sound fields near sources and for deducing important information about the nature of the sources.[1–3] In planar near field acoustic holography the sound field is reconstructed from measurements at discrete positions in a finite region in a plane. It is usually the sound pressure that is measured, but in principle there is the same information in the normal component of the acoustic particle velocity. The reason for the fact that conventional near field holography is based on measurements of the sound pressure rather than the particle velocity is of course that it is easier to measure the sound pressure than the particle velocity. However, an acoustic particle velocity transducer called "Microflown" is now available,[4,5] and therefore it would be interesting to examine the potential of particle velocity-based near field acoustic holography. Thus the purpose of this paper is to compare the performance of particle velocity-based and pressure-based near field holography.

II. OUTLINE OF THEORY

Planar near field acoustic holography is based on the fact that the sound pressure in one plane (say, $z=z_p>0$) can be expressed as the two-dimensional convolution of a "propagator" and the sound pressure in another plane (say, $z=z_m>0$), provided that the sources that generate the sound field are confined to half space ($z\leqslant 0$) and that free-field conditions obtain in the source-free region. The theory was developed in the mid-1980s.[1,2] Only a brief overview of the most fundamental relations will be presented here; see, e.g., Ref. 3 for more details.

The complex sound pressure p is measured in a plane near the source under examination and a two-dimensional (2D) spatial Fourier transform is calculated. The result is the wave number spectrum,

$$P(k_x,k_y)=\int_{-\infty}^{\infty}\int_{-\infty}^{\infty}p(x,y,z_m)e^{j(k_x x+k_y y)}dxdy. \quad (1)$$

Since the pressure is given by the inverse 2D Fourier transform,

$$p(x,y,z_m)=\frac{1}{(2\pi)^2}\int_{-\infty}^{\infty}\int_{-\infty}^{\infty}P(k_x,k_y)e^{-j(k_x x+k_y y)}dk_x dk_y, \quad (2)$$

it can be seen that the wave number spectrum $P(k_x,k_y)$ for any given value of (k_x,k_y) inside the radiation circle (that is, when $k_x^2+k_y^2\leqslant k^2$, where $k=\omega/c$ is the wave number)[3] may be interpreted as the amplitude of a plane wave that propagates in the (k_x,k_y,k_z) direction, where k_z must satisfy

$$k_x^2+k_y^2+k_z^2=k^2. \quad (3)$$

Outside the radiation circle the wave number spectrum represents the amplitude of an evanescent wave. Thus the wave number transform provides an expansion of the sound field into plane and evanescent waves. It now follows that one can

[a)]Portions of this work were presented in "Near field acoustic holography based on an array of particle velocity sensors," Proceedings of Inter-Noise 2005, Rio de Janeiro, Brazil, August 2005.
[b)]Author to whom correspondence should be addressed; electronic mail: fja@oersted.dtu.dk
[c)]Electronic mail: gordan69@163.com

determine the wave number spectrum of the sound pressure in another, parallel plane, simply by multiplying the wave number spectrum in the measurement plane with an exponential propagator,

$$G(z_p, z_m, k_x, k_y) = e^{-jk_z(z_p - z_m)}, \tag{4}$$

where k_z is given by

$$k_z = \begin{cases} \sqrt{k^2 - k_x^2 - k_y^2} & \text{for } k_x^2 + k_y^2 \leqslant k^2 \\ -j\sqrt{k_x^2 + k_y^2 - k^2} & \text{for } k_x^2 + k_y^2 > k^2. \end{cases} \tag{5}$$

The sign in the last equation has been chosen so as to satisfy the Sommerfeld radiation condition with the $e^{j\omega t}$ sign convention. Eventually one can calculate the sound pressure in the prediction plane by an inverse Fourier transform. One can also calculate the particle velocity vector, and thus the sound intensity. For example, the wave number spectrum of the normal component of the particle velocity in the prediction plane equals the wave number spectrum of the pressure in the measurement plane multiplied with the propagator

$$G_{pu}(z_p, z_m, k_x, k_y) = \frac{k_z}{\rho c k} e^{-jk_z(z_p - z_m)}, \tag{6}$$

where ρc is the characteristic impedance of the medium.[2,3]

An alternative technique involves measuring the normal component of the particle velocity in a plane, transform to the wave number domain, multiply with the propagator given by Eq. (4), and transform back to the spatial domain. The result is the normal component of the particle velocity in the prediction plane. If instead the wave number spectrum is multiplied by the propagator

$$G_{up}(z_p, z_m, k_x, k_y) = \frac{\rho c k}{k_z} e^{-jk_z(z_p - z_m)} \tag{7}$$

before the inverse Fourier transform is carried out one will get the sound pressure in the prediction plane.[2,3]

The above-noted description is, of course, grossly oversimplified. In practice the measurement area must obviously be finite, the sound field is sampled only at a finite number of discrete positions, and the 2D spatial Fourier transform is approximated by a 2D discrete Fourier transform.[1–3] To reduce the influence of the finite aperture and the spatial sampling, zero padding and a tapered spatial window should be applied before the discrete spatial Fourier transform is calculated.[2] The spatial sampling must satisfy the sampling theorem, and therefore one cannot sample very close to the source where there may be high spatial frequency components. On the other hand, one should not sample too far away, because then the evanescent modes will be buried in noise.[2,3] Moreover, whereas forward prediction is numerically stable, backward prediction, which involves predicting the sound field closer to the source than the measurement plane, is an unstable "ill-posed" inverse problem that requires regularization because of the fact that the evanescent waves are amplified exponentially with the distance. The standard regularization technique involves spatial low-pass filtering (multiplying with a window in the wave number domain). See, e.g., Refs. 2 and 3. Finally, it should be mentioned that the velocity-to-pressure propagator given by Eq. (7) has a singularity on the radiation circle where k_z goes to zero.

III. A SIMULATION STUDY

A simulation study has been carried out. To obtain realistic results a model of a relatively complicated source, a simply supported vibrating steel plate in an infinite, rigid baffle, was developed. The dimensions of the plate were 0.45×0.75 m, and it was 5 mm thick, corresponding to a coincidence frequency of about 2.4 kHz. The lowest eigenfrequency of the plate was about 80 Hz. The excitation of the plate was a harmonic point source of 10 N placed near one of the corners (10 cm from each edge), and the resulting vibrational velocity was calculated using a conventional modal summation. The vibrating plate was divided into 64×64 rectangles, each of which was regarded as a point source on the baffle, and the sound pressure radiated by the plate was calculated from the corresponding approximation to Rayleigh's first integral.[3] A virtual microphone array of dimensions 1.5×1.5 m with 32×32 microphones (corresponding to a sampling distance of 4.7 cm) was placed 15 cm above the plate, and the prediction plane was 5 cm above the plate.

The spatial window was an 8-point Tukey window,[3] and zeros were added outside the measurement area to reduce wrap-around errors. The regularization was an exponential k-space low-pass window with a cut-off frequency of 0.6 times the Nyquist frequency and a value of 0.1 of the parameter α.[3] To reduce the influence of the singularity of Eq. (7) on the radiation circle the wave number spectra were smoothed as described in Ref. 6.

In what follows, "true" values of quantities in the prediction plane have been calculated directly from the approximated Rayleigh's integral, whereas predictions have been calculated from the "measured" sound pressure or particle velocity. The results are shown along a diagonal line in the prediction plane from the corner nearest the excitation point to the opposite corner.

A. Ideal transducers

Figure 1(a) shows the "true" sound pressure level at 200 Hz, a prediction based on the pressure in the measurement plane, and a prediction based on the normal component of the particle velocity in the measurement plane. There is good agreement between the "true" pressure and both predictions in a significant part of the prediction plane, but near the edges the agreement deteriorates.

Figure 1(b) shows a similar comparison of the "true" normal component of the particle velocity level and predictions based on the pressure and based on the particle velocity in the measurement plane. (Note that the particle velocity level is shown relative to a reference velocity of 50 nm/s so as to make it directly comparable with the sound pressure level.) The two predictions are in good agreement with the "true" value, but it is apparent that the velocity-based prediction is far better than the pressure-based prediction near the edges. Similar results have been found at other frequencies.

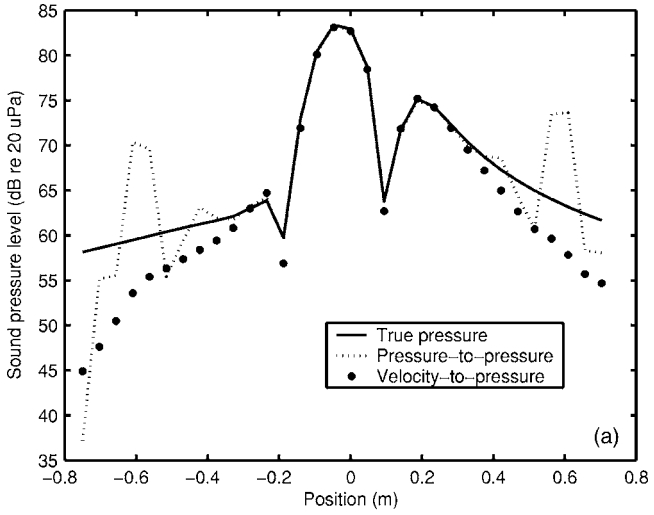

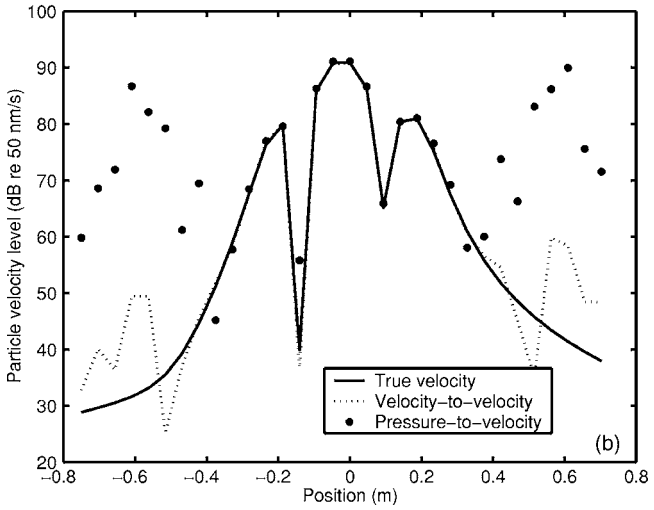

FIG. 1. "True" and predicted sound pressure level (a) and particle velocity level (b) at 200 Hz along a line across the prediction plane 5 cm from the vibrating plate.

Note also that the "true" particle velocity, not unexpectedly, decays faster toward the edges and has a larger dynamic range than the pressure. This is favorable for holography based on the particle velocity, since it means that leakage caused by the spatial window is reduced. However, the main reason for the consistent observation that velocity-based predictions of the pressure are considerably better than pressure-based predictions of the velocity is undoubtedly the fact that the wave number factor used in the former case reduces high spatial frequencies whereas the reciprocal factor used in the latter case amplifies them. These effects are demonstrated by Fig. 2, which shows the amplitude of the propagators given by Eqs. (4), (6), and (7) (except for the ρc factor), corresponding to the predictions shown in Fig. 1. Amplification of high spatial frequencies increases the inherent numerical instability in backward propagation.[3]

Figure 3 shows the "true" normal component of the sound intensity level at 200 Hz along the diagonal line across the prediction plane, a prediction based on the pressure in the measurement plane, a prediction based on the corresponding normal component of the particle velocity, and a prediction in which the pressure in the expression for

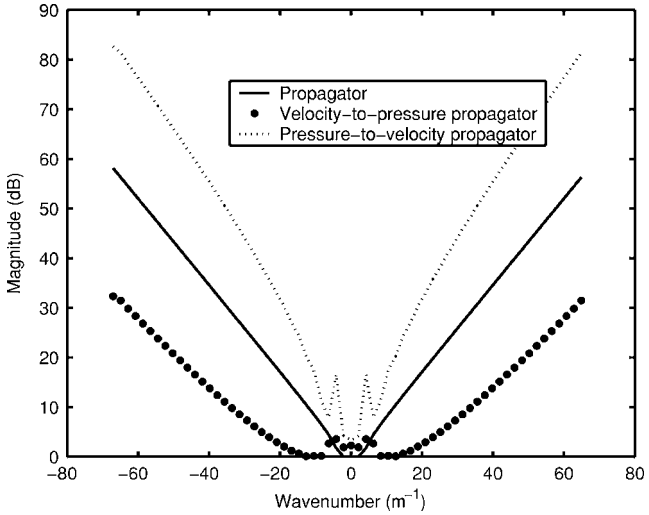

FIG. 2. The three propagators [Eqs. (4), (6), and (7)] used for the predictions shown in Fig. 1.

the intensity has been calculated from the pressure in the measurement plane and the particle velocity in the same expression has been calculated from the particle velocity in the measurement plane. Note the low level compared with the sound pressure level, and note the regions of negative intensity; the panel is a very inefficient radiator of sound at 200 Hz. It seems that the prediction in which the pressure has been based on the pressure and the velocity on the velocity is slightly better than the prediction based solely on the velocity and much better than the prediction based solely on the pressure. Similar observations have been made at other frequencies. The reason for the slightly better performance of the prediction based both on the pressure and the particle velocity compared with the prediction based exclusively on the velocity is perhaps that inaccuracies caused by the smoothing that is needed in velocity-to-pressure predictions [Eq. (7)] are avoided.

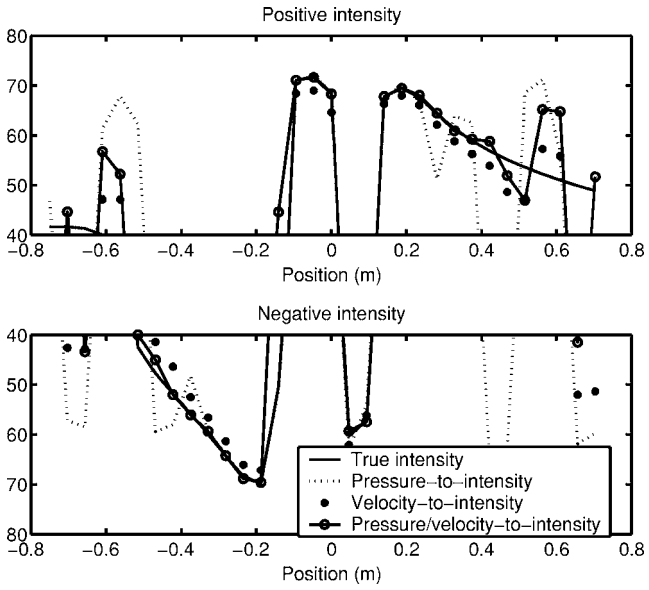

FIG. 3. "True" and predicted sound intensity level at 200 Hz along a line across the prediction plane 5 cm from the vibrating plate.

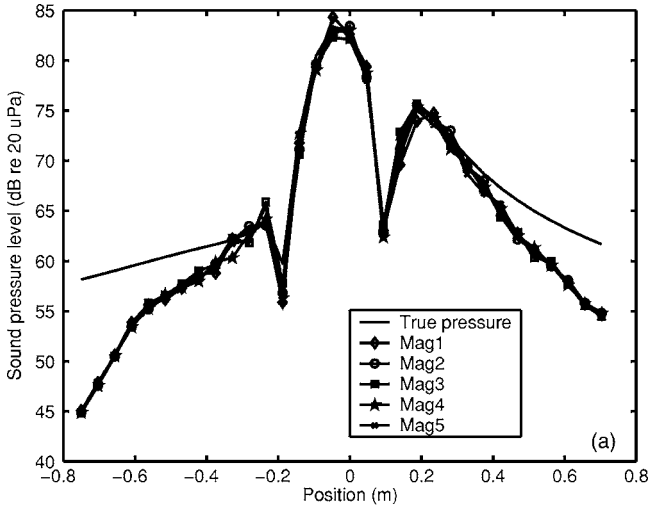

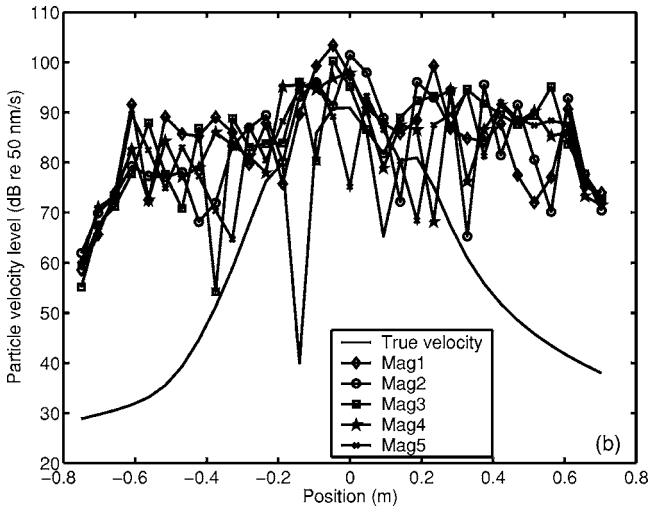

FIG. 4. "True" and predicted sound pressure level (a) and particle velocity level (b) at 200 Hz. The sound pressure level in (a) is predicted from particle velocity "measurements" in which random amplitude mismatch has been introduced, and the particle velocity level in (b) is predicted from pressure "measurements" in which random amplitude mismatch has been introduced.

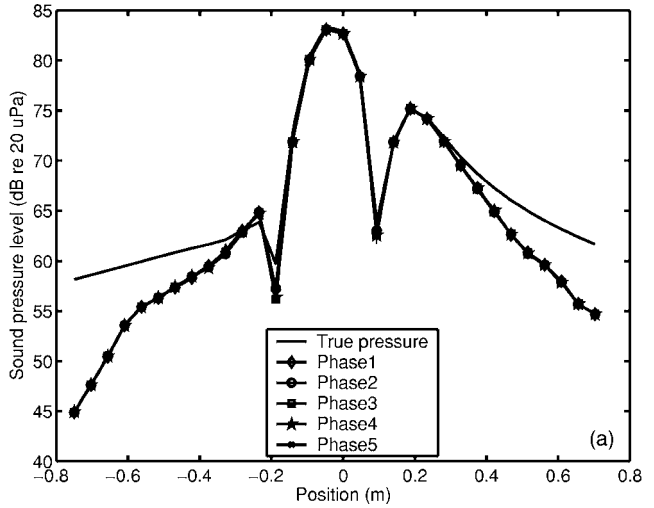

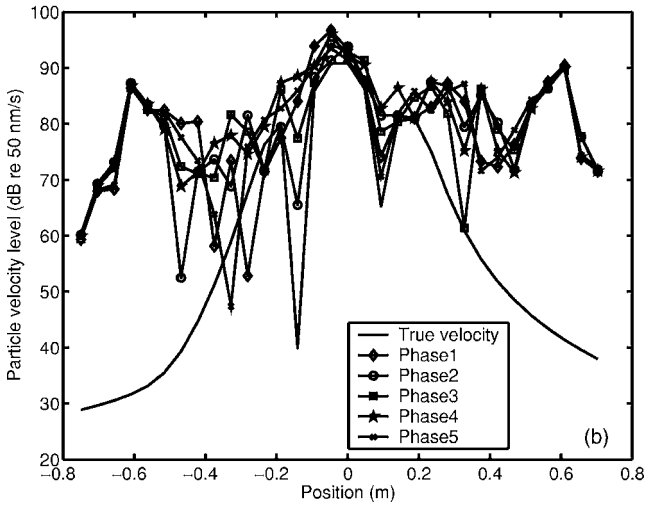

FIG. 5. "True" and predicted sound pressure level (a) and particle velocity level (b) at 200 Hz. The sound pressure level in (a) is predicted from particle velocity "measurements" in which random phase mismatch has been introduced, and the particle velocity level in (b) is predicted from pressure "measurements" in which random phase mismatch has been introduced.

B. Transducer mismatch

In stationary sound fields one can measure the pressure or particle velocity in the measurement plane point by point with a single transducer using a reference signal (or several reference signals, depending on the complexity of the source mechanism).[7] On the other hand, if the sound field is generated by a nonstationary source it is necessary to measure the complete sound field in the measurement plane at the same time, and thus a full two-dimensional transducer array must be used.[8] However, in real measurements with transducer arrays a certain amount of amplitude and phase mismatch between the transducers can be expected. The effect of such measurement inaccuracies on pressure-to-pressure predictions has been examined by Nam and Kim.[9] To examine the effect on "cross predictions," that is, predictions where the pressure is calculated from the particle velocity and the particle velocity is calculated from the pressure, random amplitude mismatch, uniformly distributed between −0.5 and 0.5 dB, has been introduced in the above-described simulations. Figure 4 shows the results of five outcomes of this stochastic experiment. It is apparent that whereas the influence on predictions from velocity to pressure is fairly moderated predictions from pressure to velocity are extremely seriously affected. The explanation is that the white noise introduced in the wave number spectrum by these errors is amplified by the wave number ratio (k_z/k) in the pressure-based cross predictions and reduced by the reciprocal factor in the velocity-based cross predictions.

Figure 5 shows the results of similar stochastic experiments in which phase errors uniformly distributed from $-2°$ to $2°$ have been introduced in the cross predictions. The results resemble the results shown in Fig. 4, but this amount of random phase mismatch appears to be slightly less serious than random amplitude mismatch in the interval from −0.5 to 0.5 dB.

IV. EXPERIMENTAL RESULTS

To examine the validity of the results of the simulations some experiments have been carried out. The sound source was a 3-mm steel plate with dimensions 39×63 cm

mounted in a large baffle. The radiating plate was one of the side plates of a box; and one of the other side plates of the box was driven via a Brüel & Kjær (B&K) 8200 force transducer by a B&K 4809 electrodynamic exciter fed with wideband pink random noise. The signal from the force transducer was passed through a B&K 2635 charge amplifier and used as a reference signal. The box was suspended from a support in such a way that it did not touch the rectangular hole in the baffle; the resulting leaks around the plate were sealed by tape. The frequency responses between sound pressure and the reference signal and between the normal component of the particle velocity and the reference signal were measured at 18×28 points in two planes using a Microflown $\frac{1}{2}$-in. *p-u* sound intensity probe. The sampling distance was 5 cm.

Since the measurements took place in an ordinary room the image source resulting from the reflecting floor had to be taken into account; that is, the sound field was sampled down to half a sampling distance above the floor, and the sound field was considered to be symmetrical about the plane of the floor.[7] Thus the resulting spatial transform was a 18×56 point transform. The phase and amplitude calibration of the Microflown particle velocity transducers was carried out in an impedance tube as described in Ref. 10. A robot moved the transducer over the two measurement planes, one typically about 12 cm from the source plane, and one typically about 4 cm from the source plane. A B&K 3560 "Pulse" analyzer in the 1/24 octave mode was used, and the measurements and the robot were controlled by B&K's program "Spatial transformation of sound fields" (STSF). The data were, however, postprocessed not with STSF but with the same MATLAB routines as used in the simulations. Each set of 1/24 octave data was processed individually and then summed so as to produce the sound pressure, the particle velocity, and the sound intensity in one-third octave bands. (With measurements directly in one-third octave bands the coherence between the force signal and the pressure and particle velocity was too poor; strictly speaking the theory outlined in Sec. II is based on pure-tone excitation, and one-third octave bands are too wide. Otherwise expressed, with one-third octave noise the physical dimensions of the source exceeded the correlation distance.[7])

Figure 6 shows an example of the results. Figure 6(a) shows a comparison of the "true," that is, directly measured sound pressure level in the 200-Hz one-third octave band along a vertical line midway through the plane close to the panel and predictions of the same quantity based on measurements of the pressure and the normal component of the particle velocity in the plane further away. Note that the sound pressure and the particle velocity increase toward the reflecting floor (the position at 0 m). It can be seen that the velocity-based prediction is acceptable and on the whole somewhat more accurate than the pressure-based prediction.

Figure 6(b) shows the "true" particle velocity in the plane close to the panel and predictions based on measurements of the pressure and the particle velocity in the plane further away. It is clear that the pressure-based prediction tends to overestimate the particle velocity and that the velocity-based prediction is by far the best.

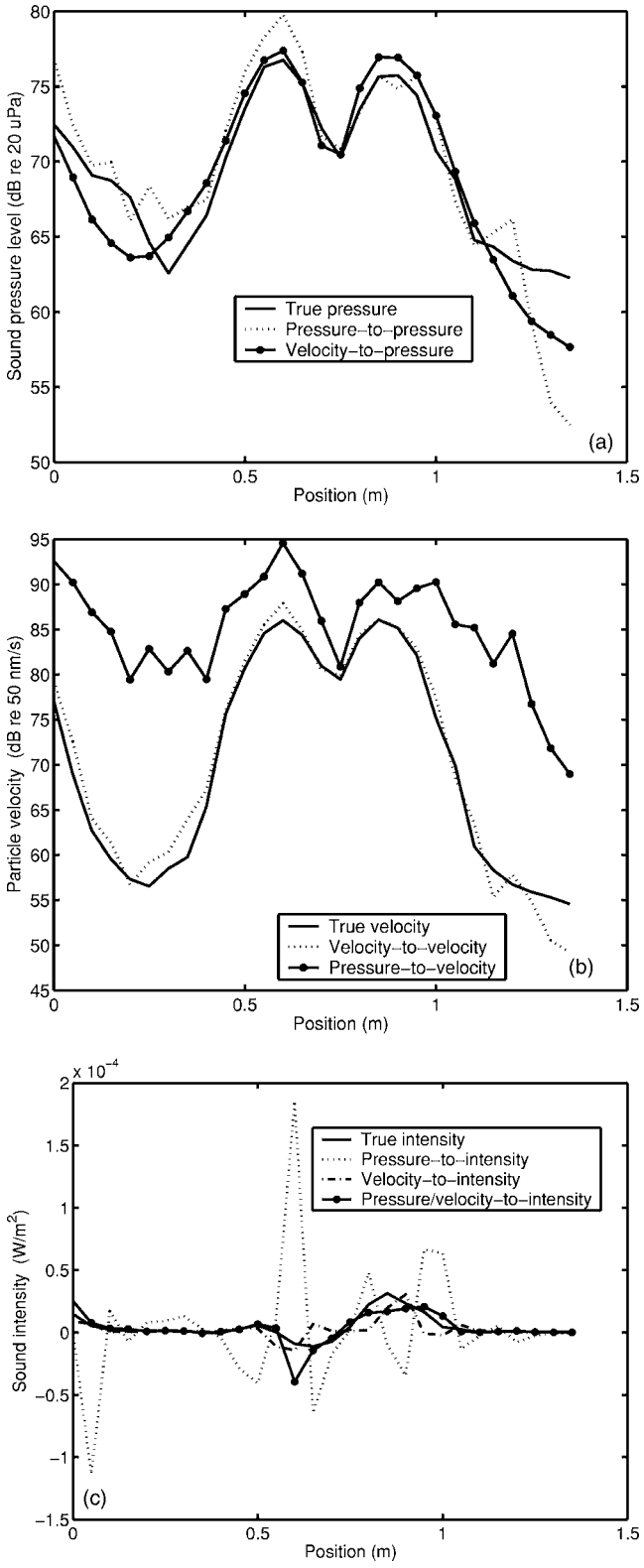

FIG. 6. Measured sound pressure level (a), particle velocity level (b), and sound intensity (c) in the 200-Hz one-third octave band compared with predictions based on the pressure and on the particle velocity in the measurement plane.

Finally Fig. 6(c) shows the "true" sound intensity in the plane close to the panel and a prediction based solely on pressure measurements in the plane further away, a prediction based solely on particle velocity measurements in the

same measurement plane, and a prediction based on both pressure and particle velocity measurements. Again the velocity-based prediction performs much better than the prediction based on measurements of the pressure, and again the prediction based on measurements of both quantities seems to be slightly better than the prediction based solely on the velocity. Similar results have been found in other one-third octave bands.

V. CONCLUSIONS

Planar near field acoustic holography has traditionally been based on measurements of the sound pressure, but since an acoustic particle velocity transducer is now available this paper has examined near field holography based on measurements of the normal component of the particle velocity.

A simulation study has revealed that the particle velocity decays faster toward the edges of the measurement region than the sound pressure and has a larger dynamic range; thus spatial windowing has less serious consequences on velocity-based holography than on conventional pressure-based holography. Nevertheless, it has generally been observed that the quality of pressure-to-pressure predictions is similar to the quality of velocity-to-velocity predictions. However, velocity-to-pressure backward predictions are far better than pressure-to-velocity backward predictions because of the fact that the wave number ratio that enters into such cross predictions reduces high spatial frequencies in the former case but amplifies them in the latter case.

For the same reason amplitude and phase mismatch, which is likely to occur in measurements with arrays of transducers, has a far more serious influence on pressure-to-velocity predictions than on velocity-to-pressure predictions: such transducer mismatch introduces high spatial frequencies, and the resulting errors are amplified exponentially with the distance if the prediction plane is closer to the source than the measurement plane.

The superiority of the method based on measurement of the particle velocity has been confirmed by an experimental study in which the sound pressure and the normal component of the particle velocity were measured at some distance from a vibrating, baffled steel panel with a Microflown *p-u* sound intensity probe and used to predict the pressure, the normal component of the particle velocity, and the normal component of the sound intensity in a plane closer to the panel. Velocity-based predictions were consistently found to be better than pressure-based predictions. Thus if only one type of transducer is available one should choose to measure the particle velocity. However, slightly better predictions of the sound intensity may be obtained if the pressure that enters into this quantity is predicted from the pressure and the particle velocity is predicted from the particle velocity.

ACKNOWLEDGMENTS

The authors would like to thank Microflown Technologies for lending us a *p-u* sound intensity probe. We are also indebted to Brüel & Kjær for lending us a robot, a multichannel "Pulse" front-end, and license to use the STSF software, and to Jørgen Hald, Brüel & Kjær, for useful advice during the project.

[1] J. D. Maynard, E. G. Williams, and Y. Lee, "Nearfield acoustic holography. I. Theory of generalized holography and the development of NAH," J. Acoust. Soc. Am. **78**, 1395–1413 (1985).
[2] W. A. Veronesi and J. D. Maynard, "Nearfield acoustic holography (NAH). II. Holographic reconstruction algorithms and computer implementation," J. Acoust. Soc. Am. **81**, 1307–1322 (1987).
[3] E. G. Williams, *Fourier Acoustics—Sound Radiation and Nearfield Acoustical Holography* (Academic Press, San Diego, 1999).
[4] R. Raangs, W. F. Druyvesteyn, and H.-E. de Bree, "A low-cost intensity probe," J. Audio Eng. Soc. **51**, 344–357 (2003).
[5] H.-E. de Bree, "The Microflown: An acoustic particle velocity sensor," Acoust. Aust. **31**, 91–94 (2003).
[6] E. G. Williams and J. D. Maynard, "Numerical evaluation of the Rayleigh integral for planar radiators using the FFT," J. Acoust. Soc. Am. **72**, 2020–2030 (1982).
[7] K. B. Ginn and J. Hald, "STSF—Practical instrumentation and applications," Brüel & Kjær Technical Review **2**, 1–27 (1989).
[8] J. Hald, "Non-stationary STSF," Brüel & Kjær Technical Review **1**, 1–36 (2000).
[9] K.-U. Nam and Y.-H. Kim, "Errors due to sensor and position mismatch in planar acoustic holography," J. Acoust. Soc. Am. **106**, 1655–1665 (1999).
[10] F. Jacobsen and H.-E. de Bree, "Measurement of sound intensity: *p-u* probes versus *p-p* probes," Proceedings of Noise and Vibration Emerging Methods 2005, Saint Raphaël, France.

Reflection and time-reversal of ultrasonic waves in the vicinity of the Rayleigh angle at a fluid-solid interface

François Vignon,[a] Fabrice Marquet, Didier Cassereau, Mathias Fink, Jean-François Aubry, and Pierre Gouedard

Laboratoire Ondes et Acoustique, ESPCI, Université Paris VII, C.N.R.S., U.M.R. 7587, 10 rue Vauquelin, 75005 Paris, France

(Received 18 January 2005; revised 15 July 2005; accepted 1 September 2005)

When sending a plane ultrasonic wave toward a fluid-solid interface, the reflected wave is affected, depending on the incident angle. Around the Rayleigh angle the reflection coefficient has a strong and rapidly varying imaginary part. This has the effect of distorting the reflected wave front. If this reflected wave is time-reversed and sent back toward the interface, the reflected wave of this time-reversed wave should not present any distortion, as the time-reversal process restores the original phases. A theoretical and experimental study of these phenomena has been done. The distortion of the reflected waves around the Rayleigh angle is observed and as expected this distortion is canceled by the time-reversal process. However a significant loss of energy in the time-reversed signal is observed for incident angles around the Rayleigh angle, as part of the energy contained in the Rayleigh wave escapes the time-reversal mirror and is lost for the time-reversal process. In a second part, it is shown by simulations and experiments how this signal distortion by reflection around Rayleigh angle influences spatial focusing of waves by time-reversal or simple time-delay methods. © *2005 Acoustical Society of America.* [DOI: 10.1121/1.2082727]

PACS number(s): 43.60.Tj, 43.20.El [DRD] Pages: 3145–3153

I. INTRODUCTION

Time reversal of acoustic waves is a robust method for field focusing that has been largely investigated in the past decades.[1–4] Its main application is focusing optimization through inhomogeneous media. A time-reversal experiment is a two-step process: first, an active source or set of sources generates a pressure field $p(\mathbf{r},t)$ that is recorded by a set of ultrasonic transducers. This recorded field is then time-reversed and sent back into the medium by the transducers, generating the field $p(\mathbf{r},-t)$ that propagates in the medium as if time was going backwards, thus recreating at the initial source location the pressure field originally emitted. Ideally the receivers should form a closed time-reversal cavity surrounding the sources, and should be able to measure the field as a function of time.[3] However, it has been shown that in practice, using time-reversal mirrors of finite size, a good approximation of the time-reversal cavity could be achieved.[4]

In this paper, time-reversal experiments are performed in a specific configuration: a fluid-solid interface is inserted between the sources and the receivers, such that the waves propagating from the sources to the receivers are reflected on the interface (Fig. 1). Specific phenomena due to this reflection appear, such as pulse shape distortion[5] and lateral shifting of the incident beam.[6–8] This phenomenon has been specifically studied by Wang *et al.* for waves transmitted through a fluid-solid interface:[9] pulse shape distortion leads to errors in speed of sound measurements in solids, and thus has to be avoided or compensated.

Here we study the pulse distortion occurring in reflection, and use a time-reversal mirror in reflection to restore the original temporal shape of the pulse. In a second part, spatial focusing capabilities of a time-reversal mirror in reflection are tested. The aim is to see how the focusing process is degraded as the waves that are transmitted into the solid are not recorded and are lost for the time-reversal process.

For this purpose, the experimental setup presented in Fig. 1 is used: two identical linear echographic arrays are mounted on articulated arms so that waves can be emitted by array 1 or 2, propagate and be reflected on the interface between water and a titanium block with an incrementable incident angle. The other array is used to record the reflected waves, that are then time-reversed and sent back, reflected on the interface and recorded by the initially emitting array in order to test temporal or spatial focusing.

First, the effect of the incident angle on the temporal shape of the reflected waves is investigated. A distortion of the reflected wave front with respect to the incident one is expected for incident angles close to the Rayleigh angle. Then time-reversal is used to restore the original shape of the wave. In a second part, spatial focusing with the time-reversal mirror is performed and compared to classical focusing based on time delays estimations.[8] The influence of the incident angle is evaluated.

II. REFLECTION AND TIME-REVERSAL OF PLANE WAVES AT A FLUID-SOLID INTERFACE, THE EFFECT OF THE INCIDENT ANGLE

The reflection and refraction phenomena occurring at an interface have already been largely studied. The theory for such phenomena can be found in Refs. 5, 10, and 11. Fur-

[a]Electronic mail: francois.vignon@loa.espci.fr

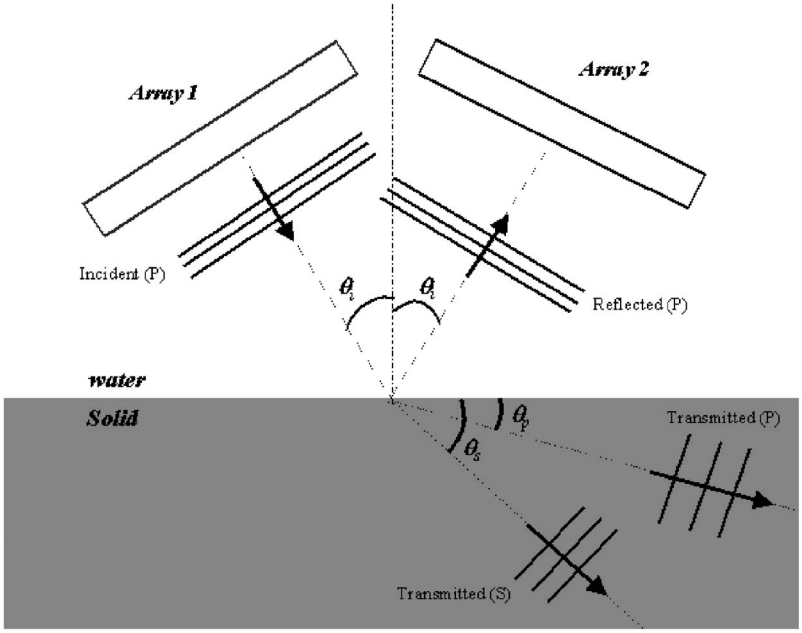

FIG. 1. The experimental setup: two echographic arrays are mounted on a circular setup fixed on a water-titanium interface, so that waves can be emitted by array 1, reflected on the interface, and be recorded on array 2, and vice-versa. The incident angle of the waves at the interface can be manually incremented. Depending on the attack angle, the compressional (P) waves generated in the fluid can give rise to P, S (Shear), and Rayleigh waves in the solid.

thermore, specific studies of pulse shape distortion at a fluid-solid interface have been performed by Wang *et al.*[9] in a framework of solid characteristics evaluation; experiments of visualization of reflected waves at a fluid-solid interface using Schlieren techniques have been done earlier by Neubauer[6] and Nagy *et al.*,[7] who observed the predicted lateral shifting of a reflected beam incident at the Rayleigh angle. Reflection of waves at a fluid-solid interface has also been carefully studied by Chen and Wu,[12] who used reflectometry (the study of the reflected amplitude as a function of the incident angle) to measure the speed of sound in solids without measuring waves that have passed through the solid.

In this section we point out some theoretical aspects of the reflection of plane waves at a fluid-solid interface. In particular it seems interesting to enlighten the differences between the fluid-solid interface and the fluid-fluid interface,[13–16] that are due to the generation of shear waves in the solid when attacking the interface with compressional waves with a nonzero incident angle. Specifically, it is shown that a temporal distortion of the emitted wave front is to be expected when the incidence is close to the Rayleigh angle.

A. Theoretical considerations

Consider that a plane ultrasonic wave is sent toward a fluid-solid interface with an incident angle θ_i. In the fluid the waves are only longitudinal (P waves) but as soon as the incidence is non-normal, shear (S) waves are generated in the solid along with longitudinal P waves, with refraction angles θ_s and θ_p, respectively (Fig. 1). Let c_f be the speed of sound in the fluid, c_p and c_s the speed of longitudinal and shear waves in the solid, respectively. The incident angle θ_i and the angle of the transmitted wave (longitudinal or shear) with the normal to the interface are linked by Snell-Descartes' law: $\theta_i = \sin^{-1}\{c_f/c_p \sin(\theta_p)\}$ for longitudinal waves, and $\theta_i = \sin^{-1}\{c_f/c_s \sin(\theta_s)\}$ for shear waves. There is no transmitted propagating longitudinal or shear wave when $\theta_{p,s} > \pi/2$, that is to say if $\theta_i > \theta_p^* = \sin^{-1}(c_f/c_p)$ for longitudinal waves, and if $\theta_i > \theta_s^* = \sin^{-1}(c_f/c_p)$ for shear waves. θ_p^* and θ_s^* are known as the longitudinal and shear critical angles respectively. For an incident angle θ_r^* (the Rayleigh angle) a little beyond the shear critical angle, a Rayleigh wave is created inside the solid. This wave is confined to the interface and radiates back into the fluid during its propagation.[10]

Let $e(t)$ be the temporal shape of the plane wave incident at the interface with an angle θ_i, and $f(t)$ the temporal shape of the reflected signals. $E(\omega)$ and $F(\omega)$, the Fourier transforms of $e(t)$ and $f(t)$, respectively, are linked by the reflection coefficient $R(\theta_i)$, which depends on the incident angle θ_i but not on the frequency of the incident wave. In fact, writing the continuity relations at the interface it comes that[5,10]

$$R(\theta_i) = (\Delta_i - \Delta_2)/(\Delta_i + \Delta_2), \tag{1}$$

with

$$\Delta_1 = [1/2(1/C_s)^2 - \alpha^2]^2 + \nu_p \nu_s \alpha^2, \tag{2}$$

$$\Delta_2 = \rho_f \nu_p / 4 c_s^4 \rho_s \nu_f, \tag{3}$$

ρ_f and ρ_s being the volumic masses of the fluid and the solid, respectively, and

$$\alpha = (1/c_f)\sin(\theta_i), \tag{4}$$

$$\nu_j = [(1/c_j)^2 - \alpha^2]^{1/2} \quad (j = f,p,s). \tag{5}$$

Note that ν_j can be complex as soon as $(1/c_j)^2 - \alpha^2 < 0$, i.e., $\theta_i > \theta_p^*$ or θ_s^*. The immediate consequence is that the reflection coefficient $R(\theta_i)$ becomes complex as the incident angle becomes greater than one of the critical angles (for longitudinal or shear waves). The real and imaginary parts of $R(\theta_i)$ as a function of the incident angle θ_i are presented in Fig. 2. As $R(\theta_i)$ becomes complex, the reflected signals $F(\omega)$ are affected with a phase shift with respect to the emitted signals $E(\omega)$. This phase shift is equal to the phase of $R(\theta_i)$ and is frequency-independent, as can be checked in Eqs. (1)–(5).

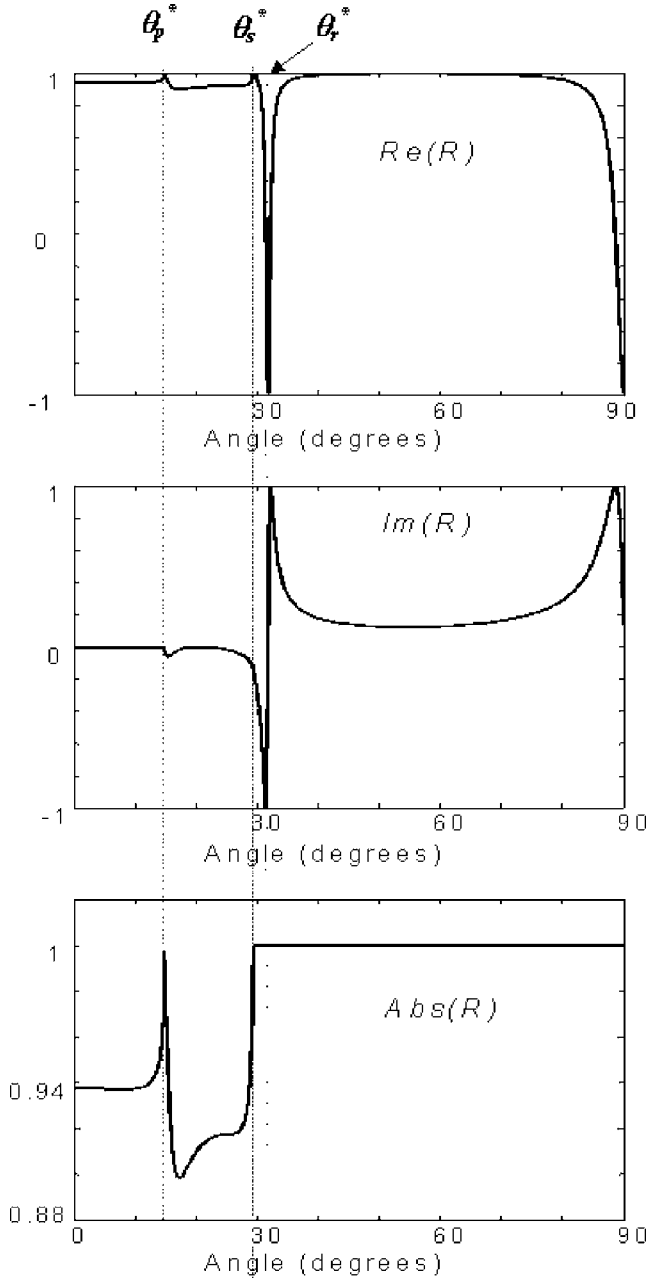

FIG. 2. The reflection coefficient R as a function of the incident angle θ_i. Top panel: real part of $R(\theta_i)$, middle panel: imaginary part of $R(\theta_i)$, bottom panel: modulus of R. θ_p^*=longitudinal critical angle, θ_s^*=shear hear critical angle, θ_r^*=Rayleigh angle.

When emitting $E(\omega)$ with an incident angle θ_i, $E(\omega)$ and $F(\omega)$ are linked by the relation

$$F(\omega) = R(\theta_i)E(\omega) \Leftrightarrow F(\omega) = [\mathrm{Re}(R(\theta_i)) + i\,\mathrm{Im}(R(\theta_i))]E(\omega). \quad (6)$$

We cannot directly calculate the inverse Fourier transform of Eq. (6) in order to obtain the temporal shape $f(t)$ of the reflected signals: it would give a complex-valued function, which has no sense for physical measurable signals. Taking into account the fact that $e(t)$ and $f(t)$ must be real-valued functions, their Fourier transforms must be Hermitian ($E(\omega)^* = E(-\omega)$, $F(\omega)^* = F(-\omega)$, E^* standing for the complex conjugate of E). In fact, Eq. (6) leads in temporal domain to

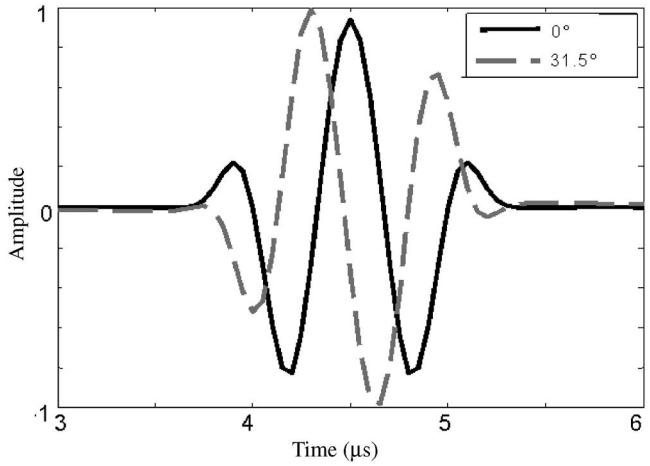

FIG. 3. The temporal shape of the reflected signals $f(t)$ for an incidence of $\theta_i = 0°$ (black line) and $\theta_i = \theta_r^* \approx 31.5°$ (gray, dashed line). [The reflected signals at normal incidence have the same temporal shape as the emitted signals $e(t)$].

$$f(t) = \mathrm{Re}(R(\theta_i))e(t) + \mathrm{Im}(R(\theta_i))\mathrm{HT}[e(t)], \quad (7)$$

HT denoting the Hilbert transform operator. The equivalence of Eqs. (7) and (6) is demonstrated in the Appendix.

One can see from Eq. (7) that as soon as the reflection coefficient becomes complex, the reflected signals $f(t)$ are no longer proportional to the emitted signals $e(t)$: a pulse distortion occurs because of the Hilbert transform operator.

The reflection coefficient has a significant imaginary part near the Rayleigh angle (see Fig. 2). In fact, the phase of the reflection coefficient is shifted by 2π as passing the Rayleigh angle. Thus, it is possible to visualize the passing of the Rayleigh angle by looking at the temporal shape of the reflected signal $f(t)$ as a function of the incident angle θ_i. Using the theoretical formulation presented earlier for the reflection coefficient $R(\theta_i)$, the reflected signals $f(t)$ when attacking the interface with a plane wave of temporal shape $e(t)$ with an incident angle θ_i have been calculated and the results are presented in Fig. 3 for normal incidence ($\theta_i = 0°$) and Rayleigh incidence ($\theta_i = \theta_r^* \approx 31.5°$), the distortion of the reflected signal at Rayleigh incidence is visible. Then, the reflected signals $f(t)$ for any incident angle between 0 and 90° have been represented in Fig. 4(a): the distortion of the reflected signals as passing the Rayleigh angle is visible. The following acoustic parameters for fluid (water) and solid (titanium) have been used for simulation: $\rho_f = 1000$ kg m^{-3}, $c_f = 1460$ m s^{-1}; $\rho_s = 7890$ kg m^{-3}, $c_s = 2991$ m s^{-1}, $c_p = 5765$ m s^{-1}.

The reflected wave $f(t)$ [$F(\omega)$ in Fourier domain] can then be recorded and time-reversed: in time-domain formalism the time-reversal operation is equivalent to the variable change $t' = -t$, and in frequency domain to a complex conjugation. The time-reversed signals are sent back with the same incident angle toward the first array, and the resulting wave $s(t)$ [$S(\omega)$] recorded on the first array is then

$$S(\omega) = R(\theta_i)F(\omega)^* \Leftrightarrow S(\omega) = R(\theta_i)[R(\theta_i)E(\omega)]^* \Leftrightarrow S(\omega) = |R(\theta_i)|^2 E(\omega) \Leftrightarrow s(t) = |R(\theta_i)|^2 e(t) \quad (8)$$

if $e(t)$ are symmetrical signals, so that $E(\omega)^* = E(\omega)$.

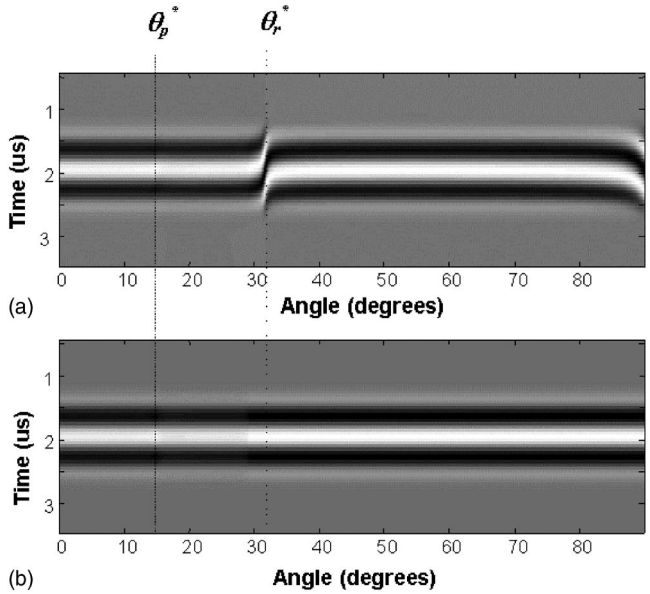

FIG. 4. (a) The temporal shape of the reflected signals $f(t)$, as a function of the incident angle (theory). (b) The temporal shape of signals $s(t)$ after time-reversal and backpropagation of $f(t)$ and backpropagation, as a function of the incident angle. On each column is presented on gray level the temporal shape of the pressure wave received after reflection, for a given incident angle. The Longitudinal critical angle θ_p^* and the Rayleigh angle θ_r^* are indicated.

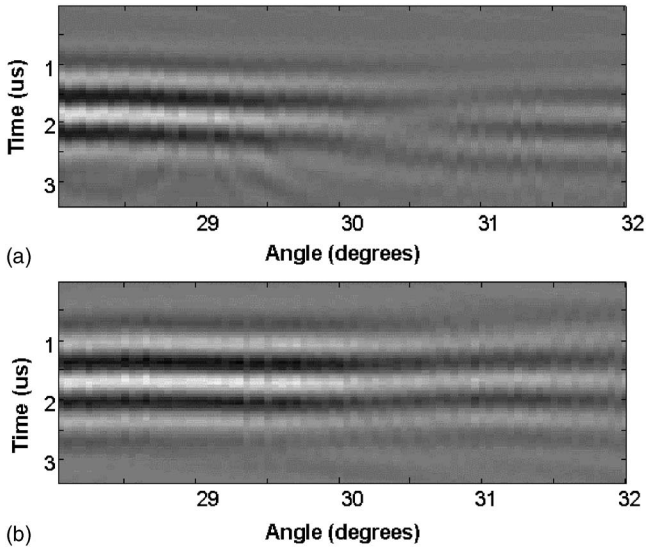

FIG. 5. Time-reversal of "plane" waves (experiment). (a) The temporal shape of the reflected signals $f(t)$ recorded on array 2, as a function of the incident angle, when emitting a "plane wave" $e(t)$ from array 1. (b) The temporal shape of signals $s(t)$ recorded on array 1 after time-reversal of $f(t)$ and backpropagation, as a function of the incident angle.

The recorded signals $s(t)$ at the end of this time-reversal process should then be proportional to the originally emitted signals $e(t)$, and the proportionality factor is $|R(\theta_i)|^2$: no distortion happens for the time-reversed and backpropagated signals $s(t)$ as passing the critical angle, as time-reversal restores the phases [Fig. 4(b)]. Nevertheless, those signals are not identical to the primarily emitted ones, as energy is lost during the time-reversal process: as long as the incident angle θ_i is lower than the second (shear) critical angle θ_s^* the two arrays located on the same side of the interface do not make up a closed time-reversal cavity. When $\theta_i > \theta_s^*$, $|R(\theta_i)|=1$ and $s(t)=e(t)$: as no propagating wave is transmitted, no information is lost in transmission for the time-reversal process and the two arrays make up a closed time-reversal cavity.

B. Experiment

In order to put experimental evidence on the above-noted considerations, the experimental setup presented in Fig. 1 is used: two identical arrays (arrays 1 and 2, respectively) of 64 transducers each, central frequency 1.5 MHz, array pitch 1 mm, are placed in front of a titanium block so that a "plane" wave can be emitted by array 1, reflected by the solid, and recorded on array 2. The whole setup is immersed in water. The waves that are obtained by using an array of finite aperture are not rigorously plane waves. The "plane" waves that are emitted are obtained exciting all the transducers of an array at the same time with the same signal.

The incident angle can vary around the Rayleigh angle, so that a distortion of the reflected signals is expected. The signal recorded on array 2 is then time-reversed and sent back toward array 1. The theory of time-reversal indicates that this operation should restore the original shape of the wave,[1–3,17] but we have to be aware that in our case the cavity is not closed: first, the time-reversal mirror in reflection does not allow us to record the wave that is transmitted into the solid; and part of the Rayleigh wave. Those waves cannot be used in the time-reversal focusing. In order to have a closed time-reversal cavity,[3] a third array should be located inside the solid (to receive end time-reverse the transmitted waves) or parallel to the interface (to receive and time-reverse the Rayleigh wave). Second, because the array used as time-reversal mirror has a finite extension, some energy escapes them that cannot be time-reversed either.

From Figs. 2 and 4 one expects to visualize the distortion of the reflected wave only on a small angular span around the Rayleigh angle. Indeed, beyond the Rayleigh angle, the reflection coefficient presents a nearly constant imaginary part with respect to the incident angle (Fig. 2). This results in a one-wavelength dephasing of the reflected wave, that cannot be detected (the reflected waves obtained with $\theta_i=20°$ and $\theta_i=50°$ superimpose perfectly in Fig. 4). In practice, in order to detect a change of the temporal shape of the wave when passing the Rayleigh angle, it will be necessary to vary the incident angle on a small angular span around this angle.

The temporal shape of the directly reflected signals $f(t)$ and of the time-reversed and backpropagated signals $s(t)$ as a function of incident angle are presented in Fig. 5. As expected, a distortion of the reflected signals $f(t)$ is observed for incident angles between 30° and 31° [Fig. 5(a)], whereas this distortion is compensated in $s(t)$ [Fig. 5(b)]. We also observe a strong energy decrease of the time-reversed and backpropagated signals $s(t)$ for incident angles around the Rayleigh angle, that was not predicted by the theory [compare Fig. 5(b) and Fig. 4(b)]: at the Rayleigh angle, the reflected beam is spatially shifted, and more energy escapes the time-reversal mirror. This energy decrease would certainly

not be visible if we were able to record and time-reverse the Rayleigh wave. The theory is based on plane waves: in order to reach experimentally the predictions of the theory we would have to work with arrays of infinite extent, which would also record the Rayleigh wave as it reradiates into the fluid.

III. SPATIAL FOCUSING BY CYLINDRICAL LAW OR TIME-REVERSAL AROUND THE RAYLEIGH ANGLE

In this section, spatial focusing with cylindrical law or time-reversal using a time-reversal mirror in reflection is tested. We observe and qualitatively discuss the influence of the attack angle on focusing quality (*the attack angle* is the angle θ_i between the normal of the interface and the normal of the echographic arrays, see Fig. 1)

Theory and simulations of spatial focusing by time-reversal in the presence of an interface have been done by Cassereau and Fink[16] in the case of a fluid-fluid interface and at near-normal incidence, and thus no pulse shape distortion was observed. Parallel to that work, theory and experiments of the reflection of a focused beam at a fluid-solid interface at Rayleigh angle have been done by Matikas *et al.*:[8] they predicted and observed a lateral shift of the focal spot when focusing at the Rayleigh angle; they explained the observed shift of the focal spot by the shift that the ultrasound beam experiences at the reflection at the Rayleigh angle.

Here, the aim is to focus the ultrasonic field on the central element of array 2 by sending a wave from array 1, using the experimental setup presented in Fig. 1. Two different techniques have been tested for such a focusing. First, a cylindrical law is sent from array 1: each element of the array emits the same temporal signal, with the appropriate time delay so that the waves originating from all elements of array 1 arrive at the same time on the central element of array 2 (the desired focal point). Time delays are calculated geometrically, assuming a constant speed of sound in water of 1.46 mm/μs, and neglecting the effects of the variations of the reflection coefficient with the incident angle. Such a wave front is presented in Fig. 6(a). Second, the focusing by time reversal is investigated: a pulse is emitted from the desired focal point, the acoustical wave is then recorded on array 1, time-reversed, and sent back in direction of array 2. The focusing wave front calculated by time reversal is presented in Fig. 6(b) for an attack angle close to the Rayleigh angle. The focusing patterns associated to both wave fronts are compared to a reference focusing: the focusing obtained by sending a cylindrical law from the first toward the second array, located directly in front of it, so that there is no fluid-solid interface on the waves' path between the arrays.

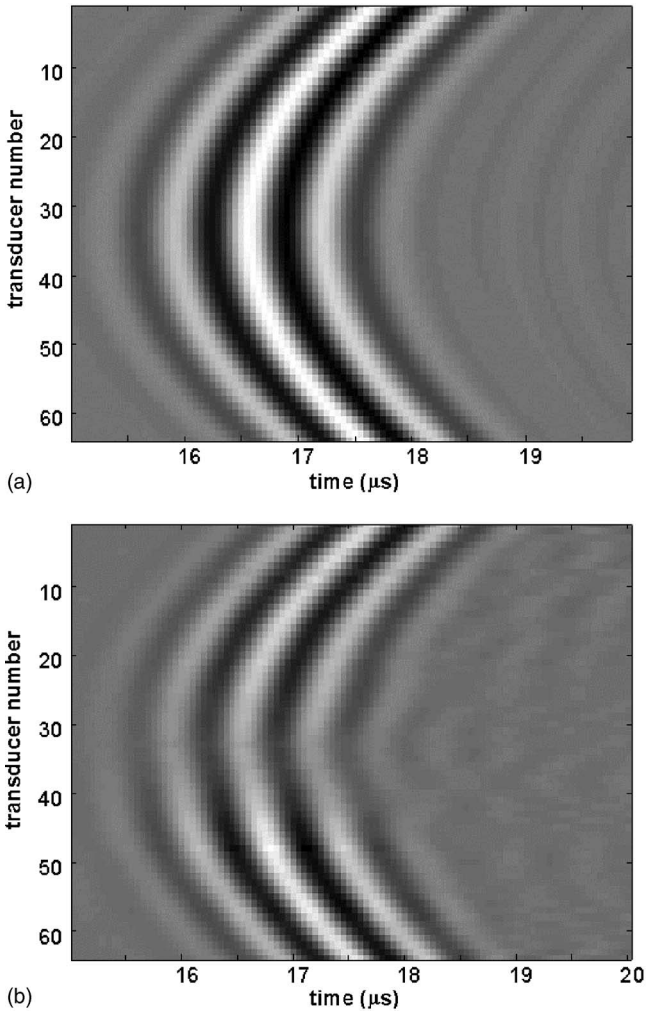

FIG. 6. Focusing wave fronts to be sent by array 1 to focus on central element of array 2 (experimental data). (a) Prefocused (cylindrical) wave front, built by computing the geometrical time delays to be applied to all the transducers on array 1 in order to arrive in phase on the central transducer of array 2. (b) The focusing wave front deduced from time reversal. On line i is presented in gray level the temporal shape of the signal that has to be emitted by element i of focusing array.

A. Simulation

First, simulations are performed in order to better understand how the spatial focusing can be affected by the reflection at the fluid-solid interface. Given the geometry of the experiment and the variations of the reflection coefficient with the incident angle, one can derive all the Green's functions between any elements of arrays 1 and 2 taking into account the reflection on the interface. Using these Green's functions the propagation of any wave going from array 1 to array 2 and from array 2 to array 1 is calculated for any attack angle by convoluting the emitted signals by the Green's functions. We use this technique to simulate the focusing on array 2 by sending from array 1 the wave fronts corresponding to the three methods described earlier: (a) reference cylindrical focusing, (b) time-reversal focusing near the critical angle, (c) cylindrical focusing near the critical angle. The resulting focal spots for an attack angle close to the Rayleigh angle are plotted in Fig. 7.

Looking at Fig. 7(b), we observe that focusing with a cylindrical law leads to a dissymmetrical focal spot, with higher residual pressure on the right-hand side of the main lobe than on its left-hand side (or in other words, less contrast on the right than on the left). Because of the reflection near the critical angle, focusing with a symmetrical cylindrical law in an apparently symmetrical geometry surprisingly results in a dissymmetrical focal spot. The dissymmetry of the focal spot can be explained: the cylindrical law can be

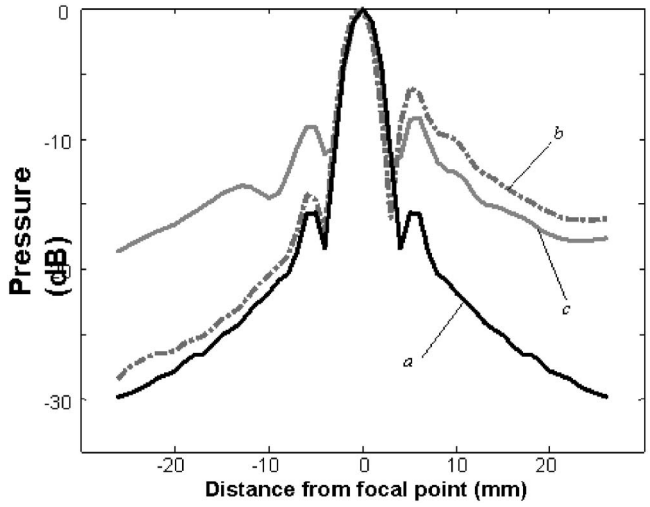

FIG. 7. Scan of the focal spots obtained with different focusing methods (simulation results): (a) reference: cylindrical law through water, (b) cylindrical law with reflection near critical angle, (c) time-reversal with reflection near critical angle. The curves represent the temporal maximum of the pressure received on array 2 as a function of the distance to focal point, in dB.

decomposed in a sum of plane waves with different incident angles on the interface. Those of the plane wave components that have an incident angle close to the Rayleigh angle will be affected: as the incident beam "slips" on the interface as experiencing reflection at Rayleigh angle, the transducers of the other array that should receive the part of the wave front incident at Rayleigh angle will receive less energy when their neighbors will receive more energy; moreover there will be a phase distortion of the wave front. The interface thus breaks the symmetry of the focusing wave front by distorting and dephasing part of it, and it results in an asymmetrical focal spot with less energy at one side of the main lobe than the other side. See Fig. 8 for an illustration of these phenomena.

Focusing with time-reversal restores the symmetry of the focal spot, but there is contrast loss (higher residual pressure levels) on both sides of the main lobe [Fig. 7(c)]. One can understand the recovery of the symmetry analyzing the two steps of the time-reversal process: in the first step, a

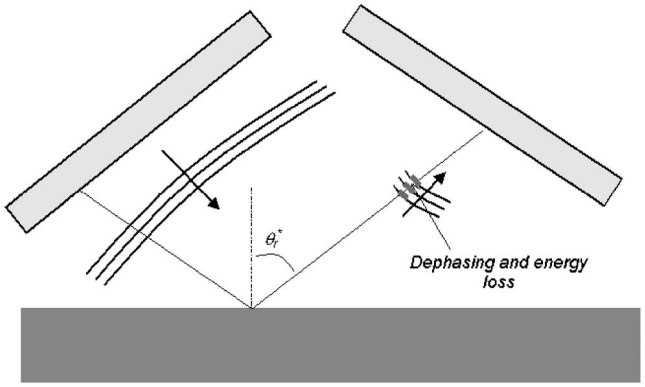

FIG. 8. Spatial focusing of a cylindrical law for an attack angle close to the Rayleigh angle. The plane wave components from the decomposition of the cylindrical law are not affected in equal way by the focusing because their incident angles cover a wide angular span, so that after reflection the focusing wave front is distorted, resulting in a dissymmetric focal spot.

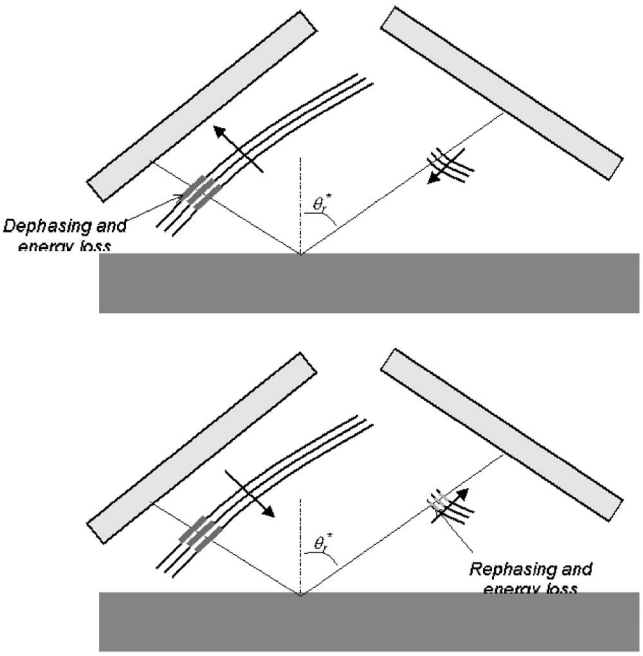

FIG. 9. Spatial focusing by time reversal for an attack angle close to the Rayleigh angle. Top panel: an impulse is emitted from the target (central) element of array 2, the emitted cylindrical wave is reflected at the interface which induces a distortion, and the distorted field is recorded by array 1. Bottom panel: the recorded field is time-reversed and sent back toward array 2, thus experiencing another reflection at the interface that restores the phases of the wave front, leading to a symmetric focal spot.

cylindrical wave is emitted from the central element of array 2. This wave can be decomposed as a sum of plane wave components. These components are not affected in the same manner by the reflection, so that the cylindrical wave that is reflected and then recorded on array 1 is dissymmetrical. A time-reversal focusing wave front is presented in Fig. 6(b): the wave arriving on elements 30–40 has been particularly affected (energy loss, temporal distortion and dephasing with respect to a cylindrical wave front). During the focusing step, the phase and temporal shape of the angular components altered in the first step are restored, and the resulting focal spot is symmetrical. However, the amplitude of those plane wave components suffers again the same energy loss as in the first step. The system behaves as if the aperture of the focusing array was modulated by a transfer function with lower values around elements 30–40 and higher values at the edges. Such an anti-apodization leads to higher residual pressure levels on both sides of the main lobe of the focal spot than in the reference experiment. See Fig. 9 for an illustration of these phenomena.

B. Experiment

The corresponding experiment has been done with an attack angle close to the Rayleigh angle. The focal spots obtained with the three focusing techniques—(a) reference cylindrical focusing, (b) time-reversal focusing near critical angle, (c) cylindrical focusing near critical angle—have been obtained and plotted in Fig. 10. We observe the same features as in the simulation: a dissymmetrical focal spot when focusing with the cylindrical law and a restoration of the

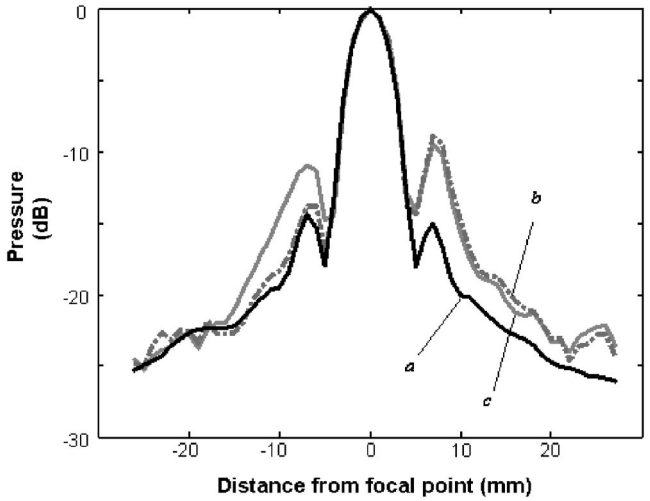

FIG. 10. Scan of the focal spots obtained with different focusing methods (experimental results): (a) reference: cylindrical law through water; (b) cylindrical law with reflection near the Rayleigh angle; (c) time-reversal with reflection near the Rayleigh angle. The curves represent the temporal maximum of the pressure received on focal plane as a function of the distance to focal point, in dB.

symmetry of the focal spot with a loss of contrast when focusing by time-reversal. As in the simulation, the focal spot obtained by focusing with the cylindrical law near the critical angle looks like the reference focal spot on the left-hand side of the main lobe and like the time-reversal focal spot on its right-hand side. Note that no spatial shift of the focal spot is observed here, neither when focusing by cylindrical law nor by time reversal.

IV. SPATIAL FOCUSING WITH TIME REVERSAL WELL BEYOND THE RAYLEIGH ANGLE: FROM THE TIME-REVERSAL MIRROR TO THE TIME-REVERSAL CAVITY

When focusing with time reversal near the Rayleigh angle, a contrast loss in the focal spot with respect to the reference focusing is observed. This contrast loss is mainly due to the fact that during the time-reversal process, part of the Rayleigh wave escapes the time-reversal mirror and the information contained in it is thus lost for the time-reversal process. Theoretically, if we were able to record and time reverse the transmitted waves and all the Rayleigh waves as well as the reflected ones, we would obtain such a good focusing quality as in the reference experiment.[3] The Rayleigh wave could be recorded, for instance, by placing a set of transducers parallel to the interface in order to receive it as it radiates back into the fluid.

Our electronics do not allow us to work with more than two arrays of transducers at the same time. It is however possible to make a time-reversal cavity (implying no information loss) using only the presented experimental setup, by ensuring that no propagating wave is transmitted into the solid or no Rayleigh wave is generated. This occurs when the maximum incident angle of the plane wave components resulting from the decomposition of the focusing wave front is much greater than the shear critical angle and the Rayleigh angle.

We performed the same simulations and experiments as in the previous section, focusing by (a) reference focusing, (b) time-reversal focusing, (c) cylindrical focusing, but with an attack angle 1—near the Rayleigh angle and 2—much greater than the Rayleigh angle. The corresponding focal spots are plotted in Figs. 11 (simulation results) and 12 (experimental results). For incident angles greater than the Rayleigh angle, no wave propagates into the solid and the incident wave suffers no distortion in reflection (cf Sec. II A): in both simulation and experimental results, one can check that focusing by time-reversal or cylindrical law are equivalent and of equal quality as the reference focusing (Figs. 11 and 12, right). It confirms the fact that the time-reversal cavity materialized by the two arrays placed on the same side of the interface is perfect when the attack angle is much greater than the Rayleigh angle. Evanescent waves are created inside the solid for incident angles greater than critical angles. A small part of the incident energy goes with them and the time-reversal mirror in reflection is only a *nearly* perfect time-reversal cavity.

The focal spots obtained when working near the Rayleigh angle (Figs. 11 and 12, left) present the same features

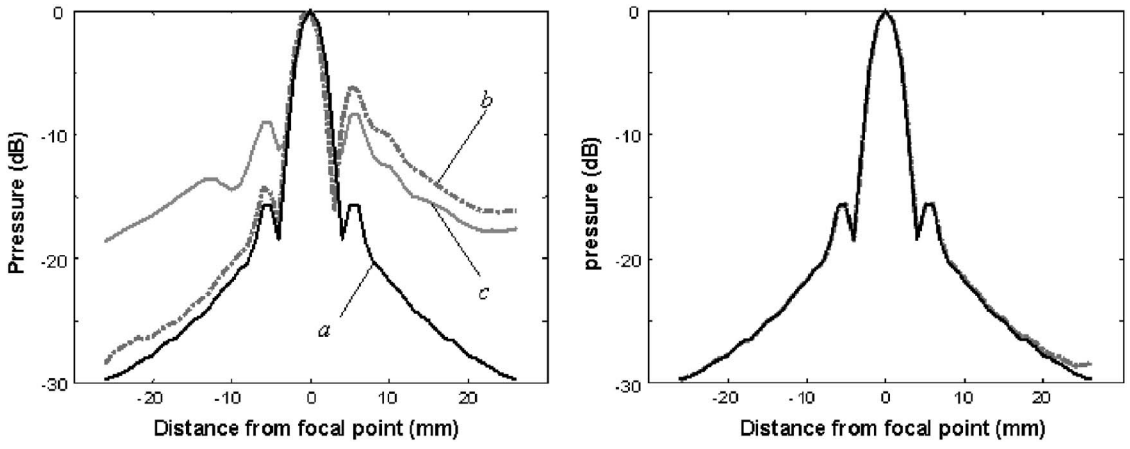

FIG. 11. Scan of the focal spots obtained with different focusing methods (simulation results): (a) reference: cylindrical law through water; (b) cylindrical law with reflection; (c) time-reversal with reflection. Left: incident angle $\theta_i = 31° \approx \theta_r^*$, right: incident angle $\theta_i = 42° > \theta_r^*$. The curves represent the temporal maximum of the pressure received on focal plane as a function of the distance to focal point, in dB.

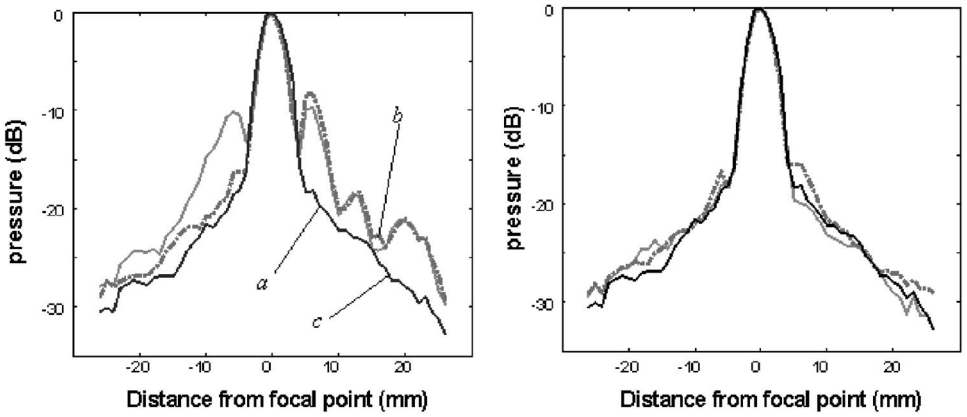

FIG. 12. Scan of the focal spots obtained with different focusing methods (experimental results): (a) reference: cylindrical law through water; (b) cylindrical law with reflection; (c) time-reversal with reflection. Left: incident angle $\theta_i = 31° \approx \theta_r^*$, right: incident angle $\theta_i = 42° > \theta_r^*$. The curves represent the temporal maximum of the pressure received on focal plane as a function of the distance to focal point, in dB.

as the ones described in previous section: dissymmetrization of the focal spot when focusing with the cylindrical laws, symmetry recovery with contrast loss when focusing by time-reversal: the two arrays do not make up a closed time-reversal cavity, as the waves transmitted into the solid cannot be recorded.

V. CONCLUSIONS

Time-reversal experiments around the Rayleigh angle have been performed. First, the effects of a reflection of plane waves on a fluid-solid interface have been described, and a distortion of the temporal shape of the signals for incident angles close to the Rayleigh angle has been observed. Time reversal of such distorted waves leads to pulse shape recovery. This recovery occurs even when using a time-reversal mirror in reflection, made of two arrays located on the same side of the interface: it is not necessary to use a closed time-reversal cavity with a third array to record and time-reverse the transmitted waves. In a second part, we studied the influence of the presence of the interface on spatial focusing of waves. It has been shown that when sending prefocused fronts toward the interface with incident angles close to the Rayleigh angle, focusing quality was affected and a dissymmetric focal spot was observed even though the experimental setup had a symmetrical geometry. However, no spatial shift of the focal point position has been observed. Focusing with time-reversal restores the symmetry of the focusing: such a property could be interesting in nondestructive testing configurations where several arrays are used in reflection. However, the focusing with time-reversal presents a significantly lower contrast than the reference focusing: the fact that the time-reversal mirror in reflection is not a closed time-reversal cavity affects the spatial focusing quality. Optimal spatial focusing by time-reversal can be achieved in conditions where the time-reversal mirror makes up a closed cavity, i.e., when there is no wave transmitted into the solid. This occurs when incident angles are beyond the Rayleigh angle.

ACKNOWLEDGMENTS

The authors would like to thank Dominique Clorennec and Daniel Royer, as well as the reviewers for useful discussions helping us to understand the experimental results.

APPENDIX

Demonstration of Eq. (7) from Eq. (6).

We have

$$F(\omega) = [\mathrm{Re}(R(\theta_i)) + i\,\mathrm{Im}(R(\theta_i))]E(\omega), \tag{A1}$$

$F(\omega)$ and $E(\omega)$ being the Fourier transforms of real-valued functions, they must be hermitic ($F(-\omega) = F(\omega)^*$ and $E(-\omega) = E(\omega)^*$). Complex conjugating Eq. (6) leads to

$$F(-\omega) = [\mathrm{Re}(R(\theta_i)) - i\,\mathrm{Im}(R(\theta_i))]E(-\omega). \tag{A2}$$

Taking into account Eqs. (6) and (A1), linking $E(\omega)$ and $F(\omega)$ for positive and negative frequencies, respectively, we obtain

$$F(\omega) = [\mathrm{Re}(R(\theta_i)) + i\,\mathrm{sign}(\omega)\mathrm{Im}(R(\theta_i))]E(\omega). \tag{A3}$$

This equation is valid for positive and negative frequencies.

Taking the inverse Fourier transform of Eq. (A3) leads directly to[18]

$$f(t) = \mathrm{Re}(R(\theta_i))e(t) + \mathrm{Im}(R(\theta_i))HT[e(t)]. \tag{A4}$$

[1] M. Fink, "Time reversal of ultrasonic fields. I. Basic principles," IEEE Trans. Ultrason. Ferroelectr. Freq. Control **39**, 555–566 (1992).
[2] F. Wu, J. L. Thomas, and M. Fink, "Time reversal of ultrasonic fields. II. Experimental results," IEEE Trans. Ultrason. Ferroelectr. Freq. Control **39**, 567–578 (1992).
[3] D. Cassereau and M. Fink, "Time reversal of ultrasonic fields. III. Theory of the closed time-reversal cavity," IEEE Trans. Ultrason. Ferroelectr. Freq. Control **39**, 579–592 (1992).
[4] D. Cassereau and M. Fink, "Focusing with plane time-reversal mirrors: An efficient alternative to closed cavities," J. Acoust. Soc. Am. **94**, 2373–2386 (1993).
[5] L. M. Brekhovskikh, *Waves in Layered Media* (Academic, New York, 1960).
[6] W. G. Neubauer, "Ultrasonic reflection of a bounded beam at Rayleigh and critical angles for a plane liquid-solid interface," J. Appl. Phys. **44**, 48–55 (1973).
[7] P. B. Nagy, K. Cho, L. Adler, and D. E. Chimenti, "Focal shift of convergent ultrasonic beams reflected from a liquid-solid interface," J. Acoust. Soc. Am. **81**, 835 (1987).
[8] T. E. Matikas, M. Rousseau, and P. Gatignol, "Experimental study of focused ultrasonic beams reflected at a fluid-solid interface in the vicinity of the Rayleigh angle," IEEE Trans. Ultrason. Ferroelectr. Freq. Control **39**, 737–744 (1992).
[9] L. Wang, A. I. Lavrentyev, and S. I. Rokhlin, "Beam and phase effects in angle-beam-through-transmission method of ultrasonic velocity measurement," J. Acoust. Soc. Am. **113**, 1551–1559 (2003).
[10] D. Royer, *Ondes Élastiques dans les Solides*, (Masson, 2000), Vol. **1**, pp. 217–223.
[11] A. H. Nayfeh, *Wave Propagation in Layered Anisotropic Media* (North

Holland, Amsterdam, 1995).
[12]W. Chen and J. Wu, "Reflectometry using longitudinal, shear and Rayleigh waves," Ultrasonics **38**, 909–913 (2000).
[13]H. Lindh, "Transmission of a transient spherical wave at a plane interface," Acustica **12**, 108–112 (1962).
[14]D. H. Towne, "Pulse shapes of spherical waves reflected and refracted at a plane interface separating two homogeneous fluids," J. Acoust. Soc. Am. **44**, 65–76 (1968).
[15]D. Cassereau and D. Guyomar, "Reflection of an impulse spherical wave at a plane interface separating two fluids," J. Acoust. Soc. Am. **92**, 1706–1720 (1992).
[16]D. Cassereau and M. Fink, "Time-reversal focusing through a plane interface separating two fluids," J. Acoust. Soc. Am. **95**, 3145–3154 (1994).
[17]M. Tanter, J. L. Thomas, and M. Fink, "Breaking of time reversal invariance in nonlinear acoustics," Phys. Rev. E **64**, 016602 (2001).
[18]F. de Coulon, *Théorie et Traitement des Signaux* (Dunod, 1984).

Underwater temporary threshold shift in pinnipeds: Effects of noise level and duration

David Kastak
Institute of Marine Sciences, University of California, Santa Cruz, Long Marine Laboratory, 100 Shaffer Road, Santa Cruz, California 95060

Brandon L. Southall
Institute of Marine Sciences, University of California, Santa Cruz, Long Marine Laboratory, 100 Shaffer Road, Santa Cruz, California 95060 and NOAA Acoustics Program, National Marine Fisheries Service, Office of Protected Resources, 1315 East-West Highway, SSMC3 13754, Silver Spring, Maryland 20910

Ronald J. Schusterman and Colleen Reichmuth Kastak
Institute of Marine Sciences, University of California, Santa Cruz, Long Marine Laboratory, 100 Shaffer Road, Santa Cruz, California 95060

(Received 1 April 2005; revised 20 July 2005; accepted 4 August 2005)

Behavioral psychophysical techniques were used to evaluate the residual effects of underwater noise on the hearing sensitivity of three pinnipeds: a California sea lion (*Zalophus californianus*), a harbor seal (*Phoca vitulina*), and a northern elephant seal (*Mirounga angustirostris*). Temporary threshold shift (TTS), defined as the difference between auditory thresholds obtained before and after noise exposure, was assessed. The subjects were exposed to octave-band noise centered at 2500 Hz at two sound pressure levels: 80 and 95 dB SL (*re*: auditory threshold at 2500 Hz). Noise exposure durations were 22, 25, and 50 min. Threshold shifts were assessed at 2500 and 3530 Hz. Mean threshold shifts ranged from 2.9–12.2 dB. Full recovery of auditory sensitivity occurred within 24 h of noise exposure. Control sequences, comprising sham noise exposures, did not result in significant mean threshold shifts for any subject. Threshold shift magnitudes increased with increasing noise sound exposure level (SEL) for two of the three subjects. The results underscore the importance of including sound exposure metrics (incorporating sound pressure level and exposure duration) in order to fully assess the effects of noise on marine mammal hearing. [DOI: 10.1121/1.2047128]

PACS number(s): 43.64.Wn, 43.66.Ed, 43.80.Nd [WWA] Pages: 3154–3163

I. INTRODUCTION

The pinnipeds (seals, sea lions, and walruses) are amphibious carnivores that spend a significant amount of time foraging at sea. All pinnipeds tested thus far are sensitive to sound in air and under water; therefore, they are likely to be susceptible to the harmful effects of loud noise in both media. It has recently been shown that moderate levels of underwater noise can induce a temporary reduction of hearing sensitivity (temporary threshold shift or TTS) in some marine mammals, provided that the exposure duration is relatively long. Noise-induced TTS has been examined in some pinnipeds and odontocete cetaceans (dolphins and other toothed whales) exposed to fatiguing stimuli of varying durations and bandwidths (Finneran *et al.*, 2000; 2002; Kastak and Schusterman, 1996; Kastak *et al.*, 1999; Nachtigall *et al.*, 2003; 2004; Schlundt *et al.*, 2000). In these studies the magnitude of TTS was generally small (<20 dB), and hearing sensitivity recovered rapidly. While it would be helpful to predict the auditory effects of different noise exposures on the hearing of marine mammals, there are no data from which extrapolation can be made from small TTS at low-level, short-duration noise exposures to TTS resulting from louder, longer exposures. Data that show relationships between sound level and TTS exist for some terrestrial mammals, but models of TTS growth in these subjects have not been applied to marine mammals.

One purpose of TTS experiments with marine mammals is to provide data that will aid regulatory agencies in determining potentially harmful levels of anthropogenic noise. Because exposure to anthropogenic noise in the marine environment is sporadic and interrupted, it is necessary to examine variables associated with varying noise sound pressure levels, intermittence of exposure, and total acoustic energy of exposure, in order to accurately predict the effects of noise on marine mammal hearing.

Various models of the effects of interrupted noise exposures on TTS have been proposed (Harris, 1991; Kryter, 1994). An equal energy model predicts that two noise exposures will induce similar threshold shifts if the exposures are matched in sound energy, regardless of the temporal patterning of exposure. Thus, according to an equal energy rule, a doubling of exposure duration and a 3-dB increase in amplitude should induce similar threshold shifts. Use of the 3-dB duration-level exchange rate for determining noise risks under intermittency of exposure is advocated in the most recent noise exposure criteria put forth by the U.S. Department of Health and Human Services (NIOSH, 1998).

A modified equal energy, or 5-dB rule, was formulated under the assumption that some recovery occurs during periods of exposure intermittency; thus, a doubling in exposure duration could be approximated by a 5-dB increase in amplitude. Though incorporated into various noise exposure criteria, exchange rates based on acoustic energy have been called into question by numerous studies (Harding and Bohne, 2004; Patuzzi, 1998; Strasser *et al.*, 2003). Because energy-based exchange rules cannot consistently predict the degree of noise-induced hearing loss, the influence of other acoustic characteristics on TTS must be examined. Specifically, the frequency and amplitude distribution, temporal patterning, and bandwidth/duration properties (e.g., continuous vs impulsive) of fatiguing sounds appear to all be important in determining the potential for noise-induced hearing loss (Ahroon *et al.*, 1993; Hamernik *et al.*, 1991; 1993; 2002).

The goal of this study was to examine the interactions between noise amplitude and duration in inducing TTS in pinnipeds under water, partly to determine whether a simple time-intensity trade-off rule can be applied to marine mammal noise exposure criteria. The experiments reported here were intended to build upon data obtained earlier from the same three subjects (Kastak *et al.*, 1999), using octave-band noise exposure levels of 65–75-dB SL (sensation level, referenced to absolute auditory threshold at center frequency). This study employed octave-band noise at 80 and 95 dB SL, with net exposure durations ranging from 22 to 50 min. It is important to note here that, as in the previous study, the sound levels chosen were based upon the hearing sensitivity of the subjects. Therefore, the absolute exposure conditions across subjects differed by up to 22 dB (the difference between pure-tone thresholds for the sea lion and harbor seal). Threshold shift was assessed at the center frequency of the exposure octave band, as well as one-half octave above the center frequency, where other studies have reported maximal threshold shifts (McFadden, 1986; Moore *et al.*, 2002). Results were analyzed by examining the relationship between TTS and sound pressure level and exposure duration. Additionally, a third metric, sound exposure level, was used to clarify some of the variability in TTS levels that was not explainable by sound pressure level or duration alone. The data reported here will contribute to the understanding of pinniped TTS and to the prediction of certain auditory effects of intense noise exposure on free-ranging marine mammals.

II. METHODS

A. Subjects

Three pinnipeds were used in this study: a 16-years-old female California sea lion (*Zalophus californianus*), a 14-years-old male harbor seal (*Phoca vitulina*), and a 7-years-old female northern elephant seal (*Mirounga angustirostris*). All three subjects had extensive experience performing acoustic signal detection tasks, and each had previously undergone audiometric testing in water (Kastak and Schusterman, 1996; Southall *et al.*, 2000). The animals were housed at the University of California, Santa Cruz, Long Marine Laboratory in outdoor concrete pools filled with running seawater. All audiometric testing and noise exposures were conducted with the approval of the UCSC Chancellor's Animal Research Committee.

B. General procedure

Auditory thresholds were obtained from each subject prior to noise exposure (baseline thresholds), immediately following noise exposure (exposure thresholds), and 24 h following noise exposure (recovery thresholds). Each test sequence spanned 2 days in order to incorporate all testing conditions. Two series of experiments were completed. In the first experiment, net noise exposure duration was held constant at 22 min and noise amplitude was held constant at 80 dB SL. Prior to testing, hearing thresholds at 2500 Hz were obtained for each subject. All noise levels (in SL) were referenced to the mean of these baseline hearing thresholds. The fatiguing stimulus was an octave band of continuous, Gaussian white noise centered at 2500 Hz. Thresholds were measured at the center frequency and at a frequency one-half octave above center frequency (3530 Hz). Twelve test sequences were completed for each of the two testing conditions. In the second experiment, the noise level was held constant at 95 dB SL, while the exposure duration was varied from 25 to 50 min. Thresholds were measured at 2500 Hz for both exposure durations and at 3530 Hz for the 50-min exposures. Eight replicates were completed for each of the three testing conditions.

C. Threshold testing

The stimuli used for threshold testing were 500-ms pure tones (40-ms rise/fall times) that were generated by and manually triggered from a function generator (Stanford Research Systems DS345—40-kHz update rate, 16-bit precision). Signals were attenuated (HP 350C), amplified (Realistic MPA-20), and projected from one of two underwater transducers (NUWC J-9 or Lubell Laboratories LL-1424). The projectors were suspended in the circular test pool (7.5-m diameter, 2.5-m depth) by a PVC harness that was moved along a steel pipe support for positioning. The projector was positioned approximately 5 m behind the testing apparatus, at a depth of about 1 m.

Calibration was conducted daily before and after noise exposure, in the absence of the subjects, by placing a hydrophone (H-56 or International Transducer Corporation ITC-8212) in the position occupied by the subjects' heads during testing. Calibration tones were projected via the function generator from one of the two projecting transducers. The received signal was measured using a PC-based signal analysis software package (SPECTRA PLUS, Pioneer Hill) through the PC sound card. Because of the reverberant characteristics of the testing environment, signal levels were mapped at multiple locations surrounding the center position to ensure that spatial variability in the tonal signal was not greater than 3 dB in the sound field surrounding the chin station.

Underwater thresholds for each animal were estimated using behavioral psychophysical techniques. The subjects were trained using operant conditioning to respond by pressing a paddle when presented a pure tone and to withhold response in the absence of a tone (go/no-go procedure). At

the beginning of a trial, the subject was signaled by a trainer to dive to the test apparatus, which consisted of a chin cup (to prevent movement of the subject's head) and a response paddle. The position of the subject's head while stationed in the chin cup was approximately 1 m below the surface of the water. The "go," or paddle press response, when occurring in the presence of a signal, was recorded as a hit. Withholding response, or a "no-go," in the absence of a signal, was recorded as a correct rejection. Responding in the absence of a signal was recorded as a false alarm, and failure to respond to a signal was scored as a miss. Hits and correct rejections were reinforced with a piece of fish. Subjects were recalled without reinforcement following false alarms and misses. The trial sequence was balanced (i.e., the number of signal-present trials equaled the number of signal-absent trials), and the first-order conditional probability of either trial type was 0.5 (modified from Gellermann, 1933).

The first signal trial of each session was preselected at a level of 20–30 dB above the estimated threshold, ensuring a hit. On subsequent signal trials, the level was decreased by 4 dB following each hit, until the first miss. Following the first miss, the step size was changed to 2 dB, and the signal level was increased following a miss and decreased following a hit (staircase procedure). Each change in the direction of the signal adjustment constituted a reversal. Thresholds were defined as the mean of ten reversals, corresponding to 50% correct detections (Dixon and Mood, 1948).

D. Noise exposures

The subjects had previously been trained to station in front of a platform used to project moderate levels of band-limited noise under water (Kastak *et al.*, 1999). Conditioning techniques were used to gradually increase the noise exposure durations and levels tolerated by the subjects. A single projector (Ocean Engineering Enterprises DRS-8) was mounted on the exposure apparatus, which was placed against the side of the testing pool, approximately 4 m from the testing apparatus. The distance between the subject's head and the noise projector was 0.5 m.

Continuous, Gaussian white noise was generated using the PC software package COOLEDIT (Syntrillium Software) and digitally filtered over the octave band to ensure that the noise spectrum was flat to within ±3 dB. The noise was projected from the DRS-8 transducer. Calibration of the noise stimuli took place daily before and after noise exposure using the same procedure described for calibrating the test stimuli. Figure 1 shows a typical exposure spectrum recorded in the absence of the subject, at the position occupied by the subject's head during exposure. Received octave band levels were either 80 or 95 dB SL. Sound pressure levels corresponding to these SLs differed because of the differences in auditory sensitivity of the three subjects. For the 80-dB SL condition, SPLs were 159 dB *re*: 1 μPa for the sea lion, 137 dB *re*: 1 μPa for the harbor seal, and 149 dB *re*: 1 μPa for the elephant seal. SPLs corresponding to 95-dB SL were 174 dB *re*: 1 μPa for the sea lion, 152 dB *re*: 1 μPa for the harbor seal, and 164 dB *re*: 1 μPa for the elephant seal. The net exposure durations were 22 min (80-dB SL), 25, and 50 min (95-dB SL).

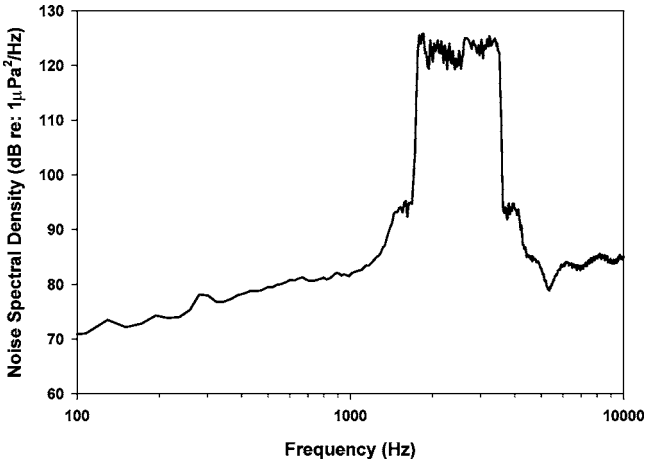

FIG. 1. Noise spectral density of the fatiguing stimulus, recorded from the calibration position in the test pool. The center frequency of the octave band is 2500 Hz and the octave-band level is approximately 159 dB *re*: 1 μPa.

For each exposure condition, the number and duration of dives into the noise field were matched within subjects. Because each of the subjects had to surface to breathe, making sound exposure intermittent, surface intervals between dives were controlled as carefully as possible, to minimize recovery effects and to avoid variability during sequence replications. Net exposure duration was determined by subtracting surface intervals from the overall exposure duration. Across all exposures, the sea lion spent an average of 75% of the total exposure interval on station in the noise field, the harbor seal spent 87%, and the elephant seal spent 84%.

E. Control sessions

During control sessions, subjects completed entire testing sequences, without exposure to noise, for net durations corresponding to each experimental exposure condition (22, 25, or 50 min). Surface intervals in control sessions were similar to those in experimental sessions. Control sequences were conducted to ensure that physiological, motivational, or emotional factors related to session length, dive duration, or satiation, as opposed to the presence of fatiguing noise, could be eliminated as causative factors for observed threshold shifts. During the first experiment, each subject completed a total of six control sequences, each with a sham exposure of 22 min. During the second experiment, each subject completed a total of ten control sequences, four with sham exposures of 25 min and six with sham exposures of 50 min.

F. Data analysis

Threshold shifts were calculated by subtracting pre-exposure thresholds from those obtained immediately following noise exposure. Recovery was assessed by comparing thresholds obtained 24 h following noise exposure to both baseline and exposure thresholds. A within-subjects, repeated measures design was used. If an overall significant difference between thresholds among the three conditions was found using a one-way, repeated measures ANOVA, a Student–

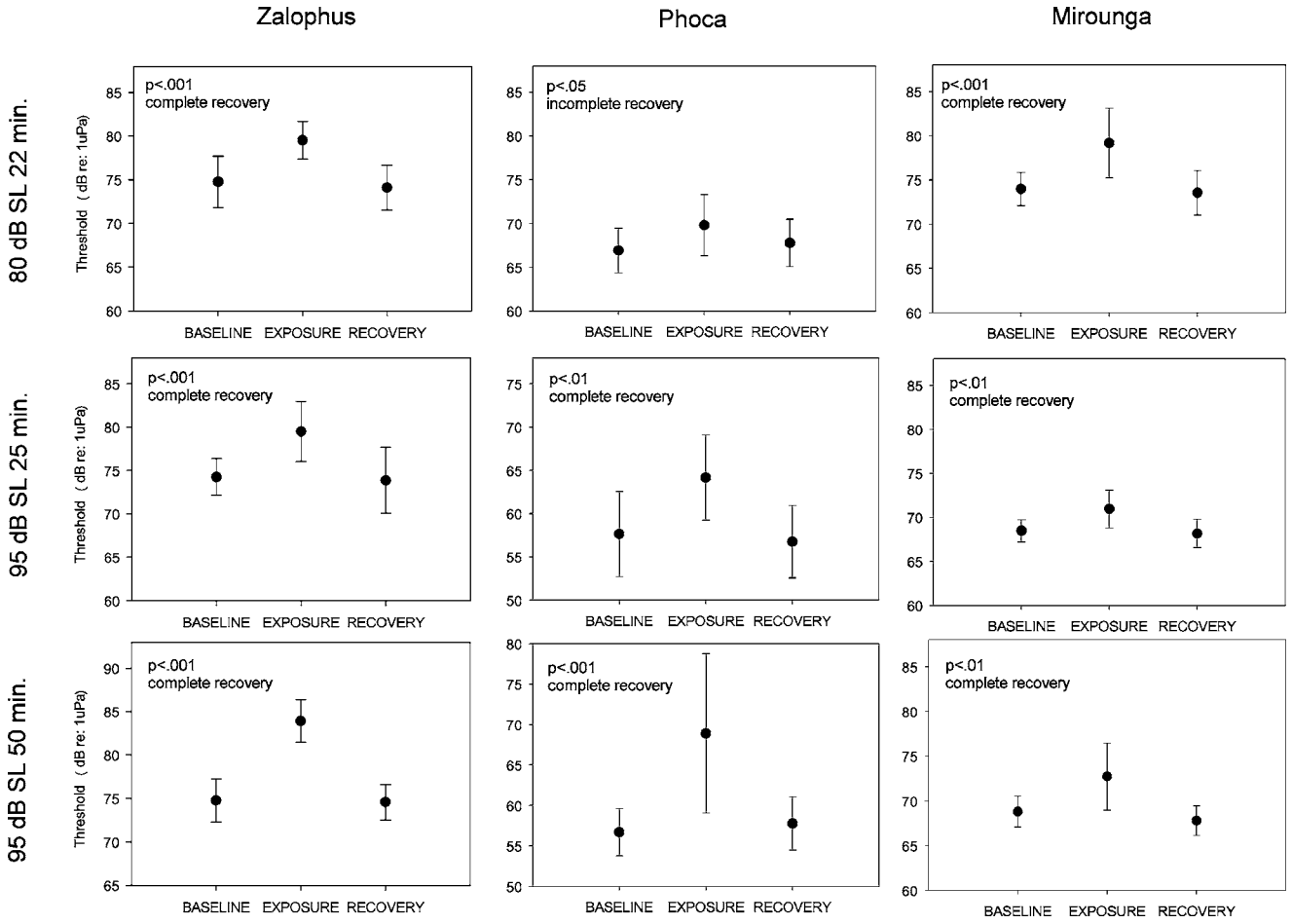

FIG. 2. Baseline (pre-exposure), exposure, and recovery thresholds for a sea lion, a harbor seal, and an elephant seal exposed to octave-band noise centered at 2500 Hz. The test frequency was 2500 Hz. The p values indicate statistical significance of comparisons between conditions. In all cases, exposure thresholds were significantly greater than baseline thresholds, and there was no difference between baseline and recovery thresholds. In all but one case, recovery thresholds were significantly lower than exposure thresholds. Points refer to mean thresholds obtained over multiple sessions; error bars denote standard deviations.

Newman–Keuls test was performed for each individual comparison. Mean threshold shifts in experimental and control conditions were compared using a Student's t-test, as were differences between control session shifts and a hypothetical condition of 0-dB shift. For purposes of analyzing the effects of exposure duration, the 22- and 25-min conditions were combined. This grouping is justified in that the 3-min difference between the exposure conditions translates into a negligible difference in sound energy or sound exposure level of approximately 0.5 dB.

III. RESULTS

A. Exposure vs control conditions

When tested at the center frequency of the exposure band, all subjects showed evidence of a significant mean threshold shift under all exposure conditions (Fig. 2). Sessions used to estimate thresholds for each of the subjects generally lasted about 15 min; therefore, it was common to find that recovery occurred during these sessions. Recovery was usually seen as a progressive decrease in the level of signals required to elicit a "go" response. Because all of the tracking data for a given session (ten reversals) were used to estimate thresholds, it is likely that the mean TTS levels presented here are underestimates of TTS that would have been recorded at earlier postexposure levels. For example, TTS_2, the threshold shift measured 2 min following exposure, is commonly cited as representing the peak postexposure TTS (Hirsch and Ward, 1952); threshold shifts recorded 15 min later are usually smaller in magnitude.

There was a statistically significant relationship between exposure condition and threshold—mean exposure thresholds were greater than mean baseline thresholds and recovery thresholds. Auditory sensitivity recovered fully within 24 h, with the exception of the 2.9-dB mean threshold elevation following recovery in the harbor seal (for the 22-min, 80-dB SL, 137-dB *re*: 1-μPa condition). Figure 3 shows that threshold shifts measured one-half octave higher than the noise band center frequency were significantly smaller than those measured at center frequency for the sea lion and elephant seal, but were not significantly different for the harbor seal.

B. TTS growth with sound pressure level and duration

Threshold shifts as a function of increasing noise exposure level are shown in Fig. 4. For the sea lion and harbor

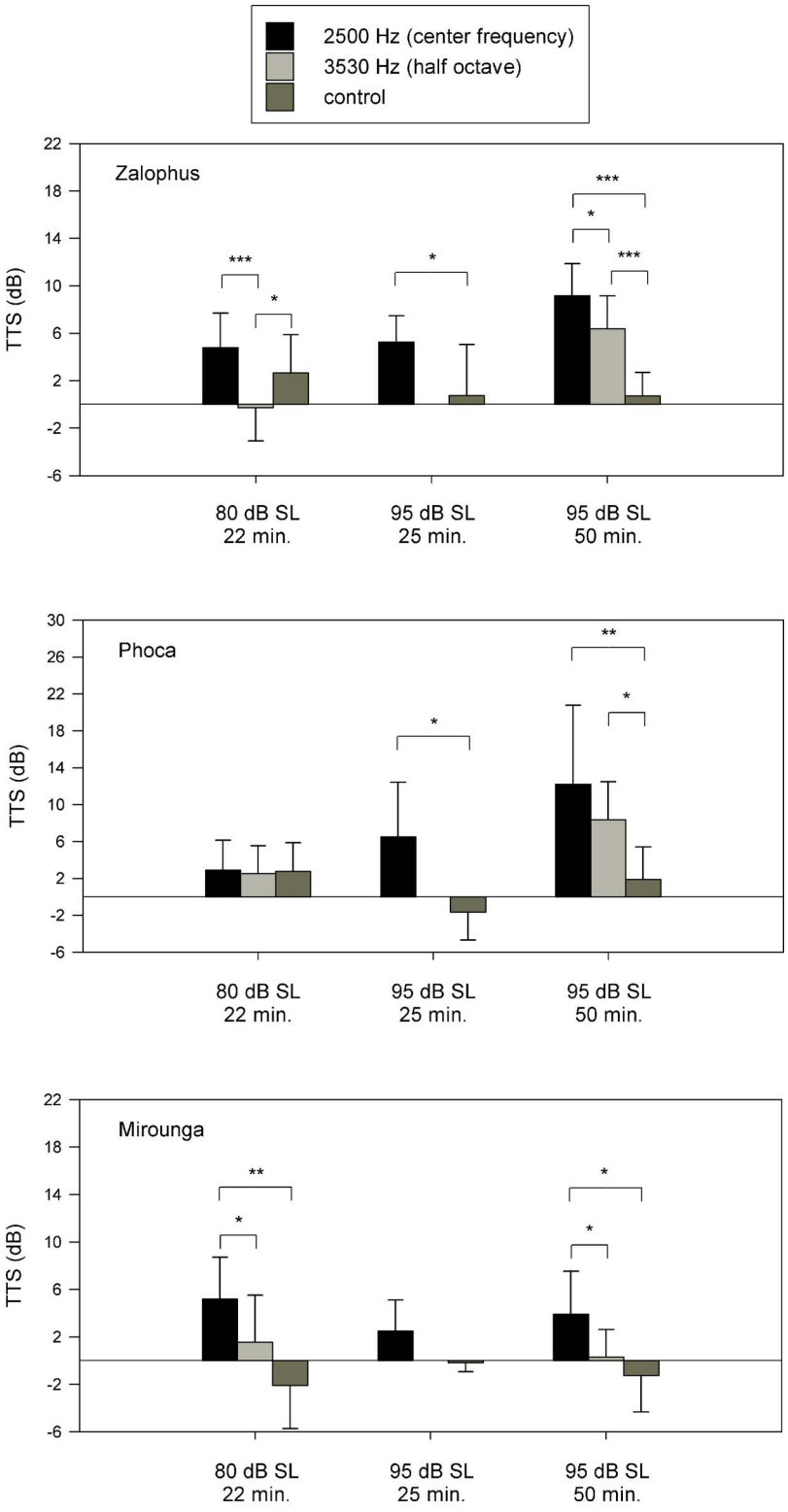

FIG. 3. Mean threshold shifts for three exposure levels and three exposure durations. Threshold shifts were measured at 2500 or 3530 Hz following exposure to octave-band noise centered at 2500 Hz. Control sequences duplicated the exposure sequences, with the exception that no noise was presented. Brackets show differences between individual groups of data. ($^{*}=p<0.05$; $^{**}=p<0.01$; $^{***}=p<0.001$; all other comparisons are not significant.)

seal, threshold shifts at center frequency increased by 0.5 and 3.6 dB, respectively, when duration was held constant (22–25 min) and noise SPL was increased from 80 to 95 dB SL. Neither of these differences was statistically significant. For the elephant seal, the magnitude of threshold shift decreased by 2.7 dB when the noise SPL was increased from 80 to 95 dB SL. This difference was also not significant.

Threshold shifts as a function of noise exposure duration are shown in Fig. 5. Threshold shifts increased significantly with an increase in exposure duration from 20 to 50 min, with exposure level held constant at 95 dB SL for the sea lion (3.9 dB). For the harbor seal, the difference between mean threshold shifts at 25 and 50 min at 95-dB SL was 5.7 dB. However, because of high levels of variability, the difference was not significant. Similarly, a difference of 1.4 dB for the elephant seal under the same conditions was not significant. Doubling the exposure duration (+3-dB sound exposure level) had a greater effect on threshold shift

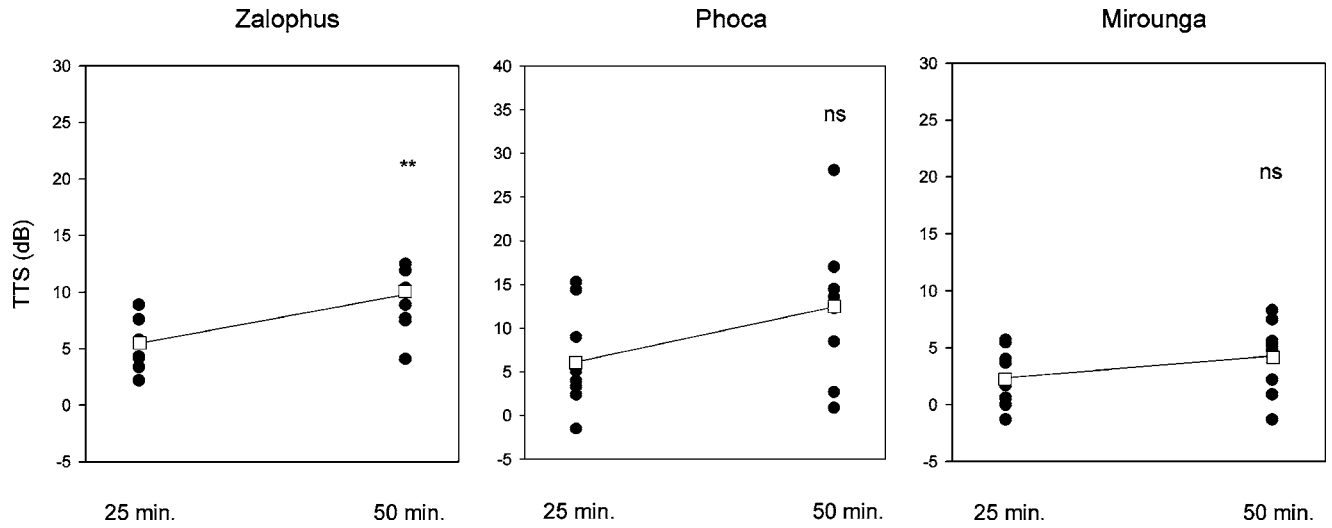

FIG. 4. Threshold shifts at center frequency of noise band following 25 and 50 min of 95-dB SL noise exposure. Points denote individual threshold shifts determined from test sequences. Open squares denote mean threshold shifts. ($^{**}=p<0.001$; ns=not significant.)

than an increase of 15 dB in exposure level, even though for two subjects the change failed to meet statistical significance.

C. Sound exposure level

Figure 6 shows TTS magnitude plotted against sound exposure level (SEL), a metric that incorporates both sound pressure level and duration. SEL is calculated as 10 times the logarithm of the integral, with respect to duration, of the mean-square sound pressure, referenced to 1 μPa^2 s. Using this metric, 0-dB SEL corresponds to a continuous sound whose rms sound pressure equals the reference pressure of 1 μPa at a duration of 1 s (Morfey, 2001). For the sea lion and the harbor seal, there was a significant linear relationship between SEL and TTS magnitude, with slopes of 0.16- and 0.39-dB TTS per dB SEL. These slopes are smaller than slopes of exposure level vs TTS that have been obtained in similar studies (Carder and Miller, 1972; Mills *et al.*, 1979; Ward *et al.*, 1958), illustrating that a linear fit to the data, though significant, is inadequate to describe the relationship between sound exposure and threshold shift at the low threshold shift magnitudes obtained in this study. For the elephant seal, the slope of the regression line was not significantly different from zero.

A curvilinear fit, modified from the exponential form of an equation developed by Maslen (1981) to describe the relationship between asymptotic threshold shift and sound pressure level, has the advantage of illustrating the relationship between shift and sound exposure at low levels, with a lower asymptote of 0-dB shift. The equation used in this study was

$$\mathrm{TTS} = (10m1)\log_{10}(1 + 10^{(\mathrm{SEL}-m2)/10}).$$

The parameter $m1$ corresponds approximately to the slope of the linear portion of the curve relating noise level to threshold shift, while $m2$ corresponds to the x intercept of the extrapolation of the linear portion of the curve, or what can be considered the approximate onset of TTS. In all cases, the fit of this curve was better than that of a simple exponential.

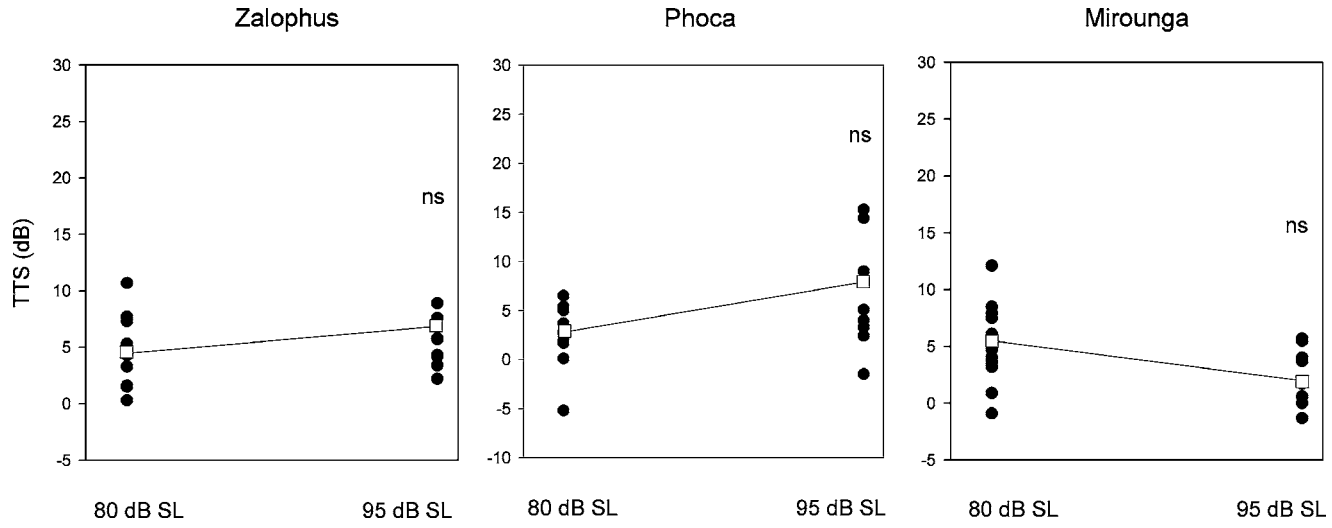

FIG. 5. Threshold shifts at center frequency of noise band following 22 min of exposure at 80-dB SL and 25 min of exposure at 95-dB SL. Points denote individual threshold shifts determined from test sequences. Open squares denote mean threshold shifts. (ns=not significant.)

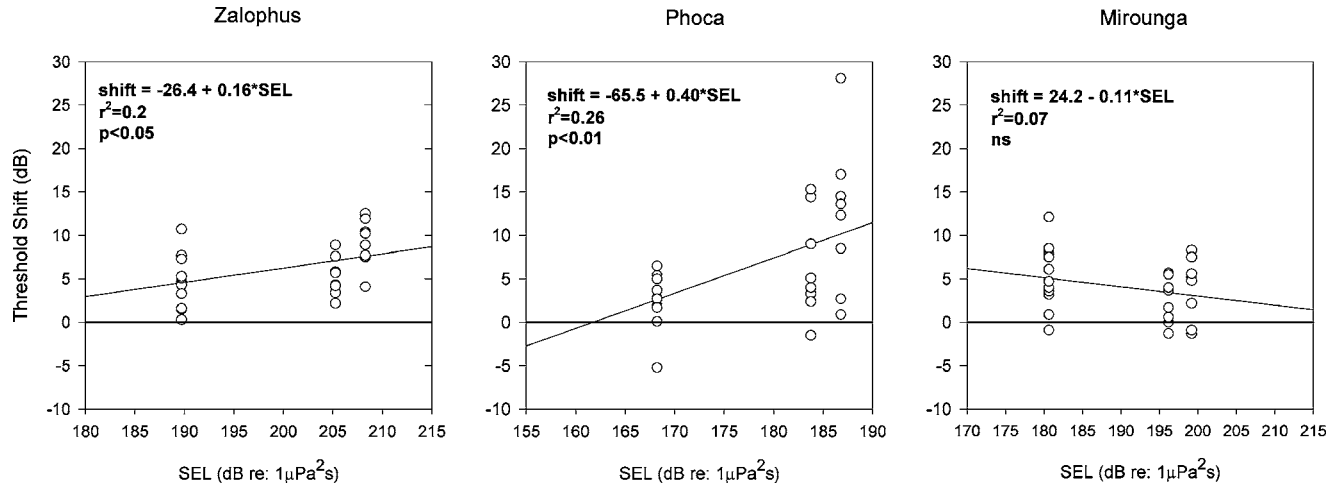

FIG. 6. Linear regression plots of TTS vs sound exposure level at center frequency of noise band for the three subjects. Line slopes, significance, and *r*-squared values are provided in the legends. The horizontal lines are zero-shift lines provided for reference.

When curves of this form are applied to the center frequency TTS data obtained from the sea lion and harbor seal, the value of $m2$ is 205.6 dB *re*: 1 μPa^{2}s for the sea lion ($r^2=0.27; F_{1,26}=9.45; p<0.01$) and 182.3 dB *re*: 1 μPa^{2}s for the harbor seal ($r^2=0.30; F_{1,26}=11.05; p<0.01$). The best fits resulting in $m2$ estimates were obtained by fixing $m1$ at 2 dB/dB. Poorer fits were obtained at both higher and lower values of $m1$ ranging from 1.0 to 3.0, values that we considered reasonable limitations based on data from terrestrial animals. An attempt to fit this equation form to the elephant seal center frequency data did not converge on estimates for either $m1$ or $m2$, probably because of outlying threshold shift values at low exposure levels.

Better fits to all three data sets were obtained by including the half-octave shifts along with center frequency shifts (Fig. 7). The best-fit curves have essentially unchanged parameters for the sea lion ($m2=206.5; r^2=0.32; F_{1,46}=27.07, p<0.0001$) and the harbor seal ($m2=183.1; r^2=0.37; F_{1,46}=21.77, p<0.0001$). With the half-octave threshold shifts included, the elephant seal data provided an estimate for $m2$ of 203.9 with $m1$ fixed at 2.0; however, the fit was still nonsignificant.

In order to determine whether differences in TTS onset represented by differences in individual hearing levels can be normalized to allow a combination of data from subjects with varying sound detection thresholds, SELs were converted to SL, in the same way that the absolute noise exposure levels were determined. Normalization here simply provides a common reference so that, with exposure levels equalized, the effects of duration can be examined. For example, the harbor seal's detection threshold for a 2500-Hz, 500-ms pure tone was about 57 dB *re*: 1 μPa. The sound exposure level of a tone of this duration at threshold is 54 dB *re*: 1 μPa^2 s. Likewise, SELs for the sea lion and elephant seal at threshold were 75.5 and 66.3 dB *re*: μ Pa^2 s, respectively. When the thresholds are subtracted from the onset of TTS, the differences are 129.1 dB for the harbor seal, 131 dB for the sea lion, and 137.6 dB for the elephant seal.

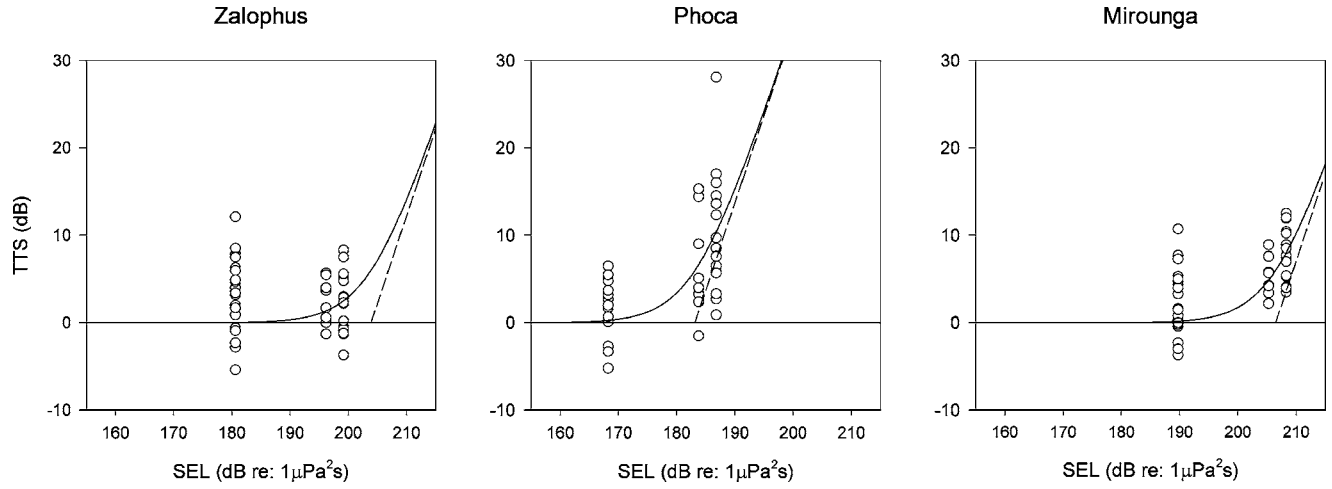

FIG. 7. Nonlinear regression plots of TTS vs sound exposure level at center frequency of noise band and one-half octave higher for the three subjects. See the text for an equation and significance of the model parameters. Solid curves represent exponential increase of TTS with increasing SEL. The horizontal lines are zero-shift lines. Dotted straight lines project TTS onset to linear portion of curve at higher exposure levels.

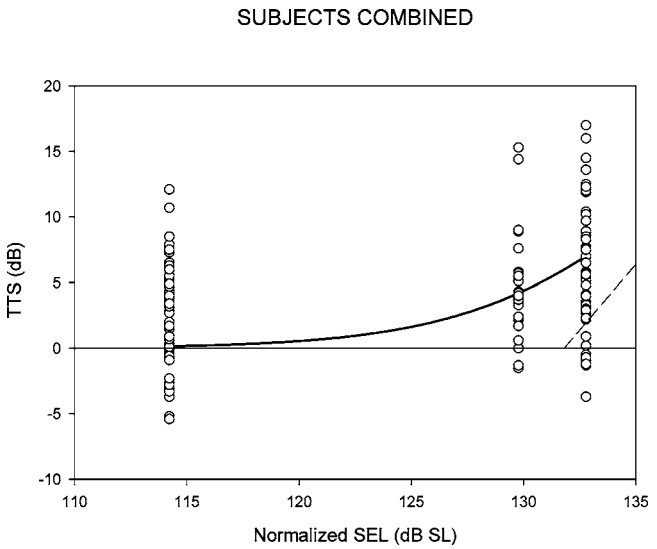

FIG. 8. Combined nonlinear regression plot of TTS vs normalized sound exposure level (referred to individual thresholds; includes half-octave data). See the text for details.

A curve fit to the normalized data combined for all subjects ($r^2=0.13$; $F_{1,142}=21.9$; $p<0.0001$) is shown in Fig. 8. The parameter $m1$ is again fixed at 2, and the resulting estimate for $m2$ is 131.8 $SL_{(e)}$ (the subscript e denotes that sensation level is referred to a threshold sound exposure level).

IV. DISCUSSION

Building upon results from previous work with the same subjects (Kastak *et al.*, 1999), the data presented here show that TTS can be induced in pinnipeds under water following exposure to moderate levels of noise for durations of up to 50 min. The mean threshold shifts in this experiment were generally small relative to experimentally induced threshold shifts in other mammals, with mean (statistically significant) shifts ranging from 2.49 to 12.2 dB, and maximum individual threshold shifts of 28.1 dB (harbor seal), 12.5 dB (sea lion), and 12.1 dB (elephant seal). A linear relationship between the amplitude of the fatiguing stimulus and TTS has been shown in some, but not all species, but primarily at durations and levels greater than those used in this study (see, e.g., Smith *et al.*, 2004). Because at low threshold shift levels there is a curvilinear rather than a linear relationship between noise level and threshold shift, extrapolating these data in order to predict TTS at higher exposure levels should be approached cautiously. Applying a simple linear model to describe the relationship between TTS and SEL at low exposure levels will most likely result in underestimates of TTS at longer exposure durations and higher noise levels. Like a simple linear model, the adapted exponential model used here is limited in terms of predictive power. The limitations arise not through the use of the model itself, but from the highly variable, relatively low TTS levels and the small number of sound exposure levels used. Nonetheless, the increase in TTS of 2 dB per dB SEL in this study is approximately the same as values from prior studies of humans (Mills *et al.*, 1979; Ward *et al.*, 1958). The significance of this result must be taken with caution, however, because of the high degree of variability and the relatively small number of SELs used. As more data are obtained by using higher sound exposure levels, different patterns of intermittency, and additional subjects, the fit of this or other models should improve.

Increasing the noise exposure duration and amplitude independently resulted in increases in the magnitude of the threshold shift for two of the three subjects of this experiment. Increasing the exposure duration from 25 to 50 min had a greater effect on threshold shifts than increasing the exposure level from 80 to 95 dB SL. These results are inconsistent with an equal energy model (3-dB exchange rate), and suggest that moderate levels of long duration sounds may have a greater impact on hearing than equal-energy sounds of greater amplitude but shorter duration. Preliminary results from the same subjects tested in air also support this conclusion (Kastak, 2003; Kastak and Insley, 2005); however, more testing at various combinations of exposure level and duration needs to be completed before definitive conclusions can be reached.

Also of interest is the finding that mean threshold shifts one-half octave above center frequency were smaller than the corresponding shifts at center frequency in all subjects, contrasting with previous findings (McFadden, 1986) which showed a maximal shift one-half octave above the frequency of the exposure stimulus. The half-octave effect has been shown to occur after exposures to pure tones; in fact, TTS at the exposure frequency may not be evident, even in the presence of a significant threshold shift one-half octave higher. Consistent with observations of this effect, Schlundt *et al.* (2000), using brief tones as fatiguing stimuli, found that threshold shifts measured in odontocetes (bottlenose dolphins and beluga whales) generally occurred at frequencies above the exposure frequency. This type of upward spread in affected frequency has been attributed to the basalward spread in the peak of the cochlear traveling wave under the influence of an increasingly intense sinusoid, and partially attributed to cochlear amplification (McFadden and Yama, 1983; McFadden, 1986; Moore *et al.*, 2002). Although Nachtigall *et al.* (2004) recently found maximal threshold shifts approximately one-half octave above the upper limit of a 7-kHz-wide noise band in bottlenose dolphins, this finding has not been shown by some other studies using bands of noise (e.g., Neilsen *et al.*, 1986). It is possible that exposure to bands of noise does not result in a shift in the peak of the cochlear partition response because of phase differences between individual frequency components, explaining why some experiments fail to demonstrate this effect.

Although the limited evidence from this study does not support an equal-energy exchange model, threshold shifts *were* proportional to overall sound exposure level, indicating an effect of noise energy. There are two interesting findings associated with this relationship. First, assuming that threshold shift magnitudes have a lower asymptote at 0 dB, and that a curvilinear, modified exponential curve describes the relationship between SEL and threshold shift, there should be an increase of approximately 2-dB threshold shift per dB of sound exposure level, at noise levels moderately more intense than those used in this study. This 2-dB relationship appears to hold for all three subjects and may be tentatively

used to predict threshold shifts at much higher noise levels. Second, there is a consistency in TTS onset, represented by the second parameter of the fit equation, in sound exposure level (SEL). When the noise levels are referenced to each subject's hearing level, these numbers fall within ±4 dB of a mean value of 132.5-dB $SL_{(e)}$, while the combined data provide an overall onset level of 131.8-dB $SL_{(e)}$. It is important to note that the normalization procedure for sound exposure level was conducted to show that the effects of increasing duration appear to be the same for all subjects, regardless of baseline hearing level, and not to make any inferences about the relationship between an auditory threshold and the sound energy resulting in TTS. In this case, auditory threshold is simply a benchmark that equalizes exposures between subjects with different hearing sensitivities. Testing at a number of different sound pressure level/duration combinations will help to determine whether these numbers can be used as onset levels for TTS in pinnipeds.

In most respects, noise-induced threshold shifts in pinnipeds follow trends similar to those observed in other mammals. The data are characterized by variable shifts at low noise levels; increasing shifts with increasing exposure duration, sound levels, and sound exposure levels; and complete, rapid recovery of sensitivity. In many cases, complete recovery appeared to occur within 15 min of noise cessation, and in no case was there an overall, long-term change in thresholds (indicating permanent threshold shift or PTS), despite numerous, repetitive noise exposures (Southall *et al.*, 2005). In the absence of better predictive models, the data included here indicate that sound exposure levels resulting in TTS onset range from about 183 to 206 dB *re*: 1 μPa^2 s, these levels being dependent on absolute hearing sensitivity. Future studies examining the effects of noise on pinniped hearing will likely have to rely on longer duration or more intense stimuli in order to adequately assess models that relate sound energy or sound exposure level to TTS. Additionally, because the pinniped auditory system functions amphibiously, future studies should examine the effects of airborne noise on pinniped hearing. Data generated by this and other studies should be taken into account by regulatory agencies attempting to mitigate the adverse effects of noise on these marine mammals.

ACKNOWLEDGMENTS

The authors would like to thank Rio, Sprouts, and Burnyce for participating in these experiments. Shannon Spillman provided invaluable assistance with animal training, and Marla Holt and James Grayson helped to collect and analyze data. The authors also gratefully acknowledge the help of the many volunteers at the Pinniped Cognition and Sensory Systems Lab at Long Marine Laboratory. This work was supported by Office of Naval Research awards N00014-95-10936 and N00014-99-1-0164 to R.J.S.

Ahroon, W. A., Hamernik, R. P., and Davis, R. I. (**1993**). "Complex noise exposures: An energy analysis," J. Acoust. Soc. Am. **93**, 997–1006.

Carder, H. M., and Miller, J. D. (**1972**). "Temporary threshold shifts from prolonged exposure to noise," J. Speech Hear. Res. **15**, 603–623.

Dixon, W. J., and Mood, A. M. (**1948**). "A method for obtaining and analyzing sensitivity data," J. Am. Stat. Assoc. **43**, 109–126.

Finneran, J. J., Schlundt, C. E., Dear, R., Carder, D. A., and Ridgway, S. H. (**2002**). "Temporary shift in masked hearing thresholds in odontocetes after exposure to single underwater impulses from a seismic watergun," J. Acoust. Soc. Am. **111**, 2929–2940.

Finneran, J. J., Schlundt, C. E., Carder, D. A., Clark, J. A., Young, J. A., Gaspin, J. B., and Ridgway, S. H. (**2000**). "Auditory and behavioral responses of bottlenose dolphins (*Tursiops truncatus*) and a beluga whale (*Delphinapterus leucas*) to impulsive sounds resembling distant signatures of underwater explosions," J. Acoust. Soc. Am. **108**, 417–431.

Gellermann, L. W. (**1933**). "Chance orders of alternating stimuli in visual discrimination experiments," J. Gen. Psychol. **42**, 206–208.

Hamernik, R. P., Ahroon, W. A., and Hsueh, K. D. (**1991**). "The energy spectrum of an impulse: Its relation to hearing loss," J. Acoust. Soc. Am. **90**, 197–204.

Hamernik, R. P., Ahroon, W. A., Patterson, J. H. Jr., and Qiu, W. (**2002**). "Relations among early postexposure noise-induced threshold shifts and permanent threshold shifts in the chinchilla," J. Acoust. Soc. Am. **111**, 320–326.

Hamernik, R. P., Ahroon, W. A., Hsueh, K. D., Lei, S. F., and Davis, R. I. (**1993**). "Audiometric and histological differences between the effects of continuous and impulsive noise exposures," J. Acoust. Soc. Am. **93**, 2088–2095.

Harding, G. W., and Bohne, B. A. (**2004**). "Noise-induced hair-cell loss and total exposure energy: Analysis of a large data set," J. Acoust. Soc. Am. **115**, 2207–2220.

Harris, C. M. (**1991**). *Handbook of Acoustical Measurements and Noise Control* (McGraw-Hill, New York).

Hirsch, I. J., and Ward, W. D. (**1952**). "Recovery of the auditory threshold after strong acoustic stimulation," J. Acoust. Soc. Am. **24**, 131–141.

Kastak, D. (**2003**). "Noise-induced temporary threshold shift in pinnipeds: Effects of exposure medium, intermittence, duration, and intensity," in *Environmental Consequences of Underwater Sound* (San Antonio, TX).

Kastak, D., and Insley, S. (**2005**). "Noise effects on pinniped hearing," in *Environmental Consequences of Underwater Sound* (Washington, D.C.).

Kastak, D., and Schusterman, R. J. (**1996**). "Temporary threshold shift in a harbor seal (*Phoca vitulina*)," J. Acoust. Soc. Am. **100**, 1905–1908.

Kastak, D., Schusterman, R. J., Southall, B. L., and Reichmuth, C. J. (**1999**). "Underwater temporary threshold shift induced by octave-band noise in three species of pinniped," J. Acoust. Soc. Am. **106**, 1142–1148.

Kryter, K. D. (**1994**). *The Handbook of Hearing and the Effects of Noise: Physiology, Psychology, and Public Health* (Academic, San Diego).

Maslen, K. R. (**1981**). "Towards a better understanding of temporary threshold shift of hearing," Appl. Acoust. **14**, 281–318.

McFadden, D. (**1986**). "The curious half octave shift: evidence for a basalward migration of the traveling-wave envelope with increasing intensity," in *Basic and Applied Aspects of Noise-Induced Hearing Loss*, edited by R. J. Salvi, D. Henderson, R. P. Hamernik, and V. Colletti (Plenum, New York), pp. 295–312.

McFadden, D., and Yama, M. F. (**1983**). "Upward shifts in the masking pattern with increasing masker intensity," J. Acoust. Soc. Am. **74**, 1185–1189.

Mills, J. H., Gilbert, R. M., and Adkins, W. Y. (**1979**). "Temporary threshold shifts in humans exposed to octave bands of noise for 16 to 24 hours," J. Acoust. Soc. Am. **65**, 1238–1248.

Moore, B. C., Alcantara, J. I., and Glasberg, B. R. (**2002**). "Behavioural measurement of level-dependent shifts in the vibration pattern on the basilar membrane," Hear. Res. **163**, 101–110.

Morfey, C. L. (**2001**). *Dictionary of Acoustics* (Academic, London).

Nachtigall, P. E., Pawloski, J. L., and Au, W. W. (**2003**). "Temporary threshold shifts and recovery following noise exposure in the Atlantic bottlenosed dolphin (*Tursiops truncatus*)," J. Acoust. Soc. Am. **113**, 3425–3429.

Nachtigall, P., Supin, A. Y., Pawloski, J., and Au, W. W. L. (**2004**). "Temporary threshold shifts after noise exposure in the bottlenose dolphin (*Tursiops truncatus*) measured using evoked auditory potentials," Marine Mammal Sci. **20**, 673–687.

Neilsen, D. W., Bauman, M. J., and Brandt, D. K. (**1986**). "Changes in auditory threshold during and after long-duration noise exposure: Species differences," in *Basic and Applied Aspects of Noise-Induced Hearing Loss*, edited by R. J. Salvi, D. Henderson, R. P. Hamernik, and V. Colletti (Plenum, New York), pp. 281–293.

NIOSH (**1998**). *Criteria for a Recommended Standard: Occupational Noise Exposure, Revised Criteria 1998*, NIOSH Pub. 98–126 (NIOSH, Cincinnati, OH).

Patuzzi, R. (**1998**). "A four-state kinetic model of the temporary threshold shift after loud sound based on inactivation of hair cell transduction channels," Hear. Res. **125**, 39–70.
Schlundt, C. E., Finneran, J. J., Carder, D. A., and Ridgway, S. H. (**2000**). "Temporary shift in masked hearing thresholds of bottlenose dolphins, *Tursiops truncatus*, and white whales, *Delphinapterus leucas*, after exposure to intense tones," J. Acoust. Soc. Am. **107**, 3496–3508.
Smith, M. E., Kane, A. S., and Popper, A. N. (**2004**). "Acoustical stress and hearing sensitivity in fishes: Does the linear threshold shift hypothesis hold water?" J. Exp. Biol. **207**, 3591–3602.
Southall, B. L., Schusterman, R. J., and Kastak, D. (**2000**). "Masking in three pinnipeds: Underwater, low-frequency critical ratios," J. Acoust. Soc. Am. **108**, 1322–1326.
Southall, B. L., Schusterman, R. J., Kastak, D., and Reichmuth Kastak, C. (**2005**). "Reliability of underwater hearing thresholds in pinnipeds," ARLO **6**, 243–249.
Strasser, H., Irle, H., and Legler, R. (**2003**). "Temporary hearing threshold shifts and restitution after energy-equivalent exposures to industrial noise and classical music," Noise Health **5**, 75–84.
Ward, W. D., Glorig, A., and Sklar, D. L. (**1958**). "Dependence of temporary threshold shift at 4 kc on intensity and time," J. Acoust. Soc. Am. **30**, 944–954.

Informational masking of speech in children: Effects of ipsilateral and contralateral distracters

Frederic L. Wightman[a] and Doris J. Kistler
Heuser Hearing Institute and Department of Psychological and Brain Sciences, University of Louisville, Louisville, Kentucky 40292

(Received 8 April 2005; revised 30 August 2005; accepted 30 August 2005)

Using a closed-set speech recognition paradigm thought to be heavily influenced by informational masking, auditory selective attention was measured in 38 children (ages 4–16 years) and 8 adults (ages 20–30 years). The task required attention to a monaural target speech message that was presented with a time-synchronized distracter message in the same ear. In some conditions a second distracter message or a speech-shaped noise was presented to the other ear. Compared to adults, children required higher target/distracter ratios to reach comparable performance levels, reflecting more informational masking in these listeners. Informational masking in most conditions was confirmed by the fact that a large proportion of the errors made by the listeners were contained in the distracter message(s). There was a monotonic age effect, such that even the children in the oldest age group (13.6–16 years) demonstrated poorer performance than adults. For both children and adults, presentation of an additional distracter in the contralateral ear significantly reduced performance, even when the distracter messages were produced by a talker of different sex than the target talker. The results are consistent with earlier reports from pure-tone masking studies that informational masking effects are much larger in children than in adults. [DOI: 10.1121/1.2082567]

PACS number(s): 43.66.Dc, 43.71.Ft [JHG] Pages: 3164–3176

I. INTRODUCTION

The ability to attend selectively to individual objects in the auditory world is undeniably one of the most important and complex skills possessed by hearing adults. In spite of the fact that relevant and irrelevant auditory events are commingled acoustically before arriving at the ears, the auditory system and the brain can, in most instances, parse the auditory "scene." This auditory source segregation process requires identification and segregation of the constituents of a scene, attention to one target sound source, and suppression of other distracting sources. For example, at a social gathering, successful interaction requires that we listen to the individual with whom we are talking while simultaneously disregarding the clamor of other voices around us. Similarly, a child must be able to attend to his or her teacher while disregarding the various sources of noise in the classroom. The mechanisms and processes that subserve source segregation and selective attention in adults are not yet fully understood, in spite of a substantial research effort over the last quarter century. [See Bregman (1990) for a comprehensive introduction to auditory source segregation.] Relatively little research has focused on the development of either auditory source segregation or auditory selective attention in children.

Experiments that measure detection or discrimination of tones in the presence of simple maskers or distracters (other tones or noise) tap a very basic form of auditory source segregation and selective attention. Even in these simple tasks, children up to the ages of 6 to 7 years perform more poorly than adults (Allen, 1991; Allen and Nelles, 1996; Allen and Wightman, 1992, 1995; Allen *et al.*, 1989; Bargones and Werner, 1994; Bargones, Werner, and Marean, 1995; Schneider *et al.*, 1989; Stellmack *et al.*, 1997; Wightman and Allen, 1992; Willihnganz *et al.*, 1997). However, simple tone detection paradigms do not present the kind of source segregation challenge that we face in real life, primarily because the "distraction" is typically relatively static and has a very different quality than the target signal. It is now well documented that, if a detection paradigm is modified to introduce uncertainty and signal-like quality in the distracter stimulus, the segregation/attention problem becomes much more difficult. For example, when adult listeners are asked to detect a tone masked by a complex of other tones, randomizing the frequencies and levels of the masker tones produces a significant decrement in performance, represented by as much as a 40 dB threshold elevation in some conditions and some listeners (Neff and Callaghan, 1988; Oh and Lutfi, 1998). This effect has been called "informational masking" to distinguish it from "energetic masking," which is masking thought to be caused by overlap of signal and masker spectra. Large individual differences characterize informational masking data. Some adult listeners show little or no informational masking, while others show a great deal (Oh and Lutfi, 1998). Recent results from our laboratory (Oh, Wightman, and Lutfi, 2001; Wightman *et al.*, 2003) suggest that informational masking is much greater in young children. Moreover, the individual differences in the data from children of the same age are also large. Even among teenagers, the data from some are like preschoolers and from others are like adults (Wightman *et al.*, 2003).

[a]Electronic mail: fred.wightman@louisville.edu

The recent models of informational masking, developed in the context of the pure-tone detection paradigms, suggest that listeners base their detection decisions on the weighted sum of outputs of a bank of auditory filters or channels (Lutfi, 1989, 1993; Lutfi *et al.*, 2003a; Oh and Lutfi, 1998; Richards, Tang, and Kidd, 2002; Tang and Richards, 2003; Wright and Saberi, 1999). The large differences in informational masking between children and adults and the large individual differences in thresholds are well predicted by the version of the model proposed by Oh and Lutfi (1998). In this model individual differences are explained by changes in channel weights and in "weighting efficiency," a measure that represents the difference between a listener's weights and those of an ideal observer in the same task. In most cases, the ideal observer would place nearly all weight on the signal channel and little or no weight on the channels passing the masker components. Data from our laboratory suggest that children display more informational masking because they place much more weight than adults on the nonsignal channels (Oh *et al.*, 2001). In other words, children appear to listen less selectively than adults.

The hypothesis that children listen less selectively than adults is generally consistent with the data from numerous studies of the development of selective attention as assessed in dichotic listening paradigms. In a typical dichotic listening experiment, a listener is asked to attend to the message presented to one ear and to ignore a distracting message presented in the other ear. Two kinds of results emerge from these studies. First, there is a consistent "right-ear advantage" (REA) which is revealed by higher performance when the target is presented to the right ear than when it is in the left ear. Most of the evidence suggests that the magnitude of the REA is the same in children as in adults (Bryden and Allard, 1981; Geffen, 1976, 1978; Geffen and Sexton, 1978; Hiscock and Kinsbourne, 1977, 1980; Sexton and Geffen, 1979), but this is still a controversial issue (Hugdahl, Carlsson, and Eichele, 2001; Morris *et al.*, 1984; Pohl, Grubmuller, and Grubmuller, 1984). A second consistent finding is that children do not perform as well as adults in dichotic listening tasks. The poorer performance is a result of more intrusions from the distracter message in the opposite ear, thus suggesting poorer attentional selection in children. This is taken as evidence that some of the brain processes that mediate performance in an auditory selective attention task are not mature in children (Doyle, 1973; Maccoby, 1969; Maccoby and Konrad, 1966). Data from recent studies of event-related brain potentials evoked during a selective attention task (Berman and Friedman, 1995; Coch, Sanders, and Neville, 2005) are consistent with this view. These results suggest that the N1 attention effect first reported by Hillyard *et al.* (1973) is not adult-like until after age 8 (Coch *et al.*, 2005). However, it is not clear whether this developmental effect originates in mechanisms of executive control, sustained attention, stimulus selection, or some other process that subserves selective attention (Gomes *et al.*, 2000).

A previous study of dichotic listening using pure tones as targets and distracters (Wightman *et al.*, 2003) reports results that are qualitatively consistent with those from the above-cited studies. When the target is presented to one ear and the distracter to the other, children produce much higher detection thresholds (poorer performance) than adults. These results, as well as the results from studies in which a pure-tone target and distracter are presented to the same ear (Lutfi *et al.*, 2003a, 2003b; Oh and Lutfi, 1998; Oh *et al.*, 2001), offer a useful picture of the developmental course of pure-tone informational masking. However, it is not clear how the results from pure-tone detection experiments might generalize to a more realistic everyday selective attention task.

Attending to a target speech signal in the presence of other speech distracters is a good example of an everyday auditory selective attention task. Listening to speech is probably the primary vehicle for learning among young hearing children, and speech is rarely heard in a quiet environment. Given the pure-tone detection results one might predict that children would have more difficulty than adults with this task. Although there is some support for this prediction in the literature, the details have yet to be revealed. The dichotic listening literature (cited earlier) offers some clues, but only for the unnatural case in which target and distracter are in different ears. Data from two recent studies (Fallon, Trehub, and Schneider, 2000; Hall *et al.*, 2002) do suggest that children have more difficulty than adults attending to speech that is presented with a speech distracter in the same ear.

One complexity of the speech task is the fact that both energetic and informational masking are likely to be involved. Because interfering speech overlaps the target both temporally and spectrally, energetic masking is to be expected. However, the focus here is on informational masking, which in the speech task would be caused both by the similarity of the target and distracter speech signals and by the uncertainty of the distracter from trial to trial. It is difficult, if not impossible, to disentangle energetic and informational masking effects completely, but previous research offers some useful techniques that may be applied to studies with children.

A series of experiments recently reported by Brungart and colleagues (Brungart, 2001a, 2001b; Brungart and Simpson, 2002, 2004; Brungart *et al.*, 2001; Kidd *et al.*, 2003) uses a novel speech intelligibility task that offers sensitive measures of "purely" informational masking effects. The "Coordinate Response Measure" (CRM) is a task in which listeners are asked to attend to a spoken target message of the form, "Ready *call sign*, go to *color number* now." The target "call sign" is fixed for a block of trials (or for the entire experiment) and is chosen from a group of eight (e.g., "baron," "ringo," "arrow," "tiger"). The target "color" and "number" are chosen randomly for each trial, from a set of four colors (red, blue, green, and white) and eight numbers (1–8). One or more distracter messages is mixed with the target message and has exactly the same form as the target but different call sign(s), color(s), and number(s). Target and distracter messages are temporally aligned at the beginning, and are roughly the same total duration. Typically the target talker (one of eight, four males and four females) is fixed for a block of trials (often the entire experiment), and the distracter talker(s) is either the same as or different from the target. If different, the distracter can be either the same or the opposite sex. In the CRM task listeners are asked to report

the target color and number on a computer screen. The ratio (T/D, in dB) of overall target rms to overall ipsilateral distracter rms is varied, and percent correct is recorded at each T/D. The articles describing the development and early experiments with the CRM (Bolia *et al.*, 2000; Brungart, 2001a) describe the task and stimulus materials in detail and show how the results compare with other more traditional measures of speech intelligibility.

The experiments described by Brungart (2001b) provide convincing evidence that masking in the CRM task is dominated by informational masking. The initial experiments investigated the masking effects of a single distracter presented in the same ear as the target. When the distracter was a speech-shaped noise with its envelope modulated by a CRM message, performance was considerably better (near perfect performance down to T/D of −6 dB) than with any of the speech distracters. The noise presumably approximated the energetic masking components of the speech distracter stimuli. Since performance was much poorer with the speech distracter, the assumption is that the overall masking effect with the speech distracter was primarily informational. When the distracter and target speakers were of opposite sexes, there was a dramatic improvement in performance over the condition in which both target and distracter speakers were of the same sex. This was most likely a result of the fact that male and female voices were perceptually very different, thus reducing informational masking. There was a smaller performance improvement when the target and distracter talkers were different, but of the same sex. The same arguments could be made in this case about reductions in target and distracter similarity. Finally, indications of the dominance of informational masking in the CRM task were found in the shapes of the psychometric functions (% correct vs T/D) in the various conditions. With a modulated noise distracter the psychometric functions were monotonic ogives, from chance (3% correct) to perfect performance, typical of detection or other speech intelligibility results. However, when the distracter was speech, the psychometric function displayed a prominent plateau from about 0 dB T/D to about −10 dB T/D. In other words, over a 10 dB range in which the target was progressively less intense than the distracter, performance remained constant. Brungart explained this in the context of informational masking. Especially in the conditions in which the target and distracter talkers were the same, intensity (loudness) could have provided information that might have allowed the listener to segregate target and distracter, since all other attributes of the two voices were the same. Thus, when the target was less intense than the distracter, so long as it was audible, a listener might be able to adopt the strategy of "listening to the softer voice." This strategy is clearly inconsistent with the principles of energetic masking.

The assertion that the masking effects of a speech distracter in the CRM task are primarily informational is strengthened by a detailed analysis of the listeners' errors. Brungart (2001b) shows that the color or number errors are not random, as might be expected if the masking were primarily energetic. Rather, the vast majority of errors come from the distracter message. For example, in one condition (same sex distracter) approximately 70% of the number responses were correct at a T/D of 0 dB. From the 30% number errors at this T/D ratio, approximately 28% (thus, nearly all of them) were from the distracter message. This suggests that listeners could hear both target and distracter messages but made errors because of an inability either to segregate the two messages or to remember which message was the target.

The experiment reported here explores informational masking in children using the CRM task. The aim is to understand both the extent and character of informational masking with speech stimuli and the development changes in the effects that occur from preschool age to young adulthood.

II. METHODS

A. Listeners

Eight adults and 38 children served as participants in this experiment. An additional 3 adults were recruited but did not complete the experiment. Preschool children were recruited from the University of Wisconsin's Waisman Early Childhood Program. Older children and adults were recruited from the University of Wisconsin community. The adults ranged in age from 20 to 30 years. For convenience in data interpretation, the children were divided into five age groups: 8 children were in the age range 4.6–5.7 years; 6 in the 6.6–8.5 year group; 8 in the 9.6–11.5 year group; 8 in the 11.6–13.5 year group; 8 in the 13.6–16.0 group. All adults and children passed a 20 dB HL screening for hearing loss. The preschool (4.6–5.7 years) children were tested for middle-ear problems (routine tympanometry) before each session, and the other children were tested similarly before the first session and irregularly thereafter. Sessions were canceled whenever there were indications of middle-ear problems. All children who were recruited completed the experiment.

B. Stimuli

The target and distracter speech messages were drawn from the corpus of CRM stimuli made available by Bolia *et al.* (2000). The corpus includes 2048 phrases of the form, "Ready, *call sign*, go to *color number* now." Eight talkers (4 male, 4 female) are recorded, each speaking 256 different phrases (eight call signs, "baron," "ringo," "tango," etc.; eight numbers, 1–8; four colors, "red," "white," "green," "blue"). For this experiment, the target phrase was always spoken by talker 1 (male) from the corpus, using the call sign "baron." The distracter phrases always used a different talker, call sign, color, and number. In some conditions the sex of the distracter talker was male, and in other conditions female. With the exception of the distracter talker's sex, the distracter phrases(s) used on each trial were chosen randomly from the available, nontarget phrases.

All conditions involved trials in which a single target and single distracter were presented to the listener's right ear. In some conditions an additional distracter phrase was presented to the left ear. Another condition involved presentation of a Gaussian noise with a speech-shaped spectrum to the left ear. The overall level (rms) of the distracter in the target ear was held constant for all conditions at approxi-

mately 62 dB SPL. When a speech distracter was present in the nontarget ear, it was presented at this same rms level. When a noise distracter was present in the nontarget ear, its rms level was 77 dB SPL. The rms level of the target was varied from trial to trial. Depending on listener and condition the target/distracter ratio (T/D) ranged from +24 to −24 dB. Thus the highest rms level of the target was 86 dB SPL.

The stimulus materials were produced digitally (CRM stimuli taken from the distribution CD, noise synthesized on a PC), converted to analog form (44.1 kHz sample rate) by Tucker-Davis Technologies (TDT) DD1 D/A converters, mixed, amplified and presented to listeners via calibrated Beyer DT990-Pro headphones. Target and distracter levels were controlled by programmable attenuators (TDT PA-4) prior to mixing. The target and distracter phrases were time-aligned on the distribution CD such that the word "ready" for target and distracter phrases started at the same time.

C. Conditions

The experiment involved three distracter conditions. In all conditions a target phrase and a simultaneous distracter phrase (different talker, call sign, color, and number than the target) were presented to the listener's right ear. A monaural condition involved no stimulus presented to the contralateral ear. The second distracter condition added a speech-shaped noise distracter to the contralateral ear. In the third distracter condition a speech distracter (CRM phrase with different talker, call sign, color, and number than either the target or the ipsilateral distracter) was presented to the contralateral ear. Each distracter condition was tested with both male and female distracters. Thus, there were six total conditions in the experiment. The youngest children were not tested with male distracters since pilot testing suggested that, with a contralateral distracter stimulus, target levels in excess of 90 dB SPL would be required to obtain above-chance performance.

D. Procedure

Listeners sat in a sound-isolated room (IAC 1200) in front of a computer display. The display showed a start button and 32 response buttons arranged in four colored matrices of 8 buttons each, numbered 1–8. Individual trials were initiated by the listener by a mouse-click on the start button, except for sessions involving the youngest (preschool) children, in which case the experimenter (seated beside the child) initiated the trial once the listener was quiet and appeared attentive. After hearing the phrases, the listener moved the mouse cursor to the matrix of the heard color and clicked on the number corresponding to the heard number. The preschoolers pointed to the color-number of the heard phrase and the experimenter entered the response. Visual feedback was given ("smiley face" on computer screen) for a correct response. The preschool children were also verbally reinforced after each trial.

The level of the target was varied in an up-down staircase fashion (5 levels) from trial to trial so that an entire psychometric function, from near perfect performance to chance, could be estimated during each session. The highest level was presented first. Then the level was decreased on each of the next 4 trials, after which it was increased for 4 trials. This down-then-up sequence was then repeated for the duration of the run. In this way the highest and lowest levels were tested on half as many trials as the intermediate levels. For the preschool children, the 5 levels were 4 dB apart, so a 16 dB range was covered. For the older children and adults, the levels were 8 dB apart, and the total range of target levels was 32 dB. The highest target level was chosen (based on pilot testing with each listener) in order to assure near perfect performance. Practice runs with no distracter were also tested to assure perfect performance at each target level. In any given run only 5 levels were presented, but for some adults and children the starting levels were different on different runs to evaluate both perfect and near-chance performance.

Both children and adults completed at least 1 practice run in each of the six conditions (and one with no distracter) before data were collected. Children were tested in an additional practice run if it appeared necessary. Most young children were tested in two practice runs. Following practice, runs from the six conditions were tested in a pseudorandom order, such that for each run a random choice was made among all the remaining runs across all conditions.

For children the total number of trials in each condition ranged from 256 to 384. For adults, the total number of trials in each condition ranged from 512 to 640. Testing was conducted over the course of several sessions. The preschool children were tested in 32-trial runs, and they would normally complete 2 such runs in a session. Older children and adults were tested in 64 or 128 trial runs depending on the listener. For the preschool children, the sessions were always less than 30 min and were held once per week. Completion of the experiment required as many as 12 sessions for these children. The adult sessions were 1.5–2.0 h long and were scheduled at the participant's convenience, usually twice per week. Most adults completed the experiment in 4–6 sessions. For children at intermediate ages, sessions were 1–2 h, depending on the participant, and the number of sessions required to complete the experiment ranged from 3 to 5. Frequent breaks were encouraged for all participants.

Children in the youngest age group were given a small toy at the end of each session. All other participants were paid $7/h for their participation.

III. RESULTS AND DISCUSSION

A. Data analysis

Interpreting psychometric function data from children is complicated by several factors. First, young children cannot be tested as extensively as older children and adults, so comparing results across age groups is not always straightforward. Second, individual differences are often larger in the younger age groups (Oh *et al.*, 2001; Wightman and Allen, 1992; Wightman *et al.*, 2003). Third, the upper asymptote of many psychometric functions obtained from children does not reach 100% correct, even for very strong signals, implying a certain degree of inattention. Finally, in the current paradigm, the same numbers of trials were not run at all T/D ratios because of the nature of the staircase procedure. In

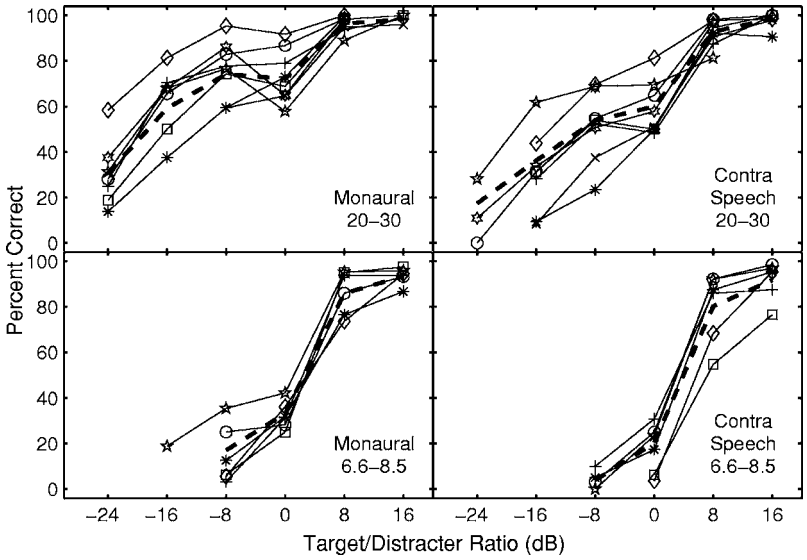

FIG. 1. Psychometric functions from individual listeners in two age groups (adults—top panels; children 6.6–8.5 years—bottom panels) and two male distracter conditions (monaural—left panels; contralateral—right panels). Functions plotted with different symbols represent data from the different listeners and the dashed line represents the mean. Data are plotted as a function of the target/distracter ratio in the target ear.

previous studies (Wightman *et al.*, 2003) these problems were mitigated by fitting a smooth curve (logistic) to the psychometric function data from each listener in each condition and extracting estimates (with confidence limits) of the parameters of those fitted functions (Wichmann and Hill, 2001a, 2001b). This allowed interpretation of the thresholds (T/D ratio producing 75% correct) for each listener. In the current study, complete psychometric functions were also obtained from each listener in each condition. However, it is not meaningful to compute the parameters of best fitting functions from these data. Many of the functions are irregular in shape, either nonmonotonic or having a plateau, similar to what has been reported before (Brungart *et al.*, 2001; Brungart and Simpson, 2002). For these reasons, we will show complete psychometric functions when discussing the results.

In order to reduce the data set from the 38 children and 8 adults to a manageable size, the children were assigned to age groups spanning roughly 2 years, as described earlier. The psychometric functions from all the children in each of the six age groups and each of the six conditions were plotted (a total of 36 plots) and examined visually for homogeneity. Figure 1 shows four representative examples. The data from individual listeners are plotted along with the means (weighted according to the number of trials included for each listener at each T/D), for two conditions and two age groups. Our conclusion from this informal analysis was that in spite of large individual differences in percent correct at specific T/D ratios, the shapes of the individual psychometric functions in each age group are well represented by the mean. Thus, all further analyses are based on the group mean psychometric function in each condition.

Although the experimental design did not allow a systematic assessment of potential training effects, an informal analysis suggested that, even for the youngest children tested, performance was approximately constant for the duration of the experiment.

B. Male distracter conditions

Figure 2 shows mean psychometric functions obtained from five of the six age groups (the preschool children were not tested in these conditions) in the three male distracter conditions. To facilitate comparison across age groups, only partial psychometric functions are shown. It is important to note in this context that all listeners reached near 100% correct performance at high T/D ratios and approached chance at low T/D ratios. The stimulus configurations represented in this figure are nearly identical to those in the Brungart and Simpson (2002) study of adults. The main differences are that the Brungart and Simpson experiment used a contralateral noise distracter 5 dB more intense than what was presented here. Consider first the current data from the adults. These are entirely consistent with those shown in Fig. 2 of Brungart and Simpson (2002). With no distracter in the contralateral ear, performance is nearly perfect at a T/D ratio of +8 dB, decreases to about 70% correct at T/D of 0 dB, remains at 70% until a T/D of about −8 dB, and falls for lower T/D ratios. The plateau in performance between a T/D of 0 and −8 dB has been reported before (Dirks and Bower, 1969; Egan, Carterette, and Thwing, 1954) and probably reflects these listeners' abilities to segregate target and distracter on the basis of intensity. The addition of a noise distracter to the contralateral ear has no effect, also as shown in the Brungart and Simpson (2002) experiment, but the addition of a contralateral speech distracter has a substantial negative effect, reducing performance by as much as 30% at some T/D ratios. Even though, as shown by Brungart and Simpson (2002), a contralateral speech distracter has no impact when presented alone, its simultaneous presence with an ipsilateral distracter apparently interferes with listeners' abilities to segregate the target and the ipsilateral distracter.

The mean data from the four groups of children (Fig. 2) suggest increasing amounts of informational masking in all conditions as age decreases. At a T/D ratio of +8 dB, performance is quite good (over 80%) in all age groups, but the youngest group (6.6–8.5 years) obtains less than 35% correct at the 0 dB T/D ratio. The performance plateau between T/D ratios of 0 and −8 dB is not evident in the data from the youngest group but is obvious in the data from the other groups. Thus, from these data, we might conclude that only listeners 9 years of age or older use the intensity-based target-distracter segregation strategy. The lack of an effect

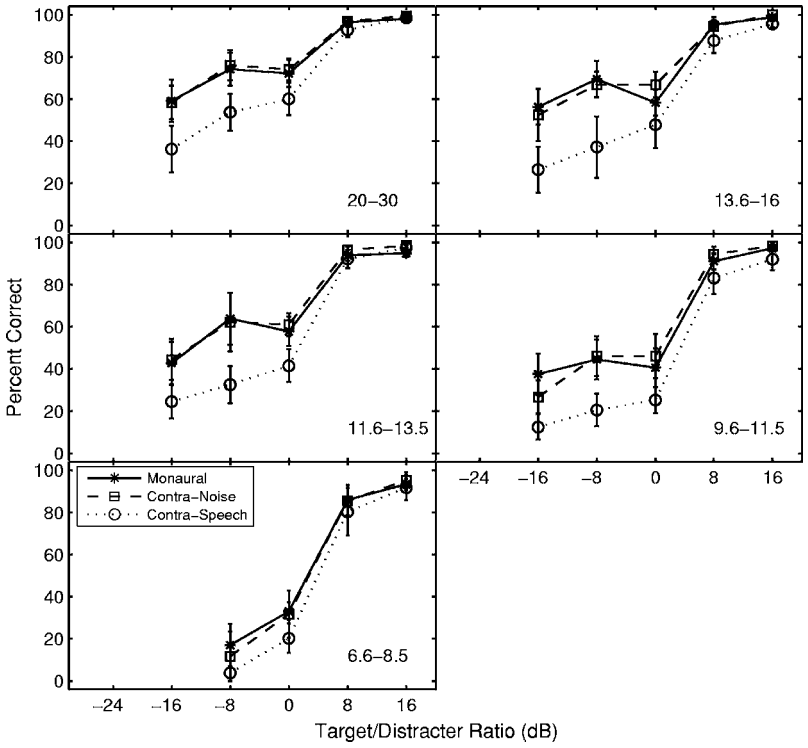

FIG. 2. Mean psychometric functions for listeners in five age groups in the three conditions that used a male distracter talker. The age ranges are indicated in each panel and the conditions are indicated in the lower left panel. Error bars represent 95% confidence intervals of the mean.

caused by the additive contralateral noise appears in all age groups. Finally, the substantial decrement in performance caused by the addition of a contralateral speech distracter is roughly constant across the age groups, but slightly smaller for the youngest group tested (probably a floor effect). The constancy of the contralateral speech effect is somewhat surprising. Even though the data from this and previous experiments (Oh *et al.*, 2001; Wightman *et al.*, 2003) suggest that informational masking decreases as the age of the listener increases, the added component of informational masking contributed by a contralateral distracter seems not to be age dependent.

The age effects in each of the three male distracter conditions are shown more clearly in Fig. 3. This figure shows the same data as Fig. 2, but displayed differently. The three panels represent the three distracter conditions and the different symbols represent the different age groups. Note that with few exceptions, at each T/D ratio performance decreases monotonically with decreasing age, although there is virtually no difference in performance between the two oldest age groups of children. Note also that the plateau effect is evident in both the monaural and contralateral noise conditions in all age groups except the youngest tested.

The masking effects shown in Figs. 2 and 3 are almost certainly dominated by informational, not energetic, masking. Brungart (2001b) offers several kinds of evidence supporting this assertion. First, when the ipsilateral distracter in his experiment was a speech-shaped noise modulated by the envelope of a CRM phrase, adult listeners' performance was near perfect at a T/D ratio of 0 dB, only decreasing to about 60% at a T/D of −8 dB. It is reasonable to assume that the masking produced by the modulated noise would represent an upper bound on energetic masking in these conditions. Thus, the masking effects observed in the Brungart (2001b) experiment, at least down to T/D of −8 dB, would be primarily informational. Brungart (2001b) also presented an analysis of errors that strongly implicated informational masking. The overwhelming majority of color and/or number errors made by his adult listeners with an ipsilateral speech distracter consisted of colors and/or numbers that were present in the distracter phrases. If energetic masking were at work, one might expect the listener to choose a response randomly, thus producing a chance distribution of errors. A similar analysis of errors for the adult listeners in the current experiment is shown in Fig. 4. Color and number errors are combined, and the number of color and/or number errors expected to be present by chance (random errors) in the distracter is shown by the dashed lines. Note that in both the monaural and contralateral noise conditions (upper panels), for T/D ratios greater than −8 dB, more than 90% of the total responses (both correct and incorrect) were contained in either the target or distracter phrases. The same is true for the contralateral speech condition (lower panels). The data from the contralateral speech condition are plotted twice in this figure to clarify the number of errors expected by chance to be contained in both the ipsilateral and contralateral distracters. The contralateral plot (right panel) shows that for T/D ratios between −8 and +8 dB most of the errors came from the ipsilateral distracter, as represented by the fact that the number of errors from the contralateral distracter at these T/D ratios is less than would be expected by chance. The ipsilateral plot (left panel) confirms this by showing that the number of errors contained in the ipsilateral distracter is greater than would be expected by chance. In summary, the fact that at T/D ratios greater than −8 dB most of the errors were contained in the distracter(s) is entirely consistent with

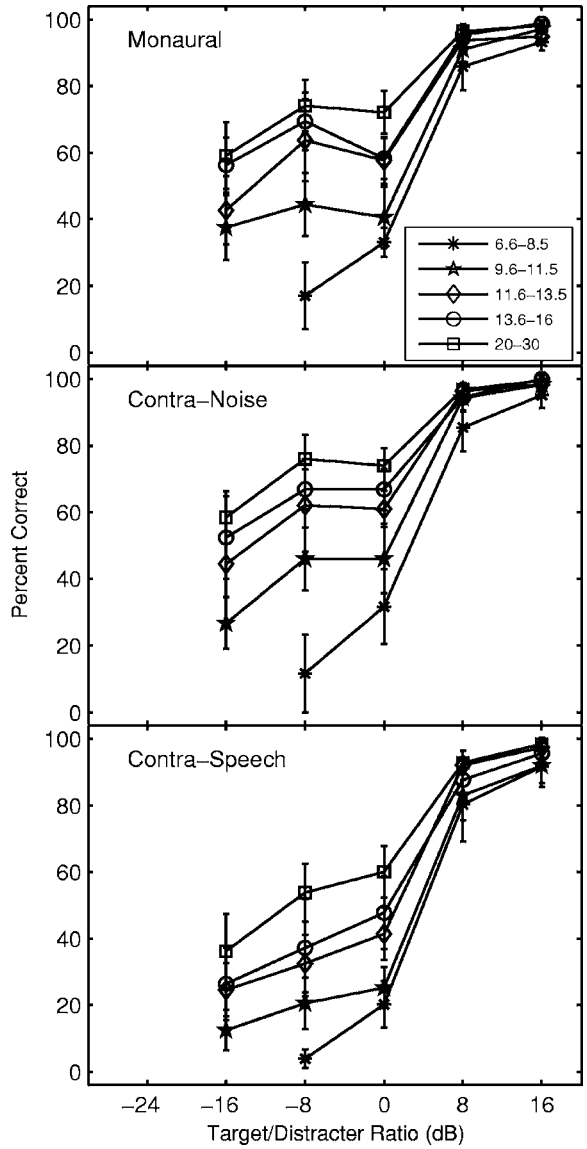

FIG. 3. Mean psychometric functions from the three male distracter conditions plotted with age group as the parameter in each panel. Error bars represent 95% confidence intervals of the mean.

what was reported by Brungart (2001b) and argues that the masking effects are primarily informational at these T/D ratios.

The error analyses shown in Figs. 5 and 6 provide evidence that the masking effects for the children are also dominated by informational masking. Figure 5 shows the data from the oldest age group (13.6–16 years). Note that except for a slightly lower performance level (as represented by fewer correct responses) the distribution of responses is indistinguishable from that seen in the adult data (Fig. 4). As was the case in the adult data, for T/D ratios of −8 dB and higher, most of the errors made by the children come from the distracter(s). In addition, most of the errors in the contralateral speech condition come form the ipsilateral distracter. Thus it appears that both the adults and the older children can effectively ignore the distracter in the nontarget ear, since the number of errors contained in the contralateral distracter never rises above that expected by chance. However, the pattern of errors also suggests that both adults and older children can hear and understand both target and distracter messages at T/D ratios of greater than −8 dB, and that the masking effects seen at these T/D ratios are thus informational.

Figure 6 shows the error analysis for the youngest group of children tested in the male distracter conditions. Note that this figure shows no data for T/D ratios below −8 dB; performance for nearly all of these listeners was at chance below this value. Although the pattern of errors is different for these young children than for the adults (Fig. 4) and older children (Fig. 5), the conclusions to be drawn from the error analyses are not fundamentally different. When performance is substantially above chance (at T/D ratios of 0 dB and above), most of the errors are contained in the distracter(s). In the monaural and contralateral noise conditions (upper panels of Fig. 6) the number of errors contained in the distracter is well above chance at T/D ratios of 0 dB and below. In the contralateral speech condition (lower panels of Fig. 6), although performance was near chance at −8 dB T/D ratio, the vast majority of errors at this T/D ratio and above came

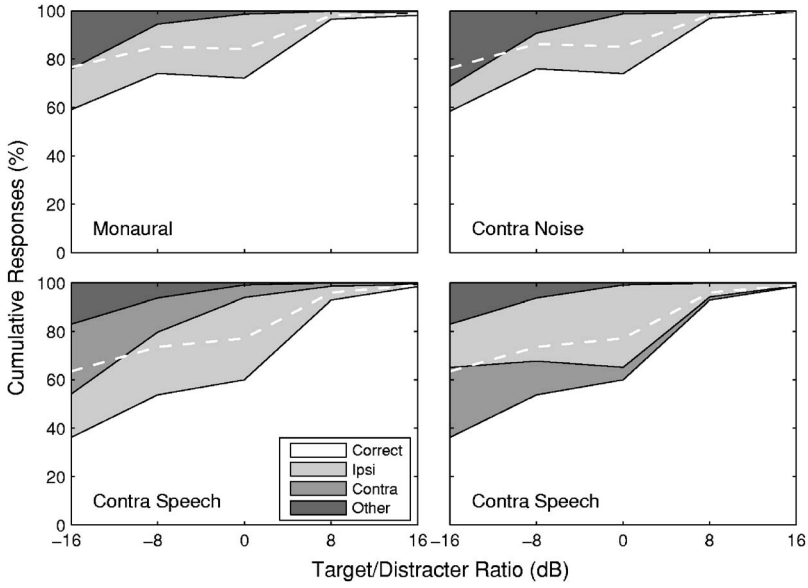

FIG. 4. Response analysis of the data from the adult listeners in the three male masker conditions. The upper panels show responses from the monaural condition (left) and the contralateral noise condition (right). Lower panels show responses from the contralateral speech distracter condition. Correct responses are indicated by the lightest shading. Color and/or number errors contained in the ipsilateral distracter, contralateral distracter, or neither are indicated by darker shadings. The light dashed lines indicate the number of color and/or number errors expected if the listener were responding randomly. The same data are plotted in the two lower panels to facilitate comparison of actual responses to expected random responses from the ipsilateral (left) and contralateral (right) distracters.

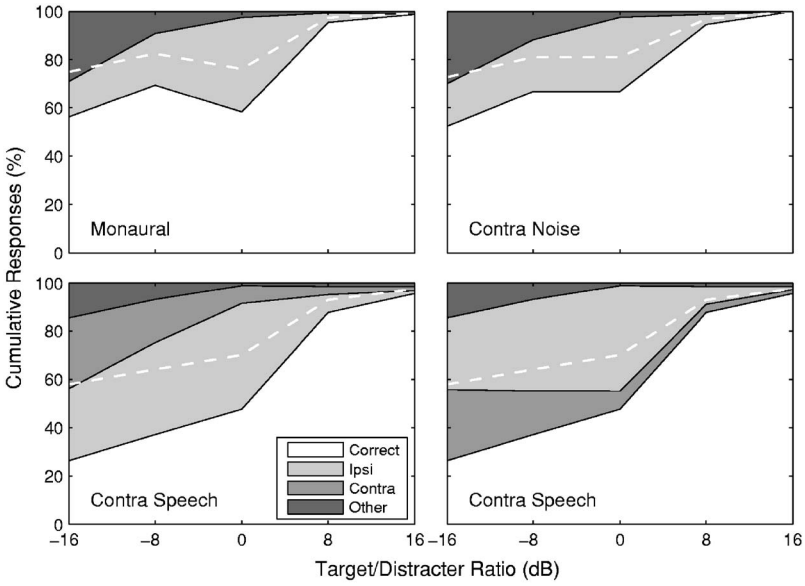

FIG. 5. Same as Fig. 4, except that the response analysis of the data from the children in the 13.6–16.0 year age group is shown.

from the distracter(s). As with the adults and older children most of the errors came from the ipsilateral distracter. As shown in Fig. 6 (lower panels), at T/D ratios above 0 dB the number of errors contained in the contralateral distracter was no greater than would be expected by chance, and at lower T/D ratios was much less than chance. Thus, even the youngest children appear to focus attention on the target ear and thus limit intrusions from the message in the nontarget ear. This result may appear to contradict the findings of our previous study of pure-tone informational masking in children (Wightman *et al.*, 2003), which suggested that children could not ignore the stimulus in the contralateral ear. However, there are many differences between the current experiment and the previous one, not the least of which is the fact that in the current experiment distracters were present in both ears. Thus, the apparent contradiction is not viewed as serious. Moreover, as will be shown in the results from the female distracter conditions, there is evidence here that in some cases children do attend to the contralateral ear when it is not appropriate to do so.

Error analyses for the two intermediate age groups of children are not shown here since the patterns of errors are not substantially different than those shown for the other groups. Performance in all conditions declines systematically with age, as can be seen in Fig. 3, and the error analyses reveal nothing inconsistent with the other error analyses. In all conditions most of the errors for T/D ratios greater than −8 dB are contained in the distracter presented to the target ear.

The main result from the male distracter conditions, that informational masking is greater in children than in adults, agrees with the results of other developmental experiments in the literature on speech recognition with same-sex speech distracters. For example, Hall *et al.* (2002) reported higher speech recognition thresholds in both adults and children with a 2-talker speech distracter than with a noise distracter. This is clear evidence of informational masking. The same authors also reported that the effect is greater in their 5–10 year olds than in their adults. Fallon *et al.* (2000) obtained higher speech recognition thresholds from children

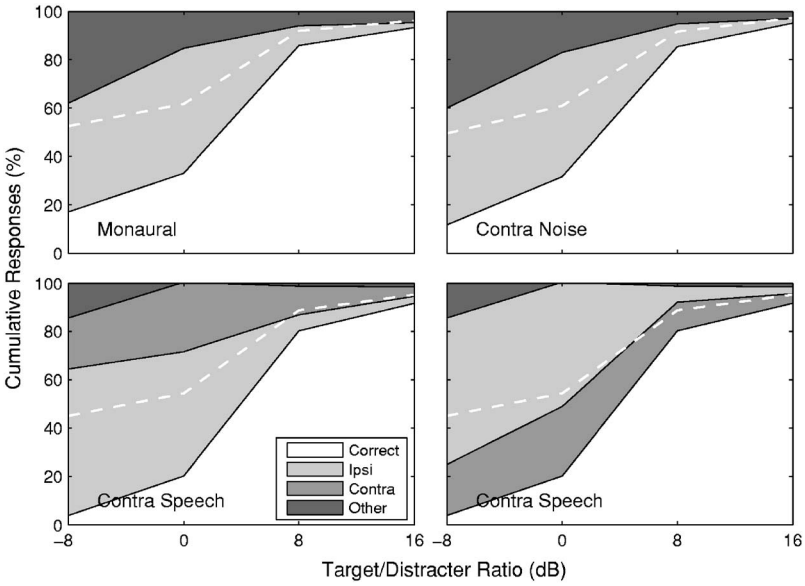

FIG. 6. Same as Fig. 4, except that the response analysis of the data from the children in the 6.6–8.5 year age group is shown.

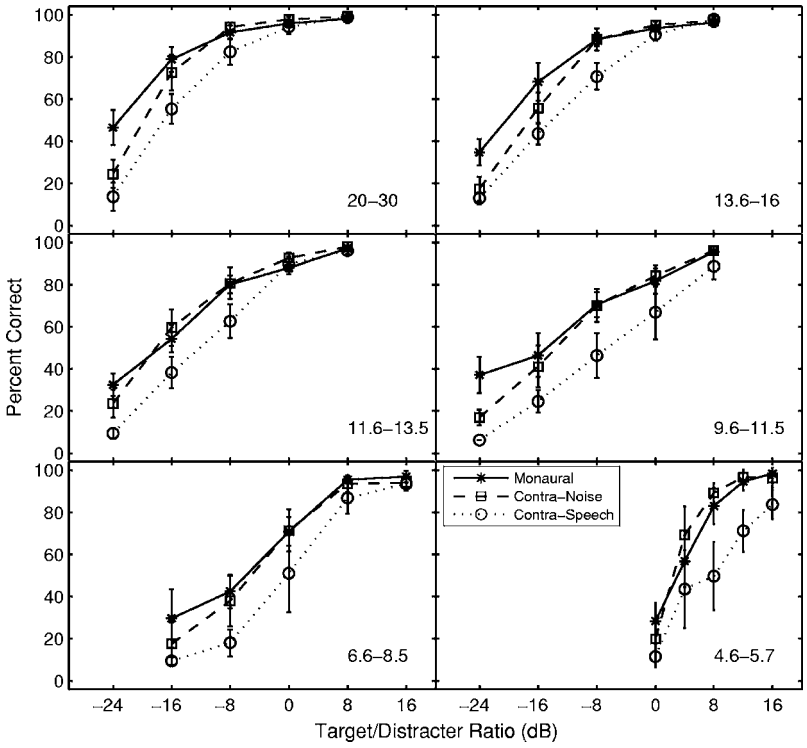

FIG. 7. Mean psychometric functions from listeners in all age groups from the conditions that used the female distracter talker. Labeling is the same as in Fig. 2. Error bars represent 95% confidence intervals of the mean.

than from adults with a multitalker babble distracter, but no control condition was run with a noise distracter to assess the extent of informational masking in this experiment.

C. Female distracter conditions

In the female distracter conditions the ipsilateral and, if present, the contralateral speech distracters were spoken by a female, randomly selected on each trial from the four possible female talkers in the corpus. If there were two distracters they were spoken by two different female talkers. The target talker was the same male (Talker 1 from the corpus) in all conditions. Thus, this condition was similar to the "different sex" condition in the experiment reported by Brungart (2001b), except that in the Brungart study, the sex of the target talker was also allowed to vary from trial to trial.

The mean data from all six age groups (including the preschoolers, who were not tested with male distracters) are shown in Fig. 7. The format of this figure parallels that of Fig. 2. Several features of these data are noteworthy. First, comparing the data from Figs. 2 and 7, it can be seen that for the adults in the monaural condition there is a substantial release from informational masking when the target is male and the distracter is female. At a T/D ratio of 0 dB for example, performance is near perfect with the female distracter and only 70% correct with a male distracter (Fig. 2). Moreover, at a T/D ratio of −16 dB, adult performance with the female distracter is about 75% correct and with a male distracter it was no more than 55%. At this low T/D ratio energetic masking is almost certainly playing a significant role, so a complete release from masking is not to be expected. For the children there is also a substantial release from informational masking when the target talker is male and the distracter talker is female (compare Figs. 2 and 7). At 0 dB T/D ratio with the male distracter, children in the 6.6–8.5 year old group obtained about 30% correct, but with the female distracter performance was above 70% correct. This corresponds to approximately 9 dB of improvement in the T/D ratio required for 50% correct. The release from informational masking in the female distracter conditions was similar in the other groups of children.

Consistent with the diminished contribution of informational masking at low T/D, there is no evidence of the plateau effect that was observed with male distracters at T/D ratios between 0 and −8 dB. The lack of a performance plateau is similar to what was reported by Brungart (2001b) in the "different sex" condition of his experiment. Those data show a gradual decline in performance from 100% at a T/D ratio of +12 dB to about 80% at a T/D of −12 dB, similar to what is shown here for the adult listeners (Fig. 7). It is reasonable to suggest that for the adults and older children, target-distracter segregation is facilitated so much by the difference in target and distracter sex that no further improvement is to be had by the use of the level-segregation strategy.

The impact of the contralateral noise and the contralateral speech distracters in the female distracter conditions was very similar to what was observed with male distracters. Adding noise to the contralateral ear had little or no effect, except at the lowest T/D ratio (−16 dB) where it caused a slight drop in performance in each age group. However, in spite of the release from informational masking in the target ear caused by the use of a different sex distracter, adding female speech to the contralateral ear caused a substantial drop in performance, about 20%, for all groups except the youngest, at T/D ratios near the midpoint of the psychometric functions. The 20% drop was somewhat smaller in some age groups than with male distracters, as might be expected. However, in the 6.6–8.5 year old group the impact of the contralateral female distracter (Fig. 7) appears to be some-

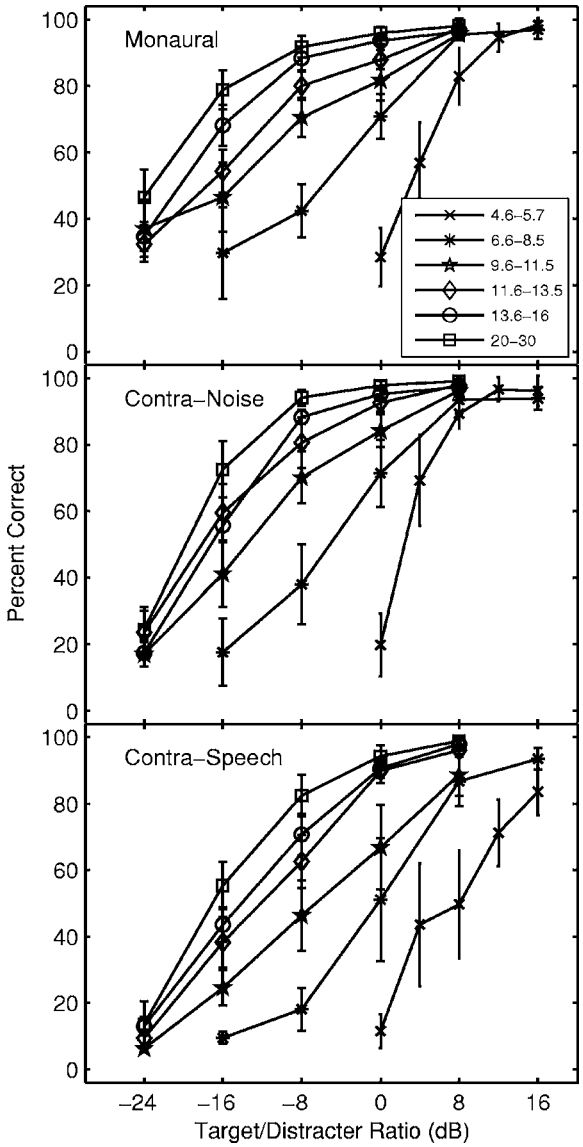

FIG. 8. Same as Fig. 3 except for the female distracter conditions. Error bars represent 95% confidence intervals of the mean.

what greater than the impact of the contralateral male distracter (Fig. 2). Overall, the effect of adding a contralateral female masker was largely age independent. The youngest children (preschoolers), who were the poorest performers overall, showed a slightly larger effect of the added contralateral female speech masker (30%–40% near the midpoint of the psychometric function).

The age effect in the female distracter conditions is shown in Fig. 8. As in the male distracter conditions (Fig. 3) performance in all conditions declines systematically and monotonically as age decreases. At a T/D ratio of 0 dB for example, the adults scored around 95% correct in the monaural condition, while the children in the youngest age group scored no higher than 30% in the same condition. As in the male distracter conditions, there is almost no difference in performance between the two oldest age groups of children.

An error analysis of the adult data from the female distracter conditions is shown in Fig. 9. These data suggest that the masking effects produced by the ipsilateral distracters were primarily energetic. Note that the number of errors contained in the distracter(s) never exceeds that expected by chance. Note also that at the lowest T/D ratios the number of errors contained in the ipsilateral distracter was lower than would be expected by chance. This suggests that at this T/D ratio, although the target was probably inaudible, the listener could hear and understand the ipsilateral distracter and thus eliminate it from the set of possible responses. The same strategy was apparently not used for the contralateral distracter, since the number of responses contained in this message was never different from chance.

Figure 10 shows the error analysis of the data from the oldest group of children (13.6–16). There are only slight differences between the error patterns shown here and those from the adults (Fig. 9). The same can be said of the error patterns for the children whose errors are not shown (ages 6.6–13.5). However, one minor difference emerges in the error data from the 6.6 to 8.5 year group. This group does not show a lower than chance frequency of errors contained in the ipsilateral distracter at low T/D ratios. In the adults and

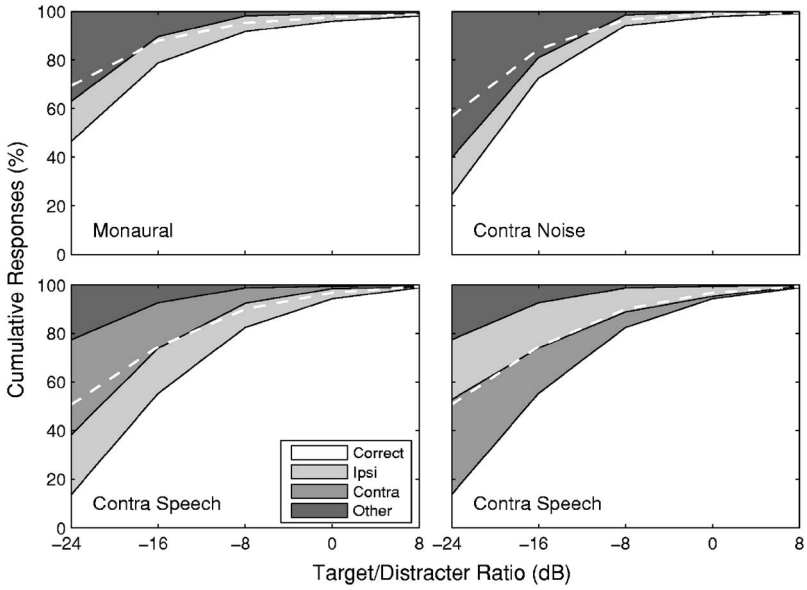

FIG. 9. Same as Fig. 4 except that the response analysis of the data from the adults in the female distracter conditions is shown.

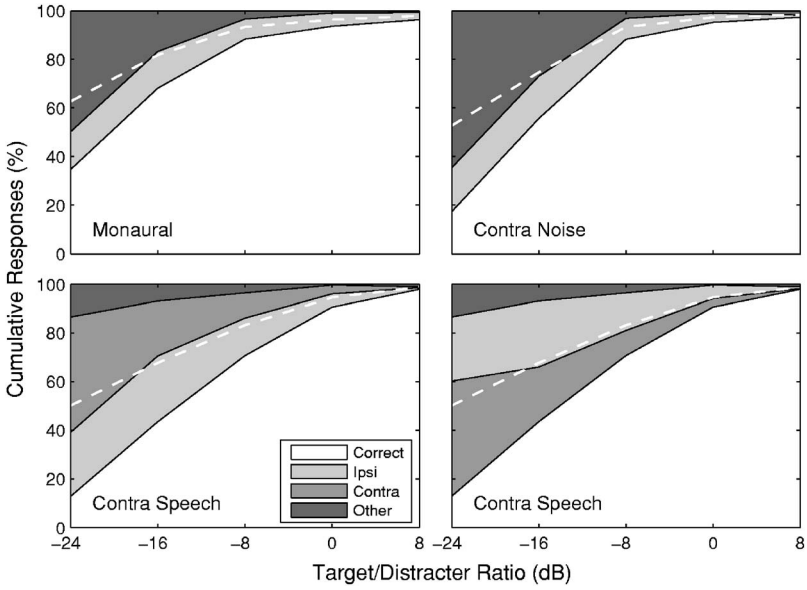

FIG. 10. Same as Fig. 4 except that the response analysis of the data from the children in the 13.6–16.0 year age group in the female distracter conditions is shown.

other groups of children this is interpreted as evidence of the ability to eliminate the ipsilateral distracter message from the set of response alternatives.

Figure 11 shows an error analysis for the 4.6–5.7 year old age group in the female distracter conditions. Note that for the monaural and contralateral noise distracter conditions (upper panels), the overwhelming majority of errors came from the distracter phrases, suggestive of informational masking. Since it is probably safe to assume that at the positive T/D ratios represented here both target and distracter were audible and understandable, one must conclude that the children simply could not determine or remember which was the target phrase and which was the distracter or could not disentangle the two. In the error analysis from the contralateral female speech distracter condition (lower panels), an especially intriguing result can be seen. As in the monaural condition, most of the errors in this condition were contained in the distracter(s). However, in contrast with the data from adults and older children, a large number of errors were contained in the contralateral distracter phrase. This could mean that young children forgot or could not determine which was the target voice, and, in addition, could not segregate the two messages in the ipsilateral ear. Thus, their only remaining choice was the contralateral distracter. This is qualitatively consistent with previous results from our laboratory (Wightman *et al.*, 2003) that indicated an inability of preschoolers to focus their attention on a single ear. The Wightman *et al.* (2003) experiments involved detection of a pure-tone signal which was presented with a random multicomponent tonal distracter. Children in the preschool age group demonstrated large amounts of informational masking when the distracter was in the target ear and only a modest release from masking when the distracter was presented to the nontarget ear.

The results from the female distracter conditions agree with those from other studies in the literature on speech-speech masking in which different sex target and distracter talkers were used. For example, in the experiment described by Doyle (1973), children (8, 11, and 14 years old) shad-

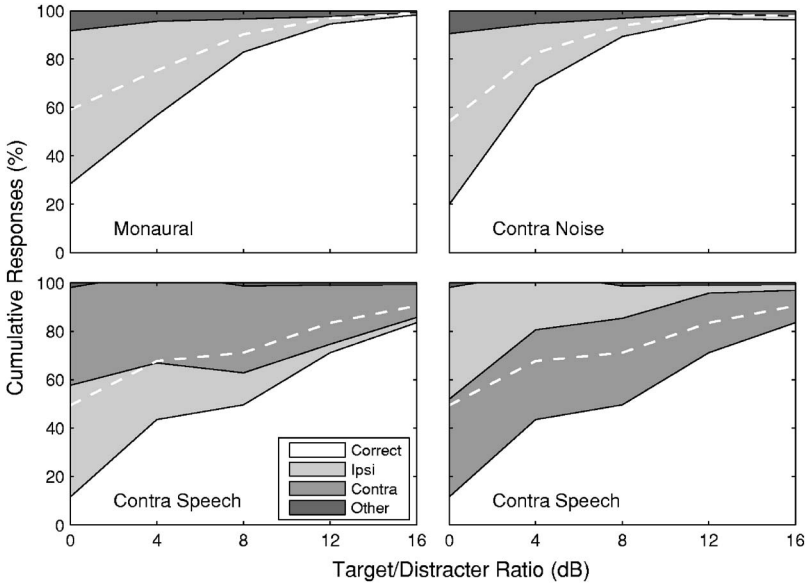

FIG. 11. Same as Fig. 4 except that the response analysis of the data from the children in the 4.6–5.7 year age group in the female distracter conditions is shown. Note that the abscissa represents different T/D ratios than in the other figures.

owed a male target talker in the presence of a single female distracter. Intrusions (errors) from the distracter talker were much more frequent in the younger children than in the older children, a result that appears consistent with ours. However, our results do not appear consistent with those from the recent study reported by Litovsky (2005). In that experiment children and adults identified target spondees produced by a male talker with either sentences (female talker) or modulated speech-spectrum noise used as distracters. Recognition thresholds were higher with the noise distracter for both children and adults, and there was no difference in amount of masking between children and adults. Thus, for reasons that are not obvious, it seems likely that informational masking was not a factor in the Litovsky (2005) study. The T/D ratios reported as thresholds in the Litovsky (2005) study are very low (−16 dB or poorer) compared to most of those tested here. Brungart (2001b) has shown that at such low T/D ratios, energetic masking exceeds informational masking in the case of different sex target and distracter talkers.

IV. CONCLUSIONS

Auditory selective attention was measured in 38 children (ages 4–16 years) and 8 adults using a closed-set speech-recognition task. The results suggested that listener performance was dominated by informational masking when the distracter was speech from a talker of the same sex as the target talker, and they confirmed earlier findings that children are much more influenced by informational masking than are adults. For the youngest children informational masking with the single ipsilateral distracter was more than 15 dB greater than in adults. A clear and monotonic age effect was also shown, with some children as old as 16 years still not performing at adult levels. For older children and adults, the added informational masking produced by a contralateral distracter amounted to about a 5 dB shift in the psychometric function toward poorer performance. For the youngest children the effect was somewhat smaller. Using a male target talker and female distracter(s) produced a considerable release from informational masking for all age groups tested.

ACKNOWLEDGMENTS

The authors would like to thank Michael Callahan, Jen Junion Dienger, and the teachers at the University of Wisconsin Waisman Early Childhood Program for their contributions to the research. The research was supported financially by a grant to F.L.W. from the National Institutes of Health (Grant No. R01-HD023333-14).

Allen, P. (**1991**). "Children's detection of auditory signals," Doctral dissertation, University of Wisconsin-Madison.

Allen, P., and Nelles, J. (**1996**). "Development of auditory information integration abilities," J. Acoust. Soc. Am. **100**, 1043–1051.

Allen, P., and Wightman, F. (**1992**). "Spectral pattern discrimination by children," J. Speech Hear. Res. **35**, 222–233.

Allen, P., and Wightman, F. (**1995**). "Effects of signal and masker uncertainty on children's detection," J. Speech Hear. Res. **38**, 503–511.

Allen, P., Wightman, F., Kistler, D., and Dolan, T. (**1989**). "Frequency resolution in children," J. Speech Hear. Res. **32**, 317–322.

Bargones, J. Y., and Werner, L. A. (**1994**). "Adults listen selectively; Infants do not," Psychol. Sci. **5**, 170–174.

Bargones, J. Y., Werner, L. A., and Marean, G. C. (**1995**). "Infant psychometric functions for detection: Mechanisms of immature sensitivity," J. Acoust. Soc. Am. **98**, 99–111.

Berman, S., and Friedman, D. (**1995**). "The development of selective attention as reflected by event-related brain potentials," J. Exp. Child Psychol. **59**, 1–31.

Bolia, R. S., Nelson, W. T., Ericson, M. A., and Simpson, B. D. (**2000**). "A speech corpus for multitalker communications research," J. Acoust. Soc. Am. **107**, 1065–1066.

Bregman, A. S. (**1990**). *Auditory Scene Analysis* (MIT, Cambridge, MA).

Brungart, D. S. (**2001a**). "Evaluation of speech intelligibility with the coordinate response measure," J. Acoust. Soc. Am. **109**, 2276–2279.

Brungart, D. S. (**2001b**). "Informational and energetic masking effects in the perception of two simultaneous talkers," J. Acoust. Soc. Am. **109**, 1101–1109.

Brungart, D. S., and Simpson, B. D. (**2002**). "Within-ear and across-ear interference in a cocktail-party listening task," J. Acoust. Soc. Am. **112**, 2985–2995.

Brungart, D. S., and Simpson, B. D. (**2004**). "Within-ear and across-ear interference in a dichotic cocktail party listening task: Effects of masker uncertainty," J. Acoust. Soc. Am. **115**, 301–310.

Brungart, D. S., Simpson, B. D., Ericson, M. A., and Scott, K. R. (**2001**). "Informational and energetic masking effects in the perception of multiple simultaneous talkers," J. Acoust. Soc. Am. **110**, 2527–2538.

Bryden, M. P., and Allard, F. A. (**1981**). "Do auditory perceptual asymmetries develop?," Cortex **17**, 313–318.

Coch, D., Sanders, L. D., and Neville, H. J. (**2005**). "An event-related potential study of selective auditory attention in children and adults," J. Cogn Neurosci. **17**, 605–622.

Dirks, D. D., and Bower, D. R. (**1969**). "Masking effects of speech competing messages," J. Speech Hear. Res. **12**, 229–245.

Doyle, A. B. (**1973**). "Listening to distraction: A developmental study of selective attention," J. Exp. Child Psychol. **15**, 100–115.

Egan, J. P., Carterette, E. C., and Thwing, E. J. (**1954**). "Some factors affecting multi-channel listening," J. Acoust. Soc. Am. **26**, 774–782.

Fallon, M., Trehub, S. E., and Schneider, B. A. (**2000**). "Children's perception of speech in multitalker babble," J. Acoust. Soc. Am. **108**, 3023–3029.

Geffen, G. (**1976**). "Development of hemispheric specialization for speech perception," Cortex **12**, 337–346.

Geffen, G. (**1978**). "The development of the right ear advantage in dichotic listening with focused attention," Cortex **14**, 169–177.

Geffen, G., and Sexton, M. A. (**1978**). "The development of auditory strategies of attention," Dev. Psychol. **14**, 11–17.

Gomes, H., Molholm, S., Christodoulou, C., Ritter, W., and Cowan, N. (**2000**). "The development of auditory attention in children," Front. Biosci. **5**, D108–D120.

Hall, J. W., III, Grose, J. H., Buss, E., and Dev, M. B. (**2002**). "Spondee recognition in a two-talker masker and a speech-shaped noise masker in adults and children," Ear Hear. **23**, 159–165.

Hillyard, S. A., Hink, R. F., Schwent, V. L., and Picton, T. W. (**1973**). "Electrical signs of selective attention in the human brain," Science **182**, 177–180.

Hiscock, M., and Kinsbourne, M. (**1977**). "Selective listening asymmetry in preschool children," Dev. Psychol. **13**, 217–224.

Hiscock, M., and Kinsbourne, M. (**1980**). "Asymmetries of selective listening and attention switching in children," Dev. Psychol. **16**, 70–82.

Hugdahl, K., Carlsson, G., and Eichele, T. (**2001**). "Age effects in dichotic listening to consonant-vowel syllables: Interactions with attention," Dev. Neuropsychol. **20**, 445–457.

Kidd, G., Jr., Mason, C. R., Arbogast, T. L., Brungart, D. S., and Simpson, B. D. (**2003**). "Informational masking caused by contralateral stimulation," J. Acoust. Soc. Am. **113**, 1594–1603.

Litovsky, R. (**2005**). "Speech intelligibility and spatial release from masking in young children," J. Acoust. Soc. Am. **117**, 3091–3099.

Lutfi, R. A. (**1989**). "Informational processing of complex sound. I. Intensity discrimination," J. Acoust. Soc. Am. **86**, 934–944.

Lutfi, R. A. (**1993**). "A model of auditory pattern analysis based on component-relative-entropy," J. Acoust. Soc. Am. **94**, 748–758.

Lutfi, R. A., Kistler, D. J., Callahan, M. R., and Wightman, F. L. (**2003a**). "Psychometric functions for informational masking," J. Acoust. Soc. Am. **114**, 3273–3282.

Lutfi, R. A., Kistler, D. J., Oh, E. L., Wightman, F. L., and Callahan, M. R. (**2003b**). "One factor underlies individual differences in auditory informational masking within and across age groups," Percept. Psychophys. **65**, 396–406.

Maccoby, E. E. (**1969**). "The development of stimulus selection," Minnesota Symposia on Child Psychology **3**, 68–96.

Maccoby, E. E., and Konrad, K. W. (**1966**). "Age trends in selective listening," J. Exp. Child Psychol. **3**, 113–122.

Morris, R., Bakker, D., Satz, P., and Van der Vlugt, H. (**1984**). "Dichotic listening ear asymmetry: Patterns of longitudinal development," Brain Lang **22**, 49–66.

Neff, D. L., and Callaghan, B. P. (**1988**). "Effective properties of multicomponent simultaneous maskers under conditions of uncertainty," J. Acoust. Soc. Am. **83**, 1833–1838.

Oh, E. L., and Lutfi, R. A. (**1998**). "Nonmonotonicity of informational masking," J. Acoust. Soc. Am. **104**, 3489–3499.

Oh, E. L., Wightman, F., and Lutfi, R. A. (**2001**). "Children's detection of pure-tone signals with random multitone maskers," J. Acoust. Soc. Am. **109**, 2888–2895.

Pohl, P., Grubmuller, H. G., and Grubmuller, R. (**1984**). "Developmental changes in dichotic right ear advantage (REA)," Neuropediatrics **15**, 139–144.

Richards, V. M., Tang, Z., and Kidd, G. D., Jr. (**2002**). "Informational masking with small set sizes," J. Acoust. Soc. Am. **111**, 1359–1366.

Schneider, B. A., Trehub, S. E., Morrongiello, B. A., and Thorpe, L. A. (**1989**). "Developmental changes in masked thresholds," J. Acoust. Soc. Am. **86**, 1733–1742.

Sexton, M. A., and Geffen, G. (**1979**). "Development of three strategies of attention in dichotic monitoring," Dev. Psychol. **15**, 299–310.

Stellmack, M. A., Willihnganz, M. S., Wightman, F. L., and Lutfi, R. A. (**1997**). "Spectral weights in level discrimination by preschool children: Analytic listening conditions," J. Acoust. Soc. Am. **101**, 2811–2821.

Tang, Z., and Richards, V. M. (**2003**). "Examination of a linear model in an informational masking study," J. Acoust. Soc. Am. **114**, 361–367.

Wichmann, F. A., and Hill, N. J. (**2001a**). "The psychometric function. I. Fitting, sampling, and goodness of fit," Percept. Psychophys. **63**, 1293–1313.

Wichmann, F. A., and Hill, N. J. (**2001b**). "The psychometric function. II. Bootstrap-based confidence intervals and sampling," Percept. Psychophys. **63**, 1314–1329.

Wightman, F. L., and Allen, P. (**1992**). "Individual differences in auditory capability among preschool children," in *Developmental Psychoacoustics*, edited by L. A. Werner and E. W. Rubel (American Psychological Association, Washington, DC), pp. 113–133.

Wightman, F. L., Callahan, M. R., Lutfi, R. A., Kistler, D. J., and Oh, E. (**2003**). "Children's detection of pure-tone signals: Informational masking with contralateral maskers," J. Acoust. Soc. Am. **113**, 3297–3305.

Willihnganz, M. S., Stellmack, M. A., Lutfi, R. A., and Wightman, F. L. (**1997**). "Spectral weights in level discrimination by preschool children: Synthetic listening conditions," J. Acoust. Soc. Am. **101**, 2803–2810.

Wright, B. A., and Saberi, K. (**1999**). "Strategies used to detect auditory signals in small sets of random maskers," J. Acoust. Soc. Am. **105**, 1765–1775.

The interaction of glottal-pulse rate and vocal-tract length in judgements of speaker size, sex, and age[a)]

David R. R. Smith and Roy D. Patterson
Centre for Neural Basis of Hearing, Department of Physiology, University of Cambridge, Downing Street, Cambridge CB2 3EG, United Kingdom

(Received 15 April 2005; revised 2 August 2005; accepted 3 August 2005)

Glottal-pulse rate (GPR) and vocal-tract length (VTL) are related to the size, sex, and age of the speaker but it is not clear how the two factors combine to influence our perception of speaker size, sex, and age. This paper describes experiments designed to measure the effect of the interaction of GPR and VTL upon judgements of speaker size, sex, and age. Vowels were scaled to represent people with a wide range of GPRs and VTLs, including many well beyond the normal range of the population, and listeners were asked to judge the size and sex/age of the speaker. The judgements of speaker size show that VTL has a strong influence upon perceived speaker size. The results for the sex and age categorization (man, woman, boy, or girl) show that, for vowels with GPR and VTL values in the normal range, judgements of speaker sex and age are influenced about equally by GPR and VTL. For vowels with abnormal combinations of low GPRs and short VTLs, the VTL information appears to decide the sex/age judgement. © *2005 Acoustical Society of America.* [DOI: 10.1121/1.2047107]

PACS number(s): 43.66.Lj, 43.71.Bp, 43.71.An [RLD] Pages: 3177–3186

I. INTRODUCTION

When the radio or the telephone presents us with a previously unknown speaker, we rapidly develop a distinct impression of whether the speaker is an adult or a child, and if an adult, whether it is a man or a woman. This paper is concerned with the acoustic cues that people use to make these judgements. One highly-salient cue is voice pitch; adult men have low pitches, young children have high pitches, and adult women lie in the middle. Pitch is determined by the rate of opening and closing of the vocal folds [glottal-pulse rate (GPR)]. Another potent cue is vocal-tract length (VTL); large adult men have the longest VTLs, children have the shortest VTLs, and women have intermediate VTLs (Fitch and Giedd, 1999). Differences in VTL lead to shifts in the frequency of the prominent spectral peaks (formants) of speech (Fant, 1970). We have shown that changes in simulated VTL of as little as 7% can be reliably discriminated (Smith, Patterson, Turner, Kawahara, and Irino, 2005). It is unclear how the different effects of GPR and VTL are combined to influence the perception of speaker size, sex, and age. The purpose of this paper was to measure the interaction of GPR and VTL in judgements of speaker size, and to the categorization of speakers according to sex and age (man, woman, boy, or girl).

Recently, we have shown that when listeners are given two sequences of four vowels, and the simulated VTL for one sequence is longer than for the other, listeners are capable of discriminating VTL differences of 6–10%, over a wide range of GPR and VTL values (Smith *et al.*, 2005). The experiments used a 2AFC discrimination task which only requires the listener to make a relative size judgement. A second motivation for the present paper was to determine the extent to which listeners can make consistent judgements about speaker size, and consistent judgements about the sex and age of the speaker (man, woman, boy, or girl).

A. Background

Much of the variability between the voices of men, women, and children is due to differences in the mass of the vocal folds and the length of the vocal tract. For a given vowel, these differences lead to significant differences in both the GPR (perceived as voice pitch) and the frequencies of the most prominent spectral peaks (formants). The length and shape[1] of the vocal tract (VT) causes certain frequencies to be reinforced and attenuated. The length of the supralaryngeal VT is highly-correlated with speaker height, increasing with both age and sex (Fitch and Giedd, 1999). The longer the VT, the more the formant frequencies are shifted towards lower frequencies (Fant, 1970). As a child grows between the ages of 4 and 12 (puberty), there is a steady increase in VTL with a concomitant decrease in the formant frequencies. The formant frequencies of adult males decrease by about 32% from their values at age 4, while the formant frequencies of adult females decrease by about 20% (Huber, Stathopoulos, Curione, Ash, and Johnson, 1999). Within groups of adult men and women, the correlation between speaker height and formant frequency weakens (González, 2004). Nevertheless, a quantitative analysis by Turner and Patterson (2003) of the variability in the classic vowel data of Peterson and Barney (1952) shows that, within a given vowel cluster, speaker size is the largest source of variation. There is also a strong correlation between body size and formant-related parameters in rhesus monkeys (Fitch, 1997),

[a)]Portions of this work were presented in "The perception of sex and size in vowel sounds," British Society of Audiology, UCL London, United Kingdom, 2004, and "Perception of speaker size and sex of vowel sounds," Acoustical Society of America, Vancouver, Canada, 2005.

and in the vowel-like grunts of baboons, the formants of adult males are about 25% lower in frequency than those of the females (Rendall, Owren, Weerts, and Hienz, 2004). Indeed, the presence of size information has been demonstrated in a diverse range of vertebrate species (e.g., frogs, Fairchild, 1981, Narins and Smith, 1986; birds, Fitch, 1999; lions, Hast, 1989; dogs, Riede and Fitch, 1999).

The relationship between GPR and speaker size is more complex. Certainly, there is a strong link between speaker sex and pitch (Darwin, 1871; Morton, 1977). Adult males have pitches about an octave lower than adult females primarily because the vibrating segments of the male vocal folds are about 60% longer than those of the female and, thus, they are much more massive (Titze, 1989). This sexually dimorphic difference in pitch is also present in the vowel-like grunts of adult baboons (Rendall *et al.*, 2004). In a statistical clustering analysis of human adult male and female speech sounds, both GPR and VTL were highly successful as single-factors for classifying speaker sex. However, GPR was much less effective than VTL in correctly classifying individual speakers (Bachorowski and Owren, 1999). The sexual dimorphism in GPR is attributable to increased testosterone at puberty in males which stimulates growth in the laryngeal cartilages (Beckford, Rood, and Schaid, 1985). However, there is no direct correlation between body size and GPR within adult men and women (e.g., Lass and Brown, 1978; Künzel, 1989; Hollien, Green, and Massey, 1994). This is to be expected because VTL is dictated by the size of the cranium whilst the vocal folds are not constrained by any bony structure (Negus, 1949). The correlation between GPR and speaker size is also weakened by our use of GPR variation to make prosodic distinctions, such as the rising pitch contour of the interrogative sentence. Thus, while GPR provides a strong cue to speaker sex in adults (cf. Bachorowski and Owren, 1999), it provides a more variable cue to speaker size.

B. The interaction of GPR and VTL in judgements of speaker size, sex, and age

We wished to determine how GPR and VTL interact in the perception of speaker size. Given the strong correlation of VTL with speaker size, we would expect that VTL has a substantial effect on the perception of speaker size. There is also a correlation between GPR and size, although it is not as strong, and pitch is a highly salient property of a person's voice. With regard to the perception of speaker sex and age, we wished to determine the combinations of GPR and VTL that are associated with the categories used naturally by people, that is, man, woman, boy, and girl. Specifically, we wished to demonstrate that listeners would reliably assign combinations of GPR and VTL found in the normal population to the expected category, and we wished to investigate how they would extend the use of the categories to combinations of GPR and VTL well beyond the range normally encountered. Finally, we wanted to compare the listener's speaker-size judgements with their use of the categories, man, woman, boy, girl, particularly in the extended region of GPR and VTL values.

II. METHOD

Listeners were presented isolated vowels scaled over a large range of GPR and VTL values, and requested to make two judgements about each vowel: the height of the speaker (seven point descriptive rating) and their natural category (man, woman, boy, or girl).

A. Stimuli

The five English vowels (/a/, /e/, /i/, /o/, /u/) of an adult male (author, R.P.) were recorded in natural /hVd/ sequences (i.e., *haad*, *hayed*, *heed*, *hoed*, *who'd*), using a high-quality microphone (Shure SM58-LCE) and a 44.1 kHz sampling rate. The vowels were sustained (e.g., *haaaad*) to allow isolation of a stationary vowel component of relatively long duration, which was free of co-articulation with the preceding /h/ and the following /d/.

The speaker's vocal-tract shape determines the vowel type. The speaker's VTL determines the scale of the resonance and, thus, the position of the vowel pattern along the frequency dimension. The scaling of the vowels was performed by STRAIGHT (Kawahara, Masuda-Kasuse, and de Cheveigne, 1999; Kawahara and Irino, 2004). This sophisticated speech processing software uses the classical source-filter theory of speech (Dudley, 1939) to segregate GPR information from the spectral-envelope information associated with the shape and length of the vocal tract. Liu and Kewley-Port (2004) have reviewed STRAIGHT and commented favorably on its ability to manipulate formant-related information. STRAIGHT produces a GPR-independent spectral envelope that accurately tracks the motion of the vocal tract throughout the utterance. Once STRAIGHT has segregated a vowel into a GPR contour and a sequence of spectral-envelope frames, the vowel can be resynthesized with the spectral-envelope dimension (frequency) expanded or contracted, and the GPR dimension (time) expanded or contracted. Moreover, the operations are largely independent. Utterances recorded from a man can be transformed to sound like a women or a child; examples are provided on our web page.[2] The resynthesized utterances are of high quality even when the speech is resynthesized with GPR and VTL values well beyond the normal range of human speech (provided the GPR is not much greater than the frequency of the first formant, cf. Smith *et al.*, 2005). STRAIGHT is reviewed in Kawahara and Irino (2004).

The scaling of GPR consists of expanding or contracting the time axis of the sequence of glottal events. The scaling of VTL is accomplished by compressing or expanding the spectral envelope of the speech linearly along a linear frequency axis. On a logarithmic frequency axis, the spectral envelope shifts along the axis as a unit. The change in VTL is described by the spectral envelope ratio (SER), that is, the ratio of the unit on the new frequency axis to that of the axis associated with the original recording. Values of SER less than unity indicate lengthening of the vocal tract to simulate larger men, and SERs greater than unity indicate shortening of the vocal tract to simulate smaller men, women, and children. The SER values of STRAIGHT can be converted to VTL values by noting that (a) the speaker of our original

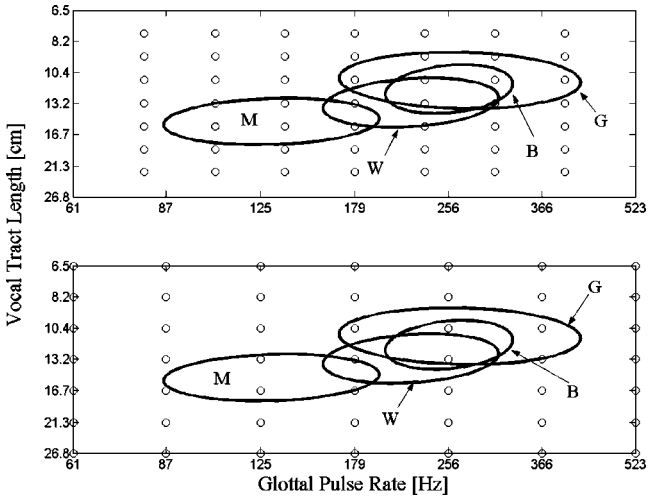

FIG. 1. The open circles show the GPR and VTL combinations of the stimuli used in the speaker size and sex/age categorization experiments. The circles in the top panel show the "narrower" range of (7×7) sample points (GPRs of 80, 105, 137, 179, 234, 306, and 400 Hz; VTLs of 7.8, 9.3, 11.0, 13.2, 15.7, 18.7, and 22.2 cm). The bottom panel shows the "wider" range (GPRs of 61, 87, 125, 179, 256, 366, and 523 Hz; VTLs of 6.5, 8.2, 10.4, 13.2, 16.7, 21.3, and 26.8 cm). The four ellipses show the normal range of GPR and VTL values in speech for men (M), women (W), boys (B), and girls (G), derived from the data of Peterson and Barney (1952). Each ellipse contains 99% of the individuals from the respective category.

vowels was of normal height, (b) that the VTL of the average-sized adult male is 15.5 cm (cf. Fitch and Giedd, 1999), and (c) assuming that formant frequencies scale linearly with VTL (Fant, 1970). The data in this study are reported in GPR and VTL units.

Following the scaling of GPR and VTL by STRAIGHT, a cosine-squared gating function (10-ms onset, 30-ms offset, 465-ms plateau) was used to select a stationary part of the vowel. The RMS level was set to 0.025 (relative to maximum ±1). The stimuli were played by a 24-bit sound card (Audigy 2, Sound Blaster), through a TDT anti-aliasing filter with a sharp cutoff at 10 kHz and a final attenuator, and presented binaurally to the listener over AKG K240DF headphones. Listeners were seated in a double-walled, IAC, sound-attenuating booth. The sound level of the vowels was 66 dB SPL.

B. Procedures

The experiments were performed using a single-interval, two-response paradigm. The listener heard a scaled version of one of five stationary English vowels (/a/, /e/, /i/, /o/, /u/), and had to make one judgement about the *size* of the speaker (very short, short, quite short, average, quite tall, tall, very tall)[3] and a second judgement about the *sex/age* of the speaker (man, woman, boy, girl). The order in which the judgements were made was left to the listener. Size and sex/age judgements were made by selecting the appropriate button on a response box displayed on a monitor in the booth. The level of the vowel was roved in intensity over a 10 dB range. Since the judgements are subjective there was no feedback.

The experiment was performed for two ranges of GPR and VTL values as shown in Fig. 1. The narrower range [Fig. 1(a)] was chosen to encompass the range of GPR and VTL values encountered in the normal population; GPR varied from 80 to 400 Hz in six logarithmic steps (seven sample points), and VTL ranged from 22.2 to 7.8 cm in six logarithmic steps (seven sample points). The four ellipses show estimates of the normal range of GPR and VTL values in speech for men, women, boys, and girls, derived from the Peterson and Barney (1952) vowel database. In each case, the ellipse encompasses 99% of the individuals in the Peterson and Barney data for that category of speaker.[4] The wider range [Fig. 1(b)] was chosen to extend the judgements well beyond the values encountered in everyday speech; GPR varied from 61 to 523 Hz in six logarithmic steps, and VTL ranged from 26.8 to 6.5 cm in six logarithmic steps. These VTLs simulate speakers ranging from a small child 0.6-m high (VTL=6.5 cm) to a giant 3.7-m high (VTL=26.8 cm).[5]

A run of judgements consisted of one presentation of each GPR-VTL combination for all five vowels, presented in a pseudo-random order (a total of 7 GPRs $\times$7 VTLs $\times$5 vowels, or 245 trials). Each run took approximately 30 min to complete. Each listener contributed a block of five runs to the database for the narrower range of judgements about speaker size and sex/age, and a block of five runs to the database for the wider range of judgements about speaker size and sex/age. The starting range [cf. Fig. 1(a) or Fig. 1(b)] was counterbalanced across listeners. The overlap in GPR and VTL values in the two ranges allows an across-condition test of the consistency of size and sex/age judgements. This helps us to see how different ranges of input sounds are stretched to the available seven point response, and how that mapping is influenced by the frames of reference provided by the two different ranges of GPR and VTL of the vowel sounds.

Eight listeners participated in the experiments, three male and five female. They ranged in age from 21 to 39 years. All had normal absolute thresholds at 0.5, 1, 2, 4, and 8 kHz.

III. RESULTS

Broadly speaking, the results from the two stimulus ranges show the same effects (Fig. 2), and they show that judgements of speaker size (Fig. 3) and sex/age (Fig. 4) are affected both by GPR and VTL. Listeners reliably reported that vowels spoken with a very low GPR and a very long VTL came from a very tall person (Fig. 3), and increasing the GPR or shortening the VTL reliably reduced the reported size of the speaker (Fig. 3). The influence of VTL upon these size judgements was very strong, as shown by the marked fall-off in reported speaker size as VTL shortened. Examination of the speaker size judgements over the course of the experiment showed little evidence of learning; listeners can do the task at near asymptotic levels almost straightaway. In the perception of sex and age (man, woman, boy, or girl), GPR and VTL had about the same influence in the narrower range about the normal ellipses (Fig. 4), but in the wider range, for the more unusual combinations of GPR and VTL, it is VTL information which appears to decide the sex/age judgement (Fig. 4).

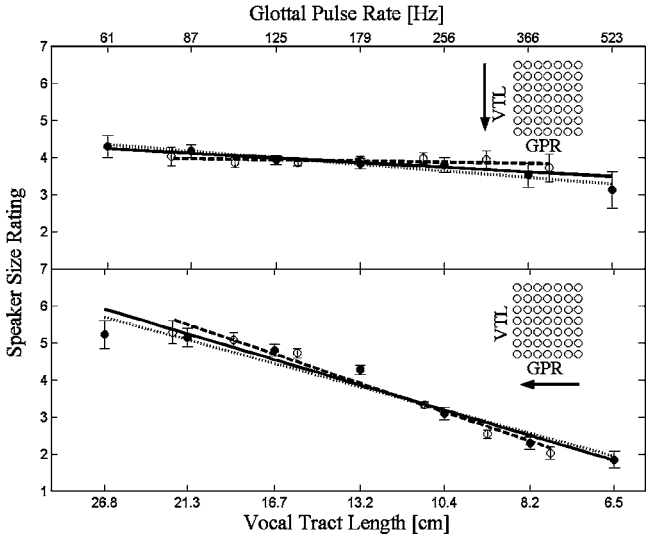

FIG. 2. Speaker size judgements collapsed across VTL (upper panel) and GPR (lower panel), separately for the narrower and the wider ranges (cf. Fig. 1). The arrows on the inset show the dimension over which the data were collapsed. The open circles show the data from the narrower range and the solid circles from the wider range. The dotted line is the best fitting line for the wider range; the dashed line is the best fitting line for the narrower range, and the solid thick line is the best fitting line for the combined data. The error bars are ± one standard error of the mean (calculated from the average of the eight listeners, where each listener's average is based on the seven values per point over which the data were collapsed). Each datum point is based on 1400 trials.

A. The effect of stimulus range on speaker size judgements

We will begin by comparing the size judgements obtained from the two ranges of GPR and VTL values [cf. Fig. 1(a) and 1(b)] because the results show that they are essentially sampling the same size surface, and so the data from the two ranges can be combined for subsequent analyzes. Figure 2 shows the column and row averages for both the narrower and the wider ranges; specifically, the upper panel shows the data for the two ranges collapsed across VTL (column averages), and the lower panel shows the data collapsed across GPR (row averages), as indicated by the inset schematic. In both panels, the data from the two ranges are seen to fall along similar lines (dashed and dotted for the narrower and wider ranges, respectively). For the GPR column averages in the upper panel, the slope of the line fitted to the data from the narrower range is slightly shallower than the slope of the line fitted to the data from the wider range. For the VTL row averages in the lower panel, the reverse is true; the slope for the wider range is slightly shallower than that for the narrower range. In both cases, when a single line (solid) was fitted to the combined data from the two ranges, it was found to provide an excellent fit to the full data set. Accordingly, the data from the two ranges were combined for subsequent analyzes.

B. The interaction of GPR and VTL in judgements of speaker size

The size judgements for both the wider and narrower ranges are presented in Fig. 3 as a 2D surface plot, averaged over the five vowels and eight listeners. The abscissa is GPR and the ordinate is VTL, both on logarithmic axes; color shows perceived speaker size. The GPR-VTL points where speaker size ratings were measured are shown by the open circles; between the data points, the surface was derived by interpolation.[6] The consistency of the size ratings across the two ranges (cf. Fig. 1) is shown by the similarity of the ratings for adjacent stimuli from the two data sets. The seven categories of the size rating scale, from "very short" to "very tall," were assigned ordinal values from 1 to 7, and they are represented by the spectrum of colors from dark-blue (1) to brown-red (7). The surface shows, as expected, that the combination of a long vocal tract with a low pitch is consistently heard as a large or very large person, and the combination of a short vocal tract with a high pitch is consistently heard as a small or very small person. The four ellipses show the normal range of GPR and VTL in speech for men, women, boys, and girls (Peterson and Barney, 1952). In each case, the ellipse encompasses 99% of the individuals in the Peterson and Barney data for that category of speaker (man, woman, boy, or girl). The figure shows that, although the perception of speaker size is affected both by VTL and GPR, the effect of VTL is stronger than that of GPR, at least in this coordinate system. For instance, for a constant GPR of 61 Hz, as we move vertically from a long VTL of 26.8 cm to a short VTL of 6.5 cm, the size rating goes from 6.2 ("tall") to 1.7 ("short"). The greatest change in perceived size as a function of change in GPR is for a VTL of 26.8 cm, where the size rating goes from 6.2 ("tall") at 61 Hz to 4.0 ("average") at 523 Hz.

The change in the perception of speaker size as a function of GPR and VTL was quantified in terms of the slopes of lines across the size surface in Fig. 3 parallel to the GPR and VTL axes. Perceived speaker size is shown as a function of GPR for three values of VTL in Fig. 5, namely, the two extreme VTLs (6.5 and 26.8 cm) associated with very short and very tall people, and a central value (13.2 cm) associated with an average-sized woman. Regression lines were fitted to the speaker size ratings as a function of the natural logarithm of GPR (solid lines in Fig. 5). They show that changes in GPR have the most effect when VTL is at its longest (26.8 cm; slope of −1.04). As VTL decreases to 13.2 cm, the slope decreases by about 60% (slope of −0.40), and as it decreases further to 6.5 cm, the slope becomes flat (0.01), indicating no change in speaker size whatsoever. The negative correlation between GPR and perceived speaker size is highly significant at the longer VTLs of 13.2 and 26.8 cm ($\rho < 0.001$ and $\rho \ll 0.001$, respectively, based on a one-tailed Spearman's rank order correlation test for nonparametric variables); the correlation is obviously not significant when VTL is 6.5 cm.

Similarly, perceived speaker size is shown as a function of VTL, for three GPR values in Fig. 6; namely, 61, 179, and 523 Hz. Again, they are the extreme values from the wider range (61 and 523 Hz), and the central value associated with an average-sized woman (179 Hz). Regression lines were fitted to the speaker size ratings as a function of the natural logarithm of VTL (solid lines in Fig. 6). The slopes of these VTL lines are all steeper than those of the GPR lines in Fig. 5. The slopes of these VTL lines become steeper as GPR

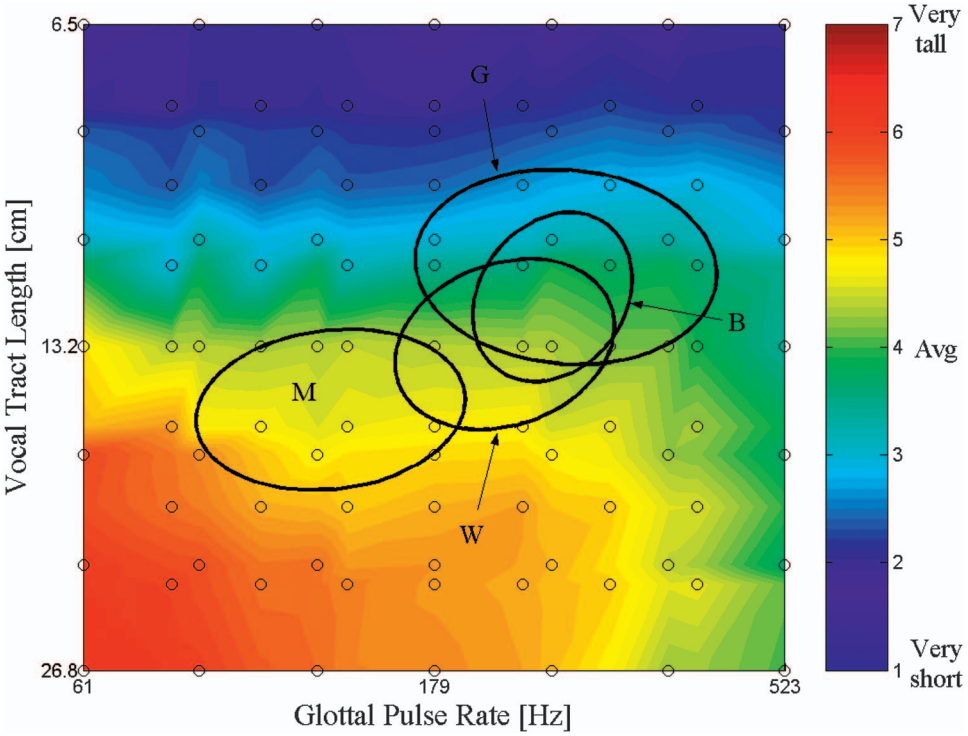

FIG. 3. Perceived size (in color) as a function of GPR and VTL on logarithmic axes. The size scale from "very short" to "very tall," is represented by the spectrum of colors from dark-blue (1) to brown-red (7). The points where speaker size ratings were measured are shown by the open circles; between the data points, the surface was derived by interpolation. The data were averaged across all five vowels and eight listeners, so each point is based on 200 trials. The four ellipses show the range of GPR and VTL in speech for men (M), women (W), boys (B), and girls (G), as derived from the data set of Peterson and Barney (1952).

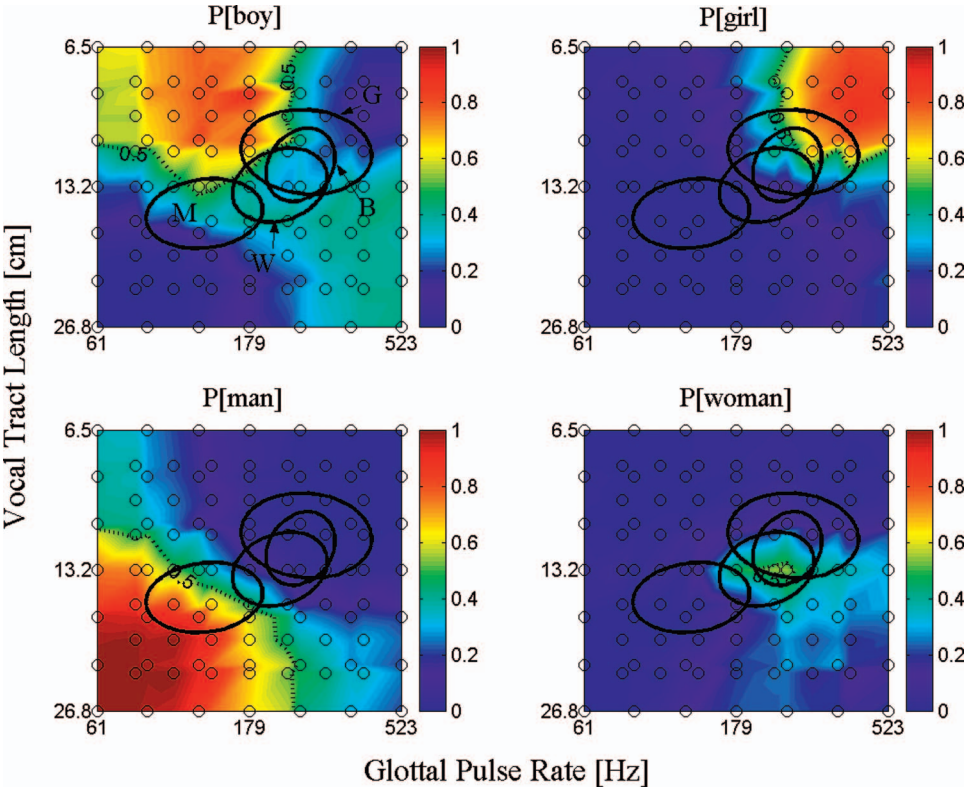

FIG. 4. Sex and age categorizations. The data are presented as 2D surface plots with color showing probability of assigning a given GPR-VTL combination to one of four categories (man, woman, boy, or girl). The points where sex/age judgements were collected are shown by the open circles; between the data points the surface was derived by interpolation. At each GPR-VTL point, the probabilities from the four panels sum to 1 (imagine the four separate 2D maps stacked vertically and aligned over each other). The data is averaged across all five vowels and eight listeners (each sample point probability based on 200 trials). The dotted black contour line marks the classification threshold, that is, a probability ≥ 0.50 of consistently choosing one category out of the four available. The region of GPR-VTL values enclosed by this line defines a region categorized as one particular sex or age. The four ellipses show the range of GPR and VTL in speech for men (M), women (W), boys (B), and girls (G), as derived from the data set of Peterson and Barney (1952).

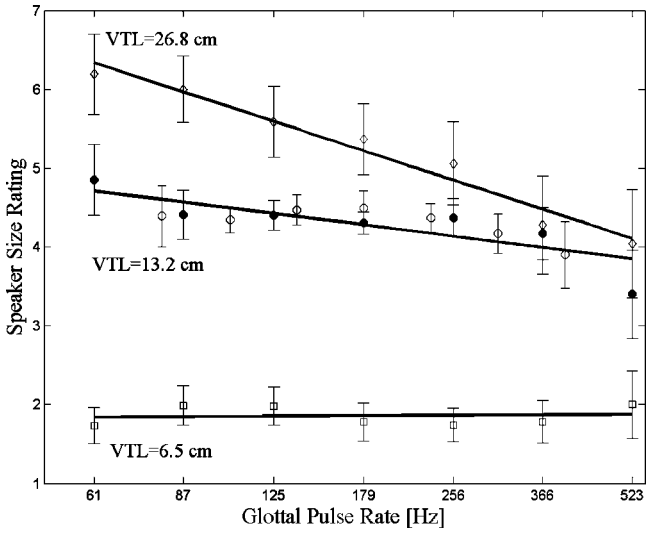

FIG. 5. Perceived speaker size as a function of GPR, for VTLs of 6.5, 13.2, and 26.8 cm. The open and solid circles show data from the narrower and wider stimulus ranges, respectively. The solid lines show the best-fitting regression lines for perceived speaker size rating as a function of the natural logarithm of GPR. The error bars are ± one standard error of the mean (calculated from the average of the eight listeners). Each datum point is based on 200 trials.

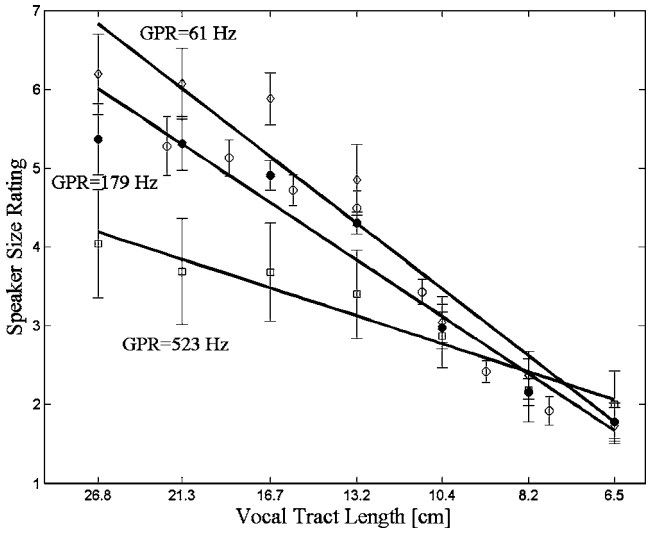

FIG. 6. Perceived speaker size as a function of VTL, for GPRs of 61, 179, and 523 Hz. The solid lines show the best-fitting regression lines for speaker size rating as a function of the natural logarithm of VTL. For all other details see Fig. 5.

decreases; the gradient is 1.50, 3.06, and 3.57 for GPRs of 523, 179, and 61 Hz, respectively. The correlation between VTL and perceived speaker size is highly significant for all three lines ($\rho \ll 0.001$ based on a one-tailed Spearman's rank order correlation test for nonparametric variables).

Figures 5 and 6 show an interaction between GPR and VTL in the perception of speaker size, especially at extreme GPR or VTL values. Simulated speakers that would only stand two feet tall, with very short VTLs (Fig. 5, VTL =6.5 cm), are always judged as short regardless of their GPR. Simulated giants of 12 feet (Fig. 5, VTL=26.8 cm) are always heard as above average height, but their estimated height declines as GPR increases. Figure 6 shows that the perception of speaker size is strongly affected by VTL, but that the effect weakens as GPR increases (cf. the decrease in slope for GPRs of 61, 179, and 523 Hz).

C. The interaction of GPR and VTL in judgements of sex and age

The speaker sex and age judgements from both the narrower and wider ranges of GPR-VTL values (cf. Fig. 1) are presented as 2D surface plots in Fig. 4; the results have been averaged over the five vowels and eight listeners. The results from the two ranges are entirely compatible, just as they were in the size rating experiments. The four panels show the probability of classifying a vowel with a specific GPR-VTL combination as a man, woman, boy, or girl. The probability of classification is shown by color, ranging from 0 (dark-blue) to 1 (brown-red). For each combination of GPR and VTL, the probabilities from the four panels sum to 1.0. The abscissa is GPR and the ordinate is VTL, both on logarithmic axes. The open circles show the combinations of GPR and VTL presented to the listeners; between these data points, the surfaces have been generated by interpolation. The dotted black lines bound regions of GPR-VTL where listeners consistently choose one category out of the four available to them. Within these regions, the probability of choosing the given combination of sex and age is greater than 0.5. The four ellipses show estimates of the normal range of GPR and VTL in speech for men, women, boys, and girls (Peterson and Barney, 1952). The ellipse for men does not intersect with the ellipses for girls and boys, whereas the ellipse for women intersects with the ellipses of all of the other groups. The ellipse for boys lies almost entirely within that for girls, and the overlap of the ellipses for boys and women is about 50%. Figure 4 shows that both GPR and VTL affect the perception of a speaker's sex and age, as expected, and that they interact, producing consistent responses in different regions across the GPR-VTL plane.

In the two quadrants of the GPR-VTL plane that represent the majority of normal human voices (lower left and upper right), the relationship between the sex/age category that the listener perceives and the combination of GPR and VTL in the vowel is straightforward. Vowels with low GPRs and long VTLs, in the lower left-hand quadrant of the GPR-VTL plane, are overwhelmingly categorized as men (lower left-hand panel of Fig. 4), and this quadrant contains the ellipse for men. This quadrant also contains vowels with lower than normal GPRs and longer than normal VTLs, and listeners consistently adopt the nearest category which is "man," as would be expected. Outside the $p \geqslant 0.5$ contour (dashed line), the probability of responding "man" drops rapidly, and only a small proportion of the "man" responses occur in the region above the negative diagonal.

Vowels with high GPRs and short VTLs, in the upper right-hand quadrant of the GPR-VTL plane, are predominately categorized as girls (upper right-hand panel of Fig. 4); this quadrant contains the ellipse for girls *and* the ellipse for boys, but the ellipse for girls extends to higher GPRs and shorter VTLs, so it is arguably the more natural category to adopt. This quadrant also contains vowels with higher than

normal GPRs and shorter than normal VTLs, and once again, listeners consistently adopt the nearest category which in this case is "girl." Outside the $p \geq 0.5$ contour, the probability of responding "girl" drops rapidly and the response "girl" is almost never used in the region below the negative diagonal. So, the categories "man" and "girl" are used consistently, and the combinations of GPR and VTL associated with these sex/age categories are mutually exclusive.

In the two remaining quadrants of the GPR-VTL plane (upper left and lower right), the majority of the vowels have combinations of GPR and VTL that are not typical of the normal population of voices; this is a consequence of the experimental design in which two related responses (size and sex/age) are obtained on each trial. It means that, as the GPR and VTL values become more extreme, the listener has to make a projection from normal experience, and decide which of the four categories of speaker would be most likely to produce the sound presented. As a result, the relationship between the sex/age category perceived and the combination of GPR and VTL in the vowel is not as straightforward as for the other two quadrants. Nevertheless, the use of the category names is consistent and seems entirely reasonable. Vowels with low GPRs but short VTLs, in the upper left-hand quadrant of the plane, are predominantly categorized as boys (upper left-hand panel of Fig. 4); the probability of "boy" is greater than 0.5 throughout most of this quadrant (although the ellipse for boys in the normal population does not even fall in this quadrant). In retrospect, the reason is not difficult to deduce; these voices with their short VTLs and low GPRs sound like males who, for some reason, are unusually short. This condition exists for male dwarves who are quite uncommon, but not unknown. Their pitch drops significantly at puberty but their vocal tract does not increase proportionately in length because their bodies do not grow in the usual way. There is no corresponding vocal category for female dwarves; they continue to sound like girls because they do not grow to the normal height and, although their pitch may decrease in the normal way, this decrease is relatively small, and the drop in pitch would rarely be so great as to shift the voice into the left-hand section of the GPR-VTL plane. The listeners rarely use the categories "woman" or "girl" for vowels in this quadrant; on the border where the pitch is 179 Hz, the response "boy" is far more likely than "woman" or "girl."

In the final quadrant of the GPR-VTL plane (lower right-hand), where the vowels have high GPRs in combination with *long* VTLs, the most common responses are "man," when the GRP is relatively low and the VTL is long (lower left-hand panel of Fig. 4), and "boy" when the GRP is relatively high and the VTL is long (upper left-hand panel of Fig. 4). The "man" responses are just the natural extension of the large "man" region in the lower, left-hand quadrant of the GPR-VTL plane. "Boy" responses seem reasonable for voices that have a high pitch and are perceived to come from tall people.

The response "woman" is predominant only in one small region near the center of the GPR-VTL plane as shown in the lower right-hand panel of Fig. 4. In this region, the probability of the response exceeds the criterion value of 0.5. Moreover, the peak of the region is close to the center of the ellipse for women (although the listeners had no knowledge of these distributions other than their personal experience). The response "woman" is also used for a proportion of the vowels produced with GPRs that are greater than those for normal women, *provided* the VTL is the same, or longer, than that for normal women; these responses appear in the lower, right-hand quadrant of the lower, right-hand panel. If the VTL becomes shorter, listeners consistently use "girl" instead of "woman," and if it becomes longer, they consistently use "boy" instead of "woman." Nevertheless, the relationship between the response category, "woman," and the combination of GPR and VTL in the vowel seems reasonable.

The four panels of Fig. 4 also make it clear that the distribution of responses across the four sex/age categories is not uniform; the overall probabilities for man, woman, boy, and girl, are 0.36, 0.11, 0.36, and 0.17, respectively. The relatively low probability of responding "woman" in the women's ellipse is consistent with the large degree of overlap of the woman's ellipse with the boy and girl ellipses. The nonuniform distribution of response is largely attributable to the fact that the GPR and VTL values span a rectangular plane of combinations, whereas the normal population of voices is concentrated on combinations that cluster the central section of the positive diagonal in the GPR-VTL plane. The listener has to extend the use of the normal categories to the novel stimuli and, in general, they do this reasonably and consistently, but it does lead to a nonuniform distribution of responses across the four categories.

All of the vowels in these experiments were synthesized from the vowels of one adult male speaker, and so the formant ratios for a given vowel are the same for all combinations of GPR and VTL in the experiment. This has the advantage of minimizing one source of variability in the experiment; however, it is not typical of the human population (Diehl, Lindbolm, Hoemeke, and Fahey, 1996). For a given vowel, the formant ratio $F2/F1$ increases slowly as height increases because throat length grows relatively more than mouth length as we grow up. The effect is illustrated in Turner, Walters, and Patterson (2004) using MRI measurements of mouth and throat length from Fitch and Giedd (1999). It is not entirely clear what effect this might have on judgements of size and sex/age like those in this paper. However, we might expect that, if the experiment were rerun using vowels from an adult female speaker, listeners would hear a difference and the proportion of "woman" responses would be higher over much of the range of our measurements. In the end, however, although the effects of the sex and size of the original speaker on these judgements are interesting, they are beyond the scope of this paper.

IV. DISCUSSION

The size rating experiments show that listeners make consistent judgements about speaker size given a sequence of vowel sounds (Fig. 3). Both GPR and VTL affect judgements of speaker size (Figs. 5 and 6), and the effect of VTL is strong enough to change speaker size estimates from tall to

short. The sex and age judgements are also affected both by the GPR and the VTL of the vowels (Fig. 4). The data show that sex and age are not dictated solely by GPR or VTL; rather, there is an interaction between these variables that means that specific combinations of GPR and VTL act as robust indicators of sex and age.

A. Speaker size - interaction of GPR and VTL

Previous studies on the perception of speaker size were limited by the restricted range of heights of the speakers. For instance, listeners were asked to judge the height of speaker of recordings made from adult men only (Lass and Davis, 1976; van Dommelen and Moxness, 1995; Collins, 2000). Although listeners made consistent judgements about the size of these adult speakers, these estimates were not very accurate (van Dommelen and Moxness, 1995; Collins, 2000), though Lass and Davis (1976) did report better than chance correct categorization. These studies only used normal-range adult voices which have recently been reported to show a significant but weak correlation between speaker size and formant frequency within same sex adults (González, 2004). Given the weak correlation between speaker size and formant frequency in same sex adults, the task of accurately judging the physical height of same sex adults might prove difficult (Rendall, Vokey, Nemeth, and Ney, 2005). Nevertheless, listeners make consistent perceptual decisions as if they were receiving strong valid acoustic cues to speaker size (e.g., Collins, 2000). One way to reconcile this apparent conflict is to hypothesize that the correlation between speaker height, VTL and formant frequency, observed in close hominoid species such as rhesus monkeys (Fitch, 1997), has become disassociated in adult humans, possibly because of human-specific vocal-tract changes such as the descent of the larynx in adult men (Fitch, 1997; Fitch, 2000).

A better mapping between perceptual judgements of speaker size and physical speaker size might arise if a wider range of speaker heights were used, say from very small children to very large men. However, for all natural recorded voices there will always be the problem that GPR and VTL cues are confounded. To tease out the separate effects of each of the cues, and to simultaneously provide listeners with a suitably wide range of potential heights, it is necessary to use synthetic speech. Fitch (1994, Ph.D. thesis) used a rating scale to gather listeners' judgements of speaker size using computerized vowels. Even though the vowels were restricted to the middle to upper normal range for men only, he found main effects of both GPR and VTL on listeners' size ratings. Our study uses a much greater range of GPR and VTL values, simulating tiny children, giants, castrati, and dwarves, as well as everyday speech combinations. It was made possible by the recent development of the high-quality vocoder, STRAIGHT (Kawahara *et al.*, 1999; Kawahara and Irino, 2004).

GPR can be used to distinguish between male and female speakers (Bachorowski and Owren, 1999) but not to draw reliable *intra*-sex inferences about speaker size. Unlike the vocal tract, which is related to the size of the cranium and hence body size, the vocal folds are not constrained by any hard bony structure (Negus, 1949; discussed in Fitch, 1997). Prosody is also routinely used to make sentence distinctions, e.g., "The baby is happy" with constant pitch is a statement, but the same sentence with rising pitch is a question. The advantage of vocal-tract information is clear. Measurements made with magnetic resonance imaging show that VTL is highly correlated with speaker height (Fitch and Giedd, 1999). There is a highly significant correlation between age and formant frequency in humans (Huber *et al.*, 1999), and a strong relationship between body size and formant-related parameters in rhesus monkeys (Fitch, 1997). The reliability of VTL for speaker size (as signalled by perceptually salient shifts in formant frequency) may have weakened within human adults of the same sex (González, 2004), but it is still strong between groups of children, women, and men. Within group, the correlation between GPR and speaker size is surprisingly weak, both in humans, and close hominoid species (Fitch, 1997; Rendall *et al.*, 2004).

The strong effect of VTL on the perception of speaker size may reflect the extremely wide range of VTL values used in our study. In normal speech, pitch is more salient than vocal tract length, perhaps because the just noticeable difference for voice pitch is about 2%, whereas the just noticeable difference for a change in VTL is 6–10% (Smith *et al.*, 2005). STRAIGHT enabled us to simulate the vowels of very small children and giants. This could have the effect of encouraging listeners to lend additional weight to VTL, especially if VTL has more natural relevance to speaker size than GPR.

Our earlier size discrimination experiments showed that listeners were capable of discriminating changes in speaker size of 6–10% when the sounds were presented in two temporal intervals of a forced choice experiment (Smith, Patterson, and Jefferis, 2003; Smith and Patterson, 2004a; Smith *et al.*, 2005). The size perception experiments reported in this paper show that listeners can also make consistent and sensible size judgements about vowels which are presented in a single temporal interval. The listener in this rating task cannot discriminate speaker size *relative* to another vowel sound presented immediately after the first vowel sound; rather, they have to make a judgement about speaker size relative to the frame of reference provided by all the other vowel sounds in the set (and presumably all the vowel sounds they have experienced over their lives). That our listeners can do this task as well as they do, supports our belief that size information can be extracted from individual voiced sounds to inform perceptual decisions.

B. Speaker sex and age: the interaction of GPR and VTL

Previous research attempting to identify those acoustic properties of male and female voices responsible for our perception of sex type, have used either statistical clustering methods (e.g., Childers and Wu, 1991; Wu and Childers, 1991; Bachorowski and Owren, 1999) or perceptual categorization experiments (e.g., Schwartz, 1968; Schwartz and Rine, 1968; Ingemann, 1968; Lass *et al.*., 1976). The statistical clustering studies have consistently highlighted GPR

and vocal tract related variables as explaining most of the variance between the speech sounds of adult males and females (Childers and Wu, 1991; Bachorowski and Owren, 1999). Some studies have shown that vocal tract information alone can be used to identify speaker sex (Schwartz, 1968; Ingemann, 1968; Schwartz and Rine, 1968). Other studies have reported that GPR is a much stronger cue to speaker sex than VTL (Lass *et al.*, 1976). Statistical clustering studies suggest that GPR and VTL are highly correlated (Childers and Wu, 1991; Wu and Childers, 1991). Other studies suggest that formant information can be important in discriminating speaker sex (Coleman, 1976; Whiteside, 1998) but generally pitch is dominant (Whiteside, 1998). Recently, Bachorowski and Owren (1999) have shown that sex classification accuracy is excellent using only GPR or only VTL, but best using both.

Our reasons for wishing to measure the interaction of GPR and VTL in sex/age judgements were based on two main factors. First, we believe that the auditory system employs a scale invariant neural transform to normalize natural sounds for size prior to more central processes like speaker identification (e.g., Irino and Patterson, 2002; Turner, Al-Hames, Smith, Kawahara, Irino, and Patterson, 2005). We have recently reported evidence that human listeners are able to discriminate and use size information in speech sounds (vowels), suggesting that size information is actively used in auditory perception (Smith, Patterson, and Jefferis, 2003; Smith and Patterson, 2004a; Smith *et al.*, 2005). We were thus interested in how speaker size information, as mediated by VTL and GPR cues, influenced decisions in natural sex/age categorization (man, woman, boy, or girl). Second, both statistical and perceptual classification studies are limited to databases of sounds that are from *normal* groups, i.e., recorded from largely homogeneous (usually adult) males and females. Thus the range over which the independent variables could be manipulated was necessarily limited. The vocoder STRAIGHT (Kawahara *et al.*, 1999; Kawahara and Irino, 2004) enabled us to manipulate the GPR and VTL of vowels independently of each other over a huge range. These speech sounds are of high quality even when pushed well beyond the normal range of speech. This allows unprecedented control over our main experimental variables, across a much wider range of GPRs and VTLs than has been used previously.

We found that *both* GPR and VTL contribute to listeners' perception of the sex and age of a speaker (Fig. 4). If GPR was the *sole* perceptual determinant of the sex and age of the speaker (man, woman, boy, or girl), then listeners would only be able to reliably classify most men (GPR $\lesssim$155 Hz) and the higher-pitched girls (GPR$\gtrsim$330 Hz). If VTL was the *only* perceptual marker to sex and age then listeners would only be able to reliably classify taller men (with VTL$\gtrsim$16 cm) and shorter girls (with VTL$\lesssim$10 cm). The sex classification performance of our listeners is much better than this.

V. SUMMARY AND CONCLUSIONS

Listeners were presented with vowels in a single-interval, two-response paradigm. The listener heard a vowel scaled in GPR and VTL, and had to make one judgement about the size of the speaker (on a seven-point ordinal scale ranging from "very short" to "very tall") and a second judgement about the sex/age of the speaker (man, woman, boy, or girl). The results from the speaker size judgement experiment show that VTL has a strong influence upon perceived speaker size (Figs. 3, 5, 6). The strength of this effect presumably reflects the high correlation of VTL with speaker size. The results of the sex/age categorization experiments show that judgements of speaker sex/age are influenced by the interaction of GPR and VTL (Fig. 4). In the normal range of GPR and VTL values, judgements of sex/age are consistent with listeners combining both GPR and VTL information about equally to give a robust indicator of sex and age. When listeners are presented with unusual GPR and VTL combinations, where low GPRs are combined with short VTLs, the VTL information appears to decide the sex/age judgement.

ACKNOWLEDGMENTS

This research was supported by the UK MRC (G9901257; G9900369) and the German Volkswagen Foundation (VWF 1/79 783). Some of the data were reported in abstract form (Smith and Patterson, 2004b; Smith and Patterson, 2005). We thank Richard Turner for providing the ellipses showing the GPR-VTL values for men, women, boys, and girls as derived from the data of Peterson and Barney (1952).

[1]The shape of the vocal tract is largely determined by the placement of the tongue within the oral cavity. The shape affects the positioning of the formants relative to each other—different vowels having different vector angles in a multi-dimensional vowel space. For the purposes of our argument, we assume the same fixed vocal tract shape across all speakers, i.e., the speakers are uttering the same vowel.

[2]http://www.mrc-cbu.cam.ac.uk/cnbh/web2002/framesets/Soundsframeset.htm. Click on "Scaled vowels."

[3]In British English, "quite" means "to some extent" in this context. Since the size scale was presented graphically and continuously, it is very likely that the responses involving the word "quite" were interpreted as meaning half way between the sizes above and below them in each case.

[4]The set of formant values for each of the 76 speakers in the classic study of Peterson and Barney (1952) were converted to VTL values using the VTL data that Fitch and Giedd (1999) extracted from magnetic resonance images of a large population of subjects. Each ellipse represents the mean ± three standard deviations for each category of speaker. The calibration details are presented in Turner, Walters, and Patterson (2004); this poster can be found at http://www.mrc-cbu.cam.ac.uk/cnbh/web2002/framesets/posters_talksframeset.htm.

[5]An estimate of the size of speaker for a given SER was derived by extrapolating from the VTL *versus* height data in Fitch and Giedd [1999 cf. Fig. 2(a)]. In Fitch and Giedd, the average VTL for seven men aged 19 to 25 was 15.54 cm. An SER of 0.58 means that the spectral envelope of the initial vowel has been compressed by a factor of 1.72 (=1/0.58), while an SER of 2.39 means that the spectral envelope has been dilated by 0.42. Assuming linear scaling between VTL and formant frequency, these SER values are equivalent to VTLs of 26.8 and 6.5 cm, respectively. The former would be a giant and the latter a tiny child.

[6]The two 7×7 ranges (cf. Fig. 1) were merged to form one 13×13 matrix (the middle row and column of both ranges is the same). Any empty cell in the matrix was filled by the average of all adjoining cells where a speaker size rating had been collected. The data surface was derived by interpolation between the sample points and their averaged neighbors.

Bachorowski, J., and Owren, M. J. (**1999**). "Acoustic correlates of talker sex and individual talker sex identity are present in a short vowel segment produced in running speech," J. Acoust. Soc. Am. **106**, 1054–1063.
Beckford, N. S., Rood, S. R., and Schaid, D. (**1985**). "Androgen stimulation and laryngeal development," Ann. Otol. Rhinol. Laryngol. **94**, 634–640.
Childers, D. G., and Wu, K. (**1991**). "Gender recognition from speech. Part II: Fine analysis," J. Acoust. Soc. Am. **90**, 1841–1856.
Coleman, R. O. (**1976**). "A comparison of the contributions of two voice quality characteristics to the perception of maleness and femaleness in the voice," J. Speech Hear. Res. **19**, 168–180.
Collins, S. A. (**2000**). "Men's voices and women's choices," Anim. Behav. **60**, 773–780.
Darwin, C. (**1871**). "The Descent of Man and Selection in Relation to Sex" (Murray, London).
Diehl, R. L., Lindbolm, B., Hoemeke, K. A., and Fahey, R. P. (**1996**). "On explaining certain male-female differences in the phonetic realization of vowel categories," J. Phonetics **24**, 187–208.
Dudley, H. (**1939**). "Remaking speech," J. Acoust. Soc. Am. **11**, 169–177.
Fant, G. (**1970**). "Acoustic Theory of Speech Production", 2nd ed. (Mouton, Paris).
Fairchild, L. (**1981**). "Mate selection and behavioural thermoregulation in Fowler's toads," Science **212**, 950–951.
Fitch, W. T. (**1994**). "Vocal tract length perception and the evolution of language," Ph.D. dissertation, Brown University.
Fitch, W. T. (**1997**). "Vocal tract length and formant frequency dispersion correlate with body size in rhesus monkeys," J. Acoust. Soc. Am. **102**, 1213–1222.
Fitch, W. T. (**1999**). "Acoustic exaggeration of size in birds by tracheal elongation: Comparative and theoretical analyses," J. Zool. (London) **248**, 31–49.
Fitch, W. T. (**2000**). "The evolution of speech: a comparative review," Trends in Cognitive Science **4**, 258–267.
Fitch, W. T., and Giedd, J. (**1999**). "Morphology and development of the human vocal tract: A study using magnetic resonance imaging," J. Acoust. Soc. Am. **106**, 1511–1522.
González, J. (**2004**). "Formant frequencies and body size of speaker: a weak relationship in adult humans," J. Phonetics **32**, 277–287.
Hast, M. (**1989**). "The larynx of roaring and non-roaring cats," J. Anat. **163**, 117–121.
Hollien, H., Green, R., and Massey, K. (**1994**). "Longitudinal research on adolescent voice change in males," J. Acoust. Soc. Am. **96**, 3099–3111.
Huber, J. E., Stathopoulos, E. T., Curione, G. M., Ash, T., and Johnson, K. (**1999**). "Formants of children, women and men: The effects of vocal intensity variation," J. Acoust. Soc. Am. **106**, 1532–1542.
Ingemann, F. (**1968**). "Identification of the speaker's sex from voiceless fricatives," J. Acoust. Soc. Am. **44**, 1142–1144.
Irino, T., and Patterson, R. D. (**2002**). "Segregating information about the size and shape of the vocal tract using a time-domain auditory model: The stabilised wavelet-Mellin transform," Speech Commun. **36**, 181–203.
Kawahara, H., and Irino, T. (**2004**). "Underlying principles of a high-quality speech manipulation system STRAIGHT and its application to speech segregation," in *Speech Separation by Humans and Machines*, edited by P. Divenyi, Kluwer Academic, Massachusetts, 167–180.
Kawahara, H., Masuda-Kasuse, I., and de Cheveigne, A. (**1999**). "Restructuring speech representations using pitch-adaptive time-frequency smoothing and instantaneous-frequency-based F0 extraction: Possible role of repetitive structure in sounds," Speech Commun. **27**, 187–207.
Künzel, H. J. (**1989**). "How well does average fundamental frequency correlate with speaker height and weight?" Phonetica **46**, 117–125.
Lass, N. J., and Brown, W. S. (**1978**). "Correlational study of speakers' heights, weights, body surface areas and speaking fundamental frequencies," J. Acoust. Soc. Am. **63**, 1218–1220.
Lass, N. J., and Davis, M. (**1976**). "An investigation of speaker height and weight identification," J. Acoust. Soc. Am. **60**, 700–703.
Lass, N. J., Hughes, K. R., Bowyer, M. D., Waters, L. T., and Bourne, V. T. (**1976**). "Speaker sex identification from voiced, whispered, and filtered isolated vowels," J. Acoust. Soc. Am. **59**, 675–678.
Liu, C., and Kewley-Port, D. (**2004**). "STRAIGHT: a new speech synthesizer for vowel formant discrimination," ARLO **5**, 31–36.
Morton, E. S. (**1977**). "On the occurrence and significance of motivation-structural rules in some bird and mammal sounds," Am. Nat. **111**, 855–869.
Narins, P. M., and Smith, S. L. (**1986**). "Clinal variation in anuran advertisement calls—basis for acoustic isolation," Behav. Ecol. Sociobiol. **19**, 135–141.
Negus, V. E. (**1949**). *The Comparative Anatomy and Physiology of the Larynx* (Hafner, New York).
Peterson, G. E., and Barney, H. L. (**1952**). "Control methods used in a study of the vowels," J. Acoust. Soc. Am. **24**, 175–184.
Rendall, D., Owren, M. J., Weerts, E., and Hienz, R. D. (**2004**). "Sex differences in the acoustic structure of vowel-like grunt vocalizations in baboons and their perceptual discrimination by baboon listeners," J. Acoust. Soc. Am. **115**, 411–421.
Rendall, D., Vokey, J. R., Nemeth, C., and Ney, C. (**2005**). "Reliable but weak voice-formant cues to body size in men but not women," J. Acoust. Soc. Am. **117**, 2372.
Riede, T., and Fitch, W. T. (**1999**). "Vocal tract length and acoustics of vocalization in the domestic dog Canis familiaris," J. Exp. Biol. **202**, 2859–2867.
Schwartz, M. F. (**1968**). "Identification of speaker sex from isolated, voiceless fricatives," J. Acoust. Soc. Am. **43**, 1178–1179.
Schwartz, M. F., and Rine, H. E. (**1968**). "Identification of speaker sex from isolated, whispered vowels," J. Acoust. Soc. Am. **44**, 1736–1737.
Smith, D. R. R., and Patterson, R. D. (**2004a**). "The existence region of scaled vowels in pitch-VTL space," *18th International Conference on Acoustics*, Kyoto, Japan, Vol. I, 453–456.
Smith, D. R. R., and Patterson, R. D. (**2004b**). "The perception of sex and size in vowel sounds," paper presented at British Society of Audiology, UCL London P49..
Smith, D. R. R., and Patterson, R. D. (**2005**). "Perception of speaker size and sex of vowel sounds," J. Acoust. Soc. Am. **117**, 2374.
Smith, D. R. R., Patterson, R. D., and Jefferis, J. (**2003**). "The perception of scale in vowel sounds," paper presented at British Society of Audiology, Nottingham P35.
Smith, D. R. R., Patterson, R. D., Turner, R., Kawahara, H., and Irino, T. (**2005**). "The processing and perception of size information in speech sounds," J. Acoust. Soc. Am. **117**, 305–318.
Titze, I. R. (**1989**). "Physiologic and acoustic differences between male and female voices," J. Acoust. Soc. Am. **85**, 1699–1707.
Turner, R. E., Al-Hames, M. A., Smith, D. R. R., Kawahara, H., Irino, T., and Patterson, R. D. (**2005**). "Vowel normalisation: Time-domain processing of the internal dynamics of speech," in *Dynamics of Speech Production and Perception*, edited by P. Divenyi (IOS Press) (in press).
Turner, R. E., and Patterson, R. D. (**2003**). "An analysis of the size information in classical formant data: Peterson and Barney (1952) revisited," J. Acoust. Soc. Am. **33**, 585–589.
Turner, R. E., Walters, T. C., and Patterson, R. D. (**2004**). "Estimating vocal tract length from formant frequency data using a physical model and a latent variable factor analysis," paper presented at British Society of Audiology, UCL London P61.
van Dommelen, W. A., and Moxness, B. H. (**1995**). "Acoustic parameters in speaker height and weight identification: sex-specific behaviour," Lang Speech **38**, 267–287.
Whiteside, S. P. (**1998**). "Identification of a speaker's sex from synthesized vowels," Percept. Mot. Skills **86**, 595–600.
Wu, K., and Childers, D. G. (**1991**). "Gender recognition from speech. Part I: Coarse analysis," J. Acoust. Soc. Am. **90**, 1828–1840.

Listening experience with iterated rippled noise alters the perception of 'pitch' strength of complex sounds in the chinchilla

William P. Shofner,[a] William M. Whitmer,[b] and William A. Yost
Parmly Hearing Institute, Loyola University Chicago, Chicago, Illinois 60626

(Received 11 February 2005; revised 10 August 2005; accepted 11 August 2005)

Behavioral responses obtained from chinchillas trained to discriminate a cosine-phase harmonic tone complex from wideband noise indicate that the perception of 'pitch' strength in chinchillas is largely influenced by periodicity information in the stimulus envelope. The perception of 'pitch' strength was examined in chinchillas in a stimulus generalization paradigm after animals had been retrained to discriminate infinitely iterated rippled noise from wideband noise. Retrained chinchillas gave larger behavioral responses to test stimuli having strong fine structure periodicity, but weak envelope periodicity. That is, chinchillas learn to use the information in the fine structure and consequently, their perception of 'pitch' strength is altered. Behavioral responses to rippled noises having similar periodicity strengths, but large spectral differences were also tested. Responses to these rippled noises were similar, suggesting a temporal analysis can be used to account for the behavior. Animals were then retested using the cosine-phase harmonic tone complex as the expected signal stimulus. Generalization gradients returned to those obtained originally in the naïve condition, suggesting that chinchillas do not remain "fine structure listeners," but rather revert back to being "envelope listeners" when the periodicity strength in the envelope of the expected stimulus is high. © *2005 Acoustical Society of America.* [DOI: 10.1121/1.2049107]

PACS number(s): 43.66.Gf, 43.66.Hg, 43.66.Lj, 43.80.Lb [RAL] Pages: 3187–3197

I. INTRODUCTION

Pitch is the perceptual dimension in human listeners that is related to the periodicity of a sound, whereas the pitch strength is the perceptual dimension that is related to the periodicity strength of a sound. Periodicity strength is a measure of the degree of temporal periodicity and can be quantified as the normalized correlation at the appropriate time lag in the autocorrelation function (e.g., Shofner and Selas, 2002). The pitch strength is how strong or salient a listener perceives the sensation of pitch to be, and in human listeners, pitch strength can be quantified using scaling techniques such as magnitude estimation (Fastl and Stoll, 1979; Yost, 1996; Shofner and Selas, 2002).

Rippled noises are a class of stimuli that have become important test stimuli for understanding pitch perception. A rippled noise is generated when wideband noise (WBN) is delayed, attenuated, and the delayed noise is added to the original, undelayed version of the noise. Each successive delay and add operation is referred to as an iteration, and a rippled noise having infinite iterations is generated by adding the delayed noise to the original noise through a positive feedback loop. With one exception, the rippled noises used in the present study are generated using the positive feedback loop. For convenience, these infinitely iterated rippled noises (IIRNs) will be referred to using the following notation: IIRN[+, *T*, dB atten], where + indicates the delayed noise is added to the undelayed version, *T* is the time delay in ms, and dB atten is the attenuation in dB of the delayed noise. More negative values of dB attenuation indicate greater attenuation. The one exception is a rippled noise generated using one iteration of the delay-and-add operation. This type of rippled noise has also been called cosine noise (CN), because the shape of the power spectrum can be described by a cosine function, and therefore it will be referred to as CN[+, *T*, dB atten] in order to distinguish it from IIRN[+, *T*, dB atten]. Increasing the number of iterations or decreasing the amount of the delayed noise attenuation results in an increase in the periodicity strength of the rippled noise as measured using autocorrelation, and a related increase in the strength of the rippled noise pitch as measured in human listeners by magnitude estimation (Yost, 1996; Shofner and Selas, 2002). These studies concluded that the temporal information in the waveform fine structure largely influences the perception of pitch strength.

In animals, questions regarding perceptual dimensions, such as pitch strength, can be addressed using stimulus generalization paradigms. In stimulus generalization paradigms, an animal is trained to respond to a specific stimulus, and then responses are measured to test stimuli that vary systematically along some stimulus dimension (Malott and Malott, 1970). A systematic change in behavioral response along the physical dimension of the stimulus is known as a generalization gradient and implies that the animal possesses a perceptual dimension related to the physical dimension (Guttman, 1963). A generalization gradient is often interpreted to indicate perceptual similarities between test and training stimuli. Test stimuli that evoke similar behavioral responses as the training stimulus indicate a perceptual equivalence or perceptual invariance (see Hulse, 1995) among these stimuli. In other words, stimuli that are perceptually equivalent contain a stimulus feature that is perceived to be functionally

[a]Present address: Dept. of Speech and Hearing Sciences, 200 South Jordan Ave., Indiana University, Bloomington, IN 47405.
[b]Present address: GN ReSound, 4201 W. Victoria St., Chicago, IL 60646.

equal among the stimuli (Hulse, 1995). Thus, data from stimulus generalization paradigms can be used to indicate what stimulus features control the behavioral response of the animal and can give insights into what features of the stimulus are being attended to or analyzed during testing. Comparing and contrasting the stimulus features that influence animal perceptions with those that influence human perceptions can then give insights into the similarities and differences in the mechanisms underlying the perceptual dimensions. In this paper, pitch strength (i.e., no quotes) will be used when referring to the human perception, and 'pitch' strength (i.e., single quotes) will be used when referring to the animal perception.

The stimulus generalization paradigm used in the present study is a modification of our previous discrimination task (Shofner and Yost, 1995; 1997) and is similar to a procedure used by Ohlemiller *et al.* (1999) to study categorical perception of consonant-vowel syllables in chinchillas. The procedure is based on positive reinforcement in an operant conditioning paradigm. Chinchillas first learn to discriminate a signal stimulus from a standard stimulus. In the generalization paradigm, animals are presented the signal stimulus on most trials and receive rewards for correct responses. Thus, it is likely that the animal expects to hear the signal stimulus and receive a reward during a testing session. The standard stimulus is presented on a fixed number of trials in order to estimate false alarms. On an infrequent number of trials, the test stimuli are presented to the animal. The infrequent presentation of test stimuli is similar to the probe-signal method of Greenberg and Larkin (1968). Behavioral responses to the test stimuli are not rewarded, because they are considered to be neither correct nor incorrect (i.e., they are subjective responses).

Shofner (2002) studied 'pitch' strength in chinchillas using this stimulus generalization paradigm in which animals were trained initially to discriminate a cosine-phase harmonic tone complex from WBN. Chinchillas were then tested with random-phase tone complexes and IIRNs as test stimuli. The generalization gradients obtained from most animals were consistent with the hypothesis that the temporal information in the stimulus envelope had a large influence on 'pitch' strength. In contrast, information in the fine structure appears to dominate pitch strength in human listeners as determined from scaling studies using the identical stimuli (Shofner and Selas, 2002). Thus, it would appear that chinchillas and human listeners have different listening strategies for these stimuli. Chinchillas seem to rely more heavily on high-frequency auditory filters where periodicity information about the stimulus envelope is dominant, whereas human listeners seem to rely more heavily on low-frequency auditory filters where periodicity information about the fine structure is dominant. It is interesting to note that one of the chinchillas (C7) used in the stimulus generalization experiment described above also had been used in earlier experiments in which chinchillas discriminated IIRNs from WBN (Shofner and Yost, 1995; 1997). C7 was the only animal in the generalization study to have had previous listening experience with IIRN stimuli of various delays and delayed noise attenuations. The generalization gradients obtained from this animal were clearly different from those obtained from the other animals (see Figs. 5 and 6 of Shofner, 2002) and were consistent with the hypothesis that the temporal information in the waveform fine structure had a large influence on 'pitch' strength. The difference in the generalization gradients from C7 and those obtained from the other chinchillas suggests that there may be a difference in listening strategy between animals with and without previous experience listening to stimuli like IIRNs. The present study examined the effect of listening experience on the 'pitch' strength perception in chinchillas. The results suggest that for broadband stimuli, chinchillas may normally analyze periodicity information in the stimulus envelope, but can learn to analyze information in the fine structure when trained with a stimulus having weak periodicity strength in the envelope, but strong periodicity strength in the fine structure.

II. GENERAL METHODS

A. Subjects

Adult chinchillas (*Chinchilla laniger*) were generally maintained at 80%–90% of their normal body weight and received food pellet rewards during behavioral testing. Their diets were supplemented with chinchilla chow to maintain their body weights. All animals had served as subjects in previous generalization studies in which they had been trained to discriminate a cosine-phase harmonic tone complex from WBN (Shofner, 2002; Shofner and Whitmer, 2005). The care and use of the chinchillas and the procedures employed were approved by the Institutional Animal Care and Use Committee of Loyola University Chicago.

B. Stimuli

Wideband noise (WBN) was generated (Model 132 Wavetek VCG/Noise generator) and then divided into two channels. The parameters of the noise generator were set to produce a pseudorandom noise that repeated itself every 6.55 s and had a bandwidth of 10 kHz. The two channels were then fed into a digital delay line (Model PD 860 Eventide Precision Delay Line)where channel B was delayed relative to channel A; the sampling rate was 62.5 kHz. The outputs of the two channels were each low-passed filtered (FT5 Tucker-Davis Technologies) at a cutoff frequency of 15 kHz. The attenuation of the delayed noise (channel B) was varied using a programmable attenuator (PA4 Tucker-Davis Technologies), and the two channels were added together (SM3 Tucker-Davis Technologies) to produce CN[+, *T*, dB atten]. For generating IIRN[+, *T*, dB atten], the delayed version was added to the WBN through a positive feedback circuit. For WBN, IIRN[+, *T*, dB atten] and CN[+, *T*, dB atten], 5 s of the waveforms were resampled at 50 kHz and stored on disk as stimulus files. Harmonic tone complexes were generated on a digital array processor at a sampling rate of 50 kHz and stored on disk. Harmonic tone complexes were comprised of the fundamental frequency ($F0$) and all higher harmonics up to and including 10 kHz, and thus had the same bandwidth as the noises described above. Individual components were of equal amplitude and either added in cosine-starting phase or random-starting phase. For random-phase

stimulus conditions, a new tone complex was generated for each block of trials (see below). The root-mean-squared amplitudes of the WBN, IIRN[+, *T*, dB atten], CN[+, *T*, dB atten], and harmonic tone complexes were scaled to be equal in order to eliminate the use of overall level as a cue during testing.

Stimulus periodicity strength was measured from autocorrelation functions of the waveform and envelope. Stimulus envelopes were extracted by using a Hilbert transform. The height of the first peak in the autocorrelation function (AC1) is the normalized correlation at the appropriate time lag and was used as an estimate of periodicity strength of the waveform and envelope. Examples of autocorrelation functions and the height of AC1 for the stimuli used in the present study have been previously published (see Figs. 1 and 2 of Shofner, 2002).

C. Behavioral testing

Stimulus presentation and data acquisition were controlled by a Gateway computer system with Tucker-Davis Technologies System II modules. Stimuli were played through a D/A converter at a conversion rate of 50 kHz, low-pass filtered at 15 kHz, attenuated, amplified (Rotel or Bryston Power Amplifier) and played through a loudspeaker (Realistic Optimus Pro X7 or RCA Pro-X880AV from Radio Shack). Sound level was monitored by placing a condenser microphone (Ivie 1133) in the approximate position of an animal's head and measuring the A-weighted sound pressure level with a sound level meter (Ivie IE-30-A Audio Spectrum Analyzer). Overall sound level was fixed at 73 dB SPL for all stimuli.

Chinchillas were placed inside a cage (16 in. $\times$ 12 in. $\times$ 10 in.) in a single-walled, sound-attenuating animal test chamber lined with acoustic foam during a testing session. Animals were not restrained and were free to roam around the cage. At one end of the cage was a pellet dispenser with a reward chute attached to a response lever. A loudspeaker was placed near the pellet dispenser approximately 6 inches in the front of the animal at approximately 30 degrees to the right of center. Transfer functions of the acoustic system have been previously published (see Fig. 3 of Shofner, 2002).

The stimulus generalization paradigm is a modification of our previous discrimination task (Shofner and Yost, 1995; 1997) and is based on positive reinforcement in an operant conditioning paradigm. Chinchillas first learned to discriminate a training or signal stimulus from a WBN-standard stimulus. Bursts of the WBN (500 ms with 10 ms rise/fall times) were presented continually once per second throughout the testing session regardless of whether the animal initiated a trial. The animal initiated a trial by pressing down on the response lever and holding the lever down for a specified duration of time. This duration of time is referred to as the hold time. After a trial was initiated, the WBN was presented continually for an additional 1–8 bursts resulting in a hold time of 1150–8150 ms for each trial. The number of WBN bursts presented after a trial was initiated varied randomly for each trial and was determined from a rectangular probability distribution. If the animal released the lever before the random hold time, the countdown for the hold time was halted; that trial began again with the next press of the lever using the same hold time. If the animal held the response lever down for the duration of the hold time, then either a signal interval or a blank interval (i.e., nonsignal interval) occurred. A signal interval consisted of two bursts of the signal stimulus, while a blank interval consisted of two additional bursts of the WBN stimulus. The response window was coincident with the duration of the signal/blank interval, but began 150 ms after the onset of the first burst and lasted until the onset of the next WBN burst. Consequently, the duration of the response window was 1850 ms. Whenever the animal released the lever during the response window, the release was scored as a positive response; that is, a lever release was the animal's way of saying "there was a signal presented."

In an experimental block of 40 trials, the signal stimulus was presented on 24 trials (60% of the trials) and the WBN-standard stimulus was presented on eight trials (20% of the trials). If the animal released the lever during a signal interval, then the positive response was treated as a hit, while a lever release during a nonsignal interval when the two additional bursts of WBN were presented was treated as a false alarm. If the animal continued to hold the lever down for the duration of the response window during a nonsignal interval, then this nonresponse was treated as a correct rejection. Chinchillas were rewarded with food pellets for hits and correct rejections. On each of two sets of four trials (10% of the trials each) two different test stimuli were presented in the block during the test interval. Animals received no food pellet rewards for behavioral responses to test stimuli, regardless of whether the response was a release of the lever or continuing to press the lever down. Thus, animals could receive food pellet rewards for 32/40 trials (24 signal stimuli +8 nonsignal stimuli) or 80% of the total trials. Generalization data were collected for a minimum of 50 blocks; this resulted in at least 200 trials for each test stimulus.

III. EXPERIMENT 1: 'PITCH' STRENGTH FOLLOWING TRAINING WITH INFINITELY ITERATED RIPPLED NOISE

A. Methods

In the previous study (Shofner, 2002), stimulus generalization gradients were obtained from chinchillas that were trained to discriminate a cosine-phase harmonic tone complex from WBN. The purpose of Experiment 1 was to determine the effect that listening experience with IIRN stimuli may have on the perception of 'pitch' strength in chinchillas. In this experiment, animals that had been trained originally to discriminate a cosine-phase harmonic tone complex from WBN were retrained to discriminate IIRN[+, *T*, −1 dB] from WBN. In the generalization paradigm, the standard stimulus was the WBN, the signal stimulus was IIRN[+, *T*, −1 dB] and the test stimuli consisted of cosine-phase and random-phase harmonic complex tones as well as other IIRN[+, *T*, dB atten] with delayed noise attenuations between −8 dB and −2 dB. In this experiment, chinchillas re-

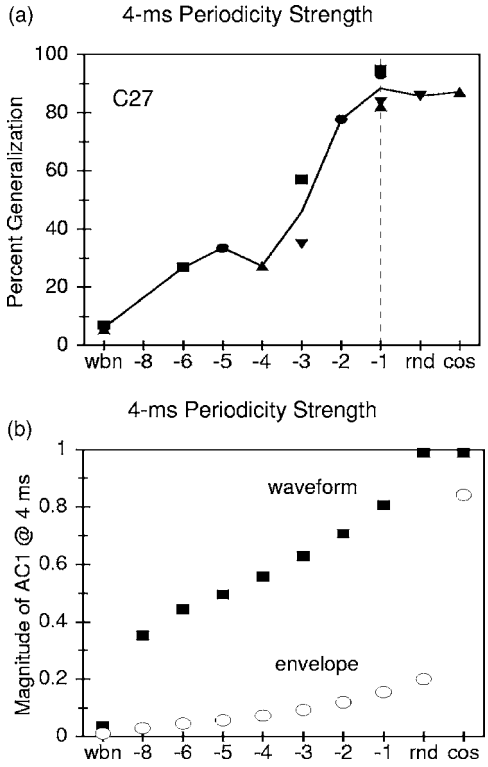

FIG. 1. (a) The behavioral responses obtained for animal C27 for stimuli having a period or delay of 4 ms. Behavioral responses are shown as percent generalization (see text). Symbols indicate the stimuli that were presented together during a testing session. The vertical dashed line at −1 indicates that the signal stimulus was IIRN[+, 4 ms, −1 dB]. The solid line through the data points is used to group the data together and is not meant to imply a continuous function, since the *x* axis is a nominal scale. For stimuli that were repeated, the solid line goes through the average percent generalization. (b) The height of the peak at a time lag of 4 ms (AC1) from the autocorrelation functions of the stimuli. Filled-squares show AC1 for the waveform fine structure; open circles show AC1 for the envelope as defined by the Hilbert transform. In this and subsequent figures, stimuli are labeled along the *x* axis, wideband noise (WBN), infinitely iterated rippled noises having delayed noise attenuations of −8,−6,−5,−4,−3,−2,−1 dB, and random-phase (RND) and cosine-phase (COS) harmonic tone complexes.

ceived food pellet rewards for responses to IIRN[+, *T*, −1 dB], but no reinforcement for responses to either harmonic tone complexes or other IIRNs. Generalization gradients were obtained for three conditions in which the delays of the IIRNs and periods of the complex tones were fixed at 2 ms, 4 ms, and 8 ms.

B. Results

Figure 1(a) illustrates the stimulus generalization gradient obtained from animal C27 for the 4 ms periodicity condition. The signal stimulus was IIRN[+, 4 ms, −1 dB] and the standard stimulus was WBN. The test stimuli consisted of cosine-phase and random-phase harmonic tone complexes each having a period of 4 ms (i.e., *F*0 of 250 Hz) and other IIRN[+, 4 ms, dB atten] of varying delayed noise attenuations. The different symbols indicate the stimuli that were presented together during a testing session. For example, the filled squares indicate the responses that were obtained when the standard stimulus was WBN, the signal stimulus was IIRN[+, 4 ms, −1 dB], and the two test stimuli were IIRN[+, 4 ms, −3 dB] and IIRN[+, 4 ms, −6 dB]. The *x* axis indicates each stimulus presented and is a nominal scale; the solid line is merely used in order to facilitate the grouping of data points and does not imply any functional relationship. Behavioral responses to the stimuli are shown as percent generalization which is defined as the percentage of trials the animal released the lever during the response window for each stimulus presented. For stimuli that were repeated (i.e., WBN and IIRN[+, 4 ms, −1 dB]), the line goes through the average values of percent generalization. For example, the squares in Fig. 1(a) indicate that WBN, IIRN[+, 4 ms, −6 dB], IIRN[+, 4 ms, −3 dB], and IIRN[+, 4 ms, −1 dB] were presented together in one set of stimuli, whereas the inverted triangles indicate that WBN, IIRN[+, 4 ms, −3 dB], IIRN[+, 4 ms, −1 dB], and random-phase tone complex were presented as another set of stimuli. Note that in these examples, WBN, IIRN[+, 4 ms, −3 dB] and IIRN[+, 4 ms, −1 dB] were repeated.

Figure 1(a) illustrates the generalization gradient obtained for C27 after the animal was trained using IIRN[+, 4 ms, −1 dB]. For the condition of 4 ms periodicity strength, the percent generalization is 87.3%, 85.8%, and 88.5% for IIRN[+, 4 ms, −1 dB], random-phase harmonic complex tones, and the cosine-phase harmonic complex tone, respectively. Thus, only small differences in percent generalization are observed among IIRN[+, 4 ms, −1 dB], the cosine-phase harmonic complex tone and the random-phase harmonic complex tones after training with IIRN[+, 4 ms, −1 dB]. Also note that the percent generalization for IIRN[+, 4 ms, −2 dB] is relatively high with a value of 77.8%. Percent generalization decreases as the amount of delayed noise attenuation changes from −2 dB to −6 dB with values above those for WBN. For comparison, Fig. 1(b) shows the periodicity strength as measured by the height of the peak at a time lag of 4 ms for the waveform and envelope of each stimulus. Note that the height of AC1 for IIRN[+, 4 ms, −1 dB] is high and that there is a systematic decrease as the amount of delayed noise attenuation changes from −2 dB to −8 dB. The generalization gradient shown in Fig. 1(a) is more similar in shape to the waveform AC1 gradient shown in Fig. 1(b) than the envelope AC1 gradient.

Figure 2 compares the generalization gradients obtained from each of six animals after retraining with IIRN[+, 4 ms, −1 dB] with those obtained initially after training with the cosine-phase harmonic complex tone. For each animal, the behavioral responses to the IIRN test stimuli are larger after retraining with IIRN[+, 4 ms, −1 dB]. That is, the generalization gradients are shifted horizontally to the left. Similar shifts in the generalization gradients were obtained after retraining with IIRN for periods of 2 ms (Fig. 3) and 8 ms (Fig. 4). These behavioral data indicate that chinchillas order complex sounds along the physical dimension of periodicity strength, and thus, possess a perceptual dimension similar to pitch strength in human listeners. It should be noted in Figs. 2–4, that some animals gave behavioral responses to the cosine-phase tone complex that were below those of the IIRN[+] signal stimulus (e.g., C28 in Fig. 2, C29 in Fig. 3, C29 and C35 in Fig. 4). These responses can be interpreted to indicate that the cosine-phase tone complex was not perceived to be similar to the IIRN signal stimulus.

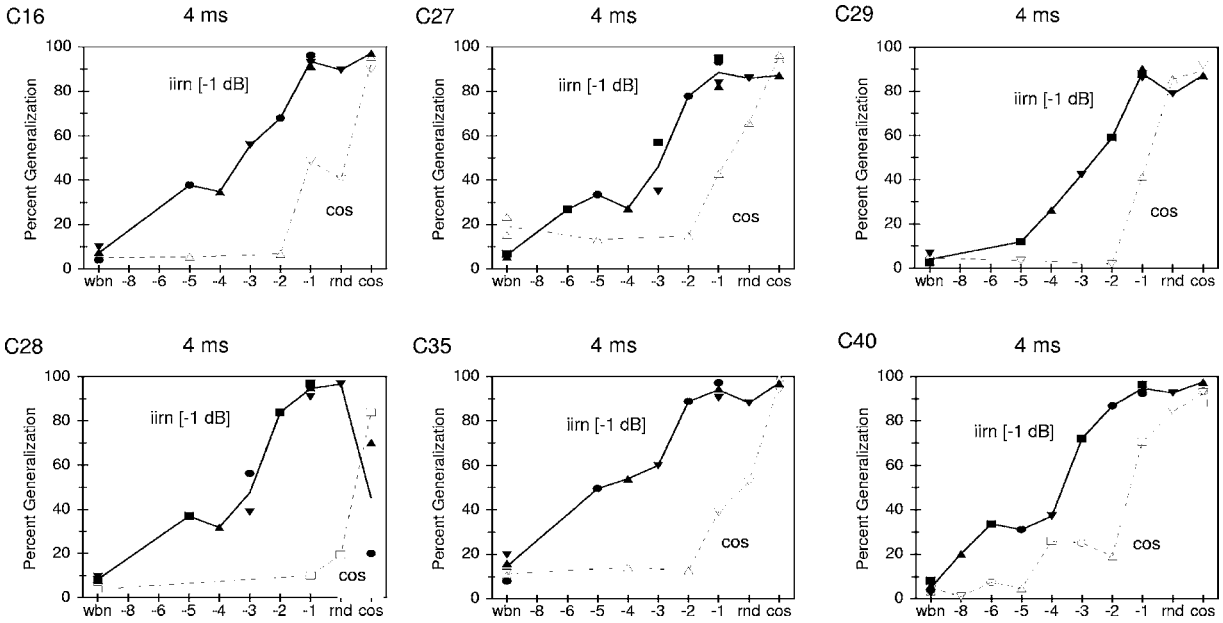

FIG. 2. Percent generalizations obtained from six chinchillas studied using stimuli having a period or delay of 4 ms. Filled symbols and solid lines indicate data obtained when IIRN[+, 4 ms, −1 dB] was used as the signal stimulus; open symbols and dashed lines indicate data obtained when the cosine-phase harmonic tone complex was used as the signal stimulus.

IV. EXPERIMENT 2: 'PITCH' STRENGTH OF COSINE NOISE

A. Methods

The purpose of Experiment 2 was to obtain an estimate of 'pitch' strength in chinchillas for CN[+, 4 ms, 0 dB] relative to that of IIRN[+, 4 ms, −1 dB]. The standard stimulus was WBN and the signal stimulus was IIRN[+, 4 ms, −1 dB]; the two test stimuli were CN[+, 4 ms, 0 dB] and IIRN[+, 4 ms, −5 dB]. In this experiment, chinchillas received food pellet rewards for responses to IIRN[+, T, −1 dB], but no reinforcement for responses to CN[+, 4 ms, 0 dB] or IIRN[+, 4 ms, −5 dB].

Figure 5 compares the spectra for the signal and test stimuli and shows that there are large spectral differences between the two test stimuli. The spectrum for CN[+, 4 ms, 0 dB] is characterized by broad peaks at frequencies corresponding to integer multiples of $1/T$ with a large peak-to-valley ratio, whereas the spectrum for IIRN[+, 4 ms, −5 dB]

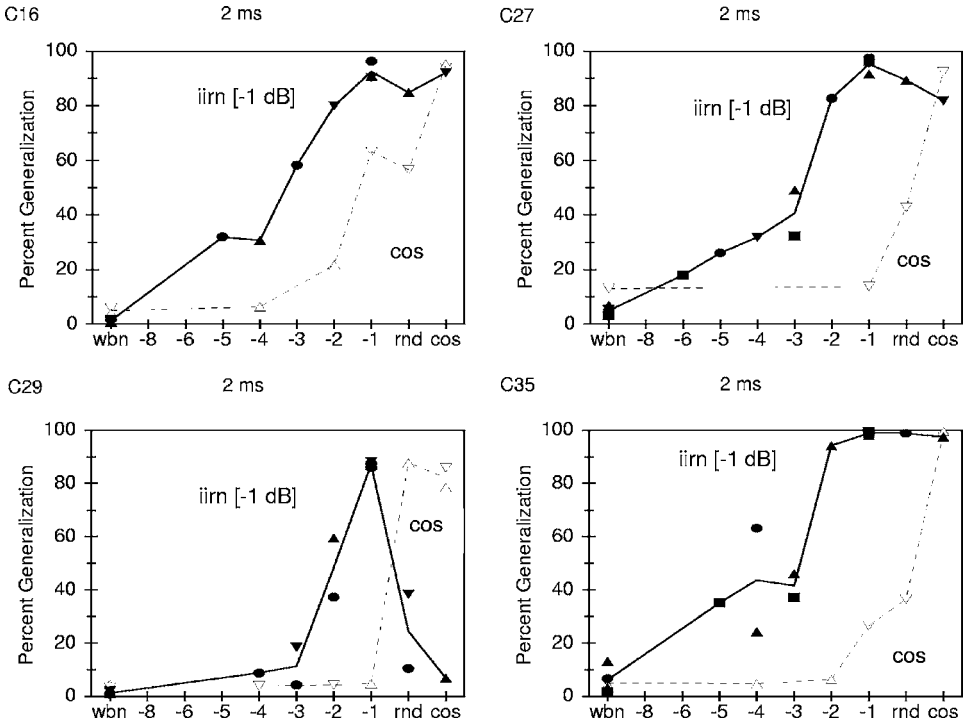

FIG. 3. Percent generalizations obtained from four chinchillas studied using stimuli having a period or delay of 2 ms. Filled symbols and solid lines indicate data obtained when IIRN[+, 2 ms, −1 dB] was used as the signal stimulus; open symbols and dashed lines indicate data obtained when the cosine-phase harmonic tone complex was used as the signal stimulus.

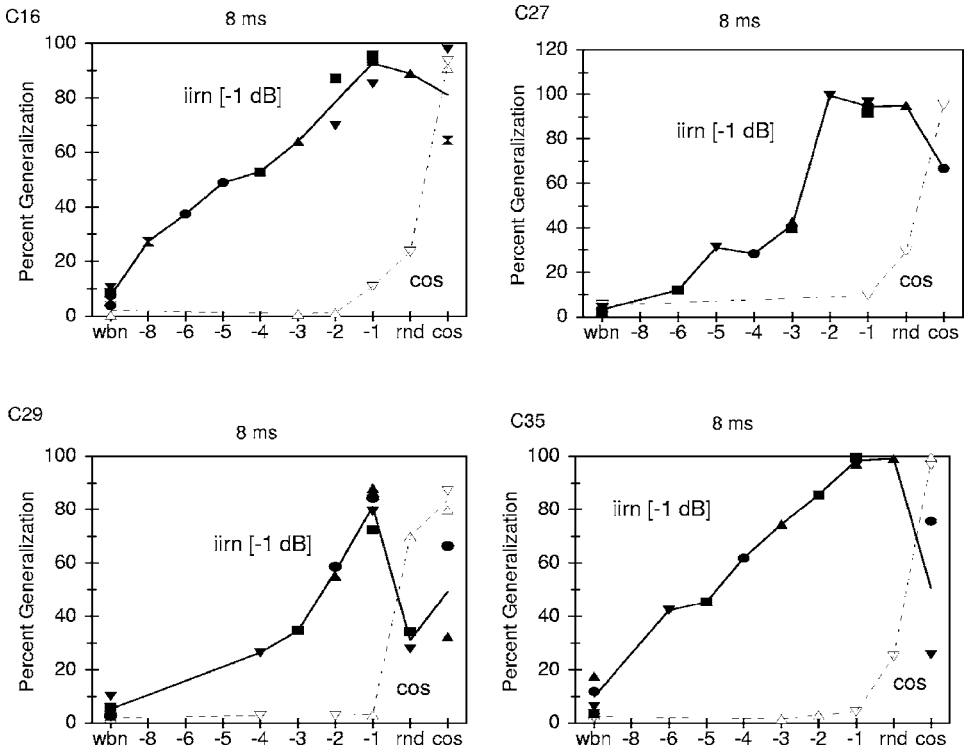

FIG. 4. Percent generalization obtained from four chinchillas studied using stimuli having a period or delay of 8 ms. Filled symbols and solid lines indicate data obtained when IIRN[+, 8 ms, −1 dB] was used as the signal stimulus; open symbols and dashed lines indicate data obtained when the cosine-phase harmonic tone complex was used as the signal stimulus.

shows sharp peaks at frequencies corresponding to integer multiples of $1/T$ with a smaller peak-to-valley ratio. Comparing these test stimuli to the signal stimulus, it can be noted that the peak-to-valley ratios of CN[+, 4 ms, 0 dB] and IIRN[+, 4 ms, −1 dB] are similar, although they do differ in their spectral shapes. However, IIRN[+, 4 ms, −5 dB] and IIRN[+, 4 ms, −1 dB] have similar spectral shapes (i.e., sharp peaks, broad valleys), but differ in their peak-to-valley ratios. Figure 5 also compares autocorrelation functions for the signal and test stimuli. The autocorrelation function of CN[+, 4 ms, 0 dB] has a single peak at a time lag of 4 ms, whereas the autocorrelation function of IIRN[+, 4 ms, −5 dB] has several peaks at integer multiples of 4 ms. However, the heights of the peaks at a 4 ms lag time are similar for the test stimuli. The average peak height at 4 ms is 0.495 for IIRN[+, 4 ms, −5 dB] and is 0.493 for CN[+, 4 ms, 0 dB]. Thus, the two test stimuli differ greatly in terms of their spectra, but show similarities in terms of the 4 ms periodicity strength.

B. Results

Figure 6 compares the percent generalization for CN[+, 4 ms, 0 dB] and IIRN[+, 4 ms, −5 dB] obtained from five chinchillas. First, it can be observed that the responses of CN[+, 4 ms, 0 dB] are much less than the responses to the

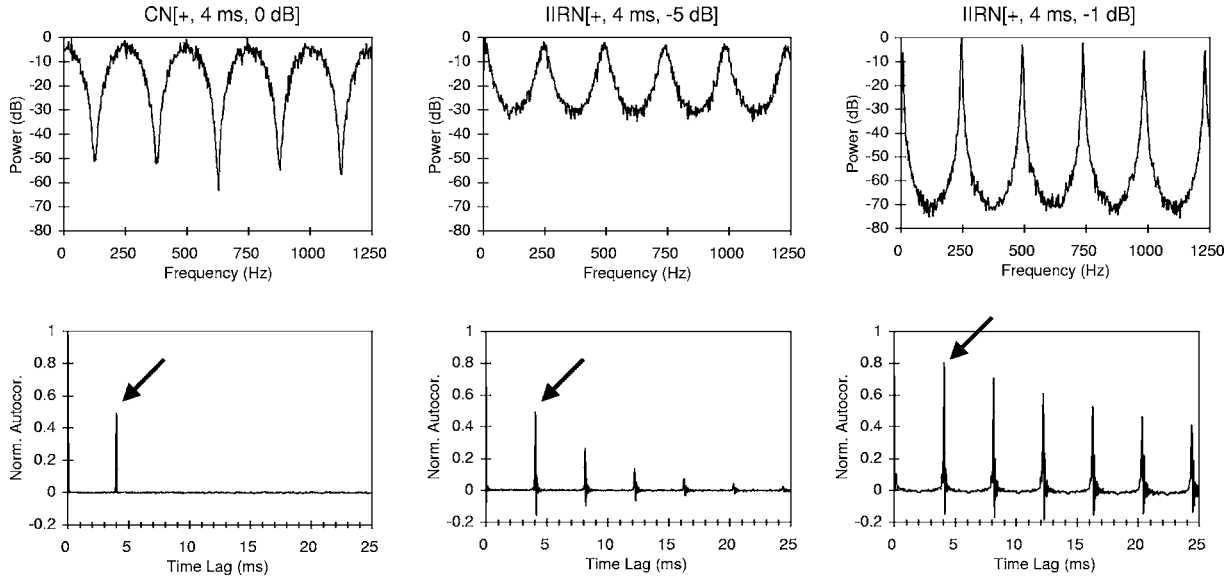

FIG. 5. Spectra (top row) and waveform autocorrelation functions (bottom row) for CN[+, 4 ms, 0 dB], IIRN[+, 4 ms, −5 dB], and IIRN[+, 4 ms, −1 dB]. Note that the spectra of IIRN[+, 4 ms, −5 dB] and CN[+, 4 ms, 0 dB] differ, but that the height of AC1 is similar for these stimuli. The arrows indicate AC1.

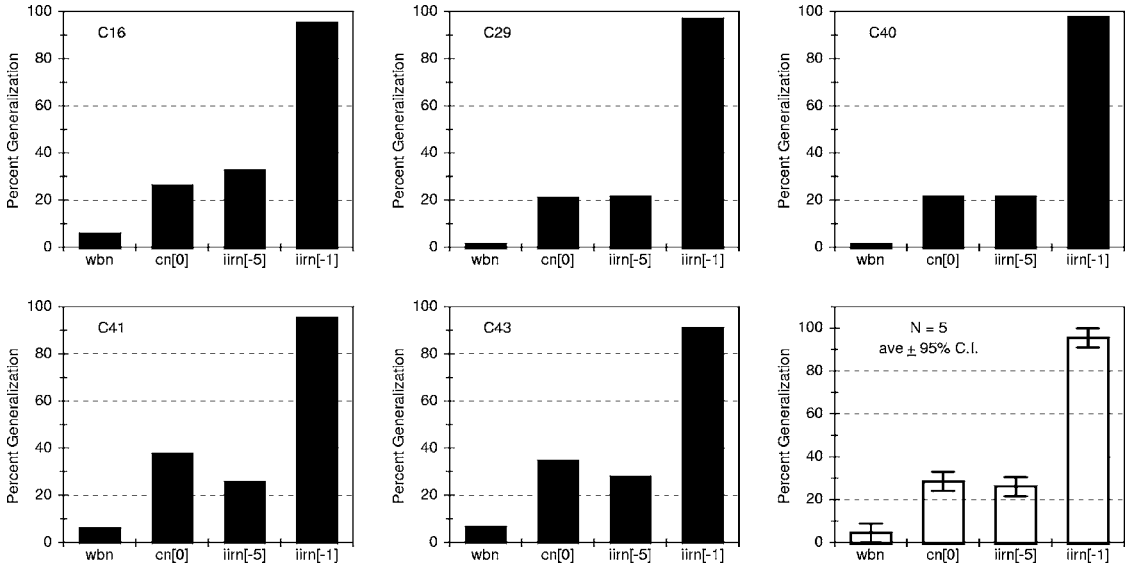

FIG. 6. Percent generalization obtained from five chinchillas for the stimuli shown in Fig. 5. Responses from individual animals are represented by the filled bars; the average responses are shown by the open bars in the lower right-hand panel. Error bars indicate the 95% confidence intervals based on Tukey's standard error.

IIRN[+, 4 ms, −1 dB] signal stimulus for each animal. Second, the responses of the CN[+, 4 ms, 0 dB] and IIRN[+, 4 ms, −5 dB] test stimuli are similar for each animal. Note also that the responses to CN[+, 4 ms, 0 dB] and IIRN[+, 4 ms, −5 dB] are greater than those to WBN. The lower-right-hand panel in Fig. 6 shows the average and 95% confidence intervals determined using the Tukey's standard error. A repeated-measures analysis of variance showed a significant effect of stimuli ($F=373.5; p \ll 0.0005$). Pairwise comparisons based on Tukey's test showed a significant difference ($q=34.01; p<0.001$) between the IIRN test stimulus and the IIRN signal stimulus (i.e., IIRN[+, 4 ms, −5 dB] vs IIRN[+, 4 ms, −1 dB]). There was also a significant difference ($q=32.84; p<0.001$) between the CN test stimulus and the IIRN signal stimulus (i.e., CN[+, 4 ms, 0 dB] vs IIRN[+, 4 ms, −1 dB]). However, there was no significant difference ($q=1.17; p>0.5$) in percent generalization between the two test stimuli (i.e., CN[+, 4 ms, 0 dB] vs IIRN[+, 4 ms, −5 dB]).

V. EXPERIMENT 3: RETESTING 'PITCH' STRENGTH USING COSINE-PHASE HARMONIC TONE COMPLEX AS THE SIGNAL

A. Methods

In the previous study (Shofner, 2002), chinchillas were trained to discriminate the cosine-phase harmonic tone complex from WBN and then tested in the generalization paradigm using the cosine-phase tone complex as the signal stimulus. In Experiment 1 above, chinchillas were retrained to discriminate IIRN[+, 4 ms, −1 dB] from WBN and tested in the generalization paradigm using IIRN[+, 4 ms, −1 dB] as the signal stimulus. In both of these experiments, the training stimulus and the signal stimulus were identical. In Experiment 3, chinchillas that had been retrained with IIRN[+, 4 ms, −1 dB] were then tested in the generalization paradigm using the cosine-phase harmonic tone complex as the signal stimulus. Thus, in Experiment 3, the training stimulus and the signal stimulus were not the same. In this experiment, chinchillas now received food pellet rewards for responses to the cosine-phase tone complex, but no reinforcement for responses to either random-phase tone complexes or other IIRNs, including IIRN[+, *T*, −1 dB]. Experiment 3 examined how animals with listening experience with IIRNs would respond when the testing conditions were identical to those used in the previous study (Shofner, 2002) in which animals had no prior listening experience with IIRNs.

B. Results

Figure 7 shows the stimulus generalization data for animal C27 for responses obtained during the first 6 week period of data collection in Experiment 3. The filled symbols indicate the responses obtained in Experiment 3, whereas the solid line indicates the generalization gradient obtained from Experiment 1 using IIRN[+, 4 ms, −1 dB] as the signal stimulus and the dashed line indicates the generalization gradient from the previous study (Shofner, 2002) in which the cosine-phase tone complex was used as the signal stimulus. Note that the responses obtained during this time period are scattered around the gradient obtained in Experiment 1 when IIRN[+, 4 ms, −1 dB] was the signal stimulus. In particular, the responses are high when the test stimuli are either random-phase harmonic tone complexes or IIRN[+, 4 ms] at delayed noise attenuations of −1 dB and −2 dB. Figure 7 also shows the generalization data obtained from C27 in Experiment 3 over the next 8 week period. Again, the symbols show the responses obtained in Experiment 3, whereas the solid and dashed lines indicate the generalization gradients obtained from Experiment 1 and the previous study (Shofner, 2002), respectively. Now it can be observed that the responses are scattered around or fall below the generalization gradient obtained in the previous study when the cosine-phase tone complex was used as the signal stimulus

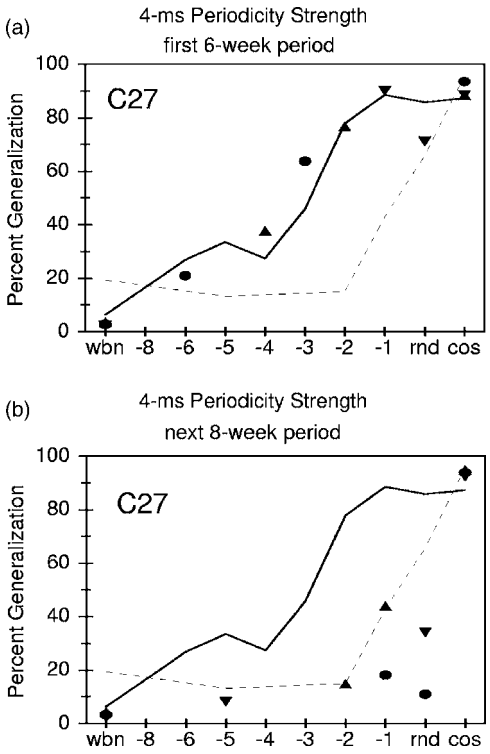

FIG. 7. Percent generalization determined for C27 over two different periods of time. The dashed lines indicate the general gradient obtained when the animal was trained with the cosine-phase harmonic tone complex and tested with the cosine-phase tone complex as the signal. The solid lines indicate the generalization gradients obtained when the animal was retrained with IIRN[+, 4 ms, −1 dB] and tested using IIRN[+, 4 ms, −1 dB] as the signal stimulus. The symbols indicate the behavioral data obtained following retraining with IIRN[+, 4 ms, −1 dB], but using the cosine-phase tone complex as the signal stimulus. (a) The percent generalization obtained over an initial 6 week period; (b) data obtained during the next 8 weeks.

(Shofner, 2002). In particular, the behavioral responses are small when the test stimuli are either the random-phase tone complexes or IIRN[+, 4 ms] at delayed noise attenuations of −1 dB and −2 dB.

Figure 8 shows the average percent generalization obtained from four chinchillas for the IIRN[+, 4 ms, −1 dB], random-phase and cosine-phase harmonic tone complexes under three different training/signal conditions. The purpose of Experiment 3 was to determine if the change in listening strategy that occurred after training with IIRN was a permanent change in listening strategy or whether animals return over time to their previous strategy when the IIRN is replaced with cosine-phase tone complex. As such, the most relevant behavioral responses are those to IIRN[+, 4 ms, −1 dB], random-phase and cosine-phase tone complexes. In order to simplify the data presentation, only the responses to those specific stimuli are shown in bar graph format. Error bars indicate ±1 standard deviation. The open bars show behavioral responses from the initial condition in which animals were trained with the cosine-phase harmonic tone complex and tested in the generalization procedure with the same cosine-phase tone complex used as the signal. For this condition, it can be seen that the behavioral responses to the random-phase tone complex and IIRN[+, 4 ms, −1 dB] were smaller than those to the cosine-phase tone complex. The black-filled bars show behavioral responses from the condition in which animals were retrained with IIRN[+, 4 ms, −1 dB] and tested in the generalization procedure with IIRN[+, 4 ms, −1 dB] as the signal. For this condition, it can be clearly seen that the behavioral responses were high when animals were tested using this IIRN as the signal stimulus, and that the behavioral responses were also high to the cosine-phase and random-phase test stimuli. Finally, the gray-filled bars show the behavioral responses from animals which had been retrained using the IIRN[+, 4 ms, −1 dB], but were then tested using the cosine-phase tone complex as the signal stimulus in the generalization paradigm. For this condition, the training and signal stimuli are not the same. The data shown are the average of four chinchillas for the final values of percent generalization obtained. For example, for C27, these final values correspond to the filled circles shown in Fig. 7(b). Figure 8 (gray-filled bars) shows that when the animals that had been retrained with the IIRN stimulus were then tested using the cosine-phase tone complex as the signal stimulus (rather than IIRN), the behavioral responses remain high only for the cosine-phase tone complex (signal stimulus); the responses to the random-phase tone complex and IIRN[+, 4 ms, −1 dB] (i.e., the test stimuli) decrease dramatically.

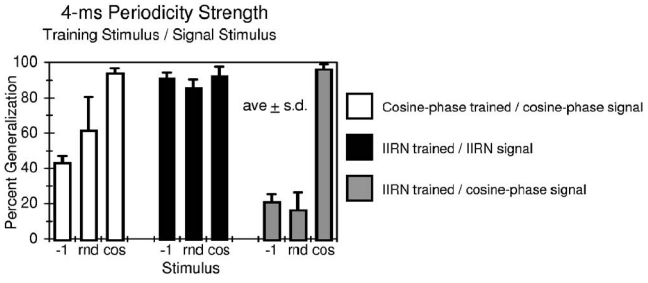

FIG. 8. Average percent generalization from four chinchillas for IIRN[+, 4 ms, −1 dB] and random-phase and cosine-phase harmonic tone complexes. Error bars indicate ±1 standard deviation. Open bars show responses when chinchillas were trained with the cosine-phase tone complex and tested in the generalization procedure using the cosine-phase tone complex as the signal stimulus. Black-filled bars show responses when chinchillas were retrained with IIRN[+, 4 ms, −1 dB] and tested in the generalization procedure IIRN[+, 4 ms, −1 dB] as the signal stimulus. Gray-filled bars show responses when chinchillas were retrained with IIRN[+, 4 ms, −1 dB] and tested in the generalization procedure using the cosine-phase tone complex as the signal stimulus.

VI. DISCUSSION

Behavioral responses to complex sounds that varied in periodicity strength were measured from chinchillas using a stimulus generalization paradigm. In a stimulus generalization paradigm, an animal is first trained to respond to a signal stimulus, and then behavioral responses to test stimuli are measured (Malott and Malott, 1970; Hulse, 1995). The stimuli that are presented typically vary systematically along some physical dimension, and a systematic gradient in behavioral responses suggests that the animal possesses a perceptual dimension related to the stimulus dimension (Guttman, 1963). The gradient in behavioral response is often interpreted to imply how closely test stimuli are perceived to be similar to the signal stimulus. In the present experiment,

the physical dimension that was varied systematically is the periodicity strength of the stimulus. Stimulus periodicity strength is measured as the height of the first peak in the autocorrelation function for both the waveform fine structure and the stimulus envelope.

In the present study, chinchillas were trained to discriminate IIRN with −1 dB of delayed noise attenuation from WBN. IIRN[+, 4 ms, −1 dB] has a relatively large periodicity strength in the waveform fine structure, but a relatively small periodicity strength in the envelope (see Fig. 1). The results of Experiment 1 of the present study indicate that chinchillas order complex sounds along the physical dimension of periodicity strength, and thus, possess a perceptual dimension similar to pitch strength in human listeners. That is, there is an increase in behavioral response as the periodicity strength of the stimulus increases. More importantly, there are generally small differences in behavioral responses between IIRN[+, 4 ms, −1 dB] and random-phase tone complexes and between IIRN[+, 4 ms, −1 dB] and cosine-phase tone complexes. The behavioral responses among these three stimuli are typically large for most animals. That is, most animals perceive random-phase and cosine-phase harmonic tone complexes to be functionally similar to IIRN[+, −1 dB] suggesting that there is a perceptual equivalence (Hulse, 1995) among these three stimuli. In this case, the perceptual equivalence is presumably related to the similarity in periodicity strength in the waveform fine structure among these three stimuli (see Fig. 1).

The generalization gradients obtained in Experiment 1 of the present study clearly differ from those obtained when the chinchillas were first trained to discriminate a cosine-phase harmonic tone complex from WBN (Shofner, 2002). Among all the stimuli, the cosine-phase tone complex has the largest periodicity strength in both the fine structure and the envelope [see Fig. 1(b)], whereas WBN noise has a periodicity strength of 0 as measured by autocorrelation. The previous results (Shofner, 2002) showed that for most chinchillas, IIRN[+, *T*, −1 dB] and random-phase harmonic tone complexes were not perceived to be similar to the 'pitch' strength of cosine-phase tone complexes, and the behavioral data suggested that the stimulus envelope had a greater influence than waveform fine structure on the perception of 'pitch' strength in chinchillas. In contrast, however, the generalization gradients obtained from Experiment 1 of the present study suggest that periodicity information in the waveform fine structure now has a greater influence than envelope on the perception of 'pitch' strength in chinchillas.

In order to gain some insight into the question regarding the dominance of information in the fine structure following listening experience with IIRN[+, *T*, −1 dB], generalization gradients were analyzed using the auditory image model (AIM) of Patterson *et al.* (1995) as previously described (see Shofner, 2002 for details). The filter functions of AIM are based on the bandwidths described by Glasberg and Moore (1990) obtained using simultaneous masking with notched noise (see Patterson *et al.*, 1995). Because the auditory filter functions for chinchillas and human listeners are similar under conditions of simultaneous masking with notched noise (Niemiec *et al.*, 1992), no attempt was made to change the

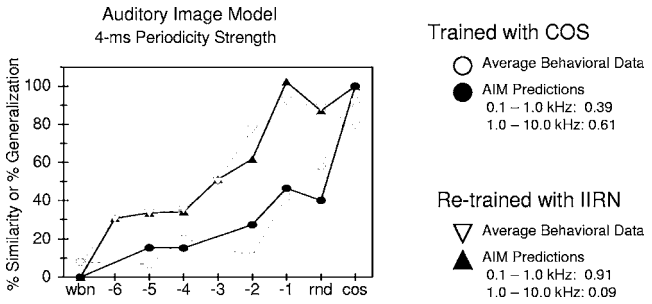

FIG. 9. Percent similarity (as defined in the text for the auditory image model) computed for stimuli having a period or delay of 4 ms. Open circles indicate data obtained when animals were trained with the cosine-phase harmonic tone complex; open inverted triangles indicate data obtained when animals were retrained with IIRN[+, 4 ms, −1 dB]. The behavioral data are the average percent generalization from the six chinchillas in Fig. 2. Filled symbols show the best fitting model predictions under the corresponding training conditions. The weights for low frequencies (0.1–1.0 kHz) and high frequencies (1.0–10.0 kHz) are indicated on the right-hand panel for the two training conditions.

bandwidth of the simulated auditory filters in AIM. Briefly, 10 ms summary autocorrelograms were obtained at the output of AIM for auditory filters with center frequencies between 0.1–1.0 kHz and for auditory filters between 1.0–10.0 kHz. These two summary autocorrelograms were assumed to represent the processed temporal information in the waveform fine structure and envelope, respectively. Fine structure and envelope summary autocorrelograms were obtained for WBN and all stimuli for the 4 ms periodicity strength condition. The similarity index (SI) is defined as

$$\mathrm{SI} = \sum_{0}^{10\ \mathrm{ms}} \left(Y_{(t,\mathrm{stimulus})} - Y_{(t,\mathrm{WBN})}\right)^2,$$

where $Y_{(t,\mathrm{stimulus})}$ and $Y_{(t,\mathrm{WBN})}$ are the normalized amplitudes of the summary autocorrelograms at times, t, between 0 and 10 ms for any given stimulus and WBN, respectively. Relative similarity in terms of percent is then defined as

$$S(\%) = \frac{\mathrm{SI}}{\mathrm{SI}_{(\cos)}} \times 100$$

where $\mathrm{SI}_{(\mathrm{COS})}$ is the similarity index of the cosine-phase harmonic tone complex. Similarity will be 100% if the stimulus is the cosine-phase tone complex and will be 0% if the stimulus is WBN. Figure 9 shows average percent generalization obtained from the six chinchillas for the 4 ms periodicity condition when animals were initially trained with the cosine-phase tone complex (open circles, dashed line) and then retrained with the IIRN (open inverted triangles, dashed line). Also shown in Fig. 9 are the best fitting model predictions based on a simple weighted average of the relative similarities of the low-frequency (0.1–1.0 kHz) and high-frequency (1.0–10.0 kHz) auditory channels. These model predictions were obtained by first fixing the weight for the low-frequency channels at 0 and the weight for the high-frequency channels at 1. A sum of squares difference between the behavioral data and model predictions based on those weights were obtained. The weights were varied in steps of 0.01 until the mini-

mum sum of squares difference between the model predictions and behavioral data was obtained. For animals trained with the cosine-phase tone complex, the relative weight given to the low-frequency channels is 0.39 and the weight given to the high-frequency channels is 0.61. The listening strategy in this case is to combine information across auditory channels, but to weigh more heavily the information in high-frequency channels where temporal information about the stimulus envelope is dominant. In contrast, for animals retrained with IIRN, the relative weight given to the low-frequency channels is now 0.91 and the weight given to the high-frequency channels is only 0.09. The listening strategy in this case is to combine information across auditory channels, but to weigh more heavily the information in low-frequency channels where temporal information about the waveform fine structure is dominant. Thus, the behavioral results indicate that listening experience can alter the perception of 'pitch' strength in chinchillas, and the simulation results indicate that chinchillas can become "fine structure" listeners when trained using a broadband stimulus like IIRN, which has a large periodicity strength in the fine structure, but not in the envelope.

The results of Experiment 1 of the present study suggest that the listening strategy of chinchillas following training with IIRN is more like the listening strategy used by human listeners. Shofner and Selas (2002) had human listeners judge the pitch strength of the same complex sounds presented in the present study using a magnitude estimation procedure. A modified version of Stevens' power law based on temporal information in both the waveform fine structure and envelope was used to model the judgments of pitch strength. These results suggested that the perception of pitch strength in human listeners is also largely influenced by the temporal information in the waveform fine structure. The results of Experiment 2 are consistent with this conclusion. The average percent generalization to CN[+, 4 ms, 0 dB] is identical to IIRN[+, 4 ms, −5 dB] when animals discriminate IIRN[+, 4 ms, −1 dB] from WBN and suggests that CN[+, 4 ms, 0 dB] and IIRN[+, 4 ms, −5 dB] evoke equal 'pitch' strength relative to IIRN[+, 4 ms, −1 dB]. The similarity in 'pitch' strength is predicted based on the similarity in the magnitude of AC1 for these two stimuli. However, the similarity in 'pitch' strength is not as clearly predicted based on the spectral differences for the stimuli. This conclusion that the perception of 'pitch' strength in chinchillas can be accounted for based on temporal processing is similar to that described for human listeners (Yost *et al.*, 1996; Yost, 1996).

Although when trained using IIRN stimuli, chinchillas develop a listening strategy that does appear to be similar to that of human listeners, this is not necessarily a permanent change in listening strategy. The results of Experiment 3 of the present study show that when retested in the generalization paradigm using the cosine-phase harmonic tone complex as a signal following retraining with IIRN, the responses to random-phase complex tones and IIRN eventually become lower than those previously obtained when tested using IIRN as the signal. That is, the generalization gradients become more like those obtained originally from naive animals trained with the cosine-phase tone complex, suggesting that "fine structure listening" has reverted back to "envelope listening." Thus, it would appear that the periodicity strength of the stimulus envelope is a very salient cue for the perception of 'pitch' strength in chinchillas.

The audiograms of chinchillas and humans are similar, indicating that chinchillas have good low frequency hearing abilities (Heffner and Heffner, 1991). Also, the bandwidths of chinchilla auditory filters are similar to those of human listeners as measured using simultaneous masking methods (Niemiec *et al.*, 1992). Given these similarities between human and chinchilla auditory systems, why is there such a difference in the perceptions between humans and chinchillas. That is, why is the envelope such a salient cue in chinchillas whereas the fine structure is more important in humans?

Recently, the similarities in auditory filter functions among human listeners and nonhuman mammals have been questioned. As previously described, filter bandwidths are similar between chinchillas and human listeners when measured using simultaneous masking procedures (Niemiec *et al.*, 1992). However, based on data from otoacoustic emissions, it has been suggested that the filter functions of human listeners are narrower than previously thought and that the auditory filters of nonhuman mammals are wider than those of human listeners (Shera *et al.*, 2002). Wider auditory filters in chinchillas would suggest that for a given harmonic stimulus, there would be more unresolved components along the chinchilla cochlea than a long the human cochlea. Because temporal information about the envelope is dominated by the unresolved components, more unresolved components in chinchillas than in humans could explain the predisposition of chinchillas to weigh more heavily on the temporal information in the stimulus envelope. However, the results from a recent experiment in which chinchillas and human listeners discriminated a cosine-phase tone complex from random-phase tone complexes argue that spectral resolvability for these types of broadband stimuli is similar for the two groups (Shofner *et al.*, 2005).

There is an interesting difference between the human and chinchilla cochleae that could potentially account in part for the differences in human and chinchilla perceptions of pitch strength. Namely, there are differences in the innervation densities of the chinchilla and human cochleae. There are approximately 10 myelinated nerve fibers per inner hair cell along the entire length of the human cochlea (Nadol, 1988). However, the chinchilla cochlea has an average of 9.4 fibers per inner hair cell in the apex, which increases systematically to 18.8 fibers per inner hair cell in the basal regions (Bohne *et al.*, 1982). Thus, in the chinchilla cochlea, there may be a greater number of auditory nerve fibers carrying information about the envelope than about the fine structure, since envelope periodicity processing is dominated by high frequency auditory channels.

Does the predisposition of chinchillas to use envelope cues compared to the use of fine structure cues by human listeners reflect species differences in central neural mechanisms? Behavioral studies from the chinchilla suggest that that the neural mechanisms underlying the discrimination of

IIRNs from WBN are not fundamentally different between chinchillas and human listeners (Shofner and Yost, 1995; 1997). The ability of the chinchilla to adopt a different listening strategy after training with rippled noise stimuli presumably reflects experience-dependent plasticity in the central auditory system, and this presumed experience-dependent plasticity appears to occur in humans as well. Normal-hearing human listeners are exposed constantly to speech and music from the time of birth, and Terhardt (1974) has argued that virtual pitch is acquired through learning processes related to speech. Unlike human listeners, the chinchillas used in laboratory studies are raised in acoustically impoverished environments. Perhaps the listening experience with rippled noise stimuli derived by chinchillas reflects experience-dependent plasticity that is similar to that which occurs in human infants through exposure to speech and music. The loci of any experience-dependent plasticity related to 'pitch' strength in the chinchilla will require future physiological studies. It seems likely that some plasticity will occur in the auditory cortex (e.g., Weinberger, 2004), but could also occur at the level of the cochlear nucleus (e.g., Woody *et al.*, 1992; 1994). It is unclear as to why it might be more adaptive for the chinchilla to use information in the envelope rather than fine structure as in human listeners. Chinchillas are good low frequency hearing animals as shown by their audiograms, and one might predict that they would attend to the fine structure more than the envelope. Perhaps the predisposition for chinchillas to weigh envelope information over fine structure reflects the importance of high frequency listening for sound localization. Heffner *et al.* (1995) have shown that high frequencies are necessary for front/back and vertical sound localization in chinchillas.

In summary, the generalization gradients obtained from chinchillas are dependent on the type of training stimulus employed. When animals are trained to discriminate a stimulus in which the fine structure and envelope both contain strong periodicities (i.e., cosine-phase tone complex) from an aperiodic stimulus (i.e., WBN), the gradients obtained suggest that animals are largely processing information about the stimulus envelope. That is, when periodicities are strong in both the fine structure and envelope, chinchillas seem to have a predisposition for using envelope information. However, when animals are trained to discriminate a stimulus with strong fine structure periodicity, but weak envelope periodicity (i.e., IIRN) from an aperiodic stimulus (i.e., WBN), the gradients obtained suggest that animals are largely processing information about the fine structure. That is, chinchillas can learn to use the information in the fine structure to do the discrimination and consequently, their perception of 'pitch' strength is altered.

ACKNOWLEDGMENTS

Supported by NIDCD Grants Nos. P01 DC00293 and R01 DC005596.

Bohne, B. A., Kenworthy, A., and Carr, C. D. (**1982**). "Density of myelinated nerve fibers in the chinchilla cochlea," J. Acoust. Soc. Am. **72**, 102–107.

Fastl, H., and Stoll, G. (**1979**). "Scaling of pitch strength," Hear. Res. **1**, 293–301.

Glasberg, B. R., and Moore, B. C. J. (**1990**). "Derivation of auditory filter shapes from notched-noise data," Hear. Res. **47**, 103–138.

Greenberg, G. Z., and Larkin, W. D. (**1968**). "Frequency-response characteristic of auditory observers detecting signals of a single frequency in noise: The probe-signal method," J. Acoust. Soc. Am. **44**, 1513–1523.

Guttman, N. (**1963**). "Laws of behavior and facts of perception," in *Psychology: A Study of A Science*, edited by S. Koch (McGraw-Hill, New York), pp. 114–178.

Heffner, R. S., and Heffner, H. E. (**1991**). "Behavioral hearing range of the chinchilla," Hear. Res. **52**, 13–16.

Heffner, R. S., Heffner, H. E., and Koay, G. (**1995**). "Sound localization in chinchillas. II front/back and vertical localization," Hear. Res. **88**, 190–198.

Hulse, S. H. (**1995**). "The discrimination-transfer procedure for studying auditory perception and perceptual invariance in animals," in *Methods in Comparative Psychoacoustics*, edited by G. M. Klump, R. J. Dooling, R. R. Fay, and W. C. Stebbins (Birkhauser-Verlag, Basel, Switzerland), pp. 319–330.

Malott, R. W., and Malott, M. K. (**1970**). "Perception and stimulus generalization," in *Animal Psychophysics: The Design and Conduct of Sensory Experiments*, edited by W. C. Stebbins (Appleton-Century-Crofts, New York), pp. 363–400.

Nadol, J. B., Jr. (**1988**). "Comparative anatomy of the cochlea and auditory nerve in mammals," Hear. Res. **34**, 253–266.

Niemeic, A. J., Yost, W. A., and Shofner, W. P. (**1992**). "Behavioral measures of frequency selectivity in the chinchilla," J. Acoust. Soc. Am. **92**, 2636–2649.

Ohlemiller, K. K., Jones, J. B., Heidbreder, A. F., Clark, W. W., and Miller, J. D. (**1999**). "Voicing judgments by chinchillas trained with a reward paradigm," Behav. Brain Res. **100**, 185–195.

Patterson, R. D., Allerhand, M. H., and Giguère, C. (**1995**). "Time-domain modeling of peripheral auditory processing: A modular architecture and a software platform," J. Acoust. Soc. Am. **98**, 1890–1894.

Shera, C. A., Guinan, Jr., J. J., and Oxenham, A. J. (**2002**). "Revised estimates of human cochlear tuning from otoacoustic and behavioral measurements," Proc. Natl. Acad. Sci. U.S.A. **99**, 3318–3323.

Shofner, W. P. (**2002**). "Perception of the periodicity strength of complex sounds by the chinchilla," Hear. Res. **173**, 69–81.

Shofner, W. P., and Selas, G. (**2002**). "Pitch strength and Stevens' power law," Percept. Psychophys. **64**, 437–450.

Shofner, W. P., Sparks, K., Wu, Y. E., and Pham, E. (**2005**). "Similarity of spectral resolvability in chinchillas and human listeners based on phase discrimination," ARLO **6**, 35–40.

Shofner, W. P., and Whitmer, W. M. (2005). "Effect of listening strategy on the 'pitch' strength of complex, harmonic sounds in chinchillas: stimulus generalization with split-test stimuli," 28th Midwinter Meeting Association for Research in Otolarlyngology, p. 255.

Shofner, W. P., and Yost, W. A. (**1995**). "Discrimination of rippled-spectrum noise from flat-spectrum wideband noise by chinchillas," Aud. Neurosci. **1**, 127–138.

Shofner, W. P., and Yost, W. A. (**1997**). "Discrimination of rippled-spectrum noise from flat-spectrum wideband noise by chinchillas: evidence for a spectral dominance region," Hear. Res. **110**, 15–24.

Terhardt, E. (**1974**). "Pitch, consonance, and harmony," J. Acoust. Soc. Am. **55**, 1061–1069.

Weinberger, N. M. (**2004**). "Experience-dependent response plasticity in the auditory cortex: issues, characteristics, mechanisms and functions," in *Plasticity of the Auditory System*, edited by T. N. Parks *et al.* (Springer, New York), pp. 173–227.

Woody, C. D., Wang, X.-F., Gruen, E., and Landeira-Fernandez, J. (**1992**). "Unit activity to click CS changes in dorsal cochlear nucleus after conditioning," NeuroReport **3**, 385–288.

Woody, C. D., Wang, X.-F., and Gruen, E. (**1994**). "Response to acoustic stimuli increases in the ventral cochlear nucleus after stimulus pairing," NeuroReport **5**, 513–515.

Yost, W. A. (**1996**). "Pitch strength of iterated rippled noise," J. Acoust. Soc. Am. **100**, 3329–3335.

Yost, W. A., Patterson, R., and Sheft, S. (**1996**). "A time domain description for the pitch strength of iterated rippled noise," J. Acoust. Soc. Am. **99**, 1066–1078.

Forward masking of amplitude modulation: Basic characteristics[a)]

Magdalena Wojtczak[b)] and Neal F. Viemeister
Department of Psychology, University of Minnesota, 75 East River Rd., Minneapolis, Minnesota 55455

(Received 20 April 2005; revised 27 July 2005; accepted 1 August 2005)

In this study we demonstrate an effect for amplitude modulation (AM) that is analogous to forward making of audio frequencies, i.e., the modulation threshold for detection of AM (signal) is raised by preceding AM (masker). In the study we focused on the basic characteristics of the forward-masking effect. Functions representing recovery from AM forward masking measured with a 150-ms 40-Hz masker AM and a 50-ms signal AM of the same rate imposed on the same broadband-noise carrier, showed an exponential decay of forward masking with increasing delay from masker offset. Thresholds remained elevated by more than 2 dB over an interval of at least 150 ms following the masker. Masked-threshold patterns, measured with a fixed signal rate (20, 40, and 80 Hz) and a variable masker rate, showed tuning of the AM forward-masking effect. The tuning was approximately constant across signal modulation rates used and consistent with the idea of modulation-rate selective channels. Combining two equally effective forward maskers of different frequencies did not lead to an increase in forward masking relative to that produced by either component alone. Overall, the results are consistent with modulation-rate selective neural channels that adapt and recover from the adaptation relatively quickly. © *2005 Acoustical Society of America.* [DOI: 10.1121/1.2042970]

PACS number(s): 43.66.Mk, 43.66.Dc [GDK] Pages: 3198–3210

I. INTRODUCTION

Envelope fluctuations provide important cues in the perception of auditory stimuli. Envelopes that differ in their temporal structure may help perceptually segregate sounds with overlapping spectra (Grimault *et al.*, 2002; Roberts *et al.*, 2002), and thus extract the target sound from the background. On the other hand, interference between concurrent temporal envelope fluctuations may adversely affect speech intelligibility, especially in listeners with reduced spectral resolution, such as hearing-impaired listeners (Hedrick and Jesteadt, 1996) or cochlear-implant users (Hedrick and Carney, 1997; Kwon and Turner, 2001).

Most sounds have envelopes that are complex waveforms and can be represented by a combination of sinusoidal amplitude modulations. An important question is whether the auditory system performs a spectral analysis on envelopes by processing different modulation components in modulation-rate selective channels or whether processing of envelopes is based on a purely temporal code.

Studies of modulation masking have demonstrated that the auditory system exhibits modulation-rate selectivity (Houtgast, 1989; Bacon and Grantham, 1989), albeit limited, as indicated by relatively broad masking patterns. This finding has inspired models of auditory processing that implement a bank of modulation filters at the output of individual peripheral channels (Dau *et al.*, 1997a, b; Ewert and Dau, 2000). Modulation-rate selective channels could be realized by neurons that have bandpass modulation transfer characteristics. Such neurons have been found in the cochlear nucleus (Frisina *et al.*, 1990; Rhode and Greenberg, 1994), in the inferior colliculus (Rees and Møller, 1983; Langner and Schreiner, 1988), and in the auditory cortex (Schulze and Langner, 1999; Liang *et al.*, 2002). Langner and Schreiner (1988) reported systematic mapping of best modulation frequencies (BMFs) in the inferior colliculus (IC) of the cat. That mapping, however, is not robust to changes in carrier level. Krishna and Semple (2000) observed that the BMF in the IC varies substantially across carrier levels, even over a relatively small (20-dB) range. Interpretation of the physiological data is further complicated by the fact that neural representations at all processing stages above the auditory nerve are nonhomogeneous and that different cell types exhibit different characteristics in their response to AM stimuli (for a review see Joris *et al.*, 2004). It is also unclear which characteristics of the response to AM are important for the perception of envelope fluctuations. Comparisons between psychophysical data from a variety of tasks involving modulation detection and discrimination and different response characteristics measured physiologically are, therefore, crucial for elucidating the mechanisms that underlie AM processing.

In this study we demonstrate a forward-masking effect in which a highly detectable AM raises the threshold for the detection of subsequently presented AM. The effect is analogous to forward masking in the domain of audio frequencies. Nonsimultaneous interference in modulation detection has been observed in numerous studies of adaptation to AM (Kay and Matthews, 1972; Regan and Tansley, 1979; Tansley and Suffield, 1983). Experiments in those studies were designed

[a)]Portions of these data were presented at the XXVII Midwinter Research Meeting of the ARO (M. Wojtczak and N. F. Viemeister, Abstract No. 838).
[b)]Send correspondence to Magdalena Wojtczak, Psychoacoustics Lab, Elliott Hall, N218, 75 East River Rd., Minneapolis, Minnesota 55455.

to produce the maximum amount of adaptation and thus, very long durations of adapting modulations were used (20–30 min). It was found that such long exposures to a sinusoidal AM decreased sensitivity to an ensuing modulation of the same rate. It is not clear whether the observed effect of adaptation plays any role in the perceptual processing of envelopes, since only negligible threshold elevation was observed after just a few minutes of exposure (Tansley and Suffield, 1983). More recently, Sheft (2000) observed significant threshold elevation (up to 7 dB) using a 3-min adapting AM before trials began and then interspersing the adaptor for 16 s between trials. However, long durations of uninterrupted exposure to a constant pattern of a temporal envelope are not commonly encountered. In addition, it has been questioned whether or not the adaptation paradigm is valid for elucidating the mechanisms responsible for encoding and processing AM. It has been demonstrated that for FM and frequency sweeps, the loss of sensitivity due to long prior exposure to these features, considered initially as reflecting neural adaptation, disappears with training (Moody *et al.*, 1984), or is small enough to be explained in terms of nonsensory factors (Wakefield and Viemeister, 1984). Recently, Lorenzi *et al.* (2004) measured adaptation to AM and found that a post-exposure impairment of AM detection, although initially in agreement with the data reported in earlier studies of adaptation, also disappears after extensive training.

Early studies that measured adaptation to AM have used the same modulation rate for the adapting AM and the signal to be detected. Thus, modulation-rate selectivity of the adaptation effect was not investigated. There is a hint in the study by Richards *et al.* (1997) that the effect of adaptation in AM detection is modulation-rate selective. They used only two modulation rates of the adapting AM: one that was equal to the modulation rate of the test AM (16 Hz), and the other that was substantially different from the test AM (56 Hz), and found that only the 16-Hz adaptor significantly decreased sensitivity to the 16-Hz test AM. However, their data do not allow for an inference about the sharpness of tuning. More recently, rate selectivity of adaptation to AM was shown by Sheft (2000) for AM detection (thresholds were elevated when the rate separation between the adapting and test AM was within one to two octaves) and by Wojtczak and Viemeister (2003) for the effect of an adapting AM on the perception of *suprathreshold* modulation depth. The tuning they observed was sharper than that observed in simultaneous modulation masking.

Forward masking of AM newly demonstrated in this study may be potentially very relevant to the processing of real-world auditory stimuli since the effect can be observed for relatively short durations of masking modulations (e.g., 150 ms), durations comparable to those observed in speech sounds. Our main focus in this study was to determine the basic characteristics of the effect, primarily the temporal and spectral region over which prior exposure to AM affects sensitivity to ensuing AM.

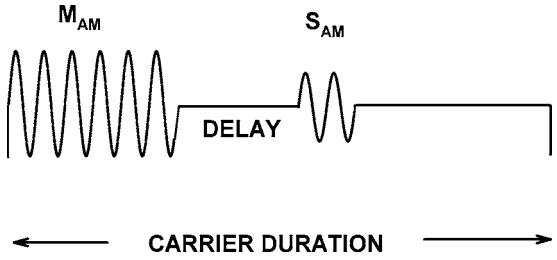

FIG. 1. Schematic illustration of the stimulus envelope in the signal interval. The envelope contains the masker AM (M_{AM}) and signal AM (S_{AM}) imposed on the same uninterrupted carrier.

II. EXPERIMENT 1: RECOVERY FROM AM FORWARD MASKING

Our purpose in this experiment was to measure the shape of the recovery function for AM forward masking. Figure 1 schematically illustrates the envelope of a stimulus containing both the masker AM (M_{AM}) and signal AM (S_{AM}). The detection of S_{AM} was measured as a function of the delay between the offset of M_{AM} and the onset of S_{AM}. To ensure that strong envelope fluctuations associated with gating the carrier off and on did not affect detection of the signal AM, both the masker and signal AM were sequentially imposed on the same uninterrupted carrier.

When attempting to measure the recovery function, it is desirable to use a very short signal so that the function can be measured with good resolution. This requires using a high modulation rate, since at least one cycle of modulation needs to be presented. However, the detection of modulation deteriorates with a decreasing number of modulation cycles (Sheft and Yost, 1990) and, for noise carriers, it also deteriorates with an increasing modulation rate above about 30 Hz (Viemeister, 1979). Thus, using just one cycle of a very high modulation rate could impose an artificial limit on the observed size of AM forward masking because it would limit the available range of modulation depths above the unmasked AM detection threshold. For these reasons, very low and very high modulation rates could not be used in the experiment.

A. Stimuli and procedure

The detection of a 40-Hz sinusoidal AM (S_{AM}) was measured using an adaptive three-interval forced-choice (3IFC) procedure that estimated the 79.4% point on the psychometric function (Levitt, 1971). Feedback indicating the correct response was provided on each trial. The signal modulation S_{AM} was presented alone in one condition, and after a 40-Hz M_{AM} in another condition. In the signal interval, the modulations were imposed sequentially on an uninterrupted noise carrier whose bandwidth extended from 0.1 to 10 kHz. The noise carrier had a spectrum level of 25 dB SPL measured at 1 kHz. For delays between S_{AM} and M_{AM} up to 210 ms, a carrier duration of 500-ms was used. A longer duration of the carrier (750 ms) had to be used when it was observed that the AM masked threshold was still elevated when S_{AM} was separated from M_{AM} by the longest delay permissible with the 500-ms carrier duration. The stimulus envelope shown in Fig. 1 was described by

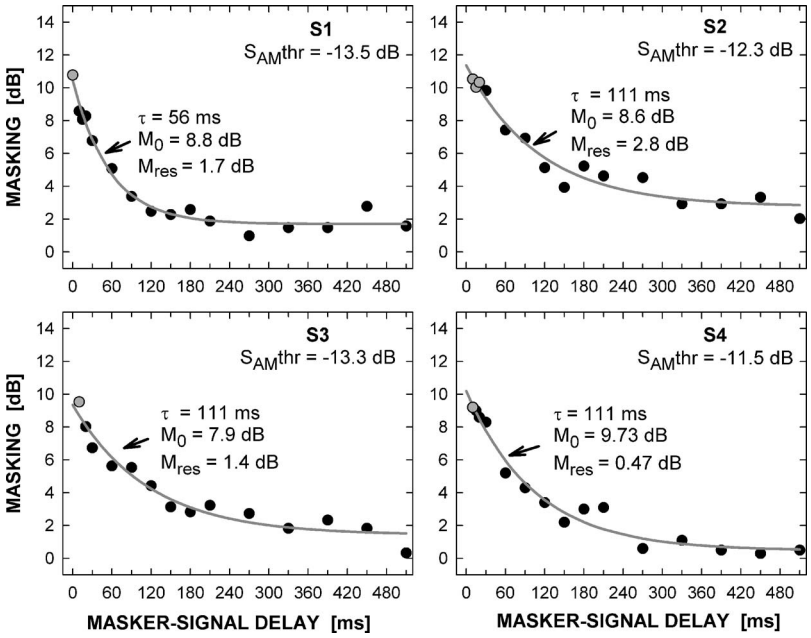

FIG. 2. AM forward masking (symbols) measured as a function of the delay between the offset of M_{AM} and the onset of S_{AM}. Gray lines represent the best fitting function described by Eq. (2). The amount of masking above the residual at the delay of 0 ms, the residual amount of masking, and the time constant describing recovery are provided in each panel. Also, the threshold for detecting unmasked S_{AM} is shown for each subject.

$$e(t) = 1 + m\sin(2\pi f_m t + \Phi) \text{ during the modulated portions of the carrier, and}$$

$$e(t) = 1 \text{ during the unmodulated portions,} \quad (1)$$

where m, f_m, and Φ are the modulation depth, modulation rate, and the modulation starting phase, respectively. M_{AM} occupied the initial 150 ms of the carrier and its modulation depth was 1 ($20\log m = 0$ dB). S_{AM} had a duration of 50 ms and its modulation depth was varied adaptively to find the threshold. Both M_{AM} and S_{AM} started at phase $\Phi = 0$ rad. Thresholds were measured for delays between the offset of M_{AM} and the onset of S_{AM}, ranging from 0 to 510 ms. When M_{AM} was not present, the unmasked detection of S_{AM} was measured with S_{AM} starting 150 ms after the carrier onset. The adaptive tracking procedure used a 2-dB step ($20\log m$) until the first four reversals were obtained. The step size was reduced to 1 dB afterward. A total of 12 reversals were obtained and the threshold estimate was computed as the mean of the last eight reversals. Six to nine threshold estimates were averaged to compute the final threshold for each masker-signal delay. The run was aborted when the adaptive procedure called for a modulation depth greater than 0 dB, to avoid overmodulation. For delays at which more than three runs were aborted, thresholds were deemed immeasurable. When three or fewer runs were aborted, the threshold was computed as the mean of the remaining three to six runs. Those thresholds are distinguished by using gray symbols.

For delays up to 210 ms, the forward-masking functions were also measured with two types of a cue that was used to help perceptually segregate S_{AM} from M_{AM}. This was done to evaluate a potential role of temporal confusion that has been shown to affect the amount of forward masking in the audio-frequency domain (Moore and Glasberg, 1982; Neff, 1985, 1986). In one case a 4-kHz tone was presented ipsilaterally at 75 dB SPL and gated (with 5-ms ramps) for the duration of M_{AM}. In another case, an independent sample of the noise carrier modulated by M_{AM} was presented to the contralateral ear in each observation interval.

The stimuli were generated digitally on a PC using a 24-bit soundcard (Echo-Gina 24/96) and a sampling rate of 44.1 kHz. The noise carrier was generated in the frequency domain, with the components outside the passband set to zero. The amplitude and phase of the components inside the passband were randomly selected from the Rayleigh and rectangular distributions, respectively. The real part of the inverse FFT was then multiplied by the modulating waveforms. A different sample of noise was presented in each observation interval. The stimuli were presented monaurally to the left ear via Sony MDR-V6 earphones, except the condition where the noise carrier modulated by M_{AM} was presented to the opposite ear to eliminate possible temporal confusion.

B. Subjects

Six listeners with normal hearing participated in experiment 1. Four listeners were used to measure the recovery functions and two additional listeners were used to compare recovery for delays up to 210 ms with versus without a cuing stimulus. The listeners had audiometric thresholds to within 10 dB of laboratory norms at octave frequencies between 250 and 8000 Hz (thresholds better than 15 dB HL). Subject S3 (the first author) was highly trained in psychoacoustic tasks. The other subjects were naïve and were given at least 10 h training on selected conditions before data collection commenced.

C. Results

Modulation thresholds for detecting the unmasked 40-Hz S_{AM} were subtracted from thresholds measured for S_{AM} presented after M_{AM} to compute the amount of AM forward masking. Figure 2 shows the amount of AM forward

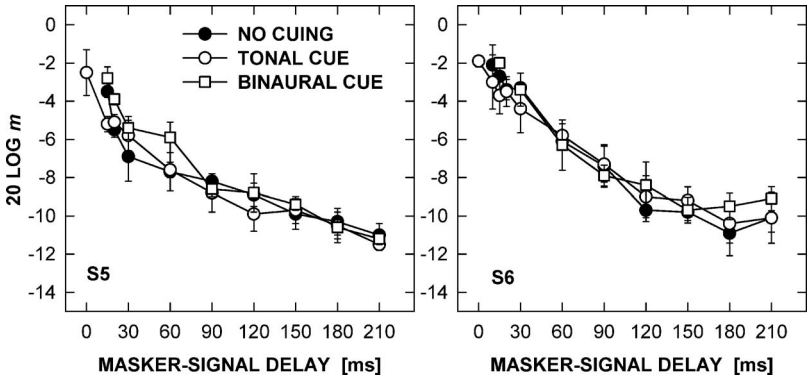

FIG. 3. Thresholds for the detection of S_{AM} plotted as a function of the delay between the offset of M_{AM} and the onset of S_{AM} measured without a cuing stimulus (filled circles), with a 4-kHz tone gated for the duration of M_{AM} (open circles), and with a contralateral noise modulated by M_{AM} (open squares). The error bars in this and all subsequent figures indicate one standard deviation. Data from two subjects.

masking (symbols) as a function of the delay between the offset of M_{AM} and the onset of S_{AM}. Standard deviations for the masked thresholds (not shown) estimated from six to nine runs were less than 1 dB in 94% of all cases (all delays and subjects). The maximum standard deviation did not exceed 1.2 dB. The unmasked thresholds are shown in the insert of each panel (S_{AM} thr). The mean unmasked threshold of −12.7 dB obtained by averaging thresholds from the four listeners is about 2 dB higher than the mean threshold for two listeners measured by Sheft and Yost (1990) using two cycles of 40-Hz AM imposed on a noise carrier. The difference could reflect the effect of a longer fringe (500 ms versus 150 ms used in this study) or slightly worse average sensitivity of our listeners.

For the 0-ms delay, a valid estimate of the masked threshold could not be obtained from any of the subjects. Subject S1 was the only one who successfully completed three out of six runs, but three other runs were aborted due to the adaptive procedure calling for a modulation depth greater than 0 dB. Since the duration of S_{AM} was 50 ms, this result indicates that over a period of 50 ms listeners could not reliably detect a 40-Hz AM when it followed AM of the same rate. Similarly, some runs were aborted at other short delays for subjects S2 (for a 10, 15, and 20-ms delay), and S3, S4 (for a 10-ms delay), indicated by gray symbols. Generally, the masking effect decays rapidly within the first 100–150 ms (offset to onset) and then gradually asymptotes. Subjects S1 and S2 exhibited a small residual amount of masking at the longest delay (510 ms).

To determine the time constant characterizing recovery from AM forward masking, the data in Fig. 2 were fitted with an exponential function given by the following equation:

$$M(d) = M_0 \cdot e^{-d/\tau} + M_{res}, \quad (2)$$

where $M(d)$ is the amount of masking in dB at a delay d, M_{res} is the residual masking, M_0 is the amount of masking at a 0-ms delay relative to the residual masking, and τ is the time constant describing the rate of recovery. The parameters yielding the best fit are given in the insert of each panel. The proportion of variance accounted for by the exponential fit (r^2) was 0.98 for S1, 0.96 for S2, 0.95 for S3, and 0.97 for S4.

Since the rates of M_{AM} and S_{AM} were identical, the masked thresholds measured at the shortest delays might have been artificially raised by the listeners' inability to determine when the masker ended and the signal began. Thresholds affected by temporal confusion are expected to decrease when a stimulus cuing the temporal end of the masker is used (Moore and Glasberg, 1982). Figure 3 shows recovery functions measured in two subjects with two types of cuing stimuli added to investigate a potential role of temporal confusion. Neither subject could detect the signal without a cuing stimulus for the 0-ms delay and both showed improvement in this condition when the 4-kHz cue was presented during the masker modulation. Subject S6, however, still required a modulation depth greater than 0 dB in two out of six runs. S5 also showed a slight (less than 2 dB) decrease in threshold for a 15-ms delay, and S6 showed a less than 1-dB improvement for 10- and 15-ms delays when the cuing tone was present. The cuing tone led to an improvement in performance in no other condition. The contralateral noise (open squares) did not reduce the threshold at any delay. For shorter delays, it may have provided distraction, causing a slight increase in forward masking compared with that observed without the noise. Overall, the data suggest that the observed AM forward masking is not affected by temporal confusion, at least for delays greater than 15 ms. It is possible, however, that the cues were not effective enough in eliminating temporal confusion (this issue is addressed in Sec. IV).

After data collection was completed, at least 30 additional blocks were run in selected conditions to make sure that the amount of masking could not be eliminated or substantially reduced by training. The data showed that the training given prior to data collection was sufficient and the amounts of masking presented in Fig. 2 likely reflect the asymptotic performance.

III. EXPERIMENT 2: RATE SELECTIVITY IN AM FORWARD MASKING

Masking patterns obtained for the simultaneously presented masker and signal AM show a clear peak for signal modulation rates that are similar to the masker modulation rates (Bacon and Grantham, 1989; Houtgast, 1989; Takahashi and Bacon, 1992; Dau *et al.*, 1997a, b; Ewert and Dau, 2000; Ewert *et al.*, 2002). This tuning of masking may reflect the processing of AM by rate-selective neural channels. However, some aspects of modulation masking cannot be explained by spectral models of masking. For example, when the rate of the masker AM is low and the rate of the signal AM is much higher, the presence of the masker facilitates

signal detection and thus leads to thresholds that are lower than the unmasked thresholds. The "negative masking," seen in the data of Bacon and Grantham (1989) and Strickland and Viemeister (1996), was explained in terms of detecting "local temporal features." This strategy for detecting the signal would require that listeners are able to evaluate their decision variable over short temporal intervals ("looks") and improve their performance by detecting the signal in the troughs of the masker modulation, where the effective modulation depth of the signal is the greatest. The same explanation could account for the fact that for a masker rate much lower than the signal rate, detection improves as the modulation depth of the masker increases, which is also seen in the two studies. Another aspect of AM masking that cannot be explained in terms of spectral models is that simultaneous AM masking depends strongly on the relative starting phases of the signal AM and the masker AM when the signal and masker rates differ by a factor of 2 (Strickland and Viemeister, 1996). Moreover, in simultaneous AM masking, listeners can improve their performance by detecting beats between the masker and signal AM component (Strickland and Viemeister, 1996; Ewert *et al.*, 2002). The beat rate, although not represented in the modulation spectrum, can be introduced in the internal representation of the envelope as a result of compressive nonlinearity and possibly other nonlinearities in the auditory system (Shofner *et al.*, 1996; Moore *et al.*, 1999; Füllgrabe *et al.*, 2005).

Using a forward-masking paradigm to measure tuning prevents listeners from detecting the signal AM in local dips of the masker AM and from using any other local temporal cues, because the two modulations do not overlap in time. In addition, modulation distortion products are unavailable as cues when the masker and signal AM are temporally separated. Thus, forward masking may potentially provide a valid assessment of tuning in AM processing, if it is assumed that the mechanism underlying the forward masking does not depend on the modulation rate of the masker (an assumption that has not been verified for AM).

In this experiment, the detection of S_{AM} was measured as a function of the modulation rate of M_{AM} for a short (fixed) temporal delay between S_{AM} and M_{AM}.

A. Stimuli and procedure

Masked-threshold patterns (with the signal rate fixed and the masker rate varied) were measured for S_{AM} rates of 20, 40, and 80 Hz. In all cases, S_{AM} had a duration of 50 ms so the number of cycles in the signal increased from 1 to 4 as the modulation rate increased. The noise carrier had the same bandwidth as that used in experiment 1, and was gated for 600 ms. The masker AM had a duration of 500 ms and a modulation depth of 0 dB (100% modulation). A masker duration of 500 ms was necessary so that at least one cycle of M_{AM} could be presented for each masker modulation rate. The detection of S_{AM} was measured for modulation rates of M_{AM} selected from the range between 2 and 256 Hz in one-octave steps. The delay between the offset of M_{AM} and the onset of S_{AM} was fixed for a given S_{AM} rate but was not always the same across subjects or S_{AM} rates. In each case, the shortest delay was used for which a subject was able to perform the task for the M_{AM} rate that produced most masking (which happened sometimes for unequal rates of M_{AM} and S_{AM}). All delays were in the range between 20 and 40 ms.

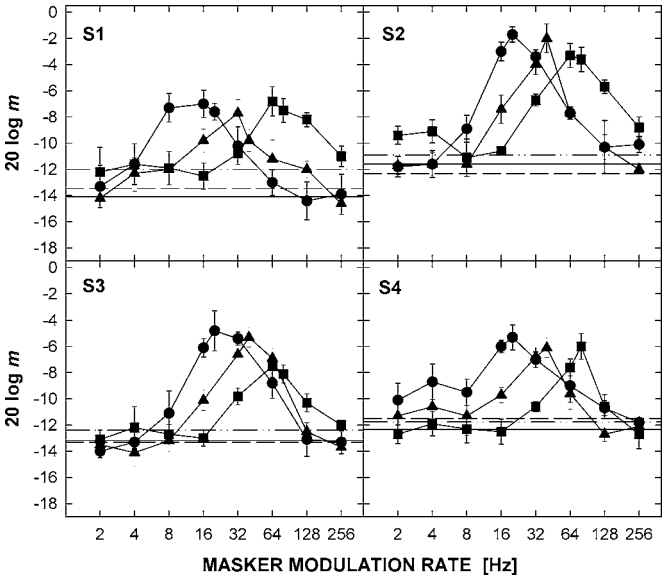

FIG. 4. Thresholds for the detection of S_{AM} plotted as a function of the rate of M_{AM}, for S_{AM} rates of 20-Hz (circles), 40 Hz (triangles), and 80 Hz (squares). Also shown are unmasked thresholds for the S_{AM} of 20 Hz (solid line), 40 Hz (dashed line), and 80 Hz (dotted-dashed line). In most cases the delay between M_{AM} and S_{AM} was fixed at 20 ms, except the 20-Hz data were collected at a 30-ms delay for S2 and S4, and the 80-Hz data were collected at a 40-ms delay for S2, and a 30-ms delay for S4.

The experimental procedure, generation, and presentation of the stimuli were the same as in experiment 1.

B. Subjects

The four subjects for whom recovery functions were measured in experiment 1 participated in this experiment.

C. Results

Figure 4 shows forward-masked AM thresholds, for all three modulation rates of S_{AM}, plotted as a function of the modulation rate of M_{AM}. The horizontal lines indicate the unmasked thresholds. The data reveal tuning of the forward-masking effect. The masker-signal delays at which the masked-threshold patterns were measured are given in the caption of Fig. 4. In some cases, the peak of the masking function is shifted toward lower rates relative to the rate of S_{AM} (S1 for the 20- and 80-Hz S_{AM}, and S2 and S3 for the 80-Hz S_{AM}). The peaks of the masking patterns are generally similar across the three modulation rates of S_{AM}, with the exception of S2 and S3, who showed a slightly lower peak threshold for the 80-Hz rate. There is a slight trend for the amount of masking, computed as a difference between the masked and unmasked threshold, to decrease with the increasing modulation rate of S_{AM}.

Not surprisingly, negative masking is not observed when the masker rate is much lower than the signal rate. Since the masker and the signal were not presented simultaneously,

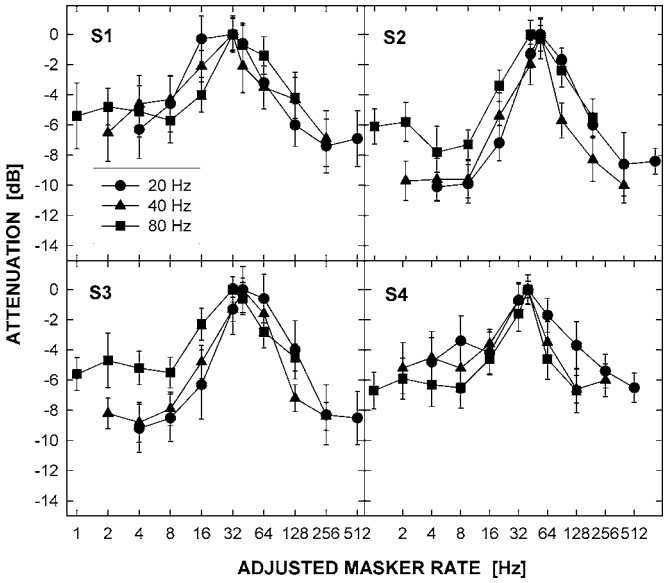

FIG. 5. Attenuation functions derived from data in Fig. 4. Functions for the 20-and 80-Hz S_{AM} are shifted to have their peak correspond to 40 Hz for the purpose of comparison.

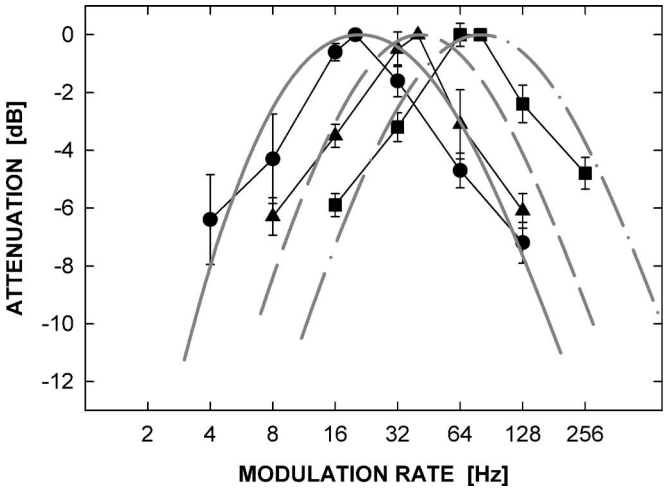

FIG. 6. Attenuation functions averaged across listeners for S_{AM} rates of 20, 40, and 80 Hz. The gray lines show the shapes of second-order bandpass filters fit to the data.

listeners could not take advantage of the larger local effective modulation depth of S_{AM} in the troughs of M_{AM}. No other local temporal features could be used to improve performance for M_{AM} differing in rate from S_{AM} relative to the performance observed for equal rates. Thus, the tuning of the forward-masking effect suggests that envelope processing is performed by rate-selective channels.

Figure 5 shows attenuation functions derived from the masked-threshold patterns. The functions were derived assuming that a masked threshold is obtained when the ratio of the S_{AM} amplitude to the M_{AM} amplitude at the output of the channel processing the signal reaches a constant criterion value. It was also assumed that the masker that produces the most masking is not attenuated by the channel processing the signal (0-dB attenuation). As mentioned above, the maximally effective masker was not always the on-frequency masker. Under these assumptions, the attenuation functions approximate the shape of hypothetical modulation filters, for the three modulation rates used in this study. To facilitate a comparison of the sharpness of tuning at the three modulation rates, the attenuation functions shown in Fig. 5, for the 20- and 80-Hz rates, are shifted upward and downward, respectively, to have their peak at the 40-Hz rate. The three functions would overlap if the filters had a constant Q value. Since the tails of the functions are limited by the unmasked threshold, the sharpness of tuning should be compared only around the peak, i.e., for the adjusted masker rates between 8 and 128 Hz. The data in Fig. 5 indicate that there is no systematic dependence of the relative bandwidth of a hypothetical modulation filter on the center frequency of the filter, over the range of the rates tested.

To quantify tuning, a second-order bandpass Butterworth filter, symmetric on the log frequency scale, was fitted to the adjusted attenuation functions in the range between 8 and 128 Hz. MATLAB's *fminbnd* function was used to find a ratio of the filters' cutoff frequencies that produced the smallest rms error between the data and the fitted filter. The Q values of the filters fitted to the individual data and the rms errors of the fits are given in Table I.

Figure 6 shows attenuation functions obtained by averaging the amounts of attenuation across the four listeners separately for each of the three signal modulation rates. The gray lines show the attenuation characteristics of the second-order Butterworth filters fitted to the averaged data. The fitted filters are clearly too broad near the peak, which results from fixing the order of the fitted filters at 2. This was done in order to compare the Q values of the fitted filters with those used to fit AM masking data in studies that measured simultaneous masking (Ewert and Dau, 2000). A higher order of the filter would produce a better fit to the data. As in studies of AM simultaneous masking, the filters were as-

TABLE I. Q values of second-order bandpass filters and the rms errors of the fits to the individual and mean data for S_{AM} rates of 20, 40, and 80 Hz.

	20 Hz		40 Hz		80 Hz	
	Q	rms_err	Q	rms_err	Q	rms_err
S1	0.35	1.45	0.36	1.40	0.41	1.12
S2	0.62	1.30	0.71	2.12	0.50	0.71
S3	0.47	1.31	0.55	1.28	0.41	0.76
S4	0.35	2.10	0.42	2.02	0.53	2.06
Mean	0.36	1.21	0.44	1.56	0.41	1.06

TABLE II. Thresholds and standard deviations for detecting S_{AM} for different starting phases.

	$-\pi/2$	0	$\pi/2$	π
S1	−6.6 (0.8)	−6.1 (0.8)	−6.2 (0.4)	−6.0 (0.4)
S2	−2.5 (0.7)	−2.2 (1.3)	−2.3 (0.9)	−2.1 (1.2)
S3	−6.6 (0.9)	−5.9 (0.6)	−6.2 (1.0)	−6.0 (0.5)

sumed to be symmetrical in log frequency. This assumption also contributed to the fitting error, since the measured attenuation functions for the 40- and 80-Hz S_{AM} appear to have a slightly steeper slope on the high-frequency side than on the low-frequency side, when plotted against log frequency. The Q values and the rms errors for the filters fitted to the averaged functions are shown in the bottom row of Table I. The Q values indicate very broad tuning. Data from tasks measuring simultaneous masking of AM suggest Q values between 1 and 2 (Dau *et al.*, 1997a; Ewert *et al.*, 2002). The much sharper tuning in simultaneous masking may result from listeners' ability to use local temporal features or distortion modulation components to enhance their performance in cases where M_{AM} and S_{AM} have different rates.

Caution is necessary in speculating about the mechanism underlying forward masking of AM, since the exact mechanism involved in coding AM in the auditory system has not been yet elucidated. One possibility is that it reflects ringing of the channels processing AM. Although broad tuning observed in modulation masking implies very short ringing times, a control condition was run to evaluate a potential effect of the modulation starting phase on the detection of S_{AM} (Sek and Moore 2002). Thresholds were measured at a fixed delay between M_{AM} and S_{AM} of 30 ms, with the S_{AM} starting phase set to $-\pi/2$, 0, $\pi/2$, and π rad. The 0-rad condition (the data point for the 30-ms delay in experiment 1) was rerun to assess a potential training effect. Data from three listeners (S4 was unavailable for testing) are shown in Table II. Although thresholds appear consistently lower for $-\pi/2$ and $\pi/2$ than for the 0 and π phases, a one-way ANOVA showed that the effect of the starting phase was not significant ($F=0.08, p=0.97$). This result suggests that the forward-masking effect does not result from a simultaneous interaction between the masker and signal AM due to ringing, in which information about the modulation phase is preserved.

IV. EXPERIMENT 3: MASKING BY COMBINED AM FORWARD MASKERS

This experiment compares the amount of masking produced by an on-frequency masker (40-Hz M_{AM}) with the amount of masking produced by that same masker paired with a masker having a different modulation rate. The aims of this experiment are (1) to test the hypothesis that the size of the forward-masking effect is determined by the total power of the modulation masker at the output of the channel tuned to the signal modulation rate; (2) to further test to what extent the perceptual similarity between M_{AM} and S_{AM} affects tuning observed in AM forward masking.

Regarding the first aim, results from previous experiments suggest that modulations with different rates are processed in modulation-rate selective channels. In this experiment, additivity of forward masking is tested by comparing the amounts of masking produced by simultaneously present similarly effective maskers with the amount of masking produced by either masker presented separately. If the size of forward masking is determined by the total power of the modulation masker at the output of the channel tuned to the signal modulation rate, then combining two maskers that separately produce similar amounts of masking should result in an increased masked threshold compared with that produced by either masker alone.

Regarding the second aim, combining a 40-Hz AM with a distinctly different rate may facilitate the perceptual segregation between the masker and signal AM. In the second part of experiment 1, a 4-kHz tone was presented during M_{AM} to mark the temporal end of the masker. Such a cue was expected to reduce a potential effect of temporal confusion between M_{AM} and S_{AM}, when the two modulations are similar perceptually. It is possible that the tonal cue was not sufficient to help listeners distinguish between the masker and the signal. In that case, tuning of the masking effect could reflect

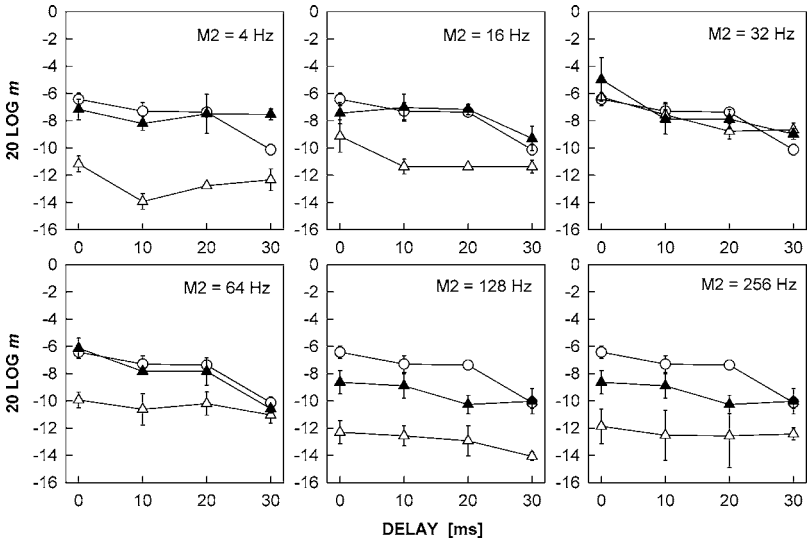

FIG. 7. Thresholds for detecting 40-Hz S_{AM} presented after a single-component M_{AM} (open symbols) and after a two-component M_{AM}. Data for the 40-Hz masker alone are shown by open circles, data for an off-frequency masker alone are shown by open triangles, and data for the two sinusoidal maskers combined are shown by filled triangles. Data for S1.

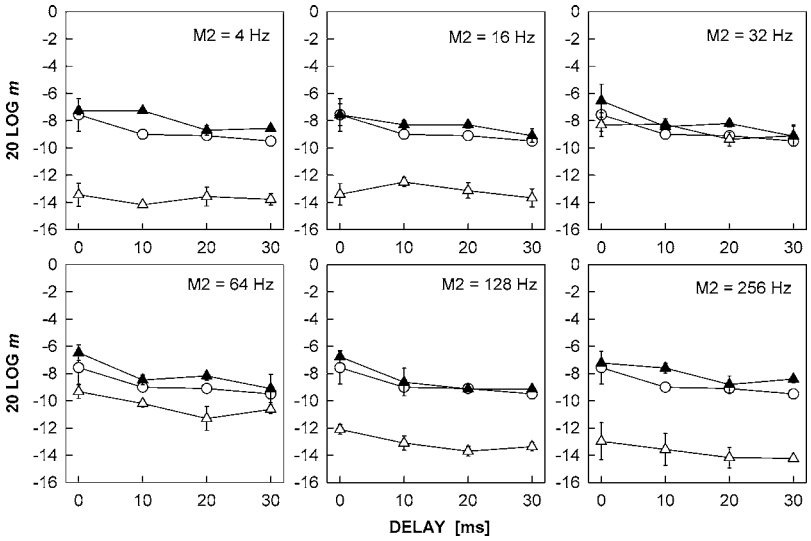

FIG. 8. The same as in Fig. 7, but for listener S3.

a decreasing perceptual similarity between M_{AM} and S_{AM} as the difference between their rates increases. Adding a modulation that has a different modulation rate from S_{AM} (one that does not produce any forward masking of S_{AM} on its own) to an on-frequency M_{AM} (with the same rate as that of S_{AM}) may provide a more efficient cue for perceptual segregation between M_{AM} and S_{AM}. If that were the case, and if forward masking reflected perceptual confusion, then the threshold would be expected to decrease in the presence of the modulation added to the on-frequency masker. Thus, measuring masking by two combined maskers could provide an insight into the nature of the forward-masking effect.

A. Stimuli and procedure

The experimental procedure, the carrier, and the durations of the masker and signal modulations were the same as in experiment 2. The masker modulation was either sinusoidal AM or a combination of two sinusoidal AMs. The combined masker AM consisted of a 40-Hz sinusoid paired with one of the following modulation rates: 4, 16, 32, 64, 128, and 256 Hz. In all conditions, each sinusoidal AM had a modulation depth of −6 dB (20 log m). All signal and masker modulations started with a phase of 0 rad. Thresholds for detecting S_{AM} were measured for four delays between the masker and signal, 0, 10, 20, and 30 ms. The method for the generation and presentation of the stimuli was the same as in the previous experiments.

B. Subjects

Three listeners completed the task. All of them participated in the first two experiments. Subject S2 was not available for testing at the time of the experiment.

C. Results

Data from the three listeners are shown in Figs. 7–9. Open symbols show data for individual maskers presented alone and filled symbols show thresholds obtained for two maskers combined. For the 40-Hz masker, the amount of masking is less than that measured in experiment 1. This is not surprising because the modulation depth of M_{AM} used here was 6 dB lower than that used in the previous experiments. Since the 32-Hz AM produced an amount of masking most similar to that observed for the 40-Hz masker, the ad-

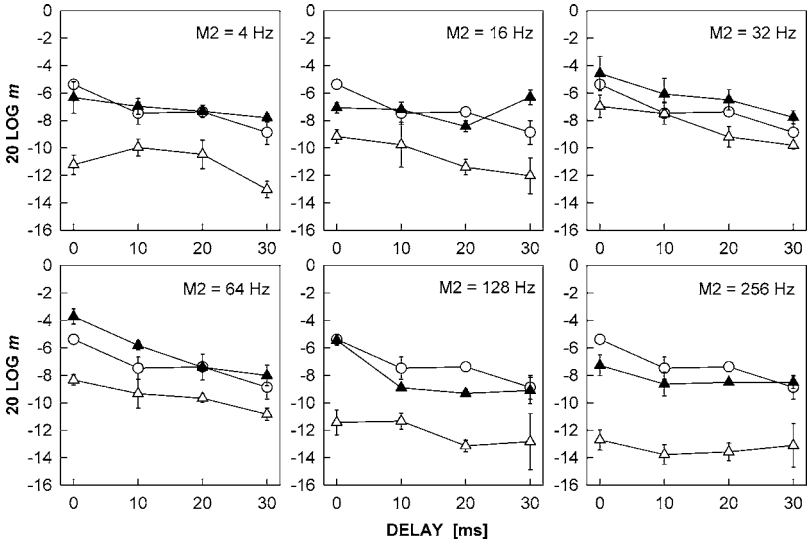

FIG. 9. The same as in Fig. 7, but for listener S4.

ditivity of masking would be expected to be revealed when these two masker rates are combined. A two-way ANOVA was performed separately on each listener's data with the masker modulation rate and the masker-signal delay as the main factors. For the 32- versus 40-Hz masker presented separately, the ANOVA revealed no significant effect of the masker rate for S1 ($F=0, p=0.96$) and S3 ($F=0.02, p=0.90$), but listener S4 showed significantly more masking produced by the 40-Hz rate ($F=17, p=0.001$). For equally effective maskers, a simple additivity of envelope power would predict a 3 dB increase in the masked threshold. The data do not show an increase of forward masking when the 32- and 40-Hz maskers were presented together, in comparison with the forward masking produced by the 40-Hz masker alone. A two-way ANOVA with the type of masker (40 Hz alone versus 32+40 Hz), and the delay as the main factors revealed no significant effect of the masker type for listener S1 ($F=0.47$, $p=0.50$) and S3 ($F=2.5$, $p=0.13$) and only a marginally significant increase in forward masking for S4
($F=10.11$, $p=0.006$). There was no significant interaction between the delay and the masker type for any of the three listeners. The lack of a significant increase in masking produced by two equally effective maskers compared with either masker alone argues against the possibility that forward masking depends on the total power of the forward masker at the output of the modulation channel processing the signal rate.

For M_{AM} other than 32 and 40 Hz presented alone, masked thresholds were substantially lower than the thresholds for the 40-Hz masker presented alone, reflecting tuning in AM forward masking. Thus, pairing an off-frequency masker with the 40-Hz masker should result in masked thresholds that are similar to those produced by the more effective masker. This was generally the case, except for some conditions where combining the 40-Hz masker with maskers of higher rates (128 and 256 Hz) led to some improvement in performance relative to that for the 40-Hz masker alone. This effect was the strongest for listener S1 (Fig. 7) at the three shortest delays, 0, 10, and 20 ms, but S4 (Fig. 9) also showed a slight decrease in threshold for the same delays when the off-frequency rate was 256 Hz, and for the 10- and 20-ms delays when the off-frequency rate was 128 Hz. The possible reasons for this improvement in signal detection will be discussed in the following section. In contrast, S3 (Fig. 8) showed a slight elevation in threshold when the off-frequency masker was added, but the change in threshold was only marginally significant ($F=12.5$, $p=0.003$).

V. DISCUSSION

There is ample evidence demonstrating masking between concurrent sinusoidal modulations of similar rates (Houtgast, 1989; Bacon and Grantham, 1989; Dau *et al.*, 1997a, b; Ewert and Dau, 2000; Ewert *et al.*, 2002). This interference between spectral components within a temporal envelope determines the amount of temporal information that is available to the listener. In a dynamically changing envelope, that information might be further limited by interference between modulations that occur nonsimultaneously. Data presented in this study convincingly demonstrate an effect that is analogous to forward masking of audio frequencies. A highly detectable modulation raises the threshold for detection of 50-ms modulation with the same or a similar rate when the latter follows it immediately after delays less than about 150 ms. The effect is referred to here as AM forward masking because of the apparent analogy and because the exact mechanism underlying the effect is presently unknown (thus, the term "adaptation" has been avoided here).

A. The temporal extent of AM forward masking

Data from the first experiment show that listeners could not consistently detect a 50-ms 100% modulation that immediately followed a 150-ms modulation of the same rate. Thresholds decreased with an increasing delay between M_{AM} and S_{AM} but in all listeners, thresholds remained elevated by more than 2 dB over at least a 150-ms interval. It is unclear to what extent this forward-masking effect plays a role in the processing of real-world auditory stimuli. The function representing recovery from AM forward masking was measured for a modulation rate of 40 Hz and the tuning of the effect was measured for rates between 20 and 80 Hz. Although such high rates are not the most prevalent in speech, they have been shown to contribute to speech recognition, especially when all spectral cues are removed and listeners have to rely on information contained in the temporal envelope (van Tasell *et al.*, 1987). Durations of the masker and signal AM used in this study fall within the range of durations for speech tokens (e.g., vowels). For modulation rates that are dominant in speech (below 16 Hz), one cycle of modulation approaches the time interval over which the auditory system recovers from forward masking, and thus the AM forward masking may not appreciably affect their perception.

The recovery times estimated from an exponential fit to the data in experiment 1 were remarkably consistent across three listeners (111 ms). One subject showed a faster recovery (56 ms). The time constants characterizing recovery from AM forward masking in all four listeners are very similar to those describing recovery from forward masking of audiofrequencies for listeners with sensorineural hearing losses (Nelson and Freyman, 1987) and recovery from forward masking in electrical stimulation for cochlear-implant users (Nelson and Donaldson, 2002). Since the two groups of listeners have reduced or nonexistent peripheral compression, the time constants reported in those studies are not affected by the effect of peripheral compression on the slope of the forward-masking curve measured behaviorally (Plack and Oxenham, 1998). Thus, those time constants may accurately describe the recovery of the mechanism underlying forward masking. Under this assumption, it is tempting to speculate that the similarity between the time constants describing recovery from AM forward masking and those characterizing forward masking of audio frequencies in the auditory system without peripheral compression may suggest that

the two effects have the same type of underlying mechanism, e.g., they both may be mediated by neural adaptation.

The relatively fast recovery from the forward-masking effect explains why Tansley and Suffield (1983) did not see a substantial change in threshold after a few minutes of uninterrupted exposure to AM, since they used a 7 s test AM. When the signal is substantially longer than the time that the system needs to recover from forward masking, no threshold elevation is observed because a large portion of the signal is unaffected by the masker. Thus, even if the amount of masking depends on masker duration, the signal was likely long enough to be detected at its unmasked threshold level.

B. Tuning of AM forward masking

When sinusoidal modulations with different rates are simultaneously present in an envelope, listeners apparently can use local temporal features to detect the signal modulation in the presence of a masker. There is evidence that listeners can take advantage of troughs in the masker modulation to detect higher-rate modulations that are effectively magnified during low-level portions of a fluctuating stimulus envelope (Strickland and Viemeister, 1996). The availability of such local temporal cues affects the shape of masked-threshold patterns, and thus the bandwidth of a modulation filter derived from the masking data. One might argue that a more accurate estimate of the filter shape and bandwidth could be obtained from forward-masking data. This would require an assumption that the rate of recovery does not depend on the frequency of the masker modulation. While this assumption has not been specifically tested, our limited data at masker-signal delays shorter than those used in experiment 2 suggest that it might be justified.[1] Functions relating the masked threshold to the modulation rate of the masker AM have a distinct peak around the rate of the signal AM. The second-order Butterworth filters fitted to the data in Fig. 6 reveal very broad tuning. The Q values of the filters fitted to the attenuation functions averaged across listeners were less than 0.5 at all three signal modulation rates. Although such low Q values have been reported in some studies that used noise carriers (Ewert and Dau, 2000), most data from simultaneous modulation-masking experiments imply sharper tuning of AM, described by Q values between 1 and 2 (Dau *et al.*, 1997a, b; Ewert *et al.*, 2002). The sharper tuning in simultaneous masking may reflect the availability of local temporal cues that may lead to an improvement in performance as the signal and masker rates become more dissimilar and availability of modulation distortion components that could lead to a sharper peak of the measured filter.

As shown in Fig. 6, the data that presumably approximate the modulation-filter shapes are slightly asymmetric on a log frequency scale, with a steeper high-frequency side. Such asymmetry was also revealed in the data of Ewert and Dau (2000). To model the asymmetry of attenuation functions obtained from their simultaneous-masking data, Ewert and Dau applied a low-pass filter with a cutoff frequency of 150 Hz to the output of a bandpass modulation filter that was symmetric on a log-frequency scale. The choice of the cutoff frequency was dictated by modulation-detection data obtained for high-frequency tonal carriers that suggest "sluggishness" in envelope processing for modulation rates above 150 Hz (Kohlrausch *et al.*, 2000). The attenuation functions measured in experiment 2 may reflect the combined symmetric bandpass processing of modulation rates and lowpass filtering due to the sluggishness of temporal processing, but to predict the asymmetry at the 40-Hz rate seen in Fig. 6, a cutoff frequency lower than 150 Hz would have to be used.

C. Ringing in modulation channels

An implication of processing AM by modulation-rate selective channels is that those channels have a finite impulse response (ringing) of the modulation channels. One reason for forward masking could be an overlap of M_{AM} and S_{AM} due to ringing in the filter processing both modulations. If the modulation phase was preserved in ringing and if ringing mediated the forward-masking effect, then the detection of S_{AM} would be expected to depend on its starting phase. Data shown in Table II demonstrate that was not the case; at a 30-ms delay, at which substantial forward masking was observed, threshold was independent of the S_{AM} starting phase. The interpretation of this result is not straightforward given that the mechanism for coding AM is still unknown. Physiological data suggest that the coding mechanism changes as the stimulus moves from peripheral processing stages to more central sites. At the auditory periphery, responses to AM exhibit a high degree of synchronization to the phase of the stimulating AM (Cooper *et al.*, 1993; Wang and Sachs, 1993), but at the level of the Inferior Colliculus (IC) that code becomes partially converted to one based on the average firing rate (Langner and Schreiner, 1988; Krishna and Semple, 2000). Subsequently, the rate-based code becomes dominant at the level of the Primary Auditory Cortex (e.g., Liang *et al.*, 2002). Although the synchrony-to-rate conversion in AM coding may not occur in some species [e.g., guinea pig, Middlebrooks (2005)], it is possible that such conversion occurs in the human auditory system. The tuning of rate-based responses may imply a more complicated form of ringing that would be insensitive to the phase of modulation. Thus, the lack of phase effects in forward masking does not allow for unequivocal rejection of a role of persistence of the response to M_{AM} beyond the physical offset of that modulation.

D. "Additivity" of AM forward masking

It is sometimes useful to use a simple model of channel processing such as the envelope power spectrum model (EPSM) proposed by Ewert and Dau (2000). When applied to simultaneous-masking data, the model does not produce accurate predictions when temporal cues (such as beats between modulation components or enhanced local modulation depth in the troughs of the masker AM) can be used to improve detection. Those temporal cues are not available in forward masking, and thus one might expect that a spectral model of AM processing could be more successful in accounting for forward-masking data.

The envelope power spectrum model assumes that the detection of a certain signal AM rate is determined by the

total power of envelope components that are processed by the modulation filter tuned to the signal rate. Comparing the amount of forward masking produced by the 100% (0-dB) 40-Hz AM in experiment 1 with that produced by the 50% (−6 dB) AM of the same rate in experiment 3 suggests a decrease in the amount of forward masking with decreasing power of the masker. The EPSM would predict such a decrease. If the system were linear, then combining two equally effective maskers should produce a 3-dB increase in the masked threshold. This was not observed in experiment 3, where thresholds for the 32- and 40-Hz masker presented separately did not differ significantly, and, yet, combining the two maskers did not lead to an increase in the masked threshold. Thus, a model assuming the integration of envelope power within a modulation filter cannot predict the data from experiment 3.

Two listeners showed a decrease in the amount of forward masking when an off-frequency modulation producing very little or no masking on its own was added to the 40-Hz masker modulation. One explanation for this effect is in terms of temporal confusion. As mentioned in the introduction to experiment 1, forward masking at short delays may be elevated due to the listener's inability to temporally separate the masker from the signal. A pure tone presented during the masker modulation in experiment 1 produced only a slight improvement (1–2 dB) in performance at the shortest delays. It is likely that in the case of two modulation maskers combined, the high-frequency modulation also provides a cue by changing the percept of the masker AM and making it less similar to the signal AM. One might argue that modulations with very low rates should provide a similar cue that would lead to an improvement in signal detection, but this is not seen in the data in Figs. 7–9. In that case, however, listeners reported being able to hear the low-frequency modulation and the 40-Hz modulation as separate. This may result from the fact that the two modulations produce percepts that fall into separate categories, temporal following for the low rate, and roughness for the higher rate (Wright and Dai, 1998). Consequently, the low-frequency AM does not change the percept of the 40-Hz AM enough to eliminate confusion between the masker and the signal. In contrast, high off-frequency rates produce a percept that falls into the same category as that produced by the 40-Hz rate. Listeners reported that when the 128 or 256 Hz are combined with the 40-Hz AM, the 40-Hz modulation component could not be heard out separately, and thus the combined masker led to a percept that was dissimilar from the signal AM. The explanation based on a reduction of temporal confusion is supported by the fact that listener S3, whose performance for the 40-Hz masker alone was the best, did not show an improvement when a modulation that could help distinguish between the signal and masker AM was presented with the 40-Hz AM. For the other two listeners, no improvement was observed when the masker-signal delay was increased to 30 ms.

Another explanation is in terms of inhibition of the response to the 40-Hz AM by a higher-rate AM. Physiological measurements show that neurons at more central processing sites can respond strongly to a relatively narrow range of modulation rates, but the response of the same neurons shows strong inhibition when they are stimulated by other rates (Krishna and Semple, 2000). Although Krishna and Semple did not stimulate their neurons by two modulation rates simultaneously, it is plausible that in the case of simultaneous stimulation by a rate that produces a strong response and by an inhibitory rate, the resulting response would be reduced. Since the decrease in threshold for S1 and S2 depended on the masker-signal delay, the explanation based on inhibition is less likely.

E. Final remarks

The mechanisms underlying AM forward masking are uncertain, especially since the mechanisms involved in AM coding have not been determined. One possible explanation could be in terms of the adaptation of neurons responding to AM. A recent physiological study by Bartlett and Wang (2005) found an effect of prior exposure to AM on subsequently presented AM of the same and different rates in cortical responses of marmoset monkeys. Although AM durations they used were longer than those in the experiments conducted within this study (from 500 to 2500 ms), the data are consistent with the adaptation as a mechanism underlying forward masking in modulation processing. Bartlett and Wang found that for equal masker and signal rates, cortical responses to the ensuing AM were strongly suppressed, with the strength of that suppression decreasing as the temporal separation between the two modulations increased. They also observed the tuning of that effect. The apparent similarity between their and our data has to be treated with caution since the parameters of the stimuli were very different, and in their study the carrier was gated with each modulation, which was not the case in our experiments. No other physiological studies that would allow more elaborate speculations are available at present.

VI. SUMMARY

The observed results can be summarized as follows.

(1) Data from our experiments demonstrate an effect analogous to forward masking observed for auditory frequencies. The sensitivity to AM is substantially decreased following even a relatively brief exposure to AM of the same (or similar) rate.
(2) The function fitted to the signal modulation depth at threshold plotted against a linear delay between the masker and signal AM reveals exponential recovery from forward masking with the time constants falling in the range between 56 and 111 ms, for the four subjects used in the study.
(3) The AM forward masking effect shows tuning. The tuning appears to be broader than that observed in the simultaneous masking of AM. The broader tuning might result from the unavailability of cues based on local temporal features and modulation distortion products that may facilitate the detection of signal AM in simultaneous masking. The tuning does not depend on the signal modulation rate over a range of rates studied (20–80 Hz).

(4) The tuning is consistent with processing AM by rate-selective modulation channels and with a notion that neural activity in such channels adapts or persists after the offset of the AM that has stimulated the channel.
(5) For a single-rate AM, a 50% AM produces less forward masking of the same rate than a 100% AM, suggesting a monotonic relationship between the power of the masker and the amount of masking. Surprisingly, combining two equally effective masker AMs does not produce an increase in the amount of forward masking relative to that observed for either of the component maskers alone. This result is inconsistent with predictions by an envelope power spectrum model.

ACKNOWLEDGMENTS

We thank the editor Gerald Kidd, Jr., and two anonymous reviewers for their helpful comments on an earlier version of this paper. This work was supported by NIH/NIDCD Grant No. DC00683 and Grant No. DC006804.

[1]Masked-threshold patterns were first measured at a delay of 20-ms for all listeners and all rates of S_{AM}. When for the same (or similar) rates of S_{AM} and M_{AM}, the masked threshold could not be measured at the 20-ms delay due to the listener's inability to detect the signal at a 0-dB modulation depth, a delay longer by 10 ms was used. This was done because attenuation functions could not be derived without estimating the peak of the masking function. For those short delays, data points (not shown) were obtained for masker rates that did not produce the maximum amount of masking. A visual comparison of the shape of the attenuation functions measured at 20 ms with those measured at 30 or 40 ms shown in Fig. 4, suggests a parallel shift of the attenuation functions with increasing masker-signal delay. A parallel shift implies that the rate of recovery is independent of the stimulating modulation rate.

Bacon, S. P., and Grantham, W. D. (**1989**). "Modulation masking: Effects of modulation frequency, depth, and phase," J. Acoust. Soc. Am. **85**, 1575–2580.
Bartlett, E. L., and Wang, X. (**2005**). "Long-lasting modulation by stimulus context in primate auditory cortex," J. Neurophysiol. **94**, 83–104.
Cooper, N. P., Robertson, D., and Yates, G. K. (**1993**). "Cochlear nerve fiber responses to amplitude-modulated stimuli: variations with spontaneous rate and other response characteristics," J. Neurophysiol. **70**, 370–386.
Dau, T., Kollmeier, B., and Kohlrausch, A. (**1997a**). "Modeling auditory processing of amplitude modulation. I. Detection and masking with narrow-band carriers," J. Acoust. Soc. Am. **102**, 2892–2905.
Dau, T., Kollmeier, B., and Kohlrausch, A. (**1997b**). "Modeling auditory processing of amplitude modulation. II. Spectral and temporal integration," J. Acoust. Soc. Am. **102**, 2906–2919.
Ewert, S. D., and Dau, T. (**2000**). "Characterizing frequency selectivity for envelope fluctuations," J. Acoust. Soc. Am. **108**, 1181–1196.
Ewert, S. D., Verhey, J. L., and Dau, T. (**2002**). "Spectro-temporal processing in the envelope-frequency domain," J. Acoust. Soc. Am. **112**, 2921–2931.
Frisina, R. D., Smith, R. L., and Chamberlain, S. C. (**1990**). "Encoding of amplitude modulation in the gerbil cochlear nucleus. II. Possible neural mechanisms," Hear. Res. **44**, 123–142.
Füllgrabe, C., Moore, B. C. J., Ewert, S. D., Sheft, S., and Lorenzi, C. (**2005**). "Modulation masking produced by second-order modulators," J. Acoust. Soc. Am. **117**, 2158–2168.
Grimault, N., Bacon, S., and Micheyl, S. (**2002**). "Auditory stream segregation on the basis of amplitude-modulation rate," J. Acoust. Soc. Am. **111**, 1340–1348.
Hedrick, M. S., and Carney, A. E. (**1997**). "Effect of relative amplitude and formant transitions on perception of place of articulation by adult listeners with cochlear implants," J. Speech Lang. Hear. Res. **40**, 1445–1457.
Hedrick, M. S., and Jesteadt, W. (**1996**). "Effect of relative amplitude, presentation level, and vowel duration on perception of voiceless stop consonants by normal and hearing-impaired listeners," J. Acoust. Soc. Am. **100**, 3398–3407.
Houtgast, T. (**1989**). "Frequency selectivity in amplitude-modulation detection," J. Acoust. Soc. Am. **85**, 1676–1680.
Joris, P. X., Schreiner, C. E., and Rees, A. (**2004**). "Neural processing of amplitude-modulated sounds," Physiol. Rev. **84**, 541–577.
Kay, R. H., and Matthews, D. R. (**1972**). "On the existence in human auditory pathways of channels selectively tuned to the modulation present in frequency modulated tones," J. Physiol. (London) **225**, 625–667.
Kohlrausch, A., Fassel, R., and Dau, T. (**2000**). "The influence of carrier level and frequency on modulation and beat-detection thresholds for sinusoidal carriers," J. Acoust. Soc. Am. **108**, 723–734.
Krishna, B. S., and Semple, M. N. (**2000**). "Auditory temporal processing: Responses to sinusoidally amplitude-modulated tones in the Inferior Colliculus," J. Neurophysiol. **84**, 255–273.
Kwon, B. J., and Turner, C. W. (**2001**). "Consonant identification under maskers with sinusoidal modulations: Masking release or modulation interference," J. Acoust. Soc. Am. **110**, 1130–1140.
Langner, G., and Schreiner, C. (**1988**). "Periodicity coding in the inferior colliculus of the cat. I. Neuronal mechanisms," J. Neurophysiol. **60**, 1799–1822.
Levitt, H. (**1971**). "Transformed up–down methods in psychoacoustics," J. Acoust. Soc. Am. **49**, 467–477.
Liang, L., Lu, T., and Wang, X. (**2002**). "Neural representations of sinusoidal amplitude and frequency modulations in the auditory cortex of awake primates," J. Neurophysiol. **87**, 2237–2261.
Lorenzi, C. (2004). personal communication.
Middlebrooks, J. C. (2005). "Transmission of temporal information from a cochlear implant to the auditory cortex," XXVIII Midwinter Research Meeting of ARO, Abstract No. 253.
Moody, D. B., Cole, D., Davidson, L. M., and Stebbins, W. C. (**1984**). "Evidence for a reappraisal of the psychophysical selective adaptation paradigm," J. Acoust. Soc. Am. **76**, 1076–1079.
Moore, B. C. J., and Glasberg, B. R. (**1982**). "Contralateral and ipsilateral cuing in forward masking," J. Acoust. Soc. Am. **71**, 942–945.
Moore, B. C. J., Sek, A., and Glasberg, B. R. (**1999**). "Modulation masking produced by beating modulators," J. Acoust. Soc. Am. **106**, 908–918.
Neff, D. L. (**1985**). "Stimulus parameters governing confusion effects in forward masking," J. Acoust. Soc. Am. **78**, 1966–1976.
Neff, D. L. (**1986**). "Confusion effects with sinusoidal and narrow-band noise forward maskers," J. Acoust. Soc. Am. **79**, 1519–1529.
Nelson, D. A., and Donaldson, G. S. (**2002**). "Psychophysical recovery from pulse-train forward masking in electric hearing," J. Acoust. Soc. Am. **112**, 2932–2947.
Nelson, D. A., and Freyman, R. L. (**1987**). "Temporal resolution in sensorineural hearing-impaired listeners," J. Acoust. Soc. Am. **81**, 709–720.
Plack, C. J., and Oxenham, A. J. (**1998**). "Basilar-membrane nonlinearity and the growth of forward masking," J. Acoust. Soc. Am. **103**, 1598–1608.
Rees, A., and Møller, A. R. (**1983**). "Responses of neurons in the inferior colliculus of the rat to AM and FM tones," Hear. Res. **10**, 301–310.
Regan, D., and Tansley, B. W. (**1979**). "Selective adaptation to frequency-modulated tones: Evidence for an information-processing channel selectively sensitive to frequency changes," J. Acoust. Soc. Am. **65**, 1249–1257.
Rhode, W. S., and Greenberg, S. (**1994**). "Encoding of amplitude modulation in the cochlear nucleus of the cat," J. Neurophysiol. **71**, 1797–1825.
Richards, V. M., Buss, E., and Tian, L. (**1997**). "Effects of modulator phase for comodulation masking release and modulation detection interference," J. Acoust. Soc. Am. **102**, 468–476.
Roberts, B., Glasberg, B. R., and Moore, B. C. J. (**2002**). "Primitive stream segregation of tone sequences without differences in F0 or passband," J. Acoust. Soc. Am. **112**, 2074–2085.
Schulze, H., and Langner, G. (**1999**). "Auditory cortical responses to amplitude modulations with spectra above frequency receptive fields: evidence for wide spectral integration," J. Comp. Physiol. [A] **185**, 493–508.
Sek, A., and Moore, B. C. J. (**2002**). "Mechanisms of modulation gap detection," J. Acoust. Soc. Am. **111**, 2783–2792.
Sheft, S. (2000). "Adaptation to amplitude modulation," XXIII Midwinter Research Meeting of ARO, Abstract No. 5058.
Sheft, S., and Yost, W. A. (**1990**). "Temporal integration in amplitude modulation detection," J. Acoust. Soc. Am. **88**, 796–805.
Shofner, W. P., Sheft, S., and Guzman, S. J. (**1996**). "Responses of ventral cochlear nucleus units in the chinchilla to amplitude modulation by low-

frequency two-tone complexes," J. Acoust. Soc. Am. **99**, 3592–3605.
Strickland, E. A., and Viemeister, N. F., (**1996**). "Cues for discrimination of envelopes," J. Acoust. Soc. Am. **99**, 3638–3646.
Takahashi, G. A., and Bacon, S. P., (**1992**). "Modulation detection, modulation masking, and speech understanding in noise in the elderly," J. Speech Hear. Res. **35**, 1410–1421.
Tansley, B. W., and Suffield, J. B., (**1983**). "Time course of adaptation and recovery of channels selectively sensitive to frequency and amplitude modulation," J. Acoust. Soc. Am. **74**, 765–775.
van Tasell, D. J., Soli, S. D., Kirby, V. M., and Widin, G. P., (**1987**). "Speech waveform envelope cues for consonant recognition," J. Acoust. Soc. Am. **82**, 1152–1161.
Viemeister, N. F., (**1979**). "Temporal modulation transfer functions based upon modulation thresholds," J. Acoust. Soc. Am. **66**, 1364–1380.
Wakefield, G. H., and Viemeister, N. F., (**1984**). "Selective adaptation to linear frequency-modulated sweeps: evidence for direction-specific FM channels?," J. Acoust. Soc. Am. **75**, 1588–1592.
Wang, X., and Sachs, M. B., (**1993**). "Neural encoding of single-formant stimuli in the cat. I. Responses of auditory nerve fibers," J. Neurophysiol. **70**, 1054–1075.
Wojtczak, M., and Viemeister, N. F., (**2003**). "Suprathreshold effects of adaptation produced by amplitude modulation," J. Acoust. Soc. Am. **114**, 991–997.
Wright, B. A., and Dai, H., (**1998**). "Detection of sinusoidal amplitude modulation at unexpected rates," J. Acoust. Soc. Am. **104**, 2991–2996.

The temporal effect in listeners with mild to moderate cochlear hearing impairment[a)]

Elizabeth A. Strickland[b)] and Lata A. Krishnan
Department of Speech, Language and Hearing Sciences, Purdue University, West Lafayette, Indiana, 47907

(Received 29 March 2005; revised 27 July 2005; accepted 22 August 2005)

This study examines the relationship between a temporal masking effect and cochlear hearing impairment. The threshold level of a long-duration broadband masker needed to mask a short-duration tonal signal was measured for signals presented 2 ms (short-delay) or 202 ms (long-delay condition) after masker onset. The difference between these thresholds is the temporal effect. In two previous studies with normal-hearing listeners, estimates of gain of the cochlear active process derived from such data suggested a decrease in gain during the course of the masker. This hypothesis was further examined in the present study by testing listeners with mild to moderate cochlear hearing impairment. Results are consistent with a decrease in gain in the short-delay condition with increasing hearing impairment, and also less change in gain with increasing hearing impairment. © *2005 Acoustical Society of America.* [DOI: 10.1121/1.2074787]

PACS number(s): 43.66.Mk, 43.66.Dc, 43.66.Ba, 43.66.Sr [JHG] Pages: 3211–3217

I. INTRODUCTION

Under certain conditions, a brief tone may be more difficult to detect when it is presented at the onset of a masker than when it is delayed from the onset of the masker. This has been referred to as "overshoot" (Zwicker, 1965; Elliott, 1965) or the temporal effect (Wright, 1995). The term temporal effect will be used here. Although the temporal effect may well be due to processes at several levels of the auditory system, it has been of particular interest of late because of evidence that it may be partially due to a decrease in the gain of the cochlear active process during acoustic stimulation.

Evidence for this hypothesis comes from studies showing reductions in the temporal effect subsequent to temporary hearing loss induced by noise exposure (Champlin and McFadden, 1989) and aspirin use (McFadden and Champlin, 1990; Bacon and Hicks, 2000). McFadden and Champlin (1990) also tested the effect of shifting thresholds with a background noise; however, this did not affect the temporal effect as did the use of aspirin or the induced temporary threshold shift, suggesting that the cochlear amplifier had to be altered.

Further evidence for the role of cochlear gain in the temporal effect comes from studies of listeners with permanent cochlear hearing loss. In general, studies with hearing-impaired listeners have shown a reduced temporal effect with pure-tone maskers (Bacon *et al.*, 1988; Kimberly and Nelson, 1989) and broadband maskers (Bacon and Takahashi, 1992). In contrast to the preceding studies, Carlyon and Sloan (1987) evaluated the temporal effect in six listeners with unilateral or asymmetric hearing impairment and reported that the temporal effect was not influenced significantly by the hearing impairment. However, they used a single high masker level. Since the temporal effect varies with signal and masker level (e.g., Bacon, 1990), the high level used may not have shown the maximum amount of temporal effect. In addition, while two of their six listeners had normal hearing in one ear, the other four listeners had bilateral hearing loss. Examination of their data reveals that three of their six listeners did indeed demonstrate a reduced temporal effect in the poorer ear; while all of their listeners (including those with normal hearing) demonstrated a very small temporal effect, possibly due to the choice of masker level.

The relationship between the temporal effect and the active process was examined in a different way by von Klitzing and Kohlrausch (1994), by measuring the temporal effect across a range of signal and masker levels. They noted that the change in threshold signal-to-masker ratio with masker level in the short-delay condition could reflect the input-output characteristics of the basilar membrane (BM). For a tone presented at the characteristic frequency of a given place on the BM, this input-output function can be divided into three regions: at low levels, up to about 40 dB SPL, the response has a slope near one; at intermediate levels from about 40 to 80 dB SPL, the response is strongly compressive; and at high levels above 80 dB SPL, the response may become steeper again. They noted that the temporal effect tends to be seen for short-duration signals, when the signal level at threshold is considerably higher than the masker level. Suppose a signal at less than 40 dB SPL can be detected at a certain signal-plus-masker to masker ratio. If the signal level is increased, it will be on the compressive part of the function, and so the output level will increase at a slower rate than the output level of the masker, which is still on the lower part of the function. Therefore the signal-plus-masker to masker ratio should increase at mid levels. In the long-delay condition, this hypothesis would suggest that the input-output function becomes more linear, because the

[a)]Portions of this paper were presented at the Twenty-Third Midwinter Meeting of the Association for Research in Otolaryngology, February 2003.
[b)]Electronic mail: estrick@purdue.edu

TABLE I. Audiometric thresholds (dB HL) of hearing-impaired listeners. Test frequency thresholds shown in bold. For L4, two frequencies at which hearing thresholds were normal were also tested.

Listener	Ear	Age	250	500	1000	2000	3000	4000	6000	8000	Type of loss
L1	R	30	15	10	5	10	5	20	25	15	Notched
L2	L	51	5	20	20	20	10	**30**	20	15	Notched
L3	L	53	10	5	5	10	10	**20**	15	35	Sloping
L3	R	53	30	20	20	15	50	**50**	55	60	Sloping
L4	L	44	10	5	10	15	**5**	15	5	5	Normal
L4	R	44	5	5	5	10	**20**	15	**10**	0	Notched
L5	R	73	15	20	25	30		**35**		35	Sloping
L6	L	53	0	0	5	5	15	25	25	30	Sloping
L6	R	53	0	5	5	15	15	20	**30**	35	Sloping
L7	L	54	10	10	10	15	30	**55**	55	45	Sloping
L7	R	54	10	10	10	15	20	**25**	40	45	Sloping
L8	L	51	5	15	5	10		**25**		25	Sloping

signal-to-noise ratio at threshold becomes more constant. Strickland (2001, 2004) tested this idea quantitatively for normal-hearing listeners, by fitting input-output functions to data measured at a range of signal and masker levels, assuming a constant signal-plus-masker to masker ratio at the output. Input-output functions fit to the data had lower gain in the long-delay condition than in the short-delay condition.

The purpose of the present study was to evaluate the temporal effect in listeners with cochlear hearing impairment using this same technique. In the above-reported studies, when the masker was a broadband noise, temporary and permanent cochlear hearing loss caused a decrease in the signal-to-noise ratio at threshold in the short-delay condition, but not in the long-delay condition.[1] This would be consistent with a decrease from the normal amount of gain in the short-delay condition. In this study, signal levels from near threshold to 90-95 dB SPL will be used, so that input-output functions may be estimated from the data. Previous studies with hearing-impaired listeners have utilized single (Carlyon and Sloan, 1987, Bacon *et al.*, 1988) or few (Bacon and Takahashi, 1992) masker levels. The use of input-output functions will also allow the examination of small changes in the temporal effect in listeners with milder degrees of hearing impairment. Previous studies have tended to use listeners with moderate degrees of hearing impairment, to look for clear differences from normal data.

II. METHODS

A. Subjects

Eight listeners with cochlear hearing impairment participated in the study. Cochlear hearing impairment was determined using a test battery. To qualify for the study, listeners had to have air conduction hearing thresholds outside the normal range ($>$15 dB HL) at least at one audiometric frequency in at least one ear, with no significant difference between air conduction and bone conduction thresholds. Tympanometric results had to indicate a type A (normal) tympanogram, and acoustic reflex thresholds had to be consistent with the hearing level. Retrocochlear involvement was ruled out in listeners with asymmetric hearing loss using an auditory brainstem response evaluation. Both ears of three listeners were evaluated for a total data set from eleven ears at frequencies with hearing impairment. One listener (L4) was also evaluated at frequencies at which he had normal hearing. Listeners had hearing thresholds ranging from 0 to 60 dB HL (normal at certain frequencies to a moderate sensory hearing loss at other frequencies: see Table I). The pattern of hearing impairment with frequency was categorized as sloping or notched based on the pattern of thresholds across frequency. Listeners with sloping hearing losses (eight ears) showed hearing thresholds increasing with increasing frequency above 3000 Hz. Listeners with notched hearing impairment (three ears) had normal or near-normal hearing in the low to mid frequencies (500–2000 Hz) and an increase in thresholds at 3000–6000 Hz with recovery to normal thresholds (15 dB HL or less) at 8000 Hz. Audiometric thresholds at the experimental frequency ranged from 5 to 55 dB HL. Listeners ranged in age from 30 to 73 years and there were five male and three female listeners. All listeners were paid for their participation. Two listeners were excluded from the investigation: one who demonstrated large variability in responses (standard deviations $>$5 dB) and another who had a mild unilateral notched hearing impairment at 2000 Hz and demonstrated no temporal effect at this frequency even in his normal-hearing ear.

B. Stimuli

The signal was a sinusoid with a frequency of 3, 4, or 6 kHz. The signal frequency was chosen for each individual listener so that it would be in a region of hearing loss. One listener was also tested at two normal frequencies as a control. The duration of the signal was 10 ms including 5-ms $\cos^2$ onset and offset ramps. This duration was chosen to be brief, yet long enough to preclude the effects of spectral splatter (Bacon and Viemeister, 1985). The masker was a flat-spectrum broadband noise with a bandwidth of 0.2 f to 1.8 f, where f is the signal frequency. The masker duration was 200 ms (short-delay condition) or 400 ms (long-delay condition) including 5-ms $\cos^2$ onset and offset ramps. The signal onset was either 2 ms after masker onset (short-delay condition) or 202 ms after masker onset (long-delay condi-

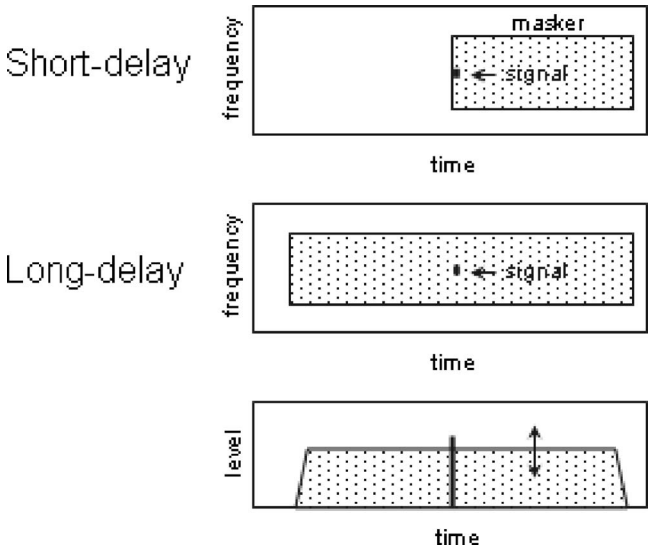

FIG. 1. Schematic showing the temporal and spectral characteristics of the masker and signal.

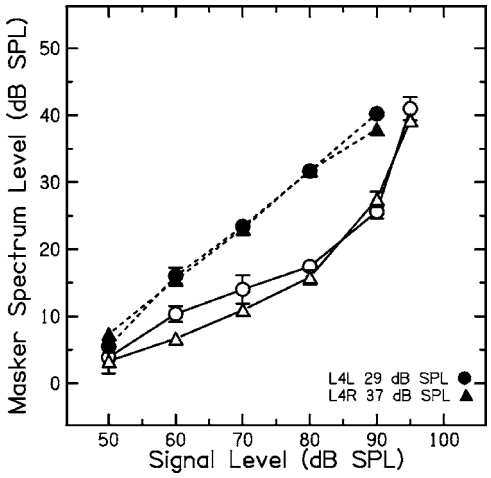

FIG. 2. Threshold masker levels at which the signal was just detectable for two ears (L4) at normal hearing frequencies. Closed circles represent the long-delay condition and open circles represent the short-delay condition. The difference between the thresholds for the two conditions is the temporal effect. Threshold for the short-duration signal is listed next to the symbols.

tion). This was done to maintain the same duration between the signal and the offset of the masker to avoid offset effects (e.g., Wright and Dai, 1994). See Fig. 1 for stimulus characteristics.

All signals and maskers were generated digitally and produced through two separate D/A channels at a rate of 25 kHz (TDT DA1). Stimuli were low-pass filtered at 10 kHz (TDT FT5 and TDT FT6-2). Signal and masker levels were adjusted by programmable attenuators (TDT PA4). Stimuli were presented through one of two Etymotic ER-2 insert earphones to the listener seated in a double-walled sound-attenuating booth.

C. Procedures

Signal levels were fixed from as low as 50 dB SPL to as high as 95 dB SPL, with the provision that the signal level had to be at least 5 dB above quiet threshold for the short-duration tone. Masker levels were varied to determine the masker level at which the signal was just detectable. Threshold masker levels were measured using a three-interval-forced-choice task with a two-up, one-down stepping rule to estimate the 71%-correct point on the psychometric function (Levitt, 1971). Listeners were given visual information regarding the timing of stimulus presentations as well as feedback regarding their responses on a computer screen. Listeners responded via a computer keyboard. The initial step size was 5 dB, and this was decreased to 2 dB after the first two reversals. Fifty trials were presented and threshold was taken as the average of the last even number of reversals at the 2-dB step size.

Previous studies in this laboratory have found that listeners do not typically show improvement with training when the masker is a broadband noise, so no training blocks were run. All listeners were first tested in the long-delay condition, to familiarize them with the procedure. Each data point is the average of two blocks of fifty trials. Blocks were discarded if the standard deviation was 5 dB or greater. Threshold masker levels obtained on the two trials from hearing-impaired listeners were within 2 dB 92% of the time.

III. RESULTS

Over the next few figures, results are shown for listeners with increasing amounts of hearing loss. In Fig. 2, the threshold masker level is plotted for the short-delay (open symbols) and long-delay (closed symbols) conditions, for signals at two frequencies at which the listener had normal hearing. The temporal effect is the difference in threshold masker level between the long-delay and short-delay conditions. As has been shown in previous studies, data for the long-delay condition are similar and approximately linear with a slope near one. Functions for the short-delay condition show a shallow slope at low signal levels, and a steep slope at high signal levels. Therefore, the temporal effect is largest at mid signal levels, with a maximum of close to 15 dB, which is consistent with previous studies (Bacon, 1990; Strickland, 2001, 2004). This figure also demonstrates that, at least for this listener, the temporal effect is similar at 3000 (L4L) and 6000 (L4R) Hz.

Figure 3 shows results for listeners with sloping hearing losses in order of increasing hearing thresholds in quiet. This figure illustrates why listeners with such mild hearing loss were recruited to the study. The first four listeners in the legend have audiometric thresholds of 20 to 25 dB HL, which are just on the borderline of what is considered the normal range. Yet these listeners clearly show a smaller temporal effect than normal. As hearing loss increases, the lowest signal level that can be tested increases, so only a few data points can be measured. Even with just a moderate hearing loss, however, the temporal effect is almost gone. Although the long-delay functions are all approximately linear with a slope near one, the functions shift slightly upward with increasing hearing loss. Thus, there are systematic changes in the short-delay and long-delay functions with increasing hearing loss.

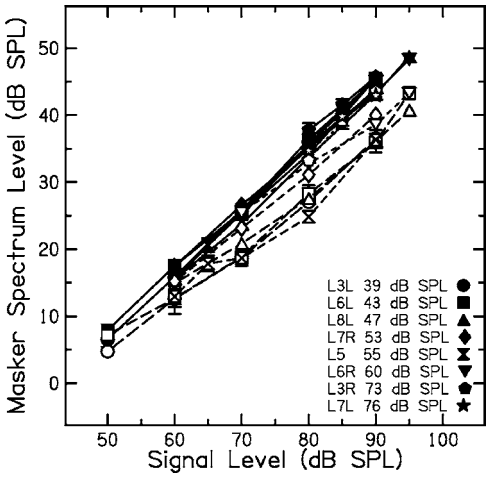

FIG. 3. Same as in Fig. 2 for eight ears (of five listeners) with sloping hearing loss.

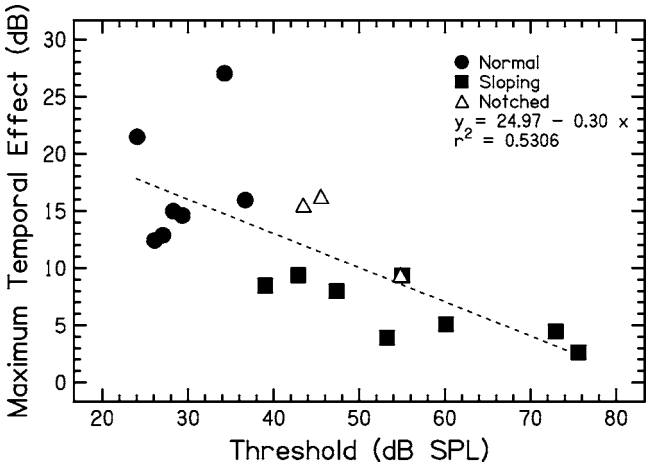

FIG. 5. The maximum temporal effect as a function of quiet threshold for the short-duration tone. The dashed line is a regression line fit to the data.

In Fig. 4, results are shown for the three listeners who had notched hearing losses. These listeners showed a small, nearly constant temporal effect for signal levels below 70 dB SPL, and then an increasing temporal effect up to a signal level of 90 dB SPL. For L2, the long-delay function had a slope steeper than one, in contrast to all of the other listeners in this and the previous figures.

In Fig. 5 the maximum temporal effect is shown as a function of hearing threshold in quiet for the short-duration tone for each listener. The maximum temporal effect was usually at a signal level of 80 dB SPL. Data from five normal-hearing listeners tested at 4000 Hz from Strickland (2001) are also included. The temporal effect tends to decrease with increasing degree of hearing loss. With a given quiet threshold, listeners with notched hearing losses tend to show a greater temporal effect than those with sloping hearing losses. As has been found in previous studies, the size of the temporal effect varies over a wide range in listeners with normal audiometric thresholds.

Measurements made at a range of signal levels allowed the data to be fit using input-output functions. Previous experiments (Strickland, 2001) have shown that data for the short- and long-delay conditions can be fit using a modification of the model of the compressive input-output function of the basilar membrane used by Glasberg and Moore (2000). Thresholds are assumed to be based on a constant internal difference between the response to the signal-plus-masker and the response to the masker alone. It is also assumed that the masker energy at or near the signal frequency dominates in masking the signal in this condition. Thus, the signal-plus-masker and the masker are assumed to follow the same input-output function at the signal frequency. The level of the masker was estimated to be the level passing through an equivalent rectangular bandwidth (ERB) filter centered at the signal frequency. The goal of the fitting procedure was to find the input-output function which produced a constant difference between the signal-plus-masker and masker levels at the output.

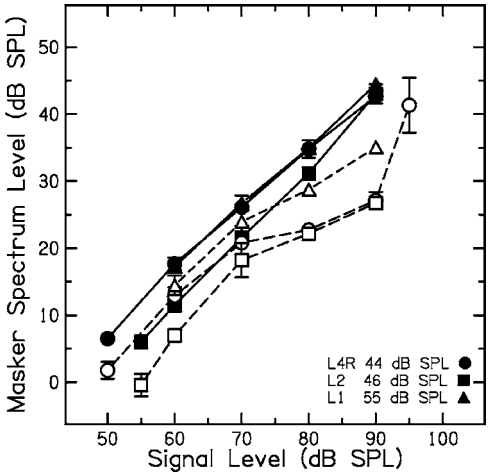

FIG. 4. Same as in Fig. 2 for three ears with notched hearing loss.

The gain formula used was

$$G_{\mathrm{dB}} = -0.1\ L + A + B(1 - (1/(1 + \exp(0.05(60 - L)))))$$

where L is the input level in dB, and

$$A = -0.1430\ G_{\max} + 11.430,$$

$$B = 1.1999\ G_{\max} - 11.999.$$

A and B depend on the maximum gain $G_{\max}$ such that G_{dB} is equal to $G_{\max}$ when $L=0$ and zero when $L=100$. The total output level, O, is equal to L plus G_{dB}.

In the fitting procedure, $G_{\max}$ was adjusted to make the difference between the output level of the signal plus masker (O_{S+M}) and the output level of the masker alone (O_M) as constant as possible across the range of signal levels. If no initial criterion was specified for this difference, however, the function would converge to an unrealistically high level of $G_{\max}$ to drive $O_{S+M} - O_M$ close to zero. Therefore, an initial estimate of $G_{\max}$ was used to fit the average normal data from Strickland (2004). The value of $G_{\max}$ for 4 kHz was set to 47.7 dB, an estimate from Glasberg and Moore (2000) in fitting data from Baker *et al.* (1998). The ERB estimates were also taken from this paper, and were 413, 453, and 717 Hz for center frequencies of 3, 4, and 6 kHz. The rms error

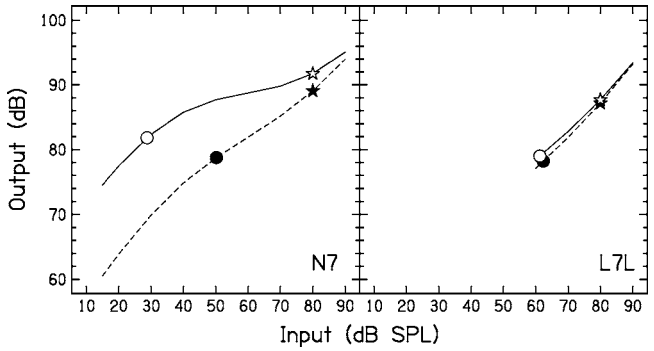

FIG. 6. Schematic illustrating input-output functions fit to data for two listeners for the short-delay and long-delay conditions. Stars represent the signal-plus-masker level, and circles the masker level. Open symbols and solid lines are the short-delay condition, and closed symbols and dashed lines the long-delay condition. Functions are only shown over the range of input levels for the signal and masker in the data.

of $O_{S+M} - O_M$ was 9.45 dB, and this was set as the criterion. In fitting all the data, the criterion was fixed, and G_{max} was allowed to vary.

Figure 6 illustrates the fitting procedure schematically for two listeners, N7 and L7L. These two listeners were chosen because they had the lowest and highest thresholds for the short-duration tone in quiet. Symbols are shown for an 80-dB SPL signal and the threshold masker level for that signal. Symbols for the short-delay condition are open, while those for the long-delay condition are closed. The functions are fit so that the difference between the signal-plus-masker and the masker level at the output is 9.45 dB for all levels, although only one signal level is shown. The solid line is the fit for the short-delay condition, and the dashed line for the long-delay condition. For a given listener and a given condition (short-delay or long-delay) a single input-output function was fit to the data for all signal levels. G_{max}, the rms error of the fit, and the difference in G_{max} between the short-delay and long-delay condition are presented in Table II. For all listeners, G_{max} in the long-delay condition is lower than G_{max} in the short-delay condition, consistent with the hypothesis that a decrease in cochlear gain may mediate the temporal effect.

If fitting the data in this way truly does reflect cochlear gain under some conditions, it would be expected that gain in the short-delay condition would decrease with increasing hearing thresholds. The regression line fit to the data was

$$\text{Short-delay gain} = 65.97 - 0.35 \times \text{threshold}$$

$$r^2 = 0.6254.$$

Estimated gain does decrease with increasing hearing threshold in quiet. The rate of decrease in gain with hearing thresholds is less than that found by Plack *et al.* (2004), who found a slope of −0.65. Gain in the Plack *et al.* study was estimated from forward masking, while in the present study it is estimated from simultaneous masking, and thus includes the effects of suppression. This may tend to decrease the highest amount of gain that will be seen.

In Fig. 7, the change in gain between the short- and long-delay conditions is shown as a function of gain in the short-delay condition. It can be seen that the change in gain decreases with decreasing short-delay gain. This is not because gain is always decreased to the same level in the long-delay condition. As can be seen in Table II, listeners with hearing impairment had lower gain than the listeners with normal hearing even in the long-delay condition. This is also

TABLE II. Results obtained using the model to fit the data from normal-hearing (Strickland, 2004) and hearing-impaired listeners. Frequencies at which L4 had normal hearing are shown in bold. The numbers for the normal-hearing listeners correspond to the numbers used in Strickland (2004). Long-delay fits are shown for two hypotheses, discussed in the text.

						Criterion held constant			Gain held constant	
Listener	Ear	Frequency	Threshold	SD gain	rms error	LD gain	rms error	Change in gain	LD criterion	rms error
N1	L	4000	28.28	57.36	1.36	46.61	1.62	10.75	6.48	1.67
N4	L	4000	26.11	51.28	1.02	43.54	1.11	7.74	7.70	1.35
N5	L	4000	27.07	52.15	1.84	47.60	1.76	4.55	9.41	1.84
N6	L	4000	34.26	64.36	1.62	48.92	1.24	15.44	4.99	1.83
N7	L	4000	24.08	64.15	1.22	49.27	1.33	14.88	4.55	1.33
L4	L	3000	**29.35**	54.56	1.87	42.67	1.38	11.89	6.26	1.33
L4	R	3000	43.45	52.47	2.30	38.50	1.35	13.97	6.15	1.34
L3	L	4000	39.01	47.17	1.31	37.60	0.97	9.57	7.32	1.06
L6	L	4000	42.88	47.94	1.88	35.11	0.81	12.83	6.69	0.92
L2	L	4000	45.50	53.79	1.89	44.48	0.63	9.31	6.89	0.85
L8	L	4000	47.38	48.87	2.30	41.27	1.23	7.60	7.76	1.42
L7	R	4000	53.25	42.88	1.46	36.61	1.28	6.27	8.07	1.30
L5	R	4000	55.04	47.08	1.67	37.16	0.63	9.92	7.11	0.81
L3	R	4000	72.95	42.40	0.55	36.37	0.86	6.03	8.31	0.89
L7	L	4000	75.64	41.67	0.90	38.75	0.52	2.92	8.94	0.56
L4	R	6000	**36.7**	53.74	1.68	39.17	1.96	14.57	5.73	1.57
L1	R	6000	54.8	43.32	2.35	31.29	1.12	12.03	7.06	1.18
L6	R	6000	60.15	44.08	2.40	37.01	1.40	7.07	8.18	1.53

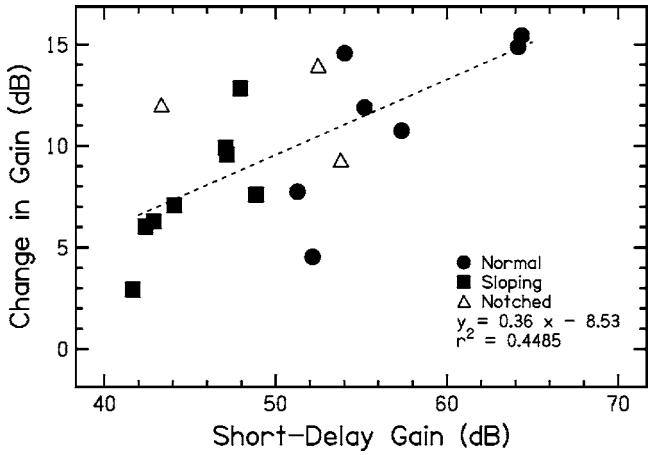

FIG. 7. The change in gain between the short- and long-delay conditions as a function of gain in the short-delay condition as estimated by the fitting of input-output functions to the data obtained from each listener. The dashed line is a regression line fit to the data.

evident in the difference between the long-delay functions seen in Fig. 3.

Even though the data fit the hypothesis that the temporal effect is consistent with a decrease in gain between the short-delay and long-delay conditions, an alternative hypothesis was considered. The difference in thresholds for the short-delay and long-delay conditions could also be produced by changing the criterion signal-plus-masker to masker ratio while keeping the gain constant. This could reflect some more central decision process. In order to test the hypothesis that the data resulted from a constant change in criterion across listeners, the long-delay data were fit again, with the gain held constant at that fit to the short-delay condition, and the criterion allowed to vary. The results are shown in the last two columns of Table II. They do not support the hypothesis of a constant change in criterion. The criterion decreased by as little as 0.04 dB to as much as 5 dB.

IV. DISCUSSION

The main findings of the present study are that the temporal effect decreases in a graded manner with increasing hearing impairment. Although previous studies have reported a decrease in the temporal effect in hearing-impaired listeners (Bacon and Takahashi, 1992), these studies did not use degree of hearing loss as a parameter and did not examine changes in the temporal effect relative to the degree of hearing impairment. The present study used a wide range of signal levels which allowed the fitting of input-output functions to the data obtained from the hearing-impaired listeners. These input-output functions demonstrate a trend for the gain of the cochlear amplifier as well as the change in gain between the long- and short-delay conditions to decrease with inreasing hearing loss.

It has been previously suggested that a mechanism for this frequency-specific decrease in gain could be feedback to the cochlea via the medial olivocochlear bundle of the efferent system (Schmidt and Zwicker, 1991; von Klitzing and Kohlrausch, 1994; Strickland, 2001, 2004). This branch of the efferent system feeds back to the outer hair cells from the level of the superior olivary complex (Warr and Guinan, 1979; Warr, 1980), and appears to decrease gain during the course of stimulation by sound, with a time constant of 50–100 ms (Liberman *et al.*, 1996). The results of the present study would be consistent with this hypothesis. A reduced change in gain with cochlear hearing impairment might be expected for two reasons. First, if there is less gain at a certain frequency region in the cochlea, there will be less afferent activity feeding into the efferent system. Second, the efferent system is also feeding back to damaged OHCs, and thus might produce less change in gain. Figure 6 supports the second hypothesis. At threshold in the short-delay condition, the masker output level is nearly the same in the normal ear, in the left panel, and the hearing-impaired ear, in the right panel. Therefore the input to the efferent system would not be substantially different in the two cases, suggesting that the reduced change in gain is due to damaged OHCs. Figure 6 also illustrates why efferent feedback might be important. As can be seen in the left panel in the short-delay condition, compression allows the auditory system to respond to a wide range of sound levels. In comparing the normal-hearing ear in the left panel to the hearing-impaired ear in the right panel, one of the costs of compression is that for a given signal level, the noise level must be lower in the normal ear than in the hearing-impaired ear. By decreasing the gain in response to ongoing noise, as seen in the left panel, the signal is detectable in a higher level of noise in the long-delay condition.

Although the results in the present study have been examined using changes in gain only at the signal frequency, this is likely an oversimplification. For listeners with approximately the same threshold at the signal frequency, those with notched hearing losses tended to have a larger temporal effect at the higher signal levels than those with sloping hearing losses. This indicates that the gain in the cochlea at frequency regions above the signal frequency plays a role in the temporal effect, which complements some previous results. Bacon *et al.* (1988) evaluated the temporal effect using tonal maskers in hearing-impaired listeners with the signal and masker at regions of normal and impaired hearing. They reported that the temporal effect was reduced when either the masker or masker and signal were in a region of hearing loss. Strickland (2004) suggested that in this condition, the masker might be suppressing the signal, and the temporal effect might reflect a decrease in gain at the masker frequency, rather than the signal frequency. It is possible that suppression plays a role even when the masker is broadband, as in the present study. Schmidt and Zwicker (1991) showed that with noise maskers, the largest temporal effect was seen when the noise encompassed frequency regions just above the critical band around the signal frequency. Taken together, the results of this and previous studies suggest that to have a maximal temporal effect, the masker must encompass frequency regions above the signal frequency, and the gain in those frequency regions must be high.

ACKNOWLEDGMENTS

We thank the editor, Chris Plack, and an anonymous reviewer for their comments. This research was supported by a grant from the Kinley Trust.

[1]The Bacon and Hicks (2000) study is an exception to this. With tonal maskers at frequencies above the signal frequency, and fixed at 80 dB, signal threshold *increased* with ingestion of aspirin, but less for the short-delay condition than for the long-delay condition. This is still consistent with a decrease in gain, but in this particular case it affects the signal more than the masker. See the lower left panel in Fig. 10 of Strickland (2001) for a schematic representation of this case.

Bacon, S. P. (**1990**). "Effect of masker level on overshoot," J. Acoust. Soc. Am. **88**, 698–702.

Bacon, S. P., Hedrick, M. S., and Grantham, D. W. (**1988**). "Temporal effects in simultaneous pure tone masking in subjects with high-frequency sensorineural hearing loss," Audiology **27**, 313–323.

Bacon, S. P., and Hicks, M. L. (**2000**). "The influence of aspirin on temporal effects in simultaneous masking with noise and tonal maskers," J. Acoust. Soc. Am. **107**, 2914–2915(A).

Bacon, S. P., and Takahashi, G. A. (**1992**). "Overshoot in normal-hearing and hearing-impaired subjects," J. Acoust. Soc. Am. **91**, 2865–2871.

Bacon, S. P., and Viemeister, N. F. (**1985**). "Simultaneous masking by gated and continuous sinusoidal maskers," J. Acoust. Soc. Am. **78**, 1220–1230.

Baker, R. J., Rosen, S., and Darling, A. M., (**1998**). "An efficient characterisation of human auditory filtering across level and frequency that is also physiologically reasonable," in Psychophysical and Physiological Advances in Hearing, edited by A. R. Palmer, A. Rees, A. Q. Summerfield, and R. Meddis (Whurr, London).

Carlyon, R. P., and Sloan, E. P. (**1987**). "The 'overshoot' effect and sensory hearing impairment," J. Acoust. Soc. Am. **82**, 1078–1081.

Champlin, C. A., and McFadden, D. (**1989**). "Reductions in overshoot following intense sound exposure," J. Acoust. Soc. Am. **85**, 2005–2011.

Elliott, L. L. (**1965**). "Changes in the simultaneous masked threshold of brief tones," J. Acoust. Soc. Am. **38**, 738–746.

Glasberg, B. R., and Moore, B. C. J. (**2000**). "Frequency selectivity as a function of level and frequency measured with uniformly exciting notched noise," J. Acoust. Soc. Am. **108**, 2318–2328.

Kimberly, B. P., and Nelson, D. A. (**1989**). "Temporal overshoot in simultaneous-masked psychophysical tuning curves from normal and hearing-impaired listeners," J. Acoust. Soc. Am. **85**, 1660–1665.

Levitt, H. (**1971**). "Transformed up-down methods in psychoacoustics," J. Acoust. Soc. Am. **49**, 467–477.

Liberman, M. C., Puria, S., and Guinan, Jr., J. J. (**1996**). "The ipsilaterally evoked olivocochlear reflex causes rapid adaptation of the 2 f1 - f2 distortion product otoacoustic emission," J. Acoust. Soc. Am. **99**, 3572–584.

McFadden, D., and Champlin, C. A. (**1990**). "Reductions in overshoot during aspirin use," J. Acoust. Soc. Am. **87**, 2634–2642.

Plack, C. J., Drga V., and Lopez-Poveda, E. A. (**2004**). "Psychophysical evidence for auditory compression at low characteristic frequencies," J. Acoust. Soc. Am. **113**, 1574–1586.

Schmidt, S., and Zwicker, E. (**1991**). "The effect of masker spectral asymmetry on overshoot in simultaneous masking," J. Acoust. Soc. Am. **89**, 1324–1330.

Strickland, E. A. (**2001**). "The relationship between frequency selectivity and overshoot," J. Acoust. Soc. Am.. **109**, 2062–2073.

Strickland, E. A. (**2004**). "The temporal effect with notched-noise maskers: Analysis in terms of input-output functions," J. Acoust. Soc. Am. **115**, 2234–2245.

von Klitzing, R., and Kohlrausch, A. (**1994**). "Effect of masker level on overshoot in running-and frozen-noise maskers," J. Acoust. Soc. Am. **95**, 2192–2201.

Warr, W. B. (**1980**). "Efferent components of the auditory system," Ann. Otol. Rhinol. Laryngol. Suppl. **89**, 114–120.

Warr, W. B., and Guinan, J. J. Jr. (**1979**) "Efferent innervation of the organ of corti: Two separate systems," Brain Res. **173**, 152–155.

Wright, B. A. (**1995**). "Detectability of simultaneously masker signals as a function of signal bandwidth for different signal delays," J. Acoust. Soc. Am. **98**, 2493–2503.

Wright, B. A., and Dai, H. (**1994**). "Detection of unexpected tones in gated and continuous maskers," J. Acoust. Soc. Am. **95**, 939–948.

Zwicker, E. (**1965**). "Temporal effects in simultaneous masking by white-noise bursts," J. Acoust. Soc. Am. **38**, 653–663.

Comparing monaural and interaural temporal windows: Effects of a temporal fringe on sensitivity to intensity differences

Mark A. Stellmack,[a] Neal F. Viemeister, and Andrew J. Byrne
Department of Psychology, University of Minnesota, Minneapolis, Minnesota 55455

(Received 27 October 2004; revised 2 August 2005; accepted 9 August 2005)

In an effort to provide a unifying framework for understanding monaural and binaural processing of intensity differences, an experiment was performed to assess whether temporal weighting functions estimated in two-interval monaural intensity-discrimination tasks could account for data in single-interval interaural intensity-discrimination tasks. In both tasks, stimuli consisted of a 50-ms burst of noise with a 5-ms probe segment at temporal positions ranging between the onset and offset of the overall stimulus. During the probe segment, one monaural interval or binaural channel of each trial contained an intensity increment and the other contained a decrement. Listeners were instructed to choose the interval/channel containing the increment. The pattern of monaural thresholds was roughly symmetrical (an inverted U) across temporal position of the probe but interaural thresholds were substantially higher for a brief time interval following stimulus onset. A two-sided exponential temporal window fit to the monaural data accounted for the interaural data well when combined with a post-onset-weighting function that described greatest weighting of binaural information at stimulus onset. A second experiment showed that the specific procedure used in measuring fringed interaural-intensity-difference-discrimination thresholds affects thresholds as a function of fringe duration and influences the form of the best-fitting post-onset-weighting function. © *2005 Acoustical Society of America.* [DOI: 10.1121/1.2047247]

PACS number(s): 43.66.Pn, 43.66.Mk, 43.66.Fe [AK] Pages: 3218–3228

I. INTRODUCTION

The temporal resolution of the auditory system is limited in that the system smoothes rapid fluctuations in intensity. One manifestation of this smoothing is that the just-detectable change in intensity of a tonal or noise pedestal increases as the duration of the change decreases. This limitation in temporal resolution can be modeled as a temporal window that integrates intensity information over a brief time interval. A number of attempts have been made to characterize the duration and shape of the temporal window on the basis of data for monaural detection of a click in noise (e.g., Penner *et al.*, 1972; Penner and Cudahy, 1973), monaural tone-in-noise detection data (e.g., Moore *et al.*, 1988; Plack and Moore, 1990) and monaural intensity-discrimination data (e.g., Oxenham, 1997). The temporal window often is modeled as asymmetrical in order to account for differences in the influence of information that precedes and follows the signal or intensity change to be detected. While models incorporating temporal windows have been used to account for the results of various detection and discrimination tasks such as those just cited, the parameters of the best-fitting temporal window depend on the specific task.

Temporal resolution for changes in the interaural intensity difference carried by a stimulus also is limited (Grantham, 1984; Zurek, 1980; Bernstein *et al.*, 2001). In conditions similar to the monaural increment- and decrement-detection studies just described, Zurek (1980) and Akeroyd and Bernstein (2001) measured the sensitivity of listeners to changes in the binaural information of a 5-ms burst of broadband noise that was embedded in an otherwise-diotic 50-ms noise burst (their "Both-fringe" conditions). In both sets of results, sensitivity to changes in either the interaural time difference (ITD) or interaural intensity difference (IID) of the probe segment was greatly diminished when the onset of the probe segment occurred just after and within about 10 ms of the overall stimulus onset. In separate conditions, Akeroyd and Bernstein (2001) presented a 5-ms probe that was either preceded or followed by a diotic noise of varying duration (a forward or backward fringe; their "Forward-only" and "Backward-only" conditions) such that the probe occurred at the offset or onset of the overall stimulus. In both cases, they found that sensitivity to changes in the binaural information of the probe decreased with increasing duration of the diotic forward or backward fringe. Akeroyd and Bernstein were able to fit their data and those of Zurek with a model that consisted of a combination of a temporal window and a post-onset-weighting function that described a decrease in the weighting of information following the onset of the stimulus, although different best-fitting parameter values were estimated in order to account for the two sets of data. Furthermore, while Zurek posited that sensitivity to changes in the interaural configuration of the probe segment was determined only by the diotic noise that preceded the probe, the data of Akeroyd and Bernstein as well as their model results showed that processing of the binaural information carried by the probe was influenced by diotic portions of the stimulus that both preceded and followed the probe.

[a]Electronic mail: stell006@umn.edu

The present study, motivated by the study of Akeroyd and Bernstein (2001), seeks to determine whether a relationship exists between sensitivity to changes in the IID of a brief segment of a stimulus like that described earlier and sensitivity to changes in the monaural intensity of a stimulus with similar temporal characteristics, or more specifically, whether a common set of weighting functions can account for data gathered in the two listening conditions. The comparison is made using data gathered in a two-interval monaural intensity-discrimination task and a single-interval IID-discrimination task. Stellmack *et al.* (2004) observed that monaural and interaural comparisons of intensity both exhibit Weber's law for broadband noise and the near-miss to Weber's law for pure tones when monaural and binaural performance is measured using procedures that facilitate direct comparison of the data. The underlying assumption was that monaural intensity-discrimination thresholds measured in a two-interval forced-choice procedure and IID-discrimination thresholds measured in a single-interval task involve the presentation of equal amounts of information on each trial. Both procedures present two samples of intensity to the listener on each trial, samples that are separated in time in the monaural task and separated across ears in the binaural task. As a result, the presumed decision statistics in the two tasks are identical. [Unlike the Akeroyd and Bernstein (2001) study, ITD-discrimination thresholds were not measured in the present study.] It will be seen that a temporal window alone accounts well for the monaural intensity-discrimination thresholds while a temporal window with the same parameters combined with a weighting function that described greatest weighting of binaural information at stimulus onset yielded good predictions of the binaural intensity-discrimination thresholds. This yields a simple framework for understanding the relationship between the auditory processing that underlies the monaural and binaural intensity-discrimination tasks. A second experiment described in the following assesses the effects of procedural differences between the present study and those of Zurek (1980) and Akeroyd and Bernstein (2001) in order to attempt to account for differences between the weighting functions derived for the various sets of data.

II. EXPERIMENT 1: MONAURAL AND INTERAURAL TEMPORAL WINDOWS

A. Methods

The temporal and spectral characteristics of the binaural stimuli were similar to those in the "Both-fringe" conditions of Akeroyd and Bernstein (2001) and the stimulus envelopes are depicted in the upper portion of Fig. 1. In the single-interval binaural procedure used here, the signal was a 50-ms burst of broadband noise that was diotic except for a 5-ms probe segment that carried a nonzero IID. Listeners were instructed to indicate whether the IID of the probe on each trial favored the left or right ear. (In contrast, Akeroyd and Bernstein used a multi-interval procedure in which listeners discriminated diotic stimuli from dichotic stimuli.) The IID in the probe segment was produced by decrementing the intensity of the signal in one ear and incrementing the intensity at the other ear during the probe segment (relative to the fringe), with the ear receiving the incremented probe chosen randomly from trial-to-trial.

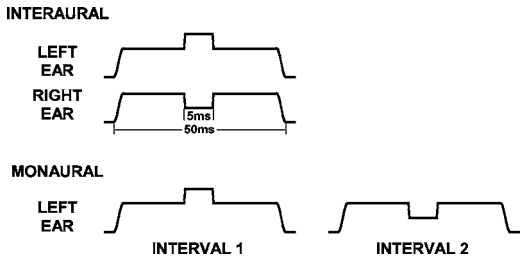

FIG. 1. A schematic illustration of the envelopes of the stimuli (noise bursts) presented in the IID-discrimination task (upper portion) and monaural intensity-discrimination conditions (lower portion). Stimuli are not drawn to scale. See the text for a complete description.

The envelopes of the stimuli presented in the two-interval monaural intensity-discrimination procedure are depicted in the lower portion of Fig. 1. The monaural condition can be considered as a situation in which the left- and right-ear stimuli of the binaural condition were presented to only the left ear in two separate temporal intervals of each trial. The interval that contained the incremented probe was varied randomly from trial-to-trial and the listeners' task was to identify which interval contained the intensity increment.

For each stimulus presentation, a 50-ms broadband noise signal was generated in the frequency domain by drawing amplitudes from a Rayleigh distribution and starting phases from a uniform distribution for all components below 8 kHz. A time-domain signal was produced by applying an inverse fast Fourier transform (FFT) to the resulting spectrum. Cosine-squared ramps, 1 ms in duration, were applied to the onset and offset of each noise signal. Thresholds were measured for forward-fringe durations of 0, 0.5, 1, 2.5, 5, 7.5, 10, 15, 20, 25, 30, 35, 40, and 45 ms. (In this paper, the term "forward fringe" refers to temporal portions of the stimulus that precede the probe while "backward fringe" refers to portions that follow the probe.) In each case, the duration in milliseconds (ms) of the backward fringe was computed as follows: overall duration of stimulus (50 ms) minus probe duration (5 ms) minus forward-fringe duration. (The exact durations described could not be achieved because of the 44.1-kHz sample rate. As a result, the durations of the forward fringe, probe, backward fringe, and ramps in ms were rounded up to the duration corresponding to the nearest integer number of samples.) No ramps were applied to the onset or offset of the 5-ms probe segment (unless those coincided with ramps at the onset or offset of the entire 50-ms signal).

The difference in intensity between the incremented and decremented probe segments was varied adaptively from trial-to-trial using a three-down-one-up procedure designed to track to the 79.4% correct point on the psychometric function (Levitt, 1971). The intensity difference between the incremented and decremented probe segments was expressed in decibels (dB) relative to the intensity of the decrement $[10 \log(\Delta I/I)]$. These units were chosen because they commonly are used to express monaural intensity-discrimination thresholds. Furthermore, because there is no absolute zero in

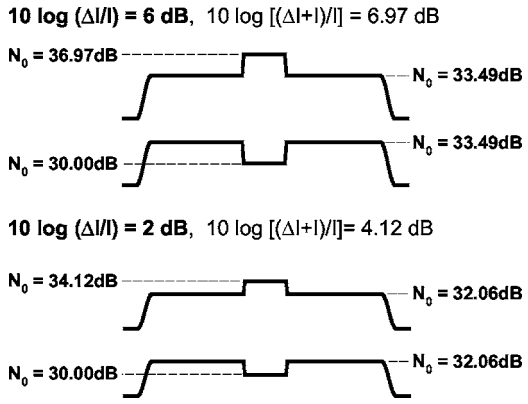

FIG. 2. A schematic illustration of how levels were determined for two different signal levels, $10\log(\Delta I/I)=6$ dB (upper portion) and 2 dB (lower portion). The absolute level of the decrement was held constant and the levels of the fringe and increment were adjusted based on the signal level determined by the adaptive procedure.

these units as there is for the dB difference between intensities $\{10\log[(\Delta I+I)/I]\}$, units in which IID is usually expressed, there is no concern that the adaptive procedure will track to zero. In each block of trials, the intensity difference initially was varied in steps of 4 dB and reduced to 2 dB after four reversals until a total of 12 reversals occurred. The intensity difference at the start of each block of trials was set to a well-detectable level (6–8 dB above the expected threshold) and adjusted as necessary in subsequent blocks based on the ongoing performance of each listener. The mean of the intensity differences in units of $10\log(\Delta I/I)$ at the final eight reversals was computed as the estimate of threshold. Four such estimates were obtained in each experimental condition and the mean of those four estimates was taken as the final threshold estimate.

Although the lower-intensity probe segment is described here as a "decrement" or "decremented," that lower intensity was fixed across trials. Thus, the decrement was relative to the fringe, not in absolute terms. This was done so that threshold intensity differences (between the higher- and lower-intensity probe segments) could be specified, if desired, relative to a fixed reference intensity (that of the lower-intensity probe), as in Stellmack *et al.* (2004). Therefore, in the course of the adaptive procedure, the intensity of the decremented portion of the probe was held constant (30 dB spectrum level) and the intensities of the fringe and incremented portion of the probe were adjusted appropriately (see Fig. 2). After the spectrum level of the incremented probe was determined (based on the magnitude of the current increment in the adaptive procedure), the spectrum level of the fringe was set to the mean of the spectrum levels of the incremented and decremented probes. Thus the difference between the fringe and decrement was equal to the difference between the increment and fringe in terms of both the dB difference $\{10\log[(\Delta I+I)/I]\}$ and Weber fraction $[10\log(\Delta I/I)]$. Akeroyd and Bernstein (2001) held the spectrum level of the fringe constant and varied the spectrum levels of the incremented and decremented probes while in the present experiment the spectrum level during the decrement was held constant. Given that Stellmack *et al.* (2004) found no level effects for binaural intensity-discrimination thresholds with noise, it is believed that this procedural difference is not important.

Stimuli were generated digitally within MATLAB at a sample rate of 44.1 kHz and converted to analog signals on a PC equipped with a high-quality, 24-bit sound card (Echo Audio Gina). Stimuli were presented over Sony MDR-V6 stereo headphones to listeners seated in an IAC sound-attenuating chamber. Each block of trials was initiated by the listener. On each trial, a "ready" light flashed on the computer screen for 250 ms followed by a 100-ms pause after which a trial was presented. Listeners entered their responses on the computer keyboard at which time the correct response was indicated on the screen. Listeners were run in 2-h sessions, during which approximately 12–14 blocks of trials were run, until all stimulus conditions were completed.

In case performance in the single-interval binaural task could be facilitated by allowing each listener to establish an estimate of the perceptual midline, before each block of binaural trials each listener was allowed to listen to a diotic broadband noise burst (500 ms, 20 dB spectrum level) and he or she was instructed to adjust the headphones so that the stimulus produced an intracranial image at the center of his or her head. Listeners were allowed to listen to the diotic stimulus until they were satisfied that the headphones were positioned properly at which time a block of binaural trials was initiated.

The four listeners consisted of the first and third authors (S2 and S1, respectively) and two undergraduate students (one female and one male) from the University of Minnesota who were paid to participate in the study. All listeners had pure-tone thresholds of 15 dB HL or better at octave frequencies from 250 to 8000 Hz. Listeners were allowed to practice in a variety of the monaural and binaural conditions until their thresholds stabilized. Very little practice was required for this set of listeners to reach asymptotic performance. Listener S1 ran two blocks of all the monaural conditions in a pseudorandom order followed by two blocks of all the binaural conditions in a pseudorandom order, and then he ran two additional blocks of the monaural and binaural conditions. Listeners S2, S3, and S4 ran two blocks of all the monaural conditions in a pseudorandom order followed by two additional blocks of the same monaural conditions, then they ran all of the binaural conditions in the same way.

B. Results

The individual data are shown in Fig. 3 and the mean data are shown in Fig. 4. Thresholds are plotted in units of $10\log[(\Delta I+I)/I]$, the difference between the spectrum levels of the decrement and increment. The right-hand ordinates of Figs. 3 and 4 scale these values as the Weber fraction $10\log(\Delta I/I)$, the units in which thresholds were measured adaptively, where ΔI is the just-detectable increment in intensity and I is the intensity of the decremented probe. In both figures, the monaural and interaural thresholds for the 5-ms probe segment in isolation are plotted as separate sym-

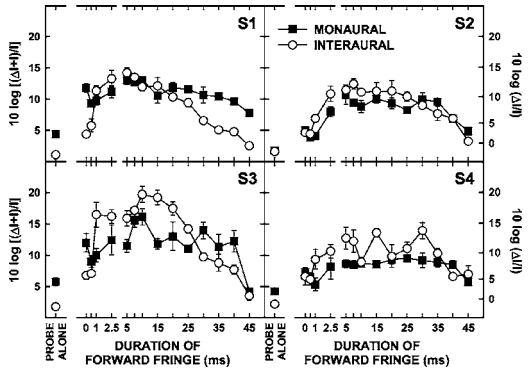

FIG. 3. Monaural (filled symbols) and interaural thresholds (open symbols) for four individual listeners as a function of forward-fringe duration. The ordinate is scaled in units of $10\log[(\Delta I+I)/I]$ on the left-hand side and $10\log(\Delta I/I)$ on the right-hand side. Thresholds for the probe alone are represented by the individual symbols on the left-hand side of each panel. Error bars represent standard errors of the mean for the four threshold estimates in each condition. Note the change in scale along the abscissa to expand the plots of the functions for short forward-fringe durations.

bols on the left-hand side of each panel. Note the breaks in the abscissas such that the scale is expanded between 0 and 2.5 ms.

The mean thresholds reflect the general trends of the individual data reasonably well, so the remaining comments will deal exclusively with the mean data of Fig. 4, although it should be noted that the individual data carry some exceptions to the trends of the mean data. All of the mean thresholds for the fringe conditions are higher than those for the corresponding "probe alone" conditions. The patterns of thresholds as a function of forward-fringe duration are similar for the monaural data (an inverted U) and interaural data (an asymmetrical inverted U) and are consistent with the data of Akeroyd and Bernstein (2001). The interaural thresholds are higher than the monaural thresholds for forward-fringe durations from 1 to 25 ms, while the monaural thresholds are higher than the interaural thresholds for the remaining (shorter and longer) forward-fringe durations. The monaural threshold for a 0-ms forward fringe was slightly elevated relative to monaural thresholds with forward fringes of 0.5 or 1 ms. The IID data of Akeroyd and Bernstein showed a similar upturn for a 0-ms forward fringe while the present interaural data did not. (It is difficult to compare the threshold values across studies because of procedural differences, a point that will be addressed in Experiment 2.)

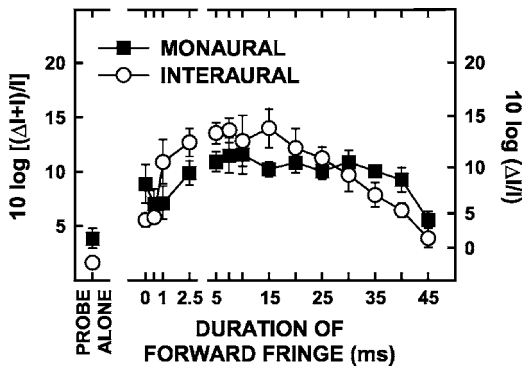

FIG. 4. Mean thresholds for four listeners in the same format as Fig. 3. Error bars represent standard errors of the mean.

C. Quantitative analysis: Methods

A quantitative analysis of the data was undertaken in the manner described by Akeroyd and Bernstein (2001). They showed that their interaural data were fit well by an asymmetric temporal window in combination with a post-onset-weighting mechanism that represented decreased weighting of binaural information for a brief period of time after the onset of the stimulus. Akeroyd and Bernstein performed a least-squares nonlinear regression on their data to estimate the parameters of the functions that would best fit their data. All fits in the present paper were performed on the mean data shown in Fig. 4. All equations and fitting procedures described in the following are identical to those described by Akeroyd and Bernstein unless otherwise noted. [See Akeroyd and Bernstein (2001) for additional details.]

Akeroyd and Bernstein (2001) gathered data only in binaural conditions so their fitting procedure operated on functions describing the instantaneous IID of their stimuli. In the present paper, functions were fit to the IID functions for the binaural stimuli and to functions describing the instantaneous intensity difference between corresponding temporal positions of the monaural stimuli. That is, for the monaural stimuli, the function describing the instantaneous intensity of the waveform containing the decrement was subtracted from that for the waveform containing the increment (as for the left- and right-ear stimuli of the binaural conditions) and the fitting procedure operated on this difference function. The instantaneous intensity differences were expressed in terms of $10\log[(\Delta I+I)/I)]$, the dB difference, for both the monaural and binaural conditions. In the following, the term "intensity difference" refers generally to a value of the difference function for the monaural or binaural conditions. The nature of these intensity-difference functions are discussed further at the end of this section.

The asymmetric temporal window was defined as follows:

$$w(\tau)=\begin{cases} e^{\pi/T_1}, & \tau<0 \\ e^{-\pi/T_2}, & \tau\geqslant 0 \end{cases}, \qquad (1)$$

where τ is the time relative to the peak of the temporal window and T_1 and T_2 are the time constants determining the slopes of the temporal window before and after, respectively, the peak of the temporal window. It was assumed that the temporal window integrates the values of intensity difference carried by the probe segment with those of the surrounding noise, with the temporal window defining the relative weight given to the intensity difference at each temporal location within the window. The output of the temporal window, W, is

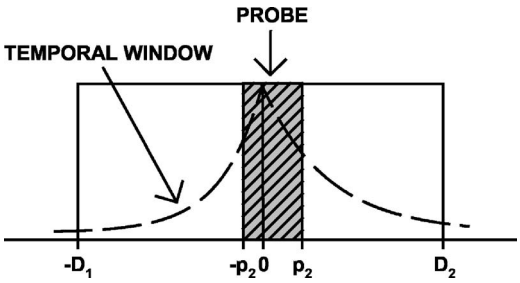

FIG. 5. A schematic illustration of the temporal regions represented by the limits of integration in Eq. (2).

$$W = \text{probe intensity difference} \frac{\int_{-p_1}^{p_2} w(\tau)d\tau}{\int_{-D_1}^{D_2} w(\tau)d\tau}, \tag{2}$$

where $-p_1$ and p_2 are the times between the peak of the temporal window and the onset and offset of the probe, respectively, and $-D_1$, and D_2 are the times between the peak of the temporal window and the onset and offset of the entire stimulus, respectively. These times are illustrated schematically in Fig. 5 (which is based on Fig. 3 of Akeroyd and Bernstein, 2001). W in Eq. (2), then, is the probe intensity difference weighted by the ratio of the area under the temporal window occupied by the probe segment to the area under the temporal window occupied by the entire stimulus. The temporal position of the window was fixed so that the value of W was maximized. The position of the temporal window at which W was maximized was found by moving the peak of the window between the onset and offset of the probe segment in 0.1-ms steps and computing W for each peak position. Then it was assumed that the threshold intensity differences measured in the experiment corresponded to a constant "effective" intensity difference, W_0, at the output of the temporal window. Equation (2) can then be rearranged to give the predicted intensity difference at threshold:

$$\text{probe intensity difference at threshold} = W_0 \frac{\int_{-D_1}^{D_2} w(\tau)d\tau}{\int_{-p_1}^{p_2} w(\tau)d\tau}. \tag{3}$$

The MATLAB Optimization Toolbox function "lsqnonlin" was used to estimate values of T_1, T_2, and W_0 in order to fit the temporal window to the data. The parameters were estimated in order to minimize the mean-squared error between the predictions and the data, with the mean-squared error computed using the predicted and observed values of intensity difference in units of $10\log[(\Delta I+I)/I]$. All integrals were evaluated analytically.

The post-onset-weighting function was

$$f(t) = ae^{-t/T_a} + be^{-t/T_b} + 1, \tag{4}$$

where t represents the time relative to the onset of the stimulus. Incorporating Eq. (4) into the fitting procedure, Eq. (3) becomes[1]

$$\text{probe intensity difference at threshold} = W_0 \frac{\int_{-D_1}^{D_2} f(\tau + D_1)w(\tau)d\tau}{\int_{-p_1}^{p_2} f(\tau + D_1)w(\tau)d\tau}. \tag{5}$$

Note that $f(t)$ is fixed with respect to the onset of the overall stimulus while $w(\tau)$ is positioned optimally for each temporal position of the probe. When the post-onset-weighting function was included in this way, the fitting procedure amounted to estimating the parameters a, b, T_a, and T_b in addition to those of the temporal window of Eq. (1).

For all fits to the data, the percentage of variance in the actual data for which the predicted values accounted was computed as follows:

$$100 \times \left(1 - \frac{\sum (O_i - P_i)^2}{\sum (O_i - \bar{O})^2}\right) \tag{6}$$

where O_i and P_i are the observed and predicted threshold values, respectively, and $\bar{O}$ is the mean of the observed threshold values.

The instantaneous IID function represents the presumed output of an ongoing differencing process occurring at a level of binaural interaction in the auditory system. The type of process to which the monaural intensity-difference function can be attributed is less evident. As noted by Stellmack *et al.* (2004), the two-interval monaural intensity-discrimination task depends on memory in a way that the single-interval binaural task does not, namely, a representation of the first interval of the two-interval stimulus must be stored in memory so that the difference between it and a representation of the second interval can be computed for temporally corresponding points. The present model operates on this representation of instantaneous intensity differences. In both the monaural and binaural cases, the fitting procedure considers the output of the temporal window positioned with respect to the instantaneous intensity-difference function such that the weighting of the intensity difference of the probe is maximized. However, applying the temporal window to the difference function is computationally equivalent to applying the temporal window to the individual stimuli and then computing the difference between the outputs. It is more plausible that the smoothing effects of the temporal window are due to processes occurring prior to a comparison of the two monaural intervals in memory. Given that the temporal order of the windowing and differencing procedures in the present analysis is unimportant, in the binaural conditions, windowing might be considered as occurring prior to binaural interaction as well.

TABLE I. For the set of data shown in the first column, shown are values of the parameters of the temporal window (T_1 and T_2 in ms), effective IID at the output of the temporal window (W_0 in dB), and parameters of the post-onset-weighting function (a, b, T_a, T_b, the latter two in ms). The percent of variance in the observed thresholds that the estimated parameters account for is shown in the final column. The parameter values that were allowed to vary in each nonlinear regression analysis are shown in bold type. The thresholds to which the functions were fit were expressed in units of $10\log[(\Delta I+I)/I]$.

Data set	T_1	T_2	W_0	a	b	T_a	T_b	% accounted
1) Monaural	**4.3**	**6.8**	**4.0**					80.3
2) Interaural	4.3	6.8	**4.3**					53.6
3) Interaural	4.3	6.8	**3.2**	**47.6**	**1299.5**	**5.3**	**0.4**	93.4
4) Akeroyd and Bernstein (2001) "Both fringe"	4.1	7.4	2.7	1.8	−0.8	1.8	13.0	85.2
5) Zurek (1980)	9.8	6.6	2.1	24.9	−0.6	0.7	31	97.2

D. Quantitative analysis: Results

Because up to seven parameters were estimated to produce fits to the data (as in Akeroyd and Bernstein, 2001), numerous combinations of parameter values accounted for nearly the same proportion of variance in the actual data. As a result, independent regression analyses performed on different sets of data that appear to be similar in form can yield very different "best-fitting" function parameters. Furthermore, the nonlinear regression analysis could produce very different results for the same set of data when the analysis was initialized with different sets of starting parameters. (This variation in best-fitting model parameters did not occur when only the temporal window was fit to a set of data by estimating the best-fitting values of the three free parameters T_1, T_2, and W_0.) As a result, the test of interest is whether the best-fitting parameters estimated for one set of data can account for another set of data, that is, whether two different sets of data can be described reasonably well by the same functions. Specifically, in the present analysis, the best-fitting values of the parameters of the temporal window [described by Eq. (1)] were estimated for the monaural data and then predictions of the interaural data using the same temporal window combined with the best-fitting post-onset-weighting function [described by Eq. (4)] were evaluated.

The parameters T_1, T_2, a, b, T_a, and T_b determine the shape of the functions defined by Eqs. (1) and (4) and the shape of the threshold curves that predict the observed data in Fig. 4. The parameter W_0 effectively represents the sensitivity of the observer and simply determines the vertical position of the predicted threshold curve without changing its shape. As a result, in the analyses that follow, whenever a particular temporal window and/or post-onset-weighting function that was derived from one set of data is used in a subsequent fit to the same or another set of data, the parameter W_0 is estimated once again in order to shift the predicted threshold curve up or down to produce the best fit to the data.

As a first step in the quantitative analysis of the data, only the asymmetric temporal window was fit to the monaural data. The best-fitting values of T_1, T_2, and W_0 are shown in line 1 of Table I. The temporal window defined by these parameters accounted for 80% of the variance in the observed data.

When both the temporal window and post-onset-weighting function were included in the analysis for the monaural data (introducing four additional parameters to the fitting procedure), the resulting fit accounted for a larger percentage of the variance (82%) in the monaural data. The difference between the percentage of variance accounted for with and without the post-onset-weighting function corresponds to threshold predictions that are only about 1 dB better than those for the temporal window alone for five of the seven shortest forward-fringe durations. The parameters of the temporal window estimated without the post-onset-weighting mechanism (Table I, line 1) were used in subsequent fits to the interaural data for two reasons: (1) the inclusion of the post-onset-weighting mechanism does not improve the predicted thresholds substantially, and (2) the post-onset-weighting mechanism was posited to account for purely binaural phenomena such as the precedence effect (Zurek, 1987; Houtgast and Aoki, 1994) and, as a result, there is no apparent theoretical justification for including it in the predictions of the monaural data. [While the phenomenon of overshoot (Zwicker, 1965) involves a change in sensitivity over time, it does not seem to apply to the present situation in that lowest sensitivity resulting from overshoot occurs at stimulus onset and the effect is seen in situations involving detection of a tonal signal in a noise masker and not for noise signals.]

As Akeroyd and Bernstein (2001) observed for their own data, the temporal window alone accounted for a very low percentage of the observed variance in the present interaural data (54%; see Table I, line 2). In contrast, when the best-fitting values of the temporal window parameters (T_1 and T_2) estimated from the monaural data (Table I, line 1) were fixed and parameters for the post-onset-weighting function were estimated, the resulting functions accounted for about 93% of the variance in the interaural data (Table I, line 3). The thresholds predicted by these parameters are represented by the solid line in the upper panel of Fig. 6, plotted among the mean interaural data replotted from Fig. 4. For the present data, as Akeroyd and Bernstein (2001) observed for their own data and those of Zurek (1980), the combination of a temporal window and a post-onset-weighting mechanism can account for a large proportion of the variance in the interaural data. Furthermore, the temporal window that was

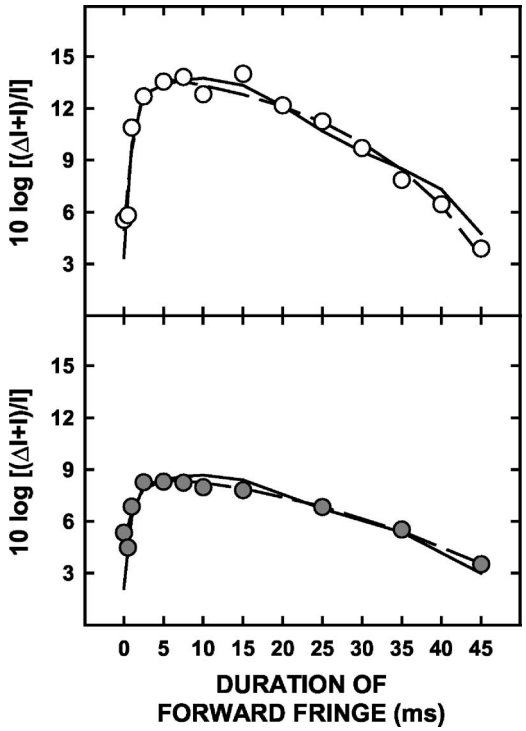

FIG. 6. The data in the upper panel are the mean interaural data replotted from Fig. 4. The data in the lower panel are the "Both-fringe" data of Akeroyd and Bernstein (2001) from their Fig. 5, panel C, open squares. The solid line in the upper panel represents thresholds predicted using the temporal window estimated from the monaural data combined with the post-onset-weighting function that produces the best fit to the interaural data. The solid line in the bottom panel shows the predictions for the data in that panel using the same temporal window and post-onset-weighting function, where the effective output of the temporal window, W_0, was allowed to vary in order to obtain the best fit. The dashed lines in both panels represent the predicted thresholds when the parameters of both the temporal window and post-onset-weighting function were allowed to vary to produce the best fit to the data in each panel.

estimated from the monaural data provides an excellent fit to the interaural data when paired with the appropriate post-onset-weighting function.

For comparison to the present data, the data of Akeroyd and Bernstein (2001) are plotted as the symbols in the lower panel of Fig. 6. [The observed threshold values were estimated from Akeroyd and Bernstein (2001), Fig. 5, panel C, open squares.] The thresholds measured by Akeroyd and Bernstein were lower than those reported in this paper, which would be expected given that they used a cued two-interval task and their adaptive procedure tracked to a lower value of percent correct. Furthermore, Akeroyd and Bernstein utilized a task involving discrimination between diotic and dichotic stimuli while the present task was a single-interval task that required discrimination between IIDs favoring the left and right ears. (As will be discussed in Sec. III, these procedural differences may limit the ability to compare thresholds obtained in the two tasks.) The temporal window and post-onset-weighting function that best fit the interaural data in Fig. 4 (defined by the parameters shown in line 3 of Table I, with W_0 free to vary) accounted for only about 58% of the variance in the IID data of Akeroyd and Bernstein (2001). The thresholds that were predicted using these function parameters are shown as the solid line in the lower panel of Fig. 6. However, when the data point for the forward-fringe duration of 0 ms is excluded, the weighting functions described by the same parameters account for over 93% of the variance in the data of Akeroyd and Bernstein. The increase in the variance accounted for is attributable to the fact that the functions used in the present fitting procedure describe large relative weight given to IIDs at stimulus onset and they cannot account well for the relative increase in threshold at stimulus onset observed in the data (noted in Sec. II B). The best-fitting parameters of the temporal window that Akeroyd and Bernstein estimated for their data are similar to the parameters estimated for the present data. The primary difference between the two fits resides in the best-fitting parameters of the post-onset-weighting function, which will be discussed in Sec. II E 2.

In all of the above-described conditions, the best-fitting parameters were estimated from the thresholds measured for the probe in the presence of diotic temporal fringes. In all cases, the parameter W_0 is the effective IID after application of the relative weights to the probe and fringe IIDs. Therefore, W_0 represents a prediction of the threshold for the corresponding probe alone condition. The value of W_0 estimated for the monaural data (4.0 dB) is very close to the mean probe alone threshold (3.8 dB), but W_0 estimated for the binaural data (3.2 dB) is somewhat higher than the observed value (1.6 dB). The value of W_0 estimated by Akeroyd and Bernstein (2001) for their IID data (2.7 dB) appears to be quite close to the observed value. It is uncertain why the estimated value of W_0 overpredicted the observed probe alone threshold for the present binaural data. One possibility raised by the results of Experiment 2 to follow is that listeners are particularly insensitive when discriminating the left-right direction of a nonzero probe IID for a brief time following stimulus onset (as opposed to discriminating a diotic from dichotic stimulus, as in Akeroyd and Bernstein, 2001). This will be discussed further in Sec. III B.

E. Discussion

1. Accounting for monaural and interaural data

The question addressed by the present experiment was whether a common set of temporal weighting functions could account for data gathered in monaural and interaural intensity-discrimination tasks in which the probe to be discriminated was preceded and followed by a temporal fringe that was fixed in intensity and, in the binaural task, diotic. The analysis showed that the double-sided exponential window that predicted the best-fitting thresholds for the monaural data also produced a very good fit to the interaural data when paired with a post-onset-weighting function that gave relatively greater weight to the binaural information at the onset of the stimulus. (The inclusion of a post-onset-weighting function did not substantially improve the predictions of the monaural data.) In other words, the relatively symmetric functions describing the monaural thresholds could be predicted well by a two-sided exponential temporal window, while it was necessary to combine a post-onset-weighting function with the same temporal window in order to account for the sharply higher thresholds after onset and

the resulting asymmetry of the function describing the binaural thresholds. The fact that a common temporal window provided good predictions for both sets of data indicated that the discrimination of intensity in a brief temporal segment of a stimulus might be affected in a similar way in monaural and binaural tasks by information temporally surrounding the segment to be discriminated.

If monaural temporal resolution is limited simply by the characteristics of a temporal window that integrates intensity over time, similar estimates of the parameters of the window should be obtained from data gathered in increment- and decrement-detection tasks. However, Oxenham (1997) showed that thresholds for detection of very brief intensity increments are lower than detection thresholds for decrements of the same magnitude. Oxenham also showed that if one assumes that listeners detect increments and decrements on the basis of the output of a temporal integrator, a common two-sided exponential function does not account well for the differences. That is, estimates of the parameters of the temporal window differ when calculated separately for the two sets of data. Oxenham assumed that the time constant that determined the slope of the temporal window for times before the peak was 1.5 times the value of the time constant that determined the slope of the function after the peak. He then estimated the best-fitting equivalent rectangular duration (ERD) of the temporal window that predicted his increment- and decrement-detection data. Oxenham found that the best-fitting ERDs were many times longer for the decrement-discrimination data than for the increment-discrimination data. Oxenham's data were fit better by assuming that listeners detect increments and decrements in intensity on the basis of the positive-going slopes (the onsets of the increments and offsets of the decrements) at the output of a temporal integrator. With this assumption, Oxenham was able to account for the fact that thresholds for increment detection were lower than for decrement detection.

The preceding discussion raises two issues with respect to the present data. First, because discrimination thresholds were measured in the present experiment by simultaneously varying the (equal) magnitudes of the increments and decrements, it is possible that discrimination was performed on the basis of detection of the increments (in one interval in the monaural task and in one ear in the binaural task) while the decrements were undetectable at discrimination threshold. The same possibility exists for the data of Zurek (1980) and Akeroyd and Bernstein (2001). This issue cannot be resolved on the basis of the present data.

The second issue involves interpretation of the temporal window used in the present fitting procedure. If estimates of a temporal window differ for increment and decrement detection, the single temporal window estimated for the present discrimination task must be considered as a simple description of the data rather than of a mechanism for integrating intensity information within a single interval or channel. In other words, the temporal window measured for the discrimination task represents the net effects of the integration of intensity information in the increment and decrement of each trial, either in the two intervals of the monaural task or in both ears of the binaural task. Despite these qualifications in the interpretation of the temporal window estimated here, it remains the case that a temporal window estimated from the data in the monaural task accounts well for the interaural data when combined with an appropriate post-onset-weighting function.

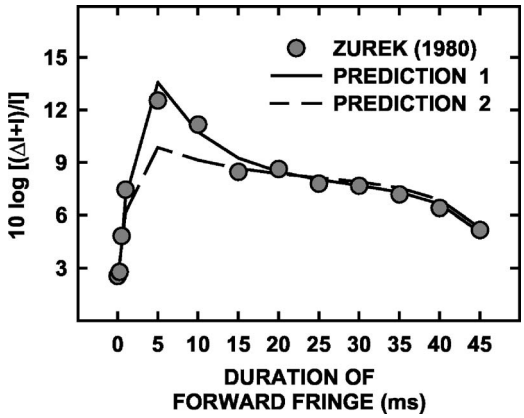

FIG. 7. Mean threshold IIDs from the two listeners of Zurek (1980) estimated from Fig. 7 of Akeroyd and Bernstein (2001). The solid curve shows predictions produced using the best-fitting weighting-function parameters estimated by Akeroyd and Bernstein. The dashed curve shows predictions generated using the same parameters but without the second term of Eq. (4). See the text for details.

2. Form of the best-fitting post-onset-weighting function

The post-onset-weighting function defined by the best-fitting parameter values estimated by Akeroyd and Bernstein (2001) for their entire body of data (their Both-fringe, Forward fringe only, and Backward fringe only data) is nonmonotonic and indicates large weight given to binaural information at the onset of the stimulus, then reduced weight (less than unity) given to information for a brief period following the onset of the stimulus after which the value of the weighting function returns to unity. For all of the post-onset-weighting functions estimated in the present paper, the functions indicate maximum weight at the onset of the stimulus, but the weight decreases monotonically to unity. In other words, the post-onset-weighting functions estimated here do not indicate a minimum in the weight applied to binaural information for a brief period following the onset of the stimulus. In fact, the parameter values estimated by Akeroyd and Bernstein only account for about 89% of the variance in their "Both-fringe" data alone (Table I, line 4), while the parameter values computed here account for over 93% of the variance in those same data (excluding the threshold for the probe at stimulus onset from the data for both fits, as previously noted in Sec. II D). Likewise, the parameter values estimated by Akeroyd and Bernstein account for only about 77% of the variance in the interaural data of the present experiment.

In their analysis of Zurek's (1980) data, Akeroyd and Bernstein (2001) found, as for their own data, that the parameters of the best-fitting post-onset-weighting function (Table I, line 5) also describe a nonmonotonic function like that described earlier. The thresholds predicted using these parameter values are plotted as the solid line in Fig. 7. The

data points in Fig. 7 are the average data of Zurek estimated from Fig. 7 of Akeroyd and Bernstein (2001). It can be seen that the predicted thresholds provide a very good fit to the data.

The nonmonotonicity in the post-onset-weighting function defined by the parameters in Table I, line 5 can be removed by eliminating the second term in the function [i.e., setting b in Eq. (4) to zero]. The result is a post-onset-weighting function that is simply an exponentially decreasing function. The predicted thresholds using this post-onset-weighting function are shown by the dashed line in Fig. 7. By comparing the solid and dashed lines in Fig. 7, it can be seen that the nonmonotonicity in the post-onset-weighting function produces large changes in threshold predictions (increases) for probes with onsets shortly after the overall stimulus onset. This nonmonotonicity is necessary in order to predict the sharp peak in the thresholds of Zurek's listeners for a forward-fringe duration of 5 ms. The thresholds reported by Akeroyd and Bernstein in their "Both-fringe" conditions do not exhibit as large a peak at 5 ms relative to surrounding thresholds (lower panel of Fig. 6) and, accordingly, the data could be predicted well by a post-onset-weighting function that decreases monotonically, as was the case for the present data. Thus the common characteristic of the best-fitting post-onset-weighting functions for all of the data considered here describes a maximum weight at onset followed by a rapid decrease immediately after onset. Whether the best-fitting function reaches a minimum after onset or decreases monotonically throughout the stimulus appears to depend on individual differences in sensitivity of the listeners to probe IID shortly after stimulus onset.

The best-fitting post-onset weighting functions for the present interaural data and those of Zurek (1980) are the sum of decaying exponentials such that one with a short time constant is weighted very heavily relative to the other with a longer time constant (see Table I, lines 3 and 5). In other words, these post-onset-weighting functions give very large relative weight to the IID at the onset of the stimulus and the relative weight decays very rapidly after stimulus onset. The best-fitting parameters represent very fast and large changes in sensitivity that may be biologically unrealistic, suggesting that the functions derived here may not correspond directly to underlying biological processes.

One factor that led to a very large peak value for the post-onset-weighting function is that, in the fits to the interaural data of the present paper, the parameters of the temporal window were fixed at the best-fitting values determined from the monaural data. If the parameters of the temporal window were allowed to vary as well, the peak value of the best-fitting post-onset-weighting function is similar to that obtained for Zurek's (1980) data. In all cases, a large peak value in the post-onset-weighting function (or, more accurately, a large difference between the initial value of the post-onset-weighting function and the value of the function after several ms) is necessary to account for the relatively large difference between thresholds measured for probes at the stimulus onset (forward fringe duration=0 ms) and thresholds measured with forward fringe durations between about 2.5 and 20 ms (as illustrated in Fig. 7). When the difference between minimum and maximum thresholds is smaller [as in the data of Akeroyd and Bernstein (2001)], the best-fitting post-onset-weighting function has a smaller peak value. Experiment 2 explores the possibility that the range of thresholds across forward fringe durations may be related to the specific experimental procedure.

III. EXPERIMENT 2: COMPARISON OF PROCEDURES

The three sets of data considered in this paper were collected using different procedures. In this section, it will be shown that some of the differences between the data that were compared earlier in this paper can be attributed to these procedural differences.

In the interaural task of Experiment 1, a single-interval procedure was used in which an intensity increment occurred at one ear (chosen randomly on each trial) while a decrement was simultaneously presented to the other ear. The listener's task was to identify which ear the resulting nonzero IID favored, a left-right discrimination task. Zurek (1980) used a three-interval procedure in which the signal interval presented an intensity increment to one ear and a simultaneous decrement to the other while in the nonsignal intervals the increment and decrement were presented to opposite ears relative to the signal. Thus, Zurek's task also was a left-right task in which the signal carried an IID favoring the right ear and the nonsignals carried an IID favoring the left ear.

Akeroyd and Bernstein (2001) used a four-interval task that essentially amounts to a two-interval forced-choice task with cue (nonsignal) intervals added to the beginning and end of each trial. The signal, which could appear in either the second or third interval of a trial, contained an intensity increment to one ear and a simultaneous decrement to the other. (The ears to which the increment and decrement were presented presumably were held constant.) The remaining intervals of each trial were diotic. If one arbitrarily assumes that the IID in the signal interval favored the right ear, this task can be described as a center-right task, one in which the listener discriminates a dichotic stimulus from diotic stimuli. An added feature of the Akeroyd and Bernstein procedure was the fact that the nonsignal intervals also carried diotic increments or decrements (determined randomly for each interval) at the same temporal position as the signal nonzero IID that was designed to minimize monaural, energy-based cues to detection of the dichotic stimulus. This experiment examines the relevance of the primary differences between the left-right and center-right procedures as well as the effects of the diotic increment or decrement in the nonsignal intervals of Akeroyd and Bernstein.

A. Methods

Thresholds were measured in three different conditions, all of which were two-interval, forced-choice tasks. In the left-right condition, designed to mimic the task of Zurek (1980), the signal interval contained an increment to the right ear and a decrement to the left ear while in the nonsignal interval the ears of presentation of the increment and decrement were reversed. In the center-right condition, as in the experiment of Akeroyd and Bernstein (2001), the signal in-

terval contained an increment to the right ear and a decrement to the left ear while the nonsignal interval contained a diotic increment or decrement (chosen randomly on each trial) at the same temporal position as the signal nonzero IID. In a third condition, "flat-right," the signal interval contained an increment to the right ear and a decrement to the left while the nonsignal contained no increment or decrement. While the diotic, nonsignal increment or decrement of the center-right condition, in theory, minimizes a potential monaural detection cue, the flat-right condition seeks to establish whether listeners utilize this cue.

In Experiment 1, the stimulus spectrum level during the decrement was held constant across trials and the spectrum levels during the fringe and increment were varied as dictated by the adaptive procedure. In this experiment, the spectrum level of the fringe was held constant (at 30 dB) and the spectrum levels during the increment and decrement were varied according to the adaptive procedure. A three-down, one-up adaptive procedure that tracked to the 79.4% correct level was used (Levitt, 1971). The increments and decrements in each trial were equal in magnitude in units of $10\log[(\Delta I+I)/I]$. The increments and decrements were varied adaptively in those units as well. The initial step size was set to 1 dB and was reduced to 0.5 dB after four reversals. A block of trials was terminated after 12 reversals and the mean increment/decrement size (in dB) at the final eight reversals was taken as threshold. Four blocks of trials were run in each condition and the four resulting threshold estimates were averaged to produce the final threshold for that condition. Thresholds were measured for forward fringe durations of 0, 5, 25, and 45 ms.

All remaining details of stimulus generation and threshold estimation were the same as those of Experiment 1. As in Experiment 1, the fine structures of the noises were identical at the two ears. [The noise bursts used by Zurek (1980) were interaurally uncorrelated while the noise bursts of Akeroyd and Bernstein (2001) and the present study were diotic. The effects of this difference are not examined here.] Only listeners S1 and S2 (the third and first authors, respectively) ran these conditions.

B. Results and discussion

In Fig. 8, thresholds are plotted in terms of the change in IID across intervals in units of $10\log[(\Delta I+I)/I]$ as a function of forward-fringe duration for the flat-right (circles), center-right (squares), and left-right (triangle) conditions. In other words, the magnitude of the IID within each interval of the left-right task was half the value plotted in the figure. For example, for a left-right threshold plotted as $\Delta\text{IID}=18$ dB in the figure, the IID at threshold was +9 dB in one interval and −9 dB in the other. The data for the two listeners were very similar so only the means are shown in Fig. 8.

There is little or no difference between the data of the flat-right and center-right conditions (circles and squares in Fig. 8). This suggests that these listeners generally made no use of the available monaural cues in the flat-right task.

The thresholds in the flat-right, center-right, and left-right conditions (all three symbol types in Fig. 8) are in perfect agreement for forward-fringe durations of 0, 25, and 45 ms. This suggests that performance in these conditions was determined by the magnitude of the change in IID across intervals. For a forward-fringe duration of 5 ms, the left-right thresholds are substantially larger than would be predicted from the flat-right and center-right thresholds assuming that listeners' performance is determined by the magnitude of the change in IID across intervals. As a result, across forward-fringe durations, sensitivity appears to be lower for probe IIDs just after stimulus onset in the left-right task relative to the flat-right and center-right conditions. The larger peak in the left-right function is reminiscent of that shown for Zurek's data in Fig. 7. It may be the case that the effects of procedural differences are the source of the apparent relative insensitivity of Zurek's listeners to probe IIDs shortly after stimulus onset. Dr. Zurek (private communication) suggests that an important difference between the left-right task and the other two tasks is that the left-right task requires discrimination of the direction of IID in the two intervals while the center-right and flat-right tasks can be performed by a processor that discriminates diotic from dichotic stimuli. In this context, the differences between the post-onset-weighting functions computed in Experiment 1 for data gathered with left-right and center-right procedures may reflect a greater loss in sensitivity to the (left-right) direction of a nonzero IID than to the difference between diotic and dichotic stimuli for a brief time period following stimulus onset. Given the differences between the data of the left-right condition and those of the center-right and flat-right conditions and the apparent differences in listener strategies that they represent, it is probably unreasonable to expect that the data gathered with the different procedures can be predicted by common weighting functions. The fact that the best-fitting parameter values for the left-right data of Experiment 1 accounted for the center-right data of Akeroyd and Bernstein (2001) reasonably well may have been merely fortuitous.

Recall that the estimate of W_0 obtained for the binaural data of Experiment 1 over-predicted the probe-alone threshold, while the estimate of W_0 for the IID data of Akeroyd and

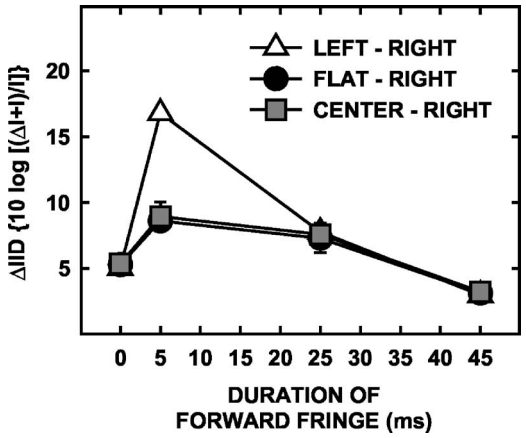

FIG. 8. Mean thresholds (of two listeners) plotted as the change in IID across intervals as a function of forward-fringe duration for the flat-right (circles), center-right (squares), and left-right (triangles) conditions of Experiment 2.

Bernstein (2001) was very close to their observed probe-alone threshold. As suggested earlier, perhaps decreased sensitivity to the direction of IID following stimulus onset contributed to drive thresholds higher in the left-right conditions of Experiment 1 in which a fringe was present. This factor was not present in the center-right discrimination task of Akeroyd and Bernstein (2001).

Another difference between the procedures that produced the data considered in this paper that might be expected to have differential effects on the data is related to the number of intervals. In Experiment 1 of this paper, a single-interval binaural task was used while Zurek (1980) and Akeroyd and Bernstein (2001) used multi-interval tasks. As a result, the stimuli of the latter two studies and those in Experiment 2 may have produced a perception of movement across intervals that was not present in the single-interval task. (The single-interval thresholds of Experiment 1 are somewhat larger than the two-interval left-right thresholds of Experiment 2.) Yost *et al.* (1974) showed that the introduction of a movement cue in a two-interval lateralization task can lead to results that are not directly predictable from data gathered with a single-interval procedure. The absence of a movement cue in the single-interval binaural task contributes to its utility in comparisons to the two-interval monaural intensity-discrimination task.

IV. CONCLUSIONS

(1) The function describing mean monaural intensity-discrimination thresholds for a 5-ms probe in a 50-ms stimulus as a function of forward-fringe duration was a roughly symmetrical, inverted U with lowest thresholds when the probe segment was near the onset or offset of the overall stimulus. The function describing interaural intensity-discrimination thresholds for a probe of the same duration in a diotic fringe was more asymmetrical with highest thresholds measured when the probe segment occurred shortly after the onset of the overall stimulus. A temporal window fitted to the monaural intensity-discrimination data provides a very good fit to the IID-discrimination data when combined with a post-onset-weighting function that produces maximum sensitivity to binaural information at the stimulus onset. That is, the symmetrical monaural data can be predicted very well through a model incorporating a temporal window alone while predictions of the more asymmetrical binaural data require both the temporal window and post-onset-weighting function.

(2) When an individual listener is particularly insensitive to binaural information shortly after stimulus onset (as in Zurek, 1980), the post-onset-weighting function that provides the best fit to the data contains a nonmonotonicity with a minimum after stimulus onset.

(3) Thresholds measured as a function of forward-fringe duration with center-right and left-right procedures differ in form to the extent that it is probably inappropriate to attempt to fit both sets of data with common weighting functions. Thresholds in the two tasks for forward-fringe durations of 0, 25, and 45 ms are consistent with the notion of listeners performing the task on the basis of cues determined by the difference in IID between intervals, while the change in IID across intervals could not account for the data in both center-right and left-right tasks for a forward-fringe duration of 5 ms. Left-right thresholds were larger than center-right thresholds, suggesting that differences between the best-fitting parameters of the post-onset-weighting mechanisms in the two cases may represent a decrease in directional (signed-IID) sensitivity for a brief time following stimulus onset in the left-right task.

ACKNOWLEDGMENTS

The authors would like to thank Dr. Armin Kohlrausch, Dr. Pat Zurek, and two anonymous reviewers who provided helpful comments and suggestions for improving this paper. This work was supported by Research Grant No. R01 DC 00683 and Research Grant No. R03 DC 05343, both from the National Institute on Deafness and Communication Disorders, National Institutes of Health.

[1]Equation (5) also was used in the fitting procedure of Akeroyd and Bernstein (2001), as the present authors have confirmed with Dr. Akeroyd (private communication).

Akeroyd, M. A. (2005). (private communication).
Akeroyd, M. A., and Bernstein, L. R. (**2001**). "The variation across time of sensitivity to interaural disparities: Behavioral measurements and quantitative analyses," J. Acoust. Soc. Am. **110**, 2516–2526.
Bernstein, L. R., Trahiotis, C., Akeroyd, M. A., and Hartung, K. (**2001**). "Senstivity to brief changes of interaural time and interaural intensity," J. Acoust. Soc. Am. **109**, 1604–1615.
Grantham, D. W. (**1984**). "Discrimination of dynamic interaural intensity differences," J. Acoust. Soc. Am. **76**, 71–76.
Houtgast, T., and Aoki, S. (**1994**). "Stimulus-onset dominance in the perception of binaural information," J. Acoust. Soc. Am. **72**, 29–36.
Levitt, H. (**1971**). "Transformed up-down methods in psychoacoustics," J. Acoust. Soc. Am. **49**, 467–477.
Moore, B. C. J., Glasberg, B. R., Plack, C. J., and Biswas, A. K. (**1988**). "The shape of the ear's temporal window," J. Acoust. Soc. Am. **83**, 1102–1116.
Oxenham, A. J. (**1997**). "Increment and decrement detection in sinusoids as a measure of temporal resolution," J. Acoust. Soc. Am. **102**, 1779–1790.
Penner, M. J., and Cudahy, E. (**1973**). "Critical masking interval: A temporal analog of the critical band," J. Acoust. Soc. Am. **54**, 1530–1534.
Penner, M. J., Robinson, C. E., and Green, D. M. (**1972**). "The critical masking interval," J. Acoust. Soc. Am. **52**, 1661–1668.
Plack, C. J., and Moore, B. C. J. (**1990**). "Temporal window shape as a function of frequency and level," J. Acoust. Soc. Am. **87**, 2178–2187.
Stellmack, M. A., Viemeister, N. F., and Byrne, A. J. (**2004**). "Monaural and interaural intensity discrimination: Level effects and the 'binaural advantage'," J. Acoust. Soc. Am. **116**, 1149–1159.
Yost, W. A., Turner, R., and Bergert, B. (**1974**). "Comparison among four psychophysical procedures used in lateralization," Percept. Psychophys. **15**, 483–487.
Zurek, P. M. (**1980**). "The precedence effect and its possible role in the avoidance of interaural ambiguities," J. Acoust. Soc. Am. **67**, 952–964.
Zurek, P. M. (**1987**). "The precedence effect," in *Directional Hearing*, edited by W. A. Yost and G. Gourevitch (Springer, New York).
Zurek, P. M. (2005). (private communication).
Zwicker, E. (**1965**). "Temporal effects in simultaneous masking by white-noise bursts," J. Acoust. Soc. Am. **37**, 653–663.

The effect of diotic and dichotic level-randomization on the binaural masking-level difference

G. Bruce Henning
Hearing Research Center, Biomedical Engineering Department, Boston University, Boston, Massachusetts 02215 and the SRU, Department of Experimental Psychology, Oxford University, Oxford OX1 3UD, United Kingdom

Virginia M. Richards
Department of Psychology, University of Pennsylvania, Philadelphia, Pennsylvania 19104

Jennifer J. Lentz
Department of Speech and Hearing Sciences, Indiana University, Bloomington, Indiana 47405

(Received 27 April 2004; revised 8 August 2005; accepted 8 August 2005)

Detection thresholds for tones in narrow-band noise were measured for two binaural configurations: N_oS_o and N_oS_π. The 30-Hz noise band had a mean overall level of 65 dB SPL and was centered on 250, 500, or 5000 Hz. Signals and noise were simultaneously gated for 500, 110, or 20 ms. Three conditions of level randomization were tested: (1) no randomization; (2) diotic randomization—the stimulus level (common to both ears) was randomly chosen from an uniformly distributed 40-dB range every presentation interval; and (3) dichotic randomization—the stimulus levels for each ear were each independently and randomly chosen from the 40-dB range. Regardless of binaural configuration, level randomization had small effects on thresholds at 500 and 110 ms, implying that binaural masking-level differences (BMLDs) do not depend on interaural level differences for individual stimuli. For 20-ms stimuli, both diotic and dichotic randomization led to markedly poorer performance than at 500- and 110-ms durations; BMLDs diminished with no randomization and dichotic randomization but not with diotic randomization. The loss of BMLDs at 20 ms, with degrees-of-freedom (2WT) approximately 1, implies that changes in intracranial parameters occurring during the course of the observation interval are necessary for BMLDs when mean-level and mean-intracranial-position cues have been made unhelpful. [DOI: 10.1121/1.2047167]

PACS number(s): 43.66.Pn [AK] Pages: 3229–3240

I. INTRODUCTION

The binaural masking-level difference (BMLD) is usually measured as the difference (in decibels) between the threshold level for detecting a signal when there are interaural differences in some aspect of the stimulus, and the threshold obtained when the signal and masker are identical at the ears. For example, large BMLDs occur between configurations with diotic noise and signal (N_oS_o) and configurations in which the masking noise is identical at the two ears but the signal is presented 180° out-of-phase at the ears (N_oS_π) (Colburn and Durlach, 1978).

Some explanations of the BMLD suggest a model in which an "equalization and cancellation" preprocessor creates, in the N_oS_π configurations, an improved signal-to-noise ratio (Durlach, 1963). One extension of Durlach's model assumes that detection is performed using an energy detector following the equalization device (Green, 1966; Henning, 1973). However, monaural masking studies indicate that energy-detector models do not correctly predict the detection of a tone added to narrow bands of noise under either monaural or diotic listening conditions (Kidd *et al.*, 1989; Richards, 1992; Green *et al.*, 1992; Richards, 2002). The incorporation of information associated with dynamic changes in envelope pattern improves the predictions of detection models, but still further modifications may be required if a full account of detection is to be achieved (Kidd *et al.*, 1993; Richards and Nekrich, 1993; Richards, 2002). Further, several experiments have suggested that for high-frequency, narrow-band maskers, binaural unmasking in the N_oS_π condition may depend on differences in envelope patterns, or correlations, at the two ears (Zwicker and Zwicker, 1984; Bernstein and Trahiotis, 1992; van de Par and Kohlrausch, 1997; Breebaart *et al.*, 2001a).

To examine the relative importance of interaural envelope differences for the BMLD, thresholds have been measured using N_oS_o and N_oS_π configurations with and without level randomization (Richards and Henning, 1994; Bernstein and Trahiotis, 1997). (In addition, Bernstein and Trahiotis randomized interaural delay.) In the experiments of Richards and Henning, fully reported here, two types of level randomization were used, diotic and dichotic. For the diotic randomization, the level of the stimulus, either masker-alone or signal-plus-masker, was randomly chosen on each stimulus presentation. As a result, the overall level of the stimulus did not reliably indicate the presence of the added signal (cf. Green, 1988). For the dichotic randomization, the levels of the stimuli presented to the left and right ears were randomly and independently chosen on each stimulus presentation. Dichotic level randomization prevents both mean monaural

and mean interaural level differences for each stimulus from indicating the presence of the (anti-phase) signal. To the extent that mean interaural level differences are used to detect anti-phase signals, dichotic level-randomization should lead to increased thresholds in the N_oS_π condition, thereby decreasing the BMLD provided that the randomization does not hurt performance in the N_oS_o condition. Dichotic level randomization does not alter the interaural phase spectra, nor are interaural envelope correlations altered, provided that the estimate of interaural correlation includes a normalization component (Bernstein and Trahiotis, 1996; van de Par *et al.*, 2001).

The effect on the BMLD of differences in the level of stimuli across the ears has been studied before. McFadden (1968) reported two effects of level on the size of BMLDs: (1) the reduction in the size of the BMLD with lower masker levels (related to our diotic-randomization condition). The effect of masker level on the size of the BMLD, however, depends on the range over which levels are manipulated and is small at high levels (Hall and Harvey, 1984). The other effect is (2) an additional reduction in the size of the BMLD with fixed differences in interaural level [a condition of McFadden's (1968) but related to our dichotic-randomization condition]. In McFadden's elegant experiments using broadband noise maskers at a noise-power spectral density of 45 dB SPL in one ear and a lower but fixed level in the other, the differential effect of the fixed interaural level difference arose when the interaural level difference was 10 dB or more. The reduction in the magnitude of the BMLD with an increasing interaural-level difference was faster than when the level in both ears decreased by the same amount. This effect is predicted by the model of Breebaart *et al.* (2001a, b).

On the other hand, Witton *et al.* (2000), using narrowband but higher level (80-dB SPL) stimuli, found that fixed interaural level differences of up to 60 dB had no effect on the binaural advantage in the detectability of monaural phase modulation in the presence of an unmodulated tone at the frequency of the carrier of the phase modulation. It is not known whether this effect can be predicted by the model of Breebaart *et al.* (2001a). However, in the current study with maskers having a bandwidth of 30 Hz and signal durations both longer and shorter than the 250 ms used by McFadden (1968), we found BMLDs to be very little affected by dichotic randomization of the masker even over the 40-dB range we used.

In addition to removing cues associated with mean differences in interaural level, dichotic level randomization makes the perceived intracranial lateral position of the sound vary. Shifts in lateral position were once implicated as the basis of the BMLD (Hafter and Carrier, 1975; Jeffress and McFadden, 1971; Zwicker and Henning, 1985) although it now appears unlikely that shifts in lateral position directly determine the BMLD (Henning, 1973; Zwicker and Henning, 1984; 1985).

In their randomization study, Bernstein and Trahiotis (1997) used stimuli with "temporal fringes" and randomly assigned the mean interaural delays as well as mean interaural level differences prior to each stimulus presentation. Both manipulations normally lead to random changes in intracranial position that prevent mean intracranial position being of use in detecting signals in the N_oS_π condition. But Bernstein and Trahiotis found that neither type of randomization had much effect on the size of the BMLD. The use of a temporal "fringe" increases the size of the BMLD (McFadden, 1966), but having a temporal "fringe" that extends both before and after the signal to be detected with the value of the randomized variable makes the interpretation of the effects of randomization difficult.

Consider that, on each observation interval, the fringe had the interaural level difference that was chosen by Bernstein and Trahiotis' randomization procedure. The addition of the signal in the N_oS_π condition changed the mean interaural level difference from the value that it had during the fringe period to a different value when the signal was also present. This means that is was possible for their observers to base their decisions on the changes in average value that occur whenever the signal is added. Further, our sensitivity to such changes is very little affected by the lateral position from which they begin. Domnitz and Colburn (1977) and Koehnke *et al.* (1995) show that the positioning of images laterally through static interaural level differences has little effect on observers' ability to detect changes from that position over the range of randomized values used by Bernstein and Trahiotis (1997).

We cannot know, of course, whether Bernstein and Trahiotis' observers used the cues resulting from changes away from the interaural level differences in the fringes, but the fact that the observers may have used the changes makes Bernstein and Trahiotis' results equivocal and means that many of their conclusions are not a logical consequence of their experimental results. That is not to imply that we do not believe the conclusions of Bernstein and Trahiotis; indeed, as far as the conclusions reached on the basis of level randomization go, they follow from our results (Richards and Henning, 1994) and the current paper.

The masker used in this study was a 30-Hz-wide band of noise centered at the signal frequency. By using narrow bands of noise, it may be assumed that (a) observers could not rely on across-frequency differences in level (or across-frequency differences in interaural level) in detecting the added tone [profile analysis (Green, 1988)], and (b) it would still be possible, with long-duration signals, for the observers to use interaural differences in the dynamic envelope patterns even at high frequencies (Henning, 1974; McFadden and Pasanen, 1974; Henning and Gaskell, 1981; Bernstein and Trahiotis, 1992; van de Par and Kohlrausch, 1997; Breebaart *et al.*, 2001a).

Three signal frequencies were tested: 250, 500, and 5000 Hz so that detection could be measured in frequency regions where sensitivity to interaural phase differences in pure tones is either present (250 and 500 Hz) or absent (5000 Hz). Most investigators agree that interaural phase differences in the fine structure of waveforms do not play a role in the BMLD at high frequencies (van de Par and Kohlrausch, 1997). The agreement is based on the lack of sensitivity to interaural phase difference in pure tones, and the lack of robust phase-locking measured in eighth-nerve

fibres for high-frequency tones (Kiang *et al.*, 1965; Rose *et al.*, 1987). As a result, when high-frequency stimuli were tested and dichotic level-randomization applied, only dynamic interaural differences in envelope patterns would be expected to be available to support the BMLD for the longer-duration stimuli.

Three stimulus durations were tested: 500, 110, and 20 ms. When very short-duration stimuli were used, dynamic envelope and dynamic fluctuations in the characteristics of stimulus fine structure were not available because 30-Hz-wide bands of masking noise have only slowly varying envelopes [expected maxima every 52 ms (Rice, 1954)] and slowly varying instantaneous frequencies. As a result, for the 20-ms stimuli, only relatively static differences in the envelope and phase across ears could contribute to detection (for N_oS_π stimuli). Consequently, when dichotic level randomization was applied with 20-ms stimuli, the BMLD was expected to be absent for high-frequency stimuli and, in all likelihood, small even at low frequencies.

II. METHODS

A. Procedures

A two-interval two-alternative forced-choice procedure was used with two observation intervals separated by an approximately 300-ms pause. The signal was as likely to occur in the first as in the second observation interval. Following each response, feedback was provided. A two-down, one-up adaptive staircase algorithm (Levitt, 1971) was used to estimate the signal level for 71% correct responses. The signal level started 5–15 dB above the eventual threshold and was initially altered in 4-dB steps. After the third reversal of the staircase, the step size was reduced to 2 dB. Observers completed 50-trial sets, and the last even number of reversals, excluding at least the first three, were averaged to generate a threshold estimate. The average of ten such threshold estimates provided the final threshold estimate.

B. Experimental conditions

Stimulus durations of 500, 110, and 20 ms and signal frequencies of 250, 500 and 5000 Hz were used. The maskers were bands of Gaussian noise, 30 Hz wide, centered arithmetically at the signal frequency. The masker and signal were gated on and off synchronously, and the total duration included 40-ms cosine-squared onset and offset ramps for the 500- and 110-ms stimuli and similar 5-ms ramps at 20 ms.

Two interaural phase configurations were examined, N_oS_o and N_oS_π, and three types of level randomization were used: none, diotic and dichotic. In the first randomization condition, no external level randomization was applied. In the second, the diotic condition, a single randomly selected gain factor was chosen for each observation interval and applied to both signal and noise for both ears. In the interval in which no signal was added, the factor was applied to the noise. The gain factor was randomly chosen on every observation interval from an uniform distribution with a 40-dB range (0.1-dB steps) centered on a gain of zero dB. In the third, the dichotic condition, two gain factors, one for each ear, controlled the levels of the stimuli; the gain factors were chosen independently for each ear on each observation interval again from uniform distributions of 40-dB range centered on zero dB. The gain factors for each ear were applied to both the signal and noise of the appropriate ear and were applied to the masking noise in the interval in which no signal was added. The difference between the diotic and dichotic level randomization was that, in the dichotic condition, the random levels were chosen independently for the left and right ears, thereby introducing randomization in the apparent intracranial position of the stimuli in addition to randomization of average level.

C. Stimulus generation and presentation

The maskers were generated digitally in real-time by summing sinusoids ranging from approximately 15 Hz below to 15 Hz above the signal frequency. A 2-Hz fundamental frequency was used for the 500-ms stimuli, and a 5-Hz fundamental for the 110- and 20-ms stimuli. The magnitudes of the component tones of the maskers were chosen randomly from a Rayleigh distribution, and their phases were chosen randomly from an uniform distribution ranging from zero to 2π rad. The signal was also generated in real time with random starting phase.

The stimuli were presented at a digital-to-analog output rate of 20.4 kHz for the 110- and 20-ms durations and 16.4 kHz for the 500-ms durations. The signal and masker were played through separate digital-to-analog converters. The two analog outputs were then low-pass filtered using matched filters (Kemo VBF-8) with attenuation skirts of approximately 85 dB/oct and a cutoff frequency of 6000 Hz. After filtering, the signal and masker were attenuated using computer-controlled attenuators, and the output of each attenuator split into two channels—left and right. When the signal and masker were in phase at the two ears (N_oS_o), the signal and maskers were summed for each of the two channels. When the signal was inverted to one ear (N_oS_π), the signal and masker were summed for the left channel, but the signal was inverted prior to addition in the right channel. The outputs of both channels were then passed through separate computer-controlled attenuators and gates (synchronous to within 5 μs) and finally routed to the left and right Sennheiser HD410 earphones driven in phase. The average masker power was 65 dB SPL (corresponding to an average noise-power density of 50 dB/Hz).

D. Observers and order of data collection

The three observers who participated ranged in age from 24 to 29 years and were paid for their participation. They all had hearing thresholds better than 15 dB HL for frequencies ranging from 500 to 6000 Hz. Observer 1 had prior experience in psychoacoustic experiments, including BMLD experiments. In the N_oS_π condition, two observers showed sudden decreases in thresholds mid-way through data collection and so were required to repeat all previously completed conditions.

Extensive preliminary experiments suggested that our initial goal should be to examine only the 110- and 20-ms

TABLE I. Thresholds for 500-ms duration.

	No randomization			Diotic randomization			Dichotic randomization		
Frequency	250	500	5000	250	500	5000	250	500	5000
OBS 1									
N_oS_o	61.8	61.5	61.3	64.4	62.4	64.1	62.8	64.6	62.8
	(0.6)	(0.9)	(0.9)	(0.6)	(0.7)	(0.5)	(0.9)	(0.3)	(0.6)
N_oS_π	45.1	46.3	52.8	47.1	46.9	55.6	50.4	50.0	58.3
	(0.7)	(0.5)	(0.7)	(1.1)	(0.9)	(1.4)	(1.1)	(0.7)	(0.5)
BMLD	16.7	15.2	8.5	17.3	15.5	8.5	12.4	14.5	4.4
	(1.2)	(1.1)	(1.2)	(0.7)	(1.2)	(1.3)	(1.4)	(0.7)	(0.9)
OBS 2									
N_oS_o	63.8	62.8	61.6	66.3	66.4	66.3	67.0	65.3	65.7
	(0.7)	(1.0)	(0.4)	(0.6)	(0.9)	(0.4)	(0.5)	(0.5)	(1.4)
N_oS_π	43.2	42.9	52.6	42.3	42.9	55.0	48.9	47.6	57.4
	(0.8)	(0.6)	(1.0)	(1.1)	(0.5)	(1.4)	(0.7)	(0.7)	(1.1)
BMLD	20.6	19.9	9.0	24.0	23.5	11.3	18.1	17.7	8.3
	(1.3)	(1.0)	(0.9)	(1.1)	(1.3)	(1.4)	(1.0)	(0.6)	(2.2)
OBS 3									
N_oS_o	64.4	62.6	55.5	62.9	60.4	62.9	63.6	63.9	61.7
	(0.6)	(0.8)	(1.5)	(0.6)	(1.1)	(1.2)	(0.5)	(0.7)	(1.3)
N_oS_π	46.9	49.4	54.0	52.3	53.1	54.2	55.0	53.9	51.7
	(1.7)	(1.2)	(0.9)	(0.7)	(0.6)	(1.2)	(0.9)	(1.0)	(2.0)
BMLD	17.5	13.2	1.5	10.7	7.3	4.1	5.9	8.0	4.8
	(1.7)	(1.6)	(1.7)	(0.9)	(1.1)	(1.4)	(0.9)	(1.5)	(2.3)
Average									
N_oS_o	63.3	62.3	59.5	64.5	63.1	62.9	63.6	63.9	61.7
	(0.8)	(0.4)	(2.0)	(1.0)	(1.8)	(2.4)	(1.8)	(1.1)	(2.7)
N_oS_π	45.1	46.2	53.1	47.2	47.6	54.9	51.4	50.5	55.8
	(1.1)	(1.9)	(0.4)	(2.9)	(2.9)	(0.4)	(1.8)	(1.8)	(2.1)
BMLD	18.3	16.1	6.4	17.3	15.5	8.0	12.1	13.4	5.8
	(1.2)	(2.0)	(2.4)	(3.9)	(4.7)	(2.1)	(3.5)	(2.9)	(1.2)

conditions (the 500-ms condition had previously been completed by another group of observers). However, as time allowed, the three observers also completed the condition with the 500-ms stimuli after the other data collection finished. For the 110- and 20-ms conditions, the data were obtained in the following sequences: observer 1, who also participated in the pilot work, completed the N_oS_π conditions first. Observers 2 and 3 completed the N_oS_o before the N_oS_π conditions. Within each binaural configuration, observers first completed the conditions associated with no randomization, then diotic randomization, and then dichotic randomization. Within each type of level randomization, the order of the stimulus duration was random and, for each duration, the order in which the frequencies were tested was random.

For the 500-ms stimuli, observers 1 and 2 completed the N_oS_π condition first; observer 3 completed the N_oS_o condition first. In other respects, the data collection followed the method described for the 110- and 20-ms stimuli.

III. RESULTS AND DISCUSSION

The graphs presented in this section represent averaged data taken from Tables I–III which contain the mean and standard errors of the means for each observer and each condition. [Tables I–III show the results for the individual observers for the 500-, 110-, and 20-ms stimulus durations, respectively. For each table there are three groups of three columns: each group contains the data for a given condition of level randomization and, within each group, the data for each signal frequency are shown in a separate column. Results for each observer are grouped in rows. For each observer, thresholds (in dB) for N_oS_o and N_oS_π are presented in separate rows with the standard errors of the mean across ten threshold estimates indicated in parentheses. The average BMLDs, in decibels (the N_oS_o minus N_oS_π thresholds), are also shown with an estimate of the standard error of the mean BMLD shown in parentheses. [This estimate reflects the standard error of the mean for the BMLDs across the first threshold estimates ($N_oS_o - N_oS_\pi$), then the second, etc.]. The bottom portion of each table presents the data averaged across observers, with standard errors of the mean indicated in parentheses.]

Figure 1 shows the average signal level corresponding to the 71% correct performance level as a function of frequency. We shall refer to this signal level as the detection "threshold." The results for the 500-, 110-, and 20-ms durations are shown separately in the top, middle, and bottom

TABLE II. Thresholds for 110-ms duration.

	No randomization			Diotic randomization			Dichotic randomization		
Frequency	250	500	5000	250	500	5000	250	500	5000
OBS 1									
N_oS_o	64.8	64.2	64.5	66.1	65.7	69.2	63.6	65.2	66.4
	(0.5)	(0.4)	(0.5)	(0.9)	(0.7)	(0.7)	(1.9)	(1.3)	(0.9)
N_oS_π	54.8	57.6	59.7	57.4	58.4	60.2	64.4	61.4	61.4
	(1.2)	(0.9)	(1.0)	(1.3)	(1.2)	(1.1)	(1.2)	(1.4)	(1.1)
BMLD	10.0	6.6	4.9	8.7	7.3	9.0	−0.8	3.7	5.0
	(1.4)	(0.8)	(1.3)	(1.7)	(1.0)	(1.4)	(1.8)	(1.6)	(1.5)
OBS 2									
N_oS_o	65.2	65.3	65.5	67.9	68.9	67.2	66.3	65.7	67.9
	(0.6)	(0.6)	(0.4)	(0.2)	(0.7)	(1.0)	(0.6)	(0.8)	(0.8)
N_oS_π	50.7	49.1	62.9	52.4	50.2	63.2	56.1	56.1	65.4
	(0.8)	(0.8)	(2.5)	(1.0)	(1.6)	(0.6)	(0.9)	(1.4)	(0.9)
BMLD	14.4	16.1	2.7	15.5	18.7	4.1	10.2	9.7	2.5
	(0.5)	(1.1)	(2.3)	(0.9)	(1.8)	(1.1)	(0.7)	(1.5)	(1.5)
OBS 3									
N_oS_o	65.6	63.8	61.9	66.7	65.7	68.1	67.0	67.2	67.7
	(0.7)	(1.1)	(0.8)	(0.8)	(0.8)	(0.5)	(0.7)	(0.8)	(1.2)
N_oS_π	54.1	58.1	58.3	59.2	58.3	62.2	62.0	59.8	62.3
	(0.7)	(0.9)	(0.6)	(0.4)	(0.8)	(1.2)	(0.9)	(0.9)	(0.6)
BMLD	11.5	5.7	3.7	7.4	7.4	5.8	5.0	7.4	5.3
	(1.2)	(1.6)	(1.0)	(0.7)	(1.3)	(1.6)	(1.0)	(1.3)	(1.2)
Average									
N_oS_o	65.2	64.4	64.0	66.9	66.8	68.2	65.6	66.0	67.3
	(0.2)	(0.4)	(1.1)	(0.6)	(1.1)	(0.6)	(1.1)	(0.6)	(0.5)
N_oS_π	53.2	54.9	60.3	56.3	55.7	61.9	60.9	59.1	63.0
	(1.3)	(2.9)	(1.4)	(2.0)	(2.7)	(0.9)	(2.5)	(1.6)	(1.2)
BMLD	12.0	9.5	3.7	10.6	11.1	6.3	4.8	6.9	4.3
	(1.3)	(3.3)	(0.6)	(2.5)	(3.8)	(1.4)	(3.2)	(1.7)	(0.9)

panels, respectively. Error bars show ± twice the standard error of the average and thus enclose 95% confidence intervals for the average thresholds. The unfilled symbols represent thresholds obtained in the N_oS_o condition, and the filled symbols, those obtained in the N_oS_π condition. Squares represent the thresholds obtained with no level randomization, circles represent thresholds obtained with diotic level randomization, and triangles, thresholds from dichotic level-randomization conditions. The results for no-randomization and dichotic randomization have been offset left and right for clarity.

Figure 2 shows BMLDs (in dB) as a function of signal frequency. The average BMLDs for the 500-, 110-, and 20-ms durations are plotted on the same scale in different panels (top, middle, and bottom, respectively), and for each panel BMLDs obtained with no, diotic, and dichotic level randomization are indicated using square, circular, and triangular symbols, respectively. The data for the no- and dichotic-randomization conditions have again been offset for clarity and the error bars delimit the 95% confidence intervals for each average BMLD shown. As is usually the case, most changes in the size of the BMLD result from changes in performance in the N_oS_π condition.

A. 500-ms duration

The top panel of Fig. 1 shows the thresholds, and the top panel of Fig. 2 shows the associated BMLDs, for the 500-ms conditions. In the N_oS_o condition, there are no significant differences across randomization conditions. This result is inconsistent with energy detection models of detection and has, of course, been seen before (Green *et al.*, 1992; Richards, 1992; Kidd *et al.*, 1993). In the N_oS_π conditions, the thresholds are also relatively unaffected by level randomization, except, possibly, for dichotic randomization at 250 Hz. Note that the large confidence interval around the diotic threshold at 250 Hz encloses both the dichotic- and no-randomization thresholds. With this possible exception, the BMLDs depend in the usual way on the frequency of the signal—larger at low frequencies and decreasing to smaller values at 5000 Hz.

The effect of diotic randomization on the BMLD is small even with such a large (40 dB) range of levels. BMLDs are generally smaller with lower masker levels (McFadden, 1968) although the decrease in the size of the BMLD for a given change of level depends on the level from which the reduction is made (Hall and Harvey, 1984); for a

TABLE III. Thresholds for 20-ms duration.

	No randomization			Diotic randomization			Dichotic randomization		
Frequency	250	500	5000	250	500	5000	250	500	5000
OBS 1									
N_oS_o	66.8	67.4	68.5	75.5	74.3	75.6	71.6	72.8	72.0
	(0.9)	(0.5)	(0.8)	(1.0)	(0.8)	(1.4)	(1.0)	(0.7)	(1.0)
N_oS_π	63.8	64.9	66.6	69.7	72.4	74.0	72.7	72.5	75.3
	(0.6)	(0.8)	(1.5)	(1.1)	(1.7)	(1.5)	(1.4)	(1.0)	(0.7)
BMLD	3.1	2.5	1.9	5.8	1.8	1.6	−1.1	0.3	−3.4
	(1.1)	(0.9)	(1.3)	(1.3)	(2.0)	(2.3)	(1.8)	(1.1)	(0.9)
OBS 2									
N_oS_o	68.2	68.7	69.6	80.7	79.1	78.0	74.8	75.7	72.6
	(0.6)	(0.5)	(0.5)	(1.6)	(1.1)	(1.5)	(1.6)	(1.8)	(1.6)
N_oS_π	55.5	57.2	66.8	63.1	61.0	73.5	70.4	70.7	73.3
	(1.1)	(1.0)	(0.8)	(1.1)	(1.7)	(1.6)	(1.2)	(1.4)	(0.7)
BMLD	12.7	11.5	2.8	17.6	18.1	4.5	4.4	5.0	−0.7
	(1.3)	(1.0)	(0.9)	(2.2)	(1.5)	(2.2)	(2.1)	(2.7)	(1.6)
OBS 3									
N_oS_o	66.4	65.7	65.4	76.5	75.1	76.4	73.3	71.4	69.9
	(0.7)	(0.6)	(0.8)	(0.9)	(1.0)	(2.0)	(1.9)	(1.0)	(1.0)
N_oS_π	63.4	63.6	66.5	71.3	67.3	71.6	71.8	71.3	71.3
	(0.7)	(0.6)	(0.5)	(1.4)	(2.0)	(1.6)	(1.9)	(1.1)	(1.3)
BMLD	3.0	2.1	−1.1	5.2	7.8	4.8	1.5	0.1	−1.4
	(1.0)	(0.9)	(1.0)	(1.8)	(2.8)	(2.5)	(2.5)	(1.3)	(1.6)
Average									
N_oS_o	67.1	67.3	67.8	77.6	76.1	76.7	73.2	73.3	71.5
	(0.5)	(0.9)	(1.3)	(1.6)	(1.5)	(0.7)	(0.9)	(1.3)	(0.8)
N_oS_π	60.9	61.9	66.6	68.1	66.9	73.0	71.6	71.5	73.3
	(2.7)	(2.4)	(0.1)	(2.5)	(3.3)	(0.7)	(0.7)	(0.5)	(1.2)
BMLD	6.2	5.4	1.2	9.5	9.3	3.6	1.6	1.8	−1.8
	(3.2)	(3.1)	(1.2)	(4.1)	(4.7)	(1.0)	(1.6)	(1.6)	(0.8)

given decrease in level, the reduction in the BMLD is less for higher initial levels. It is clear from the diotic randomization condition that the removal of monaural cues based on the average level in an observation interval does not affect the size of the BMLD. Thus the modifications required for the energy-detector model of monaural signal detection might also need to be made to the energy detector sometimes assumed to follow the equalization device in Durlach's equalization and cancellation model.

It is surprising that BMLDs should be so little affected by 40 dB of dichotic randomization. (The BMLDs across frequency are, on average, 3 dB smaller for the dichotic randomization conditions than for the average of the other two conditions, but the change is chiefly due to the reduction at 250 Hz—a change of 5.7 dB compared with a mean of 1.9 at the other two frequencies.) This result is surprising because dichotic randomization with our range of randomization leads to interaural level differences that might be expected, whatever their sign, to reduce the size of the BMLD. However, although fixed interaural level differences make the BMLDs smaller with broadband maskers (McFadden, 1968), fixed interaural-level differences have little effect on the binaural advantage obtained with very narrow-band stimuli (Witton *et al.*, 2000). Our 30-Hz bandwidths are neither broad nor very narrow and centered on an average noise-power density of 50 dB/Hz. The fact that dichotic randomization has so little effect on the BMLD suggests that our conditions were, in effect, more like those of Witton *et al.* (2000) than like those of McFadden (1968) and that static interaural level differences only affect detection when the level in the ear receiving the lower level falls to within 40 dB of the monaural threshold. Regardless of frequency, the reduction in the BMLD associated with dichotic level randomization of 500-ms signals reflects an increase in the N_oS_π thresholds.

B. 110-ms durations

The center panels of Figs. 1 and 2 show the thresholds and the BMLDs for the 110-ms condition. The dotted horizontal line in Fig. 1 is based on computer simulations using the same conditions as the experiment. It represents the expected threshold that would be obtained from a decision rule based on differences in energy in the N_oS_o condition in which diotic randomization was present. The analytic solution provided by Green (1988) yields similar estimates. Thresholds at or above this line indicate that energy or loudness cues alone could account for the detectability of the

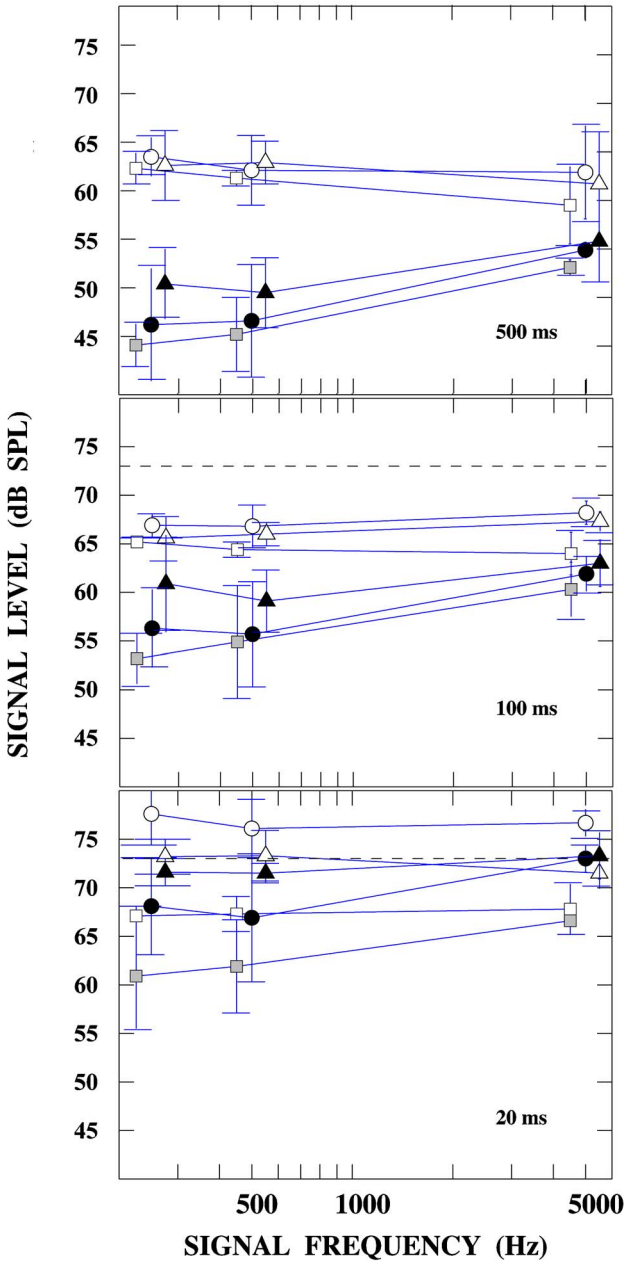

FIG. 1. (Color online) Average signal thresholds in dB SPL are plotted as a function of signal frequency for the 500-, 110-, and 20-ms conditions in the top through bottom panels, respectively. Level randomization is either diotic (circles), dichotic (triangles), or absent (gray squares). (The squares and triangles have been offset left and right for clarity.) The signal configuration is either in-phase across ears (unfilled, N_oS_o) or anti-phase across ears (filled, N_oS_π). Error bars indicate ± twice the standard error of the mean across observers ($n=3$), and the horizontal dotted lines in the center and bottom panels indicate thresholds expected for an energy-based decision rule in the N_oS_o condition with diotic randomization.

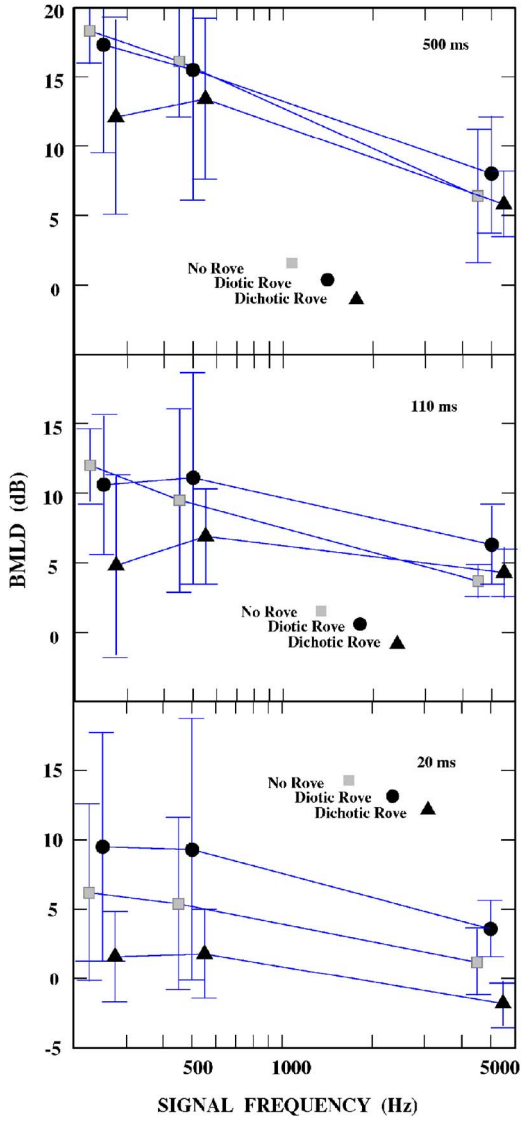

FIG. 2. (Color online) Average BMLDs (dB) are plotted as a function of signal frequency for the 500-, 110-, and 20-ms conditions in the top through bottom panels, respectively. Level randomization is diotic (circles), dichotic (triangles), or absent (gray squares). Error bars indicate ± twice the standard error of the mean across observers.

added tone. (The line is not included for the 500-ms condition because thresholds for all observers are at least 10 dB below its level.)

The results for 110-ms stimuli mirror those obtained at 500 ms: the N_oS_o thresholds were better than those predicted by the energy model (the dotted lines), indicating that changes in energy are very unlikely to account for detection with diotic randomization. Again in parallel with the 500-ms condition, thresholds are relatively unaffected by diotic level randomization, the low-frequency BMLDs are smaller at the 110-ms duration but the high-frequency BMLDs do not change very much. The BMLDs in the dichotic randomization conditions are on average 3.5 dB smaller than the average of the other two conditions, and again the largest effect occurs at 250 Hz; the small effect of dichotic randomization on the BMLD is again associated with increases in thresholds in the N_oS_π condition.

C. 20-ms durations

For the 20-ms duration, BMLDs in the dichotic-randomization condition become very small. The thresholds and BMLDs are shown in the bottom panels of Figs. 1 and 2 (where the horizontal dotted line again represents the prediction of energy-based detection in the N_oS_o condition). In contrast with the results obtained for the longer-duration stimuli, both diotic and dichotic level randomization led to

increases in thresholds compared to no level randomization. Moreover, for the 20-ms stimuli, most observers' thresholds in the N_oS_o conditions were either near or above the horizontal dashed line when level randomization was present (bottom panel of Fig. 1, unfilled symbols). This means that observers could have been detecting the signal on the basis of increases in level even when level randomization was present.

For the N_oS_o configuration, thresholds tend to be lower for the dichotic than the diotic level randomization. The difference may reflect differences in the average distributions of level across the ears particularly because the signal levels at threshold have become so large that energy or loudness base detection is possible in spite of the randomization. For example, if overall loudness contributes to detection in this condition at this duration, and if binaural loudness is treated as being based on the average of the stimulus levels (in dB) at the two ears, then independently choosing the level presented to the two ears will result in a triangular distribution of values across presentations. Because the resulting triangular distribution has a smaller variance than the original uniform distribution, a reduction in threshold relative to that obtained in the diotic randomization condition would result. Both computer simulations and analytic solutions indicate that such an averaging procedure could support loudness-based thresholds approximately 3 dB below the horizontal line shown in the bottom panel of Fig. 1. While this is an overly simple model of binaural loudness, it suggests an explanation of the surprising result that detection performance in the dichotic randomization condition tends to be better than in the diotic randomization condition with the N_oS_o stimuli of 20-ms duration.

For the brief signals at 5000 Hz, the BMLDs were small regardless of the roving level condition. However, BMLDs are evident for the lower-frequency stimuli when there was either no or diotic level randomization. Only one observer (OBS. 2, Table III) showed a slight BMLD when the randomization was dichotic. Two factors contribute to the diminished magnitude of the BMLDs obtained with the short-duration stimuli and dichotic randomization: relative to thresholds obtained in the dichotic randomization condition, thresholds in the diotic-randomization condition increase somewhat in the N_oS_o condition and decrease somewhat in the N_oS_π condition. On average, changing from diotic to dichotic randomization led to a 2.8-dB increase in threshold in the N_oS_π condition and a 4.1-dB decrease in threshold in the N_oS_o condition, yielding a net decrease in the BMLD of 6.9 dB.

IV. GENERAL DISCUSSION

A. Detection of a tone added to narrow bands of noise: N_oS_o

Consistent with other reports, the current data at 500- and 110-ms duration demonstrate a failure of the energy model for the detection of a tone added to noise. Several researchers (Kidd *et al.*, 1989, 1993; Richards, 1992; Green *et al.*, 1992) have suggested that the detection of a tone added to a narrow band of noise depends, at least in part, on changes in envelope modulation concomitant with the addition of the signal tone. As in most noise-masking experiments, the signal is added in random phase relative to the noise component of the same frequency. A 30-Hz-wide band of noise is only expected to have a maximum in its envelope once every 52 ms on average (Rice, 1954). At 20-ms durations then, with, in effect, no envelope variation over the signal duration, the detection task is approximately equivalent to the detection of a tone added to a tonal masker of the same frequency—a task that, in N_oS_o, must surely require changes in level for signal detection. Thus, in our experiments, changes in energy account for performance only when stimulus presentations are short relative to the rate at which envelopes change so that usable dynamic envelope cues are lacking. Our results are consistent with this line of reasoning and, for the 20-ms duration, are consistent with level-based detection.

For the 500- and 110-ms stimuli, the 40-dB interval-by-interval diotic level variations generated an average increase in threshold (relative to no level variation) of 2.3 dB consistent with those obtained previously (Kidd *et al.*, 1989; Richards, 1992). The effect of dichotic level randomization, 1.6 dB, was also small. Thus the perceptual consequence of dichotic randomization—that the sounds to be discriminated (narrow-band noise alone versus a different sample of the same noise plus a tone) were presented at different apparent intracranial positions—did not greatly influence binaural thresholds.

B. The BMLD

In general, there are two reasons why detection in the N_oS_π condition might be superior to detection in N_oS_o: (1) improvement due to quasi-independent (i.e., bounded above by independence) stimuli at the two ears and (2) a binaural advantage associated with the comparison of some aspect of the stimuli—related to delay or interaural correlation, say—across ears. In the following, the results will be considered separately for the high-(5000 Hz) and low-(500 and 250 Hz) signal frequencies. In addition to considering whether the BMLD depends on improvement associated with quasi-independent channels versus an additional binaural advantage, each subsection contains considerations of the basic results (a) that for the 500- and 110-ms stimulus durations, dichotic randomization had only small effects on the magnitude of the BMLD relative to that obtained when diotic randomization was present, and (b) that for short-duration stimuli, dichotic randomization abolished the BMLD. In a third section, the results are considered in light of some models of detection.

1. High-frequency (5000-Hz) stimuli

For the 5000-Hz signal at durations of 500 and 110 ms, level randomization did not influence the BMLD. Thus, because level randomization makes cues based on interaural-level differences unreliable, we can infer that static interaural-level differences are not required for high-frequency BMLDs. On the other hand, high-frequency BMLDs at least at the longer durations might result from

changes in envelope patterns across ears—dynamic envelope changes in either interaural time or intensity or both (Bernstein and Trahiotis, 1996; van de Par and Kohlrausch, 1997; van de Par *et al.*, 2001). Cues related to dynamic envelope changes, however, become ineffectual at short durations (Richards, 1992).

The degrees of freedom in the noise sample, $2WT$, where W is the bandwidth and T is the duration, are 1.2 for our 20-ms stimuli so that, in effect, only about one independent sample of the envelope is available at the short duration. At 110 ms, there are between six and seven independent samples available and that appears to be sufficient information for cues based on envelope changes to become effective. The degrees of freedom for the 100-Hz-wide noise of 17-ms duration used by Bernstein and Trahiotis (1997) are 3.4. That observation, coupled with the current results, suggests either that 3 degrees of freedom provide a sufficient number of independent samples or that their observers were able to use the additional information provided by changes from the brief temporal "fringes" of noise before and after the signal. In any case, at sufficiently short durations or sufficiently narrow bandwidths (Henning and Zwicker, 1984), interaural envelope cues should be ineffectual so that with dichotic roving levels, small BMLDs should result. That is what is observed.

A second possible explanation of the high-frequency BMLD—that of "probability summation" or the integration of the quasi-independent cues derived separately from the ears—is very unlikely given that the BMLDs are usually much larger than probability summation would predict (van de Par and Kohlrausch, 1999).

We conclude that, except possibly at short durations, high-frequency BMLDs in the presence of level randomization are based on cues that are not derived from energy or from (time average) interaural level differences; the cues in the N_oS_π condition may be derived from the characteristics of the temporally varying envelopes as Bernstein and Trahoitis (1996) and van de Par and Kohlrausch (1997) have suggested.

2. Low-frequency (250- and 500-Hz) stimuli

With low frequencies, dynamic changes in carrier phase across ears become available and these interaural differences are not influenced by diotic level randomization. There are only very small differences between the size of the BMLDs with no- and diotic-randomization for the low-frequency signals; the BMLD decreases with decreasing duration, but performance with diotic level randomization remains within the 95% confidence intervals of the no-randomization condition. The similarity in performance could result from the observers using cues based solely on interaural phase (or time) differences, on interaural correlation, on envelope-based cues, or combinations of the three. Changes in the cues used by the observers may account for the differential effect of duration on performance in the diotic- and no-randomization conditions. With no randomization, the BMLD decreases between 110 and 20 ms but with diotic randomization it does not. This suggests that the different cues used in the two cases depend differently on duration.

There are not many data concerning the way in which sensitivity to interaural cues depends on signal duration. Tobias and Zerlin (1959) reported slightly more than a factor of 2 deterioration in their mean jnd for interaural delay as duration decreased from 500 to 20 ms. Their observers, however, were lateralizing wideband noise and it is consequently difficult to determine which of many possible characteristics they might have been using.

As with envelope modulation, interaural phase differences are not influenced by dichotic level randomization. Thus, if BMLDs are based solely on, or strictly depend on, cues derived from interaural phase, neither static interaural-level differences nor dichotic level randomization should affect the size of the BMLDs (McFadden, 1968).

Our results with dichotic randomization are duration dependent: At 500 ms, BMLDs with dichotic randomization are slightly smaller than with diotic or no randomization (particularly at 250 Hz) and the detrimental effect of dichotic randomization increases with decreasing duration. At 20 ms, the BMLDs approached zero for the 250- and 500-Hz signals with dichotic level randomization. The reduction in the BMLD principally reflects an increase in thresholds for the N_oS_π condition. This could be the result of the loss in effectiveness of dynamic envelope-based cues coupled with a loss in sensitivity to interaural-delay related cues (Tobias and Zerlin, 1959) and thus a forced reliance on level-based cues so that the interaction between interaural phase and interaural level differences in determining the bearing of the stimuli could be the cause.

To elaborate, a 20-ms stimulus duration leads to relatively impoverished time-varying characteristics for 30-Hz-wide bands of noise. Not only is the average interval between envelope maxima large relative to the stimulus duration, but the average rate of change of the instantaneous phase is also slow relative to the duration of the stimulus. For the 20-ms duration, then, both the dynamic interaural phase differences in the fine structure and differences in the envelope patterns approach static conditions. If "static" interaural time differences were necessary to produce a BMLD, one would expect thresholds in the diotic and dichotic randomization conditions to be equal. This was not the case at short durations, and, as with the longer-duration stimuli, two possible explanations in the N_oS_π conditions with short durations are (a) that detection depends on interaural differences in intensity and/or (b) that detection depends on shifts in lateral position.

For the 20-ms stimuli, the second account is consistent with one observer's report of relying on lateral position with short-duration stimuli except when dichotic randomization was present. A second observer, however, indicated that she primarily used "spread-in-the-head" as a cue for the signal in the N_oS_π condition, even for short-duration stimuli. This observation is consistent with the notion of dual images (Hafter and Carrier, 1975; Jeffress and McFadden, 1971) or with width-of-image cues (Bernstein and Trahiotis, 1997). Both observers, however, indicated reliance on both general clarity or roughness as well as on binaural or "spatial" cues for the

500- and 110-ms duration N_oS_π conditions. The cues of clarity and roughness were similarly reported to be used for N_oS_o conditions.

3. Implications for models of the BMLD

The data have implications for several models of the BMLD (e.g., Durlach, 1963; Osman, 1971; Jeffress, 1972; Colburn, 1973; Henning, 1973; Colburn and Durlach, 1978; Stern and Colburn, 1978; Zwicker and Henning, 1985; Bernstein and Trahiotis, 1992; Breebaart *et al.*, 2001a). Here, only three classes of models of the BMLD are briefly considered: (a) equalization and cancellation (EC) models stemming from Durlach (1963), (b) the "vector" model stemming from Jeffress (1972), and (c) the bearing-channel model (Zwicker and Henning, 1985). The latter model is a simple development of Jeffress' model in which the bearing of the combined signal and masker in the N_oS_π condition does not provide the cue for the presence of the signal as in early versions of Jeffress model. Rather, the bearing of the combined signal and masker serves as an address "pointer" directing the information in the combined signal and noise stimulus to a bearing-tuned mechanism which then processes that information (Henning and Wartini, 1990; Henning, 1991). A much better developed model that includes detailed characterizations of the contributions of both interaural delay and interaural amplitude differences as well as gain control and temporal smoothing may be found in Breebaart *et al.* (2001a).

First, consider Durlach's EC model (Durlach, 1963). As applied to the current experiment and, in its simplest form, the EC model subtracts the waveforms presented to each ear after adjusting their levels to equalize the mean magnitudes of the masker. These operations, used only when they improve detection, produce an effective increase in the signal-to-noise ratio in the N_oS_π condition. Extensions of the model (Green, 1966; Henning, 1973) assume subsequent detection to be based on energy detection, thus the extensions have all the failings of the energy detector. But the equalization and cancellation mechanisms need not be followed by energy detection—the improved signal-to-noise ratio in the N_oS_π conditions would benefit whatever mechanism supported detection. Thus, taken to its extreme, the EC model predicts BMLDs at all durations and in all conditions of randomized level. Overall level is irrelevant in the model (except insofar as BMLDs are reduced at lower masker levels) and dichotic randomization is approximately compensated by the equalization mechanism. For this model, the reduction in the BMLD with the very short presentation durations (which were shorter than those suggested in Durlach's description of the model) might be taken to reflect the time required for the equalization device to operate or the "sluggishness" that is an integral part of Breebaart *et al.*'s (2001a) adaptation of Dau's model (Dau *et al.*, 1996). Were either to be the case, a clear prediction for large reductions in the BMLD with static interaural-level differences and short-duration stimuli follows.

Second, consider Jeffress's "vector" model (Jeffress, 1972) as well as models that, although not depending directly on either the bearing of the stimuli or the interaural delay, rely on differences in the timing of responses (envelope or fine structure) across the ears (e.g., Stern and Colburn, 1978). For such models, a BMLD is obtained for low-frequency tones because the observer is sensitive to the nonzero interaural phase differences in the fine structure of the stimuli in the N_oS_π condition. The failure of dichotic randomization to abolish the low-frequency BMLDs for moderate and long-duration stimuli is consistent with this, but the small BMLDs obtained for short-duration stimuli are not—unless the decision axis stemming from differences in the timing of responses across the ears is also sensitive to interaural level differences for short- but not for long-duration stimuli. In considering Jeffress's model we might, as with the EC model, imagine that laterality estimates require long durations to develop; there is certainly evidence for binaural sluggishness in localization (Grantham and Wightman, 1978; Grantham, 1986; Witton *et al.*, 2000; Bernstein *et al.*, 2001). But, for Jeffress's model and contrary to our findings, binaural "sluggishness" with 20-ms signals should, but does not, abolish BMLDs in no- and diotic-randomization conditions as well. This finding may also offer some easily remediable difficulties for the model of Breebaart *et al.* (2001a) because of the combination of early low-pass filtering and/or the (relatively) long time for the appropriate "weight" to develop (right-hand panel; their Fig. 7). As described above, however, the reduction in the BMLD for the short-duration stimuli is not inconsistent with a dependence on a spatially determined decision.

Finally, consider the model of Zwicker and Henning (1985). Their model relies on differences in the output of "bearing channels" and thus indirectly on the spatial location of a sound (lateral position in this case). The very small BMLDs with dichotic randomization with 20-ms signals are consistent with this model. However, because the model depends on channels tuned for stimuli coming from different bearings, the robust BMLDs obtained with dichotic randomization at longer durations are not consistent with it. On the contrary our results are consistent with bearing channels' being determined solely by interaural phase or time differences. Then, in the fashion of Jeffress and McFadden (1971), the extraneous perceptually varying laterality, produced on the intensity image by dichotic level randomization, would not affect performance. Alternatively, an extension of the model to include information processing across various bearing channels (Breebaart *et al.*, 2001a) [in the way that profile analysis operates across frequency-tuned channels (Green, 1988)] might bring this model into accord with the current results.

V. SUMMARY

Thresholds were measured for the detection of a tone added to a narrow band of noise for both N_oS_o and N_oS_π conditions in three conditions: (a) no level randomization, (b) diotic level randomization, and (c) dichotic level randomization. For 500- and 110-ms stimuli and diotic randomization, the effects of level randomization were small and BMLDs were unaffected by level randomization. At the same durations, dichotic level randomization reduced the

size of the BMLD slightly at 250 and 500 Hz. With 20-ms stimuli, the introduction of diotic level randomization led to increased thresholds in both the N_oS_o and N_oS_π conditions relative to thresholds obtained with no level randomization; diotic level randomization increased the size of the BMLD relative to that obtained with no randomization. Dichotic level randomization at 20-ms durations led to better performance in the N_oS_o conditions and poorer performance in the N_oS_π conditions resulting in very small BMLDs.

ACKNOWLEDGMENTS

This research was supported by Grant No. RO1 DC 02012 from the National Institutes of Health, a grant from the University Research Foundation of the University of Pennsylvania, by Grant No. RO1 DC00100 from the National Institute on Deafness and Other Communication Disorders, and by the Wellcome Trust. We should like to thank Dr. Emily Buss and Dr. Armin Kohlrausch for comments on earlier versions of this paper and for drawing our attention to the relevance of McFadden's 1968 paper, and Professor McFadden himself for kind, insightful, and helpful criticism of an earlier version of this paper.

Bernstein, L. R., and Trahiotis, C. (**1992**). "Discrimination of interaural envelope correlation and its relation to binaural unmasking at high frequencies," J. Acoust. Soc. Am. **91**, 306–316.

Bernstein, L. R., and Trahiotis, C. (**1996**). "Binaural beats at high frequencies: Listeners' use of envelope-based interaural temporal and intensitive disparities," J. Acoust. Soc. Am. **99**, 1670–1679.

Bernstein, L. R., and Trahiotis, C. (**1997**). "The effects of randomizing values of interaural disparities on binaural detection and on the discrimination of interaural correlation," J. Acoust. Soc. Am. **102**, 1113–1120.

Bernstein, L. R., and Trahiotis, C., Akeroyd, M. A., and Hartung, K. (**2001**). "Sensitivity to brief changes of interaural time and interaural intensity," J. Acoust. Soc. Am. **109**, 1604–1615.

Breebaart, J., van de Par, S., and Kohlrausch, A. (**2001a**). "Binaural processing model based on contralateral inhibition. I. Model structure," J. Acoust. Soc. Am. **110**, 1074–1088.

Breebaart, J., van de Par, S., and Kohlrausch, A. (**2001b**). "Binaural processing model based on contralateral inhibition. II. Dependence on spectral parameters," J. Acoust. Soc. Am. **110**, 1089–1104.

Colburn, H. S. (**1973**). "Theory of binaural interaction based on auditory nerve data. I. General strategy and preliminary results on interaural discrimination," J. Acoust. Soc. Am. **54**, 1458–1470.

Colburn, H. S., and Durlach, N. I. (**1978**). "Models of binaural interaction," in *Handbook of Perception*, edited by E. C. Carterette and M. P. Friedman (Academic, New York).

Dau, T., Püschel, D., and Kohlrausch, A. (**1996**). "A quantitative model of the 'effective' signal processing in the auditory system. I. Model structure," J. Acoust. Soc. Am. **99**, 3615–3622.

Domnitz, R. H., and Colburn, H. S. (**1977**). "Lateral position and interaural discrimination," J. Acoust. Soc. Am. **61**, 1586–1598.

Durlach, N. I. (**1963**). "Equalization and cancellation theory of the binaural masking level difference," J. Acoust. Soc. Am. **35**, 1206–1218.

Grantham, D. W. (**1986**). "Detection and discrimination of simulated motion of auditory targets in the horizontal plane," J. Acoust. Soc. Am. **79**, 1939–1949.

Grantham, D. W., and Wightman, F. L. (**1978**). "Detectability of varying interaural temporal differences," J. Acoust. Soc. Am. **63**, 511–523.

Green, D. M. (**1966**). "Signal-detection analysis of the equalization and cancellation model," J. Acoust. Soc. Am. **40**, 833–838.

Green, D. M. (**1988**). *Profile Analysis: Auditory Intensity Discrimination* (Oxford Science, Oxford).

Green, D. M., Berg, B. G., Dai, H., Eddins, D. A., Onsan, Z., and Nguyen, Q. (**1992**). "Detecting spectral shape in very narrow frequency bands," J. Acoust. Soc. Am. **95**, 2586–2597.

Hafter, E. R., and Carrier, S. C. (**1975**). "Masking-level differences obtained with a pulsed tonal masker," J. Acoust. Soc. Am. **47**, 1041–1047.

Hall, J. W., and Harvey, A. D. G. (**1984**). "N_oS_o and N_oS_π thresholds as a function of masker level for narrow-band and wideband masking noise," J. Acoust. Soc. Am. **76**, 1699–1703.

Henning, G. B. (**1973**). "Effects of interaural phase on frequency and amplitude discrimination," J. Acoust. Soc. Am. **54**, 1160–1178.

Henning, G. B. (**1974**). "Detectability of interaural delay in high-frequency complex waveforms," J. Acoust. Soc. Am. **55**, 84–90.

Henning, G. B. (**1991**). "Binaural amplitude discrimination and the binaural masking level difference," Hear. Res. **55**, 188–194.

Henning, G. B., and Gaskell, H. (**1981**). "Binaural masking level differences with a variety of waveforms," Hear. Res. **4**, 175–184.

Henning, G. B., and Wartini, S. (**1990**). "The effect of signal duration on frequency discrimination at low signal-to-noise ratiosin different conditions of interaural phase," Hear. Res. **48**, 201–208.

Henning, G. B., and Zwicker, E. (**1984**). "Effects of the bandwidth and level of noise and of the duration of the signal on binaural masking-level differences," Hear. Res. **14**, 175–178.

Jeffress, L. A. (**1972**). "Binaural Signal Detection Theory," in *Foundations of Modern Auditory Theory*, edited by J. V. Tobias (Academic, New York), Vol. **II**.

Jeffress, L. A., and McFadden, D. (**1971**). "Differences in interaural phase and level in detection and lateralization," J. Acoust. Soc. Am. **49**, 1169–1179.

Kiang, N. Y-S., Watanabe, T., Thomas, E. C., and Clark, L. F. (**1965**). *Discharge Patterns of Single Fibers in the Cat's Auditory Nerve* (MIT, Cambridge).

Kidd, G., Mason, C. R., Brantley, M. A., and Owen, G. A. (**1989**). "Roving-level tone-in-noise detection," J. Acoust. Soc. Am. **86**, 1310–1317.

Kidd, G., Uchanski, R. M., Mason, C. R., and Deliwala, P. S. (**1993**). "Discriminability of narrow-band sounds in the absence of level cues," J. Acoust. Soc. Am. **93**, 1028–1037.

Koehnke, J., Culotta, C. P., Hawley, M. L., and Colburn, H. S. (**1995**). "Effects of reference interaural time and intensity differences on binaural performance in listeners with normal and impaired hearing," Ear Hear. **16**, 331–353.

Levitt, H. (**1971**). "Transformed up-down methods in psychoacoustics," J. Acoust. Soc. Am. **49**, 167–177.

McFadden, D. (**1966**). "Masking-level differences with continuous and with burst masking noise," J. Acoust. Soc. Am. **40**, 1414–1419.

McFadden, D. (**1968**). "Masking-level differences determined with and without interaural disparities in masker intensity," J. Acoust. Soc. Am. **44**, 212–223.

McFadden, D., and Pasanen, E. G. (**1974**). "High-frequency masking-level differences with narrow-band noise signals," J. Acoust. Soc. Am. **56**, 1226–1230.

Osman, E. (**1971**). "A correlation model of binaural masking level differences," J. Acoust. Soc. Am. **50**, 1494–1511.

Rice, S. O. (**1954**). "Mathematical analysis of random noise," in *Selected Papers on Noise and Stochastic Processes*, edited by N. Wax (Dover, New York), pp. 133–294.

Richards, V. M. (**1992**). "The detectability of a tone added to narrow bands of equal-energy noise," J. Acoust. Soc. Am. **91**, 3424–3435.

Richards, V. M. (**2002**). "Varying feedback to evaluate decision strategies: the detection of a tone added to noise," J. Assoc. Res. Otolaryngol. **3**, 209–221.

Richards, V. M., and Henning, G. B. (**1994**). "The effects of two types of level variation on the size of the binaural masking level difference," J. Acoust. Soc. Am. **95**, 3003 [A].

Richards, V. M., and Nekrich, R. D. (**1993**). "The incorporation of level and level-invariant cues for the detection of a tone added to noise," J. Acoust. Soc. Am. **94**, 2560–2574.

Rose, J. E., Brugge, J. F., Anderson, D. J., and Hind, J. E. (**1987**). "Phase-locked response to low-frequency tones in single auditory nerve fibers of the squirrel monkey," J. Neurophysiol. **30**, 769–793.

Stern, R. M., and Colburn, H. S. (**1978**). "Theory of binaural interaction based on auditory-nerve data. IV. A model for subjective lateral position," J. Acoust. Soc. Am. **64**, 127–140.

Tobias, J., and Zerlin, S. (**1959**). "Lateralization thresholds as a function of stimulus duration," J. Acoust. Soc. Am. **31**, 1591–1594.

van de Par, S., and Kohlrausch, A. (**1997**). "A new approach to comparing binaural making level differences at low and high frequencies," J. Acoust. Soc. Am. **101**, 1671–1680.

van de Par, S., and Kohlrausch, A. (**1999**). "Dependence of binaural making level differences on center frequency, masker bandwidth, and interaural

parameters," J. Acoust. Soc. Am. **106**, 1940–1947.
van de Par, S., Trahiotis, C., and Bernstein, L. R. (**2001**). "A consideration of the normalization that is typically included in correlation-based models of binaural detection," J. Acoust. Soc. Am. **109**, 830–833.
Witton, C., Green, G. G. R., Rees, A., and Henning, G. B. (**2000**). "Monaural and binaural detection of sinusoidal phase modulation of a 500-Hz tone," J. Acoust. Soc. Am. **108**, 1826–1833.
Zwicker, E., and Zwicker, U. T. (**1984**). "Binaural masking-level differences in non-simultaneous masking," Hear. Res. **13**, 215–219.
Zwicker, E., and Henning, G. B. (**1984**). "Binaural masking level differences with tones masked by noises of various bandwidths and levels," Hear. Res. **14**, 179–183.
Zwicker, E., and Henning, G. B. (**1985**). "The four factors leading to binaural masking-level differences," Hear. Res. **19**, 29–47.

Precedence-based speech segregation in a virtual auditory environment

Douglas S. Brungart[a] and Brian D. Simpson
Air Force Research Laboratory, Wright-Patterson AFB, Ohio 45433

Richard L. Freyman
University of Massachusetts, Amherst, Massachusetts 01003

(Received 2 September 2004; revised 20 July 2005; accepted 29 August 2005)

When a masking sound is spatially separated from a target speech signal, substantial releases from masking typically occur both for speech and noise maskers. However, when a delayed copy of the masker is also presented at the location of the target speech (a condition that has been referred to as the front target, right-front masker or F-RF configuration), the advantages of spatial separation vanish for noise maskers but remain substantial for speech maskers. This effect has been attributed to precedence, which introduces an apparent spatial separation between the target and masker in the F-RF configuration that helps the listener to segregate the target from a masking voice but not from a masking noise. In this study, virtual synthesis techniques were used to examine variations of the F-RF configuration in an attempt to more fully understand the stimulus parameters that influence the release from masking obtained in that condition. The results show that the release from speech-on-speech masking caused by the addition of the delayed copy of the masker is robust across a wide variety of source locations, masker locations, and masker delay values. This suggests that the speech unmasking that occurs in the F-RF configuration is not dependent on any single perceptual cue and may indicate that F-RF speech segregation is only partially based on the apparent left-right location of the RF masker. [DOI: 10.1121/1.2082557]

PACS number(s): 43.66.Pn, 43.66.Qp, 43.66.Dc [GDK] Pages: 3241–3251

I. INTRODUCTION

When a target speech signal is masked by a second competing speech signal, two distinct types of masking interfere with the listener's ability to comprehend the target speech (Kidd *et al.*, 1998; Freyman *et al.*, 2001; Brungart *et al.*, 2001; Arbogast *et al.*, 2002). The first is traditional "energetic" masking, which occurs when the masking speech overlaps in time and frequency with the target speech, thus rendering some of its acoustic elements undetectable. This type of masking is typically attributed to constraints in peripheral processing. The second is "informational" masking, which occurs when the listener has difficulty segregating the audible acoustic components of the target speech signal from the audible acoustic components of a perceptually similar speech masker. Informational masking is often attributed to more central auditory processing constraints. Multitalker speech stimuli may involve both informational and energetic masking components, so traditionally it has been very difficult to experimentally isolate the contributions of these two types of masking. However, a general assumption that has been employed in a number of recent studies on multitalker speech perception is that the masking that occurs when a speech signal is masked by random noise is purely energetic and, consequently, that the informational component of speech-on-speech masking can be indirectly evaluated by comparing the effects that different target and masker manipulations have on speech intelligibility with speech maskers to those that occur for random noise maskers (Hawley *et al.*, 2000; Freyman *et al.*, 1999; 2001; Brungart, 2001b; Brungart *et al.*, 2001; Arbogast *et al.*, 2002).

Comparisons between speech and noise maskers can be particularly valuable in cases where a particular stimulus variation can be shown to influence performance with one type of masker but not the other type, thus allowing the effects of the stimulus change to be attributed entirely to one of the two types of masking. One example of stimulus manipulation that *has* consistently been shown to produce a large release from speech masking while at the same time having no measurable effect on noise masking is the precedence-based speech segregation paradigm first developed by Freyman *et al.* (1999). That manipulation involves the addition of a delayed and spatially displaced copy of the masking signal that reduces the overall signal-to-noise ratio of the stimulus but causes the masker to appear to originate from a different spatial location than the target. The three basic conditions of this experimental paradigm are illustrated in Fig. 1. The baseline condition is the F-F configuration, shown in the leftmost panel of the figure, where both the target and masking signals are presented from the same front loudspeaker. The middle panel depicts the F-R configuration, where the masking signal is moved 60° to the right of the listener. Predictably, this manipulation results in a substantial release from masking with both speech and noise maskers. However, when a 4-ms delayed copy of the 60° masker is then added back to the front loudspeaker (the F-RF configuration shown in the right panel of the figure), the resulting performance is no better than the F-F configuration when the

[a]Electronic mail: douglas.brungart@wpafb.af.mil

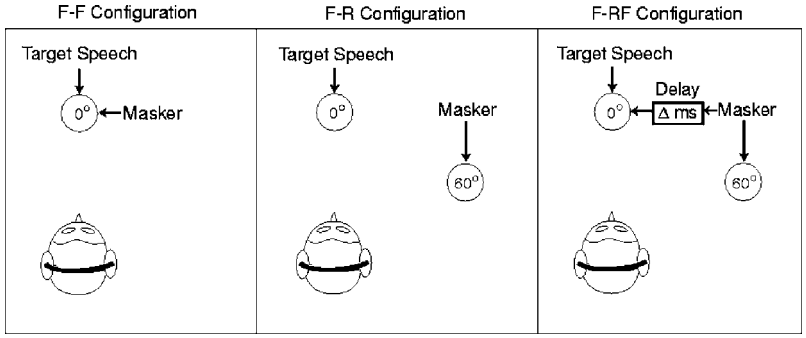

FIG. 1. Spatial configurations tested in Experiments 1 and 2. See the text for details.

masking sound is noise, but substantially better than the F-F configuration when the masking sound is speech. Freyman and his colleagues attributed this difference to the precedence effect causing listeners to perceive the RF masking stimulus lateralized well to the right of the front target. They believed that this difference in the apparent locations of the target and masking signals made it easier to segregate the similar-sounding target and masking voices in the speech masking conditions, but that it had no effect on the masking of speech by noise. However, they also acknowledged that other factors, such as a change in the apparent source width or timbre of the RF masker, might also have contributed to this effect.

Since this initial experiment (Freyman *et al.*, 1999), the F-RF paradigm has been used to examine a variety of different target and masker stimulus configurations, including configurations with more than one masking voice, masking voices in foreign languages, modulated noise maskers (Freyman *et al.*, 2001, 2004), and, in at least one case, configurations with both the target and masking speech signals located in the listener's median plane (Rakerd and Aaronson, 2005). However, little effort has been made to systematically examine the effects that different stimulus parameters such as the masker delay value and the target location have on the release from masking that occurs in the F-RF paradigm, or to determine which perceptual cues are primarily responsible for this effect. In this paper, we present the results of a series of experiments that used virtual synthesis techniques to further explore the limitations inherent in the F-RF masking paradigm, and to determine which perceptual cues are primarily responsible for the speech unmasking that occurs in the F-RF configuration.

II. EXTENDING THE F-RF LISTENING PARADIGM TO VIRTUAL ACOUSTIC SPACE

To this point, most of the research that has examined speech segregation in the F-RF listening configuration has been conducted with stimuli generated by loudspeakers in a free-field environment. While such free-field experiments unquestionably have merit, they also introduce a host of potential complications, such as unwanted reflections off of equipment in the anechoic space and inadvertent subject head motion, which can make it difficult to determine the precise cues that listeners are using to perform the speech segregation task. Free-field studies also limit the range of possible stimulus presentations to those that can be physically realized from the configuration of loudspeakers used in the experiment. Consequently, many recent studies of speech perception have instead used digitally implemented head-related transfer functions (HRTFs) (Wightman and Kistler, 1989) to generate headphone reproductions of the spatial auditory cues that normally occur in free-field listening (Crispien and Ehrenberg, 1995; Hawley *et al.*, 1999, 2004; Drullman and Bronkhorst, 2000; Shinn-Cunningham *et al.*, 2001; Brungart and Simpson, 2002a; Brungart *et al.*, 2002; Brungart and Simpson, 2003; Best, 2004). In this series of four experiments, virtual synthesis techniques were used to replicate and expand the experimental conditions reported in the original precedence-based speech segregation study by Freyman and his colleagues (1999).

A. General methods

1. Listeners

Eleven paid volunteer listeners, five male and six female, participated in the experiments. All had normal hearing ($<$15 dB HL from 500 Hz to 8 kHz), and their ages ranged from 19 to 55 years. All of the listeners had participated in previous experiments with the same speech materials used in this study.

2. Stimuli

a. Speech materials. The speech stimuli were taken from the publicly available Coordinate Response Measure (CRM) speech corpus for multitalker communications research (Bolia *et al.*, 2000). This corpus, which has been shown to be particularly sensitive to the effects of informational masking (Brungart, 2001b), consists of phrases of the form "Ready (call sign) go to (color) (number) now" spoken with all possible combinations of eight call signs ("arrow," "baron," "charlie," "eagle," "hopper," "laker," "ringo," "tiger"), four colors ("blue," "green," "red," "white"), and eight numbers (1–8). Thus, a typical utterance in the corpus would be "Ready baron go to blue five now." Eight talkers (four male, four female) were used to record each of the 256 possible phrases, so a total of 2048 phrases are available in the corpus. Variations in speaking rate were minimized by instructing the talkers to match the pace of an example CRM phrase that was played prior to each recording. The phrases were time-aligned to ensure that the word "ready" started at the same time in all the speech signals in the stimulus, but no additional efforts were made to synchronize the call signs, colors, and numbers in the competing CRM phrases. Note that all of the phrases in the CRM corpus have been processed with an 8-kHz low-pass filter, and that in this experi-

ment their sampling rate was reduced from 40 to 25 kHz in order to minimize the processing time required between consecutive stimulus presentations.

b. Speech-shaped noise. Some conditions of the virtual synthesis experiments employed a speech-shaped noise masker rather than a normal-speech masker from the CRM corpus. The spectrum of this speech-shaped noise masker was determined by averaging the log-magnitude spectra of all of the phrases in the CRM corpus.[1] This average spectrum was used to construct a 71-point, 25-kHz finite impulse response (FIR) filter that was used to shape Gaussian noise to match the average spectrum of the speech signals (Brungart, 2001a).

3. Spatial processing

The stimuli were processed with head-related transfer functions (HRTFs) that were designed to simulate the 0° and 60° source locations used in the earlier free-field experiment by Freyman and colleagues (1999). These HRTFs were derived from measurements that were made every 1° in azimuth in the horizontal plane with a compact sound source located 1 m away from a Knowles Electronics Manikin for Acoustic Research (KEMAR) (Brungart and Rabinowitz, 1999). The raw HRTFs were corrected for the response of the headphones used in the experiment (Sennheiser HD-540) and used to construct 251-point, 44.1-kHz linear-phase FIR filters matching the magnitude and phase responses of the original HRTFs over the frequency range from 100 Hz to kHz. These filters were then resampled to the appropriate sampling frequency[2] and convolved with the target and masker stimuli to simulate the 0° and 60° source locations tested in this experiment. This HRTF processing procedure has been described in greater detail in an earlier paper by Brungart and Simpson (2002b).

4. Spatial configurations

The HRTFs were used to spatially process the stimuli to replicate three of the free-field spatial configurations tested by Freyman and colleagues (1999), as illustrated at the top of Fig. 1. In the F-F configuration (left panel), both the target phrase and the masker were processed with the left and right ear HRTFs measured at 0° azimuth. In the F-R configuration, the target was processed with the left and right ear HRTFs measured at 0° and the masker was processed with those measured at 60°. In the F-RF configuration, the target and masker were processed as in the F-R condition, and an additional copy of the masker was shifted in time (delayed or advanced), processed with the HRTF measured at 0°, and added into the stimulus.

5. Procedure

The data were collected with the listeners seated in front of the CRT of a Windows-based control computer in one of two quiet, sound-treated listening rooms. Prior to each trial, the control computer randomly selected a target phrase from the 128 phrases in the corpus that were spoken by a male talker and contained the call sign "Baron" (4 talkers $\times$ 4 colors $\times$ 8 numbers = 128). Then, in the conditions with a speech masker, a masking phrase was randomly selected from the 441 phrases in the corpus that were spoken by a different male talker than the target phrase and contained a different color, number, and call sign (3 talkers $\times$ 7 call signs $\times$ 3 colors $\times$ 7 numbers = 441). In the conditions with a noise masker, a speech-shaped noise was constructed that was the same length as the target phrase. The overall rms levels of these target and masking wave forms were then scaled to produce one of five different signal-to-noise ratios (SNRs): −8, −4, 0, +4, and +8 dB with the speech masker, and −16, −12, −8, −4, and 0 dB with the noise masker.[3] Finally, the scaled target and masking signals were convolved with the appropriate HRTFs to replicate the appropriate spatial configurations and played to the listeners over headphones at a comfortable listening level (roughly 70 dB SPL) through a D/A converter (TDT RP2) connected to a headphone buffer (TDT HB7).

The listener's task in each trial was to listen for the target phrase containing the call sign "Baron" and respond by using the mouse to select the color and number contained in that target phrase from an array of colored digits displayed on the screen of the control computer.

B. Experiment 1: Precedence-based speech segregation in virtual acoustic space

The first virtual-synthesis experiment was designed to replicate the conditions that Freyman and colleagues (1999) first used to examine precedence-based speech segregation.

1. Methods

A total of 30 different conditions were examined in the experiment, including all combinations of three spatial configurations (F-F, F-R, and F-RF as shown in Fig. 1), two masker types (speech and speech-shaped noise), and five signal-to-noise ratios (−8 to +8 dB in 4-dB steps for the speech masker, and −16 to 0 dB in 4-dB steps for the noise masker). The data were collected in blocks of 60 trials with the same spatial configuration in every trial of a block, and each listener completed 4 blocks in each spatial configuration with each type of masker. The order of the blocks was randomized across the different listeners.

2. Results

The overall results of Experiment 1 are shown in Fig. 2. The left panel of the figure shows the percentage of correct color and number responses as a function of SNR for the speech masker. The right panel shows the same data as a function of SNR for the noise masker. In each case, the error bars represent the 95% confidence intervals calculated from all the raw data at each data point.

In general, the results were consistent with those of the earlier experiments by Freyman and colleagues that have tested similar listening configurations with different kinds of speech stimuli (Freyman *et al.*, 1999, 2001). In the speech masker condition, the addition of the delayed copy of the masking signal in the F-RF condition improved performance significantly relative to the baseline F-F condition at all SNR values between −4 and +4 dB (comparing the squares and

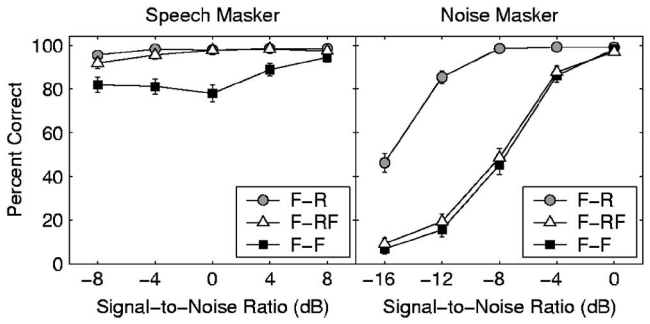

FIG. 2. Results from Experiment 1. The left panel shows the results in the trials with a speech masker, and the right panel shows results in the trials with a noise masker. The curves within each panel show the percentages of correct color and number identifications as a function of signal-to-noise ratio for each of the spatial configurations shown in Fig. 1. In each case, the masker delay value (Δ) was fixed at +4 ms. Each data point represents a total of 48 trials from each of the 11 listeners in the experiment. The error bars show 95% confidence intervals calculated from all the raw data at each data point.

triangles in the left panel of Fig. 2) [Tukey HSD post-hoc test, $p < 0.05$], while in the noise masker condition, there was no difference between the F-RF and F-F conditions at any SNR value (comparing the same points in the right panel of the figure).

There is, however, one important distinction between these data and the earlier data. In this experiment, performance in the F-RF condition with the speech masker was nearly as good as it was in the F-R condition, while, in the original experiment, performance in the F-RF condition fell roughly halfway between the F-R and F-F conditions (Freyman *et al.*, 1999). This difference probably occurred because the CRM sentences used in this experiment were substantially less sensitive to the energetic component of speech-on-speech masking than the nonsense sentences used in the 1999 study. Because the CRM uses a very small vocabulary of only four colors and eight numbers, there are many phonetically redundant differences between the keywords in the CRM task that make it less sensitive to the effects of energetic masking than most other speech intelligibility tests (Brungart, 2001a). Indeed, in this experiment, CRM performance with a noise masker in the F-F configuration was near 100% when the SNR was 0 dB (right panel of Fig. 2). In comparison, the nonsense sentence task used by (Freyman *et al.*, 1999) produced only about 75% correct responses in the same configuration. If one assumes that speech-on-speech masking consists of both an informational component that is reduced by the F-RF configuration and an energetic component that is unaffected by the F-RF configuration, then it is not surprising that the F-RF configuration caused a greater release from masking with the CRM used in this experiment (which produces a relatively slow decrease in performance at negative SNR values with a noise masker) than with nonsense sentences used in the 1999 experiment (which produced a much more rapid decrease in performance at negative SNR values).

Other than this difference in the magnitude of the F-RF masking release for the speech maskers, the results of Experiment 1 indicate that the effects of precedence-based speech segregation in virtual acoustic space are comparable to those that have been reported in earlier free-field experiments. In part, this result can be viewed as a verification that the virtual synthesis techniques and CRM speech materials used in Experiment 1 were adequate to capture the acoustic cues that the listeners were using to perform the F-RF speech segregation task in the free field. However, the result can also be viewed as a verification that the free-field results were indeed based on the direct acoustic interactions between the F and RF target and masking signals, and not on some spurious acoustic cues generated by unwanted room reflections or inadvertent listener head movements.

C. Experiment 2: Variations in delay value

Once our virtual synthesis techniques were validated in Experiment 1, the next logical step was to expand the virtual synthesis technique to examine new stimulus conditions that might provide some insight into the perceptual cues listeners use to segregate the target and maskers in the F-RF condition. Specifically, the technique was used to evaluate how the precedence-based masking release varied with the delay introduced between the F and R copies of the masking signal. In the 1999 experiment, Freyman and colleagues examined only two delay values between the masker presentations at the front and right speaker locations: a 4-ms lead at the right loudspeaker, which, due to the precedence effect, should have produced the illusion that the masking talker was located near 60°, and a 4-ms lag at the right loudspeaker which produced the illusion that the masking talker was located near the target location at 0°. Somewhat surprisingly, the results showed little difference between performance in these two configurations, despite the apparently much smaller spatial separation between the target and masker locations in the F-FR configuration. Experiment 2 was conducted to extend this experiment to a broader range of delay values and determine more generally how F-RF speech segregation varies with the delay value introduced between the two masking loudspeaker locations.

1. Methods

Experiment 2 was conducted to extend the results of the 0-dB SNR F-RF speech-masking condition of the first experiment to delay values other than the 4-ms value tested by Freyman and colleagues (1999). Thus a total of 14 different delay conditions were tested in the experiment: 12 different delay (Δ) values (−64, −4, −0.5, 0, 0.5, 1, 2, 4, 8, 16, 32, and 64 ms) plus the F-R and F-F control conditions. In this context, note that negative delay values imply that the 0° copy of the masker occurred before, and not after, the masker at 60° (a condition that has previously been referred to as the F-FR condition).

This range of delays was selected to cover the entire span of values that have traditionally been associated with the precedence effect. According to Blauert (1983), the delays of −0.5, 0 and +0.5 ms are in the range of "summing localization," where the auditory image is perceived to be between the two loudspeakers at a position dependent on the delay and the details of the stimulus. At delays of 1 ms and greater, the auditory image is heard very close to the leading

loudspeaker consistently across stimuli, the phenomenon known as the "law of the first wavefront" or precedence effect [see Litovsky *et al.* (1999) for a review]. Detailed measurements reveal that the image is often pulled slightly toward the location of the lag loudspeaker. This small contribution of the lag toward the perceived location of the image has been quantified for several different stimuli by Shinn-Cunningham *et al.* (1993), and is generally found to be between 0 and 20%, compared with 80%–100% for the lead. At sufficiently long delays, the image breaks up into the original sound plus an "echo." The delay at which this transition occurs, the "echo threshold," is dependent both on the stimulus characteristics and on the instructions given to the subject [see Blauert (1983), pp. 223–231). For speech stimuli, an estimate of 20 ms is provided in Blauert (1983) from the experiment of Cherry and Taylor (1954). Thus, the delays selected for the current study span the entire range of delays from summing localization, to precedence, to delays at which two images are likely to be perceived.

Each of the 14 delay conditions was tested with three different masking signals: (1) A one-talker speech masker, which was similar to the 0-dB SNR speech masker from Experiment 1 but with the masking phrase spoken by the same talker as the target phrase to make the baseline F-F condition more difficult. (2) A two-talker speech masker, where the masker consisted of a mixture of two randomly selected CRM phrases spoken by the same talker as the target phrase, with the rms level of each individual masking phrase scaled to match the overall rms level of the target speech. (3) A noise masker, identical to the −8-dB SNR noise-masking condition of Experiment 1. Data collection in each masking condition was divided into 56-trial blocks, with four replications of each delay condition in each block, and 12 blocks of trials collected from each listener in each condition. The data were first collected in the one-talker speech masker condition with the same 11 listeners used in Experiment 1. Data were then collected in the two-talker speech masker condition and the noise masker condition with a different panel of 10 listeners.[4]

2. Results

The results of Experiment 2 are shown in Fig. 3, which plots the percentage of correct color and number identifications as a function of the onset delay (Δ) of the front (F) masker relative to the onset time of the right (R) masker for each type of masker. For comparison purposes, the 95% confidence intervals for the F-R and F-F control conditions are shown by the gray regions at the top and bottom of each panel.

a. Noise masker. The top panel of the figure shows the results from the noise masking condition of the experiment, where performance in the task was presumably driven primarily by energetic masking effects. At most of the delay values tested, performance was as bad or worse in the F-RF configuration as it was in the baseline F-F configuration. However, significant releases from masking did occur (i.e., performance was significantly better than in the F-F configuration) when the delay was set to −0.5, +1.0, or +2.0 ms (Tukey HSD post-hoc test, $p < 0.05$).

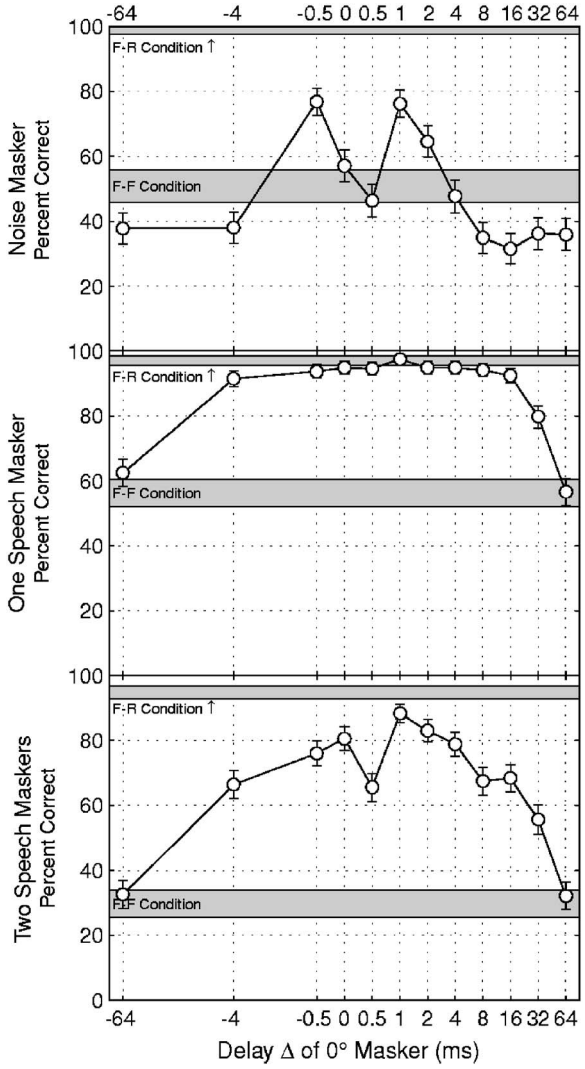

FIG. 3. Percent correct color and number identifications in the F-RF configuration of Experiment 2 as a function of the delay value Δ. The top, middle, and bottom panels show performance in the noise masker, one-talker speech masker, and two-talker speech masker conditions of the experiment. Each data point represents a total of 48 trials from each listener in the experiment. The error bars show 95% confidence intervals calculated from all the raw data at each data point, and the gray bands at the top and bottom of the figure show the 95% confidence intervals from the F-R and F-F control conditions.

A priori, one might expect more energetic masking to occur in the F-RF configuration than in the F-F configuration because the addition of the second masking stimulus (the masker presented at 60 deg to the right) increases the total energy in the masking stimulus. However, the addition of the delayed right side masker can in some cases improve performance when it produces periodic comb-filtered "notches" in the spectrum of the masker [with center frequencies spaced every $(1/\Delta)$ Hz in the frequency spectrum starting at $(1/2\Delta)$ Hz] that allow the listener to get glimpses of the target speech signal in one or both ears. These notches can be particularly useful if they occur at different frequencies in the listener's two ears because listeners are known to be able to benefit from the ear with the highest SNR within each frequency band (Zurek, 1993). However, the practical advantages of these comb-filtered notches in the masker spectrum

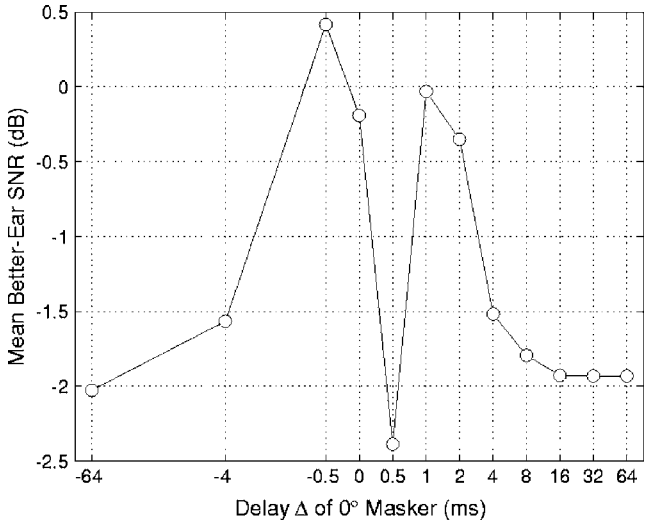

FIG. 4. Mean better-ear SNR in each delay condition of Experiment 2. The data were calculated by convolving the HRTFs from the experiment with speech-shaped noise, processing the resulting signals with a 50-band ERB filterbank, and averaging the SNR values at the better ear within each frequency band. See the text for details.

are limited to a relatively small range of masker delay values. When the delay value Δ is very high ($\geqslant$4 ms) or very low ($\leqslant$−4 ms), the comb-filtered notches are spaced so closely together in frequency that they cannot be resolved within a single critical band. This explains why no release from masking is seen for the high or low delay values in Fig. 3. There are also certain delay values that cause the initial and delayed copies of the masker to arrive at one of the listener's ears at the same time, thus producing a constant decrease in the effective SNR value at all frequencies in that ear. In the stimuli used in this experiment, an in-phase combination of the front and right copies of the masker occurred in the listener's right ear when the delay value was 0 ms, and in the listener's left ear when the delay value was +0.5 ms (which almost exactly matched the interaural time delay in the 60° HRTF used in this experiment).

In order to determine the extent to which the binaural integration of the signal from the ear with the best SNR within each critical band could explain the general pattern of performance seen in the top panel of Fig. 3, the target and masking HRTFs used in each delay condition of Experiment 2 were convolved with speech-shaped noise and processed with a 50-band ERB filterbank [using the MATLAB functions in the Auditory Toolkit (Slaney, 1998)]. The resulting output signals were used to determine the SNR in the better-ear within each frequency band; these values were averaged across all the bands to determine the mean better-ear SNR ratio for each delay condition. The resulting values, plotted in Fig. 4, indicate a pattern of performance that is nearly identical to the one seen in the top panel of Fig. 3. This strongly suggests that better-ear SNR effects are primarily responsible for the release from masking seen at the −0.5, +1.0, and +2.0-ms delay values of Experiment 2.

b. One speech masker. The middle panel of Fig. 3 shows performance in the single speech masker condition of Experiment 2. These results indicate that substantial releases from masking occurred across a broad range of delay values in the F-RF spatial configuration when the masker was speech. Performance was in excess of 90% correct responses at delay values ranging from −4 ms to as high as +16 ms. Some release from masking still occurred at +32 ms, but little or no release occurred at ±64 ms. Subjective listening by the experimenters indicated that the initial and delayed copies of the masker sounded like they were spoken by two different spatially separated talkers in the ±64 ms conditions, suggesting that the fusion of the echoed masking phrase may have broken down at those delay values. Note that in Experiment 2 the same talker was used for both the masker and the target, resulting in a decrease in performance in the baseline F-F condition of the experiment to roughly 60% correct responses as compared to roughly 80% in Experiment 1. Similar results have been reported in other two-talker experiments using the CRM stimuli (Brungart, 2001b).

c. Two speech maskers. The bottom panel of Fig. 3 shows performance in the two speech masker condition of Experiment 2. This condition was much more difficult than the single-masker condition, and led to substantially worse performance in the F-F condition (30%) as compared to performance in the same condition with only one masker (roughly 60%). This increased difficulty also resulted in a much larger variation in performance with the delay value of the masker than the one-masker condition, suggesting that performance in the one-masker condition of the experiment may have been limited by a ceiling effect. In the two-masker condition, performance was best when the delay value was equal to 1 ms, where it was significantly better than for all other delay values less than 0 ms or greater than 4 ms but still significantly worse than in the F-R control condition (Post-hoc Tukey HSD test, $p=0.05$). When the delay was set to 0.5 ms, performance was significantly worse than when the delay was 0 ms or 1 ms (Tukey HSD, $p<0.05$). This dip in performance was probably related to the increase in energetic masking that occurred at that delay value (e.g., see top panel of Fig. 3 and Fig. 4). As in the one-masker condition, the results of the two-masker condition show that the F-RF listening configuration produces a release from speech-on-speech masking across a broad range of delay values, spanning from −4 to +32 ms.

d. Discussion. One of the most compelling aspects of the original experiment by Freyman and colleagues (1999) was that the F-RF configuration produced a substantial increase in performance with a speech masker but no increase in performance (or even a slight decrease in performance) with a noise masker. This made it possible to attribute the entire release from masking that occurred in the F-RF configuration with a speech masker to a release from informational, rather than energetic masking. Although the results in Fig. 3, along with those of a similar experiment conducted in the free field by Rakerd and Aaronson (2004), clearly suggest that the F-RF configuration produces a significant release from masking across a broad range of delay values, it is equally clear that a release from energetic masking can account for part of this effect at some delay values (−0.5, +1, and +2 ms in this case). Thus it is only possible to argue that the release from masking in the F-RF configuration is a purely informational effect at a subset of the delay values

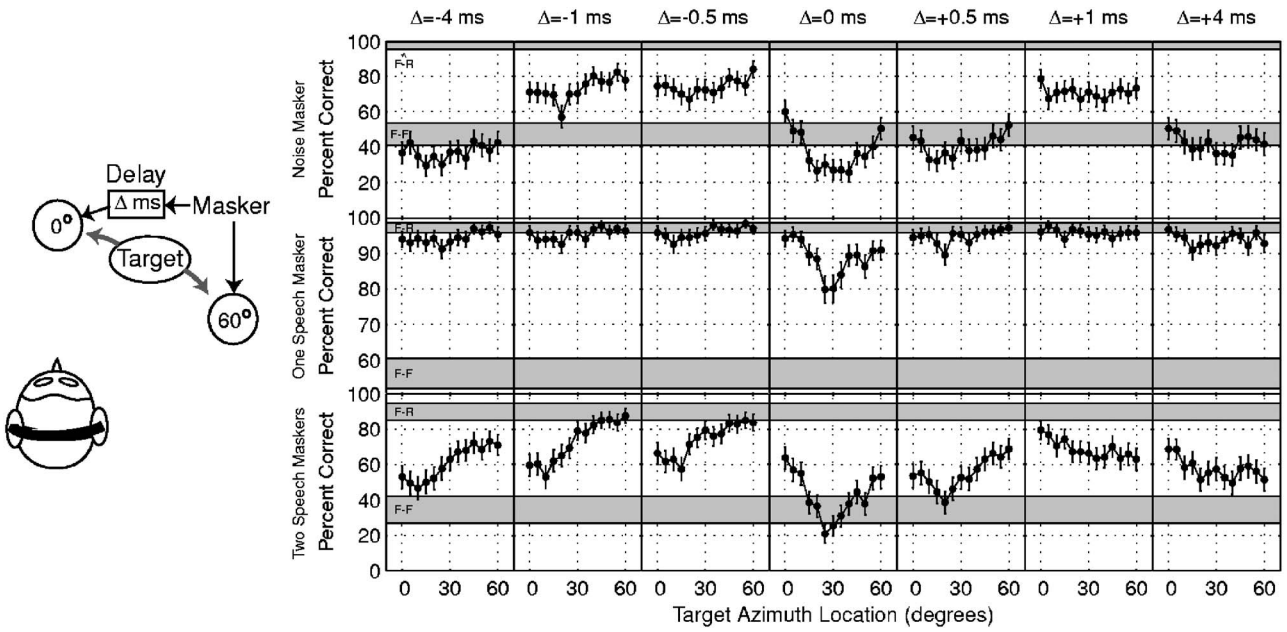

FIG. 5. Percent correct color and number identifications in the configurations of Experiment 3 with a RF masker and a target that varied in location from 0° to 60° (as illustrated at the left-hand side). The top row shows results from the noise masker condition, the middle row shows the single speech masker condition, and the bottom row shows two talker speech masker condition. The error bars show 95% confidence intervals calculated from all the raw data in each bin.

tested in Experiment 2. However, even if we exclude those delay values where significant releases from energetic masking may have occurred, it is apparent that the release from informational masking in the F-RF condition with a speech masker extends over a much wider range of delay values than the ±4-ms values that have previously been examined by Freyman and colleagues (1999, 2001). Furthermore, the results show relatively little difference in performance between the +4-ms condition, where there was a time lead in the right copy of the masker and precedence presumably should have shifted the apparent location of the masking voice toward 60° and away from the location of the target talker, and the −4-ms condition, where there was a lead in the front copy of the masker and precedence presumably should have shifted the apparent location of the masking voice toward the target talker (Blauert, 1983). Yet, despite the relatively large predicted difference in the apparent spatial separation of the target and masking talkers in these two conditions, there was effectively no difference between the +4- and −4-ms conditions in the one-talker masking condition, and only about a 12 percentage point advantage in the +4-ms condition in the two-talker masking condition. This result could potentially be explained in either of two ways (Freyman *et al.*, 1999): (1) The F-RF segregation is based on indirect source cues like apparent "source width" or nonspatial cues like timbre that are not directly related to apparent location in the horizontal plane; or (2) even when the delay value was −4 ms, the RF masker appeared to be displaced far enough to the right of the 0° target speaker to allow the listener to successfully segregate the target and masking talkers. If the latter argument is true and the F-RF segregation occurs because the target talker is heard at 0° and the masking talker is heard *between* 0° and 60°, then one might expect the F-RF segregation cue to break down if the location of the target talker were laterally shifted to match the apparent location of the RF masker. Experiment 3 was conducted to test this hypothesis explicitly.

D. Experiment 3: Variations in target location

1. Methods

Subjectively, the most salient difference between the F-F stimuli and the F-RF stimuli is that the masker in the F-RF configuration appears to originate from a spatial location somewhere between the front and right loudspeaker locations. This suggests that the RF masker might interfere more with a target signal located somewhere between 0° and 60° than it does with the 0° target in the standard F-RF configuration. In Experiment 3, this hypothesis was tested by varying the HRTFs used to process the target stimulus to move its apparent azimuth location from 0° to 60° in 5° increments (left panel of Fig. 5). The delay in the RF masker was set to one of seven different values: −4, −1, −0.5, 0, 0.5, 1, and 4 ms. As in Experiment 2, the same talker was always used for both the target and masking phrases, and the experiment was conducted with three different kinds of maskers: a speech-shaped noise masker at a SNR value of −8 dB, a single-talker speech masker at a SNR value of 0 dB, and a two-talker speech masker with the rms level of each interfering talker set to match the rms level of the target speech. The experiment was divided into 52- to 78-trial blocks, with two to three different delay values within each block. Data were collected first in the single-talker speech masking condition with 9 of the 11 listeners used in Experiment 1. They were then collected in the two-talker speech masker condition and the noise masker condition with the 10 listener panel used in the corresponding conditions of Experiment 2. In all, a total

of 24 trials were collected with each listener at each of the 72 combinations of target location, masker delay value, and masker type tested in the experiment.

2. Results and discussion

The results from the individual listeners in each masking condition of Experiment 3 were subjected to a repeated-measures analysis of variance on the two factors of target angle and delay value. These ANOVAs revealed significant main effects of both target angle and delay value, and a significant interaction between these factors, in all three of the masking conditions of the experiment ($p < 0.001$).

Figure 5 plots the percentage of correct color and number identifications in Experiment 3 as a function of the angle of the target talker for each of the seven values of the delay Δ tested in the experiment. The top panel of the figure shows performance in the condition with a noise masker. In this condition, it is apparent that the delay value had a substantially greater impact on performance than target location: performance was universally good (i.e., better than the F-F baseline condition) when the delay value was −1, −0.5, or +1 ms, and was almost always as bad as, or worse than, the F-F control condition when the delay value was −4, 0, +0.5, or +4 ms. This pattern of predicted performance is generally consistent with the one found for the noise maskers in Experiment 2, and it probably reflects variations in the effective better-ear SNR across the different delay values tested in the experiment.

The middle panel of Fig. 5 shows performance in the single-masking talker condition of Experiment 3. As in Experiment 2, these results show that the listeners performed extremely well in almost every condition. Even in the worst case tested, where the delay was set to 0 ms, performance never fell below 80% correct responses. Furthermore, the 0 ms condition was the only one where the target angle seemed to have any meaningful effect on performance.

Target talker location did, however, have a significant effect on performance in the two-masking-talker condition, which is shown in the bottom panel of Fig. 5. In that masking condition, target location had a substantial greater effect on performance than in the single speech masker condition for every delay value tested. This suggests that a ceiling effect, rather than a true lack of perceptual sensitivity, may have accounted for the relatively angle-independent performance that occurred at most delay values in the single-talker masking condition. Furthermore, the two-talker masking results seem to support the hypothesis that speech segregation in the F-RF configuration is influenced in part by differences in the apparent locations of the target and masking talkers. In the conditions with a leading front masker (negative delay value), for example, where the listeners should have heard the interfering talkers somewhere near to the front masker location, performance was consistently 20 percentage points better when the target was located near 60° than when it was located near the front. Similarly, when the masker from the right led (delay values greater than or equal to 1 ms), where the listeners should have heard the masking talkers somewhere near 60°, they performed roughly 20 percentage points better when the target talker was located toward the front than when it was located toward the side. Both of these results support the notion that listener performance in the F-RF listening configuration is influenced by the spatial separation between the apparent locations of the target and masking speech signals. In the negative delay configurations, there is also some indication that a local minimum occurred in the performance curve at a location slightly to the right of target speech signal (located at 10° in the −4 ms delay condition and at 15° in the −1-ms condition). Although we did not measure the perceived locations of the masking talkers in these conditions, these minima might represent the points where the apparent location of the target matched the apparent location of the masker.

The most puzzling results are those associated with delays of 0 and 0.5 ms. In these conditions, one would expect summing localization to cause the masking talker to appear to be located somewhere near the midpoint of the 0° and 60° masker locations, and the local minima in performance that occurred near 30° in those two conditions are consistent with this. However, these conditions also produced U-shaped performance curves in the noise-masker condition, suggesting that energetic masking effects might also have contributed to the decrease in performance that occurred at intermediate target locations in these conditions. At the present time, it is simply not possible to determine the relative contributions that informational and energetic masking might have made to the performance curves in these conditions of the experiment.

E. Experiment 4: An F-FF listening configuration

Although the results in the two-masker condition of Experiment 3 suggest that the apparent location of the F-RF masking voice played an important role in helping the listener segregate the target speech signal from the masking stimulus, the results in the one-masker condition were nearly perfect in the conditions with a nonzero delay value regardless of the actual location of the target speech. This strongly suggests that the delayed copy of the masker that was added to the stimulus in the F-RF listening configurations provided some segregation cues that were not directly related to the apparent lateral locations of the competing talkers. For example, the addition of a delayed copy of the masker may have changed the apparent width of the masking voice or it may simply have changed the timbre of the masking voice enough to help distinguish it from the target voice. Experiment 4 was conducted to determine whether some release from masking might still occur in the single-talker masking condition even when the potential spatial location cues were minimized by placing both the original and delayed copies of the masking signal at the same location as the target speech (as illustrated in the left panel of Fig. 6).

1. Methods

A total of ten conditions were tested in this experiment: an F-FF configuration with each of nine different delay values (0, 0.25, 0.5, 1, 2, 4, 16, 32, and 64 ms) plus the standard F-F baseline condition. As in Experiments 2 and 3, the data were all collected at a SNR value of 0 dB, and the same

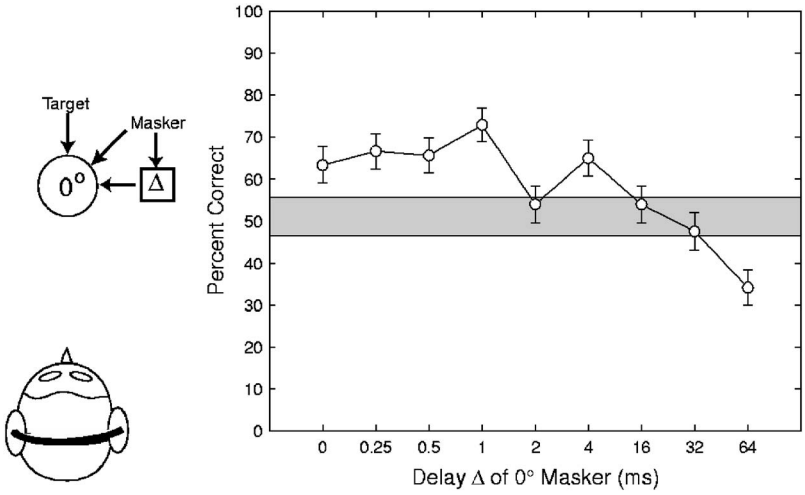

FIG. 6. The left panel depicts the F-FF configuration used in Experiment 4, in which the original and delayed copies of the masking signal were added together and presented from the same location as the target speech (0°). The right panel shows the percent correct color and number identification scores for each delay value tested in the experiment. Each data point represents 48 trials from each of the 11 listeners, and the error bars show 95% confidence intervals calculated from all the raw data in each bin. The gray area shows the 95% confidence interval of the baseline F-F condition of the experiment.

talker was always used for both the target and masking phrases. The data were divided into blocks of 54–66 trials, with each of the 11 listeners participating in 48 trials in each of the 10 conditions of the experiment.

2. Results

The results for each of the 10 conditions of Experiment 4 are illustrated in Fig. 6. As in Fig. 3, the shaded region indicates the 95% confidence interval of the baseline FF condition. Although the effect is relatively small, the results clearly show that there was some improvement in performance when an additional copy of the masker was added at the same location as the target signal. A one-factor, within-subject ANOVA on the individual results of the 11 listeners in each condition revealed that the main effect of delay was significant ($F_{(9,81)}=19.0, p<0.0001$) and a post-hoc test (Tukey HSD)indicated that the F-FF conditions with delay values of 0–1 ms and 4 ms all produced a significant increase in performance relative to the baseline F-F configuration. In the 0-ms delay condition, the addition of the second copy of the masking signal effectively produced a uniform 6 dB reduction in the SNR value of the stimulus. Such a reduction in SNR would always lead to a monotonic decrease in performance with a noise masker, so the increase in performance that occurred in the 0-ms F-FF condition in this experiment cannot be explained by a release from energetic masking. A more likely explanation is that the 6-dB level difference reduced the effects of informational masking by allowing the listener to selectively focus attention on the quieter talker in the stimulus. Although it is not clear what strategy the listeners were using in the 0.5-, 1-, and 4-ms delay conditions, it is apparent that the available segregation cues in the F-FF configuration are much weaker than those in the F-RF configuration: performance with a single speech masker never exceeded 72% in the F-FF configuration, while performance in the F-RF configuration was better than 80% in the worst condition tested (with a 0-ms delay value and the target talker at 30°) and better than 90% in almost every other condition tested. Thus it seems that spatial separation of the two masking signals is necessary to obtain a substantial speech segregation benefit from the addition of second copy of the masker in the F-RF configuration.

III. SUMMARY AND CONCLUSIONS

In this series of experiments, we have explored the release from masking that occurs when a time-advanced or delayed, spatially offset copy of the interfering voice(s) are added to a stimulus containing two or three spatially colocated competing speech signals. Knowledge about the release from masking that occurs when this second copy of the masker is added was extended in several ways.

First, the effect, previously tested only with nonsense target sentences recorded by one individual female talker, has been extended to a new set of stimuli (the CRM corpus) that utilized four different male talkers. The release from masking due to the precedence-based masker was, if anything, clearer with these stimuli, and nearly equal to the improvement obtained by simply moving a single-source masker away from the target location (Fig. 2, left). This is presumably attributable to the large informational component and small energetic component in the masking of one CRM utterance by another (Brungart, 2001a, 2001b).

Second, the release from masking effects for speech-on-speech masking, and the lack of effect for noise maskers (Fig. 2, right) were extended to conditions in which the spatial manipulations were created virtually and the stimuli were presented via headphones. This eliminated the possibility that the original effects were spurious, due to head movements or reflections off equipment in an anechoic room.

Third, the release from masking was found to be extremely robust with respect to the delay of the second copy of the masker (Fig. 3, middle and bottom panels). Release from masking was observed with the delay in the summing localization range (e.g., 0 or 0.5 ms) and across a wide range of delays in the precedence range (1–16 ms). The only delays at which an effect was not observed were at ±64 ms, where it is assumed that fusion of the two-source masker into a single image broke down. At this long delay it is likely that the masker was perceived to be at two locations, one in the front (matching the target) and one near the 60° loudspeaker.

Fourth, while the absence of energetic masking release at the ±4-ms delays used by Freyman *et al.* (1999) was confirmed, at some other delays the release from energetic masking was quite substantial (Fig. 3, top panel). This release from masking was probably due to improvements in signal-

to-noise ratio created by comb filtering (Fig. 4). Thus, it cannot be assumed without measurement that improvements in speech recognition resulting from the addition of a copy of the masker are, in general, entirely attributable to a release from informational masking.

Fifth, with regard to conditions in which it was clear that the addition of a second masker location produced a release from informational masking, the current data confirm that differences in perceived location between target and masker often play an important role. This was most obvious in the more difficult two-masking talker conditions where it was found that speech recognition depended on target location in a manner generally consistent with the assumed differences in target-masker perceived location (Fig. 5, bottom).

Finally, in less difficult conditions of the experiment (i.e., those with a single masking talker), it is not clear that perceived spatial separation was required to achieve a release from informational masking. Considerable release from masking was found even when a single-source target was moved through the range of angles assumed to include the perceived locations of the two-source maskers (Fig. 5, middle). This suggests that the two-source masker was relatively easy to distinguish from the single-source target even when both the target and masking auditory images originated from approximately the same apparent location. However, spatial separation between the two copies of the RF masker did seem to play a significant role in the precedence-based unmasking effect—relatively little release from masking occurred in Experiment 4 where the original and delayed copies of the single-talker masker were presented at the same location as the target speech (Fig. 6). These results seem to indicate that some spatial attribute of the RF masker other than its apparent location (perhaps its apparent spatial width) was sufficient to produce a high level of performance in the single-talker masking conditions of the experiment.

ACKNOWLEDGMENTS

Portions of this research were funded by AFOSR Grant No. HE-01-COR and NIDCD Grant No. DC01625.

[1]Note that this included the four female talkers, who were not used in these experiments, so one might expect the noise to have a slightly greater high-frequency emphasis than our speech stimuli.

[2]The sampling frequency used in the experiment was 25 kHz, but through a technical oversight the KEMAR HRTFs used for the convolution were inadvertently resampled to 22.05 kHz. The effect of this resampling was to scale down the effective size of the KEMAR manikin by 12%. While this certainly caused a change in the HRTFs relative to those of an unscaled KEMAR manikin, the magnitude of this change was within the range that would be expected to occur due to size variations in a population of real human listeners [Algazi, *et al.* (2001), for example, measured variations in 24 anthropomorphic parameters in 45 listeners and found an average percentage standard deviation of ±13%]. Thus, the rescaling that occurred was practically equivalent to selecting nonindividualized HRTFs measured on an arbitrarily selected human head that was slightly smaller than that of the KEMAR manikin. For reference, note that the intertragal distances of the 11 subjects used in this experiment ranged from 12.3 to 14.4 cm, compared to 14 cm with the standard KEMAR manikin and 12.6 cm for the effectively rescaled KEMAR manikin used in this study.

[3]The range of SNRs was lowered by 8 dB with the noise masker because previous experiments have shown that speech-in-noise performance with the CRM task is near 100% at SNR values greater than 0 dB (Brungart, 2001b).

[4]This new panel included 3 of the listeners from Experiment 1 and 8 listeners who did not participate in the first experiment.

Algazi, V. R., Duda, R. O., Thompson, D. M., and Avendano, C. (**2001**). "The CIPIC HRTF Database," Proceedings of 2001 IEEE Workshop on Applications of Signal Processing to Audio and Acoustics, New Paltz, NY, 21–24 October, pp. 99–102.

Arbogast, T., Mason, C., and Kidd, G. (**2002**). "The effect of spatial separation on informational and energetic masking of speech," J. Acoust. Soc. Am. **112**, 2086–2098.

Best, V. (2004). "Spatial hearing with simultaneous sound sources: A psychophysical investigation," Ph.D. thesis, University of Sydney.

Blauert, J. (**1983**). *Spatial Hearing* (MIT, Cambridge).

Bolia, R., Nelson, W., Ericson, M., and Simpson, B. (**2000**). "A speech corpus for multitalker communications research," J. Acoust. Soc. Am. **107**, 1065–1066.

Brungart, D. (**2001a**). "Evaluation of speech intelligibility with the coordinate response measure," J. Acoust. Soc. Am. **109**, 2276–2279.

Brungart, D. (**2001b**). "Informational and energetic masking effects in the perception of two simultaneous talkers," J. Acoust. Soc. Am. **109**, 1101–1109.

Brungart, D., Ericson, M., and Simpson, B. (**2002**). "Design considerations for improving the effectiveness of multitalker speech displays," Proceedings of the International Conference on Auditory Display (ICAD 2002), Kyoto, Japan, 2–5 July, pp. 169–174.

Brungart, D., and Rabinowitz, W. (**1999**). "Auditory localization of nearby sources. I. Head-related transfer functions," J. Acoust. Soc. Am. **106**, 1465–1479.

Brungart, D., and Simpson, B. (**2002a**). "The effects of spatial separation in distance on the informational and energetic masking of a nearby speech signal," J. Acoust. Soc. Am. **112**, 664–676.

Brungart, D., and Simpson, B. (**2002b**). "Within-channel and across-channel interference in the cocktail-party listening task," J. Acoust. Soc. Am. **112**, 2985–2995.

Brungart, D., and Simpson, B. (**2003**). "Optimizing the spatial configuration of a seven-talker speech display," Proceedings of the International Conference on Auditory Display (ICAD2003), Boston, MA, 6–9 July.

Brungart, D., Simpson, B., Ericson, M., and Scott, K. (**2001**). "Informational and energetic masking effects in the perception of multiple simultaneous talkers," J. Acoust. Soc. Am. **110**, 2527–2538.

Cherry, E., and Taylor, W. (**1954**). "Some further experiments upon the recognition of speech, with one and two ears," J. Acoust. Soc. Am. **26**, 975–979.

Crispien, K., and Ehrenberg, T. (**1995**). "Evaluation of the 'Cocktail Party Effect' for multiple speech stimuli within a spatial audio display," J. Audio Eng. Soc. **43**, 932–940.

Drullman, R., and Bronkhorst, A. (**2000**). "Multichannel speech intelligibility and talker recognition using monaural, binaural, and three-dimensional auditory presentation," J. Acoust. Soc. Am. **107**, 2224–2235.

Freyman, R., Balakrishnan, U., and Helfer, K. (**2001**). "Spatial release from informational masking in speech recognition," J. Acoust. Soc. Am. **109**, 2112–2122.

Freyman, R., Balakrishnan, U., and Helfer, K. (**2004**). "Effect of number of masking talkers and auditory priming on informational masking in speech recognition," J. Acoust. Soc. Am. **115**, 2246–2256.

Freyman, R., Helfer, K., McCall, D., and Clifton, R. (**1999**). "The role of perceived spatial separation in the unmasking of speech," J. Acoust. Soc. Am. **106**, 3578–3587.

Hawley, M., Litovsky, R., and Colburn, H. (**1999**). "Speech intelligibility and localization in a multi-source environment," J. Acoust. Soc. Am. **105**, 3436–3448.

Hawley, M., Litovsky, R., and Culling, J. (**2000**). "The 'cocktail party' effect with four kinds of maskers: Speech, time-reversed speech, speech-shaped noise, or modulated speech-shaped noise," Proceedings of the Midwinter Meeting of the Association for Research in Otolaryngology, p. 31.

Hawley, M., Litovsky, R., and Culling, J. (**2004**). "The benefit of binaural hearing in a cocktail party: Effect of location and type of interferer," J. Acoust. Soc. Am. **115**, 833–843.

Kidd, G. J., Mason, C., Rohtla, T., and Deliwala, P. (**1998**). "Release from informational masking due to the spatial separation of sources in the iden-

tification of nonspeech auditory patterns," J. Acoust. Soc. Am. **104**, 422–431.
Litovsky, R., Colburn, H., Yost, W., and Guzman, S. (**1999**). "The precendence effect," J. Acoust. Soc. Am. **106**, 1633–1654.
Rakerd, B., and Aaronson, N. (**2004**). "Spatial release from informational masking," J. Acoust. Soc. Am. **115**, 2597.
Rakerd, B., and Aaronson, N. (**2005**). "Spatial release from informational masking along the front-back dimension," J. Acoust. Soc. Am. **117**, 2537.
Shinn-Cunningham, B., Schickler, J., Kopco, N., and Litovsky, R. (**2001**). "Spatial unmasking of nearby speech sources in a simulated anechoic environment," J. Acoust. Soc. Am. **110**, 126–134.
Shinn-Cunningham, B., Zurek, P., and Durlach, N. (**1993**). "Adjustment and discrimination measurements of the precedence effect," J. Acoust. Soc. Am. **93**, 2923–2932.
Slaney, M. (**1998**). "Auditory Toolbox, Version 2," Technical Report No. 1998-010. Tech. Rep., Interval Research Corporation.
Wightman, F., and Kistler, D. (**1989**). "Headphone simulation of free-field listening. II. Psychophysical validation," J. Acoust. Soc. Am. **85**, 868–878.
Zurek, P. M. (**1993**). "Binaural advantages and directional effects in speech intelligibility," in *Acoustical Factors Affecting Hearing Aid Performance*, 2nd ed., edited by G. Studebaker and I. Hochberg (Allyn and Bacon, Portland).

Thresholds for second formant transitions in front vowels[a)]

Diane Kewley-Port[b)] and Shawn S. Goodman
Department of Speech and Hearing Sciences, Indiana University, Bloomington, Indiana 47405

(Received 22 August 2003; revised 3 August 2005; accepted 29 August 2005)

Formant dynamics in vowel nuclei contribute to vowel classification in English. This study examined listeners' ability to discriminate dynamic second formant transitions in synthetic high front vowels. Acoustic measurements were made from the nuclei (steady state and 20% and 80% of vowel duration) for the vowels /i,I,e,ɛ,æ/ spoken by a female in /bVd/ context. Three synthesis parameters were selected to yield twelve discrimination conditions: initial frequency value for F2 (2525, 2272, or 2068 Hz), slope direction (rising or falling), and duration (110 or 165 ms). F1 frequency was roved. In the standard stimuli, F0 and F1–F4 were steady state. In the comparison stimuli only F2 frequency varied linearly to reach a final frequency. Five listeners were tested under adaptive tracking to estimate the threshold for frequency extent, the minimal detectable difference in frequency between the initial and final F2 values, called ΔF extent. Analysis showed that initial F2 frequency and direction of movement for some F2 frequencies contributed to significant differences in ΔF extent. Results suggested that listeners attended to differences in the stimulus property of frequency extent (hertz), not formant slope (hertz/second). Formant extent thresholds were at least four times smaller than extents measured in the natural speech tokens, and 18 times smaller than for the diphthongized vowel /e/. © *2005 Acoustical Society of America.* [DOI: 10.1121/1.2074667]

PACS number(s): 43.71.Es, 43.66.Fe [PA] Pages: 3252–3260

I. INTRODUCTION

According to a traditional description of vowel sounds, the steady-state formant frequencies F1 and F2 have been considered the most important perceptual cues (Peterson and Barney, 1952). For over 20 years, however, research has shown that for American English (AE) dynamic formant information also plays an important role in vowel recognition (Strange, Verbrugge, Shankweiler, and Edman, 1976; Strange, 1989; Andruski and Nearey, 1992; Strange, Jenkins, and Johnson, 1993; Hillenbrand, Getty, Clark, and Wheeler, 1995; Hillenbrand and Nearey, 1999). Vowels, of course, usually occur in consonantal context, for example the common syllable type in AE, the CVC. Two kinds of voiced formant movement occur in CVCs: movement during the transition portion between consonants and vowels, and movement in the center portion (nucleus) of the vowel. Formant transitions carry acoustic cues for both consonants and vowels (Liberman and Mattingly, 1985; Nearey, 1989; Kewley-Port, 1995; Ohde and Abou-Khalil, 2001). During the initial and final portions of the syllable, formant transitions are characterized by short duration and usually rapid movement across large frequency ranges. Vowel nucleus dynamics are characterized by longer durations and slower changes across smaller frequency ranges, most clearly seen in vowels like [e^I] and [o^U]. Fully diphthongized vowels such as /ɑɪ/ and /oɪ/ are characterized by long durations with extensive changes in frequency. Perhaps because of the more limited movement in non-diphthongized vowels, the nucleus dynamics have often been characterized as 'quasi-steady state.' However, it has been shown that systematic movement does occur (Nearey, 1989; and Hillenbrand *et al.*, 1995).

The dynamic cues in syllables available in either the consonantal transitions alone (Strange, 1989) or the nucleus region alone (Nearey and Assmann, 1986) have been shown sufficient to produce high vowel identification rates (Hillenbrand *et al.*, 1995; Andruski and Nearey, 1992; Hillenbrand and Nearey, 1999). A complete theory of vowel perception must explain the roles of both types of formant movement in vowel identification. In fact, to model the underlying processing mechanisms of vowel perception, the ability to discriminate small differences in vowel dynamics should also be known. A reasonable hypothesis is that dynamic formant cues cannot be used for vowel identification if they cannot be perceived. Yet little is known about how much formant movement is needed to exceed thresholds for discriminating dynamic changes. The purpose of the present study is to estimate the psychophysical thresholds for discrimination of formant movement in the vowel nucleus. With few exceptions, previous threshold studies that used dynamic stimuli investigated transitions more similar to consonantal dynamics, i.e., transitions that are short and rapid. For instance, work has been done using short-duration tone glides (e.g., Summers and Leek, 1995; Madden and Fire, 1996, 1997; Sek and Moore, 1999) and rising or falling single-formant, speech like transitions (Porter, Cullen, Collins, and Jackson, 1991; van Wieringen and Pols, 1994). Porter *et al.* (1991) measured jnds for speech formant transitions. Stimuli consisted of a single formant modeled after F2 consonantal transitions connected to a steady-state portion. Because of the great temporal and spectral differences, interpretation of

[a)]Portions of this work were presented in a talk given at the 138th meeting of the Acoustical Society of America on June 4, 2000 in Atlanta, GA.
[b)]Electronic mail: kewley@indiana.edu

TABLE I. Average F1 and F2 formant values in hertz for the female talker for three repetitions of the words shown. Measurements were made at three intervals, 20%, the steady-state (SS, visually identified from spectrograms) and 80% of the total vowel duration.

	F1			F2		
	20%	SS	80%	20%	SS	80%
/bid/	319	303	320	2525	2600	2646
/bɪd/	358	363	391	2253	2251	2038
/bed/	486	452	347	2291	2438	2666
/bɛd/	519	588	621	2060	2068	1893
/bæd/	684	698	784	2075	2115	1846

these results for nucleus dynamics is probably not predictive of thresholds of formant dynamics in vowel nuclei.

A related study has examined dynamics in nonspeech stimuli, namely, harmonic profiles (Drennan and Watson, 2001). Thresholds were estimated for profile stimuli that were harmonically spaced (200 Hz) when fundamental frequency was swept over time. The duration was similar to that of a long vowel nucleus (400 ms). No consistent differences in thresholds for static versus dynamic stimuli were found.

Previous studies in this series have examined thresholds for formant frequency in stimuli that represent steady-state vowel nuclei. Kewley-Port and Watson (1994) measured thresholds for frequency difference in steady-state first and second formants of isolated female vowels. Their stimuli were comparable in length to vowel nuclei (160 ms). In that study, thresholds for discrimination were constant over the F1 region at about 14 Hz, and constant in the F2 region with a Weber ratio $\Delta F/F$ of 1.5%. Other studies (e.g., Sinnott and Kreiter, 1991; Hawks, 1994) have reported similar results. Kewley-Port and her colleagues have extended these studies to examine thresholds in CVC context, and in phrases and sentences. Together these studies have yielded systematic descriptions of the degrading effects of phonetic context and other experimental variables on the ability for humans to discriminate small differences in vowel formants. However, the vowel nuclei in all these studies used steady-state formants (i.e., frequency in the vowel nucleus did not change over time), while the formants in the nuclei of most natural AE vowels vary in frequency over time.

The present study was designed to examine the discrimination of formant transitions that more closely resemble natural AE vowel nuclei. An important issue for a theory of vowel perception is to determine the stimulus conditions in which nucleus dynamics are the information-bearing properties of vowels. If the observed vowel dynamics are not above threshold, then these differences cannot contribute information to vowel classification. Specifically, this study determined the smallest amount of frequency change in a second formant that could be discriminated under nearly optimal listening conditions by well-trained listeners. A working hypothesis for this study was that if formant dynamics in the nucleus contribute to vowel identification, they should exceed optimal thresholds for discriminating formant transitions by an amount sufficient to be salient in running speech, e.g., at least a factor of two. Because vowels are often modeled with steady-state formants, the standard vowels used as the basis for the formant transition comparisons were chosen to have static (flat) formant frequencies. Synthesis parameters manipulated in the comparison stimuli, based on measurements of natural vowels from a female talker, included initial frequency of F2, slope direction, duration, and F1 frequency. This study determined thresholds using psychophysical procedures for dynamic changes in F2 frequency for five synthetic front vowels.

II. METHOD

A. Participants

Six young (under 35 years) listeners with normal hearing participated in this study. All listeners had audiometric thresholds of 15 dB HL or better at octave intervals from 250 to 4000 Hz. Listeners were paid for their participation. One listener could not produce consistent thresholds and voluntarily terminated participation. This study reports on data obtained from the remaining five listeners.

B. Stimuli

To select the acoustic parameters to manipulate in these psychoacoustic studies of vowel nuclei, we derived the stimulus parameters from natural speech. The American English front vowels, /i,ɪ,e,ɛ,æ/, recorded digitally at a 10 kHz sample rate, were analyzed. The vowels in the original utterances were produced by a female talker from the North Midland dialect region (Labov, 2004) in /bVd/ context in short sentences. Formants were measured for each word using linear predictive coding (LPC) analysis with a 128-point Hamming window, preemphasis, and 12 coefficients. To specify vowel formant change primarily in the nuclei and reduce the consonantal effects, formant values for F1 and F2 were measured at 20% and 80% of vowel duration, following Hillenbrand *et al.* (1995) for three repetitions of each vowel ($n=15$). Also, the apparent F2 steady-state value was determined visually and measured from spectrograms. These measures are shown in Table I.

Based on these acoustic measurements, synthesis parameters were selected with the goal of producing vowels that resembled the intended vowels even though various simplifications were imposed. It was observed that the initial F2 values of /ɪ/ and /e/ (at 20%) were very close in frequency (2253 and 2291 Hz), as were the initial F2 values of /æ/ and /ɛ/ (2060 and 2075 Hz). Thus to simplify the experiment, the mean value of each pair was used as the initial frequency value to represent both vowels. The measured initial F2 fre-

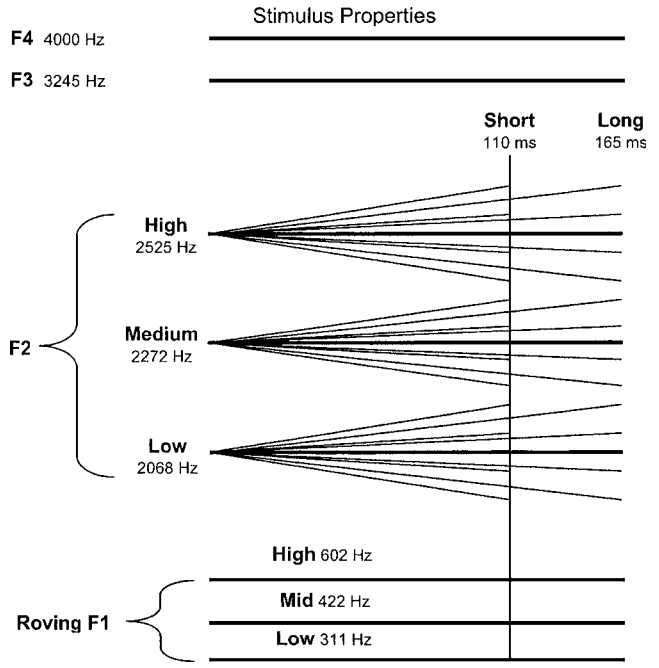

FIG. 1. Stylized formants represent the major stimulus variables for the synthetic vowels used in this study; three values of F1, three onset values of F2, rising and falling slope direction, and short or long duration.

quency of /i/ was substantially higher than the others. Thus, the resulting initial second formant frequency values were 2525 Hz for /i/, 2272 Hz for /I-e/, and 2068 Hz for /ɛ-æ/.

From the acoustic analysis, it was noted that across the nucleus portion, each vowel had either a general rise or fall in F2 frequency (Table I). Thus a second experimental variable of either a rising or a falling F2 slope was chosen. The set of vowels analyzed contained both long (/i,e,æ/) and short (/I,ɛ/) vowels. In order to examine possible effects of vowel length, two durations were calculated from the average of the long vowels (154, 166, 173 ms) and the average of the short vowels (100, 124 ms), rounded to 5 ms: long (165 ms) and short (110 ms). Together these three factors yielded 12 stimulus conditions: initial F2 frequency (×3), direction of formant movement (×2), and duration (×2). Clearly some of the combinations do not occur in AE vowels, but the intention of this study was to systematically investigate the effects of all three factors. The general pattern of these 12 F2 transitions is shown in Fig. 1.

Normally a change in second formant frequency is coupled to a change in first formant frequency. F1 frequency was also of interest as a parameter, but in order to focus on the movement in F2 with simpler acoustic stimuli, it was decided to fix F1 as a steady-state parameter. Because the F1 values measured in the original 15 words ranged over 370 Hz, it appeared necessary to select several F1 values in order to have the stimuli resemble AE vowels. Three values of F1 were calculated using a similar grouping strategy as for F2 (/i/,/I-e/, and /ɛ-æ/). This resulted in three steady-state frequency values for F1: low (/i/, 311 Hz), medium (/I-e/, 422 Hz), and high (/ɛ-æ/, 602 Hz). Since the front vowels used in this experiment have a wide separation between F1 and F2, it was hypothesized that F1 frequency would not affect thresholds for F2 formant movement; therefore F1 frequency was roved randomly throughout the experiment. Steady-state values were chosen for F3 (3245 Hz) and F4 (4000 Hz). The bandwidths of the first three formants were 70, 90, and 170 Hz, for F1, F2, and F3, respectively.

The fundamental frequency was chosen to be steady state at 200 Hz (appropriate for this female talker). Although this choice also compromised the naturalness of the stimuli, a steady-state F0 was chosen to avoid possible undesirable interactions between shifting harmonics and their placement relative to the moving F2 formant peaks.

Using the above parameters, the vowel nuclei were synthesized with the cascade branch of the KLTSYN synthesizer (see Klatt, 1980). Stimuli had a length of either 165 or 110 ms with an additional 15 ms rise time and a 20 ms fall time. Eighteen *standard vowels* were synthesized with steady-state F1 and F2 values (3 F2 Frequencies × 2 lengths × 3 F1 frequencies). Of course these standard stimuli sounded unnatural because of the various constraints imposed to systematically manipulate the stimulus factors. Nonetheless, to document how these 18 synthetic stimuli would be identified by naïve American English listeners, a brief identification experiment was performed. Besides the 18 standard vowels, another set of stimuli was included that more carefully preserved the parameters measured from the recorded utterances. This set of five "original" stimuli were synthesized with both F1 and F2 formant frequencies linearly changing from the average 20% to the 80% intervals measured for each of the five natural syllables (shown in Table I), and with the appropriate long (165 ms) or short (110 ms) duration, although F0, F3, and F4 were still steady state. Eight naïve, normal-hearing American English listeners from Indiana were recruited for the identification task. The keyword responses included the ten monophthongal vowels in order to provide a wide choice of vowel responses. Following a short training task with another female speaker's syllables, listeners heard six repetitions of the 28 vowels.

Overall subjects selected the five front vowels from the ten-vowel response set 78% of the time. Identification results showed that the original stimuli modeling the F1 and F2 transitions were correctly identified at 58% on average, with /i/ most accurately identified at 88%. The 18 standard vowels, all with fixed formants, had no predicted category labels. Two results were notable. The stimuli with the high F2 and low F1 were categorized 95% as /i/. Second, in all cases changes in F1 from low to mid to high values radically altered the perceived vowel quality. For example, for a stimulus with about 40% classification of a vowel with one value of F1, the percentage responses dropped to 15% and then 0% as F1 changed.

Summarizing, although the values for the parameters of F1, F2, vowel duration and formant movement were derived from natural speech, the resulting compromises in stimulus construction yielded stimuli that were not well categorized as AE vowels except for /i/. Clearly, however, the acoustic parameters manipulated in this study of thresholds for formant movement are information bearing properties of AE vowels.

Sets of test stimuli were also synthesized for the comparison conditions. Each test set had F2 values that either

increased or decreased in frequency over the entire stimulus. These changes in F2 were specified as the amount of frequency change in hertz between onset and offset (called *frequency extent*). The shape of the F2 transition was determined by linear interpolation calculated by KLTSYN between the initial and final values. Stimuli for each F2 transition were synthesized three times, once for each of the F1 frequencies. Thus there were 36 sets, of stimuli (3 F2 frequencies $\times$ 2 lengths $\times$ 3 F1 frequencies $\times$ 2 slope directions). For each set, the change in frequency of the F2 extent varied in 14 steps. Based on pilot work, unequal step sizes were used to change the frequency of F2 extent. The largest steps used increments of around 50 Hz, while the smaller steps had 5 Hz increments for rising F2s and 8 Hz decrements for falling F2s. During testing a few vowel stimuli proved more difficult than expected for some listeners, and to ensure that accurate thresholds were being measured, new sets were synthesized wherein the smaller steps had 7 Hz increments for rising F2s and 10 Hz decrements for falling F2s.

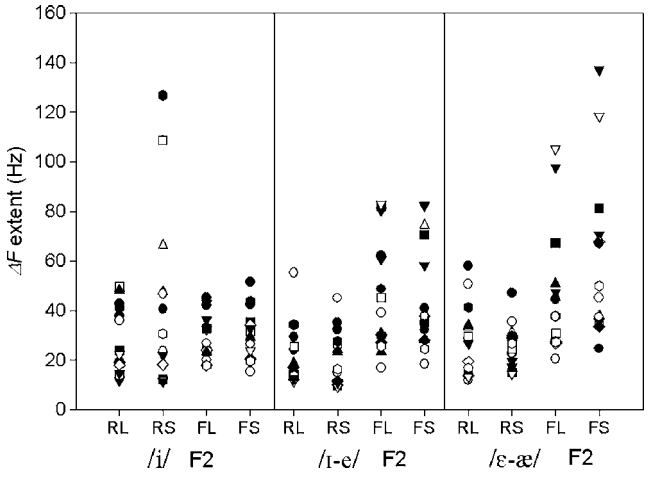

FIG. 2. Each symbol is a threshold estimated for ΔF extent for one listener for all 180 data points [F1(3) $\times$ F2(12) $\times$ listeners(5)]. Panels are organized by the onset of F2 frequency, and within panels for rising long (RL), rising short (RS), falling long (FL), and falling short (FS) formants for a total of 12 stimulus conditions.

C. Apparatus

Listeners were seated in a sound-treated booth facing a computer monitor and keyboard. Stimuli were presented monaurally to the right ear through a TDH-39 headphone. Up to three listeners were tested simultaneously, each listening to a separate output through a Tucker-Davis Technologies (TDT) array processor in a 486 computer. Stimuli were output through a 16-bit digital-analog (D/A) converter at a 10-kHz sample rate (TDT DA1) followed by a 4.3 kHz lowpass filter with a 96 dB/octave rolloff uploaded to a TDT PF1.

One standard vowel (medium F2=2272 Hz, medium F1=422 Hz) was selected as the calibration vowel. Output gain was set so the sound pressure level measured in an NBS-9A coupler with a Larson Davis sound level meter (model 800B) on linear weighting was 70 dB SPL. The levels of the other eight standard vowels [(3 values of F2 $\times$ 3 values of F1)-1] were adjusted via the overall gain parameter of the KLTSYN synthesizer so that their overall rms energy was within ±1 dB of the calibration stimulus. One standard could not meet this tolerance level without undergoing severe peak clipping in the synthesis. Its level was accordingly adjusted to within ±2 dB of the calibration stimulus.

D. Procedure

A two-down-one-up adaptive tracking procedure (Levitt, 1971) estimated the difference in F2 offset frequency between standard and comparison stimuli at 70.7% correct. On each trial, listeners heard three successive stimuli. The standard stimulus was always presented first, followed by presentation of the standard and comparison stimuli in random order. Listeners indicated which of the last two intervals contained the stimulus that sounded different from the original reference by pressing the appropriate key on a keyboard. Feedback for correct resonses was provided following each trial. Each block consisted of 90 trials. To obtain nearly optimal thresholds, only one of the 12 stimulus conditions for F2 was presented per block, although the three F1 frequencies were roved randomly within a block.

In order to obtain reliable thresholds, listeners were highly trained. Listeners were trained with the parameters of the stimuli set to medium F2, long duration, and rising slope. This condition was chosen as the training stimulus because rising slopes were easier than the falling slopes in pilot work. During training, listeners completed an estimated 3500 trials each over four sessions.

Following training, listeners were tested five days per week and were allowed to proceed at their own pace. A test session lasted for approximately 1.5 h per day, including breaks. On average, listeners completed 11 blocks of 90 trials each day. The 12 stimulus conditions were tested in random order across subjects. For each condition, blocks were run until it was judged that stable values had been achieved based on examination of block-by-block plots of the reversal means. The stopping rule was near-asymptotic performance over four blocks. Wide variability was seen in the amount of time spent on each condition. The average time spent on each condition was 14.43 blocks (1299 trials), but ranged from 6 to 30 blocks (540 to 2700 trials). No clear patterns emerged to explain this variability.

For each block, a value ΔF in hertz was calculated as the difference in the formant frequency extent between the standard and test stimuli, using the average of the reversals, excluding the first three reversals. A threshold for formant frequency extent, ΔF extent, for each listener was averaged over the last four blocks.

III. RESULTS

Results, reported as ΔF extent, were first examined for individual variability. Figure 2 displays the 180 independently measured data points for the 12 F2 conditions, each with three F1 formants, from the five listeners (15 points/condition). As can be seen in Fig. 2, ΔF extent values had narrow distributions for seven of the 12 conditions while in

TABLE II. ΔF extent thresholds in hertz for F2 transitions for the four factors of initial F2 frequency (low, mid, high), vowel length (short, long), slope direction (rising, falling), and fixed value of F1 (low, mid, high). The F1 values were calculated as arithmetic averages over the five subjects. The pooled data across the five subjects and three values of F1 ($N=15$) were calculated from the antilog of the means of the $\log_{10}$ thresholds (see text). All values in hertz.

		F2 Short			F2 Long		
Slope	F1	/ɛ-æ/ 2068	/I-e/ 2272	/i/ 2525	/ɛ-æ/ 2068	/I-e/ 2272	/i/ 2525
Rising	Low=311	31.7	26.4	51.3	38.7	29.1	28.7
	Mid=422	25.3	16.2	40.9	22.0	17.0	31.6
	High=602	21.8	19.0	46.6	21.1	16.7	29.4
	Mean (antilog)	19.6	15.8	38.6	18.8	16.3	23.6
Falling	Low=311	65.7	44.1	34.8	49.0	40.9	31.9
	Mid=422	58.4	42.3	27.8	48.2	41.7	24.3
	High=602	51.9	50.8	26.9	41.7	54.4	32.6
	Mean (antilog)	45.6	44.2	25.0	38.1	44.0	30.0

the other five conditions there was a positive skew in the distributions. This presence of a few highly elevated thresholds is similar to that reported for other complex stimuli, for example, vowel formant thresholds (Kewley-Port and Watson, 1994) and dynamic profiles (Drennan and Watson, 2001). However, this resulted in a high correlation ($r=0.80$) between the means and the variances of the data. The data were therefore subjected to a $\log_{10}$ transform. This transform created a more normal distribution and reduced the correlation between means and variances ($r=0.26$). Thus statistical analyses were carried out on the $\log_{10}$ transform of the 180 individual data points. Average thresholds are reported in hertz (e.g., Table II and in subsequent figures) by taking the antilogs of the transformed values, an averaging method that dampens the effect of the skewed thresholds. A Mauchley Sphericity test was also performed on the data, and results suggested that the assumption of sphericity was violated (Max and Onghena, 1999). A multivariate analysis of variance (MANOVA) was therefore preferred to the univariate three-way repeated measures ANOVA. The results of the MANOVA may be interpreted in much the same way as the results of an ANOVA.

A four-factor MANOVA was calculated for F1 frequency, F2 frequency, slope direction, and length, treated as within-subject factors, and $\log_{10}\Delta F$ extent as the dependent variable. The ΔF extent thresholds for these four factors, and their means, are shown in Table II. Results showed a significant main effect only for F2 frequency [$F(2,3)=14.96$, $p<0.028$]. A significant two-way interaction was obtained for F2 frequency $\times$ slope [$F(2,3)=22.36$, $p<0.016$]. There was also one significant three-way interaction for F1 frequency $\times$ F2 frequency $\times$ length [$F(4,1)=11\,818.15$, $p<0.007$].

A. Effect of F1

In this experiment it was not anticipated that F1 frequency would affect discrimination of F2 transitions. Indeed, no main effect was found for F1, or for any two-way interactions involving F1. The values of ΔF extent for F1 averaged over listeners are shown in Table II. Given the significant three-way F1 $\times$ F2 $\times$ length interaction, results were scrutinized for specific F1 effects. The largest effects were for long stimuli when F1 was low and for F2 for /i/ or /ɛ-æ/ stimuli. Overall the effect of F1 on F2 transition thresholds was small and not systematic.

B. Effect of F2 frequency and slope direction

The significant main effect for F2 frequency reflected that ΔF extent was smaller for the /i/ and /I-e/ frequencies compared to the /ɛ-æ/ F2 frequency. Although there was no effect of the F2 slope direction overall [$F(2,3)=3.94$, $p>0.10$], the significant interaction for F2 frequency $\times$ slope direction reflected that ΔF extent was smaller for rising than falling second formants for /I-e/ F2 and /ɛ-æ/ F2 as shown in Fig. 3. For /i/ F2, however, ΔF extent was nearly the same for rising and falling. Given these results were based on the $\log_{10}$ transformed data, additional analyses of the data were conducted to verify that the above interpretation was correct. For example, the medians of the ΔF extent values in hertz represented in Fig. 3 produced a display with the same pattern of interactions.

Note that in Fig. 3 it appears that thresholds for falling F2 transitions increase as frequency decreases. It is unlikely

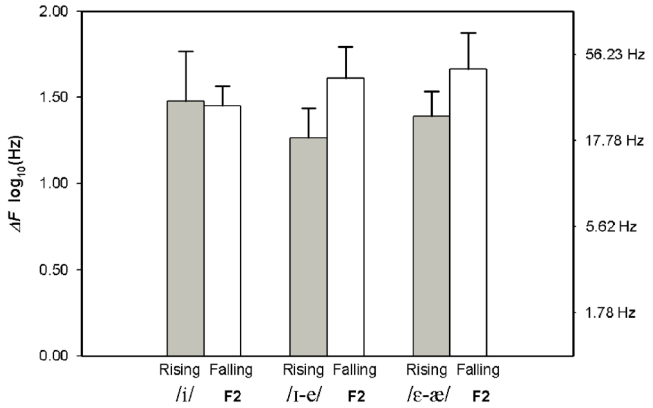

FIG. 3. ΔF extent thresholds calculated from the $\log_{10}$ transformed data to show the interaction between the F2 onset frequencies and slope direction. Error bars indicate standard deviation in the $\log_{10}$ units. The right-hand axis indicates equivalent values in hertz.

that the increase in threshold for falling slopes was due to a closer proximity of F1 than for rising slopes, because the highest F1 center frequency was 602 Hz and the lowest F2 center frequency was 2011 Hz. Thus there was always at least 1329 Hz separating the F1 and F2 formants for the vowels investigated here.

C. Effects of duration

There was no significant difference between thresholds for the long and short durations. Thus slope is not the primary acoustic property used in discrimination, because the slopes for the short conditions are markedly steeper than the slopes for the long conditions (0.167 versus 0.280, 0.167 versus 0.247, 0.191 versus 0.328 Hz/ms for increasing F2). Apparently listeners pay attention to the extent of formant frequency movement (hertz) rather than the slope of formant movement (hertz/milliseconds), a conclusion compatible with those of Nearey and Assmann (1986).

IV. DISCUSSION

A. Formant transition thresholds

The purpose of this study was to determine thresholds for discriminating dynamic changes in the second formant frequency of front vowels. Four acoustic properties that contribute to the accurate identification of American English vowels were manipulated, F1 frequency, F2 frequency, slope direction, and length. Thresholds differed primarily as a result of manipulating onset of F2 frequency and for specific combinations of F2 onset with the slope of the formant transitions. Given our psychophysical approach to investigating these formant transitions, it is of theoretical interest to know how auditory sensitivity for frequency change in formants compares to that for simple tones (tone glides). The most comparable research is that of Dooley and Moore (1988). In the Dooley and Moore (1988) second experiment, tone glides started at 2000 Hz, with durations of either 100 or 200 ms long. Similar to our formants, duration had little effect on thresholds for either set of stimuli. They obtained thresholds around 15 Hz in comparison to our F2 thresholds ranging from 19–52 Hz. Thus the lowest thresholds in Fig. 3 for the rising /I-e/ F2 were similar in magnitude to those for tone glides, while the highest F2 thresholds were about 300% higher than for tones. These threshold differences reflect our significant F2 X slope interaction. However, slope direction appears to affect dynamic formants differently than tone glides because slope direction had no effect in Dooley and Moore (1988) for their shorter tone glides in experiment 2. However, their results for longer glides are the opposite of ours, with thresholds being smaller for falling tone glides than for rising glides.

Summarizing, thresholds for our F2 transitions were roughly similar to those for tone glides with similar parameters, except that thresholds for falling formant transitions increased as F2 frequency decreased. While it is unclear what reasons might underlie such differences in the effect of slope direction for simpler versus more complex vowel stimuli, we suspect that the presence of the fixed formants (F1, F3, and F4) are an important factor, as well as a possible interaction between F0 and F2.

How do formant thresholds patterned after vowel nuclei compare to those patterned after stop consonants? The most comparable data for stop transitions is that of Porter *et al.* (1991). They used a single formant transition rising or falling to 1800 Hz followed by about a 200 ms steady-state segment. For their 120 ms transition, the thresholds range from 50 to 150 Hz. These single formant thresholds are about 300% greater than for ours for vowel formant stimuli. Of the many differences between experiments, one reason for the higher thresholds may be that listeners in Porter *et al.* (1991) participated for 1–2 h, while our listeners were trained extensively before data collection started (5 h training, and an average of 24 h testing). Another difference between vowel and stop transitions is that thresholds were also smaller for falling single formants than rising ones in Porter *et al.* (1991). Thus auditory processing of stop-like, single formant stimuli appears to be different from that of vowel-like, multiformant stimuli.

An important question for understanding the processing of dynamic stimuli is whether transition slope or frequency extent provides the information to differentiate frequency transitions. For our vowel transition stimuli, the short (110 ms) versus long (165 ms) duration did not have an effect on the ΔF extent thresholds, and therefore frequency extent was the distinguishing acoustic property. These results are similar to those reported for tone glides by both Madden and Fire (1997) and Moore and Sek (1998) who found no threshold difference between the 50 and 400 ms stimuli. An earlier study by Nábělek and Hirsh (1969) also found that ΔF extent was an important acoustic property in the perception of tone glides. Results are not as clear for single formant studies. While Porter *et al.* (1991) and van Wieringen and Pols (1994) reported that thresholds increased significantly as the single formants shortened, additional experiments by van Wieringen and Pols (1994) did not reveal whether ΔF extent or transition rate was the primary acoustic property for these short stimuli. Thus it appears that for several different types of dynamic stimuli including vowels, the perceptually salient acoustic property is the frequency achieved at the end of the transition, ΔF extent, not transition slope or rate.

B. Comparison to steady-state formants

Given that most sounds are dynamic, but most frequency thresholds are measured from static stimuli, it is important to understand differences in auditory processing of dynamic versus static stimuli. The present thresholds for dynamic formants can be directly compared to static vowel thresholds reported by Kewley-Port and Watson (1994). They used F2 frequency values of 2900, 2500, and 1950 Hz to represent the vowels /i, e, æ/ measured from the same talker used here. Using experimental procedures similar to those of the present study, they estimated ΔF, the minimum frequency change in a steady-state F2 needed to detect either an increment or decrement in frequency from a steady-state standard. Vowel duration for the steady-state stimuli was 160 ms com-

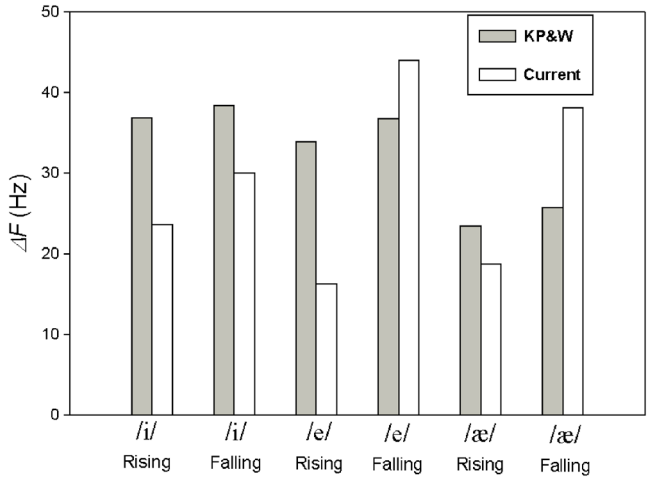

FIG. 4. F2 thresholds from two studies are displayed. The light grey bars are ΔF thresholds for steady-state formants from Kewley-Port and Watson (1994). The white bars are ΔF extent thresholds from the current study. Note that the onset frequencies are somewhat different between the two studies. The labels rising or falling indicate a positive or negative frequency shift for the steady-state formants, and the slope direction of the formant transitions.

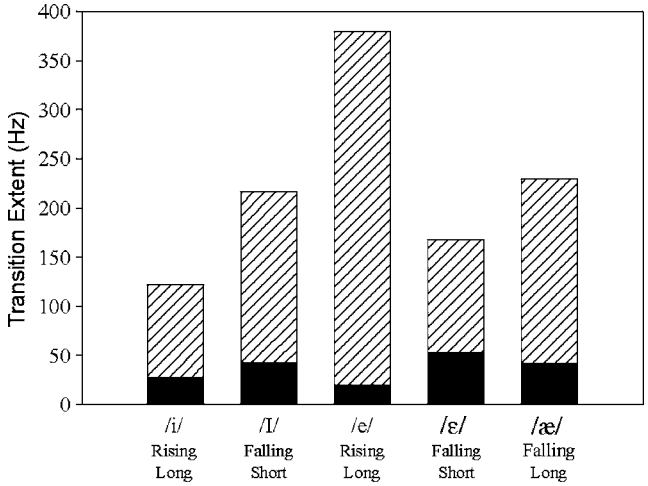

FIG. 5. The height of the black bars displays the ΔF extent thresholds in this study for the stimulus conditions as labeled. The length of the hatched bars displays the average F2 transition extent measured from 20% to 80% of the vowel duration for the female talker's vowels recorded for this study.

pared to 165 ms in the present study. Thresholds are plotted for both experiments in Fig. 4 for both the rising and falling changes in frequency.

For the six formant comparisons, the differences between ΔF extent thresholds and steady-state thresholds ranged from −14.2 to 16.1 Hz. While this variability is somewhat high, the overall means of the thresholds were similar [30.9 versus 32.5 Hz for dynamic versus steady-state, $t(10) = 0.36$, $p = 0.73$, two-tailed]. Moreover, no general pattern of differences in thresholds in Fig. 4 between the dynamic and steady-state F2s is apparent. These results are similar to those for another type of complex stimuli, harmonic profiles. Drennan and Watson (2001) also observed no significant pattern of differences in amplitude detection thresholds between static and dynamic harmonic profiles. However, these results for harmonic complexes contrast with those for single sinusoids where thresholds for glides were significantly greater than for static tones (Dooley and Moore, 1988). Summarizing, although auditory processing appears to be influenced by several factors for harmonic complexes, static versus dynamic stimulus parameters do not produce consistent effects.

C. Comparison to natural vowel transitions

Thresholds for formant transitions in this study were obtained under nearly optimal listening conditions. In natural speech it must be assumed that formant movement substantially exceeds optimal perceptual thresholds in order for communication to be robust in ordinary listening conditions. To quantify this relationship, the ΔF extent thresholds were compared to natural F2 transitions measured from the three original recordings of /bVd/ stimuli (Table I). Of the 12 conditions tested, five correspond to the natural vowels /i,I,e,ɛ,æ/ measured from the original talker when the factors of F2 initial frequency, vowel duration, and F2 slope are matched. The length of the black bars in Fig. 5 represents the ΔF extent thresholds, and the measured change in F2 from 20–80 % of vowel duration is shown by hatched lines. Thresholds for ΔF extent were rather constant and small relative to the amount of naturally occurring movement. The amount of naturally occurring movement was on average more than four times larger than the thresholds for ΔF extent for the vowels /i,I,ɛ,æ/. For the highly diphthongized vowel /e/, the amount of naturally occurring movement was 18 times larger than the threshold for ΔF extent. One reason for the large increase in the /e/ ratio was that the ΔF extent threshold was smallest for /e/. Clearly naturally occurring vowel F2 transitions are perceptually very salient, given that the thresholds are better by a factor of at least four than the actually observed vowel transitions.

Although the present study examined only a small number of F2 transitions from a female talker's vowels, an intriguing hypothesis is suggested by the above analysis. It is clear from numerous reports that dynamic formants improve accurate vowel identification (c.f. Hillenbrand and Gayvert, 1993). In fact, Hillenbrand and Nearey (1999) showed that larger formant dynamics in their synthetic vowels correlated with more accurate vowel identification. Presumably, when formant dynamics are particularly important cues to vowel identity, a corresponding difference in the sensory abilities to process formant transitions should be observed. In the present data the best sensitivity to F2 transitions was for /e/, both in terms of the absolute lowest threshold and in relation to the amount of naturally occurring F2 transition (Fig. 5). A plausible hypothesis for the large differences in sensitivity is that the auditory system becomes more sensitive to formant dynamics for just the vowels, such as /e/, where formant change is a more important cue to vowel identity. This hypothesis is in agreement with one suggested by Guenther, Nieto-Castanon, Ghosh and Tourville (2004), namely, that the brain puts more neural resources into regions of the acoustic space where differences in sound are behaviorally more important. Additional data on formant transitions are needed to determine whether this hypothesis generalizes to all American English naturally produced vowels.

Another issue examined in this study was the effect F1 had on F2. In our perceptual study, there was no systematic

effect of F1 manipulation on the discrimination of F2 vowel transitions. Given that F1 and F2 onsets were widely separated by more than 1300 Hz, this was the expected result. However, F1 differences alone can affect vowel categorization. The classification of some American English vowels appears to rely primarily on differences in F1 when F2 values are very similar (Hillenbrand *et al.*, 1995). In a vowel perception study, Johnson, Fleming, and Wright (1993) reported that when F2 is fixed, listeners selected different vowel categories when F1 was manipulated. Our small identification experiment also had stimuli in which only F1 varied, and large changes in vowel identification were obtained. Thus we expect to observe significant interactions between F1 and F2 in formant discrimination for some other vowels, particularly for the back vowels where formants are close together such that changes in one formant clearly affect the amplitude and shape of the other.

D. Relation between formant extent and formant transition thresholds

The concept of a behavioral threshold implies that differences between a standard and its comparison are all equally detectable by the listener. Thus spectral differences between the flat formant standard and the just discriminable formant transition at threshold across formants are in some sense perceptually equivalent. One possibility is that the actual acoustic differences are the same, i.e., formant extent thresholds in hertz were constant for different formants. Clearly this was not true because variability in the formant extent thresholds exceeded 280% over the 12 conditions, ranging from 15.8 to 45.6 (Table II). Formant extent is a value in hertz based on the difference in *synthesis parameters*, offset minus onset of F2. The actual acoustic differences among stimuli resulting from the specified parameters still need to be measured. Note that the F0 for all vowel stimuli was constant at 200 Hz so that the frequencies of the harmonics for each stimulus were the same, namely, the 25 harmonics from 200 to 5000 Hz. Thus the primary physical differences between the standard and comparison stimuli were intensity level differences for the 25 harmonics. Although these intensity differences can be fit with a formant resonance (e.g., using LPC), the present analysis focuses on the intensity differences. To measure the harmonic component level differences, a discrete Fourier transform (DFT) was taken of each pitch pulse of the stimuli. For each harmonic component, the DFT of the standard was subtracted from the DFT of the comparison stimulus nearest threshold, as shown Fig. 6 for /ɛ-æ/ F2 long, rising transition. The results showed a linear increase or decrease over time in the decibel level, primarily for the two harmonics closest to the formant peak.

To quantify the spectral differences between the standard and comparison at threshold, two metrics were calculated. They were the intensity differences in decibels for the harmonics with the maximum decrement and the maximum increment at the stimulus offset. Given that intensity changed linearly over time, any measures at other proportional intervals (i.e., 1/2, 1/3 etc) of the total duration would yield the same relative metrics. Across all 12 conditions at offset, the decrement metric ranged from 1.53 to 2.69 dB, while the increment metric ranged from 1.5 to 3.58 dB. Not only are these two metrics far from constant, each correlated highly with ΔF extent, namely, $r=0.71$ for the increment metric and $r=0.48$ for the decrement metric (both $N=12$). Examining these metrics and other spectral-temporal measures of the transitions, we concluded that stimulus differences derived from acoustic measures could not yield a constant metric that captured the perceptual equivalence of the transition thresholds. Rather, some processing of this information in the auditory system must transform the physical differences into some internal representation that is more constant.

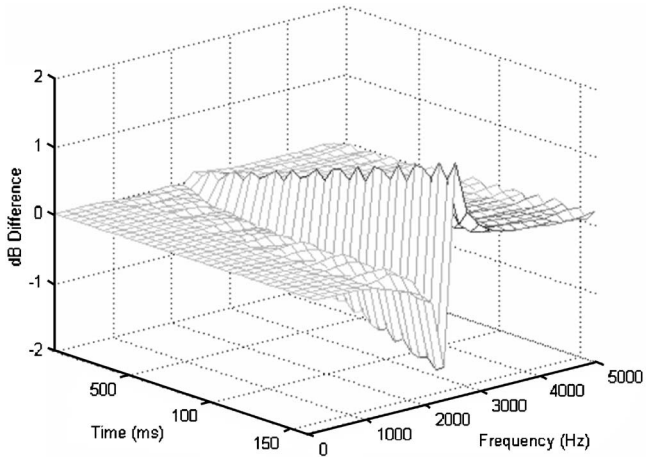

FIG. 6. For the /ɛ-æ/ F2 long, rising stimulus, the acoustic difference between the DFTs of the standard and the comparison vowel nearest to threshold is displayed (see text).

Obvious choices of models for auditory processing are the excitation and loudness pattern models developed by (Glasberg and Moore, 1990). We have previously been successful in applying them to find a constant metric for formant threshold data for steady-state vowels (Kewley-Port and Zheng, 1998; Liu, 2002). However, there appear to be no guidelines or logical extensions on how to apply these models to our stimuli with dynamic formants, and our modest efforts to apply these models to ΔF extent thresholds were not successful. We note the application of excitation pattern models to tone glide discrimination (e.g., Moore and Sek, 1998) focused on changes in frequency while our stimuli had fixed-frequency harmonics with variable level differences. Thus, it appears that it is premature to adapt auditory models developed for frequency glides of sinusoids to the harmonic changes in formant transitions.

V. CONCLUSIONS

Listeners' ability to discriminate F2 transitions that are found in the nucleus of front vowels were reported for the manipulation of four factors, F1 frequency, initial F2 frequency, rising versus falling slope direction, and short versus long vowels in synthetic speech. The major results are summarized as follows:

- Changes in F2 onset affected ΔF extent thresholds, but changes in F1 frequency, F2 slope direction, and length did not. An interaction between F2 onset and slope direction was seen for some conditions.
- Listeners attended to differences in the stimulus property of the frequency extent at the offset of the transition, not the formant slope.
- ΔF thresholds for vowel transitions were roughly similar to those for steady-state formants.
- Estimated ΔF extent thresholds in hertz were similar to those obtained for tone glides with analogous acoustic parameters.
- The effects of several stimulus factors, e.g., rising versus falling slope, on ΔF extent thresholds were the opposite of one another for vowel transitions versus tone glides, suggesting that the underlying perceptual mechanisms for discriminating frequency change are different for harmonic versus simple stimuli.
- Vowel transitions measured in natural speech exceeded the ΔF extent thresholds in synthetic speech by at least a factor of four, indicating that formant dynamics observed in American English vowel nuclei are perceptually very salient.

ACKNOWLEDGMENTS

This research was supported by NIHDCD-02229.

Andruski, J. E., and Nearey, T. M. (**1992**). "On the sufficiency of compound target specification of isolated vowels and vowels in /bVb/ syllables," J. Acoust. Soc. Am. **91**, 390–410.

Drennan, W. R., and Watson, C. S. (**2001**). "Sources of variation in profile analysis. II. Component spacing, dynamic changes, and roving level," J. Acoust. Soc. Am. **110**, 2498–2504.

Dooley, G. J., and Moore, B. C. (**1988**). "Duration discrimination of steady and gliding tones: A new method for estimating sensitivity to rate of change," J. Acoust. Soc. Am. **84**, 1332-1337.

Glasberg, B., and Moore, B. C. J. (**1990**). "Deviation of auditory filter shapes from notched-noise data," Hear. Res. **47**, 103-138

Guenther, F. H., Nieto-Castanon, A., Ghosh, S. S., and Tourville, J. A. (**2004**). "Representations of sound categories in auditory cortical maps," J. Speech Lang. Hear. Res. **47**, 46-57.

Hawks, J. W. (**1994**). "Difference limens for formant patterns of vowel sounds," J. Acoust. Soc. Am. **95**, 1074–1084.

Hillenbrand, J., and Gayvert, R. T. (**1993**). "Vowel classification based on fundamental frequency and formant frequencies," J. Speech Hear. Res. **36**, 694–700.

Hillenbrand, J., Getty, L. A., Clark, M. J., and Wheeler, K. (**1995**). "Acoustic characteristics of American english vowels," J. Acoust. Soc. Am. **97**, 3099–3111.

Hillenbrand, J. M., and Nearey, T. M. (**1999**). "Identification of resynthesized /hVd/ utterances: Effects of formant contour." J. Acoust. Soc. Am. **105**, 3509–3523.

Johnson, K., Flemming, E., and Wright, R. (**1993**). "The hyperspace effect: Phonetic targets are hyperarticulated," Lang. **69**, 505–528.

Klatt, D. (**1980**). "Software for cascade/parallel formant synthesizer," J. Acoust. Soc. Am. **67**, 971–995.

Kewley-Port, D. (**1995**). "Thresholds for formant-frequency discrimination of vowels in consonantal context," J. Acoust. Soc. Am. **97**, 3139–3146.

Kewley-Port, D., and Watson, C. S. (**1994**). "Formant-frequency discrimination for isolated English vowels," J. Acoust. Soc. Am. **95**, 485–496.

Kewley-Port, D., and Zheng, Y. (**1998**). "Modeling formant frequency discrimination for isolated vowels." J. Acoust. Soc. Am. **103**, 1654–1666.

Labov, W. (**2005**). *Atlas of North American English* (Mouton de Gruyter, New York) in press.

Levitt, H. (**1971**). "Transformed up-down methods in psychoacoustics," J. Acoust. Soc. Am. **49**, 467–477.

Liberman, A. M., and Mattingly, I. G. (**1985**). "The motor theory of speech perception revised," Cognition **21**, 1–36.

Liu, C. (2002). "Modeling vowel discrimination in quiet and noise for natural speech," unpublished doctoral dissertation, Indiana University.

Madden, J. P., and Fire, K. M. (**1996**). "Detection and discrimination of gliding tones as a function of frequency transition and center frequency," J. Acoust. Soc. Am. **100**, 3754–3760.

Madden, J. P., and Fire, K. M. (**1997**). "Detection and discrimination of frequency glides as a function of direction, duration, frequency span, and center frequency," J. Acoust. Soc. Am. **102**, 2920–2924.

Max, L., and Onghena, P. (**1999**). "Some issues in the statistical analysis of completely randomized and repeated measures designs for speech, language and hearing research," J. Speech Lang. Hear. Res. **42**, 261–270.

Moore, B. C., and Sek, A. (**1998**). "Discrimination of frequency glides with superimposed random glides in level," J. Acoust. Soc. Am. **104**, 411–421.

Nàbělek, I. V., and Hirsh, I. J. (**1969**). "On the discrimination of frequency transitions," J. Acoust. Soc. Am. **90**, 1510–1519.

Nearey, T. M. (**1989**). "Static, dynamic, and relational properties in vowel perception," J. Acoust. Soc. Am. **85**, 2088-2113.

Nearey, T., and Assmann, P. (**1986**). "Modeling the role of inherent spectral change in vowel identification," J. Acoust. Soc. Am. **80**, 1297–1308.

Ohde, R. N., and Abou-Khalil, R. (**2001**). "Age differences for stop-consonant and vowel perception in adults." J. Acoust. Soc. Am. **110**, 2156–2166.

Peterson, G. E., and Barney, H. L. (**1952**). "Control methods used in a study of the vowels." J. Acoust. Soc. Am. **24**, 175–184.

Porter, R. J., Cullen, J. K., Collins, M. J., and Jackson, D. F. (**1991**). "Discrimination of formant transition onset frequency: Psychoacoustic cues at short, moderate, and long durations," J. Acoust. Soc. Am. **90**, 1298–1308.

Sek, A., and Moore, B. C. (**1999**). "Discrimination of frequency steps linked by glides of various durations." J. Acoust. Soc. Am. **106**, 351–359.

Sinnott, J. H., and Kreiter, N. A. (**1991**). "Differential sensitivity to vowel continua in Old World monkeys (Macaca) and humans," J. Acoust. Soc. Am. **89**, 2421–2429.

Strange, W. (**1989**). "Dynamic specification of coarticulated vowels spoken in sentence context." J. Acoust. Soc. Am. **85**, 2135–2153.

Strange, W., Jenkins, J., and Johnson, T. (**1993**). "Dynamic specification of coarticulated vowels," J. Acoust. Soc. Am. **74**, 695–705.

Strange, W., Verbrugge, R. R., Shankweiler, D. P., and Edman, T. R. (**1976**). "Consonant environment specifies vowel identity." J. Acoust. Soc. Am. **60**, 213–224.

Summers, V., and Leek, M. R. (**1995**). "Frequency glide discrimination in the F2 region by normal-hearing and hearing-impaired listeners," J. Acoust. Soc. Am. **97**, 3825–3832.

van Wieringen, A., and Pols, L. C. (**1994**). "Frequency and duration discrimination of short first-formant speechlike transitions," J. Acoust. Soc. Am. **95**, 502–511.

Intelligibilities of 1-octave rectangular bands spanning the speech spectrum when heard separately and paired

Richard M. Warren,[a] James A. Bashford, Jr., and Peter W. Lenz
Department of Psychology, University of Wisconsin-Milwaukee, Post Office Box 413, Milwaukee, Wisconsin 53201-0413

(Received 7 April 2005; revised 8 August 2005; accepted 9 August 2005)

There is a need, both for speech theory and for many practical applications, to know the intelligibilities of individual passbands that span the speech spectrum when they are heard singly and in combination. While indirect procedures have been employed for estimating passband intelligibilities (e.g., the Speech Intelligibility Index), direct measurements have been blocked by the confounding contributions from transition band slopes that accompany filtering. A recent study has reported that slopes of several thousand dBA/octave produced by high-order finite impulse response filtering were required to produce the effectively rectangular bands necessary to eliminate appreciable contributions from transition bands [Warren *et al.*, J. Acoust. Soc. Am. **115**, 1292–1295 (2004)]. Using such essentially vertical slopes, the present study employed sentences, and reports the intelligibilities of their six 1-octave contiguous passbands having center frequencies from 0.25 to 8 kHz when heard alone, and for each of their 15 possible pairings.
 [DOI: 10.1121/1.2047228]

PACS number(s): 43.71.Es, 43.71.Gv, 43.71.An [RLD] Pages: 3261–3266

I. INTRODUCTION

The relative contributions to intelligibility made by the different regions of the speech spectrum is of major interest for theory and for practical applications such as telephony, hearing aids, cochlear implants, and architectural acoustics. There has been considerable research devoted to determining passband intelligibilities since the pioneering work at Bell Telephone Laboratories in the early twentieth century (see Fletcher, 1929; French and Steinberg, 1947; Fletcher and Galt, 1950). These studies have led to the development of a widely used method for estimating passband intelligibilities heard singly and together. This was accomplished by employing calculations based upon intelligibility measurements of high-pass and low-pass speech partially masked by noise. The procedure was used to construct the American National Standard Institute's Articulation Index (AI) (ANSI S3.5, 1969) and its updated successor, the Speech Intelligibility Index (SII) (ANSI S3.5, 1997). At the time the AI/SII procedure was being developed, it was recognized that the intelligibility of speech bands was determined by contributions from both the passband and the flanking transition bands produced by filters available at that time (see Kryter, 1960). However, the design of the AI/SII procedure minimized the contribution of the transition bands and permitted the use of shallow filter slopes: The instructions for deriving AI state: "For the purpose of this standard, the slope of the filter skirts should be equal to or greater than 18 dB/octave" (ANSI S3.5, 1969, p. 7). The AI/SII calculations were amended by the Speech Transmission Index (STI) (Steeneken and Houtgast, 1980; 2002) to compensate for distortions such as echoes and reverberation and also to permit evaluation of speech transmission quality. The Speech Recognition Sensitivity (SRS) model (Müsch and Buus, 2001a; 2001b) amended the AI/SII calculations to account for both the "synergistic and redundant interactions among spectral bands of speech."

Although there have been many estimates, there have been no direct measurements of the intelligibilities of passbands spanning the speech spectrum. The present study was undertaken to obtain such measurements for passbands heard singly and in pairs. In order to avoid confounding the passband information with out-of-band input, it was necessary to eliminate contributions from the transition-band slopes that accompany all filtering. Despite dwindling amplitude and distortions of normal spectral profile, transition bands can provide considerable information. This is demonstrated by the high intelligibility of narrow-band speech consisting solely of transition bands. Everyday sentences restricted to a wedge-shaped band consisting of high-pass and low-pass filter slopes of 48 dBA/octave meeting at a common cutoff frequency of 1.5 kHz were reported to have ceiling intelligibility scores of over 95% (Bashford, Riener, and Warren, 1992), and when, in a subsequent study, the slopes of this wedge-shaped band were increased to 115 dBA/octave (quite steep for analog filtering), scores remained quite high at 77% (Warren, Riener, Bashford, and Brubaker, 1995).

To measure the relative contributions of passbands and transition bands in determining the intelligibility of narrow-band speech, a series of experiments was conducted using FIR (finite impulse response) digital filtering to produce nearly vertical slopes without the passband distortions accompanying high-order analog filtering. In the first of these studies, Warren and Bashford (1999) separated the passband from the flanking 100 dBA/octave transition bands of everyday sentences centered at 1.5 kHz. This was done using 2000-order FIR filtering that produced filter slopes averaging approximately 1000 dBA/octave. It was found that the high-pass and low-pass slopes separated by a 1/3-octave gap had

[a]Electronic mail: rmwarren@uwm.edu

an average intelligibility more than three times that of the excised passband that had occupied the gap. Subsequent experiments substituted word lists for the everyday sentences; intelligibilities were reduced as would be expected, but the ratio of transition-band scores to passband scores was equivalent to that obtained with sentences (Bashford, Warren, and Lenz, 2000). Another study also employed the 1/3-octave everyday sentences centered at 1.5 kHz with transition bands of 100 dBA/octave, and truncated the filter skirts at a series of increasing distances from the cutoff frequency using 2000-order FIR filtering. It was found that statistically significant contributions from these transition bands could be made for frequencies attenuated by 30 dBA, so that the nominal 1/3-octave band had a much larger effective bandwidth (i.e., the range of frequencies contributing to intelligibility) that extended to almost one octave (Warren, Bashford, and Lenz, 2000). While these experiments using 2000-order FIR filtering demonstrated the major role played by transition bands in determining intelligibilities of filtered speech, none of these experiments employed filter slopes steep enough to remove all contributions from transition bands, and so permit measurement of passband intelligibilities.

In order to determine the transition-band slopes necessary to ensure that passband contributions were not conflated with transition-band contributions, Warren, Bashford, and Lenz (2004) systematically increased transition-band slopes of a 1/3-octave band of everyday sentences centered at 1.5 kHz by starting at 150 dBA/octave, and continuing until further increases no longer reduced intelligibility. It was found that transition bands of 4800 dBA/octave for both high-pass and low-pass slopes (produced by FIR orders that exceeded 7000 for each slope) were needed to eliminate significant transition-band contributions and reach asymptotic scores. Even with both high-pass and low-pass transition bands as steep as 1200 dBA/octave, frequencies lying outside the passband still contributed over 30% of the 1/3-octave band's intelligibility. In keeping with this information, 8000-order FIR filtering was used throughout the present study (except for[1] that employed 20 000-order FIR filtering).

Experiment 1 obtained intelligibility judgments for six 1-octave rectangular passbands that covered the range of frequencies from 0.25 to 8 kHz. To determine the effect of amplitude upon intelligibility, separate groups of listeners were employed for each of four levels, 80, 70, 60, and 50 dB. On the basis of the results obtained in this experiment, 60 dB was selected as the optimal level to be employed in each of the subsequent experiments. Experiment 2 determined the intelligibility scores for the five adjacent pairings of the six 1-octave bands; Experiments 3a and 3b taken together obtained the scores for each of the 10 possible nonadjacent pairings.

II. METHOD

A. Subjects

The 212 listeners employed in Experiments 1, 2, 3a, and 3b (plus an additional 30 listeners used to obtain the data presented in[1]) were students at the University of Wisconsin-Milwaukee who received payment for their participation in the study. All were native English speakers who reported having no hearing problems and were screened to ensure that they had normal bilateral hearing as defined by pure tone thresholds of 20 dBA HL or better at octave frequencies from 250 to 8000 Hz.

B. Stimulus processing

The speech stimuli were sentences drawn from the "low-predictability" (LP) sublist of the revised Speech Perception In Noise (SPIN) test (Bilger, Nuetzel, Rabinowitz, and Rzeczkowski, 1984). These sentences are from five to eight words in length, and each ends with a monosyllabic noun serving as the keyword for scoring of intelligibility. In these LP sentences, the identity of the keyword is not predictable from sentence context (e.g., "The boy might consider the trap."). The digitally recorded sentences (44.1 kHz sampling, 16-bit quantization) were produced by a male speaker having an average voicing frequency of about 100 Hz and having no obvious regional accent.

A total of 180 of the 200 LP SPIN sentences were used as experimental stimuli, and an additional five sentences were used as practice stimuli. Prior to filtering, the sentences were transduced by a Sennheiser HD 250 Linear II headphone and their slow-rms peak levels were matched to within 0.2 dB using a flat-plate coupler in conjunction with a Brüel and Kjaer model 2230 digital sound-level meter set at A-scale weighting (as were all level measurements reported).

All filtering to produce six 1-octave bands centered at 0.25, 0.5, 1, 2, 4, and 8 kHz was done using the *fir1* function in MATLAB 5.2.1 running on a Macintosh G4 computer. As discussed in Sec. I, high-order FIR filtering was necessary to avoid confounding the contributions made by the passbands with those made by filter skirts. Slopes of 3.2 dBA/Hz, produced by two successive passes through 4000-order FIR filtering, ensured that filter slopes did not contribute to the intelligibility of any of the 1-octave bands.[1] The use of two successive stages for the 8000-order filtering reduced all frequencies within the stopbands to levels below threshold. Figure 1 shows the effectively vertical slopes of the long-term averaged spectrum for the midfrequency 2 kHz band superimposed upon that of broadband speech.

After filtering, the speech stimuli were again adjusted in level so that the slow-rms peaks of all of the sentences were matched to within 0.2 dBA SPL. The mixing of bandpass signals was done using Sound Designer II software running on a Macintosh G3 computer.

C. General procedure

A repeated measures design was used in each experiment. Before receiving each stimulus condition in an experiment, listeners were familiarized with the effects of filtering by listening to the set of five practice stimuli. These were first presented broadband, and then filtered in the same manner as the test stimuli. The test sentences in each experiment were grouped into sets, and these sets were presented in a

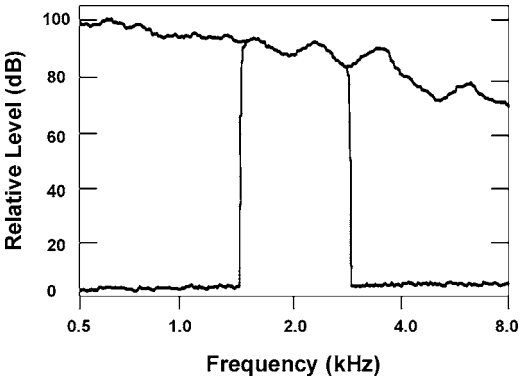

FIG. 1. Long-term average spectrum of 180 LP SPIN sentences, subjected to two successive stages of 4000-order FIR filtering that produced a 1-octave rectangular band centered at 2-kHz. This plot for the filtered band is superimposed and coincides with the spectrum of the parent broadband stimulus. The plots were generated offline via discrete Fourier transform (DFT) with linear averaging of spectra using a 64 000-point (0.7 Hz resolution) Blackman window across the entire set of digitally recorded stimuli. Metric Halo Laboratories, Inc. produced the DFT software.

balanced pseudorandom order, so that each center frequency was applied an equal number of times in each serial position to each sentence set across listeners.

After audiometric screening, subjects were tested singly while seated with the experimenter in an audiometric chamber. The stimuli were delivered diotically through Sennheiser HD250 Linear II headphones, with each of the speech bands, whether heard singly or in combination, presented at a fixed slow-rms peak level. The levels of the bands were varied from 50 to 80 dBA SPL for separate groups of listeners in Experiment 1, and each of the individual bands was delivered at 60 dBA when paired in Experiments 2, 3a, and 3b. Subjects were told to repeat the final word of each sentence as accurately as they could, and to guess if unsure. The keywords reported accurately were recorded by the experimenter. Testing occurred in a single session lasting approximately 30 minutes.

III. EXPERIMENTS

A. Experiment 1: Intelligibilities of the six 1-octave bands spanning the important frequencies of the speech spectrum at levels of 50, 60, 70, and 80 dBA

Four separate groups of 30 subjects each received 180 keywords (six sets of 30 keywords) at peak-rms levels of either 50, 60, 70 or 80 dBA. The six sets of sentences presented at each level were reduced to 1-octave bands having center frequencies of 0.25, 0.5, 1, 2, 4, and 8 kHz. Based upon the results obtained in Experiment 1, 60 dBA was used in Experiments 2, 3a, and 3b.

B. Experiment 2: Intelligibilities of adjacent pairs of 1-octave bands

The 30 subjects each received 180 keywords (5 sets of 36 keywords). Each set consisted of one of the five contiguous pairings of the 1-octave bands. These pairs were 0.25 +0.5 kHz, 0.5+1 kHz, 1+2 kHz, 2+4 kHz, and 4+8 kHz.

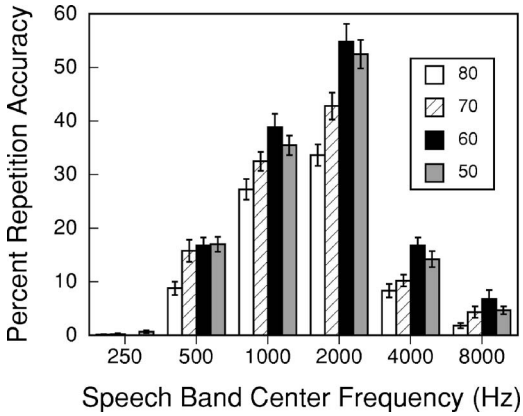

FIG. 2. Experiment 1: Mean percent intelligibility scores and standard errors as measured for the six 1-octave rectangular passbands presented at four different intensity levels to separate groups of listeners ($N=30$ at each level).

C. Experiment 3: Intelligibilities of paired nonadjacent 1-octave bands

Experiment 3a: Pairs separated by spectral gaps of one octave. The 32 subjects each received 180 keywords (4 sets of 45 keywords). Each set consisted of one of the following four pairs of the nonadjacent 1-octave bands: 0.25+1 kHz, 0.5+2 kHz, 1+4 kHz, and 2+8 kHz.

Experiment 3b: Pairs separated by spectral gaps of two, three, and four octaves. The 30 subjects each received 180 keywords (six sets of 30 words each). These sets consisted of the three pairs of 1-octave bands separated by two octaves (0.25+2 kHz, 0.5+4 kHz, and 1+8 kHz), the two pairs separated by three octaves (0.25+4 kHz, 0.5+8 kHz), and the single pair separated by four octaves (0.25+8 kHz). Experiments 2, 3a, and 3b taken together represent all of the 15 possible pairwise combinations of the six 1-octave bands in Experiment 1.

IV. RESULTS

A. Experiment 1

Figure 2 shows the average intelligibility scores (defined as the percent correct repetition of keywords) and standard errors for the six 1-octave bands at each presentation level. It can be seen that except for the 0.25 kHz band (having scores less than 1%), the highest intelligibility was obtained when the speech bands were presented at the two lowest levels of 60 and 50 dBA SPL. It also can be seen that intelligibility was highest for the 2 kHz band, and that the scores for the higher and lower bands decreased with the extent of their separation from the 2 kHz band. The data were subjected to a two-factor (speech level X center frequency) mixed analysis of variance, which yielded significant main effects of presentation level $[F(3,116)=19.4, p<0.0001]$ and speech band center frequency $[F(5,580)=523.9, p<0.0001]$, and a significant interaction of those factors $[(F5,580)=4.9, p<0.0001]$. Simple-effects comparisons yielded significant effects of presentation level at each speech band center frequency $[F(3,116)\geqslant 3.5, p<0.02]$ or better], and subsequent Tukey HSD tests (Hays, 1988) revealed ($p<0.05$) that the effect of presentation level was due primarily to lower per-

TABLE I. Intelligibilities of individual rectangular 1-octave passbands spanning the speech spectrum and their synergistic or redundant interactions when paired. The matrix summarizes the results obtained in Experiments 1, 2, 3a, and 3b for bands presented at 60 dBA. The dark diagonal boxes show the intelligibility scores and standard errors for the six 1-octave rectangular passbands when heard alone. The boxes to the left of the diagonal show the dual-band intelligibility scores and standard errors (in parentheses) for all 15 possible pairings of the six bands. The boxes to the right of the diagonal show the percentage difference ($\Delta\%$) between the dual-band scores and the predicted scores based on the scores of the two component bands when heard alone, $+\Delta\%$ values indicate synergy, $-\Delta\%$ values (none found) would indicate redundancy (for further details see text). Note that the matrix exhibits reflection (or mirror) symmetry, so that if folded over on the major diagonal, the dual-band intelligibilities and their $\Delta\%$ values are superimposed.

Dual-Band intelligibility & (SE) / Dual Band Synergy

	.25 kHz	.5 kHz	1 kHz	2 kHz	4 kHz	8 kHz
8 kHz	9.2% (1.0)	40.7% (2.5)	68.1% (2.2)	71.2% (2.3)	23.5% (1.3)	6.8% (1.7)
4 kHz	17.9% (1.3)	66.8% (1.5)	82.8% (1.5)	75.6% (2.3)	16.8% (1.5)	Δ+5%
2 kHz	65.6% (2.4)	89.9% (1.0)	90.0% (1.1)	54.8% (3.3)	Δ+21%	Δ+23%
1 kHz	50.8% (1.4)	71.3% (1.3)	38.8% (2.5)	Δ+24%	Δ+69%	Δ+59%
.5 kHz	18.5% (1.3)	16.8% (1.5)	Δ+45%	Δ+44%	Δ+122%	Δ+81%
.25 kHz	0.0% (0.0)	Δ+10%	Δ+31%	Δ+20%	Δ+1%	Δ+35%

formance in the 80 dBA condition at all center frequencies except 250 Hz. For that speech band the 50 dBA level produced higher intelligibility than all other levels. The effect of center frequency also was subjected to simple-effects tests, which were significant at all presentation levels [$F(5,145) \geqslant 116.7, p < 0.0001$]. Subsequent Tukey HSD tests indicated ($p < 0.05$) that intelligibility at each presentation level was highest for the 2 kHz band, next highest for the 1 kHz band, lower for the 0.5 and 4 kHz bands (which did not differ significantly at any presentation level), and lowest for the 0.25 and 8 kHz bands.

B. Experiment 2

The average percent intelligibility scores and standard errors for the five adjacent pairs of 1-octave bands (0.25 +0.5, 0.5+1, 1+2, 2+4, 4+8 kHz) are shown in Table I, along with the scores for the nondjacent band conditions to be discussed below. The data for the adjacent bands were subjected to a repeated measures analysis of variance, which yielded a significant effect of band composition [$F(4,116) = 459.5, p < 0.0001$]. Subsequent Tukey HSD tests indicated ($p < 0.05$) that intelligibility was highest for the 1+2 kHz pair, next highest and equivalent for the 0.5+1 kHz pair and 2+4 kHz pairs, and lowest for the 0.25+0.5 kHz and 4 +8 kHz pairs, which did not differ significantly.

C. Experiments 3a and 3b

The data for the pairs of speech bands separated by a 1-octave spectral gap were subjected to a repeated measures analysis of variance, which yielded a significant effect of band composition [$F(3,93) = 165.3, p < 0.0001$]. Subsequent Tukey HSD tests indicated that all pairs differed significantly ($p < 0.05$). The data for the band pairs separated by more than a 1-octave spectral gap were subjected to a similar analysis, which also yielded a significant effect of band composition [$F(5,145) = 226.3, p < 0.0001$]. Subsequent Tukey HSD tests indicated ($p < 0.05$) that intelligibility was highest, and equivalent, for the 0.25+2 kHz, 0.5+4 kHz, and 1 +8 kHz pairs. The next highest intelligibility was obtained for the 0.5+8 kHz pair, and the lowest performance was obtained for the 0.25+4 kHz and 0.25+8 kHz pairs, which did not differ significantly.

Table I shows the average intelligibility scores and standard errors for all 10 nonadjacent pairs of 1-octave bands

presented in Experiment 3. Since the table also shows the scores for the five adjacent pairs of bands presented in Experiment 2, all possible pairings of the octave bands are represented in a single matrix. These values all appear on the left-hand side of the black boxes lying along the table's diagonal. These black boxes contain the intelligibility scores and standard errors for each of the six 1-octave bands presented individually in Experiment 1. The boxes on the right-hand side of the main diagonal show the extent of synergy or redundancy produced when the individual bands are paired. The synergy/redundancy values were calculated based on the assumption that the error probability given by (1-proportion correct) for one band (P_1) and for the other (P_2) were independent and multiplicative. The "expected" dual-band score (S_E) is then $100(1\text{-}P_1xP_2)$. The obtained dual-band score (S_O) is shown on the left-hand side of the table's major diagonal. The ratio S_O/S_E indicates whether the dual bands exhibit synergy or redundancy, with values greater than unity signifying synergy, and less than unity signifying redundancy. The extent of synergy or redundancy is shown to the right of the diagonal as $\Delta\% = 100[(S_O/S_E) - 1]$, with positive values indicating synergy, and negative values indicating redundancy. It can be seen that none of the dual bands exhibit redundancy, and that all of the 15 dual-band combinations show synergy.

V. SUMMARY AND DISCUSSION

The effectiveness of speech as a means of communication depends upon the great redundancy provided by multiple dynamic cues, coupled with opportunistic strategies adopted by the listener. This can result in appreciable intelligibility even when some of the broadband information is severely distorted or missing. Some cues occur simultaneously across the entire spectrum (see Rosen and Fourcin, 1986); these include the presence or absence of voicing (e.g., /v/ vs /f/), the duration of noise bursts before the onset of voicing (e.g., /d/ vs /t/), and the duration of articulatory closure and pauses. There are also frequency-specific cues, (1) the peaks in spectral envelopes corresponding to the three most important formants each have limited spectral ranges, and each can sweep across critical bands, with the individual formants following different trajectories (see Peterson and Barney, 1952); (2) cross-frequency integration of patterns of low-frequency amplitude fluctuation can provide significant information (see Cole and Scott, 1974; Shannon *et al.*, 1995; Healy and Warren, 2003); (3) phase locking of auditory-nerve fibers can provide local timing and fine-structure information for the three principal vowel formants *F*1, *F*2, and *F*3 (Sachs and Young, 1979, 1980). As will be discussed, the current study provides information concerning the effectiveness of these cues when bands are heard singly and paired.

Experiment 1 was conducted to determine the optimal amplitudes for this study. Six 1-octave bands were presented at four different levels, 50, 60, 70, and 80 dBA. As shown in Fig. 2, scores were generally highest for the 60 dBA level, and scores declined somewhat at 70 dBA, indicating saturation of neural firing rate, and decreased still further at the 80 dBA level. Based on these results, the individual bands were presented at slow-peak levels of 60 dBA in all of the subsequent experiments.

The decrease in intelligibility starting at the high-to-moderate level of 70 dBA is in agreement with the observation reported by Bashford, Warren, and Lenz (2005) that the intelligibility of a rectangular speech band starts to decline at 65 dBA corresponding to the spectrum level it had in broadband speech at 80 dBA. Although broadband speech intelligibility can remain nearly perfect at levels exceeding 90 dBA, bandpass speech excised without a change in its spectrum level exhibits the effects of neural saturation, apparently due to the lack of lateral suppression normally evoked by flanking components of the bandpass speech. Evidence supporting the role of lateral suppression was provided by a series of experiments employing flanking stochastic noise.

Table I contains all of the experimental data concerning dual-band intelligibility obtained in Experiments 2, 3a, and 3b with individual bands at a level of 60 dBA, as well as the single band data obtained at that level from Experiment 1. In Experiment 1, the octave band centered on 2 kHz had the highest intelligibility. This band has the advantage of lying within the transit range of two formants, the upper range of *F*2 and the lower range of *F*3 (see Peterson and Barney, 1952). It can be seen that intelligibility decreases monotonically as the separation of the lower and higher octave bands from the 2 kHz band increases.

The finding, shown in Table I, that all of the 15 dual bands exhibit synergy is not in agreement with earlier studies using pairs of band-limited speech. But in each of the previous studies, contributions of the passbands and transition bands were conflated. Experiments by Pollack (1948), Licklider (1959), Kryter (1960), Grant and Braida (1991), Steeneken and Houtgast (1999), and Müsch and Buus (2001a, 2001b) taken together, found that dual-band scores exhibited redundancy when bands were adjacent, and synergy when bands had sufficient separation. Grant and Braida suggested that when the bands were adjacent, there would be overlapping of transition bands, so that some of the information present in the individual bands would become redundant. When the bands were separated by spectral gaps, there would be "new" information, the extent of which depended upon the degree of separation.

Müsch and Buus (2001a, see also 2001b) stated that a "particularly impressive example of synergistic interaction was reported by Warren *et al.* (1995)." The study they referred to employed two widely separated 1/20-octave speech bands having slopes of approximately 100 dBA/octave. The band centered at 370 Hz had an intelligibility score of 0.9% and the band centered at 6 kHz had a score of 10.4%; when heard together, the intelligibility score was 27.8%. This measured score for the paired bands was considerably greater than the predicted score (11.2%) calculated by Müsch and Buus, based upon the same multiplication of error rates of the individual bands used in the present study. When expressed as $\Delta\%$ (as in Table I), the extent of synergy was Δ +148%. Müsch and Buus argued that their Statistical Deci-

sion Theory (SDT) model could predict the extent of "synergistic interaction between frequency bands measured by Warren *et al.*"

The extent of synergy for the individual pairs shown in Table I depends upon a complex interaction of cues to phonetic and lexical identity. Some cues, such as the presence or absence of voicing, occur simultaneously across the spectrum, thus confirming but not adding new information to that available in each band. However, formants provide complex dynamic frequency-specific information; the sweeps of a formant across one of the 1-octave bands and the sweeps of the same or a different formant in the other band would be expected to interact in complex and (at present) unpredictable ways.

VI. CONCLUSION

The results obtained in the present study indicate that direct measurement of passband intelligibilities using rectangular bands could provide data for testing and perhaps modifying the estimates of passband intelligibilities based upon the AI/SII procedure. Comparison of the two procedures would be facilitated by obtaining direct intelligibility measurements for the same speech stimuli and passbands that had been employed for estimates based upon the SII.

ACKNOWLEDGMENT

This work was supported by NIH Grant No. DC00208 from the National Institute on Deafness and Other Communication Disorders.

[1]In order to verify that the slopes in Experiment 1 were steep enough to eliminate out-of-band contributions for all 1-octave speech bands, the order of FIR filtering was increased from 8000 to 20 000. A separate group of 30 subjects was tested using the identical procedure employed at the 60 dBA level used in Experiment 1, except for the higher filter order that increased the slopes from 3.2 dBA/Hz to 8 dBA/Hz. Expressed in the more conventional terms of dBA/octave (rounded to two significant digits), the shallowest slope in Experiment 1 (the high-pass slope of the 0.25 kHz band) was 280 dBA/octave, and the low-pass slope of that band was 1100 dBA/octave. When the slopes were increased, the corresponding slopes for the 0.25 kHz band expressed as dBA/octave became 700 and 2700 respectively. For the five other 1-octave bands, the high-pass and low-pass bands were each doubled in dBA/octave for every increase of one octave. With careful listening by four laboratory personnel, no ringing (i.e., sound preceding the onset and following the offset of the sentences) could be heard for any of the six 1-octave bands presented in Experiment 1. However, clear ringing could be heard for the higher order filtering at center frequencies of 0.5, 1, and 2 kHz (there was no audible ringing for the other three bands). The percent intelligibilities for the six 1-octave bands follows with scores for the 3.2 dBA/Hz conditions preceding, and the 8 dBA/Hz conditions following the solidus: 0.25 kHz, 0.0/0.2; 0.5 kHz, 16.8/14.3; 1 kHz, 38.8/36.2; 2 kHz, 54.8/48.0; 4 kHz, 16.8/17.3; 8 kHz, 6.8/5.9. Increasing the slopes had no statistically significant effect upon any of the 1-octave passbands spanning the speech spectrum. It appears that 8000-order FIR filtering was sufficient to eliminate significant contributions from transition bands for each of the six 1-octave bands spanning the speech spectrum.

ANSI S3.5. (**1969**). *American National Standard Methods for the Calculation of the Articulation Index* (American National Standards Institute, New York).

ANSI S3.5. (**1997**). *American National Standard Methods for Calculation of the Speech Intelligibility Index* (American National Standards Institute, New York).

Bashford, J. A., Jr., Riener, K. R., and Warren, R. M. (**1992**). "Increasing the intelligibility of speech through multiple phonemic restorations," Percept. Psychophys. **51**, 211–217.

Bashford, J. A., Jr., Warren, R. M., and Lenz, P. W. (**2000**). "Relative contributions of passband and filter skirts to the intelligibility of bandpass speech: Some effects of context and amplitude," ARLO **1**, 31–36.

Bashford, J. A., Jr., Warren, R. M., and Lenz, P. W. (**2005**). "Enhancing intelligibility of narrowband speech with out-of-band noise: Evidence for lateral suppression at high-normal intensity," J. Acoust. Soc. Am. **117**, 365–369.

Bilger, R. C., Nuetzel, J. M., Rabinowitz, W. M., and Rzeczkowski, C. (**1984**). "Standardization of a test of speech perception in noise," J. Speech Hear. Res. **27**, 32–48.

Cole, R. A., and Scott, B. (**1974**). "Toward a theory of speech perception," Psychol. Rev. **81**, 348–374.

Fletcher, H. (**1929**). *Speech and Hearing* (McMillan, London).

Fletcher, H., and Galt, R. H. (**1950**). "The perception of speech and its relation to telephony," J. Acoust. Soc. Am. **22**, 89–151.

French, N. R., and Steinberg, J. C. (**1947**). "Factors governing the intelligibility of speech sounds," J. Acoust. Soc. Am. **19**, 90–119.

Grant, K. W., and Braida, L. D. (**1991**). "Evaluating the articulation index for auditory-visual input," J. Acoust. Soc. Am. **89**, 2952–2960.

Hays, W. L. (**1988**). *Statistics* (Holt, Rinehart and Winston, Chicago).

Healy, E. W., and Warren, R. M. (**2003**). "The role of contrasting temporal amplitude patterns in the perception of speech." J. Acoust. Soc. Am. **113**, 1676–1688.

Kryter, K. D. (**1960**). "Speech bandwidth compression through spectrum selection," J. Acoust. Soc. Am. **32**, 547–556.

Licklider, J. C. R. (**1959**). "Three auditory theories," in *Psychology: A Study of a Science*, edited by S. Koch (McGraw-Hill, New York), pp. 41–144.

Müsch, H., and Buus, S. (**2001a**). "Using statistical decision theory to predict speech intelligibility. I. Model structure," J. Acoust. Soc. Am. **109**, 2896–2909.

Müsch, H., and Buus, S. (**2001b**). "Using statistical decision theory to predict speech intelligibility. II. Measurement and prediction of consonant-discrimination performance," J. Acoust. Soc. Am. **109**, 2910–2920.

Peterson, G. E., and Barney, H. L. (**1952**). "Control methods used in a study of the vowels," J. Acoust. Soc. Am. **24**, 175–184.

Pollack, I. (**1948**). "Effects of high pass and low pass filtering on the intelligibility of speech in noise," J. Acoust. Soc. Am. **20**, 259–266.

Rosen, S., and Fourcin, A. (**1986**). "Frequency selectivity and the perception of speech," in *Frequency Selectivity in Hearing*, edited by B. C. J. Moore (Academic, London), pp. 373–487.

Sachs, M. B., and Young, E. D. (**1979**). "Encoding of steady-state vowels in the auditory nerve: Representation in terms of discharge rate," J. Acoust. Soc. Am. **66**, 478–479.

Sachs, M. B., and Young, E. D. (**1980**). "Effects of nonlinearities on speech encoding in the auditory nerve," J. Acoust. Soc. Am. **68**, 858–875.

Shannon, R. V., Zeng, F.-G., Kamath, V., Wygonski, J., and Ekelid, M. (**1995**). "Speech recognition with primarily temporal cues," Science **270**, 303–304.

Steeneken, H. J. M., and Houtgast, T. (**1980**). "A physical method for measuring speech-transmission quality," J. Acoust. Soc. Am. **67**, 318–326.

Steeneken, H. J. M., and Houtgast, T. (**1999**). "Mutual dependence of the octave-band weights in predicting speech intelligibility," Speech Commun. **28**, 109–123.

Steeneken, H. J. M., and Houtgast, T. (**2002**). "Validation of the revised STI method," Speech Commun. **38**, 413–425.

Warren, R. M., and Bashford, J. A., Jr. (**1999**). "Intelligibility of 1/3-octave speech: Greater contribution of frequencies outside than inside the nominal passband," J. Acoust. Soc. Am. **106**, L47-L52.

Warren, R. M., Bashford, J. A., Jr., and Lenz, P. W. (**2000**). "Intelligibility of bandpass speech: Effects of truncation or removal of transition bands," J. Acoust. Soc. Am. **108**, 1264–1268.

Warren, R. M., Bashford, J. A., Jr., and Lenz, P. W. (**2004**). "Intelligibility of bandpass filtered speech: Steepness of slopes required to eliminate transition band contributions," J. Acoust. Soc. Am. **115**, 1292–1295.

Warren, R. M., Riener, K. R., Bashford, J. A., Jr., and Brubaker, B. S. (**1995**). "Spectral redundancy: Intelligibility of sentences heard through narrow spectral slits," Percept. Psychophys. **57**, 175–182.

Phonetic training with acoustic cue manipulations: A comparison of methods for teaching English /r/-/l/ to Japanese adults

Paul Iverson, Valerie Hazan, and Kerry Bannister
Department of Phonetics and Linguistics, University College London, 4 Stephenson Way, London NW1 2HE, United Kingdom

(Received 5 May 2005; revised 5 August 2005; accepted 17 August 2005)

Recent work [Iverson *et al.* (2003) Cognition, **87**, B47-57] has suggested that Japanese adults have difficulty learning English /r/ and /l/ because they are overly sensitive to acoustic cues that are not reliable for /r/-/l/ categorization (e.g., F2 frequency). This study investigated whether cue weightings are altered by auditory training, and compared the effectiveness of different training techniques. Separate groups of subjects received High Variability Phonetic Training (natural words from multiple talkers), and 3 techniques in which the natural recordings were altered via signal processing (All Enhancement, with F3 contrast maximized and closure duration lengthened; Perceptual Fading, with F3 enhancement reduced during training; and Secondary Cue Variability, with variation in F2 and durations increased during training). The results demonstrated that all of the training techniques improved /r/-/l/ identification by Japanese listeners, but there were no differences between the techniques. Training also altered the use of secondary acoustic cues; listeners became biased to identify stimuli as English /l/ when the cues made them similar to the Japanese /r/ category, and reduced their use of secondary acoustic cues for stimuli that were dissimilar to Japanese /r/. The results suggest that both category assimilation and perceptual interference affect English /r/ and /l/ acquisition. © *2005 Acoustical Society of America.* [DOI: 10.1121/1.2062307]

PACS number(s): 43.71.Hw, 43.71.Es [ARB] Pages: 3267–3278

I. INTRODUCTION

Infants are born with an ability to tune their perceptual processes to the sounds of their first language (L1), but the perceptual processes of adults are much less plastic during second language (L2) learning. Although some scientists have argued that this change in plasticity is a result of a biologically delimited critical period that ends at puberty [e.g., Lenneberg (1967); Patkowski (1990)], the current evidence suggests that this change is a gradual consequence of learning one's L1. For example, Flege (1999) has shown that there is no discrete point where learning switches from "easy" to "hard;" rather, it becomes linearly harder to learn an L2 without an accent as one gets older. Learning does not become globally harder for all L2 phonemes; adults have the greatest difficulty learning L2 phonemes that are strongly assimilated into L1 categories, and are better able to produce and perceive L2 phonemes that are dissimilar from any existing L1 phonemes [e.g., Best *et al.* (1988); Flege (1995); Flege *et al.* (2003); Guion *et al.* (2000)]. It appears that plasticity for L2 speech perception progressively declines as individuals become neurally committed to processing their native language [e.g., Kuhl (2000)].

The case of Japanese adults learning the English /r/-/l/ distinction has become the canonical example of "hard" L2 phoneme learning. Japanese adults tend to be very poor at distinguishing English /r/-/l/ [e.g., Goto (1971); Miyawaki *et al.* (1975)]. Although the perception and production of English /r/ and /l/ can improve with experience and training [e.g., Bradlow and Pisoni (1999); Bradlow *et al.* (1999); Hazan *et al.* (in press); MacKain *et al.* (1981); Logan *et al.* (1991)], it can take decades of English-language experience before individuals achieve native levels of performance [Flege *et al.* (1995)]. Best and Strange (1992) hypothesized that the English /r/-/l/ distinction is particularly hard for Japanese adults because they are both assimilated into a single Japanese /r/ category. The Japanese /r/ is a lateral flap, which is much more rapid than the English /r/ or /l/, but it has a range of F2 and F3 frequencies that overlap with those of English /r/ and /l/ [Lotto *et al.* (2004)]. Best and Strange argued that English /r/ and /l/ may sound the same to Japanese adults because they both are the same in respect to the Japanese phonological system (i.e., they both are poor exemplars of the Japanese /r/). Aoyama *et al.* (2004) have further suggested that assimilation patterns can account for the finding that Japanese adults are somewhat better at learning English /r/ than /l/; they argue that English /l/ is more similar to the Japanese /r/ category than is English /r/, and learning to produce and perceive English /r/ is thus easier because it is subject to less L1 interference.

Although Best's (1994) Perceptual Assimilation Model can account for some patterns of L2 phoneme perception [e.g., Best *et al.* (2000); Harnsberger (2001)], our recent work [Iverson *et al.* (2003)] has suggested that it cannot explain the perception of English /r/ and /l/ by Japanese adults. Iverson *et al.* (2003) replicated the common finding that Japanese adults are much poorer, compared to English speakers, at discriminating /r/-/l/ differences near the category boundary. However, we found that Japanese adults were actually better than English speakers at discriminating within-category acoustic variation, and were more sensitive to acoustic variation in F2 frequency. It is thus not the case that English /r/ and /l/ stimuli all sound the same to Japanese listeners. Instead, the problem may be that Japanese adults

are particularly sensitive to acoustic differences that are irrelevant to the English /r/-/l/ categorization. Iverson *et al.* (2003) hypothesized that these patterns of perceptual sensitivities interfere with /r/-/l/ learning by making it harder for Japanese adults to focus attention on more critical acoustic cues (i.e., F3 differences near the category boundary) and more likely to form category representations based on cues that are not critical to native listeners [e.g., F2 frequency or duration differences; see Gordon *et al.* (2001); Yamada (1995)]. Learning English /r/ and /l/ may be hard because it requires Japanese listeners to alter their perceptual space for these phonemes in order to reduce these perceptual interference effects. That is, they must learn to become less sensitive to acoustic cues that are not important for the /r/-/l/ distinction.

The aims of the present study were to test whether the reliance on secondary cues (i.e., acoustic differences that are not critical for distinguishing /r/ and /l/, such as F2 and duration) is reduced during learning, and to compare the effectiveness of different training methods. The baseline method was High Variability Phonetic Training [HVPT; Logan *et al.* (1991)], which involves having subjects give identification judgments with feedback for natural recordings of words produced by multiple talkers, with target phonemes in multiple syllable positions. Pisoni and colleagues [e.g., Logan *et al.* (1991); Lively *et al.* (1993)] have argued that exposing listeners to a wide range of natural stimuli is better than training with a small number of stimuli because the distributions of natural stimuli teach individuals which cues are most reliable; listeners are thought to store individual exemplars that they hear in training, and the multidimensional categorization space for these stimuli gets stretched along dimensions where /r/ and /l/ differ and shrunk along dimensions that do not distinguish /r/ and /l/ [see Nosofsky (1986) (1987)]. This shrinking/stretching account is compatible with the notion of perceptual interference [Iverson *et al.* (2003)]; such a process is exactly what Japanese listeners would need to alter their perceptual space so that they can better attend to the F3 differences that are critical to the /r/-/l/ distinction.

Although HVPT has emphasized the importance of natural variability, it is possible to experimentally manipulate stimuli to specifically target the perceptual interference problems of Japanese listeners. For example, the Perceptual Fading technique [Jamieson and Morosan (1986)] has been used to help listeners focus on critical acoustic cues; listeners are initially trained on stimuli that are maximally contrastive (i.e., enhanced) on the primary acoustic cues used for a phonetic contrast, and the degree of enhancement is decreased as training progresses. This approach has been used to train English /r/ and /l/ for Japanese listeners [Doeleman *et al.* (2000); McCandliss *et al.* (2002); McClelland *et al.* (2002); Protopapas and Calhoun (2000)], but it has not been directly compared to HVPT. The present study used a version of Perceptual Fading that was designed to parallel HVPT; the natural stimuli used in HVPT were signal-processed to increase the difference in F3 for /r/ and /l/ at early stages of training, and decrease this difference at later stages. The study also tested a similar training technique, All Enhanced, in which subjects received enhanced F3 differences at every stage (i.e., no fading); this tested whether a lack of exposure to stimuli with natural variability in F3 would affect the learning process and/or generalization to natural stimuli.

Our work [Iverson *et al.* (2003)] suggested that too much sensitivity to secondary cues was as much a problem for learning as too little attention to the primary acoustic cues. The present study thus constructed a Secondary Cue Variability training technique that was essentially the complement of Perceptual Fading; individuals started training on stimuli that had been signal-processed to equate secondary acoustic cues (i.e., no variability in F2, closure duration, or transition duration) and the amount of random variability in these cues was increased throughout training. The intention was to keep subjects from being distracted by secondary cues at early stages of training (i.e., making it easier to pay attention to F3 differences) and then progressively teach them to ignore this kind of variation.

The study thus compared 4 training techniques (HVPT, All Enhanced, Perceptual Fading, and Secondary Cue Variability). The stimuli from all conditions were based on natural recordings from 10 talkers speaking 100 initial-position /r/-/l/ minimal pair words. The positional variability normally used in HVPT (i.e., stimuli with /r/ and /l/ in multiple syllable positions) was not used here because little is known about which acoustic cues are most important for distinguishing /r/ and /l/ in medial position and consonant clusters; to compensate, more variability was introduced by using more talkers and words than had been used in earlier studies [e.g., Logan *et al.* (1991)]. Subjects were given a battery of tests before and after training to examine how well their training generalized to new words, talkers, and syllable positions. In addition, they were tested on signal-processed stimuli to examine whether training altered their use of secondary acoustic cues.

II. METHOD

A. Subjects

A total of 73 subjects completed testing (87 began the training program but 14 did not finish all of the sessions). Of the subjects that completed, 5 were dropped from the data analysis because of computer problems (i.e., missing data), and 6 were dropped because their pre-training identification of initial-position /r/-/l/ was greater than 90% correct. There was thus a total of 62 subjects included in the data analysis (16 each in the Secondary Cue Variability and All Enhanced conditions; 15 each in HVPT and Perceptual Fading). Forty-six of these subjects participated in all pre/post tests; the other 16 subjects were given the pre/post tests using natural stimuli but not those using cue-manipulated stimuli (see Procedure) due to testing time limitations.

All subjects were native speakers of Japanese with no known hearing or language impairments. Their ages ranged from 18 to 40 years (median 20 years), and the age at which they began learning English ranged from 4 to 23 years (median 12 years). Forty-one subjects were tested in Japan; they were students taking a course in English language at Kochi University, and all but one of these participants had never lived in an English speaking country. Twenty-one subjects

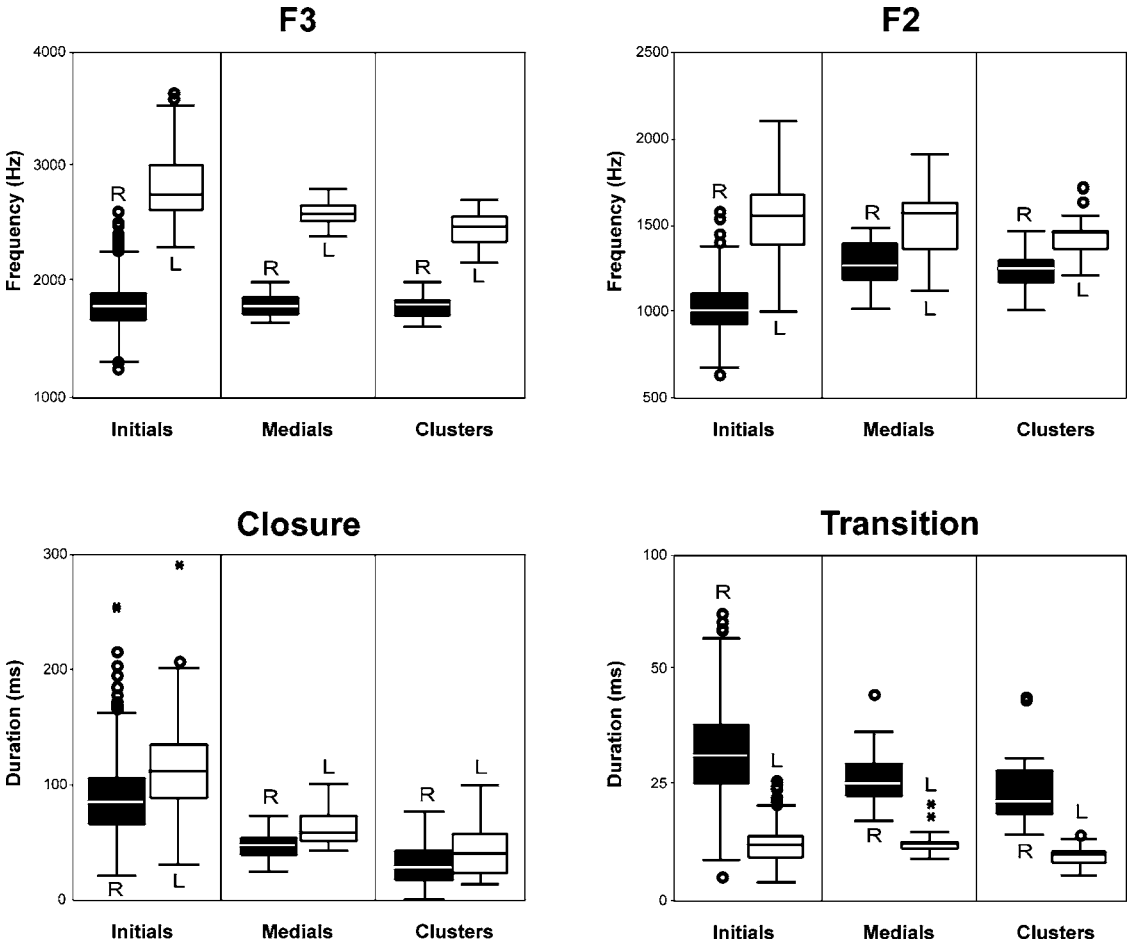

FIG. 1. Distributions of acoustic cues in natural stimuli. The boxplots represent the quartile ranges of each acoustic measure. The distributions of initials were based on 1000 stimuli (100 words each from 10 talkers). The distributions of medials and clusters were based on 40 stimuli (20 words each from 2 talkers). The formant frequency measurements (F3 and F2) were normalized to each speaker's vowel formant frequencies.

were tested in England; they were students who were attending English language or phonetics courses in London, and 5 had lived for more than 12 months in an English-speaking country (the longest for 5 years). The subjects in the two locations had very similar levels of /r/-/l/ identification accuracy (e.g., the pre-test percentage correct across all conditions averaged 60.5% in Kochi and 60.3% in London).

B. Apparatus

Subjects were tested and trained using either laboratory PCs or their own laptops and headphones. When subjects used their own laptops, a research assistant supervised the installation and checking of the software, and the subjects were able to borrow laboratory headphones if they did not own any of sufficient quality. Subjects were allowed to adjust the amplitude of the stimuli to a level that they found comfortable. Testing was completed in a quiet room under supervision of a research assistant. Training was completed by the subjects on their own (e.g., at home or in the laboratory), with the details of each session (e.g., time and date completed) automatically logged in a password-protected file that the subjects could not read or change.

C. Stimuli

1. Natural recordings

Twelve adult native speakers of British English (6 male and 6 female) were digitally recorded in an anechoic chamber with a calibrated microphone. The stimuli were recorded with 44 100 16-bit samples per second, and downsampled to 22 050 samples per second at a later stage. The words were spoken in isolation, but were presented to the talkers on a computer screen one at a time to avoid list intonation. The words were presented in a random order, mixed with words that did not contain /r/ or /l/. The training corpus was recorded by 10 speakers and consisted of 100 initial-position /r/-/l/ minimal-pair words (e.g., *rock* and *lock*). The testing corpus was recorded by two additional speakers and included 40 initial-position /r/-/l/ minimal-pair words from the training corpus, 40 initial-position /r/-/l/ minimal-pair words that were not used in training, 40 medial-position /r/-/l/ minimal-pair words (e.g., *arrive* and *alive*), and 40 consonant-cluster /r/-/l/ minimal pair words (e.g., *crash* and *clash*). The word lists are in Table A1 of the Appendix.

Acoustic measurements of the natural stimuli are displayed in Fig. 1. Formant frequency measurements were made using hand-corrected LPC analyses. For Fig. 1 (not for later signal processing), the formant frequency measure-

ments were normalized for each talker by a multiplicative factor that equated the F2 frequency that each speaker used in the vowel /i/ [which is stable between speakers; Evans (2005)]; this normalization was similar to methods that have been used to equate vowel spaces between speakers [see Adank *et al.* (2004) for a review]. The closures (i.e., the beginning of the consonant in which the articulators are held in a relatively static position) and transitions (i.e., between the consonant and the following vowel) were hand marked by inspecting F1 transitions and the amplitude envelope changes.

As expected, there was little overlap between the distributions of F3 frequencies for /r/ and /l/, although the frequency difference between /r/ and /l/ was moderately lower in medials and clusters. F2 also differed between /r/ and /l/ for initials, but there was substantial overlap between the distributions; the F2 difference was reduced further for medials and clusters. The F2 cue thus has some utility for distinguishing initial-position /r/ and /l/, and has less value in other positions [F2 may be even less useful for American English; see Lotto *et al.* (2004)]. There was substantial overlap between the distribution of closure durations for /r/ and /l/ at all syllable positions, indicating that this would be an unreliable acoustic cue for listeners. Transition duration was longer for /r/ than for /l/, with some overlap between distributions; the differences between transition durations was reduced for medials and clusters compared to initials, but the overlap between the distributions was not greater. Transition duration was thus similar to F2 frequency; both had some utility as secondary cues for distinguishing /r/ and /l/.

2. Signal processing

All of the signal processing was conducted only on the initial-position stimuli, and the processing combined changes in duration with changes in formant frequencies. The duration changes were made using the PSOLA function in Praat [Boersma and Weenink (2004)], and the duration of the closure and transition intervals were independently manipulated. The formant frequency changes were made via LPC analysis and resynthesis within Praat; the LPC parameters (e.g., prediction order and frequency cutoff) were hand selected for each stimulus so that the analysis correctly tracked the formants in the spectrogram, an LPC residual was created by inverse filtering the stimulus, a new LPC filter was created by manipulating the formant frequencies in the LPC analysis, and the final stimulus was created by filtering the LPC residual with the new LPC parameters. In order to improve the naturalness of the stimuli, the high-frequency energy that was removed by LPC (i.e., energy that was above the cut-off frequency) was added back into the signal following the LPC manipulations.

Prior to the construction of the final versions of the stimuli, the signal processing was pilot tested to make sure that it did not reduce the identifiability of these stimuli. A group of 9 native British English speaking listeners gave forced-choice /r/-/l/ identification responses for stimuli from multiple talkers and words, with the signal-processing dimensions (F3 enhancement, F2, closure duration, and transition duration) varying independently. Listeners were correct on 98.7% of the trials. Given this high level of accuracy, the final versions of the stimuli were simply screened by a research assistant to ensure that they were intelligible.

a. All Enhancement condition. Throughout training, F3 was set to extreme values during the closure (enhancing the difference between /r/ and /l/) and the duration of the closure was increased by 100 ms (ensuring that all stimuli would have a closure that was long enough to be audible; see Fig. 2 for example spectrograms, and Table A2 of the Appendix for specific values). For /r/, F3 was set to be 100 Hz higher than the median F2 frequency during the closure. For /l/, F3 was set to be 100 Hz lower than the median F4 frequency during the closure. The distribution of F3 across all stimuli was thus bimodal, with the values for /r/ and /l/ being further apart than in natural stimuli. To prevent the formants from crossing, F2 and F4 were flattened by setting them to their median values throughout the closure. During the transition, the degree of F3 enhancement was reduced linearly so that there was no enhancement at the end of the transition (i.e., the F3 frequency was the same as in the original recording by the time that the transition was over).

b. Perceptual Fading condition. On the first day of training, the stimuli were fully enhanced (i.e., the same as in the All Enhancement condition) and the amount of enhancement was linearly decreased each day until, by Day 10, the difference between /r/ and /l/ was less distinctive than normal (see Fig. 2 and Table A2 of the Appendix). The F3 values were based on the differences between the fully enhanced and normal values, such that there was 100% enhancement of F3 values on Day 1 (i.e., 100 Hz greater than F2 for /r/ and 100 Hz less than F4 for /l/), there was 50% enhancement on Day 4 (i.e., values were the average of the fully enhanced and normal), there was 0% enhancement on Day 7 (i.e., normal values), and −50% enhancement on Day 10 (e.g., for /r/, F3 was higher than normal, by an amount equal to half the difference between the fully enhanced and normal values). The "negative enhancement" in Days 8–10 lead to overlap of the F3 distributions for /r/ and /l/, but F3 remained a cue to the contrast because of vowel coarticulation (i.e., F3 in the vowel tends to be lowered following an /r/ and the vowel formant frequencies were unaffected by this manipulation). The amount of closure duration lengthening was 100 ms on Day 1, and decreased linearly to 0 ms (i.e., no lengthening) on Day 7; closure duration remained at its normal values on Days 8–10 (i.e., it was not shortened to match the negative F3 enhancement).

c. Secondary Cue Variability condition. On the first day of training, F2 during the closure, closure duration, and transition duration were set to the median values for all stimuli from the speaker; the stimuli thus had no variability and no differences between /r/ and /l/ along these acoustic dimensions. By Day 10, the stimuli randomly varied between the maximum and minimum F2 frequency, closure duration, and transition duration used by that speaker for all /r/ and /l/ stimuli (see values in Table A2 of the Appendix). That is, the stimuli had random combinations of short and long closures and transitions, and high and low F2 frequencies, for both /r/ and /l/. The distributions of values were bimodal (i.e., the values were either set to the minimum or maximum). The

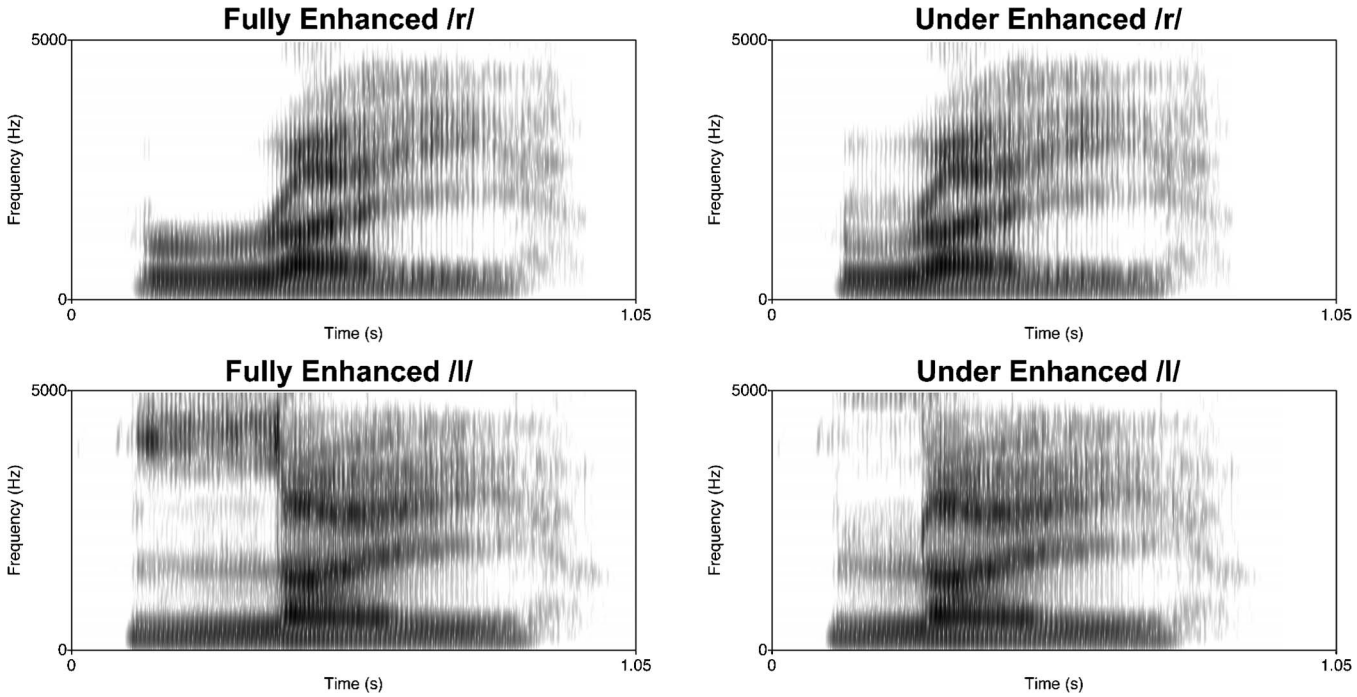

FIG. 2. Spectrographic examples of stimuli in Perceptual Fading, for the words *ray* and *lay*. The fully enhanced versions (used on the first day of training in Perceptual Fading, and on all days in All Enhanced) set F3 to extreme values and increased the duration of the initial closure by 100 ms. The under-enhanced versions (used on the last day of training in Perceptual Fading) decreased the contrast in F3 frequencies and had natural closure durations.

values of F2 were limited for each stimulus so that they were at least 100 Hz greater than F1 and 100 Hz less than F3 (e.g., if the maximum F2 frequency across all stimuli was greater than the F3 frequency for a particular stimulus, as occurred sometimes for /r/, F2 was set to be 100 Hz less than F3). The variability increased from Day 1 to Day 10 by increasing the range of the values. That is, Day 1 had 0% range (all values set to medians for that speaker), Day 10 had 100% range (all values set to the maximum or minimum), and Day 2, for example, had 11% range (all values set to 11% of the difference between the median and the maximum or minimum).

D. Procedure

1. Training

Each subject was randomly assigned to one of the 4 training conditions: HVPT, All Enhanced, Perceptual Fading, and Secondary Cue Variability. Except for the stimulus differences between the conditions, the training procedures were identical. The training comprised 10 sessions, each taking approximately 1/2 hour to complete. The subjects ran no more than one session per day, and completed the training over a 2 to 3 week period. There was a different talker each day [as in previous HVPT studies, e.g., Logan *et al.* (1991); Lively *et al.* (1993)], and each subject received the same talker order regardless of condition.

At the beginning of each session, subjects heard a greeting from the talker (e.g., "Hello, my name is Ian. You're going to hear my voice in the training today. Let's get started.") that was synchronized with an animated face. They then completed 300 trials (3 repetitions of the 100 stimuli, presented in a random order) of forced-choice identification with feedback. On each trial, subjects saw minimal pair words on the computer screen (e.g., *rock* and *lock*; the words varied for each stimulus), heard one of the words, and then clicked on the "R" or "L" button to indicate which of those words they thought they heard. If they answered correctly, they saw a "Correct!" message on the computer screen, heard a cash register sound, and heard the stimulus played again. If they answered incorrectly, they saw a "Wrong." message on the computer screen, heard two beeps with descending pitch, and then heard the stimulus played twice again. The screen displayed a running tally of the percentage of correct responses during the training session.

After each training session, subjects completed a short identification test without feedback or display of the percentage correct. This test tracked their performance as training progressed, and consisted of 20 words that were randomly selected from the training corpus. In order to directly compare the different conditions, the HVPT, Perceptual Fading, and Secondary Cue Variability conditions all used natural speech (i.e., unprocessed) from the talker that had been used in the training session. The All Enhancement condition used enhanced speech, in order to test whether subjects were able to improve when they had not heard *any* natural speech during the course of the training program.

2. Pre/Post identification testing

Before and after completing the period of training, subjects were tested in terms of their identification of natural and cue-manipulated stimuli. The format of each trial was the same as in the training (i.e., forced-choice identification of /r/-/l/ minimal pairs), except that subjects did not receive feedback.

a. Natural stimuli. Subjects first completed a practice

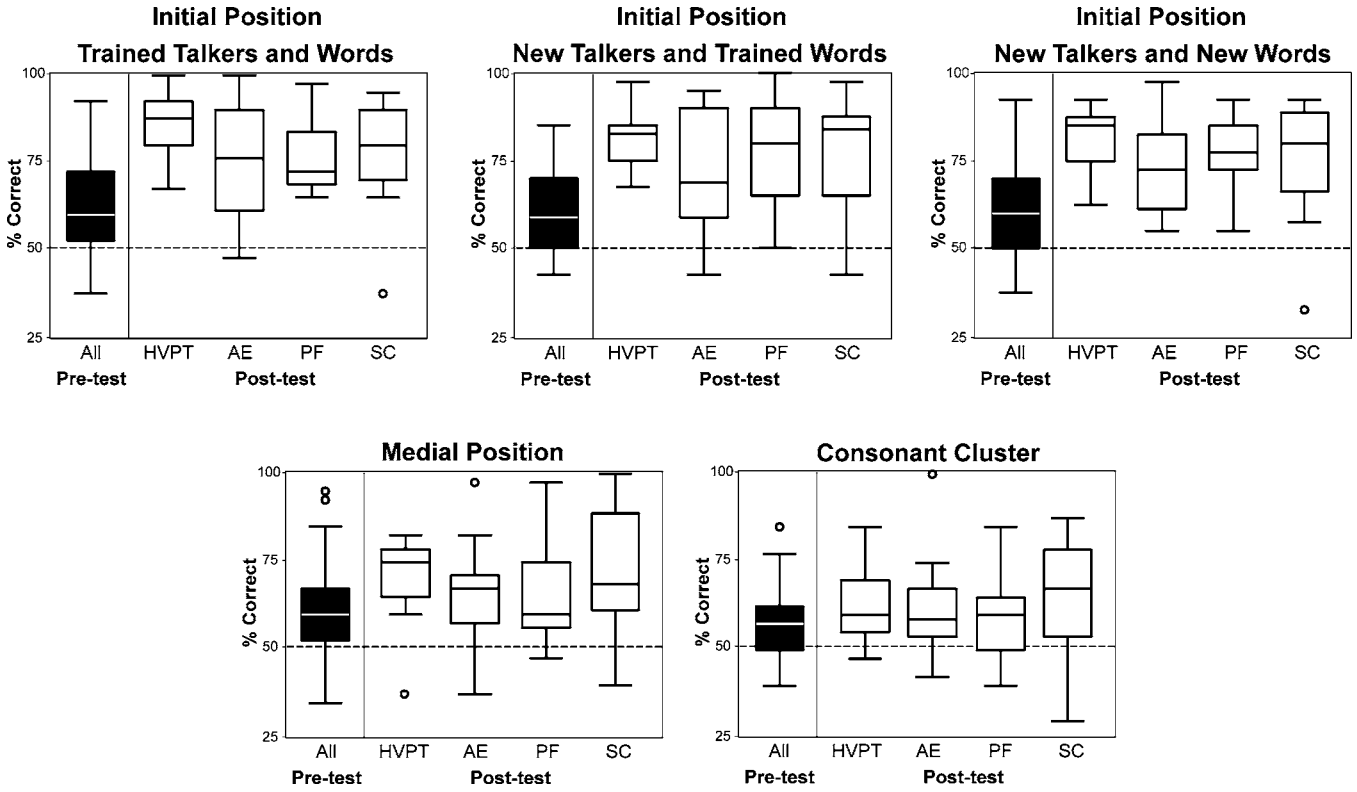

FIG. 3. Identification accuracy for natural /r/ and /l/ stimuli before and after training, for High Variability Phonetic Training (HVPT), All Enhanced (AE), Perceptual Fading (PF), and Secondary Cue Variability (SC). Pre-test scores are aggregated across training techniques, because there were no significant differences between the subjects assigned to the different techniques. Although there was high between-subject variability in pretest scores, there were reliable within-subject improvements after training. Improvement was greatest for initial-position stimuli, and this training generalized to new talkers and initial-position words. Generalization was weaker for medials and clusters. There were no significant differences between training techniques.

block of 10 trials, comprising initial-position /r/-/l/ minimal pairs from the training set. Subjects then completed 10 experimental blocks (5 conditions, with 2 talkers for each condition) of 20 trials each. The 5 conditions were: (1) trained talkers and words, (2) new talkers and trained words, (3) new talkers and new initial-position words, (4) new talkers and new medial-position words, and (5) new talkers and new consonant-cluster words. Each of the 10 blocks had a different word list (i.e., words were not repeated). All subjects received the same 10 lists of words, and all subjects were tested on the same talkers. The word lists are in Table A1 of the Appendix.

b. Cue-manipulated stimuli. Following identification testing for natural stimuli, subjects completed the same forced-choice identification task with stimuli that had been signal-processed to alter the acoustic cues. There were two talkers and 9 stimulus conditions, and the talkers and words were drawn from the training corpus. The conditions were: (1) Short Closure (i.e., closure duration set to a speaker's minimum, as in Day 10 of Secondary Cue Variability), (2) Long Closure (i.e., closure duration set to a speaker's maximum, as in Day 10 of Secondary Cue Variability), (3) Short Transition (i.e., transition duration set to a speaker's minimum, as in Day 10 of Secondary Cue Variability), (4) Long Transition (i.e., transition duration set to a speaker's maximum, as in Day 10 of Secondary Cue Variability), (5) Low F2 (i.e., F2 set to a speaker's minimum, as in Day 10 of Secondary Cue Variability), (6) High F2 (i.e., F2 set to a speaker's maximum, as in Day 10 of Secondary Cue Variability), (7) Enhanced F3 (i.e., F3 the same as Day 1 of Perceptual Fading, with no duration lengthening), (8) Negative Enhancement of F3 (i.e., F3 the same as Day 10 of Perceptual Fading), and (9) Natural stimuli (i.e., no acoustic manipulation). There were 2 blocks (1 for each talker), with 180 trials per block (20 trials per stimulus condition, with the conditions mixed randomly within each block).

III. RESULTS

A. Pre/Post identification of natural stimuli

The pre- and post-training results for initial-position words (see Fig. 3) were analyzed by MANOVA; the RAU-transformed percentages correct [Rationalized Arcsine Units; Studebaker (1985)] were analyzed with pre/post (i.e., before and after training) and stimulus condition (trained talkers and words; new talkers and trained words; and new talkers and new words) coded as within-subject factors (i.e., as a repeated measure) and training condition coded as a between-subject factor. There was a significant effect of pre/post, $F(1,58)=102.01, p<0.001$, demonstrating that identification performance improved after training (mean improvement of 18 percentage points). There was a significant effect of stimulus condition, $F(2,57)=57.00, p=0.008$; on average, accuracy for the trained talkers and words was 2.3 percentage points higher than for the other two conditions. However, there was no significant interaction of stimulus condition and

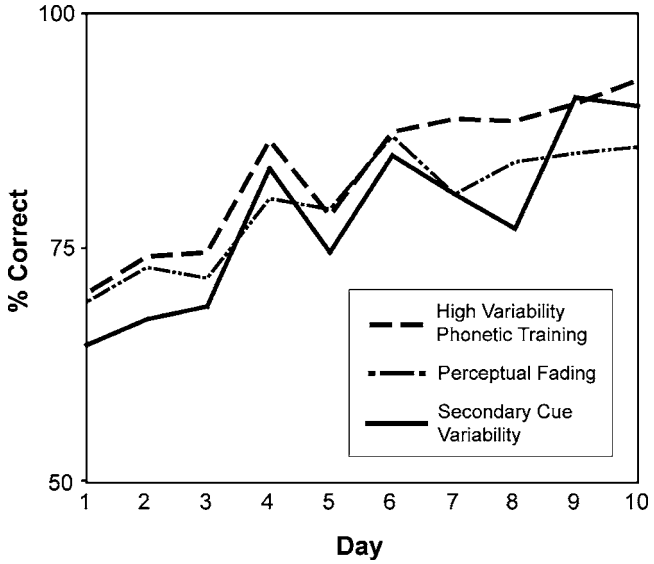

FIG. 4. Changes in identification accuracy for /r/ and /l/ over time. Subjects gradually improved in identification accuracy during the 10 training sessions. There were no significant differences between training techniques.

pre/post, $p > 0.05$, which indicated that the magnitude of improvement with training was similar across the stimulus conditions (i.e., the training generalized to new words and talkers). There was no significant effect of training condition and no significant interactions, $p < 0.05$, demonstrating that all four training conditions yielded similar levels of improvement in identification accuracy.

To further examine generalization, the pre- and post-training results for the different syllable positions (initial, medial, cluster) were also analyzed by MANOVA. There was a significant effect of pre/post, $F(1,58) = 99.65, p < 0.001$, demonstrating that identification performance improved after training. There was a significant effect of position, $F(2,57) = 42.29, p < 0.001$, demonstrating that initials were more accurately identified than were medials and clusters. There was also a significant interaction of position and pre/post, $F(2,56) = 12.61, p < 0.001$, demonstrating that the improvement in training on initials did not fully generalize to the other syllable positions (median improvement in accuracy was 18.0 percentage points for initials, 8.7 percentage points for medials, and 5.5 percentage points for clusters). There was no significant effect of training condition and no significant interactions, $p < 0.05$, demonstrating that all four training conditions yielded similar levels of improvement in identification accuracy.

B. Changes in identification performance during training

Although the pre/post analysis demonstrated that there were no differences in improvement between training methods, the results for each training session were analyzed to examine whether identification improved at different rates among the training conditions. The results for the tracking test at the end of each training session, for all conditions except All Enhanced (which did not have a tracking test with natural stimuli), are displayed in Fig. 4. Identification performance appeared to improve steadily for all conditions, without reaching asymptotic levels. There was some variation between conditions in Days 4–6 that may have been caused by differences in the intelligibility of speakers. A MANOVA analysis of the RAU-transformed percentages correct revealed that there was a significant main effect of day, $F(9,29) = 9.62, p < 0.001$, demonstrating that training improved recognition. There was no significant effect of training condition, $p > 0.05$, but there was a marginally significant interaction between day and training condition, $F(18,58) = 1.67, p = 0.072$. It is thus possible that there were some differences in the rate of learning in the different conditions, but the mean data in Fig. 4 suggests that the differences, if reliable, were small.

C. Pre/Post assessment of cue-manipulated stimuli

Figure 5 displays the percentage correct for /r/ and /l/ when the secondary cues were altered. A preliminary examination revealed that there were substantial differences in response bias between conditions (e.g., listeners gave more /l/ responses when transition durations were short than when they were long), so Detection Theory [Macmillan and Creelman (1991)] was used to calculated the sensitivity (d') and bias (c) for each condition. The bias statistic provides a way of measuring cue weighting. For example, if listeners are biased to identify stimuli with long transitions as /r/ and short transitions as /l/, this would demonstrate that the transition duration affects whether they identify the stimulus as /r/ or /l/ and thus indicate that transition duration had high weighting in the categorization decision. If listeners had zero bias for a cue, this would indicate that the cue does not affect /r/-/l/ identification, and thus had low weighting.

For each stimulus condition, a MANOVA analyzed the bias with pre/post (i.e., before and after training) as a within-subjects variable and training condition as a between-subjects variable. Although d' was also analyzed, the results are not reported here because they simply corresponded with the natural identification results (i.e., d' increased with training, but there were no interactions with training condition).

For closure duration, listeners had a strong bias before training to label long closures as /r/ and short closures as /l/, demonstrating that they had a high weighting for this cue in their categorization decision. After training, subjects had significantly reduced response bias for long closures, $F(1,42) = 2.51, p < 0.001$, but there was no change for short closures, $p > 0.05$; training thus modified their cue weightings somewhat (particularly for long closures), but they continued to use this cue. There was no main effect of training condition or significant interaction with pre/post, $p > 0.05$.

For transition duration, listeners had a strong bias before training to label long transitions as /r/ and short transitions as /l/, demonstrating that they had a high weighting for this cue. After training, subjects had significantly reduced bias for long transitions, $F(1,42) = 21.0, p < 0.001$, but had significantly increased bias for identifying short-transition stimuli as /l/, $F(1,42) = 18.0, p < 0.001$; training thus changed how they used this cue, but they continued to give high weight to this cue overall. For long-transition stimuli, there was a significant main effect of training condition, $F(3,42) = 4.4, p$

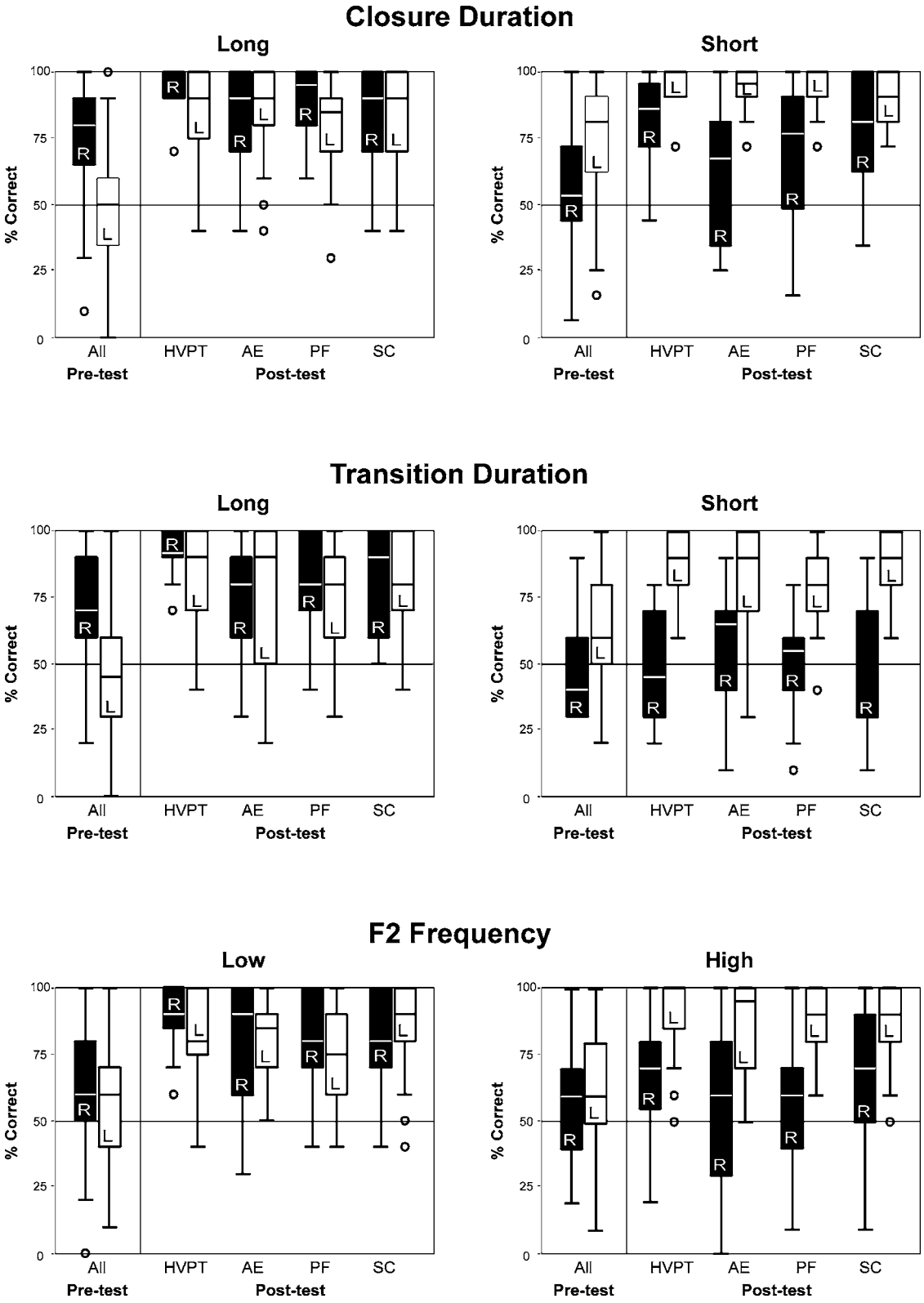

FIG. 5. Identification accuracy for cue-manipulated stimuli before and after training, for High Variability Phonetic Training (HVPT), All Enhanced (AE), Perceptual Fading (PF), and Secondary Cue Variability (SC). Subjects were biased to identify stimuli with long closures and transitions as /r/ before training, but this bias was reduced after training. Subjects were biased to identify stimuli with short closures and transitions as /l/ before training; this /l/ bias increased after training for short transitions and for high F2 frequencies.

$=0.009$, but no significant interaction with pre/post, $p > 0.05$; there were some differences in long-transition biases between subject groups (i.e., All Enhanced subjects had less bias to identify /r/) but this difference seemed more a result of the subject assignment to conditions rather than a result of training. For short-transition stimuli, there was no main effect of training condition or significant interaction with pre/post, $p > 0.05$.

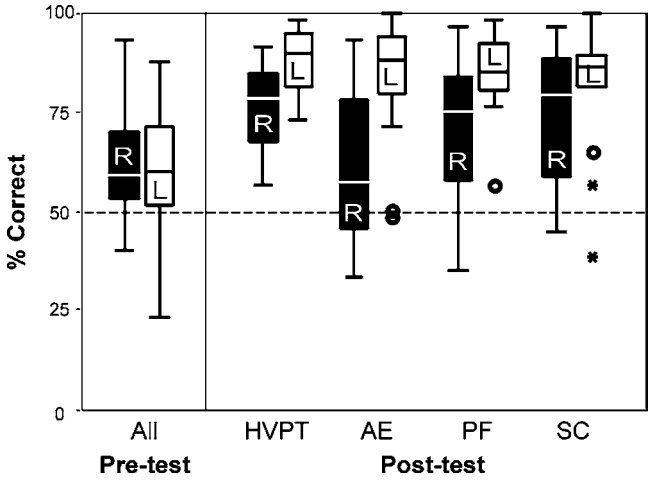

FIG. 6. Identification accuracy for natural stimuli before and after training, divided by /r/ and /l/, for High Variability Phonetic Training (HVPT), All Enhanced (AE), Perceptual Fading (PF), and Secondary Cue Variability (SC). Subjects became biased to identify stimuli as /l/ after training, leading to more accurate identification of /l/ than /r/.

For F2 frequency, listeners began with no strong biases, demonstrating low cue weighting. After training, they did not significantly change their biases for low-F2 frequency stimuli, $p>0.05$, but they increased their bias to identify high-F2 frequency stimuli as /l/, $F(1,42)=25.8, p<0.001$, demonstrating an increased weighting for this cue. There were no main effects of training condition or significant interactions with pre/post, $p>0.05$.

For the other conditions in the cue-manipulated identification tests, there was low bias before training, but a small bias to identify stimuli as /l/ after training (natural stimuli, $F(1,42)=31.6, p<0.001$; enhanced F3, $F(1,42)=11.8, p=0.001$; negatively enhanced F3, $F(1,42)=9.7, p=0.003$). Although there were no significant interactions between training condition and pre/post, $p>0.05$, there were significant main effects of training condition for enhanced F3, $F(3,42)=3.2, p=0.033$, and negatively enhanced F3, $F(3,42)=4.7, p=0.006$; subjects in the All Enhanced condition had a slightly stronger bias overall to identify stimuli as /l/.

To further explore the apparent increase in /l/-bias after training, the identification of natural stimuli in the main pre/post test was reanalyzed in terms of response bias. As displayed in Fig. 6, there was a significant increase in bias to identify stimuli as /l/ after training, $F(1,58)=46.7, p<0.001$. There was no main effect of training condition or significant interaction, $p>0.05$. The increase in /l/-bias can also be interpreted as a differential increase in identification accuracy. That is, individuals had greater improvement in identification accuracy for /l/ than for /r/.

IV. DISCUSSION

The results demonstrated that there was significant improvement of /r/ and /l/ identification by Japanese adults; the identification of initials improved by an average of 18 percentage points, which is at least as large as in previous studies that have used HVPT [Hazan *et al.* (in press); Logan *et al.* (1991); Lively *et al.* (1993); Bradlow and Pisoni (1999); Bradlow *et al.* (1999)]. There were no significant differences in how well the methods improved perception, both in terms of correct identification and in the use of secondary acoustic cues. Regarding the applied goal of aiding L2 phoneme learning, it thus appears that training with natural speech is currently the best method, because the signal processing techniques used here are more labor intensive and offer no additional gains in performance. However, the lack of significant differences between training methods also demonstrates that there is nothing particularly special about having fully natural variability; Pisoni and colleagues [e.g., Logan *et al.* (1991); Lively *et al.* (1993)] have emphasized the importance of exposing listeners to natural speech from multiple talkers in order to teach listeners how individual talkers covary their acoustic cues, but training was just as successful here using methods in which the F3 or secondary cues were varied unnaturally. Even though the specific signal-processing methods used here did not improve upon natural speech, the general approach of training with manipulated speech is supported by our results; listeners clearly could learn under these conditions. It remains to be seen whether differences between the methods would emerge if long-term retention or production were measured, if other phonetic contrasts or cues were trained that might benefit more from enhancement, or if more natural enhancement (i.e., clear speech) was used.

The changes in secondary-cue biases support the general view that secondary cues are important to L2 phoneme learning, but the changes were not as predicted by the perceptual interference account [Iverson *et al.* (2003)]. That is, there was not a general reduction in the salience of secondary acoustic cues as identification performance improved. Rather, there was a decrease in response bias for some types of secondary cues (long closures and transitions) and an increase in others (short transitions and high F2 frequencies).[1] The patterns of secondary cue weightings after training also did not correspond to their validity in natural stimuli, contrary to the patterns of shrinking and stretching predicted by exemplar models [e.g., Logan *et al.* (1991); Lively *et al.* (1993)]. For example, /r/ and /l/ have substantial overlap in terms of closure duration (Fig. 1), with /r/ having shorter closures on average, but listeners persisted in being biased to label short-closure stimuli as /l/. Moreover, the acoustic measurements revealed that F2 frequency and transition duration had some cue validity, but their natural distributions did not predict the asymmetries in subjects' cue weightings. For example, the acoustic measurements indicated that the presence of a long transition was a more reliable cue for /r/ than a short transition was for /l/ (i.e., there was more overlap between the distributions for durations <25 ms), but the subjects changed their cue weightings in an opposite way, reducing /r/-bias for long transitions and increasing /l/-bias for short transitions.

On the surface, the results are also at odds with category assimilation accounts of /r/-/l/ learning. Aoyama *et al.* (2004) claimed that English /l/ is more strongly assimilated into the Japanese /r/ category than is English /r/, and this makes English /r/ easier to learn. Our results showed the opposite pattern of learning, with /l/ identification improving more with

training than /r/. However, it is notable that all of the unpredictable cue biases described above involved stimuli that would be expected to be strongly assimilated into the Japanese /r/ category. That is, assimilation has been shown to be stronger for English /r/ and /l/ stimuli that have high F2 frequencies [Iverson *et al.* (2003)], and the short duration of the Japanese /r/ would likely produce stronger assimilation effects for English stimuli with short closures and transitions; all of these types of stimuli were biased to be identified as English /l/ after training. It is thus plausible that training caused subjects to learn to systematically label a stimulus as /l/ whenever it was strongly assimilated into the Japanese /r/ category [Japanese students are sometimes taught this strategy when learning English; Lotto *et al.* (2004)]. For stimuli that were probably not strongly assimilated (low F2 frequencies, and long closures and transitions), subjects had low biases for secondary acoustic cues after training, in accord with the predictions of perceptual interference [Iverson *et al.* (2003)] and exemplar models [e.g., Logan *et al.* (1991); Lively *et al.* (1993)]. Category assimilation and perceptual interference may therefore combine to affect how English /r/ and /l/ are learned.

This account may help explain why there were no differences between training conditions. The Secondary Cue Variability technique was designed to eliminate the validity of secondary acoustic cues, such that, for example, the distributions of transition duration would be identical for /r/ and /l/ rather than as in natural stimuli (i.e., /r/ longer than /l/, with some overlap between distributions). This technique successfully reduced /r/-bias for stimuli with long transitions, but /r/-bias was reduced by all of the other training techniques too. It seems that natural variability in transition durations was sufficient to change biases, and that the Secondary Cue Variability technique offered no additional improvement. For the stimuli that were strongly assimilated into the Japanese /r/ category, the variability in the stimuli may not have mattered very much (e.g., stimuli with short closures were biased to be labeled as /l/ even though this was unmotivated by the acoustic distribution of stimuli in any of the conditions), and hence there were no differences between training conditions.

The poor generalization of training to medials and clusters may simply have occurred because they were too dissimilar to the initial-position stimuli that were used during training. That is, they may not have mapped onto the same categorization space [cf., Lively *et al.* (1993)]. The acoustic measurements, though, suggest that category assimilation may also have played a role. That is, medials and clusters had shorter closure durations, and /r/ in those positions had higher F2 frequencies, all of which promote assimilation into the Japanese /r/ category. That being said, training did not cause subjects to identify all medials and clusters as /l/ (there was an /l/-bias, as in the other conditions), and these positions have not been shown to be particularly resistant to training in previous studies that included medials and clusters in the training set [e.g., Logan *et al.* (1991); Lively *et al.* (1993)].

In summary, the results demonstrate that listeners modify their use of secondary cues during L2 phoneme learning, and suggest that both perceptual interference and assimilation affect the learning process. Although the signal-processing methods used here did not improve the effectiveness of training, the results demonstrate that there is still room for improvement in existing methods; identification performance for most individuals did not reach ceiling after training, and category assimilation remained a barrier to learning. What may be needed are new techniques that are specifically targeted to reduce assimilation effects.

APPENDIX

TABLE A1. Words used in the experiment.

Trained words					
lack	rack	leer	rear	loaves	roves
lad	rad	lent	rent	lob	rob
lag	rag	lice	rice	lobe	robe
laid	raid	lick	Rick	lock	rock
lake	rake	lid	rid	long	wrong
lamb	ram	lies	rise	look	rook
lane	rain	life	rife	loom	room
lank	rank	lift	rift	loss	Ross
late	rate	light	right	lot	rot
laughed	raft	limb	rim	loud	rowed
laws	roars	lime	rhyme	lout	rout
lay	ray	line	Rhine	low	row
laze	raise	lined	rind	lows	rose
leach	reach	link	rink	lump	rump
leaf	reef	lip	rip	lush	rush
leak	reek	lit	writ	lust	rust
led	red	loan	roan		
New initial-position words (pre/post test)					
lace	race	lest	rest	loot	root
lamp	ramp	lewd	rude	lope	rope
lap	wrap	lied	ride	lord	roared
lapse	raps	list	wrist	lose	ruse
law	raw	load	road	lug	rug
leap	reap	loam	roam	lung	rung
lens	wrens	loon	rune		
New medial-position words (pre/post test)					
alive	arrive	elect	erect	palling	poring
allows	arouse	fairly	fairy	pilot	pirate
bawling	boring	fallow	farrow	starling	starring
believe	bereave	holler	horror	tally	tarry
bellies	berries	mallow	marrow	teller	terror
calling	coring	miller	mirror	whirling	whirring
collect	correct	palate	parrot		
New cluster words (pre/post test)					
bland	brand	flame	frame	glue	grew
bloom	broom	flesh	fresh	plank	prank
blunt	brunt	flows	froze	plays	praise
blush	brush	flute	fruit	plod	prod
clamp	cramp	glass	grass	splay	spray
climb	crime	glaze	graze	splint	sprint
cloud	crowd	glow	grow		

TABLE A2. **Ranges of acoustic cue values for each training condition and day**. The values in each box represent the minimum and maximum values for /r/ and /l/ (i.e., min-max [r]/min-max [l]); the SC condition had identical acoustic distributions for /r/ and /l/ in terms of F2, closure duration, and transition duration, so only one range of values is listed. HVPT (High Variability Phonetic Training) used natural recordings with a different talker on each day. AE (All Enhanced), PF (Perceptual Fading), and SC (Secondary Cue Variability) used signal-processed versions of these natural recordings.

Day	Condition	F2 (Hz)	F3 (Hz)	Closure (ms)	Transition (ms)
1	HVPT (natural)	719–1377/894–1538	1378–2016/2144–2810	17–92/31–108	6–44/7–20
	AE	same as natural	819–1477/2981–3423	117–192/131–208	same as natural
	PF	same as natural	819–1477/2981–3423	117–192/131–208	same as natural
	SC	1140-1140	same as natural	64-64	17-17
2	HVPT (natural)	716–1382/1638–2275	1892–2722/2954–3994	41–132/72–191	28–64/10–33
	AE	same as natural	816–1482/3470–4586	141–232/172–291	same as natural
	PF	same as natural	1040–1647/3434–4419	124–215/155–274	same as natural
	SC	1581–1754	same as natural	98–115	27–33
3	HVPT (natural)	945–1370/1616–2346	1932–2498/2656–3458	22–78/25–103	20–58/9–24
	AE	same as natural	1054–1470/4054–4686	122–178/125–203	same as natural
	PF	same as natural	1395–1760/3634–4281	89–145/92–170	same as natural
	SC	1467–1778	same as natural	43–61	19–30
4	HVPT (natural)	620–1114/1077–1692	1298–1724/2424–2998	49–186/106–167	26–78/8–30
	AE	same as natural	755–1214/3270–3967	149–286/206–267	same as natural
	PF	same as natural	1135–1408/2922–3371	99–236/156–217	same as natural
	SC	961–1318	same as natural	96–141	20–43
5	HVPT (natural)	956–1613/1317–1881	1551–2699/2402–3768	30–93/30–118	13–63/9–30
	AE	same as natural	1056–1713/3722–4389	130–193/130–218	same as natural
	PF	same as natural	1403–2287/2837–3871	63–126/63–151	same as natural
	SC	1214–1625	same as natural	54–93	15–39
6	HVPT (natural)	735–1346/1645–2151	1813–2267/2881–3925	29–91/70–137	36–69/9–29
	AE	same as natural	1019–1446/3757–4391	129–191/170–237	same as natural
	PF	same as natural	1701–2098/3056–3959	46–108/87–154	same as natural
	SC	1139–1927	same as natural	51–111	18–52
7	HVPT (natural)	619–1122/1041–1596	1216–1694/2432–2826	42–113/49–118	19–50/7–28
	AE	same as natural	719–1222/2975–3601	142–213/149–218	same as natural
	PF	same as natural	same as natural	same as natural	same as natural
	SC	777–1429	same as natural	54–104	12–44
8	HVPT (natural)	1017–1324/1415–2150	1749–2640/2924–3965	41–102/68–138	21–69/7–33
	AE	same as natural	1160–1424/3621–4658	141–202/168–238	same as natural
	PF	same as natural	1840–2874/2774–3855	same as natural	same as natural
	SC	1098–1979	same as natural	50–126	12–60
9	HVPT (natural)	602–1211/1208–2960	1507–2586/2759–3336	34–117/33–148	30–89/9–35
	AE	same as natural	862–1311/3837–4470	134–217/133–248	same as natural
	PF	same as natural	1682–3060/2277–3036	same as natural	same as natural
	SC	682–2778	same as natural	38–140	12–83
10	HVPT (natural)	835–1132/1044–1423	1105–1797/2208–2659	52–212/71–242	26–75/5–30
	AE	same as natural	995–1232/3352–3799	152–312/171–342	same as natural
	PF	same as natural	1117–2144/1507–2184	same as natural	same as natural
	SC	835–1423	same as natural	52–242	5–75

ACKNOWLEDGMENTS

We are grateful to Professor Masaki Taniguchi (Kochi University) for his help in organizing the testing sessions in Japan. This research was funded by Grant No. RES-000-22-0445 from the Economic and Social Research Council of Great Britain.

[1]The pattern of bias changes could also be interpreted as being a result of a global increase in /l/ bias, because most conditions changed bias in the direction of more /l/ responses (i.e., reductions in /r/ bias and increases in /l/ bias both result from increases in the proportion of /l/ responses). However, the /l/ bias did not change to the same extent across all conditions. For example, there was no bias change for low-F2 frequencies, but a significant increase in /l/ bias for high-F2 frequencies. This suggests that there were cue-specific changes to biases rather than a simple global increase in the proportion of /l/ responses or an overall increase in /l/ identification accuracy.

Adank, P., Smits, R., and van Hout, R. (**2004**). "A comparison of vowel normalization procedures for language variation research," J. Acoust. Soc. Am. **116**, 3099–3107.

Aoyama, K., Flege, J. E., Guion, S. G., Akahane-Yamada, R., and Yamada, T. (**2004**). "Perceived phonetic distance and L2 learning: The case of Japanese /r/ and English /l/ and /r/," J. Phonetics **32**, 233–250.

Best, C. T. (**1994**). "The emergence of native-language phonological influences in infants: A perceptual assimilation model." in *The development of speech perception: The transition from speech sounds to spoken words*, edited by J. C. Goodman and H. C. Nusbaum (MIT Press, Cambridge, MA), pp. 167–224.

Best, C. T., McRoberts, G. W., and Goodell, E. (**2001**). "Discrimination of non-native consonant contrasts varying in perceptual assimilation to the listener's native phonological system," J. Acoust. Soc. Am. **109**, 775–794.

Best, C. T., McRoberts, G. W., and Sithole, N. M. (**1988**). "Examination of

perceptual reorganization for nonnative speech contrasts: Zulu click discrimination by English-speaking adults and infants," J. Exp. Psychol. Hum. Percept. Perform. **14**, 345–360.
Best, C. T., and Strange, W. (**1992**). "Effects of language-specific phonological and phonetic factors on cross-language perception of approximants," J. Phonetics **20**, 305–330.
Boersma, P., and Weenink, D. (**2004**). "Praat: doing phonetics by computer" [Computer program]. Retrieved from http://www.praat.org/
Bradlow, A. R., and Pisoni, D. B. (**1999**). "Recognition of spoken words by native and non-native listeners: Talker-, listener- and item-related factors," J. Acoust. Soc. Am. **106**, 2074–2085.
Bradlow, A. R., Akahane-Yamada, R., Pisoni, D. B., and Tohkura, Y. (**1999**). "Training Japanese listeners to identify English /r/ and /l/: Long-term retention of learning in perception and production," Percept. Psychophys. **61**, 977–985.
Doeleman, T. J., Conley, R. J., Pruitt, J. S., Iverson, P., Kuhl, P. K., and Stevens, E. B. (**2000**). "Perceptual identification training of American English /r/ and /l/ by Japanese speakers generalizes to novel stimuli and tasks," J. Acoust. Soc. Am. **108**, 2652.
Evans, B. G. (**2005**). "Plasticity in speech perception and production: A study of accent change in young adults," Unpublished PhD dissertation, University of London, UK.
Flege, J. E. (**1995**). "Second language speech learning: Theory, findings, and problems," in *Speech perception and language experience: Issues in cross-language research*, edited by W. Strange (York Press, Baltimore), pp. 233–277.
Flege, J. E. (**1999**). "Age of learning and second language speech." In Birdsong (Ed.), *Second Language Learning and the Critical Period Hypothesis* (pp. 101–131). London: Erlbaum.
Flege, J. E., Schirru, C., and MacKay, I. R. A. (**2003**). "Interaction between native and second language phonetic subsystems," Speech Commun. **40**, 467–491.
Flege, J. E., Takagi, N., and Mann, V. (**1995**). "Japanese adults can learn to produce English /r/ and /l/ accurately," Lang Speech **38**, 25–55.
Gordon, P. C., Keyes, L., and Yung, Y. F. (**2001**). "Ability in perceiving nonnative contrasts: Performance on natural and synthetic speech stimuli," Percept. Psychophys. **63**, 746–758.
Goto, H. (**1971**). "Auditory perception by normal Japanese adults of the sounds "L" and "R"," Neuropsychologia **9**, 317–323.
Guion, S. G., Flege, J. E., Akahane-Yamada, R., and Pruitt, J. (**2000**). "An investigation of current models of second language speech perception: The case of Japanese adults' perception of English consonants," J. Acoust. Soc. Am. **107**, 2711–2724.
Harnsberger, J. D. (**2001**). "On the relationship between identification and discrimination of non-native nasal consonants," J. Acoust. Soc. Am. **110**, 489–503.
Hazan, V., Sennema, A., Iba, M., Faulkner, A. (in press). "Effect of audiovisual perceptual training on the perception and production of consonants by Japanese learners of English," Speech Commun..
Iverson, P., Kuhl, P. K., Akahane-Yamada, R., Diesch, E., Tohkura, Y., Kettermann, A., and Siebert, C. (**2003**). "A perceptual interference account of acquisition difficulties for non-native phonemes," Cognition **87**, B47–B57.
Jamieson, D. G., and Morosan, D. E. (**1986**). "Training non-native speech contrasts in adults: Acquisition of the English /ð/-/θ/ contrast by francophones," Percept. Psychophys. **40**, 205–215.
Kuhl, P. K. (**2000**). "A new view of language acquisition," Proc. Natl. Acad. Sci. U.S.A. **97**, 11850–11857.
Lenneberg, E. (**1967**). *Biological Foundations of Language* (Wiley, New York).
Lively, S. E., Logan, J. S., and Pisoni, D. B. (**1993**). "Training Japanese listeners to identify English /r/ and /l/: II. The role of phonetic environment and talker variability in learning new perceptual categories," J. Acoust. Soc. Am. **94**, 1242–1255.
Logan, J. S., Lively, S. E., and Pisoni, D. B. (**1991**). "Training Japanese listeners to identify English /r/ and /l/: a first report," J. Acoust. Soc. Am. **89**, 874–886.
Lotto, A. J., Sato, M., and Diehl, R. L. (**2004**). "Mapping the task for the second language learner: The case of Japanese acquisition of /r/ and /l/," in J. Slifka, S. Manuel, and M. Matthies (Eds.) *From Sound to Sense:* 50 +Years *of Discoveries in Speech Communication* (MIT Research Laboratory in Electronics, Cambridge, MA), pp. C-181–C-186.
MacKain, K. S., Best, C. T., and Strange, W. (**1981**). "Categorical perception of English /r/ and /l/ by Japanese bilinguals," Applied Psycholinguistics **2**, 369–390.
Macmillan, N. A., and Creelman, C. D. (**1991**). *Detection theory: a user's guide*. (Cambridge University Press, New York).
McCandliss, B. D., Fiez, J. A., Protopapas, A., Conway, M., and McClelland, J. L. (**2002**). "Success and failure in teaching the r-l contrast to Japanese adults: predictions of a hebbian model of plasticity and stabilization spoken language perception," Cognitive, Affective, and Behavioral Neuroscience **2**, 89–108.
McClelland, J. L., Fiez, J. A., and McCandliss, B. D. (**2002**). "Teaching the /r/-/l/ discrimination to Japanese adults: behavioral and neural aspects," Physiol. Behav. **77**, 657–662.
Miyawaki, K., Strange, W., Verbrugge, R., Liberman, A., Jenkins, J., and Fujimura, O. (**1975**). "An effect of language experience: The discrimination of /r/ and /l/ by native speakers of Japanese and English," Percept. Psychophys. **18**, 331–340.
Nosofsky, R. (**1986**). "Attention, similarity, and the identification-categorization relationship," J. Exp. Psychol. Gen. **115**, 39–57.
Nosofsky, R. (**1987**). "Attention and learning processes in the identification and categorization of integral stimuli," J. Exp. Psychol. **15**, 87–108.
Patkowski, M. (**1990**). "Age and accent in second language learning: A reply to James Emil Flege," Applied Psycholinguistics **11**, 73–89.
Protopapas, A., and Calhoun, B. (**2000**). "Adaptive phonetic training for second language learners," 2nd International Workshop on Integrating Speech Technology in Language Learning (InSTIL). Dundee, Scotland.
Studebaker, G. A. (**1985**). "A "rationalized" arcsine transform," J. Speech Hear. Res. **28**, 455–462.
Yamada, R. A. (**1995**). "Age and acquisition of second language speech sounds: Perception of American English /r/ and /l/ by Native Speakers of Japanese," in *Speech perception and language experience: Issues in cross-language research*, edited by W. Strange (York Press, Baltimore), pp. 305–320.

Effects and modeling of phonetic and acoustic confusions in accented speech

Pascale Fung[a] and Yi Liu
Human Language Technology Center, Department of Electrical and Electronic Engineering, Hong Kong University of Science and Technology, Clear Water Bay, Hong Kong

(Received 22 July 2004; revised 28 June 2005; accepted 21 July 2005)

Accented speech recognition is more challenging than standard speech recognition due to the effects of phonetic and acoustic confusions. Phonetic confusion in accented speech occurs when an expected phone is pronounced as a different one, which leads to erroneous recognition. Acoustic confusion occurs when the pronounced phone is found to lie acoustically between two baseform models and can be equally recognized as either one. We propose that it is necessary to analyze and model these confusions separately in order to improve accented speech recognition without degrading standard speech recognition. Since low phonetic confusion units in accented speech do not give rise to automatic speech recognition errors, we focus on analyzing and reducing phonetic and acoustic confusability under high phonetic confusion conditions. We propose using likelihood ratio test to measure phonetic confusion, and asymmetric acoustic distance to measure acoustic confusion. Only accent-specific phonetic units with low acoustic confusion are used in an augmented pronunciation dictionary, while phonetic units with high acoustic confusion are reconstructed using decision tree merging. Experimental results show that our approach is effective and superior to methods modeling phonetic confusion or acoustic confusion alone in accented speech, with a significant 5.7% absolute WER reduction, without degrading standard speech recognition. © *2005 Acoustical Society of America.* [DOI: 10.1121/1.2035588]

PACS number(s): 43.72.Ne, 43.72.Ar, 43.71.An, 43.71.−k [DOS] Pages: 3279–3293

I. INTRODUCTION

Most state-of-the-art automatic speech recognition (ASR) systems fail to perform well when the speaker has a regional accent different from that of the standard language the systems were trained on. The high error rate is largely due to the effects of phonetic confusions and acoustic confusions in accented speech. Previous studies on accented speech recognition investigated in detail the effect of phonetic confusions (Liu *et al.*, 2000; Tomokiyo, 2001) or acoustic confusions (Huang *et al.*, 2000). However, the distinction and correlation between phonetic and acoustic confusions, in particular how to model their different roles for better ASR performance, are less clear. We suggest that it is essential to distinguish phonetic and acoustic confusions, as well as understand their relationship and roles in accented speech in order to achieve better recognition performance.

Phonetic confusions in accented speech are caused by the speaker pronouncing an expected phone in a different way (for example, when /zh/ is pronounced as /z/). A phone is the fundamental sound category that is represented by a particular group of articulatory features found in languages (Stevens, 1998). In the speech production process, a speaker first retrieves the canonical pronunciation of the word from his/her mental lexicon in terms of phoneme sequence (i.e., baseform), and then forms the articulatory shape of the pronunciation in terms of phones (i.e., surface form). Due to the effect of different accents and pronunciation habits, the surface form production can be different from that of the baseform. From this point of view, phonetic confusion can be regarded as the probabilistic transformation from a baseform unit to a surface form unit. In speech recognition, it is the erroneous recognition of a baseform phone into a different surface form phone.

On the other hand, acoustic confusion arises when the accented speech is found to lie acoustically somewhere between two baseform phones and can be equally recognized as either (for example, when it is in between /zh/ and /z/). Acoustic confusion can also come from data and recognizer-related confusions (Strik and Cucchiarini, 1999; Fung *et al.*, 2000), in addition to pronunciation variation.

In this paper, we focus on accent-specific phonetic and acoustic confusions. Phonetic and acoustic confusions are common and amorphous in accented speech, which degrade the recognition performance if they are not well accounted for.

A common approach to reduce phonetic confusion in ASR is by extending the phone set and generating a dictionary with multiple pronunciations (Bacchiani and Ostendorf, 1998; Chen *et al.*, 2002, Li *et al.*, 2000). In this approach, phonetic set is extended to include more surface form variants by either using hand-defined symbols based on phonological knowledge (Li *et al.*, 2000) or by using data-driven methods (Bacchiani and Ostendorf, 1998; Chen *et al.*, 2002). For example, Li *et al.* (2000) used pre-defined SAMPA-C symbols to differentiate Wu accented Mandarin pronunciations for spontaneous speech annotation. Chen *et al.* (2002) applied the chi-square test to design additional phonetic units for phonetic confusions with short duration. Bacchiani and Ostendorf (1998) proposed a data-driven method to generate

[a]Electronic mail: pascale@ee.ust.hk

acoustic subword unit (ASU) to capture phonetic confusions. Jurafsky *et al.* (2001) showed that triphones are a good phone set for modeling multiple pronunciations.

Moreover, augmenting the pronunciation dictionary by pronunciation variations typically found in accented speech provides more hypotheses in the decoder search space which sometimes leads to better recognition results. Huang *et al.* (2000) and Liu *et al.* (2000) established accent-related pronunciation dictionaries, where the alternatives in the dictionaries are learned from accented speech data. Liu and Fung (1999) generated accent-adapted dictionary using some supra-segmental information to model the phonetic confusions in Cantonese-accented English.

To model acoustic confusions, especially those in accented speech, a commonly adopted method is to modify the acoustic parameters to cover accent variations. For example, retraining acoustic models using a large amount of accented speech data (Huang, *et al.*, 2000, Liu *et al.*, 2000), applying maximum *a posteriori* (MAP) or maximum log likelihood ratio (MLLR) on speaker-independent models to adapt to the acoustic characteristics of a particular accent (Young, 1999; Tomokiyo, 2001). Juang and Katagiri (1992), Chou *et al.* (1992) and Katagiri *et al.* (1998) proposed a discriminative training approach that uses the local error information to refine the acoustic model. Recently, Nakamura (2002) proposed restructuring Gaussian mixture density functions with Gaussian mixture sharing to restore local modeling mismatch within the confused acoustic models.

However, it is not sufficient to either model phonetic confusion or acoustic confusion exclusively as in the abovementioned methods, when phonetic and acoustic confusions are correlated but different.

Simply using extended phonetic units is insufficient in reducing a lot of phonetic confusions which also include acoustic confusions. Even though an accent-specific dictionary with multiple pronunciations provides a larger hypothesis space to cover phonetic confusions, a larger search space also leads to more lexical confusion *if* the underlying models are acoustically confusable. In other words, the increase in dictionary size can increase recognition errors if the underlying models already contain acoustic confusions. Meanwhile, the local error information used for discriminative training to reduce acoustic confusions is based on recognition errors, which may be attributed to various recognizer and data design configurations, not just because of accent. In addition, retraining and using MAP or MLLR adaptation of acoustic models lead to irreversible changes in acoustic parameters that are not suitable for native speech recognition. This results in performance degradation in speaker-independent systems.

In this paper, we propose methods to measure phonetic and acoustic confusions and reduce them for optimal speech recognition performance on accented speech without sacrificing the performance on standard speech. The paper is organized as follows. In Sec. II, we analyze a special case of Cantonese-accented Mandarin speech, which is used as our test case. Section III outlines the distinction and correlation between phonetic and acoustic confusions in accented speech. Section IV describes the mechanism of reducing both the phonetic and acoustic confusions using accent-specific units and acoustic model reconstruction. In Sec. V, experiments on accented Mandarin telephony speech are presented. We summarize our work and present our conclusions in Sec. VI.

II. CANTONESE ACCENT IN MANDARIN

Accent is a more serious problem for native Mandarin speakers than for native speakers of most other languages. In addition to the standard Chinese Mandarin (also known as Putonghua) spoken by radio and TV announcers, there are seven major language regions in China, including Guanhua, Wu, Yue, Xiang, Kejia, Min, and Gan (Huang, 1987). These major languages can be further divided into more than 30 sub-categories of dialects. In addition to lexical, syntactic, and colloquial differences, the phonetic pronunciations of the same Chinese characters are quite different between Mandarin and the other Chinese languages. Only 70% of Chinese speakers on Mainland China are native speakers of Guanhua, the language group most related to Mandarin. Among these, only a minority speak with the standard Mandarin accent. Consequently, accent distribution among Mandarin speakers can be as varied as that among European speakers of English. Cantonese is an important regional language and is spoken by tens of millions of speakers in south China, Hong Kong, and overseas. 60% of the pronunciations between Cantonese and Mandarin are not even close to each other (Huang, 1987). In this section, we focus on the phonetic and acoustic analysis of Cantonese and Mandarin, especially on the pronunciation differences of their subword units, to highlight the phonological differences between the two languages. Cantonese-accented Mandarin is used as the test case for our work in this paper.

In Chinese ASR systems, initial and final units are conventionally used as subword units instead of phonemic units. One initial corresponds to one phoneme, while one final may consist of one or several phonemes. Without taking into account tonal differences, there are 21 initials and 37 finals for Mandarin, compared to 19 initials and 53 finals in Cantonese (Lee *et al.*, 2002). Initials in both Mandarin and Cantonese consist of a single consonant. However, the initial inventories for these two languages are different. In contrast to Mandarin initials, Cantonese initials do not have retroflexed affricatives (e.g., /zh/, /ch/, /sh/, and /r/), but include one additional velar nasal /ng/. Table I gives an example of a comparison between Mandarin and Cantonese initials with respect to the place and method of articulation. The structure of Cantonese finals is more complicated than that of Mandarin. Cantonese finals have six different consonant codas (/m/, /n/, /ng/, /k/, /p/, and /t/) in contrast to the two codas /n/ and /ng/ in Mandarin finals. Cantonese finals have five categories: vowel, diphthong, vowel with nasal coda, vowel with stop coda and syllabic coda. On the other hand, Mandarin finals were comprised of a vowel or diphthong nucleus preceded by an optimal medial and followed by an optimal nasal.

Consequently, native Cantonese speakers often have difficulty pronouncing many basic Mandarin initials and finals.

TABLE I. Mandarin initials vs Cantonese initials.

Manner of articulation	Place of articulation	Mandarin initials
4 Plosive	Labial	b
	Alveolar	d
	Velar	g
Aspirated plosive	Labial	p
	Alveolar	t
	Velar	k
Affricates	Alveolar	z
	Retroflex	zh
	Dorsal	j
Aspirated affricates	Alveolar	c
	Retroflex	ch
	Dorsal	q
Nasals	Labial	m
	Alveolar	n
Fricatives	Labiodental	f
	Alveolar	s
	Retroflex	sh
		r
	Dorsal	x
	Velar	h
Laterals	Alveolar	l
Plosive	Labial	b
	Alveolar	d
	Velar	g
Aspirated plosive	Labial	p
	Alveolar	t
	Velar	k
Plosive, lip-rounded	Velar, labial	gw
Aspirated plosive, lip- rounded	Velar, labial	kw
Nasals	Labial	m
	Alveolar	n
	Velar	ng
Liquid	Lateral	l
Affricate, unaspirated	Alveolar	z
Affricate, aspirated	Alveolar	c
Fricative	Alveolar	s
	Dental-labial	f
	Vocal	h
Glide	Alveolar	j
	Labial	w

They use some of the typical strategies of language learners to compensate for such difficulties, including phonological transfer, overgeneralization, prefabrication, epenthesis, etc. For example, the pronunciation of the retroflexed affricative /zh/ is sometimes similar to that of the dental velar /z/ among Cantonese speakers. Since there is no /zh/ in the Cantonese initial set, the speaker naturally moves this pronunciation to the most similar initial unit /z/ from the Cantonese initial set. On the other hand, such pronunciation is distinct from the canonical pronunciation of /z/ since the speaker needs to distinguish the pronunciation between /zh/ and /z/. Sometimes, this intention to distinguish leads the Cantonese speaker to pronounce /zh/ as /j/. Since the speaker is trying to say /zh/ and not /z/ or /j/, the phonological transfers of "$zh \rightarrow z$" and "$zh \rightarrow j$" lead to confusable pronunciations which are correlated with yet different from the canonical pronunciations of /z/ and /j/. Moreover, this type of change is unidirectional in accented speech, i.e., there are no "$z \rightarrow zh$" or "$j \rightarrow zh$" transfers. The degree and tendency of confusions between "$zh \rightarrow z$" and "$z \rightarrow zh$", and between "$zh \rightarrow j$" and "$j \rightarrow zh$" are quite different.

III. PHONETIC CONFUSION VERSUS ACOUSTIC CONFUSION

A. Phonetic confusions and acoustic confusions are different yet correlated

There are different types of phonetic and acoustic confusions in speech recognition systems. While some phonetic and acoustic confusion are correlated with each other, others are not, and whereas some are caused by accented speech, others are due to inadequacies and idiosyncrasies in the design and implementation of the recognizer or the training data. In this paper, we focus on analyzing and reducing phonetic and acoustic confusion caused by accented speech.

Phonetic confusion is a property of relating phone instances to acoustic models whereas acoustic confusion is a property of acoustic models. In accented speech, phonetic confusion is caused by the pronunciation of an expected phone into a different one whereas acoustic confusion arises from a pronounced phone lying between two standard phones acoustically (Liu and Fung, 2003a; Tsai and Lee, 2003). For a speech recognizer trained on standard speech, phonetic confusion is then the erroneous recognition of a phonetic unit in the accented speech into another phonetic unit in the standard speech. It can be regarded as the probability of the transformation from a baseform unit to a surface form unit. Acoustic confusion, on the other hand, is at a more fundamental level and describes the distance between the phonetic unit in accented speech and phonetic units represented by two baseform models, in terms of acoustic properties.

Phonetic and acoustic confusions are different yet correlated in the speech recognition task. If the acoustic models of two phonetic units are close to each other (i.e., not easily separable), then these models have low discriminative ability and will cause phonetic confusions in the final recognition task, irregardless of whether the input speech is accented or not. However, even if the trained acoustic models have good separability, accented speech might produce a phone that lies somewhere between two models and again cause acoustic confusion, resulting in phonetic confusion. In other cases, the accented speech might produce one phone that is clearly close to another, different phone in the standard speech. This causes phonetic confusion, even though there is no acoustic confusion between models.

We use Fig. 1 to illustrate the distinction and correlation between the phonetic confusion and the acoustic confusion. Suppose "A" is a phonetic unit and "B" is another phonetic unit that is often confused with "A." Acoustic models for "A" and "B" consist of a single Gaussian component, $G_A(\mu_A, \sigma_A)$ and $G_B(\mu_B, \sigma_B)$, respectively, where μ and σ are the mean and the variance. The phonetic confusion between units "A" and "B" are measured using $P(B|A)$ which is computed using occurrence frequencies (Byrne *et al.*, 2001;

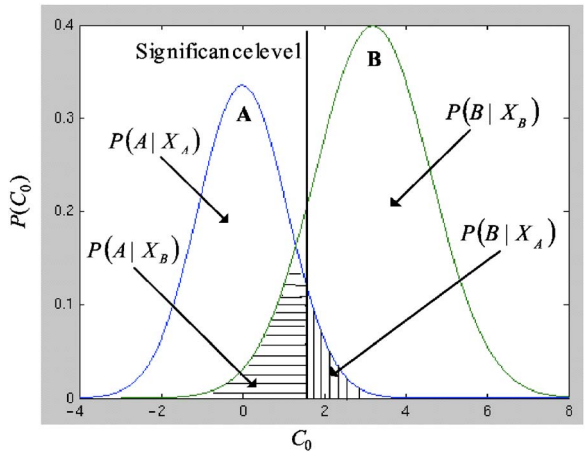

FIG. 1. An example of phonetic and acoustic confusions. C_0 is one dimension of the mean and $P(C_0)$ is the relevant output distribution.

Liu and Fung, 2003a; Chen *et al.*, 2002). The more "A" maps to "B," the higher the phonetic confusion. On the other hand, the acoustic confusion is measured using the acoustic distance between models "A"; and "B", i.e., the distance between the Gaussian components. This distance is computed using Gaussian distance measure (Li and King, 1999; Liu and Huang, 2000). In this case, the more model "A" overlaps with model "B" (the shaded area in Fig. 1), the higher the acoustic confusion between "A" and "B." Obviously, phonetic and acoustic confusions are measured differently.

Suppose the acoustic samples for phone A and phone B are X_A and X_B, respectively, in the accented speech. If the acoustic sample is located in the shaded area, it can be assigned to either $P(B|X_A)$ or $P(A|X_B)$, causing phonetic confusions. Conversely, acoustic confusion is caused by a large overlap between "A" and "B," causing the misclassification of $P(X_A|B)$ and $P(X_B|A)$.

Even if model A and model B do not have any overlap, X_A can still be recognized as phone B, if the accented speech differs from standard speech. In this case, there is phonetic confusion without acoustic confusion.

We wish to point out that there are other conditions that lead to phonetic confusions, even if the input speech has no accent: (1) models "A" and "B" are confusable even in standard speech. This corresponds to the underlying acoustic confusions (e.g., /b/ and /d/, /in/ and /ing/ in Mandarin speech). Representing this condition in Fig. 1 is the large shaded area, and the high overlap ratio. Hence, even if the speaker accurately pronounces "A" or "B," chances for mismatched outputs still exist; (2) models are poorly trained because of biased data or incorrect phonetic transcriptions due to transcriber disagreement.

Assuming the above two factors are held constant, i.e., we use the same set of training data and transcriptions and the same training methods for an ASR system, we are interested in studying how best to reduce phonetic and acoustic confusions due to the accent effect.

B. Measuring phonetic and acoustic confusions

1. Measuring phonetic confusions

Phonetic confusions are measured in terms of the *distribution* of the mapping between surface form and baseform phones. Due to the effect of accented speech, the baseform (standard speech) and surface form (accented speech) sequences of a word differ. For example, the word (China) has the standard pronunciation represented by the baseform sequence "zh ong g uo." Cantonese-accented Mandarin speech might produce different surface form representations such as "z ong g uo", "ch ong g uo" or "j ong g uo."

Aligning the baseform and surface form representations and counting the mapped phone pairs is an obvious way to estimate phonetic confusion distribution. However, as we mentioned in Sec. III A, this type of confusion can be caused by accent as well as the recognizer or training data design and implementation. As we need to focus on phonetic confusion caused by accent effect, it is necessary to impose a confidence measure on the phonetic confusion pairs. Intuitively, if a particular phone A in input speech is often misrecognized as phones B, C, D, etc., then we reason that the phone model A in the ASR system is unreliable either due to training data bias or recognizer design. Similarly, if we find multiple phones being misrecognized as B, then we have reason to believe that the phone model B is unreliable. However, if A and only A is consistently misrecognized as B, then we suspect that there is a phonetic shift from B to A in the accented speech. Of course, there might be additional acoustic confusion between A and B as well, which can then be measured using another measure described in the next section.

We use *likelihood ratio test* as a confidence measure to evaluate the phonetic confusions. We use dynamic programming to align the phone sequences in the accented speech with standard baseform phone transcriptions. For a baseform phone b which is misrecognized as s, we count the occurrences of b, s, and b_s in the aligned data, which are c_1, c_2, and c_{12}, respectively. We have the likelihoods:

$$p = \frac{c_2}{N}, \quad p_1 = \frac{c_{12}}{c_1}, \quad p_2 = \frac{c_2 - c_{12}}{N - c_1}, \tag{1}$$

where N is the total number of the phonetic units in the training set. The log of the likelihood ratio λ is then defined as follows:

$$\log \lambda = \log L(c_{12}, c_1, p) + \log L(c_2 - c_{12}, N - c_1, p) - \log L(c_{12}, c_1, p_1) + \log L(c_2 - c_{12}, N - c_1, p_2), \tag{2}$$

where $L(k,n,x) = x^k(1-x)^{n-k}$ is a binomial distribution. In general, we use $-2 \log \lambda$ instead of λ in practice (Manning and Schütze, 1999). The phonetic confusion distribution is then described as

$$D_{\text{ph}}(b,s) = \frac{C}{-2 \log \lambda} \tag{3}$$

where C is a constant estimated from data. Equation (1) shows that the likelihood of phonetic confusion depends not only on the occurrence frequency of b_s but also on the occurrence frequencies of b and s. Thus, we can distinguish between whether the models b and s are simply badly trained or there is indeed a phonetic shift from b to s. Moreover, since c_{12} differs from c_{21} (e.g., the occurrence number of

/zh/->/z/ is different from that of /z/->/zh/), this phonetic confusion distribution is asymmetric and unidirectional, in accordance with phonological knowledge about accented speech.

2. Measuring acoustic confusions

The degree of acoustic confusions can be measured by the dissimilarity or distance between two speech vectors, between a speech vector and a speech model, and between two speech models. For accented speech, we are interested in measuring the statistical dissimilarity between that of the accented speech model and the standard speech model. Common distance measures include Euclidian distance, Mahalanobis distance, Kullback-Leibler distance, etc. (Hwang, 1993; Liu and Huang, 2000). These measures assume that the distance between two vectors or models is symmetric, i.e., the acoustic distance from model "A" to model "B" is equal to that of from model "B" to model "A." However, it is well known that acoustic confusions in accented speech are asymmetric and unidirectional[1] (Liu and Fung, 2003a, Tsai and Lee, 2003). For speech recognition tasks, we need an asymmetric distance measure between continuous hidden Markov models (CHMM) with variable, multiple Gaussian components.

Tsai and Lee (2003) proposed an asymmetric acoustic distance measure that uses an asymmetric form of Mahalanobis distance, which is the averaged distance over all M mixtures and over all N states of two HMMs:

$$D_{ac}(\lambda_i,\lambda_j)=\sum_{s=1}^{N}\sum_{m_{i,s}=1}^{M} w_{m_{i,s}}\sum_{m_{j,s}=1}^{M} w_{m_{j,s}} d(g_{m_{i,s}},g_{m_{j,s}}).$$

However, the above distance measure simplifies multiple mixtures into one mixture before obtaining the *average* distance. This averaged distance sometimes does not correspond to true model distance as had been pointed out in previous research (Liu and Huang, 2000). Instead, we start from the method of parametric distance metric for mixture probability distribution function (PDF) described in (Liu and Huang, 2000), and propose an *asymmetric acoustic distance measure* for CHMM with multiple states and variable, multiple Gaussian components using a weight matrix. Suppose λ_i and λ_j are two different CHMM phonetic models which consist of N states. Each individual state is represented by a PDF representing multiple Gaussian components. Consider two different states s_{in} and s_{jn} of model λ_i and model λ_j,

$$s_{in}=\sum_{k=1}^{K} w_{in,k} g_{in,k}(\mu_k,\sigma_k)$$

and

$$s_{jn}=\sum_{l=1}^{L} w_{jn,l} g_{jn,l}(\mu_l,\sigma_l), \tag{4}$$

where $w_{in,k}$ and $w_{jn,l}$ correspond to the mixture weights of the kth and lth Gaussian components which satisfy $\Sigma_{k=1}^{K} w_{in,k}=1$ and $\Sigma_{l=1}^{L} w_{jn,l}=1$. According to the parametric distance metric for PDF, the distance $D(s_{in},s_{jn})$ is defined as

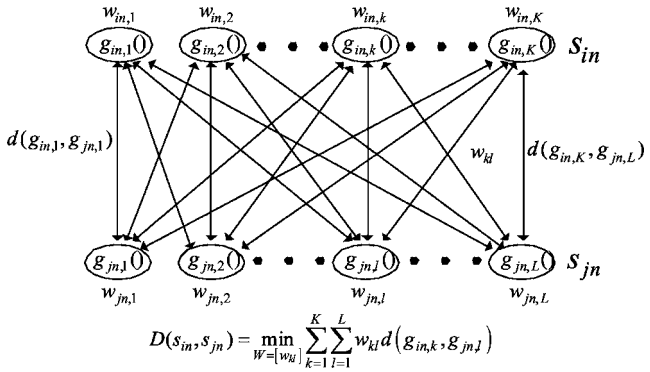

FIG. 2. Asymmetric distance measure for CHMM with multiple states and multiple Gaussian components.

$$D(s_{in},s_{jn})=\min_{W=[w_{kl}]}\sum_{k=1}^{K}\sum_{l=1}^{L} w_{kl} d(g_{in,k},g_{jn,l}), \tag{5}$$

where $W=[w_{kl}]$ is a weight matrix to be estimated by using a linear programming procedure, such as the Simlex tableau method (Cover and Thomas, 1991). $d(g_{in,k},g_{jn,l})$ is an element distance between two single Gaussian components. In order to consider the asymmetric property of acoustic confusions in accented speech, we use the asymmetric form of Mahalanobis distance:

$$d(g_{in,k},g_{jn,l})=(\mu_k-\mu_l)^T\sigma_2^{-1}(\mu_k-\mu_l).$$

The weight matrix $W=[w_{kl}]$ is determined under the constraints shown in Eq. (6):

$$\begin{aligned}
&w_{kl}\geqslant 0\\
&\sum_{k=1}^{K} w_{kl}=w_{jn,l}\quad 1\leqslant k\leqslant K,\\
&\sum_{l=1}^{L} w_{kl}=w_{in,k}\quad 1\leqslant l\leqslant L,\\
&\sum_{k=1}^{K} w_{in,k}=1,\\
&\sum_{l=1}^{L} w_{jn,l}=1.
\end{aligned} \tag{6}$$

The overall distance $D(s_{in},s_{jn})$ is then determined according to the weight matrix $W=[w_{kl}]$ and element distance between each Gaussian component, as described in Fig. 2.

Finally, the overall distance between model λ_i and model λ_j is calculated as a sum of each individual state distances:

$$D(\lambda_i,\lambda_j)=\sum_{n=1}^{N} D(s_{in},s_{jn}). \tag{7}$$

In this paper, we assume state alignment between two HMMs since the baseform and surface form models in ac-

cented speech have the same number of states. Equation (7) could be replaced by frame-to-state alignment if the models have different state numbers (Liu and Fung, 2001). Our proposed asymmetric acoustic distance measure is both computationally efficient and linguistically motivated. Owing to the different mixture weight matrices $W=[w_{kl}]$ and $W=[w_{lk}]$, as well as the asymmetric element distance, the distance $D(s_{in},s_{jn})$ is distinguished from $D(s_{jn},s_{in})$. Hence, our acoustic distance measure captures the fact that the acoustic confusion is asymmetric and unidirectional in accented speech.

Given the above-noted quantitative measures of acoustic and phonetic confusions, we can describe different classes of confusion in accented speech.

C. Combinations of phonetic and acoustic confusions in accented speech

There are four combinations of acoustic and phonetic confusions in speech recognition systems: (1) phonetic confusions and acoustic confusions are both low; (2) phonetic confusion is low and acoustic confusion is high; (3) phonetic confusion is high and acoustic confusion is low; and (4) phonetic confusions and acoustic confusions are both high.

Ideally, the subword units (e.g., phonemes and phones or initials/finals in Mandarin speech) used in ASR systems should be modeled and trained so that phonetic and acoustic confusions are both low for good discriminative-ness. Condition (1) is therefore desirable for ASR systems.

Condition (2) in which phonetic confusion is low but acoustic confusion is high is relatively rare. It happens when two phoneme models are acoustically confusable (i.e., with overlapping acoustic characteristics such as between /l/ and /n/), but accented speaker tends to distinguish the two phones very clearly, even more so than standard speakers (for example, Cantonese speakers never pronounce /l/ close to /n/). This type of confusion exists when native models are acoustically confusable (e.g., "l" and "n" in Mandarin) whereas accented speakers, by overcompensation, can separate the two pronunciations better than native speakers in their pronunciation (e.g., Cantonese speakers of Mandarin) (Huang, 1987). Under condition (2), accented speech does not adversely affect speech recognition performance. Example phone pairs in condition (2) for Cantonese-accented Mandarin are shown in the following:

1. $n \rightarrow l$,	2. $d \rightarrow p$,	3. $h \rightarrow k$,	4. $ei \rightarrow en$,
5. $ei \rightarrow ui$,	6. $ang \rightarrow iang$,	7. $c \rightarrow z$,	8. $k \rightarrow g$.

Condition (3) under which phonetic confusion is high and acoustic confusion is low indicates that phonetic confusion in this case is not caused by acoustic confusion, since acoustic models under this condition have good discriminative abilities. Accent is a predominant factor leading to phonetic confusion in this case. For instance, acoustic confusion between models /f/ and /x/ is low since there is little overlapping acoustic characteristic between standard Mandarin models of these two sounds. On the other hand, there is high phonetic confusion between /f/ and /x/ in Cantonese-accented Mandarin speech. In Cantonese-accented Mandarin speech, we have detected the following phone pairs that have high phonetic confusion but low acoustic confusions:

1. $ai \rightarrow uai$,	2. $h \rightarrow u$,	3. $ao \rightarrow ou$,	4. $t \rightarrow sh$,
5. $en \rightarrow iang$,	6. $sh \rightarrow r$,	7. $d \rightarrow zh$,	8. $x \rightarrow t$,
9. $j \rightarrow d$,	10. $h \rightarrow q$,	11. $d \rightarrow z$,	12. $ia \rightarrow e$,
13. $d \rightarrow n$,	14. $x \rightarrow t$,	15. $f \rightarrow sh$,	16. $n \rightarrow sil$,
17. $d \rightarrow m$,	18. $j \rightarrow b$,	19. $f \rightarrow z$,	20. $e \rightarrow uo$,
21. $l \rightarrow d$,	22. $x \rightarrow i$.		

Under condition (4), phonetic and acoustic confusions are both high. If most of the phonetic units are phonetically and acoustically confusable, then perhaps the unit inventory is not well defined and/or the acoustic models are not well trained. The acoustic models do not have good separability and ASR performance will suffer greatly. Another factor is again accent. In most cases, the two factors co-exist. That is, the acoustic models do not have good separability *and* the accented speech differs from standard speech.

More important, accent effect is a key contributing factor to high acoustic and phonetic confusions. For example, the articulatory features of the retroflexed affricative /zh/ are similar to those of the dental velar /z/ for Cantonese-accented speakers. Since there is no /zh/ sound in the native Cantonese initial set, Cantonese speaker naturally shifts this pronunciation to the most similar initial unit /z/, found in native Cantonese phone set. However, the pronounced /zh/ by Cantonese speaker is not exactly /z/ either, but acoustically somewhere in between /zh/ and /z/. This shift leads to phonetic confusion as well as acoustic confusion between /zh/ and /z/ in Cantonese-accented Mandarin speech. An analysis of Cantonese-accented Mandarin speech data shows us that this type of confusion is limited to a particular set of subword units, such as the retroflexed affricatives to dental velars in Cantonese-accented Mandarin speech.

To illustrate the above, we plot the two-dimensional projection of the acoustic distribution of actual MFCC samples of accented versus standard Mandarin for the baseform /zh/ in Fig. 3. We can see that while "zh-$>$z" and "zh-$>$zh" share similar acoustic properties, "zh-$>$j" and "zh-$>$ others" are clearly different in terms of acoustic cluster shape and centroid.

Note that while our visualization method cannot show all of the parameters or variations of the original acoustic (LDA compression of the features may cause the loss of some variation information), it has been found that if two phenomena are dissimilar in two dimensions, they can only be more dissimilar in the original feature space (Peters and Stubley, 1998). In other words, the characteristics of partial changes in two dimensions are in accordance with their characteristics in higher dimensions. Examples of phone pairs which belong to condition (4) in Cantonese-accented Mandarin speech are shown below:

1. $ai \rightarrow an$,	2. $c \rightarrow ch$,	3. $c \rightarrow ch$,	4. $ch \rightarrow s$,
5. $d \rightarrow j$,	6. $f \rightarrow h$,	7. $h \rightarrow g$,	8. $in \rightarrow ing$,
9. $j \rightarrow x$,	10. $j \rightarrow zh$,	11. $m \rightarrow l$,	12. $q \rightarrow x$,
13. $s \rightarrow zh$,	14. $x \rightarrow z$,	15. $zh \rightarrow q$,	16. $zh \rightarrow s$.

Since accented speech only impacts ASR systems adversely in conditions (3) and (4), our task is to analyze and

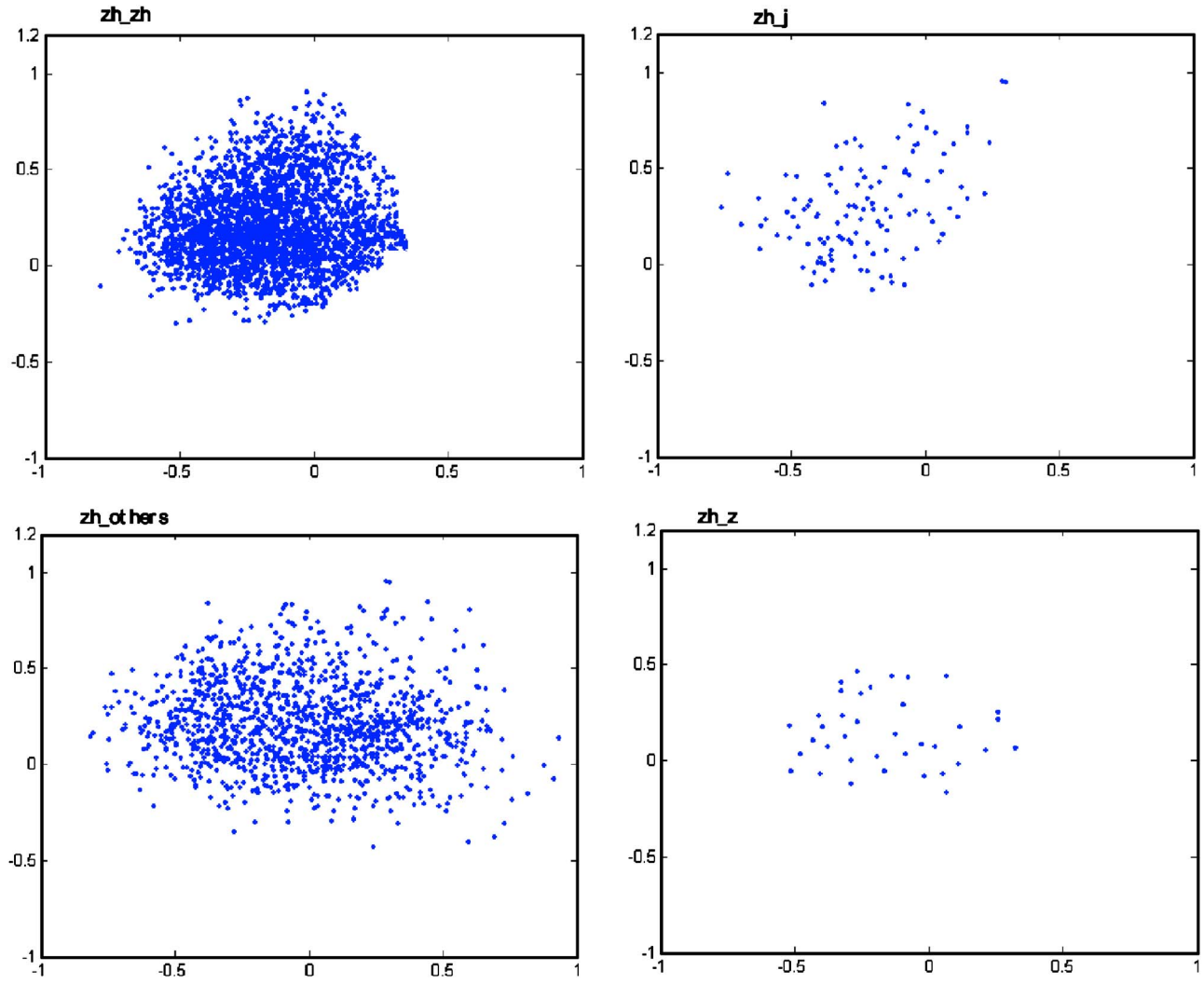

FIG. 3. Two dimensional MFCC samples of accented vs standard Mandarin for the baseform /zh/.

model accented speech with the objective of reducing phonetic and acoustic confusions under these conditions.

IV. REDUCING PHONETIC AND ACOUSTIC CONFUSIONS FOR ACCENTED SPEECH RECOGNITION

We studied four combinations of acoustic confusions and phonetic confusions in speech recognition. The investigation of these four combinations and the corresponding pronunciation phenomena in accented speech shows that the phonetic and acoustic confusions should be considered distinctively to improve recognition performance in accented speech recognition task. Figure. 4 gives examples of acoustic and phonetic distances of Chinese initials in the accent-specific units.

To model phonetic and acoustic confusions in accented speech for the task of speech recognition, we propose the following algorithm:

Modeling Phonetic and Acoustic Confusions in Accented Speech:

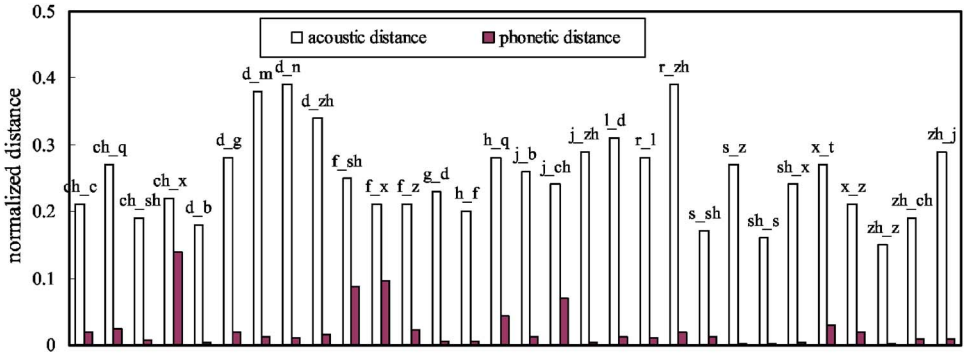

FIG. 4. Examples of normalized acoustic and phonetic distances in accent-specific units.

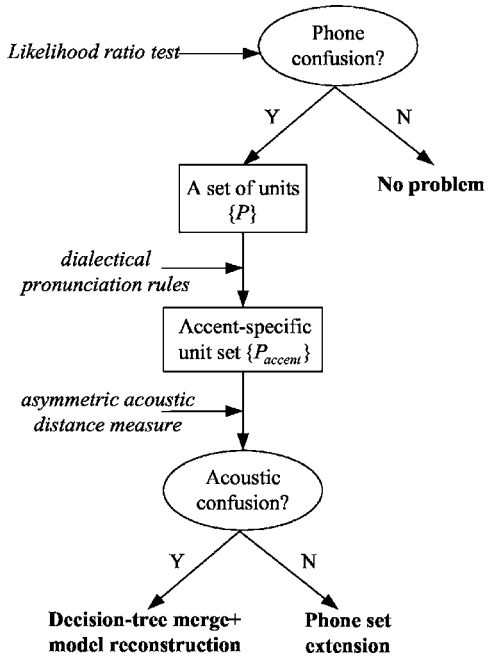

FIG. 5. State-transition charts of modeling phonetic and acoustic confusions in accented speech.

1. Identify phonetic confusion in the input speech by *likelihood ratio test* to generate a set of units $\{P\}$;
   1a. Identify accent-specific confusion pairs from $\{P\}$ by using dialectical pronunciation rules, and replace set $\{P\}$ by this new set $\{P_{\text{accent}}\}$.
2. Identify acoustic confusion from $\{P_{\text{accent}}\}$ using *asymmetric acoustic distance measure*, and form a set of units that have high phonetic confusion but low acoustic confusion $\{A\_l\}$ and another set of units with high phonetic confusion as well as high acoustic confusion $\{A\_h\}$;
3. For phonetic units in $\{A\_l\}$, form a multiple pronunciation dictionary with *extended phone set*;
4. For phonetic units in $\{A\_h\}$, use *acoustic model reconstruction* with decision-tree merging.

State-transition charts of the above-mentioned algorithms are shown in Fig. 5.

In the following sections, we first explain how to classify phone units into those with high and low phonetic and acoustic confusions in Sec. IV A. The algorithm for extending phone sets to form a multiple pronunciation dictionary units with high phonetic confusion but low acoustic confusion in $\{A\_l\}$ is described in Sec. IV B. The algorithm for acoustic model reconstruction with decision-tree merging for units with high phonetic and high acoustic confusion in $\{A\_h\}$ is detailed in Sec. IV C.

A. Classifying phone units according to accent effects

As we explained in Sec. III, only phonetic units with high phonetic confusion can lead to recognition errors, whether these confusions are caused by accented speech or other factors. Therefore the first step in modeling accented speech is to find phonetic units with high phonetic confusion during recognition. An initial set of baseform to surface form phone confusion pairs are found by dynamic programming alignment between the baseform and surface form transcriptions. The baseform transcription is a phoneme sequence corresponding to canonical pronunciations found in a standard pronunciation dictionary. The surface form transcription is a phone sequence with alternative pronunciation information, which can be obtained either by hand-labeled transcription or by a weighted finite-state transducer using a Classification and Regression Tree. In this step, we implement a flexible alignment tool that incorporates intersymbol comparison costs. These costs are based on phonetic feature distance between each pair of phone symbols, derived from linguistic rules (Fung *et al.*, 2000; Byrne *et al.*, 2001; Sproat, 2001).

Next, *likelihood ratio test* is applied to the DP-aligned baseform-surface form phone pairs to form a set of phonetically confusable units. As a result, 353 units are selected from the original 6573 initially found units. To help further distinguish between phonetically confusable units that are caused by accented speech from those caused by recognizer or data related factors, we use some linguistic rules to select a subset of the 353 units that are believed to be due to accented speech. For Cantonese-accented Mandarin, we apply the following linguistic rules in Cantonese dialectical pronunciations described in (Huang 1987):

(1) High confusions within retroflexed affricatives (e.g., /zh/, /ch/, /sh/ and /r/).
(2) High confusion between /f/ and /x/.
(3) One special velar nasal /ng/.
(4) Cantonese finals include /m/ coda.
(5) Pronunciation change in accented speech is unidirectional (e.g., /zh/ moves to /z/ and /r/ moves to /l/ but not vice versa).
(6) No medial in Cantonese finals.

These rules enable us to select 79 accent-specific units from the previous 353 pre-selected units for phonetic confusions.

These 79 phonetically confusable units are further divided into two classes: those with high acoustic confusions and the others with low acoustic confusions. The *asymmetric acoustic distance measure* is used to divide the units into high and low acoustic confusion pairs. 57 phone units are found to have high phonetic and high acoustic confusions whereas 27 phone units are found to have high phonetic but low acoustic confusions.

Having classified accent-specific phonetic units according to high and low acoustic confusions, we suggest selecting only phonetic units with low acoustic confusions to form alternate pronunciations and add into a pronunciation dictionary. For phone units with high acoustic confusions, we suggest that incorporating them into a pronunciation dictionary will further increase lexical confusions. Instead, we propose using decision tree merging with acoustic model reconstruction for this class of phone units.

B. Modeling phone units with high phonetic confusion and low acoustic confusion

When standard phonetic unit models are applied to accented speech recognition tasks, severe performance degra-

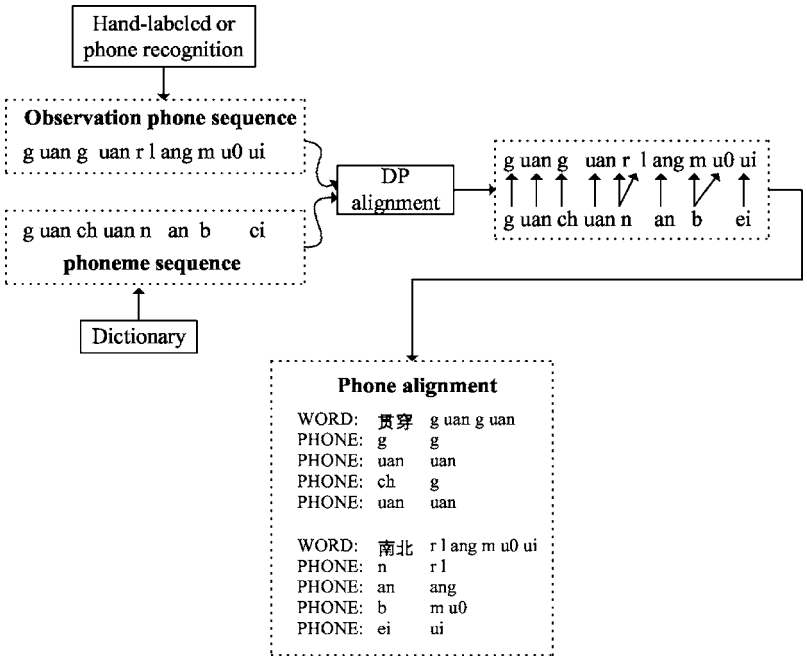

FIG. 6. Aligning baseform sequence to surface form sequence.

dation is observed (Huang, *et al.*, 2000). The increased phonetic variability in accented speech means the acoustic models of the defined units are not adequate for modeling such variability within subword units. Hence, we need to extend the original phonetic unit inventory to represent accented speech. The extended units are used to form alternate pronunciations in a pronunciation dictionary to cover phonetic variations (Holter, 1997 Riley *et al.*, 1999). Special attention must be paid to selecting units with low acoustic confusions. Our resultant multiple-pronunciation dictionary should cover only units with phonetic confusions but not those with acoustic confusions.

Adding these pronunciations, the dictionary is augmented and includes both standard initial/final units and accent-specific units. Compared to conventional multiple pronunciation dictionaries (Liu *et al.*, 2000; Huang *et al.*, 2000), our augmented dictionary uses selected units with low or no acoustic confusion. In other words, the use of such dictionary provides more chances for speech recognizer to output correct sequences without increasing lexical confusion. Moreover, pronunciation probabilities can be attached to each entry of the dictionary. These associated probabilities can be determined from training data using decision tree based structure as follows: A decision tree is constructed to predict the surface form of each reference phoneme by asking questions about its phonemic context. Each phoneme unit has a separate decision tree in which a yes/no question is attached to each node. These questions include information about the phoneme stream itself (such as stress, position, and the classes of neighboring phones), or the past output of the tree (including the identities of surface phones to the left of the current phone). From this, a probability distribution over the set of surface phone(s) for any given context can be determined by the alignment. The decision tree-based pronunciation model thus assigns probabilities to alternative surface form realizations of each phone depending on its context. When decision tree-based pronunciation modeling is carried out, it can be used to generate phone level networks to predict alternative pronunciations in terms of phone sequences. An example alignment is shown in the following Fig. 6.

C. Modeling phone units with high phonetic and high acoustic confusions

Due to high acoustic confusions and the resultant lexical confusions, the direct use of extended phone units to form alternative pronunciations in the dictionary gives no significant improvement in recognition (Liu and Fung, 2003b). To model acoustic confusions, we treat these accent-specific units as hidden models and adjust the mixture distributions of the pretrained baseform models through the use of mixture components from the hidden models by acoustic model reconstruction. The acoustic model reconstruction is equivalent to tree merging in the decision tree based triphone model structure. This approach aims at refining the pretrained baseform models to achieve a high discriminative ability for the high degree of acoustic confusions, while keeping the model robustness to cover the flexible acoustic variations in accented speech.

1. Auxiliary decision trees for accent-specific triphone units

Context-dependent triphone models are commonly used in current ASR systems for high recognition performance. To limit the model complexity and reduce redundant Gaussian components, decision tree based state tying approach is commonly used (Young, 1999; Hwang *et al.*, 1996). Decision trees for accent-specific triphone units are called *auxiliary decision trees*, compared to *standard decision trees* of baseform triphones. In our system, the structure of triphones for accent-specific units differs from that of baseform triphones only in terms of the central unit. The central unit in an accent-specific tree is a baseform to surface form pair (e.g.

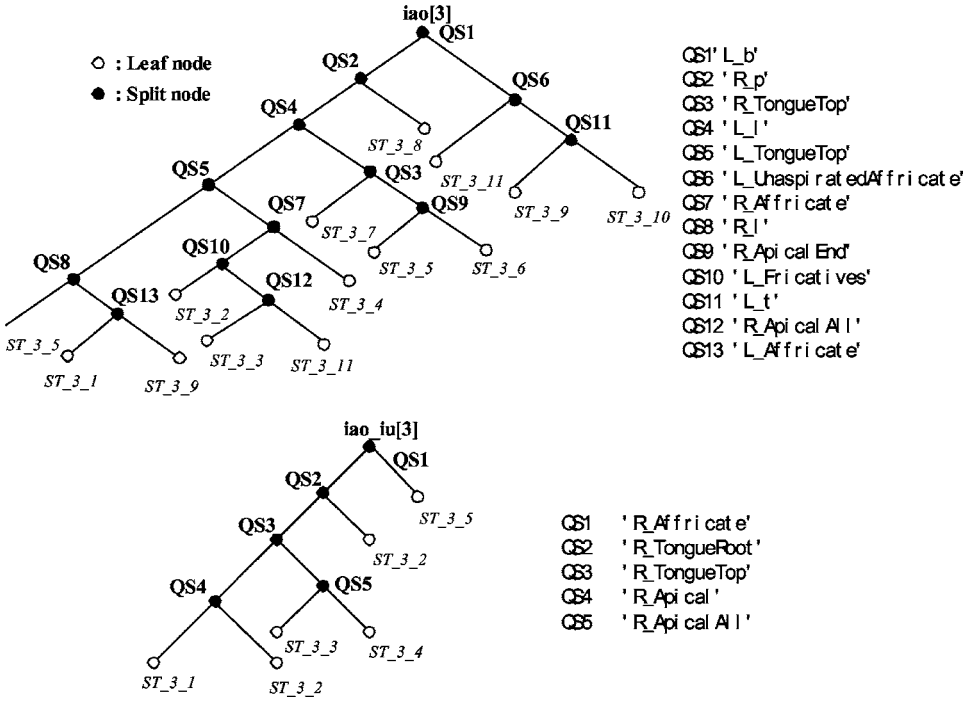

FIG. 7. The auxiliary decision tree of "iao_iu[3]" vs the standard decision tree of "iao[3]".

"*iao_iu*"). Compared to standard decision trees, auxiliary decision trees are also phonetic binary trees in which a yes/no question is attached to each node. On the other hand, the question set for auxiliary trees is enlarged to include accent-specific units. The tree size is smaller than that of standard decision trees due to the small training sample of phone units with high acoustic confusions.

The topology of the auxiliary decision trees represents accent variation characteristics. Figure 7 shows an auxiliary tree of "iao_iu" and a standard tree of "iao" at the final, state three. Nearly all the questions for tree splitting of the auxiliary decision tree are right-dependent phonetic questions, while the standard decision tree has both the right-dependent and left-dependent questions. This means that a lot of acoustic variations from /iao/ to /iu/ occur at the final end of the pronunciation. Right-context information is therefore more important than left-context information for accent-specific triphone unit "iao_iu." This is probably because Cantonese speakers tend to move /iao/ to /iu/ at the end of the phone owing to the ingrained influence of their native language.

2. Acoustic model reconstruction through decision tree merge

Auxiliary decision trees representing accented speech and standard decision trees representing standard speech are merged for better recognition of both accented and standard speech.

We merge the leaf nodes of auxiliary decision trees into the related nodes of the standard tree for acoustic model reconstruction as shown in Fig. 8. Through decision tree merge, the pretrained acoustic models are reconstructed to include Gaussian mixture distributions from accent-specific triphone models. As a result, the structure of the Gaussian distribution is adjusted and more Gaussians borrowed from tied states of auxiliary decision trees may locate at the dis-

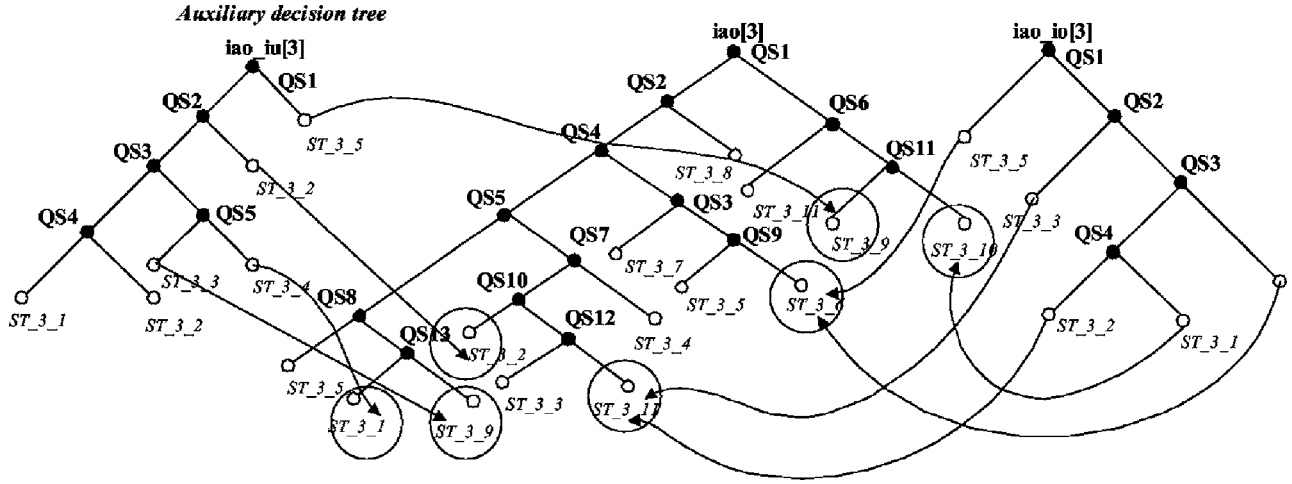

FIG. 8. Acoustic model reconstruction using decision tree merge for triphone acoustic models.

tribution boundaries to cover the variant pronunciations within the accented speech. We use acoustic distance measure of Eq. (5) to determine the mapping relation of tied states between auxiliary decision trees and their related standard trees.

Figure 8 also shows that not all leaf nodes of standard decision tree are mapped to those of auxiliary decision trees. Some nodes have more than one mapping nodes while some nodes have none. The number of mapping nodes is determined by the coverage of the original pretrained model and training samples. For example, the leaf node "ST_ 3_11" of standard decision tree includes mapping nodes from two different auxiliary decision trees in order to model the accented pronunciation changes from /iao/ to /iu/ and from /iao/ to /ao/, while leaf node "ST_3_5" has no mapping node.

According to Fig. 8, the new output distribution of the reconstructed model is represented as

$$P'(x|b) = \lambda P(x|b) + (1-\lambda)\sum_{i=1}^{N} P(x|s_i)P(s_i|b), \tag{8}$$

where $P(x|b)$ is the output distribution of the pretrained baseform model, λ is a linear interpolation coefficient for combining different acoustic models. The coefficient is the probability of the baseform model being recognized as itself. For instance, if "p[2],", i.e., the second state of the baseform unit /p/, has 70% probability to be recognized as "p[2]" and 30% probability as other alternate surface forms from the training data, then $\lambda=0.7$. In addition, $i=1,2,\ldots,N$, and N is the total number of merged nodes from auxiliary decision trees; s_i is one possible surface form state from auxiliary decision trees with respect to the baseform state. If a certain leaf node of standard decision tree has no mapping modes, then $N=0$ and $\lambda=1$. $P(s_i|b)$ is the confusion probability between the accent-specific unit model and baseform model, which can be estimated from confusion matrix or from state-level pronunciation modeling (Liu and Fung, 2003a; Saraclar, Nock, and Khudanpur, 2000).

V. RECOGNITION EXPERIMENTS

A. Experimental setup

We evaluate our algorithms in a Chinese telephony short phrase recognition task. All speech data were sampled at 8 kHz and 8 bit-rate. The baseform acoustic model was trained using 100 speakers' utterances with around 50 h of native Mandarin speech. two-thousand continuous utterances with 23 685 syllables from 20 Cantonese-accented speakers (DATA1) were used to extract the accent-specific units. The HMM topology is three-states, left-to-right without skips, and continuous. The acoustic features are 13MFCC, 13ΔMFCC and 13ΔΔMFCC. Twentyone standard initials and 38 finals were used to generate context-independent HMMs. We used the HTK decision tree based state tying procedures to build 12 Gaussian-component triphone models with 5500 tied states. The test data consist of two parts: the first test set (Test_set1) includes 9 speakers (4 females and 5 males) 900 Cantonese-accented utterances apart from DATA1; the second test set (Test_set2) consists of 900 standard Mandarin utterances selected from 9 native speakers (4 females and 5 males), and is used for performance comparison. In order to evaluate the recognition performance gains solely from phonetic and acoustic modeling, free from other high level information, all the utterances of the test sets are Chinese short phrases without word n-grams.

TABLE II. A comparison of WER of using multiple pronunciation dictionaries based on accent-specific units compared to using conventional reweighed and augmented dictionary.

System	Word error rate (WER)%	
	(Test_set1) Accented speech	(Test_set2) Mandarin speech
Baseline	20%	7.9%
Multiple pronunciation dictionary (Dict1)	17.3% (−2.7)	8.1% (+0.2)
Reweighted and augmented dictionary (Dict2)	18% (−2.0)	7.7% (−0.2)
Selected multiple pronunciation dictionary (Dict3)	**16.9% (−3.1)**	**7.7% (−0.2)**

B. Modeling accent-specific units with high phonetic confusion and low acoustic confusion

Using DATA1 as the development set, we obtained 79 accent-specific units with high phonetic confusions. We first used these units to generate a multiple pronunciation dictionary (Dict1) and compared its performance with respected to a conventional reweighed and augmented dictionary (Dict2) that is based on minimum count and minimum out relative frequency criteria (Byrne *et al.*, 2001; Huang *et al.*, 2000; Liu *et al.*, 2000). The results are shown in Table II. We can see that augmenting a multiple pronunciation dictionary with these high phonetic confusion units gives us an encouraging 2.7% absolute WER reduction compared to the baseline and a slight 0.7% absolute WER reduction with respect to using Dict2.

Furthermore, we compared the tendency of initial/final error rate (IFER) to that of word error rate (WER) by varying the extended phone unit numbers. As shown in Fig. 9, we found that lower IFER does not always lead to lower WER. In an extreme case, introducing more accent-specific units leads to the degradation of recognition performance. We believe that the inability of transferring the lower IFER to lower SER is caused by lexical confusion. The accent-specific high phonetic confusion units in Dict2 include both high acoustic confusions as well as low acoustic confusion. This shows that we need to model these two classes of phonetic units separately. Using the asymmetric acoustic distance measure, only 22 units with low acoustic confusions are selected to form alternative pronunciations and generated a selected multiple pronunciation dictionary (Dict3). Table II shows that using Dict3 is more efficient to cover phonetic confusions in accented speech than using Dict1 and Dict2, yielding additional 0.4% and 1.1% absolute WER reductions, respectively.

Moreover, we can see that the use of Dict3 on native Mandarin speech (test_set2) does not lead to any perfor-

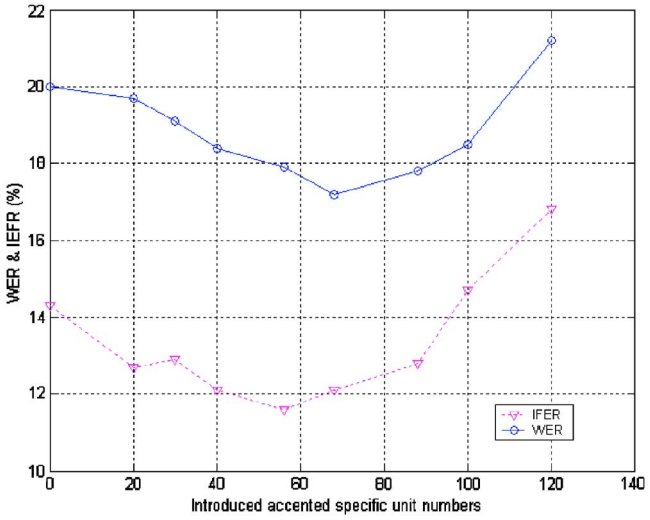

FIG. 9. WER and IFER with different amount of selected accent-specific units. Lower IFER does not always lead to lower WER.

mance degradation since there are no acoustic and lexical confusions between the additional pronunciations and the originally canonical pronunciations. On the other hand, using the conventional augmented dictionary, Dict1, with accent-specific units leads to worse performance on test_set2. That is, additional acoustic and lexical confusions are introduced when alternative pronunciations related to accent effects are added into the dictionary. These results support our claim that adding acoustically confusable phone units in an augmented dictionary leads to more decoder error in recognition.

C. Modeling accent-specific units with high phonetic confusions and high acoustic confusions

Fifty-seven units from the original 79 accent-specific units were extracted as units with high phonetic and acoustic confusions. We constructed 171 auxiliary decision trees with 967 tied states for these 57 accent-specific triphone units. Through acoustic model reconstruction, 967 tied states were merged into the pretrained 5500 tied states of 177 standard decision trees. The reconstructed model included 77 604 Gaussian components and each state has 14.1 Gaussians on average. To make a fair comparison, we generated an enhanced baseform model with 5500 tied states and 14 Gaussian-component per state. The recognition performances are shown in Table III.

TABLE III. Our approach outperforms MAP adaptation, enhanced acoustic model, and augmented dictionary.

System	Word error rate (WER) %	
	(Test_set1) Accented speech	(Test_set2) Standard speech
Baseline	20%	7.9%
Enhanced HMMs with 14 Gaussians per state	18.6% (−1.4)	7.5% (−0.4)
Baseline HMM with MAP adaptation using accented data	15.1% (−4.9)	15.7% (+6.8)
Reconstructed HMMs with selected accent-specific units	**15.2% (−4.8)**	**7.1% (−0.8)**

We can see that using the reconstructed acoustic model gives a significant 4.8% absolute WER reduction compared to the baseline, and an additional 3.4% reduction with respect to using enhanced HMM at the same model complexity. The reason lies in the fact that the mixture distribution of our reconstructed model includes borrowed Gaussians from accent-specific unit models, and adjusts the structure of the original mixture distribution and enables more Gaussians at the mixture boundaries to cover the acoustic confusions in accented speech. On the other hand, directly increasing Gaussian components in the enhanced model results in poor estimation of some Gaussians with available training data. Meanwhile, most of the increased Gaussians may converge around the global mean to handle the majority of pronunciation with small variations, and there are not sufficient Gaussians at the boundary of mixture distributions.

One advantage of using reconstructed acoustic models is that our method provides significant improvement for accented speech task without sacrificing the performance on native Mandarin speech. In comparison, the use of MAP adaptation approach gives a good 4.9%WER reduction on accented speech, while leading to a serious performance degradation (6.8% WER increase) on native Mandarin speech. Through MAP adaptation, the parameters of acoustic model are adjusted to handle accented speech and are no longer suitable for native speech. However, our reconstructed model includes its own Gaussians from pretrained acoustic model as well as those borrowed from accent-specific unit models. The borrowed Gaussians are used only to adjust the structure of original mixture distribution and not to change parameters. These two Gaussian distributions cover the acoustic samples either with small deviation in native speech or with high deviation in accented speech.

In addition, Gaussian mixture sharing and clustering across phonetic models with minimal average distortion have been shown to be efficient in improving model robustness for acoustic confusions (Huang and Jack, 1989; Nakamura, 2002). The question is whether the same amount of WER reduction can be achieved by straightforward Gaussian mixture sharing. To answer this question, a comparison of recognition performance between our acoustic model reconstruction with selected accented-specific units and Gaussian mixture sharing of baseline model is illustrated in Table IV. Note that in the decision tree-bases state tying triphone models with Gaussian sharing, based on the extended accent-specific units, an additional 7683 mixture weights are added as new parameters.

In addition, our reconstructed model gives 3% absolute WER reduction in relation to Gaussian sharing models on accented speech. In Gaussian mixture sharing, only the shared parameters are trained efficiently, while the shared Gaussians may not cover the acoustic confusions that locate at the boundary of mixture distributions. On the other hand, our reconstructed model includes more Gaussian components borrowed from accent-specific unit models at the boundary of the mixture distributions, when the confusing

TABLE IV. Our approach outperforms the baseline, and modeling phonetic or acoustic confusion alone.

System	Word error rate (WER) %	
	(Test_set1) Accented speech	(Test_set2) Standard speech
Baseline	20%	7.9%
Baseline model with Gaussian mixture sharing	18.2% (−1.8)	7.0% (−0.9)
Model trained using selective surface form tran- scriptions (modeling phonetic confusion only)	19.1% (−0.9)	7.6% (−0.3)
Reconstructed HMMs with selected accent-specific units (modeling acoustic confusion only)	15.2% (−4.8)	7.1% (−0.8)
Reconstructed HMMs and selected multiple pronunciation dictionary (our approach)	**14.3% (−5.7)**	**7.1% (−0.8)**

acoustic samples fall into this mixture distribution, a higher acoustic likelihood score is obtained compared to using Gaussian sharing models.

It was shown in Riley *et al.* (1999) that acoustic models can be trained by using the surface form transcriptions iteratively. We compare this approach with our reconstructed model in Table IV. It has been reported in Riley *et al.* (1999) and also shown here that their method gives limited performance improvement. We note that the selection of surface form transcriptions is mainly based on *phonetic confusions* not acoustic confusions. On the other hand, the recognition is primarily based on the acoustic distance, not the phonetic distance, so WER will not be reduced if the acoustic distance among the units remains unchanged. We give an example in Fig. 10 of the acoustic distance of /zh/ with respect to other Chinese initials/finals in baseline model and retrained model using selective surface form transcriptions and show that there is no distinct acoustic distance. This also explains why very limited improvement was achieved by using retrained acoustic models based on selective phone-level transcriptions in Riley *et al.* (1999). The evidence again indicates that phonetic and acoustic confusions should be treated separately in accented speech recognition. Moreover, using selected multiple dictionary as well as acoustic model reconstruction provides a significant 5.7% WER reduction without sacrificing the performance on native Mandarin speech. That is, our approach can be applied to a single system for both accented and native speech recognition.

Last but not the least, we show the performance comparison between our approach, the baseline approach, methods using only phonetic confusion modeling and a method using only acoustic confusion in Table V and show that modeling phonetic and acoustic confusable units separately gives the best performance on accented speech as well as standard speech recognition.

VI. CONCLUSIONS

We study the effects of phonetic confusions and acoustic confusions in accented speech. We suggest that phonetic and acoustic confusions are different yet correlated in accented

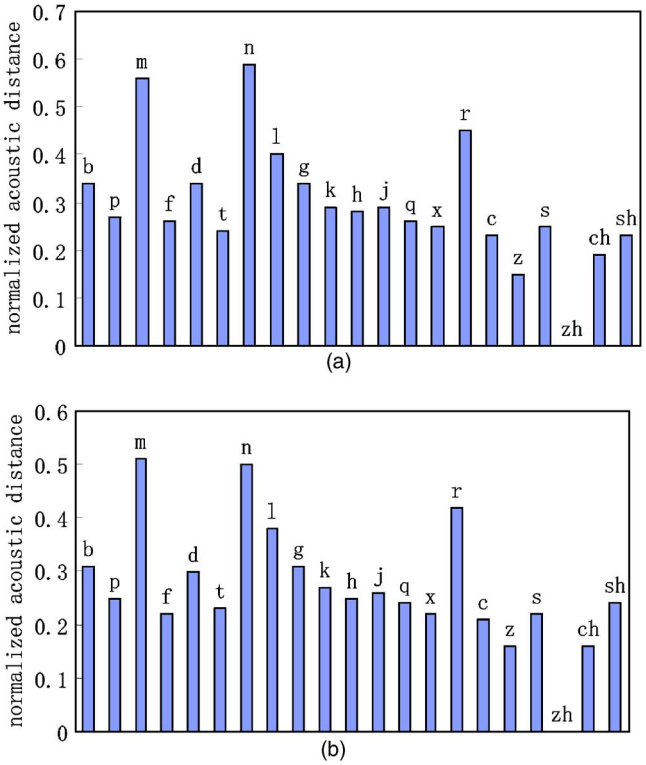

FIG. 10. The normalized acoustic distance of "zh" in relation to other Chinese initials in baseline model and surface form retrained model.

speech. We suggest that only phone units which lead to high phonetic confusions in accented speech cause recognition errors. Among these units, there are those that also have high acoustic confusions and others with low acoustic confusions. We propose to model these two classes of phone units differently for better recognition performance on both accented and standard speech. We use likelihood ratio test to select units with high phonetic confusions and we propose an asymmetric acoustic distance measure to describe the unidirectional properties of acoustic confusions in accented speech. In addition, we separated accent-specific confusions from data and recognizer-related confusions using distance measure and pronunciation phonological rules.

We propose incorporating only those accent-specific phonetic units with low acoustic confusions in a multiple pronunciation dictionary in order to reduce phonetic confusions and avoid lexical confusion at the same time. Mean-

TABLE V. Our approach outperforms the baseline, and modeling phonetic or acoustic confusion alone.

System	Word error rate (WER) %	
	(Test_set1) Accented speech	(Test_set2) Standard speech
Baseline	20%	7.9%
Multiple pronunciation dictionary (modeling phonetic confusion alone)	17.3% (−2.7)	8.1% (+0.2)
Reconstructed HMMs (modeling acoustic confusion alone)	15.2% (−4.8)	7.1% (−0.8)
Reconstructed HMMs and selected multiple pronunciation dictionary	**14.3% (−5.7)**	**7.1% (−0.8)**

while, for accent-specific units with high acoustic confusion, we propose using decision tree merging with acoustic model reconstruction to achieve a high discriminative ability for reducing acoustic confusions within phonetic unit models. This approach aims at using the selected accent-specific units as hidden models to adjust the structure of mixture distributions of standard speech baseform models to cover more acoustic variability so as to model acoustic confusions in accented speech.

Experimental results on Cantonese-accented Mandarin speech show that using the selected multiple pronunciation dictionary to model phonetic confusions provides WER reductions of 3.1% and 1.1% in absolute terms, compared to baseline and using conventional reweighted and multiple pronunciation dictionary. Through the use of acoustic model reconstruction, we achieve a significant 4.8% absolute WER reduction for accented speech compared to 1.4% using increasing Gaussian components and 1.8% by Gaussian mixture sharing. The combination of modeling phonetic confusions and acoustic confusions yields a 5.7% reduction. Compared to using MAP adaptation, our method provides a better WER reduction on accented speech recognition without sacrificing the performance on native, standard speech. Our approach can be applied to a single system to handle both accented and standard speech, and even speech with multiple accents.

ACKNOWLEDGMENTS

This work is partially supported by CERG No. HKUST6206/03E of the Hong Kong Research Grants Council, and DAG No. 03/04.EG30 of HKUST.

[1]For example, the acoustic distance from "zh" to "z" is entirely different from that of "z" to "zh" in Cantonese-accented Mandarin speech. The distance from "zh" to "z" is much smaller than that of "z" to "zh."

Bacchiani, M., and Ostendorf, M. (**1998**). "Joint acoustic unit design and lexicon generation," *Proceedings of the Workshop on modeling pronunciation variation for ASR, 1998*, 7–12.

Byrne, W., Venkataramani, V., Kamm, T., Zheng, F., Fung, P., Liu, Y., and Ruhi, U. (**2001**). "Automatic generation of pronunciation lexicons for Mandarin spontaneous speech," *Proceedings of the IEEE International Conference on Acoustics, Speech and Signal Processing (ICASSP)*, Salt Lake City, UT.

Chen, Y. J., Wu, C. H., Chiu, Y. H., and Liao, H. C. (**2002**). "Generation of robust phonetic set and decision tree for Mandarin using chi-square testing," Speech Commun. **38**, 349–364.

Chou, W., Juang, B. H., and Lee, C. H. (**1992**). "Segmental GPD training of HMM based speech recognizer," *Proceedings of the IEEE International Conference on Acoustics, Speech, Signal Processing*, San Francisco, CA, pp. 473–476.

Cover, T. M., and Thomas, J. A. (**1991**). *Elements of Information Theory* (Wiley, New York).

Fung, P., Byrne, W., Zheng, F., Kamm, T., Liu, Y., Song, Z., Venkataramani, V. and Ruhi, U. (**2000**). "Pronunciation modeling of Mandarin casual speech," Final Report, The Johns Hopkins University Summer Workshop.

Holter, T. (**1997**). "Maximum likelihood modeling of pronunciation in automatic speech recognition," Ph.D. thesis, the Norwegian University of Science and Technology.

Huang, Ch. *et al.* (**2000**). "Accent modeling based on pronunciation dictionary adaptation for large vocabulary Mandarin speech recognition," *Proccedings of the International Conference on Spoken Language Processing (ICSLP2000)*, Beijing, China.

Huang, J. H. (**1987**). *Chinese Dialects* (Xia Men University Press, Xia Men, China) (Chinese version).

Huang, X., and Jack, M. (**1989**). "Unified techniques for vector quantization and hidden Markov modeling using semi-continuous models," *Proceedings of the IEEE International Conference on Acoustics, Speech, Signal Processing (ICASSP)*, Glasgow, Scotland, pp. 639–642.

Hwang, M. Y. (**1993**). "Subphonetic acoustic modeling for speaker-independent continuous speech recognition," Ph.D. thesis, Carnegie Mellon University.

Hwang, M. Y., Huang, X. D., and Alleva, F. A. (**1996**). "Predicting unseen triphones with senones," IEEE Trans. Speech Audio Process. **4**, 412–419.

Juang, B. H., and Katagiri, S. (**1992**). "Discriminative learning for minimum error classification," IEEE Trans. Signal Process. **40**, 3043–3054.

Jurafsky, D., Ward, W., Zhang, J. P., Herold, K., Yu, X. Y., and Zhang, S. (**2001**). "What kind of pronunciation variation is hard for triphones to model?," *Proceedings of the IEEE International Conference on Acoustics, Speech, Signal Processing, (ICASSP2001)*, Salt Lake City, UT.

Katagiri, S., Juang, B. H., and Lee, C. H. (**1998**). "Pattern recognition using a family of design algorithm based upon the generalized probabilistic descent method," Proc. IEEE **86**, 2345–2373.

Lee, T., Lau, W., Wong, Y. W., and Ching, P. C. (**2002**). "Using tone information in Cantonese continuous speech recognition," ACM Transactions on Asian Language Information Processing **1**(1), 83–102.

Li, A., Zheng, F., Byrne, W., Fung, P., Kamm, T., Liu, Y., Song, Z., Ruhi, U., Venkataramani, V., and Chen, X. (**2000**). "CASS: A phonetically transcribed corpus of Mandarin spontaneous speech," *Proceedings of the International Conference on Spoken Language Processing (ICSLP)*, Beijing, China.

Li, X., and King, I. (**1999**). "Gaussian mixture distance for information retrieval," *Proceedings of the 1999 International Joint Conference on Neural Networks*, Washington DC, pp. 2070–2075.

Liu, M. K., Xu, B., Huang, T., and Li, C. (**2000**). "Mandarin accent adaptation based on context-independent/context-dependent pronunciation modeling," *Proceedings of the IEEE International Conference on Acoustics, Speech, Signal Processing, (ICASSP2000)*, Istanbul, Turkey, pp. 1929–1932.

Liu, W. K., and Fung, P. (**1999**). "Fast accent identification and accented speech recognition," *Proceedings of the IEEE International Conference Acoustics, Speech, Signal Processing (ICASSP)*, Phoenix, A2.

Liu, Y., and Fung, P. (**2001**). "Estimating pronunciation variations from acoustic likelihood score for HMM reconstruction," *Proceedings of the European Conference on Speech Communication and Technology (Eurospeech)*, Aalborg, Denmark, pp. 1425–1428.

Liu, Y., and Fung, P. (**2003a**). "Modeling partial pronunciation variations for spontaneous Mandarin speech recognition," Comput. Speech Lang., **17**, 357–379.

Liu, Y., and Fung, P. (**2003b**). "Partial change accent models for accented Mandarin speech recognition," *Proceedings of the IEEE Automatic Speech Recognition and Understanding*, St. Thomas, U.S. Virgin Islands.

Liu, Z., and Huang, Q. (**2000**). "A new distance measure for probability distribution function of mixture type," *Proceedings of the IEEE International Conference. Acoustics, Speech, Signal Processing, (ICASSP2000)*, Istanbul, Turkey, pp. 1345–1348.

Manning, C. D., and Schütze, H. (**1999**). *Foundations of Statistical Natural Language Processing* (MIT Press, Cambridge, MA).

Nakamura, A. (**2002**). "Restructuring Gaussian mixture density functions in speaker-independent acoustic models," Speech Commun. **36**, 277–289.

Peters, S., and Stubley, P. (**1998**). "Visualizing speech trajectories," *Proceedings of ESCA Totorial and Research Workshop on Modeling Pronunciation Variation for Automatic Speech Recognition*, Kerkrade, Netherlands, 1998, pp. 97–101.

Riley, M., Byrne, W., Finke, M., Khudanpur, S., Ljolje, A., Mcdonough, J., Nock, H., Saraclar, M., Wooters, C., and Zavaliagkos, G. (**1999**). "Stochastic pronunciation modeling from hand-labeled phonetic corpora," Speech Commun., **29**, 209–224.

Saraclar, M., Nock, H., and Khudanpur, S. (**2000**). "Pronunciation modeling by sharing Gaussian densities across phonetic models," Comput. Speech Lang., **14**, 137–160.

Sproat, R. (**2001**). "Pmtools: A pronunciation modeling toolkit," *Proceedings of the Fourth ISCA Tutorial and Research Workshop on Speech Synthesis*, Blair Atholl, Scotland.

Stevens, K. N., *Acoustic Phonetics* (MIT Press, Cambridge, MA, 1998).
Strik, H., and Cucchiarini, C. (**1999**). "Modeling pronunciation variation for ASR: A survey of the literature," Speech Commun. **29**, 225–246.
Tomokiyo, L. M. (**2001**). "Recognizing non-native speech: Characterizing and adapting to non-native usage in LVCSR," Ph.D. thesis, Carnegie Mellon University.
Tsai, M. Y., and Lee, L. S. (**2003**). "Pronunciation variation analysis based on acoustic and phonetic distance measures with application examples on Mandarin Chinese," *Proceedings of the IEEE Automatic Speech Recognition and Understanding*, St. Thomas, U.S. Virgin Islands, pp. 117–121.
Young, S. (**1999**). *The HTK Book* (Entropic Cambridge Research Laboratory, Cambridge).

An analytical prediction of the oscillation and extinction thresholds of a clarinet

Jean-Pierre Dalmont[a] and Joël Gilbert
Laboratoire d'Acoustique de l'Université du Maine (UMR CNRS 6613), Université du Maine, 72085, Le Mans, France

Jean Kergomard
Laboratoire de Mecanique et d'Acoustique (UPR CNRS 7051), 31 Ch. Joseph Aiguier, 13402, Marseille, France

Sébastien Ollivier[b]
Laboratoire d'Acoustique de l'Université du Maine (UMR CNRS 6613), Université du Maine, 72085, Le Mans, France

(Received 24 January 2005; revised 25 July 2005; accepted 25 July 2005)

This paper investigates the dynamic range of the clarinet from the oscillation threshold to the extinction at high pressure level. The use of an elementary model for the reed-mouthpiece valve effect combined with a simplified model of the pipe assuming frequency independent losses (Raman's model) allows an analytical calculation of the oscillations and their stability analysis. The different thresholds are shown to depend on parameters related to embouchure parameters and to the absorption coefficient in the pipe. Their values determine the dynamic range of the fundamental oscillations and the bifurcation scheme at the extinction. © *2005 Acoustical Society of America.* [DOI: 10.1121/1.2041207]

PACS number(s): 43.75.Pq [NHF] Pages: 3294–3305

I. INTRODUCTION

When a clarinet is blown with an increasing mouth pressure, for a fixed embouchure, the reed begins to oscillate for a particular pressure value, called "threshold of oscillation," and stops at another value, called here "threshold of extinction." Above this threshold the reed is held motionless against the lay. These two thresholds determine the dynamic range of the clarinet for given embouchure parameters. The threshold of oscillation has been extensively studied in the literature (see, e.g., Grand *et al.*, 1997; Kergomard *et al.*, 2000). On the contrary, the threshold of extinction has been only recently investigated (Dalmont *et al.*, 2002; Atig *et al.*, 2004) despite being of crucial importance in the playing of the clarinet. Experiments have shown that the threshold of extinction above which the oscillations stop is larger than the minimum mouth pressure p_M sufficient to maintain the reed channel closed (Dalmont *et al.*, 2000). It has also been observed that losses in the pipe and especially nonlinear losses at side holes might influence significantly the value of the extinction threshold, that is, consequently, the maximum power of a given instrument (Atig *et al.*, 2004).

The aim of the present paper is to investigate the playing range of the clarinet for the fundamental regime (first register) and to bring out the physical parameters which determine this range. To allow an analytical study, this analysis is based on a simplified model of the clarinet. The simplest model is to consider the body of the clarinet as an open straight pipe without any radiation or thermoviscous losses. This model is called here "lossless model" and has been extensively studied by Kergomard (1995) and Maganza *et al.* (1986) for example. However, it is not able to describe the extinction phenomenon at high blowing pressures since with this model, unless a nonlinear effect is introduced, there is no limit to the amplitude of the acoustic pressure when the mouth pressure is increased. Experiments and simulations suggest that losses have to be introduced in the model Atig *et al.*, (2004). In order to allow analytical calculations, losses in the pipe are introduced by means of a constant parameter, independent of the frequency. This kind of model has been extensively used for the bowed string (Raman, 1918; Schelleng, 1973; Mc Intyre *et al.*1983;Woodhouse, 1993) and appears to be useful for the study of reed woodwinds oscillations (Ollivier *et al.*, 2004, 2005), therefore it is referred to in the following as "Raman's model." In the present paper, it is shown to be sufficiently simple to allow analytical calculations, in particular of the different threshold values.

In an extended state of the art (Sec. II) the model is presented (Sec. II A) and the results for the static solution and small oscillations are reviewed (Sec. II B), as well as results obtained with a lossless model (Sec. II C). Raman's model is used to calculate the periodic solutions at the fundamental frequency from which bifurcation diagrams are derived (Sec. III). Some thresholds are calculated (Sec. III C) and stability of the periodic solutions giving the bifurcation schemes is discussed in Sec. III D. For clarity the details of calculations are given in Appendix A. Some consequences about the playing range of the musical instrument are discussed in Sec. IV.

[a]Author to whom correspondence should be addressed; electronic mail: jean-pierre.dalmont@univ-lemans.fr
[b]Present affiliation: Laboratoire de Mécanique des Fluides et d'Acoustique (UMR CNRS 5509) Ecole Centrale de Lyon, Ecully, France.

II. STATE OF THE ART

A. Equations of the model

The clarinet can be divided into two parts, each being described by a single equation: one is the body of the instrument (the pipe) and one is the reed-mouthpiece set (the generator).

1. The pipe

The pipe of the clarinet is assumed to be perfectly cylindrical. The lowest level of approximation is given by the lossless approximation in which a total reflection at the end of the pipe is assumed and losses in the pipe are ignored. The corresponding reflection function for pressure $r(t)$ at the input is given by

$$r(t) = -\delta(t-\tau), \tag{1}$$

where the delta function $\delta(t)$ is delayed by $\tau=2L/c$, that is the roundtrip travel time of a wave at speed c along the pipe of length L.

A higher level of modeling might take into account the visco-thermal dissipation and dispersion effect (see, for example, Polack *et al.*, 1987) as well as the radiation impedance (Norris and Sheng, 1989; Nederveen, 1998; Dalmont *et al.*, 2001b). An intermediate level is the so-called "Raman's model," ignoring dispersion and assuming that losses, including radiation, are frequency independent. The reflection function $r(t)$ is then given by

$$r(t) = -e^{-2\alpha L}\delta(t-\tau), \tag{2}$$

where the constant parameter α is the absorption coefficient. In the frequency domain, the Fourier transform of the reflection function is the reflection coefficient:

$$R(\omega) = -e^{-2j(k-j\alpha)L}, \tag{3}$$

where $k=\omega/c$ is the wavenumber.

The input impedance of the pipe $Z=p/u$, where p and u are the acoustic pressure and volume velocity, respectively, can be obtained from the reflection coefficient

$$Z(\omega) = Z_c\frac{1+R(\omega)}{1-R(\omega)} = jZ_c\tan[(k-j\alpha)L], \tag{4}$$

where $Z_c \approx \rho c/S$ is the characteristic impedance of the pipe, S being the cross-section area and ρ the density of air. In practice, the absorption coefficient $\alpha(f)$ is frequency dependent and is given, for a straight pipe, by

$$\alpha(f) \approx 3\cdot 10^{-5}\sqrt{f}/a, \tag{5}$$

where f is the frequency in Hz and a the radius of the pipe expressed in MKS units [see, e.g., Fletcher and Rossing (1998), p. 196]. In the present paper, the value of α is calculated at the first resonant frequency, that is for $f=c/4L$, and as α is assumed to be independent of the frequency, all the resonance peaks have the same amplitude (Fig. 1), the admittance at resonance $f_n=(2n-1)c/4L$ being real and equal to

$$Y = 1/Z = \tanh(\alpha L)/Z_c. \tag{6}$$

At zero frequency the input impedance is given by

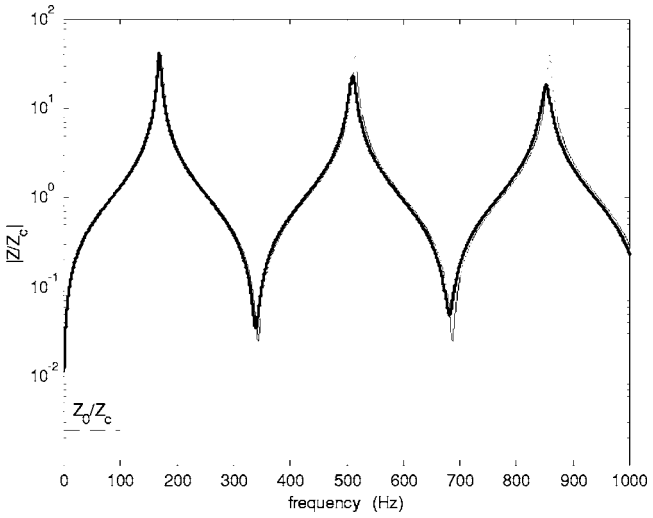

FIG. 1. Reduced input impedance Z/Z_c of an open cylinder of 50 cm length and 8 mm radius. Thick line: model with viscothermal losses. Thin line: Raman's model without dispersion and with frequency independent losses. The horizontal dotted line indicates the limit value of the impedance when frequency tends toward zero according to a Poiseuille flow.

$$Z_0 = Z_c\tanh(\alpha L). \tag{7}$$

This value is probably much larger than the real value because the value of α is not valid for $f=0$. The input impedance Z_0 could be calculated for example by using the Poiseuille equation for viscous laminar flow which leads to a much lower value [Reynolds number is shown to be lower than 500 in Kergomard (1995), p. 250]: for a 16-mm-diam pipe of length 0.5 m, $\alpha L=0.025$ at first resonant frequency and should be $\alpha_0 L=0.001\,25$ at zero frequency according to Poiseuille equation.

2. The generator

The second part of the system, the reed mouthpiece set, acts as a valve [see, for example, Wilson and Beavers (1974) or Hirschberg (1995)]. The volume velocity $u(t)$ through the reed slit is controlled by the aperture height $H(t)$ between the reed and the mouthpiece, and by the velocity of the air $v(t)$. This velocity depends nonlinearly on the pressure difference Δp equal to the mouth pressure p_m, assumed to be static, minus the acoustic pressure $p(t)$ in the mouthpiece (see Fig. 2)

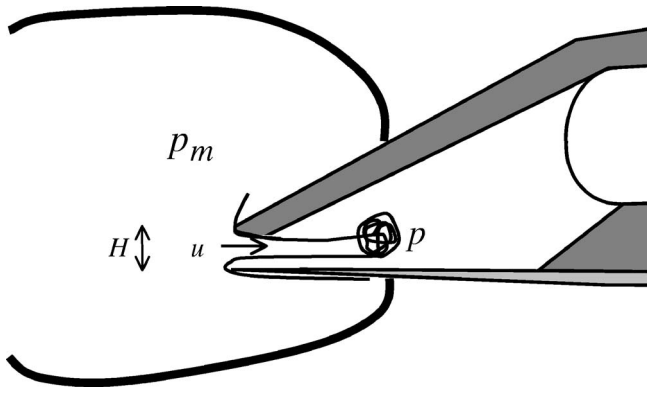

FIG. 2. Schematic view of the mouthpiece.

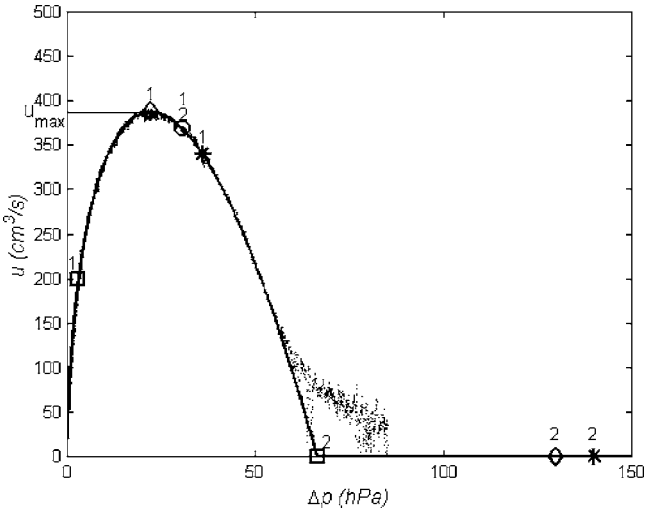

FIG. 3. Nonlinear characteristics: flow through the reed channel vs the pressure difference on both sides of the reed. Thick line: model; thin line: experiment (adapted from Dalmont *et al.*, 2003; experiment stops at $\Delta p = 85$ hPa). The points $(\Delta p_1, u_1)$ and $(\Delta p_2, u_2)$ corresponding to the different thresholds are labeled on the curve: (○) threshold of oscillation ($\Delta p_1 = \Delta p_2$); (□) beating reed threshold; (◇) saturation threshold; (∗) extinction threshold.

$$\Delta p(t) = p_m - p(t). \tag{8}$$

The nonlinear equation comes from Bernoulli equation and is based on the assumption that the kinetic energy of the jet entering in the instrument is completely dissipated into turbulence during its expansion into the mouthpiece:

$$v(t) = \sqrt{\frac{2\Delta p(t)}{\rho}}. \tag{9}$$

The volume velocity $u(t)$ is proportional to the jet cross section $S_{\text{jet}}(t)$, and is given by

$$u(t) = S_{\text{jet}}(t)v(t). \tag{10}$$

The cross section of the jet is assumed to be equal to the reed slit opening surface which is assumed to be rectangular and proportional to the height of the opening $H(t)$:

$$S_{\text{jet}}(t) = wH(t), \tag{11}$$

where w is the effective width of the slit [see Dalmont *et al.* (2003) for a detailed discussion]. The reed is assumed to behave as an ideal spring characterized by its stiffness K (in Pa/m). Then $H(t)$ is linearly dependent on the pressure difference $\Delta p(t)$:

$$H(t) = H_0\left(1 - \frac{\Delta p(t)}{p_M}\right) \quad \text{if } \Delta p(t) \leqslant p_M$$

$$H(t) = 0 \quad \text{if } \Delta p(t) \geqslant p_M, \tag{12}$$

where H_0 is the opening at rest and $p_M = KH_0$ is the lowest pressure for which the reed channel is closed, the reed being held against the lay in static regime.

Combining Eqs. (8)–(12) leads to an instantaneous relationship between the volume velocity $u(t)$ and the pressure difference $\Delta p(t)$:

TABLE I. Typical range values of the embouchure parameters.

w (mm)	p_m (hPa)	H_0 (mm)	K (hPa/mm)	p_M (hPa)	u_A (cm^3/s)
10–13	0–150	0.2–1.1	50–500	40–100	100–2000

$$u = F(p) = u_A\left(1 - \frac{\Delta p}{p_M}\right)\sqrt{\frac{\Delta p}{p_M}} \quad \text{if } \Delta p \leqslant p_M,$$

$$u = F(p) = 0 \quad \text{if } \Delta p \geqslant p_M, \tag{13}$$

where

$$u_A = wH_0\sqrt{\frac{2KH_0}{\rho}} \tag{14}$$

is a volume velocity amplitude parameter. This function $F(p)$ is the nonlinear characteristics of the embouchure. The parameter u_A is related to the maximum flow of the nonlinear characteristics $u_{\max}$ by

$$u_A = \frac{3\sqrt{3}}{2}u_{\max}.$$

Then the elementary model can be reduced to two equations, Eq. (13) characterizing the valve effect (reed) and Eq. (2) characterizing the resonator by its reflection function. Many assumptions behind this elementary model require further discussion (see Hirschberg, 1995), however, recent work has shown that this model fits rather well with the pressure flow characteristics measured in a real clarinet mouthpiece blown by using an artificial mouth setup [see Fig. 3 adapted from Dalmont *et al.* (2003)].

To summarize, seven parameters are involved in the physical model. Three are related to the pipe: the length L of the pipe, the absorption coefficient α, and the characteristic impedance of the pipe $Z_c = \rho c/S$ which depends on the cross section of the pipe. All three are fixed for a given length of the pipe. Four parameters are related to the embouchure: the effective width of the reed channel w, the reed slit opening at rest H_0, the reed stiffness K, and the mouth pressure p_m. The parameter w can be considered as almost constant. The mouth pressure p_m can be varied and controlled by the player as well as the embouchure parameters K and H_0. Typical values of the parameter ranges are given in Table I (see also Dalmont *et al.*, 2003).

B. Static solution and small oscillations for a lossy resonator

The static solution can be found from Eq. (13). This corresponds to the equilibrium state of the reed associated to each value of the mouth pressure p_m in the absence of sound. If losses at zero frequency are ignored ($Z_0 = 0$ and $p = 0$), the following values for the volume velocity u_{eq} and the aperture height H_{eq} are obtained:

$$u_{\text{eq}} = u_A\left(1 - \frac{p_m}{p_M}\right)\sqrt{\frac{p_m}{p_M}},$$

$$H_{\text{eq}} = H_0\left(1 - \frac{p_m}{p_M}\right). \tag{15}$$

The set of Eq. (15) is valid if $p_m < p_M$, otherwise the reed is held against the lay and then u_{eq} and H_{eq} are both equal to zero. The static solution is stable only for given values of the mouth pressure. Some papers have explored the equilibrium solution stability [for a review, see Fletcher and Rossing (1998)]. The main result is that the static solution is stable at low values of p_m, and becomes unstable from a particular value of mouth pressure, denoted $p_{m\text{th}}$. Applying the results of Grand *et al.* (1997) to the present model, it can be shown (Dalmont *et al.*, 2000) that a direct bifurcation is found regardless of the values of the control parameters. As a consequence, the threshold of instability of the static solution is also the threshold of oscillation. The threshold value $p_{m\text{th}}$ is reached for $\partial u/\partial p_m = -Y$ where Y is the value of the admittance at the first resonant frequency and given by Eq. (6). An elementary calculation gives the value of $\Delta p = p_m - p$ at the threshold of oscillation (Kergomard *et al.*, 2000),

$$\Delta p_{\text{th}} = \left(\frac{1}{3} + \frac{2}{3\sqrt{3}}\beta_1\sqrt{1 + \beta_1^2/3} + \frac{2\beta_1^2}{9}\right)p_M, \tag{16}$$

where

$$\beta_1 = Y\frac{p_M}{u_A} = \frac{p_M}{Z_c u_A}\tanh \alpha L. \tag{17}$$

It should be noted that Eq. (16) is obtained as well with Raman's model as with a more sophisticated model of the impedance of the pipe and despite the fact that Raman's model leads to a square signal rather than a sinusoidal one at the threshold of oscillation (see Kergomard *et al.*, 2000). In the absence of losses (i.e., $\alpha = 0$), Y is zero at the resonance, then β_1 is also equal to zero and the threshold of oscillation is found to be $p_{m\text{th}} = p_M/3$. When either losses are large or u_A/p_M (the flow parameter to closing pressure ratio) is small the threshold of oscillations tends to p_M when β_1 tends to unity. On the other hand, when the value of the mouth pressure is larger than p_M, the reed is held against the lay, and the static solution is stable again because $\partial u/\partial p_m$ and all the other derivatives are equal to zero. As a consequence since $p_{m\text{th}} > p_M$ the equilibrium state is always stable, no oscillation at all is possible. This situation is easy to obtain in practice: if the reed opening is too small no oscillation for any mouth pressure occurs despite the fact that the threshold value is finite.

C. Lossless model: Periodic solutions and stability analysis

The use of a lossless model for the resonator has been initiated independently by Friedlandler (1953) and Keller (1953) for the bowed string. This approximation cannot lead to stable periodic oscillations of the bowed string if combined with stick-slip characteristics which assume a perfect sticking of the bow on the string (Friedlander, 1953; Woodhouse, 1993). On the contrary, stable oscillations can be obtained with a lossless model of a reed instrument because of the "smoother" nonlinear characteristics plotted in Fig. 3 (Ollivier *et al.*, 2004, 2005). The use of a lossless model for the resonator cannot provide information on the evolution of the spectrum, but it is fruitful for the study of stability, transients, and bifurcations. This approach has been first used for the clarinet by Maganza (1986), who investigated period doubling mechanism. More recently Kergomard (1995) used such a model to analyze the role of the main control parameters on the oscillations of a clarinet. Lossless models have also been fruitfully applied to stepped cones [see, for example, Dalmont and Kergomard (1995) or Dalmont *et al.* (2000) for theoretical and experimental comparison].

Important results stemming from the lossless approximation and the method used to derive them are now recalled. Given the reflection function $r(t) = -\delta(t-\tau)$ [Eq. (1)], the positive and negative going plane wave pressures at the input (p^+ and p^-, respectively) are related by

$$p^-(t) = r(t)p^+(t) = -p^+(t-\tau). \tag{18}$$

The acoustical field is fully described by using the pair of variables $\{p^+, p^-\}$ or the pair $\{p, u\}$ which are related by

$$p(t) = p^+(t) + p^-(t),$$

$$Z_c u(t) = p^+(t) - p^-(t),$$

or

$$p^+(t) = \tfrac{1}{2}(p(t) + Z_c u(t)),$$

$$p^-(t) = \tfrac{1}{2}(p(t) - Z_c u(t)). \tag{19}$$

Using discrete-time representation, the acoustical field is calculated at every sampling period, by using the sampling frequency $f_s = 1/\tau = c/2L$ which is twice the fundamental resonant frequency of the pipe. In order to simplify the notations, $p(t)$ at $t = n\tau$ is written p_n, the nth sample. Then Eq. (18) is written as $p_n^- = -p_{n-1}^+$ or, using Eq. (19), as

$$p_n - Z_c u_n = -(p_{n-1} + Z_c u_{n-1}). \tag{20}$$

Searching for the periodic regimes of fundamental frequency $c/4L$, the periodicity of the solutions leads to $p_{n+1} = p_{n-1}$ and $u_{n+1} = u_{n-1}$. Applying Eq. (20) for two successive steps leads to

$$p_n = -p_{n-1},$$

$$u_n = u_{n-1}. \tag{21}$$

Using Eq. (21) and the nonlinear characteristics $u_n = F(p_n)$, the function $F(p)$ being given by Eq. (13) with $\Delta p_n = p_m - p_n$ (p_m is the mouth pressure), the solutions at the fundamental frequency can be obtained. An extensive study of the periodic solutions is done in Kergomard (1995). Two kinds of periodic regimes are distinguished: the nonbeating reed regime and the beating reed regime for which one of the two states of the reed is held motionless against the lay. The nonbeating reed regime occurs for $p_M/3 \leqslant p_m \leqslant p_M/2$. In that range of pressures it can be shown that $p_n = -p_{n-1} = \sqrt{(3p_m - p_M)(p_M - p_m)}$. The beating reed regime occurs for $p_m > p_M/2$ and it can be shown that in that case $p_n = -p_{n-1} = p_m$ and $u_n = u_{n-1} = 0$.

As explained by Kergomard (1995) or Ollivier *et al.* (2004, 2005) the periodic solutions are stable if the following inequality is true:

$$F_{\text{stab}}(p) < 0, \tag{22}$$

where

$$F_{\text{stab}}(p) = \frac{F'(p) + F'(-p)}{1 + Z_c^2 F'(p) F'(-p)} \tag{23}$$

is the stability function, F' being the first derivative of the nonlinear characteristic Eq. (13). A conclusion of the stability analysis is that the beating reed regime is always stable. The nonbeating reed regime is stable under certain control parameters conditions, that is:

$$Z_c^2 u_A^2 < \frac{2(p_M - 2p_m)p_M^3}{(3p_m - p_M)(5p_M - 6p_M)}. \tag{24}$$

For a fixed value of u_A, this condition is satisfied below a limit value of p_m. Above this limit, a range of mouth pressure is found for which the oscillation is not stable and in this range period doubling bifurcations can be found. Several regimes where periods are multiple of these of the fundamental frequency $f=c/4L$ can exist. For these regimes the reed can beat for mouth pressures lower than $p_M/2$ [see the curves for the volume velocity in Fig. 8, p. 253 of Kergomard (1995)]. So, the value $p_m=p_M/2$ which is called the beating reed threshold (for the lossless model) is the beating reed threshold only for the oscillating regime of fundamental frequency $f=c/4L$.

III. RAMAN'S MODEL: PERIODIC SOLUTIONS AND THEIR STABILITY

As discussed in Dalmont *et al.* (2002), the main weakness of the lossless model is that it allows periodic oscillations for every mouth pressure above the threshold of oscillation, showing no extinction phenomenon. Recently Atig *et al.* (2004) have shown theoretically and experimentally how losses can modify and control the saturation and extinction phenomena. The simplest way to take into account losses in a theoretical approach is to use a Raman's model in which losses are independent of the frequency and in which the dispersion phenomenon is ignored. This model, and its dynamic behavior (oscillating solutions, bifurcation diagrams) is described in the following.

A. Equations of Raman's model

Taking into account a frequency independent absorption coefficient α, and using Eq. (2), Eq. (18) becomes

$$p^-(t) = r(t)^* p^+(t) = -e^{-2\alpha L} p^+(t-\tau). \tag{25}$$

In the discrete-time representation, Eq. (20) becomes

$$p_n - Z_c u_n = -e^{-2\alpha L}(p_{n-1} + Z_c u_{n-1}). \tag{26}$$

The instantaneous relationship defining the volume velocity u [Eq. (13)] remains valid. The slight complication introduced in Eq. (26) as compared to Eq. (20) implies that Eq. (21) is no longer valid. The periodic solutions of the Raman's model cannot be derived so easily. This difficulty is overcome by a change in variables, where a new pair of variables, $\{q,w\}$, is defined as a function of the pair $\{p,u\}$, as follows:

$$q = p\cosh(\alpha L) - Z_c u \sinh(\alpha L),$$

$$w = Z_c u \cosh(\alpha L) - p \sinh(\alpha L). \tag{27}$$

The left and the right traveling pressure waves in the open end of the pipe (p_o^+ and p_o^-, respectively) can be successively written as functions of the pair $\{p,u\}$, and as functions of the pair of variables $\{q,w\}$:

$$\begin{aligned} p_o^+ &= e^{-\alpha L} p_{n-1}^+ = e^{-\alpha L}\tfrac{1}{2}(p_{n-1} + Z_c u_{n-1}) \\ &= (\cosh \alpha L - \sinh \alpha L)\tfrac{1}{2}(p_{n-1} + Z_c u_{n-1}) \\ &= \tfrac{1}{2}(q_{n-1} + w_{n-1}), \end{aligned}$$

$$\begin{aligned} p_o^-(t) &= e^{+\alpha L} p_n^- = e^{+\alpha L}\tfrac{1}{2}(p_n - Z_c u) \\ &= (\cosh \alpha L + \sinh \alpha L)\tfrac{1}{2}(p_{n-1} + Z_c u_{n-1}) \\ &= \tfrac{1}{2}(q_n - w_n). \end{aligned} \tag{28}$$

With this change of variables the problem is formally similar to that for the lossless model. Results are identical except that the instantaneous relationship defining the volume velocity u as a function of p Eq. (13) must be transformed into a new relationship between w and q:

$$w_n = G(q_n). \tag{29}$$

Function G is known only implicitly since an explicit expression is difficult to find. Nevertheless an expression of its derivative can be obtained, as shown in Sec. III D. Assuming that at the open end the boundary condition is a pressure node [Eq. (18)], Eq. (28) leads to

$$q_n - w_n = -(q_{n-1} + w_{n-1}). \tag{30}$$

The acoustical field can be calculated step by step in time, by using Eqs. (29) and (30) where the unknowns are q and w. These equations are formally identical to Eqs. (13) and (20) where the unknowns are p and u. Then searching for the periodic regimes, that is determining the two states of the periodic solution, leads to solve the following set of equations, similar to Eq. (21):

$$q_n = -q_{n-1},$$

$$w_n = w_{n-1}. \tag{31}$$

Similar to the lossless model results [Eqs. (22) and (23)], the periodic solutions are stable if the following inequality is true:

$$G_{\text{stab}}(q) < 0, \tag{32}$$

where

$$G_{\text{stab}}(q) = \frac{G'(q) + G'(-q)}{1 + G'(q)G'(-q)} \tag{33}$$

is the stability function, G' being the first derivative of G.

B. Periodic solutions and bifurcation diagrams

The periodic regimes are defined by the two different values of the acoustic pressure corresponding to the two alternate states of the reed position. Let p_1 and p_2 be the pressure in the mouthpiece for two successive states and u_1 and u_2 the corresponding volume velocities. These two pressures are solutions of Eq. (26), which, using Eqs. (6) and (7), leads to

$$p_1 + p_2 = (Z_c u_1 + Z_c u_2)\tanh\,\alpha L = Z_0(u_1 + u_2),$$

$$u_1 - u_2 = (p_1 - p_2)\tanh\,\alpha L/Z_c = Y(p_1 - p_2). \tag{34}$$

The first equation expresses that the ratio of mean value of the pressure to the mean value of the volume velocity is equal to the impedance at zero frequency. At this stage it is reasonable to consider that this impedance is low, that is to assume $p_1 \approx -p_2$. The second equation expresses that the ratio of the pressure difference to the volume velocity difference is equal to the impedance at the resonant frequencies. It is convenient, for the calculations of the solutions, to define the following dimensionless parameters:

$$\beta = Z_0\frac{u_A}{p_M} = \frac{Z_c u_A}{p_M}\tanh\,\alpha L,$$

$$\beta_1 = Y\frac{p_M}{u_A} = \frac{p_M}{Z_c u_A}\tanh\,\alpha L,$$

$$\beta_2 = \frac{2\beta_1}{1+\beta\beta_1} = \frac{p_M}{Z_c u_A}\tanh\,2\alpha L. \tag{35}$$

The first one, β, can be seen as the adimensioned impedance at zero frequency and the second, β_1, as the adimensioned admittance at playing frequency. The parameter β_2 is a combination of the two others and it can be noted that, if $\alpha L \ll 1$, which is usually the case, $\beta \approx 0$ and $\beta_2 \approx 2\beta_1$.

1. Beating reed regime

The beating reed regime is attained for $\Delta p = p_m - p \geqslant p_M$. So, the set of equations (34) is simplified by the fact that $u_2 = 0$, state 2 being arbitrarily considered as the closed state. Then it follows from Eq. (34):

$$p_1 + p_2 = Z_c u_1 \tanh\,\alpha L,$$

$$Z_c u_1 = (p_1 - p_2)\tanh\,\alpha L, \tag{36}$$

which implies

$$p_2 = p_1\frac{(\tanh^2\,\alpha L - 1)}{(\tanh^2\,\alpha L + 1)}$$

$$Z_c u_1 = p_1 \tanh\,2\alpha L. \tag{37}$$

Using Eq. (13), u_1 can be written as a function of p_1, then the second equation of Eq. (37) leads to the following nonlinear equation for the unknown p_1:

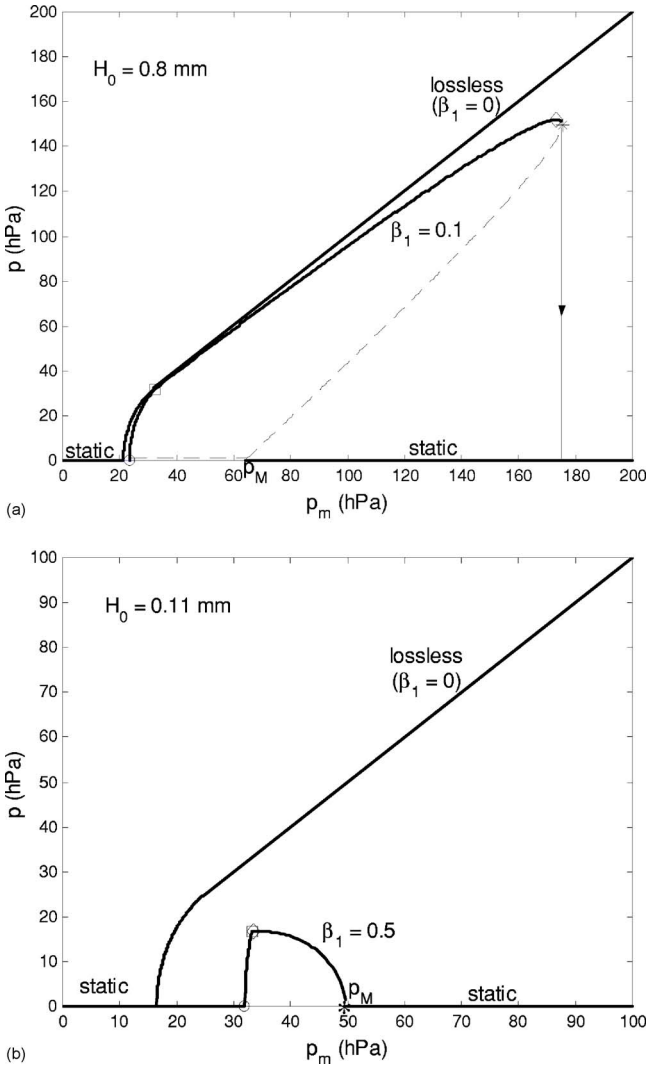

FIG. 4. Bifurcation's diagram: Pressure in the mouthpiece p vs mouthpressure p_m. Dotted line corresponds to an unstable branch and thick lines correspond to stable branches (including static solution). Losses correspond to a 50-cm-long cylindrical tube. The points corresponding to the different thresholds are labeled on the curve: (○) threshold of oscillation; (□) beating reed threshold; (◇) saturation threshold; (∗) extinction threshold. (a) Reed opening is $H_0 = 0.8$ mm ($p_M = KH_0 = 67$ hPa, $\beta_1 = 0.1$, and $\beta = 0.005 \ll 1$). (b) Reed opening is $H_0 = 0.11$ mm ($p_M = KH_0 = 50$ hPa, $\beta_1 = 0.5$, and $\beta = 0.001 \ll 1$).

$$-\beta_2 p_1 + (p_M - p_m + p_1)\sqrt{\frac{p_m - p_1}{p_M}} = 0. \tag{38}$$

From Eq. (38), p_1 can be calculated as a function of p_m. This leads to a third-order polynomial equation in $\Delta p_1 = p_m - p_1$ which can be solved by using, for example, Cardan's method. A detailed analysis, including the stability, is given in the Appendix. In the range of interest, for $\beta_2 < 1$ and $p_m > p_M$ there are two solutions, but only one is stable. In that case there is an inverse bifurcation scheme at extinction [Fig. 4(a)]. Above a threshold of extinction, written p_{me}, no solutions exist. For $\beta_2 \geqslant 1$ or $p_m < p_M$ only one solution exists, which is stable. In that case there is a direct bifurcation scheme at extinction [Fig. 4(b)].

As $\beta_2 \approx 2\beta_1$, it can be concluded that the parameter β_1, which has been shown previously to influence the threshold

of oscillations, is shown here to influence also the amplitude of the oscillations in the beating reed regime.

2. Nonbeating reed regime

By using Eq. (13), u_1 and u_2 can be written as functions of p_1 and p_2, respectively. Then Eq. (28) leads to a set of two nonlinear equations of the two unknowns $\Delta p_1 = p_m - p_1$ and $\Delta p_2 = p_m - p_2$:

$$2p_m - \Delta p_1 - \Delta p_2 = \beta[(p_M - \Delta p_1)\sqrt{\Delta p_1/p_M} + (p_M - \Delta p_2)\sqrt{\Delta p_2/p_M}],$$

$$(p_M - \Delta p_1)\sqrt{\Delta p_1/p_M} - (p_M - \Delta p_2)\sqrt{\Delta p_2/p_M} = \beta_1[\Delta p_2 - \Delta p_1]. \quad (39)$$

In the Appendix, it is shown that this system leads to the solving of a third-order polynomial equation, followed by a second-order one. Under the assumption that $\beta=0$, i.e., $Z_0=0$, a great simplification occurs, the third order being reduced to a second order. Otherwise the threshold of existence of the solutions can be checked to be the same as the instability threshold for the static regime.

3. Bifurcation diagrams

To summarize, solving the set of equations (39) gives the nonbeating regimes, and solving Eq. (38) gives the beating regimes. This means that the bifurcation diagram can be completed. As an illustration, two typical bifurcation diagrams are displayed: one shows an inverse bifurcation at extinction [Fig. 4(a)] and the other one shows a direct bifurcation at extinction [Fig. 4(b)]. For the studied example, the parameter β is assumed to be small, this assumption being realistic for practical situations. The diagram of Fig. 4(a) is very similar to what can be observed with an artificial mouth (see, e.g., Dalmont *et al.*, 2000, or Atig *et al.*, 2004).

C. Thresholds from Raman's model

As displayed in Fig. 4(a), some remarkable points in the bifurcation diagrams can be brought out. These are:

(1) the threshold of oscillation $p_{m\mathrm{th}}$ for which oscillation starts when pressure increases slowly,
(2) the beating reed threshold $p_{m\mathrm{b}}$ for which the reed starts beating (for sake of simplicity, we omit here and in the following the precision "for the periodic regime of frequency $f=c/4L$," see explanations at the end of Sec. II C),
(3) the saturation threshold $p_{m\mathrm{s}}$ for which the maximum amplitude is reached,
(4) the extinction threshold $p_{m\mathrm{e}}$ beyond which there is no oscillation, and
(5) the inverse oscillation threshold $p_{m\mathrm{in}}$ for which oscillation starts when pressure decreases after the reed have been blocked on the lay.

In what follows the pressure values of these thresholds are calculated as a function of the parameters of the model, that is p_M, β, β_1, and β_2. The parameter β is usually small compared to unity. However, all the following results are general, it means that β is not supposed to be small compared to unity. On the contrary $\beta_2 \approx 2\beta_1$ and β_1 can be larger than unity, but, as discussed in the following, if $\beta_1 \geqslant 1$ no oscillation is possible. The conditions for an inverse or a direct bifurcation at the extinction are also derived.

1. Threshold of oscillation

This threshold is discussed in Sec. II B, Eq. (16).

2. Beating-reed threshold

The beating reed threshold is defined by the condition $\Delta p_2 = p_M$. Then at the beating threshold $p_2 = p_m - p_M$ is known, and p_1 is derived from Eq. (38):

$$p_1 = (p_m - p_M)\frac{(\tanh^2 \alpha L + 1)}{(\tanh^2 \alpha L - 1)} = (p_m - p_M)\frac{(\beta\beta_1 + 1)}{(\beta\beta_1 - 1)}. \quad (40)$$

Equation (39) remains valid, and yields to the particular value of the mouth pressure p_{mb} which is the beating reed threshold:

$$p_{m\mathrm{b}} = \left(\tfrac{1}{2} + \tfrac{1}{2}[\beta\beta_1 + \beta_1^2(1 - \beta\beta_1)]\right)p_M. \quad (41)$$

In the absence of losses $\beta=\beta_1=0$ and $p_{mb}=p_M/2$. If $\beta_1=1$ then $p_{m\mathrm{b}}=p_M$ and, as discussed in Sec. II B, no oscillation is possible, for any mouth pressure.

At the beating threshold, the two states p_{1b} and p_{2b} of the periodic regime are

$$p_{1\mathrm{b}} = \frac{\beta_1}{\beta_2}(1 - \beta_1^2)p_M,$$

$$p_{2\mathrm{b}} = -p_{1b} + \beta\beta_1(1 - \beta_1^2)p_M. \quad (42)$$

3. Saturation threshold

The saturation threshold is the point for which the amplitude of the oscillation is maximum, that is $\partial p_1/\partial p_m = 0$. This occurs when the maximum flow is reached ($u_1 = u_{\max} = 3\sqrt{3}/2u_A$), that is for $\Delta p_1 = p_M/3$ (see Fig. 3). Then, using $p_m = \Delta p_1 + p_1$ and $Z_c u_1 = p_1 \tanh(2\alpha L)$, Eq. (37) shows that

$$p_{ms} = \left(\frac{1}{3} + \frac{2}{3\sqrt{3}\beta_2}\right)p_M. \quad (43)$$

At this value, the corresponding pressures p_{1s} and p_{2s} are

$$p_{1\mathrm{s}} = \frac{2}{3\sqrt{3}\beta_2}p_M,$$

$$p_{2\mathrm{s}} = -p_{1\mathrm{s}} + \frac{2\beta}{3\sqrt{3}}p_M. \quad (44)$$

If β_2 tends to zero the saturation threshold as well as the amplitude of the oscillations tend to infinity. The saturation threshold cannot be lower than the beating reed threshold. Both thresholds are equal when $\beta_1 = 1/\sqrt{3}$. So the previous result is valid for $\beta_1 < 1/\sqrt{3}$. For $1 > \beta_1 > 1/\sqrt{3}$ the beating reed threshold is equal to the saturation threshold.

4. Extinction threshold

Due to losses, when the mouth pressure p_m is too large, there is no more oscillation. The maximum value for which oscillation is still possible is defined as the "extinction threshold." It is obtained from Eq. (38) which gives the beating reed periodic solutions. Two situations are possible. The first one is obtained for $\beta_2 < 1$. In that case the extinction threshold is larger than p_M and is given by

$$p_{me} = \left(\frac{1}{9} + \frac{2}{27\beta_2}(3+\beta_2^2)[\beta_2 + \sqrt{3+\beta_2^2}]\right)p_M. \tag{45}$$

Such a situation has been observed in experiments with an artificial mouth (Dalmont, 2000; Atig, 2004). The second situation is obtained for $\beta_2 > 1$, p_{me} is equal to p_M and in that case there is a direct bifurcation at extinction, thus p_{1e} and p_{2e} vanish.

5. Inverse oscillation threshold

The threshold $p_{\min}$ is the pressure for which oscillation starts when the pressure is decreased after the reed have been held motionless on the lay. It is equal to the lowest pressure for which the reed closes the reed-mouthpiece channel, that is $p_{min} = p_M$.

All the previous results about the thresholds are summarized in Fig. 5. It can be observed that all the threshold are different for $\beta_1 < 0.5$. For $\beta_2 = 1$, that is $\beta_1 \approx 0.5$, the extinction threshold reaches p_M, which means that the bifurcation becomes direct at extinction (p_M can be seen as the direct threshold of oscillation for decreasing a pressure). For $\beta_1 = 1/\sqrt{3}$ the saturation threshold reaches the beating reed threshold which means that the maximum amplitude is obtained at the beating reed threshold. Finally when $\beta_1 \geqslant 1$ all the thresholds collapse and no oscillation is possible.

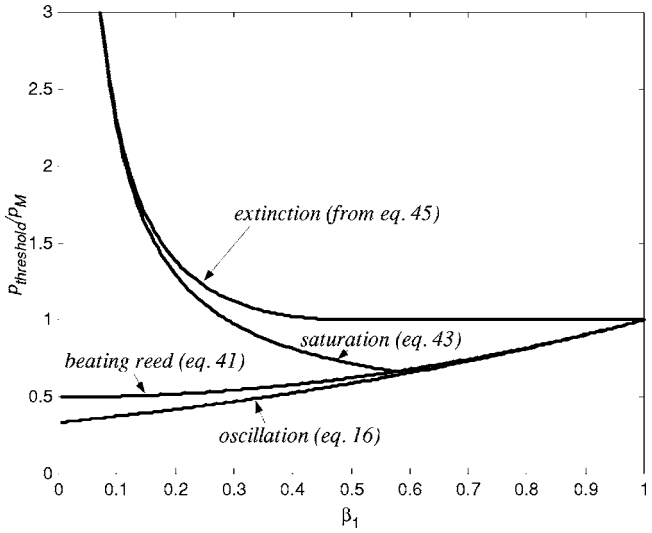

FIG. 5. Thresholds as a function of parameter β_1 with $\beta \ll 1$.

6. Instability threshold

The threshold of instability is discussed in the next section, because another dimensionless parameter needs to be introduced.

D. Stability analysis

As written at the end of Sec. III A, the periodic solutions are stable if the inequality (32) is true. The derivative of the function G defined in Eq. (29) is given by

$$G' = \frac{Z_c F' - \tanh \alpha L}{1 - Z_c F' \tanh \alpha L}. \tag{46}$$

According to Eq. (46), the stability function $G_{\text{stab}}(q)$ can be written as follows:

$$G_{\text{stab}}(q) = \frac{G'(q) + G'(-q)}{1 + G'(q)G'(-q)} = \frac{\left(\frac{Z_c F'(p_1) - \tanh \alpha L}{1 - Z_c F'(p_1)\tanh \alpha L}\right) + \left(\frac{Z_c F'(p_2) - \tanh \alpha L}{1 - Z_c F'(p2)\tanh \alpha L}\right)}{1 + \left(\frac{Z_c F'(p_1) - \tanh \alpha L}{1 - Z_c F'(p_1)\tanh \alpha L}\right)\left(\frac{Z_c F'(p2) - \tanh \alpha L}{1 - Z_c F'(p2)\tanh \alpha L}\right)}, \tag{47}$$

or

$$G_{\text{stab}}(q) = \frac{Z_c F_{\text{stab}}(p_1,p_2) - \tanh 2\alpha L}{1 - Z_c F_{\text{stab}}(p_1,p_2)\tanh 2\alpha L} \tag{48}$$

with

$$F_{\text{stab}}(p_1,p_2) = \frac{F'(p_1) + F'(p_2)}{1 + Z_c^2 F'(p_1)F'(p_2)}, \tag{49}$$

the stability condition being $G_{\text{stab}}(q) < 0$.

Because $\tanh 2\alpha L$ is positive, this condition can be split into two conditions:

$$F_{\text{stab}}(p_1,p_2) < Z_c^{-1} \tanh 2\alpha L,$$

$$F_{\text{stab}}(p_1,p_2) > Z_c^{-1} \coth 2\alpha L. \tag{50}$$

To check the stability of the periodic regimes the signs of the stability conditions (50) are first analyzed for the beating case and then for the nonbeating case. The details are given in the Appendix. For the beating case, $F'(p_2) = 0$ implies that $F_{\text{stab}}(p_1,p_2) = F'(p_1)$. For this case, it can be seen that the solutions p_1 corresponding to the upper branch of the bifurcation diagram are always stable, and the solutions corresponding to the lower branch are unstable, except for a very special case: a complete analysis could be done for the case, but it is without interest in practice, because it requires both large losses and large u_A.

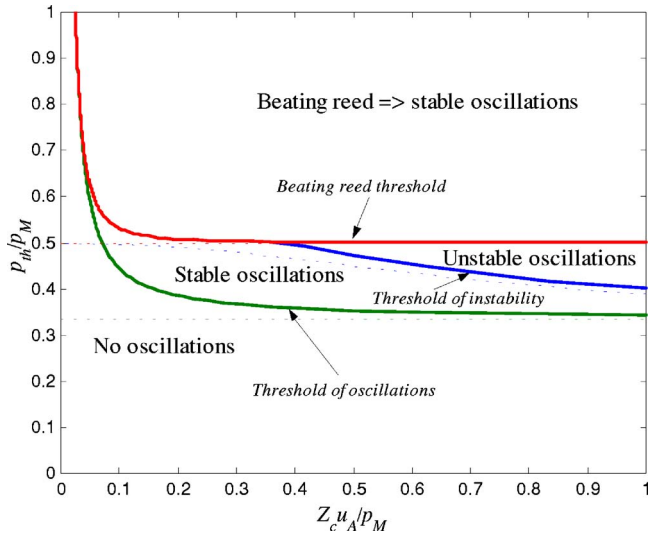

FIG. 6. (Color online) Thresholds as a function of the dimensionless flow amplitude of the nonlinear characteristics $\tilde{u}_A = Z_c u_A / p_M$. Dotted lines correspond to the lossless case. The instability region (for the fundamental regime) is between the threshold of instability and the beating reed threshold.

For the nonbeating reed ($p_{m\text{th}} < p_m < p_{m\text{b}}$), the analysis is not straightforward and the conclusion is not so simple. Nevertheless it can be checked that there is a low limit of the mouth pressure, called $p_{m\text{inst}}$, under which the oscillations are stable. If $p_{m\text{inst}} < p_m < p_{m\text{b}}$ oscillations are not stable and a period doubling can be observed as well as other regimes with larger periods, or even chaos (Kergomard *et al.*, 2004; Kergomard, 1995). The instability range is actually narrow because the beating reed threshold for the periodic regime of frequency $c/4L$ is in practice close to the threshold of instability. In the appendix the value of the threshold of instability is found for $\beta \ll 1$ [see Eq. (A32)]. This threshold is plotted in Fig. 6 as a function of $\tilde{u}_A = Z_c u_A / p_M$.

The threshold of instability increases significantly when losses increase and even disappears for some limit value of parameter $\tilde{u}_A$ depending on the value of the parameter β_1. This result confirms numerical, *ab initio* calculations given in Ollivier *et al.* (2004). The limit value of β_1 up to which there is no instability range is found to be at the second order of $\tilde{u}_A = Z_c u_A / p_M$:

$$\tanh \alpha L = \tfrac{1}{2}\tilde{u}_A^3[1 - \tilde{u}_A^2] \quad \text{for } \beta \ll 1 \tag{51}$$

This limit value is rather low, which means that period doubling might usually not be observed. Indeed, with standard values of the limit pressure $p_M = 10$ kPa and maximum flow $u_{\max} = 4.10^{-4}$ m^3/s, $\tilde{u}_A$ is found to be $\tilde{u}_A = 0.22$. This leads to $\beta_{1\text{inst}} = 0.023$, which is much lower than the actual value $\beta_1 = 0.11$ for a 16-mm-diam pipe of length 0.5 m. This means that no period doubling may be observed. However with a reed of low stiffness (a weak reed), and a rather loose embouchure the value of β_1 is decreased while the value of $\beta_{1\text{inst}}$ is increased. So, it is theoretically possible to obtain period doubling as noted by Kergomard (1995) with some unusual embouchure.

IV. DISCUSSION

Based upon a simplified model of the clarinet, solutions for the mouthpiece pressure and their stability have been found analytically. The playing range of the clarinet is found to depend on two parameters. The first one is the minimum pressure p_M sufficient to close the reed channel in static regime. The second parameter $\beta_1 = Y p_M / u_A$ is the ratio of the input admittance of the pipe at the playing frequency to the flow amplitude parameter of the nonlinear characteristic u_A divided by p_M. The definition of this second parameter β_1 shows that the playing range depends on the balance between the embouchure, characterized by its nonlinear characteristics, and the pipe characterized by its input admittance. In an extreme situation, if, for example, the reed channel cross section is small compared to the pipe cross section, no oscillation for any mouth pressure occurs. Such an extreme situation can also be reached if losses are too large. This is the case if side holes are too small since in that case nonlinear losses become large (Keefe, 1983; Dalmont *et al.*, 2001a). Parameter β_1 also determines the bifurcation scheme at extinction. If the parameter β_1 is lower than 0.5 the bifurcation is inverse at the extinction and the extinction threshold is larger than p_M, showing an hysteretic phenomenon at extinction [see Atig *et al.* (2004) for experimental evidence]. This is probably the most usual situation. On the contrary if the parameter β_1 is larger than 0.5 the bifurcation is direct at the extinction and the extinction threshold is equal to p_M. These same two parameters also determine the threshold of oscillation (Kergomard *et al.*, 2000) as well as the beating reed threshold for the periodic regime of frequency $c/4L$. However, the stability of the oscillations also depends on another parameter: the dimensionless volume velocity amplitude $\tilde{u}_A = Z_c u_A / p_M$ of the nonlinear characteristics. This parameter also expresses the balance between the embouchure and the pipe and its role has been first emphasized by Wilson and Beavers (1974) and Kergomard (1995) in the context of the lossless model. A limit value of β_1, as a function of $\tilde{u}_A$, exists up to which oscillations at the fundamental frequency are always stable. For realistic values of the physical parameters, β_1 is shown to be larger than this limit value. This might explain why period doubling is not usually observed on a standard clarinet.

V. CONCLUSION

All these results are in a good agreement with experimental observations (Atig *et al.*, 2004) showing that, despite its simplicity, Raman's model is a powerful tool for the study of the clarinet. The present results give a new enlightenment on the playing of the clarinet. In particular, it reveals the possibility of playing pianissimo by playing near the threshold of extinction when the bifurcation at extinction is direct. The way clarinet players use this possibility in performing is a subject for further investigations.

ACKNOWLEDGMENTS

We acknowledge Aude Lizée for discussions about the beating reed threshold, the clarinetist Pierre-André Taillard

for discussions on the musical consequences of our calculations, and Kees Nederveen for a careful and enlightened reading of the paper.

APPENDIX: STUDY OF THE OSCILLATING SOLUTIONS AND THEIR STABILITY

The Appendix gives the detailed calculation of the oscillating solutions and their stability. In order to simplify the presentation, dimensionless quantities are used. Pressures are divided by the limit pressure p_M and flows are multiplied by the ratio Z_c/p_M, where Z_c is the characteristic impedance of the tube.

Starting from Eq. (13), it means that the following nonlinear function $u=F(p)$ is considered:

$$u = u_A(1-\Delta p)\sqrt{\Delta p} \quad \text{if } \Delta p \leqslant 1$$

$$u = 0 \quad \text{if } \Delta p \geqslant 1, \tag{A1}$$

where $\Delta_p = p_m - p$, and $u_A = \sqrt{2} Z_c w H/\sqrt{\rho p_M}$. Note that in Kergomard (1995) p_m and u_A are denoted γ and ζ, respectively. The two cases of the beating reed and the nonbeating reed are studied successively.

1. Beating case

For one of the solutions, p_2, $F(p)=0$. The other solution, p_1, is found to be solution of Eq. (37), rewritten as follows:

$$H(X) = \frac{1}{\beta_2}(1-X^2)X + X^2 - p_m = 0, \tag{A2}$$

where $X=\sqrt{\Delta p_1}=\sqrt{p_m - p_1}$, which satisfies $0<X<1$.

The first condition of stability from Eq. (50) is first examined. If it is satisfied, the solution is stable, if not, the second condition remains to be examined. Because $F(p_2)$ is zero as well as its derivative, the condition is

$$F'(p) < \tanh 2\alpha L \quad \text{at } p = p_1. \tag{A3}$$

Using Eq. (37), we notice that

$$F(p_1) = [H(X) + p_1]\tanh 2\alpha L, \tag{A4}$$

which leads to the following stability condition:

$$H'(X) > 0$$

with

$$H(X) = 0. \tag{A5}$$

The derivative $H'(X)$ of $H(X)$ with respect to X is given by

$$H'(X) = (1-3X^2)/\beta_2 + 2X. \tag{A6}$$

For $X=0$, $H(X)=-p_m$ and $H'(X)=1/\beta_2$. For $X=1$, $H(X)=1-p_m$ and $H'(X)=2(1-1/\beta_2)$. The derivative of $H(X)$ vanishes for a unique, positive value

$$X_e = \tfrac{1}{3}[\beta_2 + \sqrt{\beta_2^2+3}]. \tag{A7}$$

Because $H'(X)$ is a second-order polynomial, above this value X_e, $H'(X)$ is negative, below, it is positive. If $\beta_2<1$, $X_e<1$. On the contrary, if $\beta_2>1$, $X_e>1$. We now distinguish the two cases:

a. First case: $\beta_2>1$

Function $H(X)$ increases from $-p_m$ for $X=0$ to $1-p_m$ when $X=1$.

If $p_m>1$, there are no solutions. If $p_m<1$, there is a unique solution, with a positive derivative, therefore the solution is stable.

b. Second case: $\beta_2<1$

Function $H(X)$ increases from $-p_m$ for $X=0$, then goes through a maximum value at $X=X_e$, and finally decreases to $1-p_m$ when $X=1$.

If $p_m<1$, there is a unique solution $X<X_e$ with a positive derivative, thus the solution is stable.

If $p_m>1$, there are no solutions if $H(X_e)<0$, and two solutions if $H(X_e)>0$. This condition can be written as $H(X_e)=\text{function}(\beta_2)-p_m>0$. Therefore there are two solutions if

$$p_m < \frac{1}{\beta_2}(1-X_e^2)X_e + X_e^2 = \frac{1}{9} + \frac{2}{27\beta_2}(3+\beta_2^2) \times [\beta_2 + \sqrt{\beta_2^2+3}] = p_{me}. \tag{A8}$$

The value p_{me} is interpreted as the extinction threshold. The solution satisfying $X<X_e$ has a positive derivative: it means that the solution such as $p_1>p_{me}$, on the upper branch in Fig. 4, is stable. The other solution, satisfying $X>X_e$, corresponding to the lower branch, has a negative derivative. It is expected to be unstable, the condition being that the second condition from Eq. (50) is not fulfilled, i.e.,

$$F'(p_1) < \coth 2\alpha L. \tag{A9}$$

Using Eq. (A4), this condition is rewritten as

$$\left[-\frac{1}{2X}H'(X) + 1\right] < \coth^2 2\alpha L,$$

or

$$\frac{1-3X^2}{2X} > -\frac{1}{u_A}\coth 2\alpha L. \tag{A10}$$

The function of the left-side member is decreasing from $X=X_e$ to $X=1$. Thus a sufficient condition is that the condition is satisfied for $X=1$. A final sufficient condition is found to be

$$u_A \tanh 2\alpha L < 1. \tag{A11}$$

We notice that for $p_m=1$, the two solutions are $X=\beta$ and $X=1$: thus the condition is also necessary. As a conclusion, for given values of u_A and α, the condition for the instability of the lower branch solution for every value of p_m lying in the interval $[1, p_{me}]$ is given by inequality (A11). This condition is satisfied for every practical case, but we notice that it is possible to have $\beta = u_A \tanh \alpha L < 1$ while $u_A \tanh 2\alpha L > 1$. As a matter of fact, this would imply a large value of

either the losses (αL) or the parameter u_A (at least u_A larger than unity), and this case is probably not encountered in practice.

2. Nonbeating case

a. Existence of the solutions

The solutions p_1 and p_2 are given by Eq. (39)

$$2p_m - \Delta p_1 - \Delta p_2 = \beta[(1-\Delta p_1)\sqrt{\Delta p_1} + (1-\Delta p_2)\sqrt{\Delta p_2}] \tag{A12}$$

$$(1-\Delta p_1)\sqrt{\Delta p_1} - (1-\Delta p_2)\sqrt{\Delta p_2} = \beta_1(\Delta p_2 - \Delta p_1), \tag{A13}$$

where $\Delta p_1 = p_m - p_1$ and $\Delta p_2 = p_m - p_2$.

Writing

$$\Sigma = \sqrt{\Delta p_1} + \sqrt{\Delta p_2}, \quad \Pi = \sqrt{\Delta p_1}\sqrt{\Delta p_2}, \tag{A14}$$

the first equation leads to

$$2p_m - \Sigma^2 + 2\Pi = \beta\Sigma(1 - \Sigma^2 + 3\Pi) \tag{A15}$$

and the second one, after elimination of $\sqrt{\Delta p_1} = \sqrt{\Delta p_2}$, corresponding to the static regime,

$$1 - \Sigma^2 + \Pi = -\beta_1\Sigma. \tag{A16}$$

Eliminating Π, Σ is found to be solution of the following equation of the third order:

$$2\beta\Sigma^3 - (1 + 3\beta\beta_1)\Sigma^2 + 2(\beta_1 - \beta)\Sigma + 2(1 - p_m) = 0. \tag{A17}$$

The solution is particularly easy to find if parameter β is small, and assumed to be zero.

The threshold of existence for the solutions is given by $\Sigma^2 = 4\Pi$. Using Eqs. (A15) and (A16), we get

$$p_m = \beta(1-\Pi)\sqrt{\Pi} + \Pi \tag{A18}$$

and

$$3\Pi - 2\beta_1\sqrt{\Pi} - 1 = 0. \tag{A19}$$

Eliminating Π, the threshold is found be equal to the threshold of instability of the static regime.

b. Stability of the solutions

In order to be stable, the solutions need to satisfy one of equations (50). After some algebra, they are found to be

$$\text{either } K < 1 \tag{A20}$$

$$\text{or } K > \coth^2 2\alpha L, \tag{A21}$$

where

$$K = \frac{2\Sigma(3\Pi - 1)}{\beta_2[4\Pi + u_A^2[(1+3\Pi)^2 - 3\Sigma^2]]}. \tag{A22}$$

Using Eq. (A19), quantity K is found to be equal to unity at the threshold of existence. Then, a numerical analysis shows that, for increasing p_m, the factor $(3\Pi - 1)$ becomes negative, and the condition (A20) is fulfilled. Then the denominator vanishes, the quantity K tending to $-\infty$, then decreases from $+\infty$. Therefore the instability threshold appears to be given by the single condition (A21), written as follows:

$$4\Pi + u_A^2[(1+3\Pi)^2 - 3\Sigma^2] = \frac{2\Sigma(3\Pi - 1)}{\beta_2 \coth^2 2\alpha} \tag{A23}$$

or

$$\frac{4\Pi}{u_A^2} + (1+3\Pi)^2 - 3\Sigma^2 = \frac{\beta_1}{1+\beta\beta_1}\Sigma(3\Pi - 1). \tag{A24}$$

An analytical solution is difficult to find, except if $\beta = u_A \tanh\alpha$ is small. With this assumption, the following equation needs to be solved:

$$\frac{4\Pi}{u_A^2} + (1+3\Pi)^2 - 3\Sigma^2 = \beta_1\Sigma(3\Pi - 1), \tag{A25}$$

where

$$2p_m - \Sigma^2 + 2\Pi = 0 \tag{A26}$$

and

$$1 - \Sigma^2 + \Pi = -\beta_1\Sigma. \tag{A27}$$

This leads to a fourth-order polynomial equation in Π, thus we limit the analytical calculation to a first-order approximation with respect to parameter β_1. The following result is obtained:

$$\Sigma^2 = 1 + \Pi + \beta_1\sqrt{1+\Pi}.$$

Then, using Eq. (A25):

$$9\Pi^2 + \left[\frac{4}{u_A^2} + 3\right]\Pi - 2 = \beta_1\sqrt{1+\Pi}(2+3\Pi). \tag{A28}$$

At the zeroth order of β_1 (no losses are present), the result corresponding to Eq. (45) of the Kergomard (1995) is obtained:

$$\Pi_0 = \frac{1}{18}\left[-\frac{4}{u_A^2} - 3 + \sqrt{\left[\frac{4}{u_A^2} + 3\right]^2 + 72}\right], \tag{A29}$$

then at the first order

$$\Pi = \Pi_0 + \frac{\beta_1\sqrt{1+\Pi_0}(2+3\Pi_0)}{18\Pi_0 + 3 + 4/u_A^2} \tag{A30}$$

and finally the threshold of instability is found to be

$$p_{m,\text{inst}} = \tfrac{1}{2}[1 - \Pi + \beta_1\sqrt{1+\Pi_0}]. \tag{A31}$$

This result has been found to be in good agreement with numerical simulation, which shows that the bifurcation corresponds to a period doubling (it is deduced that the threshold of instability increases significantly when losses increase).

An interesting point is that this threshold can reach the beating threshold when losses become larger, and the insta-

bility range disappears, as we will prove now. At the beating threshold, $\Pi=\beta_1$ and $\Sigma=1+\beta_1$, thus the equality of the thresholds is given by Eq. (A24):

$$\frac{4\beta_1}{u_A^2}+6\beta_1-2=\frac{-\beta_1}{1+\beta_1\beta}(1+\beta_1)(1-3\beta_1). \tag{A32}$$

This leads to a third-order polynomial equation:

$$3\beta_1^3u_A^2(u_A^2-2)+\beta_1^2u_A^2+\beta_1(2+2u_A^2-u_A^4)-u_A^2=0. \tag{A33}$$

For small u_A, a series expansion leads to

$$\beta_1=\frac{u_A^2}{2}\left[1-u_A^2+\frac{5}{4}u_A^4-\frac{1}{2}u_A^6\right]. \tag{A34}$$

For losses larger than this value, no period doubling occurs. For practical cases; the second order in the bracket is certainly sufficient.

Atig, M., Dalmont, J.-P., and Gilbert, J. (**2004**). "Saturation mechanism in clarinet-like instruments, the effect of the localized non-linear losses," Appl. Acoust. **65**, 1133–1154.

Dalmont, J.-P., Ducasse, E., and Ollivier, S. (**2002**). "Saturation mechanism in reed instruments," Proceedings of the Third EEA European Congress on Acoustic, Sevilla, Spain.

Dalmont, J.-P., Ducasse, E., and Ollivier, S. (**2001a**). "Practical consequences of tone holes nonlinear behaviour," International Symposium of Musical Acoustics, Perugia, pp. 153–156.

Dalmont, J.-P., Gilbert, J., and Kergomard, J. (**2000**). "Reed instruments, from small to large amplitude periodic oscillations and the Helmholtz motion analogy," Acust. Acta Acust. 86, 671–684.

Dalmont, J.-P., Gilbert, J., and Ollivier, S. (**2003**). "Non-linear characteristics of single reed instruments: Quasi-static volume flow and reed opening measurements," J. Acoust. Soc. Am. **114**, 2253–2263.

Dalmont, J.-P., and Kergomard, J. (**1995**). "Elementary model and experiments for the Helmholtz motion of single reed wind instruments," Proceedings of the International Symposium on Musical Acoustics, Dourdan, France, pp. 114–120.

Dalmont, J.-P., Nederveen, K., and Joly, N. (**2001b**). "Radiation impedance of tubes with different flanges: Numerical and experimental investigations," J. Sound Vib. **244**, 505–534.

Fletcher, N. H., and Rossing, T. D. (**1998**). *The Physics of Musical Instruments* (Springer, New York).

Friedlander, F. G. (**1953**). "On the oscillations of a bowed string," Proc. Cambridge Philos. Soc. **49**, 516–530.

Grand, N., Gilbert, J., and Laloé, F. (**1997**). "Oscillation threshold of woodwinds instruments," Acustica **1**, 137–151.

Hirschberg, A. (**1995**). "Aero-acoustics of wind instruments," in *Mechanics of Musical Instruments*, edited by A. Hirschberg, J. Kergomard, and G. Weinreich, CISM Courses and Lectures No. 355 (Springer, Wien).

Keefe, D. H. (**1983**). "Acoustic streaming, dimensional analysis of nonlinearities, and tone hole mutual interactions in woodwinds," J. Acoust. Soc. Am. **73**, 1804–1820.

Keller, J. B. (**1953**). "Bowing of violin strings," Commun. Pure Appl. Math. **6**, 483–493.

Kergomard, J. (**1995**). "Elementary considerations on red-instruments oscillations," in *Mechanics of Musical Instruments*, edited by A. Hirschberg, J. Kergomard, and G. Weinreich, CISM Courses and Lectures No. 355 (Springer, Wien).

Kergomard, J., Dalmont, J.-P., Gilbert, J., and Guillemain, P. (**2004**). "Period doubling on cylindrical reed instruments," 7ème Congrès Français d'Acoustique, Strasbourg, pp. 113–114.

Kergomard, J., Ollivier, S., and Gilbert, J. (**2000**). "Calculation of the spectrum of self-sustained oscillators using a variable truncation method," Acust. Acta Acust. 86, 685–703.

Maganza, C., Caussé, R., and Laloé, F. (**1986**). "Bifurcations, period doublings and chaos in clarinet like systems," Electron. Lett. **1**, 295–302.

Mc Intyre, M. E., Schumacher, R. T., and Woodhouse, J. (**1983**). "On the oscillations of musical instruments," J. Acoust. Soc. Am. **74**, 1325–1345.

Nederveen, C. J. (**1998**). *Acoustical Aspects of Woodwind Instruments* (Northern Illinois University Press, DeKalb).

Norris, A. N., and Sheng, I. C. (**1989**). "Acoustic radiation from a circular pipe with an infinite flange," J. Sound Vib. **135**, 85–93.

Ollivier, S., Dalmont, J.-P., and Kergomard, J. (**2004**). "Idealized models of reed woodwinds. I. Analogy with the bowed string," Acust. Acta Acust. 90, 1192–1203.

Ollivier, S., Kergomard, J., and Dalmont, J.-P. (**2005**). "Idealized models of reed woodwinds. II. On the stability of 'two step' oscillations," Acust. Acta Acust. 91, 166–179.

Polack, J.-D., Meynial, X., Kergomard, J., Cosnard, C., and Bruneau, M. (**1987**). "Reflection function of a plane wave in a cylindrical tube," Rev. Phys. Appl. **22**, 331–339.

Raman, C. V. (**1918**). "On the mechanical theory of vibrations of bowed strings," Indian Assoc. Cult. Sci. Bull., **15**(1), 1-158

Schelleng, J. C. (**1973**). "The bowed string and the player," J. Acoust. Soc. Am. **53**, 26-41

Wilson, T. A., and Beavers, G. S. (**1974**). "Operating modes of the clarinet," J. Acoust. Soc. Am. **56**, 653–658.

Woodhouse, J. (**1993**). "Idealized models of a bowed string," Acustica **79**, 233–250.

How do clarinet players adjust the resonances of their vocal tracts for different playing effects?

Claudia Fritz[a] and Joe Wolfe
UNSW, School of Physics, NSW 2052 Sydney, Australia

(Received 28 February 2005; revised 27 July 2005; accepted 29 July 2005)

In a simple model, the reed of the clarinet is mechanically loaded by the series combination of the acoustical impedances of the instrument itself and of the player's airway. Here we measure the complex impedance spectrum of players' airways using an impedance head adapted to fit inside a clarinet mouthpiece. A direct current shunt with high acoustical resistance allows players to blow normally, so the players can simulate the tract condition under playing conditions. The reproducibility of the results suggest that the players' "muscle memory" is reliable for this task. Most players use a single, highly stable vocal tract configuration over most of the playing range, except for the altissimo register. However, this "normal" configuration varies substantially among musicians. All musicians change the configuration, often drastically for "special effects" such as glissandi and slurs: the tongue is lowered and the impedance magnitude reduced when the player intends to lower the pitch or to slur downwards, and vice versa. © *2005 Acoustical Society of America.* [DOI: 10.1121/1.2041287]

PACS number(s): 43.75.Pq, 43.75.Yy, 43.75.St, 43.58.Bh [NHF] Pages: 3306–3315

I. INTRODUCTION

Acousticians (Backus,[1] Benade,[2] Hoekje,[3] Johnson *et al.*,[4] Wilson[5]) are divided over the extent of the influence of the respiratory tract in playing reed instruments, of which the clarinet is the most studied example. The reed and the airflow past it interact with acoustical waves in the bore of the instrument and with waves in the player's tract. A simple argument shows that the acoustical impedances of these are approximately in series.[2] The cross section of the clarinet bore is rather smaller than that of the tract, so its characteristic impedance is higher. Further, the resonances in the instrument have a high value of quality factor, so the peaks in impedance have high value and, to first order, usually determine the playing regime of the bore-reed-tract system.[6] Nevertheless, the effects of the impedance spectrum of the vocal tract, even if smaller than those of the clarinet, may be important, because musicians are often interested in subtle effects. For instance, a 1% change in frequency could be a large mistuning for a musician, and subtle changes in the spectral envelope may be important in controlling timbre and musical expression. Most researchers agree that the effect is small but important—even if they do not necessarily agree about how the vocal tract affects the sound production—except for Backus who considers that the player's tract has a negligible influence on the instrument tone.

Strictly speaking, it is the impedance of the entire airway of the player, from mouth to lungs, that loads the reed or lips and that drives the air flow past them. However, Mukai[7] reported that experienced players of wind instruments keep the glottis (the aperture between the vocal folds) almost closed when playing. This is very important to the possible influence of the tract: with an open glottis, the airway has relatively weak resonances, because it is terminated with the high losses in the lungs and lower airways. In contrast, an almost closed glottis provides a high coefficient of reflection for acoustic waves at all but the lowest frequencies, and so would be expected to give strong resonances, similar to those that give rise to formants in speech. For that reason, we shall refer hereafter to the player's vocal tract as the resonator that is controlled by the player.

Impedance measurements have been made previously (Benade,[2] Backus,[1] Hoekje,[3] and Wilson[5]) but are not fully exploitable or applicable due to the fact that they either were performed under conditions that do not closely resemble those used to play an instrument, or that they lacked phase information, or contained high levels of background noise. Moreover, they were made in most cases on only one subject. The measurement conditions should reproduce, as much as possible, the playing condition, so that the player can automatically adopt the tract configurations used in playing under particular conditions. For example, Benade[2] measured the impedance of a clarinettist's tract by inserting into the player's mouth a pipe containing the acoustical source and the microphone. The pipe inner diameter was 20 mm, which forces the player to open the mouth considerably more than he would when playing a clarinet. This problem was solved by Hoekje,[3] who used a similar arrangement, with the exception that he reduced the size of the part which goes into the musician's mouth. Overall, Hoekje measured somewhat low values of the impedance (maxima about 8 MPa s m^{-3}), therefore much smaller than the maxima measured for the clarinet using most fingerings (Wolfe *et al.*,[8] Backus[9]). This may be explained by the fact the player could not breathe into the apparatus, nor was the glottis aperture monitored. It is likely, therefore, that the subject may have relaxed the glottis, and thus reduced the magnitude of the airway resonances, as discussed earlier. This is the case too with Backus's[1] measurements which only give a maximum magnitude of

[a]Current address: LIMSI-CNRS, BP 133, 91403 Orsay, France; electronic mail: claudia.fritz@ens-lyon.org

5 MPa s m^{-3}. That would explain as well why he reported that the values he obtained could not be consistently reproduced, as a musician cannot be consistent with his glottis if he cannot blow. Moreover, all these studies only give the amplitude of the impedance but not the phase. Wilson[5] measured the complex impedance in a situation in which a clarinettist could mime playing while exhaling, in order, to her opinion, to keep the glottis open (in contrast with the images in Mukai's work[7]). These measurements were made with a chirp of $\frac{1}{3}$ s duration, and so have a relatively high noise component. The performers were three professional clarinettists and two advanced amateurs. She was also able to obtain values for the impedance during playing at the frequencies of the harmonics of the note played. These are interesting values but, because they are widely spaced in frequency, the give little information about the tract configuration and few data for numerical simulations. There may have been problems in consistency, because the two methods did not always give similar results.

It has not yet proved possible to make accurate impedance measurements in the vocal tract during playing because of the very high sound levels produced by the reed. (The acoustic current produced in the tract by the reed is comparable with that produced in the clarinet, so peak pressure levels are high.) Consequently, it is still necessary to measure clarinettists miming playing. In our measurements reported here, a direct current shunt was placed in parallel with the impedance head, to allow the players to blow normally, and so to adopt a tract configuration approaching that used for playing.

Our measurements were done on professional clarinettists and advanced students. They were asked to play notes on their own clarinet, set up for normal playing, and then to mime playing on the instrument containing the impedance head. Notes over the range of the instrument were chosen, and players were asked to play and to mime a range of conditions requiring different embouchures to adjust the intonation or register, or to produce other effects.

II. MATERIALS AND METHODS

A. The impedance spectrometer

The setup is based on the impedance spectrometer developed previously,[10] which uses a source of acoustic current produced from an output with high acoustic impedance (see Fig. 1) and which is calibrated using an acoustically infinite waveguide as the reference impedance. This reference is a straight, cylindrical stainless steel pipe, 7.8 mm in diameter and 42 m long, so that echos, in the frequency range of interest, return attenuated by about 80 dB or more. Several compromises were made to incorporate an impedance head

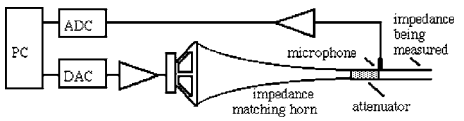

FIG. 1. A schematic of the impedance spectrometer using the capillary method.

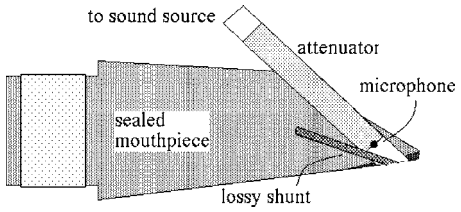

FIG. 2. Cross section of the clarinet mouthpiece containing the impedance head and a lossy shunt.

of this type into the clarinet mouthpiece so that it can measure the impedance that loads the clarinet reed without disturbing the player.

A range of impedance heads and (cylindrical) reference waveguides are available. For this experiment, we chose to use one with diameter 7.8 mm, because it yields a cross-sectional area comparable with that of the effective surface area of the reed protruding past the lower lip inside the mouth. Such an impedance head was mounted inside a modified clarinet mouthpiece as shown in Fig. 2. The angle is chosen so that the head passes through the upper surface of the mouthpiece just beyond the point where the player's teeth rest and meets the lower surface at the position of the reed tip. The end of the attenuator (the current source) and a small microphone (Countryman CAI-B6 miniature B6, diameter 2 mm) positioned $l=9$ mm from the end of the head, and the impedance at the end is calculated using the transfer matrix for a cylindrical waveguide.

This angle produces an elliptical area at the end of the measurement head. For calibration, this was simply sealed on the circular area of the reference waveguide, with the centers aligned. Several other geometries were also tried: one used a bent waveguide between the measurement plane and the reference plane. Another used straight tubes as here, but the extra volume at the ends of the ellipse were filled with modeling compound. To estimate the effect of the discontinuities thus produced, the impedance was measured for a range of waveguides with simple, known geometries (cylindrical pipes of different diameters and lengths), for which the impedance is known from other measurements to agree well with theory. The most successful fits were obtained from the geometry shown: the simple straight impedance head with the open elliptical end. For pipes of same diameter as the head, the comparison between the measurement gives an error of 1% in frequency and up to 20% in amplitude at high frequency.

The mouthpiece was sealed with epoxy so that the measurement head is connected only to the player's tract and not to the clarinet. In any case, the position of the head, which should measure the impedance in the plane of the reed near its tip, prohibits the installation of a reed. Preliminary experiments showed however that musicians could reproduce embouchures that had very similar acoustic impedance spectra. This suggested that they have a high developed sensory or muscle memory and can mime easily a configuration that they use regularly. This is not surprising: it is presumably what they must do normally before playing in order to have the desired pitch and timbre from the beginning of their first note. However, players are not usually aware of the position

of the vocal folds and the glottis and so, if they are not blowing air, they may close them or relax them. For that reason, a shunt with a dc impedance, judged by a clarinettist to be comparable with that of a clarinet under normal playing conditions, was introduced to allow subjects to blow normally. A small pipe (40 mm long and 3 mm diameter) was positioned to provide a shunt or leak from the mouth to the outside air. Its short length ensured that resonances and antiresonances fell beyond the frequency range of interest and measurement, its diameter ensures that its characteristic impedance is between 10 and 100 times larger than the maxima in the vocal tract impedance with which it is in parallel, and it was filled with acoustic wool which makes the impedance largely resistive, reduces the turbulent noise due to flow, and provides a dc resistance comparable to that of a real clarinet.

To prevent water condensation in the measurement apparatus, a low voltage electrical circuit was used to raise the temperature of the impedance head to 40 °C.

B. Procedure

Seventeen players took part in the experiment and their musical level varied between advanced student and professional. They first answered a survey about their musical backgrounds and their opinions about the influence of the vocal tract when playing. Throughout all measurement sessions, a digital audio tape recorder was used to record players comments and played sounds. The microphone was positioned 10 cm from the bell.

For measurements, each player was asked first to play a note *mezzo forte* on his/her own clarinet, and then to mime playing the same note on the modified clarinet. The notes, selected after discussion with clarinettists, were (written) G3, G4, G5, and G6. G3 is close to the lower end of the instrument range and uses almost the full length of the nearly cylindrical part of the bore. It is a good example of a note in the chalumeau register. G4 uses the fundamental mode of a relatively short section of the bore: it is an example of a note in the throat register. G5 uses the speaker or primary register key and the second resonance of a medium length tube: it is an example of the clarion register. G6 uses two open register holes and is an example of a note in the altissimo register.

The subjects then played and mimed some unusual embouchures: some peculiar configurations such as pitch bending (lowering the pitch without changing the fingering), slurring a register change and embouchures of their own suggestion used for different playing conditions. They were also asked to mime embouchures described in terms of vowels (in particular "ee" and "aw"), a description used by some clarinettists. For the slurred register change, the musicians were asked to mime over 5 s what they usually do in less than a second, during the transient between two notes.

The measurements were made over the range 0.1–3 kHz, which includes the playing range of the instrument. In this range, there are usually three vocal tract resonances, at typically 0.3, 1.3, and 2.3 kHz, although the frequency varies among different players and playing conditions. The sampling in the frequency domain was chosen as a compromise between a high signal to noise ratio and precision in frequency. The frequency resolution was set at 5.4 Hz. The measurement time was set at 10 s (except for some unusual embouchures) as it is tiring and hard for a musician to hold a constant embouchure longer.

III. RESULTS

A. The survey

Except from one amateur player, all the participating musicians consider that their vocal tract has a very important influence on the timbre. Regarding the pitch, four of them think that the vocal tract is important whereas the thirteen others regard it as very important.

For more specific details, we shall only quote here the musicians who were the most able to describe their own utilization of the vocal tract. We shall retain their own vocabulary, which often corresponds to mental and musical images. Some of the subjects, with busy schedules as performing musicians, had done no teaching for many years and were therefore not in the habit of describing what they do with the mouth.

Player B, a very experienced music teacher, reported having reflected at depth on what she does in order to explain it to her pupils. She changes the vocal tract shape for:

(1) note bending (i.e., adjusting the pitch using the mouth, rather than keys on the instrument);
(2) changing tonal colors to give character to interpretations. For that effect, she especially uses two configurations. In one, which she names for the vowel in "hee," she reports that she has the back and middle tongue in a high position, increased lip tension, the soft palate is lowered and the throat somewhat closed. This embouchure she uses and recommends for brightening the sound. In another named for the vowel in "haw," she reports a high soft palate, the back of the tongue lowered and the throat more open. This she recommends and uses for darkening the timbre;
(3) for changing articulation: the tongue has to be as close as possible to the tip of the reed to have a light articulation. So the "hee" configuration is usually more appropriate than the "haw" one.

Her tongue touches the lower lip but not usually the lower teeth. The tongue can actually touch the lip/teeth in low or clarion register but not in altissimo register. It is in general between 1 and 2 mm away from the teeth.

Player D, another experienced player and teacher, reported lifting the soft palate in order to obtain more resonance and projection which, she said, induces a richer sound. She reports that her tongue touches neither the lower teeth nor the lower lip, and is in different positions according to the register:

(1) for the low register, the tongue is low and arched, 1 cm away from the lip;
(2) for the high register: the tongue is higher in the mouth, moves a little forward (about 8 mm away from the lip), becomes wider, and flattens.

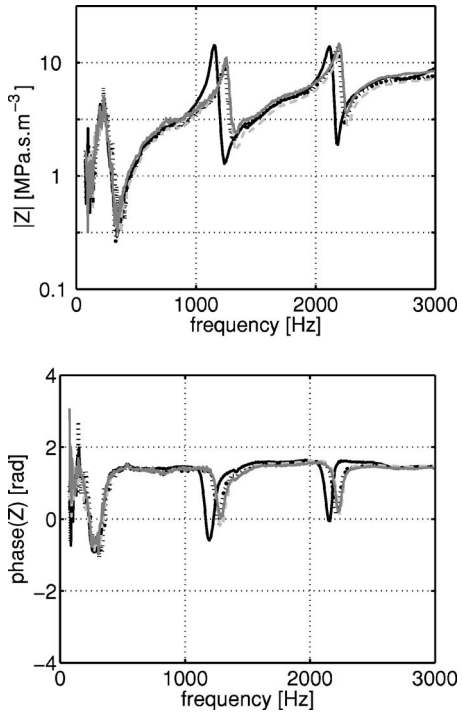

FIG. 3. Typical results of measures testing the reproducibility of the player's tract configuration: the impedance spectra of the vocal tract of the same player (player G) miming playing the note G3 on three occasions over an interval of 40 min.

One advanced student, player H, prefers having the tongue high in the mouth so the sound is more "focused." He uses changes in the vocal tract for register change, large intervals, pitch bend, and multiphonics.

Player C, a very experienced professional player, reported that he enriches the sound in high harmonics by opening the oral cavity. Further, he "opens the throat," but not necessarily the glottis, when he descends a register. Above all, however, he reports using his facial muscles in order to modify the embouchure.

Another very experienced professional player, player A, imagines, when playing, "focussing the sound through the nose." She has the impression that the more her soft palate is arched the more the sound is "focussed." (It should be remarked that the velum must be closed or very nearly closed during clarinet playing, to avoid a dc shunt through the nose that would prohibit playing. However, the muscular tension in the velum could in principle affect the impedance spectrum.)

In at least one case, disagreements among the opinions of the musicians were reported. Player D reported that large mouth cavity was useful for a "rich, focussed" sound, while others reported that they achieved such a sound by lifting the tongue close to the soft palate. One possible explanation is that the musicians in question have different meanings for "rich" and especially for "focussed" in this circumstance.

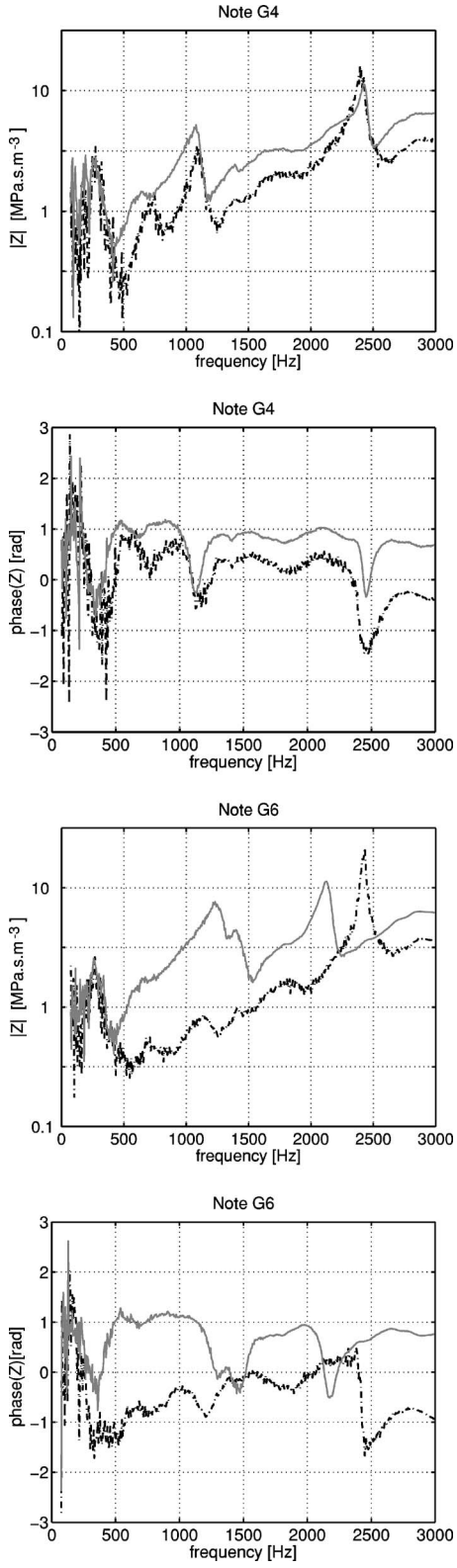

FIG. 4. The impedance spectra of the respiratory airway of two experienced professional musicians (player B in black and player E in grey), for notes G4 (top) and G6 (bottom).

B. Reproducibility of the impedance measurements

Reproducibility was tested on each musician by making about five measurements of the embouchure for the same note (written G3) over the course of a session (typically 40 min). Players were able to repeat their embouchures rather reproducibly: in the typical result shown in Fig. 3, the second resonance is obtained at 1250 Hz with a standard deviation of 3% in frequency and 15% in amplitude.

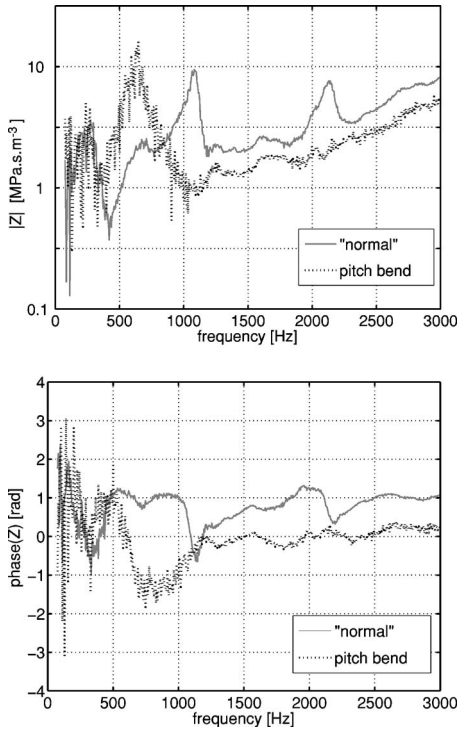

FIG. 5. A comparison of the impedance spectra measured on player C for the configurations for normal playing and for performing a pitch bend.

C. General comments

Most of the subjects in our study reported that, for normal playing, they use an embouchure that varies little over most of the range, except for the highest register. This was confirmed by the measurements: for all players, the form of the impedance spectra is quite stable over the whole register, except sometimes from the altissimo register.

The geometric average amplitude of the impedance is similar for all musicians. The first peak, whose frequency is between 200 and 300 Hz, has an amplitude between 1.8 and 5.6 MPa s m^{-3}. The next resonances are on the other hand different for both amplitude and frequency. For some player embouchure combinations, the amplitudes are in the range 30–100 MPa s m^{-3} which is of the same order as that of the impedance of the clarinet at its resonances.[8]

The difference between the impedance spectra recorded for the "normal" playing configuration and that measured for the tract configuration used for "special effects" is not very large for any of the student players measured. For some of the professional players, however, the effect was very large. However, the spectra measured for the different special effects also varied substantially among these players, just as it did for normal playing.

For several players, the "ee" configuration produced a strong peak between 560 and 1000 Hz, a peak that is associated with the constriction between tongue and palate (see Fig. 7). For many players, however, the configuration they produced when asked to mime the "ee" embouchure had no such peak and indeed resembled somewhat the impedance

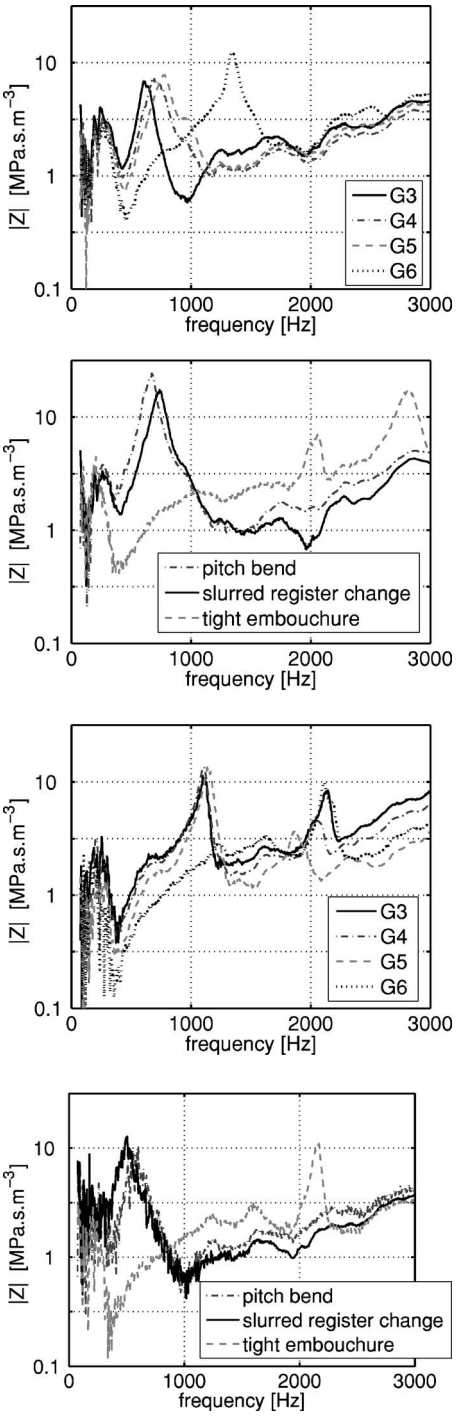

FIG. 6. A comparison between two professional players (player D above and C below) for their normal playing configurations (top) and for those used for some less usual effects (bottom).

measured when they were asked to mime the "aw" embouchure. However, the average level of impedance, even for these players, was in general higher for "ee" than for "aw." Not all players use the "ee" and "aw" terminology for the embouchure and it is possible that the instruction was in this case confusing. It is important to remark that this terminology in terms of vowels refers more to the position of the tongue in the mouth than to the real configuration of the vocal tract in speech as the mouth of the player is of course closed around the mouthpiece.

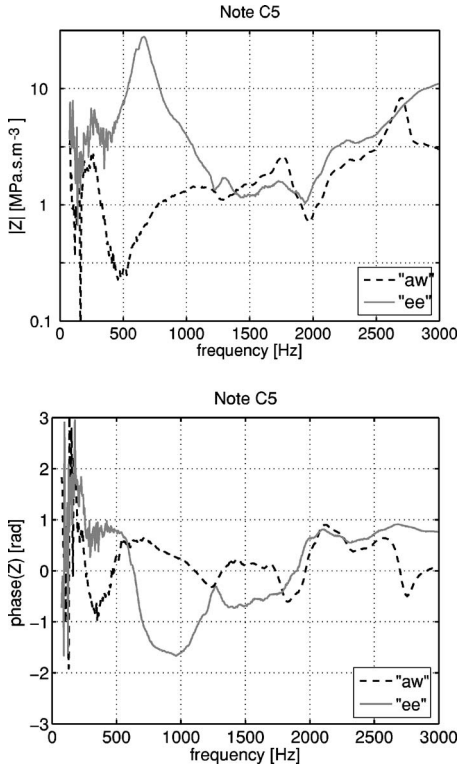

FIG. 7. The impedance spectra of player D's airway for two configurations described as "ee" and "aw," for the note C5.

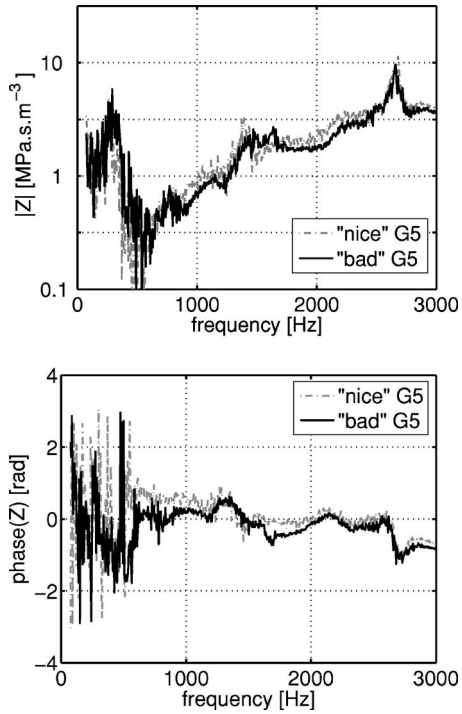

FIG. 8. The impedance spectra of the vocal tract of player A for two configurations associated with a "nice" sound or with a "bad" one, i.e., one which is to be avoided (note G5).

D. Differences among players for "normal" playing mode

We study here the configurations that musicians use in "normal" playing, which means the configuration they adopt usually, when they have no special musical intentions, in the *mezzo forte* nuance. For comparisons, we choose the note G4 which is representative of the low and medium register and the note G6 for the high register. In Fig. 4, the same two musicians mime playing each of the notes.

The configuration for the note G4 is qualitatively similar for both musicians. A few exceptions apart, it is a configuration used by many players in the normal playing mode for almost the whole range of the clarinet, as shown in the figures available in Ref. 11. However, the configuration adopted for the very high register can differ quite considerably among players: some musicians adopt a configuration that enhances the second peak and moves it into the frequency range of the note played whereas some others tend to adopt a configuration that reduces the amplitude of this peak.

E. Variations used by players

Players agree that they use different embouchures for different effects. The embouchure includes the lip and jaw position, and hence the force, the damping, and the position on the reed may vary. The aspect being studied here is the way in which the mouth or vocal tract geometry changes can affect the impedance spectrum. The substantial changes shown in Fig. 5 suggest that the latter effect may not be negligible even if the configuration in normal playing is quite stable over the whole register.

It is interesting to note the remarkable similarity in the impedances for "special effects" between two professional players who played together for several years in a major national orchestra, whereas they do not adopt the same configuration for normal playing (Fig. 6).

One of the professional players expressed her control of pitch and timbre thus: she uses an "ee" for the high register or for brightening the sound and in contrast she adopts an "aw" configuration for darkening the timbre and lowering the pitch. The differences between these two configurations are represented in Fig. 7.

F. Subtlety

In most cases, different tract configurations that were reported to be used to produce different effects on the sound were found to have different impedance spectra. However, for some of the players, the impedances measured when they were miming "good" and "bad" embouchures differed by amounts comparable with the measured reproducibility of a single embouchure. For example, Fig. 8 shows a large similarity between the impedances for embouchures described by a very experienced soloist as those corresponding to a "nice" and a "bad" sound. We presume that in this case the differences had more to do with aspects of the embouchure such as lip tension and position, and less to do with the tract configuration.

G. Summary of the measurements

The players are classified into groups for which the impedances look similar for notes G3 to G5. The results of one player contained unexpected and unexplained high levels of

TABLE I. Summary of the features of impedance spectra measured on 16 players for the vocal tract configurations they used for the different cases listed.

	Normal playing		Special effects
Players	G3, G4, G5	G6	pitch bend
A, B, C, E, and one other	Two resonances: 1000–1400 Hz (3.2×10^6–10^7 Pa s m^{-3}) and 2100–2400 Hz.	The second resonance disappears for players A, C, and D. For player F, the second resonance is lowered by 500 Hz.	Only one resonance: 600 Hz (1.3×10^7 Pa s m^{-3}) for player D, 1400 Hz (4×10^7 Pa s m^{-3}) for F, 2500 Hz for A and 2700 Hz (in the last two cases, it is actually the first resonance which disappears).
Player D	One resonance: 700 Hz, 5.6×10^6 Pa s m^{-3}.	This resonance is shifted to 1400 Hz.	Strong resonance (1.8×10^7 Pa s m^{-3}) at 700 Hz which suggests that she uses a "ee" configuration.
Players H, F and four other players	The impedance grows continuously with the frequency, withy a slope of 30 dB for 2500 Hz. Two small resonances at 1200 and 2000–2300 Hz.	The second resonance is slightly enhanced.	For half of the players, the resonances disappear; for the others (like player E), the first resonance is strongly enhanced.
Player G	G3-G4: Two acute resonances at 1200 and 2100 Hz. G5: one strong resonance at 1400 Hz.	As for G5.	As for G3 and G4.
Two players	Same configuration for all playing modes. One strong resonance at 2200 or 2500 Hz, between 3.2×10^7 and 10^8 Pa s m^{-3}.		

noise, and are omitted. Results are summarized in Table I. The first resonance is not listed. It is present for all players, its amplitude is hardly varied and its frequency only slightly little varied for playing conditions. Its frequency is between 220 and 280 Hz and its amplitude between 1.8×10^6 and 1.8×10^7 Pa s m^{-3}.

IV. THEORETICAL MODEL

A. Model for the vocal tract

This model draws on work in speech science, where scientists are more interested in what happens at the glottis and usually calculate either the transfer function or the impedance at the glottis. However, numerical simulations which were done in speech synthesis to calculate the impedance at the glottis can be used in our study by inverting the calculation and using the appropriate impedance at the glottis. The model used is the one developed by Sondhi[12,13] with yielding walls. The vocal tract is represented by concatenated cylinders and the relation between the variables at the input of cylinder $k+1$ and cylinder k (k=0 at the glottis) is the following:

$$\begin{pmatrix} p_{k+1} \\ u_{k+1} \end{pmatrix} = \begin{pmatrix} A & B \\ C & D \end{pmatrix} \begin{pmatrix} p_k \\ u_k \end{pmatrix}$$

with

$$A = D = \cosh\left(\frac{\sigma l}{c}\right),$$

$$B = \frac{\rho c}{S}\gamma \sinh\left(\frac{\sigma l}{c}\right), \quad C = \frac{S}{\rho c}\gamma \sinh\left(\frac{\sigma l}{c}\right) \tag{1}$$

with

$$\gamma = \sqrt{\frac{r + j\omega}{\beta + j\omega}}, \tag{2}$$

$$\sigma = \gamma(\beta + j\omega), \tag{3}$$

$$\beta = \frac{j\omega\omega_t^2}{(j\omega + r)j\omega + \omega_w^2} + \alpha, \tag{4}$$

$$\alpha = \sqrt{j\omega q}, \tag{5}$$

where r and ω_w are related to the yielding properties of the vocal tract and represent, respectively, the ratio of wall resistance to mass and the mechanical resonance frequency of the wall. Their values are set to $r=408$ rad s^{-1} and $\omega_w/2\pi = 15$ Hz. ω_t is the frequency of a resonance of the tract when sealed at both the glottis and the lips, and which is associated with the finite mechanical compliance of the walls (like the "breathing mode" in a string instrument): $\omega_t/2\pi=200$ Hz. The parameter q is a correction for thermal conductivity and viscosity, which is set to $q = 4$ rad s^{-1}.

The calculation was done was done using a program written by Story,[14] except that it was inverted in order to calculate the impedance at the mouth (and not at the glottis). To complete the calculation we need the glottis geometry (tube 0) as, in contrast with speech, the vocal folds are not

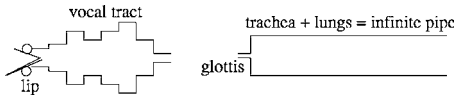

FIG. 9. A schematic of the waveguide used to model the respiratory airway. It is not to scale, and the number of elements has been reduced for clarity. The clarinet mouthpiece is inserted between the lips at left.

entirely closed. We also need the boundary condition at the glottis: $p_0 = Z_{sg} u_0$, where Z_{sg} is the input impedance of the subglottal tract.

B. The glottis

According to the laryngoscopic study by Mukai,[7] the glottis of professional wind musicians is usually a narrow slit, to which our first-order approximation is a rectangle of length $a = 10$ mm, width $b = 1.5$ mm, and thickness $e = 3$ mm.

However, the discontinuity between the cross section of this slit and that of the trachea requires an acoustic end correction. Here the glottis is treated as a tube baffled at both ends, having an effective length of $e_{\text{eff}} = e + 0.85 r_g$ where r_g is the equivalent radius of the glottis ($r_g = \sqrt{ab/\pi} = 2.2$ mm). (In principle, the end correction for a slit is greater than that for a circular aperture of the same area.[15] However, this approximation is appropriate, given the experimental uncertainties.)

Consequently, cylinder 0, which represents the glottis and thus connects the vocal tract to the subglottal tract in the model, has a length $e_{\text{eff}} = 4.7$ mm and area ab.

C. The subglottal tract

For all but very low frequencies, the results depend only very weakly on the subglottal tract, so we use a very simple model. (Fig. 9).

The lungs are very lossy at the frequencies of interest, and so reflections are minimal. For that reason, they are modeled here as a purely resistive load with the same characteristic impedance (i.e., an infinitely long pipe whose radius equals that of the trachea, $r_t = 9$ mm)

$$Z_{\text{sg}} = \frac{\rho c}{\pi r_t 2}. \tag{6}$$

D. Correction at the input of the mouth

In comparison with the cross-sectional area of the mouth, the area of the reed inside the mouth is small, as is that of the impedance head. It resembles thus a small piston vibrating in a baffle that seals a larger waveguide, or a discontinuity in waveguides, which is often modeled by adding an end correction to the smaller element. Physically, the volume of air in the end correction has an inertance comparable to that of air in the strongly diverging part of the radiation field in the larger guide. The end correction for a baffled pipe is used at this end of the vocal tract, too: an element with radius $r = 3.9$ mm and length $l = 0.85 r$.[16]

As we used mainly the MRI data from Story and Titze,[17] we divided the vocal tract, of length 170.4 mm, in finite elements of length 4 mm, giving 44 elements, plus the zeroth element representing the glottis (this one is actually divided in two elements: the first has the same length as the others whereas the second is used to adjust the effective length of the glottis). A complication is due to the insertion of the mouthpiece about 10 mm in the mouth, which puts the first two tract elements effectively in parallel with the rest. The iterative calculation of Sec. IV A is conducted on 33 tract elements, beginning at the glottis, which is loaded with the subglottal resistance. This gives the impedance Z_1. The two elements closest to the mouth and sealed at the mouth end give an impedance Z_2. The total uncorrected impedance is therefore

$$Z_{nc} = \frac{Z_1 Z_2}{Z_1 + Z_2}, \tag{7}$$

which, when the end correction mentioned earlier is added, gives

$$Z_{VT} = Z_{nc} + j Z_0 \frac{\omega}{c} l \tag{8}$$

with $Z_0 = \rho c / (\pi r^2)$.

The result of end effects and the parallel elements at the mouth are noticeable primarily at high frequency (>3000 Hz). However, at such frequencies the unidimensional model fails anyway because of its neglect of transverse modes. For example, El-Masri *et al.*[18] showed how the plane wave approximation gave poor predictions for the behavior of the tract at frequencies above 4500 Hz. Further refinement is therefore inappropriate in this simple model. What is of practical importance in these corrections is their substantial reduction of the amplitude of the resonances at high frequency, which avoids artifacts in simulations that have strong high frequency resonances that do not correspond to those of the tract made of flesh. Further, the cutoff frequency of an array of open tone holes in the clarinet is typically around 2000 Hz, so our interest need not exceed the range 0–3000 Hz.

E. Results for two vowels: Adjustment

The aim of this simulation is to "invert" the model, i.e., to obtain the area function from the impedance spectrum. Solutions to inversion are not unique, but other constraints on vocal tract shape eliminate many. An inversion was obtained with assistance from Story, which mapped the calculated impedance of the complete model, including corrections to the area function. The program begins with the first three resonance frequencies and the mapping was generated using area functions such as given by Story *et al.*[17] (using 4-mm elements). In general it was found that the impedance spectra calculated from the mapped area functions differed noticeably from the original impedance measurements. A further program was therefore written to allow iteration by local adjustment of the area function to improve the fit. By such iterations, anatomically possible area functions giving the experimental impedance spectra were obtained.

Two important results are shown. Clarinettists often refer to two tract configurations as "ee" and "aw," being those for the vowel sounds (those of "heed" and "hoard") sensibly

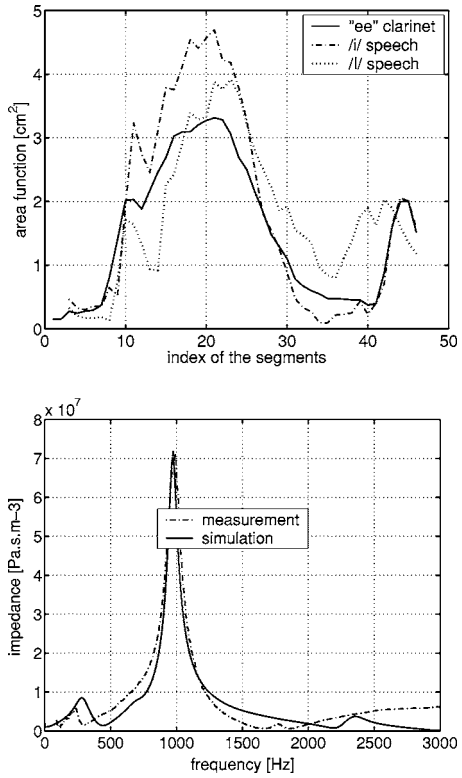

FIG. 10. Top: area function for the vowels /i/ and /ɪ/ (data from Story and Titze with glottis added). Also shown are the calculated tract configuration named "ee" by clarinettists, as determined from inversion. The abscissa is the element number: the first two are the glottis (see Sec. IV D), the next 44, of length 4 mm, comprise a tract 174 mm long. Bottom: the impedance spectrum for the "ee" tract configuration measured on one of the authors (player G) an amateur clarinettist.

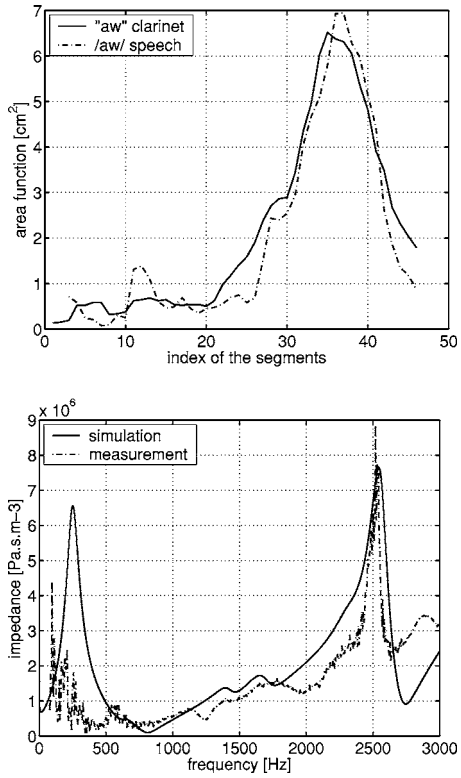

FIG. 11. Top: area function for the vowel /ɔ/ (data from Story and Titze with glottis added). Also shown are the calculated tract configuration named "aw" by clarinettists, as determined from inversion. The abscissa is the element number: the first two are the glottis (see Sec. IV D), the next 44, of length 4 mm comprise a tract 174 mm long. Bottom: the impedance spectrum for the "aw" tract configuration measured on player B.

resembled by the playing position. The resemblance is only approximate, of course: for the vowels, the mouth is open to different extents, whereas in the playing configuration the mouth is sealed by the mouthpiece of nearly constant area.

For "ee," Fig. 10 shows the plausibility of the area function, which is rather similar to that of the vowels /i/ ("heed") and /ɪ/ ("hid"). This configuration has a cross section at the palatal constriction lying between the values reported for the two vowels, which in English differ little except in their duration. At the mouth end, the area function is set equal to the cross section of the clarinet mouthpiece, 15 mm from the end.

It proved impossible, however, to fit the first peak, for which the inversion gave frequencies that were systematically too high (e.g., between 230 and 250 Hz instead of 200 Hz for "aw" and between 250 and 280 Hz instead of 230 Hz for "ee").

A resistance of 1.5 MPa s m^{-3} was added at the glottis. Although this was an empirical adjustment to fit the measured height of the peak values of impedance, it might be justified by considering that energy would be lost from propagating waves due to turbulence produced by flow through this narrow slit.

For the case of "aw" (Fig. 11) the area function found by inversion closely resembles that of the corresponding vowel. However, the magnitude of the first peak is too great, even allowing for the fact that the peak for this musician is systematically lower than that of other musicians. Thus for the same vowel, the first peak of player G has an amplitude between 5 and 7 MPa s m^{-3}, and is thus better predicted by the numerical simulation.

Overall, the inversion results have only moderate agreement, and the area functions must be adjusted "by hand" in order to give impedance spectra close to those measured. Further, some effects have been neglected, such as the fact that some players place the tip of the tongue just behind the lower lip, which might plausibly add a parallel compliance associated with the air volume under the tongue. Neverthe-

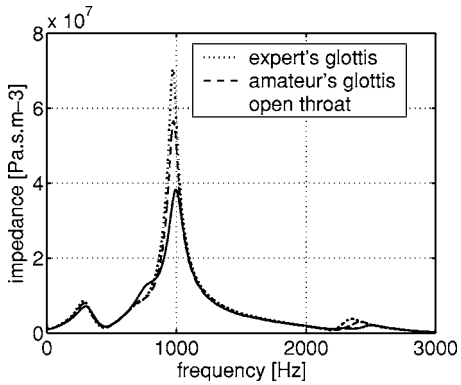

FIG. 12. Calculated impedance spectra for a tract in the configuration "ee" with three different values of the glottal opening. Two are taken from the data of Mukai for an expert and an amateur player, the third is for an open glottis.

less, this does not prevent the obtaining of approximate area functions and allows in particular the determination of a palatal constriction.

F. Influence of the glottis opening

Figure 12 shows the impedance for an "ee" configuration (as described in Fig. 10) calculated in three cases:

(1) the glottis is an expert's glottis, almost closed, i.e., a slit of area 15 mm^2;
(2) the glottis is an amateur's glottis, partially closed, of section 90 mm^2;
(3) the glottis is the same as the previous case and the cross-sectiontional area of the last two cylinders of the vocal tract (just above the glottis) was increased for more realism: it is indeed very likely that the amateur not only opened the glottis wider but also opened further the upper part of the vocal tract..

This figure shows that the opening of the glottis can have a large effect (a factor of 2 or 6 dB) on the amplitude of the peaks. The magnitude of peaks in the impedance data allow us thus to assume that in many cases, the glottis is almost closed.

V. CONCLUSION

The newly configured spectrometer permitted the measurement of the impedance spectra of the vocal tracts of experienced clarinet players in a situation that allowed them to mime the conditions of playing. In contrast with most previous measurements, the players could blow into the mouthpiece and, probably as a consequence of this, the impedance spectra showed the strong resonances that are characteristic of a nearly closed glottis, which is the case both for speech and for the playing of experience wind instrument players.[7] As the glottal opening could not be monitored, this deduction is only made on both the good reproducibility which ensures us that the glottis is well controlled by the musician during the measurement and the high level of the impedance in comparison to previous measurements.

The peak values of impedance measured were in some cases comparable with the peak values of that of the clarinet (Wolfe *et al.*,[8] Backus[9]). Moreover, the vocal tract impedance is much larger than the clarinet impedance around the even harmonics. The phase of these harmonics, when we consider the whole impedance (i.e., the sum of the clarinet impedance and the vocal tract one) is thus shifted, which may affect the playing frequency. This suggests that the acoustic effects of the vocal tract should not be neglected and that they may have a musically significant influence on the sound produced.

The combination of these measurements with a survey about the utilization by clarinet players of their vocal tract allow us to relate observed acoustical responses to the reported embouchures of the players. All players agreed that the vocal tract had a large influence on the sound, but their opinions regarding the best configuration to adopt differ considerably. This is a potentially important conclusion for musicians: many highly respected professional clarinettists achieve fine sound quality using rather different tract configurations. Nevertheless, two general trends can be observed. The players try to keep their configuration stable for most part of the register, which is in contrast to Johnson's suggestion[4] that players may tune one of the vocal tract resonances to the note played. On the other hand, the configuration can be changed substantially for special effects such as difficult slurs across registers or pitch bend: players lower the tongue and the overall magnitude of the impedance when they aim to bend the pitch down, or to slur downwards over registers, and vice versa. To examine this phenomenon in more detail, we hope that, in the future, it may be possible to make such measurements in real time in order to determine how the musician changes his configuration during a transition.

ACKNOWLEDGMENTS

We are grateful to John Smith and David Bowman for ACUZ program and to the Australian Research Council for funding. We would like to thank also Brad Story for his help with the numerical model.

[1]J. Backus, "The effect of the player's vocal tract on woodwind instrument tone," J. Acoust. Soc. Am. **78**, 17–20 (1985).
[2]A. Benade, "Air column, reed and player's windway interaction in musical instruments," in *Vocal Fold Physiology*, edited by I. Titze and R. Scherer (The Denver Center for the Performing Arts, Denver, 1983).
[3]P. Hoekje, "Intercomponent energy exchange and upstream/downstream symmetry in nonlinear self-sustained oscillations of reed instruments," Ph.D. thesis, CaseWestern Reserve University, Cleveland, OH, 1986.
[4]R. Johnston, P. Clinch, and G. Troup, "The role of the vocal tract resonance in clarinet playing," Acoust. Aust. **14**, 67–69 (1986).
[5]T. Wilson, "The measured upstream impedance for clarinet performance and its role in sound production," Ph.D. thesis, University of Washington, 1996.
[6]J. Backus, "Vibration of the reed and the air column in the clarinet," J. Acoust. Soc. Am. **33**, 806–809 (1961).
[7]M. S. Mukai, "Laryngeal movement while playing wind instruments," in Proceedings of the International Symposium on Musical Acoustics, Tokyo, Japan, 1992, pp. 239–242.
[8]J. Wolfe, Clarinet Acoustics, http://www.phys.unsw.edu.au/music/clarinet.
[9]J. Backus, "Input impedance curves for the reed woodwind instruments," J. Acoust. Soc. Am. **56**, 1266–1279 (1974).
[10]J. Smith, C. Fritz, and J. Wolfe, "A new technique for the rapid measurement of the acoustic impedance of wind instruments," in Proceedings of the Seventh International Congress on Sound and Vibration, edited by G. Guidati, H. Hunt, H. Heller, and A. Heiss, Garmisch-Partenkirchen, Germany, 4–7 July 2000, Vol. III, pp. 1833–1840.
[11]C. Fritz and J. Wolfe, Impedance measurements of clarinet player's airway, http://www.phys.unsw.edu.au/~jw/AirwayImp.html.
[12]M. Sondhi, "Model for wave propagation in a lossy vocal tract," J. Acoust. Soc. Am. **51**, 1070–1075 (1974).
[13]M. Sondhi and J. Schroeter, "A hybrid time-frequency domain articulatory speech synthesizer," IEEE Trans. Acoust., Speech, Signal Process. **35**, 955–967 (1987).
[14]B. Story, A. Laukkanen, and I. Titze, "Acoustic impedance of an artificially lengthened and constricted vocal tract," J. Voice **14**, 455–469 (2000).
[15]P. Morse and K. Ingard, *Theoretical Acoustics* (Princeton University Press, Princeton, 2000).
[16]N. Fletcher and T. Rossing, *The Physics of Musical Instruments* (Springer, New York, 1995).
[17]B. Story, I. Titze, and E. Hoffman, "Vocal tract area functions from magnetic resonance imaging," J. Acoust. Soc. Am. **100**, 537–554 (1996).
[18]S. El-Masri, X. Pelorson, P. Saguet, and P. Badin, "Development of the transmission line matrix method in acoustics applications to higher modes in the vocal tract and other complex ducts," Int. J. Numer. Model. **11**, 133–151 (1998).

Conservative numerical methods for nonlinear strings

Stefan Bilbao[a)]
Sonic Arts Research Center, Queen's University Belfast, Belfast BT7 1NN, United Kingdom

(Received 8 February 2005; revised 2 July 2005; accepted 2 August 2005)

In this article, a class of numerical schemes for the simulation of nonlinear coupled longitudinal/transverse string vibration is presented. Though there are various ways of arriving at such schemes, special attention is paid here to energy conservation in nonlinear model systems and its transfer to an analogous discrete quantity in a difference scheme. Such exact numerical energy conservation can lead to simple global stability conditions, which can be otherwise difficult to ascertain for nonlinear difference schemes—in particular, such conditions may be arrived at without any reliance on frequency domain concepts (i.e., Fourier or Laplace transforms), which are of only moderate utility in the analysis of nonlinear systems. Implementation details are discussed and numerical results are presented. © *2005 Acoustical Society of America.* [DOI: 10.1121/1.2046787]

PACS number(s): 43.75.−z, 43.40.Ga, 43.40.Cw [JBS] Pages: 3316–3327

I. INTRODUCTION

Work on nonlinear string vibration has been ongoing for more than a century, and the field has, in some respects, reached maturity. There are various partial differential equation (PDE) models which describe the large amplitude vibration of a nonlinear string, and in particular the coupling between longitudinal and transverse motion, to varying degrees of complexity. Though a complete summary is impossible in this short article, it is worth mentioning that there are two discernible families of such models: (1) general forms for which the nonlinearity is pointwise dependent on the string state,[1,2] and (2) simplified forms (referred to here as Kirchhoff-Carrier type models) for which the longitudinal motion is "averaged out" to yield a nonlinear system in the transverse motion alone, with the nonlinearity intervening in a distributed, but not spatially varying way.[3–6] It is to be noted that the formulation and study of such models is of fundamental importance, as the nonlinear string is perhaps the simplest distributed nonlinear system occurring in nature. The reader is referred to the text by Morse and Ingard[1] and the work of Vallette[7] for an overview. Nonlinear string models are intimately related to (and can often be viewed as special cases of) various models of beam vibration, and in particular, the so-called "geometrically-exact" formulation of Simo and Vu-Quoc.[8,9]

Though there do exist various established PDE models for nonlinear string dynamics, when it comes to numerical solution techniques, the situation is far less clear, and this aspect has been given relatively little attention in the literature. This is surprising, given the utility of numerical results as a means of comparing theory and measured data. Though there have been a few cursory descriptions of numerical schemes for nonlinear strings,[10–12] these are usually simple extensions of schemes for the linear wave equation; in particular, the important question of numerical stability is not addressed. (Two exceptions are the work of Furihata,[13] who employs a technique loosely related to that to be presented here to a simplified transverse-only nonlinear string model, and Rubin's work on numerical methods based on the theory of a Cosserat point;[14] in neither case is any numerical stability analysis carried out.)

In previous work, this author has described finite difference schemes for a Kirchhoff-Carrier string model in a single transverse polarization.[15–17] These schemes mirror not only the dynamics of the continuous string model, but also possess a conserved quantity analogous to an energy—this conservation property may then be used to find useful global stability conditions (i.e., stability which is independent of initial conditions), through analysis often referred to as the *energy method*,[18–21] which relies on concepts in functional analysis.[22] Stability verification for nonlinear difference schemes is otherwise difficult, and, in particular, cannot be arrived at definitively through Fourier or spectral analysis techniques (often referred to as von Neumann analysis in this context[23,24]). (The text by Gustaffson, Kreiss, and Oliger[18] discusses the ranges of applicability of spectral techniques in great detail.) Energy-based analysis and construction of numerical schemes has seen quite a bit of increased activity in recent years, and has been applied to various types of solid systems (see, e.g., Ref. 25).

Kirchhoff-Carrier type models, however, are but simplified representations of nonlinear string dynamics, and the numerical results in previous work by this author[15] exploit the spatially averaged character of the nonlinearity (the same can be said of extended digital waveguide type approaches to solutions of the so-called "tension-modulated" string[26–28] as well as quasimodal descriptions of nonlinear strings,[29,30] which lead to highly accurate energy conserving methods[17] of the spectral type[31,32]). Furthermore, as mentioned earlier, longitudinal motion is not explicitly modeled. In more realistic nonlinear string models, however, the pointwise nonlinear coupling between the transverse and longitudinal motion persists; such models are the subject of this article, and are related to so-called "geometrically exact" beam vibration formulations mentioned earlier. The case of planar motion is discussed here—an extension to full three-dimensional motion (see, e.g., Ref. 33) is immediate.

[a)]Electronic mail: s.bilbao@qub.ac.ak

The techniques earlier applied to Kirchhoff-Carrier models are here extended to the much more general case of pointwise nonlinear string equations of various types, which are given along with an energetic analysis in Sec. II. Several commonly encountered approximate forms of the nonlinear string equations are presented (see Table I), only one of which ($\mathbf{S}_4^*$) is suitable for energy-based stability analysis. In Sec. III, some basic facts regarding grid functions and finite difference operators are presented, followed by finite difference schemes of the interleaved type for the string system $\mathbf{S}_4^*$ described in Sec. II. A discussion of conservation properties ensures, and a particular scheme for which numerical stability may be guaranteed is presented (scheme $\mathbf{s}_4^{*,(c)}$, given in Table II). The section is concluded with a cursory look at boundary conditions and implementation issues. Numerical results follow in Sec. IV.

As a note, the author wishes to add that a latent goal of the present study is to develop a general methodology for the robust analysis and synthesis of sound for stringed musical instruments; such schemes are the only rigorous means of generating synthetic sound for those musical instruments whose timbre is inextricably linked to nonlinear effects (so-called "phantom partials" in piano tones[10,34] and pitch glides in plucked instruments such as the Finnish kantele[26,27] being two notable examples). Though this article is intended for a more general readership, the numerical examples are chosen so as to hint at the possibilities for musical sound synthesis.

II. MODEL EQUATIONS

A general model of nonlinear string dynamics, described by Morse and Ingard[1] and which can be related to the geometrically exact theory of beams,[35] is given by the following set of equations:

$$\rho\ddot{\xi} = EA\xi'' - (EA - T_0)\left(\frac{1+\xi'}{\sqrt{(1+\xi')^2+(\eta')^2}}\right)', \tag{1a}$$

$$\rho\ddot{\eta} = EA\eta'' - (EA - T_0)\left(\frac{\eta'}{\sqrt{(1+\xi')^2+(\eta')^2}}\right)'. \tag{1b}$$

Here, $\xi(x,t)$ and $\eta(x,t)$ describe, respectively, the longitudinal and transverse deviation of a point on the string as a function of time $t \geq 0$ and distance along the string $x \in [0,L]$. Such a point, located at Cartesian coordinates $(x,0)$ when the string is at rest, will have dynamic coordinates $(x+\xi, \eta)$. E, A, ρ, and T_0 are Young's modulus, cross-sectional area, linear mass density, and nominal tension for the string, all assumed constant here. Dots and primes indicate partial differentiation with respect to time and space, respectively. System (1) may be generalized further in various ways, including through the introduction of linear terms modeling loss and dispersion, as well as excitations, and to include motion in both transverse polarizations; all of the results on finite difference schemes which follow are affected only in a minor way by such generalizations. It may also be generalized to include more subtle higher order effects, as per the work of Narasimha;[2] such improved models may fall outside the range of the techniques presented here, and their consideration is left to a future work.

Two types of boundary conditions are be considered here. For analysis purposes, most useful are so-called periodic boundary conditions[18] of the form

$$\xi(0,t) = \xi(L,t), \quad \eta(0,t) = \eta(L,t) \tag{2}$$

As a more realistic case, conditions of the fixed type, i.e.,

$$\xi(0,t) = \xi(L,t) = 0, \quad \eta(0,t) = \eta(L,t) = 0 \tag{3}$$

are briefly examined as well.

System (1) requires the specification of four initial conditions, namely $\xi(x,0)$, $\dot{\xi}(x,0)$, $\eta(x,0)$, and $\dot{\eta}(x,0)$.

A. A transmission-line form

It is useful to rewrite system (1) as a system of four first-order equations. Defining the variables

$$p_\xi = \dot{\xi}, \quad q_\xi = \xi', \quad p_\eta = \dot{\eta}, \quad q_\eta = \eta' \tag{4}$$

it then follows that

$$\begin{aligned} \rho\dot{p}_\xi &= EAq_\xi' - (EA - T_0)\left(\frac{\partial\Psi}{\partial q_\xi}\right)', \\ \rho\dot{p}_\eta &= EAq_\eta' - (EA - T_0)\left(\frac{\partial\Psi}{\partial q_\eta}\right)', \end{aligned} \quad (\mathbf{S})$$

$$\dot{q}_\xi = p_\xi', \quad \dot{q}_\eta = p_\eta' \quad \text{(Auxiliary System)}, \tag{5}$$

where the quantity $\Psi(q_\xi, q_\eta)$ (representing a contribution to the potential energy density of the string due to the nonlinearity) is defined by

$$\Psi = \sqrt{(1+q_\xi)^2 + q_\eta^2} + a + a_\xi q_\xi + a_\eta q_\eta \tag{6}$$

for arbitrary constants a, a_ξ, and a_η [note that these constants have no effect on the solutions of system (1)]. System **S** (signifying "string"), accompanied by the *auxiliary system* (5), can be viewed as a pair of nonlinearly coupled transmission lines, one in the variables p_ξ, q_ξ, and the other in the variables p_η, q_η. The coupling occurs through the terms containing $\Psi(q_\xi, q_\eta)$.

B. Series approximations and simplifications

Slightly more tractable forms, as presented in Table I, may be obtained through the use of Taylor series approximations about $q_\xi = q_\eta = 0$ (employing the choices $a = a_\xi = -1$ and $a_\eta = 0$) to the function $\Psi(q_\xi, q_\eta)$, given in the following to fourth order:

$$\Psi = \tfrac{1}{2}q_\eta^2 - \tfrac{1}{2}q_\xi q_\eta^2 + \tfrac{1}{2}q_\xi^2 q_\eta^2 - \tfrac{1}{8}q_\eta^4 + \cdots. \tag{7}$$

As discussed in the following, the energetic behavior of the resulting system depends critically on the type of approximation made. The standard series approximation, found, e.g., in Morse,[1] is given by truncating this series approximation to fourth order, yielding the system $\mathbf{S}_4$. Truncation of Ψ to third order is also sometimes employed,[10,11] giving the form $\mathbf{S}_3$, and truncation to second order uncouples the longitudinal and transverse motion completely (see form $\mathbf{S}_2$).

The approximation Ψ_4^*, employed by Anand,[5] and given by

TABLE I. Approximations to system **S**, as well as the associated expressions for kinetic and potential energy.

	Defining equations	(aux)	Kinetic energy	Potential energy
$\mathbf{S}_4$	$\rho\dot{p}_\xi = EAq'_\xi + \frac{EA-T_0}{2}(q_\eta^2[1-2q_\xi])'$ $\rho\dot{p}_\eta = T_0 q'_\eta + \frac{EA-T_0}{2}(q_\eta^3 + 2q_\eta q_\xi[1-q_\xi])'$	$\dot{q}_\xi = p'_\xi$ $\dot{q}_\eta = p'_\eta$	$\mathcal{T}_\mathbf{S} = \frac{\rho}{2}(\|p_\xi\|^2 + \|p_\eta\|^2)$	$\mathcal{V}_{\mathbf{S}_4} = \frac{T_0}{2}(\|q_\xi\|^2 + \|q_\eta\|^2) + \frac{EA-T_0}{8}(\|q_\eta^2 + 2q_\xi\|^2 - \|q_\eta q_\xi\|^2)$
$\mathbf{S}_4^*$	$\rho\dot{p}_\xi = EAq'_\xi + \frac{EA-T_0}{2}(q_\eta^2)'$ $\rho\dot{p}_\eta = T_0 q'_\eta + \frac{EA-T_0}{2}(q_\eta^3 + 2q_\eta q_\xi)'$			$\mathcal{V}_{\mathbf{S}_4^*} = \frac{T_0}{2}(\|q_\xi\|^2 + \|q_\eta\|^2) + \frac{EA-T_0}{8}\|q_\eta^2 + 2q_\xi\|^2$
$\mathbf{S}_3$	$\rho\dot{p}_\xi = EAq'_\xi + \frac{EA-T_0}{2}(q_\eta^2)'$ $\rho\dot{p}_\eta = T_0 q'_\eta + \frac{EA-T_0}{2}(2q_\eta q_\xi)'$			$\mathcal{V}_{\mathbf{S}_3} = \frac{EA}{2}\|q_\xi\|^2 + \frac{T_0}{2}\|q_\eta\|^2 + \frac{EA-T_0}{2}\langle q_\xi, q_\eta^2\rangle$
$\mathbf{S}_2$	$\rho\dot{p}_\xi = EAq'_\xi$ $\rho\dot{p}_\eta = T_0 q'_\eta$			$\mathcal{V}_{\mathbf{S}_2} = \frac{EA}{2}\|q_\xi\|^2 + \frac{T_0}{2}\|q_\eta\|^2$
$\mathbf{S}_{T,4}$	$\rho\dot{p}_\eta = T_0 q'_\eta + \frac{EA-T_0}{2}(q_\eta^3)'$	$\dot{q}_\eta = p'_\eta$	$\mathcal{T}_{\mathbf{S}_T} = \frac{\rho}{2}\|p_\eta\|^2$	$\mathcal{V}_{\mathbf{S}_{T,4}} = \frac{EA}{2}\|q_\eta\|^2 + \frac{EA-T_0}{8}\|q_\eta^2\|^2$

$$\Psi_4^*(q_\xi, q_\eta) = \tfrac{1}{2}q_\eta^2 - \tfrac{1}{2}q_\xi q_\eta^2 - \tfrac{1}{8}q_\eta^4 \tag{8}$$

is correct to third order, but lacks one of the fourth-order terms of Ψ, and leads to the system $\mathbf{S}_4^*$. One might well ask in what sense the use of system $\mathbf{S}_4^*$ is justified. One answer follows from the energetic properties to be discussed in the next section; another relates to the relative orders of magnitude of q_ξ and q_η in system **S**. As noted by Anand[5] and Morse,[1] q_ξ is of the same order of magnitude as q_η^2, and it is perhaps more natural, then, to use a homogeneous approximation, truncated to powers of, say, q_η. Given that the term $q_\xi^2 q_\eta^2$ is clearly of sixth order in q_η, it is then justified to neglect it with respect to the term in q_η^4.

As a useful nonlinear test problem for finite difference schemes, it is also worthwhile to consider the transverse-only system (i.e., assuming $p_\xi = q_\xi = 0$) under a fourth-order nonlinearity, given as $\mathbf{S}_{T,4}$ in Table I.

C. Energetic analysis

The procedure by which one may extract a conserved energy-like quantity from a system is similar to that which was applied to a Kirchhoff-Carrier system by this author in Ref. 15. A condensed treatment is provided here.

As a notational preliminary, it is worth recalling here the definition of the spatial L^2 inner product of two real-valued functions $f(x,t)$ and $g(x,t)$ over the interval $x \in [0, L]$, as well as the associated norm:

$$\langle f, g\rangle = \int_0^L fg\,dx, \quad \|f(\cdot,t)\| = \langle f, f\rangle^{1/2}. \tag{9}$$

Consider first system **S**. Multiplying the first and second equations by p_ξ and p_η, respectively, and integrating over the range $x \in [0, L]$ gives

$$\int_0^L \rho p_\xi \dot{p}_\xi dx = \int_0^L p_\xi \left(EAq_\xi - (EA - T_0)\frac{\partial \Psi}{\partial q_\xi}\right)' dx,$$

$$\int_0^L \rho p_\eta \dot{p}_\eta dx = \int_0^L p_\eta \left(EAq_\eta - (EA - T_0)\frac{\partial \Psi}{\partial q_\eta}\right)' dx.$$

Using integration by parts on the right-hand side of these equations, and either of the boundary conditions of Eq. (2) or Eq. (3), as well as the auxiliary equations (5) gives

$$\int_0^L \rho p_\xi \dot{p}_\xi dx = -\int_0^L \dot{q}_\xi \left(EAq_\xi - (EA - T_0)\frac{\partial \Psi}{\partial q_\xi}\right) dx,$$

$$\int_0^L \rho p_\eta \dot{p}_\eta dx = -\int_0^L \dot{q}_\eta \left(EAq_\eta - (EA - T_0)\frac{\partial \Psi}{\partial q_\eta}\right) dx.$$

Finally, applying the definition of the norm as per Eq. (9) and summing the resulting equations gives

$$\frac{d}{dt}\mathcal{H}_\mathbf{S} = 0 \Rightarrow \mathcal{H}_\mathbf{S} = \mathcal{T}_\mathbf{S} + \mathcal{V}_\mathbf{S} = \text{constant} \tag{10}$$

with

$$\mathcal{T}_\mathbf{S} = \frac{\rho}{2}(\|p_\xi\|^2 + \|p_\eta\|^2),$$

$$\mathcal{V}_\mathbf{S} = \frac{EA}{2}(\|q_\xi\|^2 + \|q_\eta\|^2) - (EA - T_0)\int_0^L \Psi dx.$$

Thus $\mathcal{H}_\mathbf{S}$ is a scalar conserved quantity of system **S**; in particular, it behaves as an energy ($\mathcal{H}$ signifies "Hamiltonian"), with a kinetic part $\mathcal{T}_\mathbf{S}$ dependent on p_ξ and p_η and a potential part $\mathcal{V}_\mathbf{S}$ dependent on q_ξ and q_η.

The systems $\mathbf{S}_4$, $\mathbf{S}_4^*$, $\mathbf{S}_3$, and $\mathbf{S}_2$ all result from series approximations to Ψ, and as such, also possess conserved quantities. The kinetic energy terms remain the same in all cases, and the potential energy is given by the above-presented expression for $\mathcal{V}_\mathbf{S}$, with Ψ replaced by the series truncated form. The resulting expressions are denoted by $\mathcal{V}_{\mathbf{S}_4}$, $\mathcal{V}_{\mathbf{S}_4^*}$, $\mathcal{V}_{\mathbf{S}_3}$, and $\mathcal{V}_{\mathbf{S}_2}$, respectively, and appear at the right in

TABLE II. Finite difference schemes of the interleaved type for the systems $\mathbf{S}_2$, $\mathbf{S}_4^*$, and $\mathbf{S}_{T,4}$ as given in Table I.

	Defining equations	(Auxiliary)
$\mathbf{s}_2$	$\rho\delta_{t+}p_{\xi,i}^{n-1}=EA\,\delta_{x-}q_{\xi,i+1/2}^{n-1/2}$ $\rho\delta_{t+}p_{\eta,i}^{n-1}=T_0\delta_{x-}q_{\eta,i+1/2}^{n-1/2}$	$\delta_{t+}q_{\xi,i+1/2}^{n-1/2}=\delta_{x+}p_{\xi,i}^{n}$ $\delta_{t+}q_{\eta,i+1/2}^{n-1/2}=\delta_{x+}p_{\eta,i}^{n}$
$\mathbf{s}_4^{*,(a)}$	$\rho\delta_{t+}p_{\xi,i}^{n-1}=EA\,\delta_{x-}q_{\xi,i+1/2}^{n-1/2}+\frac{EA-T_0}{2}\delta_{x-}(q_{\eta,i+1/2}^{n-1/2})^2$ $\rho\delta_{t+}p_{\eta,i}^{n-1}=T_0\delta_{x-}q_{\eta,i+1/2}^{n-1/2}+\frac{EA-T_0}{2}\delta_{x-}([q_{\eta,i+1/2}^{n-1/2}]^3+2q_{\xi,i+1/2}^{n-1/2}q_{\eta,i+1/2}^{n-1/2})$	
$\mathbf{s}_4^{*,(b)}$	$\rho\delta_{t+}p_{\xi,i}^{n-1}=EA\,\delta_{x-}q_{\xi,i+1/2}^{n-1/2}+\frac{EA-T_0}{2}\delta_{x-}(q_{\eta,i+1/2}^{n-1/2})^2$ $\rho\delta_{t+}p_{\eta,i}^{n-1}=T_0\delta_{x-}q_{\eta,i+1/2}^{n-1/2}+\frac{EA-T_0}{2}\delta_{x-}([[q_{\eta,i+1/2}^{n-1/2}]^2+2q_{\xi,i+1/2}^{n-1/2}]\mu_{t0}q_{\eta,i+1/2}^{n-1/2})$	
$\mathbf{s}_4^{*,(c)}$	$\rho\delta_{t+}p_{\xi,i}^{n-1}=EA\,\delta_{x-}q_{\xi,i+1/2}^{n-1/2}+\frac{EA-T_0}{2}\delta_{x-}(q_{\eta,i+1/2}^{n-1/2}\mu_{t0}q_{\eta,i+1/2}^{n-1/2})$ $\rho\delta_{t+}p_{\eta,i}^{n-1}=T_0\delta_{x-}q_{\eta,i+1/2}^{n-1/2}+\frac{EA-T_0}{2}\delta_{x-}([q_{\eta,i+1/2}^{n-1/2}]^2\mu_{t0}q_{\eta,i+1/2}^{n-1/2}+q_{\eta,i+1/2}^{n-1/2}\mu_{t+}\mu_{t-}q_{\xi,i+1/2}^{n-1/2})$	
$\mathbf{s}_{T,4}^{(a)}$	$\rho\delta_{t+}p_{\eta,i}^{n-1}=T_0\delta_{x-}q_{\eta,i+1/2}^{n-1/2}+\frac{EA-T_0}{2}\delta_{x-}(q_{\eta,i+1/2}^{n-1/2})^3$	$\delta_{t+}q_{\eta,i+1/2}^{n-1/2}=\delta_{x+}p_{\eta,i}^{n}$
$\mathbf{s}_{T,4}^{(b)}$	$\rho\delta_{t+}p_{\eta,i}^{n-1}=T_0\delta_{x-}q_{\eta,i+1/2}^{n-1/2}+\frac{EA-T_0}{2}\delta_{x-}([q_{\eta,i+1/2}^{n-1/2}]^2\mu_{t0}q_{\eta,i+1/2}^{n-1/2})$	

Table I. For the simplified nonlinear transverse-only system $\mathbf{S}_{T,4}$, the kinetic and potential energies are denoted by $\mathcal{T}_{\mathbf{S}_T}$ and $\mathcal{V}_{\mathbf{S}_{T,4}}$; explicit expressions for these are also given in Table I.

D. Bounds on solution size

As a prelude to an energetic analysis of finite difference schemes, it is useful to compare the above-mentioned approximations to the system $\mathbf{S}$, especially insofar as the conserved quantities mentioned earlier lead to global bounds on the size of the solution.

Consider system $\mathbf{S}_2$, which, it is to be recalled, is the linearized form of the string equation. From the expressions given in Table I, it is clearly true that $\mathcal{T}_{\mathbf{S}}\geqslant 0$ and $\mathcal{V}_{\mathbf{S}_2}\geqslant 0$, implying $\mathcal{H}_{\mathbf{S}_2}\geqslant 0$ and, furthermore,

$$\|p_\xi\|,\|p_\eta\|\leqslant\sqrt{\frac{2\mathcal{H}_{\mathbf{S}_2}}{\rho}},\tag{11}$$

$$\|q_\xi\|\leqslant\sqrt{\frac{2\mathcal{H}_{\mathbf{S}_2}}{EA}},\quad \|q_\eta\|\leqslant\sqrt{\frac{2\mathcal{H}_{\mathbf{S}_2}}{T_0}}.\tag{12}$$

As $\mathcal{H}_{\mathbf{S}_2}$ is constant and equal to its value at time $t=0$, there are thus global bounds on the size of the solution of system $\mathbf{S}_2$ at all future times.

In contrast, for the commonly encountered approximate systems $\mathbf{S}_3$ and $\mathbf{S}_4$, such global conditions do not exist, as the energy function is not necessarily positive for all possible choices of the string state; choosing, for instance, $q_\xi=\mathrm{sgn}(T_0-EA)q_\eta^2$, then $\mathcal{V}_{\mathbf{S}_4}$ and $\mathcal{V}_{\mathbf{S}_3}$ are negative and unbounded in the limit as q_η becomes large. Because the solutions themselves cannot be bounded, it is unreasonable to expect to find finite difference schemes which are provably numerically stable under general conditions; systems $\mathbf{S}_3$ and $\mathbf{S}_4$ are not considered henceforth in this article, though it should be emphasized that they do possess a conserved energy-like quantity which can be transferred to discrete time.

System $\mathbf{S}_4^*$, however, is well-behaved in this sense, under the restricted condition

$$EA\geqslant T_0.\tag{13}$$

This is indeed the case for many systems of practical (and also musical) interest. $\mathcal{T}_{\mathbf{S}}$ and $\mathcal{V}_{\mathbf{S}_4^*}$ are both non-negative, and it follows immediately that

$$\|p_\xi\|,\|p_\eta\|\leqslant\sqrt{\frac{2\mathcal{H}_{\mathbf{S}_4^*}}{\rho}},\quad \|q_\xi\|,\|q_\eta\|\leqslant\sqrt{\frac{2\mathcal{H}_{\mathbf{S}_4^*}}{T_0}}.\tag{14}$$

It is probably possible to tighten the above-mentioned bounds through further analysis.

For the simplified system $\mathbf{S}_{T,4}$, the energy $\mathcal{H}_{\mathbf{S}_{T,4}}=\mathcal{T}_{\mathbf{S}_T}+\mathcal{V}_{\mathbf{S}_{T,4}}$ is non-negative, again under condition (13), leading to bounds

$$\|p_\eta\|\leqslant\sqrt{\frac{2\mathcal{H}_{\mathbf{S}_{T,4}}}{\rho}},\quad \|q_\eta\|\leqslant\sqrt{\frac{2\mathcal{H}_{\mathbf{S}_{T,4}}}{EA}}.\tag{15}$$

III. FINITE DIFFERENCE SCHEMES

In the following, finite difference schemes for the various nonlinear string systems discussed in Sec. II are introduced. Stability conditions which are based on discrete energy conservation, when available, are then derived. A good tutorial treatment of the energy method for finite difference schemes is given by Vu-Quoc and Li.[36,37] The reader is reminded that frequency-domain concepts are nowhere employed in this method.

A. Preliminaries

In order to approximate a real-valued function such as $f(x,t)$ which appears as a dependent variable in a PDE, a first step is to introduce a grid function f_i^n, which serves as an approximation at the coordinates $x=ih_x$, $t=nh_t$, for i and n integer. Here h_x and h_t are the grid spacing and time step, respectively. In view of the use of such grid functions in initial boundary value problems such as the string, the restrictions $n \geqslant 0$ and $i=0,\ldots,N-1$, where $N=L/h_x$, are also imposed. As the difference schemes to be discussed here are of the *interleaved* or *finite-difference time domain* variety,[38,39] it is also helpful to define grid functions such as $g_{i+1/2}^{n+1/2}$, again for integer n and $i=0,\ldots,N-1$, representing an approximation to a continuously variable function $g(x,t)$ at time $t=(n+1/2)h_t$ and at location $x=(i+1/2)h_x$.

The forward time difference operator δ_{t+} and time-mean operators μ_{t+}, μ_{t-}, and μ_{t0} are defined by

$$\delta_{t+}f_i^n = \frac{1}{h_t}(f_i^{n+1} - f_i^n),$$

$$\mu_{t+}f_i^n = \tfrac{1}{2}(f_i^{n+1} + f_i^n) \quad \mu_{t-}f_i^n = \tfrac{1}{2}(f_i^n + f_i^{n-1}),$$

$$\mu_{t0}f_i^n = \tfrac{1}{2}(f_i^{n+1} + f_i^{n-1})$$

and forward and backward spatial difference operators δ_{x+} and δ_{x-} by

$$\delta_{x+}f_i^n = \frac{1}{h_x}(f_{i+1}^n - f_i^n), \quad \delta_{x-}f_i^n = \frac{1}{h_x}(f_i^n - f_{i-1}^n).$$

For periodic boundary conditions, the spatial indices of the grid function are to be taken modulo N. For instance, $\delta_{x+}f_{N-1}^n = (1/h_x)(f_0^n - f_{N-1}^n)$.

All the discrete operators defined earlier are pairwise commutative. (The symbols δ and μ are intended as mnemonics for "difference" and "mean," respectively.)

The identities

$$(\mu_{t+}f_i^n)(\delta_{t+}f_i^n) = \delta_{t+}\left(\tfrac{1}{2}(f_i^n)^2\right), \tag{16}$$

$$\mu_{t+}\delta_{t+}f_i^n = \frac{1}{2h_t}(f_i^{n+2} - f_i^n), \tag{17}$$

$$(\mu_{t0}f_i^n)(\mu_{t+}\delta_{t+}f_i^{n-1}) = \mu_{t+}\delta_{t+}\left(\tfrac{1}{2}(f_i^{n-1})^2\right) \tag{18}$$

follow immediately from the above-presented definitions.

It is useful to define an inner product at time step n between two real-valued grid functions f_i^n and g_i^n (and the associated norm) by

$$\langle f^n, g^n\rangle = \sum_{i=0}^{N-1} h_x f_i^n g_i^n, \quad \|f^n\| = \langle f^n, f^n\rangle^{1/2}.$$

(The grid function g_i^n above may be replaced by a grid function $g_{i+1/2}^{n+1/2}$, interleaved with respect to f_i^n without affecting the above-presented definition.) It then follows that

$$\langle f^n, r^n, g^n\rangle = \langle f^n r^n, g^n\rangle \tag{19}$$

for any three grid functions f, g, and r.

Recall also the triangle inequality,

$$\|f^n + g^n\| \leqslant \|f^n\| + \|g^n\| \tag{20}$$

which implies, in particular, that

$$\|\delta_{x-}f^n\| \leqslant \frac{2}{h_x}\|f^n\|. \tag{21}$$

The useful identity

$$\langle f^n, \delta_{x-}g^n\rangle = -\langle \delta_{x+}f^n, g^n\rangle \tag{22}$$

holds for periodic boundary conditions and is the discrete analogue of integration by parts.

B. Interleaved schemes

In developing difference schemes, it is perhaps simplest to begin from the uncoupled linear system $\mathbf{S}_2$. Due to this lack of coupling, it is permissible to examine the two systems, one in p_ξ and q_ξ, the other in p_η and q_η, in isolation. A centered finite difference scheme, here called $\mathbf{s}_2$, can then be written as shown in the first row of Table II. Here, the grid functions $p_{\xi,i}^n$ and $p_{\eta,i}^n$, approximations to $p_\xi(x,t)$ and $p_\eta(x,t)$ are interleaved in time and space with respect to the grid functions $q_{\xi,i+1/2}^{n-1/2}$ and $q_{\eta,i+1/2}^{n-1/2}$, which are approximations to $q_\xi(x,t)$ and $q_\eta(x,t)$.

To see this interleaving property clearly, it is helpful to rewrite system $\mathbf{s}_2$ in update form. For the uncoupled system in $p_{\eta,i}^n$ and $q_{\eta,i+1/2}^{n-1/2}$,

$$p_{\eta,i}^n = p_{\eta,i}^{n-1} + \frac{T_0}{\rho}\alpha(q_{\eta,i+1/2}^{n-1/2} - q_{\eta,i-1/2}^{n-1/2}),$$

$$q_{\eta,i+1/2}^{n+1/2} = q_{\eta,i+1/2}^{n-1/2} + \alpha(p_{\eta,i+1}^n - p_{\eta,i}^n),$$

where the important parameter α is defined by

$$\alpha = h_t/h_x. \tag{23}$$

If the updates are performed in the order in which they are presented above, the scheme is fully explicit. The other subsystem in $p_{\xi,i}^n$ and $q_{\xi,i+1/2}^{n-1/2}$ is of the same form.

As a first example of a nonlinear difference scheme, consider the simplified transverse-only nonlinear system $\mathbf{S}_{T,4}$, which depends only on p_η and q_η. There are plainly many ways to approximate the nonlinearity. Perhaps the most straightforward choice is scheme $\mathbf{s}_{T,4}^{(a)}$, given in Table II. This finite difference scheme, like system $\mathbf{s}_2$, is again interleaved and can be updated explicitly; unfortunately, it does not possess a simple conserved quantity analogous to $\mathcal{H}_{\mathbf{S}_{T,4}}$, and its stability properties are difficult to ascertain. Another choice of difference scheme is given by $\mathbf{s}_{T,4}^{(b)}$. Many other choices are possible, but as discussed presently, scheme $\mathbf{s}_{T,4}^{(b)}$ possesses a simple conserved energy which allows for a convenient global stability condition. It should be noted, however, that scheme $\mathbf{s}_{T,4}^{(b)}$ is not fully explicit, i.e., it requires the solution of a sparse linear system at each time step. More details are provided in Sec. III F.

Returning now to the full coupled system of interest, $\mathbf{S}_4^*$, in Table II are presented, for the sake of comparison, three distinct schemes, all of the interleaved type: $\mathbf{s}_4^{*,(a)}$, $\mathbf{s}_4^{*,(b)}$ and $\mathbf{s}_4^{*,(c)}$. Scheme $\mathbf{s}_4^{*,(a)}$ is explicit, and schemes $\mathbf{s}_4^{*,(b)}$ and $\mathbf{s}_4^{*,(c)}$ are implicit. Both $\mathbf{s}_4^{*,(b)}$ and $\mathbf{s}_4^{*,(c)}$ possess conserved energy-like

quantities, but as will be seen shortly, only for scheme $\mathbf{s}_4^{*,(c)}$ may the energy function be constrained to be positive, and thus provably stable.

By virtue of the centering of difference operators, all the schemes shown in Table II are second-order accurate[23] in both h_x and h_t.

C. Conserved quantities

A good place to embark on a study of the conservation properties of the algorithms given in Table II is certainly the linear scheme $\mathbf{s}_2$; as mentioned earlier, it is composed of two uncoupled systems, one in $p_{\eta,i}^n, q_{\eta,i+1/2}^{n-1/2}$, and the other in $p_{\xi,i}^n, q_{\xi,i+1/2}^{n-1/2}$. Considering only the transverse subsystem, take the inner product of the second equation of system $\mathbf{s}_2$ with $\mu_{t+}p_{\eta,i}^{n-1}$ to get

$$\rho\langle\mu_{t+}p_\eta^{n-1},\delta_{t+}p_\eta^{n-1}\rangle = T_0\langle\mu_{t+}p_\eta^{n-1},\delta_{x-}q_\eta^{n-1/2}\rangle.$$

Using identity (16), this may be rewritten as

$$0 = \delta_{t+}\left(\frac{\rho}{2}\|p_\eta^{n-1}\|^2\right) - T_0\langle\mu_{t+}p_\eta^{n-1},\delta_{x-}q_\eta^{n-1/2}\rangle.$$

Using summation by parts Eq. (22), and commutativity of the operators δ_{x+} and μ_{t+} gives

$$0 = \delta_{t+}\left(\frac{\rho}{2}\|p_\eta^{n-1}\|^2\right) + T_0\langle\mu_{t+}\delta_{x+}p_\eta^{n-1},q_\eta^{n-1/2}\rangle$$

and finally, using the transverse auxiliary equation, and identity (17),

$$0 = \delta_{t+}\left(\frac{\rho}{2}\|p_\eta^{n-1}\|^2 + \frac{T_0}{2}\langle q_\eta^{n-1/2},q_\eta^{n-3/2}\rangle\right). \tag{24}$$

By symmetry, one may obtain, for the longitudinal subsystem,

$$0 = \delta_{t+}\left(\frac{\rho}{2}\|p_\xi^{n-1}\|^2 + \frac{EA}{2}\langle q_\xi^{n-1/2},q_\xi^{n-3/2}\rangle\right) \tag{25}$$

and combining Eqs. (24) and (25), finally, one arrives at

$$\delta_{t+}\mathcal{H}_{\mathbf{s}_2}^{n-1} = 0 \Rightarrow \mathcal{H}_{\mathbf{s}_2}^n = \mathcal{H}_{\mathbf{s}_2}^0 = \text{constant} \tag{26}$$

for the scalar function $\mathcal{H}_{\mathbf{s}_2}^n$ defined by

$$\mathcal{H}_{\mathbf{s}_2}^n = \mathcal{T}_{\mathbf{s}}^n + \mathcal{V}_{\mathbf{s}_2}^n$$

with

$$\mathcal{T}_{\mathbf{s}} = \frac{\rho}{2}(\|p_\xi^n\|^2 + \|p_\eta^n\|^2),$$

$$\mathcal{V}_{\mathbf{s}_2} = \frac{EA}{2}\langle q_\xi^{n+1/2},q_\xi^{n-1/2}\rangle + \frac{T_0}{2}\langle q_\eta^{n+1/2},q_\eta^{n-1/2}\rangle.$$

The quantity $\mathcal{H}_{\mathbf{s}_2}^n$ is clearly analogous to $\mathcal{H}_{\mathbf{S}_2}$ for the model system $\mathbf{S}_2$; it is a conserved quantity of difference scheme $\mathbf{s}_2$, but is not necessarily positive. The determination of conditions under which $\mathcal{H}_{\mathbf{s}_2}^n$ is positive is related to stability conditions for scheme $\mathbf{s}_2$. Such stability conditions will be derived in the next section.

As a first example of energetic analysis applied to a nonlinear difference scheme, consider schemes for the transverse-only system $\mathbf{S}_{T,4}$. Two such schemes are presented in Table II, $\mathbf{s}_{T,4}^{(a)}$ and $\mathbf{s}_{T,4}^{(b)}$. The first of these is purely explicit, and certainly the simpler form. Unfortunately, it does not possess a conserved energy-like quantity, and thus stability conditions are not immediately forthcoming. The implicit scheme, $\mathbf{s}_{T,4}^{(b)}$, on the other hand, does. In general, implicit schemes for nonlinear equations are very problematic, in that existence and uniqueness are not easy to show (though, interestingly, through energy-based analysis, one may often show that if a solution *does* exist, it will be stable[13]). As is shown in Sec. III F, the schemes to be discussed here do not cause these difficulties, as the implicit character of the schemes intervenes in an essentially linear way.

Beginning from $\mathbf{s}_{T,4}^{(b)}$, again take an inner product with $\mu_{t+}p_i^{n-1}$, to get

$$0 = \rho\langle\mu_{t+}p_\eta^{n-1},\delta_{t+}p_\eta^{n-1}\rangle - T_0\langle\mu_{t+}p_\eta^{n-1},\delta_{x-}q_\eta^{n-1/2}\rangle - \frac{EA-T_0}{2}\langle\mu_{t+}p_\eta^{n-1},\delta_{x-}([q_\eta^{n-1/2}]^2\mu_{t0}q_\eta^{n-1/2})\rangle.$$

Applying the same steps as for system $\mathbf{s}_2$, one obtains

$$\begin{aligned}
0 &= \delta_{t+}\left(\frac{\rho}{2}\|p_\eta^{n-1}\|^2 + \frac{T_0}{2}\langle q_\eta^{n-1/2},q_\eta^{n-3/2}\rangle\right) + \frac{EA-T_0}{2}\langle\mu_{t+}\delta_{t+}q_\eta^{n-3/2},(q_\eta^{n-1/2})^2\mu_{t0}q_\eta^{n-1/2}\rangle \\
&= \delta_{t+}\left(\frac{\rho}{2}\|p_\eta^{n-1}\|^2 + \frac{T_0}{2}\langle q_\eta^{n-1/2},q_\eta^{n-3/2}\rangle\right) + \frac{EA-T_0}{2}\langle(\mu_{t0}q_\eta^{n-1/2})(\mu_{t+}\delta_{t+}q_\eta^{n-3/2}),(q_\eta^{n-1/2})^2\rangle \\
&= \delta_{t+}\left(\frac{\rho}{2}\|p_\eta^{n-1}\|^2 + \frac{T_0}{2}\langle q_\eta^{n-1/2},q_\eta^{n-3/2}\rangle\right) + \frac{EA-T_0}{4}\langle\mu_{t+}\delta_{t+}(q_\eta^{n-3/2})^2,(q_\eta^{n-1/2})^2\rangle = \delta_{t+}\left(\frac{\rho}{2}\|p_\eta^{n-1}\|^2\right. \\
&\quad \left. + \frac{T_0}{2}\langle q_\eta^{n-1/2},q_\eta^{n-3/2}\rangle + \frac{EA-T_0}{8}\langle(q_\eta^{n-3/2})^2,(q_\eta^{n-1/2})^2\rangle\right)
\end{aligned}$$

where, in the final three steps above, the identities (19), (18), and (17), respectively, have been used. Clearly, then,

$$\mathcal{H}_{\mathbf{s}_{T,4}^{(b)}}^n = \mathcal{T}_{\mathbf{s}_{T,4}}^n + \mathcal{V}_{\mathbf{s}_{T,4}^{(b)}}^n = \text{constant}, \tag{27}$$

where $\mathcal{T}_{\mathbf{s}_{T,4}}^n$ and $\mathcal{V}_{\mathbf{s}_{T,4}^{(b)}}^n$ are as given in Table III.

Finally, consider the three schemes for the full coupled transverse/longitudinal system, as discussed in the previous section, and as given in Table II. Scheme $\mathbf{s}_4^{*,(a)}$ is explicit, but again, does not possess a conserved energy. Schemes $\mathbf{s}_4^{*,(b)}$ and $\mathbf{s}_4^{*,(c)}$ are implicit, and conservative; manipulations similar to those performed earlier may be applied in order to arrive at kinetic and potential energies. These are presented without further comment for both schemes in Table III.

TABLE III. Discrete kinetic and potential energies for the schemes given in Table II; their sum will be conserved. The closed circle (●) indicates that the scheme is not conservative.

	Kinetic energy	Potential energy
$\mathbf{s}_2$	$\mathcal{T}_{\mathbf{s}}^n=\frac{\rho}{2}(\|p_\xi^n\|^2+\|p_\eta^n\|^2)$	$\mathcal{V}_{\mathbf{s}_2}^n=\frac{EA}{2}\langle q_\xi^{n+1/2},q_\xi^{n-1/2}\rangle+\frac{T_0}{2}\langle q_\eta^{n+1/2},q_\eta^{n-1/2}\rangle$
$\mathbf{s}_4^{*,(a)}$	●	●
$\mathbf{s}_4^{*,(b)}$	$\mathcal{T}_{\mathbf{s}}^n=\frac{\rho}{2}(\|p_\xi^n\|^2+\|p_\eta^n\|^2)$	$\mathcal{V}_{\mathbf{s}_4^{*,(b)}}^n=\frac{T_0}{2}(\langle q_\xi^{n+1/2},q_\xi^{n-1/2}\rangle+\langle q_\eta^{n+1/2},q_\eta^{n-1/2}\rangle)+\frac{EA-T_0}{8}\langle (q_\eta^{n+1/2})^2+2q_\xi^{n+1/2},(q_\eta^{n-1/2})^2+2q_\xi^{n-1/2}\rangle$
$\mathbf{s}_4^{*(c)}$	$\mathcal{T}_{\mathbf{s}}^n=\frac{\rho}{2}(\|p_\xi^n\|^2+\|p_\eta^n\|^2)$	$\mathcal{V}_{\mathbf{s}_4^{*,(c)}}^n=\frac{EA}{2}\langle q_\xi^{n+1/2},q_\xi^{n-1/2}\rangle+\frac{T_0}{2}\langle q_\eta^{n+1/2},q_\eta^{n-1/2}\rangle+\frac{EA-T_0}{8}(\|q_\eta^{n+1/2}q_\eta^{n-1/2}+2\mu_{t+}q_\xi^{n-1/2}\|^2-4\|\mu_{t+}q_\xi^{n-1/2}\|^2)$
$\mathbf{s}_{T,4}^{(a)}$	●	●
$\mathbf{s}_{T,4}^{(b)}$	$\mathcal{T}_{\mathbf{s}_4}^n=\frac{\rho}{2}\|p_\eta^n\|^2$	$\mathcal{V}_{\mathbf{s}_{T,4}^{(b)}}^n=\frac{T_0}{2}\langle q_\eta^{n+1/2},q_\eta^{n-1/2}\rangle+\frac{EA-T_0}{8}\langle (q_\eta^{n+1/2})^2,(q_\eta^{n-1/2})^2\rangle$

D. Numerical stability

Given the conserved forms shown in Table III, it is relatively straightforward to arrive at bounds on the solution, provided that discrete energy may be shown to be positive. Beginning from the conserved energy for scheme $\mathbf{s}_2$, first note that

$$\langle q_\xi^{n+1/2},q_\xi^{n-1/2}\rangle=\|\mu_{t+}q_\xi^{n-1/2}\|^2-\frac{h_t^2}{4}\|\delta_{x+}p_\xi^n\|^2,$$

$$\langle q_\eta^{n+1/2},q_\eta^{n-1/2}\rangle=\|\mu_{t+}q_\eta^{n-1/2}\|^2-\frac{h_t^2}{4}\|\delta_{x+}p_\eta^n\|^2.$$

The total conserved energy for the scheme can then be rewritten as

$$\mathcal{H}_{\mathbf{s}_2}^n=\frac{1}{2}\left(\rho\|p_\xi^n\|^2-\frac{EAh_t^2}{4}\|\delta_{x+}p_\xi^n\|^2+EA\|\mu_{t+}q_\xi^{n-1/2}\|^2\right)+\frac{1}{2}\left(\rho\|p_\eta^n\|^2-\frac{T_0h_t^2}{4}\|\delta_{x+}p_\eta^n\|^2+T_0\|\mu_{t+}q_\eta^{n-1/2}\|^2\right).$$

Using inequality (21), one then has

$$\mathcal{H}_{\mathbf{s}_2}^n\geqslant\frac{1}{2}(\rho-EA\alpha^2)\|p_\xi^n\|^2+\frac{EA}{2}\|\mu_{t+}q_\xi^{n-1/2}\|^2+\frac{1}{2}(\rho-T_0\alpha^2)\|p_\eta^n\|^2+\frac{T_0}{2}\|\mu_{t+}q_\eta^{n-1/2}\|^2.$$

Under the conditions

$$\alpha<\sqrt{\rho/EA},\quad \alpha<\sqrt{\rho/T_0} \tag{28}$$

the energy is strictly positive, and, furthermore, the following bounds may be obtained:

$$\|p_\xi^n\|\leqslant\sqrt{\frac{2\mathcal{H}_{\mathbf{s}_2}^0}{\rho-EA\alpha^2}},\quad \|p_\eta^n\|\leqslant\sqrt{\frac{2\mathcal{H}_{\mathbf{s}_2}^0}{\rho-T_0\alpha^2}}, \tag{29}$$

$$\|\mu_{t+}q_\xi^{n-1/2}\|\leqslant\sqrt{\frac{2\mathcal{H}_{\mathbf{s}_2}^0}{EA}},\quad \|\mu_{t+}q_\eta^{n-1/2}\|\leqslant\sqrt{\frac{2\mathcal{H}_{\mathbf{s}_2}^0}{T_0}}. \tag{30}$$

It is simple to translate the above mentioned bounds on $\|\mu_{t+}q_\xi^{n-1/2}\|$ into a more direct bound on $\|q_\xi^{n-1/2}\|$, by using the fact that $q_{\xi,i+1/2}^{n-1/2}=\mu_{t+}q_{\xi,i+1/2}^{n-1/2}+(h_t/2)\delta_{x+}p_{\xi,i}^n$, and an application of the triangle inequality (21). A similar statement holds for $\|\mu_{t+}q_\eta^{n-1/2}\|$.

Similar stability bounds can be course be obtained in this linear case by using von Neumann (Fourier) methods;[23] Vu-Quoc and Li[37] applied such analysis to energy-conserving schemes for the Klein-Gordon equation under linear conditions.

Consider now the conserved energy for the nonlinear transverse-only scheme $\mathbf{s}_{T,4}^{(b)}$, again given in Table III. It can be expressed as

$$\mathcal{H}_{\mathbf{s}_{T,4}^{(b)}}^n=\frac{1}{2}\left(p\|p_\eta^n\|^2-\frac{T_0h_t^2}{4}\|\delta_{x+}p_\eta^n\|^2+T_0\|\mu_{t+}q_\eta^{n-1/2}\|^2\right)+\frac{EA-T_0}{8}\langle (q_\eta^{n+1/2})^2,(q_\eta^{n-1/2})^2\rangle\geqslant\frac{1}{2}(\rho-T_0\alpha^2)\|p_\eta^n\|^2+\frac{T_0}{2}\|\mu_{t+}q_\eta^{n-1/2}\|^2+\frac{EA-T_0}{8}\langle (q_\eta^{n+1/2})^2,(q_\eta^{n-1/2})^2\rangle.$$

Under condition (13) and the second of Eq. (28), all terms are positive, leading to similar bounds

$$\|p_\eta^n\| \leqslant \sqrt{\frac{2\mathcal{H}^0_{\mathbf{s}^{(b)}_{T,4}}}{\rho - T_0\alpha^2}}, \quad \|\mu_{t+}q_\eta^{n-1/2}\| \leqslant \sqrt{\frac{2\mathcal{H}^0_{\mathbf{s}^{(b)}_{T,4}}}{T_0}}.$$

The coupled scheme $\mathbf{s}_4^{*,(c)}$ can be dealt with similarly. Rewriting the expression for conserved energy as earlier, and applying similar manipulations, one arrives at

$$\begin{aligned}\mathcal{H}^n_{\mathbf{s}_4^{*,(c)}} \geqslant{}& \frac{1}{2}(\rho - EA\alpha^2)\|p_\xi^n\|^2 + \frac{T_0}{2}\|\mu_{t+}q_\xi^{n-1/2}\|^2 \\ &+ \frac{1}{2}(\rho - T_0\alpha^2)\|p_\eta^n\|^2 + \frac{T_0}{2}\|\mu_{t+}q_\eta^{n-1/2}\|^2 \\ &+ \frac{EA - T_0}{8}\|q_\eta^{n+1/2}q_\eta^{n-1/2} + 2\mu_{t+}q_\xi^{n-1/2}\|^2,\end{aligned}$$

which is positive under conditions (28) and (13). Bounds on the solution size follow as before:

$$\|p_\xi^n\| \leqslant \sqrt{\frac{2\mathcal{H}^0_{\mathbf{s}_4^{*,(c)}}}{\rho - EA\alpha^2}}, \quad \|p_\eta^n\| \leqslant \sqrt{\frac{2\mathcal{H}^0_{\mathbf{s}_4^{*,(c)}}}{\rho - T_0\alpha^2}},$$

$$\|\mu_{t+}q_\xi^{n-1/2}\|, \|\mu_{t+}q_\eta^{n-1/2}\| \leqslant \sqrt{\frac{2\mathcal{H}^0_{\mathbf{s}_4^{*,(c)}}}{T_0}}.$$

In contrast, scheme $\mathbf{s}_4^{*,(b)}$ does *not* allow such bounds on the solution size. From the form of the potential energy $\mathcal{V}_{\mathbf{s}_4^{*,(b)}}$ given in Table III, it is clear that the last term, of highest order in the state variables, is not necessarily positive, in contrast with scheme $\mathbf{s}_4^{*,(c)}$. In fact, for certain choices of the state variables, it can become unbounded and negative. Thus conservative behavior in a difference scheme is not sufficient for stability. Further comments on this topic appear in Sec. IV.

The simplicity of the nonlinear stability results presented here are a direct consequence of the series-approximated form of the nonlinearity, in which case various algebraic symmetries may be exploited. The stability analysis here is thus less general than in a case for which the form of the nonlinearity is not as simple (e.g., that carried out by Li and Vu-Quoc[36] for the nonlinear Klein-Gordon equation, with a nonlinear term of unspecified form, which is much more involved).

E. Boundary conditions

In all the above-presented analysis, periodic boundary conditions of the form of Eq. (2) have been assumed; simple fixed conditions, as given in Eq. (3) change virtually none of this analysis. These are simply incorporated into any of the schemes presented in Table II, which are used as written for $i=1,\ldots,N-1$. At $i=0$, one may simply set $p^n_{\xi,0}=p^n_{\eta,0}=0$, and the computations of $\delta_{x+}p^n_{\xi,N-1}$ and $\delta_{x+}p^n_{\eta,N-1}$ may still be performed using periodicity, under this constraint. A fuller discussion of the distinction between periodic and fixed boundary conditions in the case of energetic analysis of difference schemes for strings appears in previous work by this author.[15]

F. Implementation details

As mentioned earlier, the schemes of most interest, namely $\mathbf{s}^{(b)}_{T,4}$ and $\mathbf{s}_4^{*,(c)}$ for which numerical stability bounds can be shown, are implicit. As such, it is worth discussing a computer implementation in detail. Fixed boundary conditions, as discussed in the previous section, are assumed here.

The implicit character of scheme $\mathbf{s}^{(b)}_{T,4}$ results directly from the inclusion of the term $\mu_{t0}q^{n-1/2}_{\eta,i+1/2}$. Noting that

$$\mu_{t0}q^{n-1/2}_{\eta,i+1/2} = q^{n-1/2}_{\eta,i+1/2} + \frac{h_t^2}{2}\delta_{x+}\delta_{t+}p^{n-1}_{\eta,i}$$

scheme $\mathbf{s}^{(b)}_{T,4}$ may be rewritten as

$$\begin{aligned}\rho\delta_{t+}p^{n-1}_{\eta,i} = T_0\delta_{x-}q^{n-1/2}_{\eta,i+1/2} + \frac{EA - T_0}{2}\delta_{x-}(q^{n-1/2}_{\eta,i+1/2})^3 \\ + \frac{h_t^2(EA - T_0)}{4}\delta_{x-}((q^{n-1/2}_{\eta,i+1/2})^2\delta_{x+}\delta_{t+}p^{n-1}_{\eta,i}).\end{aligned} \quad (31)$$

Introducing vectors $\mathbf{p}^n_\eta$ and $\mathbf{q}^{n-1/2}_\eta$, defined as

$$\mathbf{p}^n_\eta = [p^n_{\eta,1},\ldots,p^n_{\eta,N-1}]^T, \quad \mathbf{q}^{n-1/2}_\eta = [q^{n-1/2}_{\eta,1/2},\ldots,q^{n-1/2}_{\eta,N-1/2}]^T \quad (32)$$

system $\mathbf{s}^{(b)}_{T,4}$ may be rewritten, in vector-matrix form, as

$$\mathbf{p}^n_\eta = \mathbf{p}^{n-1}_\eta + (\mathbf{A}^{n-1/2})^{-1}\mathbf{D}_-\mathbf{b}^{n-1/2}, \quad (33a)$$

$$\mathbf{q}^{n+1/2}_\eta = \mathbf{q}^{n-1/2}_\eta + \mathbf{D}_+\mathbf{p}^n_\eta, \quad (33b)$$

where

$$\begin{aligned}\mathbf{A}^{n-1/2} &= \mathbf{I}_{N-1} - \mathbf{D}_-(\mathbf{\Lambda}^{n-1/2})^2\mathbf{D}_+, \\ \mathbf{b}^{n-1/2} &= \left(\frac{T_0}{\rho}\mathbf{I}_N + 2(\mathbf{\Lambda}^{n-1/2})^2\right)\mathbf{q}^{n-1/2}_\eta, \\ \mathbf{\Lambda}^{n-1/2} &= \frac{\beta}{2}\,\mathrm{diag}(\mathbf{q}^{n-1/2}_\eta), \\ \beta &= \sqrt{\frac{EA - T_0}{\rho}}\end{aligned} \quad (34)$$

and the $N\times(N-1)$ matrix $\mathbf{D}_+$, which incorporates the fixed boundary condition constraints, is defined by

$$\mathbf{D}_+ = \alpha\begin{bmatrix} 1 & & & & \\ -1 & 1 & & & \\ & \ddots & \ddots & & \\ & & -1 & 1 & \\ & & & & -1 \end{bmatrix}. \quad (35)$$

The matrix $\mathbf{D}_-$ is defined by $\mathbf{D}_- = -\mathbf{D}_+^T$, and $\mathbf{I}_M$ is the $M\times M$ identity matrix. Clearly, in order to solve Eq. (33a), it is not necessary to invert the matrix $\mathbf{A}^{n-1/2}$, but merely to solve a sparse linear system (note that $\mathbf{A}^{n-1/2}$ is tridiagonal), which can be done in $O(N-1)$ operations, at each time step, which is comparable to the cost for an explicit scheme.

Difference scheme $\mathbf{s}_4^{*,(c)}$ may be treated similarly. Defining the vectors $\mathbf{p}^n_\xi$ and $\mathbf{q}^{n-1/2}_\xi$ in analogy with Eq. (32), it may be written as

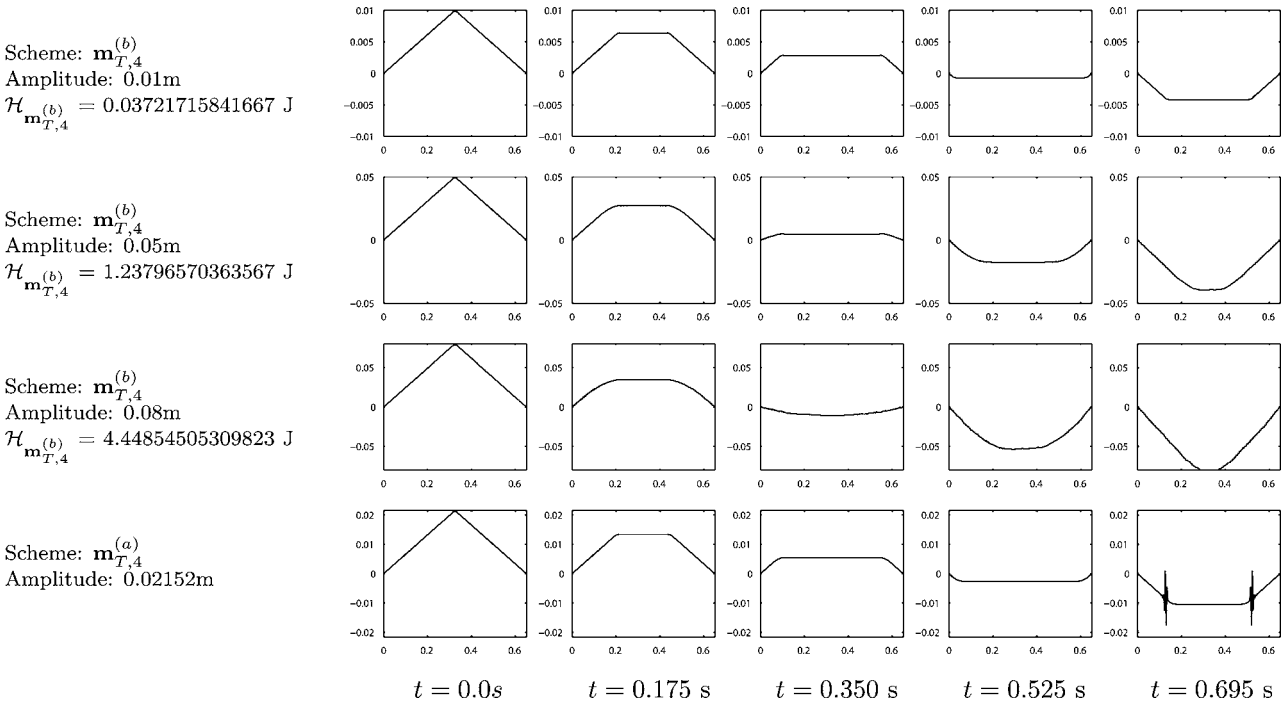

FIG. 1. Snapshots of the time evolution of the profile of a plucked string, according to the test model $\mathbf{S}_{T,4}$. The string is assumed made of steel (with $E=2.1\times10^{11}$ N/m^2 and density 7850 kg/m^3), under tension $T_0=120$ N, of length $L=0.65$ m, and of cross-sectional area $A=3.6\times10^{-8}$ m^2. The string is plucked at the center, according to the amplitudes given in the left-most column. For the first three simulations (shown in the first three rows), the energy-conserving scheme $\mathbf{s}_{T,4}^{(b)}$ is used; the conserved energy, in joules, is also given for each simulation, in the left-most column. For the fourth simulation, scheme $\mathbf{s}_{T,4}^{(a)}$ is used. In all cases, a value of $\alpha=0.85\sqrt{\rho/T_0}$ and a sample rate of 200 kHz are used. Plot units are in m.

$$\begin{bmatrix} \mathbf{p}_\xi^n \\ \mathbf{p}_\eta^n \end{bmatrix} = \begin{bmatrix} \mathbf{p}_\xi^{n-1} \\ \mathbf{p}_\eta^{n-1} \end{bmatrix} + (\mathbf{A}^{n-1/2})^{-1} \begin{bmatrix} \mathbf{D}_- & \cdot \\ \cdot & \mathbf{D}_- \end{bmatrix} \mathbf{b}^{n-1/2},$$

where

$$\mathbf{A}^{n-1/2} = \begin{bmatrix} \mathbf{I}_{N-1} & -\frac{\sqrt{2}}{\beta}\mathbf{D}_-\boldsymbol{\Lambda}^{n-1/2}\mathbf{D}_+ \\ -\frac{\sqrt{2}}{\beta}\mathbf{D}_-\boldsymbol{\Lambda}^{n-1/2}\mathbf{D}_+ & \mathbf{I}_{N-1} - \mathbf{D}_-(\boldsymbol{\Lambda}^{n-1/2})^2\mathbf{D}_+ \end{bmatrix},$$

$$\mathbf{b}^{n-1/2} = \begin{bmatrix} \frac{EA}{\rho} & \beta\boldsymbol{\Lambda}^{n-1/2} \\ 2\beta\boldsymbol{\Lambda}^{n-1/2} & 2(\boldsymbol{\Lambda}^{n-1/2})^2 \end{bmatrix} \begin{bmatrix} \mathbf{q}_\xi^{n-1/2} \\ \mathbf{q}_\eta^{n-1/2} \end{bmatrix}$$

and $\boldsymbol{\Lambda}^{n-1/2}$ and $\mathbf{D}_-$ are as defined in Eqs. (34) and (35).

It is important to note that these algorithms preserve energy exactly in exact machine arithmetic; in a finite precision machine, it will necessarily fluctuate, due to round-off error. In this respect, an important concern will be the means of solution of the linear systems mentioned earlier. Typically, this must be done using an iterative method of some sort, perhaps a variant of the conjugate gradient method;[23] if the matrix defining the linear system is poorly conditioned, convergence may be slow and, worse still, unconverged results can lead to large energy fluctuations and finally instability. More comments on this topic are to be found in Sec. IV.

Initialization of any of the above-mentioned interleaved algorithms is complicated, marginally, by the fact that the grid variables are not computed simultaneously. In general, grid variables p and q must be set at time steps 0 and 1/2, respectively. Given initial conditions $p_\eta(x,0)$ and $q_\eta(x,0)$, one may clearly set $p_{\eta,i}^0 = p_\eta(ih_x,0)$; $q_{\eta,i+1/2}^{1/2}$ requires slightly more care—from the auxiliary equation, it may be set according to a one-sided difference formula as $q_{\eta,i+1/2}^{1/2} = q_\eta(ih_x,0) + (h_t/2)\delta_{x+}p_{\eta,i}^0$. The initialization of $p_{\xi,i}^0$ and $q_{\xi,i+1/2}^{1/2}$ is similar. Other initialization strategies are also possible.

IV. NUMERICAL EXPERIMENTS

As a test of the various schemes presented in this article, several simulation results are here discussed. First, consider the test system $\mathbf{S}_{T,4}$, and the associated difference schemes $\mathbf{s}_{T,4}^{(a)}$ and $\mathbf{s}_{T,4}^{(b)}$. For a string of parameters as given in Fig. 1, simulation results are given under triangular initial displacement or "center-plucked" conditions, of various amplitudes. For the energy-conserving scheme, the discrete energy is conserved to machine accuracy (values given adjacent in the figure); recall that this scheme is stable for any initial conditions, provided $EA \geqslant T_0$ (which is true in this case), and for $\alpha < \sqrt{\rho/T_0}$. The value $\alpha=0.85\sqrt{\rho/T_0}$ has been chosen for all simulations presented in the figure. The scheme is implicit, and the stabilized biconjugate gradient method has been used in order to solve the linear system which arises, as discussed in the previous section. In the first case, for an initial displacement amplitude of 0.01 m, the problem is essentially linear, but for higher amplitudes of 0.05 and 0.08 m, nonlinear effects may be observed, in particular the increase in the propagation speed, in a gross sense. For the nonconservative, explicit scheme $\mathbf{s}_{T,4}^{(a)}$, an instability develops (bottom right panel of Fig. 1), which quickly diverges—this behavior occurs even under the relatively small amplitude of

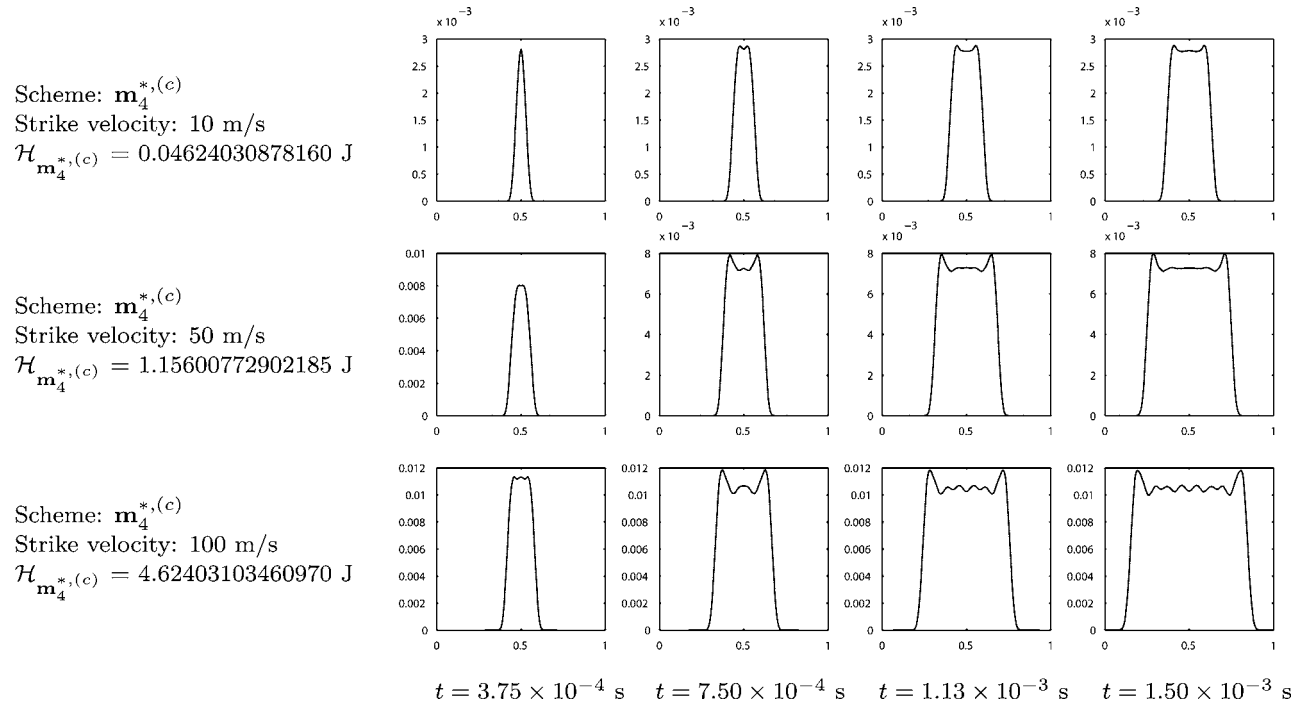

FIG. 2. Snapshots of the time evolution of the profile of a plucked string, according to the test model $\mathbf{S}_4^*$. The string is assumed made of steel (with $E=2.1\times10^{11}$ N/m^2 and density 7850 kg/m^3), under tension $T_0=120$ N, of length $L=1$ m, and of cross-sectional area $A=3.14\times10^{-6}$ m^2. The string is struck at the center, according to a raised-cosine velocity distribution, of width 0.1 m, and of peak velocity 10, 50, and 100 m/s (in the three rows, respectively). For all three simulations, the energy-conserving scheme $\mathbf{s}_4^{*,(c)}$ is used; the conserved energy, in joules, is also given for each simulation, in the left-most column. In all cases, a value of $\alpha=0.9\sqrt{\rho/EA}$ and a sample rate of 1 MHz are used. Plot units are in m.

0.021 52 m. Though this instability may be weakened through the use of lower values of α (at the expense of reduced efficiency), conditions under which it will not arise are not forthcoming.

In order to examine the results of application of scheme $\mathbf{s}_4^{*,(c)}$ for the coupled longitudinal/transverse system M_4^*, and for the sake of variety, the results of several initial velocity, or striking simulations are presented in Fig. 2, where string and striking parameters are as given in the accompanying caption. Again, energy is conserved to machine accuracy, and the scheme is globally stable, even for large strike amplitudes as shown. Note, again, the gross change in wave speed as strike velocity is increased, as well as the distinctive nonlinear distortion for high velocities—this is not a result of any kind of numerical dispersion of spurious oscillations in the numerical scheme (which was run at 1 MHz).

In analogy with the results presented in Fig. 1, it would be possible to demonstrate instability in the simple explicit scheme $\mathbf{s}_4^{*,(a)}$, even under relatively low striking velocities. More interesting, however, is the case of scheme $\mathbf{s}_4^{*,(b)}$, which is conservative, but not globally stable. In general, this scheme performs better than the explicit scheme (i.e., over a wider range of velocities), but suffers from another weakness, namely poor conditioning of the linear system which must be solved. This is an important issue which cannot be explored in any depth in this short article, but in essence, if the linear system is not adequately solved at each time step, the conservation guarantee fails, eventually leading to instabilities of the form seen when using, e.g., scheme $\mathbf{s}_4^{*,(a)}$. Both types of instability take the form of explosive oscillatory behavior, similar in character to those which occur in the last row of panels in Fig. 1; for this reason, simulation results are not presented here. As for the previous transverse-only system, decreasing α has an ameliorating effect on any stability concerns, for either of these two schemes.

V. CONCLUSION

Many interrelated issues have been raised here regarding model and difference scheme choice for nonlinear string vibration simulation. It is worth stepping back to view the main considerations, which all stem from an insistence on energy conservation, and rely in no way on frequency domain techniques. As far as model choice goes, in order to be able to arrive at difference schemes which are provably stable under an energetic criterion, the following constraints must be obeyed:

(1) The model should possess a conserved energy-like quantity.
(2) The conserved quantity should be a positive function of the state variables.

The first follows from good modeling of the system itself (though in certain models it is violated[10]); the second condition is also a very natural one, though it is not satisfied by several series-approximated forms which appear in the literature (system $\mathbf{S}_4$ in particular). As discussed in this article, form $\mathbf{S}_4^*$ does satisfy the second condition above, and is thus a more suitable candidate for the creation of a stable scheme. (A related question is: How should series approximations to nonlinearities be carried out, so as to respect the second constraint listed above? As was discussed earlier, an examination

of the relative orders of magnitude of the dependent variables is a key to this issue, but further amplification is necessary.)

If the above-mentioned conditions are observed, and a difference scheme is constructed, then the following constraints are also to be observed:

(1) The difference scheme should possess a conserved energy-like quantity.
(2) The conserved quantity should be a positive function of the discrete grid functions.

This second pair of constraints does not follow immediately for a given difference scheme, even if it is constructed from a model system which obeys the first set. In particular, often the most obvious choice of scheme (such as the explicit schemes discussed given in Table II) satisfies neither; a scheme which satisfies both of the above-mentioned conditions $\mathbf{s}_4^{*,(c)}$ has been presented. It is interesting that even if the first of these conditions is satisfied, *and* the continuous model problem itself satisfied the first set of conditions mentioned earlier, this is *still* insufficient for global stability; scheme $\mathbf{s}_4^{*,(b)}$ is an example of such a scheme. As is often the case for Lyapunov-type stability analysis (the present case of the nonlinear string being one example), it is not at all clear that there is a systematic framework for *constructing* a scheme which is energy conserving; trial and error, informed by experience and intuition appear to be the only tools available to the algorithm designer, as exemplified by other energy-based methods for related systems which appear in the literature.[13,36] Given that the number of discretization possibilities for nonlinear systems is vast, more work is clearly necessary, and an investigation of the related symplectic integration techniques[40] for Hamiltonian-type systems may be of some value.

In the present case of the string, one might ask whether difference schemes for the model system **S** may be approached directly using energy-based methods. Certain results in the literature point to an affirmative answer,[13] but the resulting schemes are either (a) explicit, and without a positivity guarantee on the discrete energy, or (b) implicit, and lacking any guarantee of existence or uniqueness of solutions.[21] For the series-truncated forms discussed here, it has been shown here that relatively simple, computationally efficient implicit globally stable schemes are available, and that existence/uniqueness issues do not arise, as the solution may always be arrived at through the solution of a linear system. This is a distinct advantage, and one that would appear to have wide applicability not merely to string vibration problems, but to other nonlinear systems of similar form which appear throughout solid mechanics (simulation of nonlinear plate vibration being a prime example).

[1] P. Morse and U. Ingard, *Theoretical Acoustics* (Princeton University Press, Princeton, NJ, 1968).
[2] R. Narasimha, "Nonlinear vibration of an elastic string," J. Sound Vib. **8**, 134–146 (1968).
[3] G. Kirchhoff, *Vorlesungen über Mechanik* (Tauber, Leipzig, 1883).
[4] G. F. Carrier, "On the nonlinear vibration problem of the elastic string," Q. Appl. Math. **3**, 157–165 (1945).
[5] G. Anand, "Large-amplitude damped free vibration of a stretched string," J. Acoust. Soc. Am. **45**, 1089–1096 (1969).
[6] J. Johnson and A. Bajaj, "Amplitude modulated and chaotic dynamics in resonant motion of strings," J. Sound Vib. **128**, 87–107 (1989).
[7] C. Vallette, "The mechanics of vibrating strings," in *Mechanics of Musical Instruments*, edited by A. Hirschberg, J. Kergomard, and G. Weinreich (Springer, New York, 1995), pp. 116–183.
[8] J. Simo and L. Vu-Quoc, "On the dynamics of flexible beams under large overall motions—The plane case: Part I," ASME J. Appl. Mech. **53**, 849–854 (1986).
[9] J. Simo and L. Vu-Quoc, "On the dynamics of flexible beams under large overall motions—The plane case: Part II," ASME J. Appl. Mech. **53**, 855–863 (1986).
[10] B. Bank and L. Sujbert, "Modeling the longitudinal vibration of piano strings," in *Proceedings of the Stockholm Musical Acoustics Conference*, Stockholm, Sweden, August 2003, pp. 143–146.
[11] B. Bank and L. Sujbert, "A piano model including longitudinal string vibration," in *Proceedings of the Digital Audio Effects Conference*, Naples, Italy, October 2004, pp. 89–94.
[12] C. Gough, "The nonlinear free vibration of a damped elastic string," J. Acoust. Soc. Am. **75**, 1770–1776 (1984).
[13] D. Furihata, "Finite difference schemes for nonlinear wave equation that inherit energy-conservation property," J. Comput. Appl. Math. **134**, 37–57 (2001).
[14] M. Rubin and O. Gottlieb, "Numerical solutions of forced vibration and whirling of a nonlinear string using the theory of a cosserat point," J. Sound Vib. **197**, 85–101 (1996).
[15] S. Bilbao and J. O. Smith III, "Energy conserving finite difference schemes for nonlinear strings," Acustica **91**, 299–311 (2005).
[16] S. Bilbao, "Energy-conserving finite difference schemes for tension-modulated strings," in *Proceedings of the IEEE International Conference on Acoustics, Speech, Sig. Proc.*, Montreal, Canada, May 2004.
[17] S. Bilbao, "Modal-type finite difference schemes for nonlinear strings with an energy-conservation property," in *Proceedings of the Digital Audio Effects Conference*, Naples, Italy, October 2004, pp. 119–124.
[18] B. Gustaffson, H.-O. Kreiss, and J. Oliger, *Time Dependent Problems and Difference Methods* (Wiley, New York, 1995).
[19] R. Richtmyer and K. Morton, *Difference Methods for Initial Value Problems* (Wiley, New York, 1967).
[20] J. Sanz-Serna, "An explicit finite-difference scheme with exact conservation properties," J. Comput. Phys. **47**, 199–210 (1982).
[21] D. Greenspan, "Conservative numerical methods for $\ddot{x}=f(x)$," J. Comput. Phys. **56**, 28–41 (1984).
[22] E. Kreyszig, *Introductory Functional Analysis with Applications* (Wiley, New York, 1978).
[23] J. Strikwerda, *Finite Difference Schemes and Partial Differential Equations* (Wadsworth and Brooks/Cole Advanced Books and Software, Pacific Grove, CA 1989).
[24] R. Vichnevetsky and J. Bowles, *Fourier Analysis of Numerical Approximations of Hyperbolic Equations* (SIAM, Philadelphia, 1982).
[25] L. Vu-Quoc and X. Tan, "Optimal solid shells for nonlinear analyses of multilayer composites II. Dynamics," Comput. Methods Appl. Mech. Eng. **192**, 1017–1059 (2003).
[26] T. Tolonen, V. Välimäki, and M. Karjalainen, "Modeling of tension modulation nonlinearity in plucked strings," IEEE Trans. Speech Audio Process. **8**, 300–310 (2000).
[27] C. Erkut, "Aspects in analysis and model-based sound synthesis of plucked string instruments," Ph.D. thesis, Laboratory of Acoustics and Audio Signal Processing, Helsinki University of Technology, 2002.
[28] V. Välimäki, T. Tolonen, and M. Karjalainen, "Plucked-string synthesis algorithms with tension modulation nonlinearity," in *Proceedings of the IEEE Int. Conf. on Acoustics, Speech, Sig. Proc.*, Phoenix, AZ, March 1999, Vol. **2**, pp. 977–980.
[29] R. Dickey, "Infinite systems of nonlinear oscillation equations related to the string," Proc. Am. Math. Soc. **23**, 459–468 (1969).
[30] R. Dickey, "Stability of periodic solutions of the nonlinear string," Q. Appl. Math. **38**, 253–259 (1980).
[31] L. Trefethen, *Spectral Methods in Matlab* (SIAM, Philadelphia, 2000).
[32] B. Fornberg, *A practical Guide to Pseudospectral Methods*, Cambridge Monographs on Applied and Computational Mathematics, Cambridge, England, 1995.
[33] J. Simo and L. Vu-Quoc, "On the dynamics in space of rods undergoing large motions—A geometrically exact approach," Comput. Methods Appl. Mech. Eng. **66**, 125–161 (1988).
[34] H. Conklin, "Design and tone in the mechanoacoustic piano. III. Piano

strings and scale design," J. Acoust. Soc. Am. **100**, 1286–1298 (1996).
[35]J. Simo and L. Vu-Quoc, "The role of nonlinear theories in transient dynamics analysis of flexible structures," J. Sound Vib. **119**, 487–508 (1987).
[36]S. Li and L. Vu-Quoc, "Finite difference calculus invariant structure of a class of algorithms for the nonlinear Klein Gordon equation," SIAM (Soc. Ind. Appl. Math.) J. Numer. Anal. **32**, 1839–1875 (1995).
[37]L. Vu-Quoc and S. Li, "Invariant-conserving finite difference algorithms for the nonlinear Klein-Gordon equation," Comput. Methods Appl. Mech. Eng. **107**, 341–391 (1993).
[38]A. Taflove, *Computational Electrodynamics* (Artech House, Boston, MA, 1995).
[39]K. S. Yee, "Numerical solution of initial boundary value problems involving Maxwell's equations in isotropic media," **14**, 302–307 (1966).
[40]J. Sanz-Serna, "Symplectic integrators for Hamiltonian problems: An overview," Acta Numerica **1**, 243–286 (1991).

High intensity focused ultrasound-induced gene activation in sublethally injured tumor cells *in vitro*

Yunbo Liu
Department of Mechanical Engineering and Materials Science, Duke University, Durham, North Carolina 27708

Takashi Kon and Chuanyuan Li
Department of Radiation Oncology, Duke University Medical Center, Durham, North Carolina 27708

Pei Zhong[a)]
Department of Mechanical Engineering and Materials Science, Duke University, Durham, North Carolina 27708

(Received 18 May 2005; revised 25 July 2005; accepted 28 July 2005)

Cultured human cervical cancer (HeLa) and rat mammary carcinoma (R3230Ac) cells were transfected with vectors encoding green fluorescent protein (GFP) under the control of hsp70B promoter. Aliquots of 10-μl transfected cells (5×10^7 cells/ml) were placed in 0.2-ml thin-wall polymerase chain reaction tubes and exposed to 1.1-MHz high intensity focused ultrasound (HIFU) at a peak negative pressure $P^-=2.68$ MPa. By adjusting the duty cycle of the HIFU transducer, the cell suspensions were heated to a peak temperature from 50 to 70 °C in 1–10 s. Exposure dependent cell viability and gene activation were evaluated. For a 5-s HIFU exposure, cell viability dropped from 95% at 50 °C to 13% at 70 °C. Concomitantly, gene activation in sublethally injured tumor cells increased from 4% at 50 °C to 41% at 70 °C. A similar trend was observed at 60 °C peak temperature as the exposure time increased from 1 to 5 s. Further increase of exposure duration to 10 s led to significantly reduced cell viability and lower overall gene activation in exposed cells. Altogether, maximum HIFU-induced gene activation was achieved at 60 °C in 5 s. Under these experimental conditions, HIFU-induced gene activation was found to be produced primarily by thermal rather than mechanical stresses. © *2005 Acoustical Society of America.*
[DOI: 10.1121/1.2041247]

PACS number(s): 43.80.Gx, 43.80.Cs, 43.25.Yw [FD] Pages: 3328–3336

I. INTRODUCTION

In recent years, high intensity focused ultrasound (HIFU) has been used successfully as a noninvasive and nonionizing therapeutic modality for the treatment of a variety of cancers, including liver (Chen *et al.*, 1999; Kennedy *et al.*, 2004), prostate (Chapelon *et al.*, 1999; Chaussy and Thuroff, 2003), ocular (Lizzi *et al.*, 1992), and breast (Hynynen *et al.*, 2001) cancers. Extensive physical and biological studies have been carried out, which demonstrate that HIFU, with a spatial peak temporal average intensity (I_{SPTA}) between 10^3 and 10^4 W/cm^2, can produce well-defined lesions in deep-sited tissue through coagulative necrosis and cavitation damage (ter Haar, 1995, 2001; Bailey *et al.*, 2003; Wu *et al.*, 2004; Kennedy *et al.*, 2003). In addition to thermal ablation, there is also preliminary yet encouraging evidence to suggest that HIFU may induce a distinct stress response in sublethally injured tumor cells surrounding the lesion. For example, following HIFU treatment in patients with benign prostatic hyperplasia, (BPH), significant up-regulation of heat shock proteins (hsps) has been observed at the border of HIFU-induced necrosis region (Kramer *et al.*, 2004). It has been further postulated that the up-regulation of hsps may play a critical role in eliciting an anti-tumor immunity (Kramer *et al.*, 2004; Wu *et al.*, 2004). Although heat shock response induced by conventional hyperthermia (42 °C for 30 min) is well documented (Hildebrandt *et al.*, 2002), the physical conditions for HIFU-induced stress response have not been thoroughly investigated. Furthermore, as we will discuss later, a synergistic combination of HIFU-induced stress response and/or gene therapy with HIFU-produced thermal ablation may help to improve the effectiveness of cancer therapy.

When cells are exposed to stressful conditions, such as hyperthermia, environmental toxicity, and even mechanical stresses, the expression of a specific family of genes that control the production of heat shock (or stress) proteins, also known as molecular chaperones, will be dramatically up-regulated (Morimoto, 1993). In cells of diverse origins, heat shock proteins are well conserved throughout evolution. In particular, it has been shown that hsp70 protein family represents the most abundant gene product in response to external stresses (Voellmy, 1996). One member of the hsp70 gene family, hsp70B, is strictly stress inducible and absent in unstressed cells (Hildebrandt *et al.*, 2002). Taking advantage of this unique property, various heat-inducible gene constructs have been developed recently for both cytotoxic and immuno-stimulatory gene therapies, which are usually activated by hyperthermia in a 42 °C water bath for 30 min (Li

a)Author to whom correspondence should be addressed; electronic mail: pzhong@duke.edu

and Dewhirst, 2002). Compared to other physical means such as radiation for gene activation, heat-regulated gene expression under the control of hsp70B promoter has excellent inducibility with very low background, making it an attractive approach for controlling gene expression both temporally and spatially (Huang *et al.*, 2000; Borrelli *et al.*, 2001).

Recently, ultrasound-induced hyperthermia has also been exploited to regulate transgene expression both *in vitro* and *in vivo* (Vekris *et al.*, 2000; Zhong *et al.*, 2003). Following exposure to 2 W/cm^2 ultrasound for 20 min, Smith *et al.* (2002) demonstrated a locally induced luciferase or FasL gene expression under the control of hsp70B promoter. Using a MRI-guided ultrasound system, Guilhon *et al.* (2003) reported heat inducible transgene (GFP) expression in a rat tumor model after ultrasound-induced hyperthermia within a thermal dose of 44 °C for 20 min to 48 °C for 3 min. However, the profile of heat shock response of tumor cells exposed to temperatures in the range of 50–70 °C for a few seconds is largely unknown. These thermal exposure conditions are most relevant to those experienced by the sublethally injured tumor cells surrounding HIFU-produced necrosis lesion. Moreover, it should be noted that heat shock response could also be induced by pulsed ultrasound without thermal effects (Barneet *et al.*, 1994; Angles *et al.*, 1990; Locke and Nussbaum, 2001) or even by cyclic mechanical shear stress (Xu *et al.*, 2000), usually for long exposure durations of 30 min to 6 h. However, the relative contribution of thermal versus mechanical stresses to ultrasound induced heat shock response in biological cells/tissue has not been systematically evaluated.

The purpose of this study was to determine the activation of transfected GFP marker gene under the control of hsp70B promoter in tumor cells that were sublethally injured during HIFU exposure *in vitro*. Specifically, the goals of this study are threefold: (1) assessing the inducibility of transfected exogenous heat-sensitive gene in sublethally injured tumor cells following HIFU treatment, (2) evaluating the optimal thermal dosage (temperature and duration) for eliciting strong and consistent gene expression both in surviving and total exposed cell populations, and (3) comparing the contribution of underlying physical mechanisms (thermal stress versus mechanical stress) for HIFU-induced gene activation.

II. MATERIALS AND METHODS

A. Cell culture and gene transfection

Human cervical cancer (HeLa) cell line was maintained routinely in minimal essential medium (MEM) with 10% heat-inactivated fetal bovine serum (FBS) and 5% antibiotics in a humidified incubator at 37 °C containing 5% CO_2. One day before HIFU treatment, HeLa cells were transfected with Adeno-hsp70B-GFP adenovirus vector at a MOI (multiplicity of infection=ratio of infectious virus particles to cells) of 10. In another set of experiments, rat mammary carcinoma (R3230Ac) cells were transfected with hsp70B-EGFP plasmid using lipofecfamine (Gibco-BRL, Bethesda, MD). To select stably transfected R3230Ac cells, G418 (400 μg/ml) was added to the transfected cell culture and hyperthermia was performed in a water bath (42 °C-30 min). Colonies that showed high level of inducible GFP expression and low fluorescence background were selected and subsequently expanded and frozen in aliquots for future use. One week before the experiment, a frozen stock of the constructed R3230Ac cells were recovered at low seeding density and cultured in T-25 flasks with DMEM containing 10% FBS and 1% penicillin-streptomycin. Before HIFU treatment, the transfected HeLa and R3230Ac cells were grown to about 60% confluence, trypsinized, pelleted (80 g, 3 min), and then suspended in culture medium with a cell density of 5 $\times 10^7$ cells/ml.

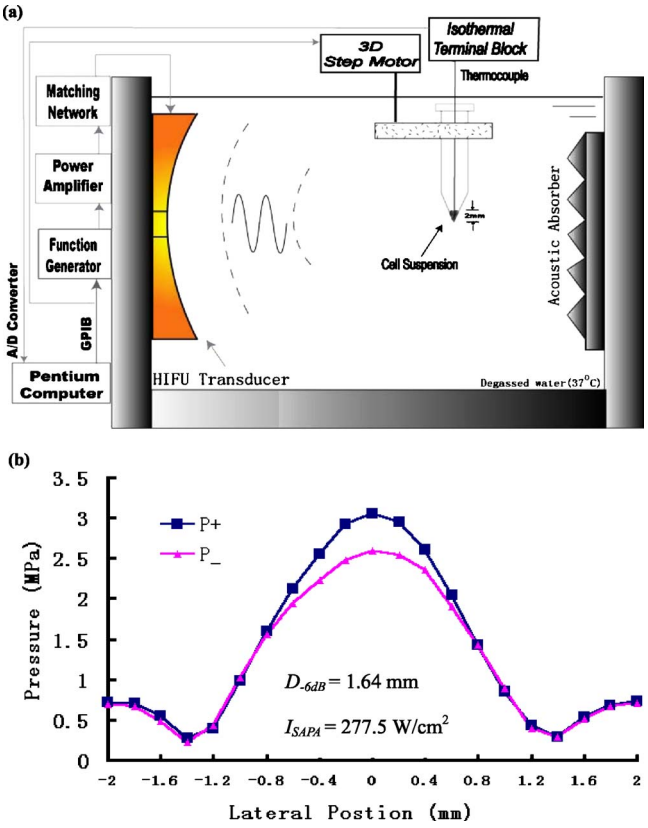

FIG. 1. (Color online) (a) Schematic diagram of the experimental system. (b) Pressure distribution across the focal plane of the 1.1-MHz HIFU transducer in water. P^+: peak positive pressure and P^-: peak negative pressure.

B. High intensity focused ultrasound (HIFU) apparatus

A 1.1-MHz HIFU transducer (H-102, Sonic Concepts, Seattle, WA) with a focal length of 62 mm was mounted horizontally inside a heated (37 °C) chamber filled with degassed water. As shown in Fig. 1(a), the HIFU transducer with its 50-Ω matching network was driven by sinusoidal tone-burst signals produced by a function generator (33120A, Agilent, Palo Alto, CA), which was connected in series with a 55-dB power amplifier (A150, Electronic Navigation Industries, Rochester, NY). The operation and exposure parameters of the HIFU system were controlled by LABVIEW programs via a GPIB board installed in a PC. A volume of 10-μl cell suspension was loaded in a 0.2-ml Polymerase Chain Reaction (PCR) thin-wall tube (Product No. 3746, Corning, NY), which was placed vertically with

its conical bottom aligned within the −6-dB beam focus of the HIFU transducer. Using a calibrated needle hydrophone (TUN001A, NTR Sys, Seattle, WA), the pressure distribution in the focal plane of the transducer was measured, which revealed a peak positive (P^+)/peak negative pressure (P^-) of 3.05/−2.68 MPa and a −6-dB beam diameter of 1.64 mm when the function generator was operated at 0.1 V_{pp} [Fig. 1(b)]. The corresponding spatial average pulse average intensity (I_{SAPA}) of the acoustic field around the beam focus was calculated to be 278 W/cm^2, based on an established protocol (Harris, 1985). At this output level, different temperature elevations in the cell suspension could be achieved by adjusting the duty cycle (10%–30%) of the tone burst signal at a fixed pulse repetition frequency of 200 Hz.

C. Temperature measurement

Temperature elevation in the cell suspension during HIFU exposure was monitored using a 0.2-mm bare-ware thermocouple (Customer designed IT-23, Physitemp Inc., Clifton, NJ), which minimizes ultrasound beam distortion and measurement artifacts due to viscous and sheathing heating (Hynynen and Edwards, 1989). The thermocouple output voltage was conditioned by an electronically compensated isothermal terminal block (TC-2190, National Instrument, Austin, TX) and registered at 6-Hz sampling rate by a Data Acquisition Board (NI4351, National Instrument, Autsin, TX) controlled by a LABVIEW program [Fig. 1(a)]. Using this system, the nonuniform spatial temperature fluctuation inside the cell suspension (2 mm medium high) was determined to be less than 3.0 °C, which was presumably caused by the inhomogeneous ultrasound absorption at the tube wall.

Figure 2 shows two representative temperature profiles that can be produced in the cell suspension during HIFU exposure—heat plateau and heat shock, both of which reached a peak temperature of 60 °C. For heat plateau scheme, the initial temperature rise was linearly proportional to the absorbed energy density in the first 5 s and subsequently the temperature rise slowed down as the local heat conduction became pronounced. With continued ultrasound exposure, a thermal equilibrium was eventually achieved to maintain a temperature plateau during the 15- to 30-s insonification. Such a heat plateau profile is most important for hyperthermia therapy. In comparison, heat shock profile is more relevant for HIFU therapy, in which the initial (5 s) temperature rise becomes dominant. Because of the high ultrasound intensity and short exposure time, a local thermal equilibrium cannot be reached before the end of HIFU exposure (Lizzi and Ostromogilsky, 1987; Hill and ter Haar, 1995).

D. Experimental design

Three series of experiments were carried out in this study. The first series of experiments were designed to provide a transition from hyperthermia-induced gene activation (heat plateau) to HIFU-elicited gene activation (heat shock). Here the temperature in the cell suspension was gradually escalated from 42 to 70 °C while the treatment time was reduced concomitantly from 30 min to 5 s. Multiple durations at 50, 60, and 70 °C temperature levels were evaluated.

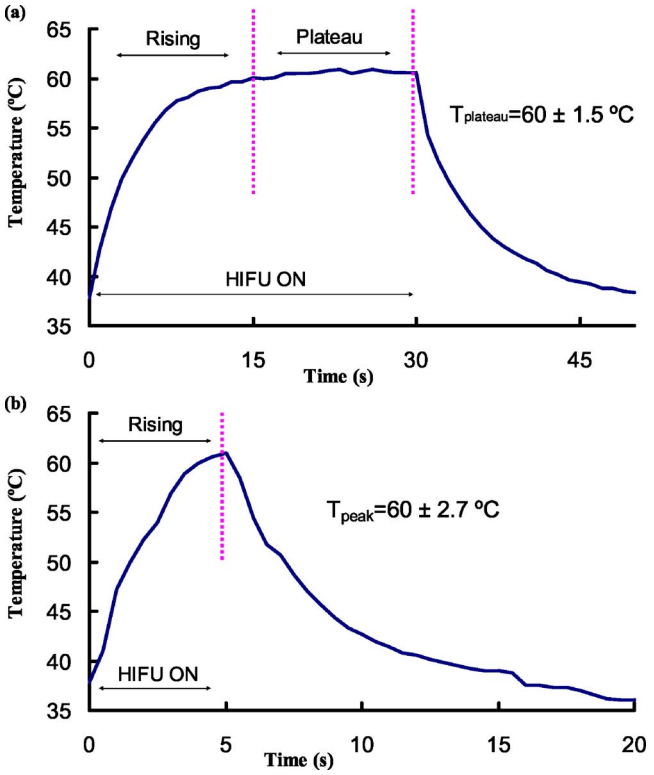

FIG. 2. (Color online) Two representative temperature profiles (a) heat plateau and (b) heat shock produced by the 1.1-MHz HIFU transducer in cell suspension.

Once the feasibility of HIFU-induced gene activation was demonstrated, a second series of experiments were carried out with HIFU-relevant heat shock exposures in which either the treatment time was fixed at 5 s while the peak temperature was increased from 50 to 70 °C or the peak temperature was maintained at 60 or 70 °C while the heat shock duration was increased progressively from 1 to 10 s. Based on these experiments, the optimal exposure conditions were identified for producing maximum gene activation either in the surviving cells or with respect to the total exposed cell population.

In the third series of experiments, the contribution of thermal stress versus mechanical stress to HIFU-induced gene activation was investigated. To evaluate the contribution of thermal stress transfected HeLa cells cultured on etched grid cover slips (Bellco Biotechnology, Vineland, NJ) were plunged rapidly into PBS solutions of 50, 60, or 70 °C, respectively, for a short immersion period of 2 s. Such exposures yielded similar cell death to the corresponding 5-s HIFU heat shock treatment. In comparison, to assess the effect of mechanical stress transfected HeLa cells were treated under the identical acoustic parameters for the 70 °C-5-s HIFU exposure except that the ambient temperature in the water bath was lowered to 5 °C. Using this approach, the peak temperature in the cell suspension during the 5-s HIFU treatment could be kept below 35 °C, thus eliminating the contribution of the thermal stress.

In addition, cavitation activity in cell suspension during

HIFU treatment was measured by passive cavitation detection (PCD) using a 15-MHz transducer (M2062, Panametrics, Waltham, MA) positioned perpendicularly to the HIFU beam and 5 mm away from the cell samples. A total of 100 acoustic emission signals (each collected in a 10-μs window) emanated from the HIFU-induced cavitation bubbles were amplified by a pulse/receiver (5052PR, Panametrics, Waltham, MA) and recorded in sequence mode on a digital oscilloscope (9310A, LeCroy, Chestnut Ridge, NY) during the 5-s exposure period (Chen *et al.*, 2004). Fast Fourier Transform (FFT) spectrums of these wave forms from ten measurements were averaged and compared for different exposure settings. rms amplitude of the broadband noise signals for each FFT spectrum between 12.5 and 17.5 MHz in frequency domain was further calculated and presented in time sequence. The level of inertial cavitation (IC) activity was quantified by computing the cumulated IC dosage (ICD), defined by the integration of the rms amplitude (12.5–17.5 MHz) over the entire exposure period (Chen *et al.*, 2003).

E. Viability and gene expression assays

Immediately following HIFU exposure, cell samples were plated and cultured on the etched-grid cover slips in a six-well plate for 24 h before assayed for cell viability and gene expression. Cell viability was determined by counting viable cells from 10 randomly selected areas of each sample under a microscope after 5 min *in situ* Trypan Blue Staining. The results from HIFU treated groups were normalized by viability of the corresponding control group.

To assess GFP gene expression, the cultured cells were trypsinized and FACS analysis was performed using a flow cytometer (FACScan, Becton Dickinson, San Jose, CA) operated at an exciting wavelength of 488 nm and emission detection wavelength of 530±15 nm.

F. Statistical analysis

Each experiment data point was averaged from six samples except otherwise indicated. Student's t-test was used to determine the statistical significance and $p<0.05$ was considered to indicate a statistically significant difference between two experimental configurations. All statistics were computed by using SIGMAPLOT 8.0 (Systat Software, Point Richmond, CA).

III. RESULTS

A. Heat plateau- and heat shock-induced gene activation

Inducible GFP gene activation was observed in both cell lines following a wide range of ultrasound exposure. Figure 3 shows the maximum gene expression in surviving cells 24-h post-treatment at four different peak temperature levels: water-bath hyperthermia (42 °C for 30 min), heat plateau (50 °C for 15 s+2 min; 60 °C for 15 s+15 s) and heat shock (70 °C in 5 s). In comparison, the transfected cells in the control group displayed a very low basal fluorescence activity (<1.5%), confirming the highly inducible nature of the hsp70B promoter. The corresponding cell viability is summarized in Table I, which reveals a graduate decrease from 84% for 42 °C-30-min hyperthermia to 13% for 70 °C-5-s heat shock treatment. In addition, the mean GFP fluorescence intensity in the GFP positive cells was calculated and used as a means to evaluate the strength of the heat shock response in each treatment group.

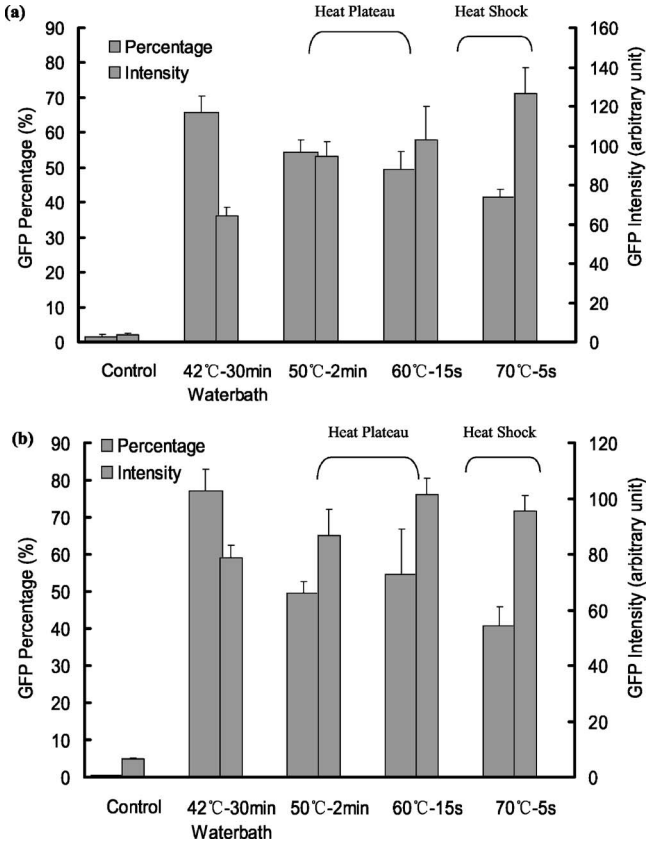

FIG. 3. Gene activation in transfected (a) HeLa and (b) R3230Ac cells following various hyperthermia and HIFU exposures.

For gene activation in the transfected HeLa cells, the percentage of GFP positive cells in the surviving population was found to be in the range of 54% to 41% for heat plateau and heat shock treatments, which are lower than 66% induced by hyperthermia treatment [Fig. 3(a)]. This is presumably caused in part by the heterogeneous temperature distribution in cell suspension produced by the ultrasound treatment, compared to the uniform temperature distribution in water-bath hyperthermia. However, the mean GFP intensity in HIFU-treated groups was found to be increased by 31-fold to 42-fold from the control group, although no statistical difference in gene expression was found within the heat plateau treatment groups ($p>0.14$). In comparison, the mean GFP intensity was increased by 21-fold in the hyperthermia treatment group. This finding suggests that stronger heat shock response can be induced in sublethally injured tumor cells that survive the insult of HIFU exposure compared to hyperthermia treatment. Similar patterns of HIFU-induced gene activation were observed in the transfected R3230Ac cells [Fig. 3(b)].

TABLE I. Cell viability of HeLa cells under HIFU exposures.

		Heat plateau			Heat shock					
	Control	42 °C 30 min	50 °C 120 s	60 °C 15 s	50 °C 5 s	60 °C 1 s	60 °C 2 s	60 °C 5 s	60 °C 10 s	70 °C 5 s
Viability (%)	100	84	64	31	95	81	80	71	47	13
STD (%)	0	±6.9	±15.1	±9.2	±6.7	±6.7	±5.7	±6.2	±9.1	±7.8

B. Effect of peak temperature on HIFU-induced gene activation

The effect of peak temperature on HIFU-induced gene activation in transfected HeLa cells for a fixed heat shock exposure time of 5 s is shown by phase contrast and fluorescence images in Fig. 4. Detectable level of GFP expression was observed as early as 4–6 h following the HIFU exposure. The gene expression level reached a maximum about 24 h and remained detectable 72 h post HIFU treatment. This temporal profile of inducible gene activation by HIFU is similar to that produced by ultrasound-induced hyperthermia (Smith *et al.*, 2000). Quantitatively, a low level of GFP expression (4%) was induced at 50 °C peak temperature and its GFP intensity increased about 3-fold compared to the control group [Fig. 5(a)]. However, as the peak temperature was increased to 60 and 70 °C, much stronger GFP expression of 38% and 41% was induced in the surviving cells with concomitant expression intensity increased by 35-fold and 42-fold, respectively [Fig. 5(a)]. However, no statistical difference in gene expression ($p > 0.09$) was found between the 60 and 70 °C treatment groups. The inducible gene expression in the surviving cells appeared to reach a saturation threshold at 60 °C peak temperature. In fact, cell viability was 95% and 71% following HIFU exposure at 50 and 60 °C peak temperatures and the corresponding value dropped significantly to 13% post-70 °C exposure (Table I). This transition in HIFU-induced cell necrosis between 60 and 70 °C is comparable to the temperature threshold for tissue necrosis (>60 °C) observed in several animal studies (Yang *et al.*, 1993; ter Haar, 1995).

For assessing the potential therapeutic effect, the gene expression efficiency with respect to the total exposed cells is most relevant. This value can be calculated as the product of cell viability and gene expression efficiency in the surviv-

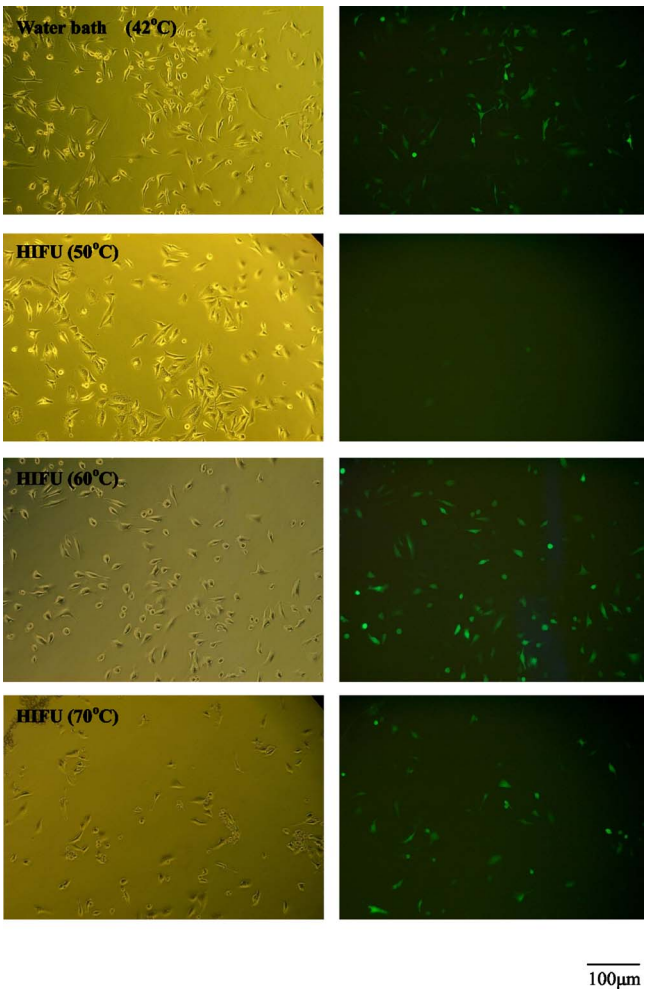

FIG. 4. (Color online) Representative phase contrast (left column) and fluorescence (right column) images of transfected HeLa cells after 5-s heat shock exposure at different peak temperatures. These images were taken 24 h after the experiment.

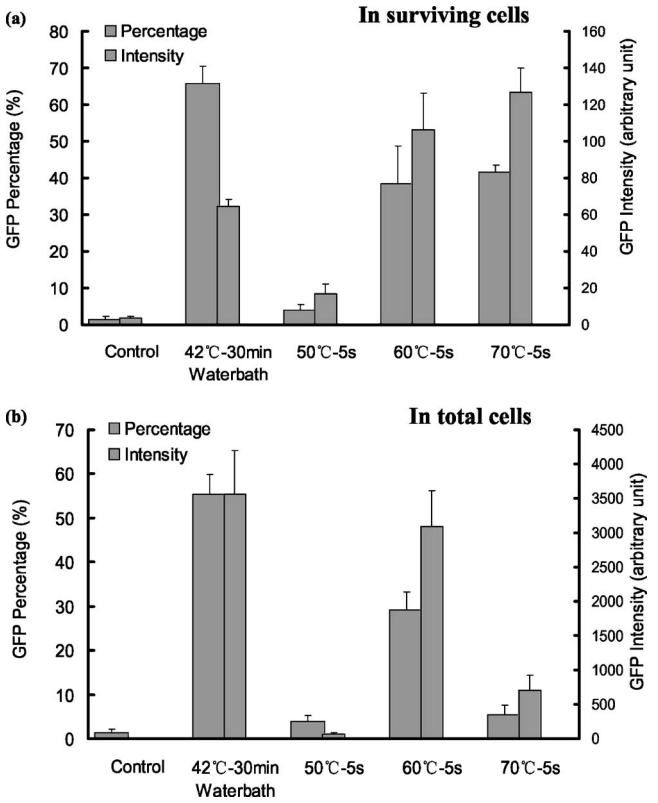

FIG. 5. Gene expression of transfected HeLa cells in (a) surviving and (b) total cell populations after 5-s heat shock exposure.

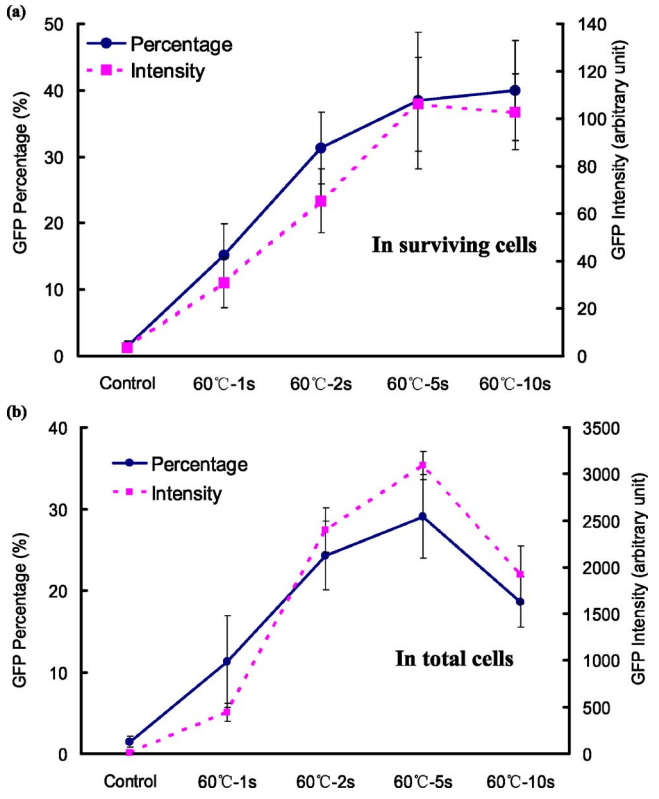

FIG. 6. (Color online) Effect of treatment duration on gene expression of transfected HeLa cells in (a) surviving and (b) total cell populations at a peak temperature of 60 °C.

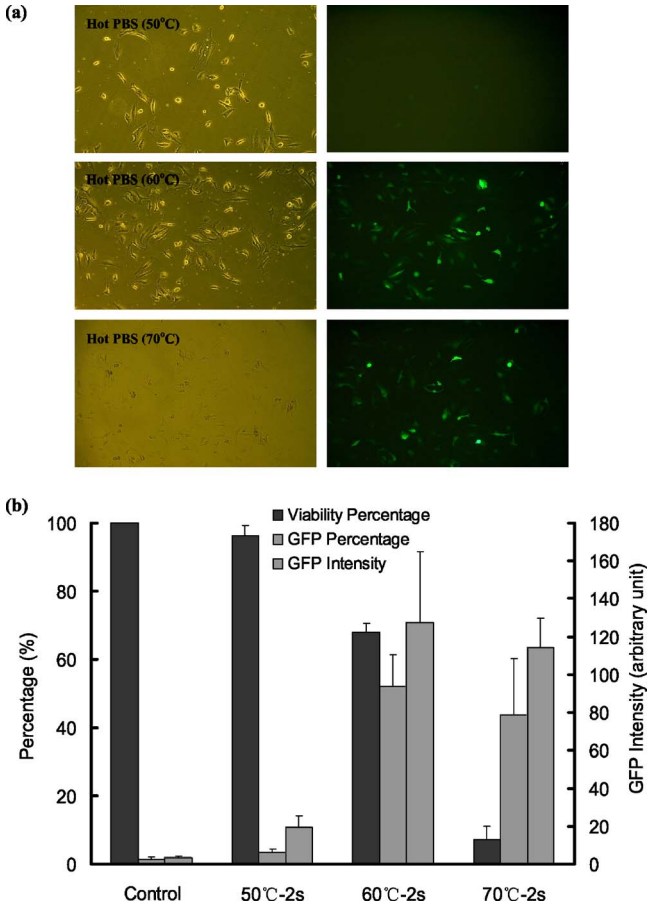

FIG. 7. (Color online) (a) Representative phase contrast (left column) and fluorescence (right column) images of transfected HeLa cells and (b) corresponding cell viability and gene expression in the surviving population after exposure to heated PBS solutions of various temperatures for 2 s. These images were taken 24 h after the experiment.

ing cells, and the results are shown in Fig. 5(b). It was found that with respect to the total exposed cells, the maximum gene expression was induced at 60 °C peak temperature. For example, a 20-fold increase (compared to control) was observed at 60 °C peak temperature, which is much higher than the corresponding results of a 3-fold increase for 50 °C and a 4-fold increase for 70 °C, respectively [Fig. 5(b)]. Altogether, these findings suggest that on the one hand, gene expression cannot be activated if the cells are not stressed sufficiently (e.g., 50 °C for 5 s). On the other hand, if cells are overstressed (e.g., 70 °C for 5 s) excessive cell death will be produced, leading to a low gene expression efficiency with respect to the total exposed cells. An optimal window of thermal dosage (around 60 °C for 5 s) exists for inducing the maximum overall gene expression following a 5-s HIFU exposure in our experimental system. It is worth noting that the maximum gene expression induced by HIFU (60 °C-5 s) is about 52% in percentage and 86% in intensity compared to the gene expression induced by 42 °C-30-min water bath hyperthermia [Fig. 5(b)]. Similar results were obtained from the R3230Ac cells following HIFU treatment (data not shown).

C. Effect of treatment duration on HIFU-induced gene activation

The effect of treatment duration on HIFU-induced gene activation in transfected HeLa cells at 60 °C peak temperature is shown in Fig. 6. It was found that gene expression in the surviving cells increased initially with the exposure duration and gradually saturated after 5-s exposure [Fig. 6(a)]. No statistically significant difference ($p > 0.1$) was observed between the gene activation levels produced by the 5- and 10-s exposures with respect to expression percentage and intensity. However, for the total exposed cells HIFU-induced gene activation showed a similar initial increase from 1 to 5 s, followed by a dramatic decline after 10-s exposure. These results suggest that an optimal dosage for HIFU-induced gene activation is 5 s at 60 °C peak temperature, and further increase in treatment time will dramatically increase cell injury and thus significantly diminish the overall inducible gene activation. A similar pattern of HIFU-induced gene activation was also observed at 70 °C peak temperature with an exposure duration ranging from 1 to 10 s; yet the corresponding gene activation efficiency in total cells was lower than its counterpart at 60 °C (data not shown).

D. Physical mechanisms: Thermal stress versus mechanical stress

The thermal stress produced by HIFU exposure was simulated by immersing transfected HeLa cells cultured on etched cover slips in hot PBS solutions with temperature of 50, 60, and 70 °C, respectively, for 2 s. As shown in Fig. 7(a), gene expression can be clearly observed in the 60 and

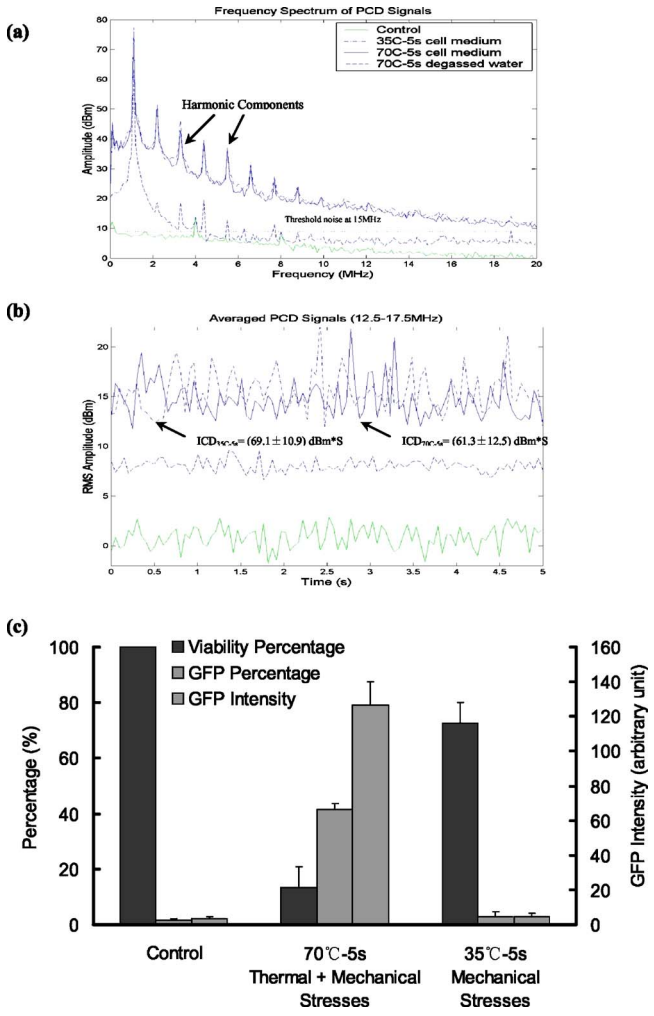

FIG. 8. (Color online) (a) Representative frequency spectrum of PCD signals measured during different HIFU exposures and medium conditions, (b) time evolution of averaged broadband noise of the PCD signals during the 5-s HIFU treatment, and (c) comparison of thermal+mechanical vs mechanical stresses on HIFU-induced cell viability and gene activation in the surviving population of transfected HeLa cells.

70 °C groups but barely in the 50 °C group. Quantitatively, GFP intensity in surviving cells was increased 42-fold and 38-fold in the 60 and 70 °C groups [Fig. 7(b)], which are comparable to the gene activation (35-fold and 42-fold) produced by the 5-s HIFU treatment [Fig. 5(a)]. Because of the much more uniform thermal exposure in the hot PBS immersion system, the resultant gene expression percentage [52% for 60 °C, Fig. 7(b)] was higher than the corresponding value [38%, Fig. 5(a)] induced by the HIFU exposure. In addition, a dramatic decrease in cell viability was also observed from 60 to 70 °C. Therefore, with respect to the total exposed cells, the maximum gene activation level was again produced at 60 °C, confirming the results from HIFU-induced gene activation [Fig. 5(b)].

To assess the effect of mechanical stress in gene activation, HIFU-induced cavitation activities in the cell suspension were measured by PCD under identical acoustic exposure conditions yet with different ambient water temperature: 70 °C-5 s($T_{\text{waterbath}}$=37 °C) and 35 °C-5 s($T_{\text{waterbath}}$=5 °C). Representative frequency spectrums of the emitted PCD signals are shown in Fig. 8(a). A significant increase of the broadband noise associated with inertial cavitation was observed during insonification, which is comparable between the two exposure conditions. In addition, subharmonics and higher harmonics (second, third, fourth, etc.) generation can be clearly identified in the frequency domain, which could be produced by the nonlinear scattering of stable cavitation bubbles in the cell culture medium (Miller and Bao, 1998). Moreover, the averaged rms amplitude of the broadband noise in the frequency range of 12.5–17.5 MHz during the 5-s HIFU exposure is plotted in Fig. 8(b), from which the integrated inertial cavitation dosages (ICD) were calculated to be 69.1±10.9 and 61.3±12.5 dBm* s, respectively. Again, no statistically significant difference was found between the two exposure conditions ($p>0.1$). It is interesting to note that all these indexes for cavitation activity dropped significantly when the culture medium was replaced by degassed water. Altogether, these results suggest that substantial cavitation activities could be induced in cell suspension during HIFU treatment, and comparable bubble activities were produced using either the 70 °C-5 s (thermal+mechanical stresses) or the 35 °C-5-s (mechanical stresses) exposure condition.

The results for cell viability and gene activation produced by the two exposure conditions are shown in Fig. 8(c). At a medium temperature of 70 °C, cell viability dropped to 13% following HIFU treatment; yet gene activation was induced in 41% of the survival cells with a concomitant 42-fold increase in expression intensity. In comparison, at a medium temperature of 35 °C cell viability was 72% with minimal level of gene activation, which is not statistically significant different ($p>0.1$) from the value in the control group. Together, these results suggest that the dominant mechanism for HIFU-induced cell necrosis and gene activation is thermal stress. The mechanical stress induced during the HIFU treatment contributes to about 1/3 of the cell damage, but it is not sufficient to elicit a measurable stress response (i.e., activation of the hsp70B promoter). However, the mechanical stress and thermal stress may interact synergistically during HIFU exposure to enhance thermal ablation of the tumor.

IV. DISCUSSION

During HIFU treatment, the peak temperature in tissue at the beam focus could increase rapidly above 80 °C, which leads to effective cell killing and coagulative necrosis even for a few seconds exposure (Kennedy *et al.*, 2003). At the boarder of the lesion, a steep temperature gradient exists and multiple layers of cells that are sublethally injured form a sharp demarcation that separate the necrotic tissue and the surrounding untreated tissue. More important, over expression of heat shock proteins in the boarder zone has been observed recently, which may incite inflammation and even stimulate an anti-tumor immune response (Kramer *et al.*, 2004). However, the thermal exposure condition that leads to the heat shock response in the boarder zone was not determined. In this study, using an *in vitro* cell exposure system we have mimicked the response of tumor cells in different temperature regions within the boarder zone of HIFU-

induced lesion. Our results suggest that heat shock response can be produced in sublethally injured tumor cells within the temperature range of 50–70 °C. The maximum heat-induced gene activation could be induced at a peak temperature about 60 °C with a 5-s exposure time. Furthermore, our results suggest that HIFU-induced gene activation is produced primarily by thermal rather than mechanical stresses because of the extremely short exposure duration in HIFU (a few seconds) compared to the long treatment duration (>30 min) in hyperthermia and physiotherapy. In future work, it would be interesting to evaluate stress response of tumor cells that are exposed to a long duration of ultrasound-induced mechanical stresses that yield a similar level of sublethal cellular damage as produced by HIFU-generated thermal stress.

HIFU-induced cell death rises rapidly as the peak temperature is increased from 60 to 70 °C (see Table I). This observation is consistent with the temperature threshold for tissue necrosis (>60 °C) observed in several animal studies (Yang *et al.*, 1993; ter Haar, 1995). However, even at a peak temperature of 70 °C or above (data not shown) a small number of tumor cells can still survive. Similarly, incomplete tissue necrosis has been observed in tissue specimens collected from prostate cancer patients following HIFU treatment (Van Leenders *et al.*, 2000). These results are presumably caused by the heterogeneity in heat conduction and biological response of the tumor cells/tissue to HIFU therapy. In light of this observation, it is desirable to combine therapeutic modalities that are effective against residual tumor cells, such as immunotherapy, with HIFU so that the overall quality of cancer therapy can be improved.

Within the population of cells that were sublethally injured by HIFU treatment, heat-induced gene activation was found to increase initially with either peak temperature (for a fixed treatment duration) or treatment time (for a fixed peak temperature) before reaching a maximum at 60 °C for 5 s. Further increase in peak temperature or treatment duration led to a rapid reduction of gene activation in the total exposed cells [see Fig. 6(b)]. This dose-dependent gene activation may be caused by the two fundamental yet opposite biological responses (i.e., survival and death) that are activated simultaneously when cells are stressed. At the molecular level, the cellular response to stress is represented by the induction of hsps that may function either as molecule chaperones or proteases (Jolly and Morimoto, 2000). When the stress is low and duration is short (e.g., <60 °C and 5 s), molecule chaperones may assist in protein folding, translocation, refolding of intermediates, and thus restoring homeostasis. In contrast, when the stress is high and the duration is long (e.g., >70 °C and 5 s), the production of proteases such as the ubiquitin-dependent proteasome may increase significantly to degrade efficiently the damaged and short-lived proteins. Furthermore, at high stress levels the induced heat shock response may also lead to apoptosis or necrosis (Barry *et al.*, 1990). The intricate balance between these two opposite pathways and their interplay will determine whether a cell exposed to heat shock will die or survive (Jolly and Morimoto, 2000).

Taking advantage of the ubiquitous heat shock response, several groups have recently exploited the use of heat-induced gene therapy for cancer treatment (Li and Dewhirst, 2002). The most significant advantage of heat-inducible gene therapy is that site-specific control of gene expression in targeted tissues can be achieved. This is particularly important for reducing the systemic toxicity of most therapeutic genes, which are toxic to both tumor and normal tissues. Moreover, significant tumor regression has been produced by hyperthermia-induced cytotoxic (Blackburn *et al.*, 1998) and immunostimulatory (Huang *et al.*, 2000) gene therapy while no such therapeutic effects are seen with hyperthermia or intratumoral injection of the transgene alone. Potentially, there is also a synergistic interaction between hyperthermia and gene therapy, which may be related to hyperthermia-induced Fas and FasL expression in the heated tumor cells (Li and Dewhirst, 2002). However, two major limitations exist for hyperthermia-regulated cancer gene therapy. First, to induce gene activation by hyperthermia the temperature in the target tissue has to be kept closely at 42 °C for a long period of time (>30 min), a condition that is difficult to maintain in internal organs due to blood perfusion (Diederich and Hynynen, 1999). Second, hyperthermia-regulated gene therapy only retards the growth but cannot eradicate the tumor completely (Blackburn *et al.*, 1998; Huang *et al.*, 2000). To be more effective, hyperthermia-regulated gene therapy has to be used in conjunction with other existing cancer treatment modalities, such as radiation or chemotherapy (Li and Dewhirst, 2002). In contrast, these limitations may be potentially overcome by HIFU-regulated gene therapy, which can be produced simultaneously with HIFU-induced thermal ablation. For example, HIFU can be used to activate cytotoxic or immuno-regulatory genes in sublethally injured peripheral tumor cells while thermally ablating (or reducing) the primary tumor mass. Because of the short exposure duration and temperature gradient produced by HIFU, no rigorous control of the tissue temperature is needed. Moreover, the heat-induced cytotoxic gene products or immunostimulatory factors may significantly improve the effective killing of residual and distal metastasis tumor cells via bystander effects or a boosted anti-tumor immune response (Li and Dewhirst, 2002). Alternatively, a pre-treatment by HIFU-induced gene activation in the target tumor at low intensity (i.e., without thermal ablation) may be used to prime the host anti-tumor immune response before a regular HIFU therapy for complete eradication of the tumor mass. With real-time monitoring of HIFU-induced thermal dosimetry in tumors by MRI (Hynynen *et al.*, 2001; Guilhon *et al.*, 2003), such new treatment strategies should be feasible and may improve the overall quality of cancer therapy by HIFU.

In conclusion, we have demonstrated the feasibility of HIFU-induced transgene activation in sublethally injured tumor cells *in vitro*. Further animal studies are warranted to identify the optimal HIFU exposure condition for maximum gene activation and to explore treatment strategies that can combine synergistically HIFU-induced gene therapy with HIFU-produced thermal ablation for overall improved quality and effectiveness in cancer therapy.

ACKNOWLEDGMENTS

This work was supported in part by NIH through Grant Nos. RO1-EB02682 (P.Z.), R21-CA91166, and RO1-CA81512 (C.Y.L.). The authors also acknowledge Dr. Wenshiang Chen for his valuable discussion about cavitation detection.

Angles, J. M., Walsh, D. A., Li, K., Barnett, S. B., and Edwards, M. J. (**1990**). "Effects of pulsed ultrasound and temperature on the development of rat embryos in culture," Teratology, **42**, 285–293.

Bailey, M. R., Khokhlova, V. A., Sapozhnikov, O. A., Kargl, S. G., and Crum, L. A. (**2003**). "Physical mechanisms of the therapeutic effect of ultrasound," Acoust. Phys., **49**, 437–464.

Barnett, S. B., ter Haar, G. R., Ziskin, M. C., Nyborg, W. L., Maeda, K., and Bang, J. (**1994**). "Current status of research on biophysical effects of ultrasound," Ultrasound Med. Biol., **20**, 205–218.

Barry, M. A., Behnke, C. A., and Eastman, A. (**1990**). "Activation of programmed cell death (apoptosis) by cisplatin, other anticancer drugs, toxins and hyperthermia," Biochem. Pharmacol., **40**, 2353–2362.

Blackburn, R. V., Galoforo, S. S., Corry, P. M., and Lee, Y. J. (**1998**). "Adenoviral-mediated transfer of a heat-inducible double suicide gene into prostate carcinoma cells," Cancer Res., **58**, 1358–1362.

Borrelli, M. J., Schoenherr, D. M., Wong, A., Bernock, L. J., and Corry, P. M. (**2001**). "Heat-activated transgene expression from adenovirus vectors infected into human prostate cancer cells," Cancer Res., **61**, 1113–1121.

Chapelon, J. Y., Ribault, M., Vernier, F., Souchon, R., and Gelet, A. (**1999**). "Treatment of localized prostate cancer with transrectal high intensity focused ultrasound," Eur. J. Ultrasound, **9**, 31–38.

Chaussy, C., and Thuroff, S. (**2003**). "The status of high-intensity focused ultrasound in the treatment of localized prostate cancer and the impact of a combined resection," Curr. Urol. Rep., **4**, 248–252.

Chen, W. S., Brayman, A. A., Matula, T. J., and Crum, L. A. (**2003**). "Inertial cavitation dose and hemolysis produced *in vitro* with or without Optison," Ultrasound Med. Biol., **29**, 725–737.

Chen, W. S., Lu, X., Liu, Y., and Zhong, P. (**2004**). "The effect of surface agitation on ultrasound-mediated gene transfer *in vitro*," J. Acoust. Soc. Am., **116**, 2440–2450.

Chen, L., ter Haar, G. R., Robertson, D., Bensted, J. P., and Hill, C. R. (**1999**). "Histological study of normal and tumor-bearing liver treated with focused ultrasound," Ultrasound Med. Biol., **25**, 847–856.

Diederich, C. J., and Hynynen, K. (**1999**). "Ultrasound technology for hyperthermia," Ultrasound Med. Biol., **25**, 871–887.

Guilhon, E., Voisin, P., de Zwart, J. A., Quesson, B., Salomir, R., Maurange, C., Bouchaud, V., Smirnov, P., de Verneuil, H., Vekris, A., Canioni, P., and Moonen, C. T. (**2003**). "Spatial and temporal control of transgene expression *in vivo* using a heat-sensitive promoter and MRI-guided focused ultrasound," J. Gene Med., **5**, 333–342.

Harris, G. R. (**1985**). "A discussion of procedures for ultrasonic intensity and power calculations from miniature hydrophone measurements," Ultrasound Med. Biol., **11**, 803–817.

Hildebrandt, B., Wust, P., Ahlers, O., Dieing, A., Sreenivasa, G., Kerner, T., Felix, R., and Riess, H. (**2002**). "The cellular and molecular basis of hyperthermia," Crit. Rev. Oncol. Hematol., **43**, 33–56.

Hill, C. R., and ter Haar, G. R. (**1995**). "High intensity focused ultrasound: Potential for cancer treatment," Br. J. Radiol., **68**, 1296–1303.

Huang, Q., Hu, J., Lohr, F., Zhang, L., Braun, R., Lanzen, J., Little, J. B., Dewhirst, M. W., and Li, C. Y. (**2000**). "Heat-induced gene expression as a novel targeted cancer gene therapy strategy," Cancer Res., **60**, 3435–3439.

Hynynen, K., and Edwards, D. K. (**1989**). "Temperature measurements during ultrasound hyperthermia," Med. Phys., **16**, 618–626.

Hynynen, K., Pomeroy, O., Smith, D. N., Huber, P. E., McDannold, N. J., Kettenbach, J., Baum, J., Singer, S., and Jolesz, F. A. (**2001**). "MR imaging-guided focused ultrasound surgery of fibroadenomas in the breast: A feasibility study," Radiology, **219**, 176–185.

Jolly, C., and Morimoto, R. I. (**2000**). "Role of the heat shock response and molecular chaperones in oncogenesis and cell death," J. Natl. Cancer Inst., **92**, 1564–1572.

Kramer, G., Steiner, G., Grobl, M., Hrachowitz, K., Reithmayr, F., Paucz, L., Newman, M., Madersbacher, S., Gruber, D., Susani, M., and Marberger, M. (**2004**). "Response to sublethal heat treatment of prostatic tumor cells and prostatic tumor infiltrating T-cells," Prostate, **58**, 109–120.

Kennedy, J. E., ter Haar, G. R., and Cranston, D. (**2003**). "High intensity focused ultrasound: Surgery of the future?," Br. J. Radiol., **76**, 590–599.

Kennedy, J. E., Wu, F., ter Haar, G. R., Gleeson, F. V., Phillips, R. R., Middleton, M. R., and Cranston, D. (**2004**). "High-intensity focused ultrasound for the treatment of liver tumors," Ultrasonics, **42**, 931–935.

Li, C. Y., and Dewhirst, M. W. (**2002**). "Hyperthermia-regulated immunogene therapy," Int. J. Hyperthermia, **18**, 586–596.

Lizzi, F. L., Driller, J., Lunzer, B., Kalisz, A., and Coleman, D. J. (**1992**). "Computer model of ultrasonic hyperthermia and ablation for ocular tumors using B-mode data," Ultrasound Med. Biol., **18**, 59–73.

Lizzi, F. L., and Ostromogilsky, M. (**1987**). "Analytical modeling of ultrasonically induced tissue heating," Ultrasound Med. Biol., **13**, 607–618.

Locke, M., and Nussbaum, E. (**2001**). "Continuous and pulsed ultrasound do not increase heat shock protein 72 content," Ultrasound Med. Biol., **27**, 1413–1419.

Miller, D. L., and Bao, S. (**1998**). "The relationship of scattered subharmonic, 3.3 MHz fundamental and second harmonic signals to damage of monolayer cells by ultrasonically activated Albunex," J. Acoust. Soc. Am., **103**, 1183–1189.

Morimoto, R. I. (**1993**). "Cells in stress: Transcriptional activation of heat shock genes," Science, **259**, 1409–1410.

Smith, R. C., Machluf, M., Bromley, P., Atala, A., and Walsh, K. (**2002**). "Spatial and temporal control of transgene expression through ultrasound-mediated induction of the heat shock protein 70B promoter *in vivo*," Hum. Gene Ther., **13**, 697–706.

ter Haar, G. R. (**1995**). "Ultrasound focal beam surgery," Ultrasound Med. Biol., **21**, 1089–1100.

ter Haar, G. R. (**2001**). "High intensity focused ultrasound for the treatment of tumors," Echocardiography, **18**, 317–322.

Van Leenders, G. J., Beerlage, H. P., Ruijter, E. T., de la Rosette, J. J., and van de Kaa, C. A. (**2000**). "Histopathological changes associated with high intensity focused ultrasound (HIFU) treatment for localized adenocarcinoma of the prostate," J. Clin. Pathol., **53**, 391–394.

Vekris, A., Maurange, C., Moonen, C., Mazurier, F., De Verneuil, H., Canioni, P., and Voisin, P. (**2000**). "Control of transgene expression using local hyperthermia in combination with a heat-sensitive promoter," J. Gene Med., **2**, 89–96.

Voellmy, R. (**1996**). "Sensing stress and responding to stress," in *Stress-inducible Cellular Responses*, edited by U. Feige, R. Morimoto, I. Yahara, and B. Polla (Birkhauser, Base, Switzerland), pp. 121–137.

Wu, F., Wang, Z., Chen, W., Zou, J., Bai, J., Zhu, H., Li, K., Xie, F., Jin, C., Su, H., and Gao, G. (**2004**). "Extracorporeal focused ultrasound surgery for treatment of human solid carcinomas: Early Chinese clinical experience," Ultrasound Med. Biol., **30**, 245–260.

Xu, Q., Schett, G., Li, C., Hu, Y., and Wick, G. (**2000**). "Mechanical stress-induced heat shock protein 70 expression in vascular smooth muscle cells is regulated by Rac and Ras small G proteins but not mitogen-activated protein kinases," Circ. Res., **86**, 1122–1128.

Yang, R., Sanghvi, N. T., Rescorla, F. J., Kopecky, K. K., and Grosfeld, J. L. (**1993**). "Liver cancer ablation with extracorporeal high-intensity focused ultrasound," Eur. Urol., **23**, 17–22.

Zhong, P., Liu, Y., Li, Z., and Li, C. (**2003**). "Control of gene expression by ultrasound," Proceedings of the Third International Symposium on Therapeutic Ultrasound, Lyon, France, pp. 136–141.

Off-axis effects on the multipulse structure of sperm whale usual clicks with implications for sound production

Walter M. X. Zimmer[a)]
NATO Undersea Research Centre, V.le San Bartolomeo 400, I-19138 La Spezia, Italy

Peter T. Madsen
Woods Hole Oceanographic Institution, Woods Hole, Massachusetts 02543

Valeria Teloni
Department of Zoophysiology, Biological Institute, University of Aarhus, DK-8000 Aarhus C, Denmark

Mark P. Johnson and Peter L. Tyack
Woods Hole Oceanographic Institution, Woods Hole, Massachusetts 02543

(Received 12 May 2005; revised 26 August 2005; accepted 31 August 2005)

Sperm whales (*Physeter macrocephalus*) produce multipulsed clicks with their hypertrophied nasal complex. The currently accepted view of the sound generation process is based on the click structure measured directly in front of, or behind, the whale where regular interpulse intervals (IPIs) are found between successive pulses in the click. Most sperm whales, however, are recorded with the whale in an unknown orientation with respect to the hydrophone where the multipulse structure and the IPI do not conform to a regular pulse pattern. By combining far-field recordings of usual clicks with acoustic and orientation information measured by a tag on the clicking whale, we analyzed clicks from known aspects to the whale. We show that a geometric model based on the bent horn theory for sound production can explain the varying off-axis multipulse structure. Some of the sound energy that is reflected off the frontal sac radiates directly into the water creating an intermediate pulse p1/2 seen in off-axis recordings. The powerful p1 sonar pulse exits the front of the junk as predicted by the bent-horn model, showing that the junk of the sperm whale nasal complex is both anatomically and functionally homologous to the melon of smaller toothed whales. © *2005 Acoustical Society of America.* [DOI: 10.1121/1.2082707]

PACS number(s): 43.80.Ka [WWA] Pages: 3337–3345

I. INTRODUCTION

Based on the observation that sperm whales produce multipulsed clicks (Backus and Schevill, 1966), Norris and Harvey (1972) advanced the idea that the hypertrophied nasal complex of the sperm whale operates as a sound generator. They suggested that a single initial sound pulse is generated at the phonic lips (Fig. 1) and then reflected from air sacs at the anterior and posterior ends of the large spermaceti compartments of the nose to produce a multipulsed click. They conjectured that the primary sound pulse of highest amplitude is projected directly into the water and that the following pulses of decaying amplitude are successively delayed by the two-way travel time between the air sacs of the nose.

Møhl (1978; 2001) amended the Norris and Harvey theory by proposing that the bulk of the sound energy is directed backwards into the spermaceti organ and that only a small fraction of energy leaks directly into the water in the creation of a weak p0 pulse. Most of the sound energy travels through the spermaceti organ and the junk complex before emission into the water as a narrowly focused p1 pulse (Møhl *et al.*, 2003; Cranford, 1999). Recent findings have corroborated the basics of this so-called bent horn model (Møhl *et al.*, 2003) by showing that sound is indeed generated in the nose (Madsen *et al.*, 2003) and that excitement of the system with a pressure transient at the phonic lips (Fig. 1) produces multiple pulses with an interpulse interval (IPI) that matches the two-way travel time back and forth between the air sacs (Møhl, 2001; Møhl *et al.*, 2003).

Møhl *et al.* (2000; 2003) have demonstrated that the p1 pulse is highly directional with some on-axis source levels in excess of 240 dB_{pp} *re*: 1 μPa, which supports both the sonar function of these clicks and the bent horn amendments to the Norris and Harvey theory. Zimmer *et al.* (2005) corroborated these findings with a different experimental approach and found, in consistency with the bent-horn model, that the weaker p0 pulse has a broad backward-directed beam whereas the highly-directional p1 pulse is projected forward from the whale (Zimmer *et al.*, 2005).

It follows from both the original Norris and Harvey theory and the bent horn model that the IPIs between outgoing pulses should be related to the distance between the reflective air sacs. Since there is an allometric relationship between the size of the nose and the overall body size of the whale (Nishiwaki *et al.*, 1963), it can be inferred that the whales may convey size information in every click they make to conspecifics and interested bioacousticians alike (Norris and Harvey, 1972).

[a)]Electronic mail: walter@nurc.nato.int

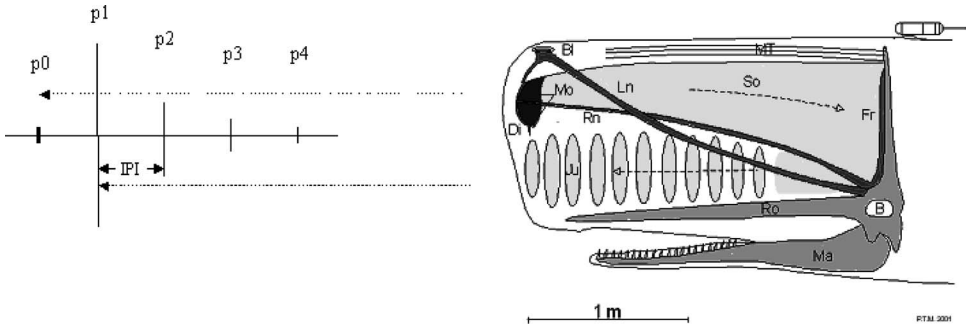

FIG. 1. Bent-horn model of sperm whale sound generation [modified from Fig. 1 of Madsen *et al.* (2002a). B, brain; Bl, blow hole; Di, distal air sac; Fr, frontal air sac; Ju, junk; Ln, left naris; Ma, mandible; Mo, monkey/phonic lips; MT, muscle/tendon layer; Rn, right naris; Ro, rostrum; So, spermaceti organ; p0, . . . , p4, pulse components of a sperm whale click showing their relative level and constant interpulse interval (IPI).

Based on photogrammetric size estimation and matched sound recordings, Gordon (1991) derived an empirical relation between sperm whale length and IPI (Goold and Jones, 1995; Goold *et al.*, 1996) using a sound speed in spermaceti oil of some 1350 m/sec (Flewellen and Morris, 1978; Goold *et al.*, 1996). Investigations on stranded animals (Møhl, 2001) and onboard recordings with acoustic tags (Madsen *et al.*, 2002a) show a good agreement between length estimates and the predictions of the Gordon equation. Recently, Rhinelander and Dawson (2004) verified the correlation between IPIs and the size of the animal. However, they also reported some discrepancy between photogrammetric length estimates and length prediction from the Gordon equation, and proposed a slightly different equation for large animals. The contention is therefore that the IPI is indeed related to the size of the animal and that such information is conveyed in all sperm whale usual clicks.

Despite the potential for acoustic size estimation of sperm whale stocks, the technique has only been employed in a few studies (Adler-Fenchel, 1980; Leaper *et al.*, 2002; Pavan *et al.*, 2000; Drouot *et al.*, 2004; Miller *et al.*, 2004; Rhinelander and Dawson, 2004). While there may be a number of reasons for this, one likely relates to the fact that recorded sperm whale clicks seldom conform to the clear multipulse structure depicted in textbooks and papers. Clicks with complex wave forms and pulse structures that cannot be accounted for on the basis of a fixed IPI must often be excluded from the analysis (Gordon, 1987; 1991; Goold, 1996; Pavan *et al.*, 1997; Drouot *et al.*, 2004, Rendell and Whitehead, 2004; Rhinelander and Dawson, 2004;).

In an attempt to explore the mechanisms behind the complex structures of sperm whale usual clicks that do not conform to the clear multipulse pattern, we analyzed acoustic data from a field experiment combining a towed hydrophone array in the far field with an acoustic and orientation recording tag attached to a sperm whale. This approach provided recordings of both the emitted clicks in a fixed recording aspect (from the tag) and in varying, but known recording aspects in the far field (from the towed array) (Zimmer *et al.*, 2005). We demonstrate that the interpulse structure of usual clicks from a sperm whale varies considerably and that sperm whale body length, therefore, is not estimated correctly from the IPI of clicks recorded off the body axis. The multipulse structure of sperm whale usual clicks can be related to the recording aspect of the whale by a more complex geometric model. We develop such a model, consistent with the bent horn hypothesis of sound production, and show that the observed variations in IPI with aspect closely follow those predicted by the model.

II. MATERIALS AND METHODS

The following analysis is based on sperm whale data recorded in the Ligurian Sea in 2001 during *Sirena-01*, a field trial organized by the NATO Undersea Research Centre (NURC) as part of its Marine Mammal Acoustic Risk Mitigation program. Data collected during *Sirena* trials included: visual observation of animals at the surface, passive sonar detection and tracking while animals were diving, and tagging of animals with a compact acoustic and orientation recorder, the DTAG, (Johnson and Tyack, 2003) developed at the Woods Hole Oceanographic Institution (WHOI).

Clicking sperm whales were detected by a passive sonar system developed at NURC consisting of a horizontal line array of 128 hydrophones, a real-time digital beamformer and sonar display system. The hydrophone array was towed just below any substantial thermocline at a depth of about 80 m. The received sound was processed and visualized in real-time on a passive sonar display (Zimmer *et al.*, 2003), and archived on a 240 MBit/s digital tape recorder, together with relevant nonacoustic data such as array depth and ship's position, heading, and speed. The hydrophones of the towed array were set to an effective saturation level of 140 dB_{peak} *re*:1 μPa and sampled with 16 bit resolution at 31.25 kHz, allowing a maximum bandwidth of about 15 kHz.

The passive sonar was able to track sperm whales throughout their foraging dives, but not to record the detailed orientation or short-term movements of the animal between clicks. For this task a DTAG was attached to the whale, recording the sounds and movement patterns of the whale with high resolution (Johnson and Tyack, 2003). Key features of the DTAG in 2001 were 12-bit analog-to-digital conversion of a hydrophone signal, a sampling rate of 32 kHz and a clipping level set to 153 dB_{peak} *re*:1 μPa. The pressure sensor, three-axis accelerometers and three-axis magnetometers were all sampled at 47 Hz and strict synchrony was maintained between audio and sensor sampling.

The procedure for tagging sperm whales was based on the following scheme: once a sperm whale was located acoustically and visually, a small workboat was deployed from the NRV *Alliance* to attempt tagging. Responses to tagging were monitored visually and acoustically from NRV

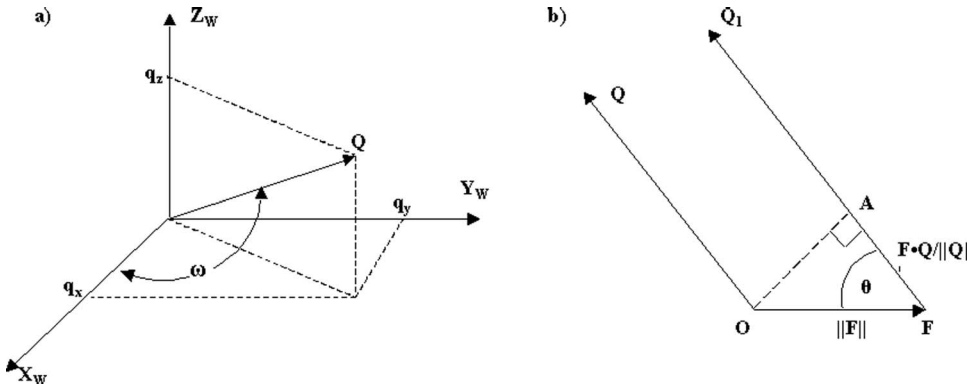

FIG. 2. (a) The general geometry of the whale coordinate system (X_W, Y_W, Z_W), indicating the range vector Q in whale coordinates $Q=(q_x, q_y, q_z)$, and the off-axis angle ω. (b) The geometry used to estimate the path length difference between two acoustic rays, with Q connecting the sound source directly to the receiver and Q_1 describing the sound path from a reflector at point F. $F \circ \hat{Q}_1$ is the dot product between vector F and the unit vector $\hat{Q}_1$ and describes the projection of vector F on vector $\hat{Q}_1$ and produces the distance between the points F and A.

Alliance as well as from the small workboat. After tagging, the whale was followed visually when it surfaced close to the ship, acoustically when it was clicking at depth, and using a radio direction finder to track a VHF radio transmitter on the tag when the whale surfaced.

On 2-October-2001, a DTAG was attached for nearly 7 h to a whale (SW01_275b) estimated by visual observation (Miller *et al.*, 2004) to be about 12 m long. While tagged, the whale performed eight complete deep foraging dives to depths of 550–900 m. Data analysis was performed in multiple steps described in detail in Zimmer *et al.* (2005), where the same data set was used to determine the beampattern of the usual sperm whale click. The underwater track of the whale was reconstructed from visual sightings, passive acoustics, and tag measurements of whale orientation and depth. Clicks made by the tagged whale were then detected in the DTAG recording and the corresponding clicks were identified in the recording from the towed hydrophone array.

The positions of source (whale) and receiver (towed array) were transformed from geo-referenced axes (i.e., east, north, zenith) to a whale-relative coordinate system (i.e., forward, left, up). The roll (α), pitch (β), and heading (γ) angles of the whale were estimated from the tag data during the reconstruction phase. Using these angles, the coordinate system of the whale is defined by the following vectors:

$$X_W = T_1,$$

$$Y_W = T_2 \cos\alpha + T_3 \sin\alpha, \tag{1}$$

$$Z_W = T_3 \cos\alpha - T_2 \sin\alpha,$$

where

$$T_1 = \begin{pmatrix} \cos\beta\cos\gamma \\ \cos\beta\sin\gamma \\ \sin\beta \end{pmatrix}, \quad T_2 = \begin{pmatrix} \sin\gamma \\ -\cos\gamma \\ 0 \end{pmatrix},$$

$$T_3 = \begin{pmatrix} -\sin\beta\cos\gamma \\ -\sin\beta\sin\gamma \\ \cos\beta \end{pmatrix},$$

where X_W points in the forward direction and defines the longitudinal axis, Y_W points to left of the whale, and Z_W points dorsally. For simplicity, we consider the whale coordinates to have their origin at the phonic lips.

The geo-referenced vector R pointing from the whale to the receiver [Fig. 2(a)] can now be expressed in whale-frame coordinates by $Q=[qx, qy, qz]^T$ where

$$q_x = X_W \circ R,$$

$$q_y = Y_W \circ R, \tag{2}$$

$$q_z = Z_W \circ R,$$

and $X \circ R$ denotes the dot product between vector X and Y. Note that while the two vectors R and Q have the same length, that is $\|R\|=\|Q\|$, they are expressed in different coordinate systems (R is geo-referenced and Q is in whale-frame coordinates). The off-axis angle ω describes the angle between the forward direction of the whale (assumed to be the acoustic axis) and the direction to the receiver and is defined by the relation $\cos\omega = q_x$ [Fig. 2(a)].

The key geometric approximation used in the following pertains to the path length difference between a direct and reflected sound ray as perceived by a distant observer [Fig. 2(b)]. If the vectors between the source and observer, and between the reflector and observer are, respectively, Q and Q_1, and F is the vector connecting the source and reflector, then the path length difference, λ, is approximated for $\|Q\| \gg \|F\|$ by

$$\begin{aligned} \lambda &= \|F\| + \|Q_1\| - \|Q\| \approx \|F\| + F \circ Q_1/\|Q_1\| \\ &= \|F\| + F \circ Q/\|Q\| = \|F\|(1+\cos\theta), \end{aligned}$$

where θ is the angle between F and Q_1 (or, equivalently, Q for a distant observer). The approximation is excellent for $k=\|Q\|/\|F\| > 100$ giving a maximum path length error of about $\|F\|/2k$.

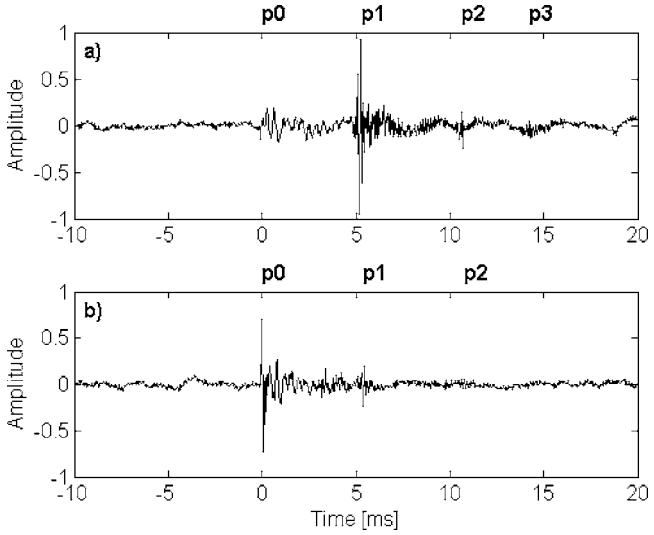

FIG. 3. Usual sperm whale clicks from forward, panel (a) and backward direction, panel (b), as measured by the remote receiver. The different component pulses in the clicks are denoted p0, p1, p2, and p3.

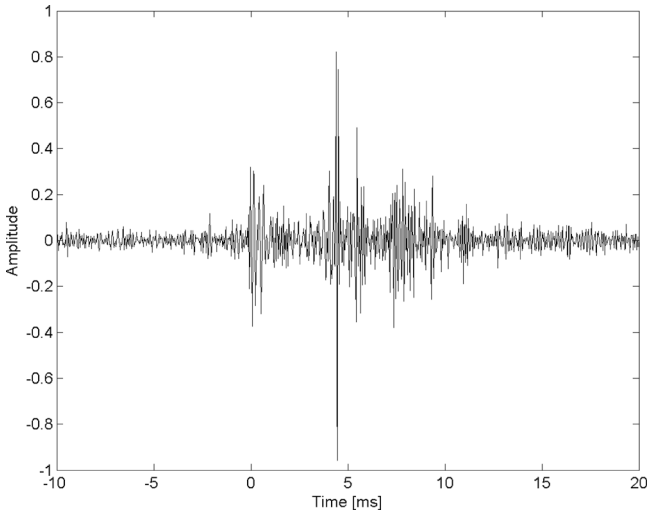

FIG. 4. Single off-axis sperm whale click as measured by the remote receiver. Time 0 corresponds to the reception of the p0 pulse.

III. RESULTS AND DISCUSSION

The combination of an orientation recording tag on the whale and an acoustic recorder in the far field allowed us to derive the off-axis aspect of the recorder with respect to the whale for each emitted click (Zimmer *et al.*, 2005). Figure 3(a) provides an example of a click recorded close to the forward direction [azimuth of 9° and elevation of 7° (Zimmer *et al.*, 2005)] and thereby close to the acoustic axis of the whale. The click structure conforms to the findings of Møhl *et al.* (2003) having a weak p0 pulse, a dominating p1 pulse followed by a weaker p2 pulse. The interpulse intervals can clearly be measured by either the time difference between p0 and p1 or p1 and p2. Figure 3(b) displays another click recorded close to the body axis, but at an off-axis angle of 160° (Zimmer *et al.*, 2005) and therefore from behind the animal. In this case the p0 pulse dominates because the recording aspect is now close to the acoustic axis of p0 and off the acoustic axis of the powerful p1 pulse (Madsen *et al.*, 2002a; Zimmer *et al.*, 2005). Note that the amplitudes are normalized in Figs. 3(a) and 3(b). In reality the on-axis source level of the p1 pulse is some 40 dB higher than that of the p0 pulse. It is evident from Fig. 3(b) that the interpulse intervals can be easily measured when recording directly behind the animal, e.g., in the footprint of a diving whale (Gordon, 1987; Goold and Jones, 1995; Rhinelander and Dawson, 2004). Thus, recordings made on the body axis of a sperm whale, whether in front or behind, will show a clear multipulse structure and consistent IPIs.

However, most sperm whale recordings are made with a single hydrophone and with the whale in an unknown orientation. When analyzing such recordings it is often painfully clear that most sperm whale clicks do not conform to the clean pattern outlined in Fig. 3, looking more like the click displayed in Fig. 4. In such complex wave forms, the click is still multipulsed, but the pulses are not evenly spaced and it is far from obvious how to number the various pulses according to the pattern of Fig. 1 with p0 to pN. Such pulses are therefore often discarded from the process of acoustic size estimation (Gordon, 1991; Goold, 1996; Rendell and Whitehead, 2004) or used uncritically which in turn renders a range of varying and sometimes unrealistic size estimates for the same animal. It is challenging to make sense of the wave forms of such off-axis clicks even when the recording aspect is known but when a large number of consecutive clicks are aligned in a stacked plot a pattern emerges (Fig. 5). In this plot, nearly 290 consecutive clicks, recorded from a single hydrophone in the towed array, were stacked together by aligning the clicks at the onset of the p0 pulses. Later arriving pulses have varying interpulse delays between 2 and 6 ms, and if such delays were used as IPI estimates for acoustic size determination (following the formulas of Gordon, 1991 or Rhinelander and Dawson, 2004), the estimated size of the whale would vary between 6 and 13 m. It should be emphasized that this variation in the pulse structure gen-

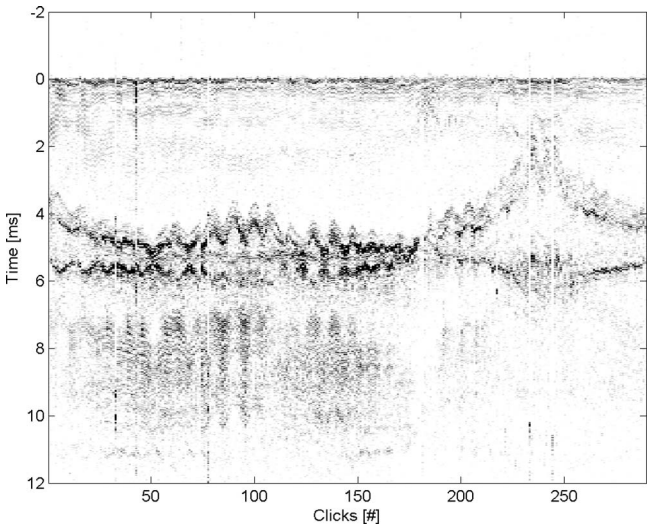

FIG. 5. Multiple sperm whale clicks, as recorded from a remote hydrophone, stacked horizontally. Each vertical slice contains the envelope of a received click aligned at the p0 pulse. The oscillating multipulse structure is visible at time delays of up to 6 ms.

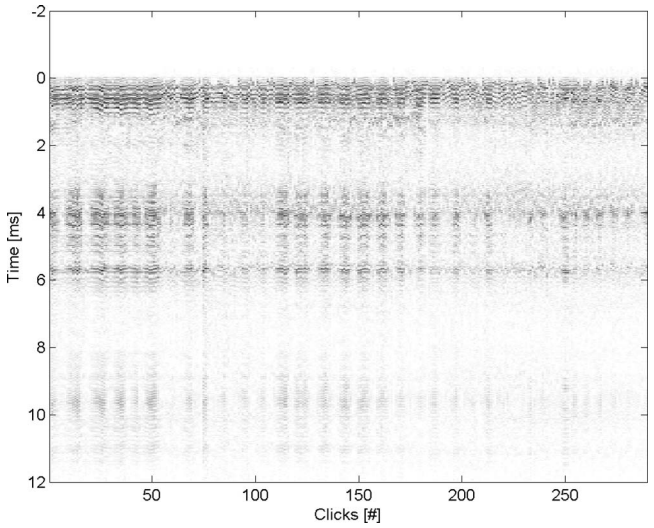

FIG. 6. Stackplot of the same consecutive sperm whale clicks shown in Fig. 5, but measured by the DTAG that was attached to the clicking whale.

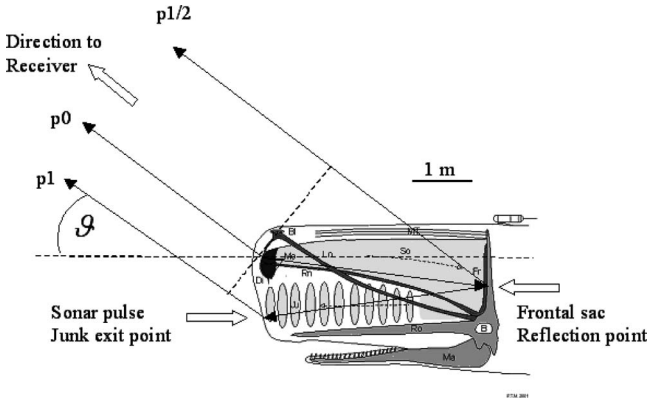

FIG. 7. Diagram of the modified bent-horn model of sound production in sperm whales; θ, off-axis angle of the receiver with respect to the acoustic axis; p0, primary pulse generated by the phonic lips; p1, highly directional sonar pulse; p1/2, pulse reflected from frontal air sac.

erally cannot be overcome by processing the received signal: both autocorrelation and cepstral analyses of isolated sperm whale clicks will yield incorrect IPIs.

Closer inspection of Fig. 5 reveals that the multipulse pattern develops over time and it seems that there is a correlation between the wave form of a click and the wave forms of the clicks preceding and following it. We hypothesize that such variability in the temporal structure can either (1) relate to variability in the sound production system or (2) be caused by changing geometry between the clicking whale and the receiver in the far field. To address the first hypothesis, we aligned the same clicks displayed in Fig. 4, but as recorded by the tag on the animal (Fig. 6). This approach ensures that the recording aspect is close to being fixed, and that changes in the received wave form most likely relate to changes in the output of the sound generator rather than aspect changes (Madsen *et al.*, 2002a). Figure 6 shows that while the received levels vary slightly over the course of time, the multipulse structure is stable with pulses at around 0, 4, and 5.7 ms. There are small fluctuations, which may relate to minor changes in the recording conformation between the tag at the dorsal fin and the sound generator in the front of the nasal complex of the swimming whale. However, compared to the large IPI fluctuations of the same clicks recorded in the far field, the pulse structure is stable, and it is safe to conclude that source modifications cannot explain the fluctuations in the multipulse structure observed in the far field (*sensu* Madsen *et al.*, 2002a).

Given that the pulse structure of the emitted wave forms is stable over time intervals of minutes, we analyzed the data for aspect-dependency in the far field. To do so, we compared the observed signals to a simplified source model based on the bent horn theory. We know from tag (Madsen *et al.*, 2002a), cadaver (Møhl *et al.*, 2002), and far field recordings (Møhl *et al.*, 2003; Zimmer *et al.*, 2005) that the sperm whale sound generator can be viewed as a sound source with two reflectors and several discrete exit paths (Fig. 7). While the functional morphology and acoustic properties are likely more complicated, a simple compartmental model of this form provides a tractable framework in which to explore the relationship between observer aspect and pulse delays in the observed signals.

If there is no leakage from the system other than at the anterior surface of the nose, it is expected from the simple pipe experiment of Norris and Harvey (1972) that the interpulse intervals would be constant irrespective of the recording aspect. On the other hand, if the sound energy is not entirely contained in the spermaceti compartments, a reflection should result from the frontal air sac and result in a new pulse, that we coin p1/2 ("p-half"), in addition to the p0 and p1 pulses predicted by the Norris and Harvey (1972) and the bent-horn amendment (Møhl, 1978; Møhl, 2001). It is predicted that the p1/2 pulse will appear in the far field with an orientation-dependent delay relative to the p0 pulse varying between 0 (i.e., merging with the p0) when recorded behind the whale, and the two-way-travel time of the nose (i.e., merging with p1) when recorded directly in front of the whale on the acoustic axis of the p1 pulse.

To predict the p1/2 time delay as a function of aspect, we first need to define the position of the reflection point on the frontal sac. This organ is posterior to the spermaceti organ and below the longitudinal axis as defined earlier, and so has a position vector $F=[f_x 0 f_z]^T$ where f_x is the longitudinal distance from the phonic lips to the frontal sac, essentially the length of the spermaceti organ. For simplicity, we model the frontal sac as a single reflection point ventral of the longitudinal axis ($f_z<0$) and with no lateral offset ($f_y=0$) with respect to the phonic lips, as justified by the lateral symmetry of the frontal sac (Madsen, 2002b).

The apparent time delay, $\tau_{1/2}$, of the p1/2 pulse, relative to p0, is the combination of two factors [*sensu* Fig. 2(b)]:

(i) the travel time of sound from the phonic lips to frontal sac. This is given by $\|F\|/v_s$ where v_s is the speed of sound in the spermaceti organ, and
(ii) the travel time difference between the path from frontal sac to observer as compared to the path from phonic lips to observer. For a distant observer (specifically, for $\|R\| \gg \|F\|$), the aspect of every point of the whale's nose is essentially the same and so the

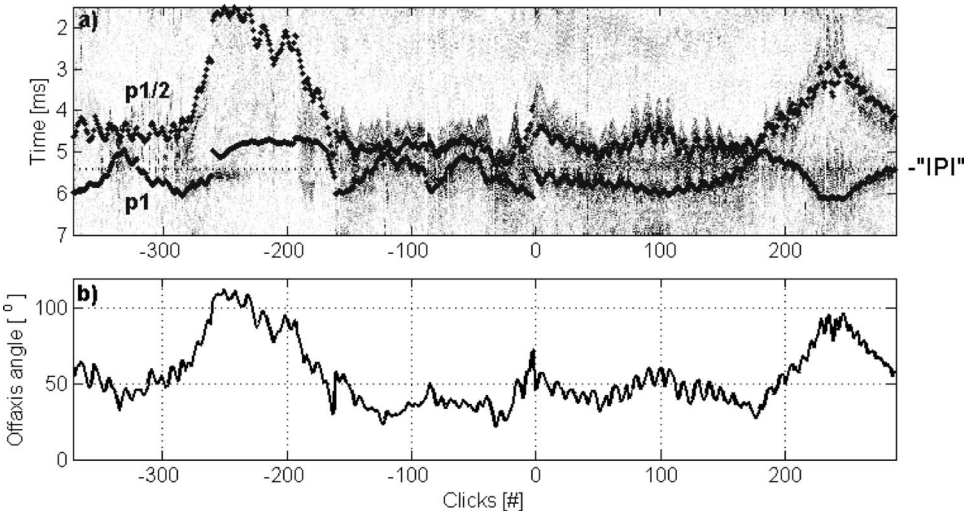

FIG. 8. (a) Multiple sperm whale clicks stacked and zoomed with model overlaid. The lower dotted line describes the modeled p1 pulse, the upper dotted line the modeled p1/2 pulse, and the horizontal dashed line corresponds to the nominal IPI. Clicks with positive click numbers correspond to the clicks shown also in Fig. 5 that were used for least-squares parameter estimation. Clicks with negative click numbers precede the clicks of Fig. 5, and are shown together with the predicted p1 and p1/2 values. (b) The estimated off-axis angle for each click.

path length difference is simply given by $\delta_{1/2}=F\circ\hat{Q}$, where $\hat{Q}=Q/\|Q\|$ is the unit vector in the direction of the observer (expressed in whale-frame coordinates). The path length difference $\delta_{1/2}$ is a function of aspect with $\delta_{1/2}\approx 0$ at broadside and $\delta_{1/2}\approx\|F\|$ or $-\|F\|$ when the aspect is 0° or 180°, respectively.

Converting path length difference to travel time is complicated by the fact that the segment of path may pass predominantly through connective tissue and water (aspects close to broadside), through the spermaceti organ (aspects close to 0°), or through the whale body (aspects larger than 90°). The speed of sound differs in these different tissues, but by using the sound speed in the spermaceti organ to convert path length to time delay, we make the least error for aspects close to 0. Combining these results, the apparent time delay of the p1/2 pulse can be expressed as: $\tau_{1/2}=(\|F\|+F\circ\hat{Q})/v_s$.

The results of the $\tau_{1/2}$ prediction for the click subset of Fig. 5 are shown by the top dotted line in Fig. 8(a) where the reflector positions were determined so as to minimize the square error between the predicted and measured delays giving $f_x=3.6$ m and $f_z=-0.6$ m. It can be seen that the predicted p1/2 delays fit the actual delays quite well, explaining the intermediate pulses in off-axis clicks such as that of Fig. 3. As demonstrated in Fig. 8(a), the predicted arrival time of the p1/2 pulse consistently matches a pulse component in the off-axis clicks supporting the p1/2 pulse hypothesis. The model is successful at predicting the arrival time of this pulse in clicks that were not used to estimate the model parameters (the negatively numbered clicks in Fig. 8) based only on the off-axis angle, an important validity test for the model. However, it is also evident in Fig. 8 that the p1/2 pulse arrives over a fairly broad spread of delays rather than a single delay as predicted by the model indicating that the reflection from the frontal sac cannot be localized to a single point, as might be expected given the size of this reflector of about 1 m (Madsen, 2002b). The presence of a p1/2 pulse is nevertheless supported by the data and we conclude that a small part of the sound energy reflecting off the frontal sac must escape from the spermaceti compartments and radiate directly into the water, giving rise to the p1/2 pulse with an aspect-dependent delay between the p0 and the p1 pulse.

In the bent-horn model and its modifications (Møhl *et al.*, 2003; Zimmer *et al.*, 2005), the majority of the sound energy propagating backwards from the phonic lips is reflected at the frontal sac and directed into the junk complex to produce the highly directional and powerful p1 sonar pulse. It is assumed in the models that this pulse exits from the flat anterior surface of the junk (Møhl, 2001) although this has not been demonstrated experimentally on a live animal. If the model is correct, then the time delay, τ_1, between the p0 and the p1 pulse as observed by a remote listener will be aspect dependent due to the vertical separation of the two exit points. In particular, τ_1 ought to vary with changes in pitch and roll. To test this hypothesis, we first define the location vector of a presumed radiation point from the junk to be $J=[00j_z]^T$, where it is assumed that the junk is located ventral to the phonic lips by j_z and that any lateral and longitudinal displacement is small in comparison. As with the p1/2 pulse, we assemble the p0-p1 time delay out of the following parameters:

(i) the travel time of sound from phonic lips to frontal sac, $\|F\|/v_s$.
(ii) the travel time of sound from frontal sac to anterior surface of the junk, $\|J\text{-}F\|/v_s$ where we use v_s as a proxy for the speed of sound in the junk.
(iii) the travel time difference between the path from junk radiator to observer (p1) as compared to the path from phonic lips to observer (p0). Again making the assumption of a distant observer, the path length difference is $\delta_1=J\circ\hat{Q}$, where $\hat{Q}$ is redefined as the unit vector from the junk radiator to the observer. δ_1 is close to zero when the observer is in the horizontal plane of the whale and is $\pm j_z$ when the observer is dorsal or ventral of the phonic lips, respectively.

For off-axis angles less than 90°, both the p0 and the p1 pulse travel mainly in water, while for off-axis angles greater than 90°, both pulses travel through whale tissue with variable sound speed. To simplify the presentation, we use the

speed of sound in water v_w, which was measured to be about 1510 m/s to the whale depth (Zimmer *et al.*, 2003). Combining these results, the apparent time delay of the p1 pulse is: $\tau_1 = (\|F\| + \|J\text{-}F\|)/v_s + J \circ \hat{Q}/v_w$.

The prediction of τ_1 using this model is superimposed on the multipulse patterns in Fig. 8(a) where, as before, the position parameter is determined by least-squares error fitting. It is evident (lower dotted line) that the modeled p1 delay is a good fit to the actual p1 delay both in clicks used for the parameter estimation (the positive click numbers in Fig. 8), and also for novel clicks (negative click numbers in Fig. 8). The temporal offset between the phonic lips and the junk surface that gave the best fit between the model and data was 0.73 ms. Using a sound speed in water of 1510 m/s, this delay corresponds to a junk exit point centered at 110 cm ventral of the phonic lips, which for a 12 m sperm whale is close to the center of the flat anterior junk surface (Fig. 7; Madsen, 2002b).

We have shown that observed far-field signals from an instrumented sperm whale are consistent with there being three, spatially separated exit paths for sound from the nasal complex. A portion of the energy in the initial p0 pulse, generated by the phonic lips, radiates directly into the water but most of the caudally directed part of the sound energy passes through the spermaceti to be reflected at the frontal sac producing a second weak sound source, dubbed here p1/2. The main part of the forward reflected energy from the frontal sac passes through the junk to form the p1 pulse, which is the primary sonar pulse for echolocation (Madsen *et al.*, 2002b; Møhl *et al.*, 2003). Results given here match the predictions of the bent horn model and are the first direct evidence from a live sperm whale that the powerful, and highly directional p1 pulse is emitted via the anterior surface of the junk into the water, a result that supports the amendment to the original Norris and Harvey model (1972) proposed by Møhl (1978; 2001). The demonstration that the junk is the exit for sonar pulses in sperm whales also supports evolutionary scenarios of the functional morphology in this species in which the junk is seen as being homologous to the sound conducting melon of smaller toothed whales (Schenkan and Purves, 1972; Cranford *et al.*, 1996). The junk of the sperm whale nose is therefore most likely both anatomically and functionally homologous to the melon of smaller toothed whales.

While the basic geometric predictions of the bent horn model have been confirmed by the data (Fig. 8), it should be noted that some components of the off-axis clicks are still unaccounted for. The energy arriving after the p1 pulse and seen at delays between 7 and 10 ms in clicks 20 through 150 in Fig. 5 has not been explained and we are unable to say unequivocally whether this is due to reflections within the whale or reflections from objects in the water column. However, they are most likely generated in the nose since reflections from the sea surface or bottom can be excluded as the delays are too short being equivalent to source-reflector separations of 10–15 m.

The empirical validation of the geometry of the bent horn model for sound propagation in the sperm whale nose may prove helpful in analyzing signals from animals of unknown orientation. An understanding of the basic geometry behind the complex pulse structure opens the possibility that animal orientation and size could be derived acoustically from off-axis clicks if a large enough sample set is analyzed as in Fig. 8. However, until a proven algorithm for this is presented, we strongly recommend that IPIs used for acoustic size estimation are derived from clicks recorded right behind a diving whale (Gordon, 1991; Goold, 1996; Rhinelander and Dawson, 2004) or close to the acoustic axis of the p1 pulse in front of the whale (Møhl *et al.*, 2003).

We have shown that the time delays $\tau_{1/2}$ and τ_1 of pulses in sperm whale usual clicks, when observed from a remote position, depend on the relative orientation of the whale. We expect that fluking is the main cause of the short-period oscillation in off-axis angle seen in Fig. 8(b) and this oscillation is consistent with delay variations in the p1/2 and p1 pulses visible in Fig. 8(a). Amplitude variations of similar scale are also evident in the clicks recorded by the tag (Fig. 6) indicating that these are related to relative motion of the tag and sound source, consistent with body flexure during fluking. The indication is that the propulsion mechanism of the whale modulates the orientation of the sound generation system and consequently the acoustic transmission axis of the biosonar. As the beamwidth of the p1 pulse has been reported to be very narrow [directivity index of 27 dB or a −3 dB beam width of about 8.3°, Møhl *et al.*, 2003, Zimmer *et al.*, (2005)], it would seem that motion-induced variation of the acoustic axis should impact sonar functionality. Our results suggest that sperm whales do not completely stabilize the direction of the p1 pulse during fluking, or perhaps intentionally use the motion-induced variation to insonify larger volumes.

The multipulse structure of sperm whale clicks has been proposed to serve the purpose of conveying information about size to conspecifics and one of the hypotheses behind the hypertrophy of the nasal complex relates to sexual selection on that basis (Cranford, 1999). Provided that the auditory system of sperm whales can cope with the problems of forward masking and the differentiation of very small time delays (Madsen, 2002a), sperm whales could tell the size of a nearby clicking whale from its usual clicks if the IPIs were stable and independent of aspect. The observed variation of IPIs with aspect will clearly complicate such size estimation. However, the predictable nature of the multipulse structure as a function of aspect angle demonstrated here, may, along with spectral cues (Møhl *et al.*, 2003), provide information to nearby whales regarding the orientation of the clicking whale similar to the situation for calls of delphinids (Miller, 2002; Lammers and Au, 2003). The low decay rate of coda clicks compared to usual clicks (Madsen *et al.*, 2002a) holds more potential for IPI decoding, but it remains to be seen how the wave forms of coda clicks appear in different recording aspects (Rendell and Whitehead, 2004). If the production of coda clicks does not involve the junk complex as suggested by Madsen *et al.*(2002a), then sound energy would principally exit from the nose at the distal and frontal sacs leading to a highly aspect-dependent variation in the multipulse structure. This is in apparent contrast to observations in the field of stable coda IPIs (Rendell and Whitehead, 2004). Fu-

ture studies should investigate this discrepancy experimentally and address the biomechanics of different sound production modes in the sperm whale nose.

IV. CONCLUSION

Remote recordings of sperm whale clicks together with simultaneous acoustic and orientation information measured by a tag on the same whale have been combined to investigate the origin of the multipulse structure in sperm whale usual clicks. These recordings were compared to a lumped-parameter geometric model for sound reflection in the sperm whale nose based on the bent-horn model developed by Møhl and co-workers (Møhl, 1978; 2001; Møhl *et al.*, 2003) and on recently reported three-dimensional radiation patterns of p0 and p1 pulses of sperm whale usual clicks (Zimmer *et al.*, 2005).

One consequence of the bent-horn model should be a small variation in time delay between the p0 and p1 pulse as a function of aspect angle due to the spatial separation between the phonic lips, where the p0 pulse is generated, and the center of the flat anterior junk surface, where the p1 pulse is hypothesized to exit. A careful analysis of off-axis measurements confirms the predicted variations and allows us to conclude that the powerful p1 sonar pulse is indeed emitted from the junk surface. Production of usual sonar clicks in sperm whales therefore involves both the spermaceti organ and the junk complex, and the latter is accordingly both anatomically and functionally homologous to the melon of smaller toothed whales.

The existence of a wide backward-oriented beam of the p0 pulse demonstrates that small amounts of sound energy leak from the spermaceti organ when the p0 pulse travels from the phonic lips to the frontal sac (Zimmer *et al.*, 2005). Similar leakage is also likely for sound that is reflected from the frontal sac back into the junk complex and spermaceti organ. We validate this prediction by the empirical demonstration of a so far undescribed intermediate pulse, called p1/2, which is characterized by a large and aspect-dependent variation in time delay relative to the p0 pulse. Fitting the observed p1/2 pulse delays to a geometric model provides a prediction for the effective reflection point which is consistent with the center of the frontal sac. A consequence of the aspect-dependent pulse structure described here is that both the size and aspect of a clicking whale are effectively coded in the pulse intervals and this may allow conspecifics to establish the size and orientation of other clicking whales. However, this coding represents a confound for field methods that estimate the size of clicking whales based on the interpulse-interval of single clicks and such estimates should be confined to clicks measured directly in front (on-axis) or directly caudal to minimize error in the apparent IPI due to the aspect-dependent p1/2 pulse.

ACKNOWLEDGMENTS

This work was carried out within the Acoustic Risk Mitigation Program of NATO Undersea Research Centre. Thanks to the science party and ship's crew on the research cruise during which these data were collected. A. Shorter, T. Hurst, and A. Bocconcelli (WHOI) provided skilled engineering support. We thank B. Møhl and M. Wahlberg for helpful discussions and constructive critique on previous versions of the manuscript. The whale was tagged under a scientific research permit No. 981-1578-00 issued by the US National Marine Fisheries Service to Peter L. Tyack. This is Contribution No. 11361 from the Woods Hole Oceanographic Institution. The Woods Hole Oceanographic Institution Animal Care Use Committee approved this research. This work was funded by grants to from the Office of Naval Research Grant Nos. N00014-99-1-0819 and No. N00014-01-1-0705, and the Packard Foundation.

Adler-Fenchel, H. S. (**1980**). "Acoustically derived estimate of the size distribution for a sample of sperm whales (*Physeter catodon*) in the Western North Atlantic," Can. J. Fish. Aquat. Sci. **37**, 2358–2361.

Backus, R. H., and Schevill, W. E. (**1966**). "*Physeter* Clicks," in *Whales, Dolphins and Porpoises*, edited by K. S. Norris (University of California Press, Berkeley), pp. 510–527.

Cranford, T. W. (**1999**). "The sperm whale's nose: Sexual selection on a grand scale?," Marine Mammal Sci. **15**, 1133–1157.

Cranford, T. W., Amundin, M., and Norris, K. S. (**1996**). "Functional morphology and homology in the odontocete nasal complex: Implications for sound generation," J. Morphol. **228**, 223–285.

Drouot, V., Gannier, A., and Goold, J. C. (**2004**). "Diving and feeding behavior of sperm whales (*Physeter macrocephalus*) in the northwestern Mediterranean Sea," Aquatic Mammals **30**, 419–426.

Flewellen, C. G., and Morris, R. J. (**1978**). "Sound velocity measurements on samples from the spermaceti organ of the sperm whale (*Physeter catodon*)," Deep-Sea Res. **25**, 269–277.

Goold, J. C. (**1996**). "Signal processing techniques for acoustic measurement of sperm whale body lengths," J. Acoust. Soc. Am. **100**, 3431–3441.

Goold, J. C., Bennell, J. D., and Jones, S. E. (**1996**). "Sound velocity measurements in spermaceti oil under the combined influences of temperature and pressure," Deep-Sea Res., Part I **43**, 961–969.

Goold, J. C., and Jones, S. E. (**1995**). "Time and frequency domain characteristics of sperm whale clicks," J. Acoust. Soc. Am. **98**, 1279–1291.

Gordon, J. C. D. (**1987**). "The behaviour and ecology of sperm whales off Sri Lanka," Ph.D. thesis, Darwin College, Cambridge.

Gordon, J. C. D. (**1991**). "Evaluation of a method for determining the length of sperm whales (*Physeter catodon*) from their vocalizations," J. Zool. Lond. **224**, 301–314.

Johnson, M., and Tyack, P. L. (**2003**). "A digital acoustic recording tag for measuring the response of wild marine mammals to sound," IEEE J. Ocean. Eng. **28**, 3–12.

Lammers, M. O., and Au, W. W. L. (**2003**). "Directionality in the whistles of Hawaiian spinner dolphins (*Stenella longirostris*): A signal feature to cue direction of movement?," Marine Mammal Sci. **19**, 249–264.

Leaper, R., Chappell, O., and Gordon, J. C. D. (**2002**). "The development of practical techniques for surveying sperm whale populations acoustically," Rep. Int. Whal. Comm. **42**, 549–560.

Madsen, P. T. (**2002a**). "Sperm whale sound production—in the acoustic realm of the biggest nose on record," in Sperm whale sound production, Ph.D. dissertation, University of Aarhus, Denmark.

Madsen, P. T. (**2002b**). "Morphology of the sperm whale head: A review and some new findings," in Sperm whale sound production, Ph.D. dissertation, University of Aarhus, Denmark.

Madsen, P. T., Carder, D. A., Au, W. W., Nachtigall, P. E., Mohl, B., and Ridgway, S. H. (**2003**). "Sound production in neonate sperm whales," J. Acoust. Soc. Am. **113**, 2988–2991.

Madsen, P. T., Payne, R., Kristiansen, N. U., Wahlberg, M., Kerr, I., and Møhl, B. (**2002a**). "Sperm whale sound production studied with ultrasound time/depth—recording tags," J. Exp. Biol. **205**, 1899–1906.

Madsen, P. T., Wahlberg, M., and Møhl, B. (**2002b**). "Male sperm whale (*Physeter macrocephalus*) acoustics in a high latitude habitat: Implications for echolocation and communication," Behav. Ecol. Sociobiol. **53**, 31–41.

Miller, P. J. O. (**2002**). "Mixed-directionality of killer whale stereotyped calls: A direction of movement cue?," Behav. Ecol. Sociobiol. **52**, 262–270.

Miller, P. J. O., Johnson, M. P., Tyack, P. L., and Terray, E. A. (**2004**). "Swimming gaits, passive drag and buoyancy of diving sperm whales

Physeter macrocephalus," J. Exp. Biol. **207**, 1953–1967.
Møhl, B. (**1978**). "Kaskelot Klik. Akustiske egenskaber, dannelsesmåde, og en mulig funktion," in *Liv og Lyd (in danish)*, edited by A. Michelsen and S. G. Dalsgaard (University of Odense Press, Odense, Denmark), pp. 201–204.
Møhl, B. (**2001**). "Sound transmission in the nose of the sperm whale Physeter catodon. A post mortem study," J. Comp. Physiol. [A] **187**, 335–340.
Møhl, B., Madsen, P. T., Wahlberg, M., Au, W. W. L., Nachtigall, P. E., and Ridgway, S. (**2002**). "Sound transmission in the spermaceti complex of a recently expired sperm whale calf," ARLO **4**, 19–24.
Møhl, B., Wahlberg, M., Madsen, P. T., Heerfordt, A., and Lund, A. (**2003**). "The monopulsed nature of sperm whale clicks," J. Acoust. Soc. Am. **114**, 1143–1154.
Møhl, B., Wahlberg, M., Madsen, P. T., Miller, L. A., and Surlykke, A. (**2000**). "Sperm whale clicks: Directionality and source level revisited," J. Acoust. Soc. Am. **107**, 638–648.
Nishiwaki, N., Oshumi, S., and Maeda, Y. (**1963**). "Changes in form of the sperm whale accompanied with growth," Sci. Rep. Wh. Res. Inst. Tokyo **17**, 1–13.
Norris, K. S., and Harvey, G. W. (**1972**). "A theory for the function of the spermaceti organ of the sperm whale (*Physter catodon L.*)," in *Animal Orientation and Navigation*, edited by S. R. Galler, K. Schmidt-Koenig, G. J. Jacobs, and R. E. Belleville, SP-262 (NASA, Washington, DC), pp. 397–417.
Pavan, G., Hayward, T. J., Borsani, J. F., Priano, M., Manghi, M., Fossati, C., and Gordon, J. C. D. (**2000**). "Time patterns of sperm whale codas recorded in the Mediterranean Sea 1985–1996," J. Acoust. Soc. Am. **107**, 3487–3495.
Pavan, G., Priano, M., Manghi, M., and Fossati, C. (**1997**). "Software tools for real-time IPI measurements on sperm whale sounds," Proc. Institute Acoust. **19**, 157–164.
Rendell, L., and Whitehead, H. (**2004**). "Do sperm whales share coda vocalizations? Insights into coda usage from acoustic size measurements," Anim. Behav. **67**, 865–874.
Rhinelander, M. Q., and Dawson, S. M. (**2004**). "Measuring sperm whales from their clicks: Stability of interpulse intervals and validation that they indicate whale length," J. Acoust. Soc. Am. **115**, 1826–1831.
Schenkan, E. J., and Purves, P. E. (**1972**). "The comparative anatomy of the nasal tract and the function of the spermaceti organ in the Physeteridae (Mammalia, Odontoceti)," Bidragen tot de Dierkunde **43**, 93–112.
Zimmer, W. M. X., Johnson, M. P., D'Amico, A., and Tyack, P. L. (**2003**). "Combining data from a multisensor tag and passive sonar to determine the diving behavior of a sperm whale (*Physeter macrocephalus*," IEEE J. Ocean. Eng. **28**, 13–28.
Zimmer, W. M. X., Tyack, P. L., Johnson, M. P., and Madsen, P. T. (**2005**). "Three-dimensional beam pattern of regular sperm whale clicks confirms bent-horn hypothesis," J. Acoust. Soc. Am. **117**, 1473–1485.

Source of the North Pacific "boing" sound attributed to minke whales

Shannon Rankin and Jay Barlow
Southwest Fisheries Science Center, National Marine Fisheries Service, La Jolla, California 92038

(Received 17 June 2004; revised 27 May 2005; accepted 2 August 2005)

During a recent cetacean survey of the U.S. waters surrounding the Hawaiian Islands, the probable source of the mysterious "boing" sound of the North Pacific Ocean was identified as a minke whale, *Balaenoptera acutorostrata*. Examination of boing vocalizations from three research surveys confirms previous work that identified two distinct boing vocalization types in the North Pacific. The eastern boing ($n=22$) has a pulse repetition rate of 92 s^{-1} and a duration of 3.6 s and was found only east of 138° W. The central boing ($n=106$) has a pulse repetition rate of 115 s^{-1} and a duration of approximately 2.6 s and was found only west of 135° W. Central boing vocalizations produced by a single source ($n=84$) indicate that variation in repetition rate and duration of the calls of the individual were not significantly different than the variation among individuals of the same boing type. Despite a slight latitudinal overlap in the vocalizations, pulse repetition rates of the eastern and central boings were distinct. [DOI: 10.1121/1.2046747]

PACS number(s): 43.80.Ka, 43.30.Sf [WWA] Pages: 3346–3351

I. INTRODUCTION

The "boing" sound was first described by Wenz (1964) from U.S. Navy submarine recordings made in the 1950s off San Diego, California, and Kaneohe, Hawaii. Despite much attention, the source of the sound has remained a mystery until now. Wenz (1964) noted variation in the duration of the signals (with a possible concurrent variation in the intervals between signals), as well as variation in frequency modulation. Thompson and Friedl (1982) tracked boing sounds made from multiple recordings from bottom-mounted hydrophones off of Oahu, Hawaii, noting long intersound intervals (6 min) for solitary sound sources, and brief intersound intervals (0.5 min) for multiple sound sources. The sources of the boing sounds typically approached the northern coast of Oahu singly, although paired or small groups were detected occasionally (Thompson and Friedl, 1982). Boings were detected seasonally, from November through March, and had an estimated sound source level of 150 dB re 1 μPa at 1 m (Thompson and Friedl, 1982). Given this information, Thompson and Friedl (1982) suggested that the sound source was likely a whale, but they did not speculate as to which species. The first suggestion that the boing may be produced by the minke whale (*Balaenoptera acutorostrata*) was made by Gedamke *et al.* (2001) based on the structural similarity of the boing and the sound produced by the dwarf minke whale in the Great Barrier Reef, Australia.

Antarctic minke whales (*B. bonaerensis*) and northern minke whales have been recorded making low-frequency downswept vocalizations in the Ross Sea (Schevill and Watkins, 1972; Leatherwood *et al.*, 1981) and the St. Lawrence Estuary (Edds-Walton, 2000), respectively. These sounds were described as sweeping from over 100 Hz down to 90 Hz (St. Lawrence Estuary) or 60 Hz (Ross Sea). Winn and Perkins (1976) recorded pulse trains and grunts in the presence of minke whales in the Caribbean. Ratchets, single pulses, and higher frequency clicks were also recorded, although less frequently. Mellinger *et al.* (2000) noted that thump trains recorded in the Caribbean occurred as "speed-up" pulse trains or less often as "slow-down" pulse trains. Pulse trains also were recorded in the presence of group-feeding minke whales in the Gulf of St. Lawrence (Zbinden and Di Iorio, 2003). High-frequency clicks as well as whistles, grunts, and other calls were recorded in the presence of minke whales in the Ross Sea (Leatherwood *et al.*, 1981), although other species may have been present. In the North Pacific Ocean, there have been no published recordings of vocalizations attributed to minke whales.

The Hawaiian Island Cetacean and Ecosystem Assessment Survey (HICEAS) was conducted in the U.S. exclusive economic zone (EEZ) surrounding the Hawaiian Islands between July and December, 2002. This survey combined visual and acoustic methods to determine the distribution and abundance of cetaceans (Barlow *et al.*, 2004) and provided a unique opportunity to investigate the source of these boing sounds. On 7 November 2002, the acoustics team located the source of a series of boing sounds and directed the ship and visual team to this location, where experienced marine mammal observers identified a minke whale. This paper details the events leading us to attribute the boing sound to the North Pacific minke whale and summarizes the characteristics of the boing vocalizations recorded during this particular encounter and during three research cruises in the North Pacific Ocean.

II. METHODS

Boings were detected during three cetacean research surveys, the 1997 Sperm Whale Abundance and Population Structure Survey (SWAPS), the 2002 HICEAS cruise, and the 2003 *Stenella* Abundance Research Survey (STAR). These research cruises combined visual and acoustic line-transect surveys of cetacean populations. Visual observation of cetaceans were conducted during daylight hours and con-

sisted of six experienced visual observers rotating between two "big eye" binocular (25×150) stations and one station observing with $7\times$ binoculars and unaided eye. The acoustics team consisted of two to four rotating acoustic technicians monitoring a hydrophone array aurally and visually (from a real-time spectrogram display).

The 1997 SWAPS survey,[1] on the R/V *McArthur*, covered the waters of the N. Pacific Ocean from 20°–45°N, from the west coast of the United States to 158°W. Emphasis was placed on detecting, locating, and recording sperm whales. The hydrophone array used during this survey consisted of a 60 m, five-element, solid array (made by Innovative Transducers, Inc) which had a relatively flat frequency response between 32 Hz and 8 kHz (±2 dB). The array was attached to a 120 kg depressor weight which was towed 600 m behind the vessel at a depth of 100 m. Signals from two hydrophone elements were monitored day and night, and recordings of sperm whales, boings, and other sounds of interest were made using DAT recorders (Sony D-7, 48 *k* samples/s). These recordings were recently reviewed and boing vocalizations were analyzed for this report.

The 2002 HICEAS survey, aboard the R/V *David Starr Jordan*, included the EEZ of the Hawaiian Island chain and transit to and from San Diego, CA (Barlow *et al.*, 2004). The STAR 2003 survey,[2] aboard the R/V *McArthur II*, surveyed the eastern tropical Pacific Ocean, from San Diego, California, south to Peru. During both of these cruises, a hydrophone array was towed 200 m behind the ship at an average speed of 10 knots and an average depth of 6 m. The arrays used during the HICEAS and STAR surveys were built inhouse and contained two elements, with 3 m spacing between elements. All hydrophones in both arrays had an effective frequency response from 500 Hz to 25 kHz (±10 dB). In addition, a small hydrophone array was installed on the bow of the Jordan during the HICEAS survey; this unit consisted of three closely spaced hydrophones. The bow hydrophones had a small range and were occasionally monitored when animals were near the bow; output from the bow hydrophones were recorded with the output from the towed hydrophone array. Hydrophone output was passed through a Mackie CR1604-VLZ sound mixer for equalization and high-pass filtering of low-frequency noise. All recordings were made using a Tascam DA-38 digital recorder, sampling at 48*k* samples/s.

Recordings from all three cruises containing boing sounds were reviewed visually using ISHMAEL software, which uses time delay between two hydrophones (estimated by cross correlation) to calculate a bearing to the sound source (Mellinger, 2001). Bearing angles were plotted relative to the ships' bow using Whaltrak, a mapping and datalogging program. The location of the sound source was determined by the convergence of beamform angles. Left/right ambiguity was addressed by making a 30° turn; angles converge on the side of the sound source. One sample from each acoustic detection of a boing series was examined for comparison of vocalizations between individuals. Measurements of beginning and end frequency, pulse repetition rate, and signal duration were taken from each sample vocalization using SpectraPlus software.

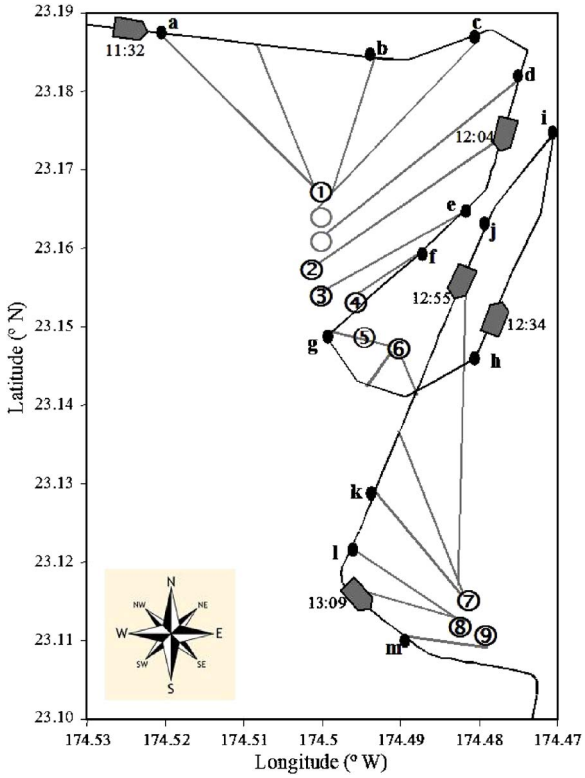

FIG. 1. (Color online) Diagram of ship movement along the trackline, with visual and acoustic detection events. Axes are in decimal degrees of north latitude and west longitude. Ship position and direction, with the associated time, are shown at intervals along the trackline. Select bearing angles and lettered points indicate events described in the text. Numbered circles indicate acoustic position for sound source and/or visual location for minke whale. Gray lines represent acoustic bearing angle to sound sources, gray circles represent probable location of sound source based on continuous acoustic tracking. For clarity of presentation, we do not show all acoustic bearing angles.

The vocalizations recorded in the presence of the single individual minke whale sighted during the HICEAS survey (sighting number 267) were identified and localized using bearing angles estimated with ISHMAEL software. Three angles from different sections of each boing vocalization were measured to determine the precision of beamform angles. The average maximum difference in bearing angles from different sections of the same boing sound was 2.8 degrees($n=99$). Vocalizations in which consistent angles to the sound source could not be verified were not used to provide location information. Boing vocalizations recorded from sighting number 267 were measured to estimate the variation in the call characteristics within a single individual, as well as to examine the intercall interval. The mean swimming speed and direction of travel was determined using the updated visual and acoustic methods independently.

III. RESULTS

A. Account of acoustic localization linked to *B. acutorostrata* sighting

At 11:32 local time on 7 November 2002, one author (S.R.) detected a distinct series of boing sounds [Fig. 1(a)].

The convergence of successive angles suggested that the sound source passed 2 km from the ship's beam at 11:53 [Fig. 1(b)]. The visual team did not detect any animals, despite good observing conditions (Beaufort sea state 2). The ship was directed 30° left of the trackline to address the left/right ambiguity of the bearing angles [Fig. 1(c)]; a subsequent 150° angle indicated that the animal had passed the ship on the starboard side at the position 23° 10.0′N and 174° 30.0′W (Fig. 1-1). A turn of 130° to the starboard was made to approach the sound source. Boing vocalizations were continuously detected during the turn; however, the increased noise from cavitation interfered with our ability to determine the angle to the sound source for 2.5 minutes. After the completion of the turn, the boing vocalizations were detected at 36° from the bow, coinciding with the expected location of the sound source [Fig. 1(d)]. Continuous detection of boing vocalizations allowed for tracking of the sound source. The acoustics team provided the visual observers with continuous updates on the estimated position of the calling animal to assist them in visually detecting the source of the boings.

The acoustics team continuously detected boings at progressively greater angles, and at 12:04 the acoustics team obtained an updated position for the sound source at 30° right and 3.7 km ahead of the ship (Fig. 1-2). This position was 1.2 km from the initial acoustic location determined at 11:53. At 12:09, computer records indicate an initial sighting of a whale at 5° left and 1.16 km from the ship. The observers did not inform the acoustics team of this detection, and this position was 1.9 km from the resighted location 2 minutes later. There were no further sightings in the vicinity of this initial sighting, and it appears that this initial sighting information was recorded in error. A turn of 30° to the right was made at 12:09 to approach the sound source. Immediately after the turn the acoustics team detected boings at 13° off of the bow [Fig. 1(e)], and notified the visual team of the updated location (Fig. 1-3). This position was 0.33 km from the latest acoustic boing location made at 12:04. At 12:11 one observer briefly detected an animal 13° to the right of the ship and identified it as a baleen whale. The dorsal fin and part of the back were seen as the animal rolled, and the animal was lost immediately. Three minutes later, the acoustics team detected seven extremely intense boings between 6° and 10° off the bow of the ship using the towed array [Fig. 1(f)]. For the first (and only) time, the sounds were detected on the bow hydrophones. The boing vocalizations ceased at 12:15 for a brief period. Less than 1 minute after the boings stopped, the observers on the flying bridge reported a baleen whale 100 m off the bow, at a position 43 m from the estimated position obtained by the acoustic team based on continuous tracking of the boing source (Fig. 1-4). The animal then breached 100 m off the starboard beam and was positively identified as a minke whale.

Several turns were made to keep the animal within view [Fig. 1(g)]. Boing vocalizations resumed at 12:20, and at 12:23 the animal was resighted at 90° and 0.7 km to the left of the ship (Fig. 1-5). At 12:25 an estimated position of the sound source using the hydrophone array was found to be 0.5 km from this resighted location (Fig. 1-6). A decision was made to launch the rigid-hulled inflatable boat (RHIB) to obtain a biopsy. During the launch procedure the main research vessel could not make course adjustments, so the observers soon lost visual contact with the whale [Fig. 1(h)]. Cavitation caused by the slow vessel speed necessary for RHIB launch made it impossible for the acoustic team to detect boings during the launch. After the launch was complete, the vessel turned towards the last known location of the whale and regained speed for acoustic survey operation [Fig. 1(i)].

At 12:46, boing vocalizations were again detected 16° off of the bow [Fig. 1(j)]. Calls were detected continuously, and the visual observers were provided with updated estimations of the bearing angles. At 13:05 the boing location was determined to be at 64° and 2.1 km from the ship [Fig. 1(k)]; at this time the left/right ambiguity prevented us from determining the exact position to the sound source (for clarity in the diagram, only the port angles and position are shown, Fig. 1-7). At 13:07 the visual team detected an animal at 70° to the left of the ship (Fig. 1-l). After the completion of the turn, the visual observers detected the animal at the same angle and within 0.3 km of the location of the boing source as determined by the acoustic team (Fig. 1-8). The turn also allowed the acoustics team to address the left/right position ambiguity; we had turned towards the direction of the sound source. During the final approach at 13:12, the source of the boing vocalizations was found to be 31° [Fig. 1(m)], which coincided with the final updated visual location at 34° to the left of the ship (Fig. 1-9). Increased ship noise due to decreased ship speed and maneuvering precluded additional acoustic detection for the remainder of the encounter. The animal remained at the surface and at this point did not appear to react to the approach of the vessels. The RHIB approached the minke whale and obtained photographs and a biopsy sample.

The mean swimming speed was determined by calculating the time interval between location updates. The mean swimming speed of the sound source was found to be 5.6 km/h based on four acoustic locations. The swimming speed of the minke whale was 5.7 km/h based on the five visual resights. The average interval between calls was 28 seconds; based on a 5.6 km/h swimming speed, the animal would have moved approximately 45 m between calls.

B. Call characterization and geographic variation

Boing vocalizations consist of a brief pulse followed by a long call that is both frequency modulated (FM) and amplitude modulated (AM) (Figs. 2 and 3). Based on our measurements of 128 boings, the calls can be grouped into two distinct call types with nonoverlapping pulse repetition rates (Fig. 4, Table I). Those with pulse repetition rates of $91-93\ s^{-1}$ were all detected east of 138°W and match Wenz's (1964) description of the San Diego boing (Fig. 5). Those with pulse repetition rates of $114-118\ s^{-1}$ were all detected west of 135°W and match Wenz's description of the Hawaii boing (Fig. 5). The distribution of these boing types clearly extend far from San Diego and Hawaii (Fig. 5), so we will refer to these as eastern and central boings, respectively.

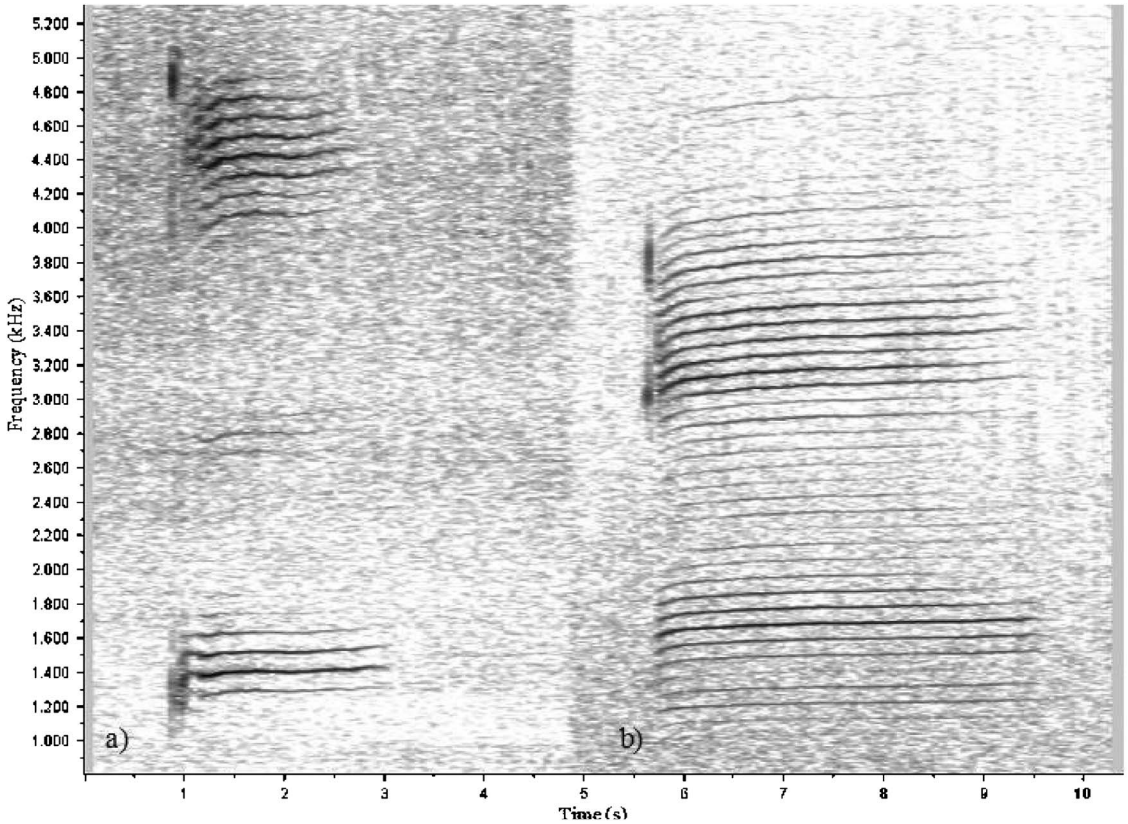

FIG. 2. Spectrogram of the (a) central boing and (b) eastern boing (sampling rate 48 kHz, FFT 8192, 75% overlap, Hanning window).

The eastern boing has a significantly longer duration (mean =3.6 s, $n=22$) than the central boing (mean=2.6 s, $n=106$) (t-test, $p<0.001$). Within each call type, no significant between-year differences were found for call duration ($p=0.61$ and $p=0.93$ for eastern and central calls, respectively) or for pulse repetition rate ($p=0.06$ and $p=0.11$ for eastern and central calls, respectively).

There were approximately 100 vocalizations made in the location of the single minke whale seen on 7 November 2002 (sighting number 267). Measurements of 84 high-quality boings from this individual indicated a variation in the pulse repetition rate that is within the range noted for the central boing (mean=114, SD=0.8, Table I). The mean duration

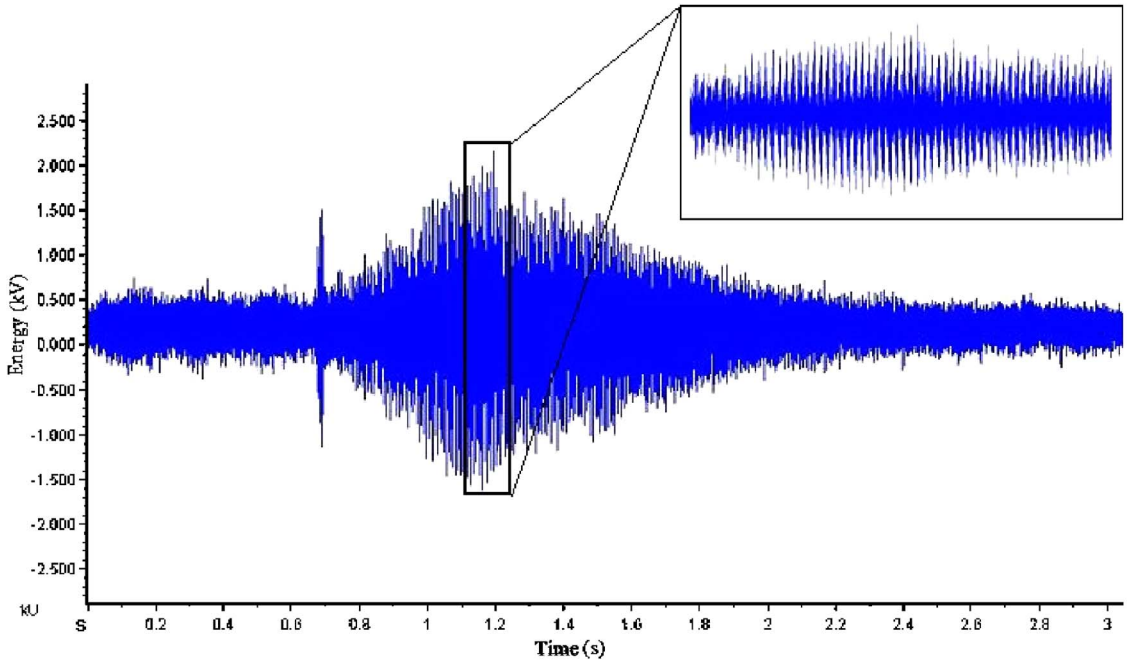

FIG. 3. (Color online) Waveform of the central minke whale boing vocalization. The pulse repetition rate can be seen clearly in the expanded waveform (inset).

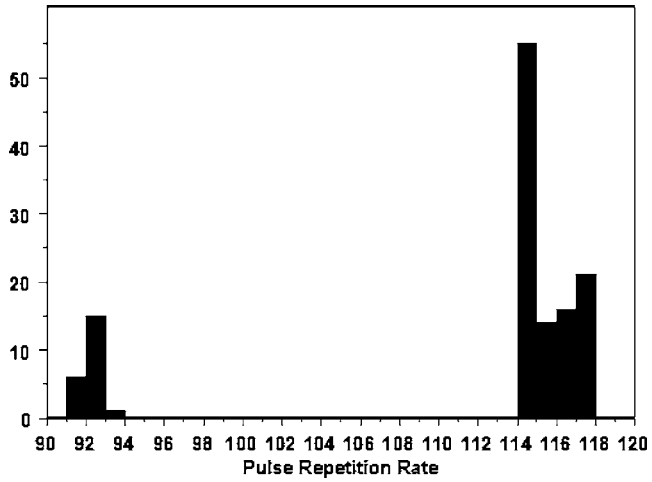

FIG. 4. Frequency distribution for pulse repetition rates of 128 boing vocalizations measured for this study. Boing sounds with pulse repetition rates of 91–93 s^{-1} are referred to as eastern boings, and those with pulse repetition rates of 114–118 s^{-1} are referred to as central boings.

(2.0 s, SD=0.5) was also typical of the central boing. The mean time interval between calls of this individual was 28.7 s (SD=14.1, n=100).

IV. DISCUSSION

Boing sounds are seasonally common in the North Pacific Ocean, yet sightings of minke whales are rare. We believe that the dearth of sightings can be explained by the difficulty in visually detecting this species in rough sea conditions. In over 326 000 km of survey search effort during Southwest Fisheries Science Center (SWFSC) cruises since 1986, 42% of 21 minke whale sightings were in Beaufort sea state 0 or 1, while only 4% of the effort was in these sea states (SWFSC unpublished data). Minke whales are the smallest of baleen whales and are typically encountered individually or in small groups of two or three. They have inconspicuous blows, and do not surface for extended periods of time. Additionally, the waters covered by these surveys are dominated by high sea states associated with the trade winds. Combined, these features reduce the probability of sighting minke whales, and may explain the discrepancy between the low visual detection of minke whales and the high acoustic detection of boings.

One author (S.R.) participated in a survey off Kauai during the peak boing season (February) on the R/V *Dariabar*. On 21 February 2005, in Beaufort sea state 1 conditions, an intense series of boing sounds were detected using a towed hydrophone array as a minke whale surfaced next to the ship. Bearing angles to the sound source agreed with those obtained independently by the visual observers. The presence of other species in the immediate area precluded confirmation that the minke produced the boing vocalizations; however, this detection supports our findings. Additional effort during the peak calling season should be made to confirm these results.

The basic call characteristics of the boing vocalizations measured in this study are similar to those described in earlier research (Wenz, 1964; Thompson and Friedl, 1982). Previous studies referred to these call types as the "Hawaiian" and the "San Diego" boings (Wenz, 1964). These names reflect recording stations rather than the distribution of call types; to avoid confusion we have referred to them as the "eastern boing" (previously the San Diego boing), and the "central boing" (previously the Hawaii boing). An unpublished paper by Turl (1980) identifies anecdotal recordings off of Japan that suggest there may be an additional "western boing" type.

Measurements from a total of 84 calls near the single vocalizing minke whale (HICEAS sighting number 267) indicate that the variation in duration and pulse repetition rate within individual sources is similar to that seen among individuals for the same call type. This suggests that differences in call characteristics found between detections is not necessarily due to individual variation. Limitations of the frequency response of the towed hydrophone array and ship noise interference did not allow for measurement of peak frequencies. Nonetheless, measurements based on the harmonics were similar to previous reports that indicated a variation in peak frequency between the eastern and central boings (Wenz, 1964). Peak frequency may have an individual-specific component that should be examined in future studies.

The swimming speed and direction of the minke whale during this encounter (sighting number 267) was found to be nearly identical based on the visual and acoustic detections (5.7 km/h and 5.6 km/h, respectively). This speed is reasonable, but higher than that found by other researchers (Stern, 1992; Folkow and Blix, 1993; Heide-Jørgensen *et al.*, 2001).

Geographic variation in vocalizations has been found for many cetacean species, including blue whales (Stafford *et al.*, 2001) and Bryde's whales (Oleson *et al.*, 2003). The

TABLE I. Measurement of repetition rate and call duration for eastern and central boing vocalizations. One sample from each clear detection was measured and divided into Eastern and Central boing types. Measurements of 84 boing vocalizations associated with sighting number 267, *B. acutorostrata* are presented for comparison.

		Repetition Rate (pulses/s)				Duration (s)			
	Count	Mean	St. Dev.	Minimum	Maximum	Mean	St. Dev.	Minimum	Maximum
Eastern boing	22	91.8	0.5	91	93	3.6	0.5	2.4	4.3
Central boing									
Overall	106	115.0	1.3	114	118	2.6	0.4	1.7	4.0
Sighting number 267	84	114.3	0.8	112	116	2.0	0.5	0.8	3.0

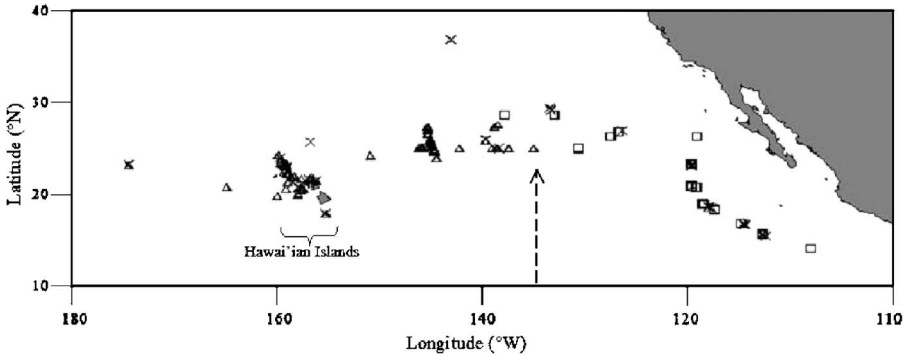

FIG. 5. Map of the location of boing sources from the SWAPS, HICEAS, and STAR surveys. The central boings are represented by open triangles, the eastern boings are represented by open squares, and the ×'s indicate the location of calls too faint for measurement of the call characteristics. The dashed arrow indicates the approximate geographic division between the eastern and central boings.

distinct differences in pulse repetition rate and duration of the central and eastern boing may indicate such geographic variation in North Pacific minke whale populations. Future research should include both acoustic and genetic sampling of minke whales throughout the North Pacific to identify different minke whale populations.

ACKNOWLEDGMENTS

Many thanks to the hard work and patience of the marine mammal observers, acoustic assistants, and crew aboard the R/V *David Starr Jordan*, R/V *McArthur* and the R/V *McArthur II*. Financial and administrative support was provided by the U. S. Navy and the Southwest Fisheries Science Center. Thanks to Tony Martinez, Katie Cramer, Julie Oswald, Carolina Bonin, Tom Norris, Mark McDonald, John Hildebrand, Olaf Jaeke, Laura Morse, and Aviva Rosenberg for their help at sea. Liz Zele assisted in analysis, and Dave Mellinger's ISHMAEL software program has been invaluable. Many thanks to Ethan Silva, Tom Norris, Ann Zoidis, Mari Smultea, and the captain/crew of the R/V *Dariabar*. Thanks to Julie Oswald, Tom Norris, and Kate Stafford for their comments on this paper.

[1]SWAPS97 Cruise Report, Southwest Fisheries Science Center, 8604 La Jolla Shores Dr., La Jolla, CA 92037.
[2]STAR03 Cruise Report, Southwest Fisheries Science Center, 8604 La Jolla Shores Dr., La Jolla, CA 92037.

Barlow, J., Rankin, S., Zele, E., and Appler, J., (**2004**). "Marine mammal data collected during the Hawaiian Island Cetacean Ecosystem Assessment Survey (HICEAS) conducted aboard the NOAA ships *McArthur* and *David Starr Jordan*, July–December 2002," NOAA/NMFS Technical Memorandum NOAA-TM-NMFS-SWFSC-362, available from Southwest Fisheries Science Center, La Jolla, CA.

Beamish, P., and Mitchell, E., (**1973**). "Short pulse length audio frequency sounds recorded in the presence of a minke whale (*Balaenoptera acutorostrata*)," Deep-Sea Res. Oceanogr. Abstr. **20**, 375–386.

Edds-Walton, P. L., (**2000**). "Vocalisations of minke whales (*Balaenoptera acutorostrata*) in the St. Lawrence Estuary," Bioacoustics 11, 31–50.

Folkow, L. P., and Blix, A. S., (**1993**). "Daily changes in surfacing rates of minke whales (*Balaenoptera acutorostrata*) in Norwegian waters," Rep. Int. Whal. Comm. **43**, 311–314.

Gedamke, J., Costa, D. P., and Dunstan, A., (**2001**). "Localization and visual verification of a complex minke whale vocalization," J. Acoust. Soc. Am. **109**, 3038–3047.

Heide-Jørgensen, M. P., Nordøy, E. S., Øien, N., Folkow, L. P., Kleivane, L., Blix, A. S., Jensen, M. V., and Laidre, K. L., (**2001**). "Satellite tracking of minke whales (*Balaenoptera acutorostrata*) off the coast of northern Norway," J. Cetacean Res. Manage. **3**, 175–178.

Leatherwood, S., Thomas, J. A., and Awbrey, F. T., (**1981**). "Minke whales off northwestern Ross Island," Antarctic J. **16**, 154–156.

Mellinger, D. K., (**2001**). "ISHMAEL 1.0 User's Guide," NOAA Technical Memorandum OAR PMEL-120, available from NOAA/PMEL, 7600 Sand Point Way, NE, Seattle, WA 98115–6349.

Mellinger, D. K., Carson, C. D., and Clark, C. W., (**2000**). "Characteristics of minke whale (*Balaenoptera acutorostrata*) pulse trains recorded near Puerto Rico," Marine Mammal Sci. **16**, 739–756.

Oleson, E. M., Barlow, J., Gordon, J., Rankin, S., and Hildebrand, J. A., (**2003**). "Low frequency calls of Bryde's whales," Marine Mammal Sci. **19**, 407–419.

Schevill, W. E., and Watkins, W. A., (**1972**). "Intense low-frequency sounds from an Antarctic minke whale, *Balaenoptera acutorostrata*," Breviora **388**, 1–8.

Stafford, K. M., Nieukirk, S. L., and Fox, C. G., (**2001**). "Geographic and seasonal variation of blue whale calls in the North Pacific," J. Cetacean Res. Manage. **3**, 65–76.

Stern, J., (**1992**). "Surfacing rates and surfacing patterns of minke whales (*Balaenoptera acutorostrata*) off Central California, and the probability of a whale surfacing within visual range," Rep. Int. Whal. Comm. **42**, 379–385.

Thompson, P. O., and Friedl, W. A., (**1982**). "A long term study of low frequency sounds from several species of whales off Oahu, Hawaii," Cetology **45**, 1–19.

Turl, C. W., (**1980**). Boing in the North Pacific Ocean: Acoustics and distribution (unpublished).

Tyack, P. L., and Clark, C. W., (**2000**). "Communication and acoustic behavior of dolphins and whales," in *Springer Handbook of Auditory Research: Hearing by Whales and Dolphins*, edited by W. W. L. Au, A. N. Popper, and R. R. Fay (Springer-Verlag, New York), pp. 15–43.

Wenz, G. M., (**1964**). "Curious noises and the sonic environment in the ocean," in *Marine Bio-Acoustics*, edited by W. N. Tavolga (Pergamon, New York), pp. 101–119.

Winn, H. E., and Perkins, P. J., (**1976**). "Distribution and sounds of the minke whale, with a review of mysticete sounds," Cetology **19**, 1–12.

Zbinden, D., and Di Iorio, L., (**2003**). Acoustic signals of group-feeding rorqual whales in the Northwest Atlantic, Abstract presented at the 2003 European Cetacean Society Conference, Gran Canary Islands (unpublished).

Target representation of naturalistic echolocation sequences in single unit responses from the inferior colliculus of big brown bats

Mark I. Sanderson and James A. Simmons[a)]
Department of Neuroscience, Brown University, Providence, Rhode Island 02912

(Received 3 April 2005; revised 26 July 2005; accepted 27 July 2005)

Echolocating big brown bats (*Eptesicus fuscus*) emit trains of frequency-modulated (FM) biosonar signals whose duration, repetition rate, and sweep structure change systematically during interception of prey. When stimulated with a 2.5-s sequence of 54 FM pulse-echo pairs that mimic sounds received during search, approach, and terminal stages of pursuit, single neurons ($N=116$) in the bat's inferior colliculus (IC) register the occurrence of a pulse or echo with an average of <1 spike/sound. Individual IC neurons typically respond to only a segment of the search or approach stage of pursuit, with fewer neurons persisting to respond in the terminal stage. Composite peristimulus-time-histogram plots of responses assembled across the whole recorded population of IC neurons depict the delay of echoes and, hence, the existence and distance of the simulated biosonar target, entirely as on-response latencies distributed across time. Correlated changes in pulse duration, repetition rate, and pulse or echo amplitude do modulate the strength of responses (probability of the single spike actually occurring for each sound), but registration of the target itself remains confined exclusively to the latencies of single spikes across cells. Modeling of echo processing in FM biosonar should emphasize spike-time algorithms to explain the content of biosonar images. © *2005 Acoustical Society of America.* [DOI: 10.1121/1.2041227]

PACS number(s): 43.80.Lb, 43.64.Bt, 43.64.Qh, 43.64.Tk [WWA] Pages: 3352–3361

I. INTRODUCTION

Echolocating big brown bats (*Eptesicus fuscus*) hunt for flying insects by ensonifying the nearby environment with trains of ultrasonic frequency-modulated (FM) signals and listening for echoes (Kick and Simmons, 1984, Masters *et al.*, 1991; Surlykke and Moss, 2000). During aerial interception of targets, the broadcast sounds (emitted pulses) undergo stereotyped changes in their duration, repetition rate, harmonic structure, and intensity according to how far the interception maneuver has progressed—that is, according to the remaining distance to the target (Griffin *et al.*, 1960; Simmons *et al.*, 1979). Three distinct stages of the aerial interception are recognizable in these adaptive changes of the sounds (Griffin, 1958; Griffin *et al.*, 1960; Kalko and Schnitzler, 1998; Schnitzler and Kalko, 1998; Simmons *et al.*, 1979). First, when in open spaces, the bat hunts for and initially detects objects in the search phase, then the bat locates and discriminates targets while moving nearer in the approach phase, and finally the bat closes in to capture the target in the terminal phase. While searching for insects in the open, the requirements of detection are paramount, and the big brown bat emits long duration (10–20 ms), relatively narrowband FM signals containing two especially prominent harmonics in the range of 25–30 and 50–60 kHz at a low rate of about 2–5 Hz. After the bat detects a target of interest, the bat's acoustic task focuses on determining the target's location and distinguishing characteristics, so the bat broadens the bandwidth of its FM sweeps to cover all frequencies from about 20 to 105 kHz in several overlapping harmonic bands. At this stage, the bat turns towards the target and begins to track the target with its head-aim while increasing the repetition rate of its sounds progressively from 5–10 Hz to about 30 Hz. The bat also progressively decreases the duration of its sounds according to the declining delay of echoes so that successive pulse durations are kept slightly shorter than successively decreasing delays. These changes in the broadcasts allow for increasingly rapid updating of target information as well as more precise resolution of target features as the maneuver progresses (Condon *et al.*, 1994; Dear *et al.*, 1993; Moss and Zagaeski, 1994). The terminal phase, which occurs at the end of the maneuver and encompasses the final several hundred milliseconds before actual capture, is characterized by very brief (0.5–1 ms) pulses emitted at rates up to 100–150 Hz. This final burst of signals is often called the "terminal buzz" for how it sounds when monitored on a bat detector. In the case of big brown bats, whose sonar operating range extends out to about 5 m (Kick, 1982), the entire interception process typically lasts for no more than 2–3 s for each target, and it occurs in repetitive cycles as the bat encounters new insects (Griffin, 1958).

The bat decodes the stream of acoustic information gathered from successive pulse-echo pairs to infer the presence, location, and identity of targets from the echoes they reflect (Moss and Surlykke, 2001). Consequently, it is of interest to know not just how biosonar *sounds* but also how biosonar *targets* are represented in the bat's auditory system. Many studies have analyzed how variations in different acoustic parameters of sounds affect the responsiveness of neurons at successive stages of auditory processing in FM bats (Casse-

[a)]Electronic mail: james_simmons@brown.edu

day and Covey, 1995; Casseday *et al.*, 2002; Haplea *et al.*, 1994; O'Neill, 1995; Suga and Schlegel, 1973). However, there is a distinction between acoustic parameters, such as duration, repetition rate, and amplitude, which the bat varies in a correlated manner during interception, and the parameters of pulse-echo pairs, such as delay and relative amplitude, that are directly affected by the location and nature of the target itself, and which the bat uses to perceive targets (Moss and Surlykke, 2001; Simmons *et al.*, 1996). Only a few neurophysiological studies on FM bats have used naturalistic stimuli that mimic pulse-echo pairs the bat actually would receive during pursuit (e.g., Friend *et al.*, 1966; Moriyama *et al.*, 1997). The results of these studies have led us to suspect that neural sensitivity to acoustic features such as duration, repetition rate, sweep rate, or amplitude may not be directly relevant to depiction of the objects themselves. Here, we explore how auditory midbrain neurons in the big brown bat's inferior colliculus (IC) respond to complex sound sequences that emulate stimuli received during aerial interception. We chose the IC because it is the first site of large-scale obligatory convergence for parallel auditory pathways where the characteristics of neural responses no longer resemble merely sharpened repetitions of responses manifested in earlier locations (Casseday and Covey, 1995; Casseday *et al.*, 2002; Haplea *et al.*, 1994), a condition that has theoretical implications relevant to echolocation (Casseday and Covey, 1996).

II. METHODS

A. Physiological procedures

Four big brown bats (*Eptesicus fuscus*; see Kurta and Baker, 1990) collected in Rhode Island were used in this study, which was carried out with a protocol approved by the Institutional Animal Care and Use Committee of Brown University and supervised by University veterinary staff. A brief description of the surgical procedure follows (described in detail by Sanderson and Simmons, 2000). Under isoflurane anesthesia, a small patch of skin and muscle overlying the bat's skull in the region of auditory cortex and IC was removed, and a stainless steel post was attached to the exposed skull with cyanoacrylate cement. This post was 19 mm long and 1.5 mm in diameter, with a 3-mm L-shaped end in contact with the skull to increase the surface area for attachment. Postoperative recovery of the bats was swift and not marred by infections or persistent inflammation, perhaps because the prolonged daily torpor of these bats in captivity, which lowers their body temperature, acts to facilitate healing. After allowing at least 5 days for recovery after surgery, recording was done by placing the bat in a sound-proof booth (Industrial Acoustics Corp.) and restraining it in a Plexiglas™ holder with its head fixed by a clamp to the previously attached post. Access to the IC was obtained by making a small hole ($\sim$100–200 μm) in the skull with a sharpened sewing needle while viewing the exposed bone through an operating microscope (Jena, type 212). The microcraniotomy and the subsequent recordings were carried out without the use of neuroleptanalgesic or anesthetic agents; this is necessary to avoid disrupting vital inhibitory inputs from the brainstem which shape the normal responses of IC neurons (Pollak *et al.*, 1977; see also Casseday and Covey, 1995). Making the hole for recording caused no apparent discomfort to the bats, which rested quietly during this procedure. Single unit activity was recorded with 3 M NaCl electrodes (2–10 MΩ), advanced by a hydraulic microdrive (Trent-Wells). The physiological signal from the electrode was amplified (WPI damp, 1000×), and filtered (Rockland Model 442 variable bandpass filter, 200–8000 Hz). Putative spike wave forms were thresholded, time-stamped (100 μs resolution), and saved to the hard disk of a PC using Datawave hardware and software. Event wave forms representing putative spikes were cluster-cut offline using Datawave software to remove any multiunit or evoked potential activity so that single-unit spikes were segregated for subsequent single-unit analysis. The indifferent electrode (tungsten, FHC) was inserted into frontal cortex. During recording sessions, if the bat showed any sign of distress that was not alleviated by an offering of mealworms or water, the experiment was terminated.

B. The pursuit sequence stimulus

A series of FM signal pairs were created in MATLAB and arranged in a temporal sequence that emulated the emitted pulses and reflected echoes from a stationary point-target being approached by a big brown bat moving at a flight velocity of $\sim$2.5 m/s [see Figs. 1(a)–1(f)]. This sequence consisted of 54 artificial FM pulse-echo pairs whose duration, repetition rate, pulse-echo delay, FM harmonic structure, and bandwidth changed to reflect observations derived from ultrasonic recordings of big brown bats pursuing insects in open air (Griffin, 1958; Kick and Simmons, 1984; Masters *et al.*, 1991; Simmons *et al.*, 1979; Surlykke and Moss, 2000). The simulated echoes were replicas of the corresponding pulse signals, delayed and attenuated according to the desired target range [Figs. 1(e) and 1(f)]. No Doppler shift was imposed on the echoes, only delay and attenuation. The resulting sequence of pulses and echoes had a total duration of 2.5 s. It was stored as a single, long digital time-series file (sampling rate 500 kHz) whose playback into sounds through a digital-to-analog converter, amplifier, and loudspeaker constituted one complete repetition of the stimulus protocol. In most cases, a total of 32 such repetitions were used to test any given neuron, with 16 or 64 repetitions used in a few instances. A silent interval lasting 1.2 s intervened between the end of one presentation of the sequence (from the last echo, in pair 54, to the first pulse, in pair 1) and the beginning of the next presentation. The total duration of each presentation cycle thus was 3.7 s.

The individual sounds making up the pursuit sequence were designed as described in Fig. 1. The timing of the numbered pulses and echoes is shown in Fig. 1(a). They consisted of two or three harmonic FM sweeps [see Fig. 1(d)] with different durations [Fig. 1(b)], instantaneous repetition-rates [Fig. 1(c)], frequency structures [Fig. 1(d)], echo delays [Fig. 1(e)], and pulse and echo amplitudes [Fig. 1(f)]. The characteristics of natural echolocation sequences can be quite variable (Surlykke and Moss, 2000), sometimes containing

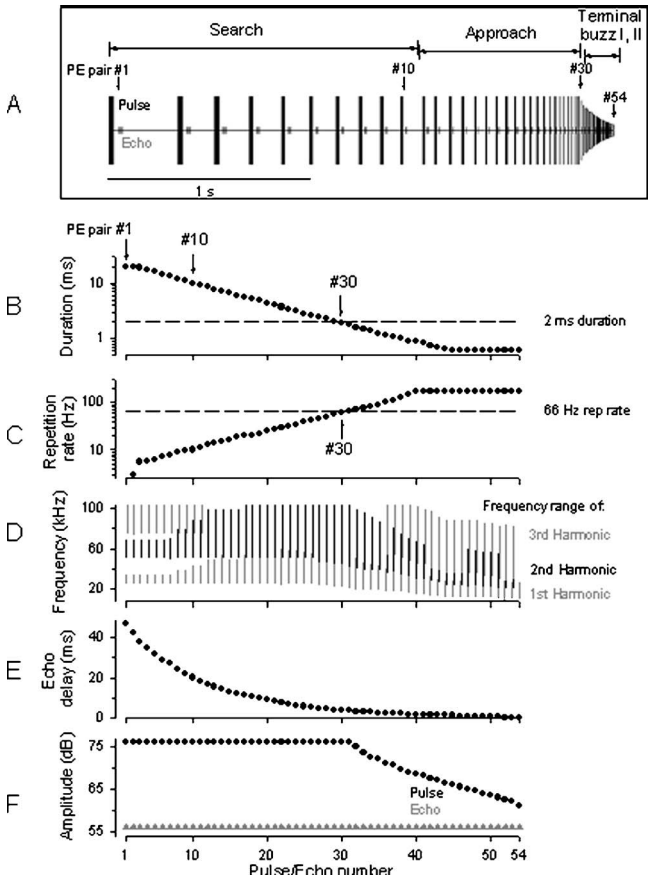

FIG. 1. Naturalistic biosonar signal sequence that simulates the acoustic stimuli received by a big brown bat (*Eptesicus fuscus*) during search, approach, and terminal stages of interception. Several parameters of these FM sounds covary to mimic the adaptive changes in biosonar sounds observed in stereotyped *Eptesicus* behavior. (a) Oscillogram trace of the whole pursuit sequence (plotted over 2.5 s total time) showing 54 numbered pairs of FM pulses and corresponding delayed, weaker echoes. The individual signals comprising the numbered simulated pulse-echo pairs (plotted against pair number, 1–54) change in duration (b), repetition-rate (c), frequency sweep organization (d), echo delay (e), and pulse and echo amplitude (f). (Signals based on Kick and Simmons, 1984.) Each echo is a delayed, attenuated replica of the preceding pulse. In the spectrograms (d), each FM harmonic is a hyperbolic downward FM sweep. Loudspeaker characteristics effectively limit the resulting acoustic stimulation of the bat's ears to the 15–90 kHz band.

smooth transitions between the search, approach, and terminal stages, and sometimes not. This stimulus sequence was constructed so that changes in duration and repetition rate were gradual [as in Figs. 1(b) and 1(c)] with progression through each of the phases [as labeled in Fig. 1(a)]. The use of smooth changes in stimulus parameters from pulse 1 to pulse 41 yielded a representative distribution of durations and repetition rates observed in the field (Surlykke and Moss, 2000).

C. Stimuli for measuring frequency tuning and latency

To measure frequency tuning and response latency for each IC neuron, an auxiliary series of sounds of varying frequency and amplitude were presented. Frequencies were presented in an ascending order as tone-bursts with durations of either 4 ms (0.44 ms linear rise/fall slopes) or 10 ms (1 ms linear rise/fall slopes). Tone-bursts in this auxiliary stimulus sequence had a presentation rate of 20 Hz and consisted of 59 frequencies spaced logarithmically from 10 to 100 kHz. As time permitted, additional tone-burst sequences were used to span a smaller frequency range around each cell's best frequency (BF) with linear frequency steps of 1 kHz at a fast (20 Hz) or slow (4 Hz) presentation rate. The tone-burst sequences initially were presented at an amplitude 20 dB above the unit's manually determined response threshold, and then as time permitted, at one or two additional amplitudes (e.g., +10, +40 dB) above threshold.

D. Stimulus generation

To generate acoustic stimuli, the digital file containing the pulse-echo sequence was loaded onto a Tucker-Davis Technologies Model QDA digital-to-analog converter board in a PC-type computer and converted into a 2.5-s stream of analog signals at a 500-kHz sampling clock rate. These signals were amplified and presented to the bat as sound through a free-field loudspeaker (Panasonic ribbon tweeter) located 38 cm from the bat, at 0° azimuth and 0° elevation in front of the bat relative to the bat's eye-nostril coordinates. The bat, loudspeaker, physiological electrodes, and supporting holders were placed inside the Industrial Acoustics Corp. sound-proof booth, which was lined inside with acoustic absorbing foam panels to minimize reverberation at ultrasonic frequencies. Instead of the free-field loudspeaker, for 29 single units the pursuit stimuli were presented diotically through a pair of Brüel and Kjaer model 4135 ("1/4 in.") condenser microphones driven as earphones. These "earphones" were polarized at 200 VDC and placed inside the bat's left and right external ears, aligned to be flush with the outer flange of each ear's pinna. No obvious differences were observed in the neural responses evoked by the pursuit stimuli from the free-field and diotic modes of presentation, so the results for the 29 diotically stimulated neurons are grouped together with the free-field-stimulated neurons in this report. (The aurality of responses in these neurons was not tested by monaural or dichotic stimulation; for binaural response properties in the IC of unanesthetized *Eptesicus*, see Haresign *et al.*, 1996.) The frequency responses for both ultrasonic delivery systems were flat in amplitude between 10 and 80 kHz (±5 dB), and frequencies above 80 kHz were attenuated by about 0.3 dB/kHz in a gradual low-pass pattern.

E. Physiological data analysis

All spike-timing data collected on-line during experiments were exported from Datawave and analyzed off-line with histogram and display routines written in MATLAB. For free-field stimulation, the 1.1-ms acoustic travel time from loudspeaker to bat was subtracted from all spike time-stamps so that latency measurements would reflect only auditory effects—middle-ear, inner-ear, and neural delays. The number of spikes evoked by successive presentations of each pulse-echo pair ($n=1-54$ in Fig. 1) was calculated by counting the number of spikes occurring in the time window from the onset of pulse n to the onset of pulse $n+1$; that is, during

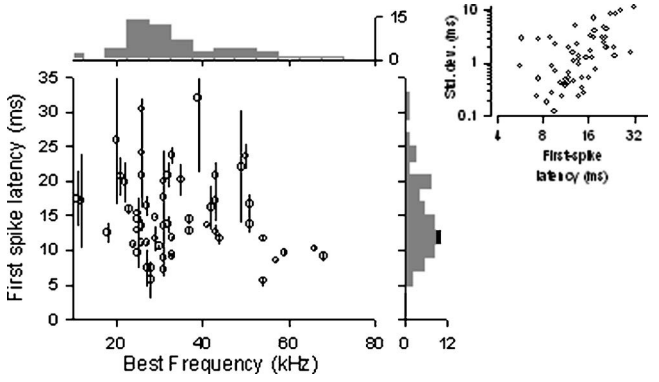

FIG. 2. Best frequency (BF) and characteristic latency for 56 IC neurons. The distributions for BF (horizontal axis) and latency (vertical axis) are projected as histograms at top and right, respectively. Error bars show 1 s.d. for first-spike latency. Inset plot (top right): standard deviation of first-spike latency decreases for neurons that respond earlier (note use of logarithmic scale for both axes).

the epoch of time defined by the instantaneous pulse repetition-rate in the sequence [Fig. 1(c)]. Due to the relatively long characteristic latency of many IC neurons (>15 ms) and the rapid repetition rate of the simulated pulses in the later portion of the pursuit sequence, some spikes evoked by stimulus n necessarily will fall into the counting window for stimulus $n+1$. To avoid this ambiguity, spike counts were not calculated separately for pulse-echo pairs after pair 30 because, at this point in the stimulus sequence, the period of the simulated pulse repetition rate decreased below 16 ms. (This precaution proved to be necessary because 70% of the IC neurons exhibited onset latencies >16 ms to tone-bursts at BF; see Fig. 2.)

Time windows different from those described just for counting spikes were necessary in order to estimate first-spike latency. Simultaneous displays of peristimulus time histograms (PSTHs, 1-ms bins) and dot raster plots were used to select appropriate start and stop times of this analysis window used for each of the first 30 pulses and echoes in the sequence. (A similar approach was used by Heil and Irvine, 1998, to deal with an analogous problem.) These windows excluded spikes falling outside the latency region most plausibly related to each pulse or echo, most of which were presumed to be spontaneous rather than evoked activity. No latency analysis was carried out on responses of units with high spontaneous activity (spontaneous rate count >1.0 spikes/s, as defined in the following). Also, estimates of first-spike latency based on less than 8 spikes across all 32 trials were discarded as being too sparse. The spike times isolated from these windows were used to construct spike-triggered average spectrograms of the effective stimuli, as illustrated in Fig. 6. Because the first and second pulse-echo pairs (Nos. 1 and 2) were identical in their spectral and duration parameters [see Figs. 1(b) and 1(d)], we did not include the first pulse or echo in these average spectrograms. Also, the first pulse-echo pair was delivered after the relatively long 1.2-s silent interval between successive presentations of the stimulus sequence, which resulted in potentially less response adaptation than for any other pairs.

Spontaneous activity was measured in two ways, one

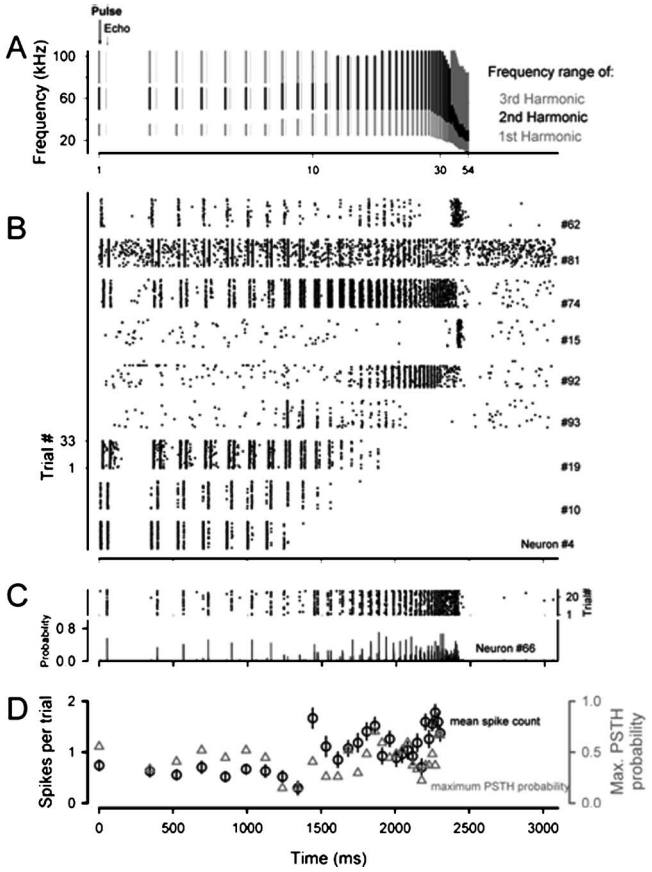

FIG. 3. Single-unit responses evoked by the pursuit sequence. (a) Spectrogram of pulses and echoes. Each pulse (thick line at left in each pair) is composed of multiple harmonics and is followed by its echo (thin line at right of each pair). (b) Composite graph of dot raster plots showing responses to the first 33 stimulus trials for 9 different single units. The unit number at the far right corresponds to the number out of 116 cells plotted in Fig. 4(a). (c) Dot rasters and corresponding peristimulus time histograms (PSTHs) for responses to each pulse-echo pair from neuron 66. Response probability shown as vertical axis of PSTHs was computed using 1 ms bins. (d) (Circles) mean number of spikes evoked for each pulse-echo pair from 1 to 30. Spikes were counted within the time window from the start of the pulse n to the start of pulse $n+1$(n=30). (Triangles) maximum spike probability from 1-ms bin with largest probability value in PSTHs. Error bars for spike counts indicate ±1 SE of mean.

based on spike counts and the other based on response probability from the PSTHs (by computing the probability of response within individual 1-ms bins over repeated trials). For the spontaneous spike rate count, we counted the number of spikes in a time window of silence after the conclusion of the pursuit stimulus [from 2680 to 3080 ms in Fig. 2(b)]. We then normalized the spike counts by the size of this measurement window (400 ms) to get an estimate of the spontaneous rate count in spikes/s. This normalized value was used to estimate the expected number of spontaneous spikes that would occur in any given time window during the stimulus. Spontaneous activity expressed as response probability was estimated from the PSTHs using the maximum PSTH response probability in any of the 1-ms bins within the silent window from 2680 to 3080 ms [see Fig. 3(c)].

Each neuron's potential for exhibiting response selectivity in any segment or region of the pursuit sequence was tested by first locating the peak in the response probability function across the 54 pulse-echo pairs. The region around

the peak response was identified as whichever neighboring and adjacent pulse-echo pairs that evoked spike counts >50% of the peak spike count. Using a criterion similar to that in our earlier studies (Ferragamo *et al.*, 1998; Sanderson and Simmons, 2000), the neuron's response was deemed selective if the spike counts of no other pulse-echo pair outside of this region evoked activity above 50% of the peak spike count.

III. RESULTS

A. Best frequencies and latencies

Spike data for responses to the pursuit stimuli were collected from 116 IC units at recording depths from 150 to 2150 μm ventral to the dorsal surface of the IC. For the majority of these single units, spontaneous activity was low (median=0.53 spikes/s; 75th percentile=4.04 spikes/s). We measured best frequency (BF) and characteristic latency for 56 of these neurons: median BF=31 kHz; interquartile range=26–43 kHz; median latency=13.73 ms; interquartile range=10.69–18.76 (Fig. 2). Response thresholds at BF ranged from 8 to 82 dB SPL peak-to-peak (mean 40 dB±20 dB SPL). The distribution of BFs was similar to that reported previously for awake big brown bats (Ferragamo *et al.*, 1998). The inset for Fig. 2 shows that the standard deviation of first-spike latency was correlated with latency (Spearman correlation coefficient=0.57, $p<0.05$). Condon *et al.* (1994) showed similar results in the little brown bat, *Myotis lucifugus*: shorter latency neurons tended to have smaller "jitter" in their spike timing.

B. Responses to simulated pursuit sequence

Figure 3(b) shows example dot raster displays for responses to the 54 pulse-echo pairs in the pursuit sequence evoked from nine different IC single units (individual cell numbers given at right). Some units discharged throughout virtually the entire pursuit sequence [e.g., Nos. 81, 74 in Fig. 3(b)]. Other units however, were active only during a restricted region of the pursuit sequence [e.g., Nos. 10, 19, 93, 92, 15, 4 in Fig. 3(b)]. Some units responded selectivity to noncontiguous sections of the pursuit sequence [e.g., No. 62 in Fig. 3(b)]. The following population analysis is based on the two metrics of spike-count and maximum response probability in the peristimulus time histograms (PSTHs). These metrics are plotted in Fig. 3(d) for the responses of the same representative single neuron (No. 66) shown in Fig. 3(c).

A spike-count metric is commonly used in neurophysiological studies of FM bats even though most stimuli evoke only ~1 spike per stimulus (Casseday *et al.*, 1994, 1996; Galazyuk *et al.*, 2000). However, a spike-count approach usually incorporates a long analysis window for accumulating spikes and therefore disregards the degree of temporal dispersion in the spike train. A neuron might discharge only one spike in response to each FM sweep, but it can do so with high or low temporal precision. The spikes sent from the IC to higher stages of processing could have different effects upon their target neurons depending upon their temporal precision in relation to the integration time of the target cells. To display the temporal organization of the spike trains evoked by the stimulus sequence, we computed aggregate PSTHs with 1 ms bins for the entire 3.7-s epoch of stimulation [example in Fig. 3(c)]. Usually, PSTHs measure neuronal firing rate within short time windows. However, because of the low number of spikes evoked by any one FM stimulus, typically less than one spike per trial, a probability measure is more appropriate than a rate measure for these responses. Thus, for Fig. 3(c), if the neuron responded on every trial with a spike that fell within the same 1 ms time bin, the response probability would be at the maximum of 1.0 for that time bin.

The aggregate PSTHs assembled across all 54 pulse-echo pairs for the entire population of 116 neurons are shown in Fig. 4(a). Across this population of single units, most neurons discharged less than two spikes for any pulse-echo pair in the pursuit sequence. The population median spike counts for the first 30 pulse-echo pairs ranged from 1.45 (pulse-echo pair 1) to 0.03 spikes per trial [pulse-echo pair 30; Fig. 4(b)]. For each of the first 30 pulse-echo pairs, we plotted the median of the maximum PSTH response probabilities in any one 1-ms bin [Fig. 4(c)]. This analysis extracts the greatest response probability occurring within the time window for a neuron's response to each pulse-echo pair for each of the 116 PSTHs. The population median response probability decreased from 0.183 (pulse-echo pair 1) to 0.027 [pulse-echo pair 30; Fig. 4(c)]. This decrease in median response probability is primarily due to the fact that the available pool of neurons activated by the pursuit stimuli decreases progressively after pulse-echo pair 15 in the pursuit sequence [Fig. 4(d)]. When the median response probabilities were plotted only for neurons that are active at each stage of the stimulus, the response probability in the approach phase was similar to that in the search phase [Fig. 4(e)].

Using the approach described in Sec. II for assessing selectivity to particular regions of the stimulus sequence, most of the neurons that exhibited such selectivity could be classified as either responding to a wide range of all the lower repetition rates and longer durations (41/116, 35%), or responding to a more restricted range at different locations within the sequence (42/116, 36%). A few of these more restricted neurons responded only during the terminal stage [e.g., No. 15 in Fig. 3(b)]. The responses for the remaining 33 neurons could not be categorized as simple filter functions in this way because multiple peaks occurred in the response functions [e.g., neuron 66, Fig. 3(d)].

C. Responses to individual pulse-echo pairs

Using specific time windows adapted to each of the 54 pieces of the stimulus sequence, we measured spike counts and onset latencies for spikes evoked by each of the pulse-echo pairs making up the sequence (Fig. 5). For this analysis, we replotted the dot raster displays from Fig. 4(a) in a stacked fashion, with the starting time for each horizontal slice fixed relative to the onset of each pulse in the pursuit sequence. This reorganization of the data is better for displaying the detailed temporal properties of each neuron's response to the pulse-echo pairs. For example, the dot rasters for the neuron in Fig. 5(a) show that the pulse and echo

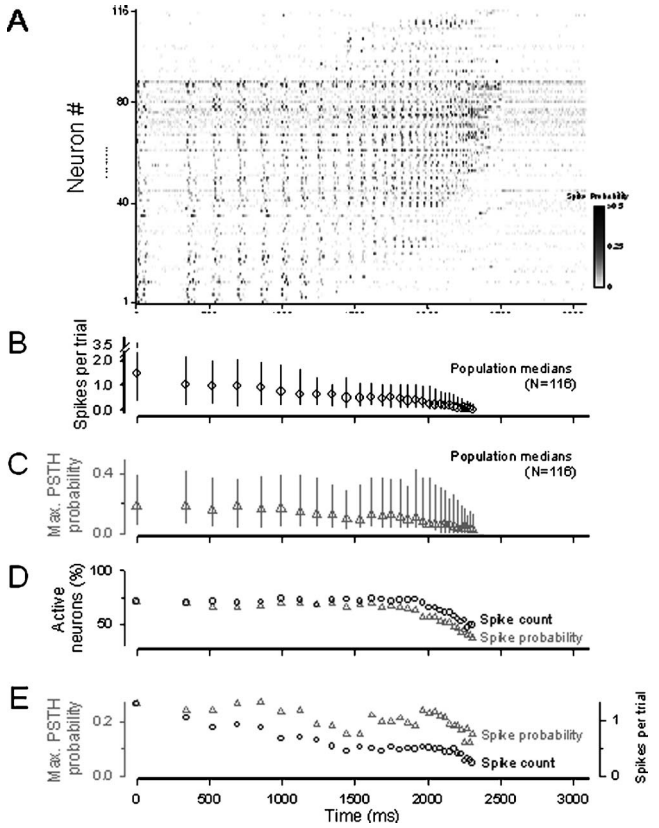

FIG. 4. Summary of all responses evoked in the entire population of 116 cells by the pursuit sequence stimulus in Fig. 1. The horizontal time axis shows an epoch of 3.088 s for each stimulus presentation (2.5 s with sounds plus 0.588 s of silence). (a) Gray-scale surface plot of PSTHs from each pulse-echo pair for each neuron (numbered from 1 to 116 at left). Each horizontal row plots a series of PSTHs for one of the 116 neurons. *Z* axis (gray scale intensity) shows response probability computed using 1 ms bins. The gray-scale map was clipped at $p=0.5$ in order to show activity for entire population. Any given pulse-echo pair typically evokes <2 spikes on a single trial. More than half of the neuronal population is active for pulse-echo pairs representing the search and approach stages [Fig. 1(a)], but most cells cease responding just before the terminal phase. (b) Median of the average spike count (spikes per sound-pair presentation) evoked by the first 30 pulse-echo pairs over the whole pool of 116 neurons. Error bars denote the interquartile range. (c) Median values for the maximum PSTH response probabilities evoked by each pulse-echo pair over the neuronal population. (d) The percentage of active neurons out of the population of 116 cells for each pulse-echo pair, tallied by comparing spike count or response probability data against spontaneous background activity. A neuron was considered active if the neural activity was greater than the expected spontaneous activity. For the first 20 pulse-echo pairs, more than half of the population exhibits activity above spontaneous level. (e) Median values for spike count and response probability recomputed for each pulse-echo pair including only data from neurons that are active in (d). Spontaneous activity was subtracted from each neuron's spike count (or response probability) for this plot. Each data point in (b)–(e) is plotted on the *x* axis aligned to the onset of the time window used to count spikes (i.e., the mean spike count for the first pulse-echo pair is plotted at the onset of pulse 1).

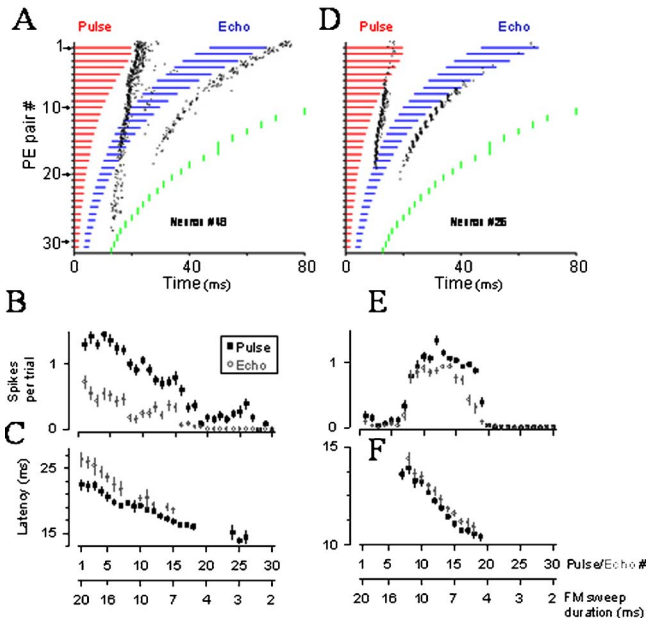

FIG. 5. (Color online) (a), (d) Dot rasters for two cells (48 and 26) replotted and stacked to show alignment of spikes to the onset time of the pulse in each pulse-echo pair. This display allows qualitative separation of evoked activity into "pulse" and "echo" responses. (a) The rasters for the first 33 pulse-echo pairs are shown with the horizontal bars below each raster indicating pulse and echo duration. The vertical lines to the right of the horizontal slices mark the start of the next pulse in the sequence (i.e., the point in time when the trial in each raster "wraps around" to the next pulse-echo pair below). (b)–(f) Mean spike counts and latencies per pulse and per echo for these two neurons derived from restacking the raster plots separately with respect to pulse onset and echo onset.

stimuli separately evoked discrete responses throughout the search and approach phases of the pursuit sequence [the corresponding spike counts are shown in Fig. 5(b)]. When this analysis was applied to each neuron in the population, we found that over half (68/116, 59%) of the population responded to both the pulse and echo [e.g., Figs. 5(a), 5(d)]. Less than a third (35/116, 30%) responded only to the pulse [e.g., neuron 62 in Fig. 3(b)]. Only 7% [8/116, e.g., neuron 92 in Fig. 3(b)] responded to the echo and not the pulse. (Four of these 8 neurons were band-pass selective neurons.) We could not categorize in this manner the responses for 5 neurons that only responded in the terminal buzz [after pulse-echo pair 30; e.g., neuron 15 in Fig. 3(b)] because the pulse interval is so short in the buzz that it is impossible to assign a given spike to any one pulse-echo pair.

Latencies to the echo were usually slightly longer than those observed for the pulse response [Fig. 5(c)], as would be expected from amplitude-latency trading because the echo always was weaker than the corresponding pulse [Figs. 1(a), 1(f)]. Variability of the mean first spike latency was measured for neurons that responded to the first 20 pulse-echo pairs and that had spontaneous rates counts of <1.0 spikes/s ($N=50$). Standard deviation for first spike latency ranged from 0.122 to 5.51 ms (median 0.49 ms). Overall, first spike latency to the onset of each pulse and echo decreased throughout the pursuit sequence [e.g., Figs. 5(c), 5(f)]. This was expected because the pursuit sequence is composed of descending FM signals. As sweep duration decreases, the time-of-occurrence of the putative effective frequency in the sweep that drives the neuron (Bodenhamer and Pollak, 1981) moves to an earlier time relative to sweep onset (Heil and Irvine, 1998). Most often, the first spike latencies did not decrease in a linear fashion with stimulus duration [e.g., Fig. 5(c)]. This was due to the hyperbolic shape of the downward FM sweeps (which is biologically more realistic than linear sweeps) and the complicated spectral parameters of the interleaved harmonics, which change in a non-continuous manner from search-stage to approach-stage to

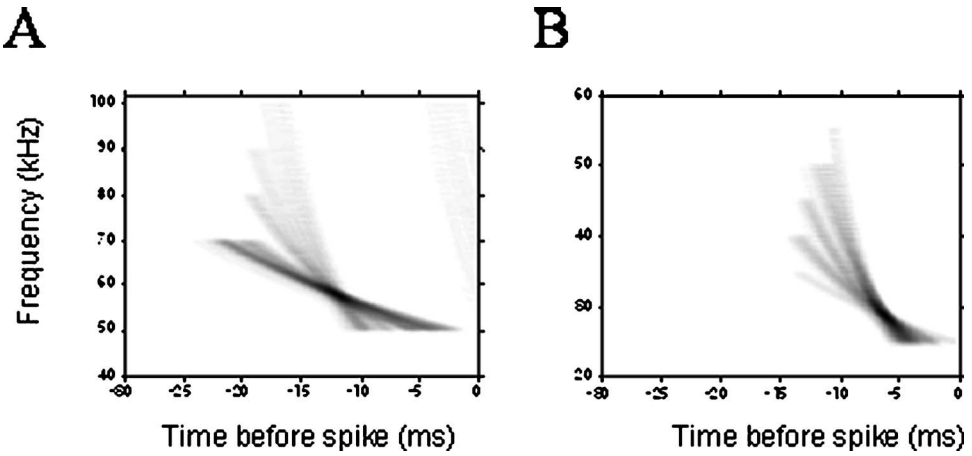

FIG. 6. Reverse-time spike-triggered average spectrograms showing a specific segment of the different FM sweeps in the stimulus sequence that is time-locked to spikes. (a) The average spectrogram for the second harmonic, calculated from a window starting 30 ms before each spike for neuron 48, of pulses 2–19 in Fig. 5(a) (based on 447 spikes). The peak at the intersection of the rotating spectrograms indicates that the neuron spiked, on average, 11.8 ms after the energy occurred at 57.4 kHz in the FM sweep. These values comprise the neuron's characteristic latency and effective frequency for the pursuit stimulus series. When tested with tone-bursts, this neuron's BF was 54 kHz and characteristic latency was 11.69 ms. (b) Same analysis for neuron 26 from spikes from the first harmonic of pulses 7–20 in Fig. 5(c) (based on 396 spikes).

terminal buzz [see Fig. 1(d)]. For example, the first 7 pulse-echo pairs are narrowband search sweeps that have no energy between 50 and 35 kHz. Cells with a BF within this frequency band ($N=14$) either did not respond ($N=9$) to these early pulse-echo pairs or responded just with a constant latency relative to stimulus onset ($N=5$).

D. Responses to specific time-frequency points in FM sweeps

To estimate characteristic latency and effective frequency for each neuron with respect to the different FM sounds, we constructed spike-triggered average spectrograms of the stimuli preceding each spike. This method is similar to a reverse correlation analysis to identify stimulus features that drive the neuron except that we are able to take advantage of the fact that all echolocation sounds of big brown bats consist of downward FM sweeps with durations of 0.5–20 ms. The more usual, much wider range of all possible combinations of frequencies in wideband noise-like stimuli does not have to be employed here because we are not interested in the neuron's generic time-frequency response profile, only its selectivity to downward-sweeping FM sounds. The average spectrogram for the spikes evoked by the FM pulse stimuli in Fig. 5(a) is shown in Fig. 6(a). From the resulting two-dimensional average time-frequency surface, we estimated the effective frequency and characteristic latency (Bodenhamer and Pollak, 1981; Felsheim and Ostwald, 1996). The peak in Fig. 6(a) for the pulse spectrograms was located at 57.4 kHz with a latency of −11.8 ms relative to spike onset time. The spike-triggered echo spectrogram had a peak at 55.8 kHz and a characteristic backward latency of −12.7 ms (data not shown). The BF and characteristic latency measured with 4 ms pure tone bursts were 54 kHz and −11.69 ms, respectively. An example from another single unit, which had a peak in its spike-triggered stimulus spectrogram at 28.7 kHz and −6.2 ms, is shown in Fig. 6(b). Pure tone data were not available for this neuron. Most neurons with a clear peak in the spike-triggered spectrogram had an effective frequency which was an average of 1.49 kHz above the BF measured with tone-bursts ($N=35$; SD=3.11 kHz). However, less than half of the population recorded from the bat's IC (49/116=42%) had clear spike-triggered spectrograms such as shown in Fig. 6. That is, for slightly more than half of the cells, the effective frequency and/or the characteristic response latency changed as a function of sweep duration and sweep rate, which jittered the overlaying of sweeps from different stimuli to obscure the emergence of any specific time-frequency point in those sweeps as the putative "excitatory event" for evoking the spikes. For rat IC neurons, Poon and Yu (2000) also found that less than half (44%) had useful spike-triggered spectrograms when driven by random FM sounds.

IV. DISCUSSION

This study examined how neurons in the big brown bat's IC respond to pulse-echo stimuli simulating a bat's pursuit sequence, which only two other reports have discussed previously. A brief section in one previous report (Friend *et al.*, 1966) showed that, in little brown bats (*Myotis lucifugus*), IC neurons responded to a recorded pursuit sequence in a variety of ways that were similar to the response patterns shown here in Fig. 3. Other than showing representative raster plots, however, that report did not quantitatively analyze the neural responses. A more recent study (Moriyama *et al.*, 1997) presented big brown bats with a tape-recorded echolocation sequence of pulse emissions from a pursuit sequence and measured activity evoked in IC neurons. There were three differences between the methods of that study and ours: (1) the stimulus sequence consisted of the echolocation emissions only, not pulses and echoes, (2) the recordings were carried out under neuroleptic analgesia, which affects spontaneous activity and onset latency, while we studied awake bats, and (3) the stimulus sequence was presented at a different overall amplitude relative to each neuron's threshold, which makes cross-neuronal population comparisons difficult. The focus was on whether IC neurons selectively re-

TABLE I. Responses to the pursuit sequence separated into stages of search, approach, and terminal buzz (I and II) according to duration, repetition rate, and amplitude of the pulses and echoes. The terminal buzz is divided into two sections (I and II; see Siemers and Schnitzler, 2000; Surlykke and Moss, 2000) based on the point in time where the duration and repetition rate of the pulses become constant [Figs. 1(b) and 1(c)]. From the PSTHs plotted in Fig. 3, the number of neurons that responded to at least 75% of the pulse-echo pairs in each of the four categories are shown. The "All" category includes those neurons that responded to at least 8 of the search phase stimuli, 15 of the approach phase stimuli, and at least 8 of the terminal buzz I or 11 of the terminal buzz II sounds.

Response category	PE pair number	Active neurons (N=116)
Search	1–10	84 (72%)
Approach	11–30	53 (46%)
Terminal Buzz I	31–40	25 (21%)
Terminal Buzz II	41–54	9 (8%)
"All"	1–⩾31	22 (19%)

sponded to one of the three phases in the echolocation sequence—the search, approach, terminal buzz stages. Spike counts were not normalized by the number of sounds within a particular phase of the stimulus sequence, which complicates making inferences about the observations. Nevertheless, at 20 dB above threshold, 59% of the neurons responded selectively to a particular phase of the sequence. The remaining neurons responded to the stimuli more broadly and did not show a large modulation in their spike counts across the sequence. In spite of methodological differences, this aspect of the results is comparable to what is shown in Fig. 3(b). A similar percentage of the neurons (53%, 62/116) in Fig. 3(b) were selective for some region of the pursuit sequence (spike count modulated by more than 50%, as defined in Sec. II).

We recorded only a few neurons that responded to the final portion of the pursuit sequence-the terminal buzz [see Fig. 3(c) or Table I, terminal buzz II]. For those cells that did respond, it does not appear that the pulse and echo evoked separate volleys of spikes. Bats clearly make corrective flight, head-aim, and postural movements based on echo information acquired during the terminal stage (Wilson and Moss, 2002), but perhaps only a small population of IC neurons is needed to handle this task. It also could be that the passive mode of our experimental paradigm (the bat does not actually emit the pulses during the experiment, it just receives artificial pulses and echoes) does not engage the auditory system sufficiently to activate neurons that would otherwise respond in the terminal buzz (Schuller, 1979). Or, perhaps our model for terminal buzz pulse-echo amplitudes [Fig. 1(f)] may be inappropriate due to the gain control effects in the vocalizing animal [Kick and Simmons, 1984].

To approximate the acoustic stimuli that the big brown bat commonly would encounter when closing in upon a small flying insect, the stimuli used in the present study covaried along multiple feature dimensions (duration, repetition rate, duration, harmonic structure, delay; see Fig. 1). Most traditional physiological studies of the auditory system employ much simpler stimuli that vary along just one of these parameters at a time to evaluate potential response selectivity. They also use long interstimulus intervals equivalent to repetition-rates of only 1–4 sounds/s (slower even than the lowest repetition rates of pulses and echoes that appear early in our sequence). Use of such long intervals leads to more spikes per stimulus and thus more "data" to pool together for more robust response profiles because response adaptation is kept low. However, in natural tasks, the big brown bat in fact is exposed to the more rapid sound sequences we used here, not the slower rates used in most physiological studies, so that its auditory system consequently operates in what can best be described as a perpetually adapted state.

In experiments with acoustic stimuli that vary one parameter at a time, about 33% of the IC population in big brown bats exhibits tuning to duration (Casseday *et al.*, 1994; Ehrlich *et al.*, 1997; Pinheiro *et al.*, 1991). For repetition rate or pulse rate, about 50% of IC neurons are tuned to specific rates (Jen and Schlegel 1982; Pinheiro *et al.*, 1991). In contrast, the results in Fig. 4(a) and Table I show that most IC neurons respond more broadly across the pursuit sequence when the duration and repetition rate of pulses and echoes covary as they would naturally [see Fig. 4(a); quantified in Table I]. Another auditory single-unit study in the big brown bat's brainstem pontine nucleus showed that repetition-rate tuning nearly disappeared when the repetition-rate protocol was made more "naturalistic" (Wu and Jen, 1995). When bats were presented with sound sequences that coupled repetition rate with stimulus duration (short durations with high repetition rates and vice versa), the percentage of repetition-rate tuned neurons decreased significantly (from 27% to just 7%). In Fig. 4(a), much of the modulation in response probability across the pursuit stimulus presumably occurs due to individual neurons' selectivity for duration and/or repetition, but the degree of selectivity is less than has been reported from experiments with simpler stimuli.

Figures 3(b) and 4(a) give support to the proposal that one function of the IC may be to organize responses to sounds for control of motor responses (Casseday and Covey, 1996). The underlying premise is that neural responses destined for control of motor events have to be made relatively slow compared to the fast following rate of responses that track rapid modulations of sounds in brainstem auditory sites. A common observation in the auditory system is that the upper limit for time-locking of responses to high stimulus repetition rates drops precipitously when ascending from the cochlear nucleus in the brainstem to the IC in the midbrain. Langner (1992) has reviewed how a temporal code for temporal events is replaced by an explicit rate (i.e., response strength) code in the IC in the context of determining pitch. Casseday and Covey (1996) argue that the transition from a temporal to a rate (response-strength) code is necessary at this stage in the auditory system in order to match the "rate of output to a rate that is appropriate for initiating or controlling motor action." In big brown bats, the brainstem phenomenon of trains of closely spaced spikes that register every sound is tempered by having IC responses distributed as single spikes across a population of neurons that respond differentially to segments of the pursuit sequence (Boden-

hamer and Pollak, 1981; Casseday and Covey, 1995; Pollak *et al.*, 1977). The IC has massive projections to the pontine gray (which, in turn, projects to the cerebellum), in addition to projecting to the superior colliculus (Schweizer, 1981). This allows for incoming echo information to rapidly modulate flight behavior. However, only a few midbrain studies in FM bats have focused on so-called filter neurons using stimuli whose properties actually relate to a target's spatial dimensions. Neurons sensitive to target azimuth (Valentine and Moss, 1997), elevation, size (Galazyuk *et al.*, 2000), and range (Dear and Suga, 1995; Feng *et al.*, 1978) would be relevant for guiding subsequent motor behavior. It is difficult to imagine how neurons sensitive chiefly to duration or repetition rate would provide useful information for guiding the bat's flight behavior.

Using the pursuit sequence as a stimulus provides a glimpse into how IC neurons participate in encoding biosonar information across a broad but relevant acoustic feature space. In spite of widely ranging signal parameters (duration, repetition rate, sweep rate), most IC neurons, if they respond at all, confine themselves to registering the timing of a particular frequency near their BF (Fig. 6) with a single spike (Fig. 4). Figures 3(b) and 4(a) emphasize how the presence of the sonar target is registered by the response latencies instead of the response strengths. As in other cases, spike timing information often is more robust and of higher fidelity for reconstructing characteristics of stimuli than response strength (e.g., Cariani and Delgutte, 1996). The probability of spiking may change dramatically across the pursuit sequence, but spike latency still conveys the existence and range of the target by registering different effective frequencies in the FM sweeps (Bodenhamer and Pollak, 1981; Pollak *et al.*, 1977). Further consideration of this latency code is essential to understand how the bat decodes target range, elevation, and shape (Matsuo *et al.*, 2001; Saillant *et al.*, 1993).

ACKNOWLEDGMENTS

This work was supported by ONR Grant Nos. N00014-01-1-0306 and N00014-99-1-0350 and an NSF grant No. (BES-9622297) to J.A.S., a NSF Predoctoral fellowship to M.I.S., and a grant from the Burroughs-Wellcome Fund to the Brown University Brain Sciences Program.

Bodenhamer, R., and Pollak, G. D. (**1981**). "Time and frequency domain processing in the inferior colliculus of echolocating bats," Hear. Res. **5**, 317–335.

Cariani, P. A., and Delgutte, B. (**1996**). "Neural correlates of the pitch of complex tones. I. Pitch and pitch salience," J. Neurophysiol. **76**, 1698–1716.

Casseday, J. H., and Covey, E. (**1995**). "Mechanisms for analysis of auditory temporal patterns in the brainstem of echolocating bats," in *Neural Representation of Temporal Patterns*, edited by E. Covey, H. H. Hawkins, and R. Port (Plenum, New York), pp. 25–51.

Casseday, J. H., and Covey, E. (**1996**). "A neuroethological theory of the operation of the inferior colliculus," Brain Behav. Evol. **47**, 311–336.

Casseday, J. H., Ehrlich, D., and Covey, E. (**1994**). "Neural tuning for sound duration: Role of inhibitory mechanisms in the inferior colliculus," Science **264**, 847–850.

Casseday, J. H., Fremouw, T., and Covey, E. (**2002**). "The inferior colliculus: A hub for the central auditory system," in *Integrative Functions in the Mammalian Auditory Pathway*, edited by D. Oertel, R. R. Fay, and A. N. Popper (Springer, New York), pp. 238–318.

Condon, C. J., White, K. R., and Feng, A. S. (**1994**). "Processing of amplitude-modulated signals that mimic echoes from fluttering targets in the inferior colliculus of the little brown bat, *Myotis lucifugus*," J. Neurophysiol. **71**, 768–784.

Dear, S. P., Simmons, J. A., and Fritz, J. (**1993**). "A possible neuronal basis for representation of acoustic scenes in auditory cortex of the big brown bat," Nature (London) **364**, 620–623.

Dear, S. P., and Suga, N. (**1995**). "Delay-tuned neurons in the midbrain of the big brown bat," J. Neurophysiol. **73**, 1084–1100.

Ehrlich, D., Casseday, J. H., and Covey, E. (**1997**). "Neural tuning to sound duration in the inferior colliculus of the big brown bat, *Eptesicus fuscus*," J. Neurophysiol. **77**, 2360–2370.

Felsheim, C., and Ostwald, J. (**1996**). "Responses to exponential frequency modulations in the rat inferior colliculus," Hear. Res. **98**, 137–151.

Feng, A. S., Simmons, J. A., and Kick, S. A. (**1978**). "Echo detection and target ranging neurons in the auditory system of the bat *Eptesicus fuscus*," Science **202**, 645–648.

Ferragamo, M., Haresign, T., and Simmons, J. A. (**1998**). "Frequency tuning, latencies, and responses to frequency-modulated sweeps in the inferior colliculus of the echolocating bat, *Eptesicus fuscus*," J. Comp. Physiol., A **182**, 65–79.

Friend, J. H., Suga, N., and Suthers, R. A. (**1966**). "Neural responses in the inferior colliculus of echolocating bats to artificial orientation sounds and echoes," J. Cell Physiol. **67**, 319–332.

Galazyuk, A. V., Llano, D., and Feng, A. S. (**2000**). "Temporal dynamics of acoustic stimuli enhance amplitude tuning of inferior colliculus neurons," J. Neurophysiol. **83**, 128–138.

Griffin, D. R. (**1958**). *Listening in the Dark* (Yale University Press, New Haven, CT).

Griffin, D. R., Webster, F. A., and Michael, C. R. (**1960**). "The echolocation of flying insects by bats," Anim. Behav. **8**, 141–154.

Haplea, S., Covey, E., and Casseday, J. H. (**1994**). "Frequency tuning and response latencies at three levels in the brainstem of the echolocating bat, *Eptesicus fuscus*," J. Comp. Physiol., A **174**, 671–683.

Haresign, T., Wotton, J. M., Ferragamo, M. J., and Simmons, J. A. (**1996**). "Converging approaches to determining sound localization in the big brown bat, *Eptesicus fuscus*," in *Neuroethological Studies of Cognitive and Perceptual Processes*, edited by C. F. Moss and S. Shettleworth (Westview Press, Boulder, CO), pp. 280–304.

Heil, P., and Irvine, D. F. (**1998**). "Functional specialization in auditory cortex: Responses to frequency-modulated stimuli in the cat's posterior auditory field," J. Neurophysiol. **79**, 3041–3059.

Jen, P. H.-S., and Schlegel, P. (**1982**). "Auditory physiological properties of the neurons in the inferior colliculus of the big brown bat, *Eptesicus fuscus*," J. Comp. Physiol. [A] **147**, 351–363.

Kalko, El. K. V., and Schnitzler, H. U. (**1998**). "How echolocating bats approach and acquire food," in *Bats: Phylogeny, Morphology, Echolocation, and Conservation Biology*, edited by T. H. Kunz and P. A. Racey (Smithsonian Institution Press, Washington, DC), pp. 197–204.

Kick, S. A. (**1982**). "Target detection by the echolocating bat, *Eptesicus fuscus*," J. Comp. Physiol. [A] **145**, 431–435.

Kick, S. A., and Simmons, J. A. (**1984**). "Automatic gain control in the bat's sonar receiver and the neuroethology of echolocation," J. Neurosci. **4**, 2705–2737.

Kurta, A., and Baker, R. H. (**1990**). "*Eptesicus fuscus*," Mammalian Species **356**, 1–10.

Langner, G. (**1992**). "Periodicity coding in the auditory system," Hear. Res. **60**, 115–142.

Masters, W. M., Jacobs, S. C., and Simmons, J. A. (**1991**). "The structure of echolocation sounds used by the big brown bat *Eptesicus fuscus*: Some consequences for echo processing," J. Acoust. Soc. Am. **89**, 1402–1413.

Matsuo, I., Tani, J., and Yano, M. (**2001**). "A model of echolocation of multiple targets in 3D space from a single emission," J. Acoust. Soc. Am. **110**, 607–624.

Moriyama, T., Wu, M. I., and Jen, P. H.-S. (**1997**). "Responses of bat inferior collicular neurons to recorded echolocation pulse trains," Chin. J. Physiol. **40**, 9–17.

Moss, C. F., and Surlykke, A. (**2001**). "Auditory scene analysis by echolocation in bats," J. Acoust. Soc. Am. **110**, 2207–2226.

Moss, C. F., and Zagaeski, M. (**1994**). "Acoustic information available to bats using frequency-modulated echolocation sounds for the perception of insect prey," J. Acoust. Soc. Am. **95**, 2745–2756.

O'Neill, W. E. (**1995**). "The bat auditory cortex," in *Hearing by Bats*, edited

by A. N. Popper and R. R. Fay (Springer, New York), pp. 416–480.
Pinheiro, A. D., Wu, M., and Jen, P. H. (**1991**). "Encoding repetition rate and duration in the inferior colliculus of the big brown bat, *Eptesicus fuscus*," J. Comp. Physiol., A **169**, 69–85.
Pollak, G. D., Marsh, D. S., Bodenhamer, R., and Souther, A. (**1977**). "Characteristics of phasic-on neurons in the inferior colliculus of anaesthetized bats with observations related to mechanisms for echoranging," J. Neurophysiol. **40**, 926–941.
Poon, P. W. F., and Yu, P. P. (**2000**). "Spectro-temporal receptive fields of auditory midbrain neurons in the rat obtained with frequency modulated stimulation," Neuro. Lett. **289**, 9–12.
Saillant, P. A., Simmons, J. A., Dear, S. P., and McMullen, T. A. (**1993**). "A computational model of echo processing and acoustic imaging in frequency-modulated echolocating bats: The spectrogram correlation and transformation receiver," J. Acoust. Soc. Am. **94**, 2691–2712.
Sanderson, M. I., and Simmons, J. A. (**2000**). "Neural responses to overlapping FM sounds in the inferior colliculus of echolocating bats," J. Neurophysiol. **83**, 1840–1855.
Schnitzler, H. U., and Kalko, El. K. V. (**1998**). "How echolocating bats search and find food," in *Bats: Phylogeny, Morphology, Echolocation, and Conservation Biology*, edited by T. H. Kunz and P. A. Racey (Smithsonian Institution Press, Washington, DC), pp. 183–196.
Schuller, G. (**1979**). "Coding of small sinusoidal frequency and amplitude modulations in the inferior colliculus of 'CF-FM' bat, *Rhinolophus ferrumequinum*," Exp. Brain Res. **34**, 117–132.
Schweizer, H. (**1981**). "The connections of the inferior colliculus and the organization of the brainstem auditory system in the greater horseshoe bat (*Rhinolophus ferrumequinum*)," J. Comp. Neurol. **201**, 25–49.
Siemers, B. M., and Schnitzler, H.-U. (**2000**). "Natterer's bat (*Myotis nattereri* Kuhl, 1818) hawks for prey close to vegetation using echolocation signals of very broad bandwidth," Behav. Ecol. Sociobiol. **47**, 400–412.
Simmons, J. A., Fenton, M. B., and O'Farrell, M. J. (**1979**). "Echolocation and pursuit of prey by bats," Science **203**, 16–21.
Simmons, J. A., Saillant, P. A., Ferragamo, M. J., Haresign, T., Dear, S. P., Fritz, J., and McMullen, T. A. (**1996**). "Auditory computations for biosonar target imaging in bats," in *Auditory Computation*, edited by H. L. Hawkins, T. A. McMullen, A. N. Popper, and R. R. Fay (Springer, New York), pp. 401–468.
Suga, N., and Schlegel, P. (**1973**). "Coding and processing in the auditory systems of FM-signal-producing bats," J. Acoust. Soc. Am. **54**, 174–190.
Surlykke, A., and Moss, C. F. (**2000**). "Echolocation behavior of big brown bats, *Eptesicus fuscus*, in the field and the laboratory," J. Acoust. Soc. Am. **108**, 2419–2429.
Valentine, D. E., and Moss, C. F. (**1997**). "Spatially selective auditory responses in the superior colliculus of the echolocating bat," J. Neurosci. **17**, 1720–1733.
Wilson, W. W., and Moss, C. F. (**2002**). "Sensory-motor behavior of free-flying FM bats during target capture," in *Advances in the Study of Echolocation in Bats and Dolphins*, edited by J. Thomas, C. F. Moss, and M. Vater (University of Chicago Press, Chicago, IL).
Wu, M. I., and Jen, P. H. S. (**1995**). "Responses of pontine neurons of the big brown bat, *Eptesicus fuscus*, to temporally patterned sound pulses," Hear. Res. **85**, 155–168.

Erratum: "The energy method for analyzing the piezoelectric electroacoustic transducers" [J. Acoust. Soc. Am. 117(1), 210–220 (2005)]

Boris Aronov
Acoustic Research Laboratory, Advanced Technology and Manufacturing Center and Department of Electrical and Computer Engineering, the University of Massachusetts, Dartmouth, 285 Old Westport Road, North Dartmouth, Massachusetts 02747–2300 and BTECH Acoustics, 1445 Wampanoag Trail, Suite 115, East Providence, Rhode Island 02915

(Received 3 August 2005; accepted 6 August 2005)

[DOI: 10.1121/1.2047149]

PACS number(s): 43.38.Ar, 43.38.Fx, 43.38.Pf, 43.10.Vx [AJZ]

Equations (8) and (9) should read

$$P(\bar{r},\omega) = \frac{\rho c}{r} e^{-j(kr-\pi/2)} U_0 \frac{ka^2}{1+jka} e^{jka}, \tag{8}$$

$$\chi = \frac{ka^2}{1+jka} e^{jka}. \tag{9}$$

Curves α_{02} and β_{02} in Fig. 11 have to be removed and the caption to Fig. 11 should read: "Nondimensional coefficients α_{01} and β_{01} for the mutual radiation impedances between zero and first modes of cylindrical transducer with 180° rigid baffle, $S_{\text{eff}} = \pi a/2$."

Erratum: "The effect of cross-channel synchrony on the perception of temporal regularity" [J. Acoust. Soc. Am. 118(2), 946–954 (2005)]

Katrin Krumbholz[a)]
Institute of Medicine (IME), Research Center Jülich, D-52425 Jülich, Germany;
MRC Institute of Hearing Research, University Park, Nottingham NG7 2RD, United Kingdom

Stefan Bleeck and Roy D. Patterson
Centre for the Neural Basis of Hearing, Department of Physiology, University of Cambridge, Downing Street, Cambridge, CB2 3EG, United Kingdom

Maria Senokozlieva, Annemarie Seither-Preisler, and Bernd Lütkenhöner
Department of Experimental Audiology, ENT Clinic, Münster University Hospital, Kardinal-von-Galen-Ring 10, D-48149 Münster, Germany

(Received 17 August 2005; accepted 17 August 2005)

[DOI: 10.1121/1.2062433]

PACS number(s): 43.66.Hg, 43.66.Mk, 43.66.Ba, 43.10.Vx [RAL]

The Acknowledgments are missing in the original version of the article.

ACKNOWLEDGMENTS

This research was supported by the UK Medical Research Council (Grant No. 9901257), the Austrian Academy of Sciences (APART project 524), and the Alexander von Humboldt Foundation.

[a)]Corresponding author. Current address: MRC Institute of Hearing Research, University Park, Nottingham NG7 2RD, UK; electronic mail: katrin@ihr.mrc.ac.uk

